Presentation Number **ES 1**
Educational Session 01: Chemistry of Contrast Media - Biologicals
September 18, 2013 / 08:00-08:35 / Room: 100

Development of antibody-based probes for molecular imaging

Anna M. Wu, *Molecular and Medical Pharmacology, David Geffen School of Medicine at UCLA, Los Angeles, CA, USA. Contact e-mail: awu@mednet.ucla.edu*

Antibodies can be produced to recognize essentially any target of interest with nanomolar affinity, making them an ideal class of molecules for the generation of molecular imaging agents. However, the use of classic mouse monoclonals for in vivo imaging has many limitations including immunogenicity, slow kinetics and clearance, etc. Recently, antibody engineering has been harnessed to produce targeting agents based on humanized and human antibodies, with tailored pharmacokinetics for rapid imaging. Antibodies can be engineered for site-specific conjugation and labeling, and clearance can be directed through hepatic or renal routes. When labeled with positron-emitting radionuclides (such as I-124, Zr-89, Cu-64, F-18), engineered antibody fragments can be employed for high resolution, sensitive, quantitative imaging by PET. ImmunoPET can be utilized for phenotypic assessment of cells and tissues in living organisms, including patients, in oncology and other diseases. Antibody-based imaging can also be applied to detection of immune cell subsets (such as CD8 T cells or macrophages), for monitoring immune responses. ImmunoPET provides a broad approach for imaging cell surface phenotype in vivo, and stands to play an expanding role in the detection and management of cancer and other diseases, for assessing key factors such as target expression, internalization and catabolism, and response to therapy and mechanism of response. Molecular imaging applications of engineered antibodies have been extended to incorporation of optical tags, by dye conjugation or generation of fusion proteins. Finally, engineered antibodies provide a versatile platform for development of targeted multimodal imaging agents including nanoparticle-based diagnostics and therapeutics.

Learning Objectives (3-4 Bullet Points): Delineate ideal properties of an antibody-based imaging agent Evaluate suitability of cell surface biomarkers as imaging targets Compare radiolabeling isotopes and methods for imaging applications

Relevant Publications: Olafsen, T. and Wu, A.M. (2010) Antibody vectors for imaging. Seminars in Nuclear Medicine, 40:167-181.

Acknowledgements/References: Dr. Wu would like to thank the members of her lab, past and present, in addition to our many collaborators, for their contributions. Support has been provided by NIH grants CA016042, CA092131, CA098010, and CA151459; DOE DE-SC0001220, and DOD W81WXH-08-0442.

Disclosure of author financial interest or relationships:
A.M. Wu, ImaginAb, Inc., Stockholder; ImaginAb, Inc., Consultant; ImaginAb, Inc., Grant/research support; Daiichi Sankyo, Consultant; Sanofi, Consultant .

DOI: 10.1007/s11307-013-0703-2
© Academy of Molecular Imaging and Society for Molecular Imaging, 2013

Presentation Number **ES 2**
Educational Session 01: Chemistry of Contrast Media - Biologicals
September 18, 2013 / 08:35-09:10 / Room: 100

Aptamer imaging

Frederic Duconge, [1]*Institut d'imagerie biomédicale, Service Hospitalier Frederic Joliot, CEA, Orsay, France;* [2]*U1023, INSERM, Orsay, France;* [3]*U1023, Universite Paris Sud, Orsay, France. Contact e-mail: frederic.duconge@cea.fr*

Sophisticated structures of nucleic acids play a key role in cells by interacting with proteins or other partners. Since 1990, several approaches of molecular evolution have been developed to study these natural properties of nucleic acid structures but also to develop non-natural ligands that bind to specific targets (amino acids, antibiotic, proteins…). The artificial ligands found by these techniques are named "aptamers", from the latin "aptus" meaning "to fit", and the method to identify them was popularized using the term "SELEX" for "Systematic Evolution of Ligands by Exponential enrichment". In vitro, it has been demonstrated that aptamers can rival antibodies as ligands, inhibitors or probes for several applications including sensors, biochips, chromatography, microscopy, flow cytometry. They present also several advantages for in vivo applications: 1- they have high specificity and affinity for their targets 2- they seem to lack immunogenicity 3- they can have an inhibitory activity on their targets, 4- they can be chemically modified in order to improve their stability against nucleases or to modify their pharmacokinetics, 5- straightforward modifications and functionalization of aptamers make them ideal targeting agents and 5- they can be selected against extracellular targets that are easier to access in vivo. Therefore, several aptamers have already been tested in vivo for therapeutic applications. Nine aptamers are already enrolled in clinical trials, and one is a commercially available treatment for age-related macular degeneration. A few experiments have been conducted in vivo to evaluate aptamers as targeting probes, mostly in small animal models of cancer. Radiolabelled aptamers have already been evaluated as radiotracers for SPECT imaging. Aptamers have also been tested as fluorescent probes including activatable probes or as targeting agent of nanoparticles for multimodal imaging or theranostic applications. These experiments provide some clues about the interest to use aptamers for molecular imaging.

Learning Objectives (3-4 Bullet Points): - properties of nucleic acid structures - methods to select aptamers - methods to label or conjugate aptamers - Biodistribution and specific targeting of aptamers

Relevant Publications: Pestourie, C., Tavitian, B. and Ducongé, F. (2005) Aptamers against extracellular targets for in vivo applications. Biochimie 87 (9-10), 921-30 Tavitian, B., Duconge, F., Boisgard, R. and Dolle, F. (2009) In vivo imaging of oligonucleotidic aptamers. Methods Mol Biol, 535, 241-259. Cibiel A., Dupont D.M. and Ducongé F. (2011) Methods To Identify Aptamers against Cell Surface Biomarkers. Pharmaceuticals. 2011; 4(9):1216-1235. Cibiel, A., Pestourie, C. and Ducongé, F. (2012) In vivo uses of aptamers selected against cell surface biomarkers for therapy and molecular imaging. biochimie, 94, 1595-1606.

Acknowledgements/References: The author would like to acknowledge grants from the FMT-XCT European program (Grant agreement no. 201792), the European Molecular Imaging Laboratory (EMIL) network (EU contract LSH-2004-503569), the "Agence Nationale pour la Recherche" under the frame of EuroNanoMed (project META) and the national project ANR-RNTS:TomoFluo3D.

Disclosure of author financial interest or relationships:
F. Duconge, LFB Biotechnologies, Grant/research support .

Presentation Number **ES 3**
Educational Session 01: Chemistry of Contrast Media - Biologicals
September 18, 2013 / 09:10-09:45 / Room: 100

HOW TO INTRODUCE REPORTER GENES IN CELLS

Christophe M. Deroose, [1]*Nuclear Medicine, UZ Leuven, Leuven, Belgium;* [2]*Imaging & Pathology, KU Leuven, Leuven, Belgium. Contact e-mail: christophe.deroose@med.kuleuven.be*

This session will focus on the different techniques available to introduce imaging reporter genes in cells, both in vitro and in vivo. Techniques discussed will include plasmid transfection, viral vectors (retro, adeno, lenti and addeno-associated) and gene locus targetting strategies. An overview will also be provided on techniques to couple reporter gene expression to expression of a gene of interest (therapeutic or disease inducing). We will further look into the quantitative aspects of reporter gene imaging and on those aspects of the gene introduction strategy on signal quantification. Finally, we will discuss how reporter gene imaging can be used to monitor gene therapy.
Learning Objectives (3-4 Bullet Points): - Knowing the different molecular biology strategies to introduce reporter genes into cells - Reconising the advantages and weaknesses of these different strategies - Critical appraisal of strategies to express more than one single gene - Influence of introduction route on signal quantification
Relevant Publications: 1. Wolfs E, Struys T, Notelaers T, Roberts SJ, Sohni A, Bormans G, Van Laere K, Luyten FP, Gheysens O, Lambrichts I, Verfaillie CM, Deroose CM. 18F-FDG Labeling of mesenchymal stem cells and multipotent adult progenitor cells for PET imaging : effects on ultrastructure and differentiation capacity. Journal of Nuclear Medicine 2013 Mar;54(3):447-54 2. Deroose C, Chitneni S, Gijsbers R, Vermaelen P, Ibrahimi A, Balzarini J, Baekelandt V, Verbruggen A, Nuyts J, Debyser Z, Bormans G, Mortelmans L. Preliminary Validation of Varicella Zoster Virus Thymidine Kinase as a Novel Reporter Gene for PET Nuclear Medicine and Biology.2012 Nov;39(8):1266-74 3. Gheysens O, Chen I, Rodriguez-Porcel M, Chan C, Rasooly J, Vaerenberg C, Paulmurugan R, Willmann J, Deroose C, Wu J, Gambhir S. Non-invasive Bioluminiscence Imaging of Myobast Mediated Hypoxia-Inducible Factor-1 Alpha Gene Transfer. Molecular Imaging and Biology, 2011; 13(6), 1124-1132 4. Vandeputte C, Evens N, Toelen J, Deroose CM, Bosier B, Ibrahimi A, Van der Perren A, Gijsbers R, Janssen P, Lambert D, Verbruggen A, Debyser Z, Bormans G, Baekelandt V, Van Laere K. A PET Brain Reporter Gene System Based on Type 2 Cannabinoid Receptors. Journal of Nuclear Medicine 2011, 52(7); 11.02-1109 5. Ibrahimi A, Vande Velde G, Reumers V, Toelen J, Thiry I, Vandeputte C, Deroose C, Bormans G, Baekelandt V, Debyser Z, Gijsbers R: Highly efficient multicistronic lentivectors with peptide 2A sequences. Human Gene Therapy 2009 Aug;20(8):845-60 6. Deroose CM, Reumers V, Debyser Z, Baekelandt V: Seeing genes at work in the living brain with non-invasive molecular imaging. Current Gene Therapy 2009; 9(3):212-38. 7. Reumers V, Deroose CM, Gijsbers R, Krylychkina O, Geraerts M, Mortelmans L, Debyser Z, Baekelandt V: Noninvasive and quantitative monitoring of adult neuronal stem cell migration in mouse brain using bioluminescence imaging, Stem Cells 2008;26(9):2382-90 8. Deroose CM, De A, Loening AM, Chow PL,, Ray P, Chatziioannou AF, Gambhir SS: Multimodality imaging of tumor xenografts and metastasis in mice with combined microPET, microCT and bioluminescence imaging, Journal of Nuclear Medicine, 2007;48(2):295-303. 9. Deroose CM, Reumers V, Gijsbers R, Bormans G, Debyser Z, Mortelmans L, Baekelandt V: Non-invasive monitoring of long-term lentiviral vector-mediated gene expression in rodent brain with bioluminescence imaging, Molecular Therapy, 2006; 14(3):423-31.

Disclosure of author financial interest or relationships:
C.M. Deroose, None.

Presentation Number **ES 4**

Educational Session 02: What Life Scientists Should Know About Imaging Modalities - Optical Imaging, Ultrasound, and Optoacoustic

September 18, 2013 / 08:00-08:32 / Room: 102

Physics of Ultrasound Imaging - Contrast Agents and Flow Imaging

Georg Schmitz, *Medical Engineering, Ruhr-Universität Bochum, Bochum, Germany. Contact e-mail: Georg.Schmitz@rub.de*

Owing to the very sensitive detection of microbubble contrast media, ultrasonic imaging has become a modality for molecular imaging. With the availability of high-frequency small animal ultrasound scanners, B-mode and contrast imaging have become important research tools. The main focus of this year's session is on ultrasound contrast media, which are micrometer-sized gas-filled bubbles that are stabilized by a soft shell (e.g. phospholipids) or a hard shell (e.g. polymers). They show characteristic behavior like non-linear scattering of ultrasound and at higher intensities also destruction in the sound fields of diagnostic ultrasound scanners. These properties can be utilized for their sensitive detection and quantification. The talk first gives a short introduction to the underlying physical principles of ultrasound imaging used in clinical scanners and laboratory small animal scanners. Then the physical properties of microbubble contrast agents like resonance, non-linear scattering, and fragmentation or cracking are presented. Based on this, different methods for their sensitive detection and scanning protocols for quantification that are used in current preclinical studies are discussed. Ultrasound contrast agents are also used for the measurement of flow by Doppler-imaging or related techniques. Therefore, a short summary of ultrasound flow measurement techniques will be given. Application examples for anatomical and molecular imaging with microbubble contrast media will be presented and discussed.

Learning Objectives (3-4 Bullet Points): - Gain basic understanding of ultrasound B-mode and Doppler imaging - Understand the physical properties of microbubble contrast agents - Learn about contrast agent detection and quantification techniques and preclinical protocols - Get an understanding of new development trends in ultrasonic imaging

Relevant Publications: [1] Ferrara, K., Pollard, P., Borden M.: Ultrasound Microbubble Contrast Agents: Fundamentals and Application to Gene and Drug Delivery. Annual Review of Biomedical Engineering. Vol. 9: 415-447 [2] Hill, Christopher Rowland / (Hrsg.): Physical Prinpiples of Medical Ultrasonics. Ellis Horward Ltd., Chichester, 1986. [3] Jensen JA. Estimation of Blood Flow Velocities Using Ultrasound. Cambridge, UK: Cambridge University Press; 1996. [4] Kiessling F, Bzyl J, Fokong S, Siepmann M, Schmitz G, Palmowski M. Targeted Ultrasound Imaging of Cancer: An Emerging Technology on its Way to Clinics. Current Pharmaceutical Design. 2012;18(15):2184-99. [5] Postema M., Schmitz G. Bubble dynamics involved in ultrasonic imaging. Expert Reviews of Molecular Diagnostics. 2006;6(3):493-502. [6] Qin, S., Caskey, C.F., Ferrara, K. W.: Ultrasound contrast microbubbles in imaging and therapy: physical principles and engineering. Phys. Med. Biol. 54, R27-R57. [7] Reinhardt M, Hauff P, Briel A, Uhlendorf V, Linker RA, Mäurer M, et al.: Sensitive Particle Acoustic Quantification (SPAQ): A New Ultrasound-Based Approach for the Quantification of Ultrasound Contrast Media in High Concentrations. Invest Radiol. 2005;40(1):2-7. [8] Schmitz, G.: Biomedical Sonography, in Biomedical Imaging: Principles and Applications (ed R. Salzer), John Wiley & Sons, Inc., Hoboken, NJ, USA. doi: 10.1002/9781118271933.ch11, 2012 [9] Shung, K. Kirk: Diagnostic Ultrasound, Imaging and Blood Flow Measurements. Taylor & Francis Group, Boca Raton, 2006. [10] Siepmann M, Reinhardt M, Schmitz G. A Statistical Model for the Quantification of Microbubbles in Destructive

Imaging. Investigative Radiology. 2010;45(10):592-9. [11] Siepmann M, Fokong S, Mienkina MP, Lederle W, Kiessling F, Gätjens J, et al. Phase shift variance imaging - a new technique for destructive microbubble imaging. IEEE Transactions on Ultrasonics, Ferroelectrics and Frequency Control. 2013;60(5):909-923. [12] Szabo, Thomas, Diagnostic Ultrasound Imaging: Inside Out. Academic Press, Burlington, 2004.

Disclosure of author financial interest or relationships:
G. Schmitz, None.

Presentation Number **ES 5**
Educational Session 02: What Life Scientists Should Know About Imaging Modalities - Optical Imaging, Ultrasound, and Optoacoustic
September 18, 2013 / 08:32-09:04 / Room: 102

Advanced Microscopy Technologies

Jorge Ripoll, *Department of Bioengineering and Aerospace Engineering, Universidad Carlos III of Madrid, Leganes, Spain. Contact e-mail: jorge.ripoll@uc3m.es*

In this educational session we will be presenting the basis of light propagation and how these affect image formation in microscopy. We shall cover new advances in microscopy such as Laser Sheet Microscopy and Optical Projection Microscopy which are capable of generating 3D images in-toto of organs and small specimens. The effect of scattering will be discussed in the context of these techniques with specific examples and applications.
Learning Objectives (3-4 Bullet Points): - Effects of scattering in microscopy - Light Sheet Microscopy - Optical Projection Tomography
Relevant Publications: [1] Colas, J.-F., & Sharpe, J. (2009). Live optical projection tomography. Organogenesis, 5(4), 211-6. [2] Sharpe, J., Ahlgren, U., Perry, P., Hill, B., Ross, A., J., H.-S., Baldock, R., et al. (2002). Optical projection tomography as a tool for 3D microscopy and gene expression studies. Science, 296(5567), 541-545. [3] Huisken, J., Swoger, J., Del Bene, F., Wittbrodt, J., & Stelzer, E. H. (2004). Optical sectioning deep inside live embryos by selective plane illumination microscopy. Science, 305(5686), 1007-1009. [4] Huisken, J., & Stainier, D. Y. R. (2009). Selective plane illumination microscopy techniques in developmental biology. Development (Cambridge, England), 136(12), 1963-75. doi:10.1242/dev.022426 [5] Keller, P. J., Schmidt, A. D., Santella, A., Khairy, K., Bao, Z., Wittbrodt, J., & Stelzer, E. H. K. (2010). Fast, high-contrast imaging of animal development with scanned light sheet - based structured- illumination microscopy. Nature Methods, (July). doi:10.1038/nmeth.1476

Disclosure of author financial interest or relationships:
J. Ripoll, None.

Presentation Number **ES 6**
Educational Session 02: What Life Scientists Should Know About Imaging Modalities - Optical Imaging, Ultrasound, and Optoacoustic
September 18, 2013 / 09:04-09:47 / Room: 102

Optical Tomography of Deep Tissues

Joseph P. Culver, *Radiology, Washington University St. Louis, St. Louis, MO, USA. Contact e-mail: culverj@mir.wustl.edu*

Who will benefit from this information? This talk is designed for people who have an interest in recent advancements in deep tissue optical imaging and Optical Tomography. -Optical Tomography (or Diffuse Optical Tomography - DOT) provides molecular- and functional- in vivo imaging in deep tissues (>1mm) well beyond the depths of advance optical microscopy methods. -The intense scattering of light by tissues means that DOT uses measurements of diffuse light or multiply scattered light. -In mouse, fluorescent molecular tomography (FMT) provides the power of fluorophore based contrast (targeted, genetic and active) with volumetric imaging. FMT can be combined with CT or MRI imaging to provide a combined molecular/anatomical data. -In humans, endogenous tissue spectroscopy is more common, and DOT is used for functional neuroimaging and tissue spectroscopy in breast cancer. How was a problem determined? These optical techniques are being developed to complement optical microscopy, positron emission tomography (PET) and fMRI techniques by addressing scenarios that are difficult to address with the alternate methods. For example: -In mouse, FMT provides a molecular imaging with a great array of activations strategies (e.g. genetically engineered mice), and greatly simplified contrast agent logistics (e.g. long shelf life ~months). -In humans, NIRS, and the more recent advancements in Diffuse Optical Tomography (DOT), provide a portable bedside technique for mapping both functional tasks and resting state functional connectivity. While historically NIRS has been limited to resolutions of >3.5 cm, new DOT imaging has demonstrated resolution of <1.5 cm with improved brain specificity and methods for co-registering function to reference anatomy. Examples of how these issues have been addressed; -In mice, initial in vivo systems used fluorescence planar reflectance imaging. Newer FMT systems provide better depth sensitivity profiles, improved resolution and a platform for integration with anatomical datasets from CT or MRI. -In humans, traditional NIRS measurements have been used in a great variety of cognitive science studies. Using the improved performance of DOT, validation studies have shown voxel-to-voxel correlations between DOT and fMRI in visual, motor and language tasks. Most recently these techniques been extended to clinical situations with initial feasibility demonstrated in functional connectivity studies of preterm infants.
Learning Objectives (3-4 Bullet Points): The attendees will understand and be able to explain the basic concepts in five areas: 1-Tissue Optics. 2-DOT Instrument Basics 3-DOT Image Reconstruction Basics 4-Mouse FMT Imaging Systems 5-Human Optical Neuroimaging Systems

Disclosure of author financial interest or relationships:
J.P. Culver, Cephalogics, Stockholder .

Presentation Number **ES 7**
Educational Session 02: What Life Scientists Should Know About Imaging Modalities - Optical Imaging, Ultrasound, and Optoacoustic
September 18, 2013 / 09:47-10:30 / Room: 102

Optoacoustic Imaging

Vasilis Ntziachristos, *[1]Chair for Biological Imaging, Technische Universität München, Munich, Germany; [2]Institute for Biological and Medical Imaging, Helmholtz Zentrum München, Munich, Germany. Contact e-mail: v.ntziachristos@tum.de*

Optical imaging is unequivocally the most versatile and widely used visualization modality in the life sciences. Yet it is significantly limited by photon scattering, which complicates imaging beyond a few hundred microns. For the past few years however there has been an emergence of powerful new optical imaging methods that can offer high resolution imaging beyond the penetration limits of microscopic methods. These methods can prove essential in cancer research. Of particular importance is the development of multi-spectral opto-acoustic tomography (MSOT) that brings unprecedented optical imaging performance in visualizing anatomical, physiological and molecular imaging biomarkers. Some of the attractive features of the method are the ability to offer 10-100 microns resolution through several millimetres to centimetres of tissue and real-time imaging. In parallel we have now achieved the clinical translation of targeted fluorescent probes, which opens new ways in the interventional detection of cancer in surgical and endoscopic optical molecular imaging. This talk describes current progress with methods and applications for in-vivo optical and opto-acoustic imaging in cancer and outlines how new opto-acoustic and fluorescence imaging concepts are necessary for accurate and quantitative molecular investigations in tissues.
Learning Objectives (3-4 Bullet Points): Learn why optoaoustic imaging is the future in optical imaging technology Principles of Multispectral photoacoustic tomography Methods for spectral absorption properties Methods for Blood oxygenation measurements Advantages and limitations Application examples
Relevant Publications: 1. Ale A, Ermolayev V, Herzog E, Cohrs C, de Angelis MH, Ntziachristos V. "FMT-XCT: in vivo animal studies with hybrid fluorescence molecular tomography-X-ray computed tomography" Nat Methods, 9(6); 615-620 (2012). 2. Van Dam G., Themelis G., Crane LMA, Harlaar NJ., Pleijhuis RG., Kelder W., Sarantopoulos A., Bart J., Low PS., Ntziachristos V., "Intraoperative Tumor-Specific Fluorescent Imaging in Ovarian Cancer by Folate Receptor-α Targeting: First In-Human Results", Nature Medicine, 17(10): 1315-9 (2011). 3. Ntziachristos V. "Going deeper than optical microscopy: High resolution photonic molecular imaging for next generation biology" Nature Methods, 7(8): 603-614, (2010). 4. Razansky D, Vinegoni C, Distel M, Ma R, Perrimon N, Koster RW, Ntziachristos V. "Multispectral opto-acoustic tomography of deep-seated fluorescent proteins in vivo", Nature Photonics 3, 412-417 (2009). 5. Vinegoni C, Pitsouli C, Razansky D, Perrimon N, Ntziachristos V. "Live imaging of Drosophila pupae with Mesoscopic Fluorescence Tomography" Nature Methods, 5(1):45-7 (2008).

Disclosure of author financial interest or relationships:
V. Ntziachristos, iThera Medical, Stockholder; SurgOptix BV, Consultant .

Presentation Number **ES 8**
Educational Session 03: Postprocessing and Cross Validation - Modeling and Quantification
September 18, 2013 / 08:00-08:45 / Room: 105

Plasma Input and Reference Tissue Compartment Models

Adriaan A. Lammertsma, *Radiology & Nuclear Medicine, VU University Medical Center, Amsterdam, Netherlands. Contact e-mail: aa.lammertsma@vumc.nl*

Molecular in vivo imaging techniques provide non-invasive measurements of regional tissue uptake and clearance of molecules of interest. The kinetic behavior of these molecules depends on several underlying physiological and/or biochemical processes. Tracer kinetic modeling is required to extract quantitative information on the specific molecular process under study. Although this will be illustrated for PET studies, the same principles apply to MRI and optical imaging. PET provides for accurate measurements of regional tissue concentrations of radioactivity, but appropriate tracer kinetic models are needed to translate these measurements of tissue tracer concentrations into quantitative values of tissue function or molecular process under study. Such a tracer model is a mathematical description of the fate of the tracer in the human body, in particular the organ under study. Although other types of models have been proposed, in practice, essentially all models used are compartment models. In these models the possible distribution of a tracer is divided into a limited number of discrete compartments. In practice, data from a single dynamic scan can only be fitted to a single or a two tissue compartment model. A single tissue compartment model would be appropriate for a blood flow (perfusion) tracer (no further interactions in tissue), but also needs to be used when kinetics between different tissue compartments are such that they cannot be identified individually. In a two tissue compartment model, a second compartment can be identified in which case the first compartment usually reflects non-displaceable tracer and the second metabolized or bound tracer. For a single tissue compartment model the outcome measure usually is the volume of distribution (V_T). For a two tissue compartment model it can also be V_T, but certainly for receptor studies non-displaceable binding potential (BP_{ND}) would be better, as it provides information on specific binding only, whilst V_T contains both specific and non-displaceable signals. Selection of both tracer kinetic model and outcome measure depends on the specific tracer being used (is a second compartment identifiable) and on accuracy and precision of the outcome measures. Both models mentioned above require a metabolite corrected arterial plasma input function. Measurement of such an input function is labor intensive (measurement of radiolabeled plasma metabolites) and rather invasive (arterial cannulation). For receptor studies, however, if a region devoid of these receptors exists, it is possible to use reference tissue models. In these models the reference region is used as an indirect input function for measuring BP_{ND} in the target region. In this contribution the mathematical background of single and two tissue compartments will be presented. In addition, the biological interpretation and validity of the various outcome measures will be discussed. Next, the mathematical background of reference tissue models will be presented, and attention will be paid to the underlying assumptions of those models. Finally, the various steps needed to select a model for a new tracer will be discussed.

Learning Objectives (3-4 Bullet Points): 1. Understanding of plasma input models 2. Understanding of reference tissue models 3. Understanding of the steps needed to select the most appropriate model

Relevant Publications: 1. Gunn RN, Gunn SR, Cunningham VJ (2001) Positron emission tomography compartmental models. J Cereb Blood Flow Metab 21:635-652 2. Innis RB, Cunningham VJ, Delforge J,

Fujita M, Gjedde A, Gunn RN, Holden J, Houle S, Huang SC, Ichise M, Iida H, Ito H, Kimura Y, Koeppe RA, Knudsen GM, Knuuti J, Lammertsma AA, Laruelle M, Logan J, Maguire RP, Mintun MA, Morris ED, Parsey R, Price JC, Slifstein M, Sossi V, Suhara T, Votaw JR, Wong DF, Carson RE (2007) Consensus nomenclature for in vivo imaging of reversibly binding radioligands. J Cereb Blood Flow Metab 27:1533-1539 3. Lammertsma AA, Bench CJ, Hume SP, Osman S, Gunn K, Brooks DJ, Frackowiak RSJ (1996) Comparison of methods for analysis of clinical [11C]raclopride studies. J Cereb Blood Flow Metab 16:42-52 4. Lammertsma AA, Hume SP (1996) Simplified reference tissue model for PET receptor studies. NeuroImage 4:153-158

Disclosure of author financial interest or relationships:
A.A. Lammertsma, Philips, Grant/research support; Hoffmann-La Roche, Grant/research support .

Presentation Number **ES 9**
Educational Session 03: Postprocessing and Cross Validation - Modeling and Quantification
September 18, 2013 / 08:45-09:20 / Room: 105

Measurement of plasma input functions using PET

Marc Huisman, *Radiology and nuclear medicine, VU medical center, Amsterdam, Netherlands. Contact e-mail: m.huisman@vumc.nl*

In order to extract physiological parameters like myocardial perfusion and glucose metabolism from PET scans kinetic models can be applied. Although the information obtained in this way is most accurate, it demands the measurement of plasma input functions. The gold standard invasive method to obtain the input function requires continuous and manual arterial sampling. The measured blood radioacitivity concentrations need to be corrected for whole blood over plasma ratios as well as for the possible presence of labelled metabolites. In addition, a delay and dispersion correction accounting for the (effect of) the time lag between arterial blood at the location of the tissue of interest and the position of measurement in an external counter is needed. A popular alternative to this invasive method is the use of an image derived input function, which would be possible if the corrections to the obtained blood radioactivity concentrations can be derived from venous instead of arterial blood samples. In this presentation the measurement of plasma input functions will be discussed and representative examples of the various methods will be given.

Learning Objectives (3-4 Bullet Points): To be able explain the role of plasma input functions in PET To be able to list the requirements on the measurements of a plasma input function To be able to assess the pros and cons or arterial and image based input functions

Relevant Publications: Characteristics of a new fully programmable blood sampling device for monitoring blood radioactivity during PET, Boellaard R, van Lingen A, van Balen SC, Hoving BG, Lammertsma AA. Eur J Nucl Med. 2001 Jan;28(1):81-9. Cerebral blood flow and glucose metabolism in healthy volunteers measured using a high-resolution PET scanner. Huisman MC, van Golen LW, Hoetjes NJ, Greuter HN, Schober P, Ijzerman RG, Diamant M, Lammertsma AA. EJNMMI Res. 2012 Nov 20;2(1):63. doi: 10.1186/2191-219X-2-63.

Disclosure of author financial interest or relationships:
M. Huisman, None.

Presentation Number **ES 10**
Educational Session 03: Postprocessing and Cross Validation - Modeling and Quantification
September 18, 2013 / 09:20-09:55 / Room: 105

Measurement of plasma input functions using MRI

Klaas Nicolay, *Department of Biomedical Engineering, Eindhoven University of Technology, Eindhoven, Netherlands. Contact e-mail: k.nicolay@tue.nl*

This presentation addresses the use of MRI for measuring the arterial (or plasma) input function (AIF). Quantitative measurements of the AIF are needed when using first-pass dynamic contrast enhanced (DCE) MRI for measuring the perfusion status of tissues in vivo. DCE-MRI refers to a very broad category of MRI acquisition techniques that dynamically monitor changes in MRI signal or MRI indices serially over time following injection of MRI contrast agent. In the specific case of quantifying the perfusion of biological tissues, the DCE-MRI recordings involve ultra-fast MRI scanning to monitor the first passage of a bolus of MRI contrast agent through the tissue of interest. The dynamic scans are converted to tissue concentration-time curves and these should subsequently be subjected to mathematical modeling to yield quantified perfusion values in units of ml/g tissue/min. To arrive at such quantified tissue perfusion values, the tissue response needs to be calibrated via deconvolution with the AIF. Willats and Calamante recently prepared a very insightful review on the use of dynamic MRI scanning for measuring tissue perfusion (1) and the different steps that are needed to conduct a meaningful study. The measurement of the AIF, i.e., the measurement of the arterial contrast agent concentration time course, presents several challenges and therefore accurate AIF quantification is an active area of research. In most cases, Gd-based MRI contrast agents are used as these are clinically approved and rapidly eliminated by renal excretion. During the presentation, examples of the use of AIF quantification for measuring perfusion of brain (2), heart (3,4) and tumors (5) will be given. It should be noted that there are also alternative MRI methods for quantifying tissue perfusion, such as Arterial Spin Labeling (ASL) (6,7). The advantage of ASL is that it makes use of an endogenous "tracer" (i.e., arterial water protons), which has certain distinct advantages. However, the relatively low signal-to-noise ratio of ASL-based perfusion mapping is a main limitation of its routine use. Nevertheless, recent advances in hardware as well as pulse sequence functionalities increasingly present ASL as an alternative for DCE-MRI-based perfusion quantification.

Learning Objectives (3-4 Bullet Points): Describe the basic MRI sequences with which arterial input function can be measured Describe the most used procedures for converting MRI contrast or parameter changes to arterial input function Describe the strengths and weaknesses of MRI-based arterial input function measurement Describe a number of key examples of the use of arterial input function measurements for the quantification of tissue perfusion in brain, heart and tumors

Relevant Publications: 1. Willats L, Calamante F. The 39 steps: evading error and deciphering the secrets for accurate dynamic susceptibility contrast MRI. NMR Biomed 2012. 2. Bleeker EJ, Webb AG, van Walderveen MA, van Buchem MA, van Osch MJ. Evaluation of signal formation in local arterial input function measurements of dynamic susceptibility contrast MRI. Magn Reson Med 2012;67(5):1324-1331. 3. Coolen BF, Moonen RP, Paulis LE, Geelen T, Nicolay K, Strijkers GJ. Mouse myocardial first-pass perfusion MR imaging. Magn Reson Med 2010;64(6):1658-1663. 4. van Nierop BJ, Coolen BF, Dijk WJ, Hendriks AD, de Graaf L, Nicolay K, Strijkers GJ. Quantitative first-pass perfusion MRI of the mouse myocardium. Magn Reson Med 2013;69(6):1735-1744. 5. Huang W, Tudorica LA, Li X, Thakur SB, Chen Y, Morris EA, Tagge IJ, Korenblit ME, Rooney WD, Koutcher JA, Springer CS, Jr. Discrimination of benign

and malignant breast lesions by using shutter-speed dynamic contrast-enhanced MR imaging. Radiology 2011;261(2):394-403. 6. Detre JA, Zhang W, Roberts DA, Silva AC, Williams DS, Grandis DJ, Koretsky AP, Leigh JS. Tissue specific perfusion imaging using arterial spin labeling. NMR Biomed 1994;7(1-2):75-82. 7. Wu WC, St Lawrence KS, Licht DJ, Wang DJ. Quantification issues in arterial spin labeling perfusion magnetic resonance imaging. Top Magn Reson Imaging 2010;21(2):65-73.

Disclosure of author financial interest or relationships:
K. Nicolay, None.

Presentation Number **ES 11**
Educational Session 03: Postprocessing and Cross Validation - Modeling and Quantification
September 18, 2013 / 09:55-10:30 / Room: 105

Measurement of plasma input functions using optical techniques

Kenneth M. Tichauer, *Biomedical Engineering, Illinois Institute of Technology, Chicago, IL, USA. Contact e-mail: ktichaue@iit.edu*

The concentration of a molecular imaging agent in the blood plasma over time - or the "plasma input function" - can provide critical information about tracer delivery to tissues of interest, and is therefore a key component to measure in more quantitative molecular imaging approaches. In optical imaging, tracers are selected based on their absorption or fluorescent properties within the visible and near-infrared range of the electromagnetic spectrum, and a variety of systems have been developed to detect concentration of optical tracers, based on one of these two mechanisms (absorption or fluorescence). Within the field of molecular imaging, optical tracers permit unique techniques to be employed in the measure of plasma concentrations. Like in nuclear medicine, it is possible to measure plasma input functions by analysing periodically sampled arterial blood; however, since the tracers are not radioactive, their concentration is typically measured by spectrophotometry or fluorimetry, rather than with a scintillator. More specifically, the blood samples are spun down to remove light absorbing and scattering red blood cells, leaving the more-or-less optically clear plasma for analysis. Light absorption properties or fluorescence properties of the plasma are then analysed at one or more wavelengths in a spectrophotometer or fluorimeter, respectively, and the results are compared to known specific absorption or fluorescence spectra of the tracer to quantify tracer concentration. Less invasive approaches have also been developed in optical imaging. Perhaps the most established of these is called pulsed dye-densitometry (PDD). This approach was initially developed from pulse oximetry methodology, wherein the oxygen saturation level of haemoglobin in the arterial blood is quantified by measuring fluctuations in light absorption in tissue (typically through a finger in adult humans) at two or more wavelengths of light in the near-infrared range. The fluctuations occurring at the heart rate are assumed to arise only from the arterial blood and differences in the absorption spectra of oxygenated and deoxygenated haemoglobin are incorporated to quantify oxygenation. This approach can be expanded to quantify changes in concentration of an optical tracer, and thus the plasma input function of a tracer, if the tracer has different absorption properties at the wavelengths measured. Other methods that have been employed to measure the plasma concentration in optical molecular imaging include direct measure from the left ventricle, which can be applied in small animals, and a dual-tracer approach wherein a second, untargeted tracer can be injected with a targeted tracer. If the tracers have different absorption or fluorescent properties, the sophistication of spectral imaging in optics can be used to resolve uptake of the two tracers simultaneously, allowing the untargeted tracer to be used as a surrogate of the plasma input function for quantitative kinetic modelling. This educational session will cover all of the points mentioned above and expand on their implementation, applications, and future directions.

Learning Objectives (3-4 Bullet Points): -Arterial sampling -Pulsed dye-densitometry -Image derived input function -Reference tracer imaging

Relevant Publications: Iijima T, Aoyagi T, Iwao Y, et al. Cardiac output and circulating blood volume analysis by pulse dye-densitometry. J Clin Monit 1997;13:81-9. Elliott JT, Wright EA, Tichauer KM, et al. Arterial input function of an optical tracer for dynamic contrast enhanced imaging can be determined from pulse oximetry oxygen saturation measurements. Phys Med Biol 2012;57:8285-95.

Disclosure of author financial interest or relationships:
K.M. Tichauer, None.

Presentation Number **ES 12**
Educational Session 04: Biology and Pathology - Central Nervous System
September 18, 2013 / 08:00-08:45 / Room: 200

Imaging of neurochemical genetics and behavior in animal models with PET and MRI

Bradley T. Christian, *Medical Physics, University of Wisconsin-Madison, Madison, WI, USA. Contact e-mail: bchristian@wisc.edu*

The nonhuman primate serves as an excellent model for studying neurodevelopment and how it relates to psychopathology. As an animal model, they live well in captivity and are very responsive to moderate perturbations such as prenatal stressors. Although they are responsive to these perturbations, they produce viable offspring that are available for longitudinal studies. And importantly, it is possible to have greater control over their rearing environment (as compared to humans), making them the most suitable animal model for studying the development of psychopathology. PET and MRI have demonstrated their utility as powerful tools for studying the development of neurochemical systems in the brain. This lecture will discuss the characterization of PET and MRI methods for studying neurochemical function with applications to disease specific rhesus models related to neurodevelopment.
Learning Objectives (3-4 Bullet Points): 1. To gain an understanding of how imaging modalities can be used to study neurodevelopment in the nonhuman primate model. 2. To gain an understanding of using pre-clinical animal models to study the relationship between behavioral endophenotypes and neurochemical function. 3. To gain an understanding of the potential of using imaging genetics to study gene x environment interactions using animal models.
Relevant Publications: Oler J, Fox A, Shelton S, Christian B, Murali D, Oakes TR, Davidson RJ, Kalin N. Serotonin Transporter Availability in the Amygdala and Bed Nucleus of the Stria Terminalis Predicts Anxious Temperament and Brain Glucose Metabolic Activity. J Neuroscience 29(32):9961-9966, 2009. PMCID: PMC2756094 Christian BT, Wooten DW, Hillmer AT, Tudorascu DL, Converse AK, Moore CF, Ahlers EO, Barnhart TE, Kalin NH, Barr CS, Schneider ML. Serotonin Transporter Genotype Affects Serotonin 5-HT1A Binding in Primates. Journal of Neuroscience, 2012. NIHMSID: NIHMS 442926. Converse AK, Moore CF, Moirano JM, Ahlers EO, Larson JA, Engle JW, Barnhart TE, Murali D, Christian BT, DeJesus OT, Holden JE, Nickles RJ, Schneider ML. Prenatal Stress Induces Increased Striatal Dopamine Transporter Binding in Adult Nonhuman Primates," Biological Psychiatry, in press, 2013. http://dx.doi.org/10.1016/j.biopsych.2013.04.023
Acknowledgements/References: NIH grants: AA017706, MH086014, AA12277, AA10079, T32CA009206, S10RR015801, P30HD003352, S10RR023033.

Disclosure of author financial interest or relationships:
B.T. Christian, Abiant, Inc, Grant/research support .

Presentation Number **ES 13**
Educational Session 04: Biology and Pathology - Central Nervous System
September 18, 2013 / 08:45-09:45 / Room: 200

Impact of Molecular Brain Imaging on Patient Management

Vikas Kotagal, *Neurology, University of Michigan, Ann Arbor, MI, USA. Contact e-mail: vikaskot@med.umich.edu*

Molecular brain imaging approaches have identified several features in patients with neurodegenerative dementias and with neurodegenerative movement disorders. These include characteristic features in measures of cerebral glucose metabolism, neuroreceptor and transporter imaging and detection of pathological protein depositions. Several of these research measures have become recently available in clinical neuroimaging, and offer the promise of improving diagnostic accuracy, informing of patient prognosis and directing the use of medical therapy. Applications in the distinction of degenerative dementia types including Alzheimer disease, dementia with Lewy bodies and frontotemporal dementia will be discussed. Additionally, distinctions among neurodegenerative extrapyramidal movement disorders on the basis of presynaptic nigrostriatal dopamine terminal lesions will be introduced. Molecular radiotracers necessary for these clinical distinctions are now FDA-approved and available.
Learning Objectives (3-4 Bullet Points): Describe the most common neurodegenerative dementia types. Identify molecular imaging characteristics that distinguish among dementias. Identify the common movement disorders with nigrostriatal degeneration. Describe molecular imaging approaches for detection of nigrostriatal lesions / damage.
Relevant Publications: Kotagal V, Albin RL, Müller ML, Koeppe RA, Frey KA, Bohnen NI. Gender differences in Cholinergic and Dopaminergic deficits in Parkinson disease. Journal of Neural Transmission. March 27th, 2013.

Disclosure of author financial interest or relationships:
V. Kotagal, None.

Presentation Number **ES 14**
Educational Session 05: What Life Scientists Should Know About Imaging Modalities - MR Fundamentals for Life Scientists
September 18, 2013 / 08:00-08:35 / Room: 203

Introduction to Magnetic Resonance II: Macroscopic and Microscopic Magnetization Effects

Truman R. Brown, *Radiology, Medical University of South Carolina, Charleston, SC, USA. Contact e-mail: trb31@musc.edu*

This presentation will cover the following areas in magnetic resonance (i) Curie law polarization; (ii) External vs.internal magnetic fields; (iii) Spectral density vs. relaxation; (iv) Chemical shifts; (v) Coupling constants.
Learning Objectives (3-4 Bullet Points): Understand the principles of magnetic susceptibility at both the macro and micro scale Understand the physical basis of relaxation Understand the physical basis of chemical shifts and J-coupling

Disclosure of author financial interest or relationships:
T.R. Brown, None.

Presentation Number **ES 15**
Educational Session 05: What Life Scientists Should Know About Imaging Modalities - MR Fundamentals for Life Scientists
September 18, 2013 / 08:35-09:10 / Room: 203

Magnets for Magnetic Resonance Imaging Systems

Michael Parizh, *MRI Technology and Systems, General Electric Global Research, Niskayuna, NY, USA. Contact e-mail: parizh@ge.com*

Magnetic Resonance Imaging (MRI) is a powerful diagnostic tool that the medical community considers as a procedure of choice for visualization of soft tissues. More than 30,000 MRI systems are installed in hospitals worldwide. Magnet is the largest and most expensive component of an MRI system. MRI was introduced in late 1970s with resistive magnets. Today, customer may choose between superconducting, permanent and electric magnets. Superconducting magnets are used in more than 75% of MRI system making MRI the largest commercial application of superconductivity. Recent decade has marked substantial progress in MRI magnets and systems. The 3.0 tesla horizontal field and high-field vertical field open whole-body MRI systems have become commercially available. Increased bore size improved patient comfort. Newer superconducting magnets typically require helium refill once in more than three years if ever. The magnet configuration is determined by numerous competing requirements including optimized functional performance, patient comfort, ease of siting in a hospital environment, minimum acquisition and lifecycle cost. The factors that drive the magnet requirements are increased center field, maximized uniformity volume, minimized stray field, magnet compactness, long helium refill period, and more. Advances in the cryogenic technology and magnet design practice provide means for improvements in magnet performance while meeting the market requirement for continuous system cost reduction.
Learning Objectives (3-4 Bullet Points): - New applications of MRI - Customer requirements to MRI scanners: critical and desirable requirements - Magnets and gradient coils

Disclosure of author financial interest or relationships:
M. Parizh, General Electric, Employment .

Presentation Number **ES 16**
Educational Session 05: What Life Scientists Should Know About Imaging Modalities - MR Fundamentals for Life Scientists
September 18, 2013 / 09:10-09:45 / Room: 203

Other Practical Considerations

W. T. Dixon, *Radiology and Imaging Science, Emory University, Atlanta, GA, USA. Contact e-mail: thomas.dixon@emory.edu*

RELAXATION T1, T2, and T2* relaxation dominate image contrast and affect temporal resolution and even spatial resolution. Resolving adjacent voxels requires putting 1/2 revolution of phase between them in ~T2, which is hard to do if gradients are weak or T2 short. In standard spin-warp imaging, T1/2 <TR <T1. Halving T1 delivers the first image in half the time and speeds up a dynamic series 2 fold. However, because the method can work on ~TR/TE slices at once, cutting T1and TR in half does not change the number of images made per minute. B0 EFFECTS Doubling B0 would quadruple signal by doubling flux and halving the precession period but it also raises noise. S/N increases by factors of 2^(7/4) in small, insulating liquid samples and 2 for large, slightly conductive, common MRI samples. High B0 gives no S/N advantage for hyperpolarized He3, C13, or Xe129. Doubling B0 can raise subject heating, SAR. If an RF pulse does the same thing in the same time, the higher field pulse deposits 4x the energy. If T2* shortening with B0 limits the high B0 pulse to half the duration, the higher field pulse deposits 8x the energy. SUSCEPTIBILITY Susceptibility complicates B0 maps greatly confounding some methods and enabling others. Diamagnetic substances, i. e. having negative susceptibility e. g. water, repel magnetic lines of force thus decreasing the field some places near a diamagnetic object and increasing it elsewhere. The effect range is about the size of the object. The complicated, shape-dependent resonant frequency change this makes is comparable to the resonant frequency difference between two lines in proton NMR. This is why frequency-based selective saturation and selective excitation methods are not robust. In some regions, information is missing and cannot be recovered. Exciting everything and keeping track of phase can make selective imaging, e. g. no fat, robust (1) and with special image processing, can even provide more information from images (2,3). The susceptibility difference between oxy-and deoxy-hemoglobin led to the first MRI method to show brain function (4). FACILITY DESIGN Facility design has grown simpler because self shielded magnets have compact fields and monitors that are unaffected by magnetic fields replaced cathode ray tubes. Room lighting was difficult because fluorescent lights made images noisy and stray fields made tungsten AC filaments vibrate and fail by fatigue, requiring trained personnel and a nonmagnetic ladder for replacement. LED's outlast imagers. SAFETY Whole body MR has hazards from energy stored in the magnet and from contrast-agent toxicity. Ear protection is needed because of rapid magnetic field gradient changes that rattle any metal in the magnet, even causing painful, direct stimulation in the body. A whole-body imager uses an RF transmitter 10x as powerful as a microwave oven. It is important to know where this power goes. FDA guidelines had to be developed before there were any easy ways to determine subject heating (5,6). Scientifically the safety problem is the same as monitoring thermal ablation or adjuvant heating during radio- or chemo-therapy.

Learning Objectives (3-4 Bullet Points): Learn relation of magnetic resonance imaging to Relaxation Field Strength Susceptibility Learn about MRI Facility Concerns MRI Safety

Acknowledgements/References: 1 Jingfei Ma. Breath-Hold Water and Fat Imaging Using a Dual-Echo Two-Point Dixon Technique With an Efficient and Robust Phase-Correction Algorithm. Magn Reson

Med 52:415-419; 2004. 2 Dixon WT, Blezek DJ, Lowery LA, Meyer DE, Kulkarni AM, Bales BC, Petko DL, Foo TK. Estimating amounts of iron oxide from gradient echo images. Magn Reson Med.61:1132-6; 2009. 3 S Mittal, Z Wu, J Neelavalli, EM Haacke. Susceptibility-Weighted Imaging: Technical Aspects and Clinical Applications, Part 2. AJNR 30:232-252; 2009. 4 S Ogawa, TM Lee, AR Kay, DW Tank. Brain magnetic resonance imaging with contrast dependent on blood oxygenation. Proc Natl Acad Sci USA 87:9868-72;1990. 5 WA Grissom, V Rieke, AB Holbrook, Y Medan, M Lustig, J Santos, MV McConnell, K Butts Pauly. Hybrid referenceless and multibaseline subtraction MR thermometry for monitoring thermal therapies in moving organs. Med Phys 37:5014-26;2010. 6 Sacolick LI, Wiesinger F, Hancu I, Vogel MW. B1 Mapping by Bloch-Siegert Shift. Magn Reson Med 63:1315-22;2010.

Disclosure of author financial interest or relationships:
W.T. Dixon, None.

Presentation Number **ES 17**
Educational Session 06: How to Succeed in Science I
September 18, 2013 / 09:45-10:30 / Room: 200

How to Write an Effective Renewal Grant Application

John Katzellenbogen, *Chemistry, University of Illinois at Urbana-Champaign, Urbana, IL, USA. Contact e-mail: jkatzene@illinois.edu*

Our ferociously challenging funding environment demands that grant applications and renewal applications be prepared with utmost care: Careful attention needs to be given to presenting them in a clear, convincing—even compelling—manner and to organizing them in a way that makes them maximally understandable and easy for a reviewer to appreciate all of their positive attributes and to construct a fair and informative review. The best reviewer is one who becomes intrigued and excited by your proposal after reading the first page and, upon further reading, becomes increasingly convinced to be a strong advocate, committed to seeing that you are able to undertake the research you propose. My presentation will be based on my own many-year experience as a researcher in medical imaging, as a generally successful grant applicant, and as a grant reviewer.
Learning Objectives (3-4 Bullet Points): How to prepare a renewal grant application that is clear and compelling. How to take the perspective of the reviewer of your grant application. How to make your grant application easy to read, to understand, and to review.

Disclosure of author financial interest or relationships:
J. Katzellenbogen, None.

Presentation Number **ES 18**
Educational Session 07: How to Succeed in Science II
September 18, 2013 / 09:45-10:30 / Room: 203

Delivering a Reasonably Interesting Talk

Martin Pomper, *Radiology, Johns Hopkins, Baltimore, MD, USA. Contact e-mail: mpomper@jhmi.edu*

Although fear is the general emotion most people experience when contemplating giving a talk, whether at a wedding, at work or at nearly every venue in which more than a few people are assembled, the actual talk itself can be enjoyable for the speaker - particularly if well prepared. Perhaps the most intimidating of talks is that delivered before one's peers, as in our case at a scientific meeting, where each slide is carefully scrutinized allowing for judgment to be passed not only on our life's work but also on our understanding of the field and the impact that our labors have on it. Accordingly, we will focus on delivering scientific talks. However, far from careful scrutiny of each slide, even when presenting our best work most of the audience remains busy on their smart phones up to and sometimes including the summary, and occasionally acknowledgments, slide. Our goal is to prevent that from happening - by maintaining the interest of the audience by obeying several simple and obvious rules - enabling not only effective communication, but also providing a positive impression of oneself, mainly through not wasting the time of those in attendance.
Learning Objectives (3-4 Bullet Points): - The key to any good talk: careful preparation. - Respect your audience. - Avoidance of data overload - How a scientific talk can seldom be too brief or too basic.

Disclosure of author financial interest or relationships:
M. Pomper, None.

Presentation Number **ES 19**
Educational Session 08: Chemistry of Contrast Media - Basic Considerations About Suitable Modalities & Probes
September 18, 2013 / 11:00-11:35 / Room: 100

Basics in pharmacokinetics: Low molecular weight probes

Arend Heerschap, *Radiology, Radboud University Nijmegen Medical Center, N ijmegen, Netherlands. Contact e-mail: a.heerschap@rad.umcn.nl*

A unique property of Magnetic Resonance is the broad range of options to monitor and image dynamic processes in the body. To derive physiologic or metabolic relevant parameters from the measured variables it is common to apply kinetic models to the data. This lecture will focus on the basics of one of the most widespread dynamic MR measurements in oncologic research: dynamic contrast MRI (DCE-MRI) to assess abnormal tumor vascularity. In this MR approach the uptake of an extracellular low molecular weight MR contrast agent (mostly Gd-DTPA) is measured by its effect on the T1 relaxation of the proton spins of water. This effect potentially can be influenced by a number of factors including physiological relevant ones, in particular blood flow, vessel permeability and the size of the extracellular compartment. In another approach called "dynamic susceptibility contrast" MRI the effect of the contrast agent on T2* relaxation is measured. This method is mostly applied to the brain and kinetic models can provide blood volume as one of its useful parameters. These methods are used for diagnostic purposes, but also to assess the effect of drugs, mostly anti-angiogenic drugs on tumor vascularity. In these applications it is important to apply some kind of calibration to eliminate as much as possible systemic and other non-relevant variations. It is possible to interprete the data of effects on water relaxation without a physiological model, but a more advanced analysis applies a physiological pharmokinetic model to extract relevant parameter values. Numerous variations and refinements of one or two compartment models for DCE-MRI have been proposed [1,2]. The most critical element in these analysis is the determination of the so-called arterial input function, which describes the blood supply by the tumor feeding arteries and allows to derive absolute parameter values. In principle this would calibrate the model output to values that are comparable among different sites, but differences in the MR methods and data analysis, as used in practice, hamper such a comparison. In the evaluation of drugs by DCE-MRI it is important to assess the reproducibility of the applied method.
Learning Objectives (3-4 Bullet Points): 1. To know which methods are used to measure the effects of low molecular weight contrast on the T1 and T2* relaxation of water spins 2. To know the main pharmacokinetic model to assess the T1 effect of low molecular weight contrast 3. To understand the meaning of the parameters derived from this kinetic modeling and limitations in measuring their values 4. To know some examples of the use of kinetic modeling to assess tumor vascularity.
Relevant Publications: 1. Dynamic Contrast-Enhanced Magnetic Resonance Imaging in Oncology. Springer 2005. Editors A. Jackson, DL. Buckley, GJM. Parker. 2. Sourbron SP, Buckley DL. Classic models for dynamic contrast-enhanced MRI. NMR Biomed. 2013 May 15.

Disclosure of author financial interest or relationships:
A. Heerschap, None.

Presentation Number **ES 20**

Educational Session 08: Chemistry of Contrast Media - Basic Considerations About Suitable Modalities & Probes

September 18, 2013 / 11:35-12:15 / Room: 100

Physical limits of optical, photoacoustic and ultrasound imaging: sensitivity, specificity and quantitation

Stanislav Y. Emelianov, [1]*Biomedical Engineering, University of Texas at Austin, Austin, TX, USA;* [2]*Imaging Physics, MD Anderson Cancer Center, Houston, TX, USA. Contact e-mail: emelian@mail.utexas.edu*

This primary purpose of this presentation is to provide a broad overview of optical, ultrasound and hybrid (i.e., photoacoustics, IVUS/OCT) imaging techniques and to discuss the strenths and weaknesses of these technologies. Basic physics of each imaging modality will be introduced, and contrast mechanisms, imaging contrast agents or imaging probes, and sources of noise and artifacts will be discussed. Finally, examples of biomedical and clinical applications of each imaging technology will be given. To achive these objectives, we will start with foundations of optical and ultrasound imaging, including brief discussion of governing equations. We will also review relevant optical/acoustic properties of the tissues. The experimental aspects of optical, ultrasound and hybrid imaging will be then discussed with emphasis on instrumentation, i.e., system hardware and signal/image processing algorithms. Specifically, penetration depth and spatial/temporal resolution of each imaging imaging modality will be anlyzed in relationship to an energy source, a sensor and other components of the imaging system. Techniques to increase contrast and to differentiate various tissues will be presented. Main emphasis, however, will be placed on design, synthesis and optimization of imaging contrast agents and probes to enable quantitative and/or molecular/cellular imaging. We will discuss design of system and contrast agents capable of multiplexed imaging, multi-modal imaging and image-guided therapy including drug delivery and release. The presentation will continue with an analysis of sensitifity and specificity of optical, ultrasound and hybrid imaging. Regulatory aspects of imaging contrast agents or probes will be presented. Finally, examples of biomedical and clinical applications of optical, ultrasound and photoacoustic imaging will be provided to stress fundamental similarities between the imaging modalities and to highlight vital differences between different imaging techniques. The presentation will conclude with the discussion of future directions in optical, ultrasound and hybrid imaging.

Learning Objectives (3-4 Bullet Points): Understand the fundamental principles of optical, ultrasound and hybrid (i.e., photoacoustic) imaging techniques Knowing how optical/ultrasound/photoacoustic images are formed Understand how imaging contrast agents can enhance contrast, signal-to-noise ratio and penetration depth in optical/ultrasound/photoacoustic imaging Understand the ability of optical/ultrasound/photoacoustic imaging system to visualize desired properties of imaged tissue using imaging contrast agents or probes Identify the role of contrast agents in basic science and clinical applications

Disclosure of author financial interest or relationships:
S.Y. Emelianov, NanoHybrids, Inc, Stockholder .

Presentation Number **ES 21**
Educational Session 09: Biology and Pathology - Systems Biology and its Link to Molecular Imaging
September 18, 2013 / 11:00-12:15 / Room: 102

An integrated-omics view of cellular regulation

Parag Mallick, *Canary Center for Cancer Early Detection, Stanford University, Stanford, CA, USA. Contact e-mail: paragm@stanford.edu*

In 1908, Archibald Garrod theorized that a gene is responsible for a particular protein and can be responsible for a disease. He suggested (correctly) that alkaptonuria results from one recessive gene, which causes a deficiency in the enzyme that normally breaks down alkapton. Beadle and Tatum subsequently demonstrated that single gene mutations could incapacitate specific enzymes and that such an incapacitation could cause a neurospora to have significantly altered physiology. Given these findings it is natural to conclude that innate diseases (e.g., alkaptonuria and cancer) result from single gene alterations. This led to the hypothesis that each gene is responsible for directing the construction of a single, specific enzyme and accordingly that disease occurs through the alteration of a gene. Decades later, this single-gene/single-enzyme view of how cells work (or break) has defined the major focus of much of biological investigation: identifying single genes whose mutation leads to pathology. In this world-view, the phenotype (disease outcome) is a sum of its parts (genotype). In much the same way that Newtonian physics explains a lot, but not all of the behavior of objects in motion, the early and ongoing views of biological regulation fail to fully explain or predict the biology. The flood of data generated by -omics technologies has given us a detailed view of the world of genes, biomolecules, and cells that we are just barely beginning to understand. Unfortunately, there is a chasm separating our knowledge of how molecular components and cellular and organismic physiology function together to enable cells to sense and respond to their environment, and to determine actions like proliferation, migration, and apoptosis. For example, the simple models of cellular regulation, driven solely by enzymatic cascades and modeled as first-order chemical processes, fail to describe the role of structural proteins (e.g., cellular cytoskeleton). Also, the emergent properties and self-organization evident in the interplay between transcription factors, DNA folding and unfolding, transcriptional machinery, and factors involved in translation and protein degradation collectively require sophisticated regulatory models to rigorously describe the diverse intermolecular interactions occurring within cells.
Learning Objectives (3-4 Bullet Points): * Understanding how to describe the genotype/phenotype relationship; * Recognizing how cellular regulation is a multi-level process and how protein levels and transcript levels are related to each other * Understanding of the history of models of cellular regulation
Relevant Publications: Integrated inference and analysis of regulatory networks from multi-level measurements. Poultney CS, Greenfield A, Bonneau R. Methods Cell Biol. 2012;110:19-56. Global quantification of mammalian gene expression control. Schwanhäusser B, Busse D, Li N, Dittmar G, Schuchhardt J, Wolf J, Chen W, Selbach M. Nature. 2011 May 19;473(7347):337-42.

Disclosure of author financial interest or relationships:
P. Mallick, None.

Presentation Number **ES 22**
Educational Session 10: Postprocessing and Cross Validation - Basics of Image Processing
September 18, 2013 / 11:00-12:15 / Room: 105

Basics of Image Processing: Image Registration and Object Tracking

Erik Meijering, *Medical Informatics and Radiology, Erasmus University Medical Center, Rotterdam, Netherlands. Contact e-mail: meijering@imagescience.org*

Imaging is playing an increasingly important role in both medicine and biology. Structural imaging modalities such as MRI, CT, and ultrasound provide detailed depictions of anatomy. PET, SPECT, and specialized MRI protocols add functional information. Optical imaging modalities, such as bioluminescence imaging and various types of light microscopy, offer an unprecedented sensitivity in visualizing molecular processes in living cells and organisms. The heterogeneity and sheer bulk of image data generated by the wealth of imaging possibilities make it impossible for a human observer to interpret and quantify the complex relationships between molecular processes and the structural and functional changes they cause. Molecular imaging studies typically involve data from multiple imaging modalities, covering a wide range of spatial and temporal scales. Differences in imaging geometry, posture, and information content occur between modalities, but also between time points in follow-up studies using the same modality. In this educational session we will discuss two important image processing techniques required to interrelate imaging data and to study dynamic phenomena occurring in these data: image registration and object tracking. Rather than going into details about available software tools, the focus will be on understanding the underlying image processing principles used by many software tools.

Learning Objectives (3-4 Bullet Points): To learn about the following aspects of Image registration: * Image transformations (rigid and nonrigid) * Image similarity metrics and optimization * Motion correction and deformation analysis * Multimodal registration and visualization To learn about the following aspects of object tracking: * Particle detection and tracking methods * Cell segmentation and tracking methods * Supra-analysis of tracking results * Applications of tracking in microscopy

Relevant Publications: The following publications are useful reviews on image registration (first three) and object tracking (last three): * Pluim JPW, Maintz JBA, Viergever MA. Mutual-information-based registration of medical images: A survey. IEEE Transactions on Medical Imaging 22(8):986-1004, August 2003. * Zitová B, Flusser J. Image registration methods: A survey. Image and Vision Computing 21(11):977-1000, October 2003. * Hill DLG, Batchelor PG, Holden M, Hawkes DJ. Medical image registration. Physics in Medicine and Biology 46(3):R1-R45, March 2001. * Meijering E, Dzyubachyk O, Smal I. Methods for cell and particle tracking. Methods in Enzymology 504:183-200, February 2012. * Meijering E, Dzyubachyk O, Smal I, van Cappellen WA. Tracking in cell and developmental biology. Seminars in Cell and Developmental Biology 20(8):894-902, October 2009. * Dorn JF, Danuser G, Yang G. Computational processing and analysis of dynamic fluorescence image data. Methods in Cell Biology 85:497-538, 2008.

Acknowledgements/References: This educational session is the second from a series of three sessions on the basics of image processing: 1) image segmentation (educated by Wiro Niessen at WMIC 2012), 2) image registration and object tracking (educated by Erik Meijering at WMIC 2013), and 3) quantitative imaging biomarkers (to be educated by Wiro Niessen and Boudewijn Lelieveldt at WMIC 2014).

Disclosure of author financial interest or relationships:
E. Meijering, None.

Presentation Number **ES 23**
Educational Session 11: How to Develop Clinical Products I
September 18, 2013 / 11:00-11:37 / Room: 200

How to develop clinical products. F-18 Florbetaben as an example of molecular imaging development

Andrew Stephens, *Clinical Research and Development, Sitz der Gesellschaft: Berlin Amtsgericht Charlottenburg HRB 136823, Berlin, Germany. Contact e-mail: andrew.stephens@piramal.com*

Development of a successful imaging agent remains a challenging endeavor. Prior to last year no PET agents had been approved since FDG. Recently there has been a great deal of activity around beta-amyloid imaging agents. This provides a unique look at what can be expected for future regulatory approvals. One must show that the agent is binding to the predicted pathologic protein or tissue. For the case of the amyloid imaging agents this meant performing a histology study on end of life patients scanned with the agent during life. After death an autopsy was performed to prove that the signal of the PET agent corresponds to the pathology. The FDA recognized that this may not represent the intended target population. Additional studies may therefore be required in the target population. Emphasis on the ability for the reader to be able to provide a dichotomous yes/no read. The Agency has not yet embraced an approval based on quantitative SUV/SUVR data. For amyloid imaging agents all sponsors have been required to produce a widely accessible training program to read scans. The sponsor must prove that nuclear medicine physicians can access a training program (e.g. web based) that would allow them to have a basic competence of the reading technique without further training or certification. The FDA required validation of the training methodology and a post-marketing commitment to assess reader training under the typical conditions of clinical practice. Although the FDA did not require clinical data assessing the effect of amyloid imaging on clinical management, this has become a sticking point for payers. Reimbursement groups have increasingly required that the results of the imaging analysis be shown to improve patient care. The biomarker hypothesis alone may be sufficient for approval, but not for subsequent market success. Sponsors should consider this early and build it into their development plans.

Learning Objectives (3-4 Bullet Points): 1) Understand the role of beta amyloid in Alzheimer's Disease 2) Be able to describe the importance of assay validity and clinica Utility 3) Be able to describe the critical pathway required by the regulatory authorities in the development of beta-amyloid Imaging agents

Disclosure of author financial interest or relationships:
A. Stephens, Piramal Imaging, Employment .

Presentation Number **ES 24**
Educational Session 11: How to Develop Clinical Products I
September 18, 2013 / 11:37-12:15 / Room: 200

Clinical Translation in Academics: Examples from Imaging Research

Martin Pomper, *Radiology, Johns Hopkins, Baltimore, MD, USA. Contact e-mail: mpomper@jhmi.edu*

Clinical translation of laboratory discoveries is difficult in any environment, but that performed in academic institutions holds its own, unique challenges. Although imaging research is arguably easier to translate - including introduction of new imaging agents to human subjects - than clinical trials involving new devices, drugs or other therapies, substantial hurdles must be overcome. We will review the process of clinical translation from project conception through the first-in-human (Phase 0/1+) trial, beyond which is generally the domain of industry.
Learning Objectives (3-4 Bullet Points): - Introduction to translational molecular imaging. - Obstacles to overcome in an academic setting. - How to gain and keep momentum by attracting industrial sponsors.

Disclosure of author financial interest or relationships:
M. Pomper, None.

Presentation Number **ES 25**
Educational Session 12: How to Develop Clinical Products II
September 18, 2013 / 11:00-11:37 / Room: 203

Monitoring and Tracking Disease Events in Small Animals using Non-invasive Optical Imaging

Kevin P. Francis, *Caliper, PerkinElmer Company, Alameda, CA, USA. Contact e-mail: Kevin.Francis@perkinelmer.com*

Since its inception in 1995, in vivo optical imaging has become a well-recognized technique for allowing disease states and complex biological processes to be non-invasively monitored in small animals. Genes encoding optical reporters, luciferases and fluorescent proteins, are engineered into cells (e.g., cancer cell lines and infectious disease agents) and animals (transgenic mice and rats) to enable them to produce light that can be visualized in vivo using highly sensitive CCD optical imaging equipment. This technique is equally amenable to imaging fluorescent dyes and particles, allowing fluorescently tagged biological entities (e.g., antibodies and peptides) to be monitored independently or in combination with genetically tagged events. An overview of this technology will be presented along with data demonstrating how in vivo optical imaging has been used by researchers worldwide to monitor a plethora of different preclinical diseases, from simple gastrointestinal infections to advanced metastatic cancers.

Learning Objectives (3-4 Bullet Points): - Understand the fundamentals of Non-invasive Optical Imaging. - Learn which optical reporters are most appropriate for preclinical imaging. - See example of how this technique has been used effectively in drug discovery and for monitoring complex biological processes in vivo.

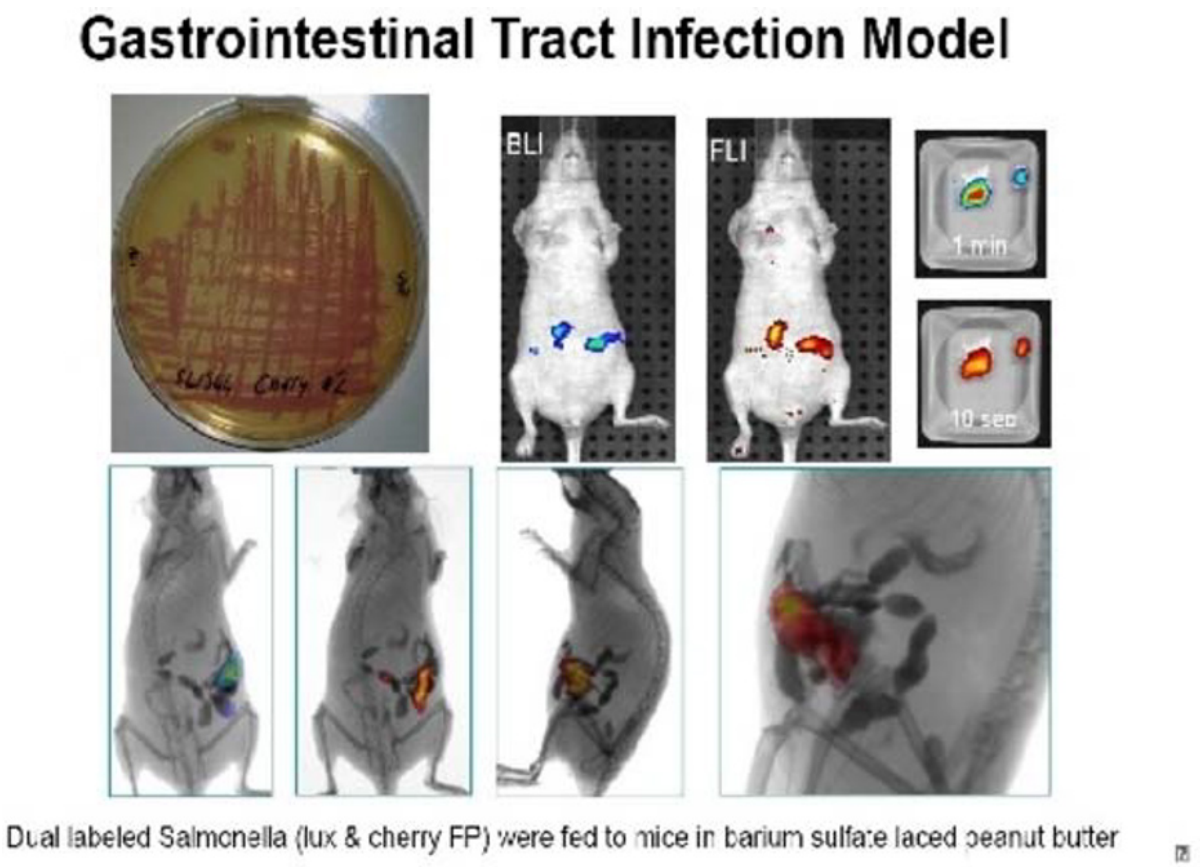

Disclosure of author financial interest or relationships:
K.P. Francis, PerkinElmer, Employment .

Presentation Number **ES 26**
Educational Session 12: How to Develop Clinical Products II
September 18, 2013 / 11:37-12:15 / Room: 203

Ultrasound Molecular Imaging: How to Develop Clinical Products?

Francois Tranquart, *Thierry Bettinger, Catherine Botteron, Christian Koller, Research and Development, Bracco Suisse SA, Plan Les Ouates, Switzerland. Contact e-mail: francois.tranquart@brg.bracco.com*

The introduction of targeted contrast agents among agents eligible for ultrasound molecular imaging (USMI) has reinforced the interest for this method and significantly broadened the scope of CEUS but in the same time, has raised significant issues with regard to the agent to be used clinically (1,4-8,11-14,16). When entering the USMI domain, the need to add a ligand to target a specific molecular marker/signature implies the validation of the targeting moiety and more precisely, the compatibility with regulatory requirements for a human use. The bubble size is not significantly modified by the presence of a ligand meaning that the specific characteristic of these agents as strict markers of the vascular bed is still a property which can be considered as a great advantage for quantification in some indications, such as therapeutic treatment monitoring. The specific issues considered for such agents are strictly related to the nature of the ligand itself and the mode of attachment to the shell membrane. Whereas preclinical tests have been performed with a biotin-streptavidin linker, the impossibility to translate this construct into clinics due to possible immunogenicity has conducted scientists to propose alternative methods compatible with human use. From a regulatory point of view, the gas microbubble is considered as the active entity meaning that each of the microbubble components should be fully characterized. The manufacture of clinical material should be carried out in compliance with the GMP guidelines. With respect to the formulation characteristics, the selection of the ingredients is of paramount importance since the use of specific components should be validated for these new drug delivery systems for parenteral administration. In that perspective, the retained formulation for clinical trials must be challenged before finalization as changing any of the components at a late stage could be difficult and costly, even impossible. Once the formulation is finalized, many steps must be accomplished before any clinical use: robustness of the manufacturing process, stability of the product, validation of the test methods. Another requirement is completing a pharma-toxicology package according to the International Conference on Harmonization (ICH) guidelines. These different steps are time-consuming and relatively expensive. Finally, when the steps above have been completed, the agent is suitable for clinical testing pending Investigational New Drug (IND) submission and Institutional Review Board (IRB) or ethical committee approval for the selected indication. At present, literature is rich of papers reporting good results with targeted UCAs in many animal models. However, only one agent BR55 (Bracco Imaging, Milan, Italy) entered clinical testing so far. This illustrates the difficulties to develop a suitable approach for clinical use. The development time of such agents does not differ significantly from what is currently reported for therapeutic drugs, i.e. at least 10 years. The translation to clinics targeted agents requires high level expertise to develop suitable agents according to the various constraints.

Learning Objectives (3-4 Bullet Points): Identify the various steps to be followed between an early development stage to a final product to be used in humans. Raise the specific issues to be considered when developing a new agent. Identify possible causes of failure when developing a new agent.

Relevant Publications: [1] Bettinger T, Bussat P, Tardy I, et al. Ultrasound molecular imaging contrast agent binding to both E- and P-selectin in different species. Invest Radiol 2012;47: 516-523.

[2] Claudon M, Cosgrove D, Albrecht T, et al. Guidelines and good clinical practice recommendations for contrast enhanced ultrasound (CEUS) - update 2008. Ultraschall Med 2008; 29: 28-44. [3] Correas JM, Claudon M, Tranquart F, Helenon AO. The kidney: imaging with microbubble contrast agents. Ultrasound Q 2006; 22: 53-66. [4] Deshpande N, Needles A, Willmann JK. Molecular ultrasound imaging: current status and future directions. Clin Radiol 2010; 65:567-581. [5] Deshpande N, Pysz MA, Willmann JK. Molecular ultrasound assessment of tumor angiogenesis. Angiogenesis 2010;13:175-188. [6] Hwang M, Lyshchik A, Fleischer AC. Molecular sonography with targeted microbubbles: current investigations and potential applications. Ultrasound Q 2010;26:75-82. [7] Kiessling F, Huppert J, Palmowski M. Functional and molecular ultrasound imaging: concepts and contrast agents. Curr Med Chem 2009;16:627-642. [8] Kircher MF, Willmann JK. Molecular Body Imaging: MR Imaging, CT, and US. Part I. Radiology 263; 3: 633-43. [9] Piscaglia F, Nolsøe C, Dietrich CF, et al. The EFSUMB guidelines and recommendations on the clinical practice of contrast-enhanced ultrasound (CEUS): Update 2011 on non-hepatic applications. Ultraschall in Der Medizin 2011; [10] Piscaglia F, Bolondi L. The safety of SonoVue in abdominal applications: retrospective analysis of 23,188 investigations. Ultrasound Med Biol 2006; 32: 1369-1375. [11] Pysz MA, Willmann JK. Targeted contrast-enhanced ultrasound: an emerging technology in abdominal and pelvic imaging. Gastroenterology 2011;140:785-790. [12] Pysz MA, Gambhir SS, Willmann JK. Molecular imaging: current status and emerging strategies. Clin Radiol 2010;65:500-516. [13] Tardy I, Pochon S, Theraulaz M, et al. Ultrasound molecular imaging of VEGFR2 in a rat prostate tumor model using BR55. Invest Radiol 2010;45:573-578. [14] Unnikrishnan S, Klibanov AL. Microbubbles as Ultrasound Contrast Agents for Molecular Imaging: Preparation and Application. AJR 2012; 199:292-299. [15] Warram JM, BS, Sorace AG, Saini R, Umphrey HR, Zinn KR, Hoyt K. A triple-targeted ultrasound contrast agent provides improved localization to tumor vasculature. J Ultrasound Med 2011; 30:921-931. [16] Willmann JK, van Bruggen N, Dinkelborg LM, Gambhir SS. Molecular imaging in drug development. Nat Rev Drug Discov 2008; 7:591-607.

Acknowledgements/References: ACKNOWLEDGMENT F Tranquart thanks his co-workers at the Geneva Research Centre for fruitful discussion and help in preparing the manuscript.

Disclosure of author financial interest or relationships:

F. Tranquart, Bracco Suisse SA, Employment; **T. Bettinger**, Bracco Suisse SA, Employment; **C. Botteron**, Bracco Suisse SA, Employment; **C. Koller**, BRACCO Suisse SA, Employment .

Presentation Number **ES 27**
Educational Session 13: Chemistry of Contrast Media - Particles and Polymers
September 18, 2013 / 13:45-14:20 / Room: 100

Targeted particles and polymers

Sjoerd Hak, *Department of Circulation and Medical Imaging, Norwegian Univeristy of Science and Technology, Trondheim, Norway. Contact e-mail: sjoerd.hak@ntnu.no*

Over the last decades a plethora of targeted particles and polymers have been developed. In this educational talk it is aimed to introduce several basic concepts and considerations in the development, characterization and applictaion of these materials. The diversity of different approaches to achieve target specificty will be outlined and several mechanisms of target interaction (e.g. cellular internalization or enzymatic activation) will be illustrated with examples from literature. Furthermore, the concepts of multivalent and synergistic targeting will be introduced.
Learning Objectives (3-4 Bullet Points): Understanding of contrast material design driven by imaging modality vs application driven choice of contrast material/imaging modality Introduction into methods for ligand conjugation Understanding of different kinds of target interactions and their pros and cons for specific applications

Disclosure of author financial interest or relationships:
S. Hak, None.

Presentation Number **ES 28**
Educational Session 13: Chemistry of Contrast Media - Particles and Polymers
September 18, 2013 / 14:20-14:55 / Room: 100

Particles and Polymers for Optical Imaging

Anthony McGoron, *Biomedical Engineering, Florida International University, Miami, FL, USA. Contact e-mail: Anthony.McGoron@fiu.edu*

Despite the limitations of poor tissue penetration and high scatter (relative to PET/PECT, CT, and MRI) optical imaging is relatively inexpensive, portable, and offers the potential for high sensitivity and spatial and temporal resolution. Near-infrared (NIR) light 700-900 nm propagates through tissues due to minimal DNA and water absorption. Most in vivo applications for optical imaging employ NIR fluorescent dyes, but gold nanoparticles, carbon nanotubes and quantum dots are also important. For optical imaging, cyanine dyes are important synthetic molecules since many fluoresce in the NIR. Of these Indocyanine Green (ICG) has the longest history and continues to garner interest because it is FDA approved for systemic delivery. However, the qualities that make it good for cardiac output measurement, i.e., plasma binding and fast plasma clearance, are poor for in imaging. It also suffers from poor stability in aqueous solutions. To improve plasma residence, stability and tissue targeting, the dyes can be loaded into polymer naoparticles and liposomes. A strong size dependent localized Surface Plasmon Resonance (SPR) absorption is observed with many metallic nanoparticles. Gold, due to its inertness and surface functionalization, has attracted much interest for imaging. Single walled carbon nanotubes (SWCNT) are also attractive for imaging. They are basically hollow cylindrical molecules of carbon atoms, open or capped at the ends, with high aspect ratios of as small as one nm in diameter to as much as several cm in length. In general, they are non-toxic and hydrophobic but can be made water soluble by surface modifications reducing the tendency to agglomerate. Surface modification can also be exploited for targeting. They possess strong absorbance in the NIR, but they have low fluorescent quantum yield relative to fluorescent dyes, gold and quantum dots, and concerns persist regarding their long-term toxicities, particularly if inhaled. Quantum dots (QDs), semiconductor crystal materials, offer the advantages of very high quantum yield, stability, almost no quenching or bleaching, and can be produced in a rainbow of colors, from visible to the NIR, depending on their size. Emission frequencies increase as QD size decreases, causing a color shift from red to blue in the emitted light and they can be made in tunable emission/excitation combinations. QDs have been studied extensively for in vitro cell imaging, but to be translated to human in vivo use problems associated with the general toxicity of semiconductor materials must be overcome. QDs tend to be hydrophobic and cannot be used in aqueous solutions unless their surfaces are modified. With surface modification their hydrophilicity can be increased and their toxicity decreased. This talk will focus on comparing imaging modalities, concentrating on optical imaging, and go into greater depth regarding the application of quantum dots and efforts to reduce their toxicity and translation to in vivo use.

Learning Objectives (3-4 Bullet Points): Understand the advantages and disadvantages of various imaging modalities Understanding of established optical probes and their uses, both clinical and preclinical Understand the synthesis and unique characteristics (e.g. preparation, spectral properties, doping and size) of quantum dots for optical imaging Understand the biocompatibility aspects (e.g., toxicity of metals and coatings) of quantum dots compared to other contrast agents used for optical imaging

Relevant Publications: 1 Srinivasan, S. R. Manchanda, A. Fernandez-Fernandez*, T. Lei*, A. J. McGoron. Near-Infrared Fluorescing IR820-Chitosan Conjugate for Multifunctional Cancer Theranostic

Applications, Journal of Photochemistry and Photobiology B: Biology 119:52-59, 2013. 2 Manchanda, R., A. Fernandez-Fernandez, D.A. Carvajal*; T. Lei*, Y. Tang, A.J. McGoron. Nanoplexes for Cell Imaging and Hyperthermia: In vitro Studies. J of Biomedical Nanotechnology. 8:699-707, 2012. 3 Fernandez-Fernandez, A, R. Manchanda, T. Lei, D. Carvajal, Y. Tang, S. Kazmi*, A.J. Mcgoron. A Comparative Study of Optical and Heat Generation Properties of IR820 and Indocyanine Green. Mol Imaging. 11(2):99-113. 2012. DOI 10.2310/7290.2011.00031 4 Fernandez-Fernandez, A., R. Manchanda, A.J. McGoron. Theranostic Applications of Nanomaterials in Cancer: Drug. Delivery, Image-Guided Therapy, and Multifunctional Platforms. Appl Biochem Biotechnol. 165(7-8):1628-51, 2011. 5 Lei, T., S. Srinivasan, Y. Tang*, R. Manchanda, A. Nagesetti, A. Fernandez-Fernandez, A.J. McGoron. Comparing Cellular Uptake and Cytotoxicity of Targeted Drug Carriers in Cancer Cell Lines with Different Drug Resistance Mechanisms. Nanomedicine: Nanotechnology, Biology and Medicine. 7(3):324-332, 2011 doi:10.1016/j.nano.2010.11.004. NIHMS 254071 6 Tang, Y., T. Lei, R. Manchanda*, A. Nagesetti, A. Fernandez-Fernandez, S. Srinivasan, A.J. McGoron. Simultaneous Delivery of Chemotherapeutic and Thermal-Optical Agents to Cancer Cells by a Polymeric (PLGA) Nanocarrier: an In Vitro Study. Pharm Res (2010) 27:2242-2253. DOI 10.1007/s11095-010-0231-6. 7 Manchanda, R., A. Fernandez-Fernandez, A. Nagesetti, and A.J. McGoron, Preparation and characterization of a polymeric (PLGA) nanoparticulate drug delivery system with simultaneous incorporation of chemotherapeutic and thermo-optical agents. Colloids and Surfaces B: Biointerfaces, 2010, 75:260-267.

Disclosure of author financial interest or relationships:
A. McGoron, None.

Presentation Number **ES 29**
Educational Session 13: Chemistry of Contrast Media - Particles and Polymers
September 18, 2013 / 14:55-15:30 / Room: 100

Novel polymeric contrast materials

David P. Cormode, *Radiology, University of Pennsylvania, Philadelphia, PA, USA. Contact e-mail: davidcormode@gmail.com*

This is the second lecture in a three year sequence on the Chemistry of Contrast Media: Particles and Polymers. The focus of this lecture is polymeric contrast agents. This lecture will cover different approaches to the formation of polymer based contrast agents, such as covalent synthesis, the use of proteins or other biopolymers, and supramolecular assembly. Agents based on dendrimers, albumin, chitosan, PLGA, PCL and PEG will be featured. Methods to integrate a range of contrast generating materials will be discussed, such as iron oxides, gadolinium chelates, gold nanoparticles, iodine and quantum dots. The use of polymers to create agents for MRI, fluorescence, CT and other imaging modalities will be covered. The advantages and drawbacks of such approaches will be described, such as the increase in relaxivity of gadolinium chelates when attached to a large polymer. The clinical utility of these agents will be discussed. For example, Gadofosveset is a gadolinium chelate that binds to albumin in the bloodstream, extending its blood circulation half-life compared to Gd-DTPA, and facilitating MRI angiography.
Learning Objectives (3-4 Bullet Points): -To know how contrast agents can be formed from polymeric materials. -To be able to explain the advantages of using polymeric contrast agents. -To be familiar with specific examples, such as albumin based agents.

Disclosure of author financial interest or relationships:
D.P. Cormode, Philips, Grant/research support .

Presentation Number **ES 30**
Educational Session 14: Biology and Pathology - Cardiovascular Diseases
September 18, 2013 / 13:45-14:20 / Room: 102

Pathobiology of myocardial infarction, healing, remodeling and heart failure -- what happens where?

Matthias Nahrendorf, *Center for Systems Biology, Massachusetts General Hospital, Boston, MA, USA. Contact e-mail: MNahrendorf@partners.org*

Myocardial ischemia creates a sterile wound which is a strong stimulus for the activation of systemic healing processes. The success of infarct healing determines whether post-MI heart failure occurs, however, we are only beginning to understand therapeutic opportunities arising in the weeks after acute MI. The talk will review aspects of infarct healing, the role of innate immune cells, and highlight the contribution of imaging to i) a better understanding of basic biology after MI and ii) improving clinical care.
Learning Objectives (3-4 Bullet Points): - time course of immune cells involved in healing - mechanisms of cell supply - therapeutic and diagnostic opportunities
Relevant Publications: Frangogiannis NG. Regulation of the inflammatory response in cardiac repair. Circ Res. 2012 Jan 6;110(1):159-73. Swirski FK, Nahrendorf M. Leukocyte behavior in atherosclerosis, myocardial infarction, and heart failure.Science. 2013;339(6116):161-6 - PMID: 23307733 Nahrendorf M, Pittet MJ, Swirski FK. Monocytes: protagonists of infarct inflammation and repair after myocardial infarction. Circulation. 2010;121(22):2437-45 - PMID: 20530020

Disclosure of author financial interest or relationships:
M. Nahrendorf, None.

Presentation Number **ES 31**
Educational Session 14: Biology and Pathology - Cardiovascular Diseases
September 18, 2013 / 14:20-14:55 / Room: 102

Molecular Imaging of Myocardial Ischemia and Remodeling

David E. Sosnovik, *Cardiology, MGH, Harvard Medical School, Boston, MA, USA. Contact e-mail: sosnovik@nmr.mgh.harvard.edu*

WMIC 2013 Syllabus David E. Sosnovik Session: Cardiac Educational Session Talk: Molecular Imaging of Myocardial Ischemia and Remodeling. Numerous molecular processes are involved in myocardial ischemia and remodeling and are amenable to molecular imaging.(1, 2) Myocardial ischemia is characterized by cell death. This can be due to apoptosis, necrosis or autophagy. Molecular MRI approaches have been developed to image apoptosis and necrosis in vivo.(3, 4) These processes can also be imaged with SPECT and PET.(5, 6) More recently, a fluorescence based approach was developed to image autophagy in vivo.(7) Cell death in ischemia is followed by inflammation. This can be imaged with iron oxide nanoparticles,(8) Gd loaded liposomes,(9) and fluorine loaded liposomes.(10) The proteolytic enzymes released by these infiltrating macrophages have been imaged with activatable MR and optical imaging agents.(11, 12) Inflammation is followed by myocardial healing during which scar formation and angiogenesis are the principal processes. Radiolabeled RGD has been used to image angiogenesis during the remodeling process.(13, 14) Gd chelates targeted to type-1 collagen and elastin and radiolabeled probes to MMP allow scar formation to be assessed noninvasively.(15-17) The remodeled heart is characterized apoptosis, fibrosis, overactivity of the renin-angiotensin system and an imbalance in cardiac sympathetic activity. Approaches have been developed to image sympathetic activity and angiotensin-II receptors in the heart.(18, 19)

Learning Objectives (3-4 Bullet Points): Learning Objectives: Become familiar with the principal molecular processes relevant to myocardial ischemia and remodeling Become familiar with the advantages and disadvantages of the various molecular imaging platforms with specific reference to myocardial imaging Review the work that has been done to date on the molecular imaging of myocardial ischemia and remodeling.

Relevant Publications: References: 1. Sosnovik DE, Nahrendorf M, Weissleder R. Molecular magnetic resonance imaging in cardiovascular medicine. Circulation. 2007;115:2076-2086. 2. Nahrendorf M, Sosnovik DE, French BA, Swirski FK, Bengel F, Sadeghi MM, Lindner JR, Wu JC, Kraitchman DL, Fayad ZA, Sinusas AJ. Multimodality cardiovascular molecular imaging, Part II. Circ Cardiovasc Imaging. 2009;2:56-70. 3. Sosnovik DE, Garanger E, Aikawa E, Nahrendorf M, Figuiredo JL, Dai G, Reynolds F, Rosenzweig A, Weissleder R, Josephson L. Molecular MRI of cardiomyocyte apoptosis with simultaneous delayed-enhancement MRI distinguishes apoptotic and necrotic myocytes in vivo: potential for midmyocardial salvage in acute ischemia. Circ Cardiovasc Imaging. 2009;2:460-467. 4. Huang S, Chen HH, Yuan H, Dai G, Schuhle DT, Mekkaoui C, Ngoy S, Liao R, Caravan P, Josephson L, Sosnovik DE. Molecular MRI of acute necrosis with a novel DNA-binding gadolinium chelate: kinetics of cell death and clearance in infarcted myocardium. Circ Cardiovasc Imaging. 2011;4:729-737. 5. Narula J, Acio ER, Narula N, Samuels LE, Fyfe B, Wood D, Fitzpatrick JM, Raghunath PN, Tomaszewski JE, Kelly C, Steinmetz N, Green A, Tait JF, Leppo J, Blankenberg FG, Jain D, Strauss HW. Annexin-V imaging for noninvasive detection of cardiac allograft rejection. Nat Med. 2001;7:1347-1352. 6. Liu Z, Zhao M, Zhu X, Furenlid LR, Chen YC, Barrett HH. In vivo dynamic imaging of myocardial cell death using 99mTc-labeled C2A domain of synaptotagmin I in a rat model of ischemia and reperfusion. Nucl Med Biol. 2007;34:907-915. 7. Chen HH, Mekkaoui C, Cho H, Ngoy S, Marinelli B, Waterman P, Nahrendorf M,

Liao R, Josephson L, Sosnovik DE. Fluorescence tomography of rapamycin-induced autophagy and cardioprotection in vivo. Circ Cardiovasc Imaging. 2013;6:441-447. 8. Sosnovik DE, Nahrendorf M, Deliolanis N, Novikov M, Aikawa E, Josephson L, Rosenzweig A, Weissleder R, Ntziachristos V. Fluorescence tomography and magnetic resonance imaging of myocardial macrophage infiltration in infarcted myocardium in vivo. Circulation. 2007;115:1384-1391. 9. Naresh NK, Xu Y, Klibanov AL, Vandsburger MH, Meyer CH, Leor J, Kramer CM, French BA, Epstein FH. Monocyte and/or macrophage infiltration of heart after myocardial infarction: MR imaging by using T1-shortening liposomes. Radiology. 2012;264:428-435. 10. Flogel U, Ding Z, Hardung H, Jander S, Reichmann G, Jacoby C, Schubert R, Schrader J. In vivo monitoring of inflammation after cardiac and cerebral ischemia by fluorine magnetic resonance imaging. Circulation. 2008;118:140-148. 11. Nahrendorf M, Sosnovik D, Chen JW, Panizzi P, Figueiredo JL, Aikawa E, Libby P, Swirski FK, Weissleder R. Activatable magnetic resonance imaging agent reports myeloperoxidase activity in healing infarcts and noninvasively detects the antiinflammatory effects of atorvastatin on ischemia-reperfusion injury. Circulation. 2008;117:1153-1160. 12. Nahrendorf M, Sosnovik DE, Waterman P, Swirski FK, Pande AN, Aikawa E, Figueiredo JL, Pittet MJ, Weissleder R. Dual channel optical tomographic imaging of leukocyte recruitment and protease activity in the healing myocardial infarct. Circ Res. 2007;100:1218-1225. 13. Meoli DF, Sadeghi MM, Krassilnikova S, Bourke BN, Giordano FJ, Dione DP, Su H, Edwards DS, Liu S, Harris TD, Madri JA, Zaret BL, Sinusas AJ. Noninvasive imaging of myocardial angiogenesis following experimental myocardial infarction. J Clin Invest. 2004;113:1684-1691. 14. Sherif HM, Saraste A, Nekolla SG, Weidl E, Reder S, Tapfer A, Rudelius M, Higuchi T, Botnar RM, Wester HJ, Schwaiger M. Molecular imaging of early alphavbeta3 integrin expression predicts long-term left-ventricle remodeling after myocardial infarction in rats. J Nucl Med. 2012;53:318-323. 15. Helm PA, Caravan P, French BA, Jacques V, Shen L, Xu Y, Beyers RJ, Roy RJ, Kramer CM, Epstein FH. Postinfarction myocardial scarring in mice: molecular MR imaging with use of a collagen-targeting contrast agent. Radiology. 2008;247:788-796. 16. Makowski MR, Wiethoff AJ, Blume U, Cuello F, Warley A, Jansen CH, Nagel E, Razavi R, Onthank DC, Cesati RR, Marber MS, Schaeffter T, Smith A, Robinson SP, Botnar RM. Assessment of atherosclerotic plaque burden with an elastin-specific magnetic resonance contrast agent. Nat Med. 2011;17:383-388. 17. Su H, Spinale FG, Dobrucki LW, Song J, Hua J, Sweterlitsch S, Dione DP, Cavaliere P, Chow C, Bourke BN, Hu XY, Azure M, Yalamanchili P, Liu R, Cheesman EH, Robinson S, Edwards DS, Sinusas AJ. Noninvasive targeted imaging of matrix metalloproteinase activation in a murine model of postinfarction remodeling. Circulation. 2005;112:3157-3167. 18. Fukushima K, Bravo PE, Higuchi T, Schuleri KH, Lin X, Abraham MR, Xia J, Mathews WB, Dannals RF, Lardo AC, Szabo Z, Bengel FM. Molecular hybrid positron emission tomography/computed tomography imaging of cardiac angiotensin II type 1 receptors. J Am Coll Cardiol. 2012;60:2527-2534. 19. Thackeray JT, Bengel FM. Assessment of cardiac autonomic neuronal function using PET imaging. J Nucl Cardiol. 2013;20:150-165.

Disclosure of author financial interest or relationships:
D.E. Sosnovik, Siemens Medical, Grant/research support .

Presentation Number **ES 32**
Educational Session 14: Biology and Pathology - Cardiovascular Diseases
September 18, 2013 / 14:55-15:30 / Room: 102

Ischemia, Myocardial Infarction and Heart Failure - Target specific contrast agents

Peter Caravan, *A. A. Martinos Center for Biomedical Imaging, Massachusetts General Hospital, Harvard Medical School, Charlestown, MA, USA. Contact e-mail: caravan@nmr.mgh.harvard.edu*

This lecture will review recent advances in the development of molecular imaging probes for cardiac applications.
Learning Objectives (3-4 Bullet Points): 1) Understand the state of the art for molecular imaging in the context of cardiac ischemia, myocardial infarction and heart failure 2) Elucidate the unmet need for molecular imaging in cardiac ischemia, myocardial infarction and heart failure and the choice of appropriate imaging modality 3) Describe the molecular imaging approaches currently in development for cardiac ischemia, myocardial infarction and heart failure

Disclosure of author financial interest or relationships:
P. Caravan, Sanofi, Grant/research support; Biogen Idec, Consultant; Factor 1A, Stockholder; Collagen Medical, Stockholder .

Presentation Number **ES 33**
Educational Session 15: Chemistry of Contrast Media - Small Molecules
September 18, 2013 / 13:45-14:20 / Room: 105

Hyperpolarized MR Probes

Matthew E. Merritt[1,2], *Craig Malloy*[1,3], *Dean Sherry*[1,4], [1]*AIRC, UTSW Medical Center, Dallas, TX, USA;* [2]*Molecular Biophysics, UTSW Medical Center, Dallas, TX, USA;* [3]*Internal Medicine, North Texas VA, Lancaster, TX, USA;* [4]*Chemistry, U of Texas at Dallas, Richardson, TX, USA. Contact e-mail: matthew.merritt@utsouthwestern.edu*

Dissolution dynamic nuclear polarization (DNP) has demonstrated the ability to identify disease and aberrant metabolic function in a variety of *ex vivo* and *in vivo* systems. The technology provides the highest MR sensitivity when operating at the lowest achievable temperatures and higher magnetic field strengths (3.35 -7 T). The enhanced sensitivity provided by DNP allows the tremendous chemical selectivity of ^{13}C MR to observe multiple steps in a reaction pathway. Taken together these factors produce a powerful molecular imaging modality.
Learning Objectives (3-4 Bullet Points): 1) Understand the physical process of hyperpolarization 2) Understand timescales for HP experiments 3) Be able to design a basic molecular imaging experiment based on the available substrates 4) Be able to differentiate between the effects of flux and pool size

Disclosure of author financial interest or relationships:
M.E. Merritt, None; **C. Malloy**, None; **D. Sherry**, None.

Presentation Number **ES 34**
Educational Session 15: Chemistry of Contrast Media - Small Molecules
September 18, 2013 / 14:20-14:55 / Room: 105

Chelate Chemistry for Molcular Imaging

Garry E. Kiefer, *N/a, Macrocyclics, Dallas, TX, USA. Contact e-mail: garry@macrocyclics.com*

Chelating agents have played an integral role in the development of contrast enhancement agents for magnetic resonance imaging (MRI) and diagnostic radiopharmaceuticals for PET and CT applications. In addition, luminescent probes based on novel cheating agents are being developed for optical imaging modalities. For these and many new applications on the horizon, the chelating agent is relied upon to form a highly stable complex with the metal ion, provide a point of attachment to bio-targeting molecules such as monoclonal antibodies, and to enhance the functionality and biodistribution for new contrast agent applications. This talk will present an overview of chelate based contrast agents in the field of molecular imaging with emphasis on emerging technologies.
Learning Objectives (3-4 Bullet Points): Selection of metal ions for imaging modality Understanding of multifunctional chelating agent platforms Potential new uses as physiological probes

Disclosure of author financial interest or relationships:
G.E. Kiefer, None.

Presentation Number **ES 35**
Educational Session 15: Chemistry of Contrast Media - Small Molecules
September 18, 2013 / 14:55-15:30 / Room: 105

Small Molecule Probes for Nuclear Medicine

Henry C. Manning, *Radiology, Vanderbilt University, Nashville, TN, USA. Contact e-mail: henry.c.manning@vanderbilt.edu*

Radiopharmaceuticals are central to all nuclear medicine studies; their development and routine production for preclinical and/or clinical use share a number of general principles. This lecture will provide a basic introduction to radiopharmaceutical design and development, beginning with initial conceptualization through scientific vetting that may lead to future clinical trials in patients. Though many types of pharmacophores can be radiolabeled for positron emission tomograpy (PET) or single photon emission computed tomography (SPECT) studies, the framework for this lecture will be developed around small, 'drug-like' molecules aimed at PET imaging in preclinical studies and humans. Approaches to incorporate common radiolabels such as cyclotron-produced fluorine-18 and carbon-11 will be discussed, including strengths and pitfalls, as well as the framework required to advance a novel PET agent through the regulatory process to early studies in humans.
Learning Objectives (3-4 Bullet Points): 1) To learn the basics of radiolabeling small molecules 2) To learn the basic biology for targeting important pathways in cancer and other diseases 3) To develop an understanding of how to develop a PET probe for a specific biological pathway or process 4) To understand hurdles of translating PET probes from the preclinical setting to the clinical setting

Disclosure of author financial interest or relationships:
H.C. Manning, None.

Presentation Number **ES 36**
Educational Session 16: Biology and Pathology - Cancer Biology
September 18, 2013 / 13:45-14:20 / Room: 200

Imaging Tumor Hallmarks

Robert Gillies, *Cancer Imaging, Moffitt Cancer Center, Tampa, FL, USA. Contact e-mail: robert.gillies@moffitt.org*

There is considerable inter- and intra- tumoral genetic heterogeneity, which is a challenge for molecularly targeted therapy. In contrast, virtually all cancers exhibit common phenotypic traits, or "Hallmarks". These hallmarks are not only useful to monitor the response to canti-cancer therapies, they are also being considered as therapeutic targets themselves. These traits, such as resistance to apoptosis, growth factor independence, altered bioenergetics, angiogenesis and invasion, call all be understood as adaptive strategies to the microenvironmental landscape that is temporally changing during the course of cancer progression. Also important is that many of these traits are imageable through molecular imaging approaches, using optical, PET and MR. In this talk, we will review the hallmarks of cancer and discuss approaches that can be used to assess their activities through molecular imaging. Over past decade there has been a significant effort to expand the armamentarium of available imaging biomarkers to those that are more sensitive to tumor metabolism, molecular expression or physiology, and following are a few examples. Some of these are directed specifically at a hallmark, such as FDG PET, which reports on altered bioenergetics, or integrin-targeted agents, which report on angiogenesis. Other approaches are more indirect, such as diffusion MRI, which reports on cellularity, perfusion imaging which reports on dysregulated vasculogenesis, and pH imaging, which is a sequela of altered bioenergetics. Hypoxia is also emerging as a common microenvironmental hallmark of cancer, and there are numerous molecular imaging approaches to visualize this parameter. In some cases, expression of a hallmark results in the altered expression of cell surface antigens, and tracers can be directed at these to interrogate, for example, cell proliferation or apoptosis/necrosis.
Learning Objectives (3-4 Bullet Points): OBJECTIVES: 1. Know the hallmarks of cancer and their related sequelae 2. Identify approaches to image these parameters with molecular imaging 3. Describe the clinico-biological significance that such imaging can provide.
Relevant Publications: Hanahan D, Weinberg RA. Hallmarks of cancer: the next generation. Cell. 144(5):646-74, 2011 Gillies RJ, Verduzco D, Gatenby RA. Evolutionary dynamics of carcinogenesis and why targeted therapy does not work. Nature reviews Cancer 12:487-93, 2012 Nowell PC. The clonal evolution of tumor cell populations. Science (New York, NY 1976;194(4260):23-8. Gerlinger M, Swanton C. How Darwinian models inform therapeutic failure initiated by clonal heterogeneity in cancer medicine. British journal of cancer 2010;103(8):1139-43. Gerlinger M, Rowan AJ, Horswell S, et al. Intratumor heterogeneity and branched evolution revealed by multiregion sequencing. The New England journal of medicine 2012;366(10):883-92. Gatenby RA, Gillies RJ. A microenvironmental model of carcinogenesis. Nature reviews 2008;8(1):56-61. Gatenby RA, Gillies RJ. Why do cancers have high aerobic glycolysis? Nature reviews 2004;4(11):891-9.

Disclosure of author financial interest or relationships:
R. Gillies, None.

Presentation Number **ES 37**
Educational Session 16: Biology and Pathology - Cancer Biology
September 18, 2013 / 14:20-14:55 / Room: 200

Imaging generic markers: proliferation, metabolism, angiogenesis, apoptosis

Michal Neeman, *Biological Regulation, Weizmann Institute, Rehovot, Israel. Contact e-mail: michal.neeman@weizmann.ac.il*

Cancer is a disease that is inherently characterized by very high heterogeneity, between patients, within a single patient, within a single tumor and also over time. Such heterogeneity implies that any information retrieved by invasive procedures based on biopsy are limited in their relevance for planning of therapy and monitoring disease progression. Clearly, non invasive tools and particularly non invasive imaging is critical for personalizing therapy. A number of generic markers show high relevance for characterization of many types of tumors and offer sensitive readout for effects of treatment. Among these, markers of cell proliferation and apoptosis provide critical information for tumor growth or regression, while imaging markers of metabolism and angiogenesis provide insight to the microenvironmental heterogeneity in tumors. Extensive progress in molecular imaging led to a wide range of contrast media for all imaging modalities, including optical, ultrasound, CT, MRI and PET.
Learning Objectives (3-4 Bullet Points): Understand the significance of changes in proliferation, metabolism, angiogenesis, apoptosis in cancer Comprehend the strategies for imaging changes in proliferation, metabolism, angiogenesis, apoptosis Review the tools for validation of imaging biomarkers for proliferation, metabolism, angiogenesis, apoptosis
Relevant Publications: 1. Hanahan, D. & Weinberg, R.A. Hallmarks of cancer: the next generation. Cell 144, 646-674 (2011). 2. Folkman, J. & Hanahan, D. Switch to the angiogenic phenotype during tumorigenesis. Princess Takamatsu Symp 22, 339-347 (1991). 3. Dvorak, H.F. Tumors: wounds that do not heal. Similarities between tumor stroma generation and wound healing. N Engl J Med 315, 1650-1659 (1986). 4. Carmeliet, P., et al. Role of HIF-1alpha in hypoxia-mediated apoptosis, cell proliferation and tumour angiogenesis. Nature 394, 485-490 (1998). 5. Shweiki, D., Neeman, M., Itin, A. & Keshet, E. Induction of vascular endothelial growth factor expression by hypoxia and by glucose deficiency in multicell spheroids: implications for tumor angiogenesis. Proc Natl Acad Sci U S A 92, 768-772 (1995).
Acknowledgements/References: This work was supported by The 7th Framework European Research Council Advanced grant 232640-IMAGO; by the European Commission 7th Framework Integrated Project ENCITE; and by the National Institutes of Health (grant R01 CA75334).

Disclosure of author financial interest or relationships:
M. Neeman, None.

Presentation Number **ES 38**
Educational Session 16: Biology and Pathology - Cancer Biology
September 18, 2013 / 14:55-15:30 / Room: 200

Imaging specific tumor markers - surface antigens

Kimberly Kelly, *Biomedical Engineering, UVa, Charlottesville, VA, USA. Contact e-mail: kak3x@virginia.edu*

Molecular imaging has already changed how tumors are diagnosed by providing clinicians with information that is difficult to obtain by other methods. The key to success of molecular imaging is the ability to identify readily accessible targets that are of high abundance on the tumor but not on normal cells or in benign conditions. In this talk, we will explore what are the ideal characteristics of a tumor biomarker and how they are currently identified.
Learning Objectives (3-4 Bullet Points): Learning objectives: At the end of this session students will be able to identify what makes a good imaging tumor biomarker. Molecular imaging has already changed how tumors are diagnosed by providing clinicians with information that is difficult to obtain by other methods. The key to success of molecular imaging is the ability to identify readily accessible targets that are of high abundance on the tumor but not on normal cells or in benign conditions. In this talk, we will explore what are the ideal characteristics of a tumor biomarker and how they are currently identified.

Disclosure of author financial interest or relationships:
K. Kelly, Astra Zeneca, Grant/research support .

Presentation Number **ES 39**
Educational Session 17: What Life Scientists Should Know About Imaging Modalities - Nuclear Imaging: Physical Principles and Instrumentation
September 18, 2013 / 13:45-14:20 / Room: 203

Principles of PET and SPECT

Roger Fulton, [1]*Medical Physics, Westmead Hospital, Sydney, NSW, Australia;* [2]*Brain and Mind Research Institute, University of Sydney, Sydney, NSW, Australia. Contact e-mail: r.fulton@physics.usyd.edu.au*

This presentation explores the principles and methods that underpin two key molecular imaging techniques based on the radioactive tracer principle: single photon emission computed tomography (SPECT) and positron emission tomography (PET). Topics covered include the radioactive tracer principle, radioisotope production and decay, radiation transport in tissue, radiation detection, PET and SPECT instrumentation and tomographic image reconstruction. On completion of this lecture, students will have a basic understanding of the imaging chain as it relates to PET and SPECT, starting with the emission of radiation in the body, leading to its external detection and, finally, a reconstructed image of the radioactive tracer distribution in the body. The factors affecting the accuracy and noise properties of molecular images will be briefly explored. Students will also have an appreciation of how to use these imaging technologies to exploit the properties of the radioactive tracer principle and make estimates of important physiological parameters.
Learning Objectives (3-4 Bullet Points): Be able to explain the tracer principle and its importance in PET and SPECT molecular imaging. Be able to explain to your peers how radiation emitted from the body is detected externally using SPECT and PET instrumentation. Be able to explain the key principles in forming a reconstructed image of the tracer distribution in the body.

Disclosure of author financial interest or relationships:
R. Fulton, None.

Presentation Number **ES 40**
Educational Session 17: What Life Scientists Should Know About Imaging Modalities - Nuclear Imaging: Physical Principles and Instrumentation
September 18, 2013 / 14:20-14:55 / Room: 203

SPECT and PET Detector Technologies

Dennis R. Schaart, *Applied Sciences, Delft University of Technology, Delft, Netherlands. Contact e-mail: d.r.schaart@tudelft.nl*

This lecture provides a basic introduction into the physical principles of the detection of gamma radiation in nuclear medicine imaging (preclinical PET and SPECT in particular). The emphasis lies on scintillation detectors, which are the most commonly applied type of detector. The interaction of the gamma quanta with the scintillation material forms the basis for the signal formation. Therefore, a basic understanding of the different types of interaction that may occur is required to understand the operation and performance of a scintillation detector. Furthermore, the physics underlying the conversion of the energy of a gamma quantum into scintillation photons will be briefly discussed. The next step in the detection chain is the conversion of the relatively weak light signal emitted by the scintillator into an electronic signal by means of a photosensor. An important aspect of detector design is the optimization of the crystal-photosensor geometry in order to achieve a good balance between multiple and often conflicting requirements on the detector performance at reasonable costs. The classical and still most widely used photosensor is the photomultiplier tube (PMT). For a long time, the relatively large internal gain and low noise of these devices made them the first, if not only, choice for the detection of very small amounts of light, down to the single photon level. However, advances in semiconductor technology have recently given birth to several new types of low-level light sensor, some of which have distinct advantages compared to PMTs for certain applications. Examples include avalanche photodiodes (APDs) and silicon photomultipliers (SiPMs). These solid state devices enable new crystal-sensor geometries, as well as new combinations of imaging modalities such as PET and MRI in highly integrated multimodality systems. For optimum detector performance, the use of dedicated front-end electronics, adapted to the specific properties of the scintillator-photosensor combination, is paramount. The readout electronics and data acquisition (DAQ) architecture furthermore need to be tailored to the imaging modality and application, as the corresponding requirements may vary greatly. The overall detector performance, expressed in terms of parameters such as spatial resolution, energy resolution, timing resolution, and detection efficiency, is the result of the design choices made with respect to each of the above components making up the detection chain (scintillation material, photosensor, detector geometry, electronics). Since the performance of the detectors impose ultimate limits on the image quality achievable with any scanner, it is not surprising that many research groups work on new and better detectors. Some of these recent developments will be briefly highlighted in this lecture.

Learning Objectives (3-4 Bullet Points): - To obtain a basic understanding of the physical principles of radiation detection - To learn the essential principles of inorganic scintillators and their most important properties - To acquire basic knowledge of photosensors and readout electronics relevant to radiation detection

Relevant Publications: - van Eijk, CWE. Inorganic scintillators in medical imaging. Phys Med Biol. 47:R85-R106, 2002 - Lewellen, TK. Recent developments in PET Detector technology. Phys Med Biol. 53:R287-R317, 2008

Disclosure of author financial interest or relationships:
D.R. Schaart, None.

Presentation Number **ES 41**
Educational Session 17: What Life Scientists Should Know About Imaging Modalities - Nuclear Imaging: Physical Principles and Instrumentation
September 18, 2013 / 14:55-15:30 / Room: 203

PET and SPECT Based Hybrid Imaging Systems

Robert Miyaoka, *Radiology, University of Washington, Seattle, WA, USA. Contact e-mail: rmiyaoka@u.washington.edu*

A theme in medical imaging is that two images combined together can often provide more than twice the information as one. The two images can be a functional (e.g., PET or SPECT) and an anatomic image (e.g., CT or MRI); images from two different pharmaceuticals or contrast agents; or images before and after therapy. In this session we will focus on nuclear medicine based hybrid imaging systems (e.g., PET/CT and SPECT/CT). We will begin with an overview of the rationale for hybrid imaging both for clinical and pre-clinical applications. We will describe the synergistic benefits of these systems. We will then discuss the different types of nuclear medicine hybrid instrumentation. The main focus will be on PET/CT and SPECT/CT as they have the largest user base. However, we will also cover PET/MRI, SPECT/MRI, and other types of hybrid imaging systems. We will cover the challenges (i.e., imaging artifacts) associated with hybrid imaging systems and also the benefits of having multiple sets of complementary data. Finally, we will go over the special data processing requirements that are necessary and available for the various imaging combinations.
Learning Objectives (3-4 Bullet Points): To become acquainted with a range of hybrid imaging methods, their rationale and principles. To develop an appreciation of the applications of clinical and preclinical hybrid imaging. To gain an understanding of technical challenges facing designers of hybrid imaging systems, and recent technological innovations. To be familiar with potential sources of artifacts in hybrid imaging and how they may be counteracted.

Disclosure of author financial interest or relationships:
R. Miyaoka, Philips Healthcare, Grant/research support; GE Healthcare, Grant/research support .

Presentation Number **LBA 2**
Late Breaking Abstract Session 1
September 19, 2013 / 11:00-11:15 / Room: Oglethorpe Auditorium

First use of Sn117m-DOTA-Annexin as a novel vulnerable plaque tracer in humans

Pilar Orellana[1], *Rodrigo Jaimovich*[1], *Leopoldo Marine*[2], *Albrecht H. Krämer*[2], *Maria Cecilia Gil*[3], *Jagat Narula*[4], *Suresh Srivastava*[5], *H. William Strauss*[6], *Nigel R. Stevenson*[7], *Gilbert Gonzales*[7], [1]*Radiologia. Unidad de Medicina Nuclear, Pontificia Universidad Catolica de Chile, Santiago, Chile;* [2]*Cirugia Vacular y Endovascular, Pontificia Universidad Catolica de Chile, Santiago, Chile;* [3]*CGM Nuclear, Santiago, Chile;* [4]*Medicine-Cardiology, Mount Sinai Hospital, New York, NY, USA;* [5]*Brookhaven Laboratory, Upton, NY, USA;* [6]*Nuclear Medicine, Memorial Sloan-Kettering Cancer Center, New York, NY, USA;* [7]*Clear Vascular Inc, The Woodlands, TX, USA. Contact e-mail: porellana@med.puc.cl*

Background: Atherosclerotic Disease (AD) is one of the most important and common causes of death and disability, especially when it is associated with the rupture of unstable or vulnerable atherosclerotic plaques. Annexin V, found on the inner cell membrane, specifically binds to phosphatidylserine (PS). When cells undergo apoptosis, the PS is exposed for binding. The targeting molecule developed for vulnerable plaque (VP) imaging and therapy is [tin-117m]-DOTA-annexin (TA). Due to its nuclear and physical properties (t½ 14days, emission of an imaging photon as well as therapeutic conversion electrons), Sn-117m labelled Annexin-V could be particularly useful for the non-invasive imaging and treatment of AD. We report the first human use of TA for imaging. Methodology: All studied patients had carotid artery stenosis (CAS), and were candidates for carotid endarterectomy (CEA). The first part of the trial involved 6 patients and the second part 9 patients. For the first part of the study a dose of 500 µCi cGMP TA was used to determine dosimetry and biodistribution. The second part of the trial was performed with 3 mCi of the tracer (determined by the first part's organ toxicity results) in order to enable a better image quality. All patients were followed with scintigraphic images up to 14 days after the injection. Blood and urine samples were collected to establish blood clearance and urinary excretion. Complete haematological, renal, biochemical and liver parameters were measured in blood weekly until 4 weeks after injection. All patients underwent endarterectomy and both groups had optical, autoradiography and histology data from excised carotid plaque tissue. Results: Tracer activity in blood cleared after 24 hours. Urine tracer excretion at day 7 was less than 5% of total urinary activity. Scintigraphic images showed mild bone marrow uptake, moderate spleen uptake and high initial uptake in liver and kidneys. Kidney activity decreased after one week and disappeared at 2 weeks. There was no change in uptake pattern in bone marrow, liver and spleen during the two-week period of observation. In three patients bowel activity was seen in the delayed images. No significant clinical changes or blood test abnormalities were detected. Imaging of atherosclerotic plaques was not achieved at these doses, although tissue analysis confirmed the presence of the tracer on all inflammatory plaques. TA uptake was seen in one patient with an abdominal aortic aneurysm (see Figure 1) and other with a previous surgical procedure at the lumbar spine. Conclusion: A novel anti-inflammatory tracer, specifically targeting vulnerable/unstable atherosclerotic plaque, is presented. Biological safety and imaging capability is demonstrated. These preliminary results showed selective uptake of TA in cardiovascular VP and other inflammation sites.

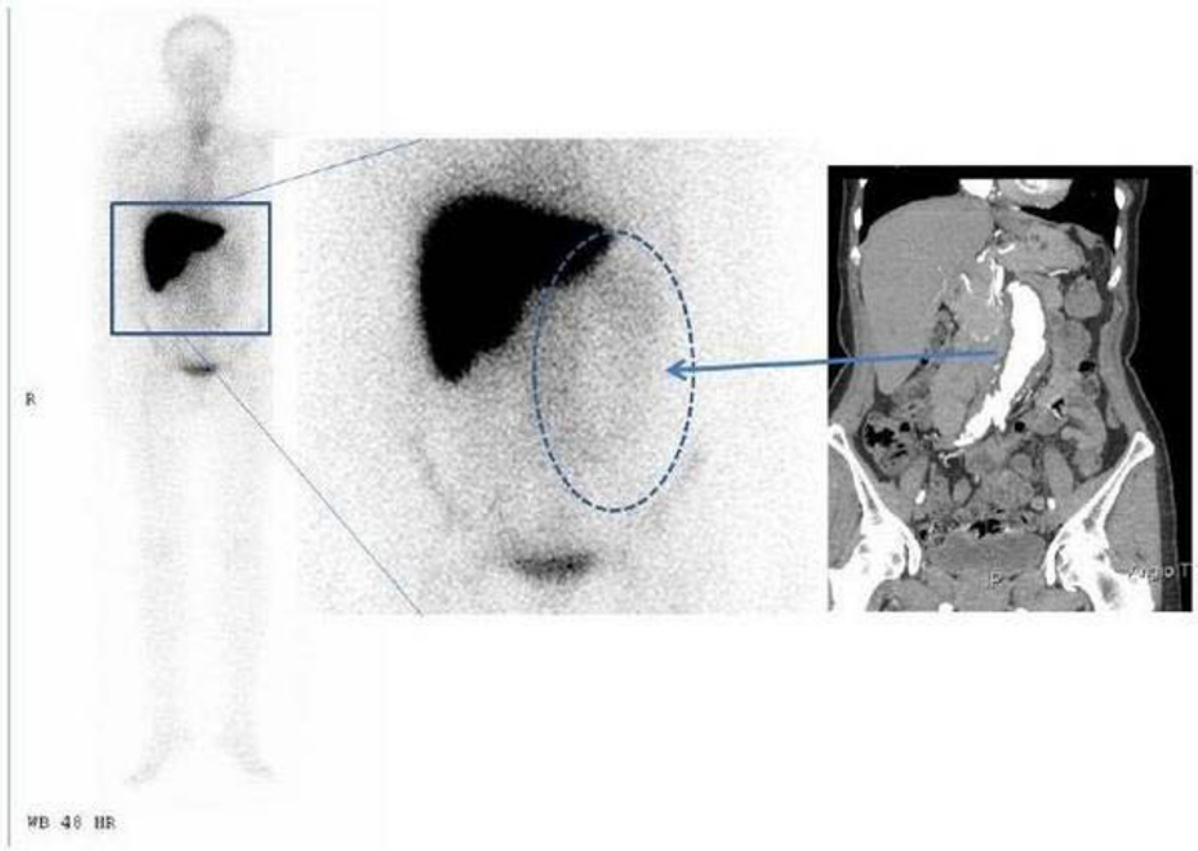

Figure 1: Detection of an abdominal aortic aneurism with [Tin-117m]-DOTA-Annexin V

Disclosure of author financial interest or relationships:
P. Orellana, Clear Vascular, Inc., The Woodlands, TX.United States., Grant/research support; **R. Jaimovich**, ClearVascular Inc., Grant/research support; **L. Marine**, None; **A.H. Krämer**, None; **M. Gil**, None; **J. Narula**, None; **S. Srivastava**, None; **H. Strauss**, None; **N.R. Stevenson**, Clear Vascular, Inc., Employment; **G. Gonzales**, Clear Vascular, Inc., Employment; Serene Oncology, LLC, Stockholder; Rheumco, LLC, Stockholder .

Presentation Number **LBA 3**
Late Breaking Abstract Session 1
September 19, 2013 / 11:15-11:30 / Room: Oglethorpe Auditorium

Proteomics Based Imaging Biomarker Discovery for Acidic Microenvironment of Breast Cancer Tumors

Mehdi Damaghi[1], *Veronica Estrella*[2], *Mark Lloyd*[3], *Robert Sprung*[4], *John M. Koomen*[4], *Robert A. Gatenby*[2], *Robert Gillies*[1], [1]*Cancer Imaging and Metabolomics, Moffitt cancer center, Tampa, FL, USA;* [2]*Radiology, Moffitt cancer center, Tampa, FL, USA;* [3]*proteomics core, Moffitt cancer center, Tampa, FL, USA;* [4]*Analytical Microscopy, Moffitt cancer center, Tampa, FL, USA. Contact e-mail: mehdi.damaghi@moffitt.org*

The physical microenvironment of tumors is heterogeneous. A combination of poor vascular perfusion, regional hypoxia and increased glycolysis leads to an acidic microenvironment. Chronic acidosis selects for phenotypic alterations and changes in protein expression. The tumor cells that acquire resistance to acid-mediated cytotoxicity have a growth advantage over non-adapted stromal cells and hence acquire an invasive and metastatic phenotype. As a consequence of its importance to cancer progression, there has been a concerted effort to develop molecular imaging probes to measure tumor and tissue pH. An alternative approach is to develop probes to target tissue response to acidosis. As a precursor to developing such probes, we have used proteomic approaches to identify proteins that are expressed in cells that have been adapted to growth in acidic conditions. Stable Isotope Labeling by Amino acids in Culture (SILAC) techniques provide an efficient method for quantitative analysis of whole proteome of paired biological samples. In this study we SILAC labeled MCF-7 breast cancer cells grown in neutral pH and adapted for growth at pH 6.7, which required more than 3 months. Using liquid chromatography and tandem mass spectrometry (LC/MS-MS) whole proteomes of neutral and acid-adapted samples were compared in a 2 set parallel "flipping" experiments, which reduces the false positive rate and increases the reliability of the data set. Analyses identified 31 proteins that have more than 2-fold higher expression in acid-adapted compared to control cells. Using Selected Reaction Monitoring (SRM) we have re-confirmed the differences in the expression levels of three of the proteins that had increased expression in acidic pH: viz. LAMP2, S100A6, and HSP72. qRT PCR and Western blots confirmed overexpression, with LAMP2 and S100A6 showing a higher increase than HSP72. To move toward to the in-vivo direction we used spheroid 3D cell culturing followed by Immunohistochemistry (IHC) to localize expression of our markers. LAMP2 showed very interesting pattern close to the hypoxic area of the spheroid that is comparable to Glut1 expression pattern. Using a Dorsal Window Chamber (DWC) we showed the overexpression of LAMP2 in more acidic area of the actual tumor inside the chamber. Finally, IHC analyses of Tissue Micro Array (TMA) of breast cancer patient samples showed staining patterns for LAMP2 that were consistent with areas suspected to be acidic. We thus suspect that LAMP2 specific ligands may be useful targeted molecular imaging probes for biological acidosis. Such agents may have potential to serve broadly for the non-invasive detection of tumor acidity, which would be a valuable in prognosis, prediction and monitoring therapy response.

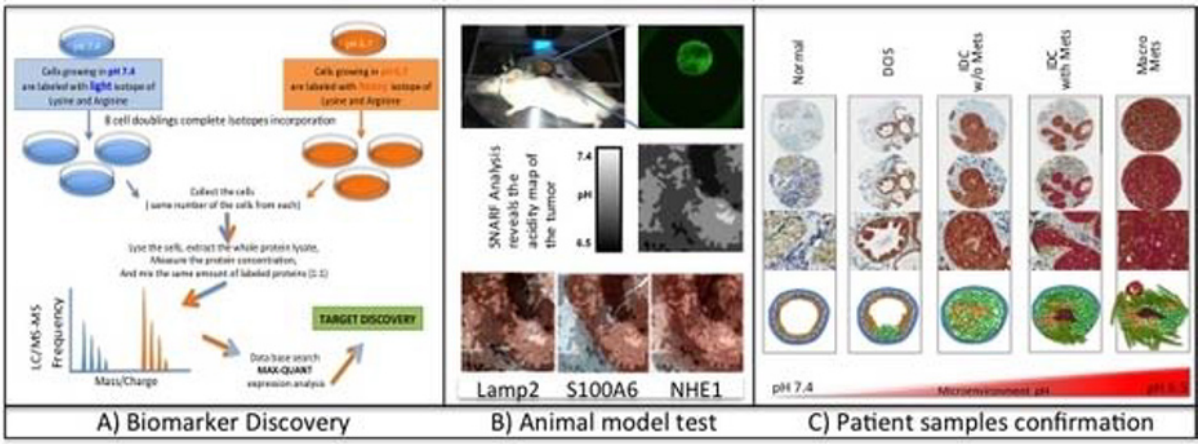

Fig1. Different steps of biomarker discovery: A, Shotgon protemoics approach on SILAC labeled acid adapted and non-adapted MCF-7 cells to find the overexpressed proteins in response of acidic media. B, Reconfirmation of discovered marker in animal model using dorsal window chamber (DWC) experiment. C, IHC of breast cancer TMA approved our findings and model.

Disclosure of author financial interest or relationships:
M. Damaghi, None; **V. Estrella**, None; **M. Lloyd**, None; **R. Sprung**, None; **J.M. Koomen**, None; **R.A. Gatenby**, None; **R. Gillies**, None.

Presentation Number **LBA 4**
Late Breaking Abstract Session 1
September 19, 2013 / 11:30-11:45 / Room: Oglethorpe Auditorium

Cu-64 Collagelin Conjugate Validation and PET Characterization of Myocardial Fibrosis

Cynthia A. Davies-Venn[1], *Sung-Jin Lee*[2], *Samuel J. Won*[1], *Jin Su Kim*[2], *Zhengsheng Yao*[4], *Songtao Liu*[1], *Insook Kim*[2], *Gang Niu*[3], *Xiaoyuan Chen*[3], *Chang Paik*[2], *David A. Bluemke*[1], [1]*Radiology and Imaging Sciences, National Institutes of Health, Bethesda, MD, USA;* [2]*Radiopharmaceutical Research, National Institutes of Health, Bethesda, MD, USA;* [3]*Molecular Imaging and Nanomedicine, National Institutes of Health, Bethesda, MD, USA;* [4]*Nuclear Medicine, National Institutes of Health, Bethesda, MD, USA. Contact e-mail: cynthiana28@gmail.com*

Introduction: Fibrosis represents a significant morbidity in cardiovascular disease and diseases of aging. Current clinical imaging modalities such as MRI and CT successfully identify discrete fibrosis. However, more diffuse and early stage fibrosis can benefit from higher sensitivity imaging as well as a more distinct threshold for distinguishing fibrotic tissue. "Collagelin" is a 22 amino acid peptide that has been shown to bind with high affinity to fibrotic collagen in a heart and lung model of fibrosis (Muzard et al., 2009). While other molecular markers of fibrosis target intermediates in the fibrosis pathway such as pro-collagen and matrix metalloproteinases (MMPs), collagelin directly targets collagen. Collagelin also has the advantage of favorable conjugation chemistry and higher affinity than other collagen targeting probes. Hypothesis: Collagelin conjugated to a PET radioisotope can be used for high sensitivity targeted imaging of fibrosis. Methods: The Blitz system, which uses interferometry to analyze binding, served as a baseline for measuring collagelin dissociation constant at different collagen concentrations. ELISA using biotin-collagelin on a collagen coated well plate was then used to assess binding affinity and specificity of collagelin for normal collagen. To assess collagelin binding to both normal and fibrotic collagen, samples of rat aorta and rat tail tissue were analyzed using biotin-collagelin and picrosirius red. A rat model of myocardial infarction was used to assess in vivo parameters of Cu-64 collagelin binding to infarcted tissue followed by autoradiography with Cu-64 collagelin labeled using 1-p-isothiocyanotobenzyl-NOTA as a bifunctional chelator. Results: The Blitz method showed the Kd of collagelin to be 10-7 M. Blitz results are currently being validated by ELISA studies. Biotinylated collagelin showed a concentration dependent increase in binding to collagen as seen from initial ELISA studies. Preliminary blocking studies, in which an excess of unlabeled collagelin was used to block binding by biotinylated collagelin showed evidence of some signal decrease by spectrophotometry and suggest collagelin specificity. Histology of cardiac tissue also showed binding of biotin-collagelin to fibrotic tissue. The rat model of myocardial infarction showed uptake of collagelin in infarct region and in the skin at week 5, while normal rats showed no uptake of Cu-64 collagelin in the heart. PET imaging results were validated by Cu-64 autoradiography while biotin-collagelin and picrosirius red histology confirmed the location of fibrotic collagen. Percent of the infarcted tissue was estimated from autoradiography to be about 20% of the left ventricle myocardium. Infarct percentage appeared similar to vivo studies with radiolabeled collagelin. Conclusion: Cu-64 collagelin shows good binding affinity to type 1 collagen models. These results show potential utility for specific binding of Cu-64 collagelin to fibrous scar secondary to myocardial infarction.

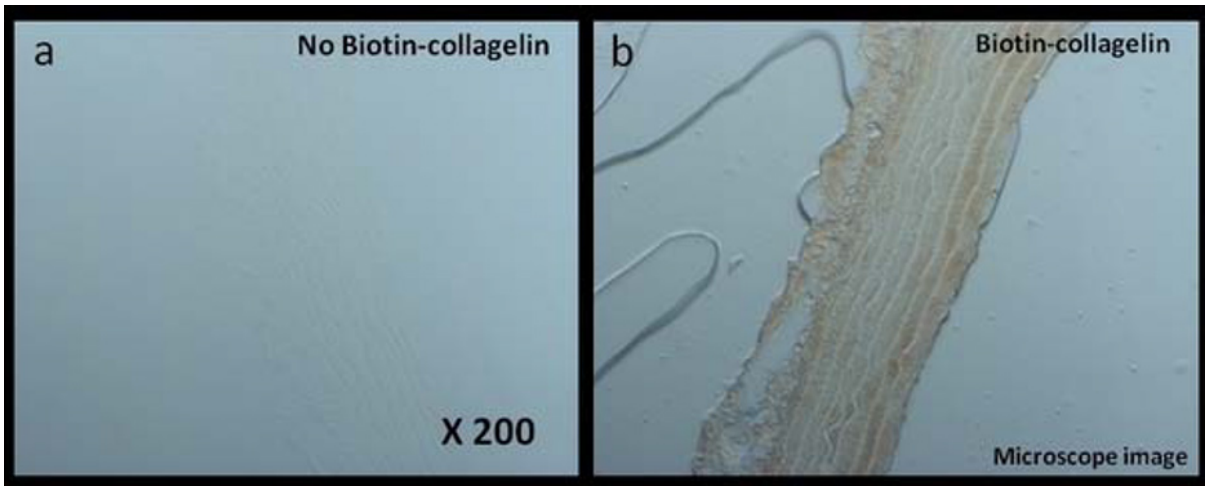

Figure 1: Biotinylated collagelin bound to collagen in rat aorta, stained by streptavidin-horseradish peroxidase (HRP) using diaminobenzidine (DAB) as a substrate; a) no biotin-collagelin, b) 200ug/ml biotin-collagelin.

Disclosure of author financial interest or relationships:
C.A. Davies-Venn, None; **S. Lee**, None; **S.J. Won**, None; **J. Kim**, None; **Z. Yao**, None; **S. Liu**, None; **I. Kim**, None; **G. Niu**, None; **X. Chen**, None; **C. Paik**, None; **D.A. Bluemke**, None.

Presentation Number **LBA 5**
Late Breaking Abstract Session 1
September 19, 2013 / 11:45-12:00 / Room: Oglethorpe Auditorium

Semiconducting polymer nanoparticle as photoacoustic molecular imaging probes in living mice

Kanyi Pu[1], *Adam J. Shuhendler*[1], *Jesse V. Jokerst*[1], *Jianguo Mei*[3], *Sanjiv S. Gambhir*[2], *Zhenan Bao*[3], *Jianghong Rao*[1], [1]*Department of Radiology, Stanford University, Stanford, CA, USA;* [2]*Department of Bioengineering and Department of Materials Science & Engineering, Stanford University, Stanford, CA, USA;* [3]*Department of Chemical Engineering, Stanford, Stanford University, CA, USA. Contact e-mail: kanyipu@stanford.edu*

Purpose. Photoacoustic (PA) imaging holds great promise for the visualization of physiology and pathology at the molecular level with deep tissue penetration and fine spatial resolution. However, the full utilization of this potential is greatly constrained by the lack of PA molecular imaging probes, particularly activatable PA probes. Herein we introduce near infrared (NIR) absorbing semiconducting polymer nanoparticles (SPNs) as a new class of PA contrast agents that outperform many existing materials for PA molecular imaging. Results. Semiconducting polymers (SPs) originally used to convert sunlight into electricity have been made into nanoparticles that produce ultrasound signals upon pulsed NIR laser irradiation. These purely organic PA nanoparticles have a unique set of advantages that derive from their precursor SPs, including a large mass extinction coefficient and high photostability. These advantages make SPN a superior PA imaging agent with stronger and more photostable PA signals in the NIR region when compared with single-wall carbon nantube (SWNT) and golden nanorod (GNR). At the same mass concentration, the intrinsic PA amplitude of the SPN at 700 nm can be more than 5-times higher than SWNT and GNR. Such a high PA brightness in conjunction with its favorable size (40 nm) enables the efficient PA imaging of major lymph nodes in living mice with a high signal-to-noise ratio of 13.3 after a single intravenous administration of a small amount of SPN. With the characteristics such as a narrow PA spectral profile, good photostability and reactive oxygen species (ROS) inert PA signal, we further develop SPN into an activatable NIR ratiometric PA probe for in vivo imaging of ROS, which are a hallmark of many pathological processes, such as cancer, cardiomyopathy, stroke and bacterial infections. This PA probe effectively detects ROS, and exhibits enhancements in ratiometric PA signals (PA700/PA820) of 25, 7.3, and 2.7-times in solution, in cells and in living mice, respectively. Conclusion. We have introduced SPNs as a new class of NIR PA contrast agents for in vivo PA molecular imaging. They can serve not only as simple accumulation-based PA probes (as demonstrated for lymph node mapping) but also as a platform to develop activatable probes (as shown by ratiometric PA imaging of inflammatory ROS in living mice). Given many key merits of SPNs such as strong signal amplitude, long-term photostability, size-independent spectral tunability, scalable and facile synthesis, compositional biocompatibility and structural diversity, we believe that SPNs can provide opportunities for advanced PA molecular imaging, from facilitating the preclinical investigation of physiological and pathological processes in living subjects to enhancing the PA imaging modality now in the process of clinical translation.

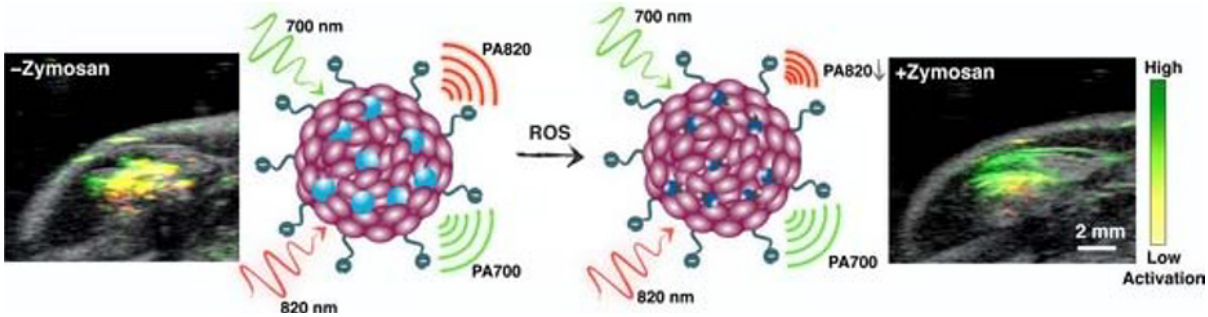

Semiconducting polymer nanoparticles are introduced as a new class of photoacoustic nanoagents, which serve not only as simple accumulation-based PA probes (as demonstrated for lymph node mapping) but also as a platform to develop NIR activatable photoacoustic probes capable of reporting the progression of pathological processes in real time (as shown by ratiometric imaging of inflammatory reactive oxygen species in living mice).

Disclosure of author financial interest or relationships:

K. Pu, None; **A.J. Shuhendler**, None; **J.V. Jokerst**, None; **J. Mei**, None; **S.S. Gambhir**, Bracco Diagnostics, Consultant; Endra, Inc, Stockholder; Cellsight, Stockholder; Enlight, Inc., Stockholder; General Electric, Grant/research support; ImaginAb, Stockholder; MagArray, Inc., Stockholder; Sanofi-Aventis, US, Grant/research support; SiteOne Therapeutics, Stockholder; VisualSonics/Sonosite, Stockholder; **Z. Bao**, None; **J. Rao**, None.

Presentation Number **LBA 6**
Late Breaking Abstract Session 2
September 19, 2013 / 13:00-13:15 / Room: Oglethorpe Auditorium

Cell-Cell Proximity Reporter

Mark A. Sellmyer[1,2,4], *Christopher Contag*[2], *Thomas J. Wandless*[1], *Jennifer Prescher*[2,3], [1]*Department of Chemical and Systems Biology, Stanford University, Stanford, CA, USA;* [2]*Departments of Pediatrics, Radiology, Microbiology & Immunology, Stanford University, Stanford, CA, USA;* [3]*Current: Departments of Chemistry and Molecular Biology & Biochemistry, University of California Irvine, Irvine, CA, USA;* [4]*Current: Radiology, University of Pennsylvania, Philadelphia, PA, USA. Contact e-mail: msellmyer@gmail.com*

Cell-cell interactions form the foundation of multicellular organism function. Processes such as developmental patterning, immune response, and cancer suppression rely on complex cellular choreography. Molecular imaging, especially optical imaging, is poised to illuminate these cellular interactions in the context of living tissues and whole organisms. We recently reported the development of a cell-cell proximity reporter, which detects when and where two distinct, engineered populations of cells come into close proximity on a whole-animal scale (1). This generalizable optical imaging strategy allows for non-invasive, longitudinal tracking of cell-cell proximity via the generation of bioluminescent light. We show the ability of this reporter to detect cell-cell proximity in vitro and in mouse models. We sought a strategy that used widely accessible reagents and detection equipment. Thus, we chose a well-described class of bioluminescent substrates, "caged" luciferins, that consist of a luciferin molecule covalently attached with a steric appendage that precludes binding of the molecule to luciferase. We repurposed the caged luciferin technology to be a cell proximity reporter by genetically encoding β-galactosidase (β-gal), the uncaging enzyme, in one cell population (termed "activator" cells) and luciferase in another population ("reporter" cells, Fig. 1A). Activator cells (expressing β-gal) catalyze the release of D-luciferin from the galactose-caged substrate Lugal. D-luciferin then diffuses out of activator cells, and into neighboring reporter cells (expressing luciferase) for light emitting catalysis. Reporter cells near the activator cells consume the most substrate, resulting in a correlation between the signal intensity and cell-cell proximity (Fig. 1B). We evaluated the system in a real-time cellular proximity assay using immobilized activator cells. Suspensions of control or activator cells in extracellular matrix (Matrigel) were placed in the middle of a tissue culture dish. Reporter cells were added in a monolayer surrounding the Matrigel. A β-gal assay confirmed the presence of active enzyme in activator cells. When human activator cells and mouse reporter cells were cultured together, a distinct border was visible by light microscopy. Upon addition of Lugal to this co-culture the reporter cells nearest the activator cells exhibited the strongest light emission. Quantification of a cross-section of the image indicated a >20-fold induction of signal closest to the activator cells. We applied the proximity reporter strategy in a mouse model of metastatic breast cancer and showed that previously difficult to identify metastasis could be highlighted with the reporter and indicate possible sites of tumor-immune interaction. The concept of using cells to illuminate the location(s) of another population of cells may lead to unique tools facilitating a better understanding of pathophysiology, human disease and treatment. 1. "Visualizing Cellular Interactions with a Generalized Proximity Reporter." Sellmyer, M.A.; Bronsart, L.; Imoto, H.; Contag, C.H.; Wandless T.J.; and Prescher, J.A, PNAS, 2013, 110, 8567-8572

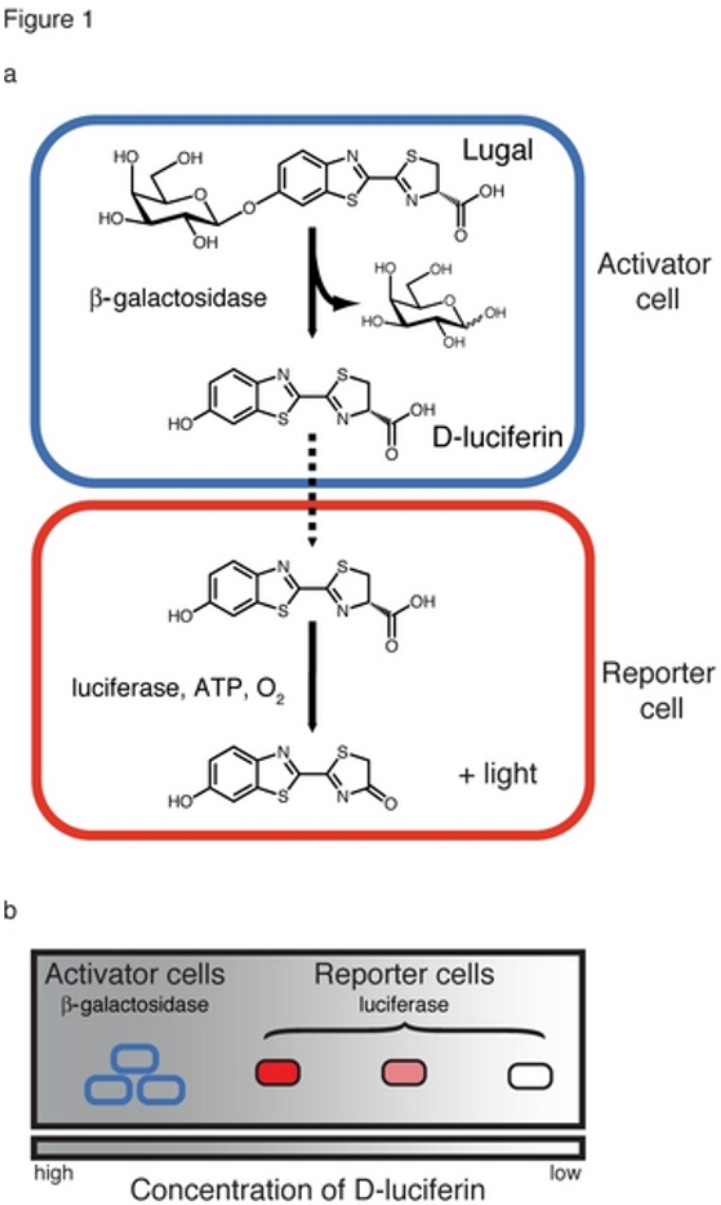

Fig. 1. Proximity reporter conceptual design (A) Visualizing cell proximity with bioluminescent tools. Activator cells (expressing β-gal) catalyze the cleavage of Lugal, ultimately releasing D-luciferin. The liberated substrate enters nearby reporter cells, where it is utilized by luciferase to produce light. (B) General strategy for visualizing the relative location of two cell populations. Activator cells potentiate the release of D-luciferin. Neighboring reporter cells use the substrate to produce light. The concentration of D-luciferin is highest near the activator cells (indicated by grayscale shading); thus, as the distance between the reporter and activator cell decreases, light production increases (indicated by the red color).

Disclosure of author financial interest or relationships:
M.A. Sellmyer, None; **C. Contag**, ConcentRx Corp, Stockholder; Olympus, Other financial or material support; **T.J. Wandless**, None; **J. Prescher**, None.

Presentation Number **LBA 7**
Late Breaking Abstract Session 2
September 19, 2013 / 13:15-13:30 / Room: Oglethorpe Auditorium

Positron Emission Tomography reporter imaging provides non-invasive monitoring of engineered hematopoietic stem cell immunotherapies expressing the hdCK3mut reporter gene

Melissa N. McCracken[1], *Owen N. Witte*[1,2,3], [1]*Molecular and Medical Pharmacology, UCLA, Los Angeles, CA, USA;* [2]*Microbiology, Immunology & Molecular Genetics, UCLA, Los Angeles, CA, USA;* [3]*Howard Hughes Medical Institute, UCLA, Los Angeles, CA, USA. Contact e-mail: mmccracken@mednet.ucla.edu*

Positron emission tomography (PET) reporter genes allow non-invasive whole-body imaging of transplanted cells by detection with radiolabeled probes. In a published study we demonstrated the use of a human deoxycytidine kinase containing three amino acid substitutions within the active site (hdCK3mut) as a reporter gene in combination with the PET probe [18F]-L-FMAU (1-(2-deoxy-2-18fluoro-β-L-arabinofuranosyl)-5-methyluracil) to monitor models of mouse and human hematopoietic stem cell (HSC) transplantation. Measurements of long-term engrafted cells (up to 32 wk) demonstrated that hdCK3mut expression is maintained in vivo with no counter selection against reporter-labeled cells. Current studies are evaluating the expression of hdCK3mut during immune cell activation and function by monitoring human models of adoptive cell therapy with engineered T cell receptors into hematopoietic stem cells. Reporter cells must mature from CD34+ stem and progenitors through a thymic graft into cytotoxic CD8 cells. We have demonstrated that we can visualize tumor infiltrating lymphocytes by [18F]-L-FMAU imaging in HLA matched tumors. During development additional lineages including myeloid and B cells also develop expressing hdCK3mut. To validate that the signal seen in antigen positive HLA matched tumors is due to engineered TCR TILs background signal seen by non-engineered reporter labeled cells expressing hdCK3mut will be observed in an HLA mismatched tumor. Additional cohorts of animals will be engineered to strictly express the reporter gene. These animals do not regress the tumor after being challenged and signal within the antigen positive HLA matched tumors is diminished in comparison to TCR engineered animals. The capability of hdCK3mut labeled engineered T cells to infiltrate and regress the antigen positive HLA matched tumors demonstrates proper T cell function and activation. Additionally, we have validated an increase in the total quantity of engineered T cells in antigen positive HLA matched tumors. Collectively these experiments demonstrate the use of a human reporter gene, hdCK3mut, to monitor immunotherapies of engineered HSCs through development and function in vivo with no discernible effect on T cell function and activation.

Disclosure of author financial interest or relationships:
M.N. McCracken, None; **O.N. Witte**, Sofie Biosciences, Consultant; Sofie Biosciences, Stockholder .

Presentation Number **LBA 8**
Late Breaking Abstract Session 2
September 19, 2013 / 13:30-13:45 / Room: Oglethorpe Auditorium

Imaging pancreatic cancer with a 89Zr-radiolabeled EGFR/HER3 dual-action antibody

Nerissa Viola-Villegas, *Sean Carlin, Kuntalkumar Sevak, Jason S. Lewis, Radiology, MSKCC, New York, NY, USA. Contact e-mail: VillegaN@mskcc.org*

Background: EGFR and HER3 are known to be expressed in pancreatic ductal adenocarcinoma (PDA). The dual-action antibody MEHD7945A was developed to target and inhibit ligand binding to both EGFR and HER3 receptors with high affinities (Kd ~ 1.9 and 0.4 nM respectively) for therapeutic purposes1. Here we explore the potential of 89Zr-labeled MEHD7945A to delineate pancreatic tumors expressing these receptor tyrosine kinases. Methods: MEHD7945A was bridged to desferrioxamine via an isothiourea linker and radiolabeled with 89Zr (t1/2~3.27 d). PET imaging was conducted on female SCID mice bearing subcutaneous BxPC3 xenografts implanted on the right shoulder at 4-120 h post-tracer injection (p.i.). To determine overall tissue uptake of the imaging probe, distribution studies in parallel tumor models were performed at 24-120 h p.i. Specificity was determined through competitive inhibition with 100-fold excess cold MEHD7945A co-administered with the tracer. Ex vivo autoradiography and histology studies examined tissue localization of 89Zr-MEHD7945A versus EGFR and HER3. Results: Conjugation of MEHD7945A to DFO was achieved via a N-succinimidyl linkage with a mAb:DFO ratio of ~ 1:4. Efficient labeling of MEHD7945A with 89Zr was obtained with excellent radiochemical yields (>80 %) and purities (>99%). The specific activity was determined to be ~ 3 mCi/mg. The final 89Zr-MEHD7945A construct proved to be robust, exhibiting an immunoreactivity of >98 %. In vivo PET imaging studies demonstrated high 89Zr-MEHD7945A uptake in BxPC3 tumors where volumes-of-interest drawn on the tumor show incremental radiotracer uptake at 4 h (11.5 ± 2.2 %ID/g), 24 h (20.5 ± 4.4 %ID/g), which reached a plateau at 72 h and 120 h p.i (24.7 ± 5.3 %ID/g and 24.5 ± 4.0 %ID/g respectively) (Fig. 1A). From the tissue distribution, tumor-to-pancreas ratios clearly show excellent contrast across all time points (i.e. 31.1 ± 9.6 at 48 h). Autoradiography and fluorescence microscopy performed on ex vivo frozen tissue sections shows clear association with well-perfused regions containing receptor-expressing tumor cells (Fig. 1B). Minimal pooling in necrotic tumor regions was observed. Conclusions: 89Zr-MEHD7945A displays an outstanding potential as a detection tool of PDA. Reference: 1Schaefer, G., et al. (2011). A Two-in-One Antibody against HER3 and EGFR Has Superior Inhibitory Activity Compared with Monospecific Antibodies. Cancer Cell, 20, 472-486.

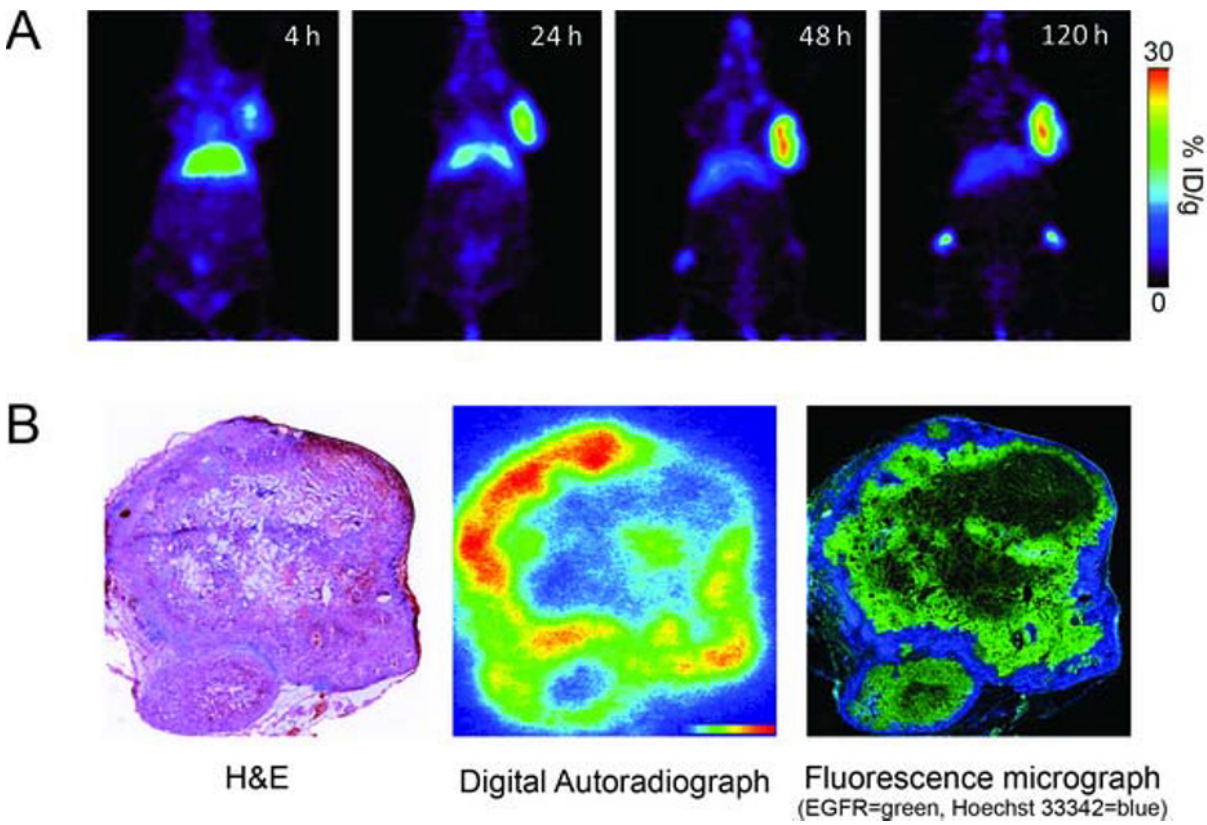

Figure 1. PET imaging with 89Zr-MEHD7945A in BxPC3 xenografts show incremental uptake of the radiotracer from 4-120 h p.i. (A); H&E staining (left) digital autoradiograph (center) and ex vivo fluorescence micrograph (right, green = EGFR, blue = Hoechst 33342). All data shown from a single frozen section obtained from a subcutaneous BxPC3 murine xenograft model treated with 89Zr-MEHD7945A (B).

Disclosure of author financial interest or relationships:
N. Viola-Villegas, None; **S. Carlin**, None; **K. Sevak**, None; **J.S. Lewis**, None.

Presentation Number **LBA 9**
Late Breaking Abstract Session 2
September 19, 2013 / 13:45-14:00 / Room: Oglethorpe Auditorium

Direct Observation of Lactate Metabolism in Skeletal Muscle with Hyperpolarized 13C-NMR

Jae Mo Park[1], *Sonal Josan*[1,2], *Dirk Mayer*[1,2], *Ralph E. Hurd*[3], *Daniel M. Spielman*[1], *David Bendahan*[4], *Thomas Jue*[5], [1]*Radiology, Stanford University, Stanford, CA, USA;* [2]*Neuroscience Program, SRI International, Menlo Park, CA, USA;* [3]*Applied Science Lab, GE Healthcare, Menlo Park, CA, USA;* [4]*Centre de Résonance Magnétique Biologique et Médicale, Marseille, France;* [5]*Biochemistry & Molecular Medicine, UC Davis, Davis, CA, USA. Contact e-mail: jaemo@stanford.edu*

Introduction Conventional biochemistry often views lactate (Lac) as a hypoxemia indicator and a dead-end product of glycolysis, which the muscle then exports to liver via the Cori cycle. Yet studies have detected Lac uptake and a correlation between Lac turnover and O2 consumption in resting and contracting muscle. The localized Lac flux/exchange in skeletal muscle suggests the presence of a Lac shuttle1. To test these underlying hypotheses, we have directly followed hyperpolarized [1-13C]Lac in rat muscle in vivo to confirm that muscle can indeed metabolize exogenous Lac. The results moderate an indiscriminate interpretation of Lac as a hypoxemia biomarker and provide insight into the idea of a Lac threshold, which underpins many athletic performance and clinical strategies. Methods [1-13C]Lac was hyperpolarized using a dynamic nuclear polarizer. Seven healthy male rats were prepared for the study. Each animal was anesthetized and placed in a clinical 3T GE MR scanner, followed by an injection of the hyperpolarized 40-mM Lac solution through the tail vein. Metabolic kinetics (517-681g,n=6) were observed from the muscle using a 13C surface coil (Ø=28mm, placed on top of right rectus femoris) and a dynamic free induction decay (FID) MR sequence (10o hard pulse, temporal resolution=3s, spectral width/points=10kHz/4096, Tacq=4min). The acquired time-curves of spectrally resolved metabolites were fit to a modified 4-site exchange model to calculate apparent conversion rate constants2. From a separate animal (320g), 2D axial images were acquired for metabolite mapping with a dual-tuned 1H-13C birdcage coil (Ø=50 mm) using a single-time point FID chemical shift imaging sequence (in-plane resolution=3x3mm2, 15-mm slice, variable flip angle scheme, spectral width/points=5kHz/256, Tacq=19s). Results & Discussion Alanine (Ala), pyruvate (Pyr), and bicarbonate (Bic) as well as Lac were detected from dynamic measurements. Metabolite ratios from the averaged (0-2min) spectra were 0.032±0.002 (mean±se) for Pyr/total carbon (tC), 0.15±0.013 for Ala/tC, 0.013±0.004 for Bic/tC, and 0.22±0.027 for Pyr/Ala. The apparent conversion rate constants were estimated from averaged time-curves as klac→pyr=0.016s-1, kpyr→ala=0.17s-1, and kpyr→bic=0.025s-1. In the imaging study, Ala and Lac signals were detected predominantly from leg muscle and blood vessels, respectively, whereas the signal-to-noise ratios of Pyr and Bic were inadequate to create reliable metabolite maps. The observation confirms that muscle converted the exogenous Lac to Pyr and Ala. Peripheral tissues and blood contributed insignificantly. Considering the much smaller pool sizes of intrinsic Pyr and Ala relative to the injected Lac pool, the detected Pyr and Ala represent a predominant metabolic flux from Lac to Pyr rather than exchange. Moreover, the Bic peak indicates Pyr dehydrogenase activity and a potential participation of Lac in the TCA to support oxidative phosphorylation. Conclusion The production of Ala and Pyr in muscle tissue from the injected hyperpolarized 13C-Lac shows that muscle can indeed metabolize exogenous Lac. Reference 1Brooks GA, J Physiol, 2009. 2Park JM et al, ISMRM, 2013.

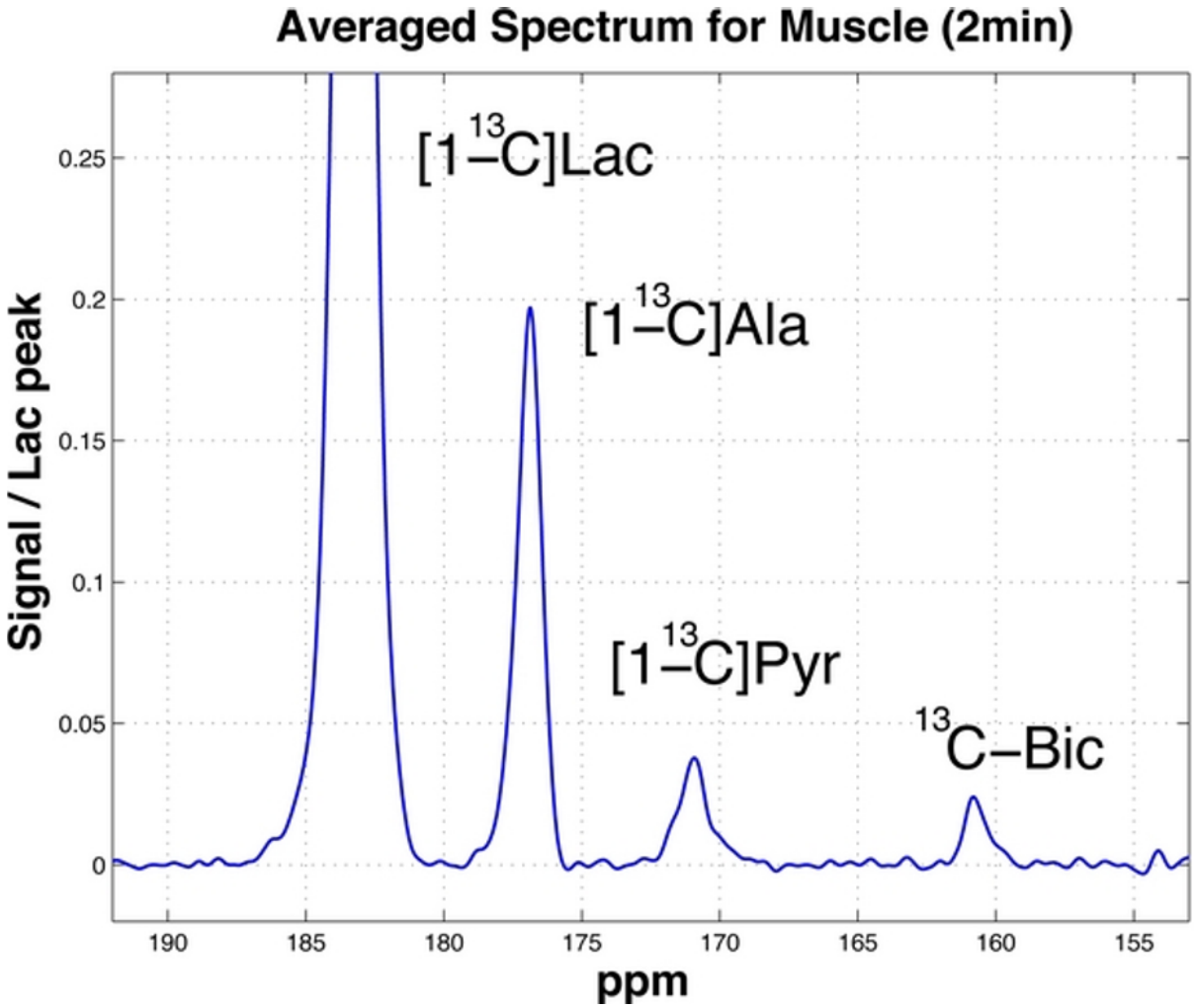

Time-averaged spectrum from rat leg muscle measured by a 13C transmit/receive coil using a fast dynamic free induction decay spectroscopy pulse sequence after an injection of [1-13C]lactate solution.

Disclosure of author financial interest or relationships:
J. Park, None; **S. Josan**, None; **D. Mayer**, None; **R.E. Hurd**, GE Healthcare, Employment; **D.M. Spielman**, None; **D. Bendahan**, None; **T. Jue**, None.

Presentation Number **LBA 10**
Late Breaking Abstract Session 2
September 19, 2013 / 14:00-14:15 / Room: Oglethorpe Auditorium

Engineered antibody fragments for ImmunoPET imaging of the B-cell compartment in a transgenic mouse model expressing human CD20

Kirstin A. Zettlitz[1], *Richard Tavaré*[1], *Felix B. Salazar*[1], *Kristopher K. Steward*[2,3], *Reiko E. Yamada*[2], *John M. Timmerman*[2,3], *Anna M. Wu*[1], [1]*Crump Institute for Molecular Imaging, Department of Molecular and Medical Pharmacology, David Geffen School of Medicine at UCLA, Los Angeles, CA, USA;* [2]*Division of Hematology and Oncology, Department of Medicine, UCLA, Los Angeles, CA, USA;* [3]*Molecular Biology Institute, UCLA, Los Angeles, CA, USA. Contact e-mail: kzettlitz@mednet.ucla.edu*

CD20 is expressed on the majority of B-cell malignancies and is a valuable target for antibody-based therapy. For diagnosis, therapy management and follow-up, an efficacious diagnostic tool is needed to assess antigen expression, tumor burden and localization in vivo. In addition, the B-cell compartment is involved in a variety of autoimmune and inflammatory diseases, e.g. rheumatoid arthritis. The non-invasive detection of CD20 expressing B-cells in vivo would enable the monitoring of immunotherapies, such as reconstitution after B-cell depletion and increase the understanding of B-cell mediated disease states. We evaluated novel antibody-based PET tracers based on the humanized type II anti-CD20 mAb GA101 in a transgenic BALB/c mouse model expressing human CD20 on B cells (huCD20TM). We engineered small bivalent antibody fragments of 55 kDa (GA101 cys-diabody, CDb) and 80 kDa (GA101 cys-minibody, CMb) with optimized pharmacokinetics for PET imaging and different clearance characteristics (renal and hepatic clearance, respectively). The antibody fragments were site-specifically conjugated to maleimide-desferrioxamine (mal-DFO) and radiolabeled with zirconium-89 (Zr-89) or radioiodinated (I-124). MicroPET images were obtained at 4, 8 and 20 hours post i.v. injection of the tracers and showed rapid and specific localization to CD20-positive organs (spleen and lymph nodes) and high contrast imaging with both I-124 and Zr-89 labeled antibody. While the cys-diabody reached good contrast earlier, the cys-minibody showed higher uptake due to its longer half-life. Smaller lymph nodes were difficult to visualize with I-124 labeled cys-diabody while Zr-89 CMb imaging resulted in clearly distinguishable lymph nodes (inguinal, brachial, axillary, mesenteric and cervical). The increased partial volume effect (PVE) due to a longer mean positron range of I-124 compared to Zr-89 (3.0 and 1.1 mm, respectively) likely contributes to these variations. Specificity was confirmed by blocking with cold antibody and by comparison to antigen negative wild type mice. Organ uptake was determined by ex vivo biodistribution at 24 h and the non-residualizing I-124 labeled antibody fragments showed lower uptake in the spleen (5.02 %ID/g for CDb and 11.5 %ID/g for CMb) compared to the residualizing Zr-89 labeled antibody fragments (17.8 % ID/g for CDb and 38.8 %ID/g for CMb). In conclusion, the humanized GA101-based antibody fragments specifically target human CD20 expressing B-cells in a transgenic mouse model and produce high contrast microPET images. The combination of antibody fragments (size, plasma half life, clearance) with radionuclides (residualizing vs. non-residualizing, physical half-life) offers optimized tracers for a variety of applications in B-cell imaging. Of particular interest could be to image biological mechanisms like CD20 internalization in vivo, B-cell response upon vaccination, in autoimmune diseases and oncological settings in the context of normal tissue expression of human CD20. We believe these tracers have great potential for translation into patients.

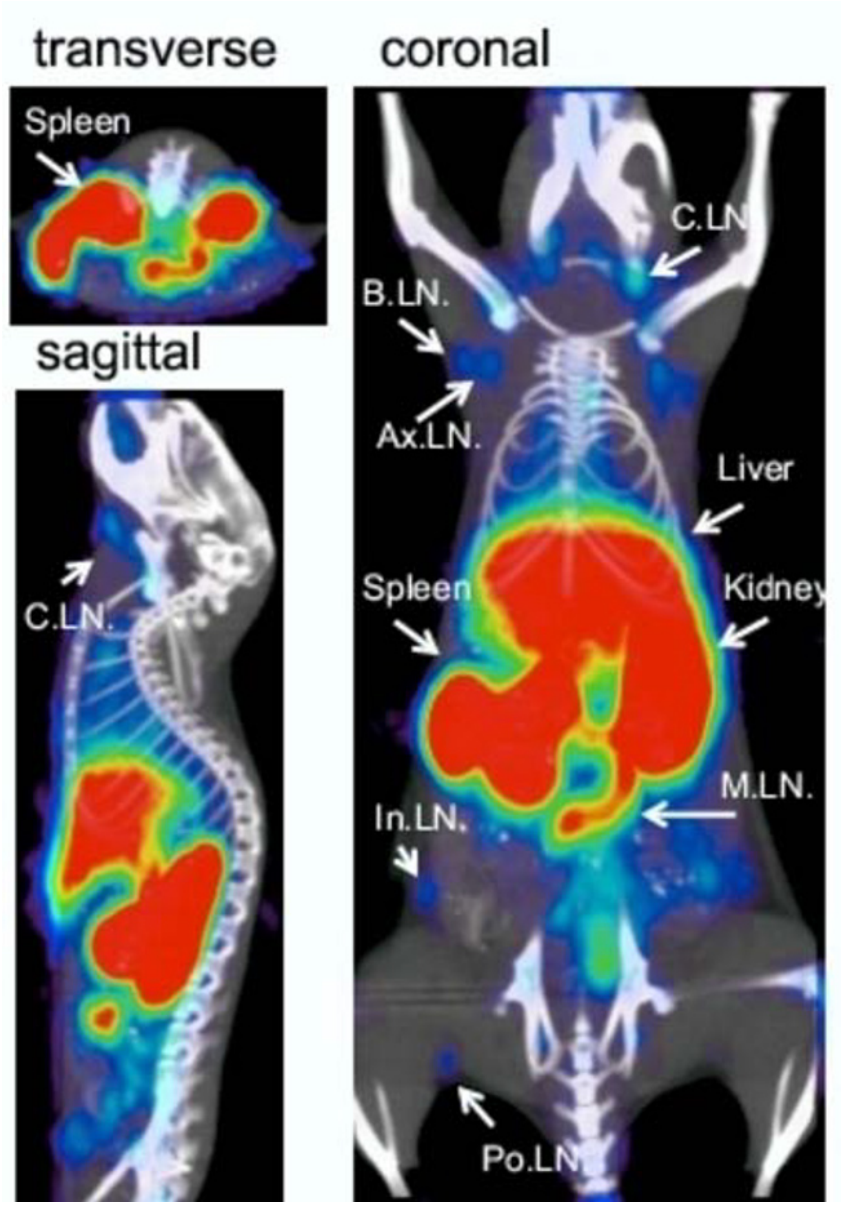

ImmunoPET images of 89Zr labeled GA101 cys-minibody in a huCD20TM model.

Disclosure of author financial interest or relationships:
K.A. Zettlitz, None; **R. Tavaré**, None; **F.B. Salazar**, None; **K.K. Steward**, None; **R.E. Yamada**, None; **J.M. Timmerman**, None; **A.M. Wu**, ImaginAb, Inc., Stockholder; ImaginAb, Inc., Consultant; ImaginAb, Inc., Grant/research support; Daiichi Sankyo, Consultant; Sanofi, Consultant .

Presentation Number **LBA 11**
Late Breaking Abstract Session 2
September 19, 2013 / 14:15-14:30 / Room: Oglethorpe Auditorium

Longitudinal evaluation of the glutamatergic pathway in a schizophrenia rat model of chronic NMDA hypofunction

Lauren Kosten[1], *Tine Wyckhuys*[1], *Jeroen Verhaeghe*[1], *Leonie Wyffels*[1,2], *Livia De Picker*[3], *Stefanie Dedeurwaerdere*[4], *Sigrid Stroobants*[1,2], *Steven Staelens*[1], [1]*Molecular Imaging Center Antwerp, University of Antwerp, Antwerp, Belgium;* [2]*Department of Nuclear Medicine, University Hospital Antwerp, Antwerp, Belgium;* [3]*Collaborative Antwerp Psychiatric Research Institute, University of Antwerp, Antwerp, Belgium;* [4]*Translational Neurosciences, University of Antwerp, Antwerp, Belgium. Contact e-mail: lauren.kosten@ua.ac.be*

AIM: N-methyl-D-aspartate receptor (NMDAR) hypofunction and neuroinflammation were recently linked to schizophrenia's etiology. Using Positron Emission Tomography (PET) the binding of the mGluR5 ligand [11C]-ABP688, microglia activation ([18F]-PBR111) and cerebral glucose metabolism ([18F]-FDG) are assessed longitudinally in a chronic schizophrenia rat model of daily MK801 injections (an NMDAR antagonist resulting in higher endogenous glutamate levels). Additionally, the potential of N-Acetyl-cysteine (NAc), modulating extracellular glutamate and presynaptic glutamate release, is evaluated as a treatment. METHODS: Sprague Dawley rats (n=24;279-302g) received a daily injection with MK801 (n=16;0.3mg/kg,ip) or saline (n=8) for 30 days. Half the animals in both groups additionally received daily NAc treatment (65mg/kg,ip), the others received control saline injections. We thus obtained four different groups (n=4): saline-saline, MK801-saline, MK801-NAc, and saline-NAc. The nondisplaceable binding potential (BPnd) was calculated at t=0d, 14d and 30d by 60 mins dynamic [11C]-ABP688 imaging (0.65±0.33mCi;<3nmol/kg,iv) using the simplified reference tissue model (SRTM) versus the cerebellum. Additionally, static [18F]-PBR111 µPET scans (0.78±0.31mCi;<0.75nmol/kg,iv) assessed microglia activation at t=0d, 14d and 30d and weekly static [18F]-FDG µPET scans (1mCi, iv) measured cerebral glucose metabolism. Percentage injected dose (pID) uptake was determined for all static scans. RESULTS: There is a clear trend that [11C]-ABP688 BPnd increases over time in the schizophrenia-related MK-801 model, which was at this time still non-significant given the small sample size (n=4). The BPnd is 9.6±17.4% and 9.6±14.1% increased compared to t=0d in the medial prefrontal cortex (MPC) and cingulate cortex (CC) respectively for the MK801-saline group. NAc does not seem to counteract this effect with a BPnd increase of 11.8±15.0% and 16.8±16.2% for MK801-NAc animals in MPC and CC respectively at t=30d. [18F]-PBR111 pID % change to t=0d tends to decrease over time for the MK801-saline group with -26.4±15.4 % and -8.7±10.8 % for MPC and CC respectively, but less under NAc treatment with -26.1±20.9 % decrease and +8.4±14.2 % increase for these same regions. Histology reveals cell loss by MK801 and potential protection by NAc, which might contribute to these [18F]-PBR111 findings. The percentage decrease in [18F]-FDG uptake compared to t=0d for the MK801 (±NAc) treated animals was significantly higher (between -21.1 and -37.0%) than for the saline (±NAc) treated animals (between -0.7 to -14.5%) for all regions in both groups at t=21d ($p<0.05$). Besides cell loss, reduced brain uptake due to weight gain (312g±13g at t=0d compared to 391g±22g at t=30d) also contributes here. CONCLUSION: Chronic exposure to higher MK801 induced endogeneous glutamate levels may upregulate the mGluR5 receptor. NAc does not seem to reverse MK801-induced effects, yet might exert tissue-preserving effects as an anti-inflammatory agent. We are currently increasing group sizes and further histology as well as TRYCAT HPLC analysis is underway to evaluate the neurotoxicity in more detail.

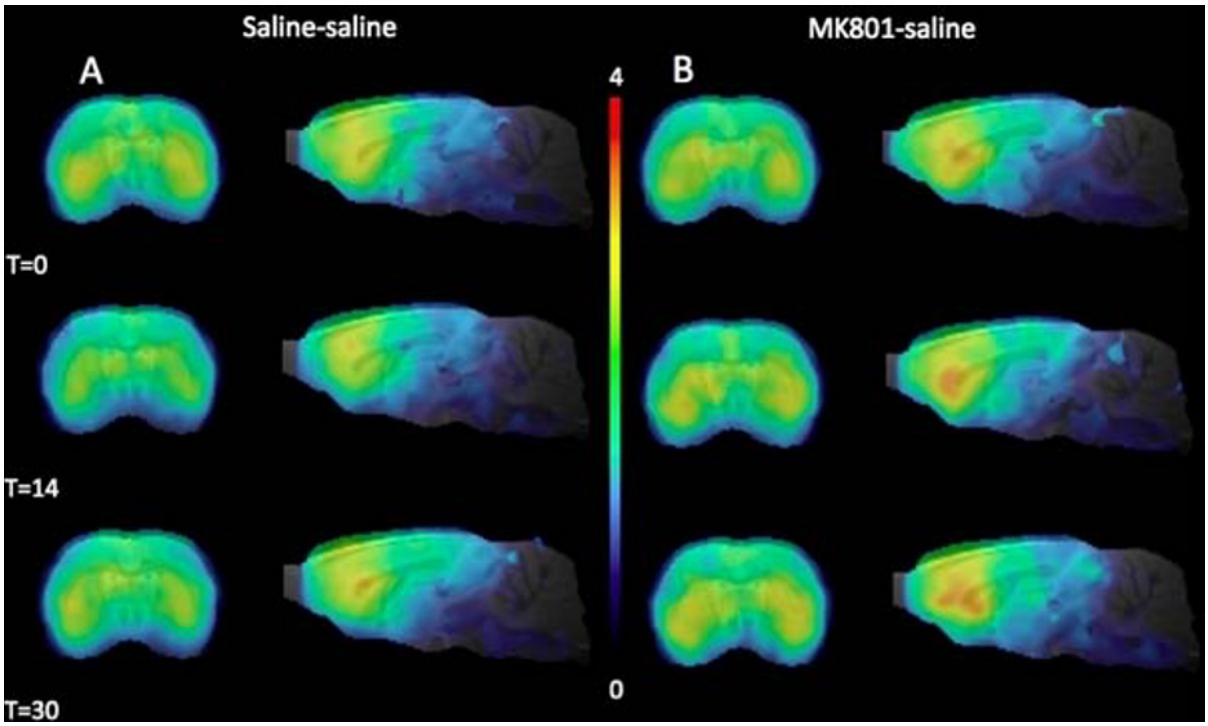

[11C]-ABP688 BPnd images calculated using SRTM with cerebellum as reference tissue, showing [11C]-ABP688 BPnd increase with MK801 treatment. Images are represented on MRI template. (A) Images from a rat in the saline-saline control group. (B) Images from a schizophrenic model (MK801-saline).

Disclosure of author financial interest or relationships:

L. Kosten, None; **T. Wyckhuys**, None; **J. Verhaeghe**, None; **L. Wyffels**, None; **L. De Picker**, Janssen R&D, Grant/research support; **S. Dedeurwaerdere**, None; **S. Stroobants**, Janssen Pharmaceuticals, Grant/research support; **S. Staelens**, Johnson & Johnson, Grant/research support .

Presentation Number **LBAP 001**
Late Breaking Abstract Poster Session
September 19, 2013 / 15:15-15:15 / Room: Exhibit Hall B

PLGA encapsulated bismuth nanocrystals for molecular CT

Eric R. Swy[1], *Aaron S. Schwartz-Duval*[1], *Matthew T. Latourette*[1], *David P. Cormode*[2], *Erik M. Shapiro*[1], [1]*Department of Radiology, Michigan State University, East Lansing, MI, USA;* [2]*Department of Radiology, University of Pennsylvania, Philadelphia, PA, USA. Contact e-mail: swyeric@gmail.com*

INTRODUCTION: High Z metal nanoparticles are recognized for their potential to transform CT into a molecular imaging paradigm, particularly if coupled with emerging spectral CT methodologies. Gold nanoparticles (Z = 79, k-edge = 80.7 keV) are the most well developed nanoparticle platform, however the cost of gold may be prohibitive for widespread use. Bismuth (Bi) nanoparticles (Z = 83, k-edge = 90.5 keV) are a cost effective alternative with potentially equal CT contrast/biocompatibility to gold. Here we describe the design, synthesis, characterization, and ex vivo CT use of new fluorescent, polymer encapsulated Bi nanocrystals for dual CT/fluorescence applications. The major innovations lie in the use of atomic Bi nanocrystals for higher contrast density, rather than BiS_2 or Bi_2O_3 and the encapsulation of nanocrystals within an FDA approved polymer. METHODS: Bi nanocrystals were synthesized via reduction of Bi dodecanethiolate (DDT) to Bi metal. DDT coated Bi nanoparticles were analyzed with X-ray diffraction (XRD) and Fourier Transform infrared spectroscopy (FTIR). Nanocrystals were sized by transmission electron microscopy (TEM). Bi nanocrystals were soaked in oleic acid, rinsed with ethanol, and suspended with fluorescent labeling agent comarin-6 in dichloromethane (DCM). Encapsulation within PLGA was then established by creating an oil-in-water emulsion and evaporation of DCM. Nanoparticles were sized by scanning electron microscopy (SEM). Bi nanocrystal encapsulation in PLGA was determined by thermogravimetric analysis. Samples for CT were prepared by suspending Bi nanoparticles in agarose at 0, 18, 60, 82 and 182 mM Bi. In vitro μCT images were acquired on a GE eXplore Locus Micro CT Scanner operating at 80 kV at 450 μA. Ex vivo μCT imaging was performed after injecting 340 μL of a 100 mM solution of Bi nanoparticles in H2O into the forearm of a chicken wing, between the radius and ulna and acquiring images as above. Clinical CT was performed on the agarose samples and chicken wing using a GE Discovery 750 HD CT scanner, operating at 80, 100, 120 and 140 kV and 100 mA. RESULTS and DISCUSSION: XRD and FTIR confirmed DDT coated Bi nanoparticles. Nanocrystal diameter was 6.2±0.8 nm (Fig 1A). The PLGA nanoparticle diameter was 124.4±20.6nm (Fig 1B). Bi content ranged from 38.7 to 73.3% w/w, with encapsulation efficiencies approaching 99%, verified by TEM (Fig 1B inset). In vitro μCT imaging of samples of 0, 18, 60, 82 and 182 mM Bi revealed a linear relationship between CT contrast and Bi concentration (R^2=0.98) with 8.1 HU/mM. CT imaging using a clinical system demonstrated a similar linear relationship of CT contrast to concentration with 5.2, 4.4, 4.2, and 4.0 HU/mM at 80, 100, 120 and 140 kV, respectively. These attenuations are comparable with that found for gold nanoparticles. CT imaging of the chicken wing with both μCT (Fig 1C,D) and clinical CT (Fig 1E) at 80 kVp detected nanoparticles as hypointense signal, measured to be 4846.2±1710.1HU on the μCT and 1272.9±195.9HU on the clinical CT. Discrepancies between the preclinical and clinical systems highlight the importance of evaluating new CT materials on clinical systems.

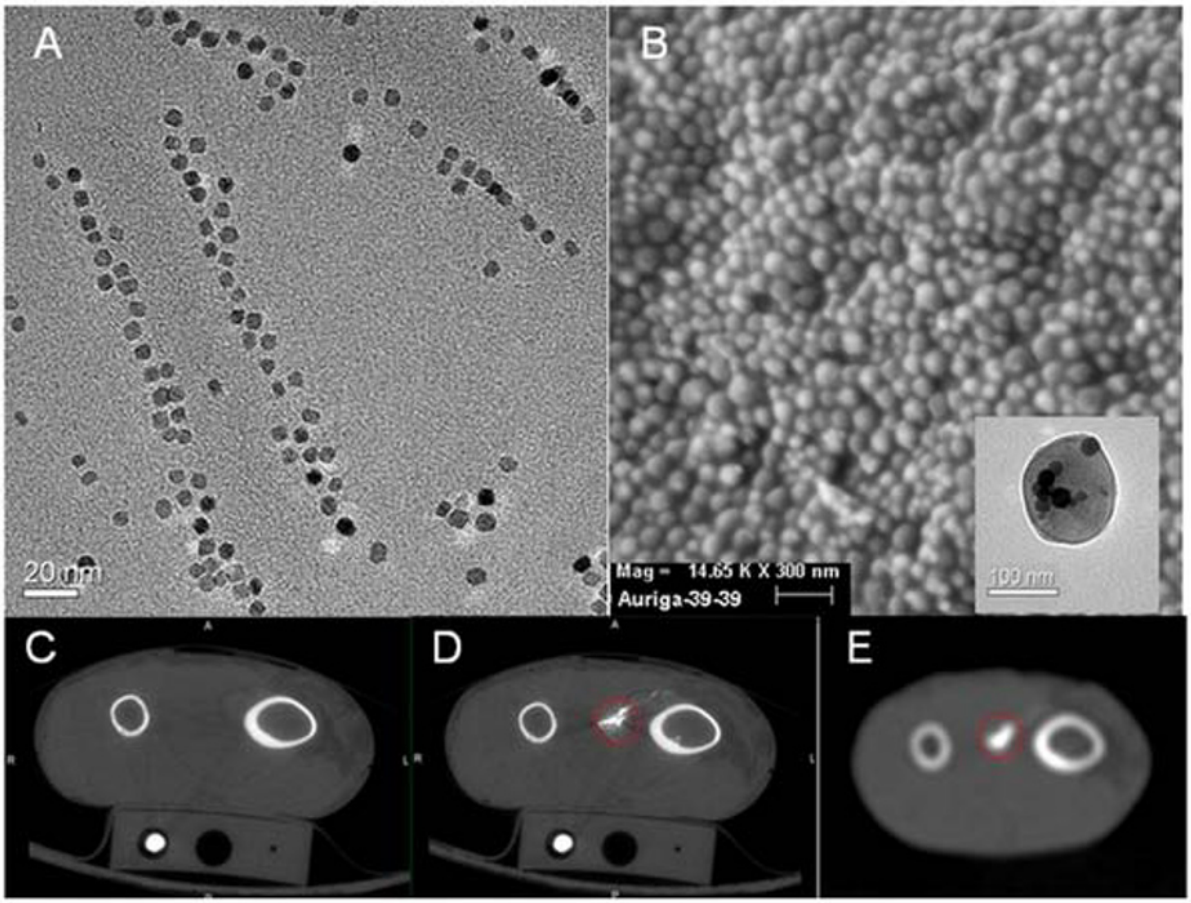

A) TEM image of nanocrystals, average diameter = 6.2 +/- 0.8 nm. B) SEM image of PLGA encapsulated Bi nanocrystals, average diameter = 124.4 +/- 20.6 nm. Inset is TEM image of a single nanoparticle with embedded Bi nanocrystals. C, D) µCT of chicken forearm C) before and D) after injection of PLGA encapsulated Bi nanoparticles, circled in red. E) Clinical CT of same view in D.

Disclosure of author financial interest or relationships:
E.R. Swy, None; **A.S. Schwartz-Duval**, None; **M.T. Latourette**, None; **D.P. Cormode**, Philips, Grant/research support; **E.M. Shapiro**, None.

Presentation Number **LBAP 002**
Late Breaking Abstract Poster Session
September 19, 2013 / 15:15-15:15 / Room: Exhibit Hall B

In vivo characterization of MV-1 magnetosomes as biogenic contrast agents dedicated to high field MRI: a dose study

Marianne Boucher[1], *Nicolas Ginet*[2], *Daniel Garcia*[2], *David Pignol*[2], *Sébastien Mériaux*[1], [1]*DSV / I2BM / NeuroSpin / UNIRS, CEA, Gif-sur-Yvette, France;* [2]*DSV / IBEB / SBVME / LBC, CEA, Saint-Paul-lez-Durance, France. Contact e-mail: marianne.boucher@cea.fr*

Introduction. Magnetosomes are superparamagnetic nanoparticles produced by magnetotactic bacteria that exhibit different characteristics of interest for molecular MRI applications: a perfectly crystalline and regular nanocrystal of magnetite coated by a natural lipid bilayer, which can be functionalized for biomarkers targeting [1] (Figure 1). Here, we demonstrate with ultra high field MRI acquisitions the very high *in vivo* contrasting efficiency of magnetosomes compared to a commercial SPIO solution (Ferumoxide). Both magnetosomes and Ferumoxide cannot pass through the blood-brain-barrier because of their relatively large diameter. Therefore, contrast efficiency of both nanoparticles has been characterized towards their ability to provide high-resolution 3D angiograms of mouse brain after intravenous injection. **Materials and methods.** *Magnetovibrio blakemorei* MV-1 strain is grown at 30 °C in defined media following an already published protocol [1]. Their magnetosomes (MV-1m) were then extracted after bacteria centrifugation using a permanent magnet. To calibrate the injected doses for *in vivo* acquisitions, we investigated the MRI contrast efficiency of both tested nanoparticles by measuring *in vitro* their transverse relaxivity r_2 at 17.2 T (BioSpec scanner, Bruker, Germany): we acquired T_2 parametric map (Multi-Slice Multi-Echoes sequence, TE=7.7 ms, 66 echoes) of phantom containing 12 tubes filled with different concentrations of contrast agent. *In vivo* experiments were carried out on Swiss mice at 17.2 T. T_2*-weighted images (Fast Low Angle Shot sequence, TE/TR= 8/680 ms, R = 90x90x180 μm^3) were acquired pre and post injection at the tail vein of MV-1m or Ferumoxide (100 µL, 20 μmol_{Fe}/kg and 200 μmol_{Fe}/kg), or control solution (100 µL of physiological serum). The post-processing included the Frangi filtering method implemented by [2] to reveal brain vasculature enhancement induced by contrast agent circulating in blood stream. **Results.** Transverse relaxivities r_2 (Table 1) show the great contrasting efficiency of MV-1m compared to Ferumoxide. 3D angiograms visualization presented in Figure 2 reveal that both high doses of MV-1m or Ferumoxide strongly highlight brain vasculature, whereas for low doses only magnetosomes do. Large vessels already detected before injection of contrast agent due to endogenous iron in the blood are enhanced, and smaller ones are only revealed by low dose of MV-1m or by high doses of MV-1m and Ferumoxide. As expected, the injection of physiological serum does not provide any vasculature enhancement (control solution). **Conclusion.** In conclusion, relaxometry measurements and *in vivo* MRI acquisitions performed at ultra high field confirm that MV-1m exhibit very high contrasting properties compared with a commercially produced SPIO solution. The observed gain enables to obtain high-resolution angiograms of mouse brain after injection of significantly lower dose than the one commonly used in rodent studies. These magnetosomes used as MRI contrast agent should provide enough sensitivity for molecular imaging studies. **References.** [1] Ginet et al, PLoS One 2011 [2] Manneising and Neissen, Inf Process Med Imaging 2005

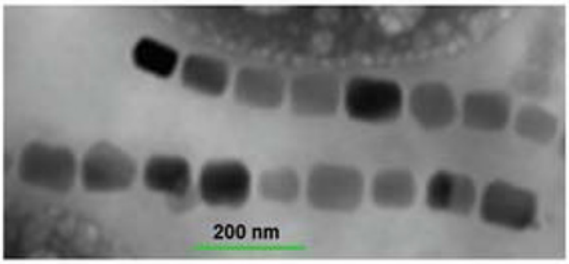

	r_2 ($mM^{-1}s^{-1}$)	R^2
Ferumoxide	173	0.999
MV-1m	724	0.992

Table 1: Transverse relaxivities r_2 measured at 17.2 T for Ferumoxide and MV-1m, with the corresponding Pearson correlation coefficient R^2 of the linear fit leading to r_2 estimation.

Figure 1: TEM image of MV-1 magnetosomes.

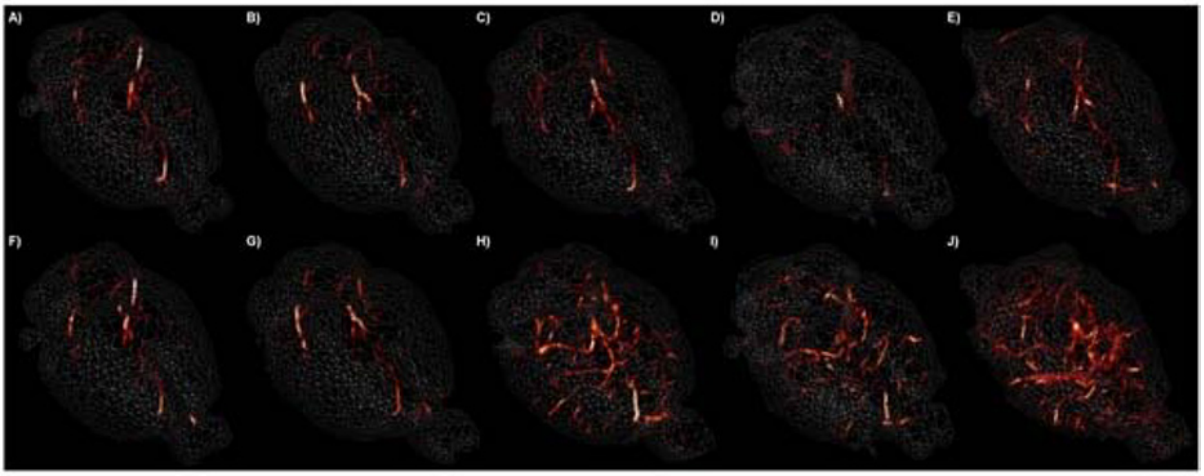

Figure 2: 3D angiograms visualization. (A-E) pre injection and (F-J) post injection angiograms. (A/F) control, 100 µL of physiological serum. (B/G) Ferumoxide at 20 μmol_{Fe}/kg. (C/H) Ferumoxide at 200 μmol_{Fe}/kg. (D/I) MV-1m at 20 μmol_{Fe}/kg. (E/J) MV-1m at 200 μmol_{Fe}/kg.

Disclosure of author financial interest or relationships:
M. Boucher, None; **N. Ginet**, None; **D. Garcia**, None; **D. Pignol**, None; **S. Mériaux**, None.

Presentation Number **LBAP 003**
Late Breaking Abstract Poster Session
September 19, 2013 / 15:15-15:15 / Room: Exhibit Hall B

Salicylic Acid and Analogues as diaCEST MRI Contrast Agents with Highly Shifted Exchangeable Proton Frequencies

Xing Yang[1], *Xiaolei Song*[1], *Yuguo Li*[1], *Guanshu Liu*[1,2], *Sangeeta Ray*[1], *Martin Pomper*[1], *Michael T. McMahon*[1,2], [1]*Radiology, Johns Hopkins SOM, Balltimore, MD, USA;* [2]*F.M. Kirby Research Center, Kennedy Krieger Instute, Balltimore, MD, USA. Contact e-mail: xyang45@jhmi.edu*

Introduction: Magnetic resonance imaging (MRI) has been widely used as a diagnostic method to detect changes in soft tissue due to its exquisite spatial resolution. One of the standard methods to detect pathologies involves injection of magnetic resonance (MR) contrast agent, such as the gadolinium(III) complexes routinely used for angiography. [1] Chemical exchange saturation transfer (CEST) contrast agents are a new alternative, which have become popular due to the unique features of these agents. [2] One of these features is that MR contrast can be produced by a variety of organic, diamagnetic compounds having exchangeable protons [3] . Herein we show that salicylic acid (1), one of the main metabolites of aspirin, and its derivatives possesses suitable exchangeable protons that resonate ~9 - 11 ppm from water, a frequency far removed from all other organic diaCEST agents reported to date. Results: The CEST contrast mechanism involves selective irradiation of labile protons on the agent to perturb their signal, with this signal change then transferred to water by exchange between these labile protons and bulk water. [5] Figure 1 displays the MTRasym spectra of salicylic acid compared to two other typical organic agents. demonstrating the strong contrast of this agent. Furthermore, the intramolecular hydrogen bonding found in salicylic acid analogues[4,5] results in strong CEST contrast properties, with these agents all shifted far from a number of common metabolites protons resonating between 1 to 3.6 ppm from water [2c]. In scheme 1, seven salicylic acid analogues (4-10) producing similar contrast to 1, with labile protons up to 10.8 ppm from water are listed. We were able to measure the proton exchange rate for 1, determine optimum saturation conditions, and detect this agent in the kidneys of mice after intravenous (IV) administration. Figure 1 d-g displays the results. About 4 minutes after injection of a 60 μL volume of a 0.25 M solution of 1, CEST contrast could be detected in the kidneys, which persisted for ~ 3 minutes. The average CEST contrast was 6.0 ± 0.8 % over the whole kidney. Conclusion: The present work demonstrates the feasibility of designing diamagnetic CEST agents with much further shifts than previously reported. Seven new agents are reported which display strong contrast at frequencies larger than 8 ppm, appropriate for detection at clinical field strengths. In addition, we show that these highly shifted agents can be detected in vivo readily after tail vein administration into mice. Supported by R21EB015609, R01EB015031, U54CA151838, R01134675 and R01EB012590. References: [1] P. Caravan, Chem, Soc. Rev. 2006, 35, 512-523.; [2] a) I. Hancu, et al., Acta Radiol. 2010, 51, 910-923.; b) E. Terreno et al., Contrast Media Mol. Imaging 2010, 5, 78-98.; c) G. Liu et al., NMR Biomed. 2013, doi:10.1002/nbm.2899; d) P. C. M. van Zijl, et al., Magn. Reson. Med. 2011, 65, 927-948.; [3] K. M. Ward et al.,, J. Magn. Reson. 2000, 143,79-87. [4] G.E. Maciel, G.B. Savitsky, J. Phys. Chem. 1964, 68, 437-438. [5] W.L. Mock, L.A. Morsch, Tetrahedron, 2001, 57, 2957-2964.

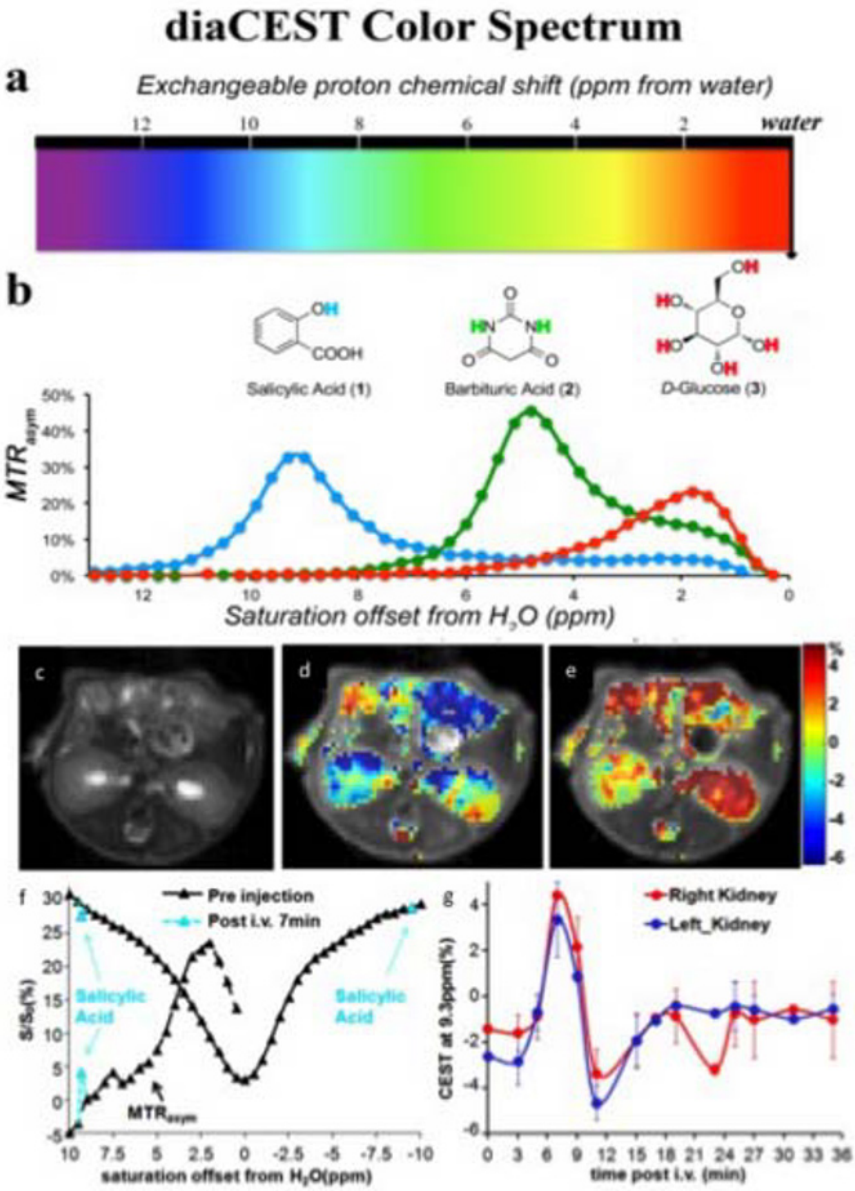

Figure 1. Schematic depicting the color spectrum for diaCEST agents and in vivo imaging results for compound 1. a) range of exchangeable proton shifts observed presently for diaCEST agents; b) CEST contrast curves for three representative agents: Salicylic Acid (1), Barbituric Acid (2), and D-Glucose (3) at concentrations of 25 mM, pH 7.0,, 37oC using ω1 = 7.2 μT, tsat = 3 s for saturation; .c) T2w image; d) overlay MTRasym (9.3 ppm) map pre-injection; e) overlay MTRasym (9.3 ppm) map at 7 min post-injection; f) Z-spectra and MTRasym for a region of interest (ROI) enclosing the entire right kidney with pre-injection data (black), 7 min post-injection; (light blue) g) dynamic time course of the MTRasym (9.3 ppm) for ROIs enclosing the whole left kidney and right kidney. ω1= 7.2 μT (n = 2).
Table 1. CEST signals [ppm] for C2-OH and contrast [%] (exchange rate [ks-1]) of salicylic acid and its analogues. Experimental conditions: concentration = 25 mm, pH 7.1-7.4, using tsat=3 s, ω1=3.6 μT.

Compound	CEST signal (ppm)	% Contrast	Exchange rate (s^{-1})
1	9.3	18	0.6
4	8.7	19	0.7
5	9.6	22	1.0
6	8.9	3	0.05
7	8.7	19	1.2
8	9.6	18	0.65
9	9.3	16	0.65
10	10.8	12	0.4
11	Not determined	0	Not determined

Disclosure of author financial interest or relationships:
X. Yang, None; **X. Song**, None; **Y. Li**, None; **G. Liu**, None; **S. Ray**, None; **M. Pomper**, None; **M.T. McMahon**, None.

Presentation Number **LBAP 004**
Late Breaking Abstract Poster Session
September 19, 2013 / 15:15-15:15 / Room: Exhibit Hall B

Hydrogels Encapsulating Highly-shifted DiaCEST Agents Readily Detectable by MRI

Xiaolei Song[1,2], *Xing Yang*[1], *Dian R. Arifin*[1], *Kannie WY Chan*[1,2], *Nikita Oskolkov*[1,2], *Jeff W. Bulte*[1], *Peter C. van Zijl*[1,2], *Martin Pomper*[1], *Michael T. McMahon*[1,2], [1]*The Russell H. Morgan Department of Radiology and Radiological Science, The Johns Hopkins University, Baltimore, MD, USA;* [2]*F.M. Kirby Research Center for Functional Brain Imaging, Kennedy Krieger Institute, Baltimore, MD, USA. Contact e-mail: lisasonger@gmail.com*

Introduction: Salicylic acid (SA) and its analogues have recently been identified as diaCEST MRI contrast agents with highly shifted exchangeable proton frequencies [1] . The large chemical shift from water displayed by these compounds should provide advantages for in vivo measurements through reducing the amount of direct water saturation, conventional magnetization transfer and endogenous CEST contrast from tissue. Hydrogels incorporating the diaCEST agent (L-arginine) previously showed that transplanted cell viability could be sensed through pH-sensitive CEST contrast.[2] SA analogues also display pH-dependent contrast, and in this work we demonstrate that hydrogels suitable for cell transplantation can be prepared with encapsulating these new probes and allow CEST-MRI detection and monitoring of the pH of their microenvironment. **Material:**Liposomes were made using the thin film hydration method, with encapsulating three SA analogues respectively, including: 4-aminosalicylic acid (a NonSteroidal Anti-Inflammatory Drug,NSAID), 2,4-Dihydroxybenzoic acid (DHB, a metabolite found in human plasma after cranberry juice consumption) and 2,5-Dihydroxyterephthalic acid which contains two exchangable protons per molecule. These liposomes were mixed with alginate to a final concentration of 1.5%-1.7% (w/v) alginate. The mixture was electrosprayed into a 20 mM $BaCl_2$ bath which resulted in the formation of alginate beads. After gelation, the capsules were crosslinked with 0.1 % w/v protamine sulfate and then coated with a second layer of alginate. **MR imaging:**CEST-MR imaging was performed on Bruker 11.7 T scanners (vertical bore for phantoms and horizontal bore for mice) with B1 = 5.9 uT. Z-spectra were acquired for both phantoms and mice to show the frequency profile of the resulting alginate capsules. The CEST contrast was quantified using MTR_{asym}= S(-Δω)-S(Δω)/ S(Δω), where Δω is the CEST peak frequency of the agent. **Results : Fig.a** shows the CEST spectra for 25mM DHB with different pHs. After encapsulation, the hydrogels containing three representative SA analogues also displayed strong CEST contrast (~20%) at 8-10 ppm from H_2O (**Fig.b**) , with the contrast maps obtained without the need for additional B0 correction (**Figs. c,d,e**). The individual capsules can also be seen on high resolution T2-w images (**Figs. c,d,e** left panel). The DHB liposome capsules (DHB-Cap) were further tested on 2 mice via i.p. transplantation, with **Fig. f** showing the high resolution T2-w image of a mouse abdomen containing capsules (coronal view). A contrast map at 9 ppm can be acquired w/o B0 correction (**Fig. h**) The MTR_{asym} contrast produced by the capsules (**Fig.g**) is lower than in phantoms, probably due to partial volume effects and the negative baseline of the MTR_{asym} in this frequency range. Nevertheless, the capsules were detected for both mice with the CEST peak easily being 'seen' in the MTR_{asym} spectrum. **Conclusion:**Our phantom study and preliminary in vivo study show that SA analogues can be embedded in alginate capsules allowing detection through CEST MRI at 8-10 ppm from water. This new type of alginate capsule has potential for monitoring cell viability with MRI.

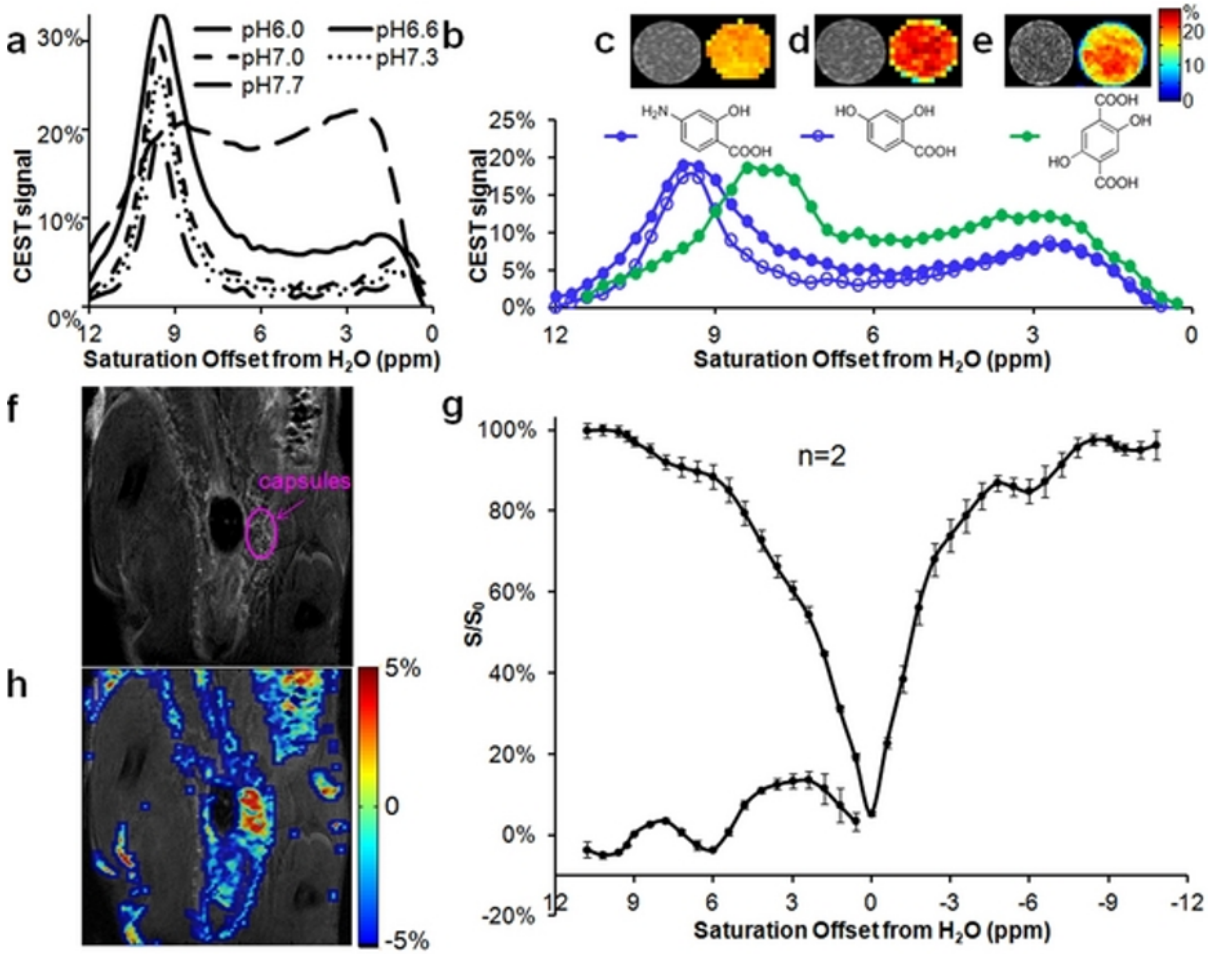

Figure. Phantoms and in vivo MR measurements of SA hydrogels: **a.** the CEST spectra for 25mM DHB with different pHs **b.**CEST MTRasym spectra for the 3 hydrogels; **c.-e.** , MR images for the 3 hydrogels **Left:** High resolution T2-w images, **Right:** CEST contrast images w/o B0 correction; **f.** In vivo high resolution T2-w image of a mouse with DHB capsules transplanted i.p. (coronal view); **g.** Z-spectrum and MTRasym spectrum of 2 mice imaged 2 days post transplantation; **h.** MTRasym at 9 ppm w/o B0 correction with overlay on **f**.

Disclosure of author financial interest or relationships:
X. Song, None; **X. Yang**, None; **D.R. Arifin**, None; **K. Chan**, None; **N. Oskolkov**, None; **J.W. Bulte**, None; **P.C. van Zijl**, None; **M. Pomper**, None; **M.T. McMahon**, None.

Presentation Number **LBAP 005**
Late Breaking Abstract Poster Session
September 19, 2013 / 15:15-15:15 / Room: Exhibit Hall B

Hydrochalarone MRI probes for enhanced contrast and molecular imaging

Zhiguo Zhou, *D. Bradford Brooks, Chris Kepley, Anthony Dellinger, Luna nanoWorks Dvision, Luna Innovations Inc., Danville, VA, USA. Contact e-mail: zhouz@lunainc.com*

Introduction: Magnetic resonance imaging (MRI) is non-invasive, is highly translatable, does not use ionizing radiation, and can provide excellent image contrast, especially in soft tissue. However, fundamental limitations of current gadolinium-based T1 contrast agents are the lack of sensitivity and the short window for data acquisition. By concentrating agent in a particular tissue, targeted contrast agents offer the potential to reduce the required systemic dose. In addition, the development of targeted agents will expand the use of MRI as an in vivo probe of detailed molecular and biological processes (i.e. molecular imaging). Effective targeting requires that these agents remain in the periphery for extended periods of time. Methods and results: Here, we report a novel platform of metallofullerene-based safer T1 contrast agents that completely eliminate the potential of Gd3+ leakage, termed Hydrochalarones, in which three gadolinium atoms are physically encapsulated inside a remarkably stable C80 carbon cage. We developed oxidative amination chemistry for surface functionalization of the Gd3N@C80 molecule enabling dramatically enhanced magnetic coupling between the Gd atoms and the surrounding water molecules outside of the carbon cage. Atomic Force Microscope (AFM) revealed that Hydrochalarones in its dry state has a molecular size of 1.2 nm, while when dispersed in solution its hydrodynamic size is 3-5 nm due to the formation of thick double layers surrounding the negatively charged Hydrochalarones core. T1 relaxivity in human plasma is 30 - 60 mM-1 s-1 (per mM of Gd) depending on the field (4.7, 3.0 and 1.5 T) with higher relaxivity at lower field. Note that each Hydrochalarones molecule contains three Gd atoms, thus the molecular relaxivity is 90 - 180 mM-1 s-1 (per mM of agent), more than 20-fold and 5-fold improvement compared to Magnevist and Vasovist, respectively (Vasovist is a blood pool agent that binds to serum albumin and has the highest relaxivity among all commercial T1 agents). Hydrochalarones also has more favorable r2/r1 ratio of 2.0-2.5 for T1-weighed imaging. In vivo mice 3T MRI pharmacokinetic analysis following a single intravenous injection showed a long blood half-life over 90 minutes. Hydrochalarone showed blood compatibility with no significant hemolysis, platelet aggregation, or complement activation, and was not toxic in an in vivo acute dose toxicity study. This platform technology has been further developed and tested for targeted MRI applications including the imaging of inflammatory macrophage biomarkers for early detection of atherosclerotic plaque. Conclusion: Hydrochalarone is a very promising contrast agent for safer MR imaging with enhanced capabilities. It may have significant utility as a blood-pool MRI contrast agent as well as for molecular imaging since it provides significantly improved relaxivity and prolonged "stealth" circulation sufficient for in vivo imaging of cellular receptors and biomarkers.

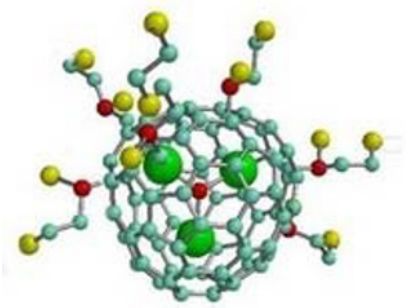

Structure of Hydrochalarone-1

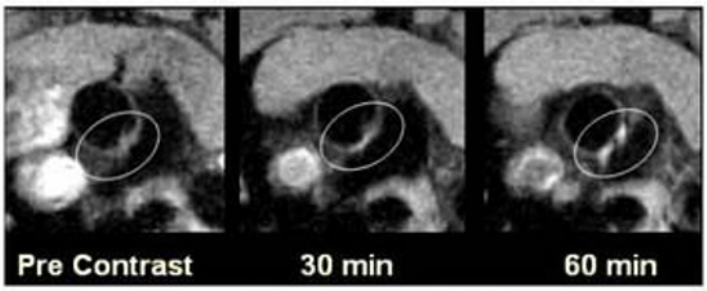

Accumulation of Hydrochalarone contrast agents (ATCA) targeting inflammatory biomarker in atherosclerotic plaque

Disclosure of author financial interest or relationships:
Z. Zhou, None; **D. Brooks**, None; **C. Kepley**, None; **A. Dellinger**, None.

Presentation Number **LBAP 006**
Late Breaking Abstract Poster Session
September 19, 2013 / 15:15-15:15 / Room: Exhibit Hall B

Iron oxide nanoparticle labeling of mesenchymal stem cells induces CXCR4 expression and improved homing to traumatic brain injury

Xinglu Huang, *Fan Zhang, Yu Wang, Gang Niu, Xiaoyuan Chen, Laboratory of Molecular Imaging and Nanomedicine (LOMIN), National Institute of Biomedical Imaging and Bioengineering (NIBIB), National Institutes of Health (NIH), Bethesda, MD, USA. Contact e-mail: xinglu.huang@nih.gov*

Objective: Bone marrow derived-mesenchymal stem cell (MSC) therapy has been shown to improve functional recovery after traumatic brain injury (TBI). The ability to fully characterize MSC population, macroscopic and microscopic cell tracking in vivo, quantification of cells localized in the lesion, and measurement of motor and cognitive function recovery, is essential to maximize the therapeutic efficacy and minimize the systemic side effects. Here we report a serendipitous finding of increased chemokine receptor CXCR4 expression after iron oxide nanoparticle (NP) labeling and subsequently improved homing of MSCs to TBI site. Methods and Results: Zinc doped iron oxide (Zn0.4Fe2.6O4) with much higher r2 relaxivity than undoped iron oxide (Fe3O4) and Feridex were encapsulated by hyaluronic acid (HA) polymer. Specific binding of HA to CD44 overexpressed on the surface of MSCs led to highly effective cellular uptake of Zn0.4Fe2.6O4 NPs. It is surprising finding that MSC labeling with various iron oxide NPs increased chemokine receptor CXCR4 expression on both MSC cell surface and cytoplasm. It has been known that interactions of stromal cell-derived factor-1α (SDF-1α) and CXCR4 chemokines or growth factors can serve as migratory cues in MSC trafficking to the injured region. As shown in Figure 1, without the need of genetic modification of MSCs, we successfully labeled mouse bone marrow derived-MSCs with HA-Zn0.4Fe2.6O4 to induce CXCR4 expression and followed the homing of MSCs in a controlled cortical impact (CCI) model of TBI by T2-weighted MRI. Conclusion: MSCs can be induced to express chemokine receptor CXCR4 in the presence of iron oxide NPs for improved TBI tropism than the unlabeled MSCs. Iron oxide especially zinc-doped iron oxide NPs labeling also allows tracking of the labeled cells in the injury site. The precise mechanism study of CXCR4 induction by iron species is currently underway. (This work was supported by the Department of Defense in the Center for Neuroscience and Regenerative Medicine, and the Intramural Research Programs of the National Institute of Biomedical Imaging and Bioengineering (NIBIB))

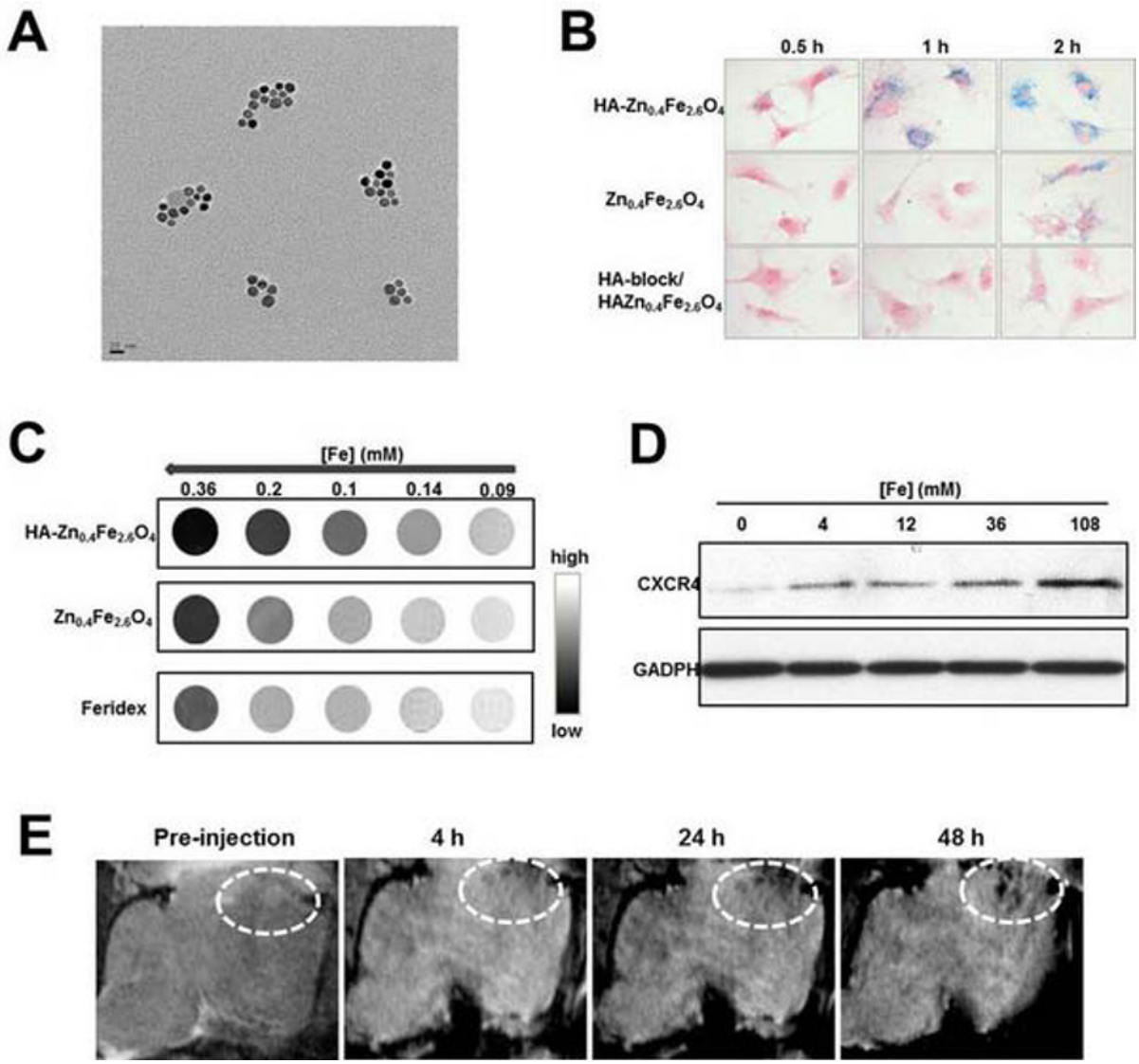

Figure 1. (A) TEM image of HA-Zn0.4Fe2.6O4 NPs. (B) Prussian blue staining show higher MSC uptake of HA-Zn0.4Fe2.6O4 over Zn0.4Fe2.6O4, also the uptake of HA-Zn0.4Fe2.6O4 can be blocked by excess amount of HA. (C) T2 effect of HA-Zn0.4Fe2.6O4 is obviously stronger than Zn0.4Fe2.6O4 and Feridex at the same Fe concentration. (D) Western blot show concentration dependent CXCR4 expression of MSCs after incubation with HA-Zn0.4Fe2.6O4. (E) T2-weighted MR imaging of TBI tropism of HA-Zn0.4Fe2.6O4 labeled MSCs at different time points after cell injection.

Disclosure of author financial interest or relationships:
X. Huang, None; **F. Zhang**, None; **Y. Wang**, None; **G. Niu**, None; **X. Chen**, None.

Presentation Number **LBAP 007**
Late Breaking Abstract Poster Session
September 19, 2013 / 15:15-15:15 / Room: Exhibit Hall B

Gd-DOTA-PAMAM G5 Dendrimer Conjugate as a Potential MRI Contrast Agent for Lymphangiography

Ana Christina Opina[1], *Karen J. Wong*[2], *Hisataka Kobayashi*[2], *Peter Choyke*[2], *Gary L. Griffiths*[2], *Olga Vasalatiy*[1], [1]*Imaging Probe Development Center, National Institutes of Health, Rockville, MD, USA;* [2]*Molecular Imaging Program, National Institutes of Health, Bethesda, MD, USA. Contact e-mail: ana.opina@nih.gov*

A compelling need exists for the accurate imaging of the human lymphatic duct system in a range of diseases, including rare genetic conditions in children mandating surgical intervention for correction. To this end, Kobayashi and co-workers (Sena et al. Nanomedicine 2010; 5:1183) developed a Gd-DTPA-PAMAM G6 dendrimer and successfully demonstrated low Gd dose MR imaging of the thoracic duct in human size-appropriate 35 kg pigs. Now, we further extend this work toward human translation by means of comprehensive chemical, physical and biological comparisons between Gd-DTPA-PAMAM G5 dendrimer and the putatively more biologically stable Gd-DOTA-PAMAM G5 dendrimer. We prepared a PAMAM G5 dendrimer conjugate using a preformed Gd-DOTA chelate via thiourea linkage with an 80 % conjugation yield, thereby ensuring all Gd was attached to dendrimer in a 1:1 complex with DOTA. After all appropriate analytical and stability testing we radiolabeled Gd-DTPA-PAMAM G5 dendrimer and Gd-DOTA-PAMAM G5 dendrimer with trace amounts of Gd-153 and compared quantitative Gd biodistributions between 1-4 days post-injection, with the latter agent displaying relatively lower liver/spleen uptakes, indicative of greater in vivo stability. However, some tissue uptakes remained higher than we wished and we determined to establish for the first time the long term disposition of Gd from the injection of a Gd-dendrimer complex, driven by the necessity to establish a biological half-life for the clinical lead prior to possible human translation. We injected Gd-153 radiolabeled Gd-DOTA-PAMAM G5 dendrimer into mice and quantitated major Gd tissue uptakes out to 90 days post-injection. Gd liver uptake during this period dropped from ~ 33 to ~ 7 % ID/g with most other tissues eliminating Gd at similar rates, with the notable exception of femur in which the observed Gd level fell from approximately 5 to 4 % ID/g at 90 days. MR imaging with 1μmol Gd/kg Gd-DOTA-PAMAM G5 dendrimer in a larger animal (monkey) showed excellent image enhancement in the mesenteric lymph nodes and ducts. Our data suggest that Gd-DOTA-PAMAM G5 dendrimer may be an excellent clinical candidate for imaging of the lymphatic system, but the eventual successful translational development of such nanomedicine agents is fraught with diverse issues, some of which will be discussed in this presentation.

Disclosure of author financial interest or relationships:
A. Opina, None; **K.J. Wong**, None; **H. Kobayashi**, None; **P. Choyke**, None; **G.L. Griffiths**, None; **O. Vasalatiy**, None.

Presentation Number **LBAP 008**
Late Breaking Abstract Poster Session
September 19, 2013 / 15:15-15:15 / Room: Exhibit Hall B

Development of the small molecule-based MRI contrast agent for atherosclerotic plaques

Shimpei Iwaki[1], *Kazuya Hokamura*[2], *Mikako Ogawa*[3], *Yasuo Takehara*[4], *Kazuo Umemura*[2], *Tetsuo Nagano*[5], *Kenjiro Hanaoka*[1], *[1]Graduate School of Pharmaceutical Sciences, The University of Tokyo, Bunkyo-ku, Japan; [2]Department of Pharmacology, Hamamatsu University School of Medicine, Hamamatsu, Japan; [3]Medical Photonics Research Center, Hamamatsu University School of Medicine, Hamamatsu, Japan; [4]Department of Radiology, Hamamatsu University School of Medicine, Hamamatsu, Japan; [5]Open Innovation Center for Drug Discovery, The University of Tokyo, Bunkyo-ku, Japan. Contact e-mail: 9839760617@mail.ecc.u-tokyo.ac.jp*

Atherosclerosis is a progressive disease characterized by thickening arterial walls due to the accumulation of lipids and fibrous elements. Cardiovascular disease due to atherosclerosis is the leading cause of mortality worldwide. In spite of its high risk, diagnosis of atherosclerosis has been possible only at advanced stages of disease. However, the most important clinical complication is acute occlusion as a result of rupture of atherosclerotic plaques, which can occur even at an early stage. Therefore, a method for early detection of atherosclerosis is required. Magnetic resonance imaging (MRI) is a noninvasive diagnostic modality that can provide three-dimensional images of the body with high resolution. MRI is based on 1H NMR signals derived mainly from water protons, and paramagnetic Gd3+ complexes and magnetic nanoparticles are widely used as MRI contrast agents, because they can enhance MRI signals via magnetic interaction with water protons. Several MRI probes for atherosclerotic plaques have been reported, and most of them are MRI contrast agents conjugated with the specific ligands or antibodies directed towards various atherosclerotic markers. However, the target molecules are generally present in atherosclerotic plaques at only nanomolar order concentration (Nature 2008, 451, 953.). Consequently, this strategy is hampered by the low sensitivity of MRI. Aiming to develop an alternative approach, we hypothesized that a MRI probe that specifically targets the atherosclerotic "environment" would be efficiently accumulated in atherosclerotic plaques regardless of the concentration of atherosclerotic markers, and thus would be suitable for sensitive detection of atherosclerotic plaques by MRI. We focused on the lipid-rich environment of atherosclerosis and developed a novel Gd3+-based MRI probe, 2BDP3Gd, for atherosclerotic plaques based on the strategy of targeting this lipid-rich environment. The design employed a lipophilic fluorophore, BODIPY, as a lipid-rich environment-targeting moiety. We first confirmed that 2BDP3Gd showed high affinity for atherosclerotic lipid-rich environments such as lipid droplets of adipocytes and foam cells. 2BDP3Gd was accumulated preferentially in atherosclerotic plaques in ApoE−/− mouse model of atherosclerosis, based on fluorescence imaging of the BODIPY moiety. Further, we showed that 2BDP3Gd could visualize atherosclerotic plaques in aorta of WHHL rabbit in T1-weighted MR images *in vivo*. These results indicate that 2BDP3Gd is an excellent candidate for sensitive MRI detection of atherosclerotic plaques even in humans.

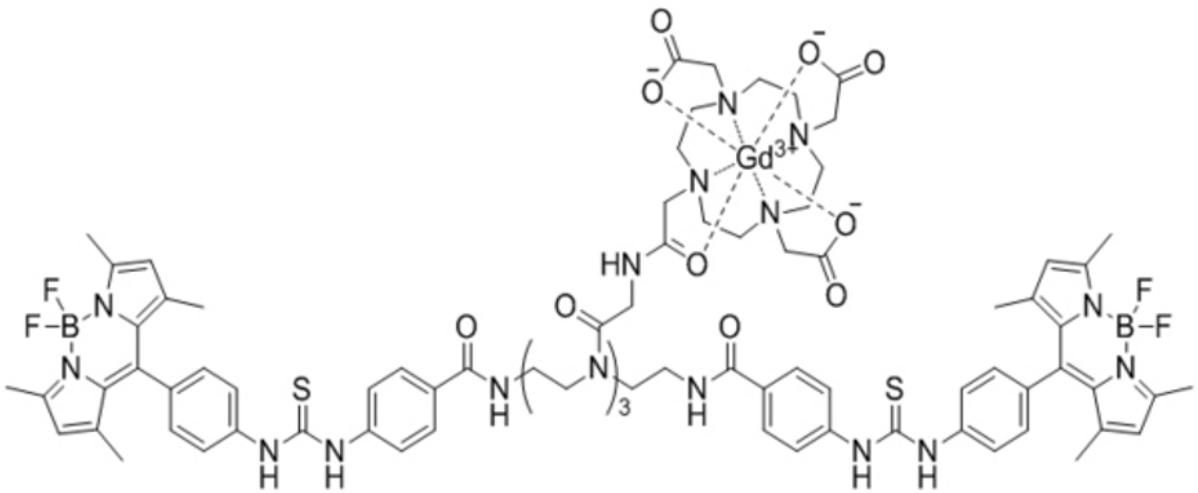

Chemical structure of 2BDP3Gd.

Disclosure of author financial interest or relationships:
S. Iwaki, None; **K. Hokamura**, None; **M. Ogawa**, None; **Y. Takehara**, None; **K. Umemura**, None; **T. Nagano**, None; **K. Hanaoka**, None.

Presentation Number **LBAP 009**
Late Breaking Abstract Poster Session
September 19, 2013 / 15:15-15:15 / Room: Exhibit Hall B

Hypotonic swelling: a "soft" route for ex vivo cellular labeling with Paramagnetic complexes

Enza Di Gregorio, *Giuseppe Ferrauto, Eliana Gianolio, Silvio Aime, Molecular biotechnologies and Health Sciences, CIM, Torino, Italy. Contact e-mail: enza.digregorio@unito.it*

Purpose: In the past decade different strategies to label cells with paramagnetic MRI contrast agents have been exploited like macropinocytosis, electroporation, receptor/transporter mediated endocytosis.1 Herein a new method, based on the application of a hypotonic treatment, has been reported as an efficient soft route to label cells with high amount of paramagnetic Gd-complexes. Methods: J774A.1 murine macrophages and k562 human myelogeneous leukemia cells have been suspended in a hypotonic solution containing Gd-containing contrast agents. The presence of a large osmotic gradient between the intra- and the extra-cellular compartments causes the swelling of the cells during which the membrane is less efficient in acting as barrier to molecular transits. After the incubation time the physiological functionality of cells has been restored by changing the osmolarity of the external solution to the isotonic conditions. This technique has been compared with pinocytosis and electroporation in term of efficiency of internalization, relaxivity, cell viability and imaging efficiency (at 7T). Results: By applying this technique, high amounts of Gd-HPDO3A (up to 10^{10} Gd^{3+} per cell) can be easily loaded into cells. The internalization efficiency depends on many factors among which the incubation time, the concentration of the probe in the hypotonic solution and the temperature. The cytoplasmatic localization of the loaded molecules has been confirmed both by MR imaging and by fluorescence imaging when Carboxyfluorescein was added to the incubation medium (Fig.1). This technique appears safe as no changes in viability, morphology and functionality have been observed after the treatments. The increase of the cellular volume during the hypotonic treatment has been measured by microscopy as well as by cytometric analysis. Conclusion: The new method here proposed for MRI cellular labeling has been proved to be very efficient and safe for cells. The cytoplasmatic confinement of the paramagnetic probe allows to overcome two major drawbacks encountered with paramagnetic labeling, namely i) the "aggressive" environment met along the endosomes/lysosomes pathway and ii) the "relaxivity-quencing" issue due to the limited exchange of water molecules across the endosomal membrane.
1)Gianolio E, Stefania R, Di Gregorio E, Aime S. Eur. J. Inorg. Chem. 2012, 1934-1944

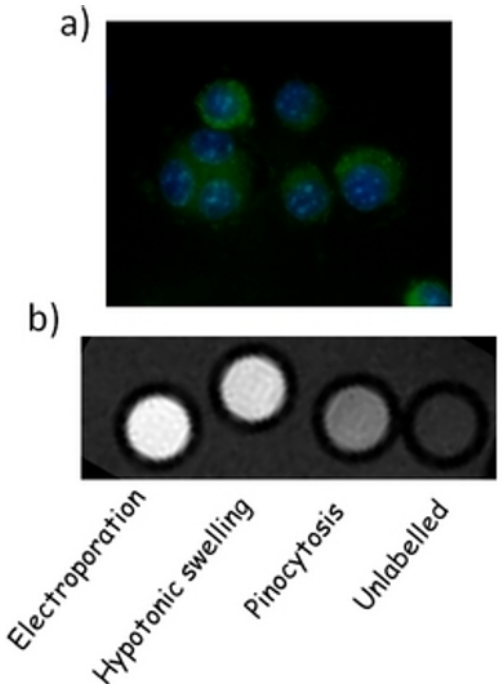

c)

Sample	Gd/cell	r1p ($mM^{-1}s^{-1}$) (300MHz at 25°C)
Gd-HPDO3A		4,2
Pinocytosis	1,39E10	2.1
Hypotonic swelling	1,49E10	4.3
Elettroporation	1,33E10	4.2

Fig.1 (A) Fluorescence microscopy image of J774A.1 cells after loading with CarboxyFluorescein by hypotonic swelling; (B)T1w image of J774A.1 cells after loading with Gd-HPDO3A with three different routes: pinocytosis, electroporation and hypotonic swelling; (C) Comparison between pinocytosis, electroporation and hypotonic swelling by using 50mM of Gd-HPDO3A

Disclosure of author financial interest or relationships:
E. Di Gregorio, None; **G. Ferrauto**, None; **E. Gianolio**, None; **S. Aime**, None.

Presentation Number **LBAP 010**
Late Breaking Abstract Poster Session
September 19, 2013 / 15:15-15:15 / Room: Exhibit Hall B

The Potential of Clustered Core Magnetic Particles for MPI

Nicole Gehrke[1], *David Heinke*[1], *Dietmar Eberbeck*[2], *Andreas Briel*[1], [1]*nanoPET Pharma GmbH, Berlin, Germany;* [2]*Physikalisch-Technische Bundesanstalt, Berlin, Germany. Contact e-mail: nicole.gehrke@nanopet.de*

INTRODUCTION: Magnetic Particle Imaging (MPI) is a promising new imaging modality, which, similarly to MRI, makes use of superparamagnetic iron oxide (SPIO) nanoparticles as tracers since it also exploits magnetic fields. It detects the tracer itself with a fast scanning speed in a quantitative and sensitive manner as is the case with SPECT and PET, but without the need of ionizing radiation. These features may provide substantial additional benefit for various applications. One prominent example is molecular imaging (MI) by MRI using target-specific SPIOs. The lower sensitivity of MRI and the challenge of tracer quantification hamper significant progress of this important research field, but these difficulties might be overcome by MPI. However, so far the MPI signal performance of SPIOs from both clinical as well as research applications is far below theoretical limits and, yet, their directed optimization is hindered by a lack of understanding of the structure-efficacy relation. In this study we synthesized different polymer-coated SPIO-based tracers and characterized their structure and magnetic properties. We recorded their magnetic particle spectra (MPS) in comparison to the two hitherto MPI gold standards to gain more insight into this relation. METHODS: The tracers were synthesized by basic precipitation in aqueous medium. For structural and magnetic characterization, dynamic light scattering, transmission electron microscopy, static, i.e. M(H), and dynamic magnetisation measurements were performed. The magnetic particle spectra (MPS) were recorded at 25 mT at a drive field frequency of 25 kHz. RESULTS: The various tracers exhibited no prominent differences in their particle structure. Their mean hydrodynamic diameter was found to be between 120 and 160 nm and their particle cores were comprised of aggregated clusters of small crystallites sized at around 5 nm. Surprisingly, their MPS amplitude, i.e. their potential efficacy as MPI tracers, varied significantly by a factor of up to 11. In comparison to the MRI contrast agents Resovist® and FeraSpin R which are so far used as gold-standards for MPI, the particle with the highest MPI efficacy synthesized here shows an improvement by a factor of up to three. Such an increase does not represent the theoretical limit, but so far a similar performance was only found for size-optimized particles obtained from the best state-of-the-art clustered core MPI tracer Resovist and FeraSpin R as well as certain mono-crystalline core particles. Static magnetization measurements help to quantitatively understand these differences, and we attribute them, among others, to the magnetic interaction between the crystallites within the core. CONCLUSION: Considering the huge range of MPI efficacies despite the similar structure of the tracers synthesized here our results indicate that the structural feature of clustered cores indeed holds a currently unknown potential for MPI tracer optimisation. With suitable tracers MPI might become a powerful alternative for fast, sensitive and quantitative molecular imaging without the need of radioactive tracers.

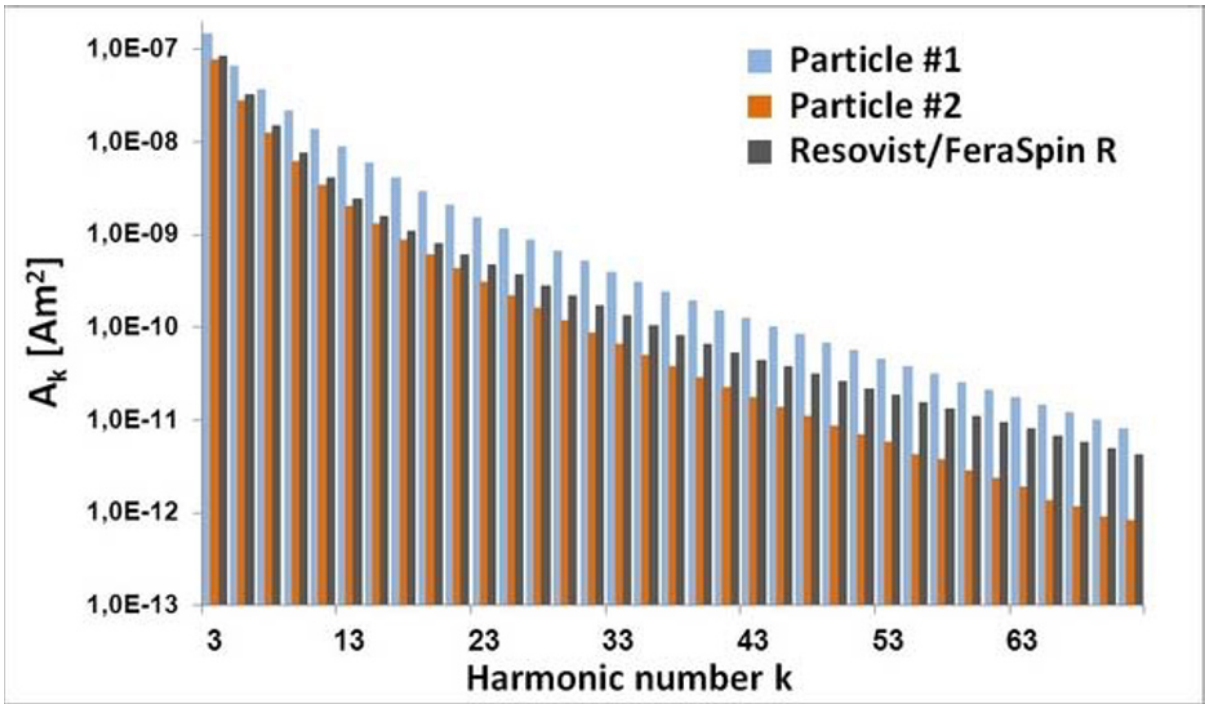

MPS of the highest (#1) and lowest (#2) MPI efficacy particles synthesized here in comparison to Resovist and FeraSpin R normalized to the iron concentration (drive field 25 mT, f0=25 kHz).

Disclosure of author financial interest or relationships:
N. Gehrke, nanoPET Pharma GmbH, Employment; **D. Heinke**, nanoPET Pharma GmbH, Employment; **D. Eberbeck**, None; **A. Briel**, nanoPET Pharma GmbH, Employment .

Presentation Number **LBAP 011**
Late Breaking Abstract Poster Session
September 19, 2013 / 15:15-15:15 / Room: Exhibit Hall B

Chemical and financial comparisons of iron oxide nanocrystal syntheses for PLGA encapsulation

Aaron S. Schwartz-Duval, *Erik M. Shapiro, Department of Radiology, Michigan State University, East Lansing, MI, USA. Contact e-mail: schwartzduval@gmail.com*

Introduction: Magnetic nanoparticles are key technologies for molecular and cellular MRI. The size of the magnetite crystals dictates the quality of the particles. Here we compare two methods for producing magnetite crystals, the Sun method(1) capable of producing 5 nm magnetite crystals and the Guardia(2) method capable of producing magnetite crystals 5 nm, 12 nm, 20 nm, and up to 160 nm in diameter (by varying the ratio of iron acetylacetonate to decanoic acid. The high level of size control, coupled with the significantly lower cost of production make the Guardia method of producing magnetite nanocrystals more beneficial for making magnetic nanoparticles. Methods: Both methods involve chemical decomposition of iron acetylacetonate in dibenzyl ether under nitrogen. In addition to iron acetylacetonate and dibenzyl ether; the Sun method requires oleylamine, oleic acid, and 1,2-hexadecenediol; while the Guardia method requires decanoic acid. Magnetite molecular identity was assessed using X-ray diffraction. Transmission electron microscopy (TEM) (figure1A-1D) was used to image the nanocrystals and size was determined with ImageJ. The iron nanocrystals were encapsulated in poly(lactic-glycolic acid) (PLGA) by first mixing oleic acid soaked iron nanocrystals with PLGA dissolved in dichloromethane (DCM). This hydrophobic solution was then added to a poly(vinyl-alcohol) (PVA) water solution while vortexing to form an emulsion. This emulsion was then tip sonicated and stirred in low percent PVA-water mixture until the DCM evaporated. Water was then removed via centrifugation and freeze drying. Particles were imaged using an AURIGA® CrossBeam Workstation Dual Column SEM-FIB to determine if nanoparticles were successfully made, and if they were of a concise size. The percent mass of iron of these particles was determined using TA instruments TGA 500, and the particles were imaged with TEM to visually determine successful encapsulation (figure 1E-1H). Results and Discussion: The average size of the magnetite nanocrystals produced with the Sun method (1A) was 6.5± 1.98 nm. Changing the ratio of iron acetylacetonate to decanoic acid ratio in the Guardia method resulted in average crystal diameters of 6.6± 1.1 nm for a 1:6 ratio (1B), 9.9± 2.36 nm for a 1:5 ratio (1C), and 20.0±6.48 nm for a 1:4 ratio (1D). Nanoparticles lacking magnetite nanocrystals were 162±52.5 nm in diameter. Nanoparticles containing magnetite nanocrystals produced using the Sun method were 139±60.0 nm in diameter, and nanoparticles containing magnetite nanocrystals produced using the Guardia method were 132±67.7 nm in diameter. The encapsulation efficiency (calculated using TGA data) of particles containing magnetite crystals made using the Sun method was 1.66 (30.7% iron by weight) and 1.41 (29.7% iron by weight) by using Guardia method. Additionally the Sun method was 12.86 times more expensive than the Guardia method by cost per gram of magnetite produced. 1. Sun, S.; Zeng, H. JACS 2002, 124, 8204- 8205 2. Guardia, P.; Pérez, N. S.; Labarta, A.; Batlle, X. Langmuir 2010, 26, 5843- 5847.

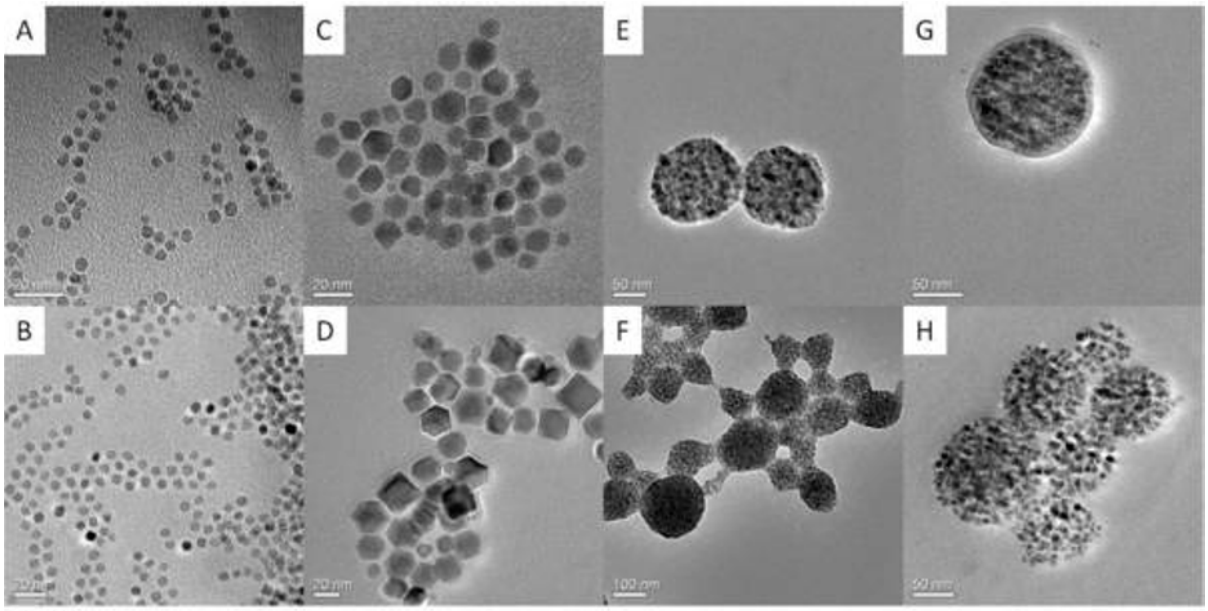

Figure 1:
A shows TEM imaging of iron oxide nanocrystals produced with the Sun method.
B, C, and D show TEM imaging of iron oxide nanocrystals produced using the Guardia method with varied amounts ratios of iron acetylacetonate to decanoic acid (1:6, 1:5, and 1:4 respectively).
E and F show TEM images of PLGA encapsulated iron crystals produced using the primary method.
G and H show TEM images of PLGA encapsulated iron crystals produced using the secondary method.

Disclosure of author financial interest or relationships:
A.S. Schwartz-Duval, None; **E.M. Shapiro**, None.

Presentation Number **LBAP 012**
Late Breaking Abstract Poster Session
September 19, 2013 / 15:15-15:15 / Room: Exhibit Hall B

Hollow mesoporous silica spheres as 19F-MRI imaging agents

Alexander Pochert[1], *Detlef Stiller*[3], *Volker Rasche*[2], *Mika Linden*[1], [1]*Department of Anorganic Chemistry, Ulm University, Ulm, Germany;* [2]*Core Facility Small Animal MRI, Ulm University, Ulm, Germany;* [3]*In Vivo Imaging, Target Discovery Research, Boehringer Ingelheim GmbH & Co, Biberach, Germany. Contact e-mail: Alexander.Pochert@uni-ulm.de*

Aim: 19F appears attractive as MRI contrast agent due its sensitivity of 83% of 1H and virtually 100% natural abundance. Perfluorocarbons (PFCs) like perfluoro-15-crown-5-ether (PF-15-c-5) are attractive due to the high 19F load and single resonance line. Liposomal encapsulation is limited by the inherent instability and dimension inflexibility. Mesoporous amorphous silica nanoparticles (MSNs) gain interest as drug carriers due to surface chemistry, flexible particle dimensions, high biocompatibility, in vivo degradation within several days, and systemic elimination by urinary excretion. For high payloads of PF-15-c-5, hollow mesoporous silica spheres (HMSS) were filled with PF-15-c-5 and tested as contrast agent for 19F MRI. Methods: Particles of 250 nm and 1500 nm diameter were synthesized. For the 1500 nm MSNs, N-hexadecylamine (1.02g) together with mesitylene (1,3,5-trimethylbenzene, 1g) was dissolved in a mixture of 100ml isopropanol and 90ml of de-ionized water at room temperature. 1.67ml of aqueous ammonia (32 wt. %) was added. The molar ratio of reaction mixture was 1.00 TEOS: 0.32 mesitylene: 0.16 n-hexadecylamine: 75 iso-propanol: 192 water: 3.3 ammonia. After stirring for 1 hour, 5.8 ml tetraethyl orthosilacate was added. After 24h the product was collected by centrifugation. Particles were dispersed in a mixture of ethanol, mesitylene and water and hydrothermal treated for 4 days at 140°C, followed by washing with acetone, ethanol and water, dried at 70°C under vacuum and calcined at 550°C for 6h to remove the surfactant template. Hallow mesoporous hollow silica spheres with a size of 250nm were prepared according to a procedure described by Rosenholm et al. in the presence of mesitylene as an etching reagent. Subsequent synthesis steps were similar to the 1500nm particls. The MRI-active particles were prepared by drying the mesoporous silica hollow spheres in a Schlenk tube under vacuum for 4h at 100°C. After cooling down, PF-15-c-5 was added and the system frozen and evacuated again and heated for 4h at 160°C. MR images were acquired by a conventional Flash technique at 224x224x1000µm3 spatial resolution with 3min acquisition time. For determination of the 19F load, quantitative MR spectroscopy was performed. Results: TEM/SEM images proof particle dimension and hollow structure. MRI images revealed an excellent 19F signal. Molecular concentration per voxel was quantified between 0.22µMol (250nm) and 1.4µMol (1500nm). A clear broadening of the MR spectra was observed, which was less pronounced for the 1500nm particle. Conclusion: In this study we could show the hollow SiO2 particle can be loaded with PF-15-c-5 for generation of a highly efficient MRI contrast agent. The broadening of the spectra may indicate a certain fraction of the PF-15-c-5 being embedded in the pores, the relevance of which gets reduced with increasing core size. With additional surface functionlization the particles are promising for molecular imaging.

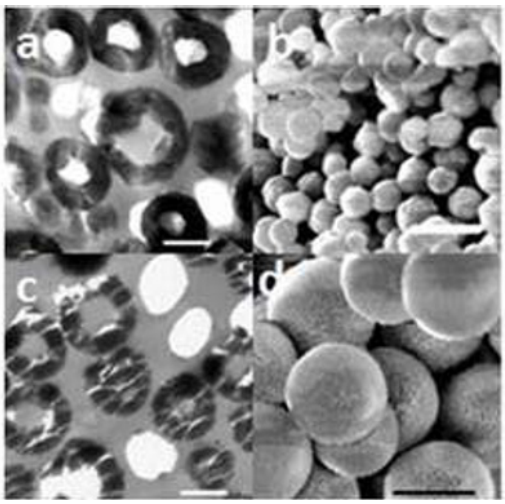

1

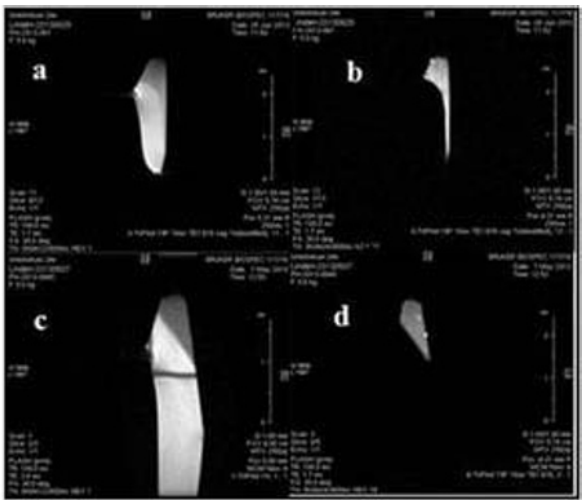

2

TEM (1 a,c) and SEM (1 b,d) pictures of 250 nm particles (scale bar = 300nm, top) and 1500 nm particles (scale bar = 1000nm, bottom). Respective 1H (2 a,c) and 19F (2 b,d) MRI images obtained at 11.7T.

Disclosure of author financial interest or relationships:
A. Pochert, None; **D. Stiller**, None; **V. Rasche**, None; **M. Linden**, None.

Presentation Number **LBAP 013**
Late Breaking Abstract Poster Session
September 19, 2013 / 15:15-15:15 / Room: Exhibit Hall B

MOLECULAR RECOGNITION OF OXY- AND DEOXY-HEMOGLOBIN BY PARAMAGNETIC Gd(III) COMPLEXES IN RED BLOOD CELLS

Giuseppe Ferrauto, *Enza Di Gregorio, Eliana Gianolio, Silvio Aime, Molecular biotechnologie and health sciences, Cim, torino, Italy. Contact e-mail: giuseppe.ferrauto@unito.it*

Introduction: Assessment of hypoxia is crucial for several major diseases (e.g. stroke, cancer) and much attention is currently devoted to the development of imaging probes able to monitor the oxygenation state of tissues. Herein, we report our studies on the binding affinity of six paramagnetic Gd(III) based MRI contrast agents (namely Gd-HPDO3A, Gd-BOPTA, Gd-DTPA, Gd-DOTP, cis-Gd-DOBP and trans-Gd-DOBP) towards oxy and de-oxy hemoglobin (Hb). In vitro and in cellulo studies have been complemented with preliminary in vivo results on a murine cancer model. Methods: Red Blood cells (RBCs) have been isolated from blood by using Ficoll Histopaque and then loaded with the Gd-complexes by applying the hypotonic swelling method. The interaction of the paramagnetic complexes with free hemoglobin has been investigated by NMR relaxation measurements (Protons Relaxation Enhancement, PRE), at 21 MHz and 25°C. By carrying out the proper titrations it has been possible to measure the binding affinity constants both for T- and R-state hemoglobin. Additionally, NMRD profiles have been acquired and analyzed for Hb/Gd complex samples at different pO_2 values. For in vivo experiments, TSA xenograft murine models have been intravenously injected with Gd-DOTP loaded RBCs and T1w images have been acquired. Results: The six compounds can be efficiently loaded inside red blood cells (ca. 1-3x10^8 Gd-complexes for cell) without affecting cells viability and functionality (no change in the main hematological parameters has been detected). Based on the results of the PRE procedure and NMRD profiles, only Gd-HP-DO3A showed no evidence of interaction with oxy- or deoxy-hemoglobin. With regard to the other investigated Gd (III) probes, the values of the dissociation constant (K_d) show a specific binding with hemoglobin, with relatively different affinity for T- and R-Hb-state. In the case of Gd-BOPTA, Gd-DTPA and Gd-DOTP a preferential interaction with the deoxy-Hb has been reported, viceversa cis-Gd-DOBP and trans-Gd-DOBP show a stronger interaction with oxy-Hb than with de-oxy Hb. Among the considered systems, Gd-DOTP showed the highest difference in the binding affinity between oxy and de-oxy Hb (K_d =2.8x10^{-3}M vs 5.5x10^{-4}M) and the largest increase of relaxivity at 20MHz. Therefor Gd-DOTP has been selected for the preliminary in vivo testing on the murine tumor model. Conclusions: The presence of the negatively charged chemical functionalities on the outer surface of the Gd-chelates allows the complexes to establish electrostatic interactions with Hb similar to the one reported for the natural allosteric effector DPG. On this basis, it appears possible to use Gd-complexes (especially Gd-DOTP and the commercial Gd-DTPA agent) to assess, by MRI, the in vivo tissue oxygenation state. The ex vivo RBCs loading with Gd-complexes is easy to perform and the stability of the complexes inside the erythrocytes does not seem to bring relevant toxicity issues.

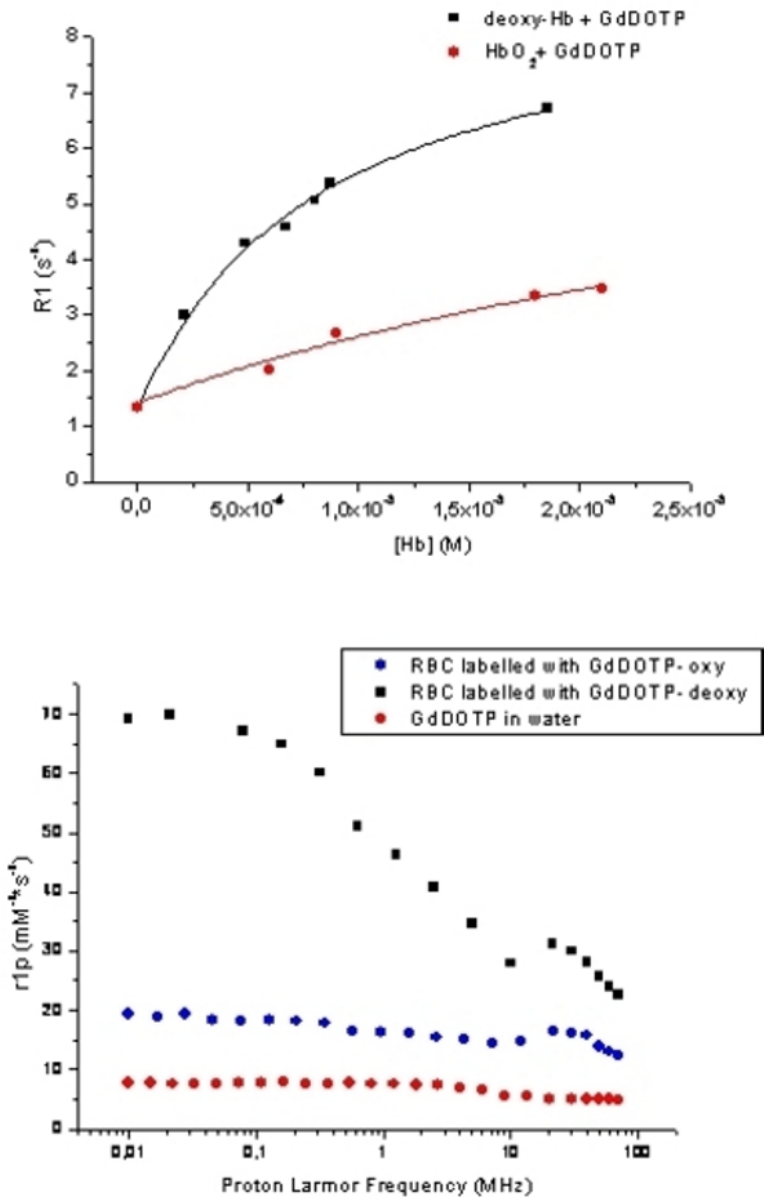

NMRD profile and R1 enhancement by using Gd-DOTP complex (oxy vs deoxy Hb)

Disclosure of author financial interest or relationships:
G. Ferrauto, None; **E. Di Gregorio**, None; **E. Gianolio**, None; **S. Aime**, None.

Presentation Number **LBAP 014**
Late Breaking Abstract Poster Session
September 19, 2013 / 15:15-15:15 / Room: Exhibit Hall B

Novel Gd-loaded Polymer Vesicles with High Longitudinal Relaxivity

Wen-Yuan Hsieh[1], *Yung-Chu Chen*[1], *Wen-Chia Huang*[3], *Hsin-Cheng Chiu*[2], [1]*Biomedical Technology and Device Research Labs, Industrial Technology Research Institute, Chutung, Hsinchu, Taiwan;* [2]*Department of Biomedical Engineering and Environmental Sciences, National Tsing Hua University, Hsinchu, Taiwan;* [3]*Department of Chemical Engineering, National Chung Hsing University, Taichung, Taiwan. Contact e-mail: hsiehw@gmail.com*

The polymer vesicle assembled from the poly(acrylic acid-co-distearin acrylate) (P(AAc-co-DSA)) exhibits high longitudinal relaxivities (r1) of 58-71 mM−1s−1 in aqueous solution through the chelation of gadolinium ions (Gd3+, an paramagnetic species) within acrylic acid (AAc) regions. The Gd3+ ions can be highly accommodated into either inner or outer surfaces of vesicles (the Gd3+-ion loading efficiency ca 80 %) through the electrostatic interaction with ionized AAc residues in the polymer vesicles. The high relaxivity value of Gd-loaded polymer vesicle solution was attributed to the prolonged rotational correlation time of the Gd3+ ions and the fast water exchange from Gd ions to bulk solution. The female C57BL/6j mice were used to investigate the in vivo biodistribution of the Gd-loaded vesicles. The in vivo mouse model showed that Gd-loaded polymer vesicles can generate similar T1 weighted MR imaging contrast as commercial Gd contrast agent, Magnevist®, but with lower Gd ion concentration. This can reduce the risk of nephrotoxicity due to less Gd dose needed

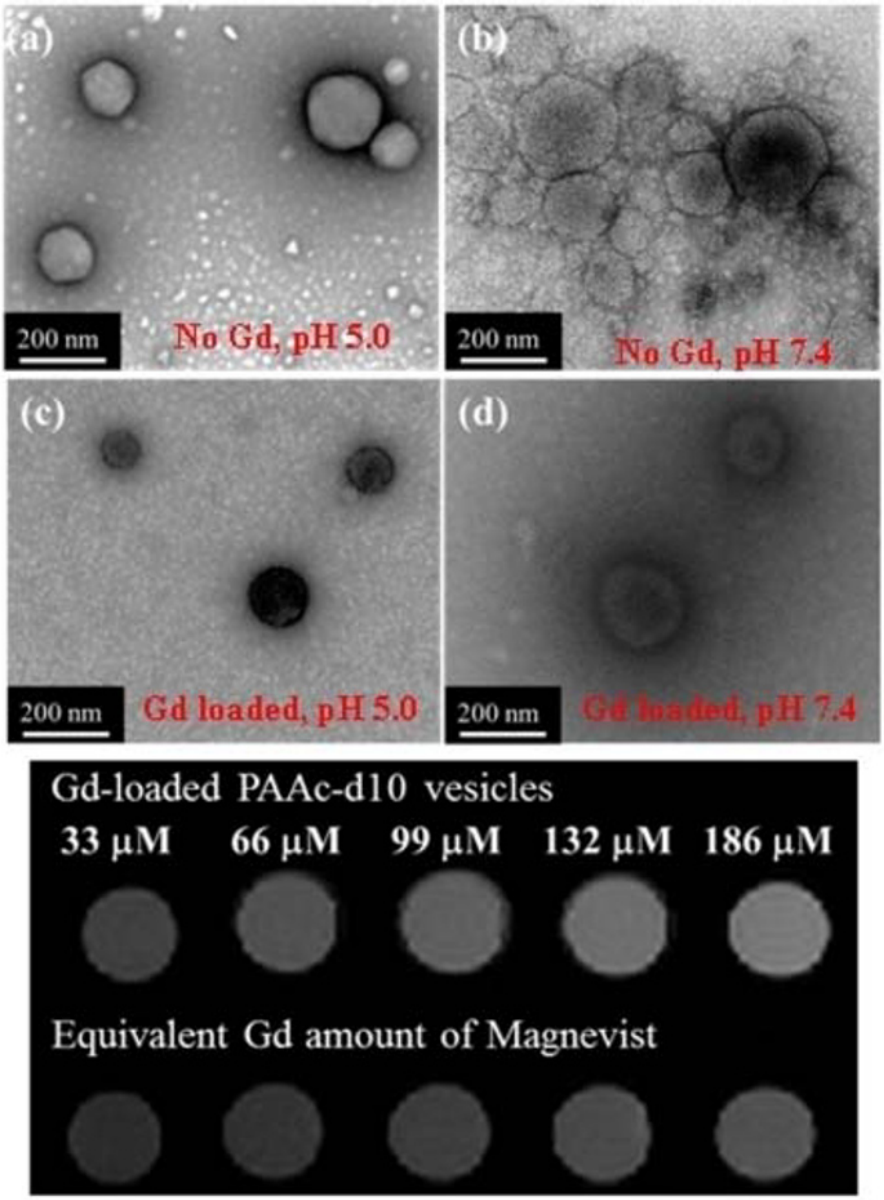

Top: TEM images of Gd-free (a, b) and -loaded PAAc-d10 vesicles (c, d) at different pH 5.0 (a, c) and 7.4 (b, d). Bottom: T1-weighted MR phantom images of the Gd-loaded PAAc-d10 vesicles and Magnevist in aqueous solutions at pH 7.4.

Disclosure of author financial interest or relationships:
W. Hsieh, None; **Y. Chen**, None; **W. Huang**, None; **H. Chiu**, None.

Presentation Number **LBAP 015**
Late Breaking Abstract Poster Session
September 19, 2013 / 15:15-15:15 / Room: Exhibit Hall B

Combined Magnetic Resonance Spectroscopy and Mass Spectrometric Imaging of Tumor Hypoxia

Asif Rizwan[1], *Lu Jiang*[1], *Nadine Mascini*[3], *Menglin Cheng*[1], *Tiffany R. Greenwood*[1], *Venu Raman*[1,2], *Zaver M. Bhujwalla*[1,2], *Ron M. Heeren*[3], *Kristine Glunde*[1,2], [1]*Radiology and Radiological Science, The Johns Hopkins University, Baltimore, MD, USA;* [2]*The Sidney Kimmel Comprehensive Cancer Center, The Johns Hopkins University School of Medicine, Baltimore, MD, USA;* [3]*FOM Institute AMOLF, Amsterdam, Netherlands. Contact e-mail: arizwan2@jhmi.edu*

The abnormal tumor vasculature causes regions of tumors to be transiently or chronically hypoxic [1-4]. Hypoxia is associated with resistance to therapy through multiple mechanisms such as cell cycle arrest, resistance to apoptosis, HIF1 stabilization, and extracellular acidification, among others [5]. In addition, clinical and pre-clinical experiments point to a fundamental role of hypoxia in metastatic progression [6, 7]. Hence, it is necessary to be able to measure tumor hypoxia to assess tumor aggressiveness and predict therapy outcome. In this work, we have used human MDA-MB-231-HRE-tdTomato breast tumor cell lines, which are genetically engineered to express red fluorescent tdTomato protein under hypoxic conditions [8, 9]. MDA-MB-231-HRE-tdTomato breast cancer cells were orthotopically grown in athymic nude mice. In vivo optical imaging of tdTomato fluorescent protein was visualized by a Xenogen IVIS 200 Spectrum system (Figure A). Mice bearing hypoxic tumors were injected with Hypoxyprobe-F6, a hexafluorinated derivative of 2-nitroimidazole. Hypoxyprobe F6 forms stable covalent bonds with proteins, peptides, and amino acids as evident from the red staining in hypoxic MDA-MB-231 cells treated with F6 (Figure B). The probe has six fluorine atoms that were detected by 19F magnetic resonance spectroscopy (MRS) in vivo for up to 6 hours following intravenous injection (Figure C). Following 19F MRS in vivo, mice were sacrificed, and tumors were excised and cryo-sectioned. Experiments are in progress to detect the distribution of the F6 probe in these tumor sections by mass spectrometric imaging (MSI). In addition, mice were injected with the hypoxia marker pimonidazole, another 2-nitroimidazole derivative [10]. The distribution of pimonidazole in these tumor sections was detected for the first time by matrix-assisted laser desorption ionization (MALDI) MSI (Figure D). For comparison, we probed the pimonidazole distribution by immunohistochemical (IHC) staining, and overlaid the pimonidazole MS image with the corresponding IHC image (Figure D), demonstrating successful detection of pimonidazole by MSI. Further experiments are underway to acquire 19F magnetic resonance spectroscopic imaging (MRSI) and to register in vivo MRSI and ex vivo MS images with IHC staining of the F6 probe in breast tumor xenografts. Our experiments indicate that hypoxyprobe F6 has the potential to be a multimodality imaging reporter for MRS/MRSI, MSI, and immunohistochemistry detection of hypoxia. References: 1.Gillies, R.J., et al., IEEE Eng Med Biol Mag, 2004. 23(5): p. 57-64. 2.Song, C.W., et al., Cancer Drug Resistance, 2006: p. 21-42. 3.Serganova, I., et al., Clin Cancer Res, 2011. 17(19): p. 6250-61. 4.Zhang, X., et al., J Nucl Med, 2010. 51(8): p. 1167-70. 5.Wilson, W.R., et al., and M.P. Hay, Nat Rev Cancer, 2011. 11(6): p. 393-410. 6.Subarsky, P., et al., Clin Exp Metastasis, 2003. 20(3): p. 237-50. 7.Rizwan, A., et al., Clin Cancer Res, 2013. 8.Krishnamachary, B., et al., PLoS One, 2012. 7(8): p. e44078. 9.Jiang, L., et al., Neoplasia, 2012. 14(8): p. 732-41. 10.Varia, M.A., et al., Gynecologic Oncology, 1998. 71(2): p. 270-277.

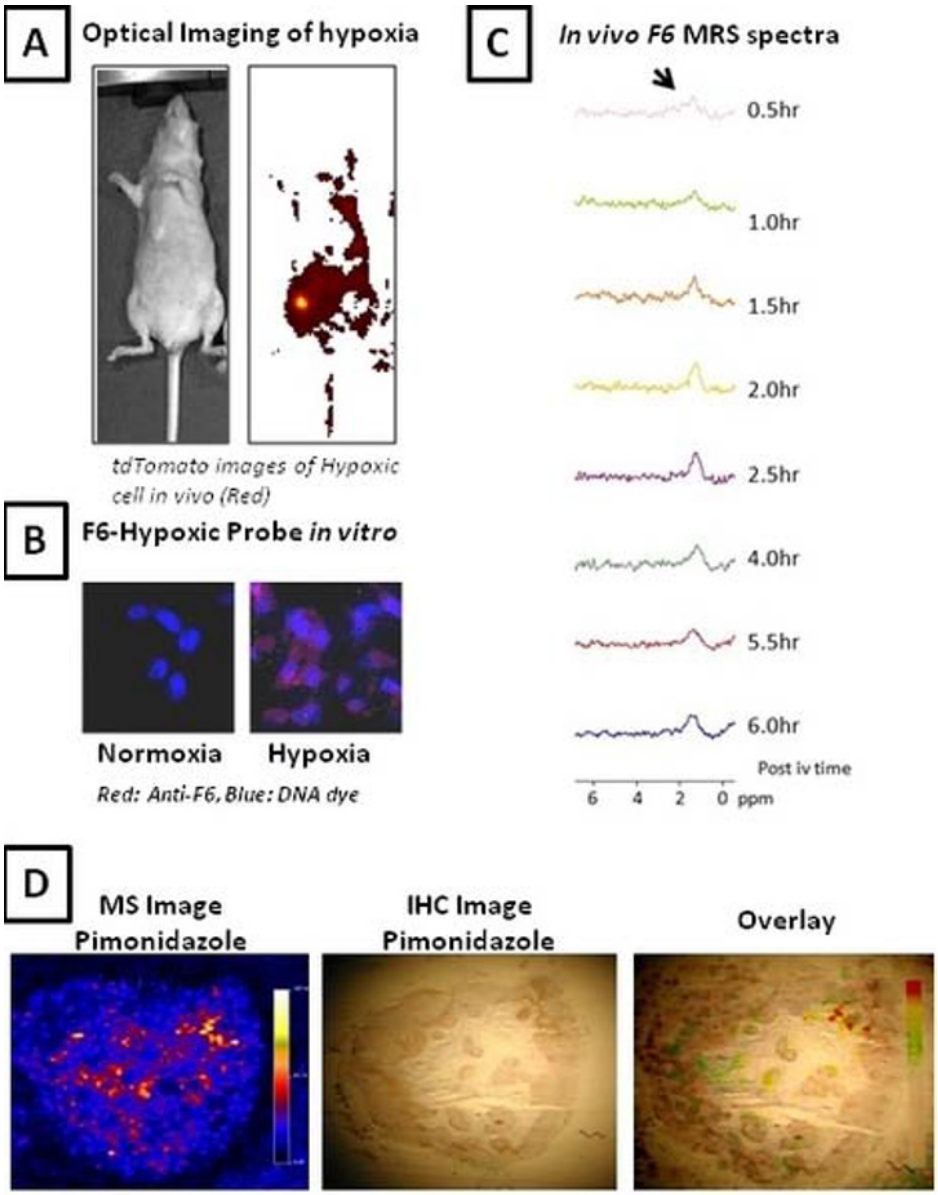

Disclosure of author financial interest or relationships:
A. Rizwan, None; **L. Jiang**, None; **N. Mascini**, None; **M. Cheng**, None; **T.R. Greenwood**, None; **V. Raman**, None; **Z.M. Bhujwalla**, None; **R.M. Heeren**, None; **K. Glunde**, None.

Presentation Number **LBAP 016**
Late Breaking Abstract Poster Session
September 19, 2013 / 15:15-15:15 / Room: Exhibit Hall B

Metabolic imaging of breast tumors with dedicated [18]FDG breast PET-CT: comparison with contrast-enhanced high-field MRI at 3T

Heinrich F. Magometschnigg, *Thomas H. Helbich, Hubert Bickel, Stephan H. Polanec, Georg J. Wengert, Katja Pinker-Domenig, Dpt. of Radiology, Division of Molecular and Gender Imaging, Medical University of Vienna, Vienna, Austria. Contact e-mail: h.magometschnigg@gmail.com*

Introduction Aim of this study was to compare contrast-enhanced high temporal and spatial resolution MRI at 3T (3T CE-MRI) with dedicated [18]FDG breast PET-CT in the assessment of breast lesions. Material and Methods 190 breast lesions classified by mammography or ultrasound as BI-RADS® 4 or 5 were included in this IRB approved prospective study. All patients preoperatively underwent dedicated [18]FDG breast PET-CT and CE-MRI of the breast. MRI protocol included: a T2-weighted sequence and contrast-enhanced high-resolution 3D-T1-weighted sequences before and after application of a standard dose Gd-DOTA (Dotarem®). A prone PET-CT dataset over the same region was acquired allowing the same patient geometry as with MRI. Patients were injected with approximately 300 MBq [18]FDG based on the patients weight. In 3T CE-MRI lesions were assessed for morphology and enhancement kinetics and classified according to BI-RADS®. Dedicated breast PET-CT was assessed for FDG avidity of lesions. Tumors were classified positive when FDG uptake was greater than blood-pool activity. Lesions within tissues demonstrating moderate/high physiologic background activity were considered positive if the activity was greater than the adjacent physiologic activity. All lesions were histopathologically verified. Results Dedicated [18]FDG breast PET-CT demonstrated a very good sensitivity of 96%, a specificity of 77% and diagnostic accuracy of 91%. CE-MRI had an excellent sensitivity of 98%, a specificity of 77% and a diagnostic accuracy of 93%. There were 47 benign and 143 malignant lesions (mean lesion size 27.44mm; range 3-97mm). False-negative lesions in PET-CT (n 6) were small and low-grade lesions (mean 11.2mm), had a very low SUVmax (mean 1.49) or were adjacent to tissue with high physiologic activity. Conclusion CE-MRI at 3T is superior to PET-CT in the assessment of breast lesions, but dedicated [18]FDG breast PET-CT is a valid alternative in patients, who are unsuitable for MRI.

3T CE-MRI vs. [18]FDG breast PET-CT

	3T CE-MRI	[18]FDG breast PET-CT
Sensitivity	98%	96%
Specificity	77%	77%
Diagnostic Accuracy	93%	91%

Disclosure of author financial interest or relationships:
H.F. Magometschnigg, None; **T.H. Helbich**, None; **H. Bickel**, None; **S.H. Polanec**, None; **G.J. Wengert**, None; **K. Pinker-Domenig**, None.

Presentation Number **LBAP 017**
Late Breaking Abstract Poster Session
September 19, 2013 / 15:15-15:15 / Room: Exhibit Hall B

Cross-linked Polyacrylamide Hydrogel Nanoparticles: New Molecular Imaging Agents for MRI and Positron Emission Tomography

Alexander G. White[1], *Jacques Lux*[2], *Minnie Chan*[2], *Adah Almutairi*[2], *Carolyn J. Anderson*[1], [1]*Molecular Imaging Laboratory, Department of Radiology, University of Pittsburgh, Pittsburgh, PA, USA;* [2]*Laboratory of Bioresponsive Materials in Therapy and Imaging, Departments of Nanoengineering and Materials Science, University of California San Diego, San Diego, CA, USA. Contact e-mail: whiteag@upmc.edu*

In recent years, increasing attention has been given to nanotechnologies within the fields of medical sciences and molecular imaging. Nanostructures of varying composition have been synthesized as both drug delivery agents and imaging tools. We hypothesize that utilization of molecular imaging agents that take advantage of the sensitivity of PET and the resolution of MRI would be supremely useful in the diagnosis of metastasis. In addition, a theranostic approach, which can not only diagnose metastasis, but also eradicate metastatic lesions, is an even more attractive feature. Thus, our group has engineered polyacrylamide-based nanogels incorporating DOTA-based chelates as crosslinkers that function as contrast agents for MRI (Gd^{3+}) or PET (^{64}Cu) and potentially also as carriers of radiotherapeutic agents, such as ^{177}Lu. The nanogels were synthesized through an inverse emulsion process using ammonium persulfate as the initiator and tetramethylenediamine to control the radical polymerization rate. Unlabeled nanogels were characterized by dynamic light scattering and yielded a hydrodynamic size of 55 to 165 nm with a polydispersity index value of 0.22. To our knowledge, our design is the first to utilize a DOTA chelating group as the crosslinker, which we believe contributes to the high stability of Gd^{3+} and ^{64}Cu nanogel complexes. The stability of Gd^{3+} chelated nanogels was confirmed by measuring the paramagnetic longitudinal relaxation rate in the presence of Zn^{2+} in a 1:1 ratio. After 60 h, no release of Gd^{3+} was observed, confirming that DOTA Gd^{3+} nanogels can be safely used as MRI contrast agents. To evaluate the stability of ^{64}Cu-DOTA nanogels, radio-TLC scans were taken of samples incubated with 0, 2.5 and 5 x molar amounts of EDTA relative to the ^{64}Cu-DOTA complex. After 24 h, <10% of ^{64}Cu was dissociated from DOTA nanogels by EDTA at 2.5 x the chelator concentration and approximately 20% was dissocated at 5 x chelator concentration. Samples incubated without EDTA were completely stable over the 24 h period. To visualize in vivo stability of ^{64}Cu-DOTA nanogels, Balb/C mice were given nanogels i.v. and imaged three times over a period of 24 h. Primary uptake of the nanogels was visualized in the heart and liver through 24 h, which we believe indicates these nanogels have a moderately long circulation half-life and are cleared via the hepatobiliary system from the body. Based on these data, DOTA nanogels show potential as a multimodal molecular imaging and a possible therapeutic agent. Tumor-targeting peptides will be attached for future imaging and therapy of cancer metastasis.

Disclosure of author financial interest or relationships:
A.G. White, None; **J. Lux**, None; **M. Chan**, None; **A. Almutairi**, None; **C.J. Anderson**, None.

Presentation Number **LBAP 018**
Late Breaking Abstract Poster Session
September 19, 2013 / 15:15-15:15 / Room: Exhibit Hall B

Self-illuminating 64Cu doped quantum dots for in vivo multimodal imaging

Xiaolian Sun, *Xinglu Huang, Jinxia Guo, Dale O. Kiesewetter, Gang Niu, Xiaoyuan Chen, Laboratory of Molecular Imaging and Nanomedicine (LOMIN), National Institute of Biomedical Imaging and Bioengineering (NIBIB),, National Institutes of Health (NIH), Bethesda, MD, USA. Contact e-mail: xiaolian86@gmail.com*

Objectives: Fluorescent quantum dots are widely used as fluorescent probes for biological imaging due to their unique optical properties. However, the use of existing quantum dots requires the excitation from external illumination sources and this is challenging for in vivo imaging because of the strong autofluorescence background arising from ubiquitous endogenous chromophores as well as the light-absorption and light-scattering properties of tissue. The objective of this research is to design self-illuminating quantum dots by doping 64Cu with quantum dots. On one hand, Cerenkov luminescence from the decay of 64Cu excites the quantum dots for optical imaging in the absence of external excitation. On the other hand, doping 64Cu into quantum dots provides a "chelator-free" method to label quantum dots for in vivo nuclear imaging. Methods: 64Cu were doped into three kinds of commercial quantum dots via cation exchange reaction in organic phase. The 64Cu doped quantum dots were then coated with SH-polyethylene glycol (PEG)-NH2 and transferred into aqueous phase for further use. The luminescence spectrum of free 64Cu, quantum dots only, the mixture of free 64Cu and quantum dots as well as 64Cu doped quantum dots were obtained on an IVIS imaging system. These 64Cu doped quantum dots were then used for in vivo luminescence and PET imaging in a U87MG glioblastoma model. Results: The specific radioactivity of the quantum dots is tunable by varying the concentration of 64CuCl2 precursor. The presence of quantum dots has red-shifted the Cerenkov light from the decay of 64Cu to the emission wavelength of quantum dots. Comparing with simply mixing 64Cu and quantum dots together, doping 64Cu inside quantum dots have significantly increased the Cerenkov resonance energy transfer efficiency. These 64Cu doped quantum dots emit bioluminescent light detectable even in deep tissues and are suitable for multiplexed in vivo imaging. PET images of U87MG tumor mice after i.v. injection of 64Cu doped quantum dots revealed a gradual increased accumulation of quantum dots in the tumor over time, reaching around 10% ID/g tumor uptake at 42 h post-injection. Conclusions: We prepared 64Cu-doped quantum dots via cation exchange reaction between 64CuCl2 and quantum dots. These quantum dots have been successfully applied for in vivo luminescence and PET imaging. Combing the nuclear imaging of 64Cu and the optical properties of quantum dots, these nanoparticles can serve as a new platform for multimodality imaging.

Disclosure of author financial interest or relationships:
X. Sun, None; **X. Huang**, None; **J. Guo**, None; **D.O. Kiesewetter**, None; **G. Niu**, None; **X. Chen**, None.

Presentation Number **LBAP 019**
Late Breaking Abstract Poster Session
September 19, 2013 / 15:15-15:15 / Room: Exhibit Hall B

Image-guided liposomes targeting m-aconitase for prostate cancer treatment

Alexander L. Klibanov[2], Galina B. Diakova[2], **Anna Moore**[1], [1]*Radiology, Massachusetts General Hospital, Charlestown, MA, USA;* [2]*Cardiovascular Division, Cardiovascular Research Center,, University of Virginia School of Medicine, Charlottesville, VA, USA. Contact e-mail: amoore@helix.mgh.harvard.edu*

Therapeutic options for treatment of advanced prostate cancer are limited to hormone therapy, followed by chemotherapy and radiation therapy; those interventions lead to serious side effects. We have developed liposome carriers to deliver zinc to prostate cancer cells with the purpose of inhibiting m-aconitase responsible for converting citrate into iso-citrate in the citric acid cycle. Normal prostate epithelial cells synthesize and secrete enormously high levels of citrate into the prostatic fluid because m-aconitase is inhibited by high levels of zinc. In prostate cancer cells a dramatic drop in zinc level activates m-aconitase responsible for the malignant "citrate-oxidizing phenotype". Zn2+ transporter in these cells is downregulated. Our hypothesis is that a liposomal carrier may provide transporter-independent intracellular Zn2+ delivery. We further hypothesize that inhibition of m-aconitase with zinc will cause a dramatic decrease in energy production by cancer cells, which will result in apoptosis and ultimately lead to cell death. To this end we synthesized positively charged liposomes containing Zn2+ in the internal aqueous core, as well as liposomes carrying fluorescent dye DiI, for intracellular uptake monitoring. Liposomes were prepared by reverse phase evaporation. Briefly, 1,2-dioleoyl-sn-glycero-3-phosphocholine (DOPC), cholesterol and positively charged DSTAP lipid were dissolved in CHCl3/ether, to which a smaller volume of ZnCl2 aqueous solution was added. Alternatively, DiI was added to the control liposome formulation containing normal saline instead of ZnCl2. Water-in-oil reverse emulsion was generated by sonication. Organic solvent was then removed on a rotary evaporator. Immediately prior to cell treatment, free unincorporated ZnCl2 was removed by centrifugation. The liposome formulation stock used for cell treatment contained 9.6 mg/ml DOPC and 0.465 mg/ml Zn2+ (7.15mM), as determined by colorimetric assays. Mean particle size was ~250 nm, as determined by dynamic laser light scattering. Zn-liposomes as well as control DiI-labeled liposomes were incubated with DU145 androgen-independent human prostate cancer cells and with SW620 human colon cancer cells (control) for 18 hours. MTT assay demonstrated dramatic kill of DU145 cells after incubation with Zn-liposomes (Fig. 1). In contrast, cell viability was virtually unchanged in DU145 cells incubated with empty liposomes or in SW620 colon cancer cells incubated with both preparations. These results demonstrate the potential of our approach to inhibit m-aconitase specifically in prostate cancer cells since no effect was seen in colon cancer cells. Additional proof of liposome uptake by the cells was obtained by fluorescence microscopy with DiI-labeled liposomes (Supplemental material). The uptake was obvious already 2 hrs after incubation (punctate staining of the cell membrane) followed by release of liposome content in the cytosol and the distribution of liposomal DiI within the cells, as it is well known for lipofectin liposomes. We are in the process of obtaining in vivo data with Gd-tagged zinc-loaded liposomes in an animal model of prostate cancer.

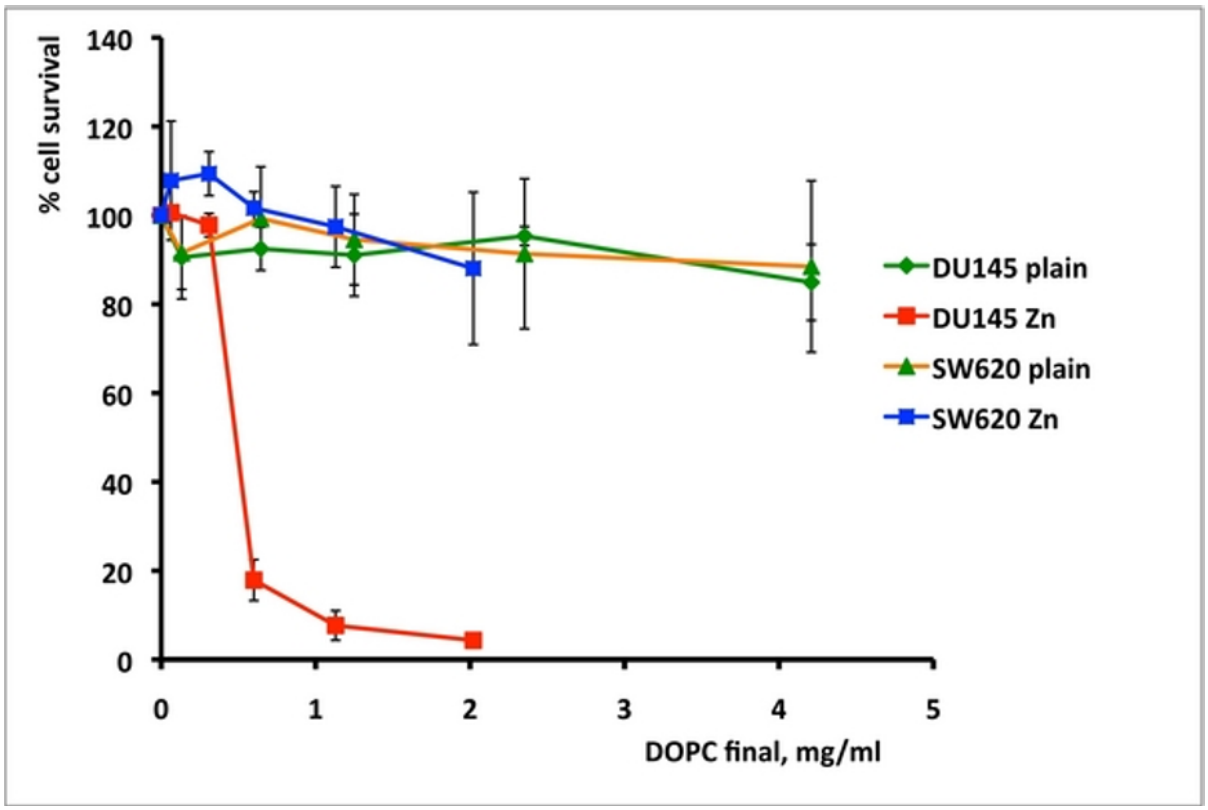

Fig. 1. MTT assay showing nearly complete prostate cancer cell kill after incubation with Zn-loaded liposomes. A: Cell survival as a function of lipid concentration; B: Cell survival as a function of zinc concentration.

Disclosure of author financial interest or relationships:

A.L. Klibanov, Philips Research North America, Grant/research support; Targeson (NIH SBIR subcontract), Grant/research support; Targeson, Stockholder; AstraZeneca, Grant/research support; **G.B. Diakova**, None; **A. Moore**, Fluoropharma, Grant/research support .

Presentation Number **LBAP 020**
Late Breaking Abstract Poster Session
September 19, 2013 / 15:15-15:15 / Room: Exhibit Hall B

Silica-coated manganese oxide nanoparticles as a platform for multifunctional imaging

He Hu[1,2], *Hong Yang*[1], *Shiping Yang*[1], *Silvio Aime*[2], [1]*Department of Chemistry, Shanghai Normal University, Shanghai, China;* [2]*Molecular Imaging Center, University of Torino, Torino, Italy. Contact e-mail: huheandy@gmail.com*

1. Introduction Manganese (II)-based nanoparticles (NPs) demonstrated to be a new kind of promising T1-weighted magnetic resonance imaging (MRI) contrast agents. The manganese (II) ion has relatively high electronic spins (five unpaired d electrons) and fast water exchange rates. On the other hands, silica has been widely used to protect the core NPs from the external environment, thereby improving the stability of the NPs. In addition, silica is highly biocompatible and its surface can be easily modified with amines, thiols, and carboxyl groups, which enables covalent modification of the particle surfaces with biological molecules. Therefore, silica-coated manganese oxide core/shell NPs would offer a great promising platform for functionalized imaging. 2. Methods The Mn3O4@SiO2 core/shell NPs were firstly prepared by encapsulating hydrophobic Mn3O4 core within amino functionalized silica shell by reversed microemulsion method. The fluorophore Rhodamine (RB) were doped in the silica shell and amphiphilic polymer poly(ethylene glycol) (PEG) were modified on the surface of the shell to improve biocompatibility, then the folate acid (FA) or apatmer AS411 were conjugated on the end of the PEG chain as targeting ligands. The final NPs were abbreviated as Mn3O4@SiO2(RB)-PEG-Apt (or FA). 3. Results: The formed Mn3O4@SiO2(RB)-PEG-Apt (or FA) core-shell NPs are water-dispersible, stable, and biocompatible when the particle concentration is below 1000 mg/mL as confirmed by cellular cytotoxicity assay. Relaxivity measurements showed that the core-shell NPs have a T1 relaxivity (r1) of 0.53 mM-1 s-1 on the 0.5 T scanner. Combined flow cytometry, confocal microscopy, and MRI in vitro studies showed that the Mn3O4@SiO2(RB)-PEG-Apt (or FA) NPs could specifically target cancer cells. By further using AS1411-conjugated Mn3O4@SiO2 NPs for in vivo MRI and quantitative biodistribution, the results demonstrated the NPs could actively targeted accumulate in tumor site. The in vivo toxicity investigation suggested the NPs could be used safely for long term body tracking. 4. Conclusions: We demonstrate a biocompatible magneto-fluorescent T1 MRI contrast agent for targeted MRI and fluorescence imaging of both in vitro (cancer cells) and in vivo (animal tumor model) based on silica-coated Mn3O4 NPs. Findings from this study suggest that the silica-coated Mn3O4 core-shell NPs could be used as a platform for multifunctional imaging (both magnetic resonance and fluorescence) in various biological systems. Acknowledgement: The Marie Curie Action of the Seventh Framework Programme of Europe Union (PIIF-GA-2011-298821). National Natural Science Foundation of China (51102171). Reference: 1. Yang H, Zhuang Y, Hu H, Du X, Zhang C, Shi X, Wu H, Yang S (2010) Silica-Coated Manganese Oxide Nanoparticles as a Platform for Targeted Magnetic Resonance and Fluorescence Imaging of Cancer Cells. Adv Funct Mater 20 (11):1733-1741 2. Hu H, Xiong L, Zhou J, Li F, Cao T, Huang C (2009) Multimodal Luminescence Core-shell Nanocomposites for Targeted Imaging of Tumor Cells. Chem Eur J 15:3577-3584

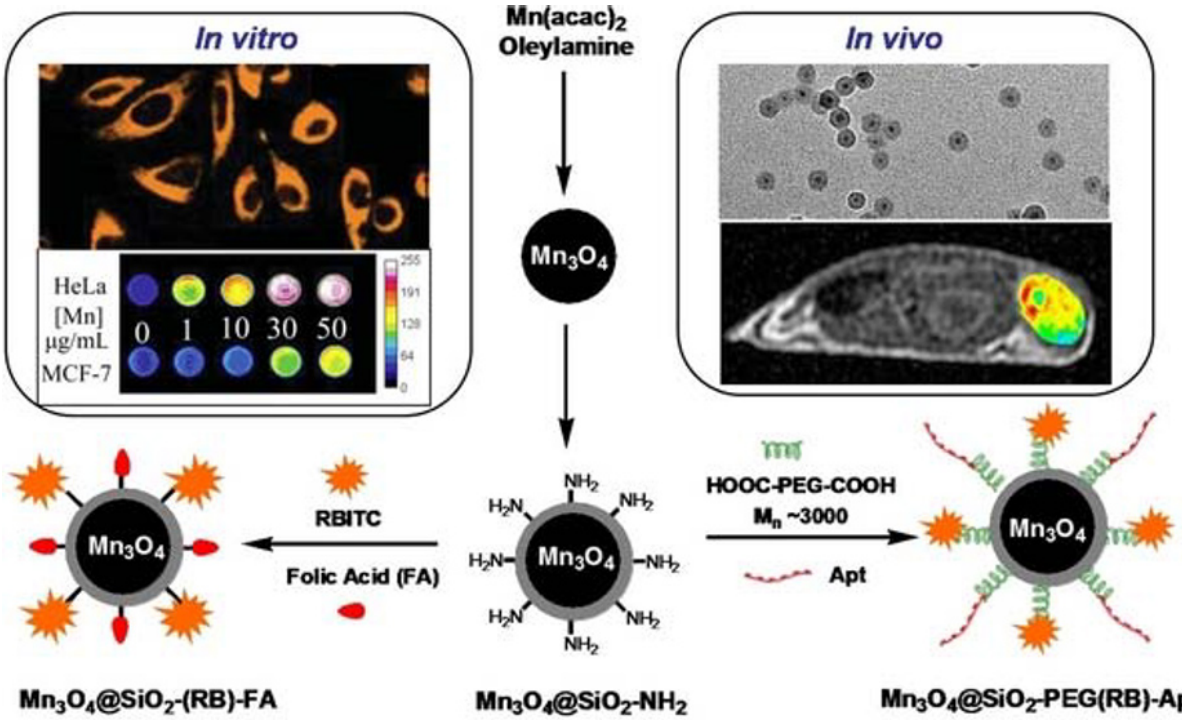

Figure 1. Mn3O4@SiO2(RB)-PEG-Apt (or FA) has been successful employed as promising bimodal fluorescence and T1-MRI probe for both in vitro (cancer cells) and in vivo (animal tumor model) imaging.

Disclosure of author financial interest or relationships:
H. Hu, None; **H. Yang**, None; **S. Yang**, None; **S. Aime**, None.

Presentation Number **LBAP 021**
Late Breaking Abstract Poster Session
September 19, 2013 / 15:15-15:15 / Room: Exhibit Hall B

Activatable Imaging of Human Colorectal Carcinoma Cell Line with a Tunable Near Infrared and Magnetic Nanoplatform

Don N. Ho, *Danielle R. McCauliffe, Xiaoyuan Chen, National Institute of Biomedical Imaging and Bioengineering, National Institutes of Health, Bethesda, MD, USA. Contact e-mail: Don.Ho@NIH.gov*

Our gold-iron oxide hybrid nanoparticle platform is designed for magnetic and optical near infrared activation of imaging agents and controlled delivery. Magnetic iron oxide is attenuated in an alternating magnetic field for controlled delivery with the addition of the NIR active gold component. Here we demonstrate the application of an external alternating magnetic field as a non-invasive, activatable imaging agent in collaboration of gold as a tunable NIR delivery source. Heterostructure nanoplatforms provide physical and chemical properties of each individual component packaged into a single unit at subcellular scales. The advantages of controlling these tools have yet to be realized in clinical applications. Our gold-iron oxide nanostructure provides a controllable method to be activated by non-invasive techniques of an alternating magnetic field and near infrared excitation. These controls allow MRI and NIR imaging as well as the potential for controlled release and delivery of imaging agents. Our examination of these materials shows the controlled activation of imaging agent and potential use as a diagnostic and surgical aid. Our multimodal imaging approach offers a platform to deliver imaging agents as well as the potential for therapeutic delivery and monitoring. We are currently examining the delivery and monitoring of therapeutics utilizing the near infrared and magnetic imaging platform.

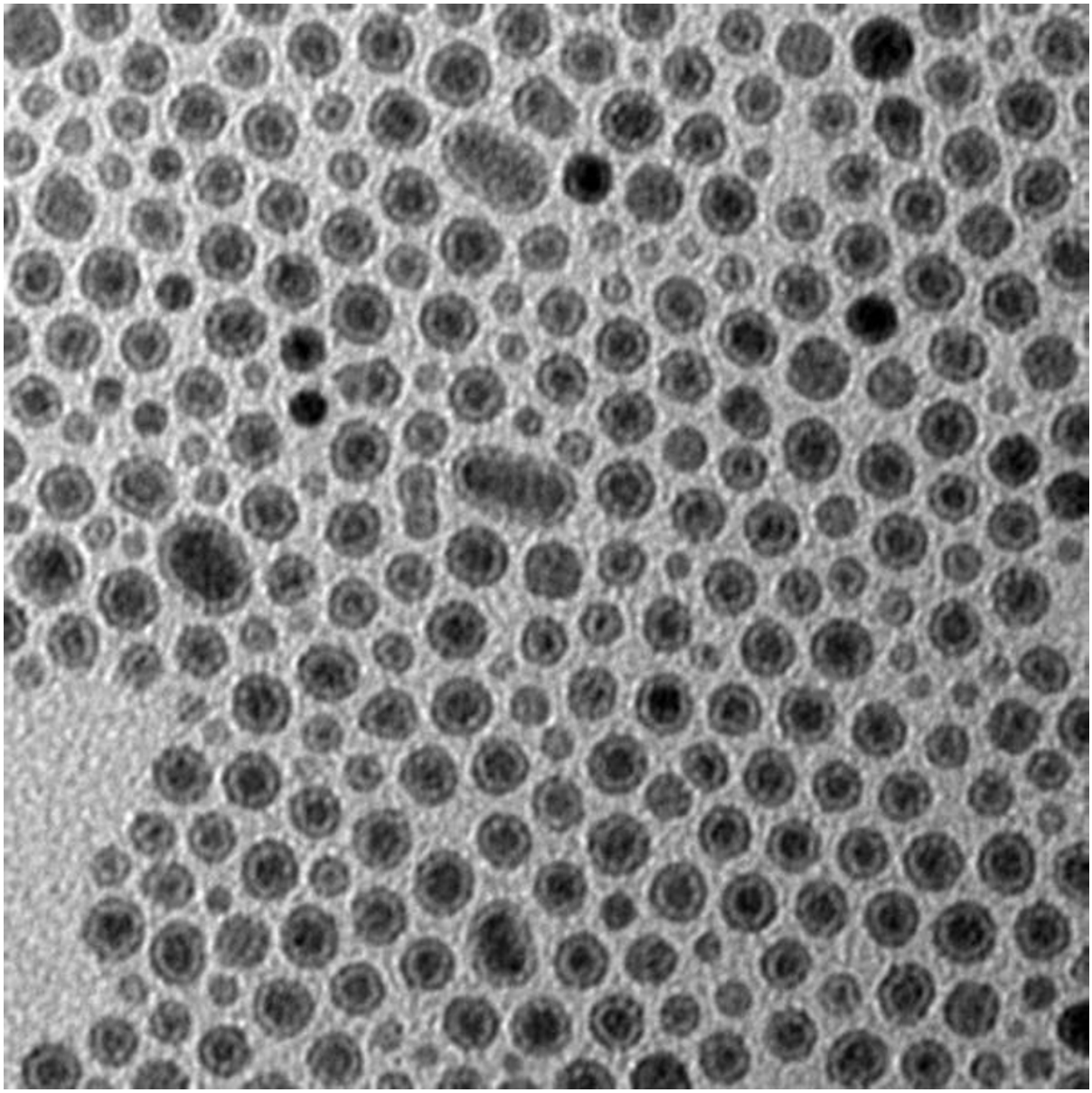

As synthesized gold-iron oxide hybrid nanoplatform

Disclosure of author financial interest or relationships:
D.N. Ho, None; **D.R. McCauliffe**, None; **X. Chen**, None.

Presentation Number **LBAP 022**
Late Breaking Abstract Poster Session
September 19, 2013 / 15:15-15:15 / Room: Exhibit Hall B

A pilot study on glucagon-like peptide 1 receptor (GLP-1R) targeted PET imaging of beta-cell mass (BCM) in Ossawbaw mini-pigs

William Silvers[1], *Saleh Ramezani*[1], *Su-Tang Lo*[1], *Amit Kumar*[1], *Jung-Mo Ahn*[2], *Bikash Manandhar*[2], *Ildiko Lingvay*[3], *Jon A. Anderson*[1], *Xiankai Sun*[1], *Orhan K. Öz*[1], [1]*Radiology, University of Texas Southwestern Medical Center, Dallas, TX, USA;* [2]*Department of Chemistry, University of Texas Dallas, Dallas, TX, USA;* [3]*Department of Clinical Science, University of Texas Southwestern Medical Center, Dallas, TX, USA. Contact e-mail: william.silvers@utsouthwestern.edu*

Within the pancreas the transmembrane G-coupled protein glucagon-like peptide receptor (GLP-1R) is uniquely expressed on beta cells. The ability to noninvasively measure and monitor relative changes in GLP-1R density would aid in the evaluation of progression and treatment response in patients with Type-1 and Type-2 diabetes. There is great difficulty in obtaining accurate quantitative measurements of the beta cell mass (BCM) in the pancreas with most non-invasive imaging. The small size of the islets of Langerhans, where beta cells reside, and the low quantity of beta cells in the pancreas (1 - 2% by weight) pose significant challenges. Positron emission tomography (PET) has superior sensitivity over other imaging techniques and has become widely used to probe biological events at cellular levels in live subjects. Its imaging specificity is rendered with specific probes. Though rodents are most commonly used in animal studies, their pancreatic anatomy differs greatly from human. Given that the pig pancreas closely approximates the human pancreas in anatomy and density we believe it is good model for pre-clinical translation imaging studies. The PET tracer we have chosen to image BCM consists of a NOTA core that selectively forms an inert complex with 68Ga (t1/2 = 68 min; β+: 90%) and is conjugated to a GLP-1R targeting peptide, EM2198. This peptide is an analogue of the endogenous GLP-1R ligand, GLP-1, with remarkably enhanced in vivo stability while maintaining specific GLP-1R binding affinity. To test the efficacy of 68Ga-EM2198 in targeting the pancreas, PET-CT imaging of the abdomen was performed as a CT scan followed by dynamic PET imaging over the abdomen immediately after injection of the radiotracer. The initial results of PET imaging in six minipigs with 68Ga-EM2198 demonstrated more rapid uptake into the pancreas as compared to the surrounding organs, leading to a reasonably high target-to-background contrast. For example, the ratio of pancreas to muscle uptake was 3.9 and pancreas to liver was 2.0. Similar to the distribution of islets in the human pancreas, uptake of the tracer varied within the major lobes of the porcine pancreas. Interestingly, lower PET signal was found within pancreatic areas of greater fat density. Pharmacokinetic modeling was applied to the PET data. Best estimates of distribution volume (VD) were obtained using the image derived input function (VD=2.05±0.4 mL/g). The binding potential, which is directly related to specific binding, was calculated as the rate of exchange between two compartments (BP=3.0±1.7). The intraclass correlation coefficient (ICC) test for consistency between the 3 readers yielded high consistency for each observer (ICC = 0.92) and low variation between observers (ICC = 0.86). From the results obtained thus far, we believe targeting GLP-1R with 68Ga-EM2198 may provide an excellent approach for non-invasive assessment of BCM.

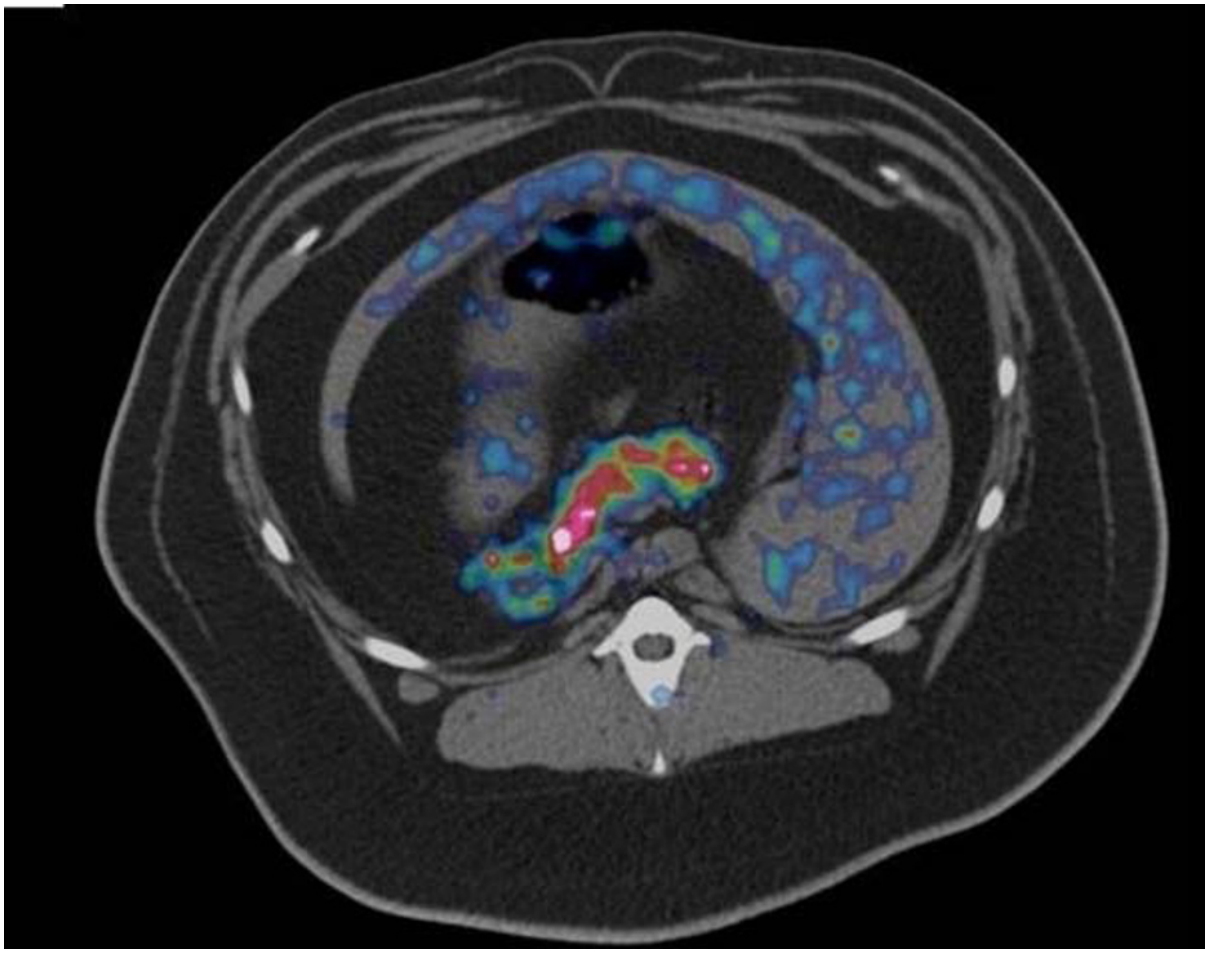

Disclosure of author financial interest or relationships:
W. Silvers, None; **S. Ramezani**, None; **S. Lo**, None; **A. Kumar**, None; **J. Ahn**, None; **B. Manandhar**, None; **I. Lingvay**, None; **J.A. Anderson**, None; **X. Sun**, None; **O.K. Öz**, None.

Presentation Number **LBAP 023**
Late Breaking Abstract Poster Session
September 19, 2013 / 15:15-15:15 / Room: Exhibit Hall B

Imaging fibroblast activation protein alpha expression using PET and Cerenkov luminescence imaging

Archibald Paillard[2], Darpan N. Pandya[2], Dongqin Zhu[3], Hong Yuan[4], Akiva Mintz[3], **Thaddeus J. Wadas[1]**, *[1]Radiology, Wake Forest School of Medicine, Winston-Salem, NC, USA; [2]Cancer Biology, Wake Forest School of Medicine, Winston-Salem, NC, USA; [3]Neurosurgery, Wake Forest School of Medicine, Winston-Salem, NC, USA; [4]Radiology, University of North Carolina at Chapel Hill, Chapel Hill, NC, USA. Contact e-mail: twadas@wakehealth.edu*

Introduction: Fibroblast activation protein alpha (FAP) is a serine protease involved with matrix remodeling that is expressed in over 90% of human epithelial cancers. The goal of this work was to characterize ^{89}Zr-DFO-F19 mAb and evaluate its potential as a PET and Cerenkov Luminescence Imaging (CLI) agent for FAP *in vivo*. **Methods:** ^{89}Zr-DFO-F19 was prepared according to standard protocols. Stability studies were conducted in human serum at physiological temperature for 7 days. The immunoreactivity and K_a of ^{89}Zr-DFO-F19 were determined using the Lindmo Method and the U87mg cell line, which demonstrates the highest endogenous FAP expression among available cancer cell lines. CLI was conducted using known procedures. Briefly, athymic nude mice (n = 6) bearing U87mg tumors xenograft tumors on the flanks received ^{89}Zr-DFO-F19 (11 MBq, (300 μCi)) and animals were imaged at 6, 24, 48 and 72 h p.i. using the fluorescence setting on an IVIS 100 optical imaging system (300 s integration time; f/stop, 1; binning, medium; field of view, B), with no light interference from the excitation lamp. Spectral analysis was obtained by measuring the optical images either with or without the use of a narrow band filter (560, 580, 600, 620, 640, and 680, or open filter) of 20 nm in full width at half maximum. **Results:** ^{89}Zr-DFO-F19 mAb was radiolabeled in high radiochemical purity and with a specific activity of 158.3 ± 1.6 MBq/mg (4.28 ± 0.04 mCi / mg, n = 6). The radiopharmaceutical remained intact in human serum at 37°C during a 6 day stability study, and Lindmo analysis revealed a K_a value of 3.03 x$10^{-8}M^{-1}$, an immunoreactive fraction of 52%, and 1.6 x 10^5 antibody molecules bound per cell. CLI imaging of female nude mice implanted with U87mg tumors in the flank revealed increasing accumulation of activity in the tumor with a concomitant decrease in background over time. *Ex vivo* analysis revealed substantially greater uptake in tumors than in other tissues such as liver, kidney, muscle or bone. **Conclusion:** ^{89}Zr-DFO-F19 represents a novel PET radiopharmaceutical for FAP positive tumors, which can be prepared in high radiochemical purity and specific activity. CLI imaging confirmed localization within tumor xenografts but not in FAP negative tissues. Biodistribution and small animal PET imaging results that corroborate the CLI and *in vitro* data will also be discussed.

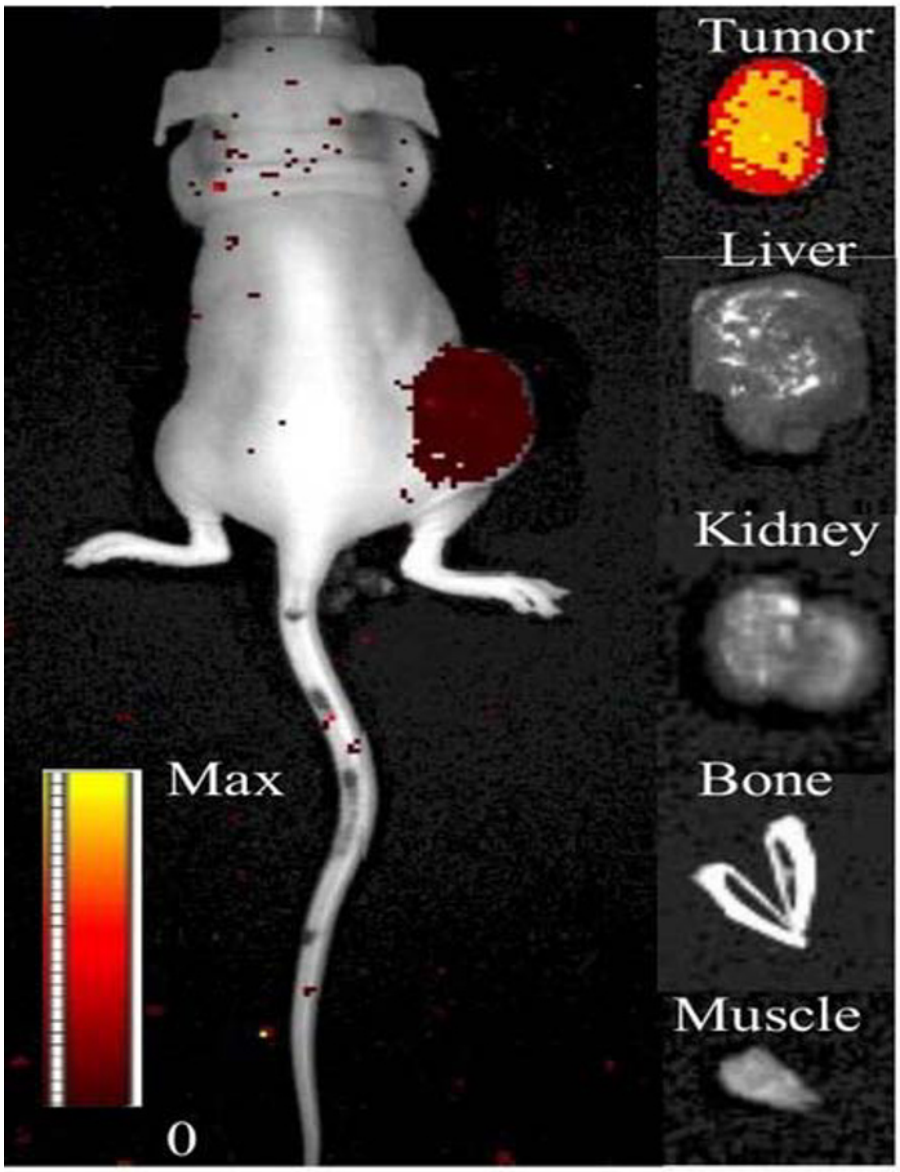

Figure 1. (Left) CLI image of a female nude mouse bearing a FAP^+ U87mg tumor xenograft. **(Right)** *Ex vivo* CLI image of tumor and selected tissues. Radiotracer accumulation was observed in FAP^+ tissue but not FAP^- tissue.

Disclosure of author financial interest or relationships:
A. Paillard, None; **D.N. Pandya**, None; **D. Zhu**, None; **H. Yuan**, None; **A. Mintz**, None; **T.J. Wadas**, None.

Presentation Number **LBAP 024**
Late Breaking Abstract Poster Session
September 19, 2013 / 15:15-15:15 / Room: Exhibit Hall B

^{89}Zr-Oxine Complex: a Long-Lived Radiolabel for Cell Tracking Using PET

Levente K. Meszaros[1], *Putthiporn Charoenphun*[1], *Krisanat Chuamsaamarkkee*[1], *James R. Ballinger*[1,2], *Greg Mullen*[1], *Trevor J. Ferris*[3], *Michael J. Went*[3], *Phil Blower*[1], [1]*Department of Imaging Chemistry and Biology, King's College London, London, United Kingdom;* [2]*Department of Nuclear Medicine, Guy's and St Thomas NHS Foundation Trust, London, United Kingdom;* [3]*School of Physical Sciences, University of Kent, Canterbury, Canterbury, United Kingdom. Contact e-mail: levente.meszaros@kcl.ac.uk*

Introduction: ^{111}In-tris(oxiquinoline) (^{111}In-oxine) has been in clinical use for decades as a long-lived radiolabel for tracking leukocytes for scintigraphic imaging of inflamed foci. A positron emitting radiolabel for cell tracking has long been sought after in order to utilise the improved resolution and quantification offered by PET to detect smaller disease foci. ^{18}F-FDG and ^{64}Cu-PTSM have been evaluated for this purpose but do not meet the requirements. Since the need for reliable high quality cell tracking is increasing with new applications in stem cell therapy and biology of immune cells, longer half life tracers with more reliable labelling and cellular retention are needed. In this study we have synthesised a novel compound ^{89}Zr-tetrakis(oxine) (^{89}Zr-oxine) and evaluated its cell labelling performance *in vitro* and *in vivo* by PET imaging using the 5T33 murine multiple myeloma model, and compared it to ^{111}In-oxine SPECT. After initial margination in lungs intravenously administered 5T33 myeloma cells are known to home exclusively in the spleen, liver and skeleton (*i.e.* haemopoietic niches) of C57Bl/KaLwRij mice. **Experimental:** Labelling efficiencies were evaluated in eGFP-5T33 cells (10^7 cells, n=4, 30 min labelling time). For *in vivo* evaluation cells were radiolabelled with ^{111}In-oxine or ^{89}Zr-oxine and injected intravenously into six-week old C57Bl/KaLwRij mice; approx. 1MBq for *ex vivo* tissue counting (n=4/tracer) and 6 MBq (^{89}Zr) or 10 MBq (^{111}In) for imaging (n=1/tracer). Mice were sacrificed 7 days post-inoculation for *ex vivo* tissue counting. One mouse from each group was imaged for up to 7 days (^{111}In) or 4 days (^{89}Zr). **Results:** Cell labelling yields for ^{111}In-oxine and ^{89}Zr-oxine were 82±6% and 32±1%. Biodistribution patterns of eGFP-5T33 cells labelled with ^{111}In-oxine and ^{89}Zr-oxine were very similar: radioactivity accumulated predominantly in the liver, spleen and skeleton whilst uptake in most other tissues and organs remained low (Fig. 1). We recovered significantly more activity from the kidneys of mice injected with 111In-oxine labelled cells than from those inoculated with the PET tracer ($p<0.99$); this was consistent with imaging data (Fig. 1). This is likely to be caused by ^{111}In released from labelled cells *in vivo*. Intravenously injected ^{89}Zr-oxalate and ^{89}Zr released from labelled compounds are known to accumulate in the skeleton. This could account for observed skeletal uptake of ^{89}Zr. However, data presented in Fig. 1d suggest that the organ-to-organ ratios with different tracers did not differ significantly suggesting that skeletal activity in mice inoculated with ^{89}Zr-oxine labelled cells is attributable to radiolabelled cells homing in the bone marrow, and the overall biodistribution of ^{89}Zr reflects the cell distribution rather than released ^{89}Zr. **Conclusions:** Cell radiolabelling yield with ^{89}Zr-oxine was adequate. At least in this model ^{89}Zr-oxine labelled cells presented higher *in vivo* stability than those labelled with ^{111}In-oxine. Radiobiological effects on labelled cells are yet to be determined but ^{89}Zr-oxine is a promising agent for cell labelling and prolonged tracking *in vivo* using PET.

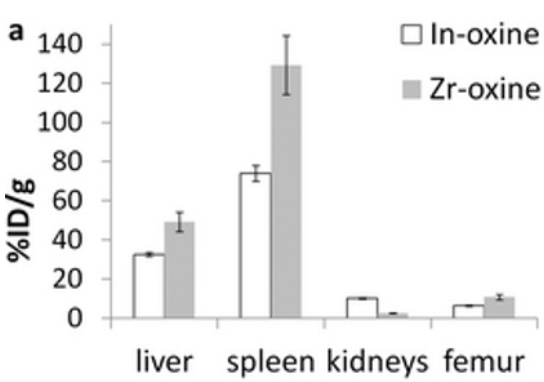

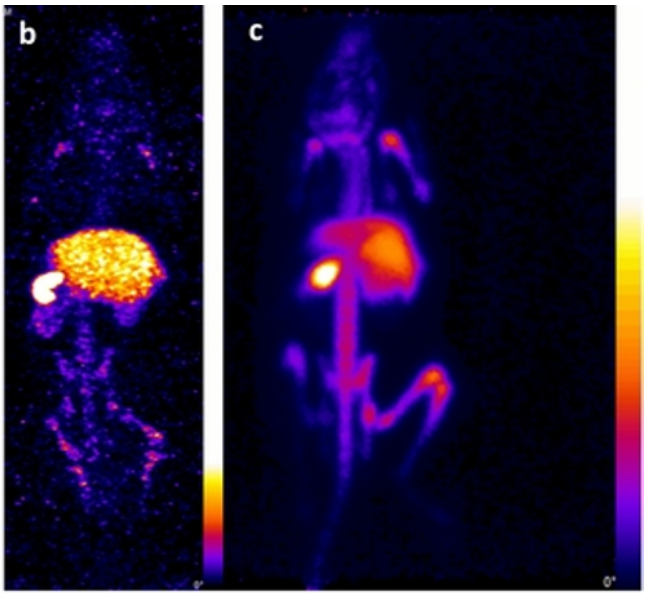

d

	In-oxine	Zr-oxine
liver:femur	5.1±0.3	4.6±0.8
spleen:femur	11.7±0.9	12.0±2.1
liver:spleen	0.44±0.03	0.38±0.06

Fig. 1: tissue distribution of ^{111}In-oxine and ^{89}Zr-oxine labelled eGFP-5T33 cells at major sites of uptake 7 days after inoculation (n=4, mean±SEM); b: SPECT scan acquired 7 days after inoculation with ^{111}In-oxine labelled eGFP-5T33 cells; c: PET scan acquired 4 days after inoculation with ^{89}Zr-oxine labelled eGFP-5T33 cells; d: table comparing organ(%ID/g)-to-organ(%ID/g) ratios with different tracers.

Disclosure of author financial interest or relationships:
L.K. Meszaros, None; **P. Charoenphun**, None; **K. Chuamsaamarkkee**, None; **J.R. Ballinger**, GE Healthcare, Grant/research support; Imaging Equipment Ltd, Grant/research support; **G. Mullen**, Mediso, Consultant; **T.J. Ferris**, None; **M.J. Went**, None; **P. Blower**, None.

Presentation Number **LBAP 025**
Late Breaking Abstract Poster Session
September 19, 2013 / 15:15-15:15 / Room: Exhibit Hall B

Visualization of the Effect of Reboxetine on the Noradrenaline Concentration in the Rat Brain using ^{11}C-yohimbine

*Vincent Keereman[1], **Nick Van Laeken**[3], Stefaan Vandenberghe[1], Christian Vanhove[1], Filip J. De Vos[3], Robrecht Raedt[2], [1]MEDISIP - Department of Electronics and Information Systems, Ghent University - iMinds, Ghent, Belgium; [2]Laboratory for Clinical and Experimental Neurophysiology, Neurobiology and Neuropharmacology - Department of Neurology, Ghent University, Ghent, Belgium; [3]Laboratory of Radiopharmacy, Ghent University, Ghent, Belgium. Contact e-mail: nick.vanlaeken@Ugent.be*

INTRODUCTION Changes in endogenous noradrenaline concentrations are associated with neuropsychiatric disorders such as depression and schizophrenia. Non-invasive visualization of the endogenous noradrenaline concentration would be of interest for the investigation of these disorders and the development of new therapies. The feasibility of using the uptake of the radiolabeled alpha2-adrenoreceptor antagonist ^{11}C-yohimbine as a measure of endogenous noradrenaline concentration has been proposed by Landau et al., showing decreased uptake in the pig brain after amphetamine challenge. However, amphetamine is a non-selective noradrenergic agent also affecting the dopaminergic system. Furthermore, validation of this tracer in rats is also of interest. In the present study we have evaluated the feasibility of using ^{11}C-yohimbine to visualize the increase in noradrenaline concentration in the rat brain after administration of reboxetine, a selective noradrenaline reuptake inhibitor. MATERIALS AND METHODS Six Wistar rats (male, 300-350g) were anesthetized using isoflurane. PET-CT acquisitions were performed on a TriFoil Triumph II system. Dynamic PET acquisitions of 90 min were started directly after i.v. administration of 61±11 MBq of ^{11}C-yohimbine (1.6±0.6 µg/kg), followed by a CT. Two scans were acquired from each rat: at baseline and 30 min after i.v. administration of 1 mg/kg reboxetine. Afterwards, T1-weighted MR images were acquired on a Bruker Pharmascan 7T and coregistered to the PET-CT images. Ten volumes of interest (VOIs - listed in table 1) were drawn on the MR images. The PET data was split up into 31 frames and reconstructed using the 3D maximum likelihood - expectation maximization algorithm with CT-based attenuation correction. The reconstructed PET images were normalized for decay, injected activity and animal weight to obtain standardized uptake values (SUVs). For statistical evaluation, the average normalized reconstructed PET activity between 15 and 45 min after ^{11}C-yohimbine injection was calculated for each scan. A pairwise Student's t-test was used to determine statistically significant differences between baseline and reboxetine scans ($p < 0.05$). RESULTS Fig. 1 shows the average time-activity curves for both groups. The average SUV in the complete brain between 15 and 45 min was 0.061±0.009 and 0.056±0.007 in the baseline and reboxetine scans respectively. The average pairwise differences are shown in table 1. Significant differences were observed in the complete brain and in the bilateral cortex and hippocampus, striatum and thalamus as well as the right amygdala, entorhinal cortex and piriform cortex. No significant differences were observed in the cerebellum and the brainstem. CONCLUSION Reboxetine 1 mg/kg induces a decrease in uptake of ^{11}C-yohimbine in the rat brain of approximately 9% compared to baseline. It has been shown that at this dose reboxetine increases the endogenous noradrenaline concentration without affecting other neurotransmitter systems. Based on these results, we believe that ^{11}C-yohimbine uptake can be used as a marker for the endogenous noradrenaline concentration in the rat brain.

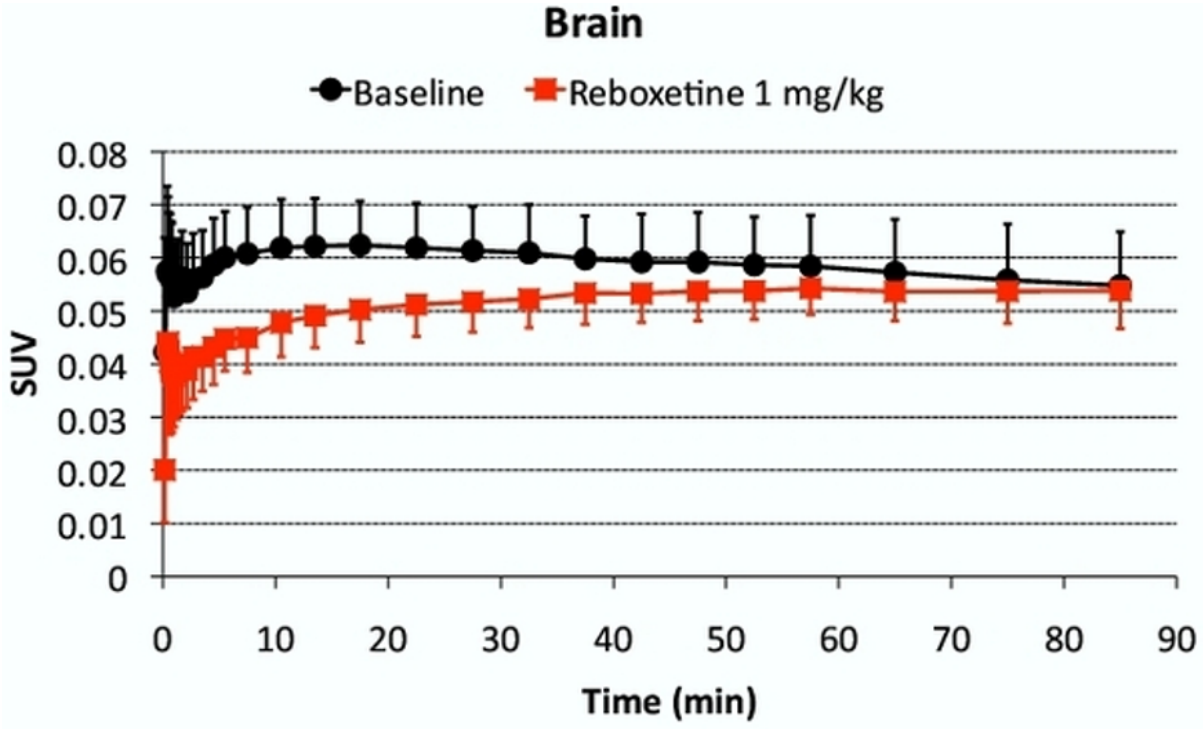

Average time-activity curves in a whole-brain VOI of ^{11}C-yohimbine PET scans performed at baseline and 30 min after administration of 1 mg/kg reboxetine.

Structure	Average difference (SUV)
Complete brain	-0.0053±0.0070*
Right cortex	-0.0074±0.0054*
Left cortex	-0.0041±0.0033*
Right hippocampus	-0.0085±0.0070*
Left hippocampus	-0.0086±0.0051*
Right amygdala/entorhinal cortex/piriform cortex	-0.0032±0.0030
Left amygdala/entorhinal cortex/piriform cortex	-0.0044±0.0040*
Striatum	-0.0091±0.0062*
Thalamus	-0.0046±0.0070*
Cerebellum	-0.0025±0.0048
Brainstem	-0.0012±0.0033

Average pairwise SUV difference in the complete brain and 10 VOIs between 15 and 45 min after ^{11}C-yohimbine injection. Statistically significant differences ($p < 0.05$) are marked with an asterisk.

Disclosure of author financial interest or relationships:
V. Keereman, None; **N. Van Laeken**, None; **S. Vandenberghe**, None; **C. Vanhove**, None; **F.J. De Vos**, None; **R. Raedt**, None.

Presentation Number **LBAP 026**
Late Breaking Abstract Poster Session
September 19, 2013 / 15:15-15:15 / Room: Exhibit Hall B

Sodium [^{18}F]Tetrafluoroborate ([^{18}F]BF4) as a sodium/iodide symporter gene therapy reporter probe: synthesis and effect of specific activity in a C6 glioma xenografted mice

Aditya Bansal[1], *Kah Whye Peng*[2], *Mukesh K. Pandey*[1], *Lukkana Suksanpaisan*[2], *Stephen J. Russell*[2], *Timothy R. DeGrado*[1], [1]*Radiology, Mayo Clinic, Rochester, MN, USA;* [2]*Molecular Medicine, Mayo Clinic, Rochester, MN, USA. Contact e-mail: bansal.aditya@mayo.edu*

Purpose Reporter gene imaging has emerged as a promising imaging strategy for non-invasive in vivo monitoring of tissue-specific gene transfer therapies or trafficking of stem cells. In this regard, the human sodium/iodide symporter (hNIS) reporter gene has shown high potential based on imaging with radioiodides or 99mTc pertechnetate. Recently, the PET radiotracer [^{18}F]BF4 was reported as a hNIS-dependent probe in a preclinical mouse model (Jauregui-Osoro et al., Eur J Nucl Med Mol Imaging 2010; 37:2108-2116). The synthesis is based on isotope exchange, limiting the specific activity to <10 GBq/mg. In this study, we developed an automated microwave-based synthesis method for [^{18}F]BF4 and evaluated the effect of specific activity in a C6 glioma xenograft mouse model. Methods [^{18}F]BF4 was prepared by isotope exchange in 0.5M HCl at 130°C for 10 min followed by neutralization on a Dionex OnGuard AG SPE cartridge and fluoride separation on two Waters neutral alumina SPE cartridges. Dynamic PET imaging was performed in hNIS-expressing C6 glioma xenografted mice following retroorbital injection ~1.1 MBq Na[^{18}F]BF4. PET scans were acquired for 60 min followed by an X-ray scan using the GENISYS4 PET imaging system (Sofie Biosciences, CA). The images from 14 hNIS-expressing C6 glioma xenografted mice were analyzed for Standardized Uptake Value in tumor, stomach, thyroid and bladder using AMIDE. Results [^{18}F]BF4 was prepared in 12-25% radiochemical yield (uncorrected) and specific activity 5-150 GBq/mg. Specific hNIS-mediated uptake was seen in thyroid, stomach and hNIS-expressing tumors. Extensive urinary clearance was also observed. Significant decreases in tumor and thyroid SUVs were noted when the injected mass dose of BF4 exceeded 1-2 mg/kg. Conclusion [^{18}F]BF4 was prepared with moderate specific activity via a microwave-assisted procedure. The PET images showed excellent properties for imaging of hNIS expressing tissues, although extensive urinary excretion was noted. Dependence of tumor and thyroid uptake on [^{18}F]BF4 specific activity should be considered in standardization of radiotracer preparations and expiration times. Further work is required in humans to determine the effect of specific activity.

Disclosure of author financial interest or relationships:
A. Bansal, None; **K. Peng**, None; **M.K. Pandey**, None; **L. Suksanpaisan**, None; **S.J. Russell**, None; **T.R. DeGrado**, None.

Presentation Number **LBAP 027**
Late Breaking Abstract Poster Session
September 19, 2013 / 15:15-15:15 / Room: Exhibit Hall B

Glucosamine based PET imaging agent for epithelial cancer diagnosis

David Ranganathan[1], *Sanjay I. Thamake*[1], *Izabela Tworowska*[2,1], *Ebrahim Delpassand*[2,1], [1]*RITA foundation, Houston, TX, USA;* [2]*RadioMedix Inc, Houston, TX, USA. Contact e-mail: dranganathan@radiomedix.com*

Introduction: Cancer is a heterogeneous disease with activation of multiple pathways leading to higher proliferation rates. However, the hallmark of growth is energy utilization, which is supported by over expression of glucose transporters in different cancer cells. Overexpression of GLUT1 transporter is predominant in breast, lung, prostate cancer as well. F-18 labeled glucose is the only currently approved diagnostic imaging molecule towards metabolic pathway of cancer. However, the limited availability of cyclotron facilities in remote areas warrants development of a chelator based agents for on-site radiolabeling. Glucosamine is structurally homologous to glucose and have been shown to bind to GLUT1 transporters. Here we synthesized a chelator based glucosamine derivative for Ga-68 based PET imaging and validated their efficacy. Methods: 4-Aminophenyl 2-Acetamido-2-deoxy-β-D-glucopyranoside was coupled to DOTA-NHS-ester; the resulting compound is called as RMX-12-GC from here on. The compound was analyzed by ESI-MS and HPLC. Their 68Ga-labeling proceeded in 0.5M NaOAc pH=4.1 at 90oC for 10min (68Ge/68Ga generator (ITG GmbH Germany)). Radiolabeled compound was analyzed by iTLC. 68Ga-labeled RMX-12-GC conjugate was validated in vivo in several types of tumor-bearing animal models (breast cancer-SKBR3, prostate cancer-PC3, lung cancer- A549, and neuroendocrine-MiaPaCa-2). Images were acquired at 30min, 60min and 90min post injection using Genysis4 microPET camera. Results: The yield of coupling reaction was 90% and radiochemical yield was 85% without decay correction with a specific activity of 1mCi/ug. In vitro uptake of RMX-12-GC was tested in human cell lines such as SKBr3, A549 and PC3. The uptake was relatively lower than FDG due to less affinity of glucosamine towards GLUT1 transporter. In vivo studies showed high tumor-specific accumulation of tracer with no uptake by normal organs. RMX-12-GC has maximum activity accumulated in tumor at 60min as quantified by analysis of PET images. Conclusions: RMX-12-GC agent has shown very specific tumor accumulation in initial PET studies. Further studies will be done to evaluate specificity and efficacy of the molecule.

Disclosure of author financial interest or relationships:
D. Ranganathan, None; **S.I. Thamake**, None; **I. Tworowska**, None; **E. Delpassand**, RadioMedix, Stockholder .

Presentation Number **LBAP 028**
Late Breaking Abstract Poster Session
September 19, 2013 / 15:15-15:15 / Room: Exhibit Hall B

^{64}Cu-labeled Antibody Vectors for Molecular Imaging and Targeting of Epithelial Ovarian Cancer

Sai Kiran Sharma[1,2], *Melinda Wuest*[2], *Monica Wang*[2], *Suzanne Lapi*[3], *Bonnie Andrais*[2], *Lars-Oliver Klotz*[1], *Frank Wuest*[2,1], [1]*Faculty of Pharmacy and Pharmaceutical Sciences, University of Alberta, Edmonton, AB, Canada;* [2]*Department of Oncology, University of Alberta, Edmonton, AB, Canada;* [3]*Division of Radiological Sciences, Mallinckrodt Institute of Radiology, Washington University in St. Louis, St. Louis, MO, USA. Contact e-mail: saikiran@ualberta.ca*

Objective: Epithelial ovarian cancer is characterized by over-expression of CA125 that serves as a tumor marker. The present work utilizes an anti-CA125 monoclonal antibody (mAb) and single chain variable fragment (scFv) to develop targeted molecular imaging probes to evaluate CA125 expression by positron emission tomography (PET). **Methods**: The B43.13 anti-CA125 mAb and scFv were purified by affinity chromatography and evaluated for antigen binding by immunostaining, western blotting, surface plasmon resonance and flow cytometry. pSCN-Bn-NOTA [S-2-(4-Isothiocyanatobenzyl)-1,4,7-triazacyclononane-1,4,7-triacetic acid] was conjugated to anti-CA125 mAb and scFv to serve as a bi-functional chelator. ^{64}Cu was obtained from Washington University (St. Louis, MO). Ovarian cancer cell lines NIH:OVCAR3 ($CA125^+$), SKOV3 ($CA125^-$) were used for immunostaining and cell binding studies. BALB/c nu/nu mice were used to develop xenograft models with OVCAR3 and SKOV3 cells and *in vivo* radiopharmacological evaluation was performed using small animal PET. **Results**: Anti-CA125 mAb and scFv were purified in yields of 7 mg/L and 0.6 mg/L from respective cell cultures. Immunostaining with unmodified, FITC-labeled and NOTA conjugated anti-CA125 mAb and scFv showed specific binding to OVCAR3 cells and no binding to SKOV3 cells as analyzed by confocal microscopy. MALDI-TOF analysis revealed 1.4 NOTA/mAb and 1.8 NOTA/scFv. ^{64}Cu-labeling and purification by size exclusion chromatography provided anti-CA125 mAb and scFv in 72% and 65% radiochemical yields with >99% purity and specific activity of 5.3 mCi/mg and 3.0 mCi/mg respectively. Lindmo assays indicated an immunoreactivity of 92% and 53% for ^{64}Cu-labeled anti-CA125 mAb and scFv respectively. Radiolabeled mAb and scFv exhibited highly specific binding to OVCAR3 cells and virtually no binding to SKOV3 cells *in vitro* over a period of 120 min. *In vivo* radiopharmacological evaluation in xenograft mice using ^{64}Cu-labeled anti-CA125 mAb provided an SUV of 5.76 ± 0.85 in OVCAR3 tumors 24 h p.i, which could be blocked upto 50% by pre-dosing the animal with 1 mg of cold anti-CA125 mAb. An EPR based SUV of 1.8 ± 0.69 was evaluated using a ^{64}Cu-labeled non-specific isotype control to account for uptake in SKOV3 tumors 24 h p.i. ^{64}Cu-labeled anti-CA125 scFv provided a SUV of 0.64 ± 0.04 in OVCAR3 tumors 24 h p.i versus 0.25 ± 0.11 in SKOV3 tumors. Both ^{64}Cu-labeled vectors showed expected biological clearance profiles: the mAb was cleared hepatically whereas scFv was cleared renally. **Conclusion**: ^{64}Cu-labeled anti-CA125 mAb and scFv could be prepared successfully with sustained *in vitro* and *in vivo* immunoreactivity. Both radiolabeled vectors presented specific tumor accumulation and expected biological clearance profiles. This renders them as potential PET probes for *in vivo* molecular imaging and targeting of epithelial ovarian cancer. **Research Support**: CREATE (NSERC), Dianne and Irving Kipnes Foundation. **References**: [1] McQuarrie SA, et al (2001) Q J Nucl Med, 45, 160-6. [2] Xiao, et al (2002) J Biotech, 94(2), 171-84

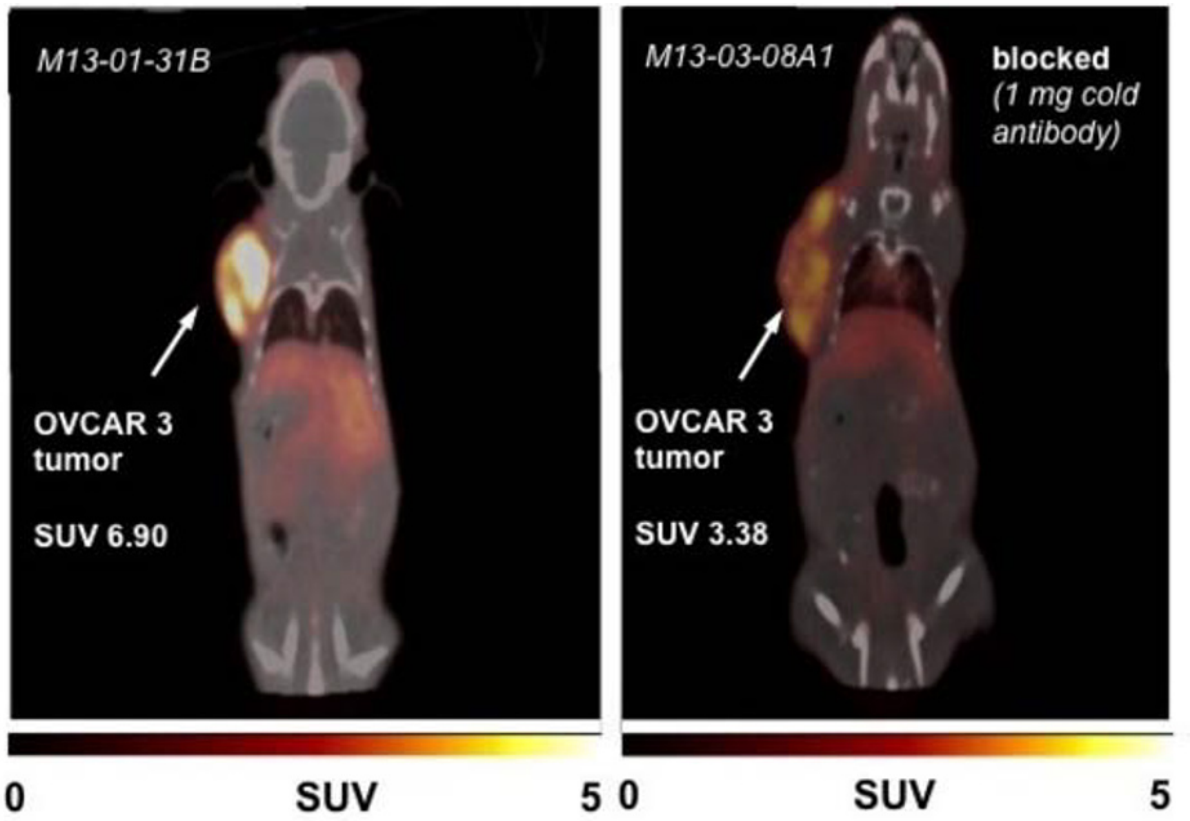

Disclosure of author financial interest or relationships:
S. Sharma, None; **M. Wuest**, None; **M. Wang**, None; **S. Lapi**, None; **B. Andrais**, None; **L. Klotz**, None; **F. Wuest**, None.

Presentation Number **LBAP 029**
Late Breaking Abstract Poster Session
September 19, 2013 / 15:15-15:15 / Room: Exhibit Hall B

Facile synthesis and biological evaluation of an 18F-labeled 4-(2-aminoethyl)benzenesulfonamide (AEBS) trimer for imaging carbonic anhydrase IX expression with positron emission tomography

Zhibo Liu[1], *Joseph Lau*[2], *Jinhe Pan*[2], *Maral Pourghiasian*[2], *Teresa R. Algara*[2], *David M. Perrin*[1], *Francois Benard*[2], *Kuo-Shyan Lin*[2], [1]*Chemistry, University of British Columbia, Vancouver, BC, Canada;* [2]*Department of Molecular Oncology, BC Cancer Agency, Vancouver, BC, Canada. Contact e-mail: rosinnju@gmail.com*

Introduction: Carbonic anhydrase IX (CA-IX), a zinc metalloenzyme catalyzing the reversible hydration of carbon dioxide to bicarbonate and proton, is overexpressed in a broad spectrum of cancers. CA-IX is a surrogate marker for hypoxia, and is a promising diagnostic/therapeutic target for cancers. Sulfonamide derivatives have been shown to inhibit CA-IX by binding to the Zn catalytic domain. We hypothesize that a tracer with multiple sulfonamide moieties will demonstrate greater binding affinity for CA-IX. Such bulky tracer is also less likely to cross cell membrane and bind to cytosolic CA isoforms I and II. Herein, we synthesized and evaluated [18F](AEBS)3-BF3¬ for imaging CA-IX expression with positron emission tomography. Methods: The radiolabeling precursor, [19F](AEBS)3-BF3 was synthesized in two steps: (1) coupling of AEBS with azidoacetic acid, (2) formation of [19F](AEBS)3-BF3 (by coupling AEBS-azide to a novel BF3-conjugated hydrophilic trimeric linker via Cu-catalyzed click reaction. For radiosynthesis, a facile kit labeling approach was developed. Prior to radiolabeling, a kit containing [19F](AEBS)3-BF3 (50-100 nmol) was resuspended with pH 2.5 aqueous buffer. After addition of [18F]fluoride to the kit, the resulting solution was incubated for 20 min at 90°C for direct 18F-19F isotopic exchange. The reaction mixture was simply purified with a C18 Sep-Pak cartridge to yield radiochemically pure [18F](AEBS)3-BF3¬. Ex vivo stability of [18F](AEBS)3-BF3¬ was assessed in mouse plasma. LogD7.4 (D: distribution coefficient) of [18F](AEBS)3-BF3¬ was determined using the shake flask method. Biodistribution and PET imaging studies were performed using NODSCID/IL2RKO mice bearing CA-IX expressing HT-29 colorectal tumours. Results: >160 mCi (31-42% nondecay-corrected yield) of [18F](AEBS)3-BF3¬ was obtained in 30 min from 500-800 mCi [18F]fluoride with > 99% radiochemical purity and 2.5-3.2 Ci/μmol specific activity. Despite bearing three lipophilic AEBS, [18F](AEBS)3-BF3¬ was still relatively hydrophilic with a LogD7.4 value of -2.4. [18F](AEBS)3-BF3¬ was stable in mouse plasma with negligible decomposition after 2 h incubation at 37 °C. Biodistribution and imaging studies showed the radioactivity was excreted primarily through the hepatobiliary pathway with the gastrointestinal tract retaining majority of the radioactivity. Based on dynamic PET imaging data, HT-29 tumours xenografts were clearly visible as early as 20 min p.i. At 22.5 min p.i. tumour uptake of [18F](AEBS)3-BF3¬ was approximately 2.09 %ID/g. At this time point, uptake ratios of tumour to blood (heart) and muscle were 1.98 and 6.02 respectively. Conclusions: We have demonstrated the feasibility of using the kit labeling approach for the preparation of [18F](AEBS)3-BF3¬ at the clinical production scale. Via 18F-19F isotopic exchange reaction, [18F](AEBS)3-BF3¬ was obtained in high radiochemical yield, purity and specific activity in a short time. [18F](AEBS)3-BF3¬ successfully targeted CA-IX expressing tumour xenografts with good contrast; however, modifications are still required to improve pharmacokinetics and reduce gastrointestinal uptake.

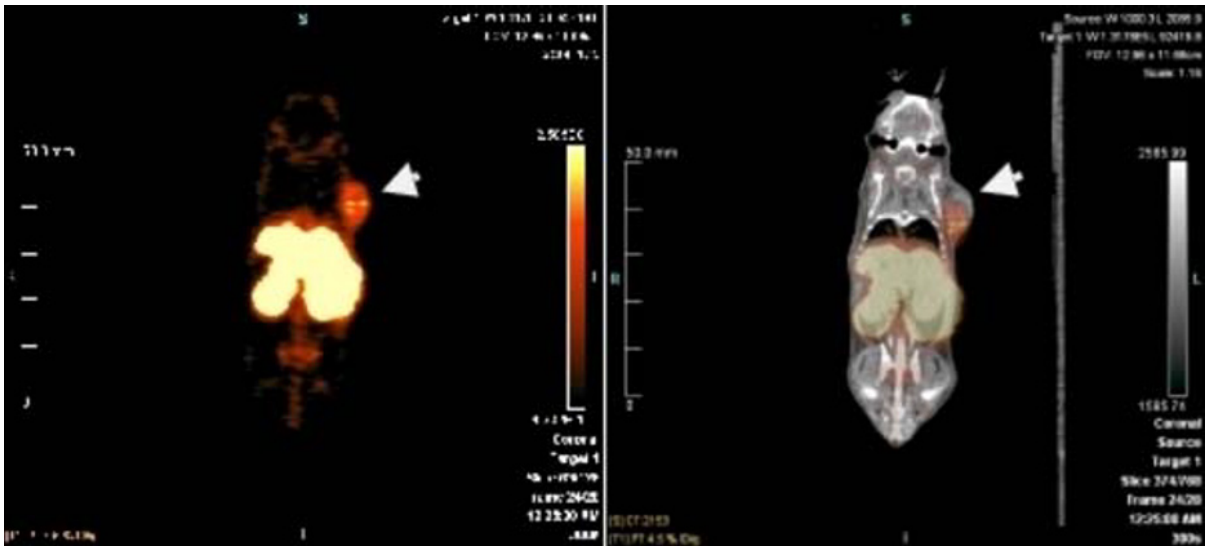

Disclosure of author financial interest or relationships:
Z. Liu, None; **J. Lau**, None; **J. Pan**, None; **M. Pourghiasian**, None; **T.R. Algara**, None; **D.M. Perrin**, None; **F. Benard**, None; **K. Lin**, None.

Presentation Number **LBAP 030**
Late Breaking Abstract Poster Session
September 19, 2013 / 15:15-15:15 / Room: Exhibit Hall B

Radiosynthesis and biological evaluation of ^{68}Ga-DOTA-AEBSA for imaging carbonic anhydrase IX expression with positron emission tomography

Joseph Lau[1], Zhengxing Zhang[1], Navjit Hundal-Jabal[1], Teresa R. Algara[1], Zhibo Liu[2], Francois Benard[1], **Kuo-Shyan Lin[1],**
[1]Department of Molecular Oncology, BC Cancer Agency, Vancouver, BC, Canada; [2]Chemistry Department, University of British Columbia, Vancouver, BC, Canada. Contact e-mail: klin@bccrc.ca

Introduction: Carbonic anhydrase IX (CA-IX) is a transmembrane metalloenzyme that mediates cell survival under hypoxic stress. Overexpressed in a broad spectrum of cancers, CA-IX drives cancer progression and its expression is negatively correlated with patient survival. Pharmacologic inhibition of CA-IX is achievable through sulfonamide-based inhibitors; however, there remains a need for an effective platform to screen for cancers that will respond to these drugs. Previously our lab demonstrated that sulfonamide derivatives can be radiolabelled with ^{18}F to image CA-IX; however, despite good tumour uptake majority of radioactivity was sequestered by the liver/gastrointestinal tract. We hypothesize that a tracer with hydrophilic tendency will reduce hepatobiliary uptake and improve image contrast. Herein, we synthesized and evaluated ^{68}Ga-DOTA-AEBSA for imaging CA-IX expression with positron emission tomography. **Methods:** The radiolabeling precursor DOTA-AEBSA was synthesized by coupling 2-bromo-N-(4-sulfamoylphenylethyl)acetamide with tri-*tert*-butyl 1,4,7,10-tetraazacyclododecan followed by deprotection and HPLC purification. ^{68}Ga labeling was performed in HEPES buffer (pH 5.1) via microwave heating for 1 min, followed by HPLC purification. *Ex vivo* stability of ^{68}Ga-DOTA-AEBSA was assessed in mouse plasma, and monitored by HPLC. $LogD_{7.4}$ (D: distribution coefficient) of ^{68}Ga-DOTA-AEBSA was determined using the shake flask method. Biodistribution and PET/CT imaging studies were performed using NODSCID/IL2RKO mice bearing CA-IX expressing HT-29 colorectal tumours. **Results:** ^{68}Ga-DOTA-AEBSA was obtained in 78% decay-corrected yield in 17 min with >99% radiochemical purity. ^{68}Ga-DOTA-AEBSA was very hydrophilic with a $LogD_{7.4}$ value of -4.37±0.08. ^{68}Ga-DOTA-AEBSA was stable in mouse plasma with >95% of the tracer remaining intact after 60 min incubation at 37 °C. Biodistribution and imaging studies showed the radioactivity was excreted primarily through the renal pathway with the kidneys and bladder being the only organs with a higher %ID/g than tumour at 60 min p.i. At this time point, tumours had a %ID/g of 0.66±0.06. This corresponded with uptake ratios of tumour to blood and muscle of 1.77 and 5.48, respectively. From the PET imaging data, HT-29 tumour xenografts were clearly visualized with good target to non-target signal. **Conclusions:** ^{68}Ga-DOTA-AEBSA was synthesized in good radiochemical yield and purity. ^{68}Ga-DOTA-AEBSA displayed favourable pharmacokinetics with rapid clearance via the kidneys and good tumour to background ratios. Although absolute uptake of the tracer in tumour was low, ^{68}Ga-DOTA-AEBSA successfully targeted CA-IX expressing tumour xenografts with good contrast. Modifications to prolong circulation time of ^{68}Ga-DOTA-AEBSA derivatives are ongoing to improve tumour uptake. Our results indicate that ^{68}Ga-DOTA-AEBSA may serve as a promising PET tracer for targeting CA-IX overexpressing or hypoxic tumours.

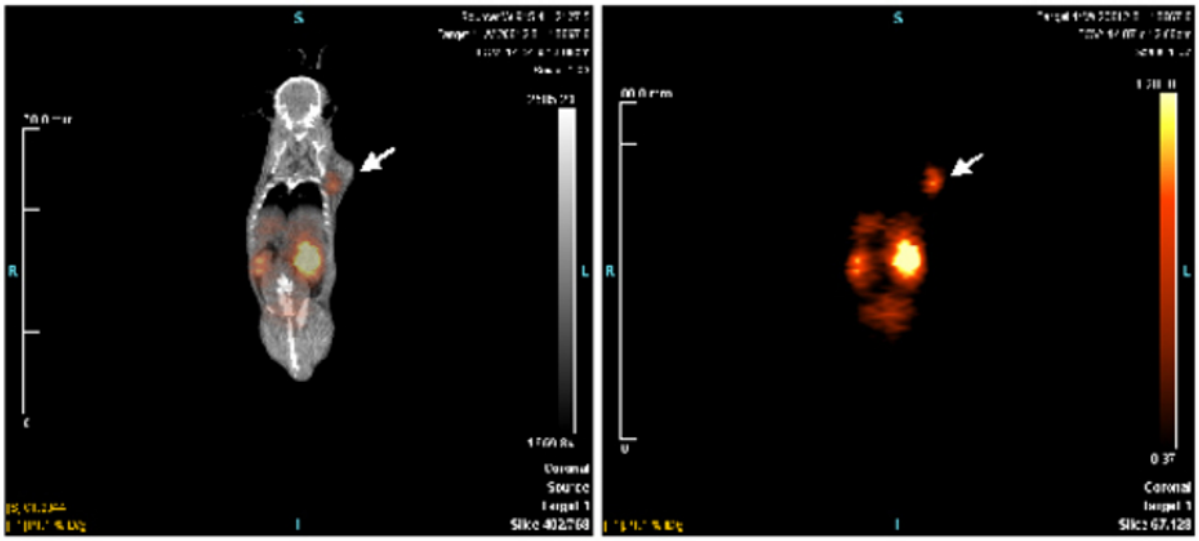

Image at 60 min p.i.

Disclosure of author financial interest or relationships:
J. Lau, None; **Z. Zhang**, None; **N. Hundal-Jabal**, None; **T.R. Algara**, None; **Z. Liu**, None; **F. Benard**, None; **K. Lin**, None.

Presentation Number **LBAP 031**
Late Breaking Abstract Poster Session
September 19, 2013 / 15:15-15:15 / Room: Exhibit Hall B

Preparation of ^{18}F-fluoride solution amenable for electrochemical reactions

Artem Lebedev, *Qinggang He, Saman Sadeghi, Molecular Pharmacology\, UCLA, Los Angeles, CA, USA. Contact e-mail: lebedevfedora@gmail.com*

Background: ^{18}F-Fluoride anion is the most commonly used source of 18F in the modern radiochemistry. Recently attempts have been made to utilize 18F-Fluoride in electrochemical transformations[1]. However, typical procedure for generating reactive fluoride was not compatible with electrochemical reactions: large quantities of base and water co-eluted with fluoride from anion exchange cartridge interfere with oxidative electroradiofluorination. As a result, ^{19}F fluoride was used to release activity from the cartridge, resulting in carrier-added radiolabeled products. Various alternative procedures have been reported for fluoride preparation[2], most relevant ones relying on the use of inert anions[3], such as mesylate or triflate. Unfortunately, these methods are not directly applicable to electrochemical transformations due to oxidation of the anions and/or use of protic solvents[4]. Here we report a method that allows for transfer of fluoride anion into an anhydrous aprotic solution using electrochemically stable salts in acetonitrile. **Results:** We found two combinations of anion exchange resin and releasing salts to release fluoride anion into organic solvent using non-nucleophilic anions. The set of anions screened included PF_6^-, ClO_4^-, OTf^-, $OMes^-$ and $HSO4^-$. It was found that dry acetonitrile solution of Bu_4NOMes (0.1 M) and Bu4NHSO4 (0.1 M) are very effective for release of ^{18}F- from BioRad MP-1 resin. Up to 95% of fluoride trapped on the resin could be washed out by 2 ml of these solutions. Bu_4NOTf was only effective in high concentration (1M) and no more than 50% of the trapped fluoride could be released after passing 5 ml of solution through 10 mg of the resin. Cartridge geometry role in the release process was also studied. It was found that increasing the packing density of the resin from 0.14 g/ml to 0.94 g/ml reduced the volume of the solution needed to release activity by 60%, but did not affect the total amount of activity released. In case of release with 1M Bu_4NOTf 50-55% of fluoride was irreversibly absorbed on the cartridge irrespective of packing density. Anions bound to the resin prior trapping of fluoride can also be a source of competing nucleophile. We studied the influence of the resin pretreatment and found no significant difference between resins pre-treated with $KHCO_3$ (0.5M), $KHSO_4$ (0.5M) or 1M Bu_4NOTf. Both trapping and release efficiency of MP-1 resin was approximately the same in all three cases. This finding indicates that inert anions can be used for pretreatment of the resin in order to reduce concentration of competing nucleophiles. **Conclusions:** Organic solution of ^{18}F fluoride suitable for electrochemical reactions can be generated by passing of target water through MP-1 resin pre-treated with $KHCO_3$, drying the resin and releasing the activity using acetonitrile solutions of Bu_4NHSO_4 (0.1 M). Less reactive salts, such as Bu_4NOTf can be used, albeit at the cost of release efficiency. 1. J. Label. Compd. Radiopharm. 48, 259-273 (2005). 2. Angew. Chem. Int. Ed Engl. 49, 3161-4 (2010). 3. J. Label. Compd. Radiopharm. 54, S475-S475 (2011). 4. Bull. Korean Chem. Soc. 32, 71-76 (2011).

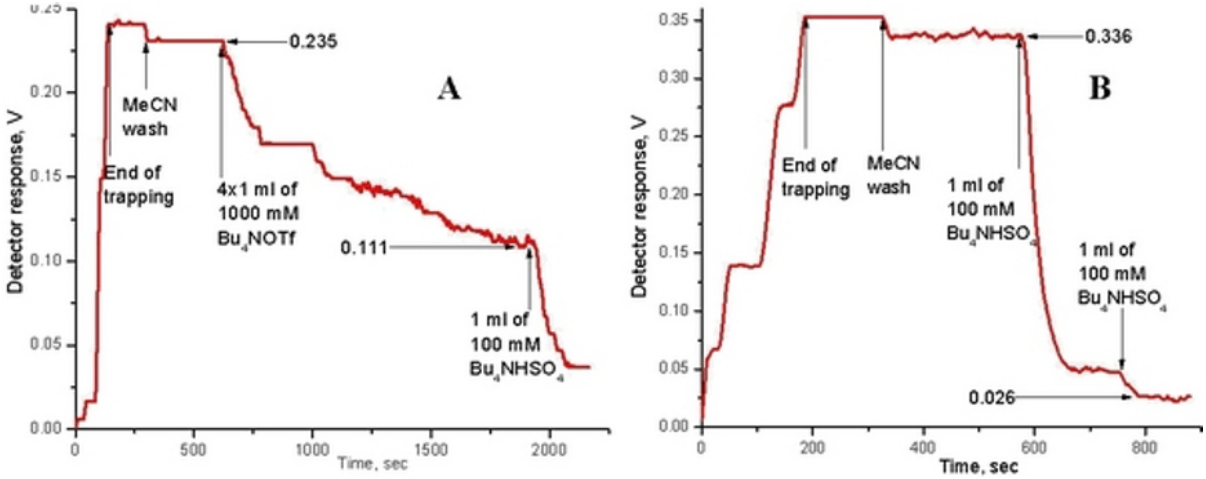

Figure 1. Radioactivity profile during a trap/release experiment: response of a radiation detector mounted on the cartridge. 0.14 g/ml of MP-1 resin. Release agent **A**: 4x1ml of 1M Bu_4NOTf, then 1ml 0.1M Bu_4NHSO_4; **B**: 2x1 ml 0.1 MBu_4NHSO_4

Disclosure of author financial interest or relationships:
A. Lebedev, None; **Q. He**, None; **S. Sadeghi**, None.

Presentation Number **LBAP 032**
Late Breaking Abstract Poster Session
September 19, 2013 / 15:15-15:15 / Room: Exhibit Hall B

First biological evaluation and facile radiosynthesis of an F-18 labeled peptide for imaging bradykinin B1R expression with positron emission tomography

Zhibo Liu[1], *Guillaume P. Amouroux*[2], *Jinhe Pan*[2], *Joseph Lau*[2], *Navjit Hundal-Jabal*[2], *Gemma M. Dias*[2], *Francois Benard*[2], *Kuo-Shyan Lin*[2], *David M. Perrin*[1], [1]*Chemistry Department, University of British Columbia, Vancouver, BC, Canada;* [2]*Department of Molecular Oncology, BC Cancer Agency, Vancouver, BC, Canada. Contact e-mail: rosinnju@gmail.com*

Objectives: Bradykinin B1 receptor (B1R), a G protein-coupled receptor, has been known to function in pain and inflammatory pathways. There is an overexpression of B1R in a variety of cancer tissue compared to normal tissue. This difference in expression makes B1R a promising diagnostic/prognostic marker and a potential therapeutic target for cancers. Therefore, we radiosynthensized a 18F-labeled BK-organotrifluoroborate (BK-B[18F]F3-) using a novel "kit-like" one-step aqueous 18F-labeling method, and evaluated BK-B[18F]F3- as a potential PET tracer for imaging B1R expression in cancers. Methods: The B1R-targeting sequence was derived from a potent B1R antagonist Lys-[Leu9,desArg10]BK with Hyp and Cha substitutions for the 3rd and 5th amino acids, respectively, to improve its in vivo stability. This sequence was elongated at the N-terminus with a PEG2 linker and an azidoacetyl moiety to form BK-azide. The radiolabeling precursor, BK-B[19F]F3 was prepared by coupling BK-azide to a novel clickable BF3 via Cu-catalyzed click reaction. The binding affinity of BK-BF3 was determined via in vitro binding assays using B1R-overexpressing CHO-K1 cell membranes. Prior to radiolabeling, an aliquot of BK-B[19F]F3 (50-100 nmol) was resuspended in pH 2.5 aqueous buffer. After addition of [18F]fluoride, the resulting solution was incubated for 20 min at 90°C for direct 18F-19F isotopic exchange. BK-B[18F]F3¬ was purified simply by solid-phase extraction. Ex vivo stability of BK-[18F]-BF3¬ was assessed in mouse plasma. LogD7.4 (D: distribution coefficient) of BK-B[18F]F3¬ was determined using the shake flask method. Biodistribution and PET imaging studies were performed using NODSCID/IL2RKO mice bearing B1R+ and B1R- HEK293T tumours. Results: Starting at 450-800 mCi [18F]fluoride, >180 mCi (21-35% nondecay-corrected yield, n=4) of BK-B[18F]F3¬ was obtained within 30 min with > 99% radiochemical purity and 2.1-3.7 Ci/μmol specific activity. BK-B[18F]F3¬ was hydrophilic with a LogD7.4 value of -2.7. BK-B[18F]F3- was stable in mouse plasma with negligible free [18F]fluoride observed after 2 hr incubation at 37 °C. Biodistribution and imaging studies showed that majority of the radioactivity was excreted through the renal pathway. Dynamic PET imaging data showed that B1R+ tumour was cleared visualized at 30-min post-injection. At 3-h post-injection, the uptake ratios of B1R+ tumour to blood, muscle and B1R- tumour were 7.58, 15.7 and 3.88, respectively. Conclusions: We have developed a high affinity B1R-trageting peptide, BK-BF3, that can be radiolabeled with F-18 with a facile kit-like labeling approach. BK-B[18F]F3- successfully targeted B1R+ expressing tumour with good contrast compared to B1R- tumour, evident in PET imaging and biodistribution. These results show that BF3- can be radiolabelled in a kit-like format with potential applications for the development of other F-18 labeled PET tracers.

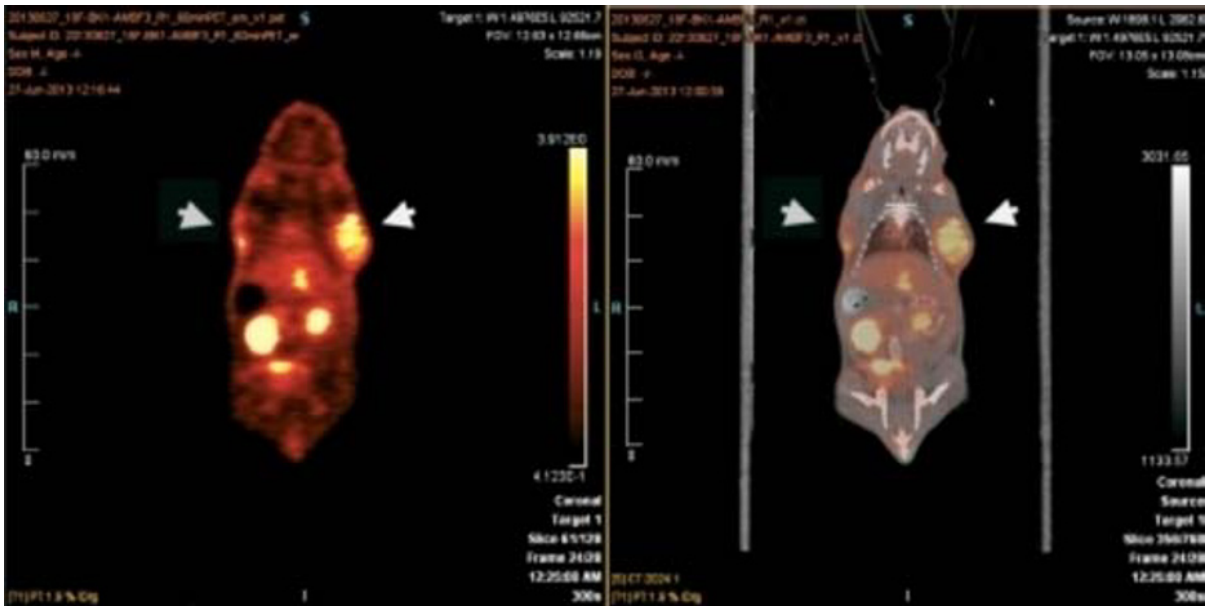

Figure 1. Left arrow: B1R-HEK293T tumour; Right Arrow: B1R+ HEK293T tumour; left image -PET image, right image - PET/CT image at 30 min post-injection

Disclosure of author financial interest or relationships:
Z. Liu, None; **G.P. Amouroux**, None; **J. Pan**, None; **J. Lau**, None; **N. Hundal-Jabal**, None; **G.M. Dias**, None; **F. Benard**, None; **K. Lin**, None; **D.M. Perrin**, None.

Presentation Number **LBAP 033**
Late Breaking Abstract Poster Session
September 19, 2013 / 15:15-15:15 / Room: Exhibit Hall B

Multimeric-presentation of a glucagon-like peptide 1 (GLP-1) analogue for beta cell mass (BCM) imaging

Amit Kumar[1], *Su-Tang Lo*[1], *Bikash Manandhar*[3], *Jung-Mo Ahn*[3], *Orhan K. Öz*[1], *Xiankai Sun*[1,2], [1]*Department of Radiology, University of Texas Southwestern Medical Center, Dallas, Dallas, TX, USA;* [2]*Advanced Imaging Research Center, University of Texas Southwestern Medical Center, Dallas, Dallas, TX, USA;* [3]*2Department of Chemistry, University of Texas at Dallas, Dallas, TX, USA. Contact e-mail: amit.kumar@utsouthwestern.edu*

Introduction: β-cell mass (BCM) in the pancreas regulate the insulin secretion for the maintenance of normal blood glucose concentrations. Currently, measurements of insulin secretion and c-peptide production serve as surrogates for the assessment of BCM; however, such measurements are not accurate. Noninvasive BCM measurements through Positron emission Tomography imaging (PET, owing to its inherent superior sensitivity and capability of imaging quantification), based on targets other than insulin, have the potential to provide real-time information on the progression and treatment of diabetes. Glucagon-like peptide 1 receptor (GLP-1R) is such non-insulin based potential target. Based on the natural GLP-1 ligand, a bicyclic peptide (EM2198) was engineered to provide greater *in vivo* stability against the enzymatic degradation while maintaining the GLP-1R binding affinity. In this work, we strive to achieve high imaging sensitivity and specificity by applying the well-accepted concept of multivalent effect to the design of GLP-1R-targeted PET probes. The multivalent probes were constructed by conjugating up to three copies of EM2198 to a bifunctional chelator scaffold of 1,4,7-triazacyclononane-1,4,7-triacetic acid (NOTA). Gallium-68 was chosen because it can be obtained as-needed from a benchtop $^{68}Ge/^{68}Ga$ generator and it forms an inert complex with the NOTA core. **Method:** Synthesis: NOTA-EM2198 conjugates carrying 1 - 3 copies of EM2198, (**NOTA-EM2198** **NOTA-(EM2198)$_2$** and **NOTA-(EM2198)$_3$**, respectively) were synthesized employing thiol maleimide conjugation and radiolabeled with ^{68}Ga. *In vitro* binding assay: The synthesized NOTA conjugates were subjected to the competitive receptor binding assay using mouse β-TC-6 insulinoma cells. *In vivo* evaluation: *In vivo* PET imaging of BCM using ^{68}Ga labeled <NOTA2198 conjugates were performed using normal C57BL/6 mice. **Results:** Synthesis: **NOTA-EM2198**, **NOTA-(EM2198)$_2$** and **NOTA-(EM2198)$_3$** were successfully synthesized. Radiolabeling procedure with ^{68}Ga for the conjugates were established with radiochemical purity of greater than 95%. *In vitro* binding assay: Results indicate that multi-presentation of EM2198 on the NOTA scaffold leads to enhancement of GLP-1R binding affinity **(NOTA-(EM2198)**: IC_{50} = 43.02 ± 0.67 nM; **NOTA-(EM2198)$_2$**: IC_{50} = 71.24 ± 15.56 nM; and **NOTA-(EM2198)$_3$**: IC_{50} = 7.35 ± 0.13 nM). PET imaging showed a valency dependent increase in pancreatic uptake. Unfortunately, a similar trend was observed for the liver uptake. Due to the elevated liver uptake and imaging intensity spillover caused thereof, it was difficult to quantitatively compare the pancreatic uptake of the ^{68}Ga labeled probes. However, the *ex vivo* PET results clearly showed an increase in pancreatic uptake with increasing valency of ^{68}Ga labeled NOTA-EM2198 derivatives [**NOTA-(EM2198)**: 0.25 ± 0.03; **NOTA-(EM2198)$_2$**: 0.42 ± 0.05; **NOTA-(EM2198)$_3$**: 0.49 ± 0.05 % ID/g)]. **Conclusion:** Multimeric-presentation of EM2198, a GLP-1 analogue, was proven as a plausible way of enhancing the desired binding affinity to GLP-1R. However, this multimeric design approach must be modified in order to obtain an optimal biodistribution profile for BCM imaging.

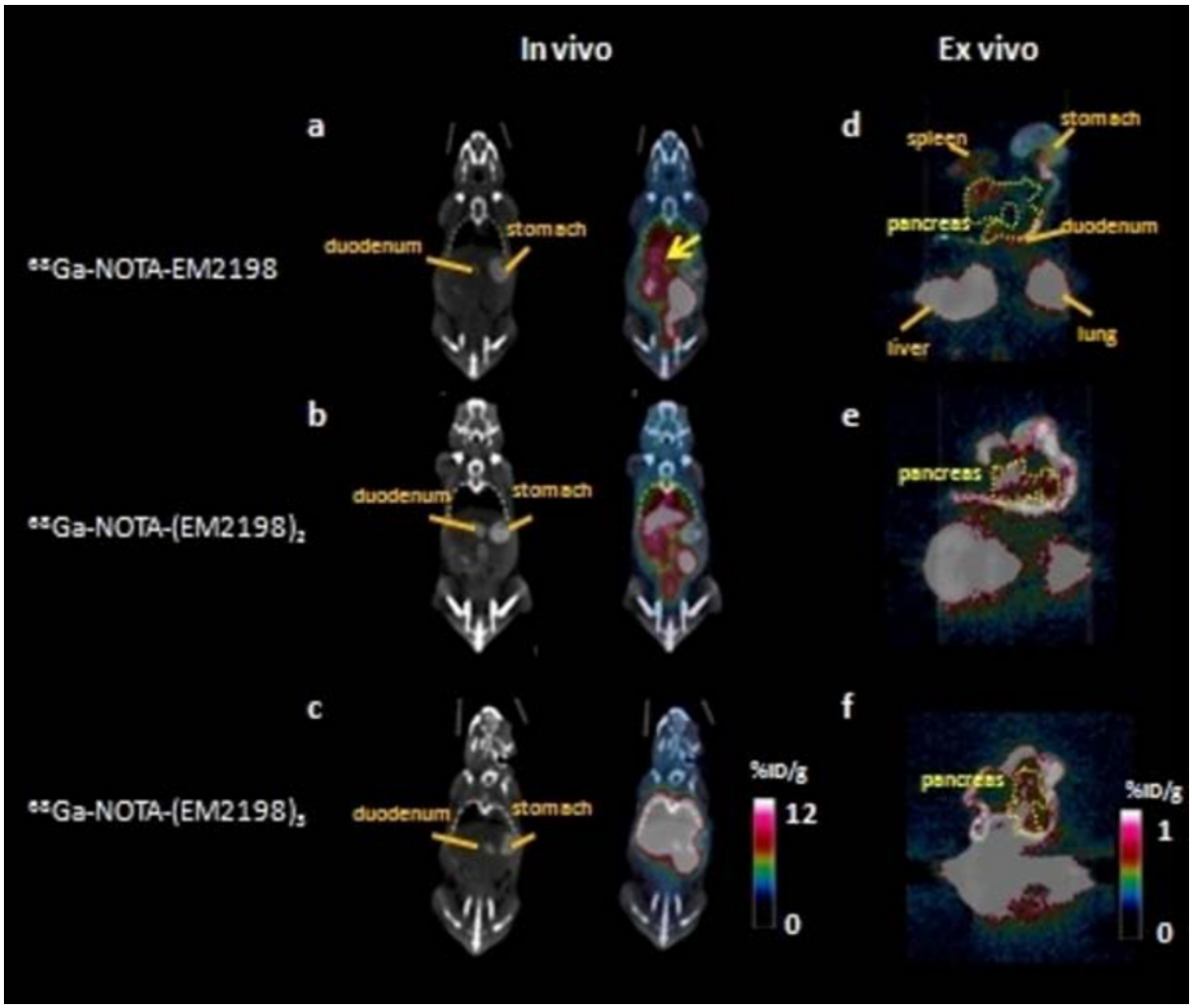

Figure 1. *In vivo* PET image (a-c) showing high liver uptake for **NOTA-(EM2198)$_2$** and **NOTA-(EM2198)$_3$** (2.9 and 6.2 % ID/g respectively) as compared to **NOTA-EM2198** (0.99 %ID/g). *Ex vivo* imaging results (d-f) showing increased pancreatic uptake with greater number of copies of EM2198 [**NOTA-(EM2198)**: 0.25 ± 0.03; **NOTA-(EM2198)$_2$**: 0.42 ± 0.05; **NOTA-(EM2198)$_3$**: 0.49 ± 0.05 % ID/g)]

Disclosure of author financial interest or relationships:
A. Kumar, None; **S. Lo**, None; **B. Manandhar**, None; **J. Ahn**, None; **O.K. Öz**, None; **X. Sun**, None.

Presentation Number **LBAP 034**
Late Breaking Abstract Poster Session
September 19, 2013 / 15:15-15:15 / Room: Exhibit Hall B

Development of an immunoPET imaging agent for pancreatic ductal adenocarcinoma

Jacob Houghton[1], *Ritsuko Sawada*[2], *Wolfgang W. Scholz*[2], *Jason S. Lewis*[1], [1]*Radiology, Memorial Sloan-Kettering Cancer Center, New York, NY, USA;* [2]*MabVax Therapeutics, San Diego, CA, USA. Contact e-mail: houghtoj@mskcc.org*

Pancreatic ductal adenocarcinoma (PDAC) is one of the most aggressive cancers, ranking fourth as a cause of cancer mortality. The development of techniques to properly diagnose, accurately stage, and effectively treat PDAC has remained elusive. Positron emission tomography (PET) is a promising technological platform for the detection and staging of PDAC. Radiolabeled immunoPET agents can provide the necessary specificity and sensitivity required to noninvasively and quantitatively image PDAC. The overexpression of CA19.9 is a key event in invasion and metastasis of many tumors, including PDAC tumors, and CA19.9 is especially attractive as a antigen target for immunoPET because it is the most highly expressed tumor antigen in pancreatic cancer, and it is minimally expressed in healthy pancreas tissue. Recent preclinical studies with a fully human antibody (5B1) that targets CA19.9 were promising and based on those results a diabody (5B1Db) was engineered. 5B1Db was stably expressed in CHO cells and purified by Ni-column chromatography. Initial studies with a fluorescein-conjugated 5B1Db (fluor-5B1Db), which was conjugated by incubating with 5B1Db with N-hydroxysuccinyl ester of fluorescein, showed that fluor-5B1Db retained over 95% of its original binding affinity with an approximately 2:1 fluorophore to diabody ratio as determined by surface plasmon resonance spectroscopy (SPR). Using fluor-5B1Db, it was also shown that 5B1Db readily binds to sLea-positive DMS79 cells, while no binding to sLea-negative H524 cells was observed by flow cytometry. 5B1Db was functionalized with p-isothiocyanatobenzyl-NOTA to form NOTA-5B1Db. Radiolabeling of NOTA-5B1Db produced an excellent yield (~85%) and good specific activity (~2 mCi/mg) as determined by iTLC and size exclusion chromatography. Cell based immunoreactivity assays using the BxPC3 pancreatic cancer cell line expressing CA19.9 showed that the diabody retained its affinity for CA19.9. In conclusion, we have generated a diabody, 5B1Db, that may be fluorescently labeled with fluorescein or radiolabeled with 64Cu. Fluor-5B1Db retains the high affinity and specificity for CA19.9, as demonstrated by SPR and flow cytometry. 64Cu-NOTA-5B1Db radiolabeled with 64Cu shows good yield and specific activity. Further studies to characterize the ability of 5B1Db as a potential immunoPET imaging agent for the delineation of PDAC using orthotopic and xenograft murine models of PDAC are currently underway.

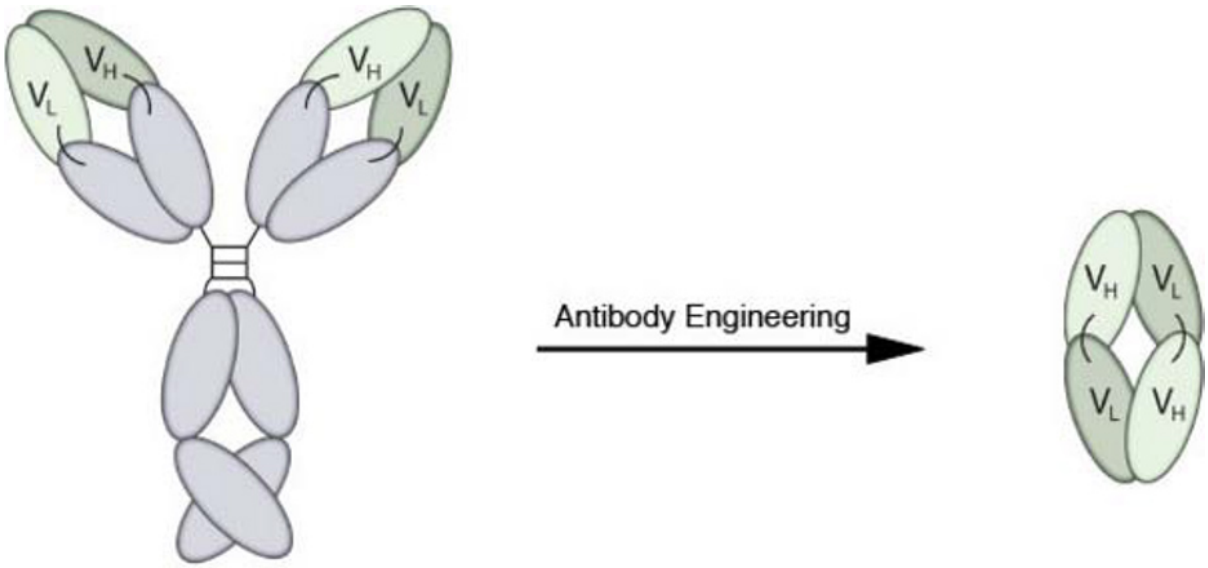

Disclosure of author financial interest or relationships:
J. Houghton, None; **R. Sawada**, MabVax Therapeutis, Employment; **W.W. Scholz**, MabVax Therapeutics, Employment; **J.S. Lewis**, None.

Presentation Number **LBAP 035**
Late Breaking Abstract Poster Session
September 19, 2013 / 15:15-15:15 / Room: Exhibit Hall B

Synthesis and Radiolabeling of Smart Peptide Probe targeting MMP-2/9

Bok-Nam Park, Kwanjae Lee, **Joon-Kee Yoon***, Nuclear Medicine & Molecular Imaging, Ajou University School of Medicine, Suwon, Republic of Korea. Contact e-mail: jkyoon3@gmail.com*

Purpose: Matrix metalloproteinase (MMP)-2 and 9 are expressed in many cancer cells and play an important role in metastasis. We synthesized and radiolabeled a smart peptide probe targeting MMP-2/9 for a tumor imaging agent. Methods: We synthesized a cleavable peptide, AcCeeeeAhxPLGLAGrrrrrKNH$_2$, which was analyzed by HPLC and LC/MS. Enzyme cleavage assay for peptide (0.35 mM) was done using LC/MS after incubation with MMP-2 (868 nM). Peptide (0.003 μM) was conjugated to 1,4,7,10-tetraazacyclododecane-1,4,7,10-tetraacetic acid (DOTA, 0.025 μM, MW=405) after succinimidylation using sulfo-NHS (0.025 μM), and then labeled to ^{99m}Tc under various condition. Succinimidylation and conjugation was tested using MALDI-TOF and LC/MS, whereas, labeling efficiency of ^{99m}Tc-DOTA-peptide was measured radio-TLC. Results: Mass and purity of peptide were 2209 (m/z) and 98.95%. After incubation with MMP-2, LC/MS revealed a single peak at 1059 (m/z) instead of 2209, which implies the cleavage of peptide. MALDI-TOF and LC/MS confirmed the production of DOTA-sulfo NHS (m/z=582). After conjugation, a single prominent peak was observed at 2596 (DOTA-peptide) by MALDI-TOF analysis. Labeling efficiency of ^{99m}Tc-DOTA-peptide reached 36% at 100°C, pH 2-3 with 30 min incubation. Conclusion: We successfully synthesized and radiolabeled smart peptide probe for MMP-2/9 with a modest labeling efficiency, which warrants a further in vitro and in vivo preclinical studies.

Disclosure of author financial interest or relationships:
B. Park, None; **K. Lee**, None; **J. Yoon**, None.

Presentation Number **LBAP 036**
Late Breaking Abstract Poster Session
September 19, 2013 / 15:15-15:15 / Room: Exhibit Hall B

Intraoperative Tumor Acidosis Imaging with a Fluorescent pHLIP Analog

Kuntalkumar Sevak[1], *Yachao Zhang*[1], *Hannah Suchy*[1], *Nerissa Viola-Villegas*[1], *Yana K. Reshetnyak*[2], *Oleg A. Andreev*[2], *Thomas Reiner*[1], *Jason S. Lewis*[1,3], [1]*Radiology, Memorial Sloan Kettering Cancer Center, New York, NY, USA;* [2]*Physics, University of Rhode Island, Kingston, RI, USA;* [3]*Molecular Pharmacology and Chemistry Program, Memorial Sloan Kettering Cancer Center, New York, NY, USA. Contact e-mail: sevakk@mskcc.org*

Objective: The 37-amino acid peptide pH Low Insertion Peptide (pHLIP) and its derivatives have been shown to be suitable imaging agents for tumor acidosis. We present a hydrophilic pHLIP derivative and investigate its pharmacokinetic and pharmacodynamic behavior. We generated the near-infrared fluorescently labeled pHLIP-FL, an analog obtained via site-selective and bioorthogonal azide-alkyne click chemistry, resulting in a metabolically stable triazole-linkage between targeted peptide and fluorescent reporter. Here, we demonstrate in vitro and ex vivo imaging with significant tumor uptake of pHLIP-FL in orthotopic 4T1 human breast cancer xenografts. Methods: The artificial amino acid 2-amino-pentynoic acid was inserted into the pHLIP-sequence, which was then allowed to react with azide-linked near infrared fluorophore via a copper click mediated conjugation to yield pHLIP-FL. For in vitro studies, pHLIP-FL was incubated with 4T1 cells at different pH levels (between 6.2 and 7.4). 4T1 orthotopic breast tumors were developed in athymic nude mice. Once achieving optimum tumor volume, mice were injected with 200 µL of 15 µM pHLIP-FL intravenously. After 1, 6, 12 and 24 hours, mice were sacrificed to collect tumor, muscle, liver and kidney tissue, which was investigated for its relative pHLIP-FL uptake using an epifluorescence imager. Results: In vitro, the cell uptake was found inversely proportional to pH levels. Increased uptake was observed at a pH of 6.2 compared to pH levels at 7.4. Ex vivo, at 1 h post injection of pHLIP-FL, we observed a total fluorescence signal of 333 ± 52% compared to the initial fluorescence. Clearance of pHLIP-FL was observed at 6 hour with a decrease in fluorescence intensity from the tumor to 208 ± 10%. Further clearance followed at 12 hours and 24 hours with 136 ± 10% and 117 ± 5%, respectively. The bulk of pHLIP-FL is being excreted renally. When looking at the absolute numbers, we saw a 2.54 fold higher signal in tumor than in muscle at 1 h, 3.28 fold at 6 h, 2.05 fold at 12 h and 1.25 fold at 24 h. Conclusion: This study shows that pHLIP-FL is a promising biomarker of extracellular acidity in malignant tissues. As an optical imaging probe it possesses suitable pharmacokinetics achieving high tumor/muscle ratios as early as 6 h post injection. Further studies will investigate whether pHLIP-FL is a suitable probe to assist in intraoperative imaging.
Funding in part by NIH CA138468-03 (JSL)

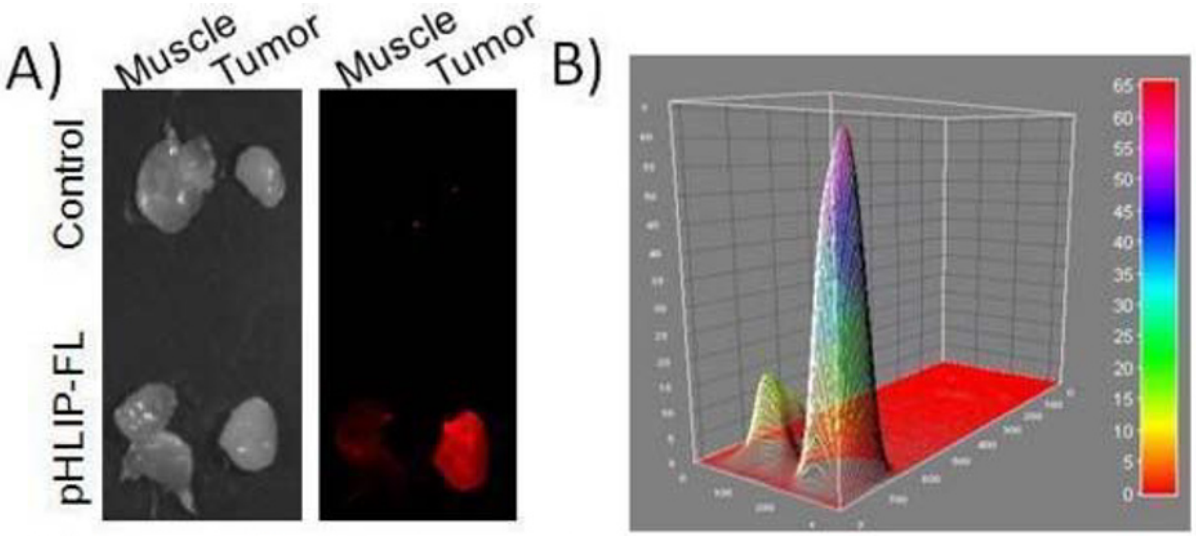

C)

Time [h]	Tumor [AU]	Muscle [AU]	Total signal increase [%]
0	8.1 ± 0.8	7.3 ± 0.8	100
1	29.3 ± 3.5	11.8 ± 1.7	332.8±52.1
6	14.9 ± 0.5	4.7 ± 0.8	207.7±9.5
12	10.2 ± 0.6	5.1 ± 0.9	136.3±9.5
24	10.3 ± 0.3	8.2 ± 0.1	116.9±4.8

Figure 1. Ex vivo pHLIP-FL imaging of 4T1 tumors. (A) White light and fluorescent images of tumor and muscle at 1 h (B) fluorescent intensity distribution at 1 h. (C) Relative surface fluorescence and signal increases for tumor and muscle.

Disclosure of author financial interest or relationships:
K. Sevak, None; **Y. Zhang**, None; **H. Suchy**, None; **N. Viola-Villegas**, None; **Y.K. Reshetnyak**, None; **O.A. Andreev**, None; **T. Reiner**, None; **J.S. Lewis**, None.

Presentation Number **LBAP 037**
Late Breaking Abstract Poster Session
September 19, 2013 / 15:15-15:15 / Room: Exhibit Hall B

ENDOSCOPIC MOLECULAR IMAGING OF HUMAN BLADDER CANCER USING CD47 ANTIBODY

Ying Pan[1,5], *Jens-Peter Volkmer*[2], *Kathleen E. Mach*[1,5], *Jen-Jane Liu*[1], *Robert V. Rouse*[3,5], *Debashis Sahoo*[2], *Timothy C. Chang*[1], *Matt van de Rijn*[3], *Eila Skinner*[1], *Sanjiv S. Gambhir*[4], *Irving Weissman*[2], *Joseph C. Liao*[1,5], [1]*Urology, Stanford University, Stanford, CA, USA;* [2]*Institute of Stem Cell Biology and Regenerative Medicine, Stanford University, Stanford, CA, USA;* [3]*Pathology, Stanford University, Stanford, CA, USA;* [4]*Radiology and Bioengineering, Stanford University, Stanford, CA, USA;* [5]*Veterans Affairs Palo Alto Health Care System, Stanford University, Palo Alto, CA, USA. Contact e-mail: yingpan@stanford.edu*

Bladder cancer (BC) is primarily diagnosed with white light cystoscopy (WLC). Well-known shortcomings of WLC include difficulty in detection of high-grade flat neoplasms such as carcinoma in situ (CIS) and differentiation of malignant lesions from benign. A combination of new imaging technologies with cancer-selective molecular imaging agents is a potentially powerful strategy to improve BC detection. Currently, approved optical imaging technologies for BC such as photodynamic diagnosis (PDD) lack molecular specificity. The cell surface protein CD47 is expressed on nearly all BC cells and was shown to be a potential therapeutic target. We theorized that CD47 might be a promising target for endoscopic molecular imaging. With IRB approval, patients with confirmed BC from prior endoscopic resection and scheduled to undergo radical cystectomy for definitive treatment were recruited. Within 60' following radical cystectomy,Qdot625 labeled anti-CD47 was instilled intravesically into unfixed intact bladders (n=19). After incubation, excess antibody was drained and the bladder washed via an inserted urinary catheter. A fluorescence cystoscope was inserted into the bladder for ex vivo cystocopy under white light and PDD. Systematic, template-based biopsy of different bladder regions, including tumors, suspicious flat lesions and normal-appearing mucosa was performed. The bladder regions and biopsy sites were analyzed by standard histopathology and co-localized with the fluorescence signals derived from anti-CD47 binding. Of the 19 bladders, urothelial carcinoma (n=14), adenocarcinoma (n=2), and no residual cancer (n=3) were confirmed. Overall, 111 sites were analyzed for co-localization of fluorescent signal and histopathology, with 31 pathologically confirmed carcinoma. Anti-CD47-Qdot625 fluorescence (pink) was observed in 26 of the 31 sites with tumor, while, 72 of 80 sites with normal, benign or inflamed mucosa had no detectable fluorescence under PDD (blue). Of the tumors that appeared papillary or sessile by WLC (n=27), 23 had pink fluorescence under PDD. Of the 4 CIS lesions, 3 with pink fluorescence under PDD. Strikingly, one of the CIS lesions appeared completely normal under WLC yet pink fluorescence was detected under PDD. Another CIS lesion with pink fluorescence was identified in the resection bed from prior endoscopic resection. Three of the tumor sites identified (2 papillary, 1 CIS) by PDD were found to have micropapillary morphology, an aggressive variant of urothelial carcinoma. Benign lesions including squamous metaplasia (n=6) and polypoid edema (n=1) appeared suspicious by WLC but lacked pink fluorescence under PDD. These results demonstrate targeted imaging of CD47 with a labeled antibody coupled with PDD technology could aid in distinguishing benign and malignant lesions including CIS, a recognized diagnostic challenge for BC. We establish CD47 as a novel bladder cancer imaging target by demonstrating fluorescence imaging of anti-CD47 in intact human bladders derived from radical cystectomy. Endoscopic molecular imaging of CD47 may improve bladder cancer diagnosis and image-guided biopsy for bladder cancer.

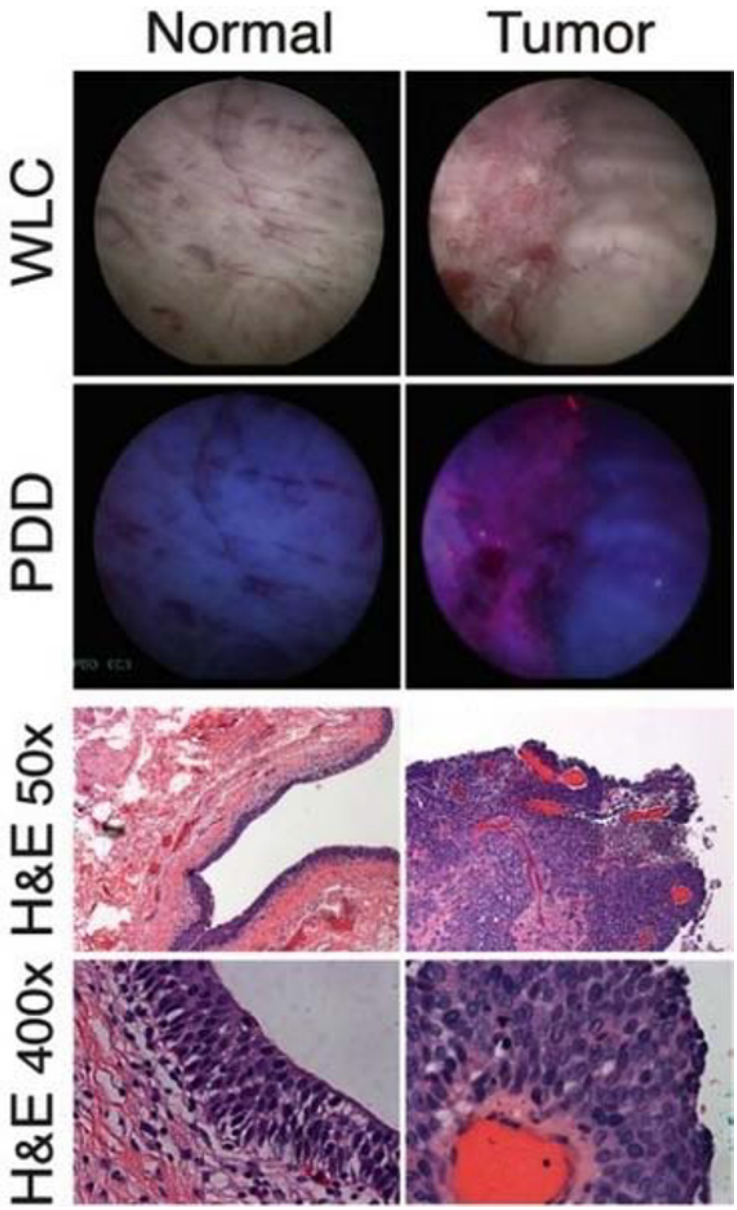

Disclosure of author financial interest or relationships:
Y. Pan, None; **J. Volkmer**, None; **K.E. Mach**, None; **J. Liu**, None; **R.V. Rouse**, None; **D. Sahoo**, None; **T.C. Chang**, None; **M. van de Rijn**, None; **E. Skinner**, None; **S.S. Gambhir**, Bracco Diagnostics, Consultant; Endra, Inc, Stockholder; Cellsight, Stockholder; Enlight, Inc., Stockholder; General Electric, Grant/research support; ImaginAb, Stockholder; MagArray, Inc., Stockholder; Sanofi-Aventis, US, Grant/research support; SiteOne Therapeutics, Stockholder; VisualSonics/Sonosite, Stockholder; **I. Weissman**, None; **J.C. Liao**, None.

Presentation Number **LBAP 038**
Late Breaking Abstract Poster Session
September 19, 2013 / 15:15-15:15 / Room: Exhibit Hall B

Development of new Bioluminogenic Firefly Luciferase substrates

Rika Obata[1], *Chihiro Miura*[2], *Satoshi Iwano*[2], *Kazuto Ito*[2], *Masahiro Kiyama*[2], *Takeshi Hirano*[2], *Shojiro A. Maki*[2], *Haruki Niwa*[2], [1]*Faculty of Pharmacy, Keio University, Minato-ku, Japan;* [2]*Department of Engineering Science, The University of Electro Communications, Chofu, Japan. Contact e-mail: robata@chem.keio.ac.jp*

Widely used bioluminescent assays are based on light-emitting enzyme, luciferase, which requires specific substrate luciferin for light production. Especially, enzyme of North American firefly *photinus pyralis* (Ppy) is universally used to detect ATP content, or as a reporter in biological assays, in cell culture, and more recently in noninvasive whole-body bioimaging. In spite of numerous studies, the mechanism of the light-emission reaction of Ppy has not been fully clarified. Modification of substrate structure will offer to probe catalytic biological reactions, results to develop synthetic luciferin having novel characteristics offer opportunities for studying biological assay. We have synthesized various luciferin analogs having different aromatic moiety for this purpose. For example, we have recently reported the simple substituted phenyl analogs (4-hydroxyphenyl and 4-dimethylaminophenyl) are capable to act as substrates, and also found the luminescence color can be controlled by the number of conjugated double bonds connecting between phenyl and thiazoline moiety. In this study, we designed various synthetic luciferin analogs as shown in figure 1. Bioluminescence intensity of these compounds was notoriously reduced compared from natural substrate D-luciferin, or some of them do not worked as substrate. Although, acceptable bioluminescence have been obtained from several compounds. Among them, 4,4'-biphenyl analog possessed bioluminescence activity emitting near-infrared biological window light at 675 nm suitable for deep site bioimaging of living animals. Interestingly, the chemiluminescence light emission maximum of the corresponding methyl ester was 500 nm. This large light emission maximum difference (175 nm) between chemiluminescence and bioluminescence implying that biphenyl and thiazolinone rings in light emitter might be placed in a co-planar conformation at the luciferase active site. To better understand this phenomenon, DFT and time-dependent (TD) DFT calculation on twisted and planar conformers were conducted at B3LYP/6-31G(d) level. The rotational energy barrier is found to be smaller than that of ethane, suggested that biphenyl moiety is easy to form planar conformation. In addition, dipole moment was diminished for the twisted conformation. These results supporting the hypothesis that the mobility of the biphenyl moiety and thiazolinone ring system is strongly restricted at the luciferase active site due to the characteristic of the molecular structure, and the dipole moment may affect the bioluminescence color. Prior to apply for biological assay with animals, these synthetic substrates require to improve water solubility, higher bioluminescence intensity, and have to check the toxicity, though these findings provide clue for further substrate design.

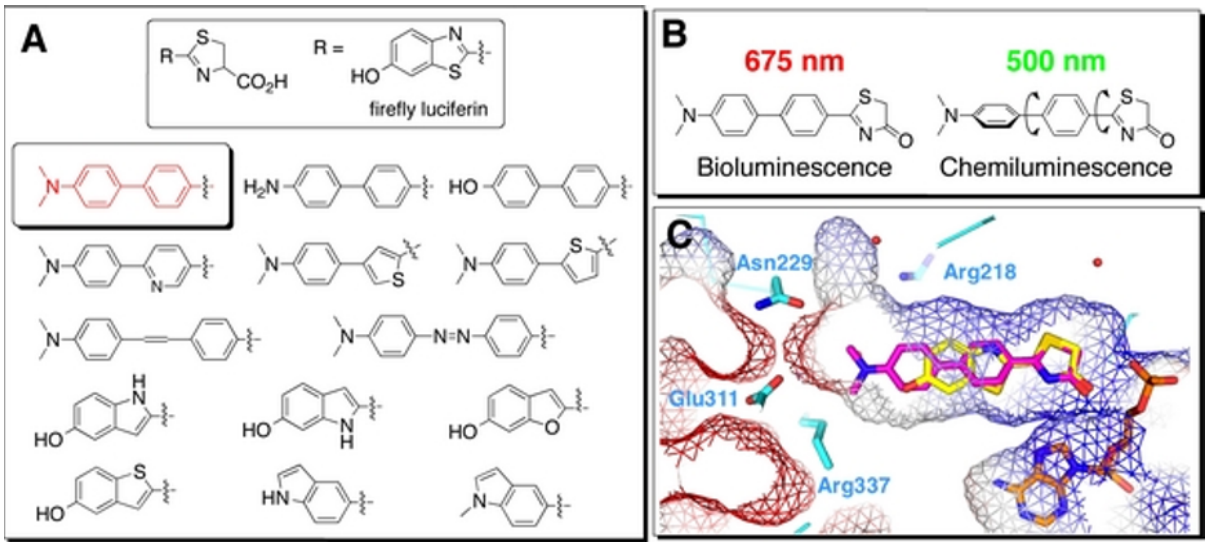

Figure 1. A) Chemical structure of synthetic substrates. B) Bioluminescence and chemiluminescence emission maximum of biphenyl analog. C) Structure around plausible ligand-binding site of *P. pyralis* luciferase and overlay model of biphenyl analog, oxyluciferin and AMP.

Disclosure of author financial interest or relationships:
R. Obata, None; **C. Miura**, None; **S. Iwano**, None; **K. Ito**, None; **M. Kiyama**, None; **T. Hirano**, None; **S.A. Maki**, None; **H. Niwa**, None.

Presentation Number **LBAP 039**
Late Breaking Abstract Poster Session
September 19, 2013 / 15:15-15:15 / Room: Exhibit Hall B

Development of Azo-based Fluorescence Probes to Detect Hypoxia

Wen Piao[1], *Satoru Tsuda*[2], *Yuji Tanaka*[2], *Toru Nakazawa*[2], *Kenjiro Hanaoka*[1], *Tetsuo Nagano*[3], [1]*Graduate School of Pharmaceutical Sciences, The University of Tokyo, Bunkyo-ku, Japan;* [2]*Department of Ophthalmology, Tohoku University Graduate School of Medicine, Sendai, Japan;* [3]*Open Innovation Center for Drug Discovery, The University of Tokyo, Bunkyo-ku, Japan. Contact e-mail: 6713775124@mail.ecc.u-tokyo.ac.jp*

Inadequate supply of oxygen is deeply related to various pathologies such as cancer, cardiopathy and vascular diseases and provokes unique biological phenomena. Therefore, tools to detect and visualize hypoxia are highly required to investigate its biological effects. Especially, hypoxia sensor with high oxygen sensitivity is preferred to detect the mild hypoxic regions where hypoxia inducible factor 1α (HIF-1α) starts to be activated. It is known that increase of reductive stress is one of the features in hypoxia and several compounds including azo compounds are selectively reduced under hypoxic condition. Besides this hypoxia-dependent reduction, azo dyes are also known to be nonfluorescent because of their ultrafast photoisomerization process to quench photoexcitation energy. Taking advantage of these phenomena, we have developed novel hypoxia-sensitive fluorescence probes, mono azo rhodamine (MAR) and mono azo Si-rhodamine (MASR), based on two different colored fluorophores. They contains azo group conjugated to the xanthene moiety of rhodamine derivatives. Under normoxic condition, the compounds are nonfluorescent due to ultrafast conformational change around the N=N bond. On the other hand, under hypoxia, the azo group is selectively reduced by reductases, releasing strongly fluorescent rhodamine derivative, which was confirmed by HPLC analysis. Furthermore, live cell assay such as fluorescence microscopic imaging and flow-cytometric analysis revealed that MAR and MASR show different hypoxia detection thresholds, i.e., their fluorescence intensity increased as the oxygen concentration fell below 5% and 1%, respectively. This is the first report of the fluorescence probes that demonstrate deferent sensitivity to hypoxia, and indicates that MAR is a useful tool to detect mild hypoxia region. Since their detection wavelength is different, simultaneous usage of two probes enabled to monitor the relative hypoxia severity by multicolor imaging method. Moreover, we successfully visualized retinal hypoxia with MAR in a rat model of retinal artery occlusion, demonstrating its usefulness in vivo. MAR and MASR are not only the practical probes to detect hypoxia in living cells, they also provide a simple design strategy which suggests that utilization of azo group would be effective to further develop fluorescence probes with different color and different threshold levels of response to hypoxia.

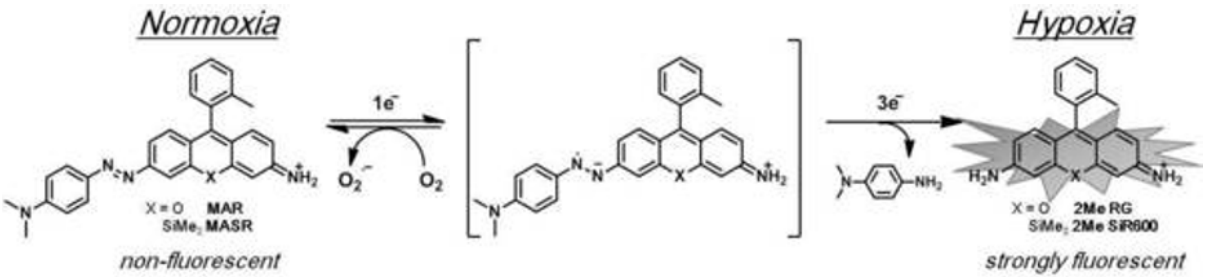

Disclosure of author financial interest or relationships:
W. Piao, None; **S. Tsuda**, None; **Y. Tanaka**, None; **T. Nakazawa**, None; **K. Hanaoka**, None; **T. Nagano**, None.

Presentation Number **LBAP 040**
Late Breaking Abstract Poster Session
September 19, 2013 / 15:15-15:15 / Room: Exhibit Hall B

Ultrabright and Ultrastable Organic Fluorescent Dots for Cell Tracing

Kai Li, *Synthesis & Integration, Institute of Materials Research & Engineering, Singapore, Singapore. Contact e-mail: lik@imre.a-star.edu.sg*

Fluorescence techniques have been extensively employed to develop non-invasive methodologies for tracking and understanding complex biological processes both in vitro and in vivo, which is of high importance in modern life science research. Among a variety of fluorescent probes, inorganic semiconductor quantum dots (QDs) have shown advantages in terms of better photostability, larger Stokes shift and more feasible surface functionalization. However, their intrinsic toxic heavy metal components and unstable fluorescence at low pH greatly impede the applications of QDs in in vivo studies. In this work, we aim to develope novel fluorescent probes that can outperform currently available QD based probes in practice. Using conjugated polymers/oligomers as the fluorescent domain and biocompatible lipid-PEG derivatives as the encapsulation matrix, the obtained organic dots have shown higher brightness, better stability in biological medium and comparable size and photostability as compared to their counterparts of inorganic QDs. More importantly, unlike QD-based probes, the organic fluorescent dots do not blink, and also do not contain heavy metal ions that could be potentially toxic when applied for living biosubstrates. Upon surface functionalization with a cell-penetrating peptide, the organic dots greatly outperform inorganic quantum dots in both in vitro and in vivo long-term cell tracing studies, which will be beneficial to answer crucial questions in stem cell/immune cell therapies. Considering the customized fluorescent properties and surface functionalities of the organic dots, a series of biocompatible organic dots will be developed to serve as a promising platform for multifarious bioimaging tasks in future.

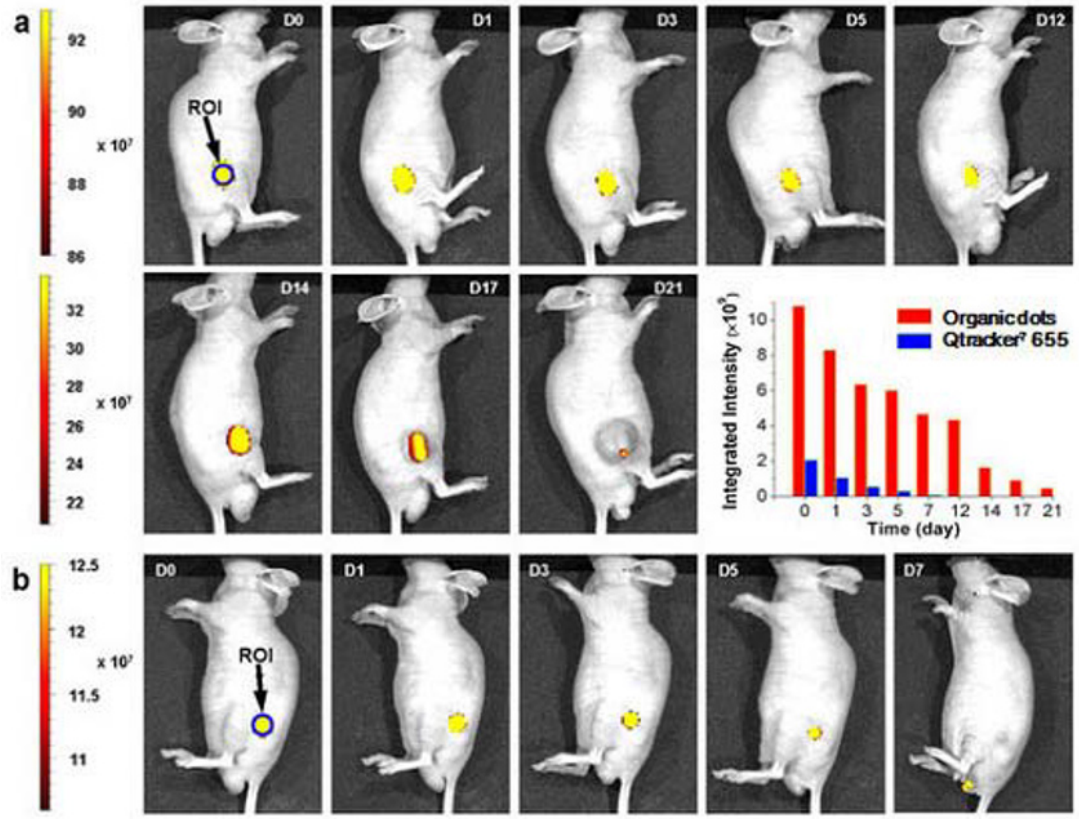

Figure 1. *In vivo* fluorescence imaging of tumor cells by organic dots. (a) Representative *in vivo* fluorescence images of the mouse subcutaneously injected with 1×10^6 of C6 glioma cells after staining by 2 nM organic dots. (b) Data for Qtracker® 655 obtained under similar conditions. The images were taken on designated days post cell injection. The inset in the middle panel shows the integrated PL intensities of the regions of interest (blue circles) at the tumor sites from the corresponding images.

Disclosure of author financial interest or relationships:
K. Li, None.

Presentation Number **LBAP 041**
Late Breaking Abstract Poster Session
September 19, 2013 / 15:15-15:15 / Room: Exhibit Hall B

A Zwitterionic Near Infrared Probe for Type 2 Cannabinoid Receptor Targeted Imaging

Ningyang Jia[1,2], *Shaojuan Zhang*[1], *Pin Shao*[1], *Mingfeng Bai*[1], [1]*Radiology, University of Pittsburgh, Pittsburgh, PA, USA;* [2]*Radiology, Shanghai Eastern Hepatobiliary Hospital, Shanghai, China. Contact e-mail: jianingyang.ehbh@gmail.com*

Introduction: The type 2 cannabinoid receptor (CB2R) plays a vital role in cancer evolution and progression, and is emerging as a therapeutic target for cancers. However, the exact role of CB2R in cancer progression and therapy remains unclear. This has driven the increasing efforts of studying CB2R and cancers using molecular imaging tools. In addition, many types of cancers over-express CB2R, and the expression levels of CB2R appear to be associated with tumor aggressiveness. Such up-regulation of the receptor in cancer cells provides opportunities in CB2R targeted imaging with high contrast and therapy with low side effects. However, the field of CB2R targeted imaging, particularly in oncology, is largely unexplored. We previously reported the first near infrared (NIR) CB2R targeted fluorescent probe, NIR-mbc94, and validated its CB2R binding in vitro. While the specific binding of NIR-mbc94 to CB2R has been demonstrated, this probe also exhibits significant non-specific binding. A recent study shows that replacement of a charged NIR dye with a zwitterionic one could significantly reduce the non-specific binding of targeted fluorescent probes. In an effort to improve the CB2R binding selectivity, in the present study, we synthesized a novel CB2R targeted probe with a zwitterionic NIR dye and investigated its specific targeting using a mouse malignant astrocytoma cell line transfected with CB2R. Methods: To develop the zwitterionic NIR CB2R probe (ZW-mbc94), we synthesized a functional CB2R ligand, mbc94, and coupled it to a zwitterionic NIR dye, ZW760. The specific binding of ZW-mbc94 to CB2R was studied quantitatively using a multi-plate reader system and the cellular localization of ZW-mbc94 was visualized using fluorescent microscopy. Results: ZW-mbc94 shows intense NIR absorption and emission in water at 762 nm and 781 nm respectively, with a fluorescence quantum yield as high as 15.2%. The uptake of ZW-mbc94 in CB2+ delayed brain tumor (DBT) cells was significantly reduced by 4-Quinolone-3-Carboxamide, a well-known CB2R ligand, indicating CB2R specific binding of ZW-mbc94. In fluorescence microscopy study, cells incubated with ZW-mbc94 showed strong fluorescence signal which was primarily localized in cytoplasm. Similarly, CB2+ DBT cells treated with ZW-mbc94 showed significantly higher fluorescence signal than challenged cells pretreated with CB2R competitor 4-Quinolone-3-Carboxamide. Conclusion: Our in vitro binding and cell imaging studies indicate that ZW-mbc94 specifically labeled CB2R with reduced non-specific binding. Such an imaging tool may have great potential in imaging various diseases that upregulate CB2R, as well as studying the regulatory functions of the receptor in disease progression.

Disclosure of author financial interest or relationships:
N. Jia, None; **S. Zhang**, None; **P. Shao**, None; **M. Bai**, None.

Presentation Number **LBAP 042**
Late Breaking Abstract Poster Session
September 19, 2013 / 15:15-15:15 / Room: Exhibit Hall B

GX1-conjugated Endostar : a new drug delivery system for anti-colorectal cancer in vivo

Qian Zhang[1], *Yaqian Li*[2], *Xiaolong Liang*[3], *Xin Yang*[4], *Yang Du*[4], *Jie Tian*[1], [1]*School of Life Sciences and Technology, Xidian University, xian, China;* [2]*Harbin University of Science and Technology, Harbin, China;* [3]*College of engineering, Peking University, Beijing, China;* [4]*Intelligent Medical Research Center, Chinese Academy of Sciences, Beijing, China. Contact e-mail: zhangqian@life.xidian.edu.cn*

Abstract Aims: (1). To verify the colorectal tumor targeting effects of GX1 peptide (CGNSNPKSC), a previous reported tumor vascular endothelial cell specific ligand identified by phage display, near-infrared (NIR) fluorescence imaging system (FMI) was used to determine the peptide distribution . (2). Endostar (endo) is a novel recombinant endostain, and has been reported to have anti-tumor growth effects. We evaluated the GX1-endo treatment efficacy in colorectal xenografts in nude mice through longitudinal bioluminescence imaging (BLI) in vivo. Methods: (1). Colo-205-Luc2-2C1 cells, which express luciferase gene and can be detected through BLI in vivo, was used for making colorectal xenografts in nude mice in our study system. (2). The peptide GX1 was conjugated to the NIR dye CW800 nanocapsules to make the molecular targeting probe. The BLI signal was first captured to detect the tumor location. Then the in vivo dynamic bio-distribution of GX1-conjugated CW800 and the unconjugated CW800 nanocapsules (as control) were evaluated through FMI. (3). For the drug treatment evaluation, endo alone and GX1-endo groups were given the corresponding drugs through intravenous tail injection. Endostar was coated with PLA (Poly lactic acid), and last amino acid of GX1 was conjugated to the Endostar-loaded PLA nanoparticles. The drug dosage was 10 mg/kg/day and was administrated for continuous 10 days. The control group was given an equal amount of 0.9% saline. In vivo BLI was carried out for every 3 days. Results: (1) As shown in Figure 1a, the ICG signal can be clearly detected in the tumor site in the colorectal tumor-bearing nude mice 5-18 hours after injection of GX1-conjugated CW800 nanocapsule, while there was no evident ICG accumulation in the tumor site in the control group. (2) The BLI data showed that the GX1-endo treated group had better tumor inhibition effects compared to the endo-treated group during the whole 10 day treatment shown in Figure 1b. Conclusion: We successfully developed a tumor specific NIR fluorescent probe, GX1-conjugated CW800 nanocapsules, which can be used for tumor angiogenesis imaging and holds a potential for the future clinical translation. The new GX1-endo drug delivery system had a better tumor targeting and anti-tumor growth efficacy than endo alone.

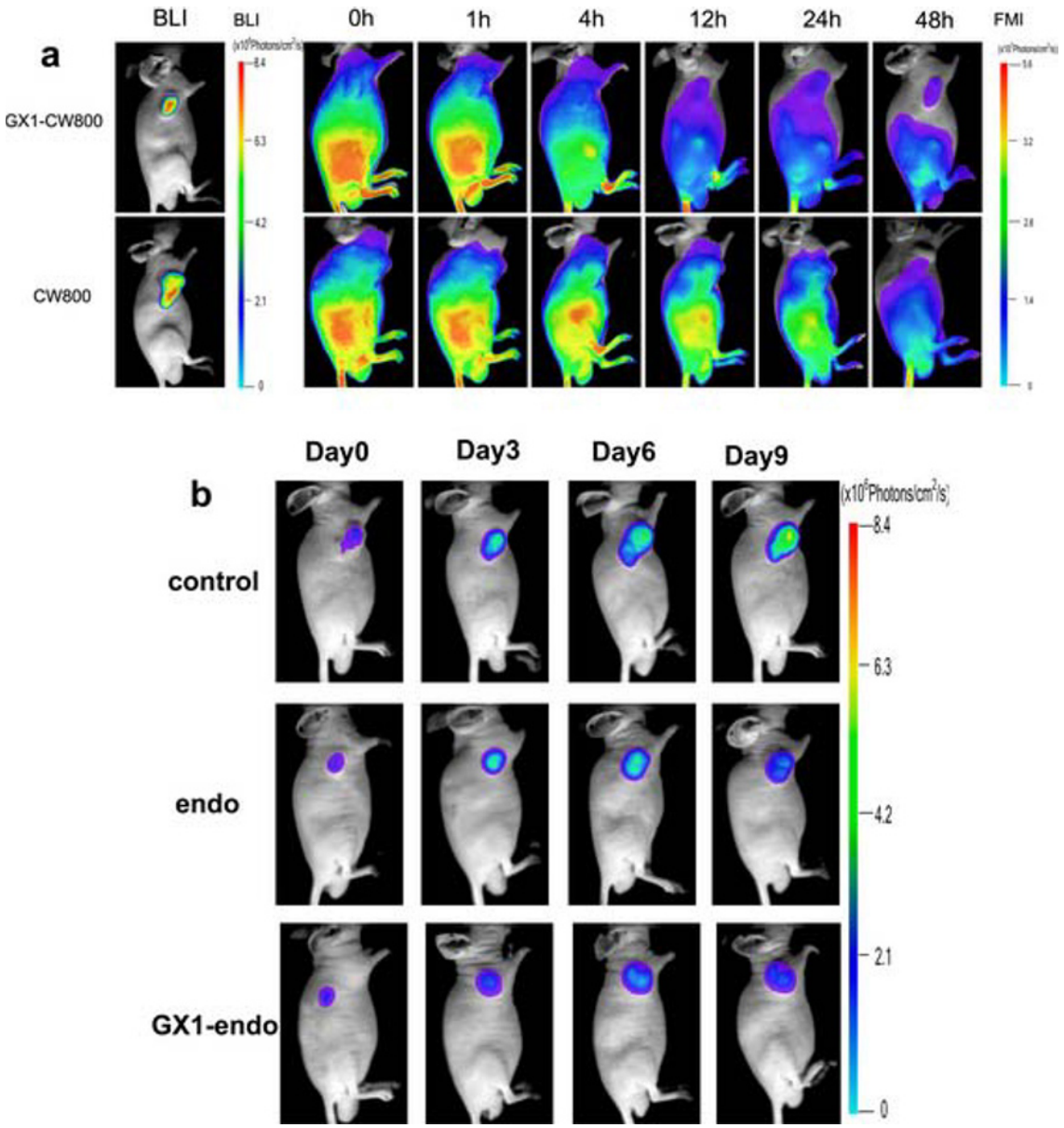

Figure 1a. Bio-distribution of GX1-conjugated CW800 nanocapsules and unconjugated CW800 nanocapsules through fluorescence molecular imaging (FMI) in colorectal tumor-bearing mice. Figure 1b. The in vivo real-time longitudinal bioluminescent imaging (BLI) of colorectal tumor-bearing mice in control,endo and GX1-endo treated groups.

Disclosure of author financial interest or relationships:
Q. Zhang, None; **Y. Li**, None; **X. Liang**, None; **X. Yang**, None; **Y. Du**, None; **J. Tian**, None.

Presentation Number **LBAP 043**
Late Breaking Abstract Poster Session
September 19, 2013 / 15:15-15:15 / Room: Exhibit Hall B

Research of fluorescent dyes and probes for staining the cellular organelles

Myeong Ju Moon, *Dong hwi Shim, Dae Su Park, Kiwon Kim, Jong Joo Na, Jin Woo Park, Affiliated Research Institute, DKC Corporation (BioActs), Incheon, Republic of Korea. Contact e-mail: mjmoon2398@bioacts.com*

Optical imaging is one of the molecular imaging techniques which utilize light for visualization at the molecular level. In particular, fluorescence imaging is the widely used imaging technique in the field of molecular biology due to its simplicity, availability and user friendly handling of the instruments and more over the various organelles can be visualized with different colors at the same time(with the help of this method). In recent years, Targeted fluorescent labeled bio probe or organic fluorescent material is used for organelle specific staining and for analyzing the cell specific marker expression with more accuracy than the normal fluorescent stains. The aim of this study is to develop a fluorescence dye which is able to specifically stain the cellular organelles. In order to selectively stain the cell membrane, we have developed a cationic hydrophobic fluorescent dyes which will be attaching to the phospholipids present in the cell membrane. Also, these functional dyes were developed to emit in the various wavelengths to satisfy the research convenience. The dyes were found to be non-toxic to the cells and the preparation of the dye for staining can be done with a relatively simple protocol. The dyes can also stain the cell walls of the microorganism through the staining of flagellins present in the outer membrane. In addition the dyes have shown more preference to the specific cell type by recognizing the cell specific markers. For instance, we have specifically labeled the immune cells by attaching mannan and glucan to the organic dyes. The mannan and glucan functionalization of the dyes will help them to specifically recognize the receptors present on the immune cells. So with in a pool of cells an immune cell can be recognized and stained with these kinds of dyes in an individual manner. HA labeled fluorescent dyes can be employed for recognizing the CD44 over expressing cancer cells, which will help in cancer cell specific visualization. We have used vinylsulfone functionalized fluorescence dye for manufacture all type of fluorescent marker. The advantage of this functionalization is that, there will be no residual material remaining after conjugation with the main body. In conclusion the organelle staining can be done in a more effective manner than the available fluorescent dyes. The target specific fluorescent dyes will increase the specificity and reduce the time for specific biomarker identification. The immune cell activity can be visualized after labeling the cells with specific probes, which will improve the monitoring in the cellular therapy. Since the dye is targeted, the cells can be visualized with the minimum quantity of fluorescent dyes and the activity of the cells will be in the native condition when they are exposed to lower quantity of staining materials.

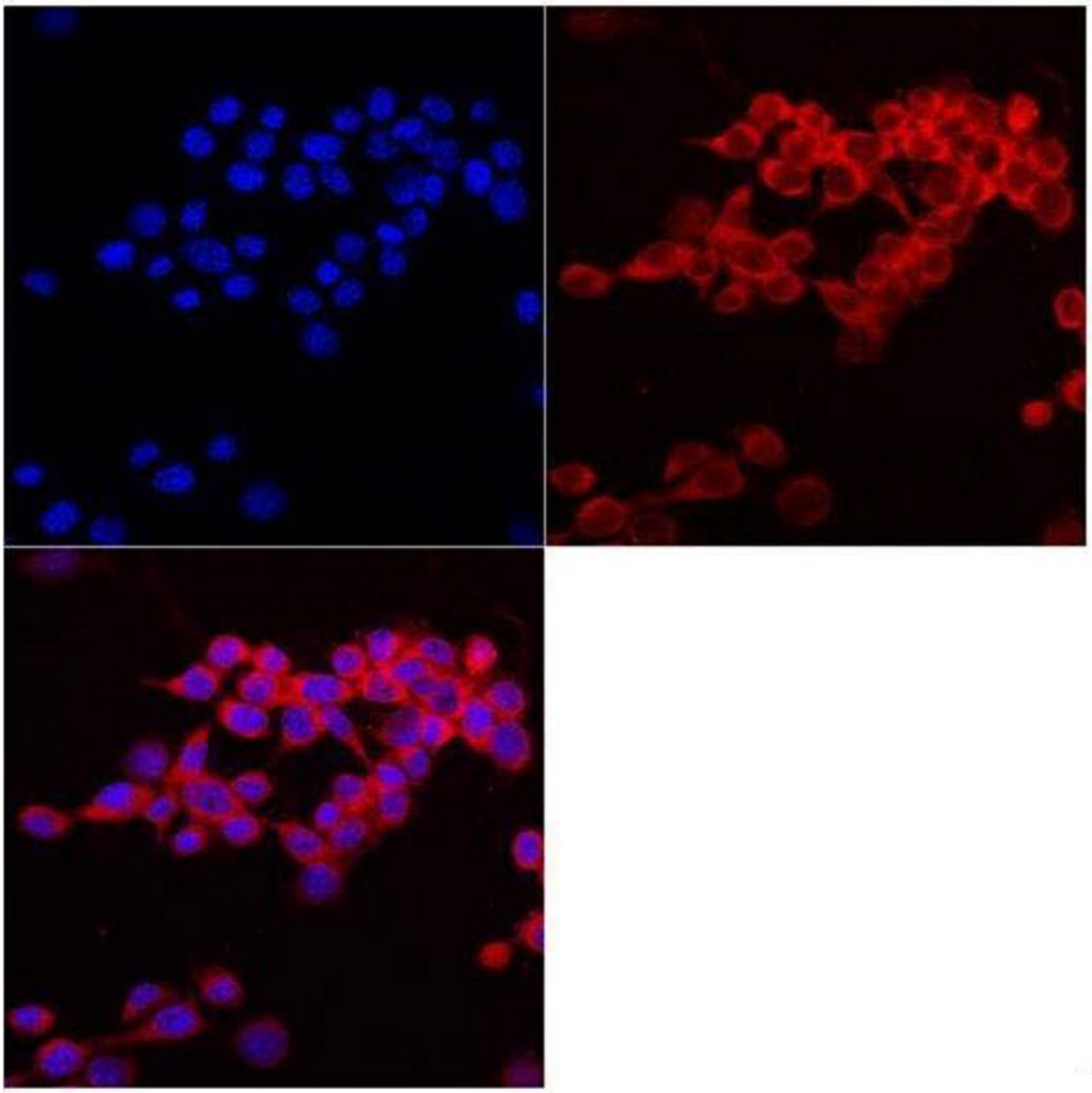

SCC7 cell line, CD44 specific fluorescent labeling of HA-Flamma

Specific target moieties for binding cellular organelles

Target Organelle	Specific targeting moieties
Nucleus	DAPI
Plasma membrane	branched polyethylenimine
Lysosome	pH indicator
Mitochondrion	OxPhos complex IV
Golgi body	golgi-97
Cytoplasm	branched polyethylenimine
Actin	phalloidin
Autophagosome	LC3B antibody
tubulin	tubulin antibody

Disclosure of author financial interest or relationships:

M. Moon, None; **D. Shim**, None; **D. Park**, None; **K. Kim**, None; **J. Na**, None; **J. Park**, None.

Presentation Number **LBAP 044**
Late Breaking Abstract Poster Session
September 19, 2013 / 15:15-15:15 / Room: Exhibit Hall B

Non-invasive Detection of Early Metabolic Remodeling in Left Ventricular Hypertrophy

Min Zhong[1,2], *Yasmin S. Hamirani*[3], *Jamieson M. Bourque*[3], *Bijoy K. Kundu*[2], [1]*Physics, University of Virginia, Charlottesville, VA, USA;* [2]*Radiology and Medical Imaging, University of Virginia, Charlottesville, VA, USA;* [3]*Medicine, University of Virginia, Charlottesville, VA, USA. Contact e-mail: mz3bs@virginia.edu*

Introduction: Diastolic heart failure is a major source of morbidity and mortality and early identification is key to prevent disease progression. We assessed the hypothesis that metabolic remodeling precedes structural and functional remodeling in hypertension-induced LVH. Methods: We recruited 18 patients, 5 with hypertension (HTN) and left ventricular hypertrophy (LVH) (group A), 5 with hypertension without LVH (group B), and 8 controls with neither LVH nor HTN (group C). The presence of hypertension was determined through chart review and LV mass, wall thickness, and left ventricular ejection fraction were assessed by echocardiography. Heart weight to body weight ratios (HW/BW) were measured using LV mass. All the patients in the 3 different groups fasted overnight for the 2-[18F]fluoro-2deoxy-D-glucose (FDG) positron emission tomography (PET) scan. A 20-minute dynamic PET scan was performed with cardiac gating on a Siemens Biograph mCT PET-CT scanner, where data acquisition was initiated a few seconds before the slow administration of 10-15 mCi FDG over 30 seconds via an intravenous catheter. A CT scan was performed before the FDG PET scan for attenuation correction. The PET images were reconstructed using an iterative reconstruction algorithm using the following dynamic frames (#, time in seconds): 12,10;8,30;8,60;2,180. Regions of interest (ROIs) were drawn in the regions corresponding to the LV blood pool and the myocardium and time activity curves were generated from the dynamic PET images. A model in which the blood input function with spill-over and partial volume corrections and the metabolic rate constants were simultaneously estimated in a 3-compartment kinetic model, were used to determine the rate of myocardial FDG uptake, Ki (ml/min/g). Mean values of Ki, HW/BW ratios and wall thickness in the 3 groups of patients were compared using ANOVA and Tukey's Studentized Range testing. Results: The mean age differed significantly between the 3 groups ($p=0.001$); it was lower in group C (35±10) than in group A (60±8, $p=0.014$) and group B (62±12, $p=0.002$). Female gender comprised 75% of the patient population in the control group with 80% and 40% respectively for groups A and B. Figures 1(A-C) indicate that significant metabolic changes precedes the development of LVH with preserved ejection fraction. The mean value for the 3 groups different significantly for the metabolic measurements, Ki ($p<0.001$); it was higher in group B compared to group A ($p<0.001$) and group C ($p=0.026$). The mean Ki for the controls differed significantly from the LVH group ($p<0.001$). The lower myocardial FDG uptake in the LVH patient population (group A) may be secondary to insulin resistance (IR). There was no significant difference in HW/BW ($p=0.311$) and septal wall thickness ($p=0.175$) measurements between the 3 groups. Conclusions: Non-invasive detection of early metabolic changes precedes the development of left ventricular hypertrophy and may allow early aggressive therapy to prevent disease progression. Further research is necessary to assess if IR is the cause of low FDG uptake in LVH. Acknowledgement: University of Virginia Thelma R. Swortzel Award

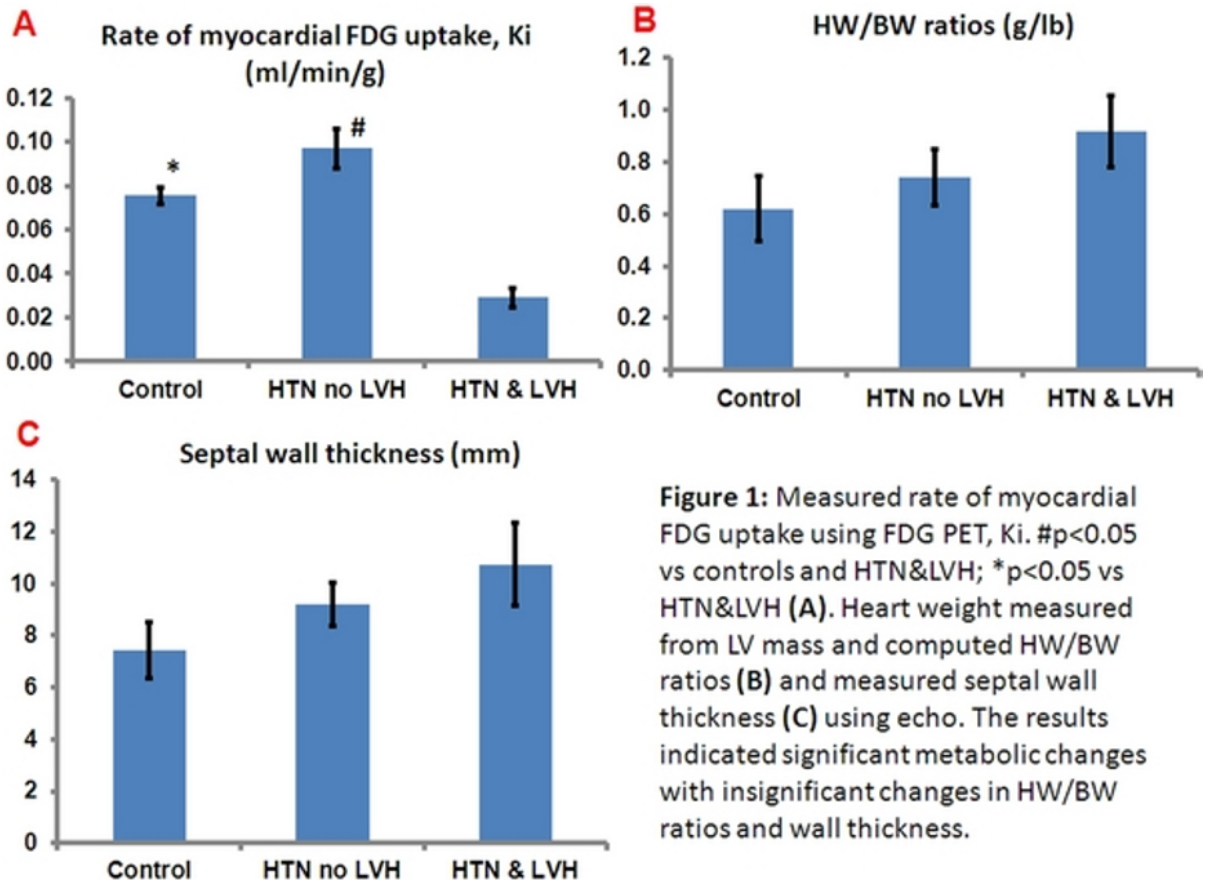

Figure 1: Measured rate of myocardial FDG uptake using FDG PET, Ki. #p<0.05 vs controls and HTN&LVH; *p<0.05 vs HTN&LVH **(A)**. Heart weight measured from LV mass and computed HW/BW ratios **(B)** and measured septal wall thickness **(C)** using echo. The results indicated significant metabolic changes with insignificant changes in HW/BW ratios and wall thickness.

Disclosure of author financial interest or relationships:
M. Zhong, None; **Y.S. Hamirani**, None; **J.M. Bourque**, None; **B.K. Kundu**, None.

Presentation Number **LBAP 045**
Late Breaking Abstract Poster Session
September 19, 2013 / 15:15-15:15 / Room: Exhibit Hall B

White matter micro structural changes in alcohol dependents: Relation to impaired visual information processing

Deepika Bagga[1], *Aakansha Sharma*[1], *Debajyoti Bhattacahrya*[2], *Mohan Garg*[3], *Subash Khushu*[1], *Namita Singh*[1], [1]*NMR Research Centre, INMAS, Delhi, India;* [2]*Psychiatry, Base Hospital, Delhi, India;* [3]*Biophysics, Panjab University, chandigarh, India. Contact e-mail: deepikabagga13@gmail.com*

Introduction: Chronic alcohol abuse is characterized by impaired cognitive abilities with a more severe deficit in visual than the verbal functions. The visual processing deficits have classically been associated with impaired function of occipital lobes, but more recently, also with alterations within the fronto-occipital circuitry [1, 2]. Disruption of this fronto occipital connectivity might lead to brain dysfunction manifested in impaired visual processing in alcohol dependents. In order to explore the relationship between white matter characteristics in the fronto-occipital circuit and visual processing in alcohol-dependent subjects, we performed a Diffusion tensor Imaging (DTI) study. Methods: The DTI study was performed on 35 alcohol dependent subjects (DSM IV criteria) and 30 healthy individuals. All images were acquired in the axial plane using 3-T MRI scanner (Magnetom, Skyra, Siemens) with a 20 channel head and neck coil. DTI data were acquired using a single-shot echoplanar dual SE sequence in 30 directions with ramp sampling. Diffusion-weighted acquisition parameters were: b-factor = 0 and 1000 s/mm2, slice thickness = 3 mm with no interslice space, number of slices = 45, FOV = 230 mm×230 mm, matrix size = 128 ×128, spatial resolution = 1.797 mm×1.797 mm×3 mm, flip angle 90degrees, TR = 8800 ms, TE = 95 ms and NEX = 2.2.3. Average ADC map, trace weighted map, FA map, and tensor data were created inline. The diffusion data was post-processed using the DTI module included in the Syngo® VD13A imaging software platform. To explore the neuropsychological status, PGIBBD (PGI-Battery of Brain Dysfunction test (an Indian version of Wechsler Scale) was performed on these subjects on the day of examination [3]. The subjects were abstained from alcohol at the time of study with an abstinent period of more than two weeks. All statistical analyses were performed using SPSS (version 11.5, SPSS Inc, Chicago, USA) statistical software. Results and discussion: A reduced FA (fractional anisotropy) and increased MD (Mean diffusivity) was observed bilaterally in inferior and superior fronto-occipital fasciculus (FOF) fiber bundles. A significant inverse correlation in Dysfunction rating score and FA values was observed in these fiber tracts whereas positive correlation of these scores was found with MD values. Our results suggest that FOF fiber bundles linking the frontal lobe to occipital lobe might be related to visual processing skills. This is the first report of an alteration of the white matter microstructure of FOF fiber bundles that might have functional consequence for visual processing in alcohol dependent subjects without manifest neurological complications. Conclusion: In conclusion, we demonstrated in alcohol-dependent subjects the marked alterations in FOF white matter bundles, which may underlie their visual processing deficits. References: 1. Modi S et al. 2011.Eur. J. Radiol. 79, 96-100. 2. Schmahmann and Pandya,2007. J. Hist. Neurosci.16, 362-377. 3. Pershad and Verma, 1990. Handbook of PGI battery of brain dysfunction (PGI-BBD). Agra, India: National Psychological Corporation.

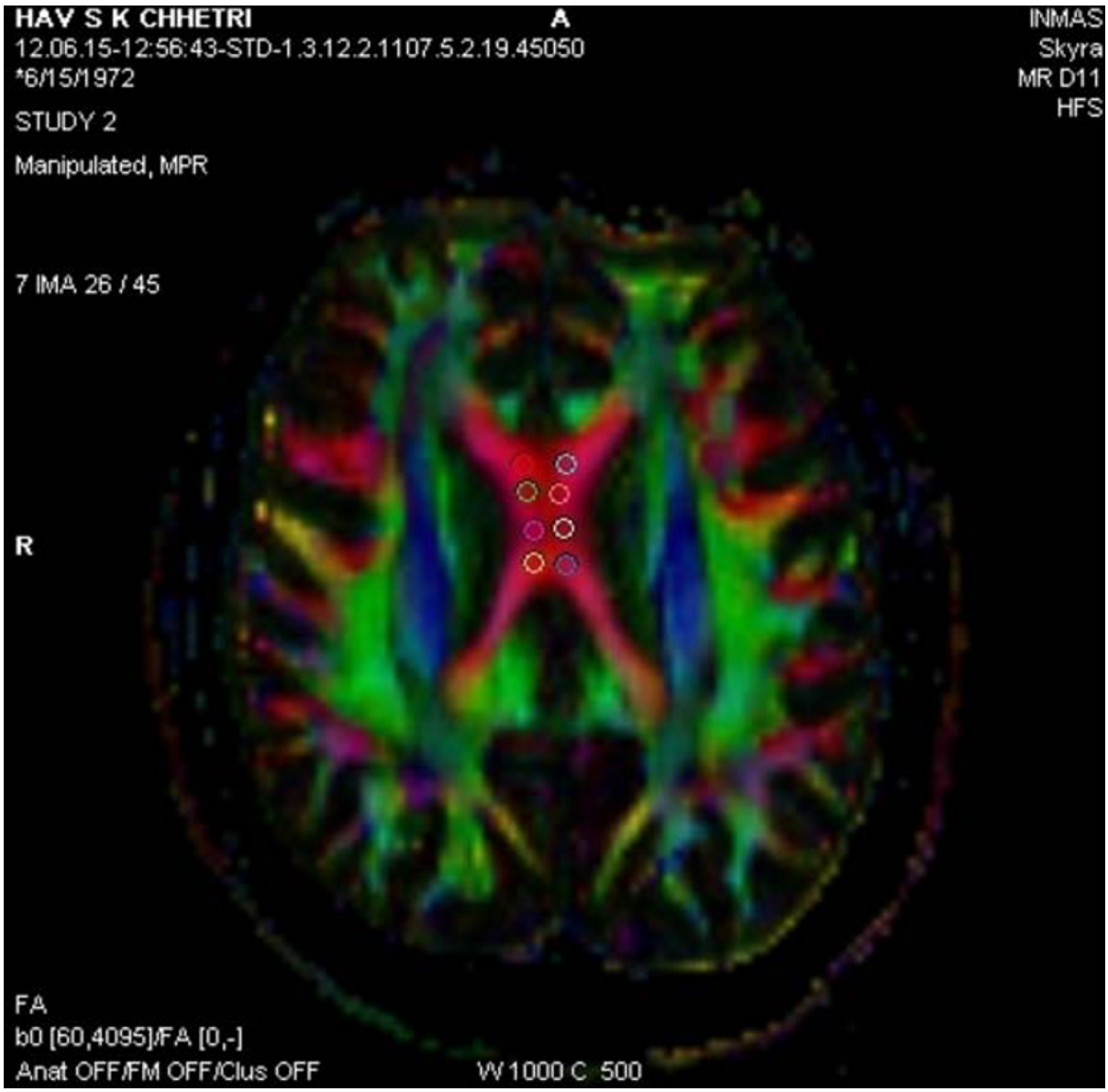

Figure1.FA map showing ROIs placed on the corpus callosum tracts.

Disclosure of author financial interest or relationships:
D. Bagga, None; **A. Sharma**, None; **D. Bhattacahrya**, None; **M. Garg**, None; **S. Khushu**, None; **N. Singh**, None.

Presentation Number **LBAP 046**
Late Breaking Abstract Poster Session
September 19, 2013 / 15:15-15:15 / Room: Exhibit Hall B

Accuracy of linearised models for measuring [^{18}F]FDG kinetics and CMR_{glu}

Marc Huisman[1], *Larissa van Golen*[2], *Hans Harms*[1], *Michaela Diamant*[2], *Adriaan A. Lammertsma*[1], [1]*Radiology & Nuclear Medicine, VU University Medical Center, Amsterdam, Netherlands;* [2]*Diabetes Center/Department of Internal Medicine, VU University Medical Center, Amsterdam, Netherlands. Contact e-mail: m.huisman@vumc.nl*

Aim Cerebral metabolic rate of glucose (CMR_{glu}) can be measured using [^{18}F]FDG and PET. The gold standard analytical method is full kinetic analysis using a two tissue compartment model with an arterial plasma input function. This allows for estimation of individual rate constants as well as net rate of influx $K_i = K_1k_3/(k_2+k_3)$ from which CMR_{glu} can be calculated as $CMR_{glu} = K_i \bullet C_{glu}/LC$, where C_{glu} is plasma glucose concentration and LC the lumped constant. Linearisations are needed to allow for parameter estimatitions at the voxel level. Indeed, Patlak graphical analysis is in common use to generate parametric maps of K_i. The Blomqvist linearisation is not in general use, although it provides a means to also determine individual rate constants, which can be used to assess the LC and brain tissue glucose concentration [1,2]. The purpose of the present study was to assess accuracy of both linearisations. **Methods** In this study 9 healthy control (HC) subjects and 28 type 1 diabetic men (T1DM) were included. Dynamic PET scans were acquired for 1 hour using an HRRT scanner (CTI/Siemens, Knoxville, USA) following injection of 185 MBq [^{18}F]FDG. For each subject the arterial plasma input function was obtained using a continuous on-line sampling device. A subject specific 3D structural MRI scan (3T Signa scanner, GE, Milwaukee, USA) was used to delineate 34 individual grey matter (GM) regions based on a standard template (PVElab [3]). For each subject, models were fitted to each regional time-activity curve and resulting parameters were averaged over all regions. For each group, $K_{i,P}/K_{i,NLR}$, $K_{i,B}/K_{i,NLR}$, $K_{1,B}/K_{1,NLR}$, $k_{2,B}/k_{2,NLR}$ and $k_{3,B}/k_{3,NLR}$ ratios were derived (P is Patlak, B is Blomqvist, mean ± SD over number of subjects per group). **Results** For the HC group $K_{i,P}/K_{i,NLR}$ and $K_{i,B}/K_{i,NLR}$ ratios of 0.96 ± 0.02 and 0.97 ± 0.02 were obtained. The $K_{1,B}/K_{1,NLR}$, $k_{2,B}/k_{2,NLR}$ and $k_{3,B}/k_{3,NLR}$ ratios were 1.11 ± 0.07, 0.97 ± 0.20 and 0.75 ± 0.10, respectively. For the T1DM group $K_{i,P}/K_{i,NLR}$ and $K_{i,B}/K_{i,NLR}$ ratios of 0.99 ± 0.08 and 1.01 ± 0.06 were obtained. For this group $K_{1,B}/K_{1,NLR}$, $k_{2,B}/k_{2,NLR}$ and $k_{3,B}/k_{3,NLR}$ were 1.24 ± 0.10, 1.08 ± 0.14 and 0.81 ± 0.06, respectively. See supplemental data for correlation plots. **Conclusion** In HC and T1DM linearisations of the two tissue irreversible compartment model lead to less than 5% bias in estimated K_i (and thus CMR_{glu}). For the individual rate constants this bias is in the range of -25% to +25%. Therefore, the use of individual rate constants cannot be recommended. **References** [1] G. Blomqvist, On the construction of functional maps in positron emission tomography, J. Cereb. Blood Flow Metab 1984 (4), 629-632. [2] J.J. Tuulari, H.K. Karlsson, J. Hirvonen et al., Weight loss after bariatric surgery reverses insulin-induced increases in brain glucose metabolism of the morbidly obese, Diabetes 2013, Mar. 14 Epub ahead of print. [3] Svarer C, Madsen K, Hasselbalch SG et al., MR-based automatic delineation of volumes of interest in human brain PET images using probability maps, Neuroimage 2005;24(4):969-979.

Disclosure of author financial interest or relationships:
M. Huisman, None; **L. van Golen**, None; **H. Harms**, None; **M. Diamant**, None; **A.A. Lammertsma**, Philips, Grant/research support; Hoffmann-La Roche, Grant/research support .

Presentation Number **LBAP 047**
Late Breaking Abstract Poster Session
September 19, 2013 / 15:15-15:15 / Room: Exhibit Hall B

Use of [^{18}F]FAU and PET to Evaluate Hepatic Toxicity in Patients Receiving FAU in a Phase I Therapeutic Trial

Anthony F. Shields[1], *Jing Li*[1], *Richard A. Wiegand*[1], *Jawana Lawhorn-Crews*[1], *Kirk A. Douglas*[1], *Thomas J. Mangner*[2], *Patricia M. LoRusso*[1], [1]*Oncology and Medicine, Karmanos Cancer Institute, Wayne State University, Detroit, MI, USA;* [2]*Radiology, Wayne State University, Detroit, MI, USA. Contact e-mail: shieldsa@karmanos.org*

FAU (1-(2'-deoxy-2'-fluoro-β-D-arabinofuranosyl) uracil) is a pyrimidine analog undergoing evaluation as an antineoplastic agent. It has been studied in patients along with imaging of its distribution using [^{18}F]FAU with emission tomography (PET) to determine tumor uptake and retention. A patient treated on a Phase I trial of FAU (NCI #7916) developed delayed fatal liver toxicity, which has been reported with other pyrimidine analogs such as FIAU. Our objective of the present analysis was to measure the liver retention of FAU and determine if it was associated with this toxicity. Methods: We studied 12 patients who received escalating doses of therapeutic FAU. Each patient was imaged with [^{18}F]FAU on the day of first treatment with therapeutic doses of FAU. [^{18}F]FAU was injected at a median of 83 min after completion of the FAU infusion on day 1. Image analysis was done on whole body scans obtained on the PET/CT starting at a mean of 93 min (range 73-120 min) after [^{18}F]FAU injection. 5 cm Regions of Interest (ROI) were drawn on three consecutive planes over the liver to calculate the standardize uptake (SUVmean). Background activity and [^{18}F]FAU blood activity were also determined. Liver/blood ratio (L/B) was calculated as the liver [^{18}F]FAU activity divided by the SUV blood activity. Levels of therapeutic FAU in plasma (Cp) were measured by LC/MS/MS. The level of therapeutic FAU in the liver was estimated as Cp x L/B, and the area under the curve (AUC) in the liver was estimated as plasma AUC x L/B, assuming the FAU blood-to-plasma ratio is 1. Results: The liver SUVmean for the first 11 patients with no liver toxicity ranged 1.20 - 2.62 (median, 1.55) and was 1.56 for patient #12 with liver toxicity. For the first 11 patients, blood counts measured in SUV at 60 minutes were obtained, and SUV mean was 1.59 (range 0.88 - 2.15) with a mean L/B of 1.04 (range 0.63 - 1.84). For patient #12, blood counts measured in SUV at 60 minutes was 1.62 with a L/B of 0.96, within the range of the patients with no noted liver toxicity. The liver to background ratios ranged 2.50 - 6.65 (mean, 4.37) for the first 11 patients and was 6.14 for patient #12. The estimated levels of therapeutic FAU in the liver ranged 1.130 - 3.552 μg/ml (mean 2.273) for the 4 patients receiving the same dose (100 mg/m^2 weekly) as patient #12 but with no liver toxicity and was 3.254 μg/ml for patient #12. The estimated AUC in the liver ranged 22.2 - 75.6 μg/ml*h (mean 40.5) for these 4 patients and was 44.2 μg/ml*h for patient #12. Conclusions: FAU liver uptake for a patient with liver toxicity was not significantly different than that for the patients with no noted liver toxicity. No difference was seen using the simple measurement of liver SUV, the liver to blood ratio, or estimates of concentration and AUC of the therapeutic FAU in the liver. The precise molecular and genetic mechanisms underlying FAU-induced delayed liver toxicity needs further investigation.

Disclosure of author financial interest or relationships:
A.F. Shields, None; **J. Li**, None; **R.A. Wiegand**, None; **J. Lawhorn-Crews**, None; **K.A. Douglas**, None; **T.J. Mangner**, None; **P.M. LoRusso**, None.

Presentation Number **LBAP 048**
Late Breaking Abstract Poster Session
September 19, 2013 / 15:15-15:15 / Room: Exhibit Hall B

Bilateral Dynamic Contrast-Enhanced MR Imaging of the Breast at 7T: First Clinical Experience

Katja Pinker-Domenig[1], *Pascal A. Baltzer*[1], *Siegfried Trattnig*[4], *Wolfgang Bogner*[4], *Stephan Gruber*[4], *Olgica Zaric*[4], *Doris Leithner*[1], *Stephan H. Polanec*[1], *Peter C. Dubsky*[2], *Zsuszanna Bago-Horvath*[3], *Thomas H. Helbich*[1], [1]*Department of Radiology and Nucelar Medicine, Division of Molecular and Gender Imaging, Medical University Vienna, Vienna, Austria;* [2]*Dept. of Sugery, Medical University Vienna, Vienna, Austria;* [3]*Dept. of Pathology, Medical University Vienna, Vienna, Austria;* [4]*Department of Radiology, MR Centre of Excellence, Medical University Vienna, Vienna, Austria. Contact e-mail: katja.pinker@meduniwien.ac.at*

Purpose To evaluate bilateral dynamic contrast-enhanced MR imaging of the breast at 7 Tesla (7T DCE-MRI) using high spatial and temporal resolution in clinical practice. Materials and Methods Twenty-seven patients with a suspicious breast lesion (BIRADS 0, 4 and 5) were included in this IRB-approved prospective study. All patients underwent bilateral contrast-enhanced DCE-MRI of the breast at 7T with a dedicated four-channel breast coil and a contrast-enhanced 3D, T1-weighted, fat-saturated TWIST sequence (spatial resolution of 0.7mm3 voxel size, temporal resolution of 14sec). In four patients, the scan had to be aborted due to severe nausea or claustrophobia. Two readers (r1; r2) independently assessed lesions according to BI-RADS®. Image quality, lesion conspicuity and artifacts were graded from 1- 5. Sensitivity, specificity and diagnostic accuracy were assessed using histopathology as the standard of reference. Results There were ten benign and 19 malignant lesions in 23 patients. Mean size was 23.9 mm (range 8-47mm). DCE-MRI at 7T had a sensitivity of 100% (19/19) and a specificity of 90% (9/10) resulting in a diagnostic accuracy of 96.6% (28/29) with an AUC of 0.95. Overall image quality was excellent in the majority of cases (27/29) and examinations were not hampered by artifacts. There was excellent inter-reader agreement for image quality parameters, ranging from κ = 0.89-1. Conclusion Bilateral DCE-MRI of the breast using high spatial and temporal resolution with excellent image quality at 7T is feasible in clinical practice. Bilateral DCE-MRI of the breast at 7T allows highly reliable and accurate breast cancer diagnosis.

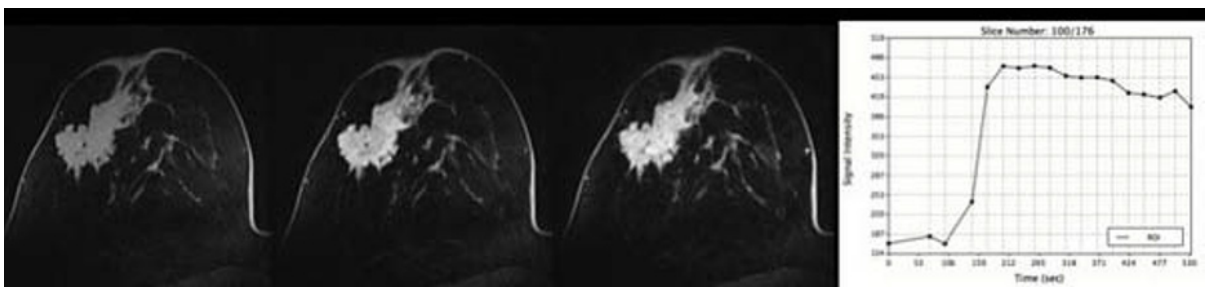

Disclosure of author financial interest or relationships:
K. Pinker-Domenig, None; **P.A. Baltzer**, None; **S. Trattnig**, None; **W. Bogner**, None; **S. Gruber**, None; **O. Zaric**, None; **D. Leithner**, None; **S.H. Polanec**, None; **P.C. Dubsky**, None; **Z. Bago-Horvath**, None; **T.H. Helbich**, None.

Presentation Number **LBAP 049**
Late Breaking Abstract Poster Session
September 19, 2013 / 15:15-15:15 / Room: Exhibit Hall B

PET/CT derived dosimetry of [^{89}Zr]cetuximab

Marc Huisman[1], *Nikos Makris*[1], *Arthur van Lingen*[1], *Willemien Menke-van der Houven van Oordt*[2], *Henk Verheul*[2], *Adriaan A. Lammertsma*[1], *Guus A. van Dongen*[1], [1]*Radiology & Nuclear Medicine, VU University Medical Center, Amsterdam, Netherlands;* [2]*Medical Oncology, VU University Medical Center, Amsterdam, Netherlands. Contact e-mail: m.huisman@vumc.nl*

Aim There is increasing interest in immunoPET, i.e. visualization of biodistribution and possible tumor targeting of positron labeled monoclonal antibodies (mAb) by positron emission tomography (PET) [1]. PET allows the visualization and quantification of the distribution of the tracer in the body [2,3]. To date, however, there has been no report on PET/CT derived dosimetry in men for a mAb labeled with a positron emitter. The advantage of the PET/CT associated low dose CT scan is a more robust organ delineation. In addition, a lumber vertebrae region of interest (ROI) allows for a non-invasive quantification of the red marrow activity concentration. It has been shown that the assumption of a constant plasma over red marrow activity concentration ratio (PLRMR) does not always hold true [4], necessitating an approach that is not based on this assumption. The aim of this study was to show the feasibility of PET/CT based dosimetry using [^{89}Zr]cetuximab as an example. **Methods** Five patients (4 males, 1 female) with histopathologically confirmed advanced colorectal cancer were scanned on a Gemini PET/CT scanner (Philips Healthcare, Best, The Netherlands). After administration of a 500 mg•m-2 therapeutic cetuximab dose, a bolus of 37.1±0.9 MBq [^{89}Zr]cetuximab was injected. PET/CT scans were obtained at 1, 24, 48, 72 and 144 hr post injection, see supplemental info. ROIs were delineated on the PET scan if they showed positive contrast (kidneys, liver and spleen) and on the low dose CT scan for lungs and red marrow (the latter delineated in five lumbar vertebrae). Residence times were derived from the time activity curves. **Results** Organ doses as well as effective doses per patient are presented in table 1. **Conclusion** For [^{89}Zr]cetuximab an effective dose of 0.62 mSv•MBq-1 was obtained, in line with previous reports [2-3]. The simplicity of this non-invasive procedure that does not make use of the assumption of a constant PLRMR makes this approach the method of choice for dosimetry of new immunoPET tracers. **References** [1] S.B.M. Gaykema, A.H. Brouwers, M.N. Lub-de Hooge et al., [89Zr]-Bevacizumab PET Imaging in Primary Breast Cancer, J. Nucl. Med. 2013 (54):1014-1018 [2] Börjesson PK, Jauw YW, de Bree R, et al. Radiation dosimetry of 89Zr-labeled chimeric monoclonal antibody U36 as used for immuno-PET in head and neck cancer patients. J Nucl Med. 2009;50:1828-1836. [3] Rizvi SN, Visser OJ, Vosjan MJ, van Lingen A, Hoekstra OS, Zijlstra JM, Huijgens PC, van Dongen GA, Lubberink M., Biodistribution, radiation dosimetry and scouting of 90Y-ibritumomab tiuxetan therapy in patients with relapsed B-cell non-Hodgkin's lymphoma using 89Zr-ibritumomab tiuxetan and PET, Eur J Nucl Med Mol Imaging. 2012 Mar;39(3):512-20. [4] N.E. Makris, R. Boellaard, A. van Lingen et al., Comparison of bone marrow dose estimation approaches based on 89Zr-PET/CT, poster presented on the SNM 2013 conference.

Absorbed organ dose and effective dose for individual subjects (mSv/MBq).

	Kidneys	Liver	Lungs	Spleen	RM	RoB	E
M_1	0.82	1.54	0.50	0.79	0.49	0.45	0.52
M_2	0.95	2.00	0.55	0.74	0.58	0.45	0.55
M_3	0.82	2.18	0.52	0.71	0.54	0.45	0.54
M_4	0.83	2.42	0.51	0.62	0.52	0.45	0.55
M_avg	0.85	2.04	0.52	0.72	0.54	0.45	0.54
M_sd	0.05	0.37	0.02	0.07	0.04	0.00	0.01
F_1	1.24	2.91	0.86	1.11	0.65	0.56	0.70

F = female; M = male; avg = average; sd = standard deviation; RM = red marrow; RoB = remainder of body; E = effective dose

Disclosure of author financial interest or relationships:
M. Huisman, None; **N. Makris**, None; **A. van Lingen**, None; **W. Menke-van der Houven van Oordt**, None; **H. Verheul**, None; **A.A. Lammertsma**, Philips, Grant/research support; Hoffmann-La Roche, Grant/research support; **G.A. van Dongen**, None.

Presentation Number **LBAP 050**
Late Breaking Abstract Poster Session
September 19, 2013 / 15:15-15:15 / Room: Exhibit Hall B

Quantification of [^{18}F]fluorocholine PET studies

Eline E. Verwer, *Daniela E. Oprea-Lager, Maqsood Yaqub, Robert C. Schuit, Albert D. Windhorst, Adriaan A. Lammertsma, Otto S. Hoekstra, Ronald Boellaard, Radiology & Nuclear Medicine, VU University Medical Center, Amsterdam, Netherlands. Contact e-mail: e.verwer@vumc.nl*

Purpose: [^{18}F]fluorocholine ([^{18}F]FCH) is a PET tracer for identifying well differentiated neoplasms, including prostate cancer (PCa). Choline is the precursor of phospathidylcholine, a major constituent of the cell membrane. Cellular transport and choline phosphorylation are usually increased in cancer. The aim of the present study was to identify the optimal plasma input pharmacokinetic model for quantifying [^{18}F]FCH uptake in PCa metastatic lymph nodes and to evaluate simplified methods. Methods: 8 patients with histologically proven metastasised PCa were included. After injection of 204±9 MBq [^{18}F]FCH, a 40 min dynamic PET/CT scan was acquired. For the duration of the scan arterial blood was withdrawn continuously, with short interruptions for collecting manual arterial blood samples at 5, 10, 15, 20, 30 and 40 min p.i. Image derived input functions (IDIF) were obtained from volumes of interest (VOI) drawn within the largest blood pool structure visible within the images. Both blood sampler curve (BSIF) and IDIF were corrected for plasma-to-blood ratios and labelled metabolites. VOI were drawn using a 50% threshold method across all visually detectable lesions. Next, several single and two tissue plasma input models were fitted to the lesion time activity curves (TAC). The preferred model was selected based on the Akaike information criterion (AIC). Finally, performance of several simplified methods, such as standardized uptake value (SUV), was compared with full kinetic modelling. Results: The irreversible two tissue compartment model with blood volume parameter yielded the best AIC values. However, more robust fits were obtained using an irreversible single tissue compartment model with blood volume parameter (1T1k+V_B). Net rate of influx parameters K_i and K_1 for the two models correlated well (R^2=0.94) with each other. IDIF derived from VOI in or near the aortic arch yielded K_1 values comparable to those derived with BSIF (R^2=0.87). In contrast, SUV showed poor correlation to parameters derived from full kinetic analysis (R^2=0.27). However, lesion activity concentration at 35-40 min p.i. normalised to mean blood activity concentration over the duration of the PET scan showed good correlation (R^2=0.83 for metabolite corrected plasma and R^2=0.66 for whole-blood activity concentrations). Conclusion: SUV cannot be used to quantify [^{18}F]FCH uptake. Quantification requires full kinetic modelling using an irreversible single tissue compartment model and an arterial input function. A reasonable alternative for clinical studies is to measure lesion activity concentration based on a whole body scan started at 30 min p.i. and normalising it to mean blood activity concentrations derived from a static scan of a large blood pool structure acquired over 0-30 min p.i.

Disclosure of author financial interest or relationships:
E.E. Verwer, None; **D.E. Oprea-Lager**, None; **M. Yaqub**, None; **R.C. Schuit**, None; **A.D. Windhorst**, None; **A.A. Lammertsma**, Philips, Grant/research support; Hoffmann-La Roche, Grant/research support; **O.S. Hoekstra**, None; **R. Boellaard**, Philips, Grant/research support .

Presentation Number **LBAP 051**
Late Breaking Abstract Poster Session
September 19, 2013 / 15:15-15:15 / Room: Exhibit Hall B

Quantitative second harmonic generation (SHG) microscopy of Col1 fiber signatures in human breast cancers predicts lymph node metastasis

Lu Jiang[1], *Samata M. Kakkad*[1], *Alireza Akhbardeh*[1], *Tiffany R. Greenwood*[1], *Meiyappan Solaiyappan*[1], *Zaver M. Bhujwalla*[1,3], *Xingde Li*[2], *Kristine Glunde*[1,3], [1]*Radiology Department, Johns Hopkins University School of Medicine, BALTIMORE, MD, USA;* [2]*Biomedical Engineering, Johns Hopkins University School of Medicine, BALTIMORE, MD, USA;* [3]*The Sidney Kimmel Comprehensive Cancer Center, Johns Hopkins University School of Medicine, BALTIMORE, MD, USA. Contact e-mail: ljiang12@jhmi.edu*

Introduction: The extracellular matrix (ECM) in breast cancers is altered and provides new biomarkers for cancer diagnosis [1] and prognosis [2,3]. Collagen I (Col1) fibers are the major ECM component in breast tumors, and increased Col1 has been found to facilitate breast tumor formation, invasion, and metastasis [2,3]. We tested the relationship between lymph node (LN) status and Col1 fibers on a tissue microarray by using second harmonic generation (SHG) imaging and image analyses. Methods: A breast tissue microarray that had 50 LN positive (LN+) and 50 LN negative (LN-) breast biopsy samples was used in this study. Z-stacks of SHG tile images were acquired on a multiphoton microscope. We analyzed the SHG images from all breast biopsies for geometric features such as fiber volume, inter-fiber distance [4], and Haralick features. K-mean clustering of a case-controlled subset (19 LN+ and 16 LN- cases with grade 2, Stage II, T2) was performed. Principal component analysis (PCA) was done to reduce data dimensions. Supervised nonlinear support vector machine (SVM) classification of 50 LN+ and 50 LN- samples with cross validation was performed on the 3D Haralick features. Results: Fig. A and B display SHG images from representative biopsies of a LN+ patient (A) and a LN- patient (B). Fig. C shows the detection of LN+ and LN- samples based on geometric and Haralick texture features, which were obtained from the analysis of the Col 1 fiber patterns of 35 case-controlled samples. Fig. D displays the receiver operating characteristic (ROC) curve of SVM classifying 3D Haralick features of 50 LN+ and 50 LN- samples. The Gaussian kernel with a sigma of 2.9 was the best model in this study, which could obtain a false negative rate of 0.13, a false positive rate of 0.31, and area under the ROC curve of 0.81. Fig. E presents detection rates for different numbers of folds in the cross validation. Discussions: The features that best differentiate LN+ and LN- samples were 3D entropy and energy in the analysis of 35 case-controlled samples. In a larger statistical analysis from 100 breast cancer samples, we performed a supervised SVM classification method with cross validation to ensure the robustness of this study and obtained a best false positive rate of 0.3. This could be because some LN- cases may have turned out as LN+ cases later on, and no follow-up data were available to us. A larger number of breast cancer samples with patient follow-up information will be needed to train a more robust statistical SVM model in the future. In our analysis, we observed that there are large areas with low Col1 fiber content that occur in regions with high cellularity in some samples. So we will modify our analysis method to consider the cellularity, which can be obtained from adjacent H&E images. The classification of tumor grade, stage, and size based on the geometric and Haralick features will also be performed. References: [1]. A. Bergamaschi et al., J. Pathol. (2008). [2] P. P. Provenzano et al., BMC Med. (2008). [3] M. W. Conklin et al., Am. J. Pathol. (2011). [4] S. Kakkad et al., J. Biomed Optics (2012). This work was supported by NIH P50 CA103175.

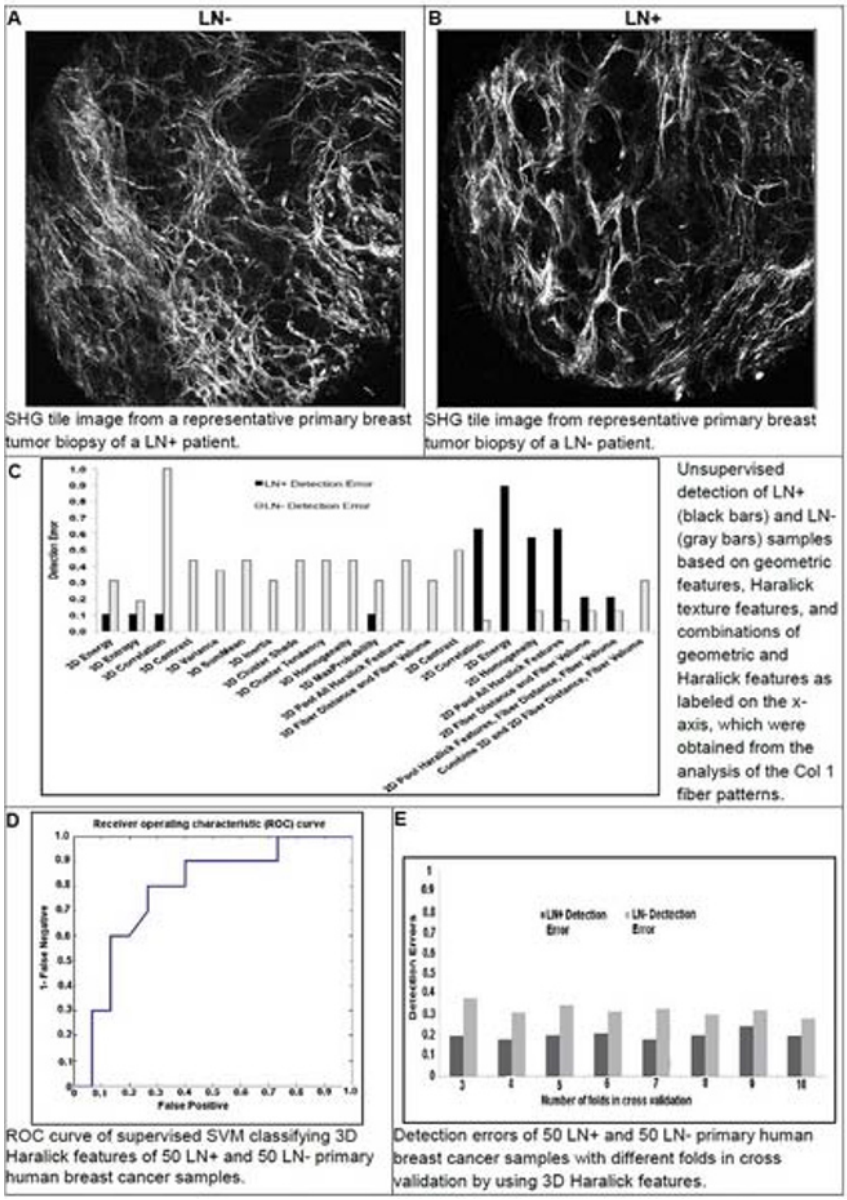

SHG tile image from a representative primary breast tumor biopsy of a LN+ patient.

SHG tile image from representative primary breast tumor biopsy of a LN- patient.

Unsupervised detection of LN+ (black bars) and LN- (gray bars) samples based on geometric features, Haralick texture features, and combinations of geometric and Haralick features as labeled on the x-axis, which were obtained from the analysis of the Col 1 fiber patterns.

ROC curve of supervised SVM classifying 3D Haralick features of 50 LN+ and 50 LN- primary human breast cancer samples.

Detection errors of 50 LN+ and 50 LN- primary human breast cancer samples with different folds in cross validation by using 3D Haralick features.

Disclosure of author financial interest or relationships:
L. Jiang, None; **S.M. Kakkad**, None; **A. Akhbardeh**, None; **T.R. Greenwood**, None; **M. Solaiyappan**, None; **Z.M. Bhujwalla**, None; **X. Li**, None; **K. Glunde**, None.

Presentation Number **LBAP 052**
Late Breaking Abstract Poster Session
September 19, 2013 / 15:15-15:15 / Room: Exhibit Hall B

Prospective open-label exploratory clinical study analyzing the potential of ex vivo injections of Indocyanine Green (ICG) in the detection of the Sentinel Lymph Node (SLN) in colon cancer: preliminary results

Gabriel Liberale[2], **Bissan K. Ahmed**[3], *Sophie Vankerckhove*[3], *Denis Larsimont*[1], *Maria G. Gomez Galdon*[1], *Pierre Bourgeois*[3], [1]*Service of Pathology, Jules Bordet Institute, Brussels, Belgium;* [2]*Service of surgery, Jules Bordet Institute, Brussels, Belgium;* [3]*Service of Nuclear Medicine, Jules Bordet Institute, Brussels, Belgium. Contact e-mail: bissan.ahmed@bordet.be*

Introduction: In colorectal cancers, the Sentinel Lymph Node (SLN) approach has been quite only based on the use of "blue" dyes injected either "in vivo", or "ex vivo". Preliminary papers have also reported the use of fluorescent molecules such as ICG to demonstrate SLN in patients with colorectal cancer using dedicated Near Infrared (NIR) Imaging camera system.The aim of the study is to evaluate the detection of the SLN in the operating room and in the department of pathology when "blue dye" and ICG were injected "ex vivo". Material and methods: Eight patients with colorectal cancer, excluding metastatic patients, were included for SLN detection. After surgical resection of the operative specimen, eight injections (four times 0.5cc of Patent Blue and four times 0.05 mg of ICG in 0.5 mL) were performed ex vivo sub-serosally at the four cardinal points around the tumour. In the operating room, the surgeon searched and marked the "blue" SLN and therafter, in a second time with the help of the NIR imaging camera PDE, the fluorescent ("Fluo") SLN. In the department of pathology, the SLN that he had so marked were excised and analyzed separately. All other LN that were thereafter found by the technician were then controlled for the "blue" and/or "fluo" characteristics. All these node were coloured using classical HE technics and so classified as pathologically either positive (pN+), or negative. Results: 4 patients had pN+ LN : two patients had 1 pN+ LN, one had 2 and one 11 out 12. In the operating room, two SLN were found blue and not "fluo" in two among these patients but these LN were not pN+ (false negative only blue SLN). One patient found in the operating room with one SLN blue not "fluo" and one "fluo" but not blue SLN had 11 out of 12 LN pN+ (true positive blue or "fluo"). The last patient had two SLN blue not "fluo", one SLN "fluo" but not blue and one SLN blue and "fluo": however, none of these SLN was pN+ (false negative blue and/or "fluo" SLN). Among the 6 patients (3 pN+) also evaluated in the department of Pathology, 2.5 SLN were found as a mean in the operating room and 4 to 14 additional LN were found blue and/or "fluo" in all in the department of pathology. The patient found falsely negative blue and/or "fluo" in the operating room was not corrected by these findings. However, the two patients where 2 SLN were found blue (and not "fluo") but false negative, one pN+ LN was found "fluo" (but not blue) in one patient and the other patient had one (different) pN+ LN blue (and not "fluo") and another pN+ LN blue and "fluo". Conclusions: These preliminary results suggest that the two approaches are at least complementary to detect SLN and that dedicated Near Infra Red (NIR) Imaging camera system can be used in the department of pathology to identify the fluorescent SLN not seen in the operating room.

Disclosure of author financial interest or relationships:
G. Liberale, None; **B.K. Ahmed**, None; **S. Vankerckhove**, None; **D. Larsimont**, None; **M.G. Gomez Galdon**, None; **P. Bourgeois**, None.

Presentation Number **LBAP 053**
Late Breaking Abstract Poster Session
September 19, 2013 / 15:15-15:15 / Room: Exhibit Hall B

Phenotypic and functional assessment of magnetically labeled pig embryonic stem cell derived hepatocytes

Neil C. Talbot[1], Paul Graninger[1], **Erik M. Shapiro**[2]*, Wesley M. Garrett[1], Thomas J. Caperna[1], [1]Agricultural Research Center, USDA, Beltsville, MD, USA; [2]Department of Radiology, Michigan State University, East Lansing, MI, USA. Contact e-mail: erik.shapiro@rad.msu.edu*

INTRODUCTION For many severe, progressive liver diseases the only effective treatment is liver transplantation. Unfortunately, due to the shortage of available donor organs, liver transplantation is not available to all patients. Metabolic liver diseases, particularly loss-of-function phenotypes affecting children, may be amenable to creative alternative treatments, such as hepatocyte transplantation. Xenotransplantation of swine cells to humans as a short-term measure is an emerging concept in regenerative medicine. Effective non-invasive imaging of transplanted cells is essential to advance this effort. Here we describe our investigation into the phenotypic and functional properties of magnetically labeled pig embryonic stem cell-derived hepatocytes for MRI-based cell tracking of regenerative liver therapy. PICM-19 cells are bipotent liver parenchymal cells derived from pig embryonic stem cells (reviewed in Talbot et al., J. Anim. Sci., 2013). PICM-19 hepatocytes exhibit serum protein production, inducible cytochrome P450 activity, γ-glutamyltranspeptidase (GGT) activity, ammonia clearance and urea production. PICM-19 cholangiocytes self-organize into 3D, multicellular ductules resembling bile ductules cultured from fetal or adult pig liver. The PICM-19 ductules express GGT at their apical cell surfaces and exhibit transcellular fluid transport to ductal lumens with in vivo-like kinetics in response to physiological levels of secretin. PICM-19 cells are promising for swine regenerative medicine models of liver disease and for potential human xenotransplantation. METHODS & MATERIALS PICM-19 hepatocytes were grown within a collagen/Matrigel sandwich in mouse STO fibroblast-conditioned medium. After 2d in culture, cells were labeled 24h by incubation with 100 particles per cell of 0.96 micron-sized iron oxide particles (MPIOs). Assays performed included 2D gel and MS analysis of serum-free conditioned medium (CM) for secreted protein identification, GGT histochemistry, forskolin and glucagon responsiveness, mitotic index, light and electron microscopy. RESULTS & DISCUSSION PICM-19 cells labeled with MPIOs (> 80%), comparable to previous work (Bennewitz, et al., Mol Im Biol, 2012). The morphology and ultrastructure were unaffected by the presence of the MPIOs. 2D gel analysis of CM showed normal serum-proteins, but also regucalcin, a cytoplasmic protein. GGT histochemistry showed intense staining at the biliary canaliculi between the cells. Forskolin and glucagon induced the expansion of the canaliculi via cAMP-dependent transcellular fluid transport. Mitotic index of MPIO-labeled and control cells were similar (0.6%). These experiments confirm that magnetic labeling of PICM-19 hepatocytes with MPIOs does not impact the phenotypic or functional properties of these cells, paving the way for their use in MRI-based cell tracking of liver regenerative medicine paradigms. Further, these experiments demonstrate the usefulness of functional assays, rather than detection of cell surface CD markers for studying effects of magnetic particles on labeled cells.

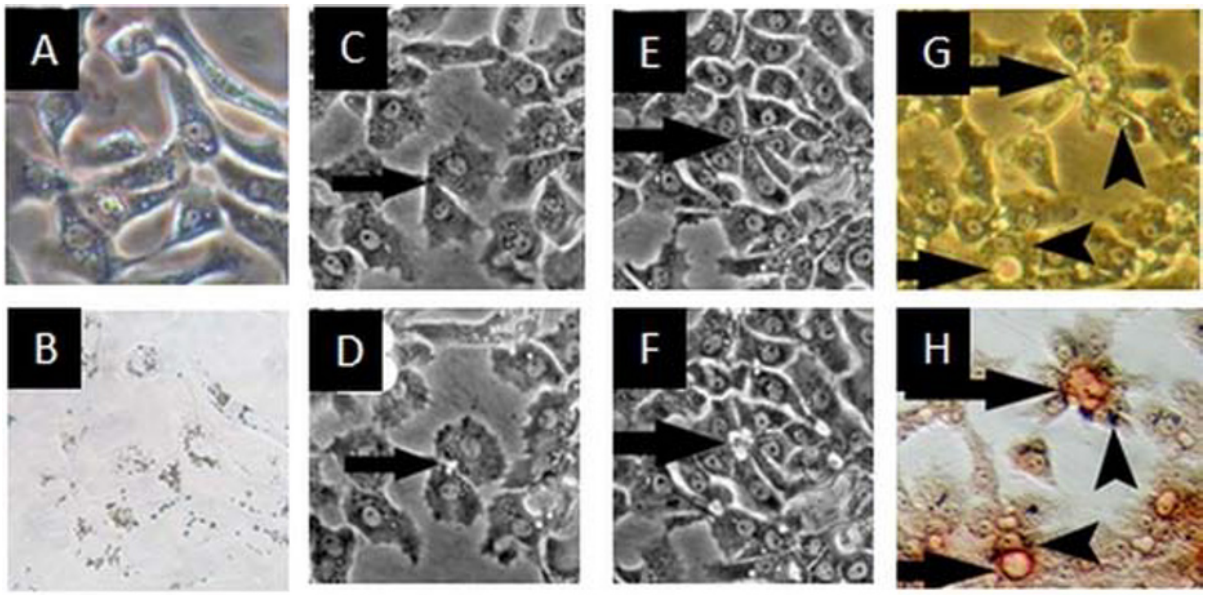

Phenotypic and functional assays of magnetically labeled PICM-19 hepatocytes. A) Phase contrast and B) dark field microscope image of labeled cells. C) Before and D) after images of forskolin response, showing the expansion of a canaliculus from the cAMP-induced transcellular fluid transport. E) Before and F) 20 minutes after glucagon was added. An expanded biliary canaliculus is shown with black arrows. G) and H) GGT stained after the addition of glucagon. G) is phase-contrast, 200x, and H) is the same area photographed with Hoffman modulation 200x. Note the intense GGT histochemical staining at the apical cell membrane surfaces surrounding the biliary canaliculi (arrows). Arrowheads indicate iron particles.

Disclosure of author financial interest or relationships:
N.C. Talbot, None; **P. Graninger**, None; **E.M. Shapiro**, None; **W.M. Garrett**, None; **T.J. Caperna**, None.

Presentation Number **LBAP 054**
Late Breaking Abstract Poster Session
September 19, 2013 / 15:15-15:15 / Room: Exhibit Hall B

Molecular Imaging of Drug Compounds in Whole Body Mouse Tissue Sections Using Laser Ablation Electrospray Ionization Mass Spectrometry (LAESI-MS)

Trust T. Razunguzwa, *Matthew Powell, Gregory Boyce, Pamela Williams, Research and Development, Protea Biosciences Inc., Morgantown, WV, USA. Contact e-mail: trust.razunguzwa@proteabio.com*

Mass spectrometry imaging (MSI) is a very powerful technique for visualizing the spatial distribution of molecules in biological samples, such as tissue sections, whole body sections, and cell colonies or populations. Using the high resolving power, high mass accuracy, and MS/MS capabilities of mass spectrometers, a wide variety of small molecules, metabolites, lipids, peptides, and proteins can be identified and characterized in tissue imaging analyses. For an MSI experiment, chemical and spatial information of a previously known or unknown compound is obtained by collecting mass spectra from many locations on a tissue section and then generating an ion map of the intensity distribution of the compound's mass signatures across every analysis location. Laser Ablation Electrospray Ionization Mass Spectrometry (LAESI) is an ambient ionization technique that has been applied to plant and animal tissue imaging, and live cell imaging (bacterial and fungal colonies). This ambient pressure technique uses an infrared 2.94 μm wavelength laser that is strongly absorbed by water to ablate the sample. The resultant ablation plume contains a population of neutral molecules from the sample. Ionization occurs via coalescence of the sample molecules with an electrospray plume above the sample, and the sample ions pass into a mass spectrometer for detection. This work demonstrates the use of the Protea LAESI DP-1000 system for tissue imaging, specifically for profiling dosed drugs in mouse tissue sections. The DP-1000 system is the first integrated instrument system using LAESI technology for tissue imaging. Imaging of whole body mouse sections on the LAESI DP-1000 Direct Ionization System connected to a Thermo LTQ VelosTM mass spectrometer was performed. The fragment peaks at m/z 129 (raclopride) and m/z 484 (fexofenadine), parent ions of the drugs, and several other endogenous ions were chosen for construction of ion distribution maps. Using LAESI-MS, distribution of two molecules, raclopride and fexofenadine could be imaged on whole mouse tissue sections. Raclopride, a widely used tracer for positron emission tomography (PET) was used to dose the animal intravenously, while fexofenadine, an antihistamine used in allergy medicines, was introduced orally into the same animal. After data acquisition in MS/MS mass spectrometry mode, the spatial distribution of the most intense daughter ions of the two drugs was visualized by mapping them in ProteaPlot imaging software. Raclopride is clearly detected in the liver and gastric organs such as the stomach and cecum 30 minutes after dosage. Fexofenadine at the same time point is shown to be mainly present in the gastric organs. The LAESI-MS data was validated using MALDI imaging data that was collected on serial sections from the same animal showing similar distributions of raclopride and fexofenadine. In addition, the path of fexofenadine through the digestive system could be imaged at 10, 30 and 60 min time points after dosing.

Disclosure of author financial interest or relationships:
T.T. Razunguzwa, None; **M. Powell**, None; **G. Boyce**, None; **P. Williams**, None.

Presentation Number **LBAP 055**
Late Breaking Abstract Poster Session
September 19, 2013 / 15:15-15:15 / Room: Exhibit Hall B

APPLICATION OF BLOCH NMR EQUATION AND PENNES BIOHEAT EQUATION TO THERANOSTICS

Michael O. Dada[1], *Bamidele O. Awojoyogbe*[1], *Simona Baroni*[2], *Moses A. Aweda*[3], [1]*Physics, Federal University of Technology, Minna, Nigeria;* [2]*Chemistry, Molecular Biotechnology Center, University of Turin, Via Nizza, 52, Turin, Italy;* [3]*Radiotherapy, College of Medicine/Lagos University Teaching Hospital, Idi-Araba, Lagos, Nigeria. Contact e-mail: das_niger@yahoo.co.uk*

INTRODUCTION Theranostics has been regarded as a key part of personalized medicine and requires considerable advances in predictive medicine; novel theranostic agents are developed and carefully designed for in vivo quantitative assessment of the amount of drug reaching a pathological region and the visualization of molecular changes due to the therapeutic effects of the delivered drug. This study intends to mathematically model a closely knitted theranostic method in which a specially selected RF field is used to heat up a tissue and at the same time cause the spins of the tissue to emit MR signals. MATHEMATICAL FORMULATION We consider bioheat flow in one direction [1, 2] given in eqn(1); where ρ is tissue density, c is the specific heat of tissue, T is the tissue temperature, t is the time, w_b is the blood perfusion rate, c_b is the specific heat of blood, T_b is the supplying arterial blood temperature, k is the thermal conductivity of tissue, and x is the distance from the skin surface. SAR is the applied RF power per unit volume. If T changes very slowly with x, we have eqn(2) and solution to eqn(2) is given in eqn(3). If the T before the application of the RF field does not defer significantly from T_b, the initial the condition for this problem is given in eqn(4) and the final solution is given in eqn(5). The RF power for the voxel volume V_{vox} is P_{rf} = (SAR) V_{vox} . The energy of the oscillating radio wave is given as E_{rf} = $(1.055 \times 10^{-34}\text{Js})\gamma B_1$, whose rate of change is expressed as in eqns(6) and (7). We can relate time dependent MRI signal to SAR using the time independent NMR equation [2] given by eqn (8) and (9). If we sample the signal when the M_y has the largest amplitude, we write $M_0 \approx 0$. Provided that the condition in eqn (10) holds, we have [2] eqn (11). From eqns (10) and (11), we obtain eqn (12). If the RF B_1 field is applied at time $t_0 = 0$, we have eqn (13). This solution is valid for the condition in eqn (14). It is always required that the M_y be finite as time tends to infinity; therefore, the solution to the problem is given by eqn (15). ANALYSIS OF RESULTS The results obtained in this study have been simulated with relaxation parameters of human liver at 1.5T [3] and the corresponding thermal properties [1, 3]: T_1 = 0.610s, T_2 = 0.057s, w_b = 2.86kg/m^{3}s, c_b = 3960J/kg.K, ρ = 1060kg/m^3, c = 3600J/kg.K. Plots a and b (SAR = 4W/m^3) give the distribution of the T and M_y on a log scale while plot c (SAR = 40000W/m^3) gives the density plot of M_y as a function of time and tissue temperature. CONCLUSION The temperature distribution and the RF power needed to generate RF $B_1(t)$ field within the medically acceptable SAR limit during MRI scanning procedure have been investigated by solving the Pennes Bioheat equation in terms of MRI parameters. The relationship between T, SAR and RF $B_1(t)$ at any given time is clearly shown in eqn (5), eqn (10) and Plots a, b, c. REFRENCES [1] Tzu-Ching Shih, Ping Yuan, Win-Li Lin, Hong-Sen Kou. MEP 29 (2007) 946-953. [2] O. B. Awojoyogbe, M. Dada, O.P. Faromika, O.E. Dada. CMRA. Vol. 38 A (3) 85-101 (2011). [3] Bottomley PA, Foster TH, Argersinger RE, Pfeifer LM (1984). Med Phys 11:425-448.

$$\rho c \frac{\partial T}{\partial t} = k \frac{\partial^2 T}{\partial x^2} + SAR - w_b c_b (T - T_b) \quad (1)$$

$$\rho c \frac{\partial T}{\partial t} = SAR - w_b c_b (T - T_b) \quad (2)$$

$$T(t) = T_b + \frac{SAR}{w_b c_b} + A \exp\left(-\frac{w_b c_b}{\rho c} t\right) \quad (3)$$

$$T(t=0) = T_b \quad (4)$$

$$T(t) = T_b + \frac{SAR}{w_b c_b}\left\{1 - \exp\left(-\frac{w_b c_b}{\rho c} t\right)\right\} \quad (5)$$

$$P_{rf} = \frac{dE_{rf}}{dt} \text{ and } E_{rf} = \int_{t_0}^{t} (SAR) V_{vox} dt \quad (6)$$

$$\gamma B_1(t) = \frac{V_{vox}}{\hbar}(SAR)(t - t_0) \quad (7)$$

$$\frac{d^2 M_y}{dt^2} + T_o \frac{dM_y}{dt} + \left(T_g + \gamma^2 B_1^2(t)\right) M_y = \frac{M_o}{T_1} \gamma B_1(t) \quad (8)$$

$$\text{where } T_g = \frac{1}{T_1 T_2} \text{ and } T_o = \frac{1}{T_1} + \frac{1}{T_2} \quad (9)$$

$$T_g << \gamma^2 B_1^2(t) \quad (10)$$

$$\frac{d^2 M_y}{dt^2} + T_o \frac{dM_y}{dt} + \gamma^2 B_1^2(t) M_y = 0 \quad (11)$$

$$\frac{d^2 M_y}{dt^2} + T_o \frac{dM_y}{dt} + \left(\frac{V_{vox}}{\hbar}\right)^2 (SAR)^2 (t - t_0)^2 M_y = 0 \quad (12)$$

$$M_y(t) = (\beta)^n (t)^n \left[C_1 J_n\left(\frac{V_{vox}}{2\hbar} t^2\right) + C_2 Y_n\left(\frac{V_{vox}}{2\hbar} t^2\right)\right] \quad n = \frac{1 - T_g}{2} \quad (13)$$

$$T_0(t - t_0) \leq 1 \quad (14)$$

$$M_y(t) = C_1(\beta)^{\frac{1-T_g}{2}} (t)^{\frac{1-T_g}{2}} J_{\frac{1-T_g}{2}}\left(\frac{V_{vox}}{2\hbar} t^2\right) \quad (15)$$

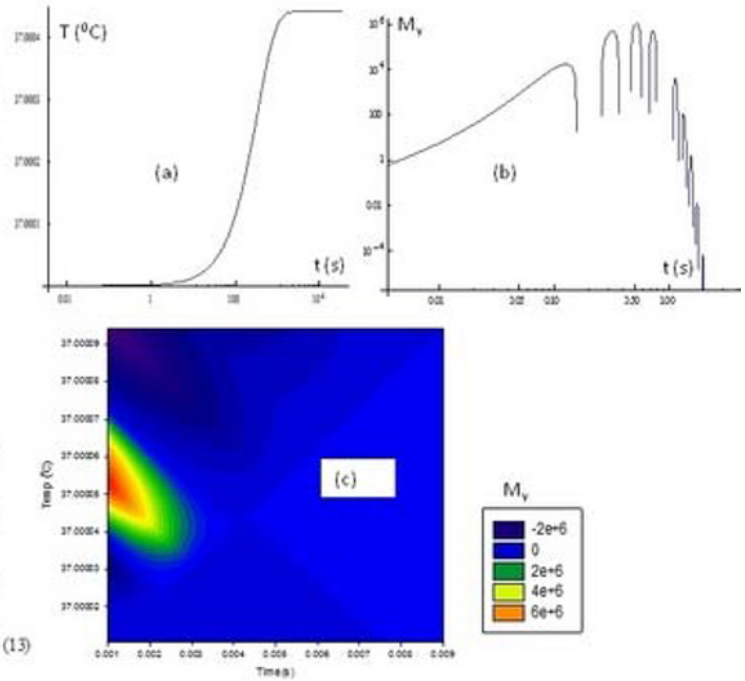

Disclosure of author financial interest or relationships:
M.O. Dada, None; **B.O. Awojoyogbe**, None; **S. Baroni**, None; **M.A. Aweda**, None.

Presentation Number **LBAP 056**
Late Breaking Abstract Poster Session
September 19, 2013 / 15:15-15:15 / Room: Exhibit Hall B

Collagen 1 fibers are a key component in the establishment of distant pulmonary metastasis by HIF silenced breast cancer cells

*Katherine M. Bruner[1], **Samata M. Kakkad**[1], Balaji Krishnamachary[1], Meiyappan Solaiyappan[1], Flonne B. Wildes[1], Kristine Glunde[1,2], Zaver M. Bhujwalla[1,2], [1]In Vivo Cellular and Molecular Imaging Center, Division of Cancer Imaging Research, The Russell H. Morgan Radiology and Radiological Science, The Johns Hopkins University School of medicine, Baltimore, MD, USA; [2]The Sidney Kimmel Comprehensive Cancer Center, The Johns Hopkins University School of medicine, Baltimore, MD, USA. Contact e-mail: skakkad1@jhmi.edu*

Introduction: We have previously observed that primary human breast cancers that have metastasized have higher collagen 1 (Col1) fiber density and volume [1]. We have also observed that severely hypoxic regions in primary human breast and prostate cancer xenografts have fewer Col1 fibers, with a dense deposition of Col1 fibers around these severely hypoxic regions [2]. Here, for the first time, we have investigated Col1 fiber patterns in metastatic lung nodules established by metastatic MDA-MB-231 breast cancer cells and their poorly metastatic subclones that have hypoxia inducible factor (HIF) silenced. Methods: Second harmonic generation (SHG) microscopy studies were performed on lung sections obtained from SCID mice five weeks post intravenous injection of MDA-MB-231 human breast cancer cells and sub-lines silenced for HIF (-1, -2)α. SHG images of 3-5 fields of view (FOV) were acquired from fixed lung sections on a Zeiss 710 multiphoton microscope and analyzed for inter-fiber distance [1]. Results: Silencing HIF-1α or -2α resulted in a significant reduction of metastatic lung burden in mice (Figures 1A and B). Representative FOV showing Col1 fibers in metastatic lung nodules in mice injected with MDA-MB-231 wild type (Fig. 2a), HIF-1 silenced (Fig. 2b), and HIF-2 silenced (Fig. 2c) cells demonstrate the significant reduction of Col1 fibers following HIF-1α or -2α silencing. Quantitative analysis of Col1 fiber density in lungs obtained from these groups is shown in Figure 3. Discussion: We have previously reported a decrease of Col1 fiber density and volume in hypoxic primary tumor regions and observed dense fibers around these hypoxic regions. Therefore in primary tumors hypoxia and upregulation of HIF resulted in fewer fibers in severely hypoxic regions. In the studies here we observed that silencing HIF in breast cancer cells resulted in fewer metastatic lung nodules containing fewer fibers. These data suggest that the ability to lay down Col1 fibers is a key requirement for the successful establishment of metastatic lesions, and that silencing the HIF pathway in MDA-MB-231 breast cancer cells affects the ability of these cancer cells to lay down a Col1 fiber scaffold suitable for cancer cell growth in the lungs. These data identify new aspects of the role of Col1 fibers and HIF in the establishment of metastatic lesions. References: [1] S. Kakkad et al., J. Biomed Optics (2012); [2] S. Kakkad et al., Neoplasia (2010). This work was supported by NIH P50 CA103175.

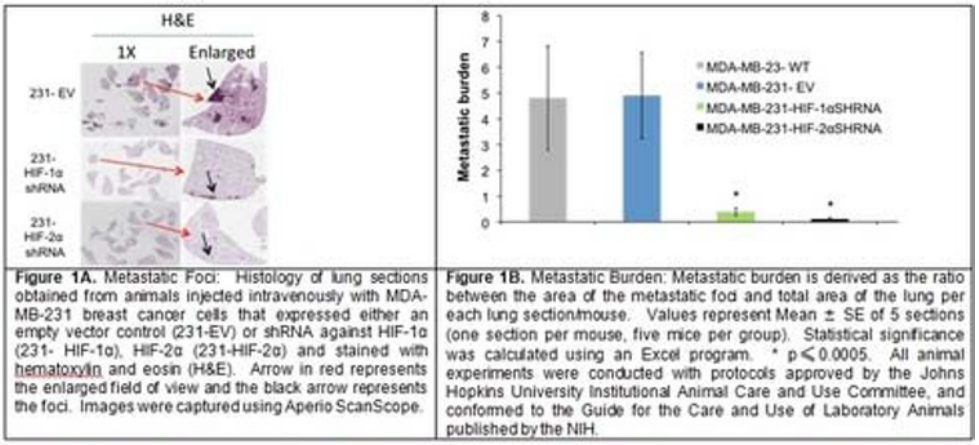

Figure 1A. Metastatic Foci: Histology of lung sections obtained from animals injected intravenously with MDA-MB-231 breast cancer cells that expressed either an empty vector control (231-EV) or shRNA against HIF-1α (231- HIF-1α), HIF-2α (231-HIF-2α) and stained with hematoxylin and eosin (H&E). Arrow in red represents the enlarged field of view and the black arrow represents the foci. Images were captured using Aperio ScanScope.

Figure 1B. Metastatic Burden: Metastatic burden is derived as the ratio between the area of the metastatic foci and total area of the lung per each lung section/mouse. Values represent Mean ± SE of 5 sections (one section per mouse, five mice per group). Statistical significance was calculated using an Excel program. * $p \leqslant 0.0005$. All animal experiments were conducted with protocols approved by the Johns Hopkins University Institutional Animal Care and Use Committee, and conformed to the Guide for the Care and Use of Laboratory Animals published by the NIH.

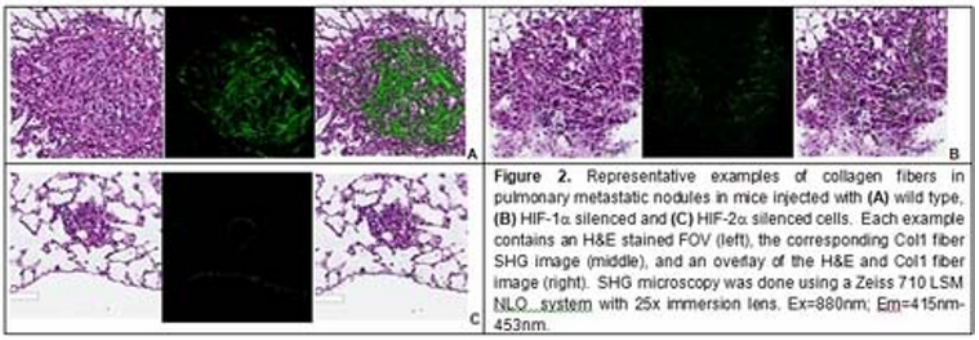

Figure 2. Representative examples of collagen fibers in pulmonary metastatic nodules in mice injected with **(A)** wild type, **(B)** HIF-1α silenced and **(C)** HIF-2α silenced cells. Each example contains an H&E stained FOV (left), the corresponding Col1 fiber SHG image (middle), and an overlay of the H&E and Col1 fiber image (right). SHG microscopy was done using a Zeiss 710 LSM NLO system with 25x immersion lens. Ex=880nm; Em=415nm-453nm.

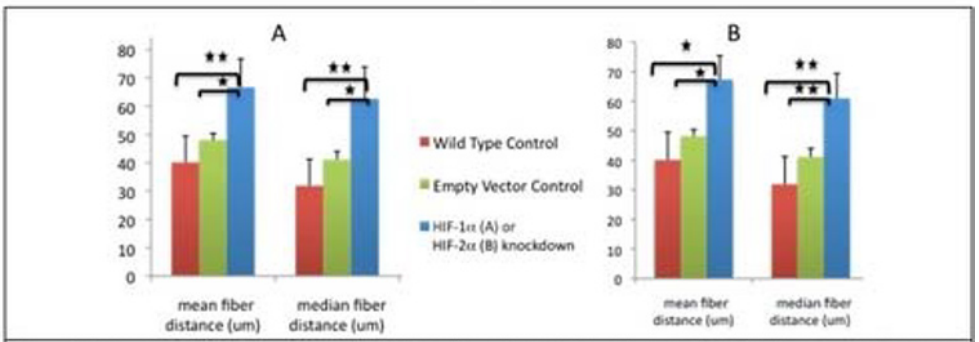

Figure 3. Comparison of the collagen content of **(A)** HIF-1α silenced metastatic nodules and **(B)** HIF-2α silenced metastatic nodules with wild type and empty vector MDA-MB-231 nodules. * p<0.05, **p<0.01. Values represent Mean +/- SE from 3-5 FOVs per lung section. Data from four wild type, five empty vector, four HIF-1α and three HIF-2α injected mice are presented.

Disclosure of author financial interest or relationships:

K.M. Bruner, None; **S.M. Kakkad**, None; **B. Krishnamachary**, None; **M. Solaiyappan**, None; **F.B. Wildes**, None; **K. Glunde**, None; **Z.M. Bhujwalla**, None.

Presentation Number **LBAP 057**
Late Breaking Abstract Poster Session
September 19, 2013 / 15:15-15:15 / Room: Exhibit Hall B

Recruitment of Endocytosis in Ultrasound-mediated Drug Delivery: a Real-time Study

Marc Derieppe[1], *Katarzyna Rojek*[1], *Baudouin Denis de Senneville*[1,2], *Clemens Bos*[1], *Chrit Moonen*[1], [1]*Imaging Division, University Medical Center Utrecht, Utrecht, Netherlands;* [2]*IMB, UMR 5251 - CNRS - Université Bordeaux 1 - INRIA, Bordeaux, France. Contact e-mail: m.derieppe@umcutrecht.nl*

Introduction. Sonoporation of cell membrane by means of ultrasound (US) waves, usually in the presence of microbubbles, proves to be an asset for local drug delivery strategies since it may locally facilitate the uptake of anticancer agents. However, transport mechanisms recruited in uptake by the cells after exposure to US remain unclear. Previous studies showed that endocytosis was involved in the uptake of macromolecules [1] and small molecules (molecular weight lower than 4 kDa) [2]; however, the observations were made at a single, fixed, time point. Here, we propose to use Fibered Confocal Fluorescence Microscopy (FCFM) [3][4] to evaluate in real-time the involvement of clathrin- and caveolin- mediated endocytosis upon US exposure by using endocytosis inhibitors. Methods. C6 rat glioma cells were preincubated for 30 minutes with either chlorpromazine (CTZ), an inhibitor of clathrin-mediated endocytosis, or genistein (GEN), inhibiting the caveolin-mediated pathway. Inhibitor cytotoxicity was assessed, varying concentration (CTZ from 10 to 40 µM - GEN from 200 to 300 µM) and incubation time (30 minutes, but also 1.5 and 3 hours, to control for increased exposure for the duration of the experiment), via XTT viability assay. For the sonoporation experiments, uptake of SYTOX Green fluorescent dye was triggered with 1.4 MHz US, (0.5 MPa p-p, Duty Cycle 10%, Pulse Repetition Frequency 1kHz), in the presence Sonovue at 20 microbubbles per cell. After detecting and tracking the nuclei, uptake in each nucleus was monitored in real-time using FCFM, as described in [3] and [4], and uptake rates were obtained from fitting a two-compartment model to the fluorescence intensity data. Statistical analyses were performed using Mann-Whitney test; results are expressed as median (interquartile range). Results. Cells incubated with endocytosis inhibitors expressed a lower SYTOX Green uptake rate after sonoporation. First, GEN inhibition resulted in a shallow but significant (MW, $p<0.05$) reduction of SYTOX Green uptake rate 1/k from 52.4s (20.1s, n=451) (no treatment) to 0'54" (0'22", n=378), 0'58" (0'21", n=455) and 0'58" (0'22", n=352) for 200µM, 250µM and 300µM of GEN, respectively (Fig 1a). CTZ had a higher inhibitory effect on SYTOX Green uptake rate than GEN. A significant (MW, $p<0.05$) uptake rate reduction was observed from 0'52" (0'22", n=946) without treatment to 1'17" (0'36", n=227), 1'32" (0'46", n=448), 1'37" (0'52", n=215), and 2'11" (1'33", n=262), for 10µM, 20µM, 30µM and 40µM of CTZ, respectively (Fig. 1b), indicating that clathrin-mediated endocytosis was recruited in sonoporated cells. Conclusion. Model drug uptake kinetics of C6 cells after sonoporation can be studied in real-time using FCFM. A reduction of US-mediated uptake rate was observed in response to GEN and especially CTZ incubation. The data provide evidence for involvement of, in this case primarily clathrin-mediated, endocytosis in US-mediated uptake of drugs. References. [1] Meijering et al., Circ. Res., 2009. [2] Zeghimi et al., ESUCI, 2013. [3] Derieppe et al., Mol. Imaging Biol., 2012. [4] Derieppe et al., EMIM, 2013.

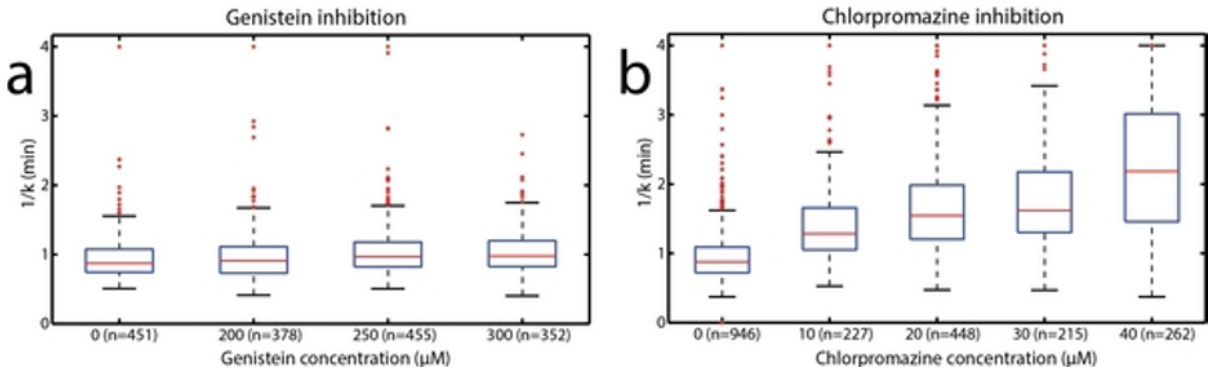

Inhibitory effect of 1a) Genistein (caveolin-mediated inhibitor) and 1b) Chlorpromazine (clathrin-mediated inhibitor) on ultrasound-mediated uptake rate of SYTOX GREEN fluorescent dye as a model drug.

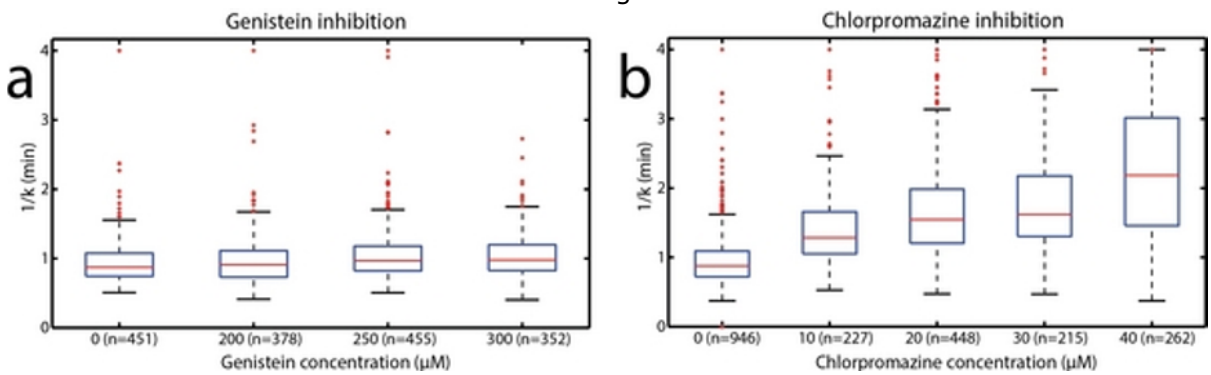

Disclosure of author financial interest or relationships:
M. Derieppe, None; **K. Rojek**, None; **B. Denis de Senneville**, None; **C. Bos**, None; **C. Moonen**, None.

Presentation Number **LBAP 058**
Late Breaking Abstract Poster Session
September 19, 2013 / 15:15-15:15 / Room: Exhibit Hall B

Cross-Talk Between Enzymes Responsible for the Elevated 1H MRS Phosphocholine Signal in Breast Cancer Cells

Franca Podo[1], *Kristine Glunde*[2], *Serena Cecchetti*[1], *Balaji Krishnamachary*[2], *Noriko Mori*[2], *Luisa Paris*[1], *Carlo Ramoni*[1], *Egidio Iorio*[1], *Zaver M. Bhujwalla*[2], [1]*Cell Biology and Neurosciences, Istituto Superiore di Sanità, Rome, Italy;* [2]*Radiology and Radiological Science, The Johns Hopkins University of Medicine, Baltimore, MD, USA. Contact e-mail: franca.podo@iss.it*

Magnetic resonance spectroscopy (MRS) in oncology has established the aberrant choline phospholipid metabolism as a novel hallmark of cancer. The accumulation of phosphocholine (PCho) in cancer cells cooperates with the dysregulated tumour growth programme, and has been attributed to a phenotype-dependent interplay between receptor-stimulated oncogenic pathways and metabolic fluxes through the phosphatidylcholine (PC)-cycle [1,2]. In breast cancer (BC) cells, emerging evidence points to the existence of functional interactions between overexpressed receptors of the EGFR family and the two PC-cycle enzymes directly responsible for PCho production, choline kinase (ChoK) [3] and PC-specific phospholipase C (PC-PLC) [4]. ChoKα has been reported to form a complex with EGFR in a c-Src-dependent manner, with consequent ChoK activation, DNA synthesis and enhanced cell proliferation [3]. Co-localization and physical binding of PC-PLC (66 kDa) to HER2 and EGFR has been detected in HER2-overexpressing BC cells [4], in which exposure to the selective PC-PLC inhibitor D609 induced down-modulation of these receptors from the plasma membrane. Both RNA interference-mediated ChoKα suppression and PC-PLC inhibition exerted antiproliferative effects and induced cell differentiation in BC cells [5,6]. This body of evidence suggests further investigation of whether cross-talk between ChoKα and PC-PLC could take place through their simultaneous binding to some EGFR family member(s). To this end, we first investigated the effects of siRNA-ChoKα silencing [5] on PCho level and PC-PLC expression in MCF-7 and MDA-MB-231 cells compared with non-tumoral MCF-12A cells. Efficient (about 75%) ChoKα silencing resulted in a 40% decrease of PCho in MCF7, 55% decrease in MDA-MB-231 cells, and unaltered PCho level in MCF-12A cells. Western blotting and confocal immunofluorescence microscopy showed increased PC-PLC protein expression in siRNA-ChoKα-treated cancer cells (e.g. 2-fold in MDA-MB-231). Our findings indicate that BC cells could compensate for the loss of ChoKα protein levels with PC-PLC upregulation, thus maintaining an intracellular PCho pool size markedly higher than that of non-tumoral breast epithelial cells. This evidence warrants further investigation to evaluate whether the here reported mechanism of cross-talk between ChoKα and PC-PLC could a) represent a key mechanism by which BC cells may maintain a growth advantage under different conditions of tumour microenvironment and treatment; and b) possibly enhance the effectiveness of a targeted anti-EGFR treatment by its combination with agents inducing down-regulation of both ChoKα and PC-PLC enzymes. Non-invasive 1H MRS approaches would provide a most suitable tool to investigate and monitor these effects in vitro and in vivo. [1] Glunde K et al Nat Rev Cancer 2011;835-48; [2] Podo F et al NMR Biomed 2011;24:648-72; [3] Miyake T and Parsons SJ Oncogene 2012; 31:1431-41; [4] Paris L et al Breast Cancer Res 2010;12(3):R23; [5] Glunde et al Cancer Res 2005;65:11034-43; [6] Abalsamo L et al Breast Cancer Res 2012;14(2):R50.

Disclosure of author financial interest or relationships:
F. Podo, None; **K. Glunde**, None; **S. Cecchetti**, None; **B. Krishnamachary**, None; **N. Mori**, None; **L. Paris**, None; **C. Ramoni**, None; **E. Iorio**, None; **Z.M. Bhujwalla**, None.

Presentation Number **LBAP 059**
Late Breaking Abstract Poster Session
September 19, 2013 / 15:15-15:15 / Room: Exhibit Hall B

Characterization and optimization of an in vitro 18F-FDG uptake assay as a pre-screening tool for in vivo studies

Maria Borland, *Donna Cvet, Daniel P. Bradley, Biomedical Imaging, Millennium Pharmaceuticals, Cambridge, MA, USA. Contact e-mail: maria.borland@mpi.com*

Objective: 2-[18F]-2-Deoxy-D-Glucose Positron Emission Tomography (FDG PET) is part of standard of care for patients in monitoring certain cancer indications and therapy. However, clinical and in vivo pre-clinical data show there is a wide range of FDG-avidity among tumor types and cell lines, respectively. In vitro FDG uptake experiments could give insight into tumor kinetics in vivo. In the present work, parameters such as cell density, nutrient conditions, glucose media levels, FDG incubation time, and normalization methods were investigated to determine optimal conditions for a 96 well in vitro FDG uptake assay. In vitro and in vivo basal FDG uptake was compared to understand the translatability of this assay to a tumor environment. In addition, cell-surface GLUT1/FDG uptake, and cell surface GLUT1 density under normal (16.7mM) and reduced (physiological; 5mM) glucose conditions were investigated. FDG Uptake Assay: Cells were seeded in a 96 well plate 24 h prior to assay. Plate was washed with media (no glucose) and 1uCi FDG was added for 1 hour at 37C. Cells were washed with DPBS and lysed with DPBS/Cell Titer Glo reagent. Lysate was read on gamma counter and Spectrum to assess uptake and viability. HCT116 cells were run in every assay to control for day-to-day variability in 18F -FDG concentration. Cell Lines: A375M , HT29, SW48, SW48G13D, T84. GLUT1 FACS Assay: Cells were grown in complete media. All cells were harvested and washed. GLUT1-FSC conjugate was added to cells in a 96 well plate and incubated at 4C for 1 hour. Cells were washed and resuspended in DPBS + 1ug/mL propidium iodide. Cell surface GLUT1 levels were evaluated using FACSCANTOII Flow Cytometer. Cell Lines: A375M, A549, CWR22RV1, DLD-1, HCT116, HT29, MDA-MB-231, OCI-Ly10, SW48.
Results/Conclusions: Basal FDG uptake in vitro is cell line-specific and trends well with in-house uptake data in subcutaneous xenograft tumor models obtained through in vivo FDG-PET imaging. Data shows that FDG uptake and cell surface GLUT1 levels are cell line dependent and GLUT1 presentation does not correlate with FDG uptake (r2=0.101). Reduced glucose growth conditions also appears to have a cell line-specific effect: HCT116 cells show an increase in cell surface GLUT1, while HT29 cells do not. While GLUT1 surface density changed with glucose conditions, FDG uptake in HCT116 and HT29 cells was unchanged regardless of glucose concentration. Future studies will include investigating other cell surface GLUT transporters, hexokinase levels/activity, and the effect of pharmacological pathway modulation and mutational status on glucose metabolism with the goal to utilize these in vitro assays to guide FDG PET drug studies in vivo.

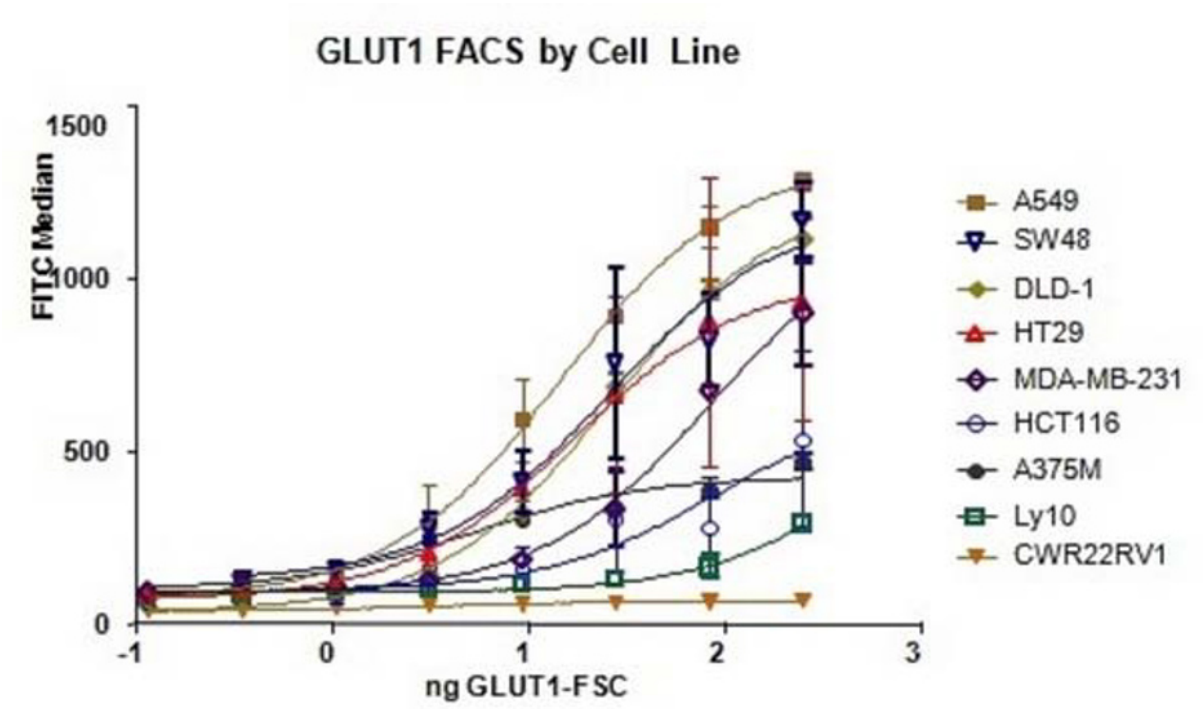

Cell Surface GLUT1 is cell line dependent

FDG uptake assay optimization and conditions

Parameter	Result	Assay Conditions
Cell density	No effect on FDG uptake	6,000 cells/well
Nutrient Conditions	Decreased cell viability when incubated without amino acids or glucose	No glucose media/10% FBS/2mM Glutamine
Glucose Concentration	Glucose competes with FDG	No glucose media/10% FBS/2mM Glutamine
FDG Incubation	Longer incubation time decreases dynamic range	1 hour at 37C
Normalization	Protein normalization and Cell Titer Glo normalization yield similar results	Cell Titer Glo

Disclosure of author financial interest or relationships:

M. Borland, None; **D. Cvet**, Takeda Cambridge US, Employment; **D.P. Bradley**, Millennium:The Takeda Oncology Company, Employment .

Presentation Number **LBAP 060**
Late Breaking Abstract Poster Session
September 19, 2013 / 15:15-15:15 / Room: Exhibit Hall B

Automated nuclear pleomorphic feature analysis and scoring for breast cancer histology in digital pathology

Munish Puri[1,3], *Marilyn M. Bui*[2,3], *Mark Lloyd*[3], [1]*Electrical Engineering, Univ Of South Florida, Tampa, FL, USA;* [2]*Pathology and Cell Biology, Univ of South Florida, Tampa, FL, USA;* [3]*Analytic Microscopy, Moffitt Cancer Center, Tampa, FL, USA. Contact e-mail: twishi03@gmail.com*

Background: Nearly 250,000 women were diagnosed with breast cancer in 2012. Nottingham Grading is the standard grading system in clinical practice. Assessment is based, in part, on irregular nuclear pleomorphic features like shape, size, color and intensity of individual cells. Computationally differentiated and classified nuclei enhance the assessment of diagnosis and grading. Histological image analysis can be used to objectively quantify tumor morphology, molecular expression, and spatial considerations in a cumulative manner, which is beginning to be used as a companion diagnostic tool to supplement current standards of predicting prognosis and make therapeutic decisions. Methods: Pathologists visually examine hundreds of slides per day under microscope. Unfortunately they are limited by the human eye which is unable to differentiate between hue, intensity and saturation to detect the nuclear level changes with exquisite precision. Computational segmentation and classification using through automated analysis and machine learning reduces the chances of error and increases prognostic precision and assessment of survival rates. Multiparametric cancer nuclei features are being developed using smart algorithms for accurate diagnosis and prognosis. Data set and grouping individual morphological features like area, size, shape, perimeter, roundness and the features of the neighboring host physical microenvironment (PME) using data classification techniques such as neural networking are the basis of automated pleomorphic feature detection. Imaging algorithms for nuclei pleomorphic classification are proposed for automated scoring and prognosis. Results: Preliminary experiments demonstrate that 17 of 25 challenging cases of breast cancer of various grades were classified identically between two practicing pathologists (68% accuracy). However, 100% of these same tumors were correctly classified using our prototypical algorithms. Separate tests are performed on breast cancer data (available online: University of Wisconsin from Dr. W.H. Wolberg) on 699 instances of 10 attributes each having benign and malignant instances. More than 98% of the breast cancer data are accurately classified using the neural network (NN) classifier. Discussion: In order to produce a more accurate prediction and prognosis for breast cancer, a more quantifiable method of automated image analysis tools like neural networking are used for nuclear feature classification. Neural network (NN) classifier`s ability to detect cancer nuclei from normal cells and learning from its errors and experience through feed forward back propagation (FFBP) algorithms, like human brain neurons, makes this a suitable candidate to assist pathologists by providing a companion diagnostic report. Back propagation learning through hidden layer neurons and assigned weights makes NN a more robust, fault tolerant module which works well even in noisy environments. Nottingham grading system is facing difficulties including a lack of precision and agreement among pathologists. Computational analysis is emerging as a reliable tool to assist pathological assessments.

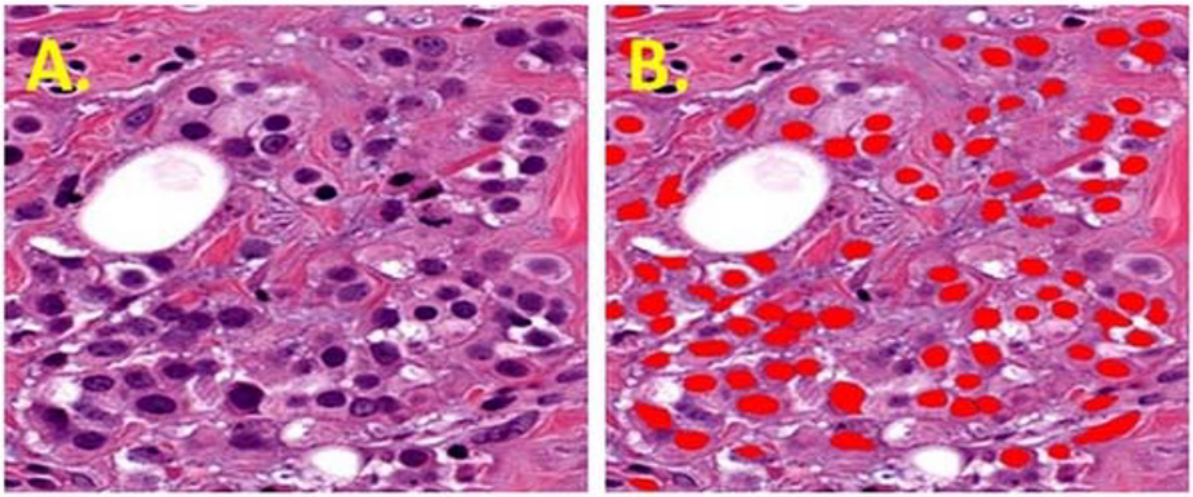

Figure. A) A hematoxylin and eosin stained Nottingham grade III breast cancer sample with B) nuclei automatically identified and segmented (masked red) and prepared for feature extraction.

Disclosure of author financial interest or relationships:
M. Puri, None; **M.M. Bui**, None; **M. Lloyd**, None.

Presentation Number **LBAP 061**
Late Breaking Abstract Poster Session
September 19, 2013 / 15:15-15:15 / Room: Exhibit Hall B

Increasing Uptake of Anti-EGFR Antibody Through Modulation of EGFR Expression

Asher M. Krell[1], *Brendan T. Eby*[1], *Kristine Day*[1], *Yolanda E. Hartman*[1], *Kurt R. Zinn*[2], *Eben L. Rosenthal*[1], [1]*Surgery-Otolaryngology, University of Alabama at Birmingham, Birmingham, AL, USA;* [2]*Radiology Chair Office, University of Alabama at Birmingham, Birmingham, AL, USA. Contact e-mail: akrell@uab.edu*

Introduction: Anti-EGFR antibody based cancer therapies have been found to have increase effectiveness when combined with conventional therapeutics including radiation or steroid therapy. The mechanism associated with additive or synergistic benefit of antibody therapies is controversial and there is limited ability to predict who will respond to therapy. We hypothesize that direct, real-time measurement of antibody delivery to the tumor may improve understanding of therapeutic mechanisms and identify tumors more likely to respond to combination therapy. Methods: Monoclonal antibodies cetuximab and panitumumab were conjugated to IRDye800CW (LICOR Biosciences). Three head and neck squamous cell lines (SCC1, OSC19, and Fadu) and three melanoma cell lines (SKMEL5, SKMEL28, and A375) were grown in culture and treated with a dose range of dexamethasone and radiation therapy. Cells underwent radiation or dexamethasone treatment prior to incubation with 2.0 μg/mL of cetuximab-IRDye800CW or panitumumab-IRDye800CW. Lysates were collected and cellular fluorescence evaluated by optical imaging of western blots using the Pearl Impulse (LICOR) system. Results: Exposure of SC¬¬C1 cells to 0.1 μg/mL of dexamethasone increased EGFR expression by 58% which correlated with an increase in fluorescence of 84% after incubation with cetuximab-IRDye800CW and 53% for panitumumab-IRDye800CW. Radiation treatment with 1 Gy had the most significant fluorescence increase in Fadu with a 19% increase in EGFR expression resulting in a fluorescence increase of 51% after cetuximab-IRDye 800CW incubation. Although the cell lines responded differently to radiation therapy, the increase in fluorescence positively correlated with elevated EGFR expression ($R2=0.65$ $P \leq 0.0001$) produced from radiation or dexametheasone treatment. Conclusion: Increased EGFR expression after dexamethasone or radiation treatment translated into increase in fluorescence after incubation with cetuximab-IRDye800. Importantly, if radiation or dexamethasone treatment among different cell lines did not produce an elevation in EGFR expression, there was no corresponding increased fluorescence. This provides evidence that EGFR expression positively correlates with incorporation of the antibody into the tumor cell.

Disclosure of author financial interest or relationships:
A.M. Krell, None; **B.T. Eby**, None; **K. Day**, None; **Y.E. Hartman**, None; **K.R. Zinn**, None; **E.L. Rosenthal**, None.

Presentation Number **LBAP 062**
Late Breaking Abstract Poster Session
September 19, 2013 / 15:15-15:15 / Room: Exhibit Hall B

Detection of impaired calcium regulation after cardiac hypertrophy using Mn-enhanced MRI

Brian B. Roman, [1]*Radiology, University of Chicago, Chicago, IL, USA;* [2]*Graduate Program Medical Physics, University of Chicago, Chicago, IL, USA. Contact e-mail: broman@uchicago.edu*

Introduction Myocardial energetics play a central role in maintaining normal cardiac function. It is well documented that the failing heart is unable to maintain the ATP/PCr ratio needed to sustain Ca2+ homeostasis in excitation-contraction coupling (E-C coupling)1,2,3,4,5. The myocardium responds to an intrinsic or extrinsic stress through hypertrophy and, in particular, left ventricular hypertrophy (LVH). Increased expression of creatine kinase (CK) has been associated with cardiac hypertrophy as a compensatory mechanism for the energetic deficits. Transgenic mice deficient in the muscle and mitochondrial CK (CK-M/Mito-/-; DBCKO) have been used to examine the metabolic aspects of hypertrophy especially alterations of the calcium handling proteins and the calcium transients. It has been recently shown that ablations or mutations of proteins of the sarcoplasmic reticulum (SR) can cause problems in Ca2¬+ handling and ultimately cardiac hypertrophy in the murine heart9,10. Unfortunately this information can only presently be obtained by use of highly invasive methods. Manganese (Mn2+) has properties similar to calcium and is a known MRI T1 relaxation agent. As such, Mn enhanced MRI (MnMRI) has been used to probe calcium regulation in preclinical models. Here we demonstrate how MnMR are used to probe post-hypertrophic changes in calcium gene expression. Methods Transgenic creatine kinase double knockout (M-CK-/Mt-CK-, n=8) and C57BL/6 (n=3) mice were imaged using a Bruker 9.4T MRI scanner with 12cm gradient inserts and a 35mm quadrature volume coil. T1 relaxation time measurements were performed using the saturation recovery Look-Locker sequence with ECG gating (FOV=2.56cm,64x64 matrix size, TR=4000/TE=2.6,NEX=1). Regions-of-interest (ROIs) were manually drawn in the left-ventricular free wall (LVFW), the septum, and a phantom placed adjacent to the animal. ROI analysis and T1 curve fitting were performed using custom written Matlab software. Ten days after initial imaging isoproterenol (47 mg/kg BW) was delivered via osmotic pumps for three days followed by reimaging. A statistical sign test was used to compare pre- and post-hypertrophic T1 relaxation times in C57 and DBKO mice, separately. Results / Discussion T1 relaxation times were significantly lowered by the presence of Mn in both control and transgenic mice. These changes mirrored changes in calcium handling gene expression. For example there was no significant difference in the LVFW of C57 mice between Mn and Mn+ISO where there was significance in the DBCKO. These are complementary to differences in both SERCA and Tridan gene expression data. These experiments indicate the power of MnMEMRI to detect changes in gene expression in the heart based on T1 relaxation maps.

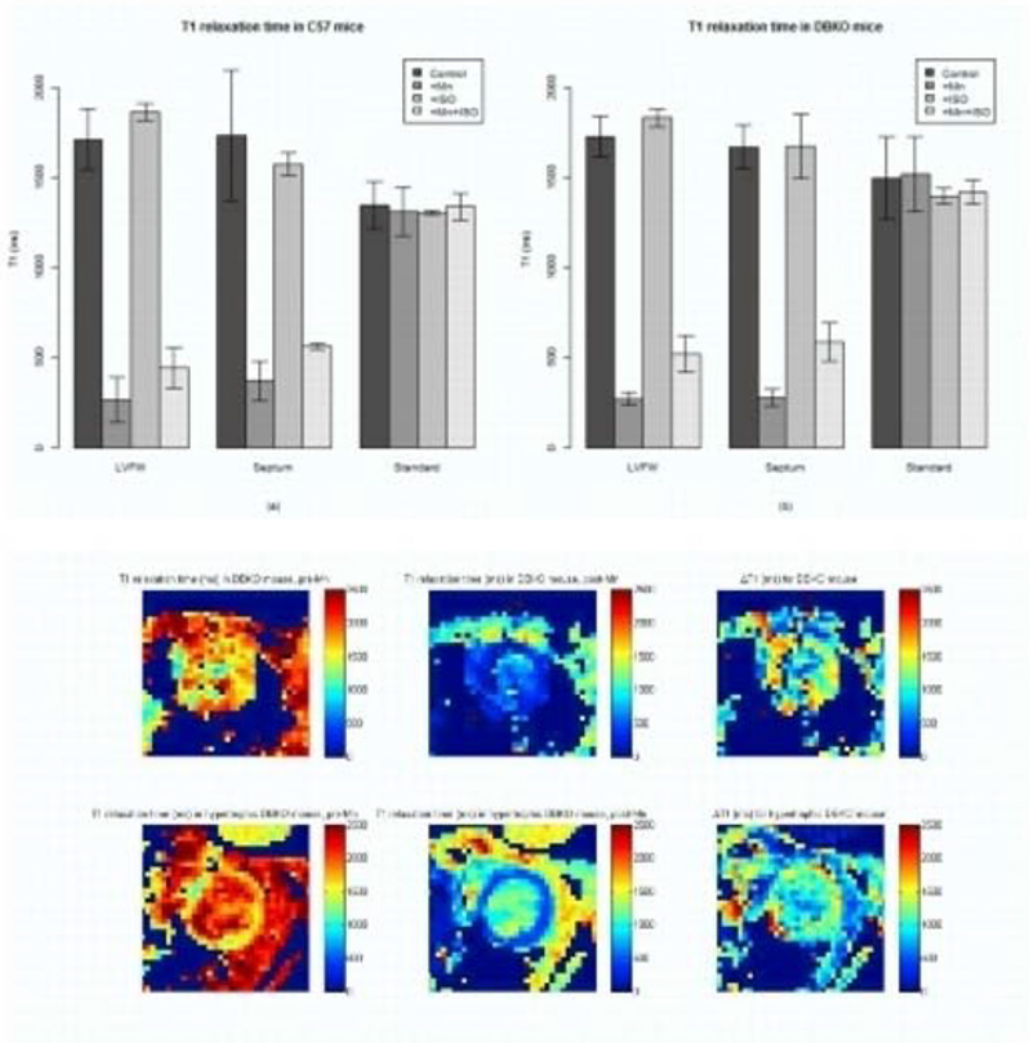

Figure 1 T1 relaxation times and maps in C57 and DBCKO mouse hearts. (Top) Average regional changes in T1 relaxation time in both C57 and DBCKO mice. *(Bottom)* Cardiac T1 maps (ms) obtained using the saturation recovery Look-Locker pulse sequence. (a) DBKO pre-Mn, control (b) DBKO post-Mn, control (c) deltaT1 DBKO (d) DBKO PRE-Mn, hypertrophic (e) DBKO post-Mn, hypertrophic (f) deltaT1 DBKO hypertrophic

Disclosure of author financial interest or relationships:
B.B. Roman, None.

Presentation Number **LBAP 063**
Late Breaking Abstract Poster Session
September 19, 2013 / 15:15-15:15 / Room: Exhibit Hall B

Rational liposomal shell design for macrophage targeting in atherosclerosis.Vaishali Bagalkot and Dr.Patrick Kee. University of Texas Health Science Center, Houston, Texas, USA

Vaishali Bagalkot, *Patrick Kee, Internal Medicine/Cardiology, University of Texas Health Science Center, Houston, TX, USA. Contact e-mail: vaishali.bagalkot@uth.tmc.edu*

Macrophages play an important role in the development and destabilization of atherosclerotic plaques. Exposed phosphatidylserine (PS) on senescent cell surface can be recognized by macrophages. Cell surface modification can be applied to lipid-based contrast agents and offers an attractive strategy for macrophage targeting and enrichment of contrast agents in vivo for molecular imaging. Dipalmitoylphosphatidylchoine (DPPC) liposomes with various amount of PS were developed. PS liposomes were labeled with rhodamine for in vitro studies by flow cytometry and fluorescence microscopy. Standard PC liposomes and 8 mol% PS liposomes containing iodixanol were prepared for in vivo pharmacokinetic analysis in New Zealand White (NZW) rabbits. To detect macrophage specific uptake of contrast agents in atherosclerotic plaques, standard PC liposomes and 8 mol% PS liposomes containing a payload of iodixanol, rhodamine lipid and near infra-red dye were injected into Watanabe Hereditary Hyperlipidemic (WHHL) rabbits. Molecular computed tomography (CT) imaging was performed using a GE Ultra flat panel CT scanner at 90kV and 150 mA at baseline and 44 hrs after injection, then ex vivo fluorescence imaging of the excised aortas was performed using small animal imaging system. Distribution of rhodamine liposomes and macrophages in the aortic wall was observed by immunofluorescence. The liposomes were 160-180 nm, with negative charge of -51.2 mV due to PS. Among the various PS liposomes (2, 8 and 20 mol% PS) enhanced targeting and uptake was seen with increasing mol% PS in J774A.1 macrophages. However, encapsulation of iodixanol was found to be impaired in the presence of 20 mol% PS in liposomes but remained intact in 8 mol% PS liposomes, which was subsequently used for in vivo CT and fluorescence imaging studies in WHHL rabbits. Liposomes were long circulating with Hounsfield units (HU) in the blood pool peaked at 211 HU at 2-8h and returned to baseline 96 HU at 44h. Molecular CT imaging showed no obvious uptake of standard or PS liposomes in the aorta in WHHL rabbits. However, ex vivo fluorescence imaging demonstrated abundant fluorescence signal along the aorta in animals injected with standard liposomes, and to lesser extent, with PS liposomes. Immunofluorescence microscopy showed similar pattern of rhodamine liposome uptake in the aortic wall with regards to both standard and PS liposomes. Distribution of both liposomal preparations was non-specific and did not co-localize with macrophages even though RAM-11 staining demonstrated abundant macrophages in the atherosclerotic lesions. Between two imaging modalities used in the current study, CT imaging appears insensitive in detecting CT-based contrast agent uptake in the aortic wall as compared with fluorescence imaging of excised tissues. Standard liposomes or modified liposomes that resemble apoptotic cells were poorly taken up by lesion macrophages even though in vitro cell culture studies demonstrated avid uptake of both liposomes. Results suggest that lesional macrophages may have defective efferocytosis and caution the reliance of the phagocytic uptake mechanism for macrophage-specific molecular imaging.

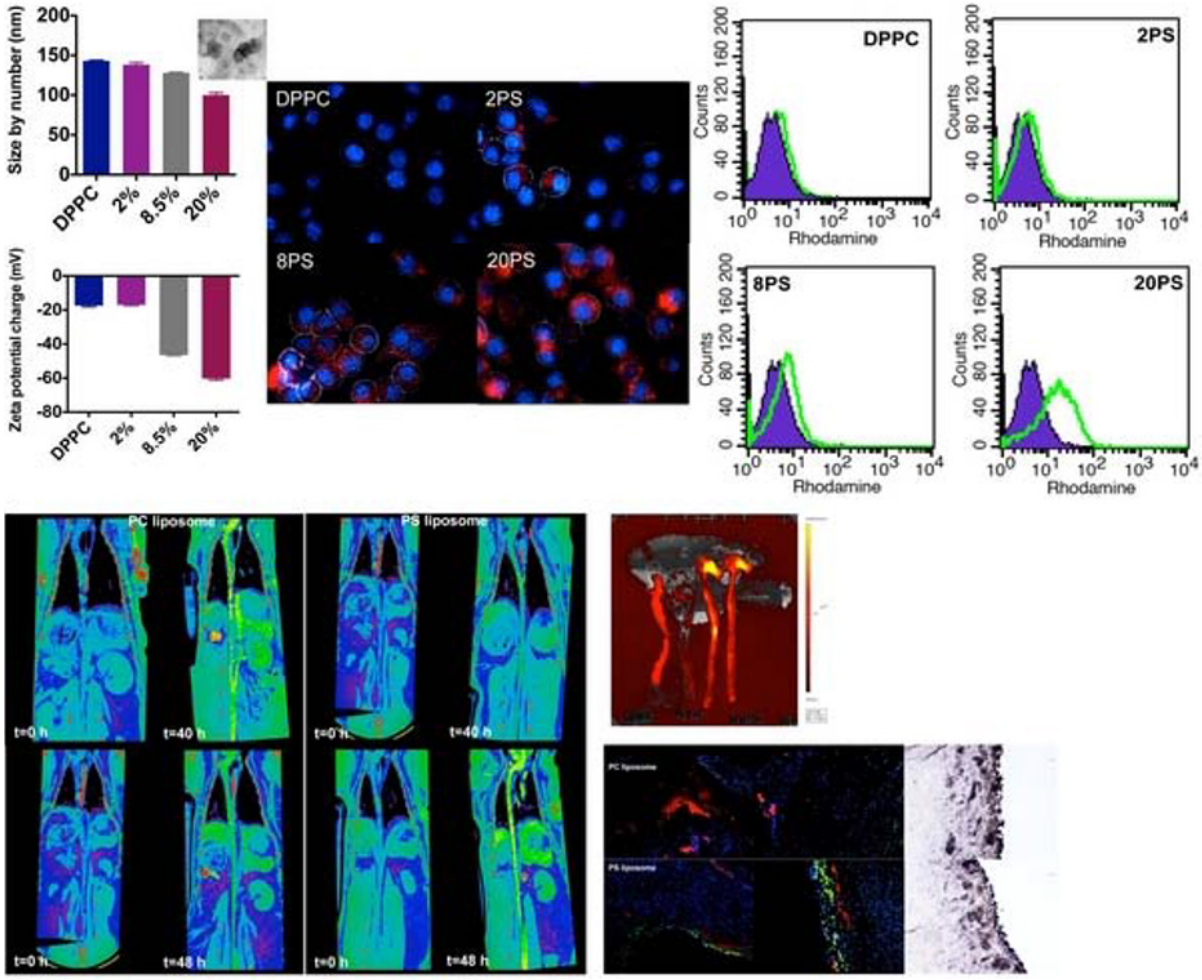

Disclosure of author financial interest or relationships:
V. Bagalkot, None; **P. Kee**, None.

Presentation Number **LBAP 064**
Late Breaking Abstract Poster Session
September 19, 2013 / 15:15-15:15 / Room: Exhibit Hall B

PET Imaging of Thrombosis using Al18F- and 64Cu-Fibrin-Binding Peptides

Francesco Blasi, Bruno L. Oliveira, Tyson A. Rietz, Nicholas Rotile, Helen Day, Richard Looby, Ilknur Ay, **Peter Caravan***, Martinos Center for Biomedical Imaging, Massachusetts General Hospital, Charlestown, MA, USA. Contact e-mail: caravan@nmr.mgh.harvard.edu*

Thrombosis is a common element of cardiovascular diseases, such as ischemic stroke, heart attack, deep vein thrombosis and pulmonary embolism, which affect millions of people worldwide. Fibrin is a major component of both arterial and venous thrombi, and represents an ideal candidate for molecular imaging of thrombosis. Recently, we demonstrated that 64Cu-labeled PET probes based on three specific fibrin-binding peptides were able to detect thrombus formation in vivo. In particular, we found that the probe FBP2, containing the cyclic, disulfide bridged peptide FHCHypY(3-CI)DLCHIL showed the best properties in terms of target uptake and imaging efficacy. However the metabolic stability of these probes was limited by some dissociation of 64Cu from the DOTA chelator resulting in persistent blood background. To address the issue of Cu dissociation, we synthesized two new PET probes by replacing DOTA with either NODAGA or NOTA, which are expected to form more inert complexes with copper. We also labeled the NOTA and NODAGA conjugates with aluminum-fluoride (Al18F). Here we describe these 4 probes (Table) and compare their biodistribution, metabolic stability, imaging efficacy and thrombus uptake in a rat model of arterial thrombosis. Thrombus was clearly visualized by all 4 probes on PET images at both 2 and 5 hours post-injection (e.g. Figure, A and B), with a 5-fold or higher thrombus to background ratio. Compared with our previous DOTA derivative FBP2, the new 64Cu probes showed substantially improved metabolic stability (>90% intact in blood from 0-4 h by HPLC) and this resulted in much greater thrombus:background ratios that increased with time post injection. In particular, the thrombus uptake was 5 to 20 fold higher than the uptake in contralateral artery, blood, muscle, lungs, spleen, large intestine and heart at 2 h post-injection, and 10 to 40 times higher at 5 h (Figure, C). Remarkably, for the 64Cu probes FBP8 and FBP9, the thrombus was the tissue with the highest uptake just after the kidneys. The Al18F derivatives were less stable (FBP10, ~35% intact probe at 2 h; FBP11, ~90% intact) but still showed high thrombus:background ratios (Figure C) that were improved relative to FBP2. The lower metabolic stability of FBP10 was associated with some accumulation of signal in bone. The improved metabolic stability of the probes resulted in a very high uptake in the thrombus (0.5 - 0.8 %ID/g) that persisted over 5 h. This high uptake resulted in a greater target-to-blood and target-to-liver ratio than DOTA derivatives. The high thrombus/contralateral ratio for all probes was also confirmed by ex vivo autoradiography (e.g. Figure, D). In summary, we demonstrated the ability of four new PET probes to detect thrombus formation in vivo. Three out of four probes showed excellent metabolic stability and high thrombus-to background ratio, and represent promising candidates for molecular imaging of thrombosis.

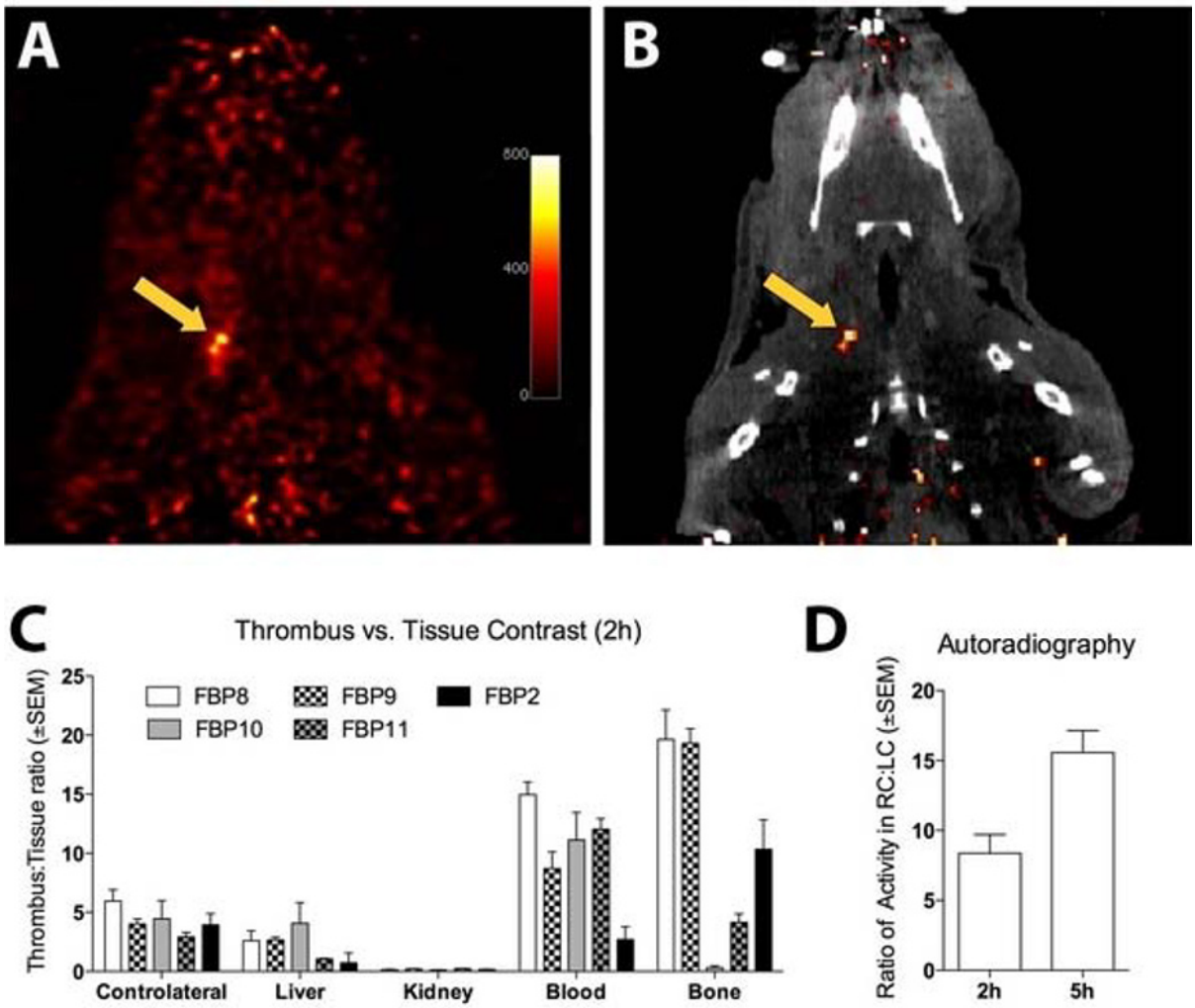

PET Imaging of Thrombosis using Al18F- and 64Cu-Fibrin-Binding Peptides Representative PET (A) and PET/CT fused (B) images showing thrombus detection (arrows) by FBP8 at 5 h post-injection. Thrombus-to-tissue ratios for FBPs (C). Ex vivo autoradiography of FBP8 (D).

Fibrin-binding probes (FBPs)

ISOTOPE	CHELATOR	PROBE
64Cu	DOTA	FBP2
64Cu	NODAGA	FBP8
64Cu	NOTA	FBP9
Al18F	NODAGA	FBP10
Al18F	NOTA	FBP11

FBP2 as in Ciesienski at al., Mol Pharm. 2013 Mar 4;10(3):1100-10

Disclosure of author financial interest or relationships:

F. Blasi, None; **B.L. Oliveira**, None; **T.A. Rietz**, None; **N. Rotile**, None; **H. Day**, None; **R. Looby**, None; **I. Ay**, None; **P. Caravan**, Sanofi, Grant/research support; Biogen Idec, Consultant; Factor 1A, Stockholder; Collagen Medical, Stockholder .

Presentation Number **LBAP 065**
Late Breaking Abstract Poster Session
September 19, 2013 / 15:15-15:15 / Room: Exhibit Hall B

Automated production and application of [11C]palmitate as a probe for myocardial fatty-acid metabolism in the stressed heart

Tao Huang[1], *Min Zhong*[2,1], *Susanna R. Keller*[3], *Stuart S. Berr*[1], *Falk Kunkel*[1], *Jiang He*[1], *Bijoy K. Kundu*[1], [1]*Radiology and Medical Imaging, University of Virginia, Charlottesville, VA, USA;* [2]*Physics, University of Virginia, Charlottesville, VA, USA;* [3]*Medicine, Endocrinology and Metabolism, University of Virginia, Charlottesville, VA, USA. Contact e-mail: th4g@virginia.edu*

Objectives: The objectives of this work are to implement the automated synthesis of [11C]palmitate with the Ecket & Ziegler modular-lab PharmTracer system and apply it as a PET probe for imaging fatty-acid (FA) metabolism along with [18F]FDG to test the hypothesis that the stressed heart preferentially uses glucose over FA. Methods: Based on the existing acetate module, modifications were made to the cassette layout and the programmed process. [11C]CO2 from the cyclotron, trapped and then released from the gas phase system, was bubbled through the precursor solutions (pentadecylmagnesium bromide in diethyl ether) at room temperature to reach the maximal radioactivity. The reaction vessel was then sealed and heated to 35°C for 3 minutes to complete the reaction. Upon quenching with HCl/Et2O, the product was purified by solid phase extraction (SPE) cartridge without solvent evaporation or distillation step. The [11C]palmitate was washed off the column with ethanol, and this solution then was formulated with bovine serum albumin(BSA). Using [11C]palmitate PET, we imaged myocardial FA uptake in male C57BL/6 mice (9-10 weeks of age) at baseline and on day 1 post transverse aortic constriction (TAC) surgery. A 20 minute dynamic PET scan was performed under 1-1.5% isoflurane using a Focus 120 PET scanner, where data acquisition was initiated a few seconds before the slow administration of about ~300-350 μCi [11C]palmitate over 25 seconds via a tail-vein catheter. The list mode data set sorted into 25 time bins (frames, time(s):12,5;8,30;4,150;1,300) was reconstructed with attenuation correction using OSEM-MAP algorithm. 90 minutes later, a 60 minute dynamic FDG PET scan was performed on the same animal. Regions of interest in the region corresponding to the LV blood pool (LVBP) and the myocardium were drawn and time activity curves generated from the dynamic PET images. Results: With the commercially available and inexpensive pentadecylmagnesium bromide solution, the modified program completed the automatic synthesis smoothly within 10 minutes.The starting radioactivity of [11C]CO2 was from 60 mCi to 250 mCi and the non-corrected yield was from 15% to 30%.The labeled product was absorbed on the cartridge without loss during sequential washing with ether, water and buffer, and finally washed off with ethanol. In this purification method, there was no solvent evaporation or liquid-liquid extraction step, which is difficult in automatic production. Preliminary imaging results using [11C]palmitate (Fig.1) and [18F]FDG PET indicate that the mouse heart under pressure overload stress exhibit increased FA and glucose uptake on day 1 post TAC. Measured standardized uptake values (SUV) for both tracers indicate FDG uptake to increase by 235.5 % as compared to 59.4% for palmitate at day 1 from baseline. Conclusions: [11C]palmitate has successfully been synthesized for the first time with the Eckert & Ziegler PharmTrace system. Preliminary results suggest that the pressure overload mouse heart preferentially utilizes glucose over FA as an adaptive response to maintain function.
Acknowledgement: NIH grant R21 HL102627.

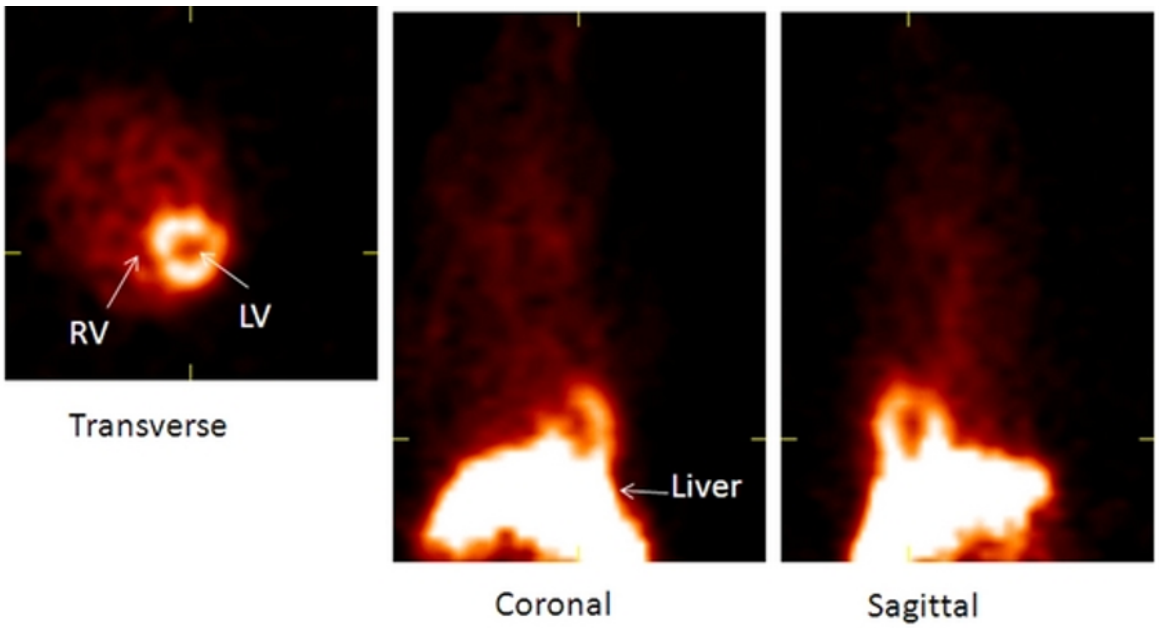

Figure 1: [11C]-Palmitate PET images of mouse heart in vivo. The images indicate a uniform uptake of the tracer in the myocardial walls. The transverse image shows the right ventricle (RV) and the left ventricle (LV). The coronal and the sagittal images also indicate elevated levels of the labeled tracer in the liver.

Disclosure of author financial interest or relationships:
T. Huang, None; **M. Zhong**, None; **S.R. Keller**, None; **S.S. Berr**, None; **F. Kunkel**, None; **J. He**, None; **B.K. Kundu**, None.

Presentation Number **LBAP 066**
Late Breaking Abstract Poster Session
September 19, 2013 / 15:15-15:15 / Room: Exhibit Hall B

Diffusion Tensor Imaging Abnormalities in HIV Transgenic Rats as Biomarkers of Cellular Death/Loss

Margaret R. Lentz[1], *Kristin L. Peterson*[1], *Wael G. Ibrahim*[1], *Dianne E. Lee*[1], *Joelle Sarlls*[2], *William Reid*[1], *Dima A. Hammoud*[1], [1]*Radiology and Imaging Sciences, National Institutes of Health/Clinical Center, Bethesda, MD, USA;* [2]*NMRI, National Institutes of Health, Bethesda, MD, USA. Contact e-mail: lentzmr@cc.nih.gov*

Background: Diffusion tensor imaging (DTI) is a non-invasive MR based technique which detects the magnitude and directionality of Brownian water motion in brain tissues, thus reflecting molecular and cellular architectural distortions associated with various CNS pathologies. In HIV-associated neurocognitive disorders, DTI has been found useful in delineating architectural brain changes between HIV+ and HIV- subjects, however it hasn't been used in a small animal model of HIV. In order to further understand the CNS pathology reported in HIV+ patients, we scanned the HIV-1 transgenic (Tg) rat and age-matched controls (ctrl) using a 7-T Bruker magnet, for the detection of DTI changes. Materials and methods: 19 rats (10Tg, 9ctrl) and 17 rats (10Tg, 7ctrl) were imaged at 3 and 9-10 months of age respectively. We measured the corpus callosum (CC) fractional anisotropy (FA) values which reflect the directionality of water diffusion and the cortical Mean Diffusivity (MD) values which reflect the average Brownian motion of water molecules moving in multiple directions simultaneously. Both values reflect the interaction of water molecules with various diffusion obstacles like white matter fiber tracts, cells, macromolecules and membranes. We correlated our findings with previous MR volumetric data obtained in a separate group of rats (using 3D-T1 weighted images) and with H&E and Neu-N (neuronal biomarker) staining in rat cohorts of the same age. Results: We previously found significantly decreased total brain and brain parenchyma volume in old Tg rats compared to age-matched controls (Generalized Linear Model, $p= 0.02$ and $p=0.04$ respectively) while no significant differences were seen in the young rats ($p= 0.28$). On DTI, significant decreases in FA values were observed in the CC of young and old Tg animals when compared to age-matched controls (Fig.1A)(Student's t-test, $p= 0.03$ and $p<0.002$ respectively). FA values were lower in the older Tg compared to the younger Tg cohort, although this was not statistically significant ($p=0.28$) In the cortex, MD values were higher in the Tg rats (young and old) when compared to age-matched controls but this did not reach statistical significance. However there were significantly higher MD values in the older Tg compared to the younger Tg rats (Student's t-test, $p=0.03$) (Fig.1B). Discussion: Concurrent with our findings of significant volume loss in older HIV-1 Tg rats compared to controls, and histological evidence of early neuronal death and secondary decreased cellularity (supplemental data), we found decreased FA values in the CC of Tg rats compared to age matched controls probably reflecting loss of myelinated fibers/oligodendroglial damage. We also found increased cortical MD in old compared to young Tg rats which we believe is due to neuronal loss resulting in less restriction of water diffusivity. The main pathophysiology underlying neuronal death in the Tg rats is probably prolonged exposure to neurotoxic levels of HIV viral proteins however more work is needed to further validate the correlation between CSF/serum viral protein levels and imaging biomarkers of cellular death and axonal loss.

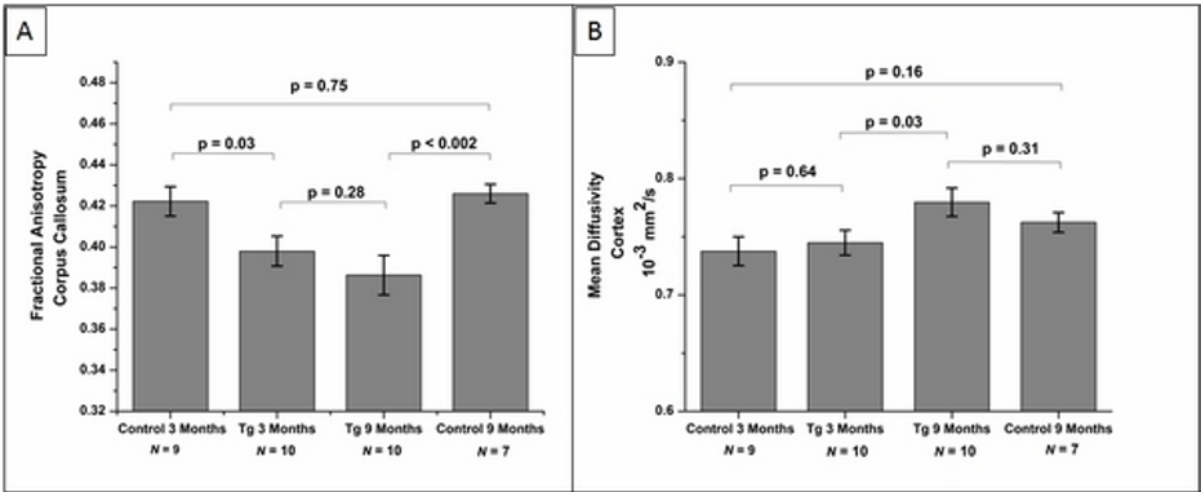

Disclosure of author financial interest or relationships:
M.R. Lentz, None; **K.L. Peterson**, None; **W.G. Ibrahim**, None; **D.E. Lee**, None; **J. Sarlls**, None; **W. Reid**, None; **D.A. Hammoud**, None.

Presentation Number **LBAP 067**
Late Breaking Abstract Poster Session
September 19, 2013 / 15:15-15:15 / Room: Exhibit Hall B

PET imaging of neutrophils in a macaque tuberculosis model

Wissam Beaino[1], *Joshua T. Mattila*[2], *Dexing Zeng*[1], *M. Teresa Coleman*[1], *Brian J. Lopresti*[1], *Joanne L. Flynn*[2], *Carolyn J. Anderson*[1], [1]*Department of Radiology, University of Pittsburgh, Pittsburgh, PA, USA;* [2]*Department of Microbiology and Molecular Genetics, University of Pittsburgh, Pittsburgh, PA, USA. Contact e-mail: beainow@upmc.edu*

Tuberculosis is an infectious disease caused by Mycobacterium tuberculosis (Mtb) that typically attacks the lungs and leads to the formation of granulomas, which are organized immune cell aggregates that mainly contain macrophages, neutrophils, T cells, B cells and dendritic cells. Studies have demonstrated that the cellular composition of granulomas can vary independently and dramatically from lesion to lesion within the same subject, and changes can over time within the same lesion. Predominance of one cell type over another yields important clues as to the microenvironmental state of a particular lesion and might predict whether a lesion is resolving or worsening naturally or in response to drug treatment. Neutrophils are the first responders and most common cell type observed in early stages of acute inflammation in TB. Our aim is to develop a Cu-64 PET probe for imaging neutrophils in a macaque model of Mtb. Formyl peptide receptor 1 (FPR1), a chemoattractant receptor, is highly expressed on neutrophils and binds formyl peptides from bacteria. Cinnamoyl-FLFLF is an antagonist of FPR1 and binds in high affinity without inducing a response in the neutrophils. We conjugated the cFLFLF peptide with a cross-bridged copper chelator developed in our laboratory (CB-TE1A1P) for labeling with Cu-64 for PET imaging. cFLFLFK-PEG12-CB-TE1AP was synthesized using solid phase peptide synthesis and obtained in high purity and good yield. The binding affinity of the peptide to neutrophils was determined by a saturation binding assay using neutrophils purified from macaque blood and the Kd was determined to be 2.3 nM. The specificity of the cFLFLF peptide for neutrophils was validated by flow cytometry using the biotinylated peptide. The peptide binds specifically to neutrophils from macaque blood and from autopsied granulomas and poorly binds to macrophages and lymphocytes. PET images of TB infected monkeys showed high uptake of the peptide in tuberculosis granulomas, the uptake correlated with the FDG uptake in the same monkey, and CT verified the presence of Mtb granulomas.

Disclosure of author financial interest or relationships:
W. Beaino, None; **J.T. Mattila**, None; **D. Zeng**, None; **M. Coleman**, None; **B.J. Lopresti**, None; **J.L. Flynn**, None; **C.J. Anderson**, None.

Presentation Number **LBAP 068**
Late Breaking Abstract Poster Session
September 19, 2013 / 15:15-15:15 / Room: Exhibit Hall B

Radioiodinated DPA-713 correlation with the Early Bactericidal Activity of a Novel TB drug regimen

Alvaro Ordonez[1,2], *Mariah Klunk*[1,2], *Supriya Pokkali*[1], *Edward Weinstein*[1,3], *Catherine Foss*[4,1], *Ronnie Mease*[4], *Martin Pomper*[4,1], *Sanjay K. Jain*[1,2], [1]*Center for Infection and Inflammation Imaging Research, Johns Hopkins University, Baltimore, MD, USA;* [2]*Department of Pediatrics, Johns Hopkins University, Baltimore, MD, USA;* [3]*Department of Medicine, Johns Hopkins University, Baltimore, MD, USA;* [4]*Russell H. Morgan Department of Radiology and Radiological Science, Johns Hopkins University, Baltimore, MD, USA. Contact e-mail: aordone2@jhmi.edu*

Background Better biomarkers are urgently needed to accelerate tuberculosis (TB) drug development. Noninvasive imaging biomarkers can provide rapid, comprehensive information to monitor the activity of TB drug regimens by providing real time data on host responses to infection. We have previously demonstrated that iodo-DPA-713, a synthetic ligand of translocator protein (TSPO), accumulates specifically in TB-associated inflammatory lesions by selective retention within macrophages and other phagocytic cells. In this study we utilized serial [^{125}I]iodo-DPA-713 single-photon emission computed tomography (SPECT) imaging as a novel imaging biomarker to monitor the host immune response and its association with the early bactericidal activity of a novel TB drug regimen. Methods C3HeB/FeJ "Kramnik" mice, that develop well defined necrotic and hypoxic lesions, were aerosol infected with *Mycobacterium tuberculosis* and administered a standard (rifampin, isoniazid, pyranizamide - RHZ) or a highly active novel drug regimen (bedaquiline, pyranizamide, clofazimine - JZC). Serial pulmonary [^{125}I]iodo-DPA-713-SPECT was compared with [^{18}F]FDG-PET and standard microbiology to monitor the activity of drug regimens. Lesion-specific standardized uptake values (SUV) were calculated by drawing regions of interest (ROI) around 3 pulmonary lesions evidenced in the CT of each animal. Five mice were used per group and per time-point. Results Pulmonary bacterial burden at the time of imaging (6-weeks post-infection) was 8.05 ± 0.02 $\log_{10}$ colony forming units (CFU). [^{125}I]iodo-DPA-713-SPECT imaging correctly identified the bactericidal activity of the drug regimens at all time-points ($p < 0.04$), while [^{18}F]FDG-PET broadly correlated with TB treatments, it was not able to distinguish the highly active regimen from the standard (Figure). [^{125}I]iodo-DPA-713-SPECT provided higher lesion-specific signal-to-noise ratios than [^{18}F]FDG-PET imaging. Conclusions These studies demonstrate that radioiodinated DPA-713, a novel imaging biomarker, could monitor the activity of drug regimens, including those for multi-drug resistant TB, and may prove to be a more specific biomarker for TB disease *in situ*. Our imaging experiments required relatively few animals, provided data on individual lesions, and could be extended to other strains of *M. tuberculosis*. The information was produced in real time, as opposed to the standard 4 week delay for CFU enumeration on solid media. By monitoring the host response to infection, failing TB regimens may be modified long before clinical microbiology data is available and the disease has progressed.

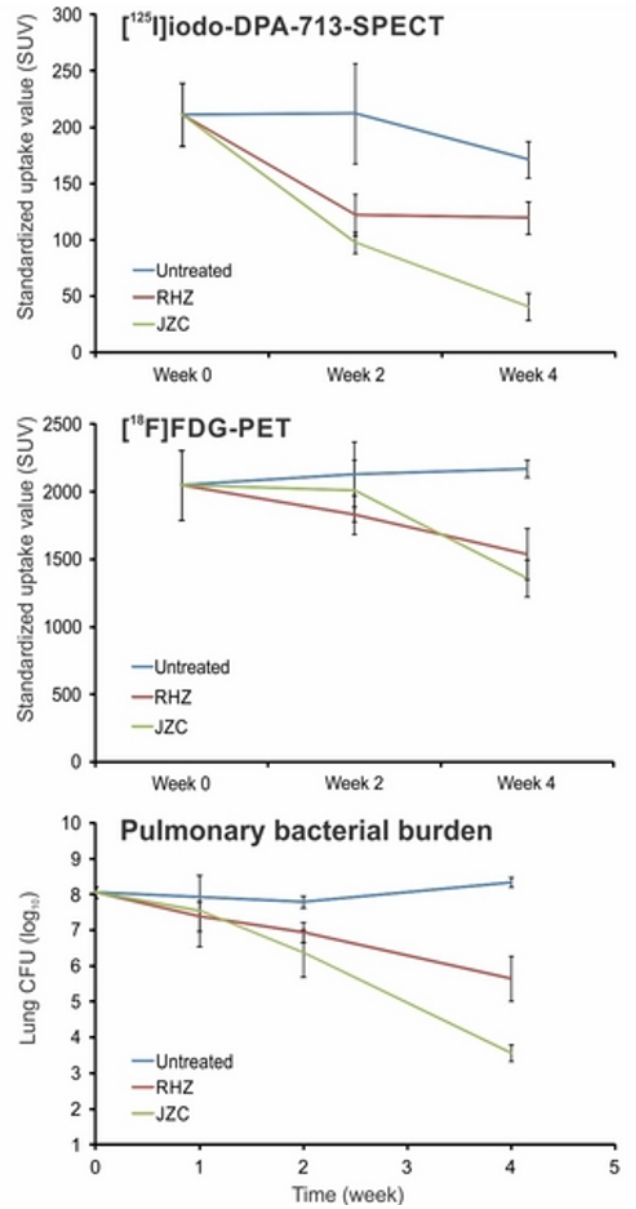

Disclosure of author financial interest or relationships:
A. Ordonez, None; **M. Klunk**, None; **S. Pokkali**, None; **E. Weinstein**, None; **C. Foss**, None; **R. Mease**, None; **M. Pomper**, None; **S.K. Jain**, NIH, Grant/research support .

Presentation Number **LBAP 069**
Late Breaking Abstract Poster Session
September 19, 2013 / 15:15-15:15 / Room: Exhibit Hall B

Quantitative Imaging of 6-OHDA-Induced Lesions in a Rat Model of Parkinsonism Using [^{11}C]PBR28

Lisa A. Wells[1], *Mona Sadeghian*[2], *Sac-Pham Tang*[1], *Christopher Coello*[1], *Christophe Plisson*[1], *Sharon Ashworth*[1], *Marija Sajic*[2], *Kenneth Smith*[2], [1]*Radiochemical Sciences, Imanova Centre for Clinical Imaging, London, United Kingdom; [2] Department for Neuroinflammation, The Institute of Neurology, University College London,, London, United Kingdom. Contact e-mail: lisa.wells@imanova.co.uk*

Objectives: Translocator protein 18 kDa (TSPO) is predominantly expressed on the outer mitochondrial membrane and is present in low quantities in healthy CNS tissue[1]. Microglia and macrophages have been shown to upregulate TSPO when activated, making TSPO an attractive target for imaging neuroinflammation in pathological states such as multiple sclerosis and Parkinsonian disorders[2]. In this novel pilot study, we quantitatively evaluate the uptake and kinetics of the second generation TSPO PET ligand, [^{11}C]PBR28, using a preclinical model of Parkinson's disease. **Methods:** 6-hydroxydopamine (6-OHDA, 12µg free base in 4µl 0.1% ascorbic acid in 0.9% saline n=4) or vehicle (control n=2) was injected stereotactically into the left medial forebrain bundle of Sprague-Dawley rats under recovery anaesthesia. Nine days post lesion, rats received an i.v. bolus of [^{11}C]PBR28 (control: 6.2±0.2MBq n=2, 6-OHDA: 9.4±2.6MBq n=4, mean±SD). Two of the four 6-OHDA-lesioned rats also underwent a PET-CT scan (dynamic, 60mins, Siemens Inveon PET-CT) and blood samples were collected to obtain a metabolite-corrected input function. After 60mins, rats were exsanguinated; blood and plasma were collected, and brain regions removed and washed in chilled saline, and the associated radioactivity was determined in all samples by a gamma counter. The PET data were reconstructed (CT attenuated, 2D FBP with scatter correction) and regions of interest were drawn on the lesion site and an equivalent contralateral area. Time activity curves (TACs) were derived and the volume of distribution (V_T) estimated. **Results:** Sixty minutes post injection of the radioligand there was increased uptake of [^{11}C]PBR28 in the 6-OHDA-lesioned hemispheres in comparison with the non-lesioned, contralateral side. There was no difference in the uptake of [^{11}C]PBR28 between the hemispheres of the control rat. Metabolism of [^{11}C]PBR28 was rapid (parent fraction, n=2: 32%, 13% and 9% at 5, 10 and 20mins respectively) and consistent between subjects. The TACs from the PET data were well described by a 1TC pharmacokinetic model. The data supported an increase in uptake of [^{11}C]PBR28 localised near the site of injection in the 6-OHDA-lesioned animals, and altered tracer washout in comparison with the contralateral side. The estimated V_T ratio between the lesion and contralateral side were 1.18 and 2.13.

Discussion: This initial data set supports an increased uptake of [^{11}C]PBR28 in the ipsilateral hemisphere of 6-OHDA-lesioned rats consistent with initial observations of increased TSPO expression in these animals. Further, *in vitro* work validating the increase in signal to an increase in TSPO expression is on-going to explore the potential utility of this ligand in the clinical imaging of neuroinflammatory diseases.

1.Banati *et al*, 2002. Glia 40, 206-217. 2.Abourbeh *et al*, 2012. J Neurosci, 32, 5728-5736

Disclosure of author financial interest or relationships:
L.A. Wells, Imanova Ltd, Employment; **M. Sadeghian**, None; **S. Tang**, None; **C. Coello**, None; **C. Plisson**, None; **S. Ashworth**, None; **M. Sajic**, None; **K. Smith**, Biogen, Grant/research support; Merck Serono, Grant/research support; Biogen, Consultant .

Presentation Number **LBAP 070**
Late Breaking Abstract Poster Session
September 19, 2013 / 15:15-15:15 / Room: Exhibit Hall B

Macrophage targeted PET imaging of muscular inflammation using 18F-DPA-714 and 18F-FAl-NOTA-PRGD2

Chenxi Wu[1,2], *Xuyi Yue*[2], *Lixin Lang*[2], *Fang Li*[1], *Gang Niu*[2], *Xiaoyuan Chen*[2], [1]*Department of Nuclear Medicine, Peking Union Medical College Hospital, Beijing, China;* [2]*LOMIN, NIBIB, NIH, Bethesda, MD, USA. Contact e-mail: cxwu2012@gmail.com*

Aims: This study aims to image translocator protein (TSPO) expression on macrophages with 18F-DPA-714 PET in acute and chronic muscular inflammations induced by turpentine-oil. 18F-FAl-NOTA-PRGD2 PET imaging was also performed to assess angiogenesis and macrophage infiltration. Methods: A mouse hindlimb muscular inflammation model was established by intramuscular injection of 20 μl turpentine-oil (day 0). Static or dynamic PET imaging was performed at day 1, 6, 10 and 22 using either 18F-DPA-714 or 18F-RGD2. For displacement study, 5 mg/kg PK11195 was administered 25 min after 18F-DPA-714 injection during a 60 min dynamic PET scan. For RGD blocking imaging, unlabeled NOTA-PRGD2 peptide (10 mg/kg) was injected at 10 min before 18F-RGD2 injection. Ex vivo autoradiography on the cryosection of the inflammatory muscle samples at day 1, 6, 10 and 22 was performed using 18F-DPA-714 with or without PK11195 blocking. Immunofluorescence staining was performed to evaluate infiltrated macrophages (TSPO, CD11b and CD68) and vasculature density (CD31) within inflammatory muscles at different time points. Results: Both acute and chronic inflammatory muscles showed 18F-DPA-714 uptakes. However, 18F-DPA-714 uptake in chronic inflammation was significantly higher than that in acute inflammation, and the highest uptake in inflammatory muscles were seen at 18 days after turpentine injection. Chronic inflammatory also showed significantly higher 18F-RGD2 uptake than acute inflammation. Time activity curves of 18F-DPA-714 uptake showed significant displacement after PK11195 injection, and autoradiography also proved that PK11195 could block 18F-DPA-714 uptake at different time-points. 18F- FAl-NOTA-PRGD2 uptake into inflammatory muscles was blocked by "cold" NOTA-PRGD2 peptides. Immunofluorescence staining showed higher degree of macrophage infiltration and vasculature density in chronic inflammation samples than those in acute inflammation, which were in accordance with PET imaging results. Conclusion: Longitudinal PET imaging using 18F-DPA-714 could reveal the dynamics of macrophage activation and infiltration in inflammatory diseases. The higher uptake of 18F-DPA-714 uptake in chronic inflammation suggests more macrophage accumulation. 18F-FAl-NOTA-PRGD2 uptake is higher in chronic inflammation, reflecting not only more inflammatory angiogenesis but probably more macrophage infiltration.

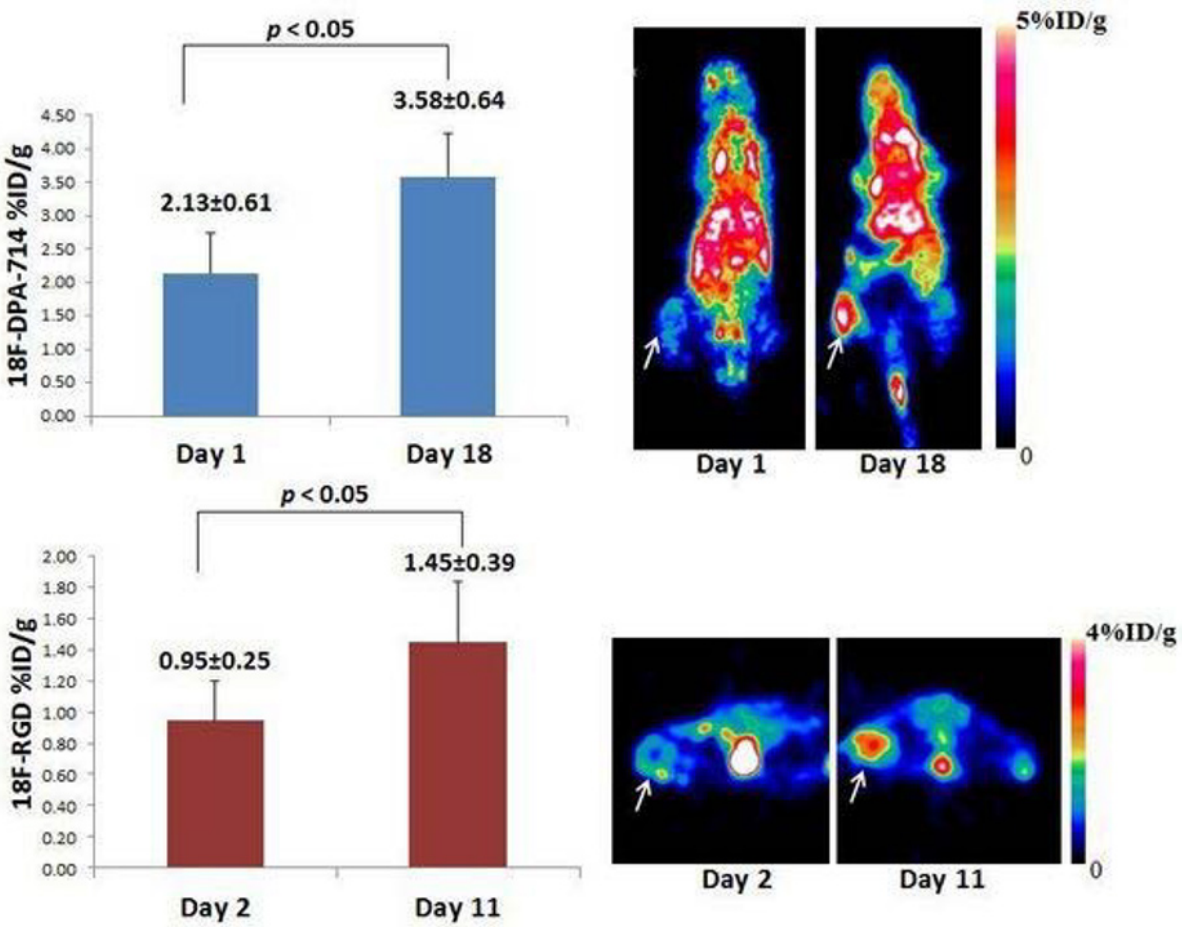

Figure 1. 18F-DPA-714 (upper row) and 18F-FAl-NOTA-PRGD2 (lower row) PET imaging of mouse acute and chronic muscle inflammation induced by turpentine-oil. Chronic inflammation saw significant higher uptake of both tracers compared to acute inflammation.

Disclosure of author financial interest or relationships:
C. Wu, None; **X. Yue**, None; **L. Lang**, None; **F. Li**, None; **G. Niu**, None; **X. Chen**, None.

Presentation Number **LBAP 071**
Late Breaking Abstract Poster Session
September 19, 2013 / 15:15-15:15 / Room: Exhibit Hall B

Inflammation Quantification in a Chronic and Acute on Chronic Murine Model of Inflammatory Bowel Disease using Ultrasound Molecular Imaging

Ferdinand Knieling[1], *Steven Machtaler*[1], *Huaijun Wang*[1], *Thierry Bettinger*[2], *Richard Luong*[3], *Juergen K. Willmann*[1], [1]*Department of Radiology, Stanford University, Stanford, CA, USA;* [2]*Bracco, Geneva, Switzerland;* [3]*Department of Comperative Medicine, Stanford University, Stanford, CA, USA. Contact e-mail: knieling@stanford.edu*

Purpose Ultrasound molecular imaging has shown promising results in imaging inflammation in murine models of acute inflammatory bowel disease (IBD). The purpose of this study was to evaluate the feasibility of ultrasound molecular imaging using a clinically translatable microbubble targeted to the inflammation markers P- and E-selectin ($MB_{Selectin}$) for quantification of inflammation in a chronic and acute on chronic murine colitis model. **Material and Methods** Acute colitis was established by rectal 2,4,6-trinitrobenzene sulfonic acid (TNBS) administration in 70 mice. Chronic colitis was established by 3 repetitive cycles of oral dextran sodium sulfate (DSS) administration in an additional 47 mice; an acute on chronic flare was simulated by rectal TNBS injection (TNBS solved in ethanol, TNBS+EtOH) in those DSS mice. All mice were imaged in contrast mode following i.v. injection of $5x10^7$ $MB_{Selectin}$ and control microbubbles ($MB_{Control}$) using a 21 MHz transducer (VisualSonics). Vehicle control groups (Ethanol, EtOH) for all experiments were also imaged using the same imaging protocol and *in vivo* imaging results were correlated with *ex vivo* immunofluorescence and histology. The specificity of $MB_{Selectin}$ binding to P- and E-selectin was tested following *in vivo* antibody blocking of both P- and E-selectin. **Results** In acute colitis mice, *in vivo* US molecular imaging signal significantly increased (day 1: 191±131a.u.) using MBSelectin compared to baseline (10±15, P < .0001) and compared to control mice (4±7). The signal decreased from day 3 (84±54, P = .01) to day 5 (6±10, P = n. s.). Imaging signal using $MB_{Control}$ (5±5, P=.001) did not increase in acute inflammation. In DSS mice with chronic background inflammation, $MB_{Selectin}$ injection resulted in a small signal increase (20±21, P = n. s.) compared to control mice. However, an acute on chronic inflammation flare resulted in significantly increased imaging signal at day 1 (306±294, P = .0002) which persisted for several days (day 3, 176±180, P=.04; day 5, 38±25, P =.84). Signal intensities decreased significantly after administration of the blocking antibodies (P = .002), confirming binding specificity of $MB_{Selectin}$ binding to P- and E-selectin. Histology and immunofluorescence confirmed inflammation and selectin expression in acute and acute on chronic inflammation in the bowel wall. **Conclusion** Selectin-targeted US molecular imaging allows inflammation assessment in an acute as well as clinically relevant acute on chronic inflammation model of IBD in mice, which simulate different disease states seen in patients with IBD. Since ultrasound is widely available and safe, ultrasound molecular imaging may be further developed as an alternative quantitative and objective approach for monitoring inflammation in particular in young patients with IBD.

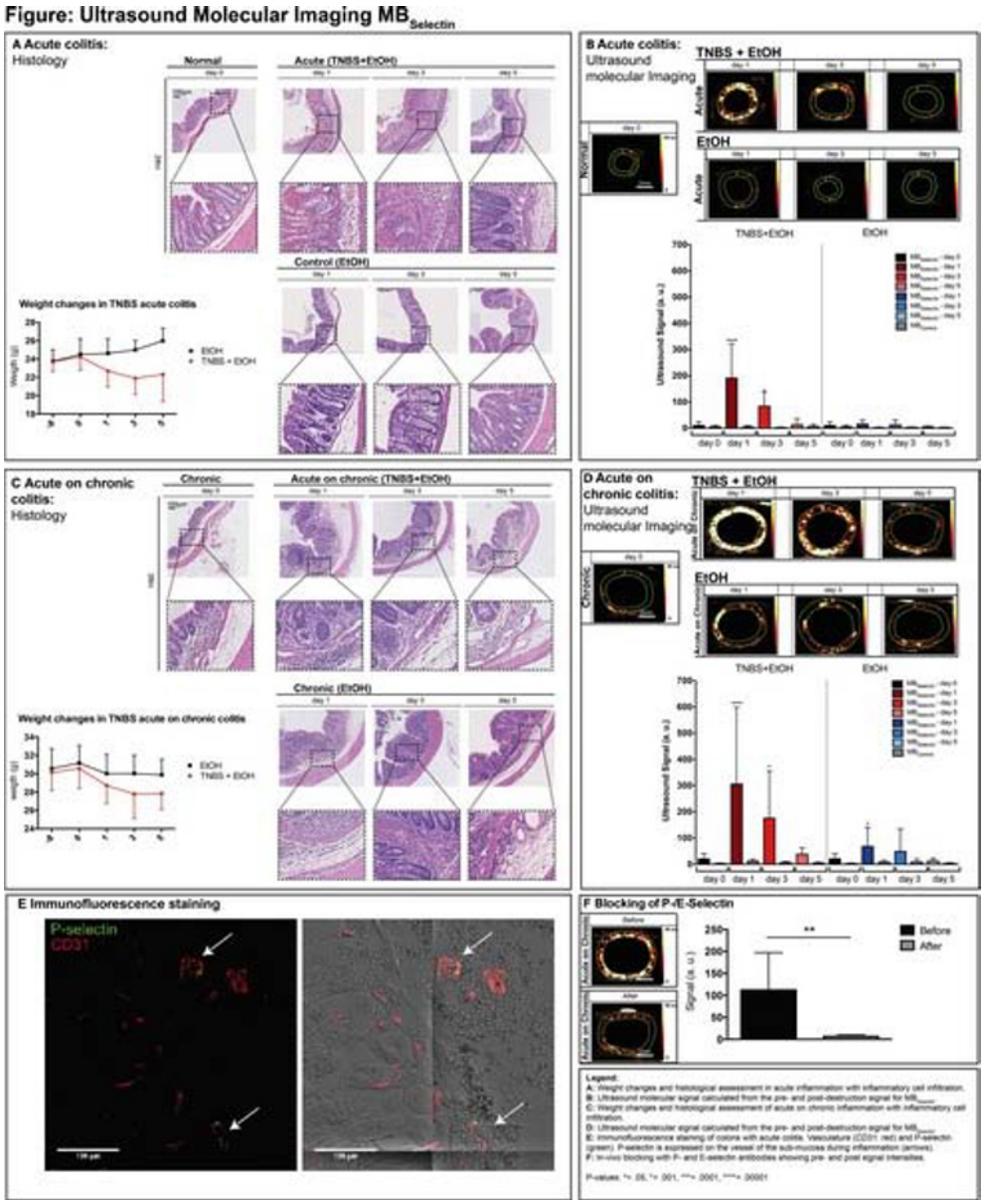

A: Weight changes and histological assessment in acute inflammation with inflammatory cell infiltration. B: Ultrasound molecular signal calculated from the pre- and post-destruction signal for $MB_{Selectin}$. C: Weight changes and histological assessment of acute on chronic inflammation with inflammatory cell infiltration. D: Ultrasound molecular signal calculated from the pre- and post-destruction signal for $MB_{Selectin}$. E: Immunofluorescence staining of colons with acute colitis. Vasculature (CD31: red) and P-selectin (green). P-selectin is expressed on the vessel of the sub-mucosa during inflammation (arrows). F: In-vivo blocking with P- and E-selectin antibodies showing pre- and post signal intensities. P-values: *< .05, *< .001, ***< .0001, ****< .00001

Ultrasound Molecular Imaging: Signal Intensities (SI)

	Day 0	Day 1		Day 3		Day 5	
	SI	SI	P-Value	SI	P-Value	SI	P-Value
Acute (THBS+EtOH)	10 ± 15	191 ± 131	< .0001	84 ± 54	.01	0 ± 10	n. s.
Control (EtOH)		15 ± 16	n. s.	16 ± 22	n. s.	5 ± 3	n. s.
Acute on Chronic (THBS+EtOH)	20 ± 21	306 ± 294	.0002	175 ± 80	.04	38 ± 25	n. s.
Chronic (EtOH)		68 ± 73	.04	49 ± 86	n. s.	13 ± 10	n. s.

Ultrasound Molecular Imaging: Signal Intensities (SI) in a.u. with corresponding P-values tested with ANOVA. n. s. = not significant

Disclosure of author financial interest or relationships:
F. Knieling, None; **S. Machtaler**, None; **H. Wang**, None; **T. Bettinger**, Bracco Suisse SA, Employment; **R. Luong** None; **J.K. Willmann**, Bracco, Consultant; Siemens, Grant/research support; Bracco, Grant/research support .

Presentation Number **LBAP 072**
Late Breaking Abstract Poster Session
September 19, 2013 / 15:15-15:15 / Room: Exhibit Hall B

Magnetic resonance imaging of chronic lymphocytic leukemia by ultrasmall superparamagnetic iron oxide nanoparticles

Gabriella Baio[1], *Giovanna Cutrona*[2], *Serena Matis*[2], *Carlotta Massucco*[2], *Simona Boccardo*[3], *Francesca Valdora*[1], *Laura Emionite*[4], *Michele Cilli*[4], *Sandra Salvi*[3], *Massimo Calabrese*[1], *Carlo Neumaier*[1], *Manlio Ferrarini*[2], [1]*Diagnostic Imaging and Senology Unit, IRCCS Azienda Ospedaliera Universitaria (AOU) San Martino - IST - National Cancer Institute, Genova, Italy;* [2]*Scientific Direction, IRCCS Azienda Ospedaliera Universitaria (AOU) San Martino - IST - National Cancer Institute, Genova, Italy;* [3]*Department of Pathology, IRCCS Azienda Ospedaliera Universitaria (AOU) San Martino - IST - National Cancer Institute, Genova, Italy;* [4]*Animal Facility, IRCCS Azienda Ospedaliera Universitaria (AOU) San Martino - IST - National Cancer Institute, Genova, Italy. Contact e-mail: gabriella.baio@istge.it*

Introduction: Chronic lymphocytic leukemia (CLL) is a type of slow growing leukaemia, characterized by a gradual increase in the number of B lymphocytes, first in the blood and bone marrow and, as the disease progresses, in the lymph nodes, liver, and spleen. Computed tomography (CT) is used as the first-line modality for imaging of lymphoid malignancies but, specifically for CLL, the role of CT has not yet been clearly defined (1). In order to prevent the exposure of the CLL patient to irradiation, we aimed to establish a specific MRI method to better visualize the presence of the disease by ultrasmall iron oxides nanoparticles (USPIO). Methods: we focused our study on a specific mouse xenogeneic transplantation model, NOD/LtSz-scid/scid (NOD/SCID), of CLL (2). Two groups of mice were injected with USPIO, as MR contrast agent: one group of healthy NOD/ LtSz-scid/scid (NOD/SCID) mice (NSG; n=5) and another group of NOD/SCID mice injected with chronic MG0248-CLLcells (NSG-CLL; n=10), which served as a xenogeneic mouse transplantation model (2). Regions of interest (ROI) were defined and the signal intensities in the liver and spleen of each mouse were calculated. Histological analysis was performed according to standard techniques on the NSG and NSG-CLL mice, 28 days and 6 days post injection (p.i.) of USPIO, respectively. Immunohistochemistry of the spleen using antihuman- CD20 antibody was performed to demonstrate the human CD20+ CLL cell aggregates. Perls' Prussian blue staining for the detection of iron was conducted. A quantitative assessment by estimation of iron-positive cells was performed using an Olympus BX4l microscope. Results: We observed in the NSG mice, at 24 hours p.i. of USPIO, a strong decrease in signal intensity (SI) in the liver (80%) and spleen (50%) (Figure A). At 28 days p.i. of USPIO, a Perls' Prussian blue staining histopathological analysis on the liver and spleen revealed only very few iron oxide nanoparticles in both organs (Figure B). This means that the nanoparticles are cleared from the liver and spleen in the healthy animal group within one month. In the NSG-CLL mice, at 24 hours p.i. of USPIO, a significant decrease in SI (60%) was observed in the liver but, in comparison, only a slight decrease in the SI (20%) was observed in the spleen (Figure C). Interestingly, iron oxide nanoparticles were detectable only in the red pulp (healthy area) of the spleen and were found to be absent in the white pulp, where the CLL cells were localized (Figure D). Conclusions: Our results demonstrate the suitability of the MRI method to detect the presence of a non-solid tumor, such as chronic lymphocytic leukemia, within the spleen. The clearance of iron oxide nanoparticles within the spleen after 28 days p.i. in the healthy group of mice offers the potential to apply this technique for the MR imaging follow-up of CLL mouse models in order to evaluate the response to therapy.

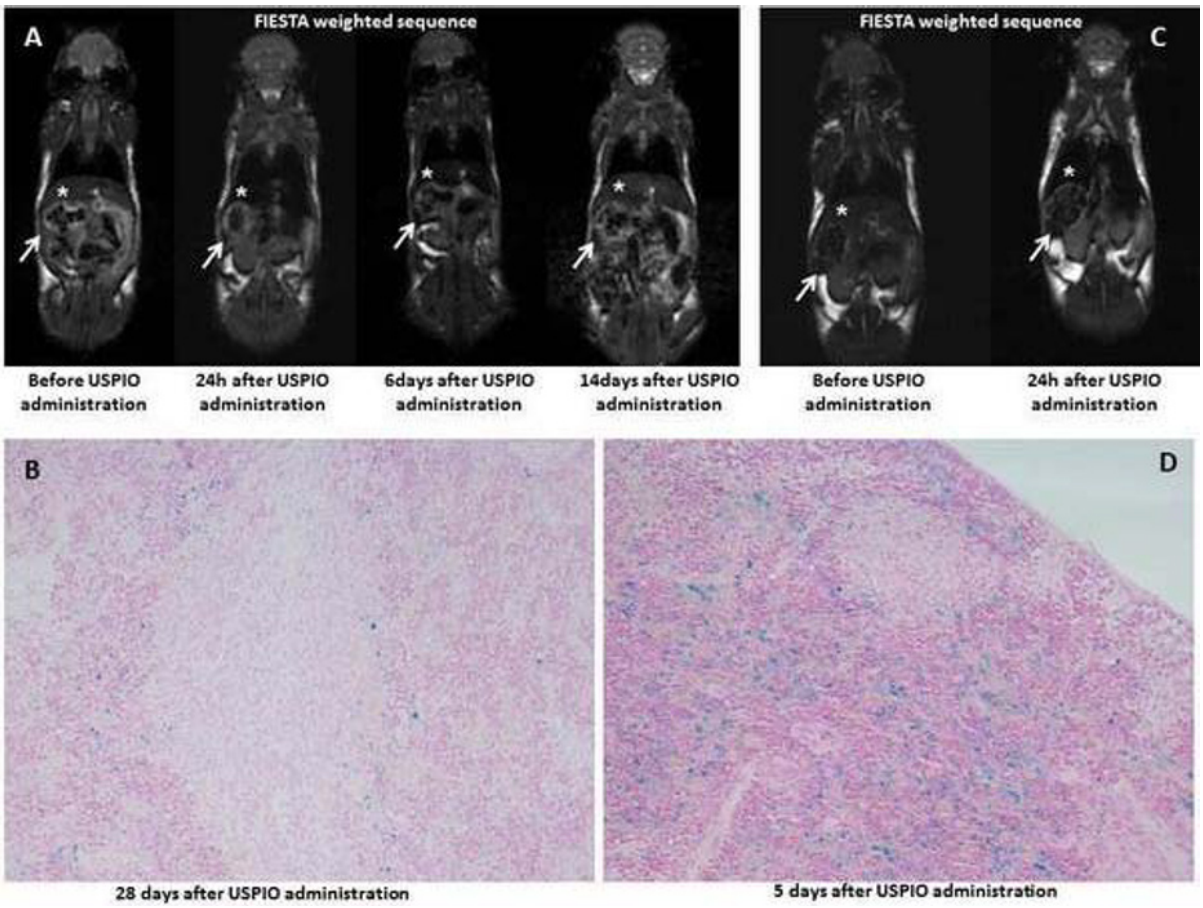

A) NSG mice: Coronal MR Images before, 24 hours, 6 days and 14 days after USPIO administration. Signal Intensity changes are observed in the liver (asterisk) and spleen (arrow). B) NSG mice: Histopatological analysis of healthy spleen by Perl' Prussian Blue staining 28 days after Feraspin XS administration reveals only few nanoparticles present. C) NSG-CLL mice: Coronal MR images before and 24 hours after USPIO administration. Signal intensity changes are observed in the liver (asterisk) and spleen (arrow). D) NSG-CLL mice: Histopathological analysis of the spleen by Perls' Prussian blue staining 6 days after USPIO administration shows that iron oxide nanoparticles are present only in the red pulp of the spleen; no nanoparticles are present in the white pulp where the CLL cells are localized.

Disclosure of author financial interest or relationships:
G. Baio, None; **G. Cutrona**, None; **S. Matis**, None; **C. Massucco**, None; **S. Boccardo**, None; **F. Valdora**, None; **L. Emionite**, None; **M. Cilli**, None; **S. Salvi**, None; **M. Calabrese**, None; **C. Neumaier**, None; **M. Ferrarini**, None.

Presentation Number **LBAP 073**
Late Breaking Abstract Poster Session
September 19, 2013 / 15:15-15:15 / Room: Exhibit Hall B

Assessment of vascular inflammation in a murine high-fat diet atherosclerosis model using VCAM-1 molecular targeted ultrasound contrast imaging

Sunil Unnikrishnan[1,3], *Zhongmin Du*[3], *Robert J. Lye*[3], *Jane V. Carrick*[3], *Nivedita K. Naresh*[1], *Carlos E. Barbery*[4], *Ayotunde Dokun*[6], *Brant E. Isakson*[5,3], *Frederick Epstein*[1,3], *Jeffrey Lysiak*[4], *Brian H. Annex*[2,3,1], *Alexander L. Klibanov*[2,3,1], [1]*Biomedical Engineering, University of Virginia, Charlottesville, VA, USA;* [2]*Cardiovascular Medicine, University of Virginia, Charlottesville, VA, USA;* [3]*Cardiovascular Research Center, University of Virginia, Charlottesville, VA, USA;* [4]*Urology, University of Virginia, Charlottesville, VA, USA;* [5]*Molecular Physiology and Biological Physics, University of Virginia, Charlottesville, VA, USA;* [6]*Endocrinology and Metabolism, University of Virginia, Charlottesville, VA, USA. Contact e-mail: sunil14@virginia.edu*

Genetically modified mice with dysfunctional lipid metabolism (e.g., ApoE-/- or LDLr-/-) are the most commonly used models of systemic atherosclerosis. Alternative approaches based on C57BL/6 mice on high-fat diet are now being studied as more relevant models for atherosclerosis. Such diet-induced obesity models exhibit disorders like hyperglycemia and insulin resistance. Assessing vascular inflammation using molecular ultrasound imaging is a non-invasive tool for detecting early events in atherosclerosis and monitoring subsequent disease progression. Purpose of this study is to compare the inflammatory status of the vasculature of the diet-perturbed model with the well-established ApoE-/- high-cholesterol diet model. C57BL/6 mice were put on lard-based high-fat diet (HFD mice, 60% caloric intake from fat) at 6 weeks of age. ApoE-/- mice were put on high-cholesterol diet at 6 weeks of age, while control mice were constantly on regular chow diet throughout. Molecular ultrasound imaging was performed on animals over 30 weeks old. Lipid microbubbles with decafluorobutane gas targeted to the inflammation marker VCAM-1 were used for contrast imaging. Biotinylated anti-VCAM-1 monoclonal antibody (MVCAM.A) or control isotype-matched IgG were conjugated to the microbubble shell with streptavidin. Microbubbles were administered via bolus intravenous injection (10^7 microbubbles) and ultrasound imaging of the carotid vasculature area was performed using Siemens Sequoia 512 (15L8 probe, 7 MHz, MI 0.2, CPS mode). To evaluate targeting, the echo intensity 10 min post-injection was quantified and normalized by the peak contrast signal. Vascular microbubble targeting was significantly higher in HFD mice than in wild type animals ($p<0.001$, $n=6$) and equivalent to ApoE-/- animals on high-cholesterol diet (Fig. 1). Isotype-matched IgG microbubbles showed negligible targeting in all animal groups. Targeted microbubble accumulation pattern was diffuse and not limited to large vessels, suggesting systemic and microvascular expression of VCAM-1 (Supplemental Data, Fig. 1). Immunohistochemistry confirmed VCAM-1 overexpression in both models. While ApoE-/- mice developed extensive atherosclerotic plaques in the aorta, the vasculature of HFD mice was free of plaques. Studies are currently underway to determine the onset and temporal evolution of VCAM-1 expression in HFD mice, in carotid and peripheral vasculature. Initial experiments indicate a trend towards higher VCAM-1 expression in animals after 3 weeks on high-fat diet (9 weeks old C57BL/6 mice), compared to age-matched animals on regular diet (Supplemental Data, Fig. 2), but it is not yet statistically significant for the number of animals tested ($n = 5$). In conclusion, using ultrasound molecular imaging, we demonstrate that inflammation marker VCAM-1 is upregulated on the vascular endothelium in a high-fat diet murine model of systemic atherosclerosis. VCAM-1 targeting in the HFD model was similar to targeting in the traditional ApoE-/- murine atherosclerosis model. Molecular ultrasound imaging is a convenient and inexpensive non-invasive tool for rapid assessment of vascular inflammation in atherosclerosis.

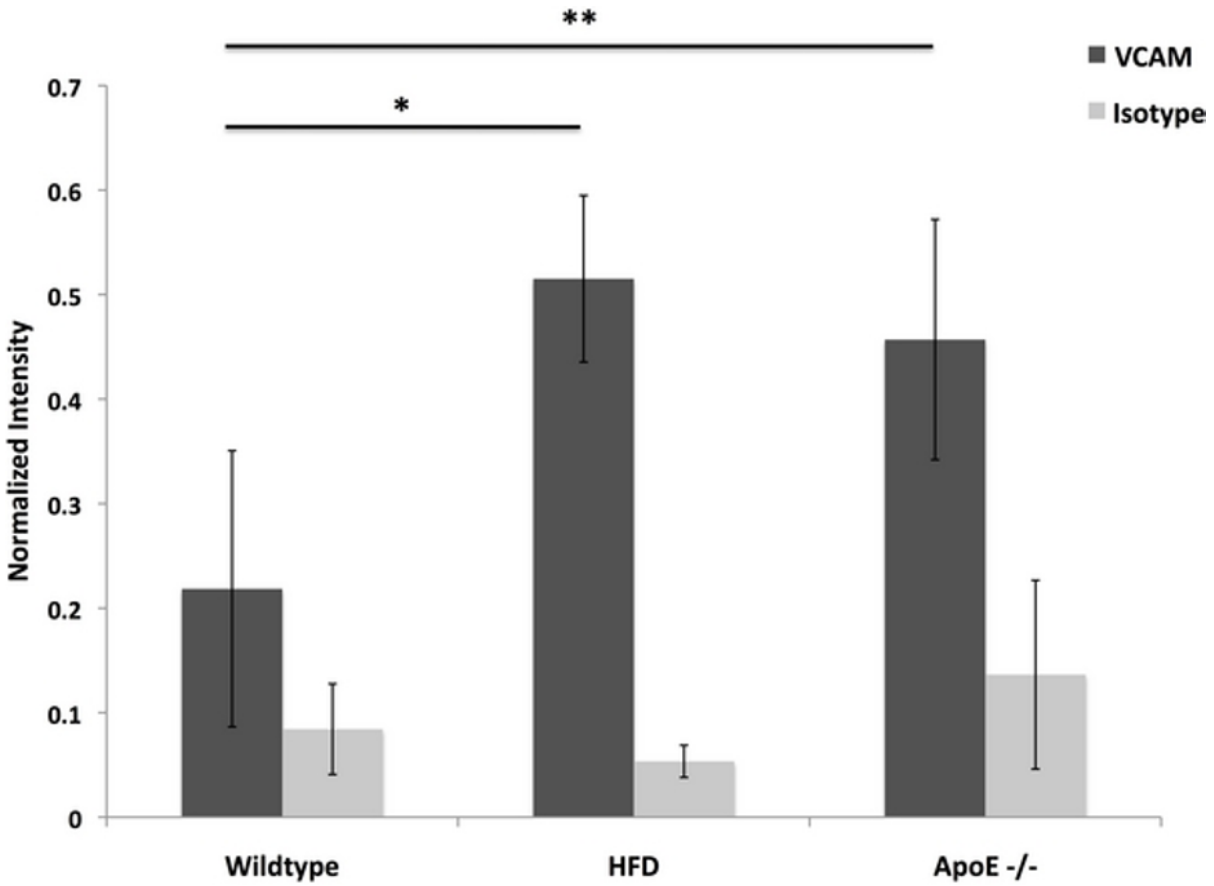

Fig. 1: Microbubble targeting to the vascular endothelium 10 min after administration of microbubbles. Echo intensity of bound bubbles was normalized to the peak signal from circulating bubbles (*p < 0.001, **p < 0.01). Animals >30 weeks of age.

Disclosure of author financial interest or relationships:

S. Unnikrishnan, None; **Z. Du**, None; **R.J. Lye**, None; **J.V. Carrick**, None; **N.K. Naresh**, None; **C.E. Barbery**, None; **A. Dokun**, None; **B.E. Isakson**, None; **F. Epstein**, AstraZeneca, Grant/research support; **J. Lysiak**, None; **B.H. Annex**, None; **A.L. Klibanov**, Philips Research North America, Grant/research support; Targeson (NIH SBIR subcontract), Grant/research support; Targeson, Stockholder; AstraZeneca, Grant/research support .

Presentation Number **LBAP 074**
Late Breaking Abstract Poster Session
September 19, 2013 / 15:15-15:15 / Room: Exhibit Hall B

Detection of Acute Cell-Mediated Rejection in Porcine kidney Transplant by Magnetic Resonance Imaging

Chih-lung Chen[1], *Hao-Chih Tai*[2], *Chen-Hsuan Lin*[1], *Wen-Yuan Hsieh*[1], *Shian-Jy Wang*[1], [1]*Biomedical Engineering devices Laboratories, Industrial Technology Research Institute, Hsinchu, Taiwan;* [2]*Surgery department, National Taiwan University Hospital, Taipei, Taiwan. Contact e-mail: gregchen@itri.org.tw*

Introduction:Organ transplantation is the preferred medical treatment for patients with end-state organ failure. Patients are generally monitored for rejection by endomyocardial biopsies that are typically obtained from the right ventricle on a periodic basis. Endomyocardial biopsy is invasive and carries significant risk of adverse side effects. Thus, there is a need in the art for a non-invasive and consistent method for detecting early signs of rejection for transplanted kidneys. If we can detect early signs of acute rejection, we may be able to reduce chronic rejection and organ loss. It would be desirable to have a non-invasive method for detecting acute rejection. Materials and Methods: Synthesis and characterization of IOPC and IOPC-CD3 particles by DLS, flow cytometry and TEM. We detected the migration and accumulation of the T cells in the cortex and medulla of graft kidney by in vivo 3TMRI. Results and Discussion: We have studied a newly synthesized iron oxide particle, IOPC-CD3, and have evaluated its potential usefulness for cellular MRI. We have found that the r2 relaxivity of ITRI-IOP is much higher than that of a variety of commonly used iron-oxide particles, thus providing a potential advantage in T2*-weighted cellular MRI. IOP-CD3 readily undergoes efficient and non-toxic uptake by non-phagocytic cells through the targeting procedures. We can monitor the infiltration of these labeled T cells at the rejection site as a non-invasive method to detect graft rejection by 3T MRI after POD 6-9. The detection time will be early 4-6 days than serum Creatinine level (Fig1A and B). Conclusion: IOPC-CD3 assisted MRI imaging method provides a non-invasive alternative to biopsy for detecting acute and chronic rejection and helps clinicians evaluate organ function after transplantation. Another clinical benefit is to help physician judge and dose properly of immune-suppressive drug.

Disclosure of author financial interest or relationships:
C. Chen, None; **H. Tai**, None; **C. Lin**, None; **W. Hsieh**, None; **S. Wang**, None.

Presentation Number **LBAP 075**
Late Breaking Abstract Poster Session
September 19, 2013 / 15:15-15:15 / Room: Exhibit Hall B

In Vivo Magnetic Resonance Imaging of acute radiation induced inflammation using ICAM1 targeted Micron-sized Particles of Iron Oxide (ICAM-MPIO)

Benedicte Descamps[1], Sara Neyt[2], Elke Decrock[3], Filip J. De Vos[2], Caroline Dumolyn[2], Caroline Van den Broecke[4], Michaël Noë[4], Julie Bolcaen[5], Ingeborg Goethals[5], Tom Boterberg[6], Christian Vanhove[1], **Karel Deblaere**[7], *[1]Infinity-MEDISIP-iMINDS, Ghent University, Ghent, Belgium; [2]Department of Radiopharmacy, Ghent University, Ghent, Belgium; [3]Department of Basic Medical Sciences, Physiology group, Ghent University, Ghent, Belgium; [4]Department of Pathology, Ghent University Hospital, Ghent, Belgium; [5]Department of Nuclear Medicine, Ghent University Hospital, Ghent, Belgium; [6]Department of Radiotherapy, Ghent University Hospital, Ghent, Belgium; [7]Department of Radiology, Ghent University Hospital, Ghent, Belgium. Contact e-mail: karel.deblaere@ugent.be*

Introduction Current magnetic resonance imaging methods lack sensitivity and specificity for imaging early post irradiation inflammatory changes in the brain. Intercellular adhesion molecule (ICAM1) plays a key role in the early inflammatory cascade following brain irradiation. ICAM1 proteins mostly express on the luminal surface of the endothelium of brain venules and capillaries and promote the recruitment and migration of leukocytes. This expression of ICAM1 is upregulated in a time-dependent manner with a peak at 48h post-irradiation (Yuan H et al. Radiat Res, 2005). Micron-sized particles of iron oxide (MPIO) consist of an iron oxide core surrounded by an inert polymer coat. Recently MPIO have been shown to be useful for molecular imaging of adhesion molecules using T2* MRI (McAteer MA et al. Nature Medicine, 2007). In this work we used 2.8 µm sized MPIO labeled with anti-ICAM1 antibodies to selectively image in vivo endothelial ICAM1 expression in an animal model of early radiation injury. **Materials and Methods** MPIOs (M-280 tosylactivated Dynabeads, Invitrogen, UK) were conjugated with monoclonal antibodies against rat-specific ICAM1 (Abcam, UK) according to Sibson et al. (Sibson N et al., Methods Mol Biol, 2011). In vitro binding of ICAM-MPIO was assessed by incubating TNF-α stimulated rat endothelial cell lines (GP8 and RBE4) with both free-MPIO and ICAM-MPIO. The right hemisphere of four young male Wistar rats (mean 93g) was irradiated with 20Gy using the Small Animal Radiation and Research Platform (SARRP, X-Strahl, UK). 48 hours later, the animals were continuously scanned before and up to 2h after injection of either ICAM-MPIO (n=2) or free MPIO (n=2) with a 3D FLASH sequence (TR=50ms, TE=10ms, isotropic resolution 120µm, NA=2,TA=31') on a PharmaScan 70/16 MR system (Bruker, Germany). Ex vivo imaging was performed on formalin fixated brains of the rats using the imaging sequence described (NA=12). **Results** In vitro tests showed binding of the ICAM-MPIO to the stimulated endothelial cell lines whereas free MPIO showed a random distribution in the cell cultures without binding to the cell walls. After administration of free MPIO no significant differences were observed between the pre and both the in vivo and ex vivo post-injection scans (Fig 1D-F). After ICAM-MPIO administration clear signal dropouts were observed on the T2* images, with the highest signal differences of the labeled MPIO during the scan of 1 to 1h30 post-injection. The ICAM-MPIO could be clearly localized in the hippocampus, the white matter of the corpus callosum and to a lesser extent the cortex of the irradiated right hemisphere (arrows Fig 1B and C). **Discussion and conclusion** Using ICAM1 labeled MPIO we were able to visualize acute inflammation following irradiation of a rat brain hemisphere with 20Gy. Free MPIO showed no binding to the activated endothelium both in vitro and in vivo. Imaging ICAM1 in acute inflammation after irradiation will allow for in vivo preclinical assessment of the impact of radiation dose and volume on the inflammatory response as well as in vivo assessment of e.g. prophylactic treatment with anti-inflammatory drugs.

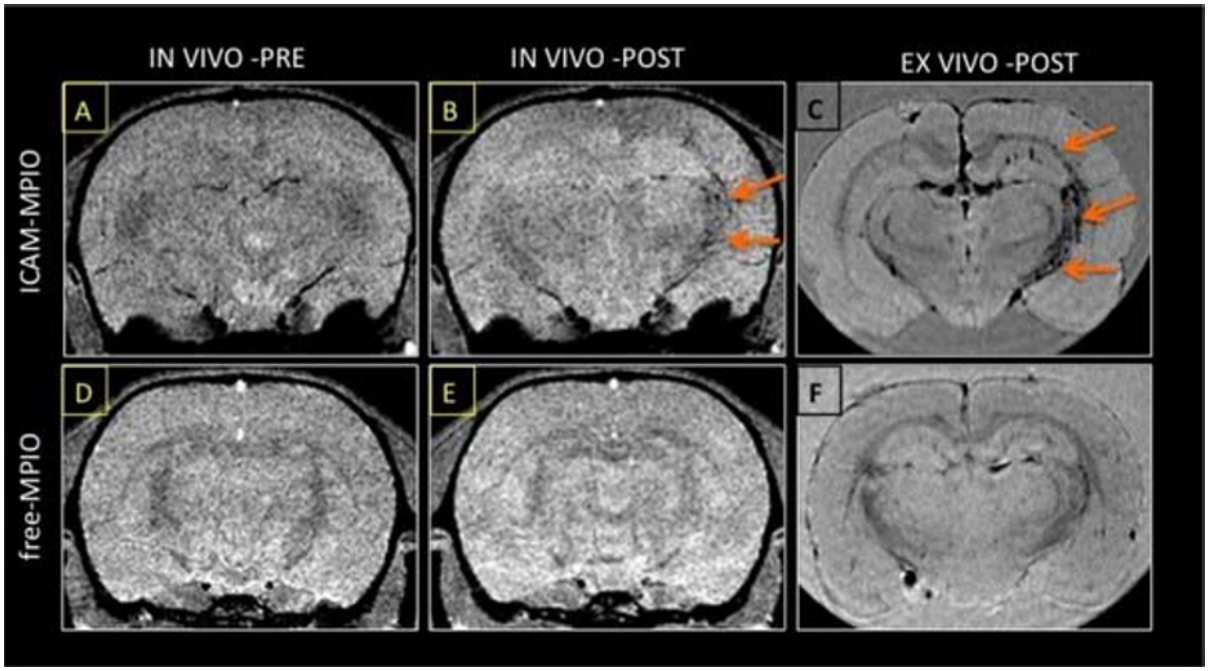

Disclosure of author financial interest or relationships:
B. Descamps, None; **S. Neyt**, None; **E. Decrock**, None; **F.J. De Vos**, None; **C. Dumolyn**, None; **C. Van den Broecke**, None; **M. Noë**, None; **J. Bolcaen**, None; **I. Goethals**, None; **T. Boterberg**, None; **C. Vanhove**, None; **K. Deblaere**, None.

Presentation Number **LBAP 076**
Late Breaking Abstract Poster Session
September 19, 2013 / 15:15-15:15 / Room: Exhibit Hall B

Imaging neuroinflammation using PET with 18F-DPA714 in an animal model of HIV infection

Dima A. Hammoud[1], *Dianne E. Lee*[1], *Margaret R. Lentz*[1], *Xuyi Yue*[3], *Wael G. Ibrahim*[1], *Frank Denaro*[5], *Kristin L. Peterson*[1], *Elaine Jagoda*[2], *Peter Choyke*[2], *Michael Kassiou*[4], *William Reid*[1], [1]*Center for Infectious Disease Imaging, Radiology and Imaging Sciences, National Institutes of Health, Clinical Center, Bethesda, MD, USA;* [2]*Molecular Imaging Program, National Institutes of Health, National Cancer Institute, Bethesda, MD, USA;* [3]*Laboratory of Molecular Imaging and Nanomedicine, National Institutes of Health, NIBIB, Bethesda, MD, USA;* [4]*Brain and Mind Research Institute, School of chemistry, The University of Sydney, Sydney, NSW, Australia;* [5]*Department of Biology, Morgan State University, Baltimore, MD, USA. Contact e-mail: hammoudd@cc.nih.gov*

Introduction: Unlike microglia and astrocytes, neurons do not express CD4 and thus are not productively infected by HIV. The neurologic damage associated with HIV is thus thought to be mediated through multiple mechanisms, mainly neuroinflammation. This however has not been shown reliably in small animal models of HIV. The goal of this study was to image neuroinflammation in the HIV-1 transgenic (Tg) rat, a model that is known to develop neurologic dysfunction at advanced age. Imaging microglial activation as a surrogate marker for neuroinflammation can be accomplished by radiolabeling ligands that target the translocator protein (TSPO), an outer mitochondrial membrane receptor known to be overexpressed in activated microglia. Recently, an 18F labeled pyrazolopyrimidine, DPA714, was found to have higher affinity to TSPO, lower non-specific binding and increased bioavailability when compared to the prototype ligand, 11C-PK11195. In this study, we used 18F-DPA714 to image neuroinflammation in vivo in the HIV Tg rat model. Materials and Methods: Seven 9-month old rats (4 Tg and 3 Ctrl) and nine 16-month-old rats (6Tg, 3Ctrl) were imaged for 60 min on the Bio PET/CT tomograph (Bioscan, Inc.) after the administration of 18F-DPA-714 (dose: 1.75 +/- 0.59 mCi, SA > 2 Ci/μmol). Dynamic images were reconstructed using OSEM-2D algorithm with scatter correction. Regional 18F-DPA714 time activity curves were generated for volumes of interest (VOI) that were drawn manually in various brain regions. As a positive control, we used the quinolinic acid (QA) unilateral striatal ablation rat model (n=3). For those rats, one VOI was selected in the left striatum at the site of QA injection, with an identical VOI drawn in the exact location in the contralateral right hemisphere as the reference region. SUV values (SUV = CPET(T) / (Injected dose / weight)) were calculated for all regions in all animals groups. Results: There were no significant differences in 18F-DPA714 SUV values of the parietal cortex, caudate, thalamus, hippocampus, pons and cerebellum between any of the four groups of animals: 9 month old Tg and controls, 16 month old Tg and controls (Fig.1). Our results were further confirmed with immunohistochemistry which did not show appreciable differential TSPO staining in the Tg compared to the ctrl animals. In the QA rat model, there was an average 1.7 fold increased 18F-DPA714 SUV in the ipsilateral VOI (lesion) compared to the contralateral VOI (range: 1.55-1.84). Discussion: We found no substantial microglial activation that can be detected using PET in the brains of HIV-Tg rats compared to age-matched controls, neither at 9 nor at 16 months of age. We validated our ligand using our positive control unilateral striatal ablation rat (with QA), which showed significant uptake corresponding to histological evidence of TSPO overexpression. Our findings suggest an alternative mechanism for neurotoxicity in this rat model, possibly chronic exposure to viral proteins. Whether viral protein neurotoxicity is a major cause of neurocognitive dysfunction in treated HIV+ is yet to be determined.

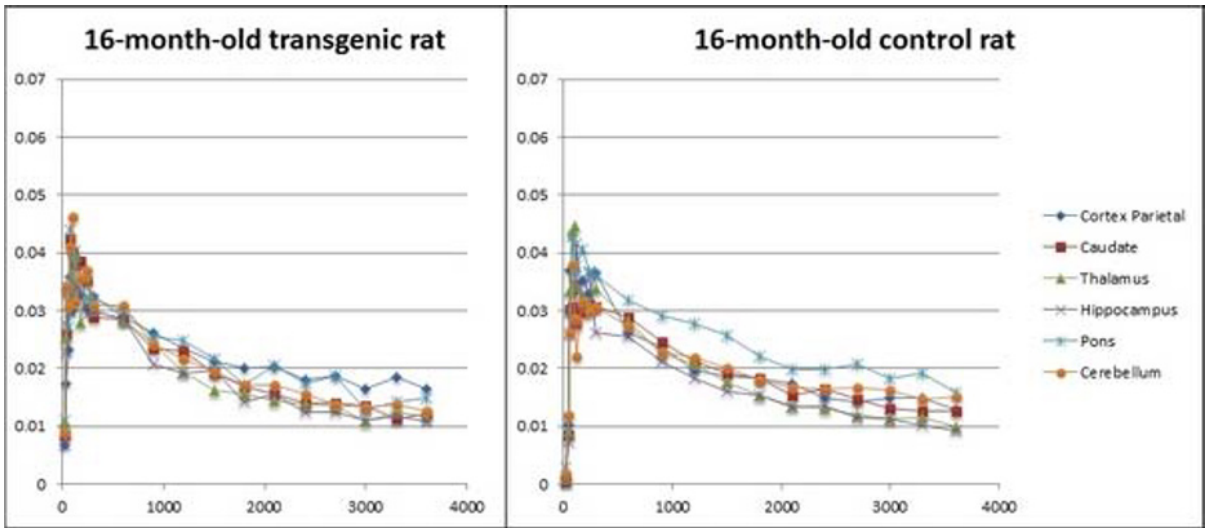

Disclosure of author financial interest or relationships:
D.A. Hammoud, None; **D.E. Lee**, None; **M.R. Lentz**, None; **X. Yue**, None; **W.G. Ibrahim**, None; **F. Denaro**, None; **K.L. Peterson**, None; **E. Jagoda**, None; **P. Choyke**, None; **M. Kassiou**, None; **W. Reid**, None.

Presentation Number **LBAP 077**
Late Breaking Abstract Poster Session
September 19, 2013 / 15:15-15:15 / Room: Exhibit Hall B

Neuroinflammation with Aging: PBR28 PET Measurements in Parkinson's Disease-related Transgenic Rats

Matthew D. Walker[1], Katherine Dinelle[2], Nathan Lee[2], Rick Kornelsen[2], Qing Miao[3], Siobhan E. McCormick[2], A Jon Stoessl[2], Matthew J. Farrer[4], **Vesna Sossi**[1], *[1]Physics and Astronomy, University of British Columbia, Vancouver, BC, Canada; [2]Pacific Parkinson's Research Centre, University of British Columbia, Vancouver, BC, Canada; [3]TRIUMF, Vancouver, BC, Canada; [4]Medical Genetics, University of British Columbia, Vancouver, BC, Canada. Contact e-mail: vesna@phas.ubc.ca*

Background Neuroinflammation is present in various neurodegenerative disorders and may contribute to disease progression. We have studied neuroinflammation in a transgenic rat model with a LRRK2-mutation, which is known to increase the risk of Parkinson's disease (PD). Measurements were made in vivo using [^{11}C]PBR28 PET over a wide range of animals' ages. The tracer binds to the 18-kDa translocator protein (TSPO) which is highly expressed on activated microglia. PET imaging using methylphenidate ([^{11}C]MP), which binds to the dopamine transporter (DAT), was also performed to assess the integrity of the dopaminergic system as a function of age. Methods The animals studied were LRRK2 G2019S over-expressing transgenic rats on a Sprague Dawley background. Nine transgenic rats were scanned on the microPET Focus120 using [^{11}C]PBR28 and 10 were scanned using [^{11}C]MP. Non-transgenic littermates (normal controls) were also studied; 11 were scanned using [^{11}C]MP, and so far 4 have been scanned using [^{11}C]PBR28. The rats spanned an age range of 3.6 to 16 months. [^{11}C]PBR28 images were quantified using the standard uptake value (kBq/mL per MBq/kg) for a region containing the whole brain (ventricles excluded), for the time range 43-90 minutes post bolus tracer injection. The region was defined using co-registration to a brain template. The SUV data were linearly regressed with age; Pearson's correlation coefficient (r) was calculated. [^{11}C]MP images were quantified using the binding potential (BP_{ND}) calculated for the striatum using the cerebellum as a reference region. Results A significant correlation (r = 0.88, p = 0.002) between age and the whole-brain SUV for [^{11}C]PBR28 was found for LRRK2 G2019S transgenic rats. The effect size was large: the SUV of 16 month old transgenic rats was 54 % higher than that of 3 month old rats. The [^{11}C]MP BP_{ND} in the striatum was not different between transgenic and non-transgenic rats, and evidenced no change with age. Discussion Our results demonstrate that after [^{11}C]PBR28 injection, the brain uptake of radioactivity in G2019S transgenic rats increases with age, as calculated relative to the injected activity per unit body weight. This suggests increased TSPO availability with age, possibly reflecting increased activation of microglia which mediate neuroinflammation. However, no evidence of DAT alteration as a function of aging was found for this transgenic model, and there was no difference in our DAT marker between transgenic and non-transgenic rats. [^{11}C]PBR28 data from non-transgenic littermates are in the final stages of being collected; they will allow us to determine whether LRRK2 mutation is associated with an abnormal increase in neuroimflammation, which could contribute to the vulnerability of the dopaminergic system suggesting a possible PD pathogenic mechanism.

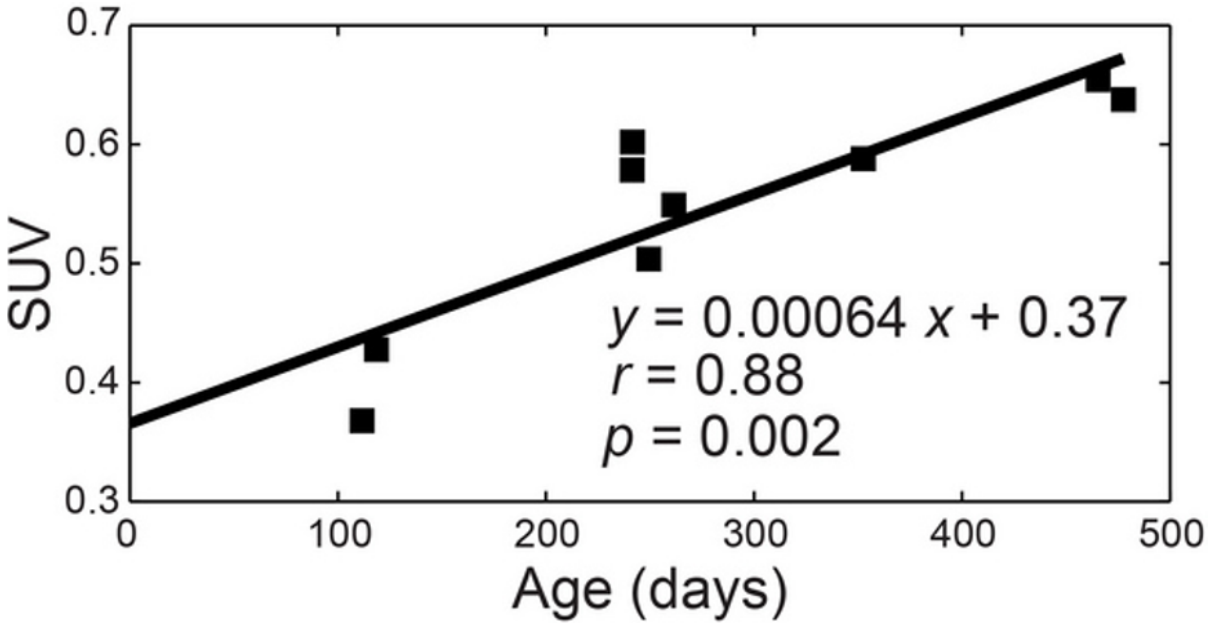

The whole-brain SUV from [^{11}C]PBR28 PET scans of LRRK2 G2019S transgenic rats, shown versus age. A linear regression is shown (solid line).

Disclosure of author financial interest or relationships:
M.D. Walker, None; **K. Dinelle**, None; **N. Lee**, None; **R. Kornelsen**, None; **Q. Miao**, None; **S.E. McCormick**, None; **A. Stoessl**, None; **M.J. Farrer**, None; **V. Sossi**, None.

Presentation Number **LBAP 078**
Late Breaking Abstract Poster Session
September 19, 2013 / 15:15-15:15 / Room: Exhibit Hall B

Dynamic Contrast-enhanced MRI of pulmonary perfusion

Laura Carrero-Gonzalez[3], Marta Tibiletti[2], Anne Kirchherr[1], Thomas Kaulisch[3], Andreas Briel[1], Volker Rasche[2], **Detlef Stiller**[3], *[1]nanoPET Pharma GmbH, Berlin, Germany; [2]Core Facility Small Animal MRI, University Ulm, Ulm, Germany; [3]In-Vivo Imaging, Target Discovery Research, Boehringer Ingelheim Pharma GmbH & Co. KG, Biberach, Germany. Contact e-mail: detlef.stiller@boehringer-ingelheim.com*

Aim: Chronic Obstructive Pulmonary Disease (COPD) is a rapidly growing chronic health condition with a current diagnosis rate of 13 % in Japan and 37 % in the EU5 (UK, France, Germany, Spain, Italy). COPD is under-diagnosed and unmet medical needs include the availability of disease-modifying drugs and improved early detection methods. Hallmarks of the disease are inflammation, airway wall thickening and excess mucus production resulting in deficits of ventilation and gas exchange. Since ventilation and blood perfusion of the lungs are linked, the assessment of lung perfusion can provide an indirect measure for ventilation deficits caused e.g. by mucus plugging. It may also serve as an alternative method for the assessment of therapeutic interventions for plug removal. In this study, the variation of pulmonary perfusion after obstruction of the right bronchus was assessed by magnetic resonance imaging (MRI) with the aid of a suitable blood pool agent, namely GadoSpinTM P, and a fast imaging sequence with a short echo time. Methods: In vivo MRI was performed in healthy male Wistar rats (n = 5) after intravenous injection of 400 µL of GadoSpin P per 350 g rat, corresponding to a dose of 100 µmol Gd/kg body weight. The right bronchus of all tested rats was obstructed for 50 min post contrast agent injection while the left bronchus was not affected and acted as the control. The relative signal intensities (SI) of the heart, aorta, muscle, right and left bronchus were assessed before and up to 75 min after injection of GadoSpin P. T1-weighted images were acquired on a 7 T Bruker BioSpec 70/30 scanner (Bruker BioSpin, Ettlingen, Germany) using a UTE-3D sequence (TR/TE = 3/0.02 ms, FA = 7°, total acquisition time 2 min 34 s). Results: Directly after injection of GadoSpin P, the SI of the heart and vessel increased significantly and then remained constant over the whole imaging time period of 75 min, whereas no changes in the SI of the muscle were observed. The SI of the right bronchus (obstructed) showed only a small increase after injection of GadoSpin P while the SI of the left bronchus (control) showed a significant initial increase followed by a slower increase up to 50 min post injection. After removal of the obstruction, the SI of the left unobstructed control bronchus decreased significantly while the SI of the right lung showed a slight increase. SI values of both lungs finally adjusted to the same level. Conclusion: In this study we were able to demonstrate a strong correlation between ventilation and perfusion of the lung providing valuable information about organ functionality. This technique may be applicable in studies of different pulmonary diseases including asthma, COPD or cystic fibrosis. However, further investigations are necessary to prove adequate sensitivity of the technique and, thus, its applicability in the detection of obstruction or plugging of small airways.

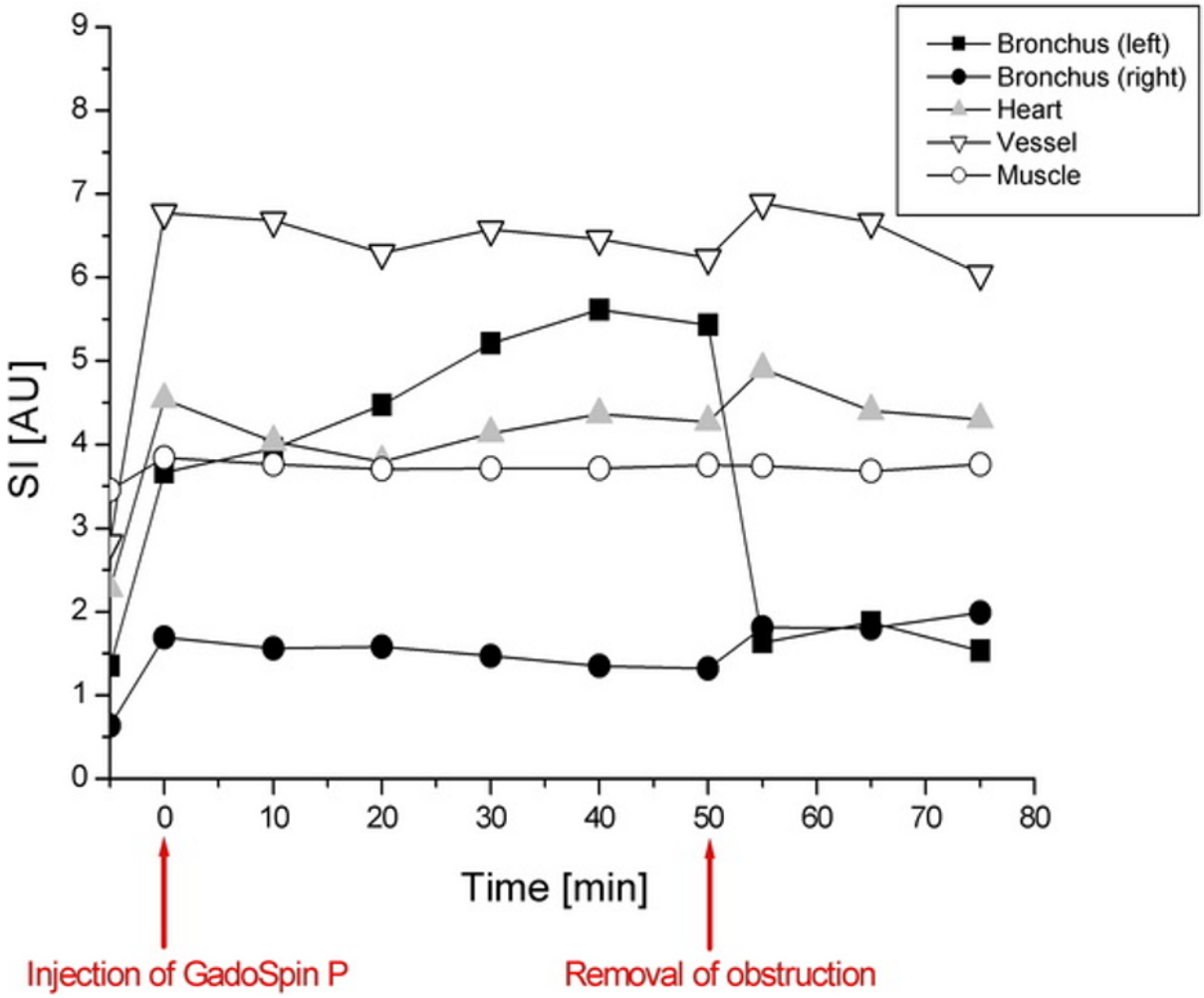

Representative time course of the signal intensity (SI) in T1-weighted images of the left and right bronchus, heart, vessel and muscle after intravenous injection of GadoSpin P in rat (100 µmol Gd/kg body weight). The right bronchus was obstructed for 50 min post contrast agent injection while the left bronchus was not affected and acted as the control.

Disclosure of author financial interest or relationships:
L. Carrero-Gonzalez, None; **M. Tibiletti**, None; **A. Kirchherr**, nanoPET Pharma GmbH, Employment; **T. Kaulisch**, Boehringer Ingelheim Pharma GmbH & Co. KG, Employment; **A. Briel**, nanoPET Pharma GmbH, Employment; **V. Rasche**, None; **D. Stiller**, None.

Presentation Number **LBAP 079**
Late Breaking Abstract Poster Session
September 19, 2013 / 15:15-15:15 / Room: Exhibit Hall B

Ribose salvage is dysregulated in metabolic syndrome

Peter M. Clark[1], *Graciela Flores*[2,4], *Nikolai M. Evdokimov*[2], *Melissa N. McCracken*[2], *Timothy Chai*[1], *Kym F. Faull*[3], *Michael Phelps*[2,4], *Michael E. Jung*[3], *Owen N. Witte*[1,2,5], [1]*Department of Microbiology, Immunology, and Molecular Genetics, UCLA, Los Angeles, CA, USA;* [2]*Department of Molecular and Medical Pharmacology, UCLA, Los Angeles, CA, USA;* [3]*Department of Chemistry and Biochemistry, UCLA, Los Angeles, CA, USA;* [4]*Crump Institute for Molecular Imaging, UCLA, Los Angeles, CA, USA;* [5]*Howard Hughes Medical Institute, UCLA, Los Angeles, CA, USA. Contact e-mail: pclark@mednet.ucla.edu*

Metabolic syndrome affects up to 25% of the world population. Despite considerable work, metabolic syndrome is still not fully understood. New positron emission tomography (PET) probes may provide a unique perspective on metabolic syndrome-associated changes in whole-body metabolism. Previous studies suggest that the metabolite ribose may be important in metabolic syndrome but have suffered from a lack of tools for studying ribose and ribose salvage in vivo. We recently developed and validated a new positron emission tomography probe to monitor ribose and ribose salvage in vivo. This probe has the same biodistribution as 14C-ribose, can compete with cold ribose for accumulation, and is metabolized through the ribose salvage pathway. Using this probe, we discovered that although ribose salvage occurs in multiple organs, it is highly enriched in the liver, where it likely contributes to gluconeogenesis. Additionally, we found that ribose salvage in the liver is significantly dysregulated in multiple mouse models of metabolic syndrome and that treating these mice with the diabetes drug metformin failed to rescue this dysregulation. Collectively, our studies suggest that changes in ribose metabolism, as measured by PET, may contribute to the etiology and complications of metabolic syndrome. We anticipate that this new PET probe will be useful for monitoring therapeutics designed to change the activity of the ribose salvage pathway.

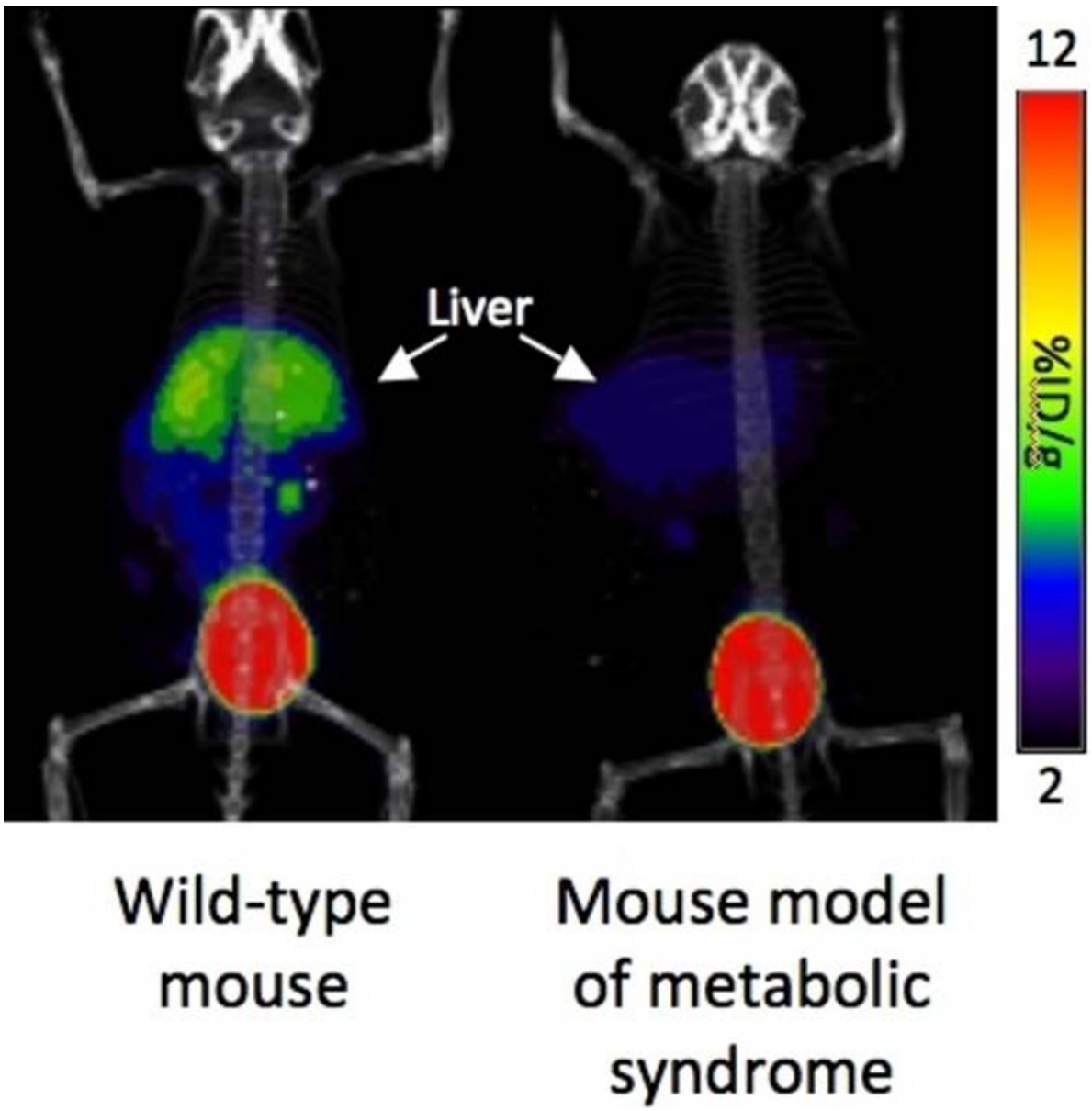

Mouse models of metabolic syndrome accumulate less ribose (as measured by PET) in the liver than wild-type mice.

Disclosure of author financial interest or relationships:
P.M. Clark, None; **G. Flores**, None; **N.M. Evdokimov**, None; **M.N. McCracken**, None; **T. Chai**, None; **K.F. Faull**, None; **M. Phelps**, None; **M.E. Jung**, None; **O.N. Witte**, Sofie Biosciences, Consultant; Sofie Biosciences, Stockholder .

Presentation Number **LBAP 080**
Late Breaking Abstract Poster Session
September 19, 2013 / 15:15-15:15 / Room: Exhibit Hall B

Reduced Oxidative Metabolism in T2DM Diabetic Skeletal Muscle as Observed by Hyperpolarized 13C-NMR

Jae Mo Park[1], *Sonal Josan*[1,2], *Dirk Mayer*[1,2], *Ralph E. Hurd*[3], *Daniel M. Spielman*[1], *James Graham*[4], *Peter Havel*[4], *David Bendahan*[5], *Thomas Jue*[6], [1]*Radiology, Stanford University, Stanford, CA, USA;* [2]*Neuroscience Program, SRI International, Menlo Park, CA, USA;* [3]*Applied Science Lab, GE Healthcare, Menlo Park, CA, USA;* [4]*Molecular Biosciences and Nutrition, UC Davis, Davis, CA, USA;* [5]*Centre de Résonance Magnétique Biologique et Médicale, Marseille, France;* [6]*Biochemistry & Molecular Medicine, UC Davis, Davis, CA, USA. Contact e-mail: jaemo@stanford.edu*

Introduction Many studies focus on non-oxidative pathways in muscle to determine the mechanisms behind the disrupted glucose homeostasis in type 2 diabetes mellitus (T2DM). In vivo 13C MR experiments have correlated the reduced glucose disposal in T2DM to a lower glycogen synthesis rate1. A new rat model2, which develops diabetes with age and obesity, has now provided an opportunity to assess with hyperpolarized 13C MR the oxidative pathway contribution. Indeed, [1-13C]lactate (Lac) does not form bicarbonate (Bic), consistent with a pyruvate (Pyr) dehydrogenase (PDH) deficiency in T2DM. Dichloroacetate (DCA), however, restores PDH function. The proposed studies yield insights into the pathogenesis of T2DM and the contribution of oxidative mechanisms. Methods UC, Davis (UCD)-T2DM rats (459-575g,n=5) and age-/weight-matched control (CRL) rats (517-681g,n=6) were anesthetized and scanned using a 3T GE MR scanner and a 13C surface coil (Ø = 28mm, placed on top of right rectus femoris). Animals in both groups were injected with a 40-mM hyperpolarized [1-13C]Lac solution, and 3 of the T2DM rats were additionally scanned following another 40-mM Lac injection 1h after a DCA infusion (200mg/kg). Moreover, 2.5h after the DCA administration, another set of data was acquired from a T2DM rat with 125-mM hyperpolarized [2-13C]Pyr to investigate the metabolic fate of the increased Pyr flux into mitochondria in the T2DM rats. Metabolic kinetics was measured from dynamic 13C MR spectroscopic data, acquired using a dynamic free induction decay (FID) MR sequence (10o hard pulse, temporal resolution=3s, spectral width/points=10kHz/4096, Tacq=4 min). Metabolite ratios relative to total carbon (tC) were used to compare metabolism in T2DM and CRL rats. Results & Discussion Alanine (Ala, 0.15±0.02 (mean±se) for T2DM and 0.15±0.01 for CRL) and Pyr (0.027±0.004 for T2DM and 0.032±0.002 for CRL) were detected at similar levels from both groups when Lac was injected. Bic, which measures Lac flux into mitochondria via Pyr with PDH, was significantly lower (P=0.015) in T2DM (0.002±0.002) than in CRL (0.013±0.004). However, Bic increased to 0.092±0.017 after DCA infusion, whereas Ala (0.076±0.007) and Lac (0.012±0.005) decreased. The restored Bic formation indicates that sufficient PDH exists in T2DM for activation. The addition of [2-13C]Pyr produced Lac (0.08) and Ala (0.024), and mitochondrial metabolites: acetyl-carnitine (0.045), acetoacetate (0.017), and glutamate (0.011). Whereas normal T2DM muscle showed undetectable oxidative metabolism, DCA activation of PDH upregulated the flow of Pyr to acetyl-CoA, which can then participate in fatty acid metabolism, ketone body formation, and the TCA cycle. Conclusion The metabolism of hyperpolarized [1-13C]Lac in the muscle is different in T2DM compared to CRL rats, in particular with respect to PDH activity. The restoration of PDH activity with DCA in UCD-T2DM rat suggests a non-negligible contribution of oxidative metabolism impairment in diabetes and a potential role for PDH activation to restore glucose homeostasis. Reference 1. Shulman GI et al, NEJM, 1989. 2. Cummings BP et al, Am J Physiol, 2008

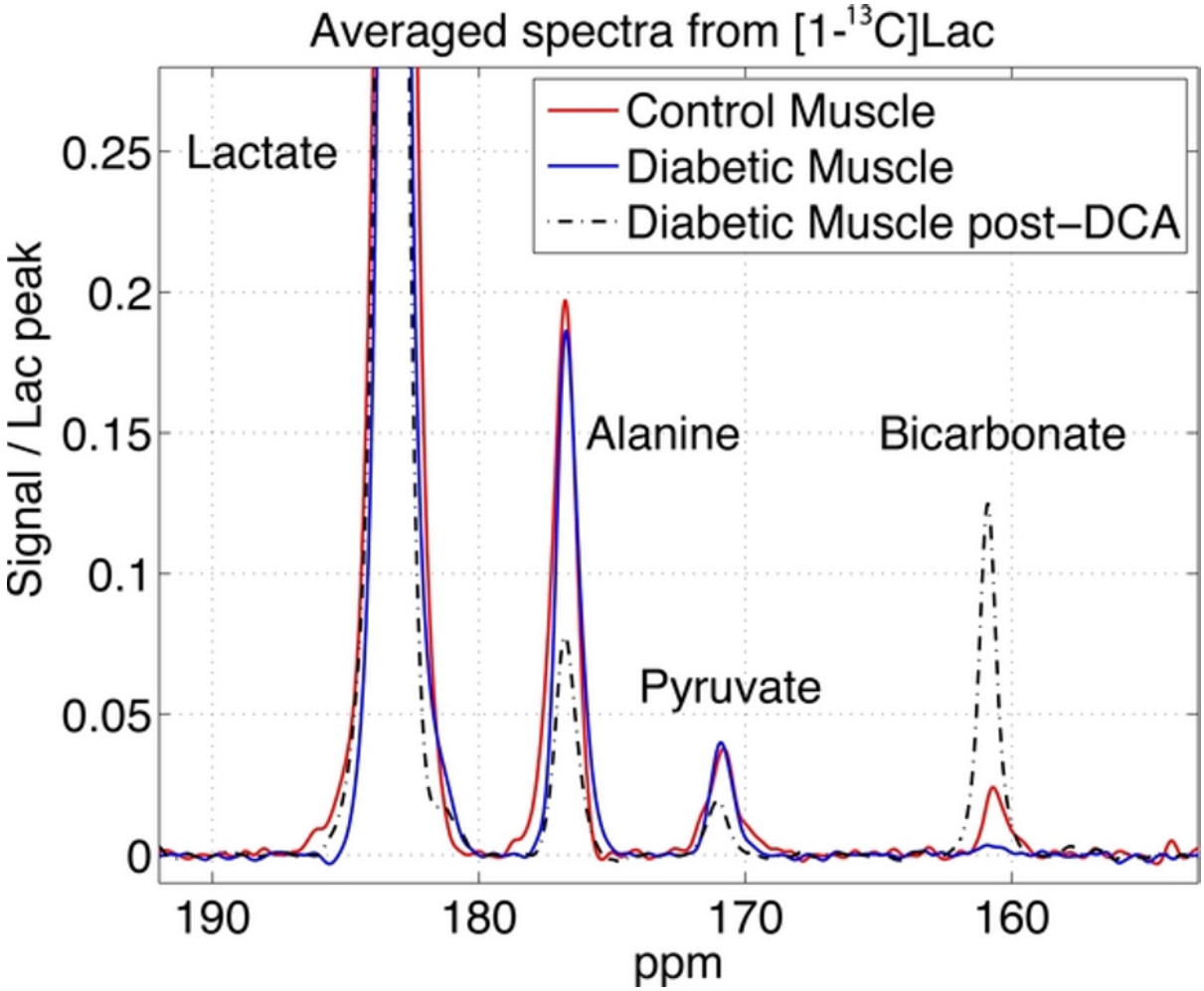

Time-averaged spectra of healthy control (red), diabetic muscle (blue), and diabetic muscle 1h after dichloroacetate infusion (dotted black) after hyperpolarized [1-13C]lactate.

Disclosure of author financial interest or relationships:
J. Park, None; **S. Josan**, None; **D. Mayer**, None; **R.E. Hurd**, GE Healthcare, Employment; **D.M. Spielman**, None; **J. Graham**, None; **P. Havel**, None; **D. Bendahan**, None; **T. Jue**, None.

Presentation Number **LBAP 081**
Late Breaking Abstract Poster Session
September 19, 2013 / 15:15-15:15 / Room: Exhibit Hall B

Imaging osteogenic and angiogenic responses in bone metabolism and defect healing using osteoporotic rat models

Yifei Liu[1], *Liji Cao*[1], *Seemun Ray*[3], *Ulrich Thormann*[2,3], *Gudrun Schlewitz*[2,3], *Parameswari Govindarajan*[3], *Jens Hillengass*[4,5], *Stefan Delorme*[5], *Reinhard Schnettler*[2,3], *Christian Heiss*[2,3], *Volker Alt*[2,3], *Tobias Baeuerle*[1], [1]*Department of Medical Physics in Radiology, German Cancer Research Center, Heidelberg, Germany;* [2]*Department of Trauma Surgery, Justus-Liebig-University, Giessen, Germany;* [3]*Laboratory of Experimental Trauma Surgery, Justus-Liebig-University, Giessen, Germany;* [4]*Department of Hematology, Oncology and Rheumatology, University of Heidelberg, Heidelberg, Germany;* [5]*Department of Radiology, German Cancer Research Center, Heidelberg, Germany. Contact e-mail: yifei.liu@dkfz.de*

Purpose: The role of angiogenesis in osteoporosis and osteoporotic bone repair mechanisms is unclear. Even less known is the influence of angiogenesis on osteoporotic bone defect healing with the intervention of implant materials. The aim of this study is to address these issues by utilizing imaging technologies in the assessment of angiogenesis and osteogenesis in designed rat models. Material and Methods: Volumetric computed tomography (VCT) in combination with dedicated calculation of density ratio between bone and nearby muscle was used to quantify osteogenesis; while dynamic contrast-enhanced VCT (DCE-VCT), dynamic contrast-enhanced MRI (DCE-MRI), diffusion-weighted MRI (DW-MRI), histology and immunohistochemistry were combined to evaluate angiogenesis. Three investigations were included in this study: (i) Sham operated rats (SHAM) and rats with osteoporosis induced by ovariectomy plus calcium and Vitamin D3 deficiency (OVXD) or plus glucocorticoid (OVXC) were imaged at 1, 3, or 12 months post surgery with a special focus on regions of lumbar vertebrae, pelvis and femur; (ii) Wedge-shaped defects were created at left distal femurs and stabilized internally by T-shaped miniplates after 3 months of SHAM (SHAM-F) or OVXD (OVXD-F) treatment. Imaging was performed in all animals 6 weeks after this procedure; (iii) Fracture gap sizes or filling materials for OVXD-F were varied among 8 different groups (OVXD-F-M), and rats were imaged at 1 week to 5 weeks post-surgery. Results: Within and among SHAM, OVXD and OVXC groups, early time points (1 and 3 months) didn't show significant difference in any of the angiogenetic parameters. After 12 months, in particular in the pelvis, the osteoporotic individuals (irrespective of the osteoporosis inducers applied) exhibited decreased permeability, significantly reduced vessel density, significantly increased vessel maturity, as well as statistically unaltered perfusion amplitude, diffusion, and vessel diameter. Bone density within the osseous defect was significantly reduced in OVXD-F as compared to SHAM-F rats. Vascularization parameters derived from DCE-MRI and DCE-VCT in the defect were significantly elevated compared to the adjacent tissues for both groups. However, comparing SHAM-F and OVXD-F rats, no statistically different values were noticed concerning any determined vascularization parameter within the bone defect. Furthermore, a slight increase of perfusion amplitude was found for OVXD-F as compared to SHAM-F within the bone marrow, which was similar to the increase seen in OVXD versus SHAM. No significant difference in vascularization parameters existed among different OVXD-F-M groups. Conclusion: The study indicates that osteoporosis influences osteogenic but not early-phase angiogenic response in bone and bone defect in rat models. With or without implant the angiogenesis

doesn't evidence any significant changes detectable for DCE-MRI and DCE-VCT technologies. Results provide insight into the relationship between angiogenesis and osteogenesis during osteoporosis-related compromised bone healing.

Disclosure of author financial interest or relationships:
Y. Liu, None; **L. Cao**, None; **S. Ray**, None; **U. Thormann**, None; **G. Schlewitz**, None; **P. Govindarajan**, None; **J. Hillengass**, None; **S. Delorme**, None; **R. Schnettler**, None; **C. Heiss**, None; **V. Alt**, None; **T. Baeuerle**, None.

Presentation Number **LBAP 082**
Late Breaking Abstract Poster Session
September 19, 2013 / 15:15-15:15 / Room: Exhibit Hall B

Response to deep brain stimulation in a rat model of obesity: in-vivo assessment of brain glucose metabolism in nucleus accumbens vs. lateral hypothalamus

María L. Soto-Montenegro[1,2], *Javier Pascau*[3,1,2], *Veronica Garcia-Vazquez*[2], *Manuel Desco*[3,1,2], [1]*Laboratorio de Imagen Médica. Unidad de Medicina y Cirugía Experimental, Instituto de Investigación Sanitaria Gregorio Marañón, Madrid, Spain;* [2]*CIBER de Salud Mental (CIBERSAM), Hospital General Universitario Gregorio Marañón, Madrid, Spain;* [3]*Departamento de Bioingeniería e Ingeniería Aeroespacial, Universidad Carlos III, Madrid, Spain. Contact e-mail: marisa@hggm.es*

Objectives: Obesity is the most common metabolic disorder in human clinical practice with a well-founded neuropsychiatric basis, being the centers of appetite and satiety in the brain the major research areas. In particular, it has been suggested that deep brain stimulation (DBS) in the lateral hypothalamus (LH) or in the nucleus accumbens (NAcc) are two possible targets for the treatment of obesity and food intake disorders. The aim of this study is to examine and selectively identify the associated networks after the treatment with DBS in LH or NAcc in a rat model of obesity. **Methods:** 18 male Zucker Obese rats (fa/fa-) were included in the study. A concentric bipolar platinum-iridium electrode was bilaterally implanted into the LH or NAcc. Four groups of animals were studied: a) NAcc control (2), b) NAcc-DBS (6), c) LH control (4), d) LH-DBS (6). After 7 days, the DBS study was performed in a constant current mode at 130 Hz and 300 μA using an isolated stimulator. DBS was applied one hour per day for 15 days. We controlled weight and intake of food and water for one month. Imaging studies with [18F]fluoro-D-glucose (FDG) were performed the day after the end of the DBS treatment with a small-animal PET/CT scanner. Images were reconstructed using a 2D-OSEM algorithm. An MR image of one animal was acquired with a 7 Tesla Bruker Biospec scanner. All images were spatially registered, smoothed with a 2 mm isotropic Gaussian kernel and masked to remove extracerebral tissues. Voxel values were normalized to the overall brain average, and analyzed with Statistical Parametric Mapping software (SPM5). **Results:** A weight decrease of 3.2% from baseline was found in LH-DBS animals compared to LH animals at day 15. This difference was maintained during the following month without DBS treatment. No effect on weight was found in NAcc-DBS animals compared to NAcc animals. There was no difference in food and water consumption in any group. LH-DBS treatment increased metabolic activity in the pituitary (t=4.12) and the hippocampus (right: t=3.95; left: t=3.47); and decreased FDG-uptake in the thalamus (t=5.24) and occipital cortex (t=4.52). NAcc-DBS treatment increased metabolic activity in the cingulate cortex (t=3.96) and the hippocampus (right: t=41.64; left: t=2.52); and decreased FDG-uptake in the orbitofrontal cortex (t=11.53) and the thalamus and striatum (t=4.21). **Conclusions:** Our results show significant FDG uptake changes in several brain regions that are associated with the control of food intake (basal ganglia, thalamus, and hippocampus). DBS treatment seems to normalize the impaired hippocampal functioning that has been described in obese rats [1], independently of the brain area stimulated. Only LH-DBS treatment has produced a reduction in weight gain in the animals, which suggest that the treatment of choice may be DBS in lateral hypothalamus. More studies are needed to clarify exactly which is the best strategy. [1] Thanos et al. Int J Obes (Lond). 2008; 32(7): 1171-1179. Supported by FIS PI11/00616, PI10/02986, TEC2010-21619-C04-01, RD09/0077/00087), CENIT-20101014, ARTEMIS S2009/DPI-1802, CIBERSAM and Fundación Mapfre.

Disclosure of author financial interest or relationships:
M.L. Soto-Montenegro, None; **J. Pascau**, None; **V. Garcia-Vazquez**, None; **M. Desco**, None.

Presentation Number **LBAP 083**
Late Breaking Abstract Poster Session
September 19, 2013 / 15:15-15:15 / Room: Exhibit Hall B

19F molecular MR imaging for detection of brain injury: in vivo validation using targeted perfluorocarbons nanoemulsion

Fan Zhang, *Ki Young Choi, Xinglu Huang, Gang Niu, Xiaoyuan (Shawn) Chen, National Institute of Biomedical Imaging and Bioengineering, National Institutes of Health, Bethesda, MD, USA. Contact e-mail: mri_zf@126.com*

Background and Purpose: Magnetic resonance imaging (MRI) with appropriate contrast agents has emerged as a promising molecular imaging approach to detect brain injury biomarkers. In particular, 19F MRI is an attractive option for imaging molecular biomarkers in vivo due to significantly low 19F MR background signals in the body. However, biomedical applications of perfluorocarbons are significantly hampered by its low solubility in physiological conditions and lack of site specificity. In this study, we engineered a perfluro-15-crown-5-ether (PFCE)-based nanoemulsion (PC-NE) using a multifunctional, hyaluronan-based biosurfactant. The PC-NE can actively target injured brain tissues known to overexpress hyaluronan receptor proteins, CD44 [1]. 19F MRI was utilized in a brain injured mouse model to investigate CD44-targeted PC-NE's potential as a contrast agent. Methods: We prepared a multifunctional, hyaluronan-based biosurfactant and fabricated PC-NE using a sonication method. To investigate the diagnostic potential of PC-NE, we prepared traumatic brain injury (TBI) mouse models. The mice were then injected intravenously with CD44-targeted PC-NE labeled with FITC or non-targeted 19F imaging agent Celsense 1000 (Celsense Inc.). 19F images were acquired at predetermined time points. Small animal MRI was conducted on a 7.0 T system (Bruker BioSpin Corp.) and with a double-tuned 1H/19F volume coil (m2m Imaging Corp). 19F images were acquired with our optimized FLASH. Brain samples were collected and sectioned after the animals were sacrificed, and brain tissue slices were examined under a fluorescence microscope (X81; Olympus) to observe the brain tissue distribution of the PC-NE. Results: The resulting PC-NEs were well-dispersed with a 150 nm hydrodynamic diameter. 19F MR effects of PC-NEs were confirmed with 19F NMR and 19F MR phantom imaging experiments. 19F MR images exhibited strong signals at TBI tissues from 4 h post injection, which further increased by 48h and decreased. On the other hand, only nonspecific signals at the superior sagittal sinus were detected in the control group injected with Celsense 1000 at 4 h time point, which was washed out from 24 h and could not be detected at 48 h after injection. MR results were also confirmed by ex vivo fluorescence imaging of the tissue. Conclusion: In this study, we successfully developed a CD44-targeted 19F MRI contrast agent based on PFCE nanoemulsion supported by a multifunctional, hyaluronan-based biosurfactant. After systemic administration of the PC-NE into the TBI mouse models, strong signals were detected at the injury sites, suggesting the great diagnostic potential of PC-NE. To the best of my knowledge, this is the first study which demonstrates the diagnostic potential of 19F MRI to detect CD44 expression in a TBI mouse model. This system may be used for the detection and characterization of brain injury and refining individualized therapy. Reference 1. Stylli SS, Kaye AH, Novak U. Induction of CD44 expression in stab wounds of the brain: long term persistence of CD44 expression. J Clin Neurosci. 2000 Mar;7(2):137-40.

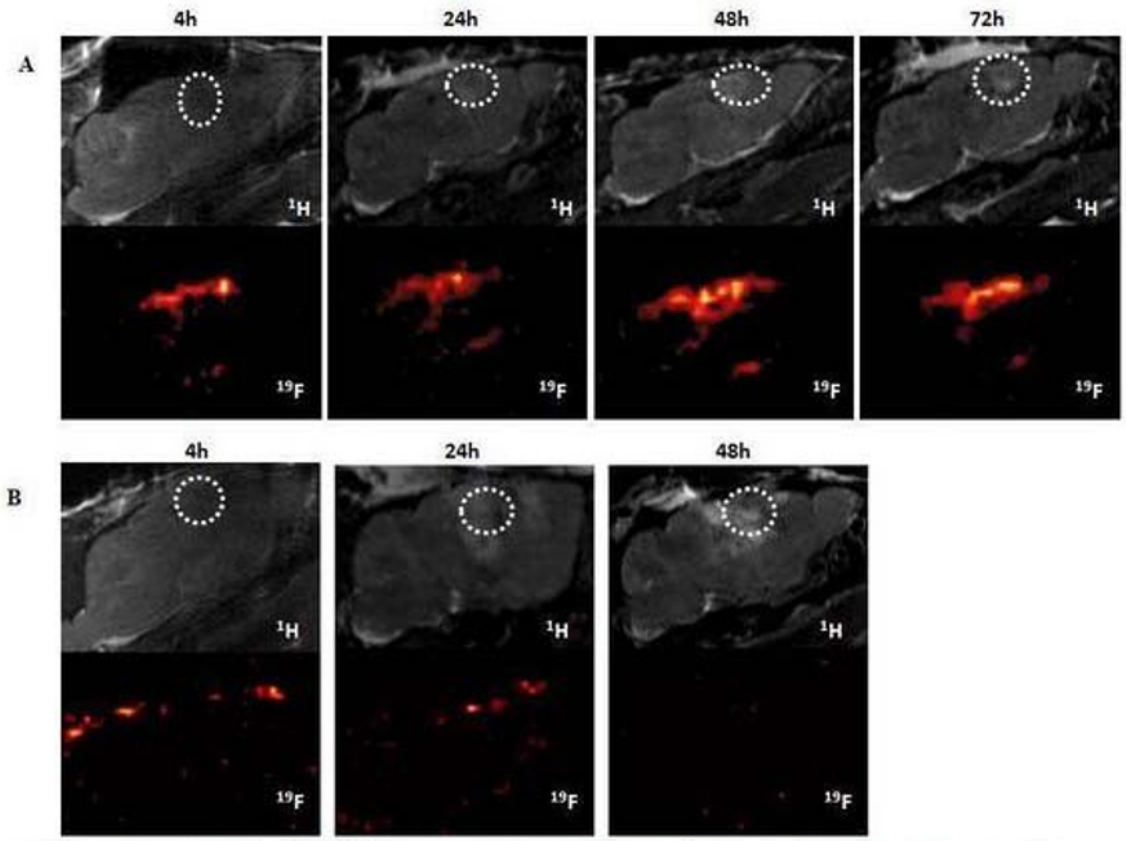

Figure. (A) Representative ^{1}H and ^{19}F (orange color was applied to the ^{19}F images) MR images of the mouse brain 4,24,48and 72 hrs after HA-perfluorocarbon /FITC nanoemulsion injection. (B) Representative ^{1}H and ^{19}F MR images of the mouse brain 4, 24 and 48 hrs after non-targeted ^{19}F imaging agent celsense 1000 injection.

Disclosure of author financial interest or relationships:
F. Zhang, None; **K. Choi**, None; **X. Huang**, None; **G. Niu**, None; **X. Chen**, None.

Presentation Number **LBAP 084**
Late Breaking Abstract Poster Session
September 19, 2013 / 15:15-15:15 / Room: Exhibit Hall B

Dopaminergic modulation in rats by Deep Brain Stimulation of the medial prefrontal cortex: quantification of [11C]-raclopride D2R binding in the caudate putamen using microPET

Joke Parthoens, *Viki Engelen, Tine Wyckhuys, Jeroen Verhaeghe, Sigrid Stroobants, Steven Staelens, Nuclear Medicine, University of Antwerp, Antwerp, Belgium. Contact e-mail: joke.parthoens@ua.ac.be*

Objective: Deep brain stimulation (DBS) is a reversible and adjustable neurosurgical intervention using implanted electrodes to stimulate specific brain structures. After its success in movement disorders, it has been proposed as a treatment for other neurological and psychiatric disorders such as epilepsy, depression and obsessive-compulsive disorder (OCD). Despite the promising results in both clinical and preclinical studies, all the optimal stimulation targets for these diseases have not yet been elucidated. The prefrontal cortex (PFC) is involved in the regulation of emotions and plays a significant role in a variety of neuropsychiatric diseases including depression and addiction. DBS of the rat medial PFC (mPFC) induces antidepressant-like behavior, reduces cocaine self-administration and induces sustained increases in hippocampal 5-HT levels [1][2]. In this study, the dopamine(DA)-inducing effects of this promising therapeutic approach are evaluated through small animal Positron Emission Tomography (microPET) using [11C]-raclopride, a D2R antagonist. Methods: One week after stereotactic implantation of a bipolar DBS electrode in the left prelimbic (PL) mPFC, the rats (n=9) were anaesthetized with isoflurane and positioned on a microPET scanner. Fifteen minutes after the start of DBS application (60 Hz) or sham stimulation, these animals were injected with 5.54 ± 0.97 MBq of [11C]-raclopride (S.A. 129.19 ± 16.86 GBq/μmol) and the dynamic PET acquisition (1h) was started using a Siemens Inveon (Siemens, Knoxville, USA). All rats underwent both a DBS and a sham scan on separate days in a randomized order, and acted as their own control. For the active DBS, the animals were continuously stimulated throughout the scan acquisition. The [11C]-raclopride binding potential (BPND) of the caudate putamen was calculated by kinetic modeling (PMOD 3.3) using the simplified reference tissue method, with the cerebellum as a reference area. The BPND values of sham versus DBS were compared using a Wilcoxon Signed Ranks test (SPSS). Results: After histological verification of the cannula placements, 7 rats were included in the image analysis. Compared to sham, left PL mPFC DBS induced a decrease in the caudate putamen [11C]-raclopride BPND (BPND-sham: 2.22, BPND-DBS: 2.07; -6.32% ± 5.45% averaged), which was more pronounced in the right (contralateral) compared to the left (ipsilateral) hemisphere (-7.70% ± 5.67% versus -5.07% ± 5.39%) (Figure 1) albeit not yet significant with n=7. More animals are being operated upon and data is underway. Conclusion: These data suggest that mPFC DBS may induce increases in striatal endogenous DA levels, adding to the promising results found in other preclinical studies and providing a rationale for further exploration of this therapy in diseases characterized by a hyposensitive reward system such as treatment-refractory addiction or OCD. [1] C. Hamani et al. BPS: 67(2) 117-124, 2010. [2] D. Levy et al. Journal of Neuroscience: 27(51) 14179-14189, 2007.

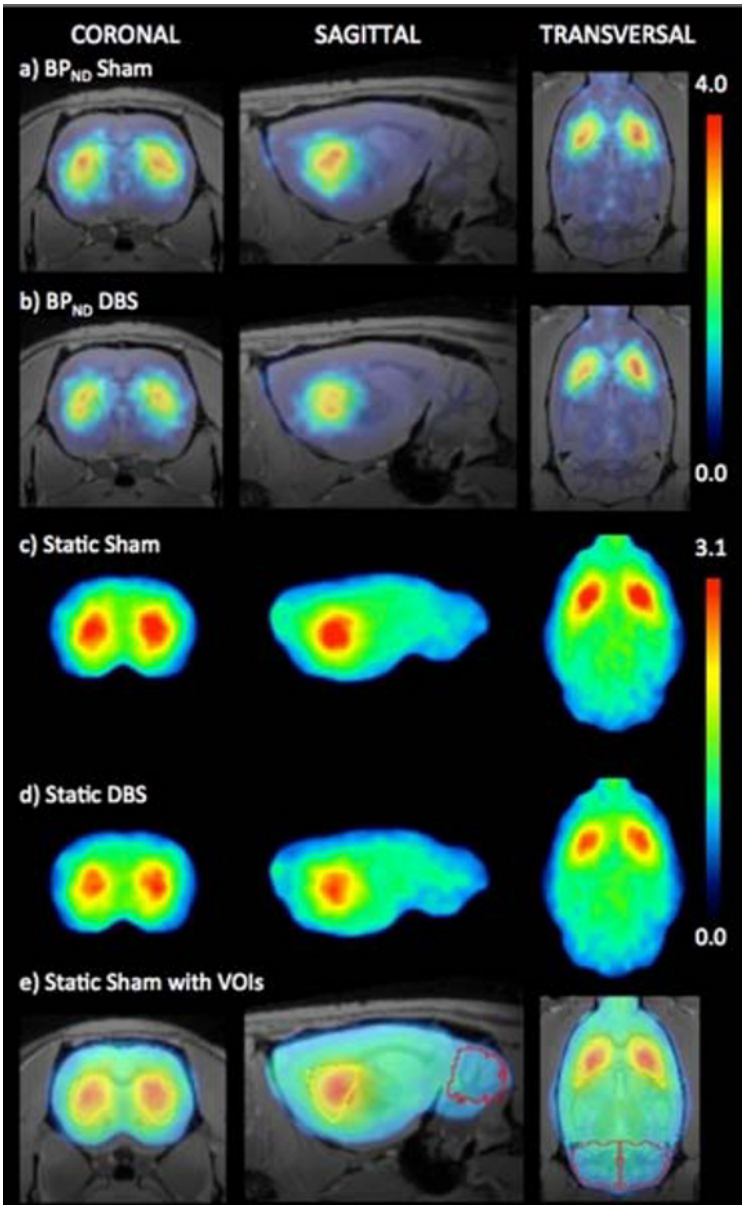

Figure 1: Average [11C]-raclopride BPND values overlaid on an MR template (a. and b.) and static images (c. and d.) for sham and DBS (n=7), e. static sham image overlaid on an MR template with caudate putamen (yellow) and cerebellum (reference area) delineated in yellow and red, respectively (n=7, Gaussian smooth factor 0.5).

Disclosure of author financial interest or relationships:
J. Parthoens, None; **V. Engelen**, None; **T. Wyckhuys**, None; **J. Verhaeghe**, None; **S. Stroobants**, Janssen Pharmaceuticals, Grant/research support; **S. Staelens**, Johnson & Johnson, Grant/research support .

Presentation Number **LBAP 085**
Late Breaking Abstract Poster Session
September 19, 2013 / 15:15-15:15 / Room: Exhibit Hall B

In vivo PET imaging of amyloid pathology and brain metabolism in a double transgenic model of Alzheimer's Disease

Ann-Marie Waldron[1,4], *Jonathan B. Kelley*[2], *Leonie Wyffels*[1], *Jeroen Verhaeghe*[1], *Jill C. Richardson*[3], *Stefanie Dedeurwaerdere*[4], *Sigrid Stroobants*[1], *Xavier Langlois*[2], *Steven Staelens*[1], [1]*Molecular Imaging Center, University of Antwerp, Antwerp, Belgium;* [2]*Neuroscience, Janssen Pharmaceutica NV, Beerse, Belgium;* [3]*R&D China U.K. Group, GlaxoSmithKline, Stevenage, United Kingdom;* [4]*Translational Neurosciences, University of Antwerp, Antwerp, Belgium. Contact e-mail: ann-marie.waldron@ua.ac.be*

Introduction: In vivo diagnostic imaging with small animal PET has the ability to bridge the gap between preclinical and clinical research. By employing shared biomarkers of disease in studies of murine models and AD patients we can facilitate the straightforward translation of results from bench to bedside. Thus the aim of the present study was to validate the use of two currently employed clinical PET tracers, Florbetapir ([18F]-AV45) and fluorodeoxyglucose ([18F]-FDG), in a murine model of amyloidosis. Methods: For this purpose we studied a double transgenic mouse model of amyloidosis (TASTPM, n=12) and wild-type controls (C57BL6J, n=12) at 12mth of age (Howlett et al. 2008). Each mouse underwent two scans; 1) with [18F]-AV-45 (17.39± 0.4MBq, S.A 63.91-78.92 GBq/umol) for the assessment of amyloid burden and 2) with [18F]-FDG (18.5±0.7MBq) for the evaluation of metabolic abnormalities. In each instance tracers were administered via tail-vein injection and after a conscious uptake of 45min a 20min static scan was performed. PET data was reconstructed using OSEM2D (4 subsets, 16 iterations) and relevant VOI's were delineated through registration of PET/CT images with a predefined mouse brain VOI template (Mirrione et al. 2007). Tracer uptake was quantified through %ID for [18F]-AV45 and SUV for [18F]-FDG. All animal studies were ethically reviewed and carried out in accordance with European Directive 86/609/EEC Welfare and Treatment of Animals. Results: PET analysis revealed significant uptake of [18F]-AV-45 in TASTPM versus controls in all brain regions investigated excluding the cerebellum. The highest significance was observed in the striatum, cortex, hippocampus, thalamus and superior colliculi (all $p<0.0001$). Additionally TASTPM mice exhibited a profound and global decline in [18F]-FDG uptake in comparison to wild-type mice with the thalamus demonstrating the most significant difference ($p= 0.0013$). Conclusion: These results support the use of [18F]-AV45 and [18F]-FDG as translational biomarkers of Alzheimer's pathology and imply that the longitudinal monitoring of TASTPM mice with these tracers would provide valuable information concerning the underlying pathology of AD. This research was performed in conjunction with the European Community's Seventh Framework Program (FP7/2007-2013) for the Innovative Medicine Initiative under the PharmaCog Grant Agreement n°115009.

Disclosure of author financial interest or relationships:
A. Waldron, None; **J.B. Kelley**, Janssen R&D, Employment; **L. Wyffels**, None; **J. Verhaeghe**, None; **J.C. Richardson**, GlaxoSmithKline, Employment; **S. Dedeurwaerdere**, None; **S. Stroobants**, Janssen Pharmaceuticals, Grant/research support; **X. Langlois**, None; **S. Staelens**, Johnson & Johnson, Grant/research support .

Presentation Number **LBAP 086**
Late Breaking Abstract Poster Session
September 19, 2013 / 15:15-15:15 / Room: Exhibit Hall B

Can MRI Measure Tissue Oxygen Content? Towards a Quantitative Measure of Hypoxia

*Scott C. Beeman[1], **Joseph J. Ackerman**[1,2], Joel R. Garbow[1], [1]Radiology, Washington University, St. Louis, MO, USA; [2]Chemistry, Washington University, St. Louis, MO, USA. Contact e-mail: ackerman@wustl.edu*

A quantitative MRI method to measure tissue oxygen content would be a significant advance. Blood oxygen level dependent (BOLD) MRI (1) has been proposed as an endogenous molecular imaging tool to determine oxygen extraction fraction (2), though quantification is challenged by susceptibility-driven field inhomogeneities. We (and others: 3, 4) are pursuing a complementary strategy, one that takes advantage of the paramagnetic property of molecular oxygen (O_2), as found dissolved in tissue. Herein, we present preliminary data suggesting that MR mapping of the tissue-water longitudinal relaxation rate constant ($R_1=1/T_1$), while modulating the oxygen and carbon dioxide content of the breathing gas, holds promise for measurement of tissue O_2 content and may provide a means to differentiate pathologies such as tumor and radiation necrosis. Healthy BALB/c mice were anesthetized with 0.8% isoflurane in either 100% O_2 (n=4) or carbogen (95% O_2/5% CO_2) (n=1). R_1 data were collected during free breathing of either pure oxygen followed by the reference gas (12.5% O_2 / 87.5% N_2) or carbogen followed by the reference gas. The experiment was repeated in a DBT mouse tumor model (n=5) and a mouse model of radiation necrosis (n=6) using only carbogen and the reference gas. A fast spin-echo pulse sequence with 32 inversion times ranging from 0.005 sec to 4.5 sec was used to collect R_1 data. The tissue R_1 was determined for each voxel and R_1 maps were generated using in-house developed Bayesian analysis software (5). Whole-brain ROIs were drawn manually to quantify the global R_1 changes. R_1 maps show that breathing of either carbogen (A) or pure oxygen (B) increased the R_1 in healthy mouse brain tissue by 5.7±3.4% and 8.6%, respectively, compared to breathing of the reference gas (C). Switching the order of administration of the breathing gases had no effect on the induced R_1 changes. Mice with tumors (D, E) and mice with radiation-induced necrosis (F, G) respond differently to the carbogen breathing-gas challenge. Interestingly, in these initial studies, this effect is not isolated to the site of the lesion, but is instead diffuse across both hemispheres of the brain. The whole-brain percentage change in R_1 (H) in mice with tumors was 0.24±0.14% (with one outlier of 3.6%) versus 6.2±2.2% in mice with radiation necrosis. Consistent with the paramagnetic nature of O_2, R_1 in the brain increases as a function of O_2 content in the breathing gas. The addition of CO_2 to a hyperoxic gas mixture further increases R_1. We hypothesize that these changes in R_1 are a function of the amount of O_2 dissolved in the brain parenchyma. Preliminary data suggest this technique can distinguish radiation damage from tumor, though it is not yet clear why the R_1 changes are not localized to only the lesion site. In vivo measurements of R_1 during breathing gas challenges may prove to be clinically valuable on their own, or in combination with qBOLD, for non-invasive quantification of O_2 and for differentiating and grading pathologies such as tumor and radiation necrosis. Refs: (1) Ogawa, et al.1990 (2) He, et al. 2007 (3) Dunn et al. 2002 (4) Winter et al. 2011 (5) Bretthorst, et al. 2005.

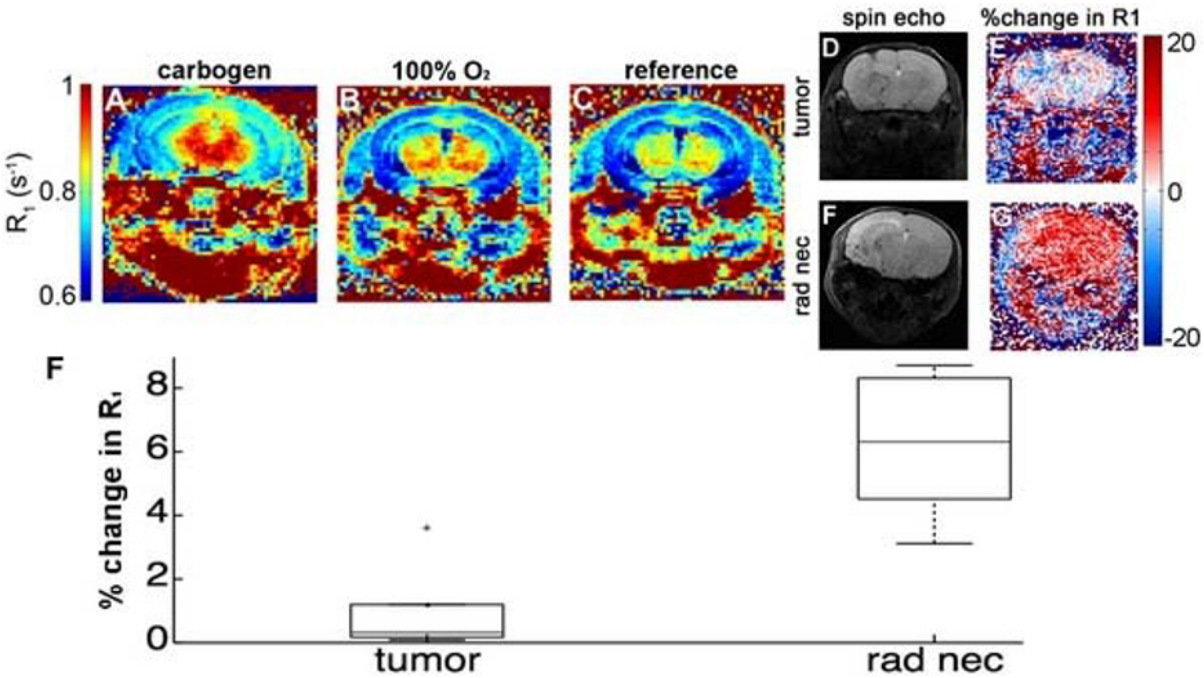

Figure 1 - R_1 maps in the brains of healthy mice breathing carbogen (A), pure oxygen (B), and the hypoxic reference gas (C). Mice with tumors (D, E) and mice with radiation-induced necrosis (F, G) respond differently to the breathing gas challenge. The whole-brain percentage change in R_1 (H) in mice with tumors was 0.24±0.14% (with one outlier of 3.6%) versus 6.2±2.2% in mice with radiation necrosis.

Disclosure of author financial interest or relationships:
S.C. Beeman, None; **J.J. Ackerman**, Agilent Technologies, Grant/research support; Sigma-Aldrich Company, Honoraria; Elsevier, Honoraria; Monsanto Company, Grant/research support; Agilent Technologies, Other financial or material support; **J.R. Garbow**, None.

Presentation Number **LBAP 087**
Late Breaking Abstract Poster Session
September 19, 2013 / 15:15-15:15 / Room: Exhibit Hall B

Characterizing vascular changes in a novel mouse model of ischemic stroke with vessel size imaging

Jonathan A. Disselhorst[1], *Salvador G. Castaneda*[1], *Mathew R. Divine*[1], *Sandra Beer-Hammer*[2], *Bernd Nuernberg*[2], *Bernd J. Pichler*[1], [1]*Werner Siemens Imaging Center, Eberhard Karls University of Tuebingen, Tuebingen, Germany;* [2]*Department of Pharmacology and Toxicology, Eberhard Karls University of Tuebingen, Tuebingen, Germany. Contact e-mail: jonathan@disselhorst.eu*

Ischemic stroke (IS) is a cerebral infarction that occurs after blocking of an arterial segment. Animal models are required to develop therapies and diagnostic tools for IS. We present an in vivo evaluation of vascular parameters using vessel size imaging (VSI) in a novel mouse model for IS which combines injection of Pertussis toxin (PTX) followed by a temporary occlusion of the carotid artery (TOC). **Methods**. C57BL/6 mice were divided into 4 groups: control, TOC, PTX, and PTX + TOC (Stroke). Group PTX was injected i.p. with 150µg/kg PTX. A vascular clamp was applied for 30 min to the left carotid artery under anesthesia to the TOC group. A stroke was induced by applying a vascular clamp 48 hours after injection of PTX. All imaging procedures were performed under general anesthesia on a 7T small-animal MRI scanner using a mouse brain surface coil. Respiratory gated T2-weighted images were acquired for anatomical reference. Diffusion-weighted images were acquired with a respiratory triggered HASTE sequence to calculate the apparent diffusion coefficient (ADC). Arterial spin labeling (ASL) images were obtained in one plane to determine perfusion. For vessel size imaging, T2 and T2* maps were acquired before, and two minutes after i.v. injection of 50 µL USPIO contrast agent (Ferumoxytol). Mice in the stroke group without apparent stroke, or mice with invalid or missing data were excluded from analysis. Calculations of the ADC, T2, T2*, perfusion and vessel parameters were performed in MATLAB. T2 and T2* pre- and post-maps were calculated and used to produce change in R2 relaxation (ΔR2) and change in R2* relaxation (ΔR2*) maps. These maps were used for the calculation of the mean vessel diameter (mVD), vessel density, and the relaxation rate shift index (Q). The median was determined in the entire scanned area of the brain. In addition, the ratio between the left and the right hemisphere (L/R) was determined. A t-test for statistical significance was performed with an alpha level of 0.05 comparing all groups to the control-group. The mice in the stroke group had additional regions of interest drawn in the affected area and on the contralateral side, with which the ratio was obtained (S/C). A one sided t-test was performed with a hypothesized mean of 1 (i.e., no difference between stroke and contralateral side). **Results**. Statistically significant differences were found between the ligation and control group in the ADC value in the entire brain (0.65±0.02 vs. 0.69±0.02 $x10^{-3}$ mm^2/s). In the stroke group as well as the pertussis group, statistically significant differences were found in the perfusion (86±24 and 90±23 vs. 157±16 mL/100g/min). Comparing L/R, statistically significant differences in the stroke group were found in the three vessel parameters (a decrease in Q and vessel density and increase in mVD). Also, the S/C ratio showed significance in these parameters in addition to the T2 before injection and ΔT2. **Conclusion**. The combination of PTX with TOC leads to ipsilateral lesions in the brain. These lesions are characterized by clear changes in vasculature, consistent with vasogenic edema as assessed by MRI.

Disclosure of author financial interest or relationships:
J.A. Disselhorst, None; **S.G. Castaneda**, None; **M.R. Divine**, None; **S. Beer-Hammer**, None; **B. Nuernberg**, None; **B.J. Pichler**, Siemens, Grant/research support; Bayer, Grant/research support; AstraZeneca, Grant/research support; BoehringerIngelheim, Grant/research support .

Presentation Number **LBAP 088**
Late Breaking Abstract Poster Session
September 19, 2013 / 15:15-15:15 / Room: Exhibit Hall B

Decreased Striatal D2/3 Receptors in HIV-1 Transgenic Rat seen with [18F]Fallypride-PET

Dianne E. Lee[1], *William Reid*[1], *Wael G. Ibrahim*[1], *Kristin L. Peterson*[1], *Margaret R. Lentz*[1], *Elaine Jagoda*[2], *Peter Choyke*[2], *Dima A. Hammoud*[1], [1]*Center for Infectious Disease Imaging, Radiology and Imaging Sciences, National Institutes of Health,Clinical Center, Bethesda, MD, USA;* [2]*Molecular Imaging Program, National Institutes of Health,NCI, Bethesda, MD, USA. Contact e-mail: dianne.lee@nih.gov*

INTRODUCTION: HIV-Associated Neurocognitive Disorders (HAND) encompass a spectrum of behavioral and cognitive deficits that occur long after the HIV virus gains entry into the brain. HIV-related neurotoxicity is probably multifactorial, however the end result of neuronal death is evident both in infected humans and SIV-infected monkeys. The dopaminergic system seems to be particularly sensitive to HIV associated damage. Previous PET imaging studies showed decreased dopamine transporter protein (DAT) in the basal ganglia of HIV+ subjects that correlated with higher plasma viral load and dementia (Wang et al., 2004). Here, we further investigated the selective vulnerability of basal ganglia dopaminergic neurons using the transgenic HIV+ rat. The goal of this work was to quantify dopamine D2/3 receptors in the HIV-1 Tg rat brain, using [18F]Fallypride-PET. METHODS: HIV-1 Tg rats (n=5; age=462 ± 3.6 days) and F344 controls (n=5; 465 ± 7.6 days) were imaged for 90 min on the Bio PET/CT tomograph (Bioscan, Inc.) under ~ 2.5% isoflurane anesthesia after the administration of [18F]Fallypride (mean= 1.2 mCi/scan, SA > 1.8 Ci/μmol) via a lateral tail vein catheter. Dynamic images were reconstructed using OSEM-2D algorithm with scatter correction. Regional [18F]Fallypride uptake was quantified as binding potential BPND using the 2T Reference Model (Watabe et al., 2000) with cerebellum as reference. Time activity curves were generated for volumes of interest (VOI) that were drawn manually in the ventral striatum(VS) , dorsal striatum (DS), thalamus (Th), and cerebellum guided by an anatomical atlas of the rodent brain (Paxinos and Watson, 1998). The kinetic analyses were performed using PMOD 3.4 kinetic modeling tool (PMOD Technologies Ltd., Zurich, Switzerland). RESULTS: The animals' age, dose and mass/dose were not significantly different between the two groups of animals. The mean body weights of the HIV-1 Tg (388 ± 30 g) were significantly lower ($p < 0.01$) compared to control rats (494 ± 30 g). The HIV-1 Tg brain [18F]Fallypride BPND values were significantly decreased in the VS (36 %, $p < 0.001$) and in the DS (33 %, $p = 0.001$), but not in the Th ($p = 0.78$) of Tg rats compared to control rats. We found little variability in our measurements using test-retest imaging on one control animal. CONCLUSION: Consistent with basal ganglia pathology in HIV patients, our findings indicate striatal but not extrastriatal D2/3 receptor deficits in HIV-1 Tg rats. Our study demonstrates HIV-1 Tg rat as a useful animal model to probe the neuronal mechanisms underlying dopaminergic dysfunction in HIV infected subjects. Further evaluation of our findings as a function of viral protein levels in the CSF and serum, and in correlation with volumetric MR measurements of the striatal structures will probably shed more light on the underlying pathology of dopaminergic dysfunction in this animal model of HIV.

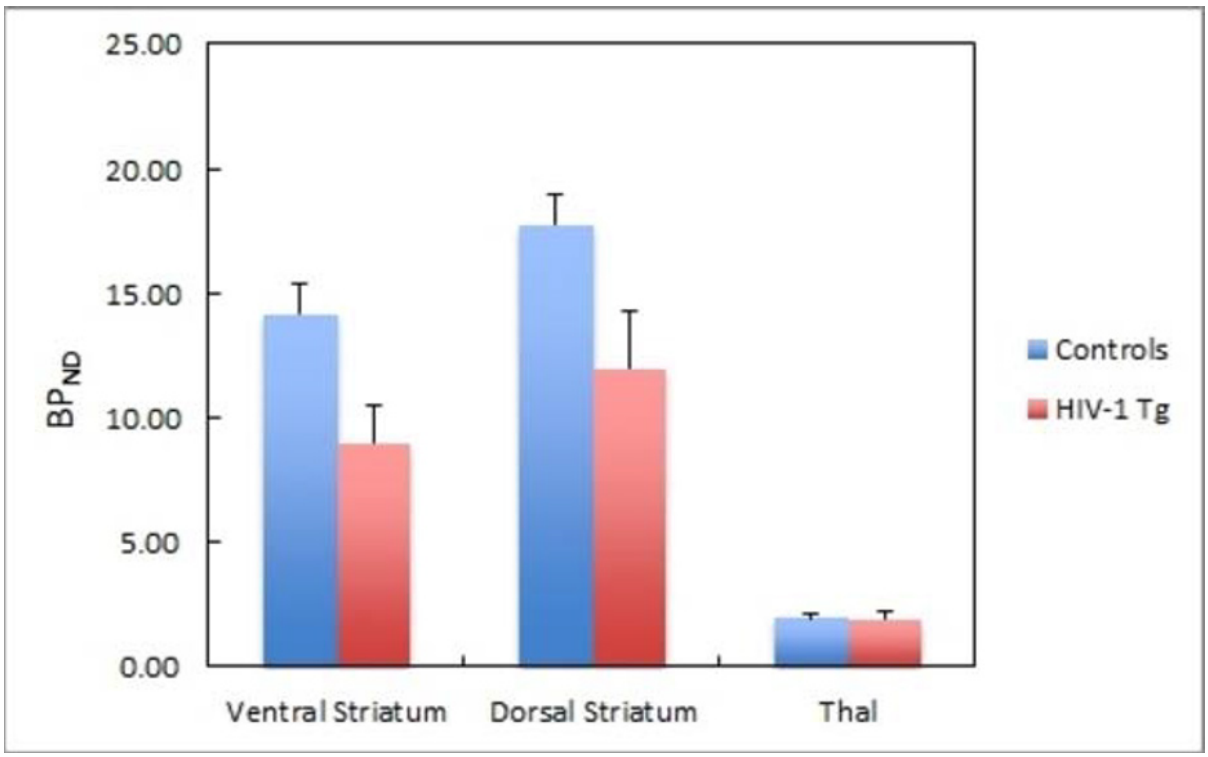

Disclosure of author financial interest or relationships:
D.E. Lee, None; **W. Reid**, None; **W.G. Ibrahim**, None; **K.L. Peterson**, None; **M.R. Lentz**, None; **E. Jagoda**, None; **P. Choyke**, None; **D.A. Hammoud**, None.

Presentation Number **LBAP 089**
Late Breaking Abstract Poster Session
September 19, 2013 / 15:15-15:15 / Room: Exhibit Hall B

PET imaging of neuroinflammation in rat TBI model with a radio-labeled TSPO ligand DPA-714

Yu Wang[2,1], *Xuyi Yue*[1], *Gao-Jun Teng*[2], *Gang Niu*[1], *Xiaoyuan Chen*[1], [1]*NIBIB, NIH, Bethesda, MD, USA;* [2]*Jiangsu Key Laboratory of Molecular and Functional Imaging, Department of Radiology, Zhongda Hospital, Medical School of Southeast University, Nanjing, China. Contact e-mail: yu.wang3@nih.gov*

Background and aims: Traumatic brain injury (TBI) can result in temporal or long-term, even lifelong physical, cognitive, behavioral problems. Inflammatory response in injured brain parenchyma after TBI is crucial to its pathologic process. In order to follow the microglia activation and neuroinflammation after TBI, herein, we performed PET imaging in a rat TBI model using 18F-labeled DPA-714, a ligand of 18 KDa translocator protein (TSPO). Materials and methods: TBI was induced in male SD rats by controlled cortical impact (CCI). The success of the TBI model was confirmed by MRI. Automated synthesis of [18F]DPA-714 was carried out using a slightly modified TRACERLab FX-FN module. In vivo PET imaging was performed at different time points after surgery by an Inveon small animal PET scanner. The specificity of PET imaging was confirmed by displacement study with an unlabeled competitive TSPO ligand, PK11195. Ex vivo autoradiography as well as immunofluorescence staining was carried out to confirm the in vivo PET results. Results: In vivo T2 weighted MR image and ex vivo TTC staining revealed successful establishment of the TBI model. Compared with the sham group, [18F]DPA-714 uptake was significantly higher in the injury brain area on PET images. Increased ipsilateral-to-contralateral ratio of [18F]DPA-714 in rat brain with TBI was observed at day 2 after surgery. The peak of ratio appeared at around day 6 and then decreased gradually to normal level at day 28. Displacement study using PK11195 confirmed the specific binding of [18F]DPA-714 to TSPO. Ex vivo autoradiography was consistent with in vivo PET imaging. The immunofluorescence staining showed the temporal and spatial distribution of microglia and astrocyte in damaged brain area. Conclusion: TSPO targeted PET using [18F]DPA-714 as the imaging probe can be used to dynamically monitor inflammatory response after TBI. The non-invasive imaging would be useful for better understanding the pathological outcome of the neuroinflammation and providing guidance for anti-inflammatory therapy for TBI.

Disclosure of author financial interest or relationships:
Y. Wang, None; **X. Yue**, None; **G. Teng**, None; **G. Niu**, None; **X. Chen**, None.

Presentation Number **LBAP 090**
Late Breaking Abstract Poster Session
September 19, 2013 / 15:15-15:15 / Room: Exhibit Hall B

[18F]-HSA PET imaging in a rat model of mild controlled cortical impact brain injury: A proof-of-principle study

Colin M. Wilson[1], *Shalini Jaiswal*[1,2], *Falguni Basuli*[3], *Sanjeev K. Mathur*[1], *Alexandru Korotcov*[1], *Asamoah Bosomtwi*[1], *Elizabeth A. Broussard*[1], *Scott Jones*[1,2], *Olga Vasalatiy*[3], *Gary L. Griffiths*[3], *Peter Choyke*[4], *Reed G. Selwyn*[1,2], [1]*Translational Imaging Facility, Center for Neuroscience and Regenerative Medicine, Uniformed Services University of the Health Sciences, Bethesda, MD, USA;* [2]*Radiology and Radiological Sciences, Uniformed Services University of the Health Sciences, Bethesda, MD, USA;* [3]*Imaging Probe Development Center, National Heart, Lung, and Blood Institute, National Institutes of Health, Rockville, MD, USA;* [4]*Molecular Imaging Program, National Cancer Institute, National Institutes of Health, Bethesda, MD, USA. Contact e-mail: colin.wilson.ctr@usuhs.edu*

Objectives: Our goal was to conduct a proof-of-principle study to evaluate blood-brain-barrier (BBB) disruption and changes in blood volume using small animal positron emission tomography (PET) imaging and 18F-labeled human serum albumin ([18F]-HSA), a novel blood pool radiotracer, in a rat model of mild controlled cortical impact (CCI) brain injury. Methods: A mild brain injury was initiated with a 5 mm craniotomy over the left motor cortex followed by a CCI with a 4 mm impactor, 5 m/s impact speed, 200 msec dwell time, and 1.5 mm piston depth. Human serum albumin (HSA) was radiolabeled with 18F via coupling to a [18F]fluoronicotinic acid tetrafluorophenyl ester in moderate radiochemical yield. Male rats (SD, 6-8 wks) were anesthetized with 2% isoflurane and injected intravenously with 37-74 MBq (1-2 mCi) of [18F]-HSA approximately 25 minutes prior to scanning. Under anesthesia, serial [18F]-HSA PET scans were acquired for 30 min with a Siemens Inveon microPET/CT at baseline and at days 1, 3, 7, 14 and 21 post-injury (N=3). Scatter and attenuation-corrected sinograms were reconstructed as a single high-resolution static frame using a 3D-OSEM algorithm. Results: Static PET/CT images demonstrate high vascular contrast, allowing visualization of blood vessels with no observed defluorination. PET images at days 1 and 3 post injury show clear enhancement at the level of the dura mater rostral and caudal to the lesion site. In addition, the Circle of Willis shows increased activity, apparent blood volume, on the ipsilateral side at day 3 when compared to the contralateral side. Also, no apparent [18F]-HSA distribution was observed in brain parenchyma, indicating minimal diffusion of serum proteins throughout the brain extracellular space within the imaging time frame (50 minutes). This finding is consistent with previous studies of BBB disruption and brain injury in rats, which show albumin confined to perivascular regions at 2 hours post contrast injection and a bi-phasic opening of the BBB at 4-6 hours and 3 days post CCI injury. Conclusions: [18F]-HSA shows promise as a sensitive blood pool agent for PET imaging of BBB disruption and small changes in blood volume following mild brain injury. Additional studies are needed to evaluate this novel radiotracer as a quantitative imaging probe, including dynamic PET imaging at earlier time points post injury. Research Support: This work was supported by the Center for Neuroscience and Regenerative Medicine, the National Institutes of Health, Molecular Imaging Program, and the intramural program of NIH.

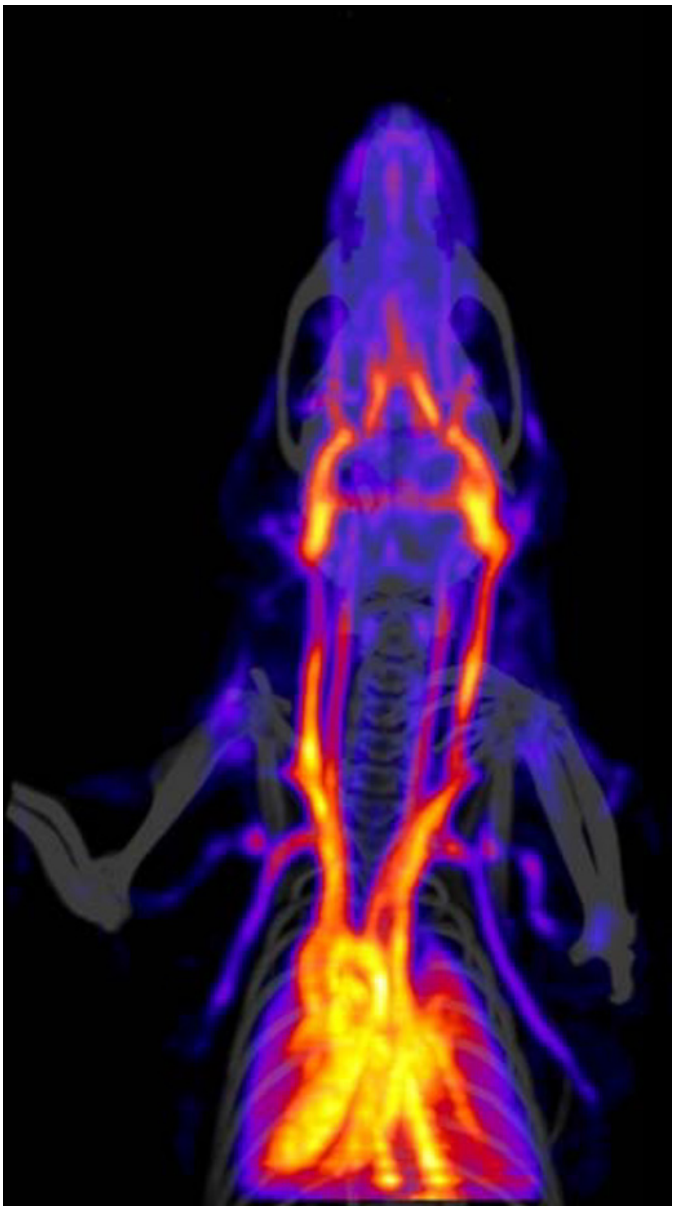

In vivo maximum intensity projection [18F]-HSA PET/CT image of a rat following a mild controlled cortical impact (CCI) brain injury.

Disclosure of author financial interest or relationships:

C.M. Wilson, None; **S. Jaiswal**, None; **F. Basuli**, None; **S.K. Mathur**, None; **A. Korotcov**, None; **A. Bosomtwi**, None; **E.A. Broussard**, None; **S. Jones**, None; **O. Vasalatiy**, None; **G.L. Griffiths**, None; **P. Choyke**, None; **R.G. Selwyn**, None.

Presentation Number **LBAP 091**
Late Breaking Abstract Poster Session
September 19, 2013 / 15:15-15:15 / Room: Exhibit Hall B

The need for in vivo experiments to investigate possible chaperone effects of pharmacological compounds

Nick Van Laeken[1], *Kathleen Van Craenenbroeck*[3], *Jeroen Verhoeven*[1], *Christian Vanhove*[2], *Filip J. De Vos*[1], [1]*Laboratory of Radiopharmacy, Ghent University, Ghent, Belgium;* [2]*INFINITY, Ghent University, Ghent, Belgium;* [3]*Laboratory of Eukaryotic Gene Expression and Signal Transduction, Ghent University, Ghent, Belgium. Contact e-mail: nick.vanlaeken@Ugent.be*

Introduction: The last decade several research groups have investigated variations in receptor expression after administration of pharmacological chaperones. As such in vitro studies using the dopamine D2-like receptor agonist quinpirole resulted in an increased dopamine D2 and D4 receptor expression which was not caused by an increased transcription or translation of receptor genes. The underlying theory is that pharmacological chaperones like quinpirole stabilize the folding of newly synthetized receptors in the endoplasmic reticulum. This results into a more quickly correct folding of the receptor and a reduced receptor degradation by the ubiquitine proteasome pathway [1]. Unambiguous data concerning the in vivo correlation of these findings are however missing. Materials and methods: An initial PET experiment was set up in male Wistar rats (N=4, 330-375g) using the dopamine D2 receptor antagonist radiotracer [11C]raclopride. Two PET scans were acquired from each rat: at baseline and 48 hours after i.p. administration of 2 mg/kg quinpirole. The PET scans were performed with an GE Triumph II scanner and were based on a 60 min dynamic acquisition starting with a bolus injection of mean 25 MBq (range 20 - 29 MBq) [11C]raclopride given over 10 seconds in the isoflurane anaesthetized rats. The acquisition consisted of 28 time frames, increasing progressively in duration from 5 s to 5 min. In each case, an additional CT-scan was taken for anatomical correlation. All data were analyzed using the Pmod software version 3.405 (PMOD Technologies). After coregistering the PET/CT data to the Rat_W.Schiffer-masked user template, the Rat W.Schiffer atlas was added to the PET data. [11C]raclopride binding potentials (BPND) in the striatum were calculated via the Simplified Reference Tissue Model (SRTM) using the cerebellum as reference region. Results and discussion: Since several in vitro experiments indicate that the administration of pharmacological chaperones results in an increased receptor expression we expected a higher BPND in the post quinpirole scan compared with the baseline scan. However, each rat showed a decrease in BPND after quinpirole administration which was on average 20.2 ± 13.8%. These preliminary findings do not confirm the in vitro data although we have to take into account other processes which can mask the chaperone effects such as: 1) agonist-mediated receptor internalization, 2) agonist-medicated effects on receptor transcription and 3) dopamine release which can compete with [11C]raclopride. Conclusion: Despite the high number of articles published on in vitro chaperone effects, our preliminary results using the pharmacological chaperone quinpirole and the [11C]raclopride PET-radiotracer show a 20.2 ± 13.8 % decrease in BPND instead of an increase. In vivo studies to investigate additional pharmacological mechanisms such as receptor internalization are of high value before an adequate estimation about the clinical consequences of these chaperone effects can be provided.

Disclosure of author financial interest or relationships:
N. Van Laeken, None; **K. Van Craenenbroeck**, None; **J. Verhoeven**, None; **C. Vanhove**, None; **F.J. De Vos**, None.

Presentation Number **LBAP 092**
Late Breaking Abstract Poster Session
September 19, 2013 / 15:15-15:15 / Room: Exhibit Hall B

Preliminary Assessment of Estrogen Receptor in the Female Rat Brain by 16α-Fluoroestradiol PET Imaging

Michel Paquette[1], *Hiba Cherifi*[2], *Jacques A. Rousseau*[1], *Otman Sarrhini*[1], *Rene Ouellet*[1], *Roger Lecomte*[1], [1]*Nuclear medicine and radiobiology, Université de Sherbrooke, Sherbrooke, QC, Canada;* [2]*UFR Biomédicale, Université Paris Descartes, Paris, France. Contact e-mail: michel.paquette@usherbrooke.ca*

There is indication that the estrogen decline during and after menopause have an effect on concentration and memory suggesting a relationship between cognition and physiological estrogen stimulation. Hence, follow-up of the estrogen receptor (ER) in the brain of an adequate animal model would be of great interest to investigate the fundamental relationship between ER expression, aging and cognition. Previous autoradiography studies showed that many areas in the rat brain either have a high ER expression or a high [^{3}H]-estradiol uptake. In a pilot study, two groups of Sprague-Dawley female rats, one untreated (control; n=3) and the other ovariectomized one week before beginning the experiment to mimic menopause (OVX; n=3), were followed by PET imaging for the brain uptake of 16α-[^{18}F]-fluoroestradiol (FES). Initial rat weight was 225-250 g. Animals were imaged on a regular basis for 5 weeks up to now and will continue to be imaged for long-term monitoring. For each scan, a 30-minute static PET image with the rat head in the center of the scanner field-of-view was acquired 60 minutes following injection of 20-25 MBq FES. The images were reconstructed using 20 MLEM iterations. Following half of the PET scans, a CT image was obtained to gain anatomical information. The control group was also imaged once using MRI at day 17 to better identify the location of PET signals in the rat brain. PET data were converted into percent injected dose per gram of tissue (%ID/g) using the scanner calibration factor. Only one region (a bifocal signal at the base of the brain) was clearly visible in the FES PET images. PET/CT and PET/MRI fusion images allowed identification of the signal as being the hypothalamus (likely the preoptic area). Uptake of this area was higher in OVX rats than in control rats for the first 3 weeks of the follow-up ($p<0.05$ for the first and third week, $p<0.005$ for the second week). Acute co-injection of 100 µg estradiol along with FES in control rats reduced the uptake of this area substantially, indicating that the uptake is ER-specific. Follow-up of the control group up to 5 weeks showed a gradual FES uptake increase in this area, with the 5-week uptake being significantly higher ($p<0.05$) than in the first week. Although preliminary, this study already shows intriguing results regarding ER expression in the female rat brain as a function of time. Based on these initial observations, further follow-up of brain ER expression on a long-term schedule has the potential to confirm the link between aging and receptor expression.

Disclosure of author financial interest or relationships:
M. Paquette, None; **H. Cherifi**, None; **J.A. Rousseau**, None; **O. Sarrhini**, None; **R. Ouellet**, None; **R. Lecomte**, None.

Presentation Number **LBAP 093**
Late Breaking Abstract Poster Session
September 19, 2013 / 15:15-15:15 / Room: Exhibit Hall B

Functional MRI in the early detection of Parkinson's disease

Chiao-Chi V. Chen, Yi-Hua Hsu, **Chen Chang***, Institute of Biomedical Sciences, Academia Sinica, Taipei, Taiwan. Contact e-mail: bmcchen@ibms.sinica.edu.tw*

Nonmotor manifestations in Parkinson's disease (PD) generally antedate the clinically diagnosed motor dysfunctions. Early detection of PD may be achieved if the prodromal nonmotor changes specific to PD can be characterized early. To test this hypothesis, the present study examined the utility of a recently proposed MRI technique as an early detection tool for it allows the characterization of a nonmotor symptom in PD(1, 2). Nociception is a sensory disturbance that is present in as many as 83% of PD patients. Using cerebral blood volume (CBV) weighted functional MRI (fMRI), nociception has been characterized as striatal CBV changes with specificity for dopaminergic dysfunction. The present study evaluated the nonmotor signals detected by CBV-weighted fMRI in the early and symptomatic stage of PD and compared those signals with the motor dysfunctions. A rat PD model induced by 6-hydroxydopamine in the unilateral substantia nigra was employed. While nonmotor manifestation was evaluated by the abovementioned fMRI technique, motor dysfunction was assessed by meth-amphetamine induced rotation behaviors. In this rat model, parkinsonism is conventionally defined by rotation more than 360 turns per hour. Parkinsonism generally occurs at two weeks after the model induction. The results showed that, at one week after the model induction, the averaged rotation of the rats were 174 ± 63 turns per hour (mean ± standard deviation). None of the rats exhibited motor abnormalities that reached the criterion of being parkinsonism. However, interestingly, these rats exhibited diminished CBV responses in the lesioned striatum with intact reactions in the unlesioned side. At two weeks after the model induction, the averaged rotation reached up to 1206 ± 316 turns per hour, indicating the presence of the motor dysfunction in these rats. In the meantime, the nonmotor changes identified as CBV alterations remained observable, with a level comparable to that of the previous time point. Tyrosine hydroxylase immunohistology confirmed that the striatal denervation and substantia nigra cell loss occurred as early as one week after the model induction, although the motor test did not indicate the lesion yet. At two weeks, the dopaminergic system showed more severe damage, while the motor dysfunction was finally observed. The results altogether indicate that the nonmotor signs revealed by fMRI antedate the motor aberrations in the rat PD model. The nonmotor abnormalities may be attributed to the lesion in the dopaminergic system to a degree where the motor aberration is yet detectable. 1. Shih YY, et al. (2009) The Journal of neuroscience. 29(10):3036-3044. 2. Chen CC, Shih YY, & Chang C (2012). Neurobiology of disease. 49C:99-106.

Disclosure of author financial interest or relationships:
C.V. Chen, None; **Y. Hsu**, None; **C. Chang**, None.

Presentation Number **LBAP 094**
Late Breaking Abstract Poster Session
September 19, 2013 / 15:15-15:15 / Room: Exhibit Hall B

Functional imaging of individual cells in deep brain regions of free-moving mice

Jesus Pascual-Brazo[1], Sarah Libbrecht[1], **Hedi Gharbi**[3]*, Chris Van den Haute[1], Zeger Debyser[2], Veerle Baekelandt[1], [1]Laboratory of Neurobiology and Gene Therapy. Department of Neurosciences, KU Leuven, Leuven, Belgium; [2]Laboratory for Molecular Virology and Gene Therapy. Department of Pharmaceutical and Pharmacological Sciences, KU Leuven, Leuven, Belgium; [3]Preclinical Research Division, MaunaKea Technologies, Paris, Belgium. Contact e-mail: hedi@maunakeatech.com*

Probe-based Confocal Laser Endomicroscopy (pCLE) uses thousands of fiber optics to transport excitation light to the tissue and emission light from the tissue. The Cellvizio® system allows to obtain images with high spatial (3 µm) and temporal (5 ms) resolution, filling the gap between traditional neuroimaging techniques and 2-photon microscopy. Recent effort in protein engineering has given rise to sensitive genetically encoded calcium indicators (GECIs) and redox sensitive GFP variants, being now comparable to calcium sensitive dyes. We employed viral vectors encoding GCaMPs or roGFP to obtain functional information from individual cells in deep brain regions of free-moving mice (hippocampus, striatum and olfactory bulb). After stereotactic injection and reporter gene expression, in vivo calcium or redox imaging was performed and the images were acquired and analyzed with the Cellvizio® microscope. In conclusion, the combination of viral vector technology with this new in vivo optical technique allows us to perform functional imaging of individual cells in the brain of free-moving animals. This work has been supported by IWT-SBO/060838 Brainstim, SCIL programme financing PF/10/019 and IWT-O&O JANSSEN-DEPVEGF projects.

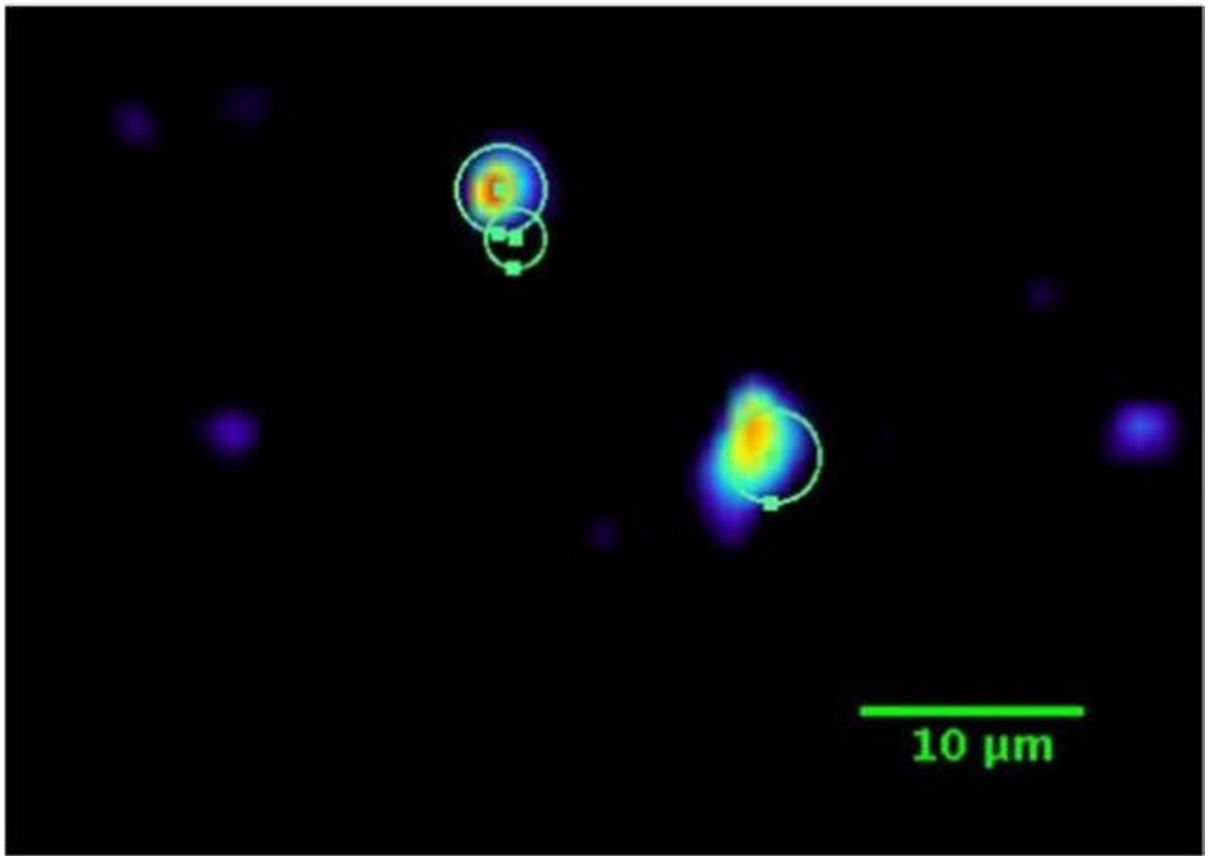

Disclosure of author financial interest or relationships:
J. Pascual-Brazo, MaunaKea Technologies, Grant/research support; **S. Libbrecht**, None; **H. Gharbi**, None; **C. Van den Haute**, None; **Z. Debyser**, None; **V. Baekelandt**, None.

Presentation Number **LBAP 095**
Late Breaking Abstract Poster Session
September 19, 2013 / 15:15-15:15 / Room: Exhibit Hall B

Response of C6 Glioma to Anti-Angiogenesis Treatment Measured by Metabolic Imaging of Hyperpolarized [1-13C]Pyruvate

Jae Mo Park[1], *Sonal Josan*[1,2], *Taichang Jang*[3], *Milton Merchant*[3], *Ralph E. Hurd*[4], *Dirk Mayer*[1,2], *Daniel M. Spielman*[1], *Lawrence Recht*[3], [1]*Radiology, Stanford University, Stanford, CA, USA;* [2]*Neuroscience Program, SRI International, Menlo Park, CA, USA;* [3]*Neurology and Neurological Sciences, Stanford University, Stanford, CA, USA;* [4]*Applied Science Lab, GE Healthcare, Menlo Park, CA, USA. Contact e-mail: jaemo@stanford.edu*

Introduction: Administration of the anti-VEGF drug bevacizumab (Avastin®) to GBM patients frequently produces a dramatic, temporary imaging response that is considered primarily due to changes in permeability rather than an anti-tumor effect1. We hypothesize that, in addition to this action, this agent also acutely and temporarily forces increased oxidative phosphorylation (OXPHOS) in glioma tissue due to nutrient depletion, increasing tumor vulnerability. To address this, flux through both the glycolytic and OXPHOS pathways must be measured in vivo. Using an optimized 13C MRSI pulse sequence, we were able to reproducibly image 13C-bicarbonate (Bic) in addition to 13C-lactate (Lac) labeling using hyperpolarized [1-13C]pyruvate (Pyr) in tumor-bearing rats, reflecting OXPHOS and glycolysis, respectively. Methods: An anti-VEGF mab B20.4.1.1 (Genentech) that binds rodent in addition to human VEGF was used as an anti-angiogenesis drug. Approximately 106 C6-glioma cells were implanted in the right striatum of male Wistar rats 10 days prior to imaging. Each animal was anesthetized and placed in a clinical 3T GE MR scanner. Hyperpolarized [1-13C]Pyr (125 mM) was injected into three groups of rats through a tail vein catheter: baseline (n=15, 220-284g) and 3h (n=8, 212-244g), and 24h (n=6, 203-229g) after a single injection of B20 (5mg/kg). Two of the rats were imaged both for baseline and 3h-post treatment. A 2D spiral chemical shift imaging sequence (4 spatial interleaves, spectral bandwidth=932.8Hz, variable flip angle leading up to 90o, in-plane resolution=2.7x2.7mm2, slice thickness=6-8mm) and a 13C/1H dual-tuned quadrature RF coil (Ø=50mm) were used for data acquisitions2. Metabolite ratios relative to total carbon (tC) signals were reported for assessment of the treatment response in glioma and normal ROIs. Results & Discussion: Bic increased from 0.011±0.004 to 0.038±0.003 at 3h-post B20 (P=0.01), and slightly decreased back to 0.032±0.005 at 24h post-B20 in tumor. On the other hand, Lac in glioma, which was 0.39±0.02 (mean±se) at baseline, showed a trend to lower levels at both 3h- (0.32±0.02) and 24h post B20 (0.33±0.03). Therefore, Lac/Bic, which reflects the balance between glycolysis and OXPHOS, decreased from 22.3±2.5 at baseline to 8.74±0.7 (3h, P=0.002), but increased back to 11.7±2.1 (24h). Neither Bic nor Lac levels were altered in normal-appearing brain on the contralateral-side (Lac/Bic: 5.98±0.31 (baseline), 5.66±0.87 (3h), 6.50±0.66 (24h)). These findings are consistent with the contention that sequestering VEGF is associated with a transient period of increased OXPHOS in glioma tissue. Conclusion: At 3h post B20, Bic levels were higher and Lac/Bic ratios were lower than those obtained at 24h, providing evidence for "forced" OXPHOS. The increased Lac/Bic at 24h relatve to 3h suggests this might be a temporary phenomenon. We suggest that real time Bic measurements may provide both a useful biomarker for anti-angiogenic therapies and a potentially exploitable therapeutic strategy. Reference: 1. Von Baumgarten LD, et al., Clin Canc Res, 2011, 2. Park JM, et al., Neuro Oncol, 2013

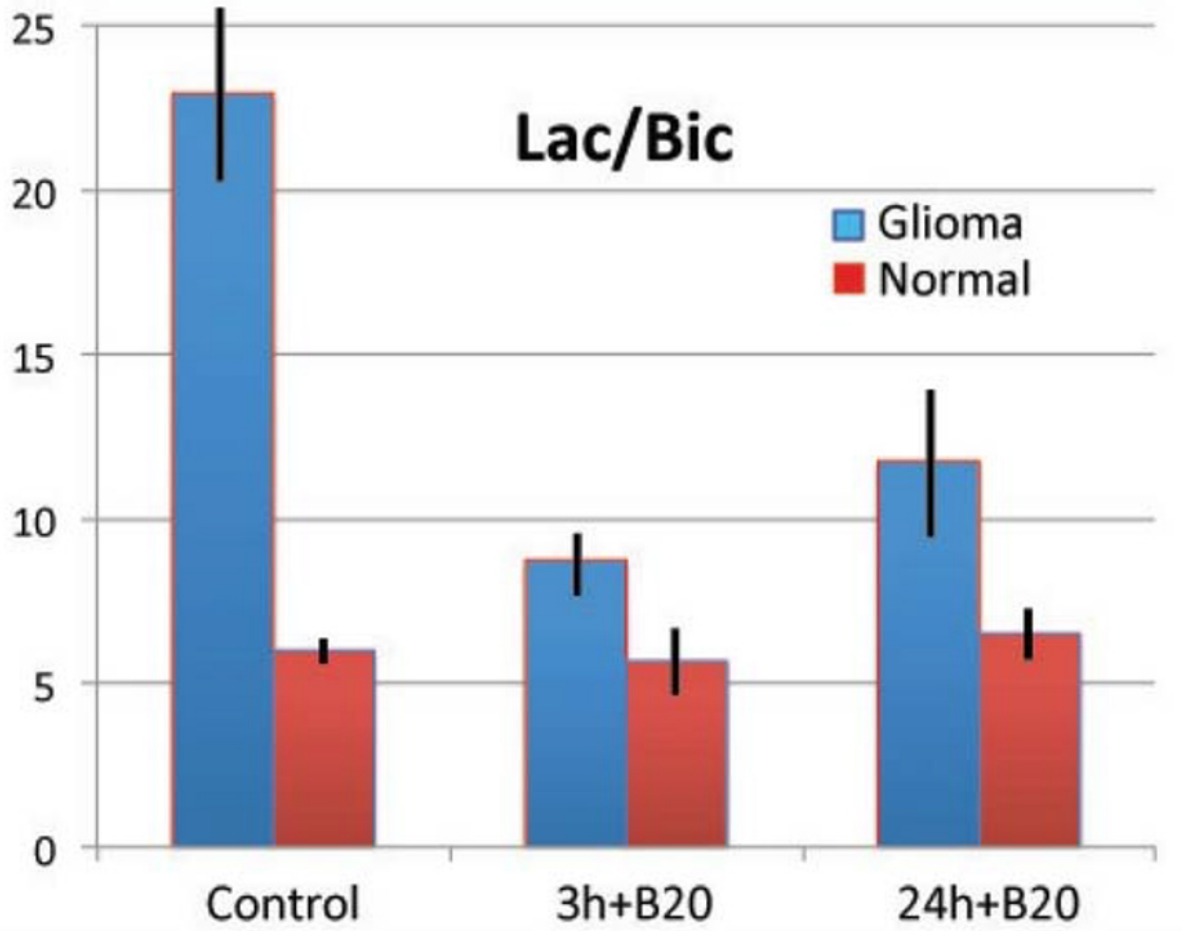

Lactate-to-bicarbonate ratios from glioma and normal-appearing brain after injection of hyperpolarized [1-13C]pyruvate. The metabolite ratio was higher in glioma (blue) than normal brain (red) at baseline, and the ratio decreased in glioma 3h-post anti-VEGF (B20) treatment, and slight increased back 24h after the treatment whereas normal brain was not significantly affected by the treatment.

Disclosure of author financial interest or relationships:
J. Park, None; **S. Josan**, None; **T. Jang**, None; **M. Merchant**, None; **R.E. Hurd**, GE Healthcare, Employment; **D. Mayer**, None; **D.M. Spielman**, None; **L. Recht**, None.

Presentation Number **LBAP 096**
Late Breaking Abstract Poster Session
September 19, 2013 / 15:15-15:15 / Room: Exhibit Hall B

Imaging The Degradome Associated With Breast Cancer Metastasis

Asif Rizwan[1], *Alexandra Payne*[3], *Menglin Cheng*[1], *Tiffany R. Greenwood*[1], *Lu Jiang*[1], *Balaji Krishnamachary*[1], *Zaver M. Bhujwalla*[1,2], *Kristine Glunde*[1,2], [1]*Radiology and Radiological Science, The Johns Hopkins University School of Medicine, Baltimore, MD, USA;* [2]*The Sidney Kimmel Comprehensive Cancer Center, The Johns Hopkins University School of Medicine, Baltimore, MD, USA;* [3]*School of Science and Engineering, Tulane University, New Orleans, LA, USA. Contact e-mail: arizwan2@jhmi.edu*

The cancer degradome is defined as the complex set of proteolytic enzymes expressed by tumors to degrade the extracellular matrix [1]. Tumor invasion and metastasis are closely associated with the activities of the degradome, which consist of protease families such as lysosomal cathepsins and matrix metalloproteases (MMPs) [2-6]. The aim of this work is to study and compare the expression and activities of these enzymes in metastatic and non-metastatic tumors. We have compared two non-metastatic human breast cancer cell lines (BT-474, T47D) to two metastatic human breast cancer cell lines (MDA-MB-231, SUM-149) (Fig A). These cell lines were genetically engineered to constitutively express tdTomato fluorescent protein to optically track the formation of spontaneous metastases from orthotopic xenograft models in athymic nude female mice (Figs B & C). Metastatic cell displayed significantly faster growth rates as compared to non-metastatic cells lines (Figure D). Metastatic cell lines displayed strong adhesion for matrigel or collagen-1 coated surfaces (Fig E). Non-metastatic BT-474 cells showed a significantly lower adhesion for matrigel or collagen-1. Although T47D cells demonstrated very weak adhesion for matrigel, it showed stronger binding with collagen-1 surfaces (Fig E). Metastatic cell lines exhibited stronger colony formation capabilities compared to non-metastatic cell lines as seen by clonogenic assay. The migratory response of cells was assessed with transwell migration and invasion assays. Both MDA-MB-231 and SUM-149 cells displayed strong migration and invasion capabilities when compared to non-metastatic BT-474 and T47D cells (Fig F). Gelatin zymography was employed to detect the activities of metalloproteinases, collagenases, and other proteases expressed in the culture medium after 24 hours of incubation without serum. Metastatic cell lines demonstrated an increased activity of MMPs compared to non-metastatic cell lines (Fig G). In vivo Optical imaging of tdTomato fluorescent protein in tumor bearing mice was performed on a Xenogen IVIS 200 Spectrum system. The enzymatically activatable near-infrared fluorescent (NIRF) probes MMPSense (activated by key matrix metalloproteinases), and Cathepsin K (activated by Cathepsin K) were employed to study enzyme activities in vivo. Imaging of angiogenesis was done by NIRF angiosense probe to account for uneven delivery of NIRF probes to tumor. Following whole-body in vivo NIRF tracking, animals were sacrificed and tumor xenografts, lungs, and lymph nodes were excised for ex vivo fluorescence microscopy. Our preliminary results showed increased enzyme activities in the metastatic tumors and metastatic nodules (Figs H and I). Further experiments are underway to study the collagen-1 fiber remodeling in the tumor models by second harmonic generation (SHG) microscopic imaging. References: 1. Edwards D, et al., Springer; 2008 2. Skrzydlewska E, et al., W J Gastroenterol 2005 3. Song F, et al., Front Biosci 2006 4. Zheng WQ, et al., Tumori 2002 5. Guinec N, et al., BCHS 1993 6. Riddick AC, et al., BJC 2005 This work was supported by NIH CA154725.

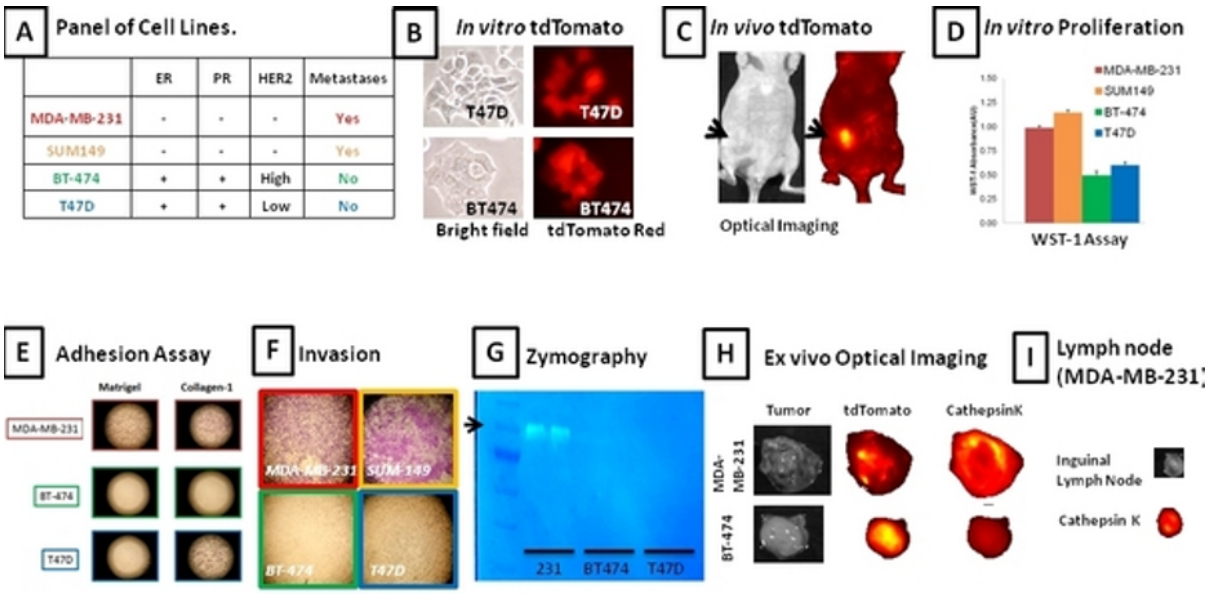

Disclosure of author financial interest or relationships:
A. Rizwan, None; **A. Payne**, None; **M. Cheng**, None; **T.R. Greenwood**, None; **L. Jiang**, None; **B. Krishnamachary**, None; **Z.M. Bhujwalla**, None; **K. Glunde**, None.

Presentation Number **LBAP 097**
Late Breaking Abstract Poster Session
September 19, 2013 / 15:15-15:15 / Room: Exhibit Hall B

Preclinical MRI Reveals Anti-VEGF Therapy Mitigates Radiation Necrosis

Xiaoyu Jiang[1], Liya Yuan[4], Joel R. Garbow[2], **Joseph J. Ackerman**[1,2]*, Robert E. Drzymala[3,4], Dinesh Thotala[3], Dennis E. Hallahan[3], Keith M. Rich[3,4], John A. Engelbach[2], [1]chemistry, Washington University in St. louis, st louis, MO, USA; [2]radiology, Washington University in St. louis, st louis, MO, USA; [3]radiation oncology, Washington University in St. louis, st louis, MO, USA; [4]neurosurgery, Washington University in St. louis, st louis, MO, USA. Contact e-mail: ackerman@wustl.edu*

Purpose: Radiation necrosis, a severe but late occurring injury to normal tissue within and surrounding a radiation treatment field, has been described as a slow, continuous process in which increased levels of VEGF-A lead to breakdown of the blood brain barrier [1]. Thus, a strategy that involves blocking VEGF-A from reaching capillaries and repairing "leaky" capillaries is a possible therapeutic approach for radiation necrosis. In this work, in concert with a novel mouse model of radiation necrosis [2], the therapeutic effects of the humanized anti-VEGF antibody bevacizumab (Avastin®, Genentech) and the murine anti-VEGF antibody B20-4.1.1 (Genentech) are monitored by magnetic resonance imaging. Methods: Hemispheric irradiation of mouse brain was performed with the Leksell Gamma Knife® PerfexionTM (GK), a state-of-the-art unit used for stereotactic irradiation of patients with malignant brain tumors. Three cohorts of 7-8 week old female mice (n=5) were irradiated with a single 60-Gy dose (50% isodose) of GK radiation. At this dose, the onset of radiation necrosis typically occurs 3-4 weeks post-irradiation. Mouse cohort #1 was an irradiated but untreated control; cohort #2 received bevacizumab (10 mg/kg, twice weekly) from 3-to-10 weeks post-irradiation; cohort #3 received B20-4.1.1 (10 mg/kg, twice weekly) from 4-to-13 weeks post-irradiation. Mice were imaged from 3-to-10 weeks post-irradiation, using an Agilent/Varian DirectDriveTM 4.7-T small-animal MR scanner. Results: The MRI-derived volumes of radiation necrosis for control, bevacizumab-treated, and B20-4.1.1-treated mice are plotted in Fig. 1 as a function of time post-irradiation. Both anti-VEGF antibodies slow the overall rate of progression ($p<0.0001$, week 10). Considering the initial 3-7 week period post-irradiation, bevacizumab has the same mitigative effect as B20-4.1.1 ($p = 0.8$, week 7). However, for the latter 3-week period (7-10 weeks post-irradiation), radiation-induced necrosis developed at a higher rate than in the B20-4.1.1-treated cohort ($p<0.0001$, week 10), indicating that the mitigative effect of bevacizumab was weaker than B20-4.1.1 in the late period following the initiation of treatment. Histology results support the MR data. The irradiated hemispheres of the control mice demonstrated many of the classic histologic features of radiation necrosis. In contrast, the irradiated hemisphere of the bevacizumab-treated mouse showed only modest tissue damage and the irradiated hemisphere of the B20-4.1.1-treated mouse displayed no visible tissue damage. Conclusion: Our data demonstrate a significant mitigative effect of bevacizumab and B20-4.1.1 in a mouse model of radiation necrosis, an effect also observed recently in a group of brain-tumor patients treated with bevacizumab [3]. Efforts to verify the mechanism of action of bevacizumab and B20-4.1.1 in the treatment of radiation necrosis in the mouse model are ongoing. References: (1) Siu A, et al. Acta Neurochirurgica 2012; 154(2): 191-201. (2) Jost SC, Hope A, et al. Int J Radiat Oncol Biol Phys 2009; 75: 527-33. (3) Levin V.A., et al. International Journal of Radiation Oncology Biology Physics 2011; 79(5): 1487-1495.

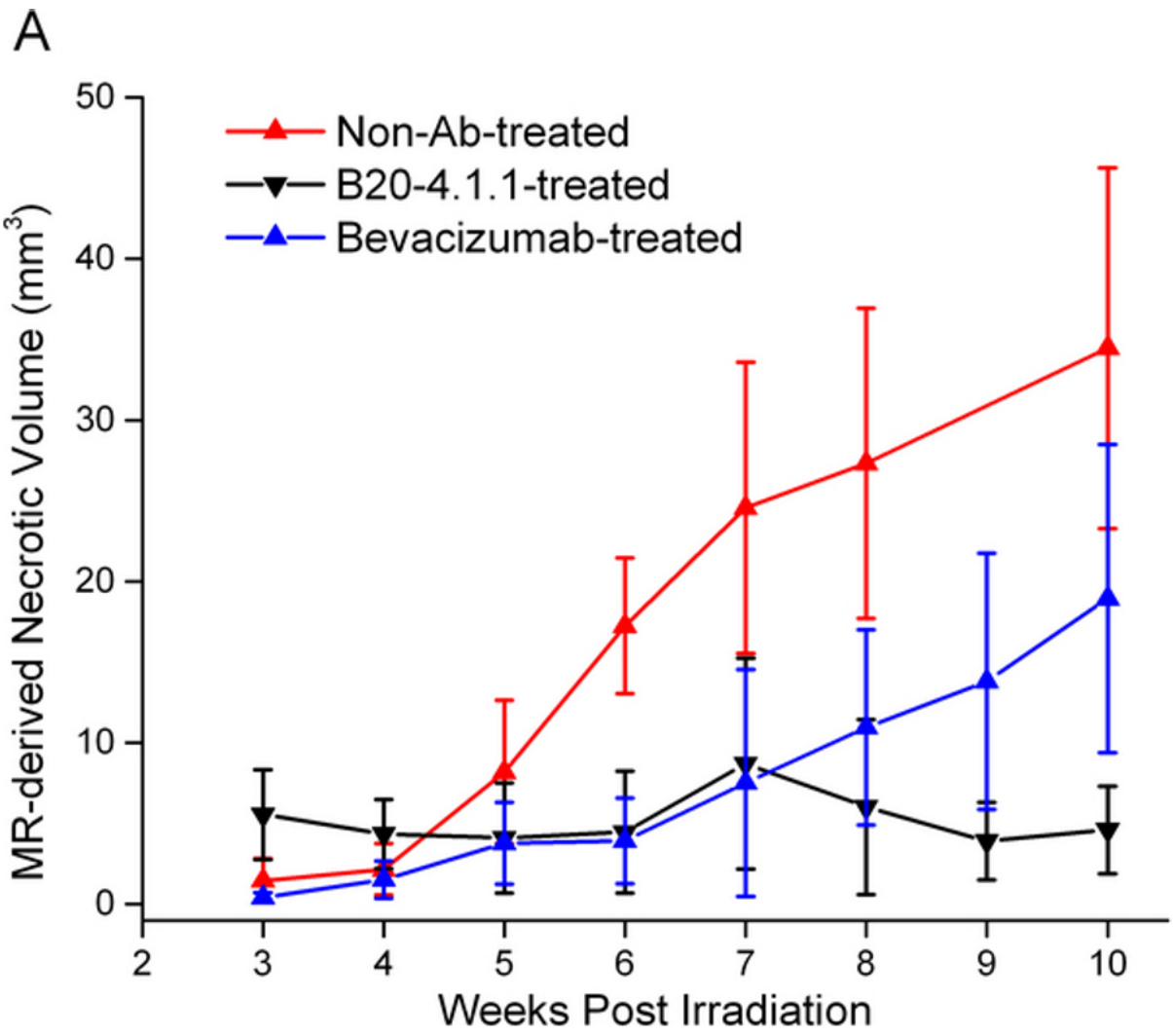

Disclosure of author financial interest or relationships:
X. Jiang, None; **L. Yuan**, None; **J.R. Garbow**, None; **J.J. Ackerman**, Agilent Technologies, Grant/research support; Sigma-Aldrich Company, Honoraria; Elsevier, Honoraria; Monsanto Company, Grant/research support; Agilent Technologies, Other financial or material support; **R.E. Drzymala**, None; **D. Thotala**, None; **D.E. Hallahan**, None; **K.M. Rich**, None; **J.A. Engelbach**, None.

Presentation Number **LBAP 098**
Late Breaking Abstract Poster Session
September 19, 2013 / 15:15-15:15 / Room: Exhibit Hall B

In Vivo Identification and Characterization of a Novel Targeted Peptide for Aggressive Breast Cancer Detection

Benjamin Larimer[1,2], *Thomas P. Quinn*[1,2], *Susan L. Deutscher*[1,2], [1]*Research, Harry S Truman Veterans Administration, Columbia, MO, USA;* [2]*Biochemistry, University of Missouri, Columbia, MO, USA. Contact e-mail: bmlyr4@mail.missouri.edu*

Molecular targeted breast cancer imaging agents offer distinct advantages over traditional detection methods such as mammography and physical exam. Vectors targeting cancer antigens consist mostly of antibodies, which present challenges due to their large size and immunogenicity. Peptides, which are small and non-immunogenic, may be ideal for a molecular imaging agent; however they are mainly comprised of natural ligands, thus limiting potential targets. Bacteriophage (phage) display is a combinatorial technique that provides a large (~109) population of potential ligands for selection with novel targets of interest. We hypothesized that phage display could be utilized in vivo to select for peptides targeting aggressive human breast cancer xenografts. This type of selection provides the benefits of selecting for peptides with favorable pharmacokinetics, as well as offering a method to select based on cancer phenotype, independent of a known target. Filamentous phage engineered to display 3-5 copies of a random 15 amino acid peptide were subjected to four rounds of in vivo selection against mice bearing BT-474 breast tumor xenografts. Individual clones were screened based on their ability to discriminate between BT-474 breast cancer and normal breast epithelial cells. The top clone (Clone 51) bound to tumor cells 18.4 times greater than control phage, and its corresponding peptide was synthesized for characterization (Fig 1). Fluorescent confocal microscopy revealed high affinity and specificity for BT-474 cells (Fig 2). These results were confirmed by flow cytometry analysis, as the peptide bound BT-474 cells with an apparent EC50 of 3.9 μM (Fig 3). Additionally, tumor targeting of the phage was confirmed in vivo by fluorescent- labeled phage imaging. At 6 hours post-injection, tumor uptake was clearly visible in nude mice bearing BT-474 tumors (Fig 4), and ex vivo analysis of tumor uptake revealed a total photon count/sec of 3.3x106, over 10 fold greater than non-targeted phage uptake in the same tumor model (Fig 5). The peptide was conjugated to the macrocyclic chelator 1,4,7,10-tetraazacyclododecane-1,4,7,10-tetraacetic acid (DOTA) for radiolabeling in order to translate the peptide to a more clinically relevant configuration. Following labeling with the SPECT imaging agent 111indium, the peptide was analyzed in vitro for retained BT-474 affinity and specificity. The peptide bound specifically to BT-474 cells, with an IC50 calculated at 16.1 nM (Fig 6). Based on these results, the radiolabeled peptide was injected into tumor bearing mice in order to ascertain its SPECT imaging capabilities. The results of this study highlight the use of phage display to develop a new candidate peptide for aggressive breast cancer. The targeted peptide is a two-tiered success. It provides a new targeted peptide for further development as a clinical imaging agent, and it can be used as a probe to determine the cancer-specific antigen to which it binds.

Disclosure of author financial interest or relationships:
B. Larimer, None; **T.P. Quinn**, None; **S.L. Deutscher**, None.

Presentation Number **LBAP 099**
Late Breaking Abstract Poster Session
September 19, 2013 / 15:15-15:15 / Room: Exhibit Hall B

Preclinical Evaluation of a Novel Vascular-Targeted Combination Strategy for Prostate Cancer

James Kalmuk[1], *Roberto Pili*[2], *Mukund Seshadri*[1,3,4], [1]*Pharmacology and Therapeutics, Roswell Park Cancer Institute, Buffalo, NY, USA;* [2]*Medicine, Roswell Park Cancer Institute, Buffalo, NY, USA;* [3]*Department of Dentistry and Maxillofacial Prosthetics, Roswell Park Cancer Institute, Buffalo, NY, USA;* [4]*Department of Head and Neck Surgery, Roswell Park Cancer Institute, Buffalo, NY, USA. Contact e-mail: James.Kalmuk@roswellpark.org*

Androgen dependency of newly diagnosed prostate cancer is highlighted by the initial clinical responsiveness of these tumors to androgen deprivation therapy (ADT). However, a majority of patients that undergo ADT relapse and present with castration-resistant prostate cancer (CRPC) that is characterized by increased aggressiveness and metastatic potential. The high mortality rate associated with CRPC underscores the need for identifying and evaluating novel treatment options for this patient population. In this preclinical study, we examined the therapeutic potential of ADT in combination with vascular disruption against prostate cancer. Experimental studies were carried out to examine the response of subcutaneous and orthotopic Myc-CaP tumors to EPC2407, a tumor vascular disrupting agent (tumor-VDA) currently undergoing clinical evaluation. A tri-modality imaging based approach based on magnetic resonance imaging (MRI), ultrasound (US) and bioluminescence imaging (BLI) (Figure 1) was employed to characterize the vascular response of tumors to castration alone and in combination with VDA therapy. Imaging data was used to guide the sequence and schedule of combination treatment. Long-term therapeutic efficacy was assessed by monitoring tumor growth over time. BLI enabled early monitoring of orthotopic tumor growth and disease recurrence in vivo prior to any visible or palpable tumor growth. Castration resulted in acute changes in vascular function evidenced by a reduction in perfusion within a 24 hour period. Treatment with the VDA also resulted in a similar reduction in contrast enhancement on both MRI and US examination. While castration alone and VDA treatment alone resulted in transient inhibition of tumor growth, combination treatment resulted in maximal therapeutic benefit with significant tumor growth inhibition and a survival benefit in both subcutaneous and orthotopic tumor models. These results demonstrate the therapeutic potential of this novel vascular-targeted combination strategy against prostate cancer.

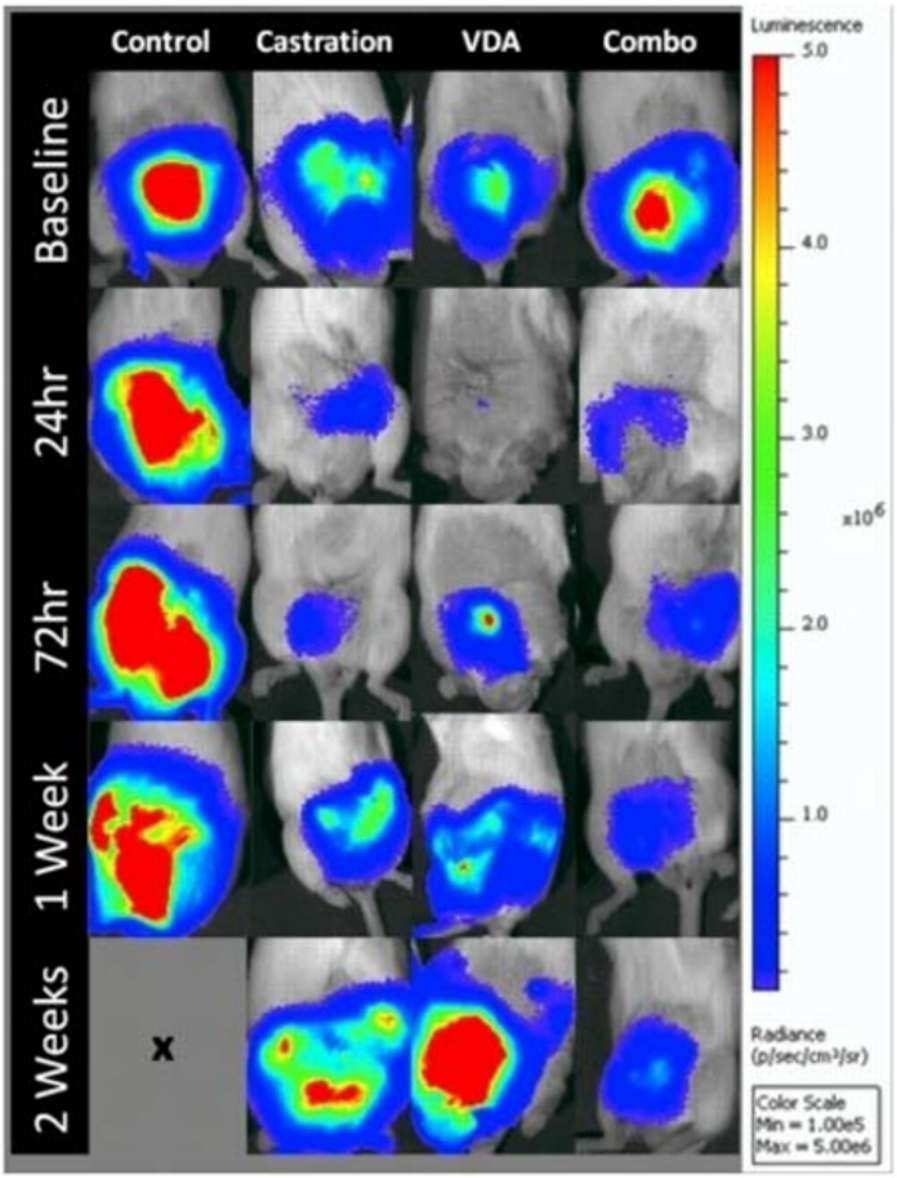

Bioluminescent Images of mice with orthotopic prostate tumors treated with single agent castration, single agent vascular-disrupting agent, combination castration+vascular disrupting agent, as well as untreated controls over time. Combination treatment led to sustained vascular inhibition compared to single agent treatment and untreated controls.

Disclosure of author financial interest or relationships:
J. Kalmuk, None; **R. Pili**, None; **M. Seshadri**, None.

Presentation Number **LBAP 100**
Late Breaking Abstract Poster Session
September 19, 2013 / 15:15-15:15 / Room: Exhibit Hall B

Spectroscopic Photoacoustic Imaging of Focal Breast Lesions in a Transgenic Mouse Model

Katheryne Wilson, *Sunitha Bachawal, Juergen K. Willmann, Radiology, Stanford University, Palo Alto, CA, USA. Contact e-mail: katheryne.wilson@gmail.com*

Introduction: Breast cancer is the second deadliest cancer in women and an estimated 232,340 new cases will be diagnosed in 2013 in the USA. However, if detected early, through mammography and ultrasound (US), mortality decreases by approximately one-fifth. For women with a genetic risk for breast cancer, routine screening often begins at an early age even though mammography is notoriously insensitive (30-48% detection) in younger women due to the presence of high density breast tissue, resulting in delayed detection and worse prognosis. Although B-mode ultrasound (US) increases the detection rates for breast cancer in patients with dense breast tissue, its positive predictive value is low resulting in a large number of unnecessary callbacks and biopsies. Thus, increasing the diagnostic accuracy of US is highly needed in particular in patients with dense breast tissue. Photoacoustic imaging can add additional tissue information to ultrasound imaging by providing the molecular composition of the tissue based on optical absorption properties. In this study, we explored the potential of spectroscopic photoacoustic (PA) imaging (the quantification of specific chromophores based on wavelength dependent absorption properties) for quantification of tissue oxygen saturation (sO2) in order to differentiate among varying breast histologies in a transgenic mouse model of breast cancer. Methods: The transgenic mouse model for breast cancer development FVB/N Tg(MMTV/PyMT634Mul was used to assess sO2 levels in four different breast histologies (normal, hyperplasia, ductal carcinoma in situ (DCIS), and invasive carcinoma) using spectroscopic photoacoustic imaging. Mammary glands of female mice at varying ages (4-10 weeks), were imaged using the VisualSonics Vevo LAZR, collecting combined ultrasound and photoacoustic data at 17 wavelengths (700-860 nm, 10 nm increments) using a 25 MHz transducer. Using in-house data analysis based on the PA signal collected at varying wavelengths, the overall average sO2 of each mammary gland was calculated. After scanning, all glands were excised, stained with H&E, and classified into the four different histologies. Results: In total, 187 mammary glands were imaged, analyzed, and classified into four disease categories: normal (n=70), hyperplasia (n=14), DCIS (n=78), and invasive carcinoma (n=25). Hyperplasia (51.9% ± 2.2%; $p<0.0001$), DCIS (41.6% ± 1.0%; $p<0.0001$), and invasive (40.2% ± 2.1%; $p= 0.0024$) lesions showed a statistically significant increase of average sO2 over normal mammary tissues (35.3% ± 0.6%). Representative ultrasound, spectroscopic photoacoustic, and histology images are presented in Figure 1. Spectroscopic analysis based on a linear least squares resulted in coefficients of determination ($R2 > 0.96$), indicating a high degree of model fit. Conclusion: Our results suggest that spectroscopic PA imaging in a transgenic mouse model of breast cancer development is feasible. Tissue oxygen saturation is increased in hyperplasia, DCIS, and invasive cancer compared to normal tissue and adding this intrinsic PA contrast to B-mode ultrasound imaging may help in focal lesion characterization in the breast.

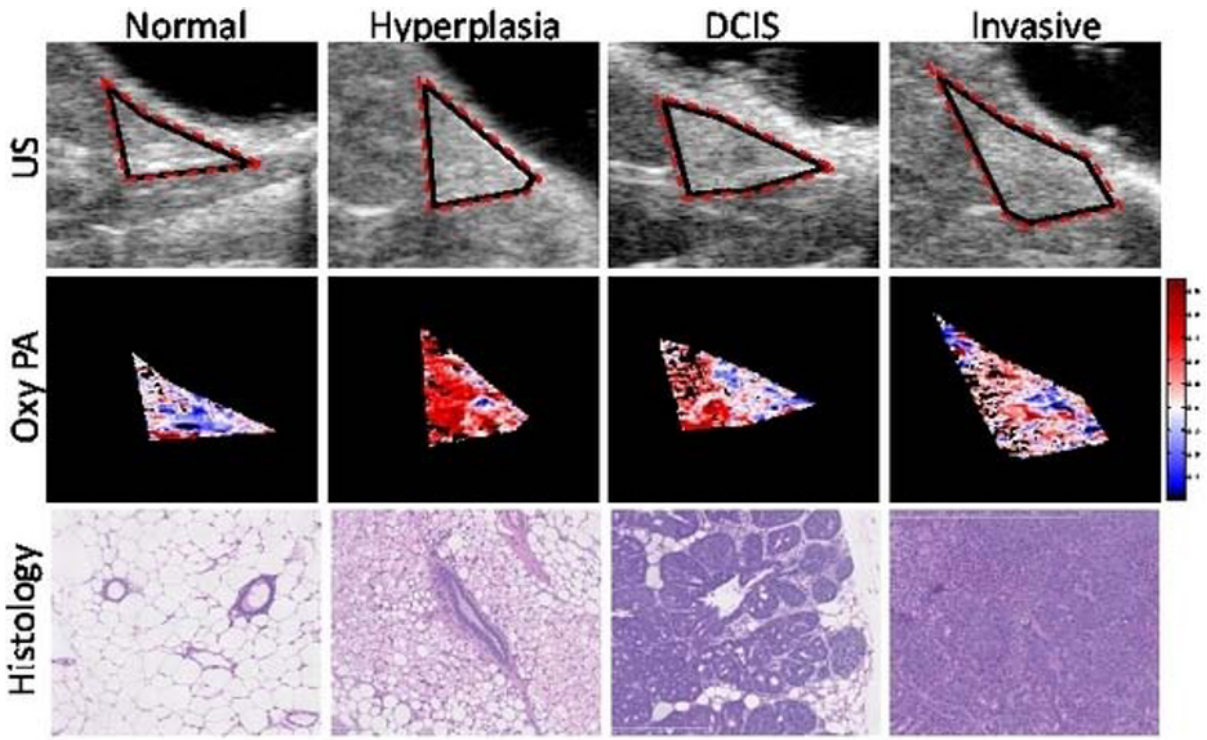

Figure 1: (Top Row) B-mode ultrasound images of mouse mammary glands at different developmental stages. Note that normal, hyperplasia, DCIS, and invasive breast cancer tissues cannot be differentiated based on B-mode ultrasound imaging. The ROIs used for spectroscopic image analysis are shown. (Second Row) Spectroscopic photoacoustic images limited to a region of interest encompassing the total mammary glands as defined by the B-mode ultrasound images. The color map is shown on the right with dark red indicating 100% sO2 and dark blue representing 0% sO2. (Bottom Row) Representative H&E tissue slides from the four different histologies.

Disclosure of author financial interest or relationships:
K. Wilson, None; **S. Bachawal**, None; **J.K. Willmann**, Bracco, Consultant; Siemens, Grant/research support; Bracco, Grant/research support .

Presentation Number **LBAP 101**
Late Breaking Abstract Poster Session
September 19, 2013 / 15:15-15:15 / Room: Exhibit Hall B

Trimodal PET/CT/MRI Imaging of EphA2 in Glioblastoma

Simon Puttick[1], *Bryan W. Day*[4], *Brett W. Stringer*[4], *Karine Mardon*[2], *Gary J. Cowin*[2], *Zara C. Bruce*[4], *Paul R. Jamieson*[4], *Kathleen S. Ensbey*[4], *Nathan R. Boase*[1,2], *Michael Fay*[7,3], *Kristofer J. Thurecht*[1,2], *Andrew K. Whittaker*[1,2], *Stephen Rose*[5,6], *Andrew W. Boyd*[4,3], [1]*Australian Institute for Bioengineering and Nanotechnology, The University of Queensland, Brisbane, QLD, Australia;* [2]*Centre for Advanced Imaging, The University of Queensland, Brisbane, QLD, Australia;* [3]*Department of Medicine, The University of Queensland, Brisbane, QLD, Australia;* [4]*Brain Cancer Research Unit, Queensland Institute for Medical Reasearch, Brisbane, QLD, Australia;* [5]*Biomedical Imaging Group, Australian e-Health Research Centre, Brisbane, QLD, Australia;* [6]*CSIRO, Brisbane, QLD, Australia;* [7]*Division of Cancer Care, Royal Brisbane and Womens Hospital, Brisbane, QLD, Australia. Contact e-mail: s.puttick@uq.edu.au*

Glioblastoma is the most common primary brain tumour and its treatment represents a significant clinical challenge. Current therapy, which includes surgical resection, radiotherapy and chemotherapy with temozolomide is rarely curative and median patient survival is between 9-12 months.[1] It is clear that new therapies are needed to increase survival rates in glioblastoma patients. The Eph receptor tyrosine kinases and their Eph receptor-interacting (ephrin) ligands have received increasing attention over the last two decades as potential targets for cancer treatment.[2] Overexpression of the EphA2 receptor tyrosine kinase in a number of cancers,[3] in particular in glioblastoma,[4, 5] makes it an attractive target for novel therapeutics. In this study we report the preparation and synchronous PET/CT and simultaneous PET/MRI imaging of a 64Cu labeled monoclonal antibody (mAb) specific to the EphA2 receptor tyrosine kinase in a U87 model of GBM. We show fast uptake, high specificity and significant activity of the EphA2-NOTA-64Cu mAb at the tumour site when compared to non-tumour controls. Purity of radiolabeled mAb was assessed by radio-TLC prior to injection and found to be > 95 %. The number of NOTA cages per mAb was calculated by isotopic dilution. [1] M. J. B. Taphoorn et al., The Lancet Oncology, 2005, 6, 937-944. [2] E. B. Pasquale, Nat. Rev. Cancer, 2010, 10, 165-180. [3] M. Lackmann and A. W. Boyd, Sci. Signal., 2008, 1. [4] J. Wykosky et al., Mol. Cancer Res., 2005, 3, 541-551. [5] E. Binda et al., Cancer Cell, 2012, 22, 765-780.

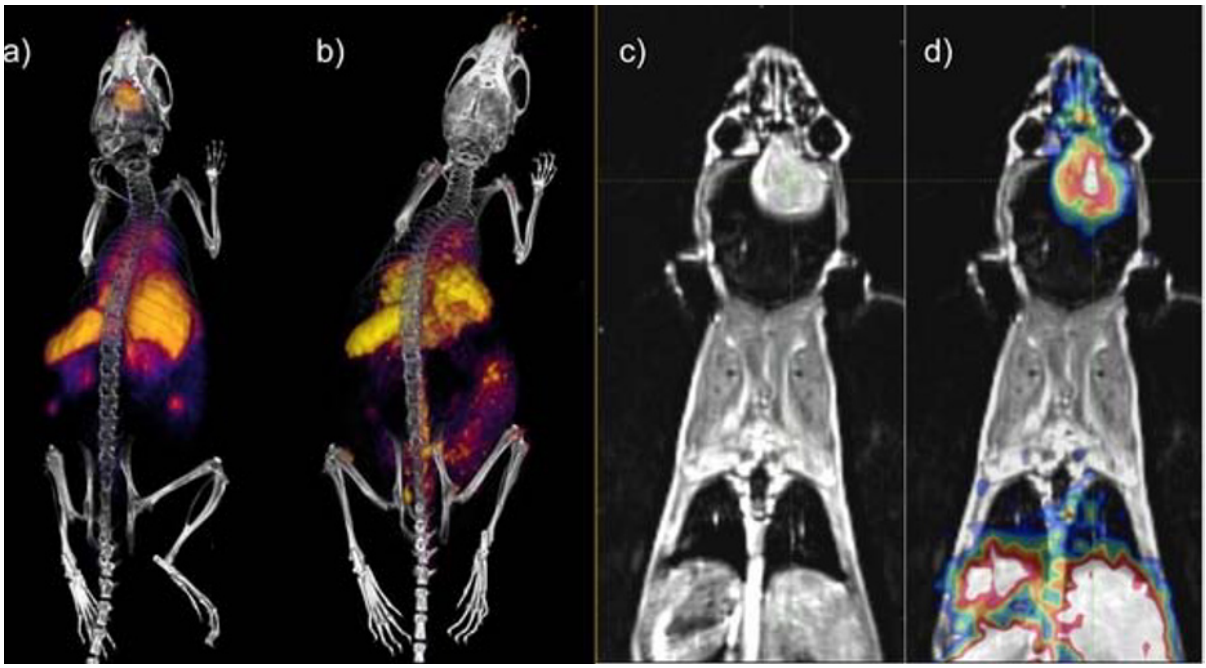

Figure 1: a) PET/CT image of a NOD/SCID mouse bearing a U87 xenograft in the right striatum 6 hours after intravenous administration of a 64Cu labeled EphA2 mAb and b) PET/CT image of a NOD/SCID mouse with an intracranial injection of laminin 6 hours after intravenous administration of a 64Cu labeled EphA2 mAb. c) Coronal slice of a contrast enhanced 3D GE image following 50 uL intravenous injection of Magnevist via the lateral tail vein. The tumour site can clearly be seen. d) Coronal slice of a contrast enhanced 3D GE image (grayscale) overlayed with a simultaneously acquired PET image. Both c) and d) were acquired 50 hours following intravenous injection via the lateral tail vein of 200 µCi of EphA2-4B3-NOTA-64Cu

Disclosure of author financial interest or relationships:
S. Puttick, None; **B.W. Day**, None; **B.W. Stringer**, None; **K. Mardon**, None; **G.J. Cowin**, None; **Z.C. Bruce**, None; **P.R. Jamieson**, None; **K.S. Ensbey**, None; **N.R. Boase**, None; **M. Fay**, None; **K.J. Thurecht**, None; **A.K. Whittaker**, None; **S. Rose**, None; **A.W. Boyd**, None.

Presentation Number **LBAP 102**
Late Breaking Abstract Poster Session
September 19, 2013 / 15:15-15:15 / Room: Exhibit Hall B

Feasibility of quantitative ^{15}O-water PET imaging in mouse models of breast cancer

Bosky Ravindranath[1], *Szeman Chan*[2], *Yuan-Chuan Tai*[1], *Kooresh I. Shoghi*[1], [1]*Mallinckrodt Institute of Radiology, Washington University School of Medicine, St. Louis, MO, USA;* [2]*Department of Pathology and Immunology, Washington University School of Medicine, St. Louis, MO, USA. Contact e-mail: ravindranathb@mir.wustl.edu*

Objective- To test the feasibility of ^{15}O-water PET measurements in mouse breast cancer tumor model. **Background**- Angiogenesis, the formation of new blood vessels on an existing vasculature is essential to tumor growth. It plays an important role in determining tumor size as well as metastatic potential and therefore is an important therapeutic target. ^{15}O-water PET is the gold standard for quantitative measurement of blood flow, which in turn reflects angiogenesis. Here, we aim to test the feasibility of acquiring the short lived ^{15}O-water radiotracer PET images in mouse breast cancer model and perform qualitative (SUV) and quantitative analyses using kinetic modeling. **Methods and Results** - Four mice implanted with the SSM3 mammary tumor cell line derived from STAT1 deficient mice were imaged with either the microPET Focus F220 or Inveon (Siemens Molecular Imaging, TN) small animal PET/CT scanner. The imaging protocol included a 10 min dynamic imaging with ^{15}O labeled CO gas to visualize the cardiac blood pool and underlying tumor vasculature. The cardiac blood pool images were used to draw regions of interest (ROI) to extract input function for use in kinetic modeling. Following the CO imaging, the mice were injected with ^{15}O-water and imaged for a period of 10 minutes. ROIs were drawn on the corresponding CT image of the tumor and used to extract ^{15}O-water PET time activity curve for characterizing tumor perfusion using a single tissue compartment model defined by the differential equation - $(dC_t)/dt = FC_a - (F/V_T)\,C_t$,where F is the blood flow in ml/gm/min, C_t is the tissue tracer concentration, C_a is the arterial blood tracer concentration, and V_T is the tissue to plasma concentration ratio in equilibrium. One set of co-registered ^{15}O-water PET/CT images along with cardiac pool images are shown in Figure 1. **Conclusion**: We have imaged four mice with SSM3 mammary tumor using ^{15}O-water and extracted the input function and tumor time activity curves for kinetic modeling of ^{15}O-water. The assessment of feasibility of ^{15}O-water measurements in mice will be beneficial to investigators wishing to use ^{15}O water for their experiments such as for evaluation of effect of therapy on tumor blood flow or angiogenesis.

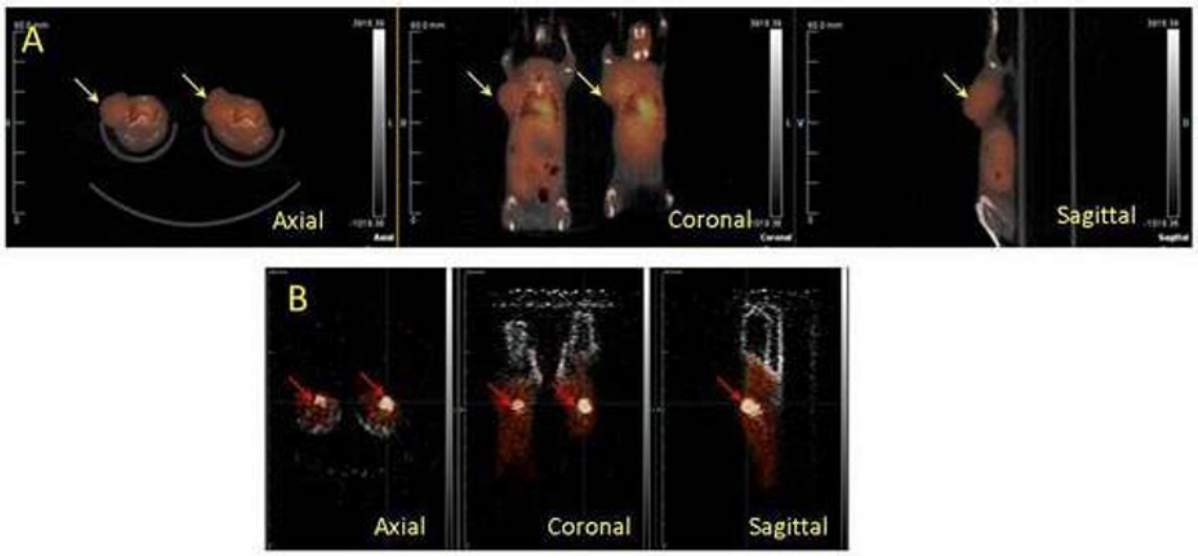

Figure 1: A-: Coregistered ^{15}O-water PET/CT images of two mice with mammary tumor (yellow arrow) imaged simultaneously. B- Cardiac blood pool images of the same set of mice using ^{15}O labeled CO imaging

Disclosure of author financial interest or relationships:
B. Ravindranath, None; **S. Chan**, None; **Y. Tai**, None; **K.I. Shoghi**, None.

Presentation Number **LBAP 103**
Late Breaking Abstract Poster Session
September 19, 2013 / 15:15-15:15 / Room: Exhibit Hall B

PET/MR Provides Complementary Information about the Tumor Micro-Environment Enabling Identification and Profiling

Mathew R. Divine, *Bernd J. Pichler, Jonathan A. Disselhorst, Preclinical Imaging and Radiopharmacy, Werner Siemens Imaging Center, Tuebigen, Germany. Contact e-mail: mathew.divine@med.uni-tuebingen.de*

Introduction Molecular imaging, especially hybrid imaging like Positron Emission Tomography (PET) and Magnetic Resonance Imaging (MRI) provide complementary information about the biochemical, as well as, the biophysical environment *in vivo*. These devices play a strong role in the clinic for making differential diagnosis of many diseases and define the most sophisticated standard of care available today. In the preclinical arena, these devices are used to expand the domain of knowledge by allowing serial, *in vivo* measurements of disease and its progression. Recently, the integration of these two devices has raised interest in finding optimal ways of utilizing both modalities together and fully understanding the complementarity of their combined measurements. We present results obtained from serial imaging of malignancies, and following tumor growth over a two week time period with PET tracers ([^{18}F]FDG, [^{18}F]FLT, and [^{64}Cu]DOTA-Cetuximab) along with anatomical and functional imaging via MRI, namely, T2-weighted Turbo Spin Echo images and Apparent Diffusion Coefficient (ADC) maps. The goal of the study was to understand the basic mechanisms of tumor progression in a xenograft tumor model as observed by PET/MR. **Methods** 8 week old NMRI-Nu/Nu (n=10) mice were injected with 1.2 million NCI-H460 NSCLC cells, and were allowed to grow until just above 100mm^3. Up to 8 serial, PET/MRI scans were made with either [^{18}F]FDG uptake 50 min post injection or [^{18}F]FLT at 90 min post injection for a 10 min static scan. This was followed by a T2-weighted Turbo Spin Echo (T2-tse) sequence and a HASTE sequence at differing b-values for ADC map calculation. The 3rd PET scan measured the uptake of [^{64}Cu]DOTA-Cetuximab to assess the presence of Epidermal Growth Factor Receptor (EGFR). At the end, tumors were excised and cut in half along a mark that coincided with the transversal axis in the MRI images. **Results** The average [^{18}F]FDG Standard Uptake Values (SUV) and the ADC values (mm^2/s x10^{-6}) in tumors were plotted against tumor size (mm^3) revealing a significant trend (p-value < 0.03) as determined by the Pearson's correlation coefficient which was 0.63 and 0.83, respectively. Plotting the [^{18}F]FDG SUV and the ADC values against each other revealed another significant, positive trend with a p-value of 0.83. Tumor images of different time points were co-registered and allowed emergence of necrotic areas to be pinpointed on early scans and their expansion could be followed. Using the [^{18}F]FDG SUV and ADC parameters, a k-means clustering algorithm segmented the tumor into distinct biological regions (2 necrotic, and 2 viable) which compared superbly to both H&E and Ki-67 histological staining. [^{18}F]FLT and [^{64}Cu]DOTA-Cetuximab hyper intense areas correlated well with each other and with [^{18}F]FDG. Additionally, [^{18}F]FLT had a similar relationship with ADC like [^{18}F]FDG. **Conclusion** ADC and [^{18}F]FDG are complementary measurements. Clustering algorithms can use the information to distinguish different viable and necrotic regions *in vivo*. PET/MR imaging detects changes in proliferation rate, glucose consumption, local EGFR expression, and early onset of necrosis *in vivo*

Disclosure of author financial interest or relationships:
M.R. Divine, None; **B.J. Pichler**, Siemens, Grant/research support; Bayer, Grant/research support; AstraZeneca, Grant/research support; BoehringerIngelheim, Grant/research support; **J.A. Disselhorst**, None.

Presentation Number **LBAP 104**
Late Breaking Abstract Poster Session
September 19, 2013 / 15:15-15:15 / Room: Exhibit Hall B

[^{18}F]fluoro-pivalic acid: a novel acetate analog for cancer detection by positron emission tomography

Timothy H. Witney, *Federica Pisaneschi, Israt S. Alam, Lisa Iddon, Frazer Twyman, Eric O. Aboagye, Surgery and Cancer, Imperial College London, London, United Kingdom. Contact e-mail: t.witney@imperial.ac.uk*

Deregulated cellular metabolism is a hallmark of many cancers. As well as increased glycolytic flux, exploited for cancer imaging with [^{18}F]fluoro-2-deoxyglucose (FDG), tumor cells display upregulated plasma membrane turnover and accumulation of cytoplasmic lipid droplets. Elevated *de novo* fatty acid synthesis can be traced with [^{11}C]acetate, whose metabolic fate is either through TCA cycle metabolism (non-specific) - resulting in loss of signal through [^{11}C]CO_2, or the accumulation in cell membranes via fatty acid synthesis (specific) [1]. [^{11}C]acetate has shown clinical utility for the imaging of non-FDG-avid tumors such as those of the prostate. Fluorinated derivatives of [^{11}C]acetate have been developed for cancer imaging with improved radioactive halflife [2]. [^{18}F]Fluoroacetate ([^{18}F]FAC) however shows a high degree of defluorination and consequent bone uptake in rodents. We have designed a new probe, [^{18}F]fluoro-pivalic acid ([^{18}F]FPIA), as an analogue of [^{11}C]acetate with longer radioactive half-life, lacking the undesired defluorination properties of [^{18}F]FAC. *In vivo* imaging of implanted EMT6 murine breast adenocarcinoma cells showed rapid and extensive tumor labeling with [^{18}F]FPIA, reaching 8.3 %ID/mL by 30 min post injection, followed by stable retention of the tracer over the 60 min dynamic imaging time course. Time course biodistribution studies demonstrated substantial uptake in the cortex of the kidney, with clearance primarily via urinary excretion. Tracer localization was also observed in the heart, liver and intestines. Notably, there was lack of bone-associated radioactivity, suggesting the absence of (or low) defluorination. Similar radiotracer biodistribution has been previously observed with [^{11}C]acetate [3], except for route of excretion: elimination via [^{11}C]CO_2 for [^{11}C]acetate and via the renal route (kidney and urine) for [^{18}F]FPIA. [^{18}F]FPIA was stable 30 min post injection in heart, liver and plasma as determined by radioHPLC. In a comparative study with FDG (Fig. 1), there was no significant difference in tumor-associated radioactivity, as assessed from the area under the time verses radioactivity curve (TAC) and tumor radioactivity at 60 min in implanted EMT6 tumors. FDG-PET, however, is not effective in all tumor types because some tumors, e.g., prostate adenocarcinoma, show low FDG uptake, whereas in others, a high background uptake by surrounding normal tissue can mask tumor uptake, for example, in the brain. We further show that [^{18}F]FPIA passes the blood brain barrier and provides superior tumor:brain ratio of 2.5 in comparison to 1.3 for FDG in subcutaneously implanted U87 human glioma tumors, providing a possible advantage of [^{18}F]FPIA over FDG for brain cancer imaging. Although the metabolic fate of [^{18}F]FPIA is yet to be experimentally determined, [^{18}F]FPIA shows great promise as an imaging agent for cancer detection. [1] R. R. Wolfe and F. Jahoor, Am J Clin Nutr, 1990, 51, 248-252 [2] D. E. Ponde et al., J. Nucl. Med., 2007, 48, 420-428 [3] Ö. Lindhe, A. et al., Eur. J. Nucl. Med. Mol. I., 2009, 36, 1453-1459

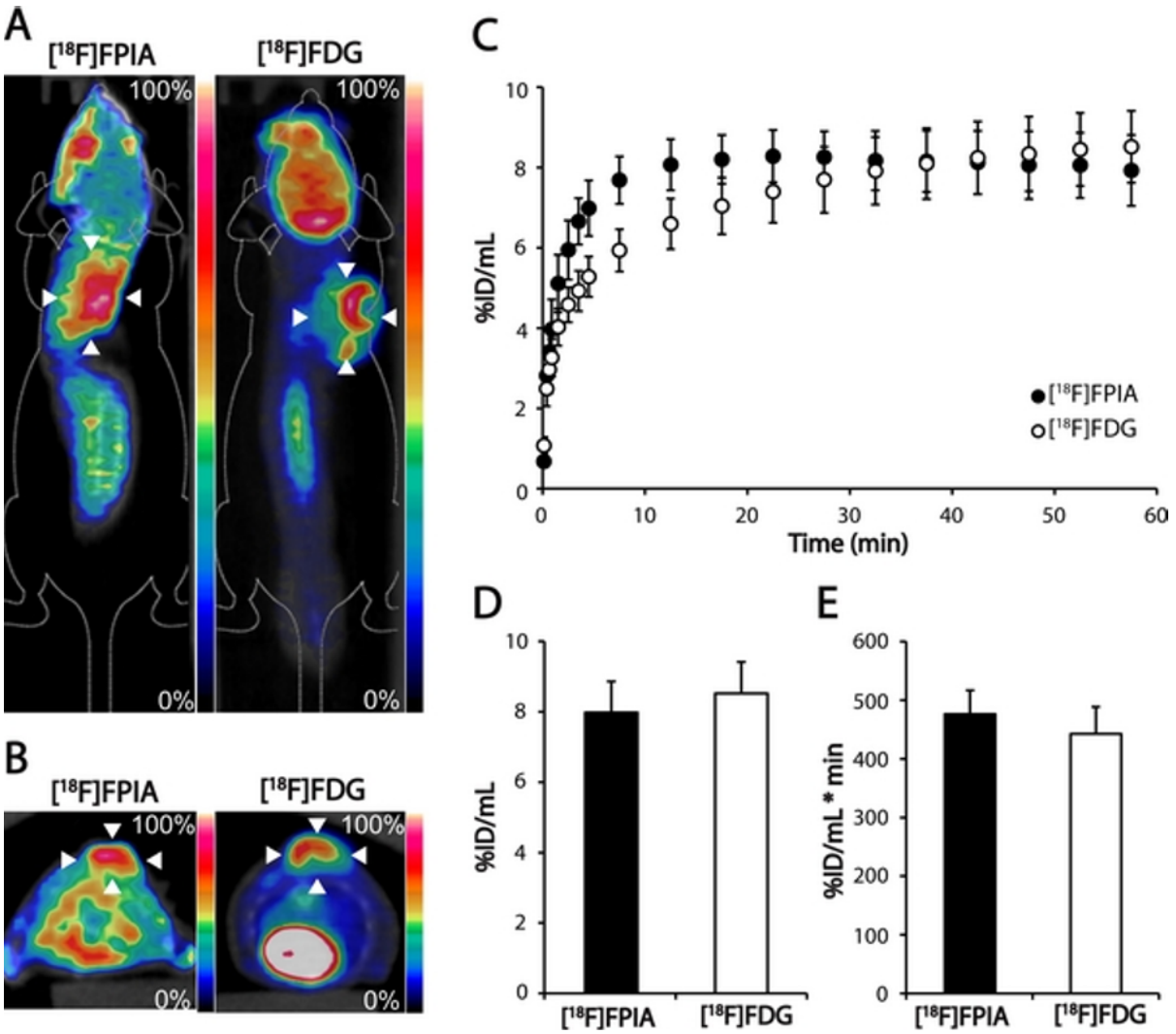

Figure 1. Dynamic [^{18}F]FPIA and [^{18}F]FDG-PET image analysis. (A) Representative coronal PET-CT images (30-60 minutes of summed activity) for [^{18}F]FPIA and [^{18}F]FDG. (B) Representative axial PET-CT images of EMT6 tumor-bearing mice (30-60 minutes of summed activity) for [^{18}F]FPIA and [^{18}F]FDG. White arrowheads indicate the tumor, identified from the CT image. (C) EMT6 tumor time versus radioactivity curve (TAC) obtained from 60-minute dynamic PET imaging. Mean ± SD (n = 5 mice per group). (D & E) Semi-quantitative imaging variables extracted from the TAC: Tumor radioactivity 60 min post injection (D) and area under the TAC, 0-60 min (E). Mean ± SD (n = 4 mice per group).

Disclosure of author financial interest or relationships:
T.H. Witney, None; **F. Pisaneschi**, None; **I.S. Alam**, None; **L. Iddon**, None; **F. Twyman**, None; **E.O. Aboagye**, None.

Presentation Number **LBAP 105**
Late Breaking Abstract Poster Session
September 19, 2013 / 15:15-15:15 / Room: Exhibit Hall B

A PSMA Specific Diabody For SPECT Imaging of Prostate Cancer

Florian Kampmeier[1], Jennifer D. Williams[1], John Maher[2,3,4], **Greg Mullen**[1]*, Phil Blower[1], [1]School of Medicine, Division of Imaging Sciences & Biomedical Engineering, King's College London, London, United Kingdom; [2]King's Health Partners Integrated Cancer Center, Department of Research Oncology, King's College London, London, United Kingdom; [3]Department of Immunology, Barnet and Chase Farm NHS Trust, London, United Kingdom; [4]Department of Clinical Immunology and Allergy, King's College Hospital NHS Foundation Trust, London, United Kingdom. Contact e-mail: greg.mullen@kcl.ac.uk*

Purpose: Sensitive and specific detection of nodal status, sites of metastases and low volume recurrent disease could greatly improve management of patients with advanced prostate cancer. Prostate specific membrane antigen (PSMA) is a well-established marker for prostate carcinoma with increased levels of expression in high grade, hormone refractory and metastatic disease. The monoclonal antibody J591 is directed against an extracellular epitope of PSMA and has been shown to efficiently target disseminated disease including metastases in lymph nodes and bone. Its use as a diagnostic imaging agent however is limited due to its long serum half life. In this study a diabody fragment of mAb J591 was developed as a single photon emission computed tomography (SPECT) tracer with improved systemic clearance for the detection of PSMA expression in prostate cancer. Experimental: A diabody in VH-VL orientation and with a C-terminal cysteine was expressed in HEK293T cells and purified by a combination of metal ion affinity- and size exclusion chromatography. Specificity and affinity were determined in cell binding studies. For SPECT imaging, the diabody was site specifically labelled with $[^{99m}Tc(CO)_3]_+$ via the C-terminal His tag and evaluated in a subcutaneous DU145/DU145-PSMA prostate carcinoma xenograft model. Results: J591C diabody binds to PSMA expressing cells with low nanomolar affinity (3.3 ± 0.2 nM). SPECT studies allowed imaging of tumour xenografts with high contrast from 4h post injection (p.i.). Ex vivo biodistribution studies showed peak tumour uptake of the tracer of 12.1 ± 1.7% injected dose (ID)/g at 8 h p.i. with a tumour to blood ratio of 8.0.

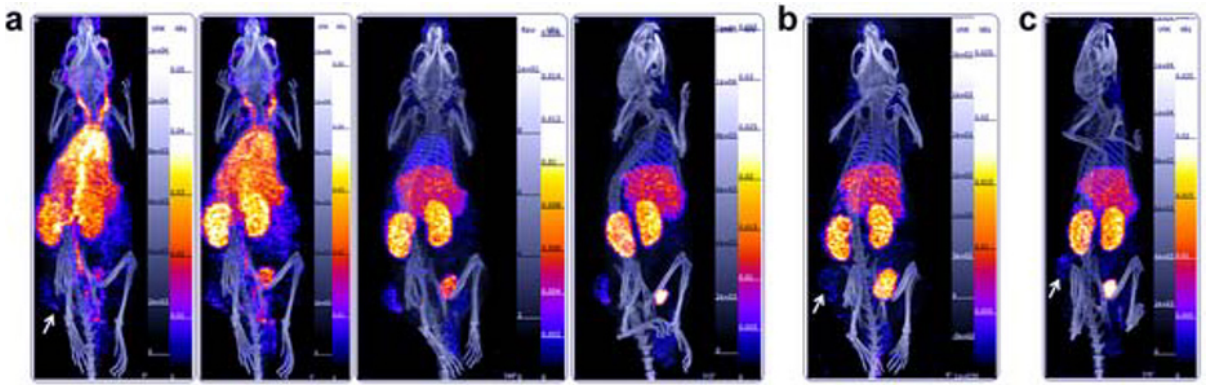

Maximum intensity projection (MIP) images of SPECT/CT scans with J591C diabody-99mTc in SCID beige mice bearing subcutaneous prostate carcinoma tumours a) Serial images at 5 min, 60 min, 4 h and 8 h post injection of a mouse with DU145-PSMA tumour. b) Mouse with PSMA negative DU145 tumour at 8h p.i.. c) Mouse with DU145-PSMA tumour; binding of J591Cdia-99mTc blocked with a 20x excess of unlabelled diabody (cold competition, at 8h p.i.).

Disclosure of author financial interest or relationships:
F. Kampmeier, None; **J.D. Williams**, None; **J. Maher**, None; **G. Mullen**, Mediso, Consultant; **P. Blower**, None.

Presentation Number **LBAP 106**
Late Breaking Abstract Poster Session
September 19, 2013 / 15:15-15:15 / Room: Exhibit Hall B

Spatio-Temporal Quantification of Sodium Iodide Symporter (NIS) Radiotracers using pre-clinical SPECT/CT and PET/CT: A Study in Healthy Scid/Beige Mouse

Krisanat Chuamsaamarkkee[1], *Seckou Diocou*[1], *Greg Mullen*[1], *Lefteris Livieratos*[1,2], *Phil Blower*[1], [1]*Imaging Sciences and Biomedical Engineering, King's College London, London, United Kingdom;* [2]*Nuclear Medicine, Guy's & St Thomas' Hospitals NHS Foundation Trust, London, United Kingdom. Contact e-mail: krisanat.chuamsaamarkkee@kcl.ac.uk*

Background:The sodium iodide symporter has been important to nuclear medicine for many years, both as a molecular target for imaging and therapy of thyroid disease, and as a reporter gene product for tracking the migration and survival of cells in vivo. A range of radiolabelled substrates have been used and these substrates are expected to show different properties leading to subtly different pharmacokinetics, yet there has not been a side by side comparison of their pharmacokinetics to identify these differences. In this study, we have used high resolution preclinical imaging to quantify the spatio-temporal distribution of the available NIS-radiotracers;Tc99m-pertechnetate, I123-iodide, Re188-perrhenate and F18-tetrafluoroborate (BF4). Furthermore, such information may be used to determine the optimal time to image and also provides a valuable tool to study cumulated activity, effective half-life and residence time for dosimetry in therapeutic applications. Methods: Quantification phantoms for all radiotracers were acquired in order to establish a calibration factor of injected activity between the imaging system and the dose calibrator. For in vivo imaging, healthy female Scid/Beige mice were used (n=3 for each radiotracer). Dynamic whole body SPECT or PET was performed continuously for 4 hour after tracer administration. Additional images at 8 and 24h were collected for pertechnetate, iodide and perrhenate. 3D ROIs were drawn at thyroid, salivary glands, stomach, left ventricle (for blood) and muscle (for background). The percentage uptake per injected dose (%ID) in each organ was calculated as the activity in the tissue divided by the injected activity with decay correction. Time-activity curves were expressed as percentage uptake and plotted for all tracers. Results: The uptake of radiotracers in thyroid can be categorised into 2 groups: metabolised and non-metabolised tracers. For non-metabolised tracers, the uptakes initially increased and gradually decreased over time. In contrast, thyroid uptake of iodide was much higher and continued to increase through 8h time point then decreasing by the 24h time point. In salivary glands similar patterns of uptake were observed for all tracers: uptake increased gradually over time then remained steady and slowly decreased. Stomach uptake was high compared with other organs due to its large size. Stomach uptake peaked at 8h, except with BF4 which showed peak values at around 3h after injection. By 24h after injection, the stomach activity was less focal and activity was more apparent in the intestinal system. Activity in muscle (not expressing-NIS) and left ventricle (representing blood activity) were low and remained so over time for all tracers. Discussion: This work has shown the capability of pre-clinical imaging for spatio-temporal tracer quantification. It has also identified distinct difference in uptake patterns between metabolised and non-metabolised tracers, and also subtle differences between the putatively non-metabolised tracers with potential implications for the development of imaging and therapeutic NIS reporter-gene radiotracers.

Disclosure of author financial interest or relationships:
K. Chuamsaamarkkee, None; **S. Diocou**, None; **G. Mullen**, Mediso, Consultant; **L. Livieratos**, None; **P. Blower**, None.

Presentation Number **LBAP 107**
Late Breaking Abstract Poster Session
September 19, 2013 / 15:15-15:15 / Room: Exhibit Hall B

Oncolytic vaccinia viruses encoding the human sodium iodide symporter facilitate long-term deep-tissue image monitoring of virotherapy

Barbara Haertl[3], *Dana Haddad*[1,5], *Markus Schiller*[4], *Pat Zanzonico*[1], *Sean Carlin*[1], *Ina Israel*[4], *Nanhai G. Chen*[2], *Chun-Hao Chen*[1], *Valerie A. Longo*[1], *Qian Zhang*[2], *Samuel Samnick*[4], *Jochen Stritzker*[2], *Yuman Fong*[1], *Aladar A. Szalay*[2], [1]*Memorial Sloan-Kettering Cancer Center, , New York, NY, USA;* [2]*Genelux Corporation, , San Diego, CA, USA;* [3]*Genelux GmbH, , Bernried, Germany;* [4]*Nuclear Medicine, University Hospital Würzburg, Würzburg, Germany;* [5]*Department of Radiology, Harlem Hospital/Columbia University, New York, NY, USA. Contact e-mail: barbara.haertl@genelux.com*

To assess therapeutic response and potential toxicity of oncolytic virotherapy, a noninvasive, deep-tissue imaging modality is needed. This study aimed to assess the feasibility, parameters, determining factors of serial imaging and long-term monitoring of systemic virotherapy together with radiotherapeutic response of cancer xenografts treated with vaccinia viruses encoding the human sodium iodide symporter (hNIS). hNIS, an intrinsic plasma membrane protein, mediates the active transport, and trapping of iodine mainly in the thyroid and some extrathyroidal tissues such as the stomach. Tumor xenografts in nude mice were treated systemically or intratumorally with hNIS-encoding viruses and serially imaged using 124I-PET and 18F-tetrafluoroborate-PET at 1, 2, 3, and 5 weeks post virus injection and 4 respectively 1 hours post radiotracer injection. The PET signal intensity was compared with tumor therapeutic response and optical imaging. The results show, that hNIS-encoding viruses successfully facilitated serial long-term imaging of virotherapy with PET signal intensity correlating to antitumor response both using 124I or 18F-tetrafluoroborate. Additionally at week 1 and 2 post virus injection, mice were also imaged at 1, 8, 24, 48, and 72 hours post radiotracer injection in order to obtain time-activity curves for dosimetry calculations of radioiodine uptake. Tumors were histologically analyzed for morphology and presence of virus particles. Autoradiography was performed utilizing technecium-pertechtenate and gamma-scintigraphy to assess determining factors for radiouptake in tumors. Successful radiouptake required presence of virus, adequate blood flow, and viable tissue, while loss of signal intensity was linked to tumor death and necrosis. hNIS-encoding recombinant Vaccina Viruses are promising oncolytic agents against cancer. Furthermore they provide the possibility for the non-invasive imaging of virotherapy and facilitate longterm monitoring of therapy.
This study was partially financed by the German Federal Ministry of Education and Research (grant 13N10451).

Disclosure of author financial interest or relationships:
B. Haertl, Genelux GmbH, Employment; **D. Haddad**, None; **M. Schiller**, None; **P. Zanzonico**, None; **S. Carlin**, None; **I. Israel**, None; **N.G. Chen**, Genelux Corporation, Employment; **C. Chen**, None; **V.A. Longo**, None; **Q. Zhang**, Genelux Corporation, Employment; Genelux Corporation, Stockholder; **S. Samnick**, Genelux GmbH, Bernried, Germany, Other financial or material support; **J. Stritzker**, Genelux Corporation, Employment; Genelux Corporation, Stockholder; Genelux Corporation, Grant/research support; **Y. Fong**, genelux Inc, Consultant; **A.A. Szalay**, Genelux Corporation, Stockholder; Genelux Corporation, Employment; Genelux Corporation, Other financial or material support .

Presentation Number **LBAP 108**
Late Breaking Abstract Poster Session
September 19, 2013 / 15:15-15:15 / Room: Exhibit Hall B

Upconversion luminescence targeted imaging of tumor xenografts *in vivo*

Majid Badieirostami, *Conroy Sun, Colin M. Carpenter, Guillem Pratx, Lei Xing, Radiation Oncology, Stanford University, Stanford, CA, USA. Contact e-mail: badiei@stanford.edu*

Near infrared (NIR) optical imaging has demonstrated significant potential as an effective modality for cancer targeted molecular imaging. Among various NIR probes currently under investigation, upconversion nanophosphors (UCNPs) possess great promise due to their anti-Stokes emission and sequential photon absorption which result in superior detection sensitivity and a simple imaging setup, respectively. Here, we report on the targeted imaging of EGFR-expression in tumor xenografts using affibody labeled UCNPs. They emit optical light upon irradiation by NIR laser, thereby allowing the detection of the molecular contrast. Initially, aqueous dispersible $NaYF_4$: Tm^{+3}, Yb^{+3} UCNPs were synthesized and their photophysical properties were characterized. The synthesized UCNPs were first modified with an amine functionalized PEG-phospholipid copolymer to improve biocompatibility and serve as a linker for biomolecules. Then, EGFR affibody conjugation attachment to the amine-functionalized UCNPs was performed using NHS linkers and thiolation chemistry. In addition, a current limitation of upconversion luminescence imaging is the lack of commercial instrumentation. To address this issue, we built a custom small-animal imaging system comprised of off-the-shelf components in a light-tight box and verified its imaging capabilities. The UCNP linear luminescence responses versus their concentrations and their depth resolving capability in a tissue-simulating phantom were examined using this imaging system. Finally, we demonstrated the use of the affibody functionalized UCNPs and the custom imaging system for targeting EGFR-expressing tumors both *in vitro* and *in vivo*. Our data suggests that NIR imaging with UCNPs can be used as a specific modality for noninvasive imaging of tumors.

Disclosure of author financial interest or relationships:
M. Badieirostami, None; **C. Sun**, None; **C.M. Carpenter**, None; **G. Pratx**, None; **L. Xing**, None.

Presentation Number **LBAP 109**
Late Breaking Abstract Poster Session
September 19, 2013 / 15:15-15:15 / Room: Exhibit Hall B

Diffusion and Magnetization Transfer in an Irradiated Glioma Model

Carlos J. Perez-Torres[1], John A. Engelbach[1], Jeremy Cates[2], Dinesh Thotala[2], Robert E. Drzymala[2], Joel R. Garbow[1], **Joseph J. Ackerman**[1,3], *[1]Department of Radiology, Washington University, Saint Louis, MO, USA; [2]Department of Radiation Oncology, Washington University, Saint Louis, MO, USA; [3]Department of Chemistry, Washington University, Saint Louis, MO, USA. Contact e-mail: ackerman@wustl.edu*

Accurate diagnosis is essential for proper treatment decisions. Standard anatomical MRI is incapable of differentiating recurring tumor from delayed radiation injury. Further studies are therefore necessary to accurately identify a robust imaging paradigm that can differentiate these pathologies. We investigated two MRI approaches that investigate cellularity through complementary properties: Diffusion Weighted Imaging (DWI), from which we calculated the apparent diffusion coefficient (ADC), and Magnetization Transfer Contrast (MTC), from which we calculated the magnetization transfer ratio (MTR). Our approach was to test these metrics longitudinally, first in each lesion type alone and then on an irradiated glioma model. All experiments were approved by the Washington University Division of Comparative Medicine and were performed on 8-9 week old female BALB/c mice. For the delayed radiation injury model, mice were irradiated with the Leksell Gamma Knife Perfexion (Elekta, Stockholm, Sweden) with a single 50-Gy radiation dose (50% isodose). For all glioma experiments, DBT cells (~10,000 in 10 µl) were injected below the cortical layers in the left hemisphere. Mice then received three radiation treatments of 7.5 Gy (50% isodose) each on days 10, 12, and 14 for a total dose of 22.5 Gy. Images were acquired with a 4.7 T small-animal Agilent/Varian DirectDrive scanner using an actively decoupled volume coil (transmit) and 1.5 cm surface coil (receive). MTC, DWI, and post-contrast T1-weighted images were acquired for each animal. For MTC analysis, proton-density-weighted images were acquired with and without the application of a 10 ms, 500 degree saturation pulse applied at a frequency offset +10 ppm from the water resonance. The MTR was calculated as the percent signal lost due to the saturation pulse. For DWI analysis, the ADC was calculated as the average of three separate diffusion datasets, acquired with diffusion encoding along three orthogonal directions, with a b-value of 1000 s/mm2. ROIs were drawn on the post-contrast T1-weighted images of the lesion and contralateral hemisphere and overlaid onto the ADC and MTR maps. Mice were imaged at multiple time points spanning the progression of radiation injury in healthy tissue or tumor growth. The MTR ratio is consistently hypointense in both lesions (Figure 1A), becoming significantly more hypointense in late radiation injury. The ADC ratio increased with progression of radiation injury and decreased with tumor growth, making it a better metric for discriminating between these pathologies. Having characterized radiation injury in healthy tissue and tumor alone, we next examined irradiated tumor. The ADC ratio in irradiated tumor increased immediately after irradiation (Figure 1B), then decreased as the tumor regrew. The MTR ratio was consistently low as would be expected based on Figure 1A. Our results suggest that ADC is a better metric than MTR for evaluating the changes that occur in the tumor in response to irradiation. MTR was more sensitive to both tumor and radiation injury than ADC and might instead be useful for detecting lesions that do not enhance strongly on T1-weighted images.

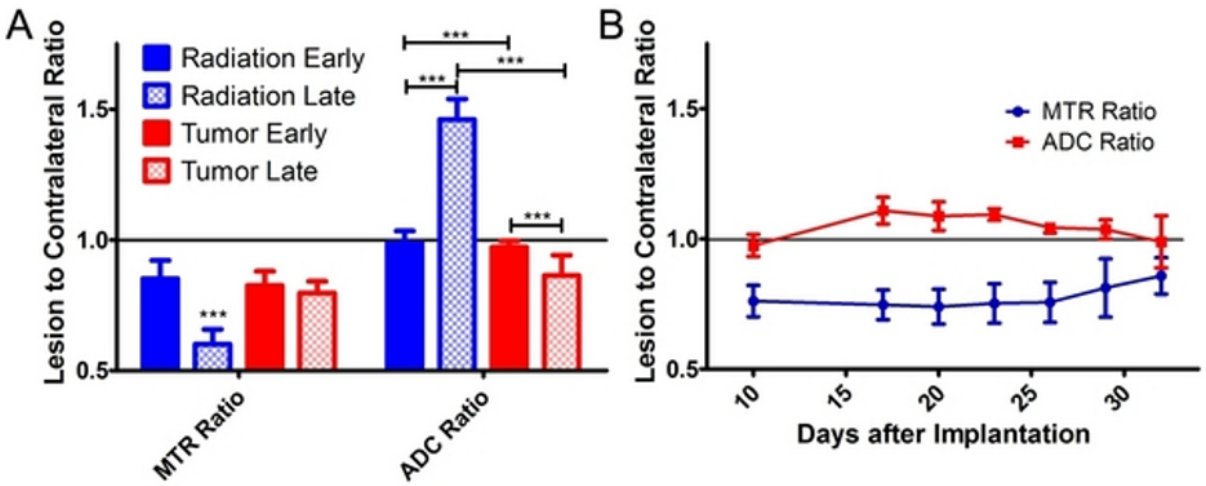

Figure 1: A. Lesion to contralateral ratios for radiation injury and glioma models at early and late time points. B. Lesion to contralateral ratios in the irradiated glioma model over time. The imaging time point at 10 days was pre-treatment and matches the early tumor time point in panel A. In both cases, lesions were defined solely by the enhancement in post-contrast T1-weighted images.

Disclosure of author financial interest or relationships:

C.J. Perez-Torres, None; **J.A. Engelbach**, None; **J. Cates**, None; **D. Thotala**, None; **R.E. Drzymala**, None; **J.R. Garbow**, None; **J.J. Ackerman**, Agilent Technologies, Grant/research support; Sigma-Aldrich Company, Honoraria; Elsevier, Honoraria; Monsanto Company, Grant/research support; Agilent Technologies, Other financial or material support

.

Presentation Number **LBAP 110**
Late Breaking Abstract Poster Session
September 19, 2013 / 15:15-15:15 / Room: Exhibit Hall B

Intraoperative Tumor-Specific Fluorescence Imaging Using Clostridium Perfringens Enterotoxin Carboxi-terminal Fragment (c-CPE) to Specifically Target Metastatic Chemotherapy-Resistant Human Ovarian Cancer in Xenograft Mouse Models

Emiliano Cocco, *Sara Gasparrini, Stefania Bellone, Ileana Bortolomai, Salvatore Lopez, Alessandro D. Santin, Obstetrics, Gynecology and Reproductive Science, Yale University, New Haven, CT, USA. Contact e-mail: emiliano.cocco@yale.edu*

Ovarian Cancer is the most lethal among gynecologic malignancies. Although many patients initially respond to the standard combination of surgery and chemotherapy, nearly 90% later develop incurable recurrent chemo-resistant cancer. Currently, the degree of cytoreduction has been shown to be one of the few prognostic factors. Intraoperative tumor-specific fluorescence imaging has the potential to guide surgeons identifying residual malignant tissue therefore improving tumor resection and consequent patients' outcome. We have recently analyzed the genetic fingerprints of ovarian cancer discovering extremely high expression of genes encoding for claudin-3 and claudin-4, the epithelial receptors for Clostridium Perfringens Enterotoxin (CPE). Importantly, although the administration of the full length CPE in mice is toxic, the injection of the only carboxi-terminal fragment (c-CPE) avoids toxicity while preserving the binding to the receptors. Our previous studies demonstrated a specific in vitro and in vivo binding of FITC conjugated c-CPE (FITC-c-CPE) to multiple primary ovarian carcinomas and a time-dependent internalization of the peptide into tumor cells. In this study we have evaluated the potential of the FITC-c-CPE peptide for real-time tumor imaging applications following c-CPE injection in Xenograft mouse models harboring intraperitoneal human chemo-resistant ovarian cancer. We report fluorescence uptake into the tumor starting 30 minutes after c-CPE injection. Strong signal was retained up to 24 hours after c-CPE administration while negligible staining was detected in control organs. Importantly, when the abdominal cavity of c-CPE injected animals was visualized using a fluorescence microscope, strong signal was detected on metastatic implants of few millimeters in size. Remarkably, when mice presenting ascites were injected with FITC-c-CPE, a strong fluorescence was detected on malignant tumor spheroids isolated from the ascitic fluid (Fig. 1). Finally, we successfully attached c-CPE to a nearInfraRed Dye (CW800) and showed that CW800-c-CPE also accumulated into the tumor starting 30 minutes after intraperitoneal (IP) or intravenous (IV) injection. Ex vivo distribution analysis demonstrated a significantly higher fluorescence intensity in the tumor compared to control organs (kidney, liver, spleen, bowel, lungs, brain and heart; $p<0.01$). In vivo whole body time course fluorescence distribution was carried out on sub-cutaneous models of Xenograft human ovarian cancer after IV injection of CW800-c-CPE. Images showed an initial c-CPE uptake by all well-perfused organs. Interestingly, longer incubations (48-96 hours) resulted in c-CPE accumulation into the tumor while clearance was observed in control organs, suggesting a potential use of c-CPE for diagnostic imaging. Taken together our results demonstrate the ability of c-CPE to specifically target metastatic chemo-resistant ovarian cancer in vivo and suggest the potential use of c-CPE in an intraoperative setting for the optical detection of residual malignant tissue aimed at improving real-time staging and cytoreductive surgery in ovarian cancer patients.

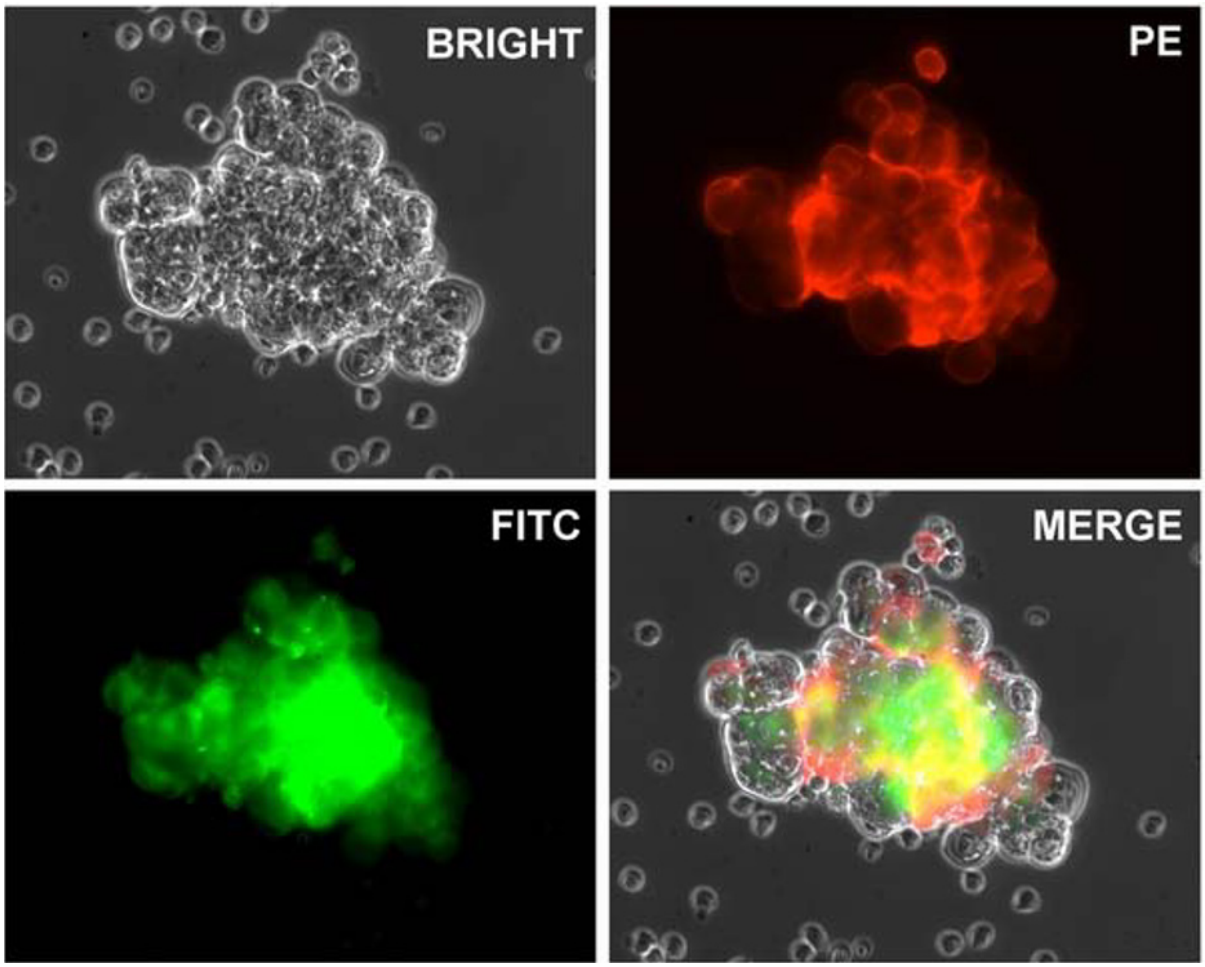

Figure 1: FITC conjugated c-CPE accumulation into tumor floating cells isolated from ascitic fluid of chemo-resistant Ovarian Cancer Xenograft mice. Representative fluorescence microscopy images depicting tumor cells collected from the mouse ascites following abdominal paracentesis 12 hours after IP injection of 10 μg of FITC conjugated c-CPE in a mouse harboring intraperitoneal chemo-resistant human Ovarian Cancer. PE conjugated anti-human EPCAM antibody was used as tumor marker (upper right panel). FITC-c-CPE specifically accumulated into EPCAM positive human tumor cells (lower left and right panels). Notably, no fluorescence was detected on the host contaminant inflammatory cells (i.e., tumor associated lymphocytes, macrophages and DC; upper left and lower right panels).

Disclosure of author financial interest or relationships:
E. Cocco, None; **S. Gasparrini**, None; **S. Bellone**, None; **I. Bortolomai**, None; **S. Lopez**, None; **A.D. Santin**, None.

Presentation Number **LBAP 111**
Late Breaking Abstract Poster Session
September 19, 2013 / 15:15-15:15 / Room: Exhibit Hall B

Nanotechnology-based approach for molecular imaging of PaCa: a MRI-distribution study

Albert Strauss[1], *Sophie Dobiasch*[2], *Klaus Felix*[2], *Ina Rosenberger*[3], *Joerg Kreuter*[3], *Mauro Comes Franchini*[4], *Jean-Paul M. Lellouche*[5], *Liron L. Israel*[5], *Rivka Ben Ishay*[5], *Ghislain Opdenakker*[6], *Jennifer Vandooren*[6], *Kauczor Hans-Ulrich*[1], *Lars Grenacher*[1], [1]*Radiology, Heidelberg University, Heidelberg, Germany;* [2]*Surgery, Heidelberg University, Heidelberg, Germany;* [3]*Institute of Pharmaceutical Technology, Biocentre Niederursel, Goethe University, Frankfurt, Germany;* [4]*Department of Industrial Chemistry "Toso Montanari", University of Bologna, Bologna, Italy;* [5]*Department of Chemistry, Bar-Ilan University, Ramat-Gan, Israel;* [6]*Rega Institute for Medical Research, KU Leuven, Leuven, Belgium. Contact e-mail: Albert.Strauss@med.uni-heidelberg.de*

Background & Purpose: MRI distribution studies were done using five different nanoparticles targeted for pancreatic adenocarcinoma (PDAC). These nanoparticles were developed as part of the EU funded SaveMe project (http://fp7-saveme.com), a consortium of nineteen european research institutions. The overall aim of the project is the development of a modular nanosystem as carrier for diagnostic as well as therapeutic agents, targeting PDAC. Material & Methods: Galectin-1 (Gal-1) has been chosen as the target molecule as this protein was shown to be strongly overexpressed in PDAC as well as in its precursor lesions pancreatic intraepithelial neoplasias but not in normal pancreas, demonstrated by QRT-PCR, Western blot, IHC and IF techniques. For targeting the tumor, four 10-20 AA long peptide-sequences derived from tissue plasminogen activator (tPA), functioning as Gal-1 ligands have been chosen and linked to different nanoparticles. Project partners have developed different nanoparticles of which five were analyzed using MRI regarding their distribution in the first 60 minutes after administration. These targeted and iron loaded nanoparticles (Core CAN-maghemite nanoparticles (Ce-Fe2O3) n=3, serum-albumin-iron-complex n=2) were tested in immunocompromized mice carrying an orthotopic as well as a subcutaneous pancreatic tumor (orthotropic & subcutaneous n=4, just orthotropic n=2, Panc-1 n=4, Su86.86 n=2). Two particles were additionally covered with MMP-9-substrates as a novel approach to cloak the particles and increase their size as a matter to escape the RES-system as far as possible. T2-weighted sequences were used prior to as well as after administration of these particles using a 1.5T MRI (Siemens Magnetom Symphony Syngo) and a custom mouse coil. T2 intensities (T2 tse) were compared preinjection and repetitively (eight different points in time) after injection of the particles over a period of 60 minutes after injection. T2-signal intensities were measured for the orthotopic and the subcutaneous tumor, as well as the liver (as reference point for the RES). The mouse was not moved between the measurements. Results: The largest signal drop for the liver was 84% (364 vs. 61 signal intensity) 44 min after injection of the particles. Signal loss in the orthotopic tumor reached a maximum of 18% (1181 vs. 974, %liver/%ortho=4,4) 60 min after injection and the subcutaneous tumor showed a maximum signal drop of 12% (998 vs. 878, %liver/%sc=6,6) 60 min after injection. Even after addition of MMP9 substrates escape of the particles into the RES (mainly liver and spleen) remained significant. Conclusions: Two of the particles showed a clear tendency of accumulation over time inside the tumor. This behavior was more marked for the orthotropic tumor. It seems that the plateau was not reached after 60 min.

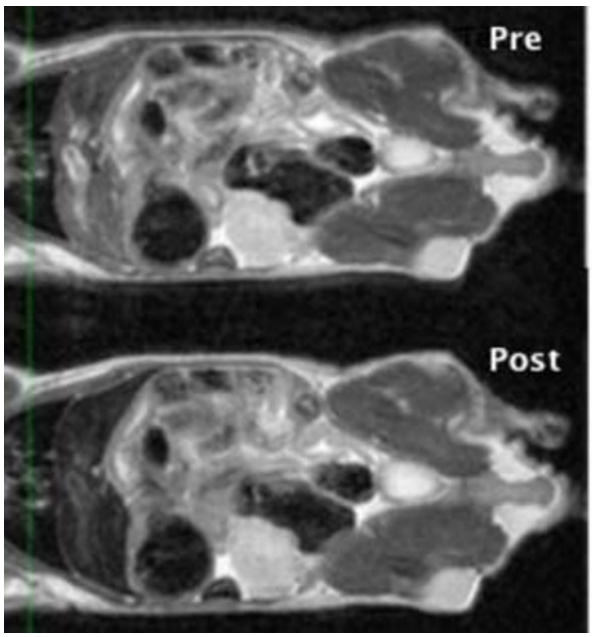

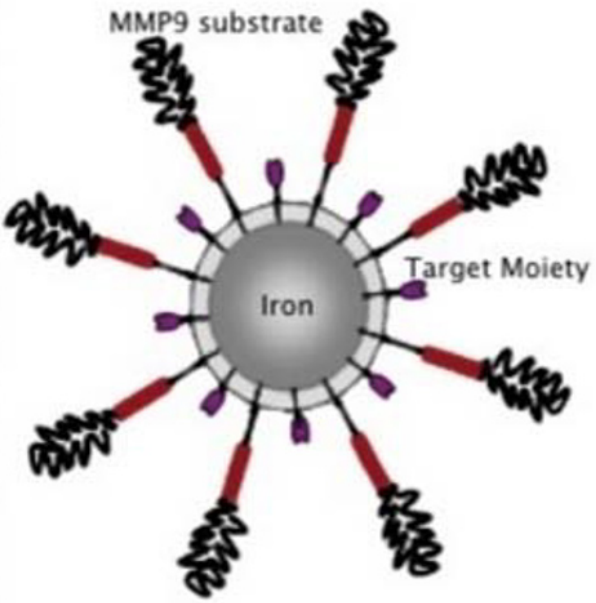

Disclosure of author financial interest or relationships:
A. Strauss, None; **S. Dobiasch**, None; **K. Felix**, None; **I. Rosenberger**, None; **J. Kreuter**, None; **M. Comes Franchini**, None; **J.M. Lellouche**, None; **L.L. Israel**, None; **R. Ben Ishay**, None; **G. Opdenakker**, None; **J. Vandooren**, None; **K. Hans-Ulrich**, None; **L. Grenacher**, None.

Presentation Number **LBAP 112**
Late Breaking Abstract Poster Session
September 19, 2013 / 15:15-15:15 / Room: Exhibit Hall B

Multitracer Assessment of an Orthotopic Colorectal Cancer Model in Mice by Multimodal Molecular Imaging

Sara Rapic[1], *Sven De Bruycker*[1], *Christel Vangestel*[1,2], *Jeroen Verhaeghe*[1], *Leonie Wyffels*[1,2], *Tim Van den Wyngaert*[1,2], *Steven Staelens*[1], *Sigrid Stroobants*[1,2], [1]*Molecular Imaging Center Antwerp, University of Antwerp, Antwerp, Belgium;* [2]*Department of Nuclear Medicine, University Hospital Antwerp, Antwerp, Belgium. Contact e-mail: sara.rapic@ua.ac.be*

Introduction. Colorectal cancer (CRC) is one of the leading causes of cancer-related death due to recurrence and metastasis as a result of therapy resistance. Non-invasive positron emission tomography (PET) imaging using dedicated tracers as predictive biomarkers may assist in early evaluation of therapy efficacy. Discrepancies between promising preclinical trial results and subsequent lack of clinical effect, have lead to the belief that traditional subcutaneous tumor models in animals are not optimal for translational cancer research. Therefore, renewed focus is on orthotopic tumors as a more natural tumor microenvironment, more reliably mimicking human disease. We aim to establish a reproducible orthotopic mouse model of CRC for a PET biomarker validation study. Materials & Methods. A human colon cancer cell line (Colo205) transfected with a firefly luciferase gene was used to create either subcutaneous (n=22) or orthotopic (n=4) tumors in athymic nude mice. Orthotopic tumors were created through microsurgical transplantation of a subcutaneously grown tumor fragment harvested from donor animals onto the caecal wall of recipient mice. Bioluminescence imaging (BLI) was performed twice a week to monitor tumor implantation and growth. Animals with subcutaneous (250±186 mm3) and orthotopic tumors (285±92 mm3) underwent static 18F-fluoro-2-deoxy-D-glucose (FDG) PET-CT imaging 2 and 3 weeks after inoculation, respectively. Three mice with orthotopic tumors underwent additional dynamic 18F-fluorothymidine (FLT) PET-CT imaging 4 weeks after transplantation. Subcutaneous tumors were delineated on CT images and maximum standardized uptake values (SUVmax) were calculated. For the orthotopic tumors, due to a general lack of soft tissue µCT contrast, we applied threshold based automated tumor delineation on PET images (VOI = 80 % of maximal value) to calculate both SUVmax and the 18F-FLT uptake rate (Ki) using a 2 tissue kinetic model and an image derived left ventricle input function. Histological examination of the tumors was done using H&E for morphological evaluation and Ki-67 for proliferation assessment. Results. PET-CT imaging showed twofold higher tumor uptake of 18F-FDG in orthotopic tumors as compared to subcutaneous tumors (SUVmax = 3.39±0.45 vs. 1.53±0.41, respectively, $p<0.005$). 18F-FLT uptake in the orthotopic tumors reached high SUVmax and Ki values (1.86±0.39 and 0.021±0.009 min-1, respectively). Macro- and microscopic evaluation showed local invasiveness of orthotopic tumors into the caecum. Immunohistochemistry revealed a high level of mitosis and proliferation and little or no necrosis. Furthermore, the tumors showed evidence of neovascularization. In subcutaneous tumors, the level of mitosis, proliferation and neovascularization was considerably lower. Conclusion. Our implementation of this orthotopic mouse model through donor fragment transplantation onto the receiving animal's caecum proves to be a promising model for the investigation of CRC and for biomarker validation. Future plans involve the inclusion of 18F-CP18, a tracer for caspase-3 activity, to examine therapy induced interaction between proliferation and apoptosis.

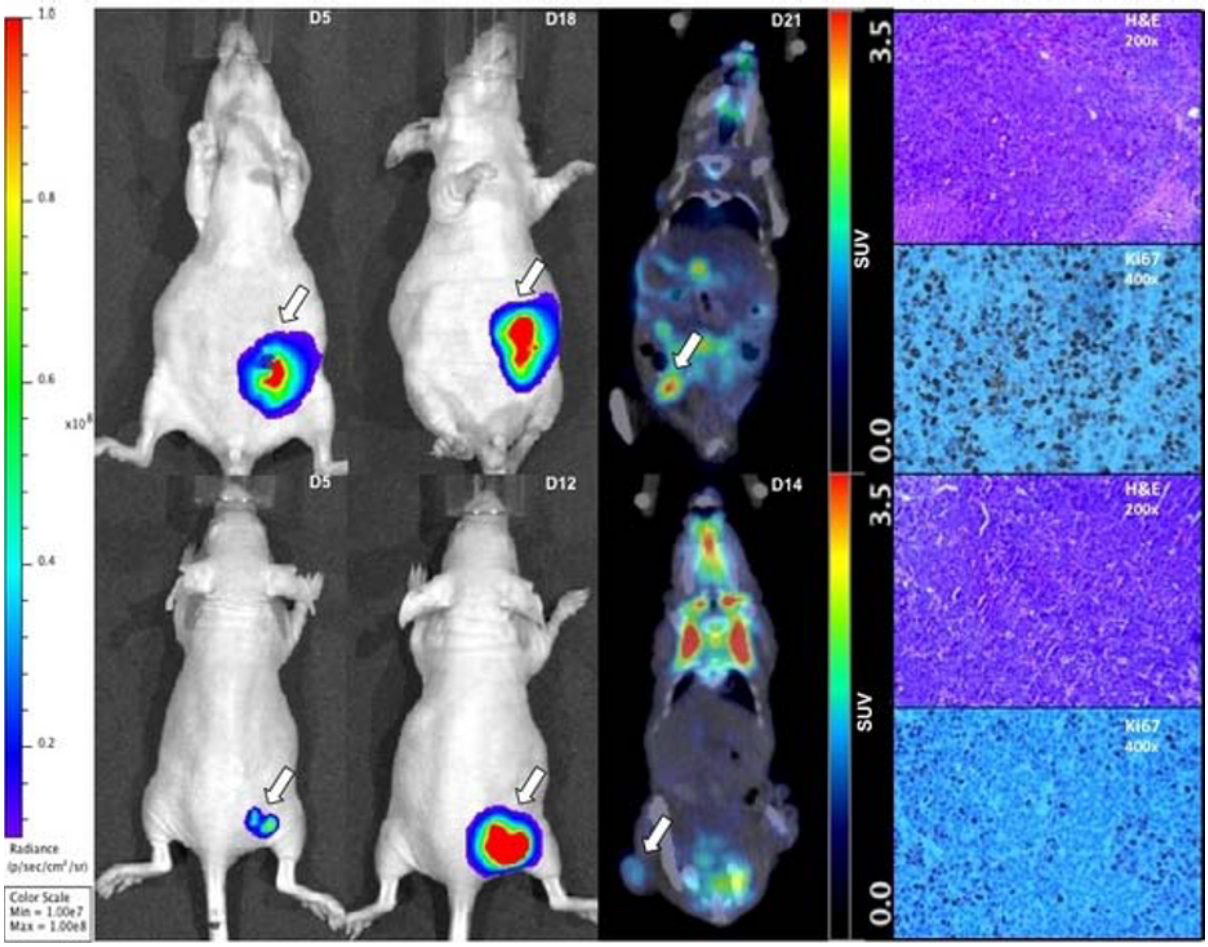

Orthotopic model (upper panel) vs. subcutaneous model (lower panel). Shown from left to right are representative images obtained from BLI, PET-CT and immunohistochemistry showing the follow-up of tumor growth, tumor metabolism as well as tumor histology (H&E) and proliferation (Ki67), respectively. Arrows indicate tumor localization.

Disclosure of author financial interest or relationships:
S. Rapic, None; **S. De Bruycker**, None; **C. Vangestel**, None; **J. Verhaeghe**, None; **L. Wyffels**, None; **T. Van den Wyngaert**, None; **S. Staelens**, Johnson & Johnson, Grant/research support; **S. Stroobants**, Janssen Pharmaceuticals, Grant/research support .

Presentation Number **LBAP 113**
Late Breaking Abstract Poster Session
September 19, 2013 / 15:15-15:15 / Room: Exhibit Hall B

Development of a Tongue Carcinoma Model Using Real-Time In Vivo Molecular Monitoring

Marisa R. Buchakjian[2,1], *Michael D. Henry*[1], [1]*Molecular Physiology and Biophysics, University of Iowa Carver College of Medicine, Iowa City, IA, USA;* [2]*Otolaryngology - Head and Neck Surgery, University of Iowa Hospitals and Clinics, Iowa City, IA, USA. Contact e-mail: marisa-buchakjian@uiowa.edu*

Objective: Head and neck squamous cell carcinoma (HNSCC) poses a significant clinical challenge, with an incidence of 600,000 cases and a survival rate of 50%. Mouse models of cancer have provided critical insights into disease mechanisms, and there remains an urgent need for translational HNSCC models. In this proposal we describe a novel viral-mediated inducible mouse model of HNSCC based on somatic induction and tongue-specific loss of TP53/PTEN. Importantly, this model is coupled with Cre-dependent luciferase expression to facilitate longitudinal, noninvasive bioluminescence imaging of gene recombination and tumor formation. Materials/Methods: C57BL/6 mice with floxed TP53/PTEN and a lox-stop-lox luciferase allele (ROSA26 LSL-luc TP53-/- PTEN-/-) were engineered for the proposed model. Adenovirus or adeno-associated virus containing a Cre-recombinase expression vector was injected directly into the tongue mucosa to promote site-specific Cre expression and gene recombination. Mice were evaluated for luciferase expression using intraperitoneal luciferin delivery and in vivo molecular imaging using the Ami X bioluminescence imager and analysis software from Spectral Instruments Imaging. Injected mice were followed longitudinally with real-time bioluminescence imaging to evaluate gene recombination and tumor development. Results: A pilot cohort of eight ROSA26 LSL-luc TP53-/- PTEN-/- mice underwent a single tongue adeno-Cre injection with a range of viral titers. Mice were imaged 24 hours post-exposure and biweekly thereafter. The Ami X imaging system was sufficiently sensitive to detect gene recombination and luciferase expression in the tongue as early 24 hours post-injection, suggesting efficient viral delivery and recombination. In addition to luciferase expression in the tongue, signal was observed in draining lymph nodes, alerting us to limitations in the specificity of our viral delivery and prompting us to evalute adeno-associated virus serotypes. Luciferase expression in the tongue as measured by in vivo bioluminescence imaging increased over time as cells with presumed TP53/PTEN loss continued to grow and divide. The initial pilot mouse, which was injected in the tongue and bilateral flanks with varying titers of adeno-Cre, developed a tumor at the site of greatest viral exposure (right flank) after 10 weeks. Bioluminescence at the flank as well as at the tongue, which received an intermediate viral dose, demonstrated an increase in bioluminescence over time, with in vivo signal significantly preceding tumor palpation or visualization. Conclusions: This proposal describes our progress in developing an innovative model of tongue carcinoma based on viral-mediated TP53/PTEN knockout coupled with luciferase expression for in vivo longitudinal tumor imaging. Successful development of this model will help us gain a better understanding of HNSCC development and progression, and real-time molecular imaging of cancer cells in vivo will allow us to monitor tumor dynamics and metastasis. In the future, this model may serve as a valuable translational tool for monitoring preclinical responses to novel treatment algorithms.

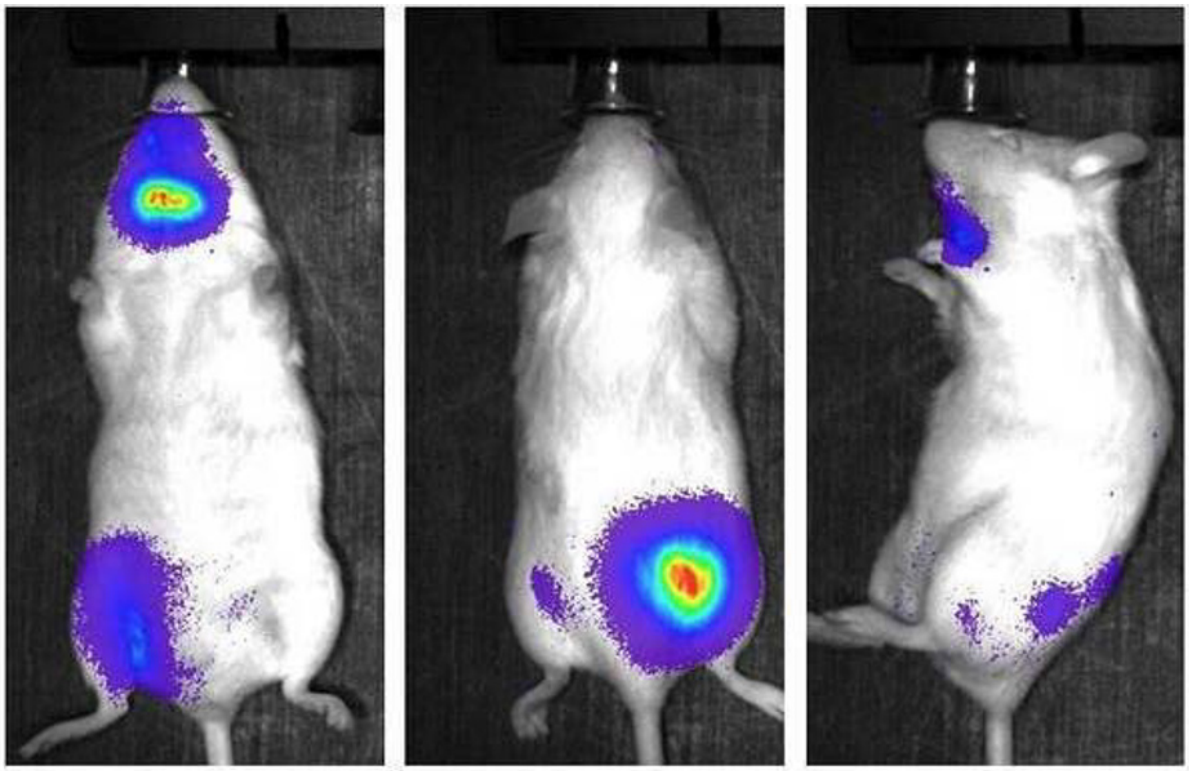

Figure 1. Luciferase expression 5 weeks post- adeno-Cre injection in tongue and bilateral flanks. Image obtained on Ami X with 5 minute exposure time following intraperitoneal D-luciferin administration.

Disclosure of author financial interest or relationships:
M.R. Buchakjian, None; **M.D. Henry**, None.

Presentation Number **LBAP 114**
Late Breaking Abstract Poster Session
September 19, 2013 / 15:15-15:15 / Room: Exhibit Hall B

Detection of orthotopic pancreatic tumors using multispectral optoacoustic tomography

Christopher England[1], *Shanice V. Hudson*[1], *Justin Huang*[1], *Wenyuan Yin*[1], *Hermann Frieboes*[2], *Lacey R. McNally*[1], [1]*Medicine, University of Louisville, Louisville, KY, USA;* [2]*Engineering, University of Louisville, Louisville, KY, USA. Contact e-mail: c0engl03@louisville.edu*

Detection of primary pancreatic tumors hinder quick diagnosis, diminishing clinical outcomes. Due to anatomical location of pancreas, along with lack of functional imaging agents, most pancreatic tumors are found during late stages. This predicament yields 5 year survival rates ~5%. While optical imaging techniques, e.g. bioluminescence and fluorescence imaging, have been employed to monitor pancreatic tumor growth in pre-clinical models, these techniques have two major disadvantages, namely limited tissue penetration and high light scattering. The newly emerging imaging technology, photoacoustic tomography, provides high optical contrast images at microscale resolution and at a reasonable penetration depth. We hypothesize that the introduction of exogenous probes could greatly enhance contrast, detection, and further enable resolution of orthotopic pancreatic tumors. S100A9 is a novel ligand for the extracellular matrix metalloproteinase inducer (EMMPRIN), a glycoprotein on tumor cells. We developed a S100A9-NIR labeled probe to target EMMPRIN for the detection of pancreatic cancer in vivo using multispectral optoacoustic tomography (MSOT) and fluorescent imaging (AMI 1000X). The bio-conjugated probe was synthesized by attaching the water soluble CF750 dye with the functionalized S100A9 ligand. To ensure activity of the probe after conjugation, flow cytometery and immunocytochemistry were performed. To measure probe accumulation in orthotopic pancreatic tumors, mice were injected with either 1 x 106 S2VP10 or 5 x 107 MiaPaCa2 cells and tumor formation occurred in 7 days (S2VP10) or (21 days) MiaPaCa2. Probe accumulation was observed within the pancreatic tumors via MSOT imaging. Accumulation of probe was further confirmed using fluorescence imaging (AMI 1000X) in vivo and ex vivo tumors. Flow cytometry revealed specific cellular uptake of S100A9 probe, with minimal uptake of the CF750 dye alone. Immunocytochemistry showed specific uptake of the probe, further ensuring the activity of the probe. Accumulation of probe within tumor was confirmed through AMI fluorescence imaging and MSOT with specific uptake in tumor regions, within minimal uptake (below detection limit) within healthy tissue in vivo. Our study demonstrates the feasibility of the combination of multispectral optoacoustic tomography and NIR-labeled probes for improved detection, both in specificity and sensitivity, of pancreatic tumors.

Disclosure of author financial interest or relationships:
C. England, None; **S.V. Hudson**, None; **J. Huang**, None; **W. Yin**, None; **H. Frieboes**, None; **L.R. McNally**, None.

Presentation Number **LBAP 115**
Late Breaking Abstract Poster Session
September 19, 2013 / 15:15-15:15 / Room: Exhibit Hall B

Tissue Localization of Cetuximab-IRDye800CW in Macaques Using Fluorescence Imaging

Asher M. Krell[2], *Melissa L. Korb*[3], *Trenton R. Schoeb*[4], *Jack O'Malley*[1], *Eben L. Rosenthal*[2], *Kurt R. Zinn*[1], [1]*Radiology Chair Office, University of Alabama at Birmingham, Birmingham, AL, USA;* [2]*Surgery/Otolaryngology, University of Alabama at Birmingham, Birmingham, AL, USA;* [3]*Surgery, University of Alabama at Birmingham, Birmingham, AL, USA;* [4]*Genetics, University of Alabama at Birmingham, Birmingham, AL, USA. Contact e-mail: akrell@uab.edu*

Monoclonal antibodies targeting over-expressed receptors on cancer cells provide important mechanisms for tumor treatment. Cetuximab targets the epidermal growth factor (EGFR) that is often used alone or in combination with other therapies. Despite its widespread use since 2005 little is known about the specific regions within tissues where the drug is localized following administration. Fluorescence tissue imaging after systemic administration of cetuximab conjugated to a near infrared fluorophore provides a novel approach to address this question. The goal of this experiment was to examine and localize fluorescence in macaques treated with cetuximab-IRDye800CW, since this agent binds equivalently to macaque and human EGFR. Cetuximab was covalently linked to IRDye800CW (LICOR Biosciences, Ab: dye ratio = 1.8), with retained immunoreactivity. Male cynomolgus macaques (~3kg) were intravenously injected with either cetuximab-IRDye800 (treatment group, n=4) or cetuximab (control group, n=4) at a dose of 20.83 mg/kg over 1 hour. At necropsy on post-infusion day 15, a total of 38 tissue samples from each primate were collected, mounted, and stained for hematoxylin and eosin (H&E). Slides containing treatment and control tissue pairs were fluorescently imaged on the Odyssey (LICOR) scanning system using the same acquisition settings. Overlays were created with high resolution photos taken of the H&E stained slides to determine localization of IRDye800 fluorescence in each tissue, as determined by comparing directly with control tissues. Fluorescence signal in each tissue section was further analyzed using ImageJ. The liver had the highest fluorescence signal consistent with high EGFR expression and known liver clearance of cetuximab (Fig. 1). The brain and GI tract showed the lowest signal above background. Cetuximb-IRDye800 fluorescence was identified within the connective tissues of the testicle but not in the seminiferous tubules with a similar pattern to collagen staining. The lymph nodes also had particularly high localization of fluorescence concentrated in the medullary portion of the node however, little to limited dye was found in the lymphoid tissue itself. Fluorescence localized within the connective tissue of the liver as well; however it was a much more diffuse pattern with additional dye remaining in the wall of the vasculature and wall of the gall bladder. In the lungs the dye was diffusely retained within the alveoli with some staining in the walls of the airways and vessels. Tissue taken from both the anterior and posterior skin had higher fluorescence in the epithelium of the hair follicles and a particularly high and diffuse pattern in all layers of the epidermis excluding the stratum corneum. ImageJ analyses results are presented in Figure 2, with liver showing the highest fluorescence, and a treatment: control ratio of 2.8. IRDye800 fluorescence was detected 15 days after administration and post fixation and H&E staining. Fluorescence was identified in the connective tissue, vessel walls, and epithelial cells of the epidermis. The low fluorescence of tissue from the brain is due to the blood brain barrier restricting passage.

Disclosure of author financial interest or relationships:
A.M. Krell, None; **M.L. Korb**, None; **T.R. Schoeb**, None; **J. O'Malley**, None; **E.L. Rosenthal**, None; **K.R. Zinn**, None.

Presentation Number **LBAP 116**
Late Breaking Abstract Poster Session
September 19, 2013 / 15:15-15:15 / Room: Exhibit Hall B

Pharmacokinetic analysis of IRDye 800CW 2-DG in the mouse kidney by photoacoustic imaging

Andrew Heinmiller[1], *Minalini Lakshman*[1], *Joy L. Kovar*[2], *Daniel Draney*[2], *Andrew Needles*[1], *Catherine Theodoropoulos*[1], [1]*FUJIFILM VisualSonics, Inc., Toronto, ON, Canada;* [2]*LI-COR Biosciences, Lincoln, NE, USA. Contact e-mail: aheinmiller@visualsonics.com*

Introduction: The ability to determine the distribution, clearance and retention of drugs, toxins or other exogenous substances within the body after their administration is vitally important for drug development and is necessary to calculate various pharmacokinetic metrics such as dose, plasma concentration and half-life. Photoacoustic (PA) imaging allows for the high-resolution visualization of optical absorbers in vivo and non-invasively1, making it an ideal tool for studying pharmacokinetics. 2-deoxyglucose (2-DG) is a glucose analogue which accumulates within metabolically active cells. 2-fluoro-2-deoxyglucose is used extensively in PET studies for various applications2 including visualizing tumor location and metabolic activity. 2-DG conjugated with the near infrared fluorophore IRDye 800CW can be used with fluorescent and photoacoustic imaging systems, taking advantage of its long half-life and lack of ionizing radiation3. In the current study, the pharmacokinetics of IRDye 800CW carboxylate and IRDye 800CW 2-DG in the kidney were analyzed using a commercially available photoacoustic imaging system and verified with histology. Methods: Photoacoustic imaging was performed on the Vevo® LAZR system (FUJIFILM VisualSonics Inc.). Kidney imaging was accomplished with a LZ250 linear array transducer (fc = 21MHz). IRDye 800CW carboxylate was imaged in a polyethylene tube phantom for spectral analysis. IRDye 800CW 2-DG or IRDye 800CW carboxylate (LI-COR Biosciences) was administered by tail vein at a dose of 0.4 mM (200ul). 2D and 3D photoacoustic imaging of the kidney was performed before, immediately, 6 hours and 24 hours after injection. The PA signal at various wavelengths was examined including 780nm and 850nm as well as the Spectro tool, which sweeps the entire wavelength range from 680nm to 970nm in one 2D slice. Quantification of signal was performed by drawing 2D and 3D ROIs around the kidney for each time point and wavelength, giving average PA intensity measurements within the ROIs. Histology was performed to verify results obtained with photoacoustics. Results: IRDye 800CW carboxylate showed a peak photoacoustic signal at approximately 785nm in the phantom. Bolus infusion showed a clear increase in signal upon injection of the dye. Spectral analysis of the kidney of the IRDye 800CW 2DG-injected animal revealed a peak signal at approximately 785nm as compared to before injection where the peak was at 760nm, strongly suggesting the presence of the conjugate. 3D analysis showed the difference in signal between 780nm and 850nm increased over time, further indicating the presence of the conjugate in the kidney which was confirmed by histology. Conclusions: We have demonstrated the use of the Vevo LAZR photoacoustic imaging system to perform pharmacokinetic studies and confirmed this use with histology. In addition, we demonstrate the use of a multi-modality agent for imaging metabolism non-invasively with high resolution in deep tissue. Future studies could involve looking at different organs such as the liver or brain as well as assessing pharmacokinetics in disease models such as cancer.

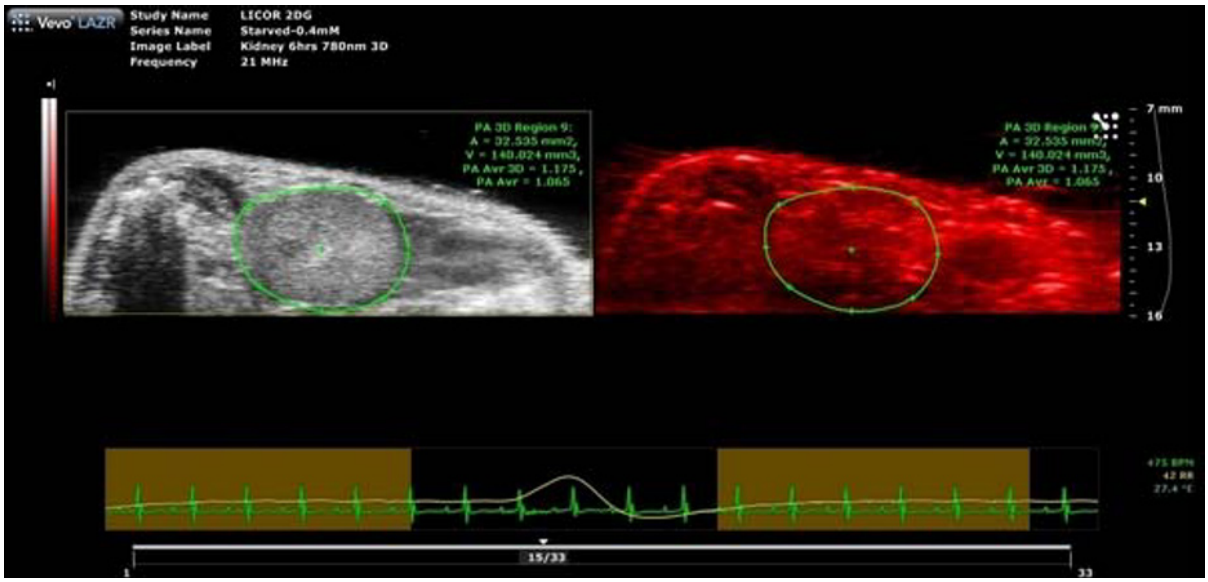

Co-registered ultrasound (left) and photoacoustic (right) image at 780nm of the mouse abdomen with an ROI drawn around the kidney.

Disclosure of author financial interest or relationships:

A. Heinmiller, FUJIFILM VisualSonics Inc., Employment; **M. Lakshman**, FujiFilm Visualsonics Inc.,, Employment; **J.L. Kovar**, LI-COR Biosciences, Employment; **D. Draney**, LI-COR, Inc., Employment; **A. Needles**, FUJIFILM VisualSonics, Inc., Employment; **C. Theodoropoulos**, Fujifilm VisualSonics Inc, Employment .

Presentation Number **LBAP 117**
Late Breaking Abstract Poster Session
September 19, 2013 / 15:15-15:15 / Room: Exhibit Hall B

PET Imaging Biomarkers to select the target and predict the response to Anti-HER-1 Therapy in Esophageal Squamous Cell Carcinoma Model

In Ho Song, *Tae Sup Lee, Kwang Il Kim, Yong Jin Lee, Joo Hyun Kang, Molecular Imaging Research Center (MIRC), Korea Institute of Radiological and Medical Science (KIRAMS), Seoul, Republic of Korea. Contact e-mail: inosong@kirams.re.kr*

Esophageal squamous cell carcinoma (ESCC) is one of the most aggressive malignant tumors of the digestive tract. High levels of epidermal growth factor receptor (EGFR) expression are observed frequently in ESCC, and it is reportedly a significant prognostic indicator for ESCC. This study is aimed to select tumor with the high EGFR expression using ^{64}Cu-labeled cetuximab (CET), and the ^{64}Cu-CET and FDG-PET monitoring to predict therapeutic efficacy by anti-HER-1 therapy in ESCC model. EGFR expression level of ESCC cell lines, TE4 and TE8, was analyzed by western blot and flow cytometry. CET was conjugated with p-SCN-Bn-PCTA and radiolabeled with ^{64}Cu. Biodistribution and PET imaging of ^{64}Cu-PCTA-CET were performed in TE4 and TE8 ESCC tumor bearing mice. ESCC bearing mice were treated with CET or isotype control for 28 days twice a week (50 mg/kg). ^{64}Cu-CET and FDG-PET images were obtained before and after anti-HER-1 therapy. FDG-PET monitoring performed once a week during CET treatment. Tumor volume and body weight were measured three times a week. Immunohistochemistry to TUNEL and phospho-Akt were performed. EGFR expression level in TE8 was higher than that in TE4. ^{64}Cu-PCTA-CET prepared by high radiolabeing yield and showed high stability in human serum. ^{64}Cu-CET showed higher uptake in TE8 tumor, compared to TE4 tumor. In CET-treated group, tumor volume and FDG uptake of TE8 tumor was markedly reduced, but those of TE4 gradually increased. In isotype control-treated group, tumor growth and FDG uptake continually increased. ^{64}Cu-PCTA-CET uptake in TE8 decreased by CET treatment , but ^{64}Cu-PCTA-CET uptake in TE4 maintained. In CET-treated group, TE8 tumor showed increased TUNEL positive and decreased phospho-Akt staining by CET treatmentr. Tumor uptake of ^{64}Cu-CET represented EGFR expression level and therapeutic efficacy in ESCC model. Change of ^{64}Cu-CET and FDG uptake showed a good correlation with therapeutic response to anti-HER-1 therapy. Evaluation of HER-1 expression in ESCC with ^{64}Cu-PCTA-CET immuno-PET may be helpful to screen ESCC patient pertinent to anti-HER-1 treatment, and ^{64}Cu-CET and FDG PET could be useful for therapeutic response monitoring of anti-HER-1 immunotherapy.

Disclosure of author financial interest or relationships:
I. Song, None; **T. Lee**, None; **K. Kim**, None; **Y. Lee**, None; **J. Kang**, None.

Presentation Number **LBAP 118**
Late Breaking Abstract Poster Session
September 19, 2013 / 15:15-15:15 / Room: Exhibit Hall B

Whole body irradiation of mice produces bioluminescence and increased ROS activity reporting chemiluminescence

Rao V. Papineni, *PACT & Health, Branford, CT, USA. Contact e-mail: papineni@graduate.hku.hk*

Earlier work from my laboratory demonstrated that molecular probes including near-IR dye conjugated bisphosphonate can monitor radiation-induced physiological changes at the target and off-target sites using in vivo molecular imaging approaches (presented at WMIC 2011). Here, we utilized sensitive in vivo imaging methodologies to determine if endogenous bioluminescence resulting from whole body irradiation can be determined. Further, using molecular probes, investigate the reactive oxygen species (ROS) activity generated in the process. Swiss albino mice without anesthesia were held in ventilated mouse pie cage and subjected to 5 Gy X-ray irradiation using commercially available X-RAD 320 irradiator (1Gy/min; F2 beam hardening filter 1.5mm Al, 0.25mm Cu, 0.75mm Sn,). The endogenous bioluminescences from the subjects were captured using cooled CCD camera. Significant increase (up to 100 fold) in the amounts of photons released as bioluminescence was detected during 5 min capture from the mice subjected to irradiation compared to that of the control. To determine the early inflammatory response, the reactive oxygen species (ROS) activity was monitored using L-012 (8-amino-5-chloro-7-phenylpyridol [3,4-d]pyridazine-1,4(2H,3H) dione), a chemiluminescence reporter. L-012 was administered (i.p) after 15 min of irradiation. Chemiluminescence resulting from the irradiation induced ROS activity, possible through the action of the polymorphonuclear leucocytes (PMN), was imaged in real-time. Robust increase in ROS activity was determined in mice subjected to 5 Gy irradiation compared to the controls (Figure-1). The relationship between chemiluminescence and the availability of the substrate (L-012) during irradiation was also assessed. The increased ROS activity and their potential role in treatment strategies will be discussed. Such molecular imaging methodologies and modalities described will be useful tools in treatment design and process. Further, such tools will be valuable in biodosimetry, assessing radiation damage in humans during nuclear terrorism or mass radiation accidents.

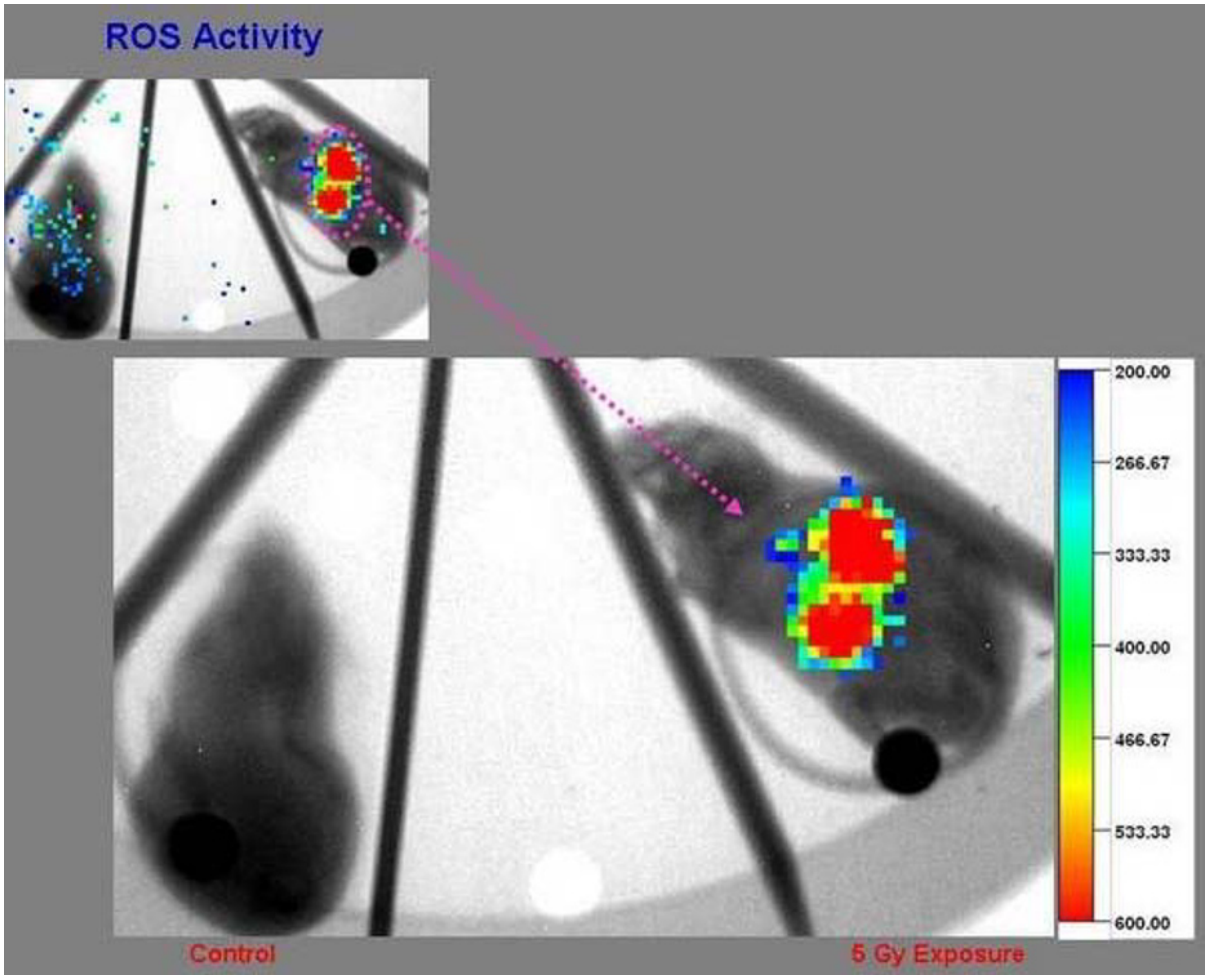

Disclosure of author financial interest or relationships:
R.V. Papineni, None.

Presentation Number **LBAP 119**
Late Breaking Abstract Poster Session
September 19, 2013 / 15:15-15:15 / Room: Exhibit Hall B

X-ray skeleton imaging in conjunction with bioluminescence imaging does not alter pancreatic tumors

Christopher England[1], *Shanice V. Hudson*[1], *Justin Huang*[1], *Wenyuan Yin*[1], *Hermann Frieboes*[2], *Lacey R. McNally*[1], [1]*Medicine, University of Louisville, Louisville, KY, USA;* [2]*Engineering, University of Louisville, Louisville, KY, USA. Contact e-mail: c0engl03@louisville.edu*

The technology for bioluminescence imaging allows for noninvasive study of biological processes in small animals. Since mammalian tissues have low intrinsic bioluminescence, images are obtained with incredibly high signal-to-noise ratio. The ease of use, along with capabilities to monitor disease progression, has prompted bioluminescence imaging as an excellent methodology for cancer research. Recently, detection of mouse skeleton via X-Ray, has become popular as a method for providing anatomical context of bioluminescence signals. Because repeated X-ray can cause DNA damage, upregulate radiation sensitive proteins, and induce cell stress, our goal was to evaluate the potential damage resulting from repeated X-ray exposure in conjunction with bioluminescence imaging. Mice were orthotopically implanted with either S2VP10L or MiaPaCa2A cells containing a luciferase reporter. Mice were imaged ten times on consecutive days using bioluminescence imaging in conjunction with either High Resolution X-ray or Low Resolution X-ray using an Advanced Molecular Imager 1000X. A dosimeter was placed inside the AMI along with each group of mice. Total radiation was measured via dosimeter. Bioluminescence signals were compared for both groups. At the end of 10 days, Rad51, H2AX, and TUNEL were evaluated on tumor and liver sections. The radiation dose for the High Resolution was 15.6mGy while the Low Resolution was 10.7 mGy. S2VP10 and MiaPaCa2 tumors did not have higher levels of double strand breaks in comparison to control tumors. Additionally, immunohistochemistry did not demonstrate a statistical difference in radiation sensitive proteins. Overall, radiation exposure obtained during animal imaging does not increase DNA damage, up-regulate radiation sensitive markers, or induce cell stress.

Disclosure of author financial interest or relationships:
C. England, None; **S.V. Hudson**, None; **J. Huang**, None; **W. Yin**, None; **H. Frieboes**, None; **L.R. McNally**, None.

Presentation Number **LBAP 120**
Late Breaking Abstract Poster Session
September 19, 2013 / 15:15-15:15 / Room: Exhibit Hall B

Preclinical evaluation of AminoMedixTM as a Kidney protective agent during peptide receptor radionuclide Therapy (PRRT)

David Ranganathan[1], *Sanjay I. Thamake*[1], *Izabela Tworowska*[2,1], *Ebrahim Delpassand*[2,1], [1]*RITA foundation, Houston, TX, USA;* [2]*RadioMedix Inc, Houston, TX, USA. Contact e-mail: dranganathan@radiomedix.com*

Introdcution: PRRT using radiolabelled somatostatin analogues shows beneficial results in patients suffering from neuroendocrine tumor (NET). One of the main dose limiting factor in PRRT is the renal reabsorption of radiopeptides to kidney, which may lead to radiation induced nephrotoxicity. The Co-infusion of lysine/arginine lowers renal retention of these radiopeptides by about 40%. Here, we report an agent, (AminoMedixTM) reducing the kidney uptake of radiopeptides by 67% without compromising the tumor uptake in mice. Methods: AminoMedixTM solution contains Amifostine trihydrate, Lysine hydrochloride and Arginine hydrochloride. In this study, we tested combinations of various amounts of all three components and tested the kidney retention of 68Ga-octreotide in mice model. The mice were give three intravenous injections of AminoMedixTM solution (200µL) at every 45 min interval and sacrificed 4 h post 68Ga-octreotide injection. The 68Ga-octreotide injection was administered 30 min after 1st AminoMedixTM injection. The kidney retention of 68Ga-octreotide was analyzed using gamma counter. We further evaluated AminoMedixTM solutions effect on tumor uptake in mice bearing pancreatic NET tumor. Results: The AminoMedixTM composition showed significant reduction in kidney uptake of 68Ga-octreotide by 67 % among all various compositions we tested. We compared the kidney protective effect of AminoMedixTM solution with individual components of AminoMedixTM, Lysine & Arginine (used in Europe) and 15% Clinisol (used in USA). The uptake of radiolabelled octreotate in somatostatin receptor-expressing normal tissues and tumor was not affected by AminoMedixTM solution. Conclusion: The AminoMedixTM resulted in maximum reduction of renal retention of 68Ga-octreotide. Tumor uptake of radiolabelled octreotate was not affected, resulting in an increased tumor to kidney ratio. More effective kidney protective agents can enhance the safety profile and probably facilitate higher maximum tolerated dose of radiopeptide in PRRT.

Disclosure of author financial interest or relationships:
D. Ranganathan, None; **S.I. Thamake**, None; **I. Tworowska**, None; **E. Delpassand**, RadioMedix, Stockholder .

Presentation Number **LBAP 121**
Late Breaking Abstract Poster Session
September 19, 2013 / 15:15-15:15 / Room: Exhibit Hall B

PET-based imaging of T cells used for immunotherapy of CD19+ malignancies

Shahriar Yaghoubi[1,3], *Amer M. Najjar*[2], *Simon Olivares*[2], *Harjeet Singh*[2], *Helen Huls*[2], *Pallavi Raja Manuri*[2], *Laurence J. Cooper*[2], *[1]CellSight Technologies, Inc., San Francisco, CA, USA; [2]Immunology, Pediatrics and Experimental Diagnostic Imaging, MD Anderson Cancer Center, Houston, TX, USA; [3]Molecular and Medical Pharmacology, UCLA, Los Angeles, CA, USA. Contact e-mail: syaghoubi@cellsighttech.com*

Introduction: Clinical immunotherapy trials using T cells expressing a CD19-specific chimeric antigen receptor (CAR) to target B cell malignancies are currently ongoing at the University of Texas M.D. Anderson Cancer Center (MDACC). Clinical-grade CAR+ T cells can be readily generated using the Sleeping Beauty (SB) system. This non-viral gene transfer approach can be readily and inexpensively adapted to co-express reporter genes that will enable repetitive and non-invasive whole-body monitoring of infused T cell kinetics in cancer patients by positron emission tomography (PET). This information will be essential in personalizing immunotherapy and maximizing its effectiveness. We are validating a PET reporter gene (PRG)/probe (PRP) technology for imaging CAR+ T cell trafficking and tumor targeting kinetics with the goal of clinical translation. Methods: On Day -26 4 X 10^6 CD19+ NALM-6 B-lineage acute lymphoblastic leukemia cells were subcutaneously implanted on the left shoulders of 14 NOD.Cg-Prkdc^scid Il2rg^tm1Wjl /SzJ (NSG) mice. On day -4 10^6 HT29 human colon carcinoma control cells were implanted on the right shoulders of 12 of the mice. The HT29 implanted in half of these 12 mice stably expressed a mutant of Herpes Simplex Virus (HSV) type 1 thymidine kinase (HSV1-sr39tk) gene (positive control). On day 0, half of the mice (N=7) were intravenously injected with 2 X 10^7 SB-modified T cells co-expressing a 2nd generation CD19-specific CAR, firefly luciferase (ffLuc) and a nuclear localization signal (NES)-truncated HSV1-sr39tk (NES-sr39tk) reporter gene. The remaining NSG mice were injected with 2 X 10^7 T cells co-expressing CD19RCD28, ffLuc and non-truncated HSV1-sr39tk (sr39tk). Results: In both mouse groups, homing of T cells to CD19+ NALM-6 tumors was observed upon intravenous injection of [18F]FHBG and PET imaging. The PET signal intensity was significantly higher in the NALM-6 tumors compared to HT29 tumors in mice that received T cells expressing NES-sr39tk ($P<0.01$) or sr39tk ($P<0.001$). The [18F]FHBG signal intensity increased significantly in the NALM-6 tumors of both groups from day 3 to day 8 (sr39tk $P<0.02$ and NES-sr39tk $P<0.05$). There was no significant difference in NALM-6-associated [18F]FHBG signal intensities between NES-sr39tk and sr39tk. The PET signal foci co-registered with ffLuc bioluminescent signals at the tumor sites. Conclusion: Trafficking of NES-sr39tk+/sr39tk+ ffLuc+ CAR+ T cells to NALM-6 tumors was detectable by small animal PET imaging with [18F]FHBG. Clinical-grade DNA plasmids of the SB system (produced at 1/10th the cost of generating viral vectors) and [18F]FHBG (approved by FDA under IND# 61,880) will be adapted to ongoing clinical trials at MDACC to infuse CAR+ T cells and monitor their biodistribution using PET.

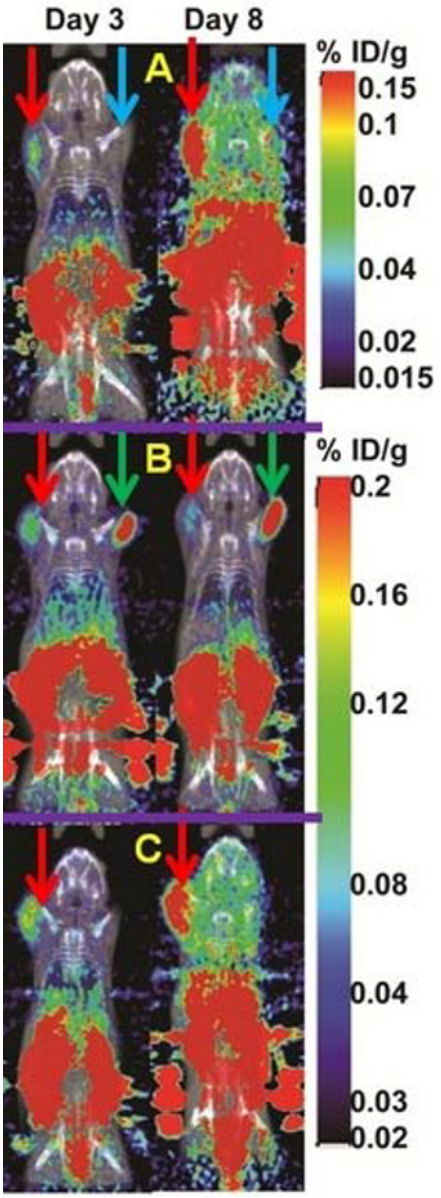

Specific tumor-targeting of CD19-CAR+ sr39tk⁺ T cells. NSG mice were injected subcutaneously with CD19⁺ NALM-6 cells (red arrows), CD19⁻ HT29 cells (blue arrows), and sr39tk⁺ CD19⁻ HT29 cells (green arrows). When the tumors reached a diameter of ~5 mm, 2 x 10^7 CD19-CAR⁺ ffLuc⁺ NES-sr39tk⁺ CTLs were infused intravenously. The mice were then imaged by PET two hours following the injection of ~200 µCi of [^{18}F]-FHBG at days 3 and 8 post-infusion of T cells. **A)** Mice injected with CD19⁺ NALM-6 cells (red arrows) and CD19⁻ HT29 cells (blue arrows) show foci of radiotracer accumulation at the site of the CD19⁺ NALM-6 tumor only at days 3 and 8. **B)** Mice injected with CD19⁺ NALM-6 cells (red arrows) and sr39tk⁺ CD19⁻ HT29 cells demonstrated foci of radiotracer accumulation at both tumor sites as expected. **C)** Mice injected with only CD19⁺ NALM-6 cells (red arrows) show accumulation at the tumor site.

Disclosure of author financial interest or relationships:

S. Yaghoubi, CellSight Technologies, Inc., Employment; CellSight Technologies, Inc., Stockholder; **A.M. Najjar**, None; **S. Olivares**, None; **H. Singh**, None; **H. Huls**, None; **P. Raja Manuri**, None; **L.J. Cooper**, None.

Presentation Number **LBAP 122**
Late Breaking Abstract Poster Session
September 19, 2013 / 15:15-15:15 / Room: Exhibit Hall B

Comparative analysis of human nucleoside kinases for PET reporter imaging with radiolabeled reporter probes FEAU, FIAU and L-FMAU

Jason T. Lee, *Maxim A. Moroz, Larissa Shenker, Juan Zurita, Vladimir Ponomarev, Radiology, Memorial Sloan-Kettering Cancer Center, New York, NY, USA. Contact e-mail: leej8@mskcc.org*

INTRODUCTION: Radionuclide-based reporter gene imaging has the sensitivity to monitor gene and cell-based therapies in human. Potential immunogenicity of current viral transgenes warrants development of human-based reporter systems. We seek here to compare a panel of human nucleoside kinase reporters, deoxycytidine kinase (dCK) and thymidine kinase (TK) mutants, expressed in human U87 glioblastoma cells across three reporter probes, 2'-deoxy-2'-fluoro-5-ethyl-1-β-D-arabinofuranosyluracil (FEAU), 2'-deoxy-2'-fluoro-5-iodo-1-β-D-arabinofuranosyluracil (FIAU) and 1-2'-fluoro-5-methyl-β-L-arabinofuranosyluracil (L-FMAU). **METHODS:** Human U87 glioblastoma cell lines were transduced with the SFG retroviral vector bearing one of the following human reporter genes fused to the green fluorescent protein (GFP): dCK-R104M/D133A (dCKDM), dCK-A100V/R104M/D133A (dCKTM), dCK-R104Q/D133N (dCKepTK16A) and TK2-N93D/L109F (TK2mut). Wild-type dCK was used as negative control and herpes simplex virus type-1 thymidine kinase with nuclear export signal (nesHSV1-TK) as clinical comparison. GFP-based fluorescence activated cell sorting was employed to yield comparable reporter gene-expressing population distributions across all cell lines. Gene expressions were confirmed by quantitative real time-PCR (RT-PCR), Western Blot and flow cytometry analyses of the surrogate GFP marker. *In vitro* uptake assays were performed using ^{3}H-FEAU, ^{124}I-FIAU, ^{3}H-L-FMAU and ^{14}C-thymidine. **RESULTS:** RT-PCR and Western Blot analyses demonstrate comparable levels of GFP mRNA and protein expression, respectively. Flow cytometry of functional GFP show overlapping population distributions. The reporter gene/probe combination dCKDM/^{3}H-FEAU exhibited the highest fold difference (72 ± 2.7) for a human-based reporter when normalized to "background" of wild type U87 cells, second only to viral-based nesHSV1-TK/^{3}H-FEAU by ~25% (96 ± 1.7). Cells overexpressing dCK exhibited three-fold higher ^{3}H-L-FMAU uptake than wild type control whereas ^{3}H-FEAU and ^{124}I-FIAU remain unchanged (other nucleoside kinases were not assessed). ^{14}C-thymidine uptake was increased at least three-fold across U87 cell lines overexpressing mutant reporter genes relative to wild type and dCK-overexpressed controls. **CONCLUSION:** *In vitro* results clearly demonstrate dCKDM/^{3}H-FEAU exhibits the highest contrast of the human reporter gene/probe combinations assessed. These data support dCKDM/FEAU in whole-body monitoring of T cell-based immunotherapy and *in vivo* evaluation is currently underway. Furthermore, the degree to which endogenous substrates, such as thymidine, are recognized by these reporter genes may affect cellular function and must be addressed. A systematic evaluation of currently available non-immunogenic reporter gene/probe combinations is necessary and conclusions should be drawn in a context pertinent to on-going clinical trials.

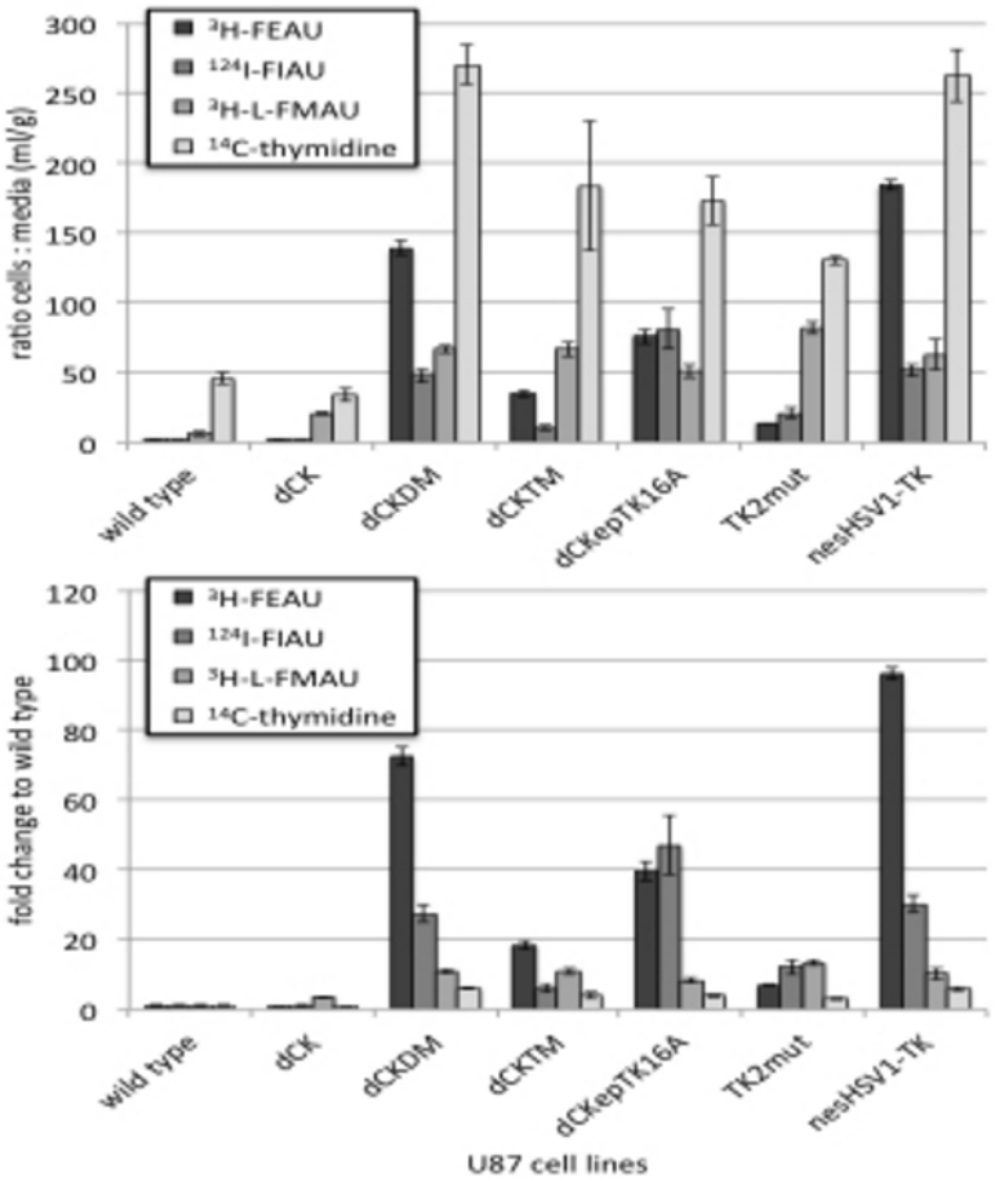

In vitro ^{3}H-FEAU, ^{124}I-FIAU, ^{3}H-L-FMAU and ^{14}C-thymidine uptake assays in a panel of U87 cell lines expressing different nucleoside kinase reporter genes.

Disclosure of author financial interest or relationships:
J.T. Lee, None; **M.A. Moroz**, None; **L. Shenker**, None; **J. Zurita**, None; **V. Ponomarev**, None.

Presentation Number **LBAP 123**
Late Breaking Abstract Poster Session
September 19, 2013 / 15:15-15:15 / Room: Exhibit Hall B

Small-animal PET imaging of human copper transporter as a novel reporter gene in tumor xenograft mouse model

Kwang Il Kim, *Yong Jin Lee, Tae Sup Lee, Kwang Sun Woo, Ju Hui Park, Hyun Park, Gwang Il An, Joo Hyun Kang, Molecular Imaging Research Center, Korea Institute of Radiological & Medical Sciences, Seoul, Republic of Korea. Contact e-mail: kikim@kirams.re.kr*

Purpose: Copper is an essential cofactor for a variety of biochemical processes including, oxidative phosphorylation, cellular antioxidant activity and elimination of free radicals. Copper transporter gene is known to be involved in ingestion of these copper ions into the cell. In this study, we evaluated the feasibility of human copper transporter gene (*hCTR1*) as a new PET imaging reporter gene with ^{64}Cu. **Methods**: The recombinant plasmid vector pCMV-hCTR1 (expressing human copper transporter gene driven by CMV promoter) was prepared. After transfection of this plasmid vector into rat glioma cells (C6) using lipofectamine, the stable transfectant (C6-hCTR1) was selected with hygromycin. The expression of *hCTR1* gene was measured by RT-PCR and Western blot analysis, and ^{64}Cu uptake assay was performed in C6 and C6-hCTR1 cells. Small-animal PET/CT images were acquired with ^{64}Cu in tumor bearing nude mouse. **Results**: The *hCTR1* gene expression in both RNA and protein levels was observed in C6-hCTR1 cells. The ^{64}Cu uptake by hCTR1 expression also increased approximately three-fold in C6-hCTR1 cells compared to C6 cells. Small-animal PET/CT imaging revealed good accumulation of ^{64}Cu in C6-hCTR1 tumor. Maximum standard uptake value (SUV_{max}) of C6-hCTR1 tumor was 1.58 fold higher than that of C6 tumor. **Conclusion**: Increase of ^{64}Cu uptake by the expression of *hCTR1* gene was validated *in vivo* as well as *in vitro*. Much more research is needed, but copper transporter gene could be used as a new imaging reporter gene for PET with ^{64}Cu.

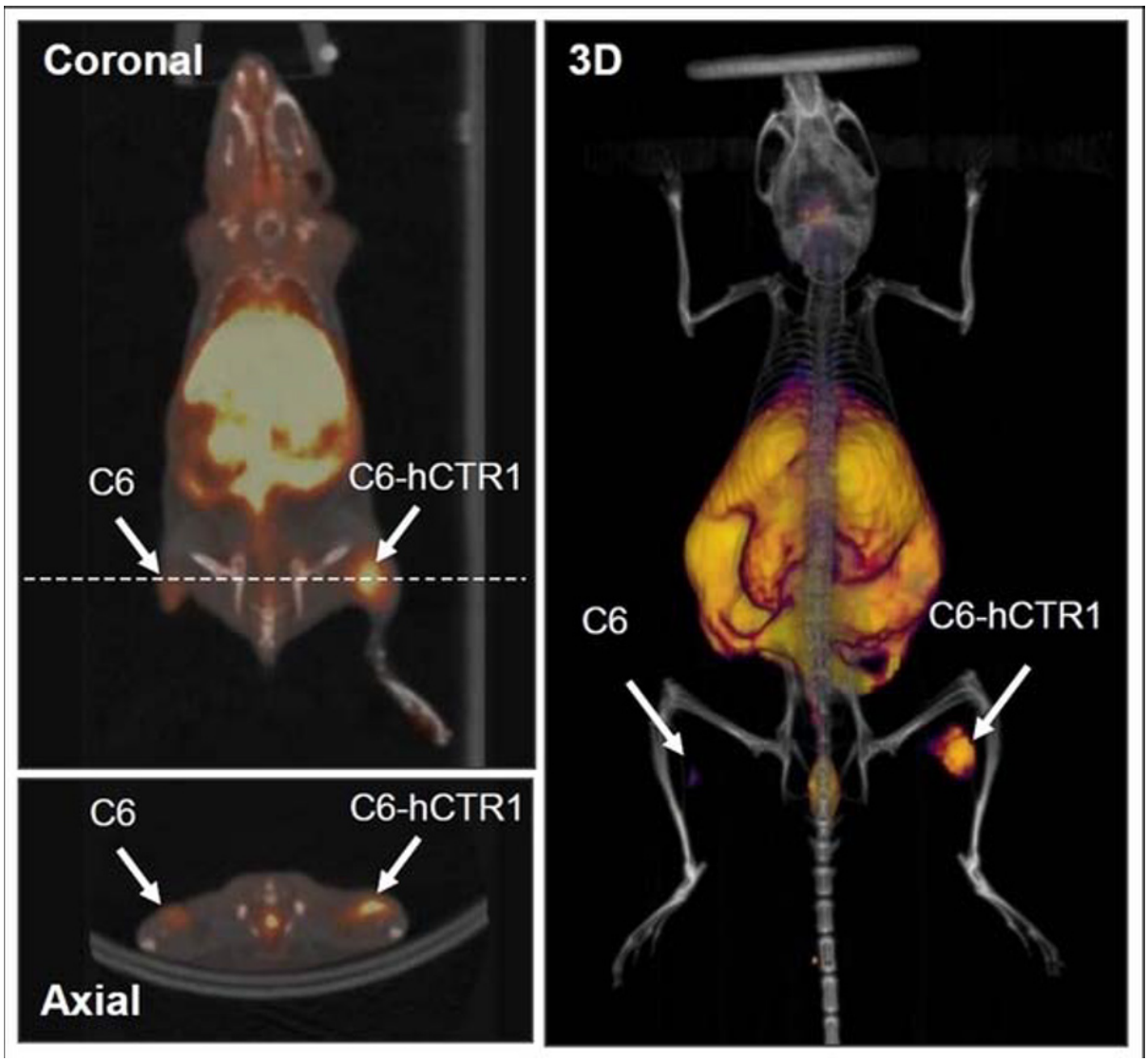

Small-animal PET imaging of human copper transporter gene expression in tumor bearing mouse with $^{64}CuCl_2$.

Disclosure of author financial interest or relationships:
K. Kim, None; **Y. Lee**, None; **T. Lee**, None; **K. Woo**, None; **J. Park**, None; **H. Park**, None; **G. An**, None; **J. Kang**, None.

Presentation Number **LBAP 124**
Late Breaking Abstract Poster Session
September 19, 2013 / 15:15-15:15 / Room: Exhibit Hall B

No-Hardware Retrospective Respiratory Gating in microCT Imaging Using Low-Dose Detector Technology

Dustin Osborne[1,2], *Alan Stuckey*[1], *Shelley N. Wilson*[1], *Jonathan S. Wall*[1], *Jens Gregor*[3], [1]*Molecular Imaging & Translational Research, University of Tennessee, Knoxville, TN, USA;* [2]*Molecular Imaging, Siemens Medical Solutions USA, Inc., Knoxville, TN, USA;* [3]*Electrical Engineering & Computer Science, University of Tennessee, Knoxville, TN, USA. Contact e-mail: dosborne@utk.edu*

Objectives : Many preclinical CT systems are limited to prospective gating because of slow gantry rotation speeds, long X-ray exposure times and complicated gating equipment and setup. Because of long scan times, dose to the animal can be a concern as well as constantly changing respiratory patterns throughout the course of the scan. This work examines the feasibility of using low-dose CT technology with short exposure times (<25 ms) for the purposes of acquiring retrospective respiratory gated data to improve imaging of the lungs without the use of complicated gating equipment. This work uses new low-dose technology on an Inveon trimodal platform to examine methods for retrospective respiratory gating while maintaining an estimated dose to the animal that is similar to a standard whole-body imaging protocol. Methods : 5 mice were imaged using low-dose detector technology. X-ray settings of 80 kVp @ 0.5 mA were used with ~ 25 ms for each exposure and 2000 exposures acquired over 220 degrees of rotation. Projections were chosen post acquisition using a semi-automated technique that selected the desired phase of the respiratory cycle using the acquired projection data. The projection selection method uses information from a region of interest drawn over the lung in the projection data. Descriptive statistics are used along with count density information to optimize the selection of CT projections. The projections were then reconstructed into 3D volumes. Comparisons were made between retrospectively "gated" and non-gated images to assess improvements. All imaging was performed using a bin factor of 4 resulting in a projection size of 512x768. Data were reconstructed using a standard Feldkamp implementation. Results : Initial results show improvement between retrospective "gated" and non-gated images. The retrospective selective projection reconstructed images show decreased motion blur and sharper regions within the lung. This is evident in the attached images by improved clarity in lung structures. 2000 exposures using low-dose imaging technology and a 25 ms exposure time results in a dose to the animal that is similar to that of a typical 220 projection acquisition over 220 degrees using standard detector technology and a 225 ms exposure time. Count density is similar between standard and low dose protocol because of the increased sensitivity of the low-dose detector technology (Osborne, et. al, 2012). Conclusions : This work shows that retrospective respiratory gating using low-dose technology with fast exposure times is feasible and may enable gating without the use of complicated and inaccurate hardware for providing respiratory gating signals. It is also shown that is possible to perform this sort of protocol using new technology that will enable maintaining the smallest dose possible. Further research is being performed on protocol optimization, projection selection methods and application specific reconstruction techniques. References: Osborne DR, Yan S, Stuckey A, Pryer L, Richey T, et al. (2012) Characterization of X-ray Dose in Murine Animals Using microCT, a New Low-Dose Detector and nanoDot Dosimeters. PLoS ONE 7(11)

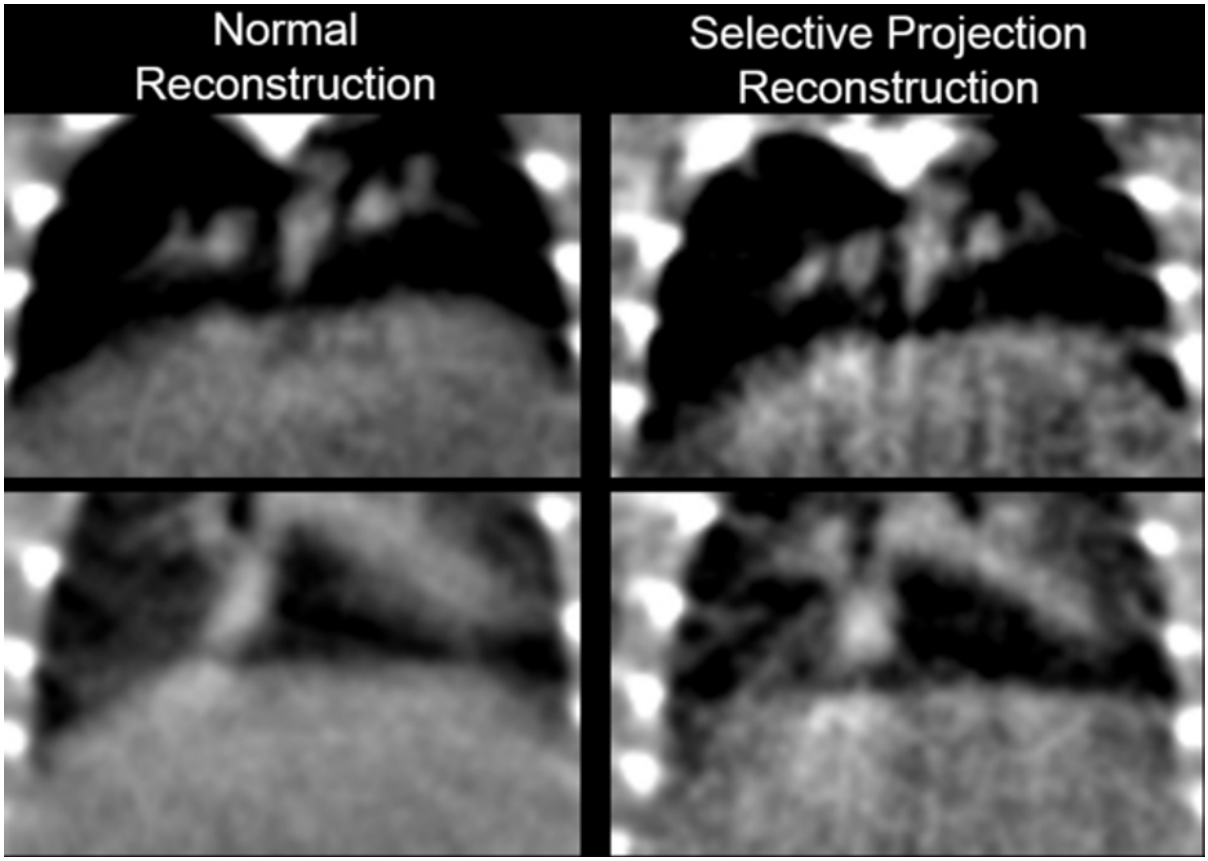

Disclosure of author financial interest or relationships:
D. Osborne, Siemens, Employment; **A. Stuckey**, Solex, LLC, Stockholder; **S.N. Wilson**, None; **J.S. Wall**, Solex Inc, Stockholder; **J. Gregor**, None.

Presentation Number **LBAP 125**
Late Breaking Abstract Poster Session
September 19, 2013 / 15:15-15:15 / Room: Exhibit Hall B

EXPLORER, an Ultrasensitive Total-Body PET Scanner: Application Feasibility Simulations

Ramsey D. Badawi[1,2], *Jonathan K. Poon*[1,2], *Suleman Surti*[3], *Xuezhu Zhang*[2], *Joel S. Karp*[3], *Bill Moses*[4], *Jinyi Qi*[2], *Michael Graham*[5], *David Mankoff*[3], *Richard L. Wahl*[6], *William Jagust*[7], *Thomas F. Budinger*[4], *Terry Jones*[1], *Simon R. Cherry*[2,1], [1]*Radiology, UC Davis, Sacramento, CA, USA;* [2]*Biomedical Engineering, UC Davis, Sacramento, CA, USA;* [3]*Radiology, University of Pennsylvania, Philadelphia, PA, USA;* [4]*Functional Imaging Center, Lawrence Berkeley National Laboratory, Berkeley, CA, USA;* [5]*Radiology, University of Iowa, Iowa City, IA, USA;* [6]*Radiology, Johns Hopkins, Baltimore, MD, USA;* [7]*Helen Wills Neuroscience Institute, UC Berkeley, Berkeley, CA, USA. Contact e-mail: ramsey.badawi@ucdmc.ucdavis.edu*

A 2-meter long PET scanner would possess a range of capabilities currently unavailable to the imaging community, including whole-body dynamic imaging with high temporal resolution, massively increased sensitivity and the ability to image at very low radiation doses. These offer opportunities to explore application spaces hitherto inaccessible, including total-body organ-specific pharmacokinetics, imaging of the brain-body connection, nutrition and biology in normal populations. Other applications such as drug microdosing would be achievable at far lower radiation and pharmacological doses. The EXPLORER initiative is a multi-institutional collaboration that aims to build such a scanner and to make it available to the community. Initial work developing the necessary technologies for this device (detectors, electronics, image reconstruction and mechanical design) is under way. In this work we simulate a variety of applications in order to quantify the advantage that EXPLORER would enjoy over conventional PET scanner designs, with a view to promoting a conversation with the molecular imaging community regarding the potential benefits, opportunities and pitfalls associated with this potentially transformative endeavor. A Monte Carlo model was used to estimate count rates for EXPLORER compared to the Siemens mCT using phantoms mimicking adult and pediatric scans. We modeled an adult-sized cylinder (27 cm diameter, 200 cm length) uniformly filled with activity. After careful optimization of the maximum acceptance angle and coincidence time-window, we determined that the gain in NEC was ~35-fold (activity range 0.1-10 mCi). Using an anthropomorphic phantom with activity in the heart only, mimicking the early frames of a dynamic study, NEC was 3.1-3.6 times higher (activity range 0.1-30 mCi). With a 6:1 activity concentration ratio between the brain and the rest of the body, NEC for the brain was 3.4-4.0 times higher (activity range 0.1-10 mCi). A 20cm diameter, 70 cm long cylinder, which has similar mass to a typical 6-yo child, showed an NEC gain of 16-19-fold (activity range 0.06-6 mCi). If a 3 to 5-fold reduction in count density compared to a typical clinical FDG study is considered acceptable, which is likely to be the case for drug biodistribution studies or whole-organ kinetic studies, then scanning could be performed using 1/100 of the activity typically used in the clinic, resulting in radiation doses of 0.07 mSv for the adult and 0.07 mSv for a 5 year old child, much less than an annual absorbed background radiation dose of 3 mSv. With a specific activity of 37 GBq/umol, for molecules of molecular weight less than ~10 kDa (FDG is ~0.2kDa), it would be possible use an injected mass below 1ugram. Of note, the regulatory threshold for toxicological concern for most non-pharmaceutical compounds is an ingested mass of 1.5 ugrams/person/ day. This has substantial implications for fast tracking first-in-human studies in drug development.

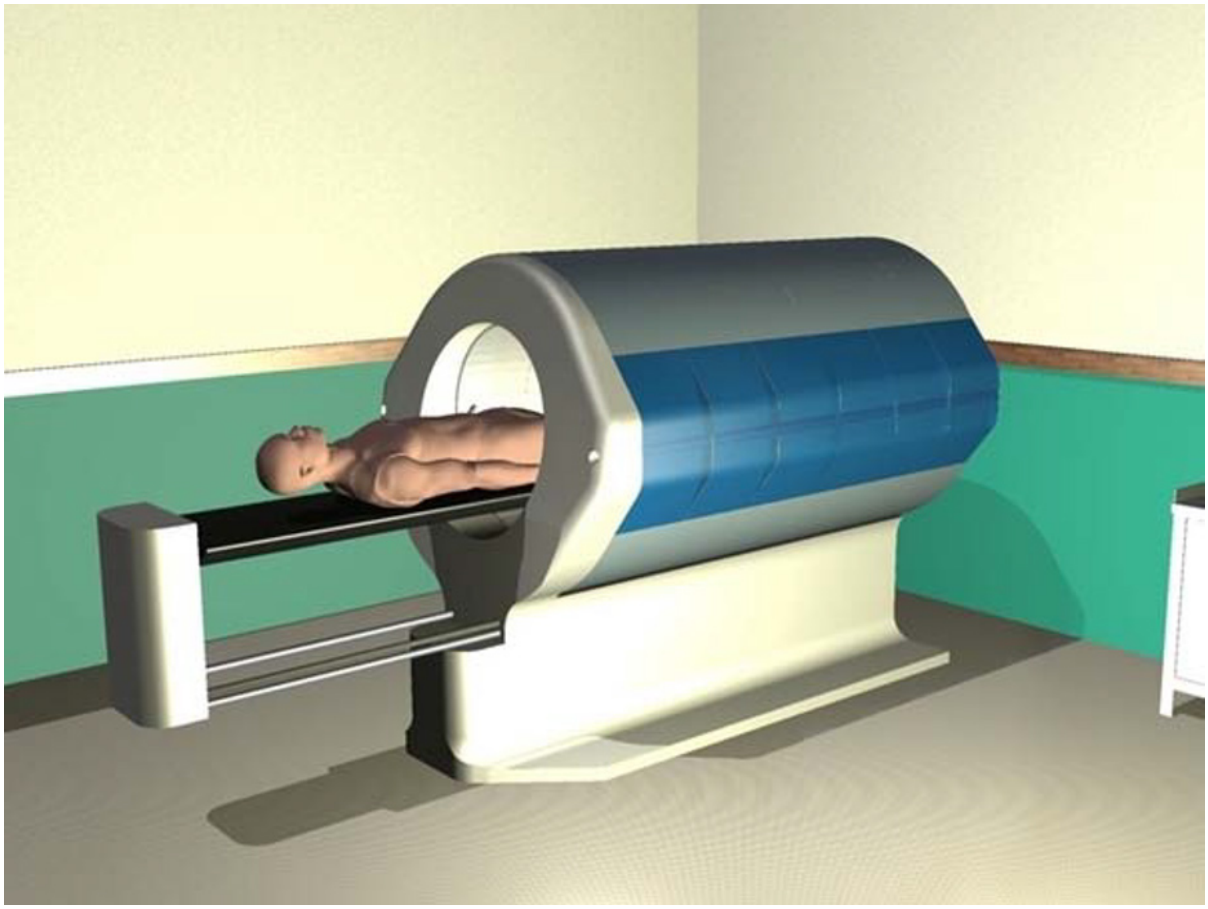

Preliminary design rendering of total-body PET scanner

Disclosure of author financial interest or relationships:
R.D. Badawi, Philips Medical, Grant/research support; Toshiba Medical, Consultant; JNJ, Stockholder; **J.K. Poon**, None; **S. Surti**, None; **X. Zhang**, None; **J.S. Karp**, Philips Healthcare, Grant/research support; **B. Moses**, None; **J. Qi**, None; **M. Graham**, None; **D. Mankoff**, None; **R.L. Wahl**, novelos, Consultant; nihon medi physics, Consultant; gsk, Other financial or material support; spectrum, Other financial or material support; naviscan PET, Other financial or material support; actinium pharmaceuticals, Grant/research support; Lantheus, Grant/research support; **W. Jagust**, Synarc, Consultant; F. Hoffman La Roche, Consultant; **T.F. Budinger**, SENO, San Antonio, TX, Consultant; Ultrsawave, Irvine, CA, Consultant; Ionetix. San Francisco, CA, Consultant; **T. Jones**, None; **S.R. Cherry**, GE Healthcare, Grant/research support; Perkin Elmer, Grant/research support .

Presentation Number **LBAP 126**
Late Breaking Abstract Poster Session
September 19, 2013 / 15:15-15:15 / Room: Exhibit Hall B

PET transparency improvements in a Neurovascular coil for MR-PET systems

Sahil Bhatia[1], *TaeYoung Yang*[1], *Gabriel M. Searles*[1], *Bijay Shah*[2], *Dmitriy Londarskiy*[1], *Darren Gregan*[1], *YunJeong Stickle*[1], *Tom Zink*[1], [1]*GE Healthcare, Aurora, OH, USA;* [2]*GE Healthcare, Waukesha, WI, USA. Contact e-mail: sahil.bhatia@ge.com*

Introduction: MR-PET combines the advantages of MRI's morphological imaging and PET's functional molecular imaging. Sequential scanners have separate gantries for PET and MR. Integrated MR-PET scanners offer several advantages such as reduction in overall scan time and elimination of patient repositioning. The challenges of an integrated MR-PET system are different from a sequential scanner. In MRI, surface coils are positioned close to the patient for achieving higher SNR. In an integrated MR-PET system, these coils are directly in the PET FOV and attenuate photons resulting in artifacts or poor quality PET images. Hence having low PET attenuation is critical to good quality PET images during simultaneous MR-PET acquisition. Surface coils have earlier not been designed to incorporate this requirement. Previous attempts have been limited to using attenuation maps to perform correction. We present a head neck coil designed specifically to be PET transparent. Methods: The first of several key strategies applied during the design was to move majority of the components outside the PET FOV. Secondly, PET attenuation was also improved by reducing the thickness of the coil former. Thirdly, every module was redesigned to be PET transparent. The 23 element coil was constructed using strips cut from 0.125 inches wide copper (thickness=0.25mm). Adjacent elements were isolated by overlap whereas next nearest elements were isolated using low input impedance preamplifiers. Elements were tuned to 127.73MHz and matched to 50Ohms. Bench measurements were collected using an RF network analyzer 8712ES (Agilent). Loaded Q was measured using a Head and Neck phantom with an internal bone structure filled with 3.3 g/L NiCl2 and 2.4g/L NaCl. Polycarbonate was used in a FDM Machine to build thin formers. Axial images of a 10cm radius spherical phantom were acquired on a 3T/70 cm G.E. scanner. (Spin echo, TR/TE=500/20msec, 256x256, FOV=45cm, st=5mm, Nav=1). PET performance improvements were measured by calculating sensitivity loss for a 10 min period over three 15cm regions that covered the entire coil length.A cylindrical phantom of 21.2cm diameter and 28.98cm height filled with 68Ge was used to calculate the average sensitivity loss. Results: MR performance was measured by comparing SNR to the industry standard 8HR Brain coil. Improvement in PET transparency was measured by comparing the sensitivity loss to G.E.'s 3T GEM Head neck coil designed for MR only imaging. We observed a 41.84%, 43.49% and 40.51% improvement in PET sensitivity loss in each of the three beds respectively. For the MR-PET coil over a large Ø= 15cm circular ROI, the signal measured was 6.1% higher; the noise standard deviation was 17% higher; making the MR-SNR within 9.5% of the 8HR brain coil. More importantly for brain imaging, in a small Ø=5.2cm ROI close to center of the phantom, the signal measured was 7.1% higher; making the SNR within 8.6% of the brain coil.

Disclosure of author financial interest or relationships:
S. Bhatia, GE Healthcare, Employment; **T. Yang**, GE healthcare, Employment; **G.M. Searles**, GE Healthcare, Employment; **B. Shah**, GE Healthcare, Employment; **D. Londarskiy**, None; **D. Gregan**, GE Healthcare, Employment; **Y. Stickle**, GE Healthcare, Employment; **T. Zink**, None.

Presentation Number **LBAP 127**
Late Breaking Abstract Poster Session
September 19, 2013 / 15:15-15:15 / Room: Exhibit Hall B

A new motorized MR-guided ultrasound system for the controlled delivery of large molecules to the rodent brain

Remi Magnin[1], *Sébastien Mériaux*[1], *Denis Le Bihan*[1], *Erik Dumont*[2], *Benoit Larrat*[1], [1]*DSV/I2BM/NeuroSpin/UNIRS, CEA, Gif sur Yvette, France;* [2]*Image Guided Therapy, Pessac, France. Contact e-mail: remi.magnin@cea.fr*

Introduction: The application of focused ultrasound combined with microbubbles injection has shown its capability to open the Blood Brain Barrier (BBB) locally, transiently and non-invasively, allowing large molecules to access the central nervous system. Performing this protocol under MRI guidance ensures a precise control of the disruption location and deposited acoustic intensity prior to BBB opening, while its visualization is followed using MR contrast agents injected after disruption. We developed a motorized setup for rodent transcranial experiments which allows the displacement of an ultrasound transducer within high field MRI preclinical systems. This system enables to perform BBB disruption at several arbitrarily chosen locations, and therefore to deliver specific drugs at different brain regions after unique systemic injection. Methods and material: After coupling the ultrasound transducer over the head, Sprague Dawley rats (n=5) were maintained under isoflurane anesthesia in stereotactic position inside 7 T preclinical scanner (Pharmascan, Bruker). T1-weighted and T1-mapping reference scans were acquired. The position of ultrasound focal point was monitored using a MR-acoustic radiation force imaging sequence [1]. We then defined an arbitrary spatial pattern for BBB opening (Figure a) by shifting the sites of disruption (displacement of the transducer) and varying the transmitted acoustic intensity. 200 µL of Sonovue (Bracco) were injected via a tail vein catheter and the sonication was performed following the defined trajectory. 200 µL of Dotarem (Guerbet) were then injected. A T1-weighted sequence was acquired to visualize the contrast enhancement at the sonoporated regions, while a T1-mapping sequence allowed, after post-processing, calculating quantitative gadolinium concentration maps at the disruption sites. Results: Due to T1 shortening effect induced by the presence of gadolinium chelate, a contrast enhancement is clearly visible at the planned locations compared to the rest of the brain (Figure b), confirming that the BBB has been opened along the programmed trajectory. The same result was obtained for different spatial patterns (circle, square, cross, dotted line). Our T1 mapping sequence enables to quantify drug uptake in brain tissue for different acoustic pressures (Figure c), confirming the absence of Dotarem penetration for acoustic pressure below opening threshold (estimated to be around 0.3 MPa [2]). Conclusion: This preliminary study demonstrates that our setup offers the unique possibility to test, on the same animal and with only one microbubbles injection, different acoustic conditions (pressure, shot duration) or the influence of region dependent physiological parameters (vessel density, size distribution). It may result in a significant reduction of both the number of animals and the acquisition time required for drug delivery experiments, and may also offer a real gain of reliability because the animal can be its own control avoiding variability due to for instance body temperature or anesthesia level fluctuations. References: [1] Larrat et al., Phys. Med. Biol., 2010 [2] Larrat et al., Proc. 4th WMIC, 2011

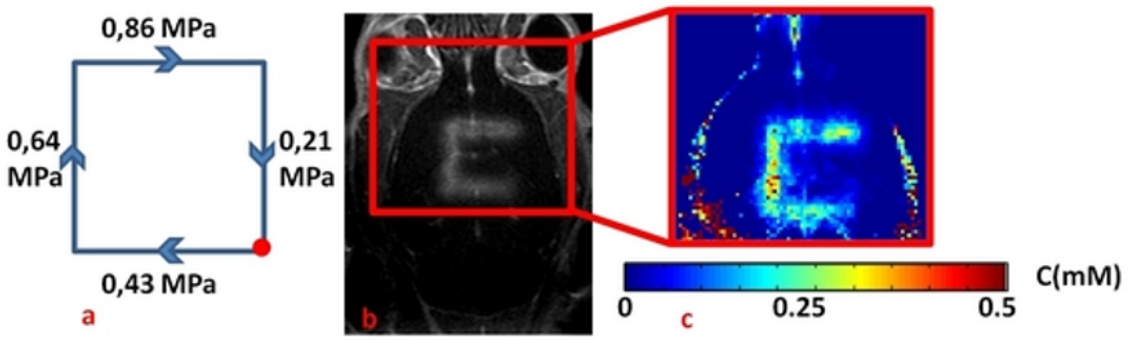

Images obtained after a BBB opening protocol and Dotarem injection, with a square trajectory where a different acoustic pressure is used for each side of the square. a. Schema of the trajectory used, the red dot represents the starting point and the approximate acoustic pressure at the focal point is given for each side. b. T_1-weighted image, showing a contrast enhancement at the disruption location. The right side of the square shows no contrast enhancement because the acoustic pressure was below the BBB opening threshold. c. Corresponding Dotarem concentration map, calculated from T_1 map acquisition.

Disclosure of author financial interest or relationships:
R. Magnin, None; **S. Mériaux**, None; **D. Le Bihan**, None; **E. Dumont**, Image Guided Therapy SA, Employment; **B. Larrat**, None.

Presentation Number **LBAP 128**
Late Breaking Abstract Poster Session
September 19, 2013 / 15:15-15:15 / Room: Exhibit Hall B

Catheter Tracking In Vivo by Magnetic Resonance Imaging Employing Hyperpolarized Silicon Nanoparticles

Jay Shah[1,2], *Nicholas Whiting*[2], *Jingzhe Hu*[2], *Pratip Bhattacharya*[2], [1]*Biomedical Engineering, University of Texas at Austin, Austin, TX, USA;* [2]*Cancer Systems Imaging, University of Texas MD Anderson Cancer Center, Houston, TX, USA. Contact e-mail: jayshah1216@gmail.com*

Catheter tracking, normally done through fluoroscopy, can pose a threat to both patients and physicians due to significant doses of ionizing radiation. Magnetic resonance imaging (MRI) offers several advantages over other imaging modalities, making it a better technique to track catheters. MRI does not cause radiation exposure as in fluoroscopy and provides excellent soft tissue contrast which can offer physicians with detailed three-dimensional images of the anatomical structures [1]. While traditional MRI presents such key advantages over other imaging modalities, this technique is unable to distinguish the catheter within the body because of the inherently low sensitivity associated with the Boltzmann polarization. This can be overcome through the use of hyperpolarized silicon nanoparticles (SiNPs), which have an increased MRI signal on the orders of 10^4-10^5 [2]. Hyperpolarization of SiNPs is achieved through low temperature dynamic nuclear polarization (DNP), which utilizes a cold environment, a high magnetic field, and microwave irradiation to polarize the sample past equilibrium. Unlike the common hyperpolarized nuclei like 13C, 3He and 129Xe, hyperpolarized SiNPs have an unusually long relaxation time (T1 ~ 40 minutes), allowing for greater than an hour of imaging time [2]. Combining the popular MRI platform, hyperpolarized SiNP, and its long-lasting signal, potentially allows catheter tracking in real-time in vivo. A commercially available SiNPs with an average mean diameter of 2000 nm was employed as reported in our earlier paper [2]. The home-built DNP polarizer situated adjacent to a 7 T Bruker small animal MRI scanner operated at ~2.9 T and ~3 Kelvin with microwave irradiation at ~81 GHz directed to the sample of SiNPs (~100 mg) through a waveguide and slot antenna. Catheters with varying diameters were obtained from a local clinic. The SiNPs are polarized for ~5 hours. The particles are then removed from the polarizer and transported to the nearby 7 T MRI scanner. For the phantom trials, we attached the SiNP sample to the catheter and pushed it through a phantom made of gelatin. Phantom results show that we can track an 8 mm wide catheter through a phantom via MRI over a period of 25 minutes. Ongoing and future experiments include testing catheters of smaller diameters in a gelatin phantom and extending this to in vivo studies on mouse models. The preliminary results demonstrate the feasibility of tracking catheter by MR utilizing the long lived hyperpolarized signal from non-toxic, non-radioactive SiNPs. When translated to clinics, this technique may allow for real-time monitoring of catheter in patients via MR, taking advantage of over 10,000 fold sensitivity as well as contrast enhancements in 29Si MRI which gives no background signal. References: [1] Lardo, A. C. (2000). Real-time magnetic resonance imaging: Diagnostic and interventional applications. Pediatric Cardiology. [2] Cassidy, M. C. (2013). In vivo magnetic resonance imaging of hyperpolarized silicon particles. Nature Nanotechnology.

Disclosure of author financial interest or relationships:
J. Shah, None; **N. Whiting**, None; **J. Hu**, None; **P. Bhattacharya**, None.

Presentation Number **LBAP 129**
Late Breaking Abstract Poster Session
September 19, 2013 / 15:15-15:15 / Room: Exhibit Hall B

Transverse Relaxation Rate (R2) Dependence on Refocusing Pulse Interval (2τ) in MagA-expressing, Breast/Melanoma Tumor Cells

Casey Y. Lee[1,2,3], *R. Terry Thompson*[1,2], *Frank S. Prato*[1,2], *Donna E. Goldhawk*[1,2,3], *Neil Gelman*[1,2], [1]*Medical Biophysics, Western University, London, ON, Canada;* [2]*Imaging Program, Lawson Health Research Institute, London, ON, Canada;* [3]*Collaborative Graduate Program in Molecular Imaging, Western University, London, ON, Canada. Contact e-mail: clee@lawsonimaging.ca*

Introduction: Gene-based iron-labeled cells produce contrast which can be detected using magnetic resonance imaging (MRI). This is a promising approach for long-term cell tracking and potential monitoring of cellular activities using a reporter gene. We have used MagA, a putative iron transport gene from magnetotactic bacteria, to enhance magnetic resonance (MR) contrast in a human tumor cell line [1]. To optimize the cellular MR signal detection and specificity, a measure that is influenced more strongly by iron in comparison to other cellular properties, is needed. Based on previous MR studies of iron containing tissues [2], we hypothesize that change in the transverse relaxation rate (R2) as a function of refocusing pulse interval (2τ) is a candidate for providing an iron-specific measure in the detection of gene-based iron-labeled cells. Methods: Stably transfected, MagA-expressing MDA-MB-435 cells were cultured in the presence and absence of iron supplementation (250 μM ferric nitrate/medium) [1]. MagA-expressing cells were compared to the untransfected parental cell line (P). Cells were harvested; washed with phosphate buffered saline pH 7.4; and centrifuged (400xg) into a compact pellet. Nuclear magnetic resonance (NMR) studies were performed with a 9.4T NMR system (Agilent Inova 400). R2 was measured using the Carr-Purcell-Meiboom-Gill sequence provided by the vendor and 2τ = 0.2, 1, 2, 8, 16 ms. The relationship between R2 and 2τ for MagA-expressing, iron-supplemented cells was analyzed using a theoretical model [2] previously developed to assess this relationship in iron-containing tissues. This model provides a value for $r_c^2/2D$, where D is the diffusion coefficient of water molecules in the sample and r_c, the spatial correlation length, is a measure of the distance scale over which the microscopic magnetic field inhomogeneities change. To establish that any changes in R2 observed for cell samples were not due to artifacts from the increasing number of refocusing pulses, R2 was also measured as a function of 2τ for 100 μM $MnCl_2$. Results and Discussion: Iron-supplemented, MagA-expressing cells show greater increase in R2 with increasing 2τ than unsupplemented cells or P (Fig. 1). In $MnCl_2$(aq), R2 does not vary as a function of 2τ. Theoretical model fitting (solid line in Fig. 1) provided a value of ($r_c^2/2D$) = 0.14 ms, which is lower than the values previously found [2] in brain tissue (2.7 - 4.8 ms) or liver (0.4 ms) suggesting that iron particles within MagA-expressing cells may be in closer proximity than those in the tissues and/or that D is greater. MRI acquisitions sensitive to changes in R2 as a function of 2τ could possibly be used to detect gene-based iron-labeled cells in small animals. To achieve short 2τ values, a train of refocusing pulses may be used for magnetization preparation prior to single slice image acquisition [3] or prior to one segment of a 3D acquisition. References: 1. Rohani R, et al., Mol Imaging Biol 2013; in press. 2. Jensen JH and Chandra R, Magn Reson Med 2000; 44:144-156. 3. Ye FQ, et al., Magn Reson Med 1996; 36:153-158.

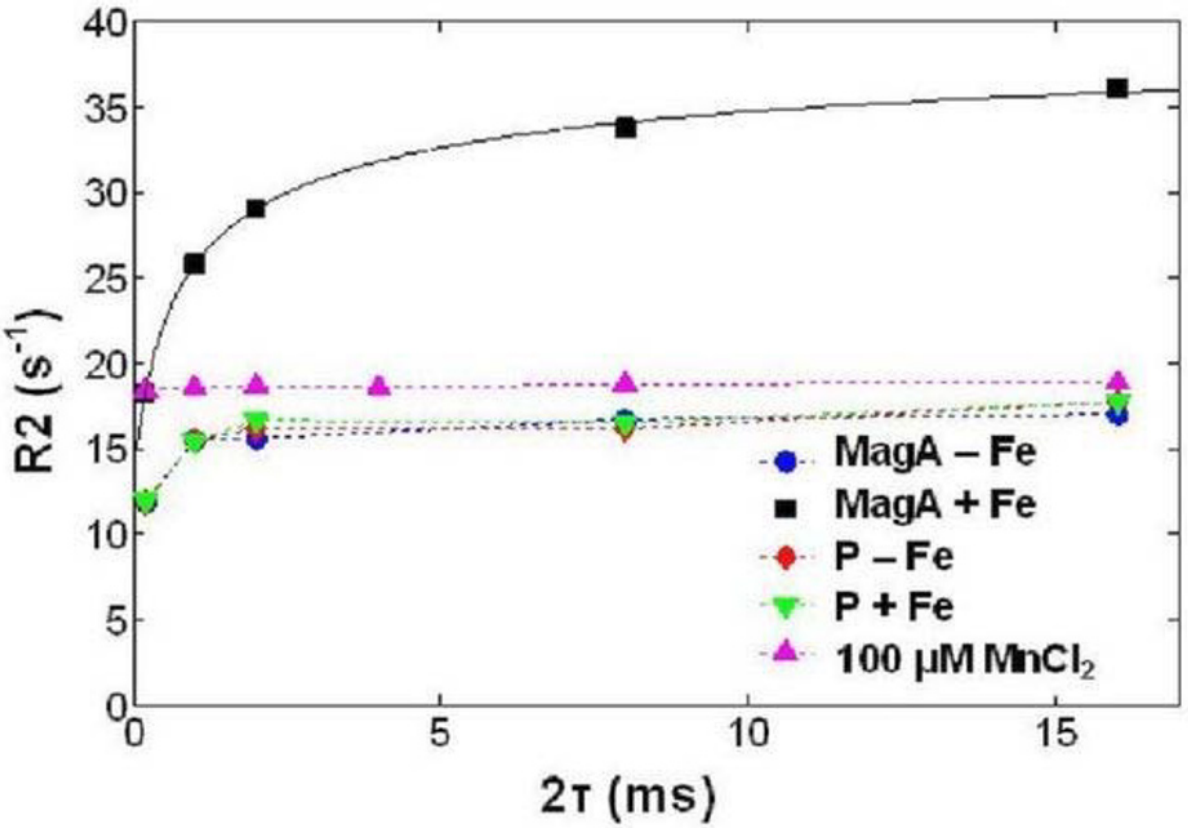

Figure 1. Influence of MagA expression on R2 dependence on 2τ. Samples consisted of MagA-expressing cells and controls, cultured in the presence (MagA + Fe, P + Fe) and absence (MagA - Fe, P - Fe) of iron-supplemented medium.

Disclosure of author financial interest or relationships:
C.Y. Lee, None; **R. Thompson**, None; **F.S. Prato**, None; **D.E. Goldhawk**, None; **N. Gelman**, None.

Presentation Number **LBAP 130**
Late Breaking Abstract Poster Session
September 19, 2013 / 15:15-15:15 / Room: Exhibit Hall B

High throughput imaging of C. elegans by combined selective plane illumination microscopy and optical projection tomography in a microfluidics device

*Matthias Rieckher[1,2], **Giannis Zacharakis**[1], Athanasios Zacharopoulos[1], Nektarios Tavernarakis[2], Jorge Ripoll[1,3], [1]Institute of Electronic Structure and Laser, Foundation for Research and Technology - Hellas, Heraklion, Greece; [2]Institute of Molecular Biology and Biotechnology, Foundation for Research and Technology - Hellas, Heraklion, Greece; [3]Dept. of Bioengineering and Aerospace Engineering, Universidad Carlos III of Madrid, Madrid, Spain. Contact e-mail: zahari@iesl.forth.gr*

Recent advances in biomedical imaging technologies have revolutionized the way we approach a variety of medical and biological questions and have unveiled several biological processes, mechanisms and functions. Optical Imaging methods facilitate the use of light for the non-invasive visualization of structure and function of biological tissue with sub millimetre resolution and at several centimetres of depth. In the field of microscopic and mesoscopic imaging pioneering new approaches have been demonstrated and implemented involving innovative illumination schemes such as Optical Projection Tomography (OPT) and Selective Plain Illumination Microscopy (SPIM). In this work we present a custom made combined SPIM and OPT system for rapid three-dimensional imaging. The system is combined with a variety of microfluidics devices to facilitate high-throughput imaging of C. Elegans in longitudinal studies. A series of cw lasers is used for excitation of the samples after passing through a cylindrical lens to create the illumination light sheet. An image intensified CCD camera is used to detect fluorescence and bright field images after focusing on the plane of illumination. The microfluidics chips have been fabricated by polydimethylsiloxane (PDMS) application on fine structured silicone wafers, which is then attached to thin glass slides and secured with a magnetic base on the imaging system. Fluidic inlets and outlets allow loading and unloading of worms through attachable tubing systems or syringes and adjusting the direction of the suction/pressure. Thus, animals can be recovered and can be grown under favourable conditions until the next imaging time point. This attachment to the microscopy system makes longitudinal imaging studies possible, which is important e.g. when studying changes in fluorescent expression during ageing. The final shape of the chip can be either cylindrical, which permits combined OPT and SPIM imaging or flat for high throughput screening. In this work we have imaged multiple worms carrying IFE-2:GFP, which is ubiquitously expressed throughout the animals in a proof of principle study. Figure 1 shows a bright field image of the microfluidics chip loaded with a worm and the corresponding fluorescence reconstructions obtained from the SPIM imaging. This setup offers significant advantages over currently available methods when imaging dynamic developmental processes and animal ageing in vivo; it permits high resolution monitoring of spatio-temporal gene expression and anatomical alterations and is readily adapted to image a wide range of model organisms.
Acknowledgements This work was funded by the Program INTERREG III, Project "YPERTHEN", financed by the European Commission through the European Regional Development Fund and by National Funds of Greece and Cyprus and Grants "Skin-DOCTor" and "Neureka!" implemented under the "ARISTEIA" and "Supporting Postdoctoral Researchers" Actions respectively, of the "OPERATIONAL PROGRAMME EDUCATION AND LIFELONG LEARNING", co-funded by the European Social Fund (ESF) and National Resources.

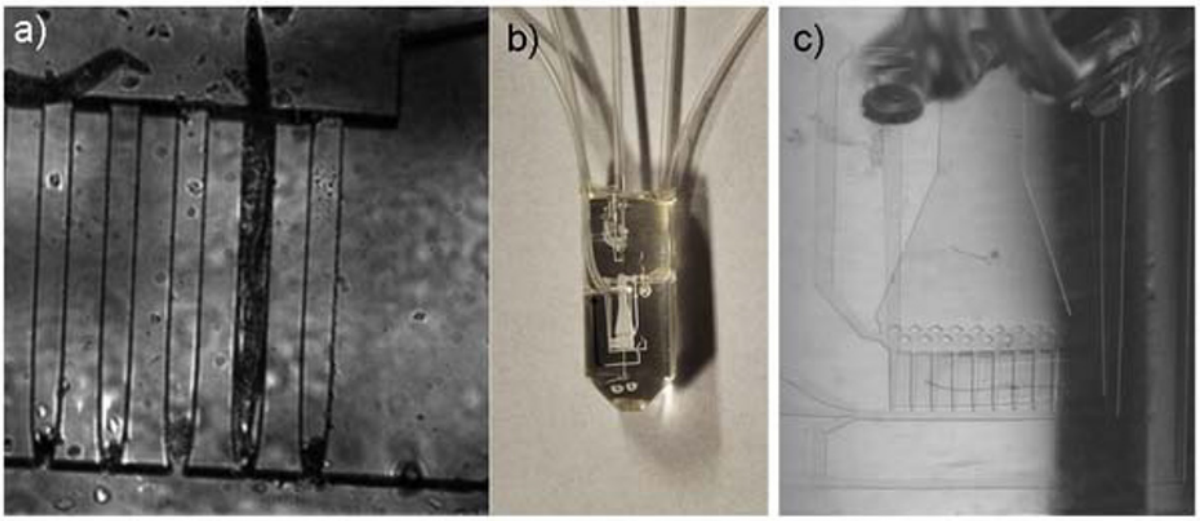

a) Bright field image of the micro-fluidics chip loaded with a worm. b) and c) Pictures of a representative micro-fluidics chip used for the high throughput SPIM micro-fluidics imaging of transgenic C. Elegans worms.

Disclosure of author financial interest or relationships:
M. Rieckher, None; **G. Zacharakis**, None; **A. Zacharopoulos**, None; **N. Tavernarakis**, None; **J. Ripoll**, None.

Presentation Number **LBAP 131**
Late Breaking Abstract Poster Session
September 19, 2013 / 15:15-15:15 / Room: Exhibit Hall B

Dynamic projection of fluorescence molecular imaging information for aiding oncologic surgery

Pinaki Sarder, Kyle Gullicksrud, Suman Mondal, Samuel Achilefu, **Walter J. Akers***, Radiology, Washington University School of Medicine, St. Louis, MO, USA. Contact e-mail: akersw@mir.wustl.edu*

Fluorescence imaging during surgical procedures has grown significantly in use during the last decade. Fluorescence contrast can augment or even replace conventional radioactive tracers in procedures such as sentinel lymph node biopsy during breast cancer surgery. In brain cancer surgery, fluorescence from natural substances can improve the accuracy of surgical margins, resulting in greater extent of resection (EOR) and longer progression-free survival. More recently, contrast from fluorescent molecular imaging agents that target cell-surface receptors has been used during open abdominal surgery to improve cytoreduction in ovarian carcinomatosis in humans. We report a novel use of digital light processing (DLP) technology for automatic real-time fluorescence projection onto the surgical field using NIR fluorescence contrast. A prototype system for direct projection of acquired fluoscence information for real-time guidance of open surgery was designed, built and evaluated in preclinical animal studies. Fluorescence guided surgery (FGS) with tumor-selective contrast agents increase tumor identification and removal. Imaging of fluorescence contrast is optimal in the NIR range which is relatively free of background tissue fluorescence and has greater depth penetration relative to visible light. . In addition, modern solid-state surgical lighting is relatively free of energy beyond 700 nm, enabling fluorescence imaging with normal surgical lighting conditions. Fluorescence imaging was performed by acquisition of fluorescence images using fast CMOS camera using, LED excitation, and longpass emission filter after injection of NIR fluorescent contrast agents in living mice. Images were smoothed and thresholded before being passed to DLP projector. Projected images were aligned digitally within the projection field. Non-invasive detection of lymphatic transport and intraoperative identification of the sentinel lymph nodes was demonstrated feasibility for use in the operating room. Subsequently, peritoneal tumors in a murine model of breast cancer metastasis were identified using the fluorescence projection system after systemic administration of a tumor-selective fluorescent molecular probe. Fluorescence imaging results were confirmed using commercial NIR fluorescence imaging system. These initial results clearly show that direct visualization of fluorescence can simplify FGS relative to existing state-of-the-art intraoperative imaging systems. This technology can easily be incorporated into oncologic surgery routine to improve surgical outcomes for cancer patients.

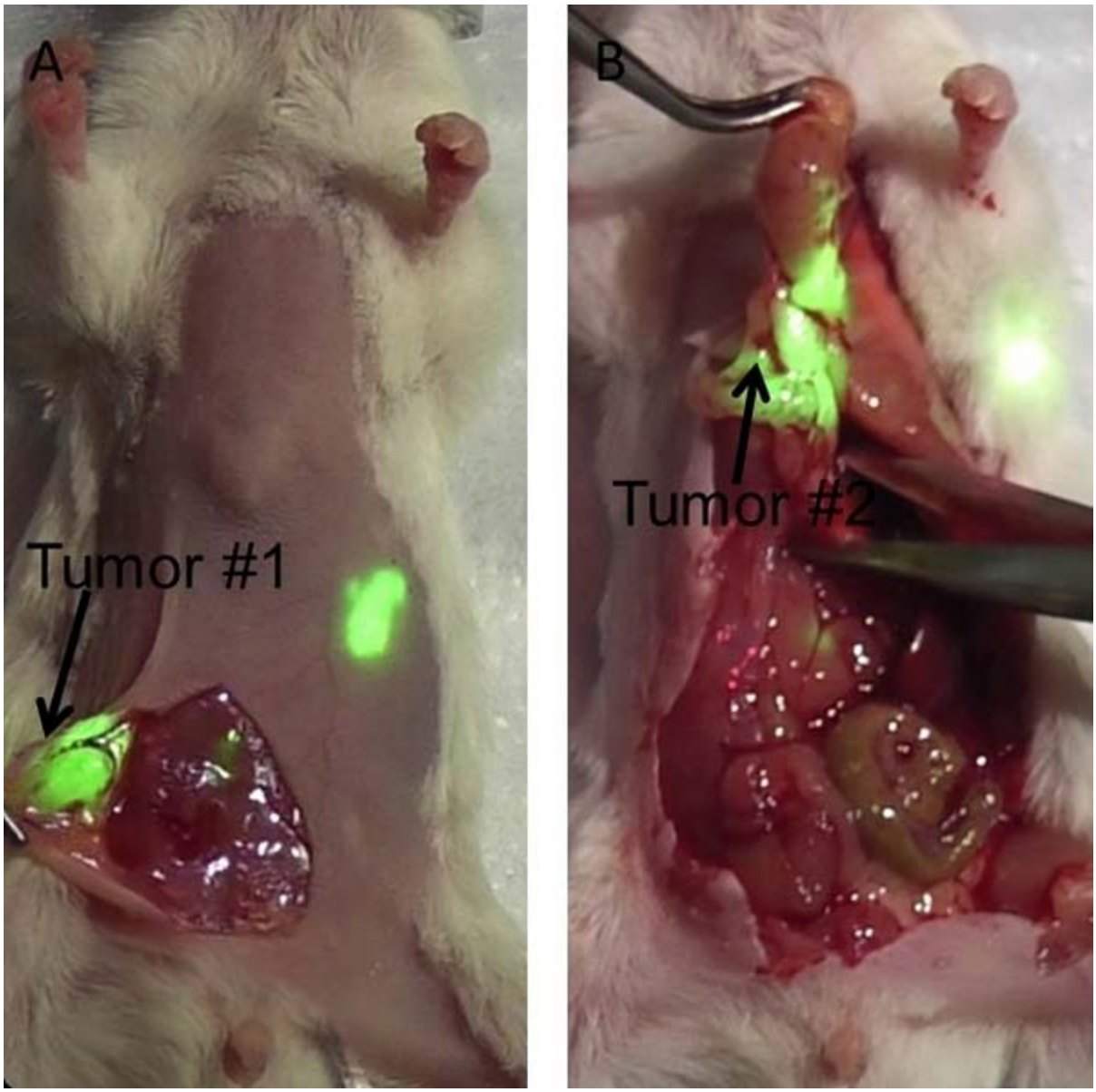

Direct projection of fluorescence signal from tumor tissue within the abdomen of a mouse. Near infrared fluorescence from an integrin-targeted molecular probe identified two tumors prior to surgery. Green light projected on the tissue surface at 1 frame per second enabled detection of one large (tumor #1) and multiple nodular (tumor #2) tumors, which were confirmed by histology.

Disclosure of author financial interest or relationships:
P. Sarder, None; **K. Gullicksrud**, None; **S. Mondal**, None; **S. Achilefu**, None; **W.J. Akers**, None.

Presentation Number **LBAP 132**
Late Breaking Abstract Poster Session
September 19, 2013 / 15:15-15:15 / Room: Exhibit Hall B

Real-Time Endoscopic Guidance using Color and Near-Infrared Fluorescent Light

Sylvain Gioux[1], *Vivek Venugopal*[1], *Alan Stockdale*[1], *Florin Neacsu*[1], *Frank Kettenring*[1], *John V. Frangioni*[1], *Sidhu Gangadharan*[2], [1]*Medicine, Beth Israel Deaconess Medical Center, Boston, MA, USA;* [2]*Surgery, Beth Israel Deaconess Medical Center, Boston, MA, USA. Contact e-mail: sgioux@bidmc.harvard.edu*

Over the past few years, there has been an increasing interest in developing real-time guidance during surgical procedures. Optical methods have proven to be particularly well suited for this purpose due to the fact that they are safe, inexpensive, and accessible to healthcare practitioners. In particular, near-infrared (NIR) fluorescence has witnessed a very rapid growth owing to the promise that targeted molecular agents could highlight with high contrast and specificity structures of interest such as tumors or nerves. Following the development of clinically compatible open surgery fluorescence imaging systems, the interest is now shifting toward minimally invasive surgery applications due the rapid growth of these procedures in patient care. In this work we present the design and validation of the first clinically compatible endoscopic imaging system capable of real time (10 fps) imaging of both color and NIR fluorescence information. A novel NIR-compatible 10 mm rigid endoscope has been used in conjunction with a custom high sensitive, handheld dual channel camera (color and NIR), and a custom light source. The system has been successfully integrated in a clinically-compatible platform and validated both on the bench and during sentinel lymph node procedures in Yorkshire pigs, and provides real-time image guidance of both color and NIR fluorescence information to the surgeon. Together, this study lays the foundation for the clinical translation of endoscopic NIR fluorescence intraoperative guidance.

Disclosure of author financial interest or relationships:
S. Gioux, None; **V. Venugopal**, None; **A. Stockdale**, None; **F. Neacsu**, None; **F. Kettenring**, None; **J.V. Frangioni**, None; **S. Gangadharan**, None.

Presentation Number **LBAP 133**
Late Breaking Abstract Poster Session
September 19, 2013 / 15:15-15:15 / Room: Exhibit Hall B

Technical characterization of one near-infrared fluorescence imaging system

Sophie Vankerckhove, **Bissan K. Ahmed***, Thomas Guiot, Bruno Vanderlinden, Pierre Bourgeois, Service of Nuclear Medicine, Jules Bordet Institute, Brussels, Belgium. Contact e-mail: bissan.ahmed@bordet.be*

Introduction: Different clinical trials using fluoroscopy with Indocyanine Green (ICG) are currently on-going in our institute. This technique allows us to observe fluorescence in different tissues such as lymph nodes or nodules. The aim of the study is to characterize the camera we use for our fluorescence imagings (Photodynamic Eye (PDE) from Hamamatsu Photonics, Japan), in order to measure the intensity of fluorescence and to estimate the quantity of ICG accumulated in each of our tissue samples. For this purpose, different parameters of acquisition need to be standardized. Material & methods: Videos of several dilutions of Indocyanine Green were acquired in plastic tubes (20 concentrations tested, from 0,1 ng/ml to 250 µg/ml in pure water), under different conditions. Different light, brightness and contrast parameters of the camera were tested and images were acquired for each condition. Intensity of fluorescence was also measured at different distances between the tubes and the camera. Finally, the influence of the position of one tube in the field of the camera was analysed. All the acquired images were analysed in order to quantify the intensity of fluorescence in the plastic tubes (see attached image). All the acquisitions were performed in a black room, without any artificial or natural light, except the light emitted by the infrared diodes of the camera. Results: Very important variations in intensity of fluorescence were observed for each dilution. According to the parameters of light and brightness of the camera, the range of concentration which can be quantified was changed when the parameters of illumination were increased, fluorescence of lower concentrations could be quantified. This characterization allowed us to quantify samples with a concentration of ICG between 1µg/ml and 1ng/ml, which means that the PDE camera is highly sensitive. On the other hand, we noticed that the intensity of fluorescence of one sample measured at a distance of 10 cm from the camera was almost two fold more intense than the same sample when it is placed at a distance of 20 cm from the camera. Furthermore, the fluorescence intensity varied up to fivefold when the tube is positioned in the middle of the field of the camera compared with the intensity of fluorescence of the tube placed at the edge of the image. Then, these parameters have also to be standardized, because they may dramatically change the fluorescence intensity measurement. Conclusions: The huge variations in intensity of fluorescence observed for each dilution, depending on the other parameters, confirm the importance to standardize the parameters of acquisition of fluorescence images. Such in vitro acquisition should be performed for each existing near-infrared camera in order to be able to compare signals-results acquired from different sources.

Disclosure of author financial interest or relationships:
S. Vankerckhove, None; **B.K. Ahmed**, None; **T. Guiot**, None; **B. Vanderlinden**, None; **P. Bourgeois**, None.

Presentation Number **LBAP 134**
Late Breaking Abstract Poster Session
September 19, 2013 / 15:15-15:15 / Room: Exhibit Hall B

Comparison of High Sensitivity BLI Imaging Systems for Ultra-weak Signal Applications

Michael D. Henry[1], **Marisa R. Buchakjian**[2,1], *Michael Cable*[3], [1]*Molecular Physiology and Biophysics, University of Iowa Carver College of Medicine, Iowa City, IA, USA;* [2]*Otolaryngology - Head and Neck Surgery, University of Iowa Hospitals and Clinics, Iowa City, IA, USA;* [3]*Spectral Instruments Imaging, Tucson, AZ, USA. Contact e-mail: marisa-buchakjian@uiowa.edu*

Bioluminescent Imaging (BLI) has become a standard laboratory tool that is particularly useful because of its high sensitivity and low background. It is used for demanding applications such as locating small tumor metastases and rapid determination of the efficacy of intracardiac (IC) or tail vein injections. For IC injections, images taken a few minutes after systemic injection can show whether the procedure, typically involving 10^4 to 10^6 luciferase-expressing cells, was done correctly. All of these applications require measurements near the threshold of detection for even the highest sensitivity imaging systems. Figure 1 shows four mice with IC injections of 10^5 22Rv1.lucPN2 cells. The two mice on the right had unsuccessful injections as evidenced by the lack of detectable signal. The two mice on the left indicate successful IC injections as observed by luminescent emission in the cardiac region. These signals are "ultra-weak" and near the limit of detection with average radiance of a few thousand photons/second/cm2/sr. For very low signal BLI images taken with a popular high sensitivity system, an IVIS 100 imager, a "halo" consisting of high background in a circular pattern around the center of the image is routinely observed. An example of this effect is seen in Figure 1. In an effort to understand this problem and how it affects quantitation and detection thresholds, similar ultra-weak images were studied with IVIS 200 (now known as the IVIS Spectrum) and Spectral Instruments Imaging Ami X systems. Measurements were made with a low level calibration light source at the center and near the corners of each system. It was observed that corner measurements had much higher levels of statistical noise on the IVIS 100. This was determined to be an artifact of the flat field correction algorithm applied to compensate for lower off-axis light collection efficiency of the lens. Since the number of photons detected decreases moving away from the center of the lens, a correction must be applied to the image to provide uniform light detection across the field of view (FOV). The background statistical noise is relatively flat across the FOV, but when the correction is applied the noise is effectively amplified resulting in the halo effect shown in Figure 1. The IVIS 100 correction factor for the measurement near the corner of the image was determined to be 4.9. The other systems have smaller flat field corrections, 1.6 for the IVIS 200/Spectrum and 1.5 for the Ami X. The halo effect was not observed on either of these systems. During the course of this work, the lower limits of these three systems for observation and quantitation of a weak BLI signal was examined. For the region of the image away from the halo effect, all three imaging system lower limits were similar and capable of quantitating ultra-weak BLI signals. Near the corners of the IVIS 100, the signal/noise for a low level signal was lower making it harder to detect a low level signal. For the other systems this effect was negligible and they were able to detect ultra-weak signals across the entire FOV.

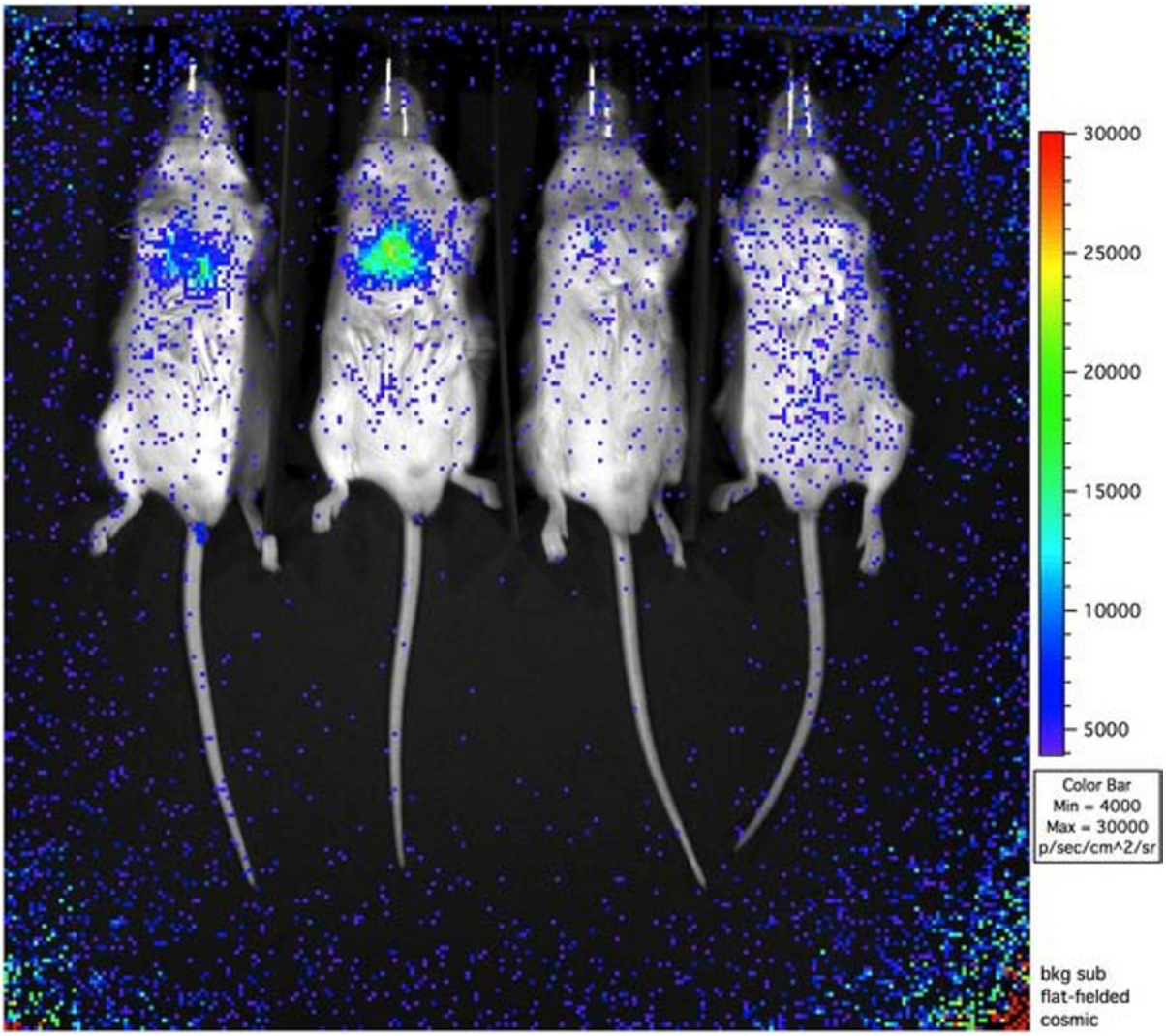

Disclosure of author financial interest or relationships:
M.D. Henry, None; **M.R. Buchakjian**, None; **M. Cable**, Spectral Instruments Imaging, Stockholder .

Presentation Number **LBAP 135**
Late Breaking Abstract Poster Session
September 19, 2013 / 15:15-15:15 / Room: Exhibit Hall B

Integration of in vivo imaging with in silico growth models can predict the distribution of viable cancer cell populations

Rosy Favicchio[1,3], Eleftheria Tzamali[2], Vangelis Sakkalis[2], Kostas Marias[2], Clio Mamalaki[3], Joseph Papamatheakis[3], Jorge Ripoll[1,4], **Giannis Zacharakis**[1], *[1]Institute of Electronic Structure and Laser, Foundation for Research and Technology - Hellas, Heraklion, Greece; [2]Institute of Computer Science, Foundation for Research and Technology - Hellas, Heraklion, Greece; [3]Institute of Molecular Biology and Biotechnology, Foundation for Research and Technology - Hellas, Heraklion, Greece; [4]Dept. of Bioengineering and Aerospace Engineering, Universidad Carlos III of Madrid, Madrid, Spain. Contact e-mail: zahari@iesl.forth.gr*

In vivo imaging modalities can readily detect heterogeneous regions in solid tumours, however, their onset and developmental pattern is highly disordered in preclinical experimental settings. This complexity is easily explained by the inconsistent balance between supply and demand of nutrients and waste products within the tumour. Mathematical models on the other hand can be designed around proliferation rates and concentrations of different cell populations. The growth predictions obtained describe the spatial distribution of tissue. An effective approach to predict heterogeneity in cancer is the integration of molecular imaging techniques with computational models. To this end we employed longitudinal in vivo imaging data obtained by Fluorescence Molecular Tomography (FMT) to validate a hybrid in silico modular predictive model of tumour progression. In this study, a custom-built FMT system was used to detect the red emitting protein Katushka, constitutively expressed in a subcutaneous xenograft HeLa model. The experimental FMT system used a diode laser emitting at 592nm and a cooled 16-bit CCD camera coupled with a 50mm Macro f/2.8 objective. Tomographic imaging was performed daily by raster-scanning the laser and acquiring two sequential measurements: the excitation and fluorescence emission, isolated using interference filters. A small tumor (typically <1mm diameter) was generally visible within 4-5 days post-injection, at which point imaging was initiated. The in silico model simulated changes of tumor cell concentration over time and space, by using two main terms: one for invasion (diffusion term), the other for proliferation (reaction term). The raw image data and the 3-dimensional FMT reconstruction obtained during the first in vivo imaging session (Day 0 of the model) was used as input for the initial spatial distribution of the viable cancer cell population. Quantitative FMT data was sensitive to changes in tumour diameter <250um with a SNR of 20:1 and a high linear correlation to electronic caliper measurements (r2=0.97). The longitudinal data therefore provided a highly precise profile of growth dynamics, for each individual tumour (Fmean vs t). The in silico model was used to compute growth curves for a combination of normoxic and hypoxic cells. Fast initial growth was observed for the first 3 days, and a subsequent plateau was reached by day7 (Figure 1). Correlation between in vivo data and in silico predictions resulted in a high linear correlation between methodologies. The integration of molecular imaging data to validate in silico models showed the importance of proper initialization in predictive models and suggests that nutrient competition is a key determinant for explaining the growth behavior of tumors. Acknowledgements This work was funded by the Program INTERREG III, Project "YPERTHEN", financed by the European Commission through the European Regional Development Fund and by National Funds of Greece and Cyprus and Grant "Skin-DOCTor" implemented under the "ARISTEIA" Action, of the "OPERATIONAL PROGRAM EDUCATION AND LIFELONG LEARNING", co-funded by the European Social Fund (ESF) and National Resources.

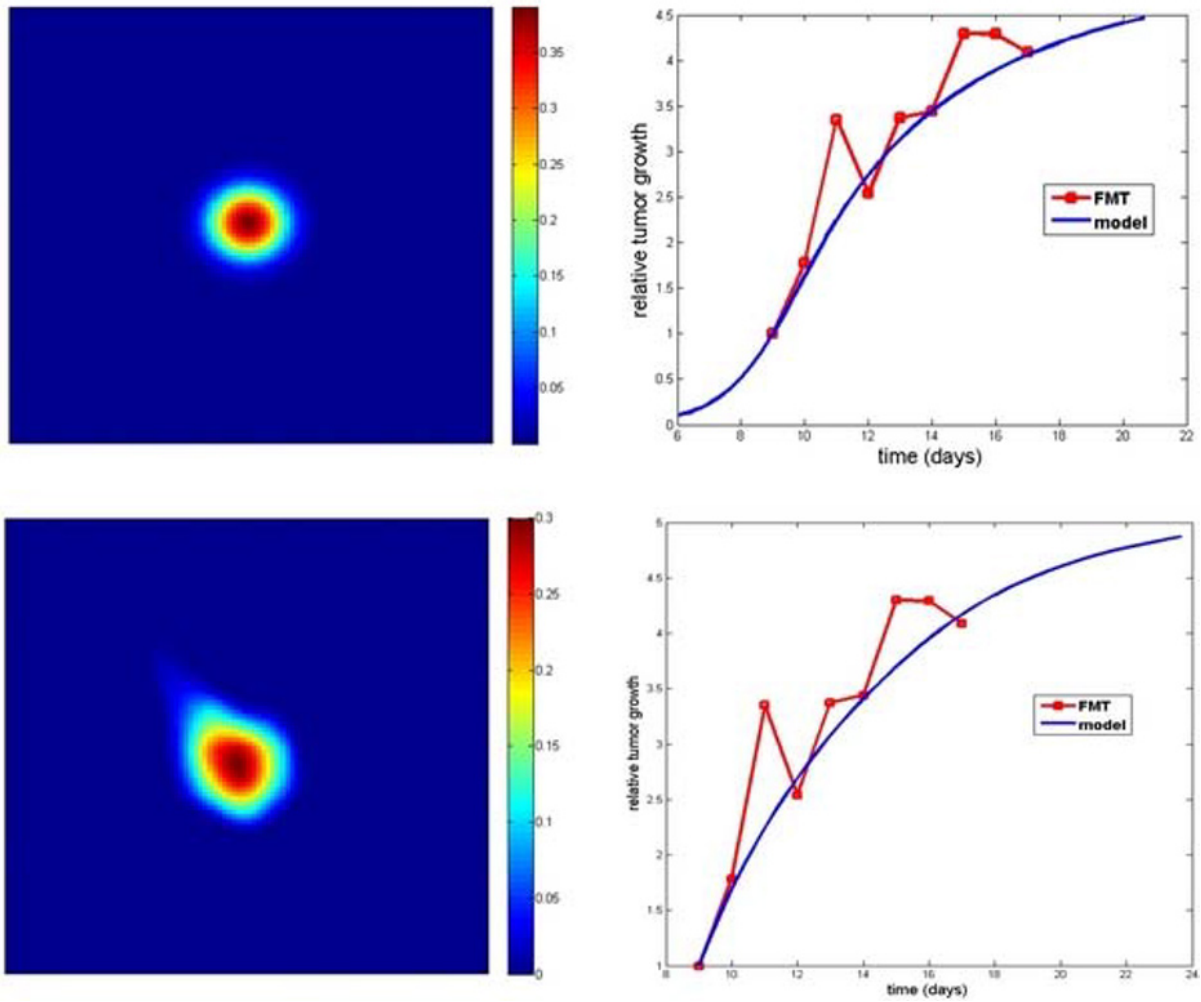

Figure 1: Tumor growth curves when a) a normal distribution of normoxic cells is assumed and b) when the distribution is obtained from the in vivo reconstructions.

Disclosure of author financial interest or relationships:
R. Favicchio, None; **E. Tzamali**, None; **V. Sakkalis**, None; **K. Marias**, None; **C. Mamalaki**, None; **J. Papamatheakis**, None; **J. Ripoll**, None; **G. Zacharakis**, None.

Presentation Number **LBAP 136**
Late Breaking Abstract Poster Session
September 19, 2013 / 15:15-15:15 / Room: Exhibit Hall B

Dicentric Chromosome Assay for Dose estimation by Microscopic Molecular Imaging

Tsui-Jung Chang[1], *Ping-Hung Yu*[1], *Kuan-Yi Yeh*[1], *Kuei-Fang Lee*[2], *Ingrid Y Liu*[2], *Chih-Hsien Chang*[1], [1]*Isotope Application Division, Institute of Nuclear Energy Research, Taoyuan, Taiwan;* [2]*Department of Molecular Biology and Human Genetics, Tzu Chi University, Hualien, Taiwan. Contact e-mail: tjchang@iner.gov.tw*

Dicentric Chromosome Assay for Dose estimation is considered to be an important first step in the medical treatment of persons exposed to radiation. Many countries around the world have been making great efforts to develop better capabilities for emergency preparedness nuclear accidents. Dose estimation is considered to be an important step in the medical treatment of persons exposed to radiation. Methods: Dicentric chromosome assay (DCA) was established by automated digital microscopic imaging as a golden standard for biodosimery estimation. Radiation dosimetry was first performed using alanine/EPR dosimetry with US National Institute for Standards and Technology (NIST) standard pellet. The blood samples were irradiated with 0, 0.5, 1, 2, 3, 4 and 5 Gy 60Co gamma rays at room temperature. Dosimetry was further validated with a thermoluminescence dosimeter (TLD). Fluorescence in situ hybridization (FISH) for translocations analysis is used when delayed sampling or suspected chronically irradiation dose assessment. Results: DCA was established by microscopic imaging. The data of Alanine/EPR dosimetry showed a high agreement with those by thermoluminescence dosimeter (R2=0.998). The dose-effect calibration curve by 60Co gamma rays was established. Our laboratory constructed a dose-effect calibration curve for the yield of dicentrics for 60Co gamma rays in the 0 to 5-Gy range, using the maximum likelihood linear-quadratic model, $Y=C+\alpha D+\beta D2$. The alpha and beta coefficients were 0.08 and 0.06, respectively. Interlaboratory comparison was also confirmed the results. For FISH, our laboratory also observed the phenomenon of chromosome translocations (chromosome 1, 2 and 4 probe used) in radiation exposed human lymphocytes. Conclusions: This study revealed low LET (60Co gamma rays) dose-effect calibration curve established in our laboratory. It is helpful in preparedness for radiological emergencies.

Disclosure of author financial interest or relationships:
T. Chang, None; **P. Yu**, None; **K. Yeh**, None; **K. Lee**, None; **I. Liu**, None; **C. Chang**, None.

Presentation Number **LBAP 137**
Late Breaking Abstract Poster Session
September 19, 2013 / 15:15-15:15 / Room: Exhibit Hall B

Optical detection and virotherapy of live metastatic tumor cells in body fluids with vaccinia strains

Huiqiang Wang[1], *Nanhai G. Chen*[1,2], *Boris R. Minev*[1,2,3], *Martina Zimmermann*[4], *Richard J. Aguilar*[1], *Qian Zhang*[1,2], *Julia B. Sturm*[4], *Falko Fend*[5], *Yong A. Yu*[1,2], *Joseph Cappello*[1], *Ulrich M. Lauer*[4], *Aladar A. Szalay*[1,2,6], *[1]R & D, Genelux Corporation, San Diego, CA, USA; [2]Radiation Medicine and Applied Sciences, Rebecca & John Moores Comprehensive Cancer Center, University of California, San Diego, La Jolla, CA, USA; [3]UCSD Division of Neurosurgery, University of California, San Diego, La Jolla, CA, USA; [4]Gastroenterology and Hepatology, Tuebingen University Hospital, Tuebingen, Germany; [5]Institute of Pathology, Tuebingen University Hospital, Tuebingen, Germany; [6]Department of Biochemistry, Rudolf Virchow Center for Experimental Biomedicine, and Institute for Molecular Infection Biology, University of Würzburg, Würzburg, Germany. Contact e-mail: huiqiangwang@gmail.com*

Metastatic tumor cells in body fluids are important targets for treatment, and critical surrogate markers for evaluating cancer prognosis and therapeutic response. Here we report, for the first time, that live metastatic tumor cells in blood samples from mice bearing human tumor xenografts and in blood and cerebrospinal fluid samples from patients with cancer were successfully detected using a tumor cell-specific recombinant vaccinia virus (VACV). In contrast to the FDA-approved CellSearch system, VACV detects circulating tumor cells (CTCs) in a cancer biomarker-independent manner, thus, free of any bias related to the use of antibodies, and can be potentially a universal system for detection of live CTCs of any tumor type, not limited to CTCs of epithelial origin. Furthermore, we demonstrate for the first time that VACV was effective in preventing and reducing circulating tumor cells in mice bearing human tumor xenografts. Importantly, a single intra-peritoneal delivery of VACV resulted in a dramatic decline in the number of tumor cells in the ascitic fluid from a patient with gastric cancer. Taken together, these results suggest VACV to be a useful tool for quantitative detection of live tumor cells in liquid biopsies as well as a potentially effective treatment for reducing or eliminating live tumor cells in body fluids of patients with metastatic disease.

Disclosure of author financial interest or relationships:
H. Wang, Genelux Corporation, Employment; **N.G. Chen**, Genelux Corporation, Employment; **B.R. Minev**, Genelux Corporation, Employment; **M. Zimmermann**, None; **R.J. Aguilar**, None; **Q. Zhang**, Genelux Corporation, Employment; Genelux Corporation, Stockholder; **J.B. Sturm**, None; **F. Fend**, None; **Y.A. Yu**, None; **J. Cappello**, Genelux Corporation, Employment; **U.M. Lauer**, None; **A.A. Szalay**, Genelux Corporation, Stockholder; Genelux Corporation, Employment; Genelux Corporation, Other financial or material support .

Presentation Number **LBAP 138**
Late Breaking Abstract Poster Session
September 19, 2013 / 15:15-15:15 / Room: Exhibit Hall B

Experimental and Simulational Study of Positron Emission Tomography for Multiple Molecular Imaging

Tomonori Fukuchi[1], *Takahisa Hanada*[2], *Hiromitsu Haba*[3], *Yasuyoshi Watanabe*[1], *Shuichi Enomoto*[1,2], [1]*Center for Life Science Technologies, RIKEN, Kobe, Japan;* [2]*Department of Pharmaceutical Analytical Chemistry, Graduate School of Medicine, Dentistry and Pharmaceutical Sciences, Okayama University, Okayama, Japan;* [3]*Nishina Center for Accelerator-Based Science, RIKEN, Wako, Japan. Contact e-mail: tfukuchi@riken.jp*

Positron Emission Tomography (PET) represents today essential role in nuclear medicine, due to its ability to provide quantitative bio-distribution of a molecular probe. However, PET works basically only for single probe simultaneously, because positron-electron annihilation results in two 511-keV photons irrespective of radionuclides. In order to overcome this limitation, we have been developing Polychrome-PET (P-PET) for multiple molecular simultaneous imaging. For the P-PET, we expect various new applications such as simultaneous performing of two or more diagnosis, analysis of the time sequence of multiple probes, analysis of additional dosage of the same drug, validation of the drag delivery system (DDS), etc. For the P-PET, β-decay radionuclides which emit de-excitation γ-ray promptly after the positron emitting are utilized as a probe. The P-PET identifies different probes by detection of this de-excitation γ-ray. In addition to γ-ray emission, β-decay half-lives are also important criteria for nuclear medicine, especially for clinical use. As a consequence, candidate radionuclides for the P-PET are the following: 38K, 44Sc, 48V, 60Cu, 76Br 82Rb, 94mTc, 124I, etc. For a feasibility study of the P-PET, we performed computer simulations using a Monte Carlo based simulator GATE (Geant4 Application for Tomographic Emission). In this simulation, semiconductor γ-ray detectors were added to the existing small animal PET (Siemens Focus 220). Using this simulator, details of various conditions such as numbers of additional γ-ray detectors, detector geometry, width of coincidence time window and energy threshold were examined. As the result, a PET system with 32 germanium semiconductor γ-ray detectors (Ge detector) in outer ring geometry, which provide about 10% of γ-ray detection efficiency, gives practical images of 2 different probe distributions in a digital rat phantom (as shown in figure). Moreover, we also carried out experimental study of the P-PET using a planer type PET system with additional Ge detector. In this experiment, standard PET probe and a positron-γ emitter were used. List-mode double- and triple-coincidence measurement was performed in parallel for annihilation and de-excitation γ-rays. The collected list-mode data was distributed into two data sets whether Ge detector detected additional γ-ray or not. These two data sets were used for image reconstruction independently. We successfully produce individual images of 2 probe distributions using this system. These experimental and simulational study support the feasibility of the P-PET and widely expand potential of the PET for multiple molecular imaging.

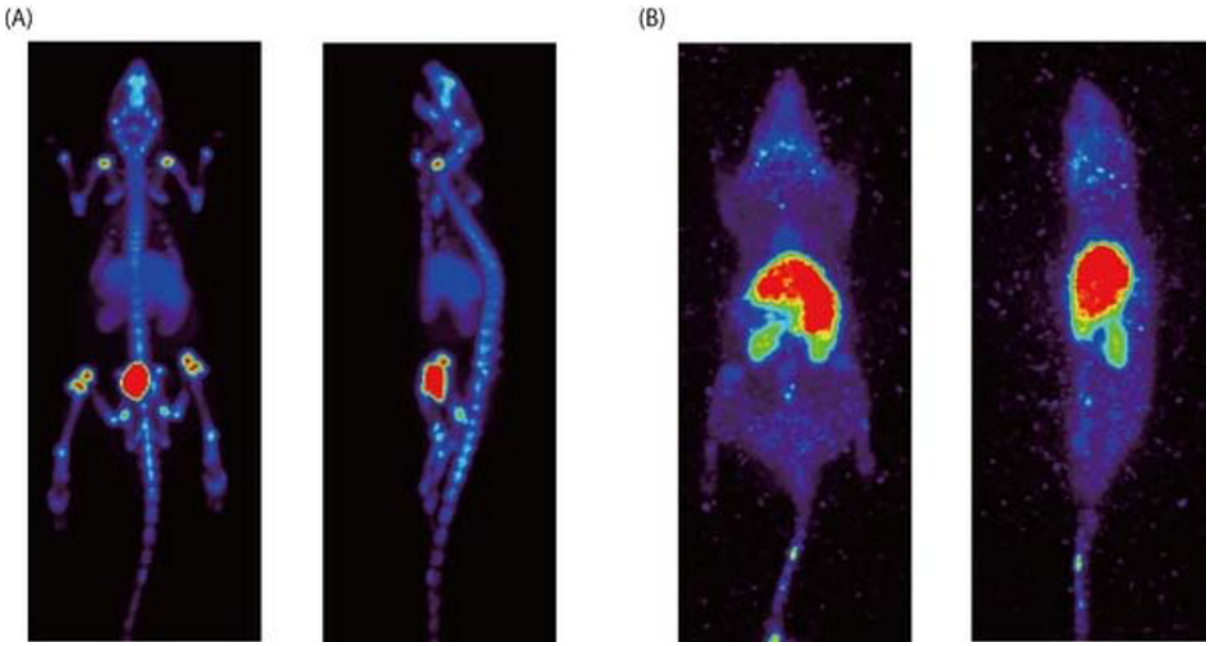

Simulated images of multiple probe distributions using P-PET. Probes of 18F (pure positron emitter) and 44Sc (positron and de-excitation γ-ray emitter) are simultaneously injected in a rat. Probe distribution without γ-ray detection (A: 18F and 44Sc). Probe distribution with γ-ray detection (B: 44Sc).

Disclosure of author financial interest or relationships:
T. Fukuchi, None; **T. Hanada**, None; **H. Haba**, None; **Y. Watanabe**, None; **S. Enomoto**, None.

Presentation Number **LBAP 139**
Late Breaking Abstract Poster Session
September 19, 2013 / 15:15-15:15 / Room: Exhibit Hall B

Sub-millimeter spatial resolution small animal PET scanner using thin monolithic scintillators: proof-of-concept

Samuel España, *Radoslaw Marcinkowski, Vincent Keereman, Stefaan Vandenberghe, Roel Van Holen, Department of Electronics and Information Systems, MEDISIP, Ghent University-iMinds-IBiTech, Ghent, Belgium. Contact e-mail: Samuel.Espana@UGent.be*

INTRODUCTION. Current dedicated small rodent PET scanners have a spatial resolution in the order of 1 mm. Most of them have a large footprint, requiring considerable laboratory space. For rodent brain imaging, a PET scanner with sub-millimeter resolution is desired. To achieve this, crystals with pixel pitch down to 0.5 mm have been used. However, fine pixels are difficult to produce and may render systems expensive. In this work we present preliminary results of a high-resolution preclinical PET scanner based on thin monolithic scintillators. The scanner will be dedicated to rat brain imaging and therefore has very compact geometry. MATERIALS AND METHODS. Four detectors were placed in a square arrangement with 34.5 mm distance between two opposing detector modules defining a field of view (FOV) of 32×32×32 mm3. Each detector consists of a thin monolithic LYSO crystal of 32×32×2 mm3 optically coupled to a DPC-3200 digital silicon photomultier (dSiPM). The outside dimensions of the system are 115×150×38 mm3. A picture of the prototype system is shown in figure 1 (a). Event positioning within each detector was obtained using the Maximum Likelihood Estimation (MLE) method leading to an average intrinsic spatial resolution of 0.6 mm FWHM as is shown in figure 1 (b) and (c). To evaluate the system performance we measured the energy resolution, coincidence resolving time, sensitivity and spatial resolution. The image quality was evaluated by acquiring a micro-Derenzo phantom filled with 18F-FDG and a rat head one hour after an 18F-FDG injection. RESULTS. We obtained a coincidence resolving time of 1 ns and an energy resolution of 20 % FWHM at 511 keV. The sensitivity and spatial resolution obtained at the center of the FOV were 2.8 cps/kBq and 0.81 mm respectively. In the reconstructed images of the micro-Derenzo phantom, the rods of 1.5, 1.2, 1.0 and 0.9 mm can be discriminated. CONCLUSION. A compact PET scanner was built using dSiPM technology and thin monolithic LYSO crystals. Excellent spatial resolution and acceptable sensitivity were demonstrated. Promising results were also obtained in terms of image quality when imaging realistic objects. As the system is still in an early stage of development, further improvements can be expected.

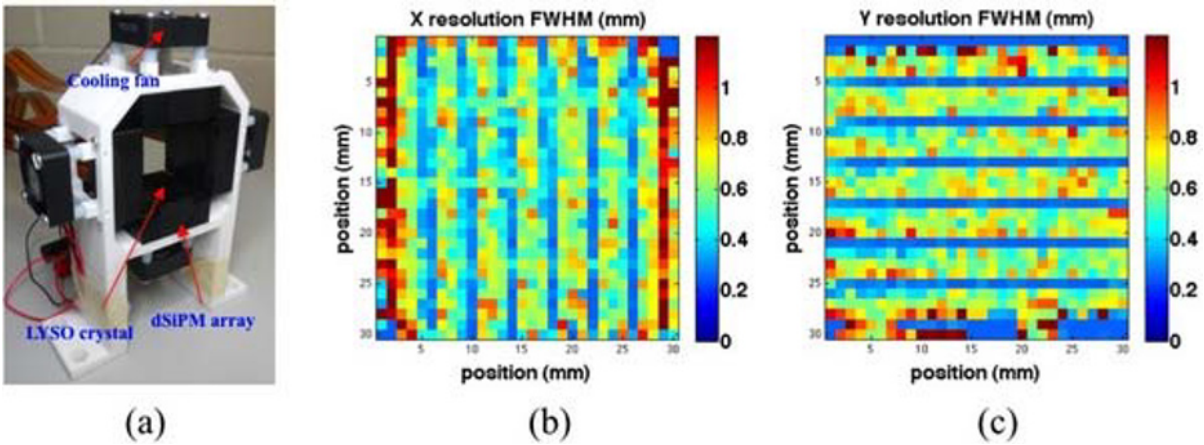

Figure 1. Picture of the PET prototype (a). Intrinsic spatial resolution in X (b) and Y (c) directions obtained for one of the detectors of the system.

Disclosure of author financial interest or relationships:
S. España, None; **R. Marcinkowski**, None; **V. Keereman**, None; **S. Vandenberghe**, None; **R. Van Holen**, None.

Presentation Number **LBAP 140**
Late Breaking Abstract Poster Session
September 19, 2013 / 15:15-15:15 / Room: Exhibit Hall B

Respiratory motion compensation in pre-clinical PET 3D registration

Poussier Sylvain[1,2,3], *Emilien Micard*[2], *Bodson Antoine*[1,2], *Pierre Yves Marie*[1,3], *Jacques Felblinger*[2], *Gilles Karcher*[1,3], [1]*GIE NANCYCLOTEP, Nancy Hospital - Nuclear Medecine, Vandoeuvre les nancy, France;* [2]*IADI, INSERM U 847, Vandoeuvre les nancy, France;* [3]*Biophysique laboratory, Lorraine University, Vandoeuvre les nancy, France. Contact e-mail: sylvain.poussier@univ-lorraine.fr*

Introduction During a PET scan on a small animal type rat, movements from respiratory cycles cause artifacts, errors on the apparent size of tumors, as quantification of voxel values, and a blur on the apparent kinetic volume observed. Due to the complex tridimensional movement organs, this work proposes to implement a 3D correction of the images based on the reconstructed PET images synchronized to the signal. Materials and methods. Our proposal is to try to correct the image set synchronized with respect to a reference image corresponding to a particular instant of the respiratory cycle. We implemented a solution using 3D optical flow to calculate the movement of voxels between each image based on the algorithm of Horn and Shunck, and its evolution by Brox. The principle of the algorithm of Horn and Schunck is based on an assumption of conservation of the intensity of the same voxel in two successive images. The optical flow equation is derived from this constraint. In 1981, Horn and Schunck expose an iterative implementation that allows them to obtain the correct optical flow computation. To do this, they assumed that there is a link between the movement of a pixel and its neighbors. Thus a set of adjacent points in a movement has a direction and a speed equivalent displacement, simulating a smooth and steady movement. The problem is then reduced to minimizing the cumulative error constraints. In 2005, T. Brox describes various improvements. He added, (i) a resolution Multiscale This technique speeds up the calculation time and reduces chances of hitting local minima without causing changes in equations algorithms, (ii) the principle of non-linearization of data by changing the shape of the Taylor development of the optical flow equation, (iii) the assumption of constant gradients, introducing the management of any change in intensity in the image and (iv) a function of strength of the non-quadratic shape data and smoothing, in order to compensate for any discontinuity in the vector field. Digital developments were carried out in C + + code to optimize the computational time. Testing different algorithms were implemented performed on digital test objects, and heart acquisitions rat and cardiac phantom on the Inveon microPET (Siemens, Knoxville, USA). Rats are under anesthesia with isoflurane (2%), injected with 70 MBq of 18F-FDG. The acquisition time is 20 minutes with a statement of cardiac and respiratory signals. Each signal is divided into 16 phases per cycle. Phantoms are filled with 5MBq of 18FDG. Respiratory motion is generated by a platform motion experimental, respiratory signal is recorded by the same sensor type for animals. Achievements and perspective With the algorithms proposed by T. Brox, results were in line with expectations products. Indeed, there is a complete recalibration of respiratory movement on a rat. We even got a good reconstruction of a phantom with an amplitude of movement even greater. Note also that the correct results were obtained in processing time quite tolerable, some ten minutes.

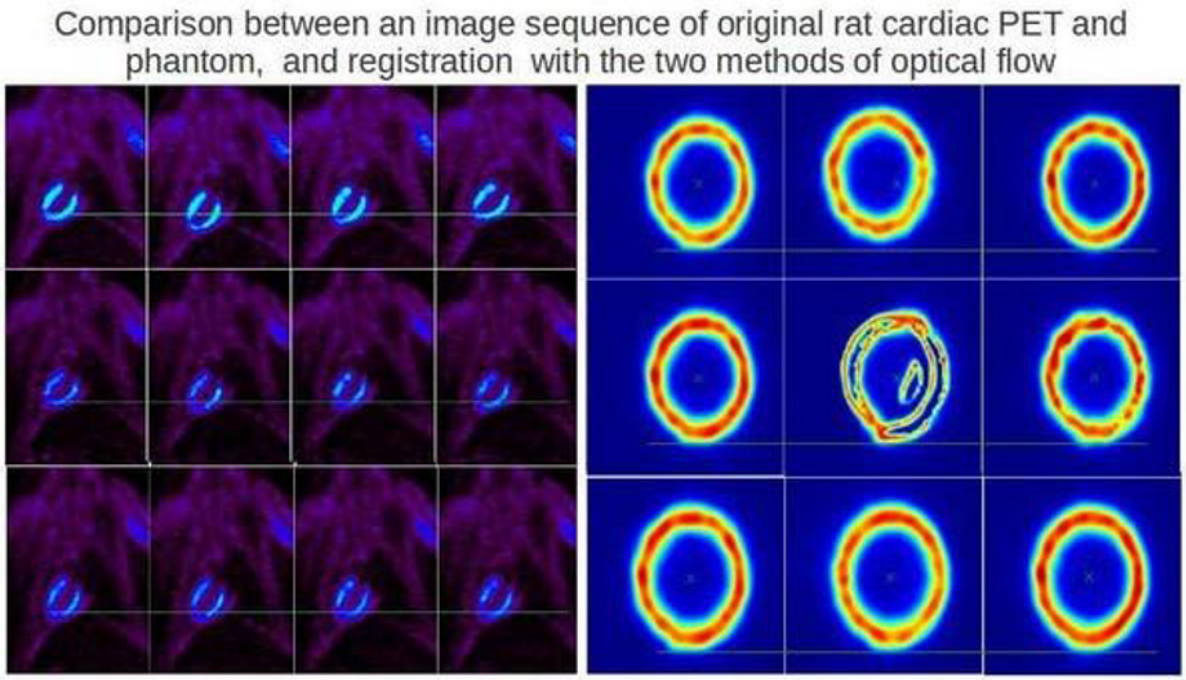

Disclosure of author financial interest or relationships:
P. Sylvain, None; **E. Micard**, None; **B. Antoine**, None; **P. Marie**, None; **J. Felblinger**, None; **G. Karcher**, None.

Presentation Number **LBAP 141**
Late Breaking Abstract Poster Session
September 19, 2013 / 15:15-15:15 / Room: Exhibit Hall B

Performance Characteristics of a Long Axial Extent, Trapezoidal Slat Crystal PET Detector

Robert Miyaoka, *William C. Hunter, Adrienne L. Lehnert, Radiology, University of Washington, Seattle, WA, USA. Contact e-mail: rmiyaoka@u.washington.edu*

Objectives: We report on the performance characteristics of a long axial extent, trapezoidal slat crystal (TSC) PET detector. Goals of the TSC detector are to provide sub-millimeter intrinsic spatial resolution, to provide depth of interaction (DOI) positioning, and to support high packing fraction for very compact PET detector systems. DOI positioning is achieved by including a model of the depth dependent light response function along the long axis of the slat crystal. The intrinsic spatial resolution goals for the design are less than 1.0 mm full width at half maximum (FWHM) along the long axis of the slat; less than 3.0 mm FWHM DOI resolution; and slat decoding with a peak to valley ratio of better than 4. Methods: The long axial extent, TSC detector is comprised of six LYSO trapezoidal, slat crystals each 8 mm tall, 40.0 mm long, and 0.68 mm on the entrance surface and 0.95 mm wide on the exit surface. Mirror film of varying lengths is used to control light sharing within the crystal array. The TSC array is coupled to a 2-by-12 array of GM-APD sensors with 3 mm by 3 mm square sensitive area and with 3.2 mm center-to-center spacing. A statistics-based method is used for three-dimensional event positioning. The detector is calibrated by stepping a finely collimated line source along the long axis of the detector. For characterizing the three-dimensional (3D) light response of the detector, simple Anger logic positioning is first used to determine the slat of interaction. Next, the width of the light distribution along the long axis of the slat crystal is used for DOI characterization. The light signal is fit to a Lorentzian function and the width term is used to group the events into DOI bins. Once the 3D light response of the detector has been characterized, the maximum likelihood method is used for event positioning. In addition to the perpendicular line source data collected to calibrate the detector and to test its positioning and energy resolution performance, a line flux incident on the detector at a 45-degree angle was used to evaluate the DOI positioning performance. Results: Crystal slat decoding of the detector was excellent. The average peak to valley ratio of the crystal map for slat decoding was 5.7. The average intrinsic spatial resolution along the long axis of the crystal was 1.00±0.17 mm FWHM after correcting for source size. The average DOI positioning was 2.4 mm FWHM, after correcting for source size and the lateral spatial resolution. Conclusions: A long axial extent, trapezoidal slat crystal PET detector has been designed and evaluated. The three-dimensional intrinsic spatial resolution performance met our design goals. We are now investigating methods to further extend the axial extent of the slat detector.

Disclosure of author financial interest or relationships:
R. Miyaoka, Philips Healthcare, Grant/research support; GE Healthcare, Grant/research support; **W.C. Hunter**, PET/X, Employment; **A.L. Lehnert**, None.

Presentation Number **LBAP 142**
Late Breaking Abstract Poster Session
September 19, 2013 / 15:15-15:15 / Room: Exhibit Hall B

Automated System for Dispensing Solutions of Beta Particle Emitting Radioisotopes

Alex A. Dooraghi[1], *David Prout*[1], *Brandon Maraglia*[1], *Nam Vu*[2], *David Stout*[1], *R. Michael van Dam*[1], *Arion Chatziioannou*[1], [1]*Crump Institute for Molecular Imaging, David Geffen School of Medicine at UCLA, Los Angeles, CA, USA;* [2]*Sofie Biosciences, Culver City, CA, USA. Contact e-mail: adooraghi@mednet.ucla.edu*

Automated protocols for measuring and dispensing solutions containing radiolabeled probes are essential not only for providing an optimum environment for radiation workers, but also to ensure a quantitatively accurate workflow. We are investigating a system for automated radioactivity distribution of beta particle emitting radioisotopes such as ^{18}F consisting of a flow cell detector in-line with a peristaltic pump. The flow cell detector consists of two 3x30 mm^2 PIN diodes operated in current mode. One diode is kept in close proximity to tubing which carries the beta source and represents a beta plus photon (background) signal, while the second diode is separated from the beta source in order to provide only a photon (background) signal. Electronic subtraction of the two signals enables measurements of radioactivity independent of background level. The integration of the detector and pump leads to a flexible system that can accurately dispense solutions containing radiolabeled probes in radioactivity concentrations directly produced from a cyclotron (~ 0.1-1 mCi/µl), to low activity concentrations intended for preclinical mouse scans (~ 1-10 µCi/µl), and anywhere in between. In this work, we present the performance and limitations of such a prototype system, and discuss a range of suitable applications.

Disclosure of author financial interest or relationships:
A.A. Dooraghi, None; **D. Prout**, None; **B. Maraglia**, None; **N. Vu**, Sofie Biosciences, Inc., Employment; **D. Stout**, Sofie Biosciences, Stockholder; **R. van Dam**, Sofie Biosciences, Inc., Grant/research support; Sofie Biosciences, Inc., Consultant; Sofie Biosciences, Inc., Stockholder; **A. Chatziioannou**, Sofie Biosciences, Stockholder .

Presentation Number **LBAP 143**
Late Breaking Abstract Poster Session
September 19, 2013 / 15:15-15:15 / Room: Exhibit Hall B

Solvent temperature during short radiochemical reactions

Mark Lazari[1,2], *Shuang Zhang*[2,3], *R. Michael van Dam*[1,2], [1]*Department of Bioengineering, UCLA, Los Angeles, CA, USA;* [2]*Crump Institute for Molecular Imaging, Department of Molecular and Medical Pharmacology, UCLA, Los Angeles, CA, USA;* [3]*Department of Chemical Engineering, UCLA, Los Angeles, CA, USA. Contact e-mail: mlazari@mednet.ucla.edu*

Background: In radiochemistry, reaction times and temperatures are optimized to increase yield and decrease overall synthesis time. In general, the oil bath or reactor temperature is measured, rather than the liquid contents of the reaction vessel. For lengthy reactions (15-30 min), the solution's temperature is assumed to stabilize near the temperature setpoint. However, this may not hold true for short reactions (1-5 min). The actual temperature reached is expected to be significantly different from the setpoint and highly dependent on the vial and heating system in this regime. As a result, translating syntheses from one synthesizer to another (e.g. the transition from developed synthesis to routine production) may require significant re-optimization, especially for temperature-sensitive reactions. We demonstrate examples to illustrate this point. **Method:** Using the ELIXYS radiosynthesizer, which employs resistive heating (300W per reaction vessel) and has been shown to have heating performance similar to an oil bath, we performed experiments with acetonitrile (MeCN) and dimethyl sulfoxide (DMSO). Clean, dry, 5 mL glass V-vials were filled with the given solvent (1 mL) and placed in the reactor. Using a specially-modified cassette (thermocouple inserted through the gasket where the dip-tube is normally placed), we measured the liquid temperatures at different reactor temperature setpoints (T_set) in the range 40-180°C. During heating, the vessel was sealed against the gasket with the thermocouple fully submerged in the solvent without contacting the glass vial. Data collection of both the reactor and solvent temperatures began as the reactor was heated to T_set. The reactor remained at T_set for 30 min and then was cooled with the standard cooling system until the liquid reached 35°C. Solvent loss was measured by mass to ensure no leaking of the reaction vessel contents had occurred. **Results:** Within 30 min, the solvent always reached a maximum temperature, T_max, lower than T_set. We have previously observed the same behavior in a vessel heating in an oil bath. A strong linear correlation was observed relating T_max to T_set ($R^2 > 0.999$). On average, both solvents required 2.5 to 3.0 min to reach 90% of T_max and 4 to 5 min for >95% of T_max. All liquid losses were < 4% (40 µL). **Conclusion:** We determined that the solvent temperature in a heated reaction vessel will reach a maximum temperature below the setpoint, as expected, for short heating times (< 2.5-3.0 min). To achieve a relatively steady temperature close to T_max using an oil bath or ELIXYS, both MeCN and DMSO should be heated for at least 3 min. We expect other synthesizers to require similar or slightly longer times to reach steady temperatures. We recommend to avoid short reaction times if rapid translation from one system to another is needed. Using a single system for both development and routine production could avoid such difficulties, and shorter reactions can be used.

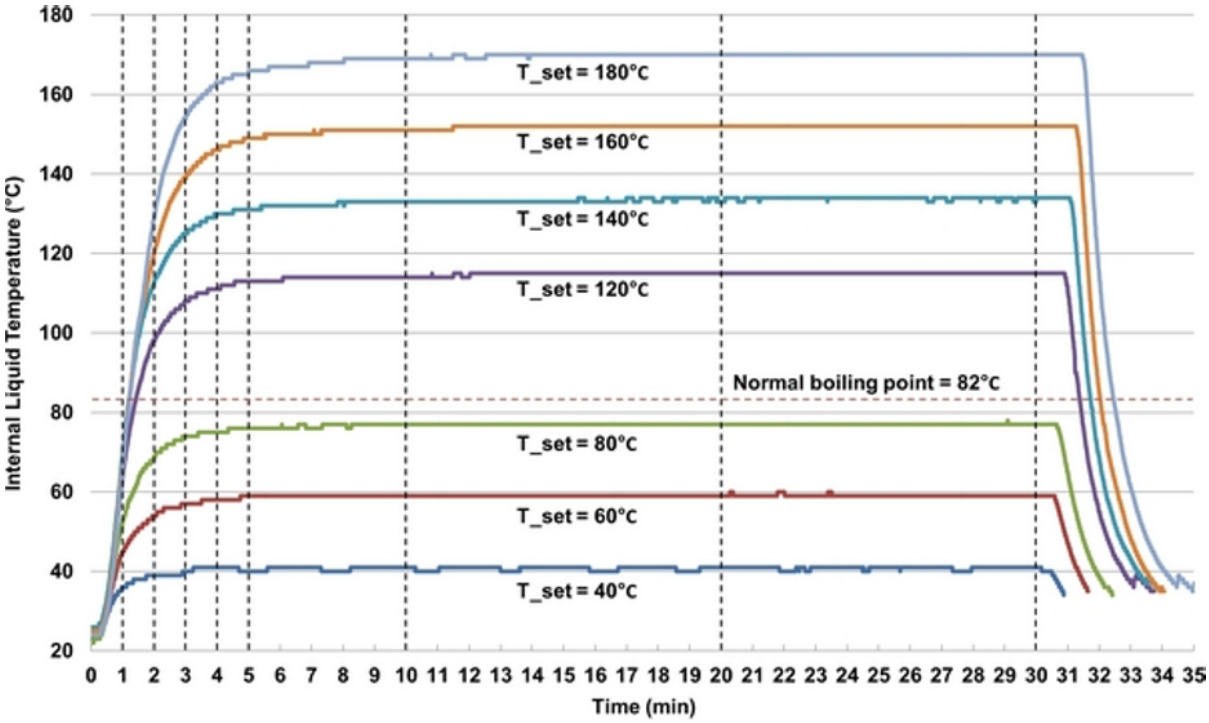

Figure 1. Internal liquid temperature profile over time for MeCN at various reactor temperature setpoints (T_set).

	T_max (°C)	
T_set (°C)	MeCN	DMSO
40	41	41
60	59	59
80	78	78
120	116	113
140	134	132
160	152	152
180	173	169

Table 1. List of the maximum solvent temperature achieved in 30 min (T_max) for given reactor set temperatures (T_set).

Disclosure of author financial interest or relationships:
M. Lazari, None; **S. Zhang**, None; **R. van Dam**, Sofie Biosciences, Inc., Grant/research support; Sofie Biosciences, Inc., Consultant; Sofie Biosciences, Inc., Stockholder .

Presentation Number **LBAP 144**
Late Breaking Abstract Poster Session
September 19, 2013 / 15:15-15:15 / Room: Exhibit Hall B

Unlocking the Full Potential of the Siemens Inveon Docked PET-CT Scanner: A Method to Increase the Useful Axial Field Of View By 33%

Nicholas Keat, *William A. Hallett, Jonathan Howard, Sac-Pham Tang, Lisa A. Wells, Imanova Centre for Imaging Sciences, London, United Kingdom. Contact e-mail: nicholas.keat@imanova.co.uk*

Introduction: The Siemens pre-clinical Inveon dedicated PET (D-PET) scanner is a standalone unit with built-in attenuation correction capability using Co-57 transmission sources. It can also be docked to an Inveon Multi-Modality (MM) system with CT scanner to perform fused PET-CT imaging of a subject placed upon the MM imaging bed. Due to limited axial bed movement range, the acquired CT and PET fields of view do not fully overlap, so CT data can only be acquired for a limited extent of the PET axial field of view (FOV). For a small CT detector in rat imaging mode, the co-scan length is only 96 mm out of the 127 mm PET axial FOV (75%). The remaining 34 mm (25%) of the PET field of view cannot be attenuation corrected. This paper demonstrates a method to extend the table movement to align PET and CT fields of view and allow the entire PET image to be used for quantitative imaging. Methods: An extra imaging position was added to the Inveon MM scanner by drilling a 3.5 mm diameter sprung ball bearing module into the sliding bed, 35 mm from the routine PET-CT imaging position. CT images were acquired with the bed in this position, and the bed moved to the standard position for PET imaging. A new transformation matrix was acquired and applied to align the CT to the PET FOV. Images were otherwise acquired and reconstructed as usual. Results: The full field of view technique was validated using two Ge-68 rod sources arranged in an 'X' shape. The modified bed position and transformation matrix were used, and automated rigid registration applied between the acquired PET and CT data sets. The standard deviation of the shifts required for alignment of the images in the x, y and z planes were 0.3, 0.1 and 0.7 mm respectively, compared to 0.5, 0.3 and 0.6 mm using an un-modified acquisition protocol. The CT images acquired with the full field of view technique provide attenuation correction information for the entire field of view. Animal images were acquired with the full field of view technique, and were attenuation corrected along the entire PET field of view, from nose to mid-liver of a 300 g Sprague-Dawley rat. Discussion: The docked Inveon D-PET and MM scanner does not normally make the most of the relatively long PET axial field of view, due to limited bed movement range. This modification to the system is a relatively simple mechanical step that increases the available FOV for attenuation corrected PET by 33%. The alignment between PET and CT fields of view was not adversely affected, as shown by the registration variability. Practical benefits include the potential for acquiring simultaneous image-derived input functions from the heart in neurological experiments with rats. For biodistribution and dosimetry studies, the extra axial length allows more organs to be imaged. Thirdly, scatter correction for PET radioligands with high liver uptake can be performed more accurately when that region is fully attenuation corrected.

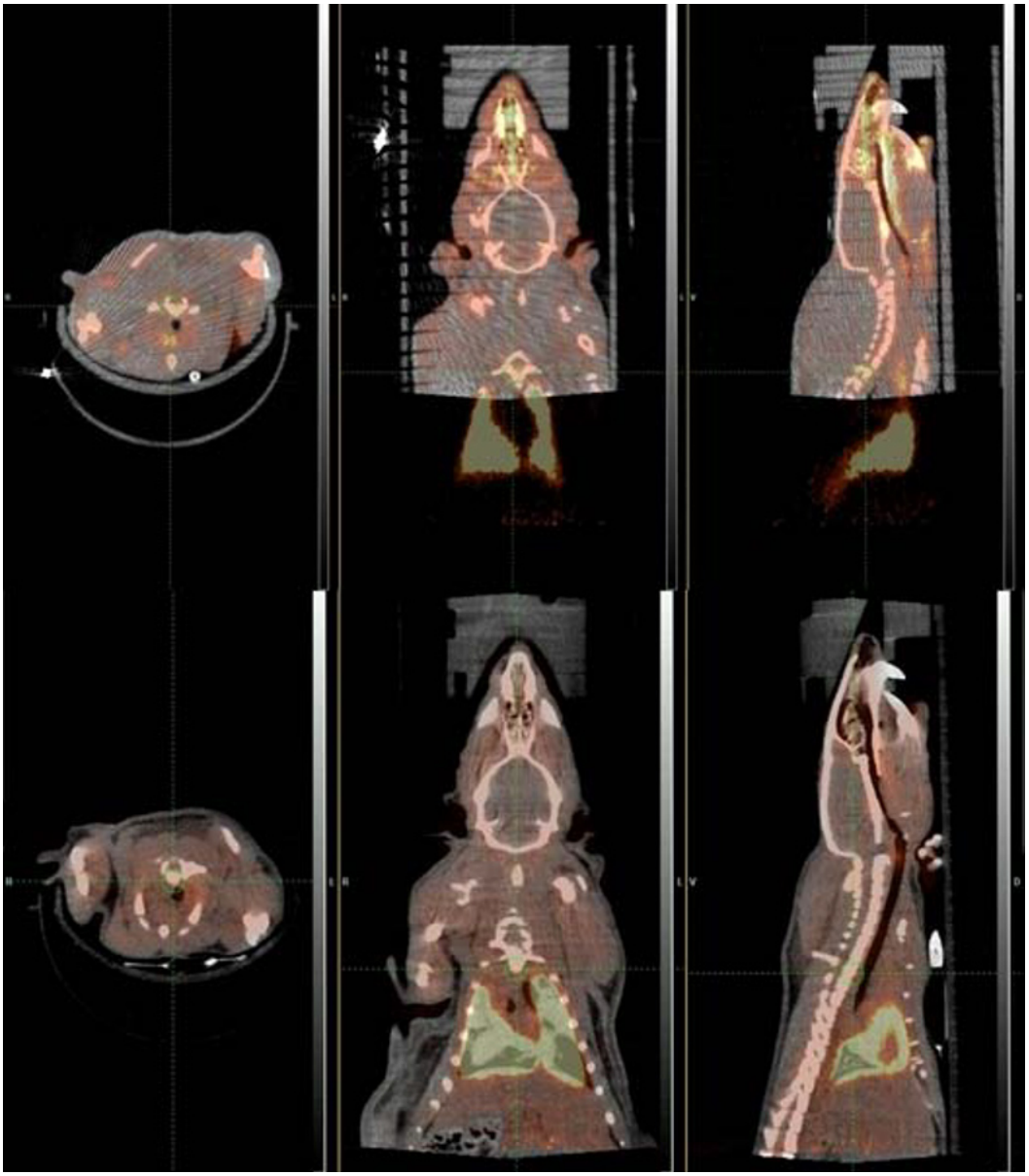

PET-CT images acquired on the Inveon D-PET scanner using the standard (top) and full field of view (bottom) techniques. Full field of view images show matching PET and CT fields of view allowing the whole PET image to be used quantitatively. Sprague-Dawley rats injected with [11C]PBR28, images summed 5-60 minutes post-injection

Disclosure of author financial interest or relationships:
N. Keat, None; **W.A. Hallett**, None; **J. Howard**, None; **S. Tang**, None; **L.A. Wells**, None.

Presentation Number **LBAP 145**
Late Breaking Abstract Poster Session
September 19, 2013 / 15:15-15:15 / Room: Exhibit Hall B

Urinary Catheterization of the Female Murine Model for Preclinical Imaging Modalities

Michelle M. Williams[1,2], *Haiming Ding*[1,2], *Michael F. Tweedle*[1,2], *Michael V. Knopp*[1,2], [1]*Radiology, The Ohio State University Wexner Medical Center, Columbus, OH, USA;* [2]*Imaging Science, Wright Center of Innovation in Biomedical Imaging, Columbus, OH, USA. Contact e-mail: Michelle.Williams@osumc.edu*

The Wright Center of Innovation in Biomedical Imaging is dedicated to advancing the scientific horizon for biomedical imaging both by creating new technology and elucidating old problems. The subject for this particular abstract is removing the pitfall for many imaging modalities involving bladder artifacts in the murine model. Many modalities benefit from the application of tracer or contrast being injected into the body. This allows for improved visualization but can develop excess excretory pooling in the bladder. Even a small level of excretion from the blood leads to high urine concentration, yielding a signal localization disparity commonly known as a bladder artifact. The high concentration of agent occludes much of the information that might be gleaned from genito-urethral and lower gastrointestinal investigation. Current techniques available to the murine model are invasive or incomplete. In most circumstances, they present more potential hazards than necessary to the subject and handler. We propose here that a retrograde adaptation to a previously utilized bladder infection technique found in Hagberg et al 1983 can serve for a murine urinary catheter. It would be safe for Magnetic Resonance, optical, PET, SPECT, and CT. The procedure requires a length of PE10 polyethylene tubing of appropriate length for access to the modality. The tube should be pulled to size, precut, and marked to indicate one centimeter of penetration prior to ethylene oxide sterilization. Under anesthesia, this procedure should be quick and effortless. Slightly part the palps on either side of the clitoral hood, and hold the tube at a 45 degree angle to gain initial entry to the urethra. The PE10 can be advanced up an adult female ureter approximately 1 cm or until slight resistance is detected. This procedure requires no metal besides a possible needle flush with a tuberculin syringe. This procedure can be performed at a safe distance inside of an MR suite with the animal quickly relocated for scanning. The materials used can be performed with plastics that do not fluoresce and thus be safe for optical imaging. The tubes can also be shielded with radiopaque materials to reduce exposure in a PET/SPECT/CT scenario. The tubing can be cut very long, so no pooling occurs within the field of view. Allowing the tubing to remain during an in-vivo scan would allow for much more detailed imaging of orthotopic bladder models as well as GI evaluations. The subsequent removal or reduction of the bladder artifact allows for better dynamic contrast across the rest of the body. This in turn, would improve the signal to noise ratio for faintly localized tracers. There are many advantages to adopting this as common practice prior to or during various imaging proceedings. The placement of the tube is simple and the materials are inexpensive. Application of a urinary catheter could drastically improve the quality of data in the preclinical community.

Disclosure of author financial interest or relationships:
M.M. Williams, None; **H. Ding**, None; **M.F. Tweedle**, None; **M.V. Knopp**, None.

Presentation Number **LBAP 146**
Late Breaking Abstract Poster Session
September 19, 2013 / 15:15-15:15 / Room: Exhibit Hall B

Ultrasound-stimulated gene therapy for improved adenovirus infection

Anna G. Sorace[1], Jason M. Warram[2], Marshall J. Mahoney[1], Kurt R. Zinn[1,2,3], **Kenneth Hoyt**[1,2,3], [1]*Biomedical Engineering, University of Alabama at Birmingham, Birmingham, AL, USA;* [2]*Radiology, University of Alabama at Birmingham, Birmingham, AL, USA;* [3]*Comprehensive Cancer Center, University of Alabama at Birmingham, Birmingham, AL, USA. Contact e-mail: hoyt@uab.edu*

OBJECTIVE: Improving the efficiency of adenovirus (Ad) delivery to target tissues has the potential to advance the translation of cancer gene therapy. Ultrasound-stimulated therapy utilizes microbubbles exposed to low-intensity US energy to improve localized delivery of systemically flowing macromolecules to the extravascular space. The goal of this study was to determine if US-stimulated gene therapy can improve Ad infection in a primary prostate tumor through enhanced tumor uptake and retention of the Ad vector. MATERIALS AND METHODS: A luciferase-based Ad on a ubiquitous cytomegalovirus (CMV) promoter (Ad5/3-CMV-Luc) was used for all experiments. In vitro studies using PC3 human prostate cancer cells were performed to analyze the degree of Ad infectivity (at various multiplicity of infections, MOIs) after application of ultrasound-stimulated gene therapy or sham ultrasound treatment. After cells were incubated with 10 μL of microbubbles (Definity), ultrasound exposure was performed with the following acoustic parameters: 1.0 MHz transmit frequency, peak negative pressures of 0.85 MPa (high pressure condition) or 0.1 MPa (low pressure condition), a pulse repetition period of 0.1 sec, 10% duty cycle, and a 5 min duration of ultrasound exposure. A murine model of prostate cancer (N = 24) with bilateral tumor growths were used to evaluate Ad transduction efficiency after ultrasound-stimulated therapy. Each animal received a 30 μL tail vein injection of microbubbles diluted to a final volume of 100 μL with saline prior to ultraosund exposure of the left flank tumor. Right tumors did not receive ultrasound treatment. Immediately following ultrasound, the Ad5/3-CMV-Luc vector was injected intratumorally in both bilateral flank tumors. Animals were divided into three groups and dosed with different Ad concentrations: 1e6 PFU (N = 12), 1e7 PFU (N = 5), and 1e9 PFU (N = 7). Bioluminescence imaging was employed for in vitro and in vivo analysis to quantify Ad infection. RESULTS: In vitro studies revealed no difference in Ad transduction between groups receiving ultrasound-stimulated therapy using high, low, or sham ultrasound intensity exposures at various MOIs ($p = 0.80$). These results suggest that ultrasound exposure has no negative effect on the infectivity potential of the Ad. However, in vivo results revealed that tumors receiving ultrasound-stimulated therapy (at low pressure conditions) after intratumoral injection with a low concentration of Ad5/3-CMV-Luc (1e6 PFU) exhibited a 95.1 ± 35.1% increase in bioluminescence expression compared to control tumors ($p = 0.03$). Again at 48 hr post treatment and at the moderate and high Ad concentrations, tumor receiving US-stimulated gene therapy demonstrated increases of 12.1 ± 6.4% and 10.1 ± 22.8% compared to control tumors ($p = 0.06$ and $p = 0.09$, respectively). CONCLUSIONS: US-stimulated therapy has significant potential to immediately impact Ad-based cancer gene therapy by improving virus bioavailability in target tissues.

Disclosure of author financial interest or relationships:
A.G. Sorace, None; **J.M. Warram**, None; **M.J. Mahoney**, None; **K.R. Zinn**, None; **K. Hoyt**, None.

Presentation Number **P 001**
Poster Session 1
September 18, 2013 / 18:00-18:00 / Room: Exhibit Hall B

Peptide-conjugated Polymer Mornitors Autophagy in Living Cells by Imaging Enzymatic Reaction of Atg4B Protease

Hyung Jun Ahn, *Ick Chan Kwon, Center for Theragnosis, Korea Institute of Science and Technology, Seoul, Republic of Korea. Contact e-mail: hjahn@kist.re.kr*

Autophagy is a regulated, housekeeping pathway that mediates the turnover of dysfunctional organelles and long-lived proteins through a lysosome-dependent degradative pathway. Autophagy has been implicated in many homeostatic, developmental, and physiological process, and also plays a critical role in clearing the cell of invading bacteria and viruses. During autophagy process, an autophagosome, which consists of a double-membrane vesicle, sequesters cytoplasmic constituents, such as mitochondria, endoplasmic reticulum, and ribosome, and then its outer membrane fuses with lysosome in mammalian cells delivering the sequestered content to the lumen of lysosome for degradation. To date, three principal methods are presently used to monitor autophagy, including electron microscope, fluorescence microscopy detection of the subcellular localization of GFP-LC3 (or RFP-LC3), and immunoblot analysis with an anti-LC3 antibody. However, there is no perfect method to monitor autophagy because they have some potential experimental pitfalls or are not applicable to living cells. Here, we describe peptide-conjugated polymeric nanoparticles for monitoring autophagic events in living cells by imaging activity of Atg4B cysteine protease, which plays a crucial role in autophagy process. Our polymeric nanoparticles including peptide derivative and lysosome dye was capable of visualizing Atg4B activation in living cells. Theses nanoparticles were specifically cleaved by Atg4B cysteine protease in cell-free condition and cell culture system. Recently, the need to test cells and/or protein extracts for autophagic activity has increased to evaluate the effectiveness of RNAi or newly developed compounds. Hence, our polymeric nanoparticle can be used to measure autophagy in cell-based high-throughtput screening for inhibitors or inducers of autophagy.

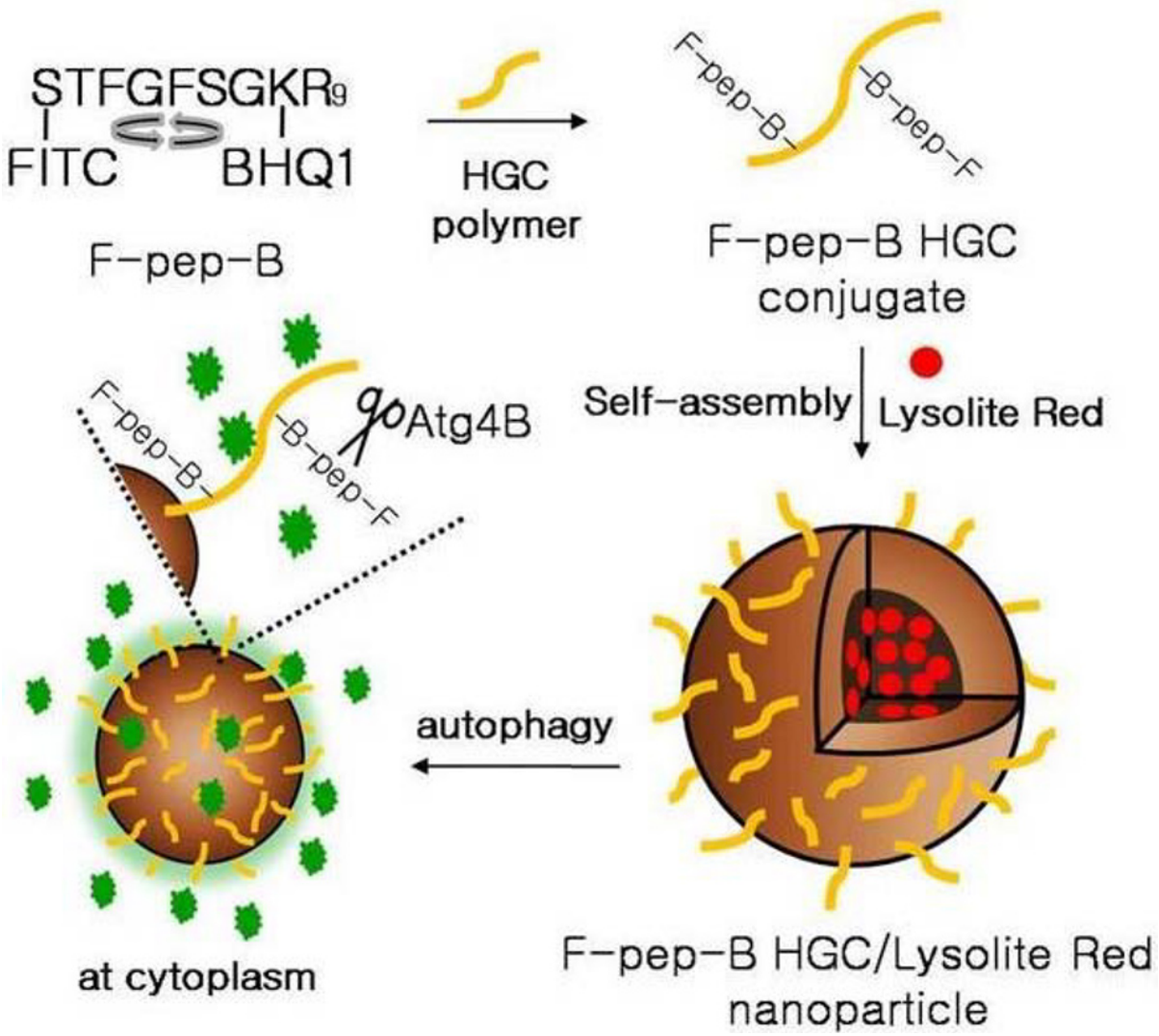

Schematic diagram of Atg4B-responsive polymeric nanoparticles for imaging autophagy in living cells.

Disclosure of author financial interest or relationships:
H. Ahn, None; **I. Kwon**, None.

Presentation Number **P 002**
Poster Session 1
September 18, 2013 / 18:00-18:00 / Room: Exhibit Hall B

Development of Nanocurcumin Conjugate to Enhance the Water Solubility and Bioavailability for non-Invasive Tumor Imaging and Therapy

Meser M. Ali, *Nadimpalli Ravi S Varma, Nipuni-Dhanesha H. Gamage, Branislava Janic, Adarsh Shankar, Thaiz F. Borin, Ali S. Arbab, Radiology, Henry Ford Hospital, Detrit, MI, USA. Contact e-mail: mesera@rad.hfh.edu*

Introduction: Curcumin (Cur), a yellow pigment present in the Indian spice turmeric (associated with curry powder) has been shown to be a potent cancer chemoprevention compound, with potential to target all steps of cancer development, including tumor initiation, promotion, and progression. In malignant glioma U87 cells, Cur down regulated anti-apoptotic proteins Bcl-2, IAPs, and NFjD to facilitate activation of both extrinsic and intrinsic caspase cascades for apoptosis. In vivo preclinical U87 xenograft models, Cur induced significant anti-tumor effects by slowing tumor growth rate and increasing animal survival time. A major limiting factor of Cur is its low solubility in water and soluble Cur molecules are extremely sensitive at physiological pH. Many preclinical and clinical studies in mice, rats and humans revealed a low bioavailability of Cur. Although 10 or 12 g/ml of curcumin administered orally in humans showed Cur levels in serum to be approximately 50 ng/ml, this resulted in a minimum availability of curcumin in the blood circulation to achieve its therapeutic effects. We have synthesized a G5-PAMAM-Succinic-Cur conjugate to increase the water solubility to enhance the bioavailability of Cur and determined the cytotoxicity in in-vitro and in-vivo studies. Methods: We have synthesized G5-PAMAM-based Cur prodrug. First, primary amines of G5 was reacted with succinic anhydride to introduce G5-PAMAM-succinic monoacid groups at the surface and then ultrapure curcumin (Sigma Aldrich) was conjugated to the functionalized G5-COOH through DMP (4-dimethylaminopyridine)/ DCC (dicyclohexylcarbodiimide) coupling method. The final conjugate, G5-Cur was purified by diafiltration using C-10 membrane filter (MW cutoff size > 10,000g) to obtain a dark yellow-orange sticky solid after freeze drying. The G5- Cur conjugate has been characterized by NMR, MADLI-TOF mass and UV-Visible absorption spectroscopic methods. The amount of Cur in G5-Cur conjugate was determined by UV-Visible absorption spectroscopy. Result and Discussion: Cytotoxicity of G5-Cur and free Cur against U251, HN26, HN48, MDA MB 231 cancer cell lines was evaluated by MTT assays. G5-Cur and free Cur at equivalent doses inhibited the cell growth in a different dose-dependent manner. We have observed that G5-Cur is capable of inducting cell death at much lower concentrations than natural Cur. G5-Cur conjugate shows lower IC50 than that of free Cur. We have created a rat model of orthotopic human glioma by implanting 4x105 human U251 glioma cells. Optical imaging of glioma bearing rat was performed. In vivo fluorescence imaging showed accumulation of the G5-Cur in the brain. The multicolor microscopy images of the glioma showed that G5-PAMAM-based nanocurcumin extravasated across the vessel lumen. Microscopy images of the contralateral tissue showed that the agent remained in the vessel lumen and did not extravasate into normal brain tissues.

Disclosure of author financial interest or relationships:
M.M. Ali, None; **N. Varma**, None; **N.H. Gamage**, None; **B. Janic**, None; **A. Shankar**, None; **T.F. Borin**, None; **A.S. Arbab**, None.

Presentation Number **P 003**
Poster Session 1
September 18, 2013 / 18:00-18:00 / Room: Exhibit Hall B

Multifunctional Micellar Platforms for Biphasic PDT Drug Delivery in Brain Tumors

Suraj Dixit[2], *Kayla Miller*[2], *Ping Zhang*[3], *Malcolm Kenney*[3], *Ann-Marie Broome*[1,2], [1]*Radiology & Radiological Science, Medical University of South Carolina, Charleston, SC, USA;* [2]*Center for Biomedical Imaging, Medical University of South Carolina, Charleston, SC, USA;* [3]*Chemistry, Case Western Reserve University, Cleveland, OH, USA. Contact e-mail: dixit@musc.edu*

Development of selectively targeted nanoparticles that can act as drug delivery vehicles is critical for improving the treatment and monitoring of glioblastoma. The widespread use of photodynamic therapy (PDT) in brain tumor therapy has been partially hampered by non-targeted phototoxicity towards healthy tissue. Improving the selectivity of tumor targeting and sustained delivery of PDT drugs will dramatically enhance the success of brain cancer therapy. The phthalocyanine Pc 4 is a highly promising PDT drug approved for clinical trials, characterized by virtual non-toxicity in the dark with high phototoxicity, and operates in the deep red spectral range, which penetrates brain tissue most efficiently for both diagnostic optical imaging and phototherapy. In order to design an efficient and effective drug carrier, we will address several issues: tailored surface on the carrier for targeted drug delivery; biocompatible coating which reduces cytotoxicity; pH-induced disruption of the carrier agent for slow and controlled drug release to the desired environment; and light activation of the photosensitizer. Liposomes and micelles are the preferred choice of carrier as they fulfill these requirements based on their composition. The potential of this conjugate platform derives from the physical and chemical protection offered to the conjugate by its liposome or micelle encapsulation during its delivery to the tumor cells, release of the conjugate by liposome/micelle breakdown when it is in the immediate vicinity of the tumor cells due to altered pH environment, and then release of Pc 4 from its prodrug formulation by photolysis. Two stage release of Pc 4 offers protection from degradation and diversion, unwanted uptake during its delivery, and accumulation of a high concentration of active drug where it is most effective. By using a biphasic-targeting drug delivery concept, we will dramatically improve PDT nanoparticle selectivity to brain cancers. Liposomes containing photolytic Pc 4 composed of HSPC, DC-cholesterol, and DSPE-PEG-amine are synthesized. Micelles containing Pc 4 drug are synthesized using PEG-PE-Amine, 1, 2-dioleoyl-sn-glycero-3-phosphoethanolamine and N-palmitoyl homocysteine (pH sensitive). Specific targeting to glioblastoma cells is achieved by cRGD coupled to the DSPE-PEG. These liposomes/micelles have an advantage of small size and reduced toxicity due to robust packaging of Pc 4 inside the core, decreasing the leaching of the drug in the intracellular environment resulting in reduced cytotoxicity. Preliminary cellular uptake studies using confocal imaging of glioblastoma cells treated with targeted and untargeted micelle or liposome-coated particles demonstrate considerable uptake of Pc 4. PDT applied to glioma cells treated with targeted micelles or liposomes carrying Pc 4 showed hemorrhagic cell death. Several Pc 4 prodrugs have been identified for encapsulation and several have been synthesized. Future experiments involve optimization of the synthesis of the Pc 4 derivatives and performing cytotoxicity assays, pharmacokinetic and tissue distribution studies in in vivo animal models.

Disclosure of author financial interest or relationships:
S. Dixit, None; **K. Miller**, None; **P. Zhang**, None; **M. Kenney**, None; **A. Broome**, None.

Presentation Number **P 004**
Poster Session 1
September 18, 2013 / 18:00-18:00 / Room: Exhibit Hall B

Near-Infrared Theranostic Probe for Detection and Selective Treatment of Dysplasia and Early Stage Oral Cancer

Laura Burgess[1], *Tracy W. Liu*[1], *Juan Chen*[2], *Alex Vitkin*[2,1], *Gang Zheng*[2,1], [1]*Medical Biophysics, University of Toronto, Toronto, ON, Canada;* [2]*Biophysics and Bioimaging, University Health Network, Toronto, ON, Canada. Contact e-mail: lajburge@gmail.com*

While there have been improvements in therapeutic management of oral cancer, there has been no improvement in prognosis over the past 50 years. Much of the failure can be attributed to late diagnosis and poor delineation of lesions. This has led to thirty percent of patients who have surgery having recurrent oral cancer. There are clinical trials underway to help better identify areas of dysplasia and early stage lesions to assist surgeons, specifically the Canadian Optically Guided Approach for Oral Lesions Surgical Trial (COOLS study). In this study, autofluorescence is used to differentiate normal from diseased tissue, allowing for negative margins during surgery. Expanding upon this idea, we have created a near-infrared theranostic probe. It is capable of detection, but also treatment of dysplastic and early stage cancerous (ESC) oral tissue at the molecular level, providing faster, less invasive and more efficient and selective treatment for early stage disease. The near-infrared theranostic probe consists of a photosensitizer (both photoactive and fluorescent) conjugated to a quencher molecule via a short disease-specific linker, named a photodynamic molecular beacon (PMB). The PMB remains fluorescence and photodynamic inactive until cleaved by the appropriate biomarker. Once becoming active, the probe is capable of both diagnostics, by its fluorescence, and therapy, by its photoactivity. Therefore, an effective photodynamic therapy can be selectively achieved by activating the fluorescent active photosensitizer and using appropriate light, in the presence of oxygen to generate cytotoxic singlet oxygen. For these studies, two biomarker targets were used. Fibroblast activation protein (FAP) is highly expressed in cancer-associated fibroblasts in human epithelial cancers and overexpressed in dysplastic and early stage oral cancer. Matrix metalloproteinase-7 (MMP-7) is an enzyme that degrades the extracellular matrix and basement membrane, the main mechanism of oral cancer invasion. Thus, once taken up by dysplastic and ESC cells, they are cleaved and fluoresce, identifying themselves and directing treatment by PDT. A hamster oral cancer model was used to study the imaging and treatment capabilities of the PMB on dysplasia and ESC. Treatment of healthy hamster cheeks with 7, 12-Dimethylbenz(a)anthracene caused the development of oral carcinoma. Once the dysplastic lesions and/or ESC had formed, they were incubated topically with either PMB. The dysplastic and ESC regions were clearly and specifically visualized in a short time period (less than 30 minutes), with fluorescence imaging, guiding PDT immediately after, selectively destroying dysplasia and ESC while sparing healthy tissue. Fluorescence imaging with highly specific PMBs targeting dysplasia and ESC allow for same-day treatment by PDT. This offers a new theranostic approach to dysplasia and early stage oral carcinoma, overcoming the hurdles that have plagued conventional treatment of this disease, providing a highly selective and effective therapy.

Disclosure of author financial interest or relationships:
L. Burgess, None; **T.W. Liu**, None; **J. Chen**, None; **A. Vitkin**, None; **G. Zheng**, None.

Presentation Number **P 005**
Poster Session 1
September 18, 2013 / 18:00-18:00 / Room: Exhibit Hall B

Development of Molecular Probes for In Vivo Imaging of DNA Repair

Allison G. Condie[1], *Jonathan D. Kenyon*[2], *Junqing Zhu*[1], *Chunying Wu*[1], *Stan Gerson*[2], *Yanming Wang*[1], [1]*Division of Radiopharmaceutical Science, Case Center for Imaging Research Department of Radiology, Chemistry, and Biomedical Engineering, Case Western Reserve University, Cleveland, OH, USA;* [2]*Hematology and Oncology, Case Western Reserve University, Cleveland, OH, USA. Contact e-mail: agc30@case.edu*

One of the challenges facing chemotherapeutic treatment of cancer is drug resistance that stems from intrinsic DNA repair pathways. Many chemotherapeutic drugs target and damage DNA in cancer cells leading to cell death. While these repair pathways have evolved to obviate damage to normal cells, they can subvert the therapeutic effect of chemotherapy. One such pathway is called the base excision repair pathway (BER), which removes DNA bases damaged by alkylating agents and leaves a free sugar residue called an abasic or apurinic/apyrimidinic (AP) site, which can be intercepted by strong nucleophiles containing a hydrazine or hydroxylamine moiety through reaction with the aldehyde group. Methoxyamine (MX) is a clinically used methylating agent for the treatment of glioma that when given to patients in conjunction with temozolomide (TMZ), has been shown to potentiate the cytotoxic effect in human tumor xenograft models.[1] In addition to the therapeutic effect of intercepting repair intermediates, we hypothesized that analogs of MX could be developed for optical and PET imaging to monitor patient response to DNA-targeted therapy and to assist in the development of new chemotherapeutic agents.[2] We have developed a small library of fluorescent MX analogs with emission in the visible and NIR range. Using fluorescent microscopy, TMZ treated T98G glioma cells showed strong nuclear uptake of the AP site-targeted imaging probes. Fluorescence spectrophotometry of DNA extracted from these cells confirmed that this signal was due to DNA binding. T98G cells were also treated with analogs of the imaging probes, which contained the same fluorophore but that did not have the AP site binding hydroxylamine or hydrazine moiety, to determine whether DNA binding occurred specifically to AP sites or through nonspecific mechanisms such as intercalation or minor groove binding. Probes were also evaluated for in vivo binding properties using optical imaging to assess the dynamics of TMZ induced BER in T98G cells. Further, the probes can be adapted for multimodality imaging combining optical imaging and positron emission tomography (PET). These results indicated proof-of-principle that these imaging probes are suitable for imaging DNA repair processes. [1] Liu, L.; Nakatsuru, Y.; Gerson, S.L. Base Excision Repair as a Therapeutic Target in Colon Cancer. *Clin. Cancer Res.* **2002**, *8*, 2985-2991. [2] Wang, Y.; Liu, L.; Wu, C.; Bulgar, A.; Somoza, E.; Zhu, W.; Gerson, S.L. Direct detection and quatification of abasic sites for in vivo studies of DNA damage and repair. *Nucl. Med. Biol.* **2009**, *36*, 975-983.

Disclosure of author financial interest or relationships:
A.G. Condie, None; **J.D. Kenyon**, None; **J. Zhu**, None; **C. Wu**, None; **S. Gerson**, None; **Y. Wang**, None.

Presentation Number **P 006**
Poster Session 1
September 18, 2013 / 18:00-18:00 / Room: Exhibit Hall B

In vivo optical imaging of inflammatory macrophages can predict the injury response following arteriovenous fistula creation: implications for dialysis access

Jie Cui, *Chase W. Kessinger, Jason R. McCarthy, Charles P. Lin, Farouc A. Jaffer, Massachusetts General Hospital, Boston, MA, USA. Contact e-mail: jcui2@partners.org*

Introduction: Arteriovenous fistula (AVF) is the most common type of hemodialysis access, but commonly fail due to neointimal hyperplasia (NH) and thrombosis. Prior studies show that inflammation plays a critical role in neointimal hyperplasia. However, the in vivo role of macrophages after AVF creation is still unclear. In this study, we mapped the distribution of macrophages post-AVF creation using intravital fluorescence microscopy (IVFM) and a near infrared fluorescence (NIRF) macrophage nanosensor. We hypothesized that the magnitude of the macrophage response early after AVF creation could predict subsequent NH scar within the AVF. Methods: AVF was created in C57BL/6J mice (n=10) by an end-to-side anastomosis between the right jugular vein and the ipsilateral carotid artery. On day 13, mice (n=5) were injected with IV 10mg/kg of the macrophage nonsensor CLIO-VT680. On day 14, IVFM was performed on the surgically exposed right AVF. Carotid blood flow was imaged using fluorescein isothiocyanate (FITC)-dextran. Second harmonic generation (SHG) images were collected to identify collagen in the adventitial-medial border. The other 5 mice that did not undergo IVFM were served as control. All mice were sacrificed at day 42, and histological analyses of resected AVF were performed using Carstair's and Von Gieson stains. IVFM Image analysis was performed using Image J software (NIH). Z-stack images were collected in the coronal plane and reconstructed in the axial plane. Mean signal intensity (MSI) measurement of CLIO signals were taken from 5 adjacent images every 60um from the anastomosis. Target-to-background ratios (TBR) were calculated as the MSI of AVF divided by the MSI of the control artery. TBR ratio was calculated as the TBRs at specific distance away from the anastomosis, divided by the TBR at the anastomotic site. Results: The survival rate of AVF mice at week 2 was 100%. By week 6, 4 mice in IVFM group had patent AVF compared to 3 mice in the control group. The penetration depth of IVFM was 200um from the adventitia of the AVF. AVF-induced macrophage inflammation was detected by IVFM at week 2. Macrophage TBRs were higher at the anastomotic AVF site compared to the remote carotid arterial side ($p=0.005$). At week 2, the IVFM macrophage TBR ratio was strongly inversely linearly related to the anastomotic distance (n=5, $R2=0.99$). At week 6, histological analyses revealed a strong linear inverse relationship between neointimal hyperplasia area and the distance away from the anastomotic site ($P<0.01$ $R2=0.83$). Macrophage inflammation at week 2 predicted the extent of NH scar area at week 6, at a given distance away from the anastomotic site (n=4, $R2=0.89$). Conclusion: AVF creation induces an intense in vivo inflammatory reaction on IVFM molecular imaging. The macrophage response is most intense at the AVF anastomosis, and linearly decreases as a function of distance from the anastomosis. The degree of inflammation in vivo at week 2 predicts the degree of AVF scarring at week 6. In vivo molecular imaging inflammation approaches could help predict the temporospatial aspects of hemodialysis access failure.

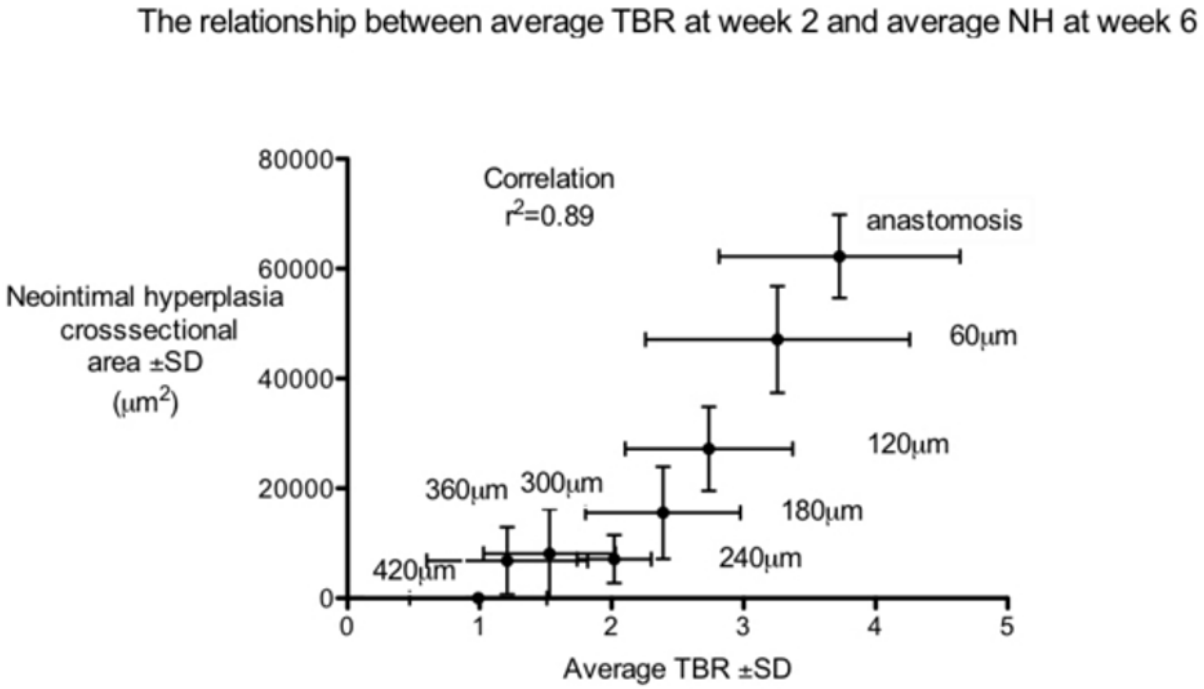

Disclosure of author financial interest or relationships:
J. Cui, None; **C.W. Kessinger**, None; **J.R. McCarthy**, None; **C.P. Lin**, None; **F.A. Jaffer**, Merck, Abbott vascular, Grant/research support; Boston Scientific, Consultant .

Presentation Number **P 007**
Poster Session 1
September 18, 2013 / 18:00-18:00 / Room: Exhibit Hall B

Deep, non-invasive imaging for surgical guidance of sub-millimeter ovarian tumors using targeted single-walled carbon nanotubes

Debadyuti Ghosh[1,2], *Angela Belcher*[1,2], *Alexander F. Bagley*[1], [1]*Koch Institute for Integrative Cancer Research, MIT, Cambridge, MA, USA;* [2]*Materials Science and Engineering, MIT, Cambridge, MA, USA. Contact e-mail: ghoshd@mit.edu*

Highly sensitive, non-invasive detection of small, deep tumors for diagnosis and surgical interventions remains a challenge for conventional imaging modalities. Second window near-infrared light (NIR2: 950-1400 nm) is promising for in vivo fluorescence imaging due to deep tissue penetration and low tissue autofluorescence. With their intrinsic fluorescence in the NIR2 regime and lack of photobleaching, single-walled carbon nanotubes (SWNTs) are highly attractive contrast agents to detect tumors. Here, targeted M13 virus-stabilized SWNTs are used to non-invasively visualize disseminated ovarian tumors in living mice. This nanoprobe demonstrates excellent tumor-to-background uptake and displays higher affinity for tumor nodules compared to underlying non-diseased tissues. Additionally, surgical excision of tumors by a gynelogical surgeon improved with SWNT image guidance and led to the identification of sub-millimeter tumor nodules. These findings demonstrate the promise of targeted SWNTs for non-invasive cancer imaging and highlight a potential clinical role in providing surgical guidance for tumors not visible to the naked eye.

Disclosure of author financial interest or relationships:
D. Ghosh, None; **A. Belcher**, None; **A.F. Bagley**, None.

Presentation Number **P 008**
Poster Session 1
September 18, 2013 / 18:00-18:00 / Room: Exhibit Hall B

In Vivo Fluorescence Imaging Of Bone Using a Multivalent Molecular Probe Bearing Iminodiacetate Groups

Kara M. Harmatys, *Erin L. Cole, Bradley D. Smith, Chemistry and Biochemistry, University of Notre Dame, Notre Dame, IN, USA. Contact e-mail: kharmaty@nd.edu*

Purpose: Molecular systems that target bone are needed for integrated imaging and therapeutic applications. The most common approach employs bisphosphonate as bone targeting groups, but they have some drawbacks such as biological action on the bone and associated toxicity. Efforts to find alternative systems have examined functional groups that chelate with Ca2+ ions exposed on the bone surface. Here, we demonstrate that a deep-red fluorescent imaging probe bearing multiple iminodiacetate groups is able to target areas of high bone turnover in a living mouse. Methods: Three fluorescent probes were studied: bis(iminodiacetate), 1; tetra(iminodiacetate), 2; or tetra(iminodipropionate), 3 as non-targeting control. The tibia and femur tissue from an SKH1 hairless mouse were excised and flash frozen in OCT media. Bone tissue was sliced, fixed in acetone and adhered to microscope slides. The tissue slices were incubated with probe (10 μM), in water for 1 h, then washed with buffer. Bright field and fluorescence images of the slices were acquired using an epifluorescence microscope. In vivo molecular imaging of bone was performed on hairless SKH1 mice after intraperitoneal injection of fluorescent probe. The mice were imaged immediately after probe dosing and also at 1, 3, 6, and 24 h time points using epi-fluorescence and planar X-ray imaging. The mice were euthanized after the 24 h time point and the skin was removed for further imaging. Another cohort of mice were co-injected with deep-red probe 2 (700 nm emission filter, 4 nmol) and OsteoSense®750 (790 emission filter, 2 nmol) to verify colocalization of the probes to the same areas of bone in living mice. Results: In vitro bone staining with probe 2 was significantly higher than staining with the control probe 3. In vivo imaging showed higher accumulation of tetravalent probe 2 than divalent probe 1 in the skeletons of living mice. Additional multicolor imaging experiments indicated strong colocalization of the deep-red probe 2 and near-infrared OsteoSense®750 at the same skeletal positions. Conclusions: A deep-red fluorescent probe bearing four iminodiacetate groups and the bisphosphonate probe OsteoSense®750 target the same regions of high bone turnover in a living mouse. Multivalent molecular probes bearing iminodiacetate groups may be useful alternative choices to bisphosphonates as bone seeking agents for imaging and drug delivery.

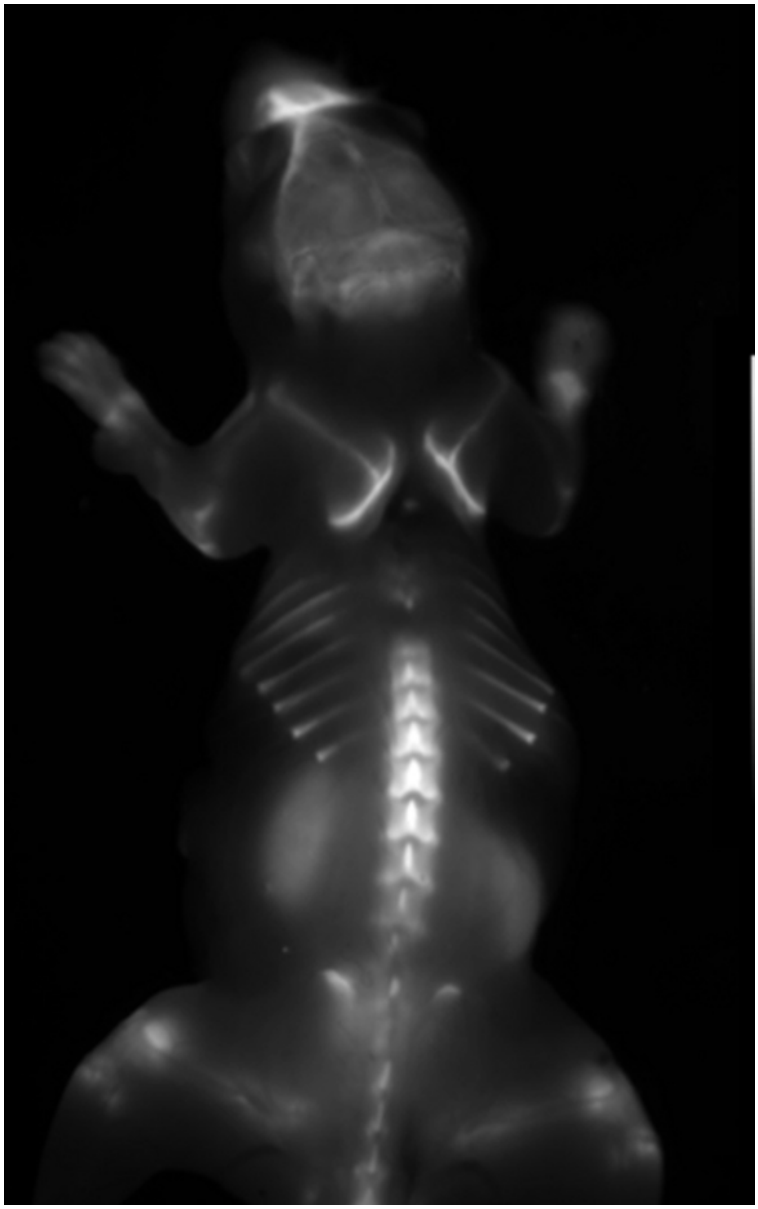

Disclosure of author financial interest or relationships:
K.M. Harmatys, None; **E.L. Cole**, None; **B.D. Smith**, None.

Presentation Number **P 009**
Poster Session 1
September 18, 2013 / 18:00-18:00 / Room: Exhibit Hall B

Detection of atherosclerotic plaques with a high affinity synthetic αvβ3 integrin targeted optical probe in a rabbit model

Julie Heroux[1], *Young-Seung Kim*[2], *Jacques Ohayon*[5], *Narasimhan S. Danthi*[3], *Ahmed M. Gharib*[1], *Roderic I. Pettigrew*[4,1], [1]*NIDDK, NIH, Bethesda, MD, USA;* [2]*NCI, NIH, Bethesda, MD, USA;* [3]*NHLBI, NIH, Bethesda, MD, USA;* [4]*NIBIB, NIH, Bethesda, MD, USA;* [5]*Laboratory TIMC-IMAG/DyCTiM, UJF, Grenoble, France. Contact e-mail: herouxj@niddk.nih.gov*

Purpose Early detection of coronary atheroma to allow for more timely therapeutic intervention remains a major challenge. αvβ3 has been identified as a key molecular target in plaque formation. This study sought to evaluate a new high affinity synthetic αvβ3 integrin targeted optical probe (ITOP), developed at the NIH, for the potential identification of early atherosclerosis. We also investigated the relationship between this ITOP and pathological observation of atherosclerotic plaques in a Watanabe heritable hyperlipidemic (WHHL) animal model. Procedures and Results For this study, experiments were performed on 7 WHHL rabbits and 1 New Zealand White (NZW) rabbit for control. The probe is a small non-peptidic carbamate integrin antagonist (RGD mimic), which is fluorescently labeled utilizing a neopentyl linker and targets the αvβ3 integrin. Previously, this compound demonstrated very high affinity for αvβ3 (IC50 of 3nM), greater selectivity towards αvβ3 compared to αIIbβIIIa, αvβ5 and αvβ6 (IC50 > 100μM), and at least 20 times higher binding affinity for αvβ3 compared to the commercially available cyclic peptide c[RGDfv][1]. Prior studies with this probe showed detection of αvβ3 receptors in vivo in cancer[2] and in vitro in a WHHL rabbit model[3]. In this study, we tested this ITOP in vivo for the detection of atherosclerotic plaques. Histological staining (H&E) of WHHL rabbit aortic tissues in transverse slices demonstrated intimal thickening of the aortic wall and plaque accumulation in some of the Watanabe rabbits. Comparisons were made with a normal New Zealand White rabbit (NZW). Fluorescence microscopy demonstrated a strong labeling of atherosclerotic plaques, which was absent in tissue without plaque or NZW rabbit control. The signal was found principally in the adventitia and proximal intima of the aortic vessel, corresponding to the expression of integrin αvβ3 as previously determined by antibody assay. Moreover, the same positive association previously seen in vitro between the distribution of the ITOP and the thickness of the adventitia was observed. Histological markers of plaque vulnerability or plaque complexity (intraplaque hemorrhage, calcifications, collagen and elastic fibers disruption) were also present at the labeling sites. Conclusions αvβ3 expression has been related to inflammatory and neovascularization processes that are characteristic features of atherosclerosis development. Our ITOP can efficiently label in vivo atherosclerotic plaques present in a WHHL rabbit model. Moreover, this labeling coincides with many histological markers of plaque vulnerability or plaque complexity. In combination with imaging techniques that evaluate stenosis, this probe has great potential for the detection of atherosclerotic plaques, including those at an early stage demonstrating endothelial activation and adventitial thickening. References: [1] Burnett CA et al. Bioorg Med Chem. 2005;13(11):3763-71. [2] Jang BS et al. Nucl Med Biol. 2007 May;34(4):363-70. [3] Heroux J et al. Mol Imaging Biol. 2010;12(1):2-8.

Disclosure of author financial interest or relationships:
J. Heroux, None; **Y. Kim**, None; **J. Ohayon**, None; **N.S. Danthi**, None; **A.M. Gharib**, None; **R.I. Pettigrew**, None.

Presentation Number **P 010**
Poster Session 1
September 18, 2013 / 18:00-18:00 / Room: Exhibit Hall B

Comparative Evaluation of Folate-Targeted Near Infrared (NIR) Dyes for Employment in Image-Guided Cancer Surgery

Mohammad Noshi[1], *Sumith A. Kularatne*[1], *Sakkarapalayam M. Mahalingam*[2], *Philip S. Low*[1,2], [1]*On Target Laboratories, LLC., West Lafayette, IN, USA;* [2]*Chemistry, Purdue University, West Lafayette, IN, USA. Contact e-mail: mnoshi@ontargetlabs.com*

Fluorescence guided surgery has been emerging as an efficient tool to assist surgeons visually identify and surgically remove malignant lesions. One of the most promising approaches to fluorescence-guided surgery is conjugation of near infrared (NIR) dyes to tumor-specific targeting ligands that bind avidly to cancer cells and clear quantitatively from most healthy tissues. Given the commercial availability of multiple NIR dyes, a true need for their comparative evaluation is crucial regarding their employment in optical imaging. In this paper we summarize a comparative analysis of NIR dyes including IR800CW (1), ZW800 (2), an analogue of ZW800 (3), LS288 (4), Kodak IRD28 (5), DyLight 750, Alex Flour 750, etc. by conjugating to folic acid (a tumor-specific targeting ligand) via either ethylene diamine (EDA) or lysine (Lys) linker. The chemical synthesis and efficiency of conjugation is demonstrated as well as product stability during the synthesis and storage. Moreover, we demonstrate comparative in vitro binding affinity for folate receptor positive cancer cells, in vivo whole body imaging and ex vivo biodistribution in mice with FR+ or FR- tumor xenografts, dose escalation and safety profile for each conjugate. The brighter dyes have great potential in the area of imaging-guided surgery especially for the visualization and subsequent surgical removal of the deeply seated tumors.

Disclosure of author financial interest or relationships:
M. Noshi, None; **S.A. Kularatne**, None; **S.M. Mahalingam**, None; **P.S. Low**, On Target Laboratories, Other financial or material support .

Presentation Number **P 011**
Poster Session 1
September 18, 2013 / 18:00-18:00 / Room: Exhibit Hall B

Monitoring of antiangiogenic tumor treatment with apoptosis imaging: Benefit of the low molecular weight phosphatidylserine-targeting ligand PSVue compared to AnnexinV

Karin Palmowski[1,2], *Anne Rix*[2], *Florian F. Behrendt*[3], *Wiltrud Lederle*[2], *Felix M. Mottaghy*[3], *Brian D. Gray*[4], *Koon Y. Pak*[4], *Moritz Palmowski*[2], *Fabian Kiessling*[2], [1]*Pneumology and Critical Care Medicine, University of Heidelberg, Heidelberg, Germany;* [2]*Experimental Molecular Imaging, RWTH-Aachen University, Aachen, Germany;* [3]*Nuclear Medicine, RWTH-Aachen University, Aachen, Germany;* [4]*Molecular Targeting Technologies, , West Chester, PA, USA. Contact e-mail: karin.palmowski@t-online.de*

Purpose: Molecular imaging of apoptosis with AnnexinV is discussed for the assessment of treatment effects in oncology. However, the reduction of the tumor neovascularization during anti-angiogenic treatments can cause a reduced delivery of the imaging probe to the tumor tissue, thus interfering with a reliable treatment response assessment. Therefore, in the present study we investigate the potential value of the low molecular weight phosphatidylserine-targeting ligand PSVue compared to the reasonably large protein AnnexinV for assessment of anti-angiogenic treatment effects. Methods: Molecular apoptosis imaging was performed by determining the accumulation of the fluorescent probes AnnexinVivo750 (750nm, 36kDa) and PSVue794 (794nm, 1.84kDa) simultaneously with 2D optical reflectance imaging in tumor mice bearing (A431). Three animal groups were investigated at day 18 after tumor induction: Untreated controls and treated tumors after either one or four days of anti-angiogenic therapy (SU11248). In additional animals, the accumulation of a nontargeted control to PSVue794 was investigated. Furthermore, the sensitivity of apoptosis imaging for assessing treatment effects was compared to 18F-FDG µPET. Imaging data were displayed as tumor-to-muscle ratio (TMR) and validated by quantitative immunohistochemistry of apoptosis (TUNEL) and vessel density (CD31). Results: TUNEL positive area fractions were significantly higher in treated tumors (0.22±0.19% and 0.27±0.10% after one ($p<0.05$) and four ($p<0.01$) days of therapy) than in untreated controls (0.03±0.02%). In line with these results, PSVue794 indicated significantly increased apoptosis after one (TMR 1.91±0.55, $p<0.05$) and four days (TMR 2.23±0.44; $p<0.01$) of therapy (TMR control group: 1.25±0.06). No significant differences in tumor accumulation were found for a control substance of PSVue794. Surprisingly, AnnexinVivo750 failed to detect significant differences between control (TMR 1.16±0.13) and treated animals (TMR day one: 1.28±0.17; day four: 1.43±0.32). In line with PSVue794, 18F-FDG µPET documented significant and highly significant treatment effects at day one and four, respectively. Conclusions: The increase in apoptosis during anti-angiogenic therapy was significantly better detected with the low molecular weight probe PSVue794 than with AnnexinVivo750. In addition, significant treatment effects were as fast detectable with apoptosis imaging using PSVue794 as with measurements of the glucose metabolism using 18F-FDG.

Disclosure of author financial interest or relationships:
K. Palmowski, None; **A. Rix**, None; **F.F. Behrendt**, None; **W. Lederle**, None; **F.M. Mottaghy**, Philips, Grant/research support; SIRTEX, Grant/research support; **B.D. Gray**, Molecular Targeting Technologies, Inc, Employment; **K.Y. Pak**, Molecular Targeting Technologies, Inc., Stockholder; Molecular Targeting Technologies, Inc., Employment; **M. Palmowski**, None; **F. Kiessling**, None.

Presentation Number **P 012**
Poster Session 1
September 18, 2013 / 18:00-18:00 / Room: Exhibit Hall B

Novel pyridazin-3(2H)-one derivatives for optical imaging of amyloid-beta plaques in Alzheimer's disease

Yong Dae Park[1,2], *Seung-Hwan Park*[2], *Min Goo Hur*[1], *Jung-Joon Min*[2], [1]*Advanced Radiation technology, Korea Atomic Energy Research, Jeongup, Republic of Korea;* [2]*Nuclear medicine, Chonnam National University, Gwangju, Republic of Korea. Contact e-mail: ydpark@kaeri.re.kr*

Objectives: Alzheimer's disease (AD), the most common form of dementia, involves the progressive accumulation of amyloid-beta (Aβ) plaques in the brain parenchyma and neurofibrillary tangles (NFTs) in neurons [1,2]. We hypothesized that the structure of 2-styrylpyridazin-3(2H)-ones could be exploited to create a probe that exhibited certain changes in fluorescence properties upon binding to Aβ plaques. Furthermore, the hydrophobic planarized system of 2-styrylpyridazin-3(2H)-ones is an advantage, promoting the binding of Aβ aggregates through hydrophobic interactions. Methods: Various 2-styrylpyridazin-3(2H)-one derivatives were prepared using the synthesis sequence. Compound 8 was reacted with benzaldehyde after treatment with potassium iodide and triphenylphosphine to produce trans-isomer. We evaluated the fluorescent properties of 28 compounds at 10 μM in PBS before and after mixing with aggregated Aβ40 peptides (10 μM, aggregated in PBS buffer for 3 days at 35 oC). Nine compounds showed a greater than 10-fold fluorescence intensity increase in their emission spectra, indicating that these compounds bind to the Aβ aggregates. To determine whether compound 9n could be used as the basis of a fluorescence probe for detecting intercellular Aβ aggregates, cells loaded with unlabeled Aβ42 were sonicated with SDS, and homogenates were incubated with 10 μM of 9n for 10 min. Fluorescent precipitates were visible by microscopy in the Aβ-loaded cell extracts. we tested 9n in brain sections from 15-month-old transgenic AD model mice (APP/PS1). Results: Dimethylamino group-containing the 2-styrylpyridazin-3(2H)-one derivative (9n) had fluorescence characteristics appropriate for imaging Aβ aggregates. Compound 9n exhibited a strong fluorescence response (FAβ/F0 = 40.84) and binding affinity (Kd = 1.84 uM) to Aβ aggregates, and it clearly stained both intracellular Aβ aggregates and Aβ plaques in the transgenic AD model mice (APP/PS1). Conclusions: 2-styrylpyridazin-3(2H)-one derivatives may have potential as alternative fluorescence imaging agents for the study of AD. Based on the above results, our next study will focus on radiolabeled 2-styrylpyridazin- 3(2H)-one derivatives as potentially useful PET imaging agents for cerebral Aβ plaques.

Disclosure of author financial interest or relationships:
Y. Park, None; **S. Park**, None; **M. Hur**, None; **J. Min**, None.

Presentation Number **P 013**
Poster Session 1
September 18, 2013 / 18:00-18:00 / Room: Exhibit Hall B

Quantitative in vivo Detection of Chlamydia Associated Inflammation in a Mouse Model using Optical Imaging Biomarkers

Manishkumar Patel[1], *Shu-An Lin*[1], *Melissa A. Wooters*[2], *Brett Connolly*[1], *Christopher DeMaula*[3], *Jeffrey Smith*[2], *Bohumil Bednar*[1], [1]*Imaging, Merck, West Point, PA, USA;* [2]*Vaccines, Merck, West Point, PA, USA;* [3]*Pathology, Merck, West Point, PA, USA. Contact e-mail: manishkumar_patel@merck.com*

Chlamydia trachomatis, is a bacterial sexually transmitted disease with over 1.3 million cases reported to the CDC in 2010. While Chlamydia infection is easily treated with antibiotics, up to 70% of infections are asymptomatic and go untreated. Consequences of untreated infection include cervicitis and pelvic inflammatory disease in females. The current mouse model relies on invasive upper genital tract pathology readouts at ~60-80 days post infection. This is a rate limiting step for the model in the development of novel therapeutics. High throughput optical imaging through the use of optical imaging biomarkers have been successfully used to quickly assess several disease processes. Here we evaluate several optical imaging biomarkers for their ability to measure Chlamydia muridarum associated inflammation in live mice. We compared optical agents NeutrophilElastase, ProsenseFAST, MMPSenseFAST and IntergriSense (Perkin Elmer) for the detection of neutrophils, cathepsins, metalloproteinase, and avb3 integrin associated with inflammation. Probe was injected via tail vein into naïve and challenged mice, then imaged after appropriate wash out period using Fluorescence Molecular Tomography (FMT). After imaging, genital tracts of naïve and challenged mice were removed for pathological and immunohistochemical analysis. Optical imaging provided a statistically significant difference in fluorescence with NeutrophilElastase and ProsenseFAST between naïve and challenged mice on days 6 and day 13 post infection ($p=0.034$). There was no significant difference between naïve and challenged mice using MMPSenseFAST and IntegriSense. Immunohistochemistry confirmed the presence of neutrophils and cathepsin expression in the uterine horns on day 6 and ovaries on day 13. In addition, we were able to differentiate uninfected, infected/untreated, and EB-immunized mice using NeutrophilElastase at day 14 post infection and this data correlated well with pathology assessment performed on the same mice 80 days post infection. In this report we demonstrated that both NeutrophilElastase and Prosense can be used as molecular imaging biomarkers for inflammation associated with chlamydial infection in a mouse model and that these biomarkers can significantly decrease the time for pathology evaluation and thus accelerate the rate of therapeutics discovery.

Disclosure of author financial interest or relationships:
M. Patel, Merck and Co, Employment; **S. Lin**, Merck, Employment; **M.A. Wooters**, Merck & Co., inc., Employment; **B. Connolly**, Merck & Co.,Inc., Employment; **C. DeMaula**, None; **J. Smith**, Merck and Co., Inc., Employment; Merck and Co., Inc., Stockholder; **B. Bednar**, Merck & Co. Inc., Employment .

Presentation Number **P 014**
Poster Session 1
September 18, 2013 / 18:00-18:00 / Room: Exhibit Hall B

Evaluation of Silicon Rhodamines: Cell Permeability and Utility for Intracellular Fluorescence Imaging Applications

Kevin Groves, *Ryan Buff, Jeannine Delaney, Garry Cuneo, Jeff Morin, Jason Hu, Sylvie Kossodo, Jeffrey D. Peterson, Wael Yared, Milind Rajopadhye, Life Sciences and Technology, PerkinElmer, Inc., Hopkinton, MA, USA. Contact e-mail: kevin.groves@perkinelmer.com*

Optical imaging with fluorescent dyes has emerged as a powerful imaging modality with significant advantages, both in vitro and in vivo. Fluorochromes that fluoresce in the far red to near-infrared (NIR) region are essential for in vivo imaging due to the superior penetration of light through tissue at these wavelengths. The most common class of NIR fluorochromes employed for in vivo imaging, the indocyanines, tend to be large in size (>750 Da) and exhibit relatively low cell membrane permeability, limiting their use for targeting intracellular markers. It has been recently shown that incorporation of a silicon atom at the 10 position of xanthene based rhodamine dyes results in a significant bathochromic shift in absorption and emission wavelengths, into the far red to NIR region, while retaining membrane permeability. Herein, we report the characterization of silicon rhodamine fluorochromes and evaluation of their properties, in comparison to commonly used cyanine fluorochromes, for utility in intracellular imaging applications. These fluorochromes showed excellent cell permeability, giving as much as 150X more fluorescence signal in HT-29 cells relative to a typical indocyanine with similar optical characteristics. The fluorochromes also showed rapid localization in cell mitochondria in as little as 5 minutes of incubation, as confirmed by co-registration with Mitotracker Green. Importantly, we demonstrate, for the first time, the incorporation of two silicon rhodamine fluorochromes into a self-quenched, protease activatable small peptide construct directed to cathepsin proteases, as a step towards imaging intracellular protease activity. The favorable optical properties, cell permeability and efficient autoquenching (> 95%) of this class of fluorochromes make them powerful new tools for interrogation of intracellular markers both in vitro and in vivo.

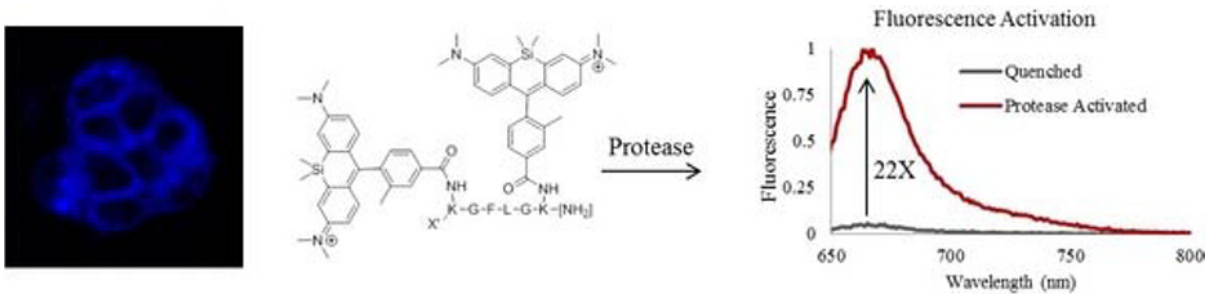

Disclosure of author financial interest or relationships:
K. Groves, PerkinElmer, Employment; **R. Buff**, PerkinElmer, Employment; **J. Delaney**, PerkinElmer, Employment; **G. Cuneo**, PerkinElmer, Employment; **J. Morin**, Perkin Elmer, Employment; **J. Hu**, PerkinElmer LST, Employment; **S. Kossodo**, PerkinElmer, Employment; **J.D. Peterson**, PerkinElmer Inc, Employment; **W. Yared**, PerkinElmer, Employment; **M. Rajopadhye**, PerkinElmer, Inc, Employment .

Presentation Number **P 015**
Poster Session 1
September 18, 2013 / 18:00-18:00 / Room: Exhibit Hall B

In vivo molecular expression is quantified using receptor concentration imaging

Kimberley Samkoe[1,2], *Kenneth M. Tichauer*[3], *Ramesh Govindan*[2], *Jason Gunn*[2], *Tayyaba Hasan*[4], *Brian W. Pogue*[2,1],
[1]*Department of Surgery, Geisel School of Medicine at Dartmouth, Lebanon, NH, USA;* [2]*Thayer School of Engineering, Dartmouth College, Hanover, NH, USA;* [3]*Biomedical Engineering, Illinois Institute of Technology, Chicago, IL, USA;* [4]*Wellman Center for Photomedicine, Massachusetts General Hospital, Boston, MA, USA. Contact e-mail: Kimberley.S.Samkoe@Dartmouth.EDU*

Current practices in cancer management rely heavily upon the presence and overexpression of molecular receptors. Knowing the amount of receptor present in a particular tumor aids in treatment stratification and prediction of a patient's response to certain therapies, particularly antibody therapies. However, current standard of care is tissue biopsy and immunohistochemical analysis, which are invasive and time-consuming analyses. Additionally, many research practices determine receptor concentrations using in vitro techniques that may not be representative of in vivo concentrations due to differences in environments and cell signaling. A method is required that can accurately and rapidly measure receptor concentrations in vivo. Here, we demonstrate that receptor concentrations can be determined in vivo using a receptor concentration imaging (RCI) technique that utilizes two simultaneously administered fluorescent tracers. One tracer is targeted to a molecular marker in the tissue of interest and the other tracer is physically similar to the targeted tracer but has no binding ability (i.e., untargeted). The similar physical characteristics of the two allow for the untargeted tracer to account for the non-specific uptake and retention of the targeted tracer. Therefore, the variation in the uptake curves of the two tracers can be attributed to receptor binding and can account for the receptor concentration of the tissue when kinetic modeling is applied. Four tumor lines with differential epidermal growth factor receptor (EGFR) expression were used to test the RCI method in vivo. A human epidermoid carcinoma (A431), human pancreatic adenocarcinoma (AcPC-1), human neuronal glioblastoma (U251) and rat gliosarcoma (9L) were chosen for known variation in EGFR expression (listed from highest to lowest expression). Each tumor line was implanted subcutaneously (A431, AsPC-1, U251 and 9L) or orthotopicaly (AsPC-1) in 6-week old nude mice (Charles River, Wilmington, MA). Affibody® (Sweden, Solna) imaging agents were chosen in this study because the targeted tracer and the untargeted tracer are similar in size (6.7 and 6.8 kDa, respectively) and are engineered to be structurally comparable. The targeted tracer, an anti-EGFR Affibody®, was labeled with IRDye® 800CW (LICOR Biosciences, Nebraska, NE) and the untargeted tracer, Affibody® negative control imaging agent, was labeled with IRDye® 680RD (LICOR). When the tumors (n=30, 6 mice/group) reached ~100 mm3, the tracers (0.2 nmol) were administered i.v. simultaneously and the fluorescence was monitored for 40 min at 2-min intervals using a two-color Odyssey scanner (LICOR). Maps of receptor concentration in vivo were created from the fluorescence images using the kinetic model (Fig. 1a). The receptor concentration determined by the RCI method correlated strongly with standard immunofluorescence staining of EGFR in excised tissue (Fig. 1b), as well as flow cytometry in vitro (Fig. 1c). These results validate that the RCI method accurately reports receptor concentration in vivo; in addition, it is demonstrated in vitro expression does not always correlate to in vivo, as demonstrated by A431 expression.

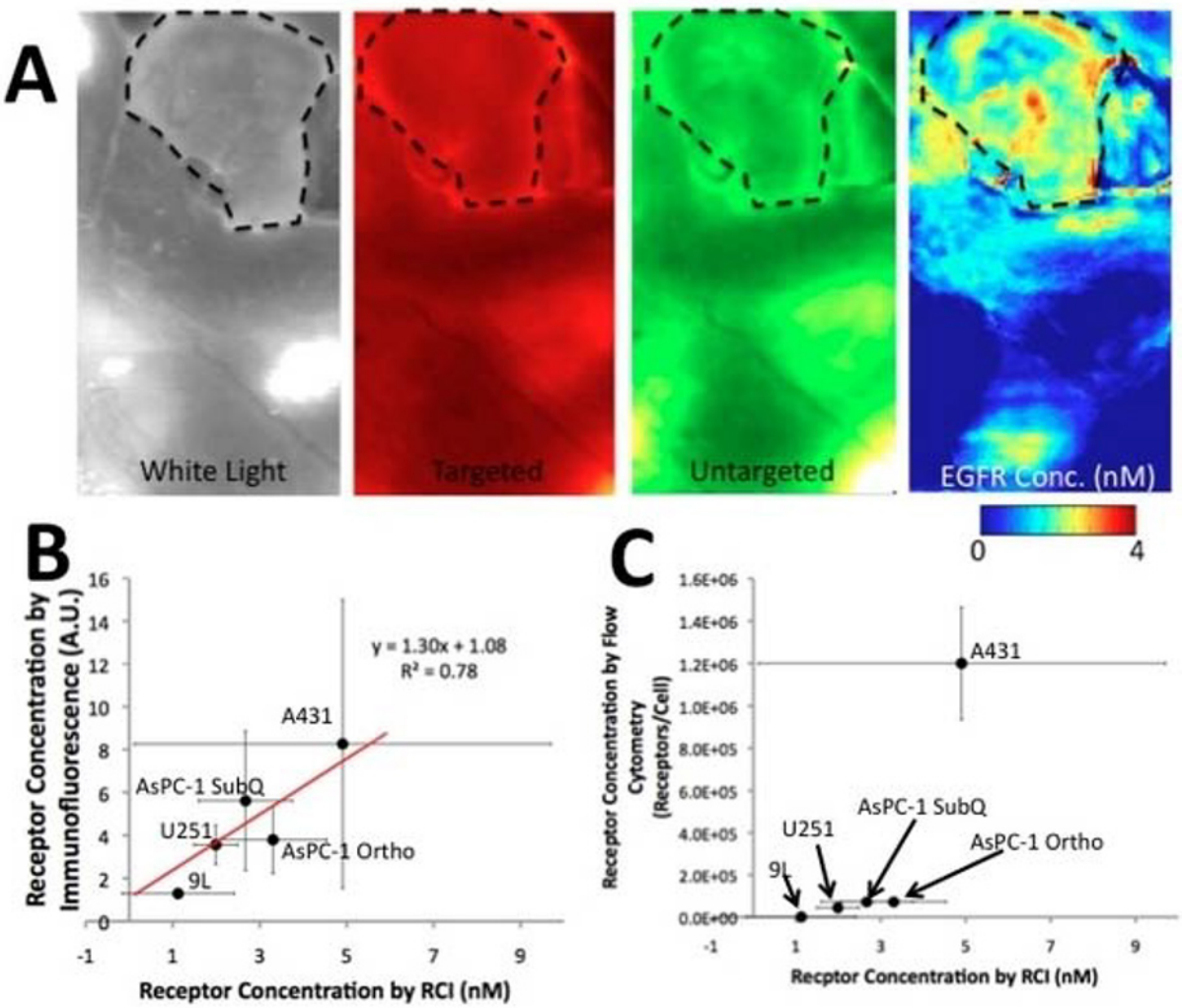

Figure 1. Receptor concentation imaging (RCI) can be used to quantify in vivo epidermal growth factor recptor (EGFR) concentration in a variety of tumors. A) U251 subcutaneous tumor images are displayed (from left to right) in white light, targeted IRDye 800CW labeled anti-EGFR Affibody®, untargeted IRDye 680RD labeled Affibody® Control Imaging Agent, receptor concentration map (in nM). B) A linear correlation exists between the receptor concentration determined by the RCI method and standard EGFR immunofluorescence. C) EGFR concentration determined by in vitro flow cytometry is unable to accurately predict the in vivo concentration.

Disclosure of author financial interest or relationships:
K. Samkoe, None; **K.M. Tichauer**, None; **R. Govindan**, None; **J. Gunn**, None; **T. Hasan**, None; **B.W. Pogue**, None.

Presentation Number **P 016**
Poster Session 1
September 18, 2013 / 18:00-18:00 / Room: Exhibit Hall B

Short PEG-Linkers Improve the Performance of Targeted, Activatable Monoclonal Antibody-Indocyanine Green Conjugates

Kohei Sano, *Takahito Nakajima, Peter Choyke, Hisataka Kobayashi, Molecular Imaging Program, National Cancer Institute, National Institutes of Health, Bethesda, MD, USA. Contact e-mail: ksano@kuhp.kyoto-u.ac.jp*

Objectives: Activatable imaging probes, which can switch from the quenched (off) to the active state (on), have potential to greatly improve imaging target-to-background ratios. Monoclonal antibody-indocyanine green (mAb-ICG) conjugates are promising activatable agents for clinical translation. The ICG derivative (ICG-Sulfo-OSu) partly forms noncovalent bonds with mAb, and is thus, gradually released from the conjugate leading to relatively high background signal especially in the liver and the abdomen. In this study, we re-engineered a mAb-ICG conjugate, using bifunctional ICG derivatives with short polyethylene glycol (PEG) linkers (ICG-PEG4-Sulfo-OSu and ICG-PEG8-Sulfo-OSu) to minimize the noncovalent fraction of ICG bound to mAb in order to decrease background fluorescence signals. Methods: ICG-PEG4-Sulfo-OSu and ICG-PEG8-Sulfo-OSu were synthesized and lipophilicity (the partition coefficient (logP)) was determined. Each ICG derivative was conjugated to anti-human epidermal growth factor receptor-1 (EGFR) mAb (Panitumumab; Pan), followed by the measurement of activation efficacy. The proportion of covalent binding was determined by SDS-PAGE. Each conjugate was evaluated in EGFR-positive MDA-MB-468 cells (breast carcinoma) *in vitro* and in an orthotopic breast cancer mouse model *in vivo*. EGFR-negative 3T3/HER2 cells were used as controls. Results: Short PEG linkers reduced the lipophilicity of ICG. Higher covalent binding (70-86%) was observed using the bifunctional ICG with short PEG linkers compared to Pan-ICG without PEG linkers (22%). The activation efficacy of Pan-ICG was decreased with longer PEG chains. In *in vitro* microscopy study, each conjugate was activated only in EGFR positive MDA-MB-468 cells which occurred after internalizaion and lysosomal degradation, a process requiring 6 h. *In vivo* fluorescence imaging demonstrated that Pan-ICG showed significantly higher signals in the liver within 3 h after injection of Pan-PEG4-ICG and Pan-PEG8-ICG due to *in vivo* dissociation of non-covalent ICG. Each conjugate clearly depicted MDA-MB-468 tumors, but, Pan-PEG4-ICG achieved the highest tumor-to-background ratios (15.8 and 6.9 for MDA-MB-468-to-3T3/HER2 tumor-to-liver ratios, respectively, at 3 d post-injection) Conclusion: Bifunctional ICG derivatives with short PEG linkers were successfully conjugated to panitumumab. ICG with PEG linkers significantly increased the proportion of covalent bonds to antibody. Conjugates with PEG-linkers were able to specifically depict target-positive tumors with high tumor-to-liver ratios compared with the conventional antibody-ICG conjugate without short PEG linkers.

Disclosure of author financial interest or relationships:
K. Sano, None; **T. Nakajima**, None; **P. Choyke**, None; **H. Kobayashi**, None.

Presentation Number **P 017**
Poster Session 1
September 18, 2013 / 18:00-18:00 / Room: Exhibit Hall B

Binding kinetics of a fluorescent bisphosphonate as a tool for monitoring bone metabolism in vivo

Robert Tower[1], Graeme Campbell[1], Olga Will[1], Marc Müller[1], Friederike Grundmann[2], Nicolai M. Purcz[3], Christian Schem[2], Claus C. Glueer[1], **Sanjay Tiwari**[1], [1]*Diagnostic Radiology, University Hospital Kiel, Kiel, Germany;* [2]*Gynecology, University Hospital Kiel, Kiel, Germany;* [3]*Oral and Maxillofacial Surgery, UK-SH, Campus Kiel, Kiel, Germany. Contact e-mail: stiwari@email.uni-kiel.de*

Introduction Bone resorption and deposition occur in a tightly regulated fashion reflecting the coupled activities of osteoclasts and osteoblasts. Several pathological conditions perturb this balance between bone synthesis and resorption, including osteoporosis and skeletal metastases. The uncoupling of remodeling activities contributes to disseminated tumor cells homing to the bone and to tumor growth in bone. Therefore, a reliable marker of bone remodeling would be useful to provide a strong correlation with the extent of skeletal disease, evaluate the effectiveness of an intervention to suppress resorption associated with metastases or menopause and to predict future bone metastases in cancer patients without malignant spread. The purpose of this study is to determine if the fluorescent bisphosphonate imaging probe Osteosense (Perkin Elmer) can predict bone turnover in ovariectomized and parathyroid hormone (PTH)-treated mice. Results While absolute fluorescence signal at the region of the proximal tibia suggests a trend of decreased Osteosense binding in ovariectomized mice, no statistical difference was observed. To determine whether mineral binding affinity, rather than total binding capacity, could serve as a more reliable marker of bone mineralization, kinetic analysis of binding was measured. Regressional analysis reveal that decreases in bone mineralization caused by ovariectomy results in significant reductions in the rates of Osteosense binding at the proximal tibia as compared to wild-type mice. This observation was found to be highly consistent between mice, showing little intra group variation. The utility of binding kinetics as a tool for monitoring changes in bone mineralization was further confirmed in a bone-gain model in which ovariectomized mice were treated intermittently with parathyroid hormone. Binding kinetics analysis revealed significant increases in Osteosense binding in mice treated with PTH as compared to control mice. Localization of Osteosense binding with GFP-positive osteoblasts revealed a prominent signal lining the epiphyseal plate and parallel to osteoblast localization at early time points. Later time points revealed the localization was no longer discrete but distributed across the entire surface of the mineralized bone. Measurement of plasma clearance of osteosense is being performed to validate skeletal uptake values. Conclusions Our data suggests a highly reproducible and sensitive method for monitoring changes in bone mineralization by monitoring the binding kinetics of Osteosense.

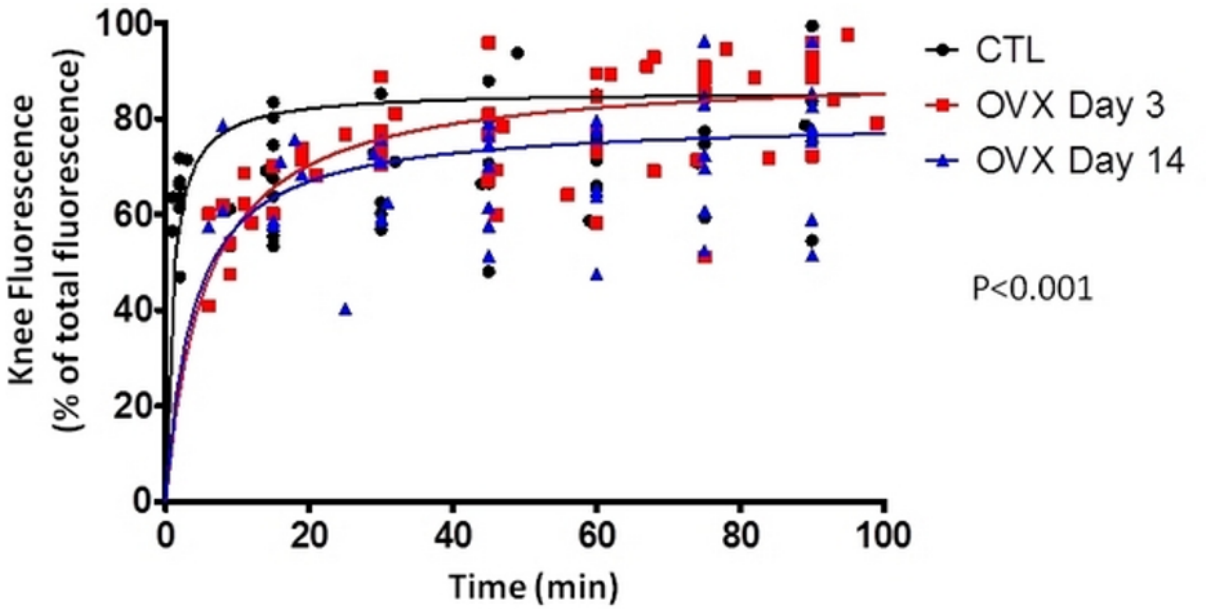

Results: Kinetics of OS750 binding in mice ovarectomized for 3 & 14 days.

Disclosure of author financial interest or relationships:
R. Tower, None; **G. Campbell**, None; **O. Will**, None; **M. Müller**, None; **F. Grundmann**, None; **N.M. Purcz**, None; **C. Schem**, None; **C.C. Glueer**, None; **S. Tiwari**, None.

Presentation Number **P 018**
Poster Session 1
September 18, 2013 / 18:00-18:00 / Room: Exhibit Hall B

Nanopartcle based gene delivery in breast cancer cell line

Nadimpalli Ravi S Varma, *Meser M. Ali, Branislava Janic, Adarsh Shankar, Asm Iskander, Ali S. Arbab, Radiology, Henry ford Hospital, Detroit, MI, USA. Contact e-mail: ravin@rad.hfh.edu*

Background: Recently, gene therapy to control breast cancer has attracted much attention in the research community. Therapeutic genes, vectors, oligonucleotides, siRNAs have emerged as great therapeutic tools to control breast cancer. In-vivo systemic delivery of these agents is hampered due to degradation by body fluids and inability for intracellular accumulation at the cancer site. The development of efficient carriers for in vivo targeted gene transfer has been one of the key challenges for gene therapy. Currently most of the gene delivery relies on viruses which have many safety concerns. Nanoparticles are an attractive alternative method for gene delivery due to their small particle size and ability to changing their surface properties. We investigated the use of our recently developed PAMAM dendrimer G5 and PEI nanoparticles ability to delivery plasmid DNA into the breast cancer cells. . Materials and Methods: pCopGFP and pFIRE plasmid (SBI,USA) was used as reporter plasmid to monitor delivery ability of nanoparticles (PAMAM dendrimer G5 and PEI). G5 /DNA nanoparticles were prepared in 250µl of a 5% dextrose solution at a ratio of 5:1 (w/w) with 50 µg of plasmid (pCopGFP) and 250 µg of dendrimer (PPIG5). To test the complex formation, the DNA/nanoparticle complex was treated with DNase enzymes and separated on agarose gel. To test in-vitro toxicity of nanoparticles, specific number of cells was incubated with different concentration of G5-dendrimer (100 to 5000 nm) up to 48 hours. Cellular viability/proliferation was determined by MTT assay. To test in-vitro gene delivery capacity of nanoparticles, MBA MD231 and T47D cells were cultured over-night and 250µl of DNA/nanoparticle complex directly added into the media. Cell transfer ability of DNA/nanoparticle was observed under fluorescent microscope for GFP expression and luciferase assay for luciferase expression. Results: PAMAM based G5 dendrimer and PEI nanoparticles were developed. DNase enzyme did not digest the nanoparticles/DNA complexes that indicate it formed strong complex with the plasmid DNA. Before applying the G5 dendrimers in gene delivery we tested in vitro toxicity. MTT assay result indicates the safety margin for G5 dendrimer below 1000nM concentrations. It is ideal to use 10-200nM concentrations of G5 dendrimers in gene delivery experiments. GFP expression was observed in the cells incubated with the DNA/Nano complexes whereas control cells did not showed any GFP expression. Similarly, luciferase expression was observed in cells incubated with DNA/Nano complexes, whereas no luciferase activity was observed in control cells. Conclusion: PAMAM based G5 nanoparticles successfully formed complex with DNA. Our in vitro studies showed that PAMAM based G5 delivered GFP or luciferase gene into MDMBA 231 cells and T47D cells.

Disclosure of author financial interest or relationships:
N. Varma, None; **M.M. Ali**, None; **B. Janic**, None; **A. Shankar**, None; **A. Iskander**, None; **A.S. Arbab**, None.

Presentation Number **P 019**
Poster Session 1
September 18, 2013 / 18:00-18:00 / Room: Exhibit Hall B

Non-invasive optical imaging of cell death in multiple in vitro and in vivo mouse models

Bang-Wen Xie[1], *Danielle Park*[2], *Martijn A. Löwik*[1], *Ermond R. van Beek*[1], *Philip Hogg*[3], *Clemens Lowik*[1], [1]*Radiology, Leiden University Medical Center, Leiden, Netherlands;* [2]*London Research Institute, Cancer Research UK, London, United Kingdom;* [3]*Lowy Cancer Research Centre and Prince of Wales Clinical School, University of New South Wales, Sydney, NSW, Australia. Contact e-mail: b.xie@lumc.nl*

Introduction: Cell death plays a pivotal role in normal physiology and in various pathological conditions. Especially, in anti-tumor therapy, imaging of cell death in tumors could facilitate the accurate monitoring of therapy efficacy. Here, we present a newly developed in vitro assay for screening of compounds with potential cell death targeting properties. Using this in vitro assay, we recently examined the properties of the membrane phosphatidylserine targeting near-infrared fluorescent (NIRF) probes: PSS794, Annexin-Vivo 750, as well as that of a HSP-90 alkylator GSAO-AF750 (Park D et al.. J Am Chem Soc 133, 2832-2835, 2011). Our in vitro findings were confirmed in vivo in a mouse brain cryo-lesion model of traumatic brain injury (TBI) (Smith BA, et al.. ACS Chem Neurosci. 3:530-537, 2012; Xie BW, et al.. Cell Death Dis 4: e473, 2013). Furthermore, GSAO-AF750 was used as a biomarker to monitor tumor response in a chemotherapy induced tumor cell death model. Methods: In vitro, we examined the cell death targeting property of the three cell death probes in a new dry-ice cell death assay using different optical imaging modules.In vivo, a liquid N2 pre-cooled metal cylinder was shortly applied to the parietal region of a mouse head to introduce a cryolesion. Subsequently, the mice were injected i.v. with the different NIRF probes and subjected to whole body fluorescence imaging (FLI) 1-24h post injection. In the chemotherapy model, a group of nude mice bearing orthotopic 4T1-luc2 breast tumors were treated with cyclophosphamide (250mg/kg). 24hr after treatment, mice were administered with 1mg/kg GSAO-AF750 intravenously and imaged over time. Finally, brain and tumor tissues were collected respectively for ex vivo FLI and subsequently histological analysis. Results: In vitro, the tested NIRF probes all strongly accumulated in the area of dead cells in the center of the culturing well but not in the living cells in the periphery. In vivo, all three NIRF probes selectively accumulated in the area of brain cryo-lesion in our TBI model. In our chemotherapy model, the uptake of GSAO-AF750 was 2.6fold ($p < 0.01$) more in treated tumors than untreated tumors, reflecting an increased tumor cell death and thus response to treatment. Moreover, the probe signal that retained in the treated tumor tissues strongly correlated with both TUNEL and cleaved Caspase-3 staining. Conclusions: A new in vitro cell death assay, in vivo mouse TBI model and chemotherapy model were successfully employed in a simple and cost-effective manner. In vitro and in vivo results obtained with different NIRF probes were consistent and suggest that these models may be employed for high-throughput screening of compounds with potential cell death targeting properties. The new NIRF death probes examined here can be employed for diagnosis purposes in all kinds of pathological conditions where cell death is involved, or they can be used to monitor treatment outcome, i.e. to investigate the efficacy of anti-tumor therapies at early time points. Acknowledgement: This study is supported by the Center for Translational Molecular Medicine, project MUSIS (grant 03O-202).

Disclosure of author financial interest or relationships:
B. Xie, None; **D. Park**, None; **M.A. Löwik**, None; **E.R. van Beek**, None; **P. Hogg**, None; **C. Lowik**, None.

Presentation Number **P 020**
Poster Session 1
September 18, 2013 / 18:00-18:00 / Room: Exhibit Hall B

The potential of hypoxia markers as target for breast molecular imaging - A systematic review and meta-analysis of human marker expression

Arthur Adams[1], *Aram van Brussel*[2], *Jeroen F. Vermeulen*[2], *Willem Mali*[1], *Elsken van der Wall*[3], *Paul J. van Diest*[2], *Sjoerd G. Elias*[1,4], [1]*Department of Radiology, University Medical Center Utrecht, Utrecht, Netherlands;* [2]*Department of Pathology, University Medical Center Utrecht, Utrecht, Netherlands;* [3]*Division of Internal Medicine and Dermatology, University Medical Center Utrecht, Utrecht, Netherlands;* [4]*Julius Center of Health Sciences and Primary Care, University Medical Center Utrecht, Utrecht, Netherlands. Contact e-mail: a.adams@umcutrecht.nl*

Background Several targets have been investigated for their potential of molecular imaging of breast cancer. A group of valid targets are membrane-bound hypoxia-related proteins, that are frequently expressed in solid tumors when tumor-growth outpaces neo-angiogenesis. Despite the potential of these proteins, expression prevalence in human breast cancer, benign breast disease and normal tissue, and expression in tumor margins and intratumoral heterogeneity is not well established. Knowledge on expression rates of these candidate imaging targets is a prerequisite for focused development of novel tumor-specific imaging tracers (such as antibodies or antibody-based molecules) and application and evaluation of these tracers in upcoming clinical trials. We therefore performed a systematic literature review and meta-analysis of hypoxia marker expression rates in human breast cancer, in order to evaluate their potential as targets for molecular imaging purposes. **Methods** We systematically searched the databases of MEDLINE and EMBASE for articles describing Carbonic Anhydrase-IX (CAIX), Glucose Transporter-1 (GLUT1), C-X-C chemokine receptor type-4 (CXCR4), or insulin-like growth factor-1 receptor (IGF1R) expression rates in human breast disease, evaluated by immunohistochemistry. We pooled study results using random-effects models and applied meta-regression methods to identify associations with clinicopathological variables. **Results** Of 1,705 identified articles, 117 matched our selection criteria, totaling 30,216 immunohistochemistry results. We found substantial between-study variability in expression rates between the studies. Invasive cancer showed pooled expression rates of 35% (95% confidence interval (CI): 26-46%) for CAIX, 46% (CI: 33-59%) for CXCR4, 46% (CI: 35-70%) for IGF1R, and 51% (CI: 40-61%) for GLUT1. Expression rates increased with tumor grade for GLUT1, CAIX, and CXCR4 (all $p<0.001$), but decreased for IGF1R ($p<0.001$). GLUT1 showed the highest expression rate in grade III cancers with 58% (CI: 45-69%). CXCR4 showed the highest expression rate in small T1 tumors with 48% (28-69%), but associations with size were only significant for CAIX ($p<0.001$; positive association) and IGF1R ($p=0.047$; negative association). Although based on few studies, CAIX, GLUT1, and CXCR4 showed profound lower expression rates in normal breast tissue and benign breast disease, and high rates in *in situ* carcinoma ($p<0.001$). Invasive lobular carcinoma consistently showed lower expression rates ($p<0.001$). Studies investigating tissue microarrays found lower expression rates compared to studies investigating full sections for CAIX ($p=0.002$) and GLUT1 ($p=0.003$). **Conclusions** Our results support the potential of hypoxia-related markers as breast cancer molecular imaging targets. Although specificity is promising, combining targets would be necessary for optimal sensitivity. The data from our systematic review and meta-analysis could help guide the choice of imaging targets for tracer development depending on the envisioned clinical application.

Systematic review, meta-analysis and meta-regression results of hypoxia membrane protein expression in breast cancer, in situ carcinoma, benign breast disease, and normal breast tissue.

	carbonic anhydrase IX (CAIX)				glucose transporter-1 (GLUT1)				C-X-C chemokine receptor type 4 (CXCR4)				insulin-like growth factor-1 receptor (IGF1R)			
	N	Prevalence (%)	(95% Confidence Interval)	p-value*	N	Prevalence (%)	(95% Confidence Interval)	p-value*	N	Prevalence (%)	(95% Confidence Interval)	p-value*	N	Prevalence (%)	(95% Confidence Interval)	p-value*
[illegible]																
Overall	[illegible]	[illegible]	[illegible]	[illegible]	[illegible]	[illegible]	[illegible]	[illegible]	[illegible]	[illegible]	[illegible]	[illegible]	[illegible]	[illegible]	[illegible]	[illegible]
[illegible]	[illegible]	[illegible]	[illegible]	-	[illegible]	[illegible]	[illegible]	-	[illegible]	[illegible]	[illegible]	-	[illegible]	[illegible]	[illegible]	-
[illegible]	[illegible]	[illegible]	[illegible]	-	[illegible]	[illegible]	[illegible]	-	[illegible]	[illegible]	[illegible]	-	[illegible]	[illegible]	[illegible]	-
Histological grade	[illegible]				[illegible]				[illegible]				[illegible]			
I		[illegible]	[illegible]	[illegible]		[illegible]	[illegible]	[illegible]		[illegible]	[illegible]	[illegible]		[illegible]	[illegible]	[illegible]
II		[illegible]	[illegible]	[illegible]		[illegible]	[illegible]	[illegible]		[illegible]	[illegible]	[illegible]		[illegible]	[illegible]	[illegible]
III		[illegible]	[illegible]	[illegible]		[illegible]	[illegible]	[illegible]		[illegible]	[illegible]	[illegible]		[illegible]	[illegible]	[illegible]
Tumor size	[illegible]				[illegible]				[illegible]				[illegible]			
T1		[illegible]	[illegible]	[illegible]		[illegible]	[illegible]	[illegible]		[illegible]	[illegible]	[illegible]		[illegible]	[illegible]	[illegible]
T2		[illegible]	[illegible]	[illegible]		[illegible]	[illegible]	[illegible]		[illegible]	[illegible]	[illegible]		[illegible]	[illegible]	[illegible]
T3		[illegible]	[illegible]	[illegible]		[illegible]	[illegible]	[illegible]		[illegible]	[illegible]	[illegible]		[illegible]	[illegible]	[illegible]
Histological type	[illegible]				[illegible]				[illegible]				[illegible]			
[illegible]		[illegible]	[illegible]	[illegible]		[illegible]	[illegible]	[illegible]		[illegible]	[illegible]	[illegible]		[illegible]	[illegible]	[illegible]
[illegible]		[illegible]	[illegible]	[illegible]		[illegible]	[illegible]	[illegible]		[illegible]	[illegible]	[illegible]		[illegible]	[illegible]	[illegible]
[illegible]	[illegible]				[illegible]				[illegible]				[illegible]			
[illegible]		[illegible]	[illegible]	[illegible]		[illegible]	[illegible]	[illegible]		[illegible]	[illegible]	[illegible]		[illegible]	[illegible]	[illegible]
[illegible]		[illegible]	[illegible]	[illegible]		[illegible]	[illegible]	[illegible]		[illegible]	[illegible]	[illegible]		[illegible]	[illegible]	[illegible]
[illegible]	[illegible]				[illegible]				[illegible]				[illegible]			
[illegible]		[illegible]	[illegible]	[illegible]		[illegible]	[illegible]	[illegible]		[illegible]	[illegible]	[illegible]		[illegible]	[illegible]	[illegible]
[illegible]		[illegible]	[illegible]	[illegible]		[illegible]	[illegible]	[illegible]		[illegible]	[illegible]	[illegible]		[illegible]	[illegible]	[illegible]
[illegible]		[illegible]	[illegible]	[illegible]		[illegible]	[illegible]	[illegible]		[illegible]	[illegible]	[illegible]		[illegible]	[illegible]	[illegible]

*p-values obtained using meta-regression (linear mixed model with subgroup indicators as fixed and the individual studies as random effects); N: Maximum number of studies evaluated for pooled estimate or meta regression.

Disclosure of author financial interest or relationships:
A. Adams, None; **A. van Brussel**, None; **J.F. Vermeulen**, None; **W. Mali**, None; **E. van der Wall**, None; **P.J. van Diest**, None; **S.G. Elias**, None.

Presentation Number **P 021**
Poster Session 1
September 18, 2013 / 18:00-18:00 / Room: Exhibit Hall B

Metabolomics approach for the detection of the leptomeningeal carcinomatosis using a nuclear magnetic resonance spectroscopy

Hye Rim Cho, *Seung Hong Choi, Radiology, Seoul National University Hospital, Seoul, Republic of Korea. Contact e-mail: hyerimcho1030@gmail.com*

Introduction Leptomeningeal carcinomatosis (LC) is a disorder caused by the seeding of the leptomeninges, the pia, arachnoid, and cerebrospinal fluid (CSF) within the subarachnoid space, by malignant cells. This disorder is the third most common metastatic complication of the central nervous system and increasingly common in cancer patients. As treatment can also improve or stabilize a patient's neurological status and maintain their neurological quality of life, an early diagnosis of LC is important to alert the oncologist to begin therapy before neurologic deterioration. Recently, our group reported the metabolomics approach for the detection of LC by using a nuclear magnetic resonance (NMR) spectroscopy in an animal model. The purpose of the present study was to apply the NMR metabolimics approach for the detection of LC using a NMR spectroscopy in patients diagnosed with LC. Materials and Methods This prospective study was approved by the institutional review board of Seoul National University Hospital, and informed consent was obtained in all patients. In the present study, 72 patients were enrolled, and we colleted CSF from each patient. Among them, 31 patients were diagnosed as LC(breast cancer (n = 11); lung cancer (n = 20)), and the CSF of 41 patients with unruptured aneurysm was analyzed as control group. Before performing the CSF collection, we obtained MR imaging in all patients, and CSF cytology was used as a reference standard. In NMR analysis, the signals were referenced to the TSP signal at 0.00ppm and normalized against the total integration values. Water and ethanol peaks were removed to prevent artifacts in downstream analysis. For the statistical analysis, partial least square regression and OPLS-DA were conducted to identify latent patterns and compare the overall metabolite profile. Results In the CSF from patiens in the control group, the concentrations of 2-hydroxybutyrate, acetone, creatin, glutamine, malonate, mannitol, and myo-inositol were higher than LC group. In contrast, the LC patients showed higher concentrations of 3-hydroxybutyrate(cancer (37.68 ± 20.02) vs control (18.10 ± 7.46), $p < 0.001$), citrate (cancer (269.66 ± 173.08) vs control (87.76 ± 19.13), $p < 0.001$), and lactate (cancer (2134.82 ± 1296.53) vs control (1151.58 ± 208.151), $p < 0.001$). In addition, we observed that the grade of the leptomeningeal enhancement was correlated with increase in 3-hydroxybutyrate, citrate, and lactate ($P < 0.01$). Conclusion The NMR metabolimics approach can be used for the detection of LC in the patients, which was firstly demonstrated on the present study.

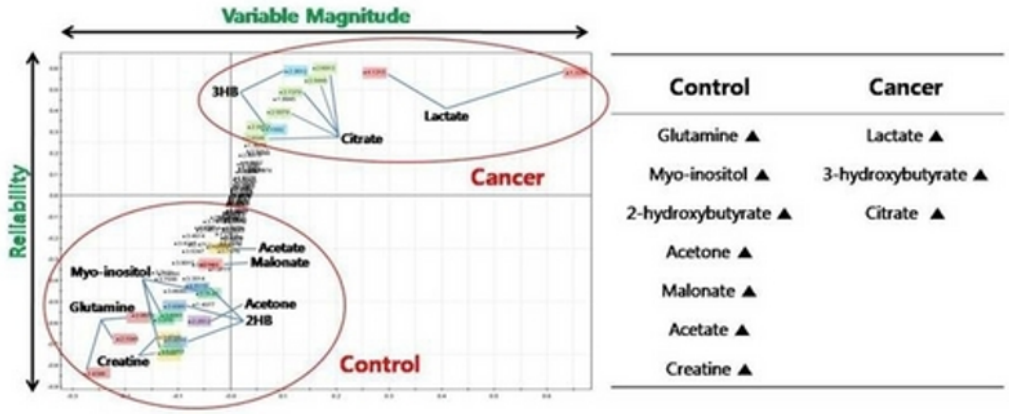

Figure 1. Signal contributing to the differentiation of control and cancer samples. S-plot (left) analysis with red colored outlines representing the highest contributing signal for the two groups. In control group, 2-hydroxybutyrate, acetone, creatin, glutamine, malonate, mannito, and myo-inositol were higher. In LC group, 3-hydroxybutyrate, citrate, and lactate were detected as markers.

Disclosure of author financial interest or relationships:
H. Cho, None; **S. Choi**, None.

Presentation Number **P 022**
Poster Session 1
September 18, 2013 / 18:00-18:00 / Room: Exhibit Hall B

Metabolic tumor volume as an early biomarker for treatment response in metastatic renal cancer

Jacob Farnebo[2], *Per Sandström*[1], [1]*Karolinska Institutet, Bromma, Sweden;* [2]*MMK, Karolinska Institutet, Solna, Sweden. Contact e-mail: jacob.farnebo@karolinska.se*

Jacob Farnebo and Per Sandström Karolinska Universitetssjukhuset Aim The purpose of this study was to test the hypothesis that early 18F-fluorodeoxyglucose-positron emission tomography/computed tomography (FDG-PET/CT) can be used to predict early response to tyrosine kinase inhibitor treatment in patient with metastatic renal cancer. Method Three FDG-PET/CT scans were conducted on 39 patients with metastatic renal cancer; before, after 2 and 4 weeks of treatment with tyrosine kinase inhibitors (Sorafenib and Sunitinib). The primary endpoint was to analyze different FDG-PET/CT parameters (SUVmax, SULmax, metabolic tumor volume, total lesion glycolysis) and correlate to response at 2 and 4 weeks with overall survival. Results We found that change of metabolic tumor volume and total lesion glycolysis after 2 weeks of treatment significantly correlated to overall survival. In contrast, the most widely used parameter SUVmax, did not correlate with overall survival. Conclusions Previous studies investigating the commonly used SUVmax parameter have had trouble to predict outcome of therapy with PET/CT. Our data indicate that tumor metabolic volume parameters such as MTV and TLG can be used as an early biomarkers of response and predict outcome as early as after 2 weeks of therapy. Since drug response is individual, side effects are common and drugs are costly, tools for early assessment are of great importance in cancer care.

Disclosure of author financial interest or relationships:
J. Farnebo, None; **P. Sandström**, Pfizer, Grant/research support; Bayer, Grant/research support; GSK, Honoraria; Pfizer, Honoraria; Bayer, Honoraria; Novartis, Honoraria; BMS, Honoraria.

Presentation Number **P 023**
Poster Session 1
September 18, 2013 / 18:00-18:00 / Room: Exhibit Hall B

Evaluation of Hepatocellula Carcinoma and Benign Liver Lesions with ^{11}C-Acetate Dynamic PET Imaging

Jinxia Guo[1,3], *Li Huo*[2], *Yonghong Dang*[2], *Jinqiao Lv*[2], *Youjing Zheng*[2], *Ning Guo*[1], *Fang Li*[2], *Xiaoyuan (Shawn) Chen*[1], [1]*NIBIB,NIH, Bethesda, MD, USA;* [2]*Nuclear Medicine, Peking Union Medical College Hospital, Peking, China;* [3]*Biomedical Engineering, Huazhong University of Science and Technology, Wuhan, China. Contact e-mail: jinxia.guo2009@gmail.com*

Introduction: ^{11}C-acetate is considered as a complementary tracer to and perhaps a better one than 18F-FDG in detection of well-differentiated hepatocellular carcinoma (HCC). However, some benign hepatic tumors also accumulate ^{11}C-acetate mimicking the malignant ones. The kinetic analysis of ^{11}C-acetate may provide more information than routine one-point metabolic observation. This study aims to investigate the potential of dynamic ^{11}C-acetate hepatic PET imaging to improve diagnosis of well-differentiated HCC from benign liver lesions by using a three-compartment dual-input model. Methods: Eleven patients were enrolled in this study, 6 cases were with well-differentiated HCCs and 5 with benign pathologies, including 2 focal nodular hyperplasia (FNH), 2 inflammations and 1 hepatic adenoma. All the patients were confirmed histopathologically after surgery. Following the CT scan, all patients underwent 10 min dynamic PET imaging simultaneously with administration of ^{11}C-acetate. The time activity curves (TAC) of normal liver tissue, tumors, portal venous (PV) and hepatic artery (HA) were generated by drawing ROIs on registered PET and CT images. A three compartment irreversible dual-input model was used to estimate the kinetic rate constant K_1-k_3, vascular fraction (VB) and the coefficient α representing the relative HA contribution to the hepatic blood flow in all tumors and normal liver tissue. The dynamic parameter Ki ($K_1 x k_3 / (k_2 + k_3)$) was calculated to evaluate the local hepatic metabolic of acetate. Results: Higher ^{11}C-acetate accumulation was found in benign liver lesion, inflammation and well-differentiated HCC in contrast with normal liver tissue. The SUV of inflammation and well-differentiated HCC in group (a) ($\alpha > 0.75$) showed more obvious increase at 3 min post ^{11}C-acetate injection compared to that of FNH and hepatic adenoma. The SUV of well-differentiated HCC in group (b) ($\alpha < 0.2$) began to decrease after 3 min. According to kinetic analysis, higher ^{11}C-acetate metabolism rate was found in well-differentiated HCC with HA as the main blood flow contribution, which is a distinctive feature different from normal liver tissue and other kinds of lesions. Conclusion: ^{11}C-acetate metabolism rate constant and the relative PV and HA contribution to the hepatic blood flow can be obtained successfully with the three-compartment dual-input model. The kinetics analysis showed the potential to improve the identification of well-differentiated HCC lesions resulting from adding arterial infusion information to metabolism. Moreover, the relative PV and HA contribution coefficient may provide a priori information for the hepatic arterial infusion therapy.

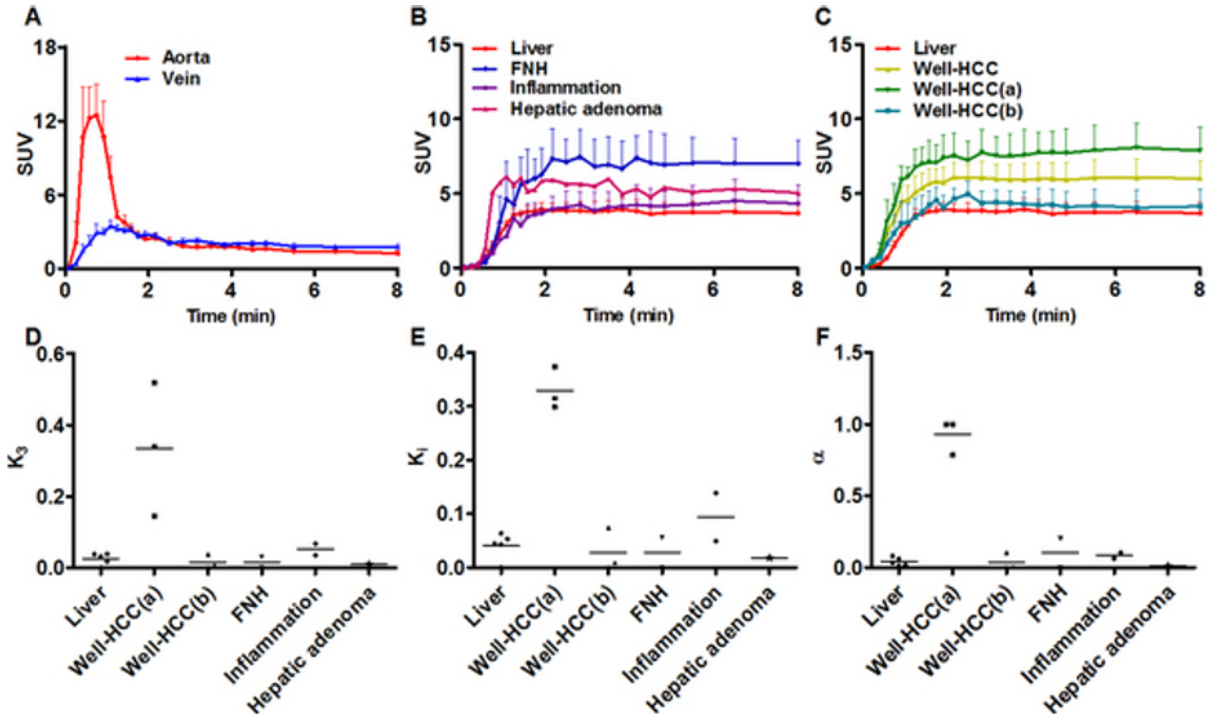

Figure 1. A) Averaged time activity curves (TACs) of ROIs drawn on aorta and vein in PET/CT registration; B) TACs for normal liver tissue, focal nodular hyperplasia (FNH), inflammation and hepatic adenoma; C) TACs for normal liver tissue and well differentiated HCC. D), E) and F) are the distribution of K_3, $K_i(K_1 x k_3/ (k_2 + k_3))$ and the hepatic artery contribution coefficient α respectively for normal liver tissue and each kind of liver lesions. Higher ^{11}C-acetate metabolism and hepatic artery contribution were found in well-differentiated HCC in group (a) (α > 0.75) than in group (b) (α < 0.2).

Disclosure of author financial interest or relationships:
J. Guo, None; **L. Huo**, None; **Y. Dang**, None; **J. Lv**, None; **Y. Zheng**, None; **N. Guo**, None; **F. Li**, None; **X. Chen**, None.

Presentation Number **P 024**
Poster Session 1
September 18, 2013 / 18:00-18:00 / Room: Exhibit Hall B

Meta-Analysis of Molecular Breast Imaging (MBI) Studies

James W. Hugg, *Rochelle Keen, Eileen Millsap, Gamma Medica, Northridge, CA, USA. Contact e-mail: james.hugg@gammamedica.com*

Objectives: Molecular Breast Imaging (MBI) uses planar imaging with single gamma photon emission from an intravenous radiopharmaceutical, such as Tc99m-sestamibi or tetrofosmin, to visualize breast cancers that are often occult on mammography in the 40-50% of women (up to 70% of Asian women) with radiographically dense breasts. Clinical results have been published since 2002 and the cumulative volume of patient studies has reached a level supporting a meta-analysis of the MBI studies in three clinical applications: diagnostic workup, extent of disease, and high-risk screening. Methods: MBI consists of a pair of opposed semiconductor (CZT, Cadmium Zinc Telluride) gamma photon cameras. Breast-Specific Gamma Imaging (BSGI) consists of a single scintillator (NaI or CsI with PS-PMT or photodiode detection) gamma camera and a compression paddle. In both MBI and BSGI the breast is mildly compressed between the bottom camera and either the top camera (MBI) or compression paddle (BSGI) in standard planar mammographic views. We performed a literature search and culled the studies until we had 19 studies and 4948 patients for diagnostic workup, 6 studies and 1405 patients for extent of disease, and 5 studies and 3013 patients for high-risk (mostly dense breast) screening. The initial analysis pools studies performed by BSGI (Dilon) and MBI (Gamma Medica or GE Healthcare). A sub-analysis to be performed will quantify the differences between a single scintillation camera (BSGI) and a pair of opposed solid-state cameras (MBI). We included a few studies from Europe that substituted the tracer Tc99m-tetrofosmin for the more common Tc99m-sestamibi. Results: Patient injected doses were 8-20 mCi for MBI and 20-44 mCi for BSGI, with a reduction in dose over time from earlier to recent studies. The diagnostic workup studies, including primarily women with suspicious lesions on screening mammography, had a sensitivity of 94% for the detection of 1652 cancers and a specificity of 85%. The extent of disease studies, including women with biopsy-proven cancer, yielded additional cancers in 7% of women, changing the clinical treatment in many cases. The high-risk (mostly dense breast) screening studies had a prevalence of 12.9 cancers detected per 1000 asymptomatic women screened by MBI or BSGI, compared to an incidence of 3.0 per 1000 for annual screening mammography. Conclusions: MBI and BSGI appear to be considerably more sensitive and specific than mammography, especially in dense breasts, and should be considered as an adjunct diagnostic and potential adjunct screening tool in breast cancer. Efforts to improve the technology and reduce the patient dose will further encourage the adoption of this new breast imaging modality.
Research Support: NIH National Cancer Institute grant R44-CA143716.

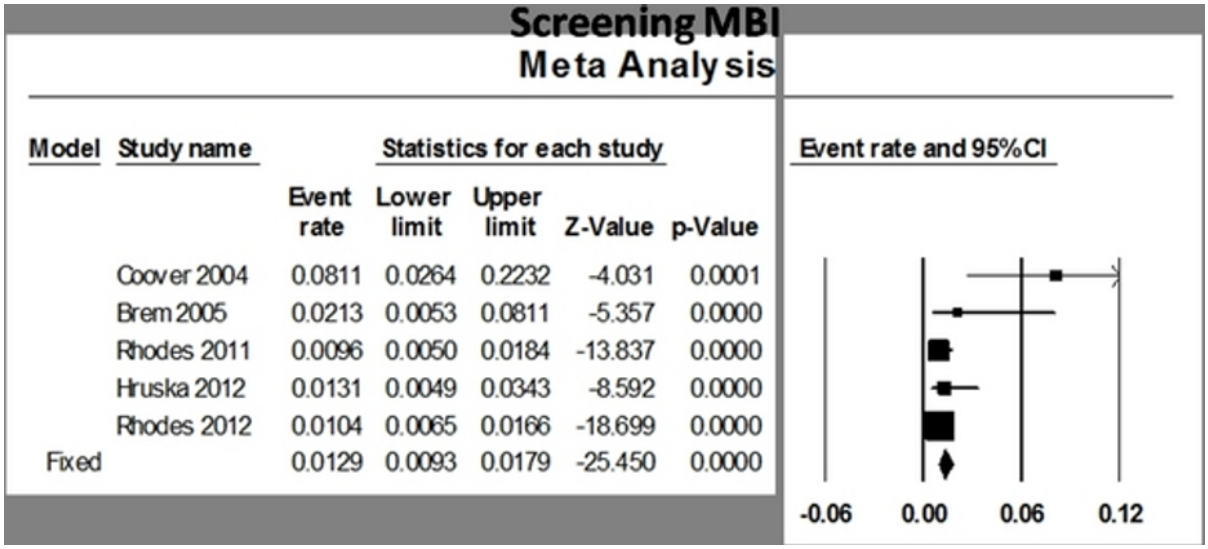

Meta-analysis of 5 MBI / BSGI high-risk (mostly dense breast) screening studies. For comparison, the incident yield for annual screening mammography is about 3 per thousand, one-fourth of the MBI prevalence yield of 12.9 per thousand..

Disclosure of author financial interest or relationships:
J.W. Hugg, Gamma Medica, Employment; Gamma Medica, Stockholder; **R. Keen**, Gamma Medica, Employment; **E. Millsap**, Gamma Medica, Employment .

Presentation Number **P 025**
Poster Session 1
September 18, 2013 / 18:00-18:00 / Room: Exhibit Hall B

Variability and Repeatability of Quantitative MRI Measurements in Normal Breast Tissue

Ella F. Jones, *Sheye O. Aliu, Ania Azziz, Sachiko A. Suzuki, John Kornak, Dorota J. Wisner, Catherine Klifa, Evelyn C. Protor, Bonnie N. Joe, Nola Hylton, University of California, San Francisco, San Francisco, CA, USA. Contact e-mail: ella.jones@ucsf.edu*

Background: Dynamic contrast-enhanced MRI (DCE-MRI) is playing an increasing clinical role in the staging and characterization of primary and locally-recurrent breast cancer. With the recent shift in treatment strategy from surgery-adjuvant chemotherapy to neoadjuvant chemotherapy prior to surgery, DCE-MRI offers high sensitivity to accurately measure early treatment response. Furthermore, the high sensitivity of DCE-MRI means it has potential to be used for screening of high-risk populations. However, the specificity of MRI is challenged by the strong background enhancement in pre-menopausal women, often associated with elevated estrogen levels that can obscure non-mass nodular malignant tissues. As we continue to develop more advanced techniques and imaging markers to improve quantitative evaluation of the breast, it is essential to gain better understanding of normal tissue characteristics measured by MRI contrasts. The purpose of this study was to characterize normal breast fibroglandular tissue (FGT) using MR background enhancement and density parameters in duplicates to evaluate the variability and repeatability of these measurements between subjects and within subjects. **Methods**: 18 normal pre-menopausal subjects underwent two breast DCE-MRI scans within 72 h (n=14) or at the same menstrual phase in two consecutive months (n=4). Fibroglandular tissue (FGT) volume was segmented from pre-contrast T1-weighted images using a fuzzy C-means clustering method. Subsequent FGT density was derived from the proportion of FGT volume in the total breast volume. Background enhancement was measured by the percent enhancement (PE). Between- and within-subject variability of measurements was assessed by the coefficient of variation (*CV*). Bland-Altman plot of difference vs. mean of measurements from visit 1 to visit 2 was used to assess the repeatability of measurements. Coefficient of repeatability (*CR* =1.96**SDdiff*, where *SDdiff* = standard deviation of measurement difference between visits 1 and 2) was used to assess the reliability of the measurements. **Results**: The between-subject variation (*bCV*) of PE and FGT density ranged from 47-63% at visit 1 and visit 2, indicating that these variations were subject dependent. The within-subject variation (*wCV*) was 21% for PE and 13% for FGT density. The repeatability of these measures was assessed by *CR* and the Bland-Altman plot (Figure 1). Both PE and FGT density measurements had a bias close to zero with narrow limits of agreement. The *CR* of PE and FGT density was 13% and 11% respectively, i.e., 95% of the observed normal subjects had changes of PE and FGT density that were within a range defined by the *CR*. **Conclusions**: Both PE and FGT density quantitative measurements of normal breast by DCE-MRI show good within-subject variability and repeatability. We anticipate expanding this analysis with a larger population and to include diffusion weighted imaging quantifiers. These estimates form the basis for interpreting normal variation of healthy breast tissue with DCE-MRI and for guiding future study design in assessing other MR parameters.

Figure 1.

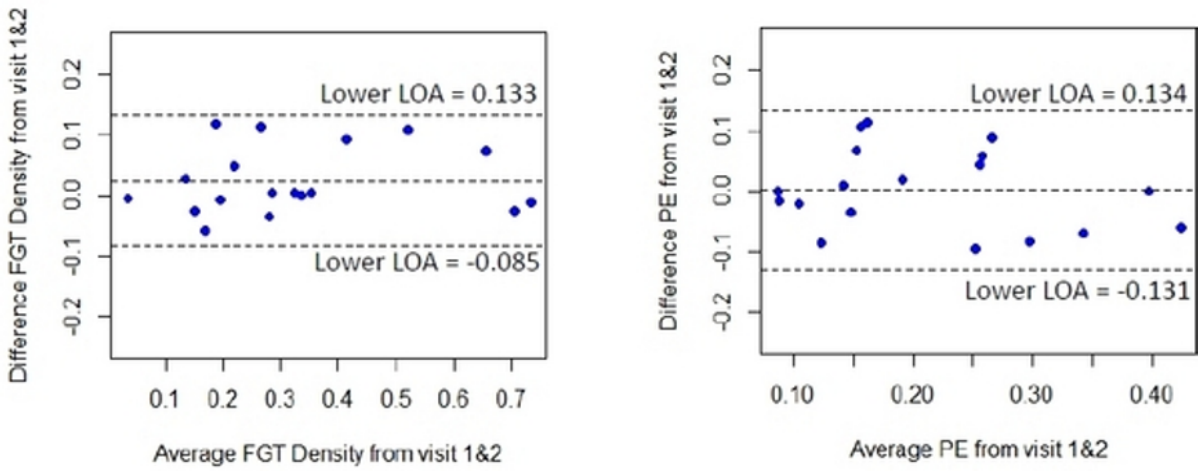

Bland-Altman plots of difference in measurements from visit 1 to visit 2 vs average of measurements from both visits. Left: FGT density measurement with mean difference at 0.024 and LOA (95% CI) = -0.085 (-0.124, -0.046) and 0.133 (0.094, 0.171). Right: PE measurements with the mean difference at 0.00161 and LOA (95% CI) = -0.131 (-0.178,-0.084) and 0.134 (0.087, 0.181).

Disclosure of author financial interest or relationships:

E.F. Jones, None; **S.O. Aliu**, None; **A. Azziz**, None; **S.A. Suzuki**, None; **J. Kornak**, None; **D.J. Wisner**, None; **C. Klifa**, None; **E.C. Protor**, None; **B.N. Joe**, None; **N. Hylton**, None.

Presentation Number **P 026**
Poster Session 1
September 18, 2013 / 18:00-18:00 / Room: Exhibit Hall B

Image based fusion SPECT/CT for pre-operative evaluation of sentinel node in esophageal cancer; comparative study of Tc-99m MSA versus Tc-99m phytate

Hyun Koo Kim[1], *Sungeun Kim*[2], *Jae Min Jeong*[3], *Young Ho Choi*[1], [1]*Thoracic and Cardiovascular Surgery, Guro Hospital, Korea University Medical Center, Seoul, Republic of Korea;* [2]*Nuclear Medicine, Korea University Guro Hospital, Seoul, Republic of Korea;* [3]*Nuclear Medicine, Seoul National University College of Medicine, Seoul, Republic of Korea. Contact e-mail: kimhyunkoo@korea.ac.kr*

Objectives : We developed a novel mannose receptor-binding agent, Tc-99m MSA and reported the feasibility for sentinel lymph node(SLN) mapping in patients with early-stage lung and esophageal cancer. The purpose of this study is to compare the role of Tc-99m MSA imaging with that of Tc-99m phytate in SLN identification in patients with esophageal cancer. Methods : Thirty patients with thoracic esophageal cancer were enrolled in this study (26 men,4 women; mean age 62.9). Patients were divided in half into two groups. Each group of patient was administered a total dose of 37 MBq (1mCi) of Tc-99m MSA and Tc-99m phytate in 0.2mL respectively, at 4 quadrants into the submucosal layer around the primary tumor under endoscopic guidance approximately 1 hour before surgery. Image based fusion SPECT/CT images were acquired within 30 minutes to 1 hour after injection. Intraoperative sentinel node sampling was subsequently followed by esophagectomy. Results : Total of 58 sentinel nodes in 30 patients were identified by surgery as follows: total 39 SLNs in 15 patients were harvested in preoperative Tc-99m MSA injected group (14 men,1 woman; mean age 63.7) and 19 SLNs in Tc-99m Phytate injected group (12 men,3 women; mean age 65.7). On the image based ananlysis, Tc-99m MSA fusion SPECT/CT and Tc-99m phytate fusion SPECT/CT identified 32 (32/39; 82.1%) and 8 (8/19; 42.15%) respectively. Tc-99m MSA fusion SPECT/CT was significantly higher SLN identification rate than Tc-99m phytate fusion SPECT/CT (Mann-Whitney test, $P<0.05$). Conclusions : In comparison with Tc-99m phytate imaging, Tc-99m MSA imaging shows higher accuracy for sentinel lymph node identification of esophageal cancer. Preoperative Tc-99m MSA may be useful in identifying sentinel lymph nodes in esophageal cancer.

Disclosure of author financial interest or relationships:
H. Kim, None; **S. Kim**, None; **J. Jeong**, None; **Y. Choi**, None.

Presentation Number **P 027**
Poster Session 1
September 18, 2013 / 18:00-18:00 / Room: Exhibit Hall B

F-18-FDG PET/CT findings of pancreas solid pseudopapillary tumor mimicking pancreas cancer

Yong-il Kim[1], *Seok-Ki Kim*[2], *Jin Chul Paeng*[1], *Ho-Young Lee*[3], [1]*Nuclear Medicine, Seoul National University Hospital, Seoul, Republic of Korea;* [2]*Nuclear Medicine, National Cancer Center, Goyang, Republic of Korea;* [3]*Nuclear Medicine, Seoul National University Bunddang Hospital, Seongnam-si, Republic of Korea. Contact e-mail: kyi821209@naver.com*

Purpose: Pancreas solid pseudopapillary tumor (SPT) is a rare disease of benign pancreas tumor and lacks data for PET/CT study. We investigated the usefulness of F-18-FDG PET/CT in evaluating pancreas SPT by multicenter data analysis. Methods: Pathologically proven eleven SPT patients were gathered retrospectively in three of our institute (age = 42.3±14.2 yrs old, M:F= 5:6). Ten subjects were primary SPT patients and one was metastatic SPT patient. Quantified parameters, maximum standardized uptake value (maxSUV), meanSUV, total leison glycolysis (TLG), and tumor-to-background ratio (TBR), was identified to PET/CT images. Tumor markers of CEA and CA 19-9 were used as laboratory parameters. Comparison study of pancreas SPT according to T-stage was performed. Results: FDG uptakes of primary SPT were variable (maxSUV, range= 2.2 - 19.7). Comparison according to T-stage of pancreas SPT showed significant result by TLG (T1 vs. T2 or T3, 10.8±4.5 vs. 369.0±587.3; p=0.017). MaxSUV and meanSUV revealed increased uptake trend according to T-stage (p=0.067, respectively). Other parameters, TBR and laboratory parameters showed no significant results. Conclusion: We found moderate to intense uptake of FDG in primary pancreas SPT. Intense uptake was observed in T2 or T3 stage of tumor and moderate uptake was detected in T1 tumor. We should think of the possibility of SPT in solid pancreas mass with FDG uptake.

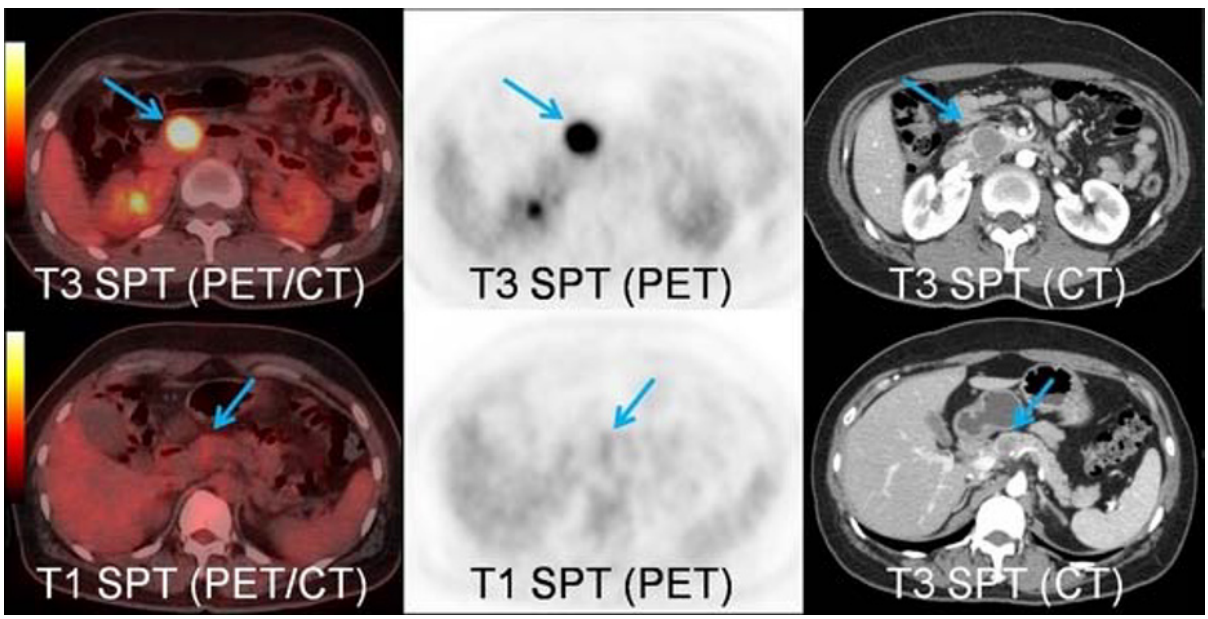

Comparison of pancreas solid pseudopapillary tumor according to T-stage

	T1 (n = 3)	T2 or T3 (n = 7)	p-value*
MaxSUV	2.3±0.3	7.4±6.4	0.067
MeanSUV	2.1±0.1	3.8±2.4	0.067
TLG	108±4.5	369.0±387.3	0.017†
TBR	2.0±0.1	2.0±0.3	0.667
CEA (ng/ml)	1.3±0.7	1.2±0.5	0.517
CA 19-9 (ng/ml)	8.0±9.5	7.8±6.3	0.833

SUV, Standardized Uptake Value; TLG, Total Lesion Glycolysis; TBR, Tumor-to-Background Ratio
*Mann-Whitney U test, †p <0.05

Disclosure of author financial interest or relationships:
Y. Kim, None; **S. Kim**, None; **J. Paeng**, None; **H. Lee**, None.

Presentation Number **P 028**
Poster Session 1
September 18, 2013 / 18:00-18:00 / Room: Exhibit Hall B

Evaluation of the L-glutamate derivative 18F-FSPG for PET imaging of various cancer indications in patients

Erik Mittra[1], *Meena Kumar*[1], *Camila Mosci*[1], *Khun Visith Keu*[1], *Andrei Iagaru*[1], *Norman Koglin*[2], *Andrew Stephens*[2], *Ludger M. Dinkelborg*[2], *Frederick T. Chin*[1], *Sanjiv S. Gambhir*[1], [1]*Radiology, Stanford University, Stanford, CA, USA;* [2]*Piramal Imaging GmbH, Berlin, Germany. Contact e-mail: erik.mittra@stanford.edu*

Objectives: (S)-4-(3-[18F]Fluoropropyl)-L-glutamic acid (FSPG) is a novel radiopharmaceutical for PET imaging (FDA eIND 108509). It is a glutamate analogue that is a marker of xC- transporter and CD44 expression that has a good dosimetric profile and shows promise for oncologic imaging. We present data on the uptake of FSPG in four different cancer indications. Methods: Subjects were recruited with brain, head and neck, lymphoma, or colon cancer (5 subjects each). Approximately 8 mCi of FSPG was given intravenously to these 20 subjects (mean age: 62.5 ± 14.5) and 3 PET/CT scans, per subject, were obtained over the next 2 hours. During this time, vitals, EKGs, and blood samples were obtained. All but the brain cancer subjects also had a routine FDG PET/CT scan within 1 month. SUV (including unpaired T-tests) and visual comparison of the FSPG and FDG scans were performed to assess relative efficacy and differences between these two tracers. Results : FSPG did not cause alterations in symptoms, vitals, EKGs, or lab values. There was similar distribution in all patients with primary clearance through the kidneys. Quantitatively, all the malignant lesions were positive with FSPG but with a range of uptake (see Figure 1). Compared to the FDG scan, the FSPG scan showed lower absolute SUV values in the lesions, but higher tumor-to-background levels. This was confirmed visually in that FSPG scan showed higher uptake than FDG for brain lesions and similar uptake for HN subjects, but with less background brain uptake. Similarly, FSPG showed similar to lower uptake than FDG in lymphoma subjects and similar uptake to FDG in colon subjects. However, these differences were not significantly different. Conclusions : FSPG was well tolerated and showed increased uptake in all cancer types evaluated including brain, head and neck, lymphoma, and colorectal cancer. Markedly lower background uptake than FDG, especially in the brain, appears to be beneficial and leads to notably higher tumor-to-background levels. These results are promising and warrant further analysis in a larger cohort of subjects for this novel tracer.

Table 1. SUV comparison between FSPG and FDG for brain and head and neck cancer subjects.

SUV Analysis (60 min p.i.)	FSPG Brain Mean ± SD	FDG Brain Mean ± SD	FSPG H&N Mean ± SD	FDG H&N Mean ± SD
Brain/primary	4.1 ± 1.9	7.16 ± 2.7	2.8 ± 2.1	4.9 ± 2.2
Metastases	2.7 ± 2	2 ± 0.42	1.4 ± 0.8	3 ± 1.5
Aorta	0.8 ± 0.2	1.5	0.8 ± 0.3	1.6 ± 0.3
Brain	0.1	6.9 ± 3	0.1	7.9 ± 1.5
Tumor:brain	41	1	27.6	0.6
Tumor:aorta	5	4.8	3.3	3
Tumor:muscle	20.5	10	12.6	7.2

Table 2. SUV comparison between FSPG and FDG for lymphoma and colon cancer subjects.

SUV Analysis (60 min p.i.)	FSPG Lymphoma Mean ± SD	FDG Lymphoma Mean ± SD	FSPG Colon Mean ± SD	FDG Colon Mean ± SD
Primary tumor	1.9 ± 3.1	2 ± 1.6	5.4 ± 1.3	7 ± 0.8
Metastases	-	-	2.5 ± 2.4	3.5 ± 3.5
Aorta	1 ± 0.3	1.8 ± 0.3	1 ± 0.4	1.9 ± 0.5
Tumor:aorta	1.9	1.1	5.7	3.7
Tumor:muscle	6.8	2.5	20.9	11.2
Tumor:liver	1.3	0.8	3.7	3

Disclosure of author financial interest or relationships:
E. Mittra, None; **M. Kumar**, None; **C. Mosci**, None; **K. Keu**, None; **A. Iagaru**, None; **N. Koglin**, None; **A. Stephens**, Piramal Imaging, Employment; **L.M. Dinkelborg**, None; **F.T. Chin**, Ground Fluor Pharmaceuticals, Consultant; **S.S. Gambhir**, Bracco Diagnostics, Consultant; Endra, Inc, Stockholder; Cellsight, Stockholder; Enlight, Inc., Stockholder; General Electric, Grant/research support; ImaginAb, Stockholder; MagArray, Inc., Stockholder; Sanofi-Aventis, US, Grant/research support; SiteOne Therapeutics, Stockholder; VisualSonics/Sonosite, Stockholder .

Presentation Number **P 029**
Poster Session 1
September 18, 2013 / 18:00-18:00 / Room: Exhibit Hall B

System A Amino Acid Transport C-11 MeAIB PET/CT Imaging for Diagnosing Prostate Cancer

Ryuichi Nishii[1,2], *Tatsuya Higashi*[2], *Shinya Kagawa*[2], *Masato Kobayashi*[3], *Shigeki Nagamachi*[1], *Yoichi Mizutani*[1], *Keiichi Kawai*[3], *Shozo Tamura*[1], [1]*Radiology, University of Miyazaki, Miyazaki, Japan;* [2]*PET Imaging, Shiga Medical Center Research Institute, Shiga, Japan;* [3]*Graduate School of Medical Science, Kanazawa University, Ishikawa, Japan. Contact e-mail: rnishii@med.miyazaki-u.ac.jp*

PURPOSE Although F-18 FDG PET is established as one of the first choice imaging modalities in the diagnosis of malignancies, there are several problems to solve in clinical practice, especially in urological field. The aim of this study was to evaluate the clinical usefulness of α-[N-methyl-C-11]-methylaminoisobutyric acid (MeAIB), a highly selective substrate of the system A amino acid transport, in the diagnosis of prostate cancers, compared with FDG and MRI. METHOD AND MATERIALS Eighteen cases (age: 67.2+/-5.8y.o.) with prostate cancer (PC) who received total prostatectomy were included. We performed preoperative whole body static PET/CT scan twice using FDG and MeAIB on each day. Qualitative analysis and quantitative analysis was performed by two well-experienced physicians and by SUVmax, respectively. MRI was also performed and diffusion-weighted image (DWI) were analyzed. RESULTS Final diagnosis was 5 unilateral and 13 bilateral PCs (Stage I: n=3, II: n=9, III: n=5, IV: n=1). In quantitative analysis, MeAIB uptake in PC was relatively lower (SUVmax=3.4+/-1.9) than FDG uptake (4.0+/-2.7). Sensitivity of each modality was MeAIB: 11/18, FDG: 8/18, and DWI: 11/18 cases. MeAIB detected two cases with negative DWI, while DWI detected two cases with negative MeAIB. In Stage I-II (n=12), all modalities showed low sensitivity (less than 50%), while in Stage III-IV (n=6), MeAIB and DWI showed higher sensitivity (5/6 and 6/6 cases, respectively). In cases with larger tumor volume (>1cm3), MeAIB and DWI showed high sensitivity (10/12), while MeAIB and DWI showed low sensitivity (1/6) in cases with smaller tumor volume (<1cm3) CONCLUSION Uptake of C-11 MeAIB was observed in prostate cancer, indicating increased expression of the system A amino acid transport. MeAIB-PET/CT showed higher sensitivity than FDG-PET/CT and showed complementary role with DWI of MRI.

Disclosure of author financial interest or relationships:
R. Nishii, None; **T. Higashi**, None; **S. Kagawa**, None; **M. Kobayashi**, None; **S. Nagamachi**, None; **Y. Mizutani**, None; **K. Kawai**, None; **S. Tamura**, None.

Presentation Number **P 030**
Poster Session 1
September 18, 2013 / 18:00-18:00 / Room: Exhibit Hall B

Added Value of Hepatobiliary Phase Gadoxetic Acid-enhanced MRI for Diagnosis of Hepatocellular Carcinoma in High-risk Patients

Sith Phongkitkarun, *Kuruwin Limsamutpetch, Diagnostic and Therapeutic Radiology, Faculty of Medicine Ramathibodi Hospital, Mahidol University, Ratchathewi, Thailand. Contact e-mail: sith.bkk@gmail.com*

Purpose: To determine the added value of hepatobiliary phase (HBP) gadoxetic acid-enhanced MRI in the evaluation of hepatic nodules among high-risk patients. Material and methods: Institutional review board approved this retrospective study and waived informed consent. The study included 100 patients with high risk for HCC and 105 hepatic nodules which size was greater than 1 cm. A blind review of two MR image sets in random order was performed: set1, unenhanced (T1- and T2-weighted) and dynamic images; set2, unenhanced, dynamic and 20-minute HBP images. Diagnostic accuracy, sensitivity, specificity, PPV and NPV were compared between 2 image sets. Univariate and multivariate analyses of MR characteristics for diagnosis HCC were performed. Results: Diagnostic accuracy was significantly higher with addition of HBP images, from 88.7% in set1 to 95.5% in set2 ($p=0.002$). Sensitivity and NPV were increased from 79.7% to 93.2% and 78.9% to 91.8%, respectively, whereas specificity and PPV were not significantly changed. Hypointensity on HBP was the most sensitivity of 93.2% and typical arterial enhancement followed by washout was the most specificity of 97.8%. Multivariate analysis showed typical arterial enhancement followed by washout, hyperintensity on T2-weighted image and hypointensity on HBP were statistically significant MRI findings for diagnosis HCC ($p<0.05$). Conclusion: Addition of hepatobiliary phase gadoxetic acid-enhanced MRI statistically improves the diagnostic accuracy for diagnosis HCC greater than 1 cm. The typical arterial enhancement followed by washout, hyperintensity on T2-weighted image and hypointensity on hepatobiliary phase are useful in the diagnosis of HCC.

Disclosure of author financial interest or relationships:
S. Phongkitkarun, None; **K. Limsamutpetch**, None.

Presentation Number **P 031**
Poster Session 1
September 18, 2013 / 18:00-18:00 / Room: Exhibit Hall B

Molecular subtyping of breast cancer using breast PET-CT

Katja Pinker-Domenig[1], *Heinrich F. Magometschnigg*[1], *Georg J. Wengert*[1], *Marius Mayerhoefer*[1], *Zsuszanna Bago-Horvath*[3], *Peter C. Dubsky*[2], *Georgios Karanikas*[4], *Thomas H. Helbich*[1], [1]*Dept. of Radiology, Division of Molecular and Gender Imaging, Medical University Vienna, Vienna, Austria;* [2]*Dept. of Sugery, Medical University of Vienna, Vienna, Austria;* [3]*Institute of Pathology, Medical University of Vienna, Vienna, Austria;* [4]*Dept. of Nuclearmedicine, Medical University Vienna, Vienna, Austria. Contact e-mail: katja.pinker@meduniwien.ac.at*

Background: Recently dedicated breast 18FDG breast PET-CT has emerged as an additional imaging tool for assessment and staging of primary breast cancer. Expression of specific molecular markers such as estrogen receptor (ER), progesterone receptor (PR), and HER2 status, has direct prognostic and therapeutic implications in patient management. This study aimed to determine whether correlations exist between 18FDG up-take of the primary breast cancer lesions and these predictive and prognostic factors. M&M: Before undergoing surgery 114 patients with primary breast cancer underwent 18FDG breast PET-CT. The maximum standardized uptake value (SUVmax) of the primary breast cancer was measured in each patient and standard immunohistochemistry was performed on a surgical specimen to characterize the receptor state of tumor cells. Appropriate statistical tests were used to test for any association that may exist among ER, PR, and HER2. Results: A significant association was found between a triple negative status and the SUVmax ($p < 0.001$) of breast tumors. ER-negative tumors (mean SUVmax, 10.4) demonstrated a significantly higher SUVmax than did ER-positive tumors (median SUV, 5.1) ($p= 0.045$). No statistical significant difference was found for SUVmax of PR-negative vs. PR-positive lesions with a mean SUVmax of 8.6 and 4.9 ($p=0.15$) respectively. No statistical significant difference was found for SUVmax of HER2-negative vs. HER2-positive lesions with mean SUVmax of 6.4 and 5.3 respectively ($p=0.55$). If either ER or PR was positive, then the other tended to be positive as well ($chi2 = 84\%$, $P < 0.01$). No such significant relationship was detected between PR or ER and HER2 ($P > 0.05$). Conclusion: ER-negative breast cancer tumors display higher 18FDG uptake than ER-positive tumors. Triple-negative breast tumors are associated with increased 18FDG uptake commensurate with their aggressive biology. The data suggest that SUVmax measurements of 18FDG breast PET-CT can provide valuable information about the state of ER, PR, and HER2 and the associated glucose metabolism of the primary breast cancer lesions. Such an association may be of importance to treatment planning and outcome in these patients.

Disclosure of author financial interest or relationships:
K. Pinker-Domenig, None; **H.F. Magometschnigg**, None; **G.J. Wengert**, None; **M. Mayerhoefer**, None; **Z. Bago-Horvath**, None; **P.C. Dubsky**, None; **G. Karanikas**, None; **T.H. Helbich**, None.

Presentation Number **P 032**
Poster Session 1
September 18, 2013 / 18:00-18:00 / Room: Exhibit Hall B

Cerenkov emission in radiation therapy to estimate skin dose and monitor tissue oxygenation

Brian W. Pogue[1,4], *Rongxiao Zhang*[4], *Scott C. Davis*[1], *Adam Glaser*[1], *Sergei Vinogradov*[3], *David Gladstone*[2], *Lesley A. Jarvis*[2], [1]*Thayer School of Engineering, Dartmouth College, Hanover, NH, USA;* [2]*Norris Cotton Cancer Center, Dartmouth-Hitchcock Medical Center, Lebanon, NH, USA;* [3]*Department of Biochemistry and Biophysics, University of Pennsylvania, Philadelphia, PA, USA;* [4]*Department of Physics & Astronomy, Dartmouth college, Hanover, NH, USA. Contact e-mail: brian.w.pogue@dartmouth.edu*

A gated intensified CCD was used to image Cerenkov emission in radiation therapy. These images have recently been proven to be linearly proportional to the deposited surface dose (R2=0.97), and so they can be used to image the dose during each fraction of treatment. This has been validated by direct comparison with ionization chamber measurements and Monte Carlo modeling. The Cerenkov image acquisition is triggered by the 5 microsecond LINAC pulses at 180Hz, allowing capture the Cerenkov emission as blue light coming from the tissue, which can be captured in normal ambient room lighting. The 3D surface registration and image correction has been worked out in patient tissue phantoms and is being initiated for in vivo monitoring of breast skin dose during whole breast irradiation at 10 MeV energy. This is the first time that in vivo dose has been able to be imaged, and the value of these images may be in tracking skin dose, which is well known to be inaccurately predicted by treatment planning systems for complex tissue shapes. Whole breast irradiation is standard of care management following breast conserving surgery to remove localized cancer. Preliminary results from this phase 1 clinical trial can be presented. In tissue phantoms and Monte Carlo simulations, the ability to monitor tissue oxygenation with luminescent dye has been examined. The signal can be measured form the surface of tissue, and by separating the beam entrance and fiber monitoring site, it is possible to probe several centimeters into the tissue. A dendritic platinum-based phosphor (PtG4) has been used at micromolar concentrations to monitor Cerenkov-induced signals, and through gating the signal to monitor the lifetime, the partial pressure of oxygen can be estimated by the Stern-Volmer equation. Tomographic recovery of a region of low oxygenation was shown in a tissue phantom, with high accuracy in pO2 estimation. Taken together the surface dose and tissue oxygenation could be monitored for subjects undergoing standard fractionated radiation to track changes which occur during the month long treatment process.

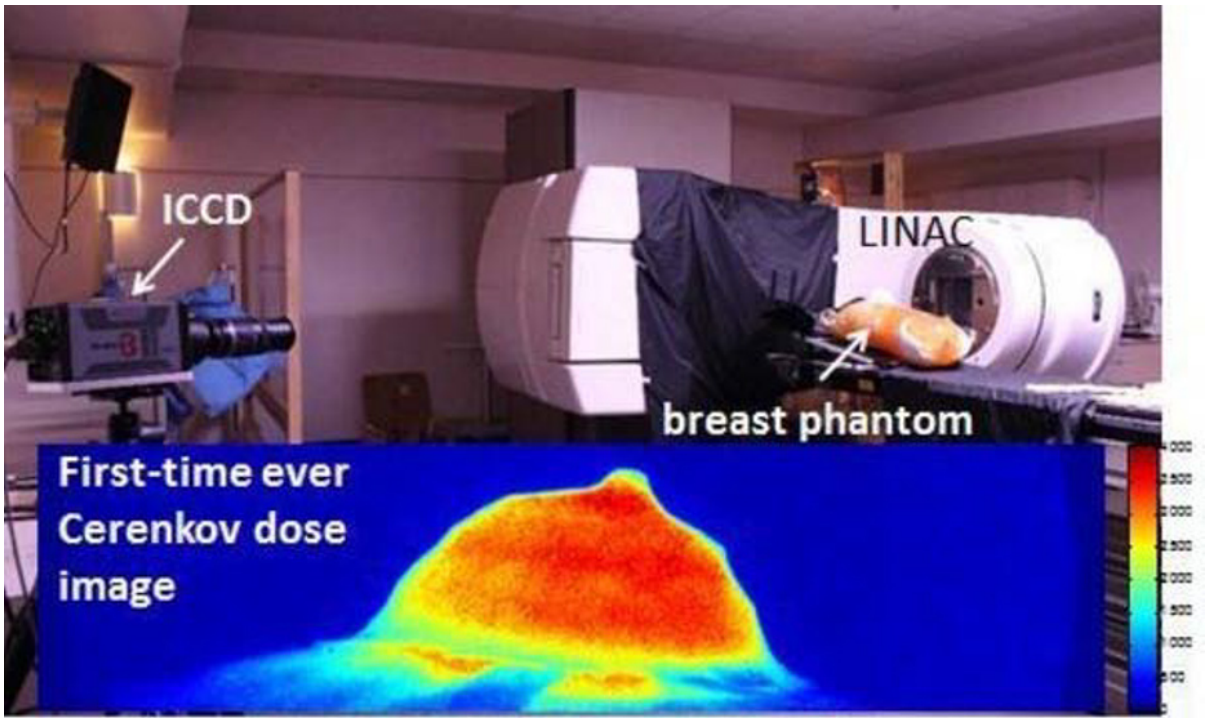

The imaging setup during linear accelerator (LINAC) irradiation is shown, with the ICCD camera at left, and the body tissue phantom with breast shown on the patient table. The first ever image is shown inset at bottom, where the intensity shown is proportional to skin dose.

Disclosure of author financial interest or relationships:
B.W. Pogue, None; **R. Zhang**, None; **S.C. Davis**, None; **A. Glaser**, None; **S. Vinogradov**, None; **D. Gladstone**, None; **L.A. Jarvis**, None.

Presentation Number **P 033**
Poster Session 1
September 18, 2013 / 18:00-18:00 / Room: Exhibit Hall B

Molecular Imaging of the Prostate using Multiparametric Functional [11C]-Acetate PET/MRI: Proof of Concept

Stephan H. Polanec[1], *Katja Pinker-Domenig*[1], *Peter Brader*[1], *Dietmar Georg*[2], *Piotr A. Andrzejewski*[2], *Heinrich F. Magometschnigg*[1], *Petra Georg*[2], *Georgios Karanikas*[1], *Thomas H. Helbich*[1], [1]*Division of Molecular and Gender Imaging, Dept. of Radiology, Vienna, Austria;* [2]*Radiooncology, Medical University Vienna /AKH, Vienna, Austria. Contact e-mail: stephan.polanec@meduniwien.ac.at*

Purpose: The potentials of multiparametric functional PET/MRI (PET/MRI) are not yet explored. We hypothesize that PET/MRI, which assess multiple pathophysiologic findings, enables an improved diagnosis of prostate cancer (PCa). Therefore the purpose of this study was to demonstrate the feasibility of multiparametric functional MRI and [11C]-Acetate PET/CT for molecular imaging of the prostate. Material and Methods: 27 patients (mean age of 68,1 yrs range from 54-79yrs; mean PSA level: 8,1ng/ml range from 0,9-23,4 ng/ml) were included in this IRB-approved prospective study. [11C]-Acetate PET/CT as well as 3T MRI of the prostate using T2-weighted, dynamic contrast-enhanced and diffusion-weighted MR imaging was performed. PET/MRI data was co-registered, fused and color-coded images were generated. PET/MRI was assessed for lesion morphology, acetate-activity and nodal status. Lesions within the prostate gland were classified as positive when [11C]-Acetate uptake was greater than blood-pool activity. The lesions were classified in the MRI with the PIRADS classification system and in all patients histopathologically verified. Results: 27 one lesions were detected by both MRI and PET/MRI. MRI classified 5 lesions as benign and 22 lesions as probably malignant. [11C]-Acetate PET/MRI upgraded the 22 suspect lesions to definite malignant, which were all histopathologically proven to be malignant. Sensitivity and specificity of PET/MRI was 100% and 95% respectively. In three patients PET/MRI revealed lymph node metastasis and in two patients additional skeletal metastasis. Conclusion: Molecular imaging of the prostate with [11C]-Acetate PET/MRI is feasible and improves diagnostic accuracy Additionally, an improved assessment of nodal status and bone metastasis is enabled.

Disclosure of author financial interest or relationships:
S.H. Polanec, None; **K. Pinker-Domenig**, None; **P. Brader**, None; **D. Georg**, None; **P.A. Andrzejewski**, None; **H.F. Magometschnigg**, None; **P. Georg**, None; **G. Karanikas**, None; **T.H. Helbich**, None.

Presentation Number **P 034**
Poster Session 1
September 18, 2013 / 18:00-18:00 / Room: Exhibit Hall B

Development of an Unbiased, Semi-automated Method for Tumor Volume Segmentation Using VelocityAI in Glioblastoma

James S. Cordova[1], *Eduard Schreibmann*[2], *Constantinos G. Hadjipanayis*[3], *Chad A. Holder*[1], *Ying Guo*[4], *Hyunsuk Shim*[1], *[1]Radiology, Emory University, Atlanta, GA, USA; [2]Radiation Oncology, Emory University, Atlanta, GA, USA; [3]Neurosurgery, Emory University, Atlanta, GA, USA; [4]Biostatistics, Emory University, Atlanta, GA, USA. Contact e-mail: j.s.cordova@emory.edu*

Currently, clinical glioblastoma (GBM) volume measurements rely on the product of orthogonal tumor diameters on contrast-enhanced, T1-weighted MR images. However, it is extremely difficult to consistently measure post-resection tumor size in this manner, especially when hyper-intense, non-neoplastic lesions are present. Though the desperate clinical need for objective, volumetric analysis was recently highlighted by the Neuro-Oncology Working Group (Wen, P.Y. et al. JCO 2010; 28,11 1963-1972), a standardized image display, processing, and analysis protocol has not been developed for a clinically-utilized volume rendering software. As such, the current work aims to standardize an MR signal-based approach for tumor segmentation using VelocityAI, an FDA 510k-approved software package that allows for the rendering, fusion, and analysis of multi-modality, 3D medical images. As proof-of-principle, we applied our volume determination method to compare the GBM extent of resection (EOR) using 5-aminolevulinic acid (ALA) fluorescence-guided resection to EOR of normal resections. Datasets consisted of high-resolution pre- and post-operative MR images (T1-weighted images pre- and post-gadolinium) from thirteen randomized patients in an Emory ALA study and thirteen controls matched for tumor location. To tabulate preoperative tumor volume, a coarse region-of-interest (ROI) was drawn around the tumor and the software was used to segment volumes of hyper- and hypo-intensity on T1-weighted MR images within the ROI in an automated fashion. To estimate the residual tumor post-surgery, image difference maps were produced by subtracting co-registered, pre- and post-gadolinium T1-weighted MR images to correct for postoperative blood accumulation. The average extent of resection for those without ALA-guidance -expressed as percent residual tumor -was 10.69 ± 7.45%, while that of ALA-guidance was 4.85 ± 3.98%. These values were found to be significantly different at $p<0.01$ using the nonparametric Wilcoxon Rank-Sum Test. These results corroborate with those seen in the literature and support the use of this semi-automated method for the unbiased and reproducible generation of contrast-enhancing tumor volumes in GBM pre- and post-resection. The comparison of our method with the current radiological assessment used in clinic is underway to illustrate precision in terms of inter-reader variability. The standardization of this method allows quantitative analysis of brain tumor response to chemo-, radiation, and surgical therapies, offering a highly precise tool for the longitudinal monitoring of patients in clinical trials. In addition, the same technology allows the selection of voxels within discrete tumor regions on T1-weighted images for the quantitative analysis of treatment-induced metabolic changes in spatially-coregistered, high-resolution MR spectroscopic images.

Disclosure of author financial interest or relationships:
J.S. Cordova, None; **E. Schreibmann**, Dr. Schreibmann is entitled to royalties derived from Velocity Medical Solution's sale of products.The terms of this agreement have been reviewed and approved by Emory University in accordance with its conflict of interest policies, Other financial or material support; **C.G. Hadjipanayis**, NX Pharmagen, Grant/research support; Meditech Inc., Consultant; **C.A. Holder**, None; **Y. Guo**, None; **H. Shim**, None.

Presentation Number **P 035**
Poster Session 1
September 18, 2013 / 18:00-18:00 / Room: Exhibit Hall B

Detection of breast cancer using near-infrared fluorescence imaging and Methylene Blue

Quirijn Tummers[1], *Floris P. Verbeek*[1], *Boudewijn Schaafsma*[1], *Martin C. Boonstra*[1], *Joost van der Vorst*[1], *Gerrit-Jan Liefers*[1], *Cornelis J. van de Velde*[1], *John V. Frangioni*[2,3], *Alexander Vahrmeijer*[1], [1]*Surgery, Leiden University Medical Center, Leiden, Netherlands;* [2]*Medicine, Beth Israel Deaconess Medical Center, Boston, MA, USA;* [3]*Radiology, Beth Israel Deaconess Medical Center, Boston, MA, USA. Contact e-mail: q.r.j.g.tummers@lumc.nl*

Background: Despite recent developments in preoperative breast cancer imaging, intraoperative localization of the tumor can be challenging. As a result, irradical resections during breast-conserving surgery are still a major problem. With Technetium(99mTc)-sestamibi (MIBI), a pharmaceutical agent used in nuclear medicine, preoperative identification of breast cancer is possible in 84-94% of patients. Based on chemical structure, we hypothesized that Methylene Blue (MB) might have a comparable biodistribution as the nuclear tracer used for a MIBI scan. Moreover, MB in low dosage can be used as a fluorescent tracer during near-infrared fluorescence (NIRF) imaging, a promising technique for intraoperative, real-time imaging. The aim of this study was to determine feasibility of MB as fluorescent tracer for the identification of breast cancer with NIRF imaging. Methods: Twenty-four patients with breast cancer, all planned for surgical resection, were included. N = 12 patients per group were administered 1.0 mg/kg MB intravenously either immediately before or 3-4 h before surgery The mini-FLARE imaging system was used to identify the fluorescent signal during surgery and on post-resected specimens transferred to the pathology department. Fluorescence microscopy images were obtained with the Odyssey Infrared Imaging System. Results: 20/24 (83%) of breast tumors (carcinoma (N=21) and ductal carcinoma in situ (N=3)) were identified in the resection specimen with NIRF. Overall tumor-to-background ratio (TBR) was 2.4 ± 0.8. There was no significant difference between TBR and background signal between administration groups (P = 0.50 en P = 0.23). Four resections were irradical (17%), and in one of these cases, tumor tissue was identified intraoperatively in the wound bed using NIRF imaging. Direct re-resection was performed, after which the tumor was radically removed. No fluorescent tumor signal was seen in the second irradical case, and in the third case, no intraoperative fluorescent images were available. In the fourth irradical case, clear fluorescent spots were identified in the wound bed, but these were characterized as benign on visual inspection. Therefore, no addition resection was performed. During histopathological assessment, the resection was found to be irradical at this margin. Histological validation with fluorescence microscopy showed a clear overlay between fluorescent signal and tumor tissue. No adverse reactions associated with the use of MB or fluorescent imaging were observed. Conclusion: This feasibility study shows that the identification of breast cancer with NIRF imaging and MB was possible in 83% of tumors. This is in agreement with the sensitivity of a MIBI scan for breast cancer of 84-94%. In 2/4 (50%) of patients, breast cancer tissue identified in the wound bed during surgery using NIRF would have changed patient management. Intraoperative NIRF imaging with MB has thereby the potency to increase the number of radical resections in breast cancer patients.

Disclosure of author financial interest or relationships:
Q. Tummers, None; **F.P. Verbeek**, None; **B. Schaafsma**, None; **M. Boonstra**, None; **J. van der Vorst**, None; **G. Liefers**, None; **C.J. van de Velde**, None; **J.V. Frangioni**, None; **A. Vahrmeijer**, None.

Presentation Number **P 036**
Poster Session 1
September 18, 2013 / 18:00-18:00 / Room: Exhibit Hall B

Navigation towards the sentinel node in the groin

Nynke S. van den Berg[1,2], *Oscar R. Brouwer*[2], *Hanna M. Mathéron*[2], *Gijs H. KleinJan*[1,2], *Thomas Wendler*[3,1], *Omgo E. Nieweg*[5], *Simon Horenblas*[4], *Henk G. van der Poel*[4], *Renato A. Valdés Olmos*[1,2], *Fijs van Leeuwen*[1,2], [1]*Radiology, Leiden University Medical Center, Leiden, Netherlands;* [2]*Nuclear Medicine, The Netherlands Cancer Institute-Antoni van Leeuwenhoek Hospital, Amsterdam, Netherlands;* [3]*Surgic Eye, Munich, Germany;* [4]*Urology, The Netherlands Cancer Institute-Antoni van Leeuwenhoek Hospital, Amsterdam, Netherlands;* [5]*Surgery, The Netherlands Cancer Institute-Antoni van Leeuwenhoek Hospital, Amsterdam, Netherlands. Contact e-mail: N.S.van_den_Berg@lumc.nl*

Background: The sentinel node (SN) biopsy procedure for various malignancies has been shown to be a valid alternative for complete lymph node resection of a certain area. Though, false-negative rates can be high. For example, for melanoma false-negative rates up to 20% have been reported. Preoperatively acquired SPECT/CT scans can be loaded into the Declipse® SPECT-system (Surgic Eye, Munich, Germany) thereby allowing intraoperative 3D SPECT/CT-virtual-reality-based navigation towards a lesion of interest. This approach might help to increase the accuracy with which a SN can be detected and as a consequence might help further reduce the false-negative outcome. This study evaluated the accuracy of the Declipse® SPECT-system in navigation towards the SN in the groin area. Methods: Fifteen patients were included in this study. Ten patients with penile carcinoma were peritumorally injected with indocyanine green (ICG)-99mTc-nanocolloid. Five patients with melanoma of the extremities were injected with 99mTc-nanocolloid surrounding the melanoma scar. Lymphoscintiography and a SPECT/CT imaging were performed to determine the number and location of the SN(s). Prior to the SPECT/CT a reference tracker (ReT) was placed on a easily reproducible anatomical location and marked with indelible ink. Prior to the start of the operation, a sterile ReT was placed on the exact same location allowing registration of the SPECT/CT image with the patient. A second ReT was placed on the gamma probe (tool to be navigated). This allowed 3D SPECT/CT-virtual-reality-based to the SN. The depth from the skin to the actual location of the SN was determined and compared to the results found with the conventional gamma probe-based approach. Results: In 14 patients the average deviation form the SN was 4.5 mm (range 0-10 mm). In 3 patients navigation of the gamma probe pointed exactly to the SN (0 mm error). In the remaining patient, the ReT was placed on the contralateral leg. This resulted in a large navigation error of 45 mm. This patient was excluded from further analysis. Conclusion: 3D SPECT/CT-virtual-reality-based navigation to the SN proved feasible and promising for the accurate localization of the SN. The accuracy with which the ReT can be placed strongly influences the accuracy of navigation.

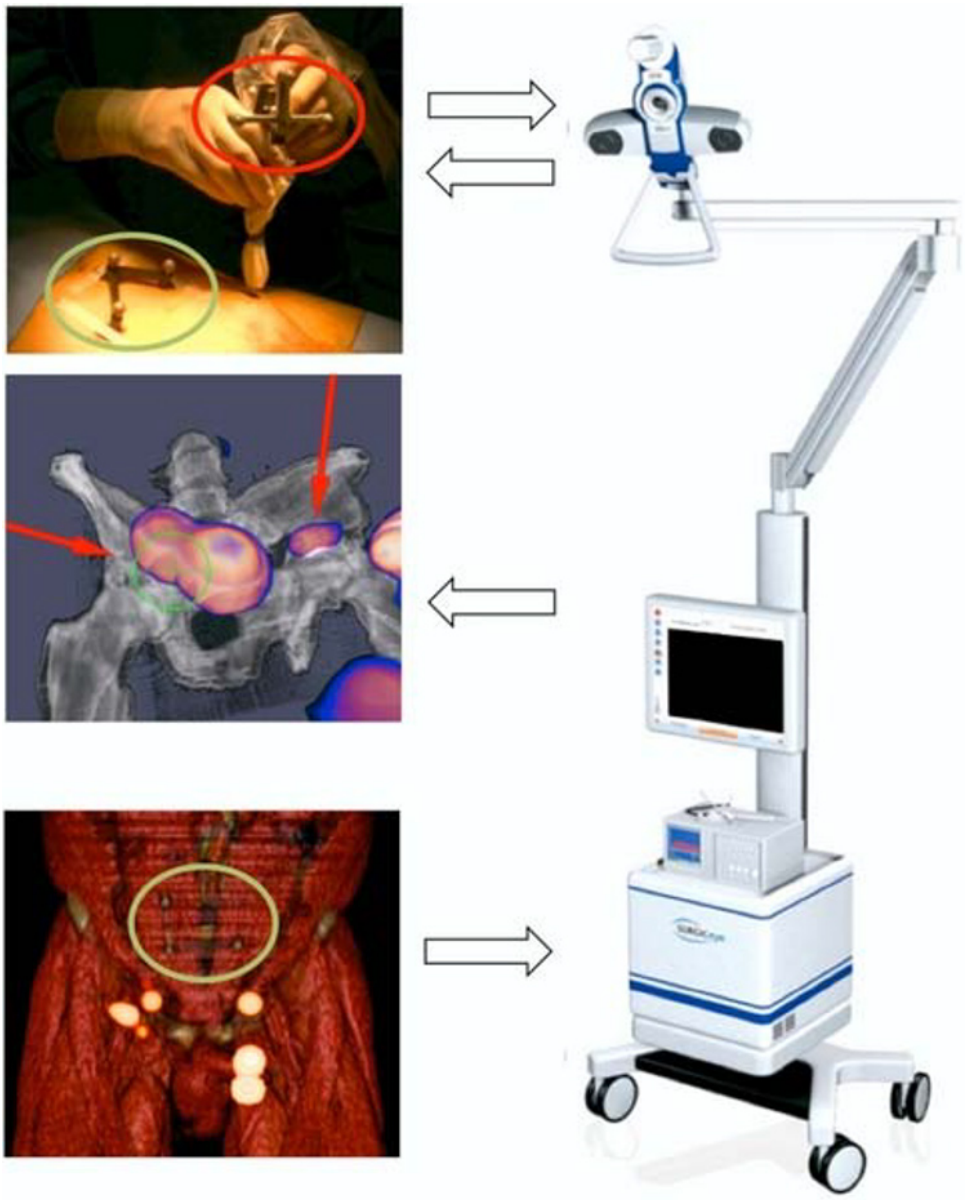

Disclosure of author financial interest or relationships:
N.S. van den Berg, None; **O.R. Brouwer**, None; **H.M. Mathéron**, None; **G.H. KleinJan**, None; **T. Wendler**, SurgicEye GmbH, Stockholder; SurgicEye GmbH, Employment; **O.E. Nieweg**, None; **S. Horenblas**, None; **H.G. van der Poel**, None; **R.A. Valdés Olmos**, None; **F. van Leeuwen**, None.

Presentation Number **P 037**
Poster Session 1
September 18, 2013 / 18:00-18:00 / Room: Exhibit Hall B

Virtual-reality-based navigation during the robot-assisted laparoscopic sentinel node biopsy procedure in prostate cancer patients

Nynke S. van den Berg[1,2], *Oscar R. Brouwer*[2], *Gijs H. KleinJan*[1,2], *Henk G. van der Poel*[3], *Thomas Wendler*[1,4], *Renato A. Valdés Olmos*[1,2], *Fijs van Leeuwen*[1,2], [1]*Radiology, Leiden University Medical Center, Leiden, Netherlands;* [2]*Nuclear Medicine, The Netherlands Cancer Institute-Antoni van Leeuwenhoek Hospital, Amsterdam, Netherlands;* [3]*Urology, The Netherlands Cancer Institute-Antoni van Leeuwenhoek Hospital, Amsterdam, Netherlands;* [4]*Surgic Eye, Munich, Germany. Contact e-mail: N.S.van_den_Berg@lumc.nl*

Background: Hybrid tracers, being both radioactive and fluorescent, facilitate preoperative surgical planning and synchronous intraoperative radio- and fluorescence guidance to the area of interest. However, the more intricate anatomy asks for improved orientation during laparoscopic surgery. This study provides a proof of concept on how intraoperative navigation based on the preoperatively acquired SPECT/CT images may facilitate radio- and fluorescence-guided surgery. In addition, the radioactive signature of the hybrid tracer may also allow for the generation of an intraoperatively generated SPECT image thereby allowing virtual-reality-based navigation towards the lesion of interest (hereafter referred to as Freehand SPECT). Methods: In 5 patients with prostate cancer scheduled for robot-assisted laparoscopic prostatectomy with subsequent (sentinel) lymph node dissection the hybrid tracer ICG-99mTc-nanocolloid was injected transrectally into the prostate under ultrasound guidance. Conventional lymphoscintigraphy and SPECT/CT were performed to determine the number and location of the sentinel lymph node(s). Prior to the SPECT/CT-scan a reference tracker (ReT) was placed on the patient and marked with indelible ink. Before starting the surgical procedure the sterile ReT was placed on the exact same location allowing registration of the SPECT/CT image with the patient. A second sterile ReT was placed on the tool to be navigated: the fluorescence laparoscope. This allowed for 3D virtual-reality-based navigation of the tip of the fluorescence laparoscope to the lesion of interest. In one patient, with a laparoscopic gamma probe (on which an ReT was placed), the area of interest could be scanned for the presence of radioactivity resulting in a Freehand SPECT image. After reconstruction of this image, the laparoscopic gamma probe could be navigated in 3D virtual-reality towards the lesion of interest (in this patient the sentinel lymph node). Results: Based on the preoperatively acquired SPECT/CT images, the tip of the fluorescence laparoscope could be navigated towards the area of interest. With decreasing distance, fluorescence intensity increased. The registration error found was approximately 1-2 cm. Laparoscopic Freehand SPECT allowed more accurate navigation towards the area of interest. Conclusion: Image navigation based on the preoperatively acquired SPECT/CT or intraoperative Freehand SPECT seem feasible. To improve the accuracy of navigation, Freehand SPECT might be favorable over SPECT/CT based navigation.

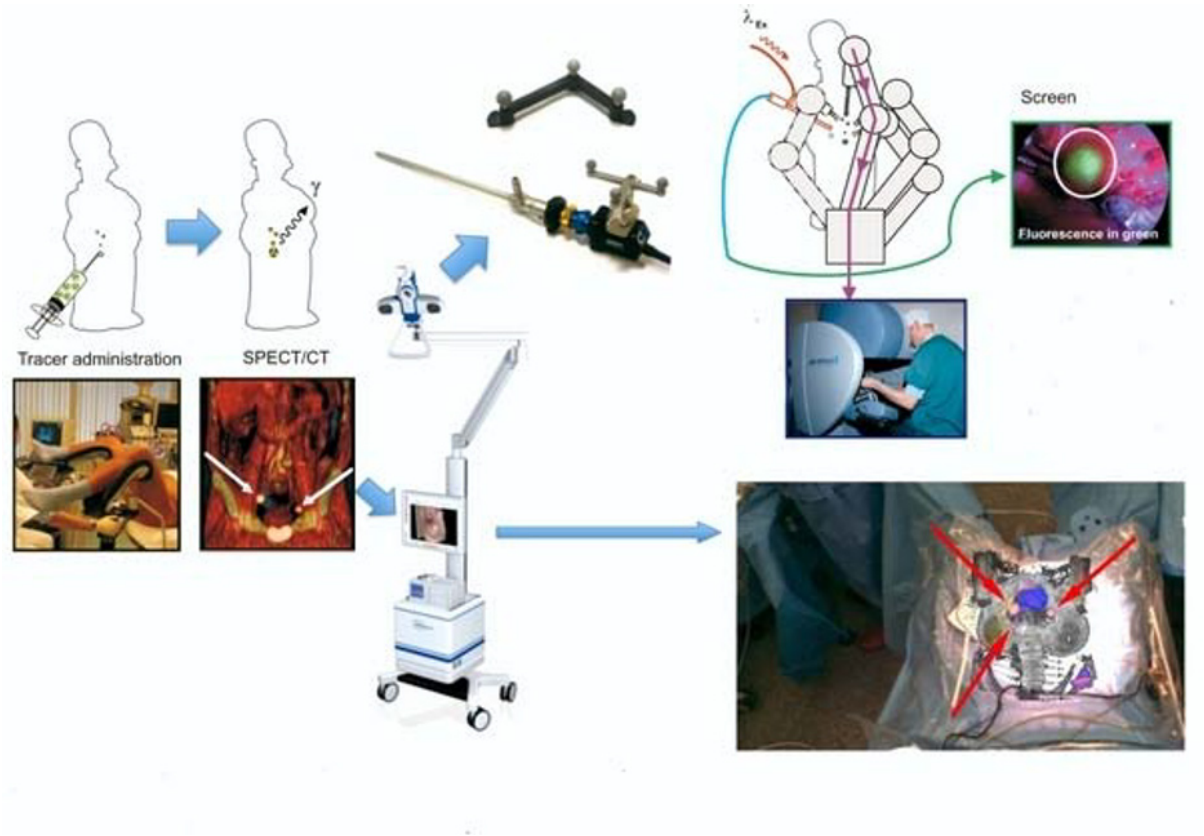

Disclosure of author financial interest or relationships:
N.S. van den Berg, None; **O.R. Brouwer**, None; **G.H. KleinJan**, None; **H.G. van der Poel**, None; **T. Wendler**, SurgicEye GmbH, Stockholder; SurgicEye GmbH, Employment; **R.A. Valdés Olmos**, None; **F. van Leeuwen**, None.

Presentation Number **P 038**
Poster Session 1
September 18, 2013 / 18:00-18:00 / Room: Exhibit Hall B

Bench to Bedside availability of Non FDG molecular imaging agents for clinical use beyond research: A clinician perspective and update of the new oncologic molecular imaging agents

Vani Vijayakumar, *Dept of Radiology, University of Mississippi Medical Center, Jackson, MS, USA. Contact e-mail: vvijayakumar@umc.edu*

Purpose and Aim: To review the new non FDG PET molecular imaging cancer agents for clinical use beyond research. Review the recent CMS decisions and MITA's recommendation to general practitioners. Methods: Proliferation Agents: FLT provides proliferative status of tumors with implications in predicting aggressiveness and monitoring therapy. Hypoxia Agents: FMISO provides the distribution of intratumoral hypoxia. 60CuATSM showing promise for imaging hypoxia in NSCLC, head and neck, rectal and cervical cancers. 64CuATSM provides higher quality images. Receptor Targeted Agents: Evaluating tumor receptor expression is important for receptor targeted therapy. Tumor receptor imaging characterizes tumor biology, therapeutic targets, pharmacodynamics of targeted cancer therapy and useful in the assessment of receptor expression of disease burden. Somatostatin is one of the tumor receptors that has been heavily studied (68Ga) agents show promising results in neuroendocrine tumor. Metabolism: Amino acid metabolic agents C11 methionine and C11 Choline Tumor specific Antibodies: 124I-A33 in colorectal cancer. Angiogenesis molecular agents: VEGF, Fibroblast Growth Factor (FGF), and αvβ3 integrinSummary: Ideal to directly derive radiobiological information from a single molecular imaging. FLT appears to be more specific to viable tumor cells. Hypoxia tracers are proving to be relevant in prognosis. Amino acid metabolic agents C11 methionine and C11 Choline showing promise in Brain Tumors and Brain Metastases and C11 Choline in prostate cancer. Tumor specific antibodies may provide accurate tumor cell distribution. Example: 124I-A33 in colorectal cancer Conclusion: Translation of imaging agents and technologies from preclinical into the clinic has been much slower due to considerable regulatory hurdles, market forces, lower profit margins for imaging than for therapeutic drugs, and the lack of reimbursement strategies for newer imaging agents. Despite these hurdles, several new technologies are entering into clinical trials. With the continued understanding of the molecular basis of disease detected by imaging studies and the recent advances in detection technology, imaging systems, reconstruction algorithms and visualization tools, the imaging transformation is going to be a reality. Applying the new molecular imaging tools to humans will make a dramatic improvement in how cancer is understood in vivo and which can allow earlier detection, stratification of patients for treatment, and objective evaluation of new therapies. CMS removed the national non-coverage decision for PET for FDA-approved oncologic applications. However, CMS stopped short of including cardiac and neurologic applications in the decision. The decision removes the national non-coverage determination for FDA-approved labeled oncologic uses of radiopharmaceuticals that are not more specifically determined nationally, according to CMS. MITA urged CMS to continue to evaluate the evidence and "avoid lengthy, bureaucratic reviews." (Health Imaging)

Disclosure of author financial interest or relationships:
V. Vijayakumar, None.

Presentation Number **P 039**
Poster Session 1
September 18, 2013 / 18:00-18:00 / Room: Exhibit Hall B

99mTc-HYNIC-trastuzumab based SPECT imaging for diagnosing advance gastric cancer

Xuejuan Wang, *Peking University Cancer Hospital, Beijing, China. Contact e-mail: xuejuan_wang@hotmail.com*

Purpose: On the basis of the results of the ToGA trial, HER2 status is included in the diagnostic workup of patients presenting with advanced gastric cancer. Trastuzumab, a humanized monoclonal antibody against HER2, is found to improve response rate and survival of those patients. Our aim was to synthesize 99mTc-HYNIC-trastuzumab to provide opportunities for noninvasive imaging HER2-positive lesions in advanced gastric cancer patient. Methods: Trastuzumab was conjugated with both a radiometal chelating group (HYNIC) and radiolabeled with 99mTc. Purity, stability, immunoreactivity, internalization, and biodistribution were evaluated in HER2+ cells and tumors. Four patients with HER2-positive gastric cancer were performed 99mTc-HYNIC- trastuzumab based SPECT imaging. Results: 99mTc-HYNIC-trastuzumab demonstrated high purity by both chemical and radioactive determinations. Both flow cytometry and the Lindmo assay demonstrated a high binding affinity of 99mTc-HYNIC-trastuzumab to HER2-overexpressing cells. 99mTc-HYNIC-trastuzumab was stable in PBS and in the serum after 24h at 37° C. Biodistribution studies revealed tumor-specific accumulation of 99mTc-HYNIC-trastuzumab in NCI-N87 tumors, and tumor uptakes 3.76±0.30%ID/g, 3.55±0.59%ID/g and 3.44±0.49%ID/g at 4h, 8h, and 24h postinjection, respectively. T/muscle ratio was 15.94. Only Two of four gastric patients (50%) had been visualized in HER2-positive lesions in patients with advanced gastric cancer. Conclusion: 99mTc-HYNIC-trastuzumab may not be an effective diagnostic biomarker that can be translated into clinical practice for identifying HER2+ lesions of gastric cancer

Disclosure of author financial interest or relationships:
X. Wang, None.

Presentation Number **P 040**
Poster Session 1
September 18, 2013 / 18:00-18:00 / Room: Exhibit Hall B

Breast density as a marker of breast cancer risk: assessment with MRI and correlation to standard mammographic density estimation

Georg J. Wengert[1], *Thomas H. Helbich*[1], *Wolf-Dieter Vogl*[1], *Wolfgang Bogner*[3], *Stephan H. Polanec*[2], *Heinrich F. Magometschnigg*[1], *Katja Pinker-Domenig*[1], [1]*Department of Radiology, Division of Molecular and Gender Imaging, Medical University of Vienna, Vienna, Austria;* [2]*Division of Gender and Molecular Imaging, Department of Radiology, Medical University, Vienna, Austria;* [3]*MR Centre of Excellence, Medical University, Vienna, Austria. Contact e-mail: georg.wengert@meduniwien.ac.at*

PURPOSE Development of a fully automated quantitative volumetric MRI breast density measurement system at 3 Tesla using the Dixon sequence and to correlate with standard mammographic density estimation using standard ACR-BIRADS classification and a user-assisted thresholding technique (Cumulus) METHOD AND MATERIAL 43 healthy women were included in this prospective IRB-approved study. Breast density was estimated qualitatively using the ACR-BIRADS categories and measured quantitatively from digitized mammograms using Cumulus, a user-assisted interactive thresholding technique, and with radiation- and compression free 3T Tesla MRI using the Dixon sequence, which acquired two datasets one representing the fatty and the other the fibroglandular tissue. The MRI approach uses a fully automated segmentation of the anatomic region of the breast and generates a combined plot resulting in two discriminable clusters of fatty and fibroglandular breast tissue. The system automatically calculated the percentage of fatty and fibroglandular tissue (%) and the total volume (cm3) of the breast. Mean values using student's T-test, and descriptive statistics using the 25-75% percentile were used to define the typical range of MRI density and MG density readings corresponding to the four BIRADS categories (ACR 1 <25%, ACR 2 25-49%, ACR 3 50-64%, ACR 4 >75%). RESULTS Percentage MRI breast density correlated with percentage mammographic breast density (r=0.99; P<0.0001). MRI measurements ranged from 2.19% to 75.39% (mean 26.05%) and mammographic measurements from 5.42% to 85.05% (mean 44.27). Compared with the BIRADS categories, 25-75% percentile assessment demonstrated a MRI interquartile range of 3.47-7.84% and a MG interquartile range of 8.42-33.84% for BIRADS-1, 7.84-25.88% (26.71-41.38%) for BIRADS-2, 26.25-44.15% (41.99-63.86%) for BIRADS-3 and 39.86-71.20% (61.75-79.91%) for BIRADS-4. Quantitative MRI breast density readings were consistently lower than qualitative BIRADS assessment. CONCLUSION Fully automated quantitative volumetric MRI BD measurement correlates well with mammography-based breast density readings; it is fast, user-independent and radiation- and compression-free and a reliable way of breast density estimation.

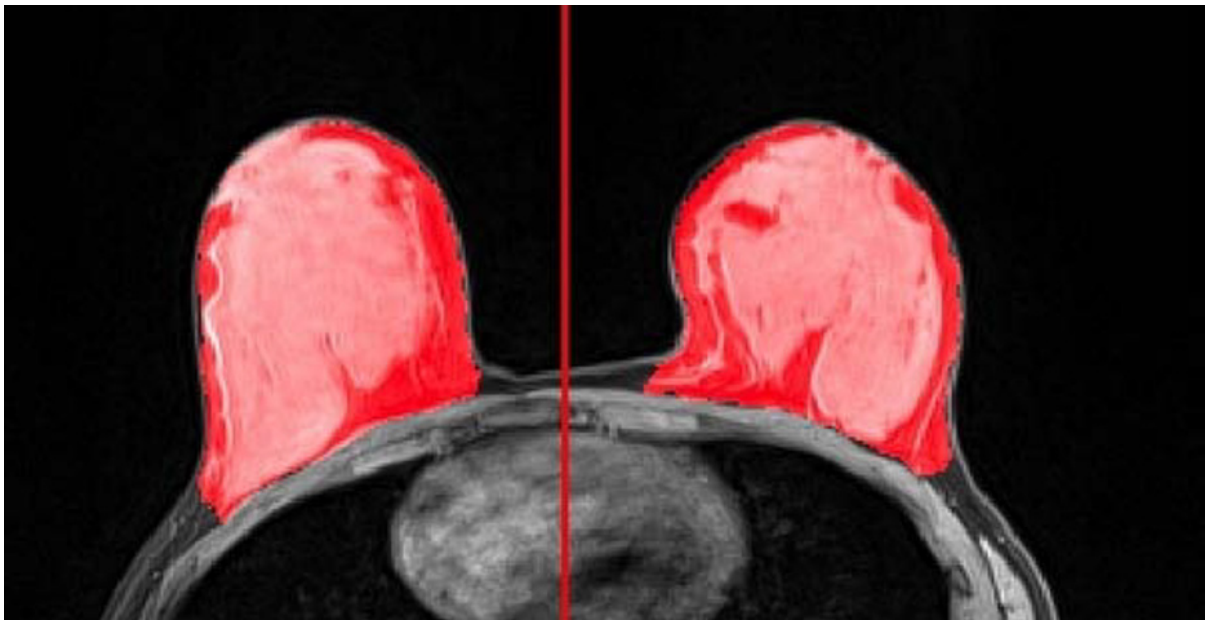

Example of fully-automated segmentation of anatomic breast region, used for MRI breast density assessment.

Disclosure of author financial interest or relationships:
G.J. Wengert, None; **T.H. Helbich**, None; **W. Vogl**, None; **W. Bogner**, None; **S.H. Polanec**, None; **H.F. Magometschnigg**, None; **K. Pinker-Domenig**, None.

Presentation Number **P 041**
Poster Session 1
September 18, 2013 / 18:00-18:00 / Room: Exhibit Hall B

Differences in Glucose Sensitivity in Normal Liver and Hepatic Metastasis Measured by FDG PET-CT Imaging

Prashant Jolepalem, *Lesley Flynt, John Rydnerg, Ching-yee O. Wong, Diagnostic Radiology & Molecular Imaging, Oakland University William Beaumont School of Medicine, Royal Oak, MI, USA. Contact e-mail: Prashant.Jolepalem@beaumont.edu*

Objective: To investigate the differences in glucose sensitivity in normal liver and hepatic metastasis. Methods: 76 patients (age 42-95 years, M:F=35:41) with 134 hepatic lesions who were referred for evaluation of metastatic disease by F-18 FDG PET-CT were analyzed. The serum glucose level [Glc] was recorded prior to FDG PET-CT imaging, and the maximum SUV in the metastasis and average SUV in normal liver were determined. For image acquistion, the mean FDG dose was 16+/-2 mCi and the average uptake time was 114+/-24 min. The glucose sensitivity, as described by Wong et al (2005) is defined as follows: g=d{ln(SUV)/d{ln[Glc]} Thus the rate of change of SUV over glucose: d(SUV)/d[Glc]=g*SUV/[Glc] Simulations using glucose level from 90 to 120 mg/dl were performed to evaluate the effects of [Glc] on the SUV of metastasis and normal liver. Pair t-tests were used for testing the signficance at $p<0.05$. Results: The mean [Glc] was 107+/-27 mg/dl. By logarithmic regression, the group average of g for metastasis was significantly higher than that for normal liver (3.61+/-2.80 vs 0.14+/-0.06, $p<0.0001$). The rate of change of SUV over [Glc] was also significantly larger in metastasis than that in normal liver (0.13+/-0.12 vs 0.0028+/-0.0011 dl/mg, $p<0.0001$). Simulation studies showed that the SUV in metastasis was easily affected by change in [Glc] beyond the normal range. Conclusion: The tumor FDG uptake is much more sensitive to ambient glucose level variation than the background liver. When using the tumor to background ratio for the diagnosis of hepatic metastases on F-18 FDG PET/CT, the sensitivity may be decreased by an abnormally high glucose level.

Disclosure of author financial interest or relationships:
P. Jolepalem, None; **L. Flynt**, None; **J. Rydnerg**, None; **C.O. Wong**, None.

Presentation Number **P 042**
Poster Session 1
September 18, 2013 / 18:00-18:00 / Room: Exhibit Hall B

Maximum standardized uptake value of preoperative F-18 FDG PET/CT as a predictor of BRAF V600E mutation in papillary thyroid cancer

Seok-Ho Yoon, *Joon-Kee Yoon, Kyung Sook Jo, Dong Hyun Lee, Su Jin Lee, Young-Sil An, Ajou University School of Medicine, Suwon, Republic of Korea. Contact e-mail: yoon.seokho@gmail.com*

BRAF V600E mutation is found frequently in recurrent papillary thyroid cancer (PTC) with increased F-18 fluorodeoxyglucose (FDG) uptake in the absence of radioiodine uptake. Furthermore, this mutation is associated with a high expression of glucose transporter 1 gene. The aim of the present study was to evaluate the usefulness of maximum standardized uptake value (SUVmax) on preoperative F-18 FDG PET/CT as a predictor of BRAF V600E mutation in PTC. 164 PTC patients (M/F=37/127; mean age ±SD=52.3±12.4) were enrolled for F-18 FDG PET/CT before total thyroidectomy. The presence of BRAF V600E mutation was analyzed by Polymerase chain reaction - restriction fragment length polymorphism (PCR-RFLP) on surgical specimens. Both univariate and multivariate analyses were performed to evaluate the association between SUVmax of PTC lesions on preoperative F-18 FDG PET/CT and the presence of BRAF V600E mutation. Association was also analyzed between SUVmax and other clinicopathologic features such as age (≥45 years or <45 years), sex, tumor size, TNM stage, preoperative unstimulated thyroglobulin, differentiational degree (well-differentiated or intermediate differentiated) and presence of accompanying thyroid disorders which can show increased F-18 FDG uptake (nodular goiter, thyroiditis or adenomatous hyperplasia). BRAF V600E mutation was found in 134 patients (134/164, 81.7%). SUVmax was significantly different between BRAF V600E mutation-positive and negative groups ($p<0.005$; mean±SD of positive group=9.51±1.5, negative group=5.0±4.1). Tumor size, T stage and N stage showed positive correlation with SUVmax ($p<0.005$). Multiple logistic regression indicated that tumor size ($p<0.005$) and presence of BRAF V600E mutation ($p=0.014$) were significantly correlated with SUVmax. In the present study, presence of BRAF V600E mutation was significantly correlated with SUVmax of preoperative F-18 FDG PET/CT in PTC. Therefore, SUVmax of preoperative F-18 FDG PET/CT may be a potential predictor of BRAF V600E mutation in PTC patients.

Disclosure of author financial interest or relationships:
S. Yoon, None; **J. Yoon**, None; **K. Jo**, None; **D. Lee**, None; **S. Lee**, None; **Y. An**, None.

Presentation Number **P 043**
Poster Session 1
September 18, 2013 / 18:00-18:00 / Room: Exhibit Hall B

A comparative Study on Post-operative Evaluation of Hepatocellular carcinoma After Radiofrequency Ablation By Gd-EOB-DTPA Dynamic Enhanced MRI and Dual Source CT

Lin Zhang, *southwest hospital, Chongqing, China. Contact e-mail: zhanglinxm@gmail.com*

Objective: to study application of Gd-EOB-DTPA dynamic enhanced MRI in evaluation of hepatic residual lesion and new lesion after radiofrequency ablation(RFA) by comparison with dual source CT(DSCT). Materials and Methods: 28 patients with hepatic carcinoma were performed with retrospective analysis after RFA. All the patients underwent DSCT and Gd-EOB-DTPA dynamic enhanced MRI. Sensitivity, specificity and accuracy of these two kinds of imaging were evaluated in activities of the residual lesions and new lesions after the RFA. Results: The sensitivity, specificity and accuracy of Gd-EOB-DTPA dynamic enhanced MRI in the diagnosis for the residual lesions were 91.2%, 97.8% and 95.1%, which of DSCT were 57.1%, 83.3% and 66.7%, respectively. The sensitivity and accuracy of Gd-EOB-DTPA dynamic enhanced MRI in the diagnosis for the new lesions were 95.5% and 87.8%, which of DSCT were 45.5% and 42.9%, respectively. There were significant differences. ($P<0.05$) Conclusions: For HCC patients after RFA, Gd-EOB-DTPA Dynamic Enhanced MRI is significantly superior to DSCT in diagnosis for the residual lesions and new lesions. Key words: hepatocellular carcinoma; radiofrequency ablation; Gd-EOB-DTPA; MRI; DSCT

Disclosure of author financial interest or relationships:
L. Zhang, None.

Presentation Number **P 044**
Poster Session 1
September 18, 2013 / 18:00-18:00 / Room: Exhibit Hall B

A novel αvβ3-integrin receptor imaging method 99mTc-3PRGD2 SPECT/CT in diagnosis, staging, and response evaluation of lung cancer: comparison with 18F-FDG PET/CT

Xiaona Jin[1], Ximin Shi[1], Bing Jia[2], Fang Li[1], Fan Wang[2], **Zhaohui Zhu**[1], [1]*Nuclear Medicine Department, Peking Union Medical College Hospital, Beijing, China;* [2]*Medical Isotopes Research Center, Peking University, Beijing, China. Contact e-mail: zzh_1969@yahoo.com.cn*

Avβ3-integrin receptor plays an important role in tumor angiogenesis, invasion, and metastasis. A novel αvβ3-integrin receptor imaging method, 99mTc-3PRGD2 SPECT/CT, was prospectively studied in diagnosis, staging, and response evaluation of lung cancer, which was compared with 18F-fluorodeoxyglucose (FDG) PET/CT in the same patients. METHODS: Sixty-five patients (M 41, F 24, 60±11 y) with suspicious lung lesions or biopsy proven non-small cell lung cancer (NSCLC) were recruited with informed consent. They underwent whole-body planar scanning and chest SPECT/CT successively 40 minutes after intravenous injection of 99mTc-3PRGD2 in 11.1 MBq/kg body weight. 18F-FDG PET/CT was performed within one week for comparison. Twenty-one proven NSCLC patients underwent repeated examinations after 1 cycle and 3 cycles of platinum-based chemotherapy, respectively. Obtainable specimens were stained with integrin αvβ3, CD34, and Ki67 to correlate with the image findings. RESULTS: 99mTc-3PRGD2 SPECT/CT showed comparable diagnostic accuracy as 18F-FDG PET/CT in differentiation of lung lesions (P=0.410). It was significantly better in assessment of lymph-node involvement (P<0.0001), in which the sensitivity, specificity, and accuracy were 87.5%, 98.2%, and 89.5%, respectively, versus 82.2%, 66.1%, and 79.3%, respectively for 18F-FDG PET/CT. However, whole-body 99mTc-3PRGD2 planar scan detected less (55/72, 76.4%) remote metastases than 18F-FDG PET/CT. The two methods were identical in response evaluation of chemotherapy in 16/21 (76.2%) patients, while either mothod showed advantages and disadvantages in evaluation of the other patients. 99mTc-3PRGD2 uptake was in positive correlation with integrin αvβ3 receptor expression (r=0.837, P<0.001) and the microvessel density (r=0.633, P=0.011). CONCLUSIONS: 99mTc-3PRGD2 SPECT/CT is a useful method for integrin receptor imaging of lung cancer, which may fulfill the lack of tumor-specific agents for SPECT. Moreover, it shows a preferable value over 18F-FDG PET/CT in assessment of lymph-node involvement, which may merit better surgical decision-making.

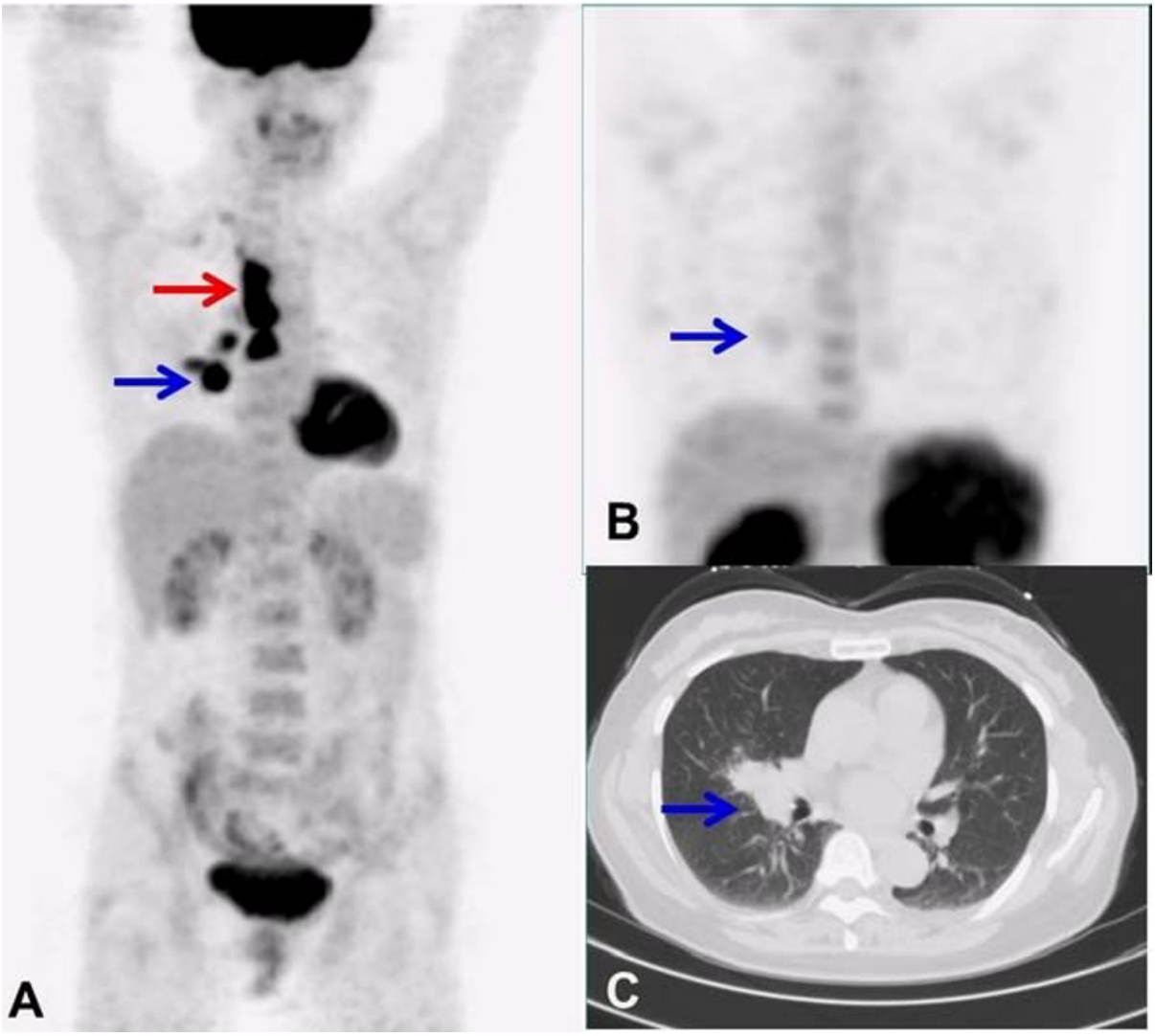

Figure. Comparison of 99mTc-3PRGD2 SPECT with 18F-FDG PET and CT in a 40-year-old woman with an inflammatory lesion near the right hilum and chronic inflammatory lymph nodes at the right hilar region and mediastinum. A: MIP of 18F-FDG PET showed intense 18F-FDG uptake at both the lung lesion and the lymph nodes. B: On the MIP of 99mTc-3PRGD2 SPECT, only mild 99mTc-3PRGD2 accumulated at the lung lesion and no uptake was found in the lymph nodes. C: A CT image showed the lung lesion and enlarged lymph nodes at the right hilar region.

Disclosure of author financial interest or relationships:
X. Jin, None; **X. Shi**, None; **B. Jia**, None; **F. Li**, None; **F. Wang**, None; **Z. Zhu**, None.

Presentation Number **P 045**
Poster Session 1
September 18, 2013 / 18:00-18:00 / Room: Exhibit Hall B

Magnetoliposomes for longitudinal follow up of pancreatic islets by MRI

Ashwini Atre[1], *Karim Louchami*[2,1], *Ting Yin*[1], *Tom Struys*[1], *Marcel DeCuyper*[3], *Willy J. Malaisse*[2], *Uwe Himmelreich*[1], [1]*Biomedical MRI, KU Leuven, Leuven, Belgium;* [2]*Laboratoire d'Hormonologie Expérimentale, ULB, Brussels, Belgium;* [3]*Lab of Bio NanoColloids, KULAK, KU Leuven, Kortrijk, Belgium. Contact e-mail: ashwini.atre@med.kuleuven.be*

Introduction Transplantation of Pancreatic Islets (PIs) have been considered an alternative therapy for patients with type 1 diabetes mellitus (T1DM). The exact location and functional status is usually unknown and makes it difficult to assess the fate of islet graft post transplantation. Thus use of a non invasive, reproducible and sensitive imaging technique is critically needed in order to determine possible causes for the graft rejection. Some studies could follow transplanted islets for longer duration with MR contrast agent (CAs) in clinical settings (1). Disadvantages of those labeling methods are the longer duration for incorporation of CAs- and subsequent potential adverse effects on PI functionality and the fact that those agents are not available any longer (2). This surges the necessity of determining a replacement CAs for such tracking studies. In this study, we have compared uptake efficiency of cationic magnetoliposomes (MLs) with Endorem and Resovist by labeling insulinoma cell lines and freshly isolated rat PIs. Methods Pancreatic Islets: Pancreatic islets were isolated from female Sprague Dawley rats (body weight 175 -299 g) with collagenase digestion. In Vitro studies: Insulinoma INS-1 and freshly isolated rat islets were labeled with Resovist, Endorem (+/- PLL) and cationic MLs at 50 µgFe/ml for 4 - 72hrs. MLs were synthesized as described in (3). All labeled samples were collected for MR scanning, viability testing (FDA-Propidium iodide staining), functional assays (insulin storage and secretion) electron microscopy, prussian blue staining (for label confirmation) and ICP-OES (for iron quantification). In vivo experiments: Labeled islets were transplanted in the kidney capsule and monitored with MRI longitudinally for 1 week. MRI: MR images were acquired from agar phantoms containing labeled cells/ PIs and from mice using a 9.4T Biospec small animal MRI scanner (Bruker Biospec, Ettlingen, Germany). T2-weighted spin echo and gradient echo images were acquired (Resolution = 200µm). (TE= 12 ms, TR= 150 ms.). Results NS-1 labeled with different labeling conditions showed varying uptake with different particles. MR detectable and non toxic uptake was achieved when MLs were incubated only for 4hrs, whereas Resovist and Endorem needed either longer duration or addition of PLL to achieve the same. No particles showed detectable toxic effects post labeling on insulinoma cells. Only cationic MLs showed very good uptake after 24hrs with of 50 µg Fe/ml without affecting insulin secretion and the viability. Longitudinal detection of MLs labeled cells and PIs was possible in in vivo in mice with 3D T2* w MRI. Conclusion: MLs were incorporated in shorter duration compared to commercially available CAs. Also it was observed that MLs are safe CAs for longitudinal and reproducible in vivo visualization of engrafted pancreatic islets in rodent models. References: (1) Jirak D.et.al. MRIM, 2004; (2) Cromer-Berman S. WIREs Nanomedicine and Nanobiotechnology, 2011; (3) Soenen S., et.al.ChemBioChem 2009

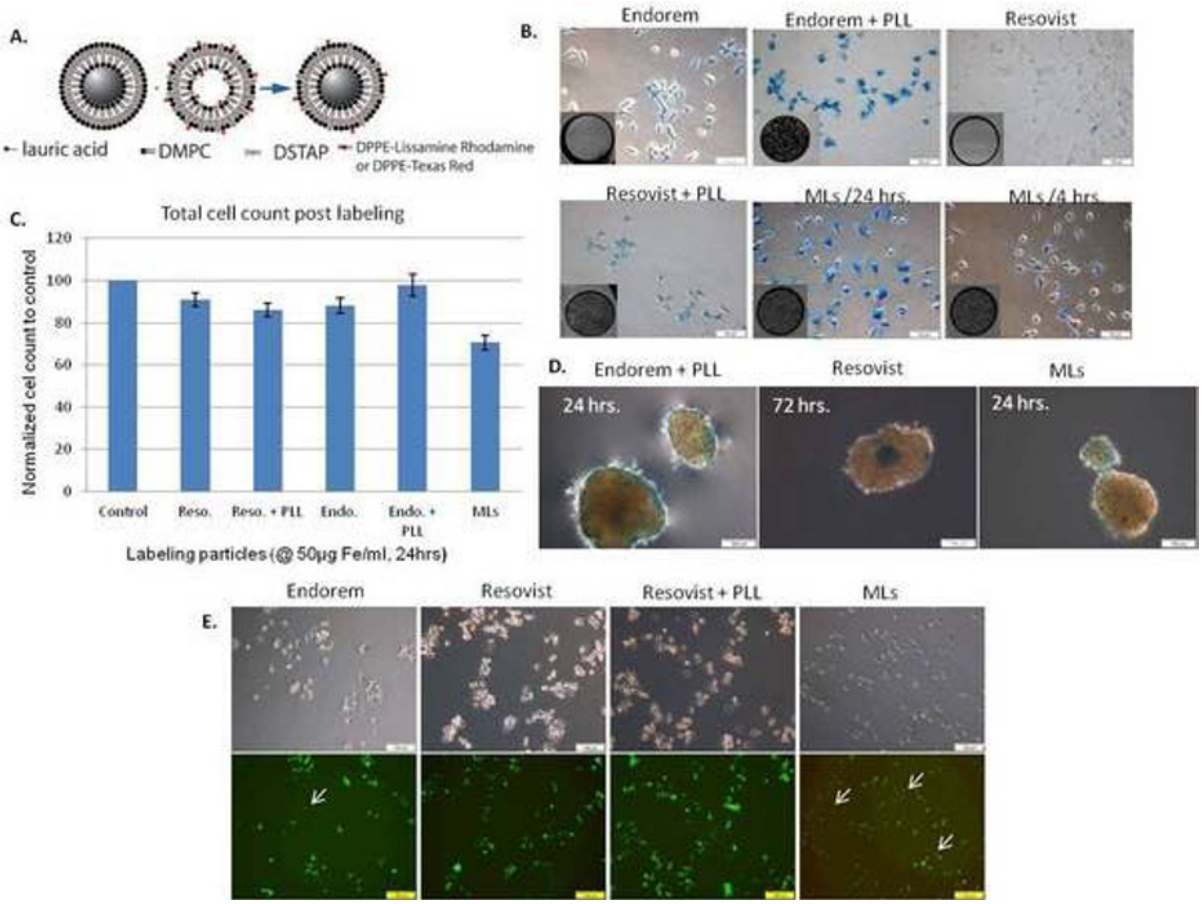

(A) Typical layout of MLs, (B) Prussian blue staining and MR 3D_T2* confirming uptake with different labeling conditions, (C) Total cell count indicating no effect on the cell proliferation, (D) Prussian Blue of islets post labeling, (E) No effect on the viability of INS-1 labeled with different labeling conditions

Disclosure of author financial interest or relationships:
A. Atre, None; **K. Louchami**, None; **T. Yin**, None; **T. Struys**, None; **M. DeCuyper**, None; **W.J. Malaisse**, None; **U. Himmelreich**, None.

Presentation Number **P 046**
Poster Session 1
September 18, 2013 / 18:00-18:00 / Room: Exhibit Hall B

Tracking 111In-labeled human Mesenchymal Stem Cells after intraperitoneal administration combining SPECT and MRI: a pilot study

Lorena Cussó[1,2], *Isabel Mirones*[4], *Santiago Peña Zalbidea*[2], *Luisa M. López-Sánchez*[1,2], *Veronica Garcia-Vazquez*[3,2], *Javier García-Castro*[4], *Manuel Desco*[2,1], [1]*Dept. Bioingeniería e Ingeniería Aeroespacial, Universidad Carlos III de Madrid, Leganes, Spain;* [2]*Instituto de Investigación Sanitaria Gregorio Marañón, Madrid, Spain;* [3]*Centro de Investigación Biomédica en Red de Salud Mental (CIBERSAM), Madrid, Spain;* [4]*Unidad de Biotecnología Celular (Área de Genética Humana, IIER), Instituto de Salud Carlos III, Madrid, Spain. Contact e-mail: lcusso@mce.hggm.es*

Human mesenchymal stem cells (hMSCs) migrate towards sites of inflammation and tumors as part of tissue remodeling processes. This behavior of hMSCs has been exploited as a tumor-targeting strategy for cell-based cancer therapy. Intraperitoneally (i.p.) injected hMSCs in mice migrate away from the peritoneal cavity, homing in tumor beds, although it is challenging to visualize this process in vivo. Labeling hMSCs with 111In-oxine provides a noninvasive method to longitudinally track and quantify the fate of administered hMSCs in vivo. Methods: For cell labeling, 7.5 million cells were incubated during 30 min with 111In-oxine in 1ml of PBS (10 Bq per cell). Labeling yield was calculated by dividing activity linked to cells by total activity (activity in cells and supernatant). Five BalbC-SCID immunodeficient mice with a subcutaneous xenograft of a neuroblastoma cell line (NB 1691) were used in this study: Four received 1 million 111In-labeled hMSC in 0.5 mL PBS i.p.; one control animal received 3.3 MBq of free 111In-oxine i.p. SPECT (uSPECT, MyLabs) and MRI (7T Bruker Biospin) images were obtained 24 and 48 hours after the injection (SPECT parameters: 1.5-2 h acquisition time, 80-500 keV window; MRI parameters: TurboRARE T2, TE=15.9 ms, TR=3425 ms, FOV= 6 x 4.13 cm). In order to co-register the SPECT and MRI images, each animal was placed on a homemade multimodal bed surrounded by three capillaries filled with a mixture of 99mTc and CuSO4, thus being visible in both modalities. Using two different SPECT radiotracers allowed us to reconstruct separately the capillaries and animal images, using the respective radioisotope photopeaks (140 keV for 99mTc and 171 + 245 keV for 111In). The spatial transformation between the SPECT and MRI images was obtained by segmenting the three capillaries in both modalities and applying the Iterative Closest Point (ICO) algorithm to both point sets. Registrations were applied to MRI images. Regions of interest (ROIs) were selected on tumor and abdomen in the MRI at each time point and these ROIs were applied to the SPECT in order to obtain the mean activity. Direct organ-activity counting was performed in the control and one hMSCs-injected animal. Results and discussion: Incubation of hMSCs resulted in a labeling efficiency of 80±6.9%, previous experiments showed survival of 80% of labeled hMSCs immediately after labeling. Figure 1 shows the mean activity in the tumor and in the abdomen 24 and 48 hour after the injection. hMSCs-injected animals showed an increased uptake in the tumor area at 48h, while the control just showed some activity at 24 h (perhaps due to spill over from the abdominal cavity), decreasing at 48 h. After injection, a number of cells seem to get trapped in the reticuloendothelial system (liver, bone marrow) thus reducing the available number of homing cells. The decrease of abdominal activity in animals 2 and 4 could indicate a migration from the abdomen to different organs. In conclusion, we have been able to detect homing of hMSCs towards a tumor in 24/48 h. Cell trapping when using intravenous or intraperitoneal administration might be overcome through direct intracardiac injection.

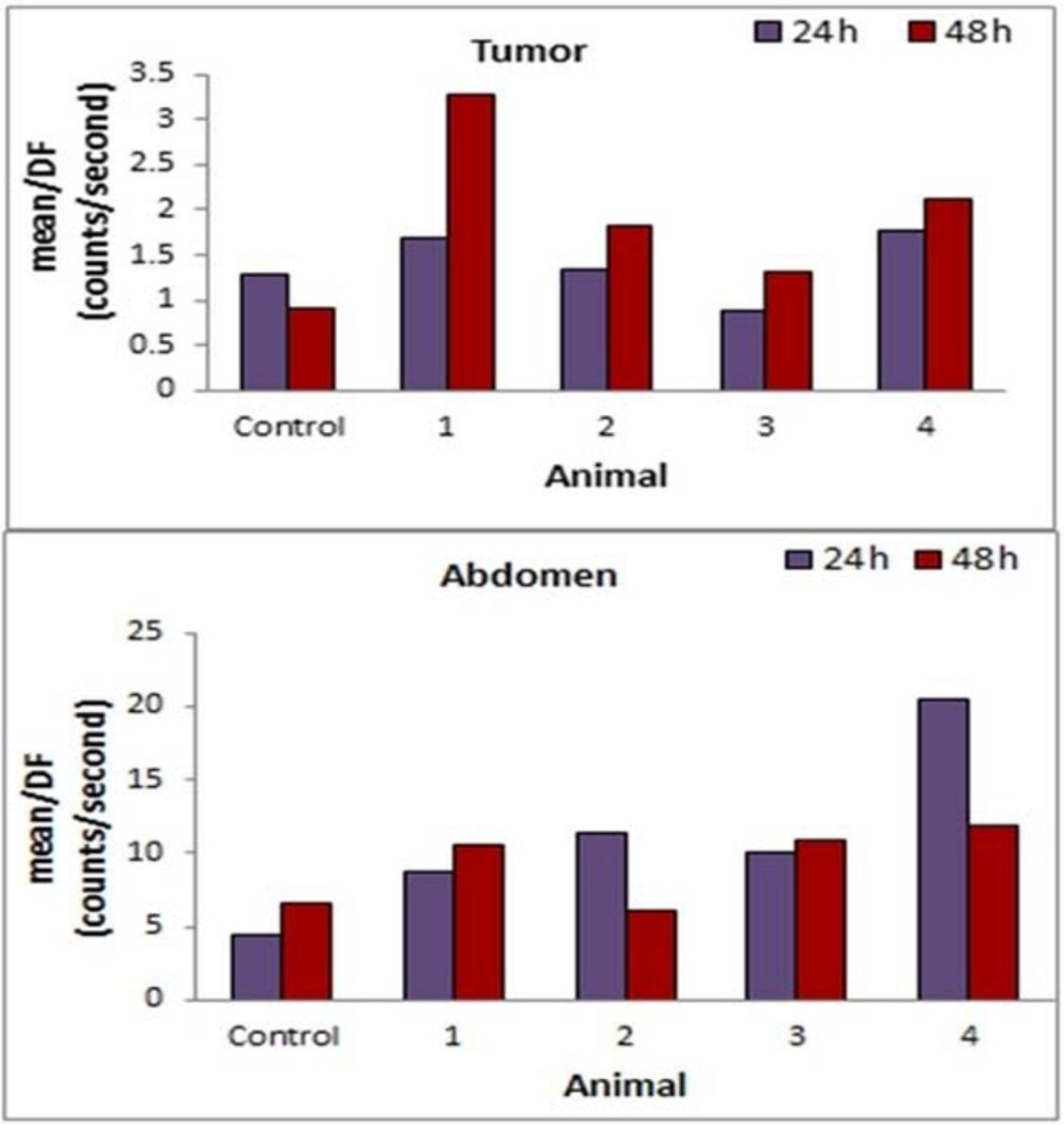

Figure 1. Both plots represent the mean activity corrected by the decay factor (DF) per animal. Top: Tumor activity increases 48 hours after the 111In-labeled hMSCs injection. Bottom: animals show similar uptake at both time points. Cells in animals 2 and 4 could migrate from the abdomen to different organs.

Disclosure of author financial interest or relationships:
L. Cussó, None; **I. Mirones**, None; **S. Peña Zalbidea**, None; **L.M. López-Sánchez**, None; **V. Garcia-Vazquez**, None; **J. García-Castro**, None; **M. Desco**, None.

Presentation Number **P 047**
Poster Session 1
September 18, 2013 / 18:00-18:00 / Room: Exhibit Hall B

Tracking of mesenchymal stem cells labeled with Gd-DTPA by MR imaging in cerebral ischemia model

Kuan Geng, De-xiao Huang, **Renhua Wu**, *Department of Medical Imaging, Shantou University Medical College, Shantou, China. Contact e-mail: gszhang_1@163.com*

Objective Recent developments in stem cell and gene therapy will require methods to monitor stem cell survival and integration repeatedly and non-invasively with a high temporal and spatial resolution in vivo.The aim of the study was to explore the possibility of the rat mesenchymal stem cells (MSCs) labeled with standard contrast agents (Gd-DTPA) for stem cell tracking. Methods MSCs from bilateral femur of rats were cultured and propagated.Intracellular uptake of Gd-DTPA was achieved by using a non-liposomal lipid transfection reagent (Effectene) as the transfection agent. Electron microscopy was performed to detect the distribution of Gd-DTPA particles in MSCs, and labeling efficiency of Gd-DTPA particles on MSCs was evaluated using spectrophotometric.Viability and proliferation of labeled MSCs were evaluated using MTT assay.Labeled MSCs were detected with T1-weighed MR imaging in vitro and in rat brain. Results The presence of Gd-DTPA particles inside the MSCs was definitely detected by transmission electron microscopy.Labeling efficiency was highly.There was no difference in viability and proliferation between the labeled and unlabeled confirmed by MTT values of light absorption.The labeled MSCs demonstrated the high signal intensity on T1-weighted MRI in vitro. Conclusion Rat MSCs can be labeled with Gd-DTPA particles without changing the cell viability and proliferation.Obviously labeled MSCs can be imaged in vitro and vivo. Gd-DTPA shows no evident adverse effect on the function of labeled MSCs. Gd-DTPA can be used for the MR imaging tracking of labeled MSCs

Disclosure of author financial interest or relationships:
K. Geng, None; **D. Huang**, None; **R. Wu**, None.

Presentation Number **P 048**
Poster Session 1
September 18, 2013 / 18:00-18:00 / Room: Exhibit Hall B

Effect of Mesenchymal Stem Cells on the Vascularization of the Artificial Cavity Used as a Site for Islet Transplantation

Daniel Jirak, *Andrea Galisova, Vít Herynek, Jan Kriz, Eva Fabryova, Milan Hajek, Department of Diagnostic and Interventional Radiology, Institute for Clinical and Experimental Medicine, Prague, Czech Republic. Contact e-mail: daji@ikem.cz*

Introduction It is estimated that at least 50% of pancreatic islets (PI) transplanted by portal vein infusion are destroyed within the first days owing to Instant Blood Mediated Inflammatory Reaction. In order to improve transplantation outcome, artificially created sites for PI transplantation are studied. The aim of our study was to verify the effect of isogeneic mesenchymal stem cells (MSC) on vascularization of the artificial cavities intended for PI transplantation implanted subcutaneously or into the greater omentum in a preclinical rat model by dynamic contrast-enhanced magnetic resonance imaging (DCE-MRI). Methods Two polymeric meshes shaped in rounded scaffolds (24x6 mm) were implanted both subcutaneously and into the greater omentum of Brown-Norway male rats (n=9). 15x106 syngeneic MSCs were injected into the scaffolds in 6 animals (+3 controls). MSC were isolated from epididymal fat and cultured for 4 weeks. MSC were characterized by specific antigens and by differentiation kit. The animals were scanned at a 4.7 T MR scanner 1 day and 1, 3, and 4 weeks after scaffold implantation. To assess the actual blood supply at the transplantation site, we analyzed the changes of the signal intensity observed within the scaffolds after the intravascular administration of a contrast agent Gadofosveset (60 µl) by DCE-MRI (3D gradient echo sequence was used with 32 repetitions, evolution delay = 5.0 s, resolution = 0.2x0.5x0.4 mm3). The regions of interest were manually outlined and mean pixel intensity was assessed for every cycle. All outcomes measured in the implanted devices were normalized to the signal intensity of kidney. Results/Discussion The significant production of VEGF by our MSCs and detection of specific surface markers by flow cytometry and the ability to differentiate into adipocytes and chondrocytes was confirmed. The implanted polymeric devices induced no adverse effects and did not cause any image artifacts. One week after the implantation, the connective tissue penetrated and covered the porous devices. On the day of implantation, no signal enhancement was detected in any device. However, over the following weeks, a signal increase in the omental device without MSC was detected (to 34% of the signal of the kidney week 1, 21% week 3, and 14% week 4). Within the subcutaneously implanted devices without MSC a signal increase of 11% (week 1), 10% (week 3), and 7% (week 4) of that detected in the kidney was detected. With MSC use, the signal intensity was higher in scaffolds both in great omentum (week 1: 42%, week 3: 41%, and week 4: 64%) and in subcutaneous tissue (week 1: 23%, week 3: 54%, and week 4: 52%). Conclusion MSCs isolated from adipose tissue demonstrated the considerable supportive effect of neoangiogenesis within polymeric scaffolds. Higher blood supply, crucial for PI graft survival, was verified by DCE-MRI. This method could also indicate the optimal time for islet implantation. Acknowledgement The study was supported by a grant project No. FR-TI3/521 (Ministry of Industry and Trade Czech Republic), MC grant - Beta Train, and by an Institutional grant 00023001IKEM (Ministry of Health, Czech Republic).

Disclosure of author financial interest or relationships:
D. Jirak, None; **A. Galisova**, None; **V. Herynek**, None; **J. Kriz**, None; **E. Fabryova**, None; **M. Hajek**, None.

Presentation Number **P 049**
Poster Session 1
September 18, 2013 / 18:00-18:00 / Room: Exhibit Hall B

Metabolite profiling of five kinds of human breast carcinoma cells in vitro 9.4T high resolution magnetic resonance (MR) spectroscopy

Miao miao Zhang[1], *Jie Zhang*[2], *Zhi-feng Xu*[3], *Yibing Chen*[4], *Yeyu Xiao*[1], *Ren hua Wu*[1], *Yaowen Chen*[5], [1]*Shantou University, Shantou, China;* [2]*Mental Health Center, the Medical College of Shantou University, Shantou, China;* [3]*Department of Medical Imaging, the First People's Hospital of Foshan, Foshan, China;* [4]*tSunYat-sen University Cancer Center, guang zhou, China;* [5]*The Central Laboratory of Shantou University, Shantou, China. Contact e-mail: zhangmmvip@hotmail.com*

Objective To get a more detailed understanding of the metabolic profiles and mechanisms of human breast carcinoma cells using 9.4T MR spectroscopy. Methods Five human breast carcinoma cell lines were used :lumina A (ER+/HER2-):MCF-7 /T47D cell lines;luminalB (ER+/HER2+) : ZR-75-1 cell line ; basical like(ER-/HER2-) : MDA-MB-231 cell line ;HER2-(ER-/HER2+): SKBR3 cell line . Cells were grown up to 80%-85% confluence at passage 4, the cells are cultured and collected(about 1.5×107,samples were n=10,the primary cells were bought from ATCC). The metabolics were extracted by perchloric acid and prepared for MRS analysis.1H proton spectra were acquired on 9.4T high resolution magnetic resonance (MR) spectroscopy and the concentrations of the main metabolites were quantified. Results Good 1H MR spectra of perchloric acid extract from five kinds of human breast carcinoma cells were obtained.MCF-7 and T47D cells significantly presented higher concentration of lactate and phosphocholine among five cells. Conclusion 9.4T MRS is an effective tool to measure the metabolic profiles of five kinds of human breast carcinoma cells .luminalA subtype could be distinguished by the higher concentration of lactate and phosphocholine among cell lines .representative of four subtype of breast cancer.

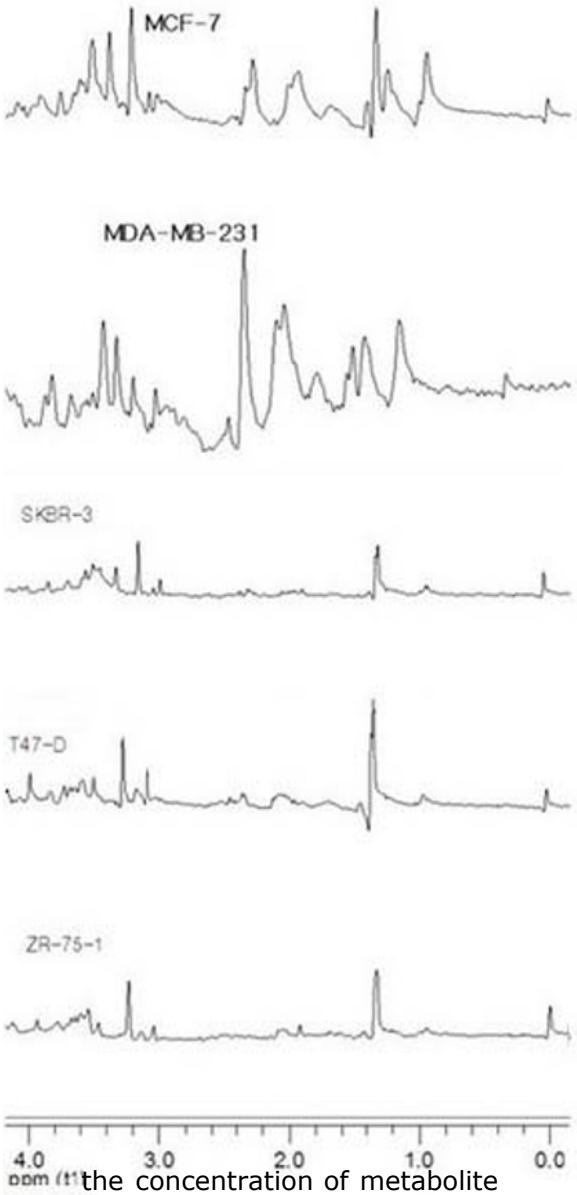

the concentration of metabolite

metabolite( )	MCF-7(1=8) nmol/mg	MDA-MB231(1=8) nmol/mg	T47-D(1=9) nmol/mg	SK-BR-3 (1=7) nmol/mg	ZR-75-1 (1=5) nmol/mg
myo-inositol(3.62ppm)	0.00670±0.0024	0.00006±0.00005	0.00843±0.002302	0.0051143±0.000935	0.00092±0.0003232326
Lysine (1.33ppm)	0.1012±0.00178** P=0.0092	0.0023±0.0009	0.008935±0.001481	0.0023857±0.000667	0.0034533±0.00078
scyllo-Inositol (3.35ppm)	0.02340±0.00471	0.00743±0.00131			
Phosphocholine (3.23ppm)	0.21130±0.04661* P=0.025	0.00218±0.00060	0.03437±0.003692	0.0064716±0.002141	0.0013222±0.000820(
Phosphocreatine (3.94ppm)	0.00755±0.00381	0.00068±0.00022	0.00929±0.003709	0.0012209±0.001765	0.0005915±0.00285
Valine (2.27ppm)	0.01778±0.00346	0.01024±0.00187			
Glutamate	0.007488±0.004016	0.0042725±0.001314			
Isoleucine (0.94ppm)	0.00139±0.00039	0.00024±0.00006			
Lysine	0.00228±0.00117	0.00015±0.00004			

Disclosure of author financial interest or relationships:

M. Zhang, None; **J. Zhang**, None; **Z. Xu**, None; **Y. Chen**, None; **Y. Xiao**, None; **R. Wu**, None; **Y. Chen**, None.

Presentation Number **P 050**
Poster Session 1
September 18, 2013 / 18:00-18:00 / Room: Exhibit Hall B

Detection of Antibacterial Response in Human Breast Milk

Rao V. Papineni, *University of Miami (adjunct), Branford, CT, USA. Contact e-mail: papineni@graduate.hku.hk*

Human milk apart from contributing to the growing nutritional requirements of infant also influences the infant immune system along with a degree of protection against pathogens. In addition, milk components are also postulated to play a major defense role in lactating breast against conditions such as mastitis. Substantial amounts of macrophages, neutrophils and lymphocytes along with epithelial and stem cells exist not only in colostrum, but also in mature milk. Further, milk is also a good source of microbes required to colonize the babies gut and likely play a role in the maturation of the infant's immune system. The bacterial genera include Weissella, Leuconostoc, Staphylococcus, Streptococcus and Lactococcus. The early response towards staphylococcus aureus (S. aureus) by the components in the breast milk is evaluated here in situ. The reactive oxygen species (ROS) activity was monitored real-time using L-012 (8-amino-5-chloro-7-phenylpyridol [3,4-d]pyridazine-1,4(2H,3H) dione), a chemiluminescence reporter. Mature breast milk collected from lactating caucasian mother at different days were challenged with S.aureus along with the ROS reporter. Luminescence resulting from the antibacterial activity of the breast milk, possible through the action of the polymorphonuclear leucocytes (PMN) within, is imaged real-time with the entire cellular, microbiome, and other milk components. Such methodologies described will be useful to assess the physical status of the breast milk especially when utilizing as a source for stem cells.

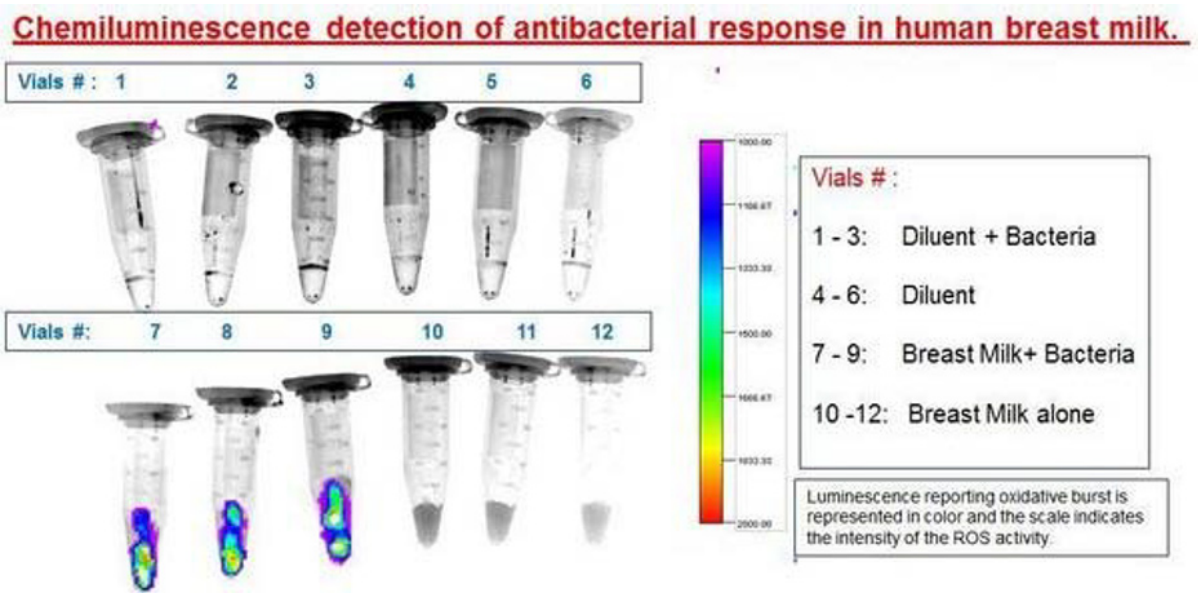

Disclosure of author financial interest or relationships:
R.V. Papineni, None.

Presentation Number **P 051**
Poster Session 1
September 18, 2013 / 18:00-18:00 / Room: Exhibit Hall B

Evaluation of Fluorescent Membrane Markers for Stem Cell Tracking

Yuzhen Wang[1], Brian D. Gray[2], Miles P. Smith[1], Koon Y. Pak[2], **Mary Rusckowski**[1], [1]*Radiology, University of Massachusetts Medical School, Worcester, MA, USA;* [2]*Molecular Targeting Technologies Inc., West Chester, PA, USA. Contact e-mail: Mary.Rusckowski@umassmed.edu*

Objectives: We are investigating a family of DiD dyes (ex 648 nm, em 667 nm) with variable length lipophilic aliphatic tails and carrying a DOTA for ^{111}In labeling to serve as a dual labeled membrane marker for cell tracking. The goal here is to optimize cell labeling efficiency and minimize dye transfer to neighboring cells to identify a stable membrane dye marker for cell tracking studies. **Methods**: Six dyes were synthesized each with the DiD fluorophore and two aliphatic tails of lengths from C3 to C22. LS174T colon cancer cells serving as a model cell were mixed with dyes at 2 uM and 10 uM. After incubation for 10 min at room temperature the labeled cells were combined with an equal number of unlabeled cells and co-cultured. Before and after labeling, cell viability was determined by trypan blue. Samples were collected at 0 h, 24 h and 48 h after initiation of co-culture in preparation for flow cytometry analysis. Unlabeled cells and a commercial dye served as reference. **Results**: Cells with each dye showed normal growth through 48 h with no obvious effects on proliferation and viability. The efficiency of the dyes for labeling cell membranes, based on fluorescence intensity per cell, was in the following order based on length of aliphatic tails: C14/C3> C22/C3> C22/C12> C14/C14> C22/C22> C20/C20. However, dyes showing the most efficient labeling also proved to be the ones with the greatest dye transfer which was shown to be the highest for C14/C3 and C22/C3. The dyes that showed good fluorescent intensity per cell and the least amount of dye transfer were C14/C14 and C22/C12, with about 5% and 10% transfer, respectively, through 48 h. Conversely, the two dyes with the two most lipophilic tails C20/C20 and C22/C22 showed similarly low fluorescent intensity per cell and dye transfer of about 20%-25% in 48 h. Transfer to an unlabeled cell population was most significant within 24 h with little change thereafter. In the case of these more lipophilic dyes the adherence to the cell membrane may be in part as micelles that with time dissociate and then partition within the membrane. **Conclusions**: The fluorescent markers identified here with carbon tails C14/C14 and C22/C12 provided the best staining intensity and lowest dye transfer of this series. These findings are critical to advance the dual stem cell marker for potential use in cell based therapy applications.

Disclosure of author financial interest or relationships:
Y. Wang, None; **B.D. Gray**, Molecular Targeting Technologies, Inc, Employment; **M.P. Smith**, None; **K.Y. Pak**, Molecular Targeting Technologies, Inc., Stockholder; Molecular Targeting Technologies, Inc., Employment; **M. Rusckowski**, None.

Presentation Number **P 052**
Poster Session 1
September 18, 2013 / 18:00-18:00 / Room: Exhibit Hall B

Flexible, mask-free, and semi-automated image processing protocol for quantification of in vivo single cell MRI following cell transplant

Margaret Bennewitz[3], *Ronen Globinsky*[2], *Xenophon Papademetris*[2], *Erik M. Shapiro*[1,2], [1]*Department of Radiology, Michigan State University, East Lansing, MI, USA;* [2]*Department of Diagnostic Radiology, Yale University School of Medicine, New Haven, CT, USA;* [3]*Department of Biomedical Engineering, Yale University, New Haven, CT, USA. Contact e-mail: maggiebe@mit.edu*

INTRODUCTION: Here we introduce an image processing method for semi-automated quantification of transplanted single cells in vivo using MRI. This method was validated on in vitro samples and implemented in vivo in rat brain. METHODS: Rat MSCs were labeled in culture with fluorescent MPIOs and CFSE, which labels the cytoplasm of live cells green. Labeled MSCs were suspended in 0.5% agarose with 1 mM gadoteridol at 100,000 cells/ml. A model of single, dispersed cells in the rat brain was created by intracardiac injection of 200,000 magnetically labeled, CFSE labeled MSCs. Animals remained under anesthesia for 1 - 1.5 hours before being imaged at 11.7T. Controls received unlabeled cells. 3D T2* gradient echo MRI of the agarose samples were acquired at 4.0 T at 50 μm3 and 100 μm3 isotropic resolution. MRI of live rats was performed at 11.7T using T2* weighted 3D gradient echo MRI at image resolution = 100 x 100 x 133.3 μm. Brain histology was performed and sections were analyzed for green CFSE stained MSCs with red MPIOs. Automated spot detection and quantification was accomplished using similar techniques as automated vessel detection (Joshi, et al, IEEE Trans. Vis. Comput. Graph.). In short, the Hessian matrix, or second derivative, and the associated Eigenvalues were calculated from the 3D T2* MRI data. The filter then selected for spherical shape (the signal voids of iron labeled cells are roughly spherical) by sorting and evaluating Eigenvalues for each voxel. The resulting Hessian images were thresholded to form 2D binary spot images, according to the image histogram, which isolated dark spots in the original MRI. Spots were quantified from the binary images through cluster thresholds. RESULTS and DISCUSSION: The iron content in labeled cells was 14 ± 0. 4 pg. Magnetically labeled single cells suspended in agarose produce dark spots on T2* weighted MRI. Comparison of the input and output images shows that the filter identifies nearly all of the spots present in the input image. A 3D output image is shown with all of the detected signal voids. Using clustering thresholds, 1,400 signal voids, or MPIO labeled MSCs, were enumerated. MRI of rats injected with labeled MSCs showed dark spots distributed throughout the whole brain - control animals had no spots. In vivo MRI was thresholded at two levels. The spot counts in the brain for low and high thresholds were: 7,765 signal voids were detected for the low threshold and 1,504 were detected at the higher one. This means that the true number of labeled MSCs in the brain after intracardiac injection is between 0.8% to 3.9% of the total number of injected cells. Histology was analyzed within imaging windows of 300 μm wide (which is 3x larger than a voxel on in vivo high resolution MRI). Out of 70 MSC identifications in histology slices, 67% were 1 labeled cell, 26% had 2 labeled cells, and 7% had 3 labeled cells. The results clearly indicate a dependence on image quality and contrast due to requirement of thresholding, yet for some applications, this level of accuracy may be sufficient. The benefit of this method over existing methods is that it requires no mask and can accommodate any spot size.

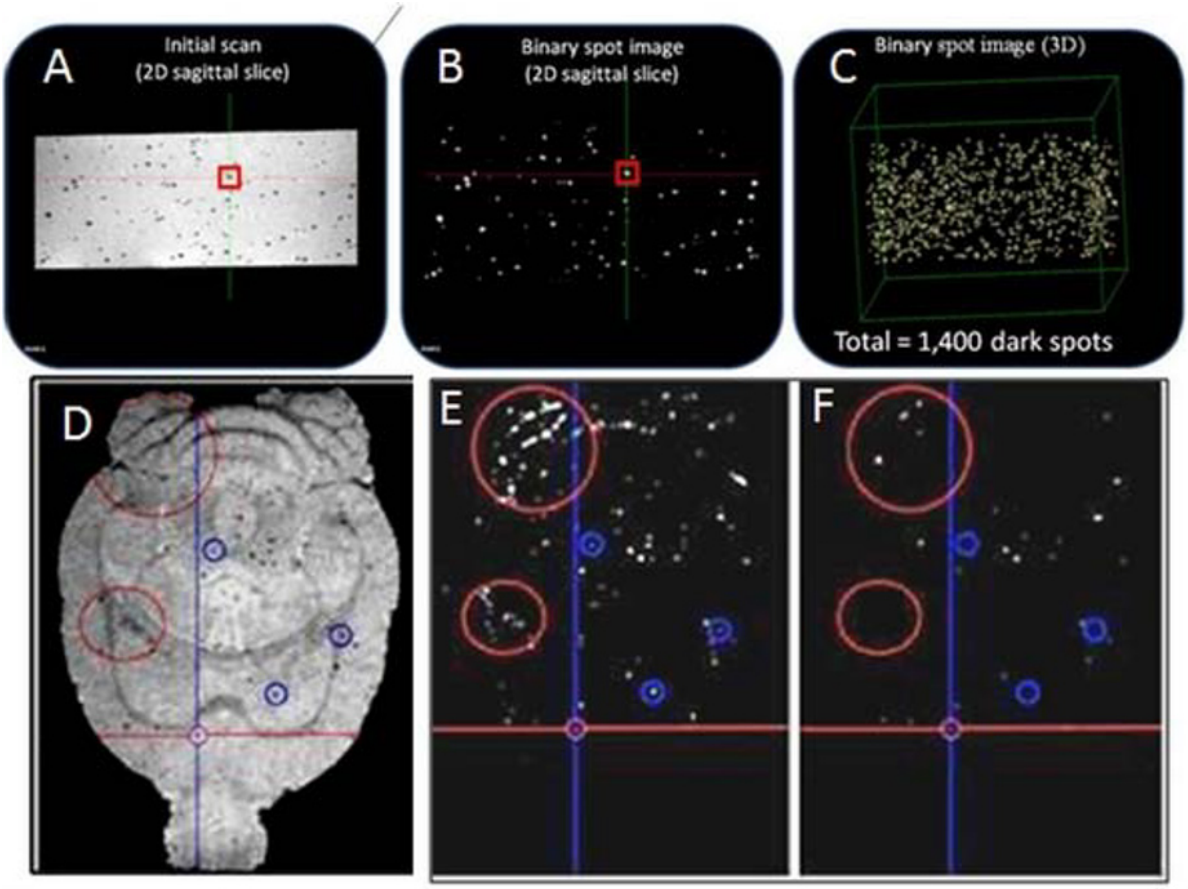

Figure 1: Automated sphere detection and quantification *in vitro* using image processing. A) 2D sagittal MRI slice of a 3D T_2* gradient echo scan of MPIO labeled cells in agarose. B) Corresponding spots identified by the automated sphere detection program, based on intensity and geometry. The output image shown here is a binary spot image. C) 3D compilation of detected spots (i.e. magnetically labeled cells) within the agarose sample. D) in vivo MRI of rat brain with labeled MSCs. E) Low threshold and F) high threshold detection of dark spots from single cells, in vivo.

Disclosure of author financial interest or relationships:
M. Bennewitz, None; **R. Globinsky**, None; **X. Papademetris**, None; **E.M. Shapiro**, None.

Presentation Number **P 053**
Poster Session 1
September 18, 2013 / 18:00-18:00 / Room: Exhibit Hall B

Mesenchymal Stem Cell Immunomodulation Effects on Graft-Versus-Host Disease as Determined with Cryo-imaging

Patiwet Wuttisarnwattana[1], *David L. Wilson*[1,2], *Kenneth R. Cooke*[3,4], *Saada Eid*[3,4], [1]*Biomedical Engineering, Case Western Reserve University, Cleveland, OH, USA;* [2]*Radiology, University Hospitals, Cleveland, OH, USA;* [3]*Pediatric Hematology and Oncology, University Hospitals, Cleveland, OH, USA;* [4]*Center for Stem Cell & Regenerative Medicine, National Center of Regenerative Medicine, Cleveland, OH, USA. Contact e-mail: pxw110@case.edu*

Introduction. Mesenchymal stem cells (MSCs) suppress graft-versus-host disease, and a variety of studies have shown their ability to inhibit T cell proliferation [1]. However, in vivo mechanisms of action following intravenous infusion are still relatively unknown, especially due to missing details of homing/bio-distribution [2]. In this study, we employed cryo-imaging [3] to study human MSCs (hMSCs) immunomodulation effects on T-lymphocytes (TCs) in an in vivo model of GVHD. Multispectral cryo-imaging uniquely provides 3D microscopic images of whole mouse with single cell sensitivity, enabling unique visualization/quantification of homing/biodistribution of hMSCs and their effect on TC proliferation. ***Methods.*** In experiments, we obtained splenic TCs and bone marrow cells (BMCs) from donor C57BL/6 mice. TCs were fluorescently labeled with CFSE dye [4]. After bone marrow transplantation (BMT), TCs were infused to syngeneic C57BL/6 mice (Syn, without GVHD) and allogeneic F1 hybrid mice (Allo, with GVHD). In the treatment arm, hMSCs were fluorescently labeled with red quantum dots and delivered to the mice 1 day after BMT. Mice were sacrificed and imaged at 1, 2, 3, 4, and 5 days post BMT. ***Analysis.*** We developed specialized image analysis and visualization software. Machine learning algorithms enabled detection of both red hMSCs and green TCs. Interactive visualization enabled exploration of homing/engraftment and hMSC co-localization with TC. Secondary lymphoid organs were analyzed in detail. Since TC CFSE dye disperses with clonal expansion [4], histogram analysis of TC brightness enables a TC proliferation assay. ***Results.*** Cryo-image datasets were processed and visually/quantitatively evaluated. An Allo mouse at day 2 shows the 3D biodistribution of TCs (Fig.A), hMSCs (Fig.B), and colocalization (Fig.C). Although TCs and hMSCs are found throughout the mouse, TCs are found primarily in lung, liver, spleen, lymph nodes, and GI-tract; and hMSCs are found primarily in lung, liver, spleen, and bone marrow. hMSCs home to marginal zone of the spleens. At day 4, the number of hMSCs in Allo spleens was ~8 times that in Syn spleens. Additionally, white pulp volume fraction (%WP) in Allo spleens was ~2 times that of Syn spleens. With the presence of hMSCs, the %WP was reduced by ~18% relative to the Allo without hMSCs. Moreover, we found that the percentage of high intensity TCs (%bright-TCs) in Allo spleens was ~ 54% less than that in Syn spleens, indicating rapid proliferation. With hMSCs treatment, %bright-TCs increased by ~224%. CFSE images (Fig D-F) clearly show that due to proliferation, signal intensity of Allo is much degraded as compared to Syn or Allo+hMSCs. ***Discussion.*** Cell labeling and 3D cryo-imaging uniquely allow one to determine homing/biodistribution of hMSCs and TCs. In GVHD (Allo as compared to Syn), spleens are larger, almost all due to increased white pulp. There is homing of hMSCs to spleen marginal zone in GVHD, reducing white pulp/spleen volume and TC proliferation. Results indicate that at least one mechanism for hMSC suppression of GVHD is due to MSC homing to lymphoid organs and in vivo inhibition of TC proliferation.

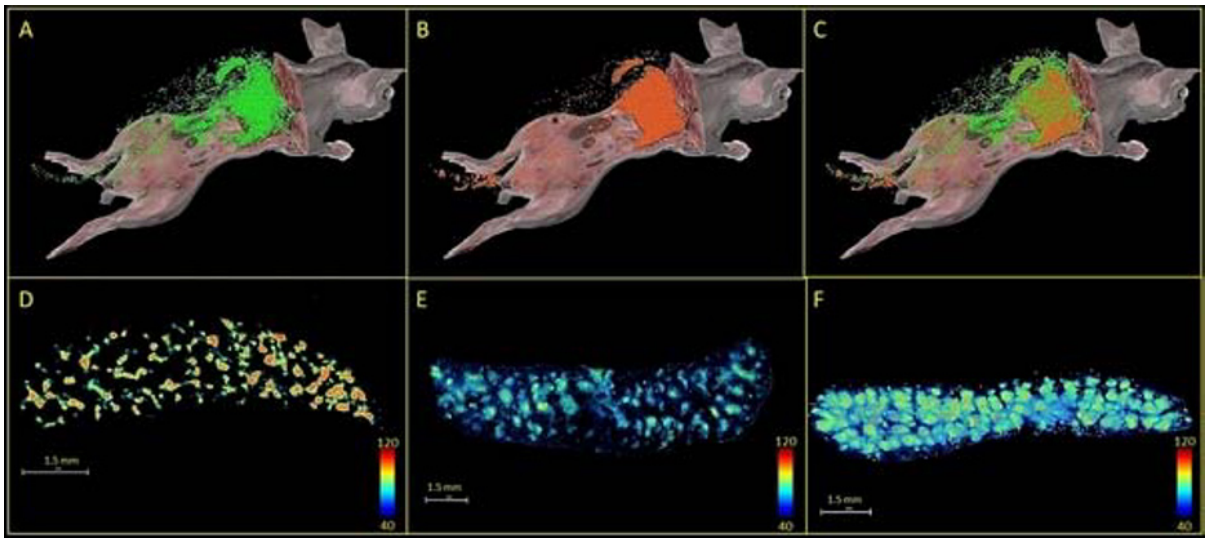

3D Visualizations of bio-distribution of CFSE-labeled T-cells (colored with green, A), redQD-labeled hMSCs (colored with orange, B) and both cell types (C) of an Allo mouse (48 hours post BMT). Colored maximum intensity projections of CFSE signals from Syn spleen (D), Allo spleen (E) and Allo+hMSCs spleen (F). The mice were imaged at 96 hours post BMT.

hMSC effect on alloT-cell proliferation in spleens

Spleen group (T=96 hrs)	Number of hMSCs or FPs found in the spleen (cells)	Splenic White Pulp size (mm^3)	% T-cells in the spleen that retained high intensity of CFSE
Syn+hMSCs	2195 ± 123.7	7.10 ± 1.6	63.4 ± 12.3%
Allo+hMSCs	1,535.5 ± 96.9	16.72 ± 1.5	28.9 ± 5.7%
Allo	62 ± 8.5	22.45 ± 3.2	12.9 ± 3.7%

MSCs homed to spleens of allogeneic mice specifically and preferentially; as observed by significantly number of hMSCs found in Allo+MSCs compare to the control. False positives were negligible small. Also T-cells that underwent clonal expansion in spleens of Allo+hMSCs was significantly less than that of Allo with no hMSCs. This can be observed by higher number of T-cells that retained more CFSE dyes.

Disclosure of author financial interest or relationships:

P. Wuttisarnwattana, None; **D.L. Wilson**, BioInVision, Inc., Stockholder; **K.R. Cooke**, None; **S. Eid**, None.

Presentation Number **P 054**
Poster Session 1
September 18, 2013 / 18:00-18:00 / Room: Exhibit Hall B

Diagnosis of Cardiac Involvement of Sarcoidosis Using 68Ga-DOTATAE Positron Emission Tomography

Ralph A. Bundschuh[1], *Constantin Lapa*[1], *Takahiro Higuchi*[1,2], [1]*Department of Nuclear Medicine, Universitätsklinikum Würzburg, Wuerzburg, Germany;* [2]*Comprehensive Heart Failure Center, Universitätsklinikum Würzburg, Wuerzburg, Germany. Contact e-mail: Bundschuh_R@klinik.uni-wuerzburg.de*

Introduction: Cardiac involvement of sarcoidosis is rare but has important influence on disease prognosis and is also of importance for therapy decisions. However accurate diagnosis is demanding and often done indirectly by cardiac function; delayed contrast enhancement in magnetic resonance tomography (MRT) provides important information but has limitations. Especially in patients with cardiac devices, diagnosis but also therapy monitoring is difficult and functional imaging may provide important information. As sarcoidosis is an inflammatory disease macrophage infiltration of the tissue may be imaged by 68Ga-DOTATAE Positron Emission Tomography/Computed Tomography (PET/CT). Methods: In this preliminary study we acquired 68Ga-DOTATAE PET/CT in 3 patients with histological proven sarcoidosis and clinical suspicion of cardiac involvement, none of the patient was under anti-inflammatory medication. Data was acquired 25 minutes after the injection of 92 - 127 MBq of 68Ga-DOTATE using a Siemens mCT 64 PET/CT. In addition to a whole body image, an additional data acquisition over the heart was performed using cardiac gated mode. Data was analyzed visually using a Siemens TrueD workstation. In addition polar maps were created to quantitatively analyze the DOTATE uptake. For comparison all patients underwent MRT examination including late contrast enhancement sequences. Results: Increased focal uptake was found in one of the three patients in the lateral wall of the left ventricle (Figure). This finding did correspond to the increased contrast uptake in the late enhancement MRT sequence. In the polar map of this patient in the corresponding segments DOTATAE uptake was 3.2 times higher as the mean value in the remaining segments. In the other two patients no increased uptake was identified visually and values in the polar map were in none of the segments higher as 0.5 times the mean value over all segments. Also in the cardiac MRT of these two patients no finding corresponding to active cardiac involvement was found. However in all patients DOTATATE uptake in the histopathological proven locations of sarcoidosis was found (mediastinal and hiliar lymph nodes in two patients and cutan lesion in one patient). Conclusions: Our preliminary study shows promising results, that 68Ga-DOTATAE may be an important tool for diagnosis and therapy monitoring of cardiac involvement of sarcoidosis. Minimal cardiac background is an important advantage of this tracer compared to for example fluorodesoxyglucose labeled with 18F. However, larger studies, perhaps including biopsy of the myocardium, are necessary to validate these findings. The relevance for therapy monitoring needs to be addressed as well in further studies.

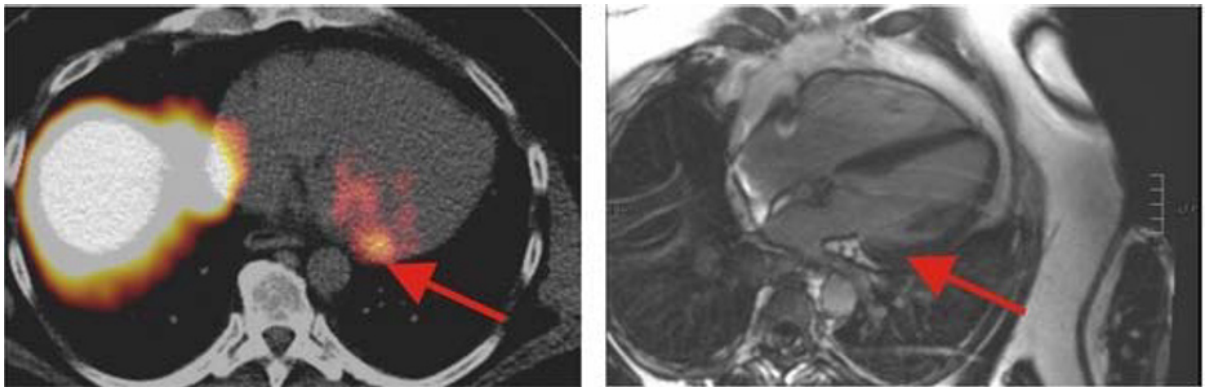

Patient 1 showing focal uptake in the lateral wall of the left ventricle in accordance with the late contrast enhancement in MRI.

Disclosure of author financial interest or relationships:
R.A. Bundschuh, Mediso Medical Imaging, Budapest, Hungary, Speakers bureau; **C. Lapa**, None; **T. Higuchi**, None.

Presentation Number **P 055**
Poster Session 1
September 18, 2013 / 18:00-18:00 / Room: Exhibit Hall B

Radiohalogenated Amino Acids Labeled with ^{76}Br and ^{123}I for Tumor Imaging with PET and SPECT

Jennifer L. Burkemper[1], *Chaofeng Huang*[1], *Liya Yuan*[2], *Amanda J. Roth*[1], *Efrem Mebrahtu*[1], *Jonathan McConathy*[1], *Suzanne Lapi*[1], [1]*Radiological Sciences, Washington University School of Medicine, Saint Louis, MO, USA;* [2]*Neurology, Washington University School of Medicine, Saint Louis, MO, USA. Contact e-mail: burkemperj@mir.wustl.edu*

Objectives: Radiolabeled amino acids are an important class of tumor imaging agents, and system A amino acid transport plays vital roles in cell growth and cellular responses to stressors. Radiotracers for system A with longer physical half-lives have the potential for achieving higher tumor to background ratios by allowing imaging at later time points and for wider ranges of distribution. The purpose of this work was to synthesize a novel ^{76}Br-labeled analogue of the previously reported compound IVAIB* and to compare the tumor imaging properties of these 2 radiohalogenated amino acids, (S)-2-amino-2-methyl-4-[^{123}I/^{76}Br]-iodo/bromo-3-(E)-butenoic acid (IVAIB and BrVAIB), in the mouse DBT model of glioma. Methods: The desired vinyl-trimethyl tin precursor was synthesized in four steps from the single isomer N-boc-α-methyl-L-serine. For iodination reactions, radiolabeling was accomplished with sodium [^{123}I]iodide, hydrogen peroxide and hydrochloric acid. Bromine labeling with successfully performed using chloramine T and ammonium [^{76}Br] bromide in phosphate buffered saline (PBS). Both compounds were deprotected under acidic conditions. Final products were isolated using ion-retardation resin in series with C-18 cartridges and then analyzed using chiral high performance liquid chromatography (HPLC). Biodistribution studies were conducted with IVAIB in BALB/c mice with subcutaneous DBT glioma tumors (n= 4 at each time point). Results: Both (S)-[^{76}Br]BrVAIB and (S)-[^{123}I]IVAIB were synthesized in good yields (50-60 % end of synthesis) with purities > 99%. Biodistribution studies demonstrated good uptake of [^{123}I]IVAIB 2.7 + 0.6 %ID/gram at 30 min in the DBT tumors with higher uptake in tumor than most normal tissues, 15.6 + 2.3 (tumor to brain) versus 1.9 + 0.1 (tumor to muscle). IVAIB showed a rapid uptake after 5 minutes and slow washout over the time studies (30 min to 24 hours) in the tumor tissue compared to more rapid washout in normal tissues. Maximal thyroid uptake occurred at the 5 min time point with 2.5 + 0.4 %ID/gram, indicating that the compound did not undergo significant de-iodination *in vivo*. Biological and imaging studies with [^{76}Br]BrVAIB are ongoing. *- Yu, W.; McConathy, J.; Olson, J.; Camp, V. M.; Goodman, M.M. J. Med. Chem. 2007, 50, 6718-6721.

Disclosure of author financial interest or relationships:
J.L. Burkemper, None; **C. Huang**, None; **L. Yuan**, None; **A.J. Roth**, None; **E. Mebrahtu**, None; **J. McConathy**, Eli Lilly/Avid, Consultant; Eli Lilly/Avid, Speakers bureau; Eli Lilly/Avid, Grant/research support; GE Healthcare, Grant/research support; **S. Lapi**, None.

Presentation Number **P 056**
Poster Session 1
September 18, 2013 / 18:00-18:00 / Room: Exhibit Hall B

Real-time handheld multispectral optoacoustic imaging on human volunteers

Andreas Buehler[1], *Neal Burton*[1,2], *Marcin Kacprowicz*[2], *Adrian Taruttis*[1,3], *Stefan Morscher*[1,2], *Vasilis Ntziachristos*[1,3], [1]*Institute for Biological and Medical Imaging, Helmholtz Zentrum Muenchen, Neuherberg, Germany;* [2]*iThera Medical GmbH, Munich, Germany;* [3]*Chair for Biological Imaging, Technische Universität München, Munich, Germany. Contact e-mail: andreas.buehler@helmholtz-muenchen.de*

Multispectral optoacoustic tomography (MSOT) promises the molecular specificity of imaging modalities such as optical imaging or PET while acquiring ultrasound signals, enabling the user to maintain resolution at depth. This molecular imaging modality has generated increasing academic interest over the last years with the availability of multiple commercial preclinical imaging systems. MSOT has recently been used to track tumor growth and metastasis using multiple genetic reporters, to track organ-specific pharmacokinetics of injected contrast agents, and detect molecular features of disease. These preclinical studies demonstrate the potential of MSOT to detect fast changes in molecular contrast in the clinic. In this work, we report on utilizing high power fast tuning laser technology, providing 100Hz pulses with a possible per pulse wavelength change, to build the first handheld video rate MSOT imaging device. We demonstrate the previously undocumented ability to dynamically resolve spectral features in the handheld imaging mode with scalable frame rates between 2 and 100 Hz and 100µm resolution, allowing the distinction in human subjects between large arteries and veins and microvasculature. We present handheld scanning of human limbs with multispectral real-time differentiation of several tissue chromophores including oxygenated and deoxygenated hemoglobin and melanin. The ability to quantify changes in oxygenation is demonstrated by induction of ischemia in a human subject with the application of a tourniquet. With the ability to perform label-free imaging and capture the fast dynamics of changes in oxygenation, MSOT is bridging the gap between preclinical and clinical imaging. Importantly, the potential of MSOT to quantify oxygenation not only in large vessels, but also in microvasculature and tissue, is demonstrated in this work.

Disclosure of author financial interest or relationships:
A. Buehler, None; **N. Burton**, iThera Medical, Employment; **M. Kacprowicz**, iThera Medical, Employment; **A. Taruttis**, None; **S. Morscher**, iThera Medical, Employment; **V. Ntziachristos**, iThera Medical, Stockholder; SurgOptix BV, Consultant .

Presentation Number **P 057**
Poster Session 1
September 18, 2013 / 18:00-18:00 / Room: Exhibit Hall B

In-Vivo Detection of activated platelets in myocardial infarction using antibody-coupled iron oxide micro particles

Moritz Braig[1], Alexander Maier[2], Marius Menza[1], Karlheinz Peter[3], Irene Neudorfer[2], Annette Merkle[1], Constantin von zur Muhlen[2], **Dominik von Elverfeldt**[1], *[1]Radiology, Medical Physics, University Medical Center, Freiburg, Germany; [2]Cardiology and Angiology I, University Medical Center, Freiburg, Germany; [3]Atherothrombosis and Vascular, Baker Heart Research Institute, Melbourne, VIC, Australia. Contact e-mail: dominik.elverfeldt@uniklinik-freiburg.de*

Localized inflammation following myocardial infarction is a cornerstone in myocardial healing and therefore great interest exists in specifically visualizing this process. Our study uses a contrast agent (LIBS-MPIO) targeted towards activated platelets in reperfused myocardium, to visualize areas of inflammation in the left ventricle after temporary ligation of the left anterior descending coronary artery (LAD) with MRI. The contrast agent consists of micro particles of iron oxide (MPIO) conjugated to a single chain antibody directed against ligand-induced binding sites (LIBS) on activated glycoprotein IIb/IIIa receptors (=LIBS-MPIO). It has already been successfully used to detect activated platelets in thrombosis1 and ruptured atherosclerotic plaques2 using the signal attenuation caused by accumulation of MPIOs. Our study utilizes LIBS-MPIO to detect activated platelets through signal attenuation in infarcted myocardium of the left ventricle. Ischemia-reperfusion injury was induced in 9-11 week old C57BL/6N mice by a 50 minute temporary ligation of the left anterior descending coronary artery (LAD). All animals were measured with the heart positioned in the iso-center using a cryocoil within a 7Tesla Bruker Biospec 70/20USR. After scouting, three slices in a pseudo short axis view were acquired using an ECG-triggered FLASH Protocol (four averages) with a slice thickness of 0.6 mm and a field of view of 2.5 cm x 2.5 cm (Matrix 256x192), resulting in an in plane resolution of 0.098 mm x 0.098 mm, with a factor of 1.34 of zero filling in phase direction (TE/TR:2.8 ms/34 ms, Flip Angle= 50°) following an intravenous contrast agent injection LIBS-MPIO or control MPIO into a tail vein. The time course of the contrast agent was followed in at least five scans over a minimum of 45 minutes. Afterwards an injection of a gadolinium based contrast agent (MultiHance™ 0.4 ml/kg) and continuous measurements for further 45 minutes with the same protocol were performed. Infarct size and accumulation of LIBS-MPIO was then validated with Histology. Image data is processed using Matlab (The MathWorks, Inc., Natick). Endo and Epicardium of the left ventricle are manually segmented and fragmented in each slice and signal intensities are compared to the septum. Evidence of LIBS-MPIO was visible through signal attenuation in parts of the myocardium of the left ventricle in the LIBS MPIO group, whereas the control group showed no signal loss within the left myocardium. Both groups showed signal enhancement in infarcted regions after MultiHance™ injection with correlation to area of signal attenuation in the LIBS-MPIO group, obtained post LIBS-MPIO contrast agent injection. Histology confirmed accumulation of LIBS-MPIO. 1. Muhlen, C. von zur et al. Magnetic Resonance Imaging Contrast Agent Targeted Toward Activated Platelets Allows In Vivo Detection of Thrombosis and Monitoring of Thrombolysis. Circulation 118, 258-267 (2008). 2. Von Elverfeldt, D. et al. In Vivo Detection of Activated Platelets Allows Characterizing Rupture of Atherosclerotic Plaques with Molecular Magnetic Resonance Imaging in Mice. PLoS ONE 7, e45008 (2012).

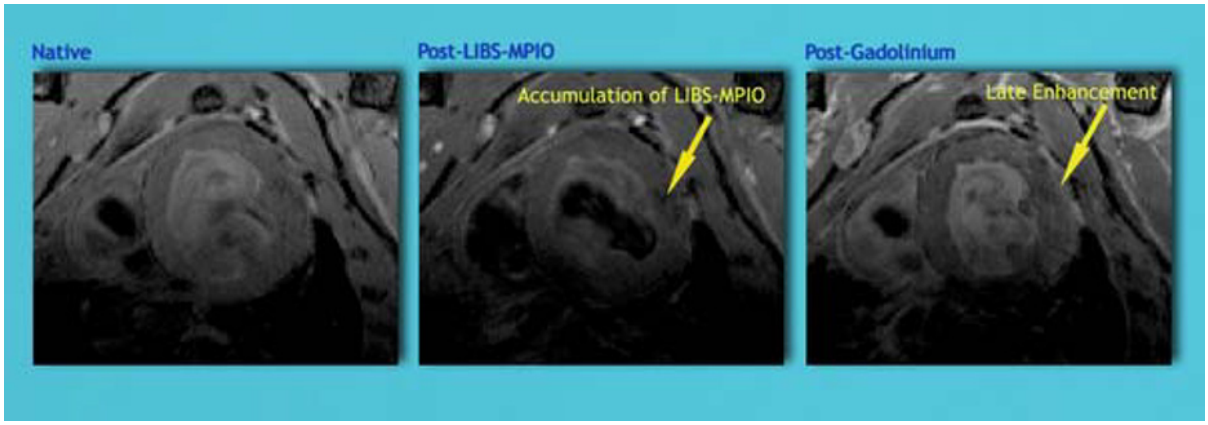

Disclosure of author financial interest or relationships:
M. Braig, None; **A. Maier**, None; **M. Menza**, None; **K. Peter**, None; **I. Neudorfer**, None; **A. Merkle**, None; **C. von zur Muhlen**, None; **D. von Elverfeldt**, None.

Presentation Number **P 058**
Poster Session 1
September 18, 2013 / 18:00-18:00 / Room: Exhibit Hall B

In vivo and in vitro imaging tracing of transplanted dual-labeled bone mesenchymal stem cells into myocardium of SD rats

Jian Cao, *Yining Wang, Hua dan Xue, Jing Lei, Zhengyu Jin, Radiology, Peking Union Medical Collage Hospital, Beijing, China. Contact e-mail: libracao@126.com*

Objective: To investigate the feasibility of in vitro and in vivo magnetic resonance imaging (MRI) and fluorescence imaging tracing of transplanted bone mesenchymal stem cells (BMSCs), dual-labeled with ultrasmall superparamagnetic iron oxide (USPIO) and firefly luciferase (Fluc) reporter gene. Methods: Fluc transfected BMSCs were incubated with 40μg/ml USPIO and 1.5μg/ml poly-l-lysine (PLL) for 24 hrs. The Prussian-blue staining, transmission electron microscope (TEM) and Trypan-Blue stain were used to determine the efficacy and safety of labeling. In vitro, T2 mapping and the T2* mapping sequence were selected to study the correlation between the number of labeled cells and MR signals, and fluorescence detector was used to detect the fluorescence intensity. Acute myocardial infarction model of SD rats (n=10) were established by ligating the left anterior descending coronary artery. The dual-labeled BMSCs were injected into the margin of the infraction myocardium. Then MR and fluorescence imaging were performed to trace the cells both in vitro and in vivo. Postmortal pathological study was carried out to observe the distribution of transplanted cells in myocardium. Results: The percentage of dual-labeled BMSCs reached up to 99% after coincubating with USPIO for 24 hrs. USPIO particles were mainly located in lysosomes. There was no significant diference in viability between the labeled and unlabeled groups demonstrated by Trypan-Blue stain. MRI was sensitive in detecting USPIO labeled cells in vitro, T2 and T2* value could be quantitatively measured by T2 and T2* mapping sequences. In addition, linear correlations between cell numbers and R2 or R2* values were calculated. The fluorescence intensity showed a cell concentration of 5.0×105/ml was strongly detectable. In vivo, the dual-labeled transplanted BMSCs showed a significant decreasing signal on MRI, and signal intensity changes had no significant difference over 4 weeks (P=0.66). In vitro cell tracing with fluorescence imaging of isolated heart from SD rats was successful, while in vivo cell tracing with fluorescence imaging was unsuccessful. Prussian blue staining showed USPIO distributed near the infracted myocardium, corresponding with the fluorescence imaging. Conclusion :MRI can be used to trace the dual-labeled BMSCs both in vitro and in vivo, while fluorescence imaging and pathological fluorescence imaging can trace the transplanted cells in vitro.

Disclosure of author financial interest or relationships:
J. Cao, None; **Y. Wang**, None; **H. Xue**, None; **J. Lei**, None; **Z. Jin**, None.

Presentation Number **P 059**
Poster Session 1
September 18, 2013 / 18:00-18:00 / Room: Exhibit Hall B

Alterations in cardiac fatty acid metabolism in non-obese type 2 diabetic rats

Sriram Devanathan[1], *Samuel T. Nemanich*[1], *Attila Kovacs*[2], *Nicole Fettig*[1], *Robert J. Gropler*[1], *Kooresh I. Shoghi*[1], [1]*Radiology, Washington University in Saint Louis, Saint Louis, MO, USA;* [2]*Medicine, Washington University School of Medicine, Saint Louis, MO, USA. Contact e-mail: devanathans@mir.wustl.edu*

Lipotoxicity of heart has been implicated as a leading cause of morbidity in Type 2 Diabetes Mellitus (T2DM). Numerous reports have demonstrated increased fatty acid (FA) utilization in cardiac cells of obese T2DM animal models. Although nearly 20% of the population with T2DM is non-obese, the phenotype of cardiac FA metabolism in non-obese animals is yet to be demonstrated. Therefore, the present study investigates the interplay between cardiomyocyte FA metabolism and cardiac function in a non-obese animal model of T2DM. Studies were conducted in Goto-Kakazaki (GK)/Wistar rats at the age of 24 weeks. Each rat was imaged with small animal positron emission tomography (PET) to estimate myocardial FA metabolism. Imaging was performed using 11C-palmitate (20 min.) to quantify myocardial fatty acid utilization. Expression levels of genes involved in fatty acid metabolism (84 genes) were measured by qPCR. Cardiac function was assessed by Echocardiograms (ECHOs). In addition, plasma levels of triglycerides (TG) and free fatty acids (FFA) were measured. Analysis of PET Data indicates that GK rats have lower myocardial blood flow and increased fatty acid utilization, primarily attributed the increase in fatty acid oxidation. Expression analysis shows that 18 of the 84 pathway specific genes involved in FA metabolism were up-regulated between 1.5 and 14 fold ($P<0.05$) in GK rat cardiomyocyte, while there were no significant differences in peripheral FFA concentrations between GK and Wistar rats. A majority of these genes were from the Acyl-CoA Dehydrogenase (Acad), Acyl-CoA Thioesterase (Acot), and Acyl-CoA Synthetase (Acsl) family, which indicates that the cardiac cells of non-obese diabetic rats have enhanced fatty acid utilization. Similarly, while we observed increased expression of genes encoding Lipase (Lipe) and Lipoprotein Lipase (Lpl), which are involved in TG catabolism, there were no measurable differences in plasma TG levels. ECHO data showed that GK rats have significantly ($P<0.05$) higher left ventricle mass index (LVMI) compared to Wistar rats suggesting increased contractile impairment and diastolic dysfunction. Furthermore, there was a significant ($P<0.05$) reduction in peak mitral annular velocity (E'), indicating further reduced diastolic function. Overall, our data supports the notion that GK rats exhibit alternations in FA utilization independent of obesity.

Alterations in cardiac fatty acid metabolism in non-obese type 2 diabetic rats

Sriram Devanathan[1], Samuel T. Nemanich[1], Attila Kovacs[2], Nicole Fettig[1], Robert J. Gropler[1], Kooresh I.

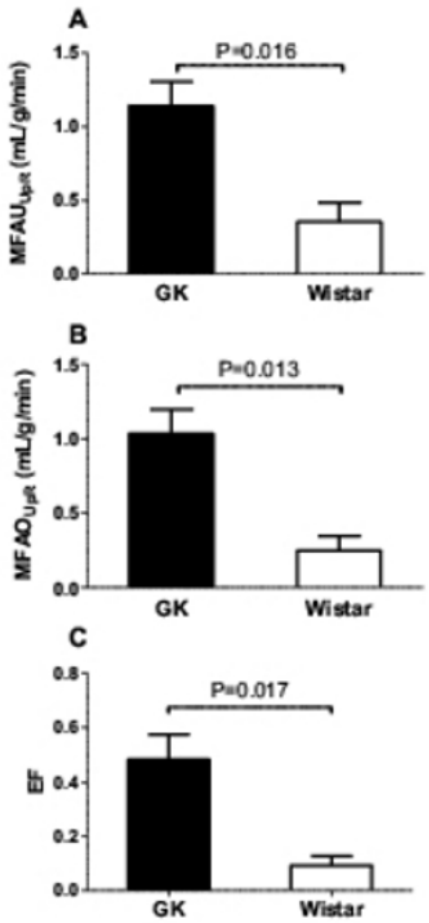

Figure 1

PET measures of myocardial fatty acid metabolism and blood flow. **(A)** Intrinsic myocardial fatty acid utilization rate ($MFAU_{UbR}$) **(B)** intrinsic myocardial fatty acid oxidation rate ($MFAO_{UpR}$), **(C)** myocardial EF in GK and control rats. $MFAO_{UbR}$ and $MFAU_{UpR}$ represent the intrinsic capacity of the heart to oxidize and utilize fatty acids, respectively, independent of the concentration of free fatty acids in plasma. *denotes that GK rats are significantly different ($P<0.05$) than Wistars for that measurement. All results are presented as mean ± 1 SEM with N=4/group.

Disclosure of author financial interest or relationships:

S. Devanathan, None; **S.T. Nemanich**, None; **A. Kovacs**, None; **N. Fettig**, None; **R.J. Gropler**, astellas, Grant/research support; avid, Grant/research support; pfizer, Grant/research support; astellas, Consultant; astellas, Speakers bureau; **K.I. Shoghi**, None.

Presentation Number **P 060**
Poster Session 1
September 18, 2013 / 18:00-18:00 / Room: Exhibit Hall B

PET Imaging of Angiogenesis in Murine Hindlimb Ischemia with a ^{64}Cu-Labeled Anti-CD105 Monoclonal Antibody

Hakan Orbay, *Yin Zhang, Hao Hong, Todd E. Barnhart, Weibo Cai, Radiology, Univ of Wisconsin, Madison, WI, USA. Contact e-mail: horbay@uwhealth.org*

Objectives : Peripheral arterial disease (PAD) affects >10% of adults in the US, which frequently involves the circulation of the lower extremities. CD105 (i.e. endoglin) is overexpressed on proliferating endothelial cells and is a promising target for in vivo vascular imaging. The goal of this study was to use ^{64}Cu-NOTA-TRC105 (TRC105 is a chimeric IgG1 monoclonal antibody that bind to both human and murine CD105 with high avidity) positron emission tomography (PET) for non-invasive and quantitative assessment of angiogenesis in a murine hindlimb ischemia model of PAD. Methods : Binding affinity and specificity of NOTA-conjugated TRC105 was evaluated by flow cytometry and microscopy. BALB/c mice (n = 15) were anesthetized and the right femoral artery was ligated to induce hindlimb ischemia, which was confirmed with laser Doppler and PET imaging (the left hindlimb served as an internal control). Ischemia-induced angiogenesis was monitored and quantified with ^{64}Cu-NOTA-TRC105 PET at postoperative days 1, 3, 10, 17, and 24. On the basis of our previous experience on in vivo PET imaging with TRC105-based agents, the time points of 4, 24, and 48 h post-injection (p.i.) were chosen for serial PET scans. Biodistribution studies were performed on days 10 and 24 in separate cohorts of mice. Histology and RT-PCR were also carried out to detect CD105 expression after ischemia. Results : NOTA-TRC105 specifically bound to CD105 in cultured endothelium. Laser Doppler imaging showed that perfusion in ischemic hindlimbs plummeted to ~10% of the contralateral hindlimb after surgery, similar as PET findings, and gradually recovered to near normal levels on day 24. The plateaued uptake of ^{64}Cu-NOTA-TRC105 in ischemic hindlimbs was observed at 48 h p.i., and was 9.0 ± 2.2, 14.1 ± 1.9, 11.4 ± 1.5, 6.2 ± 1.5, 3.4 ± 1.9 %ID/g at days 1, 3, 10, 17, and 24 after surgery (n = 3), which was significantly higher ($P<0.05$) than that of the non-ischemic control hindlimbs (2.0 ± 0.4, 1.6 ± 0.2, 2.5 ± 0.5, 0.4 ± 0.3, 0.7 ± 0.3 %ID/g at days 1, 3, 10, 17 and 24; n = 3). ^{64}Cu-NOTA-TRC105 uptake in the ischemic limbs on days 3 and 10 were significantly higher than all the other days ($P<0.05$), which correlated well with the findings based on γ-counting. Histological assessment revealed increased CD105 expression on days 3 & 10. Based on RT-PCR, there was ~50 fold increase in CD105 expression on day 3. Conclusions : This is the first report on PET imaging of CD105 expression during angiogenesis following hindlimb ischemia. Rapid, persistent, and CD105-specific uptake of ^{64}Cu-NOTA-TRC105 in the ischemic hindlimb was observed, which was validated by various in vitro and in vivo experiments. ^{64}Cu-NOTA-TRC105 PET can play multiple roles in future PAD-related research, and improve PAD patient management by identifying the optimal time for therapeutic intervention and monitoring the efficacy of therapy.

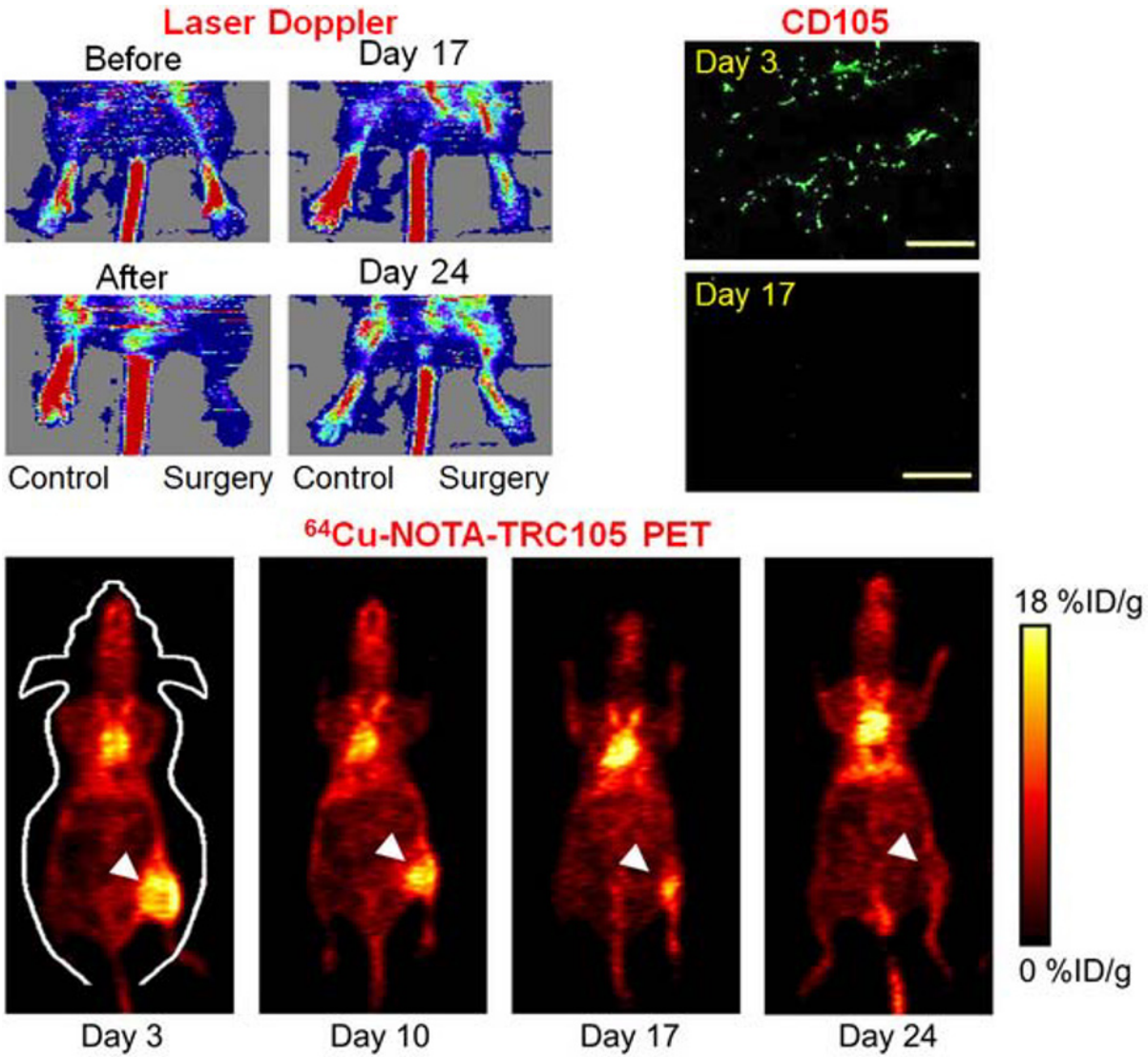

Disclosure of author financial interest or relationships:
H. Orbay, None; **Y. Zhang**, None; **H. Hong**, None; **T.E. Barnhart**, None; **W. Cai**, None.

Presentation Number **P 061**
Poster Session 1
September 18, 2013 / 18:00-18:00 / Room: Exhibit Hall B

VEGF-loaded Graphene Oxide as Theranostics for Multi-Modality Imaging-Monitored Targeting Therapeutic Angiogenesis of Ischemic Muscle

Peng Huang, *Zhongchan Sun, Jing Lin, Gang Niu, Xiaoyuan (Shawn) Chen, National Institutes of Health, Bethesda, MD, USA. Contact e-mail: penghuang2011@gmail.com*

Peripheral vascular disease (PAD) is one of most common vascular diseases in the world. PAD mainly involves the impairment of blood flow to the extremities, resulting from common cardiovascular morbidities such as atherosclerotic occlusive disease, diabetes mellitus, hyperlipidemia and so on. Therapeutic angiogenesis, which aims to stimulate new blood vessel formation via the sprouting and branching of existing vessels in ischemic tissues, has received extensive attention for PAD treatment. Successfully therapeutic angiogenesis depends on i) the targeted delivery of various growth factors such as vascular endothelial growth factor (VEGF) to ischemic tissues, and ii) the sustained high concentration of growth factors in ischemic tissues. Inspired by the targeted drug delivery for tumor therapy using nanocarriers, some efforts have been made towards the targeted delivery of VEGF to ischemic sites. Herein we report the design and synthesis of multifunctional VEGF-loaded IR800-conjugated graphene oxide (GO-IR800-VEGF) for multi-modality imaging-monitored targeting therapeutic angiogenesis of ischemic muscle. The as-prepared GO-IR800-VEGF can specifically and efficiently target ischemic muscle tissues in the murine hindlimb ischemic model. The real-time in vivo pharmacokinetics and biodistribution of GO-IR800-VEGF could be continuously monitored by near-infrared (NIR) fluorescence imaging. Both active and passive targeting of GO-IR800-VEGF can lead to highly local VEGF concentration in ischemic tissue. The successfully therapeutic angiogenesis of ischemic muscle was monitored by multiple imaging modalities including Laser Doppler Imaging (LDI), photoacoustic (PA), and PET imaging and furtherly evidenced by the immunostaining of CD31 and α-SMA. This targeted delivery of VEGF to ischemic tissue translated into potent therapeutic angiogenesis effect, which in turn led to significant therapeutic benefit in terms of oxygen delivery.

Disclosure of author financial interest or relationships:
P. Huang, None; **Z. Sun**, None; **J. Lin**, None; **G. Niu**, None; **X. Chen**, None.

Presentation Number **P 062**
Poster Session 1
September 18, 2013 / 18:00-18:00 / Room: Exhibit Hall B

RAGE imaging documents the beneficial effect of glucose control on atherosclerotic progression in apoE null mice both with and without diabetes

Yared Tekabe, *Lynne Johnson, Maria Kollaros, Medicine, Columbia University, New York, NY, USA. Contact e-mail: yt2166@columbia.edu*

Purpose: Receptor for Advanced Glycation Endproducts (RAGE) binds AGEs and other inflammatory ligands and is expressed in atherosclerotic plaques in diabetic and non-diabetic subjects. The higher expression in diabetes mellitus (DM) corresponds with accelerated course of the disease. We have previously shown that RAGE expression in aortic atheroma can be imaged in vivo in apoE null mice using Tc-99m-anti-RAGE F(ab')2 and SPECT/CT imaging and that uptake is greater in diabetic compared to non-diabetic mice. The purpose of this study was to show that control of blood glucose levels in diabetic mice would lead to reduced RAGE expression and reduced atherosclerosis compared to uncontrolled diabetics and that this difference can be detected on in-vivo SPECT imaging. Methods: Thirty apoE null mice (6 weeks) were given STZ and after 6 weeks 15 began treatment with 2 insulin implants (LinBits for mice) with weekly monitoring of blood glucose and additional implants for blood glucose > 200 mg/dL. At end of 15 weeks, all mice were injected with Tc-99m-anti-RAGE F(ab')2 (15.14 ± 1.23 MBq) and CT contrast agent (eXIA 160XL) and underwent SPECT/CT imaging (Bioscan nano-SPECT/CT). Animals were sacrificed, the proximal aorta removed and counted to calculate the percentage of injected dose per gram (%ID/g) RAGE uptake, followed by histological and immunohistochemical characterization. ROIs were drawn over uptake of radiotracer in the aorta and neck vessels using the contrast angiogram to identify vessels and quantified in mCi using InVivoScope software. Results: Radiotracer uptake in the proximal aorta, arch, and neck vessels was visibly less in the treated compared to non-treated and supported by the quantitative results for %ID: 0.45 ± 0.34 x 10-4 vs. 0.78 ± 0.28 x 10-4 (P = 0.007). The mean blood glucose levels for the duration in treated mice were 144 ± 14 mg/dL and for the controls 348 ± 60 mg/dL. RAGE uptake correlated with quantitative RAGE staining in the atheroma and there was a significant correlation between %ID from scans vs. %ID/g (R = 0.60, P = 0.023). The lesion size as percent cross sectional area was significantly smaller in the treated (14.3 ± 7.8%) vs. untreated (29.5 ± 10.9%) (P = 0.03). Conclusion: These data further support the important role of RAGE expression in atherosclerosis in diabetes, the value of in-vivo imaging of RAGE expression in atherosclerosis, and the value of glucose control to reduce atherosclerotic burden.

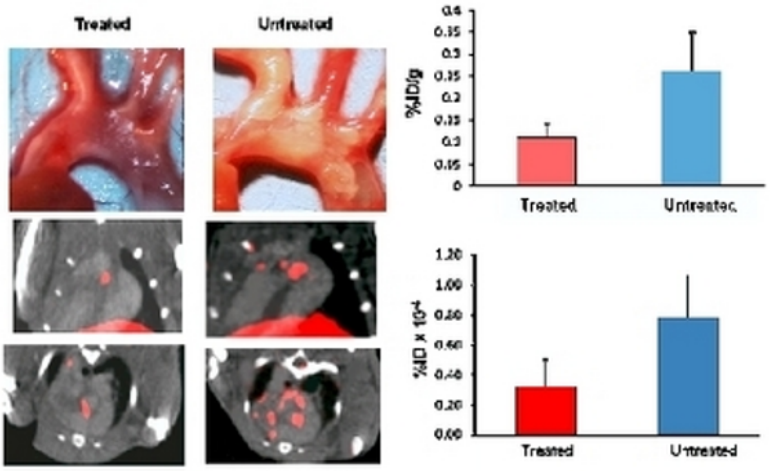

Pictures show pathology and imaging. Top panel: Dissected aortic arch and great vessels showing more extensive atheroma in the untreated compared to the insulin treated mice. Middle and lower panels show coronal (middle and transverse (bottom) slices from insulin treated mouse (on left) and untreated mouse (on right). The CT contrast outlines the ventricular cavities and arterial vessels. Uptake of the ^{99m}Tc anti-RAGE F(ab')$_2$ is seen localized to the aortic root, aortic arch and proximal branches (red color) on the untreated mouse and only to the aortic root on the treated mouse. Graphs on right show on top mean ± SD values for uptake of radioactive probe in the aortic root, arch, and proximal branch vessels from the scans in treated (red) vs. untreated (blue) experiments. The bottom graph on right shows results from well counting of tissue from treated (light red) and untreated (light blue) experiments.

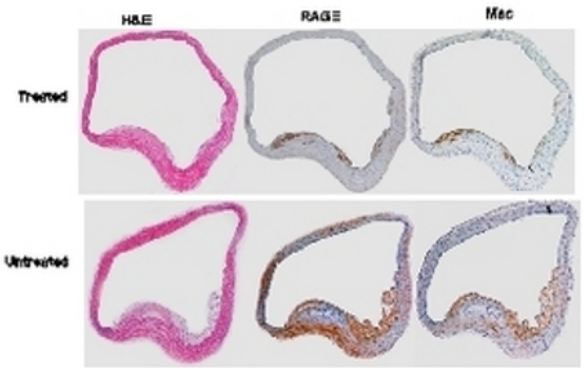

Disclosure of author financial interest or relationships:
Y. Tekabe, None; **L. Johnson**, None; **M. Kollaros**, None.

Presentation Number **P 063**
Poster Session 1
September 18, 2013 / 18:00-18:00 / Room: Exhibit Hall B

A volumetric method for quantifying progression and regression of atherosclerosis in ApoE-/- mice using Gadospin F at 7T MRI: Comparison to en face measurements

Caroline Jung, *Sabine I. Christiansen, Michael G. Kaul, Harald Ittrich, Gerhard Adam, University Hospital Hamburg Eppendorf, Hamburg, Germany. Contact e-mail: cjung@uke.de*

Purpose Despite advances in understanding of the pathogenesis of atherosclerosis and its consequences remain the main cause of mortality in industrialized nations, which makes it important to establish a noninvasive imaging technique to assess plaque burden. The aim of this study was to quantify atherosclerotic plaque by volumetric assessment at 7T MRI using Gadospin F (GDF) in comparison to en face measurements. Materials and Methods All mice were set on high fat diet (HFD) at 9 weeks of age. In-vivo MRI of the aortic vessel wall was performed at 9, 13, 17 and 21 weeks after commencement of the HFD. Therapy group was reswitched to normal rodent diet 13 weeks after starting HFD and monitored by MRI for 12 weeks (n=5 for each group). ApoE-/- and control mice were weighted and imaged before and two hours after i.v. injection of GDF (dosage: 100 µmol/kg) at a small animal MRI at 7T (Clinscan, Bruker). MRI was performed using a 3D Inversion Recovery Gradient echo MR sequence (FoV=35 x 35 mm; matrix 196 x 196, 64 slices, slice thickness 180µm; TR/TE 650/2 ms, TI 250ms; FA 20°; NSA 6, TA 9min, eff. voxel resolution (180 µm)3 in transverse orientation covering the whole aorta. Subsequently, mice were killed for en face preparation and blood samples were taken for plasma lipids analysis. MR image analyses were performed using ImageJ (V. 1.44p, NIH, USA). Total plaque volume (TPV) and total plaque volume relative to the examined area of the aorta (rTPV) were estimated. Results MRI and en face analyses showed an exponential increase of TPV and rTPV over time. The therapy group showed a slower and linear increase of TPV and rTPV. A strong correlation (r>0.8) for TPV between MRI and en face measurements was observed which was even stronger estimating the rTPV (r>0.9). In control mice no plaque volume was observed. No correlation was detectable between cholesterol and triglyceride levels in plasma and estimated plaque volume by MRI and en face. A moderate correlation was found for body weight and cholesterol and triglyceride level (r>0.6 and r>0.7, respectively). Conclusions GDF-enhanced in vivo MRI showed a strong correlation between measured plaque volume and typical en face measurements and is a powerful noninvasive imaging technique allowing reliable estimation of plaque burden, monitoring of disease progression and evaluation of therapy response in preclinical studies.

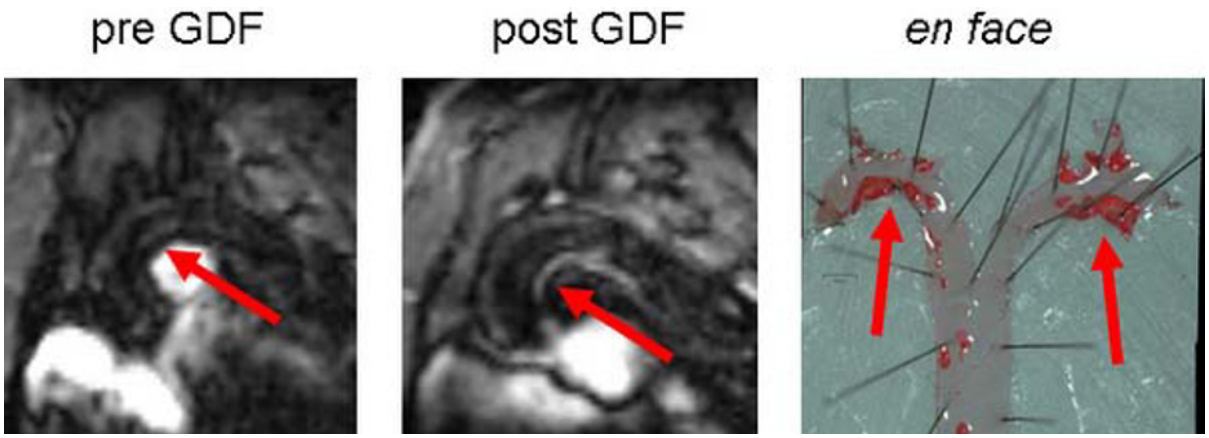

Disclosure of author financial interest or relationships:
C. Jung, None; **S.I. Christiansen**, None; **M.G. Kaul**, None; **H. Ittrich**, None; **G. Adam**, None.

Presentation Number **P 064**
Poster Session 1
September 18, 2013 / 18:00-18:00 / Room: Exhibit Hall B

Kinetic Analysis of ^{18}F-FPTP, the Novel Myocardial PET Imaging Agent, in a Rat Myocardial Infarction Model

Ji Who Kim[1], *Hyeon Sik Kim*[2], *Dong-Yeon Kim*[2,3], *Hee-Seung Bom*[2], *Dong Soo Lee*[1], *Kook-Hyun Yu*[3], *Jung-Joon Min*[2], *Jae Sung Lee*[1], [1]*Department of Nuclear Medicine, Seoul National University, Seoul, Republic of Korea;* [2]*Department of Nuclear Medicine, Chonnam National University, Gwangju, Republic of Korea;* [3]*Department of Chemistry, Dongguk University, Seoul, Republic of Korea. Contact e-mail: mwbd84@naver.com*

Objectives: (^{18}F-fluoropentyl)triphenylphosphonium salt (^{18}F-FPTP) is a promising myocardial PET imaging agent that highly accumulates in cardiomyocytes mitochondria through a negative inner transmembrane potential which is the similar uptake mechanism to ^{99m}Tc-sestamibi (Kim et al., *JNM*, 2012). As a ^{18}F-labeled myocardial PET imaging agent, ^{18}F-FPTP has advantages in longer half-life than ^{13}N and ^{15}O and better spatial resolution than SPECT agent. The aim of this study was to establish the kinetic model of ^{18}F-FPTP and compare the estimated kinetic parameters between normal and acute myocardial infarction (MI) regions. Methods: For myocardial infarction model, eight-week old male rats (n=12) underwent left coronary artery ligation. Dynamic animal PET images were acquired for 20 min after injection of ^{18}F-FPTP (37Mbq) and CT images were also acquired. Summed PET (1-18 min) and co-registered CT images were used for drawing region of interests on left ventricle, MI, and normal myocardial regions. Two-compartment model (K_1 and k_2; 2C2P) and three-compartment models with irreversible uptake (K_1-k_3; 3C3P) were compared in terms of goodness-of-fit for time-activity curves (TACs; 10- and 20-min duration) in the myocardium. Blood volume fraction (V_p) term was included in the curve fitting. Results: The 2C2P was the most suitable model for describing ^{18}F-FPTP in both the MI and normal myocardium (3C3P yielded equivalent K_1 and k_2 values to the 2C2P model and almost zero k_3 values). The average K_1, k_2, V_p and K_1/k_2 obtained from the 2C2P curve fitting on 20-min TACs in normal myocardium were 4.4, 1.4, 0.44 and 3.2, respectively. Those in MI region were 0.9, 1.3, 0.34 and 0.7. The parameters obtained using 10- and 20-min TACs were well correlated (K_1/k_2: slope = 0.99, r = 0.99). Also the average image contrast ratio between left ventricle and normal myocardium was 3.8 at 1-10 min duration. Conclusion: The results demonstrate that the fast kinetics of ^{18}F-FPTP enable the quantitative analysis of this tracer using only 10-min data with two-tissue compartment model. Normal and MI regions in rat were well discriminated based on the kinetic parameters for ^{18}F-FPTP uptake (K_1) and distribution volume (K_1/k_2). Also, the image contrast ratio was comparable with ^{13}N-ammonia which is the gold-standard in myocardial PET imaging. Therefore, ^{18}F-FPTP will be useful and remarkable for the quantitative assessment of myocardial function using PET.

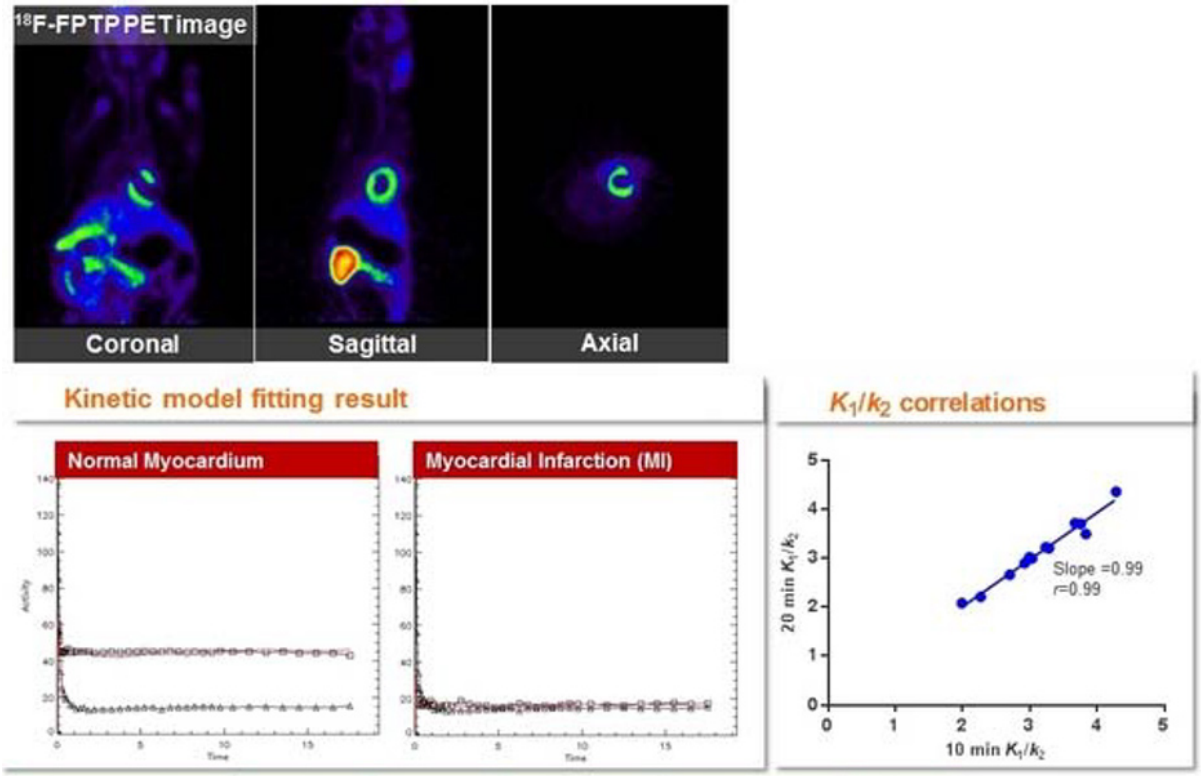

Normal	K_1	k_2	k_3	V_p	K_1/k_2
2C2P(K_1, k_2, V_p)	4.4±1.2	1.4±0.5	-	0.44±0.07	3.2±0.6
3C3P(K_1-k_3, V_p)	4.3±1.1	1.5±0.5	0.00±0.01	0.44±0.07	3.1±0.6
MI	K_1	k_2	k_3	V_p	K_1/k_2
2C2P(K_1, k_2, V_p)	0.9±0.1	1.3±0.5	-	0.33±0.10	0.7±0.2
3C3P(K_1-k_3, V_p)	0.9±0.2	1.4±0.5	0.01±0.01	0.33±0.10	0.7±0.2

Disclosure of author financial interest or relationships:
J. Kim, None; **H. Kim**, None; **D. Kim**, None; **H. Bom**, None; **D. Lee**, None; **K. Yu**, None; **J. Min**, None; **J. Lee**, Samsung Electronics, Grant/research support .

Presentation Number **P 065**
Poster Session 1
September 18, 2013 / 18:00-18:00 / Room: Exhibit Hall B

Non-invasive method to obtain blood curves of 99mTc-mebrofenin

Sara Neyt[1], *Maarten T. Huisman*[2], *Caroline Dumolyn*[1], *Maarten Vliegen*[2], *Christian Vanhove*[3], *Geert Mannens*[2], *Filip J. De Vos*[1], [1]*Laboratory of Radiopharmacy, Ghent University, Ghent, Belgium;* [2]*Drug Safety Sciences, Janssen Research and Development, Janssen Pharmaceutica NV, Beerse, Belgium;* [3]*IBITech-MEDISIP-INFINITY, Ghent University, Ghent, Belgium. Contact e-mail: Sara.Neyt@UGent.be*

Purpose: In the current study, a non-invasive image-derived method is proposed to obtain blood curves of 99mTc-mebrofenin, which can be used for kinetic modeling. Our method was validated by means of direct blood samples in wild type and Slco1a/1b knock-out mice. Methods: Wild type (n=3) and strain matched Slco1a/1b knock-out (KO) (n=3) were injected while anesthetized intravenously with 37 MBq of 99mTc-MEB. Dynamic scanning was performed on a USPECT-II/CT camera with 60 time frames of 15 seconds. Immediately after scan termination, 185 MBq of 99mTc-Tetrofosmin was injected. After 20 minutes, a static scan of 30 minutes was performed. A region of interest (ROI) was drawn around a portion of the left ventricle on the static 99mTc-Tetrofosmin data. Since the position of the mice was unaffected between the two scans, the ROI could be easily pasted on the dynamic 99mTc-MEB images to derive a blood curve. This blood curve was compared to direct blood samples (30 µL after 1, 2, 5, 7 and 10 minutes). Results: Visual inspection of the sampling blood curve and the image derived blood curve clearly showed similar curves. In wild type mice, the area under the curve (AUC) amounts 1381 ±153 MBq/mL*s for direct blood sampling and 1437 ± 182 for image derived blood concentrations. In Slco1a/1b KO mice, AUC amounts 6467 ± 834 MBq/mL*s for direct blood sampling and 6162 ± 878 MBq/mL*s for image derived blood concentrations. The AUC difference was 10.8% and 4.8% in wild-type and Slco1a/1b knock-out mice, respectively. Conclusion: Our results demonstrated that a combination of dynamic 99mTc-mebrofenin and static 99mTc-tetrofosmin scanning is useful to obtain an image derived blood curve of 99mTc-mebrofenin. These results were confirmed by manual blood samples. In the future, these image derived input functions can be used for kinetic modeling of 99mTc-mebrofenin and are superior to manual blood samples, since manual samples cannot been taken during scanning.

Disclosure of author financial interest or relationships:
S. Neyt, None; **M.T. Huisman**, None; **C. Dumolyn**, None; **M. Vliegen**, None; **C. Vanhove**, None; **G. Mannens**, None; **F.J. De Vos**, None.

Presentation Number **P 066**
Poster Session 1
September 18, 2013 / 18:00-18:00 / Room: Exhibit Hall B

Platelet aggregations associated with endothelium disruption visualized by in vivo imaging

Satoshi Nishimura, *Mika Nagasaki, ther University of Tokyo, Tokyo, Japan. Contact e-mail: snishi-tky@umin.ac.jp*

The thrombotic cellular mechanisms associated with cardiovascular events remains unclear, largely because of an inability to visualize thrombus formation. To elucidate the molecular processes underlying thrombotic vessel occlusion and relationships to endothelial cell (EC) disruption, we developed in vivo imaging technique based on single- and multi-photon microscopy, and we assessed dynamic cellular interplay in thrombosis models. We visualized that rapidly developing thrombi composed of discoid platelets without EC disruption was triggered by ROS photochemically induced by moderate power laser irradiation, and high power laser induced EC erosion and extravasatoin of circulating leukocytes. Inflammatory cytokine, adhesion molecules dynamically control these processes. Inflammatory cytokine, adhesion molecules dynamically control these processes. Thrombus formation was initiated by the binding of platelet GPIb-alpha to endothelial von Willebrand Factor in our model, and actin linker talin-dependent activation of alphaIIb-beta3 integrin in platelets was required for late phase thrombus stability. In addition, we visualized the cell dynamics of human iPS-derived artificial platelets and transfused bloods in living animals. In sum, using our imaging system can be a powerful tool to analyze thrombus formation and evaluate the therapeutic strategies.

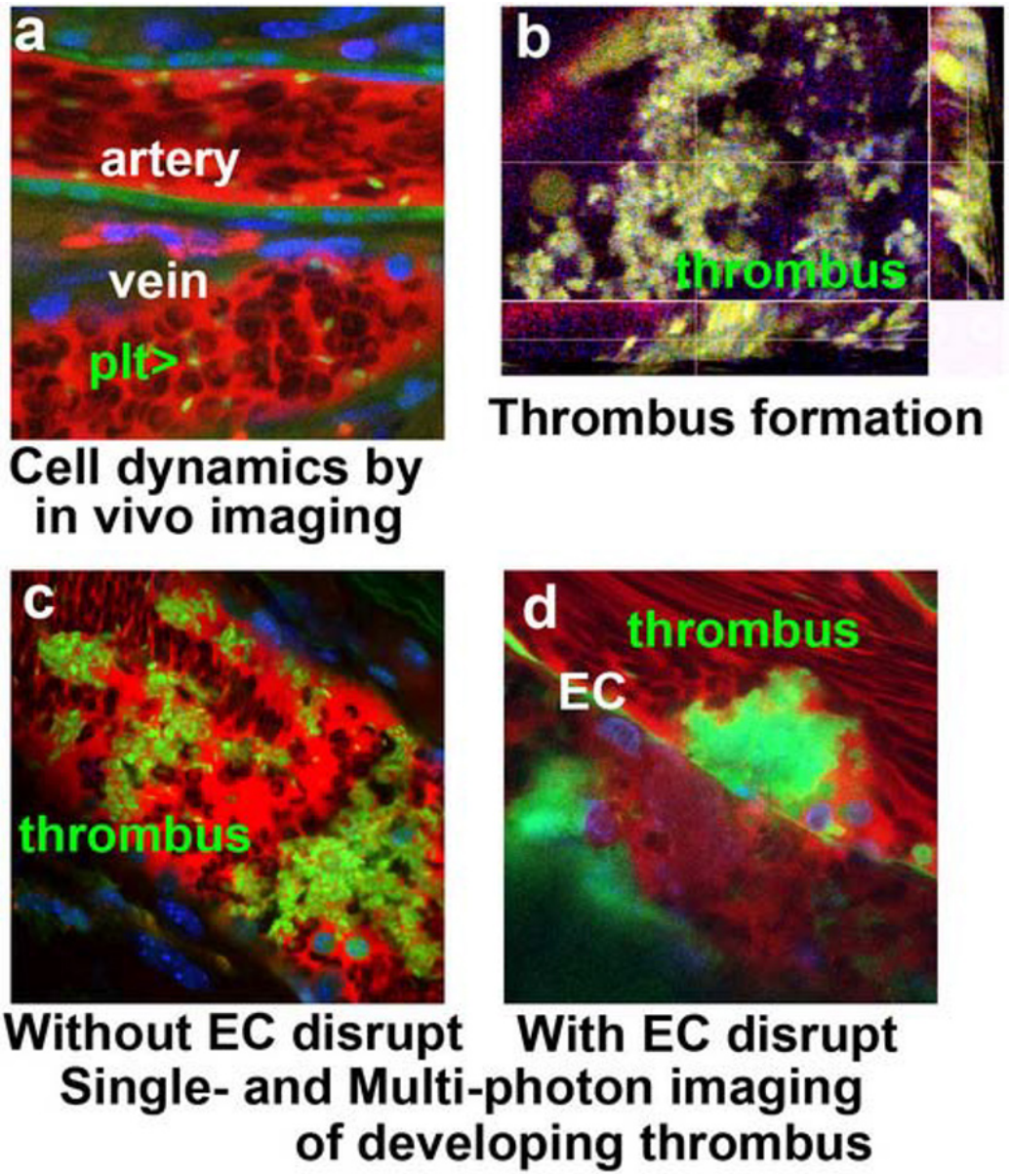

Disclosure of author financial interest or relationships:
S. Nishimura, None; **M. Nagasaki**, None.

Presentation Number **P 067**
Poster Session 1
September 18, 2013 / 18:00-18:00 / Room: Exhibit Hall B

Receptor targeted, high-throughput optical imaging of atherosclerotic plaque progression

Dolonchampa Maji[1], Metasebya Solomon[1], Annie L. Nguyen[2], Tauseef Charanya[1], Kexian Liang[1], Walter J. Akers[1], Pamela K. Woodard[1], Joseph P. Culver[1], Samuel Achilefu[1], Dana Abendschein[2], **Monica Shokeen**[1], [1]*Mallinckrodt Institute of Radiology, Washington University School of Medicine, Saint Louis, MO, USA;* [2]*Department of Internal Medicine, Washington University School of Medicine, Saint Louis, MO, USA. Contact e-mail: mshokeen@wustl.edu*

Introduction: Carotid artery atherosclerosis is the single most important cause of stroke. Non-invasive and longitudinal molecular imaging of plaque progression in atherosclerosis would allow further risk stratification of patients already at risk for atherosclerosis, potentially identifying patients with vulnerable plaque at risk for rupture. Natriuretic peptide receptor-clearance (NPR-C) receptor is a potential marker for plaque imaging that is present in vascular smooth muscle cells (VSMC), endothelial cells and macrophages and is up-regulated in vascular injury and atherosclerosis. Here, we demonstrate proof-of-principle optical imaging of focal atherosclerosis in a rabbit model using a NPR-C targeted probe and fluorescence molecular tomography (FMT) system. Methods: Endothelial denudation of right femoral artery was induced by air desiccation of the luminal surface of New Zealand white rabbits maintained on a high-cholesterol diet (>200 mg/dL). Post-surgery, the animals were maintained on a cholesterol diet and plaque formation was imaged by FMT system at day 3 and weeks 1, 2, 4, 6 and 8 respectively following surgery. Imaging scans were performed 24 h post injection of (0.02 mg/Kg) C-ANF-Cypate conjugate (C-ANF is a high affinity peptide for NPR-C; Cypate is a near-infrared dye). Imaging data was acquired as scans for 5 min and in triplicates for the respective injured and non-injured femoral artery. Cell microscopy studies were performed in stably transfected NPR-C and NPR-A cells using C-ANF-Cypate. Results: In vitro- Microscopy data demonstrated specific uptake of C-ANF-Cypate conjugate in NPR-C cells as compared to the control NPR-A cell line. In vivo- The fluorescence intensity decay curve from serial blood sampling showed optimal clearance of the targeted probe at 24 h. The tomographic FMT data showed changes in the signal intensity as the plaque progressed in the air-desiccated vessel as compared to the control vessel. Western blot analysis performed on select animals at 8 weeks demonstrated at least a 2-fold increase in the expression of NPR-C receptor concentration (ratio of injured to non-injured and normalized to beta-actin). Conclusions: Proof-of-principle studies demonstrate potential of FMT platform to perform high-throughput, longitudinal imaging of atherosclerotic focal lesions.

Disclosure of author financial interest or relationships:
D. Maji, None; **M. Solomon**, None; **A.L. Nguyen**, None; **T. Charanya**, None; **K. Liang**, None; **W.J. Akers**, None; **P.K. Woodard**, None; **J.P. Culver**, Cephalogics, Stockholder; **S. Achilefu**, None; **D. Abendschein**, None; **M. Shokeen**, None.

Presentation Number **P 068**
Poster Session 1
September 18, 2013 / 18:00-18:00 / Room: Exhibit Hall B

Targeted Delivery of Growth Factor by Nanoparticles to Reperfused Ischemic Heart for Therapeutic Angiogenesis

Zhongchan Sun, *Guang Tong, Peng Huang, Gang Niu, Xiaoyuan (Shawn) Chen, National Institute of Biomedical Imaging and Bioengineering, Bethesda, MD, USA. Contact e-mail: zhongchan.sun@nih.gov*

Objectives: Inadequate myocardial reperfusion post ischemia injury, owing to dysfunction of the microcirculation, known as the 'no-reflow' phenomenon, is associated with larger myocardial infarct, adverse left ventricular remodelling and death. Here, we design and synthesized a VEGF-loaded IR800-conjugated graphene oxide (GO-IR800-VEGF) nanoparticle for specifically delivery of VEGF into reperfused myocardium to promote angiogenesis, which is able to effectively prevent microvascular dysfunction and improve cardiac function. Methods: Myocardial ischemia/reperfusion (MI/R) model was established in C57BL/6 mice by left anterior descending coronary ligation with subsequent reperfusion. GO-IR800, free VEGF or GO-IR800-VEGF was injected via tail vein after 24h of reperfusion, respectively. The accumulation of nanoparticles in reperfused myocardium was detected by Near-infrared (NIR) fluorescence imaging ex vivo. The cardiac function post surgery was measured by Echocardiography. Small-animal PET analysis of 18F-RGD uptake within cardiac tissue was employed to evaluate the angiogenesis process post myocardial ischemia. The pro-angiogenetic effect of GO-IR800-VEGF treatment was further confirmed by immunostaining of CD31 (marker for endothelial cell). Results: Compared with sham operation group, VEGF-loaded GO-IR800 nanocarriers could substantially target to I/R myocardium, suggesting targeting of VEGF loaded nanoparticles to I/R myocardium. Meanwhile, both positron emission tomography (PET) imaging of 18F-RGD and immunostaining demonstrated more significant angiogenesis in the border area of ischemic myocardium in GO-IR800-VEGF treated group versus GO-IR800 and free VEGF treated group. In addition, compared with MI/R group treated with GO-IR800 and free VEGF, cardiac function was significantly improved in GO-IR800-VEGF treatment group. Conclusion: Growth factors such as VEGF can be loaded on nanoparticles and successfully targeted to reperfused myocardium, most likely through the enhanced permeability and retention (EPR) effect. GO nanoparticles conveying VEGF can be specifically and efficiently delivered to the reperfused mice MI heart, which can be translated into potent therapeutic angiogenesis effect, leading to significant therapeutic benefit in terms of cardiac function and remodelling.

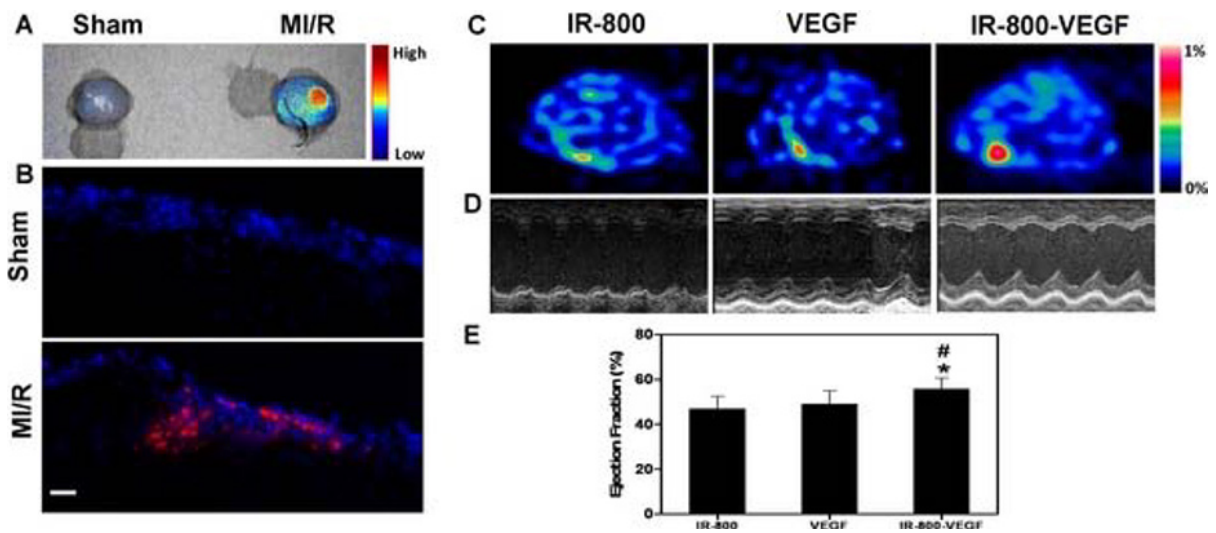

Figure 1. Accumulation of VEGF-loaded GO-IR800 nanocarriers in reperfused myocardium and its

therapeutic effects. (A) Representative ex vivo fluorescent image of heart from sham-operated group (left) and MI/R group (right) 4h post injection of GO-IR800-VEGF. (B) Fluorescence images of reperfused cardiac tissue in sham-operated group (up) and MI/R group (down). GO-IR800 nanoparticles are in red and nuclei are in blue. (Scale bar = 20 μm). (C) Representative PET images at 1 h after intravenous injection of 18F-RGD in IR-800, free VEGF and IR-800-VEGF treated groups, respectively. (D) Representative Echocardiography images at 2 weeks after surgery in three groups above. (E) Quantitative analysis of ejection fraction value (EF) in three groups above. *P < 0.05, as compared with GO-IR800 group; #P < 0.05, as compared with free VEGF group.

Disclosure of author financial interest or relationships:
Z. Sun, None; **G. Tong**, None; **P. Huang**, None; **G. Niu**, None; **X. Chen**, None.

Presentation Number **P 069**
Poster Session 1
September 18, 2013 / 18:00-18:00 / Room: Exhibit Hall B

Development of ultrasonic thrombus imaging agent using active targeting nanobubbles

Ryo Suzuki[1], *Yoshikazu Sawaguchi*[1], *Kohsuke Hagisawa*[2], *Yusuke Oda*[1], *Daiki Omata*[1], *Mutsumi Seki*[1], *Hitoshi Uruga*[1], *Kazuo Maruyama*[1], [1]*Drug and Gene Delivery System, Faculty of Pharma-Sciences, Teikyo University, Tokyo, Japan;* [2]*Physiology, National Defense Medical College, Tokorozawa, Japan. Contact e-mail: r-suzuki@pharm.teikyo-u.ac.jp*

BACKGROUND: Intravascular ultrasound imaging provides more detailed pictures of thrombi due to its higher frequency; however, thrombi within the vessel lumen can often be mistaken for soft plaques, unless they are distinguished from soft plaques by mobility, lobular edges and movement away from the vessel wall during the cardiac cycle. Therefore, it is essential to improve the diagnostic accuracy of echocardiography for detecting thrombi in vivo. Recently, we developed novel liposomal nanobubbles (Bubble liposomes (BLs)) containing ultrasound (US) imaging gas, perfluoropropane. It is confirmed that BLs could enhance echo signals with cardiosonography. In addition, we can easily optimize BLs such as modification of lipid composition and targeting ability. In this study, we developed BLs with Arg-Gly-Asp (RGD) sequence-containing peptides, which bind to activated platelet glycoprotein IIb/IIIa complexes. And the ultrasonic imaging effects of thrombus was observed with these targeted BL. METHODS: Liposomes composed of DSPC and DSPE-PEG-Maleimide were manufactured, and RGD sequence contained peptide (CGGcyclo(RGDfK)) was attached by a covalent coupling reaction between cysteine and DSPE-PEG-Maleimide. RGD conjugated liposomes were sonicated with perfluorocarbon gas to form BLs. In vitro, activated platelets were co-cultured with fluorescence labeling RGD conjugated BLs and binding activity of BLs to activated platelets was observed with flowcytometory. In vivo, we administered targeted BL to rats with acute thrombi model with iron chloride solution in the carotid artery. Thrombi were imaged using a sonography. Ultrasound images were digitized, and mean pixel gray-scale level was measured. RESULTS: In vitro, RGD conjugated BLs were more effective binding to thrombi than non-targeted BLs. In vivo, mean pixel gray-scale level of the thrombi in RGD conjugated BLs was higher than in control and non-targeted BLs. CONCLUSIONS: Perfluorocarbon gas-containing BLs with RGD peptide represent a novel echo contrast agent, which can markedly enhance ultrasonic thrombus imaging in vivo, and may be useful for noninvasively diagnosing acute thrombi.

Disclosure of author financial interest or relationships:
R. Suzuki, None; **Y. Sawaguchi**, None; **K. Hagisawa**, None; **Y. Oda**, None; **D. Omata**, None; **M. Seki**, None; **H. Uruga**, None; **K. Maruyama**, None.

Presentation Number **P 070**
Poster Session 1
September 18, 2013 / 18:00-18:00 / Room: Exhibit Hall B

In Vivo Molecular MR Imaging of Free Radicals in Diabetic Cardiomyopathy in Mice

Rheal Towner[1], *Nataliya Smith*[1], *Debra Saunders*[1], *Jorge Carrizales*[1], *Florea Lupu*[2], *Robert Silasi-Mansat*[2], *Kenneth Humphries*[3], *Shraddha Vadvalkar*[3], *Marilyn Ehrenshaft*[4], *Ronald P. Mason*[4], [1]*Advanced Magnetic Resonance Center, Oklahoma Medical Research Foundation, Oklahoma City, OK, USA;* [2]*Cardiovascular Biology, Oklahoma Medical Research Foundation, Oklahoma City, OK, USA;* [3]*Free Radical Biology and Aging, Oklahoma Medical Research Foundation, Oklahoma City, OK, USA;* [4]*Laboratory of Pharmacology and Chemistry, National Institute of Environmental Health Sciences, Research Triangle Park, NC, USA. Contact e-mail: Rheal-Towner@omrf.org*

Introduction: Evidence suggests that oxidative stress contributes an important role in the pathogenesis of cardiac complications in diabetes. The opportunity to observe these oxidative stresses in vivo would be beneficiary. This study reports on in vivo imaging of protein/lipid radicals using molecular MRI (mMRI) and immune-spin trapping (IST) in diabetic cardiac muscle. Methods: C57BL/6J mice (n=20) were treated with streptozotocin (STZ), and assessed for glucose levels. Severe diabetes was characterized when glucose levels were >300 mg/dl (n=10). For control groups, (1) non-diabetic mice were given the radical trapping agent, 5,5-dimethyl-pyrroline-N-oxide (DMPO) (non-disease control), and administered anti-DMPO probe (n=6), (2) diabetic mice were given DMPO and administered anti-DMPO probe (n=5), or (3) diabetic mice were given DMPO but administered the non-specific IgG contrast agent (contrast agent control) instead of the anti-DMPO probe (n=7). DMPO administration started at 7 weeks following STZ treatment for 5 days, and then anti-DMPO probe was administered one week later. The contrast agent, biotin-anti-DMPO-BSA (bovine serum albumin)-Gd-DTPA, was used (200µg anti-DMPO and 100µg biotin-BSA-Gd-DTPA). Non-specific mouse-IgG conjugated to biotin-BSA-Gd-DTPA was used as a control contrast agent. MR experiments were carried out under general anaesthesia on a Bruker Biospec 7T horizontal imaging spectrometer. Cardiac images were obtained using a 72 mm quadrature multi-rung RF coil. Mice were imaged at 8 weeks following STZ administration. Multiple 1H MR image slices were taken in the horizontal plane using a gradient echo multislice (FLASH); repetition time (TR) 250 ms, echo time (TE) 6 ms, 256x256 matrix, 2 steps per acquisition, 3x3 cm2 field of view (FOV), 1 mm slice thickness), with motion suppression. Mouse hearts were imaged at 0 (pre-contrast) and at 90-100 min post-contrast agent injection. Mice were injected i.v. with anti-DMPO or normal mouse IgG antibodies tagged with a biotin-Gd-DTPA-albumin-based contrast agent (200 µl/kg; 1 mg antibody/kg; 0.4 mmol Gd+3/kg). Relative MR signal intensities were calculated for the selected ROIs, and difference images were obtained between before and 90 min after injection of the anti-DMPO probe or IgG contrast agent. Results: MRI was used to detect the presence of the anti-DMPO adducts by either a significant sustained increase ($p<0.001$) in MR signal intensity. The biotin moiety of the anti-DMPO probe was targeted with fluorescently-labeled streptavidin to locate the anti-DMPO probe in excised cardiac tissues, indicating elevated fluorescence only in cardiac muscle from mice administered the anti-DMPO probe. A non-specific IgG antibody covalently bound to the albumin-Gd-DTPA-biotin construct was used as a negative control. Discussion: With mMRI and an anti-DMPO probe for DMPO-protein/lipid radical adducts combined with a Gd-DTPA-albumin-based contrast agent, MR signals associated to protein/lipid radicals in diabetic cardiac tissue were detected. Diabetic mice have more radicals in cardiac tissue, as measured by the presence of the anti-DMPO probe and molecular MRI, than non-diabetic mice.

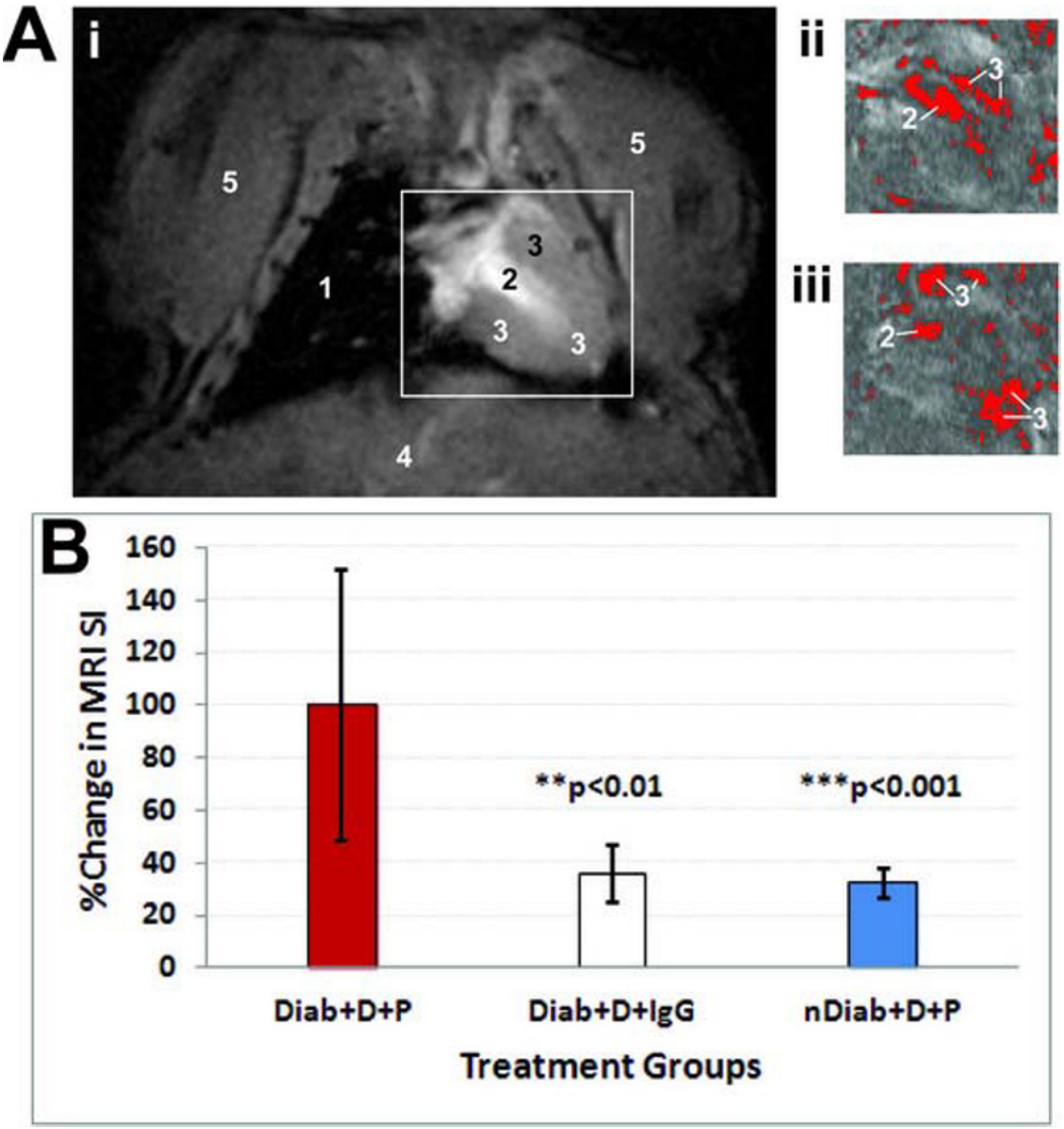

Disclosure of author financial interest or relationships:

R. Towner, None; **N. Smith**, None; **D. Saunders**, None; **J. Carrizales**, None; **F. Lupu**, None; **R. Silasi-Mansat**, None; **K. Humphries**, None; **S. Vadvalkar**, None; **M. Ehrenshaft**, None; **R.P. Mason**, None.

Presentation Number **P 071**
Poster Session 1
September 18, 2013 / 18:00-18:00 / Room: Exhibit Hall B

Evaluation of SPECT detection of cardiac amyloidosis in mice by using ^{125}I-p5R+14 peptide or ^{125}I-SAP

Jonathan S. Wall[1], *Tina A. Richey*[2], *Alan Stuckey*[3], *Craig Wooliver*[2], *Sallie D. Macy*[2], *Dustin Osborne*[3], *Emily B. Martin*[2], *Stephen J. Kennel*[1], [1]*Medicine and Radiology, University of Tennessee Graduate School of Medicine, Knoxville, TN, USA;* [2]*Medicine, University of Tennessee Graduate School of Medicine, Knoxville, TN, USA;* [3]*Radiology, University of Tennessee Graduate School of Medicine, Knoxville, TN, USA. Contact e-mail: jwall@utmck.edu*

Amyloid is a complex pathology associated with a growing number of diseases including Alzheimer's disease, type 2 diabetes, rheumatoid arthritis and myeloma. The distribution and extent of amyloid deposition in body organs establishes the prognosis and can define treatment options; therefore, determining the amyloid load by using non-invasive molecular imaging is clinically important. In patients with visceral systemic amyloidosis, the presence of cardiac amyloid deposits is particularly relevant for determining prognosis. Cardiac amyloidosis is observed principally in patients with immunoglobulin light chain (AL) amyloidosis, familial transthyretin (ATTRm - mutant) amyloidosis and as a consequence of aging (ATTRwt - wild type). Although ATTRm is considered a rare disease, the pro-amyloid V122I amino acid mutation occurs in ~3.5% of the US African American population, and may be widely underdiagnosed. Therefore, a facile, non-invasive method for detecting cardiac amyloidosis would have clinical import. We have identified amyloid-reactive, synthetic peptides, e.g. peptide p5R+14, that, when radioiodinated, are capable of selectively detecting amyloid deposits in vivo. The goal of this study was to evaluate the ability of peptides and the visceral amyloid imaging agent serum amyloid P component (SAP) to specifically detect cardiac amyloidosis in mice by using SPECT/CT imaging. Peptides p5R, p5R+14 and SAP were radioiodinated using chloramine T oxidation and ~ 100 μCi injected into mice with cardiac ApoA2c amyloidosis. The mice receiving ^{125}I-labeled peptides were imaged at 4 h post injection and ^{125}I-SAP mice at 24 h post injection. Tissue biodistribution measurements were performed following necropsy. Microautoradioraphy of tissue sections was used to validate the specific co-localization of the radiotracers with the cardiac amyloid. Peptide ^{125}I-p5R+14 and ^{125}I-SAP accumulated sufficiently in the cardiac ApoA2c amyloid to allow visualization by whole body SPECT imaging. The less-charged peptide ^{125}I-p5R was less impressive and provided ambiguous imaging. ^{125}I-p5R+14 was found at 4.5 +/- 0.8 %ID/g (range 3.7 - 5.3) representing a tissue:muscle ratio of 4.2 at 4 h post injection. ^{125}I-SAP T:M ratio was 3 at 24 h but with accumulation of only 0.19 +/- 0.05 %ID/g. Amyloid was visualized with ^{125}I-SAP due to the clearance of unbound material by 24 h post injection. SAP was shown to be capable of imaging cardiac amyloid albeit with low total probe accumulation. The novel, synthetic peptide p5R+14 also provided excellent cardiac amyloid imaging with T:M ratios >4 at 4 h post injection. Thus, this peptide or a similar variant may provide a rapid, non-invasive, cost-effective tool for detecting cardiac amyloidosis by using SPECT imaging.

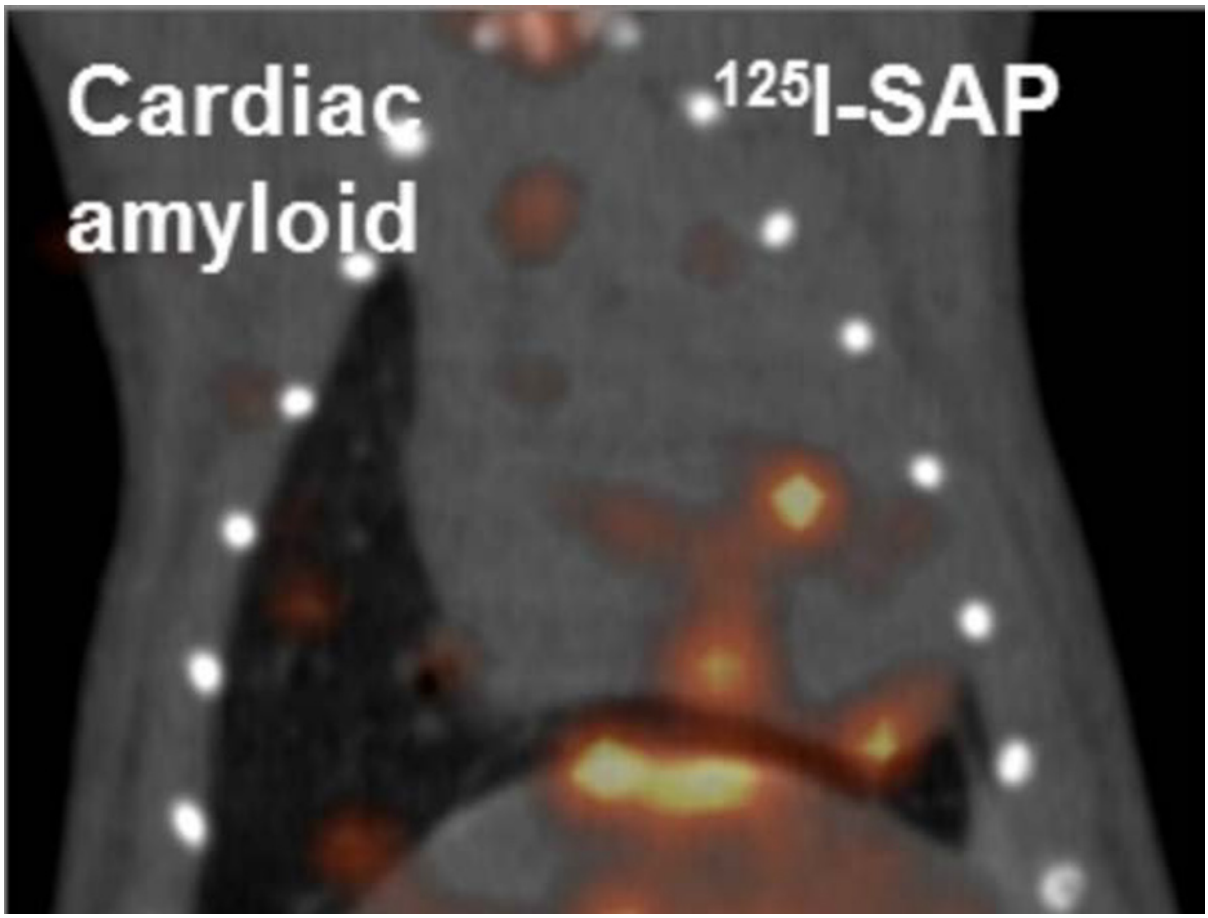

Disclosure of author financial interest or relationships:
J.S. Wall, Solex Inc, Stockholder; **T.A. Richey**, Solex Biomedical, Stockholder; **A. Stuckey**, Solex, LLC, Stockholder; **C. Wooliver**, None; **S.D. Macy**, None; **D. Osborne**, Siemens, Employment; **E.B. Martin**, Solex LLC, Stockholder; **S.J. Kennel**, Solex,lld, Stockholder .

Presentation Number **P 072**
Poster Session 1
September 18, 2013 / 18:00-18:00 / Room: Exhibit Hall B

Dual-modality imaging of microbubbles targeted to atherosclerotic plaques

Zhuojun Wu[1,2], *Adelina Curaj*[1,2], *Twan Lammers*[1,3], *Fabian Kiessling*[1], *Marc van Zandvoort*[2,4], [1]*Department of Experimental Molecular Imaging, RWTH-Aachen University Clinic, Aachen, Germany;* [2]*RWTH-Aachen University Clinic, Institut for Molecular Cardiovascular Research, Aachen, Germany;* [3]*University Twente, Department of Targeted Therapeutics, Enschede, Netherlands;* [4]*Maastricht University, Department of Genetics and Molecular Cell Biology, Maastricht, Netherlands. Contact e-mail: zwu@ukaachen.de*

Introduction Non-invasive imaging of incipient atherosclerosis and monitoring of arterial recovery after therapeutic interventions, such as balloon angioplasty and endarterectomy, are two of the main goals in current cardiovascular research, in order to reduce disease-related morbidity and mortality. The overexpression of adhesion molecules, such as ICAM-1 and VCAM-1, is characteristic for endothelial dysfunction and inflammation during the early stages of plaque growth and after therapeutic interventions. Contrast-enhanced ultrasound (CEUS) imaging using targeted microbubbles (MB), which remain strictly within the vascular compartment, is a very promising approach for the non-invasive monitoring of such molecular biomarkers. However, CEUS in major arteries, such as the carotis, is challenging due to very high flow and shear forces. Methods Two different models were used for the activation of the endothelium. HUVEC and murine carotid arteries were stimulated with TNFα for in vitro and ex vivo perfusion of ICAM-1 targeted MB (n=5). Furthermore, we investigated the in vivo application of the MB in the more physiological high fat diet - wire injury atherosclerosis model, where VCAM-1 presented a better targetv(n=5). The shell of the MB was loaded with rhodamine, to enable dual-modality imaging with CEUS and Two-Photon Laser Scanning Microscopy (TPLSM). The deep-tissue submicron resolution of TPLSM offers the visualization of single MBs and consequently quantify the total number of MBs bound to the endothelial surface in the field of view, whereas molecular CEUS imaging demonstrates the potential for clinical translation. Results Perfusion studies with ICAM-MB on TNFα-stimulated HUVECs in vitro and in freshly excised murine carotid arteries ex vivo showed specific binding at low flow rates and shear stresses of up to 0.25 ml/min (1.25 dyn/cm2 in vitro and 20 dyn/cm2 ex vivo). Moreover, even at higher (physiological) flow rates and shear stresses, of up to 35-60 dyn/cm (0.6 ml/min), MB binding is not significantly reduced (Figure 1A-C), presenting a 7.5-fold higher accumulation of MB compared to controls. In the wire injury model, VCAM-1 expression was found to be highly upregulated within the first 3 d after vascular injury. Using VCAM-1 targeted MB and CEUS/in vivo TPLSM (Figure 1D-F), we were able to visualize local inflammation and follow the re-endothelialization process (Figure 1G), which is a major indicator for arterial recovery after intervention surgery. Conclusion We show that non-invasive CEUS and the application of targeted MB is a suitable option for molecular imaging of high shear stress areas prone for atherosclerotic lesions. ICAM-1/VCAM-1 targeted MB bound efficiently and specifically to inflamed endothelium under physiological flow conditions in mice, and furthermore allowed us to track the degree of inflammation/arterial regeneration. Our findings contribute to a better understanding of MB behavior in major arteries, as well as to the establishment of clinically relevant imaging protocols for the non-invasive detection of inflammatory markers in cardiovascular disease, as the shear stress in human decreases by a factor of 6.

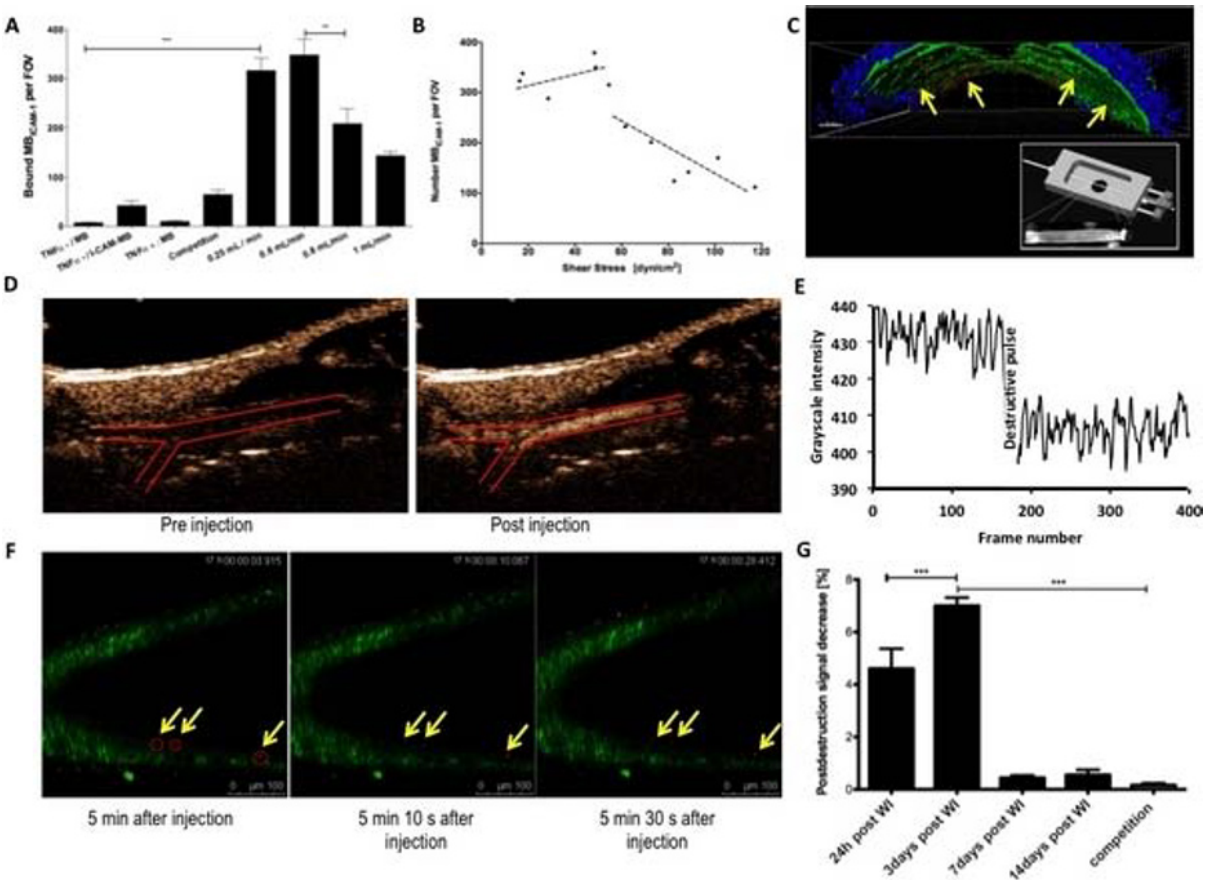

Figure 1: TPLSM/CEUS analysis of ex vivo and in vivo MB binding A) Statistical analysis of MB-ICAM binding to explanted carotids at different flow rates n=5. B) Graph depicting the shear stress-dependent binding of MB-ICAM-1. C) Reconstructed z-stack TPLSM image exemplifying bound MB-ICAM (red) to a TNFα-stimulated murine carotid artery mounted in a flow chamber (indicated by yellow arrows). Collagen is shown in blue and elastin in green). Scale bar = 50 μm. D) In vivo CEUS of wire injured carotid artery before and after MB-VCAM injection. E) Graph depicting the in vivo CEUS destruction of bound MB-VCAM 5 min post injection. F) In vivo TPLSM showing stationary MB-VCAM at the vascular wall 5 min after injection (green = vascular wall, red = MB, indicated by yellow arrows). G) Statistical analysis of MBVCAM binding using in vivo CEUS at time point 1, 3, 7 and 14 days post wire injury n=5.

Disclosure of author financial interest or relationships:
Z. Wu, None; **A. Curaj**, None; **T. Lammers**, None; **F. Kiessling**, None; **M. van Zandvoort**, None.

Presentation Number **P 073**
Poster Session 1
September 18, 2013 / 18:00-18:00 / Room: Exhibit Hall B

Imaging of Tissue Redox Activity from Early to Terminal Stage of Cancer Development Using Nitroxide-enhanced MRI

Rumiana Bakalova[1], *Zhivko Zhelev*[1,2], *Daisuke Kokuryo*[1], *Ichio Aoki*[1], *Veselina Gadjeva*[2], *Tsuneo Saga*[1], [1]*Molecular Imaging Center, National Institute of Radiological Sciences, Chiba, Japan;* [2]*Medical Faculty, Trakia University, Stara Zagora, Bulgaria. Contact e-mail: bakalova@nirs.go.jp*

Background: Redox signalling is crucial for carcinogenesis and tissue redox activity has emerged as an important sensing platform for cancer diagnosis and planning of therapeutic strategy. The cells and tissues of healthy mammals are characterized by low level of reactive oxygen species (ROS) and some constant (reference) level of reducing equivalents. Increasing of ROS above the critical level provokes genomic instability and uncontrolled proliferation, which causes normal cells to become malignant. The present study aimed to clarify the dynamics of tissue redox activity (TRA) in cancer progression and assess the importance of this parameter for therapeutic strategies. Methods: The experiments were conducted on brain tissues of neuroblastoma-bearing, glioma-bearing and healthy mice. TRA was visualized *in vivo* by nitroxide-enhanced magnetic resonance imaging (MRI) on anesthetized animals or *in vitro* by electron paramagnetic resonance (EPR) spectroscopy on isolated tissue specimens. Two biochemical parameters were analyzed in parallel: tissue total antioxidant capacity (TTAC) and plasma levels of matrix metalloproteinases (MMPs). Results: In the early stage of cancer, the brain tissues were characterized by a shorter-lived MRI signal than that from healthy brains (indicating a higher reducing activity for the nitroxide radical), which was accompanied by an enhancement of TTAC and MMP9 plasma levels. In the terminal stage of cancer, tissues in both hemispheres were characterized by a longer-lived MRI signal than in healthy brains (indicating a high oxidative activity) that was accompanied by a decrease in TTAC and an increase in the MMP2/MMP9 plasma levels. Cancer progression also affected the redox potential of tissues distant from the primary tumor locus (liver and lung). Their oxidative status increased in both stages of cancer. Conclusions: This study demonstrates that tissue redox balance is very sensitive to cancer development and can be used as a diagnostic marker of carcinogenesis. The method is simple and applicable on isolated tissue and blood specimens. The method demonstrates the potential for promising application in molecular imaging diagnostic *in vivo* on humans following the development of cell-penetrating nitroxide probes with high contrast, low toxicity and minimal side effects. The most important observations are that the oxidative status of noncancerous tissues (even those distant from the primary tumor locus) increases with cancer progression and that these tissues become susceptible to oxidative stress and damage.

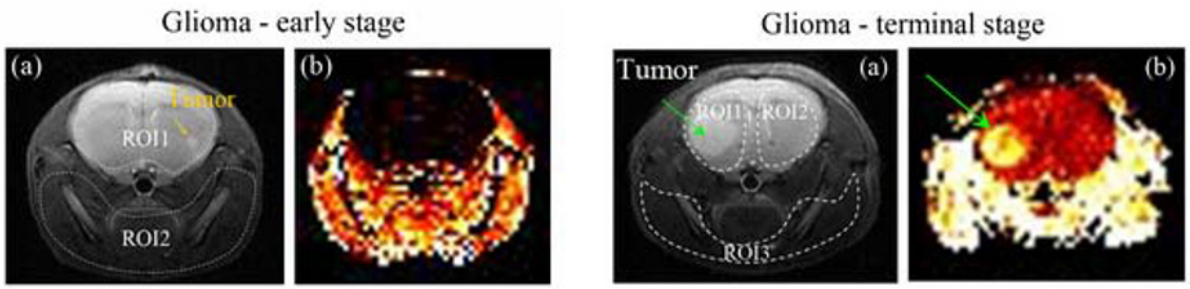

Magnetic resonance imaging of brain glioma in early and terminal stage of cancer development: (a) MR image (spin-echo sequence); (b) extracted nitroxide-enhanced MRI signal (normalized to the baseline), obtained 10 min after intravenous injection of nitroxide probe in cancer-bearing mice.

Disclosure of author financial interest or relationships:
R. Bakalova, None; **Z. Zhelev**, None; **D. Kokuryo**, None; **I. Aoki**, None; **V. Gadjeva**, None; **T. Saga**, None.

Presentation Number **P 074**
Poster Session 1
September 18, 2013 / 18:00-18:00 / Room: Exhibit Hall B

Evaluation of the effect of OKN-007 on gliomas using 1H MR spectroscopy and diffusion-weighted imaging

Krithika Balasubramanian[1], *Patricia Coutinho de Souza*[1], *Nataliya Smith*[1], *Debra Saunders*[1], *Charity Njoku*[1], *Randy L. Jensen*[2], *David L. Gillespie*[2], *Andrea L. Schwager*[3], *Osama Abdullah*[4], *Edward Hsu*[4], *Changho Choi*[5], *Rheal Towner*[1], [1]*Advanced Magnetic Resonance Center, Oklahoma Medical Research foundation, Oklahoma City, OK, USA;* [2]*Huntsman Cancer Institute, Univ. of Utah Health Sciences Center, Salt Lake City, UT, USA;* [3]*Dept. of Bioengineering, Univ. of Utah, Salt Lake City, UT, USA;* [4]*Interdepartmental Program in Neuroscience, Univ. of Utah, Salt Lake City, UT, USA;* [5]*Advanced Imaging Research Center, Univ. of Texas Southwestern Medical Center, Dallas, TX, USA. Contact e-mail: Krithika-Balasubramanian@omrf.org*

Introduction: Gliomas are a common form of adult primary brain tumors. OKN-007 (2,4-disulfophenyl-PBN) is a nitrone that has demonstrated anti-glioma effects in rodent models and is currently a clinical investigational drug for recurrent gliomas. In this study, we evaluated anti-tumor effects of OKN007 in F98 rat glioma model by assessing metabolite alterations and water mobility by using MRS and DWI. We hypothesize that 1H MRS and conventional DWI are useful methods to assess the response of varied glioma models to anti-tumor treatments. Methods: F98 cells were injected into the cortex in male Fisher 344 rats. OKN-007 was given at a concentration of 0.018% (10 mg/Kg body weight/day in drinking water) and it was administered starting from 15 days after F98 glioma cell implantations.MRI experiments were performed on a Bruker Biospec 7 T magnet imaging system. Glioma metabolites [e.g. total creatine (tCr), total choline (tCho), glutamine (Gln), glutamate (Glu), myo-inositol (mIns), N-acetyl aspartate (NAA), taurine (Tau), total lipids and macromolecules at 1.3 ppm (MM14+Lip13a+Lip13b), at 0.9 ppm (MM09+Lip09)] were acquired from 1H MRS using Stimulated-Echo Acquisition Mode (TE = 4.400 ms; TR = 3000.0 ms, 256 averages, Acquisition time = 511.18 ms, Number of Points = 2048, Spectral width = 4006.41Hz) and measured using LCModel. To calculate the apparent diffusion coefficient (ADC), uniform circular regions of interest (ROIs) were drawn on the ADC map in the various regions of the tumor as well as the normal contralateral regions. Results: There was a significant decrease in the lipid concentration in OKN-007-treated gliomas compared to untreated gliomas ($p=0.049$) (see Figure 1A for representative spectra). Other metabolites although demonstrating altering trends were not found to be significant when comparing treated vs. untreated animals. These results demonstrate that OKN-007 could affect tumor metabolism, which was denoted by significant changes in major metabolite concentrations in lipids in the F98 glioma model. Similar results have been described previously in several different glioma models (Rat C6, 9 L/LacZ, F98 and RG2, and mouse GL261) by our group. Different tumor regions could be distinguished from each other based on ADC values. Between untreated and treated groups, a significant decrease was observed in the tumor core ADC in treated animals compared to untreated rats (see Figs 1B-C for representative ADC maps). The ADC of the tumor core in treated rats also showed a significant decrease, although not significant, compared to the untreated group. Conclusion: The results of this study demonstrate that OKN-007 could affect tumor metabolism, which was denoted by significant changes in major metabolite concentrations in lipids in F98 glioma model following treatment. Moreover, the study indicates that OKN-007 mediates varying effects on different regions of the tumor. Diffusion MR enables clear distinction of tumor heterogeneity and aid in the assessment of therapeutic response. Finally, 1H MRS and DWI along with conventional MRI, are useful methods to assess and follow the response of the F98 glioma model treated with OKN-007.

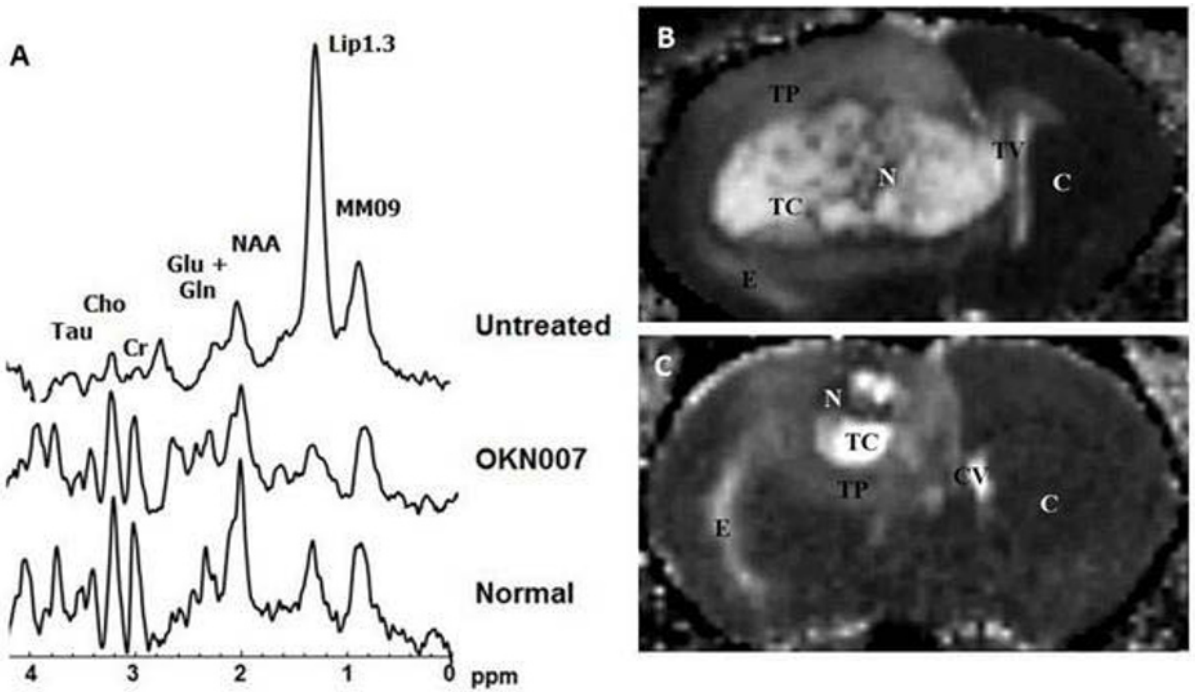

Figure 1 - (A) Representative spectra from F98 gliomas depicting alterations in metabolite ratios from normal brain and treated and untreated glioma tissues. (C) A significant decrease was observed in the ADC values of the tumor core in the OKN-007 treated group when compared with that of the untreated group (B).

Disclosure of author financial interest or relationships:

K. Balasubramanian, None; **P. Coutinho de Souza**, None; **N. Smith**, None; **D. Saunders**, None; **C. Njoku**, None; **R.L. Jensen**, None; **D.L. Gillespie**, None; **A.L. Schwager**, None; **O. Abdullah**, None; **E. Hsu**, None; **C. Choi**, None; **R. Towner**, None.

Presentation Number **P 075**
Poster Session 1
September 18, 2013 / 18:00-18:00 / Room: Exhibit Hall B

Radioactive labeling and homing of Endothelial Progenitor Cells

Lotte B. Bertelsen[1], *Michael Horsman*[2], *Lise Falborg*[3], *Hans Stødkilde-Jørgensen*[1], [1]*The MR-Research Centre, Aarhus University Hospital, Skejby, Aarhus, Denmark;* [2]*Dept. Experimental Clinical Oncology, Aarhus University Hospital, NBG, Aarhus, Denmark;* [3]*Dept. Nuclear Medicine, Aarhus University Hospital, NBG, Aarhus, Denmark. Contact e-mail: lotte@mr.au.dk*

Background and Aim: Endothelial Progenitor Cells (EPC) are believed to be crucial in the process of forming new blood vessels in tissue suffering from ischemia. To elucidate the degree of EPC homing in tumor tissues in vivo, radioactive labeled cells were injected in a mouse model carrying an implanted tumor, and their distribution traced in the mouse. Materials and Methods: EPCs were isolated from Human umbilical cord blood using anti-CD34 magnetic beads and incubated with ^{111}Indium-tropolon equal to 0.37 MBq per 3x10^{6} cells. After radioactive labeling, the EPCs were injected intravenously into mice bearing a C3H mammary carcinoma implanted on their right rear foot. Following euthanasia at various time points after cell administration, the mice were dissected and the ^{111}Indium activity in the individual organs were quantified by gamma counting. Results and Discussion: Indium activity was primarily found in the lung, liver, spleen, kidneys and tumor. The high activity in the kidneys could indicate a substantial loss of indium from the cells. Our results show that cell retention of indium decreased over time, and that injected free indium has a distribution pattern much like the one seen with injected indium labeled EPCs. A small percentage of the injected activity was located to the tumor area, however, it can still be discussed whether this ^{111}Indium activity originated from homing of living EPCs or if it, to a certain degree, corresponded to free ^{111}indium Chloride.

Disclosure of author financial interest or relationships:
L.B. Bertelsen, None; **M. Horsman**, None; **L. Falborg**, None; **H. Stødkilde-Jørgensen**, None.

Presentation Number **P 076**
Poster Session 1
September 18, 2013 / 18:00-18:00 / Room: Exhibit Hall B

Tracking SPIO-Labeled Effector and Regulatory Cell Migration with MRI

Kimberly D. Brewer[1,4], *Olivia Stanley*[2], *Christa B. Davis*[2], *Iulia Dude*[2], *Genevieve Weir*[1], *Mohan Karkada*[1], *Marc Mansour*[1], *Chris Bowen*[2,3], [1]*Immunovaccine Inc., Halifax, NS, Canada;* [2]*IWK Health Centre, Halifax, NS, Canada;* [3]*Radiology & Biomedical Engineering, Dalhousie University, Halifax, NS, Canada;* [4]*Radiology, Stanford University, Palo Alto, CA, USA. Contact e-mail: brewerk@stanford.edu*

Introduction - A growing area of interest in cancer research is the behavior of regulatory cells such as myeloid derived suppressor cells (MDSCs) and regulatory T cells (Tregs). These regulatory cells suppress both inherent and induced immune responses resulting in underperformance of many anti-cancer treatments. To assess the response of effector and regulatory cells to vaccination, we tracked MDSCs, Tregs and active cytotoxic T cells (CD8+) in a mouse C3-HPV16 cervical cancer model. The objectives of this study were 1) to demonstrate reliable homing of regulatory and effector cells to tumors and lymph nodes (LNs) using MRI, and 2) to use a semi-quantitative analysis to evaluate changes in these patterns over time, and in response to cancer immunotherapy with the cancer vaccine DepoVax^{TM}. ***Methods*** - C3 tumors were implanted in female C57BL/6 mice. Treg and CD8+ T cells were isolated from LNs of tumor bearing mice, and MDSCs from spleens. Cells were labeled with 35nm SPIO-Rhodamine B and injected i.v. into mice. Two mice from each cell type group received contralateral DepoVax^{TM} vaccinations with 5μg R9F. Injected cell-count was varied based on iron uptake efficiency and isolation yield. 3T MRI scans were performed prior to injection and daily for 3 days post injection. Sagittal images of tumors, vaccination sites and left & right inguinal LNs were obtained using a 3D true-FISP (bSSFP) sequence (TR/TE = 8/4 ms, flip angle = 30°, 150μm^3 isotropic resolution). The tumors were segmented in 3D using Mango and a semi-quantitative estimate for iron mass (M_{Fe}) was obtained by voxel-wise summation of iron-induced relaxation rate enhancements observed from baseline histograms using the formula: $M_{Fe} = \Sigma(\ln(I_0/I))$ where I_0 is the mode signal intensity of the tumor signal and I is the intensity at a given pixel. This value will be positive for tumors with strong negative contrast (e.g. due to SPIO) and 0 for tumors with normal relaxation rate distributions (e.g. no external source of contrast). ***Results*** - In naïve mice, both MDSCs and CD8+ cells were seen to migrate to tumor sites post-injection (see Figure). Tregs were also clearly visible at both the tumor and at several different lymph nodes throughout the mouse, particularly the inguinal LNs (tumor draining and contralateral). The semi-quantitative analysis further showed that for each cell type there was significant drop in signal intensity within the tumor one day post-injection, but M_{Fe} had significantly decreased again by three days post-injection. MDSC migration also significantly varied with treatment. While MDSCs were visible at the tumor site in naïve mice, none of the vaccinated mice showed evidence of MDSCs having migrated to the tumor. However, there did not appear to be any change in migration of CD8+ cells to the tumor site in response to vaccination. ***Conclusions*** - By understanding the effect that various immunotherapies have on tumor progression and *in vivo* recruitment of these cells at the preclinical level, it will be possible to undertake more focused efforts on developing novel anti-cancer treatments and studying their effects on immune cells.

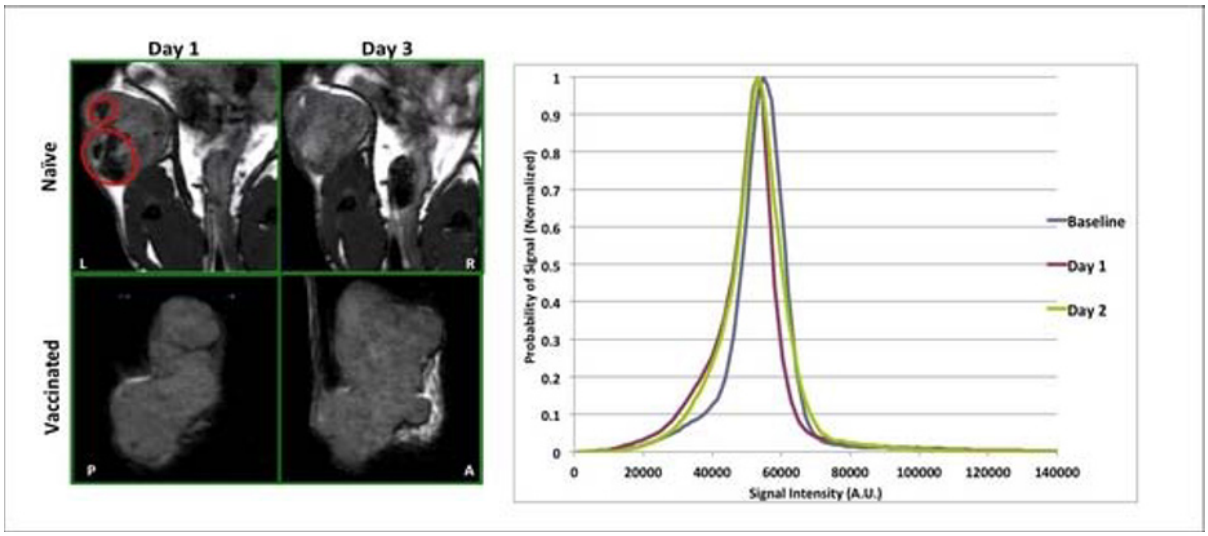

Figure 1 - ***Left*** - MR images of SPIO-labeled MDSCs. For naïve mice, these cells have migrated to the tumor on day 1, but have cleared from the site by day 3. However, for vaccinated mice, no iron-loaded cells appear to have migrated to the tumor (image is zoomed to tumor for clear visualization). ***Right*** Probability distribution of signal from a tumor after injection of CD8+ cells. Curves show a significant leftwards skew presumably due to the presence of iron one day post-injection (M_{Fe} = 0.07) that has begun to return to equilibrium two days post-injection (M_{Fe} = 0.02).

Disclosure of author financial interest or relationships:
K.D. Brewer, Immunovaccine Inc., Employment; **O. Stanley**, None; **C.B. Davis**, None; **I. Dude**, None; **G. Weir**, Immunovaccine, Grant/research support; **M. Karkada**, Immunovaccine Inc., Employment; **M. Mansour**, Immunovaccine Inc, Stockholder; **C. Bowen**, Immunovaccine Inc., Grant/research support .

Presentation Number **P 077**
Poster Session 1
September 18, 2013 / 18:00-18:00 / Room: Exhibit Hall B

Treatment of brain metastases combining ultrasound, microbubbles, and therapeutics

Charles F. Caskey[1,2], *Chun-Yen Lai*[1], *Brett Fite*[1], *Frits Thorsen*[3], *Shengping Qin*[1], *William Grissom*[2], *Lisa M. Mahakian*[1], *Katherine Ferrara*[1], [1]*Biomedical Engineering, University of Califorina at Davis, Davis, CA, USA;* [2]*Biomedical Engineering, Vanderbilt University, Nashville, TN, USA;* [3]*Department of Biomedicine, University of Norway, Bergen, Norway. Contact e-mail: cfcaskey@ucdavis.edu*

Introduction The blood brain barrier (BBB) is a selectively permeable interface that regulates the entry of molecules into the brain, making delivery of therapeutic agents beyond the BBB a significant challenge. Focused ultrasound in conjunction with microbubbles is a promising strategy to safely and noninvasively deliver drugs beyond the blood brain barrier and has been repeatedly verified in healthy animals. In this study, we applied this technology to deliver chemotherapeutics to a murine model of metastatic melanoma. Melanoma has a high incidence of metastasis to the brain with poor prognosis and limited treatment efficacy with chemotherapeutics, especially after establishing contact with astrocytes and growing to diameters greater than 250 μm. We hypothesize that ultrasound-based BBB disruption can deliver chemotherapeutics to melanoma metastases. In our study, we used contrast-enhanced ultrasound to deliver doxorubicin to brain metastases to reduce the growth of tumors in mice and have applied MRI and PET imaging to evaluate the pharmacokinetics of delivery. Methods and Results We used a dual-mode imaging (5 MHz) and therapeutic (1.5 MHz) transducer to localize and treat a single hemisphere of a mouse brain after injection of 25 μL of Targeson microbubbles designed for drug delivery (Targeson, Inc., San Diego, CA). The therapeutic acoustic pulse consisted of 15 0.3 msec bursts with a PRF of 100 Hz for 5 seconds at a peak negative pressure of 600 kPa. Tumor-bearing mice were inoculated with H1 luciferase-expressing melanoma cells, and treatments began three weeks afterwards, twice a week for two weeks. Following insonation, 3mg/mL of doxorubicin was injected IV. MRI and 18F-FLT PET demonstrated the increased tumor burden over time. Tumor burden was assessed with weekly bioluminescence (BLI) imaging (IVIS, Xenogen Corp., Alameda, CA) by measuring the total BLI counts in a circular region of interest around the head of a mouse in the supine position after luciferin injection. BLI counts decreased in 3 of the mice, reached a plateau in 1, and continued to increase in 2 mice (Fig. 1a). The decrease in BLI counts between weeks 3 and 4 occurred throughout the body in mice where tumor burden was reduced (Fig. 1b,c). Discussion and Conclusion Few studies have examined the delivery of chemotherapy with ultrasound contrast-enhanced BBB disruption in animal models of disease. In our study, we delivered doxorubicin resulting in significantly altered growth of melanoma metastases and also found the vasculature of tumor-bearing mice to be more sensitive to BBB disruption. As this research progresses, we have begun to develop MRI methods to screen high-risk populations for small melanoma metastases. The combination of ultrasound-based BBB disruption with chemotherapy and screening for small metastases with 7T MRI may provide a window for therapy that would dramatically increase the survival of patients that currently have a very poor prognosis.

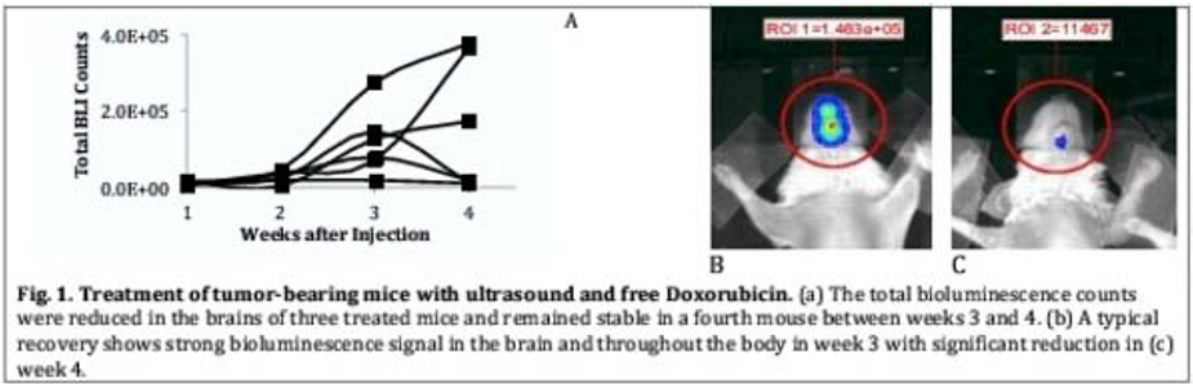

Fig. 1. Treatment of tumor-bearing mice with ultrasound and free Doxorubicin. (a) The total bioluminescence counts were reduced in the brains of three treated mice and remained stable in a fourth mouse between weeks 3 and 4. (b) A typical recovery shows strong bioluminescence signal in the brain and throughout the body in week 3 with significant reduction in (c) week 4.

Disclosure of author financial interest or relationships:
C.F. Caskey, None; **C. Lai**, None; **B. Fite**, None; **F. Thorsen**, None; **S. Qin**, None; **W. Grissom**, None; **L.M. Mahakian**, None; **K. Ferrara**, None.

Presentation Number **P 078**
Poster Session 1
September 18, 2013 / 18:00-18:00 / Room: Exhibit Hall B

Development of an optical assay to study the effect of upstream pseudohypoxic molecular factors on HIF1α

Manoj N. Desai[1,2], *Divya Vats*[1], *Steffi Lehmann*[1], *Ruth Keist*[2], *Markus Rudin*[1,2], [1]*Institute of Biomedical Engineering, ETH Zurich, Zurich, Switzerland;* [2]*Institute of Pharmacology and Toxicology, University of Zurich, Zurich, Switzerland. Contact e-mail: desai@biomed.ee.ethz.ch*

Introduction Tumor hypoxia is now recognized to be an important contributor to tumor growth, metastasis formation and angiogenesis. The key factor that responding to changes in cellular oxygen level is Hypoxia-Inducible Factor (HIF), the levels of which are regulated by the oygen sensitive prolylhydroxylase domain (PHD) protein. It is known that HIF signaling may also arise under normoxic conditions. One upstream factor associated to the HIF pathway is the mammalian target of rapamycin (mTOR), though the molecular mechanism and biological relevance of oxygen-independent HIF activation by mTOR are poorly understood. To get more insight, we developed in vivo fluorescence imaging assays for studying different molecular events involved upstream of HIF-pathway and cancer progression. Methods Mouse breast metastatic carcinoma cell line, 4T1 and murine colon cancer carcinoma cell line, C51 were stably transfected with HRE (hypoxia responsive element) and CMV driven mCherry reporter construct. The expression system was validated in vitro by fluorescent microscopy and in vivo by and 2D fluorescence imaging (CRI-Maestro 500). To elucidate the HIF regulation by mTOR, rapamycin treatment was carried out under hypoxia (2%, using a hypoxic chamber) and normoxia (using dimethyloxalylglycine, DMOG, an inhibitor of PHD) by Western blot. This was further investigated under in vivo conditions by generating subcutaneous (C51 and 4T1) and orthotopic (4T1) tumors from the stably transfected C51 and 4T1 cells expressing HRE-mCherry and CMV-mCherry cells, respectively, and treating them with either vehicle, rapamycin. Ex vivo studies were performed with excised tumors by immunofluorescence assessing the regulation of HIF1α, mTOR, CD31, GLUT1 and CA9. Results Pretreatment of mCherry labeled C51 and 4T1 cells with the mTOR inhibitor rapamycin significantly reduced the degree of endogenous HIF1α induction upon administration DMOG. This was confirmed in vivo in tumor bearing mice: treatment with rapamycin at a dose of 2mg/kg/day led to reduced HIF activity, as reflected by reduced expression levels of mCherry under the control of HRE (normalized to the tumor volume), and to a significant decrease in tumor growth both in subcutaneous (C51 and 4T1) and orthotopic (4T1) tumors. Immunofluorescence revealed reduced levels of the HIF downstream products CD31, CA9 and GLUT1 reflecting the efficacy of the treatment. While both HIF1a and mTOR levels apparently depend on the degree of cell oxygenation, we did not observe a clear correlation between the two readouts. Conclusions and outlook Regulation of both mTOR and HIF pathway activity appears to be a function of oxygen availability. The lack of correlation between HIF signaling and mTOR levels might indicate the existence of positive and negative feedback loops, the understanding of which appears essential for understanding the interplay of HIF and mTOR regulation on tumor angiogenesis and tumor growth progression. References Lehmann S. et al (2009), Longitudinal and multimodal in vivo imaging of tumor hypoxia and its downstream molecular events. PNAS, 106 (33), p 14004-9.

Disclosure of author financial interest or relationships:
M.N. Desai, None; **D. Vats**, None; **S. Lehmann**, None; **R. Keist**, None; **M. Rudin**, Hoffmann-LaRoche AG, Basel, Switzerland, Grant/research support; Roche-Glycart AG, Schlieren, Switzerland, Grant/research support .

Presentation Number **P 079**
Poster Session 1
September 18, 2013 / 18:00-18:00 / Room: Exhibit Hall B

Imaging Primary and Metastatic Murine Ovarian Tumors with 18F-FDG PET and Oral Contrast CT

Rehan Ali[1], Katherine Fuh[1], Anthony Vega[2], Daveeta Marcellin[3], Marjan Rafat[1], Denise A. Chan[4], Amato Giaccia[1], **Edward E. Graves**[1], *[1]Radiation Oncology, Stanford University, Stanford, CA, USA; [2]Physics and Earth Sciences, St. Mary's University, San Antonio, TX, USA; [3]Veterinary Medicine, Tuskegee University, Tuskegee, AL, USA; [4]Radiation Oncology, UCSF, San Francisco, CA, USA. Contact e-mail: egraves@stanford.edu*

AIMS: To develop improved PET/CT imaging protocols for detecting and quantifying tumor burden in primary and metastatic murine models of ovarian cancer. RATIONALE: 18F-FDG PET/CT has been used to measure tumor response to novel GLUT-1 inhibitors that induce selective cytotoxicity in tumor cells [1], however its effectiveness is limited by high physiological FDG uptake in the gut. This can be overcome through the use of contrast-enhanced CT to highlight the bowels and image processing to quantify gastrointestinal (GI) FDG uptake. METHODS: Primary ovarian tumor models were created by injecting adenoviral Cre recombinase into the ovaries of transgenic LSL-KRAS PTENfloxed/floxed mice, and grown for 11 weeks. Metastatic tumor models were formed by injecting 1 million SKOV3.ip1 cells intraperitoneally, and grown for 3 weeks. For imaging, mice were fasted overnight, and 500 µl of 7% w/v barium sulphate was then administered via oral gavage 2-3 hours prior to imaging. Mice were injected intravenously with 200 µCi 18F-FDG, kept anesthetized for one hour, and imaged using a Siemens Inveon microPET/CT. Image processing was performed using RT_image software. Gut regions of interest (ROIs) were drawn to cover the region constrained by the heart, kidneys and bladder, and mean %ID/g values were measured. The GLUT-1 inhibitor STF-31 [1] was evaluated on mice exhibiting metastatic ovarian tumors (n=15), with FDG PET images acquired pre-treatment and at time points between 1 to 24 hours after two separate treatments. Gut ROI values were measured at each time point. RESULTS: Contrast CT enabled the assignment of physiological bowel FDG uptake and facilitated tumor detection. For primary tumors, large FDG-avid tumors were located (n=6). Excised tumors had a mean weight of 0.42g (s.d. 0.19) and a mean CT volume of 0.34 cm3 (s.d. 0.20) (r2 = 0.56). Two excised tumors were imaged using PET and the ex vivo tumor:muscle ratios were found to correlate with in vivo values (mouse 1: 1.48 in vivo vs 1.74 ex vivo; mouse 2: 3.59 in vivo vs 2.91 ex vivo). For metastatic tumors, large FDG-avid masses were detected and found to correspond with ex vivo tumor locations (shown in Figure). Gut ROI analysis of mice treated with STF-31 revealed a decrease in 18F-FDG uptake between 6-16 hours before recovering by 24 hours. Maximum intensity projection images confirmed a corresponding reduction in 18F-FDG hotspots in the abdominal region during these times. Serial imaging enabled the detection of smaller focal tumors, suggesting a minimum detection volume of 0.01 cm3. CONCLUSIONS: The use of oral contrast CT and ROI-based image analysis in conjunction with 18F-FDG microPET is promising for facilitating the detection of primary and metastatic murine ovarian tumors in the GI tract, and for quantifying their response to therapy. We are currently evaluating this technique with luciferase-labeled SKOV3.ip1 cells in order to validate our in vivo PET measurements against bioluminescent signals. [1] Chan et al, "Targeting GLUT1 and the Warburg effect in renal cell carcinoma by chemical synthetic lethality", Sci Trans Med 2011, 3(94)

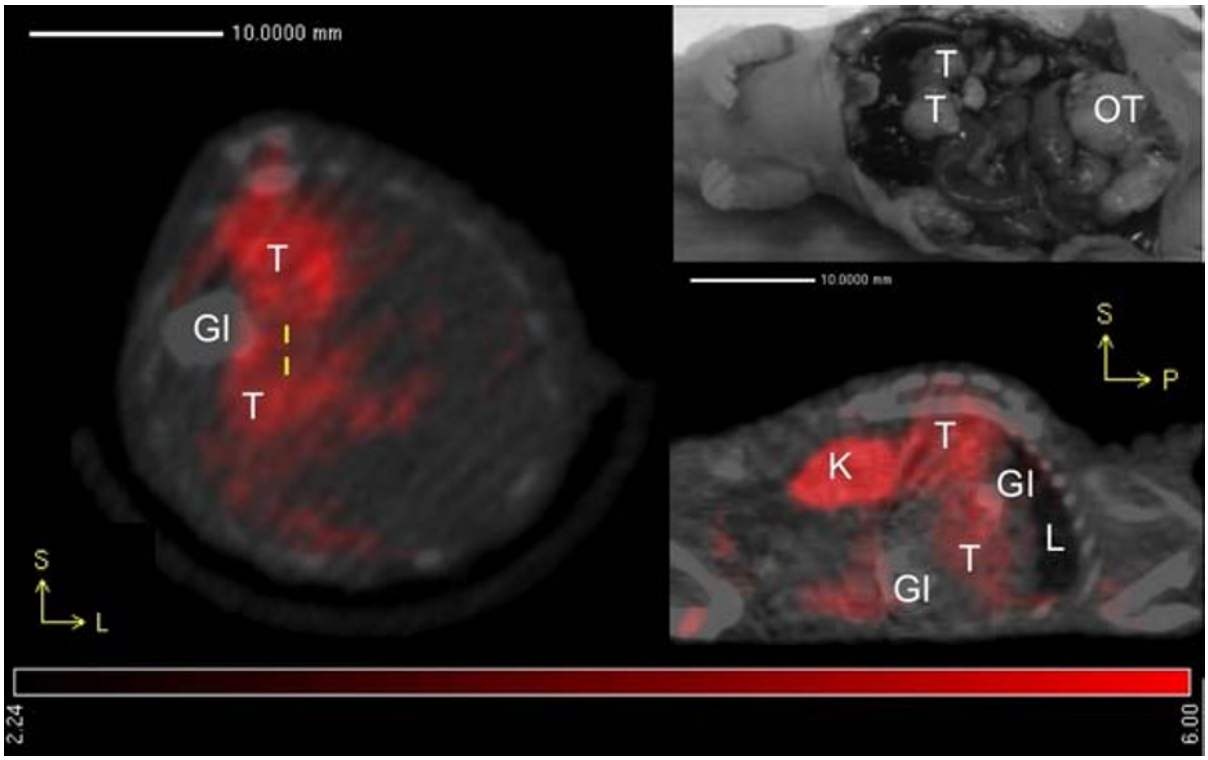

(left) Axial PET/CT section of mouse showing tumor FDG uptake (red, T) surrounding the bowel (GI) which is contrast-enhanced using BaSO4. (bottom-right) Corresponding sagittal slice, with kidney (K) and lung (L) labelled. (top-right) Photo of mouse with tumors highlighted. Tumor shown in PET images (T) is located dorsal to the liver, in the omentum. Large ovarian tumor also visible (OT). Colorbar units are %ID/g (range 2.2-6.0).

Disclosure of author financial interest or relationships:

R. Ali, Bell Biosystems, Inc., Consultant; Bell Biosystems, Inc., Stockholder; **K. Fuh**, None; **A. Vega**, None; **D. Marcellin**, None; **M. Rafat**, None; **D.A. Chan**, Ruga, Inc., Consultant; Ruga, Inc., Stockholder; **A. Giaccia**, RUGA, Stockholder; Proacta, Stockholder; **E.E. Graves**, Bell Biosystems, Stockholder .

Presentation Number **P 080**
Poster Session 1
September 18, 2013 / 18:00-18:00 / Room: Exhibit Hall B

Detecting the therapeutic efficacy of photodynamic therapy (PDT) of tumors - the necessity of a multiplexed imaging approach to visualize different molecular targets

Katja Haedicke[1], Susanna Gräfe[2], Frank G. Lehmann[3], Werner A. Kaiser[1], **Ingrid Hilger**[1], *[1]Experimental Radiology, Institute of Diagnostic and Interventional Radiology I, Jena, Germany; [2]Research & Development, biolitec research GmbH, Jena, Germany; [3]Dyomics GmbH, Jena, Germany. Contact e-mail: Ingrid.Hilger@med.uni-jena.de*

Introduction: Photodynamic therapy (PDT) is a minimally invasive tumor treatment modality which uses laser light as the therapeutic tool. After administration of a photosensitizing agent the tumor is illuminated with light to induce reactive oxygen species within the tumor cells. Subsequently, tumor elimination is expected to be the result of both, the formation of apoptotic cells and the destruction of the tumor vascularization. In this study we sought to evaluate whether these two processes are important parameters for the assessment of the therapeutic efficacy of PDT in an in vivo multiplexed fluorescence optical imaging approach. Methods: The internalization of the photosensitizer formulation Foslip® into tongue-squamous epithelium carcinoma (CAL-27) cells was examined in the in vitro and in vivo situation to comply with the requirements for a successful PDT. To detect apoptosis, annexin V was labeled with the near-infrared fluorescent dye DY-734 and characterized spectroscopically. The binding affinity was evaluated by flow cytometry and by determining the dissociation constant. In vivo, the annexin probe was injected in CAL-27 tumor bearing mice at two days and two weeks after PDT and the fluorescence intensity was evaluated semiquantitatively with time. The tumor vascularization was detected with the commercial contrast agent IRDye® 800CW RGD over a time up to three weeks after PDT, which was injected into the same animals once a week. Statistical significance of fluorescence signals ($p \leq 0.05$) was analyzed by a two-tailed Students t test. Results: In vitro, Foslip® showed a peri-nuclear enrichment in CAL-27 cells and in vivo a strong enrichment in mice tumors. After labeling with annexin V, the spectroscopic properties of the dye DY-734 were not shifted and our probe showed an absorption maximum at 715 nm and an emission maximum at 750 nm. The binding of our probe was much stronger and thus specific to apoptotic in comparison to non-apoptotic tumor cells (17 % vs. 1 %). The very high affinity binding could be corroborated with a dissociation constant of 20 nM. With our multiplexed imaging approach, the therapeutic efficacy of PDT via apoptotic cells could be detected just shortly after therapy at two days but not longer time thereafter. In contrast, the tumor vascularization illustrated the therapeutic efficacy at later time points after PDT, especially with a decrease of the fluorescence signal in the central tumor area. Conclusion: The simultaneous detection of different molecular targets allows us to understand molecular mechanisms of tumor response to PDT. The multiplexed imaging of more than one effect is essential to prevent false negative statements. When imaging molecular targets in tumor cells, the probe accessibility from the vasculature particularly at longer periods of time after therapy needs to be determined as well.

Disclosure of author financial interest or relationships:
K. Haedicke, None; **S. Gräfe**, Biolitec Research GmbH, Employment; **F.G. Lehmann**, Dyomics GmbH, Stockholder; Dyomics GmbH, Employment; **W.A. Kaiser**, None; **I. Hilger**, None.

Presentation Number **P 081**
Poster Session 1
September 18, 2013 / 18:00-18:00 / Room: Exhibit Hall B

In Vivo Molecular Optical Imaging of Apoptosis Reveals Early Response to Treatment in New Therapies for Gastrointestinal Stromal Tumors

*Lori Rink[1], **Harvey Hensley**[1], Karthik Devarajan[1], James R. Johnson[2], David Piwnica-Worms[2], Andrew Godwin[3], Margaret vonMehren[1], [1]Fox Chase Cancer Center, Philadelphia PA, PA, USA; [2]School of Medicine, Washington University, St. Louis, MO, USA; [3]School of Medicine, University of Kansas, Kansas City, KS, USA. Contact e-mail: harvey.hensley@fccc.edu*

Introduction: Gastrointestinal stromal tumors (GISTs), with an estimated annual incidence of ~6,000 new cases each year in the United States, are the most common mesenchymal tumors of the gastrointestinal tract. The current treatment for advanced GIST is imatinib mesylate (IM).The efficacy of IM in GIST is attributed to the presence of gain of function mutations of the target of IM, KIT, in approximately 75% of GISTs. Other common mutations in GIST include gain-of-function in PDGFRA and BRAF. Response to IM treatment has been correlated with the site of the mutation in KIT, with patients with tumors possessing an exon 11 (KIT) or 12 (PDGFRA) mutation demonstrating the strongest responses to therapy. Unfortunately, primary and/or secondary resistance to IM occurs in most patients within 2 years of treatment. An additional six months in median patient survival can be gained with the addition of Sunitinib treatment, but it is clear that an improved treatment protocol is needed. Such an approach would be facilitated by a better understanding of imaging as it correlates with biologic markers of response. In particular, imaging that informs more directly about cell death may be superior to current techniques. Here, we use molecular imaging technology employing (NIR) imaging probes in combination with three-dimensional fluorescence molecular tomography (FMT) for assessing therapeutic response, ultimately optimizing our understanding of the biologic effects of these agents. Methods: GIST-T1, a human patient-derived cell line, was grown as a xenograft in the flanks of nude mice. We evaluated the potential of two NIR probes, PSVue794, (Molecular Targeting Technologies) and KcapQ647 to detect apoptosis, and compared this to tumor size measured by magnetic resonance imaging (MRI) in response to IM treatment. PSVue794, used as a marker of apoptosis, binds to phosphatidylserine residues exposed on the cell surface of apoptotic cells and, in addition, binds to negatively-charged necrotic regions found in various tumors through its zinc (II)-dipicolylamine (Zn-DPA). KcapQ647, a cell penetrating activatable probe was used to detect apoptosis-associated caspase acitivity. Determination of the tumor boundaries was made by choosing regions of interest based on the distribution of Intergrisense680 (PerkinElmer), an αVβ3 integrin targeted imaging agent. Three dimension FMT image sets were made with a PerkinElmer2500. Results:Our studies revealed statistically significant increases in the rate of apoptotic activity due to IM treatment (compared to control) using both the PSVue TM794 and KcapQ647 probes (p= 0.002, 1.41e-04 respectively) as early as 24 hours post IM treatment. This preceded the observation of tumor shrinkage as measured by MRI. Validation: These findings have been confirmed by IHC. Conclusion:We believe that this methodology will allow for faster and more effective screening of novel therapies in preclinical GIST models.

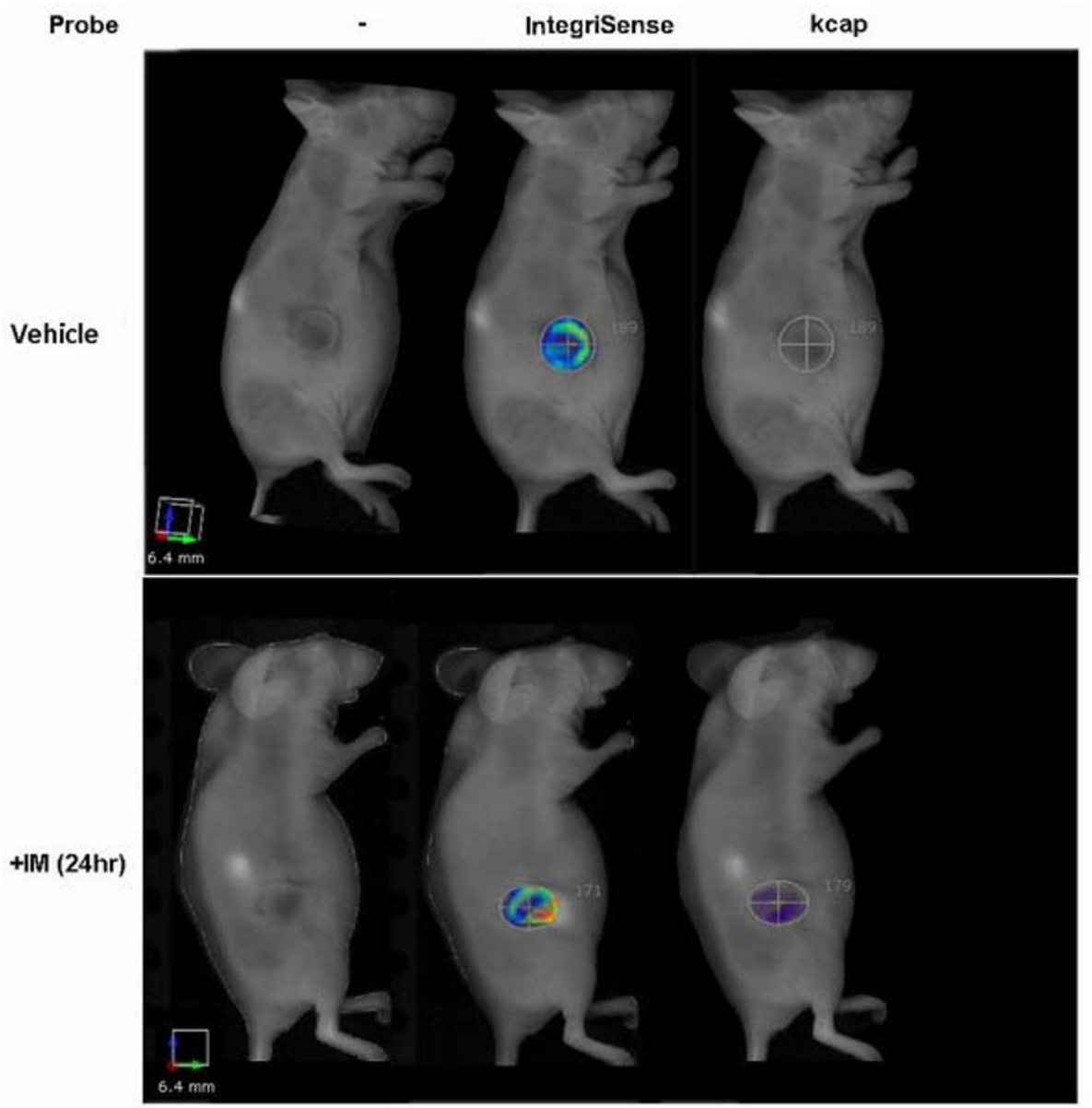

Imaging a Gist T1 tumor grown in a nude mouse. Left: external image of the mouse, middle: integrisense680 (used to mark the tumors on the FMT datasets) right: KcapQ647. At 24 hours post treatment we saw a marked increase in KcapQ647 uptake, indicating increase apoptotic activity. Similar results were seen for the imaging agent PSVue794.

Disclosure of author financial interest or relationships:
L. Rink, None; **H. Hensley**, Imaginab, Grant/research support; **K. Devarajan**, None; **J.R. Johnson**, None; **D. Piwnica-Worms**, None; **A. Godwin**, None; **M. vonMehren**, None.

Presentation Number **P 082**
Poster Session 1
September 18, 2013 / 18:00-18:00 / Room: Exhibit Hall B

Validation and Workflow Enhancements for Three-Dimensional Bioluminescence Tomography

Jacob Hesterman[1], *Matthew D. Silva*[1], *Balázs Viszoczki*[1], *Tonya Coulthard*[2], *Robert Sandler*[2], *Jack Hoppin*[1], [1]*inviCRO, Boston, MA, USA;* [2]*Aspect Imaging, Toronto, ON, Canada. Contact e-mail: hesterman@invicro.com*

Bioluminescence imaging (BLI) remains the most prevalent in vivo pre-clinical imaging modality due to its high-sensitivity for detecting viable cell populations, relatively low instrument and experiment cost, capability for high-throughput experimentation, and ease of use. While 2D imaging remains the standard, increasing success has been reported with tomographic BLI reconstructions. The continued adoption of 3D BLI relies on increasing the value to the scientist and experiment in four key areas: (1) Accurate localization of signal source, (2) A quantitative link between reconstructed volume radiance and cellular light output, (3) Sustained high throughput, and (4) Continued ease of use. Building on previous example data [1], this work employed rigorous phantom experiments to test the reconstruction performance in these areas. Multiple 62x22x12 mm3 tissue phantoms of 2% agar, 0.1% sodium azide, 1% intralipid, 20μM bovine hemoglobin, and 50mM Tris-buffered saline were created with assistance from Dr. Changqing Li (Univ. of California, Merced) [2]. During construction, 1.6mm OD / 0.58 mm ID tubing was placed either at equal height length-wise or diagonally. Tubing could be exchanged to manipulate the luminescent source distribution. For phantom experiments, chemiluminescence, generated using commercial glow stick components, rather than bioluminescence was utilized to improve control over the light output (brightness and duration). A measured characterization of the chemiluminescent spectrum at the acquisition wavelengths was used as an input to the reconstruction algorithm. Data were acquired on an IVIS Spectrum (Perkin Elmer, Inc.) using a protocol in which 7 open filter images were interleaved with 6 filtered images from 560-660nm in 20 nm increments. Experimental conditions were varied during acquisition to evaluate key parameters, such as concentration/brightness, depth, volume, and ability to resolve multiple objects at varying distances. A reconstruction algorithm employing a light propagation model based on a set of high-order simplified spherical harmonics was used to generate 3D spatial maps of the underlying source distribution for all acquisitions [3]. Reconstructions accurately reflected the spatial distribution of the underlying source, including the resolution of multiple line phantoms that are indistinguishable in the 2D data (See Image 1). A strong correlation was observed in 2D and 3D signal values for sources of varying light concentration (r2 = 0.99). Acquisition times for 3D input data remain longer than for most 2D scans, however, use of a mirrored bed and automated post-processing routines (LumiQuant™, Aspect Imaging and inviCRO) streamline acquisition and reconstruction procedures, maintaining ease of use relative to 2D scanning. These encouraging phantom data are necessary to validate the operational success and limits of any reconstruction method and, along with successful implementation in preclinical cancer models, highlight the future value of this tool. References: [1] Hesterman JY, et al., WMIC 2012: P541, [2] Li C, et al., Opt Express. 2009; 17: 7571-85. [3] Klose AD, et al., Med. Phys. 2010;37:329-38.

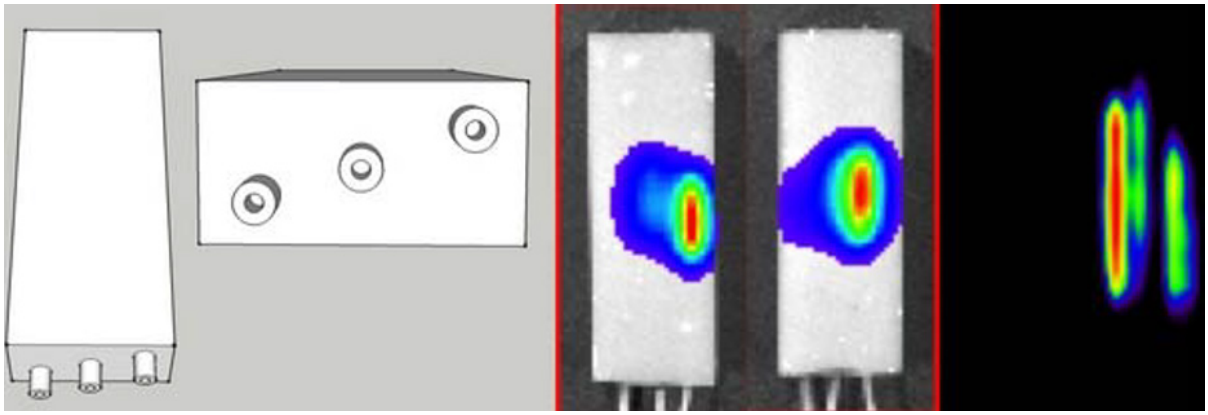

Disclosure of author financial interest or relationships:
J. Hesterman, inviCRO, LLC, Employment; **M.D. Silva**, inviCRO, LLC, Employment; **B. Viszoczki**, inviCRO LLC, Employment; **T. Coulthard**, Aspect Imaging, Employment; **R. Sandler**, Aspect Imaging, Employment; **J. Hoppin**, inviCRO, Stockholder .

Presentation Number **P 083**
Poster Session 1
September 18, 2013 / 18:00-18:00 / Room: Exhibit Hall B

In vivo tumor vasculature targeting and PET imaging with reduced graphene oxide

Sixiang Shi[1], *Kai Yang*[2], *Hao Hong*[3], *Todd E. Barnhart*[4], *Zhuang Liu*[2], *Weibo Cai*[1,3], [1]*Materials Science Program, University of Wisconsin - Madison, Madison, WI, USA;* [2]*Jiangsu Key Laboratory for Carbon-Based Functional Materials and Devices, Institute of Functional Nano and Soft Materials Laboratory, Soochow University, Suzhou, China;* [3]*Department of Radiology, University of Wisconsin - Madison, Madison, WI, USA;* [4]*Department of Medical Physics, University of Wisconsin - Madison, Madison, WI, USA. Contact e-mail: sshi9@wisc.edu*

Objectives : Graphene-based materials exhibit unique properties for biomedical applications including cancer therapy. Especially, reduced graphene oxide (RGO) is a desirable platform for photothermal therapy. Our goal was to employ RGO for in vivo tumor vasculature targeting, and quantitatively evaluate pharmacokinetics and tumor targeting with positron emission tomography (PET), using ^{64}Cu as the radiolabel. Methods : RGO sheets, with amino group-terminated polyethylene glycol (PEG) chains on the surface, were conjugated to NOTA (1,4,7-triazacyclononane-1,4,7-triacetic acid, for ^{64}Cu labeling) and TRC105 (an antibody that binds to CD105, a receptor overexpressed on tumor vasculature). FACS analyses, size measurements, and serum stability studies were performed to characterize the RGO conjugates before in vivo investigation (PET, biodistribution, and blocking studies) in 4T1 murine breast tumor-bearing mice. Imaging results were validated by histological assessment. Results : The RGO conjugate, ^{64}Cu-NOTA-RGO-TRC105, had a size range of 20-80 nm. It exhibited CD105 specificity and superb stability in vitro and in vivo. Serial PET imaging and biodistribution studies revealed that 4T1 tumor uptake of ^{64}Cu-NOTA-RGO-TRC105 was clearly visible at 0.5 h post-injection (p.i.) and remained stable over time (5.0±0.6, 5.6±0.2, 5.7±0.2, 4.5±0.4, and 4.0±0.5 %ID/g at 0.5, 3, 6, 24, and 48 h p.i.; n = 4), which gave excellent tumor contrast and was several fold higher than the non-targeted RGO conjugate. Various in vivo (e.g. blocking with TRC105), in vitro (e.g. flow cytometry), and ex vivo (e.g. histology) studies further confirmed the specificity of ^{64}Cu-NOTA-RGO-TRC105 for targeting CD105 on the tumor vasculature. Little extravasation was observed, confirming that tumor vasculature targeting is an ideal approach for RGO. Conclusions : This is the first report of in vivo tumor targeting and imaging with RGO. This proof-of-principle study opened up new perspectives for future research and cancer theranostics using graphene-based materials, which are desirable nanoplatforms for biomedical applications because of the versatile chemistry and low toxicity.

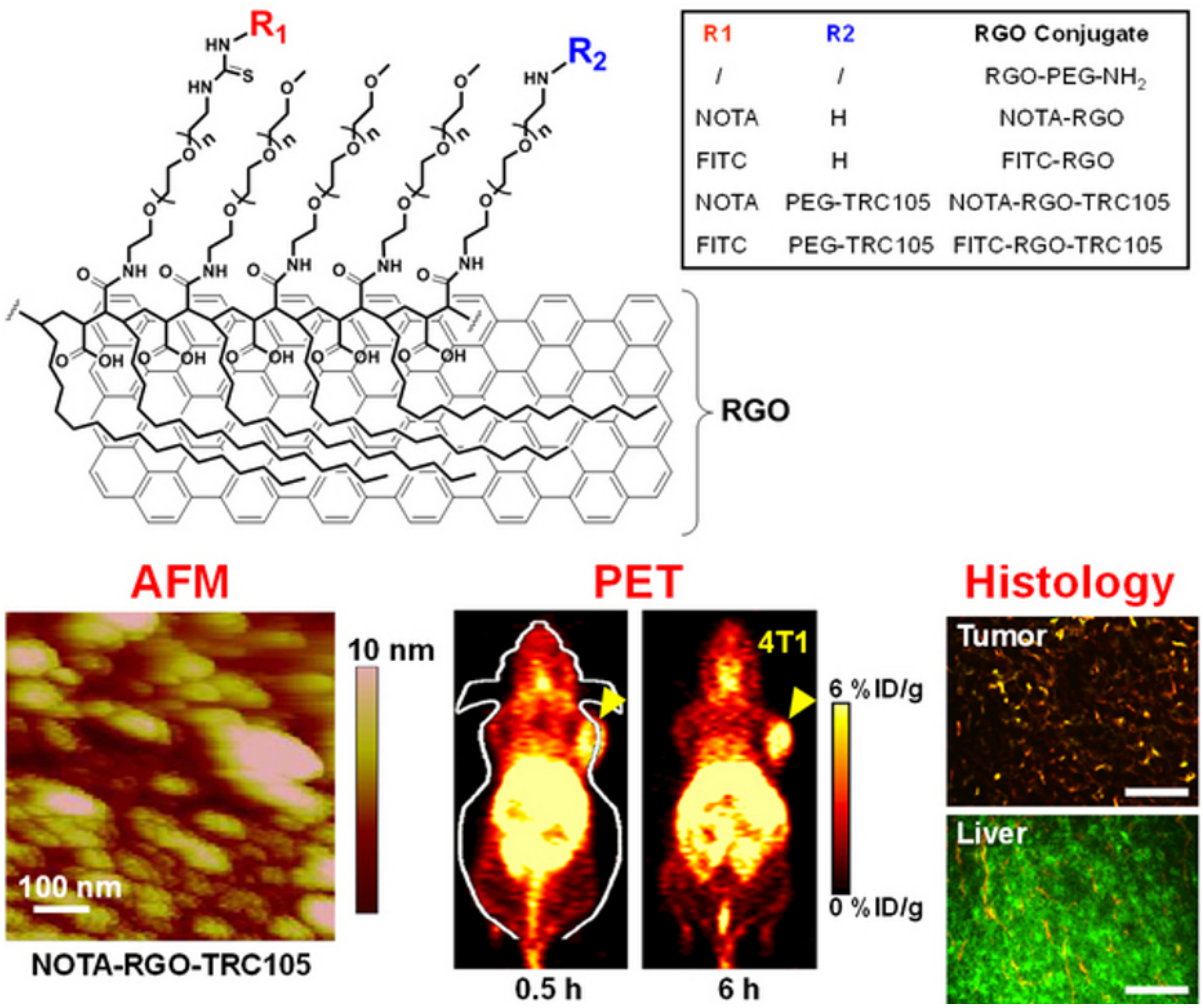

Disclosure of author financial interest or relationships:
S. Shi, None; **K. Yang**, None; **H. Hong**, None; **T.E. Barnhart**, None; **Z. Liu**, None; **W. Cai**, None.

Presentation Number **P 084**
Poster Session 1
September 18, 2013 / 18:00-18:00 / Room: Exhibit Hall B

A Toll-like Receptor 2 (TLR2) Targeted Probe for Imaging Pancreatic Cancer

Amanda Shanks Huynh[1], *Valerie E. Moberg*[1], *Jennifer M. Morse*[2], *Xuan Huang*[1], *Haibin Tian*[1], *Barbara A. Centeno*[3], *Josef Vagner*[4], *David L. Morse*[1], [1]*Cancer Imaging & Metabolism, H, Lee Moffitt Cancer Center & Research Institute, Tampa, FL, USA;* [2]*Comparative Medicine, H. Lee Moffitt Cancer Center & Research Institute, Tampa, FL, USA;* [3]*Anatomic Pathology, H. Lee Moffitt Cancer Center & Research Institute, Tampa, FL, USA;* [4]*Bio5 Institute, University of Arizona, Tucson, AZ, USA. Contact e-mail: amanda.huynh@moffitt.org*

A major goal for improving survival rates of cancer research is to employ new methods for detection, diagnosis and treatment. To achieve this goal, it is necessary to develop probes that specifically target cancer relative to normal non-neoplastic tissue. Fluorescent molecular imaging probes can be used for intraoperative surgical guidance and cancer staging. We have reported Toll-like receptor 2 (TLR2) as a bona fide cell-surface marker for pancreatic adenocarcinoma. We then developed a high-affinity TLR2 binding ligand conjugated to a near-infrared fluorescent (NIRF) dye: TLR2L-800 (IR800CW-mercaptoproprionic acid-PEGO-Cys(S-[2,3-bis(palmitoyl)oxy-(R)-propyl])-Gly-DSer-PEGO-NH2) exhibits high binding affinity (11 nM Ki) and high agonist activity (34 nM EC50) in genetically engineered overexpressing human TLR2 cells; while binding affinity is still high (67 nM Ki) in human pancreatic cancer (SU.86.86 cells) that endogenously overexpresses TLR2. We have also demonstrated the use of TLR2L-800 for intraoperative detection of pancreatic cancer. TLR2L also has potential in cancer immunotherapy as an immune adjuvant. Thus, we chose to further characterize this agent's potential as a fluorescence molecular imaging probe. We determined that TLR2L-800 is highly hydrophilic by determining the distribution coefficient (logD pH7.4 = -2.90+0.15); we also evaluated the stability of TLR2L-800 using plasma stability assays. To evaluate the pharmacokinetics and biodistribution of TLR2L-800, fluorescence imaging was performed on multiple optical imaging systems (PerkinElmer IVIS 200 and FMT2500XL, and ART Optix MX3) using various TLR2 expressing pancreatic tumor xenograft mouse models (subcutaneous and orthotopic). Tumor specificity was observed (Figure 1A, B, D, E) with a maximum 3.3 fold of enhancement (TLR2+ tumor/TLR2 - tissue) occurred at 24 h (Figure 1C); while fluorescence signal was retained in the TLR2 expressing tumor xenografts up to 96 h post-injection. Ex vivo fluorescence images determined uptake in other major organs (kidneys, liver, heart, lungs, GI tract, spleen and pancreas) by the TLR2L-800 probe (Figure 1F), excretion of probe by the kidneys, bladder and liver is indicated by these results. Excised tumors and surrounding pancreas tissue were IHC stained for TLR2 expression. The human orthotopic xenograft tumors in mice exhibited a similar IHC & histological staining pattern compared to human pancreatic cancer tissue samples (Figure S1 E). We anticipate that the clinical use of TLR2L-800 will improve pancreatic cancer survival by intraoperative fluorescence guided detection. Future studies include studying tumor uptake, penetration, and extravasation by intravital confocal microscopy using dorsal window chamber mouse models.

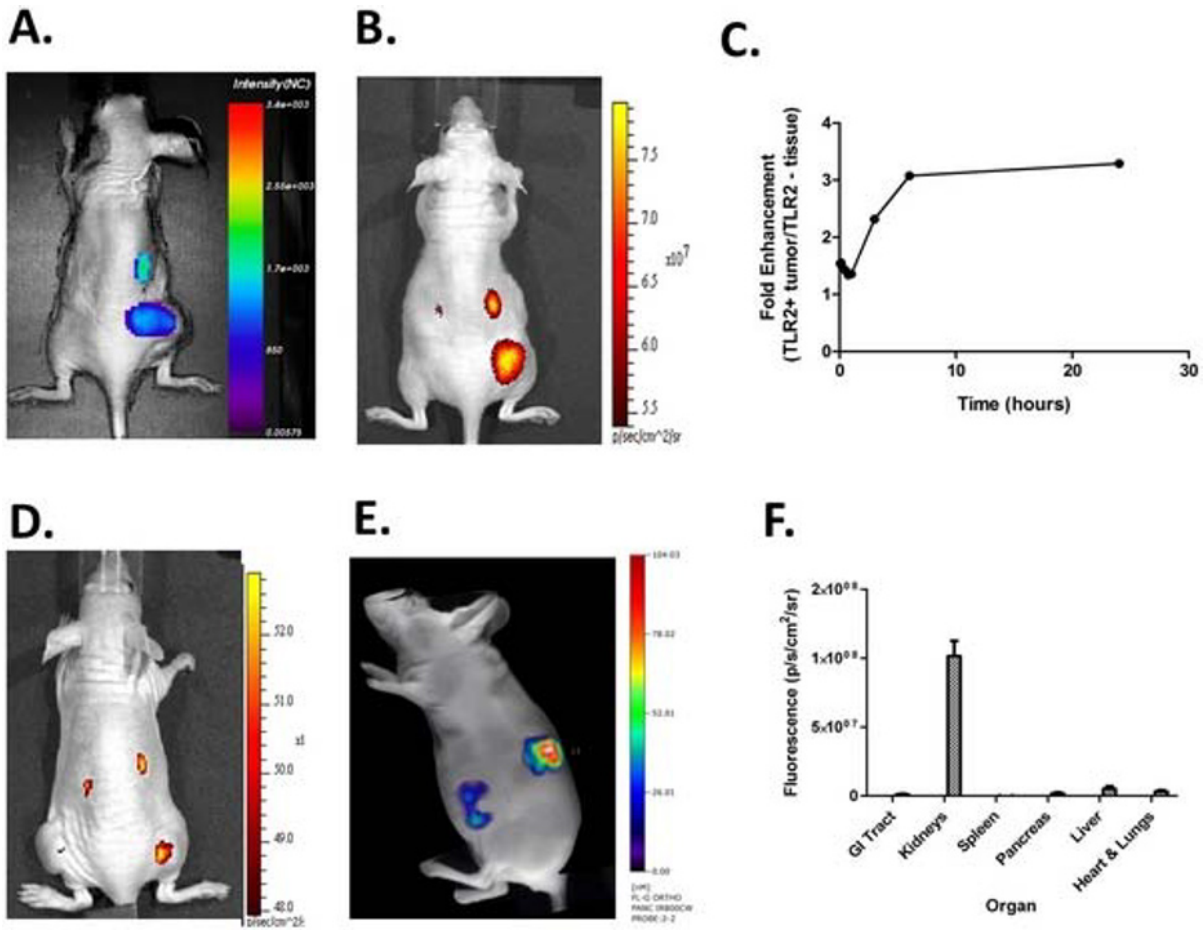

Figure 1. Fluorescence images acquired on A) Optix MX3, ART and B) IVIS 200, Perkin-Elmer at 24 h post-injection of 100 nmol/kg dose of TLR2L-800 showing uptake of probe in human pancreatic cancer xenograft tumors with endogenous TLR2 expression (SU.86.86 cells) on the right flanks. C) Graph shows the fold of enhancement (TLR2 + tumor / negative tissue) of fluorescence signal from TLR2L-800, with the highest FOE=3.3 at 24 h (n=9). D) Pancreatic tumor selectivity of TLR2L-800 is shown in a bilateral -/+ tumor xenograft model with TLR2 negative (MiaPaca-2) tumor on left flank and TLR2 positive (MiaPaca-2/hTLR2) tumor on the right flank at 24 h post-injection. E) TLR2L-800 identifies the orthotopic pancreatic tumor (SU.86.86 cells) at 24 h post-injection. F) Graph shows the biodistribution of TLR2-800 in organs imaged ex vivo at 24 h.

Disclosure of author financial interest or relationships:
A. Huynh, None; **V.E. Moberg**, None; **J.M. Morse**, None; **X. Huang**, None; **H. Tian**, None; **B.A. Centeno**, None; **J. Vagner**, None; **D.L. Morse**, LiCor Biosciences, Grant/research support .

Presentation Number **P 085**
Poster Session 1
September 18, 2013 / 18:00-18:00 / Room: Exhibit Hall B

Monitoring of NK cells immunotherapy using in drug resistance of human breast adenocarcinoma MCF-7/ADR cells

Mi-hye Hwang, *Jung Eun Kim, Shin Young Jeong, Sang-Woo Lee, Jaetae Lee, Byeong-Cheol Ahn, Department of Nuclear Medicine, Kyungpook National University,School of Medicine, Daegu, Republic of Korea. Contact e-mail: hye6887@nate.com*

Objective: We attempted to monitor therapy effect human breast adenocarcinoma MCF-7 cell line and adriamycin-resistant MCF-7/ADR cell line by NK-92MI cells using renilla luciferase. Methods: We established Human breast cancer cell line (MCF-7/RC and MCF-7/ADR-RC, as a target) expressing renilla luciferase and mCherry. NK92-MI cell line (as effector) was purchased from ATCC. To evaluate apoptosis induction by NK92-MI cells using an MCF-7/RC and MCF-7/ADR-RC, effector and target cell were co-cultured at E/T ratio of 2, 5, and 10/1 for 16 h and then bioluminescence was measured. Viability of target cell was determined using a CCK assay. In vivo bioluminescence imaging was monitored therapeutic effect by NK92-MI cells using the renilla luciferase. Results: Bioluminescence in MCF-7/RC and MCF-7/ADR-RC cells was decreased in an effectors-number dependent manner and a moderate correlation was observed between bioluminescence and E/T ratio (Fig 1. E/R ratio relative cell viability ; media, 2:1, 5:1 and 10:1, 72.5%, 60%, 56.1% (MCF-7/RC cells) and 39%, 34.9%, 36.5% (MCF-7/ADR/RC cells) , respectively). CCK assay showed the decreased both cells viability by number increase of NK92-MI cells. The therapeutic effect was assessed by bioluminescent imaging at 15, 21 and 28 days after tumor xenograft. Conclusions: We successfully established MCF-7/RC and MCF-7/ADR-RC cell line expressing renilla luciferase and monitored therapeutic effect by NK92-MI cells using the luciferase activity in vitro and in vivo. These results suggest that NK cells mediated immunotherapy can be use in breast cancer cells or drug-resistant breast cancer cells.

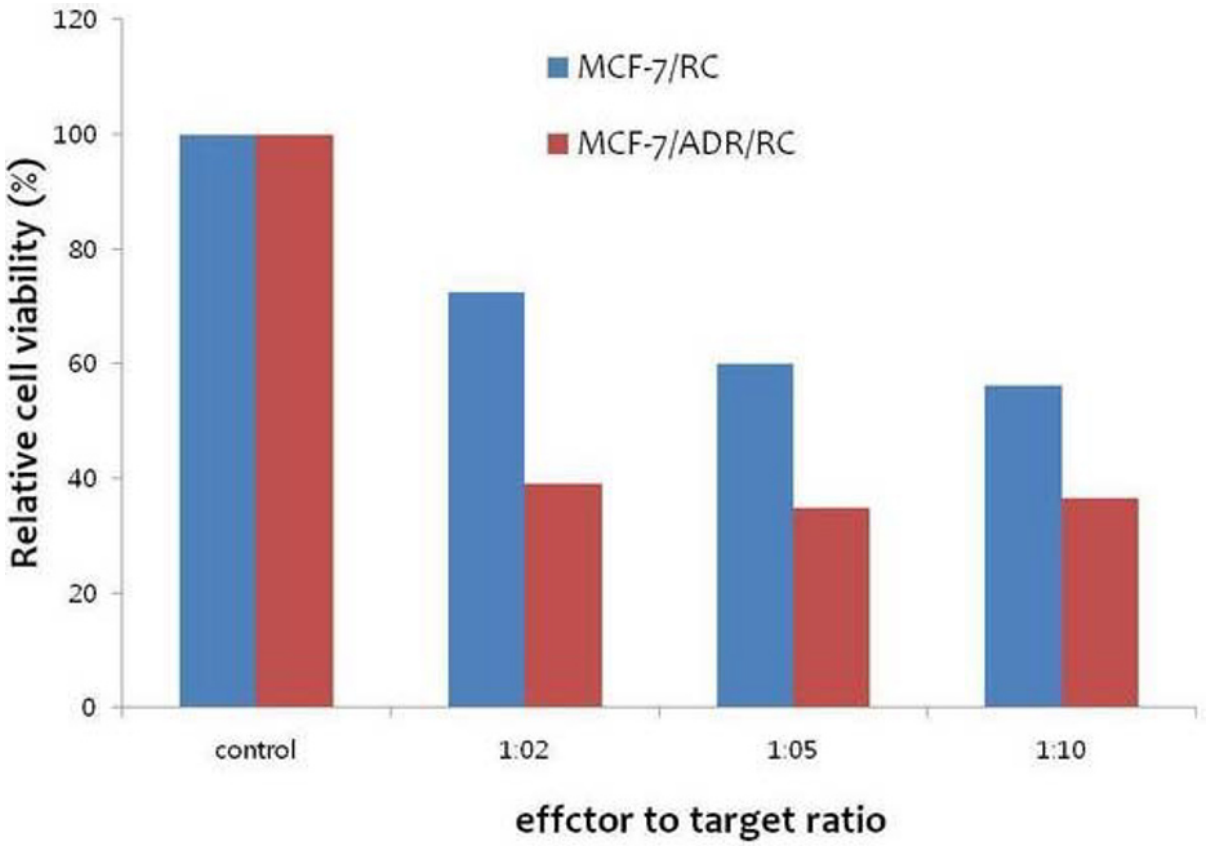

Disclosure of author financial interest or relationships:
M. Hwang, None; **J. Kim**, None; **S. Jeong**, None; **S. Lee**, None; **J. Lee**, None; **B. Ahn**, None.

Presentation Number **P 086**
Poster Session 1
September 18, 2013 / 18:00-18:00 / Room: Exhibit Hall B

Evaluation of ^{18}F-albumin as a potential PET vascular imaging agent

Elaine Jagoda[1], *Falguni Basuli*[2], *Mark Williams*[1], *Karen J. Wong*[1], *Michael V. Green*[1], *Jurgen Seidel*[1], *Biying Xu*[2], *Frank Kuo*[1], *Gary L. Griffiths*[1], *Peter Choyke*[1], [1]*Molecular Imaging program, NCI, Bethesda, MD, USA;* [2]*Imaging Probe Development Center, NHLBI, NIH, Bethesda, MD, USA. Contact e-mail: ejagoda@mail.nih.gov*

Objectives: A PET blood pool imaging agent could potentially have broad medical diagnostic and prognostic applications, e.g. in assessing cardiac function, vascular integrity, and the vascular status of cancerous lesions. Such an agent could also, in principle, allow near real time estimation of absolute organ or tissue blood volume changes associated with trauma or the efficacy of targeted anti-angiogenic cancer therapies. Since native albumin possesses a long blood biological half-life, ^{18}F radiolabeled albumin (F-ALB) may exhibit suitable retention and in vivo stability for such measurements. In these studies we determined the biodistribution, pharmacokinetics, and imaging characteristics of F-ALB in normal rats. **Methods**: F-ALB was synthesized using an indirect method via coupling of [^{18}F] 2, 3, 5, 6-tetrafluorphenyl 6-fluornicotinate to rat albumin (amino groups). For the biodistributions, rats were injected with F-ALB and blood and tissue uptakes were determined at 0.5, 1, 2 or 4 h post injection. Uptakes were expressed as differential uptake ratios (DUR): [(%Injected Dose/tissue (g))*(body weight (g))]/100. For the PET studies rats were injected (IV) with F-ALB and imaged from 0.5 to 4h post injection. **Results**: In normal rats the highest retention (DURs) of F-ALB occurred in the blood: 11.5, 10.0, 8.5, and 6.8 at 0.5, 1, 2 and 4 h, respectively (Table 1). The next highest uptakes (DURs) over the same time course were observed in lungs and heart ranging from 5.1 to 3.0 and 3.4 to 2.4, respectively. The lungs and heart DURs were decreased 56% to 60% and 65% to 70%, respectively compared to blood DURs at the same times. Although liver and kidney DURs were similar at 0.5 h, liver DURs decreased 40% from 0.5h (2.4 DUR) to 4h (1.5 DUR), whereas kidney uptakes decreased 20% from 0.5h (2.5 DUR) to 4h (2.0 DUR). Femur DURs ranged from 1.5 to 1.2 over the time course exhibiting little change indicating minimal defluorination. In the PET images the rat vasculature was clearly visualized with the ventricles of the heart the most prominent (Fig. 1); the lungs, kidney, and liver could be discerned but with lower uptakes. Although the anesthetized imaged rats at 4h had higher blood and tissue DURs compared to blood and tissues of awake rats at similar times, the blood to tissue ratios were comparable except for the kidneys indicating that anesthesia had slowed the rate of F-ALB clearance. In some images, unusually high uptakes were observed in normally low uptake tissue regions which appeared to correspond visually to hematomas or inflammation. These results would suggest that this inadvertent tissue trauma experienced by the rat during the study had resulted in vessel disruption leading to an increase of F-ALB in these regions. **Conclusions**: F-ALB was well retained in rat vasculature ($t_{1/2}$ = 5.97 h) exhibiting suitable in vivo retention for tissue blood volume determinations. These data also suggest that ^{18}F labeled human albumin may have clinical diagnostic and prognostic utility for determining tissue vascular changes due to treatment or trauma.

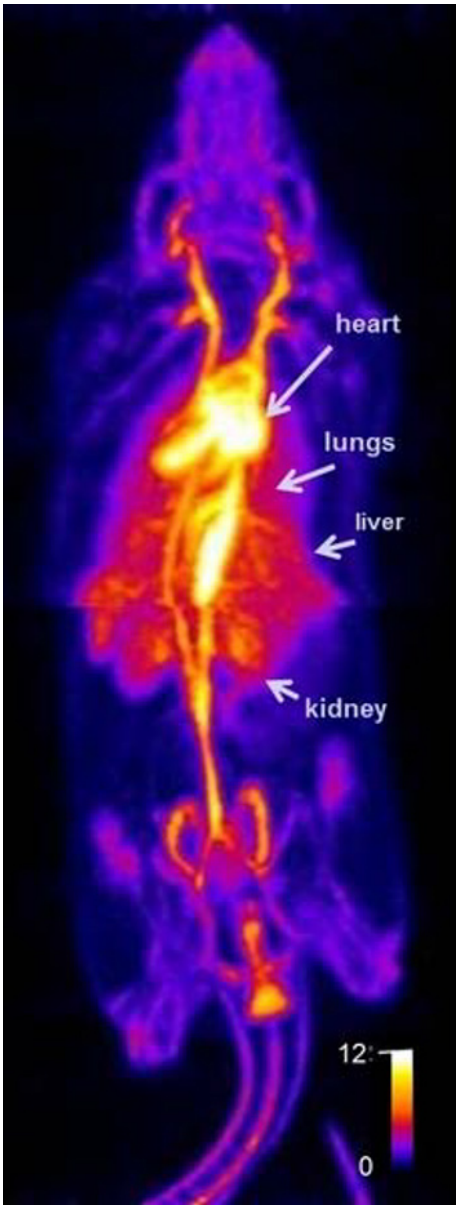

Fig.1. Rat microPET image (MIP whole body projection image) obtained 0.5 h after IV injection of ^{18}F-albumin (~700 μCi)

Table 1 Biodistribution of ^{18}F-albumin in normal rats

^{18}F-albumin Blood and Tissue Uptakes (mean DUR (SD)) [1] n=5				
Time (h) post ^{18}F-albumin injection	0.5	1	2	4
Blood	11.5 (1.3)	10.0 (0.7)	8.5 (0.4)	6.8 (1.3)
Heart	3.4 (0.2)	2.9 (0.3)	2.8 (0.3)	2.4 (0.5)
Lungs	5.1 (0.9)	4.1 (0.5)	3.4 (0.3)	3.0 (0.5)
Liver	2.4 (0.3)	2.1 (0.2)	1.8 (0.1)	1.5 (0.4)
Kidney	2.5 (0.4)	2.5 (0.2	2.3 (0.2)	2.0 (0.4)
Femur	1.5 (0.2)	1.4 (0.2)	1.5 (0.2)	1.2 (0.2)

[1]DUR(Differential Uptake ratio) each value represents: mean DUR(SD),n= 5; DUR= [(%Injected Dose/tissue (g))*(body weight (g))]/100

Disclosure of author financial interest or relationships:

E. Jagoda, None; **F. Basuli**, None; **M. Williams**, None; **K.J. Wong**, None; **M.V. Green**, None; **J. Seidel**, None; **B. Xu**, None; **F. Kuo**, None; **G.L. Griffiths**, None; **P. Choyke**, None.

Presentation Number **P 087**
Poster Session 1
September 18, 2013 / 18:00-18:00 / Room: Exhibit Hall B

A Novel Dual-contrast MRI Nanoprobe for Characterizing Tumor Extracellular Matrix Integrity

Arvind P. Pathak[1,2], **Yoshinori Kato**[1,2], [1]*Division of Cancer Imaging Research, JHU ICMIC Program, The Russell H. Morgan Department of Radiology and Radiological Science, The Johns Hopkins University School of Medicine, Baltimore, MD, USA;* [2]*Department of Oncology, The Sidney Kimmel Comprehensive Cancer Center at Johns Hopkins, Baltimore, MD, USA. Contact e-mail: ykato@mri.jhu.edu*

Purpose: Active targeting of cytotoxic agents to cancer cells using nanocarriers is an attractive strategy for efficient and safe cancer chemotherapy. However, direct access of nanocarriers to cancer cells is restricted *in vivo* due to elevated interstitial fluid pressure, poor tumor perfusion and hindrance from the extracellular matrix (ECM). This poses a serious hurdle for carrier-based targeted cancer therapy. The goal of this study was to assess the ability of dual-contrast MRI nanoprobes (Lip-Fe/Gd) to characterize differences in tumor ECM integrity via their differential intratumoral distribution and stability. **Methods:** Novel dual-contrast liposomes (Lip-Fe/Gd) encapsulating both, superparamagnetic iron oxide (SPIO) nanoparticles and GdDTPA were synthesized. This was based on the fact that co-encapsulation of small molecule T_1 and large molecule T_2 MRI contrast agents into liposomes enables us to distinguish between intact and degraded liposomes [1]. Therefore on *in vivo* MRI images, the SPIO helps identify the location of the liposomes in the tumor ECM, while released GdDTPA acts as an indicator of the *in vivo* stability of the liposomes. Liposomes were prepared using the sonication method, followed by extrusion. Two different human breast cancer (MCF-7 and MDA-MB-231) xenografts were grown in female SCID mice by injecting cancer cells into the mammary fat pad. All MR studies were carried out on a horizontal bore 9.4T scanner. MR images were acquired over time before and after i.v. injection of Lip-Fe/Gd. To visualize the intratumoral distribution of liposomes (i.e. by detecting SPIO), a 3D gradient echo sequence was used. A 3D fast spin echo sequence was also acquired to check *in vivo* stability of liposomes (i.e. by detecting GdDTPA released from liposomes). After *in vivo* MRI, tumors were excised, fixed, cut into 10 μm sections and their ECM characterized using second harmonic generation (SHG) microscopy. Region of interest analysis were carried out on the MRI data. SHG data were analyzed using a customized macro written for ImageJ.
Results/Discussion: I.v. injection of Lip-Fe/Gd resulted in successful delivery of MR probes to tumor tissue as detected in T_2*-weighted MR images. Immunohistochemistry confirmed that SPIO did not diffuse far from tumor vessels and was mostly localized to tumor vessel lumina. *In vivo* MRI also revealed a decrease in T_1 of the tumors, indicating degradation of liposomes within the tumor ECM. Although our SHG data demonstrated differences in extracellular matrix fibrillar collagen structure between the two types of tumors, we could not detect a corresponding difference in the intratumoral distributions of liposomes between them with *in vivo* MRI (**Fig. 1**). This was due to the limited resolution and low sensitivity of MRI combined with instability of the MRI probe in the tumor ECM. Future perspective: Developing a nanoprobe that is stable until it is taken up by cancer cells will permit more accurate noninvasive characterization of the tumor ECM. **References:** 1. Kato Y. et al. Magn Reson Med 2009;61:1059-1065. **Acknowledgement:** Grant support from EB008162, CA128793, and KG090640.

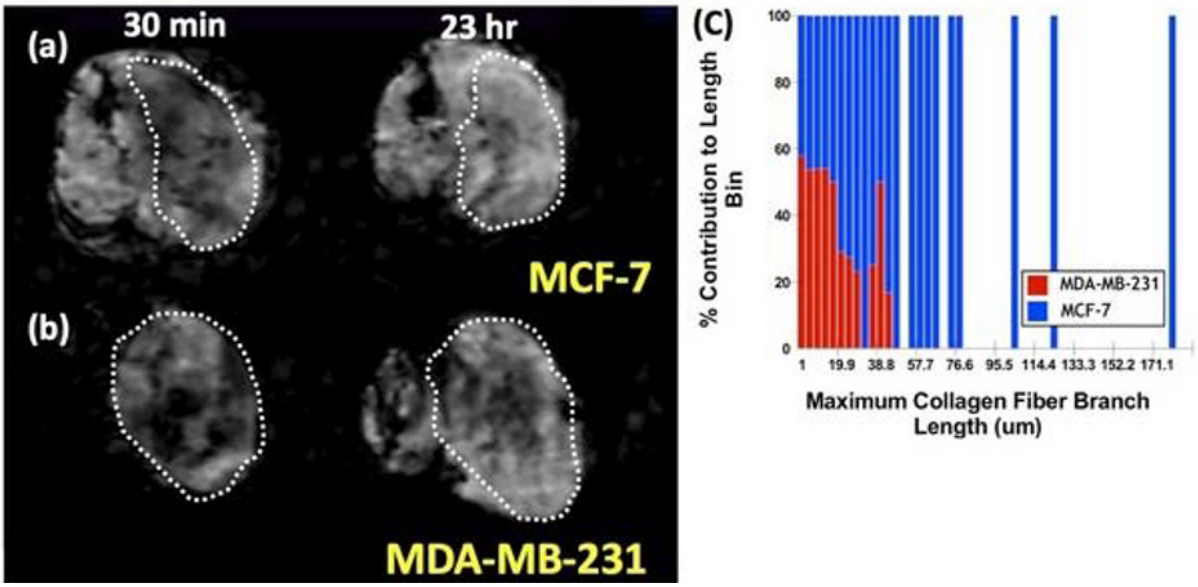

Fig. 1. (a) T_2*-weighted images of an MCF-7 tumor xenograft (white hashed line) for post-contrast time points. One can clearly see darkening in the hashed tumor ROI corresponding to successful delivery of iron nanoparticles. **(b)** T_2*-weighted images of an MDA-MB-231 tumor xenograft (white hashed line) for post-contrast time points. One can again see darkening in the hashed tumor ROI corresponding to iron nanoparticle delivery. **(C)** Stacked plot of the maximum collagen fiber branch length for the SHG image stacks, wherein one can clearly see that the MCF-7 tumors exhibit longer fibers than the MDA-MB-231 tumors.

Disclosure of author financial interest or relationships:
A.P. Pathak, None; **Y. Kato**, None.

Presentation Number **P 088**
Poster Session 1
September 18, 2013 / 18:00-18:00 / Room: Exhibit Hall B

Preclinical evaluation of single-photon emission computed tomography (SPECT) targeting EGFR in orthotopic breast tumor mouse models

Thomas Krüwel[1], *Joanna Napp*[2,1], *Christian Dullin*[1], *Joachim Lotz*[1], *Walter Stühmer*[2], *Frauke Alves*[2], [1]*Department of Diagnostic Radiology, University Medical Center Goettingen, Göttingen, Germany;* [2]*Max-Planck-Institute for Experimental Medicine, Göttingen, Germany. Contact e-mail: thomaskruewel@googlemail.com*

An early detection of cancer is important to ameliorate the overall prognosis. A prerequisite for successful therapeutic interventions is to retrieve as much accurate information on tumor load and spread as possible, as well as to assess different molecular characteristics of tumor lesions as early as possible, allowing the application of targeted therapeutic strategies tailored to specific patients in oncology. Here, we present first results of the development and preclinical evaluation of an imaging approach using single-photon emission computed tomography (SPECT) to target epidermal growth factor receptor (EGFR), which is highly overexpressed e.g. in colorectal-, mammary- or squamous cell carcinoma. A clinically approved antibody, Cetuximab, was used for the evaluation of EGFR targeting on tumors with SPECT in orthotopic mammary carcinoma mouse models. For this purpose the following cell lines with different EGFR expression levels were selected for application, validated by Western blotting and flow cytometry: MDA-MB-468 (+++), MDA-MB-231 (+) and MCF7 (-). First, the labeling of anti-EGFR antibody Cetuximab with 99mTc was optimized. The bioactivity of the labeled antibody (99mTc-Cetux) was verified after every derivatisation or labeling step using flow cytometry. The purity of the 99mTc-Cetux was analyzed by radio-HPLC. In vivo SPECT scans were performed at certain time points in tumor bearing mice after intravenous application of approx. 18 µg of 99mTc-Cetux corresponding to an activity of 100 MBq. Furthermore, in order to exclude false-positive signals, control mice received 100 MBq of the 99mTc-pertechnetate and biodistribution and clearance of unbound radionuclide was investigated over a period of 24 hours post injection. Cetuximab was efficiently labeled with 99mTc, yielding 99mTc-Cetux with a specific activity of approx. 6 MBq per µg of antibody. 99mTc-Cetux had a purity higher than 98% and showed almost unaltered binding to the EGFR in comparison to the unlabeled antibody. In vivo, 24 h after injection of 99mTc-Cetux a clear tumor-derived signal could be identified in all mice bearing orthotopic MDA-MB-468 tumors. The size of the tumors was assessed during the autopsy and ranged from 19 to 60 qmm, pointing to the feasibility of 99mTc-Cetux to detect even small tumor lesions. In addition, a strong liver derived signal was observed 24h post injection, presumably due to the removal of the unbound antibody from the body via hepatic excretion. In contrast, no tumor uptake and no liver signal could be observed after injection of the unbound 99mTc-pertechnetate. Instead, a strong uptake of 99mTc was observed in the thyroids after 5 min post injection, as well as in stomach and bladder. These results show, that 99mTc-Cetux can be applied in vivo for the detection of EGFR-expressing tumor lesions with sizes below 20 qmm and may therefore be a powerful tool to improve early detection of breast cancer.

Disclosure of author financial interest or relationships:
T. Krüwel, None; **J. Napp**, None; **C. Dullin**, None; **J. Lotz**, None; **W. Stühmer**, None; **F. Alves**, None.

Presentation Number **P 089**
Poster Session 1
September 18, 2013 / 18:00-18:00 / Room: Exhibit Hall B

Visualizing the Prostate Gland by MR imaging in Young and Old Mice

Murali K. Ravoori, Jyoti Duggal, Mihai Gagea, Lin Han, Sheela P. Singh, Liu Ping, Wei Wei, Dustin K. Ragan, James A. Bankson, Jingfei Ma, **Vikas Kundra**, *Department of Diagnostic Radiology, University of Texas-M.D. Anderson Cancer Center, Houston, TX, USA. Contact e-mail: vkundra@mdanderson.org*

Purpose: Prostate imaging requires optimization in young and old mouse models. We tested which MR sequences and field strengths best depict the prostate gland in young and old mice; and, whether prostate MR signal, size, and architecture change with age. Technique: Magnetic resonance imaging (MRI) of the prostate of young (2 months) and old (18 months) male nude mice (n=6) was performed at 4.7 and 7 T and SCID mice (n=6) at 7 T field strengths, using T1, fat suppressed T1, DWI, T2, fat suppressed T2, as well as T2-based- and proton density-based Dixon "water only" sequences. Images were ranked for best overall sequence for prostate visualization, prostate delineation, and quality of fat suppression. Prostate volume and signal characteristics were compared and histology was performed. Results: T2-based-Dixon "water only" images ranked best overall for prostate visualization and delineation as well as fat suppression (n=6, $P<0.001$) at both 4.7 T and 7 T in nude and 7T in SCID mice. Evaluated in nude mice, T2-based Dixon "water only" ranked higher at 7 T than 4.7 T (n=6, $P<0.038$, n=6). Prostate volume was less in older than younger mice (n=6, $P<0.02$ nude mice; n=6, $P<0.002$ SCID mice). Prostate T2 FSE and T2-based-Dixon "water only" signal intensity was higher in younger than older mice ($P<0.001$ nude mice; $P<0.01$ SCID mice) both at 4.7 and 7 T. This corresponded to an increase in glandular hyperplasia in older mice by histology ($P<0.01$, n=6). Conclusion: T2-based Dixon "water only" images best depict the mouse prostate in young and old nude mice at 4.7 and 7 T. The mouse prostate decreases in size with age. The decrease in T2 and T2-based Dixon "water only" signal with age corresponds with glandular hyperplasia. Findings suggest age should be an important determinant when choosing models of prostate biology and disease.

Disclosure of author financial interest or relationships:
M.K. Ravoori, None; **J. Duggal**, None; **M. Gagea**, None; **L. Han**, None; **S.P. Singh**, None; **L. Ping**, None; **W. Wei**, None; **D.K. Ragan**, None; **J.A. Bankson**, None; **J. Ma**, None; **V. Kundra**, None.

Presentation Number **P 090**
Poster Session 1
September 18, 2013 / 18:00-18:00 / Room: Exhibit Hall B

Multimodality Imaging Assessments of Response to Metformin Therapy for Breast Cancer in Nude Mice

Yi Mao, *Rui Xia, Wei Wang, Yuqing Wang, Fabao Gao, department of radiology, west china hospital,sichuan university, Chengdu, China. Contact e-mail: 363085431@qq.com*

Purpose: Metformin: A Therapeutic Opportunity in Breast Cancer? Metformin in Cancer Therapy: A New Perspective for an Old Antidiabetic Drug? But there is few creditable studies have assessed the in vivo effects of metformin in cancer. We assessed the usefulness of diffusion-weighted imaging (DWI) and bioluminescence imaging (BLI) in evaluating tumor response to metformin. Materials and Methods: A luciferase-engineered human breast cancer cell line MDA-MB-231 was inoculated into the mammary fat pad of nude mice. Twelve female nude mice bearing tumors were divided into two groups. The mice in the treatment group were administered metformin (2 mg/mL in drinking water on each day) after tumor inoculation, and the mice in the control group were offered drinking water without any drug added. We performed 7T magnetic resonance imaging and optical imaging every week, which included T1- and T2-weighted imaging, DWI, and BLI. After imaging, the tumors were collected and subjected to histological analysis. Results: Compared to the control group, the mean photons/secod of tumor in treatment group is 3.00±0.43 E+06 at 1day, 1.01±0.14 E+07 at 2weeks, 5.79±1.42 E+07 at 4weeks, 2.33±0.70 E+07 at 8 weeks ;The mean photons/secod of tumor in control group is 3.29±0.59 E+06 at 1day, 3.59±0.63 E+07 at 2 weeks, 3.87±0.56 E+08 at 4 weeks, 4.12±1.72 E+08 at 8 weeks(supplemental data). Compared to the control group, the treatment group showed an obvious decrease in the mean bioluminescence (photons/s) of the tumors and fewer metastases(fig.1). Histological examination confirmed the metastasis(supplemental data). DWI showed that the apparent diffusion coefficient (ADC) value of the tumors ,the mean (standard deviation) ADC value was 0.9287 ± 0.04346 × 10-3 (mm2/s) in the treated tumors and 0.7553 ± 0.01804 × 10-3 (mm2/s) in the untreated tumors (P = 0.0013)(Tab.1), the ADC value of tumor in the treatment group is higher than the control tumors, there was a statistically significant difference between the control and treatment groups. Conclusion: The growth and metastasis of MDA-MB-231 breast cancer may be inhibited by metformin. DWI and BLI have great potential in the evaluation of the early response to metformin treatment. BLI has a high degree of sensitivity, is able to detect micrometastases, can be used for tumor metastasis assessment in vivo.

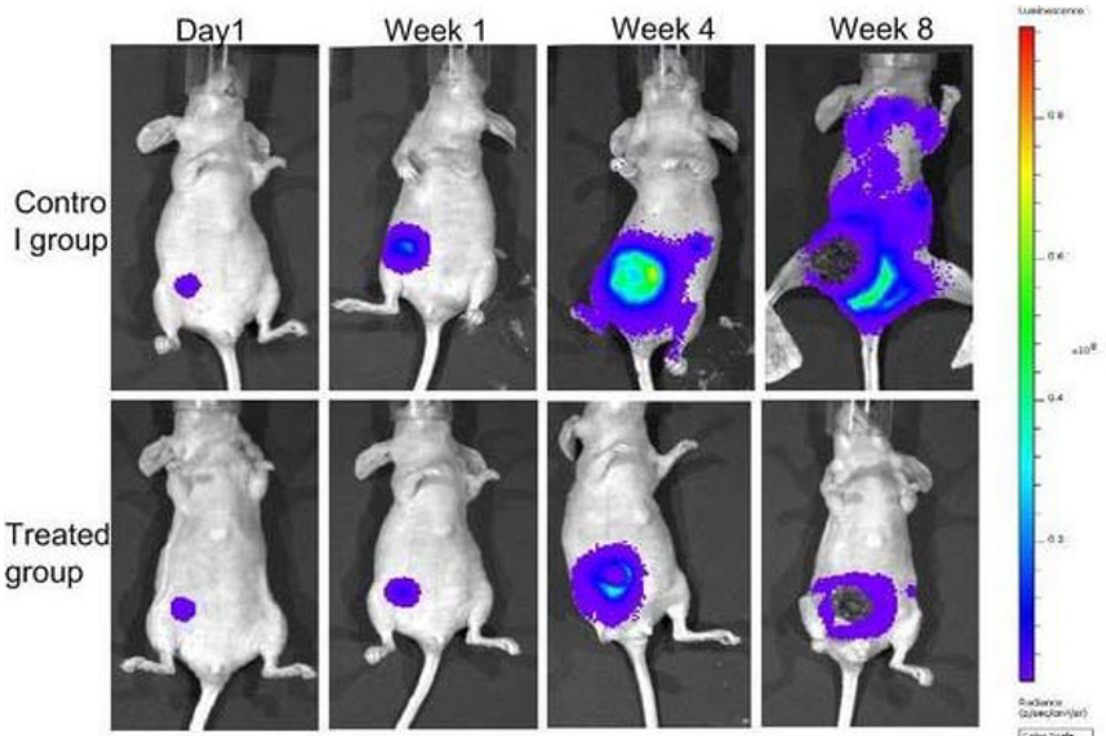

Images of representative mice from the control and treatment groups are shown from day 0 to 8 weeks after cell implantation. Tumor growth was monitored and quantified weekly by bioluminescent imaging (BLI). The tumors in the treatment group grew at a slower rate than the control group. In the control group and metastatic signals also gradually appeared at 4weeks, showed spontaneous metastasis to the abdominal lymph nodes, and then spontaneous metastasis to the lungs and thoracic lymph nodes at 8 weeks. In contrast, the mice showed spontaneous metastasis to the abdominal lymph nodes at 8 weeks;

The ADC values in the Control and Treatment groups

	mean(mm2/s)	P
Control group	0.9287 ± 0.0434 6 × 10-3	0.0013
Treatment group	0.7553 ± 0.01804 × 10-3	

Apparent diffusion coefficient (ADC) values in the treatment and control groups were analyzed using the Student t-test. The p value of 0.0013 was considered to indicate a statistically significant difference between the control and treatment groups.

Disclosure of author financial interest or relationships:
Y. Mao, None; **R. Xia**, None; **W. Wang**, None; **Y. Wang**, None; **F. Gao**, None.

Presentation Number **P 091**
Poster Session 1
September 18, 2013 / 18:00-18:00 / Room: Exhibit Hall B

Imaging Enhancement of Models of Disseminated Multiple Myeloma for Drug Discovery

Deanne Lister, Meridith Baugher, Jeni Baranski, Christopher Bull, Deepa Balagurunathan, Noah A. Winchell, Darren Shaw, Erin Trachet, **Patrick McConville***, Wilbur R. Leopold, Molecular Imaging, Inc., Ann Arbor, MI, USA. Contact e-mail: pmcconville@molecularimaging.com*

Multiple Myeloma is a cancer of the plasma cells that is characterized by multiple localized lesions in the marrow, particularly of the spine, skull, and pelvis, although soft tissue lesions also occur. It is the second most common blood cancer, affecting approximately 45,000 people in the US. Most preclinical modeling of myeloma employ SC xenografts that mimic the less common plasmacytoma form of the disease. Systemic (IV) implants are also used, but studies are typically limited to a single survival endpoint, limiting knowledge about the progression and response of the disease under treatment. There are also relatively few reliable and available models for multiple myeloma. We have characterized two human (JJN3 and MM1S) and one murine (5TGM1) myeloma models that have been modified to express luciferase, in order to more quantitatively monitor disseminated disease progression and response to treatment. All models were characterized by 100% tumor take rates and focal dissemination of the disease to the spine and skull that mimicked clinical experience. These models showed individual and reproducible patterns of spread to other sites, and differed in their sensitivities to standards of care. Analysis of tumor doubling times, tumor titrations, luminescence-based growth delay, and survival all indicated that the bioluminescence signal was a reliable quantitative indicator of viable tumor burden and a predictor of lifespan, and response to clinical standard of care agents. Luciferase labeling and the tight correlation between luminescence signal and viable tumor burden and lifespan also aid differential real time tracking of tumor progression and response at individual tissue sites.

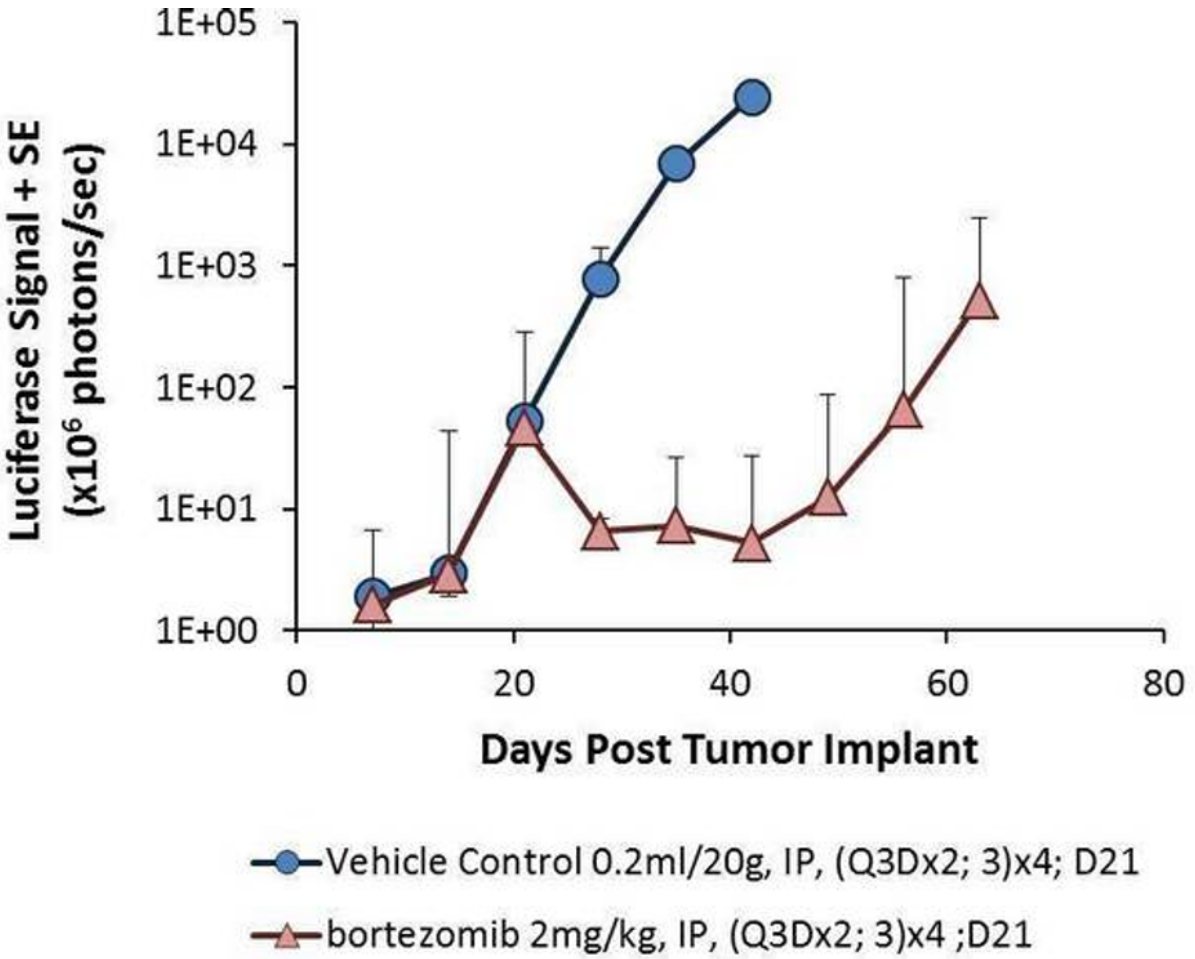

MM.1S model of disseminated multiple myeloma: whole body bioluminescence signal for standard of care treatment vs vehicle control.

Disclosure of author financial interest or relationships:
D. Lister, None; **M. Baugher**, Molecular Imaging, Inc., Employment; **J. Baranski**, None; **C. Bull**, None; **D. Balagurunathan**, None; **N.A. Winchell**, Molecular Imaging, Inc., Employment; **D. Shaw**, None; **E. Trachet**, None; **P. McConville**, Molecular Imaging, Inc., Employment; **W.R. Leopold**, None.

Presentation Number **P 092**
Poster Session 1
September 18, 2013 / 18:00-18:00 / Room: Exhibit Hall B

Molecular Colonography

Valerie E. Moberg[1], *Parastou Foroutan*[1], *Mikalai Budzevich*[2], *Gary Martinez*[1], *Kamini Sewda*[1], *Domenico Coppola*[3], *Geoffrey G. Zhang*[2], *Eduardo G. Moros*[2], *Mokenge P. Malafa*[4], *Robert Gillies*[1], *Eugene A. Mash*[5], *David L. Morse*[1], [1]*Cancer Imaging and Metabolism, Moffitt Cancer Center and Research Institute, Tampa, FL, USA;* [2]*Radiation Oncology, Moffitt Cancer Center and Research Institute, Tampa, FL, USA;* [3]*Anatomic Pathology, Moffitt Cancer Center and Research Institute, Tampa, FL, USA;* [4]*Gastrointestinal Oncology, Moffitt Cancer Center and Research Institute, Tampa, FL, USA;* [5]*Chemistry and Biochemistry, University of Arizona, Tucson, AZ, USA. Contact e-mail: Valerie.Moberg@moffitt.org*

Colorectal cancer (CRC) is the 2nd leading cause of cancer related death in men and women combined. Mortality can be reduced from 6% to over 70% 5-year survival if found in stage I rather than stage IV. Improved screening procedures can lower death rates by reducing non compliance and false negatives. To this end, we have discovered several cell-surface markers for use in CRC screening, and have developed contrast agents for MRI and CT targeted imaging probe development and an appropriate orthotopic CRC xenograft model in mice for agent evaluation. By expression profiling, immunohistochemistry (IHC) and Western blot of patient samples and cell lines, we have confirmed protein expression of cell-surface markers in CRC. For use in MRI, a sucrose-based gadolinium (Gd) scaffold was prepared and evaluated in vivo at 7T. To test feasibility of imaging small polyps in CT, gold nanoparticles (GNP) were scanned at varying concentrations and energy levels to determine if detection is achievable in vivo. By injection of luciferase expressing HCT 116 cells into the submucosal lining of the rectum, an orthotopic CRC xenograft model was developed and evaluated for use in MRI and CT imaging. Six markers were identified as over expressed in CRC, but not surrounding tissues-CLDN1, GPR56, GRM8, LY6G6D, SLCO1B3 and TLR4. At least one of the markers CLDN1, GPR56 or TLR4 was over expressed in 100% of patient tissue sample mRNA. Confirmation by IHC revealed the same 3 markers scored >4 (range 0 to 9) in 92% of patient sample protein expression. These cell surface proteins will be used for targeting MRI and CT probes. We currently have contrast agents under development for both modalities. For MRI, we have developed a sucrose-based Gd agent with a molar relaxivity (r1) of 212.8 mM/s inducing significant signal enhancement (>10-fold) in T1-weighted datasets of the mouse GI-tract in vivo. For CT, in-phantom measurements determined the lower limit of detection of GNP to be a concentration of 5 mg/ml gold in clinical scanners (97 HU at 120 kVp), and 1.5 mg/ml in the small animal micro CT scanner (137 HU at 80 kVp). We have addressed the feasibility of achieving this concentration in vivo based on known data concerning cell density, receptor number, and gold atoms per nanoparticle. In addition to our work in validating targets and contrast agents, we have evaluated an orthotopic mouse model for assessment of CRC probes. SCID mice, injected with HCT 116/luc cells, were followed for a period of 19 days and tumor growth was observed by bioluminescence and MRI imaging. Solid tumor growth was visible by MRI in less than two weeks. Passage of our Gd-Sucrose agent through the digestive tract was observed post gavage, and through the circulatory system post tail vein injection. Post-mortem gross dissection confirmed location of the tumor, with 100% of injected mice developing solid rectal tumors. We have discovered and validated 6 markers for targeting CRC, demonstrated the feasibility of using both MRI and CT contrast agents, and developed an orthotopic CRC mouse model. We are currently developing CRC targeted contrast agents.

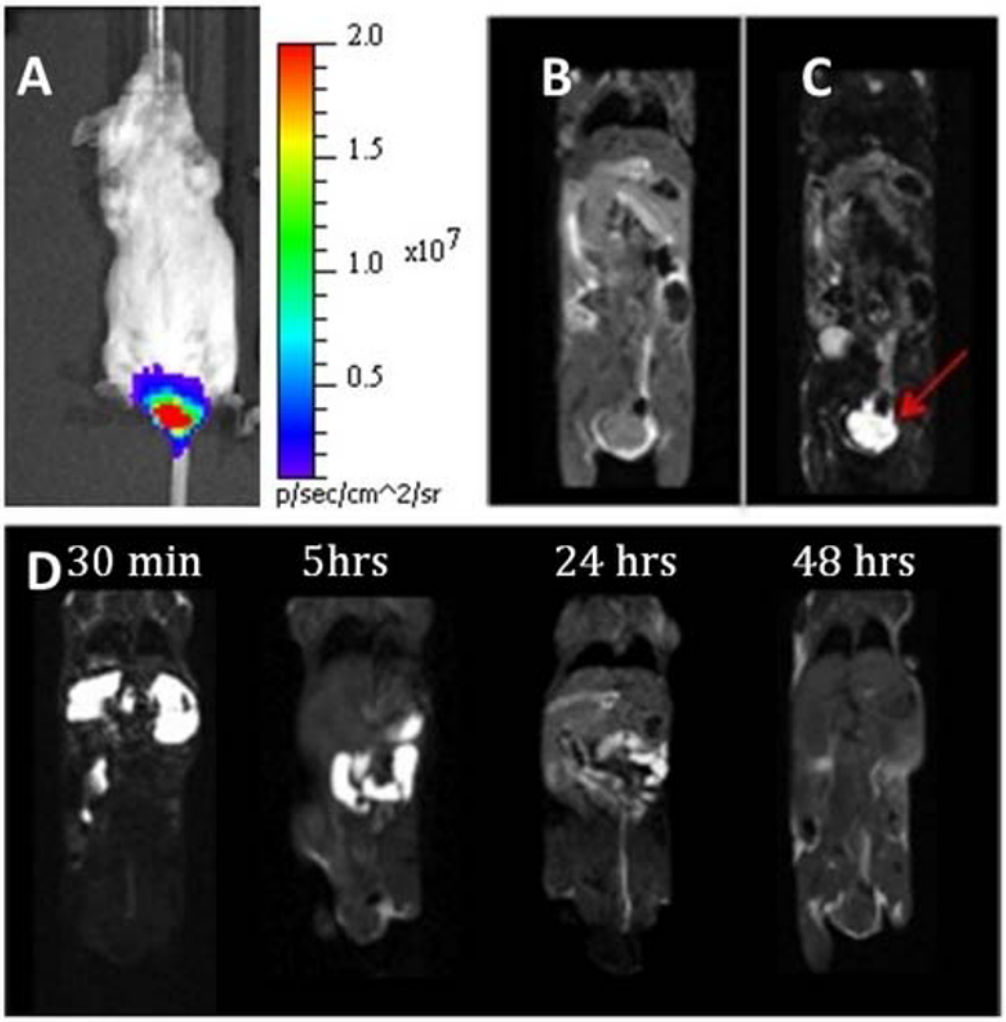

Figure 1. Images of a single SCID mouse bearing orthotopic HCT 116/luc xenograft tumor. A) Bioluminescence image, 9 days after injection. B)T1-weighted 2D Multislice Spin Echo Sequene (SEMS) with TE/TR = 14/270 ms, FOV=45x90 mm, M=128x256 and slice thickness of 1 mm acquired in coronal slice orientation, and C) corresponding T2-weighted dataset acquired with same geometry and TE/TR=72/1400 ms demonstrating the colorectal tumor (red arrow) pre-gavage. D) 3D Spin Echo (SE) datasets with T1-weighting demonstrating the passage of the contrast agent at select time points following the gavage administration. Acquisition parameters were TE/TR = 7.6/25 ms, FOV=45x90 mm, M=128x256, slice thickness of 1 mm acquired in 7 min.

	15 mg/ml	10 mg/ml	5 mg/ml	2.5 mg/ml	1.25 mg/ml	
140 kVp	318	244	88	44	42	[illegible] HU
120 kVp	374	239	90	48	40	[illegible] HU
80 kVp	318	277	97	60	55	[illegible] HU

CT numbers for gold nanoparticles as a function of kVp and density.

Disclosure of author financial interest or relationships:

V.E. Moberg, None; **P. Foroutan**, None; **M. Budzevich**, None; **G. Martinez**, None; **K. Sewda**, None; **D. Coppola**, None; **G.G. Zhang**, None; **E.G. Moros**, None; **M.P. Malafa**, None; **R. Gillies**, None; **E.A. Mash**, None; **D.L. Morse**, LiCor Biosciences, Grant/research support .

Presentation Number **P 093**
Poster Session 1
September 18, 2013 / 18:00-18:00 / Room: Exhibit Hall B

MRI Characterization of the Responses of Brain Metastatic Breast Cancer Cells to Whole Brain Micro-irradiation in Mice

Donna Murrell[1], *Amanda M. Hamilton*[2], *Michael D. Jensen*[1], *Niloufar Zarghami*[1], *Ann F. Chambers*[3], *Eugene Wong*[4], *Paula Foster*[2,1], [1]*Department of Medical Biophysics, Western University, London, ON, Canada;* [2]*Imaging Research Laboratories, Robarts Research Institute, London, ON, Canada;* [3]*London Regional Cancer Program, Victoria Hospital, London, ON, Canada;* [4]*Department of Physics and Astronomy, Western University, London, ON, Canada. Contact e-mail: dmurrell@robarts.ca*

INTRODUCTION: The prospect of being diagnosed with brain metastases is terrifying; the median time from diagnosis with brain metastases to death is between 1 and 6 months. Most systemic therapies for breast cancer are unable to cross the blood-brain barrier (BBB). In the absence of effective systemic therapies, radiotherapy is the main treatment for brain metastases. Studies have suggested that radiation may increase permeability of brain metastases to systemic therapy. Here we explore these ideas, using MRI, micro-irradiation and a mouse model of breast cancer metastasis to the brain. **STUDY DESIGN:** 100,000 human breast cancer cells (231BR-HER2) were administered by intracardiac injection to 9 female nude mice. Cells were either labeled with micron-sized iron oxide nanoparticles (MPIO) or unlabeled. Six mice received whole brain radiotherapy (WBRT) (20Gy in two fractions) on days 21 and 22 post cell injection using a modified GE Explore micro-CT. All mice were imaged at 3T on days 0, 20, and 29; three mice were also imaged the next week. First, balanced steady state free precession (bSSFP) images were acquired to visualize the fate of individual MPIO-labeled cancer cells and the development, size, and distribution of all brain metastases. Next, post gadolinium (Gad) T1-weighted images were acquired to assess the permeability of the BBB associated with individual metastases. Mice were sacrificed and brains were excised for histology. **RESULTS:** Brain metastases were detected in bSSFP images at day 20 in 8/9 mice. There was no significant difference in the numbers of metastases in mice injected with MPIO-labeled cells versus unlabeled cells. Of the total 73 metastases detected in bSSFP images for all mice on day 20, only 1 metastasis was visible in the T1w post Gad images. The total number of brain metastases, the percentage of enhancing metastases and the size of the metastases increased with time. Representative MR images are shown in Figure 1. At day 29, however, there was no significant difference between mice that had received WBRT and controls. There was a trend for smaller volumes at day 29 in the WBRT treated mice. In mice that received MPIO-labeled cells a reduction in the number of voids detected occurred with time. WBRT had a more substantial effect on metastases at later time points. After day 29 the growth of metastases continued in control mice, in terms of an increase in the number of metastases, their mean volume, and the number that enhanced. Contrarily, for WBRT treated mice tumour growth was halted; there are few new metastases detected and the volumes did not increase much, some decreased; quite unlike the control situation (Figure 2, supplementary). Furthermore, the number of enhancing metastases decreased with time after WBRT (Figure 3, supplementary). Histological analysis of H&E stained brain sections correlates well with our imaging observations and indicated tumour necrosis post-WBRT (Figure 4, supplementary). **SIGNIFICANCE:** This research offers important information about metastatic tumor growth and permeability in response to WBRT. We hope to advance treatment options for those diagnosed with brain metastases.

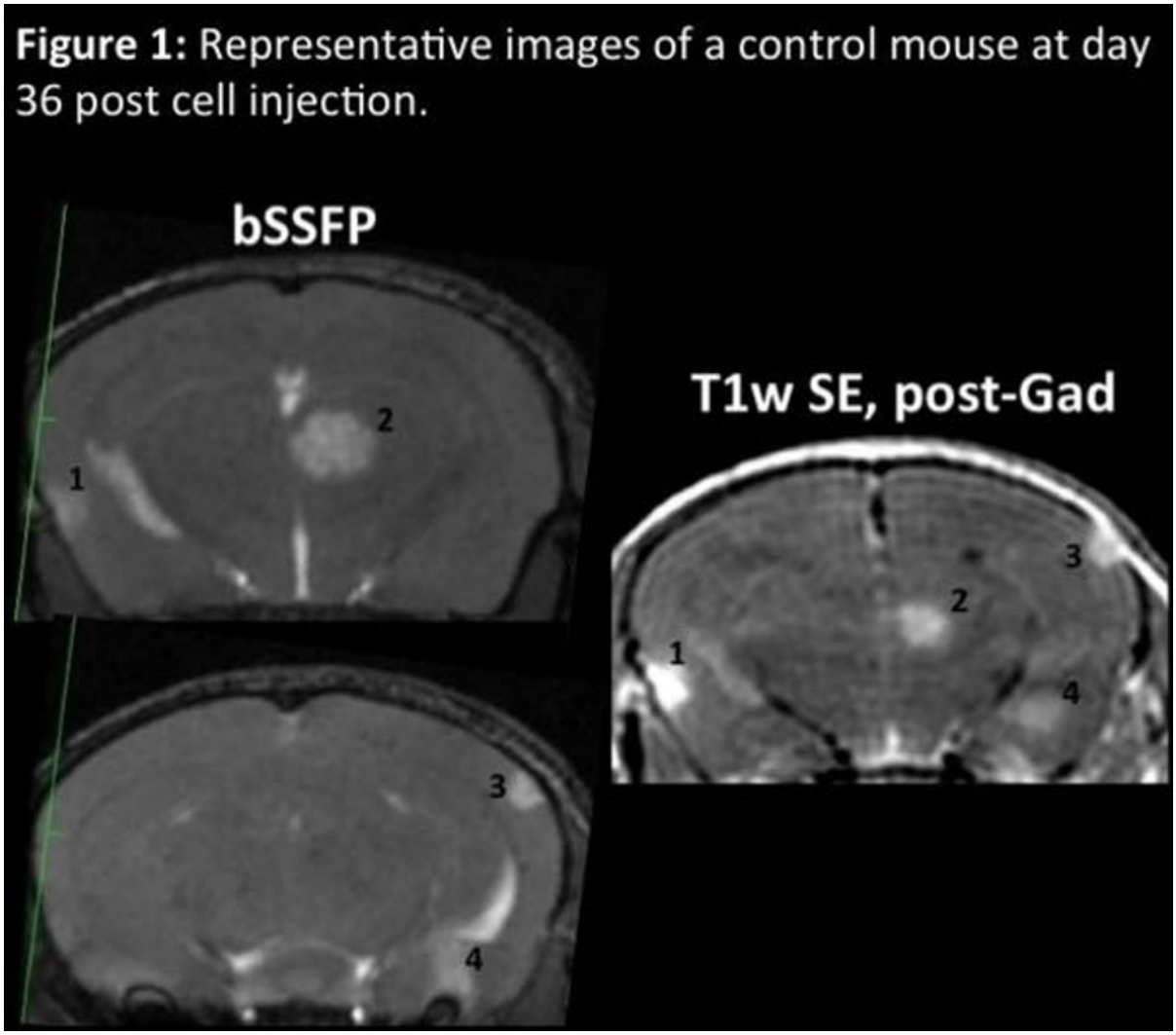

Figure 1: Representative images of a control mouse at day 36 post cell injection. Four brain metastases are visible in both the bSSFP and post Gad T1w SE images (1-4). Two of these metastases are meningeal (1,3) and two are parenchymal (2,4). Notice that the differing image resolutions for the two scans means that all 4 metastases are visible in the thicker SE image slice (400 micron) while 2 of the metastases are visible in each of the 200 micron bSSFP images. Image contrast in bSSFP images is related to T2/T1 and the brightness is due to associated edema. Signal hyperintensity in SE images indicates the metastasis is permeable to Gad (leaky BBB).

Disclosure of author financial interest or relationships:
D. Murrell, None; **A.M. Hamilton**, None; **M.D. Jensen**, None; **N. Zarghami**, None; **A.F. Chambers**, None; **E. Wong**, None; **P. Foster**, None.

Presentation Number **P 094**
Poster Session 1
September 18, 2013 / 18:00-18:00 / Room: Exhibit Hall B

Improving Efficacy of Image-Guided Photoimmunotherapy (PIT) Using a Cocktail of Antibody Conjugates in a Tumor Model with Multiple Targets

Takahito Nakajima, *Kohei Sano, Peter Choyke, Hisataka Kobayashi, National Institutes of Health, Bethesda, MD, USA. Contact e-mail: nakajimat@mail.nih.gov*

Tumors are characterized by a high degree of diversity and heterogeneity in receptor expression. Monoclonal antibodies (mAbs) are well-established therapeutic or diagnostic methods of targeting cell surface receptors. However, high affinity antibodies targeting highly expressed receptors are often prevented from distributing evenly throughout the tumor due to the "binding site barrier" whereby antibody is trapped peripherally before it can reach deeper into the tumor leading to inhomogeneous micro-distribution. The aim of this study is to investigate whether a cocktail of two monoclonal antibodies (mAbs) against two distinct antigens, one with high and one with low cell surface expression, would improve the homogeneity of overall mAb-binding in vivo. Panitumumab (Pan) and basiliximab (Bas) were conjugated with a phthalocyanine dye, IRDye700DX (IR700). ATAC4 cells with high expression of human epidermal growth factor receptor (EGFR) and low expression of interleukin-2 receptor-alpha (CD25) underwent photo-immunotherapy (PIT), using a cocktail of Pan-IR700 and Bas-IR700. Upon exposure to near infrared light, these armed antibodies produce rapid cell death only when bound to their respective receptors. There was no significant difference in PIT effects between Pan-IR700 and Pan-Bas-IR700 in vitro. However, an in vivo PIT showed that a cocktail of Pan-Bas-IR700 achieved more homogeneous distribution in the tumor and significantly suppressed tumor growth resulting in prolonged survival of ATAC4 tumor-bearing mice compared with either Pan-IR700 or Bas-IR700 alone. In conclusion, a cocktail injection of two different antibody-IR700 conjugates induced superior therapeutic effects after PIT compared with the use of a single antibody-IR700 conjugate due to improved distribution of the antibody binding within the tumor.

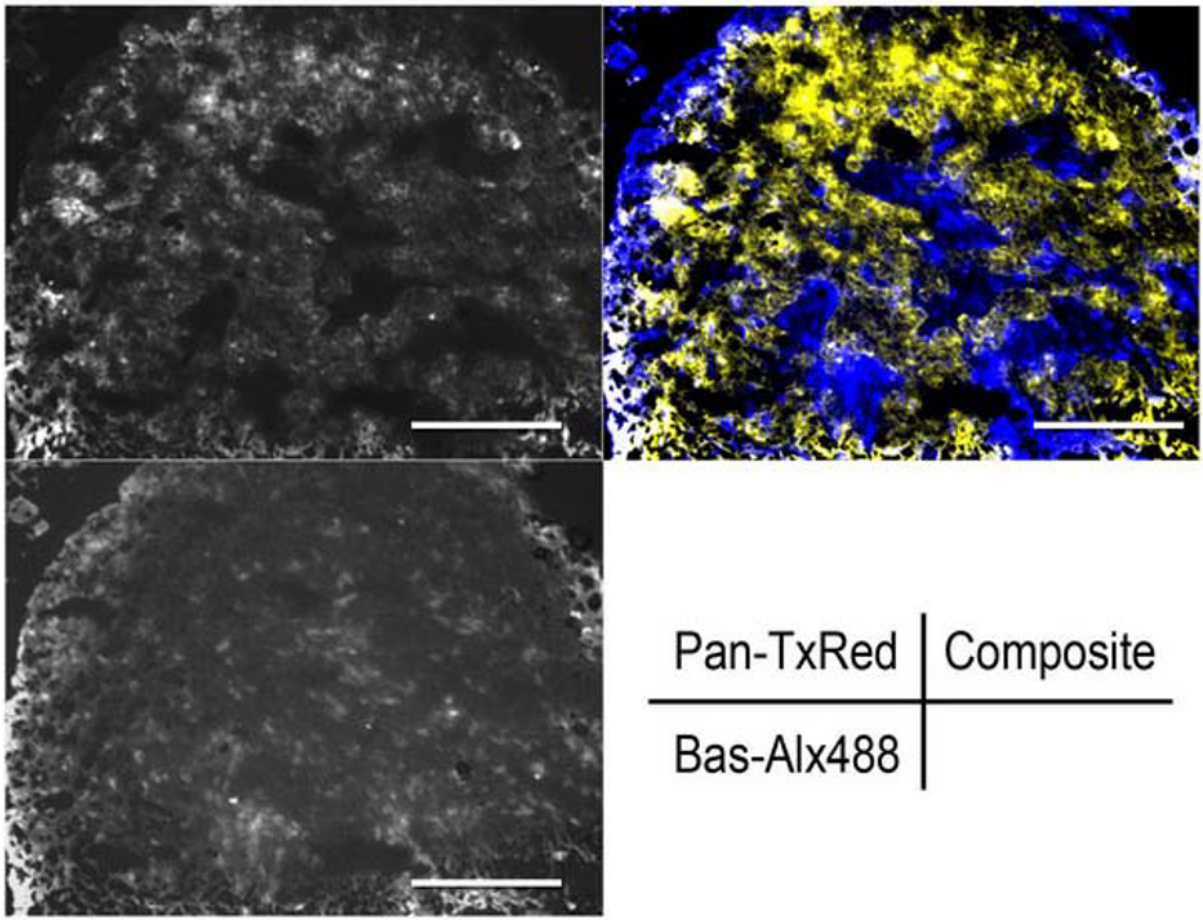

A cocktail of Pan-TexRed (yellow) and Bas-Alx488 (blue) was injected to tumor-bearing mice intravenously 24 hours before tumors were harvested. Frozen sections of A431 tumors were examined by fluorescence microscopy. Bas-Alx488 penetrated into deep area while Pan-TexRed was trapped in shallow area due to binding site barrier.

Disclosure of author financial interest or relationships:
T. Nakajima, None; **K. Sano**, None; **P. Choyke**, None; **H. Kobayashi**, None.

Presentation Number **P 095**
Poster Session 1
September 18, 2013 / 18:00-18:00 / Room: Exhibit Hall B

MRI GUIDANCE OF DOXORUBIN RELEASE FROM LIPOSOMES STIMOLATED BY LOW INTENSITY NON FOCUSED ULTRASOUND

Silvia Rizzitelli[1], Pierangela Giustetto[1,2], Juan C. Cutrin[3], Valeria Menchise[4], Cinzia Boffa[1], Marta Ruzza[1], Daniela Delli Castelli[1,2], Silvio Aime[1,2], **Enzo Terreno**[1,2], [1]*Department of Chemistry, University of Turin, Torino, Italy;* [2]*Center for Preclinical Imaging, University of Torino, Colleretto Giacosa (TO), Italy;* [3]*ININCA, UBA-CONICET, Buenos Aires, Argentina;* [4]*Institute for Biostructures and Bioimages (CNR), o Molecular Biotechnology Center, University of Torino, Torino, Italy. Contact e-mail: enzo.terreno@unito.it*

Introduction:Doxorubicin is one of the clinically most used drugs to treat solid tumors, but shows a very high toxicity.To reduce side effects and improve tumor accumulation, liposomal forms of the drug have been developed.But the ability of these nanoparticles to deeply diffuse in the tumor is still debated, and several methods to promote the release of the drug at the target site have been proposed.A promising approach is to induce the release of the drug when most of the drug is still circulating in the tumor vasculature.We have recently demonstrated, both in vitro and in vivo, that the local application of pulsed low intensity non-focused ultrasound(pLINFU)can trigger a mechanical release from liposomes.Then,if a paramagnetic Gd-complex is co-encapsulated with the drug, MRI can offer the valuable opportunity to guide the release process and monitoring the therapeutic outcome. Methods:Stealth liposomes mimicking Doxyl-like formulation (DPPC, DSPC, Cholesterol and DSPE-PEG2000methoxy10:5:4:1),co-encapsulating Doxorubicin and Gadoteridol(Gd/Doxo=1:0.092), were prepared. Liposomes were i.v. injected (once a week for 3 weeks) to have a doxorubicin dose of 5 mg/kg, and a Gadoteridol dose of 0.1 mmol/kg. Balb/C mice bearing a syngeneic breast cancer were used. Tumors were locally exposed to pLINFU (3 MHz, inson. time 2 min, duty cycle 50%). T1w and T2w MR images were taken daily to measure contrast enhancement and monitoring tumor growth.After the treatment, mice from each group were sacrificed and the tumors were collected and fixed.5 μm sections were stained with hematoxylin and eosin, and examined under a light microscope to analyze histological assessments.Adjacent sections(stained with Hoescht dye)were monitored at confocal microscopy. Results:The theranostic properties of liposomes were first tested in vitro, and it has been shown that the release profile was similar for both the agents with a maximum US time of 400ms. (Fig1)Then, the imaging performance of the liposomal agent was assessed in vivo.Fig3 reports the CNR% values measured in the tumor for the treated and control mice groups that indicates the significant enhancement peak observed for the US treated tumors just after the liposomes administration.Moreover,a slower increase in the T1 enhancement was until 4 days post-injection ,related to the cellular fate of the MRI agent(the blood half-lifetime of Gadoteridol is very short)was observed.The effective release of Gadoteridol was supported by the great CNR% observed in kidneys and bladder for the treated animals only.Importantly,treated animals showed a significant delayed tumor growth(Fig2). Organs were explanted at different time-points and the diffusion of the released drug was assessed using conventional histology and immunofluorescence at confocal microscopy (Fig4)emphasizing an active role of liposomes to induce the tumor diffusion of the drug.To optimize the method,the release scheme was implemented with a sonoporation shot applied during the injection(freq.1 MHz,total inson.time1min,duty cycle 12%),and the sensitivity of the MRI detection was improved encapsulating in the liposomes Gd-agents more efficient than Gadoteridol

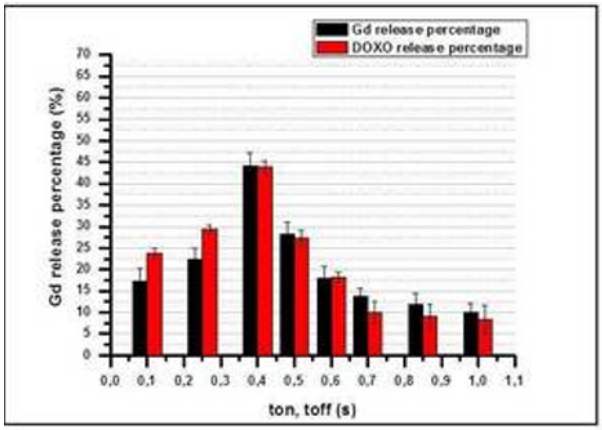

Fig.1

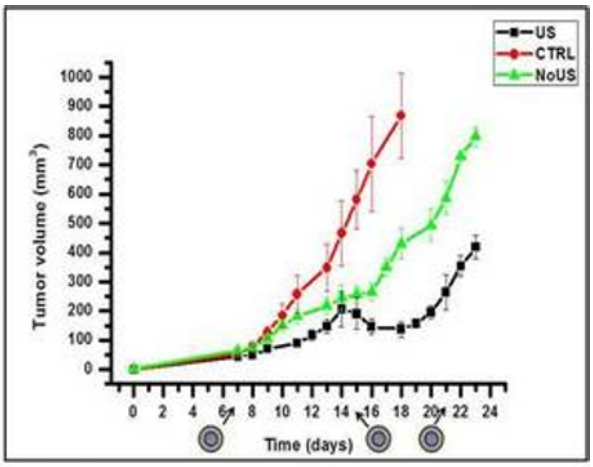

Fig.2

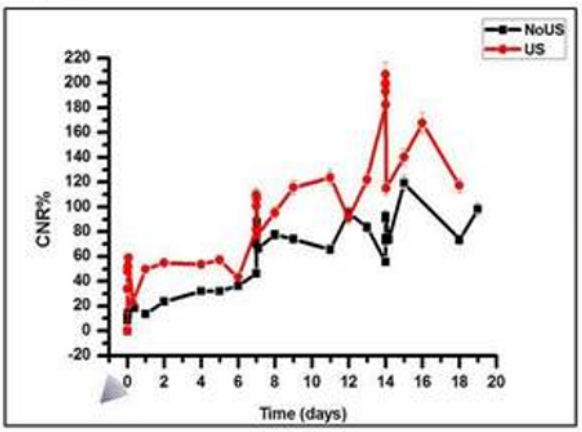

Fig.3

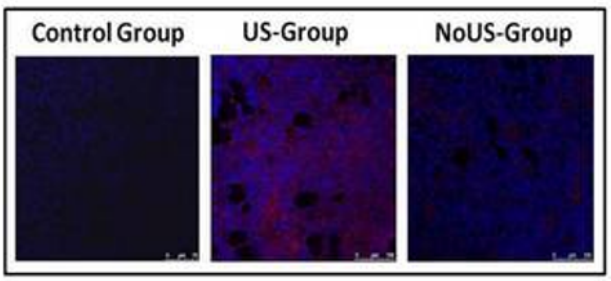

Fig.4

D.

Disclosure of author financial interest or relationships:
S. Rizzitelli, None; **P. Giustetto**, None; **J.C. Cutrin**, None; **V. Menchise**, None; **C. Boffa**, None; **M. Ruzza**, None; **Delli Castelli**, None; **S. Aime**, None; **E. Terreno**, Bracco Imaging, Consultant .

Presentation Number **P 096**
Poster Session 1
September 18, 2013 / 18:00-18:00 / Room: Exhibit Hall B

Imaging & histological changes in effects of different antiangiogenic drug treatments and timing

Adarsh Shankar[1], *Asm Iskander*[1], *Nadimpalli Ravi S Varma*[1], *Thaiz F. Borin*[1,4], *Livia C. Ferreira*[4], *Bruna Jardim*[4], *Meser M. Ali*[1], *Branislava Janic*[1], *Sanath Kumar*[2], *Hassan Bagher-Ebadian*[3], *Stephen L. Brown*[2], *James R. Ewing*[3], *Guillermo Scicli*[1], *Ali S. Arbab*[1,5], *[1]Radiology, Henry Ford Health System, Detroit, MI, USA; [2]Radiation Oncology, Henry Ford Health System, Detroit, MI, USA; [3]Neurology, Henry Ford Health System, Detroit, MI, USA; [4]Molecular Biology, Faculdade de Medicina de Sao Jose do Rio Preto - FAMERP, Sao Jose do Rio Preto, Brazil; [5]Radiology, Wayne State University School of Medicine, Detroit, MI, USA. Contact e-mail: adarshs@rad.hfh.edu*

Introduction & Purpose: There have been many challenges with antiangiogenic drugs which have attempted to normalize blood and control angiogenesis in glioblastoma (GBM). A new drug which has recently been implemented is (N-hydroxy-N'-(4-butyl-2methylphenyl) formamidine (HET0016). HET0016 is a highly selective inhibitor of 20-HETE synthesis that involves enzymes of the CYP4A and CYP4F families. HET0016 with preliminary results found to inhibit angiogenic response to many growth factors, as well angiogenesis in cornea induced by human U251 GB cells. Previously we used PTK787 (vatalanib),, which is a receptor tyrosine kinase inhibitor and interferes VEGF-VEGFR signal transduction pathway. The purposes of the studies were to determine the effect of HET0016 or vatalanib alone or in combination in the rat model of GBM using magnetic resonance imaging (MRI) by calculating different vascular, diffusion, and relaxation parameters, and compare the findings with IHC and protein array results. Materials & Methods: Sixty-four orthotopic animals were randomly divided into two treatment schedules: 1) seven days after tumor implantation the rats received either vehicle, vatalanib, HET0016, or combined treatment (8-21), and 2) the rats received treatments from the day of tumor the implantation (0-21). All the animals underwent MRI scanning 22 days after tumor implantation, and were analyzed for tumor volumes and various vascular (Ktrans, Kb, Vp, Ve), diffusion and relaxation parameters. Half of the animals from the groups were euthanized for protein extraction and the other half for histology. Proteins were extracted separately from the center and periphery of the tumors. Custom designed protein array kits, which consisted of 20 different cytokines/factors were used to analyze the expression. ELISA was also performed to determine the HIF-1α and MMP-2 protein expression. We stained histology sections for vWF (neovascularization), CD44 (invasion), MMP-2 (invasion), MHC-1 (human cells) and others. All the data was analyzed by one way ANOVA. A p-value of < 0.05 was considered significant. Results & Conclusion: First, we noticed that all values for tumor volume, Vp, Ktrans, Kb, and Ve were lower in the animals that were treated from day one, compared to the animals that were treated seven days after. HET0016 had the greatest control over the tumor volume in both treatment conditions. We observed that vatalanib could not control tumor volumes when treated seven days after. We believe that it was too late for vatalanib to resist the VEGF-VEGFR signaling pathways that had already been established. We also noticed that all the factors were at lower levels, when animals were treated from day 1, rather than seven days after. HIF-1 and MMP-2 ELISA results proved there was no significance as well. Histology showed us that vatalanib treated animals had tortuous, leaky, and large blood vessels, while the other groups had smaller, non-leaky blood vessels. We concluded that timing of treatment is important in many aspects. MRI including vascular parametric analysis could able to determine the effects of therapy.

Disclosure of author financial interest or relationships:
A. Shankar, None; **A. Iskander**, None; **N. Varma**, None; **T.F. Borin**, None; **L.C. Ferreira**, None; **B. Jardim**,

None; **M.M. Ali**, None; **B. Janic**, None; **S. Kumar**, None; **H. Bagher-Ebadian**, None; **S.L. Brown**, None; **J.R. Ewing**, None; **G. Scicli**, None; **A.S. Arbab**, None.

Presentation Number **P 097**
Poster Session 1
September 18, 2013 / 18:00-18:00 / Room: Exhibit Hall B

Experimental and Computational Approaches to Probe Nanoparticle Extravasation Design Principles

Bryan R. Smith[1], *Preyas Shah*[3], *Eric S. Shaqfeh*[2], *Sanjiv S. Gambhir*[1], [1]*Radiology/Molecular Imaging, Stanford University, Stanford, CA, USA;* [2]*Chemical Engineering, Stanford University, Palo Alto, CA, USA;* [3]*Mechanical Engineering, Stanford University, Palo Alto, CA, USA. Contact e-mail: brsmith@stanford.edu*

Nanoparticles (nps) administered intravenously are an important class of diagnostic and therapeutic agents for many diseases. Nps are often expected to leak, or extravasate, from tumor blood vessels through vessel pores associated with the Enhanced Permeability and Retention (EPR) effect. Yet shape- and size-dependent np extravasational behavior is poorly understood. Thus we integrated np experiments in live subjects across multiple tumor types with both in vitro experiments and computational simulations in order to deeply understand the physical behavior of nps and ultimately to enable computationally-directed design of np physical parameters (e.g., shape) for its specific purpose. To probe extravasation, we used two nps types (1) spherical quantum dots (qdots, ~20-25 nm) in diameter, and (2) cylindrical single-walled carbon nanotubes (SWNTs, 2nm X 200nm) conjugated to Cy5.5. We injected nps intravenously into mice with 3 different tumor types (U87MG, LS174T, and SKOV-3; n=30 mice) and quantitatively monitored extravasation using fluorescence. No extravasation occurred in SKOV-3 with either np. In U87MG tumors, SWNTs extravasated rapidly while qdots extravasated minimally. However, intriguingly in LS174T tumors the opposite occurred: qdots extravasated rapidly, while SWNTs extravasated minimally (see Fig). To put our experiments in live animals into context, we performed diffusion experiments in well-controlled in vitro conditions to understand the effects of np geometry on flux through a pore. Qdots and SWNTs were placed in inlet chambers with a membrane containing nanopores of 100 and 200 nm diameter separating them from the outlet chamber. We measured np fluxes across the nanopores using a spectrofluorometer. In 100 nm pores, SWNT flux was 3.5 times that of qdots; for 200 nm pores, SWNT flux was 1.3 times that of qdots, revealing shape and pore diameter dependence. In order to better understand the physical basis of our findings in living subjects and in vitro, we developed computational simulations. We sought to simulate both the diffusive conditions of the nanopore experiment and for a simplified Stokes flow over a pore. Using Brownian Dynamics (validated with analytical theory), we quantified the ability of qdots and SWNTs of all sizes to extravasate through pores. Interestingly, we found that i) when rod-shaped np length is of the order of the pore radius, rods display higher pure diffusion flux than spheres, ii) as convective flow increases, rod transport dominates over sphere transport (see Fig), and iii) oncotic pressure-driven suction dominates the physics of np transport (e.g., rod length minimally affects its extravasation rate). In summary, we explored np extravasation with a novel toolkit, combining high-resolution extravasation studies in live animals with in vitro studies designed to isolate key parameters and computational studies to deeply probe the underlying physics. With these tools, we demonstrate increased physical understanding of how nps extravasate: in general, rod-shaped nps are superior to spheres. These studies are key to enabling cancer nanotechnology to improve np-based cancer imaging and therapy.

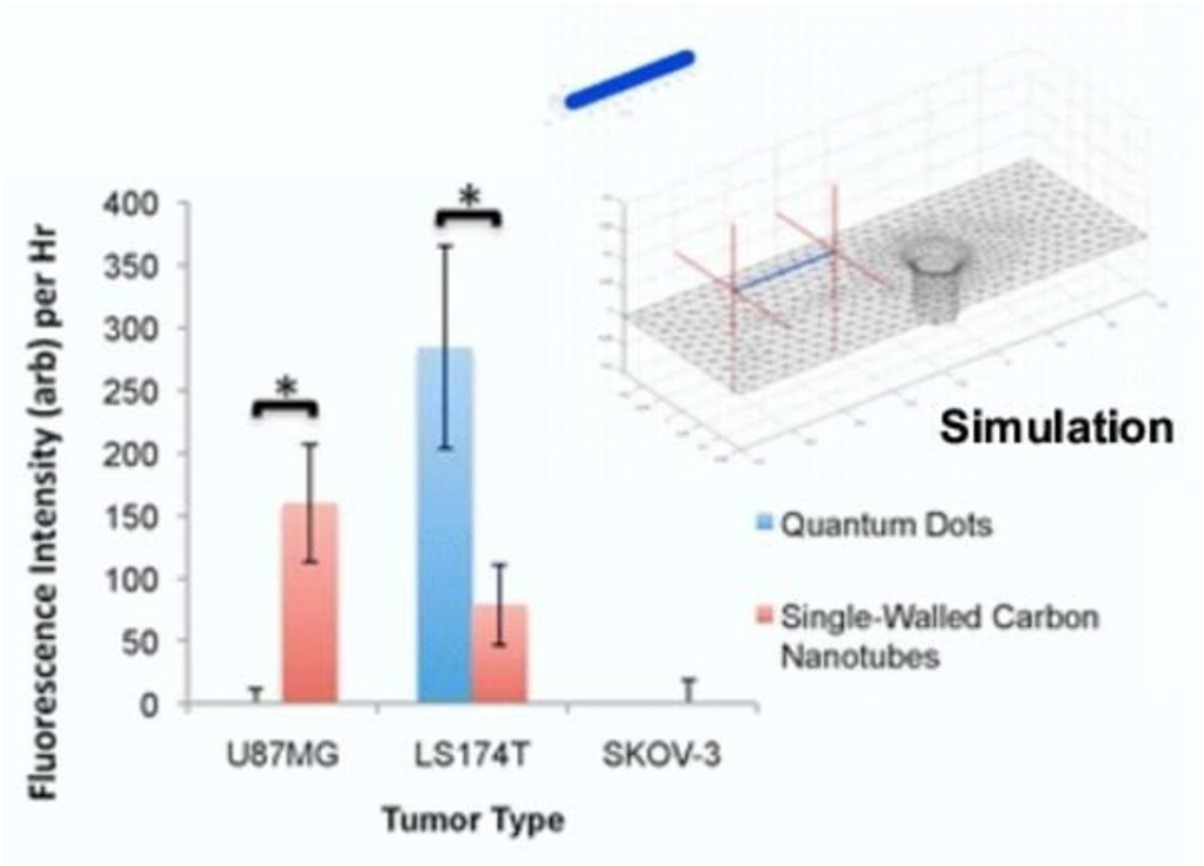

Figure. In live mice injected with SWNTs and qdots, experiments show that SWNTs extravasate more than qdots in U87MG tumor, while qdots extravasate more than SWNTs in LS274T tumors (*$p<0.05$). In vitro experiments indicate that SWNT diffusion through smaller (~100 nm) pores is more rapid than qdots, which may physically help explain the higher SWNT extravasation in U87MG tumors (which have smaller pores than LS174T tumors). (Inset) Still picture from an example simulation of a rod (single-walled carbon nanotube here, shown in blue) moving toward a pore in the meshed plane wall.

Disclosure of author financial interest or relationships:

B.R. Smith, None; **P. Shah**, None; **E.S. Shaqfeh**, None; **S.S. Gambhir**, Bracco Diagnostics, Consultant; Endra, Inc, Stockholder; Cellsight, Stockholder; Enlight, Inc., Stockholder; General Electric, Grant/research support; ImaginAb, Stockholder; MagArray, Inc., Stockholder; Sanofi-Aventis, US, Grant/research support; SiteOne Therapeutics, Stockholder; VisualSonics/Sonosite, Stockholder .

Presentation Number **P 098**
Poster Session 1
September 18, 2013 / 18:00-18:00 / Room: Exhibit Hall B

In Vivo Imaging of Nanoparticle Targeting of Aberrant Glycosylation and Glycoprotien Expression in Ovarian Cancer

Jeffrey S. Souris[1], *Shih-Hsun Cheng*[1,2], *Nai-Tzu Chen*[1,2], *Chin-Tu Chen*[1], *Leu-Wei Lo*[2], [1]*Department of Radiology, The University of Chicago, Chicago, IL, USA;* [2]*Division of Medical Engineering Research, National Health Research Institutes, Zhunan, Taiwan. Contact e-mail: sourisj@uchicago.edu*

In the tumorigenesis and neoplastic progression of many forms of cancer, deviations in the composition, structure, and areal density/distribution of glycosylation-associated molecules on cell surfaces are common phenomenon; often strongly correlating with tumor invasiveness, metastatic potential, and the evasion of host immuno-surveillance. To determine the utility of targeting aberrant glycosylation for the detection of metastatic ovarian cancer (CaOV) *in situ*, we have recently begun to design, synthesize, and evaluate mesoporous silica nanoparticles (MSNs) for use as CaOV-specific contrast agents. MSNs were synthesized via conventional sol-gel chemistry, with the incorporation of the fluorophore fluorescein isothiocyanate (FITC) within the MSN's silica framework during co-condensation - to protect the fluorophore from photobleaching and O_2 quenching, and to maximize the nanoparticle's available surface area for targeting ligand conjugation. Following nanoparticle synthesis, the exteriors of MSNs were PEGylated (5 kDa) and labeled with one of two aberrant glycosylation targeting moieties: the lectin *Ulex Europaeus Agglutinin 1* (UEA-1), to target α-L-fucose, or the monoclonal antibody CC49, to target Tumor Associated Glycoprotein 72 (TAG-72). Morphologies of the resulting functionalized MSNs were then characterized by transmission electron microscopy (TEM), dynamic light scattering (DLS), N_2 adsorption-desorption isotherm analysis, and zeta potential measurement. TEM studies revealed discrete, uniformly sized mesoporous silica nanoparticles with an average pre-PEGylated diameter of 55 nm (average post-PEGylated diameter of 172 nm). N_2 adsorption-desorption isotherm studies yielded average MSN pore diameters of 4.7 nm, calculated using the Barrett-Joiner-Halenda (BJH) method, and average surface areas and pore volumes of 980 m^2 g^{-1} and 0.38 cm^3 g^{-1} respectively, calculated using the Brunauer-Emmett-Teller (BET) method. Zeta potential measurements varied little with PEGylation status, averaging -5.15 mV before and -6.57 mV following targeting ligand amine / PEG maleimide conjugation. Athymic nude male mice, 8 weeks of age, were intraperitoneally injected with $1x10^6$ SKOV3ip.1-luc human ovarian cancer cells 42 days prior to contrast agent administration. Immediately preceding *in vivo* imaging, mice were anesthetized with gaseous isoflurane and intraperitoneally injected with 16 mg/kg of either MSN-FITC-UEA-1 or MSN-FITC-CC49 in 500 µl sterile saline. Serial *in vivo* fluorescence imaging of the FITC emission was then conducted for 2 hours after which mice were injected with 150 mg/kg luciferin, in 200 µl sterile saline, and bioluminescence imaged for 1 hour. Tissues were then harvested for microscopic examination and correlation to *in vivo* imaging studies. As shown in the figure below, both UEA-1 and CC49 labeled MSNs selectively targeted CaOV, with high spatial correlation found between the fluorescence imaging of nanoparticles and the bioluminescence imaging of transduced SKOV3ip.1 ovarian cancer metastases.

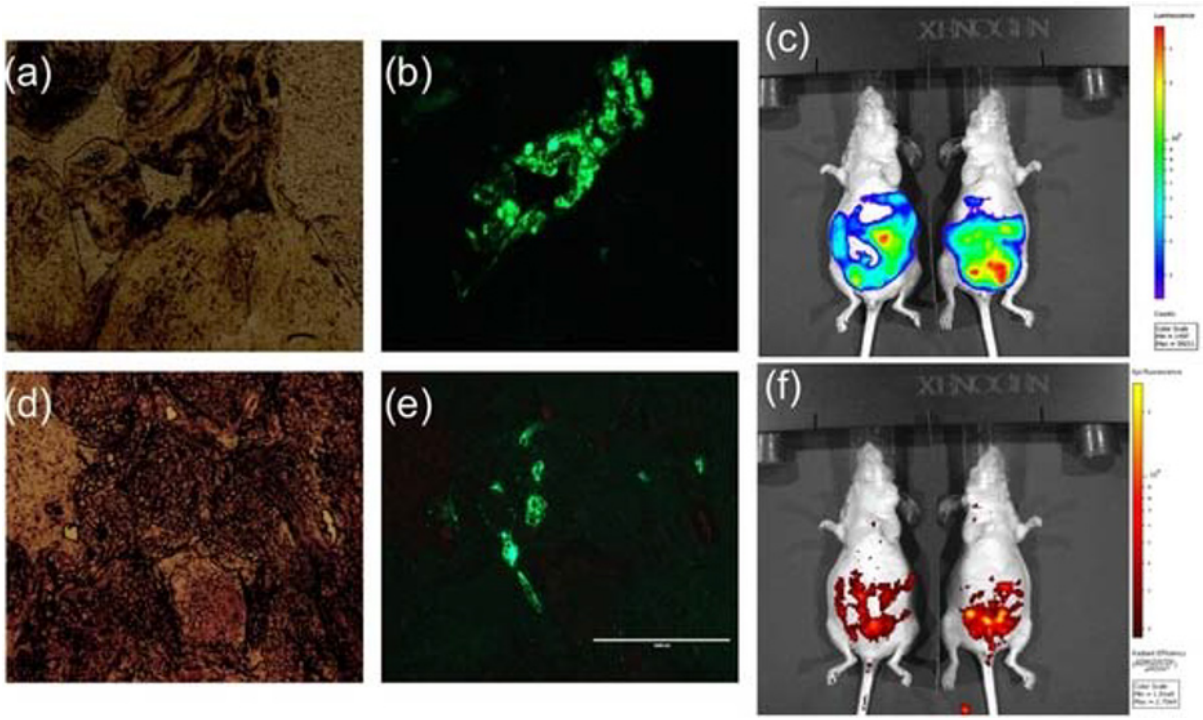

Figure 1. Bright-field (H&E stained) and fluorescence microscopy of harvested (a,b) FITC-MSN-UEA-1 sub-hepatic omentum tissue and (c,d) FITC-MSN-CC49 sub-hepatic omentum tissue, respectively. (e) *In vivo* bioluminescence imaging of human ovarian cancer metastases 42 days post i.p. injection of $1x10^6$ SKOV3ip.1-luc cells. (f) *In vivo* fluorescence imaging of FITC-MSN-CC49 (L) and FITC-MSN-UEA-1 (R), showing pathology co-registration with targeted nanoparticles.

Disclosure of author financial interest or relationships:
J.S. Souris, None; **S. Cheng**, None; **N. Chen**, None; **C. Chen**, Cell>Point, Grant/research support; RefleXion Medical, Consultant; DxRay/Photon Imaging, Consultant; **L. Lo**, None.

Presentation Number **P 099**
Poster Session 1
September 18, 2013 / 18:00-18:00 / Room: Exhibit Hall B

Evaluation of Carbonic Anhydrases IX and XII as surrogate markers of hypoxia in breast cancer

Narges K. Tafreshi[1], *Mark C. LIoyd*[3], *Joshua Proemsey*[3], *Jongphil Kim*[2], *Robert Gillies*[1], *David L. Morse*[1], [1]*Dept. Cancer Imaging and Metabolism, Moffitt Cancer Center, Tampa, FL, USA;* [2]*Department of Biostatistics, Moffitt Cancer Center, Tampa, FL, USA;* [3]*Analytic Microscopy Core Facility, Moffitt Cancer Center, Tampa, FL, USA. Contact e-mail: narges.tafreshi@moffitt.org*

Solid tumors have heterogenous regions of hypoxia (reduced pO2). Hypoxia has been associated with tumor initiation, malignant progression and resistance to chemo- and radio-therapies in many tumor types. Expression of cell surface carbonic anhydrases IX (CAIX) and XII (CAXII) are associated with tumor cell hypoxia in a variety of human tumors. As potential hypoxia imaging agents, we used our previously developed CAIX and CAXII imaging probes to investigate whether CAIX and CAXII are suitable hypoxia biomarkers in vitro, in vivo and ex vivo. Our imaging probes are two fluorescently labeled anti-CA antibodies, CA9Ab-680 and CA12Ab-680. Immunocytochemistry (ICC) and flow-cytometry of breast cancer cell lines using the probes showed high induction of CAIX expression in hypoxic conditions relative to normoxia for all cell lines surveyed, while only a slight induction of CAXII was observed in a subset of cells. These results were in complete agreement with qRT-PCR. By immunohistochemistry (IHC) of ZR-75.1 breast cancer xenograft tumors, the regional distributions of CAIX and CAXII expression were analyzed with respect to staining of the exogenous hypoxia marker, pimonidazole. CAIX was invariably induced in regions adjacent to necrosis, while CAXII was only sporadically and slightly induced (Fig. 1A). Additionally, the accumulation of CA9Ab-680 increased when animals were kept in a hypoxia environment relative to normoxia, and decreased when animals were treated with nicotinamide and kept in a hyperoxic carbogen (95% O2, 5% CO2) environment, respectively ($P<0.05$) (Fig 1B, LEFT). Tumor accumulation of CA12Ab-680 was not significantly increased by hypoxia (Fig. 1B, RIGHT). These results were in agreement with IHC and pimonidazole staining of tumors from the same animals (Fig 1C and 1D, respectively). We confirmed that CAIX is a robust hypoxia marker compared to CAXII. Since CAXII is generally more highly expressed in normoxia and less responsive to induction by hypoxia relative to CAIX, caution should be taken when using compounds that non-specifically target the CAs active site such as sulfonamide-based imaging probes as hypoxia surrogates. Our CAIX specific imaging probe has potential to serve broadly for the non-invasive detection of hypoxic volumes and prediction of response to hypoxia modulated therapies.

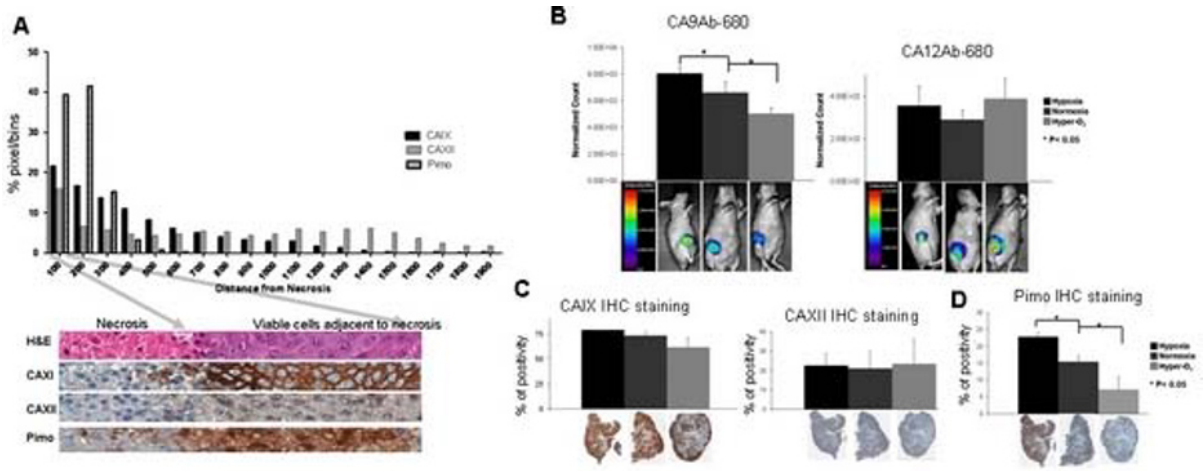

Disclosure of author financial interest or relationships:
N.K. Tafreshi, None; **M.C. LIoyd**, None; **J. Proemsey**, None; **J. Kim**, None; **R. Gillies**, None; **D.L. Morse**, LiCor Biosciences, Grant/research support .

Presentation Number **P 100**
Poster Session 1
September 18, 2013 / 18:00-18:00 / Room: Exhibit Hall B

Improved ^{64}Cu ImmunoPET targeting of an anti-ALCAM Cys-diabody using site-specific maleimide-DOTA conjugation

Richard Tavaré, *Wei Wu, Felix B. Salazar, Anna M. Wu, Crump Institute for Molecular Imaging, UCLA, Los Angeles, CA, USA. Contact e-mail: rtavare@mednet.ucla.edu*

Activated leukocyte cell adhesion molecule (ALCAM), a 100 kDa cell surface glycoprotein, has gained interest as a prospective pan-cancer biomarker for its overexpression in breast, colorectal, prostate, ovarian and pancreatic cancer. ImmunoPET imaging of cell surface markers using antibodies and their fragments, such as diabodies, can aid in the detection of tumors for diagnosis and monitor the change in cell surface expression during response to therapy. Here, the internalizing ACLAM diabody with a C-terminal Cys (cDb) is analyzed as a ^{64}Cu ImmunoPET imaging agent due to its robust potential to be used as a diagnostic marker for multiple cancer types. Due to the ability of chelators and conjugation strategy to change the pharmacokinetics of antibodies and their fragments in vivo, two conjugation strategies were compared for the ability of the radiolabeled diabody to target the colon cancer cell line LS174T. The ACLAM cDb was conjugated non-site-specifically to lysines using NHS-DOTA and site-specifically to the engineered cysteines using malemide-DOTA, resulting in ALCAM-amide-DOTA-cDb and ALCAM-thioether-DOTA-cDb, respectively. The ability to conjugate metal chelators site-specifically is of importance due to the loss of function if non-site-specific modification occurs to lysine residues in the antigen-binding site of the diabody. Mass spectrometry confirmed the addition of between 2-4 DOTA's per diabody for the ALCAM-amide-DOTA-cDb and exactly 2 DOTA's per diabody for the ALCAM-thioether-DOTA-cDb. These conjugated ALCAM cDb's retained their ability to bind the ALCAM-expressing colon cancer cell line LS174T. When radiolabeled with ^{64}Cu, ALCAM-amide-DOTA-cDb and ALCAM-thioether-DOTA-cDb achieved specific activities of 12.5 and 8.6 μCi/μg, respectively. The immunoreactive fraction of both ALCAM cDb's were about 83%. ~11.5 μg cDb was injected into mice bearing ALCAM-positive LS174T tumors and antigen negative C6 tumors. Four hours post-injection, ImmunoPET images were acquired and biodistributions were performed. Uptake in the LS174T tumor was 1.37±0.15 %ID/g and 2.64±0.53 %ID/g for ALCAM-amide-DOTA-cDb and ALCAM-thioether-DOTA-cDb, respectively, and 0.97±0.11 %ID/g and 1.36±0.15 %ID/g for the antigen negative tumor. Corresponding LS174T tumor-to-blood ratios were 1.4 and 1.9. Interestingly, the different conjugation strategies altered both the liver and kidney uptakes; ALCAM-amide-DOTA-cDb had kidney and liver uptakes of 50.9±5.7 %ID/g and 32.5±2.9 %ID/g while the ALCAM-thioether-DOTA-cDb had kidney and liver uptakes of 94.7±9.5 %ID/g and 20.2±2.5 %ID/g. As shown here, conjugation strategy greatly effects the phamacokinetics of cDb fragments and the site-specific conjugation strategy of the ALCAM cDb allows for increased tumor uptake and higher tumor-to-blood radios than non-site-specifically conjugated cDb.

Disclosure of author financial interest or relationships:
R. Tavaré, None; **W. Wu**, None; **F.B. Salazar**, None; **A.M. Wu**, ImaginAb, Inc., Stockholder; ImaginAb, Inc., Consultant; ImaginAb, Inc., Grant/research support; Daiichi Sankyo, Consultant; Sanofi, Consultant .

Presentation Number **P 101**
Poster Session 1
September 18, 2013 / 18:00-18:00 / Room: Exhibit Hall B

Molecular imaging in gold-nanoshelled microcapsules photothermal therapy evaluation

Qian Zhang[1], *Hengte Ke*[3], *Yang Du*[2], *Jie Tian*[1,2], [1]*School of Life Sciences and Technology, Xidian University, Xi'an, China;* [2]*Medical Image Processing Group, Institute of Automation,CAS, Beijing, China;* [3]*Nanomedicine and Biosensor Laboratory, School of Sciences State Key Laboratory of Urban Water Resources and Environment Harbin Institute of Technology, Haerbin, China. Contact e-mail: zhangqian@life.xidian.edu.cn*

Abstract Aim: As the enhanced permeability and retention (EPR) effect, the gold-nanoshelled microcapsules(GNS-MC) stay in the solid tumor, molecular imaging was applied in the photothermal therapy assessment non-intrusive and continuous. Methods: Green fluorescent protein (GFP) labled human hepatocellular carcinoma cells (HCC-LM3- GFP) were used to establish the subcutaneous liver tumor models. After the tumor cells were implanted 14 days, 150ul GNS-MC (4 mg/ml) or normal saline were administered through an intravenous tail injection (Figure.1.Step1). 2 hours later, the subcutaneous tumors were illuminated with an 808 nm and 2W/cm2 NIR laser for 10min (Figure.1.Step2). Then the fluorescence molecular imaging (FMI) was used to evaluate the photothermal therapy. Results: As shown in Figure.1.Step3, the tumor treated with GNS-MC under irradiation at the laser powers of 2W/cm2 was effectively ablated, leaving black scars at their original sites without showing reoccurrence. In marked contrast, tumors in control group showed normal growth speed, suggesting that laser irradiation at this power density (2W/cm2) does not affect the tumor development. The subcutaneous tumor light intensity was assessed through FMI. The result showed that there was no recurrence of the experiment group until day7 (Figure.2). Conclusion: we demonstrate that GNS-MC can be used for photothermal ablation of cancer in vivo. FMI allows for continuous and non-invasive photothermal therapy evaluation.

Figure. 1

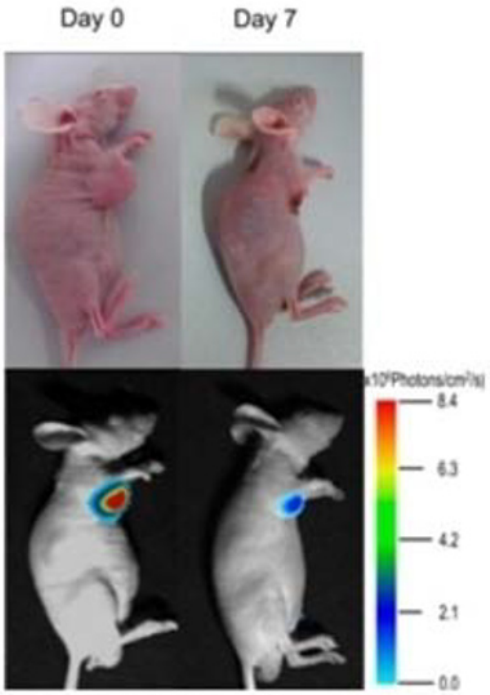

Figure. 2

Disclosure of author financial interest or relationships:
Q. Zhang, None; **H. Ke**, None; **Y. Du**, None; **J. Tian**, None.

Presentation Number **P 102**
Poster Session 1
September 18, 2013 / 18:00-18:00 / Room: Exhibit Hall B

Radiolabeled isoflavone derivatives as novel PET imaging agents

David Ranganathan[1,2], *Sanjay I. Thamake*[2], *Izabela Tworowska*[1,2], *Ebrahim Delpassand*[2], [1]*RadioMedix inc., Houston, TX, USA;* [2]*RITA Foundation, Houston, TX, USA. Contact e-mail: dranganathan@radiomedix.com*

Herbal isoflavone derivatives have been shown multiple pharmacological properties such as antitumor, antioxidant, antiviral activities and have been used as food supplements in chinese natural medicine for many years. Recent studies have confirmed their effect on different cellular targets and pathways overexpressed in cancer cells, e.g. glucose transporter-GLUT-1, estrogen receptors and tyrosine kinases. RadioMedix Inc. has developed novel class of isoflavone derivatives. They have been synthesized by coupling isoflavone glucuronides either directly to DOTA chelator (RMX-SC-11) or through-hydrophilic polyethylene glycol spacer (RMX-SC-12). RMX-SC agents have been labeled with 68GaCl3 in 0.5M NaOAc pH=4.1 at 95oC for 10min using 68Ge/68Ga generator (ITG GmbH-Germany). Their cellular uptake has been determined in several cancer cell lines e.g. breast-(SKBR-3, MCF-7), prostate-(PC-3, LNCaP) and lung-(A549). 68Ga-labeled agents were validated in xenograft model of SKBR-3, PC3 and A549 in microPET imaging studies recorded at different time intervals. They were further evaluated in biodistribution studies in SKBR-3 tumor bearing mice. Conjugation of the isoflavone to DOTA chelator significantly increased aqueous solubility and pharmacological stability of isoflavone and permitted its evaluation as tumor targeting ligand. Cellular uptake of both 68Ga-RMX-SC agents has been higher than 7 %ID/mg in all tested cancer cells lines (breast-MCF-7, SKBr3; prostate-LnCap, PC3; lung-A549). Their uptake was reduced more than 50% in the presence of increasing concentrations of GLUT1-transporter's inhibitor genistein (100-600uM). PET imaging studies of both 68Ga-agents have shown their fast and stable tumor-specific accumulation for as long as 120 minutes post-administration with elimination through liver and kidney. Both RMX-SC agents showed promising uptake in tumor with limited uptake by other organs, except liver and kidney. RMX-SC-11 and SC-12 conjugates have shown very promising tumor-targeting properties and potential as novel PET diagnostic agents. Further work is required to determine their detailed mechanism of action in cancer cells.

Disclosure of author financial interest or relationships:
D. Ranganathan, None; **S.I. Thamake**, None; **I. Tworowska**, None; **E. Delpassand**, RadioMedix, Stockholder .

Presentation Number **P 103**
Poster Session 1
September 18, 2013 / 18:00-18:00 / Room: Exhibit Hall B

In vivo Imaging to Evaluate the Biodistribution of Radioactive Gold Nanoparticles (S-NBI-29) in Normal Beagle Dogs

Anandhi Upendran[1,2], *Cathy S. Cutler*[2], *Wynn A. Volkert*[1], *James C. Kelsey*[1], *Dae Young Kim*[1], *Maryna Kuchuk*[2], *Margaret Bryan*[1], *Jimmy C. Lattimer*[1], *Raghuraman Kannan*[1,3], [1]*Nanoparticle Biochem, Inc, Columbia, MO, USA;* [2]*Physics, University of Missouri, Columbia, MO, USA;* [3]*Shasun-NBI LLC, Columbia, MO, USA. Contact e-mail: upendrana@missouri.edu*

The objectives of the study were to evaluate the pharmacokinetics and toxicity in normal healthy beagle dogs following intra-prostatic injection of gum arabic coated radioactive gold nanoparticles (S-NBI-29) using scintigraphic imaging. The pharmacokinetics of S-NBI-29 was followed by scintigraphic imaging at different post injection time points. From imaging, it is evident that minimal amounts of the intra-prostate injected S-NBI-29 leaks from the prostate into the blood. Clearance from the prostate to the urinary bladder began immediately following intra-prostatic injection. Minimal activity was found in vital organs (e.g. heart, lungs, liver, spleen and kidneys) at any time point. It is important to note that there was no detectable leakage of S-NBI-29 to the RES system at any time post intra-prostatic injection. The primary clearance of S-NBI-29 was into the bladder. After 8 days post injection, ~5 % of injected dose was retained in the prostate. The significant radioactivity transport into the bladder is thought to be due to the presence of acini ducts found throughout the normal healthy prostate glands that are directly connected to the urethra. From the urethra retrograde flow into the bladder occurs as well as antegrade flow out of the urethra. Clearance of S-NBI-29 via the acini ductal system results in efficient transport into the bladder due to the high urethral tone present in the penile urethra of dogs and the effects of anesthesia and sedation on urethral sphincter tone. Radio TLC of urine samples collected at the initial time point showed that the nano-particulate nature is retained with no measurable free 198Au ions found. No radioactivity in the blood was observed at any time point. Histological data revealed no evidence of toxicity to vital organs by 8 days post injection. Autoradiography performed on the excised prostate sections showed minimal retained radioactivity. The detailed biodistribution demonstrates that intra-prostate injection of S-NBI-29 is well tolerated in normal dogs with no evidence of acute toxicity in normal organs. The major fraction of intra-prostate injected dose clears rapidly into the urethra/bladder from the prostate via the acinar ducts. Autoradiography of the individual slices showed some diffusion of S-NBI-29 by the minimal activity retained in the prostate from the point of injection. We have shown that scintigraphic imaging can be used to ascertain the biodistribution of nanoparticles in a large animal model. Acknowledgements: NIH SBIR Phase II Contract NO. HHSN261201000100C awarded to Nanoparticle BioChem, Inc., Shasun-NBI LLC, Columbia, MO-65203. References: [1] Chanda N, Kan P, Watkinson LD, Shukla R, Zambre A, Carmack TL, Engelbrecht H, Lever JR, Katti K, Fent GM, Casteel SW, Smith CJ, Miller WH, Jurisson S, Boote E, Robertson JD, Cutler C, Dobrovolskaia M, Kannan R, Katti KV. Nanomedicine. 2010; 6 (2):201-9

Figure 1 Scintigraphic Images Recorded at Different Time points Following Intra-prostatic Injection; Yellow arrow- prostate

Disclosure of author financial interest or relationships:
A. Upendran, Nanoparticle Biochem, Inc, Stockholder; **C.S. Cutler**, None; **W.A. Volkert**, Nanopaticle BioChem, Inc, Employment; **J.C. Kelsey**, None; **D. Kim**, None; **M. Kuchuk**, None; **M. Bryan**, None; **J.C. Lattimer**, Isotherapeutics, Grant/research support; **R. Kannan**, Nanoparticle Biochem, Inc, Stockholder; Shasun-NBI, LLC, Stockholder .

Presentation Number **P 104**
Poster Session 1
September 18, 2013 / 18:00-18:00 / Room: Exhibit Hall B

MRI-only based workflow for 3D conformal small animal radiation therapy

Christian Vanhove, *Benedicte Descamps, Pieter van Mierlo, Vincent Keereman, Roel Van Holen, Stefaan Vandenberghe, iMinds - IBITech - MEDISIP - INFINITY - GROUP-ID, Ghent University (UGent), Gent, Belgium. Contact e-mail: Christian.Vanhove@UGent.be*

Introduction. Computed tomography (CT) is the standard imaging modality for radiation therapy planning (RTP) because of its ability to provide information on electron density. However, magnetic resonance imaging (MRI) provides superior soft tissue contrast, facilitating the precise selection of the target volume. This makes the technique interesting for irradiation of brain tumors. The aim of this study is to present an MRI-only based workflow for RTP on a small animal radiation research platform (SARRP), where MRI is used for target selection and for dose calculation in the rat brain. Methods. Three Wistar rats (male, 382±26g) were anesthetized using 2% isoflurane in pure oxygen before starting MRI and CT acquisitions. MRI measurements were performed on a 7T system (Bruker PharmaScan 70/16, Ettlingen, Germany) using a rat brain volume coil. Anatomical images of the rat brain were collected using a T1-weighted MDEFT sequence (TR 3000ms, TE 3.5ms, TI 1100ms, 200x200µm, 26 contiguous slices of 500µm, NA 2, TA 20'48"), directly followed by a ZTE sequence (TR 2ms, TE 0, matrix 2303, 200x200x304µm, NA 6, TA 6'21"). ZTE offers the opportunity to acquire images from proton-poor structures with short transverse relaxation times, such as bone, by using a "zero" echo time and rapid readout of the fast decaying signal. Following MRI, the animals were moved to the SARRP to start a cone-beam CT by acquiring 720 projections over 360°. Cone-beam CT projection data were reconstructed by filtered back-projection to obtain the standard-CT for RTP. ZTE and MDEFT images were co-registered with the standard-CT by rigid body transformation obtained using maximization of normalized mutual information. The co-registered ZTE images were segmented into two (soft tissue and air) or three (bone, soft tissue and air) tissue classes to obtain two different pseudo-CT data sets, providing the required electron density information. Image segmentation was done using thresholding. MDEFT images, standard-CT and both pseudo-CTs were imported in the RTP software of the SARRP. On the MDEFT images, the right motor cortex was selected as target and a dose plan was calculated to deliver 10Gy using 4 beams in combination with the 3x3mm collimator. The dose distribution was computed using the standard-CT and using the two pseudo-CTs. Differences in dose delivery were quantified. Results. The total exposure time to deliver the prescribed dose using the standard-CT was 276±2 seconds compared to 266±1 ($p<0.05$) seconds and 275±2 ($p=NS$) seconds when the pseudo-CT with two tissue and three tissue classes were used, respectively. An average absolute deviation of -40±10 cGy ($p< 0.05$) and -2±11 cGy ($p=NS$) was measured between RTP by standard-CT and by pseudo-CT using two and three tissue classes, respectively. Conclusion. We have demonstrated the feasibility of an MRI based workflow for RTP on a SARRP. Segmentation of ZTE images offers the ability to obtain electron density information from MRI, which is a requirement for RTP. Three tissue classes are necessary to obtain accurate dose calculations in the rat brain.

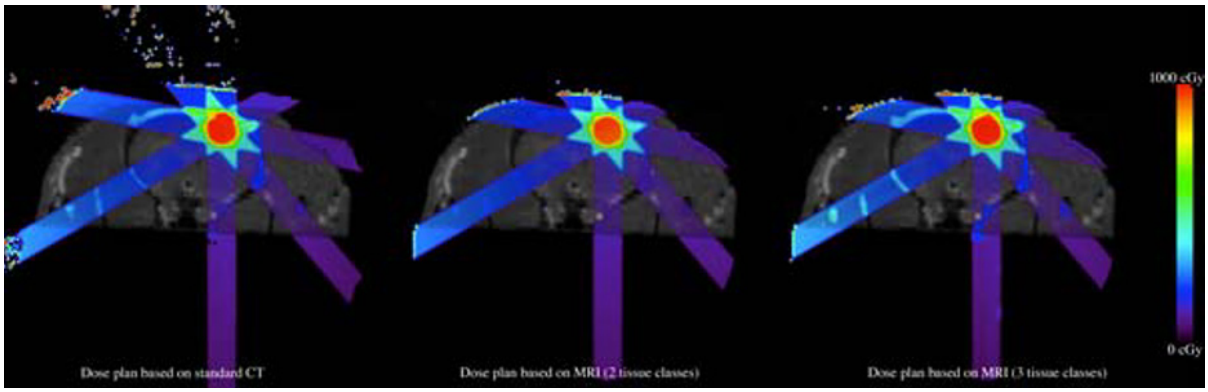

Calculated dose distribution co-registered with MDEFT T1-weighted MRI images. Left: Dose distribution computed using standard-CT. Middle: Dose distribution computed using pseudo-CT with 2 tissue classes. Right: Dose distribution computed using pseudo-CT with 3 tissue classes.

Disclosure of author financial interest or relationships:
C. Vanhove, None; **B. Descamps**, None; **P. van Mierlo**, None; **V. Keereman**, None; **R. Van Holen**, None; **S. Vandenberghe**, None.

Presentation Number **P 105**
Poster Session 1
September 18, 2013 / 18:00-18:00 / Room: Exhibit Hall B

Dynamic observation of a long term antitumor immunity by bioluminescence imaging with peptide LTX-315 in rat competent model

Mengyu Wang[1], *Janne Nestvold*[2], *Bent Rolstad*[2], *Øystein Rekdal*[3,4], *Gunnar Kvalheim*[1], [1]*Cell Terapy, Oslo University Hospital, Oslo, Norway;* [2]*Anatomy, Oslo University, Oslo, Norway;* [3]*Institute for Medicine, Tromsø University, Tromsø, Norway;* [4]*Lytix Biopharma AS,, Tromsø, Norway. Contact e-mail: Meng.Yu.Wang@rr-research.no*

Bioluminescent imaging (BLI) is the most widely used molecular imaging technique in preclinical animal model. Immunotherapy is powerful for inducing killing of tumor cells. However, the efficacy of immune response to cancer stem cells still is not very clear. Here we demonstrate an induced immune response in a novel rat tumor stem cell model following treatment with peptide LTX-315. Method: Firstly, rat transformed mesenchymal stem cells (rTMSCs) were transduced with GFP-Luciferase fusion reporter gene by retrovirus infection. High proliferation colonies were selected with high percentage of side population (SP) for assessment of the effect of LTX-315 in rat PVG and PVG7b. Before CCD camera was used for dynamic living imaging, substrates D-Luciferin Firely, potassium salt, 150mg/kg were given to rats by i.p. The animals were scanned twice each week. RTMSCs (2x105 cells) were subcutaneously inoculated into PVG rats and established tumors were treated i.t. with LTX-315 (50 µl of 20mg/ml). Treatment 5-7 times with the peptide LTX-315 resulting a total tumor regression in all treated animals (n=6). After 6 weeks the tumor-free rats were re- challenged with rTMSCs inoculation s.c. or i.p. After 9-10 months tumor free rats were given the third re-challenged by inoculating s.c. and i.p. 2x104 cells. All tested rats and control rats were scanned with IVIS by D-luciferine injection i.p. and none of the initially cured rats show regrowth of the tumor after re-challenging Conclusion: IT imaging of antitumor immunity by labeling Fluc reporter gene is very effective and represent an important method for the judgment of targeting the cancer stem cell treatment in vivo. It can dynamically used to prove long-term effect of the therapy. This method is depending on injection of D-Luciferin, a substrate of firefly luciferase, luciferase-expressing cells generate bioluminescence signal. The signal distribution can be detected by the in vivo imaging with instrument IVIS and allows for non-invasive method of monitoring of tumor growth, spread and metastasis, and regression. Our data suggest that intratumor injection with Peptide LTX-315 might be a new immune therapeutic treatment for cancer. LTX-315 can stimulate tumor specific immune responses leading to a tumor-specific protection for at least for 10-11 months. The immune cells infiltrating the tumor processed by two photons imaging is under investigation.

Disclosure of author financial interest or relationships:
M. Wang, None; **J. Nestvold**, None; **B. Rolstad**, None; **. Rekdal**, None; **G. Kvalheim**, None.

Presentation Number **P 106**
Poster Session 1
September 18, 2013 / 18:00-18:00 / Room: Exhibit Hall B

Biodistribution of P-selectin Targeted Microbubbles

Jason Warram[1], *Anna G. Sorace*[2], *Marshall J. Mahoney*[2], *Sharon Samuel*[1], *Bryant Harbin*[2], *Madhura Joshi*[2], *Amber Martin*[1], *Lee Whitworth*[1], *Kenneth Hoyt*[1,2], *Kurt R. Zinn*[1,2], [1]*Radiology, University of Alabama at Birmingham, Birmingham, AL, USA;* [2]*Biomedical Engineering, University of Alabama at Birmingham, Birmingham, AL, USA. Contact e-mail: mojack@uab.edu*

Targeted ultrasound microbubbles (MB) have the potential to deliver therapeutic agents to vascular targets associated with the cancer phenotype. The cellular adhesion molecule, P-selectin, has been shown to be overexpressed on activated endothelial cells in the tumor vasculature. To evaluate the potential for P-selectin targeted-MB to preferentially accumulate in tumor vasculature, Tc-99m labeled anti P-selectin antibodies (Ab) were avidin-bound to lipid-shelled, perfluorocarbon gas-filled MB and i.v. injected into mice bearing 2lmp breast tumors. Tc-99m radiolabeling was done using the HYNIC method. Whole-body biodistribution was performed at 5min (n=12) and 60min (n=4) using a gamma counter. Tc-99m-labeled IgG bound control-MB group (n=12 at 5min; n=4 at 60min), Tc-99m-labeled IgG control Ab group (n=5 at 5min; n=3 at 60min), and Tc-99m-labeled anti P-selectin Ab group (n=5 at 5min; n=3 at 60min) were also evaluated. Planar gamma camera imaging was also performed at each time point. Utilizing the specific activity, number of MB injected, and the injected dose; P-selectin MB were calculated to contain 3.36x109 Ab molecules per MB. Tissues from the 4 groups were compared for the Tc-99m retention in terms of %-injected dose per gram (%ID/g). The results showed lung uptake remained highest in the MB groups at both time points, however control-MB was significantly higher ($P<0.05$) than targeted-MB. This trend was confirmed using planar imaging. For the spleen, levels were greater for the MB groups compared with Tc-99m-labeled Ab groups with no significant difference ($P>0.05$) between MB groups at the 5min and 60min time points. Liver retention was significantly higher ($P<0.05$) for the control-MB group compared to the 3 other groups and retention in all groups remained stable from 5min to 60min. For the tumor, there was significantly higher ($P<0.05$) retention of targeted-MBs (1.28 %ID/g ± 0.38) over control-MBs (0.39 %ID/g ± 0.15) at 5min. Overall retention in tumor for all groups was higher at 60min than 5min, which was unique to tumor. This was also confirmed during planar imaging. Targeted-MB retention in tumor (60min: 1.77 %ID/g ± 0.31) was significantly greater ($P=0.01$) than targeted-MB levels in adjacent skeletal muscle at both time points (5min: 0.65 %ID/g ± 0.2; 60min: 0.19 %ID/g ± 0.12) while there was no significant difference ($P=0.17$) between muscle and tumor retention for the control-MB group at 5min. For the kidneys, there was significantly greater ($P<0.05$) retention for the targeted-MB over control-MB at the 5min time point, however targeted-MBs were significantly cleared ($P<0.05$) at the 60min time point while the control-MB retention remained unchanged from 5min to 60min. Blood clearance from 5min to 60min was greatest ($P<0.01$) for the targeted-MB group (87%) while the control-MB group was not significantly different ($P>0.05$). Likewise, the blood clearance was significantly greater ($P<0.05$) for the P-selectin Ab (79%) over the control Ab (42%). In summary, P-selectin targeted MBs were shown to preferentially accumulate in tumor tissue over adjacent skeletal tissue and outperform IgG control labeled MB in tumor uptake.

Disclosure of author financial interest or relationships:
J. Warram, None; **A.G. Sorace**, None; **M.J. Mahoney**, None; **S. Samuel**, None; **B. Harbin**, None; **M. Joshi**, None; **A. Martin**, None; **L. Whitworth**, None; **K. Hoyt**, None; **K.R. Zinn**, None.

Presentation Number **P 107**
Poster Session 1
September 18, 2013 / 18:00-18:00 / Room: Exhibit Hall B

In vivo metabolic characterization of a repeatable rat glioma model using 1H Magnetic Resonance Spectroscopy at 7.0 tesla

Mei zhi Yi, *Gen Yan, Renhua Wu, Shantou University, Shantou, China. Contact e-mail: ymz317@126.com*

Objectives: This study aimed to establish a repeatable rat glioma model and monitor cerebral metabolism changes during the growth of glioma using 1H magnetic resonance spectroscopy (MRS) at 7.0 tesla (7T). Methods: Healthy male Sprague-Dawley (SD) rats were randomly and equally divided into two groups. The C6 glioma cells were stereotaxically implanted into the right basal ganglia region of SD rats in the treatment group. In seven control rats, only normal saline was injected. The SD rats were sequentially followed up by 1H MRS in vivo once before operation and then once a week until they died. Brain metabolites were measured in regions of tumour and control brain tissue. All spectra were collected using a high resolution 7T MR Scanner and then quantified by LCModel fitting software. Lastly, hematoxylin-eosin (HE) staining and glial fibrillary acidic protein (GFAP) immunohistochemical were employed to detect and confirm the changes of brain tissue. Results: This model was pathological considered to resemble certain characteristics of human glioma. Glioma in the SD rats presented as T2 hyperintense in MRI. As the tumour size increased, it was characterized by decreases in N-acetyl aspartate (NAA), creatine (Cr), glutamic acid, macromolecule and increases in choline (Cho), lactate, lipid. In contrast, metabolite concentrations in rats received normal saline remained unchanged during the whole observation. There was no significant difference in inositol peak between the two groups. Moreover, reduced NAA/Cr, NAA/Cho and increased Cho/Cr were found in the treatment group during tumour growth. Conclusion: These brain metabolite profiles closely mirror those reported from human glioma confirming that SD rats provide a repeatable model for investigating biochemical specificity of this disease. The acquired MRS data of this model at 7T may not only provide valuable information about glioma metabolism, but also potentially aid the development of the clinical diagnosis and treatment of glial tumour.

Disclosure of author financial interest or relationships:
M. Yi, None; **G. Yan**, None; **R. Wu**, None.

Presentation Number **P 108**
Poster Session 1
September 18, 2013 / 18:00-18:00 / Room: Exhibit Hall B

Imaging fructose transport through GLUT5 in breast cancer: A radiopharmacological study

Melinda Wuest[1], *Vincent Bouvet*[1], *Brendan J. Trayner*[3], *Olivier M. Soueidan*[2], *Monica Wang*[1], *John Mercer*[1], *Alexander J. McEwan*[1], *Frederick West*[2], *Frank Wuest*[1], *Chris I. Cheeseman*[3], [1]*Dept. of Oncology, University of Alberta, Edmonton, AB, Canada;* [2]*Dept. of Chemistry, University of Alberta, Edmonton, AB, Canada;* [3]*Dept. of Physiology, University of Alberta, Edmonton, AB, Canada. Contact e-mail: mwuest@ualberta.ca*

Aim: According to several studies up to 50% of breast cancers are GLUT1 transporter negative and therefore possess a low sensitivity for the glucose analog [^{18}F]FDG. As an alternative approach for PET, GLUT5 was proposed. Although there has been controversy regarding overexpression of GLUT5 in human breast cancer cell lines, it remains to be established whether the present amounts of GLUT5 would represent a feasible alternative approach for PET imaging of breast cancer patients. In this study several fluoride-labeled compounds designed for transport through GLUT5 have been studied in preclinical models in vitro and in vivo in order to analyze their potential for imaging breast cancer. *Materials and Methods:* The three compounds designed for transport through GLUT5 1-deoxy-1-fluoro-D-fructose (1-FDF), 6-deoxy-6-fluoro-D-fructose (6-FDF) and fluoro-2,5-anhydro-D-mannitol (1-FDAM) were radiolabeled with F-18 to yield 1-[^{18}F]FDF, 6-[^{18}F]FDF and 1-[^{18}F]FDAM and analyzed in vitro and in vivo. 3-deoxy-3-fluoro-D-fructose (3-FDF) was only available as a non-radiolabeled compound. Radiopharmacological experiments were carried out in murine EMT-6 cells and mice bearing EMT-6, MCF-7 or MDA-MB 231 tumor xenografts. Potential metabolism of the three radiolabeled compounds was analyzed in vitro. *Results:* All three radiolabeled compounds designed for transport through GLUT5 are taken up into the breast cancer tumors in vivo. After injection of 6-[^{18}F]FDF a maximum SUV of 1.22±0.11 (n=3) was determined in EMT-6 tumors after 10 min while 1-[^{18}FF]FDF and 1-[^{18}F]FDAM only reached values of 0.48±0.07 and 0.59±0.09 (n=3) after 20 min p.i. In vitro cell uptake studies supported this finding. Inhibiting cellular uptake of 6-[^{18}F]FDF with the different compounds resulted in lower IC_{50} values compared to fructose. Over time radioactivity was cleared from tumor tissue reaching SUVs of 0.54±0.06 (6-[^{18}F]FDF), 0.28±0.01 (1-[^{18}F]FDAM) and 0.31±0.06 (1-[^{18}F]FDF, n=3) after 120 min p.i. indicating no intracellular trapping. This was explained with an enzymatic assay showing that none of the three radiotracers was phosphorylated by hexokinase II and only 6-[^{18}F]FDF by ketohexokinase (KHK), which was, however, absent in all three breast cancer cell lines investigated. Interestingly, in human xenograft tumor tissue radioactivity uptake after injection of 6-[^{18}F]FDF showed retention indicating that a trapping mechanism may be independent of KHK. Also, while uptake and retention of [^{18}F]FDG was higher in estrogen receptor (ER)-positive MCF-7 tumors versus ER-negative MDA-MB231, fructose transport trough GLUT5 and retention is opposite to that when analyzed with 6-[^{18}FF]FDF. *Conclusion:* Although the importance of GLUT5 expression and analysis of the retention mechanisms of the three investigated radiotracers in human breast cancer tissue remains to be elucidated, the present results support that imaging with a compound designed for transport through GLUT5, most likely 6-[^{18}FF]FDF, should be pursued in a clinical PET study.

Imaging fructose transport through GLUT5 in breast cancer: A radiopharmacological study

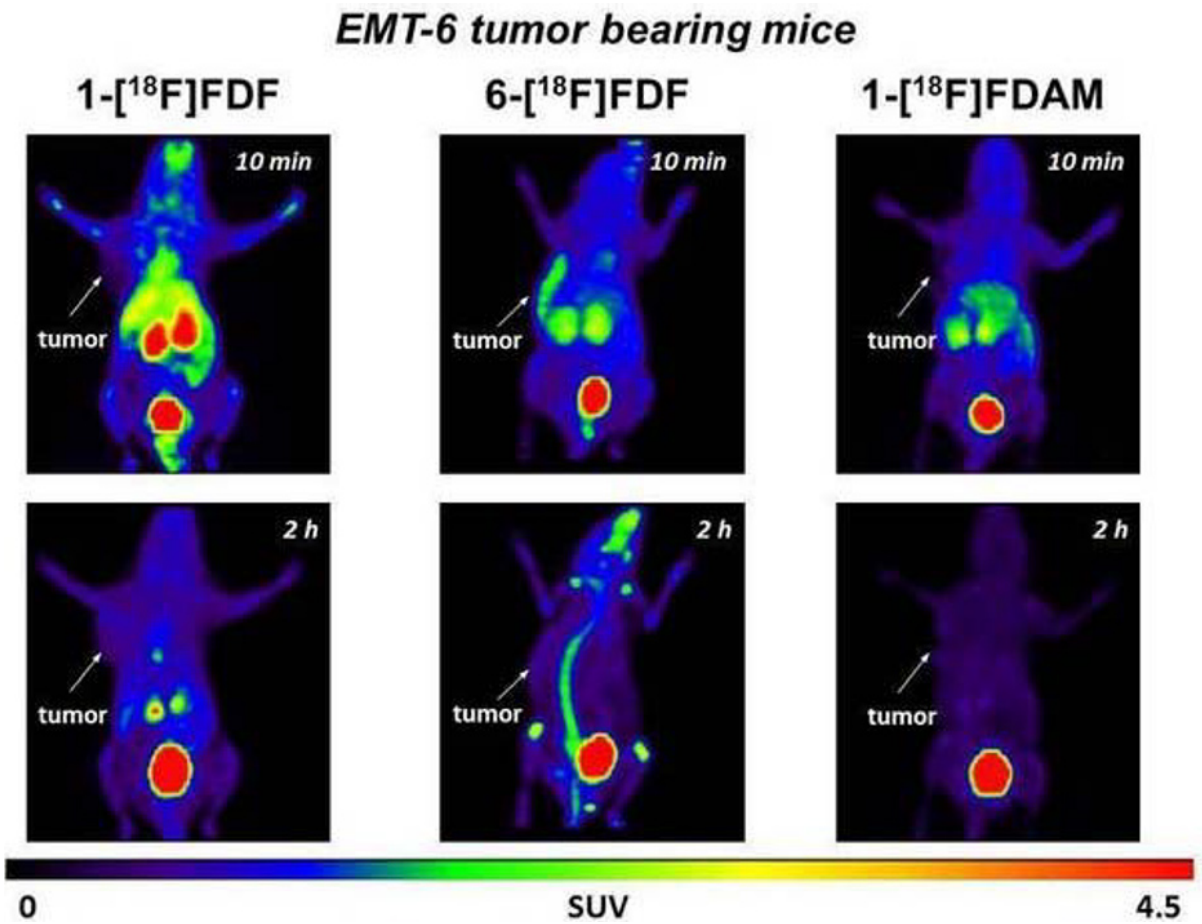

Disclosure of author financial interest or relationships:
M. Wuest, None; **V. Bouvet**, None; **B.J. Trayner**, None; **O.M. Soueidan**, None; **M. Wang**, None; **J. Mercer**, None; **A.J. McEwan**, None; **F. West**, None; **F. Wuest**, None; **C.I. Cheeseman**, None.

Presentation Number **P 109**
Poster Session 1
September 18, 2013 / 18:00-18:00 / Room: Exhibit Hall B

Suppression and inactivation of MGMT for temozolomide sensitization in glioblastoma model

Byunghee Yoo, *Marytheresa Ifediba, Subrata K. Ghosh, Zdravka Medarova, Anna Moore, MGH/MIT/HMS Athinoula A. Martinos Center for Biomedical Imaging, Massachusetts General Hospital and Harvard Medical School, Charlestown, MA, USA. Contact e-mail: byunghee@nmr.mgh.harvard.edu*

Introduction: Glioblastoma multiforme (GBM) is grade IV malignant glioma characterized by high invasiveness and low survival. Temozolomide (TMZ) is the only drug showing improved survival when administered with concomitant radiotherapy. The responsiveness of GBM to TMZ has been linked to the activity of O6-methylguanine-DNA methyltransferase (MGMT). The goal of this study is to silence MGMT to sensitize GBM to TMZ treatment using theranostic nanoparticle probe. Methods: Theranostic dextran coated magnetic nanoparticles (NP) were conjugated to siRNA against MGMT or scrambled siRNA and decorated with chlorotoxin (CTX) for glioma cell targeting and Cy5.5 for correlative microscopy (termed CTX-NP-siMGMT or CTX-NP-siSCR). MGMT gene and protein expression in T98G human glioma cells were assessed after incubation with the probe by real-time PCR and Western blot. MGMT activity was quantified by the transfer of 3H-methyl from calf thymus DNA. Intracranial glioma model was generated by stereotactic injection of T98G cells in the right hemisphere of 5-6 wk old athymic nude mice (Cox-7, MGH). Intratumoral injections of CTX-NP-siMGMT (n=6), CTX-NP(Cy5.5) (n=5) or PBS control (n=3) were followed by i.p. injections of TMZ (50 mg/kg/day) for the next 5 consecutive days (repeated three weeks totally) and TMZ alone during the fourth week. Periodic T2w-MRI was used to monitor probe injections. Histology was performed at the end of the study. Results and Discussion CTX-NP-siMGMT reduced MGMT mRNA expression by 38.3% relative to NP(Cy5.5) treatment and 26.2% relative to CTX-NP-siSCR treatment in vitro. The MGMT gene silencing induced by CTX-NP-siMGMT at the mRNA level directly correlated with downregulation of MGMT protein expression, which was reduced by 52%. These results were in agreement with a decline in MGMT activity, which was > 64% reduced following CTX-NP-siMGMT treatment relative to NP(Cy5.5) treatment. In vivo imaging of nanoparticle-treated tumors revealed abundant uptake of CTX-NP-siMGMT and CTX-NP(Cy5.5). Notably, mice treated with CTX-NP-siMGMT had the most pronounced response to TMZ, with a final tumor size that was on average only 124% of initial volume. This is in marked contrast to PBS-treated mice that increased in volume by approximately 15-fold after TMZ treatment. Interestingly, tumor sizes in CLX-NP(Cy5.5)-treated mice increased by 316%, but they were significantly reduced relative to PBS-treated mice. Histological staining and fluorescence microscopy of tumor tissues revealed abundant nanoparticle uptake in tumor cells treated with CTX-NP-siMGMT and CTX-NP(Cy5.5). In both types of nanoparticle-treated tumors there was evidence of degenerated tumor nuclei and tissue degradation associated with internalized nanoparticles. Conclusion: We have demonstrated the effect of MGMT suppression on the sensitization of malignant glioma to TMZ treatment in vitro and in vivo. MGMT-specific siRNA was effectively delivered intratumorally to GBM and induced robust knockdown of endogenous MGMT levels that, in combination with TMZ, induced widespread tumor destruction.

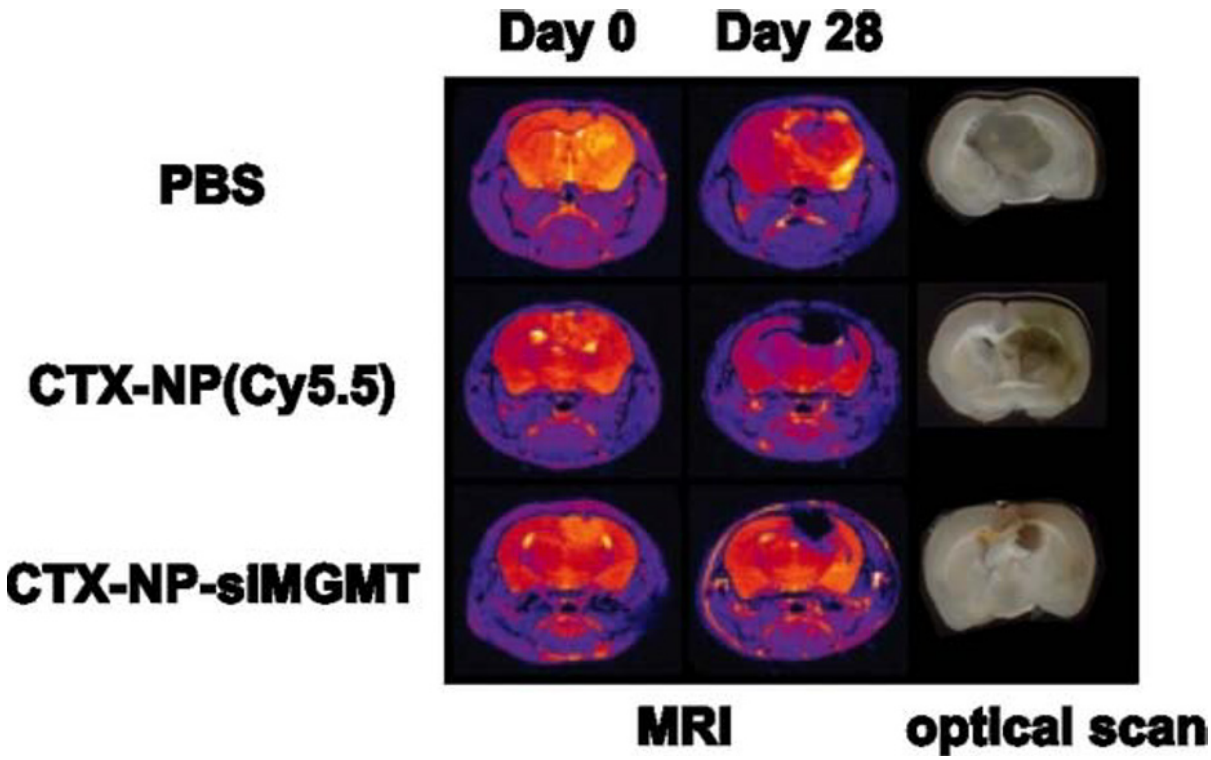

Disclosure of author financial interest or relationships:
B. Yoo, None; **M. Ifediba**, None; **S.K. Ghosh**, None; **Z. Medarova**, None; **A. Moore**, Fluoropharma, Grant/research support .

Presentation Number **P 110**
Poster Session 1
September 18, 2013 / 18:00-18:00 / Room: Exhibit Hall B

Development and validation of multimodal imaging of intestinal adenomas in APC/min+ mouse model

Kevin Guley[1], Shengli Ding[2], Pauline K. Lund[2], **Hong Yuan**[1], [1]*Biomedical Research Imaging Center, UNC Chapel Hill, Chapel Hill, NC, USA;* [2]*Department of Cell and molecular physiology, UNC Chapel Hill, Chapel Hill, NC, USA. Contact e-mail: yuanh@med.unc.edu*

Background: Mice with mutation in Apc gene (Apc/Min+) develop multiple adenomas in small intestine and colon, and are widely used to study gastrointestinal carcinogenesis and therapeutic intervention. Current assessment of tumor progression and treatment efficacy largely depends on histology after dissection or colonoscopy which only evaluates distal colon. Improved non-invasive in vivo imaging of intestinal adenoma could greatly benefit gastrointestinal research. However few studies have been conducted to develop in vivo imaging of mouse intestinal tumors due to technical challenges. We have developed a multimodal imaging method of imaging mouse intestinal and colon adenomas using microCT and 3D fluorescence imaging, and validated 3D fluorescence imaging with near infra red (NIR) cathepsin probe on Apc/min+ model. Method: First, phantom with both CT contrast agent and optical probe was imaged using microCT scanner (eXplore CT120, Gamma Meidca, Inc.) and 3D fluorescence tomography system (FMT2500, Perkin Elmer, Inc.). The registration method was developed and validated on the phantom images. Secondly, bowel preparation method and contrast enhanced microCT imaging protocol was developed to image intestinal and colon tumor adenomas on aged Apc/min+ mice. Several CT contrast agents including iodine-based and barium-based compounds were tested. Dose and timing was optimized for best contrast enhancement and tumor delineation. Finally, multi-modal imaging using microCT and FMT imaging method was conducted on aged Apc/min+ mice to delineate intestinal and colon adenomas. Mice were injected with NIR cathepsin-activatable probes 24hrs before imaging. Iodine based contrast agent was orally gavaged into mice 1.5 hours prior to CT imaging. Mouse was imaged with microCT scanner first followed immediately by 3D fluorescence imaging. Intestine was later dissected for ex-vivo fluorescence imaging for validation. Results: Rigid registration method based on fiducial markers was applied successfully on microCT and 3D fluorescence images of phantom. Oral gavage of Iodine-based contrast agent produced best CT images, and intestinal polyps in Apc/min+ mice were clearly detected in contrast enhanced microCT images. Results from in vivo microCT imaging correlated well with ex-vivo fluorescence imaging on intestine and colon specimens. In vivo imaging showed some visual correlation between tumor location detected from microCT and fluorescence signal from FMT imaging, however discrepancies between fluorescence signal and tumor location in the CT images were presented, indicating limitations in 3D fluorescence imaging (Fig. 1). Conclusion: We have developed multimodel imaging method using microCT and 3D FMT imaging to image intestine adenomas on Apc/Min+ mice. Contrast enhanced CT imaging has proven to be an efficient method of screening and localizing intestinal adenomas, and will facilitate future methods to quantify tumor volume and load. The discrepancy between CT and optical/NIR signal location indicates a need for improved 3D fluorescence imaging, and caution in interpretation of in vivo 3D fluorescence imaging in mouse intestinal tumor models.

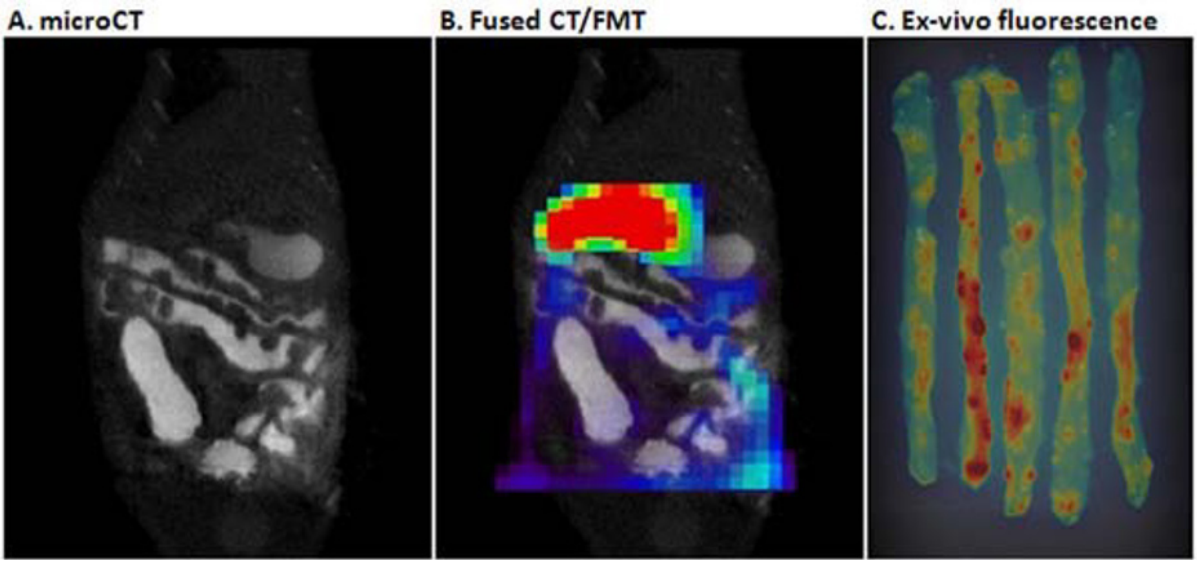

Fig. 1. Multimodal CT/FMT imaging on intestinal adenomas in Apc/Min+ mice. A: Tumor nodules were detected from contrast-enhanced microCT imaging. B: 3D fluorescence molecular tomography (FMT) imaging was taken at 24hours after injection of cathepsin-activatable NIR probe, and fused with microCT image for anatomical co-localization. C: Intestines were collected at the end of in vivo imaging and imaged ex vivo with FMT system for validation.

Disclosure of author financial interest or relationships:
K. Guley, None; **S. Ding**, None; **P.K. Lund**, None; **H. Yuan**, None.

Presentation Number **P 111**
Poster Session 1
September 18, 2013 / 18:00-18:00 / Room: Exhibit Hall B

[18F]FAZA-PET Detection of Hypoxia Changes following Anti-cancer Therapy

Jinzi Zheng[1], *Stephan G. Klinz*[2], *Raquel De Souza*[1], *Michael Dunne*[1], *Jonathan Fitzgerald*[2], *David A. Jaffray*[1,3], [1]*STTARR Innovation Centre, Princess Margaret Cancer Centre, Toronto, ON, Canada;* [2]*Merrimack Pharmaceuticals, Cambridge, MA, USA;* [3]*Radiation Oncology, University of Toronto, Toronto, ON, Canada. Contact e-mail: jinzi.zheng@rmp.uhn.on.ca*

Introduction: Tumor hypoxia is strongly linked to aggressive disease progression and resistance to therapy. Positron emission tomography (PET) imaging with hypoxia tracers such as [18F]fluoroazomycin arabinoside (FAZA) allows for non-invasive quantification of tumor hypoxia before, during and after treatment. Here, we report the use of FAZA-PET for longitudinal monitoring of tumor hypoxia changes in a mouse xenograft model of colon cancer over a 21-day period following weekly chemotherapy administrations. **Methods:** Fifteen female mice bearing bilateral subcutaneous colon xenograft tumors were employed in this study. Each treatment group was composed of a total of 10 tumors (5 animals bearing two tumors each). Seven FAZA-PET/CT imaging sessions were performed on days 0, 2, 4, 7, 10, 16 and 21 post treatment initiation using a high-throughput triple mouse imaging bed. [18F]FAZA was produced by CanProbe (Ontario, Canada) with a radiochemical purity of 95.7 ± 3.7% (calculated over 7 productions). PET imaging (Focus 220, Siemens) was performed at 2 hours post FAZA administration (0.79 ± 0.06 MBq/g of body weight). Each PET acquisition consisted of a 20-minute emission scan followed by an 8-minute ^{57}Co transmission scan for attenuation and scatter correction. Immediately post-PET imaging, a CT scan (GE Locus Ultra, 80 kVp, 50 mA) was performed with animals in the same position in order to provide anatomical data for image registration. The PET and CT datasets were registered, contoured and analyzed using the Inveon Research Workplace software (IRW 4.0, Siemens). A total of three complete treatment cycles were administered to each animal (days 0, 7 and 16). Confirmation of tumor-specific hypoxia status at the study end point (day 21) was performed using an intraperitoneal administration of EF5 (0.1 mM of EF5 per g of body weight) 2 hours before euthanizing the animals. The excised tumors were fixed, sectioned and stained for EF5. **Results:** The FAZA-PET uptake measured in the 30 tumors (15 mice) ranged between 0.83 and 4.29 %ID/g over the course of 21 days and 7 imaging session. The mean FAZA uptake was calculated to be 1.73 ± 0.58 %ID/g across all measurements. No correlation between tumor volume and FAZA uptake was observed at baseline (day 0). The background FAZA level in the muscle was consistent over time across the three treatment groups (0.78 ± 0.18 %ID/g, 0.81 ± 0.11 %ID/g and 0.71 ± 0.20 %ID/g). Significant differences in tumor FAZA uptake (%ID/g) between treatment groups were detected as early as day 7 post treatment initiation, whereas differences in tumor volume only became statistically significant on day 16 ($p < 0.05$). **Conclusion:** This study demonstrated the feasibility of performing longitudinal and repeated tumor hypoxia assessment using FAZA-PET imaging. Specifically, differences in hypoxia within tumor-size matched groups in response to treatment were successfully detected. Hypoxia changes following anti-cancer therapy has the potential to provide an early assessment of treatment activity.

Disclosure of author financial interest or relationships:
J. Zheng, None; **S.G. Klinz**, Merrimack Pharmaceuticals, Employment; **R. De Souza**, None; **M. Dunne**, None; **J. Fitzgerald**, Merrimack Pharmaceuticals, Employment; Merrimack Pharmaceuticals, Stockholder; **D.A. Jaffray**, Precision X-ray Inc., Other financial or material support .

Presentation Number **P 112**
Poster Session 1
September 18, 2013 / 18:00-18:00 / Room: Exhibit Hall B

Monitoring targeting and efficacy of novel anti-CEA-IL2v immunocytokine by in vivo imaging in tumor bearing mice

Philine M. Zumstein, *Steffi Lehmann, Valeria Nicolini, Inja Waldhauer, Anne Freimoser-Grundschober, Olivier Freytag, Erwin van Puijenbroek, Sabine Lang, Christian Klein, Pablo Umana, Christian Gerdes, Pharma Research and Early Development (pRED), Roche Glycart AG, Schlieren-Zurich, Switzerland. Contact e-mail: philine.zumstein@roche.com*

GA504 (CEA-IL2v) is a novel monomeric tumor-targeted IL-2v immunocytokine based on a single, engineered IL-2 variant (IL-2v) with abolished IL-2Rα (CD25) binding that is fused to the C-terminus of a heterodimeric Fc-part of the humanized high affinity CEACAM5 antibody CH1A1A. FcγR and C1q binding is completely abolished by incorporation of a novel mutation. This immunocytokine is supposed to act as a tumor targeted immune-modulator to locally support anti-tumor immune responses by activating tumor associated T-cells, NK cells and macrophages. Having shown increased immune cell proliferation and recruitment induced by GA504 by cell-based assays in vitro, we here set out to investigate the biodistribution and pharmacokinetic (PK) properties of GA504 and its tumor targeting capacity in vivo by non-invasive fluorescence imaging (FLI) combined with blood ELISAs. GA504, a homologous CEA targeted IgG lacking IL2v coupling, a non-targeted IL2v fusion and a non-targeted control antibody lacking IL2v were labeled with Alexa Fluor 647. Mice bearing CEA+ LS174T subcutaneous tumors were injected iv with a single dose of these molecules and FLI was performed using the IVIS® Spectrum (Perkin Elmer). The detected FLI signal was normalized to the injected dose of antibody as measured by ELISA to correct for differences in blood antibody concentration. To investigate the PK properties of all antibody constructs, animals were bled at several time points after antibody application. To further confirm our in vivo imaging data, we also investigated the presence of therapeutic antibodies by ex vivo fluorescence microscopy. In a next step, therapeutic effects of GA504 were assessed in a liver metastatic model where LS174T cells, stably expressing luciferase as reporter, were injected intra- splenically into SCID/bg mice. Both therapeutic and control antibodies were applied iv 3q7d at a dose of 1mg/kg. Tumor growth was monitored by bioluminescence imaging (BLI) every 3 days. In our experiments, we observed differences in both the targeting behavior and the basic PK of the tested compounds: IL-2 coupling resulted in a much shorter half-life of the molecule as compared to the respective IgG. This construct also displayed a more persistent tumor targeting normalized to its untargeted equivalent than the uncoupled IgG control. These differences in targeting and PK properties between the various constructs were confirmed ex vivo by conventional microscopy. Bioluminescence imaging of tumor growth and the assessment of survival showed good therapeutic efficacy of GA504 in the LS174T liver metastatic colon carcinoma model. Using non-invasive optical imaging approaches, we were able to obtain a better understanding of the binding characteristics and PK properties of the CEA targeting immune-modulator bearing IL2v. Our data demonstrate the utility of using targeted immune-modulators as anti-cancer therapeutic agents, locally stimulating anti-tumor immune responses, and allow for the identification of optimal therapeutic time windows for the combination with additional cancer immune therapies.

Disclosure of author financial interest or relationships:
P.M. Zumstein, Pharma Research and Early Development (pRED), Roche Glycart AG, Employment; **S. Lehmann**, Roche Glycart, Employment; **V. Nicolini**, Roche-Glycart, Employment; **I. Waldhauer**, Roche Glycart AG, Employment; **A. Freimoser-Grundschober**, Roche Glycart AG, Employment; **O. Freytag**, Roche Glycart AG, Employment; F.Hoffmann La Roche, Stockholder; **E. van Puijenbroek**, Roche Glycart AG, Employment; Hoffmann-LaRoche AG, Stockholder; **S. Lang**, Roche Glycart AG, Employment; **C. Klein**, Roche Glycart AG, Employment; Roche Glycart AG, Stockholder; **P. Umana**, Roche Glycart, Employment; **C. Gerdes**, Roche Glycart, Employment .

Presentation Number **P 113**
Poster Session 1
September 18, 2013 / 18:00-18:00 / Room: Exhibit Hall B

Gold nanoparticles for atherosclerotic plaque characterization via monocyte tracking using computed tomography

Peter Chhour[1], *Pratap C. Naha*[1], *Muredach Reilly*[2], *Victor Ferrari*[2], *David P. Cormode*[1], [1]*Radiology, University of Pennsylvania, Philadelphia, PA, USA;* [2]*Cardiology, University of Pennsylvania, Philadelphia, PA, USA. Contact e-mail: pchhour@gmail.com*

Introduction: Atherosclerosis is characterized by the development of plaques in the arterial wall. The migration of monocytes into the arterial wall is a key process in the early development of atherosclerotic plaques. Soon after migrating into the intima, monocytes differentiate into macrophages, then foam cells, which cause instability in the plaque and eventually lead to plaque rupture. When these events occur in a coronary artery, it can lead to myocardial infarction and death. Computed tomography (CT) is one of the best techniques for imaging the coronary arteries. The use of gold nanoparticles as a CT contrast agent is a recently explored field due to gold's high biocompatibility and strong X-ray absorption. The development of gold nanoparticles for monocyte tracking via CT may lead to early detection of rupture prone atherosclerotic plaques, informing therapeutic strategies. Methods: Gold nanoparticles (AuNPs) were synthesized through the Turkevich method. Briefly, chloroauric acid was boiled with disodium citrate for 15 minutes. The resulting nanoparticles are not stable in salt based solutions such as phosphate buffered saline (PBS) but can be stabilized through surface ligand exchange (A). AuNPs were treated with various ω-thiol ligands (see supporting information) at a final concentration 0.47 mM of ligand for 1 hour. AuNPs were purified via centrifugation and stabilization was examined by resuspension in PBS. The final concentrations of AuNPs were determined with ICP-OES. TEM images of AuNPs were taken with a JEOL 1010 electron microscope. To assess cell viability, RAW 264.7 monocytes incubated for 24 hours with various concentrations of AuNPs were stained with LIVE DEAD solution and imaged with fluorescence microscopy. To determine monocyte uptake of AuNPs, RAW 264.7 cells were treated with ligand stabilized AuNPs for 24 hours, washed, fixed with paraformaldehyde, formed into pellets and imaged with a clinical CT scanner. Results: TEM of AuNPs revealed them to have an average diameter of 15 nm (B). From a range of ω-thiol ligands, a group of five stabilized AuNPs were further studied, i.e. 11-mercaptoundecanoic acid (11-MUDA), 16-mercaptohexadecanoic acid (16-MHDA), 4-mercapto-1-butanol (4-MB), poly(ethyleneimine) (PEI), and 11-mercaptoundecyl-tetra(ethylene glycol) (MTEG). Stabilization of AuNPs can be visualized as a color change (C). Our experiments showed that AuNPs are well tolerated by monocytes, for example, concentrations of 11-MUDA AuNPs up to 0.5 mg/ml did not affect cell viability (D). The X-ray attenuation of monocytes resulting from internalization of AuNPs can clearly be seen in CT images (E). Analysis of CT images revealed high uptake of 4-MB and 11-MUDA stabilized AuNPS compared to the others (F). Conclusion: We have identified a variety of ligands that provide robust stability to AuNPs in biological media. Our results demonstrate that some of these ligands result in low AuNP toxicity and high uptake/CT contrast in monocytes. This work presents the basic principle of labeling monocytes for CT detection. Future work will include analysis of cytokine release from monocytes and in vivo experiments.

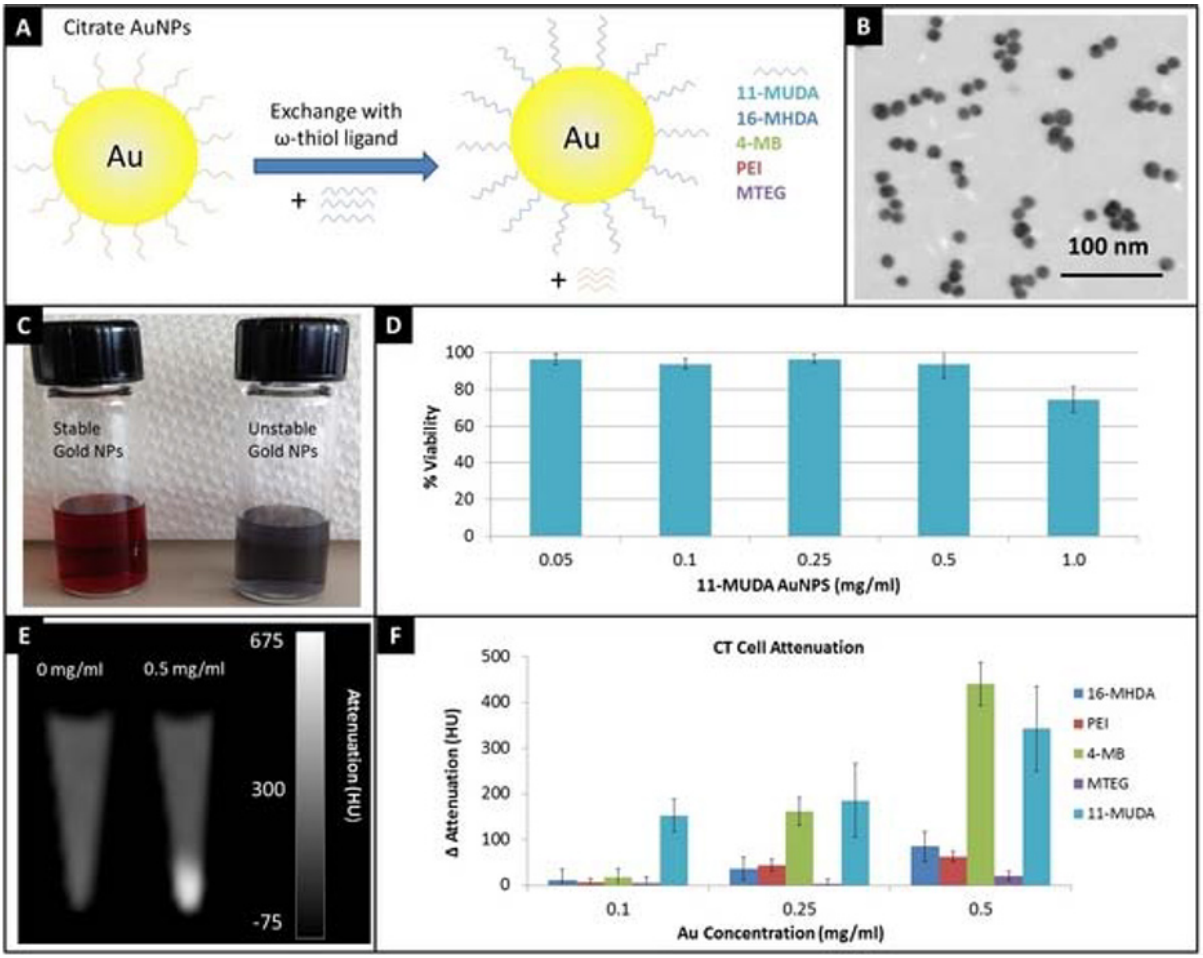

(A) Schematic depiction of AuNP ligand exchange. (B) TEM images of AuNPs. (C) Visible color difference between stable AuNPs vs unstable AuNPs. (D) Viability of RAW 264.7 monocyte cell line incubated with 11-MUDA for 24 hours. (E) CT image of pellets of RAW264.7 cells incubated with media only (left) or 0.5 mg/ml 11-MUDA (right). (F) Change of CT attenuation in pellets of RAW264.7 cells incubated with AuNPs with various coatings.

Disclosure of author financial interest or relationships:

P. Chhour, None; **P.C. Naha**, None; **M. Reilly**, None; **V. Ferrari**, None; **D.P. Cormode**, Philips, Grant/research support .

Presentation Number **P 114**
Poster Session 1
September 18, 2013 / 18:00-18:00 / Room: Exhibit Hall B

A novel CT blood pool imaging agent with the feature of myocardial uptake for in vivo small animal imaging

Alexander Kraupner[1], *Danielle Franke*[1], *Stefan Sawall*[2,3], *Jan Kuntz*[3], *Marc Kachelriess*[2,3], *Andreas Briel*[1], [1]*nanoPET Pharma GmbH, Berlin, Germany;* [2]*Institute of Medical Physics, Friedrich-Alexander-University Erlangen-Nürnberg, Erlangen, Germany;* [3]*Medical Physics in Radiology, German Cancer Research Center (DKFZ), Heidelberg, Germany. Contact e-mail: alexander.kraupner@nanopet.de*

Objectives: Cardiac imaging in small animals is rather challenging because this organ and its vasculature are relatively small. Therefore, an imaging agent that provides high blood contrast combined with an image reconstruction method, which enables high image quality is required.[1] Furthermore, for evaluation of cardiovascular function, differentiation between the blood in the heart chambers and the myocardium is required. In this work we present a novel CT imaging agent, which provides optimal blood pool properties, a high drug loading capacity and shows significant myocardial enhancement. Combined with a noise-reduced LDPC (low-dose phase-correlated) image reconstruction method, high quality CT images can be obtained [2]. Methods: The polymeric nanoparticular system was prepared using an interfacial deposition method of a polymer, followed by solvent displacement [3]. The iodine-based contrast moiety is incorporated in the polymeric system and colloidal stability is achieved by steric stabilization. The osmolality and pH value of the formulation were adjusted to physiological conditions and the imaging agent was finally sterilized. In vivo imaging studies were performed in standard wildtype mice using 200 µL of the imaging agent per 25 g mouse (intravenous injection). The images were acquired using a VolumeCT prototype (Siemens Healthcare, Forchheim, Germany). Results: Nanostructures with a mean hydrodynamic diameter of 180 nm and a high iodine content (~200 mg I/mL) were used. In vivo results in mice show that the nanoparticular formulation provides strong contrast enhancement in the vascular system with a blood half-life of approximately 40 min and a maximum contrast enhancement of about 800 HU. The maximum contrast enhancement in the myocardium was reached between 3-4 h p.i. (about 360 HU). Notably, the contrast enhancement in the myocardium persisted even after the imaging agent had been cleared from the blood. The imaging agent was mainly excreted via the liver (RES system) and was cleared completely from the body within 24 h, enabling the possibility of multiple injections. Conclusion: In this study we report on an iodine-based nanoparticular CT imaging agent, which provides high contrast enhancement in the myocardium as well as optimal blood pool properties. Of particular interest, the contrast enhancement in the myocardium persisted even after the imaging agent had been completely cleared from the blood. Therefore, using this contrast agent, CT-studies relating the myocardium and the estimation of cardiac parameters are possible. The high iodine content and the specific uptake characteristics make the polymeric nanoparticular contrast agent an ideal agent in studies involving the evaluation of cardiovascular function in small animals. References: [1] Kraupner et al.; World Molecular Imaging Congress Meeting Program; 2012 [2] Sawall et al.; Med Phys; 2011; 38(3): 1416-24 [3] Fessi et al.; Nano Int J Pharm; 1989; 55; 1:R1-R4

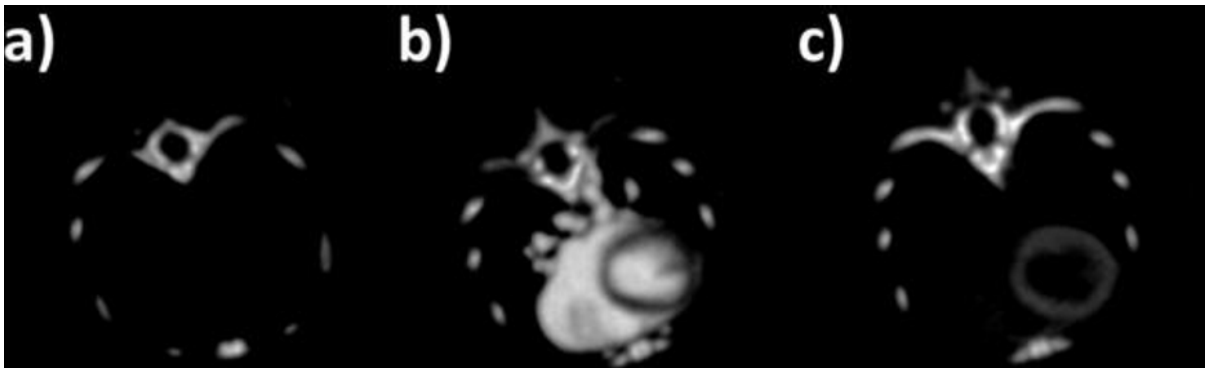

Fig. 1: Axial slices of the mouse thorax region a) pre-contrast, b) during the blood pool phase of the nanoparticular formulation and c) after uptake in the myocardium. Images were reconstructed, using a phase-correlated low-dose reconstruction method (LDPC).

Disclosure of author financial interest or relationships:
A. Kraupner, nanoPET Pharma GmbH, Employment; **D. Franke**, nanoPET Pharma GmbH, Employment; **S. Sawall**, None; **J. Kuntz**, None; **M. Kachelriess**, None; **A. Briel**, nanoPET Pharma GmbH, Employment .

Presentation Number **P 115**
Poster Session 1
September 18, 2013 / 18:00-18:00 / Room: Exhibit Hall B

Ultra high payload bismuth nanoparticles as a novel computed tomography contrast agent

Pratap C. Naha[1], *Anna Brown*[2], *Harold I. Litt*[1], *David P. Cormode*[1], *Andrea M. Goforth*[2], [1]*Radiology, University of Pennsylvania, Philadelphia, PA, USA;* [2]*Department of Chemistry, Portland State University, Portland, OR, USA. Contact e-mail: Pratap.Naha@uphs.upenn.edu*

Introduction: Interest in the area of nanoparticles as contrast agents for computed tomography (CT) is growing. Compared to clinically available iodinated small molecules, nanoparticles can carry a vastly higher payload of contrast producing agents and can have much longer circulation half-lifes. Also, it can be possible to incorporate other functionalities in the core or at the surface of nanoparticles to provide contrast for additional imaging methods. Gold nanoparticles have been proposed as CT contrast agents due to their high X-ray attenuation and biocompatible nature. The high cost of gold has encouraged the exploration of nanoparticles based on other strongly X-ray attenuating elements, such as bismuth. The synthesis of large, dense bismuth nanoparticles (Bi-NP) preferred for CT, however, is comparatively under explored. In this study, we present the synthesis of 50-90 nm, glucose coated Bi-NP (A), evaluation of their CT contrast generating properties and in vitro biocompatibility. Methods and Results: Glucose coated Bi-NP were prepared by dissolving bismuth nitrate and α-D-glucose in 1,2-propane diol, then adding borane morpholine. The resulting Bi-NP were purified by dialysis and concentrated. Bi-NP was characterized with transmission electron microscopy (TEM) and dynamic light scattering. The cores were found to be nearly 72 nm in diameter, while the hydrodynamic diameter was 90 nm (B). Proton nuclear magnetic resonance and fourier transform infrared spectroscopy confirmed that glucose is present on the nanoparticle surface. Imaging of a phantom with a clinical CT scanner showed Bi-NP to produce high X-ray attenuation (C). Incubations with Bi-NP were performed in both HeLa and J774A.1 cells at a concentration of 0, 0.1, 0.25 or 0.5 mg/ml. After 24 hours incubation, cell pellets were formed and were scanned with a clinical CT scanner (140 kV, 160 mA). Images were analyzed using Osirix 64-bit (v3.7.1). The attenuation in each cell pellet in three slices was recorded and averaged. Stronger attenuation was observed in J774A.1 cells than HeLa cells, indicating greater Bi-NP uptake (D). These cells were also imaged with TEM, which confirmed that Bi-NP uptake. Bi-NP seem to be accumulated in early endosomes and lysosomes (E). The cytotoxicity of Bi-NP was investigated using the MTS assay in HeLa and J774A.1 cells. Briefly, 10000 cells were seeded in each well of 96 well plates and were incubated with different concentrations of Bi-NP (0.0061 to 0.5 mg/ml, n=6 per condition). No cytotoxic response was seen in either of the cell lines after 1 hour exposure to Bi-NP (F). Conclusion: We have developed large, dense, glucose coated Bi-NP that produce strong x-ray attenuation. Bi-NP are more strongly taken up in J774A.1 than HeLa cells and seem to be localized in early endosomes/lysosomes. Cytotoxicity assays indicate that Bi-NP are biocompatible. Glucose coated Bi-NP are potentially an good platform to be used for future in vivo targeted imaging applications.

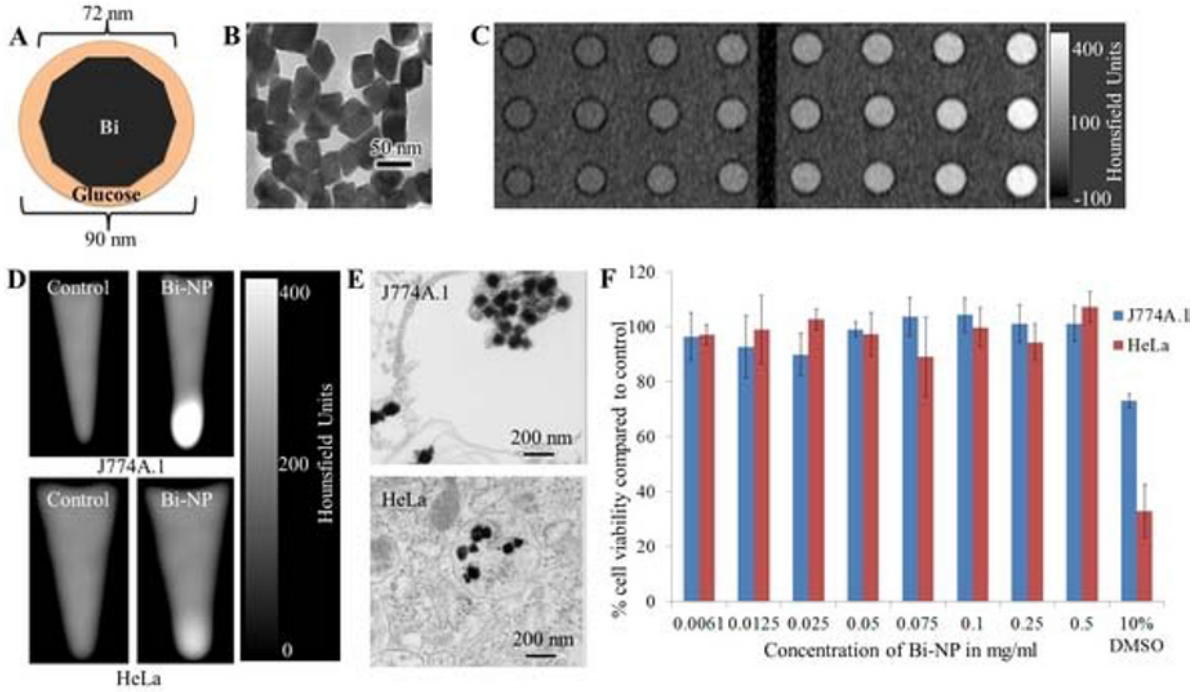

A: Schematic of glucose coated Bi-NP, B: TEM images of Bi-NP, C: CT phantom image of Bi-NP, D: *In vitro* CT image of Bi-NP in J774A.1 and HeLa cells, E: TEM of Bi-NP in HeLa and J774A.1 cells, F: Cell viability result of Bi-NP in HeLa and J774A.1 cells.

Disclosure of author financial interest or relationships:

P.C. Naha, None; **A. Brown**, None; **H.I. Litt**, Siemens Medical Solutions, Grant/research support; **D.P. Cormode**, Philips, Grant/research support; **A.M. Goforth**, None.

Presentation Number **P 116**
Poster Session 1
September 18, 2013 / 18:00-18:00 / Room: Exhibit Hall B

A semi-automated image processing work-flow to quantify longitudinal change in muscle volume using X-ray computed tomography

Prashant Bansal[1], *Michael St. Andre*[3], *Peter Bialek*[3], *Carl Morris*[3], *Jeremy Wellen*[2], [1]*Global Sciences & Technology, Pfizer, Andover, MA, USA;* [2]*Precision Medicine, Pfizer, Cambridge, MA, USA;* [3]*Rare Diseases, Pfizer, Cambridge, MA, USA. Contact e-mail: prashant.n.bansal@pfizer.com*

In vivo studies of tissue morphology often utilize X-ray computed tomography (CT) or magnetic resonance (MR) based imaging modalities due to their ability to generate high spatial resolution data-sets. These techniques have been widely applied to study changes in tissue morphology due to the effects of aging, disease progression or therapeutic intervention. In order to sensitively and efficiently detect longitudinal change in tissue morphology, a highly reproducible and semi-automated analysis methodology is necessary. Hence, the objective of this study was to develop an image processing work flow (Fig. 1, Top Panel) to longitudinally quantify measures of appendicular muscle volume in juvenile cynomolgus macaques, a common species for testing safety and efficacy of potential therapeutic compounds prior to Phase1 clinical trials. As a means of validating the developed methodology, repeated measurements of the same animal showed very low coefficient of variations (COV = 0.02, Fig.1, Middle Panel, Left) and excellent agreement between two observers (intra class correlation = 0.99, $P < 0.01$, also see Middle Panel, right). Furthermore, when the stifle joint of this animal was deliberately hyper-flexed and hyper-extended, it was shown that the COV increased by more than 2x (COV = 0.05, Fig1, Middle Panel, middle), signifying the importance of consistent positioning across imaging sessions. In addition, we conducted a temporal imaging study (four time points, Baseline, Week 4, Week 8 and Week 17) in juvenile cynomolgus monkeys (N=5) on a calorifically rich diet. With these animals, DEXA imaging also applied to validate the findings obtained using CT. Statistically significant ($P < 0.001$) and strong correlations ($R2 = 0.91$) were observed between the muscle volume measurements obtained using CT and the muscle mass obtained using DEXA imaging (Fig.1, Bottom Panel, Right). While the high correlations suggest excellent agreement between CT and DEXA, the CT approach may be more useful when regional changes in muscle volume need to be evaluated due to its ability to obtain cross sectional measurements. We have developed a semi-automated image processing workflow for precise appendicular muscle volume measurements in NHPs which may find applicability in evaluating effects of aging, skeletal muscle disorders, and therapeutics on regional muscle morphology.

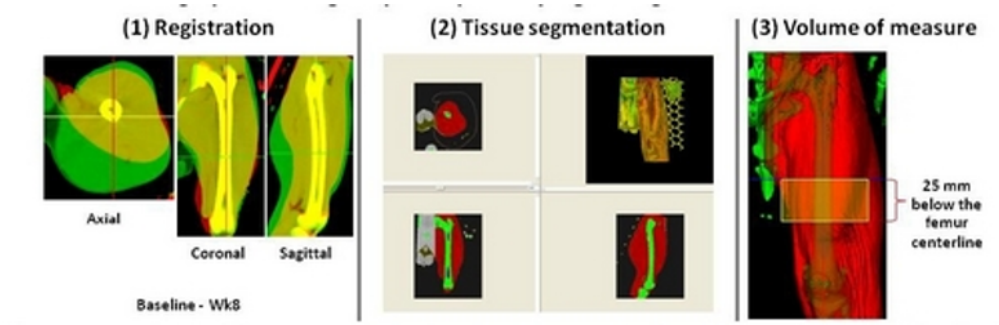

Image processing workflow used to obtain volumetric measurements of appendicular muscles in NHPs. Panel (1) shows the registration operation between two time points for the same animal. Panel (2) shows the segmented tissues (muscles (red), bone (green), intra-medullary canal (blue) and fat tissue (yellow). The region of interest that was used for volume computation is shown in panel (3)

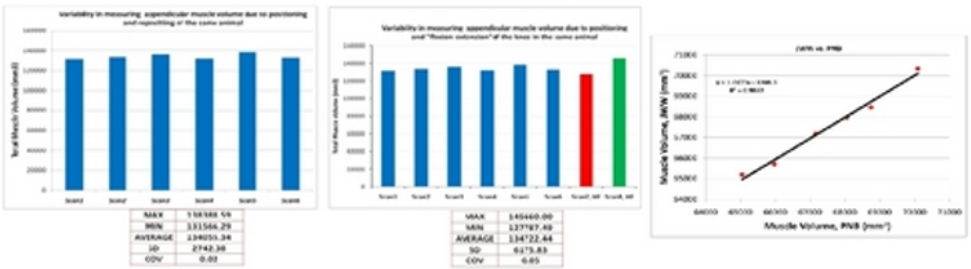

(L) Bar plots showing the total appendicular muscle volume in the same animal for the six repeat scans. **(M)** Shows additional data points for hyper flexion (HF, Red) and hyperextension (HE, Green). The tables below each plot contain basic statistics for the data depicted in the plots. **Note the increase in the COV from 0.02 to 0.05 due to the addition of the HF and HE data. (R)** Inter-observer variability in measuring appendicular muscle volumes.

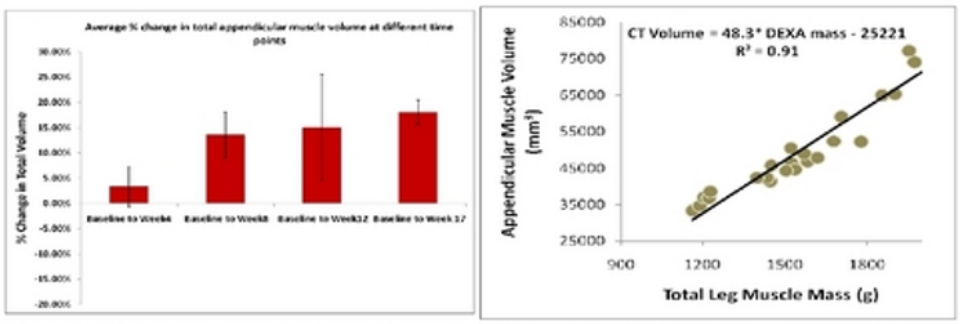

(L) Quantitative changes in muscle volume expressed as % in NHPs using CT for seventeen weeks. Error bars indicate SD **(R)** Correlation between changes in the appendicular muscle volume (CT) & muscle mass (DEXA). Data collected at each time was pooled together to generate the correlation plots.

Figure1: Overview of the image processing methodology and results

Disclosure of author financial interest or relationships:

P. Bansal, None; **M. St. Andre**, None; **P. Bialek**, Pfizer, Employment; **C. Morris**, Pfizer, Employment; **J. Wellen**, Pfizer, Employment .

Presentation Number **P 117**
Poster Session 1
September 18, 2013 / 18:00-18:00 / Room: Exhibit Hall B

Iterative Reconstruction Approach to Minimize Metal Artifacts in a Rotating Turntable CT System

Stanley Liang, **Jeffrey A. Meganck**, *PerkinElmer, Alameda, CA, USA. Contact e-mail: jeff.meganck@perkinelmer.com*

Visualization and quantification of Computed Tomography (CT) scans is ideally performed on artifact free images. However, backprojection reconstruction algorithms are prone to artifacts such as beam hardening, scattering and aliasing. These artifacts are common when a material with a high linear attenuation coefficient, such as metal, is in the patient. Many algorithms have been investigated to minimize these artifacts and improve visualization of the image for clinical needs, but relatively little work has been done in preclinical systems. This problem frequently arises in orthopedic models that require metal implants and/or screws to stabilize a trauma site, scaffolds to augment bone loss or in joint replacements. Dental implant models have similar challenges, particularly when the bone-implant interface is of interest. In addition, animal identification and tracking systems are frequently used and are sometimes unavoidable. There are several unique challenges in preclinical instruments. Conventional gantry based μCT systems are similar to clinical geometries and may be suitable to slightly modified versions of clinical metal artifact reduction algorithms. However, some preclinical μCT systems that are designed to support multi-modality imaging use a rotating turntable configuration that changes the imaging geometry significantly, potentially impacting the sinogram in a more complicated fashion. The aim of this project is to test the hypothesis that metal artifact reduction algorithms developed in the literature for gantry based systems can be adapted to this unique rotating turntable imaging geometry. Many of the iterative reconstruction approaches previously published use an iterative reconstruction approach to remove metal from the sinogram before the final reconstruction. To investigate sinogram adjustment methods, our first step was to implement several different algorithms and evaluate the results using a simulation package. Simulations were run for cases of a RFID tag implanted subQ (with and without a simulated skeleton), and three equidistant metal objects implanted simultaneously. The results indicate a basic linear interpolation and the approach by Mazin et al. (Med Phys. 2009) using a subsequent soft tissue layer can both reduce blooming artifacts around the metal. However, both are prone to some streak artifacts. The approach described by Karimi et al. (Med Phys. 2012) involving a more complicated segmentation to create a prior image minimizes these streaks but has some blooming artifacts. To extend these simulation results into a real scenario, we attached ear tags, implanted RFID tags, or implanted intramedullary pins (both SS and Ti) in the femurs of mice. CT images were acquired using the rotating turntable approach in the multi-modality IVIS SpectrumCT instrument. Results indicate it is also possible to minimize metal artifacts in these images. Furthermore, BMD values for bone near the implant have less error when these metal artifact reduction methods are used.

Disclosure of author financial interest or relationships:
S. Liang, None; **J.A. Meganck**, PerkinElmer, Employment .

Presentation Number **P 118**
Poster Session 1
September 18, 2013 / 18:00-18:00 / Room: Exhibit Hall B

Three dimensional blood vessel centerline extraction method based on distance coding

Fengjun Zhao[1], Junting Liu[1], Xiaochao Qu[1], Xianhui Xu[1], Xueli Chen[1], Jimin Liang[1], **Jie Tian**[2,1], [1]*School of Life Sciences and Technology, Xidian University, Xi'an, China;* [2]*Medical Image Processing Group, Institute of Automation,CAS, "Beijing,100190", China. Contact e-mail: tian@ieee.org*

The change of vascular morphology and topology takes responsibility for various pathological diseases. The study of vascular centerline extraction that facilitates the quantitative analysis of vascular network, is very significant for the vascular pathological process. The x-ray angiography is convenient for imaging of two dimensional blood vessel, which so far has played an important role in preclinical and clinical trials. However, the projection images are actually the overlapped result of blood vessel in space and hence restrict their accuracy. Because of the capacity of computed tomography for three dimensional imaging, it is used for the imaging of blood vessel. Based on computed tomography, a number of three vascular centerline extraction methods have developed. Currently, the three dimensional centerline extraction methods are approximately classified into two categories, topological thinning and distance coding. The topological thinning adopts the iteratively peeling layer by layer, which turns out to be time-consuming and cannot guarantee the central tendency of centerlines. Moreover, the thinning preserves too many endpoint voxels such that lots of spurious short branches are brought in. The distance coding also termed as distance transform enjoys great popularity due to the advantages of simpleness and speediness. This study proposed a centerline extraction algorithm based on the distance coding of two fields. The algorithm includes four steps: the construction of single point seeded field, the construction of boundary seeded field, the main centerline extraction, and the branch centerline extraction. The proposed method are not only more efficient, but also almost free of noise, whose results are given as Fig. 1. Compared with the previous methods, the connectivity of the proposed distance coding based algorithm is readily satisfied without complex post-processing.

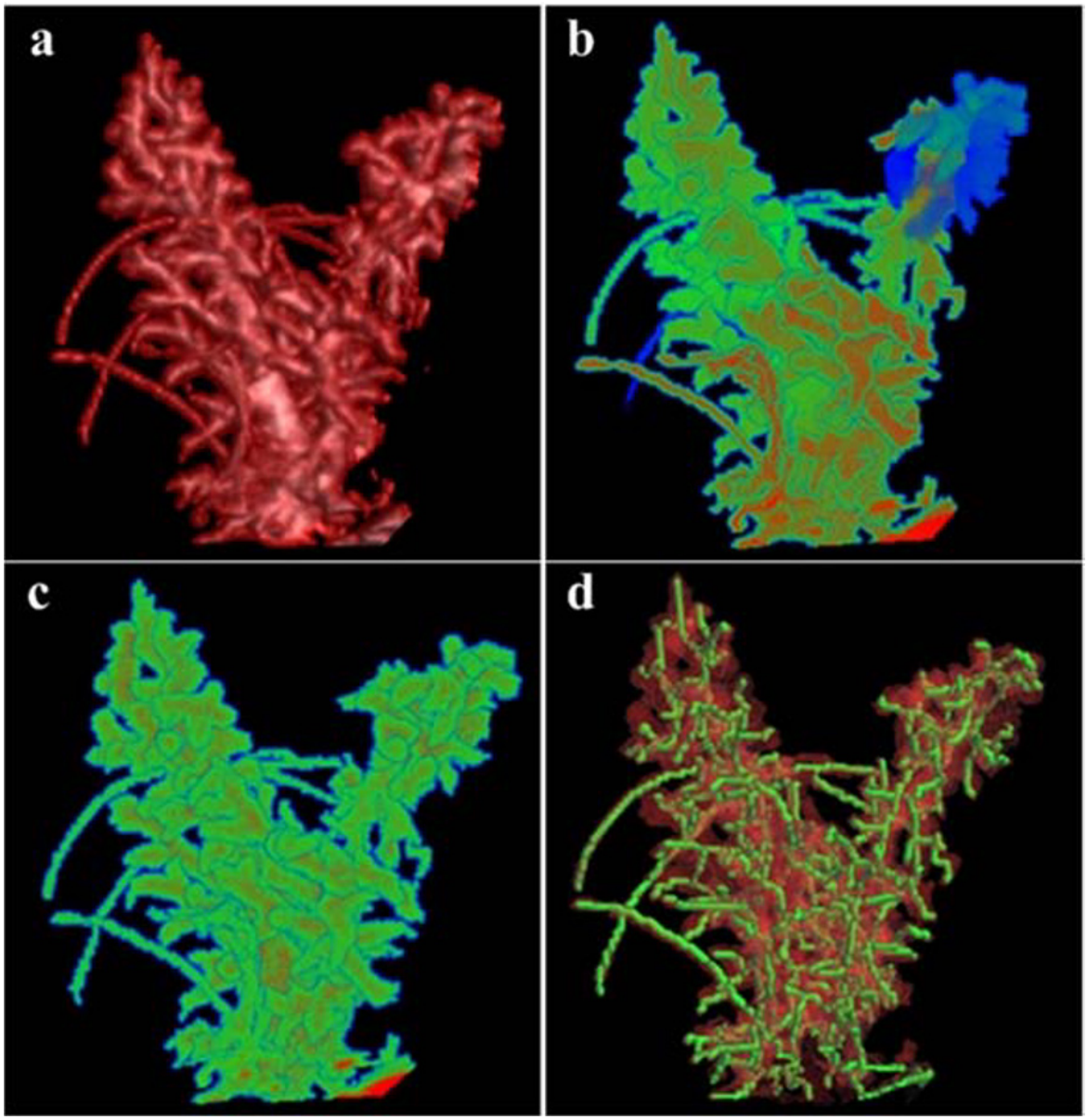

Having constructed the single point seeded field (b) and the boundary seeded field (c) of the vascular casting (a), the centerline is extracted (d).

Disclosure of author financial interest or relationships:
F. Zhao, None; **J. Liu**, None; **X. Qu**, None; **X. Xu**, None; **X. Chen**, None; **J. Liang**, None; **J. Tian**, None.

Presentation Number **P 119**
Poster Session 1
September 18, 2013 / 18:00-18:00 / Room: Exhibit Hall B

In Vivo Cerebral Plaque Visualisation in Mice with Polychromatic Iterative microCT Reconstruction

Bert Vandeghinste[1], *David De Wilde*[2], *Carole Van der Donckt*[3], *Guido De Meyer*[3], *Patrick Segers*[2], *Roel Van Holen*[1], *Stefaan Vandenberghe*[1], *Christian Vanhove*[1], [1]*MEDISIP, Ghent University-iMinds-IBiTech, Ghent, Belgium;* [2]*bioMMeda, Ghent University-IBiTech, Ghent, Belgium;* [3]*Physiopharmacology, University of Antwerp, Antwerp, Belgium. Contact e-mail: bert.vandeghinste@ugent.be*

INTRODUCTION: Recently, a new mouse model of atherosclerotic plaque rupture was developed, leading to stroke, neurological symptoms and sudden death. These mice carry a mutation (C1039G+/-) in the fibrillin-1 (Fbn1) gene, which results in elastin fragmentation, increased vascular stiffness and atherogenesis in apolipoprotein E deficient (ApoE-/-) mice. Although this mouse model shows promising results, its complete phenotype is not fully understood. Some mice show signs of head tilt, stress and panting with time, which could be indications of cerebrovascular problems. In the present study, we investigated whether it was feasible to detect anomalies in the brain vasculature with in vivo μCT imaging. Although ex vivo techniques (i.e. dissection) may be able to pinpoint the underlying cause, in vivo measurements would allow for longitudinal data during plaque growth and disease development. METHODS: Ten female ApoE-/-Fbn1C1039G+/- mice (6-8 weeks old) were fed a Western-type diet for up to 20 weeks. At week 10, and thereafter every 5 weeks, the mice were imaged pre and post injection with a gold-nanoparticle contrast agent (Aurovist, Nanoprobes, New York, USA), on a Triumph X-O CT scanner (NT Imaging Inc., Northridge, USA). Data was acquired at 70 kVp and 240 μA with zoom 3, 1024 angles over 360°, detector pixel size 50 μm and a focal spot size of 50 μm. This setup leads to a theoretical image resolution of 17 μm. The images were reconstructed with the Iterative Maximum-Likelihood Polychromatic Algorithm for CT (IMPACT) [1] on a GPU to remove beam hardening. To reduce the computational complexity, we included Volume of Interest (VOI) reconstruction into this algorithm [2]. This allowed us to reconstruct only the brain, without inducing inner tomography artifacts. Furthermore, we applied an edge-preserving prior to minimize image noise. Images were compared to conventional filtered back projection (FBP). RESULTS: Fig. 1 compares FBP to IMPACT, for one of the mice presenting head tilt. The total reconstruction time was reduced from 6 hours to just 30 minutes by reconstructing only the VOI. Applying the prior doubles the total reconstruction time and reduces the noise from 5.5% to 3.5%, whereas FBP reconstruction reached 14.1% noise. The transverse slice shows some contrast even on the pre-contrast scan (arrows). From previous studies we know that macrophages contained in plaques have the tendency to internalize the Aurovist contrast agent, even 5 weeks after the first injection. The anomalies seen here may be dislodged carotid artery plaques that moved into the cerebral vasculature. Although one such spot can be found on the FBP image, IMPACT shows multiple anomalies. CONCLUSION: Fast iterative reconstruction allows the visualization of brain vasculature in mice at better resolution and decreased noise compared to FBP, making it possible to detect the presence of anomalies more accurately. [1] B. de Man et al. "An iterative maximum-likelihood polychromatic algorithm for CT," IEEE TMI:20(10) 999-1008, 2001. [2] A. Ziegler et al. "Iterative reconstruction of a region of interest for transmission tomography," Med Phys:35(4) 1317-1327, 2008.

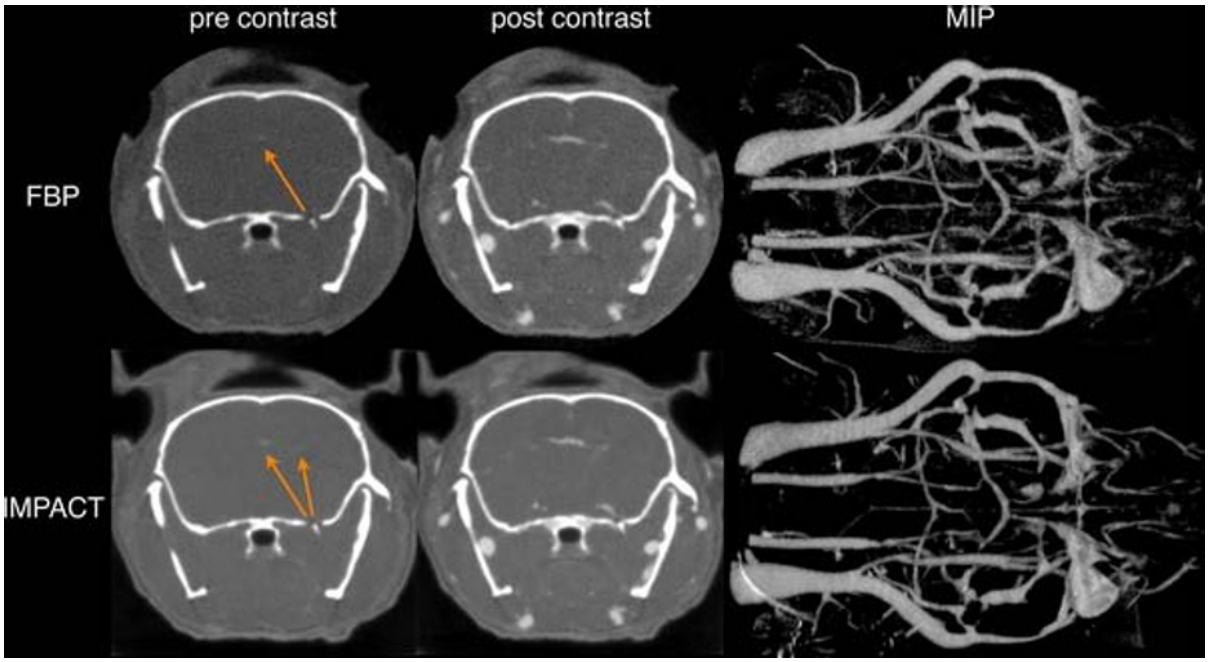

Comparison of FBP and IMPACT reconstruction. More anomalies are seen with IMPACT than with FBP. The MIP renderings are better defined when based on IMPACT images, in contrast to when based on FBP.

Disclosure of author financial interest or relationships:

B. Vandeghinste, None; **D. De Wilde**, None; **C. Van der Donckt**, None; **G. De Meyer**, None; **P. Segers**, None; **R. Van Holen**, None; **S. Vandenberghe**, None; **C. Vanhove**, None.

Presentation Number **P 120**
Poster Session 2
September 19, 2013 / 15:15-15:15 / Room: Exhibit Hall B

Synthesizing Manganese doped Zinc Sulfide nanoparticles as bimodal contrast agents

Rashin Namivandi Zangeneh[2], Mohammad Ali Oghabian[2], **Reza Ahmadi**[1], [1]*Materials Science and Engineering, Sharif University of Technology, Tehran, Islamic Republic of Iran;* [2]*Research Center for Molecular and Cellular Imaging (RCMCI), Tehran University of Medical Sciences, Tehran, Iran, Tehran, Islamic Republic of Iran. Contact e-mail: reahmady@yahoo.com*

Synthesizing Manganese doped Zinc Sulfide nanoparticles as bimodal contrast agents Rashin Namivandi Zangeneh,Reza Ahmadi, Mohammad Ali Oghabian, Introduction M: Mn nanoparticles (M is a biocompatible metallic or non metallic element such as Au or Si) have been recently considered as positive MRI contrast agents for in vivo and in vitro purposes. The presence of manganese ion as a dopant element increase R1 due to the large area of physical contact between the ion and hydrogen protons of lipid or water in the body. On the other hand, ZnS quantum dots are potential candidates for fluorescence imaging of the target. In this study, ZnS: Mn nanoparticles have been synthesized and characterized for bimodal imaging of the target tissues. It seems that these particles are suitable for simultaneously MR and fluorescence imaging for in vitro and in vivo aims. The performed characterizations show suitable capability of these particles for the above-mentioned purposes. Methods ZnS: Mn nanoparticles have been synthesized via coprecipitation method from Chloride salts of Zinc and Manganese in the presence of Sodium Sulfide as the reducing agent. UV and PL characterizations verified the excitation and emission wavelengths equal to 360 and 590 nanometers, respectively. Changing Mn concentration and particle size, some emission spectra in the range of green to orange have been observed. Using the Brus equation, the particles sizes have been calculated in the range 2-3 nm that has been verified with STM results. Conclusion Presence of Mn as a dopant element in the structure of the ZnS synthesized particles make them suitable for bimodal MR and fluorescence imaging. The preformed characterizations show that the particles are suitable for the cell tracking and molecular imaging. References 1- Weilnau, J.N., Black, S.E., Chehata, V.J., Schmidt, M.P., Holt, K.L.ZnSnanocrystal cytotoxicity is influenced by capping agent chemical structure and duration of time in suspension, Journal of Applied Toxicology 33 (2013) 227-237. 2- Mohammadikidh, M., Davar, F., Synthesis and characterization of hierarchical ZnS architectures based nanoparticles in the presence of thioglycolic acid, Ceramics International 39 (2013) 3173-3181. 3- Shu, C., Huang, B., Facile synthesis and characterization of water soluble ZnSe/ZnS quantum dots for cellar imaging, SpectrochimicaActa - Part A: Molecular and Biomolecular Spectroscopy 104 (2013) 143-149.

Disclosure of author financial interest or relationships:
R. Namivandi Zangeneh, None; **M. Oghabian**, None; **R. Ahmadi**, None.

Presentation Number **P 121**
Poster Session 2
September 19, 2013 / 15:15-15:15 / Room: Exhibit Hall B

R-ELISA: A quantitative relaxometric version of the ELISA test for the measurement of cell surface biomarkers based on the water proton T_1 measurements

Diego Alberti, *Mark van't Erve, Stefanìa Rachele, Maria Rosaria Ruggiero, Simona Baroni, Simonetta Geninatti Crich, Silvio Aime, University of Turin, Turin, Italy. Contact e-mail: albertidiego@hotmail.com*

Introduction Quantitative measurement of marker expression in diseased cells is still a topic of considerable interest and different methodologies are currently under intense scrutiny. Our work aims at developing an in vitro method based on the release of paramagnetic species from relaxometrically "silent" liposomes operated by the action of a Phospholipase A_2 (PLA_2) previously targeted to the epitope of interest. The release of the paramagnetic species is proportional to the number of PLA_2 bound to the cell outer surface. The released paramagnetic species causes an increase of the longitudinal water proton relaxation rate. Thus the quantification of the epitopes of interest relies on the amplification effect associated to the release of the paramagnetic payload from the liposomes operated by the action of the targeted phospholipase. The measure of water proton T_1 is a well established methodology and can be carried out on any NMR instrument. Multiple samples can be simultaneously measured by acquiring T_1-weighted MR images by extrapolating T_1 values from the observed signal intensity values. Methods Stable liposomes were prepared using the following lipid composition: 95% DSPC, 5% DSPE-PEG 2000. Their inner aqueous cavity contains a Gd-HPDO3A solution (200mM). The used phospholipid formulation yielded systems characterized by a very low water exchange rate (relaxometrically "silent" liposomes). PLA_2 was conjugated to folic acid residue through a PEG 3000 linker (folate-PLA_2). IGROV and Hela cells with different folate receptor (FR) expression have been incubated with the folate-PLA_2. After washing out of the unbound enzyme, aliquots of "silent" liposome were added to the cells. Enzyme induced liposome destabilization has been measured by relaxometry at 0.5T (Stelar Spinmaster) and at 1 T (Aspect M2). Results Gd-loaded "silent" liposome suspension yielded a stable, low relaxivity of $0.6 mM^{-1}s^{-1}$.Upon adding PLA_2 (1.5uM) to this suspension, the observed relaxivity increases to $4.2 mM^{-1}s^{-1}$ in ca. 40h. The attained value corresponds to the known relaxivity of free Gd-HPDO3A. Two millions IGROV cells were incubated in the presence of folate-PLA_2 for 1h. After washing, the amount of the enzyme that remained bound to cells was assessed by adding Gd-loaded "silent" liposomes for 20h. The observed relaxation rate increased from $0.55 s^{-1}$ to $1.4 s^{-1}$. On the basis of this result it was possible to estimate the number of FR expressed by the different ovarian cancer cell lines. Conclusions R-ELISA assay can detect in cell suspension nM receptor concentrations. Its sensitivity can be further improved using more efficient contrast agents (i.e. Mn^{2+} ions) inserted the inner aqueous cavity of "silent" liposomes.

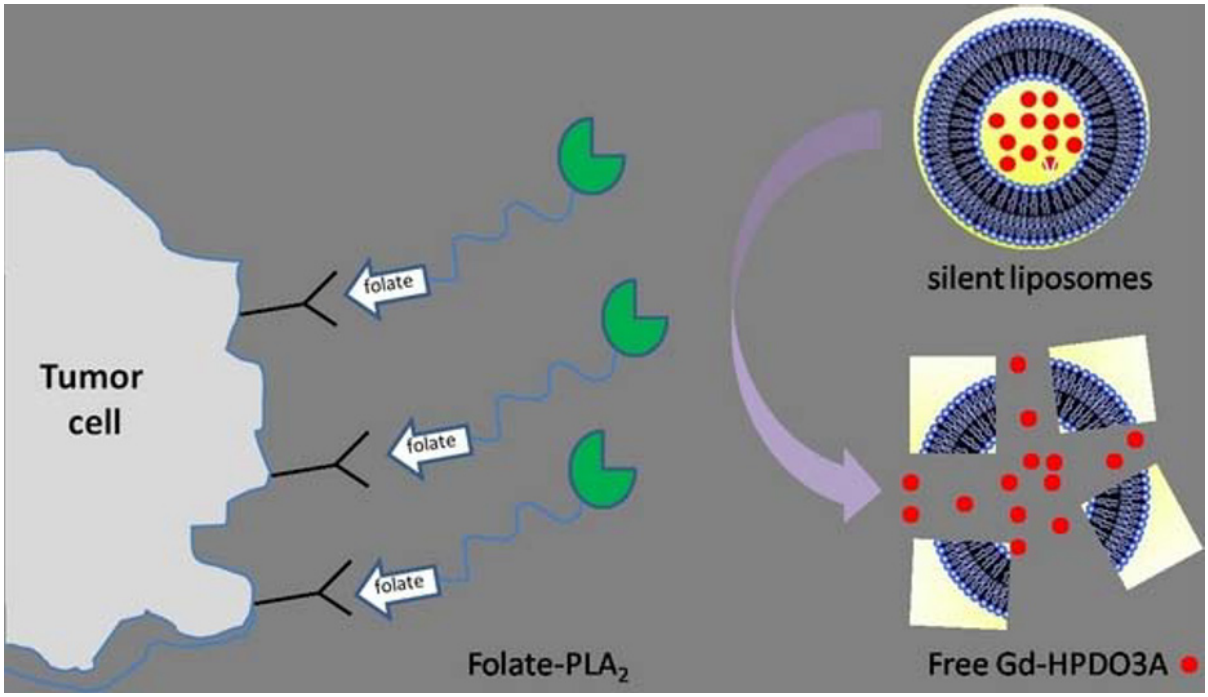

R-ELISA assay: Synthetic representation of the method

Disclosure of author financial interest or relationships:
D. Alberti, None; **M. van't Erve**, None; **S. Rachele**, None; **M. Ruggiero**, None; **S. Baroni**, None; **S. Geninatti Crich**, None; **S. Aime**, None.

Presentation Number **P 122**
Poster Session 2
September 19, 2013 / 15:15-15:15 / Room: Exhibit Hall B

Developing a dual MRI-optical reporter gene system using a single substrate

Amnon Bar-Shir[1,2], *Jeff W. Bulte*[1,2], *Assaf A. Gilad*[1,2], [1]*Division of MR Research, the Russell H. Morgan Department of Radiology and Radiological Sciences, Johns Hopkins University School of Medicine, Baltimore, MD, USA;* [2]*Cellular Imaging Section, Institute for Cell Engineering, Johns Hopkins University School of Medicine, Baltimore, MD, USA. Contact e-mail: abarshi2@jhmi.edu*

Introduction: Non-invasive monitoring of transgene expression is crucial for a basic understanding, and treatment of various diseases. The gene encoding the enzyme Herpes Simplex Virus type 1 Thymidine Kinase (HSV1-TK) is widely used for gene therapy, PET imaging[1] and has already been used in the clinic[2]. Moreover, recently a synthetic analog of thymidine has been used for monitoring the HSV1-TK expression with CEST MRI[3]. The Drosophila melanogaster 2'-deoxynucleoside kinase (Dm-dNK) enzyme phosphorylates a wider range of nucleoside analogs, including the fluorescent nucleoside pyrrolo-2'-deoxycytidine (pyrrolo-dC)[4] (Fig. 1a). We show here that pyrrolo-dC generates high CEST contrast and may be used as a CEST reporter probe for monitoring the Dm-dNK reporter gene expression in vivo. **Methods**: In vitro MRI: Pyrrolo-2'-deoxycytidine (pyrrolo-dC) was dissolved in 10 mM PBS at 10 mM concentration. CEST MRI experiments were performed as previously described.[3] pyrrolo-dC uptake: 9L rat glioma, engineered to Dm-dNK ($9L^{Dm\text{-}dNK}$) and control, non-expressing wild type cells ($9L^{wt}$), 5×106 cells per group, were incubated for 4 hours in cell-culture medium containing 2mM pyrrolo-dC. Cells were washed with PBS, lysed, and the fluorescence was measured using a plate reader (λex355nm/λem460nm). In vivo MRI: $9L^{Dm\text{-}dNK}$ and $9L^{wt}$ cells were transplanted bilaterali into the brain of adult NOD-SCID mice. One week later, 0.2 mL of pyrrolo-dC (160 mg/kg) was injected i.v and CEST-MRI data were acquired as described previously[3] 4.5 hours after i.v. injection. **Results and Discussion**: Fig. 1b shows the MTRasym plot of pyrrolo-dC (red) compared to that of PBS (gray). The NH proton of the pyrrolo-dC generates a well-defined peak at the 5.8 ppm frequency offset from water. The MTRasym maps obtained at Δω=5.8 ppm (Fig. 1c) demonstrate the high CEST contrast generated by pyrrolo-dC. The sharp NH peak at 5.8 ppm is a major advantage, since it minimizes the contribution from endogenous CEST contrast sources and direct water saturation. The optical properties of the pyrrolo-dC also allowed the assessment of its accumulation as a monophosphate derivative in Dm-dNK-expressing cells. As clearly shown in Fig. 1d, only the lysate of incubated $9L^{Dm\text{-}dNK}$ cells provides a high fluorescence level, while fluorescence could not be detected for incubated $9L^{wt}$. Fig. 1e shows an in vivo CEST-MR image in which the pyrrolo-dC accumulation could be detected only in Dm-dNK expressing cells ($9L^{Dm\text{-}dNK}$) and not in control cells ($9L^{wt}$) at 4.5 hours after i.v.iInjection. **Conclusion**: Synthetic fluorescent nucleosides, such as pyrrolo-dC, can be applied for real-time monitoring of gene expression with CEST MRI. The optical properties of Pyrrolo-dC allows in vitro quantification of both cellular gene expression as well as accurate measurement during preparation of vehicles (e.g. liposomes, polymers or stem cells) for better probe delivery. References:(1) Gambhir, S. S. et al. Proc Natl Acad Sci U S A 1999, 96, 2333. (2) Yaghoubi, S. S. et al. Nat Clin Pract Oncol 2009, 6, 53. (3) Bar-Shir, A. et al. J Am Chem Soc 2013, 135, 1617. (4) Liu, L. et al. Nucleic Acids Res 2009, 37, 4472.

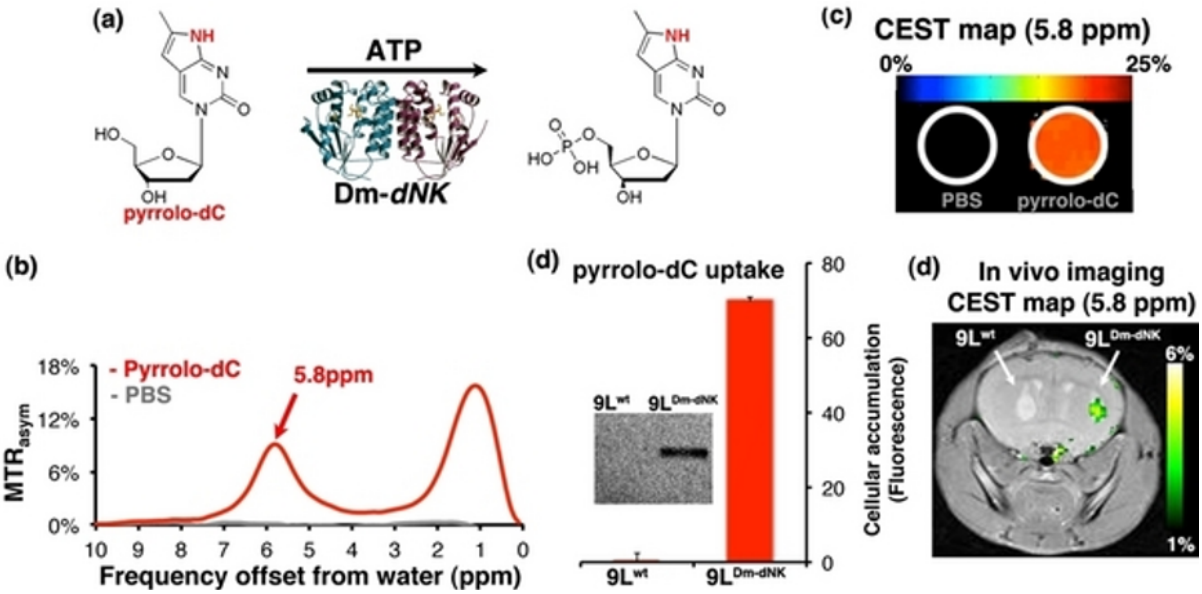

Fig 1. a) Illustration of pyrrolo-dC phosphorylation by Dm-dNK. b) MTR_{asym} plots of pyrrolo-dC (red) and PBS (gray). c) MTR_{asym} maps of pyrrolo-dC and PBS at $\Delta\omega$=5.8 ppm. d) Fluorescence as measured from the cell lysates after 4.5 h incubation of $9L^{wt}$ and $9L^{Dm\text{-}dNK}$ cells (inset, western blot) with pyrrolo-dC. e) In vivo CEST-MR image of the distribution of pyrrolo-dC 4.5h after i.v injection.

Disclosure of author financial interest or relationships:
A. Bar-Shir, None; **J.W. Bulte**, None; **A.A. Gilad**, None.

Presentation Number **P 123**
Poster Session 2
September 19, 2013 / 15:15-15:15 / Room: Exhibit Hall B

Superpositively Charged Green Fluorescent Proteins as Bimodal Reporter Genes for CEST MRI and Optical Imaging

Amnon Bar-Shir[1,2], *Yajie Liang*[1,2], *Assaf A. Gilad*[1,2], *Jeff W. Bulte*[1,2], [1]*Division of MR Research, the Russell H. Morgan Department of Radiology and Radiological Sciences, the Johns Hopkins University School of Medicine, Baltimore, MD, USA;* [2]*Cellular Imaging Section, Institute for Cell Engineering, the Johns Hopkins University School of Medicine, Baltimore, MD, USA. Contact e-mail: abarshi2@jhmi.edu*

Introduction: Recent advances in molecular MR imaging have revolutionized our ability to monitor gene expression[1-5]. One such example is the Lysine-Rich-Protein (LRP), a prototype artificial reporter gene that produces MRI contrast based on the chemical exchange saturation transfer (CEST) mechanism[6]. The positively charged amino acids (mostly lysine and arginine) in peptide and proteins, enable their use as CEST-based contrast agents or reporter genes. We investigated whether superpositively charged mutants[7] of the green fluorescent protein (GFP) reporter gene could be used as a CEST reporter gene, based on their high content of lysine and arginine residues. **Methods**: E. coli-optimized genes encoding to wild type GFP (wt) and its superpositively-charged variants (+36 and +48), achieved by modifying the solvent-exposed amino acids to lysine or arginine[7], were obtained from Dr. David R. Liu (Harvard University, Cambridge, MA[7]). The proteins were expressed in BL21 (DE3) E. coli and purified using cobalt-based immobilized metal affinity chromatography. Pure proteins were dialyzed against PBS and their CEST-MRI characteristics were measured using a modified RARE sequence and WASSR method for B_0 correction as previously described[1]. **Results and Discussion**: Fig. 1a shows fluorescence images of solutions containing the wt, +36, and +48 GFP variants. The high purity of the three proteins was validated by SDS-PAGE (Fig. 1b). The CEST MRI characteristics of the three examined GFPs (wt, +36, and +48) showed that both superpositive GFPs (+36 and +48) generated higher MTR_{asym} values as compared to wt-GFP at both 1.5 ppm (guanidine protons of arginine) and 3.3 ppm (amide protons) (Fig. 1d-f). The +48 GFP generated higher MTR_{asym} values at the amide frequencies (3.3 ppm) than the +36 mutant. Fig. 1e-f display MTR_{asym} maps that reveal the correlation between the protein charge and the CEST contrast. Both mutants contain an equal number of arginine residues (20 and 21, respectively) and therefore generated the same MTR_{asym} value from the guanidine exchangeable protons at $\Delta\omega$=1.5 ppm. In contrast, as +48-GFP mutant has more lysines as compared to +36-GFP (42 and 36, respectively), it generated higher MTR_{asym} values at the resonance of the amide protons at $\Delta\omega$=3.3 ppm. **Conclusion**: Superpositively-charged GFP has potential for use as a CEST MRI reporter gene while retaining its optical properties. **References**: (1) Bar-Shir et al. J Am Chem Soc 2013, 135, 1617. (2) Cohen, B. et al. Nat Med 2007, 13, 498. (3) Genove, G. et al. Nat Med 2005, 11, 450. (4) Kodibagkar, V. D. et al. Magn Reson Imaging 2006, 24, 959. (5) Zurkiya, O. et al. Magn Reson Med 2008, 59, 1225. (6) Gilad, A. A. et al. Nat Biotechnol 2007, 25, 217. (7) Lawrence, M. S. et al. J Am Chem Soc 2007, 129, 10110.

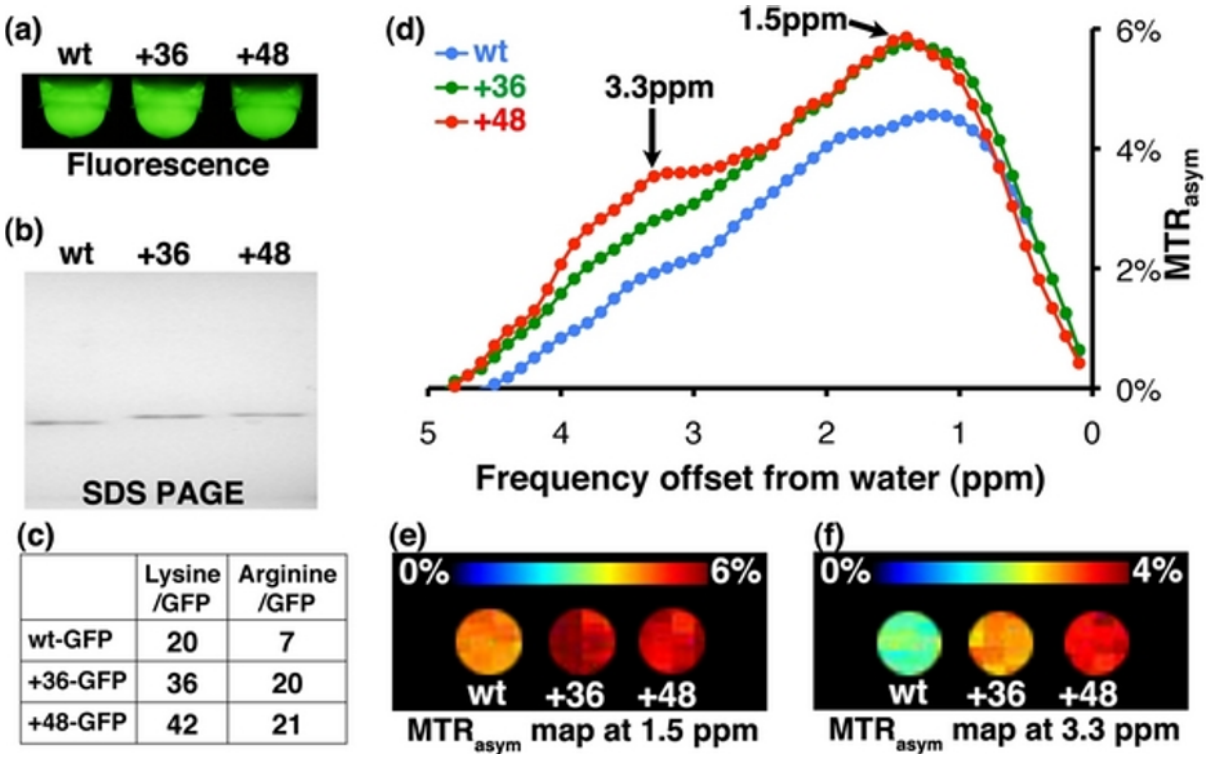

(c)

	Lysine /GFP	Arginine /GFP
wt-GFP	20	7
+36-GFP	36	20
+48-GFP	42	21

Fig 1. Characterization of wt-GFP and its superpositive mutants +36-GFP and +48-GFP. a) Fluorescence. b) SDS-PAGE of purified GFPs. c) Number of lysine and arginine amino acids in each GFP (total 239 amino acids). d) MTR_{asym} plots. e) MTR_{asym} maps ($\Delta\omega$=1.5 ppm). e) MTRasym maps ($\Delta\omega$=3.3 ppm).

Disclosure of author financial interest or relationships:
A. Bar-Shir, None; **Y. Liang**, None; **A.A. Gilad**, None; **J.W. Bulte**, None.

Presentation Number **P 124**
Poster Session 2
September 19, 2013 / 15:15-15:15 / Room: Exhibit Hall B

MRI contrast enhancement of coated GdF_3 nanoparticles

Mauro Botta, *Fabio Carniato, Kalaivani Thangavel, Lorenzo Tei, Dipartimento di Scienze e Innovazione Tecnologica, Universita` del Piemonte Orientale ''Amedeo Avogadro'', Alessandria, Italy. Contact e-mail: mauro.botta@mfn.unipmn.it*

Introduction: Gd-based MRI nanoprobes allow delivering to the site of interest a large number of metal ions, thus increasing the sensitivity of the technique.[1] Moreover, the paramagnetic nanoparticles (NPs) can incorporate different functionalities, such as a vector for specific targeting, dyes or drugs for multimodality imaging or therapeutic delivery. Among the large number of inorganic NPs investigated, GdF_3 (and $NaGdF_4$) attract growing interest due to their chemical versatility and high r_{1p} values.[2] In addition, they show the ability to exchange both cations and anions on the surface which enables multimodal imaging approaches. GdF_3 NPs with size < 5 nm and coated with citrate, EDTA, EDTA-PEG and polyacrylate (PAA) ligands were prepared and their relaxometric behaviour was investigated in order to unravel the mechanisms underlying the magnetic interaction with water. **Methods**: GdF_3 NPs were prepared in aqueous solution by reacting NaF and $GdCl_3$ in the presence of the different ligands. The solutions were stirred at 348 K (3h) and mixed with ethanol to promote precipitation of the NPs. For the characterization we measured X-ray diffraction patterns, HRTEM images, IR spectra, TG and DLS data. The magnetic field dependency of r_{1p} (NMRD profiles) was measured in water and in Seronorm™. ^{17}O NMR R_2 data were measured as a function of temperature at 11.4 T. A MRI phantom study was also carried out at 7 T on a Bruker scanner. **Results**: GdF_3 functionalized with citrate, polyacrylate and EDTA-PEG show in water a high hydrophilicity, whereas EDTA-based GdF_3 tends to aggregate in aqueous suspension as a consequence of the reduced charge density. In fact, the NMRD profile of citrate-based GdF_3 NPs presents a shape typical of slowly tumbling systems, with a peak centred at 80-120 MHz ($r_{1p} \sim 5.8\ mM^{-1}s^{-1}$). Similar behaviour is found for GdF_3 NPs functionalized with polyacrylate and EDTA-PEG. Instead, EDTA-based GdF_3 shows a completely different profile, characterized by a decrease of r_{1p} value with increasing frequency. The combined ^1H and ^{17}O relaxometric data demonstrate the presence of Gd-bound water molecules and a significant contribution from water molecules H-bonded to the organic coating in addition to highlighting the predominant role of the metal ions exposed on the surface. **Conclusions**: The nature of the organic coating on GdF_3 NPs surface can significantly affect the r_{1p} values of these nanomaterials and then their MRI contrast enhancement. We think this information will help to guide the synthetic design in order to optimize the characteristic of the NPs as MRI probes. **References** 1. M. Botta and L. Tei, Eur. J. Inorg. Chem., 2012, 1945. 2. N.J.J. Johnson et al., Chem. Mater., 2011, 23, 3714.

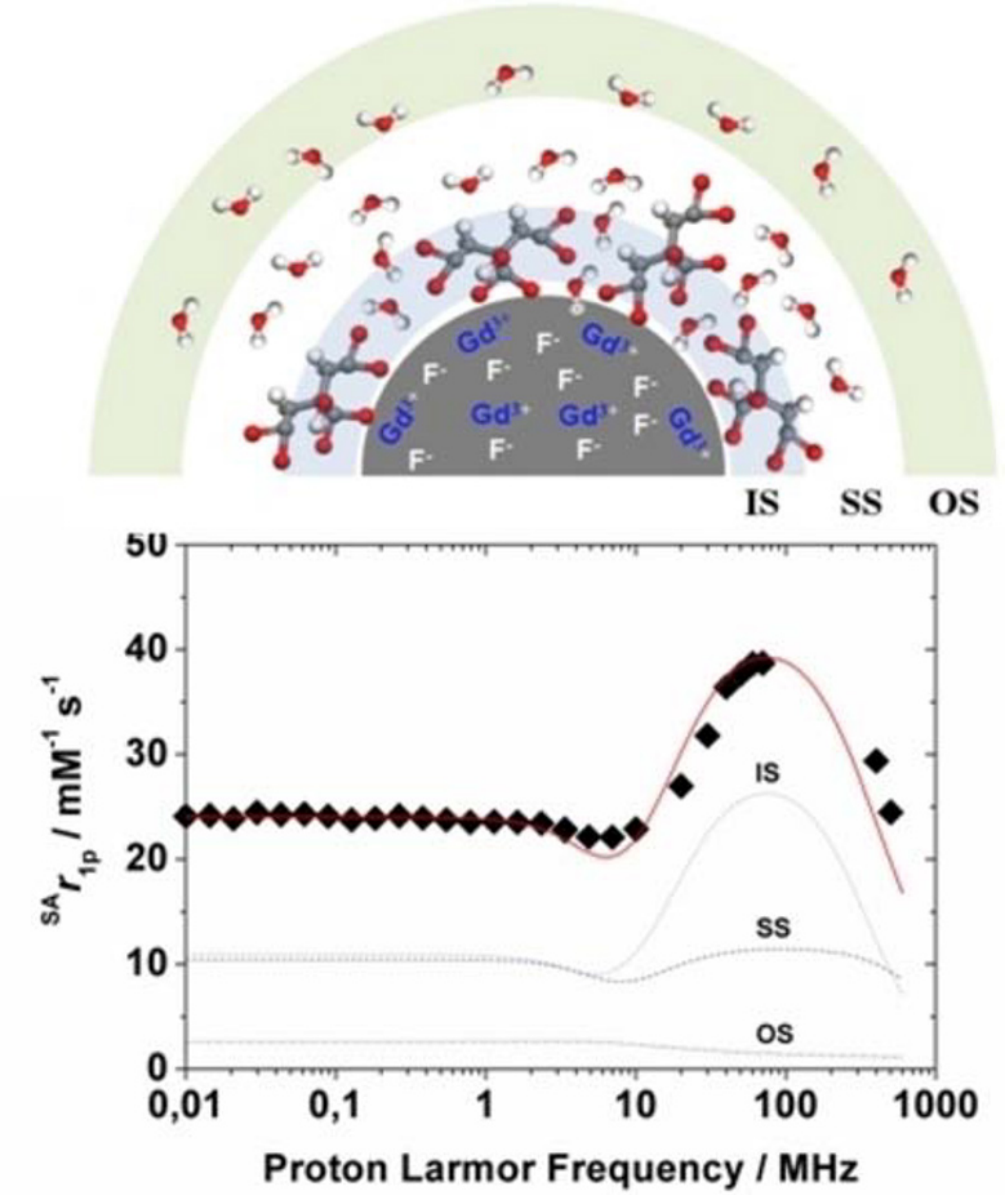

Figure 1: (top) schematic representation of the hydration layer of the Gd-NPs; (bottom) NMRD profile at 310 K for Gd-NPs considering only the metal ions exposed on the surface of citrate-coated NPs.

Disclosure of author financial interest or relationships:
M. Botta, None; **F. Carniato**, None; **K. Thangavel**, None; **L. Tei**, None.

Presentation Number **P 125**
Poster Session 2
September 19, 2013 / 15:15-15:15 / Room: Exhibit Hall B

CD163-Targeted Gold-Coated Iron Oxide Nanoparticles for in vivo MRI Imaging of Atherosclerosis

Monica Carril[1], *Carlos Tarin*[2], *Irati Markuerkiaga*[3], *Jose Luis Martín-Ventura*[2], *Daniel Padró*[3], *Juan Antonio Moreno*[2], *Isabel García*[1,4], *Nuria Genicio*[1], *Sandra Plaza*[3], *Luis Miguel Blanco-Colio*[2], *Jesus Egido*[2], *Soledad Penadés*[1,4], [1]*Biofunctional Nanomaterials Unit, CIC biomaGUNE, San Sebastian, Spain;* [2]*Laboratorio de Patología Vascular y Renal, IIS Fundación Jiménez Díaz, Universidad Autónoma, Madrid, Spain;* [3]*Molecular Imaging Unit, CIC biomaGUNE, San Sebastian, Spain;* [4]*Biomedical Research Networking Center in Bioengineering, Biomaterials and Nanomedicine (CIBER-BBN), CIC biomaGUNE, San Sebastian, Spain. Contact e-mail: mcarril@cicbiomagune.es*

Background: Atherosclerosis is a chronic inflammatory disease of the arterial wall. It is a major cause of morbidity and mortality in western societies, and the underlying cause of the majority of cardiovascular events, such as myocardial infarction or stroke. Depending on the atheroma plaque composition, it may remain stable and asymptomatic for years or evolve into vulnerable plaques, e.g. with hemorrhaged sites, leading into thrombus release and artery occlusion. Hence, gaining information about the content of the plaque is crucial for a diagnosis of its stage of development and its potential risk of rupture. Imaging probes have gained relevancy in order to detect targets that inform about the characteristics of the plaque. In this context, CD163 (a macrophage receptor) has emerged as a potential biomarker of hemorrhaged sites of the atheroma plaque due to its capability to scavenge free hemoglobin. Aim: Our aim was to design conveniently functionalized contrast agents for the detection of novel atherosclerosis biomarkers, such as CD163. Herein, we present the preparation of gold-coated iron oxide nanoparticles (NPs) functionalized with anti-CD163 antibodies and their validation both in vitro and in vivo as contrast agents for MRI. Materials and Methods: Biocompatible gold-coated iron oxide NPs were prepared as described before and converted into targeted NPs by further functionalization with protein G and incubation with anti-CD163 antibodies or isotype IgG as negative control. For the in vitro studies, CD163 (+) and (-) macrophages were incubated with the probe (NP-CD163) and its negative control (NP-IgG). Additionally, atherosclerotic ApoE-/- mice fed for 8 weeks on a high-fat diet and healthy Wt control mice were injected with 2mg of Fe/Kg of the different probes, and the abdominal aorta was monitored by MRI before the injection and at 1, 24 and 48 hours afterwards. The MRI sequence employed was a respiratory triggered flow compensated gradient recalled echo at 11.7T. The vessel wall intensity was normalized to the signal intensity in the adjacent muscle to compare pre- and post-contrast values. Differences between pre- and post-contrast mean values were evaluated by ANOVA analysis. Results: The NPs were prepared, conveniently characterized by standard techniques and functionalized with 1 to 2 units of antibody per nanoparticle. The in vitro studies showed that the nanoparticles bearing the anti-CD163 antibody could selectively detect CD163 expressing macrophages over CD163 non-expressing ones. For the in vivo studies, we observed an accumulation of the probe in ApoE-/- mice that increased over time, being significant at 48 hours after the injection. However, no accumulation was observed in the negative controls neither when injecting the NP-IgG nor when using Wt mice (Figure 1). Figure 1. Conclusions: We have developed a highly sensitive targeted probe based on gold-coated iron oxide NPs, capable of detecting a small subpopulation of macrophages present at a certain stage of the atheroma plaque evolution.

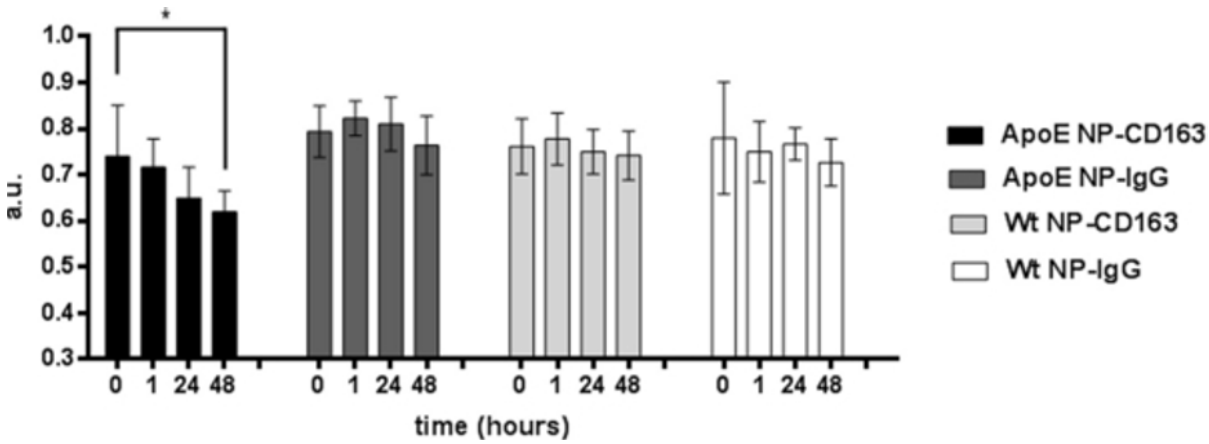

Figure 1. Evaluation of the in vivo contrast changes over time at 0, 1, 24 and 48 hours in ApoE-/- and Wt mice with NP-CD163 and NP-IgG probes.

Disclosure of author financial interest or relationships:
M. Carril, None; **C. Tarin**, None; **I. Markuerkiaga**, None; **J. Martín-Ventura**, None; **D. Padró**, None; **J. Moreno**, None; **I. García**, None; **N. Genicio**, None; **S. Plaza**, None; **L. Blanco-Colio**, None; **J. Egido**, None; **S. Penadés**, None.

Presentation Number **P 126**
Poster Session 2
September 19, 2013 / 15:15-15:15 / Room: Exhibit Hall B

Gd-loaded erythrocytes as blood pool contrast agent

Enza Di Gregorio, *Giuseppe Ferrauto, Eliana Gianolio, Silvio Aime, imaging molecular center, Torino, Italy. Contact e-mail: enza.digregorio@unito.it*

Introduction: Different MRI contrast agents (CAs) have been tested as blood pool CAs and some of them are currently used in clinical and/or pre-clinical applications to visualize tissue vascularization. One of the drawback associated to the use of these agents deals with their extravasations. One route to internalize molecules inside red blood cells relies on the application of an "osmotic shock " . Herein this methodology has been applied to label RBCs with Gd-HPDO3A (commercialized as ProHance, Bracco Imaging S.p.A.). These magnetic erythrocytes can then be used as blood pool contrast agents for the acquisition of Contrast Enhanced Magnetic Resonance Angiography (CE-MRA) and for the assessment of vessel size index maps in xenografted subcutaneous tumors. Tumor vasculature is probably the most intensively investigated aspect of the tumor microenvironment since tumors need to develop its own blood vascular network to obtain enough amount of nutrients and oxygen and the evaluation of tumor vascularization important for the staging of the disease and for the evaluation of anti cancer treatments. **Methods:** Murine RBCs have been isolated by centrifugation. Erythrocytes were then placed for 30 min at 4°C into a hypotonic solution (160mOsm/l) containing the paramagnetic agent to be loaded. The normal morphology of erythrocytes was then restored by changing the osmolarity of the solution to an isotonic condition (280mOsm/l) with the addition of a proper concentration of PBS. After this treatment RBCs were extensively washed to eliminate the not internalized molecules. Mouse tumour models were prepared by the subcutaneous injection of TSA murine breast cancer in balb/c mice. Gd-labelled RBCs were successively injected into mouse tail vein and T1w images were acquired on a Bruker Avance 300MHz spectrometer (7T). The contrast enhancement has been evaluated voxel by voxel and vascularization maps been obtained. **Results:** MR images of the tumor region obtained with Gd-loaded RBCs have been compared with those ones attained upon the addition of Gd-HPDO3A(that diffuses freely in the extracellular space) and of a HAS-binding Gd-complex. The latter agent reaches, upon time, the same distribution shown by Gd-HPDO3A. Conversely Gd-loaded RBC "light-up" a limited number of voxel as the result of their compartimentalization in the vasculature. On this basis an accurate quantification of vessels density in the tumor region has been achieved (Fig.1). It is worth to mention that the induced contrast by Gd-loaded RBC in MR Angiografhic images is markedly high to allow the visualization of vessel that could not be detected in MRA-TOF acquisitions (Fig.2).
Conclusions: The herein reported work shows that, upon loading with Gd-based contrast agents, erythrocytes can act as blood pool MRI contrast agents. This system can be efficiently used as reporter of vessels size index in tumor region. More in general, their outstanding sensitivity makes them excellent reporters for CE-MRA experiments.

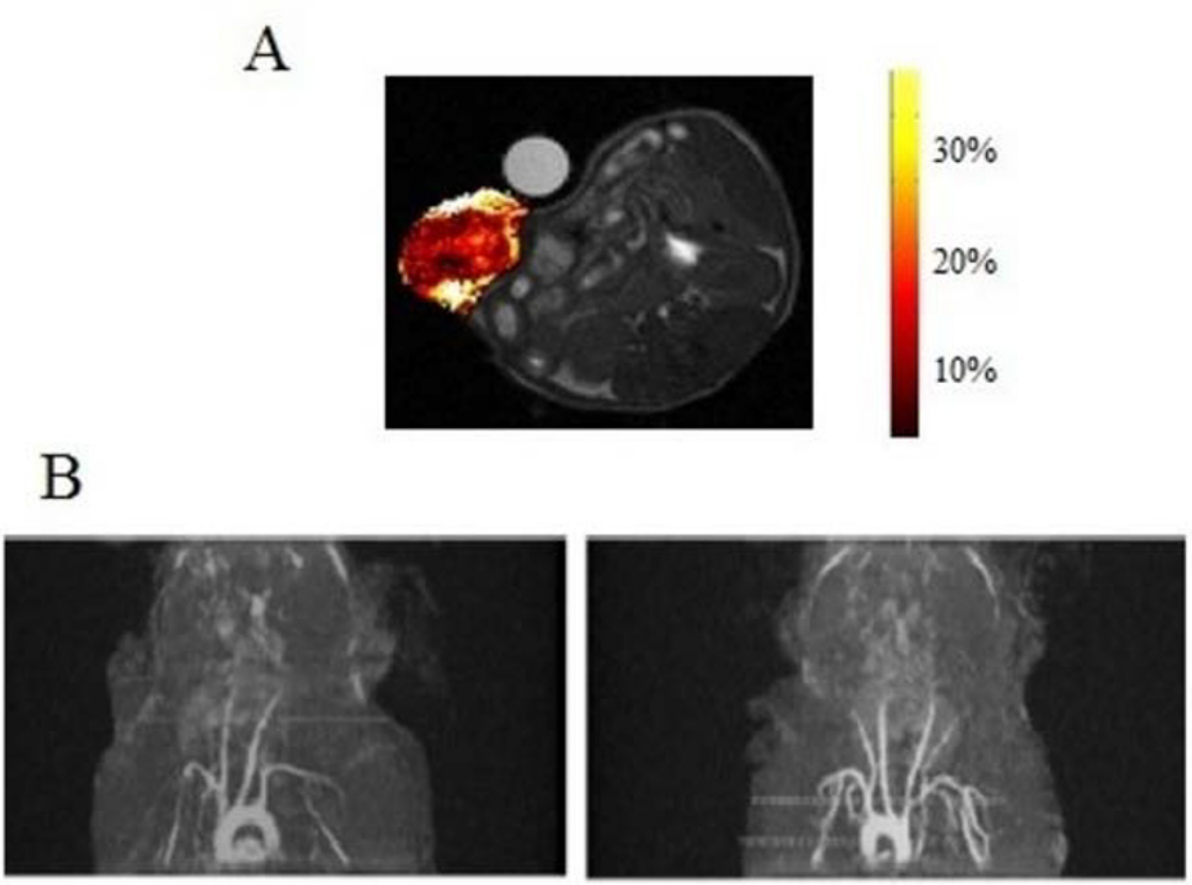

A)False color map of vessels distribution inside tumor region overlapped to T1w image of mouse. B)Magnetic Resonance Angiography of murine aortic region pre- (left) and post- (right) injection of Gd-labelled RBCs.

Disclosure of author financial interest or relationships:
E. Di Gregorio, None; **G. Ferrauto**, None; **E. Gianolio**, None; **S. Aime**, None.

Presentation Number **P 127**
Poster Session 2
September 19, 2013 / 15:15-15:15 / Room: Exhibit Hall B

Noninvasive Assessment of Myocardial Inflammation by Cardiac Magnetic Resonance Imaging in a Rat Model of Cardiorenal Syndrome Type IV

Chang Di, *Department of Radiology, Zhong-Da Hospital, Southeast University, Nanjing, China. Contact e-mail: august_changdi@163.com*

Purpose: Cardiorenal syndrome (CRS) type IV is a condition of primary chronic kidney disease (CKD) worsening cardiac function, which in turn further accelerates the failure progression of both. Monocyte-macrophages contribute to the myocardial inflammatory progression caused by CKD. The purpose of this study was to detect and quantify macrophage-related inflammation within the inflamed heart in a CRS type IV rat model using superparamagnetic iron oxide (SPIO) nanoparticle enhanced, high-resolution cardiac magnetic resonance (MR) imaging. Materials and Methods: Subtotal nephrectomy (SNx) was performed to induce chronic kidney failure in this CRS type IV rat model. 4 weeks after surgery, rats were intragastric administrated vehicle (SNx+Veh, n=12), Ramipril (SNx+Ram, n=12) or Telmisartan (SNx+Tel, n=12) for an additional 12 weeks. A group of sham-operated rats (Sham, n=8) was taken as control. In week 16, T2*-weighted MR images (7.0T) were performed before (pre-SPIO) and 24 hours after (post-SPIO) administration of SPIO (10 mg/kg via tail vein), which was used to label monocyte-macrophages. Contrast-to-noise ratios (CNR) were massured and the changes of contrast-to-noise ratios (CNR) were calculated as the difference between pre-SPIO and post-SPIO. Cardiac structure and function were assessed by cine-MR and systolic blood pressure (SBP), urine albumin excretion (UAE), serum creatinine (Scr) and blood urea nitrogen (BUN) values were measured every 4 weeks to evaluate renal function. Hematoxylin-Eosin, masson's trichrome and sirus red stain were used to observe left ventricular hypertrophy and cardiac fibrosis. Perl's Prussian blue, CD68 immunohistochemistry staining were performed to confirm labeled macrophages and detect if they infiltrated the inflamed tissue of heart. Results: SNx surgery with vehicle treatment significantly increased SBP, UAE, Scr and BUN in week 4,8,12 and maximun in week 16 ($P < .001$ vs sham, $P < .05$ vs SNx+Ram and SNx+Tel), and these changes yielded similar alterations of left ventricular wall thickness, macrophages infiltrating and myocardial fibrosis ($P < .01$ vs sham, $P < .05$ vs SNx+Ram and SNx+Tel), which demonstrated that this model was successful. Changes of CNR between pre- and post-SPIO were significantly greater in SNx+Veh rats (1.08±0.10 vs 0.62±0.13; $P < .001$), and there were no statistical differences in other groups (SNx+Ram 1.24±0.34 vs 1.02±0.20; $P > .05$; SNx+Tel 1.19±0.24 vs 0.98±0.37; $P > .05$; sham 1.05±0.32 vs 1.0±0.12; $P > .05$). CNR of SNx+Veh group significantly increased compared with other three groups ($P < .001$ vs sham, $P < .05$ vs SNx+Ram and $P < .05$ vs SNx+Tel). However, there was no statistical difference between the two treatment groups ($P > .05$). Histologic analysis demonstrated that infiltrating macrophages engulfed SPIO, resulting in altered myocardial T2* effect, and the in vivo CNR was significantly correlated to the absolute macrophages content in rats' heart ($r2 = 0.785$, $P < .001$). Conclusion: SPIO enhanced cardiac MR imaging can noninvasively assess myocardial monocyte-macrophages burden, and potentially can monitor therapy-mediated myocardial changes in CRS type IV.

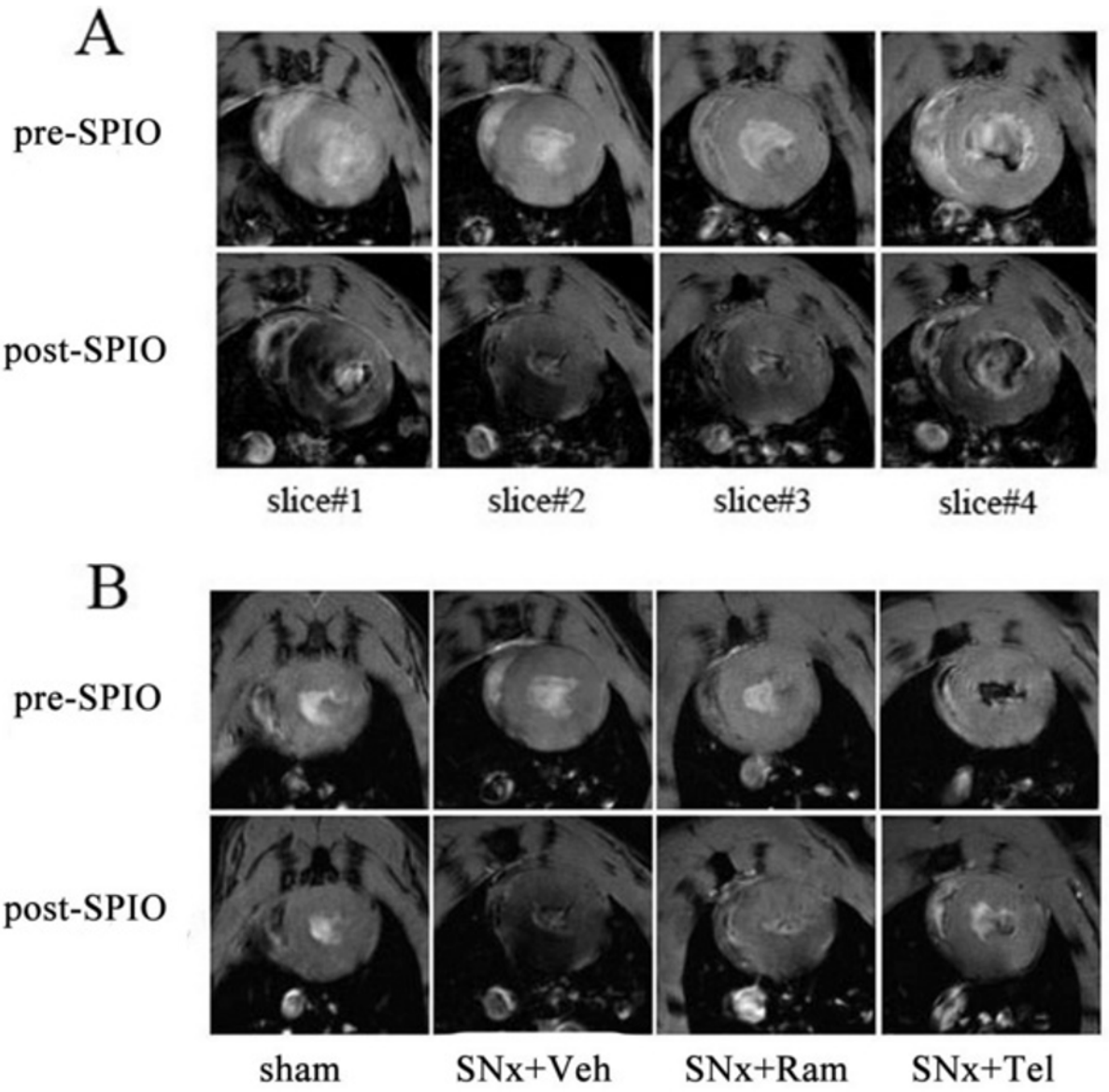

Disclosure of author financial interest or relationships:
C. Di, None.

Presentation Number **P 128**
Poster Session 2
September 19, 2013 / 15:15-15:15 / Room: Exhibit Hall B

Cell labeling by sonoporation: boosting effect of liposomes

Giuseppe Ferrauto, *Pierangela Giustetto, Marta Ruzza, Daniela Delli Castelli, Silvio Aime, Enzo Terreno, Chemistry, Molecular Imaging Center- University of Turin, Torino, Italy. Contact e-mail: giuseppe.ferrauto@unito.it*

Purpose: The development of strategies for cell labeling with Ln-based MRI contrast agents (CAs) is of huge interest in the emerging field of cell tracking. Among the other available routes for the internalization, the ones that confine the MRI probe into the cytoplasm are favorites because they allow the circumvention of the problem of the "quenched" relaxivity that invariantly occurs when the probe is internalized in cellular organelles like endosomes. Sonoporation can be successfully used to permeabilize cell membranes, thus allowing the passage of molecules from the external solution to the cytosol. This work was aimed at evaluating the efficiency of this labeling approach when liposomes are added in the incubation medium. **Methods:** Murine breast cancer cells were incubated with the clinically approved MRI agents Gadoteridol (or other Gd-complexes), and then sonoporated in the presence of differently formulated liposomes. Sonoporation was carried out by using a 1 MHz non-focused transducer, upon varying duty cycle, sonoporation time, and voltage. The experimental set-up was changed to optimize the interaction between US waves and cell membranes, without reducing cell viability. The amount of the internalized agent was evaluated relaxometrically. Cell viability was determined by trypan blue or Bradford assays. The effective cellular localization of the labeling agent was assessed by both relaxometry and confocal microscopy (using fluorescent probes). **Results and conclusions:** Liposomes mediate the interaction between US and cell membranes. In particular, cationic liposomes significantly increased the labeling efficiency allowing the internalization of high amount of Gadoteridol (in the order of 10^9-10^{10} Gd^{3+} per cell, depending on the kind of probe that was used). The size of the labeling agent played a key role in the efficiency of internalization, and smaller probes displayed higher internalization. Furthermore, the opening/closing kinetics of the pores formed on the cellular membranes by the sonoporation showed a different behavior in the presence of liposomes. Two distinct effects were observed: i) the amount of the internalized agent increased, and ii) a faster pore closing, which could explain the increased cell viability observed. The results obtained suggest that the increased internalization efficiency induced by the liposomes could be accounted for in terms of a more active transient pore formation mediated by cationic vesicles interacting with the negatively charged cellular membrane.The results here presented may pave the way for the design of more efficient, and less harmful, procedures for labeling cells with MRI agents, with the final scope to improve the detection sensitivity in cell tracking experiments. Moreover, these observation can be very useful to develop new therapeutic schemes where ultrasound can be used not only to trigger the release of a drug from the nanocarrier, but, at the same time, to facilitate the diffusion of the drug in the target tissue. **References:** J.Wu Ultrasound in Med. & Biol., 2006, 32, 3, 429-437.

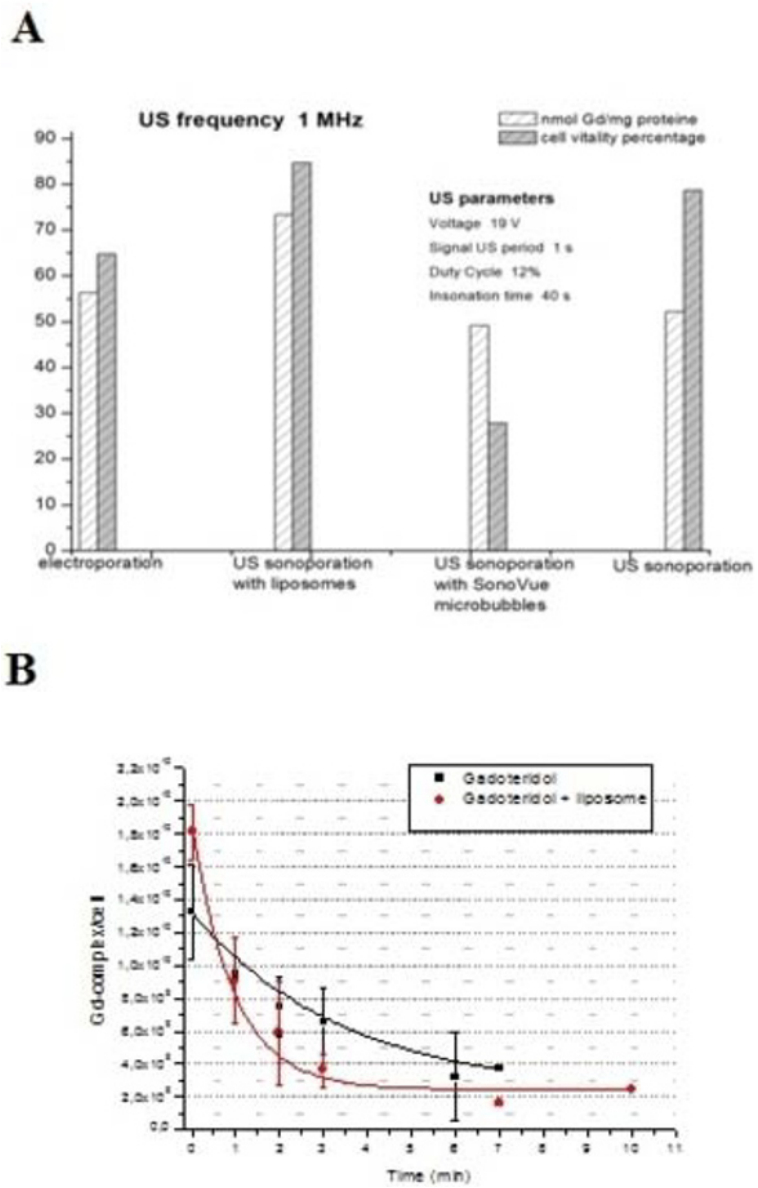

A)Comparison between electroporation and sonoporation (in presence of microbubbles, cationic liposomes or without vescicels) in terms of amount of internalized Gadoteridol and cell viability; B) Internalization of Gadoteridol by changing the time delay after US insonation.

Disclosure of author financial interest or relationships:

G. Ferrauto, None; **P. Giustetto**, None; **M. Ruzza**, None; **D. Delli Castelli**, None; **S. Aime**, None; **E. Terreno**, Bracco Imaging, Consultant .

Presentation Number **P 129**
Poster Session 2
September 19, 2013 / 15:15-15:15 / Room: Exhibit Hall B

Tumor ablation using theranostic nanoparticles

Vít Herynek[1], *Pavla Jendelova*[2], *Karolina Turnovcova*[2], *Emil Pollert*[3], *Pavel Veverka*[3], *Daniel Jirak*[1], *Eva Sykova*[2], *Milan Hajek*[1], [1]*MR Unit, Department of Diagnostic and Interventional Radiology, Institute for Clinical and Experimental Medicine, Prague, Czech Republic;* [2]*Department of Neuroscience, Institute of Experimental Medicine, Prague, Czech Republic;* [3]*Department of Magnetics and Superconductors, Institute of Physics, Prague, Czech Republic. Contact e-mail: vit.herynek@medicon.cz*

Introduction Theranostic ferromagnetic nanoparticles with low Curie temperature and high relaxivity represent a suitable agent for MRI-guided magnetic fluid hyperthermia applicable for tumor treatment. The method is based on a deposition of stable and nontoxic suspensions of the magnetic nanoparticles inside the tumor followed by an exposure to a high frequency (HF) electromagnetic field. Magnetic hysteresis losses result in local heating by the particles and consequently to apoptosis of cells in their vicinity. The aim of our study was to verify the possibility of tumor thermoablation using the ferromagnetic particles in experimental animals in vivo. Methods Perovskite nanoparticles (La1-xSrxMnO3), coated by SiO2 were synthesized, characterized in vitro and tested in vivo. Animal model: 2 millions of rat glioblastoma cells were implanted subcutaneously to six rats (Brown Norway). Nanoparticle suspension (50 μL, 4mM Mn) was injected into the tumor 2 weeks after tumor implantation. Sagittal and transversal T2-weighted MR images were obtained using a 4.7T MR imager before and immediately after the nanoparticle injection. The rats were exposed to a HF electromagnetic field (480 kHz, 11 mT) for 30 minutes. Temperature in the vicinity of the tumor was measured by an optical fiber inserted through a catheter. The animals were sacrificed 1 day after ablation. Apoptosis in the tumor was assessed by terminal deoxynucleotidyl transferase dUTP nick end labeling (TUNEL). Three control animals with tumors underwent HF field exposition without nanoparticles, or application of nanoparticles without exposition to eliminate an influence of the HF field or nanoparticles themselves. Results MRI confirmed presence of the nanoparticles in the tumor (see Fig.). Temperature in the tumor with injected nanoparticles increased to 41.5°C. Control animals without nanoparticles reached 40°C. TUNEL confirmed massive apoptosis in the tumor in animals with injected nanoparticles after exposition to HF field corresponding to distribution of the nanoparticles. Discussion Distribution of nanoparticles can be easily tracked using MRI. Although temperature increase in animals with nanoparticles is small compared to controls, we suppose that due to uneven distribution of nanoparticles, temperature increase is locally much higher. Moreover the subcutaneous measurement of temperature is strongly affected by temperature inside the chamber. Local thermoablation was confirmed by TUNEL, which revealed apoptosis in the tumor in animals treated by nanoparticles and field exposition. Thus we confirmed that the nanoparticles are suitable for MRI-guided thermoablation. Conclusion Experiment proved that ferromagnetic perovskite nanoparticles can be easily tracked in vivo by MRI. When exposed to high frequency field, they can locally heat the tissue and induce cell apoptosis in their vicinity. The tested particles potentially represent a tool for non-invasive tumor ablation. Acknowledgement The study was supported by a grant project No. FR-TI3/521 (Ministry of Industry and Trade, Czech Republic), and by an Institutional grant 00023001IKEM (Ministry of Health, Czech Republic).

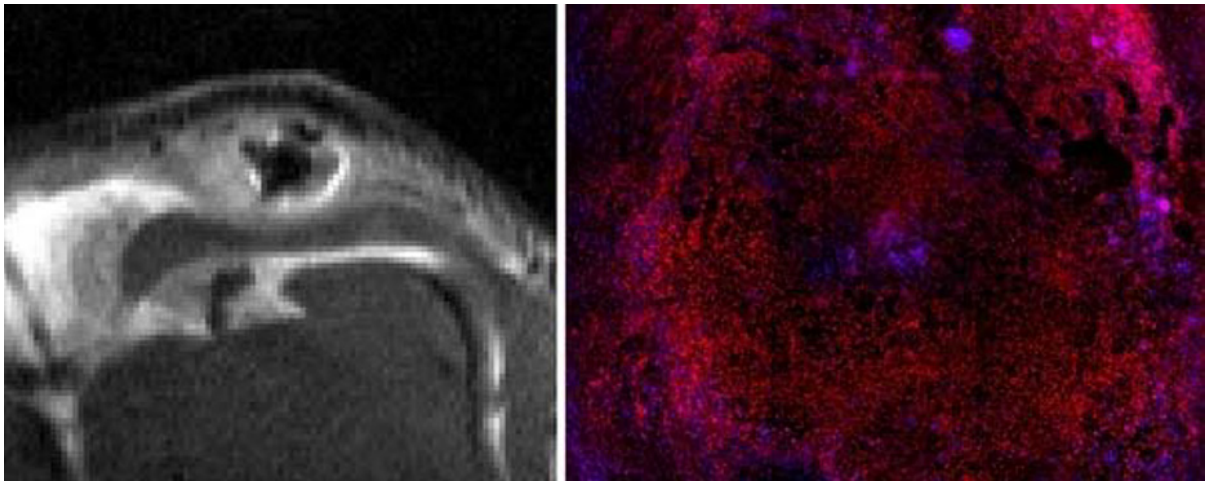

Left: T2-weighted MR image of the subcutaneous tumor after injection of nanoparticles. Right: Composed image of TUNEL (marker of apoptosis, red) and DAPI (DNA marker, blue) staining.

Disclosure of author financial interest or relationships:
V. Herynek, None; **P. Jendelova**, None; **K. Turnovcova**, None; **E. Pollert**, None; **P. Veverka**, None; **D. Jirak**, None; **E. Sykova**, None; **M. Hajek**, None.

Presentation Number **P 130**
Poster Session 2
September 19, 2013 / 15:15-15:15 / Room: Exhibit Hall B

An Enzyme-Responsive PARACEST MRI Contrast Agent That "Turns On" After Catalysis

Dina V. Hingorani, *Edward Randtke, Chemistry and Biochemistry, University of Arizona, Tucson, AZ, USA. Contact e-mail: dinah@email.arizona.edu*

INTRODUCTION Transglutaminase (TGase) is an important biomarker of tumor vascular normalization that can cross-link extracellular matrix proteins by coupling lysine and glutamine side chains [1]. A T1 MRI contrast agent was used to detect TGase by monitoring the accumulation of the agent in tumor tissue, although this approach lacks specificity for enzyme activity [2]. For comparison, CEST MRI contrast agents can detect enzyme activity with good specificity by measuring a change in CEST caused by cleavage of a specific bond of the agent by an enzyme [3-8]. We have designed a paramagnetic CEST (PARACEST) agent, consisting of Tm(III) chelated with 1,4,7,10-tetraazacyclododecane-1,4,7-triacetic acid-10-cadaverine (Tm-DO3A-cad), to detect the activity of TGase. Unlike most other enzyme-responsive CEST agents that show a disappearance of CEST after enzyme cleavage of a covalent bond, Tm-DO3A-cad is designed to show the appearance of CEST after the creation of a covalent bond by TGase. METHODS Tm-DO3A-cad was synthesized by alkylating DO3A with bromopentylamine and using the product to chelate Tm(III). A total of 0.5 units of recombinant microbial TGase (Zedira GmbH) was incubated with 20 mM of Tm-DO3A-cad, 0.75 mM of the albumin, and 8 mM of glutathione (GSH) in tris-HCl buffer at pH 7.0 and 37oC for 24 hours. We also did the reaction by replacing albumin with 20mM of ZQG peptide or 20mM of Boc-Q-OH. CEST Spectra were acquired for each reactant, GSH, and the reaction mixture before and after adding TGase. CEST Spectra A series of 1D NMR spectra were acquired using a 4 s saturation pulse applied at 20μT power with saturation frequencies spanning +35 to -35 ppm in 0.25 ppm increments (NEX=4, 37.3oC, 11.7T). Water peak heights were used to construct CEST spectra of a sample before and after adding TGase. MTRasym analysis was used to measure the magnitude of CEST from reactants and Tm-DO3A-cad-albumin product (Fig. 1). MTRasym analysis and Bloch analysis was performed to measure CEST and chemical exchange rates. RESULTS The synthesis intermediates and product prior to chelation, and the reactants and products of the enzyme reactions, were confirmed with Mass Spectrometry and NMR spectroscopy. The TGase reaction with albumin caused CEST to appear at -11 and +4 ppm (Fig. 1). The TGase reaction with ZQG caused CEST to appear at +22, +11, and +4 ppm. The catalysis with Boc-Q-OH caused CEST to appear at 31 and 21 ppm. Chemical Exchange rate analyses were used to assign PARACEST arising from proximity to Tm(III) or DIACEST arising from a non-paramagnetic reactant. Comparisons of CEST spectra of reactants and products were also used to validate the identify of each CEST effect. DISCUSSION The appearance of CEST successfully detected bond creation via TGase activity. Catalysis with hydrophilic substrate albumin, produced CEST at -11 ppm. Catalysis with more hydrophobic substrates, ZQG and Boc-Q-OH, produced multiple CEST effects at positive MR frequencies, indicating different, multiple conformations relative to the products with albumin. This result demonstrates the outstanding specificity of CEST or different molecular conformations.

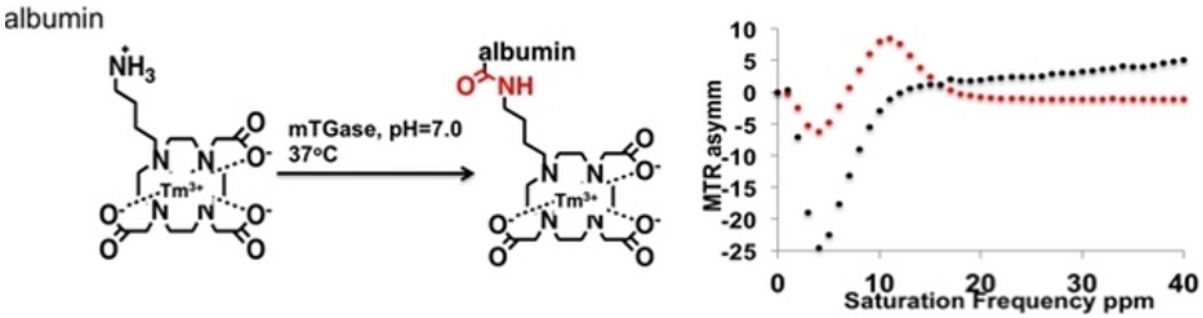

Fig (1): CestMRI detects Tgase activity: The reactants show a MTRasymm effect at 4ppm due to the amide backbone. After Tgase action, cest is appears at -11ppm reduces at 4ppm.

Disclosure of author financial interest or relationships:
D.V. Hingorani, None; **E. Randtke**, None.

Presentation Number **P 131**
Poster Session 2
September 19, 2013 / 15:15-15:15 / Room: Exhibit Hall B

Cell Apoptosis Induced T2-T1 Contrast "Switching" in MR Imaging of Supersmall Magnetic Iron Oxide Nanoparticle (sSIO) Labeled Cells

Jing Huang, *Liya Wang, Hui Mao, 1Department of Radiology and Imaging Sciences, Emory University Schoole of Medicine, Atlanta, GA, USA. Contact e-mail: jing.huang@emory.edu*

Iron oxide nanoparticles (IO) have gained increasing attention on tracking cells by magnetic resonance imaging (MRI). Labeling cells with IOs enables localizing cell implants and monitoring migration in vivo using MRI. This is typically done by taking advantage of strong T2 weighted contrast, or signal drop, caused by increased susceptibility and shortened T2 in cells engulfing IOs. However, one of the main limitations of MRI tracking IO-labeled cells is lack of ability to report cell functions, cell death and differentiation. T2 contrast from labeled cells can be found related to many other events and imaging artifacts. Here we describe a proof-of-principle application of our new developed super small superparamagnetic IO (sSIO, core size ~ 3 nm) in detecting apoptosis of labeled cells based on T2-T1 contrast "switching" that only occurs with such sSIO. Monodispersed hydrophobic sSIO were prepared by pyrolysis and surface modified by in situ polymerization of oligosaccharides. These sSIO exhibits a high r1 value (4.2 mM-1s-1) and a higher r1/r2 ratio (0.28) than those of typical IOs with larger core sizes (r1/r2< 0.1). When used for cell labelling, high cellular uptake of sSIO was demonstrated by transmission electron microscopy (TEM) and MRI. In T1 weighted spin echo imaging, sSIO suspension exhibited strong T1 contrast enhancement (bright signal). However, when labelling cells with sSIO, such bright T1 contrast is diminished, instead, signal drops as T2 weighted contrast was observed. Interestingly, significant bright contrast enhancement was observed in T1-weighted MRI when the labelled cells were lysed and sSIO were released, suggesting that there is a "contrast switch" between sSIO internalized/clustered in cells and released from cells when cell broke down. For further investigating cell death induced T1-T2 switching in sSIO labelled cells, we examined MRI contrast changes from clustered sSIO to the single disperse form, using model systems of milk protein micelle and liposome encapsulating sSIO to emulate the cellular internationalization of sSIO. Similarly, both the micelle and liposome exhibit the T2-dominated contrast effect when loaded sSIO. TEM images showed sSIO were engulfed and internalized, which led to signal drops, or darkening, in both T1 and T2-weighted spin echo images. In contrast, rapture of liposome to release sSIO led prominent T1 contrast enhancement as sSIO dispersed in solution. In addition, such T1-T2 switch phenomenon was not observed in the cells labelled with larger sized IOs (~20 nm) with the same coating. Therefore, the current study demonstrated that it is possible to not only track sSIO labelled cells with conventional T2 weighted MRI, but also can monitor the fate (apoptosis) of the labelled cells in vivo based on the T1-T2 contrast switch exhibited in sSIO. This newly developed sSIO may provide a tool for us to overcome the current limitations in MRI tracking of cell migration, apoptosis and differentiation.

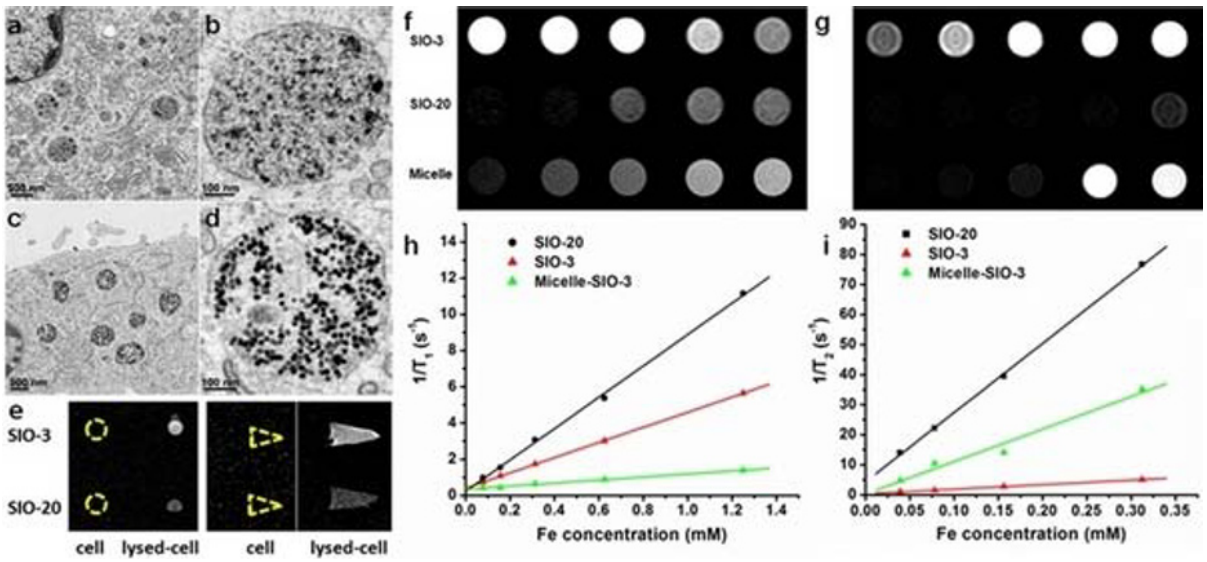

Figure 1. a, b) TEM images of cells after uptake of sSIO (SIO-3) and c, d) SIO-20 (core size 20 nm); e) T1-weighted MR images of cells after uptake of nanoparticles with different sizes; f)T1- and g) T2-weighted MRI phantom image of sSIO (SIO-3), and large sized nanoparticle (SIO-20) and Micelle incorporated SIO-3 (Micelle-SIO-3), and corresponding change of 1/T1 (h) and 1/T2 (i) at different concentrations which were used for r1 and r2 calculations.

Disclosure of author financial interest or relationships:
J. Huang, None; **L. Wang**, None; **H. Mao**, None.

Presentation Number **P 132**
Poster Session 2
September 19, 2013 / 15:15-15:15 / Room: Exhibit Hall B

129Xe MRI response and cellular labeling properties of bimodal contrast agents

Jabadurai Jayapaul, *Christopher Witte, Stefan Klippel, Leif Schröder, Molecular Imaging Group (ERC project BiosensorImaging), Leibnitz Institute for Molecular Pharmacology (FMP), Berlin, Germany. Contact e-mail: jayapaul@fmp-berlin.de*

Despite of being able to produce images with high spatial and temporal resolution, Magnetic Resonance Imaging (MRI) lacks sensitivity to contrast agents. To surpass this limitation, hyperpolarized 129Xe gas MRI can be used with 10^5 fold signal enhancement compared to conventional MRI. In this context, cryptophane-A -based contrast agents (biosensors) are utilized to achieve highly sensitive 129Xe MRI contrast via the host-guest interactions occurring between cryptophane-A as cage and xenon. In this study, we report synthesis of bimodal cryptophane constructs and study their MR contrast enhancement properties and their in vitro cellular uptake behavior, respectively. Fluorescent biosensors based on cryptophane-A are synthesized by using different amino acids with protective groups via solid phase peptide synthesis (SPPS) technique. Fluorophores (e.g. fluorescein (hydrophilic), coumarin (hydrophobic)) are introduced into the biosensor constructs in order to check their influence on the hyperCEST (Chemical Exchange Saturation Transfer) response and further to validate cellular uptake through fluorescence. The fluorophores are separated from the cage by using hetero-bi-functional PEG spacer of appropriate chain lengths. The as-synthesized biosensors are purified by using reverse-phase HPLC and structurally characterized using MALDI-TOF. MRI experiments were performed on a 9.4 T NMR micro-imaging setup. Hyperpolarized 129Xe was generated by spin exchange optical pumping in a custom-designed continuous flow set up using a gas mixture containing 2% Xe, which was directly bubbled into solution prior to xenon imaging. The cell viability of HeLa cells after incubation with fluorescent biosensors was checked using Trypan blue staining. The cellular uptake of fluorescent biosensors by HeLa cells was investigated using confocal microscopy. Fluorophore-tagged biosensors starting from glycine-loaded resins were successfully synthesized and a NH2-PEG3-CH2COOH spacer unit was suitable for preventing the undesirable steric interactions between cage and fluorophore (Fig. 1A-B). 129Xe spectra of purified fluorescein- and coumarin- conjugated biosensors and free cage (total conc. 50 µM in 10% DMSO and 90% H2O) at 290 K referenced to xenon in solution showed distinct peaks at 62, 63 and 60 ppm, respectively, thereby showing the multispectral xenon imaging possibilities of different components. In line with this, different hyperCEST response (z spectra) pattern of the hydrophilic and hydrophobic constructs and cage measured at 50 µM in 10% DMSO and 90% H2O was in close agreement to 129Xe spectra (Fig. 1C-D). Trypan blue staining showed that there is no observable change in the viability of HeLa cells after 3 h incubation with biosensors at 50 µM. The confocal microscopy showed that the biosensor was mostly localized in the cytoplasm of HeLa cells (Fig. 1E-F). In conclusion, we show biocompatible fluorescent biosensors that displayed unique 129Xe MR response and cell labeling efficacy. These constructs can serve as building blocks for biosensors with different targeting units addressing various biomedical questions.

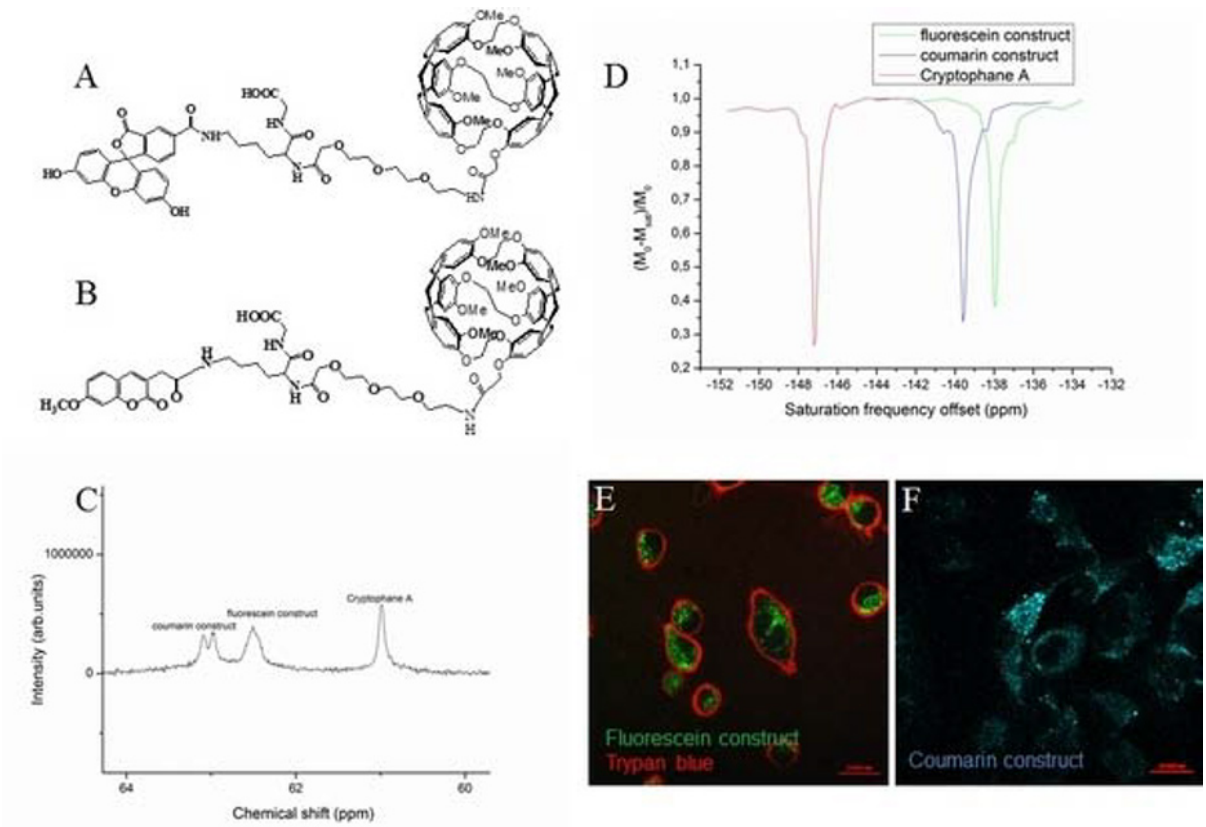

Figure 1. Schematic diagram of the generated bimodal biosensors: (A) fluorescein and (B) coumarin constructs, respectively. C: The direct 129Xe NMR read out of the solution containing cryptophane A, coumarin- and fluorescein- constructs at 16.7 μM each at 290 K confirms the multispectral detection possibilities of different components. D: HyperCEST experiments (z spectra (indirect NMR read out)) results obtained at 50 μM of different constructs and cage from individual experiments displayed patterns similar to that of direct counterparts. E-F: Confocal microscopic evaluation showed no change in viability (Trypan blue staining (red)) of HeLa cells after 3 h incubation with biosensors. The fluorescein construct was localized mostly in the cytoplasm while the coumarin construct was localized likely in the cellular membrane and cytoplasm of HeLa cells, respectively.

Disclosure of author financial interest or relationships:
J. Jayapaul, None; **C. Witte**, None; **S. Klippel**, None; **L. Schröder**, None.

Presentation Number **P 133**
Poster Session 2
September 19, 2013 / 15:15-15:15 / Room: Exhibit Hall B

Imaging of murine myocardial infarction using elastin binding MRI contrast agents

Katja Kosanke[1], *Isabella Bielicki*[1], *Marcus Settles*[1], *Armin Huber*[1], *Ernst J. Rummeny*[1], *Rene M. Botnar*[2], *Moritz Wildgruber*[1], [1]*Department of Radiology, Klinikum Rechts der Isar, Munich, Germany;* [2]*Division of Imaging Sciences and Biomedical Engineering, King's College, London, Germany. Contact e-mail: katja.kosanke@gmx.de*

Goal: Successful establishment of myocardial infarction imaging in a murine mouse model using an elastin binding contrast agent for MRI Material and methods: Myocardial infarctions were induced in C57BL/6J mice by permanent ligation of the left coronary artery. MRI imaging was performed on days 7 and 21, respectively, after infarction using a clinical 1.5T MRI scanner. Myocardial perfusion imaging was performed using a phase-sensitive inversion recovery sequence (PSIR) over 90 minutes after injection of elastin binding contrast agent CP-1052. For intraindividual comparison the same experiment was repeated with standard MRI contrast agent Gd-DTPA. Competition experiments were performed using the contrast agent analog La-1052, an agent missing the central Gd-ion being replaced by non-paramagnetic Lanthanum. Results of the in vivo imaging were validated by Triphenyltetrazoliumchlorid (TTC)-staining and histology. Results: Signal-to-noise-ratio of infarction and healthy myocardium showed peak enhancement 10 minutes after injection of Gd-DTPA. After injection of elastin binding CP-1052 an extended accumulation in the infarcted myocardium with a signal-to-noise-ratio higher than that of Gd-DTPA was detected. Competition experiments with La-1052 showed significantly lower contrast-to-noise-ratios after injection of elastin binding contrast agents, which accounts for specific binding. Ex vivo TTC-staining as well as Elastica-van-Gieson staining showed a good correlation with in vivo elastin imaging. Conclusion: In vivo targeting of elastin after experimental induction of ischemia allows high-contrast in vivo visualisation of acute myocardial infarction in mice. This is due to the higher relaxivity of the molecular contrast agent and its specifity to elastin. Therefore, remodeling of elastic fibers may be successfully monitored in vivo in future.

Disclosure of author financial interest or relationships:
K. Kosanke, None; **I. Bielicki**, None; **M. Settles**, None; **A. Huber**, None; **E.J. Rummeny**, None; **R.M. Botnar**, None; **M. Wildgruber**, None.

Presentation Number **P 134**
Poster Session 2
September 19, 2013 / 15:15-15:15 / Room: Exhibit Hall B

Cleaved Iron Oxide Nanoparticles Mediated Cancer Imaging and Therapy

Min Kyung Chae, *Janggeun Cho, Chulhyun Lee, Korea Basic Science Institute, Chungbuk, Republic of Korea. Contact e-mail: mkchae@kbsi.re.kr*

Iron oxide nanoparticles as magnetic resonance imaging (MRI) contrast agents have a variety of characteristics that penetrate effectively biological membranes, circulate for a long time in blood vessel, and conjugate with targeted peptides. We synthesized nontoxic cracked iron oxide nanoparticles (CIONPs) from hydrophobic FeO nanoparticles (HIONPs) via 3 steps. It showed improved r2 relaxivities and potential application as a drug delivery system by surface modification. Peptides are valuable targeting probes and therapeutic molecules because of their small size and low immunogenicity. CIONPs was introduced two types of peptide, RGR peptide and polo-like kinase 1 (Plk-1) targeted peptide, for targeting and therapy cancer. A tumor-homing peptide (RGR peptide) is specifically binding to PDGF receptor-beta on endothelia cells of solid tumor. It was reported that inhibition of Plk-1 which is a regulator of cell growth by using PLK1 targeted peptide cause tumor cell death but not normal cell. By selectively binding to cancer cell and inhibiting Plk-1, these nanoparticles could be multi-modality imaging agents.

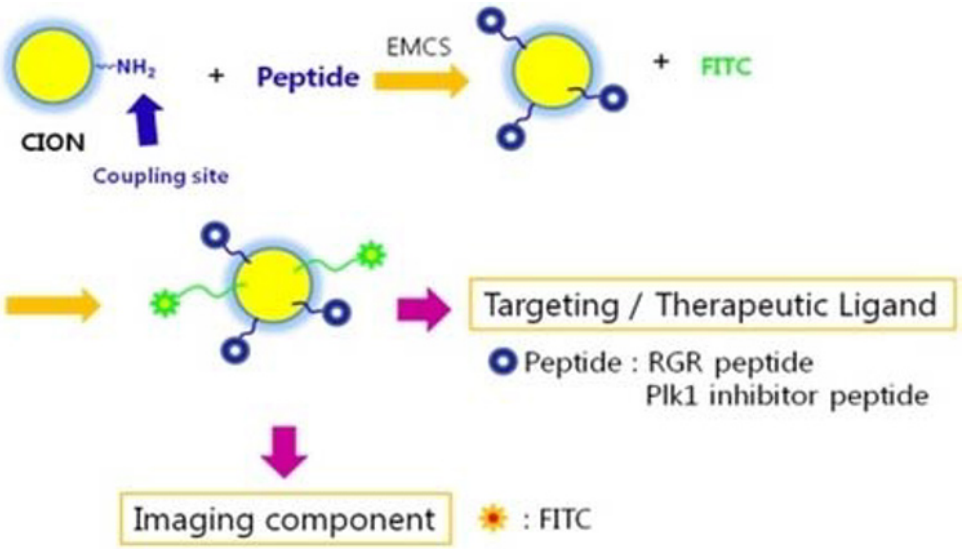

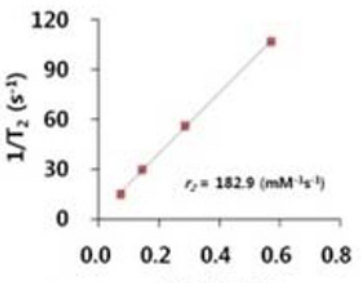

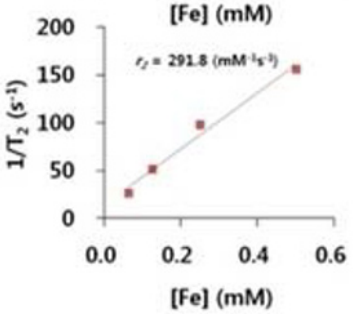

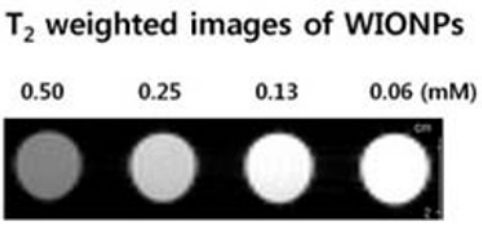

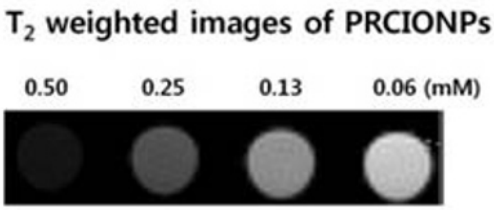

Disclosure of author financial interest or relationships:
M. Chae, None; **J. Cho**, None; **C. Lee**, None.

Presentation Number **P 135**
Poster Session 2
September 19, 2013 / 15:15-15:15 / Room: Exhibit Hall B

A Novel Anti-fouling Poly Ethylene Glycol Based Copolymer Coated Iron Oxide Nanoparticle MRI Contrast Agent for Reducing Non-specific uptake and Improving Cell Targeting

Yuancheng Li[1,2], *Run Lin*[1,2], *Liya Wang*[1,2], *Hui Mao*[1,2], [1]*Radiology and Imaging Sciences, Emory University, Atlanta, GA, USA;* [2]*Center for Systems Imaging, Emory University, Atlanta, GA, USA. Contact e-mail: yli41@emory.edu*

Magnetic resonance imaging (MRI) has been widely used in diagnostics in the past a few decades. While small molecule Gadolinium complexes are commonly used as contrast agents in clinical applications. However, increasing effort has been focused on developing novel biocompatible nanoparticle based contrast agents, such as superparamagnetic iron oxide nanoparticles (SPIONs), given the advantages of superb contrast enhancing effect, functionalization through surface modification and prolonged blood circulation and tumor retention. However, several challenges for the development of SPIONs for in vivo imaging remains, such as the stability of the nanoparticles in physiologic environment, and the non-specific uptake of the nanoparticles by the reticuloendothelial system (RES), e.g. liver and spleen. Such nonspecific uptake may lead to a substantial reduction in the efficiency of target directed imaging, and the introduction of interfering background signal from reticuloendothelial organs. The latter will become crucial when the target spot locates in such organs. To address these problems, a poly ethylene glycol (PEG)-b-poly allyl glycidyl ether copolymer coated SPION has been made and tested as a MRI contrast agent with specific need of reducing non-specific uptake and eventually improving the tumor targeting when functionalized with tumor targeting ligands. By introducing PEG group, the stability of this water-soluble nanoparticle is improved, and the nonspecific binding and uptake are also alleviated. Transmission electron microscopy (TEM) experiment indicates the size of the coated nanoparticle to be 18 nm (with 10 nm SPIONs used). Dynamic light scattering (DLS) experiment also confirmed the size distribution around 20 nm. Cell uptake experiments of the nanoparticles with macrophage and different cancer cell lines indicate an excellent antifouling property after coating. After the systemic administration of transferrin-functionalized SPIONs into tumor bearing mice, selective accumulation of functionalized SPIONs within tumor mass was observed by optical imaging, MRI, and histologic analysis. Normal tissues from a variety of organs including brain, lung, liver, and spleen are investigated as well after the administration of both functionalized and unfunctionalized SPIONs to examine the nanoparticle distribution.

Disclosure of author financial interest or relationships:
Y. Li, None; **R. Lin**, None; **L. Wang**, None; **H. Mao**, None.

Presentation Number **P 136**
Poster Session 2
September 19, 2013 / 15:15-15:15 / Room: Exhibit Hall B

Influence of coating materials of USPIO on biodistribution and particle depletion in vivo - comparison of four different coatings at 7T MRI

Nina Raabe[1], *Thomas M. Ernst*[1], *Markus Heine*[3], *Sunhild C. Salmen*[4], *Barbara Freund*[2], *Rudolph Reimer*[5], *Michael G. Kaul*[1], *Gerhard Adam*[1], *Harald Ittrich*[1], [1]*Department of Diagnostic and Interventional Radiology, University Medical Center Hamburg-Eppendorf, Hamburg, Germany;* [2]*Department of Biochemistry and Molecular Biology II, University Medical Center Hamburg-Eppendorf, Hamburg, Germany;* [3]*Department of Anatomy II: Experimental Morphology, University Medical Center Hamburg-Eppendorf, Hamburg, Germany;* [4]*Institute of Physical Chemistry, University Hamburg, Hamburg, Germany;* [5]*Heinrich-Pette-Institute for Experimental Virology and Immunology, Hamburg, Germany. Contact e-mail: nraabe@uke.de*

Purpose: To evaluate the influence of different coating materials of ultrasmall iron oxide particles on the biodistribution and relaxometric properties in vivo at 7T MR at different points of time. Materials and methods: Four diverse coated (two polymeric coatings, carboxydextran and PEG), monodisperse USPIO (hydrodynamic diameter: 20-30nm) were i.v. injected in mice at two different iron concentrations (n = 3 per concentration)(25 and 50 µgFe). The injection was performed during dynamic susceptibility MR imaging (DSC-MRI) and relaxometric measurements were performed before and after USPIO application on a 7T small animal MR scanner. Further relaxcometric measurements were performed 24h after the initial injection and after two weeks and evaluation was performed for liver, spleen, kidneys and muscle. One mouse of each USPIO and iron concentration was sacrificed on day one and two for comparison of MR data with histology and transmission electron microscopy. Results: There was an organ- and concentration dependent biodistribution for all USPIO with the highest uptake in the liver, followed by the spleen. The polymeric coated particles showed an initial fast signal drop in the liver with the following formation of a stable phase (after ~ 300s). The carboxydextran coated particles showed a slower, more linear signal drop in the liver while the PEG-coated USPIO circulated longest, with a late formation of a stable phase after ~40min. The absolute signal change was concentration dependent for all particles. Those results were in accordance to the relaxometric measurements, with a slight increase of ΔR2* in the liver of mice with PEG-USPIO after 24h. There was no significant difference between the two polymeric coated USPIO on day one and day two, while there was a small decrease of ΔR2* in the liver for only one polymeric coated particle after two weeks (n = 1). The relaxometric measurements in the liver of mice with pegylated and the carboxydextran coated particles showed a higher decrease of R2*. Cellular uptake was proven by ultra structural analysis. Conclusion: Coating materials have an important influence on the biodistribution of USPIO in vivo, which can be followed by DSC-MRI and it seems that the degradation of particles also dependents on the kind of coating material.

Disclosure of author financial interest or relationships:
N. Raabe, None; **T.M. Ernst**, None; **M. Heine**, None; **S.C. Salmen**, None; **B. Freund**, None; **R. Reimer**, None; **M.G. Kaul**, None; **G. Adam**, None; **H. Ittrich**, None.

Presentation Number **P 137**
Poster Session 2
September 19, 2013 / 15:15-15:15 / Room: Exhibit Hall B

Gd-Based Magnetic Resonance Imaging Agents Targeting the Prostate-Specific Membrane Antigen (PSMA)

Sangeeta Ray[1], *Tariq Shah*[1], *Matthew Rotz*[2], *Victoria Harrison*[2], *Richard Pracitto*[1], *Mrudula Pullambhatla*[1], *Keith MacRenaris*[2], *Marie-France Penet*[1], *Zaver M. Bhujwalla*[1], *Thomas J. Meade*[2], *Martin Pomper*[1], [1]*Radiology, Johns Hopkins University, Baltimore, MD, USA;* [2]*Chemistry, Northwestern University, Evanston, IL, USA. Contact e-mail: sray9@jhmi.edu*

MR-based molecular imaging has been hampered by the low sensitivity for detection of gadolinium (III) (Gd(III)) complexes relative to radiotracers and optical agents. However, outstanding spatial resolution, MR molecular imaging agents - if provided with a suitable signal amplification mechanism - are a worthy goal for imaging prostate cancer (PCa). Prostate-specific membrane antigen (PSMA) is an excellent target for imaging and therapy of PCa. We hypothesized that PSMA would be good target for MR molecular imaging agents because of the high target concentration per cell volume (~3 μM) and the extra-cellular location of the ligand binding site. Previously we demonstrated successful radiometal-based PET and SPECT imaging using radiolabeled, urea-based PSMA inhibitors in mice employing a tripartite strategy, containing a targeting moiety, a linker for pharmacokinetic tuning and chelator to enable attachment of radionuclides. Here we have used the same urea-linker construct with Gd(III) and increased the number of chelates (mono-, di- and trimeric Gd(III)) to optimize the sensitivity as well as binding affinity, to investigate systematically the possibility of PSMA-based MR imaging of PCa. Methods. Multi-step organic syntheses were employed in preparing monomeric **Gd-1**, dimeric **Gd-2** and trimeric **Gd-3** PSMA-targeted contrast agents. The T_1 relaxation rate of aqueous solutions of **Gd-1**, **Gd-2** and **Gd-3** were evaluated at 9.4 T using a saturation recovery method combined with fast T_1 SNAPSHOT-FLASH imaging (flip angle, 10^o, echo time, 2 ms). Images of 5 slices with 1mm slice thickness were acquired with 9 relaxation delays. The relaxivity, r1 (mM^{-1} s^{-1}), of the complexes was determined from the slope of the plot of $1/T_1$ vs. [agent] in PBS buffer. PSMA binding affinities of compounds of **Gd-1**, **Gd-2** and **Gd-3** were evaluated by a competitive protein binding assay. For cell imaging, isogenic human PCa cell lines PC3 PIP (PSMA+) and PC3 flu (PSMA-) were used. ICP analysis was done to determine [Gd] both in cells pellets (n=3) for each concentration at 1 and 2 h incubation times and for tissue samples using PSMA+ PC3 PIP and PSMA- PC3 flu tumor bearing mice (n=3) at 4 h and 24 h after intravenous injection of 150 mg/Kg of **Gd-1** per mouse. Results. All three compounds were synthesized in high yield and purity and demonstrate high binding affinities to PSMA (**Table 1**). Cell imaging studies of **Gd-1** revealed moderate contrast enhancement for the PSMA+ PC3 PIP cell pellet at 50 μM. ICP analysis showed high nonspecific uptake of Gd in PSMA- flu cells with increased concentration of **Gd-1**. A biodistribution study at 4 h and 24 h post-injection showed high and specific Gd-mediated contrast in PSMA+ PIP tumor compared to PSMA- flu tumor with PIP-to-flu tumor ratios of 4:1 and 3.6:1 at 4 h and 24 h post-injection, respectively. Conclusion.Three PSMA targeted, high-affinity, low-molecular-weight, Gd-based MR contrast agents were prepared. Monomeric **Gd-1** showed moderate contrast enhancement in PSMA+ cell pellets and specific Gd uptake in PSMA+ tumor at 4 h and 24 h post-injection. Detail in cellulo and in vivo characterization of **Gd-2** and **Gd-1** are currently in progress.

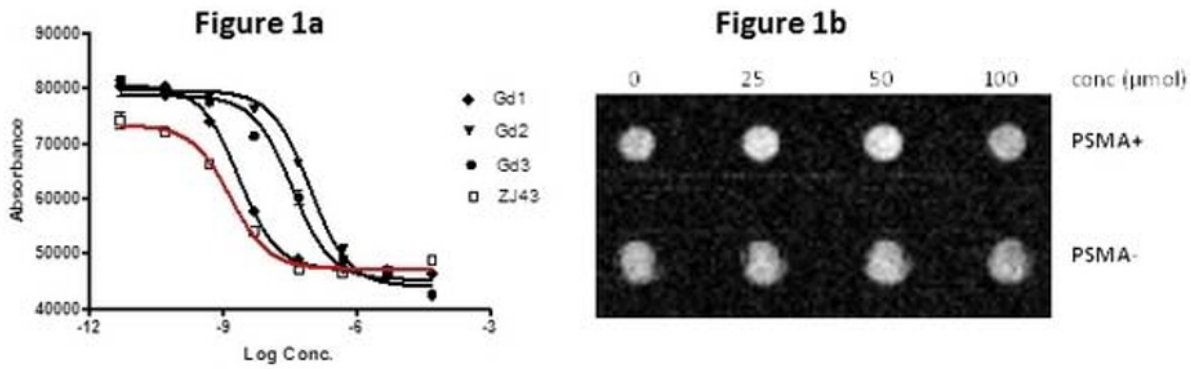

Figure 1a. IC50 curves for Gd-1, Gd-2, Gd-3 and ZJ43; Figure 1b. T1-weighted imaging of PSMA+ and PSMA- cell pellets of Gd-1

Table 1. Selected physical properties of **Gd-1**, **Gd-2**, **Gd-3**

Compound	Mol Wt	T_1 ($mM^{-1}s^{-1}$)	K_i [nM]*	95% CI of K_i
Gd-1	1230.40	2.65	0.43	0.30 nM to 0.55 nM
Gd-2	1819.13	5.44	18.18	14.07 nM to 22.16 nM
Gd-3	3651.03	12.47	7.19	5.17 nM to 10.01 nM

*ZJ43 (Ki 0.29; 95% CI of Ki 0.22 nM to 0.39 nM)

Disclosure of author financial interest or relationships:

S. Ray, None; **T. Shah**, None; **M. Rotz**, None; **V. Harrison**, None; **R. Pracitto**, None; **M. Pullambhatla**, None; **K. MacRenaris**, None; **M. Penet**, None; **Z.M. Bhujwalla**, None; **T.J. Meade**, None; **M. Pomper**, None.

Presentation Number **P 138**
Poster Session 2
September 19, 2013 / 15:15-15:15 / Room: Exhibit Hall B

Genetically Engineered Molecular Sensors for Non-Invasive Imaging of Glutamate in MRI

George L. Sun[1,4], *David V. Schaffer*[1,3], *Mikhail G. Shapiro*[1,2], [1]*Bioengineering, University of California, Berkeley, Berkeley, CA, USA;* [2]*Miller Institute, University of California, Berkeley, Berkeley, CA, USA;* [3]*Chemical and Biomolecular Engineering, University of California, Berkeley, Berkeley, CA, USA;* [4]*Electrical Engineering and Computer Science, University of California, Berkeley, Berkeley, CA, USA. Contact e-mail: mr_sunny@berkeley.edu*

Research aimed towards understanding nervous system function and improving the diagnosis and treatment of neurological and psychiatric disease will benefit from technologies enabling direct observation of neural signaling in living mammals. We are developing such technologies by engineering biological sensors for use in magnetic resonance imaging (MRI). Here, our aim is to image neural activity by monitoring glutamate neurotransmission via engineered protein contrast agents capable of selective imaging and genetic targeting to specific areas of the brain. - It has previously been shown that paramagnetic metalloproteins can be engineered to act as ligand-dependent MRI contrast agents. For example, directed-evolution was implemented to convert an iron-containing hydroxylase enzyme into a T1 sensor of the neurotransmitter dopamine (1). A key limitation of this first-generation reporter was its relatively low sensitivity, owing to the low relaxivity of its low-spin ferric iron. Here, we describe the development of a second-generation genetically engineered reporter based on a metalloenzyme containing high-spin manganese. Our protein of interest is glutamine synthetase (GS), which in a variety of organisms catalyzes the conversion of glutamate to glutamine. We cloned GS from Escherichia coli. Because this protein has previously been shown in biochemical studies to influence the paramagnetic relaxation of aqueous nuclei in a ligand-dependent fashion (2), we hypothesized that we could engineer GS to act as a sensor of the excitatory neurotransmitter glutamate (Figure 1A). - Here, we first demonstrate that GS produces glutamate-dependent effects on aqueous NMR signals under physiological conditions. At 1.5T the T1 and T2 relaxivities of GS in intracellular buffer were 12.2 mM^{-1} sec^{-1} and 29.0 mM^{-1} sec^{-1}, respectively. This T1 value is approximately 10 times higher than that of first-generation reporters (1). Upon the addition of glutamate, the T1 and T2 relaxivities increased by 12.4% and 49.3%, respectively. To engineer GS into a usable molecular sensor, we performed site-directed mutagenesis aimed at eliminating enzymatic activity and increasing specificity for glutamate over glutamine. The resulting mutant (mGS) had a 7-fold lower enzymatic function, an increase in glutamate affinity from K_d 3.1mM to .9mM, and a 30-fold reduction in glutamine binding. The measured T1 and T2 relaxivities of mGS in physiological buffer at 1.5T are 11.6 mM^{-1} sec^{-1} and 29.8 mM^{-1} sec^{-1}, and increased to 20.1 mM^{-1} sec^{-1} and 66.6 mM^{-1} sec^{-1}, respectively, in the presence of 10mM glutamate. At 60 μM of mGS, the addition of 10mM glutamate produced 32.6% and 37.1% changes in T1and T2 times (Figure 1B). - Our current work focuses on characterizing the expression and contrast properties of a codon-optimized version of mGS in mammalian cells, and its eventual use in animal models of neurological function and disease. References: 1. Shapiro, M.G. et al, Nature Biotechnology 28, 264-70 (2010). 2. Welder, F.C. et al, Biochemistry 15, 536-542 (1976)

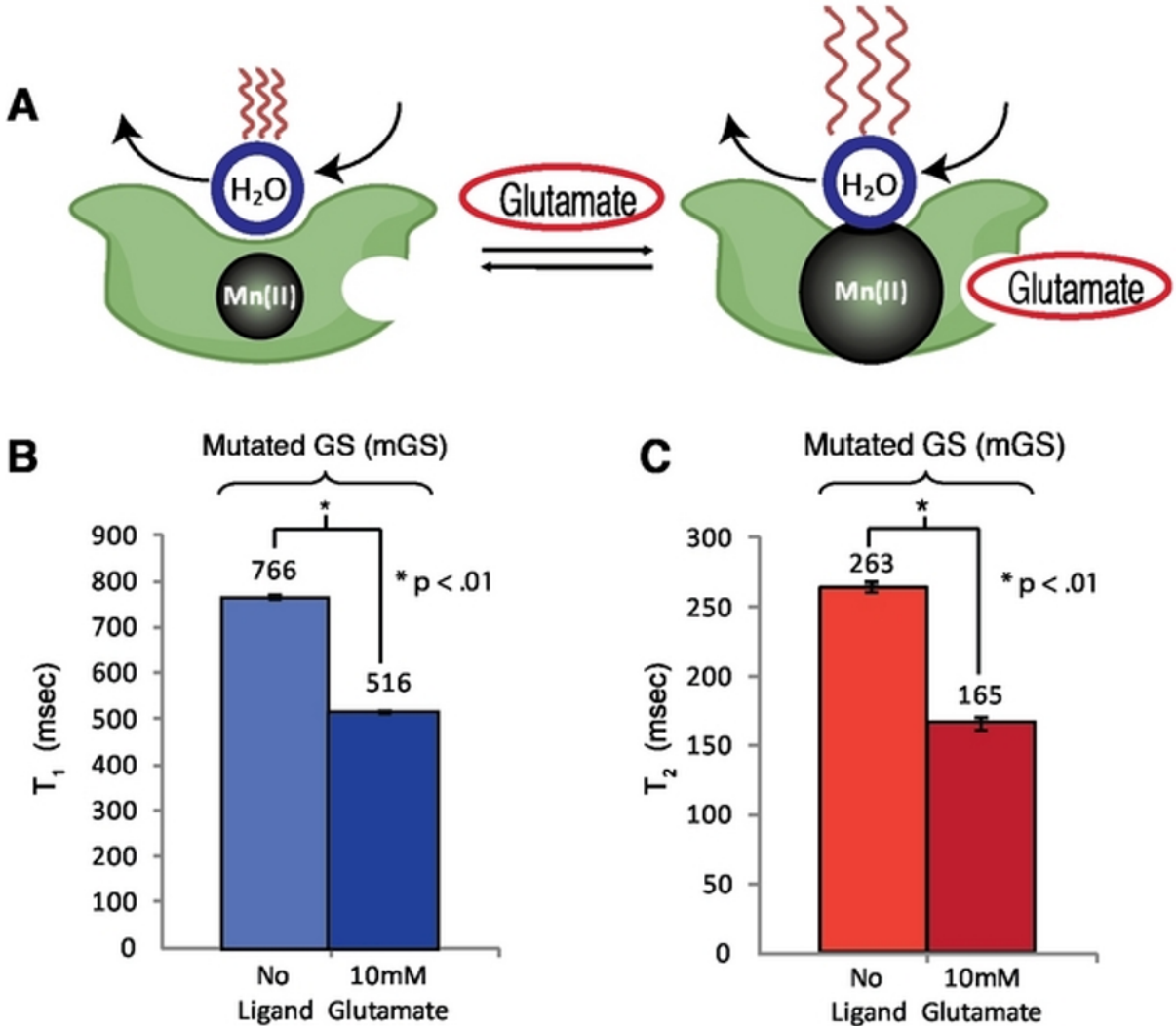

Engineered mutant glutamine synthetase (mGS) acts as a T1 and T2 sensor of glutamate. (A) Schematic depiction of a hypothetical reporter mechanism in which glutamate binding to mGS changes the interaction between its active site manganese and associated water molecules, thereby altering relaxivity. (B) T1 and T2 times measured in a physiological buffer at 1.5 T with 60μM mGS and either zero or 10mM glutamate.

Disclosure of author financial interest or relationships:
G.L. Sun, None; **D.V. Schaffer**, NIH, NSF, CIRM, Grant/research support; Bio-Rad, Avalanche, CellGS, Consultant; Valitor, Inc., Stockholder; **M.G. Shapiro**, Foundation Medicine, Stockholder; Afferent Pharmaceuticals, Stockholder; True & Company, Stockholder .

Presentation Number **P 139**
Poster Session 2
September 19, 2013 / 15:15-15:15 / Room: Exhibit Hall B

A pH-responsive PARACEST agent having a water-exchange CEST signal beyond the MT window

Xiaojing Wang[1,2], *Yunkou Wu*[2], *Piyu Zhao*[1], *Dean Sherry*[2,1], [1]*Chemistry, University of Texas at Dallas, Dallas, TX, USA;* [2]*Advanced Imaging Research Center, UT Southwestern Medical Center, Dallas, TX, USA. Contact e-mail: xiaojing.wang@utsouthwestern.edu*

Introduction: A relatively new class of MRI contrast agents (CAs) based on chemical exchange saturation transfer (CEST) offers some advantages over conventional Gd3+ agents. However, for in vivo imaging, virtually all CEST signals suffer interference from the tissue magnetization transfer (MT) signal associated with macromolecules and membranes in biological tissues. This can compromise CEST detection and quantification of both endogenous and exogenous agents. Methods: Our long-term goal is to image tissue pH without activating the broad MT signal, a new pH sensor based on the Tb(III) complex illustrated in Fig. 1 was prepared and characterized. The bis(n-butyl phosphonate) side-chain groups in this complex were introduced to slow water exchange between the inner-sphere of the central Tb3+ ion and bulk water while maintaining the pH sensitive advantages of phenolic arm.[1] The CEST properties of this new agent were measured over a range of pH values from 5 to 8 and at temperatures from 298 to 310K. The bound water lifetime (τM) of the complex was determined by the Swift-Connick T2exch method.[2] Results: The Tb3+-coordinated water CEST exchange peak in the complex was located in a region ~500 ppm upfield from the bulk water peak. The sensor responded to changes in pH similar to the previously published Eu3+ complex,[1] but, in this case, the CEST exchange signal shifted much more dramatically with changes in pH, ranging from -550 ppm at pH 8 to -494 ppm at pH 5 at 310 K. These dramatic chemical shift differences provide a direct readout of pH that is independent of agent concentration. The bound water lifetime (τM) as measured by T2exch was 104 μs at pH 5 and 53 μs at pH 8. Conclusions: Given that the chemical shift (ω) of this Tb3+-bound water exchange CEST peak is well outside the typical MT window (±100 ppm), the use of this new agent for imaging tissue pH in vivo should be dramatically simplified. Toxicity and solubility tests of the new agent are underway. References: [1] Y. Wu, T. C. Soesbe, G. E. Kiefer, P. Zhao, and A. D. Sherry, J. Am. Chem. Soc. 132, 14002-14003 (2010). [2] T. C. Soesbe, M. E. Merritt, K. N. Green, F. A. Rojas-Quijano, and A. D. Sherry, Magn. Reson. Med. 66, 1697-1703 (2011).

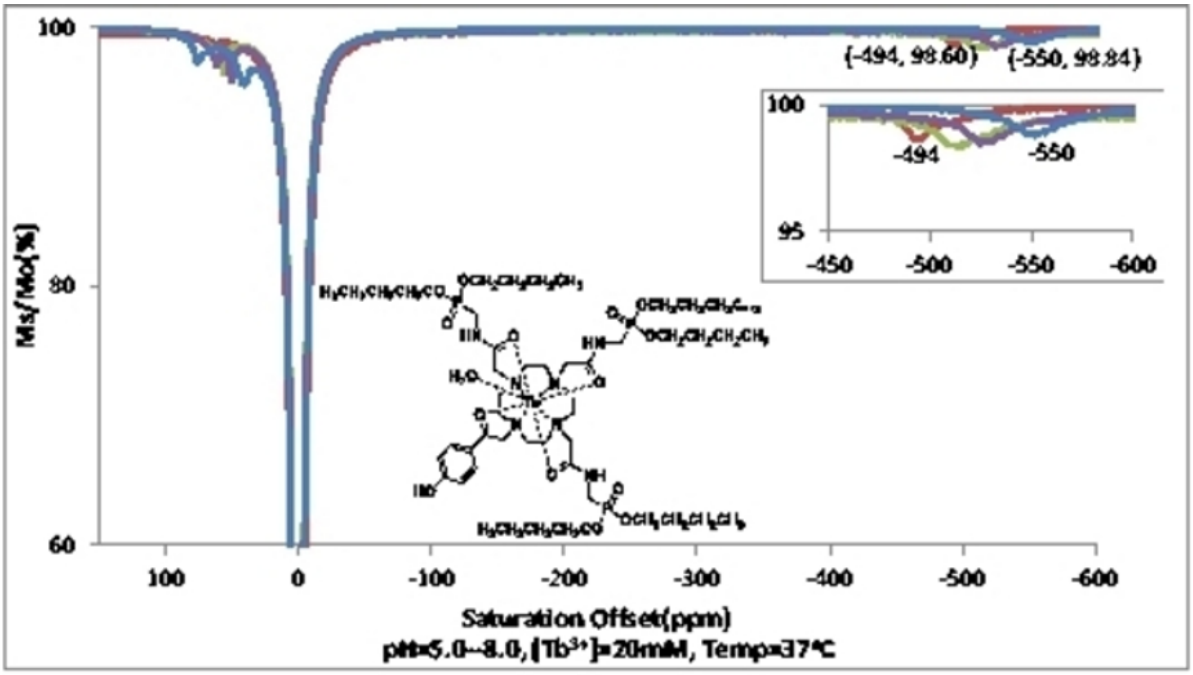

Disclosure of author financial interest or relationships:
X. Wang, None; **Y. Wu**, None; **P. Zhao**, None; **D. Sherry**, None.

Presentation Number **P 140**
Poster Session 2
September 19, 2013 / 15:15-15:15 / Room: Exhibit Hall B

Designing a novel class of protein-based MRI contrast agents (ProCAs) for molecular imaging of disease biomarkers

Jingjuan Qiao, Fan Pu, Shenghui Xue, **Jenny Yang**, *Georgia State University, Atlanta, GA, USA. Contact e-mail: jenny@gsu.edu*

MRI is a promising non-invasive imaging technique with high depth penetration and high spatial resolution. MRI contrast agents with high metal binding affinity, high relaxivity, low toxicity and targeting capabilities are highly desired for the preclinical and clinical imaging. ProCAs are newly designed MRI contrast agents with high relaxivity and tumor targeting property. The novel protein-based MRI contrast agents, ProCA, with one or multiple Gd3+ binding sites are designed based on the native protein. By optimizing Gd3+ binding ligands, the relaxivity of ProCA per particle is significantly increased compared with that of Gd-DTPA. Furthermore, we have successfully designed targeted MRI contrast agents to specifically recognize various biomarkers such as gastric release peptide receptors (GRPR), and HER2/EGFR overexpressed in different types of cancers and cell types without using antibodies. These developed targeting MRI contrast agent exhibit strong receptor-specific MRI enhancement both in tumor cells and xenograft mice models with desirable penetration of tissue and the endothelial boundary, which is much better in clearance and targeting than previously reported albumin or antibody crosslinked with Gd-DTPA. Moreover, the capability to spatially and temporally visualize intratumoral distribution and the safety profile for biostability and toxicity in preclinical models will be discussed. We can also use our targeted contrast agent to monitor the tumor progression and drug treatment. Tumor enhancement in MRI was further confirmed by immunofluorescence, immunohistochemistry analysis and ICP-OES. ProCAs present high stability, no cell toxicity and acute toxicity and proper blood circulation time for MR angiography. References: Jinjuan Qiao, Shunyi Li, and Jenny J. Yang. HER-2 Targeted Molecular MR Imaging Using a de vovo Designed Protein Contrast Agent. PLOS ONE (2011) Mar 24;6(3):e18103.PMID: 21455310 Lixia Wei, Shunyi Li, Jenny J. Yang, and Zhi-Ren Liu, Design of protein-based MRI contrast agent for molecular imaging of prostate cancer. Molecular Imaging and Biology (2010). 32(5):521-5, Jun 24. [Epub ahead of print]PMID: 20574851 Jenny J. Yang, Jianhua Yang, Lixia Wei, and Zhi-Ren Liu, Rational Design Protein Based MRI Contrast Agents with High Relaxivity Journal of the American Chemical Society (2008), 130(29):9260-7. Epub 2008 Jun 25. Shenghui Xue, Jingjuan Qiao, Jie Jiang, Lixia Wei, Shuanyi Li, Kendra Hubbard, Zhiren Liu, Jenny J. Yang, Design Protein-based MRI Contrast Agent with High Dose Efficiency and Capability for Molecular Imaging of Biomarkers. Medical Research Review, (2010), Accepted. Supported in part by NIBIB 1R01EB007268, NCI 1R21CA120181-01A1, and Pardee foundation.

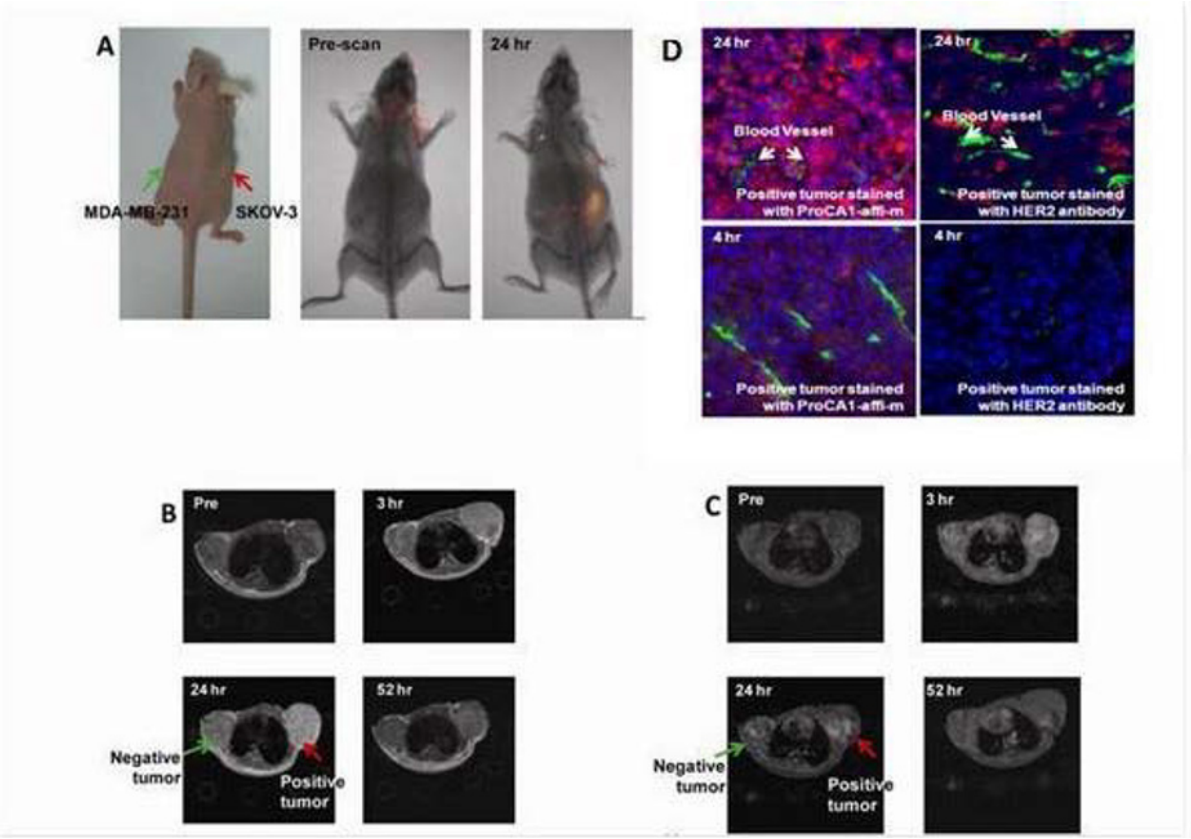

Disclosure of author financial interest or relationships:
J. Qiao, None; **F. Pu**, None; **S. Xue**, None; **J. Yang**, None.

Presentation Number **P 141**
Poster Session 2
September 19, 2013 / 15:15-15:15 / Room: Exhibit Hall B

High MRI Performance Fluorescent Mesoporous Silica-coated Magnetic Nanoparticles for Tracking Neural Progenitor Cells in Ischemic Mouse Model

Lu Zhang, **Chunfu Zhang**, *Med-X Research Institute, Shanghai Jiao Tong University, Shanghai, China. Contact e-mail: cfzhang@sjtu.edu.cn*

Multifunctional probes with high MRI sensitivity and efficiency for cell labeling is highly desirable for MR cell imaging. Herein, we fabricated fluorescent mesoporous silica-coated superparamagnetic iron oxide nanoparticles (fmSiO4@SPIONs) for neural progenitor cell (C17.2) MR imaging. fmSiO4@SPIONs was discrete and uniform in size, with clear core-shell structure. The magnetic core size was about 10 nm and the fluorescent mesoporous silica coating layer was around 20 nm. Compared with fluorescent dense silica-coated SPIONs (fdSiO4@SPIONs) with the similar size, fmSiO4@SPIONs demonstrated enhanced MR sensitivity and improved cell labeling efficiency. When implanted into stroke mice intracerebrally, contralateral to the ischemic hemisphere, a small amount of labeled cells were able to be tracked migrating to the lesion sites by a clinical MRI scanner (3T). More impressively, even administered intravenously, the labeled cells could also be monitored homing to targets, due to the high sensitivity and cell labeling efficiency of fmSiO4@SPIONs. MRI observations were corroborated by histological studies of the brain tissues. Our study demonstrated that fmSiO4@SPIONs was highly effective for cell imaging and hold great promise for MRI cell tracking in future.

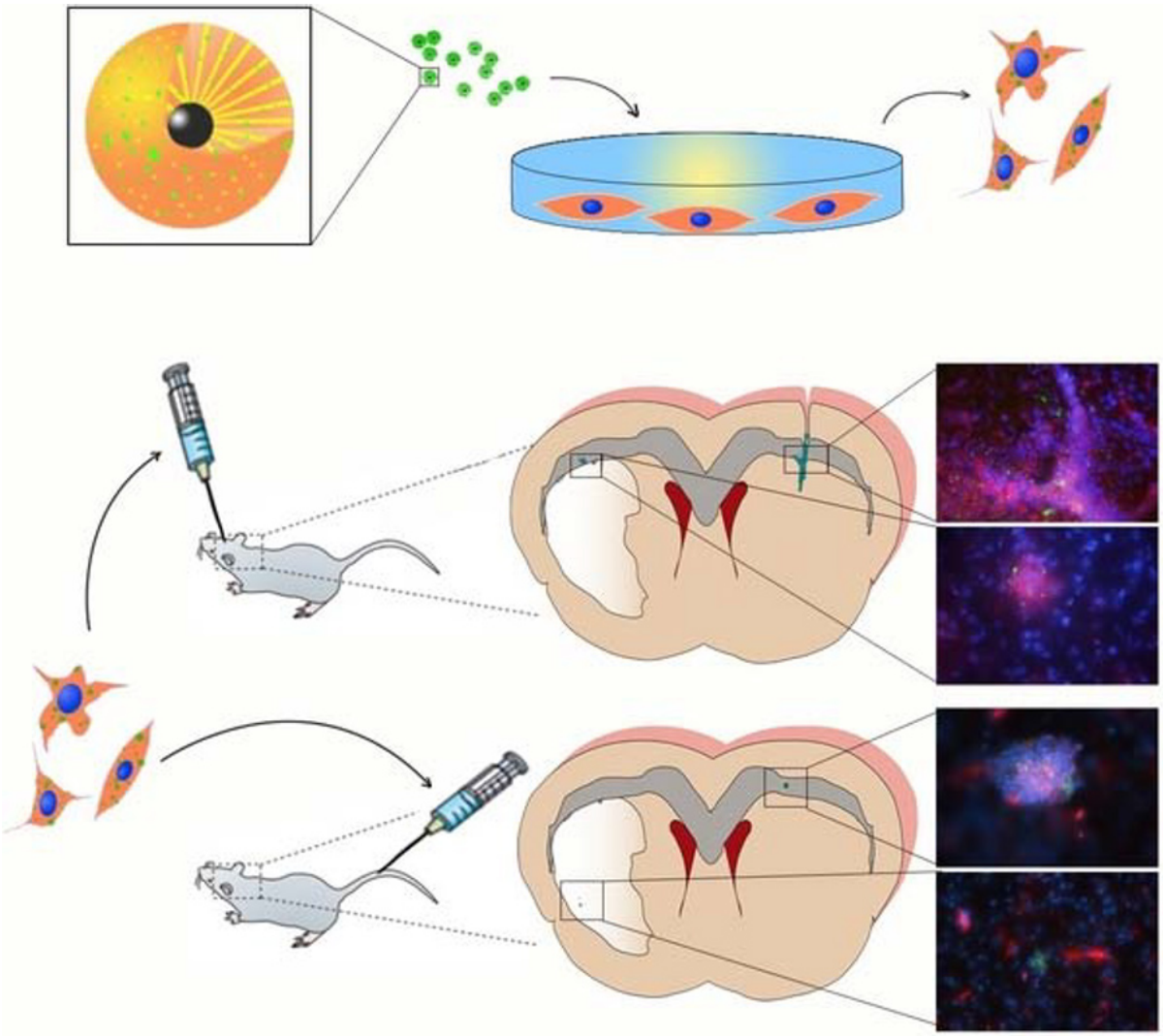

Figure 1 Scheme of high MRI performance mesoporous silica coated SPIONs for neuro stem cell labeling and tracking in stroke mouse model

Disclosure of author financial interest or relationships:
L. Zhang, None; **C. Zhang**, None.

Presentation Number **P 142**
Poster Session 2
September 19, 2013 / 15:15-15:15 / Room: Exhibit Hall B

Glioma Cells Transfected with mms6 Produce Strong Increase in Transverse Relaxivity In Vitro

Xiaoyong Zhang, *Brenda Robledo, Steven Harris, Sha Wang, Xiaoping Hu, Biomedical Engineering, Emory University, Atlanta, GA, USA. Contact e-mail: xzhan78@emory.edu*

Introduction Capable of capturing non-invasive, deep tissue images with high spatial resolution, MRI is an ideal imaging modality for in vivo studies of cancer cell proliferation, metastasization, and treatment. However, cancer cells must generate MR contrast in order to be localized. In this work, we sought to provide a gene expression marker for MRI based on bacterial magnetosomes, tiny magnets produced by naturally occurring magnetotactic bacteria. A gene, mms6, originally identified in magnetotactic bacteria, expresses a protein that is thought to initiate magnetite crystal nucleation within specialized membrane-bound organelles called magnetosomes. We hypothesized that transfecting glioma cells with mms6 would lead to magnetite formation and MR contrast. Results and Discussion Following three days of incubation in iron supplemented media, whole cell histology showed greater iron staining in mms6 positive cells (9L4S) compared to control cells (9L), suggesting increased iron uptake by these cells (Figure 1). ICP-Mass Spectrometry showed an 8.5 fold increase in intracellular iron in 9L cells that had been cultured in media supplemented with iron as compared to 9L cells cultured with no iron supplement. Under the same culture conditions, 9L4S showed a 24.7 fold increase in intracellular iron (Figure 1), 2.8 times more iron storage than the control cells. In order to investigate the location and structure of the intracellular iron, electron micrographs were acquired. Unlike in the 9L cells, particles can be found throughout the 9L4S cytoplasm, both within and outside of membrane-enclosed structures (Figure 2). To determine whether the higher density of nanoparticles observed in the electron micrographs would enhance MR contrast, the transverse relaxivity (R2) was measured. The percent increase in R2 between cells cultured without an iron supplement and the same cells cultured with an iron supplement was calculated. 9L4S showed statistically significant ($p < 0.05$) changes in R2: a 57.1% increase in R2 at 3 T and a 124.3% increase in R2 at 9.4 T (Figure 3). This increase in R2 with iron supplementation was not observed in 9L cells, which produced only a 7.8% and 18.6% increase in R2 at 3 T and 9.4 T, respectively. We then calculated the change in R2 between 9L cells and 9L4S cells, both of which had been cultured in media supplemented with iron. Relative to 9L cells, 9L4S cells showed a 46.6% and 90.6% increase in R2 at 3 T and 9.4 T, respectively. Conclusion Our results show that mms6 positive cancer cells produce significant MR contrast, possibly due to increased intracellular iron accumulation and magnetite formation. Our results suggest that mms6 may function as an MR reporter gene for cancer studies. Acknowledgements Work supported by NIH U01HL08071 and the Georgia Research Alliance.

Disclosure of author financial interest or relationships:
X. Zhang, None; **B. Robledo**, None; **S. Harris**, None; **S. Wang**, None; **X. Hu**, Siemens Medical Solutions, Grant/research support .

Presentation Number **P 143**
Poster Session 2
September 19, 2013 / 15:15-15:15 / Room: Exhibit Hall B

Ortho-phenylene phosphino-boranes for harvesting 18F fluoride anions in aqueous solutions and in vivo stability studies

Kantapat Chansaenpak[1], *Shuanglong Liu*[2], *Peter S. Conti*[2], *Zibo Li*[2], *Francois P. Gabbai*[1], [1]*Chemistry, Texas A&M University, College Station, TX, USA;* [2]*Radiology, University of Southern California, Los Angeles, CA, USA. Contact e-mail: kantapat.chansaenpak@mail.chem.tamu.edu*

Fluorine-18 (18F) is a short-lived radionuclide that has become an important label for radiotracers used in Positron Emission Tomography (PET). Since 18F has half-life of just under two hours, the synthesis and purification methods of [18F]radiotracers need to be fast and efficient to maximize activity. As part of our continuing research, we have decided to study the radiofluorination of the phosphonium aryltrifluoroborates 1 and 2 in aqueous solutions. We found that both 1 and 2 undergo 19F-18F isotopic exchange when dissolved in an acidic (pH =1.5) [18O]water solution containing [18F]fluoride. The resulting radiolabeled products [18/19F]1 and [18/19F]2 were obtained in high radiochemical yields (>87%). This synthetic protocol is significant because of its simplicity. Moreover, we found that [18/19F]1 and [18/19F]2 are stable in vivo thus indicating BF3 stabilization by proximal phosphonium group. The [18/19F]2 has better clearance activity, possibly because of its increased hydrophilicity. Encouraged by these results, we have also prepared the carboxylic functionalized phosphonium trifluoroborates 3 and 4. These compounds contain an amine-reactive carboxylic acid functionality that we are currently using for the construction of conjugates.

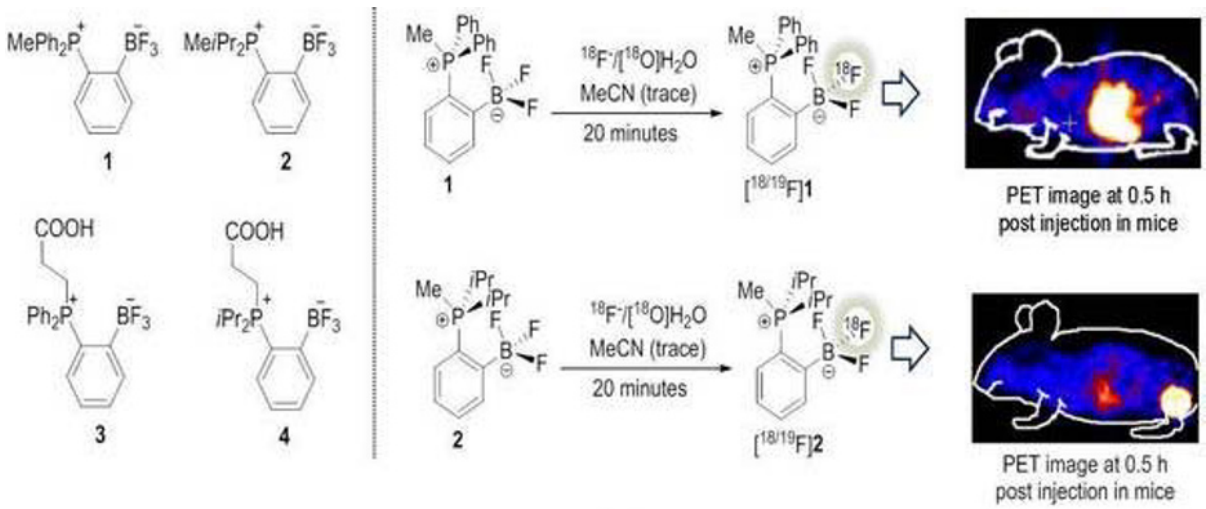

Scheme 1 Direct ^{18}F–^{19}F isotopic exchange reactions of **1** and **2**

Disclosure of author financial interest or relationships:
K. Chansaenpak, None; **S. Liu**, None; **P.S. Conti**, None; **Z. Li**, None; **F.P. Gabbai**, None.

Presentation Number **P 144**
Poster Session 2
September 19, 2013 / 15:15-15:15 / Room: Exhibit Hall B

Alternative Chelators for Zirconium-89: Radiolabeling and Evaluation of 3,4,3-(LI-1,2-HOPO) and 3,4,3-LICAM

Melissa A. Deri[1,2], *Shashikanth Ponnala*[3], *Jason S. Lewis*[1], *Lynn C. Francesconi*[2], [1]*Radiology, Memorial Sloan-Kettering Cancer Center, New York, NY, USA;* [2]*Chemistry, Hunter College and the Graduate Center of the City University of New York, New York, NY, USA;* [3]*Chemistry, Hunter College of the City University of New York, New York, NY, USA. Contact e-mail: derim@mskcc.org*

Purpose: Zirconium-89 is useful for antibody-based PET tracers due to its physical half-life of 78.41 h matching the biological half-life of antibodies. The current widely used chelator for ^{89}Zr is desferrioxamine (DFO), however there is evidence of in vivo release of ^{89}Zr which can be observed as bone uptake in mice.[1] A more robust chelation system for ^{89}Zr could eliminate the release of the osteophilic $^{89}Zr^{4+}$ cation in vivo and make for a safer PET tracer with less dose to non-target tissues. We have synthesized a pair of hydroxypyridinone (HOPO) and catechol based ligands for evaluation as potential chelators for ^{89}Zr. **Methods:** The ligands 3,4,3-(LI-1,2-HOPO) and 3,4,3-LICAM were selected from a library of published Pu chelators[2] on the basis of the fact that Zr and Pu are known to have similar chemistries. These ligands were synthesized using slightly modified procedures[3] in order to obtain extremely pure products suitable for tracer level experiments and radiolabeled with ^{89}Zr. The compound was radiolabeled with ^{89}Zr-oxalate under various conditions in order to achieve optimization. The radiolabeling was monitored using ITLC with further analysis of the ^{89}Zr-ligand complexes by HPLC and SEC. Stability studies were carried out over seven day incubations in human serum at 37°C. The non-radioactive complexes were prepared and characterized using NMR, ESI-MS, and HPLC. **Results:** The 3,4,3-(LI-1,2-HOPO) ligand has been successfully synthesized, purified, and radiolabeled with ^{89}Zr. The identity of the ^{89}Zr-ligand complex has been confirmed through HPLC co-elution with its non-radioactive analogue. The ^{89}Zr-ligand complex demonstrates high labeling efficiency and comparable stability to ^{89}Zr-DFO. Radiolabeling of 3,4,3-(LI-1,2-HOPO) initially results in two distinct species, one of which converts to the other over time. The precise nature of these two species is presently being investigated. The 3,4,3-LICAM ligand has been synthesized and the evaluation of its radiolabeling properties is currently underway. **Conclusions:** We successfully synthesized highly pure 3,4,3-(LI-1,2-HOPO) and 3,4,3-LICAM as part of an investigation of novel chelation strategies for ^{89}Zr. We have shown that the HOPO-based ligand has an affinity for ^{89}Zr and can be radiolabeled in a straightforward manner. Further evaluation of both Zr chelators is in progress. **References:** [1] Deri M. A.; Zeglis, B. M.; Francesconi, L. C.; Lewis, J. S. Nucl. Med. Biol. 2013, 40, 3-14. [2] Gorden, A. E. V.; Xu, J.; Raymond, K. N.; Durbin, P. Chem. Rev. 2003, 103, 4207-4282. [3] Xu J.; Durbin, P. W.; Kullgren, B.; Ebbe, S. N.; Uhlir, L. C.; Raymond, K. N. J. Med. Chem. 2002, 45, 3963-3971.

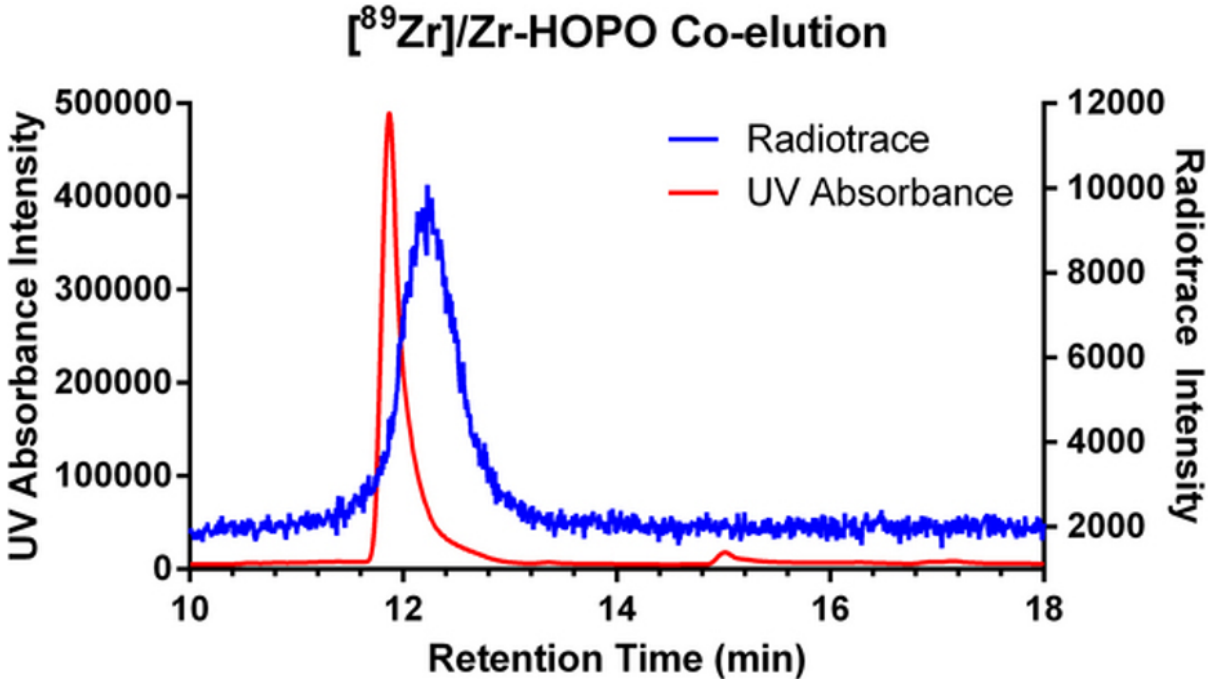

HPLC chromatogram of the co-elution of ^{89}Zr-labeled 3,4,3-(LI-1,2-HOPO) and its non-radioactive analogue.

Disclosure of author financial interest or relationships:
M.A. Deri, None; **S. Ponnala**, None; **J.S. Lewis**, None; **L.C. Francesconi**, None.

Presentation Number **P 145**
Poster Session 2
September 19, 2013 / 15:15-15:15 / Room: Exhibit Hall B

Impact of linkers on in vivo biodistribution of 64Cu/NOTA GRPR antagonists

Veronique Dumulon-Perreault, *Lidia Matei, Nematallah Mansour, Samia Ait-Mohand, Jean-François Beaudoin, Brigitte Guerin, Sherbrooke's Molecular Imaging Center (CIMS), Sherbrooke, QC, Canada. Contact e-mail: Veronique.Dumulon-Perreault@USherbrooke.ca*

Background: Recent studies have shown that radiolabelled gastrin releasing peptide receptors (GRPR) antagonists (Demobesin 1, [(D)Phe6,Leu-NHEt13,des-Met14]BNN(6-14)]) may be preferable to agonists for targeted PET imaging GRPR-positive tumors. The aim of this study was to investigate the influence of different charges to the linker (LK) on tumor uptake and excretion kinetics of the 64Cu-labeled NOTA-LK-Demobesin 1. Method: NOTA-LK-Demobesin 1 peptides bearing neutral (PEG), dicationic (2-aminoethyl-piperazine-1-carboxylic acid) or dianionic (amino-hexanedioic-1-acid) linkers were synthesized on solid phase support and radiolabeled with 64Cu. In vitro GRPR-binding affinities were determined with competitive binding assays on PC3 human prostate cancer cells. In vivo stability of radiolabeled compounds was assessed directly by radio-TLC from blood sample taken 60 min post injection in Balb/c mice. In vivo biodistribution kinetics were measured in PC3 tumor-bearing Balb/c nude mice by μ-positron emission tomography [μPET] imaging. Results: The 64Cu/NOTA-Demobesin 1 conjugates were prepared with purity of >95%. The inhibition constants of all Demobesin radiopeptides were comparable and in the low nanomolar range. The 64Cu-labeled peptides were stable up to1 hour in vivo. The tumor uptake was not significantly different between the three radiopeptides. However, the tumor-to-muscle ratio was slightly higher for the peptide with the dianionic linker. The maximum liver uptake values are similar for the three 64Cu-labeledNOTA-LK-Demobesin 1 peptides, but the tumor-to-liver ratio is higher at >30 min postinjection for the radiopeptide with the dicationic linker. Conclusions: The results from biodistribution studies show that excretion kinetics of the 64Cu-labeled NOTA-LK-Demobesin 1 can be modified with various linkers. Among the three linkers, the dicationic linker is especially useful in minimizing the radioactivity accumulation in liver.

Disclosure of author financial interest or relationships:
V. Dumulon-Perreault, None; **L. Matei**, None; **N. Mansour**, None; **S. Ait-Mohand**, None; **J. Beaudoin**, None; **B. Guerin**, None.

Presentation Number **P 146**
Poster Session 2
September 19, 2013 / 15:15-15:15 / Room: Exhibit Hall B

Development of an Imaging Probe for Molecular Imaging of Ebolavirus

Brit J. Hart[1], Ibeawuchi Oparaocha[1], Sarah M. Cheal[2], Gary L. Griffiths[3], Isis Alexander[1], Bernardo Rosa[1], Oscar J. Rojas[1], Reed Johnson[4], Joseph E. Blaney[4], Svetlana I. Chefer[1], Gabriela Kramer-Marek[5], Gerald Jennings[1], Peter B. Jahrling[1,4], **Julie Dyall**[1], *[1]DCR/IRF, NIH/NIAID, Frederick, MD, USA; [2]Department of Radiology, Memorial Sloan -Kettering Cancer Center, New York, NY, USA; [3]Imaging Probe Development Center, NIH/NHLBI, Bethesda, MD, USA; [4]Division of Intramural Research, NIH/NIAID, Bethesda, MD, USA; [5]Division of Radiotherapy and Imaging, The Institute of Cancer Research, Sutton, United Kingdom. Contact e-mail: dyallj@niaid.nih.gov*

Introduction: In the virology field, molecular imaging will allow in vivo monitoring of molecular and cellular processes during progression of viral infections. The imaging techniques can be applied to pathogenesis studies, evaluation of therapies, and diagnostics of infectious diseases. The objective of this study is to demonstrate the specificity and sensitivity of a molecular imaging probe in order to detect Ebola virus (EBOV) infection in vivo using optical imaging. The antibody KZ52-IgG1 with high affinity against ebolavirus glycoprotein (GP) has been generated previously (T. Maruyama et al., 1999). This study assesses the value of a labeled antibody against EBOV as a probe. Rather than infect the mouse with EBOV that will be recognized by the antibody, a GP-expressing tumor was implanted in the mouse. Thus, the procedure allows us to evaluate the use of an antibody as a potential probe without the need for high containment. Material and Methods: Tumor cells (1x10E7) transduced either with an adenovirus containing GP (MOI 1) (GP+ tumor) or mock infected (GP- tumor) were implanted in the shoulder of nude mice, resulting in subcutaneous palpable tumors close to the body surface. The antibody KZ52-IgG1 was labeled with IRDye800CW NHS Ester (LI-COR, NE) and injected in the tail vein on day 2 or 3 after tumor introduction. 24h after probe injection, optical imaging was performed using the IVIS-Caliper (Luminar-XR) with the filter pair 745 and 831 for excitation and emission, respectively. Following an in vivo optical imaging procedure tumors and tissues were harvested and ex vivo imaging was performed. For quantitation, ROIs were placed on GP+ and GP- -tumors and organs, average radiant efficiency was calculated within each ROI and the GP+-tumor/tissues ratios were determined. Results: Figure 1A and 1B show NIR fluorescent in vivo and ex vivo images on day 4 after tumor injection. The GP+-tumor could be clearly visualized and differentiated from surrounding normal tissue at 24h p.i. The ex vivo image of the tissues was used for quantification analysis of the ROIs. The GP+-tumor-to-tissue ratios are depicted in Fig 1C. The control tumor showed uptake, but it was consistently lower than uptake in the GP+-tumor (1.3 to 2.2 fold). The signal in control tumor may represent nonspecific retention of the probe due to the leaky vasculature in tumor tissue. A prominent signal was observed in the liver as a result of slow antibody (150kD) clearance. With continued development we hope to improve clearance of the probe and increase its sensitivity. Labeling KZ52-IgG1 with a radioisotope will allow adding in vivo PET imaging modality and help to improve clearance and signal-to-noise ratios. This is the first step in a process that will lead to a greater understanding of designing suitable probes for imaging to be used in studies of infectious diseases. Probes suitable for in vivo imaging will have great value for gathering information on disease pathogenesis in order to better design treatment and prevention strategies.

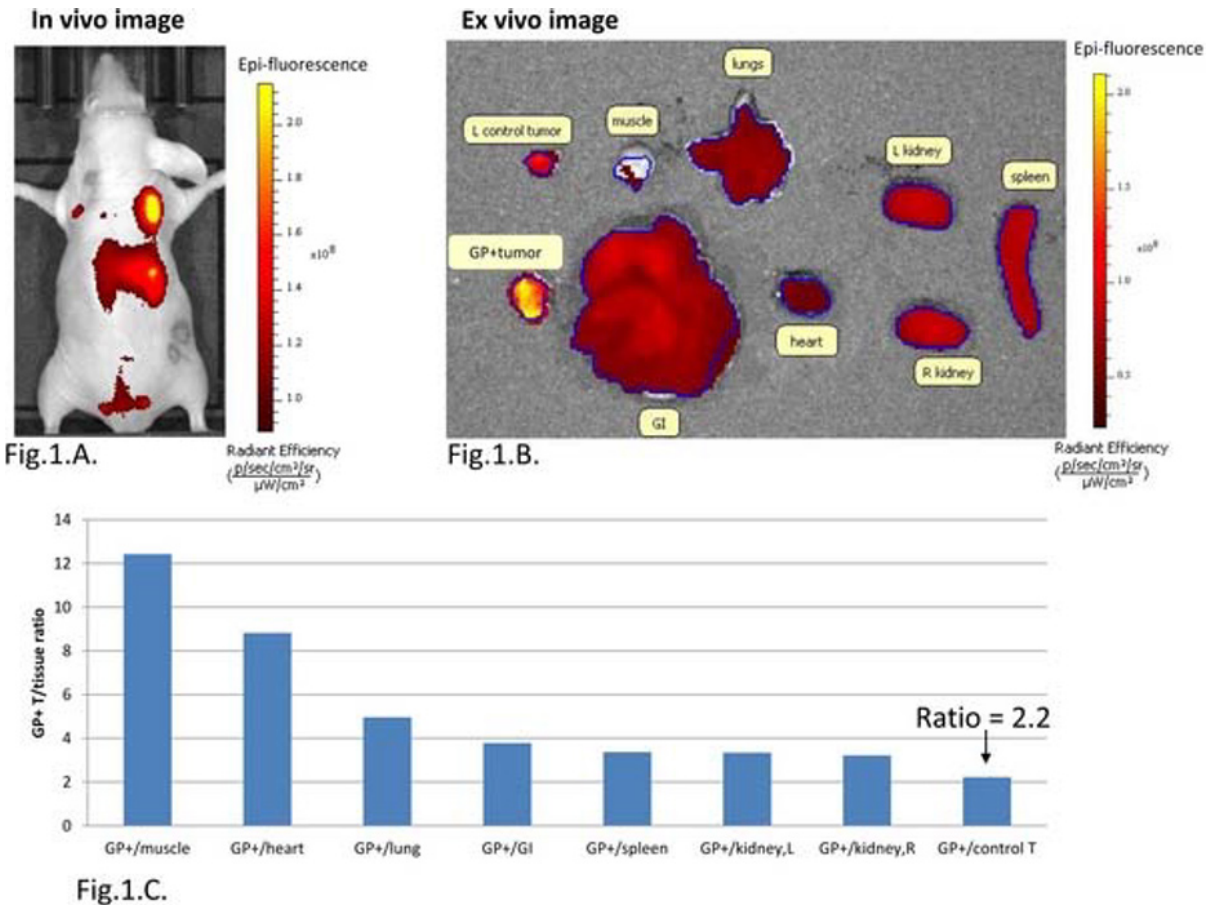

Fig. 1. GP+-tumor showed increased uptake of the KZ52-IgG1-probe on day 4 after tumor injection. A. In vivo image, 24h after probe injection. B. Ex vivo image of harvested organs, 24h after probe injection. C. GP+ tumor-to-tissue ratios of the average radiant efficiency of ROIs in Fig.1B.

Disclosure of author financial interest or relationships:

B.J. Hart, None; **I. Oparaocha**, None; **S.M. Cheal**, None; **G.L. Griffiths**, None; **I. Alexander**, None; **B. Rosa**, None; **O.J. Rojas**, None; **R. Johnson**, None; **J.E. Blaney**, None; **S.I. Chefer**, None; **G. Kramer-Marek**, None; **G. Jennings**, None; **P.B. Jahrling**, None; **J. Dyall**, None.

Presentation Number **P 147**
Poster Session 2
September 19, 2013 / 15:15-15:15 / Room: Exhibit Hall B

89Zr-transferrin, a versatile tool for the detection and monitoring of cancer

Michael J. Evans, *Jason P. Holland, Charles L. Sawyers, Jason S. Lewis, Memorial Sloan Kettering Cancer Center, New York, NY, USA. Contact e-mail: evansm1@mskcc.org*

Owing to elevated nutrient demand, many cancers are avid for the iron transport protein transferrin, a phenomenon most successfully exploited in oncology with 67Ga-citrate imaging of lymphomas. To more fully exploit this tumor-targeting strategy for PET, we developed 89Zr-transferrin (89Zr-Tf). Because the transferrin receptor is a target gene of the oncogenic transcription factor MYC, we have shown that 89Zr-Tf can be used to measure the biology of MYC, a finding with widespread implications for staging and treatment monitoring of several malignancies (e.g. prostate cancer, lymphoma, breast cancer). Of note, 89Zr-Tf can be used to interpret the pharmacology of JQ1, one of an emerging class of anticancer therapies targeting the epigenetic protein BRD4 to suppress MYC function. While 89Zr-Tf uptake can be coupled almost exclusively to MYC activity in some cancers, other malignancies are avid for this radiotracer in an ostensibly MYC-independent fashion. For instance, we have shown 89Zr-Tf demarcates many models of glioblastoma multiforme (GBM, a malignancy not commonly driven by MYC), and even small orthotopic lesions are detectable with this radiotracer. Although the biological basis for 89Zr-Tf avidity in this cancer remains to be determined, that the radiotracer detects many genetically discrete models of GBM (and uptake in normal brain tissue is negligible) suggests it could be a powerful tool to generically distinguish malignant versus normal tissue. In summary, these findings point to the potential for the widespread use of this radiotracer in cancer diagnostics, and pending its translation, its ultimate clinical utility can be assessed.

Disclosure of author financial interest or relationships:
M.J. Evans, None; **J.P. Holland**, None; **C.L. Sawyers**, Aragon, Consultant; Aragon, Stockholder; Novartis Board of Directors, Other financial or material support; **J.S. Lewis**, None.

Presentation Number **P 148**
Poster Session 2
September 19, 2013 / 15:15-15:15 / Room: Exhibit Hall B

The Effect Of PEGylation And Dendronization On Biodistribution Of Melanoma-Targeting Ligands Studied In Vivo By Nuclear Medical Imaging

Delphine Felder-Flesch, *IPCMS, UMR CNRS-UDS 7504, Strasbourg, France. Contact e-mail: Delphine.Felder@ipcms.u-strasbg.fr*

The main input of today's Nanotechnology in the biomedical field is to allow real progress in achieving temporal and spatial site-specific drug delivery, local therapy, and imaging. In this respect, creating nano-objects not only displaying very important targeting capacities thanks to a multivalent grafting of biological effectors (multivalent system), but also allowing the vectorization of diagnostic or therapeutic agents through the complexation of very diverse metallic ions is of great interest. The small size of the nanoobjects is mandatory as it allows envisaging a crossing of the capillary barrier, a urinary elimination and a favourable biodistribution. Indeed, our work shows that a dendritic platform combining a high targeting power, favorable biokinetics together with optimal biodistribution properties, drained more predominantly by lymphatic vessels after intradermal injection. We synthetized generation 0 (G0, model compound), 1 (G1) and 2 (G2) PAMAM dendrons bearing 1 (G0), 2 (G1) or 4 (G2) benzamide arylcarboxamide vectors targeting the melanine granules (2). Thanks to a radiolabeling of these dendritic nano-objects with 99mTc or 111In, we showed, that: i) the dendrimer platform improves the biodistribution of the ligand, with a lower unspecific uptake in the liver and a faster elimination of untargeted probes by both urinary and hepato-biliary ways; ii) a 4 ligands/G2 dendrimer platform allows increasing the targeting efficiency. Indeed, it reached 22.5%/g of tumour at 4h post-IV injection; iii) dendrons G1 and G2 were also radiolabeled with 99mTc, and their lymphatic drainage studied by SPECT after intra-dermic injection at the extremity of lower legs. G2 dendron presented an exclusive lymphatic drainage together with a transient uptake within lymph nodes, starting with the popliteal nodes. The washout of lymph node activity happened within a few hours, and was complete at 24 hours. (1) New Engl. J. Med. 1991, 325, 171; New Engl. J. Med. 1988, 318, 1159. (2) New J. Med. Chem. 2008, 51, 3133. Bioconjugate Chemistry 2009, 20, 760-767; New J. Chem., 2010, 34, 267-275; Biomaterials, 2011, 32, 8562-8573; New J. Chem. invited Perspective review in DENDRIMER 2, 2012, 36 (2), 310-323; Eur. J. Inorg. Chem., invited Microreview on MEMRI Contrast Agents, 2012, 1987-2005.

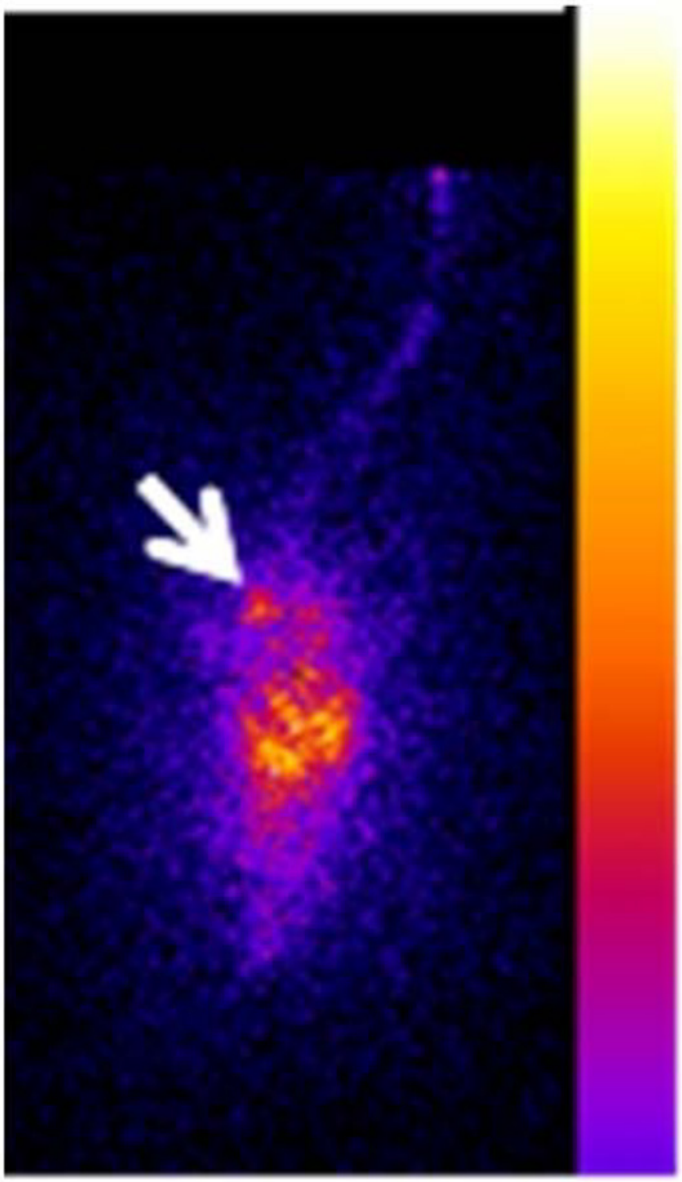

A 4 vectors(ICF01102)-G1.5 dendrimer platform allows a high uptake in tumor xenograft (arrow). The targeting efficiency reached the value of 22.5%/g of tumor at 4h (not shown) post-IV injection. The studies revealed also a very favourable biodistribution, with a low unspecific uptake especially in liver, and a high elimination (less than 6% remained in the kidneys at 24 hours post iv).

Disclosure of author financial interest or relationships:
D. Felder-Flesch, None.

Presentation Number **P 149**
Poster Session 2
September 19, 2013 / 15:15-15:15 / Room: Exhibit Hall B

Fungus mediated synthesis of protein capped, water dispersible nanoparticles and their application in small animal imaging

Sanjay Gambhir[1], *Sukanta Barai*[1], *Imran Uddin*[2], *Absar Ahmad*[2], *Veeresh Dube*[1], *Subash C. Kheruka*[1], [1]*Nuclear Medicine, S.G.P.G.I.M.S, Lucknow, India;* [2]*Biochemical division, NCL, Pune, India. Contact e-mail: gaambhir@yahoo.com*

Nano materials are being synthesized by chemical, physical and biological routes for various applications in imaging and therapy. Water solubility and protein coating makes this nanoparticles amenable to Technetium radiolabelling and thus explore their utility in animal and human system. Unlike the toxic and expensive chemical and physical protocols, the recently developed biological routes are eco friendly and cheap. We report the extra cellular biosynthesis, complete characterization and biodistribution in rats of some of so synthesized nanoparticles Nanoparticles were synthesized by challenging fungus Fusarium Oxysporum precursor salts of Bismuth (Bi), Gold (Au) and Manganese (Mn). The optical properties of nanoparticles were examined by using UV-vis spectroscopy. The measurements were performed on a Shimadzu dual-beam spectrophotometer (model UV-1601 PC) operated at a resolution of 1 nm. The nanoparticles were also characterized by using Transmission Electron Microscopy (TEM) and X-ray Diffraction (XRD) measurements and confirmed to be 10—50 nm size.Tc99m- nanoparticles were prepared by dissolving 10 mg of nanoparticles in 1 ml of distilled water followed by the addition of 100 µg of SnCl2.2H2O and the pH was adjusted to 6.5. Approximately Tc-99m (2mCi) was added to the content, mixed and incubated for 10-15min. The percent radiolabel was determined by using instant thin layer chromatography (ITLC) method. Male Sprauge Dawley rats weighing 180-220 gm were selected for evaluating the localization of the labelled complex. Tc99m- nanoparticles of 14.8 MBq (400uCi) were administered through the penile vein of rat. The biodistribution studies of labeled nanoparticles were evaluated 45 min and 2 hr. post injection. Whereas Bi biodistribution was found mainly in liver and spleen the Au nanoparticles mainly to kidneys and Mn nanoparticles were distributed to heart, liver and kidneys. The biodistribution picture remained same till 2 hour post injection, thus confirming the in-vivo stability of Technetium labeling of these nanoparticles. The natural ability of fungus to synthesize the nanoparticles of substrate and to protein coat them, offer a very simple method of obtaining water dispersible nanoparticles of various elements and to explore their possible use in imaging.

Disclosure of author financial interest or relationships:
S. Gambhir, None; **S. Barai**, None; **I. Uddin**, None; **A. Ahmad**, None; **V. Dube**, None; **S.C. Kheruka**, None.

Presentation Number **P 150**
Poster Session 2
September 19, 2013 / 15:15-15:15 / Room: Exhibit Hall B

A novel molecular agent for PET imaging angiogenesis: synthesis, in vivo biodistribution and tumor imaging of 18F-rh-Endostatin

Xudong Hu[1], *Ligang Xing*[1], *Li Ma*[2], *Shuqiang Zhao*[2], *Jujie Sun*[3], *Xindong Sun*[1], *Jinming Yu*[1], [1]*Department of Radiation Oncology, Shandong Cancer Hospital & Institute, Jinan, China;* [2]*Department of Nuclear Medicine, Shandong Cancer Hospital & Institute, Jinan, China;* [3]*Department of Pathology, Shandong Cancer Hospital & Institute, Jinan, China. Contact e-mail: xudongh@gmail.com*

Tumor angiogenesis plays an important role in tumor growth and metastasis. Endostatin is well known as a broad-spectrum, anti-angiogenic agent that specifically inhibits vascular endothelial cell proliferation. Recombinant human endostatin (rh-endostatin), which was reconstructed with an additional nine-amino acid sequence thus to form another his-tag structure, has been reported to show significant anti-angiogenesis effects in advanced solid tumors. In this study, we have been synthetized 18F-labeled rh-endostatin as a novel molecular angiogenesis agent for PET imaging, and evaluated the biodistribution and tumor imaging of 18F-rh-Endostatin in vivo. Methods: 18F-rh-Endostatin was synthetized by conjugating rh-Endostatin with a 18F-tag, N-succinimidyl 4-[18F]fluorobenzoate ([18F]SFB). 18F-rh-Endostatin was injected in mice or human glioblastoma U87MG xenografts, and radiation dosimetry was examined by ex vivo dissection or with small-animal PET/CT scanning, respectively. Results: In normal mice, the maximum %ID/g (percentage injected dose per gram of tissue) of 18F-rh-Endostatin accumulation in kidney and the peak (55.3%ID/g) at 60 min after injected agent by the tail vein. The brain and the lung tissue were shown lower 18F-rh-Endostatin accumulation. Small animal PET/CT imaging revealed that 18F-rh-Endostatin exhibited good tumor uptake and related to microvessel density (MVD) in tumor tissue. Furthermore, co-injection of 18F-rh-Endostatin with unlabeled rh-Endostatin significantly inhibited tumor uptake in U87MG xenograft models, demonstrating the novel agent having same target with rh-Endostatin in vivo. Conclusion: We synthetized 18F-rh-Endostatin firstly. 18F-rh-Endostatin showed favorable pharmacokinetic properties, good tumor uptake and related to microvessel density (MVD) in tumor tissue. 18F-rh-Endostatin is a promising PET agent for imaging tumor angiogenesis.

Disclosure of author financial interest or relationships:
X. Hu, None; **L. Xing**, None; **L. Ma**, None; **S. Zhao**, None; **J. Sun**, None; **X. Sun**, None; **J. Yu**, None.

Presentation Number **P 151**
Poster Session 2
September 19, 2013 / 15:15-15:15 / Room: Exhibit Hall B

F-18 Click Labeling of SiO_2 Nanoparticles and PET Imaging for Their Absorption and Biodistribution Following Oral Exposure

Chang-Moon Lee[1], *Tai Kyoung Lee*[2], *Su-Jin Cheong*[2], *Hwan-Seok Jeong*[2], *Hyosook Hwang*[2], *Phil-Sun Oh*[2], *Kyung Sook Na*[2], *Young-Seop Lo*[2], *Eun-Mi Kim*[2], *Jeong Il Kwon*[2], *Yeon-Hee Han*[2], *Chang Ju Na*[2], *Se Hun Choi*[2], *Hwan-Jeong Jeong*[2], *Myung-Hee Sohn*[2], *Seok Tae Lim*[2], [1]*Department of Biomedical Engineering, Chonnam National University, Yeosu, Republic of Korea;* [2]*Department of Nuclear Medicine, Chonbuk National University Medical School and Hospital, Jeonju, Republic of Korea. Contact e-mail: cmlee@jnu.ac.kr*

The wide application of SiO_2 nanoparticles in various fields has led us to address the potential risks of the nanoparticles to human health. Therefore, understanding the behavior of SiO_2 nanoparticles in the body following the exposures is very important for investigating their physiological fates and safety. The aim of this study is to label F-18 on the SiO_2 nanoparticles through click reaction and to investigate their behavior and accumulation in the body after oral administration using PET imaging. SiO_2 nanoparticles were surface-modified with hexynoic acid and click labeled with the F-18-labeled ethoxyazide compound. Radiolabeling stability of F-18-labeled SiO_2 nanoparticles was evaluated in HCl solution (pH 1.2) for 7 h. The radiolabeled SiO_2 nanoparticles (500 mg/kg of body weight) were orally administrated in normal mice. PET imaging was performed at 0.5, 2, 4, and 6 h after oral administration. To investigate the accumulation of the nanoparticles in the organic tissues, the mice were sacrificed at 2, 4, and 6 h post administration and the removed organs were imaged and counted. Radiolabeling of F-18-labeled SiO_2 nanoparticles was stable in HCl solution for 7 h without dissociation of F-18. In vivo PET images showed that F-18-labeled SiO_2 nanoparticles remained in the stomach during early time point after oral administration. After that, the nanoparticles flowed into the small intestine from the stomach and gradually moved along the gut. In ex vivo PET imaging studies, the radioactivity signals were observed in the lung and liver. Most F-18-labeled SiO_2 nanoparticles were naturally excreted from the body through feces, but some of the nanoparticles were adsorbed and translocated into systemic circulation. F-18 click labeling for SiO_2 nanoparticles is useful for monitoring and tracing the movement of the nanoparticles in the body during absorption and distribution after oral administration. Acknowledgments: This study was supported by a grant (10182KFDA991) from Korea Food & Drug Administration in 2010.

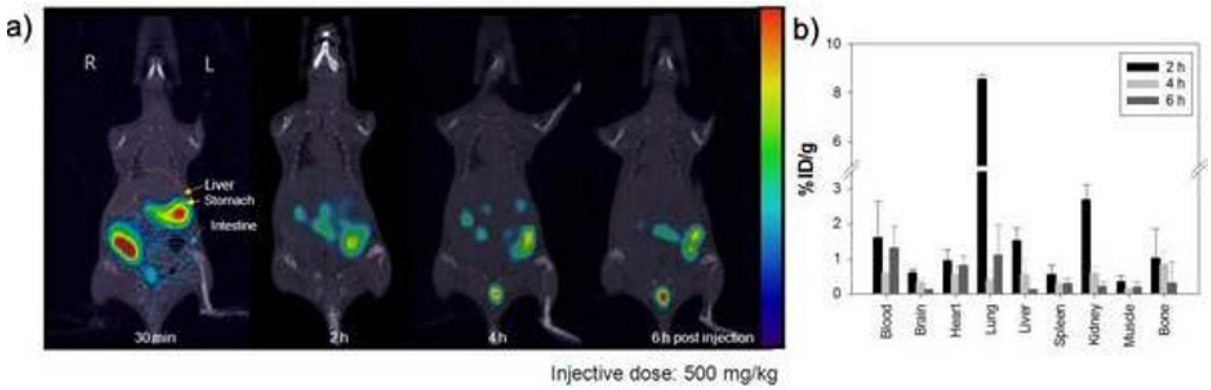

Figure 1. (a) In vivo PET/CT images and (b) Biodistribution results of mice orally administered with F-18-labeled SiO_2 nanoparticles at 0.5, 2, 4, 6 h post-administration.

Disclosure of author financial interest or relationships:

C. Lee, None; **T. Lee**, None; **S. Cheong**, None; **H. Jeong**, None; **H. Hwang**, None; **P. Oh**, None; **K. Na**, None; **Y. Lo**, None; **E. Kim**, None; **J. Kwon**, None; **Y. Han**, None; **C. Na**, None; **S. Choi**, None; **H. Jeong**, None; **M. Sohn**, None; **S. Lim**, None.

Presentation Number **P 152**
Poster Session 2
September 19, 2013 / 15:15-15:15 / Room: Exhibit Hall B

Bivalent small molecule PET probe for VEGF receptor expression imaging

Feng Li, *Zheng Li, Translational Imaging, The Methodist Hospital, Houston, TX, USA. Contact e-mail: fli2@tmhs.org*

Vascular endothelial growth factors (VEGFs) are critical regulators of vascular development during vasculogenesis and angiogenesis. In mammals, there are five VEGF ligands (VEGF A~D, and placenta growth factor, PLGF), have been identified. All members of the VEGF family stimulate cellular responses by binding to tyrosine kinase receptors (the VEGFRs) on the cell surface, known as VEGFR1 (Flt-1), VEGFR2 (Flk-1, KDR), and VEGFR3 (Flt-4). These VEGF Receptors (tyrosine kinase) act as important regulators of angiogenesis and lymph angiogenesis by inducing endothelial cell proliferation, promoting cell migration, and inhibiting apoptosis (1). Direct non-invasive molecular imaging of VEGFR expression would help to evaluate the efficacy of anti-angiogenic therapies and facilitate the selection of patients for a customized VEGFR-targeted chemotherapy. Radioligands based on VEGF/VEGFR have been labeled with various radioisotopes for the imaging of VEGFR expression in various disease models (2, 3). However, most reported VEGF imaging studies were using antibody based tracers and were limited by the slow clearance of the full-length antibodies from blood and poor extravasations and diffusion into the extracellular space (4). Multivalency is an efficient strategy for increasing the binding affinity of compounds ostensibly to increase their potency or imaging potential. In this study, a bivalent small molecule PET probe targeting VEGFR2 was developed based on the structure of anticancer drug Vandetanib (ZD6474). In vitro cell binding assay showed bivalent strategy increase its binding affinity over 100 time (with IC50 0.035 nM). 64Cu radiolabeled small molecule bivalent VEGFR targeting PET imaging probe has been developed for small-animal PET imaging and biodistribution studies using U87 Glioblastoma xenograft tumor model. MicroPET imaging of 64Cu-bivalent imaging probe clearly shows good tumor localization in comparison with 64Cu-monovalent probe.

Disclosure of author financial interest or relationships:
F. Li, None; **Z. Li**, None.

Presentation Number **P 153**
Poster Session 2
September 19, 2013 / 15:15-15:15 / Room: Exhibit Hall B

Preliminary assessment of Cu-64 labeled aptamer imaging in lung cancer: DOTA vs CB-TE2A

Junling Li, *Huaiyu Zheng, Paula J. Bates, Tariq M. Malik, Xiao-Feng Li, John O. Trent, Chin K. Ng, Univerisity of Louisville, Louisville, KY, USA. Contact e-mail: junling.li@louisville.edu*

Introduction: AS1411 is a 26-base guanine-rich oligonucleotide aptamer that specifically binds to nucleolin, a protein over-expressed in multiple cancer cells. Thus AS1411 labeled with a PET isotope can be explored as a potential imaging agent for early detection of cancers by targeting nucleolin on the cell surface. Different labeling chelators, however, could have a significant effect on the pharmacokinetics of the target molecules. Our objectives were to compare the effect of the two chelators, DOTA and CB-TE2A on the in vivo kinetics of Cu-64 labeled AS1411 by performing microPET/CT imaging and biodistribution studies in a mouse lung cancer model. Methods: Non-small lung cancer cells, HTB177 (5*10^6 and 10^7) were implanted subcutaneously into the left and right thighs of BALB/c nu/nu female mice, respectively. MicroPET/CT imaging was performed on the microPET-R4 scanner when the tumor size was about 0.5-1.0 cm3. 200 μCi of each tracer was injected intravenously to each mouse via the tail vein. Multiple static scans were obtained at 1, 3, 6, and 24 h post injection. The mice were sacrificed at 24 h after all the PET scans had been acquired. Tissues and organs of interest were removed and weighed, and the radioactivity of each sample was measured in a gamma well-counter. The percent injected dose per gram (% ID/g) was then estimated for each sample based on known standards. Results: Biodistribution data showed that the tumor-to-background ratio at 24 h post injection for 64Cu-DOTA-AS1411 was about twice that of 64Cu-CB-TE2A-AS1411, which was consistent with published in vitro cell uptake data. However, due to substantially high tracer accumulation in the liver, tumors were not visible on all the PET images for 64Cu-DOTA-AS1411 from 1 h to 24 h post injection, whereas both tumors were clearly visible from 1 h to 24 h post injection for 64Cu-CB-TE2A-AS1411. Based on the PET quantification results and the biodistribution data, 64Cu-CB-TE2A-AS1411 exhibited a faster in vivo pharmacokinetics than 64Cu-DOTA-AS1411, with lower liver uptake and higher tumor-to-background contrast. Conclusion: Our in vivo PET imaging and biodistribution data were in agreement with the published findings and CB-TE2A was shown to be a better chelator than DOTA by having more favorable kinetic properties for Cu-64 labeled AS1411.

Disclosure of author financial interest or relationships:
J. Li, None; **H. Zheng**, None; **P.J. Bates**, Antisoma, Stockholder; **T.M. Malik**, None; **X. Li**, None; **J.O. Trent**, None; **C.K. Ng**, None.

Presentation Number **P 154**
Poster Session 2
September 19, 2013 / 15:15-15:15 / Room: Exhibit Hall B

Maltodextrins image early stage bacterial infections and drug resistance by positron emission tomography

Niren Murthy, *Bioengineering, U.C. Berkeley, Berkeley, CA, USA. Contact e-mail: nmurthy@berkeley.edu*

Bacterial infections are a central cause of mortality in the world and affect all areas of medicine ranging from cardiology to oncology. Bacterial infections remain a major health problem despite the availability of effective antibiotics, because their diagnosis is challenging and because they are frequently treated with ineffective antibiotics, due to the widespread rise of bacterial drug resistance. In this report, we present a new PET contrast agent, composed of F-18 conjugated to maltodextrins (MD18F), which can for the first time image bacteria in vivo with the specificity and sensitivity needed to detect early stage infections and measure drug resistance in vivo. We show here that MD18F can detect as few as 105 E.coli colony forming units (CFUs) in rats, which is 3-4 orders magnitude higher in sensitivity than FDG, the current clinically used bacterial infection contrast agent. In addition, we demonstrate that MD18F can distinguish bacterial infections from inflammation, and has a specificity that is higher than FDG, giving it the potential to identify infections clinically without a biopsy. Finally, we demonstrate that MD18F can monitor treatment efficacy in vivo and can identify beta lactam resistance in E.coli , thus providing physicians with a powerful tool for guiding antibiotic selection. We anticipate numerous clinical applications of MD18F given the widespread use of PET and the pervasiveness of infections in medicine.

Disclosure of author financial interest or relationships:
N. Murthy, None.

Presentation Number **P 155**
Poster Session 2
September 19, 2013 / 15:15-15:15 / Room: Exhibit Hall B

A Novel Synthesis of 4-O-(α-D-glucopyranosyl)-6-deoxy-6-[^{18}F]fluoro-D-glucopyranoside (6-[^{18}F]fluoromaltose) as a PET Tracer for Imaging Bacterial Infection

Mohammad Namavari, *Gayatri Gowrishankar, Sanjiv S. Gambhir, Radiology, Stanford University, Stanford, CA, USA. Contact e-mail: namavari@stanford.edu*

We wanted to develop a novel PET agent to visualize bacterial infections and monitor the therapeutic response to bacterial infections. Maltose is a natural substrate for bacteria and not for mammalian cells. Most pathogenic bacteria have a transporter that transports maltose and maltodextrins with a high degree of specificity. We have developed a novel way to synthesize 4-O-(α-D-glucopyranosyl)-6-deoxy-6-[^{18}F]fluoro-D-glucopyranoside (6-[^{18}F]fluoromaltose) as a bacterial infection PET imaging agent. 6-[^{18}F]fluoromaltose was prepared from precursor 1,2,3-tri-O-acetyl-4-O-(2′,3′,-di-O-acetyl-4′,6′-benzylidene-α-D-glucopyranosyl)-6-deoxy-6-tosyl-D-glucopranoside (1) in 1-1.5 % radiochemical (decay corrected with 95% chemical and radiochemical purities). The synthesis utilizes the reaction between the leaving group tosylate in 1 and anhydrous [^{18}F]KF/Kryptofix 2.2.2 in DMSO at 160 oC for 50 minutes to produce 1,2,3-tri-O-acetyl-4-O-(2′,3′,-di-O-acetyl-4′,6′-benzylidene-α-D-glucopyranosyl)-6-deoxy-6-[^{18}F]fluoro-D-glucopranoside (2). Finally, acid hydrolysis of 2 followed by its basic hydrolysis produced the final 6-[^{18}F]fluoromaltose. Bacteria uptake experiments indicate that E-coli take up 6-[^{18}F]fluoromaltose. Competition assays showed that the uptake of the 6-[^{18}F]fluoromaltose was completely blocked by co-incubation with 1mM of the natural substrate maltose. In conclusion, for the first time to the best of our knowledge, we have successfully synthesized 6-[^{18}F]fluoromaltose via direct fluorination of an appropriate precursor of maltose. This methodology can also be used for the synthesis 1-[^{18}F]fluoromaltose, 2-[^{18}F]fluoromaltose and other important PET tracers.

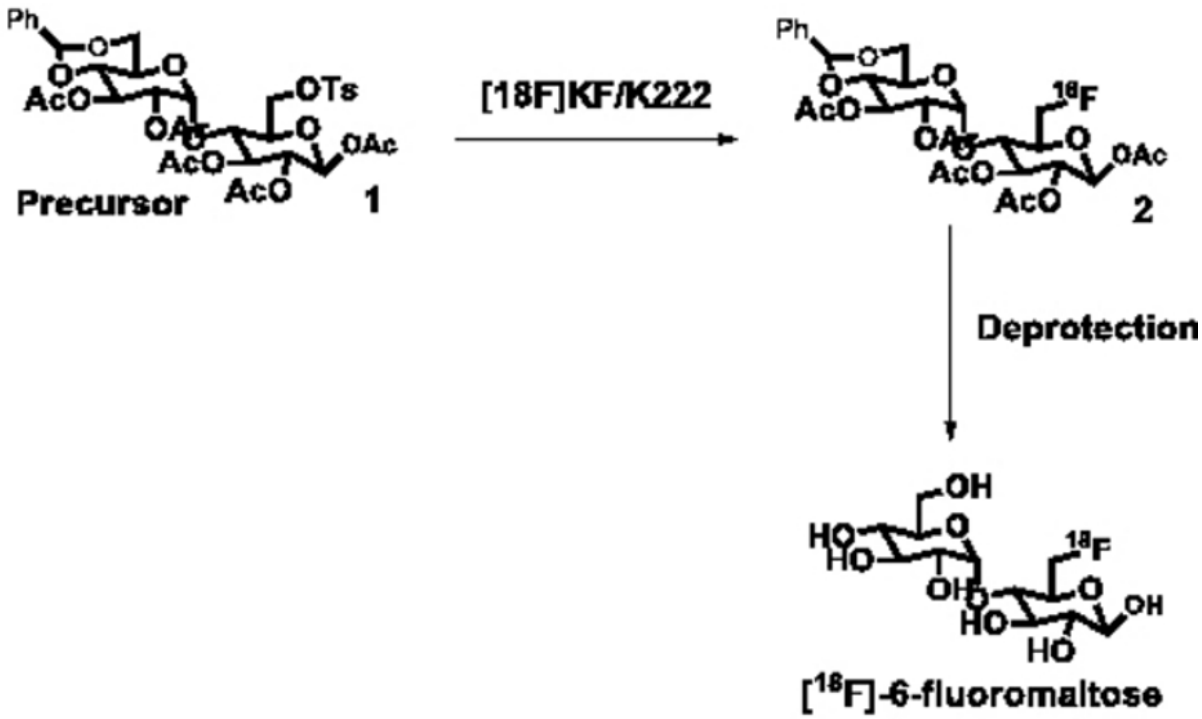

Scheme 1. Synthesis of [^{18}F]-6-fluoromaltose

Disclosure of author financial interest or relationships:
M. Namavari, None; **G. Gowrishankar**, None; **S.S. Gambhir**, Bracco Diagnostics, Consultant; Endra, Inc, Stockholder; Cellsight, Stockholder; Enlight, Inc., Stockholder; General Electric, Grant/research support; ImaginAb, Stockholder; MagArray, Inc., Stockholder; Sanofi-Aventis, US, Grant/research support; SiteOne Therapeutics, Stockholder; VisualSonics/Sonosite, Stockholder .

Presentation Number **P 156**
Poster Session 2
September 19, 2013 / 15:15-15:15 / Room: Exhibit Hall B

Preparation and in vitro and in vivo evaluation of a bombesin peptide analog linked to a cytotoxic drug for targeting of bombesin receptor-positive tumors

Subhani M. Okarvi, *Cyclotron & Radiopharm, King Faisal Specialist Hospital and Research Centre, Riyadh, Saudi Arabia. Contact e-mail: sokarvi@kfshrc.edu.sa*

Objectives: Among various tumor targeting peptides, bombesin (BN) peptides are of particular interest because of the overexpression of their receptors on various cancer cells including breast and prostate cancer. The high density BN receptors in cancer cells have created an interest in developing cytotoxic-BN conjugates for receptor-mediated tumor targeting with radiolabeled cytotoxic-BN conjugate. Targeted cytotoxic conjugates are hybrid molecules composed of a peptide carrier which binds to peptide receptors on tumors and a cytotoxic moiety. Here we report the preparation of a novel BN peptide derived from the universal sequence of BN peptide and conjugated to a well-characterized anticancer agent, methotrexate (MTX) for efficient targeting of BN receptor-positive tumors. Methods: The cytotoxic conjugate MTX-Lys-Gly-Gly-Cys-Asp-Phe-Gln-Trp-Ala-Val-βAla-His-Phe-Nle-NH2 (MTX-BN) was prepared by Fmoc/HBTU chemistry using solid-phase peptide synthesis approach. Radiolabeling with Tc-99m, a clinically-useful radionuclide, was achieved via stannous-tartrate exchange method. In vitro metabolic stability was determined in human plasma and tumor cell binding assays were conducted on various breast cancer (MDA-MB-231, MCF7, T47D) and PC3 prostate cancer cell lines. In vivo pharmacokinetics was determined on Balb/c mice and tumor targeting capacity was assessed in tumor xenografts mice models. Results and Discussion: The structure of the peptide was confirmed by mass spectrometry and its purity by HPLC analysis. The conjugate radiolabeled efficiently with 99mTc (~75%) as determined by HPLC. 99mTc-labeled conjugate exhibited a high in vitro metabolic stability in human plasma. The in vitro cell-binding demonstrated high affinity and specificity of 99mTc-MTX-BN towards both breast and prostate cancer cell lines (binding affinities in nanomolar range). In addition, the radioconjugate displayed a significant internalization (up to 35%) into the tumor cells. In vivo biodistribution and clearance kinetics in Balb/c mice displayed efficient clearance of the radioconjugate from the blood and excretion mainly by the renal route. In vivo tumor uptake in nude mice bearing MDA-MB-231 xenografts was found to be 2.70±0.44% ID/g at 1 h, whereas in nude mice with human epidermoid KB cells the accumulation in the tumor was 1.48±0.31% ID/g at 1 h post-injection. The tumor uptake was always higher than the uptake in the blood and muscle, with good tumor retention and good tumor-to-blood and tumor-to-muscle ratios. The accumulation/retention of radioconjugate in the major organs (i.e., lungs, stomach, liver, intestines, etc.) was low to moderate (<6% ID/g) in both healthy and tumor-bearing mice, except for the kidneys (up to 11% ID/g), which is undesirable, especially for radionuclide therapy. Conclusion: This initial study towards the development of a new cytotoxic BN conjugate suggest that the combination of favorable in vitro/in vivo properties may render 99mTc-MTX-BN a potential candidate for the diagnostic imaging and eventually for radionuclide therapy (when labeled with an appropriate radionuclide) of BN receptor-positive tumors and deserves further evaluation.

Disclosure of author financial interest or relationships:
S.M. Okarvi, None.

Presentation Number **P 157**
Poster Session 2
September 19, 2013 / 15:15-15:15 / Room: Exhibit Hall B

Development of thiol-reactive [F-18]FEMA for radiolabeling of biomolecules

Jun Young Park[1], *Tae Sup Lee*[2], *Jong Doo Lee*[1], *Won Jun Kang*[1], [1]*Nuclear medicine, Yonsei University Health System, Seoul, Republic of Korea;* [2]*Molecular Imaging Research Center, Korea Institute of Radiological and Medical Science, Seoul, Republic of Korea. Contact e-mail: abies60@naver.com*

Various biomolecules such as proteins, peptides and antibodies are labeled with radioisotopes for imaging and therapeutic purposes. Maleimide is the most promising linker for the labeling of biomolecule because it react selectively with thiol group. In this study, we developed a thiol-reactive 1-{2- {2-[2-(2-[18F]Fluoroethoxyethoxy}ethoxy} ethyl-4-(N-maleimidylmethyl)-1,2,3-triazole ([F-18]FEMA) for F-18 labeling of thiol-containing biomolecules. The [F-18]FEMA was prepared in two steps. [F-18]PEG-azide was first prepared via nucleophilic substitution. In the second step, [F-18]PEG-azide was labeled with N-propagyl maleimide using click chemistry. The process was performed on a modified GE TRACERlab FXFn and FXFc synthesis module. Lipophilicity of [F-18]FEMA was measured by the Octanol/water partition coefficient (logP). Conjugation of [F-18]FEMA with thiol groups was studied using cysteine-containing glutathione (GSH). In vivo PET imaging was performed using an Inveon microPET scanner. The non-decay corrected radiochemical yield of [F-18]FEMA was 5 ± 2% (n = 10) within a total synthesis time of 110 min. Further optimization for improvement on the radiochemical yield is in progress. The logP value of [F-18]FEMA was -0.52 ± 0.02. Conjugation of [F-18]FEMA with GSH was achieved in > 90% yields in a various GSH concentrations (1.0 mg/mL ~ 10 ng/mL). Small animal PET experiments showed high liver accumulation and rapid renal elimination. [F-18]FEMA showed good conjugation yield with GSH. [F-18]FEMA do not contain the aromatic moieties and logP value demonstrated that [F-18]FEMA has low lipophilicity. The results of this study suggest that [F-18]FEMA will be useful for radiolabeling of thiol groups located in a hydrophilic environment.

Disclosure of author financial interest or relationships:
J. Park, None; **T. Lee**, None; **J. Lee**, None; **W. Kang**, None.

Presentation Number **P 158**
Poster Session 2
September 19, 2013 / 15:15-15:15 / Room: Exhibit Hall B

^{99m}Tc-Pertechnetate Production Using Automated Processing of Cyclotron Irradiated ^{100}Mo Targets

Svetlana V. Selivanova[1], *Lidia Matei*[2], *Véronique Dumulon-Perreault*[2], *Jacques A. Rousseau*[1], *Jayden Sader*[3], *Erik J. van Lier*[3], *Alexander Zyuzin*[3], *Johan E. van Lier*[2,1], *Éric E. Turcotte*[1,2], *Roger Lecomte*[2,1], *Brigitte Guerin*[2,1], [1]*Sherbrooke Molecular Imaging Center, Centre Hospitalier Universitaire de Sherbrooke, Sherbrooke, QC, Canada;* [2]*Nuclear Medicine and Radiobiology, Université de Sherbrooke, Sherbrooke, QC, Canada;* [3]*Advanced Cyclotron Systems Inc., Vancouver, BC, Canada. Contact e-mail: s.selivanova@usherbrooke.ca*

Technetium-99m (^{99m}Tc) is the most widely used radioisotope in nuclear imaging with about 30 million procedures per year, which is 80% of all nuclear medicine procedures worldwide. Currently, ^{99m}Tc is obtained from a ^{99}Mo generator, which, in turn, is produced from highly-enriched ^{235}U (≥20%, typically 93%) in nuclear reactors. Recent shortage of ^{99m}Tc supply created awareness about the need to develop alternative ^{99m}Tc production technologies in time for the aging nuclear reactors become decommissioned or converted to low-enriched ^{235}U (<20%). Initial theoretical calculations and experimental results suggest that cyclotrons could provide substantial amount of required ^{99m}Tc. We investigated the irradiation parameters and ^{100}Mo target characteristics for production of useful quantities of ^{99m}Tc using a medium-energy TR24 cyclotron. Target processing and ^{99m}Tc isolation procedures were developed for a cassette-based automated synthesis unit. Enriched (>99%) ^{100}Mo targets (0.67-1.25 mm thickness) were irradiated at 20-24 MeV beam energy and 15-30 μA current to produce ^{99m}Tc via the ^{100}Mo(p,2n)^{99m}Tc nuclear reaction. Irradiated targets were dissolved in 30% H_2O_2 and basified with 2.5M $(NH_4)_2CO_3$. ^{99m}Tc was isolated from the crude mixture as sodium ^{99m}Tc-pertechnetate by passing the solution through a series of aqueous biphasic and/or ion exchange resins using a custom built cassette-based automated synthesis unit comprising of disposable 5- and 3-valve manifolds, a disposable syringe, and reagent vials. ^{100}Mo solution was collected for further recycling. A variety of resins was tested for optimal ^{99m}Tc isolation. Radiochemical yield for ^{99m}Tc was reaching 88% when calculated using gamma-ray spectrometry. Up to 75% of the radioactivity recovered from the target was in the form of 99mTc-pertechnetate with radiochemical purity >98%. A range of technetium radioisotopes (^{94}Tc, ^{94m}Tc, ^{95}Tc, ^{95m}Tc, ^{96}Tc, ^{96m}Tc, and ^{97m}Tc) is generated during proton bombardment of ^{100}Mo target. The final product contained <1% of those up to 12 h post-bombardment. Chemical purity of the final product was high (Al <10 μg/ml, Mo <5 μg/ml, and H_2O_2 <100 μg/ml).

Obtained ^{99m}Tc-pertechnetate can be used for kit labeling to produce other ^{99m}Tc-radiopharmaceuticals. The main difference of cyclotron produced ^{99m}Tc from generator source is its contamination with longer-lived ^{95}Tc, ^{95m}Tc, and ^{96}Tc, which will contribute to the additional radiation dose to patients. To resolve this issue, lower injected dose and optimization of scanning parameters may be suggested. Before cyclotron produced ^{99m}Tc will see its use in clinics, new Pharmacopoeia standards should be established and include specific limits for each co-produced technetium isotope, considering its contribution to the radiation dose increase.

Disclosure of author financial interest or relationships:
S.V. Selivanova, None; **L. Matei**, None; **V. Dumulon-Perreault**, None; **J.A. Rousseau**, None; **J. Sader**, None; **E.J. van Lier**, ACSI, Employment; **A. Zyuzin**, None; **J.E. van Lier**, None; **.E. Turcotte**, None; **R. Lecomte**, None; **B. Guerin**, None.

Presentation Number **P 159**
Poster Session 2
September 19, 2013 / 15:15-15:15 / Room: Exhibit Hall B

Radiolabeling a PSMA-specific RNA aptamer with the PET tracer zirconium-89

Travis Shaffer[1,4], *Jan Grimm*[1,2], *Matthew Levy*[3], [1]*Molecular Pharmacology and Chemistry, Memorial Sloan Kettering Cancer Center, New York, NY, USA;* [2]*Radiology, Memorial Sloan Kettering Cancer Center, New York, NY, USA;* [3]*Department of Biochemistry, Albert Einstein College of Medicine, Bronx, NY, USA;* [4]*Department of Chemistry, Hunter College of the City University of New York, New York, NY, USA. Contact e-mail: shaffert@mskcc.org*

Purpose: The purpose of our study was to radiolabel the PSMA-specific RNA aptamer A9 with the PET tracer zirconium-89 and test the ability of this probe for use as a PSMA PET imaging agent. Methods: Recently, a prostate specific membrane antigen (PSMA)-specific RNA aptamer was generated with 2'-fluoro substitutions to impart in vivo stability. The PSMA-specific RNA aptamer (A9) and a non-functional oligo control (C36) were conjugated to desferrioxamine-maleimide (DFO) via a thiol-maleimide linkage for the purpose of 89Zr chelation. 89Zr was chelated by A9-DFO and C36-DFO with the reaction monitored over serial time points, and the specific activity and purity was determined via ITLC. In vitro serum stability was performed over a 96 hour time course, and immunoreactivity of the radiolabeled A9 aptamer was evaluated on PSMA transfected PC-3 cells and the prostate cancer cell line PC-3 as a control by an immunoreactivity assay. Results: Radiolabeling of A9-DFO with 89Zr was completed at a neutral pH in one hour with successful chelation of the radiotracer. The 89Zr-labeled A9 aptamer showed a specific activity comparable to reported monoclonal antibody values and serum stability >85% over four days by ITLC. An immunoreactivity assay showed the radiolabeled aptamer sustained in vitro binding affinity. Ongoing in vivo studies are characterizing the ability of the A9 RNA aptamer to act as a novel PSMA PET agent. Conclusion: With its high specificity for the glycoprotein PSMA and ease of synthesis and radiolabeling, the PSMA-specific A9 aptamer could ultimately be used for facile PET imaging of PSMA-positive prostate cancer, with subsequent improved clinical outcome. Furthermore, due the modular nature of aptamers, this radiolabeling procedure has the potential for facilitating pharmacokinetic studies of a multitude of RNA aptamers.

Disclosure of author financial interest or relationships:
T. Shaffer, None; **J. Grimm**, None; **M. Levy**, None.

Presentation Number **P 160**
Poster Session 2
September 19, 2013 / 15:15-15:15 / Room: Exhibit Hall B

Development of F-18 labeled PET tracer for imaging early phase of inflammation

Aizhi Zhu[1], *Dinesh Shetty*[1], *Ronald J. Voll*[1], *Zhongxing Liang*[1,2], *Younghyoun Yoon*[1], *Jeffrey Ahn*[1], *James P. Snyder*[3], *Mark M. Goodman*[1,2], *Hyunsuk Shim*[1,2], [1]*Radiology, Emory University, Atlanta, GA, USA;* [2]*Winship Cancer Institute, Emory University, Atlanta, GA, USA;* [3]*Chemistry, Emory University, Atlanta, GA, USA. Contact e-mail: zhuaizhi@gmail.com*

Chemokines are small, pro-inflammatory cytokines of approximately 10 kDa that orchestrate a diverse set of activities through interaction with their cognate receptors. Coupling of stromal cell derived factor 1 (SDF-1; CXCL12) with its receptor CXCR4, which was previously identified as a major co-receptor for the entry of T-tropic HIV, plays critical roles in inflammation, as well as cancer metastasis. CXCR4/CXCL12 has been reported to play a critical role in the recruitment of inflammatory cells during early phase of malignant transformation. Therefore, in vivo imaging of CXCR4 receptor has significant potential to detect inflammation early. We have identified a novel sulfonamide and cyclic sulfonamide derivatives as small molecule CXCR4 antagonists through rational design by molecular modeling and cell-based functional assays (Mooring SR et al. ChemMedChem 2013). Sulfonamide derivatives were docked flexibly into the cavity region of the human chemokine receptor CXCR4 crystallographic structure (Wu B et al. Science 2010) devoid of small-molecule antagonist IT1t using Glide with standard precision (Schrödinger, LLC). The resulting CXCR4/benzenesulfonamide complexes were subsequently sorted energetically with the MM-GBSA approach, which provides an estimate of relative binding free energies using Schrodinger suite 2012 for Mac. Their binding potency was evaluated by an affinity binding assay using a potent peptidic CXCR4 antagonist TN14003. We found that the relative binding free energies of these compounds from Prime MM-GBSA calculation correlate with the binding assay. For the secondary functional assays, Matrigel invasion assay and cAMP assay were used to rank-order their inhibitory efficacy against CXCR4/CXCL12 interaction. We selected DS-109 (N-((1-(3-fluoropropyl)-1H-1,2,3-triazol-4-yl)methyl)-N-methyl-4-(pyrrolidin-1-ylmethyl)benzenesulfonamide to generate 18F-labeled PET tracer candidates. Briefly, 3-azidopropyl 4-methylbenzenesulfonate and N-methyl-N-(prop-2-yn-1-yl)-4-(pyrrolidin-1-ylmethyl)benzenesulfonamide were synthesized separately and conjugation was carried through click reactions under familiar conditions [Cu(II)SO4 and sodium ascorbate]. Conjugated click product was reacted with K18F in the presence of K222 under heating using acetonitrile as reaction solvent. The labeled final product was obtained by direct one step nucleophilic fluorination process. The final product F-18 labeled CXCR4 PET tracers were purified by preparative HPLC. The radiochemical purity of the product was checked by HPLC and radioTLC. Radiochemical labeling yielded higher radiochemical conversion, the radiochemical purity is more than 2 Ci/μmol. To determine the specificity of labeled antagonists, we tested them in competition assays against corresponding F-19 cold compound and CXCL12 at various concentrations. microPET images of labeled compounds in carrageenan-induced paw edema model exhibited significant radioactivity accumulation in the inflamed area. Therefore, our new CXCR4-PET tracer has a great potential to become a clinical diagnostic agent for the early detection of inflammation.

Disclosure of author financial interest or relationships:
A. Zhu, None; **D. Shetty**, None; **R.J. Voll**, None; **Z. Liang**, None; **Y. Yoon**, None; **J. Ahn**, None; **J.P. Snyder**, None; **M.M. Goodman**, None; **H. Shim**, None.

Presentation Number **P 161**
Poster Session 2
September 19, 2013 / 15:15-15:15 / Room: Exhibit Hall B

In vivo imaging of 64Cu-HSA-aptamer conjugates to target HER2 positive cancer cells

Myung Geun Song[1,2], *Hyewon Youn*[1,3], *Mee Young Kim*[1], *Yun-Sang Lee*[1,4], *Jae Min Jeong*[1,4], *Dong Soo Lee*[1,5], *June-Key Chung*[1,2], *Sunjoo Jeong*[6], *Keon Wook Kang*[1,3], [1]*Nuclear medicine, Cancer Research, Seoul, Republic of Korea;* [2]*Tumor biology, Seoul National University College of Medicine, Seoul, Republic of Korea;* [3]*Cancer Imaging Center, Seoul National University Cancer Hospital, Seoul, Republic of Korea;* [4]*Institute of Radiation Medicine, Medical Research Center, Seoul, Republic of Korea;* [5]*Molecular Medicine and Biopharmaceutical Science, WCU Graduate School of Convergence Science and Technology, Seoul, Republic of Korea;* [6]*National Research Lab for RNA Cell Biology, Dankook University, Yongin-si, Republic of Korea. Contact e-mail: bororia@hanmail.net*

Purpose: Human epidermal growth factor receptor-2 (HER2) is one of the most important cancer biomarkers. To develop a new imaging probe for targeting HER2 expressing tumor with longer blood circulation time, we designed Cu-64 labeled human serum albumins (HSA) with HER2 specific aptamer targeting small oligonucleotides and evaluated their potential for targeting to HER2 expressing cancer cells in vitro and in vivo. Methods: Her2-targeted aptamer was developed using systematic evolution of ligands by exponential enrichment technology (SELEX) and the aptamer was conjugated with human serum albumin (HSA) for effective blood circulation. FITC-labeled aptamer was used for confocal microscopy to monitor in vitro targeting. HSA was consecutively conjugated with SCN-DOTA and the bifunctional cross-linker Sulfo-SMCC, which was then covalently conjugated with HER2-targeted aptamer. The resulting DOTA-HSA-aptamer was further radiolabeled with 64CuCl2. Labeling efficiencies of 64Cu-HSA-aptamer were determined by instant thin layer chromatography (ITLC). In vivo tumor targeting was monitored with 64Cu-HSA-aptamer by PET imaging and its biodistribution was examined. Results: FITC-aptamer was clearly detected in HER2 positive cells (T47D and KPL4 cells), but not in negative cells (MCF7 and MDA-MB468 cells). Labeling efficiency of 64Cu-HSA-aptamer was over 95% and in vitro uptake test showed its specificity in HER2-positive tumor cells (3-fold increase). In tumor mice models, successful HER2-targeting was observed by PET imaging, resulting accumulation of 64Cu-HSA-aptamer in HER2 positive tumor (3-fold increase at 46h). Aptamer biodistribution were also examined to over 12% ID/g at 12 h. Conclusion: We suggest that 64Cu-HSA modified aptamer could be a promising probe for HER2 specific molecular imaging. The approach using HSA as a carrier could be applied in the design of many other radiolabeled probes.

Disclosure of author financial interest or relationships:
M. Song, None; **H. Youn**, None; **M. Kim**, None; **Y. Lee**, None; **J. Jeong**, None; **D. Lee**, None; **J. Chung**, None; **S. Jeong**, None; **K. Kang**, None.

Presentation Number **P 162**
Poster Session 2
September 19, 2013 / 15:15-15:15 / Room: Exhibit Hall B

Development of PET tracers for pretargeted imaging of tumor angiogenesis

Tiemen R. van Mourik[1], *Raffaella Rossin*[2], *Tilman Läppchen*[2], *Marc S. Robillard*[3], *Holger Gruell*[1,2], [1]*Biomedical Engineering, Eindhoven University of Technology, Eindhoven, Netherlands;* [2]*Minimally Invasive Healthcare, Philips Research, Eindhoven, Netherlands;* [3]*Tagworks Pharmaceuticals, Eindhoven, Netherlands. Contact e-mail: T.R.Mourik@tue.nl*

Introduction Radiolabeled monoclonal antibodies (mAbs) can be deployed for radioimmunoimaging via selective binding to tumors in patients. Due to the large size, however, mAbs have long blood circulation leading to a high whole body radiation dose and poor tumor-to-non tumor ratios. To overcome this, the process can be divided into two steps, an approach known as pretargeting (PT). PT uses a non-radioactive, tagged mAb which is injected in the first step. Subsequently, a small radioactive probe is injected and selectively binds the tag on the mAb while clearing rapidly from non-target organs. Nowadays, 89Zr-labeled bevacizumab is being tested in the clinic for PET imaging of angiogenesis. We wanted to evaluate whether PT with the inverse-electron-demand Diels-Alder (inv-DA) reaction can improve tumor radioimmunoimaging with bevacizumab. Therefore, the aim of this study was to develop and evaluate the pretargeting components bevacizumab-trans-cyclooctene (TCO) and 89Zr-labeled tetrazine for a head-to-head comparison with 89Zr-bevacizumab in tumor-bearing mice. Methods A tetrazine-desferal (Tz-Df) derivative was synthetized in 6 steps and labeled with 89Zr in HEPES buffer at 37°C. Bevacizumab was conjugated either with Df-NCS in a 1:3 molar ratio or with TCO-NHS in a 1:5, 1:10 and 1:15 molar ratio. The reactivity of the obtained bevacizumab-TCO in the inv-DA reaction was tested in PBS and mouse serum with both an 111In-labeled tetrazine and the 89Zr-Df-Tz. The immunoreactivity of the bevacizumab constructs towards VEGF was tested in vitro in a plate-based assay. Results Tz-Df was synthesized in an 11% overall yield, the first reaction being the limiting step (yield 22%). The conjugation of Df-NCS to bevacizumab resulted in 1.5 Df per mAb. After radiolabeling and purification, the 89Zr-mAb was obtained with >98% purity. The bevacizumab TCO-functionalization grade was found to be, respectively, 4, 9 and 11 TCOs/mAb using a titration with 111In-tetrazine. All compounds were analyzed by SDS-PAGE and IEF and the construct bearing 4 TCOs per mAb was chosen for further experiments. The reaction between bevacizumab-TCO and 89Zr-Df-Tz was complete after 10 min in both PBS and mouse serum and the obtained mAb-TCO-Tz-Df-89Zr showed retained immunoreactivity. In vivo experiments in mice bearing MDA-MB-231-LITG xenografts are in progress. Conclusion Pretargeting with the inv-DA reaction was used successfully for tumor radioimmunoimaging of cell surface associated antigens with SPECT (Robillard, AngewChemIntEd 2010) and PET (Weissleder, PNAS 2012) in mouse models of colon carcinoma. Here, we intend to apply this concept for imaging the angiogenesis related target vascular endothelial growth vector (VEGF). To that aim, we developed a new 89Zr-Df-Tz derivative and TCO-functionalized bevacizumab for a head-to-head comparison between PT and conventional radioimmunoimaging of angiogenesis with PET. PT is expected to deliver much higher tumor-to-blood and tumor-to-muscle ratios in a short time after 89Zr-Df-Tz injection compared to directly labeled 89Zr-bevacizumab.

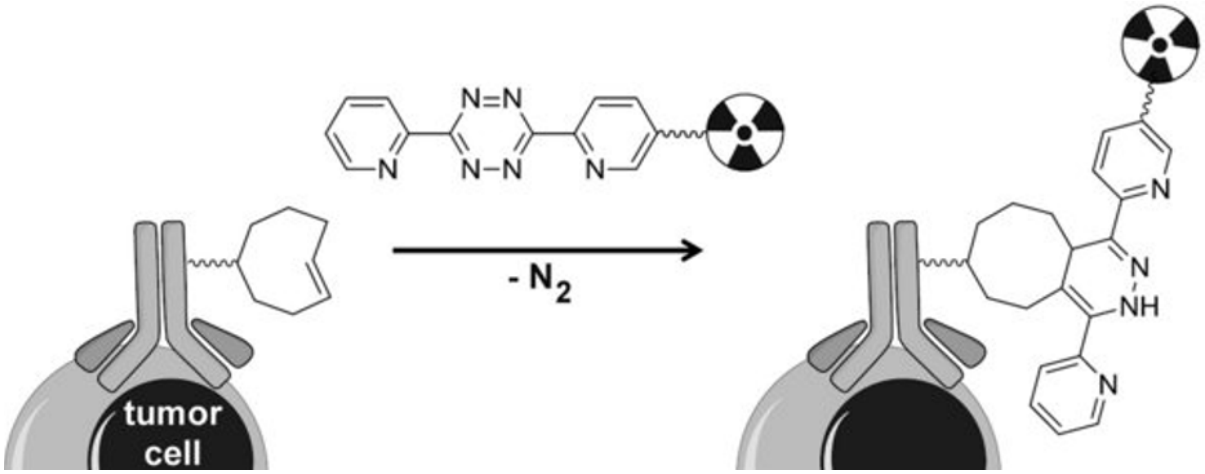

Figure 1: Graphical representation of the inverse-electron-demand Diels Alder pretargeting concept, showing the mAb modified with a TCO, which is reactive towards tetrazine labeled with a radionuclide.

Disclosure of author financial interest or relationships:
T.R. van Mourik, None; **R. Rossin**, Philips, Employment; Tagworks Pharmaceuticals, Consultant; **T. Läppchen**, Philips Electronics Nederland BV, Employment; **M.S. Robillard**, Tagworks Pharmaceuticals, Stockholder; **H. Gruell**, Eindhoven University of Technology, Employment; Philips, Employment .

Presentation Number **P 163**
Poster Session 2
September 19, 2013 / 15:15-15:15 / Room: Exhibit Hall B

Preliminary evaluation of [^{18}F]SFB- and [^{18}F]FBAM-labeled amyloidophilic peptides in mice with visceral amyloidosis

Jonathan S. Wall[1], Tina A. Richey[2], Alan Stuckey[3], Murthy R. Akula[3], George Kabalka[3], Sallie D. Macy[2], Emily B. Martin[2], **Stephen J. Kennel**[1], *[1]Medicine and Radiology, University of Tennessee Graduate School of Medicine, Knoxville, TN, USA; [2]Medicine, University of Tennessee Graduate School of Medicine, Knoxville, TN, USA; [3]Radiology, University of Tennessee Graduate School of Medicine, Knoxville, TN, USA. Contact e-mail: Skennel@utmck.edu*

Amyloidosis is a devastating pathology found not only in patients with Alzheimer's disease, but also in systemic disease in patients with multiple myeloma (AL), rheumatoid arthritis (AA) and familial transthyretin amyloidosis (ATTR). In these cases amyloid is deposited in visceral organs, notably, the spleen, liver, heart, and kidneys. The distribution and extent of amyloid deposition in body organs can establish a prognosis, inform treatment options, be used to monitor response to therapy, and act as an important end-point in therapeutic clinical trials. Therefore, non-invasive, quantitative determination of the amyloid load by using molecular imaging is valuable. We have identified polybasic amyloid-reactive peptides that, when radioiodinated are capable of selectively imaging systemic visceral amyloidosis, by using SPECT, in murine models of the disease [*PNAS* (2011) **108**(34): E586-594]. Here we describe the preliminary evaluation of radiofluorinated peptides for PET imaging using fluoro-succinimidyl benzoate (SFB) and N-[6-(4-[F-18]fluoro-benzylidene)aminooxyhexyl]maleimide (FBAM) as linkers. [^{18}F]FBAM and [^{18}F]SFB were prepared using microfluidic reactions, as previously described (*JNM* (2012) 53, 175P;*J. Label. Comps. Radiopharm*. (2011), 54, S533). Peptides were synthesized and purified by reverse phase HPLC before being reaction with FBAM at pH 6.8 in 20% acetonitrile or with SFB at pH 8.8 in borate buffer with 10% acetonitrile. [^{18}F]FBAM-p5 was recovered after reaction and purification in 30 min with a decay corrected yield of ~50% and [^{18}F]SFB-p13 in 45 min with radiochemical yields of ~7% (200 ug/mL peptide) to ~33% (2 mg/mL peptide). When injected iv into mice with systemic AA amyloidosis both peptides accumulated in the liver, spleen, pancreas and intestines, the major sites of pathology in this model. At 1 h pi [^{18}F]FBAM-p5 was found in the liver, pancreas and spleen at 6, 11 and 8 %ID/g and at 4 h pi a second group of mice were shown to have 7, 13, an 10 %ID/g. The mean AA:WT ratio for these tissues was 21, 17 and 29 at 4 h pi. Similarly the [^{18}F]SFB-p13 was present at 1 h pi in the liver, pancreas and spleen at 6, 15 and 9 %ID/g. In WT mice, both [^{18}F]SFB-p13 and [^{18}F]FBAM-p5 were present in the kidney, major the route of catabolism, at ~6 %ID/g at 1 h pi. Accumulation of both peptides was sufficient to permit visualization by PET imaging of amyloid in the major sites of deposition (see spleen and liver in the figure). These preliminary data indicate that we have developed 2 promising ^{18}F-labeled synthetic peptide candidates for the detection of visceral amyloidosis by using PET/CT imaging. These peptides interact rapidly with amyloid and will provide effective amyloid probes for PET/CT imaging of amyloid once labeling yields can be optimized.

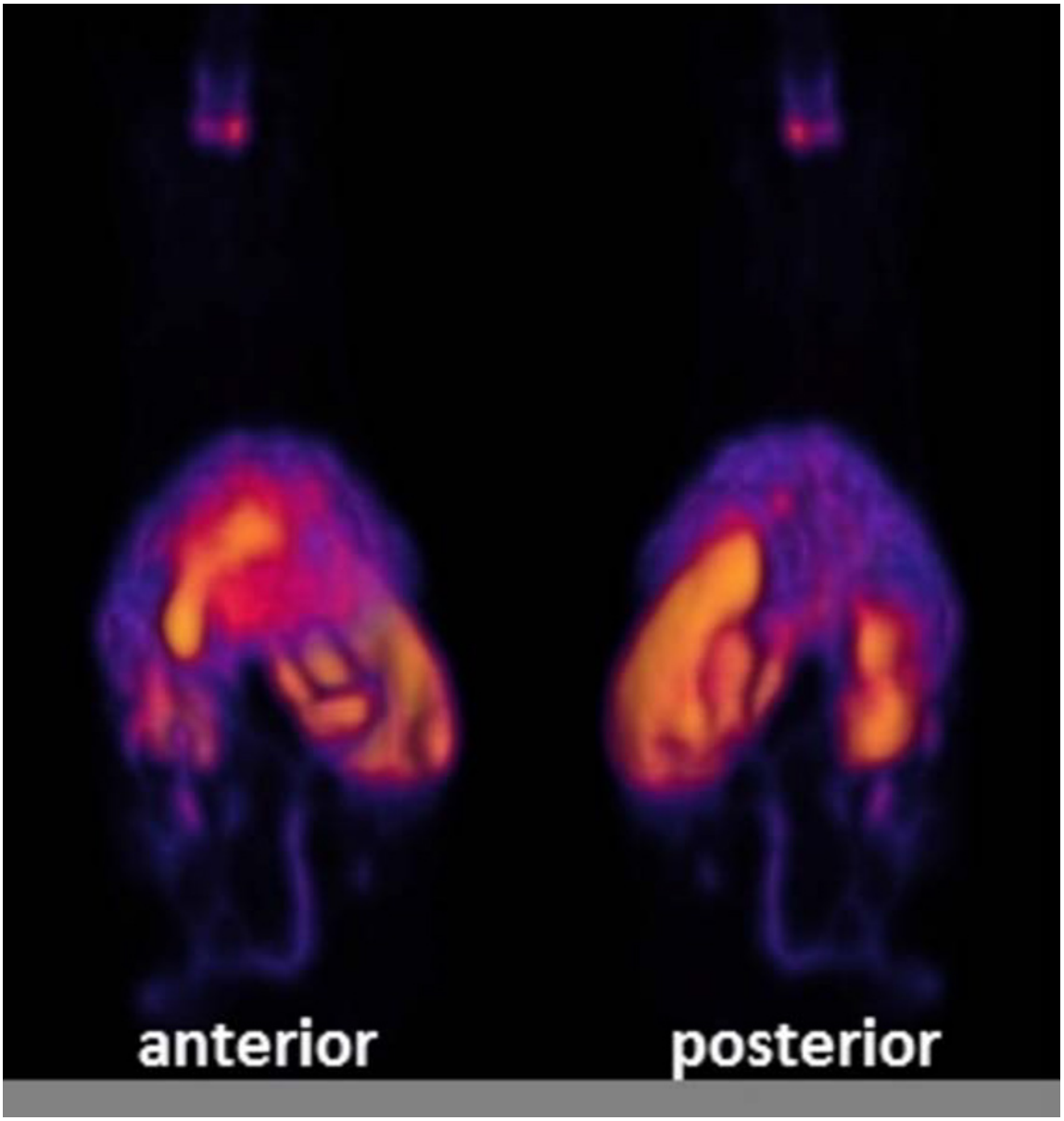

Disclosure of author financial interest or relationships:
J.S. Wall, Solex Inc, Stockholder; **T.A. Richey**, Solex Biomedical, Stockholder; **A. Stuckey**, Solex, LLC, Stockholder; **M.R. Akula**, None; **G. Kabalka**, None; **S.D. Macy**, None; **E.B. Martin**, Solex LLC, Stockholder; **S.J. Kennel**, Solex,lld, Stockholder .

Presentation Number **P 164**
Poster Session 2
September 19, 2013 / 15:15-15:15 / Room: Exhibit Hall B

In vivo evaluation of 18F-labeled TCO for pre-targeted PET imaging in the brain

Leonie Wyffels[1,2], *Jens Fissers*[2,3], *Ann-Marie Waldron*[2], *David Thomae*[2,3], *Stefanie Dedeurwaerdere*[4], *Darrel Pemberton*[5], *Mark E. Schmidt*[5], *Jurgen Joossens*[3], *Pieter Van der Veken*[3], *Koen Augustyns*[3], *Sigrid Stroobants*[1,2], *Steven Staelens*[2], [1]*Nuclear Medicine, University Hospital Antwerp, Edegem, Belgium;* [2]*Molecular Imaging Center Antwerp, University of Antwerp, Wilrijk, Belgium;* [3]*Medicinal Chemistry, University of Antwerp, Wilrijk, Belgium;* [4]*Translational Neurosciences, University of Antwerp, Wilrijk, Belgium;* [5]*Experimental Medicine, Jannsen Pharmaceutica, Beerse, Belgium. Contact e-mail: leonie.wyffels@uza.be*

Introduction: The tetrazine-trans-cylooctene ligation using radiolabeled tetrazine or radiolabeled trans-cyclooctene (TCO) has been reported to be a very fast, selective and bioorthogonal reaction that could be useful for in vivo radiolabeling of target molecules [1]. We wanted to evaluate the in vivo biodistribution profile and brain uptake of 18F-labeled TCO ([18F]-TCO) to assess its potential for pre-targeted imaging in the brain. Methods: Cold reference (F-TCO) and tosylated precursor were synthesized from the corresponding alcohol prepared by UV irradiation (UVP-CL-1000 crosslinker) [2, 3]. [18F]-TCO was synthesized by modification of the method described by Li et al [3] on a Veenstra FluorSynthon III synthesis module. Following reaction of 2mg precursor with dried [18F]KF-K2.2.2 for 10 min at 90°C, the reaction mixture was purified by HPLC using a biocompatible mobile phase. The purified [18F]-TCO was formulated for iv injection by sterile filtration and diluted with 0.9% NaCl. We performed µPET and biodistribution at 5min, 30min, 60min, 90min, 120min and 240min post tracer injection to evaluate brain uptake, ex-vivo brain autoradiography and pharmacokinetic profile. Therefore C57BL/6J mice (n=6) were injected with [18F]-TCO (18.5Mbq) for a dynamic PET (Siemens Inveon PET-CT) scan of 120 mins and a static scan at 4h. At each time point one animal was sacrificed for biodistribution completed by an extra group mice (n=12) that only underwent biodistribution (n=3 per time point in total). Results: The use of UV irradiation significantly shortened the synthetic route of F-TCO and the tosylated precursor. [18F]-TCO was obtained in a decay corrected radiochemical yield of 14±5% (n=6; decay corrected) and with a radiochemical purity of >99%. [18F]-TCO, showed an initial brain uptake of 3.8±0.6 %ID/g at 5 min pi followed by a washout to 3.0±0.6 %ID/g at 30 min pi. Subsequently the brain uptake increased again to 3.8 %ID/g at 120 min pi followed by a slow washout at 240 min pi (2.9±0.9 %ID/g). Autoradiography confirmed homogenous brain uptake. Highest tracer uptake could be detected in bone (from 2.1±0.7 %ID/g at 5 min to 15.7±2.7 %ID/g at 240 min pi). [18F]-TCO showed an initial urinary clearance followed by hepatobiliary clearance. Conclusions: Although [18F]-TCO passes the blood-brain barrier, the uptake profile in the brain and high bone uptake indicate metabolism and possible non-specific binding of radiometabolites to brain tissue. A metabolite study will be performed to identify the metabolic profile and to optimize the structure of [18F]-TCO for in vivo pre-targeted PET imaging in the brain. References: [1] Rossin et al. Angew Chem Int Ed 2010; 49, 3375-3378. [2] Keliher E.J., Chem Med Chem, 2011, 6, 424-427 [3] Li Z et al. Chem Commun 2010; 46, 8043-8045.

Disclosure of author financial interest or relationships:
L. Wyffels, None; **J. Fissers**, None; **A. Waldron**, None; **D. Thomae**, None; **S. Dedeurwaerdere**, None; **D. Pemberton**, None; **M.E. Schmidt**, Janssen Pharmaceutica NV, Employment; **J. Joossens**, None; **P. Van der Veken**, None; **K. Augustyns**, None; **S. Stroobants**, Janssen Pharmaceuticals, Grant/research support; **S. Staelens**, Johnson & Johnson, Grant/research support .

Presentation Number **P 165**
Poster Session 2
September 19, 2013 / 15:15-15:15 / Room: Exhibit Hall B

Radio-tracer techniques to distinguish choline transport inhibition from choline kinase inhibition

Sean P. Arlauckas, *Anatoliy V. Popov, Edward J. Delikatny, Radiology, University of Pennsylvania, Philadelphia, PA, USA. Contact e-mail: sarl@mail.med.upenn.edu*

Choline kinase α (ChoKα) inhibition is an emerging strategy for solid tumor treatment. The prototype ChoKα inhibitor is the choline mimetic hemicholinium-3, which is highly toxic due to its disruption of acetylcholine-related processes in the nervous system. Screens against pure ChoKα have identified several potent inhibitors that reduce the phosphorylation of choline and slow tumor growth via cancer cell-specific apoptosis. Studies in intact cancer cells have shown that ChoKα suppression via drug or siRNA not only reduces phosphocholine (PC) levels, but also lessens choline transport into the cell. Phosphorylation is a common metabolite trapping mechanism, thus, in cancers characterized by ChoKα overexpression, ChoK may drive the transport of new choline into the cell by maintaining an intracellular/extracellular gradient (Figure 1). There are a number of choline transporters; their precise mechanisms and role in cancer progression are poorly understood. Recently, we developed a near-infrared fluorophore, JAS239, which directly inhibits ChoK in breast cancer cells and has no discernible interaction with choline transport. Using this probe it is possible to identify that PC reduction in intact cells is due to ChoK inhibition, and not choline transporter inhibition. The present study explores the effect of JAS239 on phospholipid-related choline flux, and compares the results to the most-studied ChoK inhibitor in the literature, MN58b. Using 14C-choline radio-tracing in MDA-MB-231 and MCF-7 breast cancer cells, the water-soluble choline-containing metabolites were separated by TLC and quantified using autoradiography. Choline was immediately phosphorylated upon cell entry, consistent with our NMR estimates of ChoK activity in these cells. Glycerophosphocholine (GPC), a breakdown product of phosphatidylcholine, became visible by 16 h, whereupon the cycling of this metabolite back to PC was observed and presumed to be driven by the elevated expression of ChoK and mediated by GPC-phosphodiesterase. In the presence of either MN58b or JAS239, 14C-PC levels were substantially reduced 1 h and 16 h after radio-tracer addition—that is, both before and after substantial cell death was observed. MCF-7 viability was measured by Trypan Blue exclusion, and ChoKα overexpression caused no protection against cell death after 17 h treatment with MN58b or JAS239. These results were unexpected, but may be explained by the observation that both inhibitors were effective at reducing 14C-PC in ChoKα overexpressing MCF-7 cells (MCF7-CK) to levels comparable to the corresponding empty vector cells (MCF7-EV). Interestingly, JAS239 at concentrations <20 μM did not affect 14C-GPC levels at 16h of radio-tracing in MCF7-EVs, whereas MN58b significantly reduced 14C-GPC in these cells at as little as 1 μM. ChoK overexpression was sufficient to rescue the depletion of 14C-GPC induced by JAS239. MN58b does not prevent GPC from returning to PC as was seen with the transporter-independent fluorophore JAS239, thus raising the possibility that MN58b reduces PC by directly affecting one or more of the non-neuronal choline transporters actively involved in breast cancer.

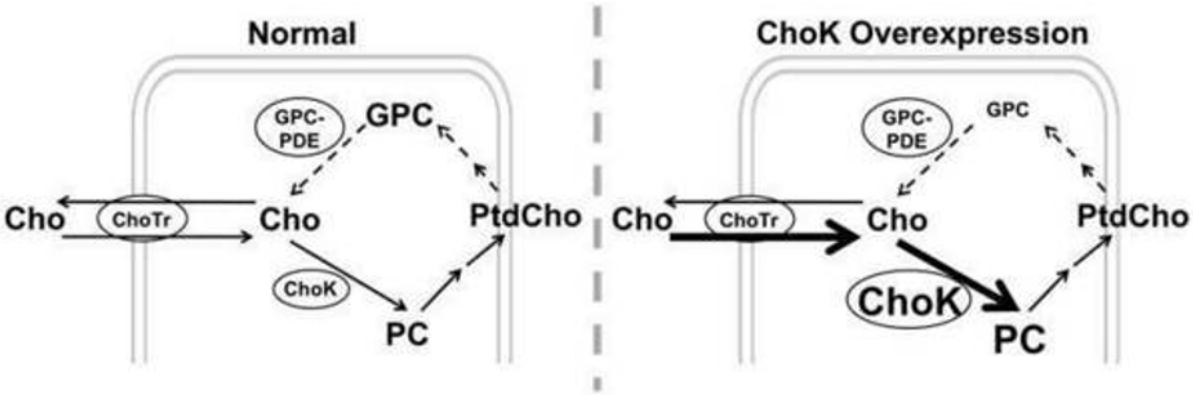

Figure 1: *Left) In normal cells choline enters through a variety of transporters (ChoTr), including the organic cation transporters (OCTs), organic cation/carnitine transporters (OCTNs), choline high-affinity transporters (CHTs), and choline transporter-like proteins (CTLs). Choline is then rapidly phosphorylated by choline kinase (ChoK) to phosphocholine (PC) in the first committed step of the Kennedy pathway leading to phosphatidylcholine (PtdCho). PtdCho can be broken down to glycerophosphocholine (GPC) and cycled back to choline and PC via a number of phospholipase and GPC-phosphodiesterase (GPC-PDE)-mediated pathways. Right) ChoK overexpression is common in many cancers and characteristically drives high choline uptake, causes high PC levels at the expense of GPC, and is associated with a more malignant phenotype, leading to the surging interest in ChoK inhibitors for cancer therapy. Disrupting choline transport and/or phosphorylation can yield similar results if the proper strategy is not implemented.*

Disclosure of author financial interest or relationships:
S.P. Arlauckas, None; **A.V. Popov**, None; **E.J. Delikatny**, None.

Presentation Number **P 166**
Poster Session 2
September 19, 2013 / 15:15-15:15 / Room: Exhibit Hall B

New Approach for Confirmation of Electrochemical Ablation by a Small Molecule Sensor

Christian Brand[1], *Christopher Irwin*[1], *Govindarajan Srimathveeravalli*[1], *Wolfgang A. Weber*[1,2], *Jason S. Lewis*[1,2], *Thomas Reiner*[1], [1]*Radiology, Memorial Sloan-Kettering Cancer Center, New York, NY, USA;* [2]*Molecular Pharmacology and Chemistry Program, Memorial Sloan-Kettering Cancer Center, New York, NY, USA. Contact e-mail: brandc@mskcc.org*

Image guided ablation is the mainstay salvage therapy for patients with unresectable tumors, chemotherapy or radiation refractory lesions, and for control of metastatic disease. Increasingly, the low morbidity rates and positive outcome following ablation has led to its adoption as a non-surgical treatment option for primary tumors in the kidney, and for non-metastatic disease in other organs (liver and lung) (1,2). Yet, although electrochemical treatment techniques (3) are becoming evermore important and even emerging as the treatment of choice for certain types of cancers, the effects of such treatments and their successful delivery can only be monitored poorly. We now report a new approach for the visualization of the amounts of energy which were deposited into tissue during ablation therapy. Based on the organometallic complex ferrocene, we designed a redox-active small molecule which acts as a molecular sensor of electrical energy. The combination of a redox-active organometallic compound and a fluorophore provides an imaging agent able to visualize the extent of radiofrequency ablation. We demonstrate that ferrocene is oxidized during the ablation process to ferrocenium (an oxidation from Fe2+ to Fe3+). The enhanced bright fluorescence, which is observed after ablation, is obtained by passed electric charge through a phantom (3% agarose gel, c(sensor): 0.5 mM). To validate the fluorescent signal increase (up to 5-fold) after electrical energy ablation of the phantom, we chemically oxidized the small molecule sensor to the ferrocenium species and compared the absorbance and emission spectra with the absorbance and emission spectra of the non-oxidized agent. One of the key novelties of this technique is the ability to observe the effects of electrical energy ablation in real time, during the clinical procedure. Ultimately, we hope to use this technique as a quantitative confirmation of therapeutic dosage - allowing diagnostics without the use of immunohistochemistry or magnetic resonance imaging. Acknowledgements: Supported by the Brain Tumor Center and the Imaging and Radiation Sciences Program of Memorial Sloan-Kettering Cancer Center (TR). Reference: [1] Lo SS, Moaffatt-Bruce SD, Dawson LA, et al. Nat Rev Clin Oncol. 2011;8:405-416. [2] McGahan JP, Dodd III GD, A J R. 2001;176:3-16. [3] Czymek R, et al. J S R. 2012;174;106-113.

Disclosure of author financial interest or relationships:
C. Brand, None; **C. Irwin**, None; **G. Srimathveeravalli**, None; **W.A. Weber**, None; **J.S. Lewis**, None; **T. Reiner**, None.

Presentation Number **P 167**
Poster Session 2
September 19, 2013 / 15:15-15:15 / Room: Exhibit Hall B

Self-Assembled Porphyrin-Lipid Nanoparticles for In Vivo Molecular Imaging via Surface Enhanced Raman Spectroscopy

Arash Farhadi[1,2], *Patrick Z. McVeigh*[1,2], *Juan Chen*[2], *Brian C. Wilson*[1,2], *Gang Zheng*[1,2], [1]*Medical Biophysics, University of Toronto, Toronto, ON, Canada;* [2]*University Health Network, Toronto, ON, Canada. Contact e-mail: arash.farhadi@utoronto.ca*

We have previously shown that optically versatile porphyrin molecules can be conjugated to a lipid backbone (pyrolipid) to produce self-assembled organic nanoparticles with unique photonic properties. Liposome constructs made of densely packed pyrolipid molecules have shown superb preclinical theranostic ability such as fluorescence, photoacoutic, and PET imaging as well as photothermal therapy capability. However, clinical translation of fluorescence contrast agents suffers from high autofluorescence background and short imaging window due to photobleaching. The use of plasmonic nanoparticles encapsulated in a self-assembled pyrolipid shell exhibit an attractive alternative to mitigate these challenges through the use of surface enhanced Raman Spectroscopy (SERS). Herein, gold nanoparticles encapsulated in a pyrolipd bilayer are used for SERS imaging of lung cancer cell surface makers. The use of pyrolipid as a SERS dye carries the advantage over traditional dyes due to its unique property of providing a distinct SERS spectrum as well as stabilizing gold nanoparticle. In this work a rapid and facile synthesis of pyrolipid SERS nanoparticles with size, signal stability and signal strength suitable for in vivo imaging of EGF receptor molecular imaging is presented. An FDA approved EGFr antagonist (Vectibix) is used to confer targeting capability to the nanoparticles wherein in vitro Raman microscopy has enabled to molecular imaging of EGF receptors on lung carcinoma cells incubated with nanoparticles; dark-field microscopy validates the high specificity of nanoparticles to target EGFr positive cells over negative cells. SERS contrast from nanoparticles can be seen in the liver and spleen of mice for up to 48 hours post injection. Dorsal skin window chamber model has been developed to preclinically mimic smoking-related early stage lung cancer disease in humans. The EGFr targeted pyrolipid SERS nanoparticles are used to provide optical contrast to tumour with minimal SERS background signal using Raman microscope.

Disclosure of author financial interest or relationships:
A. Farhadi, None; **P.Z. McVeigh**, None; **J. Chen**, None; **B.C. Wilson**, None; **G. Zheng**, None.

Presentation Number **P 168**
Poster Session 2
September 19, 2013 / 15:15-15:15 / Room: Exhibit Hall B

Novel Folate Receptor (FR)-Targeted NIR Dye: Bench to Clinic

Pravin D. Gagare[1], *Mohammad Noshi*[1], *Sakkarapalayam M. Mahalingam*[2], *Sumith A. Kularatne*[1], *Jyoti Roy*[2], *Philip S. Low*[2], [1]*Ontarget Laboratories LLC, West Lafayette, IN, USA;* [2]*Purdue University, West Lafayette, IN, USA. Contact e-mail: pgagare@ontargetlabs.com*

Surgery constitutes one of the best methods for treatment of solid tumors, such as prostate, ovarian, lung, breast, colon, and pancreatic cancer. While surgery cures 50% of patients with solid tumors in the US, chemo- and radiotherapy cure less than 5% of all cancer patients. Over 700,000 patients undergo cancer surgery every year in the US and 40% of surgical patients have a recurrence of locoregional disease within 5 years. Despite major advances in the oncology field, major hurdles must still be overcome, including: (1) resection of the primary malignant mass with entirely negative margins, (2) removal of all lymph nodes harboring metastatic cancer cells, and (3) identification of all satellite disease. In order to achieve these goals, we have recently developed a novel FR-targeted near-infrared (NIR) fluorescence probe (OTL-0038) with enhanced fluorescence intensity and photo-stability for use in image-guided tumor surgery. In this study, we summarize structure activity relationships, lead optimization, scale-up synthesis, and chiral analysis of OTL-0038. We also demonstrate the binding and specificity of OTL-0038 for FR using (1) FR+ cancer cells in culture, (2) in vivo whole body imaging and ex vivo biodistribution in mice with FR+ or FR- tumor xenografts, (3) dose escalation studies in nude mice, and (4) safety studies. We conclude that OTL-0038 not only offers a robust chemistry (efficient synthesis in small scale to multi-gram scale with high purity and high yield, ease of purification and characterization, compatibility with both organic and aqueous solvents, stability during synthesis and storage), but also exhibits excellent binding affinity, PK profile, signal-to-noise ratio for FR+ tumor tissues, and toxicity profile. With appropriate stability and toxicity data, it should qualify for examination in human clinical trials in the near future.

Disclosure of author financial interest or relationships:
P.D. Gagare, None; **M. Noshi**, None; **S.M. Mahalingam**, None; **S.A. Kularatne**, None; **J. Roy**, None; **P.S. Low**, On Target Laboratories, Other financial or material support .

Presentation Number **P 169**
Poster Session 2
September 19, 2013 / 15:15-15:15 / Room: Exhibit Hall B

NIRF imaging of fluorescent Glucan Particles in an autoimmune model of rheumatoid arthritis (CIA)

Francesca Garello[1], *Francesca Arena*[2], *Juan C. Cutrin*[3], *Luca D'Angeli*[2], *Giovanna Esposito*[2], *Sara Figueiredo*[4], *Stefanìa Rachele*[1], *Enrico Chiavazza*[1], *Silvio Aime*[1,2], *Enzo Terreno*[1,2], [1]*Molecular Biotechnology and Health Sciences, Molecular Imaging Center, University of Torino, Torino, Italy;* [2]*Center for Preclinical Imaging, University of Torino, Colleretto Giacosa, Italy;* [3]*ININCA, UBA-CONICET, Buenos Aires, Argentina;* [4]*Department of Life Sciences, FCTUC and Center for Neurosciences and Cell Biology, University of Coimbra, Coimbra, Portugal. Contact e-mail: francesca.garello@unito.it*

Glucan Particles (GPs) are hollow pseudo-microspheres (diameter 2-3 μm) obtained from common baker's yeast Saccharomyces Cerevisiae. Mannan, lipids and proteins are removed through a process of chemical extraction, leaving micron-sized porous shells made up mainly by 1,3-Beta-D-Glucan. The particles can be loaded with amphyphilic compounds through a sudden change in solvent polarity that allows the entrapment of molecules in form of microemulsion in the inner cavity. The high payload obtained and the high biocompatibility make these particles well suitable to act as carrier for contrast agents and drugs. Moreover, GPs can be considered an innovative and efficient microplatform for ex-vivo or in-vivo labelling of immune cells as they are easily recognized and taken up through dectin-1 receptor and complement receptor 3. In this work, GPs loaded with a NIRF detectable microemulsion were intravenously injected in an autoimmune model of rheumatoid arthritis (CIA) in mice to assess the potential of the system to label immune cells in vivo and detect by NIRF imaging the macrophage recruitment at the inflamed regions. Dry glucan particles were incubated overnight with a chloroform solution containing the water insoluble newly synthesized Cy5-(C16) 2 (20 μg/mL) and Rhodamine-DOPE (20 μg/mL). Next, Hepes buffer was added to change polarity and form the microemulsion. Loaded GPs were washed several times to remove the non-entrapped material. Incubation with murine macrophages J774.A1 was performed to assess the detection limit of the GP-labelled cells by NIRF. Autoimmune arthritis was induced in DBA-1 mice by immunization with an emulsion containing 0.4 mg of bovine type II collagen (CII) in CFA and 0.4 mg of mycobacterium tuberculosis. Total score, related to inflamed paws, was estimated daily and mice were recruited as soon as they showed clinical signs of inflammation. Recruited mice were intravenously injected with 150 μl of fluorescent GPs (18.5e6 GPs/μL). Animals were imaged on a LI-COR Pearl Impulse (λ exc 685 nm-λ em 720 nm) before and immediately after injection of GPs, and at 1, 3, 5, 24 and 48 h time points. Immunohistochemistry was carried out for validation purposes. A detection limit of ca. 70000 particles/μL was observed in vitro with GPs loaded with Cy5-(C16) or rhodamine-DOPE. Incubation with J774.A1 cells showed a remarkable phagocytic uptake and low cellular toxicity. Macrophages incubated with fluorescent GPs were diluted at different concentrations and imaged: a detection threshold of ca. 300 cells/μl was obtained. Cy5(C16)2-loaded GPs were injected in CIA mice with different clinical scores: a good correlation between fluorescence signal and score values was found. The highest signal was detected 3 hours post injection. Immunohistochemistry analysis was carried out to assess the co-localization between the particles and macrophages infiltrating the lesion. In conclusion, GPs may represent a promising alternative to other nano- and micro-sized labelling agents to label and track immune cells in vivo for detecting inflammation regions. Moreover, they can be successfully used as multimodal probes for several imaging technologies.

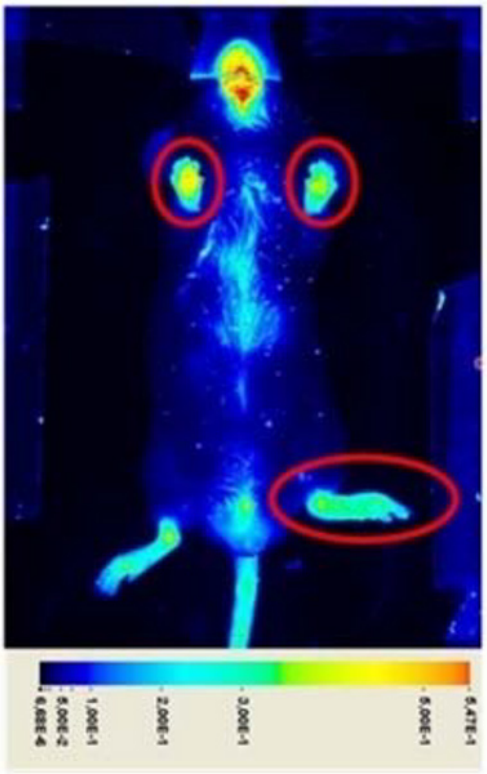

	num.inflamed fingers	thickness related values
Front paw DX	4	1.70
Front paw SX	4	1.88
Hind paw DX	1	1.70
Hind paw SX	5	2.50

Ventral optical image of a CIA mouse with a total score of 4.5. Red circles highlight paws with the highest CIA score.

Disclosure of author financial interest or relationships:
F. Garello, None; **F. Arena**, None; **J.C. Cutrin**, None; **L. D'Angeli**, None; **G. Esposito**, None; **S. Figueiredo**, None; **S. Rachele**, None; **E. Chiavazza**, None; **S. Aime**, None; **E. Terreno**, Bracco Imaging, Consultant .

Presentation Number **P 170**
Poster Session 2
September 19, 2013 / 15:15-15:15 / Room: Exhibit Hall B

Photosensitizer-Conjugated Silica-Coated Gold Nanoclusters as Photo-Theranostic for Fluorescence Imaging-Guided Photodynamic Therapy

Peng Huang, *Jing Lin, Gang Niu, Xiaoyuan (Shawn) Chen, National Institutes of Health, Bethesda, MD, USA. Contact e-mail: penghuang2011@gmail.com*

Multifunctional theranostics have recently been intensively explored to optimize the efficacy and safety of therapeutic regimens. In this work, a novel photo-theranostic based on chlorin e6 (Ce6) photosensitizer-conjugated silica-coated gold nanoclusters (AuNCs@SiO2-Ce6) is strategically designed and prepared for fluorescence imaging-guided photodynamic therapy (PDT). The AuNCs@SiO2-Ce6 shows the following features: i) high Ce6 loading efficiency due to the conjugation strategy; ii) effectively avoiding the leakage of Ce6 during its circulation in biological system; iii) significantly enhanced cellular uptake efficiency of Ce6, offering a remarkably improved photodynamic therapeutic efficacy compared to free Ce6 ; iv) the subcellular dual-localization of Ce6 via both the fluorescence of Ce6 and AuNCs; v) fluorescence imaging-guided PDT. This photo-theranostic owns good stability, high water dispersibility and solubility, non-cytotoxicity, and good biocompatibility, thus facilitating their biomedical applications, particularly for multi-modal imaging of optical, computed tomography (CT) and photoacoustic (PA) guided PDT.

Disclosure of author financial interest or relationships:
P. Huang, None; **J. Lin**, None; **G. Niu**, None; **X. Chen**, None.

Presentation Number **P 171**
Poster Session 2
September 19, 2013 / 15:15-15:15 / Room: Exhibit Hall B

The Novel Imaging Probe AZD2281-FL as a Biomarker for Ionizing Radiation-Induced DNA Damage

Christopher Irwin, *Thomas Reiner, Wolfgang A. Weber, Valerie A. Longo, Jason S. Lewis, Pat Zanzonico, Ruimin Huang, Qing Chen, Memorial Sloan-Kettering Cancer Center, New York, NY, USA. Contact e-mail: irwinc@mskcc.org*

Christopher Irwin1, Valerie Longo2, Qing Cheng2, Pat B. Zanzonico2, Ruimin Huang1, Jason S. Lewis1,3, Thomas Reiner1, Wolfgang Weber1,3 1. Department of Radiology, Memorial Sloan-Kettering Cancer Center, NY, NY 2. Department of Medical Physics, Memorial Sloan-Kettering Cancer Center, NY, NY 3. Molecular Pharmacology and Chemistry Program, Memorial Sloan-Kettering Cancer Center, NY, NY Objectives: AZD2281-FL is a novel imaging probe that has potential as a biomarker for ionizing radiation (IR)-induced DNA damage. Although radiotherapy is the treatment of choice for many human cancers [1], there is currently no non-invasive way of quantifying the amount of damage inflicted on malignant or healthy cells during treatment. AZD2281-FL is a fluorescently tagged inhibitor of the DNA damage repair protein PARP-1, which can be used to quantify levels of cellular PARP-1 [2]. Following exposure to IR, cells attempt to repair DNA by upregulating PARP-1 [3-5]. We show upregulation of PARP-1 following exposure to IR can be visualized in vitro and in vivo with AZD2281-FL. Methods: In vitro, PANC-1 cells were grown in a tissue culture dish, exposed to varying doses of IR (0-32 Gy), and then incubated with AZD2281-FL for 30 min. Fluorescent images were created with a Nikon Eclipse Ti microscope, and cellular fluorescence levels were quantified with Fiji image processing software [6]. In vivo, xenografts were grown on the left and right shoulders of nude mice. One of the tumors was irradiated with 16 Gy over 4 days via external beam radiation using X-RAD 225Cx micro irradiator (PXi Precision X-ray), while the other tumor remained untreated. After completion of the treatment the mouse was injected IV with AZD2281-FL. After two hours, the mouse was sacrificed, and tumor and muscle were resected. Levels of AZD2281-FL were determined by quantifying the fluorescence signal of the excised tissues. Results: In vitro, we observed an approximate 47% increase in average fluorescence in PANC-1 cells when treated with 32 Gy compared to the unirradiated control cells ($p<.0001$). In vivo, SKOV3 tumor treated with 16 Gy over 4 days showed an approximate 40% increase in signal compared to unirradiated tumor tissue following injection with AZD2281-FL ($p=.04$). Conclusion: These preliminary data suggest that AZD2281-FL may be used to image PARP-1 expression by cancer cells and determine its modulation by ionizing radiation. Further studies to validate these findings in other cell lines and with other radiation doses are ongoing. Acknowledgements: Supported by the Brain Tumor Center of Memorial Sloan-Kettering Cancer Center (TR). References: [1] Begg AC, et al. (2011) Nature Reviews. 4:239-53. [2] Reiner T et al. (2012) Neoplasia 14: 169-177. [3]Doucet-Chabeaud G. et al. (2001) Mol Genet Genomics 265:954-963. [4]Hagan MP et al. (2007) J Cell Biochem 101:1384-1393. [5] Redon CE, et al. (2010) Clinical Cancer Research 16:4532-4542.[6] Schindelin JRedon CE, et al. (2012) Nature Methods 9(7): 676-682

Disclosure of author financial interest or relationships:
C. Irwin, None; **T. Reiner**, None; **W.A. Weber**, None; **V.A. Longo**, None; **J.S. Lewis**, None; **P. Zanzonico**, None; **R. Huang**, None; **Q. Chen**, None.

Presentation Number **P 172**
Poster Session 2
September 19, 2013 / 15:15-15:15 / Room: Exhibit Hall B

Inspiring Performance of the Designed Firefly Luciferin Analog Emitting Near-infrared Biological Window Light

Satoshi Iwano[1], *Akane Kanamori*[2], *Takahiro Kuchimaru*[2], *Fumika Inazuka*[2], *Rika Obata*[1], *Shojiro A. Maki*[1], *Shinae Kondoh*[2], *Haruki Niwa*[1], [1]*Department of Engineering Science, The University of Electro Communications, Chofu, Japan;* [2]*Department of Biomolecular Engineering, Tokyo Institue of Technology, Yokohama, Japan. Contact e-mail: iwano@lumi.pc.uec.ac.jp*

Firefly bioluminescence is a powerful tool to noninvasively image cancer progression and metastasis in vivo. For imaging deep sites, red, or more desirably, near-infrared (NIR) biological window light is suitable due to less absorption and scattering properties in biological tissues. To improve in vivo performance of firefly bioluminescence, several variants of firefly luciferase (Fluc) with red-shifted bioluminescence emission (~620 nm) have been developed through random mutagenesis screening. However, construction of NIR firefly bioluminescence system is not achieved by combination of mutant luciferases and wild type (WT) luciferin. During past decade we designed and synthesized structurally simple luciferin analogs for color tuning of firefly bioluminescence system, culminating recently to develop a simple luciferin analog with a desirable light emission maximum in the NIR wavelength region "biological window" (Fig.1. S. Iwano, et al., Tetrahedron, 2013, in press, http://dx.doi.org/10.1016/j.tet.2013.03.050). Herein, we wish to disclose the performance of our designed NIR luciferin in in vitro and in vivo systems. First of all, we compared in vitro tissues permeability of lights produced by the NIR luciferin, amino-luciferin and WT luciferin, respectively with WT Fluc (Fig.1 B). Total bioluminescence intensity was almost comparable when we react these luciferin analogs with WT Fluc. We then measured bioluminescence intensity through a filter mimicking mammal tissues with 10 mm thickness. When using WT luciferin (λmax 565 nm) and amino-luciferin (λmax 610 nm), we observed that only 0.5 % and 1% of total light was pass through the tissue-mimicking filter, respectively. On the other hand, when using the NIR luciferin (λmax 675 nm), 5% of total light was passed through the tissue-mimicking filter, clearly indicating higher permeability of the light generated from our designed NIR luciferin. We next evaluated in vivo performance of the NIR luciferin. We intraperitoneally injected equivalent amount of WT luciferin and the NIR luciferin into nude mice subcutaneously inoculated Fluc-expressing cancer cells in the backs and hind-limbs (Fig.1 C). Surprisingly, the light from the NIR luciferin was observed over 5 folds stronger than that from WT luciferin even in subcutaneous tumors, which relatively locate relatively close to body surface. These results indicate that the NIR luciferin has great potential to detect tumors in deeper sites and will become a new powerful tool for in vivo imaging in biomedical researches.

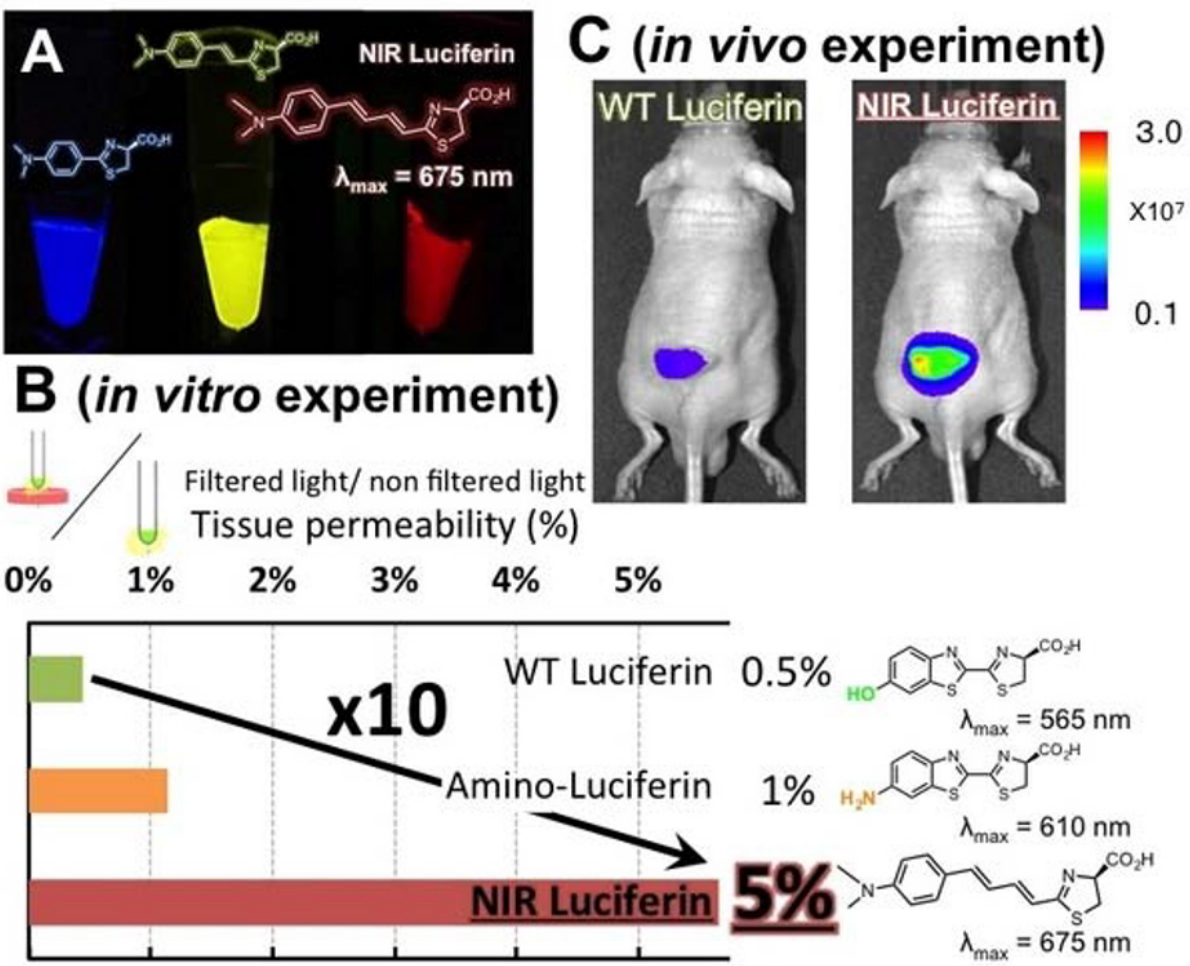

Fig. 1 A) The bioluminescence colors of our designed Firefly analogs. (B) The light permeability of Luciferin analogs through mammal tissue-mimic. The light of NIR luciferin has 10 folds higher tissue permeability than that of WT luciferin. C) Representative in vivo images of the nude mice emitting light from Fluc-expressing tumors subcutaneously inoculated. Bioluminescence substrate is WT luciferin (left) and NIR luciferin (right). The light intensity of NIR luciferin has 5 folds stronger than that of WT luciferin in vivo.

Disclosure of author financial interest or relationships:
S. Iwano, None; **A. Kanamori**, None; **T. Kuchimaru**, None; **F. Inazuka**, None; **R. Obata**, None; **S.A. Maki**, None; **S. Kondoh**, None; **H. Niwa**, None.

Presentation Number **P 173**
Poster Session 2
September 19, 2013 / 15:15-15:15 / Room: Exhibit Hall B

Liposomal Indocyanine Green as Diagnostic and Phototherapeutic Tool in Sentinel Lymph Nodes

Byungji Kim[1], *Yu Hua Quan*[3], *Yeonho Choi*[2], *Hyun Koo Kim*[3], *Ji Ho Park*[1], [1]*Bio and Brain Engineering, KAIST, Daejoen, Republic of Korea;* [2]*Biomedical Engineering, Korea University, Seoul, Republic of Korea;* [3]*Thoracic and Cardiovascular Surgery, Korea University Guro Hospital, Korea University College of Medicine, Seoul, Republic of Korea. Contact e-mail: bjkim0220@gmail.com*

Sentinel lymph node (SLN) mapping is essential in detecting cancer metastases. Current SLN mapping systems require multiple injections of different chemicals for lymph node visualization and identification, and surgical procedures for lymph node removal. All of these factors carry not only financial disadvantages, but also time consumption and patient discomfort. Herein, we engineered liposomal indocyanine green (ICG) as a biocompatible nanoparticle with potential to be used as both a diagnostic and therapeutic tool in SLN mapping. Liposomal ICG with enhanced fluorescence intensity and longevity in comparison with free-ICG was developed, which also showed photothermal properties that may be used for cancer therapy. In vivo SLN accumulation experiment was performed on 5-week old male BALB/C mice by footpad injection of liposomal ICG and free-ICG. Liposomal ICG showed SLN accumulation into the popliteal lymph node, the sentinel. In contrast, free-ICG did not show visible accumulation into SLN. Ex vivo NIR fluorescence analyses by excision of ipsilateral and contralateral popliteal lymph nodes confirmed higher accumulation by liposomes compared to free-ICG. Liposomes were tested for photothermal effect in vitro by being placed in a 96-well plate and irradiated with a 785nm laser (450mW) for 5-min under observation with an infrared camera. Both free-ICG and liposomal ICG heated up to over 50°C from room temperature, but showed photobleaching and decrease in temperature after 2-min of irradiation. In vivo photothermal effects were observed using the same laser and infrared camera system. After liposomal ICG accumulation in SLN was observed by its fluorescence, the popliteal lymph node was irradiated, and observed for extent of temperature increase. Post-irradiation, mice were sacrificed and dissected for popliteal lymph node excision. Excised ipsilateral and contralateral popliteal lymph nodes were irradiated again for ex vivo photothermal efficacy of liposomal ICG. In vivo irradiation showed notable temperature increase in popliteal lymph node despite the protective layers of skin and muscles. Ex vivo irradiation of excised popliteal lymph nodes showed temperature increases over 40°C. With use of only FDA-approved materials, we have developed a single nanoparticle with potential to perform as both the diagnostic and phototherapeutic tool ideal for SLN mapping.

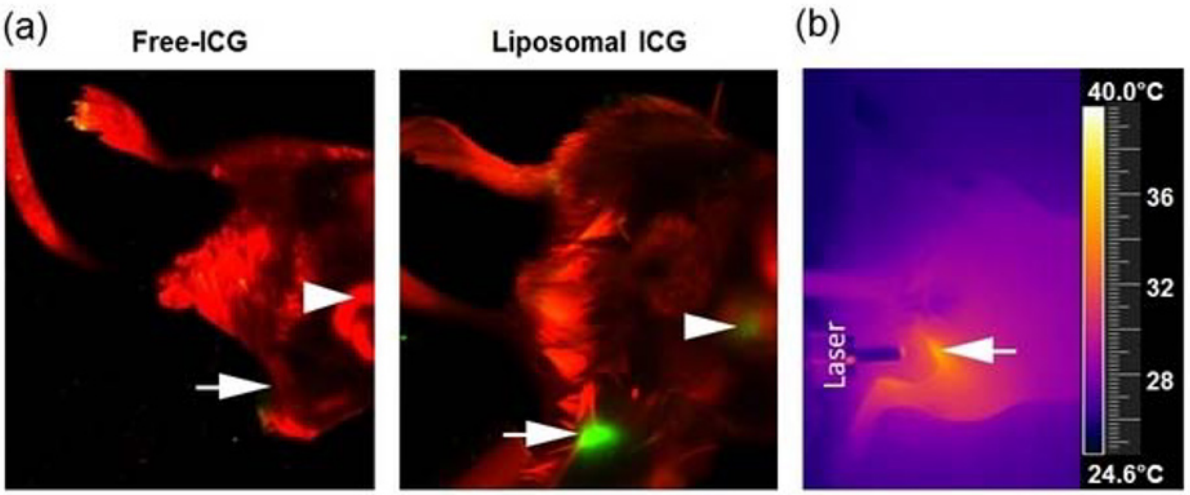

Figure 1. (a) In vivo SLN (popliteal lymph node) accumulations of free-ICG and liposomal ICG 30-min post-injection into hind footpad. Arrows indicate popliteal lymph node and arrowheads indicate second-tier medial iliac lymph node; (b) In vivo photothermal effect of liposomal ICG accumulated in ipsilateral popliteal lymph node (arrow) observed using infrared camera system; Laser information: 785nm, 450mW, 5min irradiation.

Disclosure of author financial interest or relationships:
B. Kim, None; **Y. Quan**, None; **Y. Choi**, None; **H. Kim**, None; **J. Park**, None.

Presentation Number **P 174**
Poster Session 2
September 19, 2013 / 15:15-15:15 / Room: Exhibit Hall B

Heterobivalent Affibody-scFv Fusion Protein for HER2-positive Tumor Imaging Using Universal Hapten Imaging Probes

Hye-Yeong Kim, *Xiaolei Wang, Barry Edwards, Department of Radiology, University of Pittsburgh, Pittsburgh, PA, USA. Contact e-mail: kimh6@upmc.edu*

The detection of cell surface markers with high selectivity and specificity is crucial in tumor imaging. Engineered monoclonoal antibodies (mAb) have been widely used for membrane receptor imaging and drug delivery applications due to their specific molecular recognition with high binding affinities. Pretargeting approaches have reduced nonspecific signals and enhanced tumor to normal tissue ratio. Here, the novel heterobivalent fusion protein was constructed from two small antibody fragments- an affibody (~14 kDa) and an scFv (~25 kDa) for pretargeted HER2-positive tumor cell imaging by labeling with universal hapten imaging probes. Haptens are non-immunogenic and have rapid body clearance with high specificity to anti-hapten antibody, which is favorable for target molecular imaging. The hapten peptide (histamine-succinyl-GSYK) was synthesized by solid phase peptide synthesis. Utilizing the ε-amino group of Lys for conjugation to a variety of molecules, the purified hapten peptide was used for scFv-displayed phage selections, surface plasmon resonance (SPR) evaluations, and as a ligand for optical imaging probes when conjugated to either Alexa Fluor or cypate. Hapten-specific scFvs were discovered after three rounds of biopanning with the Human Single Fold scFv Libraries (Tomlinson I + J). The purified scFvs from 78 clones were screened by SPR using hapten peptide- immobilized sensor chips in order to find high binders to the hapten. In the binding kinetics from SPR sensorgram, 12% of scFv showed KD < 10 nM from the Langmuir 1:1 binding. Interestingly, hapten-specific scFvs were found more from Library I than Library J. The identified protein sequence of anti-hapten scFv was used for the fusion protein construct. The N-terminal His-tagged HER2 affibody (ZHER2:477) was fused with the scFv by a peptide linker (Gly4Ser)3, and the resulting fusion protein HER2-scFv (~37.8 kDa) was expressed in E. coli . The bispecific binding properties of HER2-scFv will be evaluated using SPR and immunoblots. The specificity and efficiency of HER2 staining with the fusion protein and hapten optical probes by pretargeting will be conducted in vitro and in vivo optical imaging. The HER2 affibody-scFv protein would be a new class of fusion protein in tumor imaging and therapeutic applications by a pretargeting strategy with enhanced specific tumor accumulation and better pharmacokinetic profiles.
KEYWORDS: HER2- affibody, scFv fusion protein, and hapten imaging probes

Disclosure of author financial interest or relationships:
H. Kim, None; **X. Wang**, None; **B. Edwards**, None.

Presentation Number **P 175**
Poster Session 2
September 19, 2013 / 15:15-15:15 / Room: Exhibit Hall B

Naphthalic Ynimides - Novel Ratiometric, Fluorogenic Bioorthogonal Probes

Ranjith Kumar Meka, *Michael D. Heagy, Chemistry, New Mexico Institute of Mining and Technology, Socorro, NM, USA. Contact e-mail: ranjith@nmt.edu*

The development of Naphthalic Ynimide probes is intended to resolve some of the inherent problems associated with fluorescence emission intensity measurements, and difficulties associated with utilizing probes in the biological milieu for quantitative measurements. Fluorescence emission, expressed in arbitrary units, is useful only for comparative experiments and analysis under similar conditions (instrumental and experimental). In addition, it becomes increasingly difficult to control variations in probe concentration, photobleaching, and fluctuations in excitation intensities during cellular studies. Such problems are significant and can be mitigated by implementing dual fluorescent dyes. These dyes exhibit two emission maxima whose ratiometric response is independent of dye concentration and path length. This allows for a more reliable quantification of molecules or ions of interest. Among such dyes, dual emission from a single fluorophore holds a clear advantage over dual emission from two fluorophores, because each fluorophore behaves independently with respect to photobleaching and non emissive interactions with surrounding environment. In spite of the inherent advantage, the single fluorophore approach will still lack exclusivity between the dye and the analyte, as it depends on non-covalent interactions. And, in biological systems these non-specific interactions may contribute to fluctuations in the ratiometric response. However, this problem is effectively addressed by the advent of bioorthogonal "click" reactions. "Click" reaction is a two step covalent modification process, involving two small, stable coupling partners, an azide and alkyne. It is fast and regioselective, producing 1,2,3-triazole. In the first step, cells are incubated with a metabolic precursor (sugar, nucleoside, lipid or amino acid) adorned with either the azide or alkyne. Once incorporated into the target biomolecule, the second step involves coupling with the probe bearing complementary group. Most probes used in such labeling studies fluoresce continuously and show no change in fluorescent properties before and after labeling. This lowers the signal to noise ratio significantly. However, by utilizing the electronic changes associated with triazole formation, the fluorescent properties of dye scaffolds are modulated. Such response markedly improves the signal to noise ratio in a given experiment and serves as an excellent choice in biological investigations where unbound probe washing is a problem. Based on these facts naphthalic dicarboximides having N-alkyne functionality are proposed. From earlier studies, it was observed that N-aryl naphthalimides with an electron withdrawing group on the naphthalene ring and an electron donating group on the imine aryl group exhibits dual fluorescence. It is proposed that the formation of an electron rich triazole via the "click" reaction between the ynimide probe and an azide containing biomolecule, should generate a fluorogenic dual fluorescence response. Currently, we are pursuing the synthesis and spectral evaluation of a library of these novel structures and their utility as novel bioorthogonal probes.

Disclosure of author financial interest or relationships:
R. Meka, None; **M.D. Heagy**, None.

Presentation Number **P 176**
Poster Session 2
September 19, 2013 / 15:15-15:15 / Room: Exhibit Hall B

Intratympanic vs. Systemic Delivery of Fluorescent-labeled Zoledronate to the Cochlea: an Imaging Study using a Guinea Pig Model

Kim L. Nguyen[1], *Shuting Sun*[1], *Woo Seok Kang*[2], *David Jung*[2], *William F. Sewell*[2], *Boris A. Kashemirov*[1], *Charles E. McKenna*[1], *Michael J. McKenna*[2], [1]*Chemistry, University of Southern California, Los Angeles, CA, USA;* [2]*Eaton-Peabody Laboratory and Department of Otology and Laryngology, Massachusetts Eye and Ear Infirmary, Harvard Medical School, Boston, MA, USA. Contact e-mail: kimlnguy@usc.edu*

The otic capsule is unique in that it normally exhibits little or no bone remodeling. Otosclerosis is a pathology that can lead to hearing impairment characterized by an abnormal remodeling of the otic capsule. Nitrogen-containing bisphosphonate compounds (BP), such as risedronate and zoledronate, are potent inhibitors of bone remodeling, but side effects may occur with systemic administration in humans, particularly at high doses. Intracochlear and intratympanic administration offer the potential to bypass side effects implicated in systemic delivery and ensure that the drugs reach cochlear tissues and the otic capsule in the form and concentration desired. A previously proposed treatment strategy involves inner ear delivery of N-BPs directly, or via a drug-releasing polymer, such as ethylene-vinyl acetate (EVAc). Since most patients with otosclerosis receive a stapes prosthesis, the polymer formulation could be integrated into the prosthesis for intracochlear delivery. Alternatively, the polymer could be incorporated into a wafer for delivery via the round window membrane instead of the prosthesis. In order to evaluate the distribution of BP in the ear via intratympanic administration, fluorescent-labeled BP analogs were utilized. The fluoresecent-labeled BP analogs were synthesized via reaction between the appropriate 'magic' epoxide linker with the BP, followed by conjugation with an activated dye (McKenna et al., Bioconjugate Chem. 2008, 19, 2308-2310). Preliminary in vivo studies with fluorescent-labeled BPs indicate that systemic delivery results in detectable fluorescence in the cochlea at 3X the standard human dose. Using a guinea pig model, at this high dosage of fluorescent-labeled BP no prompt ototoxicity was observed. Local delivery of fluorecent-labeled BP revealed an uneven distribution of BP in the cochlea with higher concentrations of BP in the basal region and progressively lower concentrations along the length of the cochlea. Therefore, a system that delays the release of BP when intratympanically administered is indicated to achieve uniform drug delivery. In recent years, intratympanic delivery of steroid drugs for ear diseases such as dexamethasone and methylprednisolone has been investigated using Poloxamer P407 (P407), a thermo-reversible polymer, as a drug carrier. P407 was effective in prolonging the release of such drugs. Hence, P407 was investigated as a polymer that could sustain release of BP drugs in the cochlea. Model studies were conducted using a polycarbonate membrane system with UV detection of the parent N-BPs for comparison with the fluorescent drug conjugates. This allowed a direct comparison between the release profiles of parent BP and fluorescent-labeled BP using the fluorescent zoledronate imaging tools. Different alternative formulations of BP drugs were assessed with the goal of achieving uniform cochlear distribution of drugs at a known absorbed dose.

Disclosure of author financial interest or relationships:
K.L. Nguyen, None; **S. Sun**, None; **W. Kang**, None; **D. Jung**, None; **W.F. Sewell**, None; **B.A. Kashemirov**, None; **C.E. McKenna**, None; **M.J. McKenna**, None.

Presentation Number **P 177**
Poster Session 2
September 19, 2013 / 15:15-15:15 / Room: Exhibit Hall B

In Vivo NIR Imaging and Quantification of Glomerular Filtration Rate in Mice

Bagna Bao, Guojie Ho, Jun Zhang, Justin C. Jarrell, Kristine Vasquez, Jeannine Delaney, Milind Rajopadhye, **Jeffrey D. Peterson**, *R&D, PerkinElmer, Hopkinton, MA, USA. Contact e-mail: jeff.peterson@perkinelmer.com*

The measurement of glomerular filtration rate (GFR) is the gold standard in kidney function assessment and is used to determine progression of kidney disease and drug induced kidney toxicity. This is often assessed indirectly in preclinical animal models either by surrogate markers, like plasma creatinine or blood urea nitrogen. GFR is best quantified functionally by assessing plasma clearance rates of labeled inulin or labeled inulin analogs, but to-date this requires blood sampling - a fairly labor intensive process. In an effort to eliminate this procedure, we developed a near infrared (NIR) fluorescent-labeled version of inulin (GFR-Vivo 680 [GFR680]; ex/em = 670/685 nm) in a spectral wavelength that offers high tissue penetration and low background suitable for in vivo imaging. Consequently, the blood kinetics of an intravenous bolus of GFR680 is readily assessed in small numbers of mice in vivo by fluorescence molecular tomographic (FMT) imaging and quantification of mouse heart fluorescence over time (1 to 60 minutes post-injection). GFR is then accurately determined using two-compartment curve fitting (PKSolver 2.0 , an Excel Add-In), yielding average rates of 240 to 280 uL/min in normal mice. These results are comparable to those of studies in which NIR-Inulin and FITC-Inulin levels were assessed by bleeding mice at multiple time points for ex vivo assay. In comparison, uninephrectomized (UNX) mice imaged by FMT showed a statistically significant 2-fold decrease in GFR ($p < 0.005$). Similarly, FMT measurement of mice treated with Cyclosporine A (80 mg/kg/day) for 14 days showed an expected 40% decrease in GFR ($p < 0.05$). All imaging results correlated well with ex vivo plasma microplate assays showing increased levels of the surrogate markers creatinine and blood urea nitrogen (BUN). In conclusion, FMT imaging of circulating GFR680 provides a non-invasive fluorescent imaging approach that requires very few mice (3 to 10 mice per group) to generate consistent GFR measurements and detection of changes induced by nephrectomy or drug toxicity. As neither blood nor urine sampling is required, and no labor-intensive microplate assays, GFR can be determined quickly after the imaging procedure is completed. These results illustrate the potential of this imaging approach to facilitate the study of kidney disease and the monitoring of drug safety.

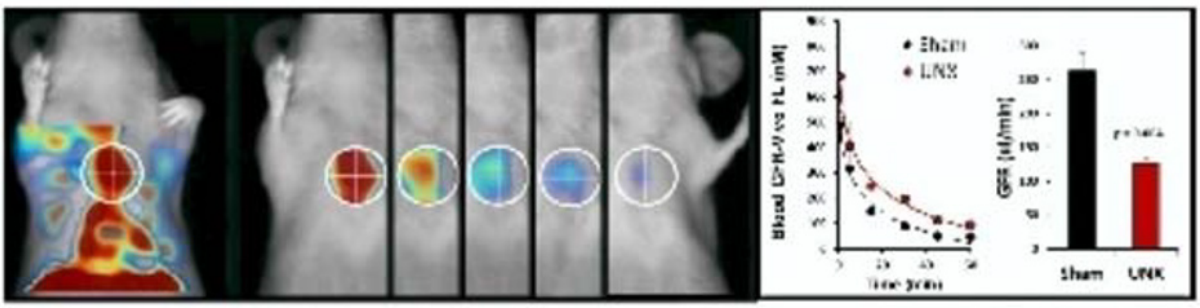

Fluorescence tomographic heart imaging to quantify blood levels of GFR680

Disclosure of author financial interest or relationships:
B. Bao, None; **G. Ho**, PerkinElmer, Employment; **J. Zhang**, PerkinElmer, Inc., Employment; **J.C. Jarrell**, PerkinElmer, Employment; **K. Vasquez**, PerkinElmer, Employment; **J. Delaney**, PerkinElmer, Employment; **M. Rajopadhye**, PerkinElmer, Inc, Employment; **J.D. Peterson**, PerkinElmer Inc, Employment .

Presentation Number **P 178**
Poster Session 2
September 19, 2013 / 15:15-15:15 / Room: Exhibit Hall B

Design and syntheses of new probes for use in super-resolution microscopy

Zhen-Dan Shi, *Biying Xu, Nalini Shenoy, Haitao Wu, Changhui Li, Kelly Lane, Andres E. Dulcey, Gary L. Griffiths, Imaging Probe Development Center, National Heart, Lung, and Blood Institute, National Institutes of Health, Rockville, MD, USA. Contact e-mail: shizh@mail.nih.gov*

Optical microscopy has become an important tool for biomedical research including exploring the structures and functions of biological molecules in living cells and tissues. However, the spatial resolution for optical microscopy is limited by the diffraction barrier. Recently, several super-resolution imaging techniques have been reported to overcome this diffraction limit, such as stimulated emission depletion (STED), stochastic optical reconstruction microscopy (STORM) and photoactivated localization microscopy (PALM). Herein we present a similar real-time super-resolution microscopy by utilizing a new class of bipartite probes with both luminescent and quenching functions. The quencher is specially designed to be in the excited state, absorbing energy from the luminescent dye (donor) and quenching the donor. One advantage of this method is that much less peak power is needed for super-resolved imaging. Moreover, it can be easily used for multicolor imaging. The detailed background, design and syntheses of the probes will be described.

Disclosure of author financial interest or relationships:
Z. Shi, None; **B. Xu**, None; **N. Shenoy**, None; **H. Wu**, None; **C. Li**, None; **K. Lane**, None; **A.E. Dulcey**, None; **G.L. Griffiths**, None.

Presentation Number **P 179**
Poster Session 2
September 19, 2013 / 15:15-15:15 / Room: Exhibit Hall B

Imaging Probe Development Center: Development of O6-benzylguanine functionalized gold nanoparticles for SNAP-tag labeling in electron microscopy

*Nalini Shenoy[1], **Agnieszka Sulima**[1], Kem Sochacki[2], Olga Vasalatiy[1], Justin Taraska[2], [1]Imaging Probe Development Center, NHLBI, NIH, Rockville, MD, USA; [2]Laboratory of Molecular and Cellular Imaging, NHLBI, NIH, Bethesda, MD, USA. Contact e-mail: agnieszs@mail.nih.gov*

The Imaging Probe Development Center (IPDC) is a chemistry core facility at the NIH. IPDC was set up to provide chemistry support (design, synthesis, characterization of imaging probes) for the intramural scientific community at the NIH. The probe development carried out at IPDC has been of a wide range, including probes to enhance understanding of basic scientific questions to translation of molecules into the clinic. The probes synthesized at the IPDC encompass the breadth of major imaging modalities, including optical, radionuclide, magnetic resonance and molecules of different sizes ranging from small molecules to biomolecules. Here we present a project involving design and synthesis of a probe to map the spatial positions of specific proteins involved in clathrin-mediated endocytosis using three-dimensional transmission electron microscopy (3D-TEM). The novel probe designed for this project is based on the SNAP-tag system, which is a variant of the human O6-alkylguanine-DNA alkyl transferase (hAGT). The SNAP tag is known to covalently react with benzyl guanine derivatives. The probe design involves derivatization of gold nanoparticles (GNP) with a ligand of O6-benzylguanine-polyethylene glycol (BG-PEG) and PEG in different ratios. The O6-benzyl-guanine functionalized gold nanoparticles would covalently react with SNAP-tag on the protein of interest and enable determining its spatial position with electron microscopy. For our investigations we chose 5 nm gold nanoparticles. In order to determine the optimal composition of the probe, gold nanoparticles were stabilized with thiol-functionalized PEG of various chain lengths including 600 Da (PEG-600), 1 kDa (PEG-1k) and 2 kDa (PEG-2k) at different molar ratio of PEG to GNP. The resulting PEGylated gold nanoparticles were characterized by UV spectroscopy, dynamic light scattering and zeta-potential. Salt induced aggregation of the PEG coated gold nanoparticles was tested by subjecting the gold conjugates to 10x PBS. The O6-benzylguanine-polyethylene glycol ligand was synthesized by coupling an amine reactive building block (BG-GLA-NHS ester) to heterobifunctionalized PEG. The O6-benzyl-guanine functionalized gold nanoparticles were prepared varying the fraction of the BG-PEG ligand in the coating mixture. The resulting BG-PEG functionalized nanoparticles will be tested for their ability to covalently attach to the SNAP-tag modified proteins.

Disclosure of author financial interest or relationships:
N. Shenoy, None; **A. Sulima**, None; **K. Sochacki**, None; **O. Vasalatiy**, None; **J. Taraska**, None.

Presentation Number **P 180**
Poster Session 2
September 19, 2013 / 15:15-15:15 / Room: Exhibit Hall B

Symmetric cyanine probe labeled GX1 peptide for near-infrared fluorescence imaging of gastric cancer

Xianghan Zhang[1], Jing Xin[1], Jimin Liang[1], Kaichun Wu[3], Hao Hu[3], Yongzhan Nie[3], **Jie Tian**[2,1], *[1]School of Life Sciences and Technology, Xidian University, Xi'an, China; [2]Medical Image Processing Group, Institute of Automation,CAS, "Beijing,100190", China; [3]State Key Laboratory of Cancer Biology and Institute of Digestive Diseases, Xijing Hospital, Fourth Military Medical University, Xi'an, China. Contact e-mail: tian@ieee.org*

Objectives: Small molecular weight, less toxicity, broad spectra tunability, and large molar extinction coefficients, cyanine dyes as fluorescence probes have been widely used for fluorescence labeling in biomedical areas. An ideal fluorescence probe should not only have superior chemical and photophysical properties but also have suitable chemical functionality for bioconjugation with specific ligands for targeting imaging. GX1, a cyclic 9-mer peptide (CGNSNPKSC), acts as a good tumor angiogenesis targeting molecule. We conjugated the GX1 peptide with cyanine dyes and evaluated the gastric tumor vasculature imaging by studying fluorescence properties and binding specificity in vitro and in vivo. Methods: The fluorescence properties and targeted ability of CyIC2-GX1 was examined by confocal laser microscopy and flow cytometry. To further evaluate the ability of CyIC2-GX1 to target a tumor and accumulate in it in vivo, fluorescence imaging was acquired after intravenous injection of 5×10-6 M CyIC2-GX1 on SGC-7901 subcutaneous xenograft models. Results: Fluorescence signals from cytoplasmic and nuclear could be easily detected in Co-HUVEC cells. The bright fluorescence and high specific staining revealed that these CyIC dyes have great potential in fluorescence labeling. Compared to GES cells, the binding percentages of CyIC-GX1 to Co-HUVEC cells have more than a 2-fold increase (85.9% vs 39.1% at a high concentration and 57.8% vs 26% at a low concentration). The results revealed that CyIC-GX1 had good binding affinity to Co-HUVEC cells. The fluorescence signal of CyIC-GX1 was significant at the tumor site (Figure 1a). We quantified the fluorescence intensity of the signals with the ROI that encompassed the tumor tissue. The accumulation of CyIC-GX1 in the tumor reached a maximum at 16-18h (Figure 1b). Each mouse in the non-blocked group as control group was intravenously injected with 5×10-6 M CyIC2-GX1 only, whereas mice in the blocked group were intravenously injected with 20 mg/kg of unlabeled GX1 and then injected with 5×10-6 M CyIC-GX1. The fluorescence signals from the non-blocked mice at the tumor sites were approximately three times higher in comparison with the blocked mice (Figure 1c). Fluorescence images of excised organs indicated that CyIC-GX1 accumulated in the tumor and kidneys (Figure 1d). Compared to the blocked group, CyIC-GX1 showed excellent tumor uptake with minimal amounts in other normal organs (Figure 1e). Conclusions: CyIC-GX1 is an excellent target-specific molecular probe and may contribute to gastric tumor metastasis detection and anti-tumor angiogenesis therapy by noninvasive targeting molecular imaging.

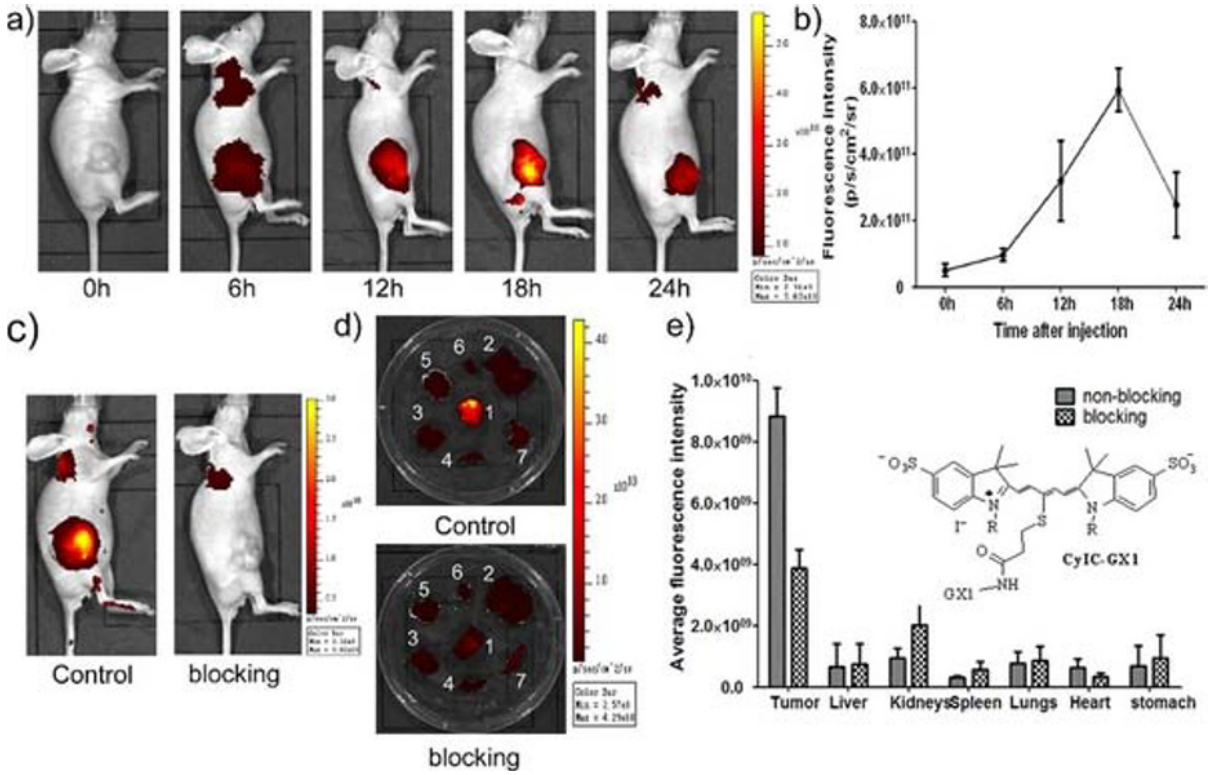

Targeting the specificity of CyIC-GX1 in vivo

Disclosure of author financial interest or relationships:

X. Zhang, None; **J. Xin**, None; **J. Liang**, None; **K. Wu**, None; **H. Hu**, None; **Y. Nie**, None; **J. Tian**, None.

Presentation Number **P 181**
Poster Session 2
September 19, 2013 / 15:15-15:15 / Room: Exhibit Hall B

A high affinity near infrared fluorescent (NIRF) probe to target bombesin receptors

Ajay Shrivastava[1,2], *Shankaran Kothandaraman*[1,2], *Shu-Huei Wang*[1,2], *Michelle M. Williams*[2,1], *Natarajan Raju*[1,2], *Keisha Milum*[1,2], *Haiming Ding*[1,2], *Michael F. Tweedle*[1,2], [1]*Radiology, The Ohio State University College of Medicine, Columbus, OH, USA;* [2]*Wright Center of Innovation, The Ohio State University, Columbus, OH, USA. Contact e-mail: asbiopro@pharmasages.com*

A NIRF probe to target bombesin (BBN) receptors is highly desirable because of well documented expression of two subtypes of this receptor family, BB1 (aka NMB receptor) and BB2 (aka GRPr receptor), in human prostate, breast, and head and neck cancers. Real time Optical Surgical Navigation using NIRF probes could potentially provide more complete removal of malignant cells and cleaner margins in these cancers. BBN is a 14-mer peptide that binds the four BBN receptor subtypes. A truncated BBN derivative, QWAVGHLM-NH2 (t-BBN), is known to bind BB1 and BB2 as an agonist when it is conjugated through an ABz4-G linker to DO3A chelating agents, and t-BBN has been studied while conjugated to two different NIRF dyes through two different linkers, GGG and GSG. Small peptide binders are often highly sensitive to subtle structure modification, and t-BBN is known to be highly sensitive to N terminal modification. In the current study, we prepared and compared three BBN receptor targeting NIRF probes. We conjugated t-BBN to IR800CW dye, which emits in the desirable 800 nm range, using three different linkers (GGG, GSG and Abz4-G) to test the linker effect on receptor binding. The three BBN targeting ligands, NH2-GGG-t-BBN, NH2-GSG-t-BBN, and NH2-G-Abz4-t-BBN were synthesized using solid phase synthesis and coupled to IR800CW-NHS ester to produce IR800CW-GGG-t-BBN, IR800CW-GSG-t-BBN, and IR800CW-G-Abz4-t-BBN. Purity and identity were verified by HPLC single peaks and MALDI parent ions, respectively. Competitive displacement binding assays with each ligand against 125I-Tyr4-BBN yielded IC50 values of 187 + 31 nM, 56 + 5 nM, and 2.6 + 0.2 nM, in PC-3 human prostate cancer cells (BB1+, BB2+), and 383+1, 57.4+1.2 and 3.1+1.1, respectively in T47D human breast cancer cells (BB2+). We thus demonstrated a strong dependency of t-BBN receptor binding ability on the linker. The IR800CW-G-Abz4-t-BBN also demonstrated the best binding among the three probes to PC-3 cells in a direct cell-binding assay, detected by fluorescence microscopy. Strongly positive binding to PC3 cells was specifically competed with by BBN but not a non-BBN binding peptide, and very little cell binding was observed to HCC1937 cells, a human breast cancer cell line lacking BBN receptors. Finally, using NIRF imaging in a CRI Maestro imager, IR800-G-Abz4-t-BBN accumulated in BBN receptor positive pancreas and receptor positive PC3 tumor xenografts in vivo in a mouse model.

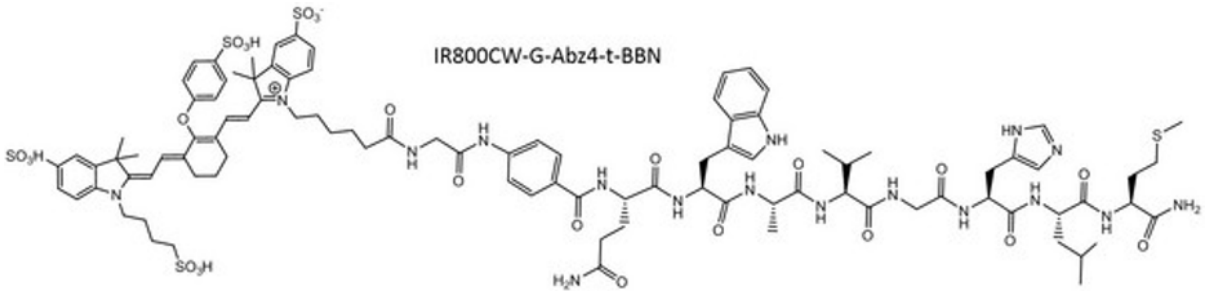

Structure of IR800CW-G-Abz4-t-BBN

Disclosure of author financial interest or relationships:

A. Shrivastava, None; **S. Kothandaraman**, None; **S. Wang**, None; **M.M. Williams**, None; **N. Raju**, None; **K. Milum**, None; **H. Ding**, None; **M.F. Tweedle**, None.

Presentation Number **P 182**
Poster Session 2
September 19, 2013 / 15:15-15:15 / Room: Exhibit Hall B

Development of a Novel Near-Infrared Imaging Agent For Prostate Cancer

Xinning Wang[1], *Steve S. Huang*[2], *Warren D. Heston*[2], *Clemens Burda*[1], *James Basilion*[1], [1]*Radiology, Case Western Reserve University, Cleveland, OH, USA;* [2]*Cancer Biology, Cleveland Clinic, Cleveland, OH, USA. Contact e-mail: xxw171@case.edu*

Approximately 238,000 new diagnoses and 29,700 deaths from prostate cancer are projected in 2013 among men in the United States. Since introduction of PSA testing, significantly more men have been diagnosed and treated for the disease. An estimated 91% of prostate cancers detected at initial screenings are clinically localized and these patients are candidates for radical prostatectomies. However, surgery fails to halt the disease in approximately 20% of the patients who undergo radical prostatectomy and can be associated with co-morbidities. We propose to develop a PSMA-target imaging probe that can be used during surgery to help define extra-capsular invasion of prostate cancer and help differentiate between diseased and normal tissues during surgery, improving prostatectomies. Prostate-specific membrane antigen (PSMA) is a type II membrane antigen. It is highly expressed in prostate cancer, especially in more advanced tumors. PSMA has an extracellular domain that is accessible to agent in the extracellular environment, making it possible to target this protein for imaging and therapy. The objective of this proposal is to design low molecular weight near infrared probe for detection of prostate cancer by targeting PSMA. Previously we have developed a 2'-5'-oligoadenylate (2'-5'-A) based PSMA ligand, RBI1033, which exhibits 10x better affinity toward PSMA than the parent ligand (S)-2-[3-((R)-1-carboxy-2-methylsulfanyl-ethyl)ureido]-pentanedioic acid (ZJ24). We hypothesized that the increased binding affinity of RBI1033 might be due to an interaction between the negatively charged phosphate backbone and the aromatic amino acid residues of PSMA. However, in vivo studies with RBI1033 showed no benefit to differentiate between tumors that expressed PSMA and those that did not. A possible explanation is that 2'-5'-A moiety is not stable in vivo. Based on our charge-charge interaction hypothesis we synthesized a presumably more stable peptide-based PSMA ligand, PSMA-1, by mimicking the negative charge and hydrogen bonding of the 2'-5'-A moiety using D-glutamic acid. A lysine residue was attached at the C-terminal end of the molecule so that large fluorescent moieties could be attached. In vitro competitive binding assays using 3H-ZJ24 showed that the new ligand, PSMA-1, had an IC50=2.3 nM which was much better than ZJ24 (IC50=9.3nM). IRDy800 was then conjugated to PSMA-1 through the -NH2 group of the lysine to generate PSMA-2, which further improved binding affinity, IC50= 1.5 nM. In vivo Maestro imaging using nude mice bearing both PSMA-positive (PC3pip) and PSMA-negative (PC3flu) tumors demonstrated selective tumor uptake in PC3pip tumors in as little as 2 hours after i.v. injection. In sharp contrast, no significant fluorescent uptake was observed in the PSMA-negative tumors. In conclusion, our study indicated that the 2'-5'-A moiety in RBI1033 can be successfully replaced by negatively charged amino acids. This change presumably increases the stability of the ligand and at the same time reduces the cost of synthesis. The NIR probe reported here has the potential to be used to provide image-guided prostatectomies.

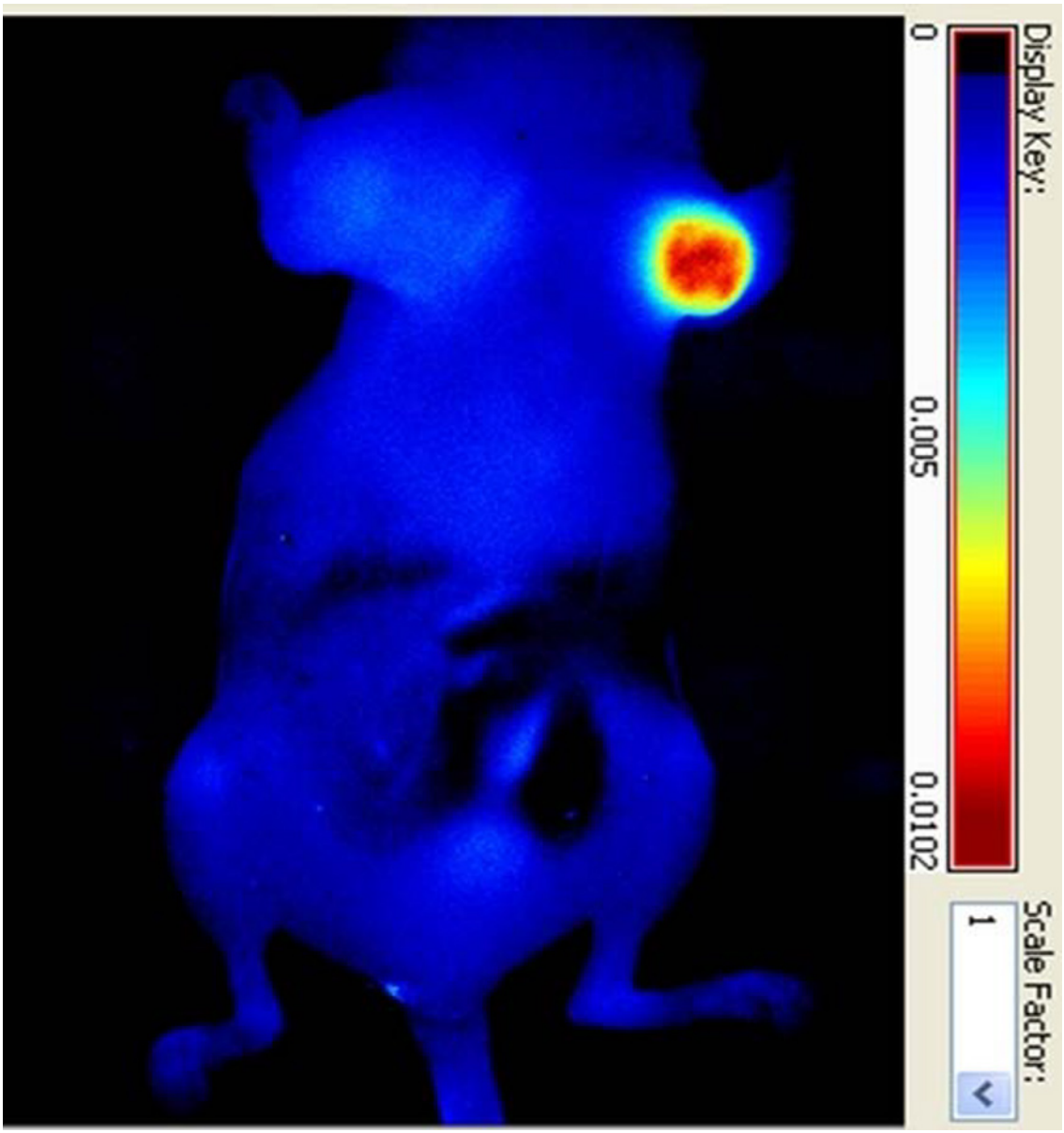

In vivo image of a nude mouse bearing both PSMA-positive PC3pip (right) and PSMA-negative PC3flu (left) tumors 24 hours after i.v. injection of 1 nmol PSMA-2.

Disclosure of author financial interest or relationships:
X. Wang, None; **S.S. Huang**, None; **W.D. Heston**, None; **C. Burda**, None; **J. Basilion**, Akrotome Imaging, Consultant; Akrotome Imaging, Stockholder .

Presentation Number **P 183**
Poster Session 2
September 19, 2013 / 15:15-15:15 / Room: Exhibit Hall B

A near-infrared fluorescent transferrin agent for quantitative imaging of transferrin receptor expression in tumor xenografts

Jun Zhang, *Guojie Ho, Kevin Groves, Ryan Buff, Jeff Morin, Bagna Bao, Jeannine Delaney, Sylvie Kossodo, Wael Yared, Milind Rajopadhye, Jeffrey D. Peterson, PerkinElmer, Hopkinton, MA, USA. Contact e-mail: jun.zhang@perkinelmer.com*

Transferrin (Tf) transports iron to all tissues, particularly those with highly metabolic cells like tumors because of their high demand for iron (for heme synthesis and as cofactors of non-heme enzymes). Given the overexpression of Tf receptors (TfR) on malignant cells, targeting TfR has been a successful approach as a strategy for pharmacological intervention in both cancer diagnosis and therapy, providing a means for selective delivery and rapid receptor-mediated internalization in tumors. While most of the imaging agents targeting TfR have involved the use of radiochemicals, in this study we generated a novel TfR-targeted agent using near infrared fluorophore labeled transferrin. This approach offered a non-radioactive alternative and exploited the favorable characteristics of optical imaging in the near infrared wavelengths that allow efficient penetration of photons through living tissue and minimizes interference from tissue autofluorescence. The agent consists of recombinant human transferrin coupled to a fluorophore (VivoTag 750, excitation 750nm/ emission 770nm) and a pharmacokinetic modifier designed to improve its plasma availability (plasma t1/2 = 10 hours). In vitro, the agent shows dose-dependent binding to HT-29 colorectal tumor cells and frozen tumor xenograft sections as quantified by flow cytometry and fluorescence microscopy, respectively. Specificity of binding was confirmed by near complete blockade of the cell/tissue labeling upon prior incubation with an excess of unlabeled transferrin. In vivo, TfR upregulation in tumors was quantified following intravenous injection of 2 nmol of the Tf agent into nude mice bearing HT-29 tumor xenografts. Imaging performed by fluorescence molecular tomography (FMT) at 2, 6 and 24 h post-injection revealed a peak of 30-40 pmol of fluorescent signal at 24 h, the time at which optimal signal-to-noise ratios were achieved. The in vivo biodistribution profile was determined by harvesting tissues from these tumor bearing mice at 24h, showing a favorable distribution dominated by tumor signal as compared to the other tissues. In vivo targeting specificity was validated by injecting mice with a 645 nm-labeled version of the Tf agent and determining appropriate co-localization in frozen tumor tissue sections with anti-TfR antibody staining. The results from these studies indicate that the newly developed agent provides a useful tool for near infrared fluorescent-based optical tumor imaging both in vitro and in vivo.

Disclosure of author financial interest or relationships:
J. Zhang, PerkinElmer, Inc., Employment; **G. Ho**, PerkinElmer, Employment; **K. Groves**, PerkinElmer, Employment; **R. Buff**, PerkinElmer, Employment; **J. Morin**, Perkin Elmer, Employment; **B. Bao**, None; **J. Delaney**, PerkinElmer, Employment; **S. Kossodo**, PerkinElmer, Employment; **W. Yared**, PerkinElmer, Employment; **M. Rajopadhye**, PerkinElmer, Inc, Employment; **J.D. Peterson**, PerkinElmer Inc, Employment .

Presentation Number **P 184**
Poster Session 2
September 19, 2013 / 15:15-15:15 / Room: Exhibit Hall B

MR Imaging and targeting of a specific alveolar macrophage subpopulation in COPD animal model using antibody conjugated magnetic nanoparticles

Achraf Al Faraj, *King Saud University, Riyadh, Saudi Arabia. Contact e-mail: aalfaraj@ksu.edu.sa*

Coupled with the use of super-paramagnetic iron oxide (SPIO) nanoparticles, MR Imaging of macrophages offers a promising noninvasive approach for an early and better assessment of the pathological and physiological impairments in chronic obstructive respiratory diseases (COPD). Inside the body, different environmental conditions will orient macrophages to have either a pro-inflammatory (M1) or immuno-modulator (M2) profile. The purpose of this study is to characterize macrophage polarization in COPD and after SPIO intrapulmonary exposition and to specifically target and monitor in vivo one macrophage subset. Mice were intrapulmonary exposed with bacterial lipopolysaccharides (LPS) to develop a COPD inflammatory model. Control and COPD mice were then exposed 24h post-LPS with either saline or PEGylated dextran coated SPIO nanoparticles. Broncho Alveolar Lavage Fluid (BALF) were collected 48h post-LPS. Flow cytometer (i.e., surface membrane receptor), ELISA (i.e., cytokines release), and Immunocytology (i.e., iNOS vs Arginase1 production) analysis were performed to have an in-depth and full characterization of macrophages polarization after LPS and/or SPIO administration. CD206 antibody was then conjugated to maleimide modified PEG SPIO to specifically target M2 macrophages subpopulations and noninvasively monitor by 4.7T Bruker MRI using ultra-short echo time (UTE) radial sequence. Finally, BALF of CD206-SPIO exposed lungs was magnetically separated and the polarization state of retained macrophages were re-characterized. Macrophages present in BALF of COPD mice have been shown to have an enhanced number of macrophages with presence of both M1 and M2 macrophages subpopulations. However, SPIO administration did not revealed any significant variation in macrophages polarization as differentiated by characteristic markers using flow cytometer, ELISA and Immunocytology analysis. Iron labeled macrophages were successfully detected in the lung using UTE radial MRI. Magnetic separation of the BALF of CD206-SPIO instilled lung confirmed that M2 macrophages subsets were specifically targeted in vivo and monitored using noninvasive MRI. Macrophages polarization was extensively characterized after LPS and/or SPIO intrapulmonary exposition and specific biomarkers were identified. Antibody conjugated magnetic nanoparticles has been shown to offer a novel approach to specifically target one subpopulation of macrophages and allow their noninvasive tracking using MRI.

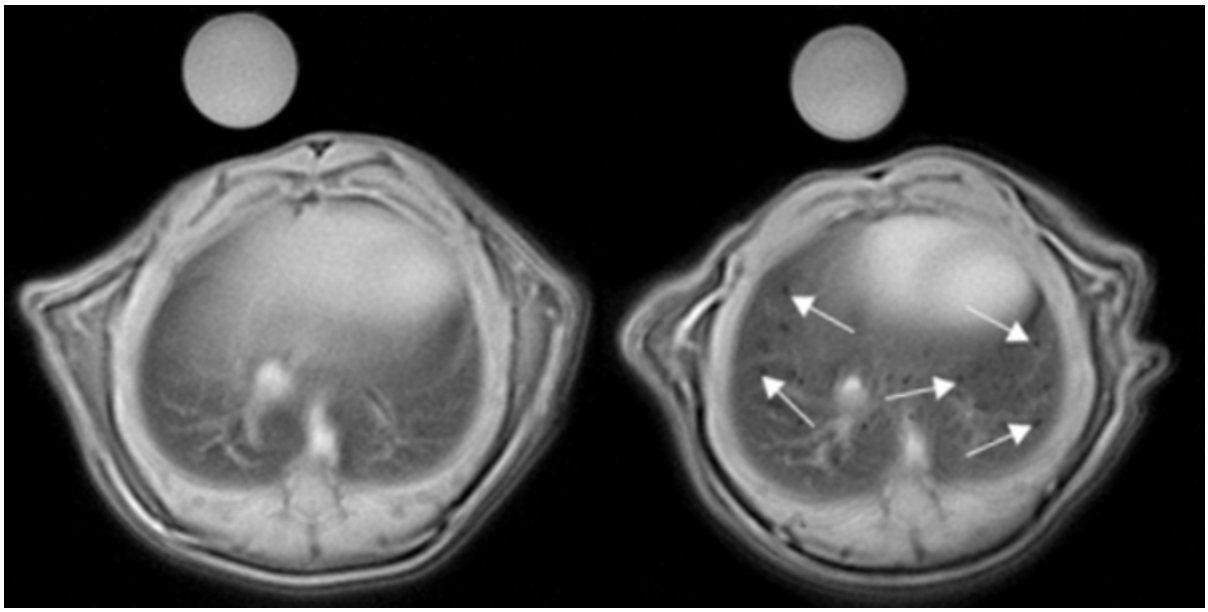

Pulmonary MR Images of control vs. CD206-SPIO intrapulmonary exposed animal revealing the detection of M2 macrophages subpopulations as void signal dots in lung parenchyma using UTE radial sequence 2 hours post exposition

Disclosure of author financial interest or relationships:
A. Al Faraj, None.

Presentation Number **P 185**
Poster Session 2
September 19, 2013 / 15:15-15:15 / Room: Exhibit Hall B

In vivo fluorescence imaging of antigen presenting cells in nonhuman primates

Biliana Todorova[1,2], Nina Salabert[1,2], Frédéric Martinon[1,2], Thierry Kortulewski[3], Raphael Boisgard[4], Antonio Cosma[1,2], Roger Le Grand[1,2], **Catherine Chapon**[1,2], [1]*Division of Immuno-Virology, iMETI, CEA, Fontenay-aux-Roses, France;* [2]*UMR E1, Université Paris-Sud, Orsay, France;* [3]*Photonic microscopy platform, IRCM, CEA, Fontenay-aux-Roses, France;* [4]*Institute of biomedical imaging, SHFJ, CEA, Orsay, France. Contact e-mail: catherine.chapon@cea.fr*

Introduction: Noninvasive and longitudinal imaging strategies are required to study the behavior of antigen presenting cells (APCs) in order to better understand the mechanisms leading to the induction of cellular and humoral immune responses to vaccination. Here we describe in vivo fluorescence imaging approaches to monitor skin APCs and evaluate their migration to draining lymph nodes (LNs) following an intradermal (id) immunization in nonhuman primates (NHP), with injection of a DNA vaccine or an adjuvant, the resiquimod (R848), an agonist of Toll-like receptor 7 and 8. Methods: Monoclonal fluorescent labelled α-HLA-DR antibody (mAb) was injected intradermally in order to specifically target skin APCs in NHP. In vivo near infrared (NIR) fluorescence imaging was performed prior to and at different times post-injection of the fluorescent mAb with or without R-848 (FluobeamTM, Fluoptics). The fluorescent intensity was measured over time in both sites of injection and LNs using ImageJ software. Epidermal APCs were also monitored at cellular level with noninvasive in vivo fibered confocal fluorescence microscopy (Cellvizio® 488, Mauna Kea Technologies) at various time points post injection (4h, 24h, 48h, 72h, 96h) with or without id DNA plasmid injection associated with noninvasive electroporation (EP). In addition, confocal fast laser scanning microscopy was performed on whole skin biopsies to monitor the behavior of fluorescent-labelled APCs in both dermis and epidermis with or without the injection of DNA vaccine or R848 adjuvant. Three-dimensional image reconstructions and image analysis (cell quantification and tracking) were performed using Volocity software (Perkin Elmer). Results: APCs were visualized by in vivo fluorescence imaging at macroscopic and cellular level after id injection of fluorescent labelled α-HLA-DR mAb for at least 48 hours in NHP. In vivo macroscopic NIR imaging allowed the visualization of the differences in term of retention of fluorescent labelled mAb at the injection site and in the LNs in the presence of R848 compared to the control. A decrease of epidermal APC density was observed over time using in vivo cellular fluorescence imaging, after vaccination with DNA plasmid. The injection of R-848 adjuvant or DNA vaccine led to APC recruitment in the dermis and to an increase of APC displacement in the dermis and epidermis compared to the control. Recruited cells were mostly identified as macrophages (CD45+CD163+CD14+/-) and inflammatory polymorphonuclear cells (CD45+CD66+) by flow cytometry. Conclusion: In vivo fluorescence imaging approaches allow us to track the skin immune cells noninvasively in their native environment, and to characterize early cellular events in different experimental settings such as vaccination and immune therapeutic interventions.

Disclosure of author financial interest or relationships:
B. Todorova, None; **N. Salabert**, None; **F. Martinon**, None; **T. Kortulewski**, None; **R. Boisgard**, None; **A. Cosma**, None; **R. Le Grand**, None; **C. Chapon**, None.

Presentation Number **P 186**
Poster Session 2
September 19, 2013 / 15:15-15:15 / Room: Exhibit Hall B

Cerenkov and fluorescence imaging of joint inflammation in a CIA mouse model of rheumatoid arthritis

Carlos A. Cotto[1], *Peter King*[1], *Shannon Hitchcock*[2], *Jeffrey Hall*[2], *Paul Acton*[1], [1]*Molecular Imaging, Janssen Research & Development, Spring House, PA, USA;* [2]*Mechanistic Pharmacology in Immunology, Janssen Research & Development, Spring House, PA, USA. Contact e-mail: ccotto@its.jnj.com*

Fluorescent optical imaging agents such as MMPSense (an activateable optical probe which emits light in the presence of matrix metalloproteinase) and positron emission tomography (PET) imaging utilizing FDG (a radioactive analog of glucose, which indicates increased metabolic activity in arthritic joints), are valuable imaging endpoints in longitudinal studies of collagen induced arthritis (CIA) mouse models of rheumatoid arthritis (RA). Cerenkov radiation from high energy positrons can be detected as visible light in sensitive optical systems, and can be used to detect and quantify Cerenkov light emission produced by PET radiotracers. This study aimed to validate the use of Cerenkov imaging in a CIA mouse model of RA, comparing the uptake of both FDG and MMPSense in the inflamed joint. For calibration, varying amounts of FDG, ranging from 1.3 uCi to 1 mCi, were placed in the wells of a 96 well plate and a Cerenkov image was acquired to test quantitative accuracy on an IVIS Spectrum optical imager. Quantification of this Cerenkov image depicted a linear relationship when comparing the light emitted and the known activity in each well (R-squared = 0.99, $p < 0.0001$). In animal studies, doses of FDG and MMPSense 750 FAST were administered via tail vein injections in CIA mice. The animals were scanned for Cerenkov light emission and fluorescence in an IVIS Spectrum, and also in an Inveon microPET scanner prior to disease onset as a baseline and after RA was established. The Cerenkov image and the MMPSense optical images revealed a strong correlation in this disease model (R-squared = 0.98, $p = 0.01$). Furthermore there was the additional benefit that the images were in perfect spatial alignment. This study demonstrated that quantitative Cerenkov images could be measured during a single scanning session with a fluorescent optical imaging agent in a mouse model of RA. Direct correlation between fluorescent probe activity and glucose metabolism on the same scan could be performed with increased throughput and reduced cost.

Disclosure of author financial interest or relationships:
C.A. Cotto, None; **P. King**, None; **S. Hitchcock**, None; **J. Hall**, None; **P. Acton**, Johnson & Johnson, Employment; Johnson & Johnson, Stockholder .

Presentation Number **P 187**
Poster Session 2
September 19, 2013 / 15:15-15:15 / Room: Exhibit Hall B

Evaluating the best treatment, calcium channel blocker or ketogenic diet, to reduce myocardial 18FDG uptake

Lorena Cussó[1,2], *Pablo Sanchéz-López*[2], *Alexandra de Francisco*[2], *Luisa M. López-Sánchez*[1,2], *Santiago Peña Zalbidea*[2], *Manuel Desco*[2,1], *Juan Jose Vaquero*[1,2], [1]*Dept. Bioingeniería e Ingeniería Aeroespacial, Universidad Carlos III de Madrid, Leganes, Spain;* [2]*Instituto de Investigación Sanitaria Gregorio Marañón, Madrid, Spain. Contact e-mail: lcusso@mce.hggm.es*

Miocardial uptake may hamper the visualization of lung infections, atherosclerotic plaques or inflammatory diseases in 18FDG studies. Some clinical studies indicate that low-carbohydrate and high-fat meal reduces myocardial uptake. In pre-clinical studies two different approaches to reduce the myocardial uptake have been proposed: ketogenic diet (KD), to switch myocardium metabolism to fatty acids, and calcium channel blocker (verapamil) administration, since myocardial glucose uptake is partly mediated by Ca2+. The aim of this study was to compare the efficacy of both approaches. Usefulness in increasing lesion detectability was assessed on an inflammatory lung model induced by lipopolysaccharide (LPS). Methods: Ten female C57BL/6 mice (Harlan) 6 to 8 weeks age were used. Respiratory gated PET scans (Argus PET-CT, SEDECAL, Madrid) were performed 60 min after intraperitoneal (ip) injection of 18.5 MBq of FDG. PET data were collected for 45 min and then a CT image was acquired. Three studies were obtained for each mouse, basal, post-verapamil (1.3 mg/kg administrated ip 1 hour prior to FDG) and post-KD (overnight 48-hour on KD, TD.96355 Harlan). LPS challenge was performed on eight animals directly administering the LPS (5 mg/kg, 100 µl), into the trachea under light anesthesia with isoflurane. Four LPS-challenged mice received KD and four were fasted overnight, as a control. Regions of interest (ROIs) were selected on right lung on basal and post LPS-challenged PETs. Results and discussion: After verapamil administration 20% of the animals showed complete myocardial uptake suppression and 40% of them exhibited a partial uptake reduction. Ketogenic diet totally suppressed myocardial uptake in 60% of the animals and induced a partial myocardial reduction in 20% of the animals. Figures 1.B and 1.C show the lung inflammation in LPS-challenged animals vs. basal image (1.A), the lung uptake doubled in LPS-challenged animals. KD had no effect on inflammation areas uptake but improved the visualization of hot areas near the heart (Figure 1.c). In conclusion, our preliminary results prove that ketogenic diet is an effective method to decrease the myocardial uptake in healthy mice, better thanverapamil administration. Also, it improves visualization and quantification of lung inflammation processes.

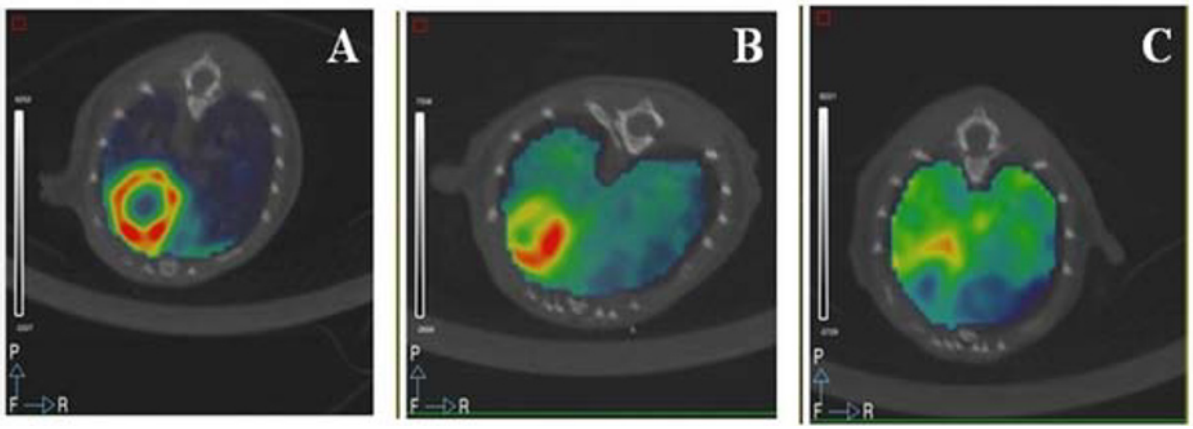

PET-CT scans: A) Basal PET scan. B) Overnight fasted animal after LPS challenge. C) LPS challenged animal after 2 days of ketogenic diet. In C) higher uptake areas in lung would be hidden by the heart if not suppressed.

Disclosure of author financial interest or relationships:

L. Cussó, None; **P. Sanchéz-López**, None; **A. de Francisco**, None; **L.M. López-Sánchez**, None; **S. Peña Zalbidea**, None; **M. Desco**, None; **J. Vaquero**, None.

Presentation Number **P 188**
Poster Session 2
September 19, 2013 / 15:15-15:15 / Room: Exhibit Hall B

Creating novel imaging tools to diagnose stem cell rejection in vivo

Christopher Dove, *Hossein Nejadnik, Heike E. Daldrup-Link, Radiology, Stanford, Stanford, CA, USA. Contact e-mail: c.g.dove@gmail.com*

Background: Stem cell transplantation has great potential across a range of regenerative medicine therapies. However, stem cell (SC) transplantation, particularly allogenic SC transplantation, carries a risk of graft rejection from host immune responses. We propose to develop an easily translatable, non-invasive tool to predict SC engraftment or rejection by measuring cellular immune infiltrate and cytokine levels in transplanted stem cells in a murine calvarial defect model. Calvarial defects in mice can be repaired by transplantation of stem cells in growth factor enriched scaffolds (Fig. 1-2). Detecting macrophage recruitment to the defect will be one of several modalities to monitor transplant rejection or engraftment. We have developed a cellular imaging technique involving ultrasmall superparamagnetic iron oxide particles (USPIO, ferumoxytol) conjugated to a fluorescent marker, which are readily phagocytosed by macrophages. This novel method of intravital microscopy offers a powerful, detailed view to better understand how individual cellular components interact with transplanted cells. To understand cell-level dynamics of pro- and anti-regenerative immune responses of macrophages, we have collected intravital imaging data of macrophage infiltration following stem cell engraftment. Methods: Prior to scaffold implantation, macrophages were loaded with USPIO by tail vein injection of 0.5mmol/kg Rho-USPIO into recipient Balb/c mice. Human or mouse adipose derived stem cells were seeded in PLGA scaffolds, implanted into mouse calvarial defects, and secured with viewing windows. Scaffolds were visualized for fluorescent signal every 7d for a period of 4 weeks. Additional studies are ongoing in conjunction with MR and PET imaging to provide important clinical markers of stem cell integration in the host environment. Results: Our preliminary results show greater in vivo macrophage inflammatory response in mismatched SC grafts as compared to matched control SC or blank scaffolds (Fig. 3). Further studies will validate this data, explore T cell infiltration, and examine macrophage subtype (M1 vs M2). Importantly, ferumoxytol is already an FDA-approved iron supplment, and has been used with MR imaging to detect macrophage infiltration in other SC engraftment models [1]. We anticipate that collecting additional data on USPIOs in this model will demonstrate that USPIO imaging technology is readily translatable to use in human subjects. [1] Khurana, A., et al., Intravenous Ferumoxytol Allows Noninvasive MR Imaging Monitoring of Macrophage Migration into Stem Cell Transplants. Radiology, 2012.

Disclosure of author financial interest or relationships:
C. Dove, None; **H. Nejadnik**, None; **H.E. Daldrup-Link**, None.

Presentation Number **P 189**
Poster Session 2
September 19, 2013 / 15:15-15:15 / Room: Exhibit Hall B

[11C]Choline-PET imaging is superior to 3'-deoxy-3'-18F-fluorothymidine ([18F]FLT) in detecting cell proliferation in experimental rheumatoid arthritis (RA)

Kerstin Fuchs[1], *Gerald Reischl*[1], *Martin Röcken*[2], *Bernd J. Pichler*[1], *Manfred Kneilling*[1,2], [1]*Department of Preclinical Imaging and Radiopharmacy, Eberhard Karls Univsersity of Tuebingen, Werner Siemens Imaging Center, Germany, Tuebingen, Germany;* [2]*Department of Dermatology, Eberhard Karls Univsersity of Tuebingen, Germany, Tuebingen, Germany. Contact e-mail: kerstin.fuchs@med.uni-tuebingen.de*

Inflammatory autoimmune diseases such as RA or psoriasis are associated with enhanced cell proliferation. Arthritic joints display a massive inflammatory cells infiltration, synovial cell proliferation and pannus formation and subsequent cartilage and bone destruction. We have recently shown that non-invasive in vivo detection of cell proliferation by [18F]FLT-PET is a powerful tool to detect even early stages of experimental RA. The intracellular target of [18F]FLT is thymidine kinase 1. A second cell proliferation detecting radiotracer is [11C]Choline which is used in the clinical setup for imaging of prostate cancer. In contrast to [18F]FLT, [11C]Choline is transported into the cell, phosphorylated by choline kinase and attached as phosphatidylcholine into the cell membrane. The aim of our study was to investigate the potential of [11C]Choline to quantify cell proliferation in vivo in experimental RA and its comparison to the already established PET tracer [18F]FLT. Naïve BALB/c mice were injected with glucose-6-phosphate-isomerase (GPI) antibody containing serum to induce inflammatory arthritis or control serum. At day 6 after onset of arthritic disease, the time point with maximum ankle swelling, animals were injected intravenously (i.v.) with [18F]FLT or [11C]Choline and dynamic PET scans were conducted for one hour. The tracer uptake in arthritic or healthy ankles was quantified by drawing standardized regions of interest. Analysis of cell proliferation in arthritic ankles by [11C]Choline-PET (3.±1.0% ID/cc, n=7) on day 6 after onset of disease revealed an impressive 6-fold enhanced [11C]Choline uptake when compared to the uptake values in healthy control ankles ([11C]Choline: 0.5±0.2% ID/cc, n=8). In comparison to [11C]Choline, the [18F]FLT uptake in arthritic ankles (3.1±0.4% ID/cc, n=5) at the identical time point was only 3.4-fold enhanced when compared to control ankles ([18F]FLT: 0.9±0.3% ID/cc; n=2). In sharp contrast to the [18F]FLT time activity curves (TACs) derived from arthritic ankles, which display an initial tracer injection peak for up to 20 minutes before reaching a plateau, the [11C]Choline TACs showed a fast kinetic and a constant tracer distribution over the 1 hour scan after tracer injection. Histological analysis of arthritic ankles, 6 days after GPI-serum injection, revealed a massive inflammatory cell infiltration, synovial cell proliferation and pannus formation. An additional major advantage of [11C]Choline is its low bladder activity, in comparison to 18F-labeled tracers such as [18F]FLT. A disadvantage of [11C]Choline is the short half-life time of the isotope 11C (20 min) compared to 18F with a half-life time of 90 min. Our data clearly prove that non-invasive in vivo [11C]Choline-PET imaging of inflammation induced cell proliferation in experimental RA is superior to [18F]FLT-PET imaging as the arthritic to healthy ankle ratios are much higher and a constant tracer distribution was evident even immediately after tracer injection.

Disclosure of author financial interest or relationships:
K. Fuchs, None; **G. Reischl**, None; **M. Röcken**, Abbott Laboratories, Honoraria; Abbott Pharmaceuticals, Honoraria; Almirall Hermal, Honoraria; Biogen Idec, Honoraria; Galderma, Honoraria; Janssen-Cilag, Honoraria; Johnson & Johnson, Honoraria; Merck, Honoraria; Novartis, Honoraria; Pfizer, Honoraria; **B.J. Pichler**, Siemens, Grant/research support; Bayer, Grant/research support; AstraZeneca, Grant/research support; BoehringerIngelheim, Grant/research support; **M. Kneilling**, None.

Presentation Number **P 190**
Poster Session 2
September 19, 2013 / 15:15-15:15 / Room: Exhibit Hall B

Optical imaging of cathepsin activity in a TNBS induced murine model of IBD

Brahma Ghosh, *Prashant Bansal, Rao Varada, Maria R. Moalli, WCM-Global Science & Technology, Pfizer Inc., Andover, MA, USA. Contact e-mail: Brahmananda.Ghosh@pfizer.com*

The 2,4,6- trinitrobenzene sulfonic acid (TNBS) induced murine colitis model of human Inflammatory Bowel Disease (IBD) mimics the human disease state symptomatically and in severity. Cathepsins have been implicated in a wide variety of inflammatory/immune diseases and are activated during TNBS-induced intestinal inflammation. Earlier studies have utilized fluorescence tomography to investigate cathepsins as biomarkers of colonic inflammation and mediators of colonic pain in C57/Bl6 mice using activity-based probes that covalently bind to the protease active site with high specificity. In our current study using the above model, we applied a pan-cathepsin activatable probe from PerkinElmer (ProSense750 FAST) to investigate induction, magnitude, and progression of inflammation in the enteric organs of TNBS-treated (intra rectal) SJL/J mice. Reported here are results from this longitudinal in vivo imaging work, which among other things, provide valuable insight to the influence of route of administration [intravenous (I.V.) vs. intraperitoneal (I.P.)] of the probe on its in vivo kinetics and distribution. Administered I.V., the probe failed to produce detectable in vivo signal over a 24h imaging time-course [up to 42h post intra-rectal challenge with 2 mg (N =6)/3 mg (N =6) TNBS in 30% EtOH; Figure 1]. The minimal uptake to G.I. tract following I.V. administered ProSense was further confirmed by ex vivo imaging of harvested intestinal organs. In contrast, I.P. delivered probe produced signal in the colonic region as early as 1.5h post administration (Figure 1). Therefore, the I.P. route of administration was chosen as the dosing approach for subsequent imaging experiments of this study. This temporal imaging window and route of administration differs from the imaging time-course (6-24h post-probe administration) and procedural recommendations (I.V. injection) provided in the PerkinElmer package insert. These findings thus support the rationale for exploring and evaluating probe dosing approaches on a case-by-case manner and for conducting a thorough temporal characterization of in vivo probe signal via pilot work prior to embarking on a full length study. Also demonstrated in this report is the usefulness of in vivo imaging to illustrate the degree of inherent variability in animal responsiveness associated with chemically-induced preclinical models of experimental colitis such as the one above.

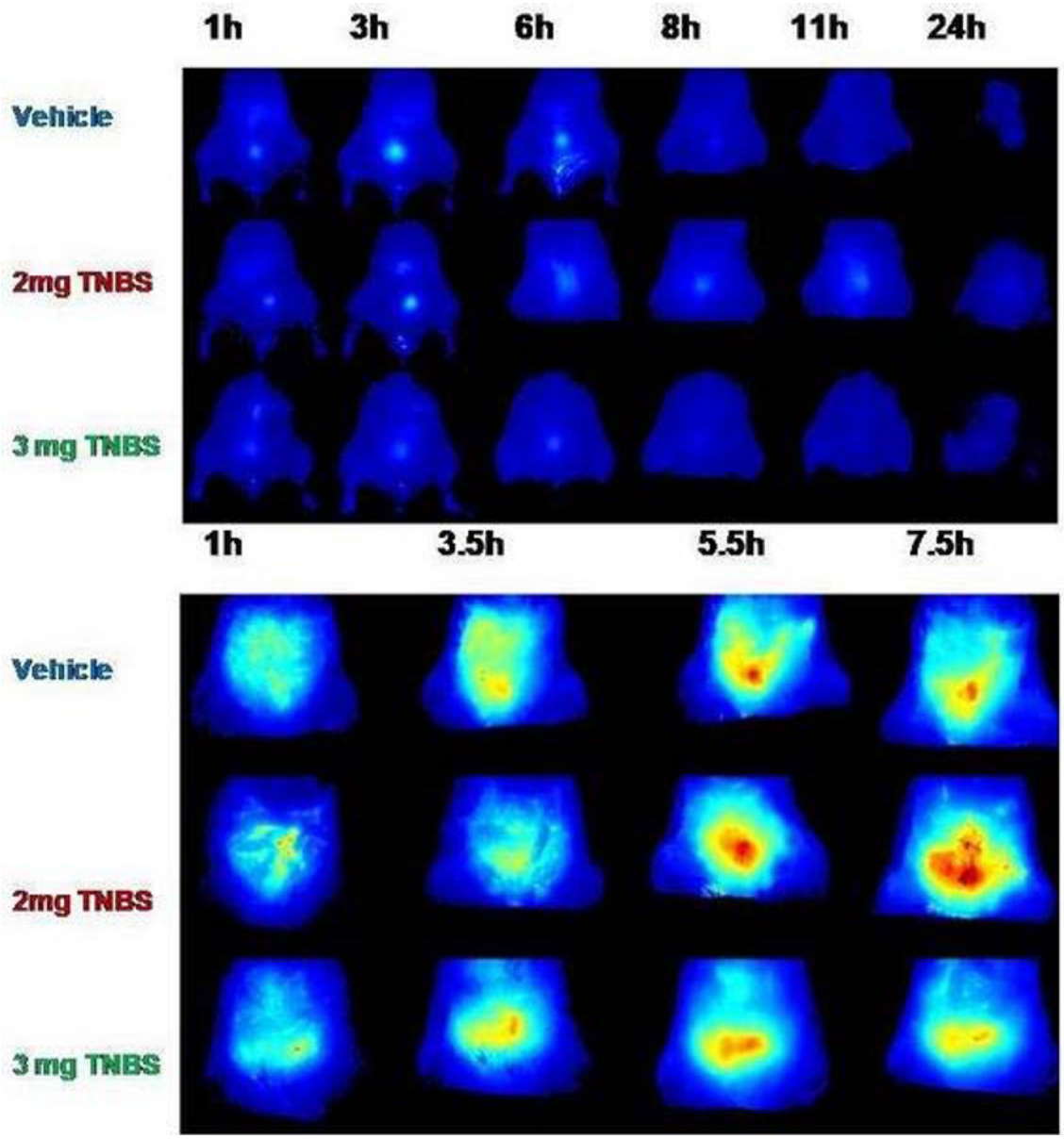

Figure 1. Representative images from Vehicle and TNBS groups showing temporal evolution of ProSense 750 FAST signal post IV (upper) and IP(lower) administration of probe.

Disclosure of author financial interest or relationships:
B. Ghosh, None; **P. Bansal**, None; **R. Varada**, None; **M.R. Moalli**, None.

Presentation Number **P 191**
Poster Session 2
September 19, 2013 / 15:15-15:15 / Room: Exhibit Hall B

Imaging Lymphatic Migration and Nodal Retention of Radiolabeled Polysaccharide-based Nanocapsule Vaccine Carriers

*Sara Vicente[2], **Beth Goins**[1], Alejandro Sanchez[2], Maria Jose Alonso[2], William T. Phillips[1], [1]Radiology, University of Texas Health Science Center San Antonio, San Antonio, TX, USA; [2]Pharmacy and Pharmaceutical Technology, University of Santiago de Compostela, Santiago de Compostela, Spain. Contact e-mail: goins@uthscsa.edu*

We have previously reported the adjuvant properties of polyglucosamine (PG) nanocapsules using the recombinant hepatitis B surface antigen (rHBsAg) as a model antigen. The aim of this study was to monitor lymphatic migration and lymph node retention of the PG nanocapsules by scintigraphic imaging after subcutaneous (s.c.) injection in New Zealand White rabbits. Methods: The nanocapsules were efficiently radiolabeled with indium-111 (In-111) (labeling efficiency of 98%). The stability of the radiolabeled nanocapsules was adequate for imaging purposes, with only a 20% release of In-111 from the nanocapsules after 48 hours of incubation in serum. The particle size of the nanocapsules was preserved after the radiolabeling process. The radiolabeled nanocapsules and the control In-111chloride in saline solution (18.5 MBq (500 µCi) in 100 µl) were injected s.c. into the foot pad of rabbits and scintigraphic images acquired at various times. Images were analyzed using Mango 2.6 software. Results: Image analysis revealed the slow clearance of the nanocapsules from the injection site and their progressive accumulation in the popliteal lymph node over time (3.8% ± 1.2 ID at 48 hours). The clearance rate of the nanocapsules from the injection site was significantly slower than that of the control (free In-111 chloride), which rapidly drained into systemic circulation and accumulated mainly in excretion organs (i.e. kidneys and bladder). In contrast, the biodistribution of nanocapsules was preferably limited to the lymphatic circulation. Conclusion: These results suggest that the immune potentiating effect previously observed for PG nanocapsules was mainly due to the formation of a depot at the injection site and their slow lymphatic drainage with prolonged retention in lymph nodes. Since In-111 is a commonly used imaging agent, studies with radiolabeled vaccine nanoparticles can be readily translated into human studies of vaccine biodistribution.

Disclosure of author financial interest or relationships:
S. Vicente, None; **B. Goins**, None; **A. Sanchez**, None; **M. Alonso**, None; **W.T. Phillips**, None.

Presentation Number **P 192**
Poster Session 2
September 19, 2013 / 15:15-15:15 / Room: Exhibit Hall B

A novel approach to image multiple sclerosis by PET

Aileen Hoehne[1], *Michelle L. James*[1], *Gayatri Gowrishankar*[1], *Zhaoqing Ding*[2], *Sanjiv S. Gambhir*[1], [1]*Radiology, Stanford University, Stanford, CA, USA;* [2]*Department of Neurology and Neurological Sciences, Stanford University, Stanford, CA, USA. Contact e-mail: ahoehne@stanford.edu*

Objectives: Glutamate excito-toxicity contributes to oligodendrocyte and CNS tissue damage in multiple sclerosis (MS). Cystine/glutamate antiporter (xCT) expression is reportedly up-regulated in cells from the monocyte-macrophage-microglia lineage in the spinal cord of experimental autoimmune encephalomyelitis (EAE) rodents, as well as in MS patients. We aim to evaluate the novel 18F-labeled xCT substrate, (4S)-4-(3-[18F]fluoropropyl)-L-glutamate (18F-FSPG), for visualizing alterations in xCT transporter activity in EAE mice by means of PET, compared to 18F-FDG accumulation in the same model. Methods: EAE was actively induced in C57BL/6 mice by s.c. injection of MOG35-55 peptide in complete Freund's adjuvant, followed by i.v. injections of pertussis toxin. Clinical signs of disease were scored daily according to a standard scoring system. Two groups of EAE and naïve mice (n=3-5 per group)underwent PET imaging following i.v. administration of either 18F-FSPG (248±20 µCi), or 18F-FDG (126±3 µCi). In contrast to 18F-FDG, 18F-FSPG normally does not cross the intact blood-brain-barrier, therefore a higher dose was used to increase sensitivity for potential changes in brain uptake. Dynamic 18F-FSPG-PET imaging was performed from 0-60 min p.i.. Static images for both tracers were acquired at 90 min p.i.. Mice were perfused and sacrificed at ~110 min p.i., and tissue-associated radioactivity was measured with a gamma-counter. Brain sections and spinal cords from one mouse per group were analyzed via ex vivo digital autoradiography (ARG). Results: In this pilot study 18F-FSPG uptake in EAE mice was elevated in most tissues compared to naïve mice, but the most prominent differences were seen in kidneys (18.7±5.0-fold, n=3, $p<0.0001$) and spinal cord (22.9±5.1-fold, n=2), as measured by ex vivo biodistribution studies. In contrast, 18F-FDG uptake did not differ much between EAE and naïve mouse tissues, with spinal cord uptake only 1.5±0.5-fold higher in EAE mice (n=4, $p>0.05$). Similarly, the ex vivo ARG results demonstrated a dramatic difference in 18F-FSPG uptake in spinal cords of EAE versus naïve mice, whereas 18F-FDG uptake was only elevated in distinct foci (Figure 1). ARG of brain sections revealed elevated 18F-FSPG uptake in brain stem, cerebellum, choroid plexus, and optic nerve of EAE mice. Increased retention of 18F-FSPG in the brain of EAE mice was confirmed by time activity curves generated during dynamic PET imaging. In the case of 18F-FDG, decreased brain uptake was observed in EAE mice (5.9±0.2 %ID/g) compared to naïve mice (7.6±0.7 %ID/g, n=5, $p=0.01$), consistent with reports about hypometabolism in several regions of the MS-affected brain. Conclusions: Uptake of 18F-FSPG in EAE spinal cord is markedly elevated compared to naïve mice, which is in agreement with xCT immunohistochemistry data. However, since absolute 18F-FSPG uptake in spinal cord is relatively low (1.1 %ID/g in EAE mice) and several adjacent tissues display high uptake, it is difficult to visualize the accumulation in mouse spinal cord via small animal PET. Further studies are warranted to explore the feasibility and ultimate utility of18F-FSPG imaging in MS patients.

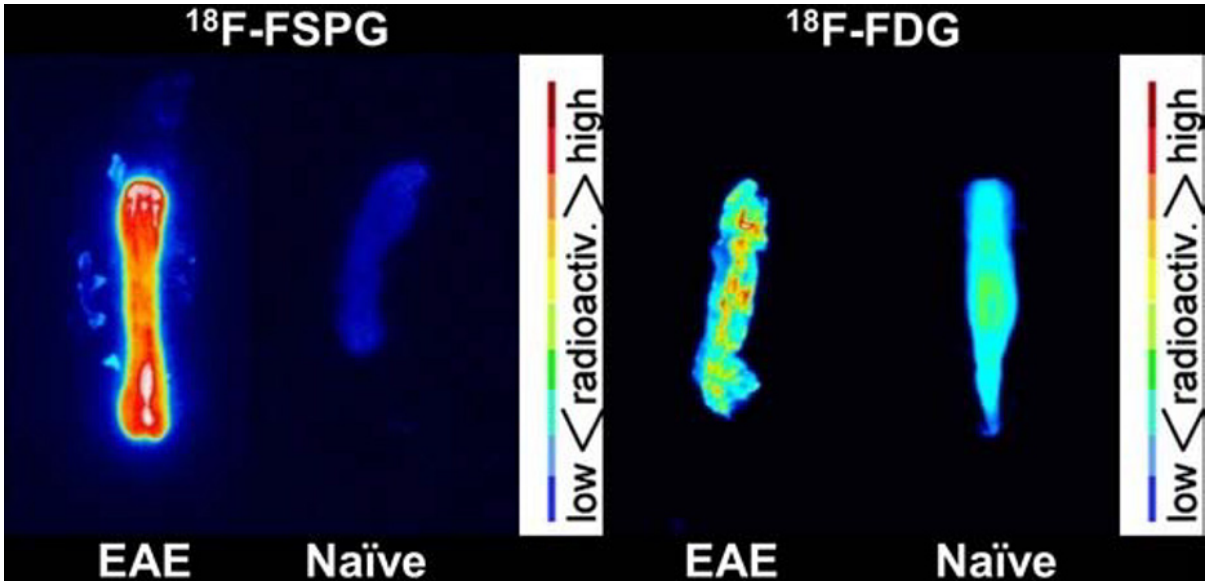

Figure 1: Autoradiography of spinal cords ~110 min p.i. of 18F-FSPG and 18F-FDG in EAE and naïve mice.

Disclosure of author financial interest or relationships:

A. Hoehne, None; **M.L. James**, None; **G. Gowrishankar**, None; **Z. Ding**, None; **S.S. Gambhir**, Bracco Diagnostics, Consultant; Endra, Inc, Stockholder; Cellsight, Stockholder; Enlight, Inc., Stockholder; General Electric, Grant/research support; ImaginAb, Stockholder; MagArray, Inc., Stockholder; Sanofi-Aventis, US, Grant/research support; SiteOne Therapeutics, Stockholder; VisualSonics/Sonosite, Stockholder .

Presentation Number **P 193**
Poster Session 2
September 19, 2013 / 15:15-15:15 / Room: Exhibit Hall B

Immunomodulation of doxorubicin on adoptive therapy with T cell functional imaging in mice

Fei-Ting Hsu, *I-Tsang Chiang, Jeng-Jong Hwang, Dept. of Biomedical Imaging and Radiological Sciences, National Yang-Ming University, Taipei, Taiwan. Contact e-mail: sakiro920@hotmail.com*

Purpose Adoptive cell therapy (ACT) is an emerging strategy for cancer treatment. Several limitations, however, exist in its applications for clinical use, such as isolation, expansion and the number of tumor-specific T cells for transfusion. On the other hand, using chemotherapeutic drug to suppress those immunosuppressive factors in the tumor microenvironment has emerged as a potential strategy to enhance T-cell-mediated tumor progression. Doxorubicin has been used to treat leukemias, Hodgkin lymphoma as well as cancers of the lung, ovary and multiple myeloma. Here, we demonstrated that low-dose doxorubicin could inhibit various immunoresponsive factors, suggesting that therapeutic efficacy of ACT may be enhanced by combination with doxorubicin. Materials and Methods OT-1 transgenic mouse and E.G7 mouse lymphoma cells with OVA-expression were used in this study. CD8+ T cells were obtained from OT-1 mouse and were transduced with pGBeLT lentivirus for monitoring the activation of CD8+ T cells by optical imaging. E.G7 cells were pretreated with 0.4 μM doxorubicin for 24 h, then co-cultured (effector-to-target ratio=25) with CD8+ T cells for another 4 h. The activation of CD8+ T cells, intracellular IFN-γ and IL-12 were evaluated by flow cytometry. The expression of immunosuppressive factors, such as TGF-β, VEGF, IL-10, CCL-2, Cox-2, IDO and CCL-22 were assayed by Western blotting. The number of tumor-infiltrated CD8+ T cells was evaluated with transwell migration assay. E.G7/OT-1 mouse model was established to evaluate the therapeutic efficacy of low-dose doxrubicin combined with ACT. Results CD8+ T cells were significantly activated when co-cultured with doxorubicin pretreated E.G7 cells. Significant increase of fluorescence intensity, IFN-γ and IL-12 production were found (**$p<0.01$ as compared with non-activated and untreated groups). The expression of TGF-β, VEGF, IL-10, CCL-2, Cox-2, IDO and CCL-22 were suppressed by doxorubicin. The number of migrated CD8+ T cells was increased in the group of doxorubicin pretreated E.G7 cells as compared with those of non-activated and untreated groups. Doxorubicin could enhance the therapeutic efficacy of ACT in E.G7/OT-1 mouse model. Tumor growth could be suppressed by doxorubicn pretreated 2 million CD8+ T cells (2T) and 5 million CD8+ T cells (5T), respectively. Since NF-κB has been reported to play an important role in immunomodulation, we also used NF-κB inhibitor as a positive control. The result showed that tumor microenvironment could be modulated by doxorubicin via NF-κB pathway. Conclusions Combination of doxorubicin pretreatment and ACT may improve the therapeutic efficacy through downregulation of NF-κB expression and its effector proteins. The pGBeLT imaging system used in this study, provides not only a potential tool for observing the development of ACT, but also a platform for the evaluation of new preclinical trial. (This study is supported by a grant 101-2321-B-010-006 from National Science Council, Taipei, Taiwan)

Disclosure of author financial interest or relationships:
F. Hsu, None; **I. Chiang**, None; **J. Hwang**, None.

Presentation Number **P 194**
Poster Session 2
September 19, 2013 / 15:15-15:15 / Room: Exhibit Hall B

In vivo imaging of apoptosis activation by NK cell-based immunotherapy using a caspase-3 biosensor in glioma caner model

Ho Won Lee[1], *Thoudam Debraj Singh*[1], *Sang-Woo Lee*[1], *Jeoung-Hee Ha*[2], *Alnawaz Rehemtulla*[3], *Byeong-Cheol Ahn*[1], *Yong Hyun Jeon*[1], *Jaetae Lee*[1], [1]*Nuclear Medicine, School of Medicine, Kyungpook National University, Daegu, Republic of Korea;* [2]*Pharmacology, School of Medicine, Kyungpook National University, Daegu, Republic of Korea;* [3]*Radiation Oncology, University of Michigan, Ann Arbor, MI, USA. Contact e-mail: howon1234@hanmail.net*

Objective: Natural killer (NK) cells-based immunotherapy is still challenging area among several strategies of cancer treatment and caspase-3 is an important effector molecule in NK cells-mediated apoptosis in cancers. Herein, we monitored caspase-3 activation in glioma cancer model by NK cell-based immunotherapy using a caspase-3 biosensor. Methods and Materials: Human glioma cell co-expressing caspase-3 sensor (as a surrogate marker for caspase-3 activation) and renilla luciferase (Rluc, as a surrogate marker for cell viability) were established (referred to as a D54-CR). NK92 cells (IL-2 independent human natural killer cell line) were used as a target cells. To determine caspase-3 activation in D54-CR cells in response to treatment of NK92 cells, effectors and target cells were co-cultured at different E/T ratio and BLI activity was measured. Inhibition study using Z-VAD (a pan-caspase inhibitor) was performed to examine the selectivity of caspase-3 sensor. After transfer of either PBS or NK92 cells to D54-CR tumor-bearing mice intravenously, BLI was performed to determine both caspase-3 activation and anti-tumor effects. Detail schematic for in vivo experiment was further illustrated in Fig. 2.A Results: Treatment of NK92 cell resulted in time- and effector number-dependent increase of BLI activity in D54-CR cells in vitro. Caspase-3 activation by NK92 treatment was blocked in D54-CR cells by pan-caspase inhibitor, Z-VAD. In vivo transfer of NK92 cells exhibited increase of caspase-3 activation in a dose- and time-dependent manner in D54-CR tumor bearing mice but not PBS-treated mice. Concurrently, sequential BLI with Rluc reporter gene revealed significant retardation of tumor growth in NK92-treated mice but not PBS-treated mice ($P<0.05$). Conclusions: We successfully visualized the activation of caspase-3-dependent apoptosis by NK cell-mediated cytotoxicity in glioma cancer in vitro and in vivo and evaluated the its anti-tumor effects using a Rluc reporter gene. Caspase-3 sensor provides a more comprehensive tool for evaluation of therapeutic efficacy as well as protocol optimization of NK cell-based immunotherapy.

Disclosure of author financial interest or relationships:
H. Lee, None; **T. Debraj Singh**, None; **S. Lee**, None; **J. Ha**, None; **A. Rehemtulla**, None; **B. Ahn**, None; **Y. Jeon**, None; **J. Lee**, None.

Presentation Number **P 195**
Poster Session 2
September 19, 2013 / 15:15-15:15 / Room: Exhibit Hall B

Tumor antigen-specifity of Interferon-γ (IFN-γ) producing CD4+ T helper cells (Th1) is essential for successful cell-based immunotherapy of solid cancer

Dominik B. Krueger[1], *Christoph M. Griessinger*[1], *Daniel Bukala*[1], *Jennifer Schmitz*[1], *Maren K. Koenig*[1], *Andreas Schmid*[1], *Heidi Braumüller*[2], *Martin Röcken*[2], *Bernd J. Pichler*[1], *Manfred Kneilling*[1,2], [1]*Department of Preclinical Imaging and Radiopharmacy, Eberhard Karls University of Tuebingen, Tuebingen, Germany;* [2]*Department of Dermatology, Eberhard Karls University of Tuebingen, Tuebingen, Germany. Contact e-mail: dominik.krueger@med.uni-tuebingen.de*

Several preclinical and clinical studies revealed the high potential of Th1 cells in mediating tumor rejection. A successful Th1 cell-based immunotherapy has been established in an endogenous pancreatic cancer mouse model (RIP1-Tag2) doubling the lifespan of mice by induction of tumor senescence through IFN-γ and TNF-α. Anti-tumoral effects were observed after both intraperitoneal (i.p.) and intravenous (i.v.) injection of tumor antigen (TA)-specific Tag2-Th1 cells, although no homing to the tumor sites could be observed after i.v. administration. Thus, a systemic effect of the Th1 cells can be assumed and the necessity of TA-specifity questioned. The aim of this study was to investigate whether unspecific Th1 cells are able to induce similar therapeutic effects and to analyze their homing patterns. CD4+ T cells were isolated from C3H mice, further activated with CD3, CD28, and APCs, and then specifically cultured over 7 days to generate a Th1 phenotype. In a second approach, CD4+ T cells were specifically cultured for 3 days and purified by negative-selection to obtain Th1 cells in an early activation state (Th1a). Following an initial 2 Gy whole body irradiation, which was repeated after 6 weeks, 10^7 unspecific Th1/Th1a cells were injected i.v. or i.p. once weekly into RIP1-Tag2 mice starting at 5 weeks of age. Control mice were sham-treated with NaCl. Blood glucose levels were determined twice weekly and MRI scans were performed to monitor the growth of the insulin producing carcinomas. Th1 cells, labeled with the fluorescence dye Cy5, were injected i.p. into 14 week old mice to follow their migration by Optical Imaging (OI) over 5 days. Subsequently, ex vivo OI as well as histological and immunofluorescence analyses were performed. The blood glucose levels decreased continuously during the treatment in all experimental groups. At 13 weeks of age, blood glucose levels achieved values of 36±3 mg/dl (±SEM) in sham-treated mice as well as 32±5 mg/dl (Th1) and 32±6 mg/dl (Th1a) in the treatment groups. MRI analyses at 14 weeks of age revealed pancreatic islet carcinomas in all groups with a similar volume (Th1: 28±6 mm^3, sham: 33±6 mm^3; Th1a: 32±4 mm^3, sham: 31±3 mm^3). Corresponding to our Tag2-Th1 cell investigations the OI migration studies yielded a strong Cy5-Th1 derived signal in the perithymic, pancreatic, mesenteric, axillary, and inguinal lymph nodes as well as in the peripancreatic lymphatic tissue, the liver, and the spleen, but not within the islet carcinomas. In summary, our data demonstrate the necessity of TA-specifity of Th1 cells for successful anti-tumoral immunotherapy. Treatment with unspecific Th1 cells was inefficient although both Tag2-Th1 and unspecific Th1 cells secrete IFN-γ and TNF-α and no differences in the migration properties were identified. Neither unspecific nor specific Th1 cells were detected within the carcinomas after i.p. administration. This raises the question of the crucial lymphatic sites in which the Tag2-Th1 cells effect the immune system of the recipient. Therefore, future studies should focus on the sites of TA-specific Th1 cell activation and TA-presentation.

Disclosure of author financial interest or relationships:
D.B. Krueger, None; **C.M. Griessinger**, None; **D. Bukala**, None; **J. Schmitz**, None; **M.K. Koenig**, None; **A. Schmid**, None; **H. Braumüller**, None; **M. Röcken**, Abbott Laboratories, Honoraria; Abbott Pharmaceuticals, Honoraria; Almirall Hermal, Honoraria; Biogen Idec, Honoraria; Galderma, Honoraria; Janssen-Cilag, Honoraria; Johnson & Johnson, Honoraria; Merck, Honoraria; Novartis, Honoraria; Pfizer, Honoraria; **B.J. Pichler**, Siemens, Grant/research support; Bayer, Grant/research support; AstraZeneca, Grant/research support; BoehringerIngelheim, Grant/research support; **M. Kneilling**, None.

Presentation Number **P 196**
Poster Session 2
September 19, 2013 / 15:15-15:15 / Room: Exhibit Hall B

Antitumor Effect of theranostic S. typhimurium expressing Vibrio Vulnificus FlaB and bioluminescence reporter gene

Jinhai Zheng[1], *Sheng Nan Jiang*[2], *Seung-Hwan Park*[1], *Yoon Soon Moon*[1], *Hee-Seung Bom*[1], *Jung-Joon Min*[1], [1]*Nuclear medicine, Chonnam National University, Gwangju, Republic of Korea;* [2]*Nuclear medicine, Central South University, Hainan, China. Contact e-mail: kingseazheng@hotmail.com*

Objectives: The application of attenuated Salmonella typhimurium for cancer therapy has been attributed to the characteristics of bacteria, tumor-specific accumulation and proliferation. Cytokines or other immune-modulators were explored to be carried by bacteria to stimulate immune cells that kill cancer cells. In the present study, we engineered attenuated S. typhimurium that carry flagellin B (FlaB) from Vibrio vulnificus that is recognized by toll-like receptor 5 (TLR5) and stimulates proininflammatory response. Methods: By employing inducible promoter such as PBAD, FlaB can be expressed in tumor-specific manner (1). We cloned V. vulnificus FlaB gene into pBAD vector system that tightly regulate gene expression by inducer L-Arabinose, and transformed attenuated S. typhimurium with this constructed plasmid. To noninvasively monitor the bacterial migration in mice, the bacterial luciferase (Lux) operon from S. typhimurium-Xen26 was transduced into the salmonellae by P22HT int transduction. Mouse colon carcinoma cells (MC38) bearing mice (C57BL/6) were i.v. injected with the engineered bacteria (1x107 CFU). Results: The engineered Salmonella successfully localized to tumor tissue and gene expression was dependent on the concentration of inducer, indicating the feasibility of peripheral control of bacterial gene expression. The bioluminescence signal permitted the localization of gene expression from the bacteria. The engineered bacteria significantly suppressed both primary and metastatic tumors and prolonged survival in mice. Conclusion: We successfully visualized the therapeutic process with these engineered bacteria and found that they often mediated complete tumor eradication on FlaB induction. The next study should be focused to elucidate the mechanism of FlaB that elicit immune reaction in tumor.

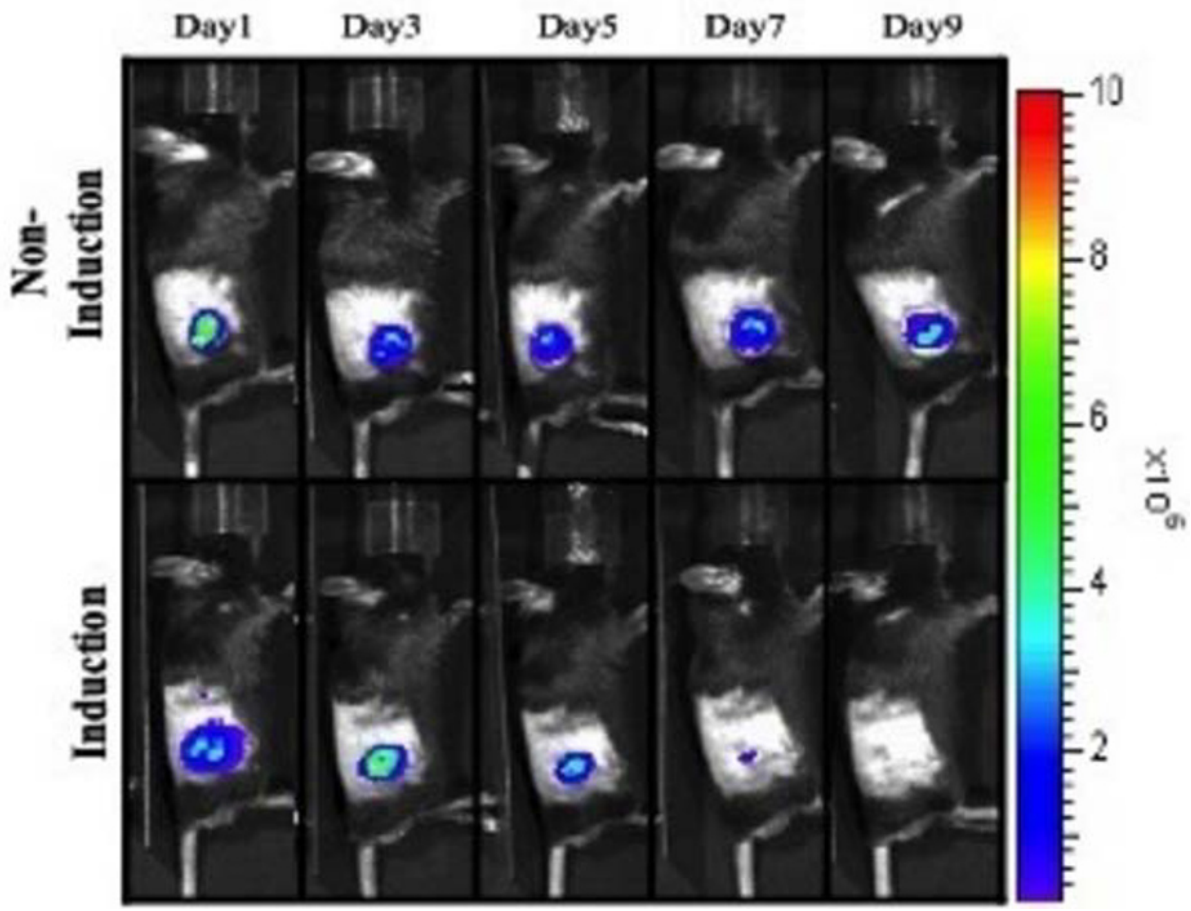

Detection of tumor-targeting S. typhimurium expressing FlaB and Lux. After induction of FlaB expression tumor growth was significantly suppressed and eventually almost eradicated. After tumor being removed, bioluminescence signal from bacteria also disappeared indicating the clearance of bacteria after removal of tumor.

Disclosure of author financial interest or relationships:
J. Zheng, None; **S. Jiang**, None; **S. Park**, None; **Y. Moon**, None; **H. Bom**, None; **J. Min**, None.

Presentation Number **P 197**
Poster Session 2
September 19, 2013 / 15:15-15:15 / Room: Exhibit Hall B

Highly Sensitive Lanthanide Based Luminescent Probes for In Vivo Imaging of ROS Species in Deep Tissues

Daniel Ansaldi, Sunetra Ray, Ed Lim, **Rajendra Singh**, *Caliper LifeSciences, a PerkinElmer Company, Alameda, CA, USA. Contact e-mail: rajendra.singh@perkinelmer.com*

Introduction: Reactive oxygen species (ROS) play a critical role in a wide variety of disease conditions like cancer, inflammation, neurodegenerative disorders and oxidative stress. Highly sensitive and specific optical probes (fluorescent, luminescent or chemiluminescent probes) are therefore required for detecting and studying the roles of different ROS in disease pathogenesis. However, very short life times of these species coupled with the presence of antioxidants in living systems make it extremely hard to detect these reactive species in vivo, especially in deep tissues. We employed the chemiluminescent properties of lanthanide acceptor beads to develop a highly sensitive probe for ROS detection by non-invasive optical imaging. In this approach when an acceptor bead comes in close proximity (200nm) to Singlet oxygen ($_1O^2$), energy is transferred from the singlet oxygen to thioxene derivatives within the acceptor bead, resulting in light production at 520-620 nm (EPRM®). The major advantages of this approach are: a. enabling detection of ROS by generating long-lived signal (half-life in seconds); b. Achieving high sensitivity due to lack of background signal and c. Generating long wavelength (620nm) signal thereby allowing deep tissue interrogations in living organisms. Results: When incubated with ROS generating systems under light-proof conditions, the EPRM beads produced high amount of chemiluminescence (signal:background 5-15 fold) in presence of singlet oxygen. As a proof-of-concept, the beads were also tested in an animal model of LPS-induced lung inflammation. When delivered intravenously the beads produced 2-3 fold higher optical signal in inflamed vs normal lungs, further confirming their potential usage as an ROS probe for deep tissue imaging applications. Summary: In conclusion, our results demonstrated the practical applicability of the probe for in vivo imaging of ROS. Future studies are aimed at targeting the beads with antibodies for investigating specific disease pathogenesis.

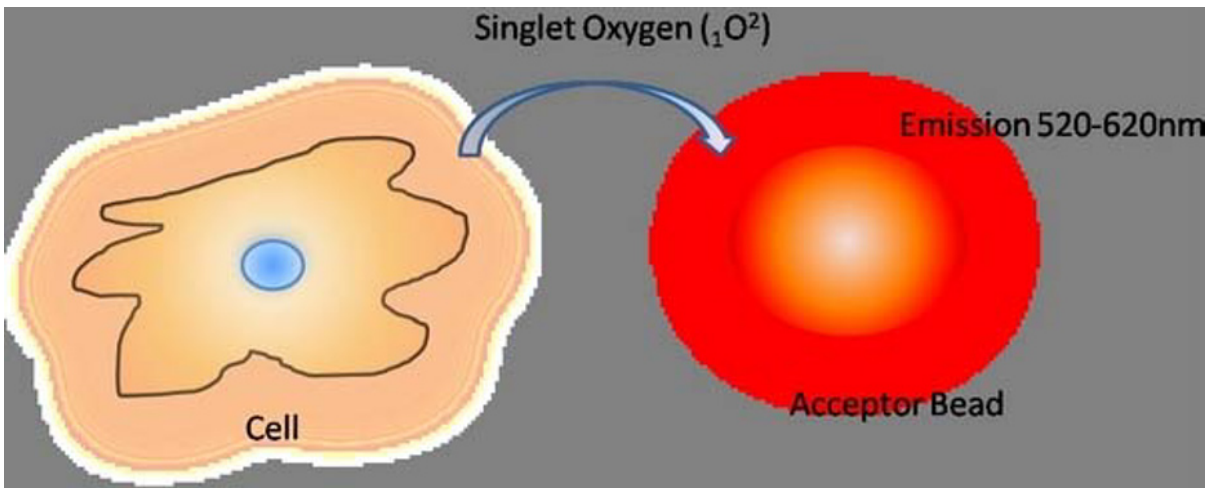

Fig 1: Lanthanide based acceptor beads for the detection of ROS species. In the presence of ROS molecules produced by cells or tissues under physiological or pathological conditions, the thioxene derivatives in the acceptor beads emits light at 520-620nm

Disclosure of author financial interest or relationships:
D. Ansaldi, Caliper Life Sciences, A Perkin Elmer Company, Employment; **S. Ray**, PerkinElmer, Employment; **E. Lim**, None; **R. Singh**, PerkinElmer, Employment .

Presentation Number **P 198**
Poster Session 2
September 19, 2013 / 15:15-15:15 / Room: Exhibit Hall B

Time-Course for Macrophage Detection in vivo by Ferumoxytol-Enhanced T2-MRI

Marina Stukova[1], *Daniel Golovko*[2], *Kendra Huber*[1], *Barbara Frederick*[3,4], *Joshua Thurman*[2], *Natalie J. Serkova*[1,4],
[1]*Anesthesiology, University of Colorado Denver School of Medicine, Aurora, CO, USA;* [2]*Medicine, University of Colorado Anschutz Medical Campus, Aurora, CO, USA;* [3]*Radiation Oncology, University of Colorado Denver School of Medicine, Aurora, CO, USA;* [4]*University of Colorado Cancer Center, Aurora, CO, USA. Contact e-mail: marina.stukova@ucdenver.edu*

In our previous studies, we have reported on magnetic resonance imaging (MRI) using 75-nm targeted super-paramagnetic iron oxide (SPIO) nanoparticles for non-invasive detection of C3-complement activation in inflamed lupus kidneys (1,2). The T2-relaxation times (RT) in C3-expressed kidneys were significantly decreased 48 hours after SPIO injection. In addition to this targeted approach, there is a significant interest to develop a non-targeted SPIO T2-MRI protocol for macrophage imaging. The use of commercially available Fe2O3 nanoparticles, such as Ferumoxytol, has its advantages since it can be directly translated into clinical trials. The aim of this study was to establish a time course (pharmacokinetics) for Ferumoxytol effects on T2-RT in control mice and mouse models of inflammation. The ability of Ferumoxytol to detect macrophages in vivo was validated in two mouse models: (i) wild-type mice after induced renal ischemia-reperfusion (I/R); (ii) athymic cancer xenograft models after radiation-induced inflammation. Ferumoxytol (10 mg iron/kg, 17-31 nm) was injected into mice intravenously. A control group (n=5) and a renal I/R model (n=8) of male C56BL/6 mice were used. Four of the animals underwent I/R with no contrast injected. Each one of the remaining mice received Ferumoxytol injections at different time points: 24 hrs before, during, 24, 48 and 72 hrs after I/R. Finally, female athymic mice (n=4) with human UMSCC2 head-and-neck squamous cell carcinoma xenografts underwent MRI scans before and after 2 Gy radiation treatments. T2-MRI maps were obtained at 4.7T MRI scanner using spin echo with 16 echo times (all MRI protocols are reported previously by our groups, (1, 2, 3)). Scans were performed at baseline, 4, 24, 48 and 72 hrs after injection of the SPIO. The T2-RTs (in ms) of various organs (muscles, kidneys and tumors) were calculated using Bruker ParaVision software. In the control group, Ferumoxytol renal clearance happens between 4 hrs and 24 hrs after injection, as seen by highly decreased T2-RT. The liver enhancement persisted beyond 48 hrs, indicating a prolonged retention of Fe2O3 by Kupffer cells (data not shown), and as expected muscle T2-RT were unchanged (Figure 1). In I/R kidneys (with well reported macrophage infiltration (4)), the decrease of T2 was less profound at 4 hrs (due to limited blood flow to the kidney), and persisted beyond 24 hrs, indicating iron retention in the macrophages (Figure 1). Finally, in UMSCC2 xenografts, there were no significant changes after injection of Ferumoxytol prior to irradiation treatment (Table 1), which correlated with minimal presence of tumor-associated macrophages by histopathology. However, 24 hrs after radiation treatment, there was a significant drop of T2-RT by Ferumoxytol (Table 1), with a positive macrophage staining for radiation-induced inflammation. The results indicate that Ferumoxytol clears from the blood within 4-24 hrs. Macrophages, if present in the kidneys or tumors, can retain Ferumoxytol for up to 48 hrs before its excretion. Ferumoxytol can be used clinically off-label as a novel negative contrast agent for inflammation and tumor MR imaging.

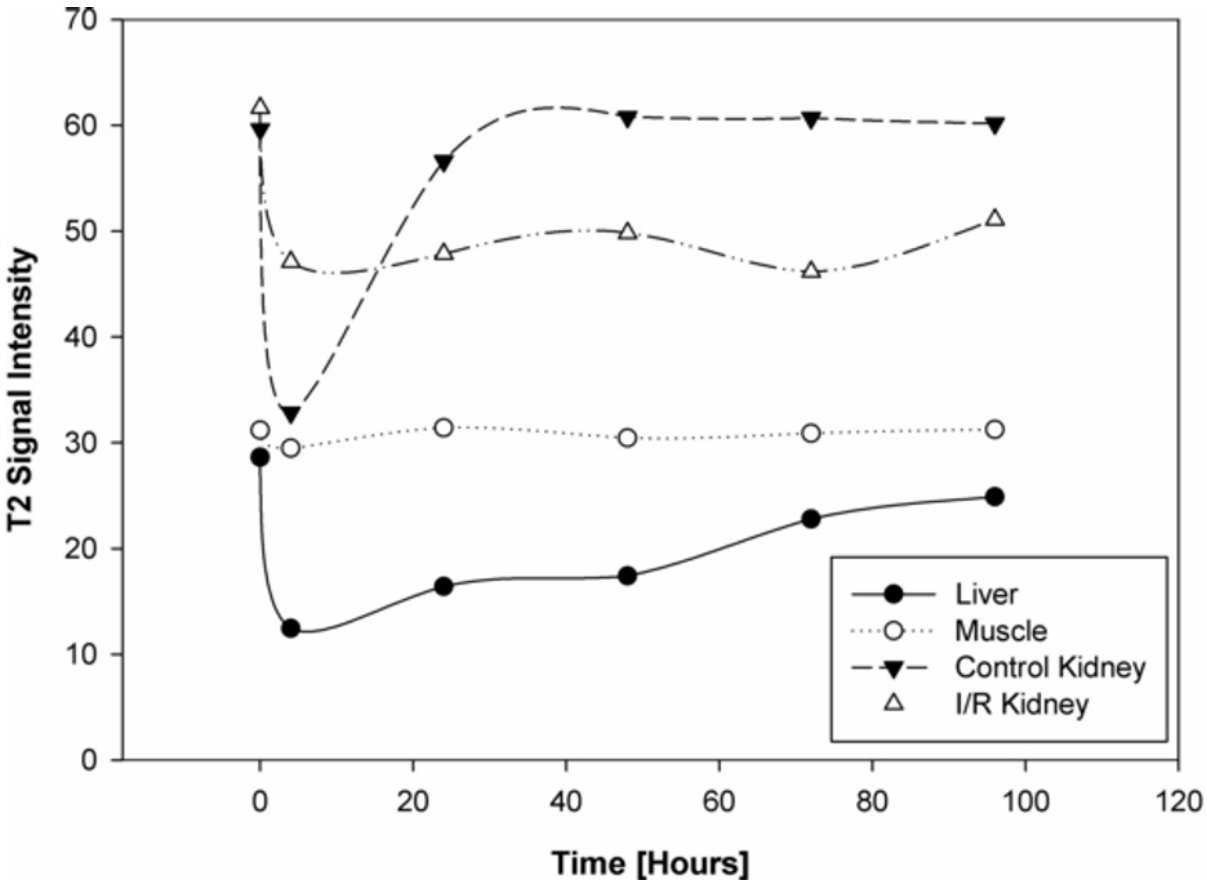

Figure 1: T2-weighted signal intensity was measured at various times in liver, muscle (as unchanged in comparison), control C56BL/6 and I/R mice. After injection with Ferumoxytol, no changes in T2 signal intensity were seen in the muscle. In contrast, significant decrease in T2 relaxation time was seen in liver and I/R kidney. Changes were observed as soon as 4 hours after injection and persisted upon 24 hours after injection.

Table 1: T2 (ms) relaxation times in human UMSCC2 head-and-neck carcinoma xenografts at baseline and 24 hours after Ferumoxytol injection in athymic mice

Prior Irradiation		After Irradiation	
Baseline	24 Hours after Injection	Baseline	24 Hours after Injection
52.0±5.4	30.2±4.2	56.3±7.6	42.5±2.7

Disclosure of author financial interest or relationships:

M. Stukova, None; **D. Golovko**, None; **K. Huber**, None; **B. Frederick**, None; **J. Thurman**, Alexion Pharmaceuticals, Inc., Consultant; **N.J. Serkova**, None.

Presentation Number **P 199**
Poster Session 2
September 19, 2013 / 15:15-15:15 / Room: Exhibit Hall B

Membrane-Bound Radicals Detected In Vivo within Septic Mouse Brains using Molecular MRI and Immuno-Spin-Trapping

Rheal Towner[1], *Nataliya Smith*[1], *Philippe Garteiser*[1], *Debra Saunders*[1], *Florea Lupu*[2], *Robert Silasi-Mansat*[2], *Dario C. Ramirez*[3], *Sandra E. Gomez-Mejiba*[3], *Ronald P. Mason*[4], *Marilyn Ehrenshaft*[4], *Fernando Bozza*[5], *Marcus Fernandes de Oliveira*[7], *Hugo C. Castro Faria-Neto*[6], [1]*Advanced Magnetic Resonance Center, Oklahoma Medical Research Foundation, Oklahoma City, OK, USA;* [2]*Cardiovascular Biology, Oklahoma Medic al Research Foundation, Oklahoma City, OK, USA;* [3]*Laboratory of Experimental Medicine and Therapeutics, National University of San Luis, San Luis, Argentina;* [4]*Laboratory of Pharmacology and Chemistry, National Institute of Environmental Health Sciences, Research Triangle Park, NC, USA;* [5]*Instituto de Pesquisa Clinica Evandro Chagas, Oswaldo Cruz Foundation, Rio de Janeiro, Brazil;* [6]*Laboratorio de Imunofarmacologia, Oswaldo Cruz Foundation, Rio de Janeiro, Brazil;* [7]*Laboratorio de Bioquimica Redox, Federal University of Rio de Janeiro, Rio de Janeiro, Brazil. Contact e-mail: Rheal-Towner@omrf.org*

Introduction: Oxidative stress, particularly involving free radicals, plays a major role in sepsis. Understanding the extent and timing of in vivo free radical triggered events is of importance regarding disease evolution and prognosis. With the use molecular magnetic resonance imaging (mMRI) and immuno-spin trapping (IST) technologies combined, in vivo radicals were monitored for the first time in a mouse model for sepsis. Methods: As cecal ligation puncture (CLP) sepsis model was used. Mice (8-10 weeks old; male; n=6; n=3 CLP and n=3 sham) were anesthetized with isoflurane (2-3%) and the cecum was exposed, ligated and punctured below the ileocecal junction. Sham operation control mice did not involve ligation and puncture of the cecum. DMPO (5,5-dimethyl-pyrroline-N-oxide) was administered (i.p.) every 1.5 h over a period of 6 hours, prior to injection of the anti-DMPO probe. A contrast agent, biotin-BSA (bovine serum albumin)-Gd-DTPA (100 µg) conjugated to an antibody against DMPO adducts (200µg) was used. Non-specific mouse-IgG conjugated to biotin-BSA-Gd-DTPA was used as a control contrast agent. MRI experiments were done on a Bruker Biospec 7.0 Tesla/30 cm horizontal-bore imaging system. Multiple brain 1H MR image slices were taken using a spin echo multislice (repetition time (TR) 0.8 s, echo time (TE) 23 ms, 128x128 matrix, 4 steps per acquisition, 3x4 cm2 field of view, 1 mm slice thickness). Mouse brains were imaged at 0 (pre-contrast), 20, 40, 60, 120 and 180 min intervals post-contrast agent injection. Mice were injected intravenously with anti-DMPO or non-immune-IgG antibodies tagged with a biotin-Gd-DTPA-albumin-based contrast agent (200 µL/kg; 1 mg antibody/kg; 0.4 mmol Gd+3/kg). T1-weighted images were obtained using a variable TR (repetition time) spin-echo sequence. Pixel-by-pixel relaxation maps were reconstructed from a series of T1-weighted images using a nonlinear two-parameter fitting procedure. The T1 value of a specified region-of-interest (ROI) was computed from all the pixels in the identified ROIs. Results: MRI was used to detect the presence of anti-DMPO adducts via a substantial decrease in T1 relaxation, measured as %T1 change (Fig. 1), within the hippocampus, striatium, occipital and medial cortex brain regions ($p<0.01$) in septic animals compared to sham controls. Fluorescently-labeled streptavidin was used to target the biotin moiety of the anti-DMPO probe to locate the targeting contrast agent in excised tissues, detecting increased signal in the brains, liver and lungs of septic animals, compared to sham controls. Ex vivo DMPO adducts were also confirmed in septic brain tissues from animals administered DMPO, compared to sham controls. Discussion: Here we used a combination of mMRI and IST to show for the first time non-invasive in vivo detection of membrane-bound radicals in neurological effects from sepsis. Using both mMRI and IST provides the advantage of in vivo image resolution and spatial differentiation of regional events in heterogeneous tissues or organs and the regional targeting of free radical mediated oxidation of cellular

membrane components.

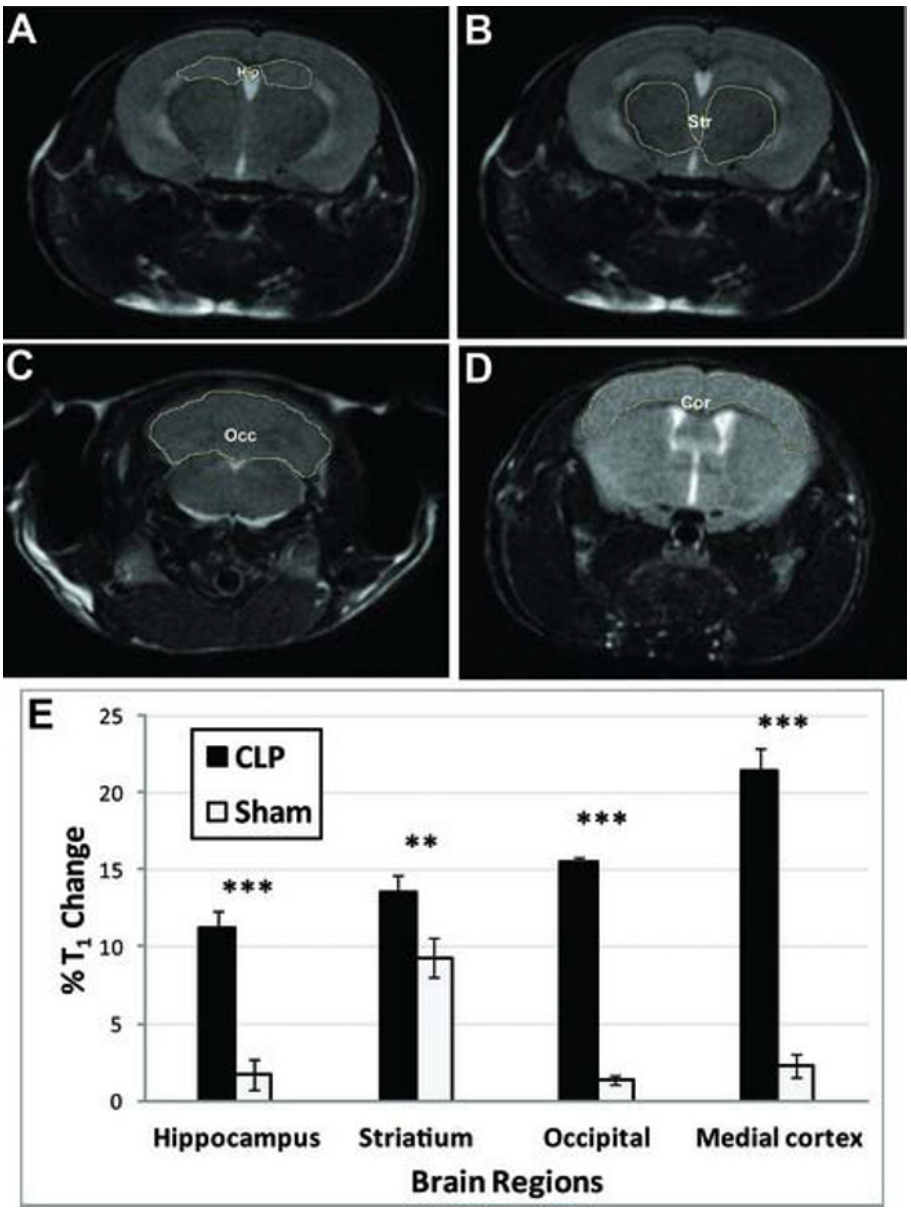

Figure 1: mMRI detection of membrane-bound radical adducts in brain regions of a CLP-induced mouse model for sepsis. Outlined brain regions including the hippocampus (A), the striatum (B), the occipital lobe (C) and the medial cortex (D). (E) Histogram of the percent T1 difference in the brains of mice with CLP-induced sepsis (CLP) or control shams (Sham). Significantly elevated % T1 differences were found in the hippocampus (*p<0.05), the striatum (**p<0.01), the occipital lobe (***p<0.001), and the medial cortex (**p<0.01).

Disclosure of author financial interest or relationships:
R. Towner, None; **N. Smith**, None; **P. Garteiser**, None; **D. Saunders**, None; **F. Lupu**, None; **R. Silasi-Mansat**, None; **D.C. Ramirez**, None; **S.E. Gomez-Mejiba**, None; **R.P. Mason**, None; **M. Ehrenshaft**, None; **F. Bozza**, None; **M. Fernandes de Oliveira**, None; **H.C. Castro Faria-Neto**, None.

Presentation Number **P 200**
Poster Session 2
September 19, 2013 / 15:15-15:15 / Room: Exhibit Hall B

Answers to potential radiotoxicity issues in longitudinal mouse lung µCT studies

Greetje Vande Velde[1], *Jennifer D. Poelmans*[1], *Ellen De Langhe*[2], *Ria Bogaerts*[3], *Rik Lories*[2], *Uwe Himmelreich*[1], [1]*Imaging and Pathology, KU Leuven, Leuven, Belgium;* [2]*Development and Regeneration, KU Leuven, Leuven, Belgium;* [3]*Oncology, KU Leuven, Leuven, Belgium. Contact e-mail: greetje.vandevelde@med.kuleuven.be*

µCT has proven to be an efficient and safe imaging method to dynamically monitor lung fibrosis and emphysema progression in mouse models of lung disease [1]. To extend µCT scanning protocols to animal models that require more frequent scanning or over longer periods of time, radiotoxicity issues that could interfere with the CT read-out for the lung must be considered. As radiation-induced lung fibrosis is an important manifestation of radiotoxic damage, this is a particularly relevant potential confounding factor when using µCT in pulmonary research. Therefore, we evaluated the potential radiotoxicity of repeated retrospectively gated CT scans for different long-term lung imaging protocols. 48 C57Bl/6 mice were subjected to 4 different CT imaging schedules (1x or 2x weekly for 5 weeks, incl./ 1x triple-dose scan, weekly for 12 weeks) or control. µCT data were acquired, processed and quantified as described before [1]. After the last time point, mice were sacrificed, ex vivo CT data acquired and lungs isolated for histological analysis and quantification of lung fibrosis and collagen content [1]. Radiation dose was measured by ionization chamber and thermoluminescent dosimeters (TLDs). Lung and skin dose were measured ex vivo by introducing TLDs in the lung or on the skin of a mouse. The average total dose for one lung scan was found to be 1.64 ±0.04 Gy, resulting in a measured skin dose of 1104 ±240 mGy and a measured lung dose of 813 ±103 mGy. For all experimental groups, no differences in aerated lung volume segmented from the CT data compared to the corresponding control groups was found. Upon visual inspection of the in vivo and ex vivo CT data for individual mice, no signs of lung injuries or focal spots of increased density that may correspond to fibrotic areas could be identified (Figure 2). The existence of fibrotic lung injuries that might not have reached the detection threshold of the µCT could be excluded based on the quantification of collagen content of lung samples and histology. Despite the relatively large radiation dose measured during a lung µCT scan, mice do not show signs of radiation-induced lung fibrosis that would potentially interfere with CT read-out for the lungs when scanned weekly during 5 and up to 12 weeks. Doubling the scanning frequency during 5 weeks remained without symptoms, indicating that the time resolution of CT scanning can be safely increased within the given time frame. A single tripling of the radiation dose also stayed without detectable symptoms after 5 weeks of scanning. This result suggests that, for instance, a failed scan can be safely repeated without jeopardizing the experimental outcome. This is the first study assessing potential radiotoxic damage after long-term µCT scanning, showing that longitudinal monitoring of mouse lungs using µCT is safe using the here evaluated imaging protocols. This opens perspectives for the long-term monitoring of lung conditions such as fibrosis, emphysema… and therapeutic response on an individual basis with high spatial and temporal resolution, without concerns for radiation toxicity. [1] De Langhe E, Vande Velde G et al, 2012, PLoS ONE 7 (8):e43123

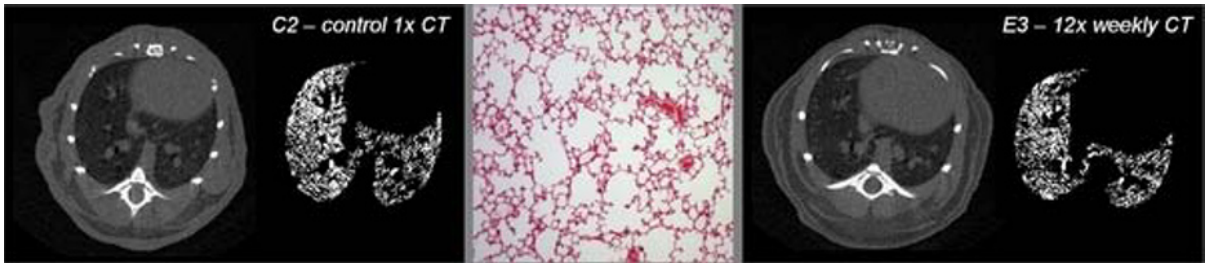

Figure 1: CT images and histology. Axial lung μCT images acquired at 12 weeks after baseline and corresponding binary images segmented for aerated lung content of a control (left panels) and weekly-scanned mouse (right panels). In the middle panel, an HE-stained histological section showing undamaged lung tissue.

Disclosure of author financial interest or relationships:
G. Vande Velde, None; **J.D. Poelmans**, None; **E. De Langhe**, None; **R. Bogaerts**, None; **R. Lories**, None; **U. Himmelreich**, None.

Presentation Number **P 201**
Poster Session 2
September 19, 2013 / 15:15-15:15 / Room: Exhibit Hall B

3D MRI-Based Histology for Pre-Clinical Toxicology Applications Using Compact, High-Resolution MRI

Yael Schiffenbauer[1], *Catherine Brami*[1], *Rinat Abramovitch*[2], *Abraham Nyska*[3], *Robert Maronpot*[4], [1]*Aspect Imaging, Shoham, Israel;* [2]*Hadassah Hebrew University Medical Center, Jerusalem, Israel;* [3]*Consultant in Toxicologic Pathology, Timrat, Israel;* [4]*Maronpot Consulting, Raleigh, NC, USA. Contact e-mail: yael@aspectimaging.com*

Magnetic Resonance Imaging (MRI) is widely used in pre-clinical research and provides a powerful method for in vivo assessment of phenotypes in small animal models of disease. MR-based Histology (MRH) (Johnson et al) of fixed tissue specimens is gaining recognition as a technique to provide complimentary information to conventional histology, as numerous digital slices from any plane can be acquired in the intact sample. Moreover, non-destructive quantification of 3D structures allows specimens to be imaged and then sectioned for conventional histology. With the advent of new compact MR systems that are designed to operate in most conventional labs without the cost, complexity and infrastructure needs of conventional MRI systems, the possibility of MRH becoming wide-spread is now viable. The purpose of this study was to investigate the capabilities of a new compact, high-performance 3D MR-based histology platform (M2, Aspect Imaging) in the field of MRH it relates to toxicology studies. Conventional toxicology studies suffer from the limitations of histology based results in which significant amount of time is required, limiting the investigation of target organs to a small number of 2D slices. MRH allows for rapid acquisition of 3D data of the entire target organ, leading to a more comprehensive assessment of the toxilogical effects. Here we present the results of in vivo MRI and ex vivo MRH of acute kidney injury (AKI) induced in mice by intra-muscular injection of glycerol, producing abrupt rhabdomyolysis, associated with rapidly progressive renal dysfunction. Time course of the changes in renal morphology and cortico-medullary differentiation were evaluated in vivo on anesthetized mice using a compact MRI scanner. High-resolution MRH of the extracted kidneys was performed using a 10mm RF coil on the same compact MRI platform followed by H&E histology and further immunostained for apoptosis (TUNEL), and proliferation (BrdU). Changes in MR contrast were readily observed in affected kidneys in vivo as well as ex-vivo indicating higher water content in the cortex as a result of edema and cell death. Administration of Gd-DTPA revealed delayed circulation, filtration and washout, demonstrating renal dysfunction. We have demonstrated the utility of compact, high-performance MRI and 3D MR-based histology (MRH) as valuable tools to complement conventional toxicological studies. While in vivo MRI provides invaluable functional, morphological and quantitative information of disease progression and regression by non-invasively imaging the same animals over time, non-destructive ex vivo MRI provides high throughput and high-resolution 3D digital data sets of intact organs, with exquisite morphological and quantitative information. With a high degree of correlation to conventional H&E, 3D MR-based histology can provide both additional insights into disease pathology as well as directing conventional histology to ensure key targets are fully assessed, considered and calculated in toxicological work-ups.

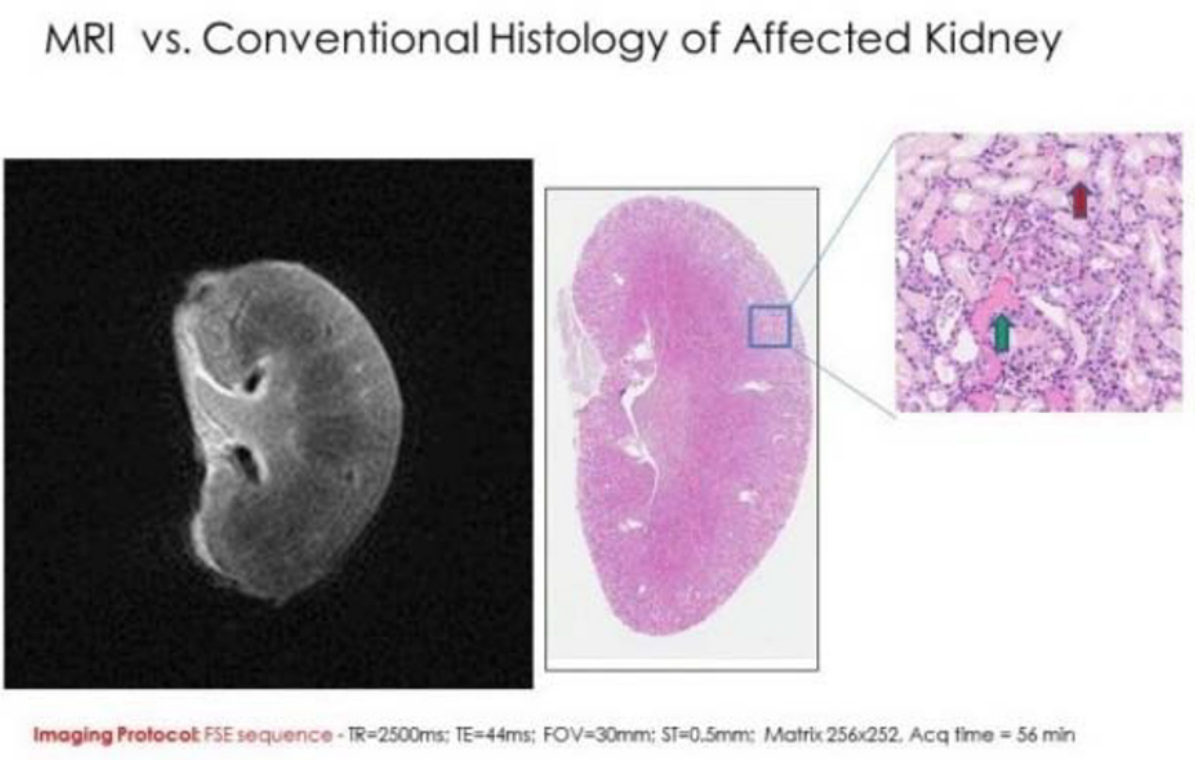

Disclosure of author financial interest or relationships:
Y. Schiffenbauer, Aspect Imaging, Employment; **C. Brami**, None; **R. Abramovitch**, None; **A. Nyska**, None; **R. Maronpot**, None.

Presentation Number **P 202**
Poster Session 2
September 19, 2013 / 15:15-15:15 / Room: Exhibit Hall B

Phenotyping TILs in situ: Tissue cytometric enumeration both activated and regulatory T cells in follicular lymphoma

James R. Mansfield[1], *Richard Byers*[2], *Lilli S. Nelson*[2], *Chris van der Loos*[3], [1]*PerkinElmer, Inc, Hopkinton, MA, USA;* [2]*Pathology, University of Manchester, Manchester, United Kingdom;* [3]*Pathology, Academic Medical Center, Amsterdam, Netherlands. Contact e-mail: james.mansfield@perkinelmer.com*

Background. In many cancers, tumor-infiltrating lymphocytes (TILs) indicate levels of tumor immunogenicity and are a strong predictor of survival. In particular, increased levels of regulatory T cells (Tregs) are associated with poorer prognosis in some cancers. An understanding of the phenotype and spatial distribution of TILs in situ within tumor regions would be advantageous. However, visual TIL assessment cannot easily determine the type of lymphocyte in situ and multimarker quantitation is difficult with standard methods. Here we present a multi-marker, computer-aided event-counting method for determining the phenotypes of lymphocytes in follicular lymphoma sections using a multispectral imaging (MSI) and automated tissue segmentation and counting approach. Methods. A single section of a tissue microarray containing 70 follicular lymphoma cores from [42 male, 28 female, 17 alive and 53 dead at the end of followup, survival range 2-171 months (median 55 months)] was stained for CD3, Foxp3, CD69 and hematoxylin. Each core was imaged using MSI and the individual staining of each marker separated from each other using spectral unmixing. The images were analyzed using software which had been trained to recognize the follicular areas based on the tissue morphology. Then the Foxp3 status of each CD3+ TIL was then determined and the number of each Treg (Foxp3+) and Tact (CD69+). Results. Results indicate that machine-learning software can be trained to accurately recognize follicular and non-follicular regions within each core. MSI enabled the accurate quantitation of two immunostains in the sample without crosstalk. The number of Tregs were determined for each core and ranged from 0 to 453 per core (median 58, stddev 97.5). There was a good correlation between Treg and Tact numbers and good outcome. Conclusion. Understanding the number and location (intra- and extra-follicular) of Tregs and Tacts is an assay with potentially important clinical prognostic implications. This study shows that an automated method for counting Tregs and Tacts can be developed for follicular lymphoma. This multimarker phenotyping and counting approach shows the potential for broad applicability in the enumeration of a wide range of specifically phenotyped TILs in situ in many solid tumors.

Disclosure of author financial interest or relationships:
J.R. Mansfield, Perkinelmer, Employment; **R. Byers**, None; **L.S. Nelson**, None; **C. van der Loos**, None.

Presentation Number **P 203**
Poster Session 2
September 19, 2013 / 15:15-15:15 / Room: Exhibit Hall B

Perfluorocarbon Nanoemulsions as a Versatile Platform for Anti-inflammatory Drug Delivery and Inflammation Imaging

Sravan Kumar Patel, *Jelena M. Janjic, Graduate School of Pharmaceutical Sciences, Duquesne University, Pittsburgh, PA, USA. Contact e-mail: patels1@duq.edu*

Chronic inflammation is an underlying process in cancer, atherosclerosis, neurological and autoimmune diseases, etc playing pivotal role in initiation, promotion and progression of the disease. Many epidemiological studies have shown that long-term use of anti-inflammatory drugs lead to reduced incidence of the mentioned diseases. By targeting molecular and cellular mechanisms of inflammation selectively with theranostic (therapeutic and diagnostic) nanomedicine can help elicit their role and contribution to the disease mechanisms. Theranostics, in which molecular imaging modality and drug are combined, can provide insight into pathways involved in chronic inflammation. Cylcooxygenase-2 (COX-2), an inducible pro-inflammatory enzyme is over-expressed in many diseases where underlying chronic inflammation is present. Nanomedicine formulations with imaging and therapeutic components together provide many advantages including tracking biodistribution of drug delivery vehicle, imaging efficacy during treatment, etc. We present a theranostic nanoemulsion with combination of 19F magnetic resonance imaging (MRI) and near-infrared fluorescence (NIRF) imaging capabilities. The combination of the two can overcome specific issues associated with each modality used alone such as low sensitivity (19F MRI) or deep tissue penetration limitations (NIR). To this end, we developed a novel triphasic perfluorocarbon /hydrocarbon/ water nanoemulsion platform aimed at studying the role of COX-2 in chronic inflammation (Patel et al, PLOS One 2013, 8(2): e55802). Imaging and therapeutic functionalities are evaluated in model mouse inflammatory cells, macrophages. Dose dependent uptake of nanoemulsion in macrophages was observed with strong correlation between imaging signals (Figure 1A). Significant inhibition ($p<0.0001$) of COX-2 enzyme with drug loaded nanoemulsion compared to drug-free nanoemulsion was obtained, Figure 1B. Fluorescence microscopy showed the presence of droplets in the cytoplasm, Figure 1C. Formulation was further modified to make in vivo image analysis and ex vivo histological studies feasible by the addition of a second optical probe fluorescing in visible region. Development, characterization and in vivo evaluation of the nanoemulsion will be presented.

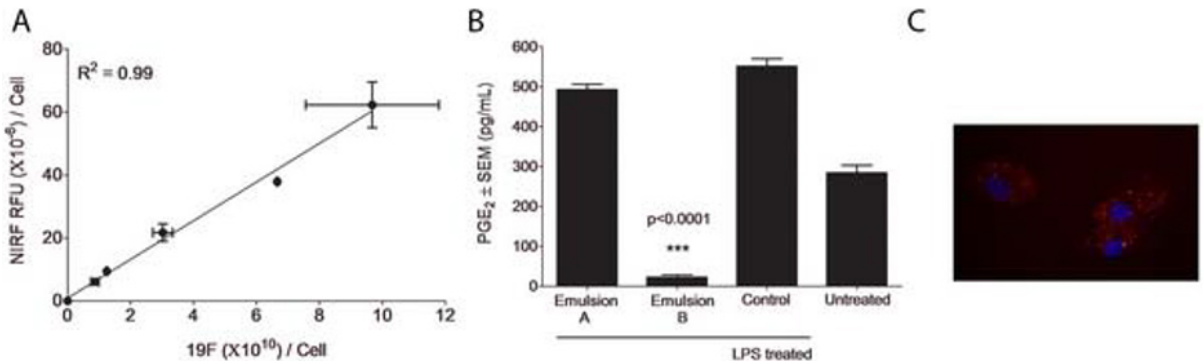

Figure 1. A) Linear correlation between NIR and 19F NMR signal in macrophages loaded with increasing concentrations of COX-2 inhibiting PFC nanoemulsion. B) Inhibition of PGE2 release from nanoemulsion treated LPS activated macrophages. Each data point represents the average of at least nine independent measurements, where the error bars are the standard error of the mean (SEM).C) Confocal image of Macrophages with NIR labeled PFC nanoemulsion (red). Nuclei are labeled with Hoescht dye (blue). Images demonstrate intracytoplasmic localization of COX-2 inhibitor loaded nanoemulsion in macrophages. (Data reproduced from Patel et al, PLOS One 2013, 8(2): e55802)

Disclosure of author financial interest or relationships:
S. Patel, None; **J.M. Janjic**, None.

Presentation Number **P 204**
Poster Session 2
September 19, 2013 / 15:15-15:15 / Room: Exhibit Hall B

Evaluation of a Novel PET Tracer for Selective Imaging of T Cells

John A. Ronald[1,2], *Gayatri Gowrishankar*[1,2], *Mohammad Namavari*[1,2], *Robert E. Reeves*[1,2], *Aileen Hoehne*[1,2], *Sanjiv S. Gambhir*[1,2], [1]*Radiology, Stanford University, Stanford, CA, USA;* [2]*Molecular Imaging Program at Stanford, Stanford University, Stanford, CA, USA. Contact e-mail: jronald1@stanford.edu*

The ability to image immune cells (e.g. activated T cells) has important applications in multiple diseases. Few imaging agents exist for the selective imaging of the immune system and specific imaging of particular immune cell lineages has been a challenge. Recently, the tracer 1-(2'-deoxy-2'-[18F] fluoroarabinofuranosyl)cytosine (18F-F-Ara-C) that is phosphorylated by cytosolic deoxycytosine kinase (dCK) was demonstrated to selectively accumulate in lymphoid organs in vivo. Unfortunately, 18F-F-Ara-C shows little selectivity towards particular immune cells within the lymphoid organs. Another tracer recently developed is 2'-deoxy-2'-[18F] fluoro-9-β-D-arabinofuranosylguanine (18F-F-Ara-G) that is preferentially phosphorylated by mitochondrial deoxyguanosine kinase (dGK). 18F-F-Ara-G is an analog of arabinosyl guanine (Ara-G) proven to have specificity towards T cells. However the T cell specificity of F-Ara-G is unknown. Here we evaluated the immune cell specificity of F-Ara-G and F-Ara-C by examining the uptake and efflux of both 18F-F-Ara-G and 3H-F-Ara-C across T cells, B cells, myeloid cells, and solid tumor cell lines. Methods and Results: The six cell lines used include CCRF-CEM (T lymphoblasts), Jurkat (T lymphocytes), Daudi (B lymphoblasts), Ramos (B lymphocytes), HL-60 (promyeloblasts), and MDA-MB-231 (breast cancer). One-hour incubation of 18F-F-Ara-G (5 μCi) resulted in similar uptake in all cells except myeloid cells (~3-fold greater) (Figure 1). Importantly, uptake of 18F-F-Ara-G could be competitively inhibited in all cell lines by 100 μM Ara-G ($p<0.05$; Figure 1). To measure efflux, cells were incubated with tracer for 1 hour and then for an additional hour without tracer. Like Ara-G, T cells preferentially retained 18F-F-Ara-G versus all other cells ($p<0.05$; Figure 1). Compared to 18F-F-Ara-G, 3H-F-Ara-C percentage efflux was the same or significantly lower ($p<0.01$) in non-T cell lines, suggesting 18F-F-Ara-G background uptake in non-T cell lineages may be minimized in vivo. Discussion: The immune system plays a critical role in many disease processes, and often the strength of the immune response can influence disease outcome. Therefore, imaging agents capable of more selective imaging of particular immune cell lineages are urgently needed. We have demonstrated for the first time that 18F-F-Ara-G is preferentially retained in T cells versus all other cells tested. Future work will study the selectivity of 18F-F-Ara-G in a variety of disease models and evaluation of this tracer for selective T cell imaging in humans is warranted. Continued development of 18F-F-Ara-G as a selective T cell tracer should have a number of broad applications including improved diagnosis of T cell mediated immunoproliferative and autoimmune diseases, imaging of T cell responses during cancer progression or organ rejection, and effective monitoring of T cell-based adoptive immunotherapies.

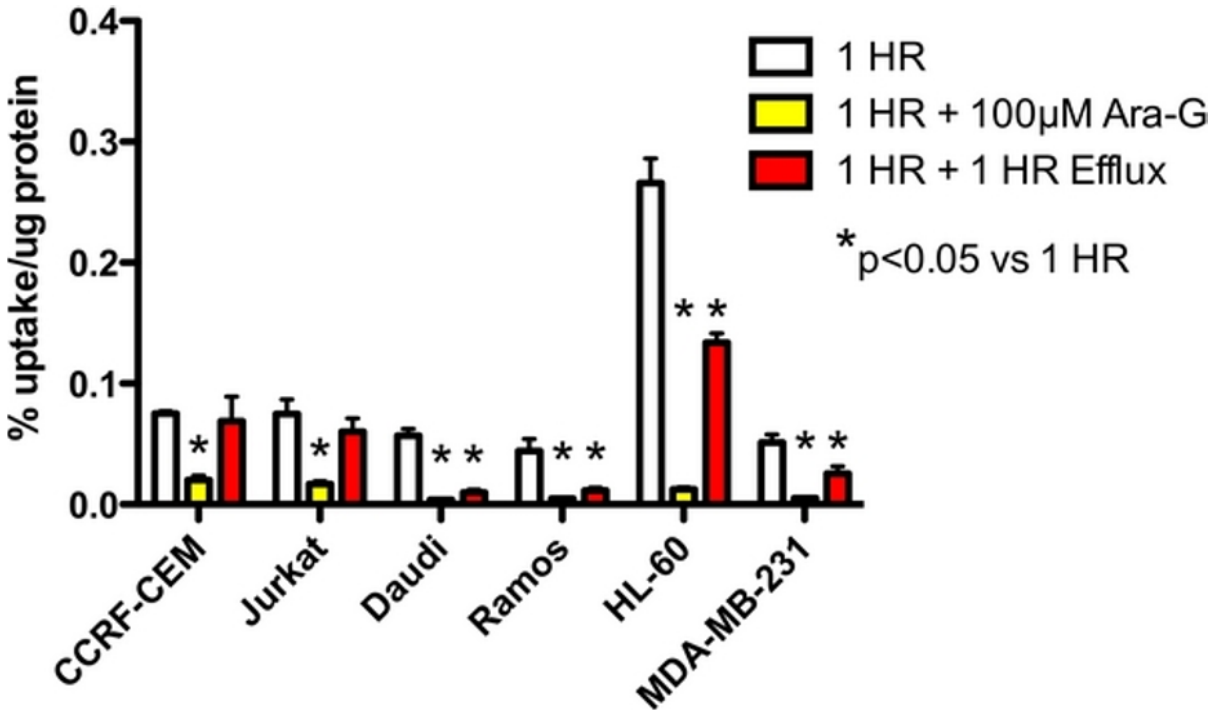

Figure 1: Competition and efflux assays of 18F-F-Ara-G uptake across T cell (CCRF-CEM; Jurkat), B cell (Daudi; Ramos), myeloid (HL-60) and breast cancer cells (MDA-MB-231).

Disclosure of author financial interest or relationships:
J.A. Ronald, None; **G. Gowrishankar**, None; **M. Namavari**, None; **R.E. Reeves**, None; **A. Hoehne**, None; **S.S. Gambhir**, Bracco Diagnostics, Consultant; Endra, Inc, Stockholder; Cellsight, Stockholder; Enlight, Inc., Stockholder; General Electric, Grant/research support; ImaginAb, Stockholder; MagArray, Inc., Stockholder; Sanofi-Aventis, US, Grant/research support; SiteOne Therapeutics, Stockholder; VisualSonics/Sonosite, Stockholder .

Presentation Number **P 205**
Poster Session 2
September 19, 2013 / 15:15-15:15 / Room: Exhibit Hall B

The Influence of COMT and TaqIA alleles on Dopamine D2 Receptor Availability following an Alcohol Challenge

Amira K. Brown[1,3], *Brittany Sumerel*[4], *Wisam Shaba*[3], *Magda Shaheen*[1,2], *Theodore C. Friedman*[1,2], *Edythe London*[4], *Mark A. Mandelkern*[5,3], [1]*Internal Medicine, Charles R. Drew University of Medicine and Science, Los Angeles, CA, USA;* [2]*Medicine, UCLA, Los Angeles, CA, USA;* [3]*Nuclear Medicine, Greater Los Angeles Veterans Affairs Healthcare System, Los Angeles, CA, USA;* [4]*Psychiatry, UCLA, Los Angeles, CA, USA;* [5]*Physics, UC-Irvine, Irvine, CA, USA. Contact e-mail: amirabrown@cdrewu.edu*

Considerable evidence suggests that alcoholism is highly heritable, and several candidate genes that affect neurotransmitter function have been identified as influencing the risk of developing alcoholism. Due to the importance of the mesolimbic dopamine (DA) system in the rewarding effects of alcohol and other drugs of abuse, alleles of the dopaminergic (DAergic) system are likely associated with the development of alcoholism. Our objective was to clarify in social drinkers using [18F] fallypride (FP) and positron emission tomography (PET), whether DAergic genotypes influence changes in DA D2-like receptor availability (RA) following an alcohol challenge in subcortical brain regions associated with reward. Methods: We examined the relationship between DAergic genetic variants with a central response to alcohol (as measured by DA D2-like RA) in 21 (ages 21-40) white male social drinkers on separate days under two conditions; 1) after ingesting an alcoholic beverage, and 2) after ingesting a placebo beverage. Image processing and volume-of-interest analyses were performed using a reference-region model with cerebellum as reference, FSL FIRST and PMOD 3.0 (Fig 1). DA D2-like RA was calculated as binding potential (BPND). In SPSS 20 we used a generalized linear mixed model approach comparing BPND in the putamen (PU), caudate nucleus (CN) and nucleus accumbens (NA) for the following genotypes: DRD2 TaqIA allele (7(A1+) vs. 14(A1-)), COMT (7(V/V) vs. 14(V/M & M/M)), DRD4 VNTR repeat alleles (9(<7R) vs. 12(7R)) and DAT VNTR (11(9/9) vs. 10(10/10)) after controlling for sequence, duration of time elapsed between the 1st and 2nd scans and the BPND for the CN, NA and PU from the placebo scan. Results: There were no significant differences between the groups in age, education, injected FP doses or specific activities for the placebo or alcohol scans (table 1). We found a significant effect of group indicating less intrasynaptic DA release in the CA, PU and NA following an alcohol challenge for the following genotypes: COMT V/M and M/M (coefficient= -2.87; p= 0.03 and TaqIA A1+ (coefficient= -3.04; p= 0.03) when compared to social drinkers with the COMT V/V and TaqIA A1- alleles, respectively. We did not find any significance for the other DAergic genotypic divisions. Discussion: Following an alcohol challenge, our study found that social drinkers with the A1+ and COMT V/M and M/M alleles have less intrasynaptic DA release (as measured by greater DA D2-like RA) in several brain regions that regulate the rewarding effects of alcohol. Our novel findings suggest that there may be a need for individuals with these DA genotypic variants to consume more alcohol to obtain the desired rewarding effects. Future investigations are necessary with larger datasets to further understand the role of the DA system in social drinkers with these DAergic genetic variants.

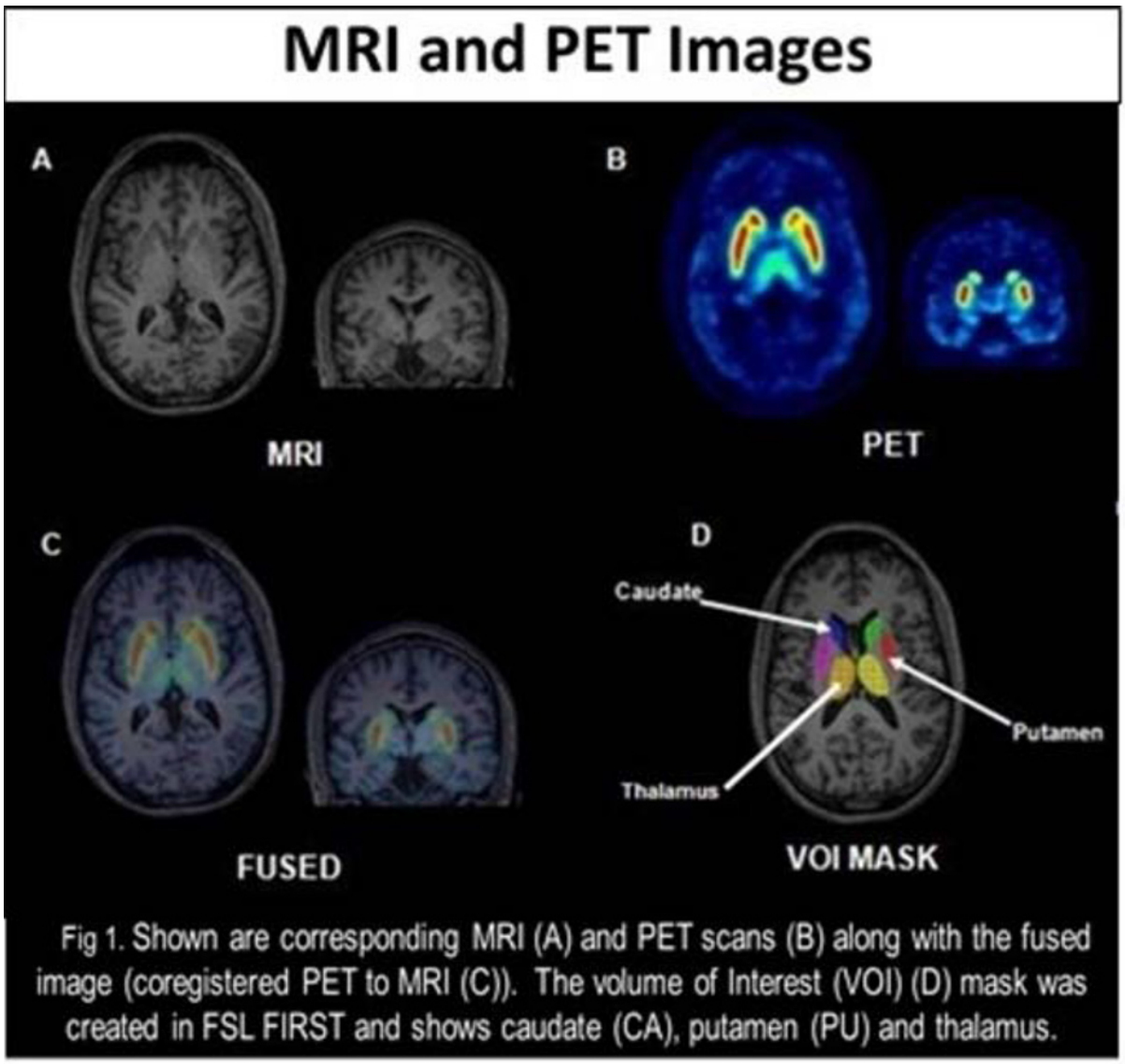

Fig 1. Shown are corresponding MRI (A) and PET scans (B) along with the fused image (coregistered PET to MRI (C)). The volume of Interest (VOI) (D) mask was created in FSL FIRST and shows caudate (CA), putamen (PU) and thalamus.

Table 1. Participant Demographics & Dose Information

Characteristics	COMT V/V (mean ± SD (N=7))	COMT V/M & M/M (mean ± SD (N=14))	F	P
Age: yrs	25.5 ± 5.5	28.1 ± 5.9	-0.97	15
Education	15.1 ± 1.3	15.9 ± 1.4	-1.47	15
Inj Dose: (mCi) placebo	4.98 ± 0.23	4.94 ± 0.22	0.41	15
SA (Ci/μmol) placebo	16.9 ± 9.4	15.8 ± 8.87	0.33	15
Inj Dose: (mCi) alcohol	4.9 ± 0.22	5.0 ± 0.33	-0.87	15
SA (Ci/μmol) alcohol	14.0 ± 7.56	17.0 ± 10.1	-0.71	15
breathalyzer alcohol scan	.136 ± .114	.194 ± .119	-1.21	15

SA= Specific activity of [18F]fallypride
Inj Dose= Injected dose of [18F]fallypride
COMT= genotype V/V valine/valine; V/M Val158Met; Met/Met

Disclosure of author financial interest or relationships:
A.K. Brown, None; **B. Sumerel**, None; **W. Shaba**, None; **M. Shaheen**, None; **T.C. Friedman**, None; **E. London**, None; **M.A. Mandelkern**, None.

Presentation Number **P 206**
Poster Session 2
September 19, 2013 / 15:15-15:15 / Room: Exhibit Hall B

Evaluation of Relative Somatotopic Arrangement and Location for Corticospinal Tract in the Human Brain using Diffusion Tensor Tractography and Functional MRI

Dong Hoon Lee[1], *Cheol Pyo Hong*[1], *Jiwon Park*[2], *Bong-Soo Han*[1], [1]*Radiological Science, Yonsei University, Wonju, Gangwondo, Republic of Korea;* [2]*Physical Therapy, Catholic University of Daegu, Daegu, Republic of Korea. Contact e-mail: ldhdaum@yonsei.ac.kr*

The corticospinal tract (CST) is the major neural fiber in the human brain associated with voluntary movement such as hand and foot. The CST passes corona radiata (CR), internal capsule (IC), and pons that is connected to the origin of the path from the motor cortex. The hand and foot fiber tracts of CST which are related to the direct movement of the human body have different origin of motor cortex, but each has a similar pathway on these locations. For the accurate management or longitudinal studies of patients who had brain injuries related with movement, more specific and relative information of location differences between the two fiber tracts on the locations are very important. In this study, we attempted to identify the hand and foot fiber tracts of the CST, and measured the relative locations and angles between two fiber tracts using functional magnetic resonance imaging (fMRI) and diffusion tensor tractography (DTT). Twelve healthy subjects participated in this study. MR dataset were obtained 1.5T Philips Gyroscan Intera scanner using following parameters: DTI (TR/TE=10726/76ms, FOV=221mm, matrix=128×128, b-value=1000s/mm2, slice thickness=2.3mm and 32 diffusion-sensitizing gradients direction), fMRI (TR/TE=2000/60 ms, FOV=210 mm, matrix=64×64, slice thickness=5 mm, reduction factor=2 and using a block paradigm (hand/foot grasp-release movements at 1Hz frequency)). The eddy currents induced image distortions were corrected by registering all diffusion-weighted images to non-diffusion weighted image using twelve-parameter affine registration. The analysis software were used FSL with 5000 streamline samples, 0.5 mm step lengths and curvature thresholds = 0.2 for DTI fiber tracking, and SPM2 with $p<0.05$ for fMRI. The ROIs were drawn in the fMRI activation areas for hand and foot movements, and pons in the color-coded DTI FA map. After, hand and foot fiber tracts of CST was reconstructed, we measured relative location and separation angles between two fiber tracts based on the hand fiber tract (origin of the coordinates) in the upper/lower CR, IC, and pons. The locations of the hand and foot fibers that showed the highest probability values in these locations were measured. In most cases, separation angles from any locations were within a 90° between two fiber tracts. The hand fibers located anterolateral to foot fibers in the upper and lower CR, relatively. In the IC and pons, the hand fibers located anteromedial to foot fibers, relatively. The ranges of the separation angles are 96.43-150° (upper CR), 91.86-180° (lower CR), 54.47-75° (IC), and 3.65-90° (pons), respectively. Our results showed that the fibers relative locations between two fiber tracts are further and wider when the slice location is getting closer to cortex. In this study, we identified the relative locations and separation tendencies of hand and foot fiber tracts of CST, and showed that two fiber tracts have the characteristics of location change in response to their unique pathway in the human brain. We believe that our results and experimental methods seem to be helpful in motor control and rehabilitation researches.

Disclosure of author financial interest or relationships:
D. Lee, None; **C. Hong**, None; **J. Park**, None; **B. Han**, None.

Presentation Number **P 207**
Poster Session 2
September 19, 2013 / 15:15-15:15 / Room: Exhibit Hall B

Microstructural alterations in mild traumatic brain injury detected by combined resting-state fMRI and diffusion tensor imaging

Hui Tan, **Wenbin Zheng***, Hongyi Zheng, Huimin Liu, Department of Radiology, The Second Affiliated Hospital of Shantou University Medical College, Shantou, China. Contact e-mail: hwenb@126.com*

Objectives: Persistent neurological and behavioral symptoms associated with a single episode of mild traumatic brain injury (mTBI) may be the result of subtle neurological alterations that are beneath the detection threshold of conventional neuroimaging techniques. In this study, we used resting-state fMRI and diffusion tensor imaging to identify white matter structural alterations consistent with functional deficits following mild traumatic brain injury. Methods: Twenty-nine patients with mTBI and twenty-seven healthy people underwent conventional MRI, rs-fMRI and DTI studies. The rs-fMRI data were preprocessed by DPARSF software and analyzed by REST software. ReHo and ALFF maps were separately calculated. For DTI, FA values and ADC values were measured in the ROIs. Results: Compared to healthy individuals, mTBI patients had more bilateral frontal lobe and cerebellum posterior lobe activation in the resting state, as revealed by rs-fMRI BOLD signals, but less activation in the right thalamus, right hippocampus, brainstem, bilateral occipital lobe, left post-central gyrus, and right corona radiate. Second, a positive correlation occurred between ALFF and ReHo in some brain regions. Moreover, we found ALFF was more sensitive than ReHo in the same comparison significance level($P \leq 0.005, K \geq 18$). Considering the results of the rs-fMRI portion of our study, we observed decreased diffusivity as evidenced by FA in the bilateral frontal lobe, brainstem, and left occipital gyrus, and by ADC in the left thalamus, bilateral hippocampus and right cerebellum posterior lobe in mTBI patients. BOLD signal changes, observed in rs-fMRI were consistent with the alteration of structural integrity within white matter in most brain regions, as judged by DTI. Conclusion: Both rs-fMRI and DTI can detect the abnormalities that are undetectable by conventional magnetic resonance/CT. Combination of rs-fMRI and DTI provides greater sensitivity in detecting microstructural alterations in mTBI, enabling detection of the underlying causes of the pathophysiological mechanisms of complicated sequela after mild brain injury. Key words: Mild traumatic brain injury (mTBI); resting-state functional MRI (rs-fMRI); diffusion tensor imaging (DTI); multi-modal neuroimaging; BOLD signal; white matter structural alterations.

Disclosure of author financial interest or relationships:
H. Tan, None; **W. Zheng**, None; **H. Zheng**, None; **H. Liu**, None.

Presentation Number **P 208**
Poster Session 2
September 19, 2013 / 15:15-15:15 / Room: Exhibit Hall B

Diffusion kurtosis imaging in different periods cerebral infarction, a preliminary clinical study

Yue-Lin Guo[1], Su-Juan Li[1], Phillip Zhe Sun[2], **Renhua Wu**[1], [1]*Shantou University, Shantou, China;* [2]*Athinoula A. Martinos Center, Department of Radiology, Massachusetts General Hospital and Harvard Medical School, Boston, MA, USA. Contact e-mail: gszhang_1@163.com*

PURPOSE: To evaluate the feasibility of diffusion kurtosis imaging (DKI) for detecting cerebral infarction in different periods and its clinical value. MATERIALS AND METHODS: Four patients with different periods cerebral infarction underwent DKI and conventional MRI (including T1WI, T2WI, FLAIR and DWI) by GE 1.5T HDx echo speed plus MRI scanner. The post-processing of DKI data was done by DKI software in GE ADW4.3 workstation, and MK, Kr, Ka maps and values were got and analysis. Fourteen regions of interest (ROI) were set in cerebral infarction regions of the 4 cerebral infarction patients, including 2 ROI of supper acute infarction, 3 ROI of acute, 6 ROI of subacute and 3 ROI of chronic. The period of infarction was judged by the attack time and the signal strength of DWI. The prognosis for infarction lesion was evaluated by follow-up MRI scan and clinical manifestations. RESULTS: One extremely high signal ROI of DKI (MK and Kr) in supper acute cerebral infarction was keep deteriorating into irreversible infarction with mild bleeding, but did not hint by DWI and ADC maps at the same period. Three low signal ROI of subacute cerebral infarction were shown pretty clear by DKI (MK and Kr) , but not found in DWI and ADC maps. The other 10 ROI of cerebral infarction in different periods were synchronously displayed by DKI and ADC maps. CONCLUSION: DKI was sensitive to super acute cerebral infarction changes, and showed different contrast than DWI and ADC maps. DKI also has the potential to complement existing cerebral infarction imaging techniques, particularly in the assessment of subacute cerebral infarction which was in the false negatives period of DWI and ADC maps.

Disclosure of author financial interest or relationships:
Y. Guo, None; **S. Li**, None; **P. Zhe Sun**, None; **R. Wu**, None.

Presentation Number **P 209**
Poster Session 2
September 19, 2013 / 15:15-15:15 / Room: Exhibit Hall B

Optimizing Confocal Imaging of Neuronal Transport in a Microfluidic Platform

Lucia LeRoux, *Leo G. Flores, Dawid Schellingerhout, Experimental Diagnostic Imaging, MD Anderson, Houston, TX, USA. Contact e-mail: lucia.leroux@mdanderson.org*

Purpose: To study neuronal transport in living axonal cultures. In this study we devised an experimental system to allow this using a specialized live culture system (Millipore, AX150) and confocal imaging. Materials & Methods: We used micro-fluidic chambers that direct the growth of axons into microgrooves (10 um each) by means of hydro-static pressure [1]. The microgroove, dual-chamber system also serves separate the neuronal cell bodies from the neurite end terminals, allowing dual-chambered experiments with differing fluid environments for the neuritis and the cell bodies. Imaging was done with an Olympus FV1000 Confocal Microscope using a PLAPO60XO3 oil objective. We optimized 3D imaging within the microfluidic grooves containing neurites at 12 bits/pixel at 20% laser power to reduce the effects of photo-bleaching. Results: We found, during our optimization that several factors were very important for the culture system: a) there had to be a tight seal (plasma bonding) between the isolation inset and the culture plate bottom, b) hydrostatic pressure had to be carefully applied to guide neurite growth, and c) to isolate the cell bodies from nerve terminals. We found that the following factors were important for the optimization of imaging: a) thin bottom (0.17 mm) glass coverslip material was needed, with b) high magnification (60x oil), c) careful Z-stack optimization to find the optimal plane of imaging and d) the choice of fluorophore needed to be matched to system sensitivities. Conclusion: We demonstrated retrograde neural transport of fluorescently labeled Tetanus toxin C fragment (TTc) in differentiated PC12 cells using this system, and were able to show foci of fluorescence (likely transport endosomes) traveling along the neurite over a 30 minute observation period during live imaging. This technique allows us to determine the rate of in-vivo neural transport in mammalian cells and will further advance our knowledge of neuronal transport (Figures 1A & B), and highlights the importance of optimized live cell culture systems and confocal imaging. References: [1] Enquist et al., A microfluidic Chamber for analysis of Neuron-to-Cell Spread and Axonal Transport of an Alpha-Herpesvirus. Plos One Vol 3 (Issue 6). E2382 (2008).

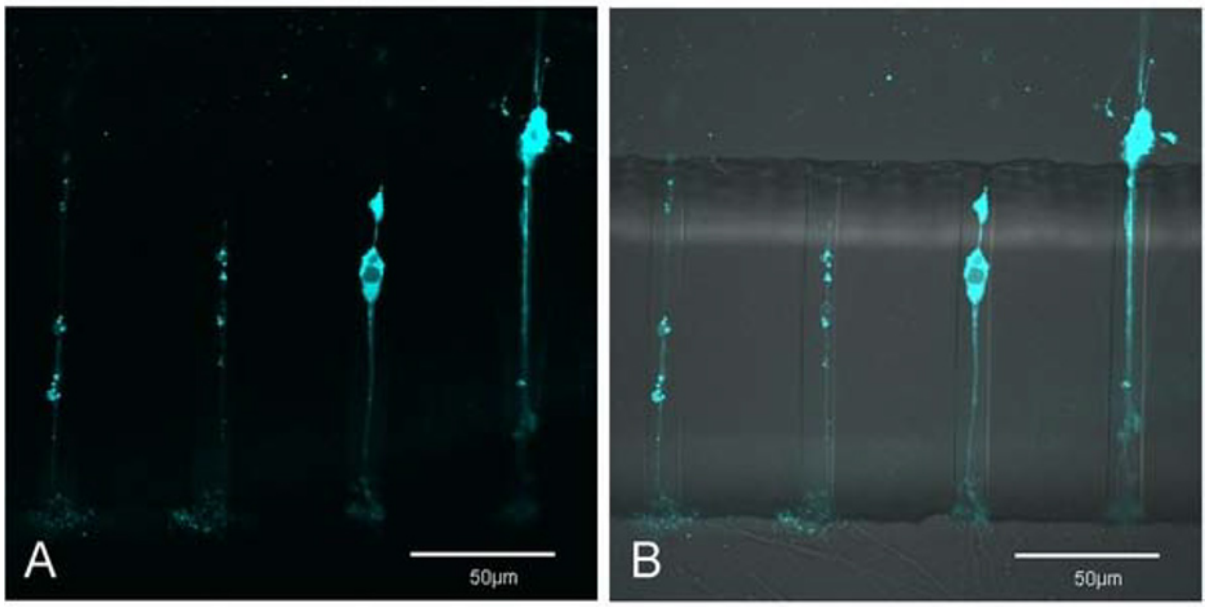

Figure 1. Imaging of individual neurites in a Micro-fluidic device (AX150) We demonstrate retrograde neural transport of Alexa488 TTc during a 30 minute live imaging session using a 60x oil objective. The directional movement of TTc molecules could be observed in the neuritis using confocal imaging (A) and in bright field overlay images (B).

Disclosure of author financial interest or relationships:
L. LeRoux, None; **L.G. Flores**, None; **D. Schellingerhout**, None.

Presentation Number **P 210**
Poster Session 2
September 19, 2013 / 15:15-15:15 / Room: Exhibit Hall B

Towards functional NMDA-receptor MR-imaging: Novel probes based on competitive antagonists

Sven Gottschalk[1,2], *Neil Sim*[3], *Robert Pal*[3], *Joern Engelmann*[2], *David Parker*[3], *Anurag Mishra*[1,3], [1]*Institute for Biological and Medical Imaging, Helmholtz Zentrum München, Neuherberg, Germany;* [2]*Magnetic Resonance Centre, Max Planck Institute for Biological Cybernetics, Tuebingen, Germany;* [3]*Department of Chemistry, Durham University, Durham, United Kingdom. Contact e-mail: sven.gottschalk@helmholtz-muenchen.de*

For neuroimaging techniques such as positron emission tomography and optical imaging brain receptor-targeting is a widely used concept, either using probes based on receptor antagonists or agonist. So far, applying competitive binding approaches for brain functional magnetic resonance imaging (fMRI) has not been demonstrated. Our idea was therefore to develop responsive MRI contrast agents (CAs) based on competitive antagonists to the N-methyl-D-aspartate (NMDA) receptor, an ionotropic glutamate receptor that plays an important role in controlling synaptic plasticity and memory function.[1] Ultimately, such CAs would allow to monitor glutamate activity at NMDA receptors (NMDARs) and thus neuronal activity itself. For such a CA to be responsive, release of glutamate from the pre-synapse will detach the CA from the receptor, in turn leading to a reduction in image contrast, followed by a restoration of equilibrium and again binding of the CA to the receptor. It has been shown, that these events happen over a period of a few seconds allowing data acquisition with modern fast MR-techniques.[2] Here we report the in vitro evaluation of a series of NMDAR targeted CAs, that are based on established competitive NMDAR-antagonists[3] coupled to DOTA-derived gadolinium chelates (Fig. 1A). Cellular labeling, cytotoxicity, receptor binding and reversibility were studied on the NMDAR-expressing (shown by immunofluorescence) neuronal cell line model NSC-34. Binding affinity in cultured cells (Fig. 1B) showed that two of the compounds (Gd.L2 and Gd.L4) increased the cellular relaxation rate R1,cell up to 170±11% and 176±4% of control, respectively (200 µM, 45min., 37°C). MRI-measurements were done on a 3T human whole body scanner. No cytotoxic effects with the concentrations used (24h incubation) were seen. Receptor binding and reversibility were demonstrated using a modified version of Gd.L4, with a trans-substituted biotin moiety appended to the macrocyclic core (Gd.L5, Fig. 1C). Cell-surface binding was visualized after adding an AvidinAlexaFluor® 488 conjugate, which binds with high specificity to the biotin moiety, while the receptor-binding moiety of the CA binds to the receptor on the cell membrane. Live cell confocal microscopy showed labeling of the cell membrane by Gd.L5 (green) in a pit-like manner and co-localization with a cell membrane specific marker (red, Figure 1D). Furthermore, a glutamate wash (1 mM) demonstrated that Gd.L5 is removed from the cell surface (Fig. 1E). In conclusion, we were able to identify two promising novel NMDAR-targeted MRI contrast agents. These CAs are based on the structures of competitive antagonists to NMDAR and we were able to demonstrate specific receptor binding and reversibility, which is essential for functional measurements of receptor-activity. Thus, our results indicate the possibility of using MRI for brain functional measurements based on competitive binding approaches. [1]Li&Tsien, N Engl J Med 361(2009)302; [2]Logothetis, Nature 453(2008)869; [3]Kinney et al., J Med Chem 35(1992)4720

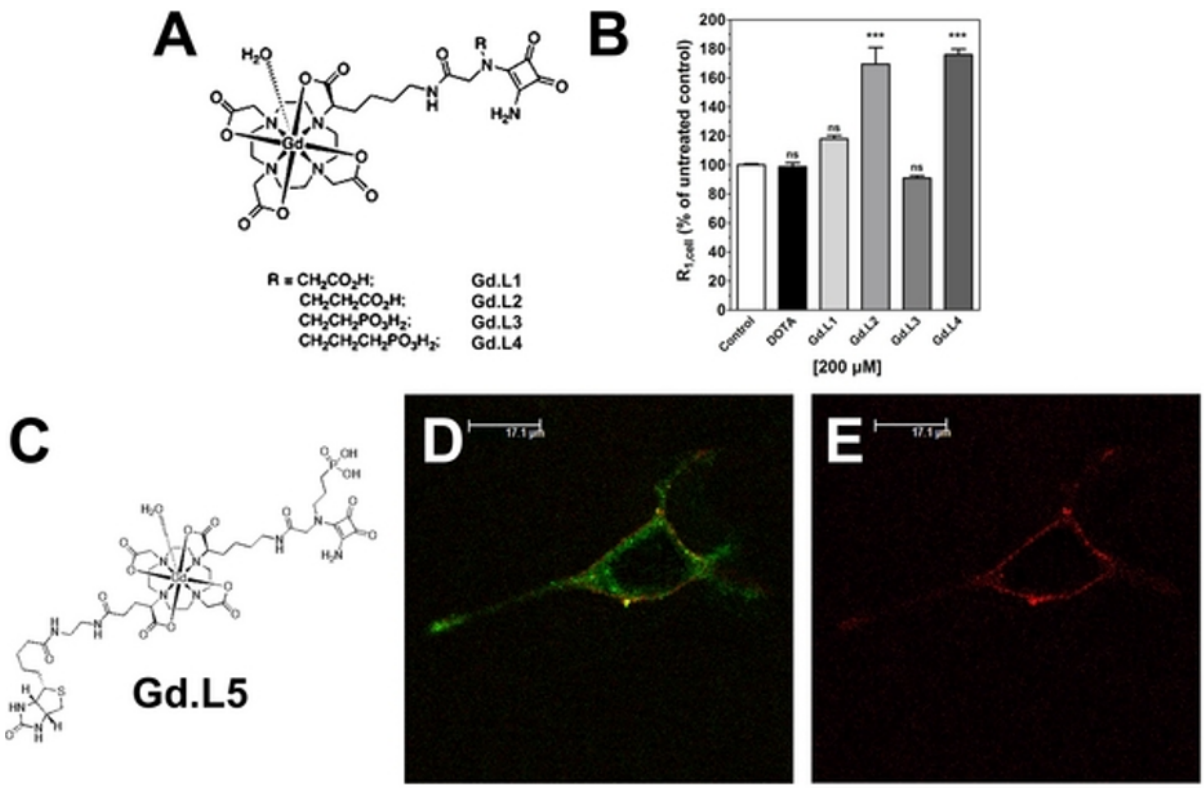

Figure 1: (A,C) Probes structures, (B) cellular relaxation rates, (D, E) binding reversibility of Gd.L5 after glutamate challenge

Disclosure of author financial interest or relationships:
S. Gottschalk, None; **N. Sim**, None; **R. Pal**, None; **J. Engelmann**, None; **D. Parker**, None; **A. Mishra**, None.

Presentation Number **P 211**
Poster Session 2
September 19, 2013 / 15:15-15:15 / Room: Exhibit Hall B

Development and Application of a Brain Atlas for Evaluation of Cognitive Decline in Canine PET-MR

Jacob Hesterman[1], *Joseph A. Araujo*[2], *Dale Araujo*[2], *Katherine L. Sokolnicki*[1], *Paige Czarnecki*[1], *Matthew D. Silva*[1], *Jack Hoppin*[1], *Howard Dobson*[2], [1]*inviCRO, Boston, MA, USA;* [2]*InterVivo Solutions, Toronto, ON, Canada. Contact e-mail: hesterman@invicro.com*

The naturally occurring dementia in the dog is being evaluated as a translational model for aging and Alzheimer's Disease (AD). Aging dogs exhibit declines in cognitive function and behavior, decreased brain volume, and neuropathology, including oxidative damage, cellular apoptosis, neuron loss, and AD-like beta-amyloid deposits [1]. In addition to cognitive and morphological changes, it has been shown that aging results in a decline in cerebral glucose metabolism as measured by 18F-FDG uptake and PET scanning [2]. The canine brain has a higher encephalization level than the rodent brain and, thus, is more elaborately structured, primarily in the cerebral cortex. Given these advantages, primarily the more accurate recapitulation of human pathophysiology and the dogs' capacity for cognitive testing, it is believed that aged dogs may have more reliable translational research value than rodent models. This study demonstrates the value of regional brain analysis in young and aged beagles by PET and MRI. To accomplish this goal it was first required to develop an anatomical atlas of the canine brain. Six T1-weighted anatomical MR scans were registered to form an average MR brain template. An expert reader assigned individual voxels to specific brain regions that were transformed into an isotropic brain atlas, consisting of 11 regions. In a pilot experiment, 18F-FDG PET-MR data were acquired on five young (average age 2.3 years) and five aged (average age 12.6 years) beagle dogs, exhibiting varying degrees of cognitive decline as assessed using a delayed non-matching to place test. PET-MR data were registered to one another and to the anatomical atlas. Analysis of the MR data confirmed the reported observations of cortical atrophy (qualitative assessment) and increased ventricle volume in aged animals [3]. Specifically, the third and lateral ventricles were segmented from the T2-weighted MR data and found to be 2.13 times larger in volume in aged animals compared to young animals with $p < 0.0001$, using a two-tailed independent samples t-test (2TIS t-test). Additionally, for the PET data, uptake in the cortical regions relative to a reference region (cerebellum) was observed to be ~1.2 times higher in young animals versus aged animals with $p < 0.0001$ for the occipital lobe (2TIS t-test). Repeatability was excellent, based on a follow-up experiment occurring 48 hours after the initial experiment with $p < 0.002$ for the occipital lobe (2TIS t-test). This work will be extended to identify differences in uptake associated with cognitive tasks of varying complexity, using both PET and MR imaging. Future studies may also include the use of novel disease-modifying medicines. References: [1] Head E., Neurobiology of the aging dog, Age (Dordr). 2011 September; 33(3): 485-496. [2] Mosconi L., et al., Multicenter Standardized 18F-FDG PET Diagnosis of Mild Cognitive Impairment, Alzheimer's Disease, and Other Dementias, J Nucl Med 2008; 49:390-398 [3] Sun M.Y., et al., A longitudinal study of brain morphometrics using serial magnetic resonance imaging analysis in a canine model of aging. Prog Neuropsychopharmacol Biol Psychiatry. 2005 Mar;29(3):389-97.

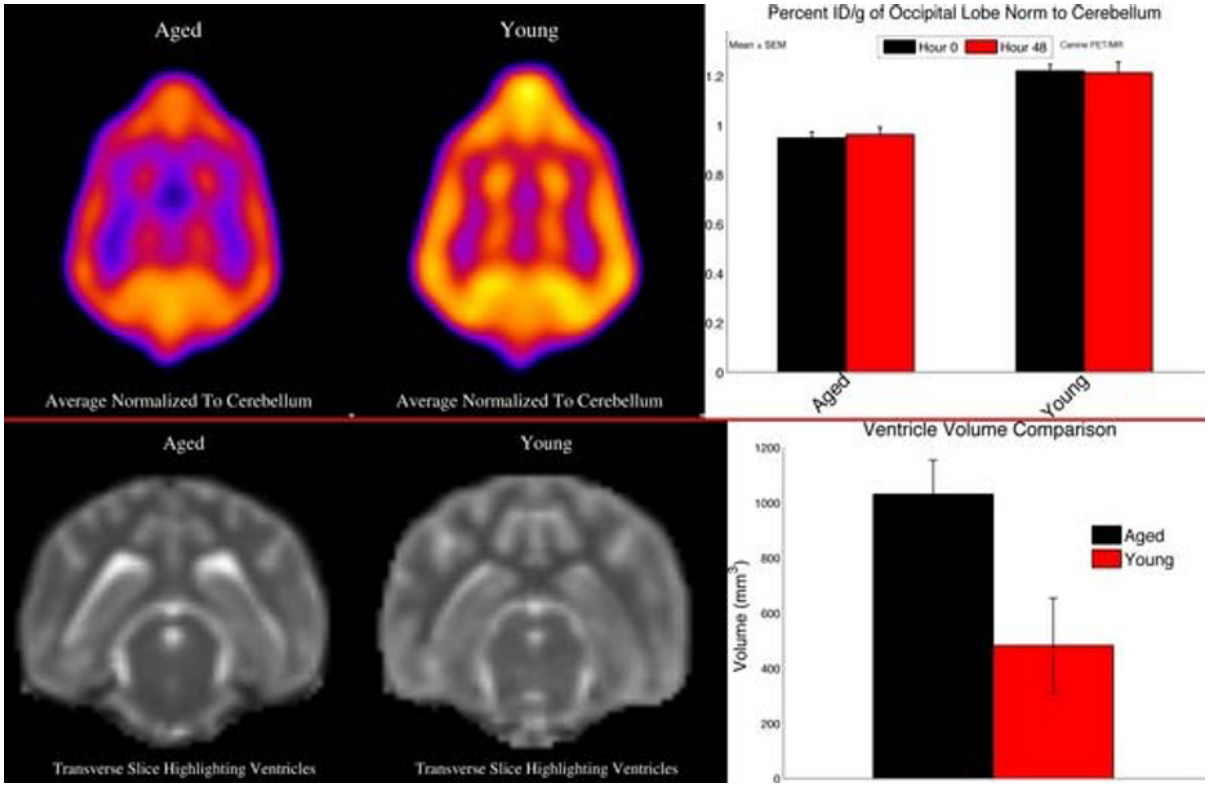

Disclosure of author financial interest or relationships:
J. Hesterman, inviCRO, LLC, Employment; **J.A. Araujo**, InterVivo Solutions Inc, Employment; CanCog Technologies Inc, Consultant; **D. Araujo**, Vivocore Inc., Employment; **K.L. Sokolnicki**, None; **P. Czarnecki**, inviCRO, Employment; **M.D. Silva**, inviCRO, LLC, Employment; **J. Hoppin**, inviCRO, Stockholder; **H. Dobson**, InterVivo Solutions, Consultant .

Presentation Number **P 212**
Poster Session 2
September 19, 2013 / 15:15-15:15 / Room: Exhibit Hall B

Imaging microglial activation in a mouse model of Alzheimer's disease using [^{18}F]PBR06-PET/MRI and *ex vivo* autoradiography

Michelle L. James[1], *Thuy-Vi V. Nguyen*[2], *Nadia P. Belichenko*[2], *Lauren Andrews*[1], *Hongguang Liu*[1], *Deepika Bodapati*[1], *Bin Shen*[1], *Zhen Cheng*[1], *Sanjiv S. Gambhir*[1], *Frank M. Longo*[2], *Frederick T. Chin*[1], [1]*Radiology, Stanford University, Stanford, CA, USA;* [2]*Neurology & Neurological Sciences, Stanford University, Stanford, CA, USA. Contact e-mail: mljames@stanford.edu*

Microglial activation is intimately associated with Alzheimer's disease (AD); however, its exact role in AD is unknown. Positron emission tomography (PET) imaging of translocator protein 18 kDa (TSPO), a biomarker of microglial activation, could enhance our understanding of the *in vivo* role of microglia in AD, and might serve as a marker of both AD progression and treatment response. Here we aim to evaluate a TSPO-specific radioligand [^{18}F]PBR06 for its ability to image alterations in TSPO and microglial activation in a transgenic mouse model of AD, Thy1-hAPP$^{Lond/Swe}$ (APP$^{L/S}$). **Methods:** One cohort of mice containing APP$^{L/S}$ and wild-type (wt) littermates underwent [^{18}F]PBR06-PET/computed tomography (CT) imaging (45-55 min post-injection of [^{18}F]PBR06, 100-150 μCi) at both 5-6 and 9-10 months of age, while another cohort underwent [^{18}F]PBR06-PET/CT imaging at 14-15 and 15-16 months of age. 7T magnetic resonance (MR) images were fused with PET/CT data (attenuation corrected) to quantify [^{18}F]PBR06 uptake in hippocampus and cortex. Brain sections from mice were analyzed via digital autoradiography, and subsequently stained to evaluate levels of microglia (CD68), plaques (ThioS), and TSPO. **Results:** Brain [^{18}F]PBR06-PET signal, normalized to arm muscle, was significantly higher in both 14-15 and 15-16 month old APP$^{L/S}$ mice compared to age-matched wts [*14-15 mo*: 2.09±0.11 (n=12) vs. 1.57±0.07 (n=11), $p<0.001$; *15-16 mo*: 2.15±0.12 (n=6) vs. 1.67±0.12 (n=5), $p<0.05$]; however, no significant difference was found between APP$^{L/S}$ mice (n=5) and wts (n=5) ≤9-10 months old ($p=0.30$). Analysis of specific brain regions, known to contain increasing levels of microglial activation in AD, revealed an even greater difference in normalized [^{18}F]PBR06 signal between 15-16 month old APP$^{L/S}$ and wt mice, as shown in Figure 1 (Cortex: 1.52±0.09 vs. 0.87±0.14, $p<0.005$; Hippocampus: 1.59±0.13 vs. 0.92±0.14, $p<0.005$). Again, no significant difference was observed between the APP$^{L/S}$ and wt mice ≤9-10 months old ($p=0.30$) (Figure 1). Similarly, autoradiography images depict a significantly higher [^{18}F]PBR06 signal in 15-16 month APP$^{L/S}$ mice compared to wts (Cortex: 1.32±0.04 vs. 1.00±0.10, $p<0.005$; Hippocampus: 1.36±0.06 vs. 1.07±0.01, $p<0.05$). Autoradiography and PET imaging results correlated well with each other ($R=0.87$) and also with immunostaining - *i.e.*, there was increased [^{18}F]PBR06 uptake in brain regions containing elevated CD68, ThioS, and TSPO staining in APP$^{L/S}$ compared to wts. Specifically, we observed a moderate correlation between normalized PET signal and TSPO levels in both hippocampus ($R=0.66$) and cortex ($R=0.67$), and a strong correlation between normalized PET signal and CD68 levels in cortex ($R=0.86$). **Conclusion:** [^{18}F]PBR06-PET/MRI shows great potential as a tool for investigating the *in vivo* role of microglia/TSPO in the progression and treatment of AD.

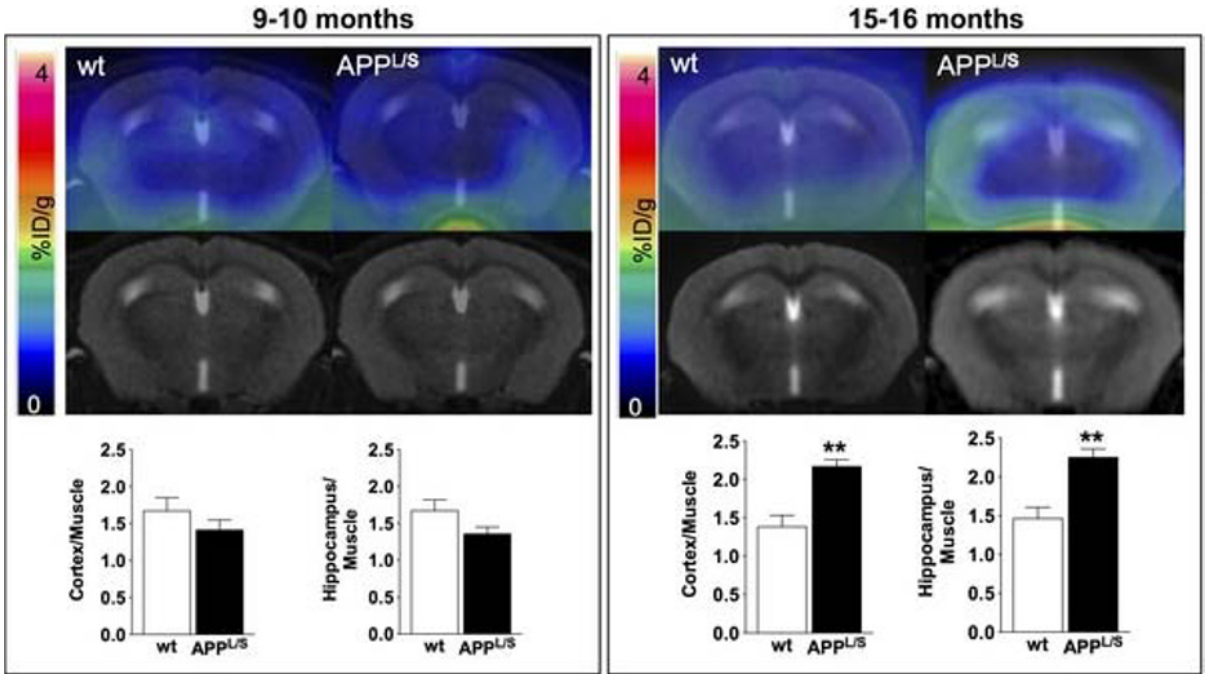

Figure 1. [^{18}F]PBR06-PET/MRI brain imaging results from a transgenic mouse model of Alzheimer's disease (APP$^{L/S}$) and age-matched wild-type (wt), at both 9-10 and 15-16 months of age. Static PET images were acquired 45-55 min post-injection of [^{18}F]PBR06 (100-150 μCi) and fused with mouse brain MRI data. Color images represent the fused coronal brain PET/MRI images, whereas, grey-scale images represent the coronal MRI brain slices alone. Graphs depict the ratio of [^{18}F]PBR06 accumulation in cortex/muscle and hippocampus/muscle in APP$^{L/S}$ versus wt mice, from both age groups. **p<0.005.

Disclosure of author financial interest or relationships:

M.L. James, None; **T.V. Nguyen**, None; **N.P. Belichenko**, None; **L. Andrews**, None; **H. Liu**, None; **D. Bodapati**, None; **B. Shen**, None; **Z. Cheng**, None; **S.S. Gambhir**, Bracco Diagnostics, Consultant; Endra, Inc, Stockholder; Cellsight, Stockholder; Enlight, Inc., Stockholder; General Electric, Grant/research support; ImaginAb, Stockholder; MagArray, Inc., Stockholder; Sanofi-Aventis, US, Grant/research support; SiteOne Therapeutics, Stockholder; VisualSonics/Sonosite, Stockholder; **F.M. Longo**, None; **F.T. Chin**, Ground Fluor Pharmaceuticals, Consultant .

Presentation Number **P 213**
Poster Session 2
September 19, 2013 / 15:15-15:15 / Room: Exhibit Hall B

Multiple Administration of Human Umbilical Cord Blood Derived AC133+ Endothelial Progenitor Cells in Rat Stroke Model - neuroprotection and neurorestoration

Branislava Janic[1], *Asm Iskander*[1], *Robert A. Knight*[2], *Zheng Gang Zhang*[2], *James R. Ewing*[2], *Adarsh Shankar*[1], *Nadimpalli Ravi S Varma*[1], *Hassan Bagher-Ebadian*[1], *Ali S. Arbab*[1], [1]*Radiology, Henry Ford Health System, Detroit, MI, USA;* [2]*Neurology, Henry Ford Health System, Detroit, MI, USA. Contact e-mail: bjanic@rad.hfh.edu*

Stem/progenitor cells hold enormous therapeutic potential for ischemic vascular diseases. Due to their pro-angiogenic characteristics, endothelial progenitor cells (EPCs) may be the best candidates for such strategies. In parallel, it is important to develop a non-invasive imaging approach for in vivo monitoring of transplanted cells. Systemically administered human Umbilical Cord Blood Cells (hUCBCs) have been shown to improve functional recovery in stroke rat models. We examined the effect of multiple doses of hUCBCs AC133+ EPCs on infarct volume, cell proliferation, angiogenesis and neurogenesis in rat model of transient middle cerebral artery occlusion (MCAo). In addition, we assessed the effect of administered cells on stroke induced neurobehavioral deficit. The objective of this study was to determine hUCBCs AC133+ EPCs' potential to provide neuroprotection and neurorestoration in rat MCAo model and to assess the capacity of magnetic resonance imaging (MRI) to track the administered cells in vivo. Animals were subjected to transient MCAo and 2 hours and 7 days later injected intravenously with 107 of magnetically and fluorescently labeled hUCBCs AC133+ EPCs. To confirm and characterize stroke lesions and to detect the administered cells MRI was performed at days 1, 7, 14, 21 and 28 after the insult. MRI showed accumulation of labeled cells in stroke affected hemispheres. Moreover, Prussian blue and immunofluorescence staining of collected brain tissues showed that administered cells localized only to the injured brain hemispheres, within and around blood vessels. Quantitative analysis of T2 maps created from T2 weighted MR images revealed that stroke volume decreased at a significantly higher rate in animals receiving cells. In addition, significantly higher numbers of cells expressing von Willebrand factor and Nestin were observed in the AC133+ EPCs treated, compared to the non-treated control animals. These results indicated that administered cells may have significantly affected angiogenesis and neurogenesis. In addition, neurological tests to assess basic sensory and motor responses were performed every 3 days during the 30 days monitoring. Analysis of the symmetry in the forelimb flexion, body proprioception and sensory functions revealed significant improvement in cell treated animals, compared to non-treated control animals. The study showed that transplanted cells can selectively migrate to ischemic brain parenchyma, where they may exert therapeutic effects on the extent of tissue damage, regeneration, time course of stroke resolution and neurobehavioral deficit.

Disclosure of author financial interest or relationships:
B. Janic, None; **A. Iskander**, None; **R.A. Knight**, None; **Z. Zhang**, None; **J.R. Ewing**, None; **A. Shankar**, None; **N. Varma**, None; **H. Bagher-Ebadian**, None; **A.S. Arbab**, None.

Presentation Number **P 214**
Poster Session 2
September 19, 2013 / 15:15-15:15 / Room: Exhibit Hall B

Real-Time MRI of Intracarotid Stem Cell Delivery in Stroke on a Time Scale of Seconds

Miroslaw Janowski[1,2], *Adam Nowakowski*[2], *Jiadi Xu*[3], *Moussa Chehade*[4], *Jeff W. Bulte*[1,5], *Barbara Lukomska*[2], *Piotr Walczak*[1,5], [1]*Radiology, Johns Hopkins University School of Medicine, Baltimore, MD, USA;* [2]*NeuroRepair, Mossakowski Medical Research Centre, Warsaw, Poland;* [3]*F.M. Kirby Research Center, Kennedy Krieger Institute, Baltimore, MD, USA;* [4]*Biomedical Engineering, Johns Hopkins University, Baltimore, MD, USA;* [5]*Institute for Cell Engineering, Johns Hopkins University, Baltimore, MD, USA. Contact e-mail: neuroibis@gmail.com*

Introduction: To date, MRI stem cell tracking has only be used for the detection of cells after the transplantation procedure has been completed. We have developed a new "snapshot" technique that allows monitoring of cell delivery in real-time on a time scale of seconds, allowing immediate intervention should cells engraft in an undesired location, or lead to the formation of a life-threatening microembolisms. Materials and Methods: An ouabain model of stroke was induced in 16 adult rats, followed by intracarotid injection of human mesenchymal stem cells (MSCs; 2x105 in 1 ml). Cells were injected at one (n=4), two (n=4), three (n=3), or seven (n=5) days after stroke induction within a magnet bore using extended catheter line. MSCs were labeled overnight with Molday ION-Rhodamine B (BioPAL, Inc.; 20 μg/ml). Immediately prior to transplantation, cells were harvested and suspended in PBS. A Bruker 7T horizontal bore magnet and a phase-array coil were used with a GE-EPI sequence (TE=17 ms, TR=2000 ms, FOV=26x26 mm, matrix=96x96, and acquisition time=2 s). This ultra-fast sequence enabled continuous monitoring of cell delivery in real-time. Standard T2 and T2*-weighted were also acquired before and after GE-EPI, as well as one day later. OsiriX and MATLAB were used for image processing. Results: We detected an inflow of cells into the brain, in real-time, characterized by a gradual, focal decrease of pixel intensities (PI) on consecutive images over a period of 300 seconds (Fig. 1, infarcted area outlined in yellow). Based on pixel intensity (PI), graphs were generated depicting a reduction in PI for selected ROIs. No change of signal was observed in the contralateral hemisphere (Fig.1 , green square). Real-time GE-EPI demonstrated that cells rapidly engrafted within the stroke periphery (Fig. 1, 100 s; orange and blue squares), with a delayed inflow into the core of the infarct (Fig. 1, 200 s; red square). At the end of the infusion (Fig. 1, 300 s), the cell distribution within the overall infarcted area was quite homogenous. In addition, dynamic real-time MRI showed that the injection of stem cells at different timepoints after stroke highly affects the velocity cell inflow ($p<0.05$) and brain coverage by cells ($p<0.05$) to the infarcted area (supplementary figure). The most efficient and fastest inflow was observed when cells were transplanted 2-3 days after stroke induction, which suggests that stroke-induced local cerebral blood flow (CBF) disturbances affect stem cell delivery. These observations may have great impact on the therapeutic outcome, and could improve the evaluation of CBF within the infarcted brain, and elucidate the influence of the CBF on cell therapy. Notably, follow-up MR images did not detect additional infarcts. Conclusions: GE-EPI enables monitoring of cell delivery in real-time to evaluate cell engraftment, and with sufficient temporal resolution to discriminate early- from late- filling areas. Monitoring the pattern and velocity of cell inflow will greatly aid in evaluating the safety and efficacy of intra-arterial cell therapy, in particular in scenario's where the stroke development is variable.

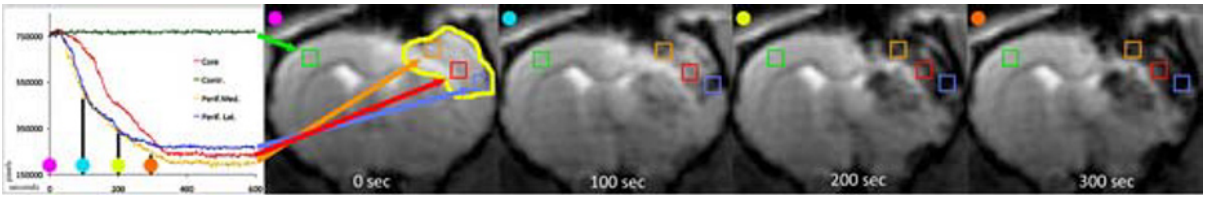

Disclosure of author financial interest or relationships:
M. Janowski, None; **A. Nowakowski**, None; **J. Xu**, None; **M. Chehade**, None; **J.W. Bulte**, None; **B. Lukomska**, None; **P. Walczak**, None.

Presentation Number **P 215**
Poster Session 2
September 19, 2013 / 15:15-15:15 / Room: Exhibit Hall B

Theranostic potential of manganese-based macrocyclic superoxide dismutase mimetic probe

Alexei A. Bogdanov[1], *Mohammed Salman Shazeeb*[1], *Giancarlo Feula*[2], [1]*Radiology, Laboratory of Molecular Imaging Probes, Worcester, MA, USA;* [2]*Worcester Polytechnic Institute, Worcester, MA, USA. Contact e-mail: alexei.bogdanov@umassmed.edu*

Endogenous manganese based superoxide dismutase (Mn-SOD) provides the primary defense against excess production of potentially toxic superoxide anion. M40401 (manganese(II)dichloro{2S,21S-dimethyl-(4R,9R,14R,19R)-3,10,13,20,26-pentaazatetracyclo[20.3.1.0.0]hexacosa-1(26),-22(23),24-triene}]), is a synthetic enzyme mimetic that has a catalytic activity rate exceeding that of the native SOD enzymes. We synthesized, purified the active enantiomer and tested the theranostic potential of M40401. Both MR imaging (Mn is paramagnetic) and SOD-mimetic properties of M40401 are enabled by a single entity, i.e. chelated Mn. The presence of a paramagnetic Mn(II) cation in M40401 suggests that the delivery and spatial distribution of this enzyme mimetic in vivo may be directly detectible using magnetic resonance imaging (MRI); however, the cardiotoxicity of Mn(II) can potentially limit the use of free M40401 in living systems. To deliver M40401 in vivo in amounts sufficient for MRI detection and to limit potential cardiotoxicity, we encapsulated M40401 into 170±50 nm liposomes composed of 90% of phosphatidylcholine and 10% PEGylated phosphatidylethanolamine to achieve extended circulation in the bloodstream. At 0.47 T, the relaxivity of M40401 was 4.44 mM-1s-1. The obtained liposomes efficiently catalyzed superoxide dismutation in vitro: at high concentration of liposome-encapsulated M40401 the SOD mimetic was dismutating superoxide more efficiently than SOD enzyme. Using 3T MRI (GRE TR/TE/FA = 192 ms/5.5 ms/75°) we investigated the biokinetics of liposome-encapsulated M40401 in mice and found that in addition to catalyzing superoxide dismutation in vitro, M40401 caused differential and region-specific enhancement of mouse brain after the systemic administration. Liposomes loaded with M40401 did not exhibit any outward toxicity and resulted in transient enhancement of the cortical and sub-cortical regions of the brain suggesting sustained release of M40401 from liposomes. The sub-cortical region of the brain generally showed greater T1 enhancement and higher signal-to-noise ratio than the cortex region, which could also indicate the potential entry of the released M40401 into the cerebrospinal fluid via the choroid plexus. Thus, liposome encapsulated M40401 is an ideal candidate for development as a theranostic compound useful for simultaneous MRI-mediated tracking of delivery as well as for neuroprotective treatment of the brain in stroke and traumatic brain injury patients.

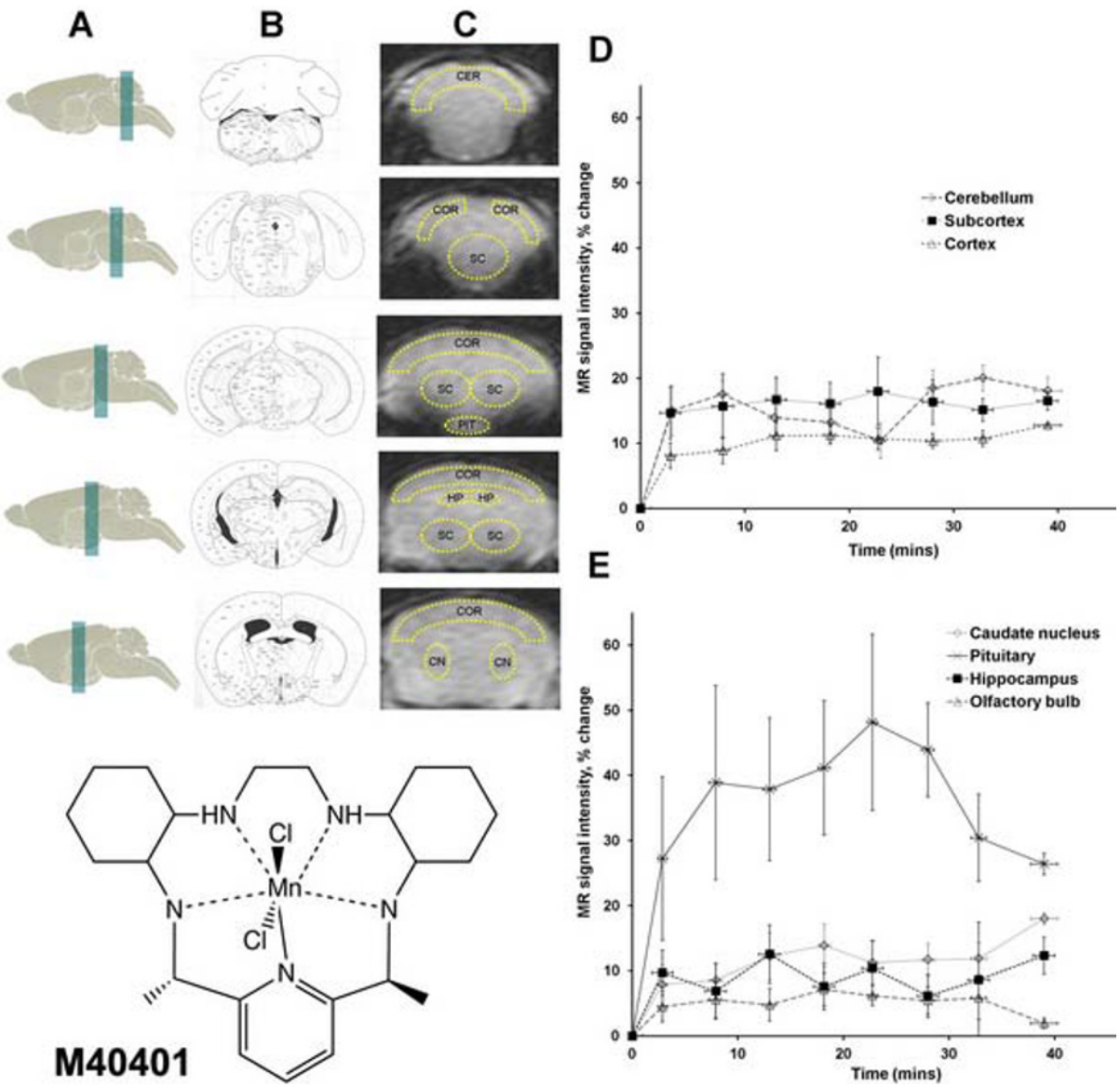

A - the position of imaging slices (B- anatomical map; C- MR imaging map), below is the chemical structure of Mn SOD mimetic M40401; D- time course of Mn-mediated MR signal enhancement showing enhanced subcortex vs. cortex; E- the comparison of pituitary MR signal enhancement vs. the enhancement of various brain structures. .

Disclosure of author financial interest or relationships:
A.A. Bogdanov, None; **M. Shazeeb**, None; **G. Feula**, None.

Presentation Number **P 216**
Poster Session 2
September 19, 2013 / 15:15-15:15 / Room: Exhibit Hall B

Cystamine Effectively Promotes Functional Recovery by Increasing Brain-Derived Neurotrophic Factor Levels in Brain after Stroke in Mouse

Peicheng Li, *Yun Jiao, Chen Qian, Xiangyu Yang, Gao-Jun Teng, Jiangsu Key Laboratory of Molecular and Functional Imaging, Department of Radiology, Zhongda Hospital, Medical School of Southeast University, Nanjing, China. Contact e-mail: lpccat@163.com*

Objective: Cystamine has been reported it is neuroprotective in Huntington disease (HD) mice by increasing Brain-derived neurotrophic factor (BDNF) levels in brain. BDNF which is mainly synthesized by neurons, plays a crucial role in neuronal survival, synaptic plasticity,learning and memory, and neuroplasticity. Thus, the beneficial effects of rehabilitation in promoting functional recovery after stroke may also depend on BDNF. The aim of this study was to examine whether cystamine could promote functional recovery after stroke in mouse by increasing brain levels of BDNF. Methods: Adult male C57B/6J mice (n=60) were subjected to photothrombotic model of focal stroke or sham operation. Cystamine (100mg/kg/day, i.p.) or saline was administered for 7 days initiated at 24 h after onset of stroke. We also administered ANA-12, a low-molecular weight TrkB antagonist that prevented activation of the receptor by BDNF with a high potency, to examine the mechanisms for rehabilitation by cystamine.The expression of BDNF mRNA and the secretion of BDNF protein in brain were examined by RT-PCR and enzyme linked immunosorbent assay at 1, 3, and 7 days after stroke. T2-weighted imaging, diffusion tensor imaging (DTI) and functional motor measurements were performed to detect lesion volumes, axonal remodeling and functional recovery from 24 h to 6 weeks after stroke. After the mouse euthanasia, brain sections were immunostained for semiquantitative analysis of myelin basic protein, synaptophysin, neurogenesis and quantification of infarct volumes. Results: Cystamine significantly increased BDNF levels in brain. Cystamine-treated animals had better functional motor recovery compared with all other groups($p<0.05$). Cystamine treatment induced axonal remodeling in the ischemic border zone and synaptophysin expression within the contralateral cortex 6 weeks after ischemia ($P<0.05$). Cystamine treatment also doubled both the number of new mature neurons and immature neurons adjacent to the stroke. Preinjection of ANA-12 abolished the beneficial effects of cystamine. Infarct volumes were not different between the groups 1 or 6 weeks after ischemia. Conclusions: Cystamine treatment improves functional recovery after photothrombotic stroke and induces neurogenesis and axonal remodeling by increasing BDNF levels in brain. Cystamine may be a promising pharmacological therapy for promoting recovery of function after stroke. Together, our results provide a novel drug to promote recovery after stroke and possibly other brain injuries.

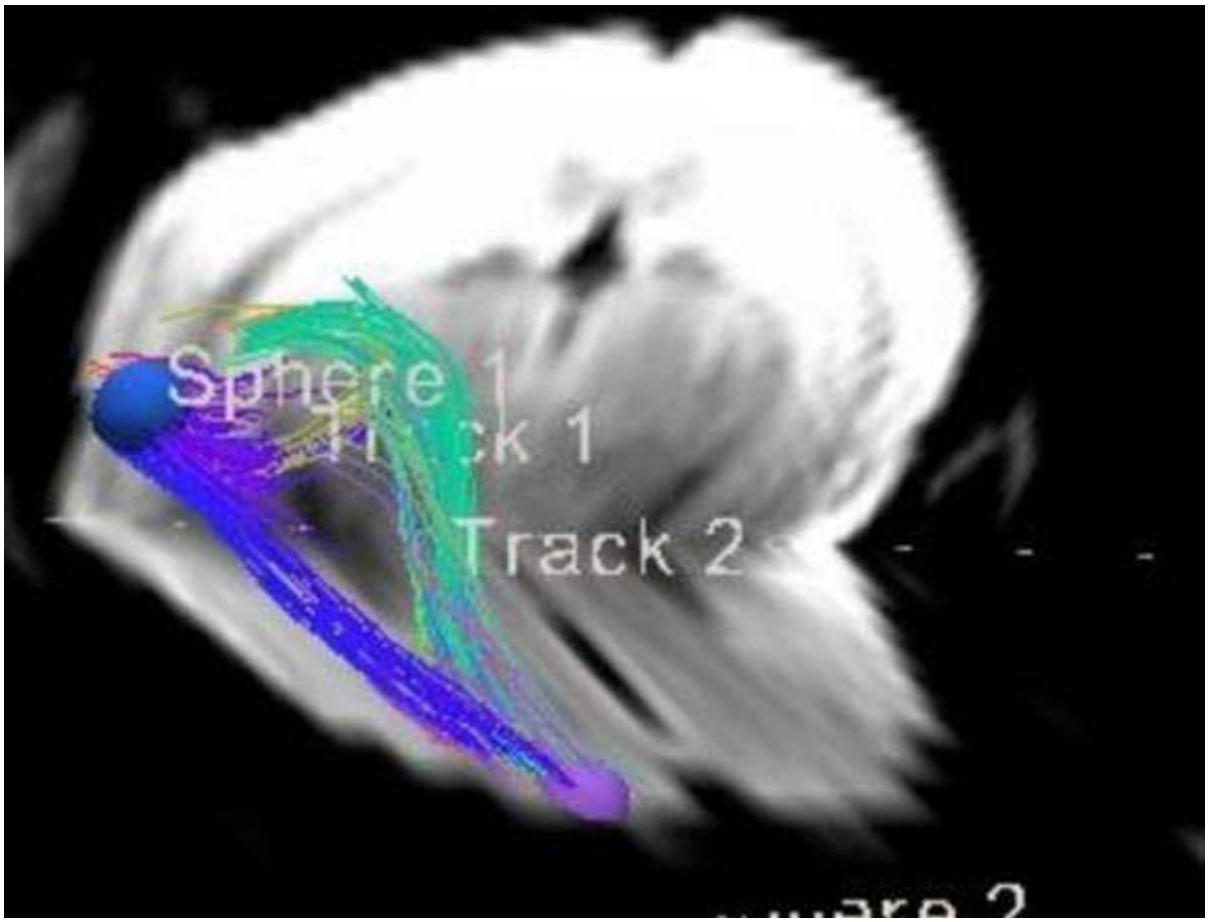

axonal remodeling in ischemic brains as measured by tractography using DTI

Disclosure of author financial interest or relationships:
P. Li, None; **Y. Jiao**, None; **C. Qian**, None; **X. Yang**, None; **G. Teng**, None.

Presentation Number **P 217**
Poster Session 2
September 19, 2013 / 15:15-15:15 / Room: Exhibit Hall B

Differential Effects of Amphetamine Exposure on Neuroglia in vivo

Philip K. Liu[1], *Christina Liu*[1,2], [1]*Radiology, Mass General Hospital, Charlestown, MA, USA;* [2]*NIBIB, NIH, Bethesda, MD, USA. Contact e-mail: philipl@nmr.mgh.harvard.edu*

Drug abuse is a major public health problem with wide range of negative health, economic, and social consequences. One of the most commonly abused types of drugs is amphetamine, a psycho-stimulant sometimes used as a performance enhancer to increase alertness and focus and may induce anxiety and psychosis. The effects of amphetamine use or abuse on brain development may last for many years, and chronic amphetamine exposure in animals and humans is known to cause hyperthermia and apoptosis, as well as leakage of the blood-brain barrier (BBB). However, the effect of amphetamine on neuroglia is not well understood, and somewhat controversial. Although there is research evidence that chronic amphetamine exposure activates striatal gliosis and overproduction of cytokines from microglia, autopsy results from human methamphetamine users have not supported those observations. We chose to investigate the effect of amphetamine exposure on the neuroglia, as these cells play critical roles in modulating injury repair, neuronal migration, and in facilitating neurotransmitter transport, BBB integrity, blood flow regulation, metabolic balance, iron homeostasis, and immune response, in learning processes, stress responses and mental health, as well as in the development of glioma, psychiatric and neurological disorders, and neurodegenerative diseases. How amphetamine affects the neuroglia in living brains is not well understood. In an effort to elucidate this effect, we investigated neuroglia in response to amphetamine exposure using antisense (AS) or sense (S) phosphorothioate-modified oligodeoxynucleotides (sODN) sequences that correspond to glial fibrillary acidic protein (GFAP) mRNA (AS-gfap or S-gfap, respectively) expression. The control is a random sequence sODN (Ran). Using cyanine 5.5-superparamagnetic iron oxide nanoparticles (Cy5.5-SPION) label and fluorescent microscopy, we demonstrated that living neural progenitor cells (PC-12.1), as well as the cells in fresh brain slices and intact brains of male C57black6 mice exhibited universal uptake of all of the sODNs, but rapidly excluded all sODN-Ran and most of S-gfap. Moreover, transmission electron microscopy revealed electron-dense nanoparticles only in the neuroglia of normal or transgenic mice (B6;DBA-Tg(Fos-tTA, Fos-EGFP*)1MmayTg(tetO-lacZ,tTA*)1Mmay/J) that had been administered AS-gfap or Cy5.5-SPION-gfap. Subtraction R2* maps from mice with acute and chronic amphetamine exposure demonstrated, validated by postmortem immunohistochemistry, a reduction in striatal neuroglia, with gliogenesis in the subventricular zone and the somatosensory cortex in vivo. The sensitivity of our unique gene transcript targeted MRI was illustrated by a positive linear correlation ($r2 = 1.0$) between in vivo MRI signal changes and GFAP mRNA copy numbers determined by ex vivo TaqMan assay. The study provides direct evidence for targeting neuroglia by antisense DNA-based SPION-gfap that enables in vivo MRI of inaccessible tissue with PCR sensitivity. We conclude that amphetamine induces toxicity to neuroglia in vivo, which may cause remodeling or re-connectivity of neuroglia.

Disclosure of author financial interest or relationships:
P.K. Liu, None; **C. Liu**, None.

Presentation Number **P 218**
Poster Session 2
September 19, 2013 / 15:15-15:15 / Room: Exhibit Hall B

In Vivo Imaging of Microglia Cells Activated by LPS-Induced Systemic Inflammation in Mouse

Domokos Mathe[1], *Ildiko Futo*[2], *Daniel Veres*[2], *Ildiko Horvath*[2], *Mariann Semjeni*[1], *Noemi Kovacs*[1], *Miklós Tóth*[3], *Ralf K. Bergmann*[4], *Krisztian Szigeti*[1], [1]*CROmed Ltd, Budapest, Hungary;* [2]*Biophysics and Radiation Biology, Semmelweis University, Budapest, Hungary;* [3]*Clinical Neuroscience, Karolinska Institute, Stockholm, Sweden;* [4]*Radiopharmacy Radiopharmaceutical Biology, Helmholtz-Zentrum, Dresden-Rossendorf, Germany. Contact e-mail: domokos.mathe@cromedresearch.com*

Introduction: The role of microglia cells in the pathogenesis of inflammations and chronic neurodegenerative disorders in the central nervous system (CNS) is an active research field in recent years. The ramified form of microglia cells is activated via inflammation markers (e.g. IL-1b, TNF-alpha). The activated form of microglia cells as a key player of the innate immune system in the CNS present MHC II and release antiinflammatory agents. The activation status of the microglial benzodiazepine (BZD) receptor system could be used to monitor the process of neuroinflammation. Methods: Healthy (n=6) and LPS induced inflamed (n=4) C57BL/6 mice were used. The activation of the microglia cells was induced by systemic injection of 0.3 g/bw kg lipopolysaccharide (LPS) 5h before the in vivo measurements. We used NanoSPECT/CT Plus and nanoScan PET/MRI (Mediso Ltd, Hungary) multimodal in vivo imaging systems. To detect dynamics and localization of microglia activation we used a micro dose partial inverse BZD agonist (125-I - Iomazenil). The change of the general metabolic state in the CNS was monitored by 18-F-FDG PET. 99m-Tc-HMPAO (hexamethylpropylene-amino-oxime) was used for the detection of altered regional cerebral perfusion. The segmentation of different mouse regions was first based on MRI measurements of the animals and for aims of standardization coregistered with an MRI atlas. Results: FDG uptake was increased by systemic LPS in every region of the brain ($p<5\%$). HMPAO uptake was decreased in several brain regions ($p<5\%$). We found that the activity concentration of 125-I-Iomazenil was increased in the hippocampus and cerebellum but not in the cortex after systemic induction of neuroinflammation. Conclusions: FDG uptake increase indicates an increased metabolic rate due to induced brain inflammation. HMPAO uptake change could show glutathione depletion generated decrease of HMPAO fixation induced by reactive oxygen species (ROS) generated by activated inflammatory cells. The surprising result of selective Iomazenil uptake increase could be attributed to a higher amount of an activated but already resident microglia cell pool in the hippocampus as an early step of acute systemic inflammation in the brain. Based on our results the LPS induced changes in the BZD system should be further monitored in neuroinflammation in concordance with ROS status and the time course of the inflammatory changes in this general neuroinflammatory model in mice. A multi-modal imaging approach combining detailed structural and functional approaches elucidates important unknown details of neuroinflammation monitoring. This work was supported in part by INMiND (HEALTH.2011.2.2.1-2 No.278850) of FP7.

Disclosure of author financial interest or relationships:
D. Mathe, CROmed Ltd, Stockholder; Mediso Ltd., Consultant; **I. Futo**, None; **D. Veres**, None; **I. Horvath**, None; **M. Semjeni**, CROmed Ltd, Employment; **N. Kovacs**, None; **M. Tóth**, None; **R.K. Bergmann**, None; **K. Szigeti**, None.

Presentation Number **P 219**
Poster Session 2
September 19, 2013 / 15:15-15:15 / Room: Exhibit Hall B

Assessment of glucose brain metabolism in a rat model of traumatic brain injury by in vivo PET imaging

Laura Reyes[1], Eliseo Taranto[3], Andrea Paolino[1], Alethia de la Fuente[1], Daniela Blanco[3], Darío Tejera[5], Maria L. Negro[5], Daniela Alí[4,5], Hugo Peluffo[5,4], Henry Engler[2], **Patricia Oliver**[1], *[1]Department of Biomedical Research, Uruguayan Center of Molecular Imaging (CUDIM), Montevideo, Uruguay; [2]General Director, CUDIM, Montevideo, Uruguay; [3]Department of Physiopathology, Faculty of Medicine, Hospital de Clínicas, Montevideo, Uruguay; [4]Department of Histology and Embryology, Faculty of Medicine, UDELAR, Montevideo, Uruguay; [5]Neurodegeneration Laboratory, Institut Pasteur of Montevideo, Montevideo, Uruguay. Contact e-mail: patricia.oliver@cudim.org*

Introduction: Until now, our country didn't have a reproducible and clinically relevant rat model of focal traumatic brain injury (TBI) for preclinical studies. TBI has a high incidence of long-term neurologic morbidity. The mechanisms of secondary TBI are only partially known and there are no specific treatments to reduce the associated histopathology and to promote post-trauma functional recovery. Modulation of the post-injury inflammation has been shown to enhance physiopathological processes. The CD300f immunoreceptor displays immune/inflammatory-modulatory properties being a promising target for gene therapy. Aim: To study glucose brain metabolism changes by serial μPET to assess the reproducibility of a rat model of TBI and to evaluate the effect of a non-viral modular gene therapy vector overexpressing CD300f. Methods: Wistar rats (250-300gr) underwent right lateral TBI using the Controlled Cortical Impactor model (CCI; n=24). Rats were injected 4hr post-injury at 3 foci with the gene therapy vector NLSCt/CD300f or NLSCt/GFP. Then, they were randomized into 3 groups (n=8 each): Saline, GFP, CD300f. Longitudinal μPET imaging with [18F]-FDG were performed to explore changes in brain glucose metabolism at baseline before CCI (control) and 3 and 94days after focal injury. PET/CT scans were obtained with a Triumph Tri-modality Scanner (Gamma Medica, Inc.). The rats were injected i.v. with 35-50MBq of [18F]-FDG and examined during 60min, 30min post-injection. Images were reconstructed with 3D-MLEM, normalized with a FDG template using PMOD software. Brain FDG uptake was analyzed in different regions and normalized to the whole-brain uptake. Results were expressed as mean ± SEM and the groups were compared by ANOVA. Results: No significant difference in whole-brain uptake was observed between CCI rats and controls ($p=0.68$). The brain areas of interest at both the impact regions (motor and somatosensory primary cortex) and the penumbra lesion (cingulate, anterior parietal, retrosplenial cortex) showed a significant decrease in FDG uptake 3days after CCI compared to control ($p<0.05$). Moreover, there was a significant increase in FDG uptake at the somatosensory and anterior parietal cortex of the left hemisphere contralateral to the injury ($p<0.05$). The FDG uptake in the center of the lesion and the penumbra of the right lesioned hemisphere in the GFP and CD300f treatment groups was not significantly different from the saline group at 3days. The results of μPET studies at 94days after CCI are currently being analyzed. These results will be verified by histology and immunohistochemistry. Conclusions: This rat model of TBI has proved to be reproducible showing a profile of FDG uptake similar to those reported previously: early hypometabolism in ipsilateral brain regions directly affected by CCI and in the penumbra area. Although monitoring with FDG-PET clearly indicated this condition, we couldn't observe any effect of this gene therapy 3days after CCI. The evaluation of its effect at 94days is still pending. The use of other tracers such as [18F]-FMISO or 15O and a modified vector, might provide more information about this subject.

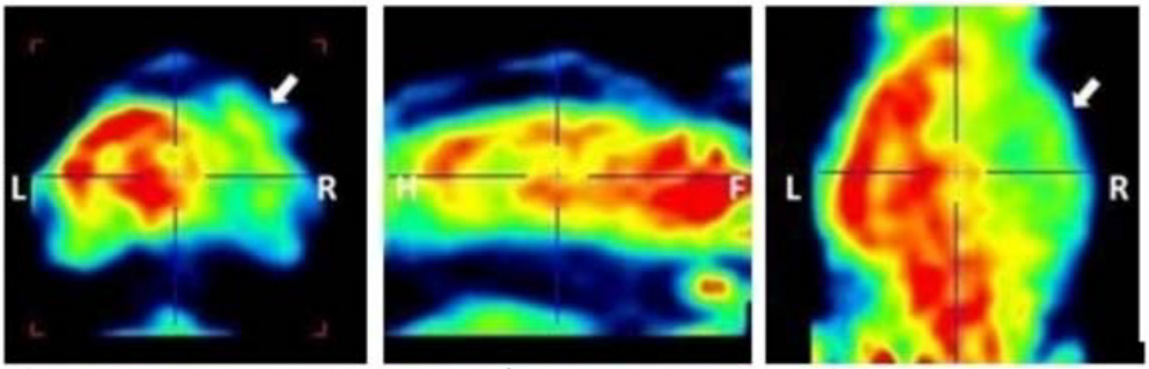

Coronal, sagital and axial image of [^{18}F]-FDG PET of a rat brain at 3 days post-TBI. It shows a significant decrease in FDG uptake in the traumatized area (right hemisphere) compared to healthy hemisphere.

Disclosure of author financial interest or relationships:
L. Reyes, None; **E. Taranto**, None; **A. Paolino**, None; **A. de la Fuente**, None; **D. Blanco**, None; **D. Tejera**, None; **M.L. Negro**, None; **D. Alí**, None; **H. Peluffo**, None; **H. Engler**, None; **P. Oliver**, None.

Presentation Number **P 220**
Poster Session 2
September 19, 2013 / 15:15-15:15 / Room: Exhibit Hall B

Kinetic Analysis of ^{18}F-FDG in Normal Dog Brain: Preliminary Review for Potential Use as a Human Model

Dustin Osborne[1], *Lindsay Wiliiams*[2], *Federica Morandi*[2], *Amy K. LeBlanc*[2], *Jonathan S. Wall*[3], [1]*Graduate School of Medicine, University of Tennessee, Knoxville, TN, USA;* [2]*Veterinary Medicine, UT College of Veterinary Medicine, Knoxville, TN, USA;* [3]*Dept. of Medicine, University of Tennessee, Knoxville, TN, USA. Contact e-mail: dosborne@utk.edu*

Objectives This works seeks to provide a preliminary review of kinetics in the brain of normal beagles as a potential model for human brain imaging using ^{18}F-FDG. Introduction Brain imaging studies involving modeling of ^{18}F-FDG in human subjects is often complex in nature and the physiological parameters required, such as blood sampling, not easily collected without causing a significant degree of discomfort for the patient. Primate models are often used as the primary substitute for human neurological studies, however, the number of facilities with access to primates is limited because of the cost and administrative overhead in maintaining that species for imaging experiments. Mice and rats are readily available to many sites but the small size of the brain creates signficant partial volume effects in measurements of local regions for use in kinetic modeling. Dogs may provide a reasonable compromise between various models by providing a cost-effective and accessible model for brain imaging studies. Materials and Methods PET/CT imaging of four healthy male beagles was performed by injecting approximately 5 mCi of ^{18}F-FDG. Listmode data acquisition was started 5-10 seconds prior to the beginning of the injection. PET data were acquired over 120 minutes and dynamically framed into 45 frames. Glucose levels were measured prior to imaging for use in calculating metabolic rates of glucose (MRGl). Regions of interest were drawn on the brain dividing it into 15 different regions using the Inveon Research Workplace software (Siemens Medical Solutions) with an additional region of interest drawn in the carotid artery as a whole blood input function measurement. Time Activity curves were generated from these regions of interest for use in Patlak analysis. The whole blood input function was corrected using the exponential whole blood to plasma correction from Wu et al. A lumped constant of 0.65 was used as only the irreversible situation was considered (k4=0). Glucose levels measured for this study were then used to calculate the MRGl for comparison to work performed in mice and humans (Phelps et al. & Wu et al). Patlak regression fits were performed over a 5-25 minute time period to reduce effects from ignoring phosphorylation. In addition, a value for the so-called $MRGl_{MAX}$ based on Williams et al. was calculated. Results Calculated average values for Ki, MRGl, $MRGl_{MAX}$ and χ^2 are presented in Table 1. Results for calculations of MRGl show a range of values from 0.22-0.55 mmol/min/g indicating agreement with the ranges of values shown for mice, rats and humans. Average values for MRGl and and $MRGl_{MAX}$ were 0.36 mmol/min/g and 0.32 mmol/min/g. Image 1 shows a parametric map created from the calculated MRGl values from one of the subjects in this study. Conclusions This work provides a preliminary look at modeling data for ^{18}F-FDG in canine brains as a potential model for human brain imaging. Additional work is needed to examine additional corrections that may be needed to provide more accurate results.

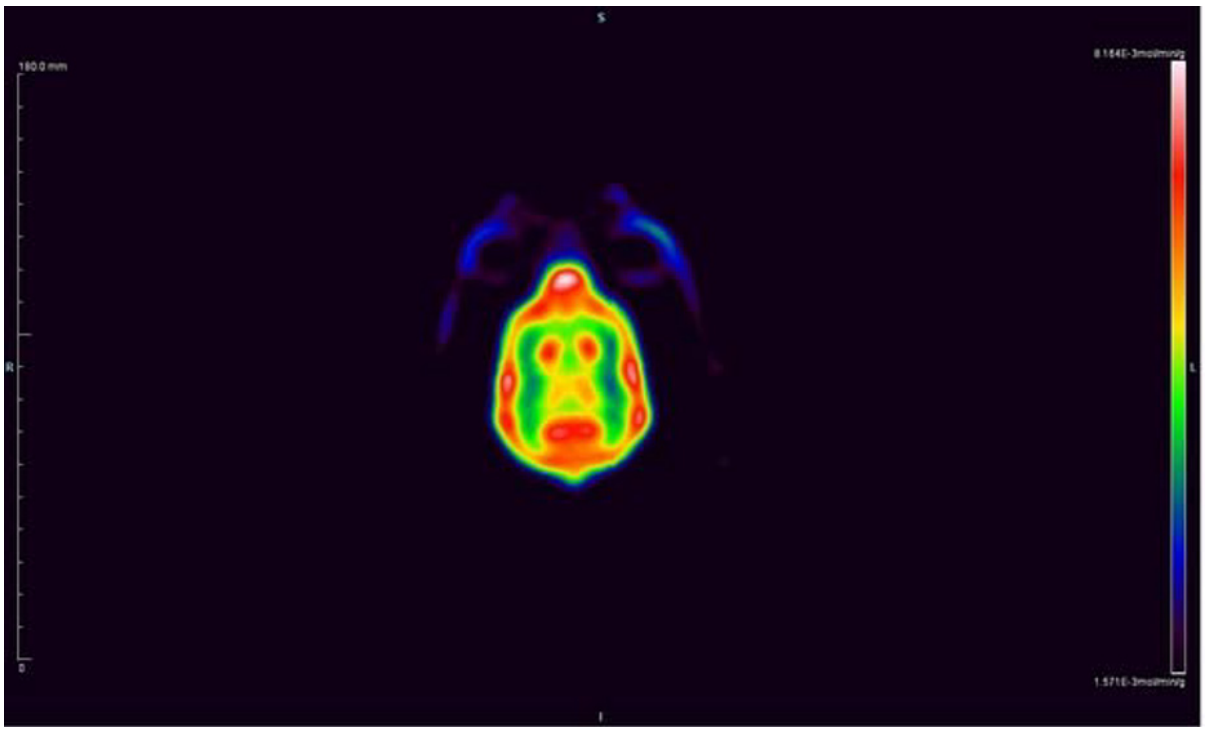

Average Ki, MRGl and Chi Sq

Average Ki (ml/g/min)	Average MRGl (mole/min/g)	Average MRGl MAX (mole/min/g)	Average Chi Square	Average Correlation (%)
0.04	0.36	0.32	0.042	84

Disclosure of author financial interest or relationships:
D. Osborne, Siemens, Employment; **L. Wiliiams**, None; **F. Morandi**, None; **A.K. LeBlanc**, None; **J.S. Wall**, Solex Inc, Stockholder .

Presentation Number **P 221**
Poster Session 2
September 19, 2013 / 15:15-15:15 / Room: Exhibit Hall B

Influence of methylphenidate on [18F]-fallypride striatal binding in C57BL/6 mice using positron emission tomography (PET)

Kennerly S. Patrick[1], *Xingju Nie*[2,3], *Michael Cdebaca*[4], *Carl Riley*[4], *David Wilson*[4], *Ann-Marie Broome*[2,3], [1]*Drug Discovery and Biomedical Sciences, Medical University of South Carolina, Charleston, SC, USA;* [2]*Radiology and Radiological Sciences, Medical University of South Carolina, Charleston, SC, USA;* [3]*Center for Biomedical Imaging, Medical University of South Carolina, Charleston, SC, USA;* [4]*Triad Isotopes, Inc., Triad Isotopes, Inc., Charleston, SC, USA. Contact e-mail: patrickk@musc.edu*

Introduction: Methylphenidate (MPH) and amphetamine are drugs of choice in the treatment of ADHD. Though both of these stimulants elevate synaptic dopamine concentrations in the striatum, their underlying mechanisms differ. Amphetamine releases dopamine from presynaptic stores, while MPH blocks impulse-released dopamine reuptake by the dopamine transporter (DAT). Previously, positron emission tomography (microPET) has been used to image competitive displacement of [18F]-fallypride from rat striatal post-synaptic D2/3-receptors following amphetamine-induced release of dopamine. The present study extends this noninvasive microPET approach to the influences of MPH on the DAT and synaptic dopamine. The reference strain C57BL/6 mouse was used. Our findings provide a proof-of-concept in advance of broader investigations into dopaminergic neuropharmacology. Methods: Male C57BL/6 mice aged 8-10 weeks (25-35 g; n=3) were gavaged with a total volume of 0.02 mL/g body weight of dH20 or MPH HCl (7.5 mg/kg). 15 min later a bolus tail vein injection of 15 MBq [18F]-fallypride (>150 GBq/umol) in 200ul normal saline was injected followed by 10 min anesthesia. [18F]-fallypride was produced daily as at Triad Isotopes Inc. using a modified ROTEM synthesis cassette and GE TRACERLab MX synthesis module. Scans were acquired with a Siemens INVEON dedicated PET (D-PET) in the undocked mode with a 90-min list mode acquisition protocol followed by a 20-min transmission scan for attenuation correction with a 57Co source. The dynamic list mode data was sorted to sinograms with 25 frames (4×30 sec, 8×1 min, 10×5 min, and 3x10 min). Dynamic emission recordings acquired in list mode were reconstructed using a combined algorithm with two OSEM3D iterations, followed by 18 MAP3D iterations with a zoom factor of 1.3 and attenuation correction, resulting in a final 256 x 256 x 159 matrix. The voxel dimensions of the reconstructed images were 0.33 x 0.33 x 0.80 mm3. The microPET files were converted to DICOM format and processed by the PMOD software (PMOD Tech, Zurich). VOIs (volume of interest) in the shape of a sphere with radius of 0.6mm were placed bilaterally in the striatum and the vermis of cerebellum. TACs (time activity curve) for each VOI were generated and BPND (nondisplaceable specific binding) (Ichise MRTM2 Ref) of [18F]-fallypride were computed from the reconstructed dynamic images with high activity in the striatum and very low activity in the cerebellum (reference region). With the Tmax and T1/2 of MPH in mice reported to be ≤ 25 min and 1.1 h, respectively, cumulative acquisition data is presented for the high MPH exposure period of 25-65 min following gavage. Results: Mean striatal [18F]-fallypride BPND was calculated to be 7.994 ± 0.4329 in the dH20 control animals and 4.147 ± 1.236 (- 48%; $P < 0.05$) in the MPH group (Fig.1). Discussion: Dopaminergic dysfunction is frequently implicated in ADHD. By using [18F]-fallypride displacement microPET, our preclinical model establishes a noninvasive imaging technology for studies of synaptic dopamine flux, MPH-drug interactions, and offers translational potential for ADHD drug optimization.

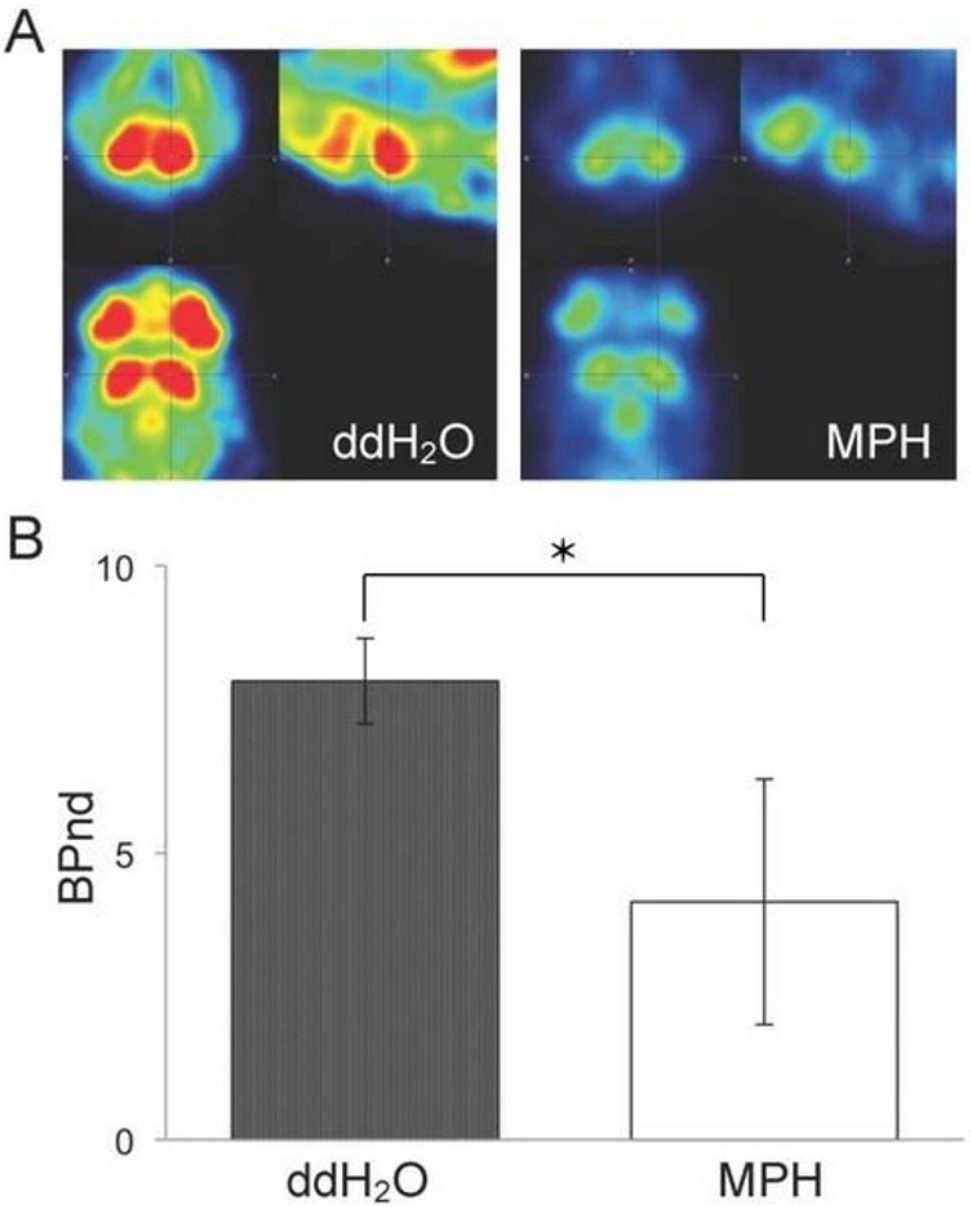

Fig.1. PET imaging of the displacement of [18F]-fallypride by MPH. (A) [18F]-fallypride binding potential maps for a representative ddH2O gavaged control mouse (left) and a methylphenidate gavaged mouse (right). (B) Mean striatal [18F]-fallypride BPND in the ddH20 control animals (n = 3) compared to the MPH group (7.5 mg/kg gavage; n = 3). *P < 0.05 (Student's unpaired t-test).

Disclosure of author financial interest or relationships:
K.S. Patrick, Noven Pharmaceutics, Inc., Consultant; **X. Nie**, None; **M. Cdebaca**, None; **C. Riley**, None; **D. Wilson**, None; **A. Broome**, None.

Presentation Number **P 222**
Poster Session 2
September 19, 2013 / 15:15-15:15 / Room: Exhibit Hall B

Neurographic Imaging with a Molecular Probe

Dawid Schellingerhout, *Sebastian Bredow, Lucia LeRoux, Departments of Radiology and Experimental Diagnostic Imaging, University of Texas M.D. Anderson Cancer Center, University of Texas M D Anderson Cancer Center, Houston, TX, USA. Contact e-mail: Dawid.Schellingerhout@mdanderson.org*

Purpose: To develop an agent for imaging retrograde axonal transport in nerve tissues based on the optical labeling of a non-toxic fragment of tetanus toxin. Materials and Methods: A His-tagged recombinant tetanus toxin fragment C (TTc) was produced in E.coli, purified, and labeled with a variety of Alexa fluorophors for optical imaging studies. Gel electrophoresis (SDS-PAGE) and quantitative immunodetection studies were performed. Cell uptake studies were performed to assess in vitro efficacy. Labeled TTF was injected into the soleus muscle of C57bl and Balb/C mice, and Wistar rats, and imaging performed with the IVIS 200 (Xenogen). In situ validation was performed with laser scanning confocal microscope FV 1000 (Olympus) utilizing intact glycerol mounted samples, and cryo-sections. Results: Gel electrophoresis and quantitative immunodetection indicated that the integrity and immune reactivity of the protein was preserved after labeling. Cell uptake assays indicated robust uptake in differentiated PC12 cells. In vivo optical imaging demonstrated the uptake of TTc-Alexa in the sciatic nerve and spinal cord. Progressive uptake and transport of the agent could be seen along the course of the sciatic nerve and spinal cord. Confocal microscopy studies on intact excised nerve segments and cryosections confirmed the compound uptake in nerve fascicles of the sciatic nerve. Axonal nerve uptake and superficial lymphatic uptake were clearly distinguishable, and transport was shown to be nerve-specific. Immunohistochemistry on cord sections demonstrated the presence of the agent in spinal cord neurons. Conclusion: Fluorescently labeled TTc is taken up into motor nerve endings after intramuscular injection, and is retrogradely transported in nerve axons. This process can be demonstrated with non-invasive in vivo imaging, and allows nerve anatomy and function to be studied.

Disclosure of author financial interest or relationships:
D. Schellingerhout, None; **S. Bredow**, None; **L. LeRoux**, None.

Presentation Number **P 223**
Poster Session 2
September 19, 2013 / 15:15-15:15 / Room: Exhibit Hall B

Accumulation of Micron Sized Iron Oxide Particles (MPIOs) in Endothelin-1 Induced Focal Cortical Ischemia in Rats is Independent of Cell Migration

Erik M. Shapiro[1,2], *Dorit Granot*[2], [1]*Department of Radiology, Michigan State University, East Lansing, MI, USA;* [2]*Department of Diagnostic Radiology, Yale University School of Medicine, New Haven, CT, USA. Contact e-mail: erik.shapiro@rad.msu.edu*

INTRODUCTION: Endogenous labeling of stem/progenitor cells via intracerebroventricular injection of micron-sized particles of iron oxide (MPIOs) is useful for MRI imaging of endogenous neurogenesis. However, it is unverified in imaging endogenous neural cell migration to injury. In a rat model of stroke, we found cell independent accumulation of MPIOs at the stroke site, likely due to leaking from the blood or CSF. Strategies aimed at pre-labeling the stem cell niche, prior to the induction of stroke, reduced cell independent MPIOs accumulation, but failed to abolish it. METHODS: ET1 induced focal cortical ischemia was induced with 600 pmol ET1 in 3 µL saline, infused into the somatosensory cortex (S1) of rats over the course of 10 mins. Saline control was infused into the contra-lateral hemisphere. In vivo labeling of endogenous neural progenitor cells was performed by stereotactically injecting 20 µL 0.86 µm green fluorescent-MPIOs into the third ventricle. Variations in ET1 and MPIO injections were performed with some animals receiving MPIOs immediately following ET1 (n=5), some animals seven days following ET1 (n=20) and some animals two days before ET1 (n=8). MRI was performed at 11.7T. To confirm stroke, T2 and ADC mapping experiments were performed. To identify MPIO labeled cells, T2* weighted MRI was performed at 100 µm isotropic voxel size. Gd-enhanced MRI probed BBB integrity. After the last MRI session, brain histology was performed: Nissl staining for general brain structure; microglia staining with anti-IBA1. RESULTS and DISCUSSION: We sought to track MPIO-labeled endogenous neuroblasts migrating from the SVZ to the stroke area, on a time scale of several days if carried by neuroblasts. Focal cortical stroke was confirmed in vivo by T2 and ADC maps, foot fault tests and eventual Nissl staining on brain sections. Dark contrast was detected rimming the infarct areas as early as 1 day post injection, suggesting cell independent accumulation of particles. To verify this, particles were injected at different time points post stroke, and scanned immediately. Immediately post injection of particles, dark contrast was observed at the rim of both ET1/saline-control infusion sites (Figure 1B). Immunohistochemistry revealed MPIOs within the injured site in association with IBA1+ microglia (Figure 1C). These results suggested cell independent leakage of particles at the site of injury. Indeed, leakage of Gd-DTPA was observed at both 1 and 14 days post ET1 infusion, demonstrating impaired BBB (Figure 1D). To determine whether cell independent delivery of particles could be prevented by pre-labeling the NPC population, MPIOs were injected 2 days prior to stroke onset. MRI revealed normal RMS migration at 1 day and 2 days post injection of MPIOs as well as clear and homogenous signal intensity at the cortex. Immediately after infusion of ET1 and saline-control, T2* weighted MRI revealed very little dark contrast around the injured sites with pre-labeling reducing the extent of leakage of particles at the stroke site over 5-fold (Figure 1E). This method should be carefully evaluated for use in any disease model that involves breakdown of BBB.

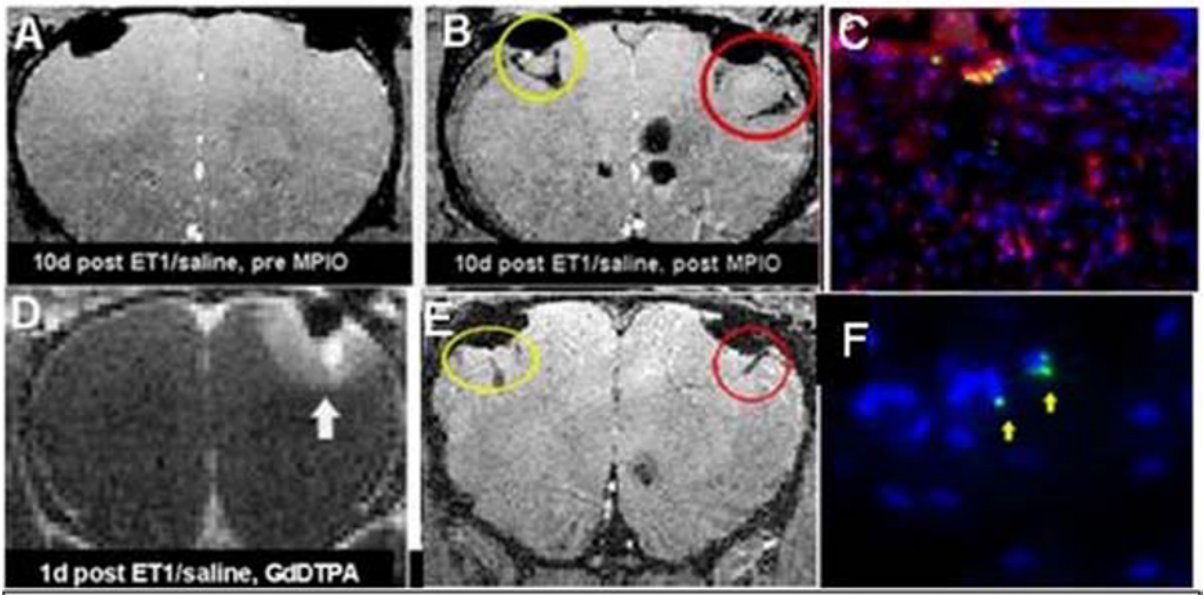

Figure 1: (A) T_2* weighted MRI 10 days post ET1 infusion, prior to MPIOs injection and (B) immediately post MPIOs injection. Red circles, ET1 infused cortex; yellow circles, saline-control infused cortex. C) IHC of injury site immediately post MPIO injection. Green, MPIOs; Red, IBA1+ cells; Blue, Dapi. (D) Gd-DTPA enhanced T_1 weighted MRI 1 day post ET1 infusion. White arrows point to bright contrast due to leakage of Gd-DTPA. E) T_2* weighted MRI 2 days post MPIOs injection, immediately after ET1 infusion. F) IHC of injury site immediately post ET1 infusion, showing instantaneous arrival of free beads into injury. Green, MPIOs; Blue, Dapi.

Disclosure of author financial interest or relationships:
E.M. Shapiro, None; **D. Granot**, None.

Presentation Number **P 224**
Poster Session 2
September 19, 2013 / 15:15-15:15 / Room: Exhibit Hall B

Selective transport of (R)-[11C]verapamil by murine and human P-glycoprotein at the blood-brain barrier

Jens P. Bankstahl[1,3], *Thomas Wanek*[2], *Kerstin Römermann*[3], *Marion Bankstahl*[3], *Maren Fedrowitz*[3], *Markus Mueller*[4], *Wolfgang Loescher*[3], *Claudia Kuntner*[2], *Oliver Langer*[2,4], [1]*Department of Nuclear Medicine, Hannover Medical School, Hannover, Germany;* [2]*Biomedical Systems, Health & Environment Department, AIT Austrian Institute of Technology GmbH, Seibersdorf, Austria;* [3]*Department of Pharmacology, Toxicology and Pharmacy,, University of Veterinary Medicine and Center for Systems Neuroscience, Hannover, Germany;* [4]*Department of Clinical Pharmacology, Medical University of Vienna, Vienna, Austria. Contact e-mail: bankstahl.jens@mh-hannover.de*

The adenosine triphosphate-binding cassette (ABC) transporter P-glycoprotein (Pgp, ABCB1), located at the blood-brain barrier (BBB), restricts cerebral uptake of several drugs by active ATP-driven efflux transport. Positron emission tomography (PET) with the carbon-11 labeled substrate (R)-[11C]verapamil ([11C]VPM) has been frequently used to measure the functional activity of Pgp, either in drug disposition studies or in brain pathologies such as epilepsy, Parkinson's disease or Alzheimer's disease. Aim of this study was to assess the selectivity of VPM in nanomolar concentration relevant for PET experiments among different ABC transporters expressed at the BBB (Pgp; breast cancer resistance protein, BCRP and multidrug resistance protein 1, MRP1). Concentration equilibrium transport assays were performed with [3H]VPM (5 nM) in LLC-PK1 or MDCK-II cell lines expressing murine or human Pgp, murine Bcrp1 or human BCRP, and human MRP1. Paired PET scans were performed with (R)-[11C]VPM in female FVB/N (wild-type), Mrp1(-/-), Mdr1a/b(-/-), Bcrp1(-/-) and Mdr1a/b(-/-)Bcrp1(-/-) mice, before and after complete Pgp inhibition with 15 mg/kg tariquidar (TQD). In vitro experiments showed directed transport of [3H]VPM exclusively in Mdr1a- and MDR1-overexpressing cells which could be inhibited by the Pgp inhibitor TQD (0.5 µM). In PET experiments, before TQD administration, brain-to-blood ratio (Kb,brain) of (R)-[11C]VPM was low in wild-type (1.3±0.1), Mrp1(-/-) (1.4±0.1) and Bcrp1(-/-) mice (1.8±0.1) and high in Mdr1a/b(-/-) (6.9±0.8) and Mdr1a/b(-/-)Bcrp1(-/-) mice (7.9±0.5). After TQD administration, Kb,brain was significantly increased relative to Kb,brain before TQD administration in Pgp-expressing mice (wild-type: 5.0±0.3-fold, Mrp1(-/-): 3.2±0.6-fold, Bcrp1(-/-): 4.3±0.1-fold) but not in Pgp knockout mice (Mdr1a/b(-/-) and Mdr1a/b(-/-)Bcrp1(-/-)). Our data demonstrate that VPM, in nanomolar concentrations, is selectively transported by Pgp and not by MRP1 and BCRP at the BBB, which supports the use of [11C]VPM as PET tracer of cerebral Pgp function.

Disclosure of author financial interest or relationships:
J.P. Bankstahl, None; **T. Wanek**, None; **K. Römermann**, None; **M. Bankstahl**, None; **M. Fedrowitz**, None; **M. Mueller**, None; **W. Loescher**, None; **C. Kuntner**, None; **O. Langer**, None.

Presentation Number **P 225**
Poster Session 2
September 19, 2013 / 15:15-15:15 / Room: Exhibit Hall B

Positron emission tomography (PET) evaluation of a transgenic mouse model expressing human MDR1

Thomas Wanek[1], *Michael Sauberer*[1], *Thomas Filip*[1], *Severin Mairinger*[1,2], *Johann Stanek*[1], *Claudia Kuntner*[1], *Markus Mueller*[3], *Oliver Langer*[1,3], [1]*Health & Environment Department, AIT Austrian Institute of Technology GmbH, Seibersdorf, Austria;* [2]*Department of Medicinal Chemistry, University of Vienna, Vienna, Austria;* [3]*Department of Clinical Pharmacology, Medical University of Vienna, Vienna, Austria. Contact e-mail: thomas.wanek@ait.ac.at*

The adenosine triphosphate-binding cassette (ABC) transporter P-glycoprotein (Pgp, ABCB1) restricts brain distribution of several drugs by active ATP-driven efflux transport which may lead to therapeutic failure of compounds targeting the central nervous system. Earliest possible prediction of Pgp efflux is important in drug development and is frequently achieved by studying drug brain distribution in rodent knockout models. However, quantitative proteomics data suggest that species differences in substrate specificity as well as in expression levels between human Pgp (MDR1) and rodent Pgp (mdr1a/b) may exist. Recently, a transgenic mouse model in which the rodent *mdr1a/b* gene is replaced by the human *MDR1* gene has been developed. In this study, we compared brain distribution of the radiolabeled Pgp substrate (*R*)-[^{11}C]verapamil in this new mouse model with their wild-type counterparts. **METHODS** (*R*)-[^{11}C]Verapamil and *T1*-weighted gradient echo MR images of female C57Bl/6 mice and humanized MDR1 mice (B6-Abcb1a$^{tm1767(ABCB1)Arte}$-Abcb1b$^{tm1767(ABCB1)Arte}$) were acquired two hours after intravenous injection of different doses (0-20 mg/kg, n=4-6 per dose group) of the Pgp inhibitor tariquidar (TQD, XR9576). At the end of the PET data acquisition period, animals were sacrificed, blood, plasma and whole brain collected and measured for total radioactivity in a gamma-counter. In addition, metabolism and plasma protein binding of (*R*)-[^{11}C]verapamil was assessed in both mouse types. Plasma concentration levels of TQD were measured with LC-MS/MS. Brain-to-plasma concentration ratios ($K_{p,brain}$) were calculated by dividing radioactivity concentrations in whole brain by radioactivity concentrations in plasma at 60 min after (*R*)-[^{11}C]verapamil injection. $K_{p,brain}$ values were plotted against TQD plasma concentrations and sigmoidal concentration-response curves were fitted using the Hill function. **RESULTS** In C57Bl/6 mice, $K_{p,brain}$ increased dose-dependently from 0.43±0.05 at baseline to 2.13±0.15 for the 15 mg/kg TQD group. Data obtained in humanized MDR1 mice showed greater variability and $K_{p,brain}$ increased from 1.28±0.28 at baseline to 1.87±0.11 for the 15 mg/kg TQD group. Blood radioactivity levels of (*R*)-[^{11}C]verapamil and TQD plasma concentration levels were comparable in both mouse types. In addition, no differences in radiolabeled metabolites and plasma protein binding of (*R*)-[^{11}C]verapamil between C57Bl/6 and humanized MDR1 mice were observed. Half-maximum effect concentrations (EC_{50}) of TQD were 842 ng/mL (Hill slope=4.1, R^2=0.96) in wild-type mice and 513 ng/mL (Hill slope=2.1, R^2=0.73) in humanized MDR1 mice. **CONCLUSION** Higher baseline $K_{p,brain}$ values of (*R*)-[^{11}C]verapamil in humanized MDR1 compared to wild-type mice points to lower function/expression of Pgp in humanized mice. A dose-dependent increase of $K_{p,brain}$ after tariquidar administration in humanized MDR1 mice suggests presence of functional Pgp at their blood-brain barrier. In order to further evaluate this transgenic mouse model, quantitative data on MDR1 expression levels is required.

Disclosure of author financial interest or relationships:
T. Wanek, None; **M. Sauberer**, None; **T. Filip**, None; **S. Mairinger**, None; **J. Stanek**, None; **C. Kuntner**, None; **M. Mueller**, None; **O. Langer**, None.

Presentation Number **P 226**
Poster Session 2
September 19, 2013 / 15:15-15:15 / Room: Exhibit Hall B

Evaluation of ethinyl estradiol (EE-3-SO_4) in a rat model of traumatic brain injury using MRI and PET/CT

Guihua Zhai[1], *Ahmar Ayub*[2,3], *Hyunki Kim*[1], *Sharon Samuel*[1], *Irshad H. Chaudry*[2,3], [1]*Dept. of Radiology, UAB, Birmingham, AL, USA;* [2]*Dept. of Surgery, UAB, Birmingham, AL, USA;* [3]*Center for surgical research, UAB, Birmingham, AL, USA. Contact e-mail: Guihua.Zhai@ccc.uab.edu*

Purpose: To assess the therapeutic potential of EE-3-SO_4 in a rat model of traumatic brain injury (TBI) using diffusion-tensor imaging (DTI), T2 mapping of the brain, FDG-PET/CT, and physiological parameters measurement. Methods: Six groups (n=4-6/group) of rats underwent craniotomy. TBI was induced by lateral fluid percussion in groups 1, 2, 4 and 5 at 24 hours after surgery. At 1 hour after TBI, EE-3-SO_4 (1mg/kg) was injected into groups 1 and 4 (treated group); saline was injected into groups 2 and 5 (vehicle group) and groups 3 and 6 (sham group). DTI, T2 mapping and FDG-PET/CT imaging were performed in groups 1-3 at 24 hours post-treatment. Fractional anisotropy (FA) maps, T2 maps and relative SUV (ratio of SUV of the injured region to that of central region) were calculated. Intracranial pressure (ICP), cerebral perfusion pressure (CPP), and brain tissue oxygen partial pressure (pbtO2) were measured in groups 4-6 at 24 hours after treatment, and the recording lasted 120 minutes. One-way analysis of variance was employed to determine statistical differences among groups. Results: The body weights in groups 1-3 were 334.2±4.8g (mean±SE), 337.4±6.5g, 330.0±8.6g, respectively, before TBI, decreasing by 3.6%, 6.6% and 0.3%, respectively, at 24 hours after treatment. The body weight was not significantly different among groups on both days; the body weight loss was significantly different ($p<0.05$) between the groups after TBI. The contralateral FA in groups 1-3 were 0.493±0.012, 0.488±0.013, 0.488±0.013, respectively, without significant differences among groups. The ratios of ipsilateral FA/contralateral FA values in groups 1-3 were 90.8±1.39%, 81.9±2.64%, and 101.05±0.59%, respectively; the values in vehicle group were significantly lower than those in treated group ($p=0.024$) and sham group ($p=0.001$), and the values in treated group were significantly different from those in sham group ($p<0.001$). The edema sizes in vehicle group (63.5±4.0 mm^3) were significantly larger than those in treated group (25.3±3.4 mm^3, $p<0.001$), while no edema was found in sham group. The relative SUV in groups 1-3 were 88.9±0.6%, 84.1±0.8%, and 99.5±1.0%, respectively; the values in vehicle group were significantly lower than those in treated group ($p=0.002$) and sham group ($p<0.001$), and the values in treated group were significantly lower than those in sham group ($p<0.05$). ICPs of groups 4-6 were 9.2±0.7, 16.0±0.4 and 4.0±0.4mmHg, respectively, while CPPs were 71.6±1.8, 63.8±1.3 and 81.3±1.5mmHg, respectively, and pbtO2 values were 35.4±3.4, 18.0±4.1 and 49.4±1.7mmHg, respectively; all values were significantly different ($p<0.05$) between groups. Conclusion: Independent multimodal imaging and physiological parameters confirmed the salutary effect of EE-3-SO_4 following TBI, significantly increasing the glycolysis of brain cells, reducing edema, and alleviating diffuse axonal injury within 24 hours of treatment.

Disclosure of author financial interest or relationships:
G. Zhai, None; **A. Ayub**, None; **H. Kim**, None; **S. Samuel**, None; **I.H. Chaudry**, None.

Presentation Number **P 227**
Poster Session 2
September 19, 2013 / 15:15-15:15 / Room: Exhibit Hall B

Protective effects of acetyl L-carnitine on inhalation anesthetic-induced neuronal damage in the nonhuman primate

Xuan Zhang[1], *Shuliang Liu*[1], *Merle G. Paule*[1], *Glenn D. Newport*[1], *Ralph Callicott*[1], *Marc Berridge*[2], *Scott M. Apana*[2], *William Slikker*[1], *Cheng Wang*[1], [1]*NCTR/FDA, Jefferson, AR, USA;* [2]*3D Imaging LCC, Little Rock, AR, USA. Contact e-mail: xuan.zhang@fda.hhs.gov*

The inhalation anesthetics nitrous oxide (N2O) and isoflurane (ISO) are commonly used for general anesthesia in human infants. Combined exposures to N20 and ISO are known to cause abnormal apoptotic cell death (neurotoxicity) in pediatric animal models. Acetyl-L-carnitine (ALC), an anti-oxidant dietary supplement, has been reported to minimize neuronal damage in some models of neurotoxicity. MicroPET/CT imaging is capable of detecting and localizing changes in cellular markers of brain damage associated with developmental exposures to general anesthetics. By monitoring changes in glial activation, thought to be a marker of neuroinflammation, it should be possible to determine the intensity, duration and location of neuronal damage associated with exposure to general anesthetics. Here we assessed the uptake of 18F-labeled fluoroethoxybenzyl-N-(4-phenoxypyridin-3-yl) acetamide (FEPPA), a ligand for peripheral benzodiazepine receptors on activated glial cells. On postnatal day (PND) 5, rhesus monkeys (4/group) were exposed to a mixture of 70% N2O, 29% oxygen plus 1% ISO, or ALC (100mg/kg given i.p.) plus this mixture for 8 hours; control monkeys with and without ALC were exposed to room air only. [18F]-FEPPA was injected intravenously and microPET/CT images were obtained one day and one and three weeks after anesthetic exposure. One day after anesthetic exposure the uptake of FEPPA was significantly increased only in the temporal lobe and one week after exposure uptake was significantly increased in only the frontal lobe. No significant differences in uptake were seen in any area after 3 weeks. Co-administration of ALC effectively blocked the increase in FEPPA uptake in both the temporal and frontal lobes. These findings suggest that microPET/CT imaging of FEPPA uptake may be useful for monitoring the time-course and location of adverse neural events that are associated with developmental exposures to general anesthetics. In addition, ALC appears to be capable of protecting against at least some of the adverse effects associated with such exposures.

Disclosure of author financial interest or relationships:
X. Zhang, None; **S. Liu**, None; **M.G. Paule**, None; **G.D. Newport**, None; **R. Callicott**, None; **M. Berridge**, None; **S.M. Apana**, None; **W. Slikker**, None; **C. Wang**, None.

Presentation Number **P 228**
Poster Session 2
September 19, 2013 / 15:15-15:15 / Room: Exhibit Hall B

In vivo fluorescence assessment of lymph nodes and peritoneum by confocal endomicroscopy: new insights to speed up the transfer into cancer surgery

Muriel Abbaci[1], *Peggy Dartigues*[2], *Monique Fabre*[2], *Odile Casiraghi*[2], *Matthieu Cazaux*[3], *Valérie Rouffiac*[1], *Mélanie Polrot*[4], *Frederic De Leeuw*[1], *Corinne Laplace-Builhé*[1], [1]*Imaging and Cytometry Platform, IR4M, IRCIV, Institut Gustave Roussy, Villejuif, France;* [2]*Department of Pathology, Institut Gustave Roussy, Villejuif, France;* [3]*Mauna Kea Technologies, Paris, France;* [4]*Preclinical Evaluation Platform, Institut Gustave Roussy, Villejuif, France. Contact e-mail: muriel.abbaci@igr.fr*

Histological analysis of tissues is essential for cancer diagnosis and the therapeutic choices. Recently, non-invasive optical technologies based on the miniaturization of imaging systems have been proposed to achieve in vivo human "optical biopsies". Among them, probe-based confocal laser endomicroscopy (pCLE) provides dynamic images of tissue architecture and cellular details. Although they show excellent capability to produce high resolution images, one of the current limitations of these technologies for dissemination into clinic is the lack of fluorescent contrast agent already approved for use in humans. Fluorescein is the only agent used in clinical pCLE imaging, but its rapid clearance in tissue severely limits the exploration time to few minutes, after which the image quality deteriorates significantly. To overcome this limitation, we explored the potential of two already approved agents; Patent Blue (BP) and Indocyanine Green (ICG), to produce endomicroscopic images that can be interpreted by the pathologists. 3 rabbits were included in the feasibility study. Lymph nodes mapping was performed using a combination of BP and ICG injected subcutaneously in the paw of the animals. Peritoneal areas were imaged after topical application of either BP or ICG. Images were achieved using pCLE (CellVizio®, Mauna Kea Tech.) with new optical probes specifically designed for either intratissular or subsurface imaging. Resulting pCLE images allowed the pathologists to discerned inflammatory cells with homogeneous distribution in lymph nodes. Highly detailed information was also described by the pathologists on the peritoneum layers as mesothelium, connective tissue and fat cells, with both dyes. Although these two fluorescent dyes require a specific far red and near infrared set up, they offer the great advantage, over Fluorescein, to provide standardized imaging sessions for at least 30 min due to their high fluorescence stability in tissues and their low sensitivity to environmental factors such as pH, which in the case of Fluorescein can significantly affect image quality. They also highlight some tissue features not shown with Fluorescein such as cell nuclei. We believe that these two contrast agents already validated for humans could open new opportunities for optical biopsies in patients until the medical regulatory agencies can approve new targeted fluorescent contrast agents.

Disclosure of author financial interest or relationships:
M. Abbaci, None; **P. Dartigues**, None; **M. Fabre**, None; **O. Casiraghi**, None; **M. Cazaux**, None; **V. Rouffiac**, None; **M. Polrot**, None; **F. De Leeuw**, None; **C. Laplace-Builhé**, None.

Presentation Number **P 229**
Poster Session 2
September 19, 2013 / 15:15-15:15 / Room: Exhibit Hall B

Comparison of imaging and molecular biomarkers in glioma

Ali S. Arbab[1,2], *Adarsh Shankar*[1], *Thaiz F. Borin*[1], *Nadimpalli Ravi S Varma*[1], *Asm Iskander*[1], *Meser M. Ali*[1], *Tom Mikkelsen*[3], *Hassan Bagher-Ebadian*[1], *Austin M. Guo*[6], *Stephen L. Brown*[4], *Guillermo Scicli*[1], *James R. Ewing*[5], [1]*Cellular and Molecular Imaging Laboratory, Henry Ford Hospital, Detroit, MI, USA;* [2]*Radiology, WSUSOM, Detroit, MI, USA;* [3]*Neurosurgery, Henry Ford Hospital, Detroit, MI, USA;* [4]*Radiation Oncology, Henry Ford Hospital, Detroit, MI, USA;* [5]*Neurology, Henry Ford Hospital, Detroit, MI, USA;* [6]*Pharmacolgy, NYMC, Valhalla, NY, USA. Contact e-mail: saali@rad.hfh.edu*

Background & Purposes: Glioblastoma (GBM) is hypervascular tumor and anti-angiogenic therapy (AAT) has widely been given as an adjuvant. However, recent reports indicate the activation of different alternative angiogenic factors during AAT and the tumor becomes resistant. Expression of different pro-angiogenic factors with or without AAT can be determined from the tumor extracts. We have recently custom designed protein array kit to determine 22 different pro-angiogenic and growth factors for tumors. We call them molecular biomarkers. Magnetic resonance imaging (MRI) has been used to determine different vascular parameters in GBM. These parameters, such as Ktrans (forward transfer constant), Kb (backward transfer constant), Vp (plasma volume) and Ve (interstitial space volume) can be called imaging biomarkers. The purpose of this study was to compare and correlate the molecular and imaging biomarkers of GBM with or without different AAT (such as vatalanib and HET0016 alone or in combination). Materials and Methods: Nude rats bearing human GBM underwent early (starting from day 0 of tumor implantation) and late (starting from day 8 of tumor implantation) treatments with different AAT. Total of 27 nude rats bearing orthotopic GBM (U251 cells) underwent MRI and their brains were collected and snapped frozen. All vascular parameters were determined for all the tumors. Proteins were extracted from the tumors. Different angiogenic and growth factors (Angiogenin, Angiostatin, Ang1/2, Tie1/2, G-CSF, RANTES, SDF-1, HIF-1, MMP-2/9, EGF, EGFR, VEGF-A, VEGF-C, VEGFR2/3, bFGF, PDGFaa, PDFGRa, and IGF1) were determined by protein array and ELISA. Simple regression analysis was performed between each of the vascular parameters and all molecular biomarkers individually to determine significant correlation. A p-value of <0.05 was considered significant. Results: All parametric values; Vp, Ktrans, Kb, and Ve were lower in the animals that were treated from day 0, compared to the animals that were treated from day 8. Vp showed significant correlation only with HIF-1α. Ktrans showed significant correlation with angiogenin and border line correlation with MMP-2 (negative correlation), EGFR, and RANTES. Kb showed significant negative correlation with MMP-2 and borderline positive correlation with MMP-9, EGFR, and angiogenin. Ve showed significant correlation with angiogenin, EGFR, G-CSF, VEGF-A, and RANTES. Ve also showed border line correlation with VEGF-C, bFGF, EGF, and SDF-1α. Conclusion: Expression of different molecular biomarkers was dependent on the timing of treatments. In vivo imaging biomarkers can predict the expression of different molecular biomarkers following AAT and determine the emergence of resistance to AAT.

Disclosure of author financial interest or relationships:
A.S. Arbab, None; **A. Shankar**, None; **T.F. Borin**, None; **N. Varma**, None; **A. Iskander**, None; **M.M. Ali**, None; **T. Mikkelsen**, None; **H. Bagher-Ebadian**, None; **A.M. Guo**, None; **S.L. Brown**, None; **G. Scicli**, None; **J.R. Ewing**, None.

Presentation Number **P 230**
Poster Session 2
September 19, 2013 / 15:15-15:15 / Room: Exhibit Hall B

Synthesis and evaluation of panitumumab-NIR dye conjugate as an immuno-fluorescence probe for HER1 expression in cancers

Sibaprasad Bhattacharyya[1], *Nimit Patel*[2], *Ling Wei*[1], *Lisa Riffle*[2], *Joseph Kalen*[2], *G. C. Hill*[3], *Paula M. Jacobs*[4], *Kurt R. Zinn*[5], *Eben L. Rosenthal*[5], [1]*ADRD, SAIC, Frederick National Laboratory for Cancer Research (FNLCR), Frederick, MD, USA;* [2]*SAIP/LASP, SAIC-Frederick, Inc., FNLCR, Frederick, MD, USA;* [3]*CMRP, SAIC-Frederick, FNLCR, Rockville, MD, USA;* [4]*DCTD, NCI, Bethesda, MD, USA;* [5]*School of Medicine, University of Alabama at Birmingham, Birmingham, AL, USA. Contact e-mail: bhattacharyyas2@mail.nih.gov*

Panitumumab (Vectibix®) is a fully human antibody (mAb) approved by the FDA for the treatment of HER1- expressing colorectal cancer. This study involves the noninvasive preclinical assessment of HER1 expression in cancer by fluorescence imaging in conjunction with Near-infrared (NIR) dye labeled panitumumab. Panitumumab was chemically conjugated to NIR dye (Li-COR 800CW) at a well-defined and limited substitution ratio (1mAb:1-2 dye molecules) for the characterization of fluorescence signals. In a typical conjugation reaction, 10 mg of panitumumab was incubated with 2.3 equivalents of aqueous NIR-dye solution at 20 °C for 2 hours. Conjugate was purified by size-exclusion chromatography using Sephadex G 25 column. After purification the yield and purity of the conjugate was 80±5% and 95±2% respectively (n= 6). Female athymic nude xenograft tumor bearing mice (n=5 per tumor model) with very low (BT-474), moderate (MDA-MB-231), and high (MDA-MB-468) HER1-expression levels were administered NIR-dye-panitumumab formulations (100 µg of mAb in 100 µL of 0.9% saline) via IV tail-vein injection. Animal imaging and biodistribution experiments were conducted on the FMT 2500 (PerkinElmer) fluorescence scanner at 24, 48, 72, 96, and 144 hours post injection. The relative uptake of the panitumumab-dye for the MDA-MB-231 and BT-474 tumors was 72% and 56% of the MDA-MB-468 (high HER1 expression) signal, respectively and resulted in a good correlation between HER1-expression and tumor uptake. Comparing the biodistribution uptake of panitumumab-NIR dye with panitumumab-[89Zr] for the solid organs (kidney, heart, lung, muscle, and brain) resulted in a good correlation at all time-points (0.99, 0.73, 0.86, 0.89, and 0.89), respectively. Figure 01shows the 2D epi-fluorescence images (FMT2500, PerkinElmer) of panitumumab-NIRdye at various time points post injection for HER1-expressing tumors (MDA-MB-468, MDA-MB-231, and BT-474). Panitumumab-NIR dye conjugate was synthesized with very high yield and purity. Immuno-fluorescence images proved the potential of this conjugate to be used as an effective probe for HER1- expression. Funded by NCI/NIH, Contract No. HHSN261200800001E References: 1) Heath CH, Deep NL, Sweeny L, Zinn KR, Rosenthal EL. Ann Surg Oncol. 2012 Nov;19(12):3879-87 2) Bhattacharyya S, Krudziel K, Wei L, Riffle L, Kaur G, Hill GC, Jacobs PM, Tatum J, Doroshow J, Joseph K. Nuc. Med. Biol. 2013, in press.

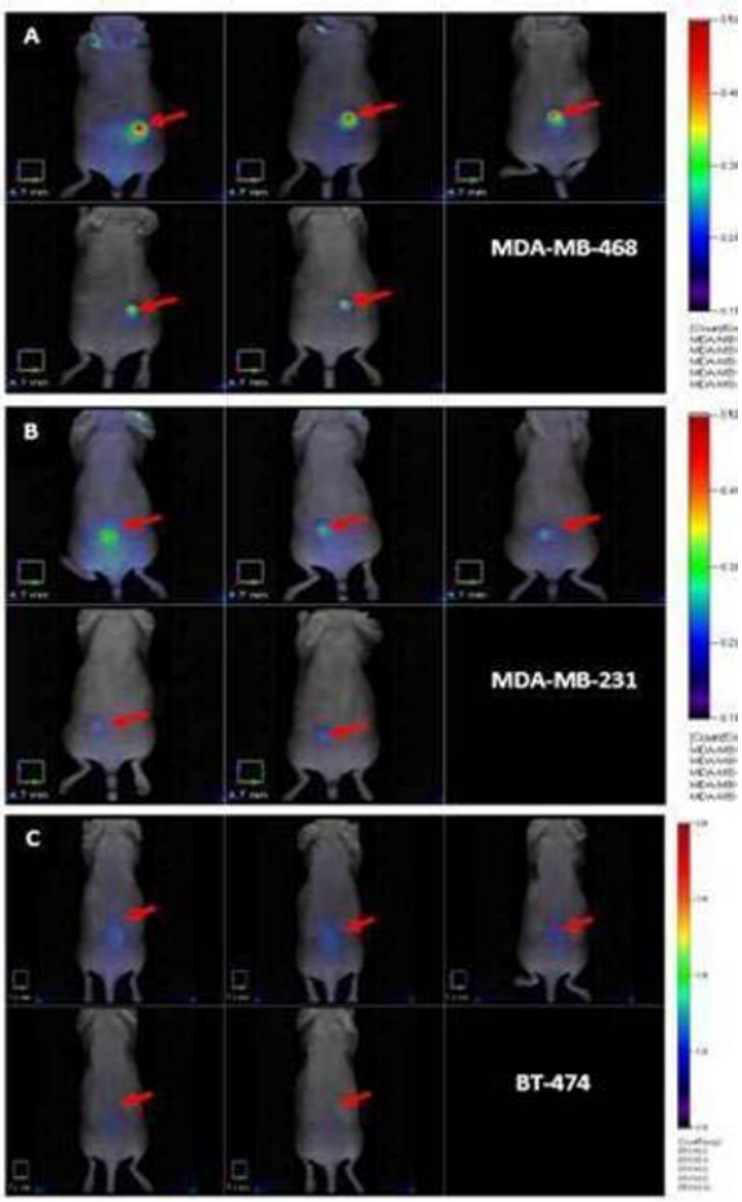

Figure 01

Disclosure of author financial interest or relationships:
S. Bhattacharyya, None; **N. Patel**, None; **L. Wei**, None; **L. Riffle**, None; **J. Kalen**, None; **G.C. Hill**, Manzanita Pharmaceuticals, Consultant; **P.M. Jacobs**, None; **K.R. Zinn**, None; **E.L. Rosenthal**, None.

Presentation Number **P 231**
Poster Session 2
September 19, 2013 / 15:15-15:15 / Room: Exhibit Hall B

[18F]FMAU as a PET Imaging Agent to Evaluate Response to Cisplatin in Pre-Clinical Lung Cancer Studies

Stephanie Blocker[1], *Kirk A. Douglas*[2], *Lisa A. Polin*[2], *Jawana Lawhorn-Crews*[2], *Thomas J. Mangner*[3], *Anthony F. Shields*[2], [1]*Cancer Biology Graduate Program, Wayne State University, Detroit, MI, USA;* [2]*Oncology, Wayne State University, Detroit, MI, USA;* [3]*Radiology, Wayne State University, Detroit, MI, USA. Contact e-mail: sblocker@med.wayne.edu*

Introduction [18F]FMAU [(1-(2′-deoxy-2′-fluoro-β-D-arabinofuranosyl)thymine] is a pyrimidine analog tracer being studied for tumor imaging with positron emission tomography (PET). Natural thymidine is incorporated in nuclear and mitochondrial DNA after phosphorylation by thymidine kinase 1 (TK1) and TK2, respectively. Thus, it has been suggested that [18F]FMAU may function as a marker of cell proliferation and DNA synthesis. However, [18F]FMAU is incorporated into mitochondrial DNA via TK2, but not nuclear DNA. Therefore, [18F]FMAU retention most likely reflects a different aspect of tumor cell biochemistry, such as metabolic stress or cell viability. Classifying the functional properties of [18F]FMAU may clarify the tumor biology reflected in these PET scans. This insight could provide dynamic profiles of tumors over time, aiding physicians in treatment selection. Our objective was to evaluate changes in FMAU retention shortly after cytotoxic drug treatment of human non-small cell lung cancer models. Methods We studied two non-small cell lung cancer cell lines, H522 (cisplatin resistant) and H460 (cisplatin sensitive). Initially, we exposed plated cells to different cisplatin concentrations for 24 hours, followed by labeling with [14C]-FMAU. Cells were washed, subjected to liquid scintillation, and radioactivity was normalized to cell counts. In vivo studies were done in CD-1 nu/nu mice inoculated with both H522 and H460 cells in either flank. Established tumors were allowed to grow to ~0.5g. Treated (n=14) and untreated mice (n=14) were scanned at baseline and after 24 hours via microPET with [18F]FMAU. Changes in [18F]FMAU uptake from scan 1 to scan 2 were compared between treated mice and controls. We also searched for differences between the two tumor types for early evidence of drug response. Untreated mice also served to verify scan reproducibility. Scans were analyzed with PMOD (Zurich, Switzerland) imaging software and SUVs were generated for tumor and shoulder (background) tissues, as well as tumor:background SUV ratios. After scan 2 mice were sacrificed and tissues were subjected to gamma counting for dosimetry. Results In vitro, both cell lines exhibited reduction in FMAU uptake following treatment, with mean decreases in retention ranging from -16.5% to -71.8% when compared to untreated cells. Mouse scan data also shows decreases in FMAU uptake 24 hours after treatment. In vivo, a statistically significant decrease in uptake was seen in the cisplatin-sensitive H460 tumors ($p=0.009$), where no significant difference was observed in the H522 tumors ($p=0.129$). Conclusions While our previous work in cell lines demonstrated early increases in FMAU uptake after relatively mild cell stress (e.g. nutritional deprivation), more rigorous treatment with chemotherapy caused declines in FMAU uptake. Our findings suggest that [18F]FMAU may provide an early measure of cell viability after chemotherapy.

Disclosure of author financial interest or relationships:
S. Blocker, None; **K.A. Douglas**, None; **L.A. Polin**, None; **J. Lawhorn-Crews**, None; **T.J. Mangner**, None; **A.F. Shields**, None.

Presentation Number **P 232**
Poster Session 2
September 19, 2013 / 15:15-15:15 / Room: Exhibit Hall B

From rapid visualization of subcutaneous tumors to the delineation of primary orthotopic tongue tumors and cervical lymph node metastases: a promising anti-EGFR nanobody for fluorescence guided surgery

Pieter B.A.A van Driel[1], Sabrina Oliveira[2,3], Joost van der Vorst[4], Floris P. Verbeek[4], **Martin C. Boonstra**[4]*, Stijn Keereweer[5], Alexander Vahrmeijer[4], Paul M. van Bergen en Henegouwen[2], Clemens Lowik[1], [1]Radiology and Molecular Imaging, Leiden University Medical Center, Leiden, Netherlands; [2]Biology, Utrecht University, Utrecht, Netherlands; [3]Pathology, University Medical Centre Utrecht, Utrecht, Netherlands; [4]Surgery, Leiden University Medical Center, Leiden, Netherlands; [5]Otorhinolaryngology- Head and Neck Surgery, Erasmus Medical Center, Rotterdam, Netherlands. Contact e-mail: m.c.boonstra@lumc.nl*

Introduction The epidermal growth factor receptor (EGFR) is overexpressed in many human cancers, therefore, EGFR is a relevant tumor target for molecular imaging. Although many monoclonal antibodies (mAbs) have been used to target EGFR, their characteristic long half-life in the bloodstream has encouraged the development of smaller agents. Recently, we have developed a near-infrared fluorescent nanobody targeting EGFR for optical molecular imaging [2]. Although smaller than mAbs (15 kDa, instead of 150 kDa), nanobodies can bind very specifically and with high affinities to their targets. This study presents the pre-clinical evaluation of an anti-EGFR nanobody 7D12 for optical imaging of subcutaneous tumors and, subsequently, for delineation of primary orthotopic oral squamous cell carcinomas (OSCC) in intraoperative imaging. Methods The anti-EGFR nanobody 7D12 and the control non-specific nanobody R2 were produced and conjugated to the near-infrared fluorophore IRDye800CW-NHS (IR, LI-COR Biosciences). Nude mice bearing A431 tumor xenografts at the hind legs were intravenously (i.v.) injected with 7D12-IR, R2-IR, or cetuximab-IR. Mice were imaged at several time points post injection (p.i.) with the IVIS Lumina. In subsequent study, OSC-19-luc2-cGFP cells were orthotopically injected in the tip of the tongue of nude mice. The size of the primary tumor and cervical lymph node metastases were followed by bioluminescence. 7D12-IR, R2-IR and IR were i.v. injected and fluorescence images were acquired using the IVIS spectrum and FLARE intraoperative system. Results A431 subcutaneous tumors were visible 30min after the injection of 7D12-IR, with best images obtained 2h p.i., whereas the negative control R2-IR did not accumulate at the tumors. Cetuximab-IR needed at least 24h p.i. for adequate delineation of tumors. With the orthotopic model, only 7D12-IR was clearly observed allowing the delineation of primary tumors and microscopic cervical metastases using the intraoperative FLARE system. In both models, tumor sections presented a tumor specific and homogeneous distribution of 7D12-IR. Conclusions Altogether, this anti-EGFR nanobody conjugated to the NIR fluorophore has excellent properties for rapid, non-invasive optical imaging. Importantly, results could also be obtained in the intraoperative context, were delineation of oropharyngeal or OSCC during surgery may improve radical resections, increasing patients' survival rates.

Disclosure of author financial interest or relationships:
P. van Driel, None; **S. Oliveira**, None; **J. van der Vorst**, None; **F.P. Verbeek**, None; **M. Boonstra**, None; **S. Keereweer**, None; **A. Vahrmeijer**, None; **P.M. van Bergen en Henegouwen**, None; **C. Lowik**, None.

Presentation Number **P 233**
Poster Session 2
September 19, 2013 / 15:15-15:15 / Room: Exhibit Hall B

Detection of Breast Cancer Metastasis using SPECT images

Thaiz F. Borin[2,1], *Debora A. Zuccari*[2], *Asm Iskander*[1], *Nadimpalli Ravi S Varma*[1], *Adarsh Shankar*[1], *Ali S. Arbab*[1,3], [1]*Radiology, Henry Ford Hospital, Detroit, MI, USA;* [2]*Molecular Biology, Faculdade de Medicina de Sao Jose do Rio Preto - FAMERP, Sao Jose do Rio Preto, Brazil;* [3]*Radiology, Wayne State University of Medicine School, Detroit, MI, USA. Contact e-mail: thaizb@rad.hfh.edu*

Introduction: Breast cancer represents the most common cancer among women with a high mortality rate mainly due to the intense tumor growth and metastatic potential. Earliest metastatic sites of breast cancer are bone, lung, pleura and liver. There are less frequently brain and adrenal metastasis. Most of the animal studies of breast cancer are done by developing tumor subcutaneously or into mammary pad. Lung or bone metastatic animal models are lacking and there has not been any systematic investigation to determine the progression of metatasis by in vivo imaging following treatments. The purposes of this study were to develop lung and bone metastasis in animals by human breast cancer cell line (MDA-MB-231), follow the metastasis development by single photon emission computed tomography (SPECT) and deternmine the effect of various agents on the development of metastatsis by SPECT. Materials & Methods: To develop bone metastasis the breast cancer MDA-MB-231 cells (2x105) suspended in 200µL sterile PBS were injected into left ventricle with a 29-gauge needle under anesthesia with Ketamine/Xylazine (100/15mg/kg) and to develop lung metastasis the same amount of cells were injected into animals via tail vein. SPECT images were obtained with Tc-99m-tetrafosmin and Tc-99m-MDP to determine lung and bone metastasis, respectively, on days 21 and 49 following administration of cancer cells. Animals that did not receive any cancer cell was considered negative control (n=5). Animals that received cancer cell but no treatment were considered positive control (n=10). Groups of metastatic animals received curcumin (n=3), melatonin (n=2) and Rock-1 inhibitor (n=3) starting from the day of cell administration. The SPECT images were acquired with the PRISM 3000 gamma camera modified for studies with laboratory animals and constructed using HiSPECT software (Bioscan). ImageJ was used to multplanar reconstruction and image analysis. The total radioactivity in the lungs or the vertebrae was calculated as the intensity of radioactivity of the lung or vertebrae minus 3 times of standard desviation. The metastases was also evaluated from multiplanar images and confirmed by hematoxylin eosin stain. The results were compared by ANOVA, followed by the Bonferroni test. Results: SPECT images showed multiple foci in the lungs (on Tc-99-tetrofomin images) and in the vertebrae (on Tc-99-MDP images) in metastatic animal models. The number of "hot" spots were significantly higher in animals that were scanned on day 49 compared to that of negative controls and the animals that were scanned on day 21, indicating more developed metastatic foci on later days. Semi quantitative analysis showed significantly lower activity in the lungs and vertebrae in animals that received treatments. Conclusion: IV or IC (intracardiac) injection of MDA-MB-231 cells can develop lung and bone metastasis. SPECT images using Tc-99m-terfosmin or Tc-99m-MDP can determine the development of lung and bone metastasis of breast cancer over time. SPECT images can also determine the effect of different treatments.

Disclosure of author financial interest or relationships:
T.F. Borin, None; **D.A. Zuccari**, None; **A. Iskander**, None; **N. Varma**, None; **A. Shankar**, None; **A.S. Arbab**, None.

Presentation Number **P 234**
Poster Session 2
September 19, 2013 / 15:15-15:15 / Room: Exhibit Hall B

Detection of COX-2 expressing cancers using novel optical imaging agent, fluorocoxib A

Maria Cekanova[1], *Md. Jashim Uddin*[2], *Joseph Bartges*[1], *Kusum Rathore*[1], *Amanda Callens*[1], *Alfred M. Legendre*[1], *Lawrence Marnett*[2], [1]*Small Animal Clinical Sciences, The University of Tennessee, College of Veterinary Medicine, Knoxville, TN, USA;* [2]*Department of Biochemistry, Vanderbilt University, School of Medicine, Nashville, TN, USA. Contact e-mail: mcekanov@utk.edu*

Identification of biomarkers for cancer screening is essential for early detection and for improved prognosis and long-term survival. Conventional scoping is not able to assess cancer in early stages such as carcinoma in situ, but only at advanced stages. Therefore, sensitivity and specificity of conventional scoping of tumors can be significantly improved by using the specific fluorescence agent recognizing tumor cells. The enzyme cyclooxygenase-2 (COX-2) is induced at high levels in tumors, but not in surrounding normal tissues, which makes it an attractive target for molecular imaging of cancer. In this study, we evaluated a newly synthesized optical imaging agent, fluorocoxib A, for detection of spontaneously-occurring canine tumors expressing cyclooxygenase-2 (COX-2) enzyme. The synthesized rhodamine-conjugated analog of indomethacin is a non-steroidal anti-inflammatory drug that selectively targets COX-2 in solid tumors (Figure 1A). None of the current imaging agent is able to provide this valuable information about the expression levels of COX-2 in tissue. Here, we show that fluorocoxib A uptake overlapped with COX-2 expression in primary canine transitional cell carcinomas (K9TCC) and canine oral squamous cell carcinomas (K9OSCC) in vitro (Figure 1B). Using subcutaneously implanted primary K9TCC in athymic mice, we demonstrate specific uptake of fluorocoxib A by COX-2-expressing K9TCC xenograft tumors in vivo (Figure 1C). Fluorocoxib A uptake by COX-2 expressing xenograft tumors was blocked by 70% ($p<0.005$) when pre-treated with the COX-2 selective inhibitor, celecoxib (10 mg/kg), 4 h before intravenous administration of fluorocoxib A (1 mg/kg). Fluorocoxib A was taken up by COX-2-expressing tumors, but not by COX-2 negative human UMUC-3 xenograft tumors. UMUC-3 xenograft tumors with no expression of COX-2 showed no uptake of fluorocoxib A. In addition, fluorocoxib A uptake was evaluated in 5 dogs diagnosed with K9TCC, 1 dog with colorectal adenocarcinoma, and 2 dogs with K9OSCC during cystoscopy/endoscopy procedures in vivo. Fluorocoxib A specifically detected COX-2-expressing canine cancers during cystoscopy/endoscopy in vivo, but was not detected in normal tissues (Figure 1D). Taken together, our findings show that fluorocoxib A selectively bound to COX-2 expressing primary canine cancer cells in vitro, COX-2 expressing K9TCC xenografts tumors in nude mice and heterogeneous canine TCC during cystoscopy in vivo. Our study focused on evaluation of fluorocoxib A in bladder, OSCC and colorectal cancer; however, data obtained from this study can be applied to other types of cancers known to express COX-2 enzyme, such as breast, lung, pancreas, and prostatic carcinomas. Spontaneous cancers in companion animals offer a unique translational model for evaluation of novel imaging and therapeutic agents using primary cancer cells in vitro and in heterogeneous cancers in vivo.

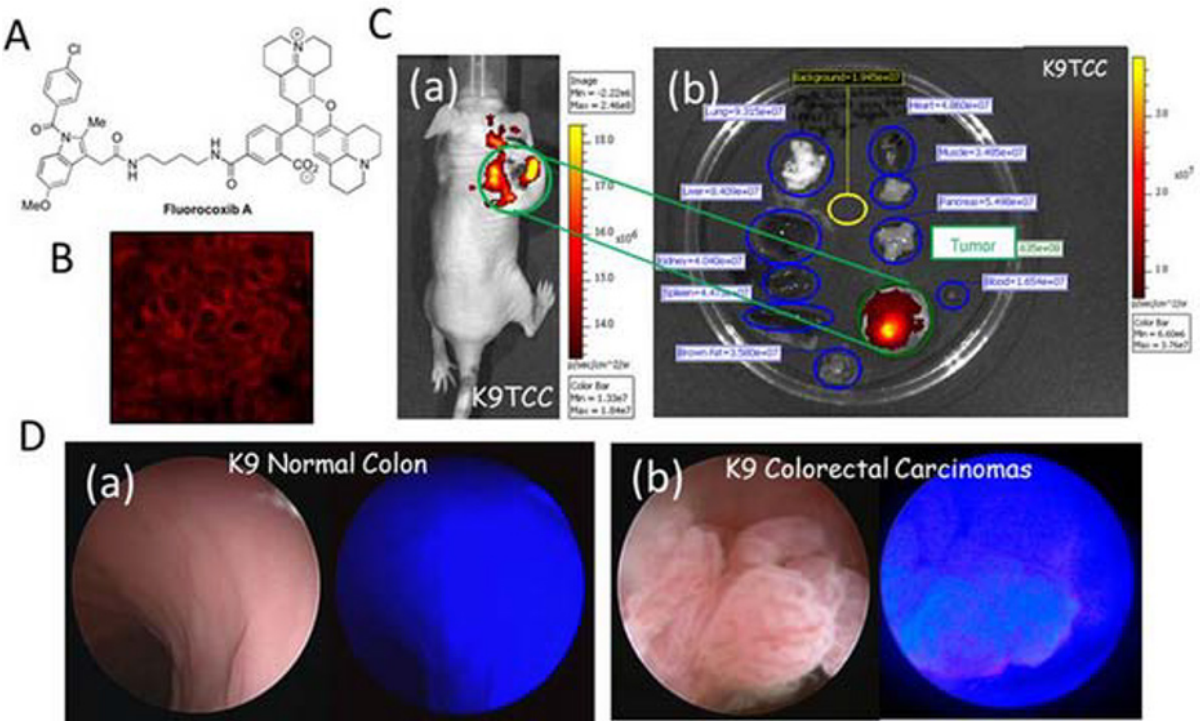

Figure 1: Fluorocoxib A uptake by COX-2-expressing canine cancers in vitro and in vivo. (A) Chemical structure of fluorocoxib A. (B) The uptake of fluorocoxib A by canine transitional cell carcinoma (K9TCC) in vitro. (C) (a) The uptake of fluorocoxib A by subcutaneous K9TCC xenograft tumor (1 mg/kg, 24h post i.v.) in vivo with (b) confirmed specific uptake by tumor as compared to normal tissues ex vivo using IVIS Lumina imaging system. (D) No detection of fluorocoxib A (a) by normal mucosa of canine colon in contrast to (b) specific uptake of fluorocoxib A (1 mg/kg, 24h post i.v.) in canine colorectal adenocarcinoma in vivo during colonoscopy procedure using Karl Storz imaging system.

Disclosure of author financial interest or relationships:

M. Cekanova, None; **M. Uddin**, Perkin Elmer Inc, Other financial or material support; **J. Bartges**, None; **K. Rathore**, None; **A. Callens**, None; **A.M. Legendre**, None; **L. Marnett**, Perkin Elmer, Other financial or material support .

Presentation Number **P 235**
Poster Session 2
September 19, 2013 / 15:15-15:15 / Room: Exhibit Hall B

High Resolution Imaging of Apoptosis within a Murine Lymph Node and Spleen in Living Mice using A Novel Self-assembling Caspase-3 Sensitive Probe

Carmel T. Chan[1], *Adam J. Shuhendler*[1], *Hui-Yen Chang*[1], *Deju Ye*[1], *Ataya Sathirachinda*[1], *Masakatsu Kotsuma*[1], *Christoph C. Miething*[2], *Scott Lowe*[2], *Jianghong Rao*[1], *Sanjiv S. Gambhir*[1], [1]*Radiology, Stanford University School of Medicine, Stanford, CA, USA;* [2]*Cancer Biology and Genetics, Memorial Sloan Kettering Cancer Center, New York, NY, USA. Contact e-mail: carmelc@stanford.edu*

Background: Mutations of the Arf tumor suppressor gene have been shown to accelerate lymphomagenesis by disabling the p53 pathway. Repetitive imaging of tumor cells within the lymph nodes and spleen provides a detailed understanding of the progression and treatment of lymphoma harboring Arf mutations. We have devised a new imaging strategy that allows direct high resolution imaging of apoptosis within the inguinal lymph node using a novel fluorescent self-assembling probe (CS3) developed in our labs. CS3 leads to increase in local fluorescence retention upon cleavage by caspase-3. Apoptosis and proliferation of lymphoma cells in other regions of the living mice in response to pharmacological intervention were also monitored by whole body bioluminescence (BLI) and fluorescence imaging (FI). Methods: Eμ-Myc Arf-/- lymphoma cells transduced with the eGFP-LUC2 imaging reporter were injected into syngenic C57/BL6 mice via tail vein to establish lymphoma tumors within 7 days. CS3 was administered i.v. to determine baseline apoptotic levels of lymphoma cells in the inguinal lymph nodes (ILN) and the spleen using intravital microscopy (IVM) and FI, respectively. Tumor vasculature within the ILN was visualized by IVM in conjunction with a blood vessels imaging agent. Prior to drug treatment, baseline cell proliferation in the spleen, renal lymph node (RLN) and ILN was determined by BLI of Firefly Luciferase (FL) activities. Mice were randomized and i.p. injected with 180 mg/kg of the DNA alkylating agent cyclophosphamide (CP) (N =3) or carrier control (PBS) for 2 days (N=3) prior to re-imaging of IVM, FI and BLI signals. Results: IVM showed that CP led to a 1.6-fold increase in CS3 signals in the lymphoma cells ($p < 0.05$ vs. carrier control-treated mice) in ILN with concurrent shrinkage of blood vessels compared to carrier control-treated mice (Figure 1a). FI showed that CP led to a 3-fold increase in CS3 signals in the spleen, relative to carrier control treated mice ($p < 0.02$, Figure 1b). Spleens were excised post-imaging for staining with cleaved caspase-3 to verify the presence of apoptotic lymphoma cells (Suppl. Figure 1). Whole body BLI also showed that CP treatment was effective in reducing lymphoma cell proliferation in spleen, RLN and ILN, relative to carrier control treated mice ($p < 0.01$) (Figure 1c). Conclusion: Using a caspase-3 sensitive self-assembling CS3 probe coupled with IVM of the ILN, we were able to directly monitor the apoptosis of lymphoma cells and shrinkage of blood vessels upon treatment with CP. Furthermore, using whole-body BLI and FI, we were able to track and monitor the effect of CP on proliferation and apoptosis of lymphoma cells in different regions of living mice. This multimodality molecular imaging strategy will allow the temporal and spatial monitoring of the response of lymphoma cells to chemotherapy, facilitates the investigation of drug resistance and accelerate drug development pertaining to lymphoma.

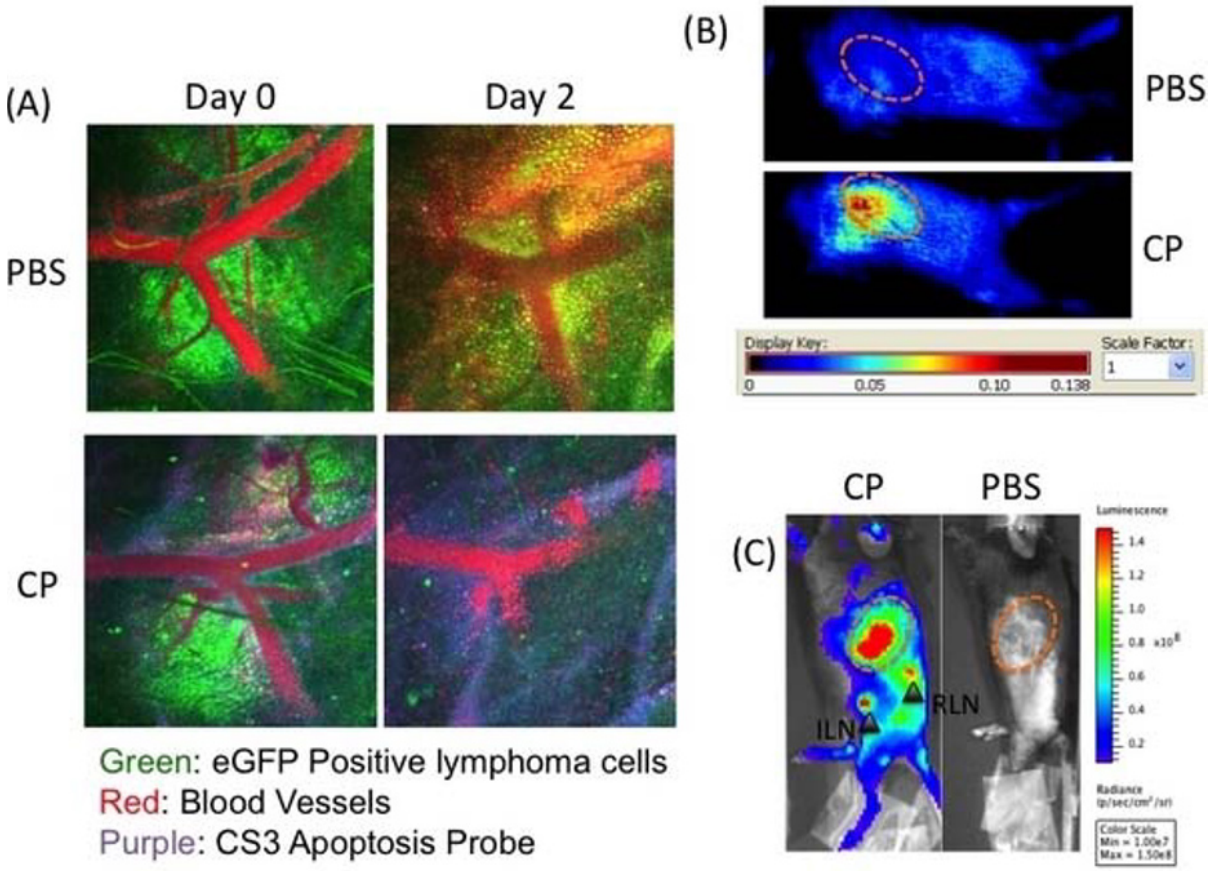

Figure 1: Multimodality Molecular Imaging of cell proliferation and apoptosis of Eμ-Myc Arf-/- lymphoma cells in living mice upon cyclophosphamide (CP) or carrier control (PBS) treatment. (A) Intravital microscopy imaging of lymphoma cells (green) with CS3 probe (purple) and blood vessels (red) pre- and post CP or carrier control (PBS) treatment. (B) Fluorescence imaging of apoptosis of lymphoma cells in the spleens using the CS3 probe. (C) BLI of lymphoma cells (Firefly Luciferase signals) in spleen, inguinal (ILN) and renal lymph nodes (RLN) post CP or carrier control treatment.

Disclosure of author financial interest or relationships:

C.T. Chan, None; **A.J. Shuhendler**, None; **H. Chang**, None; **D. Ye**, None; **A. Sathirachinda**, None; **M. Kotsuma**, None; **C.C. Miething**, None; **S. Lowe**, None; **J. Rao**, None; **S.S. Gambhir**, Bracco Diagnostics, Consultant; Endra, Inc, Stockholder; Cellsight, Stockholder; Enlight, Inc., Stockholder; General Electric, Grant/research support; ImaginAb, Stockholder; MagArray, Inc., Stockholder; Sanofi-Aventis, US, Grant/research support; SiteOne Therapeutics, Stockholder; VisualSonics/Sonosite, Stockholder .

Presentation Number **P 236**
Poster Session 2
September 19, 2013 / 15:15-15:15 / Room: Exhibit Hall B

Imaging-Guided RNAi therapy Using HDL-Like Nanoparticles

Juan Chen[1], *Qiaoya Lin*[1], *Cheng Jin*[1,2], *Huang Huang*[1], *Gang Zheng*[1,2], [1]*University Health Network, Toronto, ON, Canada;* [2]*University of Toronto, Toronto, ON, Canada. Contact e-mail: juan.chen@uhnresearch.ca*

Developing a multifunctional theranostic nanoparticle platform that combines imaging and therapeutic modalities to interact with cancer cells at the molecular level will lead toward imaging-guided cancer therapy. Herein, we developed a HDL-like theranostic nanoparticle by integrating near-infrared (NIR) fluorescence probe and therapeutic siRNA on HDL-like nanoparticles, and demonstrated this nanoplatform can selectively target to and accumulate in tumor to achieve higher target drug concentrations with lower overall body exposure. The NIR fluorescence was only observed in malignant tumor cells, whereas healthy prostate tissue, SV and testis showed little to no fluorescence, allowing in vivo detection of orthotopic tumor by non-invasive FMT/CT (Fluorescence Molecular Tomography/Computed Tomography) dual imaging technique and further assessment of drug delivery in deep tissues. Simultaneously, the ferried bcl2-siRNA significantly knocked down the bcl2 gene in tumor, induced tumor tissue apoptosis, and ultimately resulted in tumor growth hindrance. Such multimodal HDL-like nanotheranostic platform provides a useful tool in personalized medicine for detection of tumor, assessment of drug delivery, effective treatment planning, and finally evaluation of therapeutic response.

Disclosure of author financial interest or relationships:
J. Chen, None; **Q. Lin**, None; **C. Jin**, None; **H. Huang**, None; **G. Zheng**, None.

Presentation Number **P 237**
Poster Session 2
September 19, 2013 / 15:15-15:15 / Room: Exhibit Hall B

Sorafenib Enhances Therapeutic Efficacy of Vorinostat via Inhibition of ERK/NF-κB Pathway in Human HCC in vitro and in vivo

Yu-Chan Chen, *Fei-Ting Hsu, I-Tsang Chiang, Jeng-Jong Hwang, Biomedical Imaging and Radiological Sciences, National Yang-Ming University, Taipei, Taiwan. Contact e-mail: angela790126@hotmail.com*

Purpose Resistance of cancer cells to chemotherapy and/or radiotherapy is a major challenge to current anticancer treatment. The NF-κB signaling pathway plays an important role in tumor development and progression, and results in unsatisfactory treatment outcome. Some studies show that histone deacetylase (HDAC) inhibitors, such as suberoylanilide hydroxamic acid (SAHA), could induce cell-cycle arrest, and apoptosis in HCC. In addition, NF-κB inhibitor was shown to enhance the cytotoxicity of HDAC inhibitor in several cancer cell types. In our previous study, we found that sorafenib could inhibit tumor growth in HCC via inhibition of ERK/NF-κB pathway. However, whether sorafenib could increase the activity of SAHA via suppression of ERK/NF-κB pathway in HCC has not been elucidated. Here, we demonstrated the therapeutic efficacy and mechanism of sorafenib combined with SAHA in human HCC both in vitro and in vivo. Materials and Methods A human HCC Huh7 cell line transfected with NF-κB responsive element to drive dual reporter genes, herpes simplex virus thymidine kinase (tk) and firefly luciferase (luc2), and co-transfected with a third red fluorescent protein (rfp) gene, was renamed as Huh7/NF-κB-tk-luc2/rfp cells. and monitored by bioluminescent imaging (BLI) and red fluorescent protein imaging (RFPI) to evaluate the effect of sorafenib combined with SAHA on NF-κB activation and tumor growth inhibition. Cytotoxic mechanism of sorafenib combined with SAHA on HCC was also elucidated. Results Tumor growth inhibition by SAHA was significantly enhanced by sorafenib, which suppressed SAHA-induced NF-κB activity in HCC both in vitro and in vivo. On the other hand, Huh7/NF-κB-tk-luc2/rfp cells were treated by SAHA combined with different kinases (JNK, p38, AKT, ERK) inhibitors and NF-κB inhibitor. The results showed that sorafenib decreased SAHA-induced NF-κB activity via ERK dephosphoryaltion. NF-κB inhibitor could increase SAHA-induced cell cytotoxicity and apoptosis in HCC in vitro. Togethr, these results showed that sorafenib could sensitize human HCC to SAHA via suppression of ERK/NF-κB pathway. Conclusion Combination of sorafenib and SAHA could improve the therapeutic efficacy of human HCC through suppression of ERK/NF-κB pathway and NF-κB regulated downstream effector proteins. (This study is supported by a grant NSC 101-2314-B-010-045-MY3 from National Science Council, Taipei, Taiwan)

Disclosure of author financial interest or relationships:
Y. Chen, None; **F. Hsu**, None; **I. Chiang**, None; **J. Hwang**, None.

Presentation Number **P 238**
Poster Session 2
September 19, 2013 / 15:15-15:15 / Room: Exhibit Hall B

In vitro and Quantitative In vivo Dynamic Study of 188Re-perrhenate for Imaging and Treatment in NIS-expressing Tumour

Krisanat Chuamsaamarkkee[1], *Seckou Diocou*[1], *Greg Mullen*[1], *Lefteris Livieratos*[1,2], *Phil Blower*[1], [1]*Imaging Sciences and Biomedical Engineering, King's College London, London, United Kingdom;* [2]*Nuclear Medicine, Guy's & St Thomas' Hospitals NHS Foundation Trust, London, United Kingdom. Contact e-mail: krisanat.chuamsaamarkkee@kcl.ac.uk*

Background: 188Re-perrhenate is a substrate of the sodium/iodide symporter (NIS) which has been proposed for therapeutic purposes in NIS-expressing tumours. We aim to explore potential advantages of 188Re as alternative radionuclide in its biological and radiological properties, which has shorter half-life, less abundant gamma photons and higher energy beta particles than conventionally used 131I and is not organified, in order to achieve improved or equivalent treatment outcome at lower cost and less adverse effect on quality of life of the patients and their families. Methods: In vitro cell uptake was performed in the rat breast cancer cell line MnLTN3 overexpressing truncated CXCR4 and hNIS (Δ34CXCR4-NIS), with perchlorate block used as a control. For in vivo imaging, female scid/beige mice (n=3) were induced with Δ34CXCR4-NIS, with another set of healthy mice (n=3) of same strain used as a control. Whole body dynamic SPECT (NanoScan SPECT/CT, Mediso, Hungary) commenced immediately after administration of 41.96 ± 0.42 MBq of 188Re-perrhenate via the lateral tail vein with acquisition time 12-15 minute/scan, continuously for 4 hours followed by CT for anatomical localisation. 3D ROIs were drawn over thyroid, salivary glands, stomach, bladder, left-ventricle (for blood), muscle (for background) and tumour. Time-activity curves were expressed as percentage uptake and plotted in each case. Results: In vitro cell uptake in Δ34CXCR4-NIS cells was significantly (38.6 times) higher than in CXCR4 cells (31.35 ± 3.15 % for Δ34CXCR4-NIS and 0.81 ± 0.11 % for CXCR4). In vivo dynamic imaging showed similar patterns of radiotracer uptake in organs for both groups. Uptake was highest in stomach, while in the salivary glands tracer uptake was slightly higher than thyroid for both groups of mice. In the xenograft mice, kinetic tumour uptake reached its maximum (5.64 ± 1.42 %) at approximately 3 hours after injection. Activity in muscle and left ventricle remained low over time. Discussion & Conclusion: This work has shown the capability of 188Re-perrhenate for imaging in NIS-expressing tumour with potential application to treatment. However, dosimetry and treatment outcome need further studies. Additionally, this work demonstrated the ability of pre-clinical imaging for dynamic in vivo assessment of 188Re distribution. Uptake in thyroid can be distinguished from salivary glands along with high spatial resolution imaging of other NIS-expressing organs, allowing accurate and quantitative in vivo analysis for development of diagnostic and therapeutic NIS-targeting radiopharmaceuticals.

Disclosure of author financial interest or relationships:
K. Chuamsaamarkkee, None; **S. Diocou**, None; **G. Mullen**, Mediso, Consultant; **L. Livieratos**, None; **P. Blower**, None.

Presentation Number **P 239**
Poster Session 2
September 19, 2013 / 15:15-15:15 / Room: Exhibit Hall B

Fluorescent imaging of labeled monoclonal antibodies for identification of oral cavity carcinoma

Kristine Day[1], *Melissa L. Korb*[3], *Kurt R. Zinn*[2], *Eben L. Rosenthal*[1], [1]*Surgery, Division of Otolaryngology, University of Alabama at Birmingham, Birmingham, AL, USA;* [2]*Radiology, University of Alabama at Birmingham, Birmingham, AL, USA;* [3]*Surgery, University of Alabama at Birmingham, Birmingham, AL, USA. Contact e-mail: dayk500@gmail.com*

Objective: Fluorescent guided resections of oral cavity cancer may improve patient outcomes by detecting microscopic disease during surgical resection. Real-time optical imaging is a promising technique for visualization of microscopic cancer. In this study, four FDA approved therapeutic monoclonal antibodies were evaluated in order to determine the optimal targeting antibody. Methods: Mice bearing orthotopic tongue tumors (OSC19) were systemically injected with bevacizumab, cetuximab, panitumumab, trastuzumab, or non-specific IgG conjugated to a near-infrared (NIR) fluorescent probe (IRDye800CW). Primary tumors were imaged and resected under fluorescent guidance. Post-resection, the mice oral cavities were again fluorescently imaged to confirm absence of fluorescence. Tissue samples were prepared and tumor subsequently confirmed by correlation with permanent histology. Results: All fluorescently-labeled therapeutic monoclonal antibodies could adequately delineate tumor from normal tissue based on tumor-to-background ratios (TBR) compared to IgG- IRDye800CW. Cetuximab and panitumumab achieved the best average TBRs of 3.0 and 2.4 on SPY imaging and 3.2 and 3.7 on Pearl. Bevacizumab and trastuzumab, however, only attained TBRs of 1.9 and 1.4 on SPY and 2.6 and 2.3 on Pearl. On one-way ANOVA analysis of the SPY data, there was a significant difference ($p < 0.0001$) among the antibodies, the largest of which between cetuximab and trastuzumab. Analysis of the Pearl data also revealed a significant difference ($p = 0.0315$), with the biggest difference between panitumumab and trastuzumab. Conclusion: Our data suggests cetuximab and panitumumab are effective for tumor targeting of oral cavity carcinoma and in the intraoperative fluorescent detection of disease.

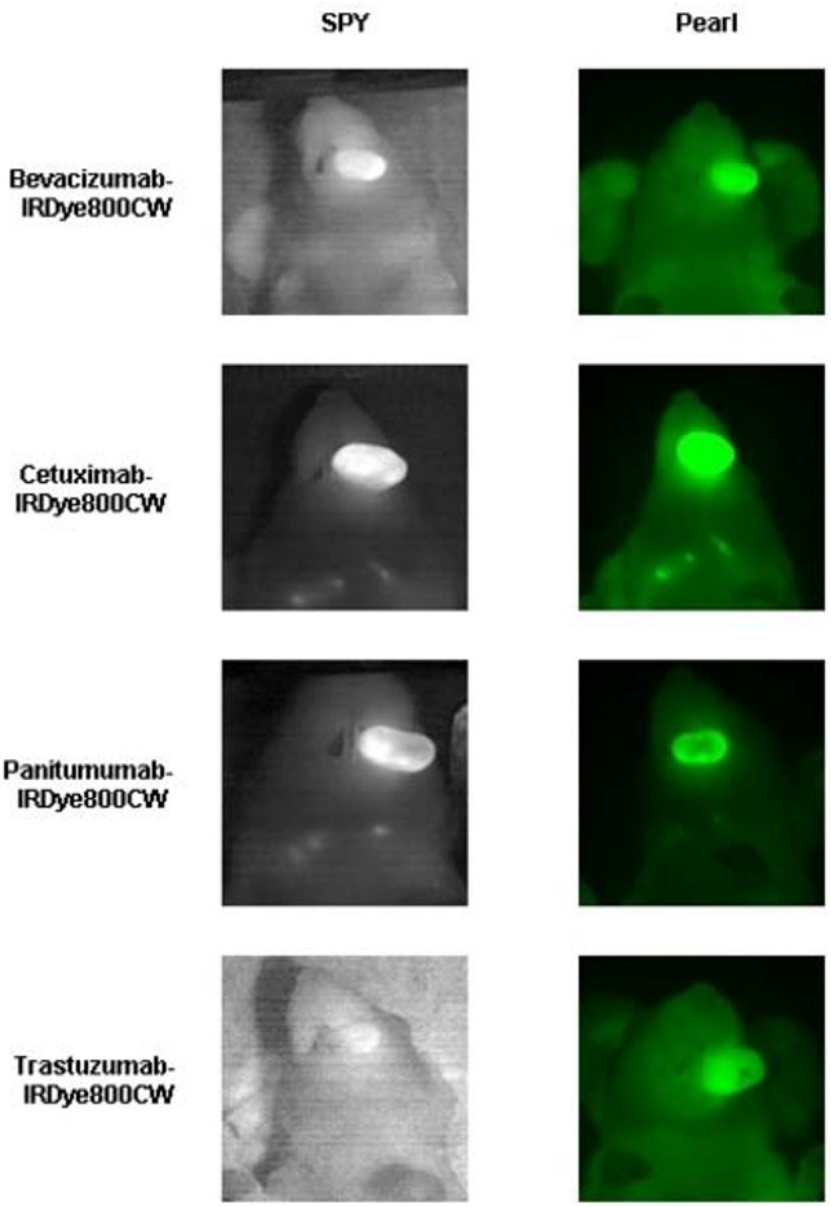

Disclosure of author financial interest or relationships:
K. Day, None; **M.L. Korb**, None; **K.R. Zinn**, None; **E.L. Rosenthal**, None.

Presentation Number **P 240**
Poster Session 2
September 19, 2013 / 15:15-15:15 / Room: Exhibit Hall B

Erythropoietin enhances the effects of platinum-based chemotherapy in human NSCLC xenograft tumors

Dennis Doleschel[1], *Anne Rix*[1], *Susanne Arns*[1], *Karin Palmowski*[1,4], *Andreas Franke*[2], *Felix Gremse*[1], *Ursula Klingmüller*[3], *Michael Jarsch*[2], *Fabian Kiessling*[1], *Wiltrud Lederle*[1], [1]*Experimental Molecular Imaging, Medical Faculty, RWTH Aachen University, Aachen, Germany;* [2]*Pharma Research, ROCHE Diagnostics GmbH, Penzberg, Germany;* [3]*Division of Systems Biology of Signal Transduction, DKFZ-ZMBH Alliance, German Cancer Research Center (DKFZ), Heidelberg, Germany;* [4]*Clinic for Inner Medicine III, Medical Faculty, RWTH Aachen University, Aachen, Germany. Contact e-mail: ddoleschel@ukaachen.de*

Introduction: Non-small-cell-lung-cancer (NSCLC) patients are commonly treated with platinum based chemotherapy leading often to anemia. Anemia is treated with Erythropoietin (Epo), but clinical studies with negative outcomes and the discovery of the Epo receptor (EpoR) in tumors have raised concerns and resulted in recommendations for restricted use. Therefore, we analyzed the effect of Epo on tumor growth during carboplatin-treatment in two NSCLC models with different EpoR-expression using longitudinal non-invasive imaging. Methods: Nude mice bearing subcutaneous A549 and H838 tumors (50 mm3) were randomly divided in the following groups: the control group received carboplatin (60 mg/kg), one group carboplatin and 5 µg/kg of Epo, the third group carboplatin and 20 µg/kg of Epo (n = 5 per group). Therapy was followed for 3 weeks by injecting carboplatin i.p. once weekly and Epo three times per week. Tumor growth and the relative blood volume (rBV) were assessed longitudinally by 3D contrast-enhanced ultrasound (3D-US). In parallel, tumor EpoR-levels were determined by FMT/µCT hybrid imaging using the NIRF-EpoR probe Epo-Cy5.5. In-vivo data were validated ex-vivo by immunohistochemistry (CD31-staining: vascularization, TUNEL-staining: apoptosis). HUVEC proliferation was assessed in vitro using similar Epo-concentrations as in-vivo. The platinum content in tumors was measured using inductively coupled plasma mass spectrometry (ICP-MS). Results: A significantly reduced tumor growth was observed in Epo-treated compared to control mice in both NSCLC models. Interestingly, the rBV was significantly higher in Epo-treated tumors. Immunohistochemistry confirmed their significantly higher microvessel density, indicating pro-angiogenic effects of Epo (Figure 1 A, C). Accordingly, Epo promoted proliferation of HUVEC in vitro. ICP-MS revealed a significantly higher platinum concentration in Epo-treated tumors compared to controls. In line with this, apoptosis was significantly enhanced in Epo-treated tumors (Figure 1 B, D). Differences between the models were recorded for the EpoR-status. Whereas in A549, it increased over time in response to Epo comparably to the controls, the EpoR-status remained significantly lower in Epo-treated H838 tumors compared to controls. Conclusion: In conclusion, Epo sensitized A549 and H838 tumors for chemotherapy potentially via increased vascularization. The enhanced vascularization obviously improved the delivery of carboplatin to the tumor, resulting in increased tumor apoptosis and reduced tumor growth.

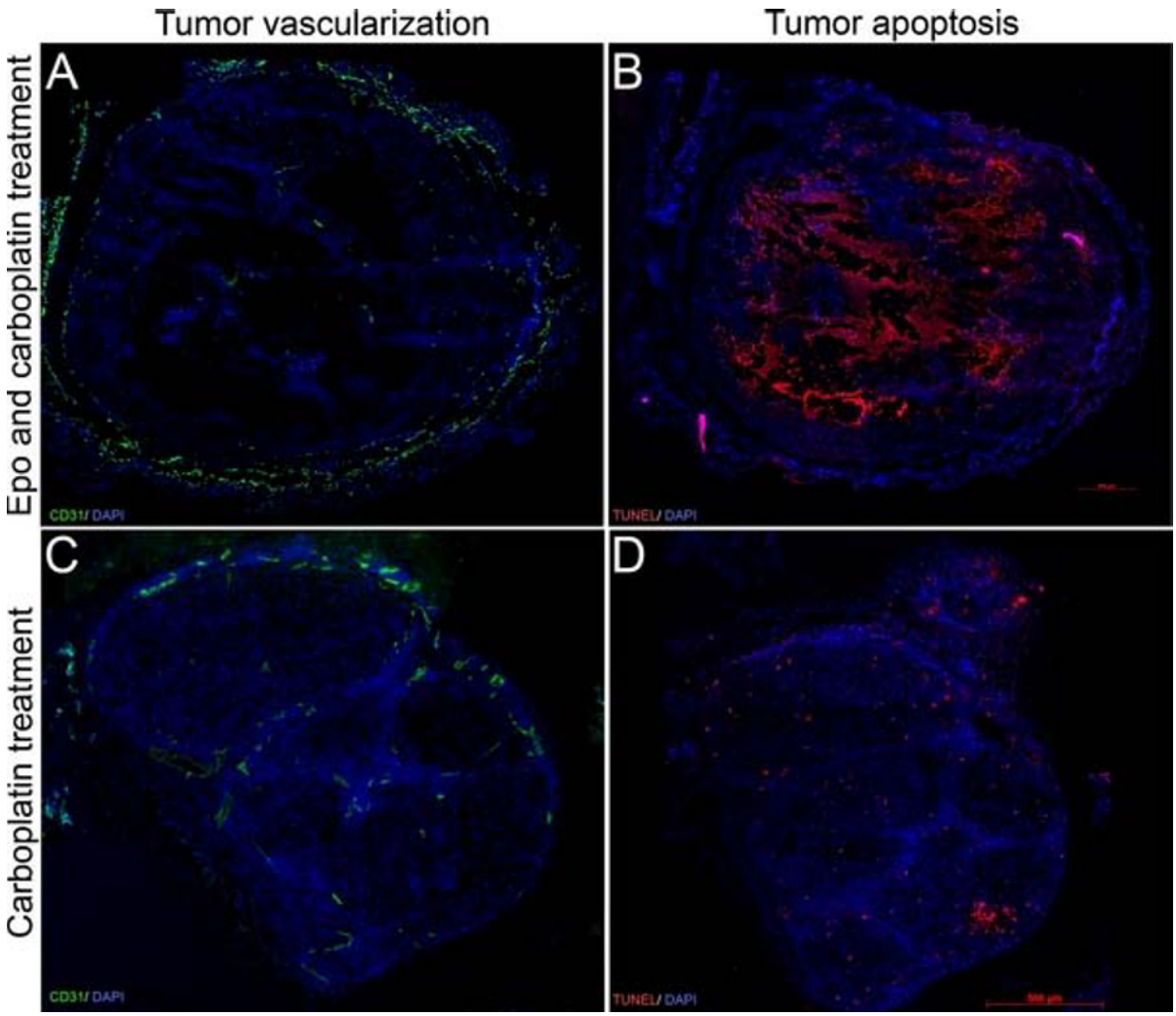

Figure 1. Epo promotes the chemotherapeutic effects by improving tumor vascularization Representative images of H838 tumors treated with Epo (5 µg/kg) and/or carboplatin (60 mg/kg) demonstrate that both, vasculature and apoptosis are enhanced by Epo-treatment. A, C: Immunohistochemical staining for tumor vascularization by CD31 (green). B, D: TUNEL-staining of apoptosis (red). Nuclei are stained with DAPI (blue).

Disclosure of author financial interest or relationships:

D. Doleschel, None; **A. Rix**, None; **S. Arns**, None; **K. Palmowski**, None; **A. Franke**, Roche Diagnostics GmbH, Employment; **F. Gremse**, None; **U. Klingmüller**, None; **M. Jarsch**, Roche Diagnostics GmbH, Employment; **F. Kiessling**, None; **W. Lederle**, None.

Presentation Number **P 241**
Poster Session 2
September 19, 2013 / 15:15-15:15 / Room: Exhibit Hall B

Prediction of VEGF expression in two tumor models using dynamic contrast enhanced ultrasound: identification of optimal imaging mode and temporal parameter

John R. Eisenbrey[1], *Christian C. Wilson*[2], *Anush Sridharan*[1,3], *Raymond Ro*[1,4], *Traci B. Fox*[5], *Ji-Bin Liu*[1], *See-Ying Chiou*[1], *Flemming Forsberg*[1], [1]*Department of Radiology, Thomas Jefferson University, Philadelphia, PA, USA;* [2]*College of Physicians and Surgeons, Columbia University, New York, NY, USA;* [3]*Department of Electrical and Computer Engineering, Drexel University, Philadelphia, PA, USA;* [4]*School of Biomedical Engineering, Sciences and Health Systems, Drexel University, Philadelphia, PA, USA;* [5]*Department of Radiological Sciences, Jefferson College of Health Professions, Thomas Jefferson University, Philadelphia, PA, USA. Contact e-mail: john.eisenbrey@jefferson.edu*

Objectives: Previously we showed that parametric imaging of ultrasound contrast agents (UCAs) correlates well to vascular endothelial growth factor (VEGF) expression in glioma and breast cancer murine xenograft models. In this study we seek to identify the optimal contrast imaging mode and temporal parameter for the prediction of VEGF expression. Methods: Spraque-Dawley rats (n=144) were inoculated with either an NMU breast cancer line or C6 glioma cell line in the thigh or abdomen. Rats were then separated into groups of 6, 8 or 10 days post implantation (12 rats per time point x 2 cell lines x 2 implant locations). Bolus tail vein injections of 0.4 ml/kg of the UCA Optison (GE Healthcare, Princeton, NJ) and ultrasound imaging were performed using 3 separate imaging modes (power Doppler imaging (PDI), harmonic imaging (HI), and microflow imaging (MFI)) using an Aplio scanner with 7.5 MHz linear array (Toshiba America Medical Systems, Tustin, CA). Parametric maps were generated for each ultrasound acquisition showing the maximum intensity projection (MIP), the time required to reach peak contrast from the time of injection (TTP), perfusion (PER), and the area under the time intensity curve, also known as time integrated intensity (TII). These parameters were then calculated over the entire tumor area and compared to VEGF expression obtained during histological staining. Strength of correlation was determined using Pearson's correlation coefficient, while statistically significant differences between correlations were determined using a Z test. Results and Discussion: Significant correlations were observed between TII and VEGF expression for all three imaging modes (R = -0.35, -0.54, and -0.32 for PDI, HI and MFI respectively). When comparing correlations with this parameter among imaging modes, HI showed statistically significant improvement over MFI ($p = 0.028$), but not over power Doppler imaging (although this was approaching significance; $p = 0.052$). This improvement is attributed to HI's increased sensitivity to UCA detection (PDI frequently resulted in blooming or motion artifacts), and HI's lack of temporal artifact (whereas MFI relies on flash replenishment sequences to create motion compensated time restricted projections of the microvasculature). Within the HI group, TII resulted in the strongest overall correlation to VEGF expression (R = -0.20, 0.10, -0.30, and -0.54 for MIP, TTP, PER and TII respectively), and this improvement was found to be statistically significant over the other three dynamic parameters ($p < 0.017$). Conclusions: Parameters from dynamic contrast enhanced ultrasound have been compared from three ultrasound imaging modes to VEGF expression in two tumor models, with HI appearing to be the best predictor of expression. Within HI, TII appears to best predict VEGF expression, and may be a potentially useful tool for monitoring angiogenesis. Acknowledgements: This work was supported by NIH CA093907 and US Army Medical Research Material Command Grant W81XWH-11-1-0630. The contrast agent was provided by GE Healthcare, Princeton, NJ, while Toshiba America Medical Systems, Tustin, CA provided the ultrasound scanner.

Disclosure of author financial interest or relationships:
J.R. Eisenbrey, None; **C.C. Wilson**, None; **A. Sridharan**, None; **R. Ro**, None; **T.B. Fox**, None; **J. Liu**, None; **S. Chiou**, None; **F. Forsberg**, Toshiba America Medical systems, Grant/research support; GE Healthcare, Grant/research support; Lantheus Medical Imaging, Grant/research support; AIUM, Other financial or material support .

Presentation Number **P 242**
Poster Session 2
September 19, 2013 / 15:15-15:15 / Room: Exhibit Hall B

The Effects of Vascular Density and Glucose Uptake on Tumor Growth: A Dorsal Window Chamber Model

Veronica Estrella, *Mark Robertson-Tessi, Tingan Chen, Mark C. LIoyd, Robert A. Gatenby, Robert Gillies, Cancer Imaging and Metabolism, H Lee Moffitt Cancer Center, Tampa, FL, USA. Contact e-mail: Veronica.Estrella@moffitt.org*

Tumor invasion into the surrounding microenvironment is governed, at least in part, by local extracellular acidosis. Increased glucose flux due to aerobic glycolysis results in elevated H+ production and excretion, which allows tumors to create an acidic environment. Flow of H+ ions along concentration gradients from the tumor into peritumoral normal tissue promotes invasion through matrix degradation, induction of normal cell death, and decrease in immune response. These observations have led to the "acid-mediated invasion hypothesis," which proposes increased glucose metabolism observed in FdG PET imaging confers an adaptive advantage, despite the loss of metabolic efficiency, by generating an acidic environment that promotes tumor survival and invasion. Using tumor imaging and pH analysis in a dorsal window chamber model, we demonstrated that regions of tumor invasion corresponded to areas of maximal acidosis at the tumor edge. In contrast, tumor invasion did not occur into regions with normal or near normal pHe. Mathematical models of acid mediated invasion predicted regional acidity in peritumoral normal tissue to be strongly dependent on vascular density. Specifically, a dense vascular network will hinder tumor growth by creating a sink for newly produced H+. We tested this prediction in HCT116/GFP cells growing in a window chamber. Spatial analyses of vessel density demonstrated that maximal tumor invasion was observed in regions with the lowest vascular density (Figure 1a). To further understand the dynamics of the tumor microenvironment, we obtained high resolution images of glucose metabolism using a home-made positron- imaging system with 0.02 mm lateral resolution. As indicated in figure 1b, we can co-register fluorescent images of tumor growth with glucose uptake and use these data to parameterize mathematical models of tumor metabolism and invasion. The models predict that increased vascularity leads to increased pH and inhibits tumor growth (Figure 1c). These findings are somewhat counter-intuitive and warrant further investigation.

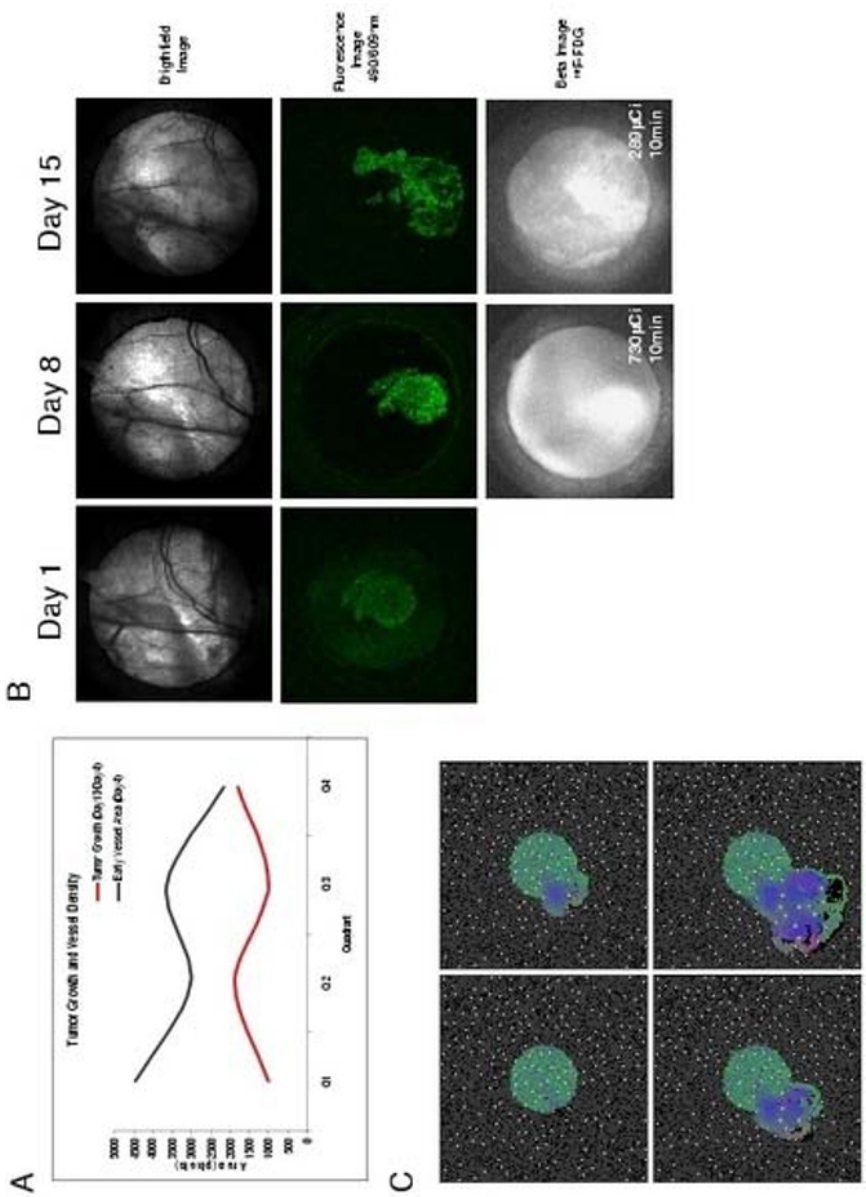

Spatial analysis, intravital imaging and mathematical modeling of vessel density and tumor growth in a murine dorsal window chamber model

Disclosure of author financial interest or relationships:

V. Estrella, None; **M. Robertson-Tessi**, None; **T. Chen**, None; **M.C. LIoyd**, None; **R.A. Gatenby**, None; **R. Gillies**, None.

Presentation Number **P 243**
Poster Session 2
September 19, 2013 / 15:15-15:15 / Room: Exhibit Hall B

Theranostic Evaluation of a Lu-177 Peptide Antagonist in Preclinical Models of Breast Cancer

Ashley Szczodroski[1], *Tammy L. Rold*[1,2], *Kelsey Richmond*[2,1], *Gary L. Sieckman*[1,2], *Lixin Ma*[3,1], *Timothy Hoffman*[1,2], [1]*R&D, U.S. Department of Veterans Affairs, Columbia, MO, USA;* [2]*Internal Medicine, University of Missouri, Columbia, MO, USA;* [3]*Radiology, University of Missouri, Columbia, MO, USA. Contact e-mail: szczodroskiaf@health.missouri.edu*

Introduction: Lutetium-177 labeled radiopharmaceuticals have potential as theranostic agents afforded by their dual emission of a therapeutic beta particle and a gamma ray suitable for imaging using conventional SPECT technology. The current study evaluates the ability of a Lu-177 labeled peptide antagonist to target the BB2 receptor (BB2r) in BB2r positive and estrogen receptor positive (ER+) / negative (ER-) human xenograft mouse models. Methods: Human cell line xenograft models were established in female SCID mice. ER+ models required implantation with 17-beta Estradiol pellets (0.50 mg - 60 day release). ER + T47D and MCF-7 as well as MDA-MB-231(ER-) human breast cancer cell inoculations (~5 million cells per flank) were performed. BB2r expression was confirmed by Western blot analysis. The BB2r antagonist peptide, DOTA-Amino-Carboxymethyl-Piperidine-DPhe-Gln-Trp-Ala-Val-Gly-His-Sta-Leu-NH2 (Eur J Nucl Med Mol Imaging 38(1):97, 2011), was synthesized with product identification verified by mass spectral analysis. Following direct radiolabeling with Lu-177, the Lu-177 product was purified using RP-HPLC. At 8-12 weeks post xenograft inoculation, pharmacokinetic and Micro-SPECT/CT studies were performed. Pharmacokinetic animals were administered 100uL containing 20-30 uCi (0.74-1.11MBq) of the Lu-177 labeled compound. Sacrifice and tissue harvesting was performed at 1hr, 4hrs, 24hrs, and 48hrs post injection. All collected tissues were weighed, radioactivity was counted, and the results were reported as %ID/g. Molecular imaging (Micro-SPECT/CT) studies were conducted at 24hrs and 48hrs post injection of approximately 1.31-3.08 mCi (48.5-11429.6-37 MBq) of Lu-177 BB2r antagonist with correlative In-111 BB2r antagonist imaging also being performed. Results: Pharmacokinetic results demonstrated significant tumor uptake in (ER+)T47D and MCF7 tumor xenograft models with 9.58±1.93 %ID/g and 7.12±1.92 %ID/g at 1 hr, respectively, and 6.04±1.48 %ID/g and 1.40±0.24 %ID/g at 24 hrs, respectively. The (ER-) MDA-MB-231 tumor xenograft model demonstrated a significantly lower initial (1 hr) tumor uptake of 1.50±0.49 %ID/g with nearly complete washout from tumor tissue at 24 hrs post injection (0.13±0.15 %ID/g). The trend observed in tumor uptake with respect to cell line origin was further substantiated by Western blot analysis. Lu-177 Micro-SPECT/CT data collected at 24 and 48 hours correlated with pharmacokinetic studies demonstrating visualization of BB2r+ tumor tissue at extended time periods reflective of individual tumor uptake. Conclusions: These studies demonstrate selective tumor targeting and prolonged retention of a Lu-177 labeled BB2r antagonist in xenograft models of ER+ human breast cancer confirmed by both pharmacokinetic studies and SPECT/CT molecular imaging. In contrast, using an ER- xenograft model of breast cancer, we observed limited tumor uptake and substantial washout of initial tumor uptake of the radiotracer. Further studies are necessary to confirm the differences observed between ER+ and ER- breast cancer cell lines with respect to BB2r expression and tumor uptake of BB2r targeted molecular imaging agents.

Disclosure of author financial interest or relationships:
A. Szczodroski, None; **T.L. Rold**, None; **K. Richmond**, None; **G.L. Sieckman**, None; **L. Ma**, None; **T. Hoffman**, None.

Presentation Number **P 244**
Poster Session 2
September 19, 2013 / 15:15-15:15 / Room: Exhibit Hall B

In vivo tumor targeting and drug delivery with mesoporous silica nanoparticles

Feng Chen[1], *Hao Hong*[1], *Hector F. Valdovinos*[2], *Sixiang Shi*[3], *Yin Zhang*[2], *Charles P. Theuer*[4], *Todd E. Barnhart*[2], *Weibo Cai*[1,2], [1]*Radiology, Univ of Wisconsin, Madison, WI, USA;* [2]*Medical Physics, University of Wisconsin - Madison, Madison, WI, USA;* [3]*Materials Science Program, University of Wisconsin - Madison, Madison, WI, USA;* [4]*TRACON Pharmaceuticals, Inc., TRACON Pharmaceuticals, Inc., San Diego, CA, USA. Contact e-mail: FChen@uwhealth.org*

Objectives: In vivo targeting of mesoporous silica nanoparticles (MSNs, or $mSiO_2$) to either tumor cells or tumor vasculature has been a major challenge since the initial demonstration using them as novel drug delivery nanoplatforms. In this work, we sought to overcome this challenge by functionalizing uniform $mSiO_2$ with a tumor vasculature targeted antibody and a radioisotope for in vivo tumor targeting and drug delivery, which was non-invasively monitored by positron emission tomography (PET) imaging. Methods: Uniform $mSiO_2$ were synthesized using a well-established soft-template method, which was functionalized with thiol groups and subsequently conjugated to TRC105 (an anti-CD105 antibody) and 1,4,7-triazacyclononane-N,N'N''-triacetic acid (NOTA) through polyethylene glycol (PEG) linkers. Transmission electron microscopy (TEM), dynamic light scattering (DLS), and zeta-potential measurements were performed to confirm successful synthesis of the NOTA-$mSiO_2$-PEG-TRC105 nanoconjugate. In vitro CD105 targeted imaging was carried out with FITC-conjugated nanoparticles in HUVECs (CD105 positive) and MCF-7 (CD105 negative) human breast cancer cells. After labeling with ^{64}Cu ($t_{1/2}$: 12.7 h), PET imaging, biodistribution, and blocking studies were performed in 4T1 murine breast tumor-bearing mice to evaluate the tumor targeting capability of ^{64}Cu-NOTA-$mSiO_2$-PEG-TRC105, and ^{64}Cu-NOTA-$mSiO_2$-PEG was used as the control. Results: Uniform $mSiO_2$ (ca. 80 nm) nanoparticles were synthesized and nearly no changes in particle size or morphology were observed during the surface functionalization, as demonstrated by serial TEM studies. Changes in zeta-potential and DLS size distribution further confirmed the success of each reaction (e.g. thiolation, PEGylation, NOTA/TRC105 conjugation). Incubation with FTIC-$mSiO_2$-PEG-TRC105 resulted in greatly enhanced fluorescence signal on HUVECs compared to FTIC-$mSiO_2$-PEG. ^{64}Cu-labeling was achieved with high yield and specific activity. Serial PET imaging revealed that 4T1 tumor uptake of ^{64}Cu-NOTA-$mSiO_2$-PEG-TRC105 peaked at 5.9±0.4 %ID/g at 5 h post-injection (n=3), significantly higher than that of ^{64}Cu-NOTA-$mSiO_2$-PEG (2.9±0.9 %ID/g), indicating successful targeting of TRC105 conjugated $mSiO_2$ to the tumor. Moreover, blocking and histology studies confirmed CD105 specificity of ^{64}Cu-NOTA-$mSiO_2$-PEG-TRC105 in vivo. We further demonstrated successful tumor-targeted delivery of doxorubicin (DOX) in 4T1 tumor-bearing mice after intravenous injection of DOX-loaded $mSiO_2$-PEG-TRC105 nanoparticles, which holds potential for image-guided drug delivery and targeted cancer therapy. Conclusion: This is the first report of in vivo tumor (vasculature) targeting with MSNs, which has long been considered as one of the most promising drug delivery nanoplatforms. Successful surface PEGylation, antibody conjugation, radiolabeling, in vitro and in vivo CD105-specific targeting was demonstrated using ^{64}Cu-NOTA-$mSiO_2$-PEG-TRC105, which opened up new perspectives on the use of biocompatible $mSiO_2$ for cancer targeted imaging and therapy. This approach is generally appliable for cancer therapy, since CD105 is overexpressed in > 10 tumor types.

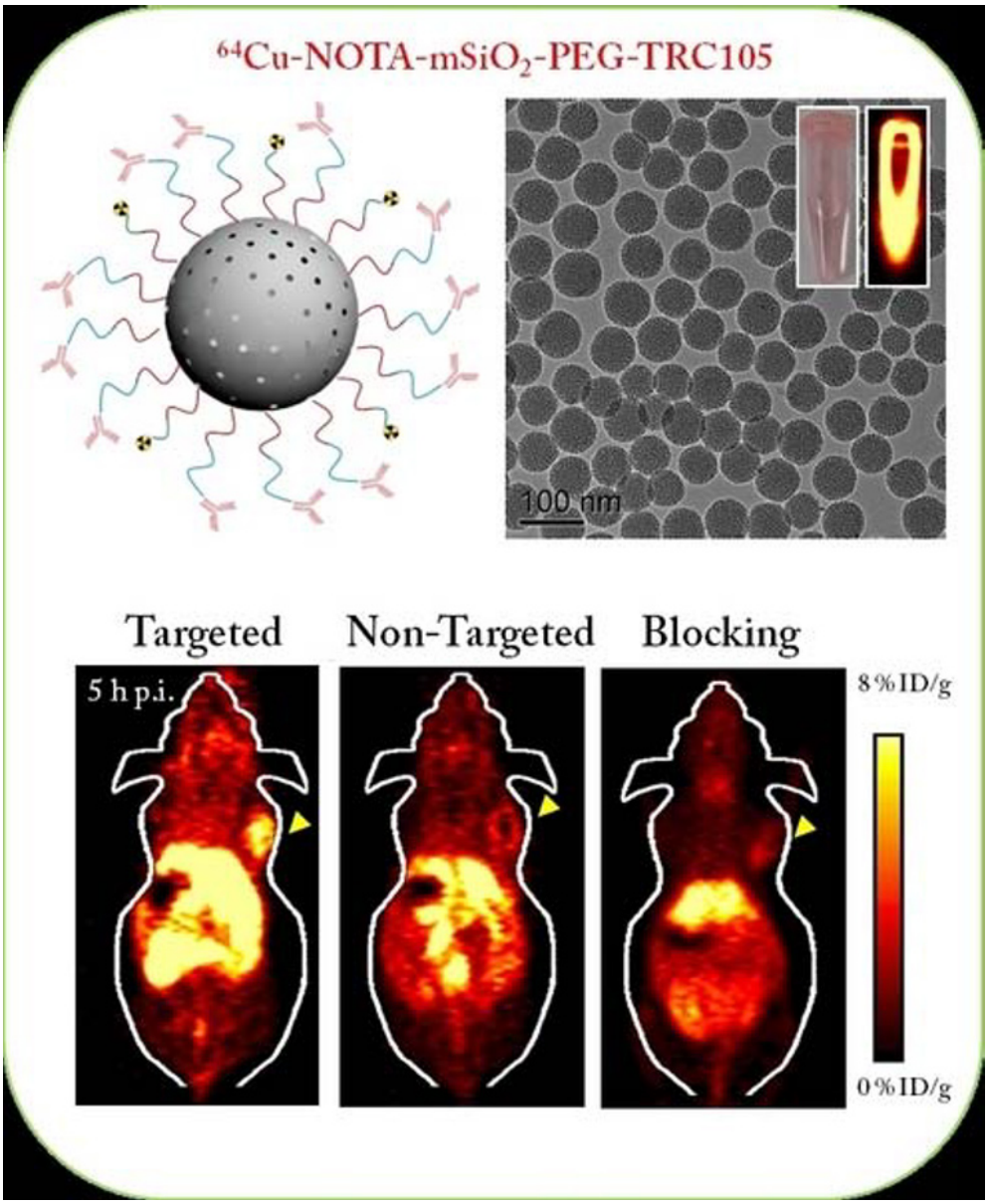

In vivo tumor vasculature targeted PET imaging and drug delivery of functionalized mesoporous silica nanoparticles

Disclosure of author financial interest or relationships:
F. Chen, None; **H. Hong**, None; **H.F. Valdovinos**, None; **S. Shi**, None; **Y. Zhang**, None; **C.P. Theuer**, TRACON Pharmaceuticals, Stockholder; TRACON Pharmaceuticals, Employment; **T.E. Barnhart**, None; **W. Cai**, None.

Presentation Number **P 245**
Poster Session 2
September 19, 2013 / 15:15-15:15 / Room: Exhibit Hall B

Novel Engineered Immuno-PET Tracers as Companion Diagnostics for Antibody Drug Conjugate Therapy

Ohad Ilovich[1], *Arutselvan Natarajan*[1], *Ataya Sathirachinda*[1], *Richard Kimura*[1], *Ananth Srinivasan*[1], *Mathias Gebauer*[2], *Jochen Kruip*[2], *Chantal Carrez*[3], *Ingrid Sassoon*[3], *Veronique Blanc*[3], *Susanta K. Sarkar*[4], *Sanjiv S. Gambhir*[1], [1]*Radiology, Stanford University, Palo Alto, CA, USA;* [2]*BioInnovation Novel Protein Therapeutics, Sanofi Aventis, Frankfurt, Germany;* [3]*Oncology, Sanofi Aventis, Vitry, France;* [4]*Oncology, Sanofi Aventis, Cambrige, MA, USA. Contact e-mail: ilovicho@gmail.com*

SAR566658 (huDS6-DM4) is an antibody-drug immunoconjugate consisting of a humanized monoclonal antibody against the tumor-associated MUC1-sialoglycotope, CA6, conjugated to the cytotoxic maytansinoid, DM4. Upon antibody/antigen binding and internalization, the immunoconjugate releases DM4, which binds to tubulin and disrupts microtubule assembly/disassembly dynamics, resulting in mitotic arrest of CA6-expressing tumor cells. SAR566658 is currently undergoing phase I clinical trial in patients diagnosed to have CA6 antigen positive solid tumors. A companion diagnostic based on huDS6 may facilitate patient stratification and early evaluation of therapeutic efficacy. The present study describes the development and preclinical evaluation of three novel Copper-64 labeled antibody fragments (a cys-diabody and two Fab fragments) derived from the DS6 antibody. Based on pre-determined imaging figures of merit (IFOM), one fragment was chosen for specificity evaluation via in vivo blocking and isotype control experiments in mouse models. All three antibody fragments and their corresponding DOTA conjugates (1.5-2.5 DOTA/fragment) had high affinity (Kd = 4-20 nM) to CA6 positive (WISH) cells, indicating that DOTA derivatization does not adversely affect the affinity towards the antigen. The fragments had low affinity towards CA6 negative (A2780) cells. The Copper-64 labeled tracers were evaluated by 24 hour human serum stability studies, in vivo imaging and 24-hour biodistribution studies in subcutaneously implanted WISH or A2780 tumor bearing nude mice. One labeled Fab fragment (64Cu-DOTA-B-Fab) was synthesized in high yield (RCY - 80%, SA - 55 GBq/μmole, >95% purity) and gave good results in serum stability (94±5%, n=3) tests. Biodistribution experiments in tumor bearing mice showed relatively high WISH tumor uptake (7.59±0.87 %ID/g, n=10, tumor mass 20-206 mg) and low A2780 tumor uptake (5.12±0.92 %ID/g, n=9, tumor mass 50-270 mg) combined with high tumor/muscle (8.7:1), tumor/blood (3.6:1) and positive/negative tumor (1.5, $p<0.05$, n=19) ratios. Tumor uptake was surpassed only by the kidneys (62.36±4.04 %ID/g) and liver (10±0.75 %ID/g). 24 hour PET images could clearly differentiate between CA6 positive and CA6 negative tumors (Figure 1). The second Fab fragment gave inferior biodistribution results and the diabody failed serum stability experiments. Two B-Fab isotype controls were labeled and evaluated in similar biodistribution experiments and both had significantly lower uptake in WISH tumors ($p<0.001$ for both) than the DS6 derived B-Fab. Specificity was further evaluated in WISH bearing tumor animals via blocking studies. Blocking was performed either by administration of B-Fab (2 mg, n=5) or DS6 (1 mg, n=4) at 2.5 or 25 hours respectively prior to the administration of the tracer. Blocking afforded a 23% ($p<0.05$, n=8) and 26% ($p<0.05$, n=7) decrease in WISH tumor uptake for B-Fab and DS6 respectively. Control tumors (n=3) were not blocked in this study. In conclusion, these preclinical studies support that 64Cu-DOTA-B-Fab may be a suitable companion diagnostic for SAR566658 in cancer patients and requires further investigation.

Novel Engineered Immuno-PET Tracers as Companion Diagnostics for Antibody Drug Conjugate Therapy

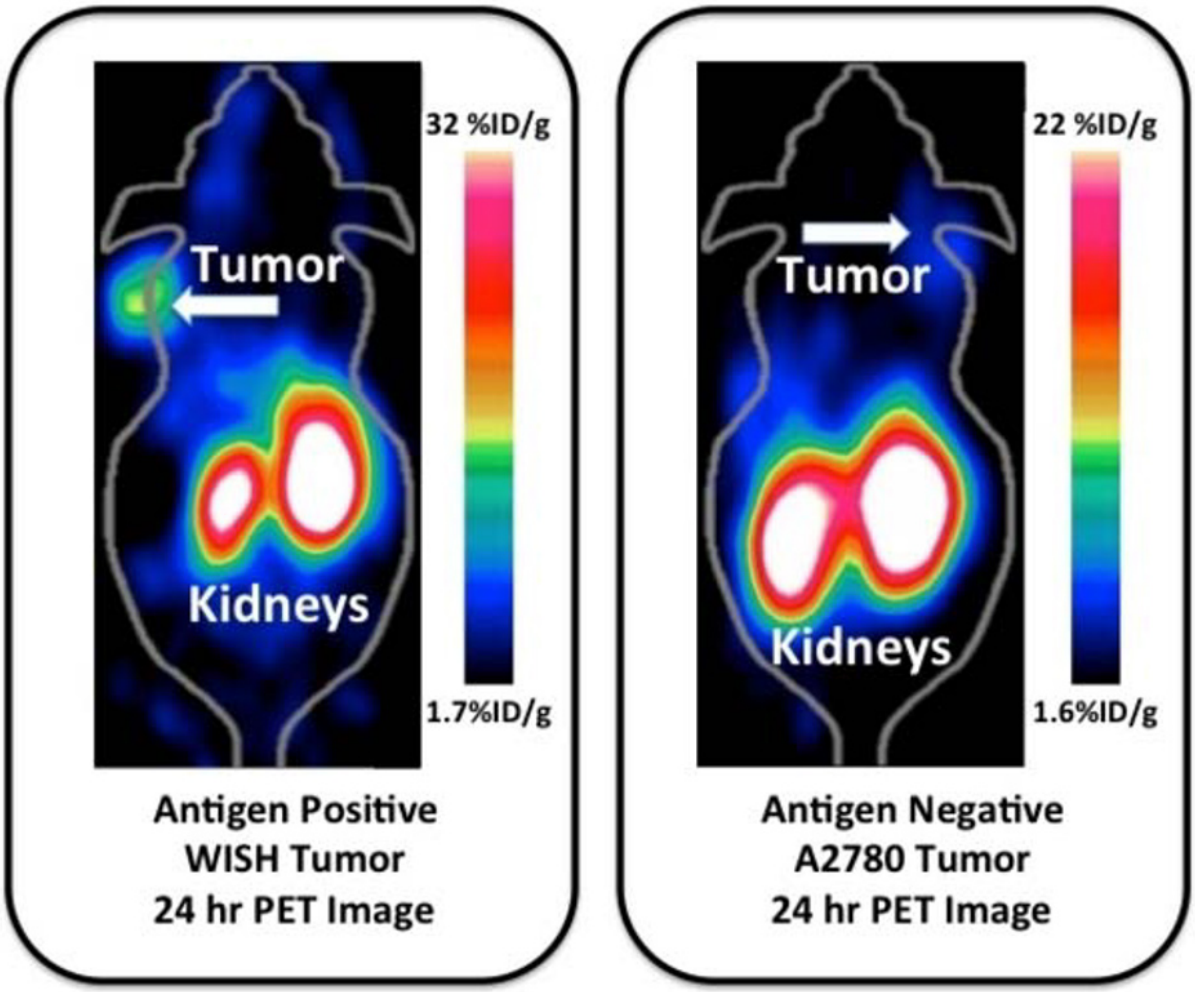

PET images of WISH and A2780 tumor bearing mice 24 hours after injection of 64Cu-DOTA-B-Fab

Disclosure of author financial interest or relationships:
O. Ilovich, Sanofi, Grant/research support; **A. Natarajan**, None; **A. Sathirachinda**, None; **R. Kimura**, None; **A. Srinivasan**, None; **M. Gebauer**, Sanofi, Employment; **J. Kruip**, Sanofi-Aventis Deutschland GmbH, Employment; **C. Carrez**, sanofi, Employment; **I. Sassoon**, SANOFI, Stockholder; **V. Blanc**, None; **S.K. Sarkar**, Sanofi, Employment; **S.S. Gambhir**, Bracco Diagnostics, Consultant; Endra, Inc, Stockholder; Cellsight, Stockholder; Enlight, Inc., Stockholder; General Electric, Grant/research support; ImaginAb, Stockholder; MagArray, Inc., Stockholder; Sanofi-Aventis, US, Grant/research support; SiteOne Therapeutics, Stockholder; VisualSonics/Sonosite, Stockholder .

Presentation Number **P 246**
Poster Session 2
September 19, 2013 / 15:15-15:15 / Room: Exhibit Hall B

Functionalization of hybrid gadolinium based nanoparticles for in-vivo targeting of chondrosarcoma

Marc F. Janier[1,3], *Jessica Morlieras*[1], *François Lux*[1], *David Kryza*[1,3], *Pauline Bonazza*[1,3], *Pierre Mowat*[1], *Aurélien Vidal*[2], *Jean-Michel Chezal*[2], *Olivier Tillement*[1], *Elisabeth Miot-Noirault*[2], [1]*Institut Lumière Matière, Lyon University - UCBL1, Lyon, France;* [2]*U990, Université d'Auvergne, Clermont-Ferrand, France;* [3]*IMTHERNAT - Hôpital Edouard Herriot, Hospices Civils de Lyon, Lyon, France.*
Contact e-mail: Marc.Janier@univ-lyon1.fr

Nanoparticles are of interest for diagnostic and therapeutic use, but many constraints (a major one concerns their size) limit their developments. Our group has developed ultrasmall hybrid nanoparticles (GBN) based on gadolinium complexes directly grafted on an inorganic matrix of polysiloxane (< 5 nm), which have demonstrated very promising biodistribution properties after IV injection. These GBN were grafted with quaternary ammonium groups (GBN-QA) in order to enable them to target proteoglycans, which are the major compound of cartilage and of chondrosarcoma. After 111In labelling of GBN-QA and GBN, in vivo imaging of an orthopic chondrosarcoma in rat (SWARM) was compared to images obtained after injection of the 99mTc-NTP15-5 (Quaternary ammonium group not linked to GBN and previously validated as an imaging tracer for chondrosarcoma). These studies demonstrated the targeting efficiency of the GBN-QA by showing tumor and joint accumulation of GBN-QA starting 10 min post-injection (See Figure). The GBN-QA uptake in tumour was similar to the one obtained after the 99mTc-NTP15-5 injection. The tumour to muscle ratio was about 4 for both targeting compounds at 1 and 3 hours after injection, while it significantly decreased after 30 minutes for GBN. Combining these results and the clear evidence of a radiosensitizing effect on radioresistant cells, we should be able to demonstrate an in-vivo therapeutic effect of targeted nanoparticles in chondrosarcoma.

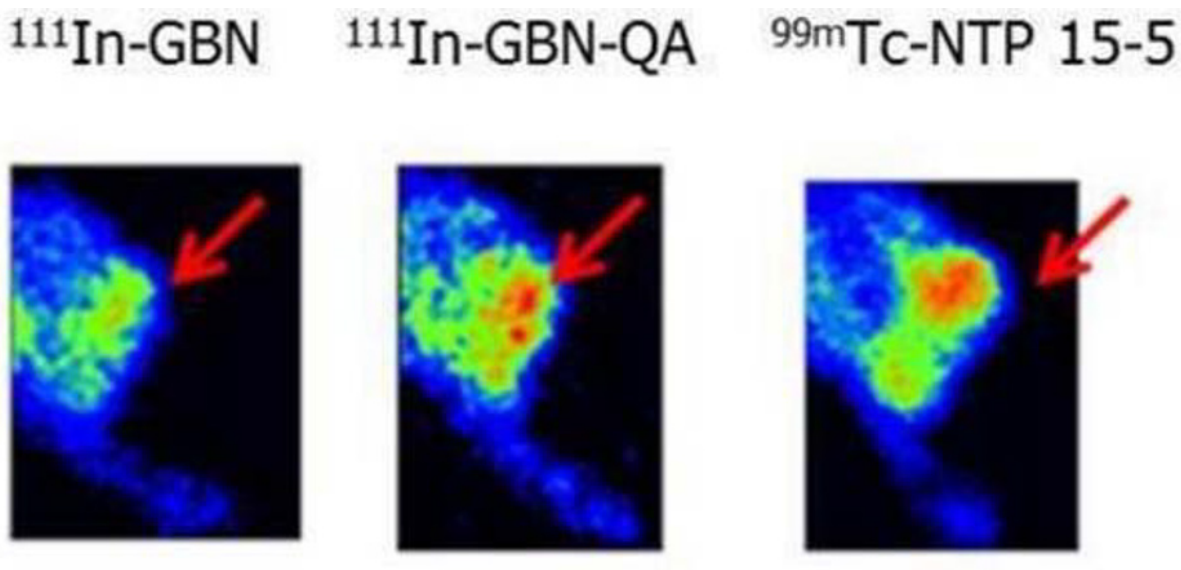

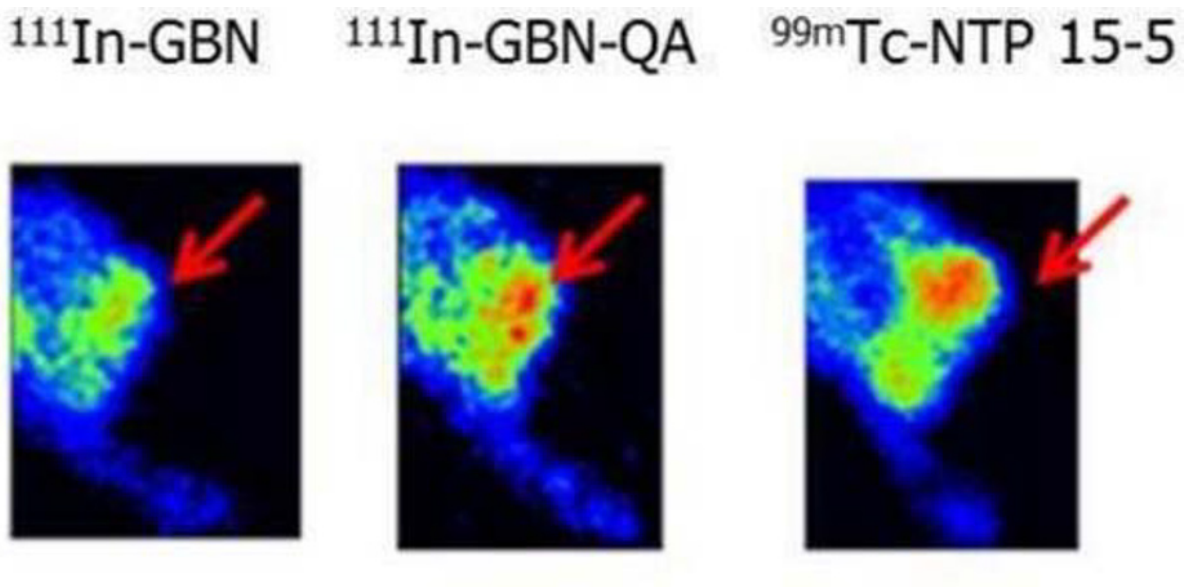

Disclosure of author financial interest or relationships:
M.F. Janier, Nano-h, Stockholder; **J. Morlieras**, None; **F. Lux**, None; **D. Kryza**, None; **P. Bonazza**, None; **P. Mowat**, None; **A. Vidal**, None; **J. Chezal**, None; **O. Tillement**, None; **E. Miot-Noirault**, None.

Presentation Number **P 247**
Poster Session 2
September 19, 2013 / 15:15-15:15 / Room: Exhibit Hall B

Validating B7-H4 as an Imaging Marker for Prostate Cancer in a Tumor Mouse Model

Narges K. Tafreshi[1], Jongphil Kim[2], David L. Morse[1], Robert Gillies[1], Robert A. Gatenby[1,3], Jung W. Choi[1,3], **Yolaine Jeune-Smith**, *[1]Cancer Imaging and Metabolism, Moffitt Cancer Center, Tampa, FL, USA; [2]Biostatistics, Moffitt Cancer Center, Tampa, FL, USA; [3]Diagnostic Imaging, Moffitt Cancer Center, Tampa, FL, USA. Contact e-mail: yolaine.smith@moffitt.org*

With over 28,000 deaths last year, prostate cancer stands 2nd among the leading causes of cancer-related mortality in men. Success rates of treatment are significantly higher in early stage prostate cancer compared to metastatic disease, demanding early detection and localization of the prostate cancer foci. Current diagnostic imaging assays for prostate cancer detection suffer from limited sensitivity and specificity. B7-H4, an immuno-costimulatory cell surface molecule, has been found to be over-expressed in a large number of human prostate cancer tissue samples and postulated to play role in immune tolerance in the disease. Furthermore, the degree of expression of this molecule has been shown to be associated with poor prognosis of prostate cancer. Therefore, present investigation was undertaken to evaluate the feasibility of in vivo imaging of a mouse tumor model with a B7-H4-specific imaging probe. HCT116 (B7-H4-negative) cells were engineered to express human B7-H4 and clone (HCT116/B7-H4) with the highest B7-H4 specific mean fluorescence intensity (1013) was identified through flow cytometry. Cell surface expression of B7-H4 by engineered cells was confirmed by immunocytochemistry. An antibody-based probe was prepared through conjugation of a near-infra-red (680nm) fluorescent dye to rabbit anti-human B7-H4 antibody (antiB7H4-680). In vivo targeting of antiB7-H4-680 was evaluated by i.v. injection of 50ug probe into each athymic nude mouse bearing bilateral subcutaneous HCT116 (B7-H4-negative) and HCT116/B7-H4 (B7-H4 positive) tumors, followed by in vivo fluorescence imaging over a 168h post-injection time course. Selective accumulation of targeted probe in the tumors expressing B7H4 compared to negative tumor and major organs was observed, demonstrating specific targeting of antiB7-H4-680 to B7-H4-positive tumor cells. Normalized signal intensities of B7-H4-expressing tumors were found to increase significantly with time before achieving a peak at the 72h post-probe injection ($p<0.05$), while no significant increase in signal intensities were observed in the non-transfected parental tumors in these mice. The difference in signal intensities between tumors expressing B7-H4 and non-transfected tumors was statistically significant ($p<0.05$) at both the 48 and 72h time points demonstrating B7-H4 selective accumulation of the probe. Seven days post probe injection, B7-H4-expressing tumors and other organs (kidneys, spleen, liver, lung and heart) were collected from the mice for ex-vivo imaging. In conclusion, initial imaging data of mice bearing B7-H4 transfected tumors confirms the potential of targeting B7-H4 as an imaging marker for prostate cancer in a mouse model. Additional imaging experiments of mice bearing metastasis from B7-H4-expressing prostate tumor cells are currently being pursued.

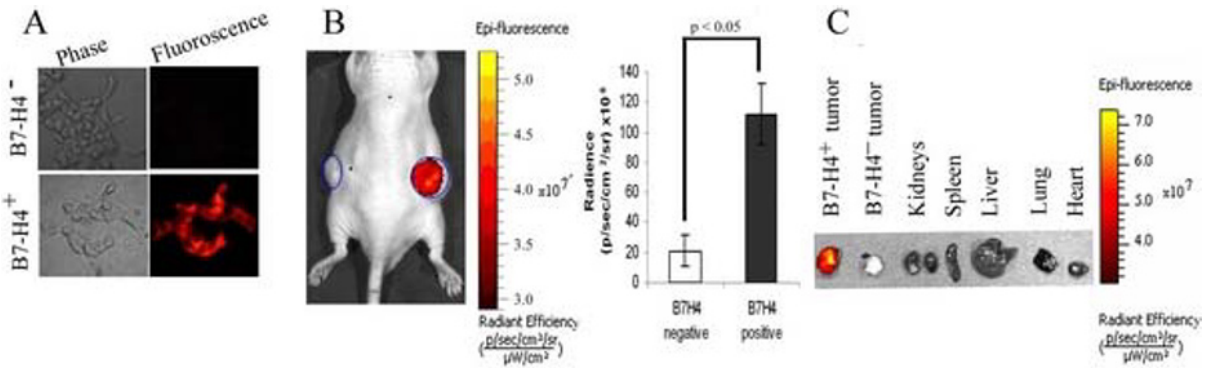

Figure 1. A) Immunocytochemistry of B7-H4 negative and B7H4 positive cells. B) In vivo targeting of B7-H4. Fluorescence overlay image of mouse bearing subcutaneous B7-H4 negative tumor in left flank and B7-H4 positive tumor in right flank, 72h post i.v. injection of antiB7-H4-680 probe with quantitation of fluorescence intensity. C) Ex-vivo fluorescence overlay image of tumors and other organs. Images shown are representative images. Data shown are mean±SD.

Disclosure of author financial interest or relationships:

N.K. Tafreshi, None; **J. Kim**, None; **D.L. Morse**, LiCor Biosciences, Grant/research support; **R. Gillies**, None; **R.A. Gatenby**, None; **J.W. Choi**, None; **Y. Jeune-Smith**, None.

Presentation Number **P 248**
Poster Session 2
September 19, 2013 / 15:15-15:15 / Room: Exhibit Hall B

Porphysome-enabled fluorescence-guided photothermal therapy to treat lung cancer: a pre-clinical study in rabbit orthotopic lung tumor model

Cheng Jin[1,2], *Takashi Anayama*[1], *Patrick Z. McVeigh*[3], *Brian C. Wilson*[1,3], *Kazuhiro Yasufuku*[1], *Gang Zheng*[1,2], [1]*Ontario Cancer Institute, University of Toronto, Toronto, ON, Canada;* [2]*Graduate Department of Pharmaceutical Sciences, University of Toronto, Toronto, ON, Canada;* [3]*Department of Medical Biophysics, University of Toronto, Toronto, ON, Canada. Contact e-mail: cheng.jin@utoronto.ca*

INTRODUCTION: Thermal ablation in the treatment of lung cancer has been developed clinically as an alternative option for local therapy due to the reduced invasiveness. To further enhance the selectivity of thermal ablation and its efficiency, we are developing a new system, using a potent photothermal enhancer, the porphysome, for efficient bronchoscopic photothermal ablation. Porphysomes are intrinsically multifunctional nanovesicles (photothermal therapy, photoacoustic imaging, fluorescence imaging), which are self-assembled from porphyrin-lipid into liposome-like nanoparticles. Porphysomes accumulated in tumor by the enhanced permeability and retention effect with high porphyrin transporting capacity, and a prototype fluorescent bronchoscope enabled the endoscopic visualization of peripheral lung cancer exhibiting porphyrin fluorescence. Therefore, we are investigating porphysome-enabled fluorescence image-guided photothermal therapy (PTT) on a pre-clinical rabbit orthotopic lung tumor model. METHODS: Porphysomes were injected intravenously into rabbits bearing peripheral VX2 lung tumors. A white light/fluorescence ultra-thin fiberoptic bronchoscope was used to image lung tumors at various time points (0 hr, 24 hr, 48 hr and 72 hr post-injection), using a 671 nm / 10 mW diode laser as excitation and a 678 nm long pass emission filter. Organs were obtained for biodistribution studies at each time point. To investigate the photothermal therapy (PTT), a thin laser fiber (200 micron diameter) was inserted to tumor area trans-bronchially with the guidance of porphyrin fluorescence for PTT irradiation at 48 hr post administration of porphysomes (671 nm, 250 mW, and 10 min). Rabbits were then sacrificed, and the irradiated lung area was collected for future histology studies including H&E staining and NADH metabolic activity staining. Tumor alone and laser alone (tumor + laser only) were used as controls. RESULTS: Porphysomes accumulated at orthotopic lung tumor passively via EPR and the tumor was clearly identified based on the bright porphyrin fluorescence using the prototype bronchoscope system. The highest tumor to normal lung fluorescence ratio was achieved at 48 hrs post-injection of porphysomes, and it provided excellent fluorescence-guidance for the following local PTT. The PTT laser ablated the orthotopic lung tumor area with the diameter over 10 mm, while the laser alone without porphysome injection only induced the minimal ablated area with less than 2 mm diameter. CONCLUSIONS: The porphysome nanoparticles not only enabled to visualize the orthotopic lung tumor following administration but also enhanced local PTT efficiency significantly, which demonstrates the potential of porphysome-based image-guided PTT for the future trans-clinical applications to lung cancer treatment.

Disclosure of author financial interest or relationships:
C. Jin, None; **T. Anayama**, None; **P.Z. McVeigh**, None; **B.C. Wilson**, None; **K. Yasufuku**, Olympus Medical Systems Corp, Grant/research support; **G. Zheng**, None.

Presentation Number **P 249**
Poster Session 2
September 19, 2013 / 15:15-15:15 / Room: Exhibit Hall B

Microenvironment-driven Drug Delivery and Imaging with Clinical Iron Oxide Nanoparticles

Charalambos Kaittanis, *Jan Grimm, Molecular Pharmacology and Chemistry, MSKCC, New York, NY, USA. Contact e-mail: kaittanc@mskcc.org*

Keywords: iron oxide nanoparticles, glycolysis, cytotoxicity, magnetic relaxation. Cancer chemotherapy relies on the effective suppression of tumor growth, ideally targeting only the pathology. Drugs, like Doxorubicin, were conjugated to polymers and targeting ligands that achieved delivery through the enhanced permeability and retention effect or the targeting of overexpressed transmembrane proteins involved in signal transduction and nutrient uptake. Alternatively, nanoparticles encapsulated drugs, without subjecting them to any chemical modification. Yet, these vehicles released their cargo upon fusion with the plasma membrane or action of enzymes after nanoparticle endocytosis. We hypothesized that clinical iron oxide nanoparticles (IONP) could serve as drug delivery vehicles, capable of retaining their cargo at physiological conditions and releasing it in tumoric glycolysis' lower pH. We further reasoned that the retained cargo might have affected IONP's magnetic properties, providing a novel way to characterize this drug delivery platform (Fig. 1). We loaded IONP with different amounts of the Taxol derivative Flutax1, and observed that there was a direct correlation between cargo concentration and the spin-spin (T2) and spin-lattice (T1) relaxation times. Utilizing MRI, we determined that the cargo obstructed the diffusion of water molecules within IONP's coating, which increased the T2 and T1. Interestingly, IONP retained the cargo via weak electrostatic interactions, and released it at slightly acidic conditions. Apart from accommodating one drug, IONP co-delivered the anti-androgen MDV3100 and the PI3K inhibitor BEZ235, and more effectively suppressed the growth of prostate cancer cells. In vivo studies with male nude mice bearing human prostate cancer xenografts showed that drug-loaded IONP were more effective than the free drug. Based on these findings, IONP can be a diverse microenvironment-responsive vehicle, which can simultaneously deliver multiple agents and facilitate the sensitive monitoring of drug levels using compact relaxometers and MRI.

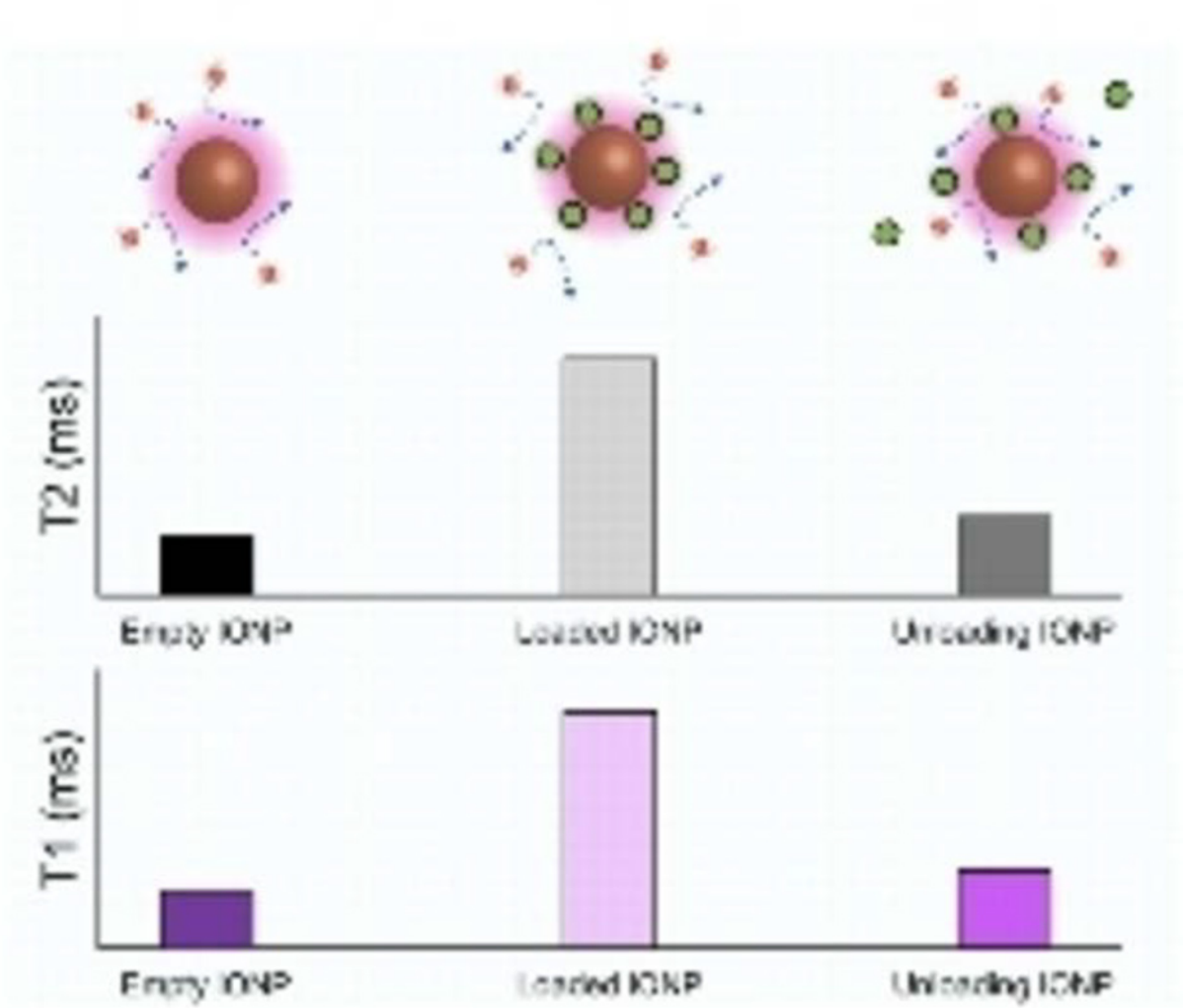

Figure 1. Iron oxide nanoparticles (IONP) can serve as multifunctional drug delivery vehicles. Once loaded, the cargo hinders the free diffusion of water molecules within the nanoparticles, causing increases in the transverse (T2) and longitudinal (T1) relaxation times. As IONP release the payload within the slightly acidic tumoric milieu, IONP recover their magnetic properties, which approach the values of the unloaded nanoparticles.

Disclosure of author financial interest or relationships:
C. Kaittanis, None; **J. Grimm**, None.

Presentation Number **P 250**
Poster Session 2
September 19, 2013 / 15:15-15:15 / Room: Exhibit Hall B

Dual combination therapy with anti-DR5 antibody and tamoxifen for Triple Negative Breast Cancer

Hyunki Kim[1], *Sharon Samuel*[1], *Guihua Zhai*[1], *Samir Rana*[2], *Kyle Lee*[3], *Amber Martin*[1], *Clinton J. Grubbs*[4], *Kurt R. Zinn*[1], *[1]Radiology, University of Alabama at Birmingham, Birmingham, AL, USA; [2]Biomedical Science, University of Alabama at Birmingham, Birmingham, AL, USA; [3]Medicine, University of Alabama at Birmingham, Birmingham, AL, USA; [4]Surgery, University of Alabama at Birmingham, Birmingham, AL, USA. Contact e-mail: hyunki@uab.edu*

Purpose: To evaluate the dual combination therapy with anti-DR5 antibody (TRA-8) and tamoxifen for triple negative breast cancer (TNBC). Methods: In vitro cell viability assay was conducted with three TNBC cell lines (2LMP, SUM159, MDA-MB-231); TRA-8 was used at 7 different concentrations (15-1000ng/ml) with/without tamoxifen (5nM), and cellular ATP signal intensity was measured. A total of 8 groups of nude mice were used for in vivo studies; groups 1-4 (n=9-10/group) were orthotopically implanted with luciferase-positive 2LMP cells (1million/site), and therapy started in 3 days thereafter (adjuvant setting). Groups 1-4 were untreated or treated with tamoxifen (400mg/kg diet), TRA-8 (0.1mg, weekly), and combination, respectively, for 3 weeks, while bioluminescence imaging was applied weekly for 6 weeks. Tumor volume was also measured with a caliper weekly for 6 weeks, and survival rate was assessed. Groups 5-8 (n=3-4/group) were subcutaneously implanted with 2LMP cells (1million/site), and therapy started when tumor size was about 9 mm in diameter (neoadjuvant setting). Groups 5-8 were untreated or treated with tamoxifen (200mg/kg diet), TRA-8 (0.2mg, semiweekly), and combination, respectively, for a week, and T2W MRI and DWI were performed at 0, 3, and 7 days after therapy initiation; tumor volume and ADC value were quantified. Results: In in vitro assay, cell viability was 20~40% reduced by tamoxifen monotherapy in all 3 cell lines ($p<0.05$), and additive efficacy was confirmed between TRA-8 and tamoxifen. In in vivo studies, however, an antagonistic effect was observed; in adjuvant setting, both tumor bioluminescence signal and tumor volume of combination group were markedly larger than those of group treated with TRA-8 alone, during entire therapeutic period. 90% of the group treated with TRA-8 alone survived for 6 weeks after cell implantation, but only 50% of combination therapy group survived during that time. Similarly, in neoadjuvant setting, tumor volume decreased 41±6% by TRA-8 monotherpay for a week, but it decreased only 16±9% during the same period when tamoxifen was added. Also, tumor ADC value increased 25±9% for 3 days after initial TRA-8 injection, but it increased only 13±9% during the same period when tamoxifen was added. Mean tumor volume change for 7 days were linearly correlated with mean tumor ADC change for 3 days ($r=-0.98$). The group treated with tamoxifen alone was not statistically different from control group in either adjuvant or neoadjuvant setting ($p>0.05$). Discussion: Tamoxifen presented high therapeutic efficacy for TNBC cell lines with/without TRA-8 in in vitro assays, but antagonistic effect in in vivo studies. All 3 TNBC cell lines express ERβ (confirmed by Western Blot analysis), and tamoxifen may induce cytotoxicity through it. However, presumably, tamoxifen could not be sufficiently delivered into the target cells in tumors due to high interstitial fluid pressure, while its antiangiogenic effect hampered the delivery of TRA-8 also. Subsequent studies will need to be followed to interpret this discrepancy more accurately.

Disclosure of author financial interest or relationships:
H. Kim, None; **S. Samuel**, None; **G. Zhai**, None; **S. Rana**, None; **K. Lee**, None; **A. Martin**, None; **C.J. Grubbs**, None; **K.R. Zinn**, None.

Presentation Number **P 251**
Poster Session 2
September 19, 2013 / 15:15-15:15 / Room: Exhibit Hall B

Imaging and quantification of bombesin receptor expression in vivo

Jeffrey D. Peterson, *Nara Narayanan, Jeannine Delaney, Jeff Morin, Milind Rajopadhye, Wael Yared, Sylvie Kossodo, LST, PerkinElmer, Hopkinton, MA, USA. Contact e-mail: jeff.peterson@perkinelmer.com*

Bombesin-like peptides, including the mammalian analogs gastrin-releasing peptide (GRP) and neuromedin B (NMB), function as growth factors in normal and neoplastic tissues. For example, GRP receptors are found in the gastrointestinal tract where they mediate hormone release and epithelial cell growth. These receptors are also overexpressed in a variety of cancers and as such have been used to develop imaging tracers and as targets in radiotherapy. As a pre-clinical alternative to using ionizing radiation, we developed a novel near infrared (NIR) fluorescent agent, BombesinRSense 680 (BRS680), designed to target and quantify bombesin receptors in vivo. BRS680 comprises a modified 7 amino-acid bombesin analog peptide labeled with a NIR fluorophore (ex/em 660/680 nm) and a pharmacokinetic modifier designed to improve its plasma availability (plasma t1/2 = 1.5 hours). In vitro labeling of human colonic adenocarcinoma HT-29 cells, which express GRP receptors, and blocking the signal by addition of unlabeled native bombesin, demonstrated the specificity of the agent by fluorescence microscopy and flow cytometry. In vivo receptor expression was quantified by fluorescence tomography after BRS680 (2 nmol/mouse) was injected intravenously into nude mice bearing HT-29 tumor xenografts. HT-29 tumors showed a high level of receptor expression with approximately 30 pmol (1.5% injected dose) quantified in the tumors at 24 hours, and lower fluorescence in other tissues except for pancreas, a tissue known for high receptor expression, and kidneys, indicating renal clearance. In contrast to the fast clearance from circulation, the tumor tissue half-life of BRS680 was shown to be approximately 42 hours. In vivo targeting specificity was confirmed by collecting tumor tissue from injected mice and co-localizing BRS680 fluorescent signal with an anti-GRP receptor antibody on frozen sections. More importantly, treatment of HT-29 tumor-bearing mice with a tumor growth-arresting chemotherapy regime decreased in vivo BRS680 signal. Six days after beginning treatment with 5-fluorouracil and oxaliplatin in mice with established tumors, BRS680 fluorescent signal was significantly decreased in treated mice as compared to control mice (21.55 + 4.89 versus 34.10 + 2.90 pmoles, p=0.043) paralleling the inhibition of tumor growth (74.25 + 7.65 versus 141 + 19.39 mm3, p=0.003). Interestingly, chemotherapy did not consistently affect the fluorescent signal associated with ProSense 750 FAST, an agent that is specifically activated by the cathepsin family of inflammatory proteases, co-injected in the same animals (6.99 +1.68 versus 10.91 + 1.73 pmoles, p=0.104). These studies demonstrate the utility of BRS680 in tracking in vivo expression of bombesin receptors and underscores its potential to serve as an in vivo real-time indicator of anti-tumor treatment efficacy.

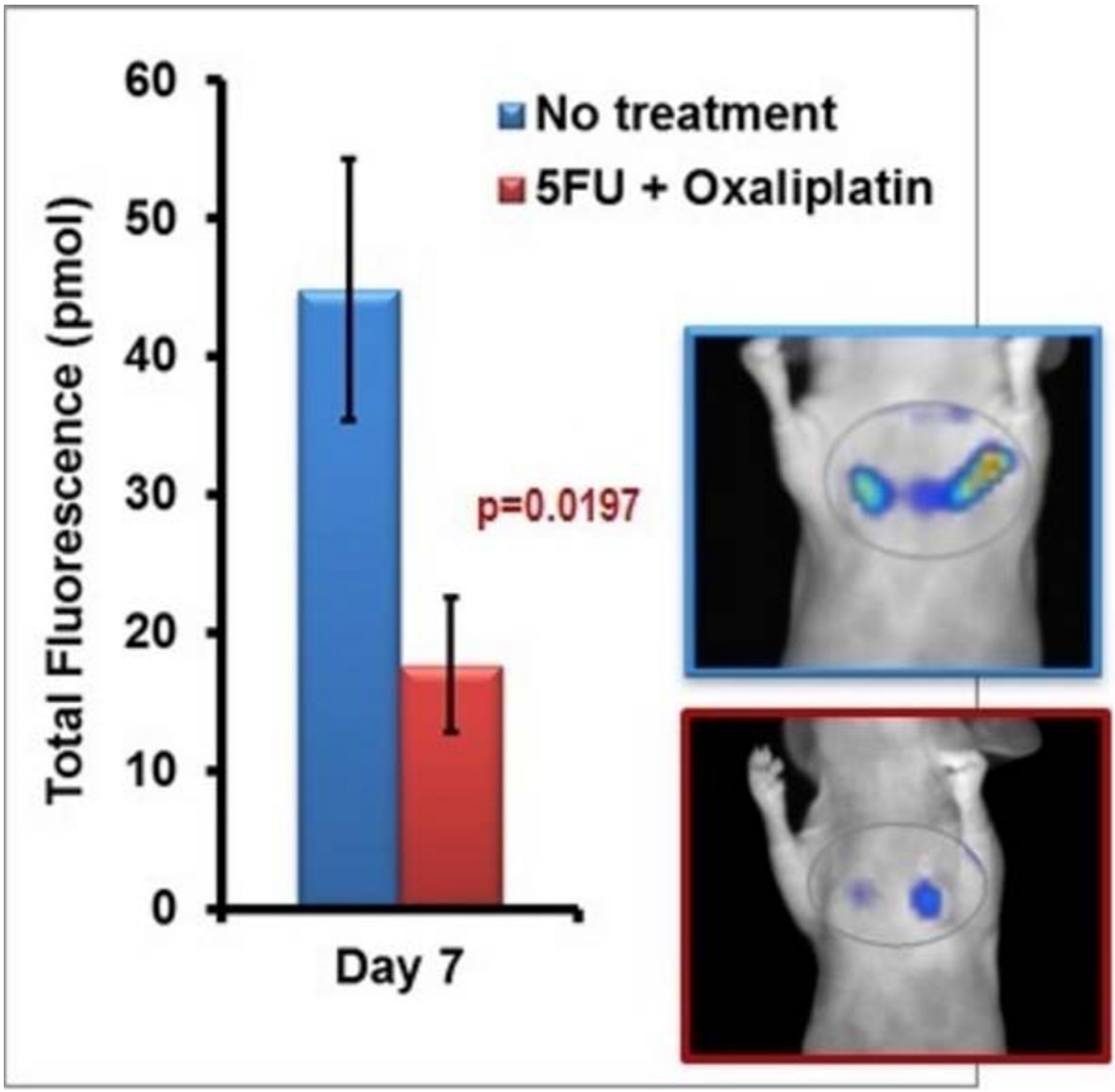

Chemotherapeutic treatment of HT29 tumor-bearing mice decreased in vivo Bombesin 680-associated tumor signal in agreement with inhibition of tumor growth

Disclosure of author financial interest or relationships:
J.D. Peterson, PerkinElmer Inc, Employment; **N. Narayanan**, None; **J. Delaney**, PerkinElmer, Employment; **J. Morin**, Perkin Elmer, Employment; **M. Rajopadhye**, PerkinElmer, Inc, Employment; **W. Yared**, PerkinElmer, Employment; **S. Kossodo**, PerkinElmer, Employment .

Presentation Number **P 252**
Poster Session 2
September 19, 2013 / 15:15-15:15 / Room: Exhibit Hall B

Detection of Hypoxia in Orthotopic Pancreatic Tumors In Vivo Using Multispectral Optoacoustic Tomography

Shanice V. Hudson[1], *Justin Huang*[1], *Christopher England*[1], *Hermann B. Frieboes*[2], *Lacey R. McNally*[1], [1]*Medicine, University of Louisville, Louisville, KY, USA;* [2]*Engineering, University of Louisville, Louisville, KY, USA. Contact e-mail: svwilliams88@gmail.com*

Noninvasive molecular and functional imaging in vivo is promising for detecting and monitoring various physiological conditions in animals and ultimately humans. Hypoxia, a condition of insufficient O2 to support metabolism, occurs when a tumor outgrows its vascular supply. When otherwise healthy tissues lose their O2 supply acutely, the cells usually die, whereas when cells gradually become hypoxic, they adapt by up-regulating the production of numerous proteins that promote their survival. To this end, we evaluated noninvasive, multispectral optoacoustic tomography (MSOT), which offers both strong optical absorption contrast and high spatial resolution. Optical contrast allows separation of signal contributions from multiple optical absorbers (e.g., oxyhemoglobin and deoxyhemoglobin), thus enabling simultaneous molecular and functional imaging. S2013 cells were implanted orthotopically into the pancreas of SCID mice. MSOT successfully detected with high resolution the distribution of a molecular contrast agent targeting αVβ3 integrin overexpressed in human S2013 cells. Simultaneously, MSOT also imaged the hemoglobin oxygen saturation and the total hemoglobin revealing hypoxic areas within the tumor. MSOT imaging can potentially lead to better understanding of the tumor microenvironment resulting in tumor progression.

Disclosure of author financial interest or relationships:
S.V. Hudson, None; **J. Huang**, None; **C. England**, None; **H.B. Frieboes**, None; **L.R. McNally**, None.

Presentation Number **P 253**
Poster Session 2
September 19, 2013 / 15:15-15:15 / Room: Exhibit Hall B

Molecular Imaging of HER2-Targeted Superparamagnetic Nanoparticles in an Orthotopic Mouse Mammary Tumor Model by Nanomagnetic Relaxometry

Steve Miller[1], *Debbie M. Lovato*[2], *Andrew D. Price*[1], *Dale L. Huber*[3], *Richard S. Larson*[2], *Edward R. Flynn*[1], [1]*Senior Scientific, Albuquerque, NM, USA;* [2]*Pathology, University of New Mexico, Albuquerque, NM, USA;* [3]*Center for Integrated Nanotechnologies, Sandia National Laboratories, Albuquerque, NM, USA. Contact e-mail: steve.miller@seniorscientific.com*

In this report, we present NanoMagnetic RelaXometry (NanoMRX™) as a novel imaging modality for in vivo detection of tumor biomarkers using an orthotopic mouse mammary tumor model and antibody conjugated superparamagnetic iron oxide nanoparticles (NPs) as the imaging agent. NanoMRX is based on brief magnetization of NPs using a small pulsed magnetic field – signal only from the bound NPs is detected by measuring the decaying magnetization of the tumor-bound NPs over time using an array of Superconducting Quantum Interference Device (SQUID) sensors (Fig. 1 Top). NanoMRX requires the production of NPs with a core size of 24 nm; following the application of a magnetizing pulse, the "Brownian" relaxation time is <1 msec and "Néel" relaxation time for bound NPs is of the order of 0.1 - 2 sec. NPs not bound to cells are not detected by the SQUID sensor array because of the rapid relaxation time due to Brownian motion allowing the unbound NPs to rotate in the fluid in which they are suspended. In contrast, the bound NPs cannot rotate because they are attached to the surface of a cell. Although the single-domain crystal is hindered in its rotation, the collective moment due to the ensemble of electron spins does realign through a process termed Néel relaxation. A method for obtaining quantitative measurements of the amount of injected iron NPs and the magnetic moment was developed to determine the location(s) and magnitude(s) of magnetic source(s) modeled by one or more magnetic dipoles and to render a 2-D contour image of the magnetic landscape for comparison with the actual physical source. For the studies reported here, the magnetic moments corresponding to the magnetic sources are extracted, the position of these dipolar sources are represented as confidence limit ellipses in the x,y plane and superimposed on the grid of the mouse photo corresponding to the same coordinate system. Methods: NPs with PEG and functionalized with carboxyl groups (Ocean Nanotech; Springdale, AR) were conjugated with an anti-human HER2/neu antibody (eBioscience, San Diego, CA) using carbodimide chemistry. Using NOD/SCID mice with mammary tumors grown from MCF7/HER2-18 cells (over-expresses HER-2) we measured the uptake of the anti-HER2-NPs by NanoMRX imaging after retro-orbital injection. Results: To illustrate our method, we show data obtained from one mouse that was imaged in the ventral position by NanoMRX (Fig. 1 Bottom). The magnetic contour map defined 3 magnetic sources. The amount of iron NPs (as percentage of the total injected) in the large tumor mass on left side was 6% and smaller mass on right side had 4%; the liver had 15% of the injected iron NPs. Conclusions: The results show that NanoMRX is a sensitive and quantitative technology for the detection of HER2-positive tumors in an orthotopic mouse model of human breast cancer. NanoMRX does not use ionizing radiation, is quantitative, with both high detection sensitivity that is linear with cancer cell number, and high contrast for tumor detection with a demonstrated in vivo localization of 0.5 mm. Studies using targeted NPs produced and optimized by us for in vivo imaging will be described.

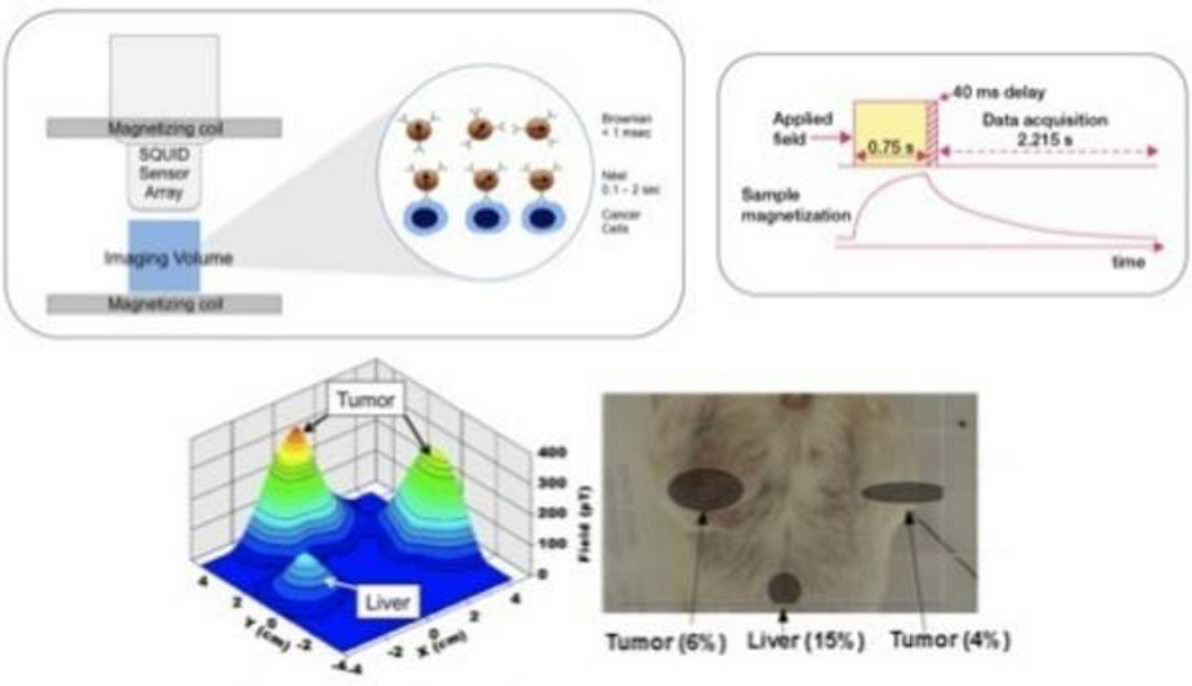

Disclosure of author financial interest or relationships:
S. Miller, Senior Scientific, Employment; Senior Scientific, Stockholder; **D.M. Lovato**, None; **A.D. Price**, Senior Scientific, LLC, Employment; **D.L. Huber**, None; **R.S. Larson**, None; **E.R. Flynn**, None.

Presentation Number **P 254**
Poster Session 2
September 19, 2013 / 15:15-15:15 / Room: Exhibit Hall B

Monitoring Extracellular pH During Tumor Growth with acidoCEST MRI

Liu Qi Chen, Christine M. Howison, Justin Jeffery, Amanda F. Baker, **Marty Pagel***, University of Arizona, Tucson, AZ, USA. Contact e-mail: mpagel@u.arizona.edu*

Introduction: Acidosis is generally considered to be a hallmark of cancer.1 However, it is unknown if different tumor models reach the same level of acidosis, and the temporal relationship between tumor growth and acidosis. In addition, the heterogeneity of acidosis throughout the tumor tissue is poorly understood. We have developed a non-invasive MRI method that can accurately measure extracellular pH (known as pHe) to assess tumor acidosis, termed "acidoCEST MRI" (acidosis - Chemical Exchange Saturation Transfer). We employed acidoCEST MRI to investigate the differences in pHe between Raji, Granta519 and Ramos lymphoma tumor cell lines, the temporal relationship between tumor growth and acidosis, and the spatial heterogeneity of tumor acidosis. Methods: Mouse models of Raji, Granta519 and Ramos lymphoma were prepared by injecting 10 x 10^6 cancer cells in 50% Matrigel™ into the subcutaneous flank of SCID mice. The mice were imaged on approximately 2.5 weeks and 4 weeks after initial injection. A CEST-FISP pulse sequence with 2.8 μT saturation power, 5 sec saturation time, 90 Hz bandwidth, and 54 saturation frequencies ranging from +10 to -10 ppm was used to acquire an acidoCEST image in 4.25 min using a 7T MRI scanner. A bolus of 200 μL of 976 mM iopromide was injected i.v., followed by an infusion of 150 μL/hour of iopromide. A series of six acidoCEST spectroscopic images were acquired within a total of 26 min. To improve the signal to noise ratio, the average of each pixel signal in the series of six acidoCEST images was determined, and groups of 2x2 pixels within this average data were binned. Pixel-wise pHe maps were created by fitting Lorentzian line shapes to the CEST spectrum for each averaged binned pixel. The average pHe and standard deviation of pHe values in each pHe map were used to compare for statistic significant using Student's T-Test. Results: The Ramos, Granta519 and Raji models had an average pHe of 6.75 ± 0.04, 6.69 ± 0.06 and 6.66 ± 0.05, respectively. The Ramos had a statistically significantly higher pHe than the Granta519 and Raji models ($p = 0.033$ and $p = 0.001$ respectively), but Granta519 and Raji tumor models were not statistically different ($p = 0.29$). The pHe changes over the two imaging sessions were statistically significant ($p < 0.01$) except for one Granta519 mouse. However there was no consistency in the pHe changes between days among mice of each tumor model. Our results showed that the tumor's pHe was spatially heterogeneous throughout the tumor volume. As a representative example, Ramos mouse #4 showed a larger region of lower acidity (< pH 6.7) on Day 18 relative to Day 25 (Fig A and B). As shown in the cumulative histogram of the pixel-wise pHe analysis on these 2 days, the pH of the tumor increased over 7 days (Fig C). Discussion: Our studies demonstrated that different tumor models can have significantly different pHe. Our studies also demonstrated that tumor pHe can show significantly different pHe values over time. We were able to obtain pH maps to demonstrate the spatial heterogeneity of tumor. The spatial heterogeneity of tumor pHe also changed over time.

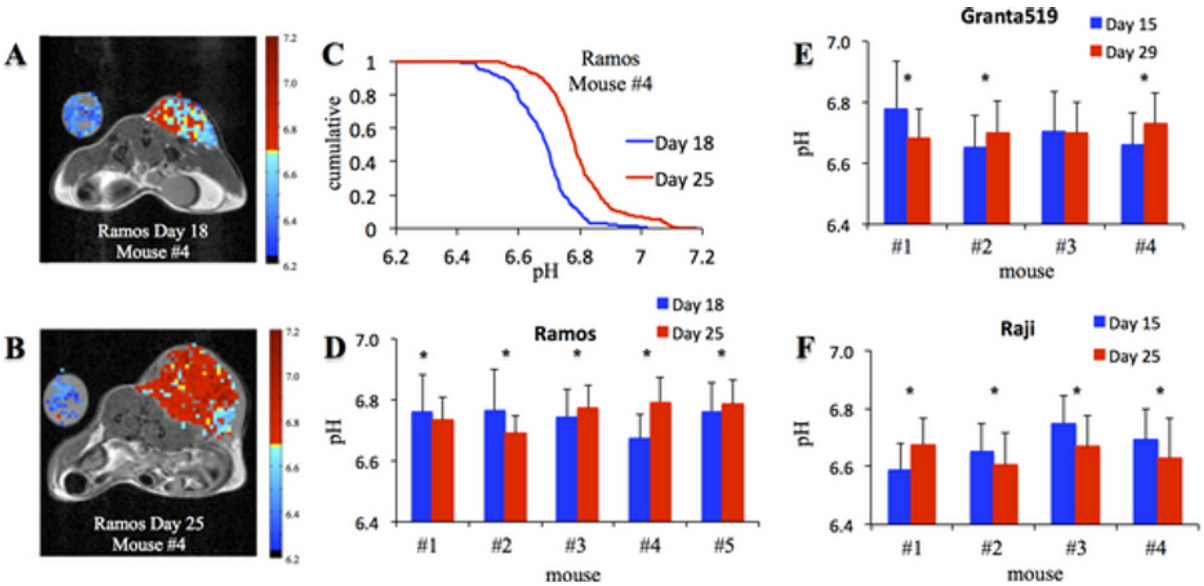

Fig A and B) pHe map of mouse model with Ramos flank tumor on day 18 and day 25. The pHe maps were simplified to show low and high pH (6.2 - 6.7 and 6.7 - 7.2 respectively). Fig C) cumulative histogram of the pixel-wise pHe of the same Ramos mouse, indicating an increase of pH of 0.12 pH units. Fig D - F) histograms of average pHe over two imaging sessions for Ramos, Granta519 and Raji flank tumor model. * p <0.01.

Disclosure of author financial interest or relationships:
L. Chen, None; **C.M. Howison**, None; **J. Jeffery**, None; **A.F. Baker**, None; **M. Pagel**, None.

Presentation Number **P 255**
Poster Session 2
September 19, 2013 / 15:15-15:15 / Room: Exhibit Hall B

Zr-75 cell line: a promising tumor model for imaging somatostatin receptor SST2a expression in breast cancer by positron emission tomography

Maral Pourghiasian, *Jinhe Pan, Navjit Hundal-Jabal, Joseph Lau, Kuo-Shyan Lin, Francois Benard, BC Cancer Research Centre, Vancouver, BC, Canada. Contact e-mail: mpourghi@bccrc.ca*

Objective: High expression of somatostatin receptor subtype 2a (SST2a) has been shown in a variety of malignancies including neuroendocrine tumors and breast cancer. Most of reported studies on the development of novel radiotracers for imaging SST2a expression used mice bearing tumors derived from either SST2a transfected cell lines or rat pancreatic cancer cell line (AR42J). The objective of this study was to screen different breast cancer cell lines of human origin, and evaluate their xenografts in mice for SST2a detection by PET. Methods: Hormone receptor positive breast cancer cell lines MCF-7 and ZR-75, were chosen for *in vitro* and *in vivo* studies. ^{68}Ga-DOTA-TATE, a potent somatostatin agonist radiotracer was prepared by microwave heating the mixture of 68GaCl3 and DOTA-TATE in HEPES buffer, followed by HPLC purification. MCF-7 and ZR-75 cells were inoculated subcutaneously in NODSCID mice. When tumors reached 5-7 mm in diameter, biodistribution and dynamic PET/CT imaging studies were carried out by injection of 0.37 MBq and 3.7 MBq of ^{68}Ga-DOTA-TATE respectively. Blocking studies were performed to determine the specificity of radioligand to the receptors. Animals were euthanized 1 h post-inj and and percentage injected dose per gram (%ID/g) of tissues of interest were determined. Time activity curves were generated from Dynamic images. Results: ^{68}Ga-DOTA-TATE was obtained in > 50 % decay-corrected radiochemical yield in 40 min starting from the elution of 68Ga, and with > 37GBq/μmole specific activity. Zr-75 tumor-bearing mice showed an excellent tumor visualization with low background at 1 h post-inj. Tumor uptake was 14.1 ± 3.5 %ID/g. Pancreas uptake was high (27.8 ± 4.8) as expected. % ID/g of blood and other tissues were minimal. Tumor uptake in MCF-7 bearing mice was only 1.5 ± 0.2 %ID/g at 1 h post-inj whereas pancreas showed a much higher uptake similar to that of pancreas of Zr-75 tumor bearing mice. In blocking studies pancreas uptake was reduced by ~90% and ZR-75 tumors by 70%. Conclusion:A high tumor to background ratio was achieved in Zr-75 tumor model, whereas very low tumor uptake obtained in MCF-7 tumor model. This study suggests that ZR-75 breast tumor-bearing mice can be used as a promising breast cancer model for SST imaging by PET. To further validate suitability of this model different radiolabeled SST agononists and antagonists will be evaluated.

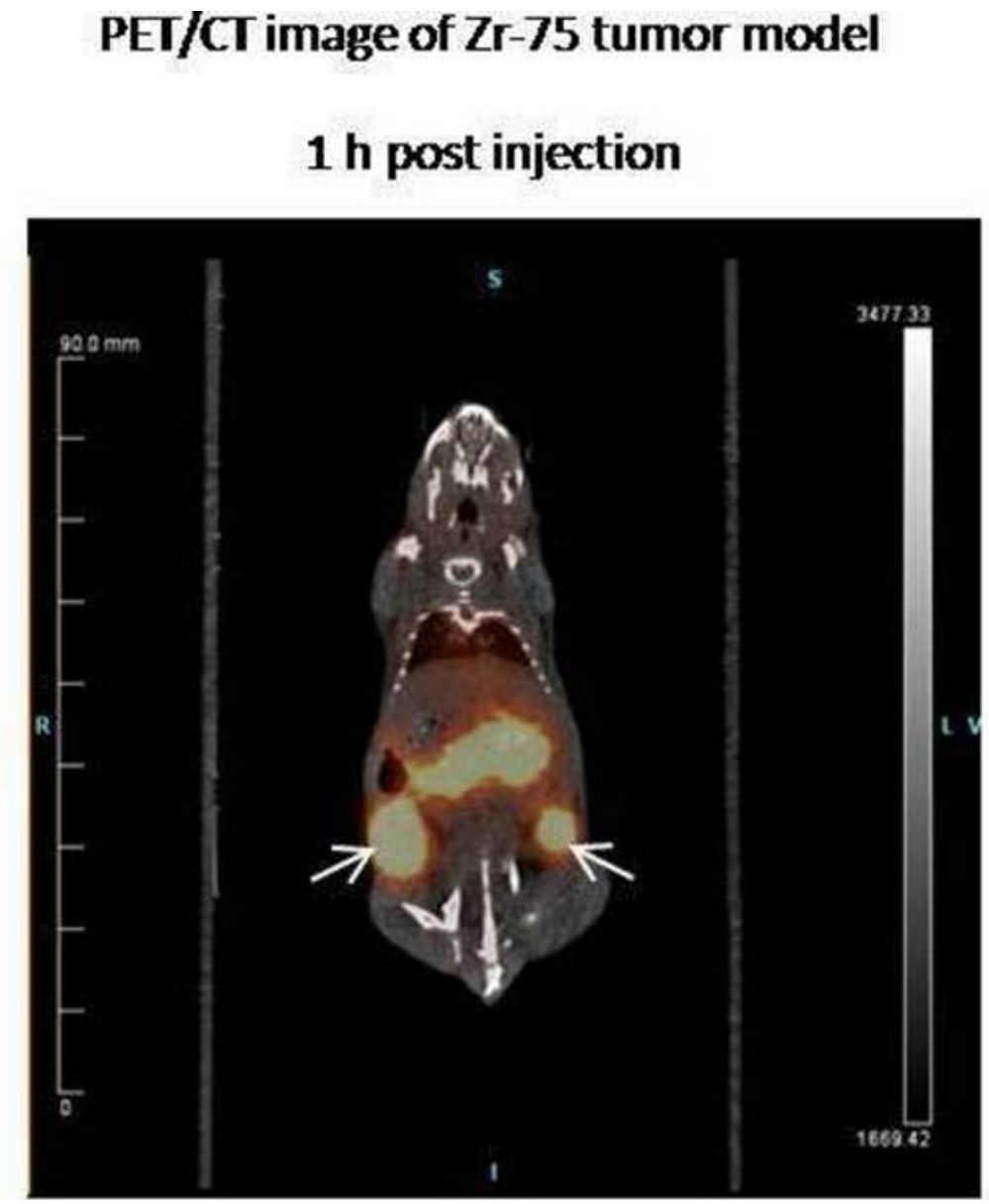

Disclosure of author financial interest or relationships:
M. Pourghiasian, None; **J. Pan**, None; **N. Hundal-Jabal**, None; **J. Lau**, None; **K. Lin**, None; **F. Benard**, None.

Presentation Number **P 256**
Poster Session 2
September 19, 2013 / 15:15-15:15 / Room: Exhibit Hall B

The pharmacodynamics of alkalinization on pH-sensitive tumor enzymes

Ian Robey, *Arthur F. Gmitro, Hui Min Leung, Justin J. Jeffery, Christine M. Howison, University of Arizona, Tucson, AZ, USA. Contact e-mail: robeyi@email.arizona.edu*

Introduction: Tumor proteases such as cathepsins and matrix metalloproteases (MMPs) serve as important biomarkers of tumor invasive potential. Proteases can be targeted using enzyme activatable fluorescence agents which are novel tools for the in vivo study of biological function and therapy monitoring1. The purpose of these experiments was to test the relationship between transient alkalinization and enzymatic activities of pH-sensitive cathepsins and MMPs in mice bearing MDA-MB-231 mammary xenografts using activatable pan-cathepsin and pan-MMP agents (MMPSense™ 750 FAST and ProSense® 750 FAST) from PerkinElmer, Inc. Methods: Mice received 4 nmol of agent via tail vein injection 24 hours prior to imaging experiments. A pre-treatment image was acquired then mice received an oral gavage of sodium bicarbonate (25 μmol/g) or PBS, and images were acquired at 0.5, 1, 2, 3, 4, and 5 hours after the gavage. Image acquisitions consisted of a 5 sec exposure for near-infrared probes (745/810 nm excitation/emission wavelength). The fluorescence images from all acquisitions were adjusted to identical minimum, maximum and threshold values. An ROI was drawn around the region of fluorescence. The photon counts in the ROIs were defined in this study as relative fluorescence units (RFU). RFU is calculated by normalizing the photon counts from each time point to the pre-treatment time point (100%) in each mouse. Results: Post-treatment images over five hours demonstrated a significant decrease in fluorescence in tumors of bicarbonate treated mice, but not PBS treated mice. Bicarbonate treated mice injected with pan-cathepsin fluorescent agent exhibited a significant reduction ($*p \leq 0.003$) in activity-based tumor fluorescence signal to 61 ± 10% in the first 30 minutes decreasing to 36 ± 8% by the first hour. Fluorescence levels remained at about 23 ± 4% between hours 2 and 5. Although there was high variability in the fluorescence signals generated from PBS treated mice, fluorescence levels were unchanged after the pre-treatment image time point with the exception of the first hour when mean fluorescence decreased to 67 ± 12% ($\dagger p = 0.014$) (Fig. 1A and B). Similar outcomes were observed in bicarbonate treated mice injected with the MMP activatable agent. Between hour 1 and 5, tumor fluorescence had decreased to 43 ± 5% of the pre-treatment time point of each mouse ($*p \leq 0.003$) (Fig. 1C and D). Discussion: The findings suggest that transient alkalinization of the tumor region resulted in a temporary reduction in cathepsin and MMP activity leading to reduced fluorescence signal from the tumors. Tumor alkalinization is proposed to provide a measure of therapeutic benefit via this mechanistic rationale. References: 1. Ntziachristos V, Tung C-H, Bremer C, and Weissleder R. Fluorescence molecular tomography resolves protease activity in vivo. Nature Med., 2002, 8(7):757-60.

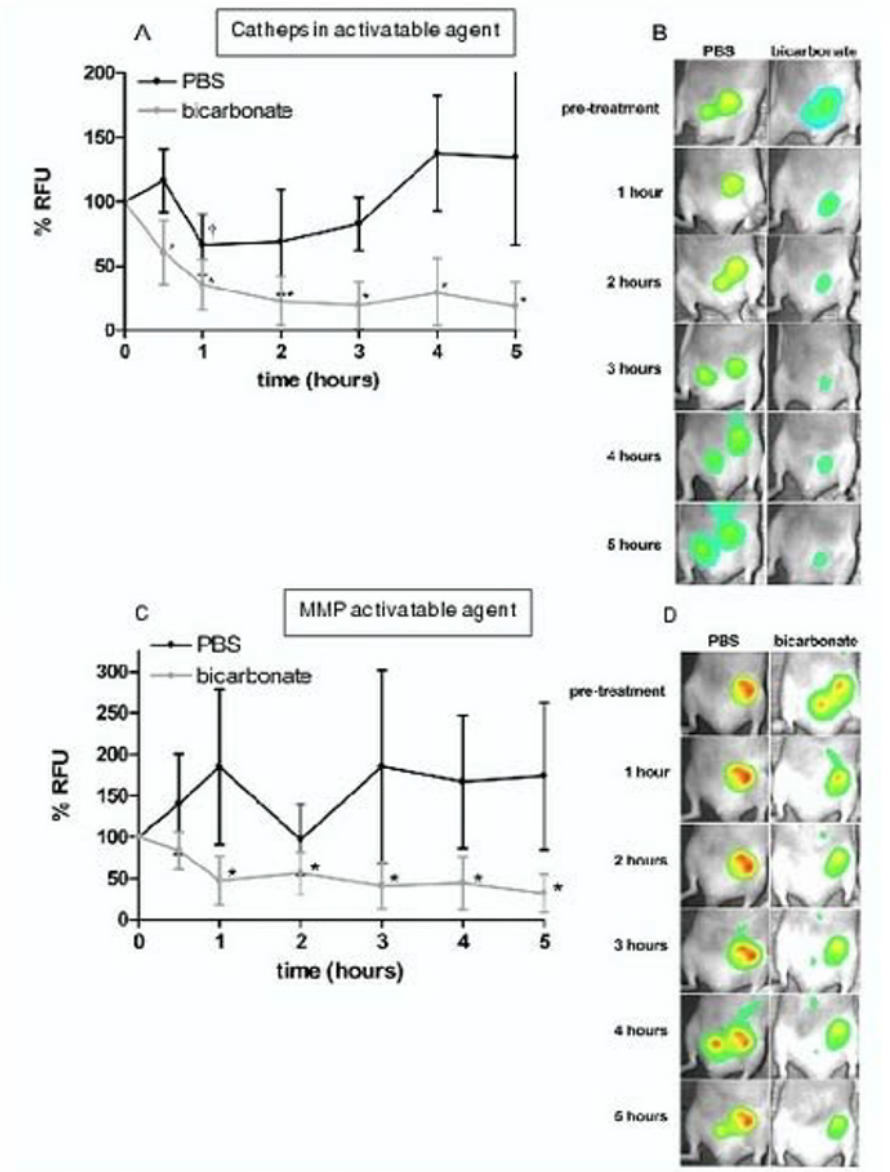

Figure 1. Effect of oral sodium bicarbonate administration on protease activity-related fluorescence in mouse xenografts. Tumor bearing mice (n = 6) were imaged prior to treatment then received 42 mg of sodium bicarbonate or PBS (p.o.). A and B) Subsequent images were taken at 30 minutes, 1, 2, 3, 4, and 5 hours. Fluorescence-based activity is expressed as a percentage of signals taken prior to treatment. The reduction in fluorescence-based activity using both pan-cathepsin and MMP agents was statistically significant in sodium bicarbonate treated mice at all time points (*P ≤ 0.003). No significant change in activation-based fluorescence was observed in PBS treated mice except at the 1 hour time point in Figure 1A (†P = 0.014). C and D) Representative image of experiment comparing PBS treated mouse to bicarbonate treated mouse.

Disclosure of author financial interest or relationships:
I. Robey, None; **A.F. Gmitro**, None; **H. Leung**, None; **J.J. Jeffery**, None; **C.M. Howison**, None.

Presentation Number **P 257**
Poster Session 2
September 19, 2013 / 15:15-15:15 / Room: Exhibit Hall B

HER-2 Affibody -conjugated Nanoparticles for In Vivo Targeting and Imaging of Primary and Metastatic Ovarian Cancers

Minati Satpathy[1], *Liya Wang*[2], *Rafal Zielinski*[3], *Weiping Qian*[1], *Malgorzata Lipowska*[2], *Jacek Capala*[3], *Gee Young Lee*[1], *Y. Andrew Wang*[4], *Hui Mao*[2], *Lily Yang*[1,2], [1]*Winship Cancer Institute, Atlanta, GA, USA;* [2]*Radiology and Imaging Sciences, Atlanta, GA, USA;* [3]*National Institutes of Health, Bethesda, MD, USA;* [4]*Ocean Nanotech, Springdale, AR, USA. Contact e-mail: msatpat@emory.edu*

Purpose: A major challenge in clinical management of ovarian cancers is the lack of sensitive and specific imaging approaches for detection of ovarian cancer. The development of targeted imaging nanoparticles offers an opportunity to apply molecular imaging for identifying ovarian cancer lesions in the peritoneal cavity, which enables accurately, differentiate between malignant and non malignant tumor before treatment, and image-guided surgery for complete tumor removal. Experimental design: We have developed HER-2 targeted magnetic iron oxide nanoparticles (IONPs) for selective delivery of the nanoparticles into HER-2 expressing ovarian tumors. A near infrared dye-labeled (NIR-830 maleimide) HER-2 affibody (ZHER2:342) was conjugated to IONPs, resulting dual imaging modality and HER-2-targeted ZHER2:342-NIR-830-IONPs. Targeted delivery of the ZHER2:342-NIR-830-IONPs in HER-2 over expressing human ovarian cancers following systemic administration was examined in an orthotopic human ovarian tumor xenograft model in nude mice. Results: ZHER2:342-NIR-830-IONPs specifically bound to and were internalized by HER-2-overexpressing SKOV3 cells but not HER-2-low OVCAR3 cells. Systemic delivery of ZHER2:342-NIR-830-IONPs led to the selective accumulation of the IONPs in primary tumors in the ovary and metastatic lesions in the peritoneal cavity and lung in the orthotopic SKOV3 tumor xenograft model, as verified by non-invasive optical and MR imaging, ex vivo optical imaging, and histological analysis of tumor and normal tissues. Conclusions: ZHER2:342-NIR-830-IONPs is a promising HER-2 targeted nanoparticle for the development of targeted imaging probes for the detection and differentiation between malignant and benign ovarian tumors using non-invasive MRI and intra-opertative optical imaging guided surgery.

Disclosure of author financial interest or relationships:
M. Satpathy, None; **L. Wang**, None; **R. Zielinski**, None; **W. Qian**, None; **M. Lipowska**, None; **J. Capala**, None; **G. Lee**, None; **Y. Wang**, None; **H. Mao**, None; **L. Yang**, None.

Presentation Number **P 258**
Poster Session 2
September 19, 2013 / 15:15-15:15 / Room: Exhibit Hall B

Development of a new highly specific targeting probe for non-invasive in vivo visualization of N-cadherin expression in prostate cancer

Christian Vanhove[1], *Caroline Dumolyn*[2], *Piet Ost*[3], *Olivier De Wever*[3], *Filip J. De Vos*[2], [1]*iMinds - IBITech - MEDISIP - INFINITY - GROUP-ID, Ghent University (UGent), Gent, Belgium;* [2]*Laboratory of radio-pharmacy, Ghent University, Gent, Belgium;* [3]*Laboratory of experimental cancer research, Ghent University, Gent, Belgium. Contact e-mail: Christian.Vanhove@UGent.be*

Purpose. Prostate cancer death results from progression from androgen receptor dependent to androgen receptor independent disease. Recently the trans-membrane protein N-cadherin showed an important role in this progression step. The aim of this study was to develop a new highly specific targeting probe for the non-invasive in vivo visualization of N-cadherin expression in prostate cancer. Today, this information can only be obtained from tissue biopsies. Methods. Three female Swiss Nu mice (21.4±1.8g) were subcutaneous injected with approximately 5-million PC3 cells. Four weeks later, animals were injected with a radiolabeled GC4 monoclonal purified anti-N-cadherin antibody, and a dose of 10.6±1.1MBq was administered intravenously in the tail vein. The antibody was labeled with I-123 (GE Healthcare, Diegem, Belgium) by incubating 10 min at room temperature using the Iodo-Gen-method. Separation of protein-bound iodine from free iodine was accomplished by purification over a PD10-column (GE Healthcare, Diegem, Belgium). Radiochemical purity was assessed by instant Thin Layer Chromatography (SG strips, Pall Corporations, Zaventem, Belgium) and by size-exclusion high performance liquid chromatography using a Shodex KW 802.5 guard column (Thomson Instrument Company, California, USA). Twenty-four and forty-eight hours after tracer injection, a 60-minutes whole-body µSPECT/µCT acquisition was started using the pre-clinical U-SPECT-II/CT system (MILabs, Utrecht, Netherlands). Mice were anesthetized with 2% isoflurane in pure oxygen for all the described procedures, and during the µSPECT/µCT acquisitions a heated bed maintained the animal body temperature. The µSPECT acquisitions were iteratively reconstructed using ordered-subsets expectation maximization; 3 iterations were used in combination with 16 subsets and the images were filtered using a Gaussian filter with 1mm full-width half-maximum. µCT images were analytically reconstructed using the Feldkamp algorithm. Volumes-of-interest were drawn over the tumor, the brain and the entire mouse body using AMIDE. Based on the average counts measured on the µSPECT images in the tumor and the brain, the tumor-to-background (T/B) ratio was calculated. Based on the global counts measured on the µSPECT images in the tumor and the entire mouse body the percent injected dose per gram tissue (%ID/g) was calculated in the tumor. Results. Results showed that the tumor could be clearly visualized on the µSPECT/µCT images (see Figure). Apart from the uptake in the tumor, tracer uptake was also present in the liver, blood pool and the thyroid. The measured T/B ratio, 24h and 48h after tracer injection was 6.5±2.0 and 5.4±2.4, respectively. The %ID/g, 24h and 48h after tracer administration was 5.6±0.3% and 4.6±0.5%, respectively. Conclusion. We developed and validated a new pre-clinically N-cadherin targeting imaging probe for molecular imaging using µSPECT. This study demonstrates that it is feasible to visualize N-cadherin expressing tumors. This predictive imaging biomarker might be able to monitor progression from androgen receptor dependent to androgen receptor independent disease in prostate cancer.

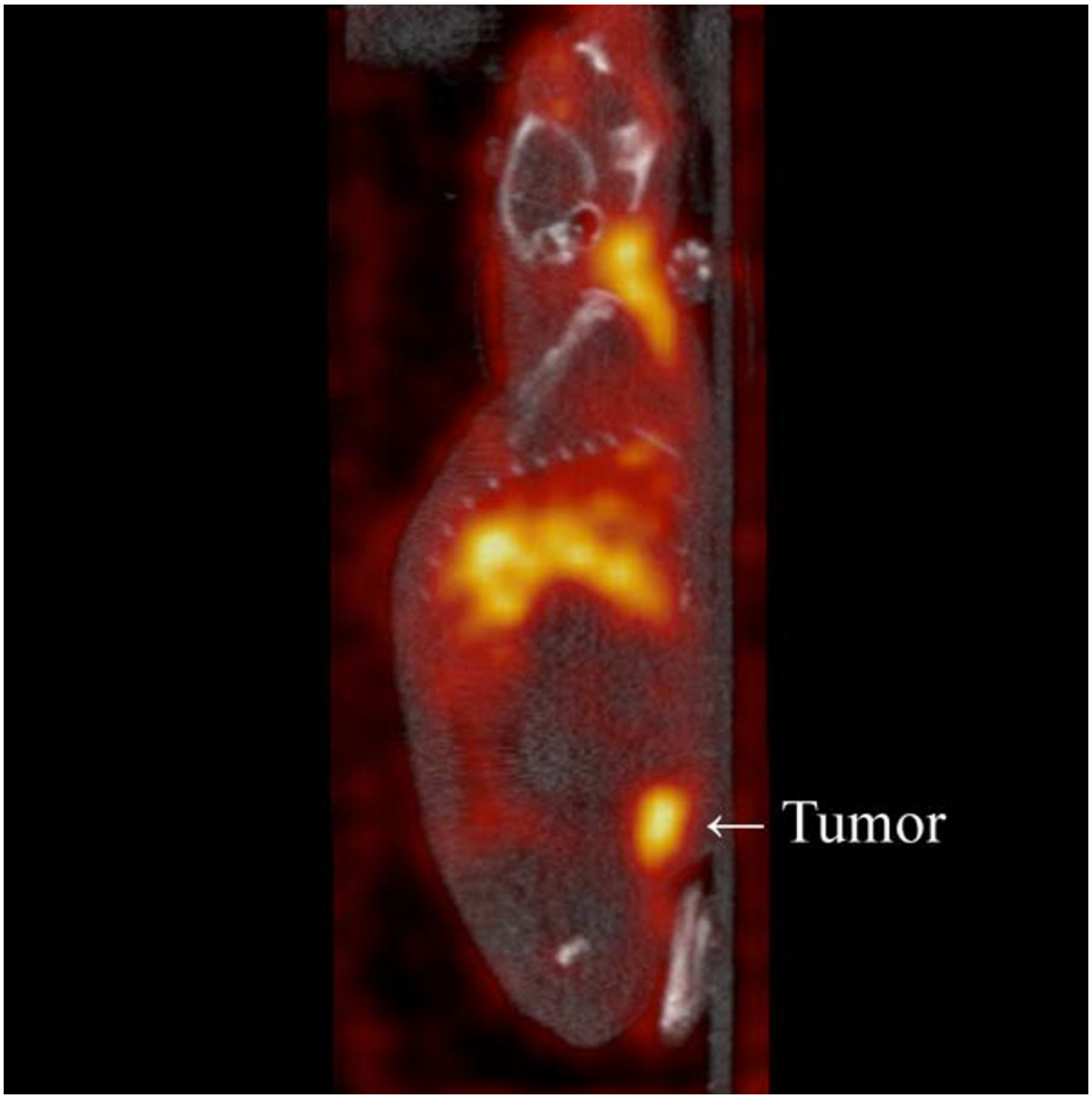

Sagittal SPECT/CT slice through one of the animals. Tracer uptake is visible on the blood-pool, liver, thyroid and the tumor.

Disclosure of author financial interest or relationships:
C. Vanhove, None; **C. Dumolyn**, None; **P. Ost**, None; **O. De Wever**, None; **F.J. De Vos**, None.

Presentation Number **P 259**
Poster Session 2
September 19, 2013 / 15:15-15:15 / Room: Exhibit Hall B

Optimizing acoustic cavitation for ultrasound-microbubble-mediated delivery of PLGA nanoparticles into tumors: phantom study and preliminary in vivo results

Tzu-Yin Wang[1], *Jung Woo Choe*[2], *Steven Machtaler*[1], *Rammohan Devulapally*[1], *Butrus T. Khuri-Yakub*[2], *Ramasamy Paulmurugan*[1], *Juergen K. Willmann*[1], [1]*Radiology, Stanford University, Stanford, CA, USA;* [2]*Electrical Engineering, Stanford University, Stanford, CA, USA. Contact e-mail: tzuyin@stanford.edu*

Introduction: Ultrasound (US) can be used to achieve targeted drug delivery via microbubble-assisted acoustic cavitation. The goal of this study was to optimize acoustic cavitation for the delivery of therapeutics encapsulated in an FDA approved drug carrier, poly(D,L-lactide-co-glycolide)-block-poly(ethylene glycol) (PLGA-b-PEG-COOH) nanoparticles (NPs), for cancer therapy. A systematic study on effects of various acoustic exposure conditions and microbubble concentration on acoustic cavitation was first performed in tissue mimicking phantoms. A preliminary in vivo study followed to demonstrate the feasibility of delivering PLGA-PEG NPs into tumor xenografts in mice. Method: Lipid shelled, perfluorocarbon encapsulated microbubbles were used as cavitation nuclei in this study. Cavitation was induced by exposing the microbubbles to US pulses with a center frequency of 1.8 MHz generated by a research US system (Verasonics). Cavitation was evaluated by passive detection of the inertial cavitation dose (ICD), and active monitoring of bubble destruction using US imaging. The effects of peak negative pressure, pulse duration, pulse repetition frequency (PRF), microbubble concentration, and focal scanning strategies, on cavitation were studied in a cavitation chamber created in an agar-based tissue mimicking phantom. Using an optimal exposure condition deduced from the parametric study, preliminary in vivo studies on the delivery of fluorescently labeled PLGA-PEG NPs into tumors were performed on hepatocellular tumor xenografts established subcutaneously on mouse hind limbs. The delivery outcomes were evaluated ex vivo using fluorescent confocal microscopy. Results: Passive cavitation detection showed that the ICD increased with pressures increasing from 0.5 to 5MPa (N=6 each), and with PRFs increasing from 10 to 100 Hz (N=6 each). The ICD also increased as the microbubble concentration increased from 4×106 to 1×108 bubbles/mL, but saturated as the concentration further increased (N=6 each). No significant effect was found for pulse lengths below 15 cycles. Active cavitation imaging confirmed more microbubble destruction with increasing pressures, as indicated by the decreased image intensity on US images. When the pressure exceeded 3MPa, more violent cavitation was observed as flickering bright spots at the center of the focal region. Compared to single focus treatment, the electronic focal steering over a large target volume resulted in more homogeneous treatment (N=4 each). Preliminary in vivo experiments showed successful delivery of PLGA-PEG NPs to a hepatocellular subcutaneous tumor (Figure, right, arrow), but not control normal hepatocytes (Figure, left). Conclusions: The peak negative pressure, pulse repetition frequency, microbubble concentration, and focal scanning strategies, have significant effects on cavitation, while no significant influence was found for short pulse lengths. Feasibility of in vivo delivery of PLGA-PEG NPs into tumor xenografts in mice was demonstrated. This study indicates that US-microbubbles-mediated drug delivery is a promising approach for targeted delivery of large drug carriers for cancer therapy.

Disclosure of author financial interest or relationships:
T. Wang, None; **J. Choe**, None; **S. Machtaler**, None; **R. Devulapally**, None; **B.T. Khuri-Yakub**, None; **R. Paulmurugan**, None; **J.K. Willmann**, Bracco, Consultant; Siemens, Grant/research support; Bracco, Grant/research support .

Presentation Number **P 260**
Poster Session 2
September 19, 2013 / 15:15-15:15 / Room: Exhibit Hall B

Functional PET imaging of Oxidative Stress

Jack M. Webster, **Christine A. Morton***, Bruce F. Johnson, Michael J. Rishel, Brian D. Lee, Andrew Torres, Global Research, GE, Niskayuna, NY, USA. Contact e-mail: morton@ge.com*

Introduction: Oxidative stress has been implicated in a wide variety of chronic conditions including cancer, diabetes, cardiovascular and neurodegenerative diseases. Therefore, development of an oxidative stress PET imaging agent could have wide clinical application. We've developed a PET tracer substrate of the cystine-glutamate transporter (System xc-), a biomarker with low expression in most normal tissues but upregulated under conditions of cellular oxidative stress. While L-cystine and L-glutamate are both natural substrates for this transporter, we decided to pursue analogs with similarities to L-cystine because it is the primary influx substrate; whereas glutamate is primarily utilized as an efflux substrate and brings potential cross-reactivity with a multitude of glutamate receptors and transporters. We've developed an analog of L-aminosuberic acid, [18F]-5-fluoro-L-aminosuberic acid ([18F]-FASu), as a PET tracer specific for uptake by System xc-. Methods: [18F]-FASu was synthesized by direct nucleophilic incorporation of [18F]F- onto a tosylate precursor and evaluated as a novel PET tracer for preclinical imaging of tumor xenografts. Quantitative biodistribution and microPET imaging studies were conducted on nude mice bearing tumor xenografts with [18F]-FASu and [18F]-FDG. Results: Renal clearance was observed to be the primary excretion pathway, while the tracer exhibited low retention in other organs with the exception of pancreas and spleen. [18F]-FASu quantitative biodistribution data showed excellent SKOV3 tumor retention (~8 %ID/g) at 1 hour post injection, with tumor-to-blood ratios of ~12 and tumor-to-muscle ratios of ~30 at 1 hour PI. These results translated well to preclinical PET imaging which showed excellent visualization of tumor xenografts with low background signal. By comparison [18F]-FDG showed SKOV3 tumor retention of ~1.5 % ID/g with a tumor-to-blood ratio of 2.6. Conclusions: [18F]-FASu is a novel PET tracer for in vivo functional imaging of a cellular response to oxidative stress conditions. Our data suggests [18F]-FASu is a promising agent for cancer imaging and may have relevance in imaging many other pathological conditions or diseases that include oxidative stress.

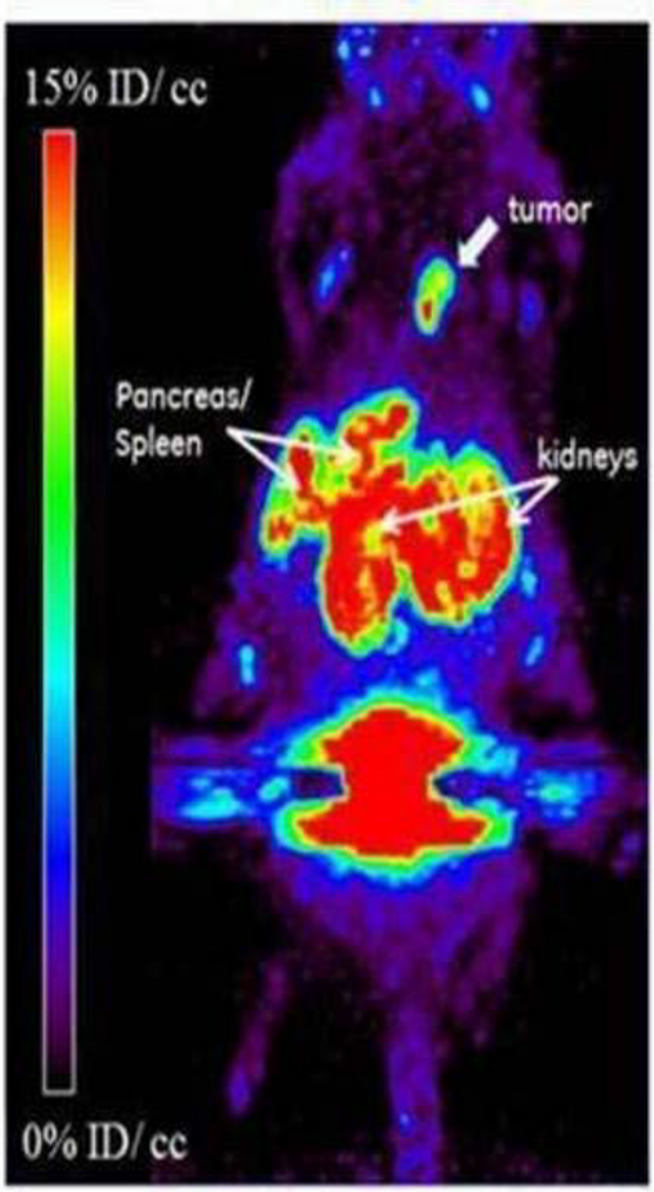

Preclinical Imaging of an SKOV3 tumor xenograft with [18F]-FASu. Tumor is labeled with a thick arrow. Kidneys, pancreas and spleen are labeled with thin arrows. Tumor ROI uptake was determined to be 8.6% ID/cc with max pixels of 16.7 %ID/cc. SUVmean and SUVmax were 2.5 and 4.9, respectively.

Biodistribution at 1 hour pi in nude mice bearing human ovarian (SKOV3) tumors

	[18F]-FDG	[18F]-FASu
Tumor % ID/g	1.55 ± 0.96	8.08 ± 2.03
Blood % ID/g	0.58 ± 0.30	0.72 ± 0.30
T:B ratio	2.61 ± 0.27	12.08 ± 0.439
Tumor size (mg)	72.60 ± 37.65	71.60 ± 39.09

n=5

Disclosure of author financial interest or relationships:

J.M. Webster, GE, Employment; **C.A. Morton**, general electric global research, Employment; **B.F. Johnson**, General Electric Global Research, Employment; **M.J. Rishel**, General Electric Co., Stockholder; General Electric Co., Employment; **B.D. Lee**, General Electric, Employment; **A. Torres**, General Electric, Employment .

Presentation Number **P 261**
Poster Session 2
September 19, 2013 / 15:15-15:15 / Room: Exhibit Hall B

Intratumoral difference of hypoxic selectivity of ^{18}F-FDG, ^{64}Cu-ATSM and ^{18}F-FMISO using sodium iodide symporter controlled by hypoxia response element expressed glioma model

Ran Ji Yoo[1,3], *Kyo Chul Lee*[1], *Sang-Kuen Woo*[1], *Kwang Il Kim*[1], *Tae Sup Lee*[1], *Kyeong Min Kim*[1], *June-Key Chung*[2], *Yang-Kyu Choi*[3], *Joo Hyun Kang*[1], *Yong Jin Lee*[1], *Sang Moo Lim*[4], [1]*Molecular Imaging Research Center, Korea Institute of Radiological & Medical Science, Seoul, Republic of Korea;* [2]*Department of Nuclear Medicine, Tumor Immunity Medical Research Center, Laboratory of Molecular Imaging and Therapy of Cancer Research Institute, Seoul National University College of Medicine, Seoul, Republic of Korea;* [3]*Department of Laboratory Animal Medicine, College of Veterinary Medicine, Konkuk University, Seoul, Republic of Korea;* [4]*Department of Nuclear Medicine, Korea Institute of Radiological & Medical Sciences, Seoul, Republic of Korea. Contact e-mail: ranjiyoo@kirams.re.kr*

Purpose: Hypoxia-inducible factor-1 (HIF-1) plays an important role in malignant tumor progression and in the development of resistance to radiotherapy. In this study, hypoxia specific radiotracers such as [^{64}Cu]diacetyl-bis(N4-methylthiosemicarbazone) (^{64}Cu-ATSM), [^{18}F]fluoromisonidazole (^{18}F-FMISO) and [^{18}F]fluoro-2-deoxy-D-glucose (^{18}F-FDG) was undertaken to compare the expression of HIF-1alpha using hypoxia response element(HRE) controlled sodium iodide symporter genes (NIS) transfected C6 glioma cell xenografted mice. Methods: C6 glioma cells were stably transfected with NIS reporter genes driven by a minimal promoter plus 5 copies of HRE(C6-5HRE-NIS; J Nucl Med 2008; 49:1489-1497). In vitro studies, hypoxic conditions were modeled by exposing a low oxygen atmosphere (<1% O2) in a hypoxic chamber. Under hypoxic condition, expression of mRNA or protein HIF1-alpha was checked by RT-PCR or western blotting assay. Uptake of ^{64}Cu-ATSM, ^{18}F-FMISO, ^{18}F-FDG or ^{125}I was measured to hypoxic or normoxic condition, respectively. At three weeks after C6-5HRE-NIS cells implantation, SPECT imaging was performed at 30 min after an intraperitoneal injection of ^{99m}Tc to confirm the expression of NIS. To detect the distribution of hypoxic, PET images were acquired for 20 min after injection of ^{18}F-FMISO and ^{64}Cu-ATSM, respectively. Additional delay scan was performed (^{18}F-FMISO: 4 hr, ^{64}Cu-ATSM: 2, 15, 24 and 40 hr). All imaging was performed using small animal scanner (Inveon, Siemens). Result: Under the hypoxic condition, uptake of ^{125}I, ^{18}F-FMISO, ^{18}F-FDG and ^{64}Cu-ATSM was increased to 2.12, 7.27, 5.15 or 2.44 times than those of normoxic condition, respectively. Also, mRNA or protein levels of HIF1-alpha or NIS increased under the hypoxic conditions. In C6-5HRE-NIS model, ^{18}F-FMISO (Early, 20min) and ^{18}F-FMISO (Delay, 4h) images were similar with those of ^{99m}Tc. In the ROI analysis, ^{99m}Tc have positive correlation with ^{18}F-FMISO as ^{18}F-FMISO (E) ($r= 0.73$, $p<0.001$), ^{18}F-FMISO (D) ($r= 0.7$, $p<0.001$). ^{64}Cu-ATSM(Delay, 24-40 hours after injection) images were similar with those of ^{99m}Tc, but the uptake distribution of ^{64}Cu-ATSM (Early, 20min) was different from ^{99m}Tc. In the ROI analysis, the uptake of ^{99m}Tc was poor correlated ($r= 0.41$) with early ^{64}Cu-ATSM uptake, but showed significantly correlation ($r= 0.69$, $p<0.001$) with ^{99m}Tc at 40 h after injection. Conclusion: ^{18}F-FMISO or ^{64}Cu-ATSM and HIF1-alpha were positively correlated in hypoxia response element controlled NIS transfected C6 glioma model. We successfully demonstrated the feasibility of evaluation of hypoxic specific radiotracers using molecular imaging of hypoxia response controlled NIS reporter gene system.

Disclosure of author financial interest or relationships:
R. Yoo, None; **K. Lee**, None; **S. Woo**, None; **K. Kim**, None; **T. Lee**, None; **K. Kim**, None; **J. Chung**, None; **Y. Choi**, None; **J. Kang**, None; **Y. Lee**, None; **S. Lim**, None.

Presentation Number **P 262**
Poster Session 2
September 19, 2013 / 15:15-15:15 / Room: Exhibit Hall B

Non-internalizing GA101 cys-diabody outperforms Rituximab cys-diabody in 124-Iodine anti-CD20 immunoPET imaging

Kirstin A. Zettlitz[1], *Richard Tavaré*[1], *Scott M. Knowles*[1], *Felix B. Salazar*[1], *Matthew Rochefort*[3], *Tove Olafsen*[2], *Anna M. Wu*[1], [1]*Molecular & Medical Pharmacology, UCLA, Los Angeles, CA, USA;* [2]*Preclinical Imaging, ImaginAb Inc, Inglewood, CA, USA;* [3]*Department of Surgery, UCLA, Los Angeles, CA, USA. Contact e-mail: kzettlitz@mednet.ucla.edu*

CD20 is expressed on the majority of B-cell malignancies and is a valuable target for antibody-based therapy. For initial diagnosis, therapy management and follow-up, an efficacious diagnostic tool is needed to assess antigen expression, tumor burden and localization. We developed and evaluated novel antibody-based PET tracers based on the anti-CD20 mAb GA101 and compared them to analogous rituximab-based PET imaging agents. GA101 is a humanized type II anti-CD20 mAb that binds CD20 in a different orientation from type I antibodies (rituximab), and is not internalized. Cell surface retention is preferable for imaging, allowing the use of radioiodinated tracers which show greatly reduced normal tissue background. We engineered small bivalent antibody fragments (cys-diabodies, CDb, 55 kDa) with optimized pharmacokinetics for PET imaging and C-terminal free cysteines that are suitable for site-specific conjugation. Both the rituximab-based Rx_CDb and the GA101-based GA101_CDb retain the cell binding characteristics (type I/II epitope, stoichiometry, apparent affinity) of their respective parental IgG but lack Fc-mediated functions and FcRn recycling. Both cys-diabodies were radioiodinated with I-124 and immunoreactivity was confirmed using CD20 expressing cells (38C13-huCD20). For in vivo evaluation we obtained microPET images in tumor-bearing mice at 4, 8, and 24 h and both fragments show high activity in the CD20-positive tumor with low normal tissue background. Tumor uptake as determined by quantitative ROI analysis and ex vivo biodistribution at 24 h was 2.75-fold higher for 124I-GA101_CDb (4.60 ±1.30 %ID/g) than for 124I-Rx_CDb (1.67 ±0.27 %ID/g) suggesting internalization and dehalogenation of the type I epitope binder 124I-Rx_CDb. In conclusion, the GA101-based cys-diabody specifically targets CD20-positive tumor cells in vivo and produce high-contrast microPET images superior to those obtained using rituximab-based cys-diabody. Labeling of both anti-CD20 cys-diabodies with residualizing radio metals and comparison of these PET tracers to 124-Iodine imaging could be used to further evaluate CD20 internalization in a variety of B-cell malignancies in vivo. As novel immunoPET imaging agent GA101_CDb could provide information on extent of disease, presence of therapeutic target, and evaluate response to therapy. Most important, as type II epitope binders, GA101-based tracers will not modulate CD20 surface molecules on the target cell and when used as a diagnostic will not influence the subsequent anti-CD20 therapy.

Disclosure of author financial interest or relationships:
K.A. Zettlitz, None; **R. Tavaré**, None; **S.M. Knowles**, None; **F.B. Salazar**, None; **M. Rochefort**, None; **T. Olafsen**, ImaginAb Inc., Employment; **A.M. Wu**, ImaginAb, Inc., Stockholder; ImaginAb, Inc., Consultant; ImaginAb, Inc., Grant/research support; Daiichi Sankyo, Consultant; Sanofi, Consultant .

Presentation Number **P 263**
Poster Session 2
September 19, 2013 / 15:15-15:15 / Room: Exhibit Hall B

In vivo MRI and Optical Imaging of Tumor Vascular Endothelial Cells using Bimodal Liposomal Nanoparticles

Liang Zhang[1], Heling Zhou[1], Philip E. Thorpe[2], **Dawen Zhao**[1], [1]*Radiology, UT Southwestern Medical Center, Dallas, TX, USA;* [2]*Pharmacology, UT Southwestern Medical Center, Dallas, TX, USA. Contact e-mail: Dawen.Zhao@UTSouthwestern.edu*

Phosphatidylserine (PS), normally restricted to the inner leaflet of the plasma membrane, becomes exposed on the outer surface of viable (non-apoptotic) endothelial cells in tumor vasculature, but not in normal blood vessels. In the present study, we report the use of in vivo molecular MRI/optical imaging to detect exposed PS on tumor vasculature based on a novel human monoclonal antibody, PGN635 that specifically targets PS. The F(ab')2 fragments of PGN635 were conjugated to polyethylene glycol (PEG)-coated liposomes. MR contrast, paramagnetic iron oxide nanoparticles (IO) were packed into the hydrophilic core of liposome, while near infrared dye, DiR was incorporated into the lipophilic bilayer. Specificity of the dual contrast liposomes (100 nm hydrodynamic diameter) bound to PS-exposed vascular endothelial cells was first studied by in vitro histological staining and MRI/optical imaging. At 9.4T MRI, significant reductions in T2-weighted signal intensity and T2 values were detected in cultured vascular endothelial cells treated with irradiation (6 Gy; $p < 0.05$), while no change was observed in nonirradiated cells, or in irradiated cells treated with control antibody conjugates or pretreated with PGN635 antibodies (blocking study). Similar results were observed by fluorescence microscopy. In vivo longitudinal MRI and optical imaging were performed after i.v. injection of the dual contrast liposomes into mice bearing subcutaneous breast MDA-MB231 tumors. NIR optical imaging revealed a clear tumor contrast in non-irradiated tumors 24 h later (tumor/normal ratio (TNR) = 3.8 ± 0.6). Irradiation significantly increased PS exposure on tumor vascular endothelial cells, resulting an enhanced tumor contrast at 24 h (TNR = 5.2 ± 0.9). At 9.4 T MRI, longitudinal T2-weighted images detected inhomogeneous signal loss in tumor at 24 h (mean TNR decrease = 15 ± 3%). Irradiation treated tumors showed significantly more hypointense regions (mean TNR decrease = 47 ± 6%; $p < 0.01$). The vascular location of IO-DiR-PGN635F(ab')2 liposomes was confirmed by Prussian blue staining and immunohistochemical staining of CD31-positive blood vessels. Localization of IO-DiR-PGN635 F(ab')2 liposomes to tumor blood vessels was antigen specific, since IO-DiR-Aurexis F(ab')2, a control probe of irrelevant specificity, showed minimal accumulation in the tumors. Our studies suggest that tumor vasculature can be successfully imaged in vivo with molecular imaging modalities to provide sensitive tumor detection. Acknowledgments: We thank Peregrine Pharmaceuticals Inc., Tustin, CA, for the provision of PGN635 antibody. This work was supported in part by DOD W81XWH-12-1-0317 and by the Gillson Longenbaugh Foundation, Dallas, TX. Imaging was conducted by DOE grant #DE-FG02-05CH11280 and NIH BTRP # P41-RR02584.

Disclosure of author financial interest or relationships:
L. Zhang, None; **H. Zhou**, None; **P.E. Thorpe**, Peregrine Pharmaceuticals, Grant/research support; Peregrine Pharmaceuticals, Consultant; Peregrine Pharmaceuticals, Stockholder; **D. Zhao**, None.

Presentation Number **P 264**
Poster Session 2
September 19, 2013 / 15:15-15:15 / Room: Exhibit Hall B

Dual-Modality CT/MR Agent for Image-Guided Radiotherapy of Liver Tumors

Jinzi Zheng[1], *Tonya Coulthard*[2], *Sharif Ahmed*[3], *Murtuza Zair*[3], *Anand Ghanekar*[3], *Christine Allen*[4], *David A. Jaffray*[1,5], [1]*STTARR Innovation Centre, Princess Margaret Hospital, Toronto, ON, Canada;* [2]*Aspect Imaging, Toronto, ON, Canada;* [3]*General Surgery, University Health Network, Toronto, ON, Canada;* [4]*Pharmaceutical Sciences, University of Toronto, Toronto, ON, Canada;* [5]*Radiation Oncology, University of Toronto, Toronto, ON, Canada. Contact e-mail: jinzi.zheng@rmp.uhn.on.ca*

Introduction: Current treatment options for unresectable liver metastases have shown to improve survival but do not control metastases permanently. Two clinical studies performed at our institution have demonstrated that stereotactic body radiation therapy (SBRT) - precise delivery of high doses of focused radiation - can be performed safely on the majority of patients with liver metastases. Specifically, treated tumors have shown a control rate of 74% (i.e. shrank or remained the same size) at one year post-treatment. Improved visualization of the tumor within the liver parenchyma using CT or MR-guided radiation therapy will further increase the precision of high dose radiation delivery and has the potential to ultimately improve patient survival. We have successfully developed a multi-modality nano-sized liposome-based contrast agent for CT and MR that provides improved visualization of liver tumors in both imaging modalities in a mouse xenograft model of intrahepatic human hepatocellular carcinoma (HCC). **Methods:** NOD/SCID mice were implanted with HCC tumor fragments obtained from a patient biopsy sample to form an intrahepatic xenograft. 200 µL of the nanosized liposome contrast agent Nanotrast-CM was administered i.v. to each mouse. CT imaging (GE Locus Ultra, 80 kVp, 50mA) and MR imaging (1T Bruker ICON Compact MRI, FLASH, TE/TR = 4.2/22.0) were performed pre-contrast administration and 1, 3 and 5 days post-injection. Histology analysis was performed on the excised livers to confirm the location of the HCC lesion. **Results:** Liver tumor bearing mice exhibited hyper and hypovascular lesions throughout the liver. Figure 1 shows an example of a mouse bearing a single hypervascular lesion in the right posterior liver lobe pre-contrast administration and 5 days post-injection imaged with CT and MR. The non-contrast enhanced lesion is seen as a hypointense region in T1-weighted MR and as a dark shadow in CT. Immediately post Nanotrast-CM administration and up to 5 days post-injection, significant positive contrast enhancement is seen in both modalities. While the contrast agent provides physically co-localized signal increase, the contrast enhancement pattern is different in the two imaging modalities. This is due to the higher sensitivity of MR compared to CT at low contrast agent concentrations, and MR's non-linear performance at high contrast agent concentrations. As a result, the HCC tumor is seen to have homogeneous contrast uptake in MR, while in CT the heterogeneous vascular supply can be visualized. Specifically, the hypervascular peripheral tumor region is visualized in CT with significant amount of Nanotrast-CM uptake, while the centre of the tumor is characterized by limited perfusion and low contrast accumulation. **Conclusion:** Clear visualization of both hyper and hypovascular liver lesions in CT and MR demonstrates feasibility of employing this novel dual-modality agent for image-guided SBRT of liver lesions. The ability of Nanotrast-CM to provide persistent signal enhancement in CT and MR will allow for radiation therapy planning and delivery to be accomplished following a single administration of contrast agent.

Disclosure of author financial interest or relationships:
J. Zheng, None; **T. Coulthard**, Aspect Imaging, Employment; **S. Ahmed**, None; **M. Zair**, None; **A. Ghanekar**, None; **C. Allen**, None; **D.A. Jaffray**, Precision X-ray Inc., Other financial or material support .

Presentation Number **P 265**
Poster Session 2
September 19, 2013 / 15:15-15:15 / Room: Exhibit Hall B

Dynamic Contrast Enhanced MRI (DCE-MRI) of Multiple-lesions in One-Time Injection Using Wideband technique

Chia-Hsin Pan, Edzer L. Wu, Yi-Fang Chen, **Wei-Er Chen***, Yeun-Chung Chang, Jyh-Horng Chen, National Taiwan University, Taipei, Taiwan. Contact e-mail: f99945013@ntu.edu.tw*

The purpose of this study was to implement Wideband MRI technique in dynamic contrast enhanced (DCE) study. This implementation allows us to monitor the perfusion of multiple organs or lesions in different anatomic locations simultaneously, therefore, we can obtain the information of the multiple organ correlation. Introduction Wideband MRI is a new technique capable of acquiring information of multiple sites simultaneously by increasing the acquisition bandwidth [1] , the number of slices can be multiplied without challenging the hardware. Each slice package can be placed far apart from each other without anatomic continuity. This approach enables simultaneously monitoring more different anatomic locations or organs in one single acquisition. DCE MRI provides important information of perfusion of organs or lesions using a series of repeated high-speed scans. Thus, the kinetic characteristics of a specific organ or lesion can be assessed by obtaining time-signal curve. Specific pharmacokinetic models are then applied to describe functional microcirculation and tumor angiogenesis [2]. There is limitation of DCE MRI to cover a large range of a specific lesion or multiple locations without sacrifice the scanning time. To cover a large region of interest within reasonable short acquisition depends on the hardware performance. In addition, long scanning time might lose kinetic information. Therefore, implementation of Wideband MR technology in DCE MRI study provides a solution not only to increase scan range and speed scanning time but also to obtain dynamic information of multiple different discontinuous anatomic sites. In this study, we implemented Wideband MR Technology into DCE MR study of a subcutaneously implanted lung cancer in a mice model to evaluate the tumor perfusion and the organ distant to the tumor simultaneously. Materials and Methods Animal preparation Male, 6-week-old, Nod-SCID mice were used. 1×106 cells of non-small cell lung cancer cell line CL1-0 transfect VEGF isoform 189 were injected intramuscularly into the right hind limb. MR scans of the mice were performed after one week of the implantation. Wideband DCE MRI The images were acquired by using a 7T MRI scanner (Biospec, Bruker, Germany). Gradient echo(FLASH) was used and the parameters are listed as follow: TR 200 ms, TE 3.628 ms, flip angle 40°, NEX=1, 15 slices for each imaging package, slice thickness=0.6mm, inter-slice distance=1mm, matrix size 256 x 128. Scan time of a single repetition was 25.4s with a total of 33 repetitions. Intra-orbital contrast medium was injected on the fifth repetition. In Wideband MR technique, the number of images acquired simultaneously is determined by a "W factor", e.g. number of locations monitored simultaneously. A W=2 was used in our experiment which made the image slices doubled (a total of 30 slices shown in Fig. (a)). Results and Discussions Figure (b) shows the kinetic change of two regions that were monitored simultaneously. According to Figure (c) the signal intensity- time curve of kidney was elevated after contrast agent injection, and followed by a sudden descent due to inverse effect of excessive amount of contrast medium accumulated. As for the limb tumor, it was positive enhanced throughout the whole experiment. Conclusions With the use of Wideband MRI, simultaneous evaluation of the kinetic information of two locations without anatomic continuity could be obtained during one single DCE MRI study. Combination of Wideband MR Technology and DCE MRI enables versatile approach to investigate perfusion characteristics of different tumor or organ. The related Ktrans characterization maps can be also derived from the DCE MRI at different sites using Tofts model in the future.

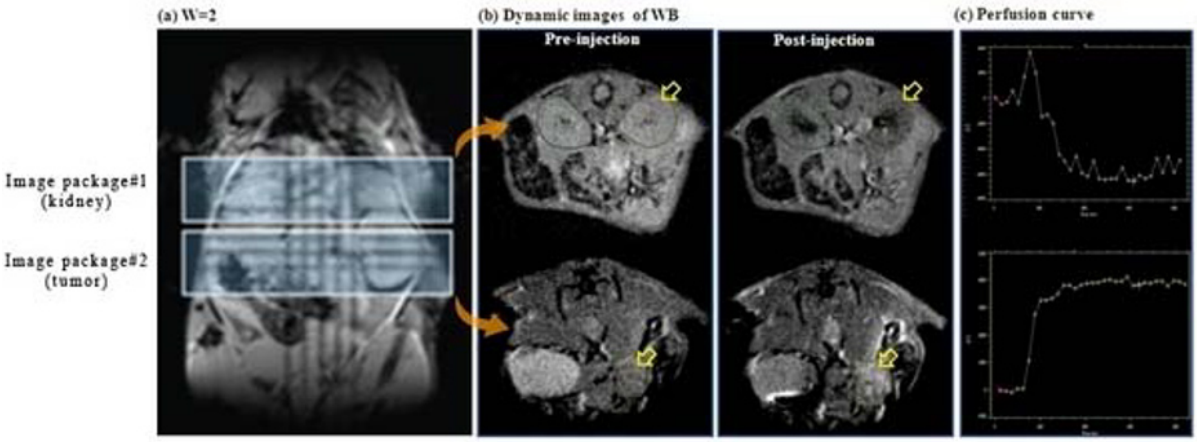

Disclosure of author financial interest or relationships:
C. Pan, None; **E.L. Wu**, None; **Y. Chen**, None; **W. Chen**, None; **Y. Chang**, None; **J. Chen**, None.

Presentation Number **P 266**
Poster Session 2
September 19, 2013 / 15:15-15:15 / Room: Exhibit Hall B

New Design of dual Tuned RF coil for Fluorine MR Molecular Imaging

Soyeon Jeon[1], *Daehong Kim*[1], *Joo-Hyuk Lee*[1], *Eunju Kim*[2], [1]*Molecular Imaging & Therapy Branch, National Cancer Center, Goyang-si, Republic of Korea;* [2]*Yonsei University, seoul, Republic of Korea. Contact e-mail: soso8504@ncc.re.kr*

Introduction The MR imaging with multi nuclei such as 19F, 13C and 23Na are very important part of MR molecular imaging. As the weak MR signal intensity of non-proton nuclei, MR images with non-proton nuclei are unsuitable to provide anatomical information. In order to use proton (1H) MR images as an anatomical guidance, multi tuned RF coils should be used. When the resonance frequencies of the nuclei are too close, it is very difficult to construct the multi tuned RF coil with typical methods. In the case, the RF coils are usually constructed with wide tuning range. In spite of the easy construction of wide tuning range RF coil, it is not of practical use that the RF coil should be tuned every time when MR signals of each nucleus are obtained alternatively. In the case of 19F, the resonance frequency of 19F(~282 MHz at 7 T) is close to the proton resonance frequency (~300 MHz at 7 T). In this study, we construct the 19F/1H dual tuned RF coil with simple structure. Methods Quadrature type RF coils and phased array RF coils consist of at least two independent RF coils. The mutual inductances of each RF coil are "0". So, each independent RF coil can be tuned in different resonance frequency without any mutual interference. This concept of multi tuning was applied to birdcage type quadrature RF coil for 19F/1H MR imaging. In the birdcage coil, there are two independent RF channels that are separated by 90o on the cylinder axis. The RF coil should be optimized for fluorine because proton MR images are acquired just for anatomical information. Balanced matching circuits are used for improving channel separation and reducing the noise. Perfluorocarbon nanoemulsions (PFC NE) made of perfluoro crown ether were synthesized for MR imaging tracer. PFC NEs were injected to normal nude mouse via tail vein. In vivo MR experiments were carried out with the constructed dual tuned RF coil. After acquisition of 1H T2WI for localization, 19F imaging was performed with true-FISP (TR/TE: 4.8/2.4 msec, FOV: 10*4 cm, resolution: 128*32, slice thickness: 4 mm, NEX: 128). Results The low-pass type 19F/1H dual tuned birdcage coil for 7 T MRI was constructed with 12 legs, 3 cm diameter, 10 cm length. 10 legs are tuned to 19F resonance frequency with capacitor and two legs are tuned to 1H frequency. The two channels were separated by more than 20 dB. The unloaded Q-values of each channel were 150 for 19F channel and 100 for 1H channel. 19F image showed a distinct signal in the spleen and liver. For more visualization, pseudo-colored 19F image was merged with 1H T2WI. Conclusions For MR molecular imaging with non-proton nuclei, it is necessary to develop some appropriate hardwares such as multi tuned RF coil. We suggested the new idea for constructing a multi tuned RF coil with simple structure. For proof of concept, the dual tuned birdcage RF coil for the fluorine MR experiments was built. Some high quality images for 19F/1H nuclei were obtained using the dual tuned RF coil. This method can be also applied to a phased array coil consisting of many independent RF coils. And, the multi tuned RF coil for various nuclei such as 13C, 31P and 23Na can be easily constructed.

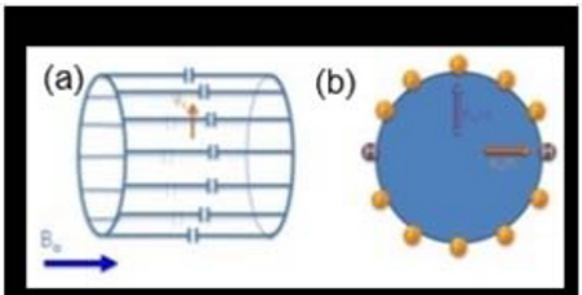

Fig.1.

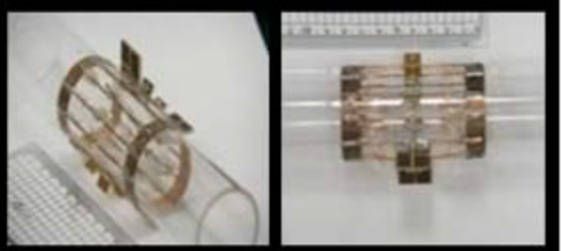

Fig.2.

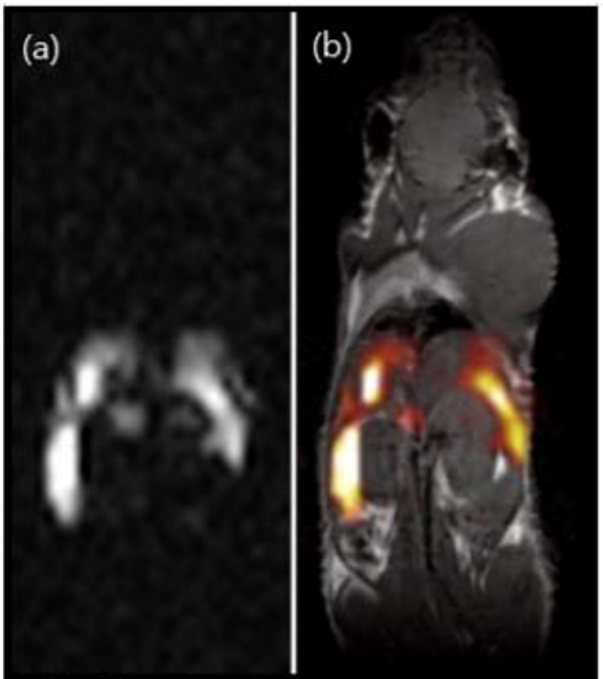

Fig.3.

Fig.1. (a). Conventional low-pass birdcage RF coil. There is a capacitor on each leg to tune the resonance frequency. (b). Two independent channels are tuned to different frequencies with different values of capacitor.(purple : 1H, orange: 19F) Fig.2. Constructed low-pass type dual tuned birdcage RF coil. Fig.3. Fluorine MR image with the constructed dual tune birdcage type RF coil. (a) Fluorine image. (b) Fluorine fusion image with proton image.

Disclosure of author financial interest or relationships:
S. Jeon, None; **D. Kim**, None; **J. Lee**, None; **E. Kim**, None.

Presentation Number **P 267**
Poster Session 2
September 19, 2013 / 15:15-15:15 / Room: Exhibit Hall B

Quantitative analysis of MRI data with ImageJ

Michael G. Kaul, *Thomas M. Ernst, Gerhard Adam, Department of Diagnostic and Interventional Radiology, University Medical Center Hamburg-Eppendorf, Hamburg, Germany. Contact e-mail: mkaul@uke.uni-hamburg.de*

PURPOSE Molecular imaging in Radiology gets more and more quantitative driven. The product software of MRI scanners does generally not provide all necessary experimental features and dedicated workstation are expensive. ImageJ (NIH, USA) is versatile and user system independent software and well known for its powerful plugin concept. We extend ImageJ for quantitative processing of DICOM data by implementing several plugins. MATERIAL AND METHODS qMapIt provides a interactive graphical user interface that embeds all practical relevant plugins. The plugin DicomSort'n'Select (DSnS) is used for the selective import of DICOM data. It can be fully automated by predefined configuration files. Importantly, DSnS extracts technical information out of the DICOM header and presents it to other plugins. The users' interaction to complete necessary information is reduced. In qMapIt several sessions can be imported and managed. A session can consist on several image stacks. Stacks are grouped images that belong together like time series. The plugins can recognize the data by the given session name. The resulting images can be saved as DICOM files (DCM4che). In this way a process chain can be built. For modeling of pharmacokinetic data for instance first T1-maps are calculated pixel by pixel from a series of different T1weighted images. The T1 maps are then combined with the dynamic contrast enhanced (DCE-) MRI data to calculate concentration maps which are used for modeling. Another process chain is realized for vessel size imaging. Remarkably, the image series are automatically aligned to the same reference coordinate system so that shifts and different scaling will be compensated. This align tool can be also used to copy drawn regions of interest for one image stack to another. Most of the quantitative analysis plugins use an underlying fitting framework. It is based on a state of the art optimization algorithm that estimates fitting errors as well and supports multi-core processors for speed reasons. The results are displayed in a single window the "hyperstack" that contains all calculated parameter maps and all slices. This hyperstack is interactive. When moving the mouse over the pixels the measured data and the calculated fit-curves are plotted offering a direct evaluation. RESULTS Currently the following plugins are available: DSnS for the DICOM import, T2RelaxIt for T2 and T2* relaxation time analysis, and T1RelaxIt for T1 relaxation analysis for three different approaches: variable flip angle, inversion-, and saturation-recovery. ADCIt extracts the apparent diffusion coefficients from a series of diffusion weighed data and IVIMIt additionally the blood volume fraction. VSIIt calculates maps representing the average vessel size taking diffusion coefficient and the changes of T2 and T2* after the application of a contrast agent into account. DCEIt will perform a pharmacokinetic modeling using the Tofts model. AlignIt will align stacks which are shifted and differently scaled. CONCLUSION The plugins offer a modular and an extensible platform for the quantitative analysis of DICOM data. The plugins interact in a way to optimize the workflow.

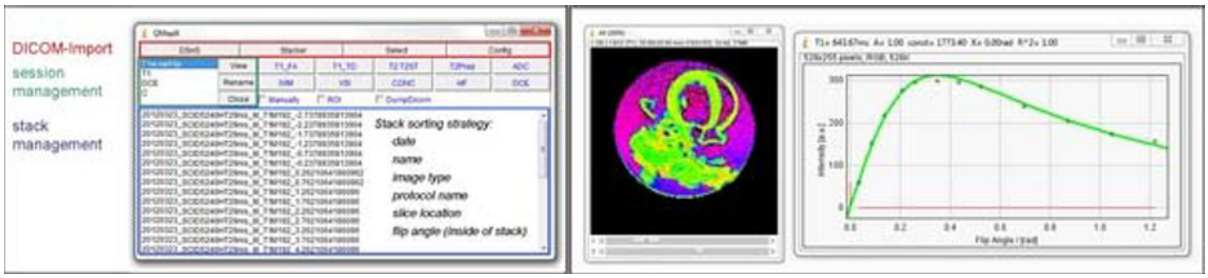

(Left) Graphical user interface of qMapIt. (Right) Fitted T1 map with an exemplary fit curve

Disclosure of author financial interest or relationships:
M.G. Kaul, None; **T.M. Ernst**, None; **G. Adam**, None.

Presentation Number **P 268**
Poster Session 2
September 19, 2013 / 15:15-15:15 / Room: Exhibit Hall B

Three-Dimensional Contrast-enhanced Magnetic Resonance Imaging of mice vasculatures: comparison of two different contrast agent injection timing protocols using 1-Tesla compact MR imaging system

Shigeru Kiryu[1], *Fang Wang*[1], *Yusuke Inoue*[2], *Kuni Ohtomo*[3], [1]*Radiology, Institute of Medical Science, The University of Tokyo, Tokyo, Japan;* [2]*Diagnostic Radiology, Kitasato University School of Medicine, Sagamihara, Japan;* [3]*Radiology, Graduate School of Medicine, University of Tokyo, Tokyo, Japan. Contact e-mail: kiryu-tky@umin.ac.jp*

Introduction T1-weighted three-dimensional fast low-angle shot sequence (3D-FLASH) is suitable for the visualization of small animal in detail due to its high spatial resolution. However, the imaging time is relatively long, and therefore to visualize the vascular structures using 3D-FLASH is a challenge. We assessed the effect of different injection timing protocols on the visualization of mouse vascular structures using a T1-weighted three-dimensional fast low-angle shot sequence. Materials and methods MR scan was performed using a 1-T permanent magnet compact MR imaging system (MRmini; MRTechnology, Tsukuba, Japan). Mice were imaged using a T1-weighted 3D-FLASH sequence in the sequential order with intravenous injection of gadopentetate dimeglumine at three different doses (standard, 0.1 mmol/kg; double, 0.2 mmol/kg; and 4 -times, 0.4 mmol/kg). We compared two different injection timing protocols. For protocol 1, the scan was started, and then the contrast agent was infused for the central 30% period of the total scan time (4 min 6 s). For protocol 2, the scan was started immediately after the completion of contrast injection. Results In the standard dose group, visual assessments did not differ significantly. In the double dose group, no significant difference was shown in visual assessments, except the flow artifacts were reduced in protocol 1. In the 4 times dose group, the visualization of left renal artery on the source images and the visualization of the aorta and intrahepatic veins on the maximum intensity projection images were better for protocol 1. The flow artifacts in the aorta were decreased for protocol 1 in 4 times dose group. The contrast ratio of the inferior vena cava was higher for protocol 1 in each of the three dose groups. The contrast ratio of the aorta was higher for protocol 1 in the standard and double dose groups. Conclusion Continuous infusion of the contrast agent at the center of data acquisition increased the contrast ratio of the inferior vena cava and aorta of mice, and decreased flow artifacts in the aorta. In combination with a high injection dose, this method improved the visualization of vascular structures.

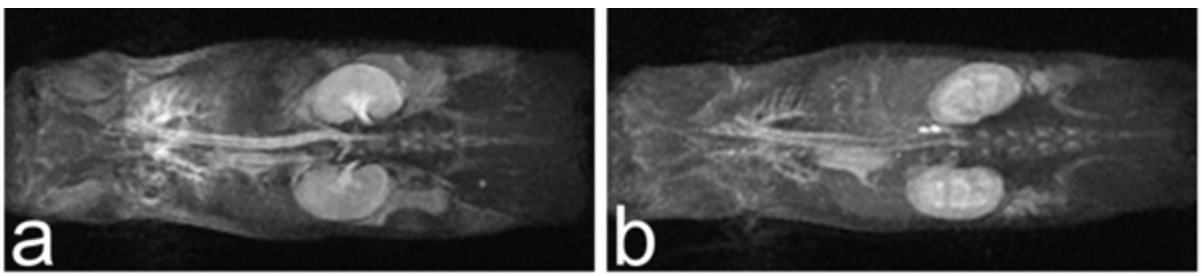

Typical partial MIP images at the 4 times dose for protocol 1 (a) and protocol 2 (b).

Disclosure of author financial interest or relationships:
S. Kiryu, None; **F. Wang**, None; **Y. Inoue**, None; **K. Ohtomo**, None.

Presentation Number **P 269**
Poster Session 2
September 19, 2013 / 15:15-15:15 / Room: Exhibit Hall B

Improved Throughput of Preclinical Hyperpolarized 13C MRS

Marc S. Ramirez[1], *Jaehyuk Lee*[1], *Chris M. Walker*[1], *Vlad C. Sandulache*[3,2], *Yunyun Chen*[2], *Stephen Y. Lai*[2], *James A. Bankson*[1], [1]*Department of Imaging Physics, The University of Texas M.D. Anderson Cancer Center, Houston, TX, USA;* [2]*Department of Head and Neck Surgery, The University of Texas M.D. Anderson Cancer Center, Houston, TX, USA;* [3]*Bobby R. Alford Department of Otolaryngology-Head and Neck Surgery, Baylor College of Medicine, Houston, TX, USA. Contact e-mail: marc.ramirez@mdanderson.org*

Introduction Hyperpolarized (HP) MR can overcome signal-to-noise (SNR) limitations of 13C MRS to probe cancer metabolism in vivo. Standard methods for dynamic nuclear polarization (DNP) require expensive consumables including cryogens, the enriched tracer, and the polarizing radical. Furthermore, polarization times of 13C metabolites (i.e. [1-13C] pyruvate) can approach one hour. For preclinical research, the cost of HP MR can be prohibitive to experimental design with high statistical power. Furthermore, a fixed dissolution volume (~4 mL) is required to counterbalance the frozen solid state tracer and yield an injectable that is at body temperature; however only 5% of the final volume (~200 µL) can be injected into murine disease models, resulting in significant waste. In this work, we evaluate the feasibility of multi-mouse dynamic HP MRS to improve study efficiency, reduce cost, and promote HP MR for routine preclinical research. Methods To permit dual-mouse 13C MRS on a 7-T Bruker Biospec MRI system, a pair of two-turn 1.5-cm inner diameter (ID) surface coils, designed to each be placed over distinct tumor sites, was developed. Low noise preamplifiers improved SNR and reduce inductive coupling between coils. Phantoms containing enriched 13C-labeled urea were used to evaluate multi-volume shimming performance. For in vivo demonstration, two mice bearing anaplastic thyroid cancer tumors were anesthetized, catheterized, and placed on a dual-mouse sled distributing 2% isoflurane in oxygen through nose cones. Because only one 13C receive channel was available, RF preamplifier outputs were combined and mice were encoded with separate slices. Animal and coil locations were staggered to achieve distinct tumor positioning along the B0 axis. Respiratory rates were monitored with a multi-animal monitoring system. 1H reference images were acquired through a 72-mm ID dual-tuned 1H/13C birdcage coil. Polarization of a 26-mg sample of pyruvic acid, containing 15-mM OX063 and 0.6 µL of 1.5-mM Prohance, was performed with a HyperSense DNP polarizer. Slice-localized dynamic 13C spectra were acquired over three minutes (TR = 2000 ms, 10° flip angle, 4960 Hz BW) and data were processed in Matlab. Two veterinary technicians injected the tracer into separate animals. Results Spatial separation of surface coils resulted in 19 dB of decoupling with an additional 22 dB from preamplifiers. Frequency differences between distinct imaging volumes and 13C linewidths were below 0.2 ppm for up to 3-cm slice offsets. Multi-animal spectra and dynamic time courses are consistent with single-animal experiments; however multi-animal SNR was slightly compromised. Conclusion We have demonstrated the initial feasibility for multi-animal HP 13C MRS. Throughput scales with simultaneously-scanned animals, potentially leading to dramatic cost reduction. Future studies will incorporate 13C imaging sequences, a multi-channel receiver, a robust tracer distribution system, and optimized receive arrays. Funding sources include CPRIT grant RP101243-P5 and NCI grant P30-CA016672. Funding as an Odyssey Fellow was supported by the Odyssey Program and The Estate of C.G. Johnson, Jr.

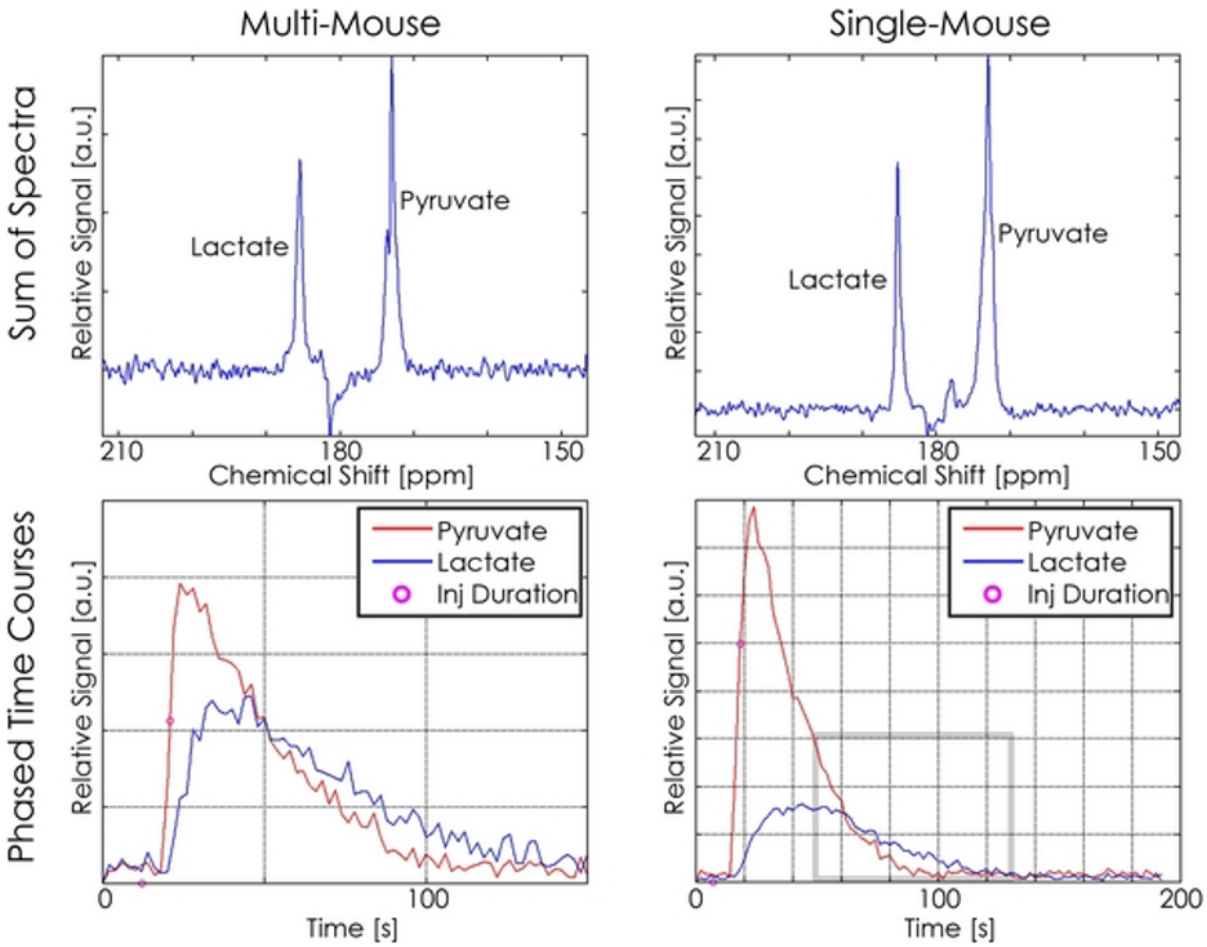

Sum of spectra (top) and dynamic time courses (bottom) from single- and multi-mouse 13C MRS acquisitions.

Disclosure of author financial interest or relationships:
M.S. Ramirez, None; **J. Lee**, None; **C.M. Walker**, None; **V.C. Sandulache**, None; **Y. Chen**, None; **S.Y. Lai**, None; **J.A. Bankson**, None.

Presentation Number **P 270**
Poster Session 2
September 19, 2013 / 15:15-15:15 / Room: Exhibit Hall B

New Analysis Methods for measuring chemical exchange rates using CEST MRI

Edward Randtke[1], *Liu Qi Chen*[1], *Marty Pagel*[2,3], [1]*Department of Chemistry and Biochemistry, University of Arizona, Tucson, AZ, USA;* [2]*Department of Biomedical Engineering, University of Arizona, Tucson, AZ, USA;* [3]*University of Arizona Cancer Center, University of Arizona, Tucson, AZ, USA. Contact e-mail: erandtke@email.arizona.edu*

Measuring the exchange rate of a Chemical Exchange Saturation Transfer (CEST) agent can be used to assess molecular biomarkers such as pH or enzyme activity (1,2). Therefore, practical methods of accurately measuring chemical exchange rates are needed to improve molecular imaging with CEST MRI. Measuring chemical exchange rates can be accomplished by fitting modified Bloch-McConnell equations to CEST spectra, but this method requires substantial time and expertise for accurate fittings (3). Chemical exchange rates can also be measured with the nonlinear QUESP method that replies on varying saturation power, or linearized versions of QUESP that improve the accuracy and analysis speed (4,5). Yet these methods are based on varying saturation power, and saturation power may vary during in vivo studies due to B1 inhomogeneities. Chemical exchange rates can also be measured with the nonlinear QUEST method that relies on varying saturation time, and saturation times are always accurately determined during a MRI protocol, so that QUEST has advantages relative to QUESP (4). However, QUEST is a non-linear analysis method that is not robust to experimental error. We have developed a Linear QUEST method that combines the advantages of the QUEST method and the robustness of the linear QUESP methods to create a simple and effective analysis method. We conducted simulations of iopromide, a diamagnetic CEST agent that has rapidly exchanging and slowly exchanging protons. CEST spectra were simulated using the Bloch-McConnell equations based on 100 mM of iopromide at pH 6.8 (6). The amplitudes of the CEST effects were analyzed with non-linear QUEST and three linear QUEST methods to estimate the chemical exchange rates. These simulated results demonstrated that the reciprocal version of the linear QUEST method (known as RL-QUEST) provided the best precision relative to the other linear QUEST methods when estimating fast exchange rates. Furthermore, the RL- QUEST method had the same behavior as the non-linear QUEST method while requiring fewer parameters for fitting. The RL-QUEST method could accurately estimate chemical exchange rates at low saturation powers, while the non-linear QUEST method required higher saturation powers for accurate measurements, which facilitates translation of this method to the clinic where saturation powers must be limited to low values. To validate the simulated results, experimental studies measured the chemical exchange rates of iopromide. CEST spectra of iopromide at 100 mM and pH 6.8 were acquired with a 600 MHz Varian NMR spectrometer with a range of saturation times and saturation powers. The RL-QUEST method accurately estimated the exchange rate of the slowly exchanging proton, using low saturation power. The RL-QUEST method estimated the exchange rate of the rapidly exchanging proton with better measurement accuracy as the saturation nutation rate (which is a function of saturation power) approached the exchange rate. The results demonstrated that RL-QUEST can accurately determine chemical exchange rates without requiring an accurate determination of saturation power. Bibliography in supplemental data.

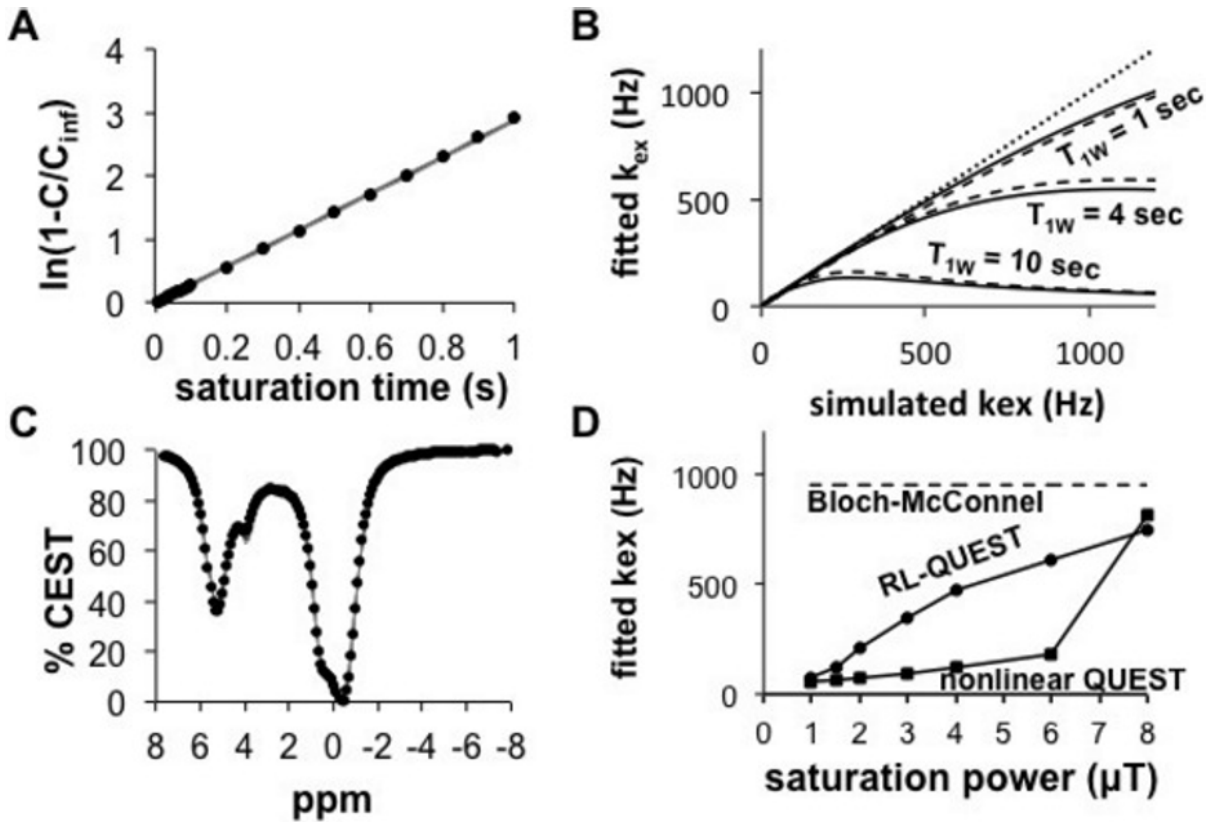

Figure 1. A) The RL-QUEST method was used to estimate chemical exchange rates from simulated CEST spectra. B) RL-QUEST (solid lines) and non-linear QUEST (dashed lines) showed the same performance when estimating chemical exchange rates from simulated results. Data was simulated with a range of exchange rates and T1w relaxation times. C) The Bloch-McConnel equations (line) were fitted to an experimental CEST spectrum of iopromide (circles). D) The RL-QUEST method estimated a chemical exchange rate of a rapidly exchanging proton of iropromide with increasing saturation power. The exchange rate estimated by Bloch-McConnel fitting was used as a gold standard for this analysis.

Experimental Exchange Rates

	4.2 ppm	5.6 ppm
Linear QUEST Slope method	65.7 (59.0,72.4)	824.8 (770.1, 879.4)
Linear QUEST Reciprocal Method	57.6 (50.0, 65.0)	753.2 (732.2, 775.6)
Linear QUEST Average Method	57.7 (47.2,68.2)	780.2 (709.6, 850.8)
Bloch Method	101.6 (98.4, 104.8)	953.3 (942.5, 964.3)
QUEST	60.0 (52.6, 68.3)	849.1 (760.3, 882.5)

Fitted exchange rates of the 4.2 and 5.6 ppm proton pools for Iopromide. The 4.2ppm exchange rates were fit with a field strength of 1.5μT, while the 5.6ppm exchange rates were fit with a power of 8μT. The Bloch method exchange rate was fit by simultaneously fitting all spectra obtained. 95% confidence intervals are in parenthesis.

Disclosure of author financial interest or relationships:
E. Randtke, None; **L. Chen**, None; **M. Pagel**, None.

Presentation Number **P 271**
Poster Session 2
September 19, 2013 / 15:15-15:15 / Room: Exhibit Hall B

Quantifying Perfusion Kinetics and Vascular Networks using DCE-MRI and CE-MRI Angiography on a Novel Compact High-Performance MRI System

Tonya Coulthard[1], *Jacob Hesterman*[2], *Jinzi Zheng*[3], *Raquel De Souza*[3], *Matthew D. Silva*[2], [1]*Aspect Imaging, Toronto, ON, Canada;* [2]*InviCRO, Boston, MA, USA;* [3]*2. STTARR Innovation Centre, Princess Margaret Hospital, University Health Network, Toronto, ON, Canada. Contact e-mail: tcoulthard@aspectimaging.com*

Magnetic Resonance Imaging (MRI) is considered the gold standard in soft tissue imaging, providing exquisite anatomical detail. Contrast enhanced (CE)-MRI provides additional functional insights into the vascular architecture of the same anatomical targets. As an additional imaging approach, Dynamic contrast enhanced (DCE)-MRI allows for quantification of perfusion kinetics, with measurements of overall perfusion as well as vessel permeability. DCE-MRI takes advantage of the pathophysiological differences between vessels, within a tumor for example which are often disorganised and leaky, compared to normal, well-organized blood vessels. In the current study, various imaging targets, including normal kidney and brain as well as an intra-peritoneal ovarian tumor, were assessed using both DCE-MRI and CE-MRI angiography. Imaging was performed on a novel compact high-performance MRI system (Bruker ICON, Germany) operating at 1 Tesla. Images were acquired using either the mouse body or head RF coil, while all contrast agents were administered through a tail vein cannulation. DCE-MRI was performed by injecting 20ul of Gd-HP-DO3A (ProHance®, Bracco Diagnositics, USA), while CE-MRI angiography was performed by injecting 150µl of a nanosized liposome agent containing gadolinium (Nanovista, STTARR, Canada). Contrast-enhanced MRI produced compelling angiography results, allowing for the assessment of the vascular network within the brain, kidney, and tumor. Percent change of signal intensity following contrast injection is used to measure perfusion in angiography images. As such, perfusion was quantified in the normal kidneys to be 59±11% compared to 11±0.3% in the hind limbs of the same animals. Heterogeneity of perfusion between IP ovarian tumors was evident both in the angiography images as well as the resulting quantification (55±31%). The blood brain barrier (BBB) restricts the passage of most molecules into the brain tissue, including MRI contrast agents, such as those used in the current study. Signal intensity changed little in the brain following contrast injection (5±2.5%) when compared to the surrounding structures of the head, including the salivary glands, palate, eyes, etc. (22±5%). Perfusion kinetics of the kidney and tumor were quantified using DCE-MRI. Specifically, Ktrans was calculated to describe vessel permeability, while the area-under-the-curve (AUC) quantifies overall perfusion. In conclusion this study demonstrates the capabilities of this novel compact high-performance MRI system in quantifying perfusion kinetics using DCE-MRI, as well as angiographic assessment of vascular networks within various anatomical and disease targets. Similar techniques could be utilized to assess the efficacy of newly developed therapeutics, as well as to study the progression or regression of pathophysiology in various disease models.

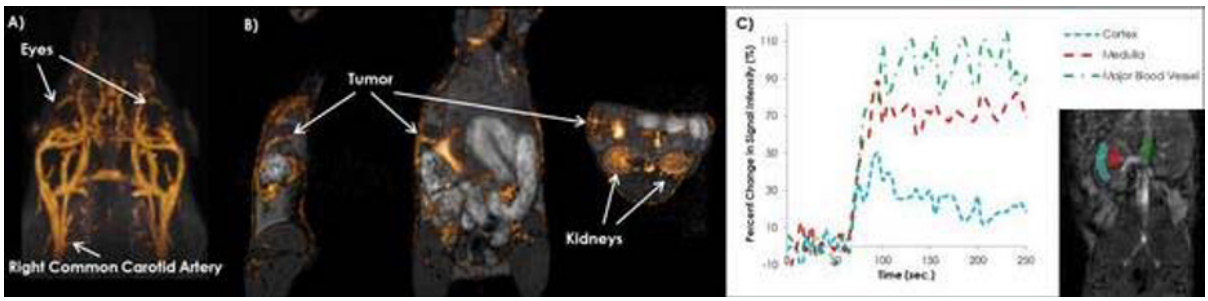

Figure 1 - Visualization of (a) vasculature within the head of a normal mouse, (b) I.P. ovarian tumor vasculature, using CE-MRI angiography; and DCE-MRI for perfusion kinetics within the normal kidney (c)

Disclosure of author financial interest or relationships:
T. Coulthard, Aspect Imaging, Employment; **J. Hesterman**, inviCRO, LLC, Employment; **J. Zheng**, None; **R. De Souza**, None; **M.D. Silva**, inviCRO, LLC, Employment .

Presentation Number **P 272**
Poster Session 2
September 19, 2013 / 15:15-15:15 / Room: Exhibit Hall B

Amide Proton Transfer Imaging of Ischemic Stroke in the First 3 Hours

Zhuozhi Dai[1], *Gen Yan*[1], *Shengkai Li*[1], *Gang Xiao*[2], *Guishang Zhang*[1], *Zhiwei Shen*[1], *Renhua Wu*[1], [1]*Shantou University, Shantou, China;* [2]*Hanshan Normal University, Chaozhou, China. Contact e-mail: s_zzdai1@stu.edu.cn*

Objective: The first 3 hours is the golden period for effective stroke treatment, and the identification of ischemic penumbra guides the treatment. Amide proton transfer (APT) MRI, a variant of Chemical exchange-depended saturation transfer imaging, is expected to detect the ischemic penumbra more precise than PWI-DWI mismatch in hyperacute cerebral infarction. But APT effect is typically small and sensitive to pre-saturation power (B1), which needs to be optimized in the first 3 hours after stroke. Methods: Five adult male Sprague Dawley rats were underwent permanent middle cerebral artery occlusion by thread embolism. MRI experiments were conducted under an Agilent 7T animal MRI system in the first 3 hours after ischemic stroke. A surface 1H coil was used. APT imaging was obtained by the home-made MT-GRE-CEST sequence. Parameters were used: Offset at 3.5 ppm and -3.5 ppm, TR/TE=26/2.5 ms, FA=5°, slice thickness=2 mm, field of view=34×34 mm^2, number of average=64, matrix=64×64 and bandwidth=50 kHz. APT MRI was optimized as functions of pre-saturation power. The pulse power (Gauss pulse, 15 ms) was serially set from 0.4μT to 1.6μT with intervals of 0.2μT. Chemical exchange saturation transfer rate (CESTR) and contrast to noise rate (CNR) were processed in Matlab. Results: The optimized pre-saturation power in the first 3 hours was about 0.4μT to 0.8μT, which had better spatiotemporal resolution and contrast than others. The best CNR was about 4. Moreover, the APT effect was almost disappeared if the pre-saturation power was more than 0.8μT. Conclusion: Our study demonstrates the optimized APT imaging in the first 3 hours of ischemic stroke, which showed the ischemic lesion well and be promising for a precise detection of ischemic penumbra.

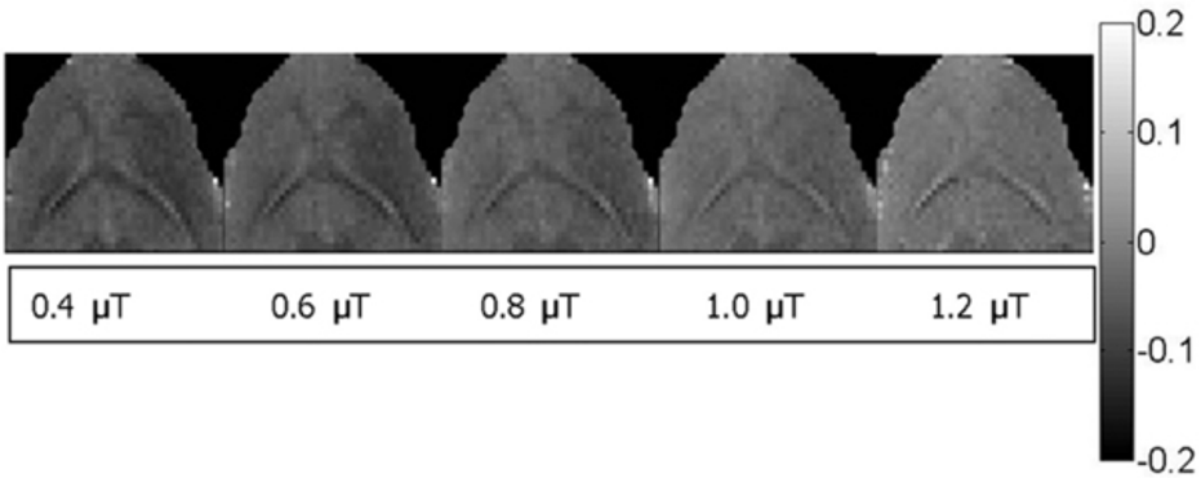

APT imaging at different pre-saturation power in the first 3 hours of ischemic stroke

Disclosure of author financial interest or relationships:
Z. Dai, None; **G. Yan**, None; **S. Li**, None; **G. Xiao**, None; **G. Zhang**, None; **Z. Shen**, None; **R. Wu**, None.

Presentation Number **P 273**
Poster Session 2
September 19, 2013 / 15:15-15:15 / Room: Exhibit Hall B

A fast method for simultaneous determination of labile proton fraction ratio and exchange rate of pulsed-CEST MRI

Gang Xiao[1], Phillip Zhe Sun[2], Zhuozhi Dai[3], **Renhua Wu**[3], [1]*Department of Math and Applied Mathematical, Hanshan Normal University, Chaozhou, China;* [2]*Department of Radiology, Massachusetts General Hospital and Harvard Medical School, Charlestown, MA, USA;* [3]*Shantou University, Shantou, China. Contact e-mail: gszhang_1@163.com*

Objective: Chemical exchange saturation transfer (CEST) imaging is sensitive to dilute proteins/peptides and microenvironmental properties, and has been increasingly evaluated for molecular imaging and in vivo applications. However, the experimentally measured CEST effect depends on the CEST agent concentration, exchange rate and relaxation time. In addition, there may be non-negligible direct radio-frequency (RF) saturation effects, particularly severe for diamagnetic CEST (DIACEST) agents due to their relatively small chemical shift difference from that of the bulk water resonance. As such, the object of the research is to demonstrate a fast method for simultaneous determination of labile proton fraction ratio and exchange rate and other parameters of CEST MRI. Methods: Mathematical models have been developed to describe pulsed-CEST contrast. We simulated pulsed-CEST MRI in Matlab (MathWorks, Natick, MA) for Z-spectra and asymmetry spectra using matrix exponential algorithm . The number of repetition of the sequence is 256. Each Gaussian-shaped pulse was divided into 101 steps, and the evolution within each step was modeled assuming a constant amplitude. In addition, the transverse magnetization was set to zero immediately before the RF pulse to represent the dephasing caused by crusher gradients. The magnetization at the end of the RF pulse was then used as the initial state for iterated simulation until the end of the RF pulse train, whereas the longitudinal magnetization relaxed toward equilibrium. We also calculated the above spectra by using the fourth/fifth-order RKF(ode45 in MatLab; The MathWorks, Natick, MA, USA) with an absolute error tolerance for each integration step of 10−6 , and compared with the results obtained by our method. Calculations were performed using MatLab on Pentium® Dual-Core CPU (2.2 GHz) with 2-GB RAM. There was a good agreement between them, and this method was much faster than the RKF method (by a factor of approximately 1000 in this study). We simulated that the error of the labile proton fraction ratio , exchange rat and other parameters less than 5%. Results: This method will be useful for determination of labile proton fraction ratio and exchange rate and other parameters, and for analyzing the pulsed-CEST contrast mechanism and/or investigating the optimal RF pulse parameters such as the RF pulse duration or pulse flip angle.

Disclosure of author financial interest or relationships:
G. Xiao, None; **P. Zhe Sun**, None; **Z. Dai**, None; **R. Wu**, None.

Presentation Number **P 274**
Poster Session 2
September 19, 2013 / 15:15-15:15 / Room: Exhibit Hall B

Stable physical phantoms for characterization of small animal photoacoustic imaging systems

Sarah Bohndiek[1,2], *Sandhya Bodapati*[1,2], *Dominique Van de Sompel*[1,2], *Sri Rajasekhar Kothapalli*[1,2], *Sanjiv S. Gambhir*[1,2],
[1]*Radiology, Stanford University, Stanford, CA, USA;* [2]*Molecular Imaging Program at Stanford, Stanford University, Stanford, CA, USA. Contact e-mail: bohndiek@stanford.edu*

Introduction: Photoacoustic imaging combines the high contrast of optical imaging with the spatial resolution and penetration depth of ultrasound. This technique holds tremendous potential for imaging in small animals and importantly, is clinically translatable. Performance evaluation and routine calibration are necessary to provide confidence in the data acquired by any imaging system. With the growing popularity of photoacoustic imaging and the advent of several commercial small animal imaging systems, it is important to develop a strategy for assessment and routine calibration of such instruments. **Aim:** To develop a range of stable phantoms with biologically relevant absorption and scattering properties for detailed performance evaluation of photoacoustic imaging systems. **Methods:** Polyvinyl chloride plastisol (PVCP) is an oil-based material insoluble in water that polymerizes and becomes translucent when heated to high temperatures. Along with easy preparation, low cost and long-term stability, the density and acoustic parameters of PVCP are equivalent to water and the speed of sound (1,400 ms^{-1}) is within 15% of the soft tissue average. Importantly, PVCP targets with defined shapes and absorbing properties can be embedded within a matrix of the same material, avoiding mismatch of acoustic, mechanical or thermoelastic properties. Tissue-mimicking phantoms were created using PVCP (M-F Manufacturing Co., USA). Optical properties were defined by adding black plastic color (BPC; M-F Manufacturing Co., USA) to adjust the absorption coefficient and titanium oxide (TiO2) powder (232033; Sigma-Aldrich) to adjust the reduced scattering coefficient. Spherical targets were formed from PVCP containing BPC concentrations from 0 to 0.256% using an aluminum mold (Fig 1A). Targets were embedded within a PVCP matrix of defined optical absorption and scattering by pouring layers and placing spheres as the matrix was solidifying (Fig 1B). **Results and Discussion:** The photoacoustic imaging systems evaluated in this study were the VisualSonics Vevo LAZR and Endra Nexus 128. Spherical targets containing BPC were clearly visible in the photoacoustic images (Fig 1C,D). We found that the two systems were reproducible (coefficient of variation <14% over 4 months), gave flat response as a function of wavelength (slope = 0.00046 ± 0.0013 nm^{-1} and 0.296 ± 1.182 nm^{-1}; neither significantly non-zero, p=0.61 and 0.81) with appropriate energy compensation, and a linear response over all wavelengths (r^2>0.92) as a function of dye concentration. Our phantoms were then used to optimize system performance, and evaluate the penetration depth, spectral accuracy and sensitivity of the two systems. Spheres placed deep in PVCP phantoms showed an exponential decrease in photoacoustic signal as a function of depth (r^2>0.96), with penetration depths found to be 16 mm and 36 mm for the LAZR and Nexus instruments, respectively. We have demonstrated that PVCP provides a stable, low cost phantom material that is appropriate for verification and validation of photoacoustic imaging instruments.

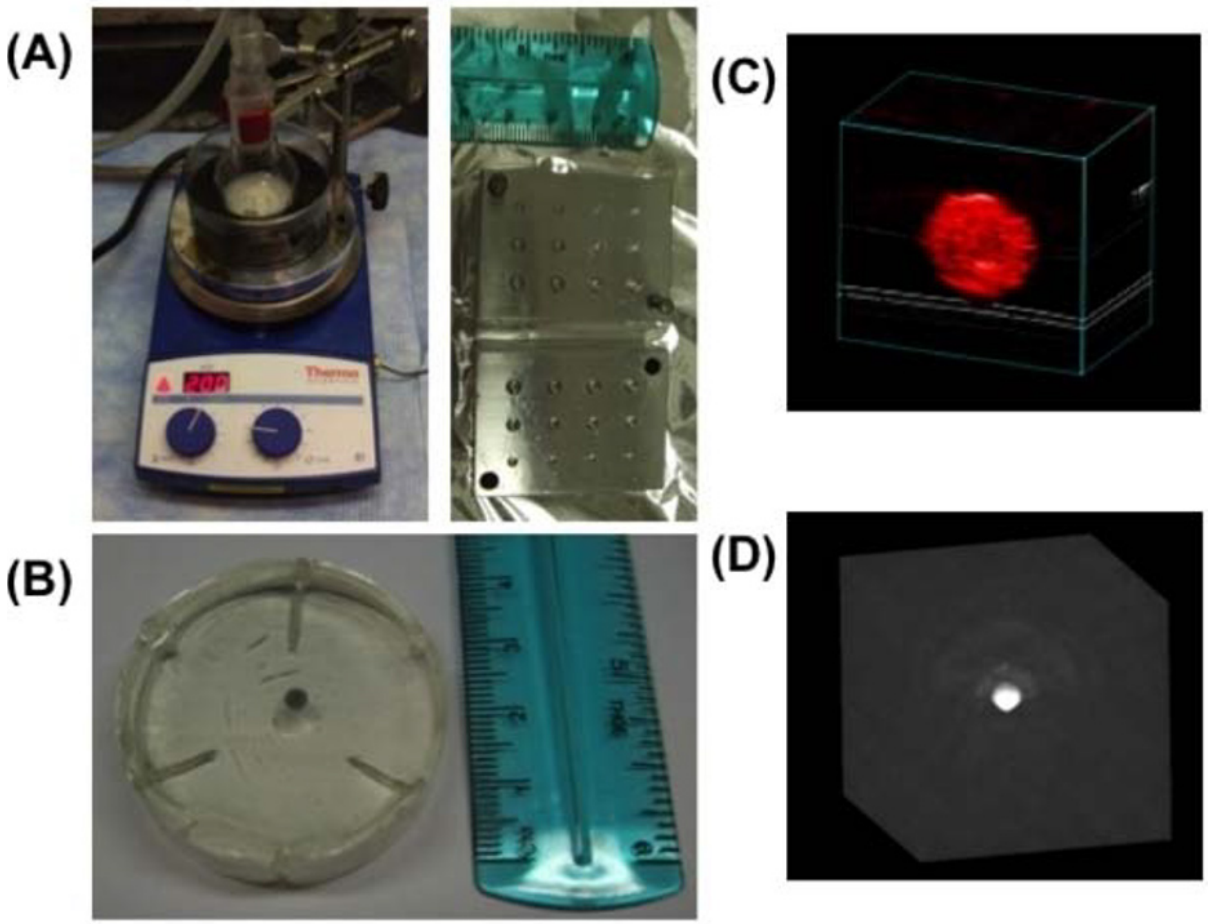

Figure 1: Polyvinyl chloride plastisol (PVCP) phantoms enable performance evaluation in small animal photoacoustic imaging systems. PVCP is prepared under vacuum by heating to 200°C (A) then is rapidly poured into the chosen mold. To produce spherical target objects with a well defined size, an aluminum mold was used. Spherical targets were then embedded within a background PVCP matrix by two phase pouring into an acrylic container (B). Spherical targets of 3.2mm diameter containing black plastic color (BPC) were clearly visible on the VisualSonics Vevo LAZR (C) and Endra Nexus 128 (D) imaging systems.

Disclosure of author financial interest or relationships:

S. Bohndiek, None; **S. Bodapati**, None; **D. Van de Sompel**, None; **S. Kothapalli**, None; **S.S. Gambhir**, Bracco Diagnostics, Consultant; Endra, Inc, Stockholder; Cellsight, Stockholder; Enlight, Inc., Stockholder; General Electric, Grant/research support; ImaginAb, Stockholder; MagArray, Inc., Stockholder; Sanofi-Aventis, US, Grant/research support; SiteOne Therapeutics, Stockholder; VisualSonics/Sonosite, Stockholder .

Presentation Number **P 275**
Poster Session 2
September 19, 2013 / 15:15-15:15 / Room: Exhibit Hall B

High rate cardiac imaging by multispectral optoacoustic tomography

Neal Burton[1,2], *Andreas Buehler*[2,3], *Marcin Kacprowicz*[1], *Wouter H. Driessen*[1,2], *Jing Claussen*[1,2], *Thomas Sardella*[1], *Daniel Razansky*[2,3], *Vasilis Ntziachristos*[2,3], [1]*iThera Medical, GmbH, Munich, Germany;* [2]*Institute for Biological and Medical Imaging, Helmholtz Zentrum Muenchen, Neuherberg, Germany;* [3]*Chair for Biological Imaging, Technische Universität München, Munich, Germany. Contact e-mail: neal.burton@helmholtz-muenchen.de*

Multispectral optoacoustic tomography (MSOT) enables the discrimination of absorbers of interest at high resolution that is maintained at depth. Based on the optoacoustic effect, absorbed light energy creates a thermoelastic expansion, producing a pressure wave that can be detected with ultrasound transducers. The use of 5MHz transducers arranged in an array allows cross-sectional imaging throughout the entire mouse with an in-plane resolution of 150um. A tunable OPO laser allows illumination within the near infrared (NIR) window. As such, the biodistribution of injected contrast agents (e.g. cyanine dyes, gold nanoparticles, carbon nanotubes) can be determined with high temporal resolution (typically 10Hz). In addition, oxygenated and deoxygenated hemoglobin have distinct absorption spectra in the NIR; therefore, the saturation of hemoglobin with oxygen can also be determined. The use of multiple wavelengths in optoacoustic imaging allows the calculation of wavelength-dependent absorption. Molecules with distinct absorption spectra can be differentiated based on the modeling of the signal as a function of known absorption spectra. This analysis is done on a pixel by pixel basis, and is susceptible to motion artifacts. The heart rate of an anesthetized mouse is 400-500 beats per minute, while the respiration rate is 60-90 respirations per minute. A commonly used method to cope with motion in such analysis is the use of averaging, which combines signals from multiple sequential laser pulses. The overall effect is motion-independent analysis; however, there is a reduction in apparent spatial resolution due to blurring. Alternatively, this study demonstrates the utility of conducting multispectral optoacoustic tomography at high repetition rates. By using an OPO laser capable of variable repetition rates from 10Hz to 100Hz, fast moving objects such as the mouse heart can be fully captured. At 10Hz, it is only possible to acquire one image per heartbeat, leading to an under-sampling of this motion. At higher repetition rates, more frames are acquired per beat, allowing for a fuller characterization of the motion of the heartbeat. Importantly, gating analysis can be performed on the data such that multispectral analysis can be performed using single wavelength images acquired at the same stages of the heartbeat (i.e. during systole or diastole). For regions of the animal where breathing artifacts occur, the use of 50Hz and higher enables the acquisition of full multispectral data sets in between respirations, obviating the need for retrospective gating. MSOT allows anatomical, functional and molecular imaging. In order to fully capitalize on the spatial resolution of any optoacoustic imaging system in vivo, it is necessary to acquire multispectral data as quickly as possible, either on a timescale where motion does not occur or by comparing equivalent points within a cycle of motion.

Disclosure of author financial interest or relationships:
N. Burton, iThera Medical, Employment; **A. Buehler**, None; **M. Kacprowicz**, iThera Medical, Employment; **W.H. Driessen**, iThera Medical, Employment; **J. Claussen**, iThera Medical, Employment; **T. Sardella**, iThera Medical, Employment; **D. Razansky**, None; **V. Ntziachristos**, iThera Medical, Stockholder; SurgOptix BV, Consultant .

Presentation Number **P 276**
Poster Session 2
September 19, 2013 / 15:15-15:15 / Room: Exhibit Hall B

Coregistration of multi-bandwidth and high resolution 3D Optoacoustic Images using Ultrasound Linear Arrays

Andrei Chekkoury, *Jérôme Gateau, Vasilis Ntziachristos, Institute for Biological and Medical Imaging, Technische Universität München and Helmoholtz Zentrum München, Munich, Germany. Contact e-mail: andrei.chekkoury@gmail.com*

Optoacoustic tomography (OAT) is a non-invasive imaging modality for high-resolution mapping of optical absorption in tissue. Absorbing structures excited with short laser pulses generate broadband ultrasound waves, which tomographically detected outside the sample enable to reconstruct an image. As light scatters in biological tissues, the excitation is three-dimensional (3D). Accurate reconstruction of the 3D distribution of optical absorption requires large solid angle detection of the ultrasonic field. Moreover, the center frequency and bandwidth of a given detector define the range of structure sizes that it is able to resolve. Therefore, detectors with different frequency bandwidths record different subsets of information. The high absorption contrast between blood (hemoglobin) and tissue in the near infrared region makes OAT suitable in particular for imaging of vessels. To image vascular structures at multiple scales and with a high 3D resolution, we developed an OAT system able to coregister successfully 3D datasets using conventional ultrasound arrays with different center frequencies. The system is based on a novel rotation/translation scan geometry (Gateau, et al. Med. Physics, 40(1) 2013). Two linear arrays (Acuson L7, Siemens Healthcare, and LA-28.0 Vermon, France) comprised of 128 elements with center frequencies respectively of 6MHz and 24MHz were used to validate the co-registration capabilities and obtain high-resolution images at different scales. Optical excitation was performed using laser pulses (<10ns) at 760nm delivered with a 10Hz repetition rate and a per-pulse energy of 70mJ. Samples were illuminated through scattering medium to ensure uniform illumination on their surface. Tomographic dataset of a volume of 7mm x 7mm x 6mm were acquired in 13 minutes and 29 minutes for the low and high frequency arrays, respectively. We report resolution capabilities of 180µm with the 6MHz array and 43µm with the 24MHz array. An excised portion of the liver of a CD1® mouse was imaged. Maximum amplitude projection (MAP) coregistered images are presented in Fig 1. The anatomical shape of the liver lobe can be distinguished for both imaging bandwidths. Moreover, blood vessels of multiple sizes can be identified. The main blood vessel (arrow) connecting the caudate lobe and other several small blood vessels are visible in the low frequency image and are better resolved and contrasted in the high-frequency image. These results demonstrate that our system can be used to obtain 3D optical contrast images of biological tissues, and to coregister multiple bandwidths. Such a system will enable the 3D localization of optical absorbers in intact samples, and therefore is expected to be of great interest for detection of specific structures, and details for diagnostic and pathology imaging. With a multispectral approach, the system could moreover perform the volumetric localization of injected biomarkers within the endogenous contrast distribution.

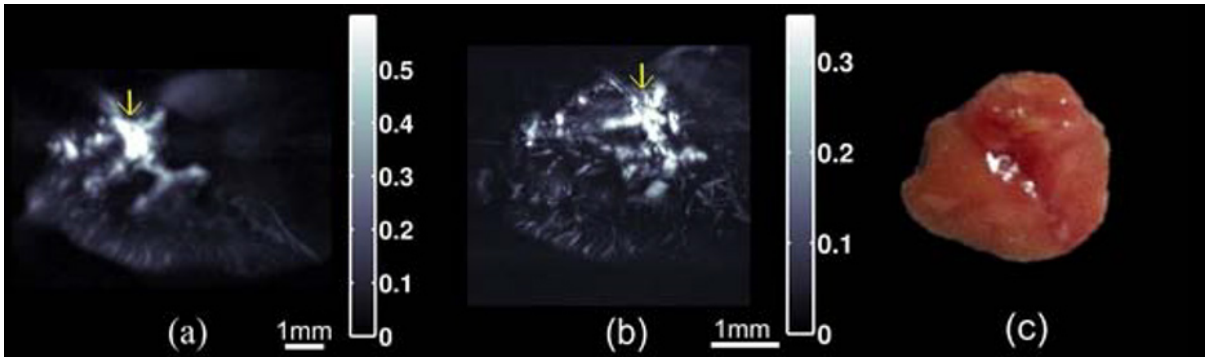

Figure 1: Excised mouse caudate liver lobe MAP image acquired with ; (a) the 6 MHz array (b) the 24MHz array (c) Photo of the excised organ

Disclosure of author financial interest or relationships:

A. Chekkoury, None; **J. Gateau**, None; **V. Ntziachristos**, iThera Medical, Stockholder; SurgOptix BV, Consultant .

Presentation Number **P 277**
Poster Session 2
September 19, 2013 / 15:15-15:15 / Room: Exhibit Hall B

Transformation-based Optoacoustic Modeling (TOM) - separating geometry and physics

Alexander Dima[1,2], *Vasilis Ntziachristos*[1,2], [1]*Institute for Biological and Medical Imaging, Helmholtz Zentrum München, Neuherberg, Germany;* [2]*Electrical Engineering and Information Technology, Technical University of Munich, Munich, Germany. Contact e-mail: alexander.dima@helmholtz-muenchen.de*

Image reconstruction in optoacoustic tomography relies on the inversion of the forward solution of the optoacoustic wave equation from a set tomographic detector positions. The most accurate and flexible approach is based on numerical forward modeling and inversion, whereby a matrix describes detection geometry and wave propagation. When faced with a large data set and number of image pixels/voxels, e.g. 3D imaging in general or 2D imaging at high-resolution over a large region, direct matrix inversion becomes challenging or outright impossible. Even iterative methods operating on the forward matrix may struggle as working memory requirements reach hundreds of GB or more. Therefore, we propose to separate the two modeling problems of wave propagation and detection geometry. We demonstrate iterative inversion using only the forward matrix of a single detector position and image transformations to describe detection geometry. Validation of our algorithm is performed in 2D against an established algorithm for model-matrix inversion using numerical phantoms and experimental mouse data acquired in vivo. Results show that it is possible to obtain the exact same image quality using only a fraction of the memory required previously. Additionally, the proposed split enables rapid development of new and more complex wave propagation models, whose elementary forward matrix can be plugged into our algorithm like a kernel. Finally, we describe how the proposed algorithm allows straight forward OpenCL implementation for use with high-end graphics cards, thus reaping the benefits of both highly parallelized computation and high-speed memory.

Disclosure of author financial interest or relationships:
A. Dima, None; **V. Ntziachristos**, iThera Medical, Stockholder; SurgOptix BV, Consultant .

Presentation Number **P 278**
Poster Session 2
September 19, 2013 / 15:15-15:15 / Room: Exhibit Hall B

Modeling Light Delivery for Improved Quantitation of Multispectral 3D Photoacoustic Imaging

Dominique Van de Sompel[1], *Hao Gao*[2], *Sanjiv S. Gambhir*[1], [1]*Radiology, Stanford University, Stanford, CA, USA;* [2]*Mathematics and Computer Science, Emory University, Atlanta, GA, USA. Contact e-mail: dominiqu@stanford.edu*

Photoacoustic tomography (PAT) combines the high spatial resolution of ultrasound with the high optical contrast of diffuse optical imaging. The literature on PAT has seen the rapid development of scanner designs and reconstruction methodologies. One of the major remaining challenges for quantitative photoacoustic tomography is to account for the effect of wavelength-dependent light attenuation. Several algorithms have been developed and tested for 2D PAT, but light fluence compensation developments for fully 3D PAT have so far remained relatively limited. In this work, we implement and test two iterative wavelength-dependent light fluence compensation algorithms based on the Diffusion Approximation, and apply them to fully 3D multispectral PAT. The light fluence model used in both algorithms employed a light fluence model developed by Gao et al. The first algorithm investigated in the current work runs the fixed point iteration (FPI) algorithm developed by Cox et al. on all wavelengths independently, and then computes a least squares fit using reference spectra of the compounds present to estimate the compounds' concentrations. This algorithm is called the fixed point iteration algorithm with post-iteration fitting (FPI-PIF). The second algorithm is novel and computes the least squares fit after each iteration of the fixed point iteration algorithm, and at each iteration sets the current solution to that least squares fit. This algorithm is called fixed point iteration with inter-iteration fitting (FPI-IIF). The two algorithms were tested on both a simulated 3D multispectral Shepp Logan phantom (see Fig. 1a) and an experimental phantom composed of gold nanoparticle-containing transparent plastic tubes immersed in tissue mimicking intralipid. Gold nanoparticles are well-suited to multiplexed imaging, as their peak absorption wavelength is easily tuned by varying their aspect ratio. The tubes were inserted at known depths up to 2 cm and contained known gold nanoparticle concentrations. The immersed tubes were then imaged using the Nexus 128 photoacoustic scanner manufactured by Endra Life Sciences, which uses a tunable near infrared laser (Nd:YAG), capable of imaging at any number of wavelengths between 690 and 980nm. In this study, we imaged the phantoms at 23 wavelengths. An example multispectral reconstruction of the gold nanoparticle-filled tubes is shown in Fig. 1(b-c). In the simulations as well as experimental tests, we made the following observations. First, image noise was amplified with each iteration for both algorithms. Second, FPI-IIF consistently achieved lower errors in the final concentration values than FPI; after 30 iterations, the error in concentration values was 58.5% less than for the FPI-IFF algorithm. This agrees with the intuitive notion that incorporating prior knowledge of the absorption spectra increases reconstruction accuracy. In conclusion, we implemented and compared two algorithms for fully 3D multispectral PAT, namely FPI-PIF and FPI-IIF. It was found that the added information provided by the absorption spectra of the compounds present improved the accuracy of the estimated compound concentrations.

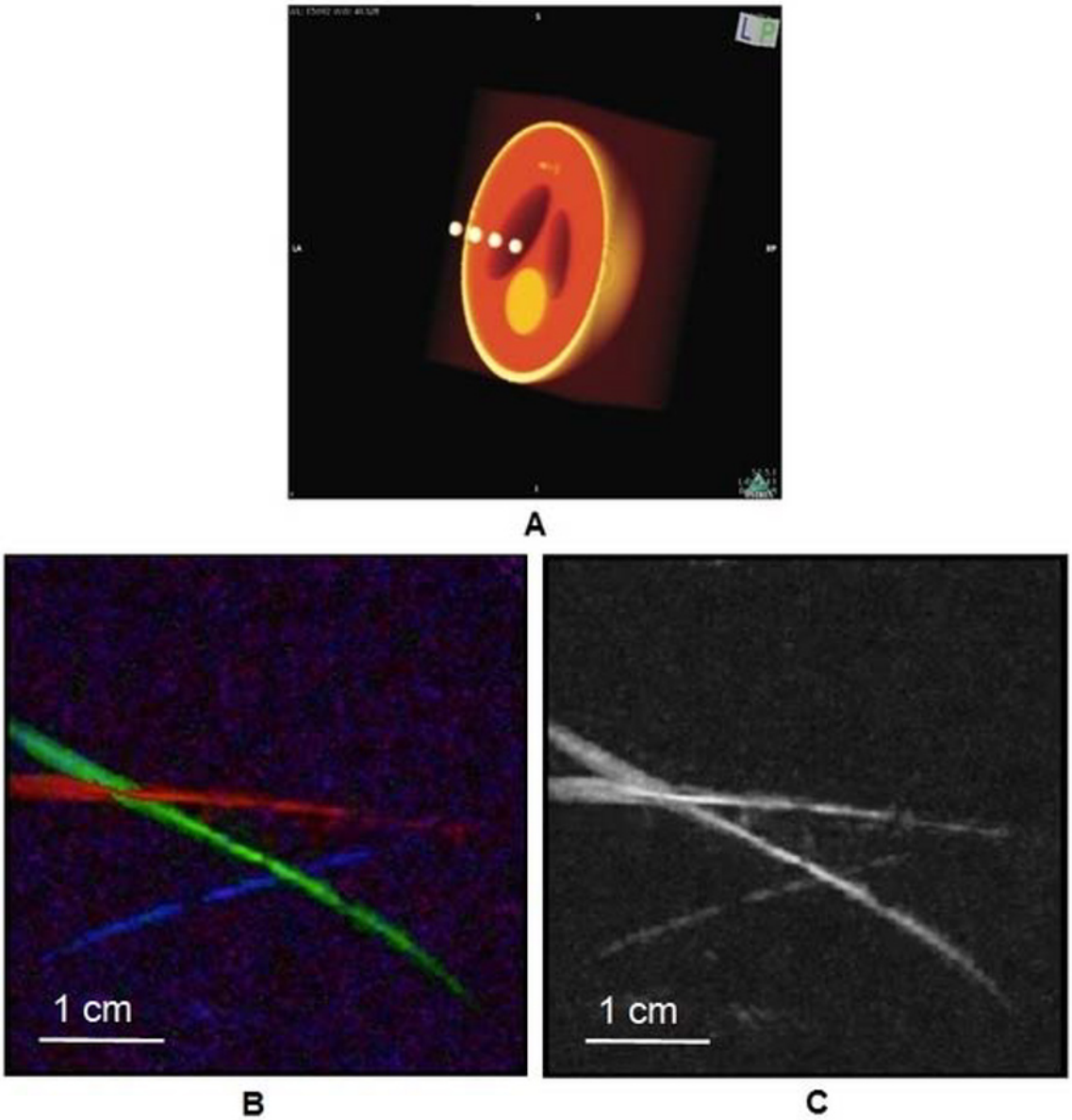

Fig. 1. (a) 3D Shepp Logan multispectral digital phantom. (b-c) Transparent plastic tubes (inner diameter of 1 mm) filled with three different gold nanoparticle solutions, each with a different absorption spectrum. (b) Multispectral reconstruction. (c) Single wavelength reconstruction.

Disclosure of author financial interest or relationships:
D. Van de Sompel, None; **H. Gao**, None; **S.S. Gambhir**, Bracco Diagnostics, Consultant; Endra, Inc, Stockholder; Cellsight, Stockholder; Enlight, Inc., Stockholder; General Electric, Grant/research support; ImaginAb, Stockholder; MagArray, Inc., Stockholder; Sanofi-Aventis, US, Grant/research support; SiteOne Therapeutics, Stockholder; VisualSonics/Sonosite, Stockholder .

Presentation Number **P 279**
Poster Session 2
September 19, 2013 / 15:15-15:15 / Room: Exhibit Hall B

Longitudinal Photoacoustic Imaging of Inducible Tyrosinase Reporter Gene Expression in Xenograft Tumors

Roger J. Zemp[1], *Andrew Heinmiller*[2], *Robert J. Paproski*[1], *Tyler Harrison*[1], *Minalini Lakshman*[2], *David Bates*[2], *Andrew Needles*[2], *Catherine Theodoropoulos*[2], [1]*Electrical & Computer Engineering, University of Alberta, Edmonton, AB, Canada;* [2]*FUJIFILM, VisualSonics Inc., Toronto, ON, Canada. Contact e-mail: rzemp@ualberta.ca*

In vivo molecular imaging of gene expression may provide powerful insights into the behavior and regulation of genes and provide a much-needed tool for researchers in a variety of fields of biological & medical research. Optical reporter gene strategies are widely used but presently suffer from imaging-depth & spatial resolution limitations associated with light scattering in tissues. Photoacoustic (PA) imaging offers a unique way to image reporter molecules with optical absorption contrast & high depth-to-resolution ratios. To leverage the fortes of PA imaging for molecular imaging we sought a reporter gene that absorbs rather than emits light. Previous efforts have included LacZ, which required a substrate, X-gal, not meant for in vivo use, & fluorescent proteins, which suffer from photostability issues, poor photothermal conversion efficiency & absorption-bleaching. Recently, tyrosinase, a principal enzyme in melanin production, has been considered as an enzymatic reporter gene for PA imaging. Here we report on longitudinal studies demonstrating the promise of PA imaging of tumors with & without doxycline-inducible tyrosinase expression. Methods: +TYR cells were created by stably transfecting MCF-7 Tet-On cells with a pTRE-Tight vector containing the tyrosinase gene. Using the Tet-On system, tyrosinase expression was inducible in the presence of doxycycline. -TYR & +TYR tumors were grown in the back right and left flanks of hairless SCID mice. When tumors reached at least 3 mm, animals were imaged with PA imaging using a Vevo LAZR platform (Visualsonics Inc) at 680, 750, 800, 850, 900 and 950nm wavelengths. Subsequently, drinking water was changed to 1 mg/mL doxycycline for 1 week after which mice were again imaged with PA imaging. Of n=6 animals imaged, n=3 were additionally given tyrosine supplementation in the drinking water. After imaging, animals were perfused with saline and another round of imaging was performed to attempt to eliminate the background hemoglobin signal & confirm the presence of melanin in the tumor. Excised tumors post exsanguination were again imaged after which tumors were sectioned for gross inspection & histology. An additional group of n=3 animals were imaged with a deeper-penetration, lower resolution custom PA imaging system and 9.4T MRI to compare image contrasts of the two modalities. Results and Discussion: Very strong PA signals were seen in +TYR tumors but not -TYR tumors after doxycline treatment. Multi-wavelength imaging showed spectral characteristics of intra-tumor regions that closely matched the absorption spectrum of melanin. Excised tumors exhibited a dark color indicative of strong melanin expression, & melanin expression levels were overall higher in animals that had tyrosine supplementation in drinking water. Phantom & animal studies indicate feasibility of detecting mere thousands of cells at 4-5cm imaging depth with PA imaging and significantly higher contrast than MRI. These data suggest unique possibilities for in vivo imaging of gene expression with PA imaging to study the tumor microenvironment, monitor cell migration & metastasis & non-invasively track expression of biomarkers.

Disclosure of author financial interest or relationships:
R.J. Zemp, None; **A. Heinmiller**, FUJIFILM VisualSonics Inc., Employment; **R.J. Paproski**, None; **T. Harrison**, None; **M. Lakshman**, FujiFilm Visualsonics Inc.,, Employment; **D. Bates**, None; **A. Needles**, FUJIFILM VisualSonics, Inc., Employment; **C. Theodoropoulos**, Fujifilm VisualSonics Inc, Employment .

Presentation Number **P 280**
Poster Session 2
September 19, 2013 / 15:15-15:15 / Room: Exhibit Hall B

In vivo frequency domain optoacoustic tomography of ICG absorption changes

Stephan Kellnberger[1,2], *Nikolaos C. Deliolanis*[1,2], *Daniel Queiros*[1,2], *George Sergiadis*[1,3], *Vasilis Ntziachristos*[1,2], [1]*Institute for Biological and Medical Imaging, Helmholtz Zentrum Munich, Neuherberg, Germany;* [2]*Chair for Biological Imaging, Technische Universitaet Muenchen, Munich, Germany;* [3]*Department of Electrical and Computer Engineering, Aristotle University of Thessaloniki, Thessaloniki, Greece. Contact e-mail: stephan.kellnberger@tum.de*

Purpose: Time domain (TD) optoacoustic imaging methods relate to the emission of broadband acoustic waves following absorption of nanosecond high energy laser pulses. Recently, frequency domain (FD) methods have been proposed which employ intensity modulated CW laser sources to excite (opto)acoustic pressure waves. Compared to TD-approaches, FD optoacoustic imaging provides more robust and economic light sources, enabling technically simpler implementations. Methods: In this work, we report on the tomographic implementation of frequency domain optoacoustics. Instead of raster scanning, the proposed method simultaneously excites and acquires optoacoustic signals at several projections around the object, enabling an extended view with diffraction limited resolution. Our frequency domain optoacoustic tomography approach consists of a 500 mW temperature stabilized laser diode emitting a collimated CW beam at 808 nm which is driven by frequency chirps covering a bandwidth of 4 MHz. Acoustic signals are acquired employing a focused ultrasound detector with a cut off frequency at ~5 MHz. Frequency domain optoacoustic signals are stimulated and acquired by simultaneous rotation of the optical fiber and the acoustic detector. To reconstruct images, we first determine the phase difference (i.e. the time lag) of each absorber before using the filtered backprojection for image formation. To validate functional imaging ability we imaged a BALB/C female mouse tail approximately 4 cm from the distal end as the tail vasculature offers a well-defined anatomical structure. During the experiments, the anesthetized mouse was immobilized and catheterized in the right lateral caudal vein at 2 cm from the distal end. FD-optoacoustic imaging was performed before injection of Indocyanine green (ICG), during and after the initial ICG administration to dynamically record changes in optical absorption. In vivo optoacoustic images were further compared to ex vivo cryosections. Results: Initial experiments were performed on graphite rods (diameter 0.35 mm) to confirm the tomographic optoacoustic imaging ability and furthermore on agar phantoms exhibiting complex geometries with defined absorption spectra. Finally, we examined the performance of the FD-optoacoustic tomography scanner to monitor optical absorption changes in vivo. Administration of ICG in the tail of a mouse revealed a twofold absorption increase compared to intrinsic hemoglobin contrast. Furthermore, FD-images taken 20 minutes after initial injection of ICG showcase reduced intensity due to clearance of ICG in the hepatobiliary tract. Conclusion: We presented a novel frequency domain optoacoustic method to visualize intrinsic soft tissue contrast and dynamically monitor absorption changes in vivo. Imaging rate and data acquisition of the proposed method can be significantly improved by using tomographic detector arrays, enabling real-time functional and molecular imaging of optical absorbers. Compared to time domain optoacoustic tomography using pulsed lasers, FD optoacoustic tomography has the potential to provide a cost effective imaging solution with more reliable and robust laser sources.

In vivo frequency domain optoacoustic tomography of the mouse tail. (A) Intrinsic contrast. (B) FD image during ICG administration. (C) FD-OAT image ~10 minutes after ICG injection. (D) ex vivo cryosection (VA - ventral caudal artery, LV - lateral caudal veins, DV - dorsal caudal vein; tail surface is approximated by dashed lines)

Disclosure of author financial interest or relationships:
S. Kellnberger, None; **N.C. Deliolanis**, None; **D. Queiros**, None; **G. Sergiadis**, None; **V. Ntziachristos**, iThera Medical, Stockholder; SurgOptix BV, Consultant .

Presentation Number **P 281**
Poster Session 2
September 19, 2013 / 15:15-15:15 / Room: Exhibit Hall B

Calibrated Spectral Unmixing for in vivo detection of melanin production using Multispectral Optoacoustic Tomography (MSOT)

Stefan Morscher[1,2], *Lorenz Kirscher*[3], *Nikolaos C. Deliolanis*[2], *Panagiotis Symvoulidis*[2], *Karin Schaefer*[2], *Qian Zhang*[4], *Ulrike Donat*[3], *Jochen Stritzker*[4], *Vasilis Ntziachristos*[2], [1]*iThera Medical GmbH, Neuherberg, Germany;* [2]*Institute for Biological and Medical Imaging, Helmholtz Zentrum München und TU München, Neuherberg, Germany;* [3]*Department of Biochemistry, Biocenter, Universität Würzburg, Würzburg, Germany;* [4]*Genelux, San Diego, CA, USA. Contact e-mail: stefan.morscher@ithera-medical.com*

Optoacoustic imaging as an emerging imaging modality, combines optical contrast in the near-infrared with high spatial resolution (~150µm in-plane for the particular imaging system) derived from ultrasound detection. Illumination at multiple wavelengths allows spectral unmixing to reveal individual absorbers such as melanin from the background contrast consisting mainly of hemoglobin. Low overall tissue absorbance of photons promotes optical imaging in the near-infrared (NIR) range, especially for deep tissue in vivo imaging. Fast image acquisition permits the collection of in vivo mouse images using multiple wavelengths, while imaging of a single, cross-sectional slice can be completed within seconds with the ability to create a 3D dataset from whole-body imaging. Oncolytic vaccinia virus strains are a valuable tool in therapeutic and diagnosic applications based on their tumor cell specific replication. In the present work, melanogenesis genes were inserted into the GLV-1h68 virus that is currently undergoing clinical phase I and II trials to create a novel theranostic agent. Based on the near infrared absorption of melanin a combination of both tools opens up a broad portfolio of applications in cancer research. In this study nude mice bearing both A549 and PC-3 tumors were injected with the modified rVACV and imaged in MSOT 2-4 weeks post, revealing specific melanin absorption in tomographic cross-sectional images in both the tumor and lymph node metastases (if present). Based on the strong hemoglobin absorption at all wavelengths it is very diificult to extract the broadband absorber melanin from this variable background. Different spectral unmixing strategies were evaluated, where an implementation of Independent Component Analysis that is calibrated on a known positive dataset performs best, both in terms of image quality and false-positive rate. All resulting images show good correlation with ex-vivo cryoslice validation imaging, control animals injected with an unmodified virus show very little melanin specific signal. In comparison to fluorescent reporter genes, melanin production has the advantage of being more stable with the added benefit of compatibility with PDT based approaches as treatment. MSOT imaging demonstrates its particular strength in real time, specific, high resolution imaging of optical absorbers such as melanin, allowing for non-invasive monitoring of tumor progression and therapy response. The demonstrated results prove both MSOT as a powerful imaging modality and the presented unmixing approach as very promising for application on large biological studies.

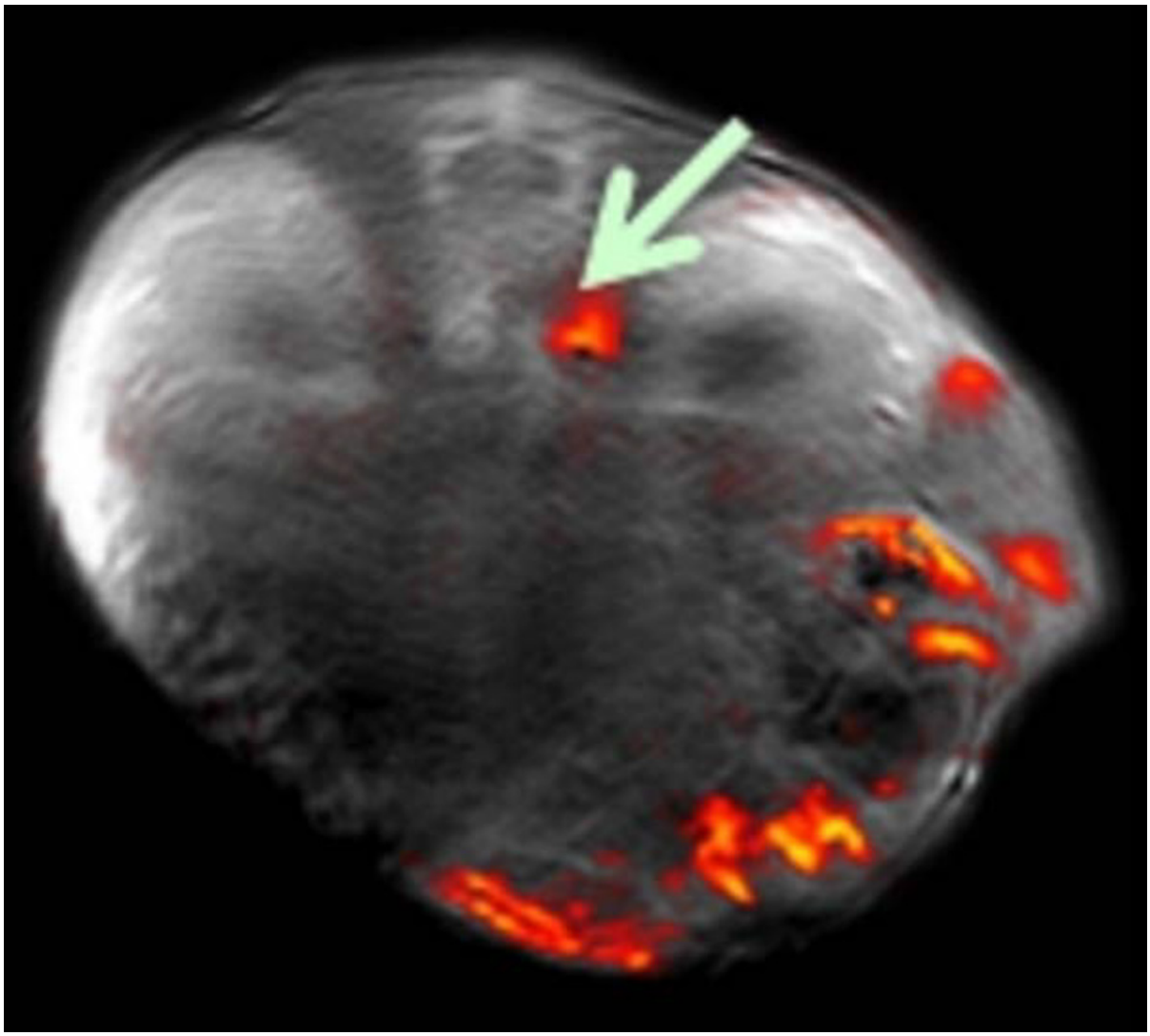

Background anatomical image overlaid with localised melanin signal revealed by multispectral unmixing

Disclosure of author financial interest or relationships:
S. Morscher, iThera Medical, Employment; **L. Kirscher**, None; **N.C. Deliolanis**, None; **P. Symvoulidis**, None; **K. Schaefer**, None; **Q. Zhang**, Genelux Corporation, Employment; Genelux Corporation, Stockholder; **U. Donat**, None; **J. Stritzker**, Genelux Corporation, Employment; Genelux Corporation, Stockholder; Genelux Corporation, Grant/research support; **V. Ntziachristos**, iThera Medical, Stockholder; SurgOptix BV, Consultant .

Presentation Number **P 282**
Poster Session 2
September 19, 2013 / 15:15-15:15 / Room: Exhibit Hall B

Water-Soluble Melanin Nanoparticles for Photoacoustic Imaging In Vivo

Quli Fan[1,2], Kai Cheng[1], Xiang Hu[1], Lihong Bu[1], **Zhen Cheng**[1], *[1]Molecular Imaging Program at Stanford, Canary Center at Stanford for Cancer Early Detection, Department of Radiology and Bio-X Program,, Stanford University, Stanford, CA, USA; [2]Institute of Advanced Materials, Nanjing University of Posts and Telecommunications, nanjing, China. Contact e-mail: zcheng@stanford.edu*

Introduction: Photoacoustic imaging (PAI) is a non-ionization and noninvasive emerging technique in molecular imaging that can provide strong optical absorption contrast and high ultrasonic resolution. Introducing exogenous contrast agents consisting of dyes or nanoparticles (NPs) such as indocyanine green ICG, carbon nanotubes and gold NPs in PAI enables its molecular imaging sensitivity and expands the functionality of the modality. Melanin, the well-known biopolymer, is found to exhibit multifunctions in biological system and especially over-expressed in melanotic melanomas. Thus it has been used as an effective molecular target as well as endogenous contrast material for PAI of melanoma. To further expand the use of melanin for molecular imaging of different diseases beyond melanoma, we herein report a facile method to prepare water-soluble melanin NPs and for the first time demonstrate their applications as exogenous organic nanoprobes for PAI in small animal models. Methods: Under the careful pH-controlling, polymeric melanin was directly dissolved in aqueous solution to prepare water-soluble melanin NPs, and their surface was further coated with polyethylene glycol (PEG5000). The melanin and PEG-melanin NPs were further characterized with Transmission Electron Microscope (TEM), Dynamic Laser Scattering (DLS), Fourier Transform Infrared Spectroscopy (FT-IR), and their PAI ability was studied in a phantom study. Moreover, their toxicity was evaluated through a preliminary cell viability test in NIH3T3 cells. The PEG-melanin NPs were then conjugated with metal chelator, 2,2'-(7-(2-((2,5-dioxopyrrolidin-1-yl)oxy)-2-oxoethyl)-1,4,7-triazonane-1,4-diyl)diacetic acid (NOTA) and radiolabeled with positron emission computed tomography (PET) radionuclide 64Cu, in order to understand the in vivo biodistribution and clearance of the NPs. Lastly, PEG-melanin NPs were injected to mice (n=3 per group) either subcutaneously or through tail vein and imaged by a PAI instrument. Results: Melanin and PEG-Melanin NPs (~4-7 nm) can be easily prepared in high water monodispersity and homogeneity (Figure 1 and 2 in Supplement Data). PEG-Melanin NPs did not show any noticeable cell toxicity, and 64Cu-NOTA-PEG-melanin NPs were found to be cleared mainly through liver and some through kidney system. More importantly, melanin NPs also produce high PAI signal in vitro and in vivo. After injection with melanin NPs for 1 h, The PAI signal of blood vessel enhanced greatly and the PAI signal also appeared on the liver surface (Figure below and Figure 3 in Supplement Data). Conclusion: Small water-soluble organic melanin NPs can be chemically prepared and used for in vivo PAI. Combined with the multifunctions of melanin, such water-soluble NPs can serve as a promising platform for molecular imaging.

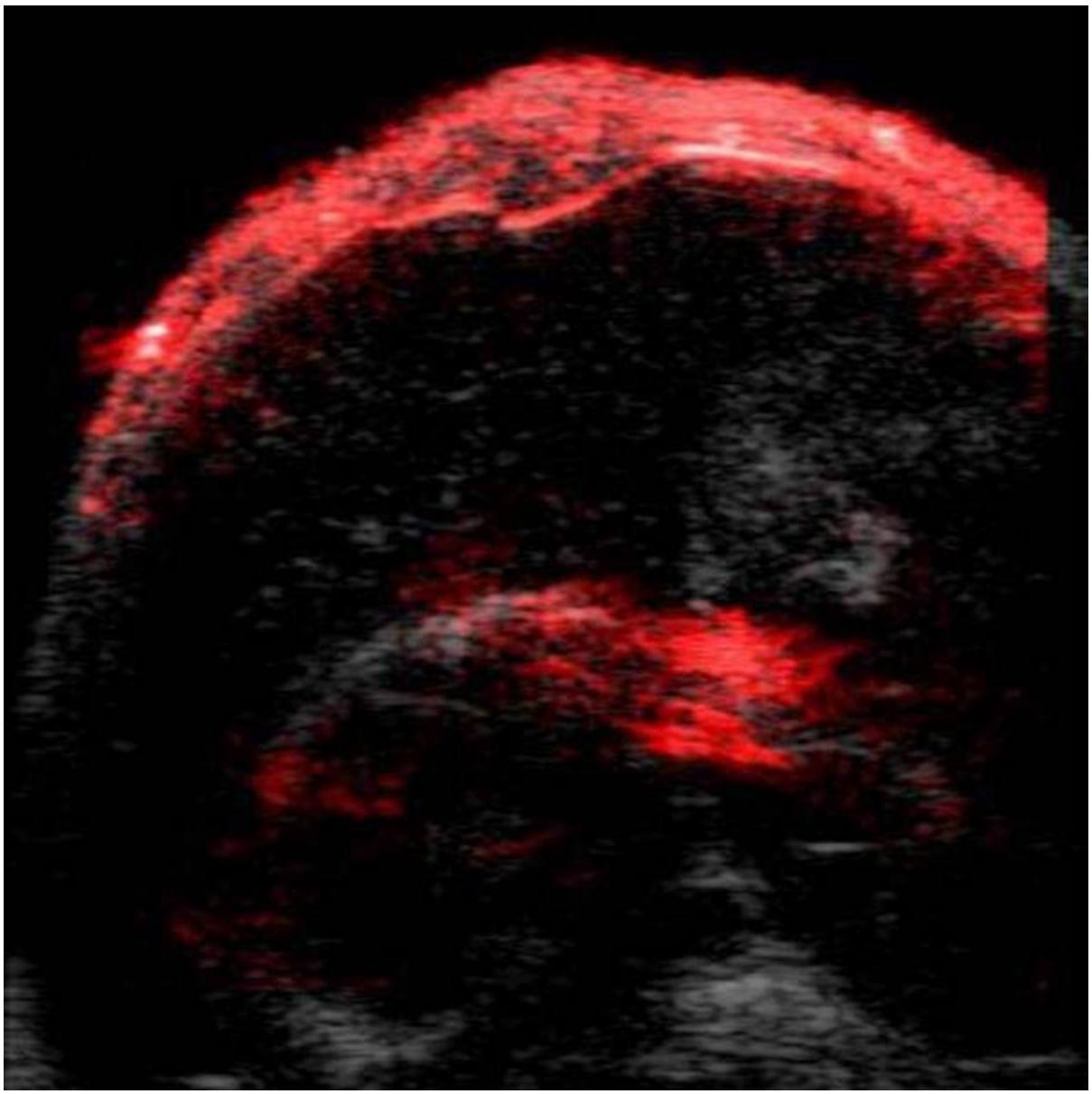

Figure: The ultrasonic (US) and photoacoustic (PA) overlaying imaging of PEG-melanin NPs in mouse liver after 1h post-injection

Disclosure of author financial interest or relationships:
Q. Fan, None; **K. Cheng**, None; **X. Hu**, None; **L. Bu**, None; **Z. Cheng**, None.

Presentation Number **P 283**
Poster Session 2
September 19, 2013 / 15:15-15:15 / Room: Exhibit Hall B

A Novel Biodegradable Nanoparticle for Enhanced Photoacoustic Molecular Imaging

Jesse V. Jokerst, *Sanjiv S. Gambhir, Radiology, Stanford University, Stanford, CA, USA. Contact e-mail: jokerst@stanford.edu*

Introduction: Photoacoustic molecular imaging combines the spatial and temporal resolution of ultrasound with the contrast of optical imaging and may employ exogenous contrast agents to enhance the signal and contrast of perturbed tissue. Nanoparticle contrast agents offer strong signal intensity and long-term stability, but are limited by poor biodistribution and clearance profiles. Conversely, small molecules offer renal clearance, but relatively low photoacoustic signal. Here we describe a cellulose-based nanoparticle with photoacoustic signal superior to gold nanorods, but that undergoes enzymatic cleavage into constituent glucose molecules for renal clearance. Materials and Methods: Cellulose nanoparticles (CNPs) were synthesized through acidic cleavage of cellulose linters and purified with centrifugation. Subcutaneous tumor xenografts of the OV2008 cell line were created in nude mice and imaged when they were 800 - 1200 mm3. Tomographic data was collected with a Nexus128 scanner from Endra LifeSciences. Spectral data used a LAZR system from Visualsonics both at 700 nm excitation. Results: The nanoparticles were 132 ± 46 nm by electron microscopy and 160-200 nm by dynamic light scattering with a polydispersity index of 0.138. Ex vivo characterization indicated a photoacoustic limit of detection of 0.02 mg/mL CNPs. The photoacoustic signal of CNPs was 1.5- to 3.0-fold higher than gold nanorods (at 700 nm resonance) on a particle-to-particle basis. Cell toxicity data with an Alamar Blue assay indicated overnight doses below 0.31 mg/mL CNPs had no significant ($p>0.05$) impact on the metabolism of OV2008 cells. Intravenous doses up to 0.24 mg were tolerated well in nude mice (n=3) with minor up-regulation of alkaline phosphatase the only measurable change in serum chemistry. When CNPs (0.024 mg, 0.048 mg, and 0.80 mg) were injected i.v. the photoacoustic signal of tumor reached maximum increase between 10 and 20 minutes—this increase was 18 to 61% higher than baseline signal depending on dose and remained elevated for at least one hour. All injected concentrations were statistically ($p<0.05$) elevated relative to the control group with n=3 mice in each group. The relationship between injected dose and the increase in photoacoustic signal was linear at $R2>0.96$ suggesting that the signal is quantitative. Biodegradation into glucose was demonstrated ex vivo with a hexokinase-based glucose assay. CNPs in the presence of cellulase were reduced to glucose in less than four hours. The glucose concentration before addition of cellulase was not-detectable and increased to 92.1 μg/mL in four hours. Cellulase-free CNPS showed no increase in glucose concentration. Small fragments of nanoparticle in the treated cohort were observed with electron microscopy (Supplement). Conclusion: There are few photoacoustic contrast agents that offer both high signal intensity and obvious clearance/biodegradation profiles. To the best of our knowledge, this is the first example of a sugar-based photoacoustic contrast agent with important implications for clinical translation of this emerging molecular imaging modality.

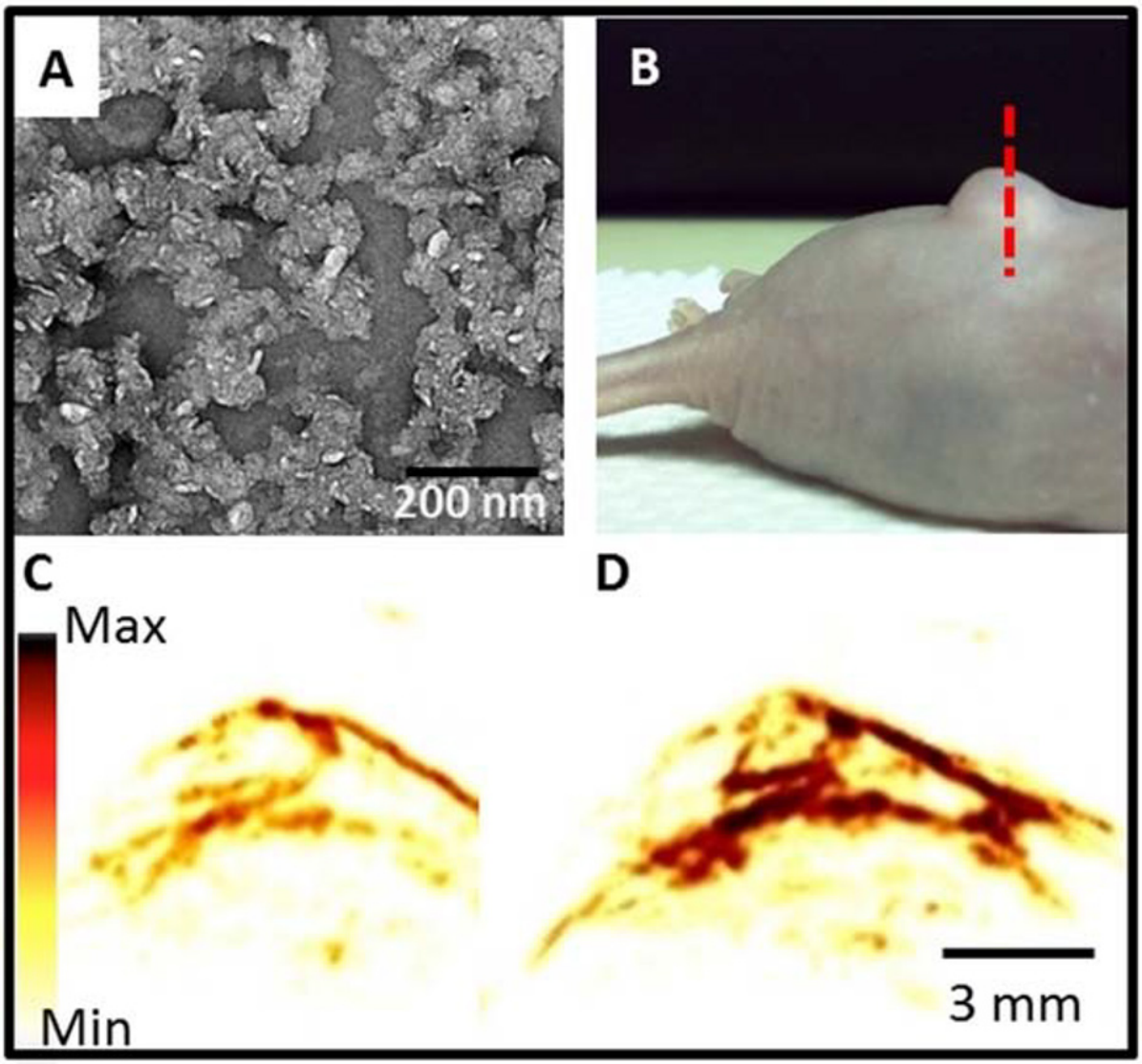

Figure 1. A) Transmission electron microscopy images of cellulose nanoparticles indicate an anisotropic morphology. B) These materials were used to image subcutaneous xenograft tumors in nude mice and increase signal in a dose-dependent fashion after intra-venous injection as illustrated by pre- (C) and post-injection (D) images of the tumor. Dashed line in B highlights the image plane projected in lower panels.

Disclosure of author financial interest or relationships:

J.V. Jokerst, None; **S.S. Gambhir**, Bracco Diagnostics, Consultant; Endra, Inc, Stockholder; Cellsight, Stockholder; Enlight, Inc., Stockholder; General Electric, Grant/research support; ImaginAb, Stockholder; MagArray, Inc., Stockholder; Sanofi-Aventis, US, Grant/research support; SiteOne Therapeutics, Stockholder; VisualSonics/Sonosite, Stockholder .

Presentation Number **P 284**
Poster Session 2
September 19, 2013 / 15:15-15:15 / Room: Exhibit Hall B

High-Yield, Silver Seed-Mediated Synthesis of Gold Nanoplates for Photoacoustic Imaging

Suraj Makhija[1], *Geoffrey P. Luke*[1,2], *Justin Harris*[3], *Kimberly A. Homan*[3], *Stanislav Y. Emelianov*[1,2], [1]*The Department of Biomedical Engineering, The University of Texas at Austin, Austin, TX, USA;* [2]*The Department of Electrical and Computer Engineering, The University of Texas at Austin, Austin, TX, USA;* [3]*NanoHybrids LLC, Austin, TX, USA. Contact e-mail: smakhija@utexas.edu*

Photoacoustic (PA) imaging is an emerging method that has potential to detect cancer in early, localized stages of development. Gold nanoparticles are commonly used as targeted contrast agents due to their inherent stability in cells and high optical absorption. In particular, triangular gold nanoplates (AuNPs) have shown great promise as contrast agents for PA imaging because of their high optical absorption, tunable optical properties, and minimal cytotoxicity. However, most current methods to fabricate AuNPs either result in substantial amounts of undesired nanospheres or a polydisperse population of AuNPs. We have developed a new high-yield, seed-mediated synthesis method to produce AuNPs. Not only does this method produce an even distribution of AuNPs with a high triangle-to-sphere ratio, but it also sheds light on the mechanisms behind the formation of planar nanostructures. In contrast to previously described methods, the developed procedure templates the growth of AuNPs on silver seeds. Silver exhibits a face center cubic lattice structure that is strikingly similar to gold and promotes the growth of gold atoms onto the silver seed. The protocol begins with the synthesis of silver nanoseeds with inherent structural defects in the lattice structure known as stacking faults. The seed particles were then added to a gold growth solution containing cetyl trimethylammonium bromide (CTAB), potassium iodide (KI), and chloroauric acid (HAuCl4) to initiate the slow, controlled adsorption of gold ions onto the seeds to form the AuNPs. Stacking faults in the seed particles were detected using X-Ray diffraction (XRD) peaks and fast Fourier transform (FFT) analysis from high resolution transmission electron microscopy (TEM) images. Forbidden {422} reflections in the FFT and short characteristic peaks in the XRD spectrum at 2θ values of 35.61 and 40.87 degrees (2.22 and 2.49 Å) differentiate the XRD of the seed particles from a typical face center cubic XRD spectrum and can be attributed to hexagonally directed stacking faults. The final particles have a peak absorption wavelength of 800 nm and an average edge length of 80 nm. The peak absorption wavelength of the final AuNPs can be reliably controlled by varying the number of silver seeds, reaction temperature, or concentration of KI. Antibodies can then be directly conjugated to the AuNPs to selectively target specific biomarkers for use in molecular PA imaging applications. The particles were characterized using TEM and Ultraviolet Visible Spectrophotometry (UV-Vis) shown in Figure 1a and 1b, respectively. The TEM images and XRD spectrum show that the silver seeds serve as the point of nucleation for AuNPs and that the inherent characteristics (i.e., presence of stacking faults) of the seeds play a major role in determining the final morphology of the particles. This ability to control nanoparticle shape for desired properties is paramount in many nanoengineering applications. Proficiency in producing optimal particles for applications will eventually lead to streamlined, cost efficient research in many nanoparticle fields.

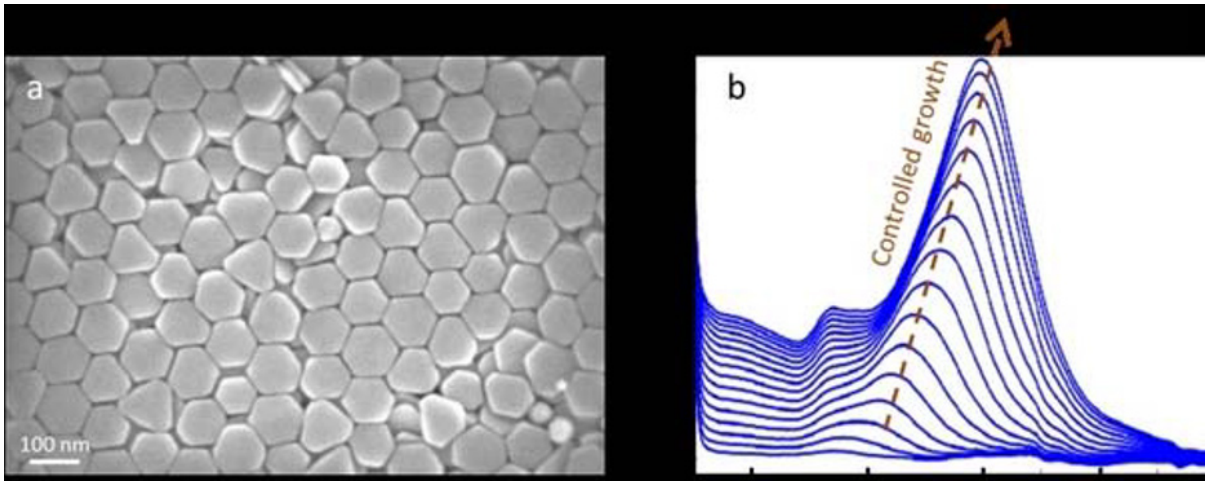

Disclosure of author financial interest or relationships:
S. Makhija, None; **G.P. Luke**, None; **J. Harris**, None; **K.A. Homan**, NanoHybrids Inc, Grant/research support; **S.Y. Emelianov**, NanoHybrids, Inc, Stockholder .

Presentation Number **P 285**
Poster Session 2
September 19, 2013 / 15:15-15:15 / Room: Exhibit Hall B

Bacteriochlorophyll nanoparticles as photoacoustic contrast agents

Mojdeh Shakiba[1,2], *Kenneth K. Ng*[2,3], *Elizabeth Huynh*[1,2], *Gang Zheng*[1,2], [1]*Department of Medical Biophysics, University of Toronto, Toronto, ON, Canada;* [2]*University Health Network, Toronto, ON, Canada;* [3]*Institute of Biomaterials and Biomedical Engineering, University of Toronto, Toronto, ON, Canada. Contact e-mail: mojdeh.shakiba@utoronto.ca*

Photoacoustic imaging (PAI) is a novel imaging modality that combines the high contrast attained in optical imaging with the high resolution attained in ultrasound at depths beyond the optical diffusion limit of ~1 mm. While endogenous chromophores can be used to create contrast, exogenous contrast agents are required for both enhancing deep tissue contrast as well as for providing additional molecular and functional information, such as those required for tumour imaging. Metallic nanoparticles have been widely used due to their high extinction coefficient and near-infrared (NIR) absorbance that together greatly enhance depth penetration of PAI. They, however, suffer from poor biocompatibility and biodegradation. Here we report synthesis and characterization of a novel organic nanoparticle for PAI using a type of porphyrin derived from photosynthetic bacteria, known as bacteriochlorophyll. These nanoparticles are shown to have a narrow, intense absorption band centred deep in the NIR at 824 nm. In order to evaluate their performance as PA contrast agents, they were imaged in agarose gel phantoms (Figure 1), where they exhibited a strong signal at the same wavelength. Interestingly, the PA signal was seen to be completely eliminated upon particle disruption, making the strong absorption and photoacoustic peak a nanoparticle phenomenon.

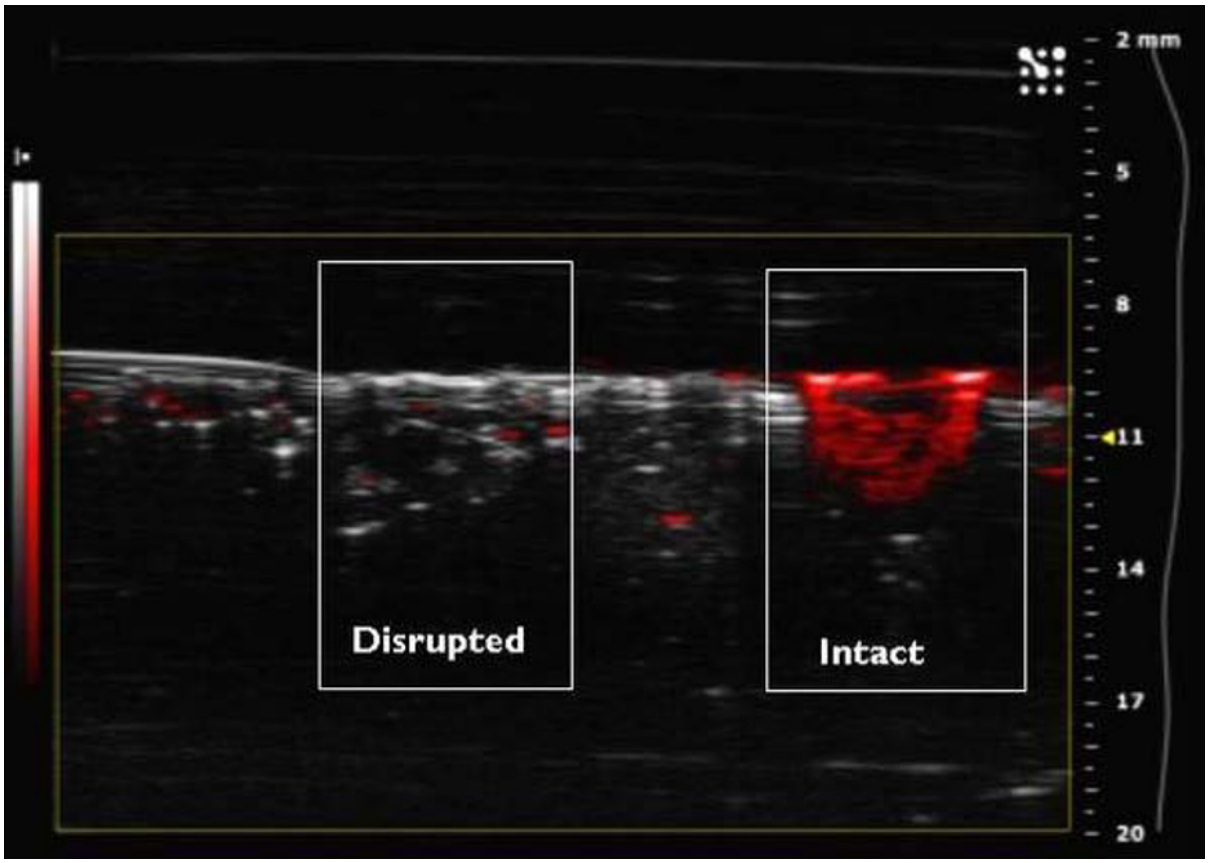

Photoacoustic image of an agarose gel phantom containing intact and disrupted bacteriochlorophyll nanoparticles. The image is obtained using Vevo LAZR photoacoustic imaging system (Visualsonics) equipped with a 21 MHz-centred transducer and a flashlamp pumped 20Hz Q-switched Nd-YAG laser, tuned to 824nm excitation wavelength.

Disclosure of author financial interest or relationships:
M. Shakiba, None; **K.K. Ng**, None; **E. Huynh**, None; **G. Zheng**, None.

Presentation Number **P 286**
Poster Session 2
September 19, 2013 / 15:15-15:15 / Room: Exhibit Hall B

Near Infrared Quaterrylenediimide-cored Dendrimers for Photoacoustic Imaging

Pin Shao[1], *Mingfeng Bai*[1], *Kang Kim*[2], *Seunghan Ha*[2], [1]*Radiology, university of pittsburgh, Pittsburgh, PA, USA;* [2]*Center for Ultrasound Molecular Imaging and Therapeutics, University of Pittsburgh, Pittsburgh, PA, USA. Contact e-mail: shaop@upmc.edu*

Photoacoustic imaging is a rapid growing biomedical imaging modality and has attracted intense interest of scientists due to its high spatial resolution and the absence of ionizing radiation. In order to image deep tissues, the near infrared (NIR) laser is typically used in the photoacoustic imaging. One of the most commonly used exogenous contrast agents in photoacoustic imaging is indocyanine green (ICG), the only FDA approved NIR dye. However, the poor chemical and photo stability of ICG greatly limits its application in photoacoustic imaging. An NIR dye with high absorption extinction coefficient, low fluorescence quantum yield and high chemical and photo stability will be more desirable. In this study, we developed two novel NIR photostable dendrimers, QR-G1-COOH and QR-G2-COOH, for photoacoustic imaging. The dendrimers are based on quaterrylenediimide with four biocompatible dendronized polyamides covalently attached to the bay regions. QR-G1-COOH and QR-G2-COOH possess twelve and thirty-six carboxyl acid groups respectively, which not only increase hydrophilicity but also introduce multilple functionality. QR-G1-COOH and QR-G2-COOH show intense absorption bands centered at 788 nm, with high molar extinction coefficients and low quantum yields and cytotoxicity. Moreover, QR-G1-COOH and QR-G2-COOH exhibit outstanding photostability. When exposed to the ambient light for 3 days, the dendrimer samples show almost no change in the absorption whereas ICG sample completely lost NIR absorption. In the preliminary in vitro photoacoustic imaging study, QR-G1-COOH and QR-G2-COOH showed significantly higher photoacoustic signal than ICG. These results indicate that our quaterrylenediimide-cored dendrimers have great potential in photoacoustic imaging research.

Disclosure of author financial interest or relationships:
P. Shao, None; **M. Bai**, None; **K. Kim**, None; **S. Ha**, None.

Presentation Number **P 287**
Poster Session 3
September 20, 2013 / 15:15-15:15 / Room: Exhibit Hall B

A comparison of functional imaging of β-cells using the Zn^{2+} sensor, GdDOTA-diBPEN, at high and low MR field strengths

Jeff R. Anderson[1], *Khaled A. Nasr*[1], *Dean Sherry*[1,2], [1]*Advanced Imaging Research Center, UT Southwestern Medical Center, Dallas, TX, USA;* [2]*Chemistry, UT Dallas, Dallas, TX, USA. Contact e-mail: j.anderson.mri@gmail.com*

The MRI contrast agent GdDOTA-diBPEN has been shown to facilitate functional imaging of pancreatic β-cells in mice (1). The functional mechanism of the contrast agent arises due to an increase in T_1 relaxivity of the complex after 1) forming a complex with zinc ions, co-released with insulin from β-cells in response to high glucose, followed by 2) binding of the resulting Zn^{2+}-sensor complex with albumin (2). Slowing of the molecular tumbling rate upon binding to the much higher molecular weight albumin (~1 kDa to ~65 kDa) results in an increase in relaxivity that should, in principle, be field dependent. In the first published study at 9.4T, the binding events described above resulted in a measurable gain in image intensity of the pancreas in T_1-weighted images following glucose-stimulated insulin secretion (1). According to basic Solomon-Bloembergen theory of paramagnetic systems, this image enhancement should not be optimal at high fields. To evaluate the field dependence, healthy C57BL/6 mice were imaged with MRI before and after GdDOTA-diBPEN injection at high (9.4T) and low (1T) field strengths. Two groups of mice were compared; mice in the experimental group (N = 3) received an injection of glucose prior to contrast agent injection while mice in the control group (N = 3) received an injection of saline prior to contrast agent injection. The timing of the glucose and contrast agent/saline injections were matched at both field strengths: IP injection of 50 µL of 20% (wt/vol) glucose or saline sham at t = 0 min, jugular vein catheter injection of 25 µL of 20 mM GdDOTA-diBPEN at t = 10 min. Imaging parameters were also matched: sequence - 3D spoiled gradient-echo, resolution - isotropic 0.5 mm, TR - 8.8 ms, TE - 2.2 ms, flip angle - 25°, number of averages - 8. A representative, composite image, presenting the results as a color enhancement overlaid on an anatomical background, is shown in the figure. The hypothesis was only partially confirmed by the experimental results. Despite a 9-fold increase in signal-to-noise at the higher field strength, image contrast between experimental and control groups was nearly identical at 9.4T and 1T. We believe this reflects a non-optimal, slow, water exchange rate in this molecular sensor. Figure 1. A representative, composite image of β-cell function after glucose stimulated insulin secretion. The color overlay is a projection image of relative signal enhancement in all slices following contrast agent injection. The grayscale background is an anatomical (pre-contrast) image of a single slice. Enhancement is seen in the pancreas (red arrow) and kidneys (due to clearance of the contrast agent; white arrows). Recall that mouse pancreas is quit diffuse (reference 1 supplemental materials). (1) Lubag AJM et al. Noninvasive MRI of β-cell function using a Zn^{2+}-responsive contrast agent. PNAS 2011, 108(45):18400-18405. (2) Esqueda AC et al. A New Gadolinium Based MRI Zinc Sensor. JACS 2009, 131(32):11387-11391.

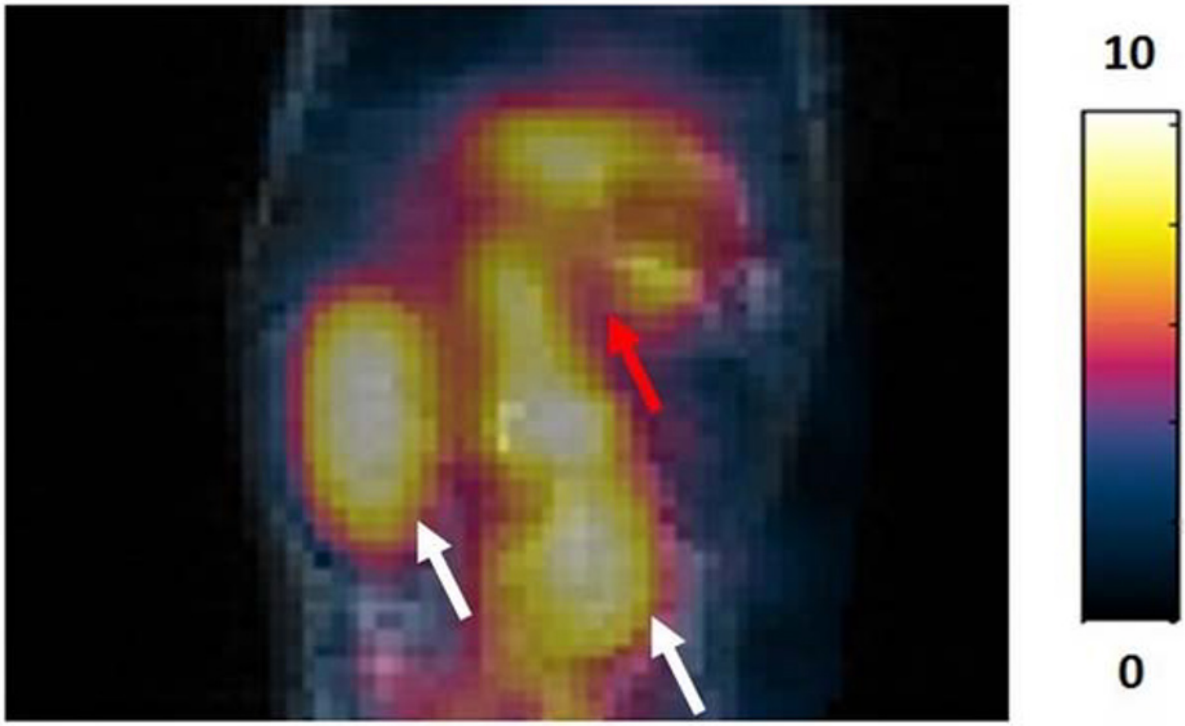

Disclosure of author financial interest or relationships:
J.R. Anderson, None; **K.A. Nasr**, None; **D. Sherry**, None.

Presentation Number **P 288**
Poster Session 3
September 20, 2013 / 15:15-15:15 / Room: Exhibit Hall B

Human Protamine-1 as an MRI Reporter Gene Based on Chemical Exchange Saturation Transfer (CEST)

Amnon Bar-Shir[1,2], *Guanshu Liu*[1,3], *Kannie WY Chan*[1,3], *Nikita Oskolkov*[1,3], *Xiaolei L. Song*[1,3], *Piotr Walczak*[1,2], *Michael T. McMahon*[1,3], *Peter C. van Zijl*[1,3], *Jeff W. Bulte*[1,2], *Assaf A. Gilad*[1,2], [1]*Division of MR Research, the Russell H. Morgan Department of Radiology and Radiological Sciences, the Johns Hopkins University School of Medicine, Baltimore, MD, USA;* [2]*Cellular Imaging Section, Institute for Cell Engineering, the Johns Hopkins University School of Medicine, Baltimore, MD, USA;* [3]*F.M. Kirby Research Center for Functional Brain Imaging, Kennedy Krieger Institute, Baltimore, MD, USA. Contact e-mail: abarshi2@jhmi.edu*

Introduction: Genetically engineered reporters have revolutionized the understanding of many biological processes. MRI-based reporter genes can improve our ability to monitor dynamic gene expression and allow co-registration of sub-cellular genetic information with high-resolution anatomical images[1-5]. We have developed a biocompatible MRI reporter gene based on a human gene, human protamine-1 (hPRM1). The arginine-rich hPRM1 (47% arginine residues) generates high MRI contrast based on CEST contrast mechanism. The high CEST contrast was demonstrated for pure synthetic protein, and in live cells expressing the hPRM1 reporter gene, which were embedded in three-dimensional culture. **Methods**: The synthesis of the 51 amino acid long hPRM1 protein was performed on a microwave-assisted peptide synthesizer and the crude peptide was purified using HPLC on a C12 reverse-phase column. Human Embryonic Kidney cells (HEK293) were engineered to express the gene encoding to hPRM1 ($293h^{PRM1}$), with non-expressing wild type cells (293^{wt}) serving as controls. Cells were lysed or encapsulated in alginate-based microcapsules using Ba^{2+} ions as the gelating cation as previously described6. CEST experiments were performed on an 11.7T Bruker Avance system, as previously described[5]. **Results and Discussions**: In order to evaluate the feasibility of hPRM1 as a CEST-based reporter gene, we initially synthesized and purified the 51-amino-acid-long hPRM1 protein and compared it CEST contrast with protamine sulfate and poly-L-lysine (Figure 1a), both of which are well-characterized CEST agents[7] with the latter having been used as a CEST reporter gene[3]. As can be concluded from both the MTR_{asym} plots and maps (Figure 1b,c), the total CEST contrast from both protamines was considerably higher than that of poly-L-lysine. This is because poly-L-lysine has a peak only at the amide proton resonance frequency ($\Delta\omega$=3.6 ppm offset with one amide per residue), while both protamine sulfate and hPRM-1 displayed two distinct peaks, specifically, for the amide protons of the protein backbone ($\Delta\omega$=3.6 ppm) and the guanidyl protons of the arginine side chain (at $\Delta\omega$=1.5 ppm with four of these protons per arginine). To demonstrate the ability to image hPRM1 expression in live cells with CEST MRI, we constructed a three-dimensional culture of alginate-encapsulated 293^{wt} and 293^{hPRM1} cells (Figure 1d). As expected, encapsulated live cells expressing the hPRM1 generated a higher CEST contrast compared to non-expressing wild-type cells (Figure 1e). This observation was found for saturation at both the 1.5 ppm or 3.6 ppm offsets from the water resonance. **Conclusion**: We have developed a novel CEST MRI reporter gene based on hPRM1 and demonstrated its expression and detection in three-dimensional cell cultures. **References**: (1) Cohen, B. et al. Nat Med 2007, 13, 498. (2) Genove, G. et al. Nat Med 2005, 11, 450. (3) Gilad, A. A. et al. C. Nat Biotechnol 2007, 25, 217. (4) Zurkiya, O. et al. Magn Reson Med 2008, 59, 1225. (5) Bar-Shir, A. et al. J Am Chem Soc 2013, 135, 1617. (6) Barnett, B. P. et al. Nat Protoc 2011, 6, 1142. (7) McMahon, M. T. et al. Magn Reson Med 2008, 60, 803.

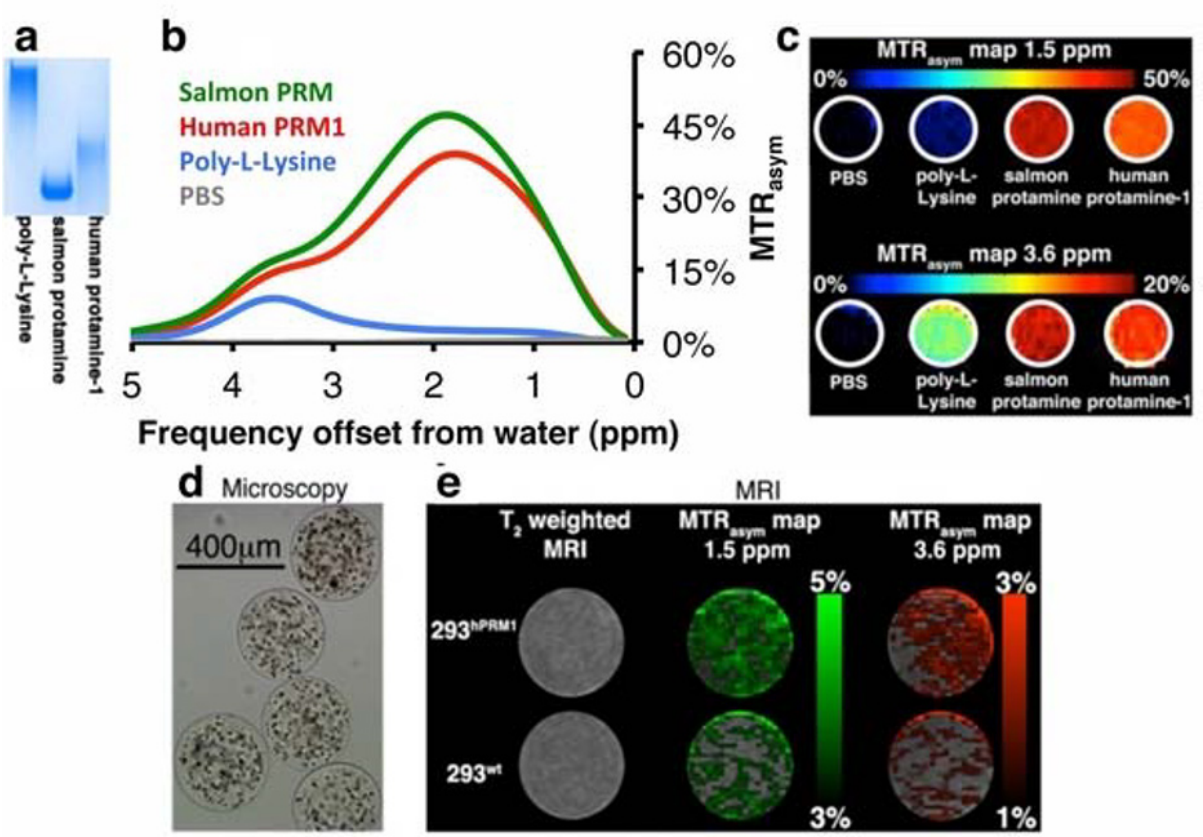

Figure 1: (a) Acetic acid-urea polyacrylamide gel electrophoresis of positively charged proteins, poly-L-Lysine, salmon protamine, and human protamine-1. The CEST MRI characteristics of 5 mg/ml protein is depicted as (b) MTR_{asym} plots and (c) MTR_{asym} maps. (d) Bright-field microscopic images of encapsulated live 293HEK cells. (e) T2-weighted images and overlaid MTR_{asym} maps of encapsulated cells obtained at 1.5 and 3.6 ppm frequency offsets.

Disclosure of author financial interest or relationships:
A. Bar-Shir, None; **G. Liu**, None; **K. Chan**, None; **N. Oskolkov**, None; **X.L. Song**, None; **P. Walczak**, None; **M.T. McMahon**, None; **P.C. van Zijl**, None; **J.W. Bulte**, None; **A.A. Gilad**, None.

Presentation Number **P 289**
Poster Session 3
September 20, 2013 / 15:15-15:15 / Room: Exhibit Hall B

Hybrid gold-iron oxide nanoparticles: the assembly via silver adapter deposition and MR imaging

Alexei A. Bogdanov, *Mohammed Salman Shazeeb, Lejie Zhang, Surong Zhang, Radiology, Laboratory of Molecular Imaging Probes, Worcester, MA, USA. Contact e-mail: alexei.bogdanov@umassmed.edu*

The major applications of stabilized colloidal iron oxides include MR imaging of lymph nodes and cell labeling in cell trafficking after transplantation. The technology of incorporating iron oxides into gold nanoparticles or gold shells is of great interest due to the potential of combining magnetic, optical and surface plasmon resonance properties in a single nanoparticle entity. Such composite nanoparticles, due to feasibility of linking of targeting molecules (a consequence of large surface energy of colloidal gold) are expected to enable several diagnostic and theranostic applications including multimodality photoacoustic and magnetic resonance imaging. We devised and tested an approach that included a greatly simplified synthesis of small gold nanoparticles with very high molar relaxivity. The synthesis was accomplished in water milieu without the need of hydrophobic adaptor molecules and similar intermediates. We used an advantage of the presence of multiple silver-reducing aldehydes that are available on the surface of freshly-prepared dextran-stabilized ultra small iron oxide nanoparticles to induce formation of the nanocolloidal silver layer after treating of 20.5±4.6 nm dextran-stabilized iron oxides with an excess of Tollens reagent (diamminesilver(I) nitrate). After size-exclusion chromatography we isolated 34.0±9.5 nm nanoparticles with unimodal size distribution and characteristic absorbance peak at 405 nm. Incubation of these silver-tagged nanoparticles in diluted solutions of tetrachloroauric acid in the presence of citrate as buffering and capping agent resulted in the formation of small, electron dense single-core negatively charged nanoparticles (30.9±9.6 nm, zeta potential - 19 mV) that were additionally purified using density gradient ultracentrifugation. The gold-iron oxide nanoparticles (Au-FeO NP) were stabilized using stable absorption of MPEG-gPLL (graft copolymer of MPEG5000 and poly-l-lysine) which resulted in stable, weakly positively charged NPs that did not aggregate in the presence of phosphate-buffered solutions. Au-FeO NPs showed a strong increase of iron molar transverse relaxivity (r2) - from 52.6 [mMs]-1 to 165 [mMs]-1 at the field strength of 0.47T. While r2 of initial iron oxide nanoparticles changed little if the filed strength was increased to 3T, the changes were dramatic with a 12-times increase of r2 for Au-FeO NP allowing the detection of nanoparticles at low concentrations of iron using MRI at 3T (Figure). The Au-FeO NP showed binding capacity for short oligonucleotide duplexes at the level of 0.3-0.6 μg (16-33 nmol)/μg NP that suggests their potential use for oligonucleotide delivery combined with imaging of their biodistribution.

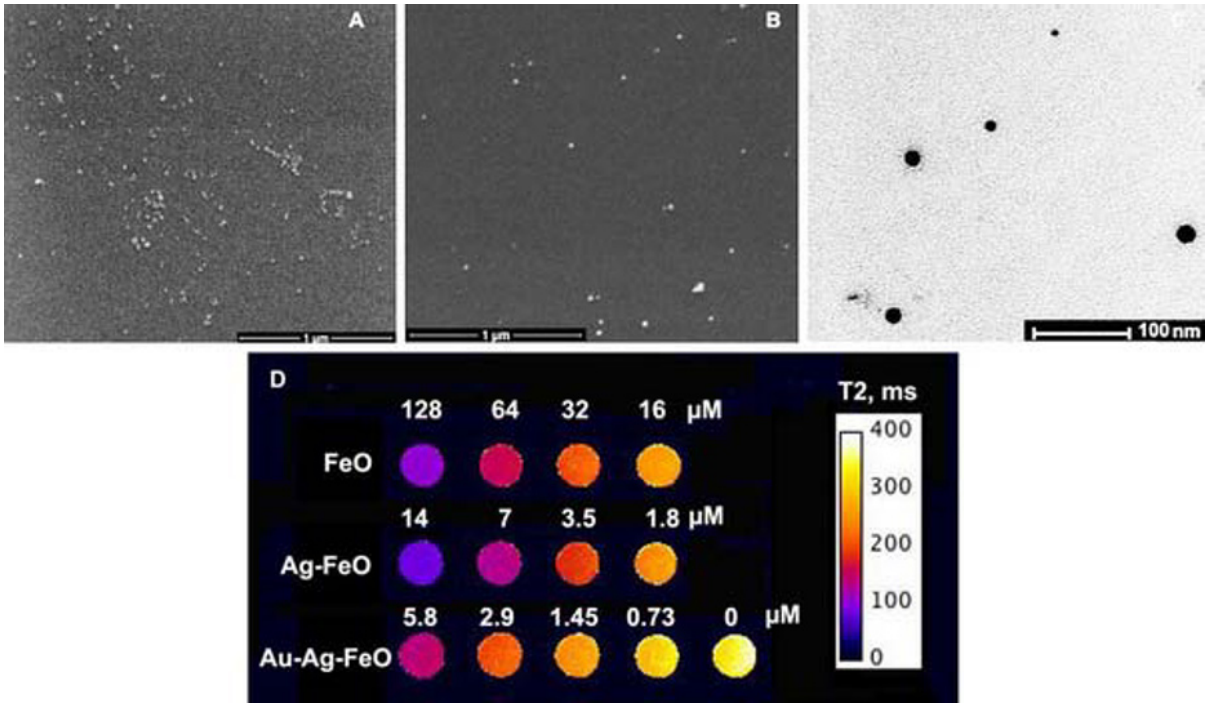

A- Scanning electron microscopy (SEM) of silver-coated iron oxide nanoparticles (Ag-FeO) showing enhanced back scatter of X-rays; B - SEM of gold(III) chloride-treated Ag-FeO showing high back scatter due to gold presence. C - A T2 map of the initial, diamminesilver(I)-treated and gold(III)-silver treated hybrid nanoparticle samples (3T MRI).

Disclosure of author financial interest or relationships:
A.A. Bogdanov, None; **M. Shazeeb**, None; **L. Zhang**, None; **S. Zhang**, None.

Presentation Number **P 290**
Poster Session 3
September 20, 2013 / 15:15-15:15 / Room: Exhibit Hall B

Mesoporous Silica Encased, Ultra-small/Aggregate Manganese Oxide Nanoparticles as Positive T1 Contrast Agents for MRI

Shih-Hsun Cheng[1,2], *Lara Leoni*[1], *Brian B. Roman*[1], *Jeffrey S. Souris*[1], *Nai-Tzu Chen*[1,2], *Leu-Wei Lo*[2], *Chin-Tu Chen*[1],
[1]*Radiology, University of Chicago, Chicago, IL, USA;* [2]*Division of Medical Engineering Research, National Health Research Institute, Zhunan, Taiwan. Contact e-mail: smallgi2002@gmail.com*

Mesoporous silica encased, ultra-small/aggregate manganese oxide nanoparticles (MnO@MSN) were synthesized for use as novel T1 magnetic resonance imaging (MRI) contrast agents. Previous studies suggested that manganese oxide (MnO) nanoparticles might serve as efficient "positive" T1 contrast agents for MRI in biological studies, due to their relaxation dynamics and biocompatibility. We postulated that nanoaggregates of individual ultra-small manganese oxide nanoparticles (USMnO; diameter ~7nm), encased within mesoporous silica nanoparticles, would significantly strengthen the T1-weighted signal via the MSN's allowance of water molecules to access and interact with internalized magnetic nanocores - resulting in the enhancement of longitudinal (R1) relaxation. MSN diameters were measured by transmission electronic microscopy (TEM) and dynamic light scattering (DLS) techniques. MnO@MSNs demonstrated excellent stability in both water and PBS. Hydrodynamic diameters of MnO@MSNs in PBS solution were determined by DLS and averaged 110 nm, while zeta potential measurements of the MnO@MSN nanoparticles yielded average surface potentials of -28.3 (mV) in PBS (pH = 7.4). Relaxometric properties of these MnO@MSN amalgam nanoparticles, in aqueous suspensions, were measured at a magnetic field strength of 9.4 T. Molar relaxivities, one metric for a moiety's effectiveness as an MRI contrast agent, were obtained by measuring the relaxation rate for increasing concentrations of nanoparticles, and calculated to be 1.29 mM-1 s-1. This relaxivity is significantly higher than those measured for isolated MnO nanoparticles (~0.28 mM-1 s-1) and nonetched mesoporous silica-coated MnO nanoparticles (~0.108 mM-1 s-1). As such these novel nanoparticles complement the currently available repertoire of nanoparticles employed as MRI contrast agents by providing positive contrast on T1-weighted images at high magnetic field strengths.

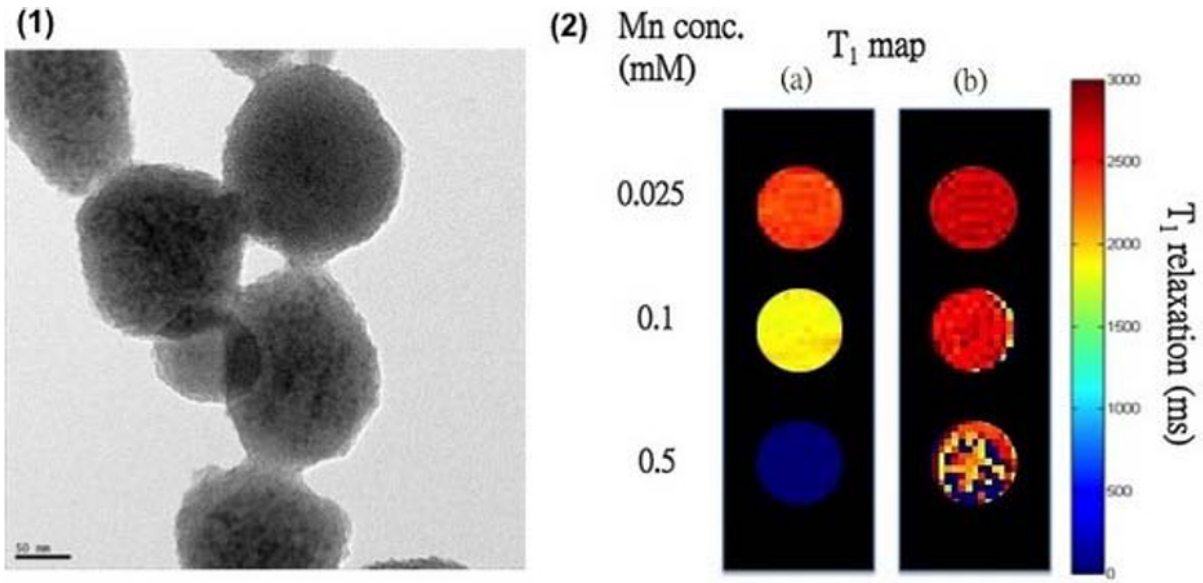

(1)TEM image of the MnO@MSN nanocomposites. (2)T1 map of (a)MnO@MSN (b)nonetched MnO@MSN suspended in water at 9.4 T with concentration varying from 0.025 to 0.5 mM.

Disclosure of author financial interest or relationships:

S. Cheng, None; **L. Leoni**, None; **B.B. Roman**, None; **J.S. Souris**, None; **N. Chen**, None; **L. Lo**, None; **C. Chen**, Cell>Point, Grant/research support; RefleXion Medical, Consultant; DxRay/Photon Imaging, Consultant .

Presentation Number **P 291**
Poster Session 3
September 20, 2013 / 15:15-15:15 / Room: Exhibit Hall B

Tale of two topological isomers: New MRI agents for targeting integrins

Quyen N. Do[1], *Zoltan Kovacs*[1,2], *Dean Sherry*[1,2], [1]*Chemistry, the University of Texas at Dallas, Dallas, TX, USA;* [2]*Advanced Imaging Research Center, The University of Texas Southwestern Medical Center, Dallas, TX, USA. Contact e-mail: quyen.do@utdallas.edu*

The RGD (Arginine, Glycine, Aspartic acid) sequence is known to be an important binding motif for various integrins on the surface of cancer cells.[1] Magnetic resonance molecular imaging of integrin receptors is hampered by the inherently low sensitivity of MRI and imaging agents consisting of Gd-complexes linearly conjugated to integrin targeting vectors generally have not worked.[2] Here, we report a novel design of integrin targeting MRI agents: cis and trans -c(RGDf-DOTA). In these complexes, the targeting peptide sequence is attached to two of the four macrocyclic nitrogens (N1 and N4 or N1 and N7, respectively) of the 1, 4, 7, 10-tetraazacyclododecane framework forming a rigid cyclic peptide which incorporates the GdDOTA unit. The rationale of this design is that binding of this Gd-complex to integrin would result in a dramatic increase in the relaxivity due to the slower tumbling rate of the bound complex. We have demonstrated in a previous publication that one should be able to detect receptors present on cell surfaces at a local concentration of ~700 nM using a single, optimized Gd agent.[3] The two ligands presented here are topological isomers with the peptide sequence (RGDf with f -D-phenylalanine) either bridged over the central metal ion (the 1,7-trans -c(RGDf-DOTA) isomer) or positioned off to one side of the Gd-complex leaving the metal ion exposed (the 1,10-cis-c(RGDf-DOTA) isomer). We have shown previously that the Lu^{3+} complex of the 1,7-trans c(DOTA-RGDf) binds to $\alpha_v b_3$ integrin with an IC_{50} values of 17.0.[4] PET imaging experiments with the $^{64}Cu^{2+}$-1,7-trans-c(RGDf-DOTA) complex in U87MG tumor bearing mice confirmed that the metal complex localizes to tumor. The water exchange properties of these two complexes in the presence and absence of integrin and the integrin binding properties of these two topological complexes will be presented and discussed.

References: (1) (a) Folkman, J., Semin. Oncol. 2002, 29, 15-18. (b) Hwang, R.; Varner, J. V. Hematol, Oncol, Clin. North Am. 2004, 18, 991-1006. (c) Brooks, P. C.; Clark, R. A. F.; Cheresh, D. A. Science. 1994, 264, 569-571. (d) Zitzmann, S.; Ehemann, V.; Schwab, M. Cancer Res. 2002, 62, 5139-5143. (2) Tan, M.; Lu, Z. Theranostics. 2011, 1, 83-101. (3) K Hanaoka, AJM Lubag, A Castillo-Muzquiz, T Kodadek & AD Sherry, J. Magn. Reson. Imaging, 26, 608-617 (2008). (4) Hao, G.; Sun, X.; Do, Q. N.; Ocampo-Garcia, B.; Vilchis-Juarez, A.; Ferro-Flores, G.; De Leon-Rodriguez, L. M. Dalton Trans. 2012, 41, 14051-14054.

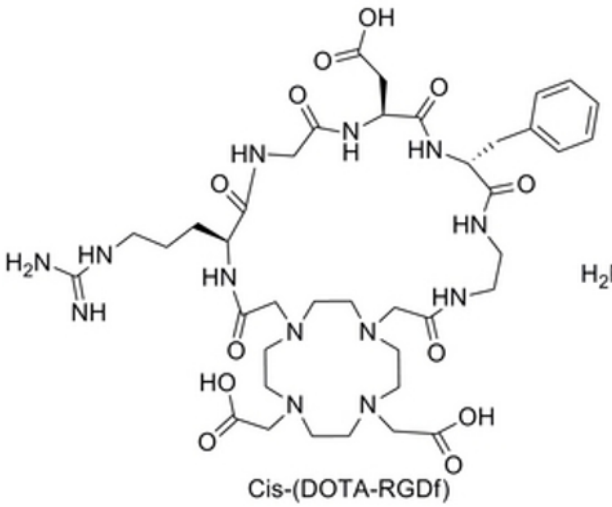

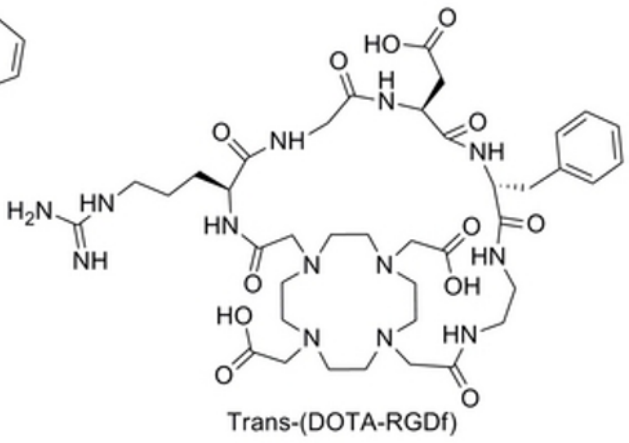

Disclosure of author financial interest or relationships:
Q.N. Do, None; **Z. Kovacs**, None; **D. Sherry**, None.

Presentation Number **P 292**
Poster Session 3
September 20, 2013 / 15:15-15:15 / Room: Exhibit Hall B

Targeting ferritin receptors using apoferritin as a selective carrier of imaging and therapeutic agents for different hepatic diseases

Simonetta Geninatti- Crich, *Juan C. Cutrin, Diana E. Burghelea, Walter Dastrù, Marta Cadenazzi, Silvio Aime, Department of Molecular Biotechnology and health Sciences, University of Torino, Torino, Italy. Contact e-mail: simonetta.geninatti@unito.it*

Ferritin is the primary iron storage protein. It is a 24-mer hollow 'nano cage' capable of sequestering iron in a nontoxic and bio-available form. Although functions of ferritin are traditionally associated with intracellular iron storage, additional roles have been recently discovered and investigated. For example, ferritin can act as a transferrin independent iron-delivery molecule to different target organs such us brain, liver and spleen by exploiting the scavenger receptor member 5 (SCARA5) for L-ferritin and TIM-2 and TfR1 for H-ferritin. Furthermore, perturbations in cellular ferritin are emerging as an important element in the pathogenesis of disease not only in the classic diseases of iron acquisition, transport, and storage, (hemochromatosis) but also in diseases characterized by inflammation, infection, injury, and repair; including neurodegenerative diseases (Parkinson and Alzheimer) vascular diseases (atherosclerosis) inflammatory states, breast, colon and liver cancers. Ferritin appears to be a key molecule that limits the extent, character, and location of the pro-oxidant stress typical of inflammatory diseases, cancer, and conditions of altered oxygenation. The link between abnormalities in ferritin regulation and onset of these diseases depends on cellular stress pathways that alter ferritin subunit composition and/or content within cells. The aim of this work is to map ferritin receptors expressed in normal and pathological tissues during the evolution of the disease by delivering imaging probes loaded into apoferritin internal cavity. In particular, the apoferritin selective internalization in hepatocytes, hepatocarcinoma, colon and breast cancer cells has been investigated. Some years ago, it was found that the assembly of ferritin, despite its rigidness under physiological condition, is pH dependent. The nanoarchitecture can be broken down in an acidic environment and restored by retuning the pH to 7.4. Apoferritin can be exploited to deliver simultaneously therapeutic and imaging agents (loaded into its internal cavity) exploiting these unique properties. Furthermore, a beta-MnOOH nanophase can be generated in the protein cavity in order to increase the number of paramagnetic ions inside the cavity. In this work the selective deliver of curcumin and GdHPDO3A (positive MRI contrast agent) has been investigated for the attenuation of thioacetamide-induced hepatitis together with the evaluation by MRI of drug delivery efficiency. Curcumin is a polyphenolic natural substance endowed with multiple pharmacological actions (namely: antioxidant, anti-inflammatory, antineoplastic). Although clinical trials have demonstrated the safety of curcumin, the clinical translation of this promising natural compound is hampered by its poor water solubility, short biological half-life, and low bioavailability in both plasma and tissues.The encapsulation of curcumin inside the apoferritin cavity significantly increases its stability and bioavailability while maintaining its therapeutic anti-oxidant and anti-inflammatory properties.

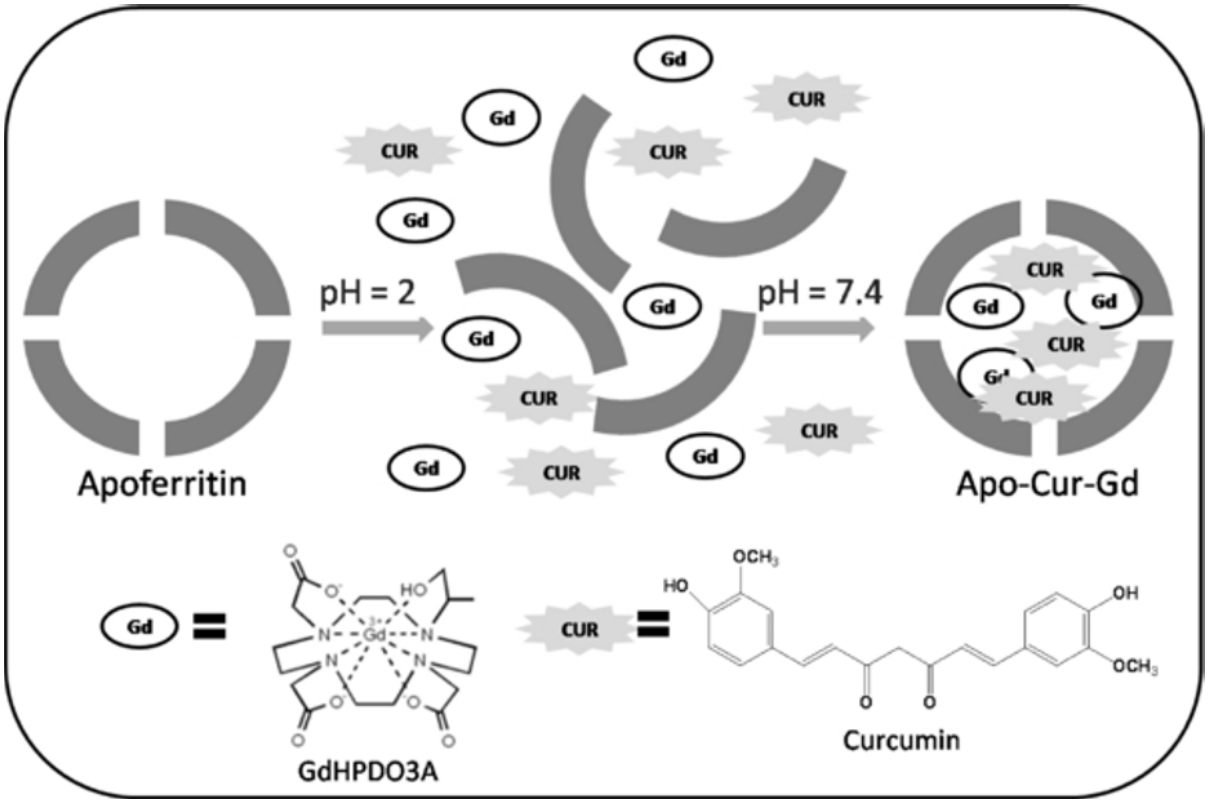

Disclosure of author financial interest or relationships:
S. Geninatti- Crich, None; **J.C. Cutrin**, None; **D.E. Burghelea**, None; **W. Dastrù**, None; **M. Cadenazzi**, None; **S. Aime**, None.

Presentation Number **P 293**
Poster Session 3
September 20, 2013 / 15:15-15:15 / Room: Exhibit Hall B

Targeting of peptide conjugated magnetic nanoparticles to urokinase plasminogen activator receptor (uPAR) expressing cells

Line Hansen[1], *Esben Larsen*[1], *Erik Holm Nielsen*[1], *Frank Iversen*[1], *Zhuo Liu*[1], *Troels Skrydstryp*[1], *Niels Christian Nielsen*[1], *Michael Ploug*[2], *Jørgen Kjems*[1], [1]*Interdisciplinary Nanoscience Center (iNANO), Aarhus University, Aarhus, Denmark;* [2]*Finsen Laboratory, Rigshospitalet & Biotechnology Research and Innovation Center (BRIC), Copenhagen Biocenter, Copenhagen, Denmark. Contact e-mail: lh05@inano.dk*

Ultrasmall superparamagnetic iron oxide (USPIO) nanoparticles are currently being used as a MRI contrast agent in vivo, mainly by their passive accumulation in tissue of interest. However, a higher specificity can ideally be achieved when the nanoparticles are targeted towards cell specific receptors and this may also facilitate specific drug delivery by an enhanced target-mediated endocytosis. Here we report efficient peptide-mediated targeting of magnetic nanoparticles to cells expressing the urokinase plasminogen activator receptor (uPAR), a surface marker shared by several cancers including breast, colorectal, and gastric cancers. Conjugation of a uPAR specific targeting peptide onto polyethylene glycol (PEG) coated USPIO nanoparticles by click chemistry, resulted in a five times higher uptake in vitro in a uPAR positive cell line compared to nanoparticles carrying a non-binding control peptide. In accordance with specific receptor mediated recognition, a low uptake was observed in the presence of an excess of ATF, a natural ligand for uPAR. The uPAR specific magnetic nanoparticles can potentially provide a useful supplement for tumor patient management when combined with MR scanning and drug delivery.

Disclosure of author financial interest or relationships:
L. Hansen, None; **E. Larsen**, None; **E. Holm Nielsen**, None; **F. Iversen**, None; **Z. Liu**, None; **T. Skrydstryp**, None; **N. Christian Nielsen**, None; **M. Ploug**, None; **J. Kjems**, None.

Presentation Number **P 294**
Poster Session 3
September 20, 2013 / 15:15-15:15 / Room: Exhibit Hall B

Biodegradable Polydisulfide Dendrimer Nanoclusters as MRI Contrast Agents

ChingHui Huang[1], *Kido Nwe*[2], *Martin Brechbiel*[2], *Andrew Tsourkas*[1], [1]*Bioengineering, University of Pennsylvania, Philadelphia, PA, USA;* [2]*Radioimmune Inorganic Chemistry Section, National Cancer Institute, Bethesda, MD, USA. Contact e-mail: chinghu@seas.upenn.edu*

Introduction: Clinically approved magnetic resonance imaging (MRI) Gd-based contrast agents are invaluable in diagnosing diseases and in enhancing MR angiographies. These agents suffer from poor sensitivity and rapid renal clearance. Macromolecular gadolinium complexes have been developed to increase the blood circulation time and enhance the longitudinal relaxivities (R_1) per gadolinium. A major concern with long circulation is the possibility of toxic side effects and the onset of nephrogenic systemic fibrosis (NSF). Efforts to develop macromolecular gadolinium based MRI contrast agents have focused on introducing biodegradable materials and/or linkages into the design, thus agents can be readily excreted after intravenous administration. We developed highly paramagnetic dendrimer nanoclusters (DNCs), which demonstrated site-specific targeting and significant contrast enhancement. To facilitate the biodegradation and excretion of DNCs, polydisulfide linkages were incorporated into the design. The polydisulfide DNCs inherit the high relaxivity and retain an extended circulation time, but are reduced to individual Gd-labeled dendrimers while in circulation and undergo efficient renal excretion, reducing the possibility of long-term particle retention. **Materials and Methods**: $SAT(PEG)_4$ was reacted with PAMAM (G3) to create sparsely thiolated dendrimers, and then cross-linked upon the addition of NH_2OH. The size was monitored by dynamic light scattering (DLS) and the reaction was quenched by adding maleimide. Pre-metalated $[Gd\text{-}C\text{-}DOTA]^{-1}$ were coordinated to the crossed-linked particles. Gadolinium concentration was determined by ICP-MS. Polydisulfide DNCs degradation and stability was studied in the presence of endogeneous thiol mixtures and at various pHs. Cell viability, biodistribution and contrast-enhanced in vivo MR imaging were studied to evaluate the potential use of polydisulfide DNCs for clinical applications. **Results and Discussion**: Polydisulfide DNCs were prepared with median hydrodynamic diameters ranging ~40nm to 200nm. A 59nm DNC, which was selected for additional study, possessed an r_1 relaxivity of 11.7 $mM^{-1}s^{-1}$. Pharmacokinetic studies indicated a circulation half-life $t_{1/2}$ > 1.6 hr and efficient renal excretion. The circulation time is significantly longer than individual gadolinium based PAMAM dendrimers, but the biodistribution is similar. These findings suggest that DNCs are slowly degraded into smaller clusters and/or individual dendrimers while in circulation. The T_1 weight images following the intravenous administration of polydisulfide DNCs revealed significant contrast enhancement in the abdominal aorta and kidneys for as long as 4 hr (Figure 1). **Conclusions**: A facile method was developed for the synthesis of size controllable and biodegradable dendrimer nanoclusters. The polydisulfide DNCs provide long blood circulation times, but undergo gradual degradation into smaller components under physiological conditions, which greatly facilitates their renal clearance. The pre-metalated, cyclic gadolinium DOTA complexes adopted in this study further minimize the increasing concern over gadolinium-mediated toxicity.

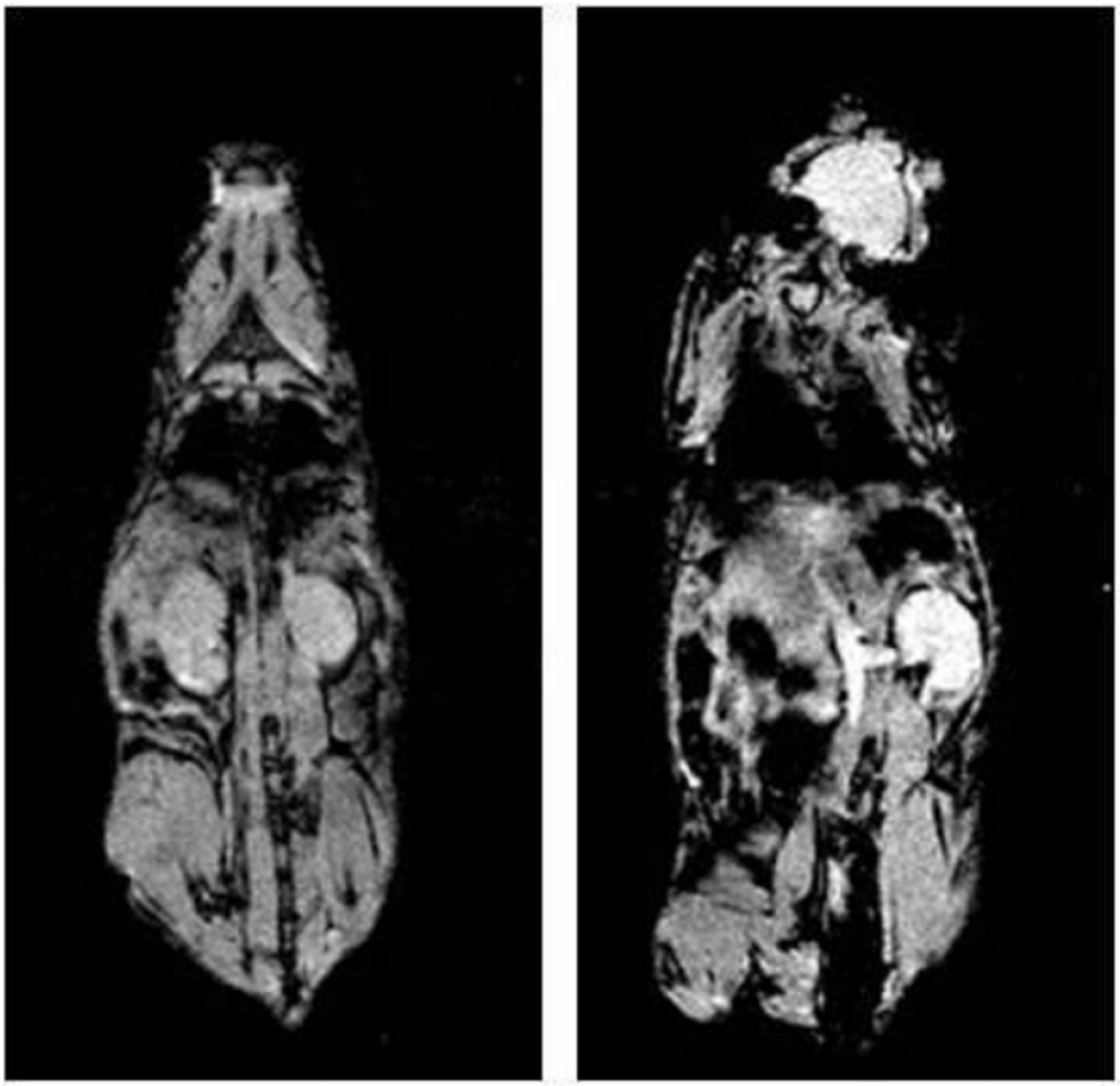

Figure 1. Magnetic resonance images of nu/nu nude mice after tail vein injection of polydisulfide DNCs. T_1 weighted images of the kidney were acquired pre-injection and 15mins post-injection. All images were acquired using a 4.7 T small animal horizontal bore Varian INOVA system.

Disclosure of author financial interest or relationships:
C. Huang, None; **K. Nwe**, None; **M. Brechbiel**, None; **A. Tsourkas**, None.

Presentation Number **P 295**
Poster Session 3
September 20, 2013 / 15:15-15:15 / Room: Exhibit Hall B

High r1 Relaxivity Sub-5 nm Supersmall Iron Oxide Nanoparticles (sSIO) as T1 Weighted MRI Contrast Agents

Jing Huang[1], *Liya Wang*[1], *Lily Yang*[2], *Hui Mao*[1], [1]*Department of Radiology and Imaging Sciences, Emory University Schoole of Medicine, Atlanta, GA, USA;* [2]*Department of Surgery, Emory University Schoole of Medicine, Atlanta, GA, USA. Contact e-mail: jing.huang@emory.edu*

Iron oxide nanoparticles have been widely used as MRI contrast agents both in clinical applications and preclinical models. Currently, most iron oxide nanoparticles are fabricated with a core size larger than 5 nm, therefore exhibit predominant shortening effect on the transverse relaxation time T2, causing signal void in T2-weighted MRI. Early studies have shown that r1 and r2 relaxivities of iron oxide nanoparitcles are size-dependent, while r1 relaxivity can be preserved in the super small iron oxide nanoparticles with size below 5 nm. Here we report a new class of high r1 relaxivity, sub-5 nm, super small iron oxide nanoparticles (sSIO, core size ~3.5 nm) with oligosaccharide coating as T1-weighted MRI contrast agents while providing reverse T2 contrast, when taken up by cells and liver. The sSIO nanoparticles were obtained from the encapsulation of iron oxide core in a thin oligosaccharide shell through in situ polymerization. Results from analyzing TEM images show that the prepared sSIO-3 has an averaged core size of 3.5 nm (Fig. 1a). The in situ modification on the iron oxide surface led to excellent water-solubility and an enhanced T1 contrast effect. The prepared sSIO has an r1 value of 4.2 mM-1s-1 and a high r1/r2 ratio (0.28), which is competitive with commercial Gd-based contrast agent (i.e. Multihance® (Gd-BOPTA), r1~5.8 mM-1s-1, r1/r2~0.85). Moreover, sSIO exhibit good biocompatibility as revealed by MTT assay with macrophage RAW264.7 cells. Significant T1 contrast enhancement in the kidney and iliac artery were evidenced in in vivo MRI experiments after intravenously administration of sSIO in mice, similar to that observed in Gd-BOPTA enhanced MRI. The positive contrast enhancement is attributed to the small size and the reduced susceptibility of the nanoparticles, as well as the excellent colloidal stability in physiological environment. Such T1 contrast enhancement is not obvious when using a larger size SIO-10 or 20. Interestingly, uptake of sSIO-3 in liver led to strong T2 effect or signal drop in liver further improves the image quality for visualizing liver tissue and hepatic vasculature (Fig. 1j) in T1 weighted MRI. Futhermore, sSIO-3 has a much longer blood retention time than small molecule Gd-chelates for prolonged imaging time for organs of interest, providing a potential long half time T1 weighted MR imaging agents for imaging of vasculture of disease tissues.

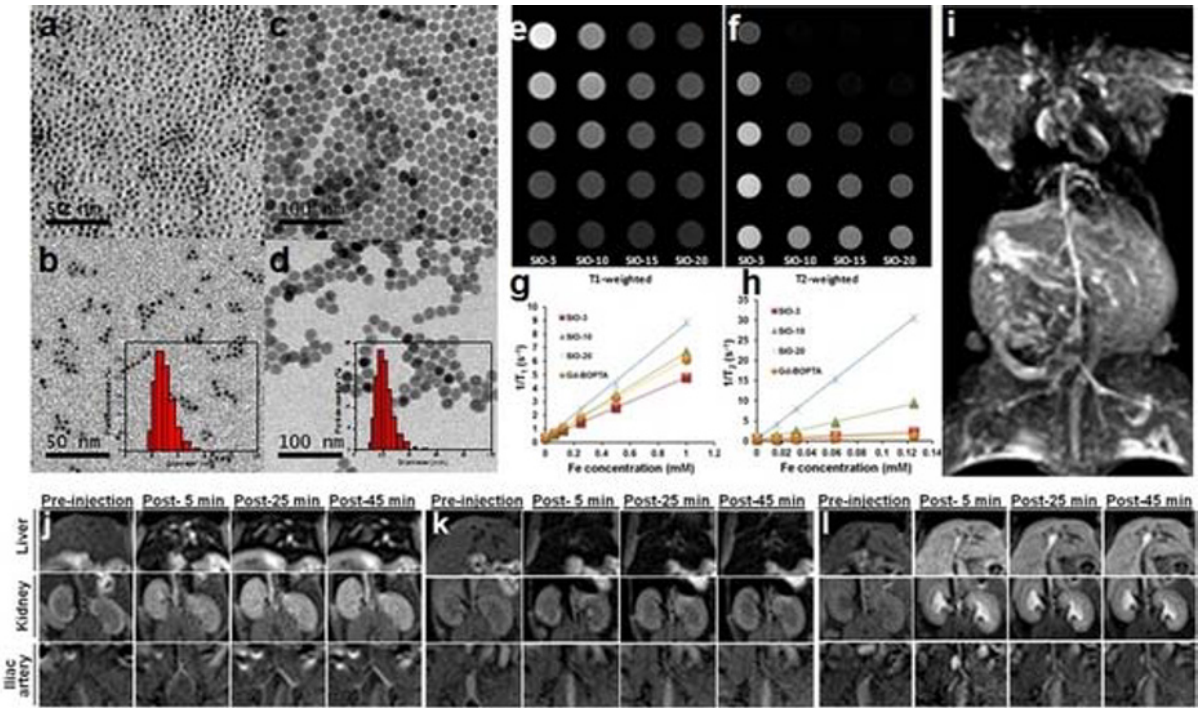

Figure 1. TEM images of a) IO-3, b) SIO-3, c) IO-20, d) SIO-20, and inset is the corresponding hydrodynamic size distribution; e) T1-weighted, and f) T2-weighted MR phantom studies of SIOs, and corresponding calculation of relaxivities g) r1 and h) r2; i) maximum intensity stacks of T1-weighted spin echo MR images of mice after administration of SIO-3 for 5 min; T1-weighted MR images of mice after administration of j) SIO-3, k) SIO-20 and l) Gd-BOPTA at different time points, pre-injection, post-5min, 25 min and 45 min.

Disclosure of author financial interest or relationships:
J. Huang, None; **L. Wang**, None; **L. Yang**, None; **H. Mao**, None.

Presentation Number **P 296**
Poster Session 3
September 20, 2013 / 15:15-15:15 / Room: Exhibit Hall B

Hyperpolarized ^{15}N Probes as pH-Sensitive MR Imaging Agents

Weina Jiang, *Lloyd L. Lumata, Wei Chen, Zoltan Kovacs, Dean Sherry, Chalermchai Khemtong, Advanced Imaging Research Center, University of Texas Southwestern Medical Center, Dallas, TX, USA. Contact e-mail: weina.jiang@utsouthwestern.edu*

BACKGROUND: The acidic tumor microenvironment is an important marker for the aggressiveness in many types of cancers. To date, several MRI probes have been developed for tumor pH imaging. Despite some success, the low sensitivity of conventional MR techniques has been the major drawback, preventing clinical translations of many pH-sensitive MRI probes. Herein, we report the development of hyperpolarized (HP) ^{15}N agents by dynamic nuclear polarization (DNP) as ultrasensitive imaging agents for the assessment of tumor pH. METHODS: A solution of pyridine (Py, 6.2 M) or 2,6-lutidine (Lut, 4.3 M) and BDPA (40 mM) in 50 µL DMSO-sulfolane (50:50) was polarized in a HyperSense. The dissolution liquid from the polarizer was rapidly mixed with a known amount of HCl or NaOH before subjecting to ^{15}N NMR (23°C). Titration curves were created by plotting ^{15}N chemical shift vs pH. For pH calculation by HP ^{15}N NMR, HP-Py or HP-Lut was mixed with an unknown amount of HCl before ^{15}N NMR. pH of the solution was calculated from the apparent ^{15}N chemical shift using the Henderson-Hasselbalch equation and the pKa from HP NMR titration. RESULTS: The ^{15}N NMR sensitivity of Py and Lut was enhanced by 4000-fold after DNP. Fig. 1A-B show ^{15}N NMR spectra of HP-Py and HP-Lut, respectively, acquired with a single scan (10-deg flip angle, top). Thermally polarized ^{15}N NMR spectra (256 scans, 90-deg flip angle) of the same agents are shown below their HP spectra demonstrating the significant sensitivity enhancement produced by DNP. The long T_1 of ^{15}N-Py (40 s) and ^{15}N-Lut (37 s) make this class of agents suitable candidates for*in vivo* applications. pH titration of these two agents by HP ^{15}N NMR revealed that their chemical shifts are very sensitive to pH and that large chemical shift difference between their free base and protonated form was observed ($\Delta\delta$ > 90 ppm, Fig. 1C). More importantly, ^{15}N chemical shifts of both agents showed a sharp change near the pKa, i.e. 5.2 for pyridine and 6.6 for 2,6-lutidine. It is important to note that the slight change in chemical functional groups near the site of protonation alters the pKa of the ^{15}N center making it possible to design an agent with pKa in the desired range. To test the accuracy of these probes, pH values of solutions containing HP-Py or HP-Lut and HCl were calculated from the Henderson-Hasselbalch equation using observed ^{15}N chemical shifts and a pKa calculated from the NMR titration. The results showed that the pH values obtained by HP ^{15}N NMR have an excellent correlation with the values obtained using a standardized pH electrode (Fig. 1D). CONCLUSIONS: Here we demonstrate for the first time the use of HP ^{15}N-pyridine derivatives as pH-sensitive probes for measuring the pH of aqueous media. A large ^{15}N chemical shift difference of HP pyridine derivatives and a sharp shift change near their pKa coupled with the significantly improved NMR sensitivity make HP pyridine derivatives highly suitable candidates for the detection of minute changes in pH in acidic tumors. REF.: Hashimay et al, NMR Biomed, 2011, 582; Lumtat et al, Chem, Eur. J., 2011, 10825.

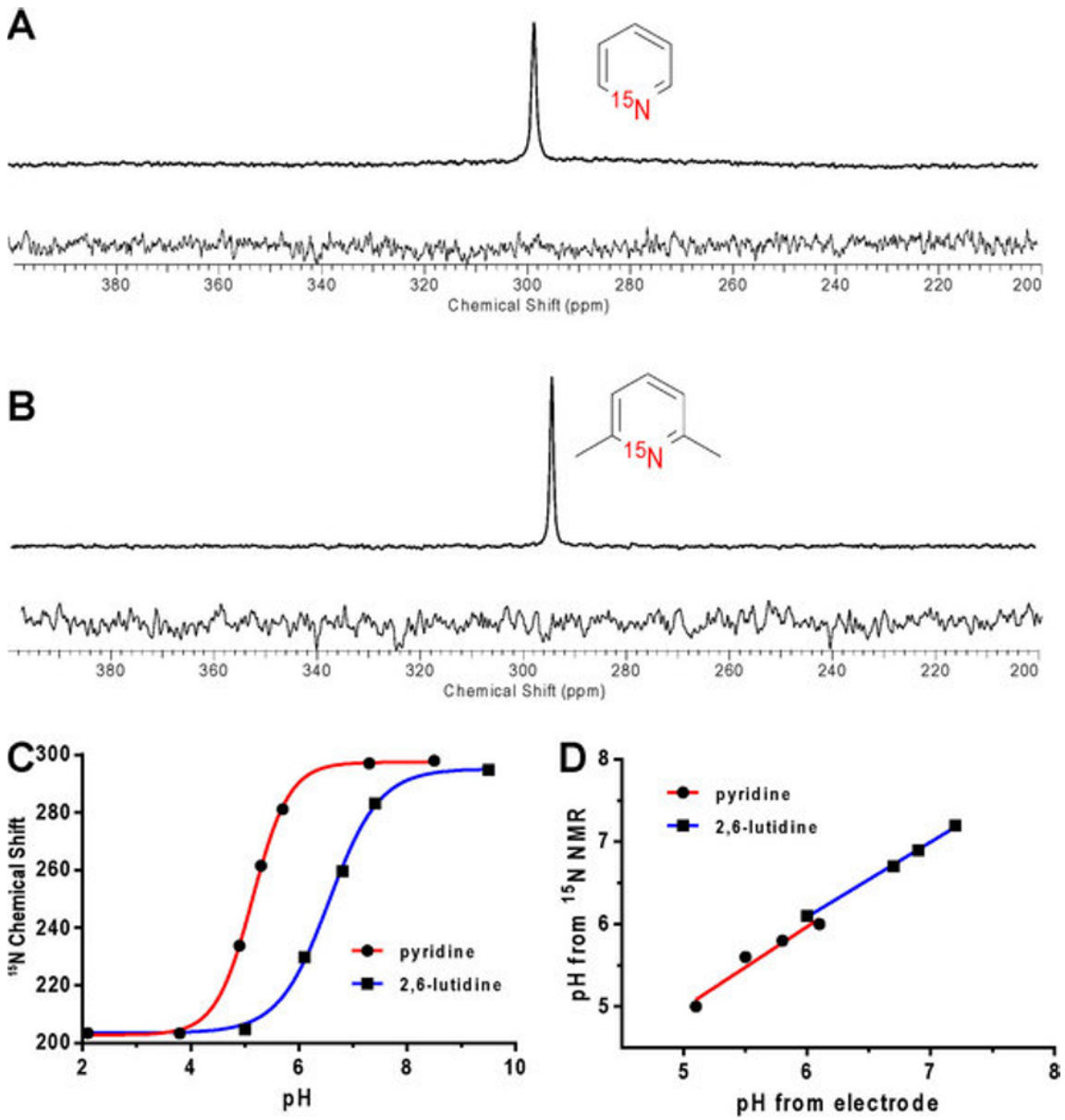

Hyperpolarized and thermal ^{15} N NMR spectra of (A) pyridine and (B) 2,6-lutidine; (C) ^{15} N NMR titration curves of HP-pyridine and HP-2,6-lutiidine; and (D) correlation of pH measured from ^{15} N NMR and the pH electrode.

Disclosure of author financial interest or relationships:
W. Jiang, None; **L.L. Lumata**, None; **W. Chen**, None; **Z. Kovacs**, None; **D. Sherry**, None; **C. Khemtong**, None.

Presentation Number **P 297**
Poster Session 3
September 20, 2013 / 15:15-15:15 / Room: Exhibit Hall B

Novel MRI Blood Pool Agents with different Chemical Structures: An *in vivo* Comparison

Anne Kirchherr[1], *Thomas Kaulisch*[2], *Detlef Stiller*[2], *Andreas Briel*[1], [1]*nanoPET Pharma GmbH, Berlin, Germany;* [2]*In-Vivo Imaging, Target Discovery Research, Boehringer Ingelheim Pharma GmbH & Co. KG, Biberach, Germany. Contact e-mail: anne.kirchherr@nanopet.de*

Objectives: Blood pool contrast agents used in magnetic resonance imaging (MRI) are characterized by their intravascular distribution and prolonged persistence in the blood in comparison to conventional clinical contrast agents. Since the size of the contrast agent molecule is a main factor determining the distribution and elimination of the agent *in vivo*, macromolecules and albumin binding molecules are excellent candidates as blood pool agents. Due to their larger size, these agents potentially overcome the limitations of small molecules such as nonspecific extravasation into surrounding tissue and poor relaxation enhancement efficiency [1, 2]. In the present work, three novel MRI blood pool agents, namely GadoSpin^{TM} P, GadoSpin^{TM} D and GadoSpin^{TM} F (Viscover^{TM}, Miltenyi Biotec, Germany) having different chemical structures, were characterized *in vitro* as well as *in vivo*. *Methods*: The structures of all three blood pool agents are based on gadolinium chelates. In GadoSpin P, the chelate is conjugated to a linear polymer, in GadoSpin D, to a dendritic polymer, and in GadoSpin F, to an amphiphilic molecule having a high albumin affinity. Relaxivity measurements were performed at 7 T on a BioSpec 70/16 scanner (Bruker BioSpin, Ettlingen, Germany) using a RARE sequence. *In vivo* experiments were performed in C57BL/6 mice after intravenous injection of 100 µL of the respective contrast agent solution per 25 g mouse, corresponding to a dose of 100 µmol Gd/kg body weight. T1-weighted images were acquired on the 7 T BioSpec 70/16 scanner using a FLASH sequence. *Results*: The longitudinal and transverse relaxivities, r_1 and r_2, of the blood pool agents in water at 37 °C, 7 T were found to be significantly higher than those of conventional contrast agents in clinical use indicating a high contrast enhancement. *In vivo* imaging in mice demonstrated that all three blood pool agents remain within the vascular space for a prolonged period of time, but differ in their pharmacokinetic properties. GadoSpin D (M_r ~ 17,000) exhibits a biphasic blood clearance with an initial half-life of about 10 min and a longer second half-life of approx. 90 min. GadoSpin F (albumin-attached, M_r ~ 70,000) and GadoSpin P (M_r ~ 200,000) exhibit blood half-lives of approx. 90 min and 120 min, respectively. *Conclusion*: In this study we report on three novel MRI blood pool agents having high contrast efficiencies as well as optimal biocompatibility. All agents remained within the vascular space for a prolonged period of time enabling higher resolution through a longer steady state period and a wide acquisition timeframe in magnetic resonance angiography (MRA). The results indicate that an increase in molecular weight of the contrast agent results in an increase of the blood circulation time. Thus, the various structural entities affecting different pharmacokinetics offer a set of unique tools for a multitude of imaging applications. *References*: [1] A. Kirchherr *et al*. Proc. Intl. Soc. Mag. Reson. Med. 20 (2012) 1205 [2] A.M. Mohs *et al*. Expert Opin Drug Deliv. 2007;4(2):149-64.

Disclosure of author financial interest or relationships:
A. Kirchherr, nanoPET Pharma GmbH, Employment; **T. Kaulisch**, Boehringer Ingelheim Pharma GmbH & Co. KG, Employment; **D. Stiller**, None; **A. Briel**, nanoPET Pharma GmbH, Employment .

Presentation Number **P 298**
Poster Session 3
September 20, 2013 / 15:15-15:15 / Room: Exhibit Hall B

Molecular imaging of autophagy-mediated chemosensitization in gastric carcinoma cell line by RGD modified quaternized chitosan encapsulated Fe3O4 magnetic nanoparticles

Xiujuan Li[1], *Xinxing Song*[1], *Yabin Wang*[1], *Hongbing Deng*[2], *Feng Cao*[1], [1]*Fourth Military Medical University, Molecular Imaging center, Xi an, China;* [2]*Wuhan University, College of resources and Environmental Sciences, Wuhan, China. Contact e-mail: lixiujuan0716@126.com*

Background Gastric cancer remains the third leading cause of mortality from all kinds of cancer. It has been reported that autophagy is a target for anticancer theraphy. The aim of this study was to use a novel molecular imaging probe which is anchoring of RGD peptides to quaternized chitosan encapsulated Fe3O4 magnetic nanoparticles (HTCC-MNPs-RGD) to assess gastric cancer by magnetic resonance imaging (MRI). Methods Transmission electron microscopy (TEM) were used to measure the particle size and shape, size distribution were measured by dynamic light scattering. Zeta potential and absorption band of probe were detected by zeta potential analysis. Cell viability was assessed by the MTTassay, the generation of the ROS and the collapse of mitochondrial transmembrane potentials were detected by flow cytometry, autophagy associated proteins were detected by western blotting.Autophagy was assessed through monitoring LysoTrcker Reduptake. In tumor models, nude mice were vaccinated by subcutaneous injection of HTCC-MNPs-RGD, MRI was performed to visualize the tumor. Histological analysis were applied to evaluate the effectiveness of the HTCC-MNPs-RGD on assessment of gastric carcinoma. Results The results showed that the mean size of HTCC-MNPs-RGD was 161 nm, the mean zeta potential was16.8±4.87 mv. HTCC-MNPs-RGD selectively induced autophagy in cancer cells (SGC7901/ADR) rather than in normal cells(GES). The generation of the ROS and the collapse of mitochondrial transmembrane potentials were reduced by the HTCC-MNPs-RGD .Pre-treatment of the cancer cells with 3-MA and NAC can promote cellular viability. The results of in vivo animal experiments by a 3.0T MRI revealed that HTCC-MNPs-RGD could give rise to a decreased T2 values ($p<0.05$) after 24 hours injection in contrast to HTCC-MNPs. Then, ex vivo histological analysis further confirmed that more HTCC-MNPs-RGD localized in lesions than HTCC-MNPs. Conclusions HTCC-MNPs-RGD can not only selectively kill cancerous cells, but also act as a novel molecular imaging probe for cancer diagnosis. .

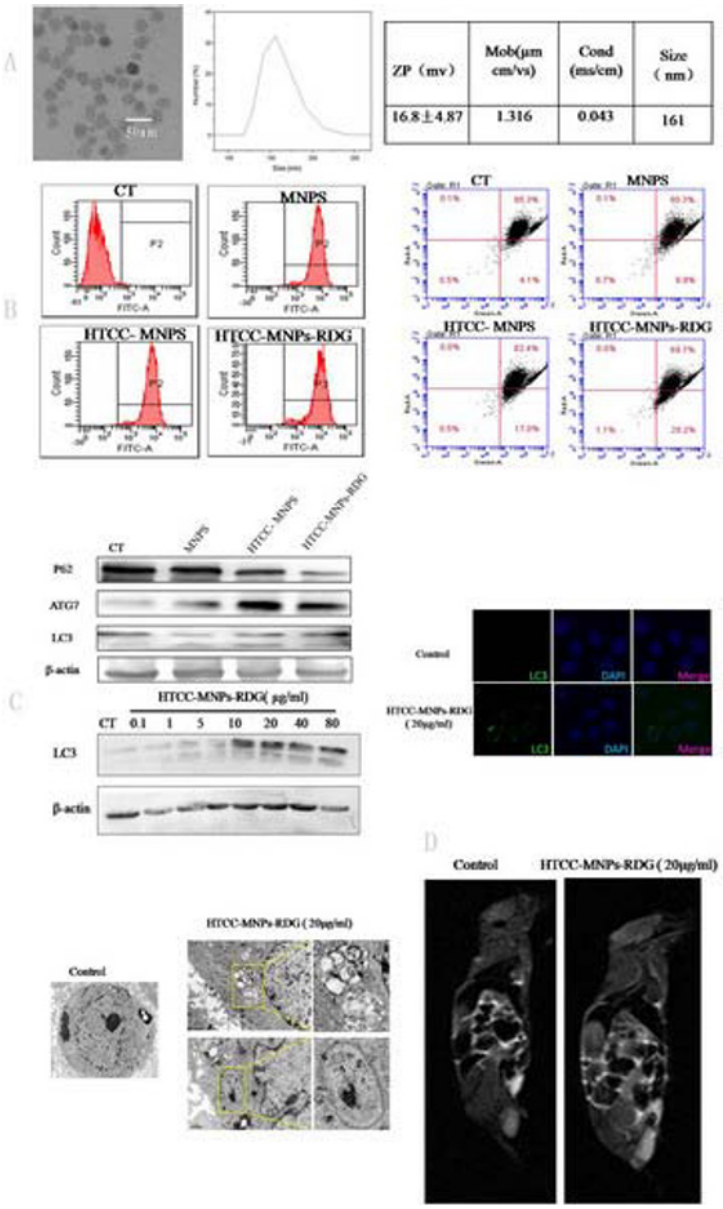

Disclosure of author financial interest or relationships:
X. Li, None; **X. Song**, None; **Y. Wang**, None; **H. Deng**, None; **F. Cao**, None.

Presentation Number **P 299**
Poster Session 3
September 20, 2013 / 15:15-15:15 / Room: Exhibit Hall B

Caspase-3 Controlled ^{19}F Signal Turn-on for Magnatic Resonance Imaging

Gaolin Liang[1], *Yue Yuan*[1], *Hongbin Sun*[2], *Mengjing Wang*[1], [1]*Chemistry, Univ. of Sci. & Tech. of China, Hefei, China;* [2]*High Magnetic Field Laboratory, Chinese Academy of Sciences, Hefei, China. Contact e-mail: gliang@ustc.edu.cn*

Abstract: One important advantage of ^{19}F comparing to ^{1}H is that in animal bodies essentially no ^{19}F is detectable by NMR spectroscopy, which therefore eliminates interference from background signals. Herein, we report a condensation system which could be controlled by caspase-3, an important protease which is associated with cell apoptosis. We designed Cys(StBu)-Asp-Glu-Val-Asp-Lys(F)-CBT (**1**) for self-assembling ^{19}F-carrying nanoparticles (^{19}F-NPs) after the reduction effect *in vivo*, which cause the 19F signal turn off (Fig. 1b). Then via caspase-3 cleavage, the ^{19}F-NPs gradually disassembled, therefore a turn-on ^{19}F signal will appear (Fig. 1c). From the High Performance Liquid Chromatography (HPLC) trace and Matrix Assisted Laser Desorption Ionization-Mass Spectrometry (MALDI-MS) analysis, the processes of condensation and enzymatic cleavage can be monitored clearly. And the ^{19}F-NMR spectroscopy show that the signal appeared at -74.8 ppm is broadened and attenuated when the molecules assemble into aggregates of high molecular mass as the condensation, but recovers on their disassembly. By means of ^{19}F signal turn-on, this provides us with a new method for detection of caspase-3.

Caspase-3 Controlled 19 F Signal Turn-on for Magnatic Resonance Imaging

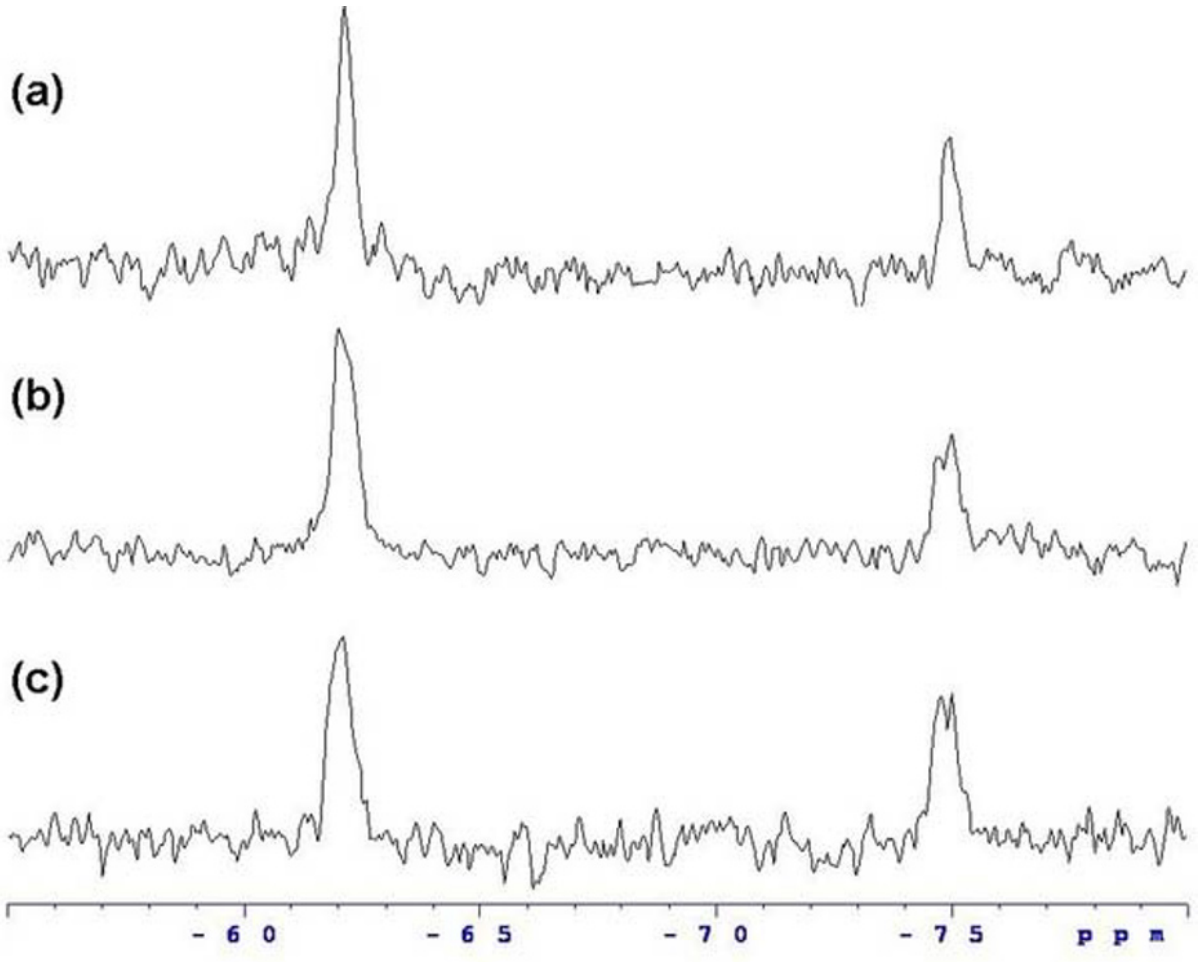

Figure 1. (a) ^{19}F NMR spectra of **1** (100 μM) alone. (b) ^{19}F NMR spectra of **1** (100 μM) after 3 h incubation with 1 mM TCEP at 37 °C. (c) ^{19}F NMR spectra of **1** (100 μM) after treatment of TCEP (1 mM) for 3 h and caspase-3 (10 nmol/U) for 5 h at 37 °C in turn.

Disclosure of author financial interest or relationships:
G. Liang, None; **Y. Yuan**, None; **H. Sun**, None; **M. Wang**, None.

Presentation Number **P 300**
Poster Session 3
September 20, 2013 / 15:15-15:15 / Room: Exhibit Hall B

In vivo Susceptibility Map of Gadolinium-based Contrast Agent Using Quantitative Susceptibility Mapping

Hsin-Chih Lo[1,2], *Meng-Chi Hsieh*[1,2], *Chia-Hsin Pan*[1,2], *Jyh-Horng Chen*[1,2], [1]*Graduate Institude of Biomedical Electronics and Bioinformatics, National Taiwan University, Taipei, Taiwan;* [2]*Interdisciplinary MRI/MRS Lab, Department of Electrical Engineering, National Taiwan University, Taipei, Taiwan. Contact e-mail: mizukinana.eadlwiacred@gmail.com*

Introduction: Dynamic contrast-enhanced (DCE) MRI has been developed to assess perfusion ability of tumour angiogenesis by injecting gadolinium (Gd) contrast agent. DCE MRI enables the depiction of physiologic alteration and morphologic changes [1]. However, it is hard to estimate the concentration of contrast agent in tumour region. Recently, quantitative susceptibility mapping (QSM) has been developed to measure susceptibility property in tissue with considerable applications, such as estimating iron, oxygen saturation in vessel and the concentration of MR contrast agent. Hence, the purpose of this study is to in vivo quantify susceptibility in tumour region using QSM technique. Materials and Methods: MR experiments were performed on a Bruker (Ettlingen, Germany) 7T Biospec 70/30 scanner. The mouse (Nod-scid, weight~20g) implanted lung cancer cell (CL1-0-189) was injected with the following two solutions, condition (a) is PBS (phosphate buffered solution) and condition (b) is gadodiamide (Omniscan, GE Healthcare, USA) with 2×10-3 mmole. The T1-weighted images were acquired by using three-dimension (3D) GEFC (gradient-echo with 1st flow compensation) sequence with image parameters: FOV = 35×15×15 mm3, MTX = 224×96×96, voxel size = 0.156 mm3, TR/TE = 50/5 ms, flip angle: 15 deg, acquisition time: 7 min 40 sec. The wrapped phase images were unwrapped with a 3D path-based unwrapping method [2]. The background fields due to air-tissue interfaces and incorrectly set shimming were removed by subtracting the data under condition (a) from that under condition (b). Finally, the local field was converted into susceptibility map compared to that of CSF by using a regularize-based method. Results: The T1-weighted image with and without contrast enhancement are demonstrated as figure A and B respectively. The estimated susceptibility map in tumour region using QSM technique is shown as figure C (unit is in ppm, relative to CSF). Measured susceptibility values are 0.277±0.043 ppm (Mean±SD) and 0.003±0.034 ppm in the periphery and the centre of tumour respectively. It illustrates that high susceptibility in peripheral region and less susceptibility change in centre region (Fig.C). It implies that not only the necrotic tumour of centre region takes less Gd, but also the tumour of peripheral region obtains more Gd due to angiogenesis. Conclusion: In this study, we have demonstrated a quantitative method for in vivo susceptibility map in tumour region of mouse. Right now, we are using this QSM technique to estimate concentration distribution of contrast agent in the targeted organs for longitudinal study of chemo therapy response. With further validation, this QSM technique could be a potential tool to estimate the tumour intake of drug and evaluate the angiogenesis and staging of tumour in the future. Reference: [1] B. Turkbey et al., Diagn. Interv. Radiol. (2010); [2] H. Abdul-Rahman et al., Applied Optics (2007); [3] Weisskoff et al., MRM (1992).

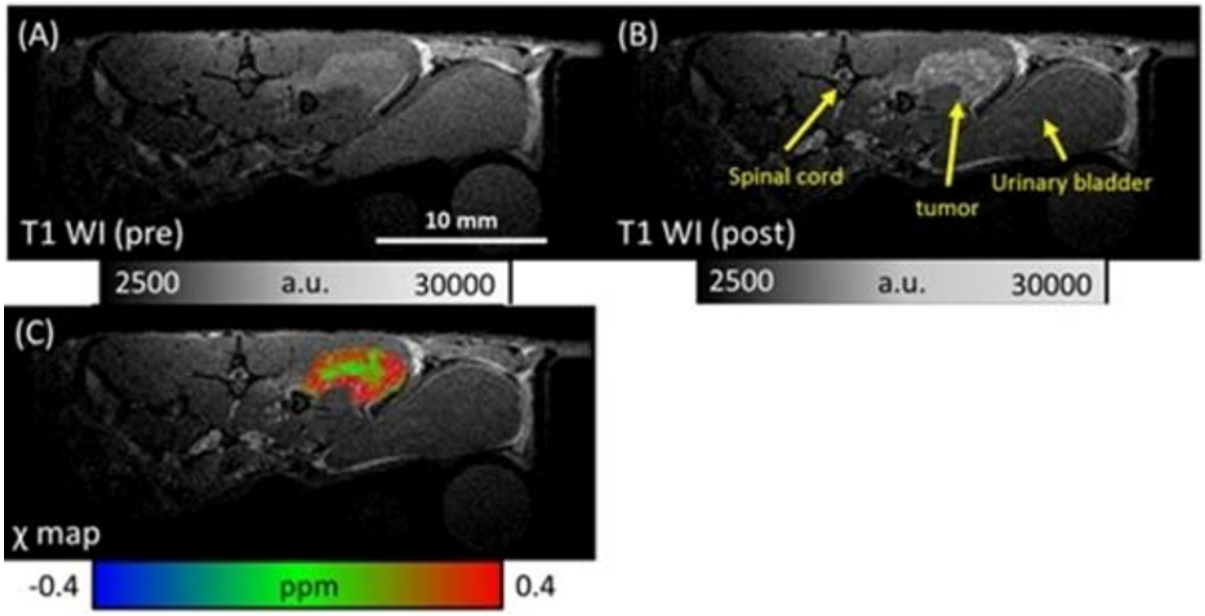

Disclosure of author financial interest or relationships:
H. Lo, None; **M. Hsieh**, None; **C. Pan**, None; **J. Chen**, None.

Presentation Number **P 301**
Poster Session 3
September 20, 2013 / 15:15-15:15 / Room: Exhibit Hall B

Synthesis and Functional Evaluation of Novel Dendrimer-triamine-coordinated Gd-MRI Contrast Agent with Aminoalcohol End Groups

Yuka Miyake[1], *Yu Kimura*[1], *Tetsuya Matsuda*[2], *Hirohiko Imai*[2], *Tetsuya Yano*[3], *Akio Toshimitsu*[4], *Teruyuki Kondo*[1], [1]*Advanced Biomedical Engineering Research Unit, Kyoto University, Kyoto, Japan;* [2]*Graduate School of Informatics, Kyoto University, Kyoto, Japan;* [3]*Canon Inc., Tokyo, Japan;* [4]*Institute for Chemical Research, Kyoto University, Kyoto, Japan. Contact e-mail: miyake.yuka.46c@st.kyoto-u.ac.jp*

Gd-MRI contrast agents can enhance the contrast of MRI images by reducing the longitudinal relaxation time (T1) of water.[1] However, since Gd-MRI contrast agents which are currently used in clinical practice have only low sensitivity, and need to be administered at high concentrations (*ca.* 0.50 M), they impose a great physical strain on the patient, and in some cases they may produce side effects such as osmotic pressure shock. Thus, there is a strong need for the development of highly sensitive MRI contrast agents based on a new principle. We have previously reported the synthesis and functional evaluation of chiral 2nd-generation dendrimer-triamine-coordinated gadolinium complexes as a highly sensitive contrast agent for MRI.[2] To accompany the specific targeting ability *in vivo*, such as cancers, introduction of antibodies and polyethyleneglycol (PEG) to the contrast agents might be effective. Here, we report synthesis and functional evaluation of novel dendrimer-triamine-coordinated Gd complexes with aminoalcohol end groups as a highly sensitive MRI contrast agent. Epoxidation of a vinyl group in 4-vinylbenzyl *p*-methoxyphenyl ether with *m*CPBA was carried out, and the obtained epoxide was treated with $TMSN_3$ in CH_3CN/H_2O to give the corresponding azidoalcohol. Then, an azido-group was reduced to an amino-group under H_2 on Pd/C catalyst. The protection of an aminoalcohol moiety with 2,2-dimethoxypropane, followed by conjugation to 1,4,7-triazacyclononane, deprotection, and complexation with $GdCl_3 \cdot 6H_2O$, gave 1st generation dendrimer-triamine-coordinated Gd complex with three aminoalcohol end groups. Although the established low-molecular-weight Gd contrast agents such as Gd-DTPA and Gd-DOTA have ionic chelating ligands that strongly suppress 8 coordination sites of Gd, a novel Gd complex has a triamine ligand and three chloride ligands, which stably occupy 6 coordination sites of Gd. Accordingly, 3 coordination sites remain for water molecules, and thus the present Gd complexes show longitudinal relaxivity that is almost 5 times higher than that of Gd-DTPA. In addition, conjugation of PEG was performed as follows: After the protection of one of the amino-end groups with a Boc group, and the conjugation of the residual two amino-end groups was carried out with PEG bearing an activated ester group (average molecular weight: 5,000) through the formation of amide bonds. The longitudinal relaxivity of the PEG-conjugated contrast agent was 30.8 $mM^{-1}s^{-1}$, which is approximately 8 times higher than that of Gd-DTPA. The slower molecular tumbling according to an increase of molecular weight by conjugation with PEG may also realize the higher relaxivity enhancement. The present results may make it possible to greatly reduce the dose of MRI contrast agents, and enhance the quality of life of patients. References [1] Caravan, P.; Ellison, J.J.; McMurry, T.J.; Lauffer, R.B. *Chem. Rev.* **1999**, *99*, 2293-2352. [2] Miyake, Y.; Kimura, Y.; Ishikawa, S.;Tsujita, H.; Miura, H.; Narazaki, M.; Matsuda, T.; Tabata, Y.; Yano, T.; Toshimitsu, A.; Kondo, T. *Tetrahedron Lett.* **2012**, *53*, 4580-4583.

Disclosure of author financial interest or relationships:
Y. Miyake, None; **Y. Kimura**, None; **T. Matsuda**, None; **H. Imai**, None; **T. Yano**, None; **A. Toshimitsu**, None; **T. Kondo**, None.

Presentation Number **P 302**
Poster Session 3
September 20, 2013 / 15:15-15:15 / Room: Exhibit Hall B

Transition Metal ParaCEST MRI Contrast Agents

Abiola O. Olatunde[1], *Joseph A. Spernyak*[2], *Janet R. Morrow*[1], [1]*Chemistry, University at Buffalo, Amherst, NY, USA;* [2]*Cell Stress Biology, Roswell Park Cancer Institute, Buffalo, NY, USA. Contact e-mail: olatunde@buffalo.edu*

The development of paramagnetic metal ions as contrast agents (CAs) for magnetic resonance imaging (MRI) is an active area of research. Paramagnetic chemical exchange saturation transfer (paraCEST) CAs are a relatively new class of contrast agents and are predominantly Ln(III) complexes. Although these Ln(III) complexes have been developed as paraCEST agents, they may contribute to health risks such as nephrogenic systemic fibrosis in patients with kidney failure. Recently, the use of transition metal ion-based paraCEST contrast agents have been reported as a new approach for creating responsive MRI contrast agents. Our progress on Ni(II) and Fe(II) based complexes for imaging (NiCEST and FerroCEST agents) will be presented. We have developed promising Fe(II) or Ni(II) contrast agents based on the 4,10-diaza-15-crown-5-ether macrocycle containing pendent groups with either exchangeable amide protons (NH) or benzimidazole (NH) protons. These rigid macrocyclic complexes produce very intense and narrow CEST peaks and are optimized for CEST at physiological pH values (6.8-7.8) for amide pendent or at acidic conditions (5.5-6.5) for the benzimidazole pendent. The Ni(II) complexes are highly stable in the presences of biologically relevant anions phosphate (0.20 mM) and carbonate (25 mM) and different ratios of cations including Cu(II) and Zn(II). An additional macrocycle, 7,13-bis(carbamoylmethyl)-1,4,10-trioxa-7,13-diazacyclopentadecane complexed to Fe(II) or Ni(II) also produces CEST contrast. Imaging experiments on a MRI 4.7 T scanner at pH 7.4 at 37°C show that the largest CEST effect corresponds to the complex with the lowest T1 and T2 relaxivity. CEST contrast was observed at sub-millimolar concentrations by using a CEST-FISP technique for MR imaging of phantoms on a 4.7 T scanner.

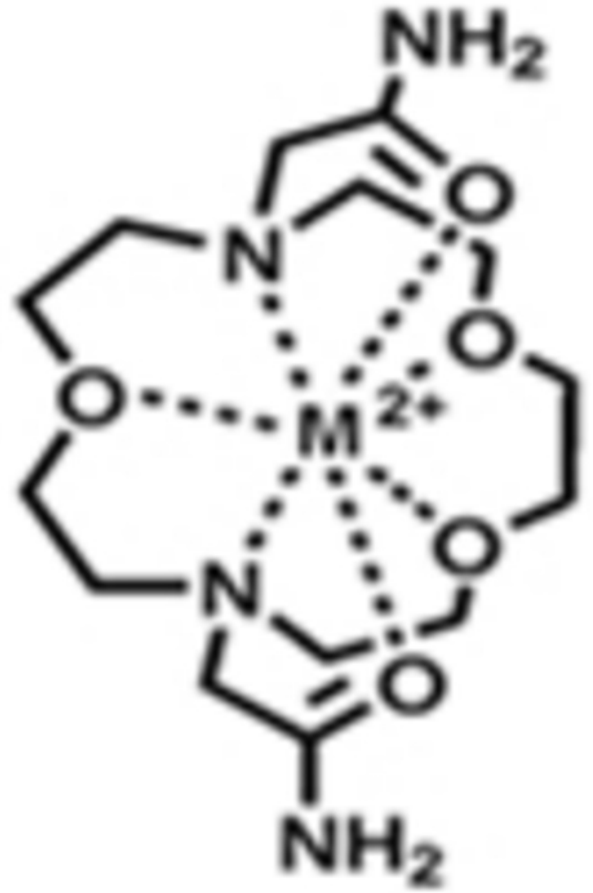

M= Fe (II) or Ni(II)

Disclosure of author financial interest or relationships:
A.O. Olatunde, None; **J.A. Spernyak**, None; **J.R. Morrow**, None.

Presentation Number **P 303**
Poster Session 3
September 20, 2013 / 15:15-15:15 / Room: Exhibit Hall B

Imaging in vivo redox status with a novel "smart" PARACEST agent

James S. Ratnakar[1], *Todd C. Soesbe*[1], *Lloyd L. Lumata*[1], *Dean Sherry*[1,2], *Zoltan Kovacs*[1,2], [1]*Advanced Imaging Research Center, UT Southwestern Medical Center, Dallas, TX, USA;* [2]*Department of Chemistry, The University of Texas at Dallas, Dallas, TX, USA. Contact e-mail: james.ratnakar@utsouthwestern.edu*

The efficiency of the paramagnetic lanthanide-based chemical exchange saturation transfer (CEST) agents has a dependency not only on the water exchange rate of that complex, but also T_1 and T_2 relaxation times of the exchanging pools.[1] The shorter the relaxation times, less efficient will be the spin transfer between the two exchanging pools, thereby reducing or diminishing the "PARACEST effect". The complex described here designed to specifically modulate CEST by altering the T_1 of bulk water by incorporation of two nitroxyl free radical moieties in the pendant arms of a DOTA-tetraamide scaffold (Figure 1). As predicted, the two stable nitroxide radicals shorten the T_1 of water protons substantially which in turn, quenches the CEST signal originating from the metal bound water protons. In the presence of a free radical scavenger (L-ascorbic acid) the PARACEST signal of the complex "turns on" due to formation of the diamagnetic hydroxylamine and lengthening of the water T_1. Nitroxyl free radicals are quite stable in water but can be deactivated in some biological environments.[2] The rates of such transformations are dependent on the tissue redox so the CEST signal of the complex could potentially be used to map tissue redox. CEST imaging of a mouse after injection of 0.2 mmol/kg of the complex showed no CEST signal in any tissues or in the bladder after an extended period of time to allow complete renal filtration. However, injection of 0.2 mmol/kg of L- ascorbic acid into the same animal after agent clearance resulted in a substantial CEST signal in the bladder. This demonstrates that the nitroxyl groups can be reduced to the diamagnetic hydroxylamine derivative in vivo and that this results in turning on the CEST signal. This preliminary work lays the groundwork for developing other EuDOTA-tetraamide free radical derivatives with proper redox properties to serve as imaging sensors of tissue redox. References 1) Viswanathan, S., Kovacs, Z., Green, K.N., Ratnakar, S.J. & Sherry, A.D., Chem. Rev., 110, 2960-3018 (2010). 2) Hyodo, F., Matsumoto, K.-i., Matsumoto, A., Mitchell, J.B. & Krishna, M.C. Cancer Res. 66, 9921-9928 (2006).

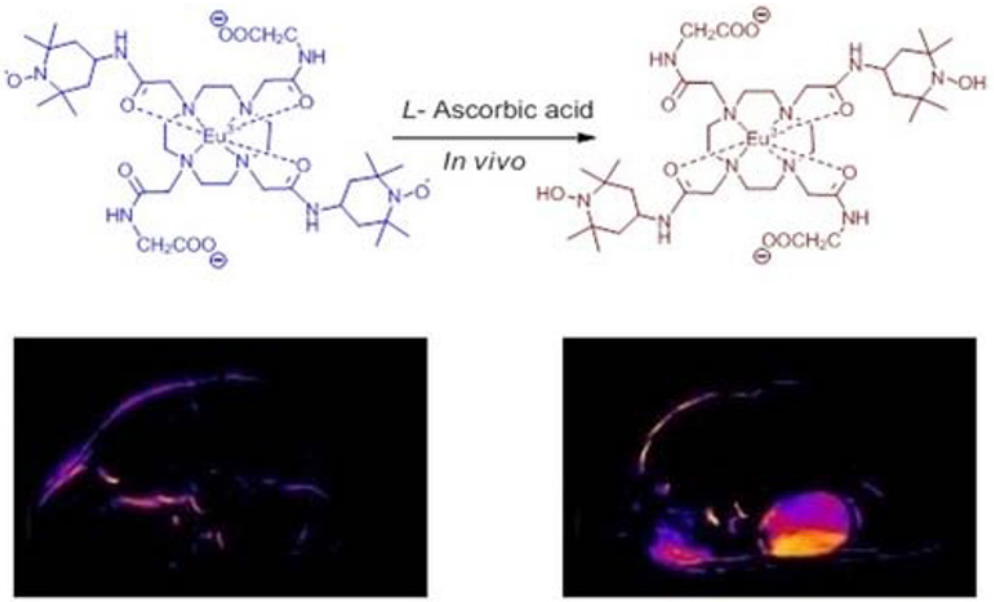

Figure 1. PARACEST imaging of the bladder of a normal female Black-6 mouse. The image on the left was taken 10 min after a 0.2 mmol/kg dose of the complex. The image on the right is recorded 1 hr after the injection of *L*-ascorbic acid in the same mouse.

Disclosure of author financial interest or relationships:
J.S. Ratnakar, None; **T.C. Soesbe**, None; **L.L. Lumata**, None; **D. Sherry**, None; **Z. Kovacs**, None.

Presentation Number **P 304**
Poster Session 3
September 20, 2013 / 15:15-15:15 / Room: Exhibit Hall B

Immune response of PEGylated nanoparticles potential use as diagnostic agent

Kouichi Shiraishi[1], *Kumi Kawano*[2], *Yoshie Maitani*[2], *Taiki Aoshi*[3], *Ken J. Ishii*[3], *Masayuki Yokoyama*[1], [1]*Research Center for Medical Science, The Jikei University School of Medicine, Tokyo, Japan;* [2]*Institute of Medicinal chemistry, Hoshi University, Tokyo, Japan;* [3]*Laboratory of Adjuvant Innovation, National Institute of Biomedical Innovation, Oska, Japan. Contact e-mail: kshiraishi@jikei.ac.jp*

Poly(ethylene glycol) (PEG) has been widely used to modify proteins and liposomes in the field of pharmaceutics. PEGylation is commonly used method to improve and control pharmacokinetics of the proteins and liposomes. Nowadays, most nanoparticles for therapeutic purpose as well as for diagnostic purpose are used PEGylation for surface coating to avoid interaction with plasma proteins and reduce uptake from reticuloendothelial system. However, recent studies have reported that antibodies against PEG have been generated by injection of PEGylated proteins and PEGylated liposomes (PEG-liposomes) in animal models. This immune responses by the PEG-liposomes exhibited the faster clearance of the subsequent PEG-liposomes from blood circulation, known as the accelerated blood clearance (ABC) phenomenon [1,2]. The produced IgM antibody binds to the second dose of PEG-liposomes, leading to enhanced uptake in the liver and thus, eliminating the intended long-circulation property. Studies on PEG-liposomes regarding the ABC phenomenon concluded that the produced IgM was PEG-main chain specific antibody, i.e., anti-PEG IgM. However, our previous results of polymer micelle MRI contrast agent exhibited no relation to the ABC phenomenon, whereas PEG is used as the outer shell [3]. So far, this immune response has not been completely elucidated yet, and further study needs to clarify for understanding of the immune response. The IgM production by the first dose of PEG-related nanocarriers will become serious issue, because PEG related diagnostic agents will lose the diagnostic ability by the IgM generation at the first dose. This ABC phenomenon must be evaded for diagnostic purpose. So far, the IgM is believed to be PEG main chain specific, the main proof of the IgM antibody has based on the results of conventionally performed ELISA. This study presents more mechanistic study regarding the ABC phenomenon by comparing PEG-liposomes and PEG possessing polymeric micelles. ELISAs and in vivo experiments involving the polymeric micelle carrier systems have yielded new findings in the ABC phenomenon. The findings should significantly strengthen our understanding of the role of produced IgM in the ABC phenomenon. Namely, the IgM does not bind to PEG main chain, but does bind to the interface between PEG and hydrophobic blocks.

Disclosure of author financial interest or relationships:
K. Shiraishi, None; **K. Kawano**, None; **Y. Maitani**, None; **T. Aoshi**, None; **K.J. Ishii**, None; **M. Yokoyama**, None.

Presentation Number **P 305**
Poster Session 3
September 20, 2013 / 15:15-15:15 / Room: Exhibit Hall B

The NIR-Fluorescent Gd-Based Silicate Nanoagents for Tumor-Specific MR and Optical Targeting Imaging

Chia-Hao Su[1], *Jui-Cheng Chang*[2], *Shu-Ting Hung*[1], *Min-Chiau Laiu*[1], *Chen-Sheng Yeh*[2,3], [1]*Center for Translational Research in Biomedical Sciences, Kaohsiung Chang Gung Memorial Hospital, Kaohsiung, Taiwan;* [2]*Department of Chemistry, National Cheng Kung University, Tainan, Taiwan;* [3]*Department of Materials Science and Engineering, National Cheng Kung University, Tainan, Taiwan. Contact e-mail: chiralsu@gmail.com*

The development of nanoscience and technology has promised researchers in successful fabrication of multifunctional nanoparticles with targeting, near-infrared imaging, and even therapeutics for biomedical applications. Additionally, near-infrared (NIR) imaging holds promise as a noninvasive and high resolution modality for *in vivo* cancer detection because of both blood and soft tissues with mild backscattering and low energy absorption, thus providing maximal tissue penetration in that wavelength region. The recent development in upconversion nanoparticles (UNPs) are able to serve as NIR fluorescence source, due to multiphoton excitation and relaxation, and can readily include additional dopant, such as gadolinium, to provide magnetic resonance (MR) imaging effect as well. However, the lanthanide composition in UNPs is always a concern for further downstream biomedical studies. It remains in its incipient area and is appealing to prepare bio-friendly NPs with ligands modified on their surfaces as simple as possible to achieve NIR-responsive multifunctionalities. Here, we report a paradigm showing three functionalities including tumor targeting, near-infrared fluorescent and magnetic resonance (MR) imaging by mean of using only a lipophilic hepatamethine cyanine dye conjugated on a porous Gd silicate nanoagent. The Gd-based silicate nanoparticle itself exhibited dual MR effect, expressing T_1-brightened and T_2-lowering effects, in lower magnetic field. Notably, in high magnetic field an abnormal enhanced transverse relaxivity (*r2*) appears, showing an effective T_2-lowering effect, likely due to concentrated Gd amount and porous architecture. For *in vivo* tumor targeting NIR and MR imaging, NIR dye conjugated Gd silicate@mSiO_2 NPs were injected i.v. to SCID/NOD mice bearing LLC/LL2 lung tumor. Successive observation at different time course displays that the increase in NIR signal associated with the implanted LLC/LL2 tumor site can be visualized as time prolonged. Addition, MR imaging was performed the T_2-weighted imaging by 9.4T animal micro MRI system, and the NIR dye conjugated NPs display effectively darkened contrast in tumor. The signal in tumor area continues drop and achieves a 44% reduction at post 7h, and even remains darkened contrast at post 24h. In conclusion, we think that NIR dye with native targeting property, in combination of inorganic NPs shall broaden current multifunctional modalities to make an important contribution and more effective in cancer diagnosis and therapeutics. The future applications of NIR fluorescent dyes could lead to important progress in the pre-clinical trial and clinical use. Interestingly, the Gd-containing silicates have highly negative enhancement. Continuing effort needs to expand the fabrication of weakly magnetized particles and study their behavior when subjected to strong magnetic field.

Disclosure of author financial interest or relationships:
C. Su, None; **J. Chang**, None; **S. Hung**, None; **M. Laiu**, None; **C. Yeh**, None.

Presentation Number **P 306**
Poster Session 3
September 20, 2013 / 15:15-15:15 / Room: Exhibit Hall B

Molecular Imaging of Atherosclerotic Plaque via GEBP11 Targeted Magnetic Nanoparticles

Tao Su[1], *Yabin Wang*[1], *Shun Qi*[2], *Junting Liu*[3], *Jimin Liang*[3], *Kaichun Wu*[4], *Feng Cao*[1], [1]*Cardiology, Xijing Hospital, Fourth Military University, Xi'an, China;* [2]*Radiology, Xijing Hospital, Fourth Military University, Xi'an, China;* [3]*Life Sciences and Technology, Xidian University, Xi'an, China;* [4]*Digestive Diseases, Xijing Hospital, Fourth Military University, Xi'an, China. Contact e-mail: sutao2001@gmail.com*

Background Angiogenesis is considered to be one of the critical features in atherosclerotic plaque progression and may exacerbate plaque vulnerability. We identified a 9-amino acid cyclic peptide named GEBP11 (CTKNSYLMC) using phage display peptides library which holds high affinity for neovascularization in gastric cancer. In the current study, we develop a 2,3-dimercaptosuccinnic acid-coated (DMSA-coated) paramagnetic nanoparticle contrast agent with GEBP11 peptide tag to assess plaque-associated angiogenesis by magnetic resonance imaging (MRI). Methods GEBP11 peptide was conjugated to DMSA-coated magnetic nanoparticles (DMSA-MNPs) by condensation of carboxyl and amine. The characterizations of the MNPs were determined by transmission electron microscopy (TEM), dynamic light scattering (DLS) and vibrating sample magnetometer respectively. In vitro cell studies were performed to investigate the binding affinity of GEBP11 peptide targeted or untargeted MNPs to human umbilical vein endothelial cells (HUVECs). Thirty New Zealand White rabbits were fed high fat diet for 12 weeks after abdominal aorta balloon injury. Ultrosound was applied to confirm the plaque formation followed by injection of GEBP11 peptide targeted MNPs introvenously. In vivo 3.0T MRI was performed at 4h after the tail vein injection of 5 mg Fe/Kg body weight MNPs. The expression of GEBP11 and CD31 in aorta section from atherosclerotic rabbits was analysed by immunofluorescence. Results Atherosclerotic lesions in the abdominal aorta were confirmed by histology stains and ultrasound imaging. The TEM image showed that DMSA-MNPs were well dispersed and the mean size of DMSA-MNPs was 20.6 nm. The GEBP11 conjugated DMSA-MNPs had greater hydrated diameters than unconjugated DMSA-MNPs (42.3 ± 3.47 nm VS. 20.6 ± 2.29 nm). The saturation magnetization value of GEBP11 conjugated DMSA-MNPs was 35.6 emu/g Fe at room temperature. In vitro HUVECs experiment showed that compared with DMSA-MNPs or unrelated peptide conjugated DMSA-MNPs, the GEBP11 conjugated DMSA-MNPs were more prone to target HUVECs. The immunofluorescence imaging confirmed the colocalization of GEBP11 and CD31 expression near the media layer by confocal microscope. In vivo MRI images revealed that after the GEBP11 conjugated DMSA-MNPs injection, the area of atherosclerotic plaque in abdominal aorta exhibited significant signal loss on T2-weighted images and the presence of MNPs was confirmed by Prussian blue staining. Conclusions In summary, the present study demonstrates that GEBP11 conjugated DMSA-MNPs, a novel molecular imaging probe, provides a potential approach for noninvasive assessment of angiogenesis in atherosclerotic plaque by MRI.

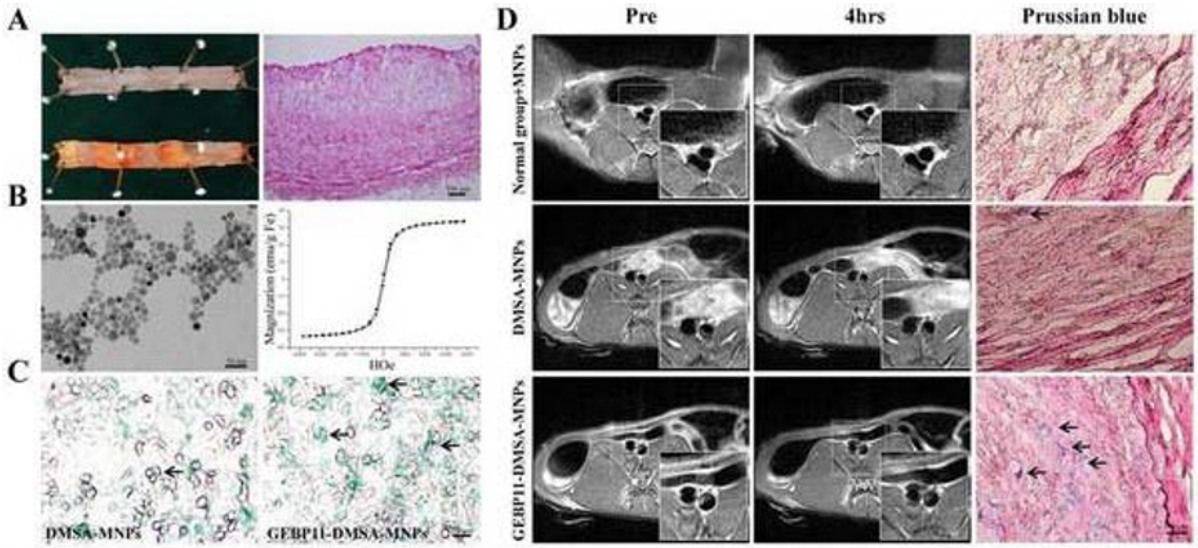

Fig 1. Histology for atherosclerotic plaque of rabbit, characterization of MNPs, HUVECs uptake of MNPs and MNPs MRI of rabbits.

A. Oil Red O and H&E stain of plaque. Bar=100 μm. B. TME image and the saturation magnetization value of MNPs. Bar=50 μm. C. *In vitro* HUVECs uptake targeted and untargeted MNPs. Bar=20 μm. D. MNPs MRI of atherosclerotic rabbit in T2 weight images and the prussian blue staining of MNPS in plaque tissue. Bar=100 μm.

Disclosure of author financial interest or relationships:

T. Su, None; **Y. Wang**, None; **S. Qi**, None; **J. Liu**, None; **J. Liang**, None; **K. Wu**, None; **F. Cao**, None.

Presentation Number **P 307**
Poster Session 3
September 20, 2013 / 15:15-15:15 / Room: Exhibit Hall B

Partially Polymerized Liposomes for Targeted Drug Delivery, Controlled Drug Release and Molecular Imaging

Xiaobing Xiong[1], *Steve H. Fung*[2], *Ching-Hsuan Tung*[2], *King Li*[1], [1]*Department of Radiology, Wake Forest University School of Medicine, Winston-Salem, NC, USA;* [2]*Translational Imaging, The Methodist Hospital Research Institute, Houston, TX, USA. Contact e-mail: xxiong@wakehealth.edu*

Introduction: A major challenge for drug delivery is to precisely control the drug release both spatially and temporally. Liposomes have been extensively used as carriers for drug delivery in cancer chemotherapy and diagnosis. However, the precise control of drug release is hindered by the limited stability at physiologic conditions against drug leakage at non-target sites. Partially polymerized liposomes (PPL) have been proposed to improve liposome stability while capable of being degraded by the liver and excreted through the biliary system into the gastrointestinal tract. Purpose: The objective of this study is to (i) assess the elimination of PPL in mice after i.v. injection, and (ii) validate that partially polymerized liposomes (PPL) can be used as a delivery platform for targeted drug delivery and controlled drug release for better cancer treatment and diagnosis. Methods: Lipid composition of DPPC and DiynePC was used as the filling lipids to control the polymerization degree of PPL. Functional lipids, i.e. DiynePE with conjugated diethylentriamene pentaacetate (DTPA), integrin αvβ3 antagonist (IA), and lipoic acid (LA) were synthesized and used for liposome functionalization. Specifically, 1) to assess PPL elimination, DTPA-functionalized PPL (DTPA-PPL) with 90% polymerization (PPL90) and 30% polymerization (PPL30) was prepared from DTPA-DiynePE, DiynePC, and DPPC, and then radio-labeled with 111Indium for SPECT imaging after i.v. injection into mice. 2) For ligand-mediated cancer targeting, IA-functionalized PPL (IA-PPL90) with packaged calcein was prepared from IA-DiynePE, DiynePC and DPPC. Cell binding and uptake was evaluated using HUVEC cells, which overexpress integrin αvβ3 on their cell membrane. 3) To achieve precise temporal and spatial control of drug release, LA-functionalized PPL with (LA-PPL90) packaged calcein was prepared from LA-DiynePE, DiynePC and DPPC and then tethered with gold nanorods on the PPL surface. Infrared laser was used to trigger drug release. 4) Gadolinium (Gd) was loaded into PPL90 to enhance tumor MR imaging. T1- and T2-relaxation times of PPL/Gd were recorded with a benchtop MR relaxometer (Process NMR Associates). MRI was also obtained with a 3.0 T MRI scanner (Ingenia, Philips Healthcare). Results: Preliminary results are summarized in Figure 1. SPECT images show PPL primarily trapped in the liver after i.v. injection and can be eliminated by hepatobiliary excretion. PPL30 showed faster excretion compared than PPL90 (Fig. 1A). IA-PPL90 can significantly enhance liposome binding and uptake into HUVEC cells (Fig 1B). Gold nanorod-tethered PPL can release encapsulated calcein by infrared laser irradiation (Fig 1C). Finally, compared to PPL/Gd, the lysed PPL/Gd showed 27% T1- and 34% T2-shortening (Fig 1D), and enhancement on T1- and T2-weighted images. Conclusions: The results of this study demonstrated that (1) PPL can be degraded and excreted in vivo, and (2) if properly functionalized, PPL can be used as a drug delivery platform for targeted drug delivery and controlled drug release.

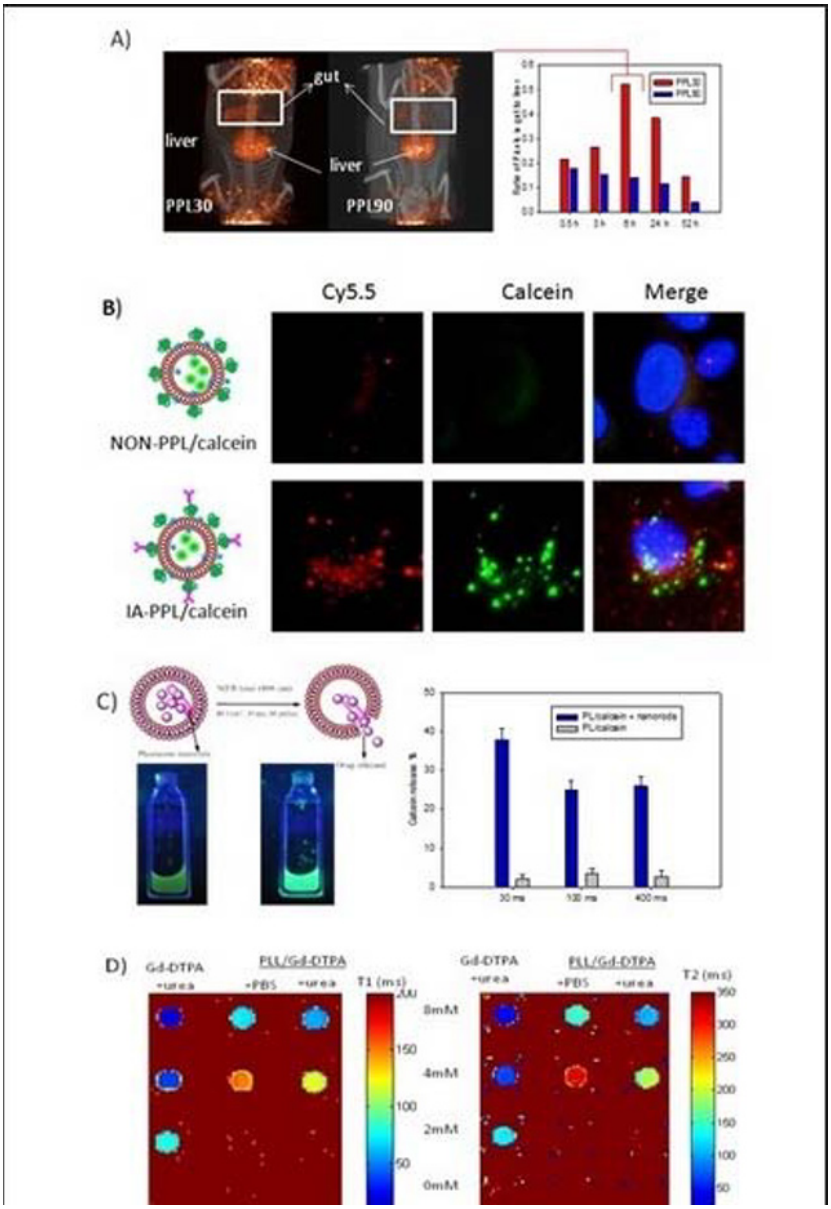

Figure 1: PPL as a drug delivery platform. A) Mice were i.v. injected with PPL30 and PPL90, and SPECT images were taken at different time points. Gut-to-liver radioactivity ratio was determined at different time points from the SPECT images. B) IA-facilitated PPL/calcein binding and uptake by HUVEC cells. Cells were incubated with PPL/calcein or IA-PPL/calcein (green). PPL was labeled with Cy5.5 (red). Cell nuclei were labeled with DAPI (blue) C) Infrared laser triggered calcein release from nanorod-teathered PPL. PPL/calcein and nanorod-tethered PPL/calcein were treated with infrared laser (Lumenis Lighsheer XC, 800 nm, 40 pulses of different pulse widths 30, 100, and 400 ms). Calcein fluorescence was measured. D) T1- and T2-maps of PPL/Gd in PBS and PPL/Gd disrupted by urea in vials surrounded by HPLC-grade water were made using a 3T MRI scanner, inversion recovery and T2 fast-spin echo sequences for T1- and T2-maps, respectively.

Disclosure of author financial interest or relationships:

X. Xiong, None; **S.H. Fung**, Lilly USA, LLC, Consultant; Lilly USA, LLC, Speakers bureau; Lilly USA, LLC, Honoraria; **C. Tung**, None; **K. Li**, None.

Presentation Number **P 308**
Poster Session 3
September 20, 2013 / 15:15-15:15 / Room: Exhibit Hall B

Design Protein-based MRI Contrast Agents (ProCAs) for Early Detection of Metastasis

Shenghui Xue[1,2], *Hua Yang*[3], *Jingjuan Qiao*[2], *Fan Pu*[2], *Hans Grossniklaus*[3], *Zhi-Ren Liu*[1], *Jenny Yang*[2], [1]*Department of Biology, Georgia State University, Atlanta, GA, USA;* [2]*Department of Chemistry, Georgia State University, Atlanta, GA, USA;* [3]*Department of Ophthalmology, Emory University, Atlanta, GA, USA. Contact e-mail: xuesh15@hotmail.com*

Lack of desired MRI contrast agents capable of enhancing the contrast between normal tissues and tumors with high relaxivity, tumor targeting, high intratumor distribution and reduced metal toxicity is one of the major barriers for the application of MRI to assess specific biomarkers for diagnosis and monitor drug effect. There is an urgent need to develop non-invasive and accurate methods for diagnosis and selection of patients and to monitor biomarker levels/distribution and their changes upon treatment by targeted drugs. We have developed a novel class of protein-based MRI contrast agents (ProCAs) by de novo design of Gd3+ binding site(s) into a stable host protein. ProCAs exhibit 10-20-fold improved MRI relaxivity, extend detection limit to less than 2.5 μM in vitro and 1.6 μmol Gd/kg body weight in vivo and excellent MR angiography. In addition, ProCAs enable to detect accurately small metastatic tumors with dual bright-and-dark enhancement. Tumor enhancement in MRI was further confirmed by immunofluorescence, immunohistochemistry analysis and ICP-OES. ProCAs have high stability, no cell toxicity and acute toxicity and proper blood circulation time with strong application in early detection and treatment of various types of cancers including image-guide surgery. References: 1. Jinjuan Qiao, Shunyi Li,Jie Jiang, Lixia Wei, Robert Liang, Liyia Wang, Hui Mao, Hua Yang, Hans Grossniklaus, Zhiren Liu and Jenny J. Yang. HER-2 Targeted Molecular MR Imaging Using a de vovo Designed Protein Contrast Agent. PLOS ONE (2011) Mar 24;6(3):e18103.PMID: 21455310 2. Lixia Wei, Shunyi Li, Jianhua Yang, Yiming Ye, Jin Zou, Omar Zurkiya, Robert Long,Julian Johnson, Jingjuan Qiao, Adriana Castiblanco, Natalie Maor, Yangyi Chen, Wangda Zhou, Hui Mao, Xiaoping Hu, Jenny J. Yang, and Zhi-Ren Liu, Design of protein-based MRI contrast agent for molecular imaging of prostate cancer. Molecular Imaging and Biology (2010). 32(5):521-5. PMID: 20574851 3. Jenny J. Yang, Jianhua Yang, Lixia Wei, Wei Yang, Omar Zurkiya, Hui Mao, Fuqian Zhao, Russell Malchow, Shunyi Li, Anna L. Wilkins Mannicia, Shumin Zhao, Jin Zou, Julian Johnson, Xiaoping Hu, Eirk Krogstad, and Zhi-Ren Liu, Rational Design Protein Based MRI Contrast Agents with High Relaxivity Journal of the American Chemical Society (2008), 130(29):9260-7. 4. Shenghui Xue, Jingjuan Qiao, Jie Jiang, Lixia Wei, Shuanyi Li, Kendra Hubbard, Zhiren Liu, Jenny J. Yang, Design Protein-based MRI Contrast Agent with High Dose Efficiency and Capability for Molecular Imaging of Biomarkers. Medical Research Review, (2013), Accepted. 5. Shenghui Xue, Jingjuan Qiao, Fan Pu, Mathew Cameron and Jenny J. Yang. Design of a novel class of protein-based magnetic resonance imaging contrast agents for the molecular imaging of cancer biomarkers. Wiley Interdiscip Rev Nanomed Nanobiotechnol (2013) 5(2):163-79. PMID: 23335551. Supported in part by NIBIB 1R01EB007268. MBD fellowship for Shenghui Xue, Georgia State University.

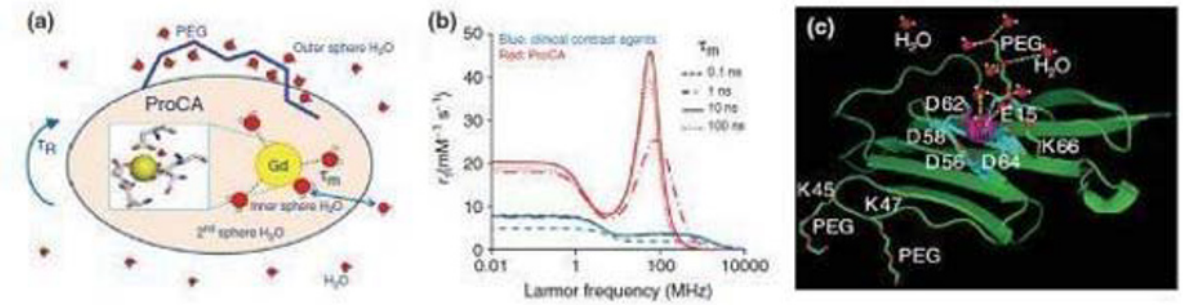

Figure 1. A. Schematic representation of a Gd3+ chelate surrounded by bulk water with one inner sphere and three second sphere water molecules and several outer sphere water molecules. Modification of contrast agents by PEG could change the water properties which could further influence relaxivity. B. Simulated magnetic field-dependent relaxivity r1 of clinical MRI contrast agents and ProCA based on SBM theory. C. Model structure of ProCA1 with PEG modification. (Adapted from ref. 5).

Disclosure of author financial interest or relationships:
S. Xue, None; **H. Yang**, None; **J. Qiao**, None; **F. Pu**, None; **H. Grossniklaus**, None; **Z. Liu**, None; **J. Yang**, None.

Presentation Number **P 309**
Poster Session 3
September 20, 2013 / 15:15-15:15 / Room: Exhibit Hall B

Detection of Enzyme Activity by 19F MRI/MRS Using A Novel Fluorous Activatable Probe

Xuyi Yue, *Lei Zhu, Dale O. Kiesewetter, Zhe Wang, Ying Ma, Xiaoyuan (Shawn) Chen, National Institute of Biomedical Imaging and Bioengineering, National Institutes of Health, Bethesda, MD, USA. Contact e-mail: xuyi.yue@nih.gov*

Strategies aimed at real time imaging and detection of enzyme activity have substantial diagnostic and prognostic value for many diseases. Dysregulation of enzymatic activities appears to play an important role in the progression of cancer, stroke and heart disease, diabetes, infections, etc. Matrix metalloproteinases (MMPs) are a class of endoproteases that are expressed in higher levels in some forms of cancer and are predominantly associated with tumorigenesis. 19F magnetic resonance imaging (19F MRI) is a promising quantitative imaging technique and is receiving great attention for application in mapping tumor oxygenation, assessing molecular expression in vascular diseases, and tracking labeled cells due to its high spatial resolution, deep tissue penetration and good soft tissue contrast. Current 19F imaging agents are based on perfluorocarbon emulsions and suffer considerable shortcomings, including complex formulation procedure with inherent instability, 19F chemical shift artifacts and excessive persistent retention of the agents in organs. We developed a novel, activatable 19F MRI probe to detect MMP activity. Conventional imaging probes used in CT, 1H MRI, 19F NMR, PET, and angiography continuously emit signals and hence are "always on". These probes emit signals regardless of their proximity to or interaction with target tissues or cells, and as a result there is considerable background signal. In order to improve signal to noise ratio, we designed and synthesized a 19F activatable MMP peptide substrate. One end of the peptide bears the 19F fluorous dendron (F3, F9, F27, or F81) that provides variable detection sensitivity. The other end of the peptide bears 1,4,7,10-tetraazacyclododecane-1,4,7,10-tetraacetic acid (DOTA) conjugated gadolinium, which can "quench" the 19F NMR signal due to its the large electron spin quantum number. In the intact MMP substrate the 19F signal will be significantly attenuated, but in the presence of MMP, the peptide will be site-specific cleaved and the influence of strong paramagnetic effect of gadolinium to fluorine will be reduced. The intensity of recovered fluorine signal, which can be directly measured by 19F MR spectroscopy (MRS) and 19F MRI, will reflect the activity of the protease. The F27 and F81 fluorous dendrons were prepared, but exhibit extreme hydrophobicity and will require compounding investigation. The activatable probe containing F9 displayed a steady increase in observed 19F signal upon treatment with MMP. Further application of the activatable probes to detect MMP activity in various cells and tumor xenograft model is ongoing. Compared to current perfluorocarbon emulsions as 19F MRI agents, our incorporation of fluorous dendron into activatable probes provide these advantages: spherically symmetrical fluorine atoms that emit a homogeneous MRI resonance; no chemical shift artifacts; tunable fluorine content; and the fluorous dendron can be easily incorporated into enzyme substrates. Acknowledgements: This research was supported by the intramural research program NIBIB/NIH.

Disclosure of author financial interest or relationships:
X. Yue, None; **L. Zhu**, None; **D.O. Kiesewetter**, None; **Z. Wang**, None; **Y. Ma**, None; **X. Chen**, None.

Presentation Number **P 310**
Poster Session 3
September 20, 2013 / 15:15-15:15 / Room: Exhibit Hall B

Facile fluorine-18 labeling of serum albumins via the coupling of [18F]fluoronicotinic acid tetrafluorophenyl ester with albumin amine groups

Falguni Basuli[1], *Olga Vasalatiy*[1], *Biying Xu*[1], *Gary L. Griffiths*[2], *Elaine Jagoda*[2], *Michael V. Green*[2], *Jurgen Seidel*[2], *Peter Choyke*[2], [1]*Imaging Probe Development Center, National Heart, Lung, and Blood Institute, National Institutes of Health, Rockville, MD, USA;* [2]*Molecular Imaging Program, National Cancer Institute, National Institutes of Health, Bethesda, MD, USA. Contact e-mail: bhattacharyyaf@nhlbi.nih.gov*

Objectives: Our objective is to develop an improved, optimized, simple, reproducible and clinically translatable method to label serum albumins with fluorine-18 for use as a blood pool imaging agent. For patient and commercial adoption, it was critical that the method we developed should produce high quality of tracer quickly with moderate to high radiochemical yield. Methods: Fluorine-18 labeling of serum albumin was achieved by an indirect method. Fluorine-18 radiolabeled fluoronicotinic acid-2,3,5,6-tetrafluorophenyl ester was prepared first by the reaction of its quaternary ammonium triflate precursor with [18F]TBAF according to a peptide F-18 radiolabeling literature method [1], with modifications. Final conjugation of the serum albumin with [18F] fluoronicotinic acid-2,3,5,6-tetrafluorophenyl ester in phosphate buffer, pH 9, for 20 min produced fluorine-18-radiolabeled albumins (rat & human). Purification of the products was done using a mini-PD MiniTrap G-25 column. Results: The conjugation yield was 92-98% within 20 min at 37-40 oC. The overall radiochemical yield of the reaction was 10-25% (n= 25, uncorrected) in a 180 minute radiolabeling time. Conclusions: Fluorine-18 labeling of serum albumins was successfully accomplished with a moderate overall radiochemical yield in a 90 minute synthesis time. No time consuming HPLC purifications of intermediates or products are required with this method. Preclinical imaging and testing will be done primarily on rat [18F]-albumin prior to planned clinical development of human [18F]-albumin. Research Support: This study was funded by the intramural program of the National Institutes of Health. References: [1] Olberg, D. E. et al. J. Med. Chem., 2010, 53, 1732-1740.

Disclosure of author financial interest or relationships:
F. Basuli, None; **O. Vasalatiy**, None; **B. Xu**, None; **G.L. Griffiths**, None; **E. Jagoda**, None; **M.V. Green**, None; **J. Seidel**, None; **P. Choyke**, None.

Presentation Number **P 311**
Poster Session 3
September 20, 2013 / 15:15-15:15 / Room: Exhibit Hall B

Preparation of USP grade 89Zr-panitumumab as an immuno-PET biomarker for monitoring the treatment of EGFR-expressing cancer

Ling Wei, Jianfeng Shi, George Afari, **Sibaprasad Bhattacharyya***, ADRD, SAIC, Frederick National Laboratory for Cancer Research, Frederick, MD, USA. Contact e-mail: bhattacharyyas2@mail.nih.gov*

Epidermal growth factor receptor (EGFR) is dysregulated in a variety of cancers, including lung, colorectal, head and neck, prostate, breast, glioma, pancreatic and ovarian cancers. Therefore, EGFR is widely recognized as promising target for the development of new drugs in oncology. In order to treat patients effectively with EGFR-targeted drug a suitable method is needed to assess the EGFR status of each patient before the treatment and monitor the effect during the treatment process. At present invasive methods such as tissue biopsy are used to identify EGFR expression in primary tumor site or metastatic sites in cancer patients. Although useful for tumor characterizations, repeated biopsy for disease management is impractical and unreliable. Essentially, there are no reliable methods for monitoring EGFR status available for everyday practice [1]. Recent preclinical evaluation [2-4] reveals that 89Zr labeled panitumumab can be used as a potential immuno-PET probe to assess the EGFR status of patient. Herein we disclose the preparation of USP grade 89Zr-panitumumab and its QC tests in our USP laboratory at Frederick for its use in early phase clinical trial. In a typical batch, 8-10 mg of panitumumab is incubated with 3 equivalents of p-isothiocyanato-benzyl desferrioxamine (SCN-Bz-DFO) for 1 hour at 37°C. The conjugate is then purified on a PD10 size exclusion chromatography column using 0.9% saline (USP) as mobile phase. Concentration (mg/mL) of the conjugate is determined by analytical HPLC. In another reaction vial, ~4.0 mCi of 89Zr-oxalate solution in 1.0 M oxalic acid (~200 µL) is neutralized by 2 M Na2CO3 solution. To this reaction vial is added 1-1.2 mg of conjugated protein, 0.2 mL of gentistic acid solution, and 0.5 mL of 0.5 M HEPES buffer. The reaction mixture is incubated for 1 hour at room temperature. The crude product is purified on a PD10 column using gentistic acid solution as mobile phase. Purified product (~2 mL) is diluted to 5 mL with 0.9% saline and transferred to a10-mL vented sterile vial through a sterile filter (0.22 µm). Vial is assayed for total radioactivity. Samples are removed for QC analysis. The preparation (bioconjugation, radiolabeling, and purification) takes 5 hours. The decay corrected radiochemical yield and purity for the qualification runs were 75.0 ± 5.0% (n=3) and 94± 4.0% (n=3) respectively. QC analysis of the product of the 3 qualification runs showed that the quality of the product was consistently meeting all the specifications of a USP grade radiotracer. Starting from clinical grade (GMP) panitumumab a quick and straight forward method has been developed to produce USP quality 89Zr-panitumumab. In this method, both bioconjugation and radiolabeling are done in same day. Details manufacturing procedure and QC test results will be presented. Funded by NCI/NIH, Contract No. HHSN261200800001E References 1.Pantaleo MA, et al. Annals of Oncology 2009, 20:213-226. 2.Bhattacharyya S, et al. Nucl Med Biol 2013, in press 3.Chang AJ, et al. Molecular Imaging 2013, 12: 1536-0121. 4.Nayak TK, et al. J Nucl Med 2012, 53: 113-120.

Disclosure of author financial interest or relationships:
L. Wei, None; **J. Shi**, None; **G. Afari**, None; **S. Bhattacharyya**, None.

Presentation Number **P 312**
Poster Session 3
September 20, 2013 / 15:15-15:15 / Room: Exhibit Hall B

[18F]Flumazenil neuroimaging of Benzodiazepine receptor in Tone-Foot Shock Pairings Anxiety Rat Model

Kai-Hung Cheng, *Yuan-Ruei Huang, Wan-I Kuo, Chieh Huang, Kang-Wei Chang, Division of Isotope Application, Institute of Nuclear Energy Research, Taoyuan County, Taiwan. Contact e-mail: kaihung@iner.gov.tw*

Objectives γ-Aminobutyric acid (GABA) is one of the most important inhibitory neurotransmitters in epliepsy, anxiety and other psychiatric disorders. Previous studies had verified that the radioactive GABA/BZR receptor antagonist, fluorine-18-labeled flumazenil ([18F]FMZ), behaves as a potential PET imaging agent for evaluation the cortical damage of brain in stroke, alcoholism and for Alzheimer disease investigation. Our aim of the study was to develop a [18F]FMZ radiosynthesis procedure and establish the nanoPET/CT imaging platform for GABA receptor in Tone-Foot Shock Pairings Anxiety Rat Model. Method(s) [18F]FMZ was synthesized from the precursor Nitromazenil in DMF at high temperature by autosyntheis system. The crude product was purified by reversed-phase preparative high-performance liquid chromatography. Tone-foot shock pairings anxiety rat model was evaluated by elevated plus maze (EPM) and freezing behavior. In the occupancy experiments, bretazenil was injected 30 min before the injection of [18F]FMZ. We evaluated the [18F]FMZ specific binding ratio from ex vivo autoradiography and nanoPET/CT. Result(s) The radiochemical yield obtained at the end of synthesis was 17.5±2.9%(EOB) with a radiochemical purity of >95%. The produced [18F]FMZ was observed to be stable for at least 8 hr. In the occupancy experiments, nanoPET/CT imaging indicated that pretreating with breazenil(benzodiazepine partial agonist)suppressed the accumulation of [18F]FMZ as compared with control rat study. The ex vivo autoradiography of tone-foot shock pairings anxiety rat model showed that the binding ratios of [18F]FMZ was significantly decreased in prefrontal cortex, hippocampus, cortex and amygdala. Conclusion We develop a [18F]FMZ autosynthesis procedure and verify the binding specificity. We also establish the imaging platforms, including ex vivo autoradiography and nanoPET/CT, for GABA/BZR receptor in rat. ex vivo autoradiograph successfully reveals the change of [18F]FMZ radioactivities in rat anxiety model. In the future, we will applied [18F]FMZ nanoPET/CT platform to the tone-foot shock pairings anxiety rat model and other disease model.

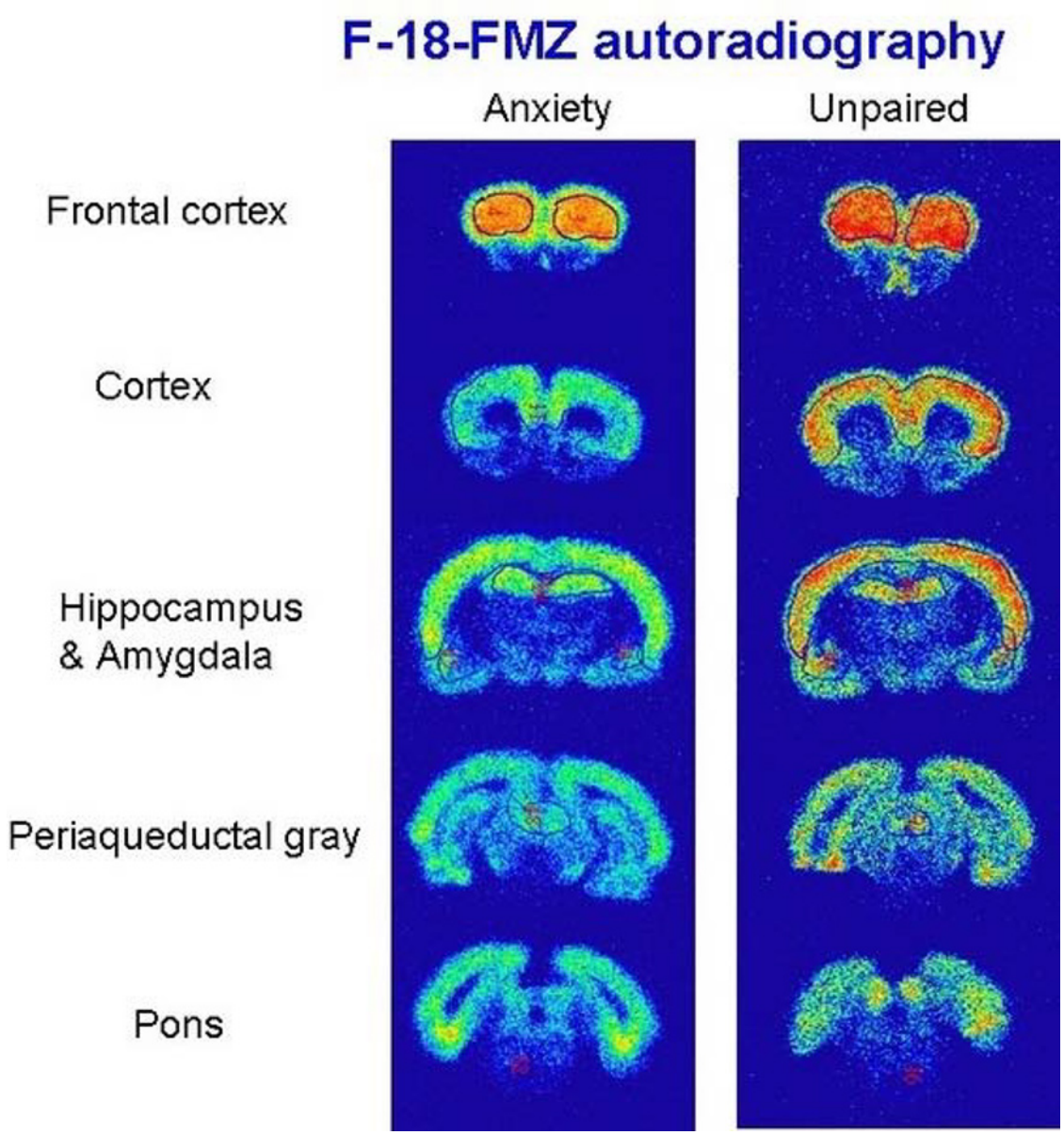

Disclosure of author financial interest or relationships:
K. Cheng, None; **Y. Huang**, None; **W. Kuo**, None; **C. Huang**, None; **K. Chang**, None.

Presentation Number **P 313**
Poster Session 3
September 20, 2013 / 15:15-15:15 / Room: Exhibit Hall B

Novel, potent and stable neuropeptide Y analog designed for Y1 receptor-targeted breast tumor imaging

Samia Ait-Mohand, **Veronique Dumulon-Perreault***, Nematallah Mansour, Brigitte Guerin, Sherbrooke's Molecular Imaging Center (CIMS), Sherbrooke, QC, Canada. Contact e-mail: Veronique.Dumulon-Perreault@USherbrooke.ca*

Background: Neuropeptide Y (NPY) Y1 receptors have been shown to be significantly overexpressed on a large proportion of breast cancers. Previously, we have developed a potent and specific ligand for NPY1R, [Pro30,Lys(NOTA)31, Tyr32, Leu34]NPY(28-36)NH2. However, the biological half-live of this 64Cu labeled truncated NPY analog was shorter than 15 min when incubated in mouse plasma. Based on the diverse metabolites identified by LC-MS-MS, we improved the design of 64Cu/ NOTA-NPY(28-36)NH2 analogs in order to increase its metabolic stability. Method: All new peptides were synthesized on solid phase and several structural modifications of the peptide backbone and linker were made to improve metabolic stability of the tracer while maintaining excellent potency for Y1 receptors. Competition assays were performed on MCF-7 human breast cancer cells after each structural modifications. In vivo stability of radiolabeled compounds was assessed in Balb/c mice. Results: A new NOTA-NPY(28-36)NH2 analog with multiple structural modifications was prepared with high purity (> 95%). The inhibition constant of this NPY analog is found to be 9.20 nM. NOTA-peptide was successfully radiolabeled with 64Cu with yields, not decay corrected, greater than 95%. The specific activities measured were 74 to 93 TBq/mmol (2,000 to 2,500 Ci/mmol). The 64Cu-labeled peptide was stable up to 1 h in vivo. Conclusion: The new NOTA-NPY(28-36)NH2 analog has been successfully synthesized and labeled with 64Cu as potential tracers for Y1 receptor-targeted breast tumor imaging by PET.

Disclosure of author financial interest or relationships:
S. Ait-Mohand, None; **V. Dumulon-Perreault**, None; **N. Mansour**, None; **B. Guerin**, None.

Presentation Number **P 314**
Poster Session 3
September 20, 2013 / 15:15-15:15 / Room: Exhibit Hall B

Cabozantinib (XL184) resolves bone scans independent of tumor response

Michael J. Evans, *David Ulmert, Michael Doran, Charles L. Sawyers, Memorial Sloan Kettering Cancer Center, New York, NY, USA. Contact e-mail: evansm1@mskcc.org*

The small molecule receptor tyrosine kinase inhibitor cabozantinib (XL184) has shown antitumor activity in many cancer models. As it principally targets MET and VEGFR2, two receptor tyrosine kinases that contribute to skeletal metastases development, several clinical trials have been initiated for cancers like castration resistant prostate cancer (CRPC) that commonly metastasize to the bone (as well as those simply harboring elevated MET and/or VEGFR2 expression). Phase I/II trials in patients with CRPC have reported that cabozantinib treatment inhibits serum markers of osteoblast or osteoclast activity with pain palliation, and solid tumor regressions. In addition to these encouraging findings, one striking result has been the complete or partial resolution of patient bone scans, an effect not even observed among androgen deprivation therapies known to confer survival benefit (e.g. enzalutamide, abiraterone acetate). Since the radionuclides (18F-NaF, 99mTc-MDP) used for clinical bone scans target bone repair mechanisms rather than tumor-intrinsic biology, we hypothesized that cabozantinib may inhibit bone remodeling independent of an authentic tumor response. Consistent with this hypothesis, serial 18F-NaF PET scans showed a reduction in radiotracer uptake post therapy in non-tumor bearing mice at a site of active bone repair (a surgically induced fracture in the tibia). To further understand the mechanistic basis of this effect, an independent cohort of mice was treated with crizotinib, a potent and selective MET inhibitor that harbors minimal potency for VEGFR2. No significant reduction in 18F-NaF accumulation at the site of the fracture was observed post therapy (compared to vehicle control), strongly suggesting that inhibition of VEGFR2 in host tissues is (at least in part) responsible for the dramatic bone scan resolution by cabozantinib. Further studies with comparatively more selective VEGFR2 inhibitors (axitinib, sunitinib) are underway to support this conclusion. In summary, these results implicate a VEGFR2-driven mechanism in host tissues to account for the dramatic bone scan resolutions observed in clinical trials, and promote the immediate use of VEGFR-directed therapies to suppress bone pain and improve quality of life for patients with CRPC (and other malignancies that propagate well in the bone microenvironment).

Disclosure of author financial interest or relationships:
M.J. Evans, None; **D. Ulmert**, None; **M. Doran**, None; **C.L. Sawyers**, Aragon, Consultant; Aragon, Stockholder; Novartis Board of Directors, Other financial or material support .

Presentation Number **P 315**
Poster Session 3
September 20, 2013 / 15:15-15:15 / Room: Exhibit Hall B

18F-fluorobenzylcystine - a novel radiotracer for monitoring apoptosis

Aileen Hoehne, *Robert E. Reeves, Judith Weber, Gayatri Gowrishankar, Ramasamy Paulmurugan, Sanjiv S. Gambhir, Stanford University, Stanford, CA, USA. Contact e-mail: ahoehne@stanford.edu*

Objectives: Molecular imaging of apoptosis allows early assessment of anti-cancer treatment as this key biological response is preceding tumor mass reduction. Induction of apoptosis is often associated with an oxidative stress response. N-(4-[18F]fluorobenzoyl)cystine ([18F]FBC), a potential substrate of the cystine-glutamate exchanger (xCT) which is known to be up-regulated under oxidative stress conditions, could serve as a novel apoptosis imaging agent. Methods: Radiosynthesis of [18F]FBC was achieved by coupling [18F]SFB with commercially available L-cystine di-tert-butyl ester hydrochloride followed by de-protection. EL4 and Jurkat cells were treated with etoposide and staurosporine, respectively, to induce late or early apoptosis. Cell uptake of [18F]FBC in treated and non-treated cells and mixtures thereof was investigated. Apoptotic level was measured by a reference Caspase-Glo assay. In blocking studies, known xCT substrates and inhibitors were added together with [18F]FBC to cells. The distribution of [18F]FBC (60-120 µCi) in EL4 tumor-bearing Balb/C mice (n = 8) 24 h after i.p. administration of etoposide and cyclophosphamide (67/100 mg/kg) or without treatment was assessed via PET/CT and gamma counting of excised organs. In vitro and ex vivo radiotracer stability was examined by HPLC analysis of mouse plasma and urine. Results: Radiochemical yields of [18F]FBC of 6.1±3.5% from [18F]SFB (n = 10, decay-corrected to end of synthesis of [18F]SFB) were achieved. The radiochemical purity was >90%. [18F]FBC uptake was 2.4-5.6-fold higher in EL4 und Jurkat cells induced for apoptosis compared to non-treated cells (p = 0.001-0.025). A strong correlation between uptake of [18F]FBC and apoptotic level as measured by Caspase-Glo assay was found for all cell types (R2 = 0.88-1.0, Figure 1). Uptake of [18F]FBC in late apoptotic EL4 could be partially blocked by co-incubation with 0.5 mM L-cystine (57%) and 1.0 mM N-acetylcysteine (71%). Ex vivo biodistribution of [18F]FBC in mice at 60 min p.i. showed no significant variation in uptake in untreated (0.21±0.14 %ID/g, n = 3) and etoposide/cyclophosphamide-treated EL4 tumors (0.17±0.04 %ID/g, n = 3). As confirmed by PET/CT imaging, it is instead almost entirely excreted by the kidneys (112-142 %ID/g). This is not due to complete degradation of [18F]FBC, as 60 min p.i. 29% and 18% of intact radiotracer were still found in blood and urine, respectively. Conclusions: Although uptake of [18F]FBC correlates well with apoptotic level in culture, its potential as apoptosis imaging agent may be limited because minimal in vivo tumor uptake during apoptosis was observed, at least in the model used in this study. This could possibly be associated with poor entrapment of the probe in this tumor cell line.

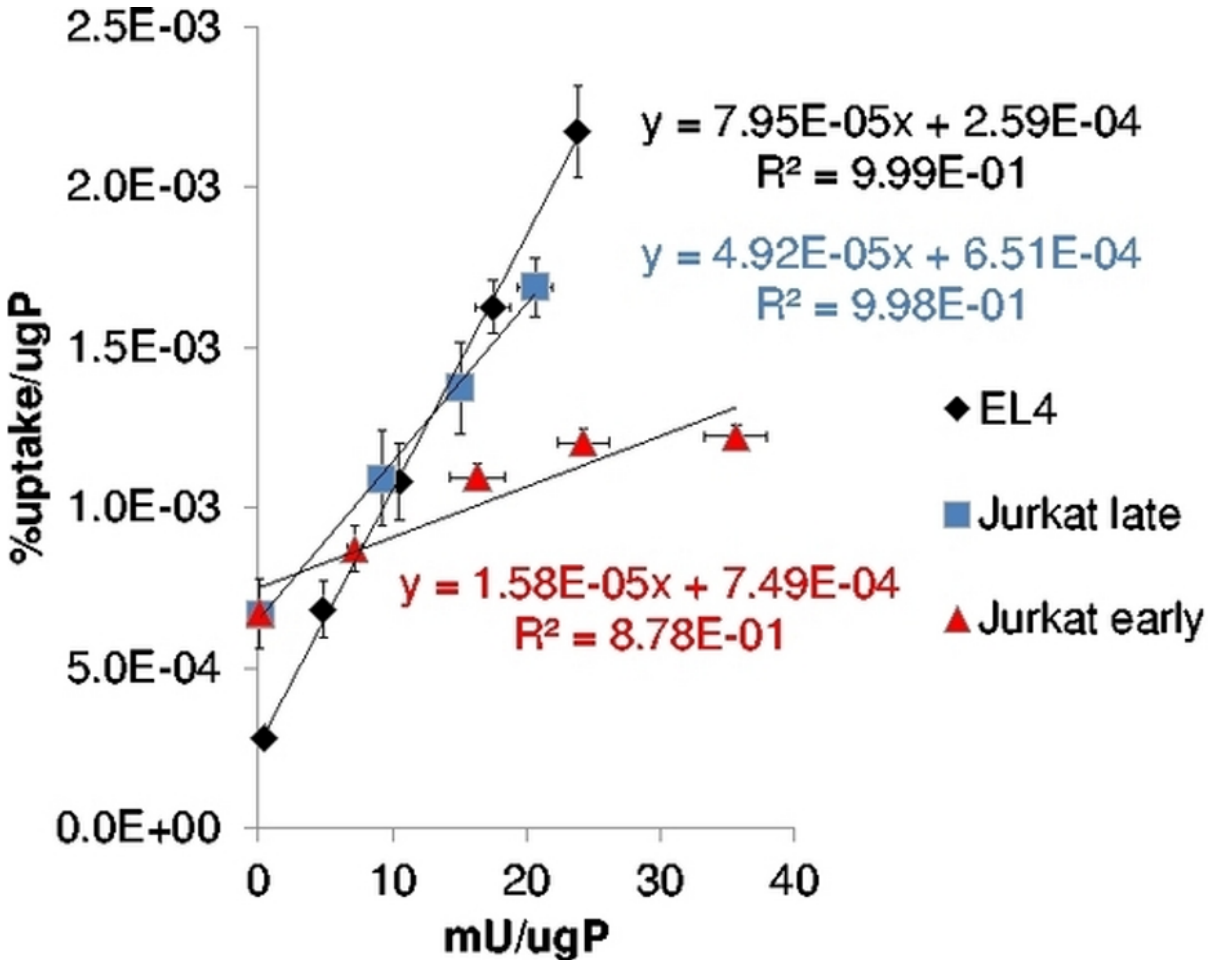

Figure 1: Cell uptake of N-(4-[18F]fluorobenzoyl)cystine after 60 min incubation correlates with increasing apoptotic levels as determined by Caspase-Glo assay.

Disclosure of author financial interest or relationships:

A. Hoehne, None; **R.E. Reeves**, None; **J. Weber**, None; **G. Gowrishankar**, None; **R. Paulmurugan**, None; **S.S. Gambhir**, Bracco Diagnostics, Consultant; Endra, Inc, Stockholder; Cellsight, Stockholder; Enlight, Inc., Stockholder; General Electric, Grant/research support; ImaginAb, Stockholder; MagArray, Inc., Stockholder; Sanofi-Aventis, US, Grant/research support; SiteOne Therapeutics, Stockholder; VisualSonics/Sonosite, Stockholder .

Presentation Number **P 316**
Poster Session 3
September 20, 2013 / 15:15-15:15 / Room: Exhibit Hall B

Optimizing the production, separation and radiochemistry of 90Nb for PET imaging

Jason P. Holland[1], *Ronald S. Moore*[1], *John A. Correia*[1], *David F. Lee*[1], *Matthew H. Stokely*[2], *Bruce Wieland*[2], *Ivan Greguric*[3], *Georges El Fakhri*[1], *Neil Vasdev*[1], [1]*Radiology, Massachusetts General Hospital - Harvard Medical School, Boston, MA, USA;* [2]*Bruce Technologies Inc, Chapel Hill, NC, USA;* [3]*Life Sciences, Australian Nuclear Science and Technology Organisation, Kirrawee, NSW, Australia. Contact e-mail: holland.jason@mgh.harvard.edu*

Niobium-90 (t1/2 = 14.6 h; I(beta+) = 51.2%; E(beta+,mean) = 0.66 MeV; E(beat+,max) =1.50 MeV) is a promising radionuclide for positron emission tomography (PET). To date, limitations in the separation chemistry have impeded attempts at exploring the radiochemistry and imaging potential of 90Nb. In addressing the problems of isolating 90Nb in a chemical form suitable for radiolabeling, we developed a simple, efficient, one-column method for separating niobium radionuclides from bulk Zr, as well as other chemical and radiochemical impurities. Niobium-90 was produced on a 16.5 MeV GE PETtrace cyclotron using a custom solid-metal target by the natZr(p,n)90Nb transmutation reaction on natural Zr foils (0.15 mm; 800 mg; 90Zr abundance = 51.45%) (1, 2). The target was dissolved in concentrated aqueous HF and purified in <45 min by using only commercially available AG-1X8 or IC-OH strong anion exchange chromatography. Radionuclidic impurities including 89Zr, 87mY and 87Y were effectively removed by washing with HF and the separation was monitored by gamma-spectroscopy. Niobium-90 was efficiently eluted (~90% total activity recovered) from the anion exchange column with citric acid (1.0 M; pH 5 - 7) giving high activity concentrations with >70% of the radioactivity isolated in <1.0 mL. Overall, improved methods for accessing 90Nb are likely to advance scientific exploration of the chemistry and biological properties of this radionuclide in PET radiotracer studies. At present, we are exploring the radiochemistry and imaging properties of 90Nb using EDTA, DTPA and DFO conjugated albumin, transferrin, antibodies and peptides in vitro and in vivo.

Disclosure of author financial interest or relationships:
J.P. Holland, None; **R.S. Moore**, None; **J.A. Correia**, None; **D.F. Lee**, None; **M.H. Stokely**, None; **B. Wieland**, Bruce Technologies Inc, Stockholder; **I. Greguric**, None; **G. El Fakhri**, None; **N. Vasdev**, None.

Presentation Number **P 317**
Poster Session 3
September 20, 2013 / 15:15-15:15 / Room: Exhibit Hall B

[18F]FMZ Neuroimaging of GABA/Benzodiazepine Receptor in Chronic MK-801 Rat Schizophrenia Model

Yuan-Ruei Huang, *Kai-Hung Cheng, Wan-I Kuo, Chieh Huang, Kang-Wei Chang, Institute of Nuclear Energy Research, Longtan Township, Taiwan. Contact e-mail: yuanruei@iner.gov.tw*

Objectives GABA is a major transmitter providing an inhibitory influence on glutamatergic principal neurons in the central nervous system. Previous immunohistochemistry studies showed the alterations of GABAergic interneurons within hippocampus and prefrontal cortex in MK-801 rat schizophrenia model. We've developed a radiosynthesis procedure for [18F] FMZ, a GABA/BZR receptor radiotracer, and established neuroimaging platforms including the nanoPET/CT imaging and ex vivo autoradiography. Aim of present study is applied the [18F]FMZ neuroimaging platform to evaluate the alteration of GABA/BZR receptor in chronic MK-801-induced rat schizophrenia model. Method(s) [18F]FMZ was autosynthesized from the precursor Nitromazenil in DMF at high temperature, and we purified the crude product by reversed-phase preparative high-performance liquid chromatography. Rats received repeated injection of MK-801 (dissolved in saline, i.p., 0.3mg/kg per day) or saline for 4 weeks. After drug treatment procedure, positive and negative symptoms of schizophrenia were assessed by open field and social interaction. We obtained [18F]FMZ neuroimages from ex vivo autoradiography and nanoPET/CT and evaluated the changes of specific binding ratio. Result(s) Radiochemical purity of [18F]FMZ was >95% determined by radio-TLC. Chronic MK-801 treatment for 4 weeks caused significantly increased local motor activity and induced an inhibition of social interaction. GABA A receptor alpha 1 subunit detection by immunohistochemistry showed the immunoactivity decreased in hippocampus after MK-801 chronic administration. [18F]FMZ nanoPET/CT neuroimaging and ex vivo autoradiography were performed on prefrontal cortex, hippocampus and midbrain. The imaging results showed statistically significant decreases in specific binding ratio (SBR) in these brain regions between saline and MK-801 group. Conclusion We establish a rat schizophrenia model by chronic MK-801 administration for 4weeks. In [18F]FMZ ex vivo autoradiography and nanoPET/CT imaging, the decrease of GABA A receptor subunits expression level might cause the lower specific binding ratio in these brain regions. Overall, the results showed [18F]FMZ from our procedure was available for tracing the GABA/BZR receptor, which could also be applied to the evaluation of MK-801-induced pathophysiology change and the effects of antipsychotics in the future.

[18F]FMZ Neuroimaging of GABA/Benzodiazepine Receptor in Chronic MK-801 Rat Schizophrenia Model

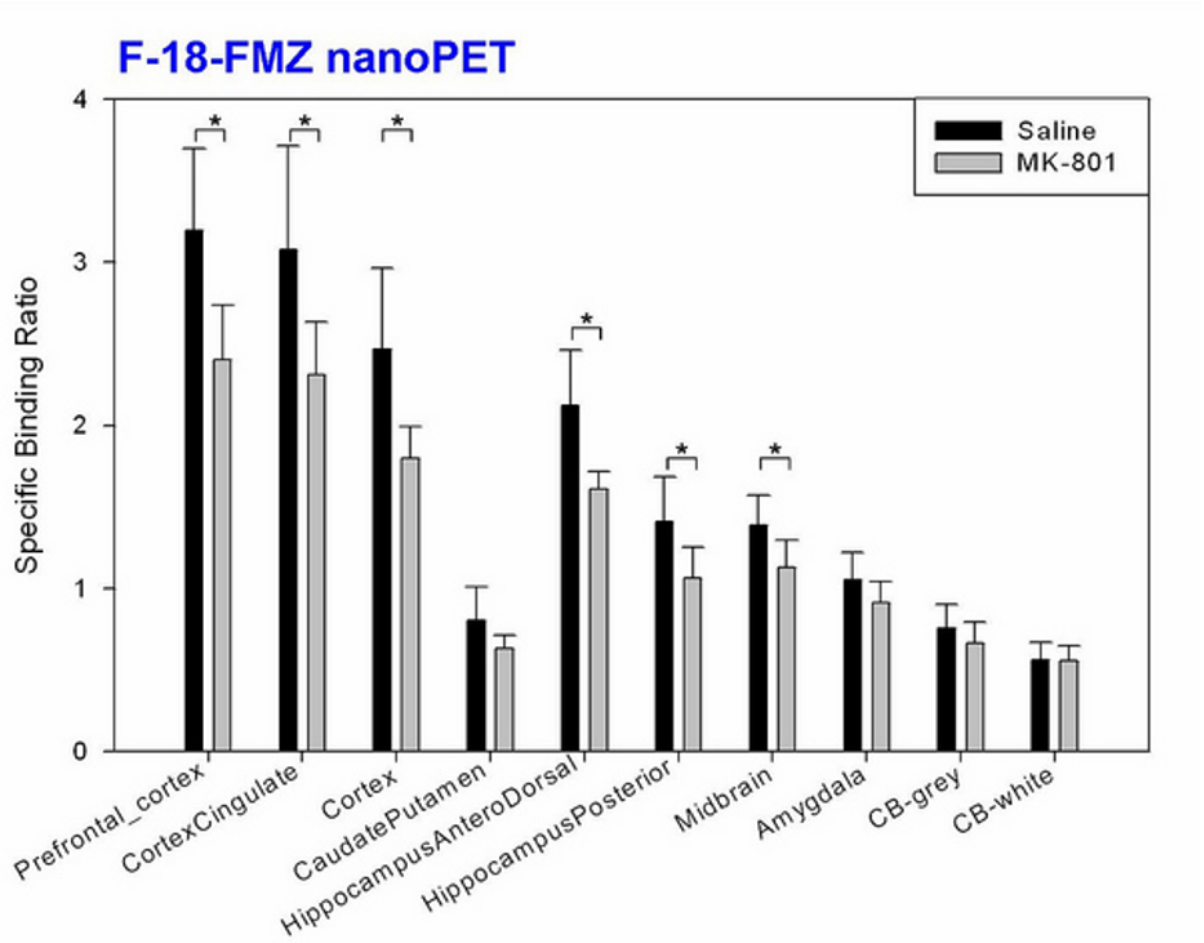

Disclosure of author financial interest or relationships:
Y. Huang, None; **K. Cheng**, None; **W. Kuo**, None; **C. Huang**, None; **K. Chang**, None.

Presentation Number **P 318**
Poster Session 3
September 20, 2013 / 15:15-15:15 / Room: Exhibit Hall B

PET imaging using a fibronectin extra domain B specific aptide as a cancer targeting agent

Sol-Ah Jang[1,2], *Myung Geun Song*[1,2], *Hyewon Youn*[1,3], *Yun-Sang Lee*[1,4], *Jae Min Jeong*[1,4], *Dong Soo Lee*[1,5], *June-Key Chung*[1,2], *Hyungjun Kim*[6], *Sunghyun Kim*[6], *Sangyong Jon*[6], *Keon Wook Kang*[1,3], [1]*Department of Nuclear medicine, Seoul National University College of Medicine, Seoul, Republic of Korea;* [2]*Laboratory of Molecular Imaging and Therapy of Cancer Research Institute, Seoul National University College of Medicine, Seoul, Republic of Korea;* [3]*Cancer Imaging Center, Seoul National University Cancer Hospital, Seoul, Republic of Korea;* [4]*Institute of Radiation Medicine, Medical Research Center, Seoul, Republic of Korea;* [5]*Department of Molecular Medicine and Biopharmaceutical Science, WCU Graduate School of Convergence Science and Technology, Seoul National University, Seoul, Republic of Korea;* [6]*Department of Biological Sciences, Korea Advanced Institute of Science and Technology (KAIST), Daejeon, Republic of Korea. Contact e-mail: sol8485@hanmail.net*

Objective: Fibronectin Extra Domain B (EDB), an alternatively spliced segment of fibronectin, is highly expressed in malignant tumors during angiogenesis and has been reported a promising cancer biomarker. To develop a new imaging probe for targeting EDB expressing tumor, we designed 18F labeled aptide (18F-aptide), protein-scaffold-based affinity molecules and oligo DNA or RNA-based aptamers and evaluated the EDB targeting possibility of 18F-aptide by PET imaging. Methods: Real time PCR and western blot analysis were performed to measure the expression of the EDB in EDB positive LLC cancer cell line and EDB negative B16F1 cancer cell line. Aptide specific fluorescence was observed in B16F1 or LLC cells using confocal microscopy and live cell imaging system. Aptide was labeled using N-succinimidyl 4-[18F] fluorobenzoate ([18F]SFB) and it was purified with Sep-Pak method. Cellular uptake of 18F-aptide was measured in B16F1 and LLC cells. 18F-Aptide was intravenously injected to BALB/c nude xenograft models and their signals were visualized in vivo by PET imaging. Results: Using confocal microscopy and live cell imaging system, aptide specific fluorescent intensity in EDB positive LLC cells was higher compared with that in EDB negative B16F1 cells. Labeling efficiency of 18F-aptide was over 90%. In vitro uptake was higher in LLC cells than in B16F1 cells. In xenograft models, 18F-aptide specific targeting was observed in LLC tumor, but not in B16F1 tumor. Conclusion: 18F-aptide specifically visualized EDB-positive tumor in vivo. Thus, it could be used as an effective imaging agent for targeting EDB positive cancers.

Disclosure of author financial interest or relationships:
S. Jang, None; **M. Song**, None; **H. Youn**, None; **Y. Lee**, None; **J. Jeong**, None; **D. Lee**, None; **J. Chung**, None; **H. Kim**, None; **S. Kim**, None; **S. Jon**, None; **K. Kang**, None.

Presentation Number **P 319**
Poster Session 3
September 20, 2013 / 15:15-15:15 / Room: Exhibit Hall B

Preparation of Lactobionic Acid Conjugated Gold Nanoparticle for Hepatocyte Imaging

Eun-Mi Kim, *Tai Kyoung Lee, Su-Jin Cheong, Hwan-Seok Jeong, Hyosook Hwang, Phil-Sun Oh, Kyung Sook Na, Young-Seop Lo, Jeong Il Kwon, Yeon-Hee Han, Seok Tae Lim, Myung-Hee Sohn, Hwan-Jeong Jeong, Chang Ju Na, Se Hun Choi, Jeong-Hoon Kim, Chonbuk National University Medical School and Hospital, Jeonju, Republic of Korea. Contact e-mail: eunmi4172@hanmail.net*

Objectives : Asialoglycoprotein receptors that specifically exist on the mammalian polygonal cell surface, situated on the liver hepatocyte membrane. ASGP-R recognizes galactose or N-acetylgalactosamine residues of desialylated glycoproteins. It is well known that degree of hepatic uptake of galactose conjugated compounds correlates well with hepatic function. Gold nanoparticles are particularly interesting for cancer diagnosis and therapy. In this study, we investigate the possibility of liver-targeted nuclear imaging with 99mTc-AuNPs bound to ASGP-R. Methods : Briefly, tiopronin (TP)-protected AuNPs were synthesized by dissolving TP and HAuCl4 into a MeOH/acetic acid solution (6:1). Sodium borohydride was added and vigorously stirred for 1 hr. The solvent was removed under vacuum, and the pH was lowered to HCl until 1. Ethylenediamine (ED) was introduced to TP terminal of AuNPs by EDC/NHS reaction. Cellobiose was coated on the AuNPs by NaBH3CN. For galactose ligand, lactobionic acid (LA) was conjugated lastly to AuNPs. After each step, the product purification was carried by dialysis. TEM, 1H-NMR, Zeta Potential, DLS, UV-vis and FT-IR was checked. The final product was labeled with Tc-99m and i.v. injected into the mice and identified in vivo distribution, respectively. Results : TP-protected AuNPs, ED-TP-AuNPs, Cellobiose-ED-TP-AuNPs and LA-cellobiose-ED-TP-AuNPs derivatives were well made and characterized. After injection, Tc-99m labeled LA-cellobiose-ED-TP-AuNPs was mainly accumulated in the liver because of galactose ligands. For in vivo inhibition, free LA was co-injected with Tc-99m labeled LA-cellobiose-ED-TP-AuNPs. The liver accumulation was greatly reduced by time. Conclusion : Tc-99m labeled LA-cellobiose-ED-TP-AuNPs specifically localized to the liver hepatocytes.

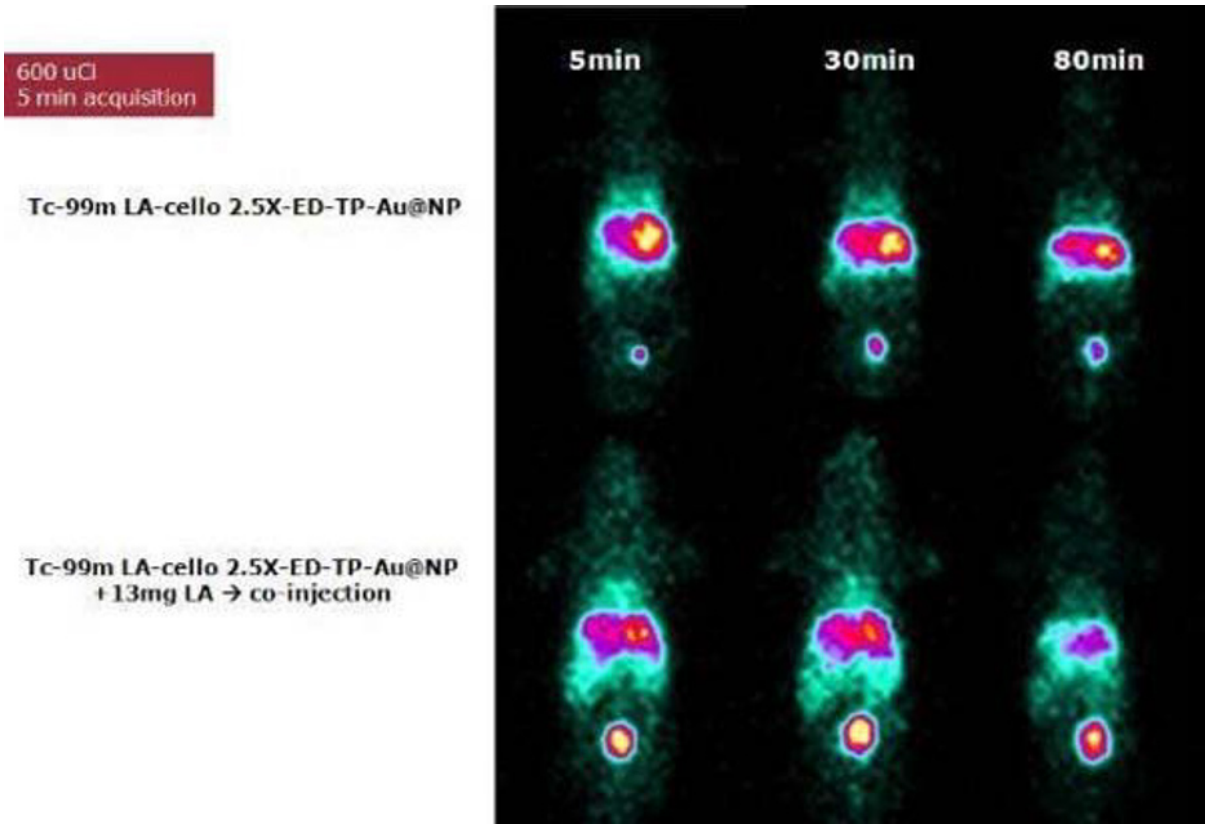

Disclosure of author financial interest or relationships:
E. Kim, None; **T. Lee**, None; **S. Cheong**, None; **H. Jeong**, None; **H. Hwang**, None; **P. Oh**, None; **K. Na**, None; **Y. Lo**, None; **J. Kwon**, None; **Y. Han**, None; **S. Lim**, None; **M. Sohn**, None; **H. Jeong**, None; **C. Na**, None; **S. Choi**, None; **J. Kim**, None.

Presentation Number **P 320**
Poster Session 3
September 20, 2013 / 15:15-15:15 / Room: Exhibit Hall B

PET imaging of bacterial infection in mouse lung using 18F-Al-DPA

Junling Li[1], *Huaiyu Zheng*[1], *Ramy A. Fodah*[1], *Brian D. Gray*[2], *Koon Y. Pak*[2], *Jonathan M. Warawa*[1], *Chin K. Ng*[1], [1]*Univerisity of Louisville, Louisville, KY, USA;* [2]*Molecular Targeting Technologies, Inc, West Chester, PA, USA. Contact e-mail: junling.li@louisville.edu*

Introduction: Several fluorescent Zn-dipicolylamine (DPA) analogues, which have been validated for targeting apoptosis in mouse models with subcutaneous bacterial infections in the thigh, can be explored as potential diagnostic imaging agents. Thus our objective was to evaluate the characteristics of DPA labeled with F-18 using the 18F-Al method by investigating its in vivo pharmacokinetics in normal mice and then performing PET imaging of the tracer in a mouse model with bacterial infection in the lung. Methods: N,N'-2,2'-(7-(4-isothiocyanatobenzyl)-1,4,7-triazonane-1,4-diyl) diacetic acid (NODA)-DPA was labeled with 18F-Al (18F-Al-DPA) and then purified with HPLC. 150-200 μCi of 18F-Al-DPA was injected intravenously into each mouse via tail vein. For normal mice, dynamic PET imaging was performed on the microPET-R4 scanner for 1 h immediately post injection and then the animals were sacrificed immediately after each scan. Tissues and organs of interest were removed and weighed. The radioactivity was measured in an automated gamma well-counter and % injected dose per gram (% ID/g) was subsequently calculated for each tissue and organ. For the C57 female mice infected with 10^5 Klebsiella pneumoniae transfected with luciferase, bioluminescence optical imaging was used to monitor the disease progression in the lung. Then dynamic PET imaging was performed for 2 h on days 2 and 3 after initial infection. Results: The radiolabeling yields for 18F-Al-DPA were between 40 and 50% (n=5) and the radiochemical purity was > 95%. For normal mice, the clearance shown by dynamic PET imaging was 50% for lung, liver and kidney and >75% for the heart within 1 h post injection. For the intestine, the clearance was 50% within the first 30 min and then reached a plateau. The biodistribution data showed that the majority of the radioactivity (% ID/g) was localized in the intestine (45%), followed by liver (10%), kidney (6%), pancreas (4%) and lung (2%) with a lung-to-muscle ratio of 2. For the infected mouse on day 2, the pharmacokinetics was similar to that of normal mice but the uptake in the lung was significantly higher than that of the normal lung (T/NT=5 vs. 2). On day 3, the ratio of lung to muscle remained at 5 but the uptake in both sides of the lungs could be more clearly visualized, especially for the right lungs. Conclusion: Our preliminary data showed that 18F-Al-DPA should be developed as an imaging agent for the diagnosis of bacterial lung infections which are considered an emerging health priority.

Disclosure of author financial interest or relationships:
J. Li, None; **H. Zheng**, None; **R.A. Fodah**, None; **B.D. Gray**, Molecular Targeting Technologies, Inc, Employment; **K.Y. Pak**, Molecular Targeting Technologies, Inc., Stockholder; Molecular Targeting Technologies, Inc., Employment; **J.M. Warawa**, None; **C.K. Ng**, None.

Presentation Number **P 321**
Poster Session 3
September 20, 2013 / 15:15-15:15 / Room: Exhibit Hall B

A GMP compliant automatic synthesizer for Ga-68-DOTATATE labeling

Ming-Hsin Li, *Isotope Application, Institute of Nuclear Energy Research, Taoyuan, Taiwan. Contact e-mail: mhli@iner.gov.tw*

The advantages of this fabricated synthesizer module are illustrated as follows. Firstly, the whole processes are operated in a closed system with a liquid nitrogen trapper used to condense the release gases of leaked radioactive material and organic solvent that can reduce the environmental radiation. Secondly, the assembly of the module is made as small as possible. Thirdly, this module is functioned with a fully automated control for synthesis of making Ga-68-DOTATATE. The process time is about 50mins. The products obtained with purity of greater than 95% is sufficient to meet the requirements of the specifications for Ga-68-DOTATATE PET in nuclear medicine applications. Other than the previous statements, the software designed can be used to execute the process step by step precisely under the command to be called. During the process performance, the temperature, pressure and variation of radiation dose can be monitored and recorded simultaneously to reflect the reaction situation at that time and compliant with the regulation of GMP.

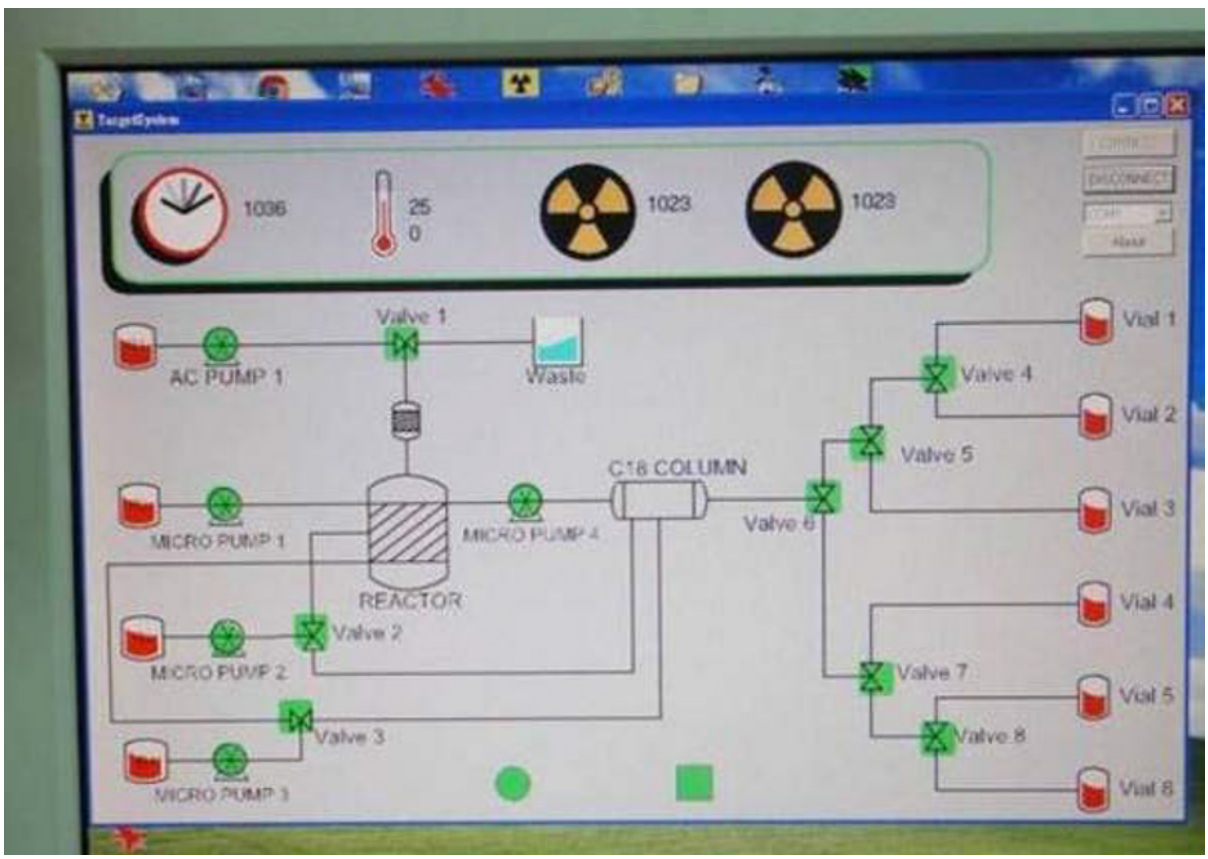

Disclosure of author financial interest or relationships:
M. Li, None.

Presentation Number **P 322**
Poster Session 3
September 20, 2013 / 15:15-15:15 / Room: Exhibit Hall B

Influence of different administration routes on ^{18}F-FBPA biodistribution

Severin Mairinger[1,2], *Thomas Wanek*[1], *Thomas Filip*[1], *Michael Sauberer*[1], *Johann Stanek*[1], *Oliver Langer*[1,3], *Claudia Kuntner*[1], [1]*Health & Environment Department, AIT Austrian Institute of Technology, Seibersdorf, Austria;* [2]*Department of Medicinal Chemistry, University of Vienna, Vienna, Austria;* [3]*Department of Clinical Pharmacology, Medical University of Vienna, Vienna, Austria. Contact e-mail: severin.mairinger.fl@ait.ac.at*

Boron neutron capture therapy is an experimental radiation therapy, where ^{10}B containing molecules are used, which should enrich in tumor tissue. 4-boronophenylalanine (BPA), an amino acid analogue, is one of the most commonly used boron carriers for treatment. In order to non-invasively measure the tissue distribution and pharmacokinetics of BPA we used a radiofluorinated analogue, 4-borono-2-[^{18}F]fluorophenylalanine ([^{18}F]FBPA). We evaluated the influence of different administration routes on whole body distribution and metabolism of [^{18}F]FBPA in mice. **METHODS** [^{18}F]FBPA was synthesized by electrophilic substitution in a modified GE Tracerlab FX synthesis module. Groups of female BALB/c mice (n=4 per group) underwent 2 hours of dynamic [^{18}F]FBPA PET scans under isoflurane anesthesia. In the first two groups the influence of fasting (6 hours) before iv bolus injection of [^{18}F]FBPA into the tail vein was investigated. In the third group [^{18}F]FBPA was continuously infused over the whole 2-hours of PET scanning. In the fourth group [^{18}F]FBPA was administered intraperitoneally. Uptake of [^{18}F]FBPA in different organs was expressed as standardized uptake value (SUV) at 120 min after radiotracer injection. Metabolism in plasma was assessed at 5, 10, 30, 60 and 120 min after iv radiotracer injection by radio-HPLC. **RESULTS** [^{18}F]FBPA was obtained in a radiochemical yield (decay-corrected) of 10% in a total synthesis time of 70 min. Radiochemical purity was >98% and specific activity at end of synthesis was 250-340 MBq/µmol. Fasting significantly increased [^{18}F]FBPA uptake in the gastrointestinal tract and spleen whereas only small changes were observed in brain, liver, pancreas, lung, muscle and heart. In the gallbladder, a 2-fold lower uptake was found following fasting. Intraperitoneal administration lead to a significantly higher uptake in pancreas, kidneys and liver as compared with iv administration. Continuous infusion led to lower uptake in stomach, gallbladder and heart but to higher uptake in pancreas and spleen. No radiolabelled metabolites of [^{18}F]FBPA could be detected in plasma over the time course of the PET experiments. **CONCLUSION** Fasting state and administration route have an effect on [^{18}F]FBPA biodistribution. As the variability of uptake data was lower in the iv bolus fasted group, all future experiments in tumor bearing animals will be performed using this protocol.

Disclosure of author financial interest or relationships:
S. Mairinger, None; **T. Wanek**, None; **T. Filip**, None; **M. Sauberer**, None; **J. Stanek**, None; **O. Langer**, None; **C. Kuntner**, None.

Presentation Number **P 323**
Poster Session 3
September 20, 2013 / 15:15-15:15 / Room: Exhibit Hall B

PET/MR Imaging of Atherosclerotic Plaque Using Dual Modality Superparamagnetic Iron Oxide Nanoparticles

Nazanin Masoodzadehgan[1], *Wonewoo Seo*[2], *Gang Bao*[1], [1]*BME, Georgia Institute of Technology, Atlanta, GA, USA;* [2]*Radiology, Emory University, Atlanta, GA, USA. Contact e-mail: nmasood@gatech.edu*

Introduction Atherosclerotic heart disease is a leading cause of death in the United States. Expression of VCAM1, which is involved in leukocyte recruitment, plays a critical role in the earliest stages of atherogenesis. Detection of VCAM-1 requires high sensitivity targeting. Nanoparticles provide a platform for targeting the markers of atherosclerosis. PET imaging is the most sensitive human molecular imaging modality for plaque detection, since it can produce whole body images for functional and molecular information. Therefore, emphasis in our in vivo imaging studies will be placed on developing nanoparticle-based contrast agents for PET imaging. In this work, we investigated the potential of the radiolabeled, targeted super paramagnetic iron oxide nanoparticles (SPIOs) in imaging atherosclerotic plaque in vivo using PET/CT. Methods To allow for PET imaging and biodistribution, SPIOs were radiolabeled using 64Cu. The particles were analyzed using radio-FPLC and radio TLC to estimate the (RCP) radio chemical purity (the percentage of the activity bound to the nano particles). The pharmacokinetics and biodistribution of 64Cu-mSPIO were evaluated in vivo. To improve the serum stability of the particles this design was modified and a chelator DOTA was conjugated instead of DTPA. Results SPIOs and DOTA-SPIOs were characterized using dynamic light scattering (DLS) and were found to have diameters of 33 and 40nm respectively. The RCP of the 64Cu-SPIOs was found to be more than 99% pure. 64Cu-SPIOs were stable in mouse serum up to 3 hr (>99%). To increase the blood circulation halflife SPIOs were covalently linked to DOTA-NHS and then labeled with 64Cu. Biodistribution studies were performed in BALB/C mice. The effect of SPIO nanoparticle size on the circulation half-life were also investigated and found that larger particles 15nm had a longer circulatin half-life compared to the 6nm SPIOs. microPET images were obtained in a carotid ligation mouse model to investigate the imaging potential of DOTA-SPIOs. Conclusions Biodistribution and in vivo PET/CT imaging studies of the probes showed a circulation half-life of 38 min for the 15nm SPIOs and 25 min for 6.8nm SPIOs, and moderate liver uptake, making them an attractive contrast agent for plaque imaging studies. Rapid elimination of contrast agents is clinically generally preferred as diagnosis can then be performed immediately after administration. This will allow for diagnostic interventions to be repeated more often and more rapidly.

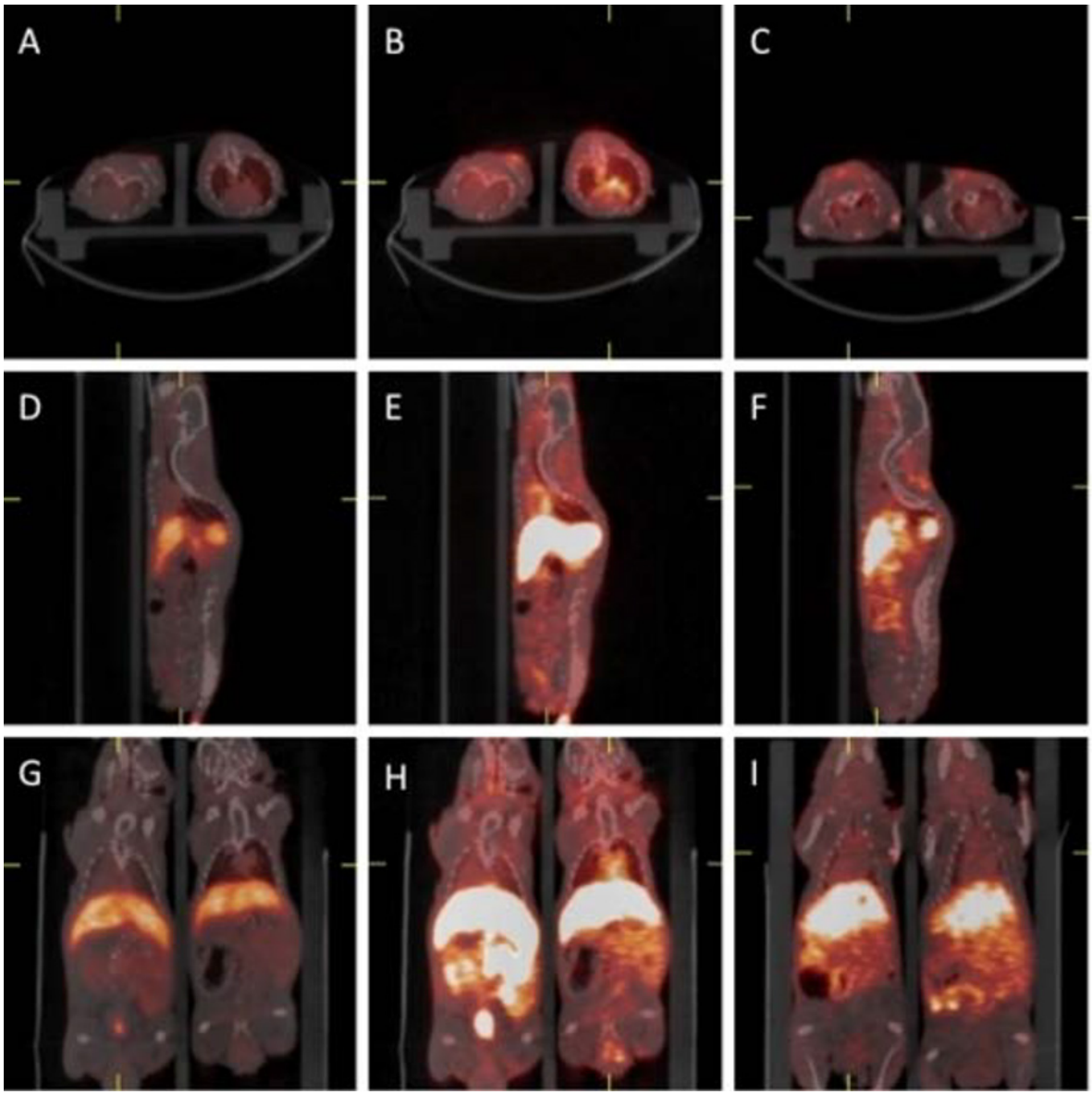

Disclosure of author financial interest or relationships:
N. Masoodzadehgan, None; **W. Seo**, None; **G. Bao**, None.

Presentation Number **P 324**
Poster Session 3
September 20, 2013 / 15:15-15:15 / Room: Exhibit Hall B

Development of atherosclerosis imaging probe for SPECT -- Effect of PEGylation of liposomes on macrophage uptake

Mikako Ogawa, *Ryuji Utino, Ayumi Kawai, Yuka Hamaya, Yasuhiro Magata, Medical Photonic Research Center, Hamamatsu University School of Medicine, Hamamatsu, Japan. Contact e-mail: mogawa@hama-med.ac.jp*

Background: We previously reported an atherosclerosis imaging probe, ^{111}In-labeled liposome. The liposome was modified with phosphatidylserine (PS), since macrophages recognize PS to phagocytize apoptotic cells in the plaque. PS modification was successful and we could visualize atherosclerotic plaques by SPECT. However, the too quick blood clearance seemed to have reduced PS-liposome accumulation to the plaque. Therefore, in this study, we PEGylated the liposome to retard the blood clearance. **Methods:** PS liposomes were prepared by lipid-film hydration method. The liposomes, sizes in 100 or 200 nm, were PEGylated with PEG2000 or PEG5000 in 1 or 5% w/w, and radiolabeled by ^{111}In. For in vitro uptake study, the liposomes were incubated with mouse peritoneum macrophages. The in vivo biodistribution studies were done in ddY mice. En face autoradiograms were obtained with ApoE-/- mice 2hr after the liposome injection. **Results:** The in vitro uptake levels to macrophages were decreased by PEGylation. 5% PEG5000 decreased the uptake to half of non-PEGylated one, but 1% PEG2000 affected less than 5%. In vivo results showed slower blood clearance in PEGylated liposomes (12 %dose/g for 5%PEG5000, 2.0 %dose/g for 1%PEG2000, and 1.0 %dose/g for non-PEGylated liposome at 60min after the injection). PS modification improved target-to-nontarget ratios, and 5%PEG2000 added 200 nm liposome showed the highest uptake to the region. **Discussion:** PEGlylation decreased macrophage uptake and blood clearance. However, we found that the effect was larger for blood clearance and decrease in macrophage uptake should be acceptable for in vivo imaging.

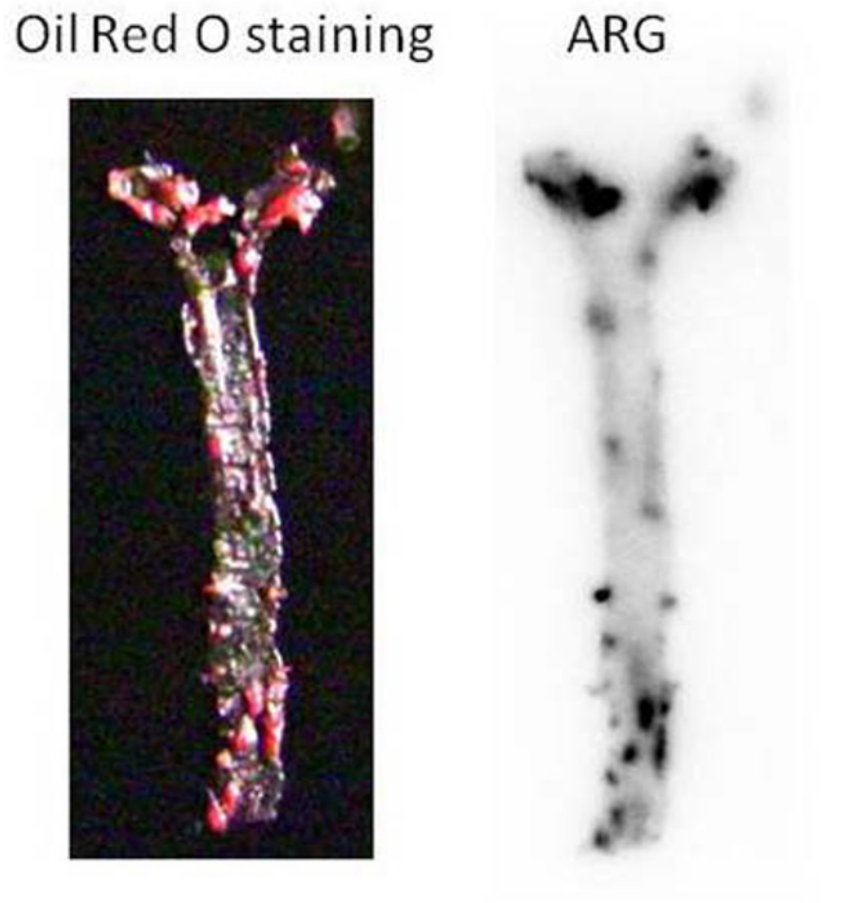

Disclosure of author financial interest or relationships:
M. Ogawa, None; **R. Utino**, None; **A. Kawai**, None; **Y. Hamaya**, None; **Y. Magata**, None.

Presentation Number **P 325**
Poster Session 3
September 20, 2013 / 15:15-15:15 / Room: Exhibit Hall B

Preparation of a 68Ga/177Lu-labeled bombesin peptide analog derived from the bombesin universal sequence for imaging and therapy of bombesin receptor-expressing tumors

Subhani M. Okarvi, *King Faisal specialist Hospital, Riyadh, Saudi Arabia. Contact e-mail: sokarvi@kfshrc.edu.sa*

Objectives: Small peptide based molecular imaging probes that target peptide receptors overexpressed on various cancer cells have attracted enormous attention for receptor-mediated tumor targeting. Among the most clinically-relevant peptide receptor systems, bombesin (BN) peptide receptors are of great clinical interest because of the overexpression of their receptors on various important human cancers including breast and prostate cancer. The high expression of receptors in cancer cells and low density in normal human tissues makes these receptors potential molecular targets with radiolabeled BN peptides. The aim of the study was to develop and evaluate a novel BN peptide analog based on the universal BN sequence (capable of targeting all four BN receptor subtypes), and radiolabeled it with both diagnostic (Ga-68) and therapeutic radionuclide (Lu-177), thus making this peptide useful for both diagnosis and therapy of BN receptor-expressing tumors. Methods: DOTA-Glu-Gln-Trp-Ala-Val-βAla-His-Phe-Nle-NH2 was prepared by solid-phase peptide synthesis following Fmoc/HBTU methodology. Radiolabeling with Ga-68 and Lu-177 was achieved in the presence of 2.5M NaOAc and 0.1M NH4OAc buffer solution, respectively. In vitro cell-binding study was conducted on BN receptor-positive T47-D breast cancer cell line. In vivo biodistribution and clearance kinetics was performed on Balb/c mice. Results and discussion: The structure and purity of the DOTA-coupled BN peptide was confirmed by mass spectrometry and HPLC analysis. Radio-HPLC analysis revealed that the BN analog radiolabeled efficiently with both radionuclides with high labeling efficiency (~98%). The radiolabeled peptide showed high radiochemical stability in excess of DTPA and a high metabolic stability (~95%) when incubated with human plasma. In vitro cell-binding assay indicated the high affinity and specificity of the radiopeptide towards T47-D human breast cancer cells (Kd=5 nM) and also significant internalization (~20%) into the breast cancer cells. In mice, the 68Ga/177Lu-labeled BN peptide displayed a fast clearance from the blood and excretion predominantly by the renal route, with some elimination through the hepatobiliary pathway. The uptake in the major organs (i.e., lungs, stomach, liver, intestines kidneys, etc.) was low (<3% ID/g). Conclusions: This initial study towards the development of a potent BN-based peptide radiopharmaceutical suggest that the BN peptide under investigation possesses favorable characteristics that need to be further explored in order to determine the real potential of this peptide for targeting tumors expressing BN receptor types.

Disclosure of author financial interest or relationships:
S.M. Okarvi, None.

Presentation Number **P 326**
Poster Session 3
September 20, 2013 / 15:15-15:15 / Room: Exhibit Hall B

Development of angiogenesis imaging and therapeutic method targeting ATP synthase

Bok-Nam Park, *Joon-Kee Yoon, Nuclear Medicine & Molecular Imaging, Ajou University, Suwon, Republic of Korea. Contact e-mail: curies@hanmail.net*

Objectives: ATP synthase which has been known as an angiostatin receptor, anti-angiogenesis, presents on the extracellular surface of a variety of tumor cells, therefore, it could be a potent theragnostic imaging target for tumors. In this study, we synthesized radioiodine 125I-labeled ATP synthase monoclonal Ab (125I-ATP mAb), evaluated its in vitro cellular binding and in vivo distribution in normal mice and tumor bearing mice models. Methods: 125I-ATP mAb was prepared using Iodogen tube method. In vitro labeling efficiencies and retention rates were measured. Cellular uptake was tested in a variety of cancer cells at 0.5, 1, 2, 4 and 24 hr after adding 125I-ATP mAb. To study the biodistribution of the 125I-ATP mAb, tumor-bearing mice models and normal mice were injected intravenously with 9.25 MBq. Pin hole gamma camera images were acquired at 2, 24 and 48 hr after intravenously injection of 125I-ATP mAb into tumor bearing mice (n=3). And then, organs were removed and counted using a gamma counter for biodistribution. Results: Average labeling efficiency of 125I-ATP mAb was gradually increased by the increment of mAb dose; 47, 69, 74, 76 and 92% at 5, 10, 20, 40 and 80 μg Ab. Retention rates of 125I-ATP mAb in tumor cell (MKN-45) were 88, 85, 79, 71 and 64% at 5, 10, 20, 30 and 60 min, respectively. Among 7 cancer cells tested, MKN-45 (human gastric adenocarinoma) showed the highest cellular binding at 24 hr (2.0±0.0%). Gamma camera images demonstrated no significant thyroid uptake at 2 hr after injeciton, whereas thyroid uptake gradually increased at 24 and 48 hr postinjection. The radioactivity measured on a gamma couter revealed similar uptake (%ID/g) between normal mice and tumor bearing mice (Fig. 1). Conclusion: ATP synthase mAb was easily labeled to radioiodine with a sufficient labeling efficiency, and its binding ability was confirmed in cancer cells. Therefore, radioiodinated ATP synthase mAb could be valuable as a target for theragnostic angiogenesis imaging.

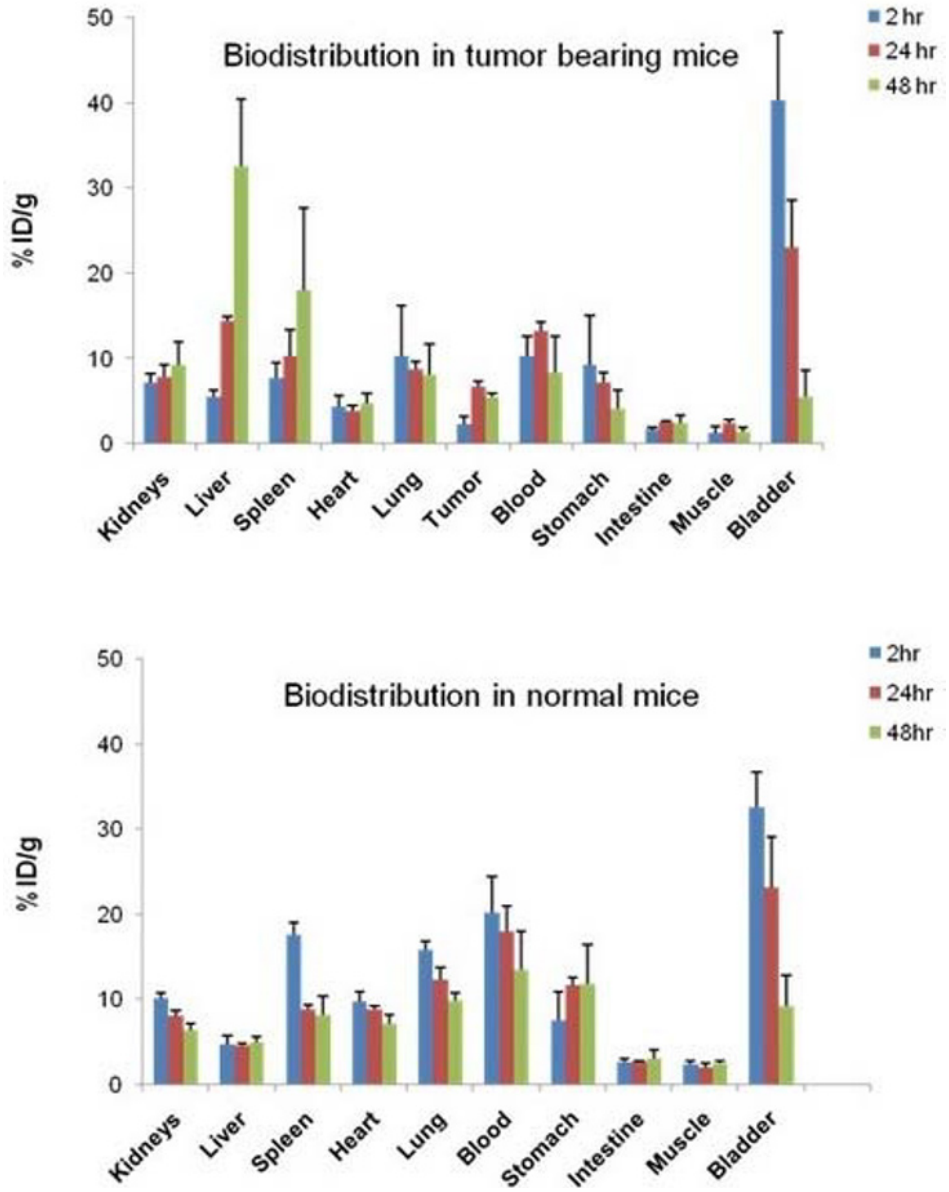

Disclosure of author financial interest or relationships:
B. Park, None; **J. Yoon**, None.

Presentation Number **P 327**
Poster Session 3
September 20, 2013 / 15:15-15:15 / Room: Exhibit Hall B

Radioiodination Via A Nickel-Mediated Halogen Exchange Reaction

Alastair Cant[1], Sue Champion[2], Rajiv Bhalla[3], **Sally Pimlott**[2]*, Andrew Sutherland[1], [1]WestChem, School of Chemistry, University of Glasgow, Glasgow, United Kingdom; [2]West of Scotland Radionuclide Dispensary, University of Glasgow, Glasgow, United Kingdom; [3]Medical Diagnostics, GE Healthcare, Amersham, United Kingdom. Contact e-mail: sally.pimlott@glasgow.ac.uk*

Labelling of small molecules for SPECT imaging with radioiodine is commonly achieved by electrophilic iodo-destannylation of aryls and alkenes. Although this produces radioiodinated compounds with excellent radiochemical purity and high specific activity, organotin compounds can be unstable resulting in unreliable radioiodination reactions. Here we report a novel nickel-mediated, single-step, halogen exchange reaction for the rapid and direct radioiodination of aryl and heteroaryl bromides. Radioiodination of 2-bromonaphthalene with [125I]-NaI was initially investigated using various sources of nickel for halogen exchange reactions; nickel(II) bromide, tri-n-butylphosphine mediated reduction of nickel(II) bromide to give a nickel(0) species and non-halogen containing sources of nickel(0) (Table 1). The highest yield for the radioiodination of 2-bromonaphthalene was obtained using bis(1,5-cyclooctadiene)nickel(0) (Ni(COD)2). The scope of this transformation was investigated for the preparation of a range of [125I]-labelled compounds. Electron-rich and electron-deficient o-, m- and p-substituted aryl compounds were all found to be compatible and converted into [125I]-labelled products in excellent incorporation yields (88-97%) using Ni(COD)2 mediated halogen exchange at 180oC. Finally we explored this new methodology for the synthesis and purification of 5-[123I]-A85380, a SPECT imaging agent for the α4β2 nicotinic acetylcholine receptor. 5-[123I]-A85380 was obtained with an end of synthesis yield of 46%, a radiochemical purity of >99% and with a specific activity of 1.0 Ci μmol-1. In summary, a novel and versatile single-step method for the incorporation of radioiodide into a various aryl compounds has been developed using a rapid nickel(0)-mediated halogen exchange reaction.

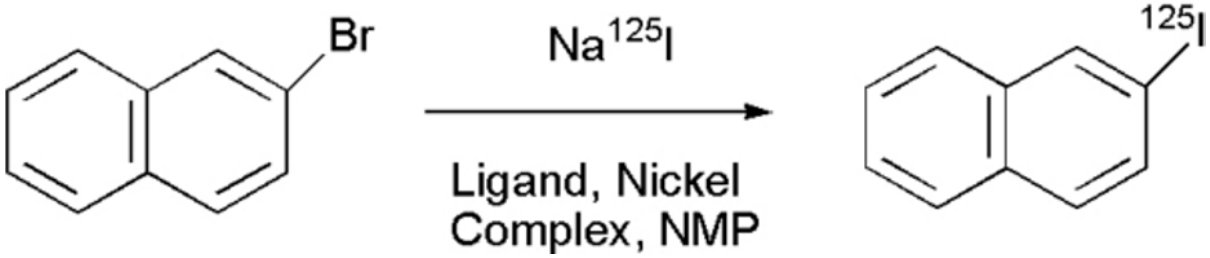

Table 1. Optimisation of the nickel(0)-mediated radioiodination of 2-bromonaphthalene

Entry	T [°C]	Nickel Complex/ Ligand	RCY (%)
1	160	NiBr2/nBu3P	7
2	160	NiBr2/dppb	19
3	160	NiBr2	19
4	130	NiBr2	29
5	130	Ni	26
6	130	Ni(COD)2	93

RYC = radiochemical yield, T = temperature

Disclosure of author financial interest or relationships:
A. Cant, None; **S. Champion**, None; **R. Bhalla**, None; **S. Pimlott**, GE Healthcare, Grant/research support; Bruker, Grant/research support; **A. Sutherland**, None.

Presentation Number **P 328**
Poster Session 3
September 20, 2013 / 15:15-15:15 / Room: Exhibit Hall B

Trapping of 2-[^{18}F]fluoroacetyl-CoA in the cell: a promising strategy for imaging enzymatic activity with positron emission tomography

Maral Pourghiasian, *Jinhe Pan, Joseph Lau, Gemma M. Dias, Navjit Hundal-Jabal, Zhibo Liu, Francois Benard, Kuo-Shyan Lin, Molecular Oncology, BC Cancer Agency, Vancouver, BC, Canada. Contact e-mail: mpourghi@bccrc.ca*

Introduction: 2-[^{18}F]fluoroethanol is known to enter cells and metabolizes into 2-[^{18}F]fluoroacetaldehyde. 2-[^{18}F]fluoroacetaldehyde is further metabolized to 2-[^{18}F]fluoroacetate, and finally to 2-[^{18}F]fluoroacetyl-CoA which is trapped inside cells. We hypothesized this trapping mechanism can be exploited for imaging enzymatic activity that leads to the formation of 2-[^{18}F]fluoroacetyl-CoA. To test this hypothesis, we synthesized 7-(2-[^{18}F]fluoroethoxy)coumarin (^{18}F-FEC, Fig. A) and 2-[^{18}F]fluoroethoxyresorufin (^{18}F-FER, Fig. B), and compared their biodistribution/imaging data in mice with known expression profiles of 7-ethoxycoumarin O-deethylase (ECOD) and ethoxyresorufin O-deethylase (EROD). Methods: FEC and the radiolabeling precursor 7-(2-tosyloxyethoxy)coumarin were prepared by coupling 7-hydroxycoumarin with 1-fluoro-2-tosyloxyethane and 1,2-bis(tosyloxy)ethane, respectively. FER and the radiolabeling precursor 2-tosyloxyethoxyresorufin were prepared similarly using resorufin. ^{18}F-FEC and ^{18}F-FER were prepared by aliphatic nucleophilic substitution reaction using their respective precursors and K^{18}F/K222. The stabilities of ^{18}F-FEC and ^{18}F-FER were determined in mouse plasma. PET imaging and biodistribution studies were performed in female Balb/C mice. Results: ^{18}F-FEC and ^{18}F-FER were obtained in 3-13 % non-decay corrected yields in 1.6 h with 1.7-5.7 Ci/μmole specific activity at EOS, and > 99% radiochemical purity. ^{18}F-FEC and ^{18}F-FER were stable in mouse plasma and remained > 93 % intact after 2 h incubation at 37 °C. Based on biodistribution and PET imaging studies, radioactivity of ^{18}F-FEC localized in the liver (45.9 ± 5.9 %ID/g, 1 h p.i.) and nasal mucosa (Fig. A). These tissues express high levels of CYP1A2, the major component of ECOD. Although ethoxyresorufin is structurally similar to ethoxycoumarin, it is deethylated mainly by CYP1A1 and CYP1B1, but not by CYP1A2. CYP1A1 and CYP1B1 are expressed in only low levels in extrahepatic tissues. This is evident in the biodistribution and PET imaging data of ^{18}F-FER, as lower liver uptake (5.56 ± 1.67 %ID/g, 1 h p.i.) was observed. The majority of the radioactivity was present in the excretory organs, intestines (17.1 ± 3.50 %ID/g, 1h p.i.) and bladder. Conclusions: The biodistribution/imaging data of ^{18}F-FEC and ^{18}F-FER in mice are consistent with the known expression profiles of ECOD and EROD. However, ECOD-facilitated uptake of ^{18}F-FEC in liver and nasal mucosa needs to be confirmed via blocking studies. Once this is verified, the strategy of using the trapping of 2-[^{18}F]fluoroacetyl-CoA could be applied to image activities of various enzymes with the identification of specific ethylated/acetylated substrates. By replacing the ethyl or acetyl group with a 2-[^{18}F]fluoroethyl or 2-[^{18}F]fluoroacetyl group, ^{18}F-labeled derivatives will have the potential to evaluate enzymatic activities of esterases, deethylase and deacetylases that generate 2-[^{18}F]fluoroethanol, 2-[^{18}F]fluoroacetaldehyde, and 2-[^{18}F]fluoroacetate, respectively in situ.

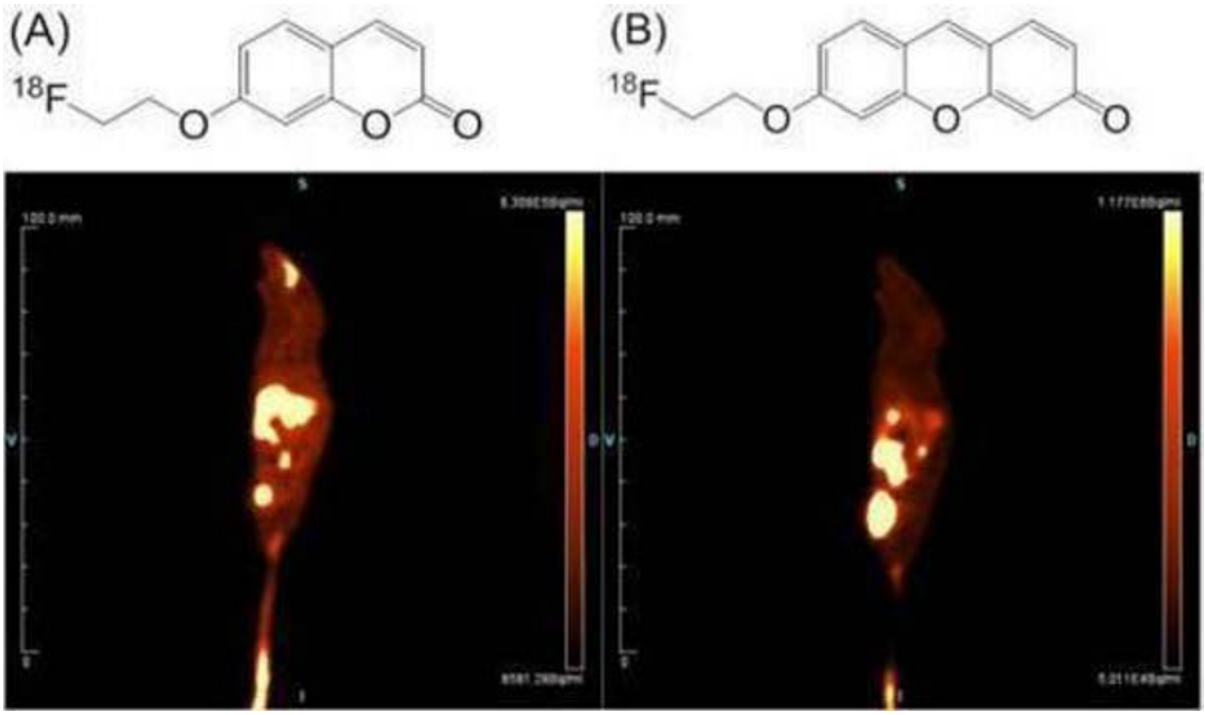

Disclosure of author financial interest or relationships:
M. Pourghiasian, None; **J. Pan**, None; **J. Lau**, None; **G.M. Dias**, None; **N. Hundal-Jabal**, None; **Z. Liu**, None; **F. Benard**, None; **K. Lin**, None.

Presentation Number **P 329**
Poster Session 3
September 20, 2013 / 15:15-15:15 / Room: Exhibit Hall B

Tetrazines/trans-Cyclooctenes and their potential as toolkit-compounds for biomedical imaging

Thomas Reiner, *Fabien Emmetiere, Nerissa Viola-Villegas, Christopher Irwin, Brian M. Zeglis, Jason S. Lewis, Radiology, Memorial Sloan-Kettering Cancer Center, New York, NY, USA. Contact e-mail: reinert@mskcc.org*

Tetrazines/trans-Cyclooctenes and their potential as toolkit-compounds for biomedical imaging Over the last years, the inverse electron demand tetrazine/trans-cyclooctene Diels-Alder cycloaddition has been used as a key reaction step for a multitude of biomedical imaging applications (1). This chemically and biologically orthogonal reaction was shown to be extremely fast and applicable in organic solvents, aqueous buffers, under physiological conditions and even in vivo. These features make tetrazines and trans-cyclooctenes an ideal platform to create key intermediates for radiopharmaceutical tracers. The reaction was shown to be selective in aqueous buffers and organic solvents, at room temperature and in the presence of biogenic amino acids. We show that tetrazines/trans-cyclooctenes can be used as a chemically orthogonal labeling platform, which makes them especially useful for conjugation of short-lived radiotracers [2-5]. We labeled small molecules, peptides, biomolecules and nanoparticles with bioorthogonal tetrazine and trans-cyclooctene tags. Methods for labeling included standard N-hydroxy succinimidyl active esters or maleimides, but also de novo design of protocols and chemical intermediates have been developed. We have shown with multiple targets and with multiple classes of tracers that radiolabeled tetrazines and trans-cyclooctenes can be superior or complement pre-existing methods and gold standards. Using traditional strategies, we compare the performance of these bioorthogonal tags to more commonly applied methodologies. The tetrazines and trans-cyclooctenes can also be used to allow the separation of unreacted starting materials during radiochemical synthesis via chemically orthogonal resins, enabling the multiplexed and high specific activity synthesis of radiolabeled tracers without HPLC support. The use of tetrazines and trans-cyclooctenes was probed in a variety of different settings and applications. These results indicate the two reaction partners can be excellent toolkit-compounds not only for radiochemical synthesis, but also for in vivo pretargeting. They yield radiolabeled targeted PET tracers with high selectivity, specific activity and purity. We show that this technique can simplify research and development and illustrate its benefits for the generation and purification of targeted tracers. Acknowledgements: Supported by NIH grant R01 CA138468 (JSL), the German Academy of Sciences grant LPDS 2009-24 (TR) and the Brain Tumor Center of Memorial Sloan-Kettering Cancer Center (TR). References: [1] Devaraj NK et al. (2011) Acc Chem Res 44:816-827. [2] Reiner T et al. (2011) Angew Chem Int Ed Engl 50, 1922-1925. [3] Keliher EJ et al. (2011) ChemMedChem 6, 424-427. [4] Reiner T et al. (2012) Neoplasia 14, 169-177. [5] Keliher EJ et al. (2012) Chem Open 1, 177-183.

Disclosure of author financial interest or relationships:
T. Reiner, None; **F. Emmetiere**, None; **N. Viola-Villegas**, None; **C. Irwin**, None; **B.M. Zeglis**, None; **J.S. Lewis**, None.

Presentation Number **P 330**
Poster Session 3
September 20, 2013 / 15:15-15:15 / Room: Exhibit Hall B

Green Synthesis of Radiopharmaceuticals

Xia Shao[1], Maria V. Fawaz[1], **Peter J. Scott**[1,2], [1]*Radiology, University of Michigan, Ann Arbor, MI, USA;* [2]*Interdepartmental Program in Medicinal Chemistry, University of Michigan, Ann Arbor, MI, USA. Contact e-mail: pjhscott@umich.edu*

Objectives: In simple terms, green chemistry is the design of products or processes that minimize (or eliminate) the use, generation, or disposal of hazardous chemical substances. Achieving this goal may include design of better synthetic pathways, use of alternative reaction conditions, and/or invention of safer (non-toxic) chemicals. Successful application of green chemistry in the chemical and pharmaceutical industries has proven beneficial from both economic and environmental safety perspectives. Recently, we have begun applying the principles of green chemistry to the preparation of radiopharmaceuticals for Positron Emission Tomography (PET) imaging, and herein report our progress in this new research area. Methods: Work to date has focused upon carbon-11 radiosyntheses. The appropriate precursor was dissolved in 100 µL of ethanol and [11C]methylated by gaseous [11C]CH3I or [11C]CH3OTf at room temperature. The reaction mixture was then purified using HPLC and/or solid phase extraction, followed by reformulation into 5% ethanol in saline for injection. Doses were filtered through 0.22 µm sterile filters and QC was performed using guidelines outlined in the U.S. Pharmacopeia. Results: To date, eleven 11C-labeled radiopharmaceuticals have been successfully prepared using only ethanol and water as solvents in entire manufacturing process (Table). Green radiochemistry is compatible with loop syntheses, reactor syntheses and sep-pak syntheses. Recent developments to be reported in this presentation also enable preparation of products from less soluble precursors such as [11C]PiB which, until very recently, were incompatible with the ethanolic methodology. All [11C]methylation reactions were carried out at room temperature for 3-5 minutes. Total syntheses time was 20-45 minutes. All final doses met release criteria for clinical use. Conclusions: Green radiochemistry represents a powerful new approach to radiopharmaceutical synthesis that greatly simplifies synthetic radiochemistry and product quality control.

Green Radiochemistry

Product	Traditional	Green
	Synthesis/Purification	Synthesis/Purification
Carfentanil	DMSO/iPrOH	
Choline	EtOH/EtOH	
DASB	MEK/MeCl	
DTBZ	DMF/EtOH	
HED	DMF/EtOH	
Methionine	Acetone/EtOH	EtOH
OMAR	DMSO/MeCl-MeOH	
PBR28	MeCl/MeCl	
PiB	3-pentanone/MeCl	
PMP	DMF/EtOH	
Raclopride	MEK/EtOH	

Disclosure of author financial interest or relationships:
X. Shao, None; **M.V. Fawaz**, None; **P.J. Scott**, SynFast Consulting, LLC, Employment; GE Healthcare, Consultant .

Presentation Number **P 331**
Poster Session 3
September 20, 2013 / 15:15-15:15 / Room: Exhibit Hall B

Usefulness of early phase washout rate of I-123 MIBG as a biomarker for cardiac sympathetic nervous system

Takuro Shiiba[1,2], *Ryuichi Nishii*[3], *Yasushi Kihara*[4], *Masayuki Sasaki*[5], *Masaji Maeda*[1], *Juniji Morishita*[5], [1]*Department of Radiological Technology, Koga General Hospital, Miyazaki, Japan;* [2]*Department of Health Sciences, Graduate School of Medical Sciences, Kyushu University, Fukuoka, Japan;* [3]*Department of Radiology, University of Miyazaki, Miyazaki, Japan;* [4]*Department of Radiology, Koga General Hospital, Miyazaki, Japan;* [5]*Department of Health Sciences, Faculty of Medical Sciences, Kyushu University, Fukuoka, Japan. Contact e-mail: tshiiba@kgh.or.jp*

PURPOSE It is widely known that the cardiac iodine-123-Metaiobezylguanidine (MIBG) scintigraphy is useful in the differential diagnosis between Parkinson's disease (PD) and other parkinsonian syndromes, and between dementia with Lewy bodies (DLB) and Alzheimer's disease (AD). Generally, planar images and SPECT images are acquired at early and delayed phases in the cardiac MIBG scintigraphy. The heart-to-mediastinum (H/M) ratio and washout rate (WR) that are obtained from anterior planar images are used as indicator of the diagnosis of abnormalities in cardiac sympathetic nervous system. The purpose of present study was to assess the diagnostic efficacy of early phase washout rate (WRearly) of MIBG as a biomarker for detecting abnormalities in the cardiac sympathetic nervous system. METHOD AND MATERIALS Sixty patients with suspected neurological disease underwent dynamic scan in early phase. The subjects were 30 males and 30 females with a mean age of 70.4±9.3 years old (range 39-85 years old). All images were acquired using a two-head gamma camera equipped with a low-middle-energy general-purpose (LMEGP) collimator. Dynamic scan were performed immediately after intravenous injection of 111 MBq of MIBG. Dynamic images were obtained in 128×128 matrix, and acquisition time was 1 frame/10 seconds for 2 minutes, since then, 1 frame/30 seconds for 26 minuets. Regions of interest (ROIs) were set over the heart and the upper third of mediastinum to obtain mean count in the respective ROIs after calculation of the H/M ratio. The WRearly calculated from images obtained at 2 minutes and 25 minutes in the dynamic scan, and the WRdelayed calculated from static images at 15 minutes and 3 hours. The relationship between WRdelayed and WRearly was evaluated using Spearman's rank correlation coefficient. Difference in WRs between negative and positive groups diagnosed based on conventional method by radiologist that was tested using the Mann-Whitney U-test. In addition, the diagnostic concordance rate of the proposed method based on WRearly and early heart-to-mediastinum (H/M) ratio was analyzed by kappa statistics, and compared to that of the conventional method by using early and delayed H/M ratios and WRdelayed. RESULTS The correlation coefficient between the WRearly and WRdelayed was 0.820 ($p<0.0001$). The WRearly of negative group was significantly lower than positive group ($p<0.0001$). When the cut-off values for negative and positive were set at 2.1 for early H/M ratio, 2.3 for delayed H/M ratio, and 23.0% for both WRearly and WRdelayed, the diagnostic concordance rate of our proposed method showed a good agreement with the conventional method. Moreover, when the cut-off value of WRearly was set at 16.3% (average of the negative group for WRearly plus 2 standard deviation), the diagnostic concordance rate was improved. CONCLUSION Our results suggest that the WRearly of MIBG has potential usefulness as a biomarker in the diagnosis of abnormalities of cardiac sympathetic nervous system.

Disclosure of author financial interest or relationships:
T. Shiiba, None; **R. Nishii**, None; **Y. Kihara**, None; **M. Sasaki**, None; **M. Maeda**, None; **J. Morishita**, None.

Presentation Number **P 332**
Poster Session 3
September 20, 2013 / 15:15-15:15 / Room: Exhibit Hall B

68Ga-labeled glucosamine click-conjugates - their synthesis and validation as novel PET imaging tracers

Izabela Tworowska[1,2], *Sanjay I. Thamake*[2], *David Ranganathan*[2], *Ebrahim Delpassand*[1,2], [1]*RadioMedix inc., Houston, TX, USA;* [2]*RITA Foundation, Houston, TX, USA. Contact e-mail: izabela.tworowska@gmail.com*

Introduction: Cancer cells preferentially use anaerobic glycolysis over mitochondrial oxidative phosphorylation for glucose dependent ATP production. Increased glucose uptake and rate of glycolysis are the key features of proliferating cancer cells compared to normal cells. These two processes are supported by overexpression of glucose transporters (especially GLUT1 and GLUT3) and hexokinase enzyme. Increased expression of GLUT1 has been observed in lung, breast, colorectal, bladder, gastric cancers and pituary hepatocellular carcinoma. There is a clinical correlation between increased GLUT1 expression and cancer initiation, progression, and poor treatment outcome that can be exploited for diagnosis and therapy of cancer. Currently, 18F-FDG is the only clinically approved diagnostic agent that targets all types of glucose transporters. Here, we present our results on development and validation our lead candidates, glucosamine-click conjugates as new PET imaging agents targeting the same binding domain of GLUT1 transporter as 18F-FDG. Methods: 2-acetamido-N-(ε-minocaproyl)-2-deoxy-β-D-glucosylamine was coupled to the "click-mate" substrates, MFCO-NHS click or BCN-NHS, followed by Cu-free click conjugation with 3-azido-propyl-monoamide DOTA to give products, RMX-GC-08 and RMX-GC-11, respectively. Both final conjugates were analyzed by ESI-MS and HPLC. Their 68Ga-labeling proceeded in 0.5M NaOAc pH=4.1 at 95oC for 10min using 68Ge/68Ga generator (ITG GmbH Germany). Radiolabeled RMX-GC compounds were purified using C18 sepak cartridges and yields of these reactions were determined by iTLC and radio-HPLC. 68Ga-labeled RMX-GC conjugates were validated in vivo in PET imaging studies performed in several types of tumor-bearing animal models (breast cancer-SKBR3, prostate cancer-PC3, lung cancer- A549, and neuroendocrine-MiaPaCa-2). Images were acquired at 30min, 60min and 90min post injection using Genysis4 PET camera. Results: Agents have shown higher than 98% radiochemical stability after incubation in FBS and PBS for 4h at 37C. Uptake of RMX-GC conjugates in tested cancer cell lines (SKBr3, A549 and 13762) was GLUT-1 specific and reduced in 50-66% in the presence of GLUT-1 inhibitors cold glucose or cytochalasin B. In vivo studies have showed high tumor-specific accumulation of both tracers with no uptake by normal organs (brain, lung or spleen). RMX-GC-08 has slower kinetics of washout that RMX-GC-11 with maximum activity accumulated in tumor at 90min for RMX-GC-08 and 60min for RMX-GC-11 as quantified by analysis of PET images. Conclusions: Both 68Ga-labeled RMX-GC (RMX-GC-08 and RMX-GC-11) agents are novel very promising tracers for PET detection of GLUT-1 over-expressing tumors. They have shown high radiochemical stability and yield of labeling. Further studies will be done to determine their pharmacokinetic in animal models.

Disclosure of author financial interest or relationships:
I. Tworowska, None; **S.I. Thamake**, None; **D. Ranganathan**, None; **E. Delpassand**, RadioMedix, Stockholder .

Presentation Number **P 333**
Poster Session 3
September 20, 2013 / 15:15-15:15 / Room: Exhibit Hall B

Characterization of peptide ^{125}I-p5R+14 as an optimized radiotracer for the in vivo detection of ApoA2c amyloidosis

Emily B. Martin[2], *Tina A. Richey*[2], *Alan Stuckey*[3], *Robert E. Heidel*[4], *Angela Lee*[2], *Brianna Rader*[2], *Dustin Osborne*[3], *Stephen J. Kennel*[1], *Jonathan S. Wall*[1], [1]*Medicine and Radiology, University of Tennessee Graduate School of Medicine, Knoxville, TN, USA;* [2]*Medicine, University of Tennessee Graduate School of Medicine, Knoxville, TN, USA;* [3]*Radiology, University of Tennessee Graduate School of Medicine, Knoxville, TN, USA;* [4]*Surgery, University of Tennessee Graduate School of Medicine, Knoxville, TN, USA. Contact e-mail: emarti15@utk.edu*

Amyloid is a complex pathology associated with a growing number of diseases and as a consequence of aging. Cardiac amyloidosis is observed principally in patients with immunoglobulin light chain (AL) amyloidosis, familial transthyretin (ATTRm - mutant) amyloidosis and as a consequence of aging (ATTRwt - wild type). Although ATTRm is considered a rare disease, the pro-amyloid V122I amino acid mutation occurs in ~3.5% of the US African American population, and it may be widely underdiagnosed as a result. Therefore, a facile, non-invasive and cost-effective method for detecting cardiac amyloidosis would have clinical import. We have identified an amyloid-reactive, synthetic peptide, designated p5R+14, that, when radioiodinated, is capable of selectively detecting amyloid deposits in vivo. APOA2c amyloid, though rare in humans, is one of only a few robust murine models of amyloidosis and so to generalize the reactivity of our peptides, we studied binding of ^{125}I-p5R+14 peptide in detail using these mice. To evaluate the affinity of p5R+14 for ApoA2c tissue amyloid, we used an ex vivo tissue homogenate binding assay in the presence of increasing NaCl (0.15 M - 2 M) concentrations. For in vivo imaging, ~150 µCi of ^{125}I p5R+14 was injected iv in ApoA2c mice (n=3). SPECT/CT images were acquired at 4 h post injection. For in vivo and ex vivo correlation studies, ^{123}I-p5R+14 was prepared and ~20 µCi administered to mice with ApoA2c amyloidosis. At 4 h pi, mice were euthanized and the tracer biodistribution measured. The organs were then frozen for 10 days, homogenized, and used as substrate for a ^{125}I-p5R+14 ex vivo binding study. Tissue samples were fixed in formalin for microautoradiography. Peptide p5R+14 bound ApoA2c amyloid-laden tissues with variable affinity (IC_{50} = 0.3 M, 0.5 M and 0.8 M NaCl for the heart, spleen, and lung, respectively). SPECT imaging confirmed that ^{125}I-p5R+14 was observed within the amyloid-laden liver, spleen, intestines and heart (with 3-7 %ID/g) of the mice. Specific co-localization with amyloid was validated using microautoradiography. Interestingly, reactivity of ^{123}I-p5R+14 peptide in vivo was dramatically reduced in the spleen, lungs and heart relative to the binding of ^{125}I-p5R+14 to the same tissues in the ex vivo assay. These data suggest that although the ^{125}I-p5R+14 peptide successfully imaged cardiac (see figure), hepatic, intestinal and splenic ApoA2c amyloid in vivo, an apparent biological or binding-site barrier hindered maximal uptake of the peptide in vivo. Therefore, we suggest that even though peptide p5R+14 can be used to image cardiac amyloid, it can be further optimized to produce enhanced in vivo reactivity and yield a valuable tool for amyloid imaging in patients with visceral amyloidosis.

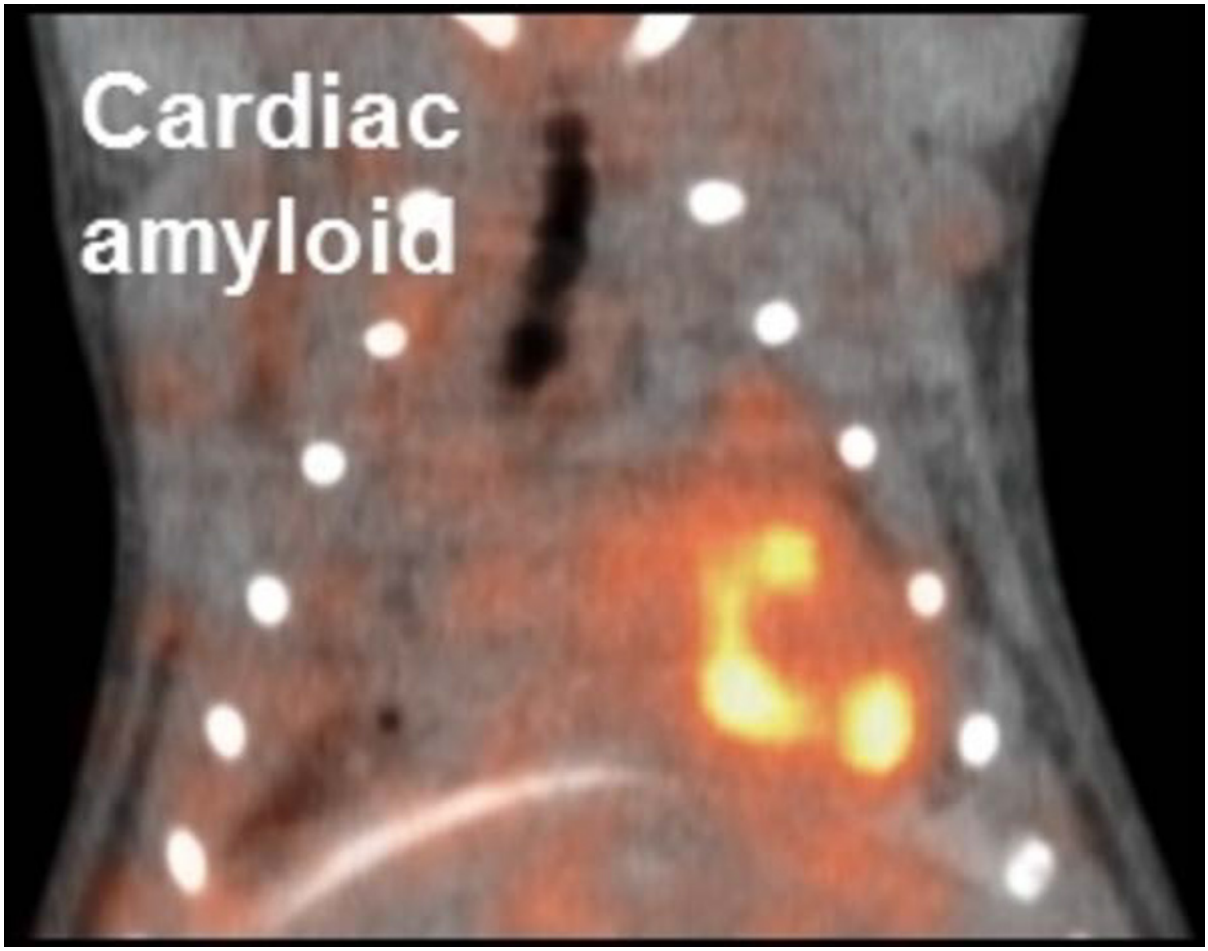

Disclosure of author financial interest or relationships:
E.B. Martin, Solex LLC, Stockholder; **T.A. Richey**, Solex Biomedical, Stockholder; **A. Stuckey**, Solex, LLC, Stockholder; **R.E. Heidel**, None; **A. Lee**, None; **B. Rader**, None; **D. Osborne**, Siemens, Employment; **S.J. Kennel**, Solex,lld, Stockholder; **J.S. Wall**, Solex Inc, Stockholder .

Presentation Number **P 334**
Poster Session 3
September 20, 2013 / 15:15-15:15 / Room: Exhibit Hall B

Decreased Dopamine D2 Receptor Availability using microPET in mice that prefer Alcohol

Amira K. Brown[1,3], *Mark A. Mandelkern*[3,4], *Judah Farahi*[3], *Monica Ferrini*[1], *Theodore C. Friedman*[1,2], [1]*Internal Medicine, Charles R. Drew University of Medicine and Science, Los Angeles, CA, USA;* [2]*Medicine, UCLA, Los Angeles, CA, USA;* [3]*Nuclear Medicine, Greater Los Angeles Veteran Affairs Healthcare System, Los Angeles, CA, USA;* [4]*Physics, UC-Irvine, Irvine, CA, USA. Contact e-mail: amirabrown@cdrewu.edu*

Alcohol abuse and dependence continues to have a tremendous impact on millions of individuals battling this debilitating disease. A major goal of alcohol addiction research is to identify biomarkers that may play a significant role in its euphoric properties. Addictive drugs (including alcohol) act in the same fashion as natural rewards in that they, release dopamine (DA) in the nucleus accumbens and other forebrain structures and mimic the effects of natural rewards thus, shaping drug-taking behaviors. In individuals with alcohol-use disorders a, lower DA D2-like receptor availability (RA) in the striatum (ST) and other brain regions associated with reward have been shown indicating that D2 receptors may play an important role in alcohol addiction or preference. Objective: The goal of our study was to determine if there are fundamental differences in the DA D2-like receptor system between mouse strains that prefer or avoid alcohol using positron emission tomography (Siemens, Inveon) and [18F]fallypride (FP) to measure in vivo DA D2-like RA. Methods: Male, drug naïve 8-week old male high alcohol preferring (HAP) (C57BL/6J) and low alcohol preferring (LAP) (DBA/2J) mice (N=11 per group) were purchased from JAX laboratories. HAP mice are characterized by their choice to voluntarily consume unsweetened ethanol, when given free-choice access to ethanol and water. LAP mice are characterized by their avoidance of ethanol even when it is administered in a sweet solution. FP was administered a bolus injection (over the course of 30 s) via the tail vein at the start of the 2 h emission scan. Dynamic emission scans were acquired in list mode, sorted to sinograms and reconstructed using two iterations of (ordered subsets expectation maximization) followed by 18 iterations of the (maximum a posteriori) reconstruction algorithm (Siemens Medical Solutions Munich, Germany). Binding potential (BPND) images of the ST were computed from the reconstructed dynamic images using PMOD software (PMOD Technologies, Zurich, Switzerland). Anatomical regions of interest (ST and cerebellum) were identified using a rodent brain atlas and manually defined in both hemispheres of PET images (Fig. 1A/1B). DA D2-like RA in the mouse ST was calculated as BPND using a reference-region method and t-tests were used for group comparisons. Results: There were no significant differences found in FP dose, weight or age between the HAP and LAP groups. DA D2-like RA in the ST of HAP mice (4.78 ± 1.0) was significantly lower (t= 2.27; p= 0.03) when compared to LAP mice (6.38 ± 2.2) (mean ± SD) (Fig. 1C). Conclusions: Our findings demonstrate that reduced DA D2-like RA exists in drug naïve HAP mice. This down-regulation of DA D2-like RA may influence the drug-seeking behaviors typically seen in alcohol-preferring mice.

Decreased Dopamine D2 Receptor Availability using microPET in mice that prefer Alcohol

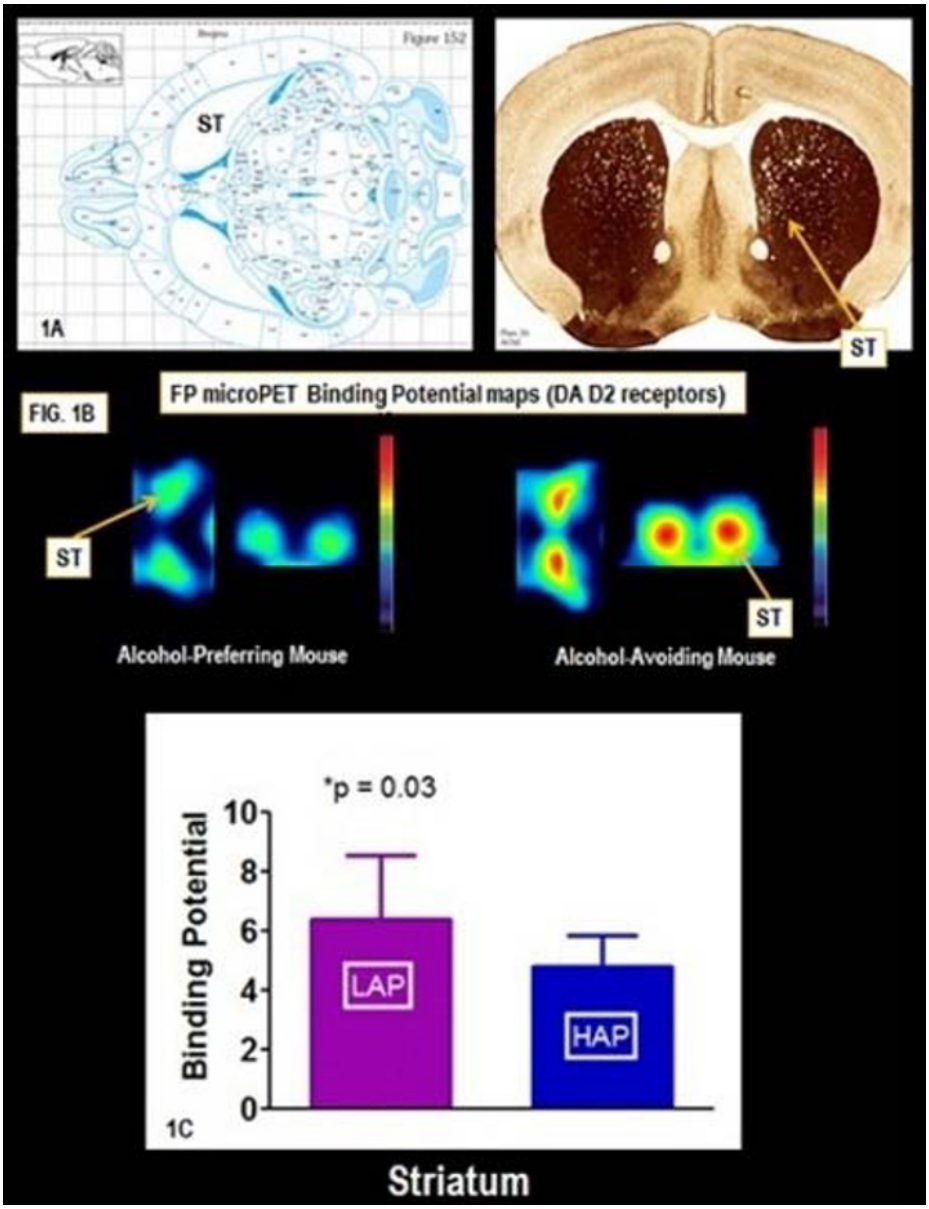

Mouse and Scan Characteristics

T-tests: Dose, Weight and BPND				
Alcohol Preference				
Characteristics	Low Alcohol mean ± SD (low-ci)	High Alcohol mean ± SD (low-ci)	t	p
Weight	24.0 ± 2.8	24.3 ± 3.0	-0.18	0.86
Dose (uCi)	183 ± 46	163 ± 43	1.01	0.31
BPND	6.38 ± 2.2	4.78 ± 1.0	2.27	003*

Dose= [18F]fallypride injected dose
BPND= binding potential

Disclosure of author financial interest or relationships:
A.K. Brown, None; **M.A. Mandelkern**, None; **J. Farahi**, None; **M. Ferrini**, None; **T.C. Friedman**, None.

Presentation Number **P 335**
Poster Session 3
September 20, 2013 / 15:15-15:15 / Room: Exhibit Hall B

A combination of Pertussis Toxin and Common Carotid Artery Occlusion produces a novel model for ischemic stroke

Salvador G. Castaneda[1], *Carsten Calaminus*[1], *Hanna Napieczynska*[1], *Sandra Schwegmann*[2], *Sandra Beer-Hammer*[2], *Bernd Nuernberg*[2], *Bernd J. Pichler*[1], [1]*Preclinical Imaging and Radiopharmacy, Eberhard Karls University of Tuebingen, Tübingen, Germany;* [2]*Experimental and Clinical Pharmacology and Toxicology, Eberhard Karls University of Tuebingen, Tübingen, Germany. Contact e-mail: Salvador.castaneda@med.uni-tuebingen.de*

Introduction Ischemic stroke (IS) is a cerebral infarction that occurs with sudden, permanent or temporary blocking of an arterial segment. Disease related animal models are crucial for development of therapies and diagnostic tools. For this, we have developed a novel model for IS by combining Pertussis Toxin (PTX) and temporary occlusion of the common carotid artery (TOCCA) which successfully reproduces MRI findings of ischemic stroke normally found in human patients. Methods 12 C57BL/6 12 week old mice were randomized and added to a "stroke group" (n=7) and a "control group" (n=5). Baseline MRI consisting of Diffusion Weighted Images (DWI), Arterial Spin Labeling images (ASL) and T2 weighted images (T2W) were used to calculate Apparent Diffusion Coefficient maps (ADC), Perfusion Weighted Images (PWI) and T2 maps one week prior to surgery. The stroke group was then injected with PTX (150µg/kg i.p.) 48h prior to surgery. Surgery was done on all mice by TOCCA applying a vascular clamp for 30 minutes, under 1.5% Isoflurane and Metamizole (100mg/kg). After 48h the mice were assessed with an open field test (15min) followed by a repetition of the MRI acquisitions. H&E staining and immunohistochemistry (IHC) for GFAP, a glial cell marker of the brains was performed subsequently. ROIs were drawn on the lesion and contralateral side as identified on T2W and overlaid with corresponding ADC, T2 maps and PWI. Analysis was done using repeated measurements ANOVA using SPSS software. Results DWI and T2W revealed hyperintense signal areas ipsilateral to the occlusion site with an average of 38% of striatum, 37% of hippocampus and 17% of cortex on 4 out of 7 mice. The control group presented no hyperintense signal areas. There were significant timepoint-treatment group interactions for ADC and T2 maps on the striatal strokes ($p=.003$ and $p=.006$ correspondingly). Striatal perfusion ipsilateral to the stroke side was low at 48h but showed only a trend towards significance ($p=.052$) when compared to the control side. Open field test demonstrated reduced movement for mice on the stroke group ($p=.009$) Analysis of the H&E presented cytotoxic edema of the striatal, hippocampal and cortical regions on the stroke mice with scattered micro bleeds. IHC showed increased glial presence on the stroke areas. Discussion and Conclusions The combination of PTX and unilateral TOCCA leads to ipsilateral brain lesions reminiscent of IS. Using ADC, DWI and T2W we have shown the stroke model presents radiological findings of vasogenic and cytotoxic edema, which are commonly found on IS lesions. Furthermore, histology and IHC has corroborated our MRI findings, along with significant behavioral abnormalities on the stroke group. This model's ease of implementation due to the low surgical skill required and the relatively large stroke areas produced offers a novel instrument for the study of stroke in the imaging field. The mechanism by which PTX combined with a 30min ligation catalyzes stroke is not yet clear and requires further research to be elucidated.

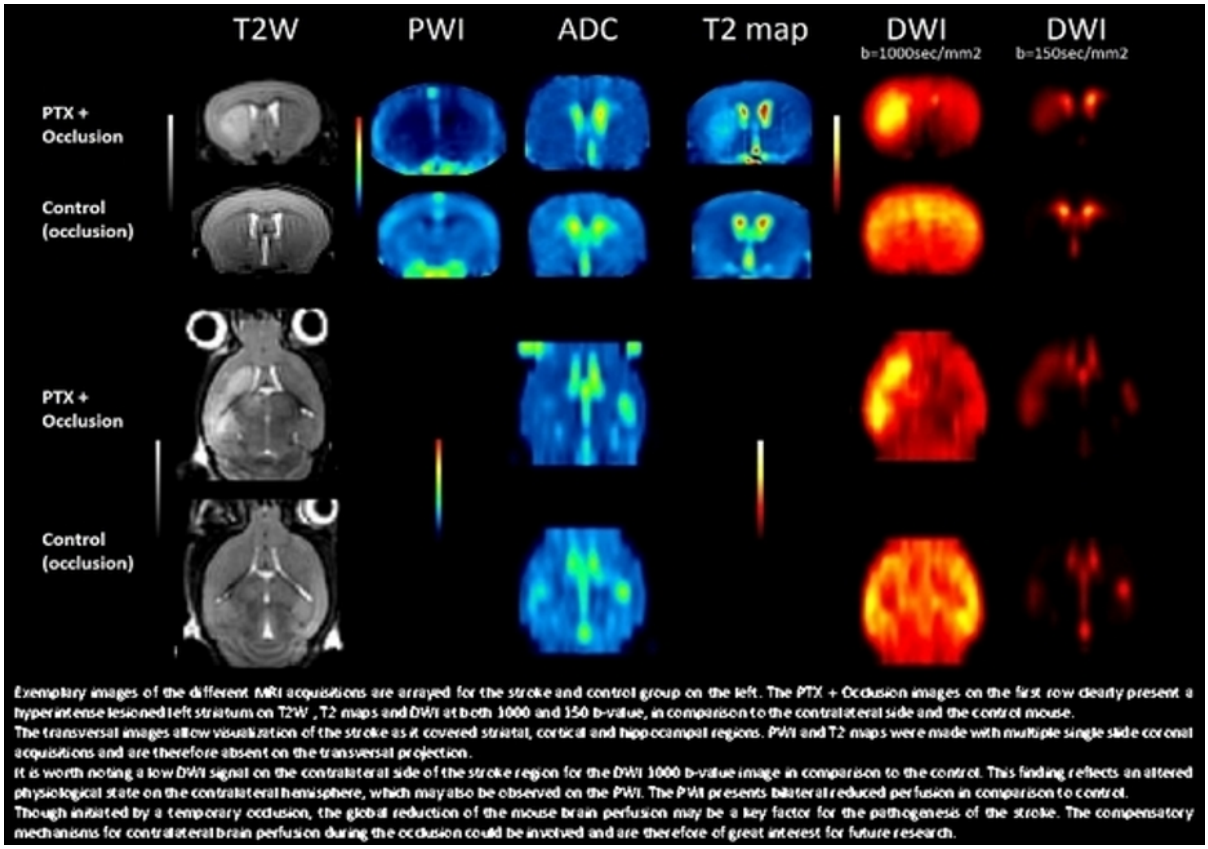

Disclosure of author financial interest or relationships:
S.G. Castaneda, None; **C. Calaminus**, None; **H. Napieczynska**, None; **S. Schwegmann**, None; **S. Beer-Hammer**, None; **B. Nuernberg**, None; **B.J. Pichler**, Siemens, Grant/research support; Bayer, Grant/research support; AstraZeneca, Grant/research support; BoehringerIngelheim, Grant/research support .

Presentation Number **P 336**
Poster Session 3
September 20, 2013 / 15:15-15:15 / Room: Exhibit Hall B

Chemical Exchange Saturation Transfer: Improving In vivo Molecular Contrast of Amine Protons without the Use of Contrast Agents

Julius J. Chung[1], *Sunyoung Chae*[1], *Jaehun Kim*[2], *Geun Ho Im*[3], *Jung Hee Lee*[1,2], [1]*Samsung Advanced Institute for Health Sciences & Technology, Sungkyunkwan University, Seoul, Republic of Korea;* [2]*Department of Radiology, Samsung Medical Center, Samsung Biomedical Research Institute, Seoul, Republic of Korea;* [3]*Center for Molecular and Cellular Imaging, Samsung Biomedical Research Institute, Seoul, Republic of Korea. Contact e-mail: juliusch@seas.upenn.edu*

Objective: Chemical Exchange Saturation Transfer (CEST) has recently been gaining interest as a tool for providing intrinsic molecular contrast tracking concentration and/or pH differences. However, due to exchange independent water signal attenuation imaging at faster exchange regimes may be difficult. A solution to this issue is spin-locking. This study examines the inconsistencies of CEST with traditional saturation such as continuous wave (CW) and demonstrates the stability of utilizing spin-locking for higher powers. Materials and Methods: Imaging was performed on a Bruker 7 Tesla scanner with a quadrature volume RF coil. Images were taken with CW or spin-locking pulses followed by EPI readout (TE = 40.71ms, TR = 8000ms). Glutamate solution phantoms (in PBS) were prepared with 50mM glutamate at varying pHs. These phantoms were imaged with a CEST preparation B1 of 500Hz and saturation length of 150 ms over a frequency range of ±5ppm with a step size of 0.2ppm. Rat MCAO models were imaged to observe amine proton contrast in vivo with CW or spin-locking pulses followed by two segment EPI readout (TE = 22.58ms, TR = 6000ms, NA = 10). CEST asymmetry was computed as follows, CESTasym=[S(-ppm)-S(+ppm)]/S0. Results: Glutamate phantoms demonstrating pH dependence are shown in Fig 1a and Fig 1b for CW and spin-locking respectively. These images show high variation across the image for CW in Fig 1a and more stable pH dependent contrast for spin-locking in Fig 1b. Fig 1c shows an inconsistent Z-spectrum with CW while Fig 1d again shows more consistency. These differences also affect their CEST asymmetries shown in Figs 1e and 1f. Figure 1g shows the pH dependencies in the images at 2.5ppm. CW shows a detection sensitivity of ~8.2% per pH while spin-locking shows ~ -14% per pH unit. In the MCAO model, CW shows a sensitivity of 8.9% whereas SL shows an improved sensitivity of 11.0% in the infarct region. Conclusion: Spin-locking is an effective method of minimizing oscillatory inconsistency resultant of an incomplete lock during standard saturation pulses in CEST. At faster exchange regimes where high power is necessary, this is crucial to ensure reliable CEST contrast.

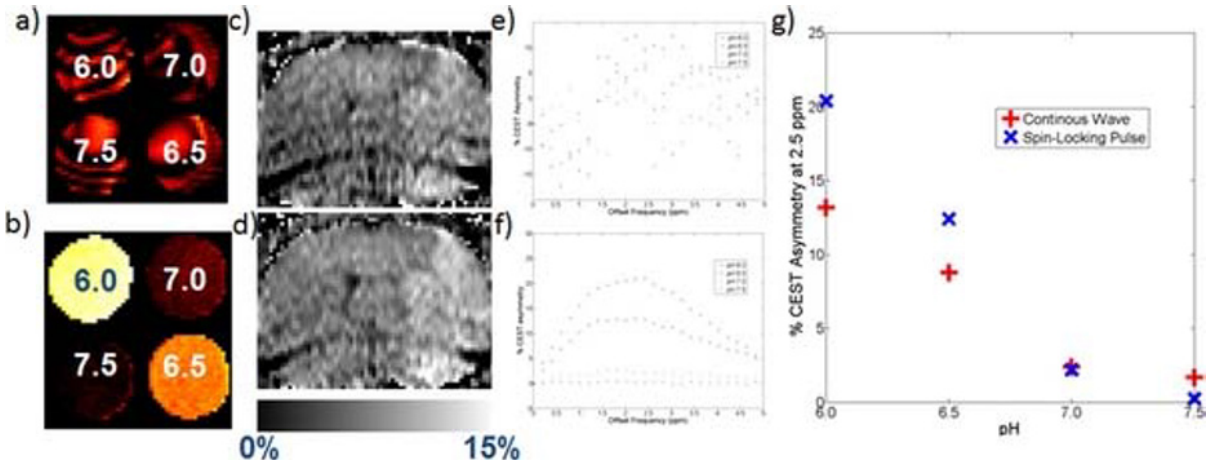

Figure 1. Comparison of CEST images between continuous wave and spin-locking preparation. CEST asymmetry images of glutamate phantoms taken at 2.5ppm using continuous wave, a, or spin-locking, b. CEST asymmetry images of a rat MCAO model taken at 2.5ppm using continuous wave, c, or spin-locking, d. CEST asymmetry curves (e and f) for continuous wave and spin-locking respectively. g shows the detection sensitivity for pH using both methods.

Disclosure of author financial interest or relationships:
J.J. Chung, None; **S. Chae**, None; **J. Kim**, None; **G. Im**, None; **J. Lee**, None.

Presentation Number **P 337**
Poster Session 3
September 20, 2013 / 15:15-15:15 / Room: Exhibit Hall B

Prenatal opiate exposure alters brain glucose metabolism in adolescent animals

Sandra R. Scherrer[1], Stergiani Agorastos[1], Christina Veith[1], Joseph Carrion[4], Wynne K. Schiffer[3], Yoon Young Choi[1], Jonathan D. Brodie[2], Amanda Talan[3], Giovanni C. Santoro[1], David Eidelberg[1], **Stephen L. Dewey**[1,4], *[1]Neurosciences, Feinstein Institute for Medical Research, Manhasset, NY, USA; [2]Psychiatry Department, NYUSOM, New York, NY, USA; [3]Neurology, University of Minnesota, Minneapolis, MN, USA; [4]Molecular Medicine, Hofstra-North Shore LIJ SOM, Hempstead, NY, USA. Contact e-mail: sdewey@nshs.edu*

Neonatal abstinence syndrome (NAS) is a drug withdrawal disorder caused by chronic maternal opiate use. Recent findings from hospitals across the U.S. suggest that the newborn addiction rate has tripled over the last decade, and that newborns with NAS spent an average of 16 days in the hospital being treated for opiate withdrawal. Symptoms of NAS include seizures, respiratory and feeding difficulties and low birth weight. While the immediate treatment of behavioral changes associated with NAS have been the focus of recent investigations, the long-term consequences remain relatively unknown. Therefore, in an ongoing effort to better understand the lifetime effects of prenatal opiate exposure on the adolescent and adult brain, we treated 4 pregnant Sprague-Dawley rats from Gestational Day (GD) 2 - GD21 (day of parturition) with an escalating dose of morphine (20 - 60 mg/kg/day). Immediately upon birth, litters were culled to 9 animals and crossed fostered to normal surrogates. Litter sizes were not significantly different between morphine and saline-treated controls. However, birth weights were significantly reduced in morphine-treated animals ($p < 0.01$). To determine if this treatment paradigm produced pups sensitive to opiate withdrawal, animals were challenged with naloxone (1.0 mg/kg) on Post Natal Day (PND) 1. Behaviors were scored (0 - 3 with 3 being highest) by 5 individuals blind to the treatment condition. Animals exposed to morphine in utero demonstrated marked withdraw behaviors following an acute naloxone challenge (saline = 1.01 ± 0.22, morphine treated = 4.91 ± 0.34, mean of the summed scores for all behaviors). At PND35 (adolescence), animals received an acute morphine challenge (10 mg/kg) 20 minutes prior to being injected with 2-deoxy-2-(18F)fluoro-D-glucose (18FDG). Scanning was performed using a Siemen's Inveon positron emission tomograph. Uptake (45 minutes) occurred in awake and freely moving animals in their home cage. Following this period, animals were anesthetized (ketamine/xylazine) and placed in the gantry. Static images were reconstructed using both filtered back projection (FBP) and maximum a posteriori (MAP) algorithms. Images were co-registered to a standard rat atlas with PMOD. Using a region of interest (ROI) and/or a statistical parametric map (SPM) protocol, data comparing the morphine-exposed group to the saline control group were obtained. Using either method of analysis, morphine-exposed animals demonstrated marked increases in 18FDG uptake in both the corpus striatum and the thalamus, bilaterally. Marked decreases, however, were noted bilaterally in the superior colliculus of these same animals. These increases and decreases were significantly different from control values ($P < 0.001$). Ongoing studies are examining whether these alterations remain into adulthood. In summary, the present findings have important implications for the abuse liability of opiates as well as the potential use of narcotic analgesics for adequate pain management in individuals with a gestational history of opiate exposure.

Disclosure of author financial interest or relationships:
S.R. Scherrer, None; **S. Agorastos**, None; **C. Veith**, None; **J. Carrion**, None; **W.K. Schiffer**, None; **Y. Choi**, None; **J.D. Brodie**, None; **A. Talan**, None; **G.C. Santoro**, None; **D. Eidelberg**, None; **S.L. Dewey**, None.

Presentation Number **P 338**
Poster Session 3
September 20, 2013 / 15:15-15:15 / Room: Exhibit Hall B

[^{18}F]Nifene is Sensitive to the Acetylcholinesterase Inhibitors Physostigmine and Galanthamine

Ansel Hillmer[1], *Dustin W. Wooten*[1], *Patrick Lao*[1], *Mohammed Farhoud*[2], *Todd E. Barnhart*[1], *Jogeshwar Mukherjee*[3], *Bradley T. Christian*[1], [1]*Medical Physics, University of Wisconsin - Madison, Madison, WI, USA;* [2]*Comprehensive Cancer Center, University of Wisconsin - Madison, Madison, WI, USA;* [3]*Department of Radiological Sciences, University of California - Irvine, Irvine, CA, USA. Contact e-mail: ahillmer@wisc.edu*

Acetylcholinesterase inhibitors (AChEIs) are drugs thought to ameliorate the cognitive symptoms of Alzheimer's disease by increasing synaptic acetylcholine (ACh) levels. [^{18}F]Nifene is an agonist PET radioligand with high affinity for α4β2* nicotinic acetylcholine receptors (nAChRs). The goal of this work is to exploit the fast kinetic properties of [^{18}F]nifene to image *in vivo* increases in ACh concentrations induced by acetylcholinesterase inhibitors (AChEIs). **Methods:** An Inveon microPET scanner was used to image two rat subjects. Bolus-constant infusion (B/I) experiments 60 min in duration were performed. A K_{bol} of 20 min was administered at the start of all studies. Drug was given once equilibrium was established 30 min following the scan start. Each subject was first scanned with 0.1 mg/kg physostigmine (PHYSO) administration. At least one week later, both subjects were scanned separately with exposure to 5.0 mg/kg galanthamine (GAL). Time activity curves (TACs) were extracted from the thalamus (TH) and cerebellum (CB). Deviations in [^{18}F]nifene binding were estimated from bound/free (B/F) ratios approximated by TH/CB-1. **Results:** After the administration of PHYSO, fast displacement of [^{18}F]nifene in both TH and CB was readily evident in the raw TACs, while B/F slightly increased before settling at a reduced level. In contrast, GAL administration resulted in a gradual decrease in B/F and TH TACs. Averaged over 24-30 min post-drug administration, PHYSO reduced B/F levels by 7% and 12% while GAL reduced B/F by 8% and 12%. **Conclusion:** This work preliminarily indicates sensitivity of [^{18}F]nifene to competition with increased synaptic ACh induced by both PHYSO and GAL. Further studies with blood sampling are required to confirm these observations, as the CB has small but significant specific [^{18}F]nifene binding in the rat.

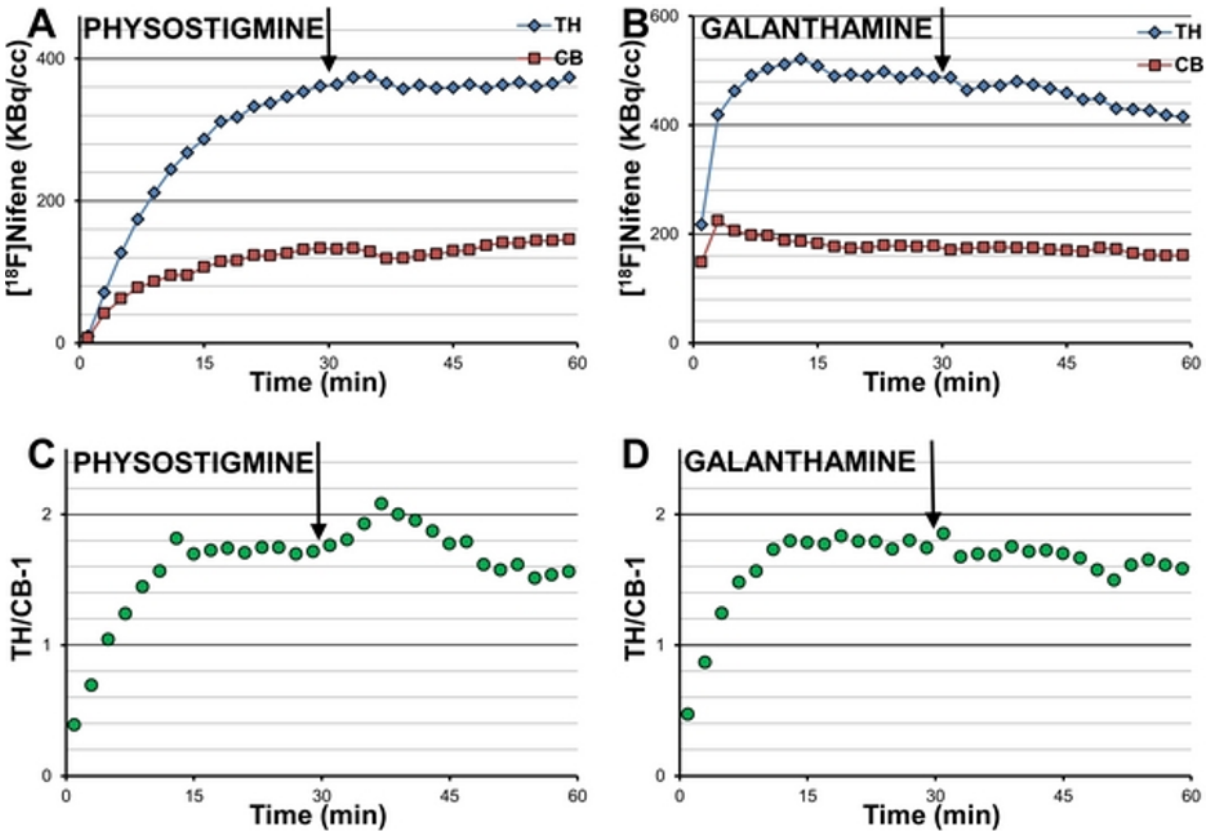

A and **B** illustrate TACs for PHYSO and GAL, respectively, in the TH and CB. **C** and **D** show B/F estimated from TH/CB-1 for the same drugs. The arrows in each figure denote the time of drug administration.

Disclosure of author financial interest or relationships:

A. Hillmer, None; **D.W. Wooten**, None; **P. Lao**, None; **M. Farhoud**, None; **T.E. Barnhart**, None; **J. Mukherjee**, None; **B.T. Christian**, Abiant, Inc, Grant/research support .

Presentation Number **P 339**
Poster Session 3
September 20, 2013 / 15:15-15:15 / Room: Exhibit Hall B

Neuroimaging the genetic effects of chromosome 13 on intrinsic thalamocortical networks by resting-state fMRI in rats with consomic technology

Zhixin Li[1,2], *Christopher P. Pawela*[1,2], [1]*Plastic Surgery, Medical College of Wisconsin, Milwaukee, WI, USA;* [2]*Biophysics, Medical College of Wisconsin, Milwaukee, WI, USA. Contact e-mail: zli@mcw.edu*

Genes are major contributors to many biological traits and diseases, the penetrance of genetic effects on systematic brain biology has been thought to be more obvious and consistent than behavioral phenotypes and clinical outcomes. The concept of Neuroimaging-based endophenotypes has emerged as a promising approach to map the genetic effects onto physiological processes in brain. The goal of this study was to reveal the effects of genetic divergence on intrinsic thalamocortical networks among three genetic strains of rat: the parental Brown Norway (BN) and Dahl salt-sensitive (SS) strains combined with a consomic SS-13BN strain(introgressed entire chromosome 13 from BN into SS with consomic strategy). Resting-state fMRI(R-fMRI)technique was employed as an objective measure of functional connectivity along thalamocortical neural pathways. Methods: Thirteen male BN, ten SS and nine consomic SS-13BN rats were anesthetized with continuous delivery of Medetomidine and Pancuronium bromide i.v.. Intrinsic BOLD-fMRI was acquired in a Bruker 9.4T animal scanner while rats were at rest. Seed-regions within thalamocortical pathways for R-fMRI network analysis were identified in a parallel study while rats were electrically stimulated on left forepaw, namely, the bilateral secondary somatosensory cortex (S2) and thalamus(TH). One-sample t-test was performed for group patterns of functional connectivity in each strain ($P<0.005$ with correction), and one-way ANOVA was used to determine the differential functional connectivity among three strains ($P<0.05$ with correction). Rat body weight and age were analyzed as nuisance covariates. Results: BN strain showed more extensive functional connectivities in cortical and subcortical regions than SS and SS-13BN strains, while SS-13BN showed less connectivities in subcortical areas compared to SS strain. Group comparison revealed differential functional connectivity in left S2, Temporal association cortex(TAC) and hippocampus(HP) within the networks of S2 and TH among three strains. Substitution of Chromosome 13 increased the synchrony of left S2 with TAC and HP, but did not change the connectivity of left S2 with right S2 and bilateral TH. Conclusion: Our results provided neuroimaging evidence for the genetic influences on the projection and integration of intrinsic thalamocortical networks among three genetic rats, and Chromosome 13 harbored gene/genes responsible for the epistatic effects on functional connectivity in specific brain regions. These findings suggest a novel strategy to visualize, specify and dissect the genetic effects on task-specific neural networks by using resting-state fMRI measures as neuroimaging endophenotypes.

Disclosure of author financial interest or relationships:
Z. Li, None; **C.P. Pawela**, None.

Presentation Number **P 340**
Poster Session 3
September 20, 2013 / 15:15-15:15 / Room: Exhibit Hall B

Quantitative evaluation of spontaneous plasticity of corticospinal projections after rat spinal cord injuries by in vivo diffusion tensor imaging

Jichun Liao[1], *Yuqing Wang*[1], *Jie Zheng*[2], *Fabao Gao*[1], [1]*Radiology, West China Hospital, Sichuan University, Chengdu, China;* [2]*Mallinckrodt Institute of Radiology, Washington University School of Medicine, St. Louis, MO, USA. Contact e-mail: ljchun2005@126.com*

Purpose: It has been recognized for some time that partial lesions to the mammalian spinal cord can be followed by remarkable and extensive recovery and such recovery can be mediated by spontaneous plasticity of intraspinal circuitry. To examine this hypothesis, we developed a rat model of T8 spinal cord hemisection, quantitatively evaluated it by in vivo diffusion tensor imaging at different time points after injury and compared the results with those from histological examinations and behavioral analysis. Materials and Methods: Healthy male SD rats were randomly assigned to 2 groups: (1) sham group (n=4), underwent laminectomy only; (2) hemisectione injury group (n=8). Briefly, laminectomy was performed at T8-T10 under 10% chloralhydrate anesthesia and right hemi spinal cord was cut transversely. All the rats were assessed using an open field rating scale and imaged by 7.0T MR scanner with a surface coil in vivo at 1 day, 3 days, 1 week, 2 weeks, 3 weeks, 4 weeks after injury. Thereafter the animals were euthanized for histological examinations. The MR sequences included RARE T2, RARE T1, and DTI. The MRI data processing were performed using ParaVision, DTI Toolkit and TrackVis software. Results: T2 weighted MRI revealed high signal intensity in the lesion of the injured spinal cord(figure A). Signal changes appeared 1 day after injury and the border became clearer as the time passed toward 4 weeks after injury. While on T1 weighted images, the signal changes were not apparent. On diffusion tensor tractography(DTT) images, the fibers were disrupted on the right side of the spinal cord, while they were intact on the other side(figure B). Quantitative analysis revealed that the number of DTT fibers at 1 day after spinal cord injuries was lower than the number of DTT fibers in sham group, and increased slightly at subsequent time points. We calculated the FA and λ1 of the lateral column of the corticospinal tract on both sides and found that the FA and λ1 values prominently decreased on the right side compared to the sham group 1day after injury and gradually increased throughout the 4weeks of observation. The FA and λ1 values were slightly decreased after injury with slightly increase thereafter on the other side. Locomotion of the right hindlimb of the injured animals was significantly decreased immediately after injury, with gradual recovery for 4 weeks. Significant correlation was observed between the open field rating scale and the number of DTT fibers and the FA, λ1 values of the right side of the corticospinal tract. Conclusions: There is spontaneous plasticity of intraspinal circuitry after spinal cord injuries in rat. DTI may become an promising tool for monitoring spinal cord injuries and evaluating the effectiveness of its treatment protocols.

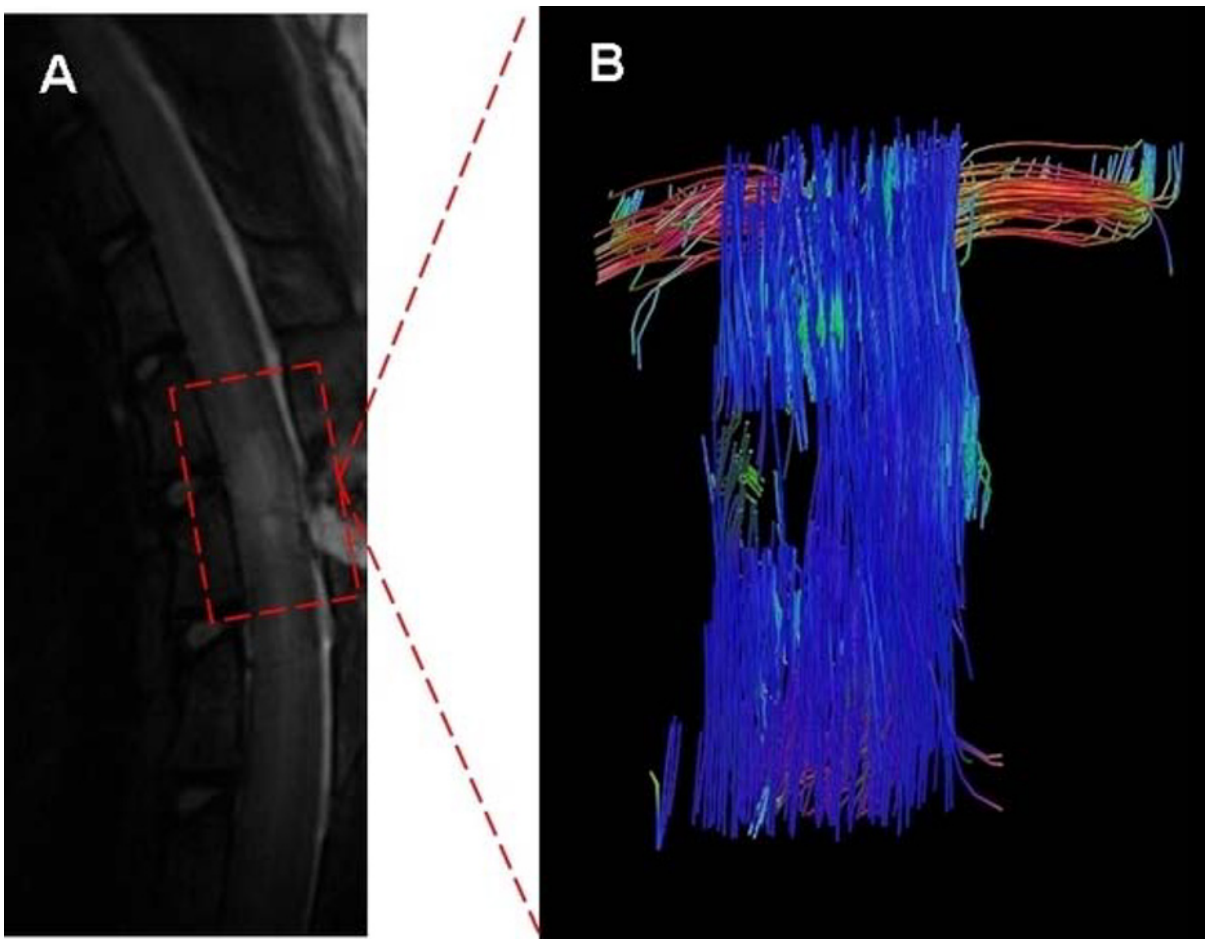

MR images of rat spinal cord 1 day after spinal cord hemisection. A: T2 sagittal image, B: diffusion tensor tractography.

Disclosure of author financial interest or relationships:
J. Liao, None; **Y. Wang**, None; **J. Zheng**, None; **F. Gao**, None.

Presentation Number **P 341**
Poster Session 3
September 20, 2013 / 15:15-15:15 / Room: Exhibit Hall B

Study of Acetyl-L-Carnitine Effects on Glucose Metabolism in Mouse Brain Using PET/MRI Imaging

*Lidia S. Cunha[3,4], **Domokos Mathe**[1], Ildiko Horvath[2], Daniel Veres[2], Krisztián Szigeti[2], Luis F. Metello[3], Teresa Summavieille[4], [1]CROmed Ltd, Budapest, Hungary; [2]Biophysics and Radiation Biology, Semmelweis University, Budapest, Hungary; [3]Nuclear Medicine Department, High Institute for Allied Health Technologies of Porto - Polytechnic Institute of Porto, Porto, Portugal; [4]Neuroprotection Lab, IBMC, University of Porto, Porto, Portugal. Contact e-mail: domokos.mathe@cromedresearch.com*

Introduction Acetyl-L-Carnitine (ALC) has important functions in mitochondrial metabolism highly affected in neurodegenerative diseases. ALC's effect on general brain glucose transport and phosphorylation was studied in vivo using healthy and metamphetamine (MET)-dosed mice. Methods Four groups of n=3 C57Bl6 mice were injected i.p. Saline, ALC-100 mg/kg and MET-10 mg/kg was injected for 3-3 animals. ALC administration as a neuroprotector agent preceded MET challenge with 30 minutes. 10.5 ± 1.1 MBq of 18F-Fluorodeoxyglucose (FDG) was injected i.v. 30 minutes after last treatment, PET for 25 minutes and a subsequent MRI scan were acquired using a sequential PET/MRI imaging system (nanoScan PET/MRI, Mediso Ltd, Hungary) in the brain after 45 minute awake FDG-uptake period. T1-weighted 3D Gradient Echo sequence was applied. PET volumes of 0.3x0.3x0.3 mm voxels were reconstructed with a proprietary 3D OSEM algorithm (Tera-TomoTM, Mediso, Hungary). Volumes of interest (VOIs) were drawn on using MRI as reference. Standardized uptake value (SUV) was calculated for 18F-FDG. VOIs were standardized by fusing the Brookhaven Laboratory Mouse MRI atlas to the PET and coregistration with the animal's own MRI scans. Prefrontal cortex, striatum and hippocampus were analysed due to their dopaminergic input together with the thalamus (striatal GABAergic inputs) and cerebellum. Results Neither ALC nor MET had a significant effect in these brain regions. In ALC+MET mice, a significant increase in glucose uptake was observed. Prefrontal cortex was one of the most affected regions, with an increase in glucose uptake in ALC+MET being significant when compared to all other conditions. Right striatum was also highly affected, displaying a very similar increase in glucose uptake in the ALC+MET group. In the left striatum differences were significant when compared to ALC ($p=0.0006$)) and MET($p=0.0083$), but not to control. Thalamus displayed an increased uptake of glucose for the ALC+MET group when compared to ALC and MET. FDG uptake in the hippocampus of the ALC+MET group showed only an increased value when compared to ALC. Conclusions The increased supply of ALC in MET-induced glucose decrease in regions with dopaminergic input leads to an acute counterbalance of glucose availability probably associated with the effect of ALC. Acetyl-L-Carnitine could represent an acute neuroprotective effect on brain metabolism.
Acknowledgement This work was supported in part by INMiND (HEALTH.2011.2.2.1-2 No.278850) of FP7.

Disclosure of author financial interest or relationships:
L.S. Cunha, None; **D. Mathe**, CROmed Ltd, Stockholder; Mediso Ltd., Consultant; **I. Horvath**, None; **D. Veres**, None; **K. Szigeti**, None; **L.F. Metello**, None; **T. Summavieille**, None.

Presentation Number **P 342**
Poster Session 3
September 20, 2013 / 15:15-15:15 / Room: Exhibit Hall B

Revealing the mouse brain functional connectivity patterns with resting state functional MRI (rsfMRI)

Anna Mechling[1], *Neele Saskia Huebner*[1,2], *Hsu-Lei Lee*[1], *Juergen Hennig*[1], *Dominik von Elverfeldt*[1], *Laura Adela Harsan*[1], [1]*Medical Physics, University Medical Center Freiburg, Freiburg, Germany;* [2]*Biology Department, Albert-Ludwigs-University, Freiburg, Germany. Contact e-mail: anna.mechling@uniklinik-freiburg.de*

A non-invasive insight into the brain's intrinsic connectional architecture of functional networks has only become possible since the development of resting-state functional magnetic resonance imaging (rsfMRI) (1). In humans, the default mode functional networks and their alterations in pathologies are intensively studied (2). However, this field is largely unexplored in the animal brain, perhaps because of methodological challenges related to the necessity of stable and comparable physiological parameters during the imaging sessions of all investigated animals, but also due to the confounding effects of anesthetic agents. To bridge this gap, we have systematically investigated here the functional connectional architecture of the mouse brain by implementing a robust, non-invasive methodological framework for the acquisition and analysis of mouse brain rsfMRI data. Our study, performed at high magnetic field (7T) and using the CryoProbe technology for the acquisition of the MR signal, demonstrate robust and reproducible patterns of mouse brain functional connectivity. First, we comparatively used 40 vs 100 independent component analysis (ICA) to identify elementary functional clusters of the mouse brain. The pure use of group ICA was extended allowing to statistically determining the reproducibility of the results via ICASSO (3) (20 repetitions of the ICA, varying initial conditions, bootstrapping and clustering - see also annex). Fig 1 (a) exemplifies a resting state network identified with 40 components group ICASSO in the anatomically well-defined somatosensory cortex (S1 and S2) areas, functionally linking these brain regions in both hemispheres (bilateral activation). Extending the analysis to 100 components, the ICASSO approach (Fig 1, b-e) was able to segregate the cortical somatosensory (SSC) network into four individual parts, separating the primary (S1) and secondary (S2) SSC and depicting unilateral (uni-hemispherical) patterns of activation. This was not only relevant for cortical regions but it was a generalized feature of subcortical areas as well. Thalamic networks clustered in one component with 40-ICASSO, were clearly split-up with 100-ICASSO into six sub-networks, corresponding to well defined thalamic nuclei. The connectional relationships between the elementary clusters obtained with ICASSO was further evaluated by partial correlation analysis and graph theory, and used to construct a graph of whole-brain neural network and to identify the most important mouse brain connectional hubs. Among them we mention the hippocampus, dorsal thalamic nuclei, cingulate and retrosplenial cortices, somatosensory cortical areas, amygdala or the hypothalamus. This whole mouse brain neuronal network exhibited the typical features of small-worldness and strong community structures seen in the human brain. Therefore our study provides a functional atlas of networks architecture of the mouse brain and demonstrates that this organization conserves fundamental topological properties that are also seen in the human brain (2). Refs:(1)Biswal BB, NeuroImage-62, 2012; (2)van den Heuvel MP et al., HBM-30, 2009; (3)Himberg et al., NeuroImage-22, 2004

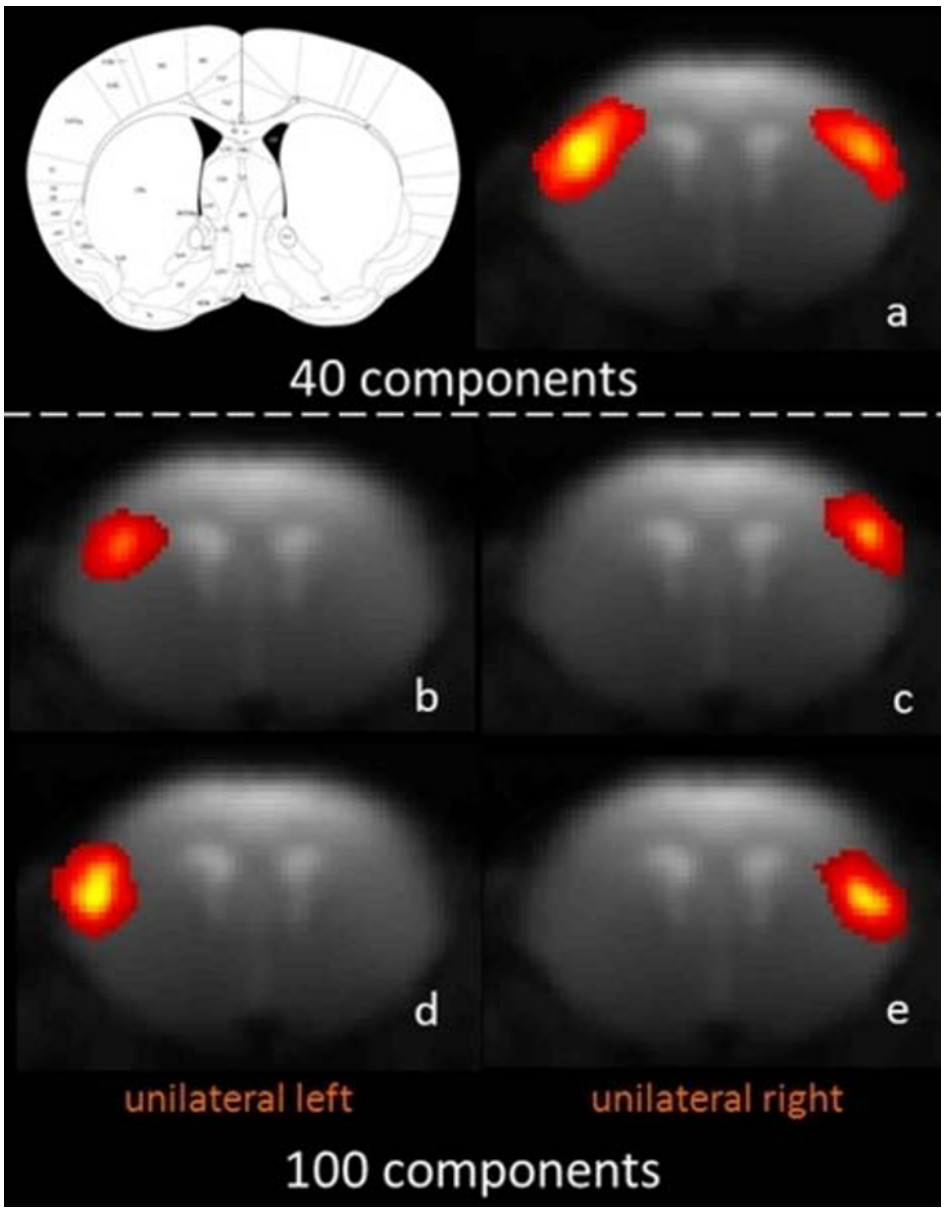

Mouse somatosensory cortex functional connectivity maps resulting form 40 (a) and 100 (b) components group ICA (ICASSO). The single cortical component (a) obtained with 40-ICASSO (bilateral pattern) is segregated into 4 meaningful components (b) when using 100-ICASSO, showing both inter- and intra- hemispherical separation of the somatosensory cortex.

Disclosure of author financial interest or relationships:
A. Mechling, None; **N. Huebner**, None; **H. Lee**, None; **J. Hennig**, None; **D. von Elverfeldt**, None; **L. Harsan**, None.

Presentation Number **P 343**
Poster Session 3
September 20, 2013 / 15:15-15:15 / Room: Exhibit Hall B

In vivo monitoring of the newly identified neurogenic microRNA related to neuronal differentiation induced by neurogenin 1 (Ngn 1) via microRNA microarray system

Hyun Jeong Oh[1], *Do Won Hwang*[1,2], *Hyewon Youn*[1], *Dong Soo Lee*[1,2], [1]*Department of Nuclear Medicine, Seoul National University College of Medicine, Seoul, Republic of Korea;* [2]*Institute of Radiation Medicine, Medical Research Center, seoul, Republic of Korea. Contact e-mail: holyhiphop@lycos.co.kr*

Purpose: MicroRNAs (miRNAs) are known as critical gene regulator and are involved in regulation of neuronal differentiation. Neurogenin1 (Ngn1) which is known as a basic helix loop helix transcription factor has been used as an activator of neuronal differentiation. To identify the novel neurogenic miRNA, we investigated the profile of miRNA during neurogenesis induced by Ngn1 via miRNA microarray. Methods: F11 cells transfected with Ngn1 were incubated in DMEM supplemented with 0.5% FBS for 1 day. MiRNA microarray was performed from isolated total RNA using agilent microarray scanner. Functional annotation for target genes of miRNAs was searched by DAVID v6.7 database. The 3'-UTR-based luciferase system containing 3 copy binding sequence for miRNA was used to observe expression of identified miRNA. Results: Microarray results in Ngn1-overexpressed F11 cells showed 240 upregulated miRNAs including miR-132 were considered as neurogenic miRNAs. We found that target genes of miRNAs were associated with neurogenesis, axon guidance and cell cycle. F11 cells generated neurite outgrowth within 3 days after the identified miRNA treatment. An in vivo study showed that bioluminescence signals were gradually decreased in identified miRNA treated group until 2 days. Immunocytochemistry and immunohistochemistry represented that βIII-tubulin, NeuroD and MAP2 neuronal marker expression was seen 3 days and 2 days after treatment of identified miRNA, respectively. Conclusions: In this study, we analyzed the miRNA expression profiling in Ngn1-treated F11 cells, via miRNA microarray. This study demonstrates that identified neurogenic microRNAs could be used as new potential inducer for neuronal differentiation in terms of stem cell-based therapy.

Disclosure of author financial interest or relationships:
H. Oh, None; **D. Hwang**, None; **H. Youn**, None; **D. Lee**, None.

Presentation Number **P 344**
Poster Session 3
September 20, 2013 / 15:15-15:15 / Room: Exhibit Hall B

Functional imaging evaluation of the neurometabolic changes in the 6-OHDA Parkinson disease model in rat

Andrés Damián[1,4], Laura Reyes[1], Gustavo Costa[2], Juan Andrés Abin-Carriquiry[2], José Pedro Prieto[3], Rodolfo Ferrando[4], Henry Engler[1], **Patricia Oliver**[1], *[1]Department of Biomedical Research, Uruguayan Center of Molecular Imaging (CUDIM), Montevideo, Uruguay; [2]Department of Neurochemistry, Biological Research Institute Clemente Estable (IIBCE), Montevideo, Uruguay; [3]Department of Celular Biology, IIBCE, Montevideo, Uruguay; [4]Nuclear Medicine Center, Clinical Hospital, University of the Republic, Montevideo, Uruguay. Contact e-mail: patricia.oliver@cudim.org*

Introduction: The 6-hydroxydopamine (6-OHDA) model is widely used to resemble selective neuronal degeneration that characterizes Parkinson's disease (PD). There is a limited amount of longitudinal studies that focus on the metabolic changes in this model. Aim: To monitor non-invasively neurometabolic changes at different time points in the 6-OHDA model using microPET and to correlate changes with behavioral evaluations and striatal dopamine (DA) levels. Methods: We performed unilateral lesions of the nigrostriatal DA system by injecting 6-OHDA in the right sustancia nigra in 9 rats. Behavioral and microPET studies were performed before, and 1 and 4 weeks after 6-OHDA lesion. All rats underwent behavioral evaluation in an Open Field system with amphetamine challenge. For microPET studies rats were intravenously injected with 63.3±13.1 MBq of [18F]-FDG; 30 minutes later animals were anesthetized and acquisition was performed in a Triumph Tri-modality Scanner (Gamma Medica, Inc.) during 60 minutes. PMOD software was used for quantification. Striatal DA levels were measured with HPLC. Results: Dopamine depletion in ipsilateral striatum was 90.8± 6 (mean ±SEM). Behavioral evaluation showed a significant increase in frequency of rotation towards the lesioned side ($p = 0.008$) 1 week post injury. A decrease in distance moved ($p = 0.05$), speed of movement ($p= 0.05$) and duration of movement ($p = 0.042$) was observed 4 weeks post injury. We found a significant correlation between ipsilateral number of turns and DA depletion (Pearson=0.74, $p=0.022$). MicroPET studies showed hypometabolism in ipsilateral striatum ($p = 0.039$), parietal cortex ($p = 0.0075$) and somatosensory cortex ($p = 0.0076$), and increased metabolism in cerebellum ($p= 0.026$) 1 week after the lesion. Significant partial reversibility of the somatosensory hypometabolism ($p = 0.032$) was found at 4 weeks. Conclusions: Our results highlight the dynamic nature of the neurometabolic changes in this model, and may contribute to understand the physiopathology of PD. Acknowledgments: National Agency for Research and Innovation (ANII), Uruguay. Biomedical Research Program (Pro.In.Bio), School of Medicine, University of the Republic, Uruguay.

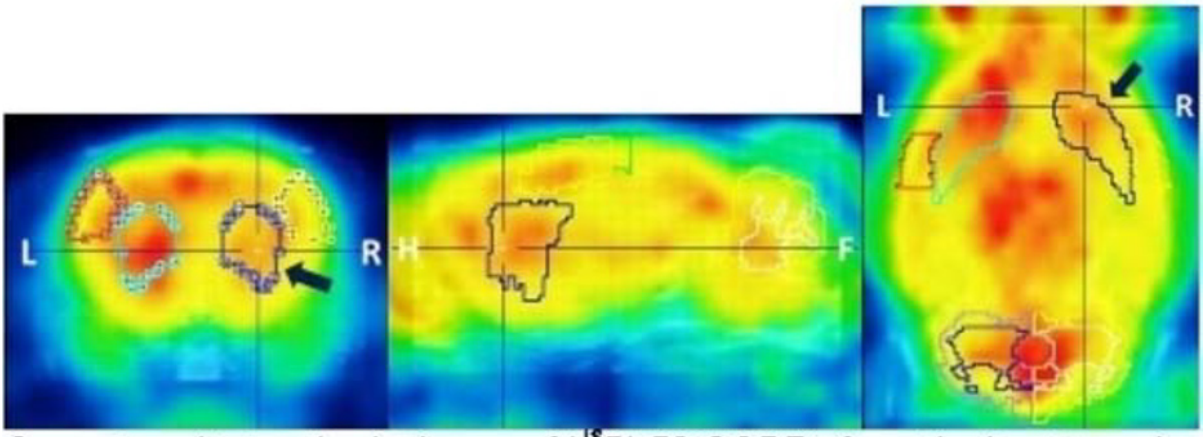

Coronal, sagittal and axial image of [^{18}F]-FDG PET of a rat brain at 1 week after injury. It shows a significant hypometabolism in the striatum ipsilateral to the lesion.

Disclosure of author financial interest or relationships:
A. Damián, None; **L. Reyes**, None; **G. Costa**, None; **J. Abin-Carriquiry**, None; **J. Prieto**, None; **R. Ferrando**, None; **H. Engler**, None; **P. Oliver**, None.

Presentation Number **P 345**
Poster Session 3
September 20, 2013 / 15:15-15:15 / Room: Exhibit Hall B

Irradiation induces molecular changes in endothelial cells of a rat AVM model

Newsha Raoufi-Rad, *Zhenjun Zhao, Joshua McHattan, Vivienne S. Lee, Michael Grace, Thi Thuy Hong Duong, Marcus Stoodley, Nirav J. Patel, Saleh R. Kashba, Australian School of Advanced Medicine, Macquarie University, Sydney, NSW, Australia. Contact e-mail: newsha.raoufi-rad@students.mq.edu.au*

Purpose: Brain arteriovenous malformations (AVMs) are abnormal connections between arteries and veins and are the leading cause of hemorrhagic stroke in children and young adults. A novel, safe and effective procedure is required to substitute the current challenging treatment of large and deep AVMs. Our hypothesis is that stereotactic radiosurgery can be utilized to selectively alter the phenotype of AVM endothelial cells, enabling targeting of AVM vessels using molecular therapies that spare normal vessels. This study examined the time course of expression of a potential target molecule by in vivo molecular imaging in a rat model of AVM after irradiation. Methods: The AVM model was created in 14 rats. Six weeks later, the AVM was irradiated with 20 Gy using a GammaKnife. The presence of phosphatidylserine (PS) on the luminal surface of endothelial cells was examined post-irradiation at day 1 and weeks 1, 3, 6, 9 and 12. Controls had an AVM fistula with no irradiation. The amount of PS on the endothelial cell surface was detected by a near-infrared fluorescent probe (PSVue 794). Results: There was an increase in PS level in irradiated rats compared to controls. PS reached the highest amount at weeks 1 and 9 in irradiated rats. Conclusion: These data support the hypothesis that stereotactic radiosurgery can alter endothelial cell phenotype in AVM vessels, potentially enabling the use of ligand-based molecular targeting therapies such as stimulation of thrombosis for AVM treatment.

Disclosure of author financial interest or relationships:
N. Raoufi-Rad, None; **Z. Zhao**, None; **J. McHattan**, Bruker, Employment; **V.S. Lee**, None; **M. Grace**, None; **T. Duong**, None; **M. Stoodley**, None; **N.J. Patel**, None; **S.R. Kashba**, None.

Presentation Number **P 346**
Poster Session 3
September 20, 2013 / 15:15-15:15 / Room: Exhibit Hall B

Prevention of Oxaliplatin-Induced Neuropathy by Minocycline: Demonstration by Imaging and Behavioral Assessment

Leo G. Flores[1], Elisabeth G. Vichaya[2], Lucia LeRoux[1], **Dawid Schellingerhout**[1], [1]*Departments of Radiology and Experimental Diagnostic Imaging, University of Texas M.D. Anderson Cancer Center, University of Texas M D Anderson Cancer Center, Houston, TX, USA;* [2]*Symptom Research, M D Anderson Cancer Center, Houston, TX, USA. Contact e-mail: Dawid.Schellingerhout@mdanderson.org*

Purpose: The purpose of our study was to utilize neurography, a new imaging technology evaluating retrograde transport, to determine if minocycline can prevent oxaliplatin-induced neuropathy, by using imaging with loss of retrograde axonal transport and pain behavior as biological readouts. Materials and Methods: Female BALB/c mice received one of four treatments vehicle/vehicle, vehicle/minocycline, oxaliplatin/vehicle, or oxaliplatin/minocycline (n=8/group). A 30 mg/kg cumulative dose of oxaliplatin or dextrose vehicle was given in 10 divided intraperitoneal doses across 3 weeks using a 5 days of treatment, 5 day rest, 5 day treatment administration paradigm. Furthermore, animals were treated daily with 50 mg/kg minocycline or 0.9% saline vehicle by oral gavage throughout the experiment beginning 48 h prior to the first oxaliplatin treatment. To assess the impact of minocycline on oxaliplatin-induced neuropathy, both imaging and behavioral (i.e., mechanical sensitivity) data was assessed at baseline and each week for 3 weeks. For each imaging session, animals received fluorescently labeled TTc-Alexa790 (15 ug/20 uL) via intramuscular injection into the calf muscle. Fluorescent imaging (Xenogen IVIS 200) was used to image the distribution of TTc over 60 minutes, with ROI measurements taken over the lower thoracic spine to quantitate fluorescent uptake. ROI measurements had background activity subtracted, and were normalized to the signal intensity at time=0. Mechanical sensitivity was assessed through the use of von Frey nylon filaments that produce calibrated force on the footpads. The 50% hind paw withdrawal threshold was calculated. At the end of the study tissue was harvested for immunohistochemical analysis. Results: Oxaliplatin/vehicle treated animals showed a decrease in transport of TTc during weeks 2 and 3, while the TTc transport of the vehicle/vehicle and oxaliplatin/minocycline remained stable across the experiment. The vehicle/minocycline group saw an increase in transport of TTc during weeks 2 and 3. Similarly, the behavioral data indicated that oxaliplatin treatment resulted in increased mechanical sensitivity, while minocycline treatment abrogated this effect, such that animals in the oxaliplatin/vehicle group showed increased sensitivity compared to all other groups. This effect emerged within the first week of treatment and remained throughout the study. At week 3 there was a significant correlation between pain behavior and TTc transport. Conclusion: Oxaliplatin causes decrease in retrograde axonal transport in the sciatic nerves and spinal cord, consistent with prior demonstrations. In this study we show that this effect can be attenuated by minocycline pre-treatment. Behavioral and imaging data were correlated. This suggests that minocyclin can prevent the painful neuropathy induced by Oxaliplatin, and that the mechanism of this effect might be related to retrograde axonal transport.

Disclosure of author financial interest or relationships:
L.G. Flores, None; **E.G. Vichaya**, None; **L. LeRoux**, None; **D. Schellingerhout**, None.

Presentation Number **P 347**
Poster Session 3
September 20, 2013 / 15:15-15:15 / Room: Exhibit Hall B

Retrograde Axonal Transport is Impaired after Radiation Injury: Demonstration with Neurographic Molecular Imaging

Dawid Schellingerhout[1], *Sebastian Bredow*[1], *David Grosshans*[2], *Lucia LeRoux*[1], [1]*Departments of Radiology and Experimental Diagnostic Imaging, University of Texas M.D. Anderson Cancer Center, University of Texas M D Anderson Cancer Center, Houston, TX, USA;* [2]*Radiation Oncology, M D Anderson Cancer Center, Houston, TX, USA. Contact e-mail: Dawid.Schellingerhout@mdanderson.org*

Purpose: The goal of this study was to determine whether molecular imaging is a suitable technique to detect changes in the spinal cord in response to radiation injury. Methods and Materials: The lower thoracic spinal cord of adult female BALB/c mice was irradiated with single doses of 2, 10, and 80 Gy. An optical imaging method utilizing the fluorescently labeled non-toxic C-fragment of tetanus toxin (TTc) was used to evaluate changes in the retrograde axonal transport mechanism, while Luxol fast blue staining served to assess demyelination in radiated cords. Results: Transport of TTc in the thoracic spinal cord was impaired in a dose-dependent manner as early as 2 days after radiation. Transport was significantly decreased by 16 d in animals exposed to either 10 or 80, while animals exposed to 2 Gy remained unaffected. Further, animals exposed to the highest dose also experienced significant weight loss by 9 d and developed posterior paralysis by 45 d. Demyelination in radiated cords could be observed after 30 d in mice exposed to 80 Gy. Conclusion: Radiation of the spinal cord induces dose-dependent changes in the axonal transport mechanism which can be monitored by molecular imaging. This approach suggests a novel diagnostic modality to assess nerve injury and monitor therapeutic interventions.

Disclosure of author financial interest or relationships:
D. Schellingerhout, None; **S. Bredow**, None; **D. Grosshans**, None; **L. LeRoux**, None.

Presentation Number **P 348**
Poster Session 3
September 20, 2013 / 15:15-15:15 / Room: Exhibit Hall B

Comparative analysis of CSF kinetics of IT injected 111In-DTPA and 99mTc-sestamibi in rats

Jenna M. Sullivan[1], *Jacob Hesterman*[1], *Matthew D. Silva*[1], *Catey L. Harwell*[1], *Jaime Tierney*[1], *Dustin Kentala*[3], *Mark R. Lane*[3], *Jack Hoppin*[1], *Ajay Verma*[2], [1]*inviCRO, LLC, Boston, MA, USA;* [2]*Biogen Idec, Inc., Cambridge, MA, USA;* [3]*Molecular Imaging, MPI Research, Kalamazoo, MI, USA. Contact e-mail: jsullivan@invicro.com*

The blood brain barrier (BBB) protects and maintains homeostasis in the central nervous system (CNS), but it may also prevent drugs to treat CNS disease from reaching the brain. Direct injection of compounds into the subarachnoid space via intrathecal (IT) injection may be able to bypass the BBB and increase drug delivery to the brain. The development of drugs for IT delivery requires an intimate understanding of pharmacokinetics in the cerebral spinal fluid (CSF). The objective of this study was to investigate pharmacokinetics in the CSF by examining the spatial distribution of IT co-injected 111In-DTPA and 99mTc-sestamibi. Sprague-Dawley rats (n=6) received IT co-injection of 111In-DTPA and 99mTc-sestamibi. Doses were administered in 20µL (n=2), 100 µL (n=2), or 30µL followed by a 40µL saline flush. Average injected activity was 804 ± 211 µCi for 111In-DTPA and 589 ± 207 µCi for 99mTc-sestamibi. Whole body SPECT scans followed by CT were acquired on anesthetized animals 0-1 (4x9min), 2, and 6 hours (1x30min) post-injection. Dual-isotope data was collected simultaneously by the NanoSPECT/CT® (Bioscan, Washington, DC) using energy windows for 111In (155.6-186.4 and 220.5-269.5 keV) and 99mTc (127.9-153.2 keV). 111In energy windows were summed for reconstruction. Spinal regions of interest (ROIs) were defined by applying a combination of manual and automated segmentation thresholds to the CT data. The spine (skeleton), sheath, and CSF were segmented and subdivided into the cervical, thoracic, and lumbar regions for analysis. The tracer activity profile over the length of the spine was plotted to examine spatial distribution of tracers within the subarachnoid space. Activity distribution along the spine varied between tracers. 111In-DTPA distributed throughout the lumbar, thoracic, and cervical subregions up to the brain, regardless of injection volume. For 20µL or 100 µL dose volumes, 99mTc-sestamibi distributed only throughout the lumbar subregion. However, for doses in 30µL followed by a 40µL saline flush, 99mTc-sestamibi distributed throughout both lumbar and thoracic subregions and into the cervical region. The limited spatial distribution of 99mTc-sestamibi along the spine compared to 111In-DTPA is likely due to its targeting of mitochondrial metabolism and uptake into cells near the site of injection.

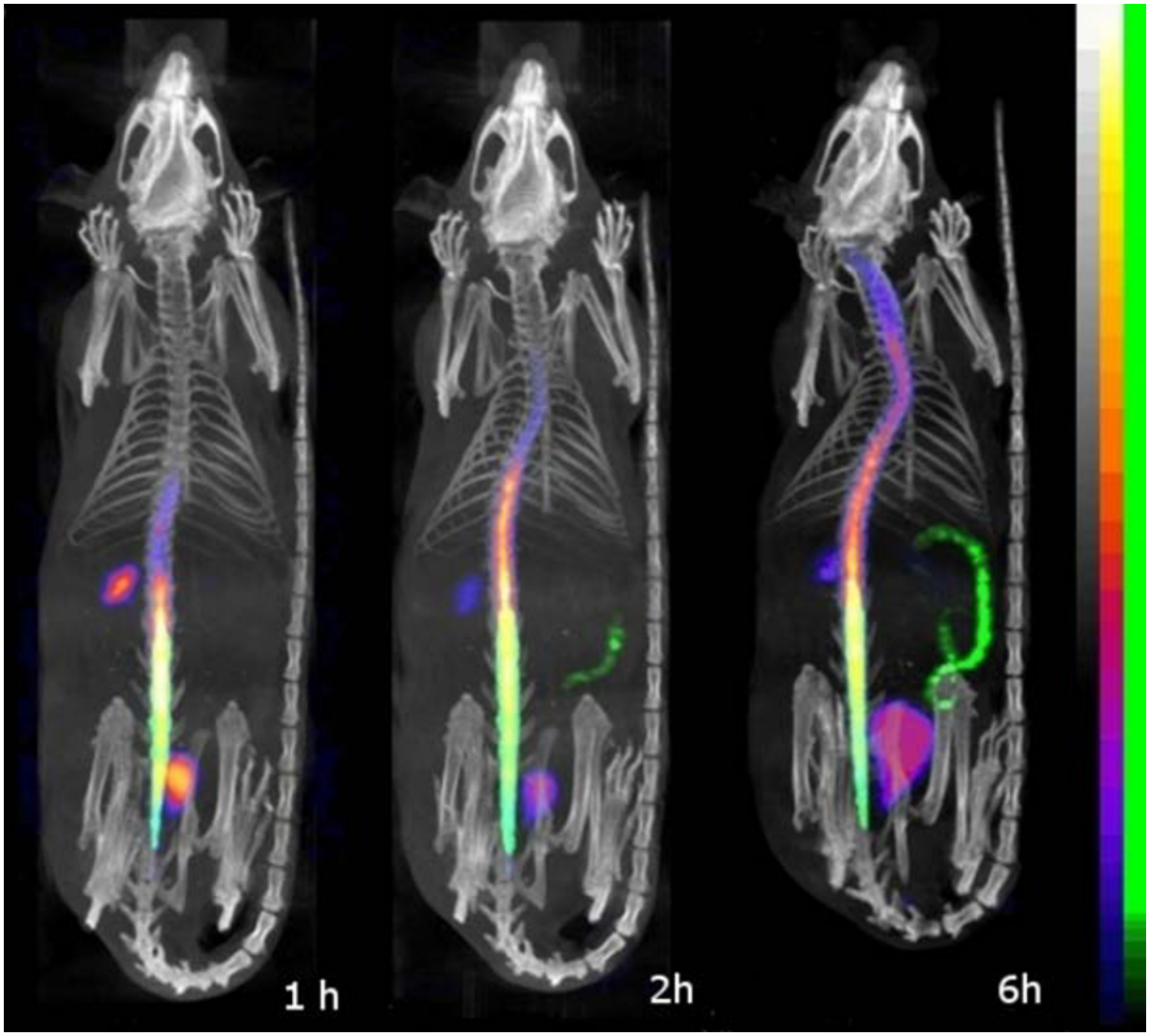

Dual-isotope 111In-DTPA and 99mTc-sestamibi maximum intensity projection (MIP) images shown superimposed on CT. Fire = 111In-DTPA, Green = 99mTc-sestamibi. Images are normalized to injected dose and scaled to a fixed max. From left to right, images show spatial distribution of tracer uptake over time. Tracers were injected IT in 20µL.

Disclosure of author financial interest or relationships:
J.M. Sullivan, inviCRO, LLC, Employment; **J. Hesterman**, inviCRO, LLC, Employment; **M.D. Silva**, inviCRO, LLC, Employment; **C.L. Harwell**, inviCRO, LLC, Employment; **J. Tierney**, inviCRO, LLC., Employment; **D. Kentala**, MPI Research, Employment; **M.R. Lane**, None; **J. Hoppin**, inviCRO, Stockholder; **A. Verma**, Bogen Idec, Employment .

Presentation Number **P 349**
Poster Session 3
September 20, 2013 / 15:15-15:15 / Room: Exhibit Hall B

In vivo basic tracer pharmacokinetic analysis for transgenic mouse models of Alzheimer's disease

Krisztián Szigeti[1], *Gellért- Szabolcs Kovács*[1], *István Varsányi*[1], *Ferenc Budán*[2], *Ildiko Horvath*[1], *Albert D. Windhorst*[3], *Domokos Mathe*[2], [1]*Biophysics and Radiation Biology, Semmelweis University, Budapest, Hungary;* [2]*CROmed Ltd, Budapest, Hungary;* [3]*Radiology, Nuclear Medicine and PET Research, Vrije University, Amsterdam, Netherlands. Contact e-mail: szigeti.krisztian@med.semmelweis-univ.hu*

Introduction: In the past years several transgenic (TG) mouse models of Alzheimer's disease (AD) were developed. This speeds up scientific research and drug development. The radiopharmaceuticals for clinical AD research appeared to be useful tools for mouse AD imaging too. There is a lack of basic pharmacokinetic parameters of these agents defined using high-resolution and high sensitivity multimodal equipments in rodent models. Such is the case of 2-(1-{6-[(2-[18F]Fluoroethyl)(methyl)amino]-2-naphthyl}ethylidene)malononitrile (FDDNP) too. Aims. In this study we aimed a) to define the mouse brain distribution of FDDNP activity concentration in time and space. Another aim b) was to create a healthy reference mouse brain database containing kinetic parameters. Materials and methods. We analyzed the distribution of FDDNP (cca. 3.0 MBq/mouse) in brain with dynamic recording using a sequential nanoScan PET/MRI system. On the other hand the blood volumes of different brain compartments were analyzed with 99mTc-labeled human serum albumin (cca. 195.5 MBq/mouse) using a NanoSPECT/CTPLUS. Experiments were performed using a PET/MRI-SPECT/CT coregistration-compatible MultiCell animal bed system in healthy C57BL6 mice (n=7). Changes of the radiopharmaceutical concentration over time were analyzed in four different brain regions- neocortex, thalamus, hippocampus, cerebellum- with own MRI volumes co-registered and measured. To determine the blood input function we applied a non-invasive method including SPECT left ventricular blood volumetry to calculate FDDNP concentration. Based on our data from 90-minute dynamic in vivo measurements we were able to set up a 1+1 and a 4+1 compartment pharmacokinetic model and could define model parameters. Results. The concentration curves over time in the analyzed brain regions are similar. The biggest activity concentration and uptake constant (0.36 1/min) was measured in thalamus. We determined that the concentration in neocortex compared to cerebellum was smaller, but there was no significant difference. Neocortex is reported to be a specific region where β-amyloid plaques appear in the Alzheimer mouse models. Therefore we expect the calculated kinetic parameters to significantly change in AD-TG mouse models. Conclusion. We built up a pharmacokinetic parametric map of healthy brain FDDNP uptake for a reference in the development of AD diagnostic and therapeutic model research. Acknowledgement This work was supported in part by INMiND (HEALTH.2011.2.2.1-2 No.278850) of FP7. We thank Mediso Ltd for technical background of NanoSPECT/CT+ and nanoScan PET/MRI.

Disclosure of author financial interest or relationships:
K. Szigeti, None; **G. Kovács**, None; **I. Varsányi**, None; **F. Budán**, None; **I. Horvath**, None; **A.D. Windhorst**, None; **D. Mathe**, CROmed Ltd, Stockholder; Mediso Ltd., Consultant .

Presentation Number **P 350**
Poster Session 3
September 20, 2013 / 15:15-15:15 / Room: Exhibit Hall B

Role of BDNF in Levodopa-Induced Dyskinesia - an in vivo PET Quantification of Serotonin Axon Terminals

Michael Walker, *Kristina Fischer, Maren K. Koenig, Sandro Aidone, Anke Stahlschmidt, Walter Ehrlichmann, Bernd J. Pichler, Lab for preclinical imaging and radiopharmacy, Tuebingen, Germany. Contact e-mail: michael.walker@med.uni-tuebingen.de*

The gold standard therapy for Parkinson's disease (PD) is still the administration of L-DOPA. PD patients taking L-DOPA for a period of 3 to 6 years develop side effects, called L-DOPA-induced dyskinesias (LID), which are caused by a non-physiological pulsatile dopamine (DA) release from striatal serotonergic (5-HT) projections of the dorsal raphe nuclei. Enhanced expression of brain derived neurotrophic factor (BDNF) has been shown to result in sprouting of 5-HT neurons which exacerbates the dyskinetic level [1]. The 5-HT transporter (5-HTT) is regarded as a measure of 5-HT neuron density and serves as the target for [11C]DASB. To further test the effect of BDNF on 5-HT neurons and the development of dyskinesias, we compared the binding potential (BPND) of [11C]DASB in wild type (wt) and heterozygous BDNF k.o. rats before and after L-DOPA priming and analyzed the LID levels of both groups in a longitudinal in vivo investigation. All animals (BDNF k.o. n=5; wt n=5) underwent an unilateral 6-hydroxy-DA lesion in the left medial forebrain bundle. 4 weeks post lesion, an apomorphine test was performed to determine lesion severity. Subsequently, MR anatomical images were acquired and a 90 min dynamic baseline [11C]DASB PET scan was performed (BDNF k.o.: n=5; wt: n=2; 55±4 MBq/kg). The BPND in the striatum and the thalamus was determined with the simplified reference tissue model using the cerebellum as a reference region. L-DOPA priming was performed over the following 3 weeks including cylinder tests (LID test) on day 1, 7, 14 and 21. A second 90 min dynamic [11C]DASB PET scan (55±6 MBq/kg) was performed after priming and BPND was calculated as described above. In BDNF k.o. rats, BPND values in the striatum were reduced by 31% on the lesioned side compared to the healthy side before L-DOPA treatment ($p=0.03$), while in wt rats no difference between healthy and lesioned side was observed. The BPND before and after L-DOPA priming showed no significant difference, but a trend towards a BPND reduction in wt ($p=0.06$) and BDNF k.o. ($p=0.07$) rats on the healthy hemisphere. In the thalamus, BPND values after L-DOPA priming were reduced by 50% in wt rats and by 23% in BDNF k.o. rats ($p<0.05$). The behavioural analysis revealed an earlier onset of the LID in the BDNF k.o. rats (day 7) than in the wt animals and reached significantly higher LID scores over time (day 14: $F(6, 48)=2.6$; $p=0.03$). The lower BPND values could be caused by internalization of 5-HTT due to the L-DOPA-priming and not as a lesion-induced effect since it was not restricted to the lesioned side and also present in the thalamus. The earlier onset of LID and the trend of the reduced BPND on the lesioned side in BDNF k.o. rats might be due to the knockout, lacking in cellular repair mechanisms. Further experiments are ongoing to increase the number of rats per group and histological analysis will be performed to confirm the in vivo findings. [1] Rylander, D., M. Parent, et al. (2010). "Maladaptive plasticity of serotonin axon terminals in levodopa-induced dyskinesia." Ann Neurol 68(5): 619-628.

Disclosure of author financial interest or relationships:
M. Walker, None; **K. Fischer**, None; **M.K. Koenig**, None; **S. Aidone**, None; **A. Stahlschmidt**, None; **W. Ehrlichmann**, None; **B.J. Pichler**, Siemens, Grant/research support; Bayer, Grant/research support; AstraZeneca, Grant/research support; BoehringerIngelheim, Grant/research support .

Presentation Number **P 351**
Poster Session 3
September 20, 2013 / 15:15-15:15 / Room: Exhibit Hall B

An in vivo comparison of 3- and 4- [^{18}F]mefway in the nonhuman primate using PET

Dustin W. Wooten[1], *Ansel Hillmer*[1], *Patrick Lao*[1], *Christopher Liang*[2], *Joanne Thio*[2], *Alisha Bajwa*[2], *Todd E. Barnhart*[1], *Mary L. Schneider*[1], *Jogeshwar Mukherjee*[2], *Bradley T. Christian*[1], [1]*University of Wisconsin-Madison, Madison, WI, USA;* [2]*University of California-Irvine, Irvine, CA, USA. Contact e-mail: dwooten@wisc.edu*

4-[^{18}F]Mefway (4-MEF) is a PET radiotracer with high affinity for the 5-HT$_{1A}$ receptor (Wooten et al, Synapse 2011). Often, radiotracers with lower affinity are desired because they are more susceptible to changes in endogenous neurotransmitter levels. In this work, we compare the in vivo kinetics of the positional isomers 3- and 4-MEF to evaluate the properties of 3-MEF as a potential lower affinity 5-HT$_{1A}$ PET radiotracer. Methods: One monkey (m, 11 kg, 16 years) was given bolus injections of both 3- and 4- MEF in separate experiments. Dynamic scans were acquired for 90 minutes using a microPET P4 scanner. Arterial blood sampling was performed to assay time course of native compound and to allow one-compartmental modeling of nondisplaceable kinetics. Time activity curves were extracted in the mesial temporal cortex (MTC), caudal anterior cingulate gyrus (cACg), raphe nuclei (RN), and the cerebellum (CB) which was validated as a reference region for 4-MEF in our previous work. The in vivo behavior of the radiotracers was compared based upon the nondisplaceable distribution volume (V_{ND}) in the CB and nondisplaceable binding potential (BP_{ND}) in specific binding regions calculated using the MRTM method. Results: Following initial rapid clearance of tracer from plasma (time > 30 minutes) exponential clearance of radiotracer was 0.015 (3-MEF) and 0.014 (4-MEF) min^{-1}. One-compartmental modeling in the CB revealed V_{ND} values of 5.4 (3-MEF) and 5.9 (4-MEF) and similar influx rate constants of 0.69 (3-MEF) and 0.71 (4-MEF) mL/mL/min. BP_{ND} values were MTC: 1.04, 3.8; cACg: 0.85, 3.5; and RN: 0.3, 2.3 for 3-MEF and 4-MEF, respectively. Conclusion: The similar kinetics in plasma and CB for 3- and 4-MEF suggests the lower BP_{ND} of 3-MEF is due to a lower affinity. Because of the lower affinity of 3-MEF, it may provide use for measuring changes in endogenous 5-HT levels, however, 5-HT competition studies will be needed to confirm 3-MEF's sensitivity to these changes.

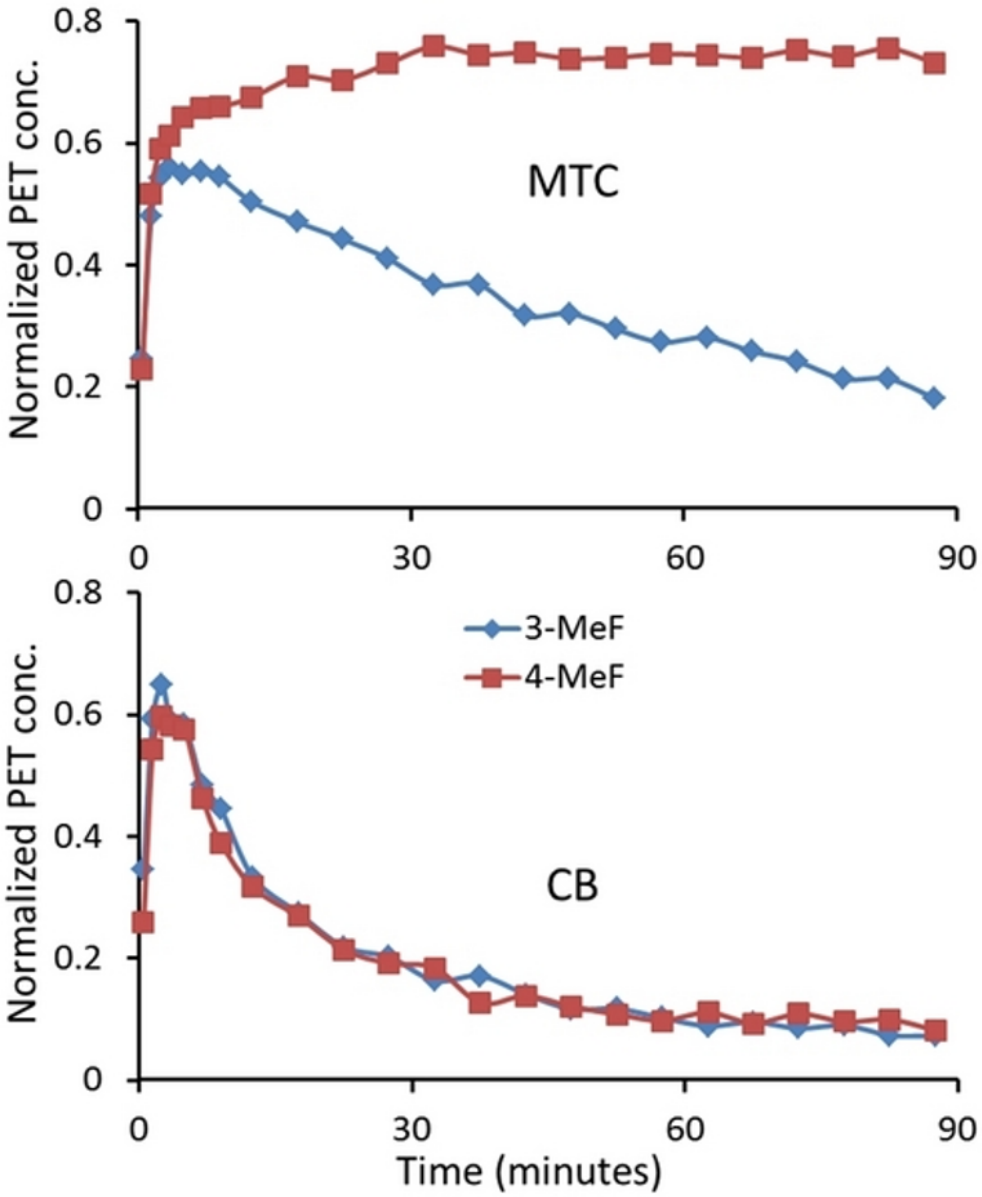

Decay corrected time activity curves of 3- and 4- MEF in the MTC (top) and CB (bottom).

Disclosure of author financial interest or relationships:

D.W. Wooten, None; **A. Hillmer**, None; **P. Lao**, None; **C. Liang**, None; **J. Thio**, None; **A. Bajwa**, None; **T.E. Barnhart**, None; **M.L. Schneider**, None; **J. Mukherjee**, None; **B.T. Christian**, Abiant, Inc, Grant/research support .

Presentation Number **P 352**
Poster Session 3
September 20, 2013 / 15:15-15:15 / Room: Exhibit Hall B

Behavioral and neurochemical alterations in C57BL/6 mice exposed to cuprizone: An in vivo 1H-MRS study at 7.0T

Gen Yan, *Zhuozhi Dai, Zhiwei Shen, Renhua Wu, Shantou University, Shantou, China. Contact e-mail: gyan@stu.edu.cn*

Recent animal and human studies have suggested that the cuprizone (CPZ, a copper chelator)-fed C57BL/6 mouse may be used as an animal model of schizophrenia. To date, few studies have used proton magnetic resonance spectroscopy (1H-MRS) to assess the effects of on mouse. In the present study we aim to assess and quantify the regional neurochemical alterations of CPZ-induced mouse model by 7T 1H-MRS. C57BL/6 mice were given 0.2% CPZ-containing diet for 5weeks while controls ate the same diet without CPZ. The animals were subjected to behavioral tests and 1H-MRS scan. An ultra short echo stimulated echo acquisition (STEAM) localization sequence (TR/TM/TE=5000/10/2.2ms) was used to measure in vivo proton spectra from the left striatum (voxel volume: 8μl) and thalamus (27 μl) of C57BL/6 mice at 7.0T and acquired proton spectra post-processed offline with LCModel. CPZ-fed mice showed significant decrease of spontaneous alternation in the Y-maze test. The concentrations of N-acetyl aspartate (NAA) and N-acetyl aspartate +N-acety laspartyl glutamate (NAA+NAAG) in the left striatum and thalamus were significantly reduced in CPZ-fed mice.. In addition, the concentration of Glu+Gln in the left thalamus of CPZ-fed mice was significantly higher than control mice. Lower NAA and NAA+NAAG levels may reflect an overall reduction of cellular processes in the caudate of CPZ-fed mice, which may be related to decreases in cell density. CPZ-fed mice show deficit in working memory as indicated by Y-maze test and have a higher Glx level in their thalamus. These features suggest that the CPZ model is a novel animal Model of schizophrenia.

Disclosure of author financial interest or relationships:
G. Yan, None; **Z. Dai**, None; **Z. Shen**, None; **R. Wu**, None.

Presentation Number **P 353**
Poster Session 3
September 20, 2013 / 15:15-15:15 / Room: Exhibit Hall B

Longitudinal coupled-imaging Alzheimer's disease mouse model using [11C]PIB and [18F]FDG PET

Yu-Ning Tang[1], *Hsin-Hsien Yeh*[1], *Tat-Wei D. Tan*[1], *Chi-Wei Chang*[2], *Hsin-Ell Wang*[1], *Irene Han-Juo Cheng*[3], *Ren-Shyan Liu*[4], [1]*Biomedical Imaging and Radiological Sciences, National Yang-Ming University, Taipei, Taiwan;* [2]*Nuclear Medicine, Taipei Veterans General Hospital, Taipei, Taiwan;* [3]*Brain Science, National Yang Ming University, Taipei, Taiwan;* [4]*Medicine, National Yang-Ming University, Taipei, Taiwan. Contact e-mail: ning217@hotmail.com*

Objectives: Alzheimer' disease (AD) is typified by deposition of β-amyloid (Aβ) within the brain accompany with cognitive decline. Imaging Aβ plaque could be useful for the development of the therapeutic and diagnosis target in AD. In this study, we aimed to access the change of Aβ and neuronal metabolism in the brain in AD mice over age by using [11C]PIB and [18F]FDG PET. Methods: The human amyloid precursor protein (hAPP) transgenic mouse lines J20 were bred and reared in our colony; littermates without hAPP were used as wild-type (wt) mice. The behavior test was applied to evaluate the change of memory and learning in APP mice. The animals (N=6/group) were imaged monthly from month 4 to month 12. The 20 min static imaging were performed after i.v. injection of [11C]PIB or [18F]FDG at 30 min. Thereafter, the animals were sacrificed, brains removed, fixed, and sectioned at 20μm for immunehistochemical staining for β-amyloid. Results: The memory and learning performance was significantly deficit in APP mice after 5-6 months. The accumulation of [11C]PIB tended higher in APP mice than the that of wt mice since month 4. The high level of accumulations of [11C]PIB were in midbrain, striatum and hippocampus where were most affected in AD. The age-dependent increased accumulation of [11C]PIB in APP mice appeared from month 4 to month 12. No difference of [18F]FDG uptake was observed between APP and wt mice in whole study period. Conclusion: [11C]PIB PET could be used to distinguish APP mice from the control ones before onset at month 5 when pathological change of Aβ in hippocampus appears. Due to the limitation of micro PET imaging, the subtle change in the brain in earlier stage (<month 4) may not be detected. [18F]FDG PET does not show the metabolic deficits in APP mice when compared to wt mice. It could be implied that the neuron loss in APP mice happens later than the β-amyloid deposition.

Disclosure of author financial interest or relationships:
Y. Tang, None; **H. Yeh**, None; **T.D. Tan**, None; **C. Chang**, None; **H. Wang**, None; **I. Cheng**, None; **R. Liu**, None.

Presentation Number **P 354**
Poster Session 3
September 20, 2013 / 15:15-15:15 / Room: Exhibit Hall B

Silica-coated superparamagnetic iron oxide nanoparticles targeting of EPCs in ischemic brain injury

Qianyun Li[2], Guanghui Tang[1], Sihan Xue[1], **Chunfu Zhang**[1]*, Guo-Yuan Yang[1], [1]Med-X Research Institute, Shanghai Jiao Tong University, Shanghai, China; [2]Department of Neurology, Ruijin Hospital, Shanghai Jiao Tong University, Shanghai, China. Contact e-mail: cfzhang@sjtu.edu.cn*

Objectives Intravenous transplantation of endothelial progenitor cells (EPCs) contributed to reduced ischemic injury, but only a small portion of transplanted cells migrated to damaged sites using this way. In the present study, we transplanted silica-coated superparamagnetic iron oxide nanoparticles (SiO4@SPIONs)-transfected EPCs intravenously to cerebral ischemic mouse to explore whether exerting an exterior magnetic field could promote the migration of SiO4@SPIONs-EPCs to cerebral ischemic region and enhanced the treatment effect. Methods SiO4@SPIONs were synthesized by coating SPIONs with silica. EPCs were isolated from human umbilical cord blood and incubated with SiO4@SPIONs for 2 hours. The effect of SiO4@SPIONs and magnetic field on EPCs was tested by CCK-8 assay, Transwell test and tube formation assay. Accumulation of SiO4@SPIONs-EPCs in flowing condition under magnetic field was tested. Adult male ICR mice (n=60) underwent transient suture middle cerebral artery occlusion (tMCAO). After SiO4@SPIONs-EPCs were injected into the mice intravenously, magnetic field was applied on the ischemic hemisphere for 2 hours. SiO4@SPIONs-EPCs migration was determined at 24 hours after tMCAO. Neurobehavioral outcomes, brain atrophy volume, microvessel counts and VEGF expression were examined at 2 and 4 weeks after tMCAO. Results The optimized concentration of SiO4@SPIONs for EPC labeling was 10 μg/ml which did not affect EPCs proliferation, migration and tube formation. SiO4@SPIONs-EPCs could be captured by exterior magnet field (0.3T) in vitro. SiO4@SPIONs-EPCs were significantly increased in the ischemic hemisphere at 24 hours after cell injection in tMCAO mice (with vs. without magnetic field, $p<0.05$). Moreover, tMCAO mice receiving SiO4@SPIONs-EPCs injection plus magnetic field application showed significantly reduced brain atrophy volume ($p<0.05$), improved neurobehavioral outcomes ($p<0.05$), increased microvessel counts ($p<0.05$) and VEGF expression ($p<0.05$) in peri-focal region compared to group without magnetic field (Figure 1). Conclusions Exterior magnetic field greatly promoted SiO4@SPIONs-EPCs migration and homing without affecting EPCs survival and function; consequently improved neurobehavioral outcomes. Our results suggested that exterior magnetic field could enhance the treatment effect of SiO4@SPIONs-EPCs in brain diseases.

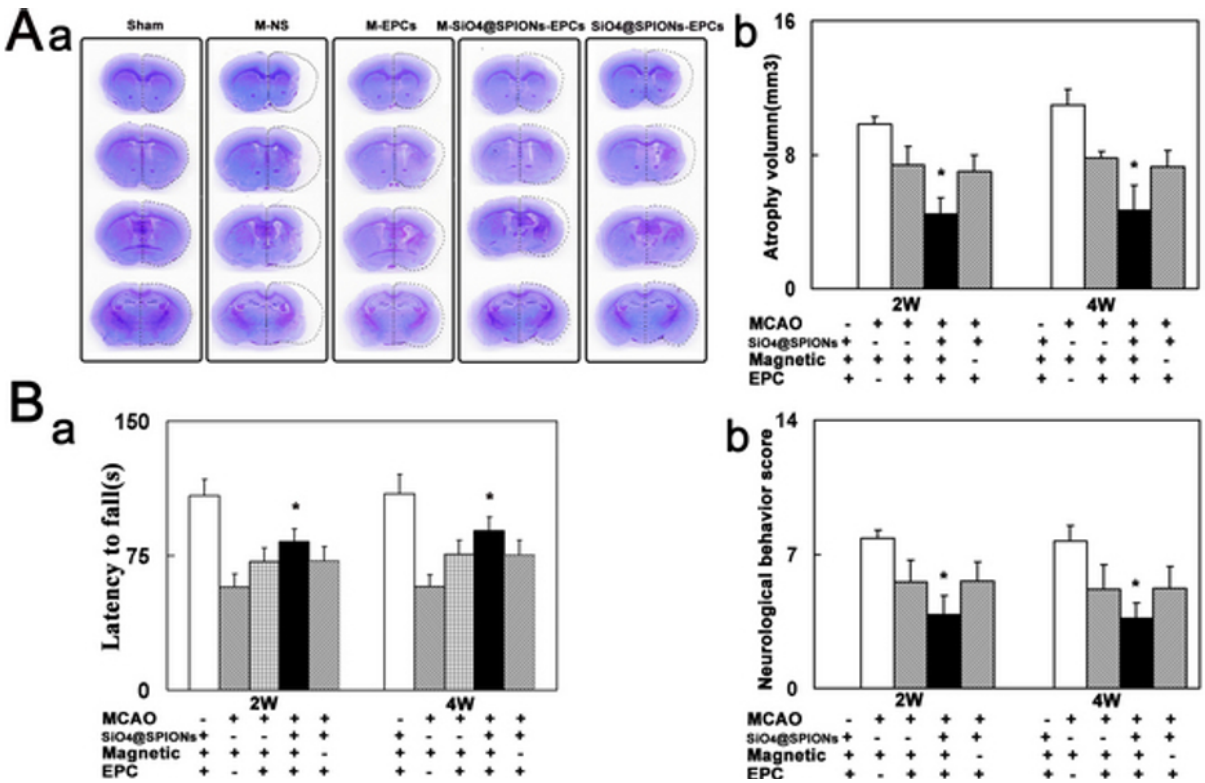

Figure 1. Ischemia-induced brain injury was attenuated in mice with M-SIO4@SPIONs-EPCs treatment A series of coronal sections represented cortical atrophy in M-NS, M-EPCs, M- M-SIO4@SPIONs-EPCs, M-SIO4@SPIONs-EPCs and sham groups, and the dotted line showed normal size of the left hemisphere. Bar graph showed calculation of cortical atrophy volume. *, $p<0.05$, data are mean± SD, n=6 in each group. B. Bar graphs showed time of mice staying on the rotor-rod (rotor-rod test) (a) and neurobehavioral deficiency (mNSS) (b) after 2 and 4 weeks of tMCAO in SIO4@SPIONs-EPCs mice with/without magnetic field. *, $p<0.05$, vs. SPIO-EPC and other three groups. Data are mean± SD, n=6 in each group.

Disclosure of author financial interest or relationships:
Q. Li, None; **G. Tang**, None; **S. Xue**, None; **C. Zhang**, None; **G. Yang**, None.

Presentation Number **P 355**
Poster Session 3
September 20, 2013 / 15:15-15:15 / Room: Exhibit Hall B

A Multi-functional Nanoplatform for Imaging, Radiotherapy, and the Prediction of Therapeutic Response

Ajlan Al Zaki[1], *Casey McQuade*[1], *Yaanik Desai*[1], *Michael J. Vido*[1], *Timothy Sakhuja*[1], *Rob J. Hickey*[2], *Daniel Joh*[3], *So-Jung Park*[2], *Gary Kao*[3], *Jay F. Dorsey*[3], *Andrew Tsourkas*[1], [1]*Bioengineering, University of Pennsylvania, Philadelphia, PA, USA;* [2]*Chemistry, University of Pennsylvania, Philadelphia, PA, USA;* [3]*Radiation Oncology, University of Pennsylvania, Philadelphia, PA, USA. Contact e-mail: ajlan@seas.upenn.edu*

Current radiation-based therapies are often limited by the maximum allowable dose tolerated by adjacent healthy tissues. Difficulty in visualizing tumor boundaries often exacerbates efforts to maximize tumor dosage while minimizing the damaging off-target effects of radiation. Here, we describe Gold and Superparamagentic iron oxide (SPIO)-loaded polymeric Micelles (GSMs)(Figure 1a) that were specifically designed to help demarcate tumor boundaries by magnetic resonance imaging (MRI), enhance radiosensitization via a gold-mediated photoelectric effect, and ultimately improve therapeutic index. GSMs were prepared with a hydrodynamic diameter of ~120nm (Figure 1a) and a transverse relaxivity (r2) of 196$mM^{-1}s^{-1}$. When human fibrosarcomma cells were incubated with GSMs and exposed to ionizing radiation, there was a significant increase in DNA double strand breaks compared with cells treated with radiation alone and non-irradiated controls (Figure 1b). Intravenous injection of GSMs into tumor-bearing mice led to the selective accumulation of GSMs in the tumors, enabling non-invasive MRI imaging and clearer delineation of the tumor margins (Figure 1c). Subsequent administration of 150 kVp X-ray therapy led to a ninety-day survival for 71% of GSM-treated mice. In contrast, the ninety-day survival for mice receiving radiation therapy alone was only 29% and it was 0% for mice receiving GSM alone and in untreated mice. In the mice that received GSMs and radiation therapy, a positive correlation was observed to exist between tumor contrast enhancement and the rate of decrease in tumor volume. The combined therapeutic, diagnostic, and prognostic characteristics of this dual-metal nanoparticle micelle system could thus enable a more personalized approach to a patient's cancer therapy and help predict tumor response.

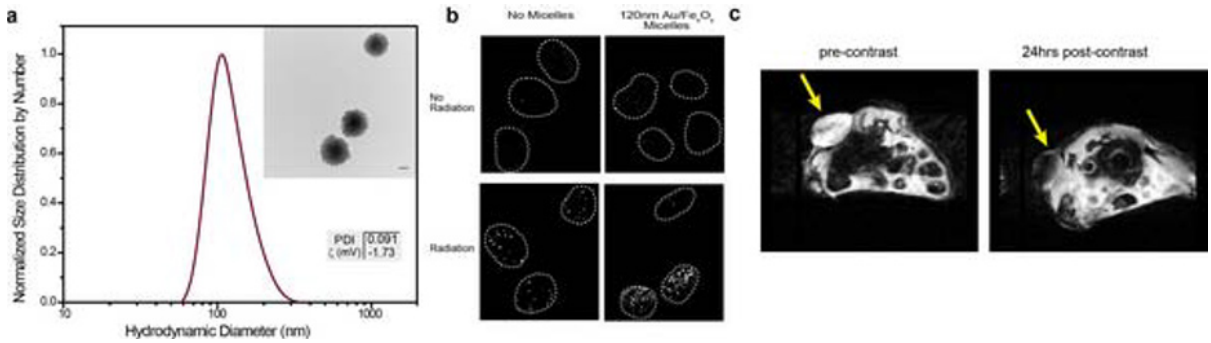

Figure 1. Gold and SPIO-loaded polymeric micelles. (a) GSMs have a peak size of 120nm and low polydispersity, as determined by dynamic light scattering. Inset. TEM of GSMs (AuNPs and SPIO are visible). (b) In vitro irradiation studies. Immunofluorescent imaging of double strand breaks (i.e. gh2ax foci) in HT1080 cells that have been incubated without and with GSMs in the absence (top row) or presence (bottom row) of radiation (4 Gy). Cells incubated with GSMs show a higher frequency of gh2ax foci 12 hrs after the administration of orthovoltage radiation. (c) In vivo MR imaging. Representative T2* weighted MR images in the axial plane prior to injection (pre-contrast) and 24 hours after injection (post-contrast) of GSMs (n=3). Tumor location is indicated by yellow arrows.

Disclosure of author financial interest or relationships:

A. Al Zaki, None; **C. McQuade**, None; **Y. Desai**, None; **M.J. Vido**, None; **T. Sakhuja**, None; **R.J. Hickey**, None; **D. Joh** , None; **S. Park**, None; **G. Kao**, None; **J.F. Dorsey**, None; **A. Tsourkas**, None.

Presentation Number **P 356**
Poster Session 3
September 20, 2013 / 15:15-15:15 / Room: Exhibit Hall B

CD276: A novel tumor specific vascular endothelial cell marker for ultrasound molecular imaging of breast cancer

Sunitha Bachawal[1], *Ferdinand Knieling*[1], *Amelie M. Lutz*[1], *Lu Tian*[2], *Juergen K. Willmann*[1], [1]*Radiology/MIPS, Stanford University, Stanford, CA, USA;* [2]*Health Research and Policy, Stanford University, Stanford, CA, USA. Contact e-mail: bachawal@stanford.edu*

Background Molecularly-targeted contrast enhanced ultrasound (US) is an emerging tool with great potential for improving the sensitivity/specificity of US for earlier cancer detection. An ideal molecular imaging target for early cancer detection is differentially expressed in cancer compared to benign pathologies. For US molecular imaging using micron-sized microbubbles (MB) as contrast agents, imaging targets need to be expressed on tumor vasculature as the size of MB precludes them from entering the extravascular compartment. CD276 (B7-H3) is a member of B7 family of immunoregulatory molecules involved in T-cell activation. In a recent proteomic study it has been shown that CD276 is differentially expressed in breast cancer compared to normal breast tissue. Furthermore, other studies indicated that CD276 is predominantly expressed on the vascular endothelial cells of various tumors, including breast cancer. Vascular endothelial growth factor receptor type2 (VEGFR2) is a general angiogenesis marker that overexpressed in breast cancer. The goal of our study was to compare the potential of US molecular imaging using MB targeted to CD276 with VEGFR2-targeted MB for assessment of breast tissue progression to early breast cancer in transgenic mice (FVB/N Tg (MMTV/ PyMT634Mul). Methods A total of 160 mammary glands were imaged each using VEGFR2- and CD276 targeted MB in the same imaging session. In vivo US imaging was performed in the non-linear mode using a 21 MHz transducer on a dedicated small-animal US imaging system (Vevo 2100). Results There was a significant ($p<0.001$) increase of in vivo imaging signal on both VEGFR2 and CD276-targeted molecular US images when breast tissue progressed over time from normal tissue (5.6 ± 0.95, 4.5 ± 0.7 a.u. respectively) to breast cancer (98.8 ± 8.78, 51.9 ± 5.3 a.u. respectively) in transgenic mice. ROC curves were constructed using logistic regression model to differentiate benign histological entities (normal and hyperplasia) from malignant forms of breast cancer (ductal carcimoma in situ (DCIS) and invasive breast cancer). Results showed that at a given sensitivity of 85%, VEGFR2 and CD276 can differentiate benign from malignant entities with specificities of 86% and 93% respectively and at 80% sensitivity with a specificity of 93% for both VEGFR2 and CD276. Overall, US molecular imaging using either VEGFR2 (AUC of 91.2) or CD276 (AUC of 90.9) targeted MB allowed the differentiation of benign from malignant diseases. Furthermore, the diagnostic accuracy was improved (AUC of 95.1) when the US molecular imaging information from both markers was utilized for differentiation. Immunofluorescence confirmed that both VEGFR2 and CD276 were expressed on the vascular endothelial cells of breast cancer. Conclusion Our results suggest that US molecular imaging using VEGFR2- and CD276- targeted MB allows non-invasive in vivo assessment of breast tissue progression from normal to breast cancer in this transgenic mouse model. Imaging tumor angiogenesis using tumor specific endothelial markers in early breast cancer may help improve diagnostic accuracy of US in early breast cancer detection.

Disclosure of author financial interest or relationships:
S. Bachawal, None; **F. Knieling**, None; **A.M. Lutz**, None; **L. Tian**, None; **J.K. Willmann**, Bracco, Consultant; Siemens, Grant/research support; Bracco, Grant/research support .

Presentation Number **P 357**
Poster Session 3
September 20, 2013 / 15:15-15:15 / Room: Exhibit Hall B

Multimodal imaging of a novel pheochromocytoma tumor model

Ralf K. Bergmann[1], *Martin Ullrich*[1,2], *Christian G. Ziegler*[2], *Torsten Kniess*[1], *Monika Ehrhart-Bornstein*[2], *Andrew V. Schally*[3], *Graeme Eisenhofer*[2], *Stefan Bornstein*[2], *Joerg Steinbach*[1,4], *Jens Pietzsch*[1,4], [1]*Institute of Radiopharmacological Cancer Research, Helmholtz-Zentrum Dresden-Rossendorf, Dresden, Germany;* [2]*Department of Medicine III, University Hospital Carl Gustav Carus, Dresden, Germany;* [3]*VA Medical Center and Dep. of Medicine, Div. of Endocrinology and Hematology-Oncology, University of Miami Miller School of Medicine, Miami, FL, USA;* [4]*Department of Chemistry and Food Chemistry, Technical University Dresden, Dresden, Germany. Contact e-mail: r.bergmann@hzdr.de*

Objective. Pheochromocytoma (PHEO) is a rare but potentially lethal neuroendocrine tumor arising from catecholamine producing chromaffin cells. Available treatment strategies are limited and, if the tumor has metastasized, not very effective. The abundant expression of peptide hormone receptors on endocrine tumor cells allows specific targeting and imaging by radioactive and highly effective anti-tumor peptide analogs. The present study focuses on the preclinical imaging and evaluation of potential therapies in the treatment of pheochromocytoma targeting peptide hormone receptors. Design and method. Somatostatin receptor 2 (SSTR2), luteinizing hormone-releasing hormone receptor (LHRH-R) and growth hormone-releasing hormone receptors (GHRH-R) were characterized by both RT-PCR and immunohistological analysis in a mouse pheochromocytoma (MPC) cell line . Based on these data, we evaluated the effects of cytotoxic peptide hormone analogs on cell viability, apoptosis, and necrosis on MPC cells. For in vivo studies, we furthermore established a new MPC mCherry transfected cell line and produced a subcutaneous mouse model of PHEO. The tumors were evaluated by multimodal imaging using PET, MRI, CT and optical imaging. Results. Our data reveal significant anti-tumor effects mediated by the cytotoxic peptide hormone analogs AN-162 and AN-238 targeting SSTR2, by the antagonist Cetrorelix targeting LHRH-R and by the cytotoxic analog AN-152 targeting as well as by the antagonist MIA-602 targeting growth GHRH-R on MPCs. Furthermore, using our newly established mouse model, we were able to visualize the growth, perfusion, metabolism, and hypoxia of MPC cell-derived subcutaneous PHEO in vivo by multimodal molecular imaging including SSTR2 PET. Additionally, histological ex vivo tumor characterization demonstrated unaltered functional peptide hormone receptor expression during in vivo tumor growth in mice. Conclusion. Our current investigation provides strong evidence for a possible future treatment of malignant PHEO using targeted peptide hormone receptor therapy. Support. This work was supported by the Deutsche Forschungsgemeinschaft (Grants BE-2607/1 (R.B. & J.P.), and ZI-1362/2-1 (C.G.Z.&G.E.).

Disclosure of author financial interest or relationships:
R.K. Bergmann, None; **M. Ullrich**, None; **C.G. Ziegler**, None; **T. Kniess**, None; **M. Ehrhart-Bornstein**, None; **A.V. Schally**, None; **G. Eisenhofer**, None; **S. Bornstein**, None; **J. Steinbach**, None; **J. Pietzsch**, None.

Presentation Number **P 358**
Poster Session 3
September 20, 2013 / 15:15-15:15 / Room: Exhibit Hall B

MRI-guided 3D-conformal arc micro-irradiation of a F98 glioblastoma rat model using a small animal radiation research platform

Julie Bolcaen[1], *Giorgio G. Hallaert*[2], *Jean-Pierre O. Kalala*[2], *Tom Boterberg*[3], *Caroline Van den Broecke*[4], *Benedicte Descamps*[5], *Karel Deblaere*[6], *Ingeborg Goethals*[1], *Christian Vanhove*[5], [1]*Nuclear Medicine, Gent University Hospital, Gent, Belgium;* [2]*Neurosurgery, Gent University Hospital, Gent, Belgium;* [3]*Radiation Oncology, Gent University Hospital, Gent, Belgium;* [4]*Pathology, Gent University Hospital, Gent, Belgium;* [5]*INnovative Flemish IN vivo Imaging TechnologY lab (INFINITY), Gent University, Gent, Belgium;* [6]*Radiology, Gent University Hospital, Gent, Belgium. Contact e-mail: julie.bolcaen@ugent.be*

Introduction: Current preclinical glioblastoma small animal models for cranial radiation therapy (RT) use simple single-beam technologies, which significantly differ from the advanced conformal three-dimensional (3D) image guided radiation techniques mostly used in clinical practice. This technological disparity presents a major hurdle in the development of new targeted therapeutic approaches. Therefore, the aim of this study was to establish a F98 glioblastoma therapeutic rat model using magnetic resonance imaging (MRI)-guided 3D-conformal arc RT with the Small Animal Radiation Research Platform (SARRP). Methods: Ten female Fisher F344 rats (169.6±8.8g) were inoculated with ± 20 000 F98 tumor cells in the right frontal lobe. Tumor growth was evaluated using a T2-weighted MRI sequence on a 7 Tesla system. When the tumor reached a volume of ± 2x2x2 mm, the animals were randomized into two groups. The first group (n=5) received RT and concomitant temozolomide (TMZ), while the second group (n=5) served as controls and received dimethyl sulfoxide (DMSO) injections. For the animals in the first group, MR images of the rat brain were collected using a contrast-enhanced T1-weighted sequence. Following MRI, the animals were moved to the SARRP, maintaining a fixed position, where a cone-beam computed tomography (CBCT) was performed. Contrast-enhanced T1-weighted images and CBCT were co-registered, and the tumor was selected as target for RT on the MR images (Figure1: A-C). CBCT was used for dose calculations. A dose plan was calculated to deliver 20 Gy using 3 non-coplanar arc beams with a 3x3 mm collimator (Figure1: D-F). For all rats, tumor volumes were evaluated on follow-up contrast-enhanced T1-weighted MRI scans at day 2, 5, 9, and 12 after therapy initiation. Results: Tumors in the control animals showed rapid proliferation during a follow-up period of 12 days. At that time tumors encompassed almost the entire right hemisphere with significant mass effect, requiring euthanasia. Animals treated with RT and concomitant TMZ showed no significant tumor growth from day 2 to 9 post-RT, with mean tumor volumes of 38.7 and 39.3 mm3, respectively (p=0,313). From day 12 post-irradiation onwards, tumor growth resumed. Hematoxylin and Eosin staining confirmed the presence of glioblastoma and revealed that the enhancing region on contrast enhanced T1 MRI corresponds to the delineation of the tumor volume. Conclusion: The results confirm the applicability of this method as a valuable model for combined radiation and chemotherapy of glioblastoma in rats similar to the approach in the clinic. This model could also be helpful in search of new targeting therapeutics for glioblastoma in combination with radiation therapy. Acknowledgements: This work is supported by Stichting Luka Hemelaere. Christian Vanhove is supported by the GROUP-ID consortium.

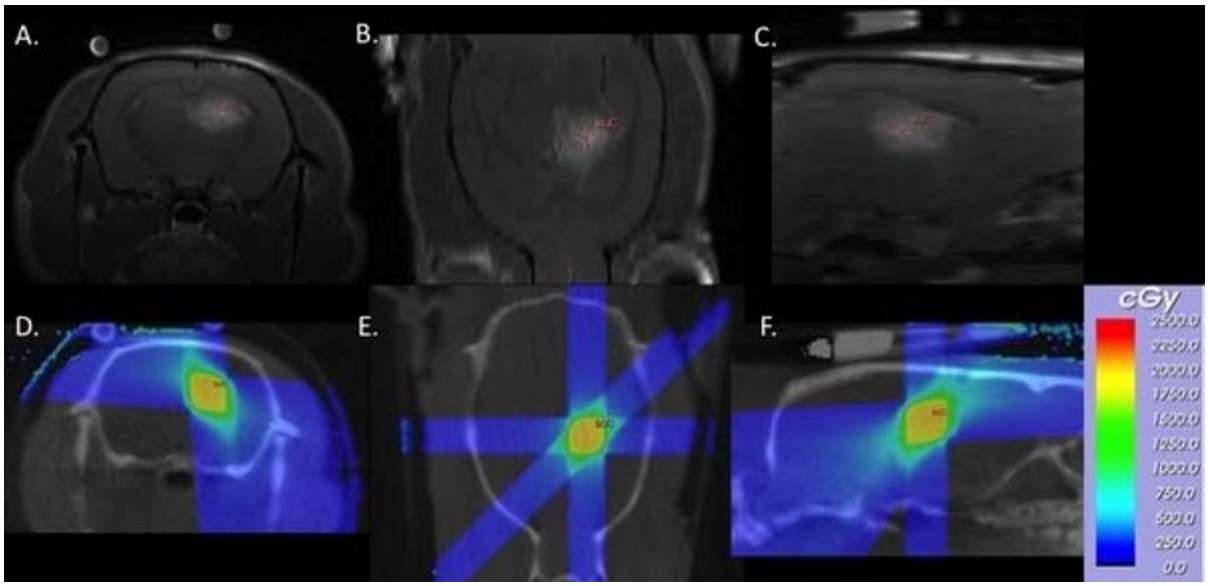

Fig 1. A-C: Selected isocenter on contrast-enhanced T1-weighted images. D-F: Dose plan for delivery of 20 Gy using 3 arc beams and a 3*3 mm collimator.

Disclosure of author financial interest or relationships:
J. Bolcaen, None; **G.G. Hallaert**, None; **J.O. Kalala**, None; **T. Boterberg**, None; **C. Van den Broecke**, None; **B. Descamps**, None; **K. Deblaere**, None; **I. Goethals**, None; **C. Vanhove**, None.

Presentation Number **P 359**
Poster Session 3
September 20, 2013 / 15:15-15:15 / Room: Exhibit Hall B

uPAR specific NIR fluorescent labeled antibody for visualization of solid tumors and metastasis

Martin C. Boonstra[1], *Quirijn Tummers*[1], *Pieter B.A.A van Driel*[2], *Floris P. Verbeek*[1], *Hendrica A.J.M. Prevoo*[1], *Danny M. van Willigen*[1], *Boudewijn Schaafsma*[1], *Andrew P. Mazar*[3], *Fijs van Leeuwen*[2], *Peter Kuppen*[1], *Cornelis J. van de Velde*[1], *Clemens Lowik*[2], *John V. Frangioni*[4,5], *Alexander Vahrmeijer*[1], *Cornelis F. Sier*[1], [1]*Surgery, Leiden University Medical Center, Leiden, Netherlands;* [2]*Radiology, Leiden University Medical Center, Leiden, Netherlands;* [3]*Chemistry of Life Processes Institute and Robert H. Lurie Comprehensive Cancer Center, Northwestern University, Evanston, IL, USA;* [4]*Medicine, Beth Israel Deaconess Medical Center, Boston, MA, USA;* [5]*Radiology, Beth Israel Deaconess Medical Center, Boston, MA, USA. Contact e-mail: m.c.boonstra@lumc.nl*

Real-time near-infrared (NIR) fluorescent imaging is a novel technique used to visualize tumor cells intraoperatively. For this purpose NIR light-emitting fluorophores are conjugated to tumor protein-specific tracers. One potential target for tracing tumors is the urokinase plasminogen activator receptor (uPAR). uPAR plays an important role in the development of cancer, tumor invasion, angiogenesis and metastasis. Over-expression of uPAR is found on the majority of human carcinomas, in cancer as well as stromal cells. This study investigates the potential of an uPAR-specific NIR fluorescent antibody for the in vivo identification of tumor cells. The dual label NIR fluorophore MSAP-ZW800-1 was conjugated to a humanized monoclonal uPAR specific antibody and an isotype IgG control. The conjugation and binding capacity of both compounds were validated in vitro using photospectrometry and plate-assay analyses on tumor cells. Athymic mice were subcutaneously injected with human colon adenocarcinoma HT-29 cells or orthotopicly in the tongue with OSC-19 cells, a metastasizing human squamous cell carcinoma. After establishment of the tumors, 1 nmol of either uPAR-specific or control IgG were injected intravenously (IV). At sequential time points up-to 120 h after injection images were obtained with the PEARL Impulse small animal imager and the intraoperative FLARETM imaging system. A dose-range study was performed with doses of 150 µg (1 nmol), 100 µg, or 50 µg per mouse. Ex vivo fluorescence imaging and histology was performed to demonstrate distribution of the compounds and tumor specificity. In vivo, the tumors were clearly fluorescently delineated, with the highest tumor-to-background ratios (TBR) at 72 hours after injection of 3.6 ± 0.4 in the HT-29 model and 2.3 ± 0.1 in the OSC-19 model respectively (n=3). The control compound showed a mean TBR of 1.8 ± 0.2 in the HT-29 model and 1.1 ± 0.2 in the OSC-19 model, whereas injection of the fluorophore alone showed a mean TBR of 0.8 ±0.1 in both animal models. In the tumor-specific compound group unexpected fluorescent spots in the cervical region of the OSC-19-injected mice were found which histologically turned out to be cervical lymph node metastases. Two-way repeated measurements ANOVA analysis showed significant differences between the tumor-specific compound and control groups in the HT-29 model at all time points later than 24 hours ($p<0.01$) and for the OSC-19 model at every time point from the start ($p<0.01$). Ex vivo evaluation showed a tumor-specific signal in both the OSC-19 primary tumors and lymph node metastases. No significant differences were found among the dose groups, indicating the potential of this anti-uPAR compound to be used in the lower micro-dose range. In conclusion, this study describes a new tumor-specific fluorescent probe, targeting uPAR, which provides visualization of solid tumors including their metastases in real time using a NIR fluorescence imaging system.

Disclosure of author financial interest or relationships:
M. Boonstra, None; **Q. Tummers**, None; **P. van Driel**, None; **F.P. Verbeek**, None; **H. Prevoo**, None; **D.M. van Willigen**, None; **B. Schaafsma**, None; **A. Mazar**, Tactic Pharma, Consultant; Tactic Pharma, Stockholder; **F. van Leeuwen**, None; **P. Kuppen**, Antibodies for Research Applications BV, Stockholder; **C.J. van de Velde**, None; **C. Lowik** None; **J.V. Frangioni**, None; **A. Vahrmeijer**, None; **C.F. Sier**, None.

,

Presentation Number **P 360**
Poster Session 3
September 20, 2013 / 15:15-15:15 / Room: Exhibit Hall B

Molecular pathology for personalized imaging of prostate cancer

Tessa Buckle, *Sharon Poort, Joeri Kuil, Fijs van Leeuwen, LUMC, Leiden, Netherlands. Contact e-mail: t.buckle@lumc.nl*

Background: The major goal of prostate cancer imaging in the next decade will be more accurate disease characterization through synthesis of anatomical and functional imaging information in order to plan the most appropriate therapeutic strategy. Similar to their use in treatment selection, individual biomarker expression patterns can be exploited to increase detection and accurate delineation of cancerous lesions via molecular pathology. As multiple consecutive biomarker imaging studies in a single patient are undesirable, a tailored selection process that identifies the most representative tumor biomarker(s) is crucial. Standard biomarker evaluation methods in tissue only provide information on the general availability of a specific biomarker, while functional factors such as the localization and level of (membrane) expression play a crucial role in the feasibility of in vivo biomarker targeting. We developed a fresh tissue based assay for simultaneous characterization and quantification of functional prostate-cancer biomarkers. Hereby, inclusion of multiple biomarkers is instrumental in addressing the heterogeneity in and between lesions. Methods: Tumor cell suspensions derived from tumors from human prostate cancer cell lines (PC3, DU145 and C4-2B4) served as a model for biopsy tissue. Cell suspensions were incubated with a CXCR4 or PSMA targeting peptide labeled with both a fluorescent dye and a DTPA chelate. Functional biomarker expression was evaluated using flow cytometry. By using fluorescent labels with different excitation and emission spectra biomarkers were evaluated simultaneously. For in vivo detection of tumor lesions, tumor bearing mice were imaged using SPECT/CT. By specifically scoring membranous staining patterns, screening-results could be validated with ex vivo (fluorescence) immunohistochemistry ((F)IHC). Results: Flow cytometric analysis after incubation of the tumor cell suspensions with revealed differences in biomarker expression between the cell lines. Expression of PSMA was only seen in C4-2B4 (ratio = 4 compared to unstained cells). CXCR4 expression was highest in the PC3 cells, however, low expression was also seen in DU145 cells. In vivo, tumors that were deemed positive for either PSMA or CXCR4, could be visualized with the biomarker specific imaging agent. Uptake of the CXCR4 targeting imaging agent in the tumor was consistent with an increase of membranous staining for CXCR4 as seen with IHC. Conclusion: The membranous fraction of the biomarkers, measured with flow cytometry, proved predictive for in vivo targeting (SPECT and fluorescence imaging) using the same (multimodal) imaging agent. The screening approach can thus enables individualized selection of a diagnostic molecular imaging approach.

Disclosure of author financial interest or relationships:
T. Buckle, None; **S. Poort**, None; **J. Kuil**, None; **F. van Leeuwen**, None.

Presentation Number **P 361**
Poster Session 3
September 20, 2013 / 15:15-15:15 / Room: Exhibit Hall B

CEST liposomes as theranostic agents for cancer therapy

Kannie WY Chan[1,2], *Tao Yu*[3,4], *Yuan Qiao*[5], *Guanshu Liu*[1,6], *Qiang Liu*[5], *Jeff W. Bulte*[1,2], *Peter C. van Zijl*[1,6], *Justin Hanes*[3], *Shibin Zhou*[5], *Michael T. McMahon*[1,6], [1]*Russell H. Morgan Department of Radiology and Radiological Science, Johns Hopkins University School of Medicine, Baltimore, MD, USA;* [2]*Cellular Imaging Section and Vascular Biology Program, Institute for Cell Engineering, Baltimore, MD, USA;* [3]*Center for Nanomedicine, The Wilmer Eye Institute, Baltimore, MD, USA;* [4]*Department of Biomedical Engineering, Johns Hopkins University School of Medicine, Baltimore, MD, USA;* [5]*The Ludwig Center for Cancer Genetics and Therapeutics, Sidney Kimmel Cancer Cente, Baltimore, MD, USA;* [6]*F.M. Kirby Research Center for Functional Brain Imaging, Kennedy Krieger Institute, Baltimore, MD, USA. Contact e-mail: kanniec@mri.jhu.edu*

Introduction: Nanoparticle-based drug delivery has great potential for improving the therapeutic index of chemotherapeutic agents in the treatment of cancer (1). The therapeutic index can be further enhanced when nanoparticle-based drugs are combined with tumor vascular therapeutics (2). However, the clinical translation of nanoparticle-based chemotherapy has experienced challenges; one of them is the lack of tools to evaluate the biodistribution and pharmacokinetics of the nanoparticle-based chemotherapeutics in cancer patients during the course of treatment. Here, we aimed to develop theranostic liposomes (i.e. endowed with both therapeutic and diagnostic properties) based on diamagnetic Chemical Exchange Saturation Transfer (diaCEST) - a molecular MRI contrast mechanism allowing the use of non-metallic and biocompatible contrast agents. Towards this end, we developed a stable formulation of liposomes that have a frequency offset further from water (at 5 ppm) than previous designs (3), and assessed their distribution and retention in a murine colon cancer model. The integration of CEST agents within nanoparticles provides a non-invasive, non-radioactive quantification, and potentially translatable way to probe nano-chemotherapeutics in tumors. Methods: DiaCEST liposome (DL): Liposomes were prepared with poly(ethylene) glycol (PEG) and corresponding phosphatidylcholines using the thin film hydration method (3), then barbituric acid (BA) and doxorubicin (DOX) were loaded. CEST: Mice bearing CT26 tumors were imaged before and 6 hrs after i.v. administration of liposomes. MR images were processed using custom-written Matlab scripts with the magnetization transfer ratio (MTRasym) for NH protons at $\Delta\omega$ = 5ppm after B0 correction. Results and Discussion: We successfully synthesized liposomes loaded with both the CEST imaging agent (BA) and the chemotherapeutic agent (DOX) (Fig. 1a). The in vitro CEST contrast of these liposomes with different phosphatidylcholines were 19-23% at 5 ppm (Fig. 1b). In order to determine if these formulations would be stable during the time course of imaging, we screened these formulations and selected the one with the highest contrast and with ~20% BA retained in the liposomes 24 h after dialysis for in vivo study (Fig. 1b; DSPC). We then imaged mice bearing colon tumors before and 6 hrs after i.v. injection of liposomes. Accumulation of CEST liposomes could be clearly visualized, with the tumor accumulation having an MTRasym value of ~1.5% at least 6 hrs post-injection (Fig. 1c). Conclusion: We developed theranostic diaCEST liposomes for imaging particle-based chemotherapy of colon tumors. Measuring the CEST contrast at 5 ppm provides information on the spatial distribution of the particles after administration and over a period of 6 hrs in vivo. We are performing further experiments to compare animals with and without treatment of a tumor vascular-active agent. References: (1) Peer D et al. Nat. Nanotechnol. 2007. (2) Qiao Y et al. Oncotarget 2011. (3) Liu G et al. Magn. Reson. Med. 2011. Supported by NIH grants R01EB015031, R01EB015032 and CA062924, and The Virginia and D.K. Ludwig Fund for Cancer Research.

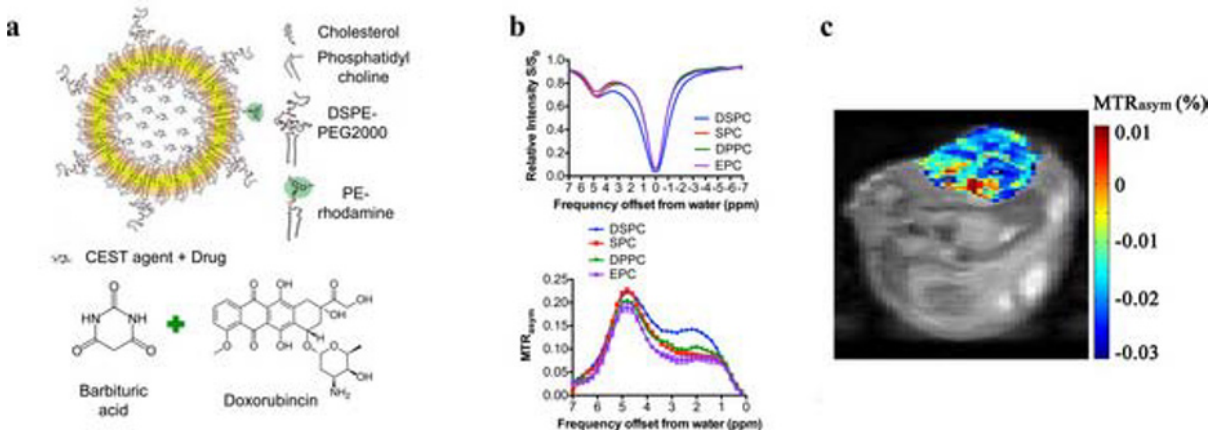

Fig. 1: a) Scheme showing the compositions of BA/DOX liposomes; b) CEST contrast for liposomes with DSPC, SPC, DPPC and EPC; c) Tumor CEST contrast at 5 ppm 6 hrs after i.v. injection of liposomes.

Disclosure of author financial interest or relationships:

K. Chan, None; **T. Yu**, None; **Y. Qiao**, None; **G. Liu**, None; **Q. Liu**, None; **J.W. Bulte**, None; **P.C. van Zijl**, None; **J. Hanes**, Kala Pharmaceuticals, Consultant; Kala Pharmaceuticals, Stockholder; **S. Zhou**, BioMed Valley Discoveries, Grant/research support; **M.T. McMahon**, None.

Presentation Number **P 362**
Poster Session 3
September 20, 2013 / 15:15-15:15 / Room: Exhibit Hall B

Using gold nanostars for a triple imaging (photoacoustic, SERS and CT) and photothermal treatment of cancer

Antoine D'Hollander[1,2], *Greetje Vande Velde*[2,3], *Evelien Mathieu*[1,4], *Elien Vermeersch*[2,3], *Hilde Jans*[1], *Jithin Jose*[5], *Pol Van Dorpe*[1], *Liesbet Lagae*[1], *Uwe Himmelreich*[2,3], [1]*Biochemistry, Imec, Heverlee, Belgium;* [2]*Biomedical MRI unit, KULeuven, Leuven, Belgium;* [3]*MoSAIC, KULeuven, Leuven, Belgium;* [4]*Solid State Physics and Magnetism, KULeuven, Heverlee, Belgium;* [5]*FUJIFILM Visualsonics Inc, Amsterdam, Netherlands. Contact e-mail: dholland@imec.be*

Introduction. Currently, the diagnosis and monitoring of cancer therapy is time-consuming, costly and complex, resulting in a need for more efficient detection, imaging and treatment techniques. Decreasing therapy complexity by combining diagnostic and treatment methods would be a big advantage in this field. Gold nanostars have potential as a contrast agent for combined photoacoustic imaging, surface enhanced raman scattering (SERS) and CT imaging as well as for photothermal therapy. In this work we demonstrate that gold nanostars can be used as a contrast agent for all three imaging techniques and photothermal therapy. Methods. In our three-step process, based on Hao et al., the nanostars are synthesized, functionalized with a SERS molecule (DTNB) and a stabilizing self-assembled monolayer. These particles are measured dry and in suspension for characterization of their SERS and PA imaging capabilities using WiteQ alpha 300 R and Vevo lazer, respectively. For in vitro validation, SKOV3 cells (ovarian cancer cell line) were plated on coverslips and incubated with gold nanostars. Using ICP-OES, darkfield microscopy, the interaction between the nanostars and cells was studied. Using a xenograft SKOV3 tumor mouse model, the nanostars were intratumorally injected and imaged with CT, PAI and SERS. The phototermal treatment effect on tumor growth was monitored in vivo with MRI and BLI. Results. Nanostars functionalized with DTNB and a SAM were successfully synthesized resulting in an absorption wavelength in the NIR-region (690 nm),an intense SERS (1333 cm-1) and PA signal. After incubating the nanostars with the SKOV3 cells for 12 hours, a significant SERS and PA signal could be detected that corresponded to an intracellular gold amount of 22 pg Au/cell (Figure 1A, 1B). Moreover, we were able to monitor in real-time the nanoparticle accumulation inside the cells using SERS, hereby confirming the delivery of the particles to the target cells (Figure 1B). We succesfully induced PTT at the laser spot, which was validated using live/dead fluorescence staining, visualizing the necrosis spot with fluorescence microscopy. Next, gold nanostars were subcutaneously injected for studying their photothermal potential in vivo (Figure 1C) . We established that a minimum of 40 ug Au is needed for a 15°C temperature increase. The injected nanostars could be visualized with CT. Nevertheless, for SERS and PA imaging, even at lower gold concentrations a significant signal could be detected, demonstrating their sensitivity for in vivo imaging. After intratumoral injection of the particles (40 ug Au), phothermal tumor therapy has been successfully induced. Monitoring of tumor therapy by BLI and MRI demonstrated a significant decrease in tumor viability and volume. However, after several days of tumor regression, tumor regrowth has been observed, indicating incomplete tumor destruction. This is validated by histology (H&E staining) . Conclusion. Both in vitro and in vivo studies proved that gold nanostars were ideally suited for combined optical PA and SERS imaging and phototermal treatment, demonstrating great theranostic potential.

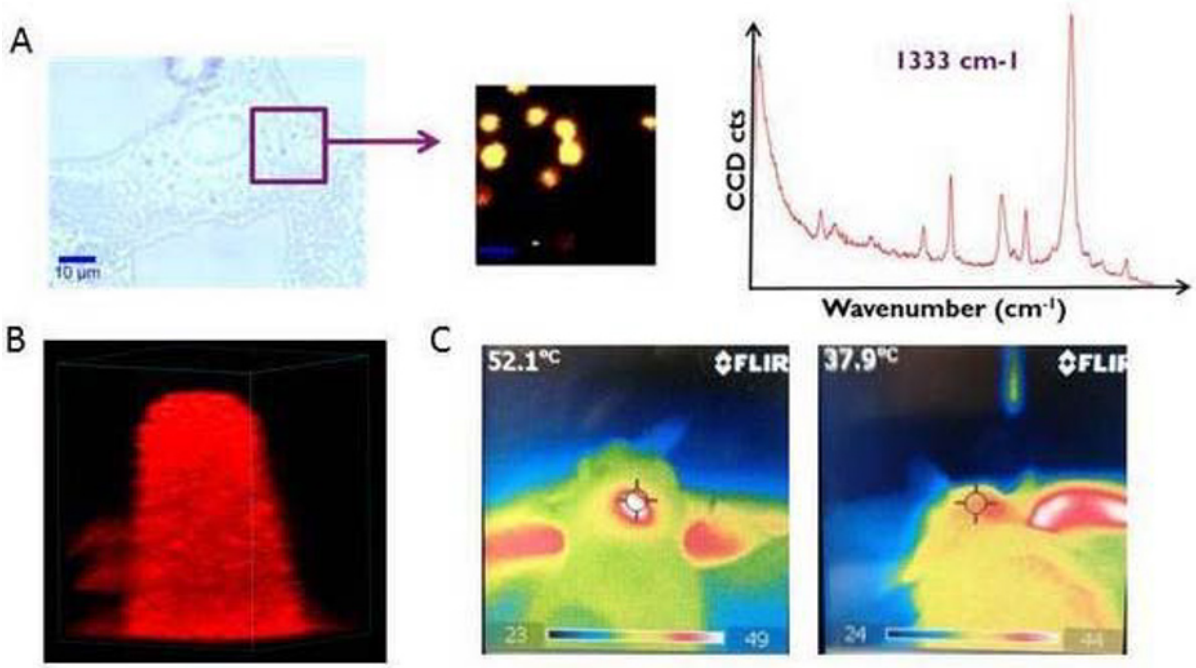

Figure 1: A. Tumor cells labeled wih gold nanostars showing the bright field image, corresponding SERS image at wavenumber 1333 cm-1 and the average spectrum. B. Photoacoustic signal of the tumor cells after labeling with the gold nanostars. C. Temperature measurement during therapytumor injected with nanoparticles (left) and control tumor injected with PBS (right)

Disclosure of author financial interest or relationships:
A. D'Hollander, None; **G. Vande Velde**, None; **E. Mathieu**, None; **E. Vermeersch**, None; **H. Jans**, None; **J. Jose**, None; **P. Van Dorpe**, None; **L. Lagae**, None; **U. Himmelreich**, None.

Presentation Number **P 363**
Poster Session 3
September 20, 2013 / 15:15-15:15 / Room: Exhibit Hall B

In-vivo assessment of LDH-A and glutaminase inhibition in tumor xenografts using hyperpolarized ^{13}C-pyruvate magnetic resonance spectroscopy

Prasanta Dutta[1], *Anne Le*[2], *Gary Martinez*[1], *Chi V. Dang*[3], *Robert Gillies*[1], [1]*Cancer Imaging and Metabolism, H. Lee Moffitt Cancer Center, Tampa, FL, USA;* [2]*Pathology, Johns Hopkins University School of Medicine, Baltimore, MD, USA;* [3]*Abramson Cancer Center, University of Pennsylvania, Philadelphia, PA, USA. Contact e-mail: Prasanta.Dutta@moffitt.org*

Hyperpolarized ^{13}C magnetic resonance spectroscopy (MRS) using the dissolution DNP (dynamic nuclear polarization) provides a unique opportunity to detect real-time metabolic fluxes as a means to measure metabolic treatment responses in vivo [1]. The aim of this study was to assess the early response of metabolically targeting therapy using ^{13}C MRS of hyperpolarized pyruvate and its downstream metabolic profiling. [1-^{13}C] pyruvic acid was mixed with 15mM trityl radical (OX63) and hyperpolarized for one hour by an Oxford DNP Polarizer (HyperSense). The polarized substrate was quickly dissolved in Tris/EDTA, NaCl and NaOH at 37°C, yielding 80 mM pyruvate at neutral pH and 350 µL was administered via a jugular-vein catheter to tumor (P493 human lymphoma xenograft) bearing mice in 12-15 sec. ^{13}C-spectra were obtained using an Agilent ASR 310 7T small animal imaging scanner utilizing a dual tuned ^{13}H - ^{13}C volume coil. Animals were treated with DMSO vehicle (control) or drugs (FX11 and BPTES) via intraperitoneal (i.p.) injection. Figure 1a & b depict a relevant metabolic pathways and the ^{13}C MR spectrum obtained from a 6 mm thick slice across the tumor after hyperpolarized pyruvate injection respectively. It displays the prominent peak of pyruvate (171 ppm) and its conversion by LDH to lactate (183 ppm) along with its conversion by glutamate-pyruvate transaminase (GPT) to alanine (176 ppm). Pyruvate hydrate (179 ppm) is formed non-enzymatically in solution and is in equilibrium with dehydrated pyruvate. Supplemental Figure 1a displays sequential dynamic spectra acquired from a 6 mm tumor slice over a total acquisition time of 100 seconds in DMSO treated mice (control), illustrating a robust tumor conversion of pyruvate-to-lactate. After six days of FX11 treatment, the pyruvate-to- lactate conversion flux in treated tumors diminished considerably (Suppl Fig. 1b). There is an overall MR signal decay due to T1 relaxation of the hyperpolarized substrate. It has observed that inhibition of lactate dehydrogenase A (LDH-A) with FX11 (a drug-like inhibitor) reduced the conversion of hyperpolarized ^{13}C-pyruvate to lactate in P493 human lymphoma tumor xenografts. By contrast, the glutaminase inhibitor BPTES decreased ^{13}C-pyruvate to alanine conversion without affecting pyruvate to lactate conversion. These changes were detected before observing any tumor volume changes between the different mice groups. The tumor volume was monitored during the treatment time window (upto seven days) using T_2-weighted MR imaging. Our results document the real-time biomarker of responses to anti-metabolic therapy, paving the way for the development of clinically tractable pharmacodynamic metabolic imaging biomarkers. References: [1]. Kurhanewicz J. et al., "Analysis of cancer metabolism by imaging hyperpolarized nuclei: prospects for translation to clinical research", Neoplasia, 13, 81-97, (2011).

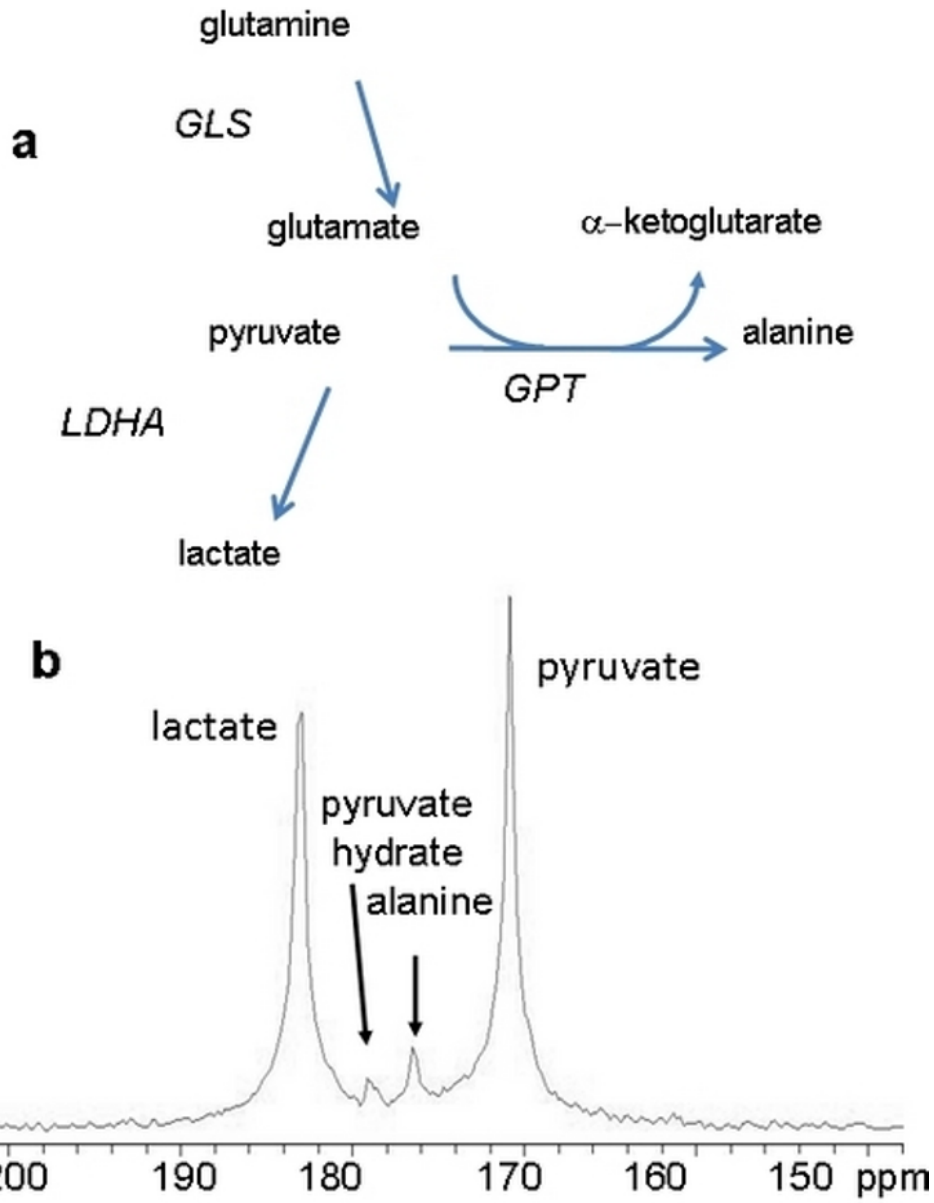

Figure 1. (a) Schematic of metabolic pathways relevant to 13C-pyruvate MRS spectra (GLS, glutaminase; GPT, glutamate-pyruvate transaminase; LDH-A, lactate dehydrogenase A). (b) Hyperpolarized 13C MRS acquired from a 6 mm thick slice across the tumor after 20 sec of pyruvate injection (i.v) into a mouse.

Disclosure of author financial interest or relationships:
P. Dutta, None; **A. Le**, None; **G. Martinez**, None; **C.V. Dang**, None; **R. Gillies**, None.

Presentation Number **P 364**
Poster Session 3
September 20, 2013 / 15:15-15:15 / Room: Exhibit Hall B

Imaging of Gastrointestinal Transit and Intestinal Mucoadhesion of Chitosan Coated Lipid Nanoparticles Following Oral Administration in Tumor Bearing Rats

Yi-Hsiu Chung, Shihong Li, Ande Bao, **Beth Goins***, Radiology, University of Texas Health Science Center San Antonio, San Antonio, TX, USA. Contact e-mail: goins@uthscsa.edu*

The goal of this study was to monitor the gastrointestinal (GI) transit and intestinal mucoadhesion of chitosan coated lipid nanoparticles (liposomes) as an oral cancer drug delivery system in a head and neck squamous cell carcinoma (HNSCC) rat xenograft model. The liposomes contain a novel asparagine-derived lipid (Asp-liposomes) to impart acid resistance during transit through the GI tract and a coating of chitosan-glutathione to enhance intestinal mucoadhesion and permeation. To monitor GI transit and bioavailability after oral administration, the liposomes encapsulated doxorubicin as a model drug and are radiolabeled with technetium-99m (Tc-99m) to permit non-invasive nuclear imaging. Methods: Tc-99m-N, N-bis(2-mercaptoethyl)-N'N'- diethyl-ethylenediamine (BMEDA) was loaded into Asp-liposomes encapsulating doxorubicin by ammonium sulfate gradient. Tc-99m-Dox-Asp-liposomes were coated with chitosan-glutathione (CS) by magnetic stirring for 1 h at 25 degC. Coating efficiency of CS-Asp-liposomes was determined after separation of free CS by centrifugation at 15000g for 30min. Uncoated Tc-99m-Dox-Asp-liposomes served as control. Coated or uncoated liposomes were given to the nude rats with HNSCC xenograft (n=5 per group) orally by gavage, followed by planar imaging and blood collection at varying time points. At 4 h after oral administration, one animal in each group was sacrificed and the intestines were fixed for doxorubicin fluorescent microscopy. The others were sacrificed immediately after 8h imaging session to determine the Tc-99m tissue biodistribution in the animal. Doxorubicin was extracted from plasma, liver and spleen and the fluorescence measured. Regions-of-interest (ROIs) of stomach and intestines were drawn on the planar images. The statistical differences between the two groups were tested by Student's t-test. Results: Coating efficiency of chitosan-glutathione on the surface of Asp-liposomes was about 86%. Coated-Asp liposome diameter increased to 1200nm from 140 nm for uncoated Asp-liposomes. Analysis of 2 h images indicated the CS-Asp-liposomes moved from stomach to intestine whereas more uncoated Asp-liposomes remained in stomach. Additionally, CS-Asp-liposomes showed less radioactivity in ROIs of intestinal images at 4 h which corresponded to more radioactivity in blood, liver, spleen and kidneys through absorption by the intestinal enterocytes. The bioavailability of extracted doxorubicin from liver ($p<0.01$) and spleen ($p<0.01$) were 34.37+/-10.21 % and 14.37+/-2.37% for CS-Asp-liposomes and 14.07+/-0.99 % and 7.76+/-1.18% for uncoated Asp-liposomes. Fluorescent microscopy of intestinal sections also showed the accumulation of higher amounts of CS-Asp-liposomes in the serosal side, in contrast to the more uniform distribution for uncoated Asp-liposomes. Conclusion: Using a combination of non-invasive nuclear imaging and fluorescent microscopy we were able to monitor and characterize the GI transit and intestinal mucoadhesion of this oral drug delivery system. Chitosan-glutathione-liposomes are a potential oral drug delivery system that can increase the bioavailability of oral cancer drugs.

Disclosure of author financial interest or relationships:
Y. Chung, None; **S. Li**, None; **A. Bao**, None; **B. Goins**, None.

Presentation Number **P 365**
Poster Session 3
September 20, 2013 / 15:15-15:15 / Room: Exhibit Hall B

Imaging and Modeling the Role of Myeloid Cells in Tumor Growth

Hansford C. Hendargo[1], *Nathan A. Koonce*[2], *Matthew J. Kan*[3], *Blanche Capel*[4], *Kingshuk Roy Choudhury*[1], *Mark W. Dewhirst*[1], *Michael D. Gunn*[5], *Gregory M. Palmer*[1], [1]*Radiation Oncology, Duke University Medical Center, Durham, NC, USA;* [2]*Radiation Oncology, University of Arkansas Medical School, Little Rock, AR, USA;* [3]*Immunology, Duke University Medical Center, Durham, NC, USA;* [4]*Cell Biology, Duke University Medical Center, Durham, NC, USA;* [5]*Cardiology, Duke University Medical Center, Durham, NC, USA. Contact e-mail: hansford.hendargo@duke.edu*

Introduction: Following sub-curative radiation treatment, tumors have been shown to regrow aggressively, observed prominently through recruitment of myeloid cells and vascularization of the tumor1. Understanding the cellular interactions that govern this growth may lead to more effective drug treatments to prevent tumor angiogenesis to be used in conjunction with radiation therapy for enhanced cancer treatments. We present work that elucidates the relationships between myeloid, endothelial, and tumor cells by using dynamic imaging methods in a mouse window chamber model to visualize cellular interactions during tumor angiogenesis. Quantitative statistical analysis is used to correlate the relationships between the different cell types. We show for the first time in vivo interactions between myeloid cells and growing tumor vasculature. Methods: Lewis lung carcinoma cells labeled with DiD were injected into the dorsal area of mice possessing fluorescent reporters for endothelial (FLK1-mcherry) and myeloid (CX3CR1-EGFP) cells. A skin fold window chamber was surgically implanted to allow for optical imaging of the tumor over time. Animals were randomized to receive either AMD3100 (6 mg/kg/day) or saline control. Tumors were imaged 1 week after implantation using a Zeiss 780 multispectral confocal microscope that enabled simultaneous in vivo imaging of the fluorescence from all 3 labeled cell types. Image sequences were acquired over 4 hours to visualize the dynamic development of the tumor. Spatial correlation between the different cell types was determined by dividing each image into a 16x16 grid and computing a predictive linear fit between the densities of the myeloid and tumor cells with the vessel densities in each location. Results: Figure 1 shows a time sequence where myeloid cells (green fluorescence) interact with endothelial cells (red) of a growing blood vessel within the tumor (purple). Following contact between the myeloid and endothelial cells, a vessel appears to elongate indicating possible association between the myeloid cells and sprouting tip cells. Spatial correlations between the different cell types were strong. Linear modeling of the densities of the myeloid and tumor cells in relation to the blood vessel density showed the myeloid cells, rather than the tumor cells, acted as a stronger predictor of the vessel density (see supplemental data). These correlations indicate that myeloid cells may play a direct role in controlling tumor vascular growth. Conclusions: We demonstrated the ability to perform in vivo cellular level imaging to study the interactions between myeloid, endothelial, and tumor cells in a mouse dorsal window chamber model. Our results indicate that myeloid cells have some influence over angiogenesis in tumors and may prove to be a suitable target for therapeutic inhibition following radiation or chemotherapy. Next steps will be to examine the effects of radiation on cell densities and associations to study the dynamics of therapeutic response. References: [1] M Kioi, H Vogel, G Schultz, RM Hoffman, GR Harsh, and JM Brown, J Clin. Invest., 120, (2010).

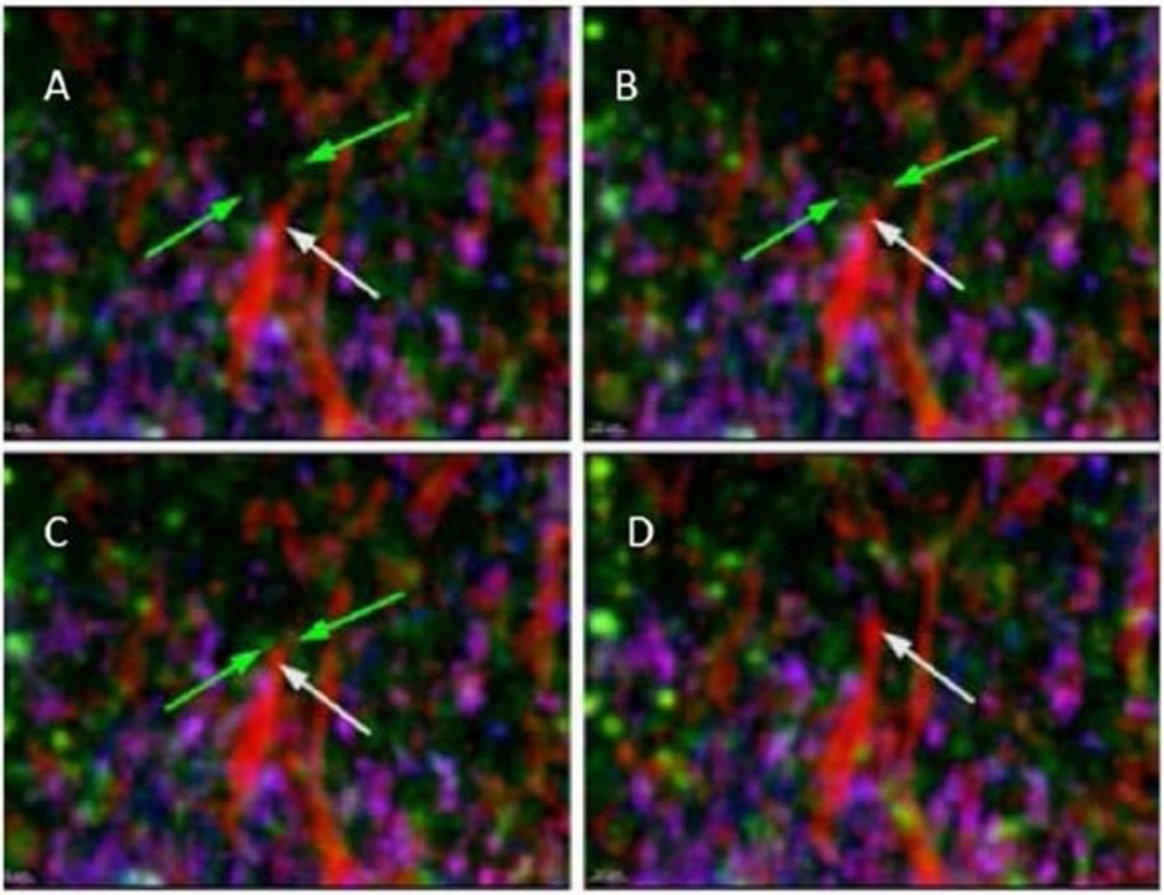

Myeloid cell interaction with sprouting tumor associated vessel. A myeloid cell (green fluorescence, green arrow) approaches and interacts with a growing vessel (red fluorescence, white arrow) within the tumor cell population (purple fluorescence). The myeloid/vessel contact appears to directly precede elongation of the vessel. Still images are captured from a time-lapsed (4 hour) movie. Order of events is A-D.

Disclosure of author financial interest or relationships:
H.C. Hendargo, None; **N.A. Koonce**, None; **M.J. Kan**, None; **B. Capel**, None; **K. Roy Choudhury**, None; **M.W. Dewhirst**, Celsion Corporation, Stockholder; Immunolite, Inc., Grant/research support; Cerulean, Inc., Consultant; Siva Corporation, Consultant; **M.D. Gunn**, None; **G.M. Palmer**, Zenalux Biomedical, Inc., Consultant .

Presentation Number **P 366**
Poster Session 3
September 20, 2013 / 15:15-15:15 / Room: Exhibit Hall B

PET of Tumor Angiogenesis with $^{61/64}$Cu-Labeled Fab and F(ab')$_2$ Antibody Fragments

Hao Hong[1], *Yin Zhang*[2], *Hakan Orbay*[1], *Charles P. Theuer*[3], *Todd E. Barnhart*[2], *Weibo Cai*[1,2], [1]*Radiology, Univ of Wisconsin, Madison, WI, USA;* [2]*Medical Physics, Univ of Wisconsin, Madison, WI, USA;* [3]*TRACON Pharmaceuticals, San Diego, CA, USA. Contact e-mail: hhong@uwhealth.org*

Aim: To characterize the in vitro and in vivo properties of the Fab and F(ab')$_2$ fragments of TRC105, a monoclonal antibody that binds with high affinity to human and murine CD105, and investigate their potential for positron emission tomography (PET) imaging of tumor angiogenesis after $^{61/64}$Cu-labeling. Materials and Methods: TRC105-Fab was generated by enzymatic papain digestion, while TRC105-F(ab')$_2$ was generated by pepsin digestion. The integrity and CD105 binding affinity of TRC105-Fab and TRC105-F(ab')$_2$ was evaluated before NOTA (i.e. 1,4,7-triazacyclononane-1,4,7-triacetic acid) conjugation and $^{61/64}$Cu-labeling. Serial PET imaging and biodistribution studies were carried out to quantify tumor targeting efficacy and distribution of $^{61/64}$Cu-NOTA-TRC105-Fab and $^{61/64}$Cu-NOTA-TRC105-F(ab')$_2$ in 4T1 murine breast tumor-bearing mice. Blocking and histology studies were performed to confirm CD105 specificity of both tracers in vivo. Results: Both TRC105-Fab and TRC105-F(ab')$_2$ were produced with high purity by enzymatic digestion of TRC105, confirmed by SDS-PAGE, HPLC analysis, and mass spectroscopy. CD105 binding affinity and specificity of both fragments were maintained based on flow cytometry analysis. ^{64}Cu-labeling of NOTA-TRC105-Fab and NOTA-TRC105-F(ab')$_2$ were both achieved with good yield and specific activity. PET imaging revealed rapid uptake of ^{64}Cu-NOTA-TRC105-F(ab')$_2$ (5.8±0.8, 7.6±0.6, 5.6±0.4, and 3.8±0.7 %ID/g at 0.5, 3, 16, and 48 h post-injection respectively; n = 4), as well as ^{64}Cu-NOTA-TRC105-Fab (3.6±0.4, 4.2±0.5, 4.9±0.3, and 4.6±0.8 %ID/g at 0.5, 2, 5, and 24 h post-injection respectively; n = 4), in the 4T1 murine breast cancer model. Since tumor uptake peaked quickly, both ^{61}Cu-NOTA-TRC105-Fab and ^{61}Cu-NOTA-TRC105-F(ab')$_2$ were also able to provide good tumor contrast at a few hours post-injection. CD105 specificity of both tracers was confirmed with blocking and histology studies. Overall, similar tumor contrast was observed for the two tracers, although the absolute tumor uptake was higher for $^{61/64}$Cu-NOTA-TRC105-F(ab')$_2$ due to bivalency, higher molecular weight, and longer circulation half-life. Conclusion: Both $^{61/64}$Cu-NOTA-TRC105-Fab and $^{61/64}$Cu-NOTA-TRC105-F(ab')$_2$ had rapid, prominent, and CD105-specific uptake in the 4T1 tumor. The use of Fab and F(ab')$_2$ fragments allowed much faster tumor uptake (peaking at a few hours after injection) than radiolabeled intact antibody (often peaking after 24 h), which may be translated for same day immunoPET imaging in the clinic. Besides a shorter t1/2 of 3.3 h that is more suitable for labeling of antibody fragments, ^{61}Cu also has much higher β+ branching ratio than $^{61/64}$Cu (62% vs 17%). Therefore,it can offer stronger signal intensity and require lower tracer dose for PET than ^{64}Cu, which will facilitate clinical translation.

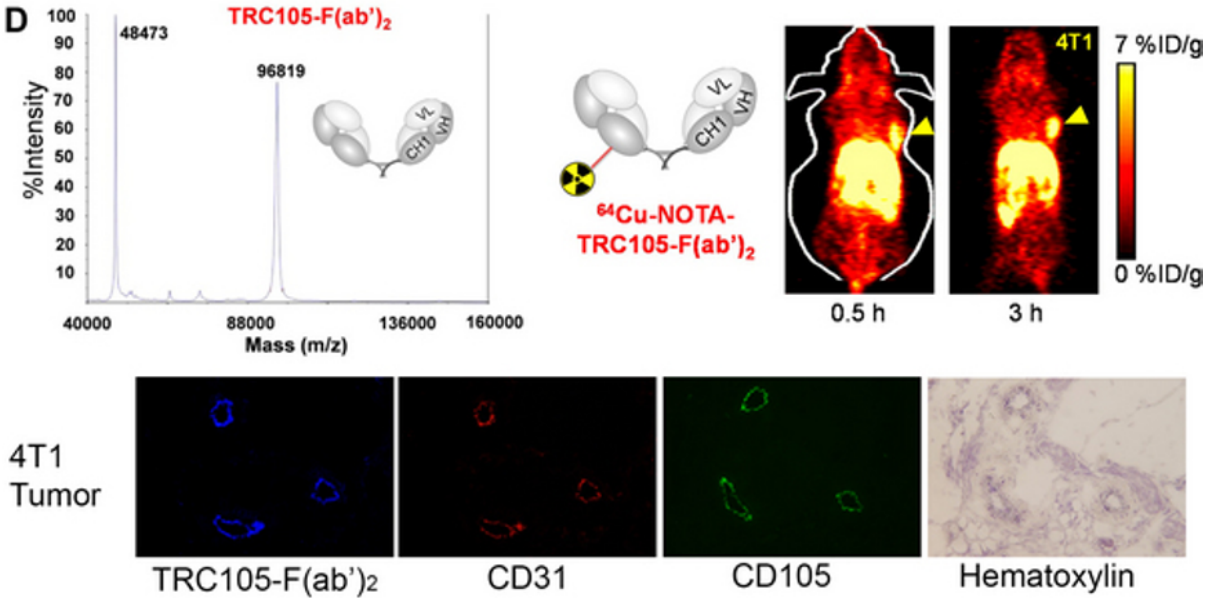

Disclosure of author financial interest or relationships:

H. Hong, None; **Y. Zhang**, None; **H. Orbay**, None; **C.P. Theuer**, TRACON Pharmaceuticals, Stockholder; TRACON Pharmaceuticals, Employment; **T.E. Barnhart**, None; **W. Cai**, None.

Presentation Number **P 367**
Poster Session 3
September 20, 2013 / 15:15-15:15 / Room: Exhibit Hall B

Non-invasive imaging of caspase-3 dependent apoptosis by adenovirus-mediated delivery of TRAIL/FasL genes in human glioma cancer model

Thoudam Debraj Singh[1], *Yong Hyun Jeon*[1], *Ho Won Lee*[1], *Sang-Woo Lee*[1], *Ha Jeoung-Hee*[2], *Alnawaz Rehemtulla*[3], *Byeong-Cheol Ahn*[1], *Jaetae Lee*[1], [1]*Nuclear Medicine, School of Medicine, Kyungpook National University, Daegu, Republic of Korea;* [2]*Pharmacology, School of Medicine, Kyungpook National University, Daegu, Republic of Korea;* [3]*Radiation Oncology, University of Michigan, Ann Arbor, MI, USA. Contact e-mail: debraj.thoudam@gmail.com*

Objectives: Here, we monitored caspase-3-dependent apoptosis by adenoviral gene therapy using a caspase-3 sensor in in vivo animal model having human glioma xenograft. Methods: Previously, we had reported high sensitive caspase-3 biosensor based on a split luciferase technology. Human glioma cancer cell line (D54) co-expressing caspase-3 sensor and renilla luciferase (Rluc) was established (referred to as a D54-CR). For in vitro experiment, Ad-TRAIL (tumor necrosis factor-related apoptosis inducing ligand)/or -FasL at 5, 25, and 50 MOI (multiplicity of infection) was transduced to D54-CR cells, followed by serial measurement of luciferase activity at designated time points. Inhibition study with Z-VAD (pan caspase inhibitor) was performed in D54-CR cells transduced with Ad-TRAIL/or -FasL to examine the selectivity of the caspase-3 sensor. FACS analysis was done to determine the percentage of 1) cleaved caspase-3/ or PARP and 2) Annexin-V positive cells in transduced D54-CR cells. After establishment of subcutaneous D54-CR tumor model, in vivo bioluminescence imaging (BLI) was acquired to determine the baseline of bioluminescence activity prior to Ad-FasL treatment. Ad-null/or -FasL (5×108 pfu/mouse) was intratumorally administered at day 1, 3 and 5 and BLI imaging was acquired at different time points post-injection. During in vitro and in vivo experiment, BLI signals of the caspase-3 sensor were divided with Rluc signals to normalize by viable cell number. Results: BLI signals in D54-CR were increased in a time- and virus dose-dependent manner post-transduction (Fig. 1 A, B) ($P<0.001$). Treatment of Z-VAD completely blocked the BLI activity in transduced cells ($P<0.005$). FACS analysis revealed increase of 1) cleaved caspase-3/or -PARP and 2) Annexin and PI positive cells in a viral dose-dependent manner. At 12 h and 24 h after intratumoral injection of Ad-FasL, in vivo BLI imaging showed ~8.2 and ~12.9 fold increase of BLI activity compared with control (Fig. 2 A, B) ($P<0.01$). The rate of apoptosis determined during the course of Ad-FasL therapy through caspase-3 sensor showed peak maximum fold ~46.6 ($P<0.01$) at day 4 post intratumoral injection. A significant reduction of Rluc activity was detected in Ad-FasL-treated tumor but not Ad-Null-treated tumors after therapy (Fig. 2 C, D) ($P<0.01$). Conclusion: To this end, we have shown the utility of a new surrogate biomarker for imaging caspase-3 mediated cell death by Ad-FasL/-TRAIL therapy in human glioma cancer model using the caspase-3 sensor.

Disclosure of author financial interest or relationships:
T. Debraj Singh, None; **Y. Jeon**, None; **H. Lee**, None; **S. Lee**, None; **H. Jeoung-Hee**, None; **A. Rehemtulla**, None; **B. Ahn**, None; **J. Lee**, None.

Presentation Number **P 368**
Poster Session 3
September 20, 2013 / 15:15-15:15 / Room: Exhibit Hall B

Vascular-based personalized anti-EMMPRIN therapy for pancreatic cancer

Hyunki Kim[1], *Christopher Rigell*[2], *Guihua Zhai*[1], *Kyle Lee*[2], *Sharon Samuel*[1], *Amber Martin*[1], *Heidi Umphrey*[1], *Cecil R. Stockard*[4], *T. M. Beasley*[3], *Long Shan Li*[5], *David A. Boothman*[5], *Kurt R. Zinn*[1], [1]*Radiology, University of Alabama at Birmingham, Birmingham, AL, USA;* [2]*Medicine, University of Alabama at Birmingham, Birmingham, AL, USA;* [3]*Biostatistics, University of Alabama at Birmingham, Birmingham, AL, USA;* [4]*Comprehensive Cancer Center, University of Alabama at Birmingham, Birmingham, AL, USA;* [5]*Radiation Oncology, University of Texas Southwestern Medical Center, Dallas, TX, USA. Contact e-mail: hyunki@uab.edu*

Purpose: To validate the differential therapeutic efficacy of anti-EMMPRIN antibody according to pancreatic-tumor vascularity when used with chemotherapy. Materials and Methods: A total of 13 groups of SCID mice (n=5-6/group) bearing orthotopic MIA PaCa-2 tumors were employed. DCE-MRI was applied for group 1 during four consecutive days, and tumor volume, Ktrans, and gadoteridol concentration at 20 minutes after injection (C20min: Interpreted as the delivery efficiency of a chemotherapeutic agent) were quantified. Subsequently, the correlation between Ktrans and C20min was determined, and tumor vascularity was stratified into hyper, iso, and hypovascular according to different Ktrans range. Groups 2-13 were used for therapy study. Groups 2-5 had hypervascular tumors, and groups 6-13 had hypovascular tumors. Groups 2 and 6 were untreated (served as control), and groups 3-5 (or groups 7-9) were treated with gemcitabine, anti-EMMPRIN antibody, and combination, respectively, for 2 weeks. The same dose schedule employed for groups 6-9 was applied to treat groups 10-13, respectively, but β-lapachone was added to the therapy regimen of each of groups 10-13. FDG-PET/CT imaging was applied weekly for all animals in groups 2-13, and tumor volume and tumor SUVmean were quantified. After treatment, all tumors were collected and Ki-67 staining was performed. Results: The averaged C20min was maximized when Ktrans value was ~0.050 min-1, and then declined with larger values. Tumors were stratified into three groups, namely hypovascular (Ktrans<0.043min-1), isovascular (Ktrans:0.043~0.060min-1), and hypervascular (Ktrans>0.060min-1) tumors; the Ktrans range of an isovascular tumor was determined when C20min became higher than 90% of its maximum value. Synergistic therapeutic effect was shown between anti-EMMPRIN antibody and gemcitabine in hypervascular tumors (Ktrans:~0.07min-1), but an antagonistic effect was shown in hypovascular tumors (Ktrans: ~0.04min-1). The antagonistic effect of anti-EMMPRIN antibody appeared more obvious when it was combined with gemcitabine and β-lapachone. Tumor volume change was significantly correlated with tumor SUVmean change either in the hypervascular tumor model (p=0.002) or hypovascular tumor model (p=0.003). Proliferating (Ki-67 stained) cell density was significantly reduced by anti-EMMPRIN antibody combined with chemotherapy in hypervascular tumors (p=0.008), but not in hypovascular tumors (p>0.05). Discussion: For hypervascular tumors, the antiangiogenic effect of anti-EMMPRIN antibody may induce the normalization of tumor microvasculature, reducing interstitial pressure and thereby improving the delivery of small-molecule chemotherapeutic agents. In contrast, for hypovascular tumors, the antiangiogenic effect may reduce the tumor vasculature excessively, decreasing the drug delivery, leading to an antagonistic effect. There may be a clinical benefit to characterize the tumor vascularity prior to therapy initiation to optimize treatment that will maximize the therapeutic effect for pancreatic cancer.

Disclosure of author financial interest or relationships:
H. Kim, None; **C. Rigell**, None; **G. Zhai**, None; **K. Lee**, None; **S. Samuel**, None; **A. Martin**, None; **H. Umphrey**, None; **C.R. Stockard**, None; **T.M. Beasley**, None; **L. Li**, None; **D.A. Boothman**, StemPAR Sciences/Bistemics, Consultant; **K.R. Zinn**, None.

Presentation Number **P 369**
Poster Session 3
September 20, 2013 / 15:15-15:15 / Room: Exhibit Hall B

I-124 labeled anti-PSCA A11 minibody for imaging bone metastases and response to androgen deprivation in prostate cancer

Scott M. Knowles[1], *Richard Tavaré*[1], *Kirstin A. Zettlitz*[1], *Felix B. Salazar*[1], *Matthew Rochefort*[2], *Robert E. Reiter*[3], *Anna M. Wu*[1], [1]*Dept. of Molecular and Medical Pharmacology, David Geffen School of Medicine at UCLA, Los Angeles, CA, USA;* [2]*Dept. of Surgery, David Geffen School of Medicine at UCLA, Los Angeles, CA, USA;* [3]*Dept. of Urology, David Geffen School of Medicine at UCLA, Los Angeles, CA, USA. Contact e-mail: sknowles@mednet.ucla.edu*

Prostate Stem Cell Antigen (PSCA) is a GPI-linked cell surface glycoprotein which has limited expression in normal tissue and prostate but is over-expressed in >90% of localized prostate cancer where its expression correlates with poor outcomes. It is also highly over-expressed in >97% of prostate cancer bone metastases. Here we use a naturally PSCA expressing LAPC-9 xenograft model to compare immunoPET imaging with the anti-PSCA A11 minibody to F-18 NaF bone scans in intratibial xenografts, and image down-regulation of PSCA in subcutaneous LAPC-9 xenografts in response to androgen deprivation. LAPC-9 intratibial xenografts were implanted by injecting ~10^5 LAPC-9 cells into the intratibial metaphysis of male SCID mice with a contralateral sham injection. At 4, 6, and 8 weeks post-injection mice underwent F-18 NaF microPET bone scans immediately followed by injection of I-124 labeled A11 minibody and microPET imaging at 44 hours post-minibody-injection. F-18 NaF bone scans shows a high degree of non-specific accumulation and no significant increase in uptake in xenograft bearing tibias between 4 and 8 weeks post-injection ($p = 0.12$, by two-way ANOVA). A11 minibody, however, shows significantly higher uptake in tibias bearing LAPC-9 xenografts than the sham control by immunoPET ($p = 0.016$, by two-way ANOVA) and by biodistribution (1.33 ± 0.38%ID/g vs 0.11 ± 0.017%ID/g, $p = 0.0290$ by t-test) with virtually no uptake in other tissues. LAPC-9 tumors, surgically implanted subcutaneously, were treated with either the anti-androgen MDV-3100 (40 mg/kg) or with a vehicle control for one week. Treatment with MDV-3100 causes a three-fold down regulation in PSCA expression in LAPC-9 tumors by quantitative ex vivo flow cytometry. Mice bearing subcutaneous LAPC-9 xenografts show no difference in A11 minibody uptake before initiation of therapy (2.31 ± 0.17%ID/g Vehicle vs 2.39 ± 0.22%ID/g MDV-3100, $p = 0.80$), however after 1 week of treatment with MDV-3100 mice show a 30% decrease in A11 minibody uptake by microPET with partial volume correction (3.70 ± 0.20%ID/g Vehicle vs 2.61 ± 0.23%ID/g MDV-3100, $p = 0.0028$) and by biodistribution (3.63 ± 0.20%ID/g Vehicle vs 2.75 ± 0.32%ID/g MDV-3100, $p = 0.03$) while no difference is seen in the tumor volumes or masses. In conclusion, immunoPET with the A11 minibody can detect osteoblastic intratibial xenografts before significant changes are seen on bone scans. A11 minibody immunoPET can also image changes in PSCA expression caused by anti-androgen therapy before changes are seen in tumor volume or mass. A11 minibody immunoPET, therefore has the possibility of detecting tumors more sensitively and specifically and measuring therapy efficacy sooner than currently used clinical imaging.

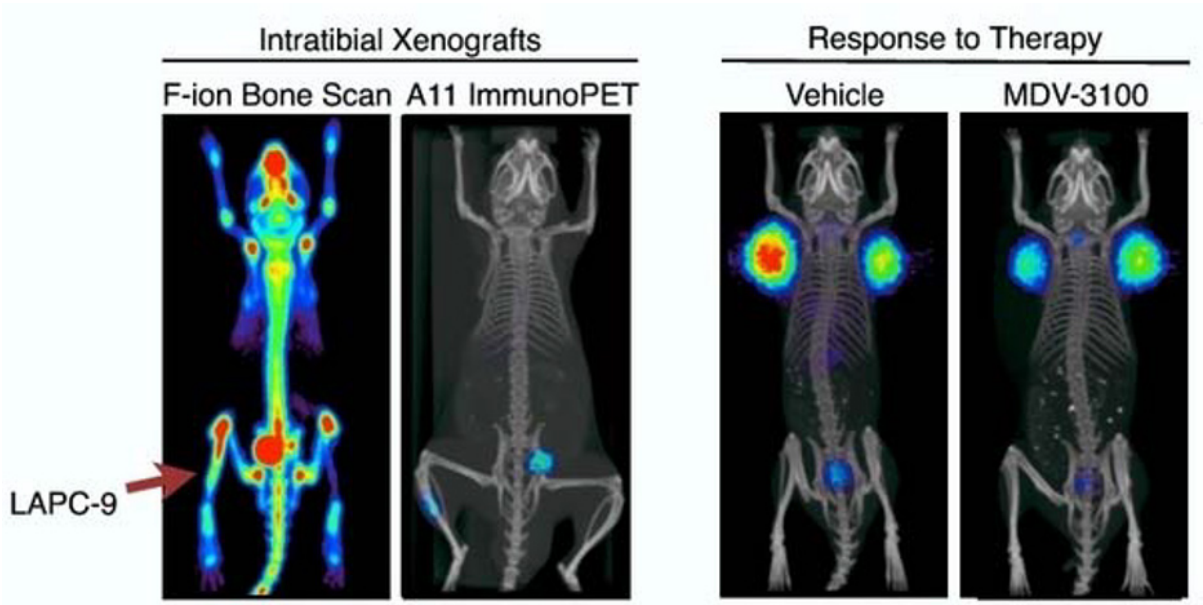

Disclosure of author financial interest or relationships:
S.M. Knowles, None; **R. Tavaré**, None; **K.A. Zettlitz**, None; **F.B. Salazar**, None; **M. Rochefort**, None; **R.E. Reiter**, ImaginAb, Stockholder; **A.M. Wu**, ImaginAb, Inc., Stockholder; ImaginAb, Inc., Consultant; ImaginAb, Inc., Grant/research support; Daiichi Sankyo, Consultant; Sanofi, Consultant .

Presentation Number **P 370**
Poster Session 3
September 20, 2013 / 15:15-15:15 / Room: Exhibit Hall B

In vivo monitoring of NIS-induction and tumor phenotyping using SPECT and MRI in extrathyroidal tumor xenograft models

Eva J. Koziolek[1], *Ivayla Apostolova*[3], *Agnieszka Tarkowska*[2], *Udo Schumacher*[2], *Winfried Brenner*[3], *Michael G. Kaul*[1], *Gerhard Adam*[1], [1]*Diagnostic and Interventional Radiology, University Hospital Hamburg Eppendorf, Hamburg, Germany;* [2]*Anatomy and Experimental Morphology, University Hospital Hamburg Eppendorf, Hamburg, Germany;* [3]*Nuclear Medicine, Charite, Berlin, Germany. Contact e-mail: ekoziole@uke.de*

Objectives: Despite the method of gene transfer, all trans retinoic acid (atRA), a vitamin A derivative, in combination with glucocorticoides has been used to stimulate the expression of the sodium iodide symporter (NIS) in some thyroid and breast cancer models to increase functional NIS and iodine accumulation. In order to apply I-131 therapy to extrathyroidal tissue, functional and sufficient NIS-expression is a pre-condition. The purpose of this study was to evaluate the potential of atRA and prednisolut (PRED) to a) induce functional NIS-expression in a NIS-negative pancreatic cancer model b) to further enhance functional NIS in a NIS-transfected breast cancer model responsive to atRA stimulation. NIS-expression was visualized in vivo by SPECT/CT using the NIS-specific tracer Tc99m. For tumor tissue characterisation multiparametric MRI was performed. Methods: For In vitro stimulation of atRA/PRED-induced NIS-expression BxPC3 (pancreas), HT29 (colon), MCF7 (breast) and NIS-transfected MCF7 cells were treated with atRA, PRED (10-6 M and 10-6 M respectively) or a combination of both for 48h. I125 Uptake was determined as described by Weiss et al.. Mouse tumor xenograft models were established over the right scapula. Daily injections of atRA/PRED (1.3mg/0.7 mg/day) treatment were given subcutaneously for up to 7 days. SPECT measurements were performed on day 0, 5 and 7 using a nanoSPECT/CTplus (Bioscan/Mediso) and 100 MBq/mouse Tc99m pertechnetate. Tumor phenotyping (T2w, ADC, DCE-MRI) was performed prior to the treatment using a 7T MRI (ClinScan, Bruker). Results: Native BxPC3, HT29 and atRA-stimulated HT29 cells showed no NIS expression. While atRA alone strongly increased the I125 uptake in BxPC3, MCF7 and MCF7/NIS cells, the combination of atRA/PRED further amplified the uptake by about 25 % for the pancreatic and breast cancer cell line. PRED alone had no effect. In vivo imaging of tumor-specific functional NIS- expression after 5 and 7 days of atRA/PRED treatment was performed by SPECT-imaging and resulted in an increase in Tc99m-uptake. The NIS-negative pancreatic cancer model resulted in an up to 3 fold increased tracer uptake (n=4) above the background (tumor tracer uptake prior to treatment) or when compared to HT29 tumor xenografts. As expected, the NIS-transfected breast cancer model (n=4) showed an initial strong tracer uptake in the tumor tissue ranging between 3 and 4 % ID/ml and further increased by 30-50%, when tracer uptake was measured on day 7 of treatment. T2w MR imaging allowed a precise delineation of tumour mass, which in turn was used to place the ROI with high accuracy for SPECT analysis. Tumor phenotyping allowed a detailed characterisation of the tumor tissue prior to atRA/PRED treatment. Conclusion: Functional NIS-expression in extrathyroidal tissues can be stimulated by atRA/PRED treatment and further increased in already NIS-transfected tissues, when tissues initially respond with NIS- expression after atRA treatment. In vivo tumor-specific NIS-induction can be visualized by SPECT/CT using a NIS-specific tracer. Multimodal imaging including SPECT and MRI generates useful complementary data.

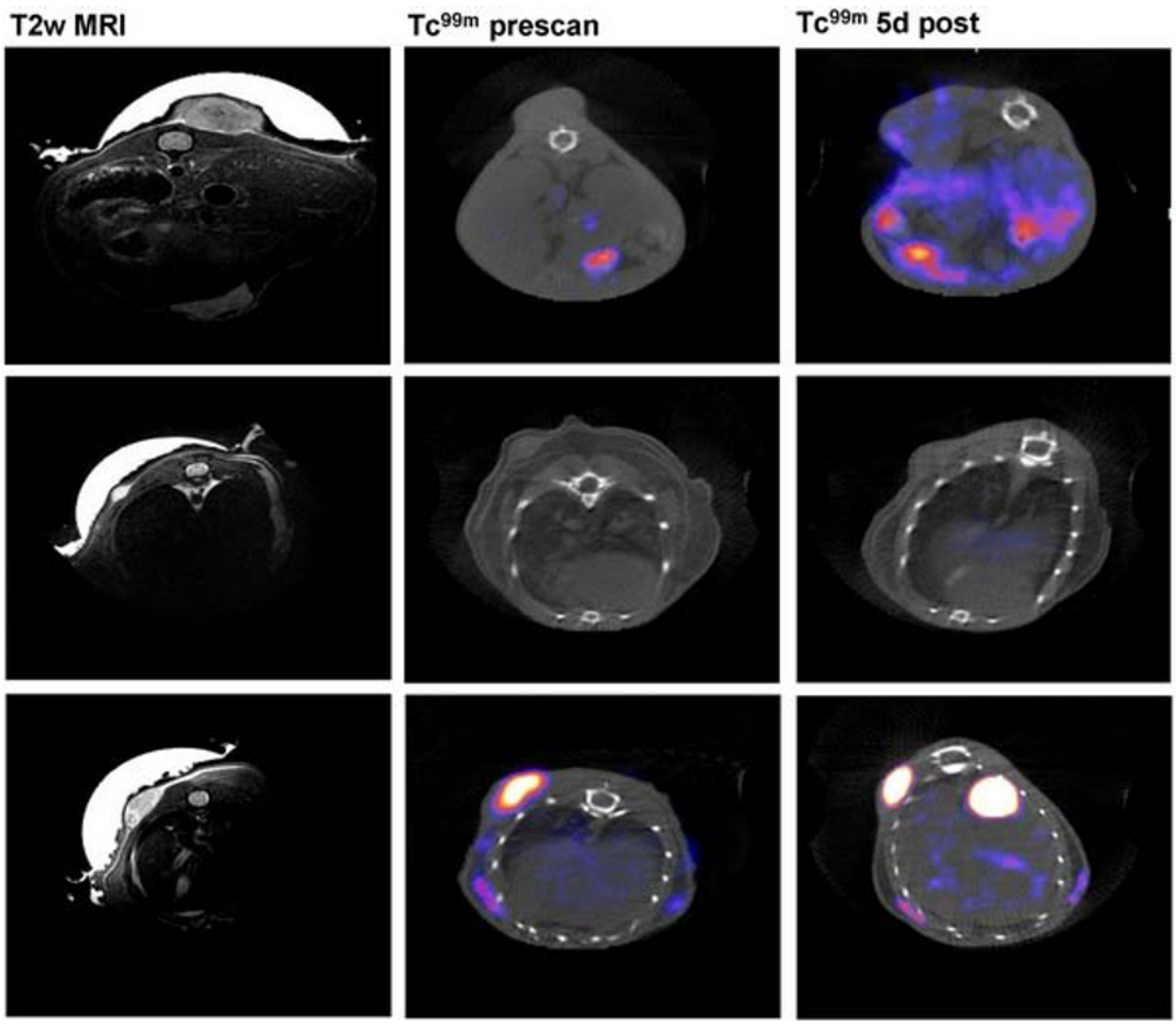

In vivo imaging of atRA/PRED stimulated NIS induction in the pancreatic (BxPC3 -upper panel) and NIS-transfected breast (MCF7 - lower panel) cancer model. As a negative control a colon carcinoma (HT29 - mid panel), not responsive to atRA/PRED, was used. T2w MR imaging allowed precise tumor delineation and was used to place the ROI for SPECT analysis. While the SPECT - prescan showed no tumor-specific tracer uptake in the pancreatic and HT29 tumor model, atRA/PRED treatment resulted in an tumor-specific Tc99m increase in the pancreatic cancer model, when compared to the negative control. The NIS-transfected breast cancer model showed a strong tumor-specific basal tracer uptake, which was further increased by about 30-50% due to atRA/PRED treatment.

Disclosure of author financial interest or relationships:
E.J. Koziolek, None; **I. Apostolova**, None; **A. Tarkowska**, None; **U. Schumacher**, None; **W. Brenner**, nanoPET, Grant/research support; **M.G. Kaul**, None; **G. Adam**, None.

Presentation Number **P 371**
Poster Session 3
September 20, 2013 / 15:15-15:15 / Room: Exhibit Hall B

Correlation of 18F-FDG-PET Imaging Changes With Expression of Glucose Transporter Genes Following Radiation Treatment

George D. Wilson[1,2], Jiayi Huang[1], Bryan J. Thibodeau[2], Sandra Galoforo[1], **Sarah A. Krueger**[1]*, Laura Fortier[2], Barbara L. Pruetz[2], John Torma[1], Brian Marples[1], [1]Radiation Oncology, William Beaumont Hospital, Royal Oak, MI, USA; [2]Beaumont BioBank, Beaumont Health System, Royal Oak, MI, USA. Contact e-mail: sarah.krueger@beaumont.edu*

Purpose: The significance of FDG-PET changes during treatment has not been an area that has been extensively studied either at the basic science level or in clinical studies mainly due to the logistics of repeat scanning during treatment. Monitoring response to radiation therapy can be complex due to post-treatment changes like inflammation and edema and therefore it is important to correlate PET parameters directly with pathology and biology. In this study we have correlated changes in FDG uptake following radiation treatment with gene expression changes in the glucose transporter family. Methods: Low passage head and neck squamous cancer cells (UT14) were injected to the flanks of female nu/nu mice to generate xenografts. After tumors reached a size of 400-500cc, they were treated with either sham RT or 15 Gy in one fraction. At different time points, day 3, 9 and 16 for controls and days 4, 7, 12, 21, 30, 40 after irradiation, 2-3 mice were assessed with dynamic FDG-PET acquisition over 2 hours. PET/CT scans were performed with a FLEX Triumph Trimodality PET/SPECT/CT system (Gamma Medica-Ideas), which has an intrinsic resolution FWHM of 850μm x 850μm x 1,200μm. Immediately after the FDG-PET, the tumors were harvested, RNA was extracted and gene expression changes studied using Human Exon 1.0 arrays in an Affymetrix GeneChip platform. Different analytical parameters were used to process the dynamic PET data including standard uptake value (SUV), SUV corrected by blood glucose (SUVglu), kinetic index (Ki), retention index (RI), and sensitivity factor (SF). The genes of particular interest were SLC2A1 (solute carrier family 2 [facilitated glucose transporter] member 1) (GLUT1), SLC2A10, SLC2A11, SLC2A12), SLC2A13, SLC2A2, SLC2A3, SLC2A4, SLC2A5, SLC2A6, SLC2A8, SLC2A9, SLC5A10, SLC5A11, SLC5A4, SLC5A9 and HK1 (hexokinase 1). Results: The UT14 xenografts showed a profound inhibition of tumor growth for two weeks after 15Gy; after that time they regrew quickly. During the period of growth inhibition period, the Ki value showed a precipitous fall on days 4 and 7 and partially recovered by day 12 after which there was a steady increase approaching pretreatment uptake levels. Fig 1 shows gene expression changes post radiation treatment. Hexokinase 1 levels remained relatively constant throughout the duration of the study. SLC2A1 and SLC2A3 showed minor changes post-irradiation during tumor inhibition and regrowth. The most significant changes were seen in SLC5A1 which was upregulated 3.8 fold on day 7 and was still 2.7 fold higher than control animals on day 12. Conclusions: The major genes involved in FDG uptake are not affected by radiation treatment and seem independent of the growth kinetics of the HNSCC xenograft in this study. The exception was SLC5A1 (SGLT1), a member of the sodium-dependent glucose transporter family. The protein is the primary mediator of dietary glucose and galactose uptake from the intestinal lumen but it has also been shown that JAK2 upregulated SLC5A1 activity which may play a role in the effect of JAK2 during ischemia and malignancy.

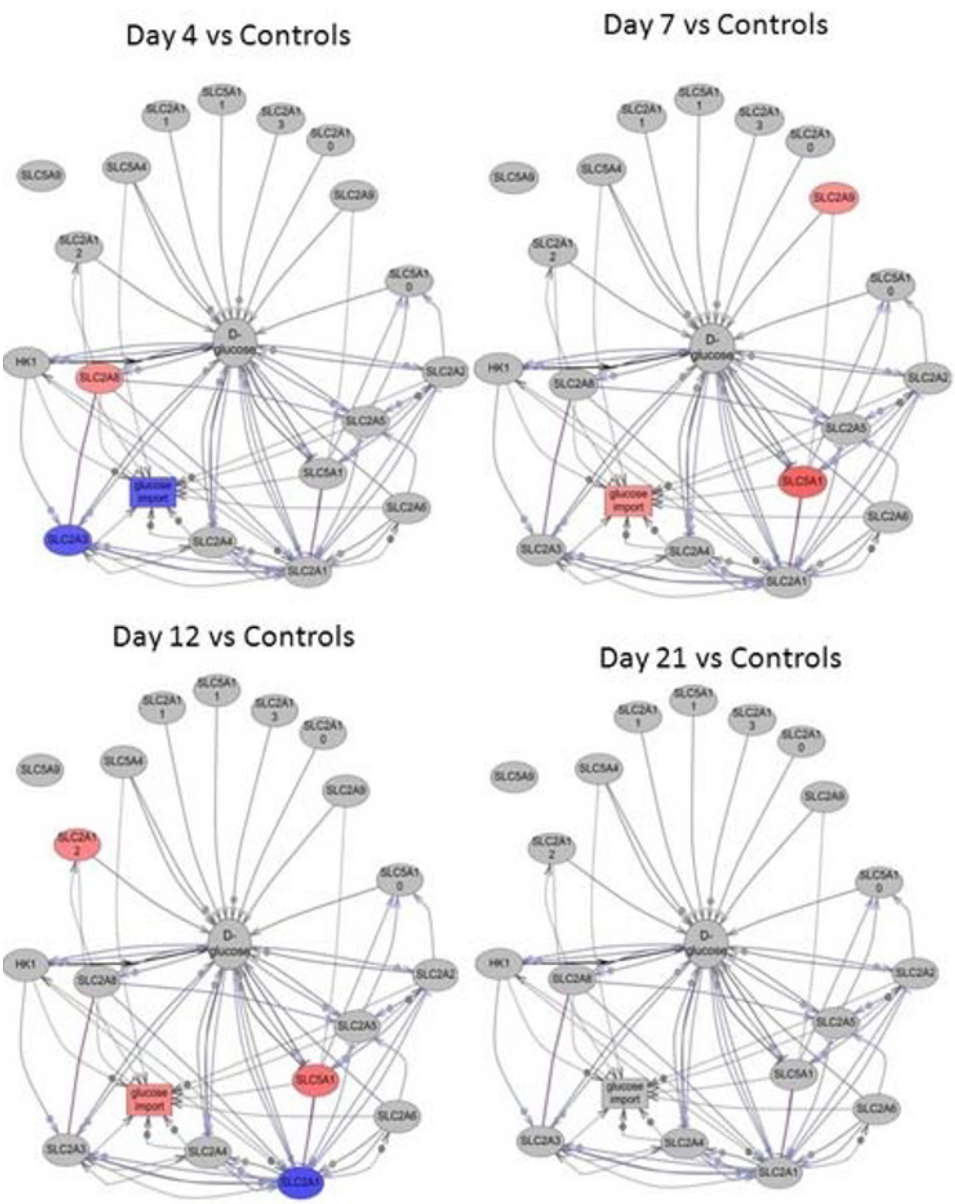

Figure 1. Gene expression changes in glucose transporter genes following radiation treatment. Red represents genes upregulated by greater than 1.2-fold with a p-value >0.10; blue are downregulated and grey are unchanged.

Disclosure of author financial interest or relationships:
G.D. Wilson, None; **J. Huang**, None; **B.J. Thibodeau**, None; **S. Galoforo**, None; **S.A. Krueger**, None; **L. Fortier**, None; **B.L. Pruetz**, None; **J. Torma**, None; **B. Marples**, None.

Presentation Number **P 372**
Poster Session 3
September 20, 2013 / 15:15-15:15 / Room: Exhibit Hall B

Targeted Gold Nanorods for Ovarian Cancer Imaging: Evaluation of RGD Targeting with Photoacoustic Imaging

Timothy Larson, *Jesse V. Jokerst, Adam J. Cole, Sanjiv S. Gambhir, Radiology, Stanford, Mountain View, CA, USA. Contact e-mail: larsonta@stanford.edu*

Introduction: Targeted nanoparticles have the ability to specifically accumulate at diseased sites, increasing efficacy and potentially reducing the required dosage. However, there are conflicting reports in the literature about whether targeting actually improves accumulation in tumors in various xenograft models. Here, we develop gold nanorods functionalized with RGD peptides targeting αvβ3 integrins, and evaluate their performance in an ovarian subcutaneous xenograft model, evaluating accumulation using both photoacoustic imaging and inductively-coupled plasma optical emission spectroscopy (ICP-OES). Both methods demonstrate that, for these nanoparticles in this specific model, there is no difference in tumor accumulation between targeted nanoparticles and a non-targeted control. Materials and Methods: Gold nanorods (GNR) were synthesized via the standard CTAB-mediated growth solution, and functionalized with either methoxy-PEG-thiol or amine-PEG-thiol and the RGD peptide via a SMCC linker. Subcutaneous tumor xenografts i of the OV2008 cell line were created in the flanks of nude mice and analyzed between 800 - 1200 mm3. GNRs were injected via tail-vein at 5 nM concentration, and photoacoustic imaging was done using a photoacoustic tomography system (Endra Inc.), and tumors were resected and dissolved in aqua regia for ICP-OES analysis. Results: GNRS were analyzed via optical spectroscopy and had peak resonances between 700 - 800 nm, and their shape was confirmed via electron microscopy, with rods having an aspect ratio of approximately 3 and a width of 10 nm. GNR targeting was verified in vitro by comparing the accumulation of GNR on adherent OV2008 cells in a 12 well plate. PEG only GNR had a zeta potential of -10 +/- 4 mV, while targeted GNR had a zeta potential of +7 +/- 3 mV. Targeted GNR binding decreased by four times in the presence of excess RGD peptide, and non-targeted GNR did not show any detectable attachment to cells. We injected 200 μL 5.4 nM GNRs into tumor-bearing mice via tail vein with n=3 mice for both targeted and non-targeted particles. Relative to baseline photoacoustic signal, these injections increased tumor signal 2.5-fold, but there was no detectable difference between targeted and non-targeted nanorods. The non-targeted GNRs accumulated at the tumor site at 2.59% +/- .45%ID/g and the targeted GNRS accumulated at 2.62% +/- 0.56% via ICP-OES analysis. In all cases, maximum signal increase occurred within 2 hours of injection with elevated photoacoustic signal persisting for at least 24 hours. To validate that this signal increase was due to the presence of GNRs in the tumor and not due to changes in hemoglobin, tumors were analyzed for gold content at 24 hours, verifying that there was no statistical difference (p value = 0.93) between targeted and non-targeted GNR. Conclusion:. RGD targeting of gold nanorods does not significantly increase GNR accumulation in this OV2008 tumor xenograft model. This is corroborated with both photoacoustic data and ICP-OES analysis. Future studies will explore if targeting may help in other mouse models including transgenic tumor models.

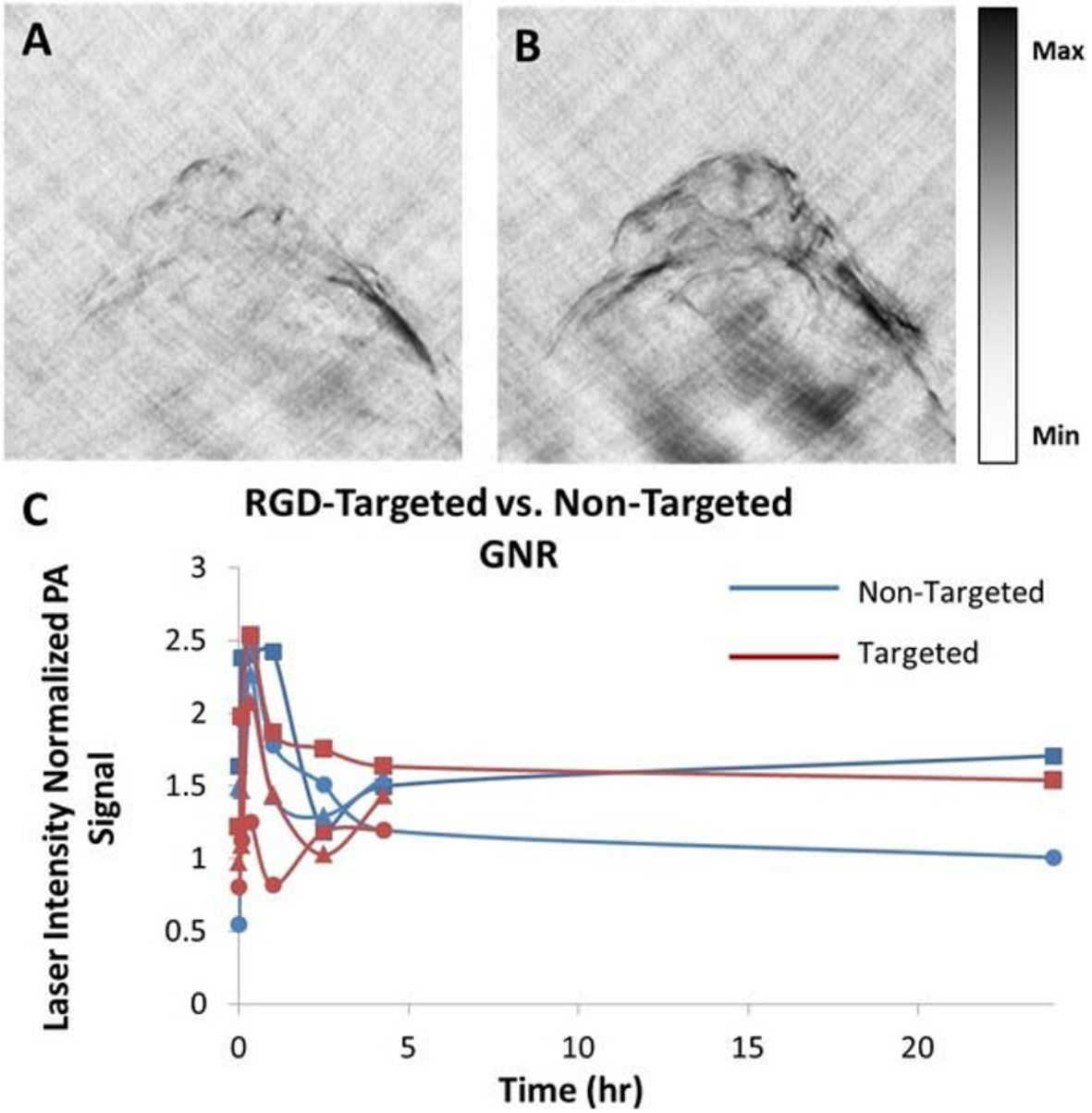

Figure 1. Photoacoustic images and signal of xenograft ovarian tumors over a period of 24 hours for n = 3 tumors of both targeted and non-targeted GNR. Images are from before (A) and 2 hours after (B) injection of non-targeted GNR. Both images are at the same intensity scale. Photoacoustic imaging was performed at 0 minutes, 20 minutes, 4.5 hours, and 24 hours.

Disclosure of author financial interest or relationships:

T. Larson, None; **J.V. Jokerst**, None; **A.J. Cole**, None; **S.S. Gambhir**, Bracco Diagnostics, Consultant; Endra, Inc, Stockholder; Cellsight, Stockholder; Enlight, Inc., Stockholder; General Electric, Grant/research support; ImaginAb, Stockholder; MagArray, Inc., Stockholder; Sanofi-Aventis, US, Grant/research support; SiteOne Therapeutics, Stockholder; VisualSonics/Sonosite, Stockholder .

Presentation Number **P 373**
Poster Session 3
September 20, 2013 / 15:15-15:15 / Room: Exhibit Hall B

Functional Imaging of the angiogenic switch in the HER-2/Neu transgenic mouse model of human breast cancer by DCE-MRI

Dario L. Longo[1,2], *Lorena Consolino*[1,2], *Walter Dastrù*[1,2], *Juan C. Cutrin*[1], *Stefania Lanzardo*[1], *Maddalena Arigoni*[1], *Federica Cavallo*[1], *Silvio Aime*[1,2], [1]*Department of Molecular Biotechnologies and Health Sciences, University of Turin, Turin, Italy;* [2]*Molecular Imaging Center, University of Torino, Torino, Italy. Contact e-mail: dario.longo@unito.it*

INTRODUCTION: Tumor progression depends on sequential events, based on a combination of genetic and epigenetic alterations. The transition from the pre-vascular hyperplasia to highly vascularized and progressively outgrowing tumors is mediated by the angiogenic switch. Among the noninvasive imaging techniques, MRI provides the best platform on which develop new functional imaging tools to observe the longitudinal progression in mammary carcinoma using transgenic mouse as preclinical in vivo model of the angiogenic switch [1]. DCE-MRI exploiting blood-pool Gd-based contrast agents is exquisitely sensitive to permeability/perfusion properties of microvessel heterogeneity and distribution in tumor [2]. In this study we evaluated how DCE-MRI can quantitatively depict different histologic stages of breast cancer development, including mammary hyperplasia, carcinoma in situ and invasive breast cancer, in the established HER-2/Neu mice model of human breast cancer. METHODS: Balb-neuT female mice develop spontaneous orthotopic mammary cancers through normal mammary glands (1-6 w - Stage 0), ductal hyperplasia (7-14 w - stage I), ductal carcinoma in situ (14-21 w - stage II) and invasive lobular carcinoma (21-28 w- stage III). In this breast cancer model the angiogenic switch occurs at weeks 8-10 [3]. Balb-neuT(n=89) mice and Balb/C (n=35) mice as control were used in this study. DCE MRI dynamic protocol was carried out with an Aspect M2 1T scanner by injecting into the tail vein a blood-pool Gd-based contrast agent and sampling T1w images for 1 hour with a Gradient Echo sequence every 60 s. The acquired raw DCE-MRI data were analyzed by a quantitative method implementing a two-compartment Tofts model, yielding the parametric maps (Ktrans, Kep, Vp). Mammary glands were excised, fixed in formalin and stained for H&E and endothelial specific factors. RESULTS AND DISCUSSION: Balb/C and Balb-neuT mice showed similar permeability and vascular volume fraction at Stage 0, before the progression of hyperplasia. After the angiogenic switch, a strong increase of permeability and vascular volume fraction was observed in Balb-neuT mice, in comparison to Balb/C ones (Ktrans= 3.0±0.7E-4 and 5.3±0.7E-4, Vp= 3.7±0.8E-2 and 7.4±0.8E-2 for Balb-neuT mice at stage 0 and I; Ktrans= 2.8±0.8E-4 and 3.1±0.5E-4, Vp= 3.4±0.3E-2 and 4.7±0.6E-2 for Balb/C at stage 0 and I). The increase of permeability remained constant during stage II and III, whereas a slight reduction was observed in Balb/C mice (Fig. 1). CONCLUSIONS: Our study showed that functional tissue parameters estimated from DCE-MRI using a blood-pool contrast agent, related to permeability and perfusion of the tumor vasculature, increase when mammary glands progress from normal tissue to all the different stages until invasive breast cancer, with clear differences when compared with normal tissues. There results provide new insights suggesting a new imaging approach for earlier breast cancer detection. REFERENCES [1] Kiessling F. et al.; Eur Radiol 2007, 17, 2136 [2] Turetscheck K. et al.; J Magn Res Imaging 2004, 20, 138 [3] Di Carlo E. et al.; Lab Investigation 1999, 79, 1261

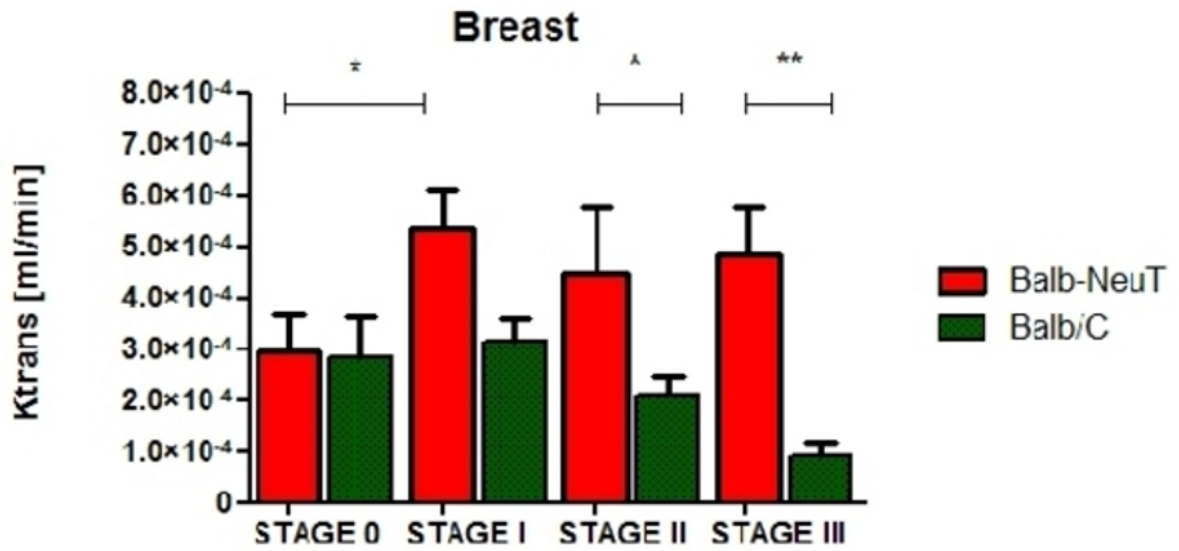

Fig. 1 Mean Ktrans values obtained for NeuT and Balb/C mice at different stages of breast cancer progression in mammary glands.

Disclosure of author financial interest or relationships:
D.L. Longo, None; **L. Consolino**, None; **W. Dastrù**, None; **J.C. Cutrin**, None; **S. Lanzardo**, None; **M. Arigoni**, None; **F. Cavallo**, None; **S. Aime**, None.

Presentation Number **P 374**
Poster Session 3
September 20, 2013 / 15:15-15:15 / Room: Exhibit Hall B

Vascular Endothelial Growth Factor Targeted Imaging with FITC-Bevacizumab-Conjugated Iron Oxide Nanoparticles

Run Lin[1,2], *Jing Huang*[1,3], *Liya Wang*[1,3], *Yuancheng Li*[1,3], *Veronica Prieto E. Veronica E*[1,3], *Kevin Kim*[1,3], *Hui Mao*[1,3], [1]*Radiology and Imaging Sciences, Emory University School of Medicine, Atlanta, GA, USA;* [2]*Department of Radiology, the First Affiliated Hospital of Sun Yet-Sen University, Guangzhou, China;* [3]*Center for Systems Imaging, Emory University School of Medicine, Atlanta, GA, USA. Contact e-mail: run.lin@emory.edu*

The formation of neovasculation is essential for malignant transformation and distant spread of cancer cells. Vascular endothelial growth factor (VEGF) is expressed at an elevated level in most human cancer which plays a pivotal role in the cascade of development of neovascular. Targeting this biomarker with antibody would be a logical strategy for cancer detection and treatment. Bevacizumab is the antibody directly against VEGF, which is presently clinically applied for the treatment of various cancers with over expression of VEGF and dependence on angiogenesis. By conjugating Bevacizumab to superparamagentic iron oxide nanoparticles, a super contrast material for magnetic resonance imaging (MRI), we have developed a VEGF targeted MRI probes that can potentially used to imaging of VEGF overexpression and delivery of Avastin for improved anti-angiogenesis treatment. In this study, we conjugated fluorescein isothiocyanate (FITC)-labeled bevacizumab onto iron oxide nanoparticle (IONP) with core size of 15 or 25 nm (as shown in the images of TEM in Figure). Conjugate efficacy of FITC labeled antibody was confirmed by gel electrophoresis, dynamic light scattering (DLS), fluorescence assay of FITC and BCA protein assay. The conjugation ratio of FITC on to each antibody ranged from 2.2 to 2.4; and for that of antibody onto IONP (10nm) is around 4.3. The characteristics such as size and surface charge were determined by DLS or transmission electron microscope (TEM). For the 25nm IONP, the size and zeta potential changed from 33.5nm, -40.3 mV to 48 nm, -30.7 mV after coupling antibody and IONP. This dual-modality imaging probe was tested for the specificity of VEGF in vitro with various cell lines and then in vivo using a mouse model of breast cancer. The targeting and affinity of FITC labeled antibody and FITC-antibody-IONP to VEGF over expressed cells were verified by cell uptake experiments with fluorescence microscopy and Prussian blue staining, respectively. The expression of VEGF is studied by western blotting and immunohistochemistry (IHC) in both cells and tumor tissues. The results showed the specific uptake of FITC-bevacizumab-conjugated iron oxide nanoparticles by VEGF-positive cancer cells. Systemic administration of VEGF-targeting IONP into tumor bearing mice resulted in selective accumulation of targeting IONPs within tumor mass compared to non-targeted IONPs, detecting by optical imaging, MRI and histological analysis. Normal tissues including brain, lung, liver, spleen, et.al, were also investigated after injection of both targeted- and nontargeted-IONPs to access their distribution. Our results demonstrated the feasibility and efficacy of FITC-bevacizumab-IONP as a molecular-targeting probe for cancer detection in vitro and in vivo.

Disclosure of author financial interest or relationships:
R. Lin, None; **J. Huang**, None; **L. Wang**, None; **Y. Li**, None; **V.E. Veronica E**, None; **K. Kim**, None; **H. Mao**, None.

Presentation Number **P 375**
Poster Session 3
September 20, 2013 / 15:15-15:15 / Room: Exhibit Hall B

Evaluation and optimization of EGFR-based ADEPT, using non-invasive time-domain near-infrared fluorescence imaging

Joanna Napp[1,2], *Thomas Krüwel*[3], *Lutz F. Tietze*[4], *Walter Stühmer*[1], *Frauke Alves*[1,2], [1]*MPI for Experimental Medicine, Goettingen, Germany;* [2]*Hematology Oncology, University Medicine Goettingen, Goettingen, Germany;* [3]*Radiology, University Medicine Goettingen, Goettingen, Germany;* [4]*Organic and Biomolecular Chemistry, University Goettingen, Goettingen, Germany. Contact e-mail: napp@em.mpg.de*

In order to reduce side effects, there is a high need to develop new approaches for specific and selective cancer treatments. One of the very promising therapy concepts is the antibody-directed enzyme prodrug therapy (ADEPT), in which a tumor-specific antibody is used to carry a drug-activating enzyme to the tumor. Subsequent enzyme-mediated activation of nontoxic prodrugs to toxic drugs only within the tumor increases the specificity of treatment and decreases the drug toxicity in healthy tissues. Here we present the design and evaluation of an ADEPT concept, in which the EGFR (Epidermal Growth Factor Receptor), highly overexpressed in e.g. colorectal-, mammary- or squamous cell carcinoma, is targeted with a construct consisting of the clinically approved antibody, Cetuximab, and the drug-activating enzyme, galactosidase. First, to test for the feasibility to deliver the drug-activating enzyme to the tumor, Cetuximab was labeled with the near-infrared (NIR) fluorophore, Alexa 647 (Cetux-Alexa) and binding of the conjugate to mammary carcinoma cell lines was analyzed in vitro using fluorescence microscopy. For this, three cell lines with different EGFR expression levels were chosen: MDA-MB-468 (+++), MDA-MB-231 (+) and MCF-7 (-). Subsequently, the biodistribution and binding-kinetics of Cetux-Alexa were studied in vivo, in tumor-bearing mice, by time-domain NIR fluorescence imaging (Optix MX2; ART, Canada). We show that Cetux-Alexa binds to the cell membrane of EGFR-expressing cells, but not to the EGFR-negative cells in vitro. In vivo, Cetux-Alexa specifically targets EGFR-expressing tumors. Cetux-Alexa-derived fluorescence measured at the tumor site was shown to be directly dependent on the EGFR-expression levels and was detectable for at least 2 weeks in vivo, with maximum fluorescence intensities reached 2-4 days after application. No unspecific accumulation of the conjugate in other organs (e.g. liver) could be observed. Localization of the fluorescent probe within the tumor was confirmed ex vivo in tumor sections using the LI-COR Odyssey imaging system and fluorescence microscopy, where strong Cetux-Alexa derived signals were detected at the plasma membrane of tumor cells, making Cetuximab a very good candidate for ADEPT. To study the feasibility of Cetuximab for ADEPT, the antibody was conjugated with galactosidase (Cetux-Gal) and the enzyme activity of the conjugate as well as its ability to convert a nontoxic prodrug into a toxic drug was analyzed in vitro. Cetux-Gal specifically binds to EGFR-expressing cells in vitro, showing a high galactosidase activity on MDA-MB-468 cells, an intermediate activity on MDA-MB-231 cells and no activity on EGFR-negative MCF-7 cells. Treatment of cells with Cetux-Gal in combination with the prodrug, showed a high toxicity to high EGFR-expressing cells, an intermediate toxicity to moderate-EGFR-expressing cells and no toxicity to EGFR-negative cells. Summarizing, we designed and evaluated tools for a novel Cetux-Gal based ADEPT concept. The efficacy of the therapy in combination with a highly potent prodrug is currently under investigation.

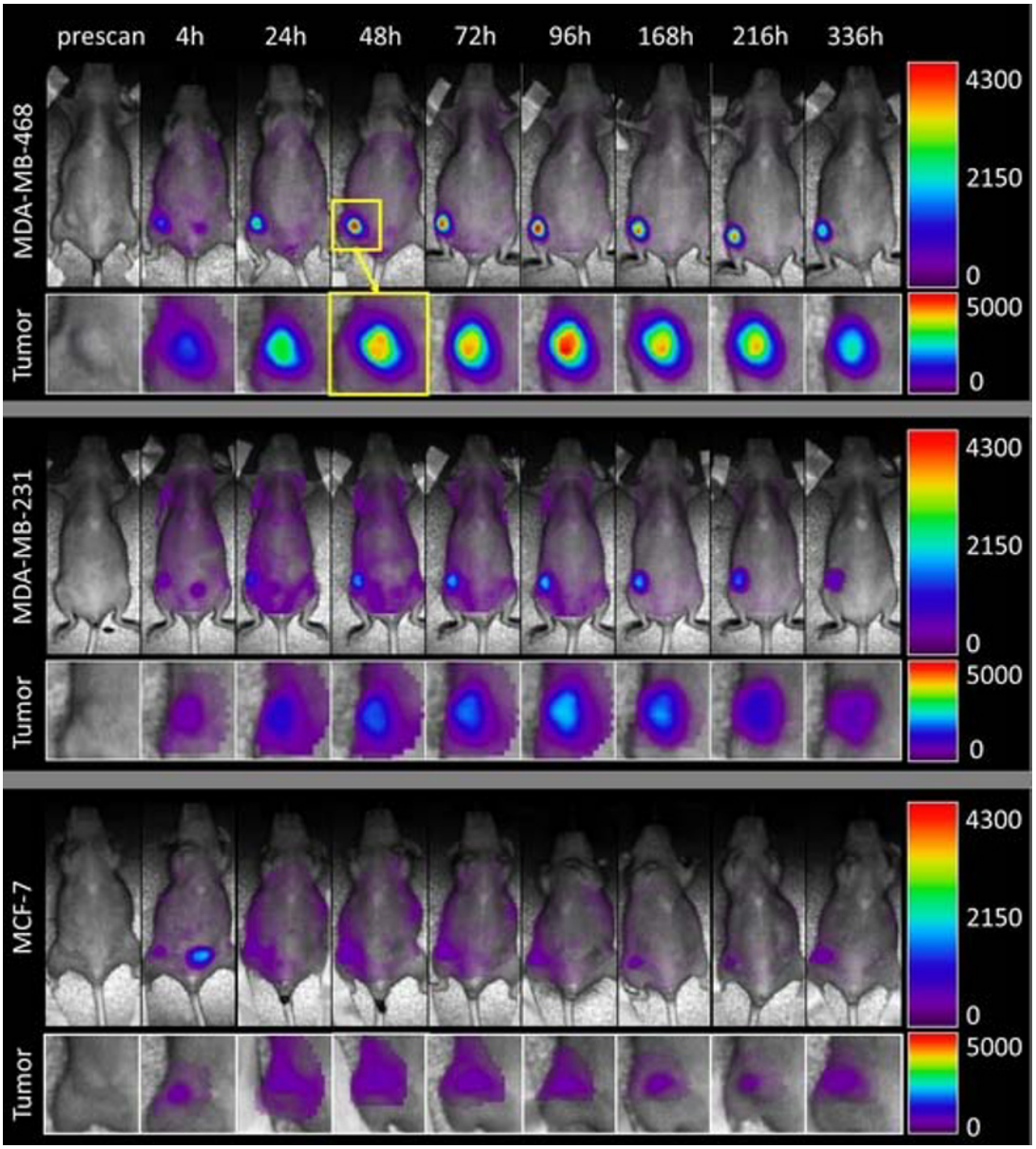

Figure 1. In vivo binding kinetics of Cetux-Alexa. The distribution and binding-kinetics of Cetux-Alexa were studied in vivo by time-domain NIR fluorescence imaging (Optix MX2; ART, Canada) in human mammary carcinoma bearing nude mice with distinct EGFR expression patterns. Cetux-Alexa targets EGFR-expressing tumors in vivo, resulting in a high tumor to background contrast for at least two weeks without an unspecific accumulation of the fluorescence conjugate in other organs such as liver.

Disclosure of author financial interest or relationships:
J. Napp, None; **T. Krüwel**, None; **L.F. Tietze**, None; **W. Stühmer**, None; **F. Alves**, None.

Presentation Number **P 376**
Poster Session 3
September 20, 2013 / 15:15-15:15 / Room: Exhibit Hall B

Evaluation of Engineered Antibody Fragments Directed to Prostate Stem Cell Antigen (PSCA) in Moderate and Low PSCA Expressing Pancreatic Tumor Xenografts Using PET Imaging

Tove Olafsen, *Edward Cabral, David T. Ho, Giti Agahi, Christian P. Behrenbruch, Jean M. Gudas, ImaginAb Inc., Inglewood, CA, USA. Contact e-mail: tove@imaginab.com*

Background: PSCA is a highly glycosylated GPI linked protein that is overexpressed in prostate, bladder and pancreatic cancers. We pre-clinically evaluated the potential for engineered antibody fragments comprised of scFv-C_H3 dimer (Minibody: Mb, 80 kDa) and scFv dimer (Cys-diabody: Cys-Db, 55 kDa) to be used for imaging pancreatic adenocarcinoma lesions that express moderate or low levels of PSCA. These engineered fragments retain equivalent binding affinity and specificity compared with the parental monoclonal antibody (mAb) but have the advantage of accelerated pharmacokinetics properties for imaging with PET. **Methods:** The parental mAb and corresponding Mb and Cys-Db engineered fragments were radioiodinated with I-124 ($t_{1/2}$ 4.2 days) using the Iodogen method. Mice bearing low (Capan-1), moderate (HPAC) and negative (MIA-PaCa-2) PSCA expressing pancreatic tumors were injected i.v. with ^{124}I-Cys-Db, ^{124}I-Mb or ^{124}I-mAb and serially imaged by PET/CT. After the final scan, mice were sacrificed and tumor, blood and organs harvested to determine the percent injected dose per gram (%ID/g). Regions of interest (ROIs) were drawn over the heart and tumors to calculate blood clearances and tumor uptakes. **Results:** The radiochemical purities of the mAb and fragments ranged from 90-99%, the specific activities from 4-6 μCi/μg and cell-based immunoreactivities up to 83%. In the low PSCA expressing Capan-1 tumor model, the Cys-Db exhibited a positive tumor to blood ratio of 9.5 at 24 hrs which was 7-fold greater than that of the Mb and 15-fold greater than that of the parental mAb as determined by ROIs. Biodistribution analyses revealed positive to negative tumor ratios of 5.7 for the Cys-Db at 24 hrs and 5.8 for the Mb and at 48 hrs and tumor to blood ratios of 4.9 and 3.1 respectively. In the moderate PSCA expressing HPAC tumor model, the Mb demonstrated a more favorable PK profile resulting in better overall ratios and image contrast. Biodistribution analysis showed an increased positive tumor to blood ratio of 9.7 for the Mb at 48 hrs with a similar for the Cys-Db (5.2) at 24 hrs. The positive tumor uptakes were 1.20±0.13% ID/g at 24 hrs for the Cys-Db and 4.06±0.62% ID/g at 48 hrs for the Mb corresponding to a 3- and 6-fold increase respectively above that of Capan-1. The elimination phase ($t_{1/2\beta}$) was determined to be 3.63, 8.66, and 80.45 hrs for the Cys-Db, Mb and parental mAb respectively. **Conclusion:** Specific targeting and high contrast images were obtained with ^{124}I-Cys-Db and ^{124}I-Mb fragments in pancreatic tumor models that express varying levels of PSCA. Different kinetics and overall results were obtained with these two imaging agents in the Capan-1 and HPAC tumor models highlighting the interplay between kinetics and tumor model / expression level when evaluating new imaging agents.

Disclosure of author financial interest or relationships:
T. Olafsen, ImaginAb Inc., Employment; **E. Cabral**, ImaginAb Inc., Employment; **D.T. Ho**, None; **G. Agahi**, None; **C.P. Behrenbruch**, ImaginAb, Inc., Stockholder; Mirada Medical Ltd., Stockholder; Ixico Ltd., Stockholder; Sofie Biosciences, Inc., Stockholder; National Cancer Institute, Grant/research support; **J.M. Gudas**, ImaginAb, Employment .

Presentation Number **P 377**
Poster Session 3
September 20, 2013 / 15:15-15:15 / Room: Exhibit Hall B

Determination of Adaptive Radiation Dose Based on the Correlation Between Bioluminescence Intensity and Radiation for 4T1 Breast Carcinoma

Ji-Yeon Park[1,2], *Magdalena Bazalova*[3,4], *Tobi L. Schmidt*[3,5], *Edward E. Graves*[3,4], *Christopher Contag*[3,5], *Tae-Suk Suh*[1,2],
[1]*Biomedical Engineering, The Catholic University of Korea, Seoul, Republic of Korea;* [2]*Advanced Research Center for Medical Physics, The Catholic University of Korea, Seoul, Republic of Korea;* [3]*Molecular Imaging Program at Stanford, Stanford University, Stanford, CA, USA;* [4]*Radiation Oncology, Stanford University, Stanford, CA, USA;* [5]*Pediatrics, Stanford University, Stanford, CA, USA. Contact e-mail: jjfortunity@catholic.ac.kr*

To pre-estimate radiation response of the cancer cells and to determine the required radiation dose during the fractionated adaptive radiation therapy, relationship of radiation dose with bioluminescence intensity was analyzed using the in-vivo bioluminescence tomography (BLT) and image registration. After a dose of 20 Gy in a single fraction was delivered by 200-kV X-ray beams to six female BALB/c mice, radiation responses of the cancer cells were monitored with BLT images in every 2-3 days. The dose distributions on mice were predicted in Monte Carlo simulation using EGSnrc codes. As the bioluminescence distributions were deformed onto the dose maps by applying the vector fields acquired in contour-based rigid and deformable registration, mathematical correlation of dose and bioluminescence was analyzed. The spatial and quantitative bioluminescence variations were also mapped on the computed tomography images to track the proliferation and metastasis characteristics particularly in tumor marginal progression. Radiation treatment showed the negative correlation between radiation dose and bioluminescence intensity with covariance of up to -0.4. By comparing and categorizing the bioluminescence responses depending on doses in treated and untreated mice group, amount of delivered dose and the field size could be adjusted for more effective control of cancer cells. Dose-related tracking of the bioluminescence variations on anatomical coordinates provided useful tool to differentiate the infiltrative cancer cells. Quantitative BLT images were a useful tool to evaluate bioluminescence responses of cancer cells according to the dose in the radiation treatment. Required effective doses would be delivered based on cancer cell responses on the BLT images.

Disclosure of author financial interest or relationships:
J. Park, None; **M. Bazalova**, None; **T.L. Schmidt**, None; **E.E. Graves**, Bell Biosystems, Stockholder; **C. Contag**, ConcentRx Corp, Stockholder; Olympus, Other financial or material support; **T. Suh**, None.

Presentation Number **P 378**
Poster Session 3
September 20, 2013 / 15:15-15:15 / Room: Exhibit Hall B

Engineered Bacteria for the Visualization of Targeted Cytolytic Cancer Therapy

Seung-Hwan Park[1], *Sheng Nan Jiang*[2], *Jinhai Zheng*[1], *Hee-Seung Bom*[1], *Yeongjin Hong*[3], *Hyon E. Choy*[3], *Jung-Joon Min*[1,3], [1]*Nuclear medicine, Chonnam National University, Gwangju, Republic of Korea;* [2]*Nuclear medicine, Central South University, Hainan, China;* [3]*Microbiology, Chonnam National University, Gwangju, Republic of Korea. Contact e-mail: biocell75@gmail.com*

Objectives: A number of recent reports have demonstrated that attenuated Salmonella typhimurium are capable of targeting both primary and metastatic tumors. The use of bacteria as a vehicle for the delivery of anti-cancer drugs requires a mechanism that precisely regulates and visualizes gene expression to ensure the appropriate timing and location of drug production. Methods: To integrate these functions into bacteria, we used a repressor-regulated tetracycline efflux system, in which the expression of a therapeutic gene and an imaging reporter gene were controlled by divergent promoters (tetAP and tetRP) in response to extracellular tetracycline. Attenuated S. typhimurium was transformed with the expression plasmids encoding cytolysin A, a therapeutic gene, and renilla luciferase variant 8, an imaging reporter gene, and administered intravenously to tumor-bearing mice. Results: The engineered Salmonella successfully localized to tumor tissue and gene expression was dependent on the concentration of inducer, indicating the feasibility of peripheral control of bacterial gene expression. The bioluminescence signal permitted the localization of gene expression from the bacteria. The engineered bacteria significantly suppressed both primary and metastatic tumors and prolonged survival in mice. Conclusion: Thus, engineered bacteria that carry a therapeutic and an imaging reporter gene for targeted anti-cancertherapy can be designed as a theranostic agent.

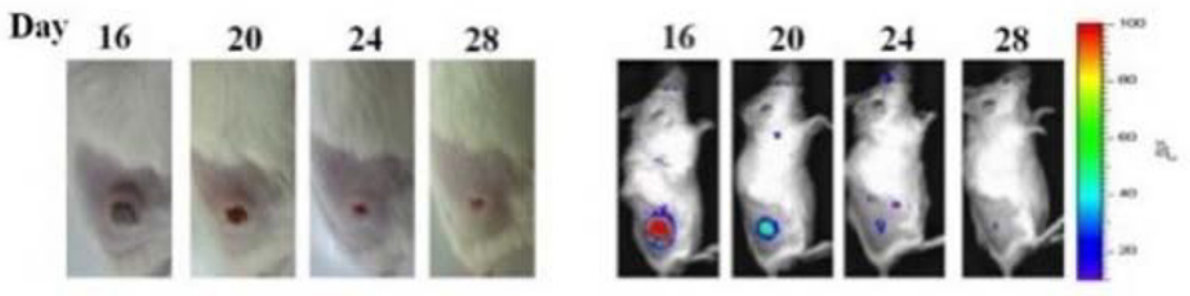

Effect of engineered salmonellae on tumor growth and visualization of bacteria-mediated cancer therapy

Disclosure of author financial interest or relationships:
S. Park, None; **S. Jiang**, None; **J. Zheng**, None; **H. Bom**, None; **Y. Hong**, None; **H. Choy**, None; **J. Min**, None.

Presentation Number **P 379**
Poster Session 3
September 20, 2013 / 15:15-15:15 / Room: Exhibit Hall B

Photoacoustic Imaging of Vascular Hemodynamics: Validation with BOLD-MRI

Laurie Rich[1,2], *Steven G. Turowski*[1], *Mukund Seshadri*[1,3], [1]*Pharmacology and Therapeutics, Roswell Park Cancer Institute, Buffalo, NY, USA;* [2]*Molecular and Cellular Biophysics Graduate Program, Roswell Park Cancer Institute, Buffalo, NY, USA;* [3]*Dentistry and Maxillofacial Prosthetics, Roswell Park Cancer Institute, Buffalo, NY, USA. Contact e-mail: laurie.rich@roswellpark.org*

Photoacoustic Imaging (PAI) [1] is an optical imaging technique that utilizes thermoelastic expansion of tissues to providing functional information (perfusion, oxygenation) pertaining to the tumor microenvironment in a time-efficient and cost-effective manner. Blood Oxygenation Level Dependent-magnetic resonance imaging (BOLD-MRI) [2] is a functional imaging technique that has been used for non-invasive assessment of oxygen status in vivo. While there has been an increased interest in developing multimodal imaging agents for PAI and MRI, to date, direct correlation and validation of PAI and BOLD MRI data has not been performed. To address this, experimental studies were carried out both in vitro (phantom) and in vivo to cross-validate PAI and BOLD-MRI based read-outs of vascular hemodynamics. Experimental ultrasound/PAI studies were performed using the Vevo® LAZR system (VisualSonics Inc., Toronto). MR images were acquired on a 4.7T/33-cm horizontal bore magnet (GE NMR Instruments, Fremont, CA). Measurement of pO2 (mm Hg) was performed using the OxyLite system (Oxford Optronix, Oxford, UK). In vitro phantom studies were performed using an agarose-intralipid based gel containing oxygenated and deoxygenated blood. In vivo studies were carried out using FaDu human head and neck squamous cell carcinoma (HNSCC) xenografts established in SCID mice (n=7). Imaging examinations were performed with animals initially breathing room air (normoxia) followed by exposure to carbogen (95% O2, 5% CO2; hyperoxia). Average percent oxygen saturation (%sO2) were obtained using PAI and correlated with percent change in signal intensity on T2-weighted BOLD acquisitions [3]. In vitro phantom experiments showed good correlation between %sO2 measurements obtained with PAI and pO2 values measured with Oxylite. Deoxygenation of blood (by exposure to nitrogen) resulted in a reduction in %sO2 levels from 21.3% to 6.6%, while measured pO2 values decreased from 141mmHg to 68.4mmHg. A strong correlation between PAI and BOLD datasets was also observed in vivo. Exposure to carbogen (hyperoxia; 6 minutes) resulted in a marked enhancement in PA signal (35.4± 10.6%) while transition back to room air resulted in a decrease in PA signal (26.1±5.0%). Consistent with this observation, BOLD-MR acquisitions showed an increase in normalized signal intensity during carbogen breathing with a subsequent decrease in BOLD-signal upon return to room air. Figure 1 shows colorized oxygen saturation maps (PAI; top panel) and BOLD maps of a tumor during exposure to room air and carbogen. Together, these results highlight the potential of combined PAI and BOLD-MRI for monitor changes in vascular hemodynamics in vivo. Ongoing studies are investigating the utility of PAI and BOLD-MRI in assess the oxygenation changes occurring within the tumor microenvironment following antivascular therapy. References 1.Zhang et al 2006. Nature Biotechnol. 24;848-51. 2.Ogawa et al, 1990. Magn Reson Med.14;68-78. 3.Seshadri et al, 2008. Clin Cancer Res.14:2796-2805

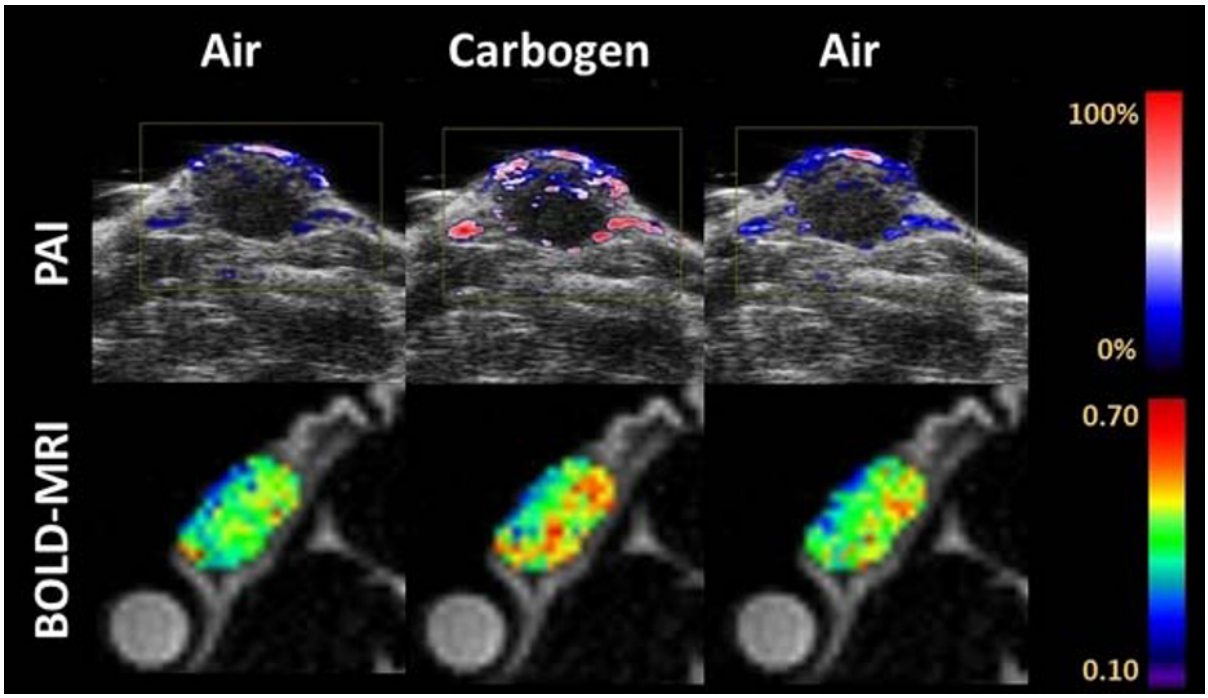

Figure 1. Colorized oxygen saturation maps (PAI; top panel) and BOLD maps (bottom panel) of a tumor during exposure to room air and carbogen.

Disclosure of author financial interest or relationships:
L. Rich, None; **S.G. Turowski**, None; **M. Seshadri**, None.

Presentation Number **P 380**
Poster Session 3
September 20, 2013 / 15:15-15:15 / Room: Exhibit Hall B

Molecular Ultrasound Imaging Enhancement by Volumic Acoustic Radiation Force (VARF): Pre-clinical in vivo Validation in a Murine Tumor Model

Nicolas G. Rognin[1], *Sunil Unnikrishnan*[2], *Alexander L. Klibanov*[2], [1]*TOSHIBA Medical Research Institute USA, Inc., Redmond, WA, USA;* [2]*Cardiovascular Division, University of Virginia, Charlottesville, VA, USA. Contact e-mail: nrognin@tmriusa.com*

Molecular ultrasound imaging, based on intravenous administration of targeted microbubbles, will reveal important outcomes in future clinical practice. These microbubbles are designed to have a high affinity with tumoral vascular molecular expression, enabling them to bind to molecular biomarkers on vascular endothelium. Potential clinical applications will range from early tumor detection to quantitative therapy monitoring, where determination of patient response to a given anti-cancer drug treatment plays a crucial role in terms of survival. In a previous work using a clinical ultrasound imaging system AplioXG (Toshiba Medical Systems, Otawara, Japan) equipped with a mechanically swept convex array transducer (PVT-681MV), we showed in-vitro under flow that Volumic Acoustic Radiation Force (VARF) improved microbubble adhesion to the endothelial layer by a factor of 6.7. Optimal settings were found as follows: 3.6 MHz, 30 kPa peak-negative-pressure, 64 cycles, 15% duty cycle. Using the same settings as above, the present study addresses the pre-clinical validation in a small animal model (non-xenograft mouse tumor). VCAM-1, which is overexpressed on the tumor vasculature, was selected as our target. Two types of ultrasound contrast agents were injected as bolus (~ 20e6 microbubbles): 1) targeted microbubbles conjugated with anti-VCAM-1 antibody and 2) control microbubbles with no ligand. Microbubble adhesion with VARF mode (exposure duration of 1 minute) was compared to Native mode (without VARF). Relative quantification of microbubble accumulation in a region of interest (CHI-Q software) 7 minutes after injection is shown in figure 1(a,b). Any remaining circulating microbubbles were removed by subtraction of post-destruction signal (destruction obtained by application of high acoustic intensity, Mechanical Index = 1.42). The average adhesion enhancement ratio was 4.8 (SD of 2.7, n=3) for targeted microbubbles and was 0.6 (SD of 0.1, n=2) for control microbubbles. A dedicated volume rendering method was developed to show the added value of VARF. Notably, volume fusion (VARF in red hues and Native in cyan hues) of figure 1(d) allows delineating additional vessels compared to the Native volume of figure 1(c). In this study, pre-clinical in vivo validation of VARF was demonstrated for the first time with a clinical ultrasound imaging system equipped with a 3D transducer, offering potential implementation into the clinic. Further processing will include advanced 3D quantification to fully characterize the vascular network of tumoral tissue. Acknowledgments: The authors would like to thank Ms. Y. Kanayama, Mr. G. Guenette, Mr. R. Woods and Mr. C. Sanders from TOSHIBA for their technical support.

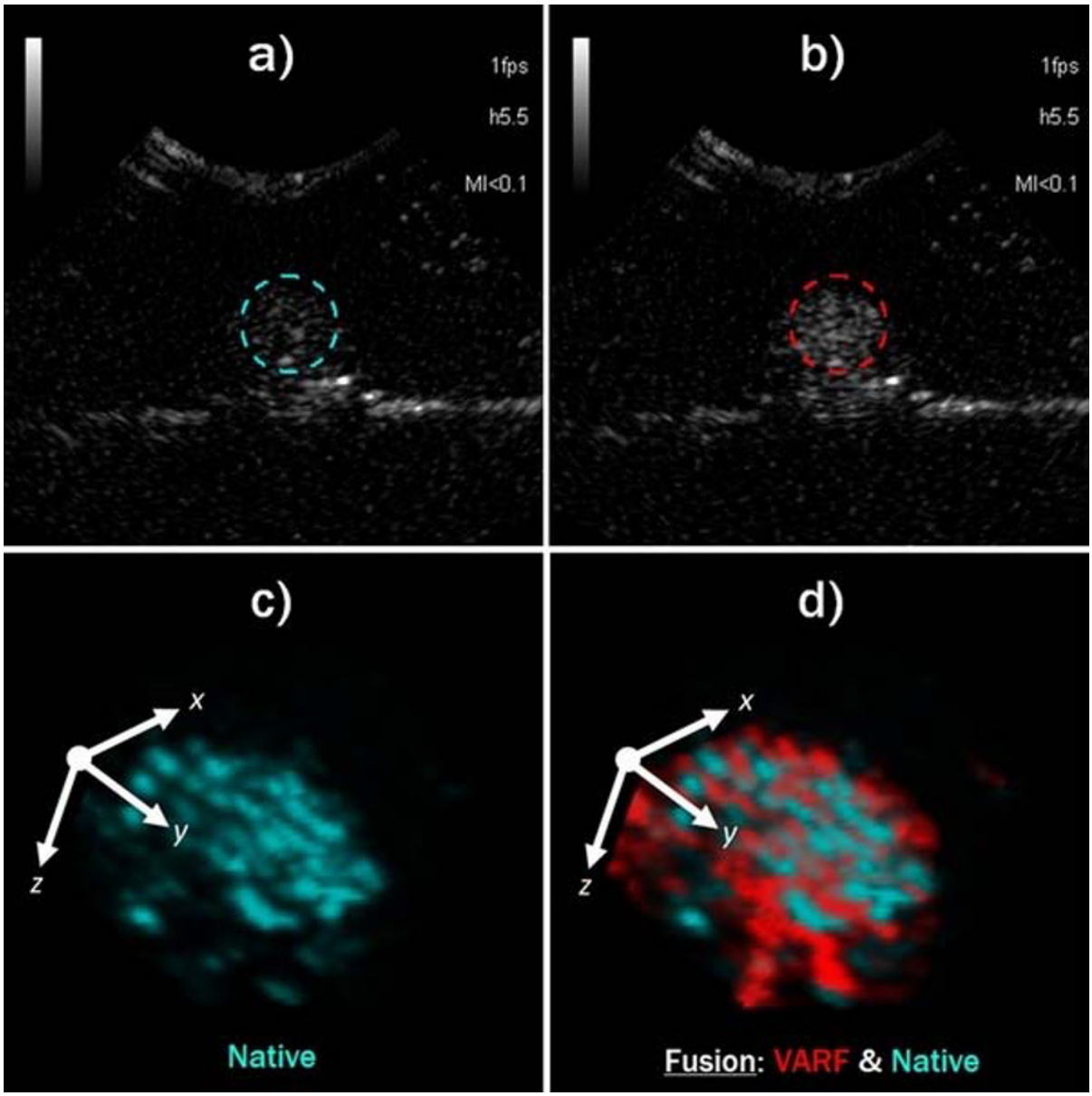

Figure 1: Ultrasound contrast image of targeted microbubbles accumulation without (a,c) and with (b,d) Volumic Acoustic Radiation Force (VARF).

Disclosure of author financial interest or relationships:
N.G. Rognin, TOSHIBA Medical Research Institute USA, Inc., Employment; **S. Unnikrishnan**, None; **A.L. Klibanov**, Philips Research North America, Grant/research support; Targeson (NIH SBIR subcontract), Grant/research support; Targeson, Stockholder; AstraZeneca, Grant/research support .

Presentation Number **P 381**
Poster Session 3
September 20, 2013 / 15:15-15:15 / Room: Exhibit Hall B

Tumor-Specific Minicircles as a Novel Safe Technology for Cancer Screening via Blood-Based and Molecular Imaging Assays

John A. Ronald[1,2], *Hui-Yen Chuang*[1,3], *Anca Franzini*[1,2], *Sharon S. Hori*[1,2], *Sanjiv S. Gambhir*[1,2], [1]*Radiology, Stanford University, Stanford, CA, USA;* [2]*Molecular Imaging Program at Stanford, Stanford University, Stanford, CA, USA;* [3]*Biomedical Imaging and Radiological Sciences, National Yang-Ming University, Taipei, Taiwan. Contact e-mail: jronald1@stanford.edu*

Background: Strategies for improved cancer diagnosis have traditionally relied on measurement of endogenous molecules that are over-expressed in cancer cells via either molecular imaging or blood-based assays. A challenge of these strategies is often significant expression within non-cancerous tissues, leading to high background levels and confounding results. An alternative strategy is to utilize promoters of tumor-specific (TS) proteins in exogenously delivered gene vectors in order to drive the expression of unique reporter genes (RGs) strictly within tumors. For this strategy to become a reality then safety, specificity, and sensitivity are of utmost importance. While safer than viral vectors, two drawbacks of non-viral vectors have been low gene transfer rates and transient expression profiles. Minicircles (MCs) are plasmids that lack a bacterial backbone and are known to overcome the above key issues. Here we have developed TS MCs driving the expression of either secretable alkaline phosphatase (SEAP) or firefly luciferase (Fluc) and validated their utility for detecting tumors after systemic administration using blood- and/or imaging-based assays. Methods and Results: Plasmids (PPs) or MCs were generated utilizing the TS Survivin promoter to drive the expression of SEAP or Fluc. SEAP PPs and MCs were transfected into MeWo and SK-MEL-28 melanoma cells and MCs lead to increased ($p<0.05$) and prolonged SEAP activity in medium. SEAP MCs administered intratumorally into MeWo subcutaneous xenografts showed higher plasma SEAP activity ($p<0.05$; $n=4$) compared to two groups of control mice ($n=6$ total). As a model of experimental metastases, MeWo cells stably expressing Rluc8.6-TurboFP (BRET6) were injected via tail-vein into mice and tumor growth was monitored with bioluminescence imaging (BLI). Mice were then intravenously administered SEAP MCs, and higher plasma SEAP activity was detected in tumor-bearing versus control mice for over 2 weeks ($n=4$). Finally, Fluc MCs were administered intravenously to both tumor-bearing ($n=5$) and control mice ($n=2$) and BLI was performed (Figure 1). By day three, 3 of the 5 tumor-bearing mice impressively showed higher Fluc signal compared to controls, and one mouse had ~5-fold higher signal. Discussion: For gene vectors to be used for cancer screening purposes many challenges need to be overcome including efficient tumor delivery, achieving potent expression for maximum sensitivity, stringent control of expression to attain tumor specificity, and minimization of safety concerns. TS MCs can overcome all of these challenges and for the first time we show that systemically administered TS MCs can be assayed via serum and non-invasive imaging to differentially identify tumor-bearing from normal subjects. Importantly, our TS MCs should have broad applicability in many patient populations since the Survivin promoter drives expression across many different tumor types. Using TS MCs, we envision a powerful new cancer management paradigm that involves tumor detection via an initial blood-based assay, tumor localization via molecular-genetic imaging, and tumor treatment using theranostic TS MCs.

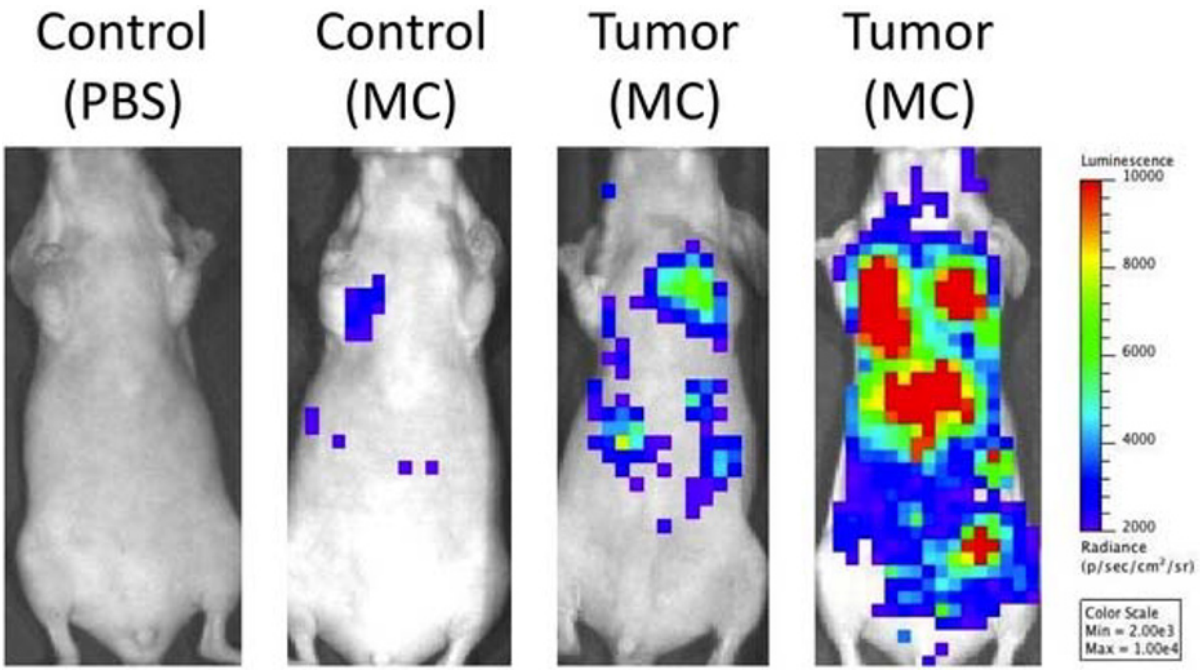

Figure 1: Bioluminescence images of firefly luciferase (Fluc) expression at day 3 following systemic administration either PBS or Fluc tumor-specific minicircles (MC) into control or tumor-bearing mice.

Disclosure of author financial interest or relationships:

J.A. Ronald, None; **H. Chuang**, None; **A. Franzini**, None; **S.S. Hori**, None; **S.S. Gambhir**, Bracco Diagnostics, Consultant; Endra, Inc, Stockholder; Cellsight, Stockholder; Enlight, Inc., Stockholder; General Electric, Grant/research support; ImaginAb, Stockholder; MagArray, Inc., Stockholder; Sanofi-Aventis, US, Grant/research support; SiteOne Therapeutics, Stockholder; VisualSonics/Sonosite, Stockholder .

Presentation Number **P 382**
Poster Session 3
September 20, 2013 / 15:15-15:15 / Room: Exhibit Hall B

Perfusion CT as a surrogate measure of dosimetry in pancreatic cancer photodynamic therapy

Kimberley Samkoe[1,2], *Jason Gunn*[2], *Errol E. Stewart*[3], *Kenneth M. Tichauer*[4], *Karen L. Moodie*[1], *Susan Kane*[1], *Jennifer Hadway*[3], *P. Jack Hoopes*[1,2], *Ting-Yim Lee*[3], *Stephen Pereira*[5], *Tayyaba Hasan*[6], *Brian W. Pogue*[2,1], [1]*Department of Surgery, Geisel School of Medicine at Dartmouth, Lebanon, NH, USA;* [2]*Thayer School of Engineering, Dartmouth College, Hanover, NH, USA;* [3]*Department of Medical Biophysics, Western University, London, ON, Canada;* [4]*Biomedical Engineering, Illinois Institute of Technology, Chicago, IL, USA;* [5]*Institute for Liver and Digestive Health, University College London, London, United Kingdom;* [6]*Wellman Center for Photomedicine, Massachusetts General Hospital, Boston, MA, USA. Contact e-mail: Kimberley.S.Samkoe@Dartmouth.EDU*

Photodynamic therapy (PDT) is being investigated in an ongoing clinical trial for the treatment of pancreatic cancer. PDT in the human pancreas involves the injection of a photosensitizing agent (here verteporfin), implantation of an optical fiber, and 690 nm light delivery to activate the photosensitizer at ~20 J/cm. The locations for fiber placement are pre-determined using X-ray computed tomography (CT) imaging and are physically placed under endoscopic ultrasound (US) guidance. In vivo light dosimetry has been attempted through these fiber ports using single measurements of localized drug concentration; however, accurate and representative measurements of photosensitizer uptake in the tumor is difficult due to the high variation in drug concentrations and the complexity and location of the disease. Previous work performed in our group has correlated contrast-enhanced magnetic resonance imaging (MRI) with verteporfin uptake in an orthotopic mouse model of pancreas cancer; however, this model is not appropriate for use with a standard human contrast agent due to physical limitations on the long scan times necessary for contrast. More recently, a rabbit model of pancreatic cancer has been established in our group using a VX2 tumor line. Using the rabbit model, we hypothesize that perfusion CT scans (using a whole body multi-slice CT scanner designed for clinic) of pancreatic tumors can accurately predict the photosensitizer delivery during PDT treatment. The tumor line is initiated subcutaneously in the right flank of a New Zealand White rabbits (3 kg) by implantation of two small pieces of solid VX2 tumor. When the tumor reaches an appropriate size (~3 weeks post-implantation), it was harvested, minced into small pieces and surgically imbedded in the pancreas of another rabbit. Contrast enhanced CT imaging was performed 7-days post-implantation to determine tumor size and location. At 10-days post-implantation, the rabbits were intubated and perfusion CT scans were performed using OmnipaqueTM (GE Healthcare) contrast agent. A two-phase imaging protocol was performed using ventilated breathing techniques: 1) a breath-hold phase for 30-seconds, and 2) a breathing phase imaged for 2 minutes. Post-CT imaging, verteporfin (1 mg/kg) was administered intravenously and allowed to distribute for one hour. The tumors were then removed, maintaining spatial alignment with the CT images, and sliced into 2.5 mm sections correlating to each CT image slice. The tumor slices were imaged on the Typhoon 9410 fluorescence scanner (GE Healthcare). CT perfusion scans were analyzed using CT Perfusion 4 (GE Healthcare) and the following hemodynamic parameters were determined: blood flow, blood volume, mean transit time, and permeability surface area product. Spatial verteporfin uptake and distribution in the fluorescent images were compared to the spatial hemodynamic parameters determined by CT. Correlation of the CT to verteporfin fluorescence could provide a surrogate measure for clinical PDT treatment planning in future work.

Disclosure of author financial interest or relationships:
K. Samkoe, None; **J. Gunn**, None; **E.E. Stewart**, None; **K.M. Tichauer**, None; **K.L. Moodie**, None; **S. Kane**, None; **J. Hadway**, None; **P. Hoopes**, None; **T. Lee**, None; **S. Pereira**, None; **T. Hasan**, None; **B.W. Pogue**, None.

Presentation Number **P 383**
Poster Session 3
September 20, 2013 / 15:15-15:15 / Room: Exhibit Hall B

Enhancement of 18F-FDG-PET in Prostate Cancer Xenografts Using Lipid Metabolic Inhibitors

Isabel R. Schlaepfer[1], *Colton T. Pac*[1], *Natalie J. Serkova*[2], *Robert H. Eckel*[3], *Scott D. Cramer*[1], *L. Michael Glode*[4], [1]*Pharmacology, University of Colorado, Aurora, CO, USA;* [2]*Anesthesiology, University of Colorado, Aurora, CO, USA;* [3]*Medicine, University of Colorado, Aurora, CO, USA;* [4]*Medical Oncology, University of Colorado, Aurora, CO, USA. Contact e-mail: isabel.schlaepfer@ucdenver.edu*

Background: It is estimated that 40 to 50 million diagnostic imaging investigations are performed annually in the world. Positron Emission Tomography (PET) with18F-deoxyglucose (18F-FDG) has gained a major role in the clinical setting for detection, staging and assessment of treatment response. However, staging of primary or metastatic prostate cancer with 18F-FDG-PET is suboptimal, likely due to the low glucose uptake and enhanced lipid metabolism characteristic of primary prostate tumors The exact mechanisms of aerobic glycolysis (Warburg effect) and lipid metabolism in prostate cancer (PCa) cells remain unknown. However, 18F-FDG-PET imaging of metastatic PCa might be enhanced by altering the intrinsic energy metabolism of involved sites. Methods: In vitro studies were carried out to confirm the specificity of etomoxir blocking lipid oxidation and enhancing glucose uptake at 24 hours. For in vivo studies, Male nude mice with palpable PCa xenografts were treated with a single dose of the lipid oxidation inhibitor etomoxir (20 mg/kg) or vehicle (saline) for 24 hours. A basal FDG-PET scan was performed before the drug treatment, followed by a second FDG-PET scan after 24 hours. Western blot analysis was used to validate the molecular mechanisms of this increased FDG uptake Results: The clinically safe drug etomoxir blocks fat oxidation within 4 hours and increases glucose uptake in cultured PCa cells. A significant increase in normalized FDG uptake (NUV) was obtained 24-hours after a single dose of etomoxir compared to basal NUV (1.4 fold change, p =0.03). This enhancing effect was not seen in mice treated with saline (vehicle). Interestingly, some xenografts were visible only after the etomoxir treatment, underscoring the glucose enhancing effect of blocking fat oxidation in PCa tumors. Protein examination of the excised tumors showed increased hexokinase-II content and activated mTOR and p70-S6 Kinase proteins in the etomoxir-treated tumors when compared to saline-treated tumors. Conclusion: blocking lipid oxidation in PCa tumors has the potential to improve diagnostic imaging, since 18F-FDG that accumulates inside the cell can enhance FDG-PET imaging of prostate cancer tumors to detectable and quantifiable levels. Translational impact: 18F-FDG is a commercially available tracer which is widely used for standard-of-care and research-based oncologic imaging. FDG-PET compromise over 95% of all clinical PET/CT studies in the US. As a result, this "bench to bedside" translational project has the potential to immediately impact and transform the management of prostate cancer through improved imaging.

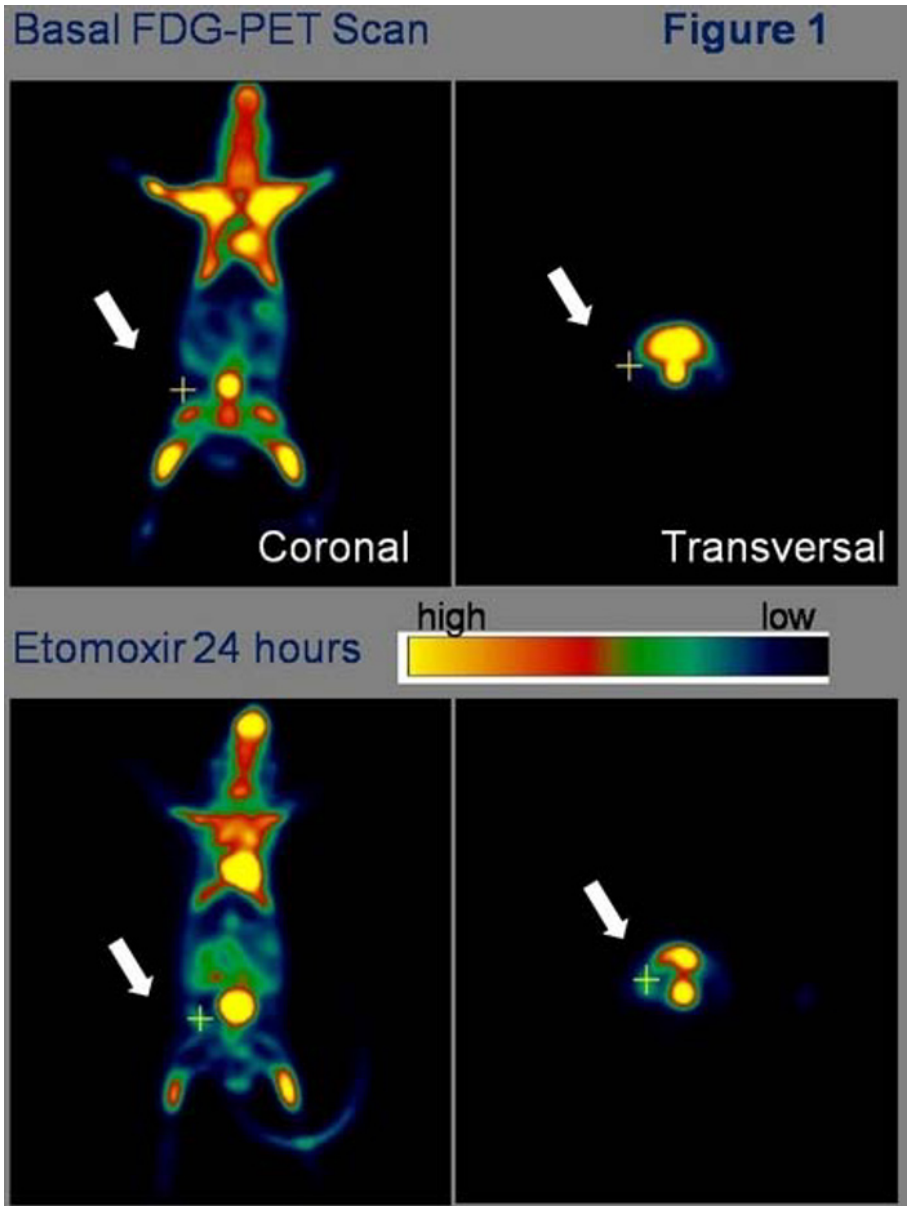

Figure 1 shows FDG-PET images of the before and after treatment in a mouse bearing a xenograft on the left side (+ symbol) and showing increased glucose uptake to detectable levels (green) after short term etomoxir treatment (24 hrs). The highest increase in glucose uptake is shown in yellow. White arrow points at left PCa xenograft.

Disclosure of author financial interest or relationships:
I.R. Schlaepfer, None; **C.T. Pac**, None; **N.J. Serkova**, None; **R.H. Eckel**, None; **S.D. Cramer**, None; **L. Glode**, None.

Presentation Number **P 384**
Poster Session 3
September 20, 2013 / 15:15-15:15 / Room: Exhibit Hall B

USPIO vs. SPIO by Differentiating Cancer from Inflammation

Perla Seyfer[1], *Axel Pagenstecher*[2], *Johannes T. Heverhagen*[3], [1]*Diagnostic and Interventional Radiology, Philipps University, Marburg, Germany;* [2]*Neuropathology, Philipps University, Marburg, Germany;* [3]*University Department of Diagnostic, Interventional and Pediatric Radiology, University Hospital of Bern, Bern, Switzerland. Contact e-mail: seyfer@med.uni-marburg.de*

Purpose: The differentiation between benign and malignant lesions is still an unsolved challenge for non-invasive diagnostic modalities. The value of USPIO (Ferumoxtran)-enhanced MRI as a diagnostic tool for differentiating abscesses from tumors has already been confirmed. Ferumoxtran-tagged monocytes cause signal intensity (SI) drops on T2*- weighted images in inflammation enabling therefore its distinction from vital tumor. The aim of our study was to compare the specificity of different superparamagnetic iron oxide substances in terms of the differentiation between abscesses and tumors and to determine the most appropriate contrast agent. Methods: This experiment was approved by the local animal care committee. VX2 carcinoma and intramuscular abscesses were implanted into the hind thighs of New Zealand White Rabbits. MR imaging was performed precontrast and serially 2, 4 and 24 hours after injecting (U)SPIOs (Sinerem®, Resovist® or Supravist®). Harvested VX2 carcinomas and abscesses were stained with Hematoxylin-eosin and Prussian blue and evaluated using a light microscope. Radiologic-histologic correlations were performed between the MR images and the corresponding histologic slices. Results: 24h after the Sinerem®-injection, a mean reduction of the contrast-to-noise ratio (CNR) of approximately 90% was measured in abscesses in T2*-weighted images, whereas no remarkable changes were observed in vital carcinomas (Fig 1). On the contrary, no significant signal intensity drops were noticed in abscesses after injecting Resovist® or Supravist®. On histopathologic examination, abscesses demonstrating a signal drop after Sinerem®-injection were found to include iron-tagged monocytes, indicating that the reduction in CNR was caused by Sinerem®-tagged monocytes. No iron-tagged monocytes were detected in the corresponding lesions after Resovist®- or Supravist®-injection. Conclusion: Merely specific (U)SPIOs enable a sensitive differentiation of abscesses from tumors, based on iron-tagged monocytes in inflamed areas. The accumulation of iron oxide particles in inflammation depends on the plasma half-life of the particles as well as on the molecular structure of the coating. Among the (U)SPIOs we tested, dextran coated ferumoxtran-USPIOs with a volume-weighted hydrodynamic diameter of 20-50 nm and a plasma half-life of 24 - 30 hours are highly sensitive for differentiating between vital tumors and abscesses.

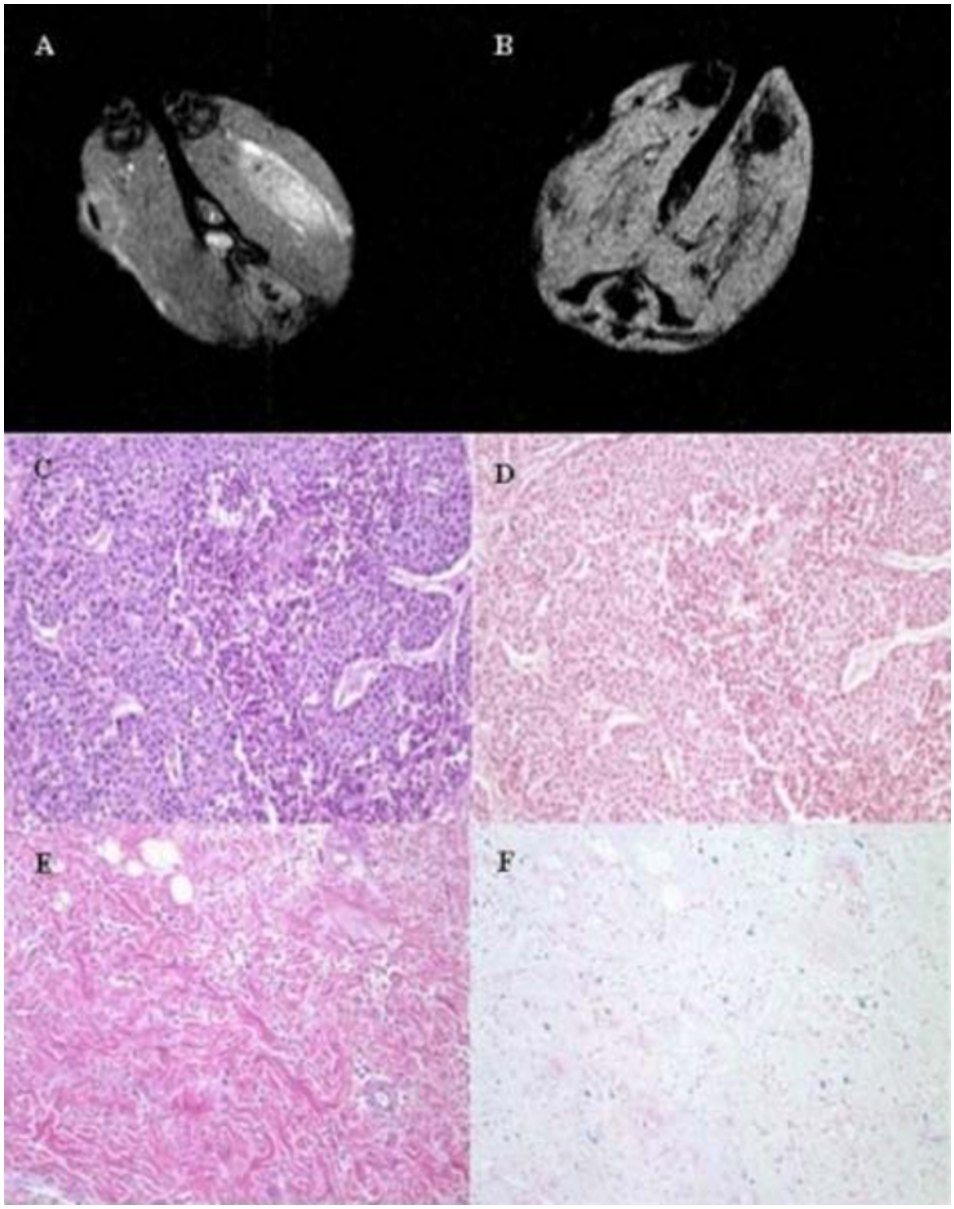

VX2 tumor in the left thigh and abscess in the right thigh of a rabbit: Precontrast (A) and postcontrast (B) transverse T2*-weighted image 24 hours after administration of Sinerem®. Hematoxylin-eosin staining (C & E) and Prussian Blue staining (D & F) of histopathologic specimen. The postcontrast T2*-weighted image (B) shows no remarkable changes in signal intensity in the tumor. The tumor remains hyperintense, whereas the abscess becomes hypointense. No intracellular iron-up take was detected by Prussian Blue staining of tumors (D) whereas blue pigment of iron oxide particles were visible in macrophages in abscesses (F).

Disclosure of author financial interest or relationships:
P. Seyfer, None; **A. Pagenstecher**, None; **J.T. Heverhagen**, None.

Presentation Number **P 385**
Poster Session 3
September 20, 2013 / 15:15-15:15 / Room: Exhibit Hall B

In Vivo Imaging of a Metastatic Ovarian Cancer Model: Monitoring tumor growth using tomographic bioluminescence images co-registered with MRI using LumiQuant

Tonya Coulthard[1], *Matthew D. Silva*[2], *Jacob Hesterman*[2], *Balázs Viszoczki*[2], *Clinton Hupple*[1], *Jinzi Zheng*[3], *Raquel De Souza*[3], *Robert Sandler*[1], *Jack Hoppin*[2], [1]*Aspect Imaging, Toronto, ON, Canada;* [2]*inviCRO, LLC, Boston, MA, USA;* [3]*STTARR Innovation Centre, Princess Margaret Hospital, Toronto, ON, Canada. Contact e-mail: tcoulthard@aspectimaging.com*

Bioluminescence imaging (BLI) is a prevalent in vivo pre-clinical imaging modality due to its high-sensitivity for detecting viable cells, low instrument and experiment cost, and high-throughput. While planar imaging is most common, there is increasing interest in tomographic (3D) imaging to enhance image visualization, signal localization, and quantification. The continued adoption of 3D BLI relies on accurate localization of the light source (i.e., tumor) and the ability to equate the signal output to the underlying biological process. In this work, we monitored metastatic tumor growth via 2D/3D BLI coupled with MRI using a custom multi-modality cassette and advanced algorithm, LumiQuant (Aspect Imaging and inviCRO). With approval from the UHN Animal Care Committee and adherence to the ethical guidelines of the Canadian Council on Animal Care, tumors were established by intraperitoneal (IP) inoculation of $3x10^6$ SKOV-3/Luc cells (human ovarian adenocarcinoma; Cell Biolabs Inc.) suspended in 100µL of medium into 6-8-week-old female SCID mice. This model results in formation of tumors throughout the abdominal and, occasionally, thoracic cavity—and pattern of tumor formation consistent with late-stage metastatic human ovarian cancer. Tumor growth was monitored every three to four days, beginning four days post-inoculation, using bioluminescence imaging (IVIS, Perkin Elmer) and MR imaging (ICON, Bruker). Prior to imaging, mice received 150mg/kg D-luciferin (Perkin Elmer) in PBS IP. The mouse was placed within a multi-modal imaging cassette (Aspect Imaging) designed to maintain consistent animal position throughout the BLI and MRI sessions. Approximately 10 minutes after IP luciferin, luminescence images were collected in both the prone and supine position using both filtered and open filter settings. The open filter images were interleaved between each filtered image (560-660nm in 20nm steps). The open filter images were used to correct the signal decline from the depletion of the luciferin substrate. After BLI, T1-FLASH and T2-RARE MRI was performed using a 1T high-performance compact MRI system using an animal handling system and RF coil (Aspect Imaging) specifically designed for the multi-modal imaging cassette. 2D data analysis of the BLI was performed using the Living Image software (Perkin Elmer) to obtain flux and radiance measures. Tomographic BLI images were produced and co-registered with the MR images using LumiQuant and VivoQuant (inviCRO) [1,2], and analysis of the 3D BLI image data was performed using automated Matlab scripts (The Mathworks). Visual inspection of the data reveals strong correspondence between the MR-visible tumors and 3D BLI reconstruction (Figure 1). These spots also correspond to the bright regions on the 2D BLI. Preliminary analysis reveals a strong correlation ($r^2 = 0.87$) between the 2D and 3D radiance calculation. Additional work to map absorption and scatter coefficients to segmented MRI is ongoing and anticipated to further improve the spatial localization and quantification. References: [1] Hesterman JY, et al., WMIC 2012: P541, [2] Klose AD, et al., Med. Phys. 2010;37:329-38.

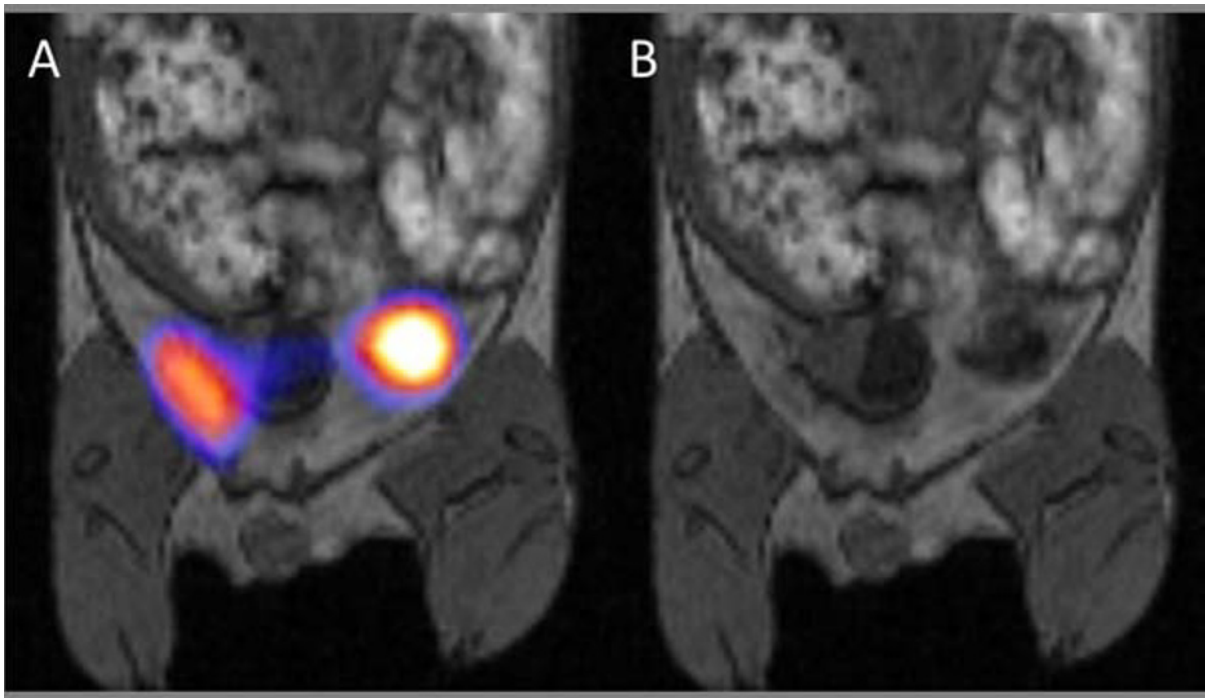

Figure 1. A: Example MRI slice with overlay slice from 3D BLI reconstruction. B: Without the overlay, the tumors are visible on the MRI.

Disclosure of author financial interest or relationships:
T. Coulthard, Aspect Imaging, Employment; **M.D. Silva**, inviCRO, LLC, Employment; **J. Hesterman**, inviCRO, LLC, Employment; **B. Viszoczki**, inviCRO LLC, Employment; **C. Hupple**, Aspect Imaging, Employment; **J. Zheng**, None; **R. De Souza**, None; **R. Sandler**, Aspect Imaging, Employment; **J. Hoppin**, inviCRO, Stockholder .

Presentation Number **P 386**
Poster Session 3
September 20, 2013 / 15:15-15:15 / Room: Exhibit Hall B

Prediction of lymphoma drug response via integration of molecular imaging and computational modeling

Bryan R. Smith[1], *Hermann B. Frieboes*[2,3], *Ken Ito*[1], *Yao-Li Chuang*[4], *Masakatsu Kotsuma*[1], *Vittorio Cristini*[4,5], *Sanjiv S. Gambhir*[1], [1]*Radiology/Molecular Imaging, Stanford University, Stanford, CA, USA;* [2]*Department of Bioengineering, University of Louisville, Louisville, KY, USA;* [3]*James Graham Brown Cancer Center, University of Louisville, Louisville, KY, USA;* [4]*Department of Pathology, University of New Mexico, Albuquerque, NM, USA;* [5]*Department of Chemical Engineering, University of New Mexico, Albuquerque, NM, USA. Contact e-mail: brsmith@stanford.edu*

A disseminated, highly malignant cancer, Non-Hodgkin's lymphoma often displays resistance to drug treatment based on molecular- and tissue-scale characteristics that are intricately linked. Partially due to such resistance, accurate prognoses are often difficult to provide for lymphoma patients prior to their treatments. To address this need, we extract parameters via molecular imaging and apply computational modeling to simulate lymphoma drug resistance in living subjects. Through this integrated experimental/computational approach we explore the links between the molecular and tissue scales to improve disease prognosis. We note that the computational model is based on the physics of tumor growth and transport, and not on fitting parameters. An important molecular-scale mediator of drug resistance is the loss of functionality in proteins such as the tumor suppressor p53. We compare two different murine tumors in live mice: drug sensitive Eμ-myc Arf-/- and drug-resistant Eμ-myc p53-/- lymphomas. We investigate the tissue-scale effects of the loss of p53 by integrating the in vivo and immunohistological data with computational modeling. We obtain the initial conditions for the simulation using cell-scale values extracted from histological staining of inguinal lymph node lymphoma tumors both in the drug-free and drug-treated states. We run the computational model and compare the results to intravital microscopy and macroscopy in live mice. We show that the model accurately predicts both the lymphoma growth and the cancer drug resistance. The findings suggest that a physical mechanism may underlie drug-resistant phenotypes: the Eμ- myc p53-/- cells pack more closely within the tumor than the Eμ-myc Arf-/- cells, potentially exacerbating diffusion gradients of oxygen and cell nutrients. This can lead to cell quiescence and subsequent resistance to cell-cycle specific drugs. Tighter cell packing may also drive steeper drug gradients and lead to locally insufficient toxicity. Transport phenomena within the lymphoma may thus contribute in nontrivial, complex ways to the difference in drug sensitivity between Eμ-myc Arf-/- and Eμ-myc p53-/- tumors, beyond what might be solely expected from molecular-level loss of functionality. Thus, we show that: 1. computational modeling tightly integrated with experimental data generates confirmable predictions of tumor growth and angiogenesis based on intravital microscopy (see Figure); 2. We accurately predict the response to drug treatment, obtaining lymphoma cell survival as a function of tumor blood volume fraction to within our system error (see Figure). In the future, the model's input parameters could be measured from a patient's biopsy specimens pre-therapy, thus our approach could ultimately help clinicians establish prognosis to chemotherapy and help save patients from ineffective, potentially deleterious treatments.

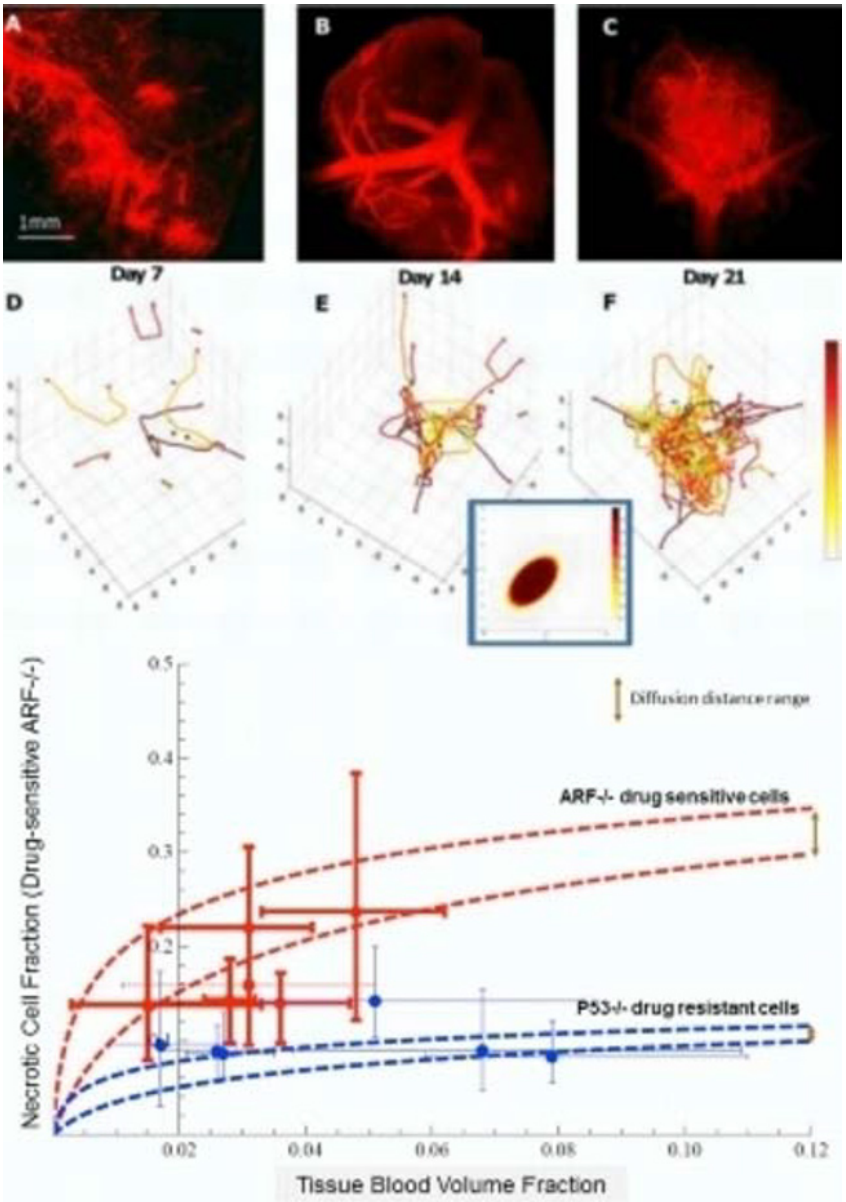

Figure. (Top two rows) Correlations between experimental intravital microscopy in live mice (A, B, C: red - functional blood vessels in Eμ-myc p53-/- tumor) qualitatively compared to simulated vessel formation (D, E, F: red - highest flow; white - lowest). Modeling of cell-substrate diffusion within the tumor enables prediction of the spatial distribution of lymphoma cells (inset, shown for one vessel cross-section; brown: highest concentration of cells) as their viability is modulated by access to oxygen and nutrients diffusing from the vasculature into the surrounding tissue. (Bottom chart) Model prediction of lymphoma cell survival after chemotherapy. Data with vertical and horizontal error bars (standard deviation from the mean) are plotted. Dashed lines indicate model prediction of necrotic cell fraction as a function of tissue blood volume fraction (blue: p53-/-; red: ARF-/-).

Disclosure of author financial interest or relationships:

B.R. Smith, None; **H.B. Frieboes**, None; **K. Ito**, None; **Y. Chuang**, None; **M. Kotsuma**, None; **V. Cristini**, None; **S.S. Gambhir**, Bracco Diagnostics, Consultant; Endra, Inc, Stockholder; Cellsight, Stockholder; Enlight, Inc., Stockholder; General Electric, Grant/research support; ImaginAb, Stockholder; MagArray, Inc., Stockholder; Sanofi-Aventis, US, Grant/research support; SiteOne Therapeutics, Stockholder; VisualSonics/Sonosite, Stockholder .

Presentation Number **P 387**
Poster Session 3
September 20, 2013 / 15:15-15:15 / Room: Exhibit Hall B

Molecular Imaging of Nanoparticles Conjugated with miNRA-16 Reverse Multidrug Resistance of Gastric Tumor in Mice

Xinxing Song[1], *Xiujuan Li*[1], *Fu Wang*[3], *Kaichun Wu*[4], *Mingyuan Gao*[2], *Feng Cao*[1], [1]*Department of Cardiology, Xijing Hospital, Fourth Military Medical University, Xi'an, China;* [2]*Institute of Chemistry, Chinese Academy of Sciences, Beijing, China;* [3]*School of Life Sciences and Technology, Xidian University, Xi'an, China;* [4]*Digestive Disease Department, Xijing Hospital, Fourth Military Medical University, Xi'an, China. Contact e-mail: song.xing86@gmail.com*

Background Gastric cancer is one of the major cause of mortality worldwide, especially in China. Chemotherapy remains the primary strategy for advanced gastric cancer. However, multidrug resistance (MDR) of cancer cells is still the major obstacle for success of chemotheraphy. It is reported that improve expression of miRNA-16 can reduce drug resistance in gastric cancer cell line SGC7901/ADR. Our study was to use a novel molecular imaging nano-probe to reverse MDR of SGC7901/ADR by multimodality imaging (BLI, FRI and MRI). Methods Magnetic nanoparticles (MNPs) were characterized by transmission electron microscopy (TEM). miRNA-16 was conjugated to (MNPs) via electrostatic interaction while cy5.5 was conjugated to MNPs via carboxyl and amine condensation. The probe was purified by high speed centrifugate. Agarose gel electrophoresis were detected to confirm whether miRNA was successfully conjugated to nanoparticles. 5x106 SGC7901/ADRfluc cells injected into the right flank of nude mice, then the nude mice were intraperitoneally (i.p.) injected with adriamycin (ADR) (1 mg/kg) twice a week for 4 weeks. cy5.5/miR16/MNPs were given by tail intravenous injection twice a week for 4 weeks. After 24h injection of cy5.5/miR16/MNPs, Bioluminescent imaging (BLI) and fluorescence imaging (FRI) were used for detecting cy5.5/miR16/MNPs. BLI were performed for monitoring tumor volume once a week for 4 weeks. Results TEM results revealed that the mean size of MNPs was 12.4±1.6nm. There is no difference in MRI between MNPs and cy5.5/miR16/MNPs. In vivo, MRI showed that the area of tumor exhibited lower T2 signal intensity compared with the signal before probe injection. BLI and FRI revealed that the probe was trapped in tumor 24 hours after injection. Results of BLI confirmed fluorescence intensity was reduced after cy5.5/miR16/MNPs injection, which suggested cy5.5/miR16/MNPs could reverse MDR in SGC7901/ADR cell lines in vivo. Conclusions Cy5.5/miR16/MNPs, a novel molecular imaging probe, provides potential for noninvasive assessment of the distribution of probe in vivo and also new sight for reversing MDR.

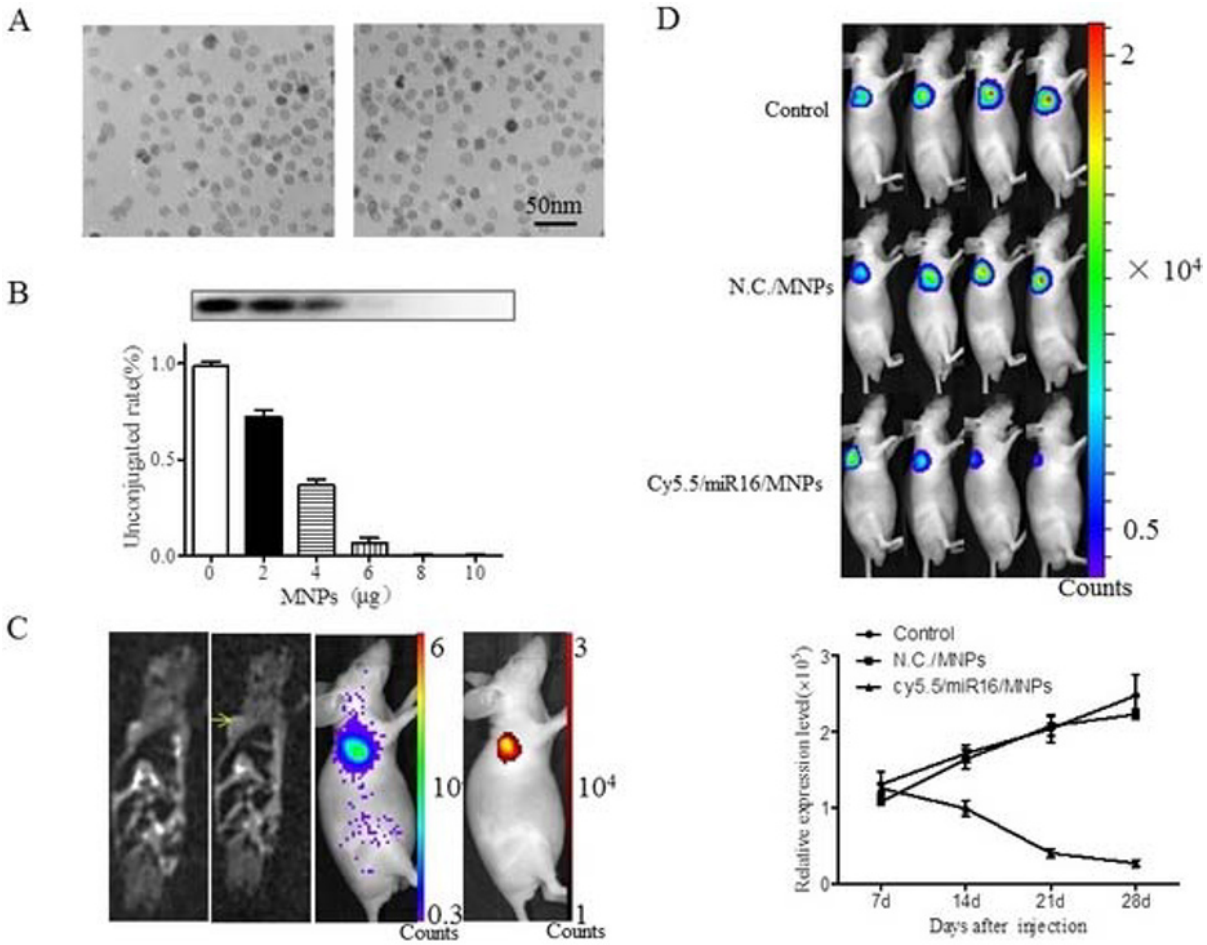

Figure 1. Characterization of probe, BLI and FRI analysis for distribution of probe in nude mice and fluorescence intensity after cy5.5/miR16/MNPs injection. A. TEM images of MNPs and cy5.5/miR16/MNPs. B. 60pmol miRNA were conjugated with different quality of MNPs (0, 2, 4, 6, 8 and 10μg). Agarose gel electrophoresis show that miRNA could conjugate with MNPs. C. MRI, BLI and FRI were used for detecting cy5.5/miR16/MNPS. D. BLI revealed fluorescence intensity was reduced after injection of cy5.5/miR16/MNPs, while fluorescence intensity was increased after injection of PBS and negative control/MNPs.

Disclosure of author financial interest or relationships:
X. Song, None; **X. Li**, None; **F. Wang**, None; **K. Wu**, None; **M. Gao**, None; **F. Cao**, None.

Presentation Number **P 388**
Poster Session 3
September 20, 2013 / 15:15-15:15 / Room: Exhibit Hall B

In vivo Detection of Membrane-Bound Radicals in Mouse GL261 Gliomas using Combined Molecular MRI and Immuno-Spin-Trapping

Rheal Towner[1], *Nataliya Smith*[1], *Debra Saunders*[1], *Patricia Coutinho de Souza*[1], *Leah Henry*[1], *Florea Lupu*[2], *Robert Silasi-Mansat*[2], *Marilyn Ehrenshaft*[3], *Ronald P. Mason*[3], *Sandra E. Gomez-Mejiba*[4], *Dario C. Ramirez*[4], [1]*Advanced Magnetic Resonance Center, Oklahoma Medical Research Foundation, Oklahoma City, OK, USA;* [2]*Cardiovascular Biology, Oklahoma Medical Research Foundation, Oklahoma City, OK, USA;* [3]*Laboratory of Pharmacology and Chemistry, National Institute of Environmental Health Sciences, Research Triangle Park, NC, USA;* [4]*Laboratory of Experimental Medicine & Therapeutics, National University of San Luis, San Luis, Argentina. Contact e-mail: Rheal-Towner@omrf.org*

Introduction: Free radicals play a crucial role in cancers, including gliomas. By combining molecular magnetic resonance imaging (mMRI) and immuno-spin trapping (IST) technologies it is possible for the first time to monitor levels of in vivo radicals in rodent glioma models. Methods: Mouse glioma cells (GL261) were implanted intracerebrally in C57BL6/J mice (n=6). The anti-DMPO probe was administered at 19 days following cell implantation. Mice (n=3) were treated with DMPO (5,5-dimethyl-pyrroline-N-oxide) for 3 days starting at day 16 prior to the administration of the anti-DMPO probe. For a control, GL261 glioma-bearing mice (n=3) were treated with DMPO, but were administered a non-specific mouse IgG-albumin-Gd-DTPA-biotin contrast agent. A biotin-BSA (bovine serum albumin)-Gd-DTPA-based contrast agent coupled to an antibody recognizing DMPO-radical adducts was used. Non-specific mouse-IgG conjugated to biotin-BSA-Gd-DTPA was used as a contrast agent control. MR experiments were carried out under general anesthesia (isoflurane). MRI studies were done on a Bruker Biospec 7.0 Tesla/30 cm horizontal-bore imaging spectrometer. Anesthetised mouse brain images were obtained using a 72 mm quadrature multi-rung RF coil. Mouse brains were imaged at at 7, 10 and 14 days following cell implantation prior to administration of the anti-DMPO probe at day 21. Multiple brain 1H MR image slices were taken using a spin echo multislice (repetition time (TR) 0.8 s, echo time (TE) 23 ms, 128x128 matrix, 4 steps per acquisition, 3x4 cm2 field of view, 1 mm slice thickness). Mouse brains were imaged at 0 (pre-contrast), 20, 40, 60, 120 and 180 min intervals post-contrast agent injection. T1-weighted images were obtained using a variable TR (repetition time) spin-echo sequence. Pixel-by-pixel relaxation maps were reconstructed from a series of T1-weighted images using a nonlinear two-parameter fitting procedure. The T1 value of a specified region-of-interest (ROI) was computed from all the pixels in the ROI. Results: MRI was used to detect the presence of the anti-DMPO adducts by either a significant sustained increase ($p<0.001$) in MR signal intensity or a significant decrease ($p<0.001$) in T1 relaxation, measured as %T1 change. The biotin moiety of the anti-DMPO probe was targeted with fluorescently-labeled streptavidin to locate the anti-DMPO probe in excised brain tissues, indicating elevated fluorescence only in tumors from mice administered the anti-DMPO probe. As a negative control a non-specific IgG antibody covalently bound to the albumin-Gd-DTPA-biotin construct was used. DMPO adducts were also confirmed in tumor tissue from animals administered DMPO, compared to non-tumor brain tissue. Discussion: In this study we used a combination of mMRI and IST to show for the first time non-invasive in vivo detection of membrane-bound radicals in gliomas. Using both mMRI and IST provides the advantage of in vivo image resolution and spatial differentiation of regional events in heterogeneous tissues or organs and the regional targeting of free radical mediated oxidation of cellular membrane components.

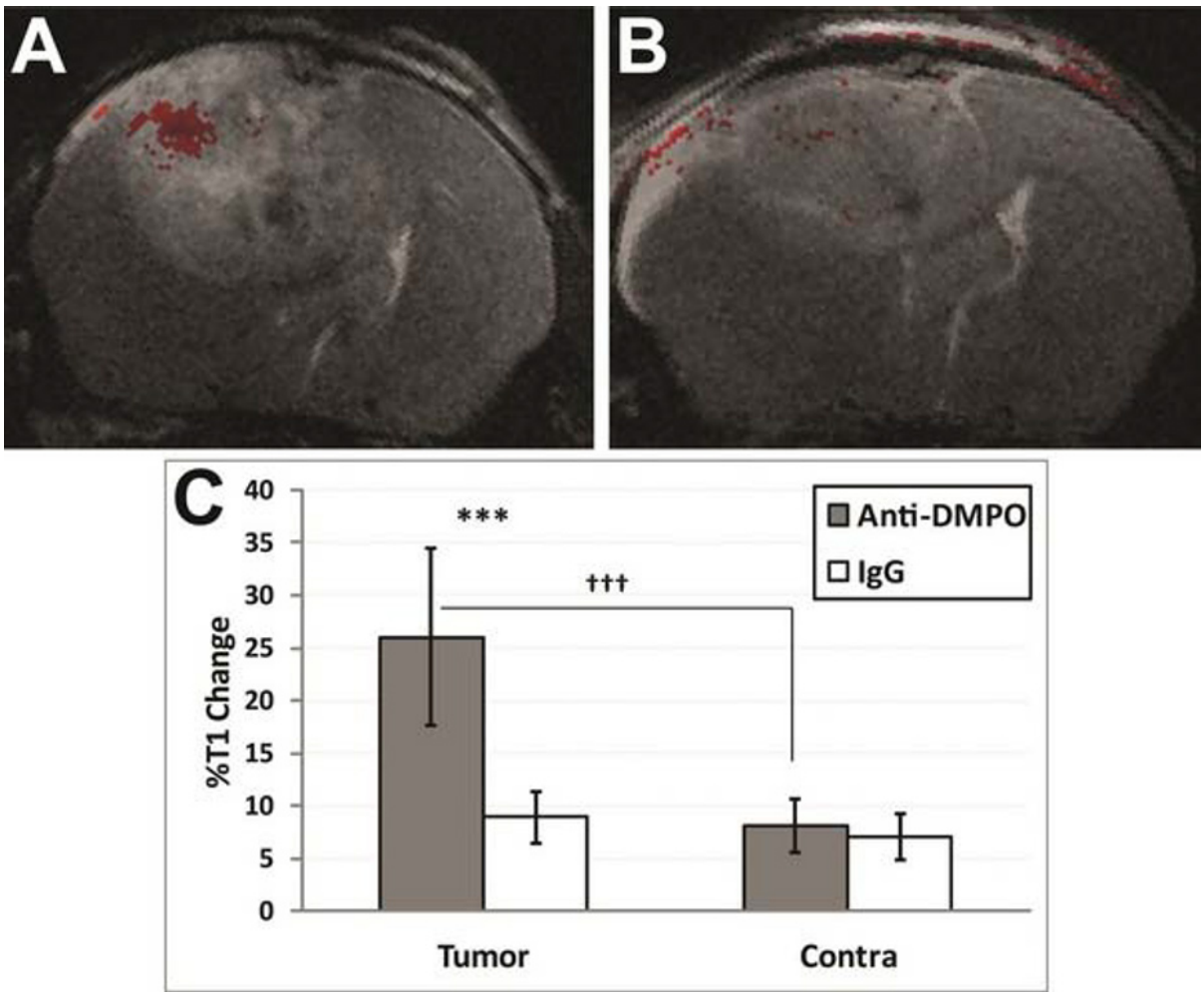

Figure 1: mMRI detection of membrane-bound radical adducts in a GL261 mouse glioma model. (A) T2-weighted MR image with an overlaid difference threshold image (120 min post- and pre-administration of anti-DMPO probe) following administration of the anti-DMPO probe, taken at 30 days after intracerebral implantation of GL261 cells in mice. Note increased uptake of the anti-DMPO probe in the tumor region. (B) T2-weighted MR image with an overlaid difference threshold image (120 min post- and pre-administration of the IgG contrast agent) following administration of the IgG contrast agent, taken at 27 days after intracerebral implantation of GL261 cells in mice. Note no specific uptake of the IgG contrast agent in the tumor region. (C) Histogram of percent T1 change in tumor and contralateral (Contra) regions of GL261 glioma-bearing mice administered either the anti-DMPO probe (Anti-DMPO) or a non-specific IgG contrast agent (IgG).

Disclosure of author financial interest or relationships:
R. Towner, None; **N. Smith**, None; **D. Saunders**, None; **P. Coutinho de Souza**, None; **L. Henry**, None; **F. Lupu**, None; **R. Silasi-Mansat**, None; **M. Ehrenshaft**, None; **R.P. Mason**, None; **S.E. Gomez-Mejiba**, None; **D.C. Ramirez**, None.

Presentation Number **P 389**
Poster Session 3
September 20, 2013 / 15:15-15:15 / Room: Exhibit Hall B

Functional Imaging of COX-2 in cancer: A challenge for designing a PET tracer and choosing the right in vivo model

Ole Tietz, Alison Marshall, Monica Wang, Sai Kiran Sharma, Jenilee Way, **Melinda Wuest***, Frank Wuest, Dept. of Oncology, University of Alberta, Edmonton, AB, Canada. Contact e-mail: mwuest@ualberta.ca*

Aim: Cyclooxygenase 2 (COX-2) represents an inducible enzyme expressed at higher levels during inflammation and development of certain types of cancer. COX-2 may play an important role in carcinogenesis. Analysis of COX-2 levels in vivo during disease development, progression and therapy with positron-emission tomography (PET) would allow non-invasive assessment of COX-2 expression. The goal of this study was to analyze a newly developed F-18 radiotracer binding to COX-2 and to characterize its radiopharmacological properties in vitro and in vivo in different COX-2 expressing cancer models. Materials and Methods: A fluorobenzyl-substituted trifluoro-pyrimidine derivative was radiolabeled with F-18 using 4-[^{18}F]fluorobenzyl amine ([^{18}F]FBA) as building block to give N-(4-[^{18}F]Fluorobenzyl)-4-(4-(methylsulfonyl)phenyl)-6-(trifluoromethyl)pyrimidin-2-amine ([^{18}F]FBA-1). Its potency and specificity was analyzed in a COX-2 binding assay and compared to celecoxib. In vitro cell uptake studies were performed in COX-2 expressing human colon adenocarcinoma (HCA-7), in ward-colon tumor (WCT) cells and in COX-2 negative murine mammary carcinoma (EMT-6) cells and in the presence of COX-2 selective inhibitors celecoxib, rofecoxib and SC58125. Dynamic PET experiments were done with Fisher rats bearing WCT and NIH III mice bearing HCA-7 tumors. In vivo blocking studies were carried out by i.p. injection of celecoxib. Results: Potency of FBA-1 was found to be higher then celecoxib: IC_{50} of 7 versus 40 nM against COX-2. In vitro uptake in WCT cells amounted to a maximum value of 40±5 % activity/mg protein after 45 min, which was blocked by 10 µM cold compound to 21±3 (n=3; $p<0.05$), but not celecoxib. However, uptake into EMT-6 cells also amounted to 40±11 % activity/mg protein (n=3) indicative of some non-specific retention of this radiotracer. In HCA-7 cells uptake of [^{18}F]FBA-1 reached 321±51 % activity/mg protein (n=6, 60 min). All three COX-2 inhibitors and also cold FBA-1 concentration-dependently reduced uptake of [^{18}F]FBA-1 reaching values of 111±34 and 155±46 % activity/mg protein (n=3; 100 µM celecoxib or cold FBA-1). In vivo only HSA-bound [^{18}F]FBA-1 passed the lungs following a fast blood clearance. The tracer was metabolically highly stable in vivo. In WCT uptake of [^{18}F]FBA-1 reached a SUV of 1.50±0.13 (n=7) after 1h and remained constant up to 2h indicating intracellular trapping. However, in muscle a SUV_{30min} of 0.69±0.06 (n=4) was determined which also remained constant for up to 2h indicating unspecific intracellular retention. In HCA-7 tumors continuously increasing uptake levels were observed (SUV_{2h} 1.09±0.04; SUV_{4h} 1.19±0.05, n=7). Pre-dosing with 1-4 mg/kg celecoxib reduced the SUV_{2h} significantly (0.96±0.05; n=7). Muscle uptake was also found to be high in mice (SUV_{2h} 0.58±0.05, n=7). Presence of celecoxib did not change the muscle uptake. Conclusion: [^{18}F]FBA-1 was shown to interact with COX-2 as its uptake into cancer cells in vitro and in vivo could be reduced by pre-dosing with celecoxib. However, a large part of its cellular uptake and retention is of unspecific nature.

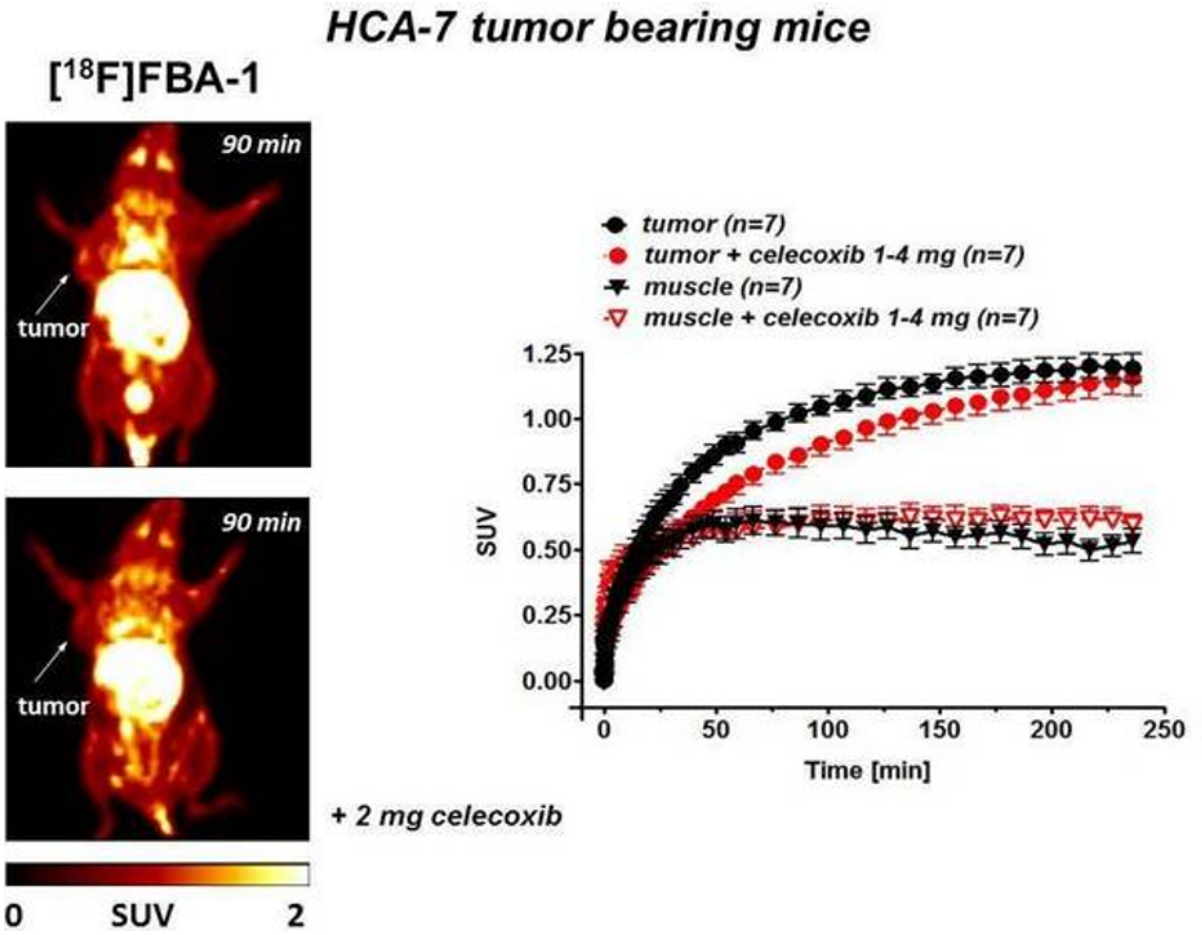

Disclosure of author financial interest or relationships:
O. Tietz, None; **A. Marshall**, None; **M. Wang**, None; **S. Sharma**, None; **J. Way**, None; **M. Wuest**, None; **F. Wuest**, None.

Presentation Number **P 390**
Poster Session 3
September 20, 2013 / 15:15-15:15 / Room: Exhibit Hall B

Dual-modality Molecular Imaging of Cholangiocarcinoma Response to Radiofrequency Heating (RFH)-enhanced Chemotherapy: Towards Interventional Molecular Imaging-Monitored RFH-enhanced Chemotherapy of Pancreatobiliary Malignancies

Feng Zhang, *Thomas Le, Han Wang, Tong Zhang, Xia Wu, Patrick Willis, Xiaoming Yang, Image-Guided Bio-Molecular Intervention Research and Section of Vascular & Interventional Radiology, Department of Radiology, university of washington, Seattle, WA, USA. Contact e-mail: fengz@u.washington.edu*

Purpose: To validate the feasibility of using 14 Tesla MRI and green protein fluorescence (GFP)-based optical imaging to monitor RFH-enhanced chemotherapeutic effect on mice cholangiocarcinomas and RFH-enhanced local chemodrug deposition in bile duct walls of living pigs. Materials and Methods: Animal studies were approved by the Institutional Animal Care and Use Committee. Initially, GFP-labeled human cholangiocarcinoma cells were treated with: (a) 30-min RFH at approximately 42 C plus gemcitabine (101 μM) and 5-fluouracil (5-FU)(95 μM); (b) 30-min RFH-only; (c) gemcitabine (101 μM) plus 5-FU(95 μM); and (d) no treatment to serve as a control. The therapeutic efficacy was evaluated by quantitative MTS assay and qualitative confocal microscopy. For in vivo study on mice, 24 nu/nu mice bearing GFP+ cholangiocarcinoma tumors were treated by: (a) intratumor injection of 25mg/kg gemcitabine and 5-fluouracil (5-FU), followed by RFH at approximately 42C for 30 mins; (b) 30-min RFH alone; (c) 25mg/kg gemcitabine and 5-FU; and (d) PBS as controls. T2-weighted imaging (T2WI), diffusion-weighted imaging (DWI) and optical imaging were used to image the tumors at day 1 before as well as days 1, 7, and 14 after treatments. For in vivo study on pigs, 8 pigs received intrabiliary local delivery of a mixture of 50mg gemcitabine and 100mg 5-FU, followed by RFH at approximately 42C for 30 mins and 8 pigs received intrabiliary delivery of the same amount of drugs only without RFH. Results: The in vitro experiments demonstrated that RFH-enhanced chemotherapy can significantly inhibit tumor cell proliferation, as compared to chemotherapy- and RFH-only groups (0.39± 0.13 VS 0.87±0.10 and 0.73±0.15, p=0.0009 and 0.001). The in vivo experiments on mice showed a significant decrease in relative tumor volume in the group with RFH-enhanced chemotherapy, compared with chemotherapy and RFH only groups (0.65±0.03 vs 1.37±0.05 and 1.30±0.021, p=0.003). ADCs in RFH-enhanced chemotherapy group decreased at day 1 but increased at days 7 and 14 after treatment, while for the chemotherapy- and RFH-only groups, there was no significant changes in ADCs between and pre-and post-treatments. Relative fluorescence signal intensities of tumors in RFH-enhanced chemotherapy group decreased after treatment. Quantitative analysis showed higher drug deposit dose in pig bile duct walls treated with intrabiliary RFH than those without RFH (Gemcitabine: 0.32±0.033mg VS 0.260±0.030mg, $p<0.05$; 5-FU: 0.664±0.060mg VS 0.52±0.050mg, $p<0.05$). Conclusions: MR DWI and optical imaging are useful techniques for assessing the early response of cholangiocarcinomas to RFH-enhanced chemotherapy, and it is feasible to use intrabiliary RFH to -enhance local chemodrugs delivery into bile duct walls.

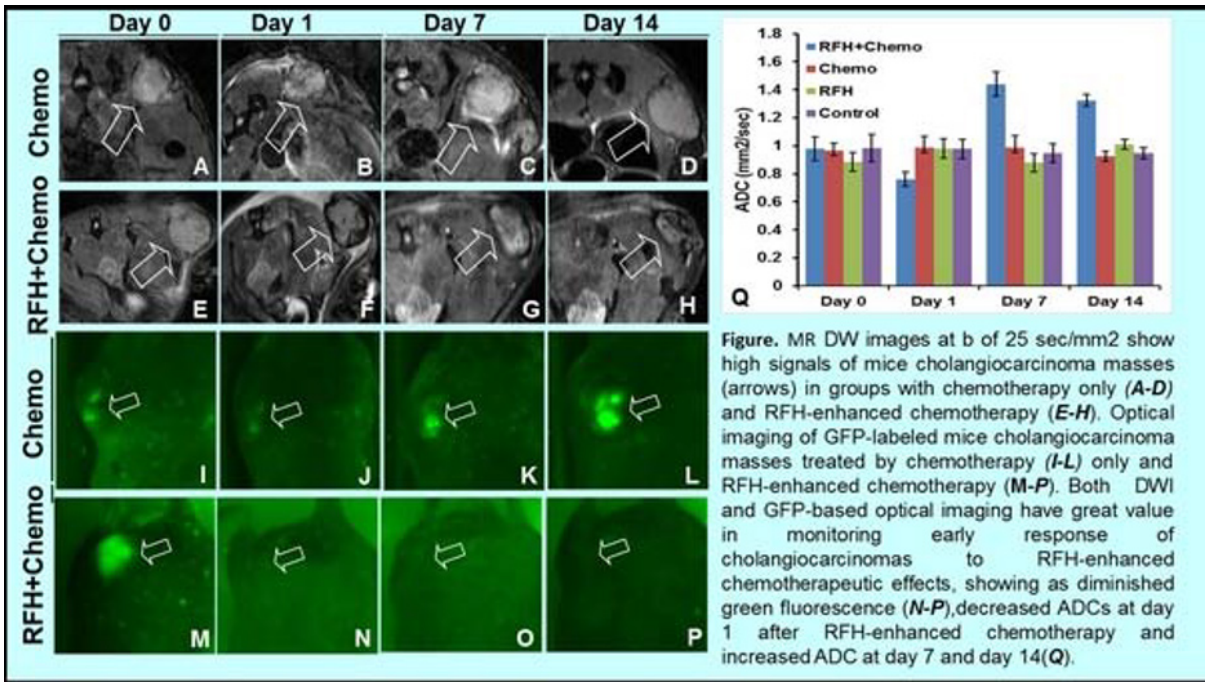

Figure. MR DW images at b of 25 sec/mm2 show high signals of mice cholangiocarcinoma masses (arrows) in groups with chemotherapy only ***(A-D)*** and RFH-enhanced chemotherapy (***E-H***). Optical imaging of GFP-labeled mice cholangiocarcinoma masses treated by chemotherapy ***(I-L)*** only and RFH-enhanced chemotherapy (**M-*P***). Both DWI and GFP-based optical imaging have great value in monitoring early response of cholangiocarcinomas to RFH-enhanced chemotherapeutic effects, showing as diminished green fluorescence (***N-P***),decreased ADCs at day 1 after RFH-enhanced chemotherapy and increased ADC at day 7 and day 14(***Q***).

Disclosure of author financial interest or relationships:
F. Zhang, None; **T. Le**, None; **H. Wang**, None; **T. Zhang**, None; **X. Wu**, None; **P. Willis**, None; **X. Yang**, None.

Presentation Number **P 391**
Poster Session 3
September 20, 2013 / 15:15-15:15 / Room: Exhibit Hall B

In Vivo Type 2 Cannabinoid Receptor Targeted Optical Imaging Using a Near Infrared Fluorescent Probe

Shaojuan Zhang, *Pin Shao, Mingfeng Bai, Radiology, University of Pittsburgh, Pittsburgh, PA, USA. Contact e-mail: shz52@pitt.edu*

Introduction: Cannabinoid receptors are G-protein coupled receptors (GPCR). The type 2 cannabinoid receptor (CB2R) overexpression is associated with many pathological conditions, such as neurodegenerative diseases, pain, inflammation and cancers. Unfortunately, the biological role of CB2R and its regulatory functions in disease progression is still unclear. This is largely due to the lack of reliable molecular imaging tools that specifically labels CB2R. Optical imaging is a relatively low-cost imaging technique with high sensitivity and resolution, suitable for cell imaging and small animal studies. The major disadvantages of optical imaging are limited tissue penetration caused by tissue absorption and scattering. This problem can be partially resolved by adapting near infrared (NIR) light (650-900 nm) under which tissue absorption and scattering is relatively low. Moreover, tissue aotofluorescence is negligible in the NIR region, allowing high-contrast optical imaging. In the present study, we synthesized a CB2R targeted NIR probe and investigated its specific targeting using an in vivo mouse tumor model. To our best knowledge, this is the first in vivo optical imaging study of CB2R using a targeted probe. Methods: To develop the NIR CB2R probe (NIR766-mbc94), we synthesized a functional CB2R ligand, mbc94, and coupled it to a NIR dye. In vitro CB2R imaging was performed using a mouse malignant astrocytoma cell line transfected with CB2R, CB2-mid DBT, which expresses CB2R at endogenous level. We then used mouse CB2-mid DBT tumor model for in vivo imaging studies. Optical images were obtained preinjection and 1, 2, 6, 12, 24, 48, 72 h post-injection of CB2R targeted probe or same amount of free dye control. For blocking experiments, mice were injected with excess amount of CB2R ligand SR144528, followed with our CB2R targeted probe. Results: CB2-mid DBT cells treated with NIR760-mbc94 showed significantly higher fluorescence signal than free dye control and challenged cells co-treated with SR144528. Similarly, NIR766-mbc94 preferentially labeled CB2-mid DBT tumors in vivo, with 3.7-fold contrast enhancement over muscle tissue at 72 h post injection, whereas fluorescence signal from the tumors of the mice treated with free dye or probe + blocking agent reached to nearly background level at the same time point. Conclusion: Our in vitro and in vivo imaging studies indicate that NIR760-mbc94 specifically labeled CB2R. Such an imaging tool may have great potential in imaging various diseases that upregulate CB2R, as well as studying the regulatory functions of the receptor in disease progression.

Disclosure of author financial interest or relationships:
S. Zhang, None; **P. Shao**, None; **M. Bai**, None.

Presentation Number **P 392**
Poster Session 3
September 20, 2013 / 15:15-15:15 / Room: Exhibit Hall B

CD47 as a potential target for cancer imaging

Alex Zheleznyak[1], *Oluwatayo Ikotun*[1], *Julie Dimitry*[2], *William A. Frazier*[2], *Suzanne Lapi*[1], [1]*Radiological Sciences, Washington University School of Medicine, St. Louis, MO, USA;* [2]*Biochemistry and Molecular Biophysics, Washington University School of Medicine, St. Louis, MO, USA. Contact e-mail: zheleznyaka@mir.wustl.edu*

CD47, also known as integrin-associated protein (IAP), is a widely expressed transmembrane protein characterized by its physical and functional association with multiple binding partners: thrombospondin-1 (TSP1), signal-regulatory protein alpha (SIRPα, CD172a), and the integrin family members αvβ3, αIIbβ3, and several beta-1 and beta-2 integrins. As a result, CD47 has been shown to participate in cellular processes such as apoptosis, proliferation, adhesion, and migration. In particular, CD47 functions as a marker of "self" by inhibiting phagocytosis of autologous cells through interaction with SIRPα expressed by professional phagocytes, such as macrophages. It has been shown that one of the mechanisms of cancer cell survival is the evasion of the immune surveillance by phagocytic cells through overexpression of CD47. CD47 over-expression was demonstrated on a number of hematologic malignancies, as well as solid tumors. Since a variety of tumors show increased expression of CD47 as means of escaping phagocytosis, detecting such overexpression may be useful for cancer detection and diagnosis; while masking CD47 to promote phagocytosis of cancer cells and elicit an immune response may provide an effective therapeutic strategy. Other researchers have suggested that the magnitude of CD47 expression could be used as a prognostic marker for recurrence and metastasis in human breast cancer, as well as aggressiveness of some leukemias. In this work we describe an in vivo evaluation of CD47 as a ubiquitous cancer immunoPET imaging biomarker. We employ xenograft (human OV10 ovarian carcinoma) and allograft (murine B16F10 melanoma) small animal models of cancer and complementary 89Zr labeled anti CD47 antibodies, B6H12 and αM-CD47, to investigate the specificity and imaging robustness of this tracer-target pair. PET image quantification demonstrated specific and similar tracer uptake in both xenograft and allograft tumors overexpressing CD47. However, liver, spleen, and kidney uptake in the allograft model was elevated, probably due to the Fc receptor binding of unmodified tracer and to tracer binding by the CD47 normally expressed in those tissues. Biodistribution studies in the xenograft model showed specific tumor uptake of the anti-human CD47 antibody and increased retention in the liver, the major clearance organ. Non-target organ uptake remained at or below the level in the circulation. Overall, CD47 demonstrates a good biomarker potential, warranting further studies and immuno-PET tracer development. These data complement the emerging new evidence which illustrates the possibility of utilizing CD47 as an immuno therapy target and support future work to establish 89Zr labeled anti CD47 antibodies as radiopharmaceuticals for detection, staging, and therapy monitoring of both, hematologic and solid malignancies, as well as for patient pre-screening to maximize the effectiveness of therapies.

Disclosure of author financial interest or relationships:
A. Zheleznyak, None; **O. Ikotun**, None; **J. Dimitry**, None; **W.A. Frazier**, None; **S. Lapi**, None.

Presentation Number **P 393**
Poster Session 3
September 20, 2013 / 15:15-15:15 / Room: Exhibit Hall B

Establishment of a mPlum-IFP 1.4 fusion protein for near-infrared based reporter gene imaging

Wang Bo-Sheng, *Liang-Ting Lin, Yi-Jang Lee, Biomedical Imaging and Radiological science, Taipei, Taiwan. Contact e-mail: humid987@gmail.com*

The bacteriophytochrome infrared fluorescent protein (IFP) has long emission wavelength that is appropriate for imaging of pathophysiological effects of deep tissues in animals. However, the brightness and photostability of IFP remain suboptimal, although exogenous supply of biliverdin (BV) can enhance these properties. In this study, we fused a far red mPlum fluorescent protein to the IFP 1.4 via a linker DNA sequence encoding seven amino acids, and investigated whether the fluorescent properties of IFP 1.4 was improved in vitro and in vivo. The confocal fluorescent microscopy demonstrated that mPlum-IFP 1.4 fusion proteins were apparently brighter than native IFP 1.4 proteins expressed in human embryonic kidney 293T cells when they were exposed to mPlum excitation wavelength. Enhanced IFP 1.4 brightness in mPlum-IFP 1.4 fusion protein is likely to be associated with Foster resonance energy transfer (FRET) based on the results of photobleaching activation and mPlum/IFP 1.4 distance measurement. Additionally, overlapping between emission spectrum of mPlum (Em. peak: 648nm) and excitation spectrum of IFP 1.4 (Ex. peak: 684nm) also supported this phenomenon in mPum-IFP 1.4 fusion protein. Use of in vivo imaging system (IVIS), we demonstrated that mPlum-IFP 1.4 fusion protein was better detected in vitro and in vivo compared to native IFP 1.4 alone, and intravenous injection of BV was not required for imaging of xenograft tumor cells expressing mPlum-IFP 1.4 fusion protein. Therefore, a fusion of mPlum to IFP 1.4 improved the fluorescent brightness of IFP 1.4 protein without BV, and this novel construct would be important for in vivo imaging of deep tissues.

Disclosure of author financial interest or relationships:
W. Bo-Sheng, None; **L. Lin**, None; **Y. Lee**, None.

Presentation Number **P 394**
Poster Session 3
September 20, 2013 / 15:15-15:15 / Room: Exhibit Hall B

Longitudinal monitoring the pharmacokinetics of rapamycin-loaded HSA nanoparticles with a split luciferase reporter gene

Fu Wang[1,2], *Zhe Wang*[1], *Ying Ma*[1], *Pengfei Rong*[1], *Gang Niu*[1], *Jie Tian*[2], *Xiaoyuan (Shawn) Chen*[1], [1]*National Institute of Biomedical Imaging and Bioengineering, National Institutes of Health, Bethesda, MD, USA;* [2]*School of Life Sciences and Technology, Xidian University, Xi'an, China. Contact e-mail: fu.wang@nih.gov*

Objectives Pharmacokinetics analysis is of great importance during early-phase clinical trials to determine the relationship between initial drug input and final drug uptake. This study aims to monitor the pharmacokinetics of rapamycin-loaded human serum albumin (HSA) nanoparticles with bioluminescence imaging (BLI) and near infrared fluorescence imaging (NIR FI) using a split luciferase reporter gene. Methods HN12 human head and neck squamous carcinoma cells were genetically modified with FRB and FKBP12 linked split firefly luciferase reporter gene. Rapamycin-loaded HSA nanoparticles were formulated with a microfluidic homogenizer. The Cy5 dye was conjugated with the HSA of nanoparticle. The size and morphology of nanoparticle were determined by the DLS and TEM. The time-dependent cell uptake of nanoparticle was evaluated by confocal microscopy and flow cytometry. NIR FI and BLI were performed to evaluate the time course of nanoparticle delivery and release of rapamycin in tumor-bearing mice. The final rapamycin concentrations in the cells or tumors were confirmed by LC/MS analysis. Results Rapamycin-loaded HSA nanoparticles were about 150 nm in diameter with narrow size distribution. Confocal microscopy revealed that HSA nanoparticles were gradually taken up from extracellular fluid into cells by endocytosis. The Cy5 fluorescence intensity from cells reached a maximal level at 24 h according to FACS analysis. After HN12 tumor bearing-mice injected intravenously with Cy5-HSA nanoparticle, the fluorescence signal in the tumor area increased over time, reached a plateau at 24 h time point, and then decreased afterwards. By contrast, the BLI signal in vivo were found to be the highest at 6 h time point and persisted for 3 days, at which point the bioluminescence signal has declined to almost the pretreatment level. Conclusions In this study, near infrared fluorescence imaging was performed to reflect HSA nanoparticle delivery and bioluminescence imaging was performed to reflect rapamycin drug uptake. BLI and NIR FI facilitate the determination of pharmacokinetics of drug-loaded nanoparticles over time in vitro and in vivo. Combination of BLI and NIR FI will be of great value for evaluating the nanoparticle based drug delivery and therapy.

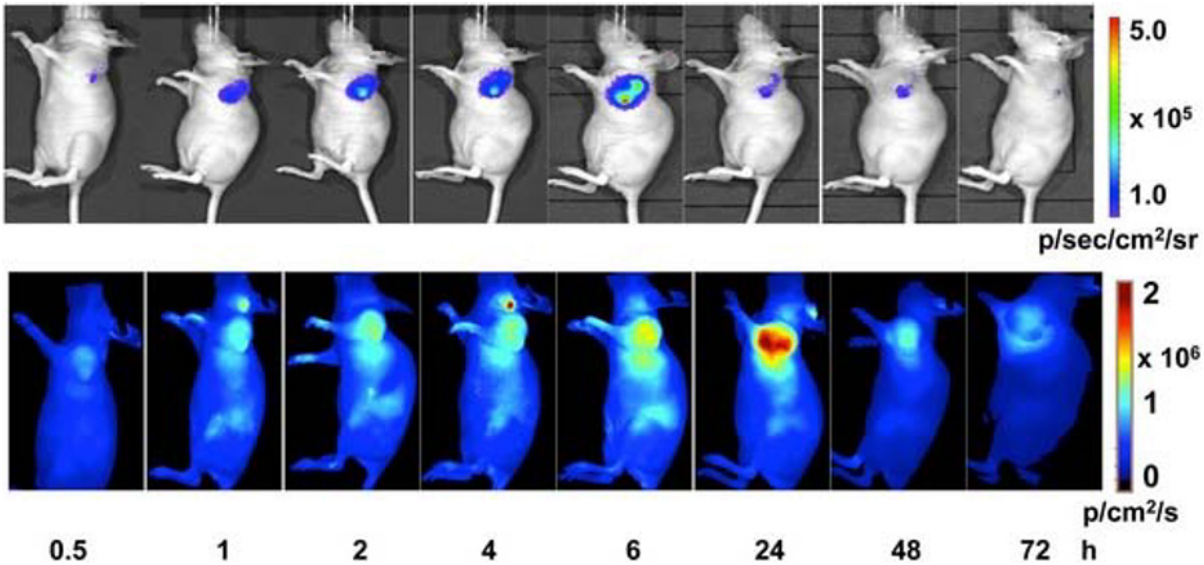

Figure. Bioluminescence imaging (Upper) and fluorescence imaging (Lower) of rapamycin loaded HSA nanoparticles delivery at different time points.

Disclosure of author financial interest or relationships:

F. Wang, None; **Z. Wang**, None; **Y. Ma**, None; **P. Rong**, None; **G. Niu**, None; **J. Tian**, None; **X. Chen**, None.

Presentation Number **P 395**
Poster Session 3
September 20, 2013 / 15:15-15:15 / Room: Exhibit Hall B

HaloTag as a Reporter Gene for Positron Emission Tomography

Hao Hong[1], *Hélène A. Benink*[2], *H. Tetsuo Uyeda*[2], *Todd E. Barnhart*[3], *Frank Fan*[2], *Weibo Cai*[1,3], [1]*Radiology, Univ of Wisconsin, Madison, WI, USA;* [2]*R&D, Promega Corporation, Madison, WI, USA;* [3]*Medical Physics, Univ of Wisconsin, Madison, WI, USA. Contact e-mail: hhong@uwhealth.org*

Objectives : To employ HaloTag technology for positron emission tomography (PET), which involves 2 components: HaloTag protein (an engineered hydrolase which covalently binds to synthetic ligands) and HaloTag ligand (HTL). Methods : 4T1 murine breast cancer cells were stably transfected to express HaloTag protein on the surface (termed as 4T1-HaloTag-ECS, extra cellulcar surface). Two new HTLs were synthesized and termed NOTA-HTL2G-S and NOTA-HTL2G-L (2G indicates second generation, S stands for short, L stands for long, NOTA denotes 1,4,7-triazacyclononane-N,N'N''-triacetic acid, for ^{64}Cu labeling). Microscopy studies were performed to determine the cellular distribution of HaloTag, using commercial AlexaFluor488-HTL. Pulse-chase experiments were conducted to evaluate the HaloTag binding efficiency of NOTA-HTL2G-S/L in vitro. ^{64}Cu-NOTA-HTL2G-S/L was studied for PET imaging in mice bearing 4T1-HaloTag-ECS or 4T1 tumors. Autoradiography and histology studies were carried out to confirm the HaloTag specificity of 64Cu-NOTA-HTL2G-S/L in vivo. Results: Microscopy confirmed surface expression of HaloTag in 4T1-HaloTag-ECS cells, which specifically bind NOTA-HTL2G-S/L. The radiochemical yield was ~25% for ^{64}Cu-NOTA-HTL2G-S and >80% for ^{64}Cu-NOTA-HTL2G-L, with purity of >95%. Uptake of ^{64}Cu-NOTA-HTL2G-L in 4T1-HaloTag-ECS tumors (4.3 ± 0.5, 4.1± 0.2, 4.0 ± 0.2, 2.3 ± 0.1, and 2.2 ± 0.1 %ID/g at 0.5, 3, 6, 18, and 24 h post-injection; n = 4) was significantly higher than that in the 4T1 tumors (3.0 ± 0.3, 3.0± 0.1, 3.0 ± 0.2, 2.0 ± 0.4, and 2.4 ± 0.3 %ID/g at 0.5, 3, 6, 18, and 24 h post-injection respectively; n = 4) at early time points. Other organs with significant tracer uptake included kidneys and liver, which indicated renal/hepatobiliary clearance. In comparison, 64Cu-NOTA-HTL2G-S did not demonstrate significant uptake in either 4T1-HaloTag-ECS or 4T1 tumors. Blocking studies and autoradiography of tumor lysates confirmed that ^{64}Cu-NOTA-HTL2G-L binds specifically to HaloTag protein in the 4T1-HaloTag-ECS tumors, corroborated by histology.

Conclusion: HaloTag protein-specific targeting and PET imaging in vivo was achieved with ^{64}Cu-NOTA-HTL2G-L, which serves as a proof-of-principle for future non-invasive and sensitive tracking of HaloTag-transfected cells with PET, as well as many other studies of gene/protein/cell function in vivo.

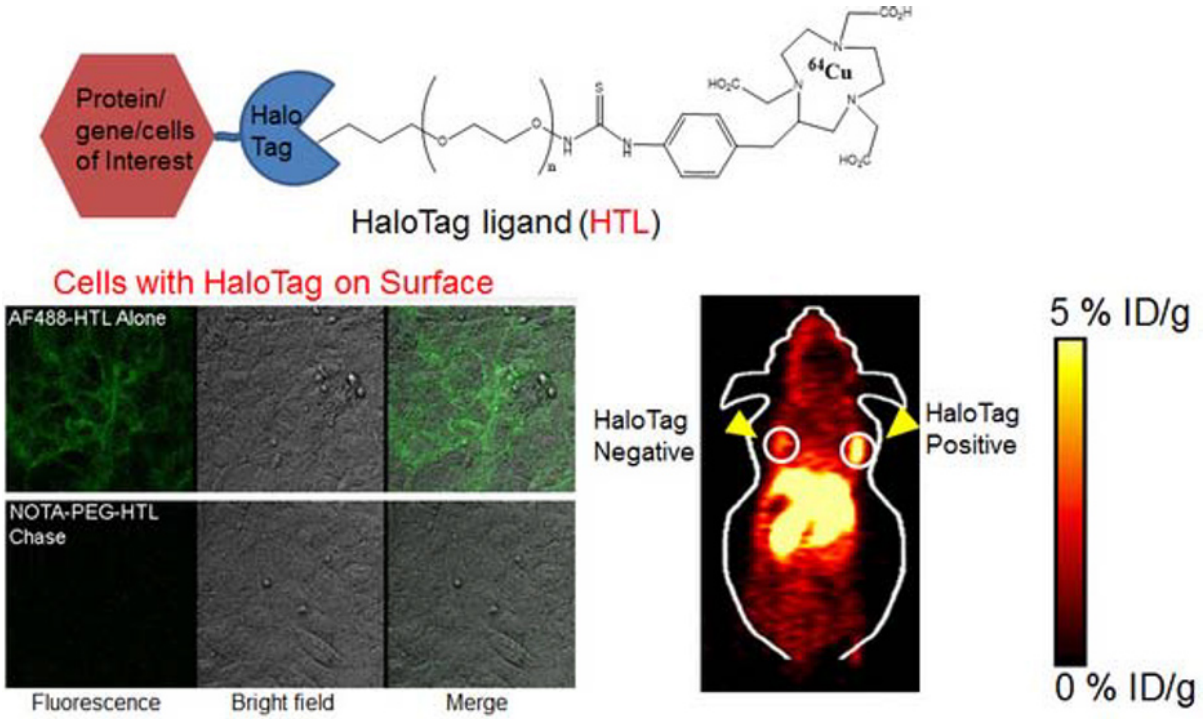

Disclosure of author financial interest or relationships:
H. Hong, None; **H.A. Benink**, Promega Corporation, Employment; **H. Uyeda**, None; **T.E. Barnhart**, None; **F. Fan**, None; **W. Cai**, None.

Presentation Number **P 396**
Poster Session 3
September 20, 2013 / 15:15-15:15 / Room: Exhibit Hall B

Discovery of Gadolinium chelate based MR Reporter Gene

Jongkai Hsiao[1], *Hon-Man Liu*[2], *Ming-Jium Shieh*[3], [1]*Medical Imaging, TzuChi General Hospital, Taipei Branch, New Taipei City, Taiwan;* [2]*Medical Imaging, National Taiwan University Hospital, Taipei, Taiwan;* [3]*Institute of Biomedical Engineering, College of Medicine and College of Engineering, National Taiwan University, Taipei, Taiwan. Contact e-mail: jongkai@gmail.com*

The importance of molecular imaging is rising because the need for imaging molecular events in vivo in drug industry, stem cell biology, caner biology and other biomedical applications. Magnetic resonance (MR) imaging is superior to other imaging modality because there is no radiation exposure and the depth of exam is not limited. Reporter gene is of biomedical importance since it can used for monitoring interesting genes. The best known reporter gene is green fluorescent protein gene that works as fluorofore. However, the in vivo application of GFP is confined to small animals because the penetration depth limitation that originates from the body absorption and reflection of the light. There is some success in the establishment of MR reporter gene based on iron oxide nanoparticles. However, the application is still limited probably due to paucity of circulating iron in the body. We established gadolinium chelate based MR reporter gene by transfecting human sarcoma cell line, HT-1080 with organic anion transporter protein (OATP) gene by lentiviral based method. The OATP is a transmembrane protein that can recognize Gd-DTPA-EOB, a clinical used MR contrast agent, and tranlocate it into cytoplasm. Under 1.5 Tesla MR scanning, the cell pallet that transfected with OATP and incubated with Gd-DTPA-EOB exhibit bright signal intensity on T1 weighted image whereas cells that incubated with other MR contrast agent remain its original signal intensity. Moreover, in spite of treating with Gd-DTPA-EOB, cells without OATP transfection remain their signal intensity. We further investigate its feasibility for in vivo application. Nude mouse implanted with HT-1080 either transfected with OATP or not were imaged under 7 Telsa MR system. Only tumors that injected intravenously with Gd-DTPA-EOB show elevated signal intensity. Tumors that without OATP treatment or given different MR contrast medium (Gd-DTPA, or Gd-DTPA-BMA) show only limited elevation of signal intensity. The success of transfection of OATP is confirmed by immunohistochemistry of excised tumors. We also noted constant expression of multiple drug resistance (MDR) protein that has been proved for transporting Gd-DTPA-EOB from cytoplasm into extracellular space. We conclude that OATP is a very good candidate for MR reporter gene and the application of the MR reporter gene is extended in embryology, transgenic or knockout animals, stem cell trafficking, drug development.

Disclosure of author financial interest or relationships:
J. Hsiao, None; **H. Liu**, None; **M. Shieh**, None.

Presentation Number **P 397**
Poster Session 3
September 20, 2013 / 15:15-15:15 / Room: Exhibit Hall B

In vivo monitoring of implanted human amniotic fluid stem cell for urethral sphincter regeneration in an animal model

Jung Eun Kim[1], *Byeong-Cheol Ahn*[1], *Mi-hye Hwang*[1], *So Young Chun*[2], *Shin Young Jeong*[1], *Sang-Woo Lee*[1], *Tae Gyun Kwon*[2], *Jaetae Lee*[1], [1]*Nuclear Medicine, Kyungpook National University School of Medicine, Daegu, Republic of Korea;* [2]*Urology, Kyungpook National University School of Medicine, Daegu, Republic of Korea. Contact e-mail: gene7302@hotmail.com*

Objective: The purpose of this study is in vivo monitoring of implanted human amniotic fluid stem cell (hAFSCs) in stress urinary incontinence (SUI) animal model. Methods: hAFSC was used to restore urethral sphincter function in a rat model. Rat underwent bilateral pudendal nerve transection to generate a SUI model and received periurethral implantation of hAFSCs/F. For in vivo monitoring, the hAFSC stably expressing enhanced firefly luciferase (effluc) was established using a retrovirus expressing effluc and Thy1.1 reporter genes driven by cytomegalovirus (CMV) promoter (hAFSCs/F). RT-PCR, confocal microscopy, and luciferase assay was performed to verify effluc expression and function in hAFSCs/F. hAFSCs/F were analyzed for stem cell characteristics and in vitro myogenic differentiation potency. Bioluminescence imaging was performed on day 1, 3, 5, 7, 14 and 21 after the implantation. Results: Expression of effluc was verified by RT-PCR and confocal microscopy. The luciferase activity from hAFSCs/F increased cell number dependently. Flow cytometry analysis was showed that hAFSCs/F were expressed mesenchymal stem cell (MSC) markers-CD 44 and CD 105, but no hematopoietic stem cell markers-CD 45. Induction of myogenic differentiation in the hAFSCs resulted in expression of PAX7 and MYOD at Day 3, and DYSTROPHIN at Day 7. In vivo bioluminescence signal was decreased over time after implantation. After 21 days, hAFSCs/F injected in urinary sphincter was confirmed by histological examination at sites in rat and the sphincter muscle had expression of Thy1.1. Conclusion: We have established hAFSC expressing effluc bioluminescence reporter gene. hAFSCs expressed MSC characteristics and could differentiate into cells of myogenic lineage. Implanted hAFSCs to restore urinary sphincter can be feasibly and non-invasively monitored with this optical molecular imaging strategy in an SUI animal model.

Disclosure of author financial interest or relationships:
J. Kim, None; **B. Ahn**, None; **M. Hwang**, None; **S. Chun**, None; **S. Jeong**, None; **S. Lee**, None; **T. Kwon**, None; **J. Lee**, None.

Presentation Number **P 398**
Poster Session 3
September 20, 2013 / 15:15-15:15 / Room: Exhibit Hall B

Intravital visualization of siRNA-mediated inhibition of gene expression in mouse skin using confocal fluorescence imaging

Robyn P. Hickerson[1], Tycho Speaker[1], Emilio Gonzalez[2], Maria F. Lara[1], Christopher Contag[2,3], **Roger Kaspar**[1,2], *[1]TransDerm, Santa Cruz, CA, USA; [2]Dept. of Pediatrics, Stanford University, Stanford, CA, USA; [3]Radiology and Microbiology & Immunology, Stanford University, Stanford, CA, USA. Contact e-mail: roger.kaspar@transderminc.com*

Small interfering RNAs (siRNAs) can be designed to specifically and potently inhibit target gene expression and are of keen interest as potential therapeutic agents and many siRNAs are progressing through clinical trials. Pachyonychia congenita (PC) is a dominant negative skin disorder caused by mutations in genes encoding keratin (K) 6a/b, K16 and K17, resulting in faulty intermediate filament formation. TD101 is a siRNA that targets a single nucleotide mutation, K6a N171K, which causes PC. This siRNA and has been evaluated in the clinic (Leachman et al., 2010, Molecular Therapy) with encouraging results. In order to better understand the pathophysiology of PC and develop a model system to study siRNA delivery and efficacy in skin, wildtype and mutant K6a cDNAs were fused to either EGFP or tomato fluorescent protein cDNA to allow co-visualization of mutant and wildtype K6a expression in mouse footpad skin, using a confocal fluorescence imaging system. Expression of mutant K6a resulted in keratin aggregates indicative of the inability to assemble properly with higher order structures, while wildtype K6a was observed uniformly throughout the cytoplasm, consistent with incorporation into intermediate filaments. Addition of TD101 siRNA, but not a non-targeting siRNA, resulted in inhibition of mutant K6a but not wildtype. The ability to intravitally image and track the effectiveness of siRNA in real time allows for detailed analysis in individual mice and should facilitate development of siRNA therapeutics for skin disorders.

Disclosure of author financial interest or relationships:
R.P. Hickerson, None; **T. Speaker**, None; **E. Gonzalez**, None; **M.F. Lara**, None; **C. Contag**, ConcentRx Corp, Stockholder; Olympus, Other financial or material support; **R. Kaspar**, TransDerm, Employment .

Presentation Number **P 399**
Poster Session 3
September 20, 2013 / 15:15-15:15 / Room: Exhibit Hall B

Visualization of gamma-irradiation induced CD44 positive cancer stem like cell in breast cancer cell line using luciferase reporter gene

Mihyun Kim[1,2], *Min Hwan Kim*[1], *Yong Jin Lee*[1], *Myung-Jin Park*[1], *Jae-Hoon Jeong*[1], *Kwang Il Kim*[1], *Tae Sup Lee*[1], *Phyl Youl Ryu*[2], *Sang Moo Lim*[1], *Joo Hyun Kang*[1], [1]*Molecular Imaging Research Center, Korea Institute of Radiological and Medical Sciences, seoul, Republic of Korea;* [2]*Department of Microbiology, Chonnam National University College of Medicine, Gwangju, Republic of Korea. Contact e-mail: tyamyn53@nate.com*

Objectives: There is increasing evidence that cancer contain cancer-initiating cells (CICs) that are capable of regenerating a tumor that has been various therapies. CD44 and CD133 like cell surface markers are used to identify CICs *in vitro* or *in vivo*. In this study aimed on noninvasive in vivo monitoring CD44 positive breast cancer cells with molecular image by fusing the bioluminescence reporter gene fLuc by the CD44 promoter. Methods: Breast cancer cell line (MCF7) was transfected with recombinant lentivirus to express luciferase by CD44 promoter. We generated to stably expressed luciferase gene controlled by CD44 promoter (MCF7-CL). After induction of CICs by sphere formation assay or gamma irradiation or both, luciferase activities of CD44 promoter were monitored by bioluminescence assay. Expression of CD44 and CD133 was investigated by flow cytometry analysis and immunofluorescence assay. Also, expression of CD44 and luciferase were investigated by RT PCR. MCF7-CL cells were injected into the fourth mammary fat pad of two groups of mice and one group was irradiated with 6Gy for one time, using a cobalt-60 source, then *in vivo* monitoring of transplated cell was each followed for 4 days by bioluminescence imaging (BLI). Results: After treatment of 6Gy irradiation, sphere formation or 6Gy irradiation and sphere formation, luciferase activity in MCF7-CL cells had increased 1.1, 1.2 or 2.6 times bioluminescence activity than those of no irradiated monolayer cells, respectively. Survived 6Gy irradiated MCF7-CL cells had increased sphere-forming capacity compared with no treated cells. Irradiated and sphere formed cells showed up-regulated expression of CD44 and CD133 by immunofluorescence and flow cytometry. Also, expression of CD44 and CD133 in 6Gy irradiated and sphere formed cells was relatively increased than no irradiated cells, no sphere formed cells or monolayer cells using RT-PCR. *In vivo* bioluminescence images, 6 Gy irradiated mice group was shown stronger signal (2.39×10^4 counts/s) than no irradiated mice group (1.82×10^4 counts/s) for four days. Conclusions: These results indicate that increased CD44 expression and caused by general feature of CICs by irradiation and sphere formation can be monitored using bioluminescence imaging. This system could be useful to evaluated CD44 expressed breast cancer by serial optical imaging (BLI) *in vivo* as well as *in vitro* noninvasively.

Disclosure of author financial interest or relationships:
M. Kim, None; **M. Kim**, None; **Y. Lee**, None; **M. Park**, None; **J. Jeong**, None; **K. Kim**, None; **T. Lee**, None; **P. Ryu**, None; **S. Lim**, None; **J. Kang**, None.

Presentation Number **P 400**
Poster Session 3
September 20, 2013 / 15:15-15:15 / Room: Exhibit Hall B

Noninvasive in vivo nuclear imaging of human T-cells bearing hNET reporter gene using Iodine- and Fluorine-labeled probes

Maxim A. Moroz[1], *Hanwen Zhang*[1], *Ekaterina Moroz*[2], *Inna S. Serganova*[2], *Juan Zurita*[1], *Jason T. Lee*[1], *Ruimin Huang*[1], *Jason S. Lewis*[1], *Ronald G. Blasberg*[1,2], *Vladimir Ponomarev*[1], [1]*Radiology, MSKCC, New Yprk, NY, USA;* [2]*Neurology, MSKCC, New York, NY, USA. Contact e-mail: morozm@mskcc.org*

Introduction: The ability to repetitively assess cell migration, targeting and expansion in vivo is critical in adoptive cell therapies. The human norepinephrine transporter (hNET) has proven to be a potent reporter gene, but is limited by the currently available probes labeled with long half-life isotopes (MIBG labeled with 123I - 13 hours, or 124I - 4.2 days), that limit sequential (e.g., daily) imaging of dynamically changing small cell populations, such as T-cells. In this study we compare the imaging characteristics of hNET-expressing T-cells across a panel of probes: the clinically approved [123I]MIBG (SPECT) and [124I]MIBG (PET) and an 18F (t1/2 = 110 minutes) MIBG analogue [18F]MFBG. Materials: Human T-cells were transduced with a vector bearing hNET and IRES-linked Green Fluorescent Protein (GFP). hNET/GFP expression levels and functionality were confirmed by Western blotting and by immunofluorescence staining. in vitro uptake studies were performed with [123I]MIBG, [124I]MIBG, and [18F]MFBG. Viable hNET-positive and negative (control) T-cells were administered subcutaneously in the shoulder areas of male rnu/rnu mice in doses ranging from 10^5 to 3x10^7 cells, diluted in 30 µl of media. Animals were separated into three imaging cohorts: [124I]MIBG-PET (n=10), [18F]MFBG-PET (n=10) and [123I]MIBG-SPECT (n=15). Each cohort received two T-cell injections in opposite shoulders over a range of increasing doses. Imaging was performed 2 and 4 hours after i.v. injection of 200 µCi of [18F]MFBG, and 4 and 24 hours after receiving 400 µCi of the iodine-labeled tracers. Results: Transduced T-cells were 88% hNET-positive and 92% viable, based on GFP expression and trypan blue exclusion, respectively. Functional assessment of hNET expression was demonstrated by rapid in vitro uptake of the probes: 6.5±0.4% of injected radioactivity for [123I]MIBG, 7.6±0.1% for [124I]MIBG and 1.9±0.2% for [18F]MFBG per 10^6 cells after two hours of co-incubation. In vivo imaging demonstrated higher hNET+ T cell uptake and faster clearance of [18F]MFBG compared to either [123I] or [124I]MIBG, and there was a linear increase in radioactivity over the range of T-cells injected (slope = 0.92 %ID increase per 10^6 T-cells for MIBG versus 0.69 %ID increase per 10^6 T-cells for MFBG). [124I]MIBG imaging at early time points showed high background in adjacent tissue, rendering accurate analysis difficult. However, at 24 hours post-injection of [124I]MIBG, all doses of T-cell injectates were observed despite the lower uptake (% dose/cc) and reduced image quality compared to that obtained with [18F]MFBG at 4 hours. [123I]MIBG SPECT imaging demonstrated less sensitivity with only the highest dose of transduced T cells (3x10^7) clearly visualized at 24 hours. Conclusion: hNET reporter-based T-cell imaging in the animal models were clearly better with [18F]MFBG compared to that with [123I] or [124I]MIBG at each of their respective optimal imaging time points. [18F]MFBG has the added benefits of rapid renal clearance, short isotopic half-life, lower radiation exposure and the ability to perform sequential (daily) studies to facilitate monitoring of adoptive T-cell therapy.

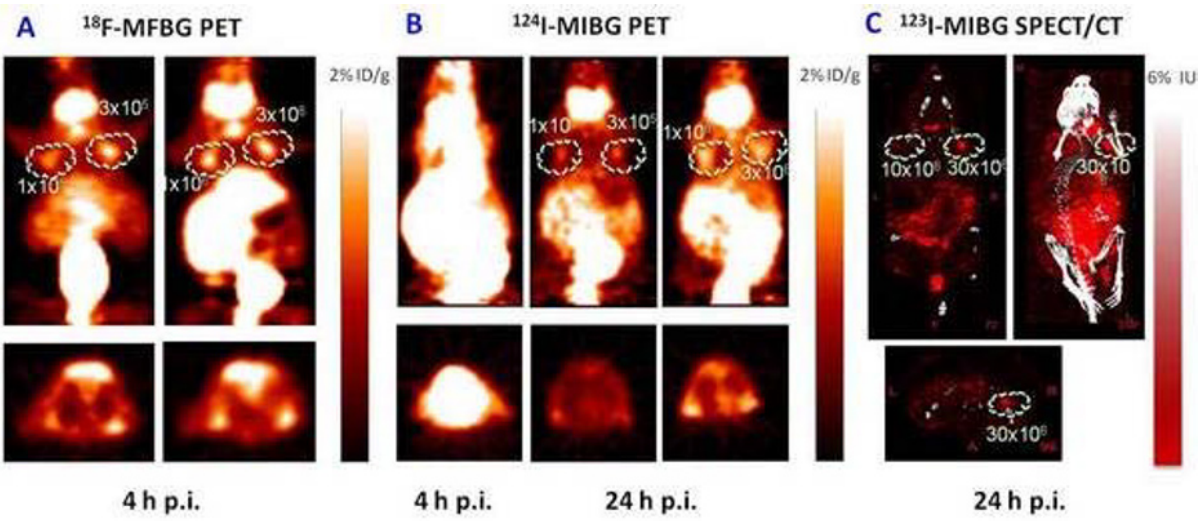

Figure. *In vivo* imaging of hNET-transduced human T cells with PET and SPECT/CT. (A) ^{18}F-MFBG PET imaging at 4 h p.i.; (B) ^{124}I-MIBG PET imaging at 4 h and 24 h p.i.; (C) ^{123}I-MIBG SPECT/CT imaging at 24 h post injection. The hNET positive human T-cells were injected subcutaneously, and 15 min later, the radiotracers were administrated by systemic injection.

Disclosure of author financial interest or relationships:
M.A. Moroz, None; **H. Zhang**, None; **E. Moroz**, None; **I.S. Serganova**, None; **J. Zurita**, None; **J.T. Lee**, None; **R. Huang**, None; **J.S. Lewis**, None; **R.G. Blasberg**, None; **V. Ponomarev**, None.

Presentation Number **P 401**
Poster Session 3
September 20, 2013 / 15:15-15:15 / Room: Exhibit Hall B

Functional Mesoscopic Fluorescence Tomography for *ex-vivo* and *in-vivo* Applications

Mehmet S. Ozturk, *Xavier Intes, Biomedical Engineering, Rensselaer Polytechnic Institute, Troy, NY, USA. Contact e-mail: ozturm@rpi.edu*

Introduction: Mesoscopic Fluorescence Molecular Tomography (MFMT) offers unprecedented potential for thick tissue imaging. Current established methods might suffer from limited field of view, providing mostly structural information, operating only with transparent or chemically decomposed samples or utilizing radioactive compounds. MFMT addresses all of these issues by allowing to image non-invasively fluorescence probes a few millimeters deep with a couple of hundred microns resolution. MFMT operates in epi-configuration so it is very well suited for in vitro and in-vivo tissue examination. In this paper, we present the development of MFMT instrumentation, image formation algorithms and its application to reporter genes imaging in tissue engineered constructs and in vivo bio-distribution of Photodynamic (PDT) drug in skin cancer model. Method: A multi-spectral MFMT system was integrated based on four illumination lasers, sequentially illuminating the tissue (λ=[488,598,658,785]nm) and raster scanned over the sample at a frame rate of 7.5Hz. Raster scanning enables a large field of view, up to 8mm by 5mm. The data set collected on the sample typically consists of 16,000 source position and for 7 off-set detectors (112,000 measurements in total). Optical reconstructions are performed using a GPU based Monte Carlo code on a desktop computer. The linearized inverse problem is solved using Conjugate Gradient Squared method (*cgs*) from MATLAB toolbox, along with vectorized measurement matrix. The overall computation to form the 3D image takes less than 5 minutes on a desktop computer. Results: We demonstrate the reconstruction of reporter gene carrying cells hosted in a 3mm thick collagen matrix in collaboration with Dr. Dai laboratory at RPI (Fig.1). Cells were printed to form two different channels, containing GFP and mCherry reporter gene expressing endothelial cells, located at different depths; 0.5mm and 2mm, respectively. Flash Red fluorescent beads (Bangs Lab Standard Intensity Kit) were pumped into the lower channel with a flow rate of 1mL/min to image the structure of the channel. The engineered collagen matrix was enclosed in perfusion chamber during imaging sessions. We also demonstrated the ability of MFMT for in vivo application by imaging the preferential accumulation of a PDT drug, HPPH, in skin cancer pre-clinical models in collaboration with Dr. Sunar laboratory at Roswell Cancer Park Institute. Concurrent ultrasound imaging was used for benchmarking and validation. Our results show that MFMT is a good candidate for molecular skin cancer imaging. Conclusion: This study demonstrates the unique potential of mesoscopic optical tomographic imaging in tissue engineering and in vivo molecular imaging applications. MFMT allows to image live tissue non-invasively with fast data acquisition, large field of view, while providing the 3D bio-distribution of optical probes up to 3-4mm deep with a couple of hundreds micron resolution. We believe that this new imaging modality has the potential to play a central role in the longitudinal characterization of tissue constructs in tissue engineering applications from in vitro to in vivo.

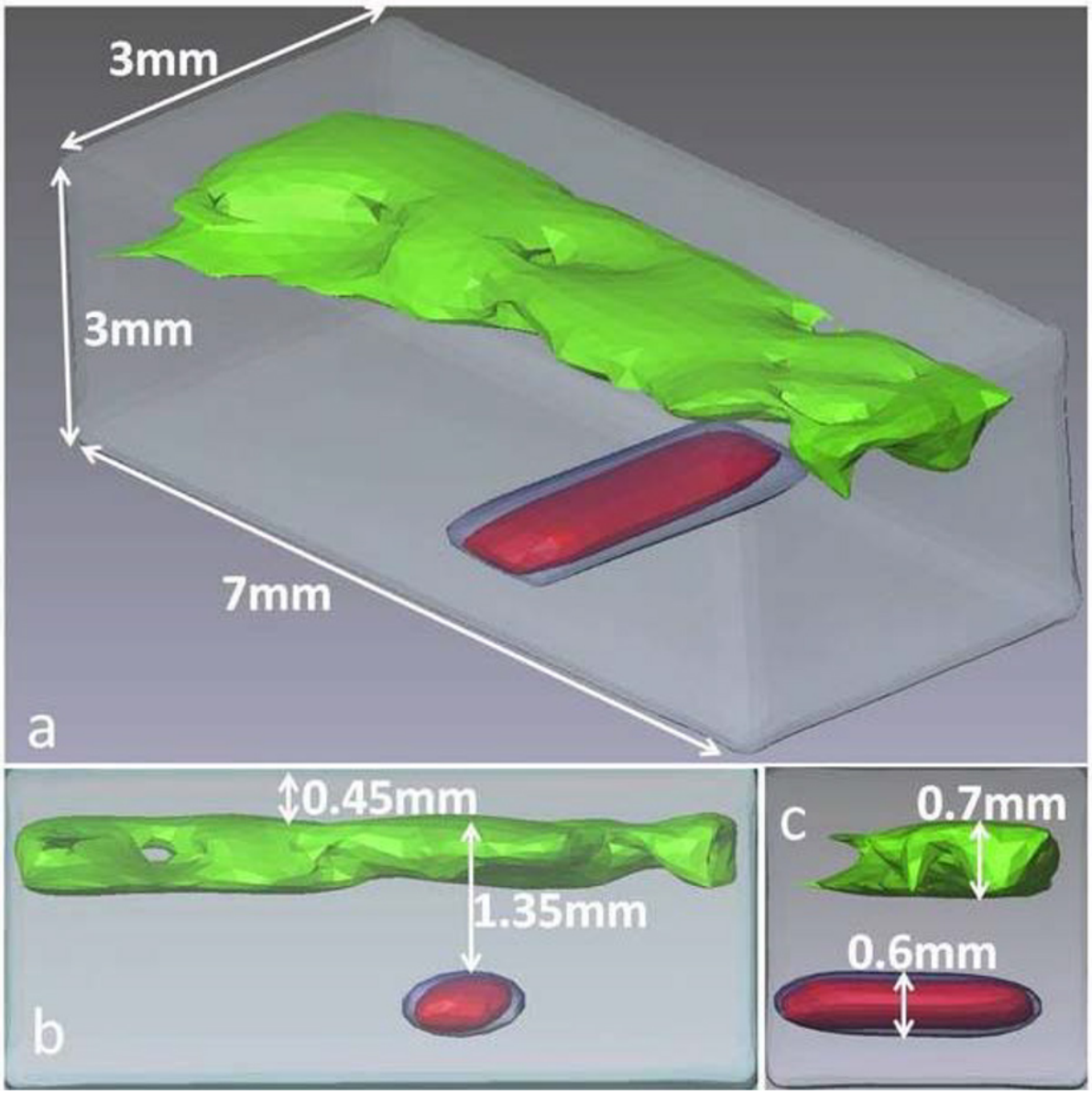

Green, Dark Blue and Red represents GFP, mCherry and Flash Red fluorescent distribution, respectively. a) Two channels (Green and Dark Blue) and perfusion (Red) is shown. b) GFP channel is placed 0.5mm below the surface, mCherry channel is located in 2mm c) Channel diameters are designed around 0.5mm. Reconstruction results, shown here, well matches with design values.

Disclosure of author financial interest or relationships:
M.S. Ozturk, None; **X. Intes**, None.

Presentation Number **P 402**
Poster Session 3
September 20, 2013 / 15:15-15:15 / Room: Exhibit Hall B

Nrf2-Luciferase Fusion Protein to Image ARE signaling in Cancer Therapy and Drug Resistance

Kira Foygel, *Ramasamy Paulmurugan, Thillai V. Sekar, Radiology, Stanford University, palo Alto, CA, USA. Contact e-mail: kfoygel@stanford.edu*

BACKGROUND AND SIGNIFICANCE. NF-E2-related factor-2 (Nrf2) is a transcription factor regulating major cellular defense mechanisms ubiquitously expressed at low levels in all human tissues. Its rapid activation in inducing phase II enzymes expression is important for preventing many diseases, including cancer. Inactive Nrf2-Keap1 complex is maintained in the cytoplasm, facilitating Keap1 mediated Nrf2 ubiquitination. During redox stress, Nrf2 is phosphorylated and translocated into the nucleus in response to the activation of protein kinase C and Map kinase, where it activates genes through AREs by interacting with the transcription factors of bZIP family. High constitutive activation of Nrf2 and its downstream gene expression has been reported in many tumors, and in cancer cell lines. Overexpression of Nrf2 in cancer cells protects them from the cytotoxic effects of anticancer therapies, resulting in chemo- and/or radioresistance. This necessitates understanding of Nrf2 regulation and identification of its activators or inhibitors that may play a role in disease prevention or cancer cell sensitization during therapy . First 435 N-terminal amino acids of Nrf2 are believed to be crucial in binding to Keap1 during its ubiquitination, but the exact binding site or the minimum N-terminal Nrf2 domain needed for efficient Keap1 binding is unknown. In the current study, we examine the efficiency of luciferase translocation into the nucleus in response to Nrf2 activators, by constructing luciferase fusion with N-terminal Nrf2 fragments of different amino acid lengths (50, 100, 150, 200, 250, and 350aa), and measuring luciferase activity in transfected cells in response to various Nrf2 activators, including anticancer drugs. RESULTS AND CONCLUSION. The construct expressing Nrf2-Fluc2 fusion protein with N-terminal Nrf2 of 100 aa was found to be significant enough in effectively translocating Nrf2-Fluc2 fusion protein, as judged by luciferase activity (50 fold basal level of activity, approximately 4 fold as compared to DMSO carrier control). Most Nrf2 activators showed maximum activity at 8-12h after exposure to the activators, it was found be an optimal time point with respect to cell viability and increase in response (up to 50 fold). Of the eight activators tested, MMS,and sodium arsenite were the most effective in activating ARE signaling. Linear response to these activators' concentration was observed, with maximum activity reached at 25 uM, and subsequent decline upon exposure to higher concentrations due to cell toxicity. The expression of superoxide dismutase (SOD), the downstream target of Nrf2, was higher upon exposure to MMS, while the expression of Nrf2 remained constant as compared to baseline. Since bioluminescence imaging can be used to monitor various biological pathways in living animals by non-invasive imaging, developed optimal Nrf2-Fluc2 fusion construct can be a valuable tool for monitoring anti-cancer therapy effect in various tumors by using tumor cell xenografts expressing truncated version of Nrf2 construct to study the role of Nrf2-ARE signaling in cancer therapy and drug resistance.

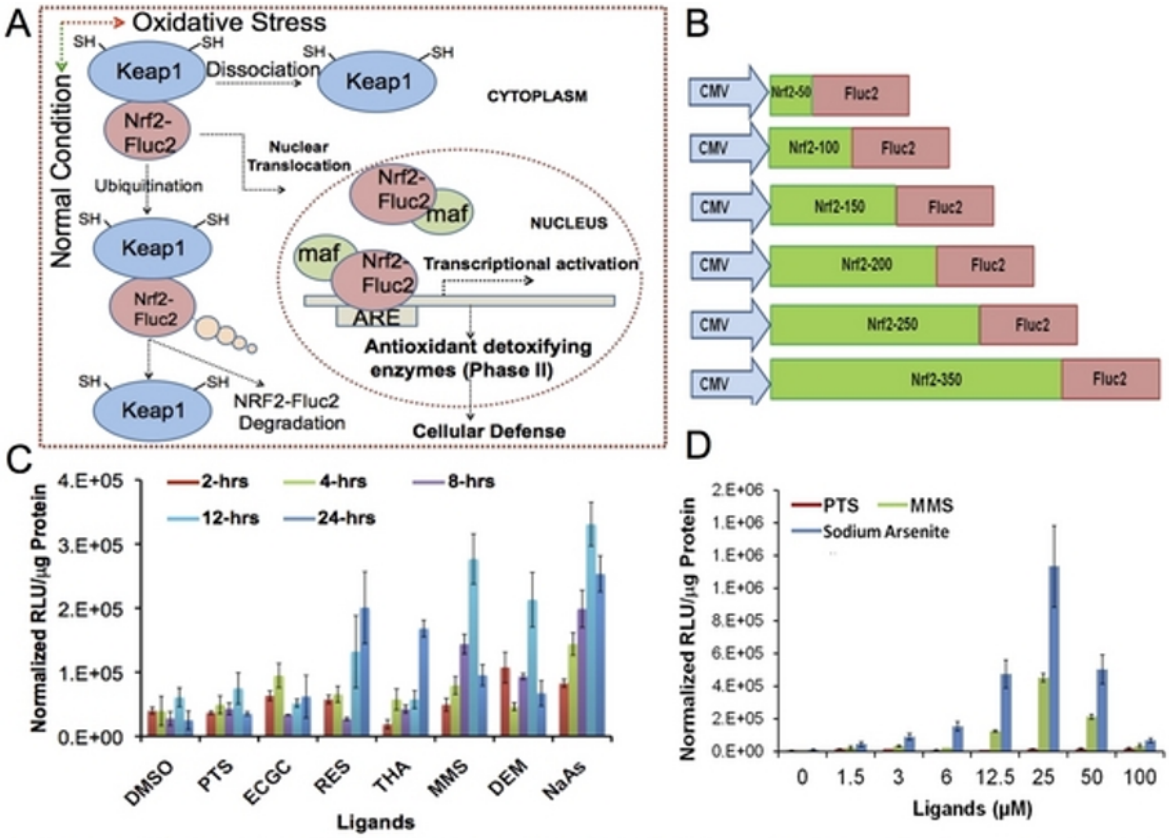

A. Mechanism of Nrf2 action in the cell. **B.** Schematics of Nrf2-Luciferase fusion constructs used for the study. **C.** Exposure of Nrf2-100-Fluc2 expressing cells to various ligands and studied at different time points. **D.** Activation of Nrf2-100-Fluc2 upon exposure to different concentration of various ligands.

Disclosure of author financial interest or relationships:
K. Foygel, None; **R. Paulmurugan**, None; **T.V. Sekar**, None.

Presentation Number **P 403**
Poster Session 3
September 20, 2013 / 15:15-15:15 / Room: Exhibit Hall B

Reporter gene imaging of exosome mediated miR-210 transfer in hypoxic tumor

Kyung Oh Jung[1,2], *Mi Jeong Kim*[1,3], *Dong Soo Lee*[1,5], *June-Key Chung*[1,6], *Hyewon Youn*[1,4], [1]*Department of Nuclear Medicine, Seoul National University College of Medicine, Seoul, Republic of Korea;* [2]*Biomedical Sciences, Seoul National University College of Medicine, Seoul, Republic of Korea;* [3]*Laboratory of Molecular Imaging and Therapy of Cancer Research Institute, Seoul National University College of Medicine, Seoul, Republic of Korea;* [4]*Cancer Imaging Center, Seoul National University Cancer Hospital, Seoul, Republic of Korea;* [5]*Molecular Medicine and Biopharmaceutical Sciences, WCU Graduate School of Convergence Science and Technology, Seoul National University, Seoul, Republic of Korea;* [6]*Tumor Microenvironment Global Core Research Center, Seoul National University, Seoul, Republic of Korea. Contact e-mail: blpg86@snu.ac.kr*

Objectives: Cancer cells actively release biological nanoscale messengers known as exosomes containing mRNAs, miRNAs and proteins to communicate signals with cancer microenvironment. It has been reported that miR-210 is specifically induced by hypoxia in cancer. In this study, we showed exosome-mediated transfer of miR-210 in hypoxia using reporter gene imaging system. Methods: 4T1 mouse breast cancer cell lines were stably cotransfected with reporter gene vectors of pCMV-EGFP and pCMV-luc2/miR-210 which luciferase signal could be turned off by binding of miR-210 to the triplicates of miR-210 binding site in the 3' end of luc2. The fluorescent and luciferase signals were measured using flow cytometry and in vivo bioluminescence imaging system (IVIS) and luciferase assay was performed. 4T1 cells were cultured under either normoxia or hypoxia (by treatment of hypoxia-inducing agents, desferrioxamine (DFO)) for 24 h. Exosomes were isolated from the conditioned media and characterized by western blot and transmission electron microscopy (TEM). Results: We characterized the isolated exosomes by size (100 nm) and protein markers such as Alix, CD63, CD9. Luciferase activity in 4T1-pCMV-luc2/miR-210 cells in hypoxia were decreased in 2.04 fold, compared to that of the cells in normoxia. Furthermore, luciferase activity in the cells treated with the exosomes isolated from the cells in hypoxia were decreased in 1.47 fold, compared to that of the control cells which were not treated with exosome. Conclusion: We developed reporter gene imaging system for monitoring miR-210 induced by hypoxia in cancer and confirmed that miR-210 was mediated by exosomes. This imaging system can be useful for monitoring exosome mediated miRNA transfer in tumor cells.

Disclosure of author financial interest or relationships:
K. Jung, None; **M. Kim**, None; **D. Lee**, None; **J. Chung**, None; **H. Youn**, None.

Presentation Number **P 404**
Poster Session 3
September 20, 2013 / 15:15-15:15 / Room: Exhibit Hall B

3D Printing for Cost Effective Customized Molecular Imaging Phantoms

Matthew Bieniosek[1,3], *David F. Hsu*[1,3], *Craig S. Levin*[2,3], [1]*Electrical Engineering, Stanford University, Stanford, CA, USA;* [2]*Radiology, Stanford University, Stanford, CA, USA;* [3]*Molecular Imaging Program at Stanford (MIPS), Stanford University, Stanford, CA, USA. Contact e-mail: mbieni@stanford.edu*

Phantoms are important tools for researchers to test molecular imaging systems without exposing patients or animals to unnecessary testing. Often researchers require customized phantoms that are easy to use and cost effective. A number of different methods have been used to manufacture imaging phantoms, including plastic or glass cavities, drilled out holes, gel suspensions, or even ink-jet printed onto 2D surfaces. Prefabricated phantoms are effective and easy to use, but are not easily customizable to different geometries and scanner applications. In addition, they can be very expensive. Drilled holes are customizable, but offer limited geometries and cannot easily achieve minuscule features required for testing high (<1 mm) resolution molecular imaging systems. Gels are customizable and offer background assessment, but require a lot of handling and are not reusable. 2D printers can build complex geometries, but only in 2 dimensions. 3D printers offer an attractive alternative to traditional phantom construction techniques. They can create almost any arbitrary geometry in 3D space. As 3D printing technology improves, the technique is also becoming increasingly accurate, versatile, and accessible. Low-end 3D printers are only a few thousand dollars. Other 3D printers can have multiple heads that can print several different materials or colors at the same time. Many molecular imaging researchers have access to 3D printers through their institutions. As a proof of concept, a 11mm long, 20mm diameter cylindrical phantom with hollow rods was fabricated with a 3D printer (see Figure 1). The hollow rods have diameters of 1.0 to 4.0mm and are sealed on one end. The other end can be closed with a cap that was also fabricated by the 3D printer, and a rubber O-ring. The 3D printer was a ProJet HD3500. It has a resolution of 750x750x890 (x-y-z) dots-per-inch and an accuracy of <0.002in per inch of part dimension. The accuracy and resolution of the printer far exceed typical molecular imaging system resolutions, making it appropriate for accurate phantoms. The phantom was successfully printed and will be used to test a 1x1x1 mm resolution clinical PET scanner under development in our lab. We have also taken X-ray projections of the phantom (see Figure 1) with a Varian PaxScan 4030CB flat panel X-ray detector, which has a pixel size of 194 microns. We plan to use the 3D printer to make different phantom geometries to test different properties of the scanner and highlight the versatility of 3D printed phantoms. The 3D printer is now an accessible tool for many researchers. It can easily be used to create custom phantoms for different scanners and applications at a low cost. Although our intent is to test the phantoms in a high resolution PET system design, the phantoms can also be used for testing high resolution, optical, photo-acoustic, CT and MRI systems.

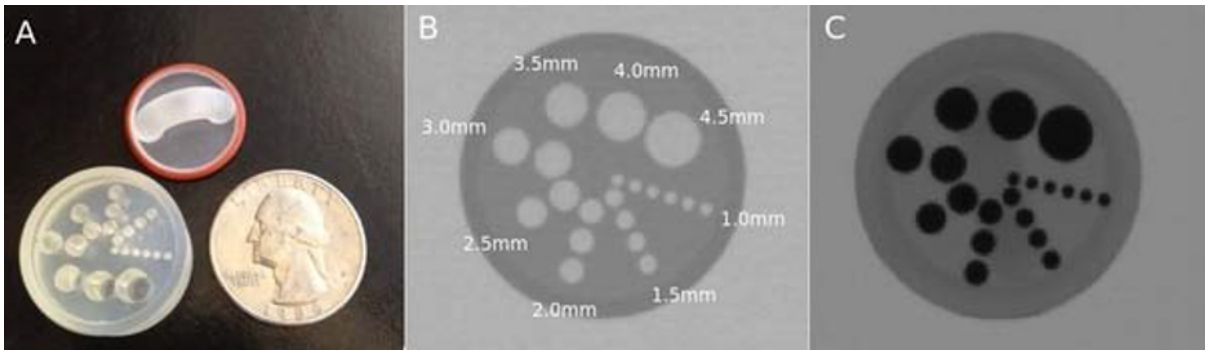

Figure 1: 3D printed molecular imaging phantom with 1.0 to 4.5mm diameter hollow rods for contrast agents. A) photograph with cap, B) X-ray projection with air in rods, C) X-ray projection with iodine contrast agent in rods.

Disclosure of author financial interest or relationships:
M. Bieniosek, None; **D.F. Hsu**, None; **C.S. Levin**, None.

Presentation Number **P 405**
Poster Session 3
September 20, 2013 / 15:15-15:15 / Room: Exhibit Hall B

A System for Preclinical Imaging Facility Management and Data Processing

*Ryan A. Bozio[1,2], **Anderson Peck**[1], Samhita Rhodes[2], Anthony Chang[1], [1]Small Animal Imaging Facility, Van Andel Institute, Grand Rapids, MI, USA; [2]College of Engineering and Computing, Grand Valley State University, Grand Rapids, MI, USA. Contact e-mail: anderson.peck@vai.org*

Introduction: Preclinical imaging laboratories are unique and specialized facilities that generally operate as service cores within large research institutions. The facilities offer non-invasive imaging technology to support and facilitate scientific research. The complexity and variety of applications for preclinical imaging creates a significant administrative burden for managing an imaging facility. Most facilities have multiple imaging modalities including PET, CT, SPECT, ultrasound, optical, and MRI each with features and administrative needs specific to the manufacturer. Large scale studies produce large amounts of data from multiple modalities requiring personnel with a variety of specializations. Imaging facility managers are responsible for managing collaborative projects, coordinating timing with other cores, scheduling machine and technician time, billing customers, implementing procedures for quality control, as well as providing meaningful and reliable results to the researchers. These challenges underscore the need for a management system that provides automated tools for designing, scheduling and overseeing the efficient completion of studies. In the Small Animal Imaging Facility of Van Andel Institute, we have developed a system for managing most aspects of an imaging facility to optimize efficiency, decrease errors, provide reliable results and to potentially provide a platform for other imaging facilities.
Methods: An entirely web-based architecture was chosen for the system to allow for ease of access from any location. The system includes tools for managing projects, data management and finance management. Project management using the system includes many aspects which accommodates for several imaging modalities. These aspects include scheduling longitudinal studies and personnel coordination such as automated emailing services for tasks and next steps in the project. Accommodating for financial management needs, the system allows the manager to automatically quote and bill the customer. Data management within the system allows for DICOM image storage, backup, retrieval and post analysis. Post analysis techniques include region of interest (ROI) drawing, image manipulation and SUV for PET data. To evaluate the system for efficiency, PET/CT studies were completed using the system as well as without the system. Scheduling, billing, and post analysis were timed for both scenarios. Results: It was found that the designed system increased scheduling efficiency by 83%, billing by 95% and post analysis by 75%. Manual intervention from the manager and users for PET/CT studies was also decreased by 82%. Conclusions: The system increased efficiency within a preclinical imaging facility and can be a model platform for other facilities as well. As a web-based system it is open architecture allowing for continual expansion as needs grow more complex. The ability to manage the imaging facility and perform image analysis as long as web-access is available makes this system easy to implement for other preclinical imaging facilities.

Disclosure of author financial interest or relationships:
R.A. Bozio, None; **A. Peck**, None; **S. Rhodes**, None; **A. Chang**, None.

Presentation Number **P 406**
Poster Session 3
September 20, 2013 / 15:15-15:15 / Room: Exhibit Hall B

FDG PET-enhances Cerenkov Surgical Image-Guidance

Colin M. Carpenter, *Guillem Pratx, Conroy Sun, Lei Xing, Radiation Oncology, Stanford University School of Medicine, Stanford, CA, USA. Contact e-mail: colincarpenter@stanford.edu*

Surgical oncologists' goal is to completely excise tumor tissue, as complete surgical resection of neoplastic tissue is critical to improving cancer outcomes. Due to the potential risk of morbidity from aggressive excision, there is a critical need to distinguish tumor from normal tissue. This is especially true in the breast, brain, skin, and in head and neck cancers. A new imaging modality, Cerenkov Luminescence Imaging (CLI), enables the imaging of PET radiotracers with conventional optics. CLI has been recently investigated for its role to guide intervention and improve surgical resection margins. Our lab has recently proposed intraoperative CLI using fiberoptics.8 This technology would enable minimally invasive endoscopic guidance for the removal of lesions; this anatomical selection also has advantages in eliminating ambient room light which is prevalent in the surgical suite. The protocol is as follows: the patient is first injected with a radiotracer, such as 18-F 2-Fluoro-2-deoxy-D-glucose. Conventional PET guidance follows. The utilization of the PET image serves to: 1) identify tumor location, and 2) identify if the selected PET tracer is appropriate for CLI. Surgical resection commences under Cerenkov guidance. In regions where the surgeon believes the tissue is free from tumor, the CLI fiberscope is introduced to locate regions of cancerous tissue. In this study, we have demonstrated that FDG-PET significantly correlates to FDG-Cerenkov in a transgenic preclinical murine model. The ability to determine tumor invasion is an unmet clinical need for prostate cancer. A transgenic adenocarcinoma mouse model of the prostate (TRAMP) was studied to compare the two modalities. The signal from organs acquired by Positron Emission Tomography (PET)/CT (Siemens Inveon) was compared to Cerenkov luminescence imaging. Six mice (four TRAMP mice, 2 healthy C57BL6 mice) were injected via the tail vein with ~1mCi of FDG. Cerenkov-guided surgery commenced immediately. All four TRAMP mice exhibited extensive tumor invasion in the prostate with subsequent invasion into the seminal vesicles. The prostate, seminal vesicles, chest wall, and subcutaneous fat were both identified with PET/CT and Cerenkov. A significant correlation ($r = 0.87$, $p<0.01$) was found between these modalities. We expect that Cerenkov may have utility in the clinic for surgical oncology. The addition of PET/CT will aid its adoption because of the ability to identify surgical regions, and the ability to guage radiotracer appropriateness. This research was funded by the National Institutes of Health (grants NCI R01 CA128908 and NIH ICMIC P50CA114747), the Department of Defense Breast Cancer Postdoctoral Fellowship BC097779, and the Center for Biomedical Imaging at Stanford (CBIS). We acknowledge the critical input and efforts of Hongguang Liu, Guillem Pratx, Conroy Sun, Zhen Cheng, and Sam S Gambhir.

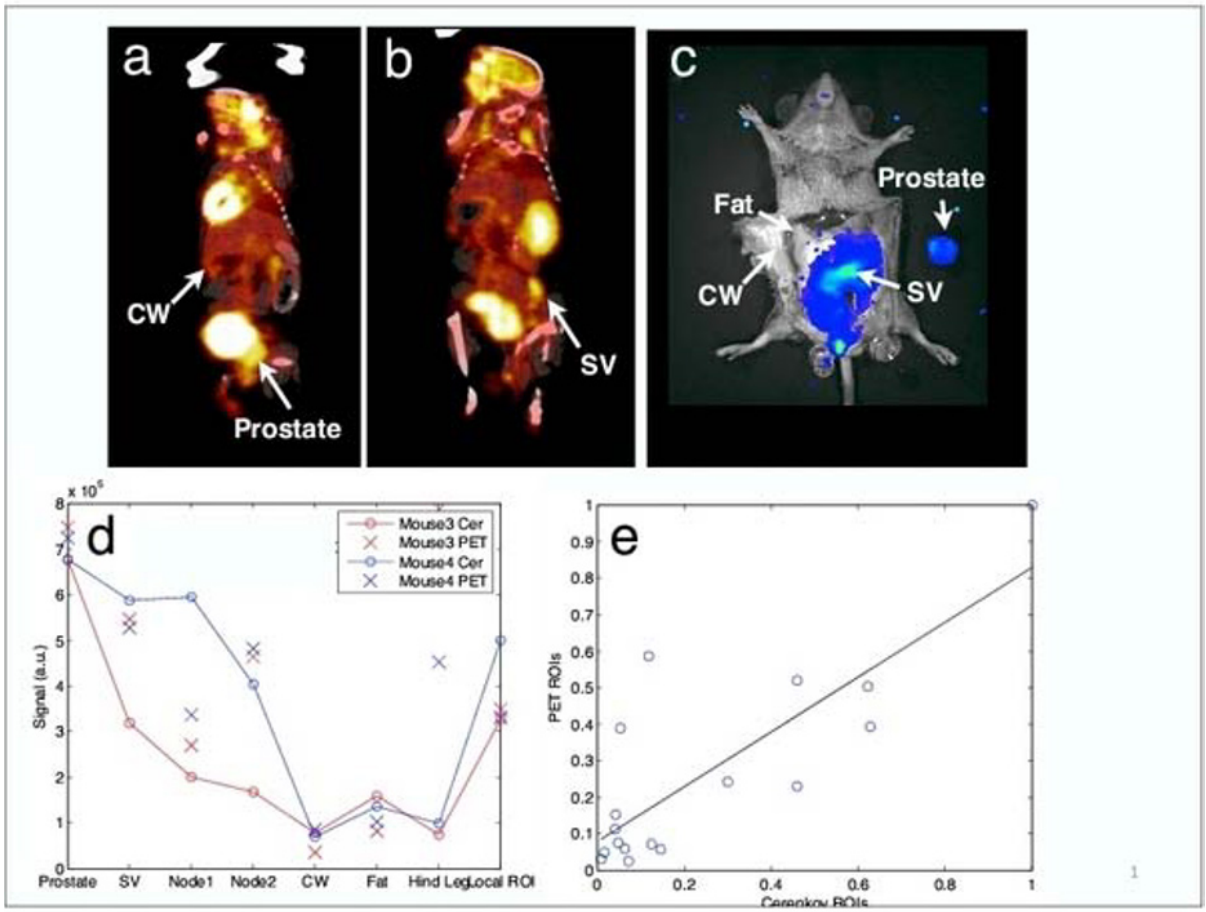

Comparison of PET/CT and Cerenkov/Ambient light overlays. (a,b) Two orthogonal views of PET/CT in a TRAMP mouse. (c) Corresponding Cerenkov/Ambient light image of the same mouse. (d) Comparison of PET and Cerenkov signals from select organs. (e) Correlation between PET and Cerenkov.

Disclosure of author financial interest or relationships:
C.M. Carpenter, None; **G. Pratx**, None; **C. Sun**, None; **L. Xing**, None.

Presentation Number **P 407**
Poster Session 3
September 20, 2013 / 15:15-15:15 / Room: Exhibit Hall B

Neutron Radiography Combined with Neutron Computed Tomography Reveals 2D and 3D Structures of Breast Cancers

Maria Cekanova[1], *Hassina Bilheux*[2], *Kusum Rathore*[1], *Jean-Christophe Bilheux*[3], *Robert L. Donnell*[4], [1]*Small Animal Clinical Sciences, The University of Tennessee, College of Veterinary Medicine, Knoxville, TN, USA;* [2]*Chemical and Engineering Materials Division, Oak Ridge National Laboratory, Oak Ridge, TN, USA;* [3]*Neutron Data Analysis and Visualization Division, Oak Ridge National Laboratory, Oak Ridge, TN, USA;* [4]*Department of Biomedical and Diagnostic Sciences, The University of Tennessee, College of Veterinary Medicine, Knoxville, TN, USA. Contact e-mail: mcekanov@utk.edu*

The early detection and appropriate staging of cancer are important factors for successful treatment of patients with cancer. Neutron radiography (NR) combined with neutron computed tomography (nCT) are novel imaging modalities that may provide additional characterization of the tumor. Neutron imaging is based on the attenuation, both scattering and absorption of a directional neutron beam by the matter, through which it passes. Hydrogen nuclei scatter thermal and cold neutrons more strongly than other atomic nuclei; thus hydrogen is a primary contributor to neutron contrast of biological specimens. We utilized NR combined with nCT to evaluate the transmission of neutrons in normal tissue and compared it with cancer tissues from dogs with naturally occurring tumors. The normal and adenocarcinomas tissues of breast were fixed in formalin and imaged by NR and nCT at the CG-1D neutron imaging prototype beam-line located at the Oak Ridge National Laboratory High Flux Isotope Reactor. Neutron radiographs of each tissue specimen were taken with 3 min exposure to neutrons. The quantification and data normalization of the neutron transmission was performed using custom-made code based on MATLAB®. The normalization procedure included removal of background effects and beam fluctuations. Mean transmission intensity values of the tissues were calculated by summing the intensity of each pixel and dividing by the number of pixels occupied by the tissue. The Octopus software was used to reconstruct the data from sinograms and thus provided nCT 3D images. As expected, the stroma containing adipose and connective tissues composed of the lipids and collagen had higher neutron transmission than areas containing hydrogen rich breast adenocarcinomas as shown in Figure 1. Using segmentation techniques, we were able to virtually remove the presence of the fat tissues from the data, allowing us to visualize the 3D structure of the tumor. The NR of 2-mm thick cancer biospecimen confirmed the detection of cancer at a spatial resolution of 50-100 μm and correlated with the obtained histology from hematoxylin and eosin stained 7-μm thick tissue section. NR and nCT are novel imaging technologies for cancer research to obtain additional information about tumors at very high spatial resolution (50-100 μm) with the ability to differentiate tumors from surrounding normal tissues. Future development of neutron imaging may be able to identify certain elements in the tissues, which may better identify tumor type, tumor margins, and assess the response to chemo- and radiotherapy evaluating the pre- and post-treatment biopsy specimens. NR using cold and thermal neutron is often described as being complementary to conventional X-ray imaging in the sense that imaging with X-rays detects heavy elements, while imaging with neutrons detect light elements. NR and nCT are complementary to currently used MRI and X-ray CT to obtain additional information about tumor structure and its cellular/molecular composition.

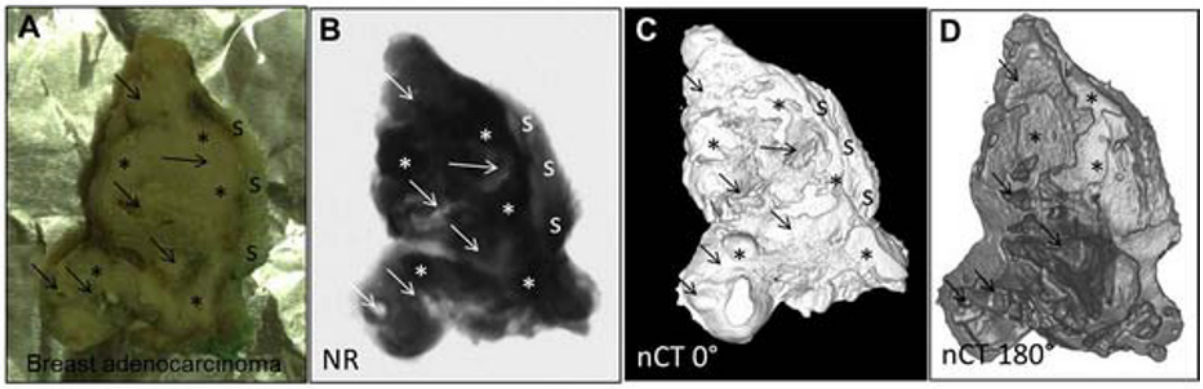

Figure 1: Neutron radiography (NR) and neutron computed tomography (nCT) of canine breast adenocarcinoma. (A) Photographic, (B) neutron radiograph, and (C, D) neutron computed tomography (nCT) images of canine breast tissue composed of adenocarcinoma (epithelial - asterisks), the stroma containing fat cells, fibroblasts, and blood vessels (stroma - arrows), and the skin with fur (s) that is shown on right side of the tissue specimen.

Disclosure of author financial interest or relationships:
M. Cekanova, None; **H. Bilheux**, None; **K. Rathore**, None; **J. Bilheux**, None; **R.L. Donnell**, None.

Presentation Number **P 408**
Poster Session 3
September 20, 2013 / 15:15-15:15 / Room: Exhibit Hall B

A 16-channel coil for simultaneous PET/MR in breast cancer

Isabel Dregely[1], Titus Lanz[2], Matthias Müller[2], Claudia Meisinger[1], Manoj Nimbalkar[1], Stephan G. Nekolla[1], **Florian Odoj**[2]*, Axel Haase[3], Markus Schwaiger[1], [1]Nuklearmedizin, Klinikum rechts der Isar der Technischen Universität München, Munich, Germany; [2]Rapid Biomedical, Rimpar, Germany; [3]IMETUM, Technische Universität München, Munich, Germany. Contact e-mail: florian.odoj@rapidbiomed.de*

Objective: To evaluate MR and PET imaging performance of a 16-channel RF-coil designed for simultaneous PET/MR imaging in breast cancer. Methods: A 16-ch breast coil (Rapid Biomedical) was designed to minimize attenuation of PET photons in a simultaneous PET/MR (3T) system (Siemens Biograph mMR). In phantom (two 1-liter water bottles) experiments MR performance was compared to two standard MR breast coils: coil-1 (7-ch, InVivo) and coil-2 (16-ch, Rapid). The effect of the coil on PET photon count statistics was evaluated by comparing PET emission counts (TA 10 min) of the phantoms (each bottle 75 MBq 18F-FDG) without vs. with presence of an RF coil. In simultaneous PET/MR, an attenuation correction (AC) map of the phantom (M_p) was obtained by segmentation of a MR-Dixon acquisition. Further, a CT-based template map of the coil (M_c) was obtained using bilinear mapping of Hounsfield units to attenuation coefficients for PET photons at 511 keV. Phantom and coil AC maps were combined yielding M_pc. For evaluation of the AC method, PET emission data were acquired without the coil present ("gold standard") and compared to with the coil present while using either M_p or M_pc. Results: The MR performance evaluation of the PET/MR coil yielded a mean [min, max] value for the channel noise correlation of 0.068 [8.7e-4, 0.39]. The mean value of a profile through the coronal (axial) SNR image yielded 46 % (8%) higher SNR for the PET/MR coil compared to the 7-ch coil-1 and 11% (0.3%) higher SNR compared to the 16-ch coil-2. The presence of the PET/MR coil caused only a 15% reduction in overall PET true counts compared to 20% for MR-only coils. Neglecting the PET/MR coil in the attenuation correction (M_p) resulted in a 19% underestimation of SUV values. Implementing the phantom-coil combined AC map (M_pc) completely recovered accurate SUV. Conclusions: The PET/MR breast coil showed state-of-the-art MR sensitivity and parallel imaging capabilities. The implementation of CT-based coil attenuation map in the PET image reconstruction enabled accurate PET quantification.

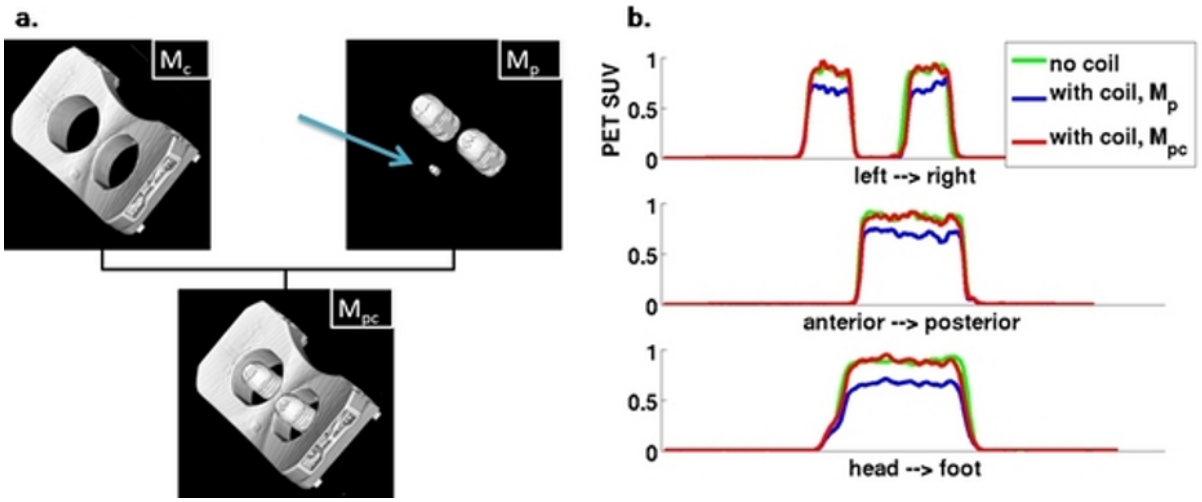

a) 3D-rendering of the AC map of the coil (M_c), the phantom (M_p) and the phantom-coil combined AC map (M_pc) obtained using an MR-visible marker (blue arrow). b) Neglecting the PET/MR coil in the attenuation correction (M_p, blue curve) resulted in 19% underestimation of SUV compared to the "gold standard" no-coil-experiment (green curve). Using the phantom-coil combined AC map (M_pc, red curve) completely recovered accurate SUV.

Disclosure of author financial interest or relationships:
I. Dregely, None; **T. Lanz**, Rapid Biomedical, Employment; **M. Müller**, Rapid Biomedical, Employment; **C. Meisinger**, None; **M. Nimbalkar**, None; **S.G. Nekolla**, None; **F. Odoj**, RAPID Biomedical GmbH, Stockholder; RAPID Biomedical GmbH, Employment; **A. Haase**, Rapid Biomedical GmbH, Consultant; GE Healthcare, Grant/research support; **M. Schwaiger**, Siemens Health care, Grant/research support .

Presentation Number **P 409**
Poster Session 3
September 20, 2013 / 15:15-15:15 / Room: Exhibit Hall B

Simulating endoTOFPET-US, the asymmetric PET for endoscopic pancreas and prostate imaging

Benjamin Frisch[1], *Etiennette Auffray*[1], *Aron Cserkaszky*[3], *Giacomo Cucciati*[4], *Erika Garutti*[2], *Paul Lecoq*[1], *Milan Zvolsky*[2], [1]*CERN, Geneva, Switzerland;* [2]*DESY, Hamburg, Germany;* [3]*SurgicEye, Munich, Germany;* [4]*University Milano-Biccoca, Milano, Italy. Contact e-mail: benjamin.frisch@cern.ch*

The endoTOFPET-US collaboration aims at the development of a multimodal imaging technique for endoscopic pancreas and prostate exams. It combines the benefits of high resolution metabolic information from Time-Of-Flight (TOF) Positron Emission Tomography (PET) and anatomical information from ultrasound (US). EndoTOFPET-US has an asymmetric layout. It requires the development of a PET head extension for a commercial US endoscope and a PET plate outside the body in coincidence with the PET head. The endoscopic PET head needs extreme miniaturization of all components to place as many individual detector channels as possible into a volume of 23 mm in diameter and at maximum 40 mm in length. The external plate is made of 256 matrices of 4x4 LYSO:Ce crystals coupled to commercial arrays of 4x4 SiPMs. The aim is to provide a coincidence time resolution of 200 ps in order to reject background signals and a spatial resolution of 1 mm in the reconstructed image. We develop a dedicated simulation framework in order to assist the collaboration for the optimization of the PET detectors. It is based on GATE, a Geant4 Application for Emission Tomography. Since the latter is not intended to be used with asymmetric geometries, we extend it with a parallel process manager and an offline custom digitizer. We implement a full-body phantom in order to provide sufficiently realistic data for the development of the reconstruction algorithm. For each position of the probe, this requires a recalculation of the phantom around the endoscopic detector, in order to avoid problems arising from overlapping volumes in Geant4. The parallel process manager allows us to split the simulation in as many processes as required and schedule them on a multi-core and multi-threaded computer or computing cluster, using available computing power in the most efficient way. The movement of the detectors is simulated by varying their position in different processes. We store exact information about the energy, position and the time of each hit in the detector. The offline digitizer smears this information and creates physically realistic coincidence pairs that are stored in an ASCII list-mode format. We present simulations indicating that the system sensitivity with a point source depends directly on the available crystal volume and varies between 2 and 6 counts per second per kBq. The availability of a depth of interaction measurement in the external plate shows to have very limited influence on the image resolution. The image resolution is better than 1 mm if full tomographic information is available. It is entirely dominated by the geometry of the endoscopic probe. In realistic conditions, with the endoscope being inserted into either the rectum or the duodenum, the detectors cannot rotate around the field of view to provide information from all angles: the resolution is severely degraded along the axis that connects both detectors. The availability of timing information with a resolution of around 200 ps improves the signal-to-noise ratio.

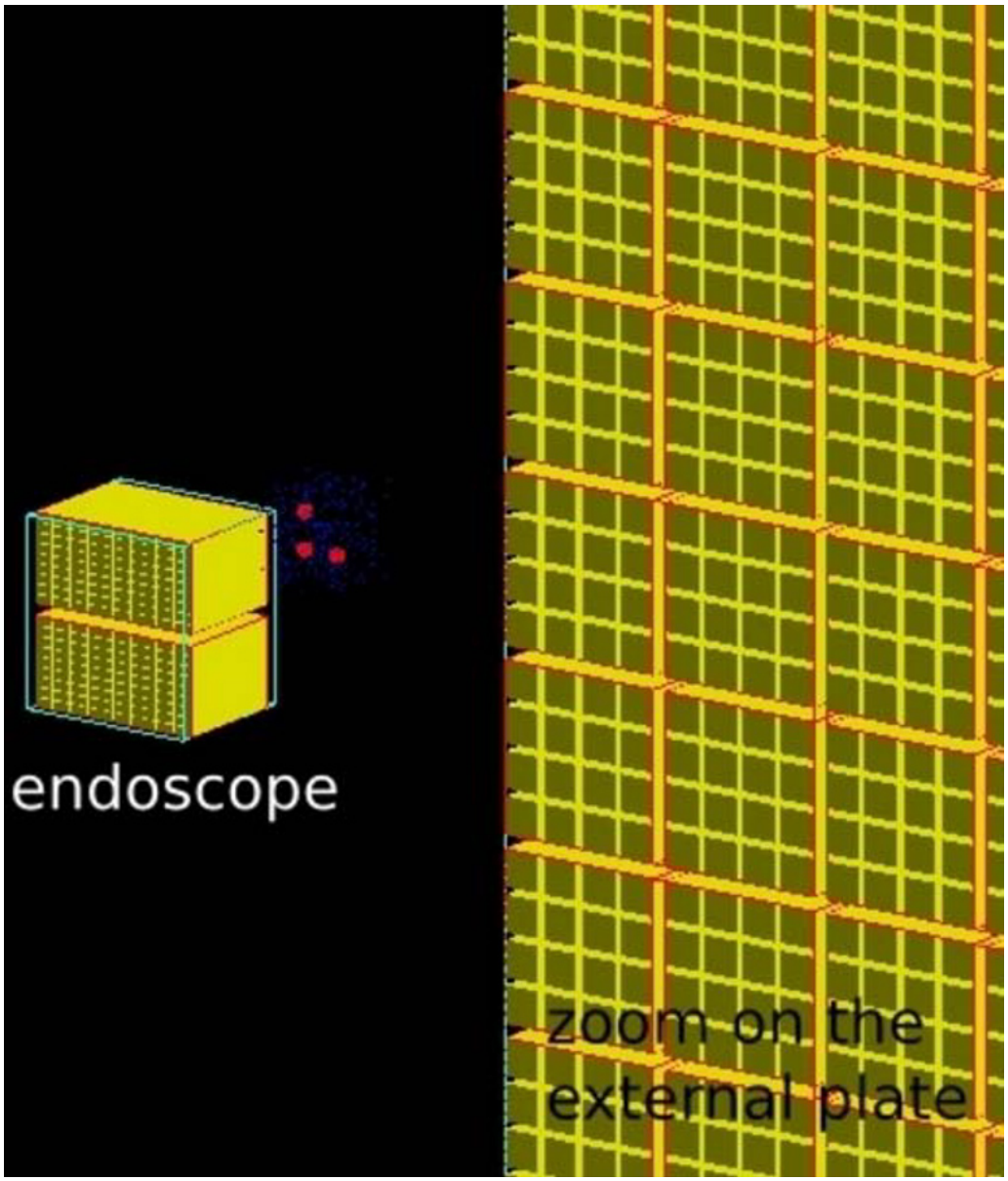

endoTOFPET-US implemented into the simulation framework

Disclosure of author financial interest or relationships:
B. Frisch, None; **E. Auffray**, None; **A. Cserkaszky**, SurgicEye Gmbh., Employment; **G. Cucciati**, None; **E. Garutti**, None; **P. Lecoq**, None; **M. Zvolsky**, None.

Presentation Number **P 410**
Poster Session 3
September 20, 2013 / 15:15-15:15 / Room: Exhibit Hall B

Multimodal molecular imaging of breast cancer tissue microarrays

Nadine Mascini, Gert B. Eijkel, **Ron M. Heeren**, *Biomolecular Imaging MS, FOM-AMOLF, Amsterdam, Netherlands. Contact e-mail: heeren@amolf.nl*

Triple-negative breast cancers are characterized by the lack of expression of the estrogen receptor, progesterone receptor and the human epidermal growth factor receptor type 2 (HER2) as defined by immunohistochemical staining. As a consequence, existing effective therapies targeting these markers cannot be used. A series of triple-negative tumor xenograft models was generated at the Netherlands Cancer Institute, to study the mechanisms involved in response to chemotherapy. At the moment there is only limited knowledge of the proteomic differences between triple-negative breast cancers. Moreover, most of the breast cancer studies published so far have compared normal tissue versus malignant tissue to investigate chemotherapy response. We have set up a workflow that uses tissue microarrays (TMAs). TMAs consist of formalin-fixed paraffin-embedded small tissue cores arranged in an array on a glass slide and are typically used for immunohistochemical analyses, to assess the capability of mass spectrometry imaging to analyze proteins associated with therapy response mechanisms,. The combined use of MSI and TMAs facilitates high-throughput analysis and limits the technical variation introduced during sample preparation. Furthermore, the use of MSI allows for direct analysis of the spatial distribution of peaks of interest. A sample preparation protocol, which includes deparaffinization, antigen retrieval and on-tissue tryptic digestion, was employed. In this way, a single experiment 25 xenograft tumors allowed the analysis of multiple technical replicates per model. As such it made the proteome of formalin-fixed paraffin-embedded tissues amenable to MSI analysis,. All tumors analyzed were untreated, but their response to cisplatin treatment was known from independent experiments. A supervised data analysis approach showed that the triple-negative tumors could be separated based on their known response to cisplatin, as shown in the figure. As such it provides a potential predictor for cisplatin treatment response. Interestingly, the largest separation was found to be between the tumor groups responding to treatment and the so-called 'non-responder' groups. Several peptide peaks correlated with specific treatment response groups were identified by on-tissue MS/MS. These include peptides from proteins as histones, structural proteins, GAPDH and HSPB1 1. In short, complex proteomic signatures correlated with different responses to cisplatin treatment based on MALDI imaging data were established. Preliminary validation results from the analysis of different tumor cores from the same tumors show the same characteristic peptide peaks correlated with treatment response. Additional validation using clinical samples will be performed and presented.

Disclosure of author financial interest or relationships:
N. Mascini, None; **G.B. Eijkel**, None; **R.M. Heeren**, None.

Presentation Number **P 411**
Poster Session 3
September 20, 2013 / 15:15-15:15 / Room: Exhibit Hall B

High throughput imaging of single-cell FDG metabolism

Laura S. Sasportas[1,2], *Guillem Pratx*[3], *Michelle L. James*[2], *Aileen Hoehne*[2], *Robert E. Reeves*[2], *Sarah Bohndiek*[2], *Sanjiv S. Gambhir*[2], [1]*Bioengineering, Stanford University, Stanford, CA, USA;* [2]*Radiology, Stanford University, Stanford, CA, USA;* [3]*Radiation Oncology, Stanford University, Stanford, CA, USA. Contact e-mail: lss@stanford.edu*

Background: Radiotracers have been instrumental to the field of molecular imaging, enabling visualization of molecular processes in living subjects with exquisite sensitivity. Despite their widespread use and clinical utility, still very little is known about how the uptake of radiotracers is modulated at a single-cell level and what factors could influence cell-to-cell variations in radiotracer uptake. Recently, radioluminescence microscopy has been introduced as a novel method to image radiotracer uptake in single-cells. Although this method is highly quantitative, sensitive and has high spatial resolution, it is not suitable for high-throughput studies. Here we aim to establish a simple, high-throughput method for measuring single-cell radiotracer uptake based on autoradiography. Methods: Live cells were glucose-starved, incubated with FDG, washed, harvested, and spread onto coated slides using a dedicated cytocentrifuge. Slides were subsequently exposed to an 18F-sensitive storage phosphor screen overnight, and scanned using a radiometric phosphor imager at a high resolution (600dpi). To quantify the amount of FDG in individual cells, a calibration ladder was included, consisting of drops (n=4) of the FDG at pre-determined concentrations (0.8-0.05 μCi/mL) absorbed onto filter paper. We were able to image ~100 cells per sample and up to 20 samples per film. The single-cell uptake of FDG by 6 different cancer cells lines (human ovarian 2008-GLS, human colon HT-29, mouse breast 4T1-GL, human breast MCF7, human prostate LnCAP cancers, and mouse lymphoma EL4) was evaluated. Results: Using this method, the uptake of FDG in single-cells was clearly resolvable. The measurements are highly reproducible between samples (n=4; CV=3.8-14.5%) and highly correlated with gamma-counter measurements (R2 = 0.90). Overall, 4T1-GL showed the highest uptake of FDG per cell (9.58×10-6 μCi/cell), while MCF7 presented the lowest FDG uptake (6.12×10-6 μCi/cell). Interestingly, within each cell population, we observed a wide heterogeneity in single-cell uptake of FDG within each cell population (CV= 37.7%-83.9%). We sought to evaluate whether this heterogeneity might have been due to different genetic material and therefore compared clonal populations derived from three 4T1-GL clones, to the parental population. There was no significant influence of the clonality on the single-cell heterogeneity (p=0.18). We also evaluated whether drug resistance can modulate FDG uptake and therefore compared a Cisplatin-resistant lineage of 2008-GL to the parental cell line. There was no significant influence of the drug resistance on the single-cell FDG uptake (p=0.10). Conclusion: For the first time, we demonstrated that autoradiography enables high-throughput imaging of FDG uptake in single cancer cells. This new method revealed a wide heterogeneity in cancer cell metabolism. We are currently evaluating the influence of several cell-specific properties (e.g., cell cycle) on the heterogeneity of FDG uptake. This method will be particularly useful for the precise, quantitative and high-throughput characterization of existing and novel radiotracers at the single-cell level.

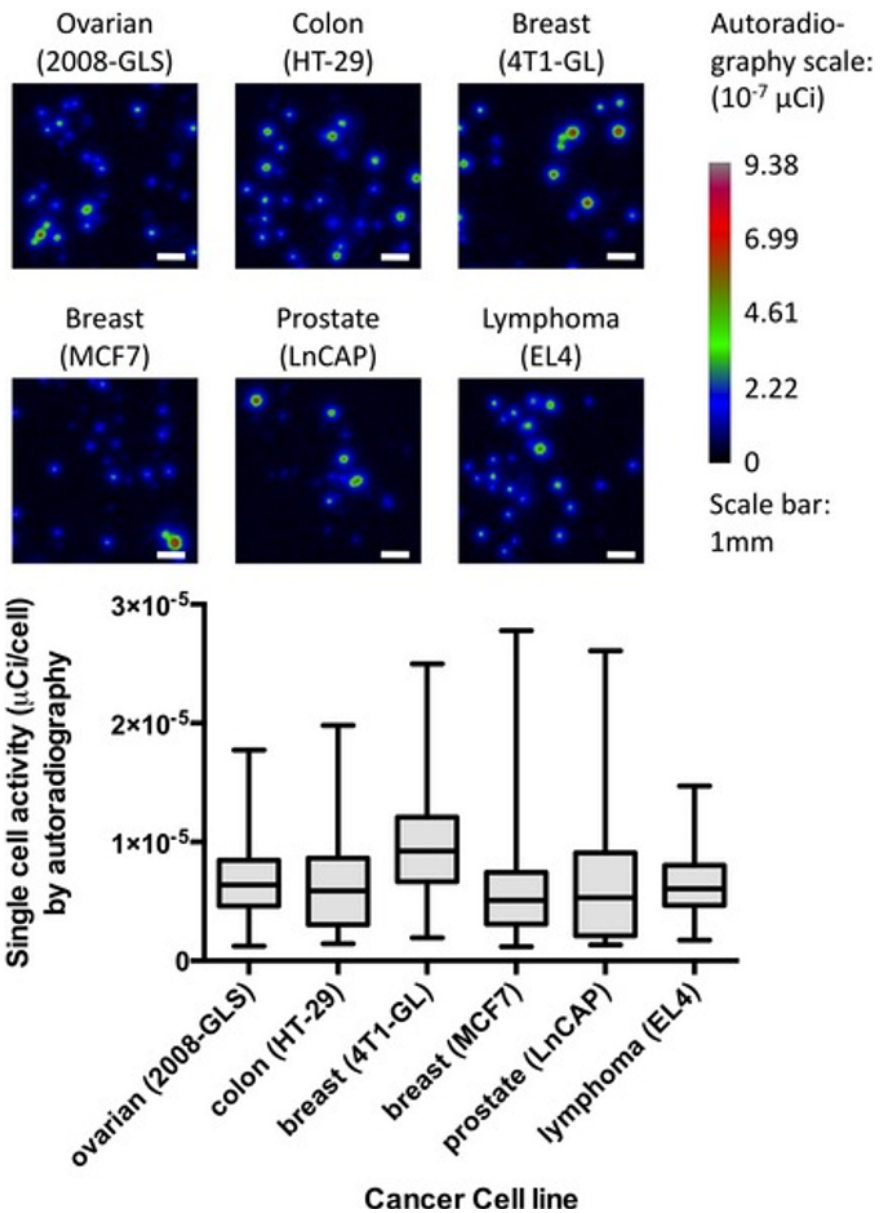

Figure. AR images of single cancer cells after 1h incubation at 25 µCi/100 µL FDG, and corresponding quantification of single -cell FDG metabolism (error bars: min to max)

Disclosure of author financial interest or relationships:
L.S. Sasportas, None; **G. Pratx**, None; **M.L. James**, None; **A. Hoehne**, None; **R.E. Reeves**, None; **S. Bohndiek** None; **S.S. Gambhir**, Bracco Diagnostics, Consultant; Endra, Inc, Stockholder; Cellsight, Stockholder; Enlight, Inc., Stockholder; General Electric, Grant/research support; ImaginAb, Stockholder; MagArray, Inc., Stockholder; Sanofi-Aventis, US, Grant/research support; SiteOne Therapeutics, Stockholder; VisualSonics/Sonosite, Stockholder .

Presentation Number **P 412**
Poster Session 3
September 20, 2013 / 15:15-15:15 / Room: Exhibit Hall B

Bioluminescence Tomography by an Iterative Reweighted l2 Norm Optimization Using Structure Priors

Ping Wu, *Yongbao Li, Xin Yang, Jie Tian, Medical Image Processing Group, Institute of Automation,CAS, "Beijing,100190", China. Contact e-mail: ping.wu@ia.ac.cn*

This article presents an iterative reweighted l2 norm optimization incorporating anatomical structures in order to enhance the performance of bioluminescence tomography. The structural information is utilized to build up a heterogeneous mouse model by extracting internal organs and tissues. To evaluate the performance of the iterative reweighted approach, several numerical simulation studies including comparative analyses have been conducted to reconstruct the same datasets based on different mouse models. The results suggest the proposed method can ensure the accuracy, robustness, and efficiency of bioluminescence tomography using the heterogeneous mouse model. Finally, an in vivo experiment has also been performed to further validate that this method is feasible in a practical application.

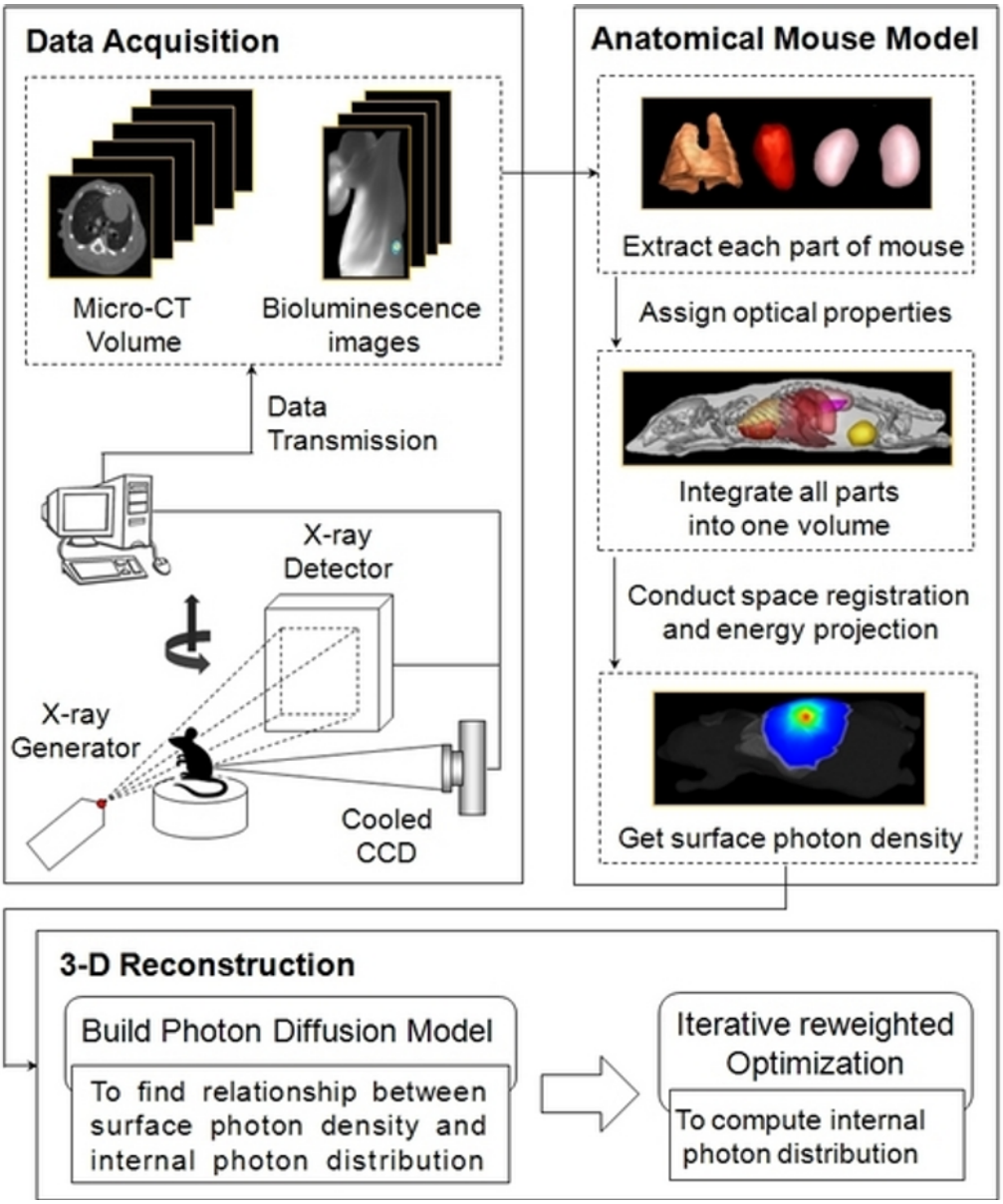

Disclosure of author financial interest or relationships:
P. Wu, None; **Y. Li**, None; **X. Yang**, None; **J. Tian**, None.

Presentation Number **P 413**
Poster Session 3
September 20, 2013 / 15:15-15:15 / Room: Exhibit Hall B

PAMA: a Parametric Articulated Mouse Atlas for Preclinical Small Animal Image Analysis

Hongkai Wang, *David Stout, Arion Chatziioannou, Crump Institute, UCLA, Los Angeles, CA, USA. Contact e-mail: hongkaiwang@mednet.ucla.edu*

Many small animal image modalities, like CT, MR, optical surface scan, PET and SPECT, require the registration of an anatomical atlas for image analysis. To serve this purpose, we developed a Parametric Articulated Mouse Atlas (PAMA) which can change its anatomy according to parameters like body weight, skeleton joint angles and bone sizes. The atlas is designed to match mice of various weights and postures. PAMA is based on a deformable surface model of mouse organs. This model is trained using contrast-enhanced CT images of 65 mice with different postures and weights (15~45g). Triangular surface meshes of the skin, skeleton and soft organs are extracted from the CT using organ segmentation and Marching Cubes method. To model the skeleton-controlled skin deformation (SSD), one of the 65 mice is selected as the reference, whose skeleton is segmented into individual bones, and the skin vertices are attached to adjacent bones so that the skin can deform along with the bones when joint angles and bone sizes are changed. To model the weight-controlled skin deformation (WSD), the skeleton of the reference subject is registered to other subjects by optimizing joint angles and bones sizes, and then the attached skin is warped along with the skeleton using SSD. The residual vertex displacements between the warped skin and the target skin are correlated with the body weights via linear regression, yielding the WSD model that controls skin deformation according to weights. SSD and WSD together control the skeleton and skin deformation. To make the soft organs deform along with the skin and skeleton, the conditional Gaussian model is used [1]. **Results** Fig.1 shows various postures and body weights generated with PAMA. (a-d) shows the adjustments of limb/head angles and spine curvatures. (e-f) shows the change of body size and abdomen girth with weight. (g-h) shows the deformation of soft organs along with the changes of posture and weight. To evaluate the accuracy of registering PAMA with mice images, 6 test subjects of different postures and weights were imaged with CT. Body surfaces were extracted from the CT images and were used as the aligning organ. The reason for using skin for registration was that skin is commonly visible in many modalities like CT, MR, surface scan, and some PET and SPECT images. For registration, the control parameters of PAMA were optimized to minimize the surface distance between the atlas skin and the subject skin. The registration error (Table 1) was measured as averaged surface distance (ASD) between the registered atlas skin/skeleton and subject skin/skeleton. The ASD of skin and skeleton of all subjects were 1.07±0.17 and 1.33±0.18mm, respectively. Skeleton was less accurate than skin because skin was the aligning organ. It seems that heavier subjects (mostly Nudes) have larger errors, implying the WSD model is slightly less accurate for larger weights. **Conclusion** PAMA is a deformable mouse atlas controlled by body weights and skeleton posture. The skin-based registration test reveals its potential to be registered with various imaging modalities. **Reference** [1] H. Wang. IEEE T MED IMAGING, 31(1), 2012.

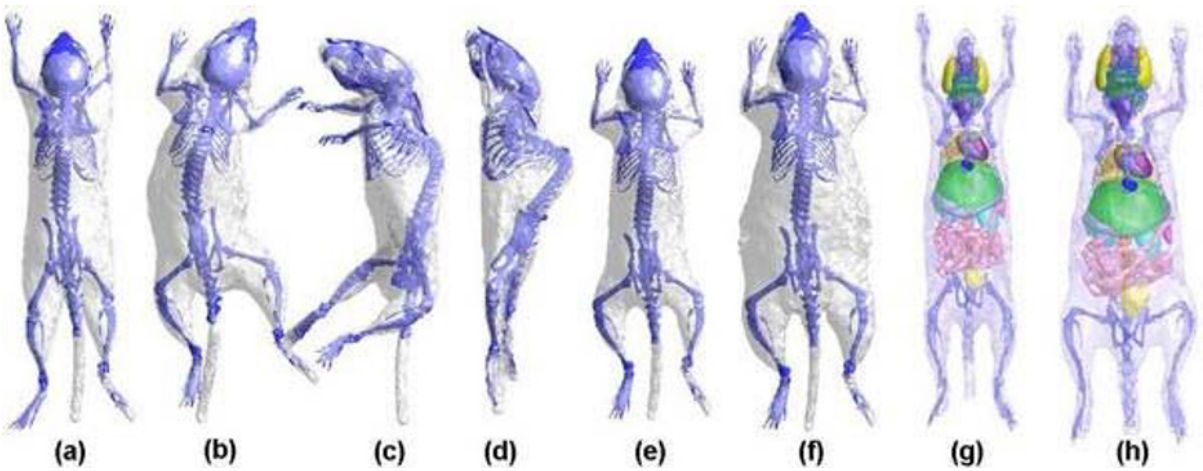

Fig.1. (a-d) PAMA deformed into different postures. (e-f) PAMA deformed into different body weights while keeping the same posture. (g-h) Internal organs deform along with the changes of body postures and weights.

Table 1. Atlas registration error (Averaged Surface Distance) of the six test subjects

	Subject 1	Subject 2	Subject 3	Subject 4	Subject 5	Subject 6	mean±std
Subject Information (Strain/Weight)	B6/18.4g	B6/28.1g	Nude/25.8g	Nude/29.3g	SCID/20.7g	SCID/21.8g	
Skin Error (mm)	0.87	1.11	0.95	1.15	0.99	1.33	1.07±0.17
Skeleton Error (mm)	1.23	1.30	1.15	1.21	1.05	1.41	1.33±0.18

Averaged Surface Distance (ASD) is defined as ASD= $\sum d_i/n$, where n is the number of vertices in the atlas surface mesh, d_i is the closest distance from vertex i of the atlas surface to the subject surface.

Disclosure of author financial interest or relationships:
H. Wang, None; **D. Stout**, Sofie Biosciences, Stockholder; **A. Chatziioannou**, Sofie Biosciences, Stockholder .

Presentation Number **P 414**
Poster Session 3
September 20, 2013 / 15:15-15:15 / Room: Exhibit Hall B

Small Animal PET/MRI Image Registration Using Information-based Algorithm with Linear Interpolation

Ji Min Kim[1,2], *Taewon Nam*[1], *Gyeong Ju Min*[1,2], *Kyeong Min Kim*[1], *Joo Hyun Kang*[1], *Sang Moo Lim*[1], *Sang-Keun Woo*[1],
[1]*Molecular Imaging Research Center, KIRAMS, Seoul, Republic of Korea;* [2]*Internet media engineering, Konkuk University, Seoul, Republic of Korea. Contact e-mail: clrkddl1@naver.com*

Registration of small animal multimodal image providing anatomical information is required for tumor segmentation and attenuation correction. The purpose of this study was to compare using same point of pixel-wise algorithm and information-based algorithm with complex mapping between two images. Small animal PET images were obtained from small animal PET scanner (InveonTM, Siemens) during 20 min after injection of 18F-FDG via tail vein and emission data was obtained under the condition of 6 nSec timing window. Acquired list mode data was reconstructed to gated PET images by ordered subset expectation maximization 2D (OSEM 2D) algorithm with four iterations. Small animal MRI images were obtained from 3-T clinical MRI (Magnetom Tim Trio, Siemens) with T1-weighted 3D-dynamic volumetric interpolated breath-hold examination (VIBE) sequence condition of TR=11.6 ms and TE=3.1 m. Registration was performed with mean squares difference (MSD), normalization correlation coefficient (NCC), mutual information (MI) and Kullback Leibler distance (KLD). MSD computes mean squared pixel-wise difference between two images and NCC normalizes pixel-wise cross-correlation. MI measures mutual dependence of intensities of two images and KLD measures relative entropy between discrete probability distributions. Performed interpolation methods were linear interpolation (LI) and B-spline interpolation (BSI). LI is a method for error fitting using linear polynomials and BSI coefficients are computed using recursive filtering and intensity at a non-grid position is computed by multiplying the B-spline coefficients. Peak signal-to-noise ratio (PSNR) value was used to evaluate algorithm performance. Dimension of PET image was 128×128×159 and voxel size was 0.78×0.78×0.8 mm. Dimension of MRI image was 640×640×200 and voxel size was 0.3×0.3×1.0 mm. PET/MRI registration was evaluated with four registration algorithms (MSD, NCC, MI and KLD) and two interpolation methods (LI and BSI). Before registration, PSNR of PET/MRI image was 32.23. After the PET/MRI registration, LI and BSI interpolation with MSD algorithm was 32.98 and 32.96, respectively. LI and BSI interpolation with NCC algorithm was 32.94 and 32.99, respectively. LI and BSI interpolation with MI algorithm was 33.04 and 33.00, respectively. LI and BSI interpolation with KLD algorithm was 33.08 and 33.07, respectively. Registration between small animal PET and MRI image with four registration algorithms and two interpolation methods was performed. Information-based algorithm showed well-suited result for multimodal registration than pixel-wise algorithm due to complex mapping capability. PET/MRI provide an advantage for diagnosis of liver cancer and it would be expected to improve accuracy of diagnosis and treatment monitoring.

Disclosure of author financial interest or relationships:
J. Kim, None; **T. Nam**, None; **G. Min**, None; **K. Kim**, None; **J. Kang**, None; **S. Lim**, None; **S. Woo**, None.

Presentation Number **P 415**
Poster Session 3
September 20, 2013 / 15:15-15:15 / Room: Exhibit Hall B

Development of an optical fiber based MR compatible block detector for SPECT/MRI system

Seiichi Yamamoto[1], *Hiroshi Watabe*[2], *Yasukazu Kanai*[2], *Katsuhiko Kato*[1], *Jun Hatazawa*[2], [1]*Nagoya University Graduate School of Medicine, Nagoya, Japan;* [2]*Osaka University Graduate School of Midicine, Suita, Japan. Contact e-mail: s-yama@met.nagoya-u.ac.jp*

Optical fiber is a promising material for integrated PET/MRI systems. However, it is unclear whether this material can be used for a SPECT/MRI system. We developed and tested an optical fiber based block detector for SPECT/MRI system and tested its performance. 1.2 x 1.2 x 6mm Y2SiO5 (YSO) pixels were combined to form a 15 x 15 block and coupled to an optical fiber image guide. The optical fiber image guide used 0.5mm diameter, 80cm long double clad fibers. The image guide had a 22mm x 22mm rectangular input and an output. The input of the optical fiber based image guide was bent for 90 degree and the output was optically coupled to a 1-inch square high quantum efficiency position sensitive photomultiplier tube (HQE-PSPMT). Parallel hole collimator made of tungsten plastic was mounted on the YSO block. The thickness of the collimator was 7mm and the collimator holes were 0.8mm diameter which positioned on-to-one coupled to the YSO pixels. Intrinsic and system performance were evaluated. We could resolve most of the YSO pixels in 2-dimensional histogram for Co-57 gamma photons (122-keV) with the average peak-to-value ratio of 1.5. Energy resolution was 38% FWHM. The system resolution was 1.7mm FWHM at 1.5mm from the collimator surface, and the sensitivity was 0.06%. Images of the Co-57 point source could be successfully obtained inside 0.3T MRI without serious interference. We conclude that developed optical fiber based YSO block detector is promising for SPECT/MRI system.

Disclosure of author financial interest or relationships:
S. Yamamoto, None; **H. Watabe**, None; **Y. Kanai**, None; **K. Kato**, None; **J. Hatazawa**, None.

Presentation Number **P 416**
Poster Session 3
September 20, 2013 / 15:15-15:15 / Room: Exhibit Hall B

Comparison between Near-Infrared (NIR) Confocal, Existing Multi-Photon, and All-NIR Multi-Photon Microscopy Modalities in Imaging Deep Tissues using Cyanine Dyes

Pinaki Sarder[1], Siavash Yazdanfar[2], **Walter J. Akers[1]**, *Gail Sudlow[1], Samuel Achilefu[1], [1]Radiology, Washington University School of Medicine, St. Louis, MO, USA; [2]Applied Optics Lab, GE Global Research, Niskayuna, NY, USA. Contact e-mail: akersw@mir.wustl.edu*

Multiphoton microscopy (MPM) enables visualization of biological structures with higher resolution and greater depths than conventional confocal fluorescence microscopy due to excitation with highly penetrating near infrared (NIR) light. All-NIR MPM is a recent addition to microscopy, and has demonstrated exceptional depth resolution in biological tissues due to 2P excitation and emission collection at NIR wavelengths. This technology uses 1550 nm excitation of NIR fluorescent dyes that emit at ~800 nm. We compared relative penetration limit of this system in imaging deep tissues with two existing fluorescence microscopic imaging modalities, NIR confocal and state-of-the-art MPM. We restricted here excitation powers and tissue conditions to be biocompatible and non-toxic. While depth resolutions of conventional NIR excitation and visible fluorescence state-of-the-art MPM system and NIR excitation single photon confocal microscope have extensively been studied, the relative abilities of these existing modalities in penetrating deep tissues were not compared yet with all-NIR MPM. We report direct comparison of the depth resolution in deep tissues in this context using cyanine-based fluorescent dyes. We demonstrate NIR confocal and state-of-the-art MPM systems perform similarly in depth resolution, whereas the newer all-NIR MPM technology enables >5-fold deeper imaging in biological tissues than these other state-of-the-art fluorescence microscopy modalities. The all-NIR MPM system imaged the whole kidney samples containing NIR fluorescent contrast agent LS288. We were able to visualize using this system renal structures based on the fluorescence alone, up to 457.2 μm below the specimen surface, and detect foreground signal at depths up to 533.4 μm. Using the NIR confocal microscope system, we were able to visualize LS288 within renal structures based on the fluorescence alone up to 80 μm below the specimen surface, and detect foreground signal at depths up to 100 μm. With the state-of-the-art MPM system, we were able to visualize similar renal structures in kidney samples containing visible fluorescent contrast agent Cy3. Structural features here were distinguished with fluorescence alone up to 75 μm below the specimen surface, and foreground signal up to 90 μm. We computed the fluorescence signal attenuation coefficient in kidney to be 19.4 mm^{-1} 20.11 mm^{-1}, 6.26 mm^{-1} for imaging them using NIR confocal microscope, state-of-the-art MPM system, and all-NIR MPM system, respectively, suggesting a >3-fold reduction in signal attenuation using the all-NIR MPM system than the other two systems. We further evaluated the potential for tissue damage in both cell and tissue viability studies, and demonstrated that laser-induced photodamage does not occur at laser powers necessary for achieving the above mentioned depth resolution using the all-NIR MPM system. This evaluation establishes that the all-NIR MPM system's depth penetration ability can be explored further clinically. Future work involves conducting deep tissue *in vivo* fluorescence imaging using the all-NIR MPM system, to characterize this system for imaging live animals.

Disclosure of author financial interest or relationships:
P. Sarder, None; **S. Yazdanfar**, General Electric, Employment; **W.J. Akers**, None; **G. Sudlow**, None; **S. Achilefu**, None.

Presentation Number **P 417**
Poster Session 3
September 20, 2013 / 15:15-15:15 / Room: Exhibit Hall B

Use of Tissue Phantoms to Validate a Multimodal Optical Imaging Device to Detect Fluorescent Integrin-Binding Peptides for Guided Resection of Brain Tumors

Adithya Balasubramanian[1], *Steven Sensarn*[2], *Jamie M. Bergen*[3,4], *Nithya Vijayakumar*[3,4], *Jennifer R. Cochran*[3,4], *Christopher Contag*[2,5], [1]*Biochemistry & Cell Biology, Rice University, Houston, TX, USA;* [2]*Pediatrics, Radiology and Molecular Imaging Program at Stanford (MIPS), Stanford University, Stanford, CA, USA;* [3]*Bioengineering, Stanford University, Stanford, CA, USA;* [4]*Chemical Engineering, Stanford University, Stanford, CA, USA;* [5]*Microbiology & Immunology, Stanford University, Stanford, CA, USA. Contact e-mail: ab27@rice.edu*

Image guidance with molecular specificity has the potential to increase precision in resection of brain cancers and preservation of critical normal tissue leading to improved outcome. While the bulk of a tumor can often be resected, the requisite sensitivity and specificity of molecular probes and the appropriate imaging devices for guided removal of residual tumor deposits at the cavity margins have yet to be realized. For this purpose, we evaluated a fluorescent, engineered integrin-binding peptide using macro- and microscopic imaging with a clinical wide-field fluorescence fiberscope and a dual-axis confocal (DAC) microscope. Collagen-based tissue phantoms containing human medulloblastoma cells (DAOY) or human T-cell lymphoma cells (Jurkat) were generated and imaged. DAOY cells express elevated levels integrins αvβ3, αvβ5, and α5β1, while the non-adherent Jurkat cells express nominal amounts. To mimic use during surgery, a solution of fluorescently labeled integrin-binding peptide was applied to the surface of the phantoms, and unbound probe was washed off prior to imaging. The wide-field fluorescence imaging system is composed of a clinical fiberscope (Boston Scientific SpyGlass), a 556-nm laser, and an EMCCD camera. After wide-field imaging, the phantoms were re-imaged with a DAC microscope for cellular-level resolution. SpyGlass videos were 9-frame averaged, background subtracted, and contrast scaled to maximize dynamic range in the fluorescence signal. Amira and MATLAB software were used to render and quantify signal from DAC image stacks. The DAOY cells in phantoms exhibited a higher fluorescent signal than did Jurkat cells or collagen-only phantoms. The ability to accurately differentiate integrin-high and integrin-low cells demonstrates that the wide-field fiberscope system is a promising tool to identify suspect regions during surgery, and subsequent DAC imaging offers confirmatory diagnosis from molecular and morphological markers with probe binding to DAOY cell membranes. The two imaging modalities are complementary and reveal the spatial distribution of stained cells. Combining the wide-field and 3D confocal images with a targeted molecular probe enables accurate mapping of tumor cell location within the phantom and supports a dual approach to enhance conventional visual inspection during surgery. Targeted contrast agents and emerging micro-optical devices have the potential to enhance resection using molecular, functional and morphological biomarkers at the margins and thus improve outcomes.

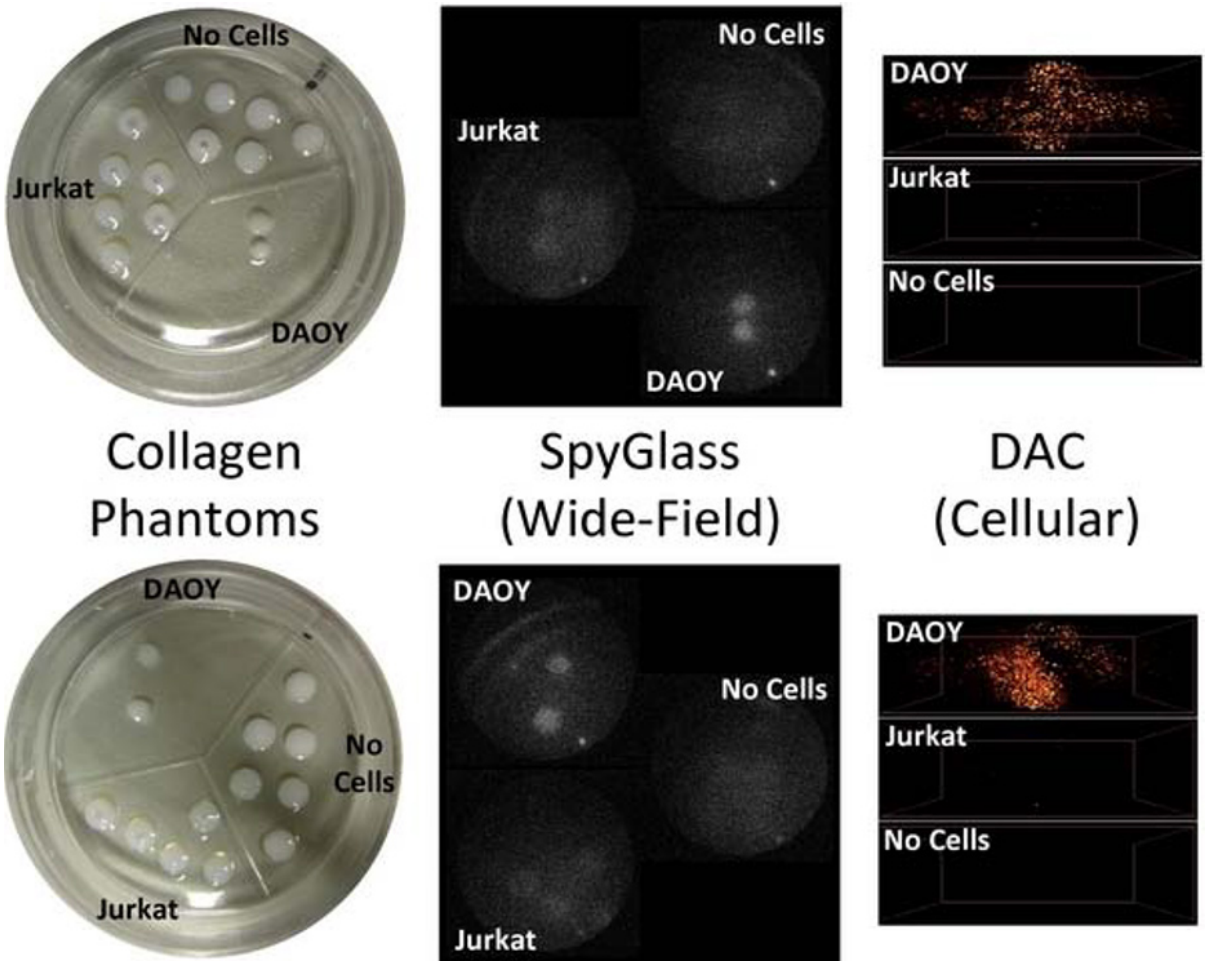

Disclosure of author financial interest or relationships:
A. Balasubramanian, None; **S. Sensarn**, None; **J.M. Bergen**, None; **N. Vijayakumar**, None; **J.R. Cochran**, None; **C. Contag**, ConcentRx Corp, Stockholder; Olympus, Other financial or material support .

Presentation Number **P 418**
Poster Session 3
September 20, 2013 / 15:15-15:15 / Room: Exhibit Hall B

Development of A Quality Control Protocol to Assess the Feasibility of Cerenkov Luminescence Imaging

Michael Dykstra[1,2], *Anderson Peck*[1,2], *Ryan A. Bozio*[1,2], *Anthony Chang*[1,2], [1]*Small Animal Imaging Facility, Van Andel Institute, Grand Rapids, MI, USA;* [2]*Physics, Grand Valley State University, Allendale, MI, USA. Contact e-mail: michael.dykstra@vai.org*

Purpose: Cerenkov radiation (CR) is the phenomenon of visible light emission that occurs when a charged particle, such as a β+ or β-, exceeds the speed of light in the medium through which it travels. Detection of this light can theoretically be achieved by an optical imager with appropriate sensitivity; however, no universal quality control protocols have been developed to ensure that a device is capable of performing Cerenkov Luminescence Imaging (CLI). The goal of this study is to develop standard protocols for testing the feasibility of optical imagers for CLI, and then to utilize the protocols to assess if the AMI-1000 (Spectral Instruments Imaging, LLC, Tucson, AZ), which has never previously been used in CLI studies, is an appropriate device to perform this imaging method. Through the development of this protocol, CLI will become more accessible to biomedical researchers by eliminating uncertainty regarding the machine and familiarizing them with necessary procedures for CLI. Methods: Two positron (β+) emitters (18F and 64Cu) were chosen for use in this investigation due to their relatively common use in imaging studies. These isotopes were then used to assess linearity, spectrum, spatial resolution, FOV homogeneity, and correlation between CLI and Positron Emission Tomography (PET). Linearity was tested by placing samples containing a range of radioactivity in the optical imager, then analyzing the correlation between radiation in the samples and detected signal. Cerenkov radiation has a well-described spectrum with intensity proportional to 1/λ^2 , which was characterized using a radioactive sample in the FOV and each of the emission filters of the AMI-1000. Spatial resolution was investigated using a Jaszczak SPECT spatial resolution phantom injected with approximately 200 μCi in a 0.25 mL radioactive solution that was placed in the FOV. The correlation between CLI and PET was obtained by designing and using a phantom that could hold multiple radioactive solutions with a range of concentrations that was consecutively placed in both the optical imager and the PET scanner. Results: A protocol for testing optical imagers for Cerenkov Luminescence Imaging was successfully developed. The linearity tests of 18F and 64Cu yielded R2 values of 0.9991 and 0.9980 respectively. After normalization to the Quantum Efficiency of the camera, experimental results matched the expected spectral curve with an R2 of 0.8446 for 18F and 0.9203 for 64Cu. Regressions between Positron Emission Tomography (PET) and CLI of a 18F source was obtained to be 0.9952. Spatial Resolution was found to be 300 μm. The uniformity analysis was complicated by high intensity spikes from interactions between gamma rays and the camera. However, after sufficient filtering and developing a unique method for uniformity assessment, the FOV was found to be highly uniform. Conclusion: Based on our experiments, the protocol we developed is an efficient and reliable way to assess the feasibility of an optical imager for CLI. Also, based on the findings in each of these areas, the AMI-1000 was determined to be a viable optical imager for Cerenkov Luminescence Imaging.

Disclosure of author financial interest or relationships:
M. Dykstra, None; **A. Peck**, None; **R.A. Bozio**, None; **A. Chang**, None.

Presentation Number **P 419**
Poster Session 3
September 20, 2013 / 15:15-15:15 / Room: Exhibit Hall B

A Mathematical Method to Estimate CCD Saturation of Cerenkov Luminescence Imaging

Michael Dykstra[1,2], *Anthony Chang*[1], [1]*Small Animal Imaging Facility, Van Andel Institute, Grand Rapids, MI, USA;* [2]*Physics, Grand Valley State University, Allendale, MI, USA. Contact e-mail: michael.dykstra@vai.org*

Purpose: The ability of Cerenkov Luminescence Imaging to obtain quantitative results is an attractive characteristic for imaging technology, especially in biomedical research. It is important to develop mathematical methods to describe these quantitative experimental results. The amount of signal expected for samples of known sizes and activities using the CLI technique has not previously been reported, but would benefit the field of Cerenkov Luminescence Imaging by theoretically validating experimental results. Rearrangement of this equation can also be used as a descriptor of the activity concentration in the field of view (FOV) required to saturate the detector. This equation could be used in the determination of the optimal dose for CLI experiments, ensuring signal maximization without exceeding the detector's ability to detect it. Methods: This derivation first began with the well-established theory of Cerenkov Radiation production. A literature review led us to several relevant quantities that will affect saturation, including the average distance from initial emission that Cerenkov light is produced, the average number of photons released per isotope decay, and the spectrum of Cerenkov light. Additional relevant quantities vary with the optical imager used and are easily obtainable from the manufacturer. This portion of the equation is comprised of the number of counts required to saturate a pixel, distance from the object to the lens, the acceptance angle of the lens, and the lens efficiency. A third category of values is the study-specific values time of scan and the geometry of the object being imaged. which will affect the percentage of charged particle path-length that occurs within the refractive medium. This theoretical basis will assist researchers in choosing the most ideal study-specific quantities. Several fundamental assumptions were made in this study. First, we assumed that no Cerenkov radiation is produced in a medium other than the primary medium of investigation. The subjects of both in vitro and in vivo studies will be primarily surrounded only by air, which does not have a sufficiently high refractive index for Cerenkov radiation production to be possible. We also assumed that no light was absorbed in the medium of interest. Water samples in in vitro studies satisfy this assumption well due to their low absorbance, but in vivo studies require more complex methodology such as Monte Carlo Simulations are required to accurately quantify absorbance. The bending of light across the boundary of water into air is also ignored. Results: Results presented are a calculation of the radioactivity required for saturation of 1 pixel; see attached figure. A direct proportionality was found between the activity and counts required for saturation, the square of the lens acceptance angle, and amount of light produced in a range of wavelengths. Activity was found to be inversely proportional to the photons released per decay, scan time, distance from the object to the lens, and the integral over wavelength of the quantum efficiency multiplied by the spectrum of Cerenkov radiation.

$$A = \frac{N_{DS}}{N_{ph/decay} * t} * \frac{{r_{lens}}^2}{4h^2} * \frac{\int_{\lambda_0}^{\lambda_f} C(\lambda)\, d\lambda}{\int_{\lambda_0}^{\lambda_f} QE(\lambda) * C(\lambda) d\lambda} * \frac{1}{T * \varepsilon(l)}$$

A = activity

N_{DS} = number of photons needed for detector saturation

$N_{ph/decay}$ = average number of Cerenkov photons produced by 1 positron decay within the refractive medium

t = time of scan

$C(\lambda)$ = Cerenkov Spectrum = $\frac{1}{\lambda^2}$

$QE(\lambda)$ = Quantum Efficiency approximation

r_{lens} = radius of acceptance angle of the lens

h = distance from object to the lens

$\varepsilon(l)$ = efficiency of Cerenkov Production based on pathlength of positrons in refractive medium

T = transmittance

Disclosure of author financial interest or relationships:
M. Dykstra, None; **A. Chang**, None.

Presentation Number **P 420**
Poster Session 3
September 20, 2013 / 15:15-15:15 / Room: Exhibit Hall B

Diffusion tensor imaging correlates with collagen 1 fiber architecture in human breast cancer specimens

Samata M. Kakkad[1,2], *Alireza Akhbardeh*[1], *Jiangyang Zhang*[1], *Meiyappan Solaiyappan*[1], *Dieter Leibfritz*[2], *Kristine Glunde*[1], *Zaver M. Bhujwalla*[1], [1]*Russell H. Morgan Department of Radiology and Radiological Science, Johns Hopkins University SOM, Baltimore, MD, USA;* [2]*Department of Chemistry and Biology, University of Bremen, Bremen, Germany. Contact e-mail: skakkad1@jhmi.edu*

Introduction: Collagen 1 (Col1) fibers are an integral part of the tumor extracellular matrix (ECM) and play an important role in macromolecular transport and cancer cell dissemination. High Col1 fiber density is a hallmark of malignant breast cancer. Here we determined the influence of Col1 fiber architecture in human breast cancer on water molecular diffusion, and evaluated the use of diffusion MRI in detecting Col1 fibers in cancer. We found, for the first time, that high Col1 fiber density regions had higher apparent diffusion coefficient (ADC) and fractional anisotropy (FA) values compared to low Col1 fiber density regions. Within high Col1 fiber density regions, dense regions with straight, aligned fibers displayed more restricted water diffusion than dense regions with a mixture of curly and straight fibers. These data suggest that diffusion MRI may be used to assess Col1 fiber architecture and density in breast cancer. Methods: Fixed infiltrating ductal carcinoma samples (stage IIb, grade 3, ER+, PR+, HEr2+) were imaged using high-resolution diffusion tensor imaging (DTI). Samples were sectioned to image Col1 fibers by second harmonic generation microscopy, acquiring a tile scan to cover the entire breast tumor section. Two structural characteristics of the Col1 fiber network were computed: 1) spatial characteristics to calculate sparseness and density; 2) pattern characteristics using textural co-occurrence matrix analysis that extracted a set of 13 Haralick features to calculate spatial inter-relations of fibers varying from straight/aligned fibers to curly/crisscross fibers. We classified the fibers based on these texture features to color-code 3D fiber information on a projected 2D image (Fig.1b&d). Col1 fiber images were superimposed on DTI images and 5 regions of interests (ROIs) were picked for each: dense, mixed and no or few fiber distribution regions. Average ADC and FA values were calculated for these regions. Additionally, the texture analysis parameters, fiber volume and inter-fiber distances were calculated for these ROIs (see supplementary data). Results & Discussions: The Haralick feature based fiber analysis gave a unique color code classification for densely, mixed and sparsely distributed Col1 fibers (Fig.1b&d). Water diffusion followed the Col1 fiber distribution (Fig.1). Regions with higher Col1 density had higher ADC and FA values than regions with few or no fibers. However, mixed fiber distribution regions had ADC and FA values higher than the densely packed fibers (Fig.1e). This may be due to mixed fibers having a larger inter-fiber distance and a sparser distribution than densely packed fibers allowing water to diffuse between the fibers more easily. In regions with no or very few Col1 fibers the ADC and FA values were significantly lower than regions with Col1 fiber present (Fig.1e). Noninvasive DTI may be used to assess Col1 fiber density in breast cancers, which is important because high Col1 fiber density is associated with mammary tumor initiation, progression, and metastasis. Acknowledgement: Work supported by NIH P50 CA103175 & P30 CA006973.

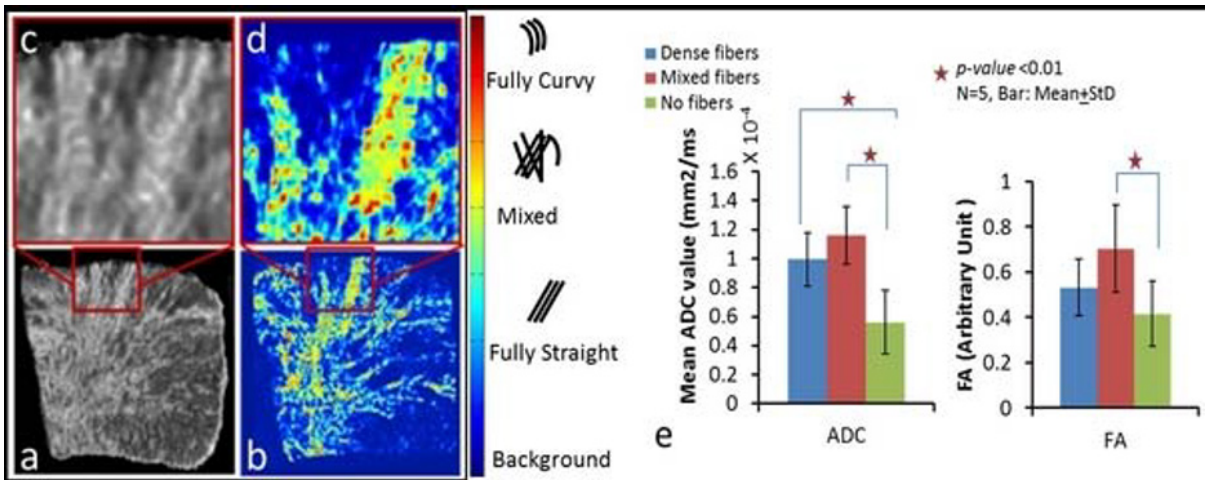

Figure1: (a) ADC map; (b) corresponding SHG tile-scan of Col1 fibers map, texture analysis color coded for high, mixed & low dense fiber distribution; (c) enlarged ADC box from (a); (d) enlarged SHG color coded Col1 box from (b). The dark red color represents dense fibers and the light blue color represents more sparely distributed fibers. (e) Graphs for apparent diffusion coefficient (ADC) and fractional anisotropy (FA) for densely, mixed and very sparsely distributed fiber ROIs, N=5.

Disclosure of author financial interest or relationships:

S.M. Kakkad, None; **A. Akhbardeh**, None; **J. Zhang**, None; **M. Solaiyappan**, None; **D. Leibfritz**, None; **K. Glunde**, None; **Z.M. Bhujwalla**, None.

Presentation Number **P 421**
Poster Session 3
September 20, 2013 / 15:15-15:15 / Room: Exhibit Hall B

A Hybrid Inversion Technique for Extremely Rapid Fluorescence Molecular Tomography Reconstructions

Joshua Kempner[1], *Jorge Ripoll*[2], *Wael Yared*[1], [1]*PerkinElmer Life Sciences, Hopkinton, MA, USA;* [2]*Dept. of Bioengineering, Universidad Carlos III of Madrid, Madrid, Spain. Contact e-mail: josh.kempner@perkinelmer.com*

Fluorescence Molecular Tomography (FMT) is commonly used in small animals, most commonly mice. A significant challenge in imaging larger anatomies is the computation time required to perform both the forward model for light propagation and the matrix inversion for computing the distribution of fluorophores in the animal. We present a technique for reducing the size of the problem through the use of hybrid computations in real space and in Fourier space, which results in a speed-up in computation time by several orders of magnitude. FMT reconstructions use a forward model for light propagation through tissue based on the commonly used diffusion approximation. This approximation uses Green's functions to model the propagation of light between a grid of excitation light source locations, the voxels within the reconstruction, and the camera detectors. Accounting for reflection and refraction at the tissue-air interface as part of this model is computationally very intensive. The "Boundary Removal" technique description by Ripoll & Nztiachristos (2006, PRL 96, 173903) simplifies this computation by in effect transforming the measurement data to how it would appear in an infinite homogeneous medium instead of a diffusive medium with a defined 3D surface. However, the weight matrix produced by this forward model is still very large (on the order of 1e8 elements), so the inversion of this matrix with the data to produce the fluorophore distribution, e.g. by the Algebraic Reconstruction Technique (ART), is very time consuming. By transforming the image data into the Fourier domain with a relatively low frequency cutoff, we can represent the data with many fewer "detectors" than if the data were represented in real space. By using on the order of 25 frequency components, compared to 1e3 detectors in real space, we reduce the size of the problem by 2 orders of magnitude. The computation time scales non-linearly with the size of the weight matrix, so the consequent speed improvement is much greater than 100-fold. We refer to this as a "hybrid" technique because the source and voxel components of the weight matrix are kept in real space. This approach also has the advantage of avoiding the reconstruction artifacts and non-quantitative results that are obtained from a pure Fourier approach such as back-projection or direct inversion techniques. Furthermore, the direct inversion approach requires O(1e3) source locations, which is not practical for in vivo imaging, whereas the hybrid approach requires only O(1e2) or fewer. A critical step in the development of this technique is optimizing the number of frequency components to strike an appropriate balance between the resolution of the final reconstruction and the computation time. The optimal resolution can be determined directly from the FWHM of a point source at the source-detector separation, as translated into Fourier space. Finally, we demonstrate that the technique maintains the quantitative nature of real-space FMT reconstructions and accurate depth recovery, both in phantoms and in vivo.

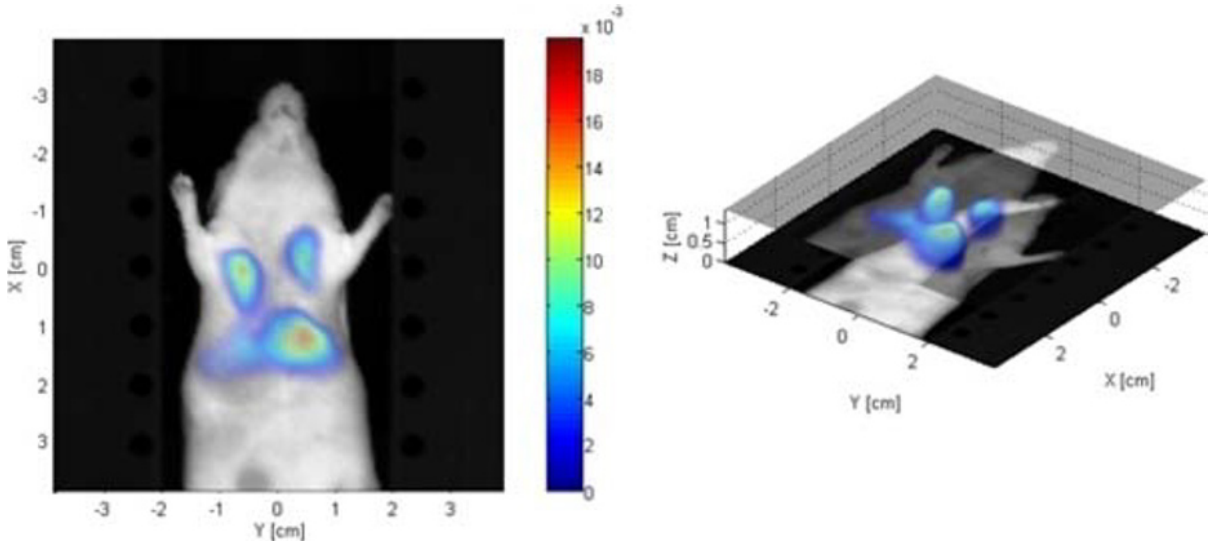

Volume renderings from two different angles of a hybrid reconstruction of a mouse with primary tumors in the upper mammary fat pads, imaged with ProSense® 750. The liver signal is also clearly visible.

Disclosure of author financial interest or relationships:

J. Kempner, PerkinElmer Life Sciences, Employment; **J. Ripoll**, None; **W. Yared**, PerkinElmer, Employment .

Presentation Number **P 422**
Poster Session 3
September 20, 2013 / 15:15-15:15 / Room: Exhibit Hall B

A Technique for Reducing Forward-Model-Induced Artifacts in Fluorescence Molecular Tomography Reconstructions

Joshua Kempner[1], *Jorge Ripoll*[2], *Wael Yared*[1], [1]*PerkinElmer Life Sciences, Hopkinton, MA, USA;* [2]*Dept. of Bioengineering, Universidad Carlos III of Madrid, Madrid, Spain. Contact e-mail: josh.kempner@perkinelmer.com*

As with any functional imaging, one of the critical factors in an investigator's ability to interpret Fluorescence Molecular Tomography (FMT) data is the reliability of the tomographic reconstructions. False negatives (missing signal) and false positives (artifacts) both hamper the accurate interpretation of data. Our study addresses the most prominent false positive artifacts with a reliable way of reducing their effect without a need for a priori assumptions about the concentration of fluorescence in the reconstruction. FMT reconstructions use a forward model for light propagation through tissue based on the commonly used diffusion approximation. This approximation uses Green's functions to model the propagation of light between a grid of excitation light source locations, the voxels within the reconstruction, and the camera detectors. The resulting weight matrix has local maxima at the locations of the excitation light sources. This matrix times the distribution of fluorophore concentrations should yield the measured images, so a matrix inversion of the image data and the weight matrix produces the reconstructed distribution of concentrations. Because of the degeneracies in this inversion, fluorescence spread evenly over a range of depths can tend to get reconstructed at the locations of local maxima in the weight matrix, i.e. at the light source locations. Sources of fluorescence that are reconstructed at other locations in the volume are presumed to be more accurately placed. Multiple reconstructions of the same volume that use data obtained from illuminating the target at different sets of source locations would therefore have similar distributions of fluorescence except for the source-related artifacts. Our technique relies on this observation. The matrix inversion is an iterative process, so in the first few inversions, N reconstructions are computed, each using a subset of the grid of sources and their associated images. After these first few iterations, the reconstructions are combined, where each voxel in the combined reconstruction is the Nth root of the product of the reconstructions at that voxel. Voxels with large values in only a subset of the reconstructions (source artifacts) are reduced in value, while voxels with consistent values across all reconstructions (real signal) retain their values. An example image shows reconstructions of a mouse with MMPSense® 680 injected intraperitoneally. Panel A shows N=1 while B shows N=3. The source artifacts in the abdomen are clearly visible in A and are dramatically reduced in B. The larger the value of N, the greater the reduction in intensity of the artifacts. However, the resolution of the resulting reconstruction degrades as the number of sources per reconstruction decreases, so the optimal value of N depends on the total number of sources for which data were acquired. Balancing these competing parameters is therefore critical. Fortunately, the set of sources in each reconstruction need not be unique, allowing larger values of N even with relatively small total numbers of sources.

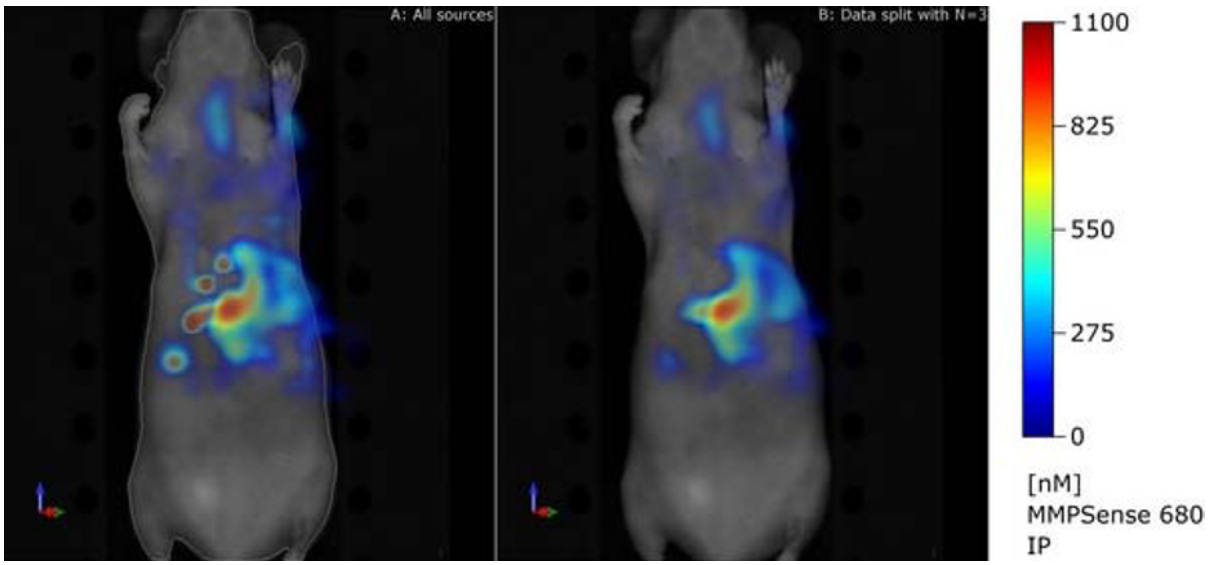

Disclosure of author financial interest or relationships:
J. Kempner, PerkinElmer Life Sciences, Employment; **J. Ripoll**, None; **W. Yared**, PerkinElmer, Employment .

Presentation Number **P 423**
Poster Session 3
September 20, 2013 / 15:15-15:15 / Room: Exhibit Hall B

Cerenkov Light Tomography of SK-NEP-1 Tumor Models Using I-131-labeled Cyclic RGD Peptides

Alexander D. Klose[1], *Yared Tekabe*[2], *Alejandro V. Garcia*[2], *Arul S. Thirumoorthi*[2], *John P. Andrews*[2], *Jessica J. Kandel*[2], *Lynne Johnson*[2], [1]*Radiology, Columbia University, New York, NY, USA;* [2]*Medicine, Columbia University Medical Center, New York, NY, USA. Contact e-mail: ak2083@columbia.edu*

Cerenkov light tomography (CLT) of radiolabeled peptides provides a bridge between optical and nuclear imaging of small animal models of cancer. While Cerenkov light imaging is mainly limited to the two-dimensional (2D) registration of the attenuated Cerenkov light intensities, CLT aims at calculating the three-dimensional (3D) Cerenkov light source distribution inside the tissue. Furthermore, CLT determines the in vivo percent injected dose per tissue weight (%ID/g) distribution and, thus, enables quantitative imaging of the radiotracer uptake via optical imaging. Our proposed CLT method is based on an expectation-maximization (EM) method and a light propagation model for Cerenkov light. The propagation model is described by the simplified spherical harmonics (SP3) equations. It is still valid beyond the diffusion limit at wavelengths <620 nm of the Cerenkov light spectrum. The SP3 equations are solved with a finite difference method. The reconstructed photon emission density of Cerenkov light is transformed into 3D maps of the %ID/g. We demonstrate the feasibility of our CLT method for quantitative imaging of aVb3 integrin over-expression in a SK-NEP-1 tumor model of early childhood cancer by using I-131 labeled cyclic Arg-Gly-Asp (RGD) peptides. 106 SK-NEP-1 cells were injected intra renally in five weeks old female NCR nude mice and showed a consistent tumor growth after six weeks. The c(RGD) peptide was labeled with 131I using the iodogen method. Briefly, 0.02 mg of the peptide was dissolved in PBS (pH 7.4) and added to borocilicate tube coated with 0.05 mg of iodogen. To the reaction mixture, Na 131I (1 mCi) was added and incubated at room temperature for 15 min. The mixture was transferred to an empty vial to terminate the iodide oxidation. The radiochemical purity was greater than 97 % by instant thin-layer chromatography. The animal was injected with 131I - c(RGD) (0.2 mCi) via femoral vein catheter. Two days prior to injection, thyroid uptake was blocked with potassium iodide. After waiting three hours for blood pool clearance, the mice were anesthetized and were secured inside an animal bed. The animal bed consisted of two optically transparent plastic plates that slightly compressed the animal between its ventral and dorsal side. The cassette was placed inside the PhotonImager (BiospaceLab, France) and light emission data at four spectral bands (575, 615, 655, and 695 nm) with 50 nm bandwidth were acquired. The image acquisition time was 10 minutes each. Following CLI, we validated the performance of the CLT method with SPECT/CT and with bioluminescence tomography (BLT). We compared the %ID/g distributions of the CLT reconstructions to the SPECT data and found good agreement. This work was supported in part by a grant (UL1 TR000040) from the National Center for Advancing Translational Science, by a grant (1R44RR030701-01) from the National Center for Research Resources (NCRR), and by a grant (1R21EB011772-01A1) from the National Institute of Biomedical Imaging and Bioengineering (NIBIB).

Disclosure of author financial interest or relationships:
A.D. Klose, InVivoAnalytics, Other financial or material support; **Y. Tekabe**, None; **A.V. Garcia**, None; **A.S. Thirumoorthi**, None; **J.P. Andrews**, None; **J.J. Kandel**, None; **L. Johnson**, None.

Presentation Number **P 424**
Poster Session 3
September 20, 2013 / 15:15-15:15 / Room: Exhibit Hall B

Advanced fluorescence imaging system for clinical translation

Soren D. Konecky, *Josh Molho, Victor Ninov, Dar Bahatt, Shashi Kamath, Jay Whalen, David Nilson, Brad W. Rice, PerkinElmer, Alameda, CA, USA. Contact e-mail: soren.konecky@perkinelmer.com*

Most small animal fluorescence imaging systems utilize a light tight enclosure to prevent ambient light from obscuring the small signals emitted from fluorescent dyes. However, there are many exciting opportunities for fluorescence imaging in which a light enclosure is not feasible. These include pre-clinical applications such as large animal imaging, plus clinical applications such as fluorescence guided surgery, skin cancer imaging, and biopsy imaging. We present initial results using a newly constructed enclosure-less imaging system which is designed to maintain the sensitivity of enclosed systems, while operating at video rates in the presence of ambient light. An array of LEDs illuminates the sample using pulse sequences which look continuous to the naked eye, but which actually consist of rapid flashes of excitation and white light. Fluorescence emission is detected by a sCMOS sensor which is synchronized with the excitation pulses, but rejects light from the white light pulses. A second camera synchronized with the white light pulses acquires color images. We eliminate background signal due to ambient light by interleaving camera exposures into the pulse sequences during which all the LEDs are off, and subtracting these frames from the emission images in real time. In addition, short camera exposures and high energy excitation pulses reduce the shot noise caused by ambient light while maintaining a large emission light signal. Multispectral imaging using a liquid crystal tunable filter combined with spectral unmixing algorithms enables us to multiplex probes and to decreasing non-specific signal due to tissue auto-fluorescence. We characterize the sensitivity of the new system over a wide range of parameters using both in vitro and in vivo imaging. We determine the minimum exposure times needed to detect small amounts of dye under the tissue surface by submerging two rods with hollow tips containing 2 and 10 picomoles of indocyanine green (ICG) respectively in a highly scattering medium with optical properties similar to human tissue. Exposure times of 20 ms and 14 ms are sufficient to achieve a signal to noise ratio per pixel (corresponding to a 100 um x 100 um area on the tissue surface using 2x2 software binning) greater than unity for the 2 and 10 picomole rods respectively when the ICG is located 1 mm under the surface. This result suggests that sub-millimeter tumors can be visualized in real time. Even at depths of up to 3 mm, both rods have SNR/pixel > 1 using 40 ms exposures. In vivo imaging of a 12 week old female nu/nu mouse two weeks after the injection of 1e6 4T1-luc2 mammary tumor cells, demonstrates that the ICG fluorescence is clearly visible at video rates (15 ms exposures) 48 hours after ICG injection. Intraoperative imaging of 3 additional mice with 4T1-luc2 mammary tumors using the CatB-680 probe enables the operator to visualize and remove residual tumor that was not removed during the initial excision. Post-surgical bioluminescence imaging immediately after surgery confirms the complete removal of the tumors, and is used to check for regrowth of the tumors at 10 and 21 days post-surgery.

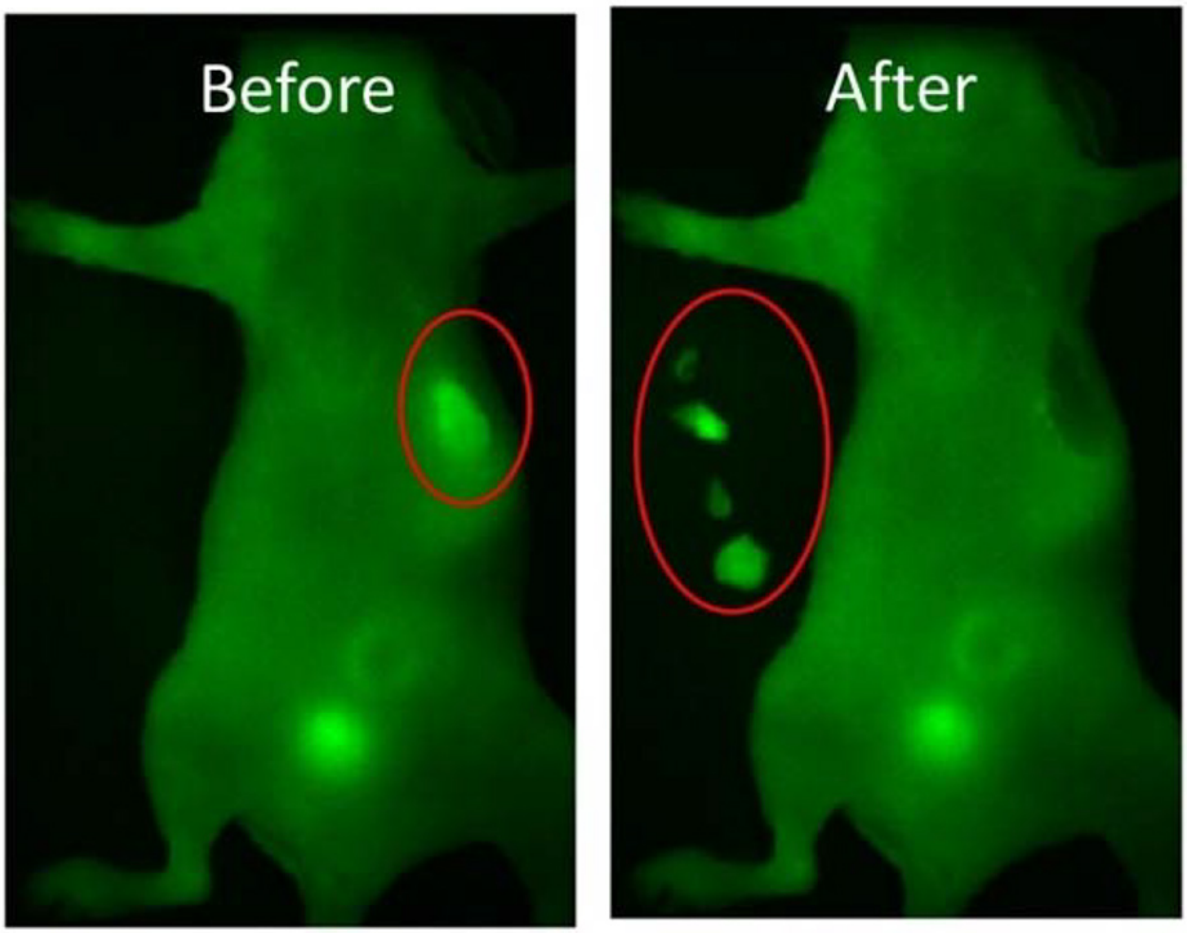

Images from a real time video of a mouse with a 4T1-luc breast tumor during surgery using the CATB-680 probe. Images correspond to before (left) and after (right) removal of the tumor. In both images, the tumor is circled in red.

Disclosure of author financial interest or relationships:
S.D. Konecky, PerkinElmer, Employment; **J. Molho**, PerkinElmer, Employment; **V. Ninov**, Perkin and Elmer, Employment; **D. Bahatt**, Perkin Elmer, Employment; **S. Kamath**, None; **J. Whalen**, None; **D. Nilson**, None; **B.W. Rice**, None.

Presentation Number **P 425**
Poster Session 3
September 20, 2013 / 15:15-15:15 / Room: Exhibit Hall B

Reduction of excitation-source coupling artifacts in diffuse fluorescence tomography reconstructions

Chaincy Kuo[1], *Ali Behrooz*[2], *Brad W. Rice*[1], [1]*In Vivo Imaging R&D, PerkinElmer, Alameda, CA, USA;* [2]*Electrical and Computer Engineering, Georgia Institute of Technology, Atlanta, GA, USA. Contact e-mail: chaincy.kuo@perkinelmer.com*

Ill-posedness of diffuse fluorescence tomography inverse problems often leads to artifacts localized near the points where excitation light is injected into the subject. These artifacts are especially problematic in systems with high levels of non-specific dye, as is often encountered after intravenous injection of targeting agents in small animal models. Earlier efforts to remove these artifacts have utilized a priori structural information to guide the reconstruction on the location of inclusions. In this work for fluorescence tomography, an algorithm to reduce excitation source coupling artifacts near the air-tissue boundary using a least-squares method in the absence of user-imposed expectation is described. This method is based on a technique developed by Kempner, Ripoll and Yared (abstract submitted to this conference) for the algebraic reconstruction technique. The fluorescence tomography problem is modeled as diffuse light propagation and homogeneous optical properties. The models compose the Green's function matrices mapping fluorescence inclusions to photon density data at the surface. The spatial sensitivity to the interior defined by these matrices is particularly high near the regions of the excitation source coupling to the volume. Due to the optical property errors and non-uniqueness, low order fluorescence background data measured at the surface can be fit by high intensity artifacts at these coupling regions. The fluorescence tomography source-detector geometry in this work is such that excitation light is directed into the animal by a 2 mm diameter beam from underneath the animal bed. A grid of excitation points is rastered, with a fluorescence emission image acquired from above the animal bed for each excitation point. This work utilizes multiple reconstructions, each using a subset of unique excitation source patterns. Pearson's correlation spatial maps between solutions are utilized to guide the final reconstruction, in which the entire excitation source grid pattern is incorporated. This scheme is naïve to any a priori expectation of fluorescence localization. Initial tests of the algorithm were performed with fluorescence tomography scans of liquid phantoms consisting of 745 mL 1.3% Intralipid and 5.6 mg of carbon for scattering and absorption, respectively. Optical properties were measured. A 2 μL of 4 μM AF680 fluorescent dye source volume was suspended in the phantom and additional fluorescent dye was added to the phantom solution as fluorescence background, giving a level of 2500:1 for the source to background ratio. The algorithm was also tested on in vivo fluorescence tomography data whereby mice were injected with a fluorescent probes targeting orthotopically implanted tumors. In comparison of reconstructions with and without the coupling artifact reduction algorithm, both the liquid phantom and in vivo identified fluorescence source intensity disagreement is ~5%. The visibility of artifacts associated with the excitation source coupling to the imaging subject is greatly reduced, contributing to increased interpretability of the fluorescence tomography reconstruction.

Disclosure of author financial interest or relationships:
C. Kuo, PerkinElmer, Employment; **A. Behrooz**, None; **B.W. Rice**, None.

Presentation Number **P 426**
Poster Session 3
September 20, 2013 / 15:15-15:15 / Room: Exhibit Hall B

Novel Endoscopic Optical System for Simultaneous Color and Fluorescence Imaging

Patricia Le Coupanec[1], *Norman Mangeret*[2], *Paul Dorval*[2], *Philippe Rizo*[1,2], *Jean-Marc Dinten*[1], [1]*DTBS, CEA-LETI-MINATEC, Grenoble Cedex 9, France;* [2]*Fluoptics, Grenoble Cedex 9, France. Contact e-mail: patricia.lecoupanec@cea.fr*

The main challenge to the transition of surgery from open to endoscopy is the loss of anatomical information as tissue palpation, texture recognition and 3D visualization are not possible through endoscopes. Thus, in minimally invasive surgery (MIS), the rendering of the video color image is critical. This white light imaging mode has been complemented by the introduction of fluorescence imaging which is helping in targeting tumors and monitoring lymphatic and blood vessels (SLN, Lymph nodes or vascularization). In laparotomy, fluorescence imaging has proven to be a valuable tool for physicians providing surgery guidance and efficient tissue differentiation and devices dedicated to laparoscopy begin to be commercialized. We are presenting here our work on the development of a novel imaging system allowing simultaneous color and NIR (800nm) fluorescence endoscopic imaging with optical performances in both modes comparable to commercialized non-simultaneous systems. This development is the extension to MIS of the technology we developed to image NIR molecular probes with surgical field white light illumination and simultaneous fluorescence imaging. With such device, high quality illumination can be achieved with IRC above 90% (FluobeamTM). The novelty in this endoscopic system is the offering of a high quality color image in addition to sensitive fluorescence imaging. The solution resides in the conception of an optimized, LED and laser based, light source coupled to a two-camera detection block. The video flows resulting from parallel acquisitions can be performed with a minimum of 10 fps. Filtering on both the illumination and detection sides ensures high performance for color imaging without compromising sensitivity to the fluorescence signal. For optimal color image rendering, a color calibration method has been implemented to generate a displayable video flow with chromatic color difference (Delta E) comparable to white light illumination with our IRC levels obtained in open surgery. Simultaneous acquisition of the fluorescence image offers better ease of use to the medical staff as there is no more need for a manual switch between white light and fluorescence imaging modes. The functional information arising from the fluorescence signal can be superposed in real time to the color image or displayed next to it. This imaging system has been designed to adapt easily onto rigid medical endoscopes with well performing color and fluorescence functionalities. We will present preclinical testing, representative of surgery, on small and large animals using our bi-modal laparoscopic imaging system with ICG.

Disclosure of author financial interest or relationships:
P. Le Coupanec, None; **N. Mangeret**, None; **P. Dorval**, Fluoptics, Employment; **P. Rizo**, None; **J. Dinten**, None.

Presentation Number **P 427**
Poster Session 3
September 20, 2013 / 15:15-15:15 / Room: Exhibit Hall B

Methodology for Validation of Imaging Agent Targeting to Tumor Metastases using Cryo-imaging

Mohammed Q. Qutaish, *Zhuxian Zhou, Zheng-Rong Lu, David L. Wilson, Biomedical Engineering, Case Western Reserve university, Cleveland, OH, USA. Contact e-mail: mqq@case.edu*

Introduction. Because current imaging modalities lack the sensitivity and/or resolution to detect small tumor metastases, we are developing new molecular imaging agents for MRI to improve contrast and enhance detection. In vivo testing requires a gold standard. Dissection can miss small tumors, and histology will necessarily have a sampling problem. In this report, we test a new preclinical platform methodology for assessing the ability of any imaging modality and agent combination to detect small tumors. We use cryo-imaging which provides 3D microscopic imaging of a mouse with the sensitivity to detect even a single fluorescent-protein-labeled tumor cell. We develop experimental methods and image registration to provide an excellent gold standard to in vivo images, enabling one to determine detection efficiency as a function of tumor size. Methods. To test the metholodolgy, we evaluated a new targeted imaging agent, CREKA-Tris(Gd-DOTA)3 designed for MR molecular imaging of breast cancer. CREKA is a tumor-homing pentapeptide (Cys-Arg-Glu-Lys-Ala) which specifically binds to fibrin and fibronectin associated with plasma protein clots in tumor stroma. A mouse model of metastatic tumor was created by implantation of 4T1-GFP breast cancer cells into mouse mammary fat-pad. 40 days later, mice were injected with the targeted probe and MRI imaged using a fat suppression T1-weighted flash 3D sequence. Then, mice were sacrificed and cryo-imaged. We have developed interactive software for registration, visualization, and analysis of image data. Registration employs the transformation system rigid→affine→B-spline, to give deformable registration of either the entire mouse or a volume of interest. By linking operations on registered image volumes, we can interactively identify tumor regions of interest in cryo and quantitatively assess corresponding imaging agent signal intensities in MR. This allows multiple evaluations such as detection rates as a function of tumor size. Results. Cryo-imaging shows that 4T1-GFP cells metastasize mainly to lungs, liver, lymph nodes, bones and adrenal gland. Fig.1A shows metastases in liver. Micro-metastases (< 200 μm) were found mostly in the lungs and bone marrow (Fig.1B). Connected component analysis shows a typical number of about 300 metastatic clusters per mouse with diameter range of 0.02-10 mm. About 70% of clusters are <1 mm. Visual inspection of preliminary results of MRI-Cryo registration data showed that the imaging agent successfully targeted larger metastases. For Example, in Fig.1C, the signal to background ratio was 1.7 for a metastatic tumor ≈2 mm diameter. To date, smaller metastases were not discernible above noise. It is believed that improved acquisition timing and MR image sequences will greatly improve small tumor detection. Conclusion. We have shown promising results for a platform technology which can uniquely characterize targeting of imaging agent to metastatic tumors. Planned improvements include enhanced registration approaches and improved MR imaging. We believe that cryo-imaigng and software will provide a very useful tool for the development of new targeted theranostics.

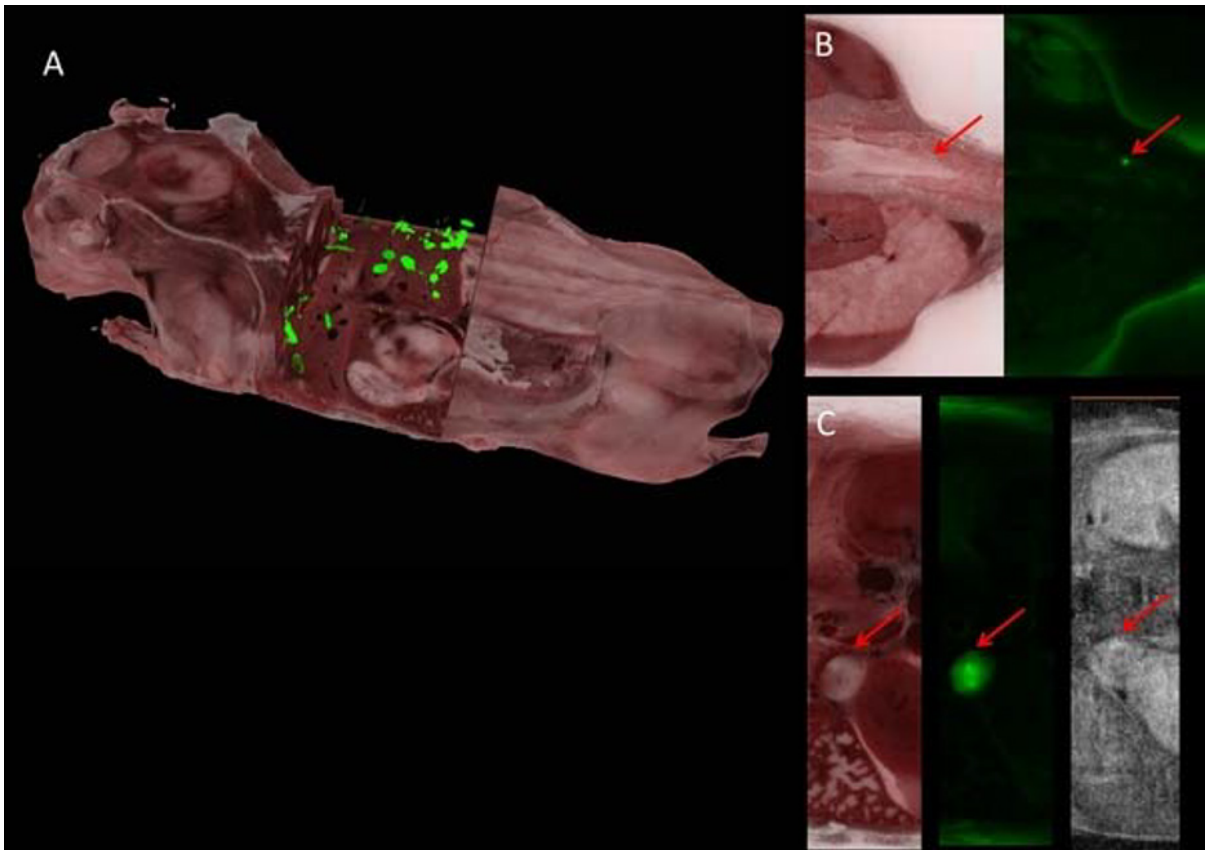

Multi resolution view of tumor metastases of 4T1-GFP cells using Cryo-imaging and MRI data. (A) shows 3D rendering of cryo-imaging data of whole mouse, Green cluster are metastatic tumors in the liver region. Arrows in (B) shows an example of micro-metastases in bone marrow of vertebra, this particular cluster is about 150 μm in diameter. Arrows in (C) show a bigger metastatic cluster in the adrenal gland above the kidney. This cluster is about 2 mm in diameter. Registered MRI image show that CREKA-Tris(Gd-DOTA)3 imaging agent generated sufficient contrast to identify this bigger cluster.

Disclosure of author financial interest or relationships:
M.Q. Qutaish, None; **Z. Zhou**, None; **Z. Lu**, None; **D.L. Wilson**, BioInVision, Inc., Stockholder .

Presentation Number **P 428**
Poster Session 3
September 20, 2013 / 15:15-15:15 / Room: Exhibit Hall B

In vivo optical projection tomography for Drosophila Melanogaster pupa

Di Dong[1], *Jin Guo*[2], *Xibo Ma*[1], *Jorge Ripoll*[3], *Jie Tian*[1], [1]*Medical Image Processing Group, Institute of Automation,CAS, "Beijing,100190", China;* [2]*School of Automation, Harbin University of Science and Technology, Harbin, China;* [3]*Universidad Carlos III de Madrid, Madrid, Spain. Contact e-mail: di.dong@ia.ac.cn*

Optical projection tomography (OPT) is a high-resolution imaging technology which can provide three-dimensional (3D) images for samples from 1 to 10 mm. Although OPT has been greatly applied to view low scattering ex vivo biological tissues, ex vivo imaging cannot record dynamic changes in biological tissues. In this paper we have developed an in vivo OPT system which can view Drosophila Melanogaster pupa expressing Green Fluorescent Protein (GFP). In our system, a 488nm laser is used for exciting the GFP in the pupa and the emission light is collected by a CCD camera which offers 1024*1024 pixels and 13μm*13μm pixel size. During the experiment, the pupa is attached to a capillary tube and exposed to air. A 3-jaw self-centering chuck is used to facilitate the location of the capillary tube. In our experiment 360 emission images are collected spanning the complete 360 degree within 2 minutes. Then a graphics processing unit (GPU) based reconstruction software is used to reconstruct the 3D structure of the pupa. Experimental results show that 3D in vivo imaging of Drosophila Melanogaster pupa is easy to implement by using our system.

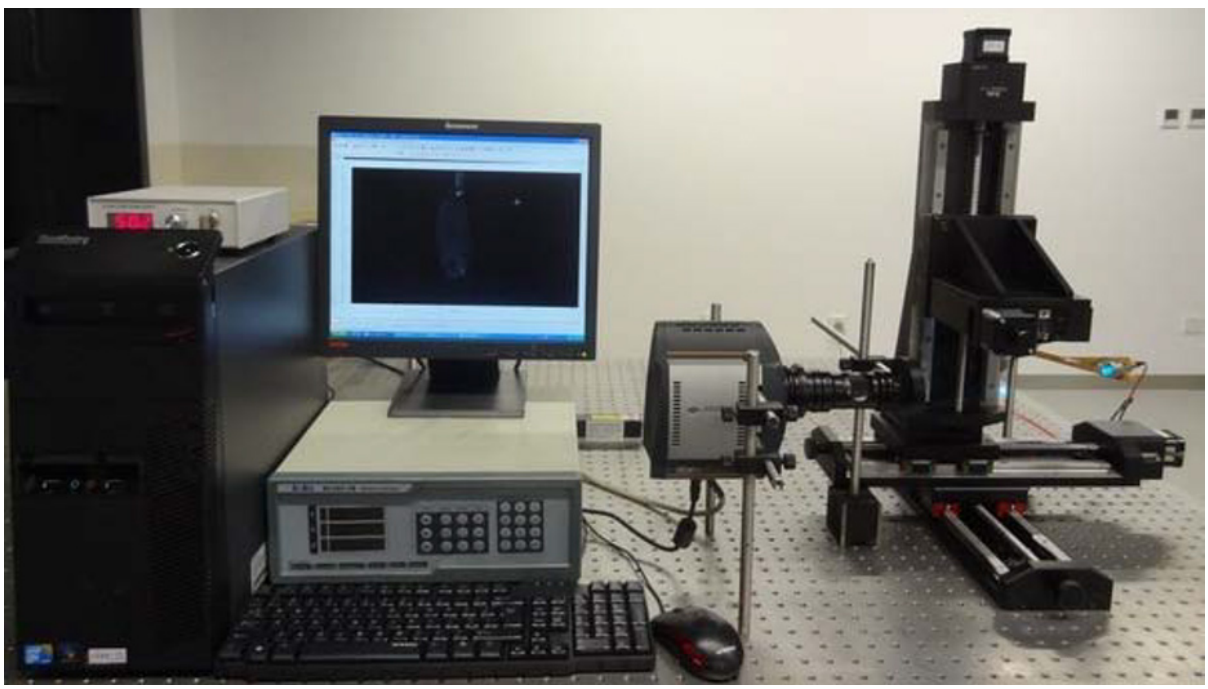

In vivo OPT system

Disclosure of author financial interest or relationships:
D. Dong, None; **J. Guo**, None; **X. Ma**, None; **J. Ripoll**, None; **J. Tian**, None.

Presentation Number **P 429**
Poster Session 3
September 20, 2013 / 15:15-15:15 / Room: Exhibit Hall B

Automatic Extraction of Region of Interest from the Emerging Cerenkov Luminescence Endoscopy Images

Wei Mu, Haixiao Liu, Wei Shen, Zhenhua Hu, Kun Wang, **Jie Tian***, Medical Image Processing Group, Institute of Automation,CAS, "Beijing,100190", China. Contact e-mail: tian@ieee.org*

Purpose: As an emerging significant way to acquire Cerenkov luminescence images of the deep tissue, Cerenkov luminescence endoscopy Imaging (CLEI) could be used to the detection of the common gastrointestinal and urinary tract cancers potentially. However, the weak Cerenkov light is attenuated distinctly due to the introduction of the endoscopy, which causes the low signal-to-noise ratio (SNR) and makes the extraction of the signal of interest very challenging. In this abstract, we proposed a novel nonlinear diffusion based method to automatically extract the region of interest (ROI) from Cerenkov Luminescence Endoscopy Images. Materials and methods: 20 EP tubes whose bottoms were injected with 18F-FDG were acquired for Cerenkov luminescence endoscopy images and anatomic (white light) images. Firstly, a nonlinear diffusion method was performed on an original luminescence image for denoising purpose. Then the intensity histogram of the processed image was calculated and a new designed automatic thresholding method based on the peaks and valleys of the obtained histogram was used. After that, the appropriate threshold was found to convert the intensity image to a binary mask image of the ROI. Finally the ROI was extracted by the automatic selection of the largest connected component. In order to validate the effectiveness of the proposed method, we compared our extraction results with the gold standard, i.e. manual segmentation of the anatomic images, by calculating the sensitivity and specificity. Results and discussion: The proposed method was evaluated on the data set of 20 Cerenkov luminescence endoscopy images, and it was feasible for all of them. The extraction results showed the high sensitivity (81.25%) and the high specificity (94.75%) of the proposed method. Conclusion: The authors proposed a novel approach for automatic ROI extraction based on nonlinear diffusion from Cerenkov luminescence endoscopy images. The encouraging results showed that this method was accurate, efficient and robust, and it could be a solution to the extraction of the low SNR images.

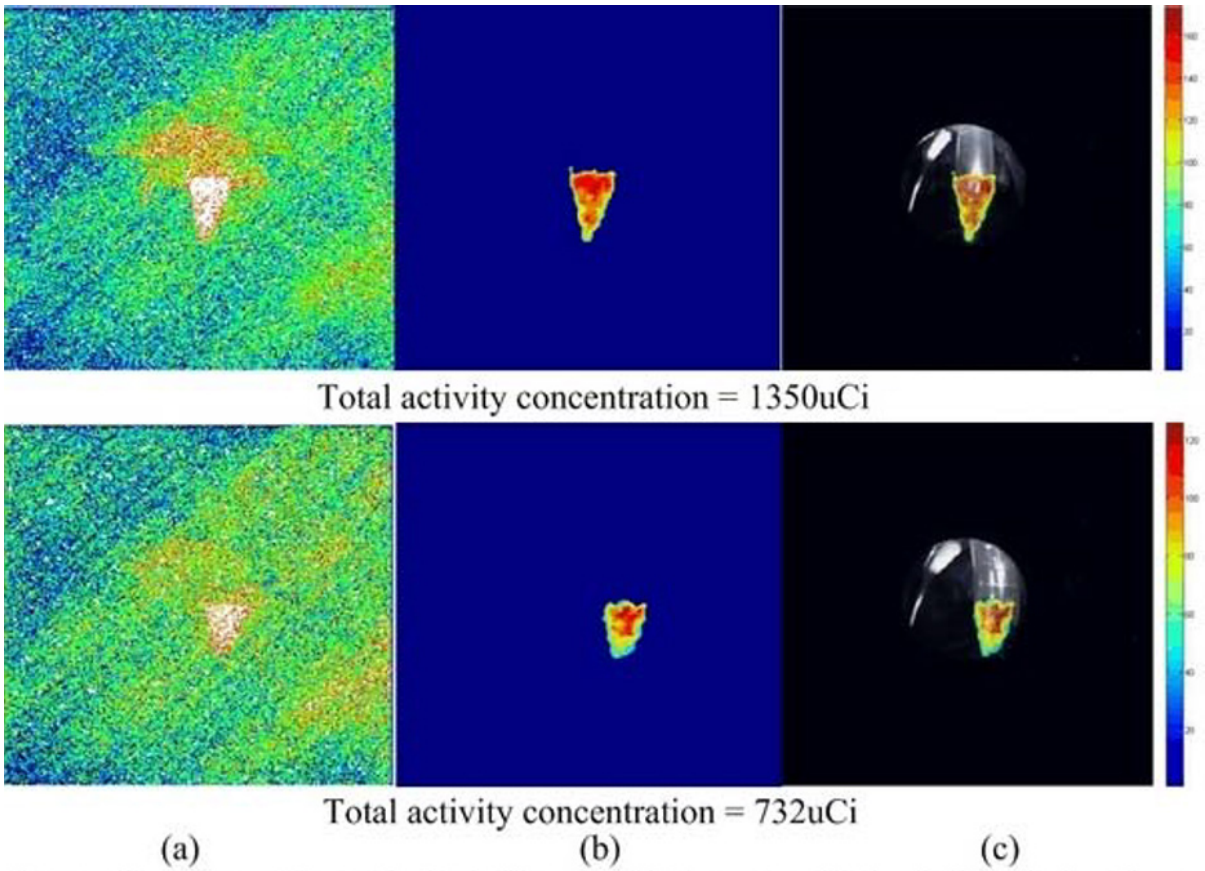

Figure. Experimental results for different activity concentration.(a) The left column are the initial fluorography.(b) The middle column are the extraction of the region of interest.(c) The right column are the photos overlaied with the extraction.

Disclosure of author financial interest or relationships:
W. Mu, None; **H. Liu**, None; **W. Shen**, None; **Z. Hu**, None; **K. Wang**, None; **J. Tian**, None.

Presentation Number **P 430**
Poster Session 3
September 20, 2013 / 15:15-15:15 / Room: Exhibit Hall B

In vivo hybrid spectral Cerenkov luminescence tomography using positron-emitting radiopharmaceutical 18F-FDG

Zhenhua Hu, Kun Wang, Haixiao Liu, Wei Mu, **Jie Tian**, *Medical Image Processing Group, Institute of Automation,CAS, "Beijing,100190", China. Contact e-mail: tian@ieee.org*

Three-dimensional (3D) Cerenkov luminescence tomography (CLT) has become a motivating topic recently due to it can provide the 3D radiopharmaceutical biodistribution in small living animals. To evaluate the performance of hybrid spectral CLT for reconstructing 3D distribution of electron-emitting radiopharmaceutical 18F-FDG, in this paper we performed an experiment by injecting a mouse with 18F-FDG, and reconstructed the 18F-FDG uptake in the mouse bladder. The fused imaging reconstruction was based on a single-view Cerenkov luminescence image acquired without using multispectral data in the experiment. Therefore the entire imaging process only took less than 10 minutes, including 5 minutes exposure and 4 minutes automated reconstruction. The results were encouraging, as shown in Fig. 1: the pseudocolor represented the reconstructed biosdistribution of 18F-FDG. It clearly demonstrated that the 18F-FDG uptake was not only happening inside the mouse bladder, and also in its neighbouring hip bones (Fig. 1 A and C, red arrows). In conclusion, our experiment showed that the hybrid spectral CLT imaging procedure and its corresponding reconstruction algorithm provided a noble way for fast imaging the metabolic activities in small animals of isotopes with short half-life periods.

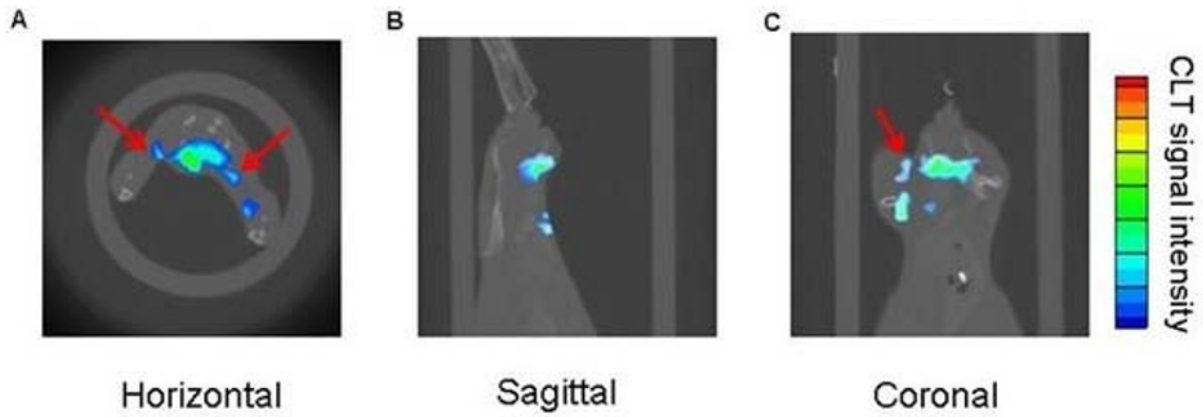

Figure 1. The biodistribution of 18FDG uptake in the mouse bladder given by hybrid spectral CLT: (A) Horizontal view; (B) Sagittal view; (C) Coronal view. Red arrows indicate the 18FDG uptake in the mouse hip bones closed to the bladder.

Disclosure of author financial interest or relationships:
Z. Hu, None; **K. Wang**, None; **H. Liu**, None; **W. Mu**, None; **J. Tian**, None.

Presentation Number **P 431**
Poster Session 3
September 20, 2013 / 15:15-15:15 / Room: Exhibit Hall B

Bronchoscopic Cerenkov luminescence imaging of the radioactive source with 18F-FDG

Zhenhua Hu[1], Haixiao Liu[1], Kun Wang[1], Wei Mu[1], XIntao Ding[2], **Jie Tian**[1], [1]*Medical Image Processing Group, Institute of Automation,CAS, "Beijing,100190", China;* [2]*School of Territorial Resources And Tourism, Anhui Normal University, Wu Hu, China. Contact e-mail: tian@ieee.org*

Objectives Cerenkov luminescence imaging (CLI) plays an important role in imaging the radiopharmaceuticals in living animals. To efficiently acquire weak Cerenkov luminescence signals, a novel bronchoscopic CLI was presented, which was expected to improve the detection depth in vivo and potentially bring new opportunities for the diagnosis of various kinds of diseases in the future. Methods Firstly, a bronchoscopic Cerenkov luminescence imaging (BCLI) system was constructed. The key component of the system was the bronchoscopic optical imaging module, in which the bronchoscopy was coupled with an electron multiplying charge coupled device (EMCCD). Inside the bronchoscopy, optical fibres were used to guide the white light from a cold light source, so that white light photographs of the imaging object can be acquired (Figure 1 A). Next to the fibres, a set of object lens were used to obtain either the Cerenkov luminescence or white light. To evaluate the performance of the BCLI system, the bronchoscopic Cerenkov luminescence images of a glass tube with 700 μCi activities inside were acquired by it. The gain was 1000, and the integration time was 300 s. After that, white light photos of the glass tube were taken by the same system. Results The picture of the BCLI system is shown in Figure 1 A. Figure 1 B illustrates the white light photo of the glass tube. Figure 1 C shows the fused bronchoscopic luminescence image with the photo. The preliminary experimental results indicated the Cerenkov luminescent image of 18F-FDG could be acquired by the BCLI system. Conclusions Our study suggested that the novel BCLI system showed promising results of detecting the weak Cerenkov luminescence signals. The design effectively reduced signal loss during the Cerenkov luminescence propagation. Based on this system, it is possible to improve the Cerenkov luminescence tomography (CLT) imaging depths.

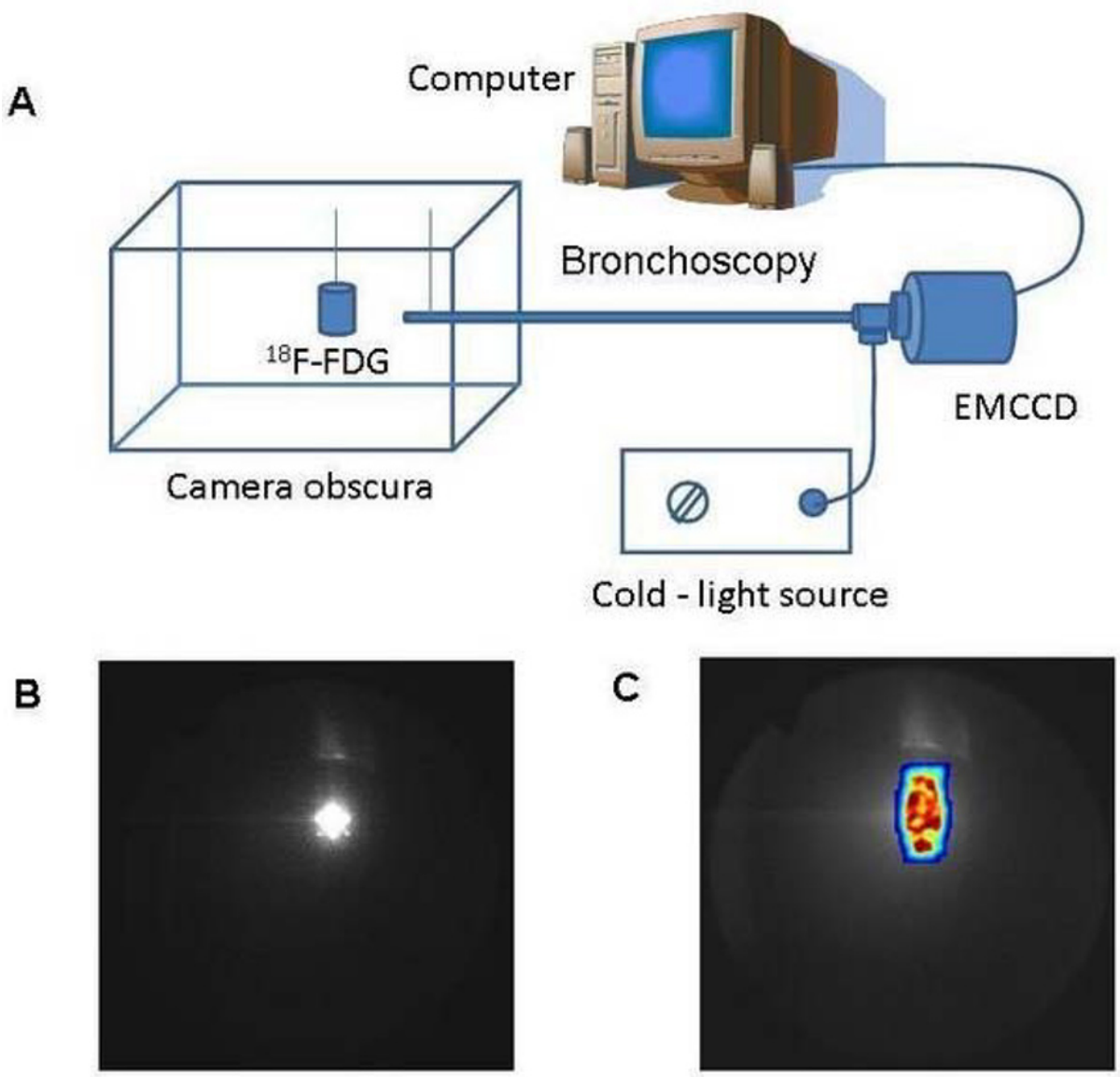

Figure 1. (A) The picture is the bronchoscopic Cerenkov luminescence imaging (BCLI) system. It was consisted of a bronchoscopic optical imaging module, a camera obscura, a cold-light source and a computer. In the imaging module, the bronchoscopy was coupled with the electron multiplying charge coupled device (EMCCD) camera. (B) The white light photo of 18F-FDG. (C) Bronchoscopic Cerenkov luminescence image of 18F-FDG in glass tube using the BCLI system.

Disclosure of author financial interest or relationships:
Z. Hu, None; **H. Liu**, None; **K. Wang**, None; **W. Mu**, None; **X. Ding**, None; **J. Tian**, None.

Presentation Number **P 432**
Poster Session 3
September 20, 2013 / 15:15-15:15 / Room: Exhibit Hall B

Tissue specificity based light transport model for three dimensional optical imaging

Defu Yang[1], *Xueli Chen*[1], *Shouping Zhu*[1], *Xianghan Zhang*[1], *Jimin Liang*[1], *Jie Tian*[2,1], [1]*School of Life Sciences and Technology, Xidian University, Xi'an, China;* [2]*Medical Image Processing Group, Institute of Automation,CAS, "Beijing,100190", China. Contact e-mail: yangdefu@life.xidian.edu.cn*

Accurate description of light transport in tissues and rapid reconstruction of target are foundation of three dimensional optical imaging. Currently, several approximation of the radiative transfer equation (RTE) based models or the hybrid light transport models, such as the hybrid Monte Carlo-diffusion model, hybrid RTE-diffusion model, and hybrid radiosity-diffusion model, were proposed and applied to optical imaging. However, these models cannot provide a compromise between accuracy and effectiveness when an organism with complicated structure and properties were considered. For this purpose, a tissue specificity based light transport model was provided for optical imaging. The concept of tissue specificity can be understood from two aspects. First, the tissues were sorted specifically. According to the discrepancy of tissues in anatomical structure and optical properties, the tissues were sorted into three categories, high scattering tissues, low scattering tissues and non scattering tissues. Second, the light transport in different categories of tissues was characterized specifically. In the proposed model, the commonly used diffusion approximation of the RTE (DE) was used to describe the light transport in the high scattering tissues, the simplified spherical harmonics approximation of the RTE (SPN) to express light transport in the low scattering tissues, and the radiosity theory was employed to process light transport in the non scattering tissues. By constructing the specific boundary conditions, the DE, SPN and radisity theory were integrated together to establish the tissue specificity based light transport model. To illustrate the accuracy of the proposed tissue specificity based light transport model, a digital mouse based simulation model, extracted from CT and cryosection data, was established. In the digital mouse model, main organs were selected to simulate the tissue's heterogeneity and tissues were divided into the high scattering, low scattering and non scattering regions according to the tissue specificity, as shown in Table 1. A solid sphere with 1mm radius was located beside the stomach and liver to simulate the internal labeled lesion. Results calculated by the proposed tissue specificity based model were compared with those simulated by the Molecular Optical Simulation Environment. The comparisons were detailed presented in Fig. 1, which shows a well agreement between the calculated and simulated results. A tissue specificity based light transport model was proposed in this work, which can provide a compromise between the accuracy and effectiveness when an organism with complicated structure and properties were considered. The primary verified results demonstrated its satisfying accuracy with a digital mouse model and showed the potential application in whole-body imaging.

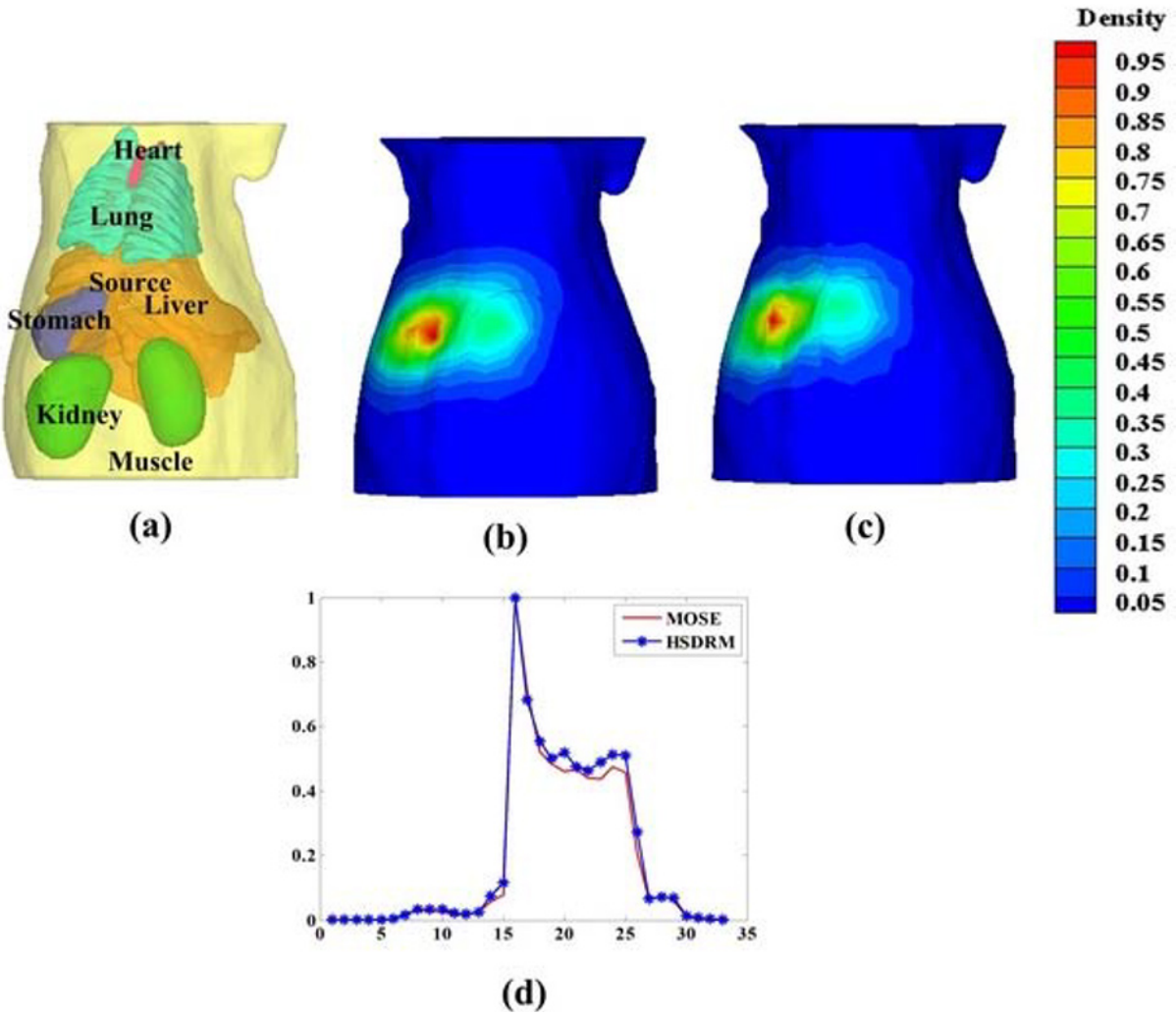

Fig.1 (a) Digital mouse model; (b)-(c) Distribution of the photon density obtained by HSDRM and MOSE respectively; (d) Profile at the height of the center of the light source.

Optical properties and the tissue specificities of the main organs of the digital mouse

Tissue	Muscle	Heart	Stomach	Liver	Kidney	Lung
Absorption	0.0644	0.04767	0.01504	0.36085	0.04904	0.14507
Scattering	3.94917	6.16113	0.000001	6.57443	1.5063	35.671
Tissue Specificity	low-scattering	high-scattering	non-scattering	low-scattering	high-scattering	high-scattering

Disclosure of author financial interest or relationships:

D. Yang, None; **X. Chen**, None; **S. Zhu**, None; **X. Zhang**, None; **J. Liang**, None; **J. Tian**, None.

Presentation Number **P 433**
Poster Session 3
September 20, 2013 / 15:15-15:15 / Room: Exhibit Hall B

Calibration of the endoscopic Cerenkov luminescence imaging system

Xin Cao[1], Yenan Lin[1], Hao Hu[2], Xueli Chen[1], Yonghua Zhan[1], Jimin Liang[1], Jing Wang[3], **Jie Tian**[4,1], *[1]School of Life Sciences and Technology, Xidian University, Xi'an, China; [2]State Key Laboratory of Cancer Biology and Institute of Digestive Diseases, Xijing Hospital, Fourth Military Medical University, Xi'an, China; [3]Department of Nuclear Medicine, Xijing Hospital, Fourth Military Medical University, Xi'an, China; [4]Medical Image Processing Group, Institute of Automation,CAS, "Beijing,100190", China. Contact e-mail: tian@ieee.org*

Currently, the gastric cancer is commonly diagnosed by the gastroscope. However, the gastroscope just provides the structural changes of the lesion and cannot provide the molecular specificity imaging at the early stage. Motivated by the widespread use of nuclide probe and the newly developed Cerenkov luminescence imaging technology, an endoscopic Cerenkov luminescence imaging (ECLI) system, which combines the advantages of gastroscope and Cerenkov luminescence imaging, has been developed. The ECLI system consists of an imaging fiber bundle, an optical coupler, and a high-sensitive EMCCD, as shown in Fig. 1. The optical imaging fiber bundle is used to transport the Cerenkov luminescence signals as well as the white-light signals acquired by a micro-size objective lens equipped at the distal end of the optical imaging bundle. The signals, emitted from the lesion deep inside the body, are received by a high-sensitive EMCCD. The optical coupler is adopted to integrate the optical imaging bundle and the EMCCD. A LED light is also fixed beside the objective lens to provide white-light illumination. The developed ECLI system has been calibrated by measuring the attenuation rate against the traditional Cerenkov luminescence system, which will provide a foundation for quantification of the system. Six wells in the 96-well plates were filled with different activity of Na131I as the radioactive sources, and the activities were 100uci, 200uci, 300uci, 400uci, 500uci, and 600uci respectively. A well filled with a non-radioactive NaI solution, as a control source, was also designed. During the experiment, each of the radioactive sources was first imaged by ECLI system and then imaged by traditional Cerenkov luminescence system, and the exposure time is 2 minutes with the binning value of 4. We believe that the calibrated ECLI system, which integrates the advantages of endoscopy and Cerenkov luminescence imaging system, will be a useful tool in preclinical study.

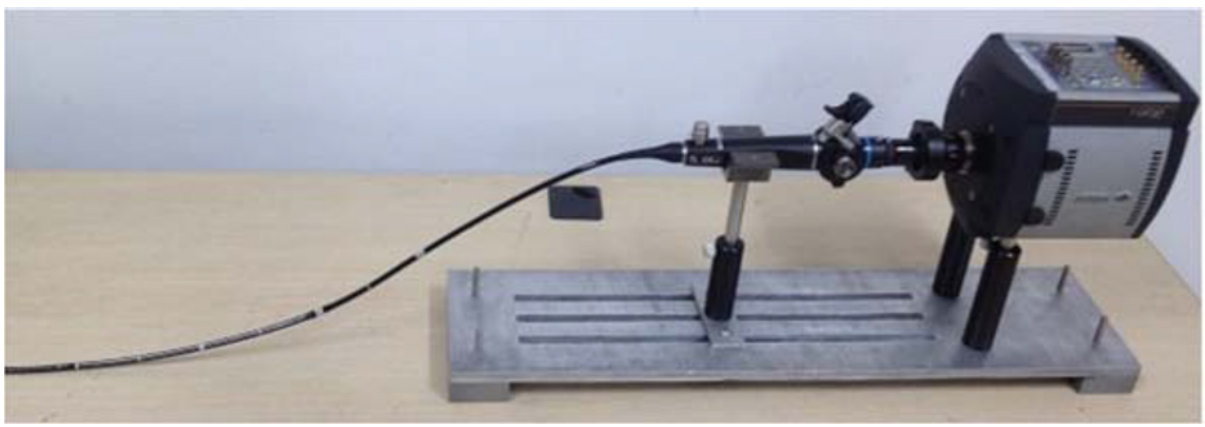

Endoscopic Cerenkov luminescence imaging system

Disclosure of author financial interest or relationships:
X. Cao, None; **Y. Lin**, None; **H. Hu**, None; **X. Chen**, None; **Y. Zhan**, None; **J. Liang**, None; **J. Wang**, None; **J. Tian**, None.

Presentation Number **P 434**
Poster Session 3
September 20, 2013 / 15:15-15:15 / Room: Exhibit Hall B

Laparoscopic Near-Infrared Fluorescence Imaging of Hepatic Uveal Melanoma Metastases using Indocyanine Green: a technical note

Quirijn Tummers, *Floris P. Verbeek, Martin C. Boonstra, Boudewijn Schaafsma, Andries E. Braat, Coen I. Baeten, Cornelis J. van de Velde, Alexander Vahrmeijer, Surgery, Leiden University Medical Center, Leiden, Netherlands. Contact e-mail: q.r.j.g.tummers@lumc.nl*

Background: Uveal melanoma is the most common primary intraocular tumor in adults and up to 50% of patients will develop liver metastases. Complete surgical resection of these metastases can improve 5-year survival, but only a few patients are eligible for a radical surgical treatment. Therefore, it is of great importance to select and treat these patients carefully, to prevent unnecessary laparotomies. Near-infrared fluorescence (NIRF) imaging using indocyanine green (ICG) is a promising technique to assist in the intraoperative identification of liver metastases in real time. However, all published cases concerning intraoperative detection of liver metastases using NIRF and ICG were performed in open procedures. A laparoscopic operation is preferable for patients with liver metastases from uveal melanoma, due to the high risk of multiple small metastases. The aim of this study was to introduce a novel, high definition, NIRF laparoscope during minimal invasive surgery for intraoperative identification of uveal melanoma liver metastases and to provide guidance during resection. Methods: Two patients previously treated for uveal melanoma, both pre-operatively diagnosed with one solitary liver metastasis are presented. Patients received 10mg indocyanine green (ICG) intravenously 24 hours before surgery (optimal timing based on a dose-finding study performed in 16 patients with colorectal liver metastases and an open imaging system). A high definition NIR fluorescence laparoscope (Karl Storz, Germany) was used to detect malignant liver lesions. After resection, ex-vivo imaging and fluorescence microscopy was performed for histological validation. Results: In both patients, laparoscopic NIR fluorescence imaging using ICG successfully identified uveal melanoma liver metastases. A clear fluorescent rim around the tumor was observed. In patient 1, seven additional lesions in both left and right liver lobe, not seen with computer tomography (CT), were identified by inspection and NIR fluorescence imaging. In patient 2, one additional lesion, not identified by CT, magnetic resonance imaging, laparoscopic ultrasonography and inspection, was seen with NIR fluorescence imaging. Importantly, NIR fluorescence imaging provided guidance during resection of these metastases. A clear fluorescent rim around tumor and metastases was seen with fluorescence microscopy. Conclusions: This study describes the successful use of laparoscopic identification and resection of uveal melanoma liver metastases using NIR fluorescence imaging and ICG. This procedure is minimal invasive, and should be used as complementary to conventional techniques for the detection and resection of liver metastases.

Disclosure of author financial interest or relationships:
Q. Tummers, None; **F.P. Verbeek**, None; **M. Boonstra**, None; **B. Schaafsma**, None; **A.E. Braat**, None; **C.I. Baeten**, None; **C.J. van de Velde**, None; **A. Vahrmeijer**, None.

Presentation Number **P 435**
Poster Session 3
September 20, 2013 / 15:15-15:15 / Room: Exhibit Hall B

Miniaturized device for real time VIS/NIR endoscopic imaging for cancer detection

Jian Xu[1], *Brad Kairdolf*[1], *James Provenzale*[2,1], *Shuming Nie*[1], [1]*Biomedical Engineering, Emory University, Atlanta, GA, USA;* [2]*Radiology, Duke University Medical Center, Durham, NC, USA. Contact e-mail: jian.xu@emory.edu*

Endoscopic imaging is a critical procedure of real time diagnosis, staging and localization of various cancers, such as esophageal cancers, gastric cancers, and lung cancers, in internal organs. For the best performance of optical imaging of biological bodies, there is a clear window in the near infrared (NIR) region between 650 nm and 950 nm, where the light has less scattering by biological tissues and lower absorption by water and lipids. In this window, there is an excellent fluorescent contrast agent, indocyanine green (ICG), the only NIR fluorescent agent approved by the Food and Drug Administration (FDA). ICG has been used in human beings for decades and is well-known for the safety profile. With the enhanced permeability and retention (EPR) effect, ICG, binding to the serum proteins, may accumulate in the tumor interstitial space and help to differentiate the tumor from the normal tissue in the oncological imaging. However, the current prevailing endoscopic imaging does not allow the NIR imaging, which makes it challenging for the accurate diagnosis and staging of cancer, especially in locating the satellite tumor, metastasis and tumor margin. Here we designed a miniaturized device, which can detect both the near-infrared and visible (VIS) signals in the endoscopic imaging of tumor. This miniaturized device has a probe with an outside diameter (O.D.) of 1.83mm (Figure 1a), which can fit into the biopsy channels of most common endoscopes, such as esophagogastroduodenoscopes, sigmoidoscopes (Figure 1b) and laparoscopes. The miniaturized device is sensitive to detect the fluorescence of ICG at the human dosage level and even lower (102 times lower). In addition, this device can also be used to detect other fluorescent agents, such as FDA approved fluorescein and quantum dots. The device has been characterized on the solution experiments, in vivo and ex vivo on the murine tumor models, with ICG as the contrast agent administered intravenously into the animal (Figure 1c); this device has shown comparable sensitivity to the regular NIR spectrometer. Further, the probe is robust to withstand the autoclave procedure, which makes it feasible for animal and human clinical trials. In summary, we have developed a miniaturized device for the VIS/NIR endoscopic cancer imaging and have demonstrated the use of various imaging contrast agents for solution experiments and animal tumor models; this device can pass the sterilization procedure and have the potential application in the intraoperative detection of tumor and metastasis in the endoscopic imaging on human.

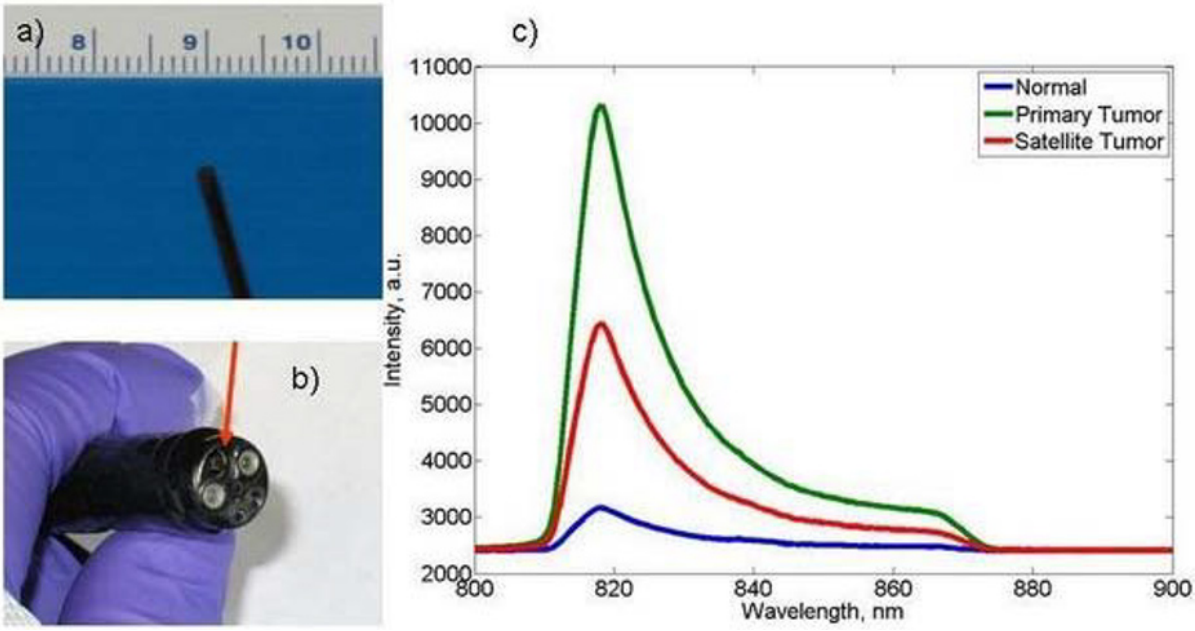

Figure 1: a) the probe of the miniaturized device; b) assembling the device probe (indicated by a red arrow) into the biopsy channel of a sigmoidoscope; c) using the miniaturized device for the in vivo detection of the primary tumor, satellite tumor and normal tissue (muscle) on a mouse with breast cancer model (4T1); 71ug/kg ICG was administered intravenously into the mouse.

Disclosure of author financial interest or relationships:
J. Xu, None; **B. Kairdolf**, None; **J. Provenzale**, None; **S. Nie**, None.

Presentation Number **P 436**
Poster Session 3
September 20, 2013 / 15:15-15:15 / Room: Exhibit Hall B

Imaging prostate tumor metastasis using spectroscopic optical coherence tomography

Miao Zhang, **Ping Yu***, Lixin Ma, University of Missouri, Columbia, MO, USA. Contact e-mail: yuping@missouri.edu*

Spectroscopic optical coherence tomography (OCT) is a potential technique for in vivo molecular imaging in biological tissue. In conventional spectroscopic OCT, the bandwidth of the light source must be large enough to cover the required wavelength range and a complicated algorithm must be used in order to get spectroscopic information. In recent years, dual-band OCT has shown to be a simple and low cost solution for spectroscopic OCT. Dual band OCT uses two superluminescent light emission diodes (SLEDs) with broadband and distinct wavelengths. Normally a single low coherent interferometer and two detectors are used for the spectroscopic detection. In this work, we developed a dual-band Fourier domain OCT (FD-OCT) system with a novel instrumental and algorithm design. We then studied prostate tumor tissues using the new system. In our system, we used two SLED light sources with the wavelengths of 750 nm and 840 nm and bandwidths of 20 and 40 nm, respectively. The small wavelength difference used in our system avoided the false spectroscopic contrast caused by the penetration depth difference in most of the existing systems, which commonly use light sources with a large wavelength difference. Therefore, in our system, the spectroscopic contrast is only related to the sample tissue properties. Furthermore, the system is simplified since only one CCD detector is used. The images from two wavelengths are intrinsically overlapped. Therefore the image processing algorithm is also simplified. We studied primary prostate tumor tissues, metastatic prostate tumor tissues, and muscle tissues excised from severely compromised immunedeficient (SCID) mice using the new dual-band FD-OCT system. The FD-OCT image of a metastatic prostate tumor tissue is shown in the figure and is compared with the histological image. Morphologically, this metastatic tumor shows characteristic porous structure both in dual-band FD-OCT images and histology image. In histological image, the cancer cells are shown in dark blue color. Spectroscopically, the tumor tissue shows color uniformity in OCT images, which can be explained by the isotropic property of tumor cells. The muscle tissue on the back side of the same tumor shows blue color which represents stronger signals at the shorter wavelength. Considering that no strong absorption found in the muscle tissue for the two wavelength bands we use, this signal difference is caused by birefringence and/or anisotropic scattering. In conclusion, we developed a new spectroscopic OCT imaging system. Tissues from SCID mice have been studied using the new imaging system. Metastatic prostate tumor tissues can be recognized according to morphological and spectroscopic features. We would like to thank financial support from the Department of Defense Prostate Cancer Research Program W81XWH-09-2-0176.

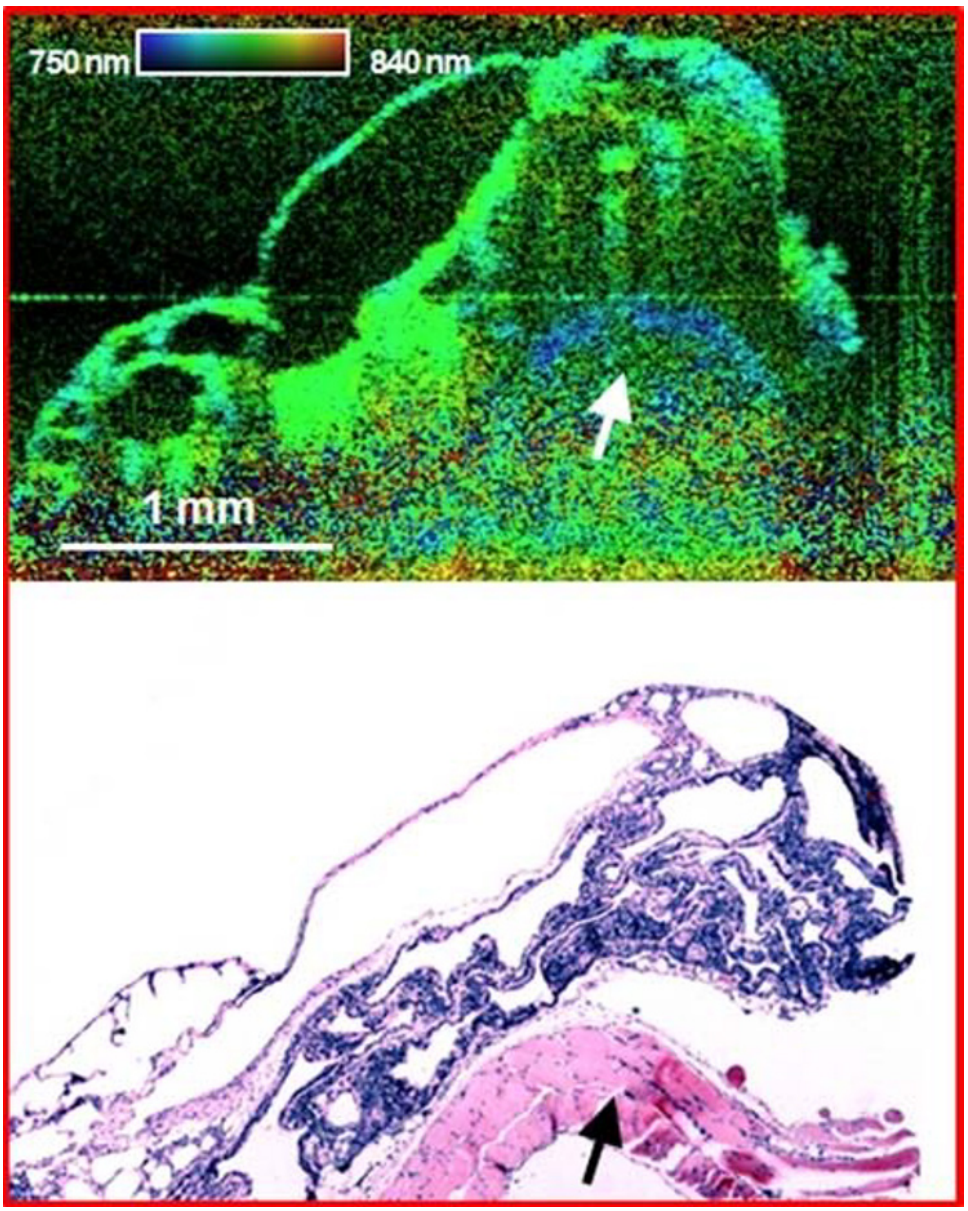

Top: FD-OCT image of a representative metastatic tumor tissue. Bottom: Histological image of the same tissue.

Disclosure of author financial interest or relationships:
M. Zhang, None; **P. Yu**, None; **L. Ma**, None.

Presentation Number **P 437**
Poster Session 3
September 20, 2013 / 15:15-15:15 / Room: Exhibit Hall B

Contrast-Enhanced Folate-Receptor-Targeted Ultrasound Imaging Using Folate-Conjugated Acoustic Droplets in a Mouse Xenograft Tumor Model

Wei-Tsung Chen[1,2], *Chien-Liang Lin*[3], *Chung-Hsin Wang*[3], *Ran-Chou Chen*[1,4], *Chih-Kuang Yeh*[3], [1]*Radiology, Taipei City Hospital, Taipei, Taiwan;* [2]*Radiology, National Taiwan University, School of Medicine, Taipei, Taiwan;* [3]*Biomedical Engineering and Environmental Sciences, National Tsing Hua University, Hsingchu, Taiwan;* [4]*Biomedical Imaging and Radiological Sciences, National Yang-Ming University, Taipei, Taiwan. Contact e-mail: wt2000.chen@msa.hinet.net*

Purpose: The purpose of this study is to validate a folate-conjugated acoustic droplet, for its ability to detect folate receptor-positive tumors in vitro and in live ultrasound imaging. Procedures: folate receptor (FR) positive KB cells, KB cells with 200-fold free folate in medium, and FR negative HT-1080 cells, were incubated with 7-nitrobenzo-2-oxa-1,3-diazole (NBD) labeled folate-conjugated droplets and with NBD-labeled blank droplets for 2 hours respectively. The acoustic droplets were constructed from phase-change perfluorocarbon, lipid-based shell materials, and folate-conjugated methoxypoly (ethyleneglycol) distearoyl- phosphatidyl ethanolamine (DSPE-PEG2000-folate). The cellular attachment ability of the folate-conjugated and blank acoustic droplets was then observed by using fluorescent microscopy and flow cytometry. An agar phantom containing acoustic droplets was made to test whether the acoustic droplets vaporization can be achieved by using a commercial available 3-12 MHz transducer (Envisor, Phillips) with a mechanical index of 1.4. Contrast-enhanced ultrasound was then performed on mice bearing both KB and HT-1080 tumors on bilateral flanks (n=6) and observed for 20 minutes after intravenous folate-conjugated acoustic droplets injection. Results: Green fluorescent acoustic droplets attachment was observed in the KB cells, but was not seen in other control settings. The acoustic droplets vaporization was demonstrated in the phantom model. In the contrast-enhanced ultrasound, the FR positive KB tumors (n=6) showed a gradual enhancement pattern during 20 minutes observation period (figure 1a-e) but the contralateral HT-1080 tumors showed persistent minimal enhancement. The frozen section of the KB tumor showed green fluorescent deposition at the periphery of the KB tumor (figure 1f), where the acoustic droplets vaporization was observed in the delayed ultrasound imaging. Conclusions: We have demonstrated the targeting ability of folate-conjugated acoustic droplets in vitro and in vivo. A gradual enhancement pattern observed in the FR positive tumors can be used to differentiate from the FR negative tumors, in which a persistent minimal enhancement pattern was revealed.

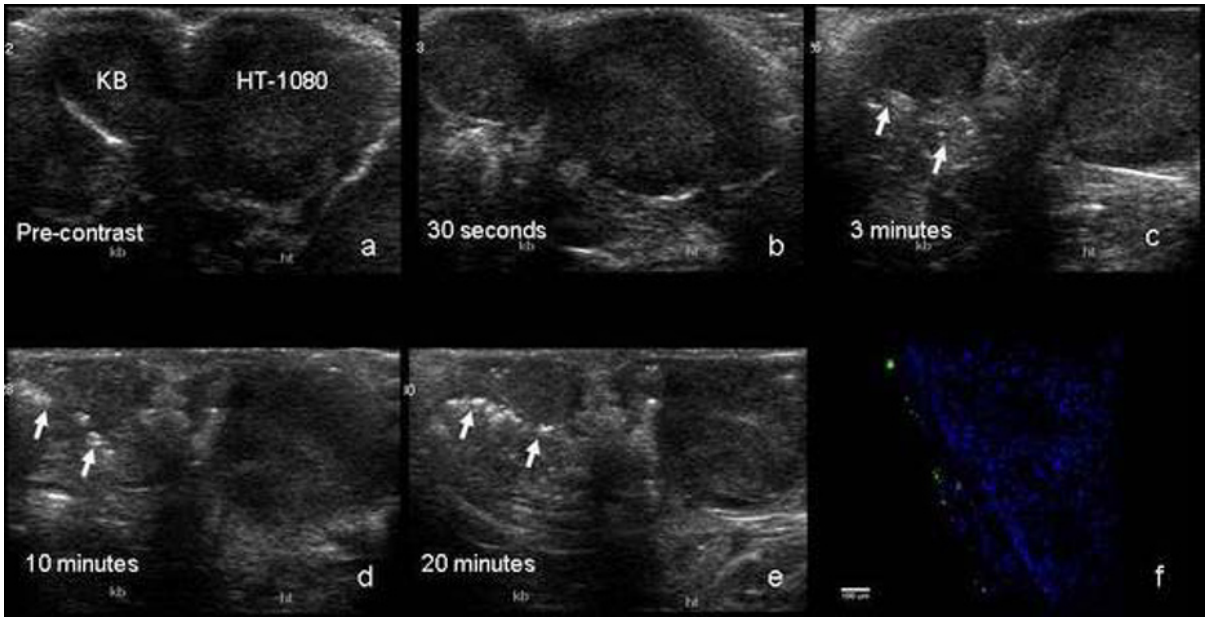

Disclosure of author financial interest or relationships:
W. Chen, None; **C. Lin**, None; **C. Wang**, None; **R. Chen**, None; **C. Yeh**, None.

Presentation Number **P 438**
Poster Session 3
September 20, 2013 / 15:15-15:15 / Room: Exhibit Hall B

Production of Albumin-stabilized Microbubbles for Ultrasound Imaging and Therapy via a Microfluidic Device

Ali H. Dhanaliwala[1], *Johnny Chen*[1], *Adam J. Dixon*[1], *Alexander L. Klibanov*[2], *John A. Hossack*[1], [1]*Biomedical Engineering, University of Virginia, Charlottesville, VA, USA;* [2]*Medicine - Cardiovascular Division, University of Virginia, Charlottesville, VA, USA. Contact e-mail: ahd3y@virginia.edu*

Introduction: Albumin-stabilized microbubbles (MBs) are a common ultrasound contrast and therapeutic agent due to the biocompatibility and stability albumin provides. MBs synthesized and administered using conventional methods (i.e. agitation or sonication and systemic intravenous injection), however, result in polydisperse sized MBs that are quickly cleared from the vasculature. As a result, MB size and concentration are unknown at the site of interest, making it difficult to optimize imaging and therapy parameters. To reduce polydispersity and minimize loss, we aim to generate MBs *in situ* via flow-focusing microfluidic devices (FFMDs) compatible with vasculature dimensions. *In situ* MB generation via FFMDs enables real-time production that can be finely tuned in both rate and diameter, while relaxing the requirement for long-term stability. Consequently, using this paradigm, we are exploring the possibility of large-diameter, short-lifetime, inherently biocompatible MBs stabilized with the albumin from a patient's own blood plasma. **Methods:** FFMD production of MBs utilizing reconstituted bovine serum albumin (BSA) or bovine blood plasma as the liquid phase and nitrogen as the gas phase was characterized for coalescence, diameter, and production rate. The acoustic lifetime of the MBs was estimated by imaging a solution of MBs under constant agitation and measuring the time to half peak B-mode image intensity. Contrast enhancement was determined by flowing whole blood containing MBs through a flow phantom and imaging the lumen with a clinical ultrasound scanner. To determine whether the MBs could enhance drug delivery, rat aortic smooth muscle cells (SMCs) were insonated in the presence of the membrane-impermeable fluorophore calcein and MBs, then imaged for fluorescence as a marker for enhanced drug uptake. **Results:** MBs with diameters between 10-20 μm at production rates between 1-6 x 10^5 MB/s were successfully generated. MBs produced with BSA or blood plasma alone coalesced soon after production (Fig 1A); however, addition of 2.5% (v/v) glycerol and propylene glycol (GP) inhibited coalescence (Fig 1B). At 37 °C, 13 μm diameter MBs were estimated to have an acoustic lifetime of 7.3 ± 3.8s. In the flow phantom, MBs increased the signal intensity within the lumen by 6.5 dB. In the presence of 11 μm diameter MBs produced at a rate of 660,000 per second and insonated at a peak negative pressure of 200 kPa, 58% of SMCs were fluorescent, compared with 0.36% when no ultrasound was applied ($p < 0.0001$). **Discussion and Conclusion:** We demonstrated FFMD production of albumin-stabilized MBs with large diameters for greater bioeffects and short half-lives to prevent gas entrapment in small vessels. FFMDs enable fine control over MB production and the potential to generate MBs in situ, thus reducing the uncertainty of MB diameter and concentration at the site of interest. Additonally monodisperse MB populations, as produced by FFMDs, may improve the imaging contrast and therapeutic potential of MBs. Most importantly, with FFMDs it may be possible to generate a biocompatible microbubble using a patient's own blood plasma directly at the point-of-care.

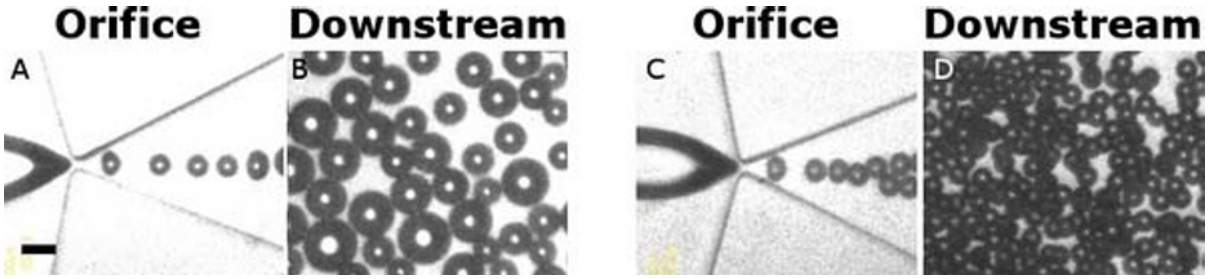

Fig 1: High speed images of MBs forming at microfluidic orifice and 1.7 mm downstream of the orifice. (A,B) MBs produced from BSA alone are initially uniform but coalesce downstream. (C,D) MBs produced from BSA plus GP do not coalesence and remain monodisperse downstream. Scale bar = 20 μm and applies to all images.

Disclosure of author financial interest or relationships:

A.H. Dhanaliwala, None; **J. Chen**, None; **A.J. Dixon**, None; **A.L. Klibanov**, Philips Research North America, Grant/research support; Targeson (NIH SBIR subcontract), Grant/research support; Targeson, Stockholder; AstraZeneca, Grant/research support; **J.A. Hossack**, None.

Presentation Number **P 439**
Poster Session 3
September 20, 2013 / 15:15-15:15 / Room: Exhibit Hall B

The study of absorption efficiency of microbubbles combines with ultrasound on skin treatment

Ai-Ho Liao, *Wan-Chun Ma, Graduate Institute of Biomedical Engineering, National Taiwan University of Science and Technology, Taipei, Taiwan, Taipei, Taiwan. Contact e-mail: aiho@mail.ntust.edu.tw*

Statement of Contribution/Methods US (sonoporation gene transfection system (ST 2000V, NepaGene, Ichikawa, Japan)) combines with microbubbles contrast agent in pig skin and agarose were penetrated by evans blue and the depths were measured by matlab software. The skins were mounted in Franz diffusion cells and determined the skin-whitening component concentration by RP-HPLC. The experimental groups were divided into four groups: (1) only penetrating drug (C); (2) ultrasound combines with penetrating drug (U) (3) ultrasound combines with microbubble contrast agent and penetrating drug (UB); (4) ultrasound combines with 10 fold diluted microbubbles contrast agent (UBD) and penetrating drug. The skin-whitening index were measured by L*a*b* system (Chroma meter CR-40 (Konica Minolta Sensing, Japan)) Results/Discussion Fig. 1 shows the penetration depth of agrose phantom (A-B) and analyzed by matlab (C-D). The penetration depth are 354μm (Fig. 1A), 521μm (Fig. 1B) of C and UBD groups. The greater penetration depth was significantly higher (30%) in UBD group than U (10%) and UB (2.5%) group in penetrating 15 minutes. The microstructure of 100x (E-H) and 400x (I-L) microscopy of the penetration depth in pig skin are presented. The penetration depth was significantly deeper in the UBD group (19.1±3 μm) than C group (10.5±1.9μm), U group (14.2±2μm) and UB group (14.6±2.6μm). Adding ultrasound contrast agent improves the skin permeability and the damages of the stratum corneum have not been observed.

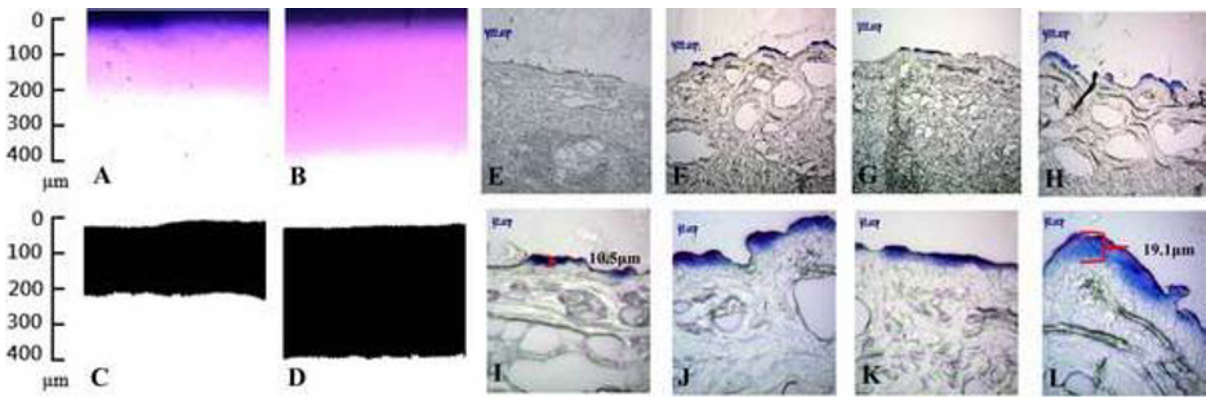

Disclosure of author financial interest or relationships:
A. Liao, None; **W. Ma**, None.

Presentation Number **P 440**
Poster Session 3
September 20, 2013 / 15:15-15:15 / Room: Exhibit Hall B

Optimizing phase-change nanodroplet formulation and synthesis for enhanced biodistribution and cell targeting

Robert J. Paproski[1], *Desmond Pink*[2], *Katia Carmine Simmen*[2], *John D. Lewis*[2], *Roger J. Zemp*[1], [1]*Electrical and Computer Engineering, University of Alberta, Edmonton, AB, Canada;* [2]*Oncology, University of Alberta, Edmonton, AB, Canada. Contact e-mail: robertpaproski@hotmail.com*

Sheeran et al (Langmuir 2011) previously described the creation of nanodroplets (NDs) which are nanosized perfluorobutane liquid droplets stabilized by a phospholipid shell. NDs exposed to high mechanical index (MI) ultrasound can phase-change into microbubbles which can provide ultrasound imaging contrast & cavitation nuclei for enhancing sonoporation of cells. We investigated the in vivo kinetics & biodistribution of Sheeran's ND formulation and realized that these NDs (containing positively charged 1,2-dipalmitoyl-3-trimethylammonium-propane) have significant non-specific cell binding properties which greatly reduces their kinetics and biodistribution. Our goal was to create new formulations of NDs optimized for enhanced 1) in vivo biodistribution, and 2) receptor specific uptake. **Methods:** Cationic & anionic (shell formulation similar to Definity® microbubbles) NDs were created with lipids containing Rhodamine B and injected in the chorioallantoic membranes (CAM) of chicken embryos followed by microscopic imaging of the CAM immediately after and 24 hours after ND injection. Chicks were sacrificed 24 hours after ND injection and tissues were dissected and visualized using confocal microscopy. A second anionic ND formulation was created containing lipids conjugated with folate. Unconjugated and folate conjugated anionic NDs (also containing lipids with Rhodamine B) were created and some NDs were forced through a 200 nm filter using a mini-extruder and sized using a Malvern Zeta sizer. NDs were incubated for 2 hours with folate receptor negative and positive ZR-75-1 and HeLa cells, respectively, and cells were washed and imaged with confocal microscopy. **Results:** Cationic NDs displayed very little flow when injected in the CAM. Many of the cationic NDs remained near the injection site as large clumps. In contrast, the anionic NDs displayed rapid flow and widespread distribution through all of the CAM vasculature. Anionic NDs also displayed significantly greater accumulation in the brain, heart, and especially lungs of chicken embryos. ZR-75-1 and HeLa cells displayed no uptake of either the folate-conjugated or unconjugated NDs which were ~530 nm in diameter. Extruded NDs were ~370 nm in diameter and only the folate-conjugated extruded NDs were taken up by HeLa cells. Extruded NDs also had ~half the polydispersity index, suggesting greater size uniformity. Phase-change NDs could be activated into microbubbles with as few as 10 cycles of 1.7MI ultrasound, or >100 cycles of 1.0MI ultrasound. Phase-change ND activation was visible using a commercial small animal ultrasound imaging system. **Conclusion:** Based on our results, cationic NDs have high non-specific cell binding properties and incorporation of anionic lipids in NDs is necessary for favorable kinetics and biodistribution for in vivo use. NDs can be sized with extrusion and must be < 500 nm for cell uptake. Ongoing experiments involving identification of ND size requirements for accumulation in tumors will also be discussed..

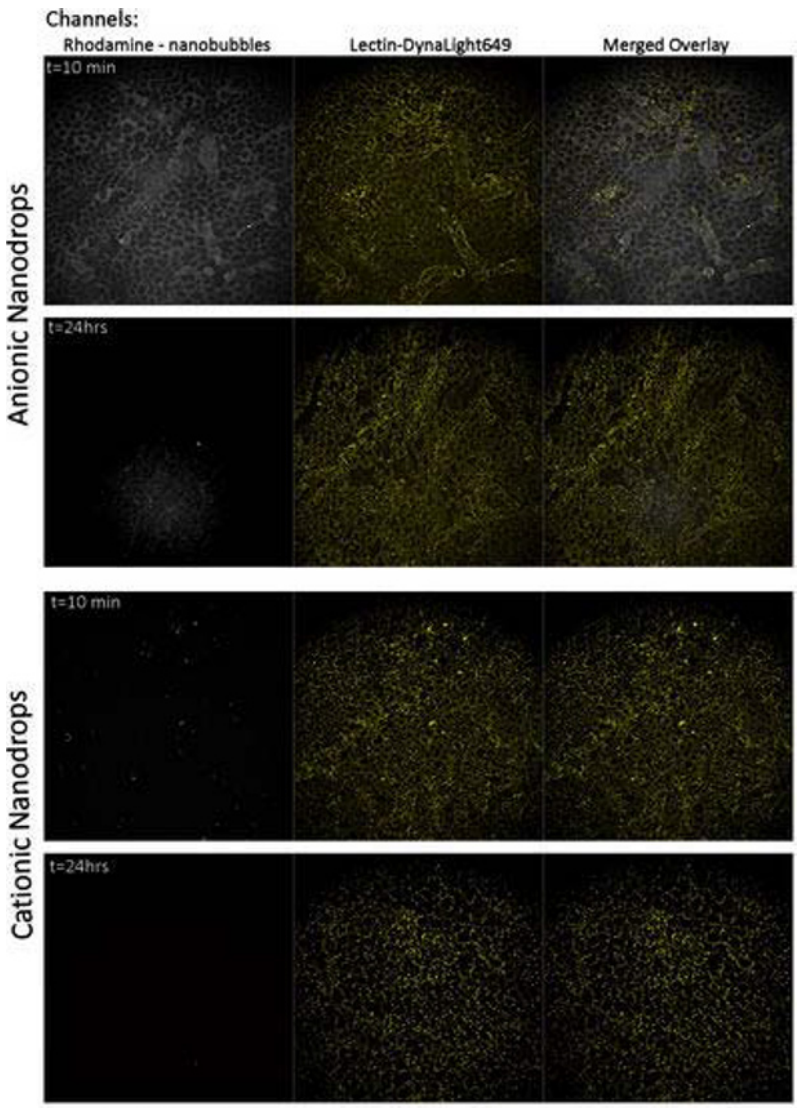

Protocol: 100uL of nanodrops diluted in PBS were injected IV. CAMs were covered with a coverslip and imaged using a confocal microscope. Exposure for the rhodamine-labelled nanodrops was held constant and contrast in post analysis was similarly held constant. Chicks were injected with lectin (lens culinaris) -Dynalight649 for visualization of the vascular bed.

Disclosure of author financial interest or relationships:
R.J. Paproski, None; **D. Pink**, None; **K. Carmine Simmen**, None; **J.D. Lewis**, None; **R.J. Zemp**, None.

Presentation Number **P 441**
Poster Session 3
September 20, 2013 / 15:15-15:15 / Room: Exhibit Hall B

Molecular Imaging of Inflammation Using Ultrasound in a Porcine Acute Terminal Ileitis Model: Moving towards Clinical Translation

Huaijun Wang[1], *Stephen Felt*[2], *Ismayil Guracar*[3], *Steven Machtaler*[1], *Thierry Bettinger*[4], *Richard Luong*[2], *Juergen K. Willmann*[1], [1]*Department of Radiology, Molecular Imaging Program at Stanford, Stanford University, Stanford, CA, USA;* [2]*Department of Comparative Medicine, Stanford University, Stanford, CA, USA;* [3]*Ultrasound Business Unit, Siemens Healthcare, Mountain View, CA, USA;* [4]*Bracco Suisse SA, Geneva, Switzerland. Contact e-mail: whjwang@stanford.edu*

Purpose: Crohn's disease is a chronic and relapsing inflammatory disease of the bowel that primarily affects young patients, peaking in the second and third decades of life. In patients with this disease, distal small bowel (terminal ileum) is the most commonly affected segment. Since multiple follow-up exams are needed, often over many years, disease monitoring should be noninvasive, radiation-free, and, above all, patient-friendly. A simple technique that meets all these requirements is not available today. Recently, it has been shown that molecularly-targeted (molecular) ultrasound (US) imaging can improve accuracy of US in assessing disease's activity in a mouse colitis model by visualizing adhesion molecules using dual P-and E-selectin-targeted contrast microbubbles ($MB_{Selectin}$). The purpose of this study was to further translate selectin-targeted US imaging from small to large animals. Materials and Methods: An acute terminal ileitis porcine model was established in 9 female pigs by intraluminal exposure of a 10-cm segment of the terminal ileum with 2,4,6-trinitrobenzene sulfonic acid (TNBS in ethanol). All pigs were imaged before (control), and 48hours after induction of acute ileitis. US molecular imaging of terminal ileum was performed in contrast pulse sequencing mode after i.v. injection of 5×10^8/kg b.w. $MB_{Selectin}$ or non-targeted $MB_{Control}$ using a clinical US machine (Acuson Sequoia 512; Siemens) and a clinical transducer (15L8W; 7MHz). Images were acquired in the transverse plane (lateral and axial resolution of 200μm each). Four minutes after contrast agent injection, US data sets were acquired for 10 sec, followed by a 3-sec high power (1.9MI) destruction pulse; this was followed by another 10-sec data acquisition. Linearized imaging signal was expressed as intensity ratio, defined as average pre-destruction signal intensity divided by average post-destruction signal intensity. After imaging, pigs were sacrificed and the terminal ileum was analyzed for inflammation grade on H&E staining and for expression of P- and E-selectin on immunofluorescence. Results: US molecular imaging of the terminal ileum was feasible in all 9 pigs. Imaging signal intensity ratio with $MB_{Selectin}$ in acute ileitis was significantly higher (increased by 106%, P=0.005) than in normal control ileum at baseline. In addition, US molecular imaging signal was significantly higher (increased by 103%, P=0.002) in acute ileitis using $MB_{Selectin}$ compared to $MB_{Control}$. In normal control ileum at baseline imaging, US molecular imaging signal was not significantly different (P=0.06) when using $MB_{Selectin}$ or $MB_{Control}$. Ex vivo analysis on H&E stained tissue samples confirmed strong inflammation in the terminal ileum at day 2. Immunofluorescence showed overexpression of selectins on the vasculature of inflamed bowel. Conclusion: US molecular imaging with $MB_{Selectin}$ can be translated to large animal imaging in an acute terminal ileitis porcine model and correlates well with extent of inflammation on histology. This study paves the way towards clinical translation of US molecular imaging for accurate and objective quantification of inflammation in the abdomen.

Disclosure of author financial interest or relationships:
H. Wang, None; **S. Felt**, None; **I. Guracar**, Siemens Medical Solutions, Employment; **S. Machtaler**, None; **T. Bettinger**, Bracco Suisse SA, Employment; **R. Luong**, None; **J.K. Willmann**, Bracco, Consultant; Siemens, Grant/research support; Bracco, Grant/research support .

Presentation Number **P 442**
Poster Session 3
September 20, 2013 / 15:15-15:15 / Room: Exhibit Hall B

Three-dimensional Ultrasound Molecular Imaging of Angiogenesis in Colon Cancer: Preliminary Feasibility Study in a Mouse Model

Huaijun Wang[1], *Osamu F. Kaneko*[1], *Vijay Shamdasani*[2], *Dimitre Hristov*[3], *Juergen K. Willmann*[1], [1]*Department of Radiology, Molecular Imaging Program at Stanford, Stanford University, Stanford, CA, USA;* [2]*Philips Healthcare, Bothell, WA, USA;* [3]*Department of Radiation Oncology, Stanford University, Stanford, CA, USA. Contact e-mail: whjwang@stanford.edu*

Purpose: Targeted contrast-enhanced (molecular) ultrasound (US) imaging is an emerging technique finding its niche among other molecular imaging approaches for earlier disease detection and treatment monitoring at the molecular level. Current US imaging equipment only supports two-dimensional (2D) US molecular imaging data acquisition. However, three-dimensional (3D) US molecular imaging capabilities can be advantageous particular for more accurate treatment monitoring of cancer response along the entire volumetric extent of tumors. The purpose of this study was to explore the feasibility of 3D US molecular imaging using a 3D clinical transducer in a human colon cancer xenograft model in mice undergoing vascular disrupting treatment. Materials and Methods: Subcutaneous human colon cancer LS174T xenografts were induced in 14 female nude mice. Mice were randomly assigned to either 1) a treatment group receiving the vascular disrupting agent ASA404 (n=8; single dose of 15 mg/kg i.v.) or 2) a control group (n=6; saline only) with no treatment. All mice were scanned with US at baseline (day 0) and at day 1 after treatment. 3D US molecular imaging was performed with a clinical US system (IU22 xMATRIX; Philips Healthcare, Bothell, WA) and a clinical transducer (X6-1; center frequency, 3.2 MHz; voxel size, $0.32\times0.11\times0.21 mm^3$; focal length, 40mm; mechanical index, 0.37; dynamic range, 40dB) at 4 min after i.v. injection of 5×10^7 VEGFR2-targeted microbubbles (MB-VEGFR2) or non-targeted control microbubbles (MB-Control) administered at the same dose in the same imaging session. After imaging, all mice were sacrificed and tumors were analyzed for VEGFR2 expression levels on ex vivo immunofluorescence. Results: 3D US molecular imaging was feasible in all 14 tumors. In the treatment group, US molecular imaging significantly ($P<0.001$) decreased from $1.3\times10^6\pm7.9\times10^5$ a.u. at baseline to $2.5\times10^5\pm2.3\times10^5$ a.u. following a single treatment with ASA404. In the control group, imaging signal was not significantly different ($P=0.67$) at baseline and at day 1. Injection of MB-VEGFR2 resulted in significantly higher ($P<0.001$) imaging signal compared to MB-Control in both treated and non-treated groups. Ex vivo immunofluorescence analysis confirmed a decrease of VEGFR2 staining in treated tumors and no substantial change in non-treated mice. Conclusion: Volumetric US molecular imaging using a clinical US system and 3D transducer is technically feasible. Preliminary data show good correlation of in vivo VEGFR2-targeted US imaging signal with ex vivo VEGFR2 expression levels in human colon cancer xenografts in mice undergoing vascular disrupting treatment. 3D imaging capabilities of US may further expand its future clinical role in molecular imaging of cancer.

Disclosure of author financial interest or relationships:
H. Wang, None; **O.F. Kaneko**, None; **V. Shamdasani**, None; **D. Hristov**, None; **J.K. Willmann**, Bracco, Consultant; Siemens, Grant/research support; Bracco, Grant/research support .

Presentation Number **P 443**
Poster Session 3
September 20, 2013 / 15:15-15:15 / Room: Exhibit Hall B

Non-invasive investigations on the biomechanical properties of mice xenograft solid tumors by Scanning Acoustic Microscopy and µCT

Ralph Pflanzer[1], *Anowarul Habib*[2], *Matthias Hofmann*[1], *Jürgen Bereiter-Hahn*[2], *Robert Sader*[3], [1]*Clinic of Dermatology, Venerology and Allergology, Goethe University Frankfurt am Main, Frankfurt am Main, Germany;* [2]*Institute for Cell Biology & Neuroscience, Goethe University Frankfurt am Main, Frankfurt am Main, Germany;* [3]*Dept. of Oral, Craniomaxillofacial and Facial Plastic Surgery, Goethe University Frankfurt am Main, Frankfurt am Main, Germany. Contact e-mail: ralphpflanzer@gmail.com*

Solid tumors grown subcutaneously in a preclinical mouse model share common abnormal biological properties which distinguish them from healthy tissue. One prominent feature is the elevated tumor interstitial fluid pressure (TIFP), which originates from a chaotically organized vessel network and insufficient tumor lymph drainage. The consequences are not only impairment in effective transport of tumor therapeutics inside the tumor, but also an increased proliferation of tumor cells induced by mechanical stress on the tumor wall. Lowering of this pressure has been experimentally undertaken and shown beneficial effects. TIFP ranges up to 40mm Hg, but is highly dependent on tumor type as well as its location and can be determined by conventional measurements methods like the wick-in-needle technique and more indirect ones, like the micropuncture method. We propose a completely non-invasive means of determination of TIFP via Scanning Acoustic Microscopy (SAM) at 30 MHz on excised as well as in-situ A431 vulva-carcinoma derived tumors. Pre-treatment of samples with various vascular endothelial growth factors (VEGF) or anti-cancer drugs like Temsirolimus or Cetuximab show different influence on the biomechanical properties of tumor tissue pertaining to angiogenesis as well. To account for the influence and structure of the supplying peripheral network of tumor-recruited blood vessels, we have investigated these with µCT on a subset of plastinated tumor models of previously perfused mice specimen. With these three-dimensional representations of the actual branching network structure of tumor vessels in conjunction with the ultrasound imaging, a characterization of tumor vessel architecture is possible. Future studies which make use of these two non-invasive modalities in conjunction are suited to improve understanding how biomechanical properties effect tumor growth and tumor therapy options.

Disclosure of author financial interest or relationships:
R. Pflanzer, None; **A. Habib**, None; **M. Hofmann**, None; **J. Bereiter-Hahn**, None; **R. Sader**, None.

Presentation Number **P 444**
Poster Session 3
September 20, 2013 / 15:15-15:15 / Room: Exhibit Hall B

Flow Shear Force-induced Decorrelation Produces a Reliable Statistical Signature of Adherent Microbubbles in Ultrasound-based Targeted Molecular Imaging

Shiying Wang, *F. W. Mauldin, Jr., John A. Hossack, Biomedical Engineering, University of Virginia, Charlottesville, VA, USA. Contact e-mail: sw7mf@virginia.edu*

Ultrasound-based targeted molecular imaging holds promise for early detection and diagnosis of stroke risk by identifying markers for atherosclerosis prior to detection of functional or anatomical response to disease. Current real-time strategies employ non-linear signal extraction (*e.g.* pulse inversion) to isolate microbubbles (MBs) from tissue and then low-pass filtering across frames to isolate adherent MBs (AMBs) from free MBs. While the success of these techniques has been well substantiated in microvasculature (*e.g.* molecular imaging of tumors), efficacy is more challenging in large blood vessel environments due to high flow rates, low MB-vessel wall contact, and bright non-linear reflections from the vessel wall. To enable enhanced performance in large blood vessel environments, we have previously demonstrated a new method called singular spectrum-based targeted molecular imaging (SiSTM), which uses changes in statistical dimensionality - quantified by normalized singular spectrum area (NSSA) - to more effectively isolate AMBs. The aim of this work is to elucidate the physical mechanism responsible for AMB separation employed in SiSTM in large blood vessels. Tissue-mimicking phantoms were constructed with 4.2 mm diameter lumen. Fluid channels were incubated with 50 μg/mL streptavidin for 5 h and then with 5% bovine serum albumin for 3 h. Experiments were performed by pulling biotinylated lipid shelled MB (~ 2 μm) solution through the channels. Custom SiSTM beam sequences were programmed on a Verasonics scanner using an ATL L12-5 38mm transducer. Plane wave imaging pulses (4.09 MHz, 50 Hz frame rate) were interspersed with transmit-focused radiation force pulses (800 Hz PRF, MI < 0.09, MBs did not burst). Different MB concentration (0.02 - 2 × 10^6/mL), radiation pulse lengths (0 - 64 cycles), and flow rates (0 - 50 mL/min) were tested systematically to examine the possible physical mechanisms: MB concentration, secondary radiation force, and flow shear force, correspondingly. In isolation from flow shear forces, neither increased MB concentration (Fig (a), $p < 0.018$; n = 5) nor increased pulse length (Fig (b), $p > 0.23$; n = 5) resulted in an increased NSSA above the vessel wall itself. However, in the presence of flow shear forces, NSSA of AMBs were observed to be significantly higher than the vessel wall and the NSSA at steady-state was a function of the flow rate (Fig (c), $p < 0.01$; n = 10). The dynamics of the NSSA closely followed the derivative of the intensity curve with maximum NSSA occurring with maximum increase in the rate of MB adhesion. The NSSA values of AMBs under flow also closely matched the measured decorrelation values (Fig (d), adjusted-$R^2 > 0.9$). These results support the hypothesis that flow shear forces are directly responsible for the NSSA signature of AMBs that is exploited in SiSTM imaging. Results further demonstrate that NSSA increases under flow conditions due to continuous aggregation and detachment of MBs along the vessel wall over time. As new MBs enter and leave the image frame, echo decorrelation is measurable - causing the observed increase in NSSA. Grant: US NIH R01 HL111077

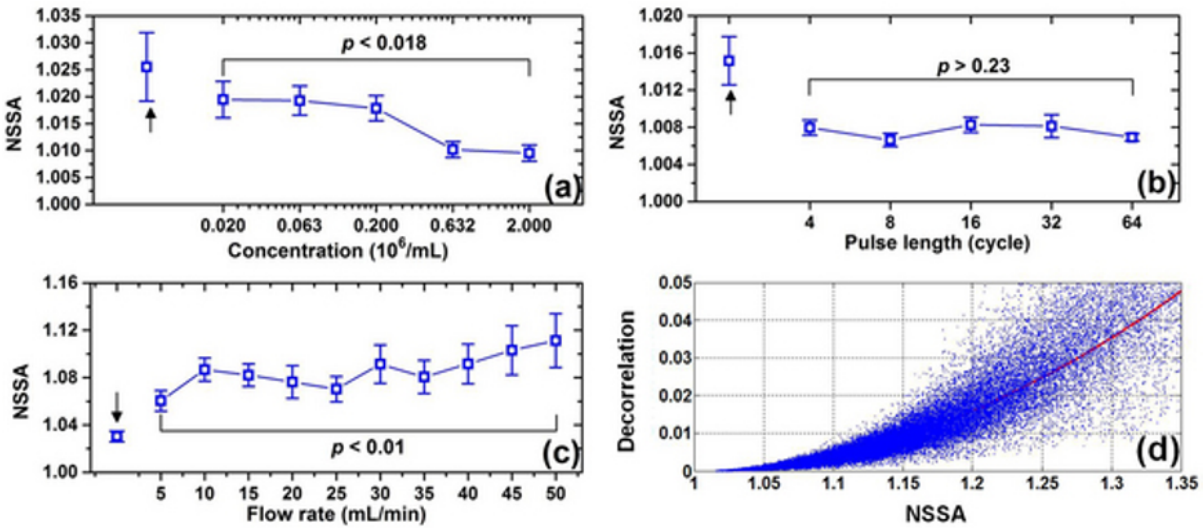

Fig: Relationships between NSSA of AMBs and (a) MB concentration, (b) pulse length, (c) flow rate and (d) echo decorrelation. Black arrows in (a) to (c) show the vessel wall without MB injection. Red line in (d) shows the quadratic fit (adjusted-R^2 = 0.9).

Disclosure of author financial interest or relationships:
S. Wang, None; **F.W. Mauldin, Jr.**, None; **J.A. Hossack**, None.

Presentation Number **P 445**
Poster Session 4
September 21, 2013 / 14:45-14:45 / Room: Exhibit Hall B

Development of a Multimodal Hyperbranched Polymer Imaging Agent for PET, 19F MRI and Optical Imaging

Nathan R. Boase[1,2], *Idriss Blakey*[1,2], *Karine Mardon*[2], *Kristofer J. Thurecht*[1,2], [1]*Australian Institute for Bioengineering and Nanotechnology, University of Queensland, Brisbane, QLD, Australia;* [2]*Centre for Advanced Imaging, University of Queensland, Brisbane, QLD, Australia. Contact e-mail: nathan.boase@uqconnect.edu.au*

Our group has recently developed hyperbranched polymer 19F MRI devices, which are able to provide high resolution images, with high signal to noise ratio *in vivo*.(1) Here we report on the further development of these hyperbranched polymers into multimodal imaging devices, including fluorescent dyes for optical imaging and radioisotopic ligands for Positron Emission Tomography (PET). These modalities have been included, to aid in the pre-clinical development of these nano-medicine devices. *In vivo* optical imaging is commonly used due to its relative low cost and high throughput capacity, but has drawbacks when moving to larger animal models or ultimately into a clinical setting. PET imaging is highly sensitive (10-11 M), but increases the radiation burden on patients and is also an expensive technique which requires access to a cyclotron. By combining these two latter imaging modalities, we are able to undertake preliminary screenings on the targeting ability of our materials with optical imaging, and then delve into more detailed investigations into the biodistribution of the polymer using PET. The hyperbranched nanoparticles in this work were synthesised using RAFT polymerisation.(2) This technique allows for control over the size and structure of the polymers and provides reactive end groups that can be later functionalised. In this work these groups were functionalised with the bifunctional ligand p-SCN-Bn-DOTA (Macrocyclics Ltd.), a near infrared optical imaging dye IR Dye 750 (LI-COR Biosciences) and folate targeting ligands. DOTA was attached to the polymer for introduction of copper-64 radioisotopes. Cu-64 was chosen for this work as it has a longer half life (12.7 hours) in comparison to other commonly used isotopes (F-18: 110 mins, C-11: 20 mins), which better matches the reported biological half life of polymers.(3) Folate provides a simple system for specific targeting for an *in vivo* B16 mouse melanoma model used in our laboratory. Characterisation of the attachment of these molecules was confirmed using 1H NMR, UV-Vis spectroscopy, with AAS for analysis of copper labelling. Preliminary *in vivo* PET and optical imaging experiments have been performed using a subcutaneous B16 melanoma model in C57/BL6 mice. For optical imaging experiments, each mouse was injected intra-venously with 50 uL of a 20 mg/mL solution of polymer in PBS and imaged with a Carestream MS-FX Pro imaging station for 24 hours followed by ex vivo analysis. For PET imaging experiments, each mouse was injected intravenously with ~7 MBq of activity in 50 uL PBS (4 µg/mL polymer concentration). These experiments have shown some specific targeting of the tumours with the folate labelled polymers, but that there is still significant signal from other organs in the body, in particular the liver. In conclusion, we have demonstrated the development of a novel polymeric multimodal imaging agent, which can incorporate optical and nuclear imaging techniques onto a core 19F MRI device. (1) Thurecht, K. et al., Am. Chem. Soc. 2010, 132, 5336. (2) Liu, B.; et al., Macromolecules 2005, 38, 2131. (3) Williams, H.; et al., Eur. J. Nucl. Med. Mol. Imag. 2005, 32, 1473.

Schematic diagram demonstrating synthesis of a targeted, hyperbranched polymer molecular imaging agent, with PET (a) and optical (b) imaging capabilities.

Disclosure of author financial interest or relationships:
N.R. Boase, None; **I. Blakey**, None; **K. Mardon**, None; **K.J. Thurecht**, None.

Presentation Number **P 446**
Poster Session 4
September 21, 2013 / 14:45-14:45 / Room: Exhibit Hall B

Engineering Colloidal Hybrid Nanostructures as Multimodal Contrast Agents for Cancer Imaging in Living Subjects

Kai Cheng, *Jesse V. Jokerst, Hongguang Liu, Sri Rajasekhar Kothapalli, Meng Yang, Jelena Levi, Joseph C. Wu, Sanjiv S. Gambhir, Zhen Cheng, Radiology, Stanford University, Palo Alto, CA, USA. Contact e-mail: kaicheng@stanford.edu*

Introduction: Multimodality imaging has attracted significant research interests since it takes advantage of strengths of each modality and provides complementary information of diseases that cannot be obtained from a single imaging modality. Most attempts to incorporate different imaging modalities [eg, positron emission tomography (PET), magnetic resonance imaging (MRI), optical, photoacoustic imaging (PAI), Raman imaging, etc.] together require the design and construction of multifunctional probes from multiple components either assembled using molecular linkers or fused together by solid-state interfaces. Recently, we have successfully synthesized plasmonic gold nanotripods (Au-tripods) with controllable size, uniform shape, and narrow size distribution, which have shown great promise as contrast agents for PAI. Here we designed and tested multifunctional Au-tripods for PET/PAI/Raman triple-modality imaging of tumors in living subjects (Figure 1a). Method: The Au-tripods were synthesized using the seed-mediated process. Raman reporter (trans-1,2-bis (4-pryidyl)-ethylene (BPE) and silica layer were coated onto the surface of Au-tripods using a reverse microemulsion procedure. The Affibody modification on the PEGylated surface of Au-tripods was used to specifically target the epidermal growth factor receptor EGFR-positive tumor (A431). Lastly, the immobilization of 64Cu chelator (NOTA) allowed us to image tumor using PET in small tumor mice models (n=4 in each group). Results: The resultant multifunctional Au-tripod-Affibody probes showed significantly enhanced photoacoustic (PA) and Raman contrast effects in both phantom and small animal imaging experiments (Figure 1b and 1c, $p < 0.01$). PET efficiently provided the in vivo pharmacokinetics and biodistribution of those nanoprobes. Compared to the Affibody blocking controls, the tumor accumulation was significant (more than 8% ID/g after 24 hour postinjection). Bio-distribution studies further demonstrated that the multifunctional Au-tripod-Affibody probes had high tumor, liver, spleen, and kidney uptakes. The hepatic and renal clearance were observed and associated with the elimination of the nanoprobes from mice (Figure 1d). The functional and molecular information of the tumor with high spatial resolution were further obtained by PAI. The images correlated well with the corresponding PET quantification (Figure 1e). Raman imaging finally provided real-time images with superior sensitivity during the procedure of image guided surgery to confirm the completion of tumor resection. Conclusion: Engineering plasmic gold nanostructures as multimodal contrast agents were successfully prepared, and it could allow us to specifically image tumors in an accurate and quantitative manner.

Disclosure of author financial interest or relationships:
K. Cheng, None; **J.V. Jokerst**, None; **H. Liu**, None; **S. Kothapalli**, None; **M. Yang**, None; **J. Levi**, None; **J.C. Wu**, None; **S.S. Gambhir**, Bracco Diagnostics, Consultant; Endra, Inc, Stockholder; Cellsight, Stockholder; Enlight, Inc., Stockholder; General Electric, Grant/research support; ImaginAb, Stockholder; MagArray, Inc., Stockholder; Sanofi-Aventis, US, Grant/research support; SiteOne Therapeutics, Stockholder; VisualSonics/Sonosite, Stockholder; **Z. Cheng**, None.

Presentation Number **P 447**
Poster Session 4
September 21, 2013 / 14:45-14:45 / Room: Exhibit Hall B

Polymersome-Based Molecular Imaging Nanoprobes

Zhiliang Cheng, *Andrew Tsourkas, Department of Bioengineering, Univ of Pennsylvania, Philadelphia, PA, USA. Contact e-mail: zcheng@seas.upenn.edu*

The development of nanoparticle-based imaging probes offers to substantially improve the specificity and sensitivity of diagnostic imaging by allowing for the non-invasive and quantitative detection of specific biomolecules in living subjects. Among the many nanoparticle imaging probes, polymersome-based molecular imaging agents possess several beneficial properties, including increased mechanical stability, the ability to solubilize larger quantities of hydrophobic compounds, and typically a complete PEG (i.e. a PEG brush) surface, offering a stealth character in vivo. Further, polymersomes can be finely tuned through polymer selection to yield vesicles with diverse functionality, i.e. biodegradability, biocompatibility, permeability, etc. As a result of these characteristics, polymersomes have garnered a great deal of interest as nanoplatforms for a range of biomedical applications, including drug delivery, in vivo imaging, and for use as cell mimetics. Here, we describe the use of nanometer-sized polymersomes to prepare two different molecular imaging probes (Figure 1): magnetic resonance (MR) contrast agents and optical imaging probes. For MR contrast agents, the Gd-labeled dendrimers were encapsulated into the large intra-vesicular volume to achieve high Gd payloads. To overcome the slow water exchange rate across the membrane bilayer, pores were introduced into the vesicle wall. As a result of the slower rotational correlation time of Gd-labeled dendrimers, the porous outer membrane of the nanovesicle, and the high Gd payload, the nanovesicles were found to exhibit a relaxivity (r1) of ~300,000 mM-1 s-1 per particle. In comparison, small Gd-DTPA possesses an r1 of only 3.9 mM-1s-1. Therefore, the polymersomes exhibited a relaxivity that was amplified by a factor of ~75,000 (per particle), which led to improved contrast enhancement for in vivo T1-weighted MR imaging. For polymersome-based optical imaging probes, fluorescent dyes were encapsulated within the vesicle lumen, incorporated within the membrane bilayer, or immobilized onto the outer membrane surface. In this work, a small percentage of phospholipids were also incorporated into these PEG-based polymersomes to dilute the density of the PEG-brush on the vesicle surface and as a result reduce the steric effect that PEG exerted on attached targeting ligands. To confer specificity for cancer cells, these lipid-polymer nanovesicles were functionalized with either folic acid or anti-HER2/neu affibodies as targeting ligands. Both in vitro and in vivo fluorescent images showed that binding of polymersomes to receptor-positive cancer cells in living subjects was highly efficient and specific.

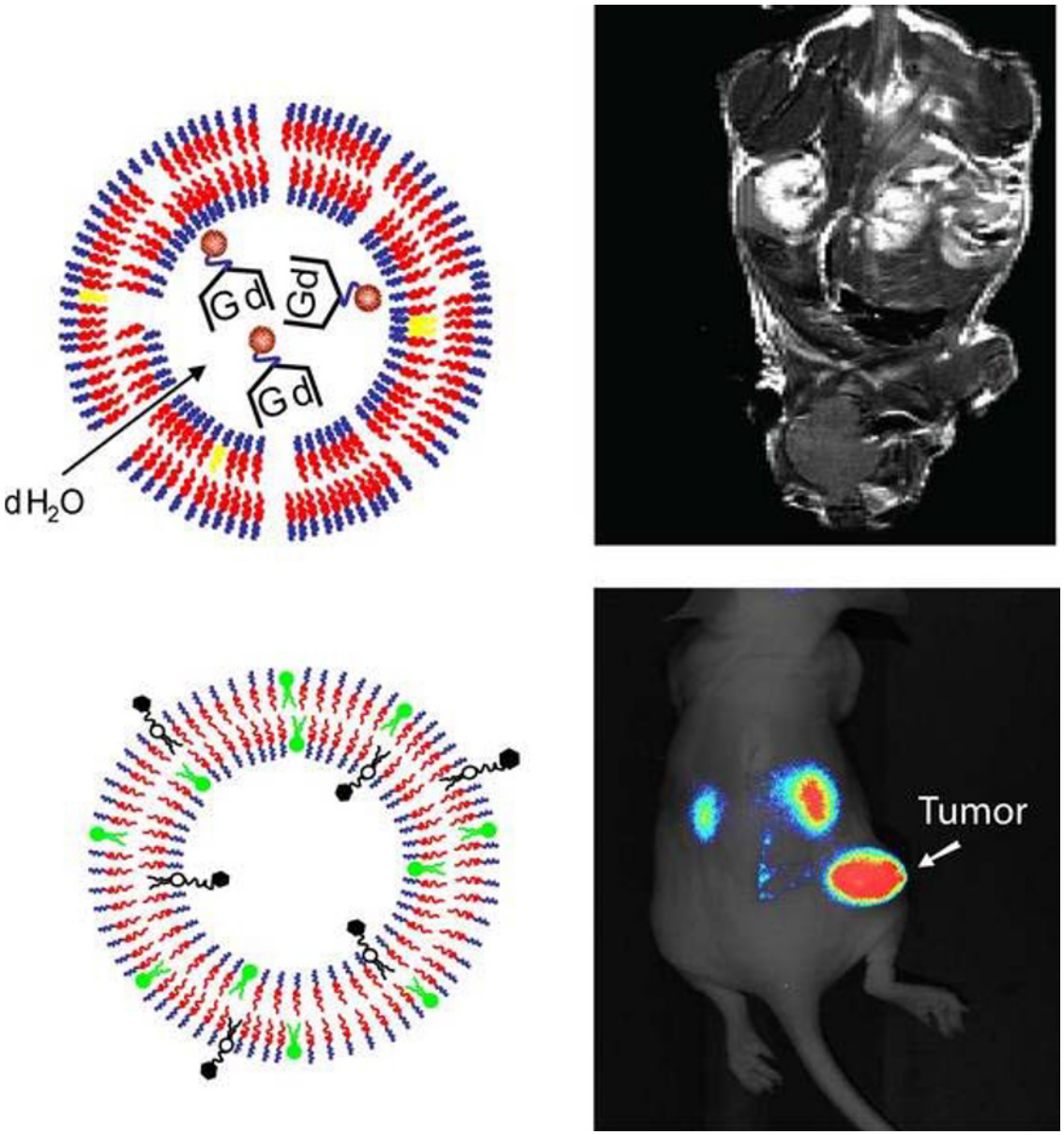

Figure 1. (Top) Polymersome-based MR contrast agents and their in vivo MR imaging. (Bottom) Polymersome-based fluorescent probes and their in vivo optical imaging.

Disclosure of author financial interest or relationships:
Z. Cheng, None; **A. Tsourkas**, None.

Presentation Number **P 448**
Poster Session 4
September 21, 2013 / 14:45-14:45 / Room: Exhibit Hall B

Loading poly (lactic acid) microbubbles with nanocrystals for multimodal imaging

Peter Chhour[1], *Nutte T. Teraphongphom*[2], *Lauren J. Jablonowski*[2], *Walter R. Witschey*[1], *Pratap C. Naha*[1], *David P. Cormode*[1], *Margaret Wheatley*[2], [1]*Radiology, University of Pennsylvania, Philadelphia, PA, USA;* [2]*Biomedical Engineering, Drexel University, Philadelphia, PA, USA. Contact e-mail: pchhour@gmail.com*

Introduction: Poly (lactic acid) (PLA) is an FDA approved polymer that can be formed into micron sized bubbles. These microbubbles entrap air which allow for utilization as contrast agents in ultrasound imaging and in sonoporation induced drug delivery. We have found that payloads can be incorporated into the PLA shell and provide contrast for multimodal imaging. We have loaded microbubbles with nanocrystals such as iron oxides, gold, or quantum dots, allowing for parallel imaging with MRI, CT, fluorescence, respectively (A). In addition, nanocrystal loaded microbubbles can be used to localize microbubble shards after sonoporation. In this study, we present the characterization and contrast generating properties of these loaded microbubbles. Methods: The microbubbles were synthesized by using a water-in-oil-in-water emulsion technique followed by a freeze drying phase to form the air filled PLA bubble. The different nanocrystals were incorporated into the PLA during the first emulsion phase of the synthesis. Iron nanoparticles coated with oleic acid were loaded into microbubbles (IOMBs) and their MRI relaxation times were assessed via relaxometry (60 MHz, Minispec, Bruker). Gold nanoparticles capped with dodecanethiol were loaded into the PLA microbubbles (AuMBs) and were characterized for CT attenuation properties using a clinical scanner. Organic quantum dots were loaded into microbubbles (QDMBs) and were assessed with an Olympus IX81 confocal fluorescence microscope. Transmission electron microscopy (TEM) was performed using a JEOL 1010. Scanning electron microscopy (SEM) was performed on a FEI XL30. Ultrasound acoustic enhancement testing was performed using a custom-built acoustic setup with a 5 MHz transducer to focus the acoustic signal that was generated by the pulser/receiver at 100 Hz in a 37oC phosphate buffered saline (PBS) solution. Results: TEM showed that the nanocrystals used could be incorporated into the shell of the PLA microbubbles (B). We found that gold nanoparticles formed large aggregates when incorporated into MBs as opposed to the disperse iron oxide nanoparticles observed in the IOMBs. SEM images (C) of non-loaded bubbles (top) and IOMBs (bottom) revealed little effect of labeling on microbubble structure. Loaded microbubbles were able to produce similar ultrasound contrast to non-loaded bubbles (~20dB)(F). Fluorescence microscopy of QDMBs revealed strong fluorescence from quantum dots incorporated into the microbubbles (D). The CT attenuation rate generated from CT phantom scanning of AuMBs (E) was 5.8 HU/mM. The relaxivity values of IO-MBs were found to be r1 = 1.667 and r2 = 118 mM-1s-1 with a r2/r1 ratio of 70.77 (G). Conclusion: In addition to ultrasound and sonoporation applications, the encapsulation of nanocrystals into microbubbles allows for dual modality imaging approaches. This work demonstrates the characterization of various nanocrystals incorporated into these microbubbles and their potential application with other imaging techniques.

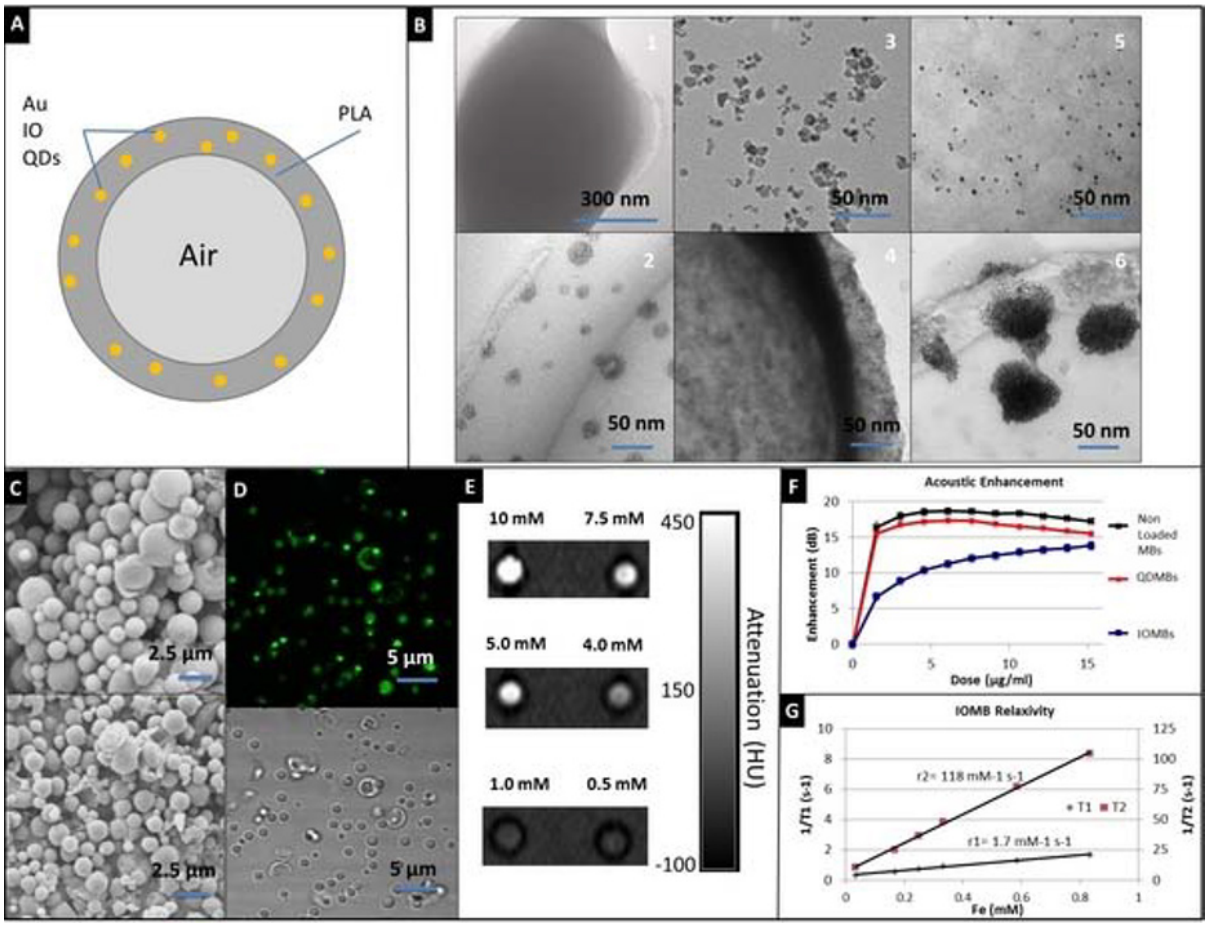

(A) Diagram of loaded microbubble. (B) TEM images of: 1-Nonloaded bubble, 2-QDMBs, 3- Free iron oxide, 4-IOMBs, 5-Free gold nanoparticles, 6-AuMBs. (C) SEM images of non loaded bubbles(top) and IOMBs(Bottom). (D) QDMBs fluorescence microscopy(top) and phase contrast(bottom). (E) CT Phantom image of AuMBs concentrations. (F) Acoustic properties of microbubbles. (G) Longitudinal and transverse relaxivity curves for IOMBs.

Disclosure of author financial interest or relationships:

P. Chhour, None; **N.T. Teraphongphom**, None; **L.J. Jablonowski**, None; **W.R. Witschey**, None; **P.C. Naha**, None; **D.P. Cormode**, Philips, Grant/research support; **M. Wheatley**, None.

Presentation Number **P 449**
Poster Session 4
September 21, 2013 / 14:45-14:45 / Room: Exhibit Hall B

PORPHYRIN-BASED BUILT-IN SENSOR FOR IMAGING LIPOSOMAL NANOPARTICLE INTEGRITY AND DRUG RELEASE

Liyang Cui[1,2], *Kenneth K. Ng*[1], *Neeshma Dave*[1], *Juan Chen*[1], *Gang Zheng*[1], [1]*Ontario Cancer Institute, University of Toronto, Toronto, ON, Canada;* [2]*Biophysics, Peking University, Beijing, China. Contact e-mail: atimocca@gmail.com*

INTRODUCTION New generation of nanocarriors that integrate site-directed imaging and drug therapy is now under intense investigation for image-guide drug delivery. Porphyrins are of special interest as imaging units in a variety of nanoscale architectures, due to their self-assembly capacity and inherent optical properties. We developed here a pyropheophorbide α aggregate (PαA) containing liposomal nanoparticles with specific optical properties to investigate the transmembrane activity and integrity of the host nanoparticles. METHODS PαA was built within various lipid environments to produce PαA liposome with different transition temperatures, size distribution and lamellarity. The formation and stucture of the PαA liposome are characterized by UV-vis, circular dichroism and optical imaging approaches such as fluorescence and photoacoustic imaging. Correlation between drug release and optical properties of PαA is further investigated. RESULTS PαA can form spontaneously in liposomes via non-covalently π-π interaction and anchor in lipid bilayer with great stability, resulting in a fingerprint red-shifted Q band in UV spectrum and distinct cotton split in CD spectrum. The aggregate is highly quenched, which leads to a unique photoacoustic signal peak at the corresponding absorbance wavelength. The specific photoacoustic property and quenching of the pyro fluorescence are highly dependent on the integrity of the liposomes and sensitive to the fine changes of the lipid layers. In the intact particle, the built-in PαA generated strong photoacoustic signals, while no photoacoutic was detected when the particle is dissociated,. On the contrary, the fluorescence of PαA was quenched by 90% in the ordered liposome bilayer and was dramaticly restored when liposome structures are disrupted. These two indices can be used to visualize transmembrane behaviors and are associated with release rate of drugs, thus establish a platform for tracking and monitoring liposome-based drug delivery system. CONCLUSIONS The spatial arrangement of pyro in lipid layers produce a set of spectrometric characteristics that reflect integrity and behaviors of the host nanoparticles. PαA-containing liposomal structure is of remarkable value in gaining insight of the transportation and in-site transmembrane activity of the particles and is of great potential as multimodality image-guided drug delivery system.

Disclosure of author financial interest or relationships:
L. Cui, None; **K.K. Ng**, None; **N. Dave**, None; **J. Chen**, None; **G. Zheng**, None.

Presentation Number **P 450**
Poster Session 4
September 21, 2013 / 14:45-14:45 / Room: Exhibit Hall B

PEGylated Core/shell Doped Fe3O4@NaYF4 Nanoparticles: Multimodality Molecular Imaging Contrast for MRI, PET/SPECT and Optical Imaging

Xianjin Cui[1], *Phil Blower*[1,2], *Mark Green*[1,3], [1]*Imaging Science, KIng's College London, London, United Kingdom;* [2]*Chemistry, Kings College London, London, United Kingdom;* [3]*Physics, Kings College London, London, United Kingdom. Contact e-mail: xianjin.cui@kcl.ac.uk*

The advent of combined modality imaging (e.g. PET/MRI) creates a need for combined modality contrast agents to bring benefits to certain clinical applications. Here we aimed to develop nanoparticulate materials offering magnetic, radionuclide and fluorescent contrast to take exploit the complementary advantages of MR, PET/SPECT and optical imaging. CoxFe3-xO4@NaYF4(Yb, Er), Fe3O4@NaYF4(Yb, Tm) and Fe3O4@NaYF4(Yb, Ho) core/shell nanostructures (NPs) with a narrow size distribution were synthesised by thermal decomposition. The CoxFe3-xO4 and Fe3O4 magnetic cores provide efficient MRI T2 contrast with r2 relaxivity up to 325.9 mM-1s-1 at 3T, while the NaYF4 shell can conveniently be radiolabelled with [18F]-fluoride or radiometal-bisphosphonate conjugates (e.g.99mTc and 64Cu) by simply incubating an aqueous 1 mg/mL particle suspension with the chosen radiotracer for 5 minutes. The NaYF4 shell offers fluorescence imaging with emissions in the near infrared region from 500 to 800 nm under excitation at 980 nm, by co-doping with Yb and Er, Tm or Ho. TEM images showed a narrow size distribution with a mean diameter of 12.2 ± 1.7 nm. Dynamic light scatter (DLS) results suggested that these NPs can be stabilised by small ligand mercaptosuccinic acid or bisphosphonate polyethylene glycol (BP-PEG), giving a hydrodynamic diameter of 43.8 nm. The feasibility and potential advantages of using these particles for sentinel lymph node imaging in vivo was demonstrated in mice with CoxFe3-xO4@NaYF4(Yb, Er)-BP-PEG (10K da) and Fe3O4@NaYF4(Yb, Tm)-BP-PEG (2 K Da) as multi-modality contrast agent, for PET, MRI and fluorescent imaging. The biodistribution of intravenously administered particles determined by PET/MR imaging suggested that negatively changed CoxFe3-xO4@NaYF4(Yb, Er)-BP-PEG NPs stay in blood pool longer than positively charged Fe3O4@NaYF4(Yb, Tm)-BP-PEG NPs.

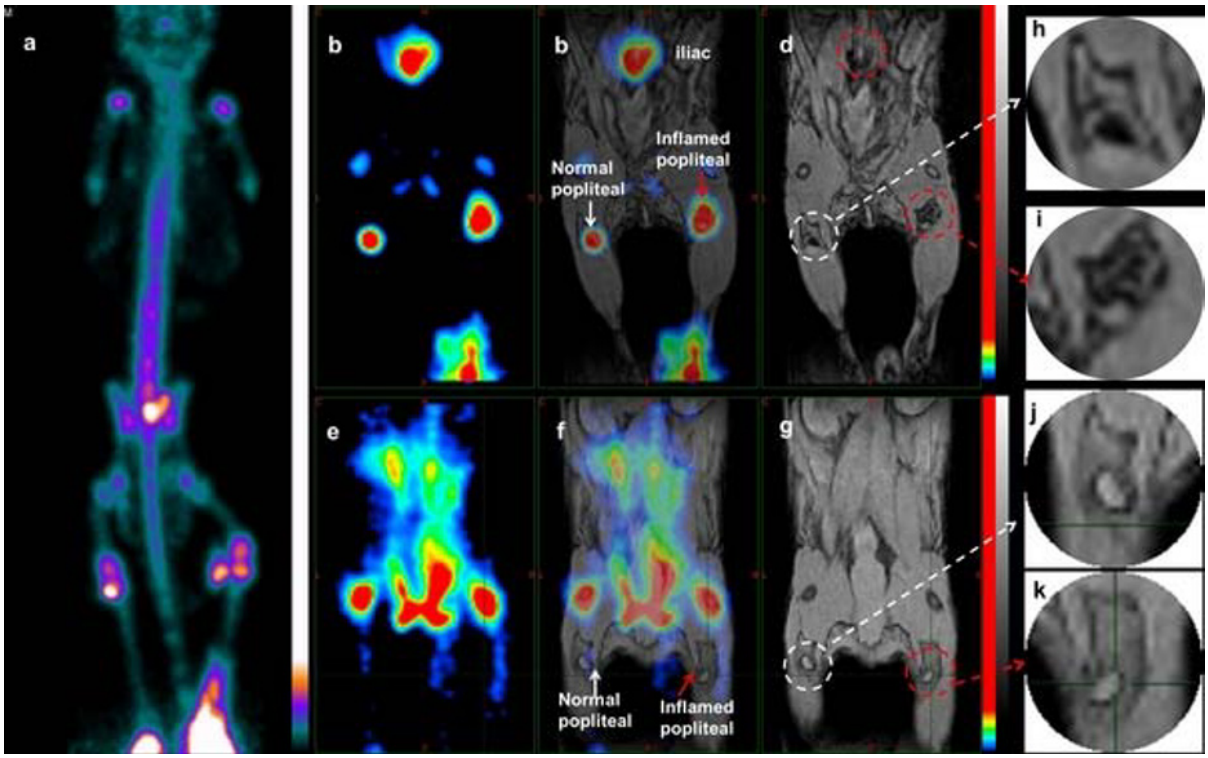

Disclosure of author financial interest or relationships:
X. Cui, None; **P. Blower**, None; **M. Green**, None.

Presentation Number **P 451**
Poster Session 4
September 21, 2013 / 14:45-14:45 / Room: Exhibit Hall B

Fluorinated carboplatin derivative for hybrid PET/MRI imaging and therapeutic applications

Gajanan K. Dewkar[1], *Purnima Jose*[1], *Narottam Lamichhane*[1], *Celina Thadigiri*[1], *Gobalakrishnan Sundaresan*[1], *Nicholas Farrell*[2], *Jamal Zweit*[1], [1]*CMI, Radiology, Virginia Commonwealth University, Richmond, VA, USA;* [2]*Chemistry, Virginia Commonwealth University, Richmond, VA, USA. Contact e-mail: gkdewkar2@vcu.edu*

DNA-damaging agents, such as cisplatin and other platinum drugs are the largest class of anti-cancer drugs. They are most important in the clinical use for the treatment of various cancers, although ovarian cancer cells often become resistant. Besides resistance, non-specific uptake in normal tissues and related toxicity is a dose limiting factor and affects their overall effectiveness. Knowledge of the drug concentration in the tumor as well as its overall concentration in the body of a patient will be helpful in accurately predicting the overall responsiveness of a patient to the drug. This type of knowledge can be accomplished by the development of a drug analog with Positron Emission Tomography/ Magnetic Resonance Imaging (PET/MRI) imaging capability, so that the accumulation of the drug in the tumor and normal organs can be tracked and quantified during the course of therapy to predict its effectiveness in a patient. Therefore, we developed a novel fluorinated carboplatin derivative, towards a hybrid agent for imaging and therapy. We synthesized 19F fluorinated carboplatin derivative using 2-(5-fluoro-pentyl)-2-methyl malonic acid by co-ordination with cis-platinum aqua complex. It was then used to treat various cell lines and compared with Cis-platin and Carboplatin at different concentrations ranging from 0.001 μM to 100 μM for 72 hrs and 96 hrs. LC50 values calculated from cell viability indicate that fluorinated carboplatin is a more potent drug than carboplatin but less effective than cisplatin. We have successfully applied our previously developed a microfluidic radiosynthesis method to synthesize [18F]-2-(5-fluoro-pentyl)-2-methyl malonic acid, which will co-ordinate with cis-platinum aqua complex to yield 18F labeled carboplatin derivative. Our approach to synthesis various derivatives of fluorinated carboplatin will allow us to develop anticancer drugs with PET/MRI imaging capabilities.

Disclosure of author financial interest or relationships:
G.K. Dewkar, None; **P. Jose**, None; **N. Lamichhane**, None; **C. Thadigiri**, None; **G. Sundaresan**, None; **N. Farrell**, None; **J. Zweit**, None.

Presentation Number **P 452**
Poster Session 4
September 21, 2013 / 14:45-14:45 / Room: Exhibit Hall B

A modular method to synthesize multimodal high-density lipoprotein-derived nanoparticle contrast agents using microfluidics

Francois Fay[1], *YongTae Kim*[2], *David P. Cormode*[3], *Brenda L. Sanchez-Gaytan*[1], *Jun Tang*[1], *Robert Langer*[2,4], *Omid C. Farokhzad*[5], *Edward A. Fisher*[6], *Zahi A. Fayad*[1], *Willem J. Mulder*[1,7], *[1]Translational and Molecular Imaging Institute, Icahn School of Medicine at Mount Sinai, New York, NY, USA; [2]David H. Koch Institute for Integrative Cancer Research, Massachusetts Institute of Technology, Cambridge, MA, USA; [3]Radiology Department, Perelman School of Medicine, University of Pennsylvania, Philadelphia, PA, USA; [4]Department of Chemical Engineering, Massachusetts Institute of Technology, Cambridge, MA, USA; [5]Department of Anesthesiology, Brigham and Women's Hospital, Harvard Medical School,, Boston, MA, USA; [6]Departments of Medicine (Cardiology) and Cell Biology (E.A.F.)., NYU School of Medicine, New York, NY, USA; [7]Department of Vascular Medicine, Academic Medical Center, Amsterdam, Netherlands. Contact e-mail: francois.fay@mountsinai.org*

High Density Lipoprotein (HDL) is a natural nanoparticle involved in the transport of cholesterol throughout the body. HDL has been shown to exhibit atheroprotective properties as it promotes cholesterol efflux from atherosclerotic plaque macrophages in the arterial wall. Various laboratories have focused on the reconstitution of HDL (rHDL) for a variety of reasons, ranging from a better understanding of the structural biology of apolipoproteins to the use of rHDL as an injectable therapeutic (1). A recent effort centers around the use of rHDL as a natural nanoparticle platform for the delivery of contrast agents such as gadolinium chelates, iron oxide or gold nanoparticles, and employing them as molecular imaging contrast agents (2). To date, multistep production protocols pose a limit on the synthesis of batch quantities and are sensitive to inter-batch variations. In order to scale up the production process and to judiciously control rHDL's composition we have developed a modular single-step approach based on recently introduced microfluidics technology (3) that enables the standardized mass production of such lipoprotein-based nanoparticles. Materials and methods Organic solutions containing phospholipids and imaging agents (QD, FeO-NP, Au-NP, DiO) were injected into a microfluidic chip alongside an aqueous solution containing ApoA1. Within the chip the controlled flow streams generate microvortices where fast mixing of the solutions leads to the instantaneous formation of HDL-like nanoparticles (Figure 1). HDL particles produced by this microfluidics method, which we refer to as μHDL, had similar physicochemical properties (size, morphology) to particles produced by conventional methods and natural HDL. Moreover cell based assays demonstrated that μHDL nanoparticles displayed a similar bioactivity profile to natural HDL. μHDL that encapsulated hydrophobic dies (DiO) or nanocrystals such as quantum dots (QD), gold (Au) or iron oxide (FeO) nanoparticles were characterized and evaluated in model murine macrophage cell line. We observed all the different versions to have excellent diagnostic properties, to be specifically taken up by macrophages and rendered these cells visible for either magnetic resonance imaging (FeO-μHDL), computed tomography (Au-μHDL), or fluorescence imaging (QD-μHDL). Conclusion We have developed a microfluidics-based method to produce bioactive multifunctional HDL-like nanoparticles that can be used for molecular imaging. This single step production process will facilitate the optimization of existing HDL nanoparticle platforms and could accelerate the development of new formulations and applications. 1. Tardif et al, JAMA. 2007: Effects of reconstituted high-density lipoprotein infusions on coronary atherosclerosis: a randomized controlled trial. 2. Cormode et al, Nano Lett. 2008: Nanocrystal core high-density lipoproteins: a multimodality contrast agent platform. 3. Kim Y et al, Nano Lett. 2012: Mass production and size control of lipid-polymer hybrid nanoparticles through controlled microvortices.

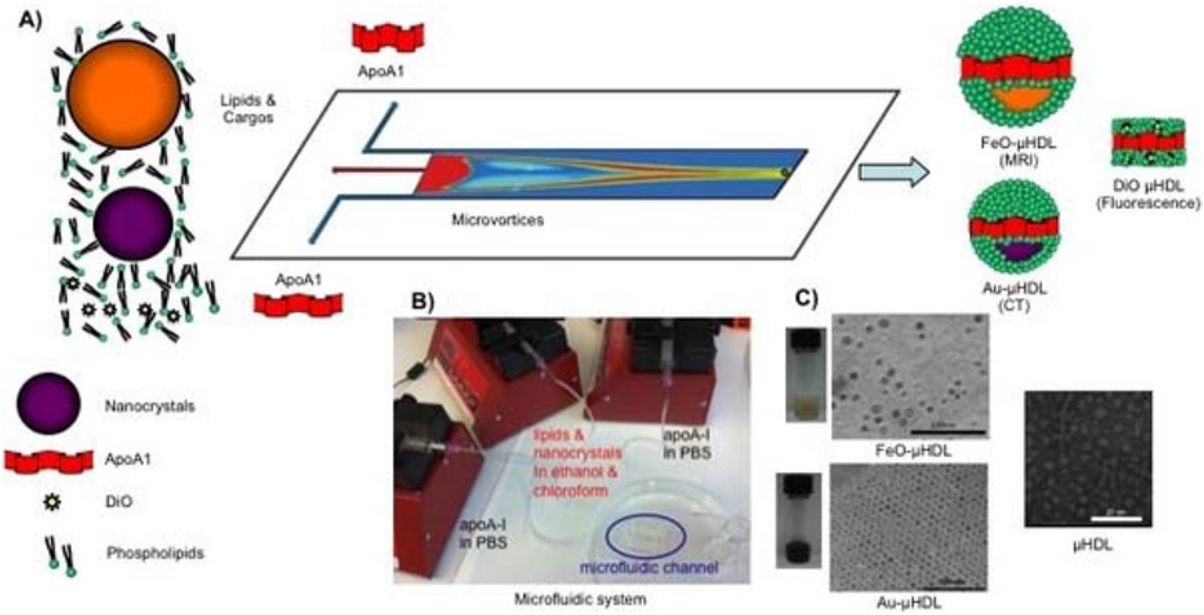

Figure 1 Microfluidic reconstitution of HDL-derived nanomaterials (μHDLs). A) The microfluidic platform allows single-step and large-scale production of the multimodal μHDLs. B) Image of the microfluidic device. C) photographs of Iron Oxide μHDL (FeO-μHDL) and Gold μHDL (Au-μHDL), Negative stain TEM images of FeO-μHDL, Au-μHDL and μHDL.

Disclosure of author financial interest or relationships:
F. Fay, None; **Y. Kim**, None; **D.P. Cormode**, Philips, Grant/research support; **B.L. Sanchez-Gaytan**, None; **J. Tang**, None; **R. Langer**, None; **O.C. Farokhzad**, None; **E.A. Fisher**, None; **Z.A. Fayad**, None; **W.J. Mulder**, None.

Presentation Number **P 453**
Poster Session 4
September 21, 2013 / 14:45-14:45 / Room: Exhibit Hall B

Hybrid Superparamagnetic Nanoparticles for Bimodal Detection and Hybrid Imaging

David Hoffman, *Likun Yang, Minghao Sun, Philip R. McDonagh, Frank Corwin, Gobalakrishnan Sundaresan, Li Wang, Celina Thadigiri, Jamal Zweit, School of Medicine, Virginia Commonwealth University, Richmond, VA, USA. Contact e-mail: david.blair.hoffman@gmail.com*

Aims: Superparamagnetic iron oxide (Fe3O4) and manganese ferrite (MnFe2O4) nanoparticles (NPs) are effective contrast agents for magnetic resonance imaging (MRI) [1]. Intrinsic incorporation of a radio-nuclide allows for bimodal detection without modifying the surface coating of the nanoparticle. Intrinsically radiolabeled [59Fe]-superparamagnetic iron oxide NPs (SPIONs) and natural manganese iron oxide NPs (MIONs) have been developed. The [59Fe]-SPION is proof of concept of a radio-intrinsic MR contrast agent, and the MION development will be used for the future incorporation of 52Mn for hybrid PET/MRI imaging. The [59Fe]-SPION is used to characterize the NP biodistribution using MRI and ex vivo gamma counting. Methods: Commercially purchased 59Fe was incorporated into the Fe3O4 NPs in the second part of a two part core/shell thermal decomposition synthesis. MnFe2O4 NPs where produced with a similar synthesis. The NPs were coated with a multidentate poly-ethylene-glycol (PEG, MW 2000) ligand. The NPs were characterized using dynamic light scattering (DLS), transmission electron microscopy (TEM), and MRI phantom studies. Nude mice (n = 15) were tail vein injected with 0.8 μCi of [59Fe]-Fe3O4 NPs (26 μg of Fe) and imaged at various time points with a 7T small animal MRI scanner. As verification of the MR data, tissues were collected after imaging, weighed, and gamma-counted, and the %ID/g was calculated. %ID/g of tissues was compared with MRI data to correlate nanoparticle uptake to MR contrast. Finally, post-injection images were deformed and coregistered with pre-injection images, to produce contrast maps of the injected mice. Results: The two part core/shell thermal decomposition synthesis of [59Fe]-SPIONs incorporates 59Fe with 95% efficiency. The R2 relaxivity of 97 ± 3 s-1mM-1 is similar to that measured from natural Fe3O4 (72 ± 10 s-1mM-1), indicating that radio-incorporation does not damage the NPs' MR contrast. The nanoparticles have 5.0 ± 1.5 nm inorganic radius from TEM and 17 ± 6 nm hydrodynamic radius from DLS. MIONs have similar size (3.3 ± 1.0 nm from TEM) and R2 relaxivity (90 ± 1 s-1mM-1). The biodistribution of [59Fe]-SPIONs is shown in the attached table. Pre-injection and 1 hour post-injection [59Fe]-SPION injection mouse MR image are attached. Signal contrast correlates well with gamma counts at all time points, with high contrast (45 ± 6 at 24 hours) in the liver, medium contrast (21 ± 5% at 24 hours) in the kidneys, and low contrast (4 ± 6% at 24 hours) in the brain. Discussion: This work demonstrates the synthesis and in vivo application of radio-intrinsic SPIONs for bimodal detection. The ex vivo gamma counts and MR imaging correspond in showing NP collection in the liver and kidneys. Future work will produce and incorporate 52Mn into manganese ferrite nanoparticles for hybrid PET/MRI contrast and explore conjugation of the NP to a targeting molecule for targeted imaging. Acknowledgements: Supported by the Virginia Commonwealth University, School of Medicine, and the Society of Nuclear Medicine Predoctoral Molecular Imaging Scholar Program Award.

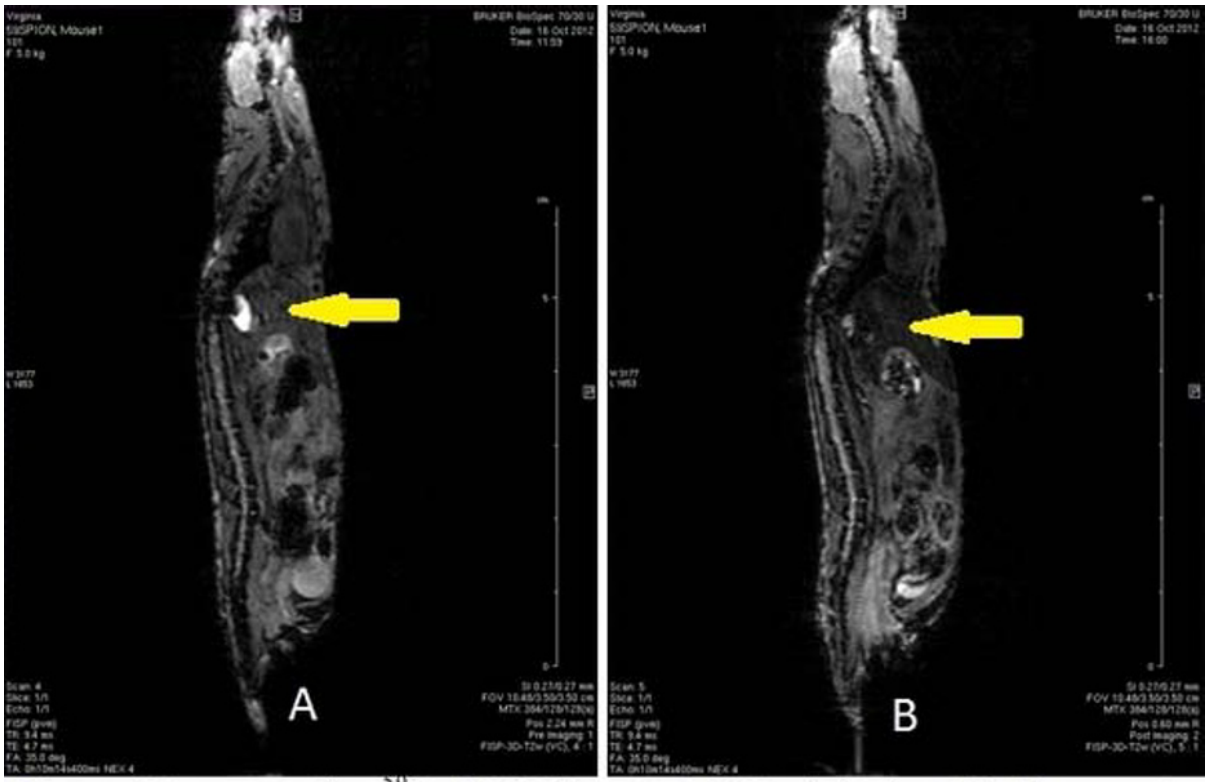

Figure 1. Represenative ^{59}Fe-SPION images: A) Pre-injection, B) 1 hour post-injection. The arrows show the liver, the main site of contrast.

Biodistribution of intravenously injected 59Fe-SPIONs in nude mice

Organs	1 Hour	4 Hour	24 Hours	72 Hours	144 Hours
Blood	3.9±0.7	1.4±0.3	2.8±0.2	4±0.4	5.5±0.7
Heart	1.2±0.2	0.48±0.07	0.51±0.02	0.8±0.3	0.9±0.2
Lungs	1.9±0.5	0.94±0.04	1.2±0.2	1.3±0.4	1.8±0.2
Liver	40±7	30±7	30±3	33±5	31±2
Spleen	16±6	19±2	17.5±0.9	14±5	15.2±0.3
Stomach	0.4±0.3	0.13±0.04	0.25±0.05	0.2±0.2	0.26±0.1
Intestines	0.7±0.2	0.9±0.1	1.4±0.1	1.3±0.4	0.8±0.1
Kidneys	1.4±0.2	0.7±0.1	0.99±0.1	0.7±0.2	1.4±0.2
Skin	0.9±0.4	0.5±0.2	0.7±0.1	0.9±0.2	0.81±0.03
Muscle	0.9±0.6	0.3±0.3	0.19±0.07	0.3±0.3	0.36±0.07
Skull	2.1±0.9	1.8±0.3	1.5±0.4	2.1±0.4	4±1
Brain	0.14±0.05	0.1±0.1	0.12±0.03	0.12±0.01	0.28±0.08
Femur	5.4±0.5	4.9±0.9	7±2	5.3±0.9	4±1

Data are presented as %ID/g (mean±stdv) values determined through gamma counting. n=3 per time point.

Disclosure of author financial interest or relationships:

D. Hoffman, None; **L. Yang**, None; **M. Sun**, None; **P.R. McDonagh**, None; **F. Corwin**, None; **G. Sundaresan**, None; **L. Wang**, None; **C. Thadigiri**, None; **J. Zweit**, None.

Presentation Number **P 454**
Poster Session 4
September 21, 2013 / 14:45-14:45 / Room: Exhibit Hall B

PET, Near-Infrared Fluorescence, and Bioluminescence Imaging of Breast Cancer Experimental Lung Metastasis

Yin Zhang[1], *Hao Hong*[2], *Tapas R. Nayak*[2], *Charles P. Theuer*[3], *Todd E. Barnhart*[1], *Weibo Cai*[1,2], [1]*Medical Physics, University of Wisconsin - Madison, Madison, WI, USA;* [2]*Radiology, Univ of Wisconsin, Madison, WI, USA;* [3]*TRACON, San Diego, CA, USA. Contact e-mail: yzhang65@wisc.edu*

Objective: Metastatic breast cancer (MBC), where lung, liver, and bone are the primary metastatic sites, is incurable. The benefit/use of anti-angiogenic therapy in MBC is hotly debated, since several large randomized prospective trials of unselected patients with MBC did not lead to significant survival benefit. Non-invasive positron emission tomography (PET) imaging of tumor angiogenesis can allow selection of MBC patients who are most likely to benefit from anti-angiogenic treatments, which will significantly increase the response rate and represent a major advance in MBC patient management. In addition, incorporation of a near-infrared fluorescent (NIRF) dye in the imaging probe can be used to guide surgical resection of tumors. The clinical gold standard for assessing tumor microvessel density (MVD), an independent prognostic marker in multiple solid tumor types including MBC, is CD105 (i.e. endoglin) immunohistochemistry on paraffin-embedded tumor specimens. The goal of this study is to develop a dual-modality PET/NIRF agent for imaging of CD105 expression (i.e. non-invasive measurement of MVD in all tumors). Methods: TRC105, an anti-CD105 monoclonal antibody, was labeled with IRDye 800CW (Ex: 778 nm; Em: 806 nm) and ^{64}Cu to yield ^{64}Cu-NOTA-TRC105-800CW. The MBC model was established by intravenous injection of luciferase transfected 4T1 murine breast cancer (fLuc-4T1) cells into female BALB/C mice. Serial bioluminescence imaging (BLI) was carried out noninvasively to monitor the burden of lung metastases. In vitro FACS analysis study was performed to compare the CD105 binding affinity of TRC105 and NOTA-TRC105-800CW. In vivo PET imaging, biodistribution, blocking, ex vivo BLI/PET/NIRF/autoradiography imaging, and histology studies were performed in the MBC model to thoroughly investigate the pharmacokinetics and tumor targeting efficacy of the PET/NIRF probe. Another chimeric antibody, cetuximab, was used as an isotype-matched control. Results: Flow cytometry studies revealed no difference in CD105 binding affinity or specificity between TRC105 and NOTA-TRC105-800CW. BLI facilitated the monitoring of lung metastases to select suitable mice for study. Serial PET imaging indicated that fLuc-4T1 lung tumor uptake of ^{64}Cu-NOTA-TRC105-800CW was 11.9±1.2 and 13.9±3.9 %ID/g at 4 and 24 h post-injection (n = 3).

Biodistribution, blocking, PET with ^{64}Cu-NOTA-cetuximab-800CW, ex vivo BLI/PET/NIRF imaging, and histology studies all corroborated the in vivo findings and confirmed CD105 specificity of the tracer. Distribution of the tracer in the lung was similar based on autoradiography and ex vivo NIRF imaging, which further confirmed stability and CD105 specificity of the tracer. A feasibility study of NIRF image-guided removal of 4T1 tumors with NOTA-TRC105-800CW was successful and straightforward.

Conclusions: Successful PET/NIRF imaging of CD105 expression in MBC with ^{64}Cu-NOTA-TRC105-800CW warrants further investigation and translation of dual-labeled TRC105-based agents, which can enable early detection of small metastases and image-guided surgery of tumor resection.

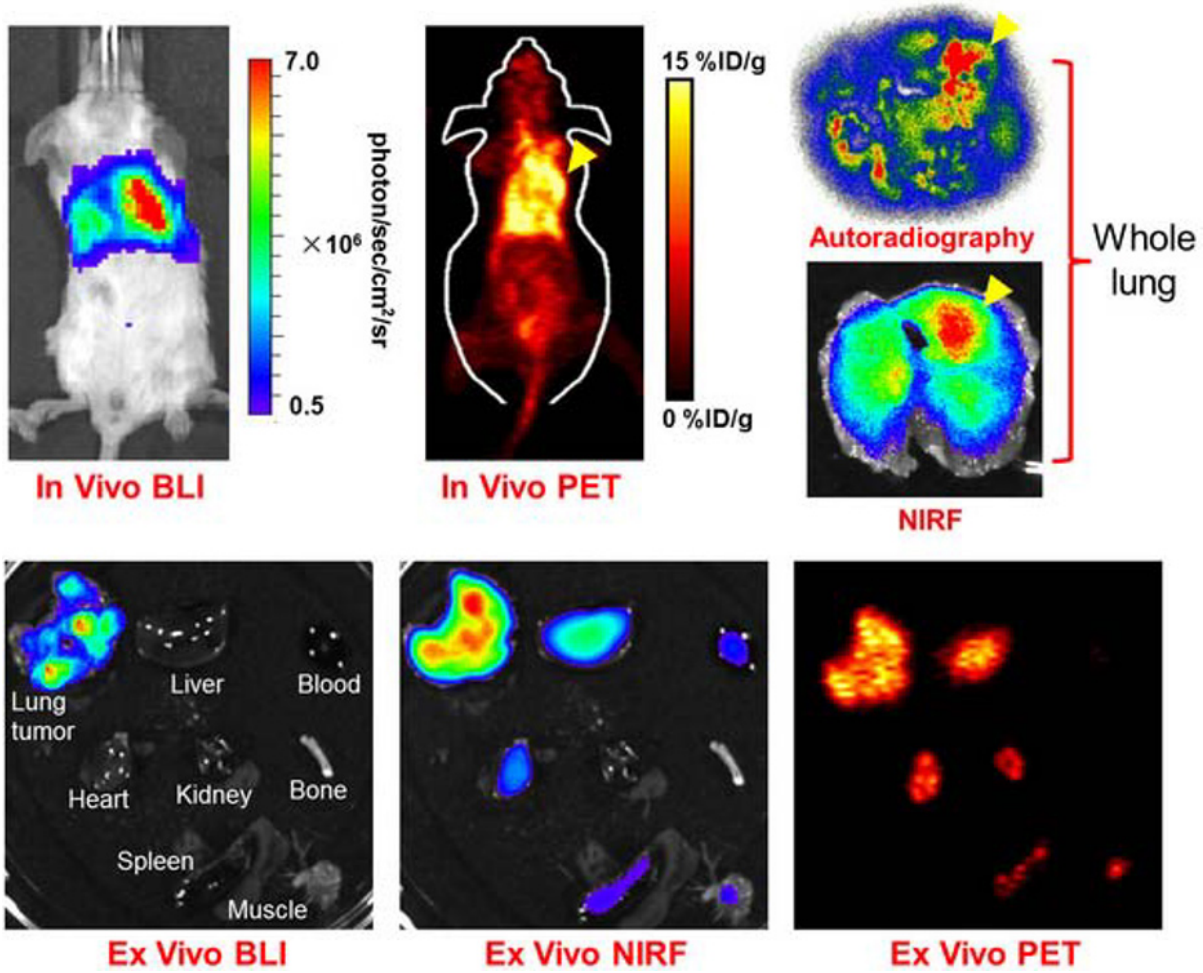

Disclosure of author financial interest or relationships:
Y. Zhang, None; **H. Hong**, None; **T.R. Nayak**, None; **C.P. Theuer**, TRACON Pharmaceuticals, Stockholder; TRACON Pharmaceuticals, Employment; **T.E. Barnhart**, None; **W. Cai**, None.

Presentation Number **P 455**
Poster Session 4
September 21, 2013 / 14:45-14:45 / Room: Exhibit Hall B

Red Fluorescent ZnO Nanoparticle as a Novel Platform for Cancer Targeting and Imaging

Hao Hong[1], *Fei Wang*[2], *Yin Zhang*[3], *Todd E. Barnhart*[3], *Xudong Wang*[2], *Weibo Cai*[1,3], [1]*Radiology, Univ of Wisconsin, Madison, WI, USA;* [2]*Materials Science, Univ of Wisconsin, Madison, WI, USA;* [3]*Medical Physics, Univ of Wisconsin, Madison, WI, USA. Contact e-mail: hhong@uwhealth.org*

Objectives : To employ intrinsically red fluorescent zinc oxide nanoparticles (ZnO NPs) for in vivo cancer targeting and imaging. Methods : Fluorescent ZnO NPs were synthesized via chemical vapor deposition, and conjugated to TRC105 (a chimeral anti-CD105 antibody) and 1,4,7-triazacyclononane-N,N'N''-triacetic acid (NOTA) through polyethylene glycol (PEG) linkers. SEM/TEM, dynamic light scattering, absorption/fluorescence spectra, and zeta-potential measurements were performed to characterize the as-synthesized and surface conjugated ZnO NPs. The intrinsic red fluorescence of ZnO NP facilitated microscopy studies, where CD105-positive HUVEC cells were incubated with NOTA-PEG-NP or NOTA-PEG-NP-TRC105. After ^{64}Cu labeling, positron emission tomography (PET) imaging, biodistribution, blocking, and histology studies were performed in 4T1 murine breast tumor-bearing mice to evaluate the tumor targeting capability of ^{64}Cu-NOTA-PEG-NP-TRC105. ^{64}Cu-NOTA-PEG-NP served as the control. Results : Significant changes in zeta-potential and absorption spectra confirmed the success of PEG and TRC105 conjugation on the surface of red fluorescent ZnO NPs (~60 nm) . Incubation with NOTA-PEG-ZnO NP-TRC105 resulted in greatly enhanced fluorescence signal on HUVECs compared to NOTA-PEG-ZnO NP. ^{64}Cu labeling was achieved with high yield and specific activity. Serial PET imaging revealed that 4T1 tumor uptake of ^{64}Cu-NOTA-PEG-ZnO NP-TRC105 was 5.7±0.6, 6.4±0.8, and 6.8±0.2 %ID/g at 0.5, 3, and 16 h postinjection respectively (n=4), significantly higher than that of ^{64}Cu-NOTA-PEG-ZnO NP (1.9±0.1, 2.5±0.2, and 2.4±0.4 %ID/g), which provided excellent tumor contrast and was corroborated by biodistribution studies. Blocking and histology experiments confirmed CD105 specificity of ^{64}Cu-NOTA-PEG-ZnO NP-TRC105 in vivo. Conclusions : We demonstrated for the first time that red fluorescent ZnO NPs can be used for fluorescence and PET imaging of cancer. With desirable properties such as biodegradability, versatile chemistry, and intrinsic fluorescence, ZnO NPs can serve as novel nanoplatforms for cancer imaging and therapy.

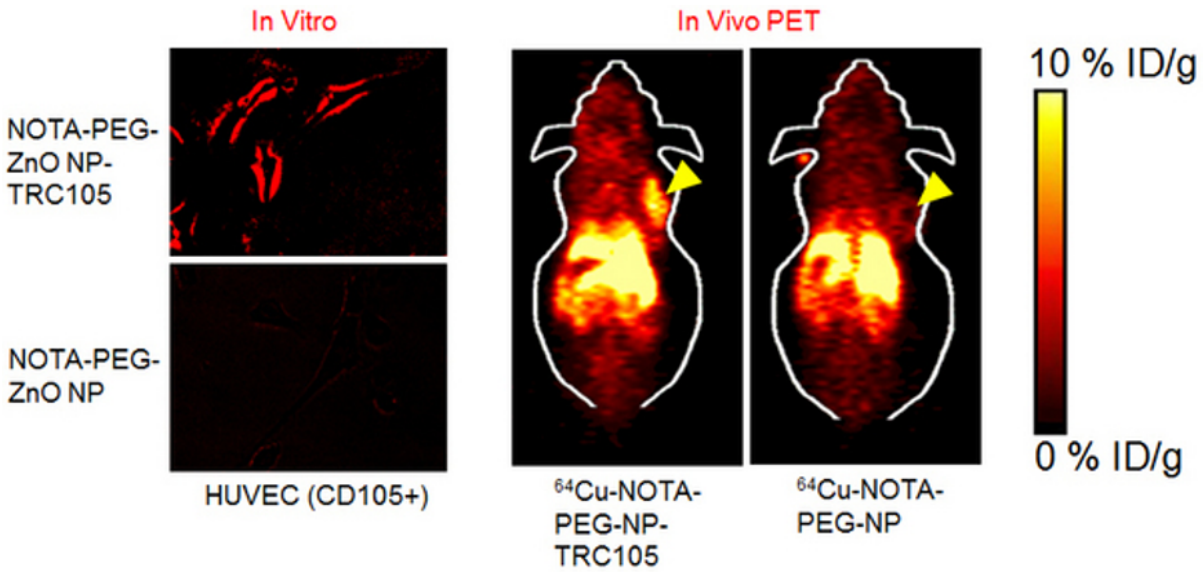

Disclosure of author financial interest or relationships:
H. Hong, None; **F. Wang**, None; **Y. Zhang**, None; **T.E. Barnhart**, None; **X. Wang**, None; **W. Cai**, None.

Presentation Number **P 456**
Poster Session 4
September 21, 2013 / 14:45-14:45 / Room: Exhibit Hall B

Photosensitizer-Loaded Gold Vesicles with Strongly Plasmonic Coupling Effect for Tri-Modality Imaging-Guided Synergistic Photothermal/Photodynamic Therapy

Peng Huang, *Jing Lin, Gang Niu, Xiaoyuan (Shawn) Chen, National Institutes of Health, Bethesda, MD, USA. Contact e-mail: penghuang2011@gmail.com*

A multifunctional theranostic platform based on photosensitizer-loaded plasmonic vesicular assemblies of gold nanoparticles (GNPs) is developed for effective cancer imaging and treatment. The gold vesicles (GVs) composed of a monolayer of assembled GNPs show a strong absorbance in the near infrared (NIR) range of 650-800 nm, as a result of the plasmonic coupling effect between neighboring GNPs in the vesicular membranes. The strong NIR absorption and the capability of encapsulating photosensitizers (i.e., Ce6) in gold vesicles (GVs) enable the tri-modality NIR fluorescence/thermal/photoacoustic imaging-guided synergistic photothermal/photodynamic therapy (PTT/PDT) with improved efficacy. The Ce6-loaded GVs (GV-Ce6) show the following features: i) high Ce6 loading efficiency (up to ~18.4 wt%) due to the hollow interior of the GVs; ii) enhanced cellular uptake efficiency of Ce6; iii) simultaneous tri-modality NIR fluorescence/thermal/photoacoustic imaging; iv) synergistic PTT/PDT treatment with improved efficacy using single wavelength continuous wave laser irradiation. In addition, the multifunctional vesicular nanocarriers have high solubility and stability in water, non-cytotoxicity, and good biocompatibility, thus facilitating their biomedical applications, particularly in cancer theranostics.

Disclosure of author financial interest or relationships:
P. Huang, None; **J. Lin**, None; **G. Niu**, None; **X. Chen**, None.

Presentation Number **P 457**
Poster Session 4
September 21, 2013 / 14:45-14:45 / Room: Exhibit Hall B

Site-Specific Conjugation of IgG onto Nanoparticles using a Recombinantly Expressed Protein A Incorporating a Non-Natural Amino Acid

James Z. Hui, *Andrew Tsourkas, Bioengineering, University of Pennsylvania, Philadelphia, PA, USA. Contact e-mail: zhui@mail.med.upenn.edu*

Background: Antibodies, commonly IgGs, have been widely used as targeting ligands in in vitro and in vivo applications due to the wide array of targets, high specificity, efficacy and biocompatibility. When conjugating antibodies onto imaging agents or nanoparticles, it is ideal to ensure that the conjugated molecules or surfaces are not attached near the antigen binding domain. Site-specific conjugations of antibody hence aim to attach conjugates near the Fc domain of the antibody. While there exist a wide arrange of conjugations methods, most of them are either non-site-specific (i.e. EDC-NHS) or complex (i.e. cysteine handle). We developed a reliable method to ensure site-specific antibody conjugation by incorporating a UV active non-natural amino acid into the Fc-binding domain of recombinantly expressed Protein A. Upon exposure to long wavelength UV light a covalent link is formed between protein A and IgG. Combining this technology with expressed protein ligation, we can achieve site-specific labeling of nanoparticles or other surfaces with IgG. Results: We have been able to use E Coli. to recombinantly express Protein A variants possessing three features: an UV active non-natural amino acid benzoylphenylalaine (BPA) at any position within the IgG binding domain, a single fluorescent label near the C terminus, a single Click-capable azide (or alkyne) group at the C terminus. We utilized an orthogonal tRNA-amino acid synthase pair in E. coli to incorporate the BPA into the Protein A during expression. Additionally, based on our previous work with expressed protein ligation (EPL), we also incorporated a fluorophore and an azide group to the C terminus of the Protein A. These allow our Protein A to be visualized and to be easily attached onto nanoparticles using the highly efficient copper-free "Click" chemistry. We have demonstrated that our Protein A variants have high expression and EPL ligation yields. We have also shown that Protein A variants can specifically bind to and be UV cross-linked (350nm) onto a broad range of IgGs, with an overall crosslinking efficiency exceeding 80%. We further demonstrated that these IgG-Protein A conjugates can be efficiently "clicked" onto dibenzocyclooctyne-coated iron oxide nanoparticles and achieve better antigen recognition activity as a result of the site-specific conjugation. Lastly, we demonstrated that the crosslinking is not inhibited in complex biological solutions. It can be easily carried out in ascites fluid and tissue culture supernatants, hence greatly simplifying the conjugation procedure with monoclonal antibodies. Conclusion: We have successfully demonstrated that recombinantly expressed, photoactive Protein A domains can be used to site-specifically and covalently conjugate IgGs onto nanoparticles. Our conjugation method is ideal for several reasons. 1. It is broadly applicable to a wide range of native full-length antibodies. 2. It conjugates IgGs at their Fc domains, hence avoiding steric hinderance or destruction of the antigen binding domain. 3. The non-harsh yet versatile nature of our technique suggests various potential applications beyond nanoparticle conjugation.

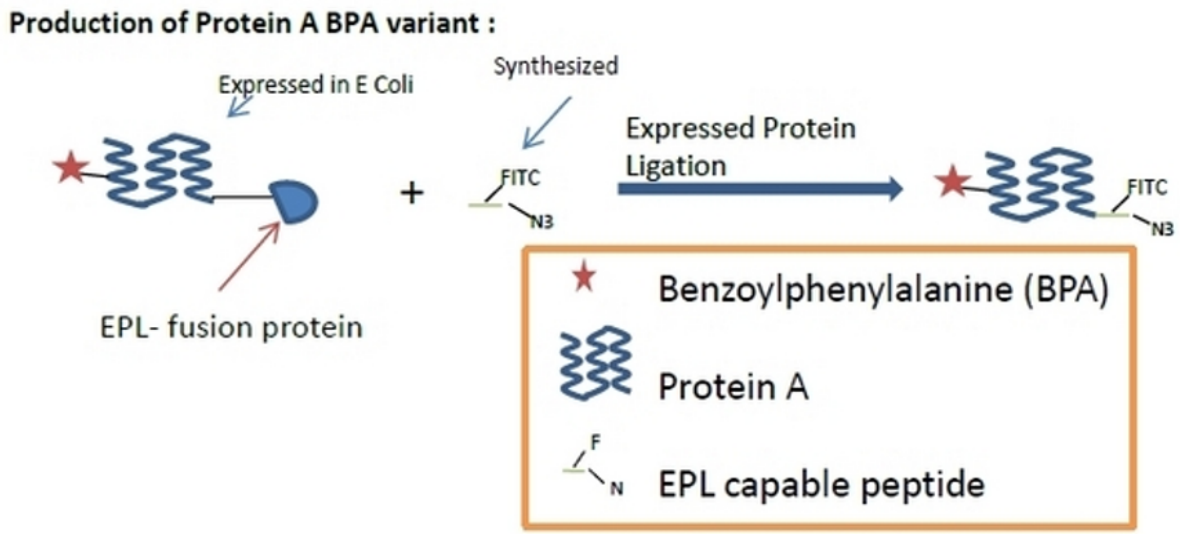

Disclosure of author financial interest or relationships:
J.Z. Hui, None; **A. Tsourkas**, None.

Presentation Number **P 458**
Poster Session 4
September 21, 2013 / 14:45-14:45 / Room: Exhibit Hall B

Targeting Ligands For Melanoma Diagnosis And Therapeutics Anyanee Kamkaew and Kevin Burgess* Department of Chemistry, Texas A & M University, Box 30012, College Station, Texas 77842, United States

Anyanee Kamkaew, *Kevin Burgess, Chemistry, Texas A&M University, College Station, TX, USA. Contact e-mail: anyanee.kamkaew@chem.tamu.edu*

A small molecule, non-peptidic, ligand was used to bind to cell surface receptors on melanoma and bring attached imaging (PET and fluorescence) or therapeutic (PDT) entities into the proximity of the tumors. Experiments with pig biopsy tissues (melanoma and normal skin tissues) for histological studies confirmed the expression of TrkC receptor in melanoma but not in normal skin tissue. Experiments in explant culture showed conjugates of the targeting agent with a PDT agent caused selective cytotoxicity against the cells isolated from tissues. Targeting of TrkC was observed, and accumulation into lysosomes was observed via cell imaging, as expected for receptor-mediated internalization. In the future, the agents will be used to increase contrast and lower dosages in PET and MRI imaging, as fluorescent probes, and to enhance the therapeutic effect of conjugated sensitizers in photodynamic therapy (PDT). They will also be tested in a pig model for melanoma that features naturally developing tumors, and does not involve surgically implants in immune-compromised subjects.

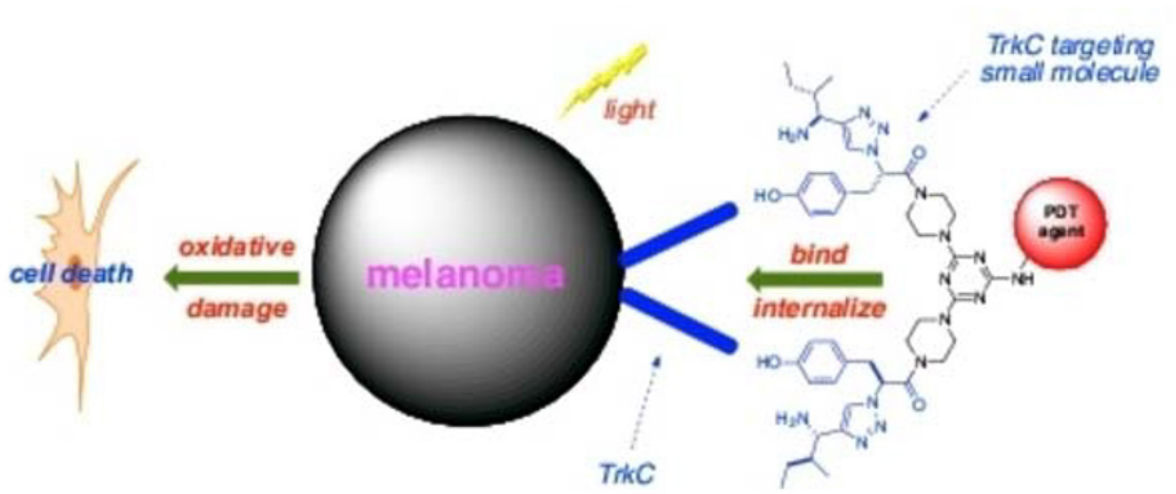

Disclosure of author financial interest or relationships:
A. Kamkaew, None; **K. Burgess**, None.

Presentation Number **P 459**
Poster Session 4
September 21, 2013 / 14:45-14:45 / Room: Exhibit Hall B

Synthesis and Functional Evaluation of Size-controlled Manganese Oxide Nanoparticles for Dual Photoacoustic and Magnetic Resonance Imaging

Yu Kimura[1], *Hiroaki Sugii*[1], *Tetsuya Matsuda*[2], *Hirohiko Imai*[2], *Yasuhiko Tabata*[3], *Akio Toshimitsu*[4], *Teruyuki Kondo*[1], [1]*Advanced Biomedical Engineering Research Unit, Kyoto University, Kyoto, Japan;* [2]*Graduate School of Informatics, Kyoto University, Kyoto, Japan;* [3]*Institute for Frontier Medical Sciences, Kyoto University, Kyoto, Japan;* [4]*Institute for Chemical Research, Kyoto University, Kyoto, Japan. Contact e-mail: ykimura@scl.kyoto-u.ac.jp*

Recently, we have succeeded in synthesis and functional evaluation of size-controlled Gd_2O_3 nanoparticles (NPs) modified with gelatin, which are a novel and highly efficient molecular probe for dual photoacoustic (PA) and magnetic resonance (MR) imaging.[1] Here, we report our further study on the synthesis and functional evaluation of novel MnO NPs modified with biocompatible surfactants based on sugar, such as glucose, glucosamine, glucronic acid, maltotriose, and pullulan. $MnCl_2 \cdot 4H_2O$ was dissolved in triethylene glycol (TEG) at 70 ^oC for 20 min under an argon atmosphere, and the mixture was heated at 200 ^oC for 6 h with stirring under basic reaction condition. After the reaction, the surfactant represented by glucosamine was added, and the mixture was again heated at 140 ^oC for 24 h with stirring. After cooling the reaction mixture, the NPs were precipitated and washed with water. X-ray diffraction analysis and TEM images of the resulting red-brown NPs showed that the NPs consist of $Mn^{II}O$. No aggregation of novel MnO NPs modified with sugars was observed in water with keeping the particle diameter constant (*ca.* 100 nm) during 10 days, which was confirmed by DLS analyses (zeta potential: -9.83 ~ -17.8 mV). Functional evaluations of the present MnO NPs are as follows. Photoacoustic signal by pulsed laser irradiation (532 nm, 100 μJ) was detected through hydrophone as a voltage variation. Glucosamine-modified MnO NP showed the strongest PA signal as 411 VM^{-1}. PA images of mice at 710 nm (laser intensity: 1.9 mJ/cm^2) before and after the subcutaneous injection of glucosamine-modified NPs(0.68 μmol Mn) clearly showed the intense image at the injected area. In addition, the relaxivity (*r1*) of the present MnO NPs was 12.3 ~ 24.7 $mM^{-1}s^{-1}$, which is higher than that of the clinically used MRI contrast agent, Gd-DTPA (4.81 $mM^{-1}s^{-1}$). In addition, the relaxivity (*r2*) of the present MnO NPs is also high (81.0 ~ 175 $mM^{-1}s^{-1}$), and the NPs are considered to be suitable as both positive and negative MRI contrast agent. In conclusion, we have succeeded in synthesis and functional evaluation of novel MnO NPs modified with biocompatible and water-dispersible surfactants based on sugar, especially by glucosamine, which are a highly promising molecular probe for dual PA and MR imaging. [1] Kimura, Y.; Kamisugi, R; Narazaki, M.; Matsuda, T.; Tabata, Y.; Toshimitsu, A.; Kondo, T., *Adv. Healthcare Mater.* **2012**, *1*, 657-660

Disclosure of author financial interest or relationships:
Y. Kimura, None; **H. Sugii**, None; **T. Matsuda**, None; **H. Imai**, None; **Y. Tabata**, None; **A. Toshimitsu**, None; **T. Kondo**, None.

Presentation Number **P 460**
Poster Session 4
September 21, 2013 / 14:45-14:45 / Room: Exhibit Hall B

MR Imaging of Sentinel Lymph Nodes Draining Lymphoma EL4 Allografts Using Size Tailored Nanostructures

Pontus Kjellman[1,3], *Rene in 't Zandt*[2,3], *Sarah Fredriksson*[3], *Sven-Erik Strand*[1], [1]*Medical Radiation Physics, Lund University, Lund, Sweden;* [2]*Lund University BioImaging Center, Lund University, Lund, Sweden;* [3]*Genovis AB, Lund, Sweden. Contact e-mail: pontus.kjellman@genovis.com*

Background: The metastatic spread, in breast cancer and malignant melanoma, mostly occurs through the lymphatic system. Histological examination of the first lymph node (LN) draining the tumor (the sentinel lymph node, SLN) reveals if the tumor is metastasizing. We have previously studied the uptake of different sized superparamagnetic iron oxide nanoparticles (SPIONs) in the LNs of healthy rats after subcutaneous injection. In order to design a multimodal SPIONs optimized for sentinel node imaging, it is necessary to investigate the uptake of SPIONs when the physiological condition of the lymphatic system is affected by the presence of a tumor. Various animal models have to be considered in order to cover a range of LNs, from healthy to severely affected by inflammation or invading tumor cells. In this study, EL4 tumor-bearing mice were injected peritumorally with SPIONs in similarity with clinical examinations. Materials and Methods: Two different sized SPIONs (29 and 58 nm) were constructed by coating 12 nm iron oxide cores with polyethylene glycol of varying molecular weight. The SPIONs were labeled with a fluorescent dye, DY-647, to enable detection in histology sections. The lymphatic uptake of the SPIONs was tested in vivo in C57BL/6 mice, that 5 days prior to particle injection were inoculated in the right flank with 3x106 EL4-cells. A 100 µL SPION injection was distributed over 4 subcutaneous injection sites at each side of the tumor. The retention of SPIONs in the SLN, in this case the inguinal lymph node, was visualized in vivo 24 h post injection. A 3D volume was acquired using a BrukerAvance II system operating at 2.4T (RARE, TR=2514 ms, TEeffective=35 ms). As SPIONs accumulate in the SLN the susceptibility effects will increase (higher T2-relaxivity), thereby leading to a loss of signal in the MR images. After the MRI measurement the animals were sacrificed and the inguinal LNs as well as the tumor were removed for histological examination. Results: The MR images revealed a clear difference in the accumulation of the two SPIONs in the SLN 24 h post injection, with the 27 nm particle generating a larger effect on the MR signal (Figure 1). Substantial amounts of particles can still be detected at the injection sites around the tumor. No obvious uptake of SPIONs could be detected in the tumor. Conclusions: The fact that the SPIONs could be seen at the injection sites is an expected result as lymphatic drainage of subcutaneous particle injections is usually small. The results confirm that the local pressure within the tumor prevents any uptake of nanoparticles, they continue to the first LN draining the tumor. The 27 nm SPION is taken up at an MRI detectable amount which indicates its potential as a SLN contrast agent. The narrow span between 27 and 58 nm is of importance as it demonstrates that even a very small size difference has an apparent impact on the localization of the particles in the lymphatics. The results also reveal that the SPIONs indeed are taken up in LNs that are affected by a tumor. The EL4 allograft will be an attractive model for future SLN studies.

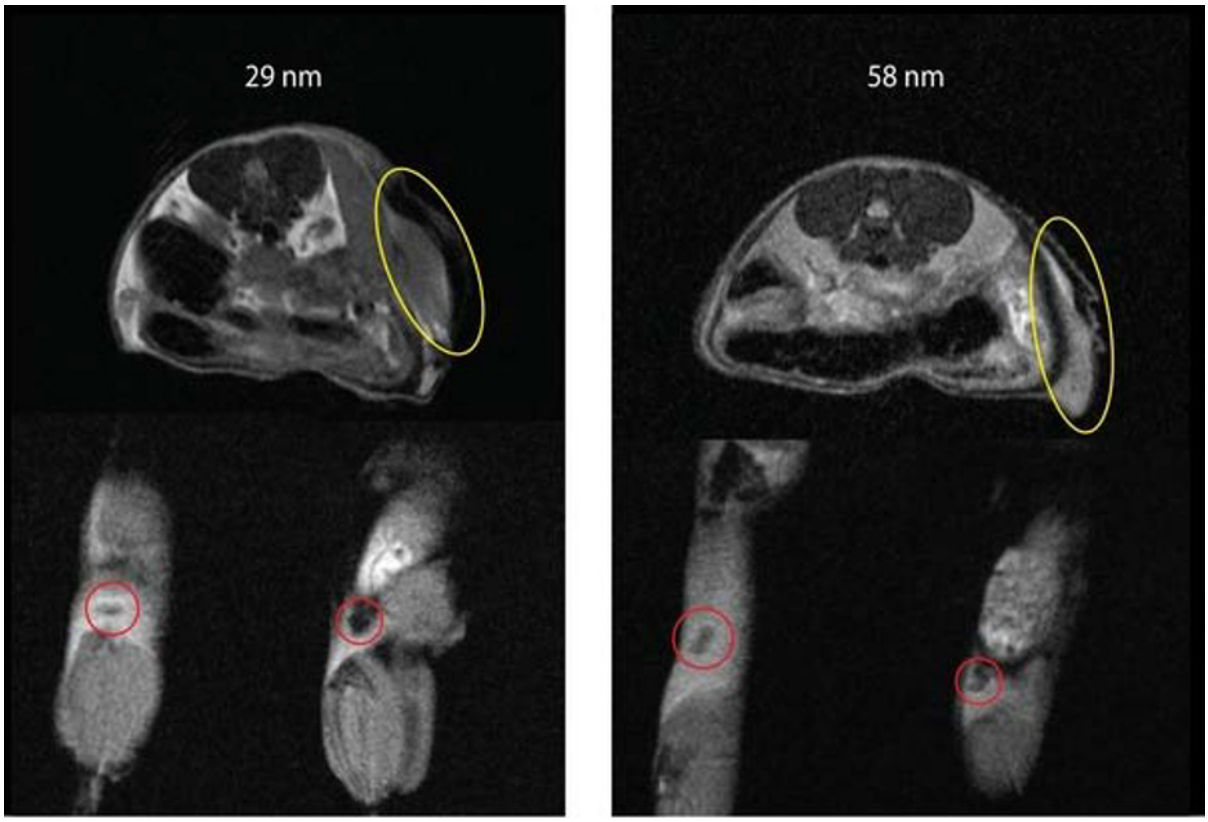

Figure 1: Top row: Axial sections highlighting the tumor (yellow ellipse). Nanoparticles injected peritumorally. Bottom row: Sagittal sections displaying inguinal lymph nodes (red circle), control side (left) and injected side (right) for the respective particles, 24 h post injection.

Disclosure of author financial interest or relationships:
P. Kjellman, Genovis AB, Employment; **R. in 't Zandt**, Genovis AB, Employment; Genovis AB, Stockholder; **S. Fredriksson**, Genovis AB, Employment; **S. Strand**, None.

Presentation Number **P 461**
Poster Session 4
September 21, 2013 / 14:45-14:45 / Room: Exhibit Hall B

Development of 111In Labeled PEGylated Liposome For Multimodal Pharmacokinetic Imaging

Narottam Lamichhane, *Gajanan K. Dewkar, Gobalakrishnan Sundaresan, Purnima Jose, Minghao Sun, Jamal Zweit, Radiology, Virginia Commonwealth University, Richmond, VA, USA. Contact e-mail: lamichhanen@vcu.edu*

DNA-damaging agents, such as cisplatin, carboplatin and other platinum drugs are the largest class of anti-cancer drugs. Although anticancer drugs show potent anti-neoplastic properties against various solid tumors, delivery of these drugs face challenges like unfavorable pharmacokinetics despite their clinical usefulness. Liposomal formulation of anticancer drugs has been proposed as a better way of delivering drugs to tumor site. Development of a drug analog with positron emission tomography (PET) imaging capability will enable us to determine the accumulation of the drug in the tumor and normal organs that can be tracked and quantified during the course of therapy to predict its effectiveness in a patient. Therefore, developing a drug delivery system comprising [18F] labeled drug in [111In] labeled liposome (ILL) will yield a quantitative tool to better understand the in vivo kinetics of drug and vehicle in tissue basis. Understanding the in vivo kinetics of liposome carrier agents helps in accessing the in vivo fate and insight on the pharmacokinetics of components of the nanocarrier, drug and construct as a whole. We recently developed ILL and studied its in vivo properties. Pentetic acid (DTPA) conjugated liposome was synthesized using film hydration method and was used to label with [111In] via post labeling procedure using 111InCl3. DTPA conjugated 1, 2-dipalmitoyl-sn-glycero-3-phosphoethanolamine (DPPE) was also labeled with 111InCl3 to synthesize 111In-DTPA-DPPE (IDD) and its in vivo property was compared with ILL. Adult female nude mice were injected with ILL through tail vein. The amount of radiotracer injected was 28- 30 µCi in 150- 200 µL PBS. At different time points post injection (1hr, 6hrs, and 48hrs); mice were anaesthetized with isoflurane (2% in oxygen) and euthanized. Tissues were harvested and were counted in gamma counter and percent injected dose per gram of the tissue was determined. The biodistribution profile of ILL was typical of a nanoparticle. Radiotracer uptake peaked in 6 hours with subsequent clearance with time. Major accumulation was observed in liver and spleen, utmost being the spleen. Minimal accumulation was observed in other major organs such as heart, lungs, kidneys etc. ILL and IDD (~ 215 µCi/230 µL in PBS) was injected intravenously in female nude mice via tail vein injection. SPECT imaging was carried out 2, 48 and 144 hours post injection. Radiotracer uptake of ILL was detected in liver and spleen, major being the spleen which corresponds to the ex vivo biodistribution data. Images showed the subsequent clearance of ILL with time. Radiotracer uptake of IDD was detected in liver, spleen and stomach. Images showed subsequent clearance of IDD with time. Thus, feasibility of synthesis of ILL and IDD and their ability of in vivo imaging was determined. Different pharmacokinetic profiles of ILL and IDD were observed. Further studies on the development of cold and radioactive analogs of platinum anticancer drugs are being studied which is presented by Dewkar et al on WMIC '13. The incorporation of these analogs on radiolabeled liposome and their in vitro and in vivo properties are being evaluated.

Disclosure of author financial interest or relationships:
N. Lamichhane, None; **G.K. Dewkar**, None; **G. Sundaresan**, None; **P. Jose**, None; **M. Sun**, None; **J. Zweit**, None.

Presentation Number **P 462**
Poster Session 4
September 21, 2013 / 14:45-14:45 / Room: Exhibit Hall B

Characterization of MPIO probes for molecular imaging of VCAM-1

Adrianna Radulska[1], Réjean Lebel[1], Witold A. Neugebauer[2], **Martin Lepage**[1], [1]*Centre d'imagerie moléculaire de Sherbrooke, Université de Sherbrooke, Sherbrooke, QC, Canada;* [2]*Department of Pharmacology, Université de Sherbrooke, Sherbrooke, QC, Canada. Contact e-mail: Martin.Lepage@USherbrooke.ca*

Introduction. Vascular Cell Adhesion Molecule-1 (VCAM-1) is an attractive molecular imaging target of cerebral vascular inflammation. Considerable efforts have been devoted to the development of microparticles of iron oxide (MPIO), useful MRI probes due to their high r2 relaxivity. VCAM-1 targeted Ab-MPIO have been tested in a model of mouse brain inflammation (1) and for the ex vivo imaging of mouse atherosclerosis (2). Here, we evaluated the impact of particle-particle interactions as a function of the hydrophobic/hydrophilic nature of the MPIO coating after derivatization with either a VCAM-1 antibody or high-affinity peptides. Next, we compared the binding affinity of these MPIOs. Material and methods. MPIO: DynaBeads MyOne(TM)Tosylactivated (polyurethane) and MyOne(TM)carboxylic Acid (glycidyl ether), 1 µm core, (Invitrogen) Control: Normal Goat IgG control (R&D), Antibody ligand: mouse VCAM-1(CD106) Antibody Antigen Affinity-purified Polyclonal Goat IgG (R&D), and the peptide VP structure is Ac-CVHPKQHKC-Peg2-K-CONH2 was synthesized using Fmoc strategy on TentaGel S RAM resin. FACS was performed (FACSCalibur cytometer, Becton Dickinson, Mountain View, CA). Fluorescence was measured using a Gemini EM 96-well spectrofluorometer (Molecular Devices, CA) (λEM, 517 nm; λEX, 495 nm). Results and Discussion. Hydrophobic (polyurethane) and hydrophilic (glycidyl ether) MPIOs were derivatized with either a VCAM-1-targeted Ab or a VCAM-1 high affinity peptide VP (3). Binding of these probes with a FITC-labelled VCAM-1 protein was assessed. In both cases protein binding was significantly higher for MPIOs derivatized with the antibody compared to peptide. The interaction of hydrophobic MPIOs to the protein was found to be the most efficient (Fig. 1). Optimal antibody orientation during coupling resulting in higher availability of antibody binding sites (4). Negligible binding was observed when using a control IgG antibody. However, aggregation of MPIOs was observed, this was much more important for hydrophobic probes. Higher oligomers were formed when derivatized with the VCAM-1 Ab. This is in sharp contrast with hydrophilic VCAM-1-Ab-MPIO. In this case protein binding efficiency was lower. Derivatization of MPIO hydrophobic with a high-affinity peptide resulted in less aggregation. Labeling the probes with the Cy5 fluorophore, which will be required for in vivo optical imaging, did not affect the probe-protein interaction. Conclusions. Based on these studies, the most suitable candidate MPIO-Cy5-VCAM-1 antibody was selected for further studies in cells and in vivo investigations. References 1. McAteer, M. A, et al. . Nat. Med. 2007, 13, 1253-1258. 2. McAteer, M. A, et al. , Arterioscler. Thromb. Vasc. Biol. 2008, 28, 77-83. 3. Nahrendorf, M.,et al. , Circulation, 2006, 3, 1504-1511. 4. Sibson, N. R., et al., Methods in Molecular Biology, 2011, 711, 379-396, - In M. Modo and J.W. Bulte (Eds.), MR Neuroimaging

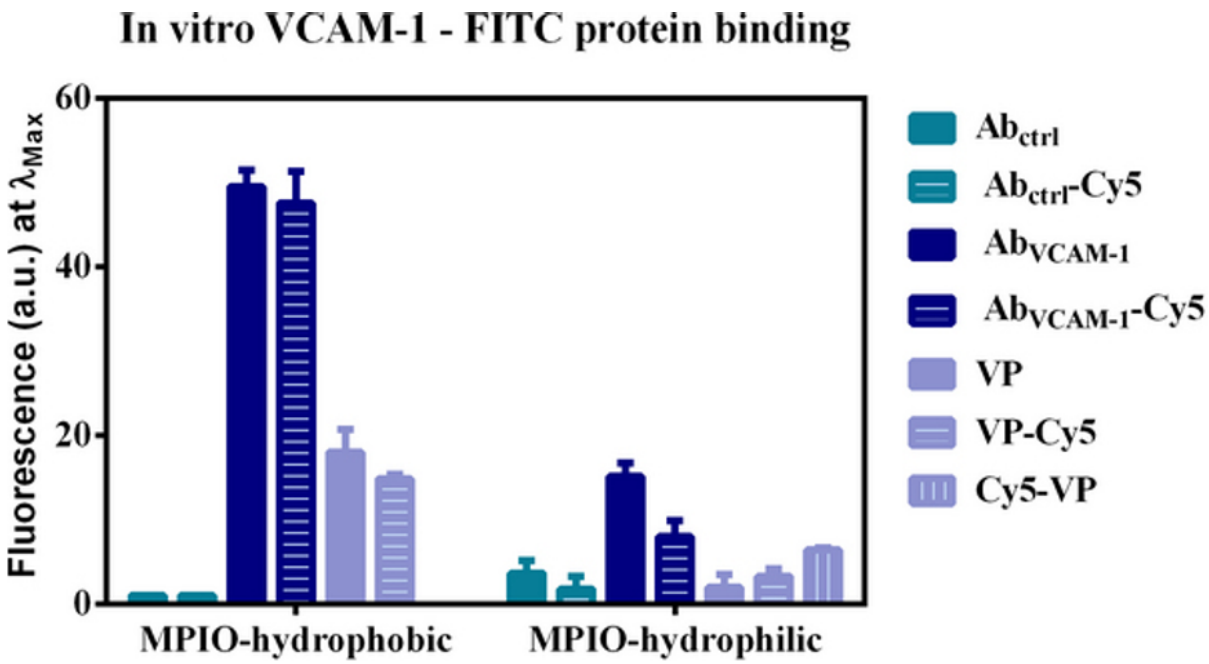

Figure1. VCAM-1 FITC binding to different MPIO probes measured by fluorescence (λEM, 517 nm; λEX., 495 nm). The interaction of the hydrophobic MPIOs to the protein was found to be more efficient compared to the hydrophilic probes. In both cases binding of MPIOs derivatized with a VCAM-1 antibody was significantly higher than for peptide-derivatized MPIOs.

Disclosure of author financial interest or relationships:
A. Radulska, None; **R. Lebel**, None; **W.A. Neugebauer**, None; **M. Lepage**, None.

Presentation Number **P 463**
Poster Session 4
September 21, 2013 / 14:45-14:45 / Room: Exhibit Hall B

Assessing tumor vasculature using a liposomal CT/MRI bimodal contrast agent

Yuguo Li[1], *Yuan Qiao*[2], *Kannie WY Chan*[1,3], *Raag D. Airan*[1], *Jiadi Xu*[3], *Jeff W. Bulte*[1,4], *Shibin Zhou*[2], *Michael T. McMahon*[1,3], *Peter C. van Zijl*[1,3], *Guanshu Liu*[1,3], [1]*Department of Radiology, Johns hopkins university, Baltimore, MD, USA;* [2]*Ludwig Center, Howard Hughes Medical Institute and Sidney Kimmel Cancer Center, Johns Hopkins University, Baltimore, MD, USA;* [3]*F.M. Kirby Research Center for Functional Brain Imaging, Kennedy Krieger Institute, Baltimore, MD, USA;* [4]*Cellular Imaging Section, Institute for Cell Engineering, Johns Hopkins University, Baltimore, MD, USA. Contact e-mail: yuguo@mri.jhu.edu*

Introduction To improve the specific biodistribution, extend the blood circulation time and reduce the nephrotoxicity of clinically-used iodinated CT/X-ray contrast agents, nanoparticulate iodine-containing contrast agents have been recently developed and showed great promises.[1] Another advantage of such system is the possibility of engineering multimodality imaging system by loading nanoparticles with multiple contrast agents.[2] Inspired by previous work,[3,4] we hypothesize that nanoparticles encapsulated with iodinated-agents can be developed to be CT/MRI bimodal contrast agents by utilizing their inherent Chemical Exchange Saturation Transfer (CEST) contrast. To this end, we first loaded liposomes with a clinical CT contrast agent iodixanol (Visipaque, GE, Fig. 1a) and then tested them in vitro and in vivo on a murine colon tumor model. **Methods** Iodixanol encapsulated liposomes (CT-lipo) were prepared according to the literature[6] using a formulation of DPPC:cholesterol: DSPE-PEG-2000=57:40:3. The size, concentration and encapsulation ratio of CT-lipo were measured following our previously published methods.[6] 24 hours before MRI and CT studies, 500 μL overnight-dialyzed liposomes (1000 mgI/kg) were injected into the tail vein of Balb/c mice carrying subcutaneous CT26 murine colon tumors. In vivo CEST MR images were acquired using previous published methods.[6] 3D CT images were acquired using an IVIS® Spectrum CT system (Perkin Elmer) with the following parameters: 50 kVp, 1 mA, and 50 msec exposure, totally 720 projections. **Results** Iodixanol (Fig.1 a) can also be detected both in liposomal (~160 nm) and non-liposomal forms, using CEST MRI with a relatively high sensitivity at an offset frequency of 4.3 ppm (Fig.1b). The detection limit was estimated to be ~ 2nM liposomes, or ~1.4mM encapsulated iodixanol. At 24 hours after i.v. injection, mice injected with CT-lipo showed marked CT contrast enhancement in the tumor region as compared to those injected with blank liposomes (blank-lipo) (Fig 1c). In MRI, the tumor of CT-lipo injected mice showed remarkable but non-uniform CEST contrast enhancement at 4.3 ppm as compared to those injected with blank-lipo (Fig. 1d), with an average tumor contrast enhancement (MTR_{asym}) of 0.8% (n=2 for each group). Studies of CT and MRI acquisitions on additional animals as well as immunohistological validation are underway. **Conclusion**The present work demonstrates the feasibility of engineering a multimodality imaging system by encapsulating single type clinically-used CT contrast agent iodixanol in nanosized liposomes. Our results showed that both CT and MRI could detect reliably the presence of iodixanol-encapsulating liposomes in tumors, enabling the bimodal assessment of tumor vasculature. **References** (1)Lusic, H.; Grinstaff, M. W. Chem Rev 2013, 113, 1641. (2)Zheng, J., et al. Invest radiol 2006, 41, 339. (3)Longo, D. L., et al. Magn Reson Med 2011, 65, 202. (4)Aime, S., et al. Magn Reson Med 2005, 53, 830. (5)Mukundan, S., Jr., et al. Am J Roentgenol 2006, 186, 300.(6)Liu, G., et al. Magn Reson Med 2012, 67, 1106. Supported by R21EB015609, R01EB015032 and R01EB012590.

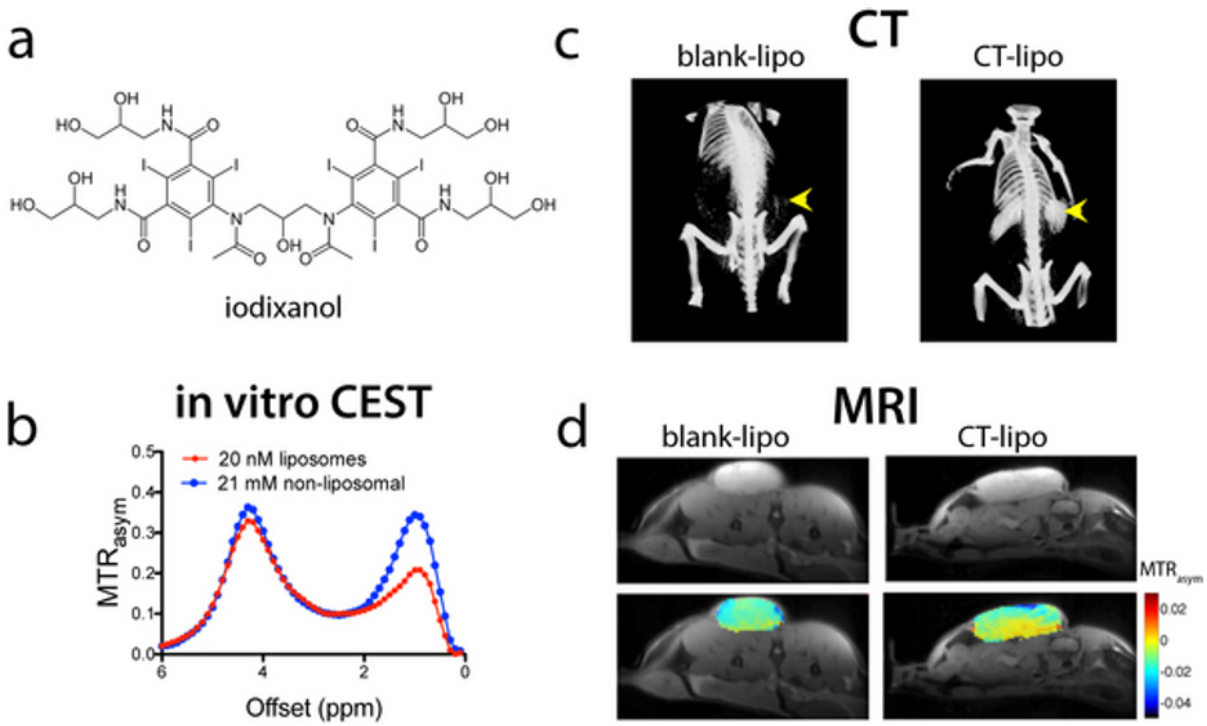

Disclosure of author financial interest or relationships:
Y. Li, None; **Y. Qiao**, None; **K. Chan**, None; **R.D. Airan**, None; **J. Xu**, None; **J.W. Bulte**, None; **S. Zhou**, BioMed Valley Discoveries, Grant/research support; **M.T. McMahon**, None; **P.C. van Zijl**, None; **G. Liu**, None.

Presentation Number **P 464**
Poster Session 4
September 21, 2013 / 14:45-14:45 / Room: Exhibit Hall B

In vitro toxicological assessment of gold nanoparticles designed for nanomedicine applications

Pratap C. Naha, *David P. Cormode, Radiology, University of Pennsylvania, Philadelphia, PA, USA. Contact e-mail: Pratap.Naha@uphs.upenn.edu*

Introduction: Gold nanoparticles (Au-NP) are increasingly being applied in the biomedical field, as therapeutics, as contrast agents, and in diagnostic systems. Due to the increasing proposed applications of Au-NP, the Organisation for Economic Co-operation and Development has therefore included Au-NP in their list of nanoparticles recommended for toxicological screening. Despite the increasing production of Au-NP for medical applications, few studies have examined their environmental toxicity. In this study, we have selected a range of Au-NP formulations proposed for use as therapeutics and as contrast agents. These formulations are PMAL coated Au-NP (CT cell labeling), m-PEG coated Au-NP (CT contrast), lipoprotein coated Au-NP (CT contrast), gold nanoshells (therapeutics), m-PEG coated gold nanorods (therapeutics) and AuroVist (CT contrast). We present the characterization and cytotoxicity of the above mentioned Au-NP at their stock concentrations in J774A.1 (macrophage), C2BBe1 (epithelial) and BJ5ta (fibroblast) cells. Methods and Results: m-PEG coated Au-NP (A), PMAL coated Au-NP (B) are synthesized in house, while lipoprotein coated Au-NP (C) was a gift from the Fayad lab. m-PEG coated gold nanorods (D), gold nanoshells (E) and AuroVist (F) were purchased from NANOPARTz, nanoComposix and Nanoprobes, respectively. Their hydrodynamic diameters and core diameters were measured using dynamic light scattering and transmission electron microscopy. The core diameter of PMAL coated Au-NP, m-PEG coated Au-NP, lipoprotein coated Au-NP, gold nanoshell, and AuroVist, was found to be 5.7±1.5, 13.7±2.0, 5.1±1.1, 145.4±12.1 and 3.6±1.2 nm respectively. The length and width of m-PEG coated gold nanorods were found to be 28.2±1.3 and 9.2±4.1 nm. The concentration of gold in each Au-NP formulation was determined using inductively coupled plasma optical emission spectroscopy. Cytotoxicity of the different Au-NP was investigated using the MTS assay in J774A.1, C2BBe1 and BJ5ta cells. Briefly, 10000 cells were seeded in each well of 96 well plates and were incubated with 2 µl Au-NP at their stock concentration (ranging from 0.9 to 61 mg/ml) per well, n=4 per condition for 24 hours at 37 °C in a CO2 incubator. No cytotoxic response was seen upon exposure of PMAL coated Au-NP, m-PEG coated Au-NP, gold nanoshell, and AuroVist to all the cells used for this study. However, an adverse response to the exposure of lipoprotein coated Au-NP and gold nanorods to J774A.1, C2BBe1and BJ5ta cells was clearly observed (G). In the case of lipoprotein coated Au-NP, this is likely due to excessive removal of cholesterol from the cells. Conclusion: Among the series of Au-NP screened, at their stock concentrations, lipoprotein coated Au-NP and gold nanorods were found to adversely affect cells, while AuroVist, PMAL coated Au-NP, m-PEG coated Au-NP and gold nanoshells were biocompatible. We plan to extend this study to more gold formulations and conditions tested. However, these experiments suggest that care should be taken during handling of lipoprotein coated Au-NP and gold nanorods.

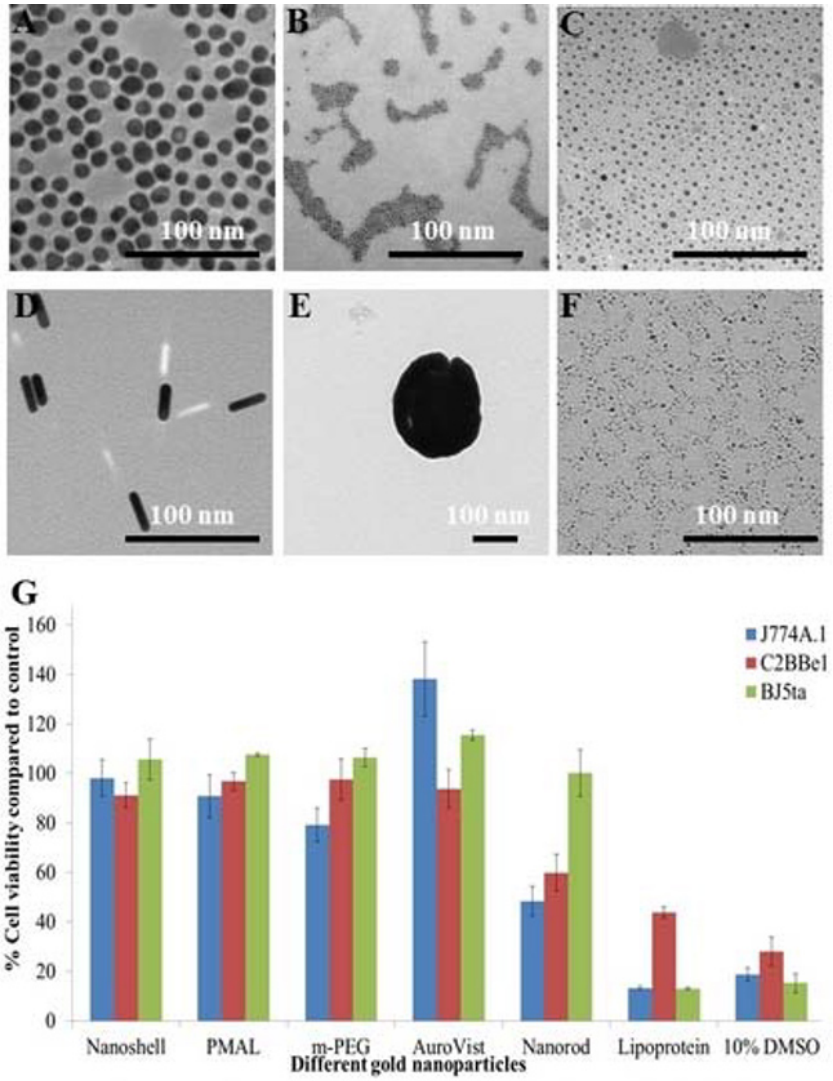

A: m-PEG coated Au NP, B: PMAL coated Au NP, C: Lipoprotein coated Au NP, D: Au nanorod, E: Au nanoshell, F: AuroVist™, G: Cytotoxicity results of different Au NP.

Disclosure of author financial interest or relationships:
P.C. Naha, None; **D.P. Cormode**, Philips, Grant/research support .

Presentation Number **P 465**
Poster Session 4
September 21, 2013 / 14:45-14:45 / Room: Exhibit Hall B

Optical Imaging of Brown Adipose Tissue in Living Mice

Douglas R. Rice, *Alexander G. White, Rachael Palumbo, Bradley D. Smith, Alexander G. White, Chemistry and Biochemistry, University of Notre Dame, Notre Dame, IN, USA. Contact e-mail: drice1@nd.edu*

Brown adipose tissue (BAT) differs from white adipose tissue (WAT) by its distinct locations and a reddish-brown color due to enhanced vascularization and a high density of mitochondria. BAT plays a key role in energy expenditure and heat generation in newborn mammals as well as adults. Recent studies have shown that BAT volume is negatively correlated with body mass index and other diabetic parameters in human adults. BAT has thus been proposed as an attractive target for anti-obesity and anti-diabetes therapy. While several positron emission tomography (PET) methods are established for detecting human BAT, there is no convenient protocol for optical imaging of BAT in small animal models. We have developed a fluorescent labeling system for BAT detection in mice. The labeling system consists of a commercially available deep red fluorescent dye encapsulated within commercially available PEGylated micelles. Mice treated with intravenous doses of the labeling system produce strong contrast in the interscapular BAT pad after a period of six hours. Additional PET imaging studies used 18FDG show strong uptake due to enhanced BAT metabolism. This enables multimodal BAT imaging where the fluorescent labeling system displays the volume of the BAT and the 18FDG reports the metabolic activity of the tissue.

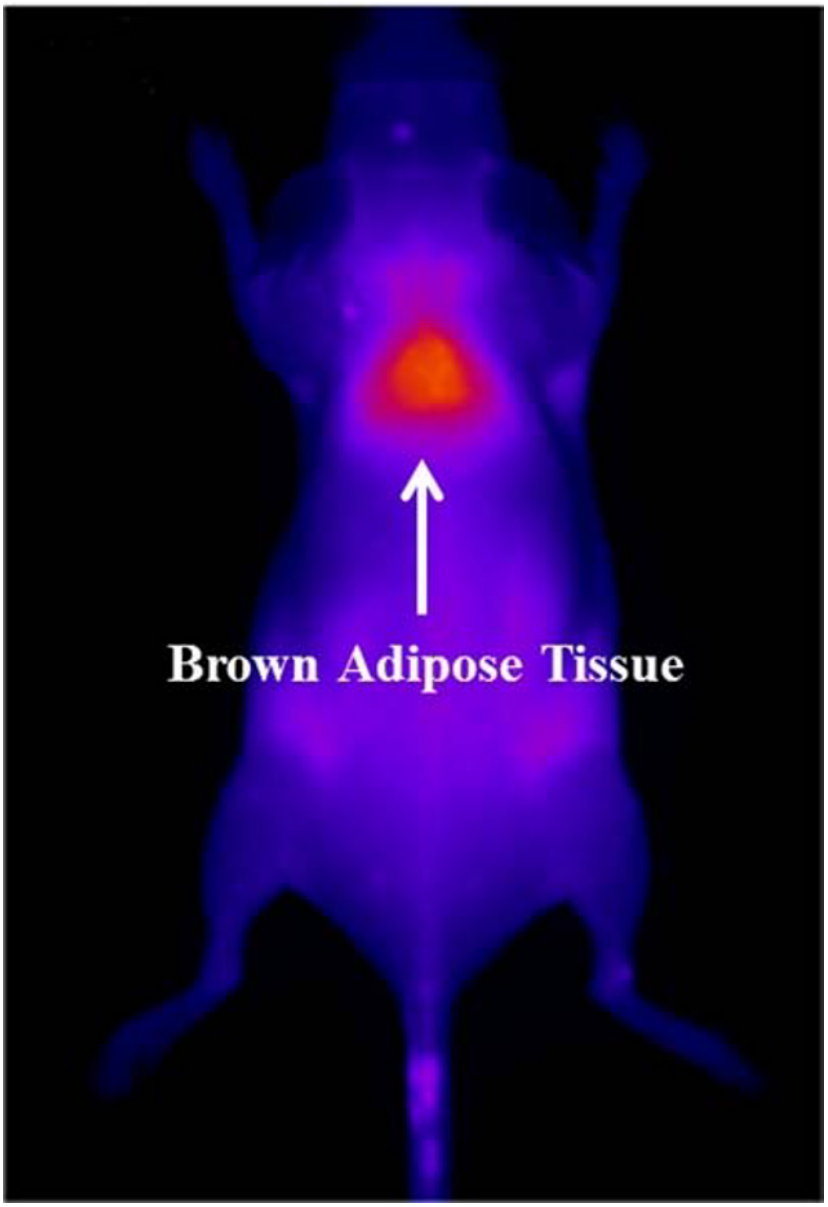

Disclosure of author financial interest or relationships:
D.R. Rice, None; **A.G. White**, None; **R. Palumbo**, None; **B.D. Smith**, None; **A.G. White**, None.

Presentation Number **P 466**
Poster Session 4
September 21, 2013 / 14:45-14:45 / Room: Exhibit Hall B

A Multifunctional Lipoprotein/Polymer Hybrid Nanoparticle for Controlled Release Drug Delivery to Atherosclerotic Plaques

Brenda L. Sanchez-Gaytan[1], *Mark E. Lobatto*[1,2], *Jun Tang*[1], *Francois Fay*[1], *Canturk Ozcan*[1], *YongTae Kim*[3], *Omid C. Farokhzad*[4], *Edward A. Fisher*[5], *Robert Langer*[3], *Zahi A. Fayad*[1], *Willem J. Mulder*[1,2], [1]*Icahn School of Medicine at Mount Sinai, New York, NY, USA;* [2]*Department of Vascular Medicine, Academic Medical Center, Amsterdam, Netherlands;* [3]*David H. Koch Institute for Integrative Cancer Research, Massachusetts Institute of Technology, Cambridge, MA, USA;* [4]*Department of Anesthesiology, Brigham & Women's Hospital, Boston, MA, USA;* [5]*Department of Medicine (Cardiology) and Cell Biology, NYU School of Medicine, New York, NY, USA. Contact e-mail: brensg@gmail.com*

Introduction 2nd generation polymeric nanoparticles have shown significant advantages in drug delivery. They can be loaded with poorly water soluble drugs,1 their size can be judiciously controlled2 and their surface can be functionalized with a PEG coating and/or targeting ligands. Importantly, the polymeric core can be loaded with drugs and/or contrast agents for which the release rates can be controlled by the choice of polymer composition and molecular weight. High-density lipoprotein (HDL) is a natural nanoparticle that transports fats through the body, which has an inherent affinity for atherosclerotic plaques. HDL-like nanoparticles labeled with contrast agents have been shown suitable for molecular imaging as they effectively target atherosclerotic plaque. In the current study we developed a novel HDL-like hybrid nanoparticle using recently developed microfluidics technology.2 The nanoparticle is comprised of a lipid/apolipoprotein coating that encapsulates a poly(lactic-co-glycolic acid) (PLGA) core suitable for the delivery of drugs in a controlled manner. The versatility of the approach also allows the incorporation of functional lipids to render multifunctional nanoparticles with imaging, therapeutic and atherosclerosis targeting properties. Methods and Results Hybrid polymer-HDL nanoparticles with a PLGA core and a coating comprised of lipids and apolipoprotein A1 (PLGA-HDL) were synthesized using microfluidics. The synthetic approach consists of the rapid injection of the components in three different channels of a microfluidics chip. Amphiphilic phospholipids and PLGA were dissolved in a mixture of ethanol and acetonitrile. This solution was injected in the middle channel of the microfluidic chip and mixed with an aqueous apoprotein A1 (ApoA1) solution injected in the two outer channels. Inside the chip, controlled nanoprecipitation occurred through microvortices, resulting in the instantaneous and continuous production of hybrid PLGA-HDL nanoparticles with high reproducibility (Fig 1A, B). The resulting PLGA-HDL nanoparticles had a hydrodynamic diameter of 75 nm with a polydispersity of 0.205 (Fig 1C). PLGA-HDL nanoparticles with imaging capabilities were formed by introducing Gd-DTPA-lipids and/or fluorescent lipids in the formulation. This allows their visualization in vitro and in vivo studies. Cells tolerated the PLGA-HDL nanoparticles very well and displayed a particular affinity for macrophages (Fig 1D). Moreover, the selective nanoparticle uptake by macrophages could be decreased by a competitive incubation with native HDL. In vivo studies carried out with ApoE knockout mouse model of atherosclerosis showed clear accumulation of PLGA-HDL nanoparticles throughout the aorta (Fig E), which were found to be colocalized with plaque macrophages (Fig F). Conclusions We developed a hybrid HDL-like nanoparticle platform with both in vivo and in vitro imaging capabilities. The nanoparticle design allows the incorporation of water soluble drugs in the polymeric core. PLGA-HDL nanoparticles displayed similar behavior as native HDLs. 1. Wang et al. Annu. Rev. Med. 2012. 185-98
2. Kim et al. Nano Lett. 2012. 3587-91

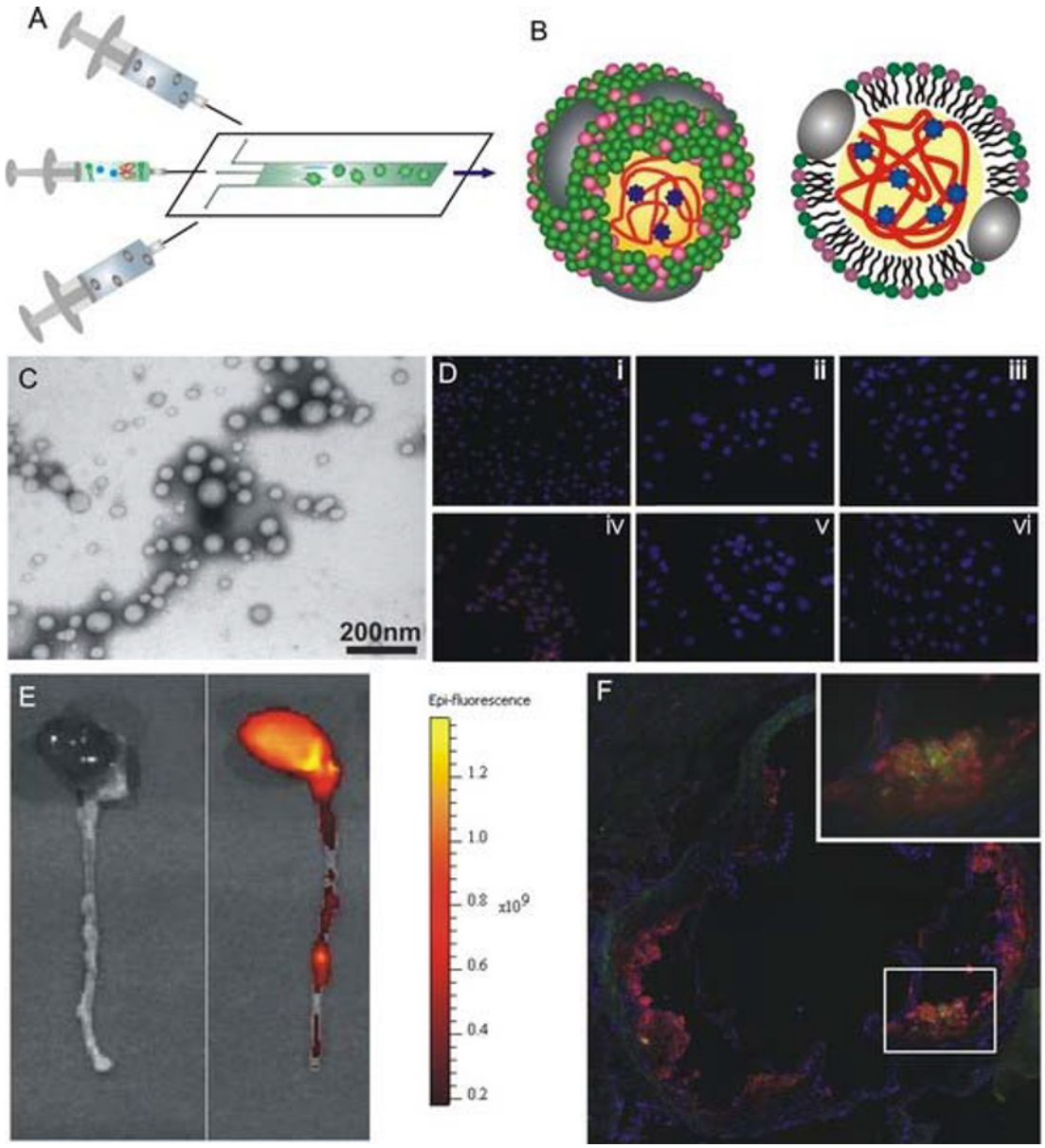

Figure 1. A) Schematic representation of the synthesis of PLGA-HDL nanoparticles using microfluidics. B) 3-D and cross-sectional view of multifunctional HDL-like nanoparticles containing functional lipids in the corona and drug molecules incorporated in the PLGA core. C) TEM image of the HDL-PLGA nanoparticles negatively stained with phosphotungstic acid. D) Micrograph of macrophages (i, iv), hepatocytes (ii, v) and pancreatic endothelial cells (iii,vi) incubated with Rhodamine-labeled HDL-PLGA (iv-vi) and Rhodamine-labelled PEG lipids in the corona and PLGA in the core (i-iii). After 2 hours of nanoparticle incubation at 37 °C, macrophages showed a preferential uptake of Rhodamine-labeled HDL-PLGA nanoparticles (iv). E) IVIS optical imaging of atherosclerotic aorta excised from a ApoE KO mice injected with saline (left) or HDL-PLGA (right). F) Fluorescence microscopy of the aortic root of ApoE KO mice revealed colocalization of HDL-PLGA (FITC) and CD68-macrophages (TRITC) 24 hours after injection.

Disclosure of author financial interest or relationships:

B.L. Sanchez-Gaytan, None; **M.E. Lobatto**, None; **J. Tang**, None; **F. Fay**, None; **C. Ozcan**, None; **Y. Kim**, None; **O.C. Farokhzad**, None; **E.A. Fisher**, None; **R. Langer**, None; **Z.A. Fayad**, None; **W.J. Mulder**, None.

Presentation Number **P 467**
Poster Session 4
September 21, 2013 / 14:45-14:45 / Room: Exhibit Hall B

Peptide Scaffolds for Multimodal Targeted Molecular Imaging Agents

Taylor M. Barrett[1], *Chelsea J. Weidman*[1], *Lauren E. Heese*[1], *Hans F. Schmitthenner*[1,2], [1]*School of Chemistry and Materials Science, Rochester Institute of Technology, Rochester, NY, USA;* [2]*Center for Imaging Science, Rochester Institute of Technology, Rochester, NY 14623, NY, USA. Contact e-mail: tmb1230@rit.edu*

Objective: Our aim is to develop versatile, differentially protected peptide scaffolds for the synthesis of diverse targeted multimodal molecular imaging agents (TMIA's) and to provide methods for the conversion of these scaffolds into discrete targeted probes containing multiple imaging and targeting agents on a single template. A second aim is the development of "TMIA tool kits" which include methods and reagents for selective deprotection, conjugation to imaging and targeting agents, and solid phase extraction (SPE) for purification. Method: The approach is based on the use of linear or cyclic peptides as scaffolds due to their facile synthesis from available protected amino acids and the inherent advantages of small peptides in bioavailability, biodistribution, and clearance, including optimization for proteolytic stability by the use of D-amino acids. By appropriate design, the differentially protected peptides allow selective unmasking and sequential conjugation to multiple imaging agents and targeting agents as illustrated below to enable the synthesis of multimodal, multi-chelating, or multi-targeting TMIA's. Results: In our initial approach, we synthesized two multi-functional scaffolds based on differentially protected lysine and glutamic acid residues, and characterized them by NMR and LC-MS. As proof of concept, we next developed methods for their conversion to multimodal TMIA's. For imaging groups we chose near infrared fluorescence (NIRF) dyes (Cy5.5, Cy7, Alexa680 or Alexa750) and the DOTA group for chelation to gadolinium (Gd-DOTA) for magnetic resonance imaging (MRI). An example of a multimodal TMIA for NIRF-MRI is shown below. The targeting approach utilizes the cyclic peptide c(RGDyK) due to its established binding to α2β3 integrin receptors in A549 and U-87 MG cancer cells. The evaluation of these is being studied by fluorescent confocal microscopy, photoacoustic (PA) measurements for MRI-PA, and measurement of spin-lattice relaxation times (T1) in NMR. Critical to our approach was developing methods for the selective deprotection of the peptide side chain groups including Cbz, Alloc, and Mtt for lysines and t-butyl ester (OtBu) for the glutamic acid, with Fmoc on the N-termini. Selective deprotection methods were developed for Alloc in the presence of Cbz and for unmasking Mtt in the presence OtBu, with each of these also being orthogonal to two or more of the other groups above. These methods were critical to enable the synthesis of multimodal TMIA's from the peptide scaffolds, as literature methods for these were inadequate or not reported. Conclusion: A synthetic approach to TMIA's is described that enables binding of multiple agents on a single template to produce discrete, targeted multimodal agents. Evaluation of these by fluorescent confocal microscopy imaging of A549 cancer cells and spin-lattice relaxation time (T1) measurements in NMR is also described.

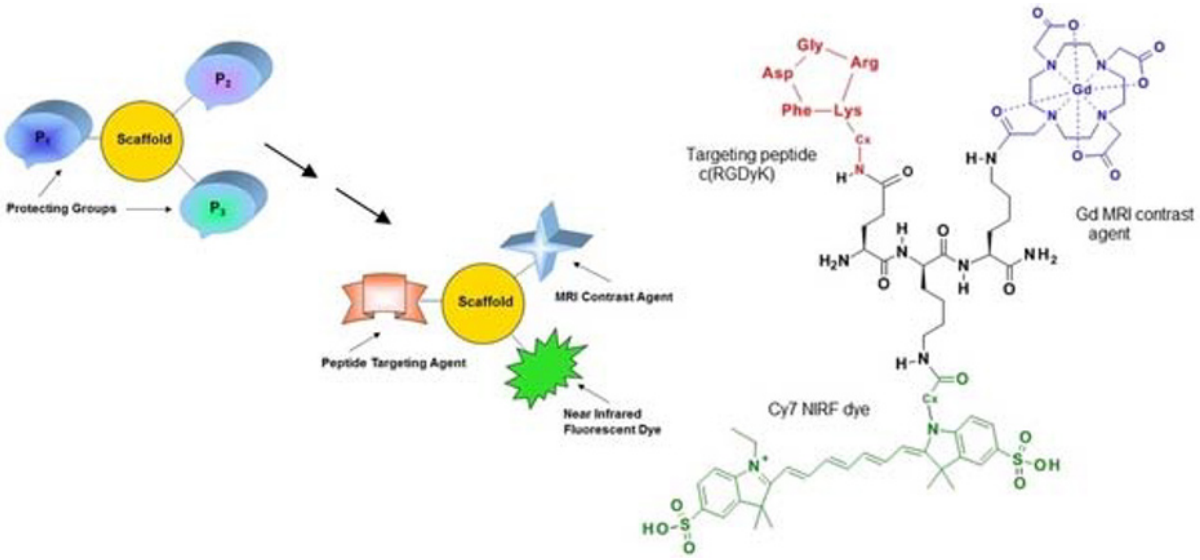

Disclosure of author financial interest or relationships:
T.M. Barrett, None; **C.J. Weidman**, None; **L.E. Heese**, None; **H.F. Schmitthenner**, None.

Presentation Number **P 468**
Poster Session 4
September 21, 2013 / 14:45-14:45 / Room: Exhibit Hall B

Development of bimodal RGD peptide conjugated radiolabeled near-infrared Cu111InSe quantum dots for αvβ3 integrin imaging

Minghao Sun, *Likun Yang, Li Wang, Purnima Jose, Gobalakrishnan Sundaresan, Jamal Zweit, Virginia Commonwealth University, Richmond, VA, USA. Contact e-mail: msun@vcu.edu*

Aims: NIR emissive, Copper-Indium-Selenium-based quantum dots (CIS-QDs) have great potential for fluorescence imaging due to their high fluorescent quantum yield and low toxicity. An intrinsic radiolabeling strategy was developed to incorporate In-111 into the crystal lattice of CIS-QDs to obtain hybrid In-111 radiolabeled CIS-QDs for in vivo SPECT/fluorescence imaging. Through specific surface modification with a multidentate zwitterionic ligand and bioconjugation with RGD peptide, this bimodal In-111 CIS-rQDs showed potential applications for targeted imaging of the αvβ3 integrin receptor. Methods: CIS-rQDs were synthesized by doping In-111 in the interface layer of the CIS core and ZnS shell. The multidentate zwitterionic ligand was synthesized through a reaction with amino-lipoic acid, N,N-dimethylethylenediamine and BOC protected PEG-NH2 with DCC activated PAA. The ligand exchange reaction was performed in a three-component reverse phase micro-emulsion system. RGD peptide was conjugated to CIS-rQDs by using DSS as cross linker. MCF-7 (breast cancer) and U87 (primary glioblastoma) cell lines were used to demonstrate the RGD conjugated CIS-rQDs targets to the αvβ3 integrin receptor. Fluorescence microscopy, flow cytometry and gamma counting were used to differentiate the uptake rate of RGD conjugated CIS-rQDs in the two cell lines. Results: In-111 radiolabeled CIS-rQDs was synthesized with high specific activity (50 Ci/mmole) and fluorescent quantum yield (~24% in chloroform). After ligand exchange with multidentate zwitterionic ligand PAA-DHLA-SB-PEG-NH2, no radioactivity loss was detected and the fluorescent quantum yield was maintained (~18%). The small HD size (~15 nm) and negative surface charge (-45 mV) reduced the interaction of zwitterionic CIS-rQDs with plasma proteins and it could potentially improve targeting to tumor in vivo. The bioconjugation of RGD peptide with CIS-rQDs was confirmed by gel electrophoresis. The cell experiments showed higher uptake of RGD-rQDs by the U87 cell line, which overexpress the αvβ3 integrin receptor compared with the MCF-7 cell line. Discussion: High efficiency synthesis, low toxicity and utilization of a clinical imaging isotope make the RGD-CIS-rQD a promising bimodal contrast agent for αvβ3 integrin receptor and tumor vasculature imaging. Surface modification of this nanoprobe could further improve the pharmacokinetics as well as tumor targeting. The strategy developed could be also used to synthesize other types of radiolabeled nanoprobes and conjugate them with various ligands for targeted multimodal molecular imaging and therapy. Acknowledgements: Supported by the Virginia Commonwealth University, School of Medicine. References: 1. Minghao Sun, David Hoffman, Gobalakrishnan Sundaresan, Likun Yang, Naru Lamichhane, Jamal Zweit. AJNMMI, 2012, 2, 122-135 2. Weibo Cai, Hong Hao. AJNMMI, 2012, 2, 122-135

Disclosure of author financial interest or relationships:
M. Sun, None; **L. Yang**, None; **L. Wang**, None; **P. Jose**, None; **G. Sundaresan**, None; **J. Zweit**, None.

Presentation Number **P 469**
Poster Session 4
September 21, 2013 / 14:45-14:45 / Room: Exhibit Hall B

Multimodal PET/MRI Ga/Gd-AGuIX® Nanoparticles for dual imaging of brain tumors

Charles Truillet[1], *François Lux*[1], *Lorenza Fugazza*[2], *Elena Castaldi*[2], *Davide Camporese*[2], *Charalambos Tsoukalas*[3], *Penelope Bouziotis*[3], *Frederic Boschetti*[4], *Pascal Perriat*[5], *Olivier Tillement*[1], *Lucie Sancey*[1], [1]*FENNEC Chemistry, ILM, Villeurbanne Cedex, France;* [2]*Research and Development, Advanced Accelerator Applications, Saint Genis Pouilly, France;* [3]*Radiochemical Studies Laboratory, Institute of Nuclear and Radiological Sciences, Technology, Energy and Safety, National Center for Scientific Research "Demokritos", Athens, Greece;* [4]*Research and Development, CheMatech, Dijon, France;* [5]*Matériaux Ingénierie et Science, Insa Lyon, Lyon, France. Contact e-mail: charles.truillet@univ-lyon1.fr*

Each imaging modality is characterized by specific resolutions on the spatial and temporal scales, as well as by the different sensitivity for contrast agents or anatomical details. The combination of resolution and sensitivity will integrate the potencies of the two modalities. This will reduce weaknesses of each individual modality, leading to improve diagnostics, therapeutic monitoring, and preclinical research using imaging approaches. The recent apparition of PET/MRI for clinical and small animal investigations requires the development of new multimodal probes. The AGuIX® Gadolinium-based nanoparticles were developed for PET/MRI imaging. The size inferior to 5 nm of this multimodal platform allows a good renal clearance in rodents . The nanoparticles are composed of silica matrix functionalized by gadolinium chelate (DOTA-Gd) and free chelate (DOTA-GA and NODA-GA), positive contrast agent for MRI, and isotopic radioactive chelate for PET or SPECT imaging. Physical and chemical properties of the AGuIX® coupled with 2,2',2''-(10-(2,6-dioxotetra hydro-2H-pyran-3-yl)-1,4,7,10-tetraazacyclododecane-1,4,7-triyl)triacetic acid (DOTA-GA) or 2,2'-(7-(1-carboxy-4-((2,5-dioxopyrrolidin-1-yl)oxy)-4-oxobutyl)-1,4,7-triazonane-1,4-diyl) diacetic acid (NODA-GA-NHS) were finely characterized. DOTA-GA and NODA-GA allow the labeling with 111In or 68Ga with high specific-activity of 50 mCi/µg and 41 Ci/µg respectively. 68Ga isotope is an excellent candidate for nuclear imaging due to its lifetime and availability. The radiolabeled 68Ga-AGuIX® were stable for more than 3 hrs in human serum solution. The purity of radiochemical assessment of the radiolabeled AGuIX® was found superior to 95% without any specific purification in agreement with required purity regulations. 68Ga-AGuIX allowed the imaging in various tumor models in particular to the brain tumor-bearing rodents. The Gd-based nanoparticles AGuIX® exhibit a real potential for multimodal imaging that should permit the PET/MRI clinical investigations with a unique nanoparticle.

Disclosure of author financial interest or relationships:
C. Truillet, None; **F. Lux**, None; **L. Fugazza**, None; **E. Castaldi**, None; **D. Camporese**, None; **C. Tsoukalas**, None; **P. Bouziotis**, None; **F. Boschetti**, None; **P. Perriat**, None; **O. Tillement**, None; **L. Sancey**, None.

Presentation Number **P 470**
Poster Session 4
September 21, 2013 / 14:45-14:45 / Room: Exhibit Hall B

A versatile agent for MRI and PET imaging of hypoxic tumors

Yunkou Wu[1], *Guiyang Hao*[2], *Xiankai Sun*[2], *Dean Sherry*[1,3], [1]*Advanced Imaging Research Center, University of Texas Southwestern Medical Center, Dallas, TX, USA;* [2]*Department of Radiology, University of Texas Southwestern Medical Center, Dallas, TX, USA;* [3]*Depatment of Chemistry, University of Texas at Dallas, Richardson, TX, USA. Contact e-mail: yunkou.wu@utsouthwestern.edu*

Introduction: Identification of hypoxic regions of tumors is critical for developing radiation treatment protocols for cancer patients. The goal of this work is to develop and evaluate a new agent for molecular imaging of tumor hypoxia with PET and MRI. Method: The new agent, HP-DO3A-NI, results from conjugation of HP-DO3A (the macrocyclic component of ProHance®) with nitroimidazole. The PET and MR imaging of A549 hypoxic tumors in mice were performed using the 68Ga(III) and Gd(III)-HP-DO3A-NI complexes, respectively, and the respective HP-DO3A complexes as controls. Results: PET images of tumor-bearing mice showed intense image contrast in hypoxic tumors at 2 hr post-injection of 68Ga(III)-HP-DO3A-NI while image contrast in tumor-bearing mice injected with the control agent was quite weak after 2 hr (Figure 1). The tumors were confirmed to be hypoxic by histology. The 68Ga(III)-HP-DO3A-NI has superior biodistribution characteristics compared to the established PET tracer 18FMISO. The tissue biodistribution results showed that the agent was cleared largely through the kidneys while heart, lung and liver tissues contained insignificant amounts of agent. The tumor/muscle ratio was 5.1 ± 0.1 at 2.5 hr post-injection. T1-weighted MR images of tumor-bearing mice were acquired using a fast spin-echo multi-slice sequence after a single IV bolus injection of either 0.4 mmol/kg ProHance or Gd(III)HP-DO3A-NI. Dynamic contrast images showed that ProHance was largely cleared from tumors by 2 hr post-injection while the hypoxia agent still steadily accumulated in tumors over this same time period but gradually cleared from tumor tissues (within detectable limits) by 5 hr post-injection. Conclusion: Hypoxic tumors were detected in mice by both PET and MRI using 68Ga(III) or Gd(III) complexes of the macrocylic ligand, HP-DO3A-NI. This versatile, new agent offers considerable potential for imaging hypoxic regions of tumors.

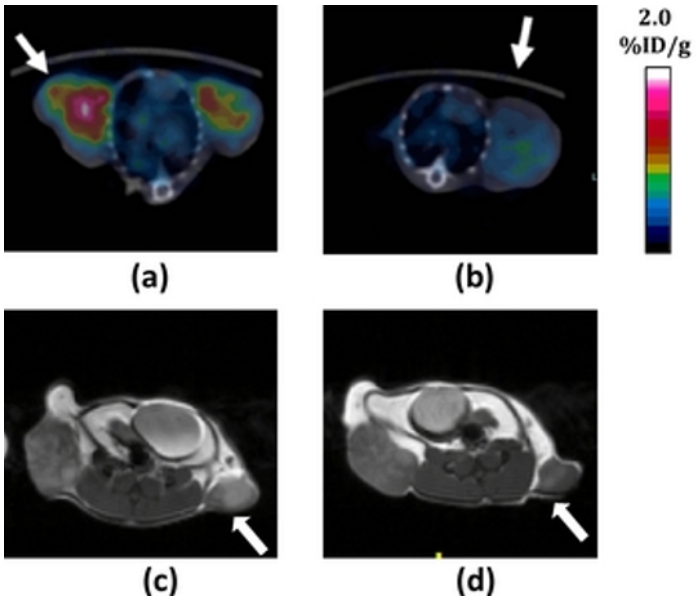

Figure 1. Axial PET (top row) and MRI (bottom row) images showing targeting of hypoxic tumors in mice. (a) and (c) show PET and MR images after 2 hr injection of either ^{68}Ga(III)-HP-DO3A-NI or Gd(III)-HP-DO3A-NI. The images in (b) and (d) show the respective controls.

Disclosure of author financial interest or relationships:
Y. Wu, None; **G. Hao**, None; **X. Sun**, None; **D. Sherry**, None.

Presentation Number **P 471**
Poster Session 4
September 21, 2013 / 14:45-14:45 / Room: Exhibit Hall B

Design of Peptide-Conjugated Gold Nanorods for Specific In Vivo Imaging of EGFR-Expressing Colorectal Tumors

Charles Caldwell[1], *Ajit Zambre*[2], *Raghuraman Kannan*[2,1], *Gerald Arthur*[3], [1]*Biological Engineering, University of Missouri-Columbia, Columbia, MO, USA;* [2]*Radiology, University of Missouri-Columbia, Columbia, MO, USA;* [3]*Pathological and Anatomical Sciences, University of Missouri-Columbia, Columbia, MO, USA. Contact e-mail: cwckc7@gmail.com*

In recent years, gold nanorods (GNRs) have been applied as high contrast agents for in vivo molecular imaging using technologies such as near-infrared (NIR) transmission imaging, photoacoustic tomography (PAT), two-photon excited luminescence (TPL) imaging, and surface-enhanced Raman spectroscopy (SERS) imaging. While these methods allow for excellent imaging of injected sites, the rise of personalized medicine has produced a need for more specific imaging agents that can image tumors in vivo as well as to also offer diagnostic insight for treatment options. One such diagnostic marker in tumors that is of high clinical interest is the presence of overexpressed epidermal growth factor receptor (EGFR). Biopsies of human tumors known to overexpress EGFR are subjected to laboratory tests to determine whether the patient would respond to target specific drugs such as Cetuximab that are specifically targeted to EGF receptors. To design a combined EGFR-targeted GNR-based diagnostic and imaging agent, we have conjugated a peptide with EGFR-avid properties to GNR functionalized with a polyethylene glycol (PEG) surface modification. In our studies we have shown the specific binding of the GNR-peptide compound (GNR-1070) to EGF receptors in numerous EGFR-overexpressing cells and human tumor tissues in vitro, such as colorectal adenocarcinoma and squamous cell carcinoma of the lung. The demonstrated efficacy and biocompatibility of EGF receptor-targeted GNR-1070, combined with the numerous imaging techniques developed for in vivo imaging of GNR in the past few years, gives promise that peptide-conjugated GNRs can be utilized as a specific diagnostic and imaging agent.

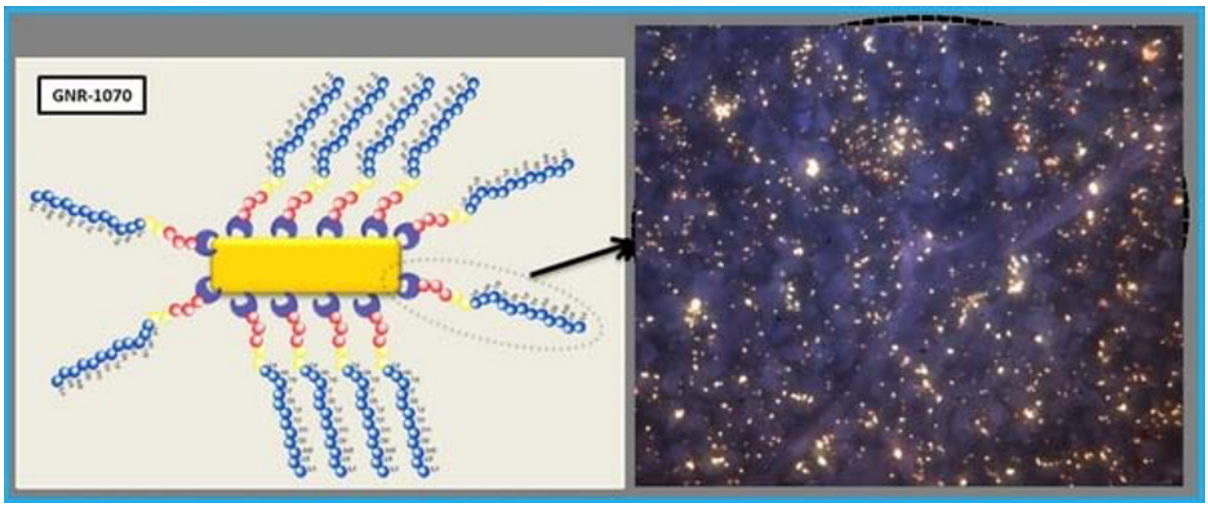

Figure 1: Schematic of GNR-1070 construct (left) and incubation of GNR-1070 construct with EGFR-overexpressing Squamous Cell Carcinoma of the Lung

Disclosure of author financial interest or relationships:
C. Caldwell, None; **A. Zambre**, None; **R. Kannan**, None; **G. Arthur**, None.

Presentation Number **P 472**
Poster Session 4
September 21, 2013 / 14:45-14:45 / Room: Exhibit Hall B

Chemical Exchange Saturation Transfer (CEST)-MRS reveals metabolite levels for monitoring the aggressiveness of breast cancer cells

Kannie WY Chan[1,2], *Lu Jiang*[1], *Jannie P. Wijnen*[1,4], *Tiffany R. Greenwood*[1], *Menglin Cheng*[1], *Peter C. van Zijl*[1,3], *Michael T. McMahon*[1,3], *Kristine Glunde*[1], [1]*Russell H. Morgan Department of Radiology and Radiological Sciences, Division of Cancer Imaging, Johns Hopkins Medicine, Baltimore, MD, USA;* [2]*Cellular Imaging Section and Vascular Biology Program, Institute for Cell Engineering, Baltimore, MD, USA;* [3]*F.M. Kirby Research Center for Functional Brain Imaging, Kennedy Krieger Institute, Baltimore, MD, USA;* [4]*Department of Radiology, University Medical Centre Utrecht, Utrecht, Netherlands. Contact e-mail: kanniec@mri.jhu.edu*

Introduction: Altered metabolism is a hallmark of cancer, in which high levels of choline-containing metabolites, such as phosphocholine (PC) and glycerophosphocholine (GPC) have consistently been detected in malignant cancer types [1,2]. In vivo assessment of these metabolite levels is important for cancer diagnosis, development of anti-cancer treatments [3], and treatment monitoring. High-resolution Magnetic Resonance Spectroscopy (HR-MRS) can be used to study metabolites. However, the MR spectra cannot be completely resolved in the in vivo MR spectroscopic imaging [3], and the free choline (Cho) levels have not been extensively investigated in cancers. Hence, there is a need for alternative methods to study these metabolite levels. Chemical Exchange Saturation Transfer (CEST) is a molecular imaging approach that enables the identification of specific groups of exchangeable protons [4]. Here we have applied CEST to monitor exchangeable protons on metabolites, such as free choline (Cho), PC and GPC, together with creatine (Cr), myo-inositol (mI), glutamine (Gln) and glutamate (Glu). Methods: CEST-MRI was acquired at 310 K using an 11.7 T Bruker Avance system, and was processed using custom-written Matlab scripts to calculate the magnetization transfer ratio (MTRasym). Fully relaxed, quantitative 1H HR-MRS of the water-soluble phases was collected and analyzed using the MestReC 4.9.9.6 software [5]. Notice that while water is located at 4.75 ppm in the normal proton spectrum, CEST spectra are referenced with respect to water at 0.0 ppm. Results and Discussion: Cho and metabolites, such as Cr, mI, Gln and Glu have CEST contrast at frequencies of 1.2, 2.0, 1.0, 1.4 and 1.8 ppm from water, respectively (Fig. 1a). The phosphorylated metabolites PC and GPC did not show any detectable CEST contrast (Fig. 1a). Next, we looked at breast cancer cell extracts, which showed CEST contrast at the frequencies of the above metabolites. The overall metabolite level was the highest in MCF-12A cells, and the lowest in MDA-MB-231 cells (Fig. 1b), which agrees with previous HR-MRS studies [6]. The CEST contrast in the cell extracts (Fig. 1b) correlates with the relative concentrations measured by HR-MRS (Fig. 1c; supplementary). The cellular Cho concentration inversely correlated with the degree of malignancy of the breast cell lines (Fig. 1d), which means that the CEST signal intensity has the potential to be used as a semi-quantitative measure for Cho and other metabolite levels. Conclusion: Our data suggest that CEST-MRI allows for the detection of metabolite levels in cell extracts, which was shown by combining and correlating CEST-MRI with 1H HR-MRS. This opens up the possibility of imaging these metabolite levels in vivo, providing information about their concentrations and spatial distributions. References: [1] Podo F et la. NMR Biomed. 1999 [2] Iorio E. et al. Cancer Res. 2010 [3] Glunde K. et al. Semin. Oncol. 2011 [4] van Zijl PCM et al. Magn. Reson. Med. 2011 [5] Glunde et al. Cancer Res 2004. [6] Tyagi et al. Magn. Reson. Med. 1996. This work was funded by NIH R01 CA134695, R01 EB015031, R01 EB015032 and the Niels Stensen Foundation.

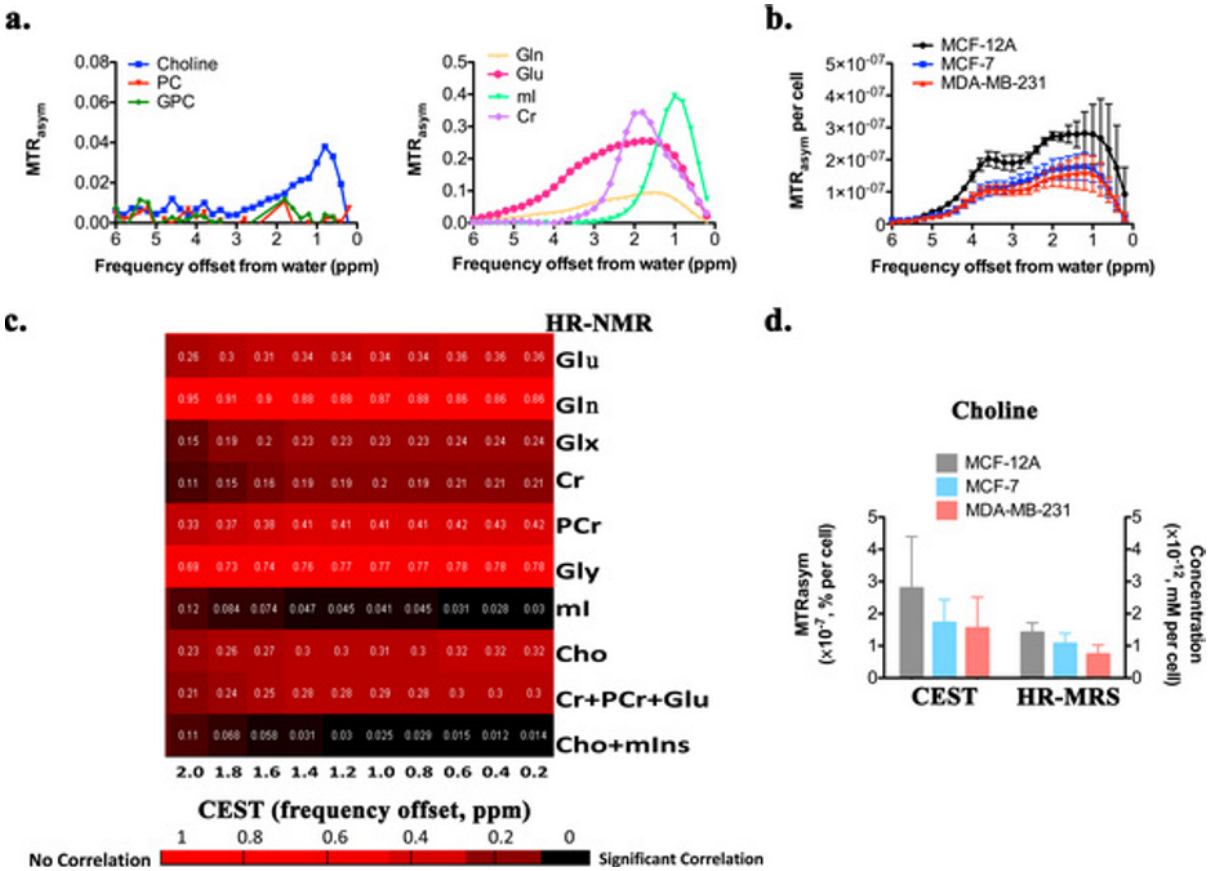

Figure 1. a, 20 mM solutions of metabolites in phosphate buffered saline at 310K. b, Aqueous phase of cell extracts of breast cell lines, including the non-malignant epithelial cells MCF-12A and malignant MCF-7 and MDA-MB-231 cells. c, Correlation heatmap (p-values) between CEST and HR-NMR in three breast cell lines (MCF-12A, MCF-7, MDA-MB-231; full panel in supplementary) d, CEST contrast at 1 ppm and the corresponding concentration measured by HR-MRS for choline.

Disclosure of author financial interest or relationships:
K. Chan, None; **L. Jiang**, None; **J.P. Wijnen**, None; **T.R. Greenwood**, None; **M. Cheng**, None; **P.C. van Zijl**, None; **M.T. McMahon**, None; **K. Glunde**, None.

Presentation Number **P 473**
Poster Session 4
September 21, 2013 / 14:45-14:45 / Room: Exhibit Hall B

In vivo reporter gene imaging of cancer stem cells-like population using piggyBac gene delivery system

Ying-Ling Chen, *Yi-Jang Lee, Shiau-yi Wang, Ren-Shyan Liu, Biomedical Imaging and Radiological Sciences, National Yang-Ming University, Taipei, Taiwan. Contact e-mail: koykogina@yahoo.com.tw*

Cancer stem cells (CSC, or named cancer initiating cells) are considered to be a rare population involved in tumor progression and relapse after therapy. However, it remains debate whether distant disseminated cancer cells in vivo would perform CSC phenotypes. In this study, we used 4T1 murine breast cancer cells to establish a syngeneic tumor model and found that liver metastatic cells exhibited several biological and molecular characteristics distinct from parental 4T1 cells, including CSC-like phenotypes. The reporter gene imaging was exploited to track the growth of living cancer cells in vivo and followed by ex vivo analysis of the metastatic cells identified by expressed reporter genes. The piggyBac transposon system was used to stably deliver multiple reporter genes including firefly luciferase, red fluorescent protein and herpes simplex virus type 1 - thymidine kinase (HSV1-tk) to 4T1 cells. The tumor growth and dissemination in vivo was tracked using the bioluminescent imaging. We isolated the liver metastatic cells (named 4T1_L cells) for further analysis. Compared to parental 4T1 cells, these cells exhibited several CSC associated characteristics, including the ability of mamosphere formation, drug resistance, higher tumorigenic potential in Balb/C mice and reduced 26S proteasome activity. We also found that 4T1_L cells exhibited stronger migrated and invasive abilities. The microarray assay showed that the Twist1, a transcription factor involved in epithelial-mesenchymal transition (EMT), was significantly up-regulated in 4T1_L cells. Interestingly, the Twist1 level was suppressed in 4T1 cells but not in 4T1_L cells after exposure to ionizing radiation. Therefore, the current data suggest that disseminated tumor cells may contain CSC and EMT related phenotypes, and this population is resistant to ionizing radiation and chemotherapy. This finding may explain the difficulty of therapy on metastatic tumors, and it would be important to design new strategy to treat this population.

Disclosure of author financial interest or relationships:
Y. Chen, None; **Y. Lee**, None; **S. Wang**, None; **R. Liu**, None.

Presentation Number **P 474**
Poster Session 4
September 21, 2013 / 14:45-14:45 / Room: Exhibit Hall B

MR Spectroscopy of Phospholipid Metabolites as Indicators of COX 2 Activation

Michael Chiorazzo[1], *Emer M. Smyth*[1], *Edward J. Delikatny*[2,1], [1]*Pharmacology, University of Pennsylvania, PHILADELPHIA, PA, USA;* [2]*Radiology, University of Pennsylvania, PHILADELPHIA, PA, USA. Contact e-mail: mchio@mail.med.upenn.edu*

Cyclooxygenase (COX) 1 and 2 are responsible for the conversion of arachidonic acid to PGH2, a precursor to the signaling molecules prostanoids. COX 2 has been shown to be upregulated in a variety of cancers including 80% of breast, colon, esophagus, liver, lung, pancreas, prostate, cervix, and head and neck cancer. Inhibition of COX 2 has been shown to decrease tumor development and is an attractive target for cancer therapy. Cytosolic phospholipase A2 (cPLA2) is the primary enzyme responsible for the release of arachidonic acid and has been shown to colocalize with COX in the synthesis of prostaglandins. We hypothesized that alterations to COX 2 activity could be measured indirectly through determination of cPLA2 activity. Alterations in cPLA2 activity can be measured using 1H NMR spectroscopy by measuring the levels of phosphatidylcholine metabolites: choline, phosphocholine (PC) and glycerophosphocholine (GPC). NMR spectra of wild type (wt) and shRNA COX 2 knock down (KD) SMF mouse mammary tumor cells showed that PC and choline are elevated in COX 2 KD cells relative to both wt and non-target (nt) shRNA cells (Fig. 1). This is consistent with a mechanism whereby the feedback inhibition of PLA2 activity causes increased flux through phospholipase C and phospholipase D resulting in higher levels of PC and choline respectively. In order to measure cPLA2 activity directly, an assay was developed utilizing phosphatidylcholine (PtdCho) labeled at the sn-2 position with 14C-arachidonic acid. Cells were incubated with liposomes containing 14C-PtdCho and cleavage was determined through autoradiography of thin layer chromatography of cell extracts. Basal PLA2 activity of nt cells was significantly higher than COX 2 KD cells. Lipopolysaccharides (LPS) were used to induce COX, and PLA2 activity was measured. Addition of LPS resulted in an increase of PLA2 activity in both cell lines. The increase witnessed in COX 2 KD cells may be a result of compensatory COX 1 activity. Together, these data suggest a direct correlation between COX activity and PLA2 activity which can be measured through changes in the choline metabolites visible with MR spectroscopy.

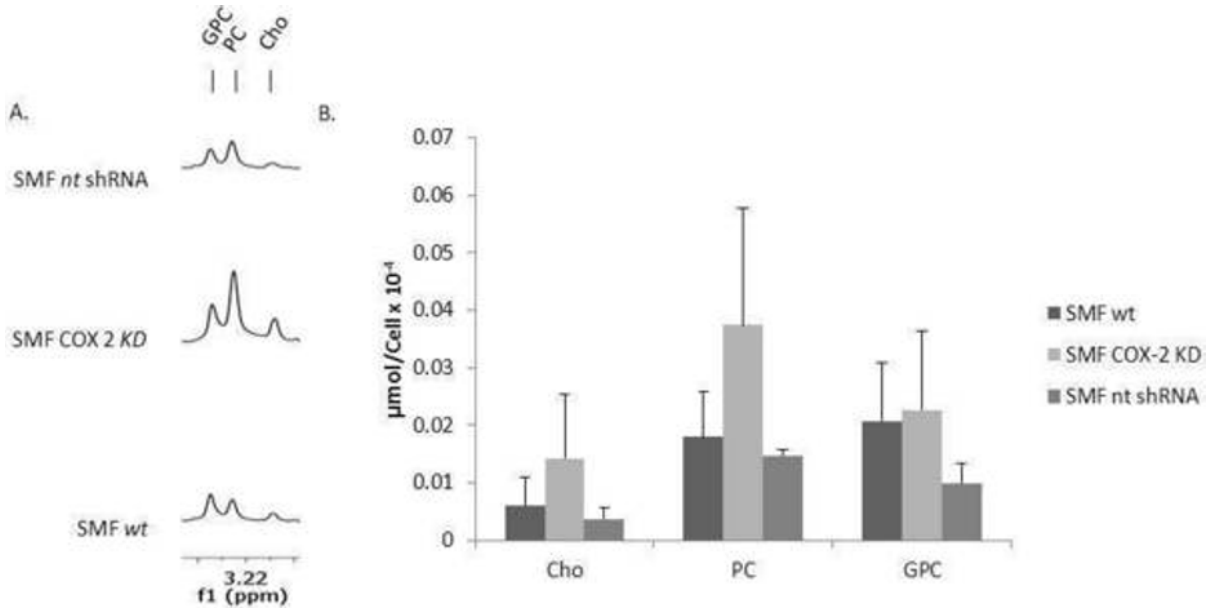

Figure 1. 1H NMR measurement of choline metabolites in wild type (wt), COX-2 knock down (KD), and non-target (nt) shRNA cells. (A) 1H NMR spectra of the choline region showing choline (Cho) at 3.21 ppm, phosphocholine (PC) at 3.22 ppm, and glycerophosphocholine (GPC) at 3.23 ppm. (B) Quantitation of integrated peak intensities shown as µmol/Cell.

Disclosure of author financial interest or relationships:
M. Chiorazzo, None; **E.M. Smyth**, None; **E.J. Delikatny**, None.

Presentation Number **P 475**
Poster Session 4
September 21, 2013 / 14:45-14:45 / Room: Exhibit Hall B

In vivo imaging of tumor angiogenesis using viral nanoparticles targeting EGFL7

Choi-Fong Cho[1], *Tienabe K. Nsiama*[2], *Nicole F. Steinmetz*[3], *Leonard G. Luyt*[2], *John D. Lewis*[1], [1]*Oncology, University of Alberta, Edmonton, AB, Canada;* [2]*Chemistry, Western University, London, ON, Canada;* [3]*Biomedical Engineering, Case Western, Cleveland, OH, USA. Contact e-mail: choifong@ualberta.ca*

Introduction: Angiogenesis is required for sustained tumor growth. The epidermal growth factor-like domain 7 (EGFL7) is a novel angiogenic marker that is highly expressed during angiogenesis and accumulates in the extracellular matrix of tumour neovasculature. Its expression is associated with poor outcome in several cancers. EGFL7 is therefore a promising target for molecular imaging and drug delivery strategies. We describe here the discovery and characterization of a novel high affinity EGFL7 peptide ligand using a "beads on a bead" combinatorial library screening approach (Cho et al., Nano Letters 2012), which were used to functionalize viral nanoparticles derived from Cowpea mosaic virus. Methods: Several novel EGFL7-homing peptides were identified from a one-bead one-compound (OBOC) library. The binding affinities of these EGFL7-targeted peptides were quantified using surface plasmon resonance (SPR). Peptides with the highest affinities were synthesized and labeled with a fluorescein dye, and their specificity for EGFL7-expressing cells were evaluated. Lead peptide E7-p72 was conjugated onto CPMV nanoparticles containing near infrared dyes and polyethylene glycol (PEG) using click chemistry. The specificity of EGFL7 targeted nanoparticles for endothelial cells were evaluated using confocal imaging and flow cytometry. The ability of these nanoparticles to target tumors and their associated blood vessels in vivo was then evaluated in a mouse xenograft model of human prostate cancer. Results: 16 novel peptides were identified in the OBOC library screen. Of, these, 4 were re-synthesized for further characterization by SPR. Lead peptide E7-p72 had a measured Kd of 13.23 ± 0.25 nM. The E7-p72 peptide specifically labeled human tumor cells and endothelial cells in an EGFL7-dependent manner as demonstrated through confocal microscopy and flow cytometry analysis. CPMV nanoparticles functionalized with PEG and E7-p72 showed significantly higher uptake in EGFL7-expressing endothelial cells compared to control nanoparticles with PEG alone. In vivo imaging of angiogenesis was conducted using E7-p72-conjugated CPMV nanoparticles in vivo in a mouse xenograft human cancer model. Conclusion: EGFL7-targeted viral nanoparticles specifically bind and are taken up by angiogenic endothelial cells. These may be useful in vivo imaging agents to identify tumors of poor prognosis, and to monitor the impact of angiogenesis inhibitors.

Disclosure of author financial interest or relationships:
C. Cho, None; **T.K. Nsiama**, None; **N.F. Steinmetz**, None; **L.G. Luyt**, None; **J.D. Lewis**, None.

Presentation Number **P 476**
Poster Session 4
September 21, 2013 / 14:45-14:45 / Room: Exhibit Hall B

Anti-Proliferative Effect of 4-Hydroxytamoxifen Loaded PLGA-*b*-PEG Nanoparticles in Human Breast Cancer Cell lines Expressing Different Levels of Her2 Receptor

Rammohan Devulapally, *Thillai V. Sekar, Ramasamy Paulmurugan, Radiology, Stanford University, Palo Alto, CA, USA. Contact e-mail: rammohan@stanford.edu*

Tamoxifen is an estrogen receptor antagonist that acts via its active metabolite 4-hydroxytamoxifen. It is extensively used in the anti-estrogen treatment of metastatic breast cancers, which are positive for estrogen receptor expression. Owing to its poor oral bioavailability and numerous adverse side effects, polymer nanoparticles (NPs) have gained great interest for the tamoxifen delivery. MicroRNA-21 is one of the key microRNAs overexpressed in cancer contributing to tumor growth and metastasis. AntagomiR-21 used to block the function of endogenous miR-21 has been reported to inhibit migration and invasion of cancer cells, and enhancing the cancer cells response to chemotherapeutic agents. In this study, we have used biodegradable poly (D,L-lactide-co-glycolide)-block-poly(ethylene glycol) (PLGA-*b*-PEG-COOH) as a carrier for the co-delivery of 4-OHT and antagomiR21 to evaluate the therapeutic potential in breast cancer (MCF7 and 4T1) cells. MCF7 cells were modified to express different level of Her2 protein, as Her2 expression has been previously linked with the variation in therapeutic response to tamoxifen treatment. 4-OHT and Cy5-conjugated-antagomiR-21 loaded PLGA-*b*-PEG-COOH NPs were formulated using an emulsion-diffusion-evaporation method with the mean size of 100-200 nm. Cy5-antagomiR-21 was used for visualization of NPs delivery in the cells by fluorescent microscopy. The effect of 4-OHT loaded PLGA-*b*-PEG-COOH NPs on proliferation of human breast cancer cell expressing different levels of Her2 (MCF7, MCF7-Her2^{low}, MCF7-Her2^{med}, MCF7-Her2^{high} and 4T1) was studied, and compared with free 4-OHT treated cells, as well as non-treated control cells. 4-OHT and Cy5-antagomiR-21 loaded PLGA-*b*-PEG-COOH NPs inhibited cell growth 2.5 folds compared to that of free 4-OHT against MCF7 cells at 1 μM concentrations. 4-OHT and Cy5-antagomiR-21 loaded PLGA-*b*-PEG-COOH NPs showed 80% and 60% cell growth inhibition activity compared to untreated cells against MCF7 and 4-T1 cells, respectively at 1 μM concentrations. These 4-OHT loaded PLGA-*b*-PEG-COOH NPs also inhibited cell growth 75% and 80% in MCF7-Her-2 (+ve)-Clone 2^{med} and MCF7-Her-2 (+ve)-Clone-14^{high} cells respectively, compared to untreated control cells at 1 μM concentrations. 4-OHT and Cy5-antagomiR-21 loaded PLGA-*b*-PEG-COOH NPs inhibited cell growth similar to that of free 4-OHT when delivered at nanomolar (1 nM to 100 nM) concentrations. Control PLGA-*b*-PEG-COOH NPs did not show considerable toxicity against all used cell lines compared to untreated cells. The results of this study indicate that the PLGA-*b*-PEG-COOH NPs are safe and efficient nanocarriers for 4-OHT delivery in vitro. The in vivo cell proliferation effects of 4-OHT in tumor xenograft of breast cancers in living animals are currently under investigation.

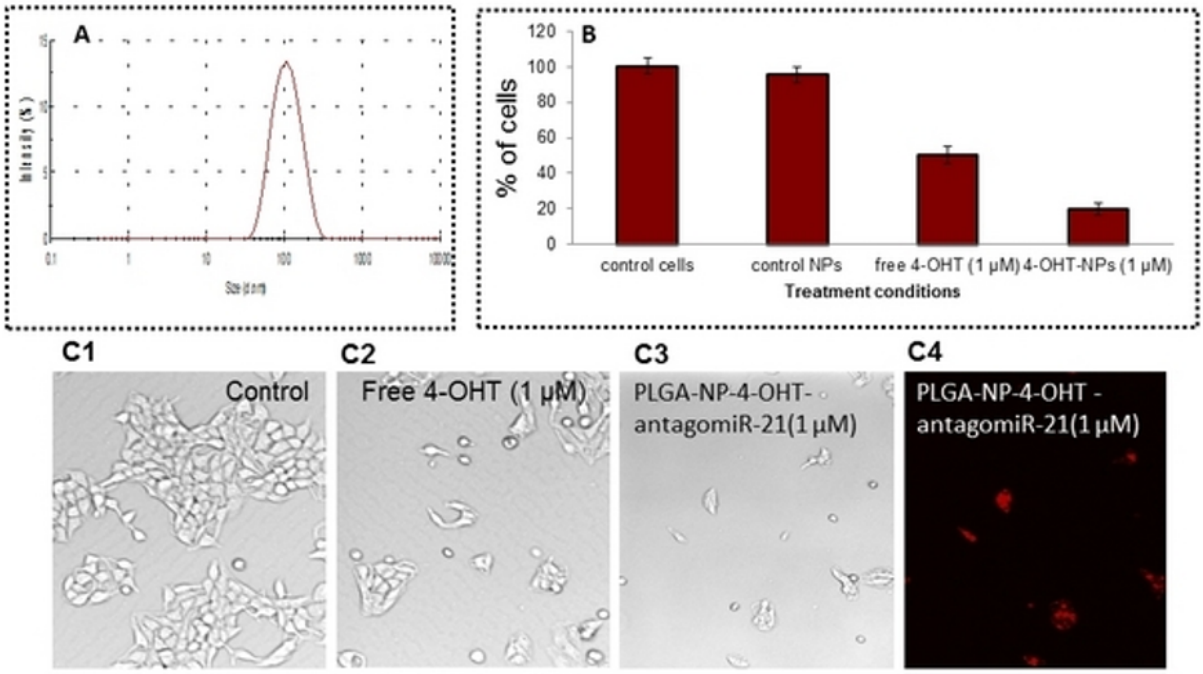

A: Dynamic light scattering (DLS) of Cy5-antagomir-21 and 4-OHT co-loaded PLGA-*b*-PEG NPs, **B:** Cell proliferation effects of free 4-OHT, and Cy5-antagomir-21-4-OHT loaded PLGA-*b*-PEG NPs in MCF7 cells, **C1-C3:** Cell density by bright field imaging, **C4:** Fluorescent microscopic images of MCF7 cells after treated with Cy5-antagomir-21-4-OHT loaded PLGA-*b*-PEG NPs

Disclosure of author financial interest or relationships:
R. Devulapally, None; **T.V. Sekar**, None; **R. Paulmurugan**, None.

Presentation Number **P 477**
Poster Session 4
September 21, 2013 / 14:45-14:45 / Room: Exhibit Hall B

Cu-ATSM versus FAZA: Intratumoral Distribution in Xenografts and Cellular Uptake

Takako Furukawa[1,2], *Yukie Yoshii*[1], *Qinghua Yuan*[1], *Yasuhisa Fujibayashi*[1,2], *Tsuneo Saga*[1], [1]*Molecular Imaging Center, Ntional Institute of Radiological Sciences, Chiba, Japan;* [2]*Biomedical Imaging Research Center, University of Fukui, Eiheiji-cho, Japan. Contact e-mail: tfuru@nirs.go.jp*

Background: The presence of hypoxia in solid tumors endows resistance to radiotherapy and chemotherapy, and also malignant transformation leading to recurrences and metastases. Accordingly, the detection of hypoxic regions in tumor is expected to provide valuable information for prognosis and treatment planning. Fluorine-18 labeled nitroimidazoles, such as fluoromisonidasole (FMISO), and Cu-diacetyl- bis(N4-methylthiosemicarbazone) (Cu-ATSM) labeled with positron emitting cuppers are the two types of positron emission tomography (PET) probes developed for hypoxia imaging. The both are reported to show hypoxia dependent cellular accumulation in cell culture studies, and the both are reported to be useful for prediction of response to therapy and/or outcome in clinical studies. The reports on their intratumoral distribution in xenograft models, however, are divided: some observed matched distribution of the two and some mismatched distribution. In this study we compared intratumoral distribution of Cu-ATSM and ^{18}F-labeled fluoroazomycin arabinoside (FAZA), a nitroimidazole with faster clearance from non-target tissues than FMISO, in xenografts of human cancer cell lines with various origins and their cellular uptake in culture. **Methods**: Intratumoral distribution of [^{18}F]FAZA and [^{64}Cu]Cu-ATSM in subcutaneous xenograft of human cancer cell lines (colorectal, lung, and breast cancers) were compared by double tracer autoradiography. In some of the tumors, Ki67 and HIF-1α expression and presence of vessels and pimonidazole adducts were examined by immunostaining and compared between the regions with high accumulation of FAZA and Cu-ATSM. Cellular uptake of the two tracers was compared by incubating the cells under normoxic(air) and hypoxic(1% and 2% O_2) conditions. **Results and discussion**: Intratumoral distribution of Cu-ATSM and FAZA were apparently different in all the xenografts tested. The region with high FAZA accumulation, which was often found surrounding necrotic region, was rich in vessels and pimonidazole adducts while the region with high Cu-ATSM lacked them. Ki67 positive cells and HIF-1a expression were more frequently found in the region with high FAZA accumulation than that with high Cu-ATSM accumulation, but the degree was varied depending on the cancer cell line used. The cellular uptake of the tracers under hypoxic condition at 2% O_2 was higher than that under normoxic condition with both Cu-ATSM and FAZA. The uptake of FAZA further increased under 1% O_2 compared with under 2% O_2, but the uptake of Cu-ATSM didn't increase. Our data indicated that Cu-ATSM and FAZA accumulate in the intratumoral regions of different characteristics: FAZA accumulation represents the area of severe hypoxia with aggressive cell proliferation overwhelming oxygen supply, while Cu-ATSM accumulation represents the area with milder hypoxia.

Disclosure of author financial interest or relationships:
T. Furukawa, None; **Y. Yoshii**, None; **Q. Yuan**, None; **Y. Fujibayashi**, None; **T. Saga**, None.

Presentation Number **P 478**
Poster Session 4
September 21, 2013 / 14:45-14:45 / Room: Exhibit Hall B

Oxygen Tension as Modifier of Prostate Cancer Cells: Potential for Identification of Novel Imaging Probes of Tumor Microenvironment

Christian Gomez[1,2], *Farhad Kosari*[3], *George Vasmatzis*[3], *Tangeng Ma*[1], *Stanimir Vuk-Pavlovic*[4], *Srinivasan Vijayakumar*[2], [1]*Pathology, University of Mississippi Medical Center, Jackson, MS, USA;* [2]*Radiation Oncology, University of Mississippi Medical Center, Jackson, MS, USA;* [3]*Department of Molecular Medicine, Mayo Clinic, Rochester, MN, USA;* [4]*Division of Hematology, Department of Internal Medicine, Mayo Clinic, Rochester, MN, USA. Contact e-mail: crgomez@umc.edu*

While extended hypoxia usually injures and kills normal cells, it can enhance the survival of tumor cells. Hence, we studied the effect of different oxygen tensions (pO_2) in prostate cancer (CaP) cells comparing the cells grown in hypoxia (pO_2=2 kPa) and normoxia (pO_2=20 kPa). At 2 kPa, cultured CaP cells designated LnCaP, VCaP and DU145 modified their proliferation rate relative to cells grown at 20 kPa ($p<0.05$), but secreted approximately twice as much of vascular endothelial growth factor ($p<0.05$). We compared transcriptomes of the cells cultured at pO_2=2 kPa and 20 kPa (assessed by Affymetrix Human U133 Plus 2.0 array) and identified the oxygen-tension-regulated genes that we related to function, pathways, networks, and unique features by Ingenuity Pathway Analysis. We found that the three cell lines cultured in hypoxia overexpressed the genes involved in molecular pathways associated with cancer and urologic diseases relative to normoxic cells ($p<0.001$) suggesting an association of low pO_2 and CaP aggressiveness. To test this hypothesis, we compared transcriptomes of cultured CaP cells with those of resected primary CaP tissues. Notably, in all three cell lines hypoxia increased transcript levels for pyruvate dehydrogenase kinase isozyme 1 (PDK1), nuclear prelamin A recognition factor (NARF), glucose phosphate isomerase (GPI), and glyceraldehyde-3-phosphate dehydrogenase (GAPDH) to the levels comparable to those found in primary bulk tissue and cells isolated from it ($p<0.005$). This finding suggests that gene expression in hypoxically, but not normoxically, cultured cells is akin to that in tumor cells in situ. Particularly, expression of molecules critical for tumor cell metabolism—a well-recognized fact of interest for selection of tumor imaging probes--was elevated both in vitro and in CaP tissues. Overall, our results suggest that variation of pO_2 can be used as a tool for identification of novel targets in tumor microenvironment relevant for the treatment, characterization and diagnosis of cancer. Our future efforts include validation of candidate probes in preclinical models and patient materials. Financial support: DOD PC094680 (CRG), PCF Creativity Award (CRG), Minnesota Partnership for Biotechnology and Medical Genomics (GV) and Mayo Clinic Prostate SPORE 5P50CA091956 (FK).

Disclosure of author financial interest or relationships:
C. Gomez, None; **F. Kosari**, None; **G. Vasmatzis**, None; **T. Ma**, None; **S. Vuk-Pavlovic**, None; **S. Vijayakumar**, None.

Presentation Number **P 479**
Poster Session 4
September 21, 2013 / 14:45-14:45 / Room: Exhibit Hall B

NMR in the study of polyherbal formulations

Rama Jayasundar[1], *Gaurav Sharma*[1], *Thirumurthy Velpandian*[2], *Shyam Chauhan*[3], [1]*Department of NMR, All India Institute of Medical Sciences, New Delhi, India;* [2]*Department of Ocular Pharmacology and Pharmacy, All India Institute of Medical Sciences, New Delhi, India;* [3]*Department of Biochemistry, All India Institute of Medical Sciences, New Delhi, India. Contact e-mail: ramajayasundar@hotmail.com*

Medicinal plants are gaining importance for treating diseases due to their safety and cost effectiveness. Many of the chemotherapy drugs used in cancer treatment are derived from natural products. Although single molecule drugs continue to be the focus of drug development, there is scientific curiosity about the use of polyherbal formulations (1). These are used in traditional systems of medicine like ayurveda, which considers synergism between the mixture of chemicals in a herbal product as a key factor in determining its therapeutic efficacy. Improved activity of crude extracts compared to isolated active fractions has been reported (1). In this context, NMR, which can study therapeutic response of cells to polyherbal formulations without fractionating the latter, can play an important role in evaluating the therapeutic efficacy of these formulations. In this study, NMR has been used to assess the response of human hepatocellular carcinoma (Hep-G2) cells to treatment with four different polyherbal formulations (labeled KG, MK, VK, GTK) indicated in ayurveda for treatment of cancer. Antiangiogenic potential of the formulations was evaluated and compared with that of thalidomide (positive control) using chick Chorio-Allantoic Membrane (CAM) assay (2). On day 1, the fertilized eggs were incubated at 37°C. On day 3, 2-3 ml albumen was aspirated from the acute pole of the egg and the egg sealed. On day 8, a small window was cut into the egg shell and sterilized cover slips coated with Thalidomide and formulations were implanted onto the CAM and the egg resealed. On day 13, angiogenesis was evaluated by measuring the area of vascularization using a digital imaging system. For NMR studies, 5x106 Hep-G2 cells were treated for 48h with 100µg/ml of formulations and 10µg/ml of synthetic chemotherapy drug paclitaxel. The cells were then extracted using chloroform-methanol and water dual phase extraction method, lyophilized and redissolved in 600µl of 100mM phosphate buffer (pH 7.0) prepared in 90%H2O - 10% deuterated trimethylsilyl propionate (TSP). Water suppressed 1D proton NMR spectra of the extracts of untreated and treated Hep-G2 cells were acquired on 700 MHz NMR spectrometer (Varian, USA) using the following parameters: relaxation delay - 4s, no. of scans - 64, spectral width - 12 ppm, data points - 32 K. All four ayurvedic formulations significantly inhibited the VEGF induced neovascularization compared to thalidomide. Proton NMR spectra of untreated Hep-G2 cells showed prominent resonances in the region between 3.5-3.8 ppm (assigned to glycerol) and also from metabolites such as isoleucine, lactate, pyruvate, citrate, dimethylamine and choline. The treatment by paclitaxel, VK and KG induced drastic reduction of the glycerol peaks. All the spectra also registered a reduction in the lactate peak, indicating response to treatment. This study serves as a scientific validation for the use of polyherbal formulations for cancer treatment. 1. H Wagner & GU Merzenich, Phytomed, 16, 97-110, 2009. 2. D Ribatti et al., J Vasc Res, 34, 455-463,1997.

Disclosure of author financial interest or relationships:
R. Jayasundar, None; **G. Sharma**, None; **T. Velpandian**, None; **S. Chauhan**, None.

Presentation Number **P 480**
Poster Session 4
September 21, 2013 / 14:45-14:45 / Room: Exhibit Hall B

High Glycolytic Activity of Multidrug Resistant Cancer Cells: A Potential Target of 18FDG-PET

Yoonseok Kam, *Robert Gillies, Robert A. Gatenby, Cancer imaging and Metabolism, Moffitt Cancer Center, Tampa, FL, USA. Contact e-mail: yoonseok.kam@moffitt.org*

P-glycoprotein (PGP), a drug effluxing pump is a major mechanism for multidrug resistance (MDR) which makes a tumor resistant to chemotherapy. Here we propose the potential use of 18FDG-PET for the diagnosis of PGP-mediated MDR based on our in vitro study results. PGP in plasma membrane enables a cancer cell to export chemotherapy drugs at the cost of 2 ATP molecules per a drug molecule. Therefore, we expect an increase in the metabolic energy demand upon the acquisition of MDR phenotype particularly when the pump protein is actively running in the presence of PGP substrate. Our in vitro study using a PGP-expressing MCF7 variant cell line (MCF7/dox) showed that the glycolytic activity as well as the glycolytic capacity of MCF7/dox is significantly elevated than the wild type MCF7 cells (MCF7/wt). Verapamil, a drug for heart disease has been suggested as very potent competitive inhibitor of chemotherapy drug export because it is a highly preferred PGP substrate. Pretreatment of MCF7/dox with verapamil could increase the glycolysis of MCF7/dox even further but not that of MCF7/wt. In an agreement with those data, 2-NBDG uptake rate of MCF7/dox appeared higher than MCF7/wt, which implies potential difference in FDG uptake in vivo. These results suggest a possible use of 18FDG-PET for MDR prediction by monitoring FDG uptake rate change upon chemotherapy and/or other PGP substrate such as verapamil. Since the drug-exclusion pattern was quite well coincided to the high 2-NBDG uptake under microscopy, it also implies a potential diagnostic use of PET in a combination with SPECT which can monitor the accumulation of 99Tc-Sestamibi, a well-known PGP substrate. In order to build a clinically practical model, in vivo experiment comparing PET/SPECT of MCF7/dox with MCF7/wt tumor is highly desired.

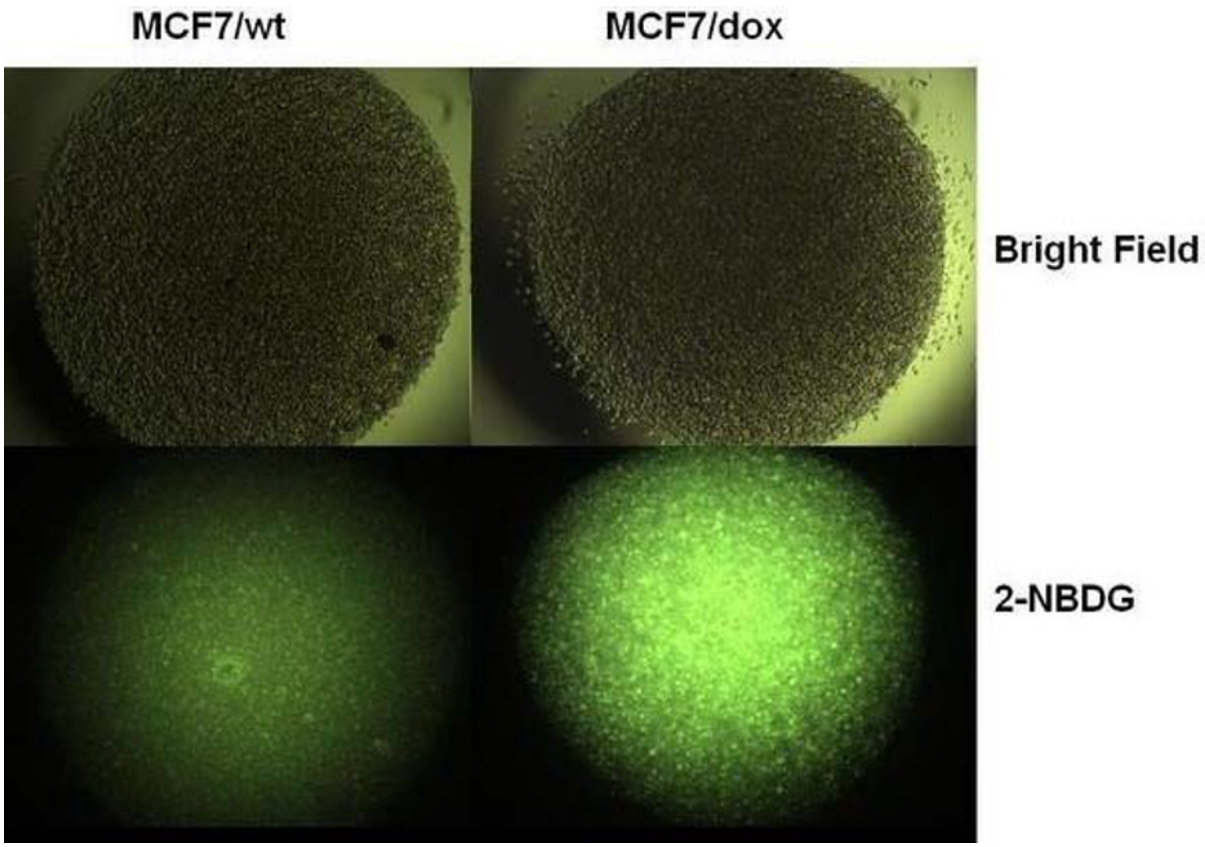

2-NBDG accumulation in MCF7/dox cells in a collage gel droplet is greater than MCF7/wt.

Disclosure of author financial interest or relationships:
Y. Kam, None; **R. Gillies**, None; **R.A. Gatenby**, None.

Presentation Number **P 481**
Poster Session 4
September 21, 2013 / 14:45-14:45 / Room: Exhibit Hall B

Proliferation assays of mesothelioma cancer initiating cells

Jae Sam Lee, *Tao Huang, Anna B. Banizs, Stuart S. Berr, Jiang He, Radiology and Medical Imaging, University of Virginia, Charlottesville, VA, USA. Contact e-mail: jsfemto@gmail.com*

Background: Malignant mesothelioma (MM) is a lethal tumor originating in the mesothelium with high chemotherapeutic resistance. Cancer initiating cells (CICs) persist in tumors and are critical targets responsible for tumor resistance and recurrence. In this study, CICs were sorted from MM subtypes by two markers (CD26 and CD24) and characterized for the proliferation and metabolism. **Methods:** MM cells (H226, H28, and MSTO) were sorted by CD26/24 expression level and their functional significances were established by small interference RNA (shRNA lentiviral vectors). CIC potential of MMs was evaluated for drug resistance, cell invasion, and cell growth rate *in vitro*. MM cells were incubated with ^{18}F-FDG for 1 or 4h at 37°C at different conditions and the ^{18}F-FDG uptake was measured to evaluate metabolism in CICs. **Results:** Knockdown of CD24 and CD26 caused noticeable reduction of phenotype expression (>95%) relative to non-targeting control vector in MMs. CD26^{high}24^{high} cells expressed significant drug resistance with up-regulated proliferative and invasive activities compared to the H28 and shRNA cells ($P<0.001$). CD26^{high}24^{high} cells also exhibited higher ^{18}F-FDG uptake than other cells either in glucose free medium or glucose containing medium. There was no statistically significant difference of ^{18}F-FDG uptake between H28 and shRNA cells. **Conclusion:** The results indicate that CD26^{high}24^{high} cells possess drug resistance, proliferation, invasion, and glucose utilization. Further investigation needs to be done on the tumor initiating capability of CD26^{high}24^{high} MM cells *in vivo* using ^{18}F-FDG and ^{18}F-FLT.

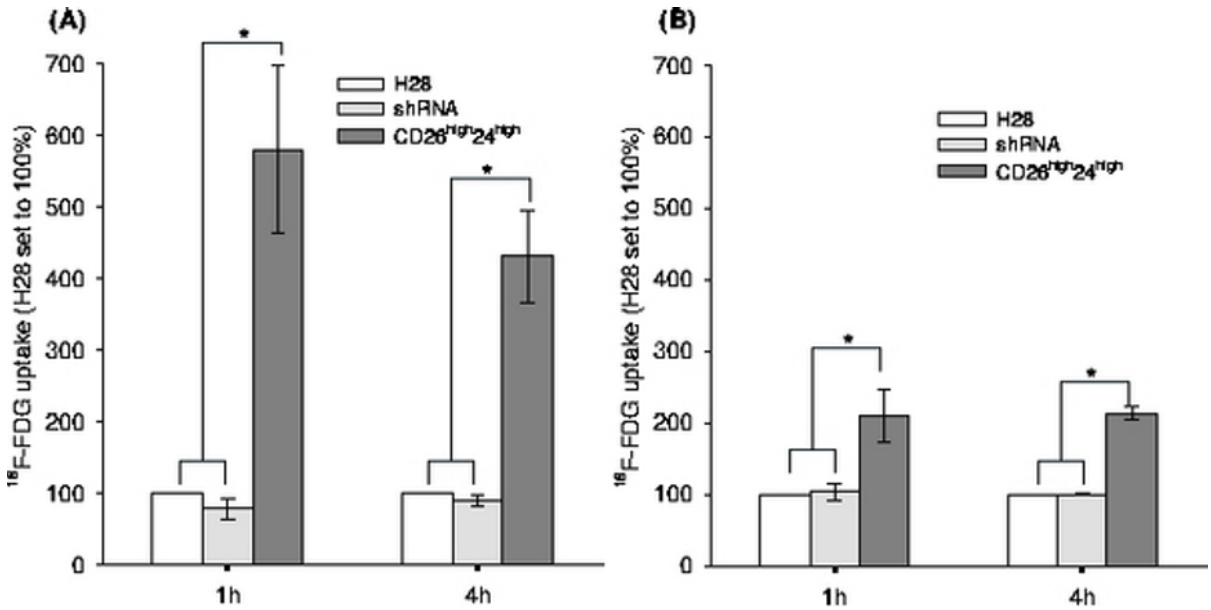

Figure 1: ^{18}F-FDG uptake in different MM cancer cells incubated in glucose free media (A) or glucose containing RPMI 1640 media (B) for 1 or 4h. The ^{18}F-FDG uptake in CD26/24 silenced (shRNA) and CD26^{high}24^{high} (sorted) cells was compared with that in H28 sarcomatoid MM cells. Mean ± SEM (n=3).

Disclosure of author financial interest or relationships:
J. Lee, None; **T. Huang**, None; **A.B. Banizs**, None; **S.S. Berr**, None; **J. He**, None.

Presentation Number **P 482**
Poster Session 4
September 21, 2013 / 14:45-14:45 / Room: Exhibit Hall B

Direct identification of drug-selected cancer stem-like cells from tumor xenografts by molecular imaging technique

Wei-Ying Kuo[1], *Luen Hwu*[1], *Chun-Yi Wu*[1], *Wen-Chen Lin*[2], *Kang-Ping Lin*[2], *Hsin-Ell Wang*[1], *Ren-Shyan Liu*[1,3], [1]*MAGIC, Nuclear Medicine, Faculty of Medicine, National Yang-Ming University, Taipei, Taiwan;* [2]*Electrical Engineering, Chung Yuan Christian University, Chungli, Taiwan;* [3]*Nuclear Medicine, Taipei Veterans General Hospital, Taipei, Taiwan. Contact e-mail: kiki0502@gmail.com*

Objectives: Cancer stem cells (CSCs) are a small subset of cancer cells capable of self-renewal and tumor maintenance and able to escape chemotherapy and metastasis. Although CSCs can be generated in vitro by non-adherent suspension culture in serum-free medium, the biologic characteristic of tumorspheres was far from CSCs in real tumors due to the distinct environmental factors, such as stroma cells, inflammation and hypoxia within tumor, which may profoundly reprogram CSCs. Histone deacetylase inhibitors (HDACIs) could induce epithelial to mesenchymal transition (EMT) and CSC characteristics in tumor cells. This study aimed to develop an in vivo CSCs-screening system using suberoylanilide hydroxamic acid (SAHA) to enrich the CSC population to facilitate the isolation of CSCs from solid tumors. Methods: We established a H1299 cell clone (non-small cell lung cancer cell, NSCLC) that stably expressed a triple fused reporter gene (DsRedm-Fluc-tTKsr39) from the control of CMV promoter. Tumor growths were tracked by in vivo luminescence imaging during continuous SAHA treatment of tumor-bearing mice. Using the Aldefluor assay, viable CSCs were isolated from xenograft tumors which co-express the reporter gene and ALDH activity. The stem cell phenotype of CSCs was assessed by a cell invasion assay, by analyzing CSC-related gene expression, and by immunohistochemical staining for ALDH1A1 in vitro. Results: Tumor tissues from SAHA-treated mice had enriched CSC population by continuous administration of SAHA. Percent increased CSCs in SAHA-treated mice relative to vehicle-treated control mice was 4.14%, v.s. 1.50%. Genes involved in the maintenance of CSCs, self-renewal and metastasis were upregulated in isolated CSCs from SAHA-treated mice. In addition, the invasive ability of these cells was also significantly elevated as compared to controls. Conclusions: Using reporter gene and differential ALDH activity may allow us to track CSCs in a real-time manner and consequently to better understand the molecular mechanism of CSCs and lead to progress in cancer management.

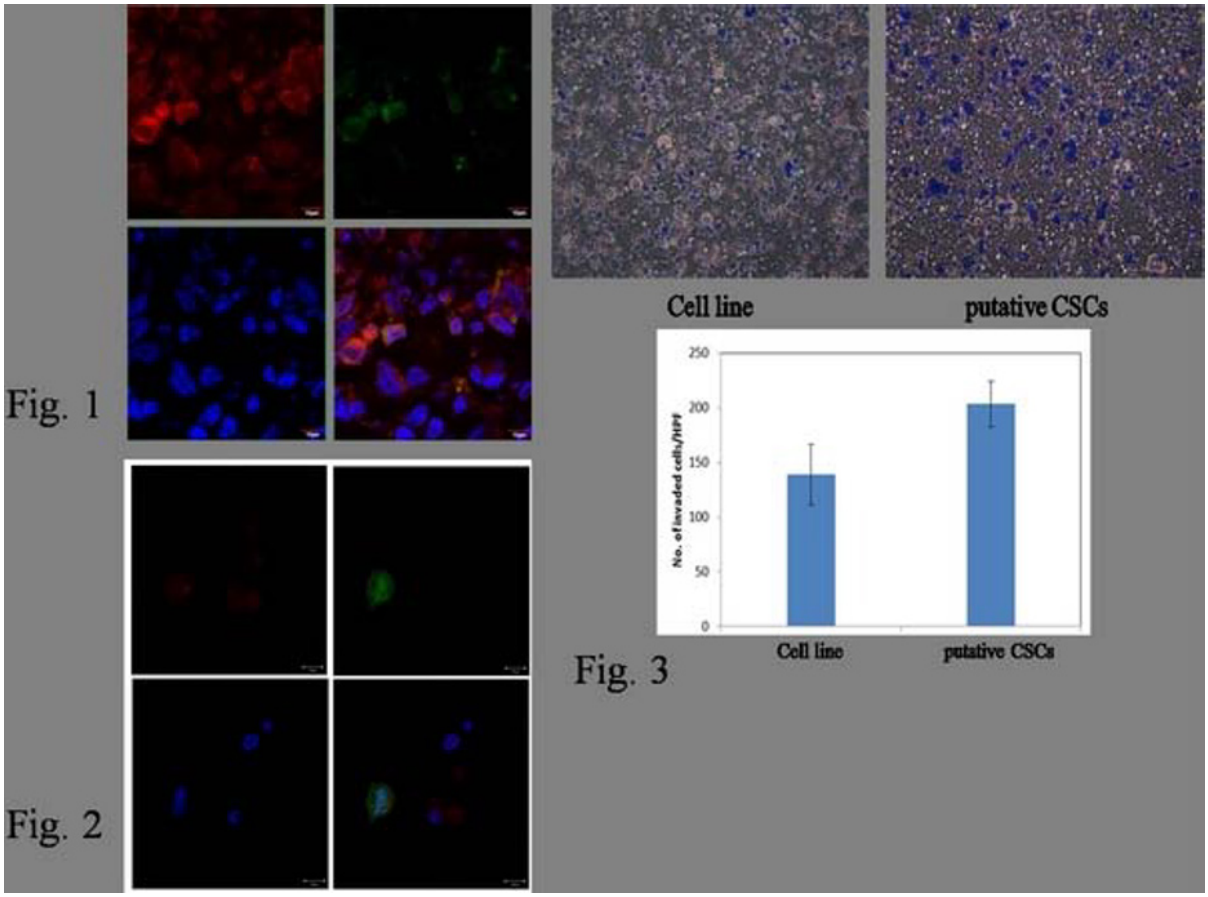

Disclosure of author financial interest or relationships:
W. Kuo, None; **L. Hwu**, None; **C. Wu**, None; **W. Lin**, None; **K. Lin**, None; **H. Wang**, None; **R. Liu**, None.

Presentation Number **P 483**
Poster Session 4
September 21, 2013 / 14:45-14:45 / Room: Exhibit Hall B

^{18}F-FAHA in assessing HDAC expression and predicting the outcome of HDAC inhibitor treatment in hepatoma

*Yi-Shuan Chen[1], **Chien-Chih Ke**[2], Luen Hwu[2], Chun-Yi Wu[1], Chi-Wei Chang[1,3], Hsin-Ell Wang[1], Ren-Shyan Liu[2,3], [1]Dept of Biomedical Imaging and Radiological Sciences, National Yang-Ming University, Taipei, Taiwan; [2]Institute of Clinical Medicine, MAGIC, Dept of Nuclear Medicine, Faculty of Medicine, National Yang-Ming University, Taipei, Taiwan; [3]Dept. of Nuclear Medicine and National PET/Cyclotron Center, Taipei Veterans General Hospital, Taipei, Taiwan. Contact e-mail: s2289.tw@yahoo.com.tw*

Objectives: Histone deacetylase inhibitors (HDACIs) are emerging as a new class of anticancer agents. Combination of HDACI with conventional chemotherapeutic drugs in treating hepatocellular carcinoma is robustly under evaluation. The activity of HDAC within HCC determine the therapeutic outcome. This study aims to test the feasibility of HDAC-specific imaging probe, 6-(^{18}F-fluoroacetamido)-1-hexanoicanilide (^{18}F-FAHA), in monitoring the HDAC activity and predicting the therapeutic outcome in hepatoma. Methods: Three hepatoma cell lines, HepG2, Huh7 and SK-Hep1, with distinct level of differentiation were used in this study. HDAC expression, drug sensitivity to TrichostatinA (TSA) and suberoylanilide hydroxamic acid (SAHA) as well as ^{18}F-FAHA uptake of these lines were analyzed. Results: The expression of class I HDACs in all cell lines was higher than that of other classes, indicating that effect of HDACI treatment may depend on the expression level of class I HDACs in the tumor. SK-Hep1, which is classified as a poorly differentiated hepatoma, showed lowest expression of all HDACs and lowest uptake of ^{18}F-FAHA in vitro among all hepatoma cells. When treated with TSA or SAHA, SK-Heplcells showed highest drug-resistance. On the contrary, HepG2 and Huh7 cells (well differentiated hepatomas) with higher expression of HDACs showed higher uptake of ^{18}F-FAHA and a higher HDACI drug sensitivity. Conclusion These results have established the relationship between the level of HDAC expression, effect of HDACI cytotoxicity and ^{18}F-FAHA uptake. We conclude that poorly differentiated hepatoma cells show decreased expression of HDACs, higher drug resistance of HDACi and lowest ^{18}F-FAHA uptake. ^{18}F-FAHA may be a potential imaging probe in detecting HDAC expression in hepatoma and the uptake level of ^{18}F-FAHA may also be a guidance for decision of HDACI treatment.

Disclosure of author financial interest or relationships:
Y. Chen, None; **C. Ke**, None; **L. Hwu**, None; **C. Wu**, None; **C. Chang**, None; **H. Wang**, None; **R. Liu**, None.

Presentation Number **P 484**
Poster Session 4
September 21, 2013 / 14:45-14:45 / Room: Exhibit Hall B

HDAC inhibitor induces re-expression of thyroid specific genes as well as dedifferentiation in anaplastic thyroid cancer

Chien-Chih Ke[1], *Ren-Shyan Liu*[1,2], *Chin-Wen Chi*[3,4], *Chen-Hsen Lee*[1,5], [1]*Institute of Clinical Medicine, MAGIC, Dept. of Nuclear Medicine, Faculty of Medicine, National Yang-Ming University, Taipei, Taiwan;* [2]*Nuclear Medicine & NPCC, Taipei Veterans General Hospital, Taipei, Taiwan;* [3]*Institute of Pharmacology, National Yang-Ming University, Taipei, Taiwan;* [4]*Medical Research and Education, Taipei Veterans General Hospital, Taipei, Taiwan;* [5]*Emergency Medicine and Surgery, Taipei Veterans General Hospital, Taipei, Taiwan. Contact e-mail: s2289.tw@yahoo.com.tw*

Objectives: With treatment of histone deacetylase inhibitor (HDACI), anaplastic thyroid cancer cells re-expressed thyroid specific genes such as sodium iodide symporter (NIS), thyroperoxidase (TPO) and thyroglobulin (Tg), and the iodide uptake and retention were restored, and consequently benefit radioiodide therapy. However, recent reports indicated that cancer cells acquired cancer stem cell properties and epithelial to mesenchymal transition (EMT) after HDACI treatment. In this study, we analyzed the multiple effects of HDACI, trichostatin A (TSA) and suberoylanilide hydroxamic acid (SAHA), on anaplastic thyroid cancer cell line, ARO. Methods: Upon treatment of different doses of TSA or SAHA for various time periods, the $CD133^+$ population was monitored by flow cytometry analysis. These TSA treated ARO cells were evaluated for the expression of thyroid specific genes as well as embryonic stem cell(ES)-related regulators by quantitative real time PCR. Results: $CD133^+$ cells in ARO whole population decreased after treatment of TSA or SAHA with a dose-dependent manner. Also, expression of thyroid specific genes, NIS, Tg and TTF1 increased after HDACi treatment. However, when analyzing the expression of various ES-related genes, expression of Oct4, nanog, sox2, Klf4 and c-Myc increased. Conclusions: In this study, we have shown that HDACI induced the re-expression of thyroid specific genes and also decreased the $CD133^+$ population in ARO cells. However, the expression of ES cell-related genes also increased after HDACI treatment. This result suggests that HDACI may not only upregulate the expression of thyroid specific genes but also potentiate the dedifferentiation of thyroid cancer cells.

Disclosure of author financial interest or relationships:
C. Ke, None; **R. Liu**, None; **C. Chi**, None; **C. Lee**, None.

Presentation Number **P 485**
Poster Session 4
September 21, 2013 / 14:45-14:45 / Room: Exhibit Hall B

Response monitoring in multiple myeloma: proteasome inhibition influences radiotracer uptake

Katharina Lückerath[1], *Constantin Lapa*[1], *Leilah Omert*[1], *Stefan Knop*[2], *Andreus K. Buck*[1], [1]*Nuclear Medicine, University Wuerzburg, Medical Centre, Würzburg, Germany;* [2]*Haematology&Oncology, University Wuerzburg, Medical Centre, Würzburg, Germany. Contact e-mail: Lueckerath_K@klinik.uni-wuerzburg.de*

Multiple myeloma (MM) is a hematologic malignancy originating from clonal plasma cells. Despite therapeutic advances, such as introduction of proteasome inhibitors, outcomes are still highly variable suggesting marked disease-heterogeneity. The role of functional imaging in therapeutic management of MM, such as 18F-FDG-PET, remains to be determined. Although some studies already suggested a prognostic value of FDG-PET, more specific tracers addressing hallmarks of myeloma tumor biology, e.g. the massively increased paraprotein biosynthesis, are needed. This study aimed at evaluating the amino acid tracers 11C-MET and 18F-FET for their potential to characterize tumor heterogeneity and response to treatment. To study the influence of proteasome inhibition on radiotracer uptake, time-activity curves of 11C-MET, 18F-FET and 18F-FDG were compared in various human myeloma cell lines (INA-6, MM1.S, OPM-2, U266) before and after treatment with either bortezomib, the first in-class proteasome-inhibitor, the novel compound MLN9708 (reversible proteasome-inhibition) or carfilzomib, a recently FDA-approved irreversible inhibitor of the proteasome. Radiotracer uptake was related to tumor cell-biology, e.g. to marker gene expression, paraprotein levels, growth rate and sensitivity towards treatment. Likewise, patient-derived CD138+ plasma cells were characterized regarding uptake- and biomedical features. Using MM cell lines and primary samples we found that the relative uptake of MET exceeded that of FDG three- and that of FET six-fold. Importantly, MET uptake differed between cell types associated with worse prognosis (e.g. deletion of chromosome 13; U266) and indolent ones (e.g. MM1.S) and could be correlated to intracellular levels of immunoglobulin light chains. Following treatment with MLN9708 or carfilzomib, but not with bortezomib, tracer-uptake was markedly reduced already at early time points. Interestingly, two groups of CD138+ plasma cells could be distinguished: one with high, the other with low 18F-FDG avidity. These data suggest that MET is a versatile biomarker for MM holding the potential to discriminate between tumor-subtypes, to detect intra- and inter-patient tumor heterogeneity and to monitor early treatment response. By transferring our findings to different mouse models we hope to confirm superiority of MET over routine functional imaging with 18F-FDG for diagnosis, risk stratification and prognosis. Together, a better understanding of myeloma-biology might allow for individualization of therapies, thereby reducing side effects as well as costs.

Disclosure of author financial interest or relationships:
K. Lückerath, None; **C. Lapa**, None; **L. Omert**, None; **S. Knop**, None; **A.K. Buck**, surgiceye, Stockholder; covidien, Grant/research support; ge healthcare, Consultant; bayer healthcare, Consultant .

Presentation Number **P 486**
Poster Session 4
September 21, 2013 / 14:45-14:45 / Room: Exhibit Hall B

An optimized near infrared fluorescent probe for folate receptor (FR) positive tumor targeted image-guided surgery

Sakkarapalayam M. Mahalingam[1], *Sumith A. Kularatne*[2], *Mohammad Noshi*[2], *Pravin D. Gagare*[2], *Philip S. Low*[1,2], [1]*Department of Chemistry, Purdue University, West Lafayette, IN, USA;* [2]*Research and Development, On Target Laboratories, LLC, West Lafayette, IN, USA. Contact e-mail: mahalins@purdue.edu*

Surgical resection of malignant disease is currently one of the most common and effective treatments for cancer. Unfortunately, quantitative tumor resection is limited by a surgeon's ability to distinguish diseased tissue from adjacent healthy tissue. Optical imaging is gaining traction in the image-guided surgery field, especially when coupled with near infrared (NIR) fluorophores that enable visualization of tumor tissue even when buried within healthy tissue. Thus, imaging in the NIR region (700-900 nm) avoids most light absorption from tissue chromophores (e.g. hemoglobin and cytochromes), minimizes light scattering by intracellular organelles, and virtually eliminates autofluorescence that primarily resides in the visible range. Although many NIR dyes are commercially available for conjugation to a tumor-targeting ligand, each of them exhibits one or more deficiencies related to conjugation efficiency, product stability or fluorescence quantum yield. To obtain the optimal tumor-targeted NIR dye for eventual clinical use, we have conjugated a modified form of folic acid (a tumor-specific targeting ligand) via a vinyl ether bridge to S0456 (a commercially available NIR dye). The resulting tumor-targeted NIR dye exhibits exhibits a quantum yield equal to the best NIR dyes available, but can be synthesized in just two steps at 98% overall yield in multi-gram quantities. Moreover, the final product is highly stable under physiological conditions. Finally, the conjugate displays ~20 nM affinity for folate receptors and concentrates exclusively in folate receptor expressing cancers in tumor bearing mice. Surgical resection of all malignant disease could be achieved with the aid of a fluorescence camera, and all resected fluorescent lesions were later confirmed by histology to be malignant. Collectively, this tumor-specific modified folate NIR probe demonstrates significant potential for use in fluorescent guided surgery by aiding in the complete resection of diseased tissue.

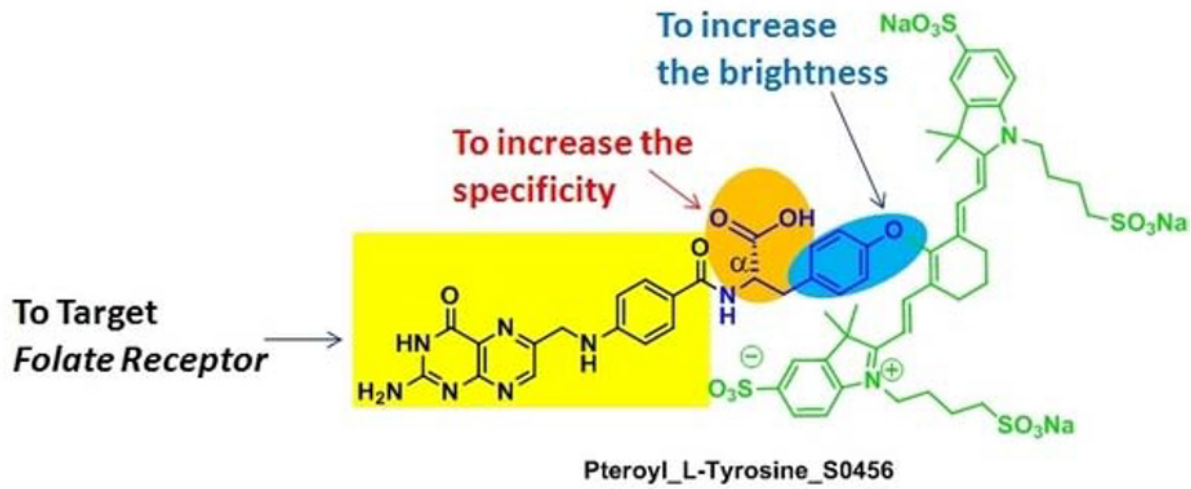

Disclosure of author financial interest or relationships:
S.M. Mahalingam, None; **S.A. Kularatne**, None; **M. Noshi**, None; **P.D. Gagare**, None; **P.S. Low**, On Target Laboratories, Other financial or material support .

Presentation Number **P 487**
Poster Session 4
September 21, 2013 / 14:45-14:45 / Room: Exhibit Hall B

Choline kinase-α protein but not its catalytic activity is important for cancer cell survival

Noriko Mori, *Flonne B. Wildes, Kristine Glunde, Zaver M. Bhujwalla, JHU ICMIC Program, The Russell H. Morgan Department of Radiology and Radiological Science, The Johns Hopkins University School of Medicine, Baltimore, MD, USA. Contact e-mail: noriko@mri.jhu.edu*

Introduction: Choline kinase-alpha (Chk-α), is the enzyme that converts choline to phosphocholine (PC) by Mg2+ and ATP-dependent phosphorylation in the Kennedy pathway. It has been evaluated as a novel target since increased levels of Chk-α and PC are consistently observed in aggressive cancers including breast cancer. Magnetic resonance spectroscopy (MRS) can detect the activated choline metabolism in cancer. We have used MRS to detect PC and glycerophosphocholine (GPC) and free choline in cell extracts. Previously we have shown that the Chk-α inhibitor, V-11-0711 (Vertex Pharmaceuticals (Europe) Ltd), which reduces the function of Chk-α by binding to the active site and inhibiting the catalytic activity but not affecting Chk-α protein levels, had no effect on MDA-MB-231 cell proliferation, although downregulation of Chk with siRNA (siRNA-Chk) reduced proliferation. Falcon et al also showed that inhibition of Chk-α catalytic activity alone by V-11-0711 in HeLa cells is not sufficient to kill cancer cells [1]. Here we have confirmed and expanded these observations in the SUM149 triple negative inflammatory breast cancer cell line. Methods and Results: The cell proliferation assay (CCK-8, Dojindo) detected no significant reduction of viability in SUM149 cells treated with up to 5μM V-11-0711 for 48 h. Fully relaxed 1H NMR spectroscopy of water-soluble phase of cell extracts performed on a Bruker Avance 500 spectrometer showed that levels of PC decreased significantly and dose dependently to almost non-detectable level after treatment with 0.1μM and 1μM V-11-0711 (Fig. 1a). Immunoblot analysis showed Chk-α protein levels in SUM149 cells were stable after 48 h treatment with 0.1μM and 1μM V-11-0711 (Fig. 1b). We have previously shown that the downregulation of Chk-α expression significantly reduced the proliferation in breast cancer cells and tumors [2-4]. Our results here indicate that reduction of PC by Chk-α inhibitor in SUM149 cells does not markedly affect breast cancer cell survival if Chk-α protein levels are not reduced. To further investigate if reduced Chk-α protein levels affect proliferation in SUM149 cells, we used siRNA-Chk to downregulate Chk-α protein level. The siRNA-Chk reduced Chk-α protein to undetectable levels and viability was significantly reduced whether 0.1μM V-11-0711 was present or not (Figure 1c). Discussion: Our results demonstrate that, similar to MDA-MB-231 cells, reduction of PC has little affect on breast cancer cell proliferation as long as Chk-α protein levels are not reduced. These data are consistent with results obtained by Miyake et al., [5] on the potential role of Chk-α as a chaperone protein that is independent of the catalytic activity, and suggest that the Chk-α protein itself may be essential in cancer cell survival. The data support the development of strategies that destabilize or downregulate Chk-α protein and provide new insights into its role in breast cancer. References: [1] Falcon SC et al, Oncogenesis, (2013) in press; [2] Glunde K et al, Cancer Res (2005); [3] Mori N et al, Cancer Res (2007); [4] Krishnamachary B et al, Cancer Res (2009); [5] Miyake T et al., Oncogene (2012).

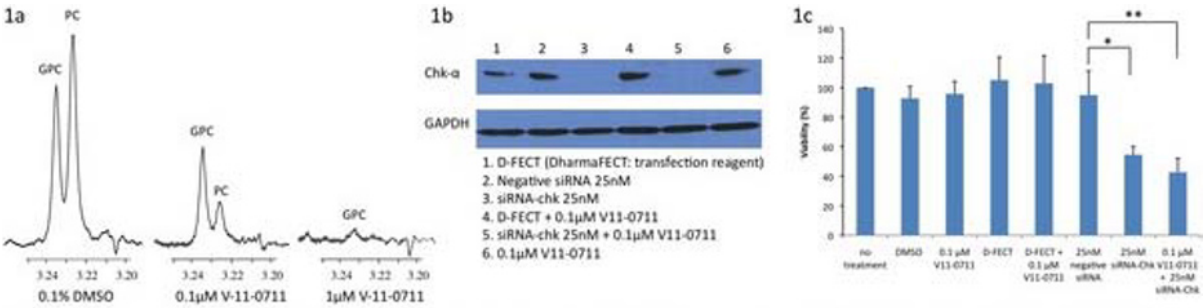

Figure 1: a) Representative ^{1}H NMR spectra expanded to show the 3.20-3.25 ppm region of SUM149 cells treated with V-11-0711. b) Chk-α protein expression levels in SUM149 cells treated with siRNA and/or V-11-0711. 50 μg of protein was loaded on 7.5% reducing SDS-PAGE gel. GAPDH: loading control. c) Cell viability/proliferation in SUM149 cells treated with siRNA and/or 0.1 μM of V-11-0711 for 48 h. Cells were treated for 2 days and changed to fresh medium, and assays were done at day 5 after starting treatment. * : $P < 0.05$ & ** : $P < 0.01$

Disclosure of author financial interest or relationships:
N. Mori, None; **F.B. Wildes**, None; **K. Glunde**, None; **Z.M. Bhujwalla**, None.

Presentation Number **P 488**
Poster Session 4
September 21, 2013 / 14:45-14:45 / Room: Exhibit Hall B

Ultrasound-mediated release of biomarker-bearing extracellular nanovesicles from human carcinoma cells

Robert J. Paproski[1], *Deborah Sosnowski*[2], *Katia Carmine Simmen*[2], *Desmond Pink*[2], *John D. Lewis*[2], *Roger J. Zemp*[1], [1]*Electrical and Computer Engineering, University of Alberta, Edmonton, AB, Canada;* [2]*Oncology, University of Alberta, Edmonton, AB, Canada. Contact e-mail: robertpaproski@hotmail.com*

Ultrasound can enhance the release of various biomarkers from cancer cells through the process of sonoporation. D'Souza et al. (PNAS, 2009) demonstrated that CEA can be released with ultrasound & detected above baseline levels in murine blood samples. Our laboratory has demonstrated that 2 W/cm^2 ultrasound can release ~0.05 & 10 mammaglobin mRNA & miR-21 molecules/cell, respectively. Microbubbles can further enhance ultrasound-mediated RNA release by up to 50-fold. Although RNA can be detected with high sensitivity (<10 molecules with TaqMan® assays), RNase in the body rapidly degrade RNA which complicates in vivo studies. Previous studies using electron microscopy have shown that sonicated cells exhibit a significant increase in membrane ruffling (Qui et al. J Control Release, 2010), suggesting that vesicles may be released from sonicated cells. Here we demonstrate that extracellular micro- and nano-particles are indeed released with ultrasound exposure and may be loaded with biomarkers from host cells useful for diagnostics. **Methods:** Confluent epidermoid HEp3-GFP cells in 12-well plates were incubated in 0.5 mL growth medium/well with or without 5% (v/v) microbubbles (formulation similar to that of Definity®) & cells were exposed to 0.25 or 0.45 mechanical index (MI) 1 MHz ultrasound at 50% duty cycle for 5 minutes. After ultrasound exposure, 0.25 mL medium/well was taken & analyzed for particles using an Apogee A50-Micro flow cytometer. Control wells without ultrasound were also analyzed for baseline levels of particles in the medium. A control experiment was also performed as described above but with no cells in the wells to verify that no particles were created upon sonicating medium with or without microbubbles. Ultrasound-released particles were sized by comparing the particles to beads with known diameters. **Results:** Sonication of medium with or without microbubbles did not increase detectable particles. In the absence & presence of microbubbles, sonication of cells with 0.25 MI ultrasound released 83 ± 570 (P = 0.91) and 5,900 ± 420 (P = 0.018) particles/cell, suggesting that microbubbles were necessary for particle release. In the absence and presence of microbubbles, sonication of cells with 0.45 MI ultrasound released 24,000 ± 1,100 (P = 0.0007) and 31,000 ± 2,700 (P = 0.003) particles/cell. Particles that were GFP+ were ~1% of total particles, suggesting that cytoplasmic GFP (here used as a model intracellular biomarker) did not partition in all vesicles and/or GFP leaked out of vesicles due to sonoporation. Particle sizes ranged from <80 -400 nm although most were ~80 nm. **Conclusion:** Our results suggest that high pressure ultrasound can liberate a significant number of micro- and nanoparticles from cells which could enhance biomarker release by several orders of magnitude. The Apogee system is capable of identifying and enumerating individual cell-derived nanoparticles. In our experiments, GFP served as a model intracellular biomarker and our data shows promise of using ultrasound-stimulated release of extracellular vesicles as a source of host tissue biomarkers.

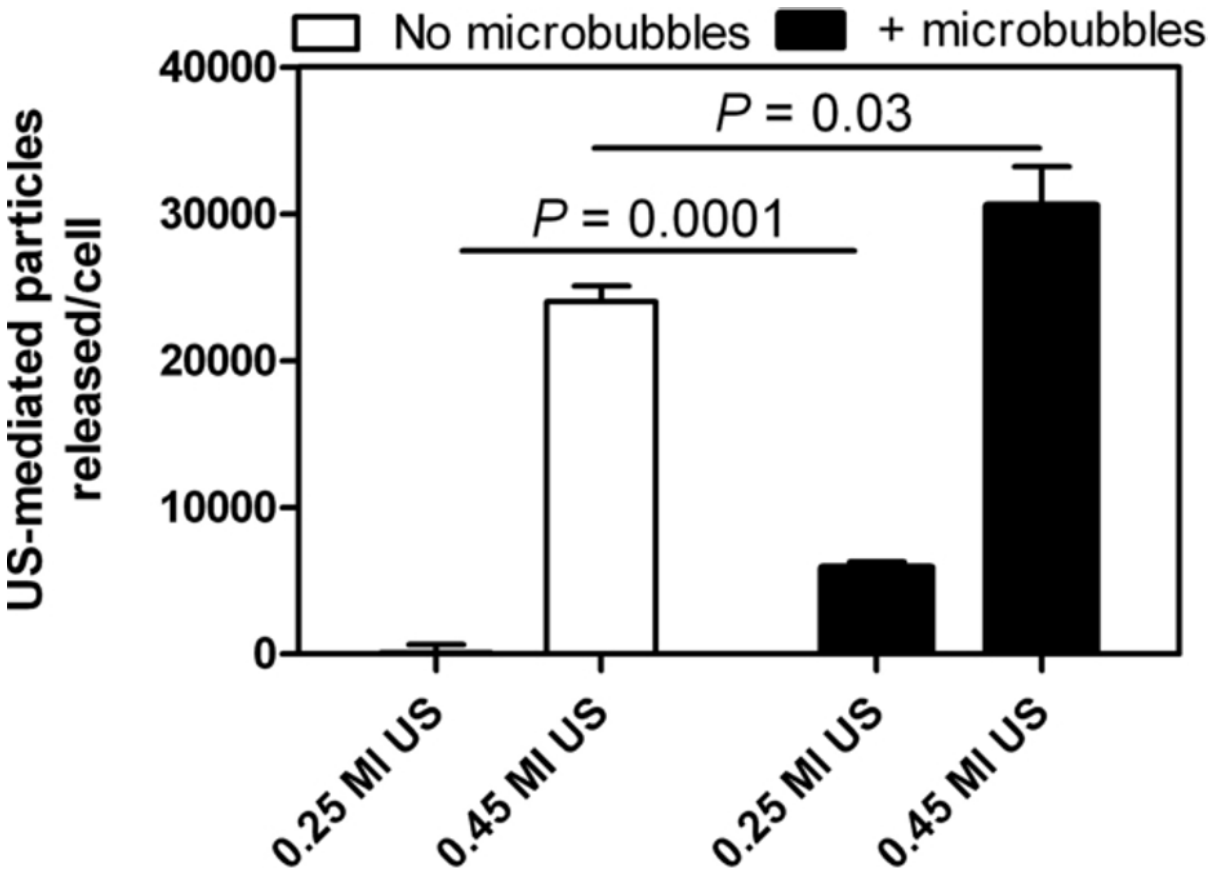

Disclosure of author financial interest or relationships:
R.J. Paproski, None; **D. Sosnowski**, None; **K. Carmine Simmen**, None; **D. Pink**, None; **J.D. Lewis**, None; **R.J. Zemp**, None.

Presentation Number **P 489**
Poster Session 4
September 21, 2013 / 14:45-14:45 / Room: Exhibit Hall B

Evaluation of Ultrasmall Gadolinium-Based Nanoparticles For Theranostic Applications: Focusing on Renal Elimination

Lucie Sancey[1,2], *Vincent Motto-Ros*[3,2], *Florence Appaix*[4], *Shady Kotb*[1,2], *Charles Truillet*[1,2], *Marie Plissonneau*[1,2], *Boudewijn V. Sanden*[4], *Jin Yu*[3,2], *Pascal Perriat*[5], *François Lux*[1,2], *Olivier Tillement*[1,2], [1]*Institute Light Matter - Team FENNEC, UMR 5306, Villeurbanne, France;* [2]*UCBL Lyon1, Univ. Lyon1, Villeurbanne, France;* [3]*Institute Light Matter - Team PUBLI, UMR 5306, Villeurbanne, France;* [4]*Grenoble intravital microscopy PF, GIN U836, Grenoble, France;* [5]*INSA-Lyon, MATEIS, CNRS UMR5510, Villeurbanne, France. Contact e-mail: lucie.sancey@univ-lyon1.fr*

Increasing therapeutic efficiency while decreasing side effects is the goal of many nanoparticles developed as anticancer agents. High-Z contrast agents, or nanoparticles such as gadolinium (Gd)-based nanoparticles increases the sensitivity of the tumor to radiation1-2. If the presence of Gd in the chemical composition of the particle can induce a positive contrast for magnetic resonance Imaging (MRI), the local concentration of the contrast agent should be high enough (close to the mM) to obtain relaxation rate effects on water protons. The Gd-based nanoparticles distribution in malignant and healthy tissues and their elimination from the organism are still unclear and their further understanding remains of very strong interest for the application of nanoparticle in cancer therapy. The renal clearance of such nanoparticles was analyzed on anesthetized animals using intravital 2-photon microscopy from 5 min to 2 weeks after administration. Tissue sections were observed after sacrificing the animals using confocal or two-photon microscopy. This analysis was completed by the quantitative mapping of Gd and Si (major constituents of the nanoparticles) on kidney and tumor sections by a very innovative method called LIBS. The Laser Induced Breakdown Spectroscopy (LIBS) provides 2-D chemical imaging with a resolution of 50 µm of the nanoparticle components as well as organic and inorganic elements in biological tissues after laser ablation 3-4. Electronic microscopy and immunohistochemistry were performed on selected samples to confirm the results. These different diagnostics shows similar and complementary results in presence or without any labeling of the nanoparticles5, allowing investigating different strategies that could help to reduce the renal retention. Moreover, the Gd-based nanoparticles exhibit an interesting potential for image-guided radiosensitization that should permit to adapt the radiotherapy to each patient, potentially reducing side effects and/or been efficient on radioresistant tumors.

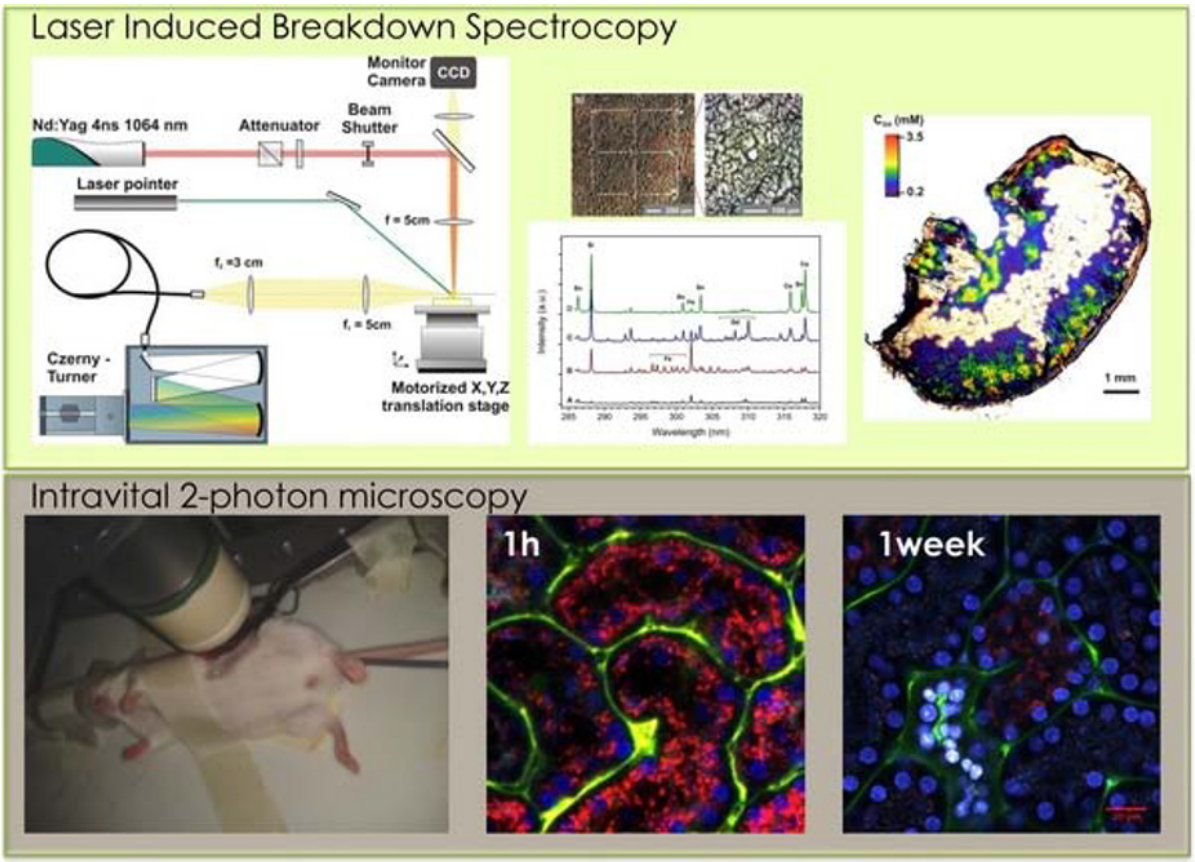

Examples of Laser induced breakdown spectroscopy and intravital 2-photon microscopy of renal sample after injection of Gadolinium-based Nanoparticles.

Disclosure of author financial interest or relationships:
L. Sancey, None; **V. Motto-Ros**, None; **F. Appaix**, None; **S. Kotb**, None; **C. Truillet**, None; **M. Plissonneau**, None; **B.V. Sanden**, None; **J. Yu**, None; **P. Perriat**, None; **F. Lux**, None; **O. Tillement**, None.

Presentation Number **P 490**
Poster Session 4
September 21, 2013 / 14:45-14:45 / Room: Exhibit Hall B

Tracking cells with multispectral optoacoustic tomography (MSOT) using different cell labelling and genetic reporter techniques

Thomas Sardella[1], *Vasilis Ntziachristos*[2,3], *Daniel Razansky*[2,3], *Stefan Morscher*[1,2], *Neal Burton*[1,2], *Wouter H. Driessen*[1,2], *Jing Claussen*[1,2], [1]*iThera Medical, Munich, Germany;* [2]*IBMI, Helmholtz Zentrum, Munich, Germany;* [3]*Biological Imaging, Technische Universität, Munich, Germany. Contact e-mail: thomas.sardella@ithera-medical.com*

MSOT is an attractive research tool for in vivo whole body mouse imaging. It provides high resolution at depth with high molecular specificity by combining the benefits of optical and ultrasound imaging modalities. Tissue is illuminated by short laser pulses and ultrasound transducers detect acoustic waves generated by the thermoelastic expansion of absorbing molecules. By illuminating the tissue at multiple wavelengths and applying spectral unmixing algorithms, it is possible to define the absorption contribution of multiple absorbers and determine their spatial distribution throughout the mouse. MSOT can potently detect endogenous and exogenous absorbers in the near-infrared spectrum (NIR). One of the most promising applications of MSOT technology is the in vivo detection of tumorigenic cells labelled with NIR absorbing molecules to investigate tumour development, immune cell migration, metastasis formation and ultimately cancer therapy approaches. This can be achieved by labelling cells with a dye or by genetically engineering the cells prior to transplantation into the mouse with gene reporters such as iRFP and Lac-z, Tyrosinase. There is a need to compare the aforementioned labelling techniques and other genetic tools with MSOT imaging using the same methodology, cell types and optoacoustic system to understand which have a higher potential for in vivo use. For this purpose we sought to compare with the inVision 256-TF MSOT system, in phantom studies, commonly used tumorigenic cell lines genetically modified to express iRFP, Tyrosinase, Lac-Z, Ferritin, the Promega HaloTag half genetic marker and common cell dies such as DiR and CellVue. For each cell type serial dilutions were performed to determine the optoacoustic detection limit and, where applicable, the intensity of the MSOT acoustic signal was adjusted to correct for the presence of cells not expressing the transgene at detectable levels, as seen by fluorescence microscopy or bright field microscopy. The above combinations were also tested in orthotopic mouse tumor models to test in vivo performance. MSOT imaging was validated post-mortem using a cryoslicer coupled with a fluorescent camera. We found that an optoacoustic signal was detected in all groups, as expected, however the detection limit of these varied significantly between cell types and optoacoustic labelling agent. While tyrosinase expressing cells provide a stronger signal, the iRFP gene is the genetic reporter with highest potential for in vivo use over extended periods of time, as it has a tight absorbance peak making it suitable for multiplexing with other absorbers. HaloTag expressing cells provide a high optoacoustic signal after addition of the NIR probe, however this limiting step makes it ideal only for transplantation of dividing cells were the primary interest is not monitoring tumour development over time, but high specificity cell tracking over shorter length experiment paradigms. The non-genetic based labelling methods we tested such as CellVue and DiR are instead suited for short-term experiments where cell division is not involved and genetic manipulation is farfetched.

Disclosure of author financial interest or relationships:
T. Sardella, iThera Medical, Employment; **V. Ntziachristos**, iThera Medical, Stockholder; SurgOptix BV, Consultant; **D. Razansky**, None; **S. Morscher**, iThera Medical, Employment; **N. Burton**, iThera Medical, Employment; **W.H. Driessen**, iThera Medical, Employment; **J. Claussen**, iThera Medical, Employment .

Presentation Number **P 491**
Poster Session 4
September 21, 2013 / 14:45-14:45 / Room: Exhibit Hall B

Lymphatic Endothelial Cells Enhances Prostate Cancer Cell Invasion of Extracellular Matrix

Tariq Shah, *Flonne B. Wildes, Dmitri Artemov, Zaver M. Bhujwalla, Division of Cancer Imaging Research, Johns Hopkins School of Mediicine, Baltimore, MD, USA. Contact e-mail: tariq196@yahoo.com*

The presence of lymph node metastasis is of major prognostic significance for many cancers, including prostate cancer. However, it is not clear how tumor-associated lymphangiogenesis is regulated and the microenvironmental factors that affect the invasion of cancer cells into lymphatic vessels. Here we have investigated the role of lymphatic endothelial cells prostate-cancer cell interaction in invasion and degradation of the extracellular matrix (ECM) under normoxic and hypoxic environments using our MR compatible cell perfusion assay, and determined the associated metabolic changes. Experiments were performed using the human prostate cancer cell line PC-3, and human dermal lymphatic microvascular endothelial cells (HMVEC-dly) maintained in EGM-2 MV medium. Before each MR experiment, $2.5X10^6$ PC-3 cells were seeded on 0.5 ml of Plastic Plus beads and grown for 3 days. Experiments were carried out either with PC-3 cells alone plated on an ECM chamber or with HMVEC-dlys layered between the PC-3 cells and the ECM. For experiments investigating lymphatic cell-cancer cell interaction, $5 X 10^4$ HMVEC-dlys were seeded on ECM gel contained in a chamber overnight before the MR experiment. This time interval allowed HMVEC-dlys to attach to the ECM gel and form a branching tubular network. MR data were acquired on a 9.4 T MR spectrometer every 12 h over a period of 2 days. T1-weighted ^{1}H MR imaging was performed to evaluate changes in ECM invasion and degradation. One-dimensional ^{1}H MR profiles of intracellular water were acquired along the length (z-axis) of the sample by diffusion-weighted (DW) MRI. These profiles were used to derive an invasion index by quantifying the number of cells invading into the ECM, as described by us previously [1]. Intracellular metabolite levels were derived from unlocalized DW ^{1}H and ^{3}1P MR spectra. Fig. 1a shows representative ^{1}H MR images of the ECM region detecting significantly increased degradation when HMVEC-dlys were layered between the ECM and the PC-3 cancer cells under normoxic condition. Fig.1b shows quantitative time-dependent invasion indices I(t). A significant increase in the invasion index of PC-3 cells was observed in the presence of HMVEC-dlys compared to PC-3 cells alone under normoxia and hypoxia ($p < 0.05$). There was also a significant decrease of PC-3 cell invasion under hypoxia compared to PC-3 normoxia ($p < 0.05$). Though hypoxia reduced the invasion of these prostate cancer cells, the presence of lymphatic endothelial cells alleviated this reduction in invasion. There was also a significant increase in phosphocholine (PC) at 48h time point in PC-3 cells grown under hypoxia versus PC-3 cells under normoxia ($p<0.05$). The enhanced degradation of ECM by PC-3 cells in the presence of HMVEC-dlys indicates that the interaction between HMVEC-dlys and prostate cancer cells play a critical role in lymphatic metastasis. Thus, the presence of HMVEC-dlys may significantly influence the metastatic potential in tumor progression. References: [1] Ackerstaff E, Gimi B, Artemov D, Bhujwalla ZM Neoplasia. 2007; 9: 222-235. Supported by NIH R01 CA73850

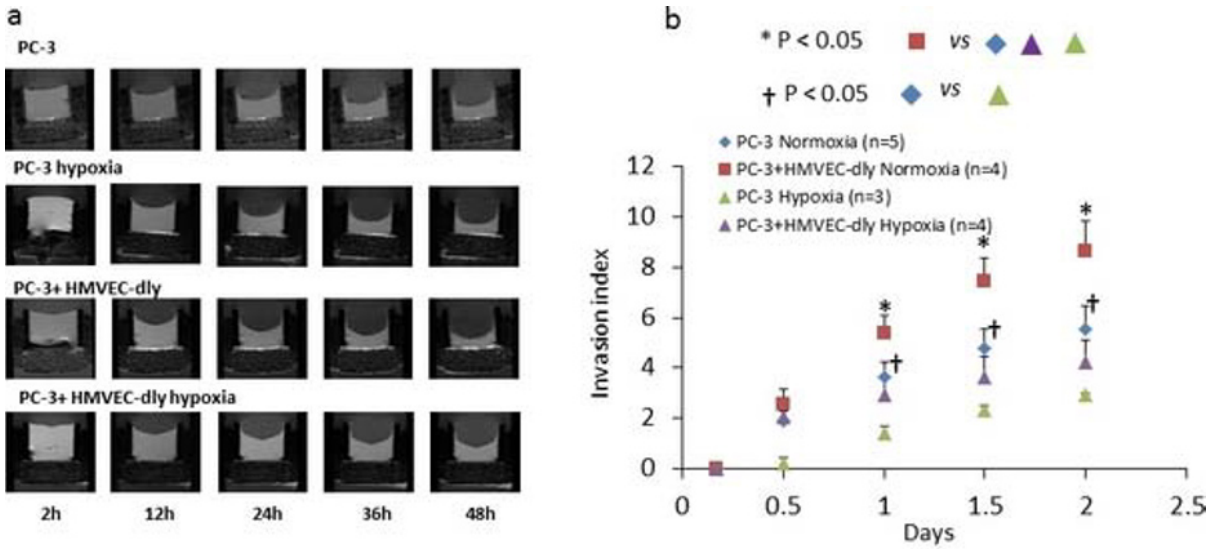

Figure 1: (a) Representative T1-weighted 1H MR images at time points zoomed into the region with the ECM chamber, showing degradation of ECM gel. (b) Invasion index obtained from intracellular water signal for PC-3 cells and for PC-3 cells in the presence of HMVEC-dlys under normoxia or hypoxia. Values are Mean ± SE.

Disclosure of author financial interest or relationships:
T. Shah, None; **F.B. Wildes**, None; **D. Artemov**, None; **Z.M. Bhujwalla**, None.

Presentation Number **P 492**
Poster Session 4
September 21, 2013 / 14:45-14:45 / Room: Exhibit Hall B

Role of Choline Kinase Isoforms in Modulation of Ethanolamine Levels in Breast Cancer Cells

Tariq Shah, *Jannie P. Wijnen, Flonne B. Wildes, Balaji Krishnamachary, Kristine Glunde, Zaver M. Bhujwalla, Radiology, JHU, Baltimore, MD, USA. Contact e-mail: tariq196@yahoo.com*

Introduction: The aberrant choline metabolism of cancers occurs, in large part, due to increased expression of choline kinase (Chk)-α, an enzyme that has been associated with malignant transformation and an aggressive phenotype. Since Chk converts choline to phosphocholine (PC), the increase of Chk results in increased phosphocholine and total choline (PC, glycerophosphocholine (GPC), and free choline) signals in cells and tumors as observed with 1H MRS. While cells in culture and tumors show increased PC, an increased signal from phosphoethanolamine (PE) is observed only in tumors but not in culture. This is because while mammalian plasma contains both choline (~10-40 μM) and ethanolamine (~50-75 μM), most culture media only contain choline (~ 1-20 μM). Although increased PE is observed in tumors almost as consistently as increased PC, understanding the role of PE in cancer is relatively unexplored. As an initial step to understanding the increase of PE in tumors here we have investigated the role of Chk-α and Chk-β in contributing to the increased PE observed in cancers, and the effect of different concentrations of ethanolamine on the activity of Chk. Materials and Methods: MDA-MB-231 human breast cancer cells were treated with various ethanolamine concentrations. In separate groups, similar numbers of cells were transfected overnight with 75 nM ChK-α specific siRNA or Chk-β siRNA and the medium changed to ethanolamine. MDA-MB-231 cells without ethanolamine or siRNA treatment were used as controls to determine the endogenous level of metabolites. Approximately 40 million cells were harvested after 24 h treatment and cell extracts were prepared using a dual-phase extraction method. ^{31}P MR spectra were acquired with a Bruker 11.7T MR spectrometer using a 60^0 pulse, a 1 s repetition time and composite pulse proton decoupling. Integrals of metabolites were determined to estimate their absolute concentration relative to PPA. Results and Discussion: Fig. 1a-c show quantitative PC and PE levels obtained from 31P MR spectra acquired under various conditions. While PC decreased consistently when cells were treated with Chk-α siRNA (Fig. 1 a,b), but in the absence of Chk--α siRNA only with an ethanolamine concentration of 1mM and 10mM in the culture media. Reduction in both PC and PE levels following treatment with ChK-α siRNA confirms the previously observed dual kinase activity of ChK-α. We additionally investigated the role of Chk-β ethanolamine kinase activity in these cells and did not find PC or PE reduction when cells were treated with Chk-β siRNA in the presence of ethanolamine (Fig. 1c). These results indicate that Chk-β does not have a significant role in choline or ethanolamine kinase activity in these breast cancer cells. This could be because Chk-β message levels are very low and 10 fold lower compared to Chk-α. We are also investigating the contribution of ethanolamine kinase to PE levels observed in vivo. These studies will further unravel mechanisms underlying aberrant choline metabolism, one of the major hallmarks of cancer. Supported by NIH P50CA103175.

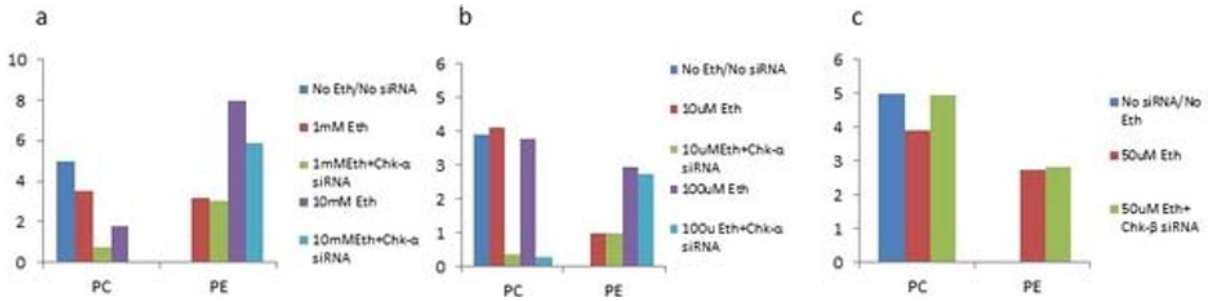

Figure 1: Quantitative PC and PE values obtained from 31P MR spectra of MDA-MB-231 cells acquired under various treated conditions.

Disclosure of author financial interest or relationships:

T. Shah, None; **J.P. Wijnen**, None; **F.B. Wildes**, None; **B. Krishnamachary**, None; **K. Glunde**, None; **Z.M. Bhujwalla**, None.

Presentation Number **P 493**
Poster Session 4
September 21, 2013 / 14:45-14:45 / Room: Exhibit Hall B

Metabolic Profiling of Pancreatic Cancer Shows Aberrant Choline Metabolism

Tariq Shah[1], *Santosh K. Bharti*[1], *Flonne B. Wildes*[1], *Yelena Mironchik*[1], *Marie-France Penet*[1], *A. Maitra*[2], *Zaver M. Bhujwalla*[1], [1]*Division of Cancer Imaging Research, The Johns Hopkins University School of Medicine, Baltimore, MD, USA;* [2]*The Sol Goldman Pancreatic Cancer Research Center, The Johns Hopkins University School of Medicine, Baltimore, MD, USA. Contact e-mail: tariq196@yahoo.com*

Pancreatic cancer has a 5-year survival rate of less than 3%, accounting for the fourth largest number of cancer deaths in the United States. Currently, there is no specific marker available for early diagnosis and there is an urgent need for biomarkers with enough sensitivity and specificity to help diagnose pancreatic cancer early. Development of novel therapeutic strategies is also critically important. Magnetic resonance spectroscopy (MRS) is being evaluated in the diagnosis of other solid malignancies such as brain, prostate and breast cancer, and for monitoring therapy in brain cancer. Here we have used 1H MRS to characterize the metabolic profile of a panel of pancreatic adenocarcinoma cell lines. Eight pancreatic adenocarcinoma cell lines and one immortalized pancreatic cell line were used to obtain cell extracts for high resolution 1H MRS. Human pancreatic nestin expressing (HPNE) cells stably expressing human telomerase reverse transcriptase (hTERT)-hTERT-HPNE cells, Panc-1 and BxPC-3 were obtained from ATCC. All other cell lines were obtained from the Johns Hopkins pancreatic Xenobank and were derived from pancreatic cancer patients and established in nude mice. While Pa02C, Pa03C were from derived from liver metastasis of adenocarcinomas, Pa04C was obtained from lung metastasis of adenocarcinomas. Panc-1, BxPC-3, Pa09C, Pa28C, Pa20C were primary adenocarcinomas. High resolution 1H spectra at 500 MHz Bruker spectrometer were acquired on water soluble cell extracts. Principal Components Analysis (PCA) on aligned NMR spectra from 0.5 to 9.0 ppm was carried out using the Unscrambler X statistical software. The water region from 4.5 to 5.20 ppm was excluded from analysis. Normalization of the metabolites peak regions to total spectral area was carried out to remove the effect of difference in cell counts. We first characterized the choline phospholipid metabolites profile in this panel of malignant pancreatic cell lines and nonmalignant pancreatic cell line. Figure 1 shows immunoblots from these cell lines with increased choline kinase-alpha (Chk-α) expression in most of the cells, relative to HPNE cells. Figure 2 shows quantitative data for choline containing metabolites obtained from water soluble cell extracts. Elevated phosphocholine (PC) and total choline were present in all adenocarcinomas relative to the immortalized pancreatic cells ($p<0.05$). PCA of the spectral data showed that we could differentiate the HPNE cells and Pa09C from the remaining pancreatic carcinoma cell lines. Free choline, PC, lactate, alanine, creatine and myoinositol were the major metabolites contributing to the principal components. There was no significant difference in the principal components between primary and secondary pancreatic adenocarcinoma cell lines. These data have identified aberrant choline metabolism as well as other metabolites in these pancreatic cancer cells lines. 1H MRS can be used to detect this altered metabolism for pancreatic cancer diagnosis, and identify new metabolism-based therapeutic strategies in pancreatic cancer.

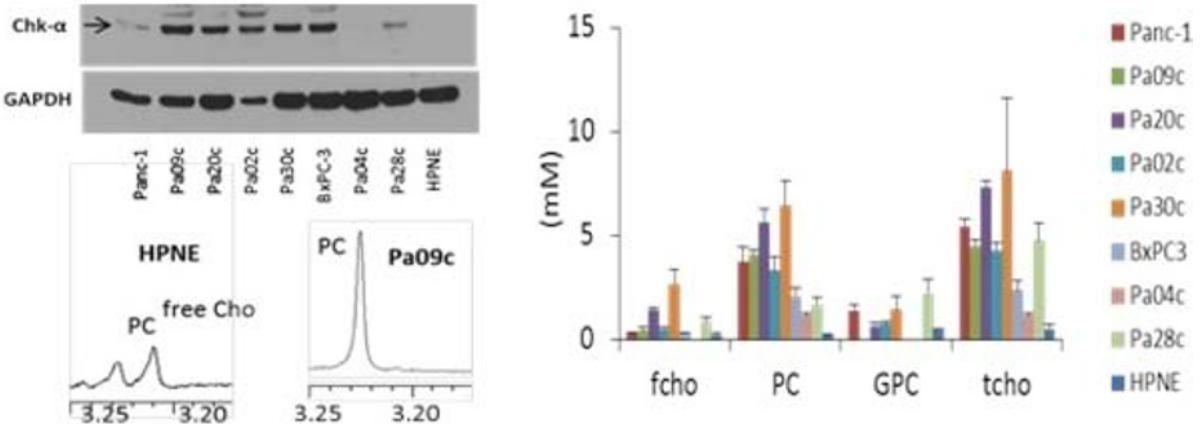

Figure1 (a) Representative immunoblots from a panel of pancreatic cell lines showing Chk-alpha expression (top panel). Representative proton spectra from HPNE and Pa09c pancreatic cancer cell lines (bottom panel).(b) Quantitative data for various choline containing compounds in a panel of pancreatic cell lines. (fCho: free choline, tcho: total choline, GPC: glycerophosphocholine).Values are Mean ± SD (n=3).

Disclosure of author financial interest or relationships:
T. Shah, None; **S.K. Bharti**, None; **F.B. Wildes**, None; **Y. Mironchik**, None; **M. Penet**, None; **A. Maitra**, None; **Z.M. Bhujwalla**, None.

Presentation Number **P 494**
Poster Session 4
September 21, 2013 / 14:45-14:45 / Room: Exhibit Hall B

Molecular CEST MR Imaging of Underglycosylated mucin-1 (uMUC-1) Tumor Cell Expression

Xiaolei L. Song[1,2], *Raag D. Airan*[1,3], *Dian R. Arifin*[1,3], *Amnon Bar-Shir*[1,2], *Deepak K. Kadayakkara*[1,3], *Guanshu Liu*[1,2], *Assaf A. Gilad*[1,3], *Peter C. van Zijl*[1,2], *Michael T. McMahon*[1,2], *Jeff W. Bulte*[1,3], [1]*The Russell H. Morgan Department of Radiology and Radiological Science, The Johns Hopkins University, Baltimore, MD, USA;* [2]*F.M. Kirby functional imaging center, Kennedy Krieger Institute, Baltimore, MD, USA;* [3]*Cellular Imaging Section, Institute for Cell Engineering, Johns Hopkins University, Baltimore, MD, USA. Contact e-mail: lisasonger@gmail.com*

Introduction Glycosylation changes on the tumor cell surface and extracellular matrix are associated with tumor proliferation, metastasis, and angiogenesis[1,2]. Several types of glycoproteins have been used as novel diagnostic and/or therapeutic targets, such as underglycosylated MUC-1(uMUC-1) antigen[2], a cell-surface glycoprotein overexpressed in many malignant adenocarcinomas such as ovarian, breast and colon cancer. CEST-MRI is an emerging imaging modality that can amplify signals from specific functional groups in proteins, peptides and sugars based on exchange of their protons with water[4]. Owing to the abundance of exchangeable protons on attached glycans (-OH) and core protein (-NH,-NH_2), mucins exhibit a characteristic CEST contrast from 0.5 ppm to 4 ppm3. **We aimed to test whether CEST- MRI is able to detect changes in mucin glycosylation levels (Fig.a) and differentiate uMUC-1 positive tumor cells (expressing underglycosylated MUC-1) from uMUC-1 negative cells (expressing normally glycosylated MUC-1)**. **Materials and Methods** Oligosaccharide chains on mucin (Sigma, M-2378) were removed using trifluoromethanesulfonic acid(TFMS) treatment4. Both deglycosylated and untreated mucin were dialyzed against water, lyophilized and dissolved at 4.0 mg/ml in PBS (pH=7.1). Three cell lines (MCF10A, non-malignant human breast carcinoma; and LS174T and HT29, both human colon carcinomas) with different MUC-1 glycosylation levels were encapsulated5 at 1000 cells/capsule in order to minimize cell sedimentation and variations in cell density. Images were acquired on a Bruker 11.7T scanner, using a RARE sequence with a CW saturation pulse of B1=3.6 μT, Tsat=3 s, and with a frequency incremented every 0.2 ppm from -6 to 6 ppm for phantoms and every 0.25 ppm from -5 to 5 ppm for cells; TR/TE=6000 ms/17.5 ms, matrix size=96x64. CEST contrast was quantified by $MTR_{asym}=(S_{-\Delta\omega}-S_{+\Delta\omega})/S0$.**Results** Untreated and deglycosylated mucin could be easily differentiated in both the Z-spectra and MTRasym spectra (**Fig.b**), with a significant reduction of CEST contrast over a broad chemical shift range, i.e. a ~80% reduction from 0.5 to 2 ppm and a ~50% loss from 2 to 4 ppm, respectively. Deglycosylation was confirmed by SDS-PAGE, where deglycosylated mucin showed a MW of 70-100kD, in contrast to untreated mucin which has an Mw >260kD6. We then compared the CEST contrast produced by LS174T and HT29, both expressing underglycosylated MUC-1 and MCF10A, expressing normally glycosylated MUC-1. Both the MTRasym spectra and contrast maps (**Fig.c**) clearly show that the underglycosylated MUC-1 tumor cell lines (LS174T and HT29) have a lower CEST contrast from 2 to 4 ppm, which corresponded to the expression levels seen on immunohistology.**Conclusions** Both mucin extracts and encapsulated cells expressing MUC-1 exhibit differential CEST contrast depending on glycosylation levels, suggesting that CEST imaging may be used to assess mucin glycosylation as a surrogate marker for tumor malignancy. Ref 1Hakomori, PNAS 2002 2Moore et al. Cancer Res. 2004 3Song et al, Proc.ISMRM 2012 4Edge Biochem J. 2003 5Barnett et al., Nat. Prot. 20116Piel et al. Reprod. Nutr. Dev. 2004

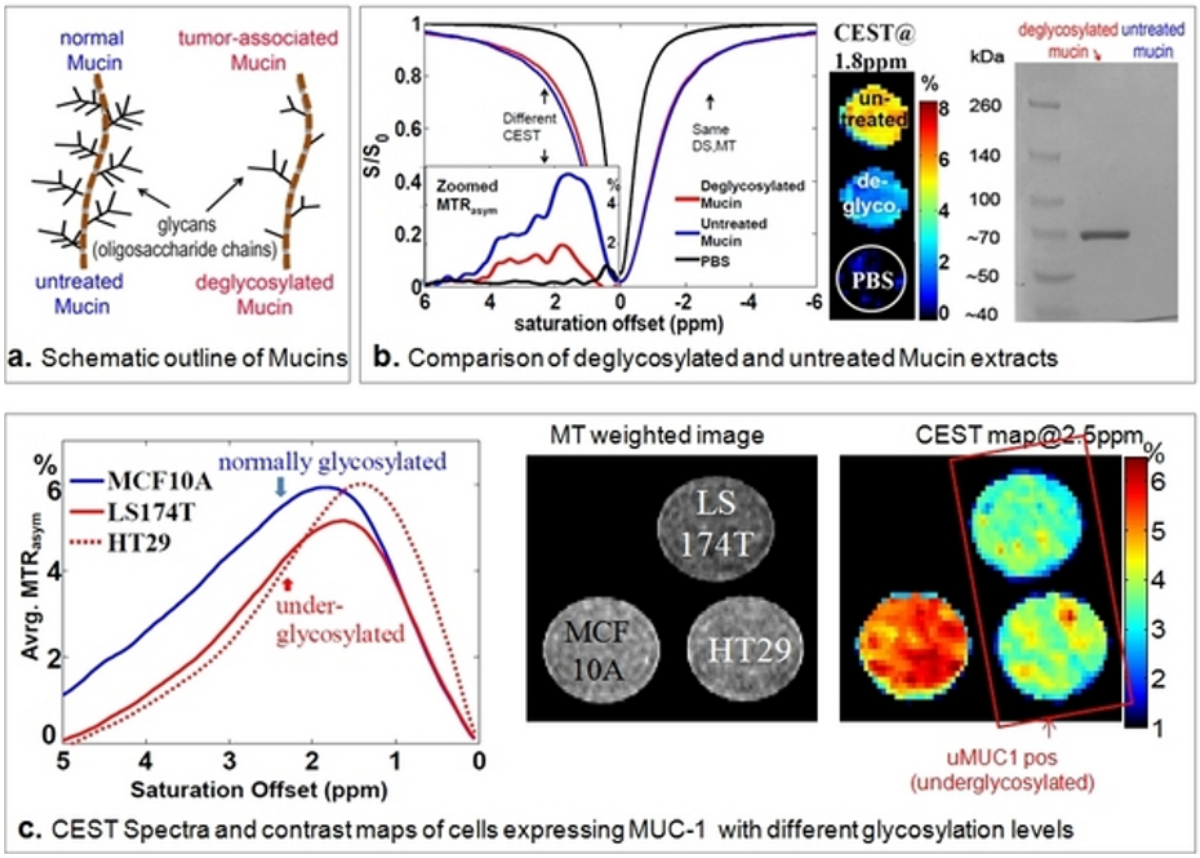

Disclosure of author financial interest or relationships:
X.L. Song, None; **R.D. Airan**, None; **D.R. Arifin**, None; **A. Bar-Shir**, None; **D.K. Kadayakkara**, None; **G. Liu**, None; **A.A. Gilad**, None; **P.C. van Zijl**, None; **M.T. McMahon**, None; **J.W. Bulte**, None.

Presentation Number **P 495**
Poster Session 4
September 21, 2013 / 14:45-14:45 / Room: Exhibit Hall B

Detection of PKM2 Activator Treatment Response in Tumor Cells using Hyperpolarized Magnetic Resonance Spectroscopy

Sui Seng Tee[1], *Jae Mo Park*[1], *Kyle R. Brimacombe*[2], *Matthew Boxer*[2], *Brian K. Rutt*[1], *Daniel M. Spielman*[1], [1]*Stanford University, Stanford, CA, USA;* [2]*National Center for Advancing Translational Sciences, National Institutes of Health, Bethesda, MD, USA. Contact e-mail: sstee@stanford.edu*

Introduction: Pyruvate (Pyr) kinase converts phosphoenolpyruvate to Pyr in the last step of glycolysis. The M2 isoform of Pyruvate kinase, PKM2, is expressed in all cancer cell lines tested so far. PKM2 exists either as a dimer or a tetramer. The less active dimer is thought to favor rapid cell division by the diversion of glycolytic intermediates into biosynthetic pathways. Recently, an activator of PKM2, TEPP46, has been shown to inhibit xenograft tumor growth. Hyperpolarization combined with a rapid dissolution process has enabled real-time investigation of metabolic kinetics non-invasively. This study proposes to detect TEPP46 treatment using hyperpolarized [1-^{13}C]Pyr magnetic resonance spectroscopy (MRS).Hyperpolarized MRS has the unique potential to quantify the efficacy of PKM2 activators by directly measuring metabolic changes in-vivo, potentially accelerating the development of this new class of drugs for use in patients. **Methods**: H1299 cells were cultured in standard media. 72 hr before Pyr injection, cells were treated with either 30μM TEPP46 or DMSO. Immediately before dissolution, approximately 1 x 10^8 cells were trypsinized and resuspended in 2ml media. This was followed by an injection of 2ml of 14mM hyperpolarized [1-^{13}C]Pyr solution polarized using HyperSense dynamic nuclear polarizer. All MR measurements were performed using 3-T GE clinical MR scanner and a custom-built surface coil. Dynamic free induction decay spectroscopic sequence (spectral width = 5,000 Hz, spectral points = 2048) with hard RF pulse excitations (pulse width = 40μs, nominal flip angle = 10^o) was used to acquire spectra with 3s of temporal resolution (T_{acq} = 4:00 min). The apparent conversion rate constants of Pyr to lactate (Lac), k_{PL}, and the apparent T_1 of Lac for both TEPP46 treated and vehicle-treated cells were estimated by a two-site exchange model **Results**: Representative spectra from TEPP46 and DMSO-treated cell suspensions, which are averaged over first 90s of acquisition and then normalized by [1-^{13}C]Pyr peaks, are shown in Fig 1. The magnitude of the Lac peak relative to the injected Pyr peak is markedly increased after treatment from 0.0043±0.0008 to 0.0066±0.0006 (p=0.03, n=3).The estimated apparent conversion rate constants from Pyr to Lac are calculated as 0.0026±0.0006s^{-1} for control cells and 0.004±0.0008s^{-1} for TEPP46 treated cells (p=0.04). **Discussion** TEPP46 treatment of cells results in viability and growth rate changes only under hypoxic conditions. Under normal oxygen levels, no detectable difference in cell growth is observed, although lower lac levels have been shown. Our experiments using hyperpolarized [1-^{13}C]Pyr were surprising as the data suggests an increase in Pyr to Lac exchange. Nevertheless, these results suggest that hyperpolarized MRS is able to detect specific metabolic alterations caused by TEPP46 treatment even with no change in cell number and viability. Further experiments are being performed to determine the biological mechanism underlying these observations.

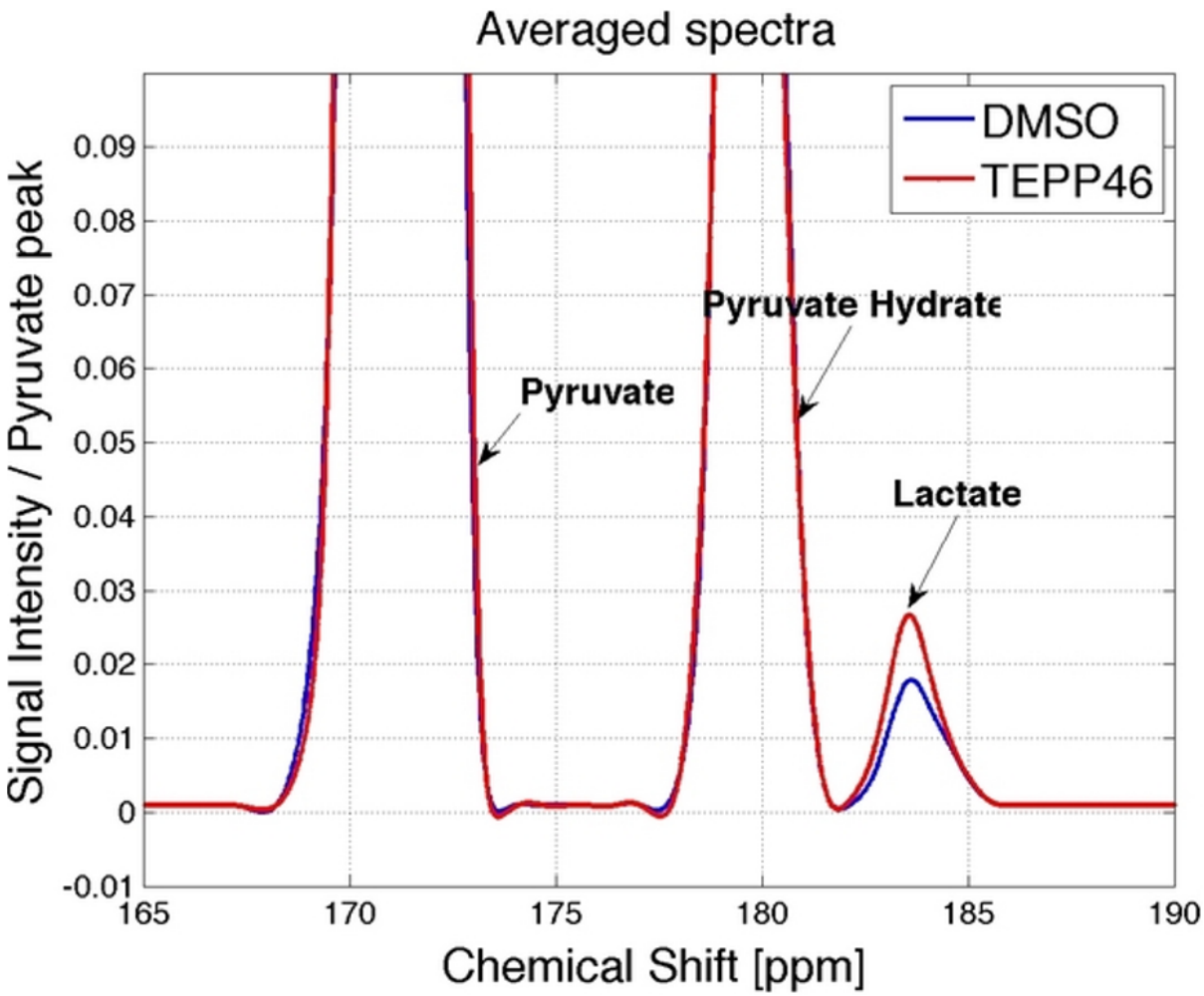

Figure 1: Representative spectra from H1299 cell suspensions averaged over the first 90s of acquisition and normalized by [1-^{13}C]Pyr peaks. A total of 1 x 10^8 cells were used for each experiment, 72 hours after treatment with 30μM TEPP46 or a corresponding, DMSO-treated control. The magnitude of the lactate peak relative to the injected pyruvate peak is increased after TEPP46 treatment.

No. of Cells	Treatment	Ratio of Lac/Pyr Signal Intensity	Pyr to Lac Conversion Rate Constant
1 x 10^8	DMSO	0.004±0.0008	0.002±0.0006 s^{-1}
1 x 10^8	30μM TEPP46	0.006±0.0006	0.004±0.0008 s^{-1}

Table 1: Summary of hyperpolarized [1-^{13}C]Pyr magnetic resonance spectroscopy on H1299 lung cancer cells treated either with the PKM2 activator, TEPP46 or DMSO.

Disclosure of author financial interest or relationships:
S. Tee, None; **J. Park**, None; **K.R. Brimacombe**, None; **M. Boxer**, None; **B.K. Rutt**, GE Heathcare, Grant/research support; **D.M. Spielman**, None.

Presentation Number **P 496**
Poster Session 4
September 21, 2013 / 14:45-14:45 / Room: Exhibit Hall B

Remodeling Intratumoral Collagen to Enhance Biodistribution of Cancer Drugs for Effective Image Guided Targeted Drug Delivery

Miguel Valdivia y Alvarado[1], **Kelvin Wong**[1], *Ki Young Choi*[2], *Xiaoyuan (Shawn) Chen*[2], *Stephen T. Wong*[1], [1]*Systems Medicine and Bioengineering, The Methodist Hospital Research Institute., Houston, TX, USA;* [2]*LABORATORY OF MOLECULAR IMAGING AND NANOMEDICINE, NATIONAL INSTITUTE OF BIOMEDICAL IMAGING AND BIO ENGINEERING/NATIONAL INSTITUTE OF HEALTH, Bethesda, MD, USA. Contact e-mail: kwong@tmhs.org*

Introduction Although molecular targeted drugs have high tumor affinity, their targeting mechanisms and effects are limited by drug biodistribution within the tumor. Since elevated levels of collagen in tumors can alter drug biodistribution within the tumor, we hypothesize that we can improve drug biodistribution by reducing collagen remodeling in the tumor with local delivery of a molecular targeted drug using a real-time image guided drug delivery system. Losartan is an angiotensin II receptor antagonist that is effective in altering type I collagen production, the most abundant in tumors. In this report, we investigated Losartan effect in collagen remodeling using a VX2 rabbit lung tumor model in order to assess drug biodistribution and enable effective intratumoral drug delivery in a large lung tumor. Materials and Methods We injected a VX2 tumor cell suspension (1x107) into the chest of rabbits using a thoracic puncture guided by fluoroscopy. Losartan Potassium (tablets 50 mg) was grinded and given to the rabbits (n=4) with food once daily for 21 days. We then selected a dose of 20 mg/kg, which was shown to be the minimum effective dose in other animal models. On day 24 post-tumor inoculation, the animals started to have respiratory distress (low O2 saturation) and were euthanized to harvest the tumor. Tumor samples were evaluated with Tri Giemsa and Picosirius red stain, as well as immunostaining (collagen I and trombospodin-1). Results and Discussion Secondary effects (e.g. hypotension and allergies) were not observed while on treatment with Losartan until day 24. When the lungs were extracted, a tumoral mass of 20-25 mm was present and no distant metastases were observed. Fluorescent staining microscopy revealed a diffuse pattern of collagen fibers and spread between each other,when normally the fibers distribution are very close between each other. In contrast, six non-treated rabbits developed extreme respiratory distress and distant metastasis after14 days post-inoculation, and they had to be euthanized. We attributed the absence of local and distant metastases to effective Losartan treatment in local tumor. The antifibrotic effects of losartan are caused, in part, by the suppression of active transforming growth factor-β1 (TGF-β1) levels via an angiotensin II type I receptor (AGTR1)-mediated down-regulation of TGF-β1 activators like thrombospondin-1 (TSP-1). Losartan blockade of AGTR1 can also reduce the production of vascular endothelial growth factor (VEGF) by cancer cells and the expression of VEGFR1 in endothelial cells, thus inhibiting tumor angiogenesis and growth. A number of drugs can also be used as collagen matrix modifiers, including bacterial collagenase, relaxin, and matrix metalloproteinase. However, these agents may produce tissue toxicity or increase tumor progression, whereas Losartan does not have any of these risks. This initial experience paves the way to investigate Losartan effects on intratumoral drug delivery as both the biodistribution and effect of the drug may be enhanced due to a better interstitial transport and intratumoral distribution caused by changes in the collagen fiber architecture.

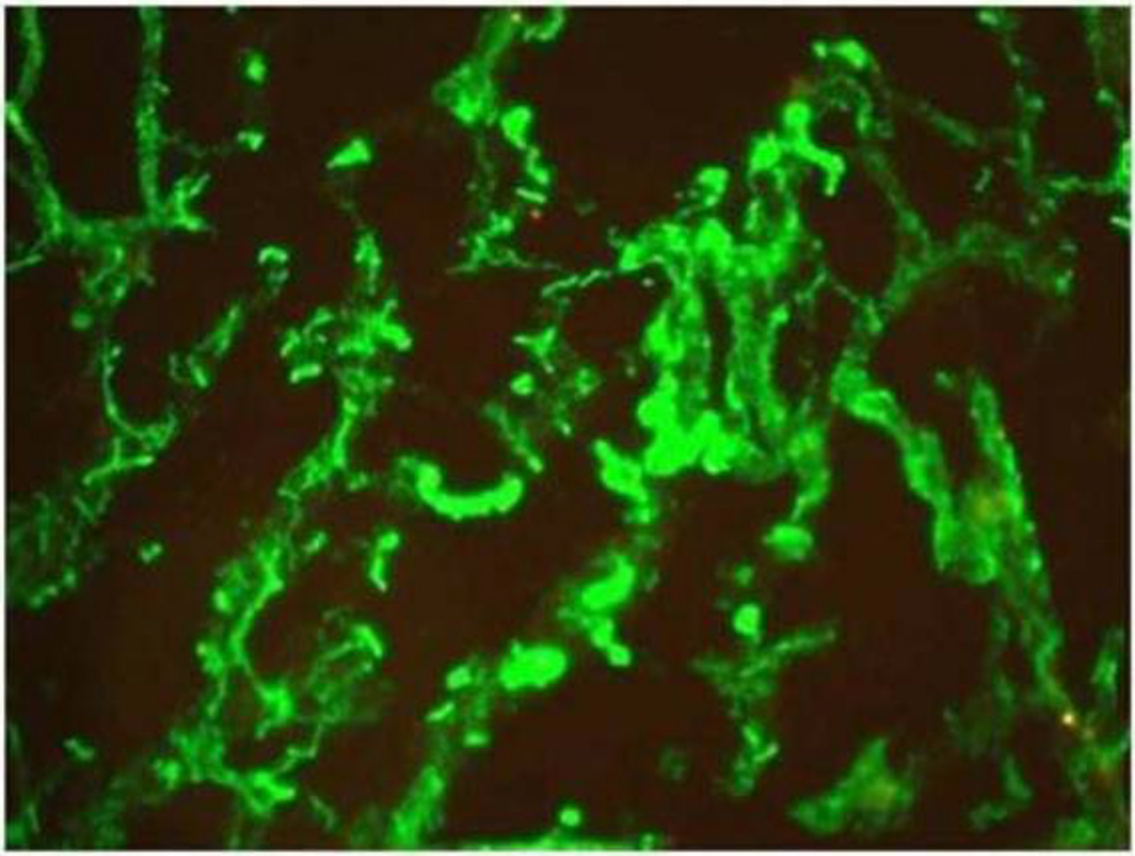

FIGURE 1: Immunohistochemistry of a frozen section of the VX2 lung tumor, Type I collagen antibody staining (x40). Sample from an external region of a VX2 tumor. This type of tumor tends to become capsular with a high deposition of fibrotic tissue over time. A very dense and tight net of collagen fibers is often seen in these areas. However the use of Losartan altered the collagen distribution and density, thus increasing the spread between the fibers as observed in this figure

Disclosure of author financial interest or relationships:
M. Valdivia y Alvarado, None; **K. Wong**, None; **K. Choi**, None; **X. Chen**, None; **S.T. Wong**, None.

Presentation Number **P 497**
Poster Session 4
September 21, 2013 / 14:45-14:45 / Room: Exhibit Hall B

Toxicity Assessment of Hyaluronic Acid-Paclitaxel Nanoparticles for Image Guided Targeted Therapy in Lung Cancer

Miguel Valdivia y Alvarado[1], **Kelvin Wong**[1], *Ki Young Choi*[2], *Xiaoyuan (Shawn) Chen*[2], *Stephen T. Wong*[1], [1]*Systems Medicine and Bioengineering, The Methodist Hospital Research Institute., Houston, TX, USA;* [2]*LABORATORY OF MOLECULAR IMAGING AND NANOMEDICINE, NATIONAL INSTITUTE OF BIOMEDICAL IMAGING AND BIO ENGINEERING/NATIONAL INSTITUTE OF HEALTH, Bethesda, MD, USA. Contact e-mail: kwong@tmhs.org*

Introduction: Image-guided nanoparticles targeted drug delivery is an emerging technology to overcome systemic chemotherapeutic toxicity by local delivery of targeted drug. This approach can effectively deliver a high dose of targeted drug and minimizing off-target effect common in targeted therapy. Hyaluronic acid (HA) is chosen as a targeting constituent since various tumor cells overexpressing receptors of HA, such as CD44 and RHAMM. Paclitaxel loaded hyaluronic acid nanoparticles (HA-NP/PTX) are constructed using an amphiphilic HA conjugate, and their hydrophobic inner cores were filled with Paclitaxel. In this paper, we studied the in vitro toxicity of Paclitaxel-loaded HA-NPs in two human non-small cell lung cancer cell lines (A549 and NCI-H460) that highly express CD44. This study will form the foundation for the subsequent in vivo studies of image-guided Paclitaxel HA-NPs delivery in orthotopic lung cancer xenograft mouse models. Materials and Methods: HA nanoparticles had a content weight of 39 wt% (e.g. 390 µg of Paclitaxel in 1 mg of HA-NP/PTX) and a hydrodynamic size of 375nm. The HA-NP/PTX dry powder was dissolved in ultra pure water at 4 mg/mL by sonication using a probe-type sonifier for 15 minutes at 90 W, and then dilute in RPMI. The concentration of nanoparticles was kept constant at 1 µg/mL. A549 and NCI-H460 cells were cultured to confluent state before trypsinized and seeded in triplet to 96-well plates at 30000 cells/well for A549 cells and at 80000 cells/well for NCI-H460 cells. Cell density was counted at day 0 manually with hemocytometer. At 24 hours after seeding, cells were washed with culture medium without any additive, and a 200 µL of HA-NP/PTX suspension was added to 96 well plates containing cell lines alone. After the cell lines were incubated for 72 hours, cells were counted again to determine the cytotoxicity. Results and Discussion: The cytotoxic effects of HA-NP/PTX on A549 and NCI-H460 cells were confirmed by cell counting. HA-NP/PTX exhibited dose-dependent cytotoxicity to both type of cells. Since both cell lines have similar doubling time (22.9 and 26 hours for A549 and NCI-H460 cells respectively), the expected cell count at day 3 for A549 should be around 32000/mL and 56000/mL for NCI-H460. Our results showed that HA-NP/PTX achieved 90% inhibition at the lowest dose tested (0.1 ug/mL). This is not surprising as previous studies have demonstrated that both lung cancer cell lines have similar high levels of CD44 receptors on the cell surface (95.62% and 91.79% for A549 and NCI-H460, respectively). HA-NP/PTX should be internalized by receptor-mediated endocytosis once bound to CD44, leading to rapid degradation of the nanoparticles by Hyal-1 and burst release of Paclitaxel intracellularly. To summarize, this in vitro study demonstrated the cytotoxicity effect of HA-NP/PTX in A549 and NCI-H460 human NSCLC cell lines. In vivo studies of HA-NP/PTX nanoparticles in orthotopic xenograft mouse models is currently underway.

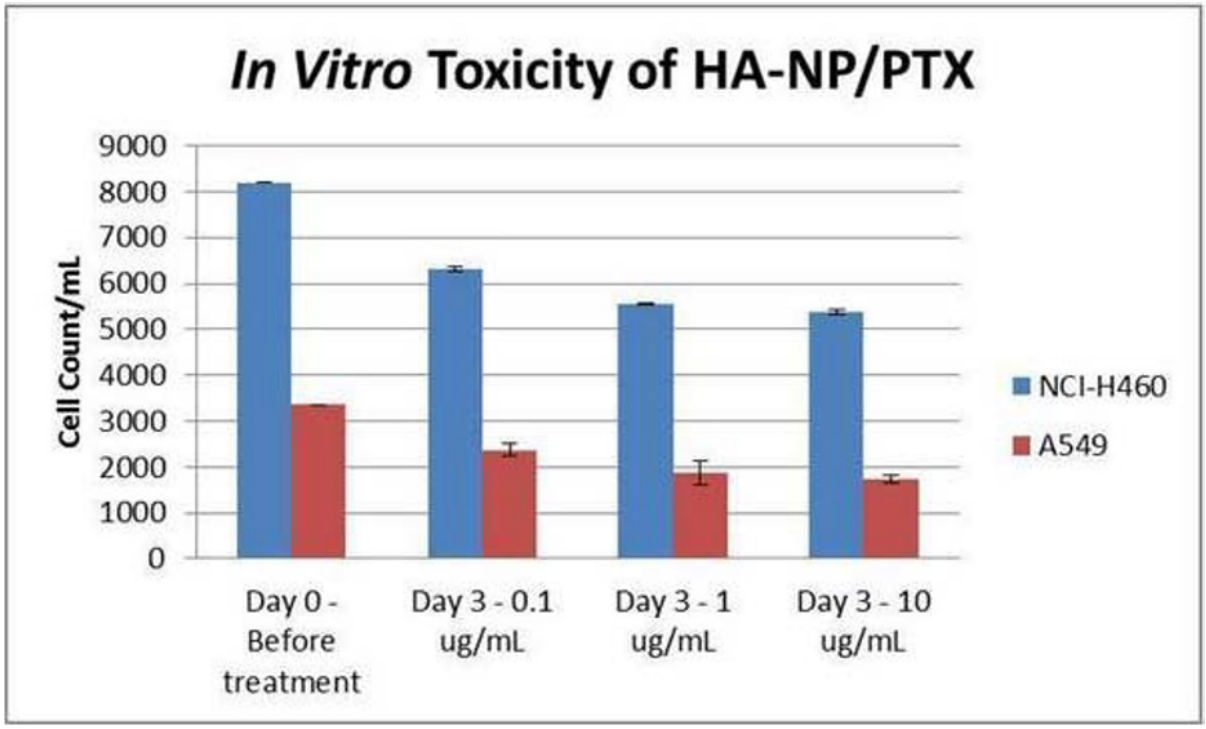

In vitro cytotoxicity of HA-NP/PTX to A549 and NCI-H460 cells. The error bar represents the standard deviation at day 0 (n=1) and day 3 (n = 3).

Disclosure of author financial interest or relationships:
M. Valdivia y Alvarado, None; **K. Wong**, None; **K. Choi**, None; **X. Chen**, None; **S.T. Wong**, None.

Presentation Number **P 498**
Poster Session 4
September 21, 2013 / 14:45-14:45 / Room: Exhibit Hall B

Study of Bombesin receptor family in breast cancer cells

Shu-Huei Wang, *Haiming Ding, Ajay Shrivastava, Michael F. Tweedle, Radiology, OSU, Columbus, OH, USA. Contact e-mail: shu-huei.wang@osumc.edu*

Four subtypes of bombesin receptors are currently identified: GRP-R(gastrin releasing peptide, BB2) receptor, NMB-R(Neuromedin B, BB1) receptor, BB3 and BB4. BB2 has been found expressed in more than 70% of human fresh frozen breast cancer tissues. BB1 is activated by binding NMB, a potent mitogen and growth factor peptide found in normal and neoplastic lung and gastrointestinal epithelial tissue. BB2 expression in breast cancer tissues and cells has been only rarely reported. There is some discrepancy on the expression levels of bombesin receptors among commonly used breast cancer cell lines. One possible reason is that a widely used binding reagent, 125I-[Tyr4]BBN preferentially binds to BB2 but not BB1. Accuracy of molecular imaging is dependent on recognizing a specific target, such as BB1 and/or BB2. Therefore, fully understanding bombesin receptor subtypes on breast cancer cells will be of importance for imaging breast cancer with various bombesin receptor-binding ligands. This study aims to understand the BB1 and BB2 subtypes' expression in commonly used human breast cancer cell lines and the possibility of inducing bombesin receptor expression for cancer imaging purposes. Using 125I-[Tyr4]bombesin, we looked for the presence of BB2 receptors (Kd and Bmax) on five triple-negative breast cancer cell lines, four non-triple-negative breast cancer cell lines, and one prostate cancer cell line. We then used 125I-[D-Tyr6, -Ala11, Phe13, Nle14]bombesin(6-14), a very potent universal ligand that binds to both BB1 and BB2 receptors, competing against non-radioactive D-Tyr6, -Ala11, Phe13, Nle14]bombesin(6-14), and against NMB, in breast cancer cell lines, with PC3 prostate cancer cell line as a known positive BB1 + BB2 control. We found that several commonly used breast cancer cell lines tested positive for both BB1 and BB2, as shown below in the Figure. A Src-family kinase inhibitor, Dasatinib, that has modest activity in triple-negative breast cancer, has been linked to upregulation of bombesin receptors. Dasatanib was tested for this ability in T47-D cells, using both 125I-[D-Tyr6, -Ala11, Phe13, Nle14]bombesin(6-14) and 125I-[Tyr4]bombesin binding. Dasatanib caused more elevation the BB1 + BB2 ligand than of the BB2 ligand, suggesting that Dasatanib upregulates both BB1 and BB2 receptors.

Disclosure of author financial interest or relationships:
S. Wang, None; **H. Ding**, None; **A. Shrivastava**, None; **M.F. Tweedle**, None.

Presentation Number **P 499**
Poster Session 4
September 21, 2013 / 14:45-14:45 / Room: Exhibit Hall B

Combined Imaging and Screening of Prostate Cancer

Jason Warram[1], *Marshall J. Mahoney*[2], *Kurt R. Zinn*[1,2], [1]*Radiology, University of Alabama at Birmingham, Birmingham, AL, USA;* [2]*Biomedical Engineering, University of Alabama at Birmingham, Birmingham, AL, USA. Contact e-mail: mojack@uab.edu*

Prostate cancer is currently the second leading cause of cancer related deaths in men with an estimated 29,720 deaths and an estimated 238,590 new cases in 2013. These statistics highlight the urgency for screening methods that can reliably detect prostate cancer. Current methods for early detection of prostate cancer are inadequate as they rely heavily on the detection of prostate specific antigen (PSA) in the blood, which is prostate-specific but not cancer specific. The PSA test lacks the specificity to differentiate aggressive cancer and using the current cut off of 3.0 ng/ml can result in up to 75% of false positives. Proposed here is a technique that uses the cancer-specific promoter, inhibition of differentiation gene 1 (Id1), to drive expression of human secreted embryonic alkaline phosphatase (SEAP) for blood-based screening and a fluorescent reporter (mCherry) for localized imaging. SEAP is present in the body only during early embryonic stages, will not illicit an immune response due to its human origin, and can be detected in blood with high levels of sensitivity. The imaging reporter, mCherry, offers superior tissue penetration and an emission wavelength that reduces the auto-fluorescence from tissue. It can also be detected by fluorescence imaging in the surgical setting, allowing for improved resection during surgery. Id1 is a helix-loop-helix protein that forms inactive heterodimers with basic helix-loop-helix (bHLH) proteins. While not expressed in normal tissues, Id1 protein expression is common in most cancers and highly expressed in aggressive prostate cancers. The level of Id1 expression also has been found to be proportional to the aggressive nature of the cancer, making it a useful indicator for specific levels of cancer aggression. To this end, a cancer-specific Ad vector (Ad5/3-Id1-SEAP-Id1-mCherry) was produced. Prostate cancer cell lines of varying degrees of aggressive behavior (Du145, CA-HPV-10) and normal prostate cell lines (WPMY-1, CA-HPV-10) were infected with Ad5/3-Id1-SEAP-Id1-mCherry and produced SEAP levels detectable over background within two days. At day four with an MOI of 10, the aggressive cancerous cell line (Du-145) had SEAP concentrations of 7.28±1.60 ng/ml that were significantly ($p<0.001$) elevated over non-aggressive and normal cell line concentrations (1.15±0.29 and 0.75±0.15 ng/ml respectively). This trend was supported by mCherry fluorescent imaging of infected cells performed two days following infection with an average pixel intensity of 5.39 for Du-145 and 2.07 the non-aggressive cell line CA-HPV-10. Also, PSA concentrations in the culture supernatant were analyzed at day 4 with no significant difference between aggressive, non-aggressive, and normal cell lines (140.4±11.49, 129.1±37.6, and 138.5±14.3 pg/ml respectively). This system that combines screening with imaging provides an effective strategy for detection of prostate cancer.

Disclosure of author financial interest or relationships:
J. Warram, None; **M.J. Mahoney**, None; **K.R. Zinn**, None.

Presentation Number **P 500**
Poster Session 4
September 21, 2013 / 14:45-14:45 / Room: Exhibit Hall B

Radiofrequency Heating-Enhanced Gene Therapy of Prostate Cancer Cells: Towards Interventional Molecular MRI-Monitored RFH-Enhanced Gene Therapy of Prostate Cancers

Xia Wu[1,2], *Feng Zhang*[1], *Xiaoming Yang*[1,2], [1]*Image-guided Bio-Molecular Intervention Research and Section of Vascular and Interventional Radiology, University of Washington School of Medicine, Seattle, WA, USA;* [2]*Radiology department, Sir Run Run Shaw Hospital, Hangzhou, China. Contact e-mail: wuxa_0@126.com*

Purpose: To evaluate the effectiveness of radiofrequency heat (RFH)-enhanced therapeutic effect of herpes simplex virus thymidine kinase (HSV-tk) genes on prostate cancers. Materials and Methods: This study was divided into two phases: the first phase for investigation of the RFH effect on gene expression and the 2ndphase for evaluation of RFH-enhanced gene therapy on prostate cancer cells (PC-3). Cells were cultured in four-chamber slides and heated by using an MR imaging-heating-guidewire (MRIHG)(Figure 1). For the first phase, different cell groups received various treatments of: (1)RFH-enhanced HSV-tk/plasmid gene transfection at approximately 42 °C for 20mins; (2)HSV-tk/plasmid only; (3)RFH only; and (4)phosphate buffer solution (PBS) only as a control. HSV/tk gene expression of cells in each group was quantified by qRT-PCR. For the second phase, cell groups received different treatments with:(1)RFH-enhanced HSV-tk/plasmid gene transfection at approximately 42 °C for 20mins, followed by ganciclovir(GCV) treatment for 72 hours; (2)HSV-tk/plasmid plus GCV with no RFH; (3) GCV only; (4)RFH only; and (v) PBS only. Each of these experiments was repeated six times. MTS assay was used to evaluate cells proliferation, with relative proliferation of cells = Aheated/ Anon-heated×100% (Aheated = absorbance of heated cells, Anon-heated = absorbance of non-heated cells). Results: Compared with HSV-tk/plasmid group, RFH significantly increased the HSV-tk gene expression of cells, as manifested by gene copy numbers (1.34×109 ± 2.22×108vs1.03×1010± 1.90×109 copies, $p<0.05$).Compared with HSV-tk/GCV group and RFH only group, RFH significantly enhanced the effects of HSV/tk gene-mediated GCV inhibition on PC-3, as manifested by inhibited relative cell proliferation (81.18±7.64% vs 39.89±4.53%, and 95.06±2.95%vs39.89±4.53%, $p<0.05$). Conclusion: This study demonstrates the feasibility of using RFH to enhance HSV-tk/plasmid gene expression in PC-3 cells and the therapeutic effect of HSV-tk/GCV on these cells, which may open new avenues of interventional molecular MRI-monitored RFH-enhanced gene therapy of prostate cancers.

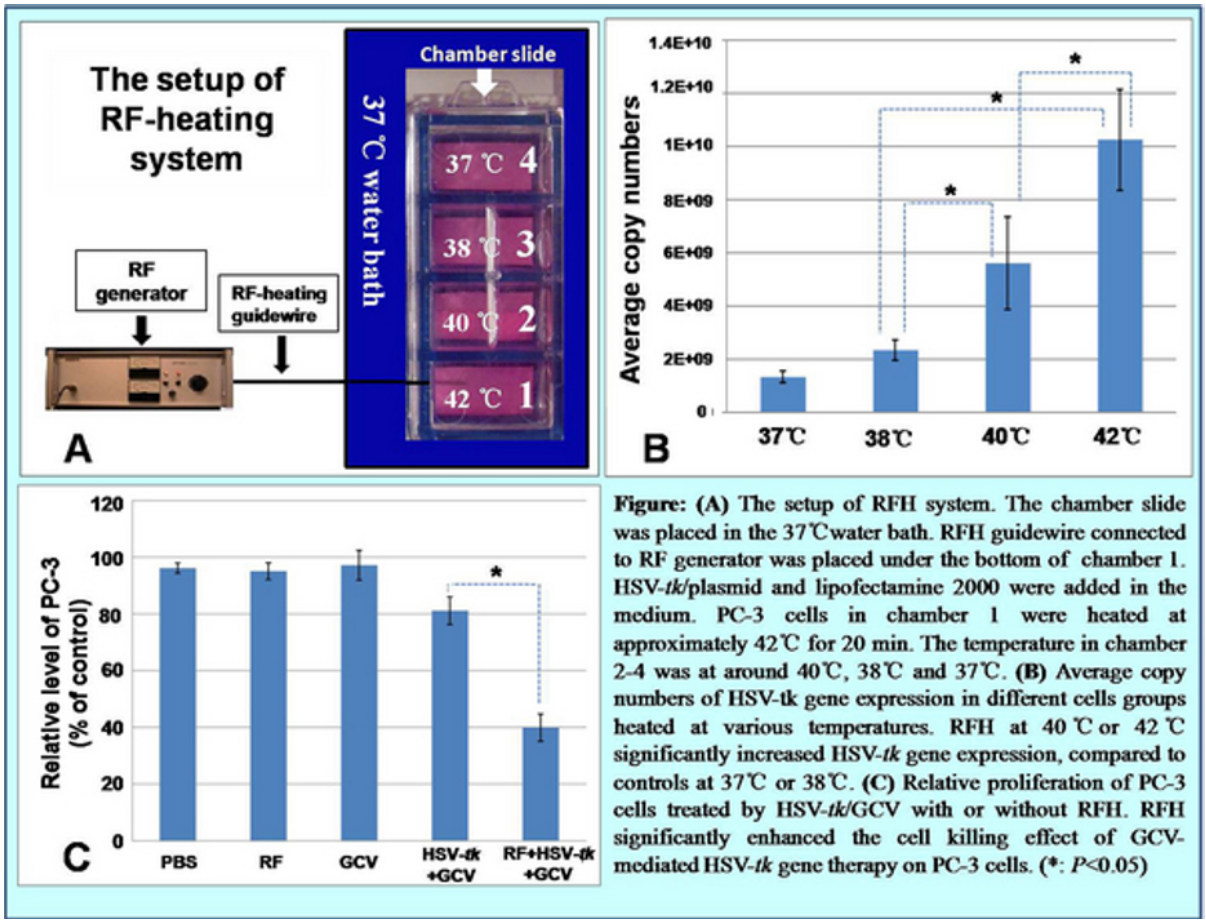

Figure: **(A)** The setup of RFH system. The chamber slide was placed in the 37℃water bath. RFH guidewire connected to RF generator was placed under the bottom of chamber 1. HSV-*tk*/plasmid and lipofectamine 2000 were added in the medium. PC-3 cells in chamber 1 were heated at approximately 42℃ for 20 min. The temperature in chamber 2-4 was at around 40℃, 38℃ and 37℃. **(B)** Average copy numbers of HSV-tk gene expression in different cells groups heated at various temperatures. RFH at 40 ℃ or 42 ℃ significantly increased HSV-*tk* gene expression, compared to controls at 37℃ or 38℃. **(C)** Relative proliferation of PC-3 cells treated by HSV-*tk*/GCV with or without RFH. RFH significantly enhanced the cell killing effect of GCV-mediated HSV-*tk* gene therapy on PC-3 cells. (*: $P<0.05$)

Disclosure of author financial interest or relationships:
X. Wu, None; **F. Zhang**, None; **X. Yang**, None.

Presentation Number **P 501**
Poster Session 4
September 21, 2013 / 14:45-14:45 / Room: Exhibit Hall B

Regulatory role of COX-2 in mechanosensing and propagation of cell traction force

A Rum Yoon[1], *Ioannis Stasinopoulos*[2], *Zaver M. Bhujwalla*[2], *Steven An*[1,2], [1]*Environmental Health Science, johns hopkin school of public health, Baltimore, MD, MD, USA;* [2]*Radiology and Radiological Science, johns hopkin school of public health, Baltimore, MD, MD, USA. Contact e-mail: ayoon@jhsph.edu*

The cytoplasmic enzyme cyclooxygenase (COX)-2 and its secondary lipid byproducts are critical determinants of cancer cell invasion and metastasis. Based on compelling evidence for the positive correlation between cancer invasion and cell traction force, here we interrogated this link in highly metastatic MDA-MB-231 breast cancer cells and the role for COX-2. Using Fourier transform traction microscopy (Fig. 1), we imaged the spatiotemporal distribution of contractile stress arising at the interface between each adherent cell and its substrate, and spanning a wide range of substrate stiffness. Poorly differentiated MDA-MB-231 cells showed progressive increases in the secretion of COX-2-generated PGE2, the expression of mechanosensitive integrin beta1, the dispersion of cell spreading, and the exertion of cell traction force with increasing substrate rigidity. These cellular responses to mechanical loading were ablated in MDA-MB-231 clone cells stably expressing COX-2 shRNA. COX-2-silenced cells were smaller in size (1769.36+1.07 parental vs 1206.67+1.06 COX-2 silenced, Geometric Mean+SE, n=63-70, $P<0.0001$) and exercised a marked reduction in cell traction force (3.00+1.14 pNm parental vs 1.20+1.15 pNm COX-2-silenced, $P<0.0001$). Both COX-2 high and silenced cells expressed EP2 and EP4 receptors, but not EP1 and EP3, and exogenous addition of PGE2 increased cell spreading area and traction force in both cells. In COX-2-silenced cells, PGE2 increased cell spreading from 1033.13+1.10 to 1421.21+1.07 ($P<0.01$) and traction force from 1.37+1.20 pNm to 3.23+1.19 pNm ($P<0.005$). These findings, taken together, establish the mechanistic role for COX-2 in the propagation of physical force and suggest as well a feed-forward mechanism involving EP-mediated signal transduction. Consistent with these observations, COX-2-silenced cells expressed a 4.6-fold lower transcript level of RhoJ, a member of the family of Rho GTPases, and displayed a slower remodeling dynamics of the underlying cytoskeletal network. To our knowledge this is the first report linking the expression of COX-2 with increased cell traction force and CSK remodeling in a highly metastatic human breast cancer

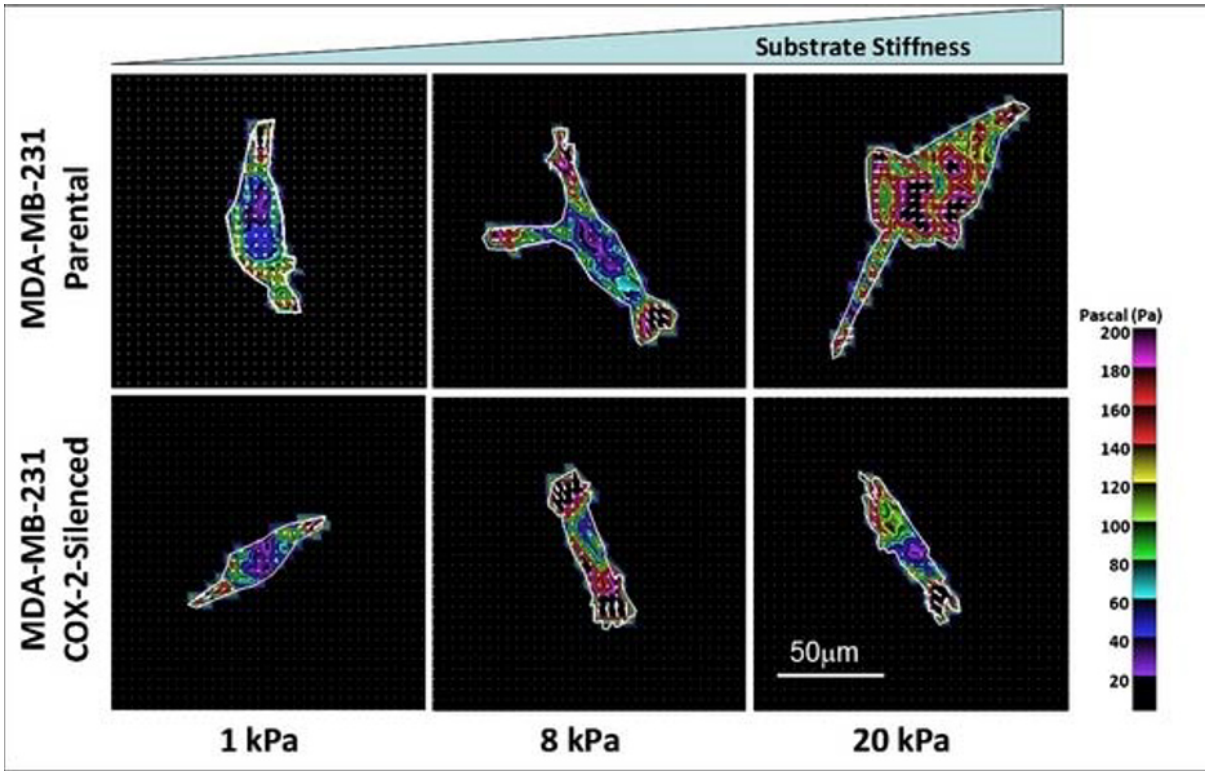

Disclosure of author financial interest or relationships:
A. Yoon, None; **I. Stasinopoulos**, None; **Z.M. Bhujwalla**, None; **S. An**, None.

Presentation Number **P 502**
Poster Session 4
September 21, 2013 / 14:45-14:45 / Room: Exhibit Hall B

Multivariate radionuclide imaging for the diagnosis of myocarditis: evaluation in a rat model

Ivayla Apostolova[1], *Nicole Gehrke*[2], *Ralph Buchert*[1], *Andreas Briel*[2], *Winfried Brenner*[1], [1]*Nuclear Medicine, University Medicine Charite Berlin, Berlin, Germany;* [2]*nanoPET Pharma GmbH, Berlin, Germany. Contact e-mail: ivaapost@hotmail.com*

Objective: Reliable diagnosis of myocarditis still requires invasive diagnostic procedures such as endomyocardial biopsy. Therefore, novel non-invasive approaches for accurate diagnosis of myocarditis are of great interest. The aim of the present study was to test a multivariate radionuclide imaging approach based on commercially available tracers to quantitatively characterize the pathological processes in an experimental autoimmune myocarditis model in the rat in which the histopathological alterations resemble those in humans. In addition, a novel 18F labelled nanoparticulate inflammation PET tracer, NPG1010, was evaluated in this model. Methods: Autoimmune myocarditis was induced in 11 male Lewis rats by intraplantar immunisation with porcine cardiac myosine emulsified in complete Freud's adjuvant. ECG-triggered SPECT with Tc99m-MIBI, FDG-PET and PET with NPG1010 were performed between days 21 and 24 after immunisation Then the rats were sacrificed and hearts were cryo-conservated for histopathological analysis. The severity of myocarditis was characterized by scores for density of inflammatory infiltration (score 0-3), degree of inflammatory destruction (0-3), occurrence of pericarditis (0-2) and degree of necrosis (0-3). A total pathology score was obtained by summing the individual scores (range 0-11). The following parameters were derived from the imaging data: ejection fraction (EF) from the gated MIBI-SPECT, the total number of segments with reduced tracer uptake from polar maps of static MIBI-SPECT and FDG-PET (threshold 60% of maximum uptake), and a score for the total uptake of NPG1010 (0-3). Histological and imaging based markers were tested for correlation by the non-parametric Spearman test. Results: Density and degree of inflammation as well as pericarditis were significantly correlated with the total uptake of NPG1010 (correlation coefficients rho = 0.74, 0.71 and 0.73, respectively, all p= 0.01). Inflammatory destruction and the extent of necrosis were correlated with the EF (rho = -0.65 and -0.86, p= 0.04 and 0.001). The spatial extent of reduced MIBI uptake correlated with pericarditis (rho = 0.68, p= 0.02) and the total histological score (rho = 0.65, p= 0.03). The FDG PET score did not show any significant correlation with histology (Fig. 1). Conclusion:PET using the novel inflammation marker NPG1010 in combination with gated perfusion SPECT is promising for the detection and detailed quantitative characterization of myocarditis. Whereas the impaired heart function detected by SPECT can have various reasons apart from myocarditis, PET with NPG1010 detects the inflammatory infiltrates and therefore has the potential to unambiguously diagnose myocarditis. PET with the glucose analogue FDG appears not to provide additional information.

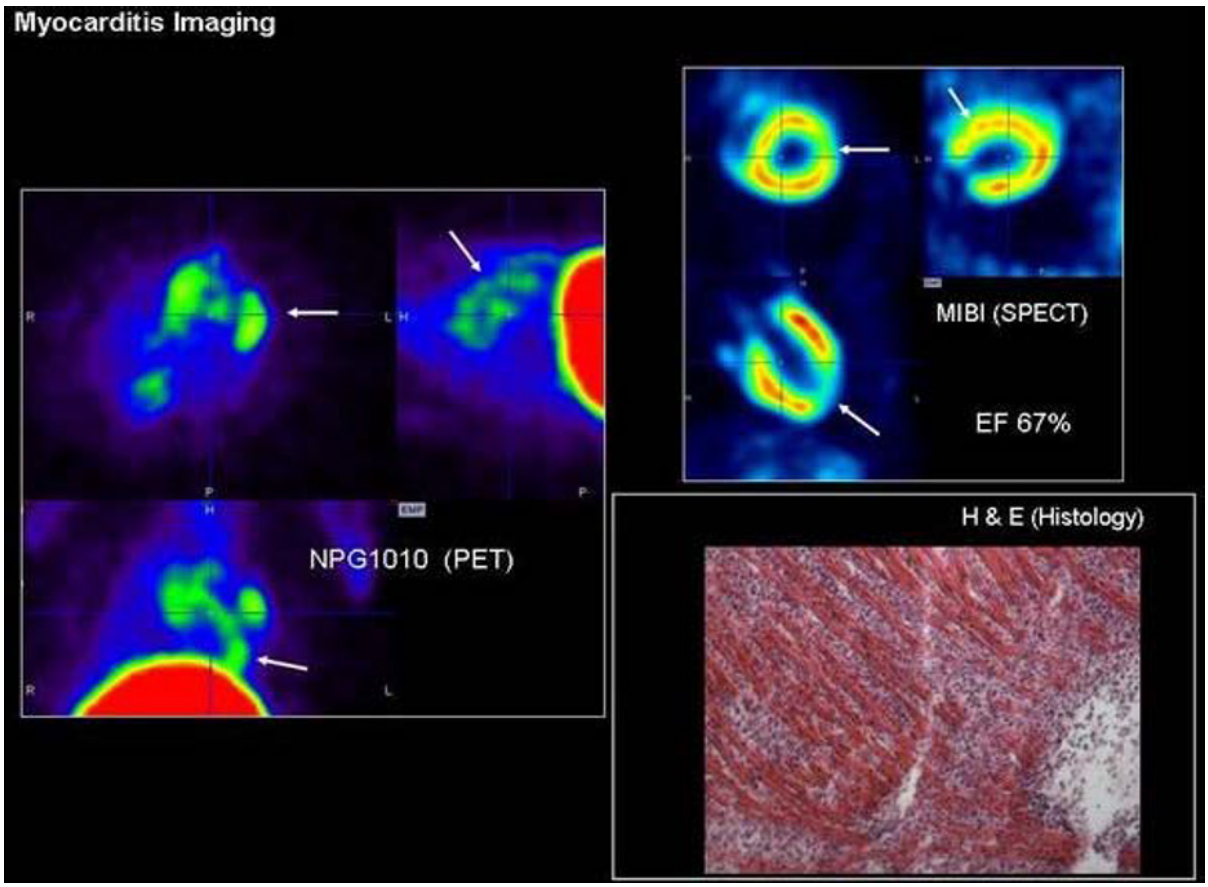

Disclosure of author financial interest or relationships:
I. Apostolova, None; **N. Gehrke**, nanoPET Pharma GmbH, Employment; **R. Buchert**, None; **A. Briel**, nanoPET Pharma GmbH, Employment; **W. Brenner**, nanoPET, Grant/research support .

Presentation Number **P 503**
Poster Session 4
September 21, 2013 / 14:45-14:45 / Room: Exhibit Hall B

Phenotyping K-RasV14I knock-in mouse by Cardiac-MRI: a pilot study

Lorena Cussó[1,2], *Isabel Hernandez-Porras*[3], *Paula Montesinos*[1,2], *Carmen Guerra*[3], *Mariano Barbacid*[3], *Manuel Desco*[2,1], [1]*Dept. Bioingeniería e Ingeniería Aeroespacial, Universidad Carlos III de Madrid, Leganes, Spain;* [2]*Instituto de Investigación Sanitaria Gregorio Marañón, Madrid, Spain;* [3]*Oncología Experimental. Centro Nacional de Investigaciones Oncológicas (CNIO), Madrid, Spain. Contact e-mail: lcusso@mce.hggm.es*

Noonan Syndrome (NS) is an autosomal dominant disorder with an incidence of 1:1,000-2,500 live births. This relatively common and genetically heterogeneous developmental disorder is clinically diverse but characterized by postnatally reduced growth, distinctive facial dysmorphism, cardiac defects and variable cognitive deficits. K-Ras mutations are found in less than 3% of NS patients but the mutations are correlated with the appearance of a more severe phenotype. These mutations result in milder activation of the K-Ras protein and are different from the somatic mutations found in human tumors. The K-RasV14I knock-in mice display some of the features observed in patients with NS, including small size, craniofacial abnormalities and cardiovascular alterations and results in milder activation of the K-Ras protein as in patients. Histological analyses have showed that 4-months-old K-RasV14I mice displayed substantially larger hearts chambers than wild type littermates and also enlarged aortic valves. Thereby, the main objective of this study is evaluating in vivo the cardiac defects induced by K-RasV14I mutation. Methods: 12 four-month-old mice were scanned in a 7T Bruker MRI (5 wild type +/+; 4 heterozygote +/V14I; 3 homozygote V14I/V14I). IntraGateFLASH sequence was performed from the aorta to the heart apex (slice thickness 0.75 mm; slice number 14-17; TE=2.691 ms; TR=8 ms; FOV=6 x 4.13 cm; matrix size=465 x 256). Left-ventricular (LV) functionality was evaluated on images in diastole and systole (Segment v1.9, R2354 software). LV epicardial and endocardial borders were manually delineated on the short-axis at each slide in order to measure the end-diastolic volume (EDV), end-systolic volume (ESV), ejection fraction (EF), left ventricle mass (LVM) and cardiac output (CO). In one slide at 3 mm from the apex we measured the wall thickness in diastole (WTd) and systole (WTs) as well as systolic wall thickening (WTn) and fractional shortening (FS). Results and discussion: Table 1 gives a summary of group averages of LV parameters. Homozygote group showed an increase of the LV wall thickness (68.48 ± 9.18) while the heterozygote group (48.03 ± 16.52) was similar to the control group (46.68 ± 7.46). Besides, the homozygote group exhibited higher EDV, LVM and CO versus control and heterozygote groups ($p < 0.05$), although these parameters also seemed elevated in the heterozygote group versus the control group as well (p N.S.). Neither heterozygotes nor homozygotes showed changes in the EF. In conclusion, MRI allows evaluating in vivo left ventricle changes induced by the expression of the mutated form K-RasV14I gen; these changes have a strong expression in homozygous animals affecting the LV function. However, heterozygote mutation show slighter effects over some LV function parameters (EDV and LVM) but heterozygotes group remains as the control in general. This methodology can be used in future work to longitudinally evaluate therapies to revert the K-RasV14I mutations effects.

Group	Control (+/+)	Heterozygote (+/V14I)	Homozygote (V14I / V14I)
Heart rate (bpm)	411.20 ± 39.11	394 ± 60.42	466.67 ± 20.43
EDV (µl)	44.4 ± 13.89	55.25 ± 15.78	74 ± 10.39*
ESV (µl)	13.4 ± 5.37	17.75 ± 9.64	20.33 ± 3.51
CO (ml min^{-1})	12.5 ± 2.91	14.9 ± 4.66	24.97 ± 2.65*
EF (%)	70.2 ± 5.17	70.2 ± 5.17	73 ± 2.65
LVM (mg)	68.4 ± 19.06	84.75 ± 23.10	112 ± 10.82
WTd (mm)	0.85 ± 0.08	0.86 ± 0.37	0.90 ± 0.13
WTs (mm)	1.32 ± 0.13	1.35 ± 0.22	1.59 ± 0.20*
WTn (%)	46.68 ± 7.46	48.03 ± 16.52	68.48 ± 9.18*
FS (%)	69.60 ± 5.18	66.00 ± 6.38	74.00 ± 4.36

*significant vs. control (p<.05)

Table 1. Group averages of LV parameters. Data are represented as mean ± SD.

Disclosure of author financial interest or relationships:

L. Cussó, None; **I. Hernandez-Porras**, None; **P. Montesinos**, None; **C. Guerra**, None; **M. Barbacid**, None; **M. Desco**, None.

Presentation Number **P 504**
Poster Session 4
September 21, 2013 / 14:45-14:45 / Room: Exhibit Hall B

Optical imaging in the development of targeted drug delivery for cardiac regeneration

Siva Sai Krishna Dasa[1], *Yaqin Xu*[2], *Marc Seaman*[2], *Brent A. French*[2], *Kimberly Kelly*[2,1], [1]*Cardiovascular Research Center, University of Virginia, Charlottesville, VA, USA;* [2]*Department of Biomedical Engineering, University of Virginia, Charlottesville, VA, USA. Contact e-mail: sd7nf@virginia.edu*

Introduction: Ischemic heart disease remains a major cause of morbidity in the world, and there are limited drugs available for the treatment of heart failure secondary to myocardial infarction (MI). None of the current drugs can reclaim the cardiac muscle lost to heart attack, making cardiac regeneration an important and unmet clinical need. Given that most strategies for cardiac regeneration will depend on targeted delivery to the infarct/border zone, we hypothesized that targeting ligands could be identified by biopanning a phage display library in vivo in a mouse model of MI. We were able to combine phage display screening with optical imaging of phage to enable rapid and efficient screening of targeted, pharmacologically relevant phage clones. In addition, we were able to streamline the manufacturing process and validation of targeted therapies using our optical imaging techniques. Methods: The in vivo phage display library screen was designed to identify peptides specific for the infarct/border zone in the heart 4 days post-MI. Three phases of in vivo biopanning were carried out and at the end of the third phase, FMT imaging was carried out to compare the specificity of selected clones against a negative phage clone. After the third round, 50 phage clones each were selected from the infarct and border zone and their DNAs were amplified and sequenced. Peptide sequences were deduced from DNA sequences and phage clones were grouped (4 clones/group) based on their phylogeny (J. Hein) and sequence similarity. Each group was then labeled with a near IR fluorescent dye (VT 680) and mixed with negative control phage clone (Panc-27) labeled with a second dye (VT 750). The specificity was determined by measuring heart: liver VT 680/ heart: liver VT 750 at times 0 and 4h post-injection on day 4 post-MI. Results: With FMT, we were able to separate the specific groups from non-specific groups. Of the 23 groups that were screened, we were able to eliminate 9 groups that had specificity value of 10 or less at t=4 h. Similarly, we determined the specificity of individual clones from groups with high specificty. Labeling the phage clones with VT 680 benefited from the fact that folowing the ex vivo imgaging of the hearts, fluorescence microscopy could be applied to the same hearts to determine the distribution of phage clones in the infarcted hearts along with the associated cell types. Conclusions: FMT imaging enabled our lab to carry out the phage screen at a faster rate while at the same time providing valuable information about the distribution of these clones in the infarct area in relation to the associated cell types. The combination of an organ-level biodistribution screen (FMT) with a tissue-level screen of phage-associated cell types provided for a power imaging tool that expedited our in vivo phage screen in post-MI mice and significantly lowered the number of mice needed to determine the specificity and distribution of phage clones.

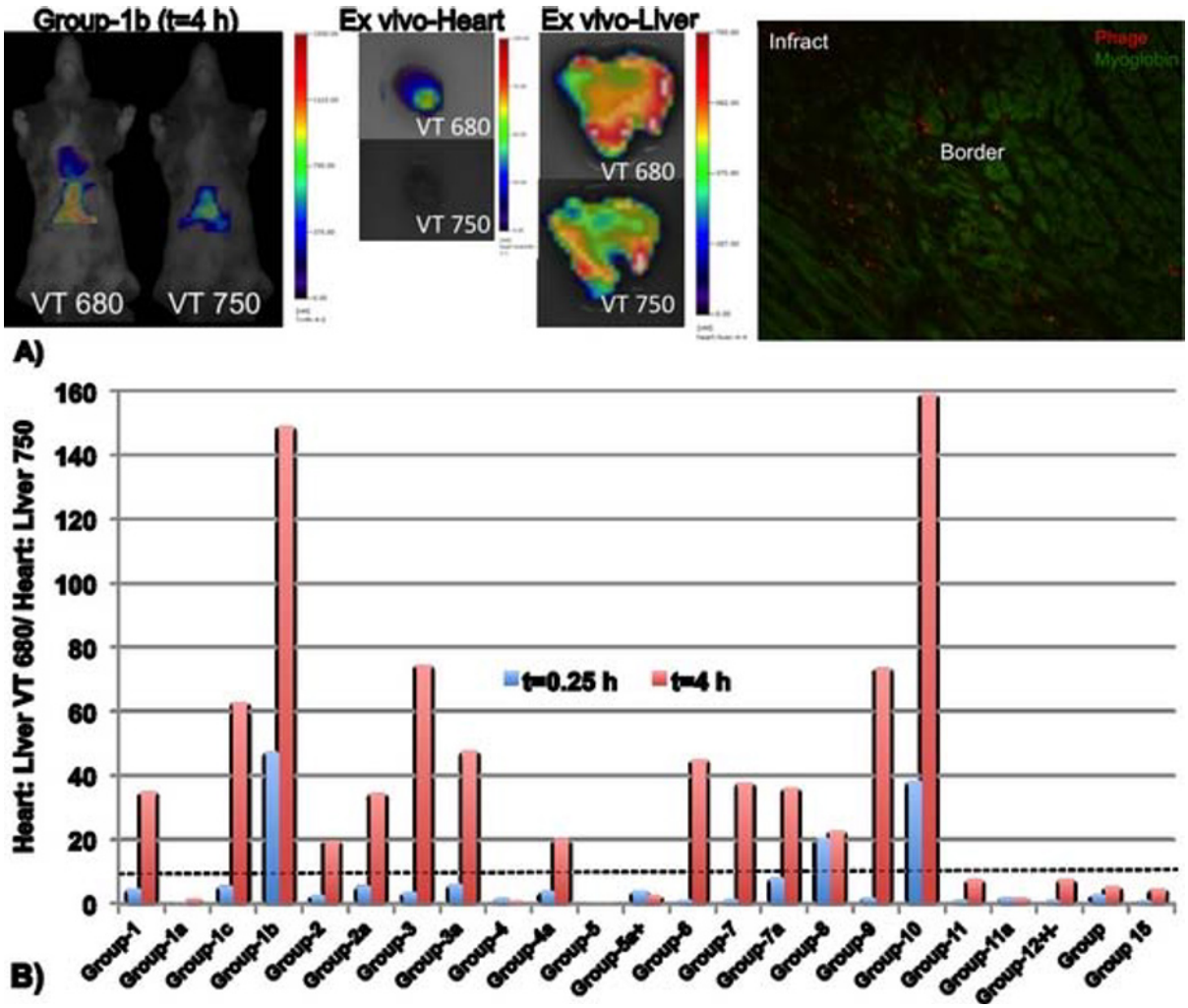

Figure 1. A) FMT image of mouse injected with group 1b phage along with control phage at t= 4 h. FMT image of mouse injected at t=4 h with phage group 1b (4 clones/group) labeled with VT 680 and a non-specific phage clone (Panc-27) labeled with VT 750. Ex vivo imaging of the heart and liver followed the in vivo imaging. The hearts were then sectioned and fluorescence microscopy was performed to determine the distribution of phage clones within the infarcted heart. B) Imaging was carried out at 0 and 4 h post injection and the specificity determined by calculating the heart to liver ratio of VT 680/ heart to liver ratio of VT750. Phage clones from groups with specificity greater than 10 (dotted line) were then screened individually to identify 44 individual clones with specificity for infarct/border region.

Disclosure of author financial interest or relationships:
S. Dasa, None; **Y. Xu**, None; **M. Seaman**, None; **B.A. French**, AstraZeneca, Grant/research support; **K. Kelly**, Astra Zeneca, Grant/research support .

Presentation Number **P 505**
Poster Session 4
September 21, 2013 / 14:45-14:45 / Room: Exhibit Hall B

The Use of High Resolution Doppler Ultrasound to Measure Hind Limb Perfusion in an Ischemia Induced Mouse Model of Peripheral Artery Disease

Brittany A. Holly[1], *Nick Duesbery*[2], *Elissa Boguslawski*[2], *Anderson Peck*[1], *Anthony Chang*[1], [1]*Small Animal Imaging Facility, Van Andel Research Institute, Grand Rapids, MI, USA;* [2]*Lab of Cancer and Developmental Cell Biology, Van Andel Research Institute, Grand Rapids, MI, USA. Contact e-mail: Brittany.Holly@vai.org*

Purpose: Rapidly growing tumors require the formation of new blood vessels to support further growth. This process of neovascularization relies on angioproliferative factors released by the tumor cells. Studying the underlying biochemical pathways responsible for neovascularization in the absence of a tumor is of great value. We have adapted a mouse model of Peripheral Arterial Disease (PAD), through surgically induced ischemia of the hind limb by femoral artery and vein ligation. High Resolution micro Ultrasound provides a non-invasive method for confirming successful ischemic injury and evaluating neovascularization through quantitative perfusion data and qualitative images. These methods aide in development of angioproliferative therapies that can be applied in cases of chronic ischemia, such as PAD in diabetic patients, or in cases of acute ischemic injury. Anti-angiogenic therapies can be applied in cases of diabetic retinopathy, retinopathy of prematurity, and tumorigenesis. Methods: Athymic Foxn1nu-/- mice underwent induced hind limb ischemia via ligation of the right femoral artery. A method was developed using Power Doppler micro ultrasound (Visual Sonics Vevo 770, Canada) to measure hind limb blood flow regularly over 5 weeks, in both ischemic and non-ischemic legs. The Visual Sonics software calculated tissue reperfusion data, reported as percent vascularity. The ratio of percent vascularity was calculated to demonstrate relative flow of experimental leg compared to control leg, and compared to baseline values at each time point. Percent Vascularity data and immunohistochemistry was used to study the biochemical pathways activated in the micro-vessel regeneration. 3-D Doppler images were rendered with Osirix software for qualitative analysis. The effects of an angiogenic inhibitor were monitored with ultrasound and used in the development of treatments to enhance or inhibit formation of blood vessels. Result: As monitored by ultrasound, ligation of the femoral artery caused a rapid and profound decrease (up to 80 %) in hindlimb perfusion, accompanied by muscle atrophy. Perfusion was gradually recovered over the course of 3-4 days, returning to or exceeding baseline values at day 7. Qualitative 3-D images of hindlimb vascularity reveal a diffuse pattern of reperfusion.(see figure) Hematoxylin and eosin staining with immunohistochemistry supports these results with marked increase in infiltrating neutrophils at day 2, focal areas of muscle regeneration at day 4, and presence of fusing myofibers at day 7. The control leg did not exhibit signs of ischemic injury, muscle atrophy, or neutrophil infiltration, and maintained baseline values of perfusion throughout the 5 week study. Conclusion: The use of micro ultrasound in this study proves to be a valuable tool in understanding the hemodynamic characteristics of this disease model. The percent vascularization obtained from micro ultrasound imaging is correlated with the inflammatory response and repair of the injury site. micro Ultrasound is a valuable tool for evaluating ischemic injury and monitoring it as it reacts and adapts through neovascularization.

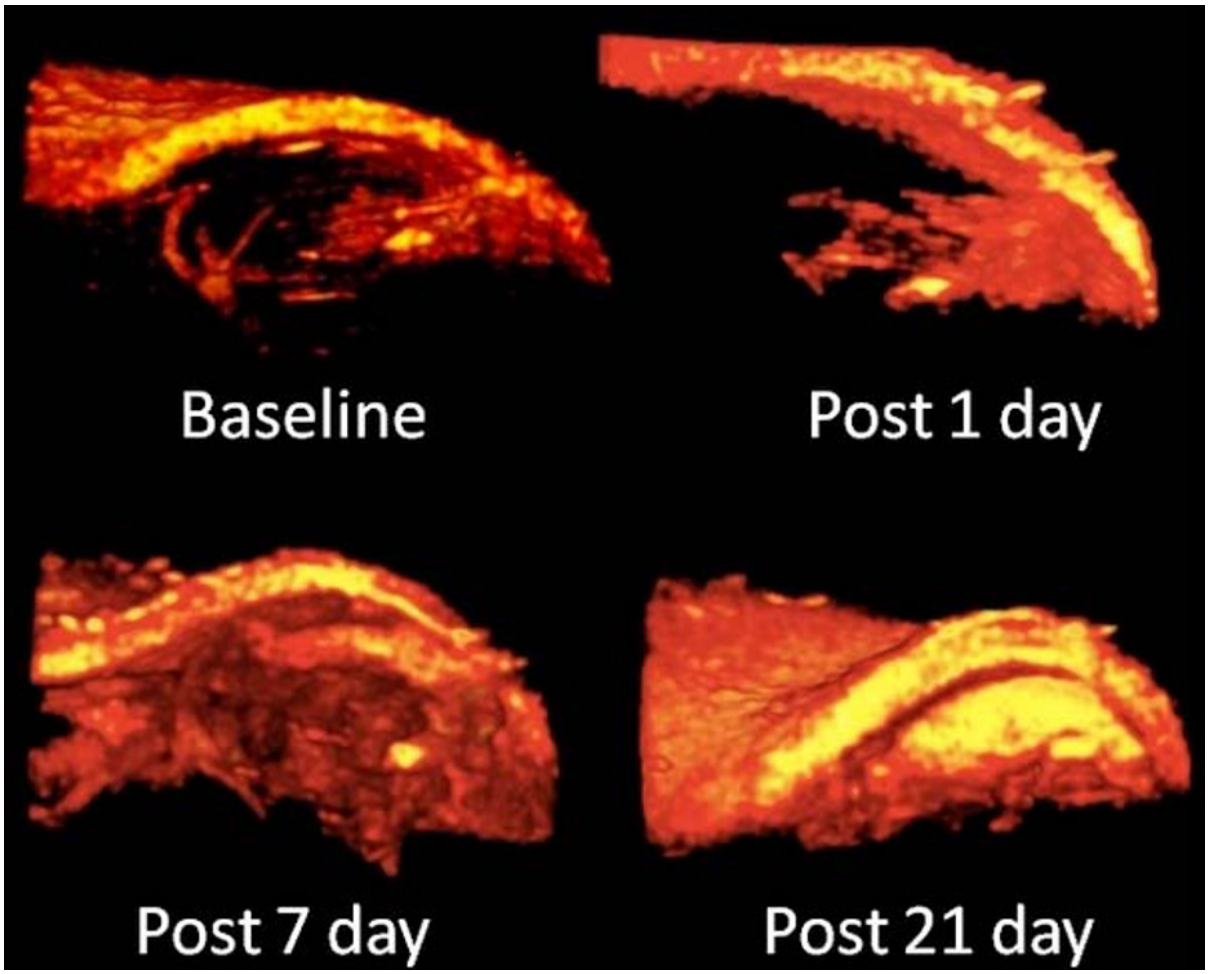

Doppler Ultrasound imaging of the femoral artery in the hindlimb at baseline, and subsequent perfusion following femoral artery ligation over 3 weeks time.

Disclosure of author financial interest or relationships:
B.A. Holly, None; **N. Duesbery**, None; **E. Boguslawski**, None; **A. Peck**, None; **A. Chang**, None.

Presentation Number **P 506**
Poster Session 4
September 21, 2013 / 14:45-14:45 / Room: Exhibit Hall B

Targeting integrins vs. targeting VEGF receptors with probes to image angiogenesis in limb ischemia

*Lynne Johnson[1], **Yared Tekabe**[1], Maria Kollaros[1], Geping Zhang[1], Qing Li[1], Joseph M. Backer[2], Roland Haubner[3], [1]Cardiology, Columbia University, New York, NY, USA; [2]SibTech Inc, Brookfield, CT, USA; [3]Radiochemistry, Innsbruck Medical University, Innsbruck, Austria. Contact e-mail: yt2166@columbia.edu*

Purpose: While avb3 integrin expression on endothelial cells of sprouting capillaries and monocytes in hypoxic tissue has been utilized as target for imaging angiogenesis in hind limb ischemia, the primary cytokines that stimulate angiogenic response are the vascular endothelial growth factors particularly VEGF-A and PGF that bind VEGF receptors 1 and 2. A VEGF modified protein binding VEGFR-1 and VEGFR-2 has been developed for radiolabeling and in-vivo imaging. We proposed to compare the signal from targeting VEGF receptors compared to targeting αvb3 to quantify the angiogenic response to hind limb ischemia. Methods: Sixteen WT (C57/BL6) mice underwent L femoral artery ligation and 5 days later 8 were injected with 0.23 ± 0.019 mCi 99mTc HYNIC-RGDs and 8 injected with 0.204 ± 0.01 mCi 99mTc scVEGF-PEG-DOTA and underwent SPECT/CT imaging of the lower limbs. From the reconstructed SPECT/CT fused images, regions are drawn on serial 5 voxel thick transaxial slices around the circumference of each hind limb from just below the hip to lower leg (approximately 8-10 sections/limb) and uptake quantified as mCi applying a calibration factor and activity from all slices are summed to obtain total for each leg which is then divided by the decay corrected ID. The mice were euthanized and the anterior tibialis muscles dissected and counted in the well counter and tissue was stained for lectin and for αv and b3 in the RGD experiments and for VEGFR1 and VEGFR2 in the scVEGF experiments. An additional 5 mice were injected and imaged with a control peptide and scans and tissue processed in a similar manner. Results: Shown in Table below. Conclusions: scVEGF PEG DOTA showed higher uptake in ischemic limbs compared to HYNIC RGDs for comparable degrees of angiogenesis based on quantitative lectin staining and each correlated with respective histological targets (VEGFR 1 and 2 for scVEGF-PEG-DOTA) and αvb3 for HYNIC RGDs. The difference in uptake in the control peptide between the ischemic and non-ischemic limbs suggests component of retention of these peptides may represent non-specific entrapment in ischemic tissue

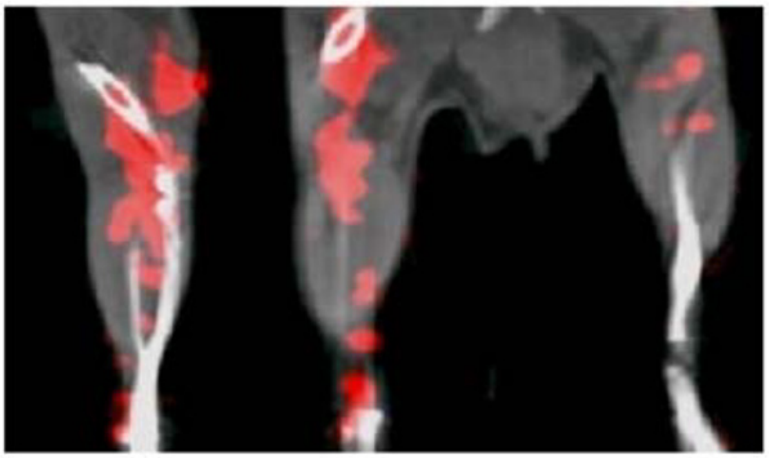

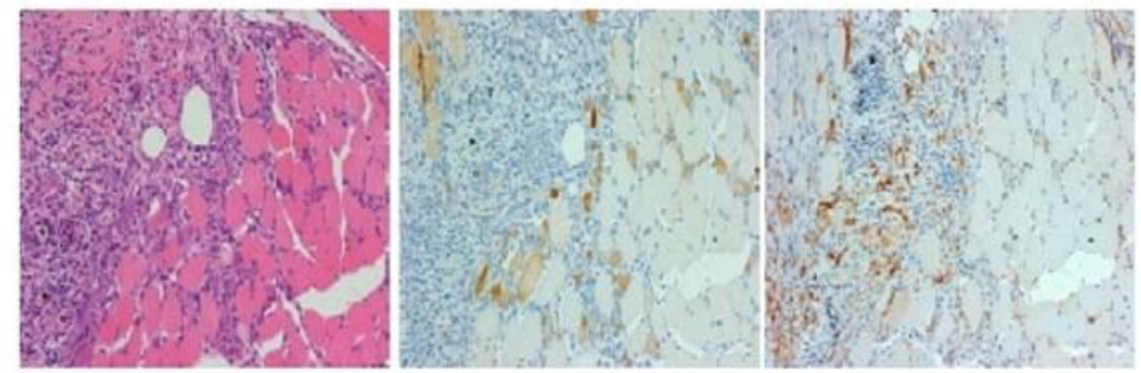

^{99m}Tc VEGF-PEG-DOTA SPECT on top with L leg sagittal on left and coronal on the right showing uptake of probe (red) in ischemic limb. Stained sections of L leg on bottom with H&E on left VEGFR1 in middle and VEGR2 on right (brown chromogen) (20x) are shown below.

Results

		L leg	R leg	Ratio L/R
1	HYNIC RGDa %ID x 10-3	2.34 ± 0.51	1.50 ± 0.24	1.52 ± 0.40
2	scVEGF PEG-DOTA %ID x 10-3	3.37 ± 0.71	1.72 ± 0.51	2.10 ± 0.38
3	control peptides %ID x 10-3	1.32 ± 0.69	0.69 ± 0.14	
	P 1 vs. 2	001	0.36	0.03
	P 1 vs. 3	003	<0.001	
	P 2 vs. 3	<0.001	0.002	

Disclosure of author financial interest or relationships:
L. Johnson, None; **Y. Tekabe**, None; **M. Kollaros**, None; **G. Zhang**, None; **Q. Li**, None; **J.M. Backer**, None; **R. Haubner**, None.

Presentation Number **P 507**
Poster Session 4
September 21, 2013 / 14:45-14:45 / Room: Exhibit Hall B

Evaluation of the Novel Myocardial Imaging Agent [^{18}F]FPTP: Comparison to [^{13}N]NH_3 in small animal models

Dong-Yeon Kim[1], *Hyeon Sik Kim*[1], *Jinhai Zheng*[1], *Hee-Jung Kim*[2], *Ayoung Pyo*[1], *Hee-Seung Bom*[1], *Jung-Joon Min*[1], [1]*Nuclear Medicine, Chonnam National University Hwasun Hospital, Hwasun, Republic of Korea;* [2]*Radiation Instrumentation Research Division, Korea Atomic Energy Research Institute, Jeongeup, Republic of Korea. Contact e-mail: blueburr@gmail.com*

Objectives: Nuclear medicine technologies by positron-emission tomography (PET) have received much attention in the myocardial perfusion imaging (MPI) studies, although single photon emission computed tomography (SPECT) using [^{99m}Tc]-sestamibi, [^{99m}Tc]-tetrofosmin, or ^{201}thallium has been validated extensively. PET has several technical advantages over SPECT, such as higher spatial resolution and quantitative measurement of myocardial tracer uptake. However, the short half-life of currently used PET cardiac tracers, including [^{13}N]NH_3, ^{82}rubidium, and [^{15}O]H_2O, limit the widespread clinical use of PET due to the need for a nearby cyclotron or generator. Because of their longer half-life, ^{18}F-labeled tracers would avoid this limitation and facilitate clinical protocols. To address this need, we developed a ^{18}F-labeled phosphonium cation, 5-([^{18}F]fluoropentyl)triphenylphosphonium salt ([^{18}F]FPTP) and compared microPET images of [^{18}F]FPTP with [^{13}N]NH_3 in myocardial infarction (MI) rat models.

Methods: We measured [^{18}F]FPTP and [^{13}N]NH_3 of the contrast ratio about each region (myocardium/blood, myocardium/liver and myocardium/lung) in normal rats. To generate MI models, eight-week old male Sprague-Dawley rats (250-260 g) underwent left coronary artery (LCA) ligation. [^{18}F]FPTP and [^{13}N]NH_3 of 37MBq were injected after 3 days of LCA ligation. We obtained the static images (30 min) that were reconstructed to short, horizontal, vertical long axial using PMOD (cardiac) program. We compared to perfusion of two tracers using polar map images and analyzed the correlation about the perfusion distribution of [^{18}F]FPTP and [^{13}N]NH_3 with 2,3,5-triphenyltetrazolium chloride (TTC) staining Results: In normal rats, difference of contrast ratio increased from 10 min after the injection. The contrast ratio of [^{18}F]FPTP was over 2 times higher than that of [^{13}N]NH_3 on 30min after the injection in each region (myocardium/blood: 4.154 vs. 2.017, myocardium/liver: 3.887 vs. 0.566, myocardium/lung: 4.670 vs. 2.436). MicroPET images of both tracers in MI rats demonstrated myocardial perfusion defects in the corresponding area. The size of myocardial defect measured by [^{18}F]FPTP polar map images revealed excellent correlation with the hypoperfused area measured by quantitative TTC staning (r^2 = 0.92, P < 0.001) as compared to that by [^{13}N]NH_3 (r^2 = 0.82, P < 0.001). Conclusions: [^{18}F]FPTP myocardial imaging provides excellent image quality and uptake properties over [^{13}N]NH_3 imaging in rats. The long half-life of ^{18}F renders this tracer useful for clinical PET/CT applications in the workup of patients with suspected or proven coronary artery disease.

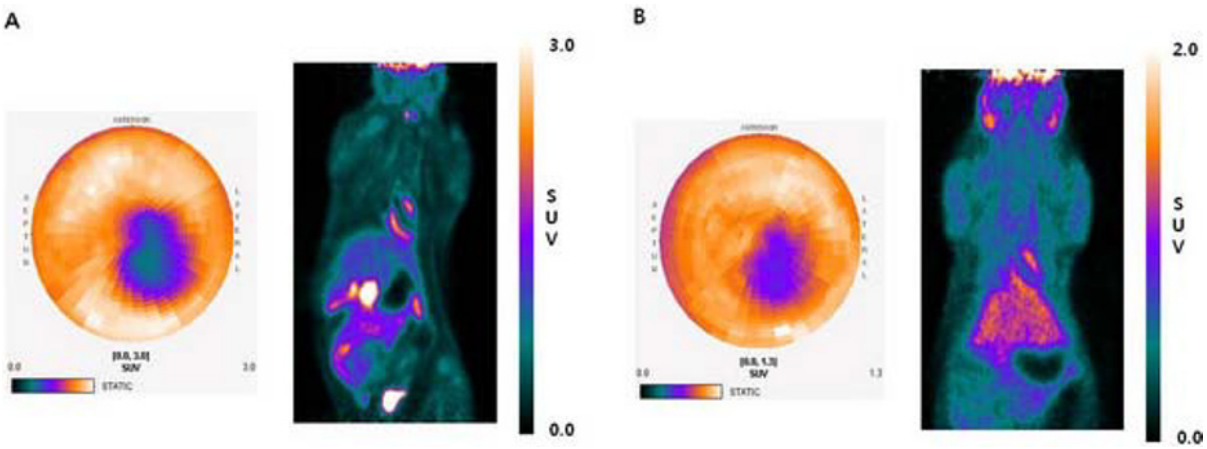

MicroPET and polar map images of MI model after injection of 37 MBq of [^{18}F]FPTP (A) and [^{13}N]NH_3 (B)

Disclosure of author financial interest or relationships:
D. Kim, None; **H. Kim**, None; **J. Zheng**, None; **H. Kim**, None; **A. Pyo**, None; **H. Bom**, None; **J. Min**, None.

Presentation Number **P 508**
Poster Session 4
September 21, 2013 / 14:45-14:45 / Room: Exhibit Hall B

Assessment of perfusion images according to the reconstruction methods using new myocardial PET agent([^{18}F]FPTP) in small animal

Hyeon Sik Kim[1], *Dong-Yeon Kim*[1], *Hyeong Ju Park*[2], *Jung-Joon Min*[1], *Hee-Seung Bom*[1], *Byeong-il Lee*[2], [1]*nuclear medicine, Chonnam National University Hwasun Hospital, Hwasun, Jeonnam, Republic of Korea;* [2]*Medical Photonics Research Center, Korea Photonics Technology Institute, Gwangju, Republic of Korea. Contact e-mail: knkc1120@nate.com*

PURPOSE: Perfusion image plays an important role for the assessment of heart function. Recent, MicroPET presents various perfusion images as reconstruction methods such as FBP, OSEM2D, OSEM3D, and 3DRP. We investigated features of perfusion images of rat as reconstruction methods by using a new myocardial perfusion imaging agent [^{18}F]FPTP. We compared infarct size and image contrast between reconstructed perfusion images and triphenyltetrazolium chloride (TTC)-stainedimages. MATERIAL AND METHODS: PET images were obtained by microPET scanner (Inveon, Siemens Medical Solutions). PMOD (PMOD technologies Ltd., Switzerland) was used for the assessment of images. The myocardial infarction (MI) models (Sprague-Dawley rat, n=10) were constructed by left circumflex coronary artery (LCX) ligation. [^{18}F]FPTP of 37MBq/200 μL was injected into the tail vain. The static images were acquired for 30 minutes, and perfusion images were reconstructed by FBP, OSEM2D, OSEM3D and 3DRP. The image contrast was calculated by the maximum perfusion score and minimum perfusion score at 17 segments polar map. The size of infarction was also calculated from polar map with low perfusion score (< 60%).The infarct size from TTC stained images was estimated by using Sobel image segmentation method. RESULT: Pearson correlation coefficients about infarction sizes between TTC stained image and each reconstructed perfusion image were obtained to 0.707 ($p<0.05$), 0.658 ($p<0.05$), 0.745 ($p<0.05$) and 0.886 ($p<0.001$), respectively. Image contrasts were obtained to 51.65 (±11.43), 52.15 (±11.80), 50.85 (±9.80) and 55.47 (±11.05), respectively. There was a significant difference between OSEM3D and FBP ($p=0.005$) or 3DRP ($p=0.005$). CONCLUSION: OSEM3D reconstruction method showed the highest correlation coefficient and image contrast in small animal images for the assessment of perfusion images using a new myocardial imaging agent, [^{18}F]FPTP.

Disclosure of author financial interest or relationships:
H. Kim, None; **D. Kim**, None; **H. Park**, None; **J. Min**, None; **H. Bom**, None; **B. Lee**, None.

Presentation Number **P 509**
Poster Session 4
September 21, 2013 / 14:45-14:45 / Room: Exhibit Hall B

Kinetic Analysis of ^{68}Ga-NOTA-c(RGDyK) and Immunohistochemical analysis in Rats with Surgically Induced Forelimb Ischemia

Joong Hyun Kim, *Young-Hwa Kim, Young Joo Kim, Bo Yeun Yang, Jae Min Jeong, Hyewon Youn, Dong Soo Lee, Jae Sung Lee, Department of Nuclear Medicine, Seoul National University, Seoul, Republic of Korea. Contact e-mail: jhkim419@gmail.com*

^{68}Ga-labeled 1,4,7- triazacyclononane-1,4,7-triacetic acid (NOTA) - cyclic Arg-Gly-Asp-$_D$-Tyr-Lys (c(RGDyK)) was developed for $\alpha_v\beta_3$ targeting, and is a promising agent for imaging of cancer and disorders related to angiogenesis. In this study, the kinetic analysis of ^{68}Ga-NOTA-c(RGDyK) in rats with surgically induced forelimb ischemia was performed, and the immunohistochemical analysis was also performed to assess $\alpha_v\beta_3$ immuno-staining level. Thirteen SD rats with forelimb ischemia (6-8 weeks) were enrolled in this study. Animal models were created by excision of the left brachial vessels, and a sham operation was performed on the right brachial region under 2% isoflurane anesthesia. To evaluate metabolic stability, HPLC profiles were analyzed from blood samples obtained 1 hour after the injection of ^{68}Ga-NOTA-c(RGDyK) in two normal SD rats (16 weeks). Animal PET scans were performed using an animal PET/CT scanner. A list mode PET scan (duration 120 min) was started with the injection of ^{68}Ga-NOTA-c(RGDyK) via the tail vein at 3, 5 and 7 days after ischemic surgery to evaluate temporal changes. Volumes of interest were drawn on the left ventricle, sham operation, control, and ischemic regions. Compartmental analysis and two graphical analyses (Logan and RE plots) were performed for kinetic parameter estimation. After the last PET scan, rats were sacrificed for immunohistochemical analysis. To quantify the intensity of αvβ3 staining, cell compartments were scored by two independent observers on a six point scale (0-negative, 1-very weak, 2-weak but clearly positive, 3-intermediate, 4- high, and 5- very high). The metabolic peak was not found in the HPLC profiles of blood samples. A 3-compartment model with reversible binding best described the tissue time-activity curves. The distribution volume of the ischemic region was about two times higher than that of the sham operation and control regions in all tested days. Both the Logan and RE plots showed high correlation with compartmental analysis (R^2=0.96 and 0.95 for Logan and RE, respectively). The temporal changes in distribution volume and binding potential were not significant. In immunohistochemical analysis, the immune-staining level of the ischemic region (4.3±0.7) was significantly higher than that of sham operation (2.4±1.1, p<0.05) and control region (1.4±0.6, p<0.05). Kinetic modeling studies with dynamic ^{68}Ga-NOTA-c(RGDyK) PET scan are feasible based on an image-derived input function in a rat ischemia model. High distribution volumes of ischemic region assessed by kinetic and graphical analysis were confirmed by immunohistochemical analysis. The kinetic modeling analysis performed in this study will be useful for the quantitative evaluation of ^{68}Ga-NOTA-c(RGDyK) binding to $\alpha_v\beta_3$ in angiogenic tissues.

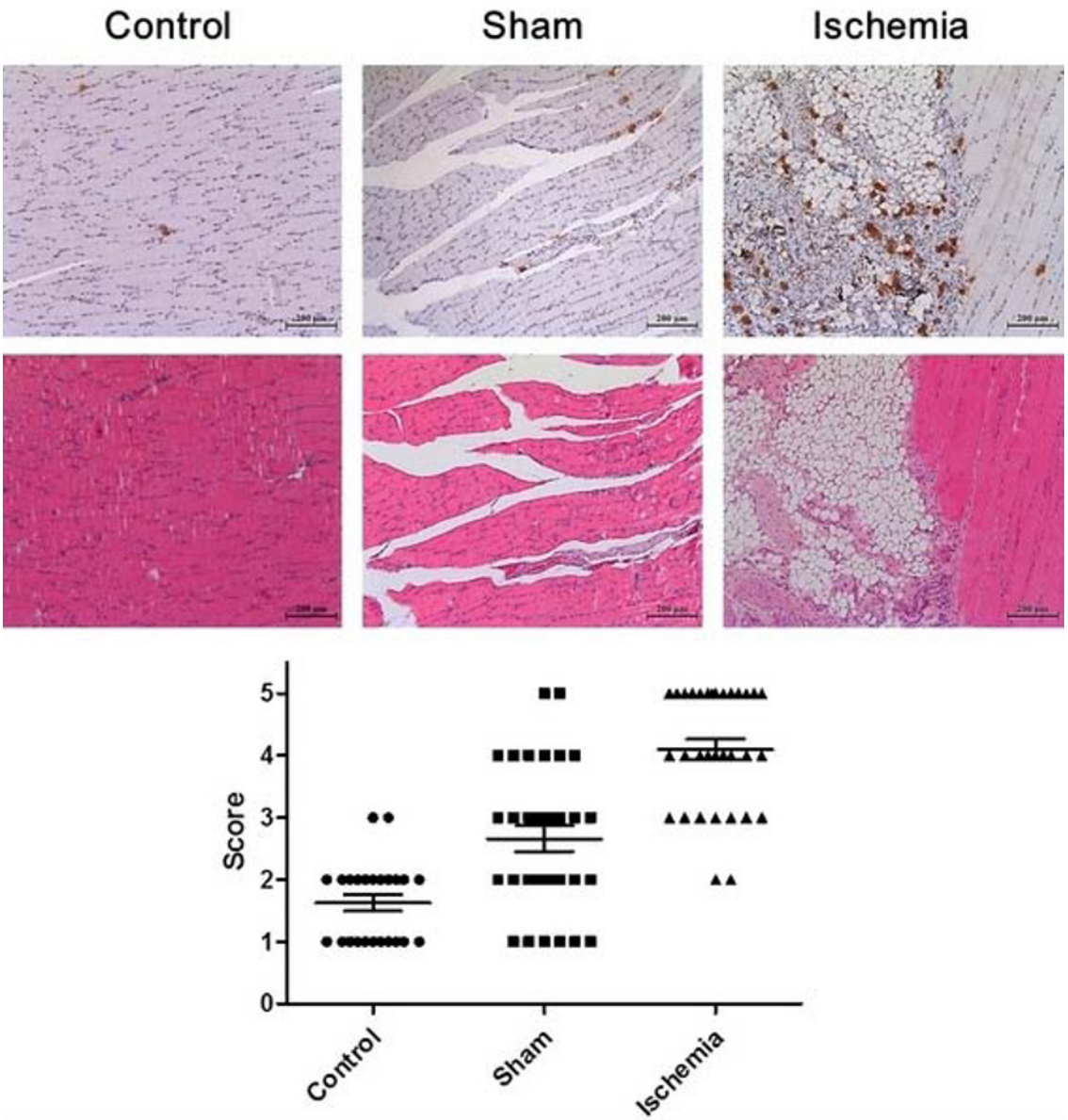

The immunohistochemical results of a representative case in 10X analysis (top). The quantified immunostaining levels were plotted (bottom). The score of ischemic region was significantly higher than sham and control region.

Distribution volumes obtained from compartmental analysis, Logan plot and RE plot. Data are presented as mean (CV)

Group	Region	Compartment model (3C5P)	Logan plot	RE plot
Day 3 (n=7)	Ischemia	0.540 (13.8)	0.561 (9.0)	0.549 (8.4)
	Sham	0.335 (67.1)	0.279 (13.4)	0.274 (12.9)
	Control	0.226 (25.4)	0.257 (10.1)	0.253 (9.6)
Day 5 (n=6)	Ischemia	0.590 (6.9)	0.613 (8.2)	0.600 (7.9)
	Sham	0.288 (18.4)	0.299 (17.0)	0.293 (15.7)
	Control	0.254 (42.6)	0.251 (9.7)	0.247 (9.1)
Day 7 (n=8)	Ischemia	0.629 (21.2)	0.579 (15.2)	0.556 (14.6)
	Sham	0.291 (31.7)	0.284 (19.1)	0.279 (18.5)
	Control	0.197 (11.4)	0.229 (13.6)	0.225 (13.2)

Disclosure of author financial interest or relationships:
J. Kim, None; **Y. Kim**, None; **Y. Kim**, None; **B. Yang**, None; **J. Jeong**, None; **H. Youn**, None; **D. Lee**, None; **J. Lee**, Samsung Electronics, Grant/research support .

Presentation Number **P 510**
Poster Session 4
September 21, 2013 / 14:45-14:45 / Room: Exhibit Hall B

Impact of Testosterone Depletion on Cardiac and Skeletal Muscle Metabolism at Fasting State in Rats

Yun Lin, *Damaris Kukuk, Maren K. Koenig, Sandro Aidone, Bernd J. Pichler, Department for Preclinical Imaging and Radiopharmacy, Eberhard Karls University Tuebingen, Tuebingen, Germany. Contact e-mail: yun.lin@med.uni-tuebingen.de*

Introduction: Testosterone plays an important role in function, performance and structural development of cardiac and skeletal muscles, but its regulation on muscle energy metabolism is still not well understood. The aim of this study was to investigate the impact of testosterone depletion through surgical castration on cardiac and skeletal muscle glucose metabolism in rats by [^{18}F]FDG-PET imaging at fasting state. The progression of the *in vivo* metabolic change was evaluated. Materials and Methods: Adult male Wistar rats (14 weeks old) were overnight fasted and scanned for 90 min with i.v. injection of 463±17μCi [^{18}F]FDG. These rats were separated into castration (bilateral surgical castration, n=4-5) and control (sham operation, n=5) groups. A baseline PET scan was performed followed by subsequent scans 8, 12 and 15 weeks post castration (*p.c.*). Before each [^{18}F]FDG-PET scan, blood glucose levels were measured. The dynamic PET data was sorted into 21 frames and reconstructed with OSEM 2D. Regions of interests (ROIs) were placed at the center 6 consecutive planes of short axial myocardium and the activities of left ventricle blood pool were subtracted. ROIs of skeletal muscle were traced from 4 consecutive planes of upper limbs in the coronal view. The tissue tracer uptake as standard uptake value (SUV) was analyzed from the final frame (15 min). Results: No significant differences were found in blood glucose levels in the fasted control rats (baseline:160.2±56.3 mg/dl; 8 weeks *p.c.*: 132.2±22.2 mg/dl; 12 weeks *p.c.*: 117.0±10.8 mg/dl; 15 weeks *p.c.*: 109.8±8.2 mg/dl) or castrated rats (baseline: 138.6±12.9 mg/dl; 8 weeks *p.c.*: 150.3±39.4 mg/dl; 12 weeks *p.c.*:135.5±16.4 mg/dl; 15 weeks *p.c.*: 123.0±9.8 mg/dl) throughout the study period. The skeletal muscle SUV of the castration group (baseline: 0.40±0.13; 8 weeks *p.c.*: 0.33±0.19; 12 weeks *p.c.*: 0.49±0.08; 15 weeks *p.c.*: 0.49±0.05) was also at the similar level as the control group (baseline: 0.38±0.13; 8 weeks *p.c.*: 0.39±0.04; 12 weeks *p.c.*: 0.42±0.04; 15 weeks *p.c.*: 0.47±0.10) before and after testosterone depletion. The myocardial SUV of the control (baseline:1.14±0.57; 8 weeks *p.c.*: 1.59±0.68; 12 weeks *p.c.*: 1.70±0.52; 15 weeks *p.c.*: 1.60±0.35) and castration (baseline: 1.21±0.53; 8 weeks *p.c.*: 1.72±0.62; 12 weeks *p.c.*: 2.60±0.11; 15 weeks *p.c.*: 1.96±0.44) groups didn't show significant changes 8 weeks *p.c.* between groups and to their baseline measurements. However, the castration group revealed a significant increasing myocardial SUV 12 weeks *p.c.* compared to its baseline ($p<0.01$). Conclusion: In our study, the blood glucose level and skeletal muscle [^{18}F]FDG uptake were not affected along the treatment. However, different from skeletal muscle, enhanced [^{18}F]FDG uptake was observed in the myocardium of the castration group. Our results indicated that testosterone may have different regulations or progressions of glucose metabolism changes in cardiac and skeletal muscles.

Disclosure of author financial interest or relationships:
Y. Lin, None; **D. Kukuk**, None; **M.K. Koenig**, None; **S. Aidone**, None; **B.J. Pichler**, Siemens, Grant/research support; Bayer, Grant/research support; AstraZeneca, Grant/research support; BoehringerIngelheim, Grant/research support .

Presentation Number **P 511**
Poster Session 4
September 21, 2013 / 14:45-14:45 / Room: Exhibit Hall B

Relationship Between Coronary Stent Inflammation and the Local Stent Healing Response Revealed by In Vivo Optical Molecular-Structural Imaging

Eric A. Osborn[1,2], *Ehsan Hamidi*[3], *Amr I. El Maghraby*[2], *Hongki Yoo*[3,4], *Adam Mauskapf*[2], *Guillermo Tearney*[4], *Farouc A. Jaffer*[2,3], [1]*Cardiology, Beth Israel Deaconess Medical Center, Boston, MA, USA;* [2]*Cardiovascular Research Center, Massachusetts General Hospital, Boston, MA, USA;* [3]*Wellman Center for Photomedicine, Massachusetts General Hospital, Boston, MA, USA;* [4]*Biomedical Engineering, Hanyang University, Seoul, Republic of Korea. Contact e-mail: eosborn@bidmc.harvard.edu*

Introduction: Stent thrombosis and restenosis are major complications of coronary artery stents that 1) occur at greater frequency in patients with diabetes mellitus and 2) result in repeat invasive procedures, myocardial infarction, and sudden cardiac death. While ex vivo studies implicate stent malhealing and inflammation in stent complications, current diagnostic clinical imaging strategies cannot accurately determine which stents are at-risk in living subjects. To address this unmet need, we simultaneously assessed in vivo stent healing and inflammation in diabetic rabbits with integrated near infrared fluorescence (NIRF)-optical frequency domain imaging (OFDI) quantitative molecular-structural imaging. Methods: A bare-metal stent (3.5x12mm) was implanted in the infrarenal aorta of alloxan-induced diabetic rabbits (n=5). Day 28 intravascular NIRF-OFDI imaging was performed 24 hours after i.v. administration of Prosense VM110 (5mg/kg; ex/em 750/780nm) for NIRF molecular imaging of inflammatory cathepsin activity. At 0.5mm intervals, OFDI stent endothelialization and neointimal area were simultaneously determined. OFDI structural data was then co-registered with quantitative NIRF molecular inflammation. Following ex vivo fluorescence reflectance imaging (FRI), stents were electrochemically dissolved for histopathology analysis. Results: Diabetic rabbits developed stable hyperglycemia ($p<0.001$ vs. controls). Compared to the non-stented aorta, day 28 stent NIRF inflammatory cathepsin protease activity was greater (50.9±2.0 vs. 26.1±0.6 nM; $p<0.0001$). At the stent edges, OFDI revealed 3-fold enhanced neointima (proximal and distal 2mm stent edge average neointimal area, 1.63±0.12 vs. mid 2 mm stent 0.50±0.05 mm2; $p<0.0001$), and 7-fold less uncovered stent struts (2.1±1.7% vs. 14.0±4.1% mid stent; $p=0.03$). NIRF inflammation was also greater at the stent edge (60.8±3.4 vs. 40.8±1.4 nM mid stent; $p=0.0005$), and correlated positively with neointimal formation ($R=0.43$; $p=0.003$), and correlated negatively with de-endothelialized stent struts ($R=-0.42$; $p=0.004$). In vivo NIRF findings were supported by ex vivo FRI showing an enhanced stent-edge NIRF pattern. Histopathology matched to OFDI images demonstrated cathepsin B and smooth muscle cell immunostaining in regions with enhanced NIRF inflammation. Conclusions: In vivo NIRF-OFDI molecular-structural imaging reveals that NIRF inflammation associates with greater neointimal formation and fewer uncovered stent struts. Intravascular molecular imaging holds potential for the clinical detection of stents at risk of stent restenosis and thrombosis.

Disclosure of author financial interest or relationships:
E.A. Osborn, None; **E. Hamidi**, None; **A.I. El Maghraby**, None; **H. Yoo**, None; **A. Mauskapf**, None; **G. Tearney**, Samsung, Consultant; Ninepoint Medical, Consultant; Ninepoint Medical, Grant/research support; iLumen, Grant/research support; Terumo Corporation, Other financial or material support; **F.A. Jaffer**, Merck, Abbott vascular, Grant/research support; Boston Scientific, Consultant .

Presentation Number **P 512**
Poster Session 4
September 21, 2013 / 14:45-14:45 / Room: Exhibit Hall B

Pharmacokinetic study of Cu-64 labeled LNA-based anti-miRNA and VHPK-liposomes in VCAM-1 expressing atherosclerotic plaque

Jai Woong Seo[1], *Karen Gagnon*[1], *Lisa M. Mahakian*[1], *Sarah Tam*[1], *Azadeh Kheirolomoom*[1], *Hua Zhang*[1], *Dong J. Son*[2], *Hanjoong Jo*[2], *Katherine Ferrara*[1], [1]*Biomedical Engineering, University of California Davis, Davis, CA, USA;* [2]*Coulter Department of Biomedical Engineering, Georgia Institute of Technology and Emory University, Atlanta, GA, USA. Contact e-mail: jwseo@ucdavis.edu*

Inhibition of miRNA is an emerging technology to treat disease; however, while miRNA has been demonstrated to effectively alter gene expression, downstream and off target effects are of significant concern. Delivery in human trials has primarily involved the direct injection of nucleic acids with a modified backbone, yet encapsulated and localized delivery to diseased regions could reduce the concerns regarding potential toxicities. The efficacy of LNA-based anti-miR712 in reducing plaque formation has been demonstrated by the Jo laboratory in a mouse model of atherosclerosis. In order to optimize the application of similar anti-miR therapeutics for human use, the pharmacokinetics resulting from direct or targeted and encapsulated delivery must be characterized. Here, we evaluated the pharmacokinetics of anti-miR712-DOTA with Cu-64 (t1/2 = 12.7 h) in an induced mouse model of atherosclerosis. We also evaluated the pharmacokinetics of 64Cu-VHPK-liposomes as a possible delivery vehicle for anti-miR712 within the same model. Methods: All in vivo studies were approved by the UC Davis Institutional Animal Care and Use Committee. A model of atherosclerosis was established in the ApoE knockout mouse (n=12) based on left carotid artery ligation, followed by a high fat diet for 1-2 weeks. 64Cu-anti-miR712 (0.3-0.2 mCi/mouse) was administered through the tail vein. After PET images were acquired at 2 or 3 hours after injection, autoradiography of aorta (figure 1a) was performed and the bio-distribution of the aortic arch (AA), carotid arteries (CA), descending aorta (DA) and other organs were assayed. For the liposomal targeting study, VHPK- and ARAL-lipopeptide (5 mol%) was formulated with 6-BAT lipid (1 mol%) in liposomes. Cu-64 labeled liposomes (0.3-0.2 mCi/mouse) were evaluated as the same manner with the same mouse model. Results: Anti-miR712 showed higher accumulation in the left carotid artery (LCA) (7.2±1.4%ID/g) than in the right carotid artery (RCA) (3.4±1.7%ID/g) or in both CAs of the normal mouse (LCA = 2.3±1.3%ID/g, RCA = 4.4±0.5%ID/g) (figure 1b). Anti-miR712 accumulation in the AA and DA were 2.4±1.2%ID/g and 1.4±0.4%ID/g, respectively. Autoradiographic images of the aorta demonstrated that anti-miR712 predominately accumulated in the ligated LCA (figure 1a). VHP-liposomal and ARAL-liposomal activity in the LCA were 9.5 ± 2.0%ID/g, and 4.5 ± 2.1%ID/g, respectively. VHP-liposomal accumulation in the RCA was 3.7±0.7%ID/g and accumulation in the AA and DA were 6.7±5.0%ID/g and 3.0±1.7%ID/g. Discussion and conclusion: LNA-based anti-miR712 was successfully labeled with Cu-64 with high chemical purity and was shown to accumulate in the heavily diseased LCA. VHPK-liposomes showed a significantly higher uptake in the LCA than control liposomes but also accumulated in other regions associated with early atherosclerosis. Acknowledgement: This publication has been funded with funds from the National Heart, Lung, and Blood Institute, National Institutes of Health, Department of Health and Human Services, under Contract No. HHSN268201000043C.

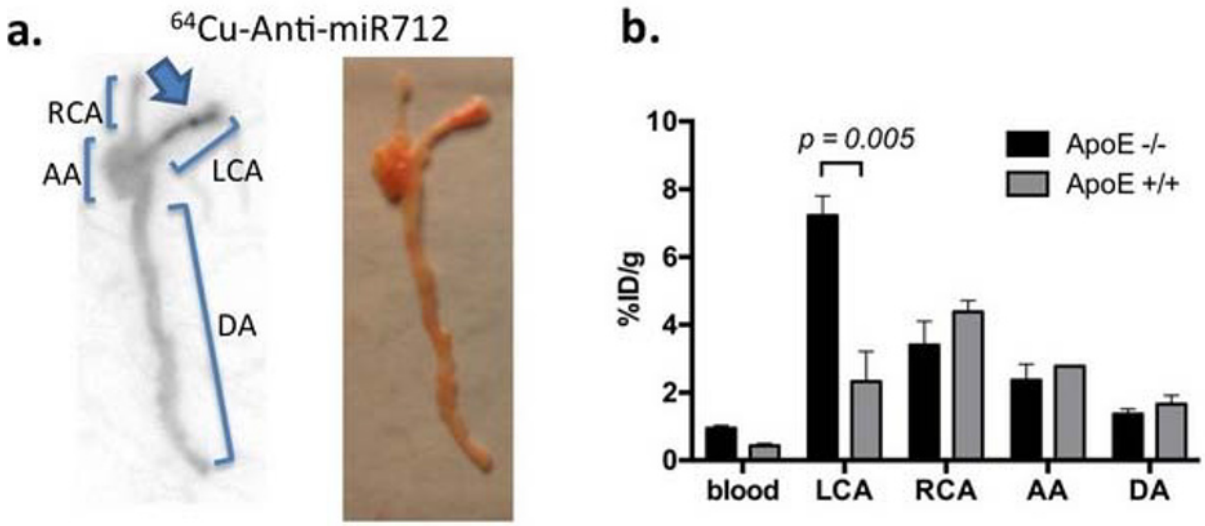

Figure 1. a. Autoradiography images of aortae obtained after intravenous injection of 64Cu-DOTA-anti-miR712. Highest signal was found in left carotid artery as black dot (blue arrow). b. biodistribution of 64Cu-DOTA-anti-miR712 at left carotid artery (LCA), right carotid artery (RCA), aortic arch (AR), and decending aorta (DA) obtained from the ApoE knockout mouse based on left carotid artery ligation (ApoE-/-, n=6) and normal mice (ApoE+/+, n=2)

Disclosure of author financial interest or relationships:
J. Seo, None; **K. Gagnon**, None; **L.M. Mahakian**, None; **S. Tam**, None; **A. Kheirolomoom**, None; **H. Zhang**, None; **D.J. Son**, None; **H. Jo**, None; **K. Ferrara**, None.

Presentation Number **P 513**
Poster Session 4
September 21, 2013 / 14:45-14:45 / Room: Exhibit Hall B

Optical molecular-structural imaging of fibrin to assess DVT age and responsiveness to fibrinolysis in vivo

Ashley F. Stein[1], *Chase W. Kessinger*[1], *Henry J. Zelada*[1], *Sibel S. Erdem*[2], *Jason R. McCarthy*[2], *Charles P. Lin*[3,2], *Farouc A. Jaffer*[1], [1]*Cardiovascular Research Center, Massachusetts General Hospital, Boston, MA, USA;* [2]*Center for Systems Biology, Massachusetts General Hospital, Boston, MA, USA;* [3]*Wellman Center for Photomedicine, Massachusetts General Hospital, Boston, MA, USA. Contact e-mail: astein5@partners.org*

Introduction: Fibrinolytic therapy with tissue plasminogen activator (tPA) is increasingly utilized for the treatment of deep vein thrombosis (DVT), a major worldwide cause of cardiovascular morbidity. Although thrombus organization over time increases resistance to fibrinolysis, the age-dependence of fibrinolysis in DVT has not been systematically assessed. In this study, we used confocal intravital fluorescence microscopy (IVFM) to dynamically study fibrinolysis of murine thigh DVT at high-resolution, using thrombus angiography and a fibrin-specific sensor, FTP11-CyAm7 (FTP11). We hypothesized that fibrinolysis could be tracked and quantified in vivo using serial IVFM and molecular imaging of fibrin, and that DVT lytic capacity would diminish over time. Methods: C57Bl/6 mice (n=23) underwent topical 7.5% ferric chloride injury to induce femoral DVT. At day 1 (n=7), day 2 (n=7), day 4 (n=5), or day 6 (n=4) post DVT generation, IVFM was performed during tPA infusion. Mice received i.v. bolus of plasminogen, tPA, and heparin, followed by a continuous 1 hour i.v. co-infusion of tPA and heparin. To enable molecular imaging of fibrin, FTP11-CyAm7 (100nmol/kg, ex/em 750/773nm) was injected 45 minutes prior to lysis. DVT area and length were quantified using FITC-dextran (MW 2000 kD, ex/em 490/520nm) venography before and after tPA infusion to quantify change in area as net lysis. IVFM image stacks were analyzed by NIH ImageJ. After sacrifice, fluorescence microscopy (FM) and Carstair's staining were performed. Results: DVT at either day 1, 2, 4, or 6, showed a day-dependent attenuation in tPA-induced fibrinolysis (net thrombus area reduction over 1 hour, 27±13%, 25±16%, 6±4%, and 7±3% respectively, p=0.003). Similar findings were noted in the fibrin FTP11 signal (net reduction in FTP11 integrated signal density over 1 hour, 52±15%, 23±18%, 11±8%, and 8±8% respectively, p=0.003). The baseline FTP11 target-to-background ratio (TBR) significantly differed among the four time points (1.8±0.6, 1.3±0.3, 1.0±0.2, and 1.1±0.2 respectively, p=0.02), consistent with increasing thrombus organization over time. Both the baseline FTP11 thrombus TBR and net change in FTP11 signal over 1 hour predicted the net lysis determined by pre/post venography (r=0.46, p=0.026 and r=0.58, p=0.004, respectively). IVFM revealed a trend of increased lysis at the thrombus edges compared to the mid segment (day 1: 33±21% vs. 22±17%, day 2: 35±20 vs. 21±13%, p>0.05). FTP11 signal on FM colocalized with fibrin-rich thrombi in Carstair's staining and the distribution of FTP11 signal was well matched to IVFM images. Conclusion: The efficacy of triggered murine DVT fibrinolysis decreases with DVT age, as assessed by dynamic IVFM molecular-structural imaging. The FTP11-CyAm7 fibrin signal differentiates DVT of different ages, and informs the magnitude of triggered fibrinolysis.

Disclosure of author financial interest or relationships:
A.F. Stein, None; **C.W. Kessinger**, None; **H.J. Zelada**, None; **S.S. Erdem**, None; **J.R. McCarthy**, None; **C.P. Lin**, None; **F.A. Jaffer**, Merck, Abbott vascular, Grant/research support; Boston Scientific, Consultant .

Presentation Number **P 514**
Poster Session 4
September 21, 2013 / 14:45-14:45 / Room: Exhibit Hall B

The potential use of Tc-99m MIBI as an imaging agent for cardiac mitochondrial toxicity: A preliminary study in isolated perfused hearts

Zaitulhusna Md Safee, *Erika Mariotti, Rodolfo Medina, Fiona Shaughnessy, Thomas R. Eykyn, Phil Blower, Richard Southworth, Imaging Sciences and Biomedical Engineering, Kings College London, London, United Kingdom. Contact e-mail: zaitulhusna.md_safee@kcl.ac.uk*

Introduction: Identification of myocardial injury due to anthracycline chemotherapy or radiotherapy is normally performed by measuring left ventricular ejection fraction. Non-invasive quantification of cardiac injury by imaging mitochondrial dysfunction may providing spatial information on cardiac injury before changes in perfusion or function can be detected. Tc-99m sestamibi (MIBI), a lipophilic cationic SPECT myocardial perfusion imaging agent is retained within viable cells by virtue of their mitochondrial membrane potential. It cannot report specifically on mitochondrial function because its distribution is also determined by perfusion. However, by correcting the perfusion with a non-mitochondrial targeting perfusion agent such as Tc-99m NOET (NOET), it may be possible to delineate and quantify mitochondrial injury. We aim to demonstrate the potential of MIBI and NOET for detecting mitochondrial dysfunction induced by either hypoxia or of mitochondrial uncouplers (CCCP) in an isolated perfused rat heart model. Methods: Isolated rat hearts were mounted onto a Langendorff perfusion apparatus and perfused with aerobic Krebs Henseleit buffer (KHB) for 20 min, followed by hypoxic KHB for 45 min. Cardiac contractile function was monitored using an intraventricular balloon. Cardiac Tc-99m retention from three 4MBq bolus injections of MIBI or NOET (during normoxia, after 5 and 20 mins hypoxia) was monitored by NaI detectors. Control studies of 65 min normoxia were performed. In a further experiment, hearts were perfused with aerobic buffer (KHB) for 20 min, before being infused with CCCP (at 200nM, 300nM or 400nM) for 30 min. Cardiac contractile function was recorded throughout, and Tc-99m retention from three separate 4MBq bolus injections of MIBI or NOET (during normoxia, after 5 and 20 min hypoxia) was monitored. Results: During normoxic perfusion, cardiac MIBI retention was 15.9 ± 0.9 % injected dose (ID). This fell significantly after 5 min hypoxia to 10.5 ± 3.4 % ID and completely abolished after 20 min hypoxia to -3.2 ± 5.4 % ID ($p<0.05$), such that even MIBI accumulated in the myocardium from the prior injections was also washed out. Tracer retention was also significantly reduced by the normoxic administration of CCCP 8.3 ± 2.1 %, 2.4 + 5.1 % ID and -2.2 ± 4.1% ($p<0.05$) after 200nM, 300nM and 400nM respectively after 5 min, although there was a rebound effect after 20 min of CCCP infusion. Cardiac NOET retention during normoxia was 25.7 ± 5.3 % ID and this was not significantly altered by either hypoxia or administration of CCCP. Discussion: Cardiac retention of MIBI was high during normoxia, and markedly reduced by hypoxic perfusion, presumably due to the collapse of the mitochondrial membrane potential; the results are closely echoed by those hearts acutely treated with CCCP. Conclusion: We have demonstrated that while cardiac retention of Tc-99m MIBI is sensitive to interventions that alter mitochondrial membrane potential, NOET is not. Using a NOET perfusion scan to correct a MIBI mitochondrial function scan therefore demonstrates some promise as a means of visualising mitochondrial damage in the myocardium.

Disclosure of author financial interest or relationships:
Z. Md Safee, None; **E. Mariotti**, None; **R. Medina**, None; **F. Shaughnessy**, None; **T.R. Eykyn**, None; **P. Blower**, None; **R. Southworth**, None.

Presentation Number **P 515**
Poster Session 4
September 21, 2013 / 14:45-14:45 / Room: Exhibit Hall B

The relationship between O2 concentration, 64Cu-BTSC retention & cardiac metabolism in graded hypoxia in isolated perfused hearts

Rodolfo Medina, Erika Mariotti, Karen P. Shaw, Maxwell G. Handley, Fiona Shaughnessy, Thomas R. Eykyn, Phil Blower, **Richard Southworth***, King's College London, London, United Kingdom. Contact e-mail: richard.southworth@kcl.ac.uk*

Introduction: The hypoxia selective 64CuATSM and other related 4Cu bis(thiosemicarbazone) (BTSC) complexes demonstrate potential for cardiac hypoxia imaging, but have only previously been investigated in isolated heart models using extreme hypoxia. Many cardiac pathologies are characterised by relatively subtle degrees of hypoxia, which limits the relevance of this approach. Here, we have determined the hypoxia selective thresholds of several promising BTSC complexes over a range of levels of hypoxia, and established the pathophysiological relevance of each with respect to cardiac contractility and bioenergetics measured by 31P NMR spectroscopy. Methods: Isolated rat hearts were Langendorff-perfused with aerobic Krebs buffer (gassed with 95% O2/5% CO2) for 20 min, then hypoxic buffer (titrated using a Linton GSM3 Gas mixer) for 45 min. Cardiac 64Cu retention from three 1 MBq bolus injections (at normoxia, 5 and 25 mins hypoxia) of either 64CuATSM, 64CuATS, 64CuCTS or 64CuATSE was measured by NaI detector. Cardiac function was monitored by intraventricular balloon. In parallel experiments, changes in cardiac bioenergetics were serially monitored by 31P NMR spectroscopy. Results: Left ventricular developed pressure started to decline within 5 minutes of perfusion with buffers of 40% O2 and below. PCr and ATP fell significantly below control after 8 min and 20 min of 30% hypoxia respectively, but achieved steady non-zero status representing metabolic compensation. Perfusion with buffers below 20% O2 resulted in exhaustion of PCr and ATP by the end of the experiment. All the BTSC compounds studied exhibited significant increases in 64Cu retention in hearts perfused with buffers gassed with <30% O2, and tracer retention increased with increasing hypoxic duration. While ATSM exhibited increased heart tracer retention after 25 minutes of perfusion with 30% O2 (29+9.5% vs 8+3% control), this was significantly outperformed by CTS which was the only tracer which demonstrated hypoxia sensitivity after 5 minutes of perfusion with 30% O2 (41+5% versus13+3% control) and exhibited the highest contrast of those tracers studied with 62+9% after 25 minutes perfusion with 30% O2, increasing to a maximum of 91+5% after 25 min of perfusion with 0% O2. Conclusion: Cardiac function and bioenergetics start to become compromised in hearts perfused with buffer gassed with <40% O2. While not capable of identifying tissue hypoxia at this threshold, 64CuATSM and 64CuCTS deposit 64Cu in tissue perfused with 30% O2 containing buffer, which is compromised but still capable of maintaining intracellular ATP, i.e. at a pathophysiologically relevant level of cardiac hypoxia. CTS exhibits a significant advantage over ATSM in this regard, both in terms of sensitivity and absolute normoxic:hypoxic contrast.

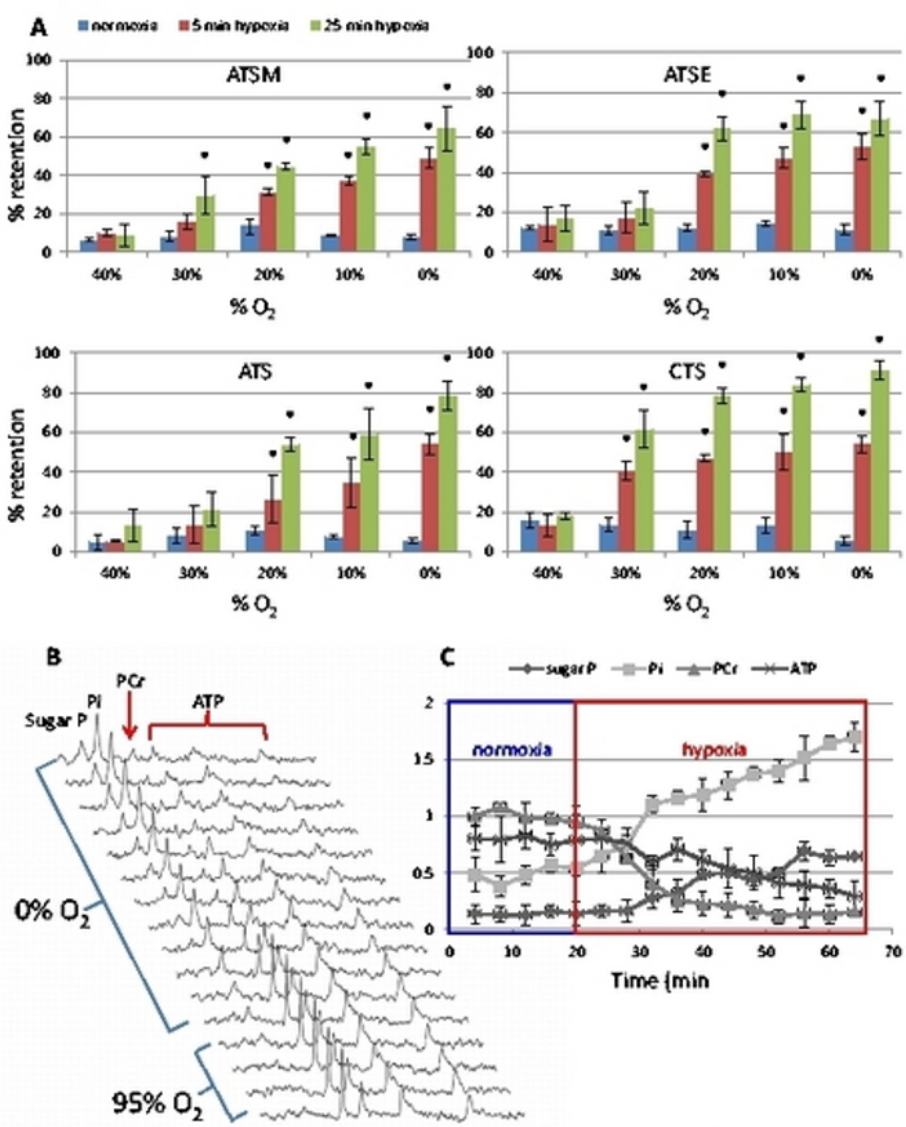

Figure 1A. ^{64}Cu-BTSC retention in hearts perfused with normoxic and hypoxic buffer. *B.* Representative NMR spectra from a heart perfused with buffer gassed with 95% O_2 followed by 0% O_2. C. Normalised NMR peak areas; sugar phosphate (sugar P), inorganic phosphate (Pi), phosphocreatine (PCr). * $p < 0.05$.

Disclosure of author financial interest or relationships:

R. Medina, None; **E. Mariotti**, None; **K.P. Shaw**, None; **M.G. Handley**, None; **F. Shaughnessy**, None; **T.R. Eykyn**, None; **P. Blower**, None; **R. Southworth**, None.

Presentation Number **P 516**
Poster Session 4
September 21, 2013 / 14:45-14:45 / Room: Exhibit Hall B

MR imaging of USPIO-labeled cardiovascular implants

Marianne E. Mertens[1], *Philipp Schuster*[2], *Valentine Gesche*[2], *Sabine Koch*[3], *Lisanne Rongen*[3], *Julia Frese*[3], *Leon Olde Damink*[4], *Anne Bühren*[4], *Fabian Kiessling*[1], *Twan Lammers*[1], [1]*Department for Experimental Molecular Imaging, RWTH Aachen, University, Aachen, Germany;* [2]*Institute for Textile Technology, RWTH Aachen University, Aachen, Germany;* [3]*Institute of Applied Medical Engineering, RWTH Aachen University, Aachen, Germany;* [4]*Matricel GmbH, , Herzogenrath, Germany. Contact e-mail: mmertens@ukaachen.de*

Introduction Non-invasive imaging holds significant potential for implementation in tissue-engineering, enabling the longitudinal assessment of functionality, acceptance and remodeling of implant materials. The availability of non-invasive imaging approaches can e.g. foster the development of improved and patient-customized tissue-engineered implants, assure functionality and safety in vivo, and facilitate the clinical translation of tissue-engineered scaffolds. Thus far, however, hardly any efforts have been undertaken to combine non-invasive imaging and tissue-engineering. Here, we present several different methods to incorporate Ultrasmall Superparamagnetic Iron Oxide (USPIO) nanoparticles into the matrix material of tissue-engineered cardiovascular grafts and patches, thereby enabling their non-invasive visualization using magnetic resonance imaging (MRI). Methods USPIO possessing different surface functionalities (terminal hydroxy-, amino- or aldehyde groups) were incorporated either physically or chemically into 3D collagen-based scaffolds. In a second approach USPIO were incorporated into a PVDF textile graft scaffold in concentrations of 0.05 and 0.2 % [w/w]. The textile structure was molded with a composite of cells and fibrinogen, and cultivated in a bioreactor system under physiological flow and pressure conditions over 14 days. Labeled vascular implants were evaluated regarding i) structural properties, ii) labeling stability, iii) MR visibility and iv) biocompatibility. Results USPIO-labeled PVDF and collagen scaffolds were successfully used to produce functional vascular patches (Figure 1 A-D) and grafts (Figure 1 E-G). USPIO incorporation was found to be highly stable, and no loss of contrast agent was observed in the course of cultivation. The grafts and patches could be imaged in T1, T2, T2*-weighted MRI. A significant increase of the relaxation rate and contrast-to-noise ratio (CNR) could be demonstrated in comparison to non-labeled grafts. Scaffold resorption could be quantitatively monitored in gelatine phantoms. Colonization by fibroblasts and endothelial cells was shown to be not affected by USPIO incorporation as demonstrated by immunohistochemical analysis. Proof-of-principle in vivo experiments are currently ongoing. Conclusions The labeling of implant material with USPIO nanoparticles has been demonstrated to be an efficient method for imaging the location and resorption of implanted scaffolds. Increased imaging characterization of scaffold material can lead to improved design of implant-based therapies and accelerate translation to clinical practice. Acknowledgement This work was supported by NRW / EU-Ziel 2-Programm (EFRE) 2007-2013: "Entwicklung und Bildgebung patientenoptimierter Implantate".

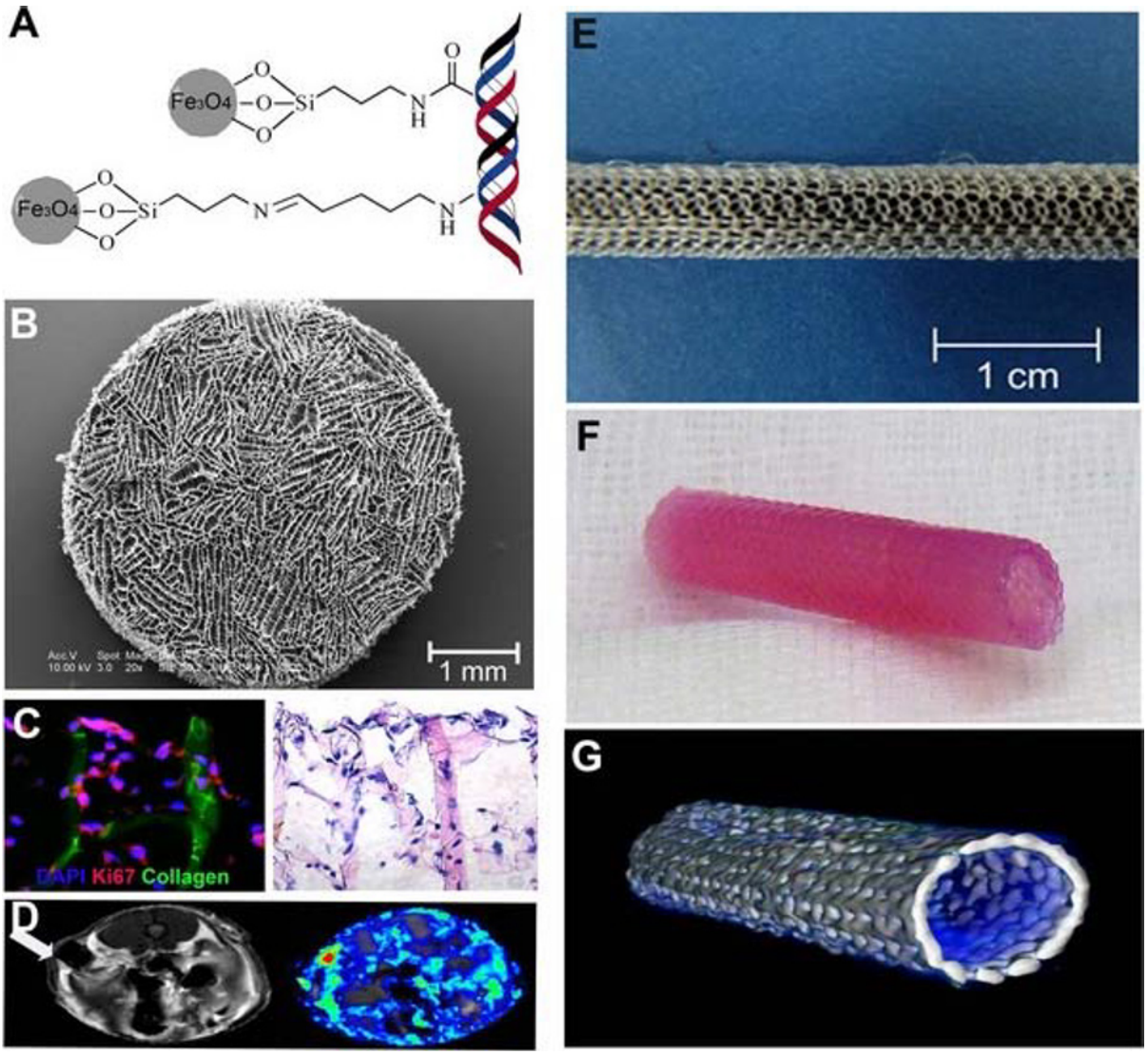

Figure 1: Labeling and imaging of a 3D collagen scaffold (A-D) and a tissue-engineered vascular graft (E-G). A) Covalent incorporation of USPIO into the collagen matrix, B) SEM image of labeled scaffold, showing that USPIO-incorporation does not affect the structural properties of the materials, C) H&E staining and IHC of a labeled scaffold colonized with NIH3T3. No qualitative and quantitative differences in colonization were observed for labeled vs. non-labeled scaffolds, D) T2 weighted MRI of a subcutaneously implanted labeled scaffold, E) PVDF based vascular graft labeled with USPIO, F) tissue-engineered vascular graft after bioreactor cultivation, G) 3D MRI rendering of a labeled textile graft.

Disclosure of author financial interest or relationships:

M.E. Mertens, None; **P. Schuster**, None; **V. Gesche**, None; **S. Koch**, None; **L. Rongen**, None; **J. Frese**, None; **L. Olde Damink**, Matricel GmbH, Employment; **A. Bühren**, Matricel GmbH, Employment; **F. Kiessling**, None; **T. Lammers**, None.

Presentation Number **P 517**
Poster Session 4
September 21, 2013 / 14:45-14:45 / Room: Exhibit Hall B

IMPACT OF ROI DEFINITION ON THE LYMPH NODE IMMUNE RESPONSE QUANTIFICATION MEASURED BY [18F]FDG /PET

Svetlana Chefer[1], *Christopher Z. Leyson*[1], *Jurgen Seidel*[1], *Reed Johnson*[2], *Joseph E. Blaney*[2], *Julie Dyall*[1], *Peter B. Jahrling*[1,2], [1]*Division of Clinical Research, Integrated Research Facility, NIAID/NIH, Frederick, MD, USA;* [2]*Division of Intramural Research, Emerging Viral Pathogens Section, NIAID/NIH, Bethesda, MD, USA. Contact e-mail: schefer@mail.nih.gov*

[18F]FDG/PET is a powerful supplement to conventional studies of infection in animal models to better characterize disease pathogenesis and to evaluate the efficacy of potential treatments. Lymph nodes (LNs) are a primarily target for monitoring the immune response over time. Similar to the methodological issues associated with image analysis in oncology, reliable assessment of the LN immune response over the course of an infection will depend on definition of the region of interest (ROI). Therefore, the current study objective is to investigate the relative merit of three different methods of determining the standardized uptake value (SUV) metric to assess LN [18F]FDG uptake as a marker of immune response in a non-human primate model of monkeypox viral infection. Imaging data were acquired using the microPET/CT scanner Focus-220 (Siemens AG) in six rhesus macaques (Macaca mulatta) infected with monkeypox virus and housed in biosafety level 3 containment. Multiple PET scans initiated 1 h after an IV [18F]FDG injection (0.25 mCi/kg) and continued for 15 min for each of two bed positions were conducted for 1.5 months (three scans before and up to six scans after virus inoculation). SUVs (SUVmax, SUVwhole and SUVcenter) in an axillary LN were measured using MIM 5.2.2. To identify an axillary LN, PET images were coregistered with CT images (Figure 1A). Following standard procedures established in the field, SUVs were derived from either a single voxel with maximal SUV (SUVmax) or all voxels inside the LN (SUVwhole). Additionally, SUVs in the center (SUVcenter) were computed by drawing three spheres in the LN center (total of 21 voxels in all three spheres) and averaging the SUVs from these spheres. The reproducibility of the baseline SUV obtained by each of the three methods and the agreement between the methods for the peak [18F]FDG uptake in LNs of survivors (day 10 after inoculation) was tested using Bland-Altman analysis. There was a good agreement between all three approaches in the pattern of [18F]FDG uptake over time with the best correspondence between SUVcenter and SUVwhole. , The lowest data reproducibility was observed for SUVmax because of adverse noise effects. SUVwhole was subject to a substantial partial volume effect associated either with radioactivity under- or over-estimation near the LN edge. Assessing the SUVs in the LN center (SUVcenter) reduced the impact of noise, minimized partial volume effect and substantially decreased the standard deviation of the mean SUV. Overall, an improvement of the accuracy of the measurement using SUVcenter revealed a 2.6 fold difference between moribund and surviving groups on day 3 postinoculation. A much smaller difference was detected by SUVmax and SUVwhole. Consequently, the results of exploratory statistical analysis using two-way ANOVA for repeated measures, demonstrated a statistically significant difference in the immune response between surviving and moribund animals with SUVcenter only. Based on these preliminary results we conclude that SUVcenter is the preferred approach rather than SUVmax or SUVwhole for quantitative analysis of LN immune response using [18F]FDG/PET.

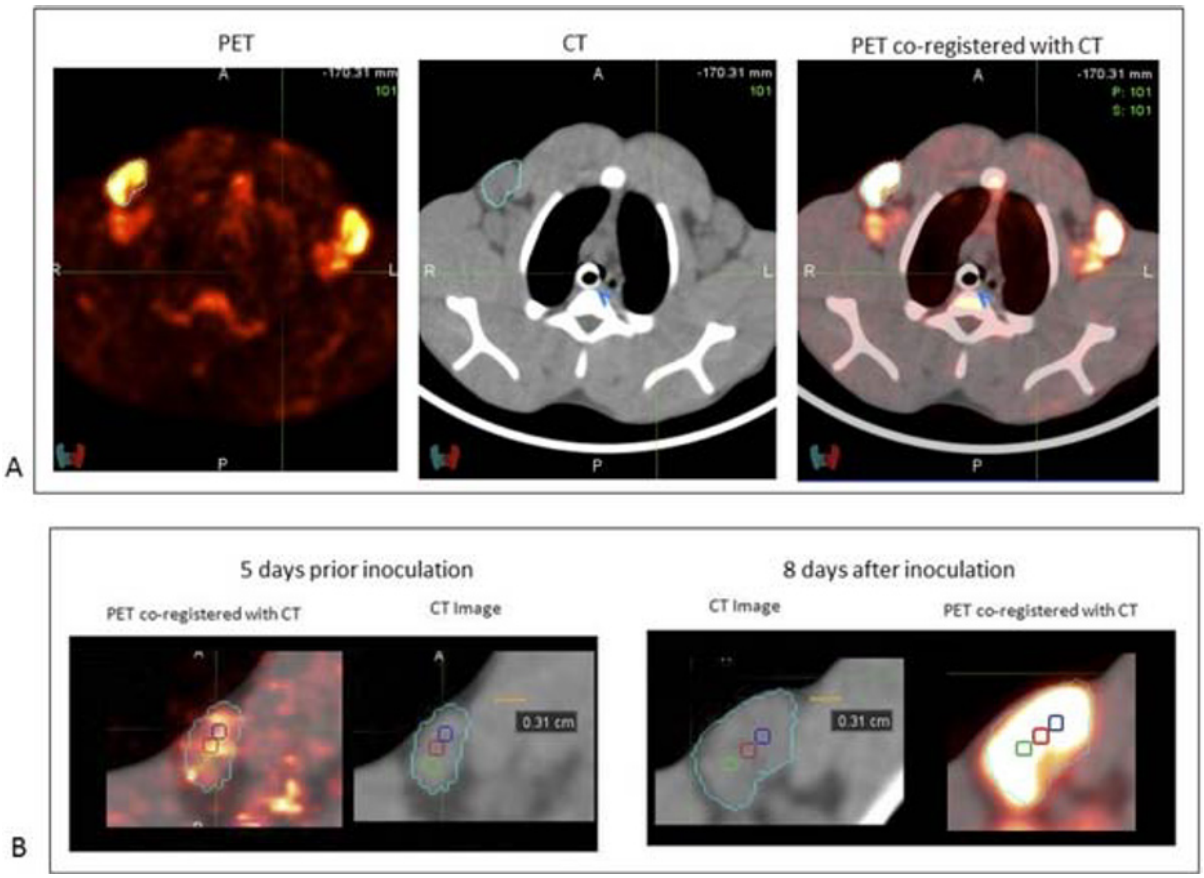

FIg.1. Definition of region of interest (ROI) used for 18F-FDG uptake quantitation in the axillary lymph node (LN) in transaxila view. (A) The ROIs were drawn on the LN identified on CT images coregistered with PET. (B) Enlarged PET and CT images of the same lymph node 5 days prior and 8 days (the same slice is shown in A using smaller magnification) after inoculation, respectively. Three sets of SUVs for each of the animal were derived from 1) a single voxel with maximal SUV (SUVmax); 2) averaging the SUVs from all the voxels inside the whole LN (SUVwhole); 3) from voxels inside three small spheres positioned in the LN center, total of 21 voxels, (SUVcenter).

Disclosure of author financial interest or relationships:
S. Chefer, None; **C.Z. Leyson**, None; **J. Seidel**, None; **R. Johnson**, None; **J.E. Blaney**, None; **J. Dyall**, None; **P.B. Jahrling**, None.

Presentation Number **P 518**
Poster Session 4
September 21, 2013 / 14:45-14:45 / Room: Exhibit Hall B

NOTA conjugation to UBI29-41 allows highly selective infection imaging with PET/CT: A feasibility study in rabbits

Thomas Ebenhan[1,5], *Jacobus D. Venter*[2], *Daniel J. Goosen*[3], *JanRijn Zeevaart*[4], *Neil Jarvis*[5], *Mike Sathekge*[1], [1]*Nuclear Medicine, University of Pretoria, Pretoria, South Africa;* [2]*Medical Research Council, , Pretoria, South Africa;* [3]*Disease Control Africa, , Pretoria, South Africa;* [4]*Science and Technology- Preclinical Drug Development Platform, North West University, Potchefstroom, South Africa;* [5]*Research and Development, South African Nuclear Energy Corporation, Pelindaba, South Africa. Contact e-mail: ebenhan@gmail.com*

Objectives Antimicrobial peptides such as ubiquicidin (UBI) are believed to differentiate between mammalian and bacterial/fungal cells. [99mTc]UBI29-41was previously tested for detecting infection in humans using SPECT imaging. For the present study, the UBI fragment UBI29-41, was conjugated to the chelator NOTA, radiolabeled with [68Ga] and investigated in a rabbit infection model. The functional radiolabeling with [68Ga] will allow acquisition of images with PET/CT. Methods [68Ga] was obtained by fractionated elution from a 1850MBq [68Ga]/[68Ge]generator (iThemba LABS, Cape Town, RSA). Animals were anesthetized with Ketamin and Rompun prior to tracer administration and placed into a clinical PET/CT scanner (Siemens Biograph True Point 40). [68Ga]NOTA-UBI29-41 was formulated in sterile saline solution and 58-150MBq were subsequently administered IV in a single bolus. [68Ga]NOTA-UBI29-41 distribution was studied by PET/CT imaging in New Zealand white rabbits: a) healthy b) bearing infection (Staph. aur. 29213 hind leg muscle) and turpentine oil induced inflammation (contra lateral hind leg muscle) and c) bearing asthmatic lung inflammation (ovalbumin treatment). The SUV quantification was achieved by 3D VOI (region of interest) analysis. For the calculation of T/NT ratios, SUV values were normalising against healthy frontal leg muscle, representing non-targeted tissue. Results PET/CT images of healthy rabbits showed biodistribution dominated by in excretion organs (Bladder SUV 26±15.6; kidneys SUV 3.2±0.89 at 30min postinjection) whereas liver, heart and spleen showed moderate declining uptake. The biological half life was determined 29min in blood. Urine samples showed accumulating activity levels of [68Ga]NOTA-UBI29-41 peaking at 3.8±0.91%ID/g at 120min with an accumulation rate of 1.72%ID/h. The total urine recovery was calculated 88±5.2%ID at 120min. [68Ga]NOTA-UBI29-41 imaging in b) was selectively visualizing the muscular infection site and was capable to differentiate from sterile inflammatory processes in the contra lateral muscle (see Figure 1). SUV ratios for infected muscle/inflamed muscle were 2.5±0.39, 3.0±0.54, 3.5±0.86 and 3.8±0.90 at 5, 30, 60 and 90min postinjection respectively. SUV ratios representing inflammation (range 0.77 to 1.22) didn't differ significantly from accumulation in normal hind muscular tissue (range 0.90 to 1.10). Lung/muscle SUV ratios of rabbit lungs with asthma showed insignificant uptake to lungs of healthy rabbits. The diseased condition for b) and c) were successfully confirmed post imaging by histo-pathological analyses. Conclusion [68Ga]NOTA-UBI29-41 was strongly localised in bacterial infected areas and minimally detected in a sterile inflammation area in rabbit muscles. The findings propose this compound to be an excellent first line PET/CT tracer to allow distinguishing of infection from inflammation as early as 30min postinjection. Also, this tracer is not expected to falsely visualize asthmatic lung inflammation.

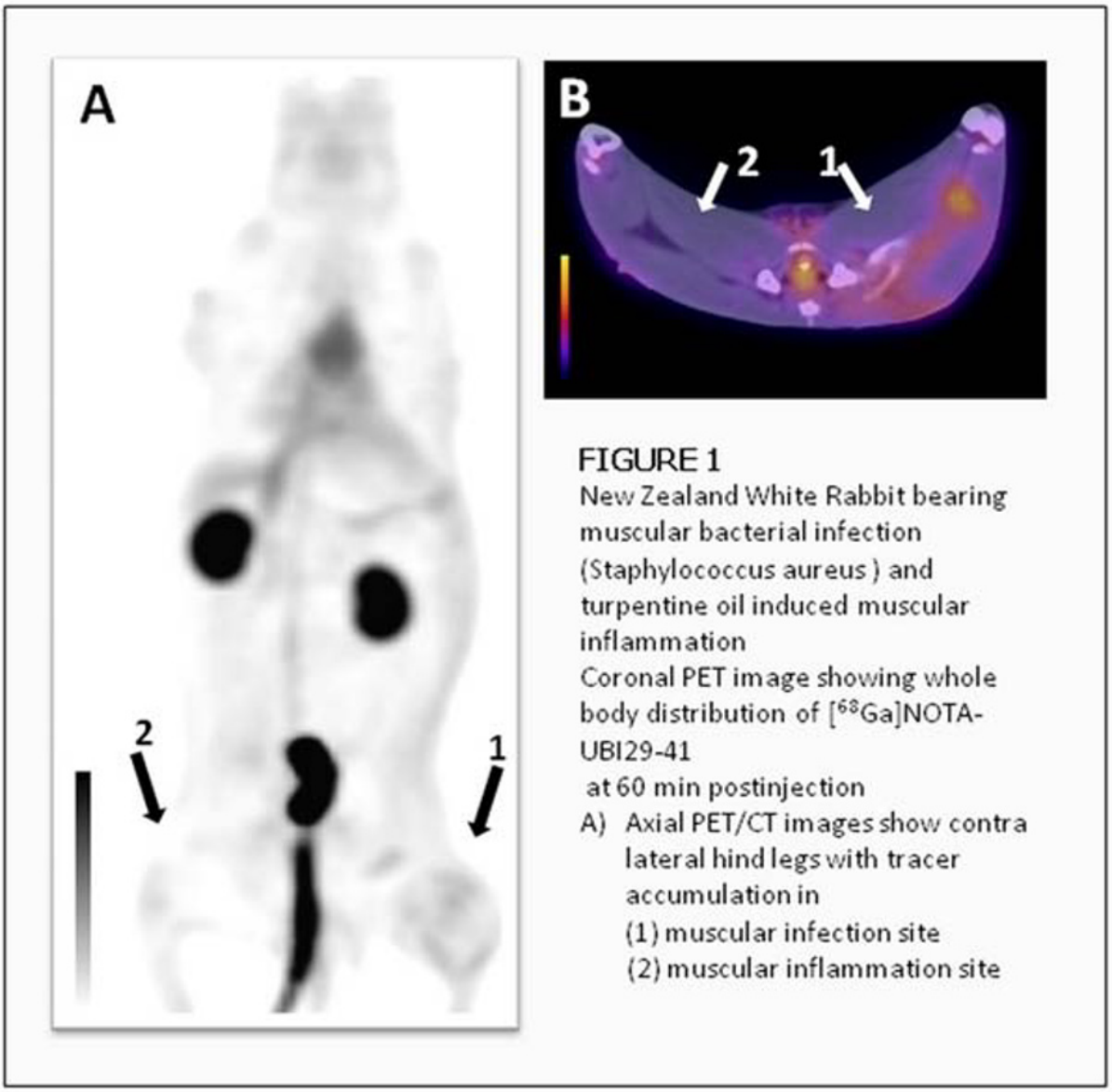

FIGURE 1
New Zealand White Rabbit bearing muscular bacterial infection (Staphylococcus aureus) and turpentine oil induced muscular inflammation
Coronal PET image showing whole body distribution of [^{68}Ga]NOTA-UBI29-41
at 60 min postinjection
A) Axial PET/CT images show contra lateral hind legs with tracer accumulation in
(1) muscular infection site
(2) muscular inflammation site

Disclosure of author financial interest or relationships:
T. Ebenhan, None; **J.D. Venter**, None; **D.J. Goosen**, None; **J. Zeevaart**, None; **N. Jarvis**, None; **M. Sathekge**, None.

Presentation Number **P 519**
Poster Session 4
September 21, 2013 / 14:45-14:45 / Room: Exhibit Hall B

3D in vivo Quantification of Uropathogenic Bacteria

Neal Paragas[1,2], *Sunetra Ray*[3], *Kevin P. Francis*[3], *Alexander D. Klose*[1,2], [1]*Medicine, Columbia University, New York, NY, USA;* [2]*Preclinical Imaging, InVivo Analytics, New York, NY, USA;* [3]*Preclinical Imaging, Caliper- a PerkinElmer Company, Alameda, CA, USA. Contact e-mail: np2014@columbia.edu*

Urogenital tract infection is a disease that annually afflicts more than 250 million people worldwide, with 90% of these infections caused by gram negative E. coli. However, the number of antibiotic resistant strains has also been increasing and thus there is an urgent public health need to validate new antibacterial agents. Testing these agents in the living mouse is the most accurate way to track organ burden overtime, however serial plating of organs is limited to a single timepoint per animal. Bioluminescent imaging (BLI) has been shown to be able to qualitatively tract bacterial infection, but it has never been shown to accurately quantify bacterial colony forming units (CFUs) in 3D in real time. Here we developed a system to quantify a pathogenic bacterial infection with the multispectral bioluminescence tomography (BLT) of a novel bioluminescent uropathogenic E. coli (UPEC-lux). UPEC-lux was generated by delivering the mini-Tn5-luxCDABE transposon to a clinical UPEC isolate (CFT073, ATCC 700928) by conjugation with the donor strain E. coli S17-1 λ-pir (pUTmini-Tn5-luxCDABE-km2). We modeled acute cystitis by implanting a vessel with 50 µl of the UPEC-lux. We then calculated the in vivo lux-bacteria count by employing BLT and a calibration protocol for quantitative in vivo imaging. First, we acquired bioluminescence images with the PhotonImager (BiospaceLab, France) at four different spectral windows centered at 575, 615, 655, 695 nm and with bandwidth of 50 nm. The PhotonImager uses an image intensified charged-coupled-devices (CCD) camera and a mirror gantry for simultaneous imaging of the dorsal and ventral view. The image data set was corrected for the nonuniform lux spectrum and the time-dependent emission kinetics of the lux-bacteria. We used five animals for our pilot imaging study. One animal was used for calibrating the unknown in vivo bacteria count. The animal was anesthesized and a 50 uL vessel with a known amount of bacteria was implanted adjacent to the animals bladder. The animal was secured into an imaging cassette and placed onto the mirror gantry. Spectral images were acquired at 3 minutes camera integration time. The light intensity imaging data became input to a BLT reconstruction algorithm based on an expectation-maximization (EM) method and the simplified spherical harmonics (SP3) equations for modeling in vivo light propagation. The EM method reconstructed the 3D photon emission density of the lux bacteria. Post reconstruction, we calculated the total photon emission density of a volume of interest (VOI) and calibrated it by using the known amount of bacteria placed in the vessel. Last, we compared the calculated in vivo bacteria count to the a priori known bacteria count and found good agreement between the calculated and given quantities (Pearson correlation coefficient R2=0.98, Figure). We further analyzed a these UPEC-lux in a model of pyelonephritis and we were able to determine the bacterial load in the kidney by BLT which correlated to CFUs from serial dilution of kidney homogenate. For the first time, we could demonstrate the feasibility of determining the unknown bacteria count inside a living animal.

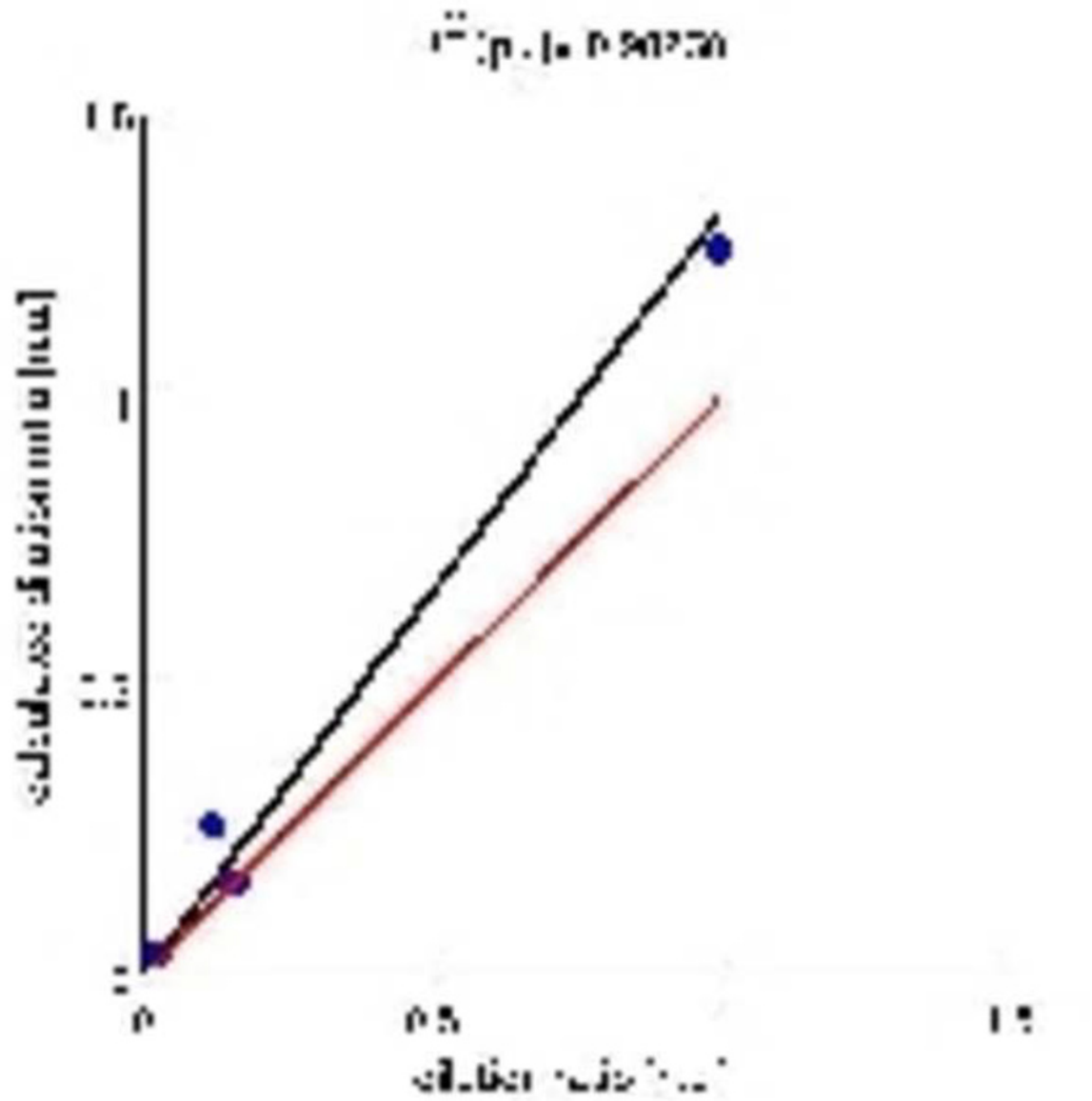

Pearson correlation coeffcient of the bacterial dilution ratio.

Disclosure of author financial interest or relationships:
N. Paragas, INVIVO ANALYTICS, Employment; **S. Ray**, PerkinElmer, Employment; **K.P. Francis**, PerkinElmer, Employment; **A.D. Klose**, InVivoAnalytics, Other financial or material support .

Presentation Number **P 520**
Poster Session 4
September 21, 2013 / 14:45-14:45 / Room: Exhibit Hall B

A simultaneous analysis method for in vivo study of pathogenesis and immune-response without pathogen-specific antibody

Pil-Gu Park, *Sang Hwan Seo, Haeseul Jeong, Min-Hee Cho, Gi-eun Rhie, Kee-jong Hong, Korea National Institute of Health, Cheongwon-gun, Republic of Korea. Contact e-mail: ppkmtg81@gmail.com*

Study on the pathogen and the pathogen-related disease require the experiments in both of organism level and cellular level. In many case, however, dispersed information of each experimental condition with variation of each animal and lack of high-quality antibodies obstruct precise analysis of in vivo mechanism. For reliable study of pathogenesis and immune-response, elaborate analysis which can provide spatio-temopral information of identical object without the concern of false-positive result and/or mis-interpretation are vital. Here, we developed tracing method of bacteria which can analyze from whole animal level to single cell level, without specific antibody for bacteria. Using this method, we traced the process of Francisella tularensis (F. tularensis) pathogenesis in organism and visualized the bacterial replication in cells. And we confirm that vaccination with LPS purified from F. tularensis live vaccine strain (LVS) greatly reduce the bacterial replication of F. tularensis LVS. Our simple and integrated analysis system would be useful for in vivo analysis of infectious diseases which have not been explained yet with technical problems.

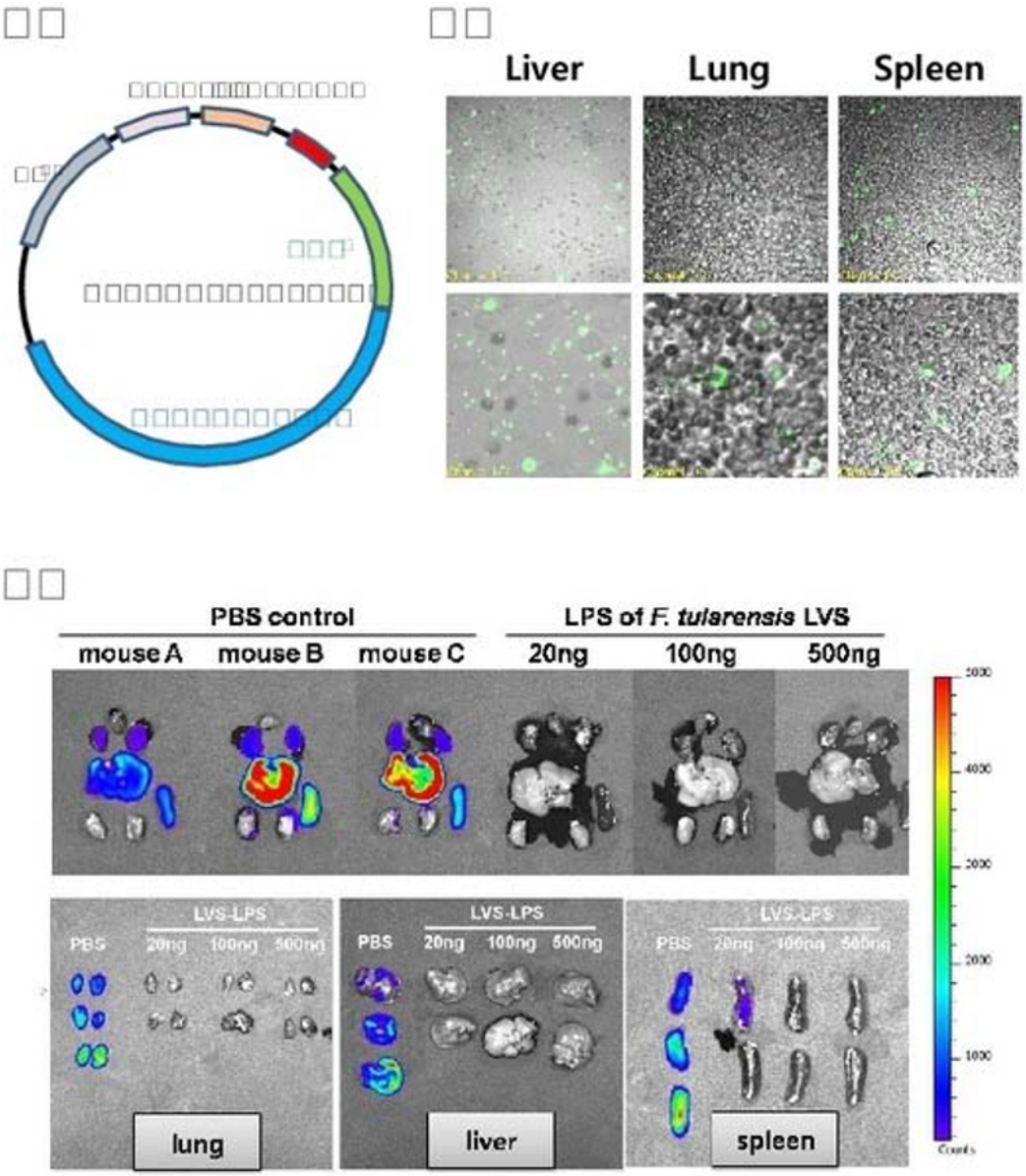

Disclosure of author financial interest or relationships:
P. Park, None; **S. Seo**, None; **H. Jeong**, None; **M. Cho**, None; **G. Rhie**, None; **K. Hong**, None.

Presentation Number **P 521**
Poster Session 4
September 21, 2013 / 14:45-14:45 / Room: Exhibit Hall B

Mouse pulmonary cryptococcosis visualized by a multimodal imaging approach

Greetje Vande Velde[1], *Jennifer D. Poelmans*[1], *Jeroen Vanoirbeek*[2], *Erik K. Verbeken*[1], *Katrien Lagrou*[3], *Tom Dresselaers*[1], *Uwe Himmelreich*[1], [1]*Imaging and Pathology, KU Leuven, Leuven, Belgium;* [2]*Public Health and Primary Care, KU Leuven, Leuven, Belgium;* [3]*Microbiology and Immunology, KU Leuven, Leuven, Belgium. Contact e-mail: greetje.vandevelde@med.kuleuven.be*

Cryptococcus neoformans and gattii are yeasts that can cause life-threatening disease in immuno-suppressed and, in the case of C. gattii, also in immuno-competent individuals. Cryptococcosis mostly affects the lung and may spread to the brain. Why, how and when the cryptococci cross an apparently intact blood-brain-barrier is still enigmatic. Histology is essential to unravel cellular and molecular interactions, but imaging techniques are indispensable to investigate dynamic events in pathogenesis. Therefore, we aimed at dynamically monitoring cryptococcosis non-invasively with MRI and CT in individual mice with cryptococcal pneumonia and meningo-encephalitis, establishing the kinetics of cryptococcal lung infection, thereby defining the critical time points for immuno- and histological analysis of key events in pathogenesis. Balb/C mice were infected with GFP+ C. gattii R265, scanned at baseline and weekly up to 5 weeks post infection (p.i.) with retrospectively gated MRI (9.4T) and CT and lung parameters quantified. We performed intravital microscopy (IVM) and functional lung tests to evaluate lung infection in vivo at a microscopical and functional level. At weekly time points p.i., lungs and brains were isolated for histology and quantification of fungal load. While the mice showed no clinical signs of cryptococcosis, progression of the lung pathology and compensatory mechanisms could be visualized non-invasively and quantified using the here evaluated MRI and CT protocols. The imaging results were in agreement with IVM and functional lung measurements and validated by histochemistry and fungal load quantification at all imaging time points. This is the first study showing that non-invasive monitoring of pneumonial cryptococcosis in mice is feasible with retrospectively gated MRI and CT. These complementary imaging approaches will allow longitudinal screening of animals, thereby visualizing infection onset and progression on an individual basis before the appearance of any phenotypical signs. IVM and functional lung tests were found to be suitable to evaluate infection, but are best considered as end-point measurements due to the invasiveness of the techniques. We will further fine-tune the timing of disease onset and correlate this with the time of traversal of C. neoformans and C.gattii cells to the CNS. This work will greatly help unraveling the still enigmatic pathogenesis of this life-threatening disease.

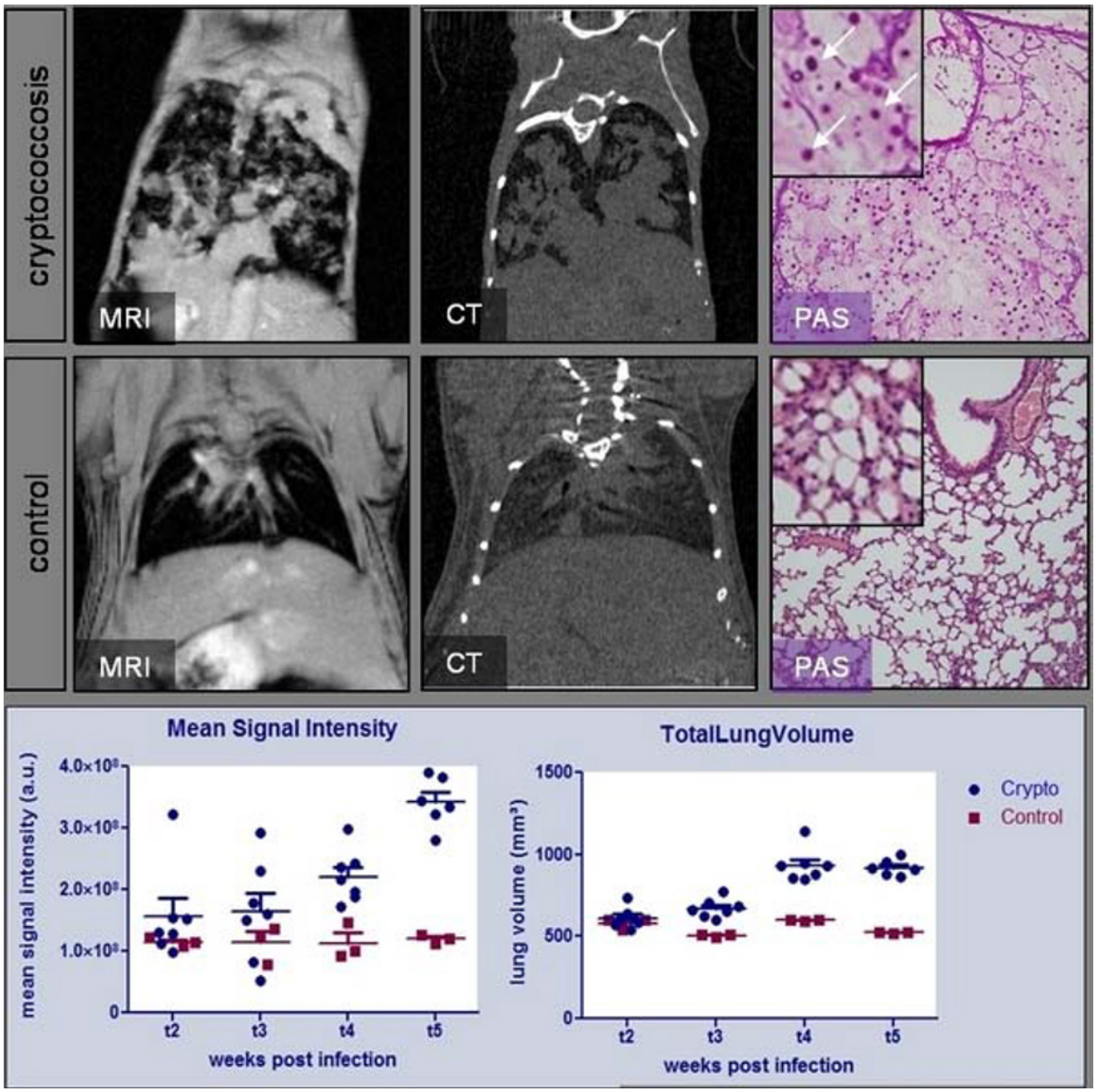

Disclosure of author financial interest or relationships:
G. Vande Velde, None; **J.D. Poelmans**, None; **J. Vanoirbeek**, None; **E.K. Verbeken**, None; **K. Lagrou**, None; **T. Dresselaers**, None; **U. Himmelreich**, None.

Presentation Number **P 522**
Poster Session 4
September 21, 2013 / 14:45-14:45 / Room: Exhibit Hall B

Taxol Enhances T cell-Mediated Therapeutic Effect in Tumor-Bearing Mice

Tzu-Chun Chen, *Jeng-Jong Hwang, Department of Biomedical Imaging and Radiological Sciences, National Yang-Ming University, Taipei, Taiwan. Contact e-mail: supersinger7981@hotmail.com*

Purpose Adoptive cell therapy (ACT) as an alternative treatment for cancers faces a serious obstacle that therapeutic activity of T cells is limited by the tumor microenvironment and immune tolerance of the host. Chemotherapy not only is a standard strategy for cancer therapy, but also can activate the immune system against cancer. Clinical chemotherapy, however, is known to suppress the immune system due to an excess of dosage. In this study, the immuno-modulating effect of ACT combined with low-dose taxol on tumor-bearing mouse model was evaluated with molecular imaging. Materials and Methods OVA-expressing E.G7 mouse lymphoma cells and OT-1 transgenic mice were used in this study. E.G7 cells were pretreated with 12.5 nM taxol for 24 h (surviving fraction was ~10%), then co-cultured with CD8+ T cells for additional 4 h. The activation of CD8+ T cells and intracellular IFN-γ and IL-2 were assayed by flow cytometry. Since the contact of T cells and E.G7 cells is necessary for activation of T cells, the chemotaxis of T cells was evaluated by transwell assay. Therapeutic efficacy of low-dose taxol combined with ACT was evaluated with molecular imaging in E.G7/OT-1 mouse model. CD8+ T cells isolated from OT-1 mice were transfected with pGBeLT lentivirus for monitoring the activation and track of CD8+ T cells in vivo. Immunosuppressive factors in E.G7 cells and the tumor, including IL-10, COX-2, TGF-β, MCP-1, IDO, VEGF, and pSTAT3 were assayed by Western blotting, respectively. Both Tregs and MDSCs immunosuppressive cells were detected with antibodies conjugated with fluorescent dyes. Results The percentage of activated CD8+ T cells and intracellular IFN-γ production were significantly increased ($p<0.001$) after co-cultured with taxol-pretreated E.G7 cells as compared with that of co-cultured with untreated E.G7 cells. The percentage of intracellular IL-2 production was also significantly increased ($p< 0.01$). In addition, the migration ability of CD8+ T cells was elevated only in the group of co-cultured with taxol-pretreated E.G7 cells. All immunosuppressive factors assayed were decreased in the taxol-pretreated E.G7 cells and the tumor. Tumor growth is significantly inhibited in mice pretreated with taxol (10 mg/kg, one day before ACT by gavage) plus 2x10^6 CD8+ T cells (2T), and 5x10^6 CD8+ T cells (5T) alone, respectively. The immunosuppressive cells, such as Tregs and MDSCs, were decreased in taxol-treated mice. Conclusions Activation of CD8+ T cells and the therapeutic efficacy of ACT in E.G7/OT-1 mouse model could be significantly improved by pretreatment with taxol. Taxol may modify the immune system of microenvironment in the tumor and the host to pave a way for ACT. Notably, the pGBeLT reporter system combined with the imaging modality provides a powerful tool for screening the potential immunomodulation compounds to support ACT. (This study is supported by a grant NSC 101-2321-B-010-006 from National Science Council, Taipei, Taiwan.)

Disclosure of author financial interest or relationships:
T. Chen, None; **J. Hwang**, None.

Presentation Number **P 523**
Poster Session 4
September 21, 2013 / 14:45-14:45 / Room: Exhibit Hall B

Continuous flushing of the bladder in small animals reduces image artifacts and improves quantification in molecular imaging: exemplified in a mouse TNBS colitis model using µPET/CT

Steven Deleye[1], *Marthe Heylen*[2], *Annemie Deiteren*[2], *Joris De Man*[2], *Benedicte Y. De Winter*[2], *Sigrid Stroobants*[3], *Steven Staelens*[1], [1]*Molecular Imaging Center Antwerp, University of Antwerp, Antwerp, Belgium;* [2]*Laboratory of Experimental Medicine and Pediatrics, Division of Gastroenterology, University of Antwerp, Antwerp, Belgium;* [3]*Nuclear Medicine Department, University Hospital Antwerp, Antwerp, Belgium. Contact e-mail: steven.deleye@ua.ac.be*

INTRODUCTION In many molecular imaging techniques (SPECT, PET, MRI,…) the accumulation of the imaging probe or contrast agent in the bladder can cause image artifacts and can hamper the quantification of the tracer in a nearby organ or region-of-interest (ROI). We have designed a device to continuously clear the bladder of small animals during in vivo scans. Here we investigate the influence of the urinary secretion of 18F-FDG (FluoroDeoxyGlucose) on the pathologic signal caused by inflammation in the colon of OF1 mice using µPET/CT in animals with and without their bladder emptied. METHODS Female OF1 mice (n=24) were scanned using µPET/CT (Siemens, Knoxville, TN) before and 3 days after induction of acute colitis by injecting 2,4,6-trinitrobenzene sulfonic acid (TNBS, 3 mg in 30% EtOH) into the colon. Mice were fasted overnight, after which they received an intravenous injection of 18.5 MBq 18F-FDG 30 min before the PET (10min) / CT scan. To visualize the colon on the CT, mice were rectally injected with gastrografin (0.5 ml) a few seconds before the acquisition. During the scans in one group (n=12) the bladder was continuously flushed using a double-lumen urethral catheter, while in the other group (n=12) no bladder flushing was performed. To insert the catheter, the animal was put in gynecological position using a dedicated in-house designed frame. Water was injected at a rate of 15 ml/h using a clinical infusion pump (Fresenius, Germany). Volumes of interest for the colon (ROI) and the brain (reference region) were outlined on the CT images. The ratio of the mean voxel counts of the PET in both aforementioned regions was calculated. As a means of in vivo validation animals also underwent colonoscopy at days 0 & 3. Additionally, on both days mice (n=6) were sacrificed to score the colonic damage micro- and macroscopically for ex vivo validation. Correlations between the PET values and colonoscopy, micro- and macroscopy were tested by Pearson's correlation coefficient. RESULTS At baseline, before induction of colitis the average count ratio colon/brain was already 0.81±0.09 for mice imaged without flushing while this was only and 0.58±0.04 if the device was used. At day 3, the ratios increased due to the fulminant inflammation respectively to 1.01±0.07 and 0.76±0.08. The correlations of mice without their bladder flushed was only 0.41, 0.12 and 0.005 for colono-, macro- and microscopy while the correlations are much higher when there is no accumulation of 18F-FDG in the bladder: 0.82, 0.73 and 0.72. CONCLUSION Without bladder flushing there is a false positive rate of 41% at day 0, while this is only 8% if the bladder is continuously flushed during the scan. High correlations with in vivo colonoscopy, micro- and macroscopic ex vivo scorings can be obtained provided the mouse bladder is flushed during the PET scan. We have performed a similar study in rats and results are underway.

Disclosure of author financial interest or relationships:
S. Deleye, None; **M. Heylen**, None; **A. Deiteren**, None; **J. De Man**, None; **B.Y. De Winter**, None; **S. Stroobants**, Janssen Pharmaceuticals, Grant/research support; **S. Staelens**, Johnson & Johnson, Grant/research support .

Presentation Number **P 524**
Poster Session 4
September 21, 2013 / 14:45-14:45 / Room: Exhibit Hall B

Functional and Molecular Imaging of Liver and Kidney Fibrosis

Josef Ehling[1], *Matthias Bartneck*[2], *Janka Bábíčková*[3], *Felix Gremse*[1], *Zhuojun Wu*[1], *Rene M. Botnar*[4], *Marc van Zandvoort*[5], *Peter Boor*[3], *Frank Tacke*[2], *Fabian Kiessling*[1], *Twan Lammers*[1], [1]*Department of Experimental Molecular Imaging, University of Aachen (RWTH), Aachen, Germany;* [2]*Department of Medicine III, University of Aachen (RWTH), Aachen, Germany;* [3]*Department of Medicine II, University of Aachen (RWTH), Aachen, Germany;* [4]*Division of Imaging Sciences and Biomedical Engineering, King's College London, London, United Kingdom;* [5]*Institute for Molecular Cardiovascular Research, University of Aachen (RWTH), Aachen, Germany. Contact e-mail: jehling@ukaachen.de*

Introduction: Fibrosis refers to the excessive deposition of extracellular matrix (ECM) proteins as a reactive process to chronic injuries and results in a pathological obliteration of organ architecture and function. Two of the most commonly affected organs are the liver and the kidney, affecting millions of people worldwide. Remarkably, however, hardly any diagnostic probes and protocols are available for the non-invasive diagnosis and staging of liver and kidney fibrosis. The aim of our efforts is to establish novel contrast agents and imaging techniques for the visualization and quantification of liver and kidney fibrosis, as well as for non-invasive therapy monitoring. Methods: Four different animal models were used, two for liver (carbon tetrachloride (CCl4) and bile duct ligation (BDL)) and two for kidney (unilateral ureteral obstruction (UUO) and Alport mice) fibrosis. Functional imaging of blood vessels in fibrotic livers and kidneys was performed by contrast-enhanced micro-CT, providing information on the relative blood volume (rBV). rBV values were determined at 2, 4, 6 and 8 weeks of repetitive CCl4 injury and 3 weeks after BDL, as well as at 1, 3, 5, 7 and 10 days after UUO, and in 6 and 8 weeks old Alport mice. For therapy monitoring, mice were imaged upon treatment with an inhibitor of CCL2, a key factor for recruiting inflammatory macrophages. Finally, ECM deposition during disease progression was imaged using a novel elastin-specific molecular imaging agent and T1-weighted molecular MRI. Findings were validated by histology, FACS and qPCR. Results: In fibrotic livers, sprouting angiogenesis was observed (Fig. 1A) and the rBV significantly increased from early- to late-stage disease (from +11% at 2 weeks to +40% at 8 weeks of CCl4 exposure). In line with this, infiltrating inflammatory macrophages highly expressed VEGF. The pharmacological inhibition of macrophage infiltration using a CCL2 inhibitor significantly inhibited fibrosis-associated angiogenesis (rBV=25% in untreated vs. rBV=18% in anti-CCL2-treated mice). In contrast, vessel rarefaction was observed in fibrotic kidneys (Fig. 1B) and the rBV significantly decreased during disease progression (from -33% at day 3 of UUO to -66% at day 10). Using an elastin-specific contrast agent (ESMA) and molecular MRI, a strong perivascular T1 signal enhancement was observed in fibrotic livers (Fig. 1C). In case of kidney fibrosis, a specific accumulation of ESMA in fibrotic kidneys could be observed in contrast to unspecific gadolinium-based contrast agents (Fig. 1D). Conclusions: Novel contrast agents and imaging protocols were established for monitoring liver and kidney fibrosis using μCT and MRI. While liver fibrosis was characterized by the infiltration of inflammatory macrophages, which promote angiogenesis, and strong perivascular elastin deposition, kidney fibrosis showed a progressive reduction of blood vessels and a strong perivascular elasting formation. Our findings contribute to a better understanding of fibrosis, and to the establishment of novel and clinically relevant imaging protocols for facilitating the diagnosis and treatment of liver and kidney fibrosis.

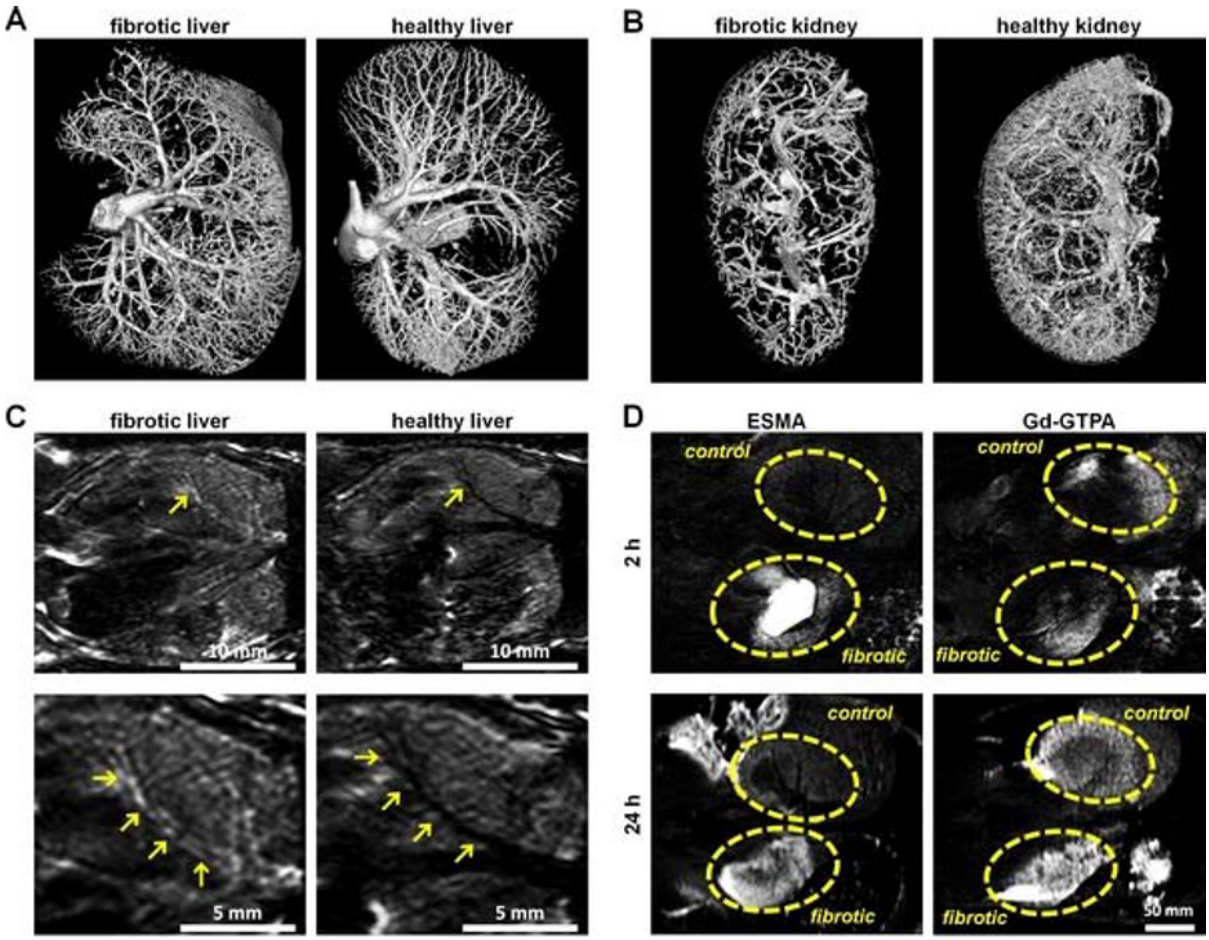

Figure 1: A+B) High-resolution contrast-enhanced μCT imaging of functional blood vessels in fibrotic and healthy livers (A) and kidneys (B). C-D) Elastin-based molecular MRI of liver and kidney fibrosis resulting in a significant perivascular T1 contrast enhancement in fibrotic livers (C; from Ehling et al. Hepatology 2013; doi:10.1002/hep.26326) and in a specific ESMA accumulation in fibrotic kidneys (D).

Disclosure of author financial interest or relationships:
J. Ehling, None; **M. Bartneck**, None; **J. Bábíčková**, None; **F. Gremse**, None; **Z. Wu**, None; **R.M. Botnar**, None; **M. van Zandvoort**, None; **P. Boor**, None; **F. Tacke**, None; **F. Kiessling**, None; **T. Lammers**, None.

Presentation Number **P 525**
Poster Session 4
September 21, 2013 / 14:45-14:45 / Room: Exhibit Hall B

Lessons learnt from reporter gene imaging of regulatory T cell therapy in transplantation: a non-invasive whole body nuclear imaging study

Ehsan Sharif-Paghaleh[1,2], John Leech[1], Robert Lechler[1], Lesley A. Smyth[1], Giovanna Lombardi[1], **Greg Mullen**[1,2], [1]*MRC Centre for Transplantation, KCL, London, United Kingdom;* [2]*Imaging Sciences, KCL, London, United Kingdom. Contact e-mail: greg.mullen@kcl.ac.uk*

Regulatory T cells (Tregs) were identified several years ago and are key in controlling autoimmune diseases and limiting immune responses to foreign antigens. Tregs are being studied for adoptive transfer immunotherapy for various diseases such preventing transplant rejection. However, key questions such as where therapeutic Tregs go and how long they stay viable in patients remains unsolved. Here we are trying to answer these questions in a pre-clinical set up with the help of nuclear medicine imaging technology. Imaging of the human sodium/iodide symporter via Single Photon Emission Computed Tomography (SPECT) has been used to image various cell types in vivo. This study addresses whether SPECT/CT imaging can be used to visualise the migratory pattern of Tregs in vivo. Murine Treg lines were retrovirally transduced with a construct encoding for the human Sodium Iodide Symporter (NIS). NIS expressing Tregs were specifically radiolabelled in vitro with Technetium-99m pertechnetate (99mTcO4-) and exposure of these cells to radioactivity did not affect cell viability, phenotype or function. In addition adoptively transferred Treg-NIS cells were imaged in vivo in mice by SPECT/CT using 99mTcO4-. After 24-hours Treg-NIS cells were observed in the spleen and their localisation was further confirmed by organ-biodistribution studies and flow cytometry analysis. Moreover, we have demonstrated that this method of imaging can be utilised to image migration of Tregs with direct and indirect allo-specificity in a skin transplant model. Interestingly, Tregs that prolonged the transplant survival demonstrated a different pattern of migration compared to Tregs that were unable to prolong the transplant survival. The data presented here suggests that SPECT/CT can be utilised in preclinical imaging studies of adoptively transferred Tregs without affecting Treg function and viability thereby allowing longitudinal studies within disease models. Moreover, this technology has also the potential to be applied to human Treg studies in future.

Disclosure of author financial interest or relationships:
E. Sharif-Paghaleh, None; **J. Leech**, None; **R. Lechler**, None; **L.A. Smyth**, None; **G. Lombardi**, None; **G. Mullen**, Mediso, Consultant .

Presentation Number **P 526**
Poster Session 4
September 21, 2013 / 14:45-14:45 / Room: Exhibit Hall B

P38-MAPK Therapy Monitoring in Experimental Arthritis by Non-invasive *In vivo* Hypoxia PET-Imaging using [^{18}F]-Fluoromisonidazole ([^{18}F]FMISO)

Philipp Guenthoer[1], *Kerstin Fuchs*[1], *Manfred Kneilling*[1,3], *Denis Lamparter*[1], *Gerald Reischl*[1], *Sandro Aidone*[1], *Maren K. Koenig*[1], *Stefan A. Laufer*[2], *Bernd J. Pichler*[1], [1]*Preclinical Imaging and Radiopharmacy, University of Tuebingen, Tuebingen, Germany;* [2]*Pharmacy and Biochemistry, University of Tuebingen, Tuebingen, Germany;* [3]*Dermatology, University of Tuebingen, Tuebingen, Germany. Contact e-mail: philipp.guenthoer@med.uni-tuebingen.de*

Various signaling pathways are involved in inflammatory immune responses. Thus, inhibition of distinct signaling pathways by specific inhibitors are powerful tools in the treatment of autoimmune diseases such as rheumatoid arthritis (RA). Protein kinases are important for innate and adaptive immune responses and can be targeted by small-molecule-inhibitors. P38-mitogen-activated protein kinases (MAPK) are one of the key kinases of inflammatory immune responses which are also regulated by hypoxia. The p38-MAPK signaling pathway is critically involved in chronic inflammatory immune responses such as RA, psoriasis and asthma. Aim of our study was to elucidate the therapeutic potential of our newly developed specific small-molecule-p38-MAPK-inhibitor (ML3595) to cure experimental RA and whether *in vivo* hypoxia [^{18}F]FMISO-PET imaging is suitable for therapy monitoring. In experiments, arthritis was induced in naïve BALB/c mice by injection of Glucose-6 phosphate-isomerase (GPI) antibody containing serum. Control mice were injected with control-serum. ML3595 (30 mg/kg mouse) or PBS-sham treatment was applied per os once daily starting three days prior to arthritis induction until the end of the experiment at day seven. The course of ankle swelling was measured daily and [^{18}F]FMISO-PET-imaging was performed on day 3 and 6 after arthritis induction to monitor therapeutic potential of ML3595 non-invasivly *in vivo*. Finally we performed histological analysis (H&E staining). Therapy studies with p38-MAPK treatment indicated significantly ($p<0.03$) reduced ankle swellings starting at day 1 after onset of arthritis (ML3595: 2.8±0.1 mm; sham: 3.0±0.1 mm). Maximum ankle swelling in the sham as well as in the ML3595-treated experimental mice was achieved at day 6 after GPI-serum injection (ML3595: 3.3±0.4 mm; sham: 3.7±0.1 mm). At this time point the ankle swelling in the ML3595-treated mice was 11% reduced compared to the sham-treated mice. At day 8 after disease onset the ankle swelling in ML3595-treated mice was 12% reduced (3.1±0.3 mm) compared to the sham-treated mice (3.5±0.2 mm). In contrast with our data for ankle swelling, *in vivo* [^{18}F]FMISO-PET imaging at day 3 after onset of disease yielded no differences in tracer uptake between the two groups (ML3595: 2.33±0.2%ID/cc, PBS: 2.28±0.2%ID/cc). On day 6 after arthritis induction we detected a decreased tracer uptake and hence less hypoxia in ankles of the ML3595-treated mice compared to sham-treated arthritic mice (ML3595: 2.34±0.4%ID/cc, PBS: 2.75±0.2%ID/cc). Histological analysis of arthritic ankles revealed a reduced joint destruction and pannus formation in ML3595-treated mice when compared to sham-treated mice. Treatment with ML3595 significantly reduced the ankle swelling in experimental RA. Thus, the selective p38-MAPK inhibitor ML3595 is a

potential new agent for treatment of experimental RA and maybe other systemic autoimmune diseases. Non-invasive *in vivo* [^{18}F]FMISO-PET imaging of hypoxia seems to be an appropriate tool for therapy monitoring not during early stages but during advanced stages of experimental RA.

Disclosure of author financial interest or relationships:
P. Guenthoer, None; **K. Fuchs**, None; **M. Kneilling**, None; **D. Lamparter**, None; **G. Reischl**, None; **S. Aidone**, None; **M.K. Koenig**, None; **S.A. Laufer**, None; **B.J. Pichler**, Siemens, Grant/research support; Bayer, Grant/research support; AstraZeneca, Grant/research support; BoehringerIngelheim, Grant/research support .

Presentation Number **P 527**
Poster Session 4
September 21, 2013 / 14:45-14:45 / Room: Exhibit Hall B

A new potential PET imaging strategy for experimental autoimmune encephalomyelitis and multiple sclerosis using an ^{18}F-acycloguanosine radiotracer

Michelle L. James[1], *Zhaoqing Ding*[2], *Jian Luo*[2], *Vidhu Mathur*[2], *Tony Wyss-Coray*[2], *Sanjiv S. Gambhir*[1], [1]*Radiology, Stanford University, Stanford, CA, USA;* [2]*Neurology & Neurological Science, Stanford University, Stanford, CA, USA. Contact e-mail: mljames@stanford.edu*

Recently we observed that ganciclovir (GCV), an approved acycloguanosine anti-viral drug, significantly attenuates disease in a mouse model of multiple sclerosis (MS), known as experimental autoimmune encephalomyelitis (EAE). This unexpected finding led to a series of *in vitro* and *in vivo* studies aimed at investigating the possible central and/or peripheral mechanism of GCV in EAE mice. As part of this work, we aimed to assess the biodistribution and kinetics of a known radiolabeled analogue of penciclovir, [^{18}F]FHBG (which is similar in structure to GCV), in EAE versus naïve mice via small animal positron emission tomography (PET), *ex vivo* gamma counting of tissues, and digital autoradiography. **Methods**: EAE was actively induced in C57BL/6 mice by subcutaneous injection of MOG35-55 peptide in complete Freund's adjuvant, followed by tail-vein injections of pertussis toxin. Clinical signs of disease were scored daily according to a standard scoring system. EAE (n=3) and naïve (n=3) mice underwent dynamic PET imaging following tail-vein administration of [^{18}F]FHBG (~100-120 µCi). Mice were perfused and sacrificed at 100 min p.i., and radioactivity from dissected tissues was measured with a gamma-counter. Additionally, brain sections and spinal cords were analyzed via *ex vivo* digital autoradiography. **Results**: Dynamic brain PET imaging demonstrated rapid accumulation of [^{18}F]FHBG in EAE mouse brain which remained at approximately the same level throughout the 60 min scan. In contrast, the time activity curve (TAC) and PET images for [^{18}F]FHBG accumulation in naïve mouse brain appeared to be indicative of blood flow - i.e., an initial peak of uptake, followed by swift washout of the radiotracer. Carrier added [^{18}F]FHBG dynamic PET in EAE mouse brain resulted in a TAC and PET image similar to that observed for [^{18}F]FHBG in naïve mouse brain. Biodistribution results reveled a dramatic difference in [^{18}F]FHBG accumulation in EAE (n=3) tissues compared to naïve (n=3) tissues - i.e., *15-fold difference* in brain (0.22±0.041 vs. 0.015±0.0034 %ID/g, $p<0.05$), *47-fold difference* in spinal cord (1.5±0.18 vs 0.032±0.014 %ID/g, $p<0.005$), *12-fold difference* in blood (4.0±0.30 vs 0.33±0.054 %ID/g, $p<0.0005$), and *8-fold difference* in muscle (2.3±0.54 vs 0.28±0.094 %ID/g, $p<0.05$). Similarly, autoradiography images illustrated markedly higher [^{18}F]FHBG signal in EAE mouse brain sections (mainly in cerebellum and brain stem - Figure 1A) and spinal cord (Figure 1B) compared to that seen in naïve mice. **Conclusion**: PET imaging results, *ex vivo* biodistribution, and digital autoradiography indicate that [^{18}F]FHBG is able to penetrate and accumulate in both brain and spinal cord of EAE but not naïve mice. Although our data suggests that [^{18}F]FHBG might be interacting with a target in the central nervous system (CNS) of EAE mice, further studies are required to fully understand the mechanism of [^{18}F]FHBG/GCV in this animal model. [^{18}F]FHBG imaging shows great potential as a possible tool for visualizing the progression and treatment of EAE and MS.

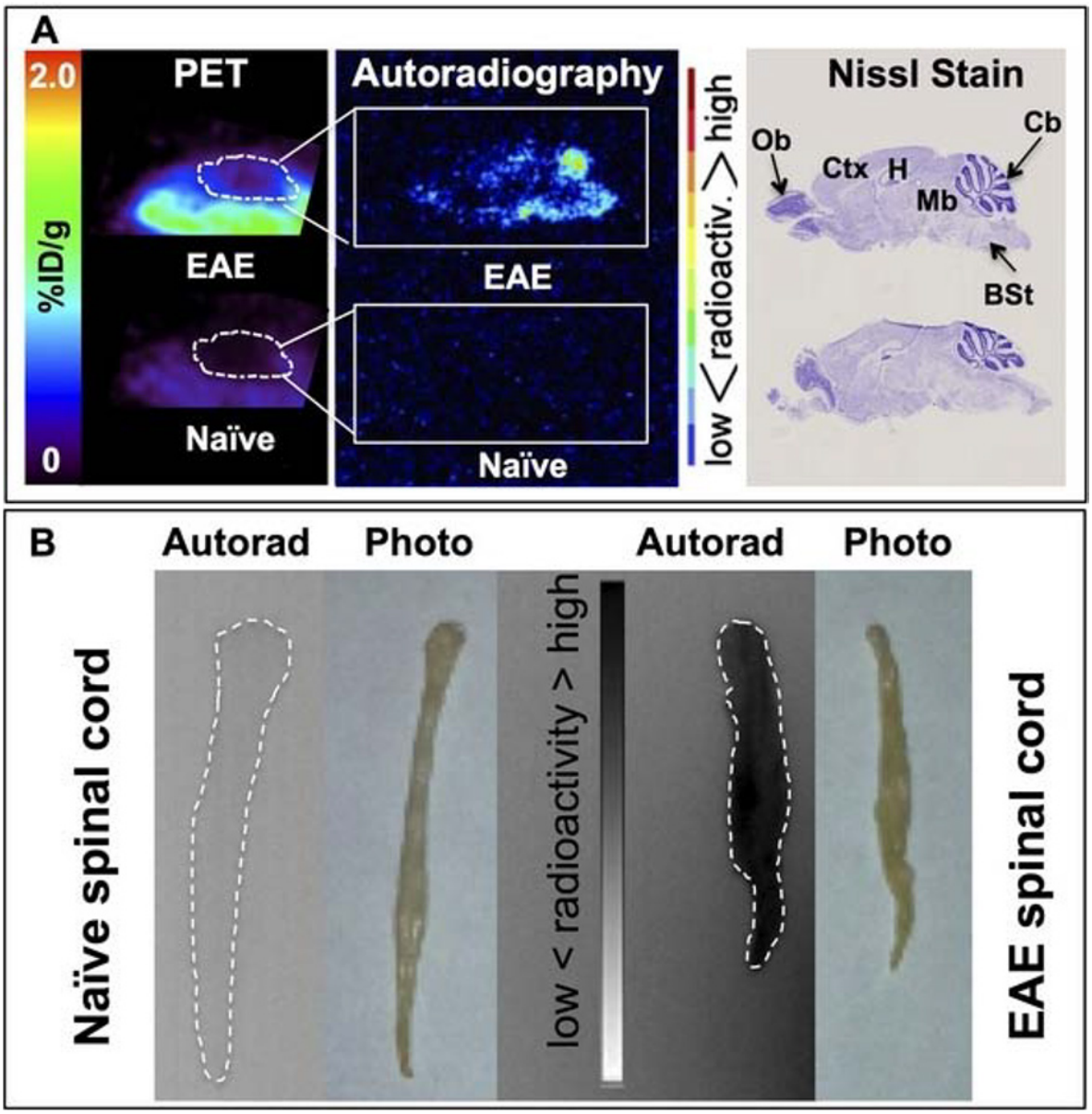

Figure 1. Mouse brain [^{18}F]FHBG-PET images and *ex vivo* autoradiography of an experimental autoimmune encephalomyelitis (EAE) mouse and age-matched naïve mouse. A) Sagittal brain PET images of [^{18}F]FHBG accumulation 90 min post-injection (p.i.) of radiotracer (~100-120 µCi) in EAE versus naïve mice (white dashed lines indicated outline of mouse brain in PET image), *ex vivo* autoradiography of sagittal brain sections (on the same scale) 100 min p.i. radiotracer, and nissl staining of same sections (for anatomical correlation); B) *ex vivo* autoradiography of spinal cords 100 min p.i. from naïve versus EAE mouse 100 min post-injection of [^{18}F]FHBG. White dashed lines indicate outline of the spinal cord in autoradiography (autorad) images. Photographs were taken of each spinal cord immediately prior to exposing them to digital autoradiography film. BSt = brain stem, Cb = cerebellum, Ctx = cortex, H = hippocampus, Mb = midbrain, Ob = olfactory bulb.

Disclosure of author financial interest or relationships:

M.L. James, None; **Z. Ding**, None; **J. Luo**, None; **V. Mathur**, None; **T. Wyss-Coray**, None; **S.S. Gambhir**, Bracco Diagnostics, Consultant; Endra, Inc, Stockholder; Cellsight, Stockholder; Enlight, Inc., Stockholder; General Electric, Grant/research support; ImaginAb, Stockholder; MagArray, Inc., Stockholder; Sanofi-Aventis, US, Grant/research support; SiteOne Therapeutics, Stockholder; VisualSonics/Sonosite, Stockholder .

Presentation Number **P 528**
Poster Session 4
September 21, 2013 / 14:45-14:45 / Room: Exhibit Hall B

In vivo tracking of primary macrophage migration toward acute inflammation lesion with combined MR/fluorescent nanoparticles

Ho Won Lee[1], *Yong Hyun Jeon*[1], *Sungmin Kang*[3], *Thoudam Debraj Singh*[1], *Yun Ju Choi*[1], *Sang-Woo Lee*[1], *Jeoung-Hee Ha*[2], *Byeong-Cheol Ahn*[1], *Jaetae Lee*[1], [1]*Nuclear Medicine, School of Medicine, Kyungpook National University, Daegu, Republic of Korea;* [2]*Phamacology, School of Medicine, Kyungpook National University, Daegu, Republic of Korea;* [3]*Nuclear Medicine, Catholic university hospital, Daegu, Republic of Korea. Contact e-mail: howon1234@hanmail.net*

Purpose: The aim of this study is to monitor the migration of near-infrared (NIR) fluorescent magnetic nanoparticle labeled primary macrophage toward carrageenan (CG)-induced acute inflammatory lesion in mice and evaluate the efficacy of anti-inflammatory drug using combined magnetic resonance and fluorescence imaging. Materials and methods: Primary peritoneal macrophage (thioglycollate-elicited) were labeled with NIR fluorescent magnetic nanoparticles (NEO-LIVETM Magnoxide 675, Ex/Em: 675nm/700nm) and cell labeling efficiency was assessed using a flow cytometry. Phenotype marker (such as F4/80, CD11b, CD86 and MHC class I), cell viability and phagocytic activity were investigated in non-labeled macrophage and labeled macrophage. Two independent animal experiments were executed as following; 1) For tracking study of macrophage in vivo, labeled macrophages were intravenously administered into mice. 24h later each mouse received either PBS or 1% CG solution in left paw and right paw, respectively and MRI/FLI was acquired. 2) For drug intervention study, mice received either a single IP dose of 30mg/kg dexamethasone (anti-inflammatory drug, DEX) or no treatment post 24h transfer of labeled macrophage. Acute inflammation was induced with CG and MR/FLI imaging was acquired. MR imaging and FLI was done with small animal 4.7T MR and IVIS 200 spectrum at designated time. Results: FACS analysis showed about ~90% labeling efficiency in macrophages and there were no significant differences in expression level of phenotype marker, cell viability and phagocytic activity between non-labeled and labeled-macrophages. In vivo imaging exhibited the increase of FLI signals in CG-injected paws in a time-dependent manner, with relative increase (%) of FLI signals up to ~20.1%, 63.8%, and 80.7% in CG-treated paw compared to PBS-treated paw at 3h, 6h and 24h post-injection. Otherwise, single dose treatment of DEX delayed the influx of labeled macrophage in CG-injected paw, with relative decrease (%) of FLI signals to ~9.7%, 15.8% and 14.9% in CG-treated paw at 3h, 6h and 24h post-injection. In accordance with FLI, T2*-weighted gradient echo pulse images showed very hypointense signals in CG-treated paw but not PBS-treated paw at 24h after CG-inflammation induction. Furthermore, reduction in the hypointense signals of CG-treated paw was observed in DEX-treated mice but not PBS-treated mice at 24h after inflammation induction. Conclusions: We successfully not only tracked the NIR fluorescent magnetic nanoparticles labeled-macrophage migration to CG-induced paw edemas using FLI and MR multi-modal imaging but also visualized the inhibition effects of its influx to edema site by treatment of anti-inflammatory drug.

Disclosure of author financial interest or relationships:
H. Lee, None; **Y. Jeon**, None; **S. Kang**, None; **T. Debraj Singh**, None; **Y. Choi**, None; **S. Lee**, None; **J. Ha**, None; **B. Ahn**, None; **J. Lee**, None.

Presentation Number **P 529**
Poster Session 4
September 21, 2013 / 14:45-14:45 / Room: Exhibit Hall B

Longitudinal [18F]PBR06 PET imaging indicates an inverse relationship between microglial activation and motor function during stroke-induced neuroinflammation in mice

Frederick M. Lartey[1], *Rehan Ali*[1], *Sahar Rosenblum*[2], *Bin Shen*[3], *Zheng Miao*[3], *Marjan Rafat*[1], *Marta Vilalta*[1], *Theo Palmer*[2], *Frederick T. Chin*[3], *Edward E. Graves*[1], *Raphael Guzman*[2], *Billy W. Loo*[1], [1]*Radiation Oncology, Stanford University, Stanford, CA, USA;* [2]*Neurosurgery, Stanford University, Stanford, CA, USA;* [3]*Radiology, Stanford University, Stanford, CA, USA. Contact e-mail: fmlartey@stanford.edu*

Objectives: [18F]N-fluoroacetyl-N-(2,5-dimethoxybenzyl)-2-phenoxyaniline ([18F]PBR06) is a radioligand that serves as a substrate for the microglial biomarker, translocator protein 18 kDa (TSPO). The objectives of this study were to characterize the time course of stroke-induced neuroinflammation (SIN) using [18F]-PBR06 PET/MR imaging and to correlate the imaging times with functional testing (rotarod tests) to investigate the role of brain microglia in learning/motor function after stroke. Methods: Stroke was induced by the middle cerebral artery occlusion (MCAO) procedure in female Balb/c mice and confirmed with MRI. Three days later, after undergoing functional rotarod tests, the mice were injected with [18F]PBR06 (200 µCi) intravenously. PET/CT imaging was performed 80 minutes post injection and the results were analyzed with RTImage, an in- house imaging software program. The functional tests and imaging runs were repeated at days 10, 17, 23 and 31 days post stroke induction (p.s.i.). After the last imaging time point, the mice were sacrificed and immunohistochemistry was performed on the brain sections using antibodies to biomarkers of microglial activation (TSPO and CD68). Results: Tracer uptake increased significantly ($p<0.05$) in the stroke regions relative to the non-stroke regions within 3 days p.s.i. and peaked at 10 days p.s.i. (Fig. 1a and b). Mean [18F]PBR06 percentage increases in the stroke over the non-stroke regions were 30, 90, 110, 100 and 100 % for days 3,10, 17, 24 and 31 respectively (Table 1). The mean times on the rotarod for the mice that underwent the MCAO procedure were 4.2, 2.8, 3.2, 2.9 and 2.4min for the respective days. When microglial uptake increased significantly from day 3 to 10 p.s.i., the time on the rotarod decreased significantly($p<0.05$). As long as microglial activation stayed high, between days 10 to 31 p.s.i., the time on rotarod remained depressed. There were no significant differences observed in [18F]PBR06 accumulation or the time on the rotarod for the control mice at the various time points. Immunohistochemistry results indicated a high degree of colocalization between the microglial proteins, TSPO and CD68 in the mice with stroke (Fig.1c). Their expression profiles were higher on the stroke hemisphere compared to the non-stroke hemisphere, reflecting an increase in activated microglia and thereby validating the imaging results. No such increases in the expression levels of TSPO and CD68 were observed for the control group. Conclusion: [18F]PBR06 PET/MR imaging shows that microglial activation during SIN peaks at 10 days p.s.i and stays relatively elevated for the next 21 days. Increased microglial activation is associated with an increase in neuroinflammation and a decrease in motor function in mice with stroke.

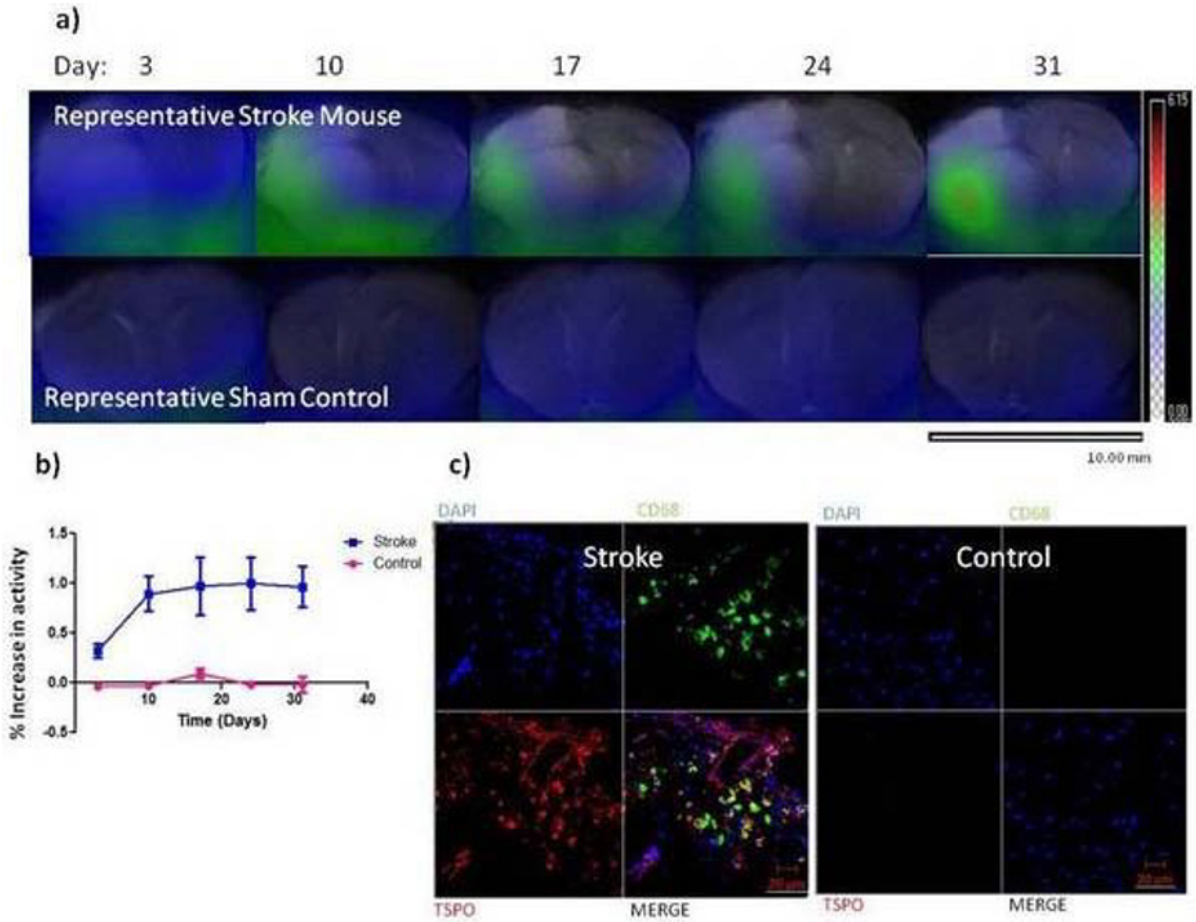

Figure 1: [18F]PBR06 PET/MR images of the time-course of microglial activation during SIN (Fig. 1a) and the graphical representation (Fig 1b) for mice with stroke and the control group. Immunofluorescent labeling (Fig. 1c) of the mouse brain using antibodies targeting TSPO and CD68.

Mean percentage increases in stroke over non-stroke regions for tracer accumulation and time on rotarod

Day	Mean [18F]-PBR06 % Increase	% Increase (over day 3)	Time on rotarod (min)	% Increase (over day 3)
3	30 ± 7.0b	-	4.2 ± 0.22a	-
10	90 ± 17.0a	200	2.8 ± 0.44b	-33
17	110 ± 29.0a	267	3.2 ± 0.46b	-24
24	100 ± 27.0a	233	2.9 ± 0.33b	-31
31	100 ± 20.0a	233	2.4 ± 0.21b	-43
p-value	P = 0.013		P = 0.003	

% Increase represents the difference in uptake between the stroke and non-stroke regions expressed as a percentage of the non-stroke region.

Disclosure of author financial interest or relationships:

F.M. Lartey, None; **R. Ali**, Bell Biosystems, Inc., Consultant; Bell Biosystems, Inc., Stockholder; **S. Rosenblum**, None; **B. Shen**, None; **Z. Miao**, None; **M. Rafat**, None; **M. Vilalta**, None; **T. Palmer**, None; **F.T. Chin**, Ground Fluor Pharmaceuticals, Consultant; **E.E. Graves**, Bell Biosystems, Stockholder; **R. Guzman**, None; **B.W. Loo**, None.

Presentation Number **P 530**
Poster Session 4
September 21, 2013 / 14:45-14:45 / Room: Exhibit Hall B

Non-invasive detection of asthma by new Itrybe near infrared nanoparticles in SKH-1 mice

Andrea Markus[1], *Joanna Napp*[2,1], *Christian Dullin*[3], *Thomas Behnke*[4], *Stephen Kilfeather*[5], *Ute Resch-Genger*[4], *Frauke Alves*[1,2], *[1]Haematology/Oncology, University Medical Centre Goettingen, Goettingen, Germany; [2]Max-Planck-Institute for Experimental Medicine, Goettingen, Germany; [3]Diagnostic Radiology, University Medical Centre Goettingen, Goettingen, Germany; [4]Biophotonics, BAM Federal Institute for Materials Research and Testing, Berlin, Germany; [5]Aeirtec, Newcastle, United Kingdom. Contact e-mail: andrea.markus@med.uni-goettingen.de*

Asthma is an inflammatory disease characterized by the recruitment of immune cells to the airways, which release proteases and pro-inflammatory factors, leading to mucus hyper secretion, bronchial hyper reactivity, and eventually to airway remodeling. Noninvasive imaging to detect and evaluate asthma in preclinical models has been difficult to date, as techniques such as CT or SPECT, either have to cope with the poor contrast of lung tissue or the use of radioactive probes. In contrast, optical imaging using near-infrared fluorescent (NIRF) probes offers a targeted and inexpensive alternative that can be additionally confirmed ex vivo by fluorescence microscopy. Here, we utilized novel NIRF nanoparticles to monitor macrophage activity in inflammatory processes in the lung in an ovalbumin (OVA)-induced new asthmatic mouse model. A conventional OVA-based model was used to induce asthma in SKH-1 mice. SKH-1 mice are hairless, but immune-competent and therefore ideal for optical imaging, as they circumvent the depilation step that is usually necessary with furred animals to avoid high background signals from the fur. We first show that this mouse strain is similarly receptive to the induction of asthma by OVA to Balb/c mice, which to date have been the strain of choice. Bronchoalveolar lavage (BAL) and Periodic Acid Schiff (PAS) staining revealed significant infiltration of immune cells (including macrophages), eosinophilia, mucus hyper production, and goblet cell hyperplasia, showing for the first time the suitability of this mouse strain for asthma research. 24h post last challenge asthmatic and control mice received intranasally 160 µg of 100 nm large Itrybe nanoparticles, i.e. amino-modified polystyrene particles loaded with the broad band emissive cyanine dye Itrybe (Behnke et al., 2013). Subsequently, in vivo whole body and lung scans were performed 1h, 5h and 24h post application using the Optix MX2 imaging system. In asthma lungs, we observed significantly higher fluorescence intensities compared to lungs of control mice, with on average two times higher signals in asthmatic mice, most prominent at 5h post application (Figure). In vivo imaging results provided an excellent indication of the presence of asthma, as validated by eosinophilia in the BAL. Mice which showed higher fluorescence in the stomach area due to swallowing of the probe had a reduced lung signal. Ex vivo measurements of the excised lungs confirmed a more than twofold higher fluorescent signal in asthma lungs compared to controls. Immunostaining of lung cryosections and cytospins from BALs with an anti-CD68 antibody, followed by fluorescence microscopy, revealed the colocalization of the Itrybe NPs with macrophages, suggesting the phagocytosis of the NPs by these cells of the innate immune system. Our results show that optical imaging using NIRF nanoparticles is a promising method to preclinically assess macrophage activity in the respiratory system in vivo.

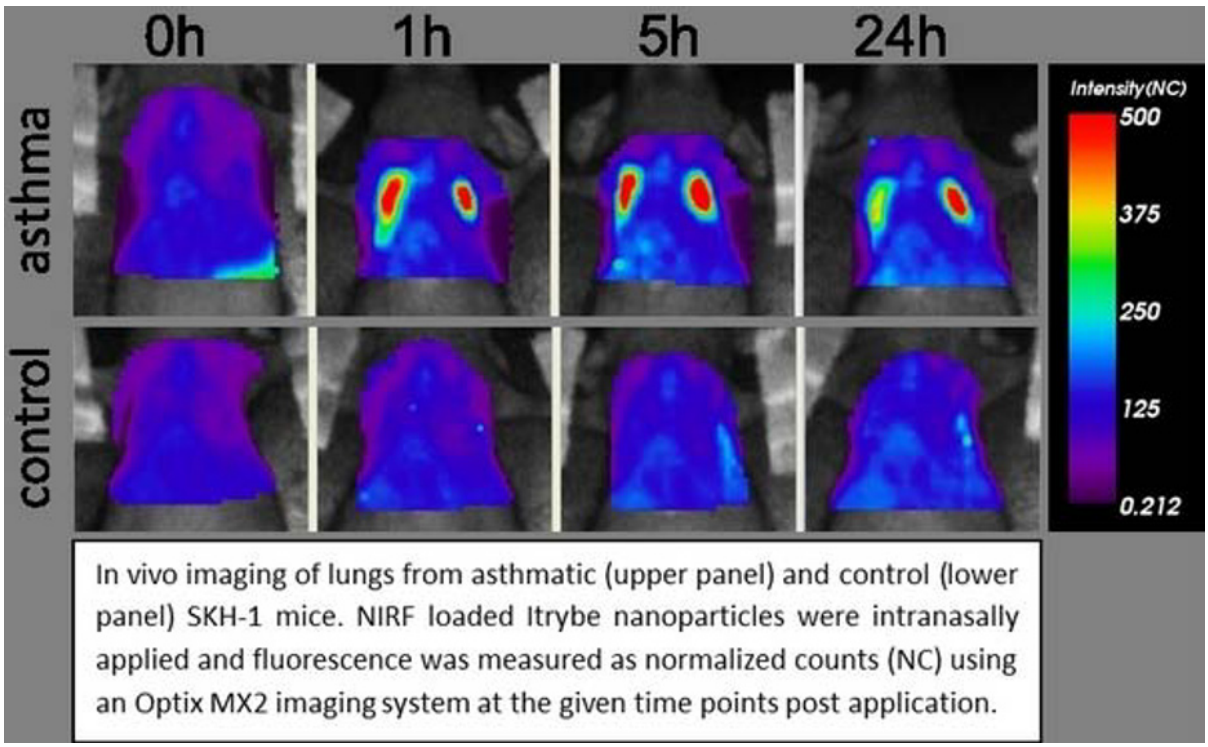

Disclosure of author financial interest or relationships:
A. Markus, None; **J. Napp**, None; **C. Dullin**, None; **T. Behnke**, None; **S. Kilfeather**, None; **U. Resch-Genger**, None; **F. Alves**, None.

Presentation Number **P 531**
Poster Session 4
September 21, 2013 / 14:45-14:45 / Room: Exhibit Hall B

99mTc-mebrofenin disposition in chimeric mice with a humanized liver

Sara Neyt[1], *Philip Meuleman*[4], *Lieven Verhoye*[4], *Christian Vanhove*[3], *Geert Mannens*[2], *Filip J. De Vos*[1], [1]*Laboratory of Radiopharmacy, Ghent University, Ghent, Belgium;* [2]*Drug Safety Sciences, Janssen Research and Development, Janssen Pharmaceutica NV, Beerse, Belgium;* [3]*IBITech-MEDISIP-INFINITY, Ghent University, Ghent, Belgium;* [4]*Center for Vaccinology, Ghent University and Hospital, Ghent, Belgium. Contact e-mail: Sara.Neyt@UGent.be*

Introduction:Interaction of drugs with hepatic transporters is an important cause of hepatotoxicity. Therefore, early identification during drug development is important. A non-invasive method to visualize and quantify hepatic transport using μSPECT imaging was recently published by our research group. We have now investigated human-type hepatobiliary transport of 99mTc-mebrofenin (99mTc-MEB) in mice with a humanized liver (chimeric urikinase-type Plasminogen Activator SCID mice), since this model could offer a better understanding of interactions of drugs with human transporters. Since the liver specific overexpression of the uPA-transgene causes extensive hepatic toxicity, a supporting environment for repopulation of healthy hepatocytes is created. Additionally, the mice are immunodeficient, allowing human hepatocyte transplantation. Several weeks after transplantation, a high proportion of diseased liver tissue, sometimes exceeding 90%, is replaced by human hepatocytes. To study the effect of liver disease, heterozygous mice of 5 and 8 weeks, which experience spontaneous somatic deletion of the transgene, thereby generating healthy mouse hepatocytes that can quickly repopulate the diseased liver, were used as controls. Methods:Wild type (WT),5 week- and 8-week old heterozygous and chimeric mice were IV injected with 99mTc-MEB (n=3 per group).Following dynamic μSPECT (60 frames of 15 seconds), time-activity curves of liver and gallbladder/intestines were obtained. Results:WT mice show rapid uptake, with a Cmax of 20.7±1 MBq followed by decrease to background levels within 15 min. At the acquisition end, the majority of 99mTc-MEB is found in gallbladder/intestines (AUC= 15010±1957 MBq*s). Heterozygous mice of 5 weeks display impaired liver uptake, due to diseased liver tissue, indicated by a 2-fold decreased Cmax,liver (10.8±0.6 MBq, p=0.04). Heterozygous mice of 8 weeks have a similar liver uptake compared to WTs, indicating restored Oatp function (20.5±0.3 MBq, p=0.51). Chimeric mice also exhibit normal liver uptake, indicating functional human OATP function (20.8±0.8 MBq, p=0.83). Heterozygous mice (5 and 8 weeks) show impaired efflux to gallbladder and intestines, indicated by respectively a 3-fold and 1.5-fold lower AUCgallbladder/intestine (5054±127 MBq*s; p=0.034 and 10438±1467 MBq*s; p=0.045 respectively). Chimeric mice show an improved efflux compared to heterozygous mice of 5 weeks (AUCgallbladder/intestine= 739±1156 MBq*s; p=0.048), but still have an impaired efflux compared to heterozygous mice of 8 weeks (p= 0.046). Conclusion:The results demonstrate that chimeric mice exhibit normal hepatobiliary uptake of 99mTc-MEB, indicating functional uptake by human OATP. Efflux from liver to gallbladder/intestines is increased compared to heterozygous mice of 5 weeks, but remained lower compared to WTs. The underlying mechanism for this decreased efflux in chimeric mice remains to be investigated. Possible differences in affinity of 99mTc-MEB for human MRP2 as compared to murine Mrp2, a lower expression of MRP2 and/or differences in bile flow might play a role here.

Disclosure of author financial interest or relationships:
S. Neyt, None; **P. Meuleman**, None; **L. Verhoye**, None; **C. Vanhove**, None; **G. Mannens**, None; **F.J. De Vos**, None.

Presentation Number **P 532**
Poster Session 4
September 21, 2013 / 14:45-14:45 / Room: Exhibit Hall B

Detection of Lymph Node using New Gadolinium Oxide based Nanoparticles for Molecuar Magnetic Resonance Imaging

Nader Riyahi Alam[1], *Gholamreza Azizian*[2], *Soheila Haghgoo*[3], *Behrouz Rafiei*[4], [1]*Medical Physics & Biomedical Engineering, Tehran university of medical sciences(TUMS), Tehran, Islamic Republic of Iran;* [2]*Medical Physics & Biomedical Engineering, Tehran university of medical sciences(TUMS), Tehran, Islamic Republic of Iran;* [3]*Pharmaceutical Department, Food & Drug Laboratory Research Center,, Ministry of Health,, Tehran, Islamic Republic of Iran;* [4]*Medical Imaging Center of Imam Khomeini Hospital,, Tehran University of Medical Sciences (TUMS),, Tehran, Islamic Republic of Iran. Contact e-mail: riahinad@sina.tums.ac.ir*

The lymph nodes can be the site of spread of metastatic disease and a pathway for the growth of most malignancies. Despite higher spatial resolution and soft tissue contrast in noncontrast MRI than CT or nuclear medicine techniques, there is still difficult to distinguish characterization of lymph node.Following the successful synthesis, high relaxivity and signal intensity of gadolinium(III) oxide(Gd2O3) nanoparticles coated with Diethylene Glycol(DEG) as new CA, the aim of this work was to evaluate Gd2O3-DEG for detection lymph node MR imaging, following subcutaneous administration to mice. For the synthesis of Gd2O3-DEG, a new supervised polyol route was peformed. Physicochemical characterization and magnetic properties of Gd2O3-DEG in comparison with conventional Gd-DTPA were verified by DLS, TEM, FTIR, vibrating sample magnetometer(VSM). The signal intensity and relaxivity measurements performed by using 1.5T-MRI scanner. In vivo study, groups of three female mice received a subcutaneous injection(5ml Gd2O3-DEG and Gd-DTPA at 2 and 20mM doses into the dorsal surface of the left hind footpad and lateral tail base. MR imaging were obtained with T1-weighted 3D-fastSPGR protocol. Quantitative and qualitative image evaluation of lymph node were done. Results of in vivo quantitative complied with qualitative image evaluation, showed an enhancement in signal intensity and CNR after injection. Proper signal enhancement(SE) was observed after 45minute of administration. Quantitative evaluation of the MR signal showed clear lymph node contrast for the Gd2O3-DEG comparison to the concentration Gd absorbed by Gd-DTPA. This study reveals contrast efficiency of magnetic nanoparticle agents for lymph node detection in molecular MRI. Groups of three female mice received a subcutaneous injection under an aesthesia with ketamine and xylazine (100 and 5 mg, respectively) for 1h. MR images obtained before and after 5, 15, 30, 24, 30 and 45 minutes of injection of the CA of Gd2O3-DEG and Gd-DTPA. A number of quantitative tissue parameters were calculated as mean differences between pre and post contrast scans repeatedly three times according to equations 1-3. The degree of enhancement at the level signal intensity was demonstrated with CNR and DeltaCNR. Results of CNR after SC injection of the 20mM Gd2O3-DEG in mice hindfoot shows a significant increase during the first 45 minutes. The lymph node/muscle(LNM) ratio was calculated by dividing signal intensities of an entire lymph node by that of adjacent muscle using a similar-sized ROI, drawn manually. CNR for each lymph node were calculated for pre and post injection according to Equations 1-3. CNRenh =SL-ST/DSB (1); CNRnon =SLnon-ST-non/DSB (2); DeltaCNR=CNRenh-CNRnon (3); Qualitative evaluation independently examined by tow radiologists who had MRI expertise according changes in signal intensity of images. The location of the lymph nodes was performed by scheme reporting localization of the lymphatic system.

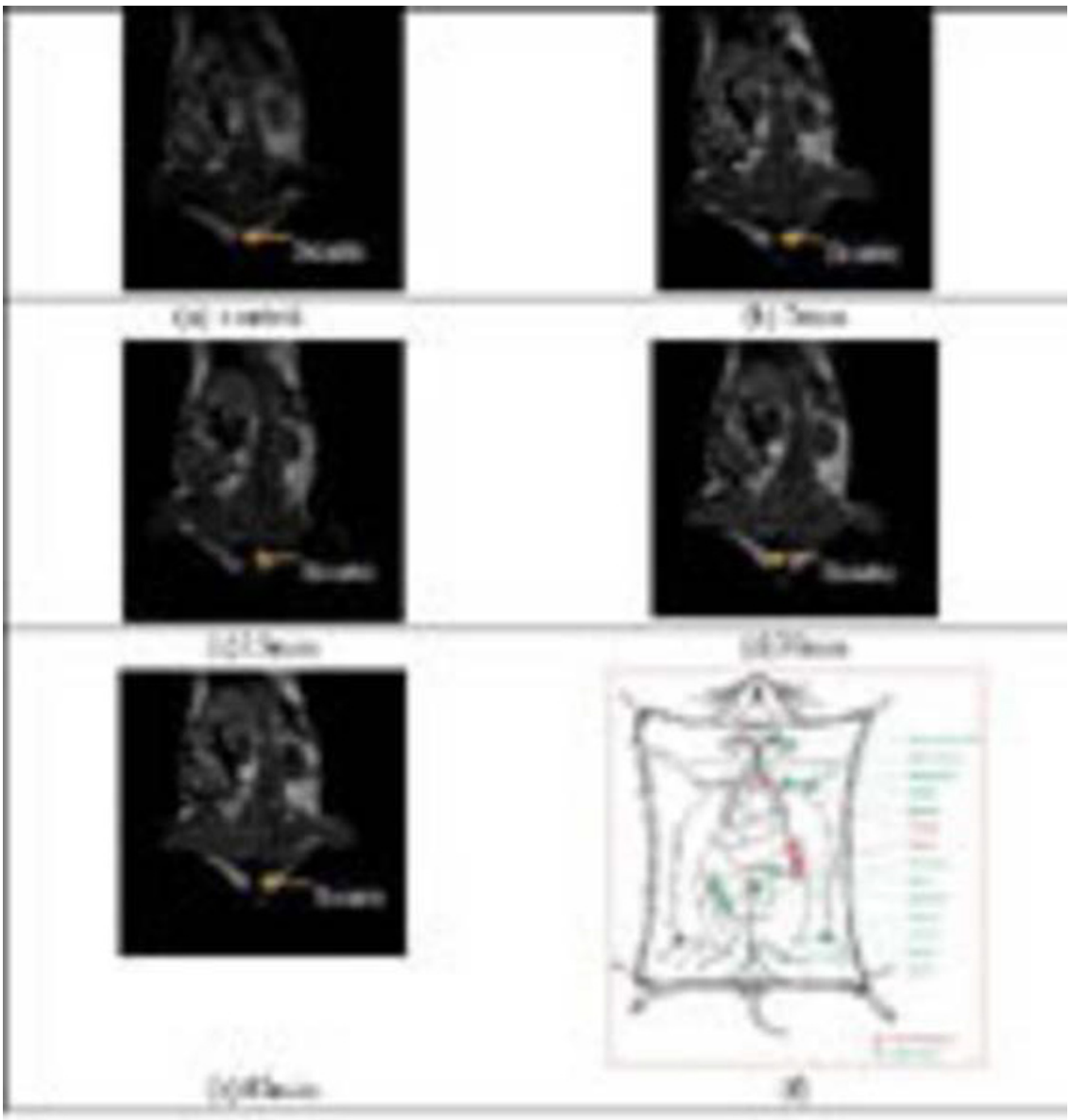

Detection of sciatic lymph node after injection of 2mM Gd2O3-DEG in lateral tail base of mice. (T1W 3D-fastSPGR) images in a mice(a) befor , after (b) 5min, (c)15min, (d)30min and (e)45 min and (f)schematically lymph node.

Disclosure of author financial interest or relationships:
N. Riyahi Alam, None; **G. Azizian**, None; **S. Haghgoo**, None; **B. Rafiei**, None.

Presentation Number **P 533**
Poster Session 4
September 21, 2013 / 14:45-14:45 / Room: Exhibit Hall B

Cell labeling using Zr-89 - comparison with In-111 oxine

Noriko Sato[1], *Lawrence P. Szajek*[2], *Peter Choyke*[1], [1]*Molecular Imaging Program, NCI, Nat'l Inst of Health, Bethesda, MD, USA;* [2]*Positron Emission Tomography Department, CC, Nat'l Inst of Health, Bethesda, MD, USA. Contact e-mail: saton@mail.nih.gov*

Cell based therapies are becoming increasingly important in the therapy of cancers and inflammatory diseases. Such therapies include dendritic cell based vaccines, adoptive immunotherapy using cytotoxic T cells or natural killer cells, and stem cell therapies. Crucial for the improvement of these therapies is a development of non-invasive, quantitative method to image and track the cells transferred. In-111 oxine has long been used as a cell labeling method to track cells by single photon emission tomography (SPECT). In order to increase the imaging sensitivity, and thus potentially lower the radioactivity dose required for *in vivo* cell tracking, we have developed a cell labeling technique with Zr-89, a positron emission tomography (PET) tracer with a half-life of 3.27 days. Optimal labeling conditions were determined and some of the characteristics were compared with the In-111 oxine labeling method. *In vivo* trafficking of Zr-89 labeled mouse bone marrow-derived dendritic cells and cytotoxic T cells were performed using a small animal PET imager. Dendritic cells and CD8 T cells were labeled with Zr-89 after neutralization of Zr-89 oxalate in combination with protamine sulfate (PS). When cells were incubated with 440 kBq of Zr-89 in PBS with PS at 37°C for 30 min, we obtained a specific activity of 148.8±13.3 kBq and 54.3±8.1 kBq per million dendritic and T cells, respectively. PS was necessary and effect of PS was inhibited by heparin, a known target of PS for direct interaction. Presence of serum and use of serum free medium inhibited the labeling by 90 and 60 %, respectively. Cells were not labeled at 4°C, indicating that the Zr-89 labeling depends on cellular active incorporation mechanisms. In fact, internalization of Zr-89 into the cells (60-84 %) was confirmed by washing the cells with acidic solution (pH 2.8) or with desferoxamine solution. Internalized fraction increased between 30 and 45 min labeling time. By contrast, In-111 oxine successfully labeled the cells even in the presence of serum or regardless of the incubation temperature, which is in accordance with its passive labeling mechanism based on its lipophilicity. Cells survived well after the Zr-89 labeling. We successfully tracked intravenously injected Zr-89 labeled dendritic cells and T cells by small animal PET imager with an injected dose as low as 148-185 kBq per 5 million cells per mouse, with a imaging time of 10 min for 2 bed positions (5 min per bed position). This was about 10 times lower activity requirement compared to In-111 SPECT imaging. The cells were initially distributed in the lungs, and then migrated to the liver and spleen. Images of Zr-89 labeled dendritic cells at 0 hour and 1 day after injection are shown in the figure. In summary, we have developed a highly sensitive method of Zr-89 cell labeling for PET. This method could be applied to various cell types and would serve as a great tool for cell tracking *in vivo* both in preclinical research and in clinical cell mediated therapies.

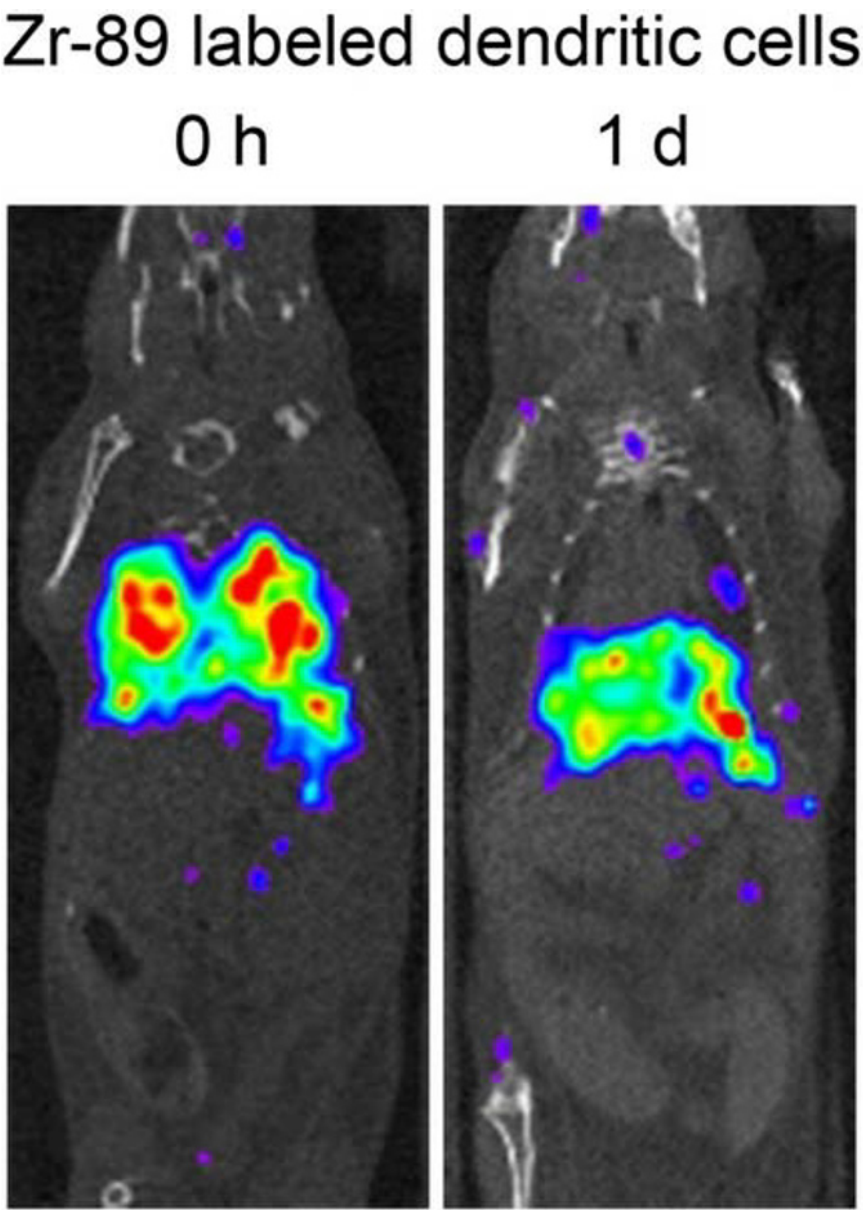

Disclosure of author financial interest or relationships:
N. Sato, None; **L.P. Szajek**, None; **P. Choyke**, None.

Presentation Number **P 534**
Poster Session 4
September 21, 2013 / 14:45-14:45 / Room: Exhibit Hall B

Magnetic Resonance Colonography with Intestine-Absorbable Nanoparticle Contrast Agents in Evaluation of Colorectal Inflammation

Jihong Sun[1], *Xia Wu*[1], *Xiaozhe Shi*[1], *Yin Jin*[1], *Shizheng Zhang*[1], *Xiaoming Yang*[1,2], [1]*Radiology, Sir Run Run Shaw Hospital, Zhejiang University School of Medicine, Hangzhou, China;* [2]*Radiology, University of Washington School of Medicine, Seattle, WA, USA. Contact e-mail: braversun@sina.com*

Purpose: Since contrast agents are not readily absorbed by the gastrointestinal tract, colonic lesions cannot be detected based on the colonic absorption of contrast agents. The purpose of this study was to develop a novel nanoparticle-based magnetic resonance (MR) colonography technique, which enabled us to evaluate ulcerative colitis via transrectal administration of intestine-absorbable nanoparticle contrast agents. Materials and Methods: Two types of solid lipid nanoparticles (SLNs) were synthesized with loading of (i) gadolinium (Gd) diethylenetriaminepenta acetic acid (Gd-DTPA) to construct Gd-SLNs as a magnetic resonance (MR) T1 contrast agent; and (ii)otcadecylamine fluorescein isothiocyanate (FITC) to construct Gd-FITC-SLNs for histologic confirmation of MR findings. Eighteen C57Bl6/J female mice were treated with 3% dextran sulfate sodium in the drinking water for 7 days to create ulcerative colitis (UC). UC mice were randomly divided into different study groups based on transrectal enema with various SLNs and control agents, including: (i) Gd-SLNs (40 mg/ml, n=6); (ii) Gd-FITC-SLNs (40 mg/ml, n=6); (iii) blank SLNs (40 mg/ml, n=6). In addition, six normal mice were administered via transrectal enema with Gd-FITC-SLNs (40 mg/ml). T1-weighted MR colonographies using a series of spin echo sequences (TR=850,700,550 and 400 msec,TE=15 msec) were then performed to detect various SLNs within the colonic walls of colitic mice. T1 mapping technique was used to evaluate T1 value of colorectal walls. MRI findings were correlated with subsequent histological confirmation. Results: MR colonographies displayed thick colorectal walls in the inflammatory mice. MRI also showed marked enhancement of colitic walls with decreased T1 relaxation times in all colitic mice treated by transrectal infusions of Gd-SLNs or Gd-FITC-SLNs. Consecutive T1WI MRI revealed the continual enhancement of colorectal walls after intracolonic administration of Gd-containing SLNs. Confocal fluorescence microscopy showed the delivered Gd-FITC-SLNs as highly-concentrated green fluorescent spots through all layers of the colonic walls of colitic mice (Figure 1). Conclusion: This study establishes the "proofs-of-principle" of a new MR colonography technique which enhances inflammatory colorectum based on absorption of nanoparticle contrast agents by colorectal wall. Solid lipid nanoparticle-based MR colonography may open new avenues for efficient management of inflammatory bowel disease.

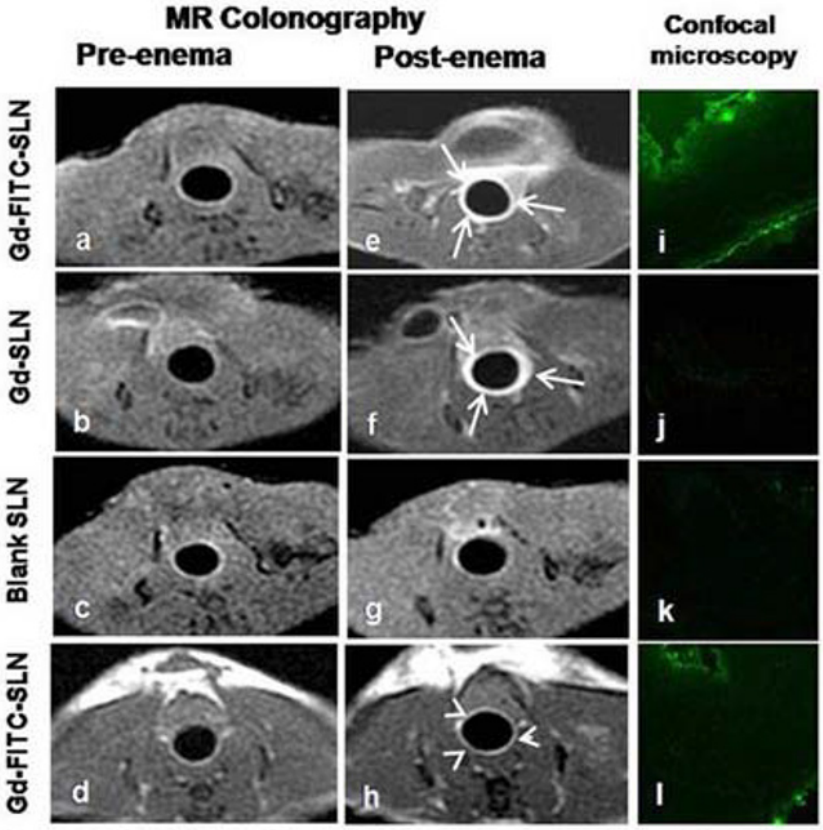

Figure 1. (a-h) Axial MR colonographics of the mouse rectums with T1-weighted spin echo sequence (TR/TE, 840/15) before (a-d) and 20 minutes after (e-h) intracolonic administration of Gd-FITC-SLNs (a&e), Gd-SLNs (b&f), and blank SLNs (c&g) in the colitic mice as well as Gd-FITC-SLNs (d&h) in the control mice. MR colonographies show thicker rectal walls with brighter contrast enhancement (arrows on e&f) in the colitic mice than the control mice (arrowheads on h) after intracolonic administration of Gd-FITC-SLNs or Gd-SLNs. This finding is not seen in the group with blank SLNs (g). Corresponding histological confirmation with confocal fluorescence microscopy (i-l) among different colitic model groups with various treatments of Gd-FITC-SLNs (i), Gd-SLNs (j), and blank SLNs (k) as well as in the control group with administration of Gd-FITC-SLNs (l). Confocal fluorescence microcopy demonstrates green fluorescent signals only in Gd-FITC-SLNs-treated colitic and normal colorectal walls (due to FITC emission, image i&l), which is not visualized in other two groups. These findings indicate the efficient absorption of SLN-based nanoparticle contrast agents by the inflammatory colonic walls via the intracolonic enema approach.

Disclosure of author financial interest or relationships:
J. Sun, None; **X. Wu**, None; **X. Shi**, None; **Y. Jin**, None; **S. Zhang**, None; **X. Yang**, None.

Presentation Number **P 535**
Poster Session 4
September 21, 2013 / 14:45-14:45 / Room: Exhibit Hall B

PET/MRI/SPECT/CT in vivo longitudinal imaging of Earthworm (Lumbricus terrestris L.), as a novel means of environmental monitoring

Ferenc Budán[2], Noemi Kovacs[2], Ildiko Horvath[1], Daniel Veres[1], Péter Engelmann[3], Peter Nemeth[3], **Krisztián Szigeti**[1]*, Domokos Mathe[2], [1]Biophysics and Radiation Biology, Semmelweis University, Budapest, Hungary; [2]CROmed Ltd, Budapest, Hungary; [3]Department of Immunology and Biotechnology, University of Pécs, Pécs, Hungary. Contact e-mail: szigeti.krisztian@med.semmelweis-univ.hu*

Introduction. Redworm (Eisenia fetida) is used widely in ecotoxicological and carcinogen tests especially with contaminated soils. Many external biomarkers as alteration in body mass and reproductive capacity and morphometric changes as well as molecular biological alterations are applied as end-points. Aims. The purpose of this study was to offer to the aforementioned tests a valuable longitudinal quantitative in vivo molecular imaging supplement based on PET/MRI and SPECT/CT. Reducing animal number, experiment duration and increasing data robustness and repeatability are all in favor of molecular imaging for environmental tests. It is important to establish proper immobilization methods for these annelids, too. Materials and methods. To visualize organs with higher resolution, larger sized earthworm Lumbricus terrestris species were used as similar environmental relevance is supposed to that of Eisenia fetida. Current rodent in vivo imaging anesthetics agents, (e.g. Isoflurane, Urethane, or Ketamin combined with Xylazine) were tested. To detect glucose metabolism after intra-coelomic (ic.) injection of cca. 3 MBq of 18F-Fluoro-D-deoxyglucose (FDG) we recorded whole body list mode PET data with a nanoScan PET/MRI (Mediso, Hungary). Data were acquired in list mode PET during 60 minutes in 4 animals. For MRI imaging T1 weighted spoiled gradient echo sequence was used with 3 dimensional acquisition scheme. [201Tl]Thallous chloride solution (cca. 12 MBq per animal) was injected ic. in other 4 animals, while in 3 animals [123I]Iodide solution was ic. applied. SPECT/CT (NanoSPECT/CTPLUS, Mediso, Hungary) imaging was performed to detect toxic heavy metal in vivo accumulation, iodine metabolism, and to obtain information on the adequacy of SPECT resolution and CT contrast. Results. Conventional immobilizing agents in the case of earthworms seemed not to be useful. After screening a wide array of pharmaceuticals and solvents on n=55 animals, one method was found employing propan-2-ol to cause immobilization; the muscles were completely relaxed during at least 20 minutes. A special bed was developed to avoid shifting of the anaesthetised animals. Using MRI the morphology of the reproductive organs of the animals was visualised. FDG-PET allowed to determine metabolic uptake in discernable organs as nehpridia, gut and genital organs. The sulfhydryl group bindig propeties of 201Tl were visualized as uptake througout the body as well as in the urinary system. Thus toxic, heavy metals could be detected in a reliable and quantificated manner. With the same modality, complete body imaging with water soluble 123I ions enabeled to elucidate the distribution of small hydrophylic molecules. Discussion. The reported tests built on multimodal imaging could supplement environmental toxicity tests with valuable information. Reproductive capacity alterations could be demonstrated. Using FDG as a biomarker, the effect of exposure to e.g. carcinogens, radioactivity or toxic heavy metals could be tested.

Disclosure of author financial interest or relationships:
F. Budán, None; **N. Kovacs**, None; **I. Horvath**, None; **D. Veres**, None; **P. Engelmann**, None; **P. Nemeth**, None; **K. Szigeti**, None; **D. Mathe**, CROmed Ltd, Stockholder; Mediso Ltd., Consultant .

Presentation Number **P 536**
Poster Session 4
September 21, 2013 / 14:45-14:45 / Room: Exhibit Hall B

Characterization of Intramuscular Inflammation using a Compact High-Performance Compact MRI System: Anatomical, Diffusion Weighted, Dynamic Contrast Enhanced and Angiography Imaging

Tonya Coulthard[1], *Jacob Hesterman*[3], *Jinzi Zheng*[2], *Raquel De Souza*[2], *Matthew D. Silva*[3], [1]*Aspect Imaging, Toronto, ON, Canada;* [2]*STTARR Innovation Centre, Princess Margaret Hospital, University Health Network, Toronto, ON, Canada;* [3]*InviCRO, Boston, MA, USA. Contact e-mail: tcoulthard@aspectimaging.com*

Inflammation is a physiological response associated with numerous disease states, including arthritis, infection, and cancer and is an important biomarker for phenotypic change and therapeutic efficacy. Inflammation is a complex biological response resulting in heat, swelling, and pain. With the exception of pain, the response results from a number of vascular changes including vasodilation and increased permeability of the blood vessels at the affected site. Magnetic Resonance Imaging (MRI) is considered the gold standard in soft tissue imaging, providing numerous imaging strategies for assessing inflammation. Anatomical details are provided by traditional T1 and T2 weighted images, with lesion size easily quantified. Diffusion weighted imaging (DWI) provides further insights into the physiological processes associated with inflammation by providing quantification of the apparent diffusion coefficient (ADC), which varies with swelling in a given area. Finally, contrast enhanced (CE)-MRI provides insights into the perfusion kinetics (DCE-MRI) as well as the vascular network (angiography) within the affected area. In the current study, acute inflammation was induced by the injection of 10µl of turpentine oil into the upper right quadriceps muscle of otherwise healthy female CD-1 mice. Imaging was performed 18 hours after induction, using a novel compact high-performance MRI system (Bruker ICON™, Germany), operating at 1 Tesla. DCE-MRI was performed by injecting 20µl of Gd-HP-DO3A (ProHance®, Bracco Diagnositics, USA), while CE-MRI angiography was performed by injecting 150µl of a nanosized liposome agent containing gadolinium (Nanovista, STTARR, Canada). Both contrast agents were administered via tail vein cannulation. Lesion size was quantified using the VivoQuant™ software analysis package (InviCRO, USA). T2-weighted fast spin echo imaging allowed for clear visualization of the inflamed area, with an overall volume increase of 72±18% (n=9), compared to the contralateral healthy muscle. DW-MRI was used to generate ADC maps. A 67±7% increase in the ADC value was observed when compared to the contralateral side. DCE-MRI was used to quantify changes in the perfusion kinetics. Specifically, Ktrans was calculated to describe vessel permeability, while the area-under-the-curve (AUC) quantifies overall perfusion. Perfusion increased by 43.6±5.6% (AUC) within the inflammatory lesion, while vessel permeability increased by 26.7±5.1% (Ktrans). CE-MRI angiography showed images of the inflammatory lesion with a marked increase in signal intensity (38±8%), a measure of perfusion (in accordance with AUC increases measured using DCE-MRI) when compared to the contralateral leg. In conclusion, this study demonstrates the capabilities of this novel compact high-performance MRI system in characterizing the various aspects of an inflammatory lesion, including size and vascular perfusion/permeability, as well as additional measures of disease pathology including the ADC value. Furthermore, this compact MRI system can be effectively used to characterize other models of inflammation and screen therapeutic compounds for their efficacy.

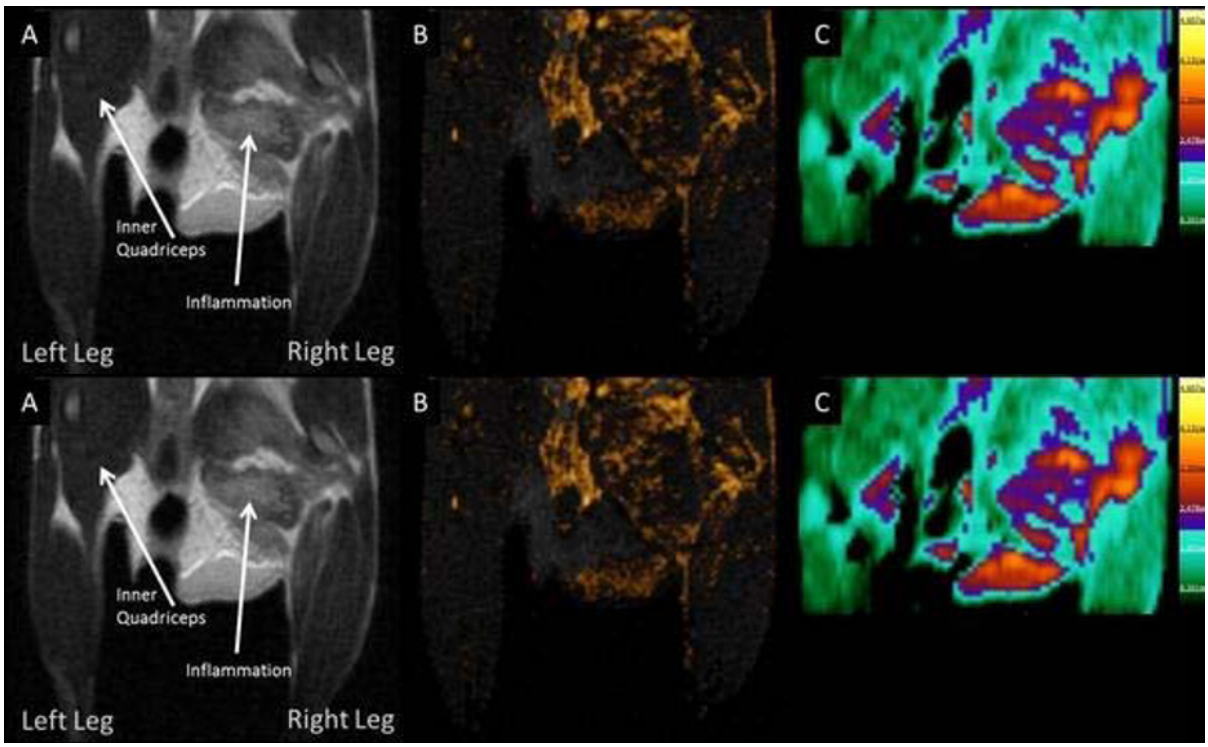

Disclosure of author financial interest or relationships:
T. Coulthard, Aspect Imaging, Employment; **J. Hesterman**, inviCRO, LLC, Employment; **J. Zheng**, None; **R. De Souza**, None; **M.D. Silva**, inviCRO, LLC, Employment .

Presentation Number **P 537**
Poster Session 4
September 21, 2013 / 14:45-14:45 / Room: Exhibit Hall B

The alarmins S100A8 and S100A9 as a promising prognostic biomarker in non-invasive molecular imaging

Tom Völler, *Michel Eisenblaetter, Johannes Roth, Thomas Vogl, Institute of Immunology Münster, Münster, Germany. Contact e-mail: tom.voeller@gmx.de*

The proinflammatory alarmins S100A8 and S100A9 are vastly released by activated phagocytes at sites of inflammation. Due to their favorable kinetics S100A8/S100A9 (calprotectin) could be characterized as a very early and sensitive biomarker in a broad spectrum of acute and chronic inflammatory disorders like rheumatoid arthritis, allergies, inflammatory bowel or lung diseases. The purpose of our study was to avail these findings for in vivo imaging of inflammation with the perspective of monitoring disease activity in clinically relevant disorders. We investigated various mouse models of inflammatory and infectious diseases using anti-S100A9-Cy5.5 antibodies. S100A9-antibody was coupled to the fluorescence dye Cy5.5 for optical imaging studies by Fluorescence Reflectance Imaging (FRI). In the contact dermatitis model injection of anti-S100A9-Cy5.5 resulted in contrast to noise ratios (CNR) which were more than ten-fold higher compared to those of knock-out-mice and also significantly higher after injection of IgG-Cy5.5 without relevant specificity. S100A9 knock-out-mice served as additional controls. With this specificity-proven marker we monitored inflammatory models of different immunological etiology, e.g. collagen-induced arthritis (CIA) or experimental leishmaniasis. In both models molecular imaging of S100A9 provides a sensitive and specific method of non-invasive monitoring even in subclinical disease stages. In addition, S100A9 is the first biomarker with a prognostic value for the Th1/Th2-driven inflammatory process in experimental leishmaniasis, even weeks prior to the clinical outcome. In conclusion S100A9 has the potential to monitor disease activities in vivo for many other inflammatory diseases associated with a high phagocyte activity.

Disclosure of author financial interest or relationships:
T. Völler, None; **M. Eisenblaetter**, None; **J. Roth**, None; **T. Vogl**, None.

Presentation Number **P 538**
Poster Session 4
September 21, 2013 / 14:45-14:45 / Room: Exhibit Hall B

Fluorescence Imaging of an Intratracheally-Induced Murine Model of Acute Pulmonary Inflammation

Jeremy Wellen[1], *Prashant Bansal*[2], *Brahma Ghosh*[2], [1]*Clinical & Translational Imaging, Pfizer, Cambridge, MA, USA;* [2]*Comparative Medicine, Pfizer, Andover, MA, USA. Contact e-mail: Jeremy.Wellen@pfizer.com*

Background and Rationale: Inflammation is an underlying pathologic feature common to many pulmonary disorders and activated immune pathways associated with pulmonary inflammation may serve as appropriate targets for *in vivo* molecular imaging of disease progression. Recent optical imaging studies have applied this rationale with the use of activatable fluorophore probes to track biological processes associated with pulmonary disease pathophysiology and pharmacological intervention in a non-invasive manner [1, 2]. The fluorogenic probe NE680 (PerkinElmer, Waltham, MA) has high specificity for neutrophil elastase (NE) and was previously evaluated in an *in vivo* model of acute pulmonary inflammation where fluorescence signal was shown to reflect endotoxin-induced NE activity following an intranasal route of administration [2]. In the current work, we expand upon this foundation and demonstrate the feasibility of an optical imaging methodology to evaluate inflammatory response induced by an intratracheal (IT) route of administration. **Study Design:** Acute pulmonary inflammation was induced in adult C57/BL6 mice (N=5) through sequential IT dosing of LPS (100 µg in 40 µL PBS), followed 18-hours later by the chemotactic peptide fMLP (400nM). Co-administered with fMLP was NE680 (4 nmoles), making the second administration a 40 µL cocktail. Following removal of animal fur with a depilatory cream, *in vivo* optical imaging was conducted with animals under isoflurane anesthesia in a supine position at discrete time-points post fMLP + NE680 cocktail administration (Maestro2, PerkinElmer, Waltham, MA). After completing the 5-hour *in vivo* time-course, animals were sacrificed and lungs were harvested for *ex vivo* imaging. **Results and Discussion:** Temporal evolution of NE680 signal was observed to increase over a 5-hour period following fMLP + NE680 cocktail administration. The images in Fig. 1 demonstrate the variability in spatial distribution and intensity of NE680 signal and how the *in vivo* signal corresponds with that obtained from excised whole lungs. Quantification of signal demonstrates a group-wise temporal increase in NE activity and a significant correlation between the *in vivo* signal at 5-hours post probe administration and the *ex vivo* signal. We attribute the variability observed between animals to a number of potential sources: variability in distribution of IT-administered compounds; anesthetic influence on immune response [3]; signal attenuation due to depilation-induced skin pigmentation [4]. Our future studies aim to explore the sources of this variability by evaluating alternative mouse strains and anesthetic regimens. Further refinement of this methodology will provide a valuable tool for the *in vivo* study of NE activity in pulmonary inflammation. **References:** [1] Cortez-Retamozo V *et al*, *J Clin Invest* **118**:4058-4066 (2008). [2] Kossodo S *et al*, *Int J Mol Imaging* **2011**:581406 (2011). [3] Reutershan J *et al*, *Anesthesiology* **104**:511-517 (2006). [4] Curtis A *et al*, *Mol Imaging Biol* **13**:1114-1123 (2011).

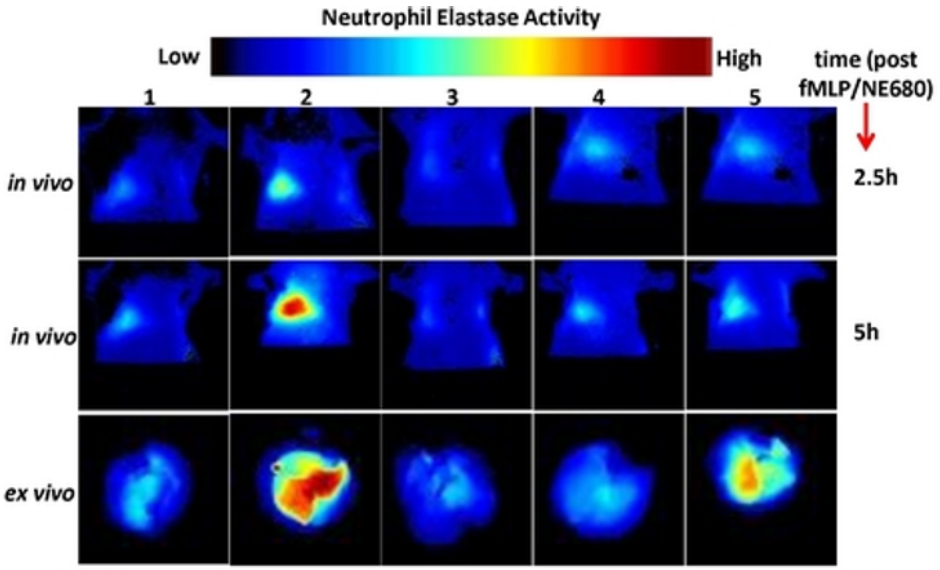

Qualitative comparison between *in/ex vivo* component images reflecting neutrophil elastase (NE) activity. *in vivo* component images at 2.5h (top row) and 5h (middle row) post fMLP+NE680 administration exhibit NE activation. Similarly, the *ex vivo* component images correspond to the NE activation observed *in vivo* (bottom row)

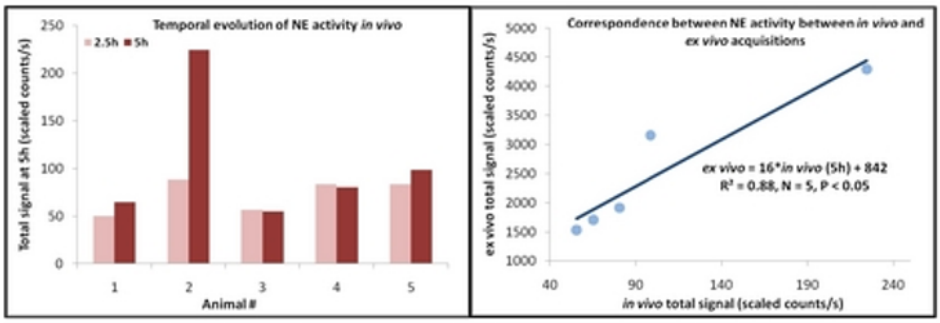

Quantitative comparison between *in/ex vivo* neutrophil elastase (NE) activity. The bar plots (left) reflect the temporal increase in NE activity at 5h compared to 2.5h. A strong correlation is observed between the *in vivo* signal (5h) and the *ex vivo* signal (right), highlighting the robustness of the image data acquisition & analysis ($R^2 = 0.88$, $P < 0.05$)

Disclosure of author financial interest or relationships:
J. Wellen, Pfizer, Employment; **P. Bansal**, None; **B. Ghosh**, None.

Presentation Number **P 539**
Poster Session 4
September 21, 2013 / 14:45-14:45 / Room: Exhibit Hall B

Therapeutic Efficacy Evaluation of Curcumin in Rheumatoid Arthritis-Bearing Mice

Wei Yu-Fen, *Jeng-Jong Hwang, Wei-Hsun Wang, Biomedical Imaging and Radiological Science, National Yang Ming University, Taipei, Taiwan. Contact e-mail: fish771018@msn.com*

Purpose It has been reported that over-activation of macrophages is highly associated with the progression of rheumatoid arthritis (RA). Furthermore, osteoclast cells will germinate differentiation of the macrophages and cause the resorption of bone. On the other hand, inflammatory-related cytokines secreted by immune cells and bone destruction both contribute to the severity of RA. Curcumin, a type of curcuminoid, has been known to have anti-inflammation and anticancer effects. In this study, we investigated the effect of curcumin on the activation of macrophages and osteoclast cells, and evaluate its therapeutic efficacy on RA with molecular imaging. Materials and Methods LPS-stimulated RAW 264.7 cells and bone marrow derived macrophages were treated with 3 μM curcumin. Inhibition of RANKL-induced formation of osteoclasts by curcumin using TRAP staining and ELISA was investigated. For in vivo study, eight weeks old DBA/1 mice were injected intradermally with bovine collagen type II. The collagen-induced arthritis (CIA) mice were intraperitoneally injected with 100 mg/kg/day curcumin and vehicle, respectively, from day 21 to day 43. The clinical RA score, serum for ELISA assay, [18F]FDG/microPET imaging, H&E staining, and immunohistochemistry were used to evaluate the therapeutic efficacy of curcumin. Results Curcumin can inhibit the RANKL-induced osteoclastogenesis and osteoclast formation. RA-bearing mice treated with curcumin exhibited the significant suppression ($p<0.05$) of inflammatory mediator production in the joint tissues and the level of serum pro-inflammatory related cytokines. Notably, curcumin ameliorates the clinical parameter and bone erosion in RA-bearing mice. [18F]FDG/microPET imaging also showed that the significant decrease ($p<0.05$) of [18F]FDG uptake in the joints of curcumin-treated mice as compared with those untreated. Conclusion Together, we concluded that the syndrome and incidence rate of RA could be significantly decreased by curcumin in a RA-bearing mouse model. The possible mechanism may via the down regulation of inflammatory cytokines and osteoclastogenesis. (We thank the Taiwan Mouse Clinic which is funded by the National Research Program for Biopharmaceuticals (NRPB) at the National Science Council (NSC) of Taiwan for technical support in [18F]FDG/microPET imaging experiment.)

Disclosure of author financial interest or relationships:
W. Yu-Fen, None; **J. Hwang**, None; **W. Wang**, None.

Presentation Number **P 540**
Poster Session 4
September 21, 2013 / 14:45-14:45 / Room: Exhibit Hall B

A Biohybrid Strategy for Improved Oxygenation of Cell Transplants and Simultaneous Monitoring of Fluorocapsule Rupture Using ^{19}F MRI

Dian R. Arifin[1,2], *Deepak Kadayakkara*[1,2], *Jeff W. Bulte*[1,2], [1]*Radiology, Johns Hopkins University School of Medicine, Baltimore, MD, USA;* [2]*Cellular Imaging Section, Johns Hopkins University School of Medicine, Baltimore, MD, USA. Contact e-mail: darifin@mri.jhu.edu*

Introduction: We engineered a biohybrid strategy for improving pancreatic islet cell therapy that allows simultaneous monitoring of the fate of encapsulated transplanted cells. While semi-permeable microcapsules immunoprotect the grafts, incorporation of perfluoro-15-crown-5-ether (PFPE) provides entrapment of oxygen. Hypoxia and rapid cell death remain one of the critical issues in the ischemic period following transplantation. The use of PFPE as an oxygen sink also enables sensitive hot spot imaging of the implants by ^{19}F MRI due to its 20 equivalent ^{19}F nuclei that yield a single NMR resonance. We hypothesized that ^{19}F MRI can offer a clinically relevant method to monitor the time course of fluorocapsule rupture and the subsequent loss of immunoprotection non-invasively (which has not been possible before), as a result of broken fluorocapsules losing their fluorine signal from PFPE release. **Methods:** Fluorine emulsions were synthesized by sonicating a mixture of 2.5% w/v lecithin and PFPE. Human islets and PFPE emulsions (12% v/v per ml of alginate) were encapsulated inside alginate/protamine/alginate microcapsules. To study the therapeutic effects of fluorocapsules, we implanted i.p. 5000 human islets with and without PFPE into diabetic NOD/ShiLtj mice (n=4) and followed the plasma human C-peptide levels every week. For *in vivo* imaging, 5000 intact fluorocapsules were implanted s.c. into normal C57Bl/6J mice. Intact fluorocapsules in 1% agarose inside a 6-mm tube (2000 capsules/ml of agarose) served as a reference. To simulate capsule rupture *in vivo*, we designed "weak" (single layer alginate without protamine crosslinking) fluorocapsules that can be rapidly degraded by alginate lyase. These were engrafted s.c. into C57Bl/6J mice. Lyase (a total of 1.2 mg) was injected into the s.c. implant one day post-transplantation. MRI was performed with a Bruker 11.7T scanner using a dual-tunable ^{19}F /^{1}H surface coil. The parameters for ^{1}H/^{19}F MRI were: RARE, TR=4/1s, TE=30/23ms, SI=2/2mm, matrix=196x128/196x128, NA=4/4, FoV=3.2x2/3.2x2cm. Mean implant signal was calculated using Voxel Tracker software (Celsense, Pittsburgh, PA). Data are reported as the ratio of the mean graft signal vs. reference. **Results:** In our stringent xenograft model, the plasma c-peptide levels were detectable up to 33 days post-implantation when PFPE was included, in contrast to 14 days without PFPE (**Fig. 1A**). The ^{19}F MR-signal of intact fluorocapsules decreased in the first week after engraftment, but remained stable for at least 44 days *in vivo* (**Fig.1B**). Fluorocapsules were intact and visible by ^{1}H and ^{19}F MRI one week post-surgery (**Fig. 1C,E**). In contrast, the T2-w MR-signal of the weak capsules disappeared one week after lyase administration (**Fig. 1D,F**). These results corresponded to that seen on hot spot ^{19}F MRI (**Fig. 1D,F**). **Conclusions:** We have demonstrated the efficacy of fluorocapsules to improve cell therapy and to monitor the capsule integrity using ^{19}F MRI. As capsule rupture leads to the loss of immunoprotection, this approach may be applied for an early determination of pending graft failure and the decision to start immunosuppression in a timely manner.

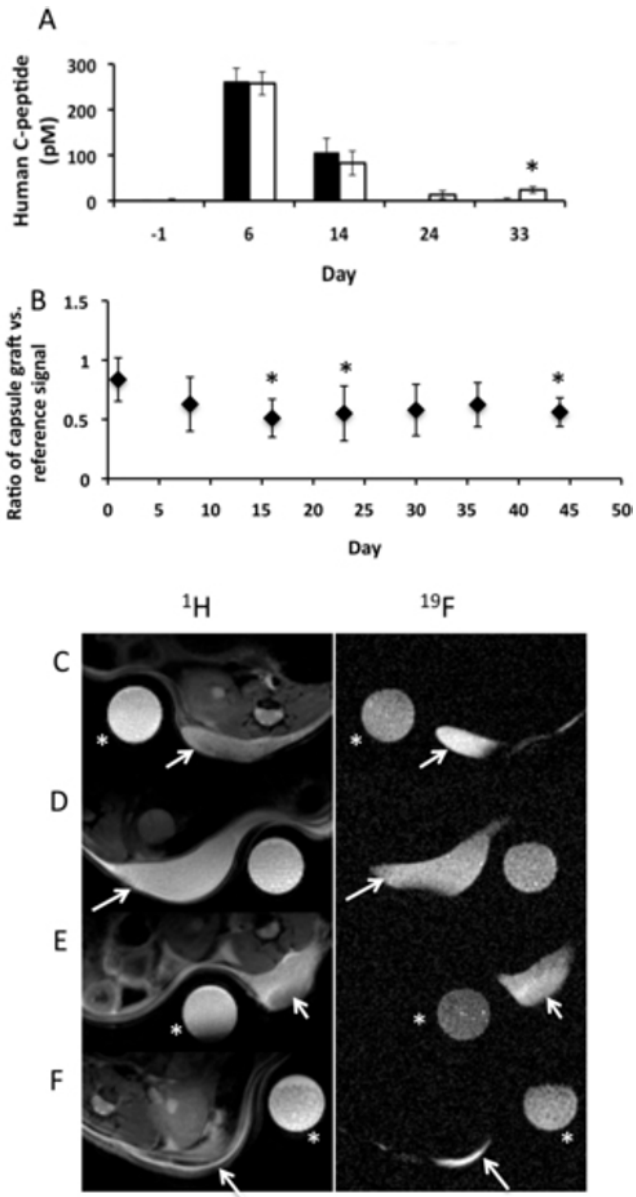

Figure 1. (A) Circulating human c-peptide levels of fluoroencapsulated islet grafts without (black bars) or with (white) PFPE. (B) The ratio of the mean signal of the capsule grafts vs. the reference over time. Asterisk indicates the day when the c-peptide levels were statistically different ($P<0.05$) or when the ratios were statistically different from day 1 ($P<0.05$). Axial ^{1}H and ^{19}F 11.7T MR images of intact fluorocapsules one day (C) and one week (E) after s.c. transplantation into a mouse. MR images of weak fluorocapsules one day after s.c. implantation (D) and one week after alginate lyase injection (F). Asterisks and arrows indicate the reference and implanted capsules, respectively.

Disclosure of author financial interest or relationships:
D.R. Arifin, None; **D. Kadayakkara**, None; **J.W. Bulte**, None.

Presentation Number **P 541**
Poster Session 4
September 21, 2013 / 14:45-14:45 / Room: Exhibit Hall B

Fluorescence lifetime change phenomena in imaging of diabetic pancreas in a mouse model

Alexei A. Bogdanov[1], *William L. Rice*[2], *Alana W. Ross*[2], *Jessica C. Lopez*[3], *Anna Moore*[2], *Anand T. Kumar*[2], [1]*Radiology, Laboratory of Molecular Imaging Probes, Worcester, MA, USA;* [2]*A. Martinos Center for Biomeidical Imaging, Massachusetts General Hospital, Charlestown, MA, USA;* [3]*Worcester Polytechnic Institute, Worcester, MA, USA. Contact e-mail: alexei.bogdanov@umassmed.edu*

Optical imaging of proteolysis in live tissues in vivo has been proven feasible as a result of the development of the "activatable" fluorophore-labeled long-circulating probes using a graft copolymer of poly(ethylene glycol) and poly-l-lysine (MPEG-gPLL) as a carrier molecule [1, 2]. The continuous wave (CW) fluorescence excitation commonly used as an imaging modality in conjunction with this class of imaging probes has been successful in detecting de-quenching of near-infrared (NIR) cyanine fluorophores in various models of human disease. The CW approach, while easy to implement has an inherent problem associated with a difficulty in differentiating between the signal of liver and other organs of chest and abdomen. Given the limited spatial resolution and diffuse nature of light propagation through the tissues, the high NIR signal of the liver compromises the accuracy of fluorescence imaging. CW imaging signal is a function of both fluorophore concentration and fluorescence lifetime (FL). Imaging in time domain (TD) allows deconvolving these two components. FL imaging is especially useful in applications developed for activatable probes, where FL reports on fluorophore microenvironment independently of concentration [3]. In this work we used SKH-1E immunocompetent mouse diabetes model for measuring the FL changes of the 800CW fluorophore linked to MEPG-gPLL resulting from the probe degradation in insulitis-associated inflammation in the pancreas. Initially we studied the magnitude and kinetics of FL changes using trypsin as a model serine protease. 800CW fluorophores after the probe activation showed a very rapid 1.5-fold increase in FL (within seconds) while CW signal developed slowly (minutes). The activation was associated with non-random cleavage of quenched MEPG-gPLL-800CW probe into smaller fragments with the larger positively charged fragments having longer FL than the negatively charged smaller ones (Figure). The cleavage of non-quenched probe with low density of linked 800CW fluorophores resulted in a decrease of FL suggesting the formation of small degradation products. The change in FL after the IV administration measured in vivo indicated that: 1) pancreas imaging in both experimental and control mice was not feasible in vivo 1-16h after injection; 2) FL in diabetic pancreas imaged at 24 h post injection ex vivo was 0.2-0.1 ns longer than in the liver; 3) the accumulation of the probe in normal pancreas was very low and FL imaging of normal pancreas using TD fluorescence was compromised by high noise. Our data indicate that: 1) whole body non-invasive FL imaging of internal organs can be greatly facilitated by using macromolecular probes with high-density linking of fluorochromes to the cleavable backbone; 2) rapid detection of FL increase is potentially feasible in internal organs with high parenchymal uptake of the imaging probe and its subsequent limited proteolysis. References: 1. Weissleder R,, et al. (1999) Nat Biotechnol 17:375-378. 2. Bogdanov A Jr, et al. (2012) Theranostics 2:553-576. 3. Goergen C, et al. (2012) J Bomed Opt 17: 056001.

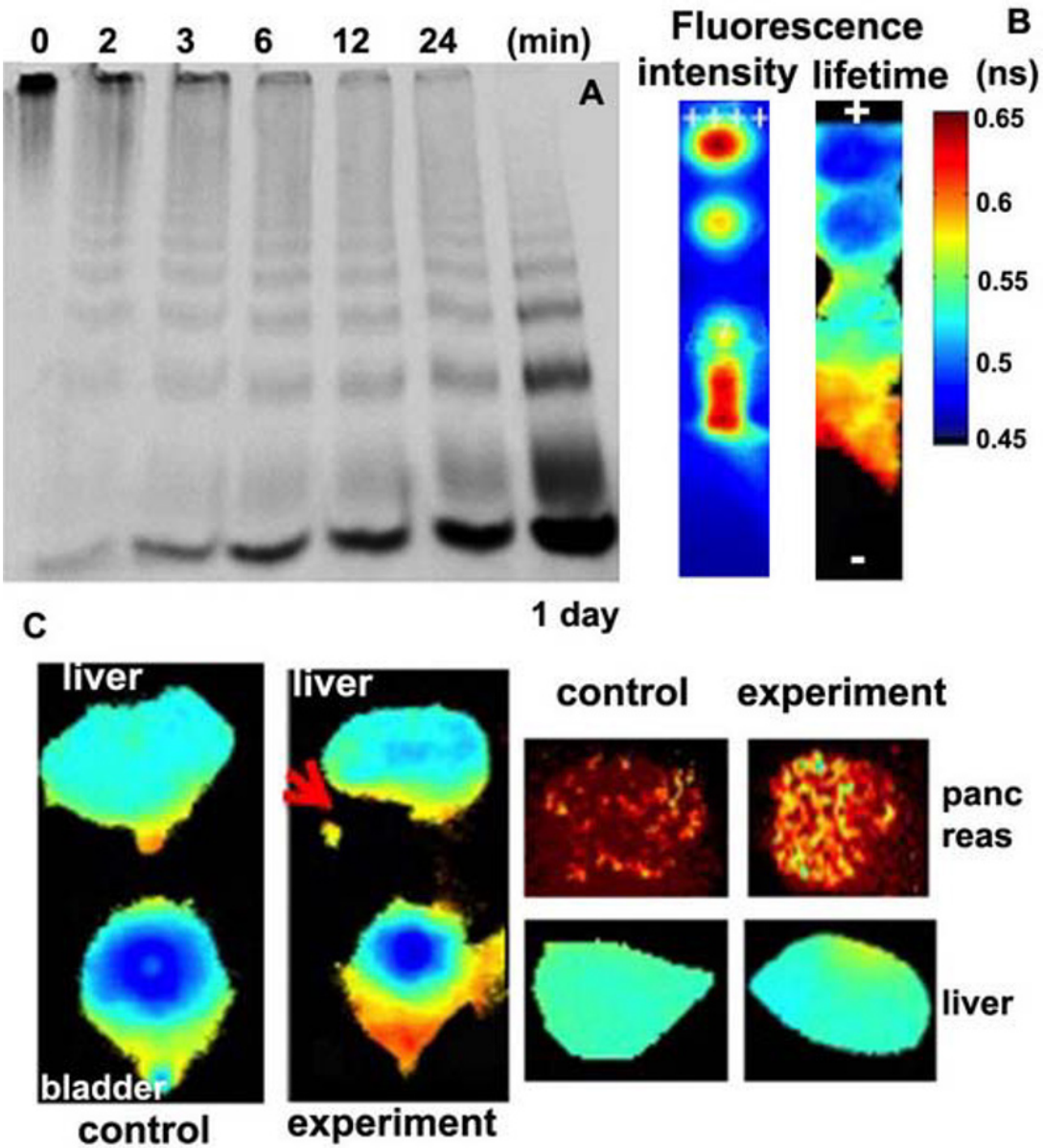

A - time course of MPEG-gPLL-800CW cleavage; B - CW and FL maps of charge/mass separation of MPEG-gPLL-800CW fragments; C-Fluorescence lifetime imaging maps of mice and isolated organs in situ.

Disclosure of author financial interest or relationships:
A.A. Bogdanov, None; **W.L. Rice**, None; **A.W. Ross**, None; **J.C. Lopez**, None; **A. Moore**, Fluoropharma, Grant/research support; **A.T. Kumar**, None.

Presentation Number **P 542**
Poster Session 4
September 21, 2013 / 14:45-14:45 / Room: Exhibit Hall B

Assessment of the Impact of the Tail Residual Activity on SUV Analysis of 18F-Fluorodeoxyglucose (18F -FDG)

Ryan A. Bozio[1,2], Michael Dykstra[1], **Anderson Peck**[1]*, Anthony Chang[1], [1]Small Animal Imaging Facility, Van Andel Institute, Grand Rapids, MI, USA; [2]College of Engineering and Computing, Grand Valley State University, Grand Rapids, MI, USA. Contact e-mail: anderson.peck@vai.org*

Introduction: Positron emission tomography (PET) is widely used for diagnosis, treatment staging and assessing therapeutic response for cancer. Preclinically, PET has demonstrated value as a tool for evaluating drug response in many disease models. 2'-deoxy-2'-18F-fluoro-D-glucose (18F-FDG) is the most popular radiotracer used for performing PET studies though its use has not been standardized across the field. Injection of 18F-FDG in rodents is predominantly performed intravenously (IV) through the tail vein. However, it is a very difficult procedure which challenges even highly experienced technicians. A poorly performed injection will leave significant amount of the radiotracer activity in the tail. A common quantitative measurement of FDG uptake is the standard uptake value (SUV) which is calculated as a ratio of measured tissue radioactivity concentration (µCi/g) to the injected dose at the time of the injection divided by the body weight. Based on the SUV formula, the quality of the tail injection and the residual activity of radiotracer in the tail could impact the SUV measurements. As a critical index for making diagnoses, evaluating therapeutic effects, and studying cell metabolism, it is essential to maintain the integrity of the SUV calculation. Methods: We investigated the quantitative effects of IV injection quality to SUV measurement by analyzing historical datasets of FDG in nude mice (n=59) from our lab. All mice included in this analysis were xenograft tumor models scanned using PET with the entire mouse body and tail in the field of view. The SUV calculation was performed after adjusting the injected activity/body weight (µCi/g) to exclude the residual activity in the tail. This tail corrected SUV value was compared to an uncorrected calculation from the same mouse to determine the impact of tail residual activity. The percent change in SUVmax¬ before and after tail activity adjustment was compared. Results: All mice displayed an increase in tumor SUVmax after excluding the residual activity in the tail as predicted. The relationship was non-linear with an R2 value of 0.9999. A 5% tail residual correlated with a 5% SUVmax increase and a 20% tail residual correlated with a 25% SUVmax¬ increase. Conclusions: The analysis showed that poor IV injections can lead to misleading quantitative results, indicating that further post analysis must be in place to ensure accurate PET results. A mouse with high residual activity in the tail and a mouse with low activity in the tail potentially have the same SUVmax after excluding the tail activity from calculations, but would otherwise be noted as different (see attached figure). Based on the result of this study, we suggest that the residual activity in the tail be excluded from future SUV calculations in PET studies.

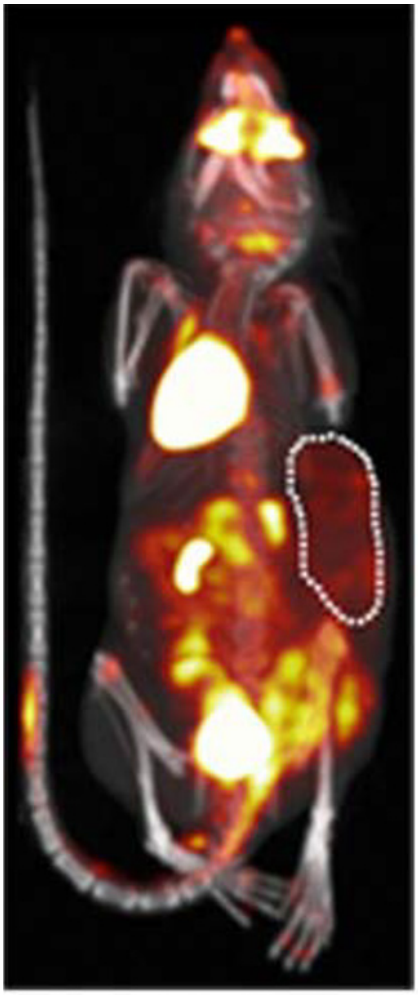

Tail Residual: 1.93%
SUVmax Before: 1.48
SUVmax After: 1.51
SUV % Change: 1.98%

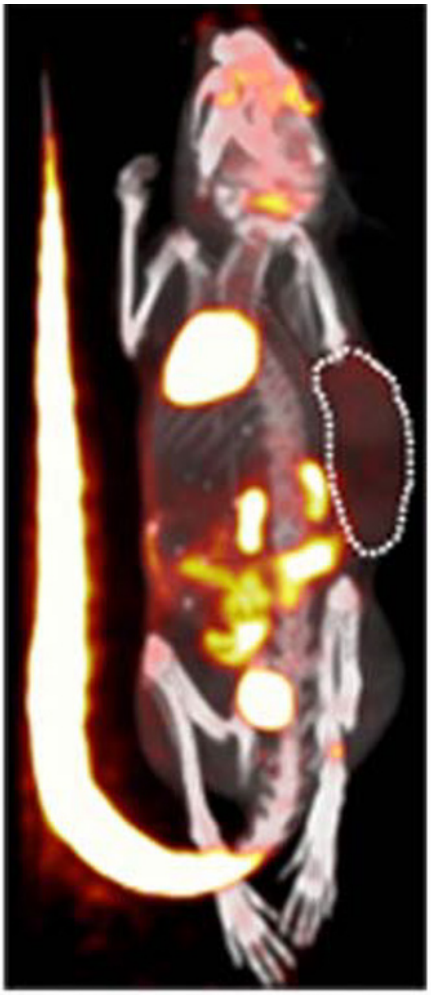

Tail Residual: 33.65%
SUVmax Before: 0.98
SUVmax After: 1.47
SUV % Change: 50.73%

Low tail residual activity versus high tail residual activity. The tumors of each scan are highlighted within the white regions.

Disclosure of author financial interest or relationships:
R.A. Bozio, None; **M. Dykstra**, None; **A. Peck**, None; **A. Chang**, None.

Presentation Number **P 543**
Poster Session 4
September 21, 2013 / 14:45-14:45 / Room: Exhibit Hall B

Probing renal pyruvate carboxylase activities with hyperpolarized [1-^{13}C]pyruvate

Albert P. Chen[1], *Charles H. Cunningham*[2,3], [1]*GE Healthcare, Toronto, ON, Canada;* [2]*Imaging Research, Sunnybrook Health Sciences Centre, Toronto, ON, Canada;* [3]*Biophysics, University of Toronto, Toronto, ON, Canada. Contact e-mail: Albert.Chen@ge.com*

Introduction: ^{13}C MR metabolic imaging utilizing hyperpolarized substrates has shown great potential to non-invasively study cellular metabolism in various organs and diseases. Majority of the studies to date utilized pre-polarized [1-^{13}C]pyruvate to investigate fluxes through pyruvate dehydrogenase, lactate dehydrogenase and alanine transaminase by measuring changes in the metabolic products ^{13}C bicarbonate, [1-^{13}C]lactate and [1-^{13}C]alanine, respectively. Recently, it has also been shown that flux through pyruvate carboxylase (PC), a key enzyme in gluconeogenesis and lipogenesis processes, can be observed in mouse liver (Merritt, ME et al. PNAS. 2011;108(47):19084-9). In this study, we demonstrate that flux through pyruvate carboxylase can be also observed in rat kidneys *in vivo*.
Materials and Methods: Three male Wistar rats (450-550 g) were scanned using a GE MR750 scanner and a dual-tuned ^{1}H/^{13}C birdcage coil (GE Healthcare). Hyperpolarized [1-^{13}C]pyruvate in solution was prepared using a SPINlab™ polarizer (GE). Approximately 0.2 mmol/kg of the substrate in (80 mM) was injected into each subject through a tail vein catheter prior to the ^{13}C MR experiment. Temporally resolved ^{13}C spectra were acquired from one axial slice through the heart and one axial slice through the kidneys (1.2 cm) in an interleaved fashion using a slice selective RF pulse (TR = 1s for each slice). Data acquisition started at the same time as the substrate injection, 64 spectra from each slice were acquired. **Results and Discussions:** ^{13}C spectra from the rat heart and kidneys are shown in Figure 1. ^{13}C signals from metabolites lactate, alanine and bicarbonate were observed in both the heart and kidneys. The resonances observed in the kidney spectra at 1.5 ppm up-field from [1-^{13}C]lactate and 1.6 ppm up-field from [1-^{13}C]alanine were assigned as [1-^{13}C]malate and [1-^{13}C]aspartate, respectively, according to the spectral data shown in Merritt et al. But contrary to the data obtained from mouse liver, malate and aspartate labeled at the C4 position were not present in these data, perhaps due to relatively lower PC activities. No evidence of ^{13}C malate and aspartate signals were found in the heart spectra, as cardiac tissue is not known to have high anaplerotic fluxes. **Conclusions:** Flux through renal pyruvate carboxylase was detected *in vivo* using ^{13}C MR spectroscopy and [1-^{13}C]pyruvate for the first time. Real time investigation of kidney metabolism with hyperpolarized metabolic imaging may aid diagnostics of diabetes, renal cancer and other renal diseases.

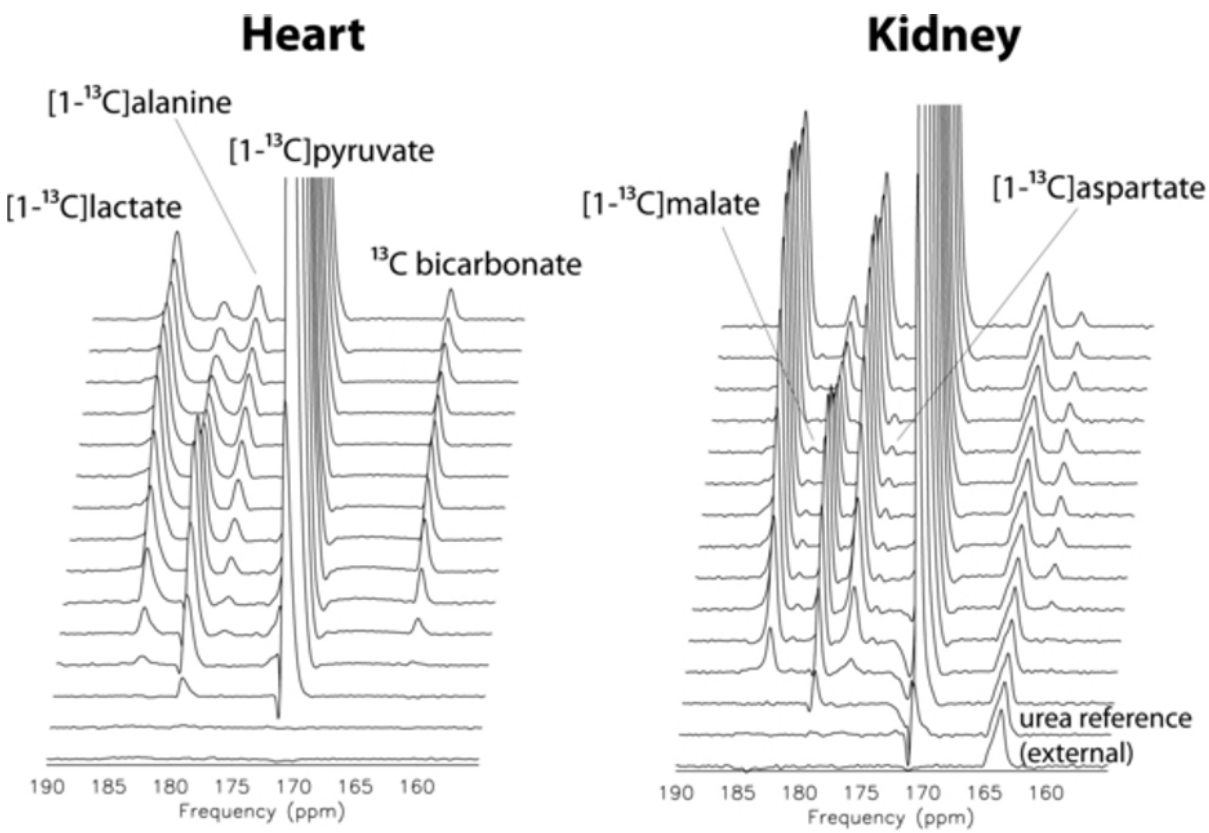

Figure 1. ^{13}C spectra from rat heart and kidneys acquired following injection of hyperpolarized [1-^{13}C]pyruvate. [1-^{13}C]aspartate and [1-^{13}C]malate signals were observed in the data from the kidneys but not the heart.

Disclosure of author financial interest or relationships:
A.P. Chen, GE Healthcare, Employment; **C.H. Cunningham**, None.

Presentation Number **P 544**
Poster Session 4
September 21, 2013 / 14:45-14:45 / Room: Exhibit Hall B

MR Imaging of the Pancreas in Streptozotocin-Induced Diabetic Rats: Comparison of Gadofluorine P and Gd-DOTA

Hye Rim Cho, *Seung Hong Choi, Radiology, Seoul National University Hospital, Seoul, Republic of Korea. Contact e-mail: hyerimcho1030@gmail.com*

Purpose The purpose of this study was to compare the enhancement pattern and diagnostic performance of gadofluorine P in the pancreas of streptozotocin(STZ)-induced diabetic rat model with those of Gd-DOTA. Materials and Methods Fifteen rats (Fischer 344) were used for the analysis of time-enhancement pattern and comparison of diagnostic accuracies between two contrast media, and nine rats were used for the monitoring of blood glucose level and weight. Diabetic rat groups were given 15 mg/kg of STZ intraperitoneally for three consecutive days (day 0, 1, 2). The rats without STZ treatment were used as controls. From day 4 to day 6, MRI was performed with a 3 Tesla human scanner using T1-weighted three dimensional gradient echo sequences. On day 4, unenhanced, immediate, and 3 minutes MR images were obtained after Gd-DOTA injection. On day 5 and 6, immediate, 30 minutes, and 24 hours MR images were obtained after Gadofluorine P injection. Enhancement ratio (ER) of the pancreas and spleen was calculated at each time point using the following equations; [ER(%) = 100×(normalized SIenhanced- SIunenhanced)/SI unenhanced]. After MRI studies, the rats were sacrificed and their pancreas were extracted for histological analysis. The mean islet size and number of each rat was determined on a light microscope using H&E staining. In addition, we used LA-ICP-MS to evaluate the distribution of Gadofluorine P within the pancreas. Results Blood glucose level elevated above 200 mg/dL from day 2 and persisted 30 days in STZ injected rats. In diabetic rat group, mean ER of the pancreas peaked at 3 minutes (9.83 ± 6.89) with Gd-DOTA and mean ER of the pancreas peaked at 30 minutes (67.71± 10.34) with Gadofluorine P. At 30 minutes after Gadofluorine P injection, the optimal ER value for differentiating diabetic rat from control was 53.16 with sensitivity 100 % (95 % CI: 54.1 % - 100 %) and specificity 100 % (95 % CI: 47.8 % - 100 %). At 3 minutes after Gd-DOTA injection, the optimal ER value was 3.04 with sensitivity 83.3 % (95 % CI: 35.9 % - 99.6 %) and specificity 80.0 % (95 % CI: 28.4 % - 99.5 %). Regarding ER of the spleen, no significant difference was found between the groups and the contrast media. On histological analysis, the mean diameter of islets was smaller in diabetic rat group than in control rat group (315.89 ± 101.44 μm vs 481.34 ± 69.32 μm; P = 0.013). The number of islet per field was smaller in diabetic rat group than in control rat group (3.67 ± 1.51 vs 6.8 ± 2.28; P = 0.023). On simple linear regression analysis, increase of ER at 30 minutes after Gadofluorine P injection was associated with decrease of the mean number of islet per field (R2 = 0.50, regression coefficient -0.101, P = 0.015). The concentration of Godaofluorine P within the diabetic pancreas tissue was higher than control pancreas tissue on LA-ICP-MS (11.16 ± 2.67 vs 4.62 ± 1.03, P < 0.05), while the Gd-DOTA was not detected in the both diabetic and control pancreas tissues. Conclusion Gadofluorine P showed better enhancement and diagnostic accuracy in the pancreas of STZ-induced diabetic rat model than Gd-DOTA.

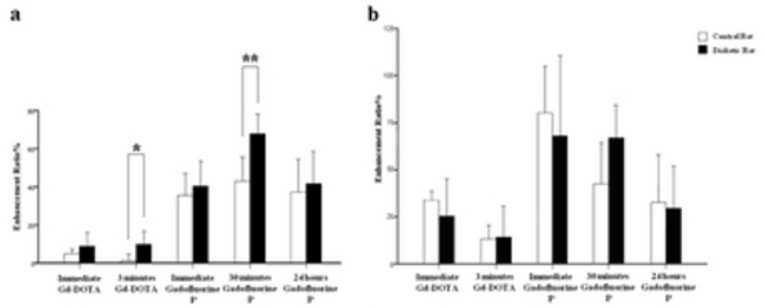

Figure 1. Mean enhancement ratio of the pancreas(a) and spleen(b) at each time point for the contrast media for comparison of control rat group and diabetic rat group. $^{*}P < 0.05$; $^{**}P < 0.01$

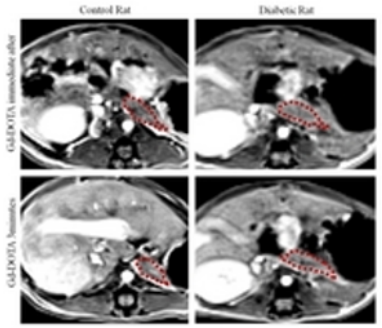

Figure 2. Gd-DOTA enhanced MRI, transverse T1-weighted 3D gradient-echo sequence image. Immediate (the upper) after, and 3 minutes (the lower) after Gd-DOTA injection images of a control rat (left column) and a diabetic rat (right column) are shown as representative images.
The area of the pancreas is outlined with red dotted line. ROIs were drawn in the pancreas while avoiding surrounding structures such as the stomach lumen, the caudate lobe of the liver and spleen. Operator-defined regions of interest (ROIs) for analysis were drawn using software NIH Image J.
The enhancement ratio at immediate after Gd-DOTA injection was 3.3 % vs 10.3 %, at 3 minutes was 1.54 % vs 3.04 % (Control vs diabetic rat).

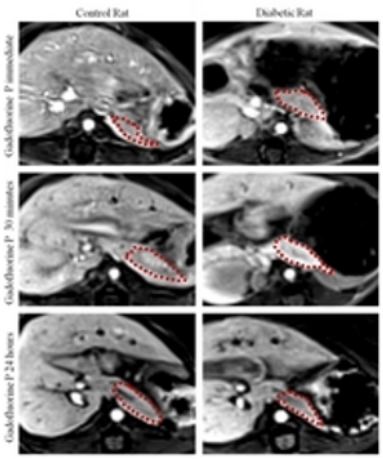

Figure 3. Gadofluorine P enhanced MRI, transverse T1-weighted 3D gradient-echo sequence image. immediate (the upper row) after, 3 minutes (the middle row) after, and 24 hours (the bottom row) after the contrast media injection of the control rat (left column) and the diabetic rat (right column) are shown as representative images.
The area of the pancreas is outlined with red dotted. ROIs were drawn in the pancreas while avoiding surrounding structures such as the stomach lumen, the caudate lobe of the liver and spleen. Operator-defined ROIs for analysis were drawn using software NIH Image J.
The enhancement ratio at immediate after Gadofluorine P injection was 36.1 % vs 47.0 %, at 30 minutes 34.7 % vs 85.30 %, at 24 hours 31.8 % vs 25.7 % (Control vs diabetic rat).

Disclosure of author financial interest or relationships:
H. Cho, None; **S. Choi**, None.

Presentation Number **P 545**
Poster Session 4
September 21, 2013 / 14:45-14:45 / Room: Exhibit Hall B

Visualisation and Quantification of brown adipose tissue activity at 7T MRI using 59Fe labelled Triglyceride-rich lipoproteins

Caroline Jung[1], *Barbara Freund*[3], *Markus Heine*[2,3], *Michael G. Kaul*[1], *Rudolph Reimer*[4], *Gerhard Adam*[1], *Jörg Heeren*[3], *Harald Ittrich*[1], [1]*of Diganostical and Interventional Radiology, University Hospital Hamburg Eppendorf, Hamburg, Germany;* [2]*of Anatomy and Experimental Morphology, University Hospital Hamburg Eppendorf, Hamburg, Germany;* [3]*of Biochemistry and Molecular Biology II, University Hospital Hamburg Eppendorf, Hamburg, Germany;* [4]*Heinrich-Pette-Institute for Experimental Virology and Immunology, University Hamburg, Hamburg, Germany. Contact e-mail: cjung@uke.de*

Purpose: It is known that cold exposure activates brown adipose tissue (BAT), that acts as a master regulator of Triglyceride-riche lipoprotein (TRL) clearance and heat generator. The aim was to determine metabolic activity of BAT with MRI at 7T using radioactively labelled superparamagnetic iron oxide nanoparticles (SPIO) embedded into the lipoprotein layer for visualisation of lipoprotein distribution and BAT metabolism after intravenous (iv) and intraperitoneal (ip) injection. Material and Methods: 59Fe labelled SPIOs were embedded into the lipid core of TRL (59Fe SPIO-TRL). Cold exposed (24h), BAT activated mice (n=10) and thermoneutral control mice (n=10) were starved for 4 hours before 59Fe-SPIO-TRL application. MRI was performed before, 1 and 24 hours after ip (n=10) and iv (n=10) injection at a 7T small animal MRI using a T2*w GRE sequence (TR/first TE 400/2ms, ETL 12, ES 1ms, FA 25°, NSA 4, 10 slices, eff. voxel volume 160x160x600µm3). T2* relaxation time, R2* and deltaR2* in liver and BAT were estimated. Ex vivo the biodistribution of 59Fe SPIO-TRL was analyzed using a large volume Hamburg whole body y counter (HAMCO). The amount of TRL in liver and BAT was calculated according to the results of percentage TRL accumulation arrived from activity measurements and correlated with MRI measurements. Uptake of TRL into tissue was confirmed by histological (Prussian blue) and TEM analyses. Results: Biodistribution after both application approaches were similar with an overall higher uptake after iv application. A significant higher uptake of TRL was detectable in BAT for cold exposed mice with deltaR2* of 104 mmol-1sec-1 after iv and 44 mmol-1sec-1 after ip application (control mice: deltaR2*<14 mmol-1sec-1). 59Fe measurements, T2* relaxation time and deltaR2* showed strong correlations for liver tissue (r>0.85) and BAT (r>0.85). Histology and TEM analyses confirmed the uptake of 59Fe SPIO-TRL within liver and BAT after both application approaches. Conclusion: BAT activity could be noninvasively determined by MRI using SPIO labelled TRL. Iv application leads to a higher uptake in all organs. The quantification of deltaR2* using 59Fe SPIO-TRL is feasible and may serve as a non-invasive tool for estimation of BAT activity, the enhancement of lipoprotein mechanisms or the detection of disorders in lipoprotein metabolism.

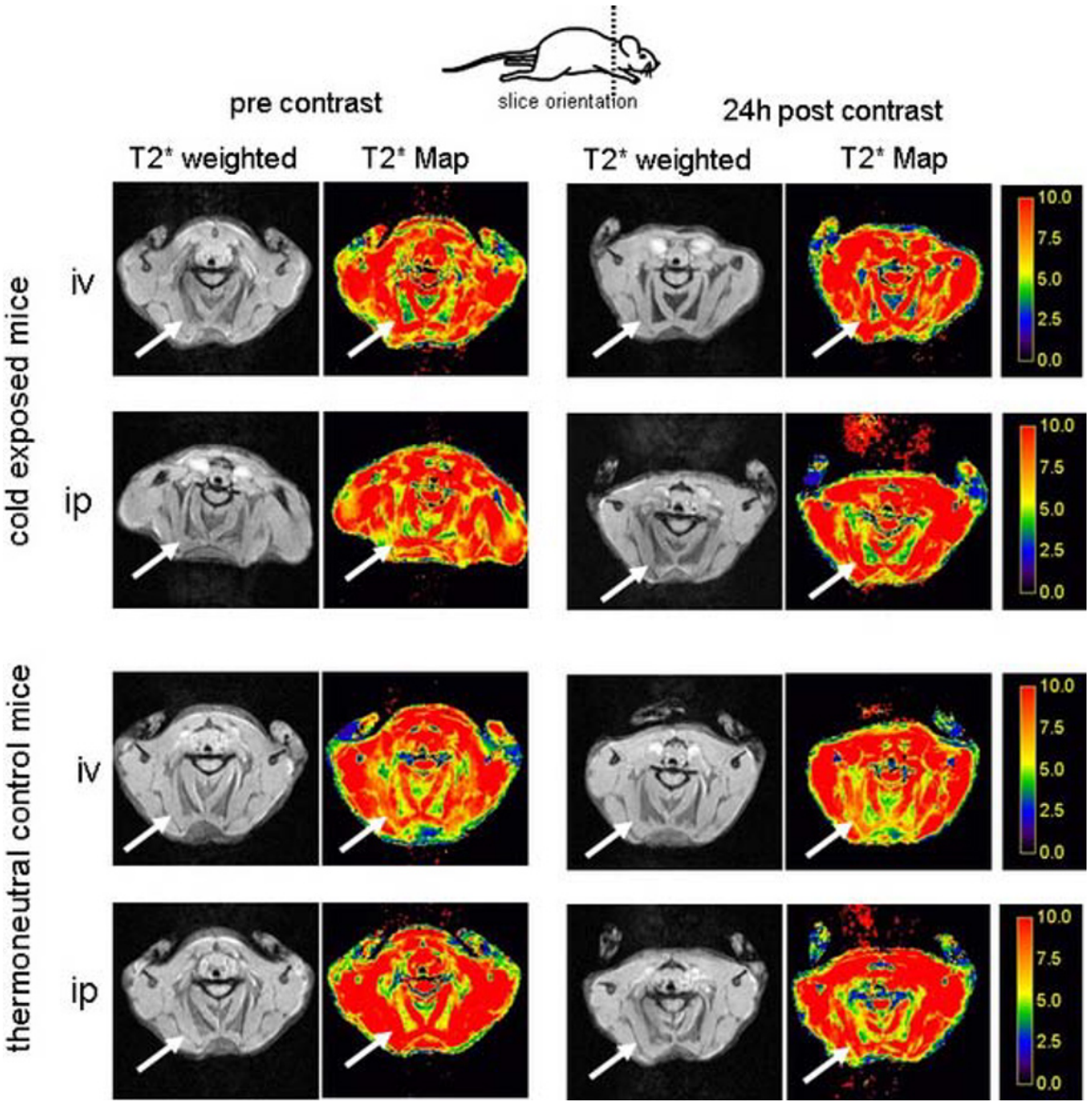

Disclosure of author financial interest or relationships:
C. Jung, None; **B. Freund**, None; **M. Heine**, None; **M.G. Kaul**, None; **R. Reimer**, None; **G. Adam**, None; **J. Heeren**, None; **H. Ittrich**, None.

Presentation Number **P 546**
Poster Session 4
September 21, 2013 / 14:45-14:45 / Room: Exhibit Hall B

Pre-Treatment with Intralipid Reducing the Reticuloendothelial System Clearance of Nano- and Micron-sized MRI Contrast Agents

Li Liu[1], *T. Kevin Hitchens*[1], *Qing Ye*[1], *Yi-Jen L. Wu*[1], *Brent Barbe*[1], *Devin E. Prior*[1], *Wendy F. Li*[1], *Lesley M. Foley*[1], *Fang-Cheng Yeh*[1], *Daniel J. Bain*[2], *Chien Ho*[1], [1]*Pittsburgh NMR Center for Biomedical Research and Department of Biological Sciences, Carnegie Mellon University, Pittsburgh, PA, USA;* [2]*Department of Geology and Planetary Science, University of Pittsburgh, Pittsburgh, PA, USA. Contact e-mail: liliu@andrew.cmu.edu*

Background and Objective: Superparamagnetic iron-oxide particles are useful as contrast agents for anatomical, functional and cellular magnetic resonance imaging (MRI), drug delivery, and diagnositic biosensors. These particles are generally cleared by the reticuloendothelial system (RES), in particular taken up by Kupffer cells in the liver, limiting particle bioavailability and in-vivo applications (1-3). Many studies have been conducted to decrease the RES clearance and increase the circulation lifetime to improve the in-vivo targeting efficiency of iron-oxide particles by modifying particle characteristics, such as the size, charge, surface property, and composition. Modifying the particle characteristics is effective in reducing RES clearance; however, each new modification calls for thorough toxicity and biomechanics studies before translating to a clinical setting. Our strategy is to target the RES, and in particular Kupffer cells, to temporarily blunt particle clearance. In this study, we set out to find if a U.S. Food and Drug Administration (FDA) approved agent could achieve this goal (4). Methods: Intralipid 20.0% (FDA approved nutritional supplement) was intravenously administered in rats at the clinical dose (2 g/kg) 1 h before intravenous injection of ultra-small superparamagnetic iron-oxide (USPIO) or micron-sized paramagnetic iron-oxide (MPIO) particles. Particle biodistribution, blood half-life, and monocyte labeling efficiency were assessed by inductively coupled plasma-mass spectrometry, histology, magnetic resonance relaxometry, and flow cytometry. Results: With Intralipid pre-treatment, there was a 49% and 45% reduction in liver uptake vs. untreated controls at 48 h for USPIO and MPIO, respectively. Pre-treatment with Intralipid resulted in a 3-fold increase in USPIO blood half-life and a 2-fold increase in USPIO-labeled monocytes. A 2.5-fold increase in MPIO blood half-life and a 5-fold increase in MPIO-labeled monocytes were observed following Intralipid treatment, with a 3-fold increase in mean iron content up to 2.6 pg Fe/monocyte. Results from USPIO studies are shown as an example in the Figure. Conclusions: Intralipid pre-treatment significantly decreases initial RES uptake and increases in-vivo circulation and blood monocyte labeling efficiency for nano- and micron-sized iron-oxide particles. Our findings can have broad applications for imaging and drug delivery applications, increasing the bioavailability of nano- and micron-sized particles to target sites other than the liver. References: 1. Tobias Neuberger, et al. Journal of Magnetism and Magnetic Materials. 2005;293:483-496. 2. Chouly C, et al. J Microencapsul. 1996;13:245-255. 3. Okon E, et al. Lab Invest. 1994;71:895-903. 4. Liu L, et al. Biochim. Biophys. Acta, doi: 10.1016/j.bbagen.2013.01.021.

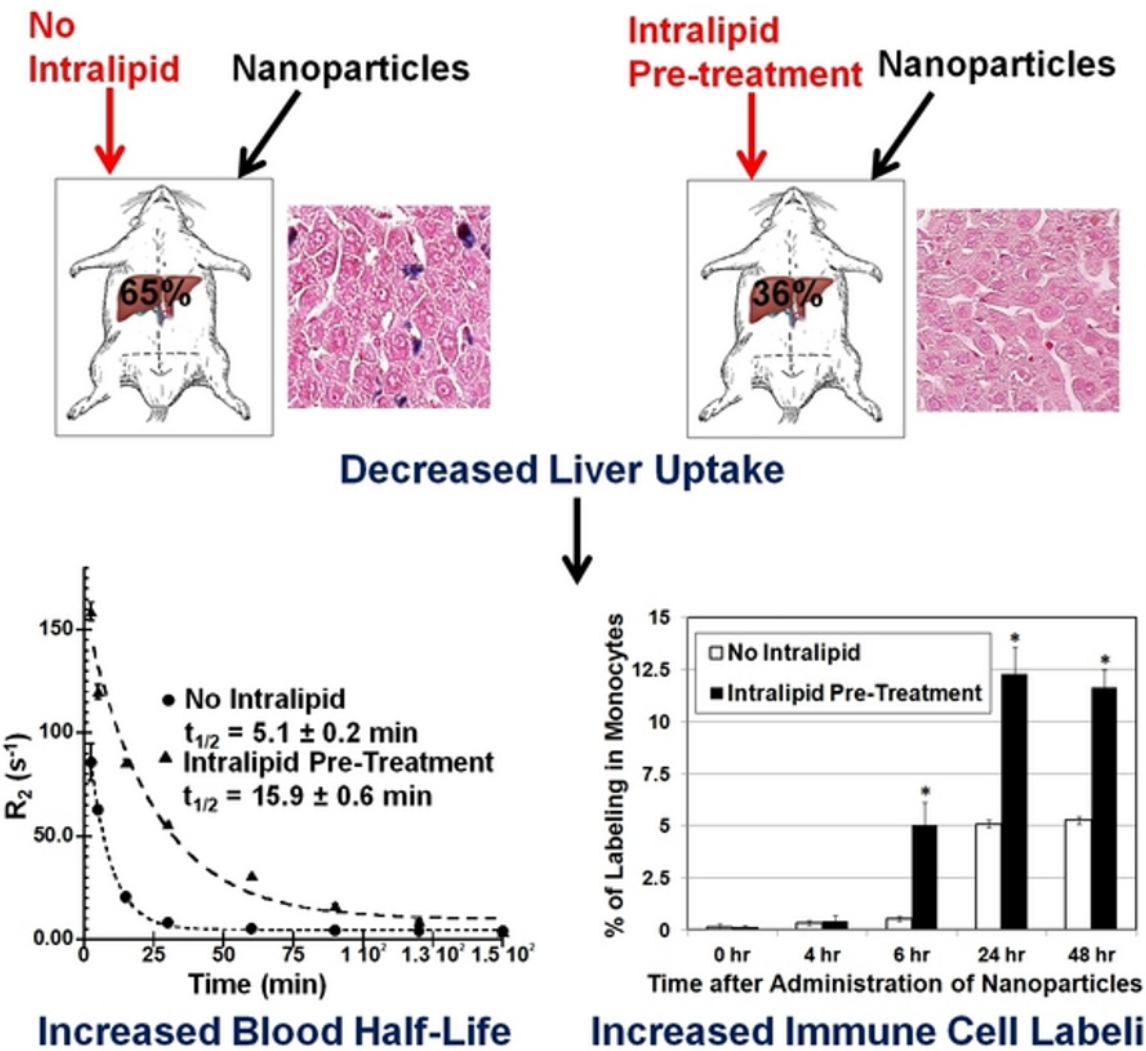

Pre-treatment with Intralipid can result a ~50% decrease in liver uptake of nano- and micron-sized MRI contrast agents, resulting a ~3-fold increase in blood half-life and a 2- to 5-fold increase in the labeling efficiency of monocytes in the blood. Results from USPIO studies are shown as an example in this Figure.

Disclosure of author financial interest or relationships:

L. Liu, None; **T. Hitchens**, None; **Q. Ye**, None; **Y.L. Wu**, None; **B. Barbe**, None; **D.E. Prior**, None; **W.F. Li**, None; **L.M. Foley**, None; **F. Yeh**, None; **D.J. Bain**, None; **C. Ho**, None.

Presentation Number **P 547**
Poster Session 4
September 21, 2013 / 14:45-14:45 / Room: Exhibit Hall B

A Novel Use of Chitosan Combines with Ultrasound for Body Weight and Local Fat Controlled in Mice

Ai-Ho Liao, *Wan-Chun Ma, Graduate Institute of Biomedical Engineering,, National Taiwan University of Science and Technology,, Taipei, Taiwan. Contact e-mail: aiho@mail.ntust.edu.tw*

Ultrasound (US) has recently been used to reduce localized adiposity in humans. The present study evaluated the combined use of chitosan, which is used to treat hyperlipidemic diseases and fatty liver, and US to control body weight and local fat deposition in normal mice over a 5-week experimental period. Female ICR mice were randomly divided into four groups (n=5 animals per group): (1) control (C), (2) US only (U), (3) chitosan only (CIS), and (4) chitosan combined with US (CU). The following measurements were made in all of the mice before and after the 5-week treatment period: body weight, epididymal fat-pad and intra-abdominal fat thicknesses (via US imaging), and plasma concentrations of high-density lipoprotein cholesterol, triglyceride, and low-density lipoprotein cholesterol. After the 5-week treatment period, body weight was decreased significantly in the CU group (-11.2%) compared to the U (-5.8%) and CIS (-9.3%) groups ($p<0.05$). The reduction in epididymal fat-pad thickness in the CU group (28.2%) was significantly more marked than in the other groups ($p<0.05$). Furthermore, in the CU group, plasma levels of triglyceride and low-density lipoprotein cholesterol were significantly decreased, by 51.5% and 26%, respectively. This is the first demonstration of the effective control of body weight and local fat by a combination of US and a putative fat-reducing dietary supplement in mice. The described method significantly decreases local fat-pad deposition, body weight, and plasma lipid levels. The experimental period was 5 weeks. High-frequency US imaging was performed using a US animal-imaging system (Prospect, S-Sharp, Taipei, Taiwan).was performed before the start of the experimental interventions to determine fat thickness and body weight. During the experimental period, body weight and food intake were recorded weekly and daily, respectively. All groups were fed corresponding diets at the beginning of the experiment. In the CU group, the inguinal portion of the epididymal fat pad was subjected to US treatment on a daily basis, together with chitosan supplementation. US was applied using the 1-MHz transducer of a sonoporation gene transfection system (ST 2000V, NepaGene, Ichikawa, Japan), using an acoustic pressure of 2 W/cm2 for 30 sec. The duty cycle was set at 10% and a 6-mm-diameter transducer was used. At the end of the 5-week intervention, high-frequency US imaging was reapplied to all of the mice to determine fat thickness, and body weight was measured. Blood was then collected, and plasma was obtained by centrifugation at 89.6 g (F2402 rotor, Beckman Coulter, Brea, CA) for 10 min. The liver and epididymal fat pad were removed, rinsed in cold saline, and then patted between paper towels. A portion of each liver was excised and fixed in 10% formalin. The plasma and liver samples were stored in a -20°C freezer until used for further analysis.

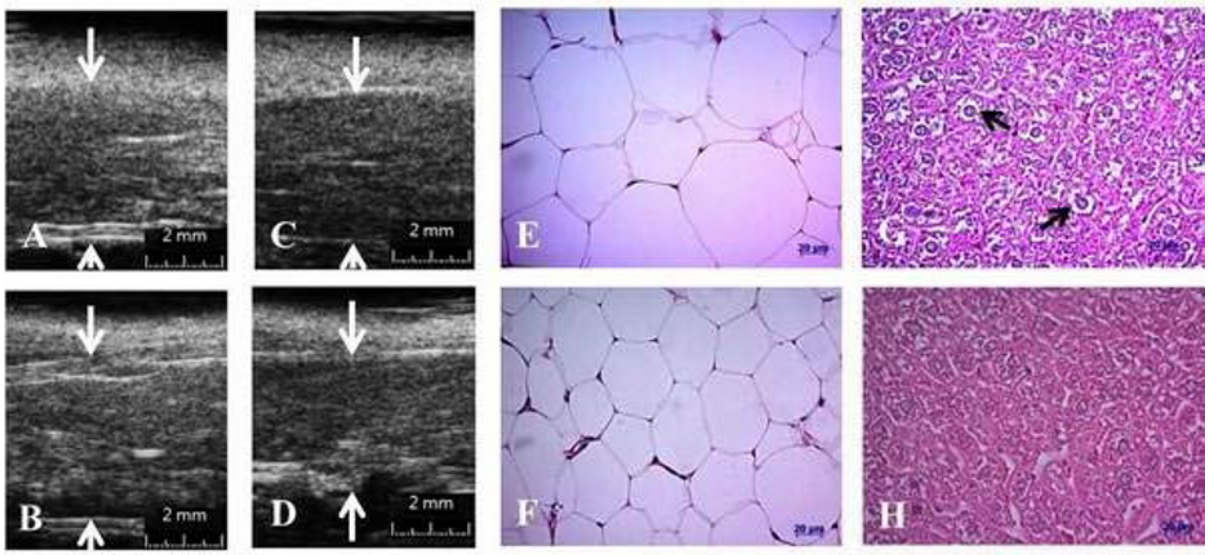

The mean thicknesses of the epididymal fat pad were 3.67 and 3.53 mm prior to the treatment interventions (Fig. 1A-B), and 3.93, 2.50 mm after treatment (Fig. 1C-D) in the C and CU groups, respectively. The reductions in epididymal fat pad thicknesses were greater in the CU group (-28.2%) than other groups. The reduction in the size of adipocytes in the epididymal fat pads (Fig. 1E-F) was 32.8μm markedly greater in the CU group than 72.1μm in the C group and the accumulation of fat vacuoles (arrows) in the liver was clearly decreased in the CU and compared with the C groups (Fig. 1G-H). CU group decreased triglyceride and low density lipoprotein cholesterol by 25% and 26%. This method could reduce the thickness of local fat and decrease the plasma levels significantly.

Mouse plasma levels of BUN, Cre, TC, TG, HDL-C and LDL-C at week 5 in the various treatment groups. The plasma levels of BUN and Cre did not differ significantly between the groups, whereas those of TC and LDL-C were markedly lower ($p<0.05$) in the U, CIS, and CU groups than in the C group. Data are mean±SD values.

Parameter	C	U	CIS	CU
BUN (mg/dl)	26.7±4.6	22.5±2.5	26.0±2.0	23.7±2.0
Cre (mg/dl)	0.83±0.04	0.75±0.10	0.75±0.05	0.80±0.05
TC (mg/dl)	171.7±15.5	128.7±13.1	126.8±9.5	125.2±4.0
TG (mg/dl)	130±24.0	78.5±10.5	123.7±32.0	63.0±5.1
HDL-C (mg/dl)	59.7±16.9	62.0±13.5	58.3±2.7	61.7±12.3
LDL-C (mg/dl)	52.3±12.0	40.8±11.1	32.3±6.7	38.7±6.4

Disclosure of author financial interest or relationships:
A. Liao, None; **W. Ma**, None.

Presentation Number **P 548**
Poster Session 4
September 21, 2013 / 14:45-14:45 / Room: Exhibit Hall B

Pharmacokinetic Modeling of Optical Markers using Multispectral Optoacoustic Tomography (MSOT)

Stefan Morscher[1,2], *Wouter H. Driessen*[1], *Neal Burton*[1], *Daniel Razansky*[2], *Vasilis Ntziachristos*[2], [1]*iThera Medical GmbH, Neuherberg, Germany;* [2]*Insitute for Biological and Medical Imaging, Helmholtz Zentrum München and TU München, Neuherberg, Germany. Contact e-mail: stefan.morscher@ithera-medical.com*

Low overall tissue absorbance of photons promotes optical imaging in the near-infrared (NIR) range, especially for deep tissue in vivo imaging. Here, conventional optical imaging suffers from low spatial resolution and long acquisition times, while multispectral optoacoustic tomography (MSOT) offers fast imaging of optical contrast at high spatial resolution inherent to ultrasound signal detection. Individual absorbers in tissue can be isolated from the acquired data set using multiple excitation wavelengths, enabling a rich portfolio of biomedical applications with clinical settings readily within reach. Image acquisition at a rate of up to 10 images per second permits the collection of a multispectral data set of a single, cross-sectional slice within seconds. Multispectral unmixing reveals the biodistribution of several absorbers with distinct spectral absorption profiles, both tissue-intrinsic (e.g. hemoglobin, melanin) and extrinsic (e.g. fluorescent dyes and probes, gold nanoparticles). These methods allow the separation of multiple injected probes at the same time, without the necessity of a baseline scan before administration of the agents. Verification of the results is achieved using ex vivo cryoslice imaging in a cryostat that enables the acquisition of whole-body color and fluorescence photographs of the mouse, resulting in cross-sectional images that are comparable with the ones acquired using MSOT. Herein we present a method to track the kinetics of dynamic processes such as the clearance and/or accumulation of injected fluorescent dyes and nanoparticles in vivo, at a high resolution. The injected agents are resolved within organs and tumors using multispectral unmixing and the temporal evolution of the signal in individual pixels is fitted to pharmacokinetic models, allowing the analysis of important kinetic parameters such as time-to-peak and half-life. Models of various complexities can be used to characterize the temporal behavior, including a simple one-compartmental model or the extended Kety model that is widely applied in DCE-MRI. The determined parameters are plotted as a parametric map overlaid on an anatomical image, allowing for easy one-glance assessment of e.g. treatment response or vascularization. The presented work emphasizes the role of MSOT as a powerful imaging modality that, in addition to whole body imaging with high spatial resolution, allows for PK modeling of injected substances non-invasively and at high temporal resolution. It is shown that MSOT enables determination of important clearance parameters such as half-life in the blood stream and organs. Furthermore, it can identify and quantify the extent of extra-vascularization of perfusion markers in tumor models. By employing expanded PK models, an even larger field of research opens up, thus enabling imaging scenarios previously limited to DCE-MRI. The demonstrated results prove MSOT as a powerful imaging modality that has the ability to revolutionize the field of biomedical imaging, enabling a large variety of applications in monitoring therapeutic efficacy and assisting drug development.

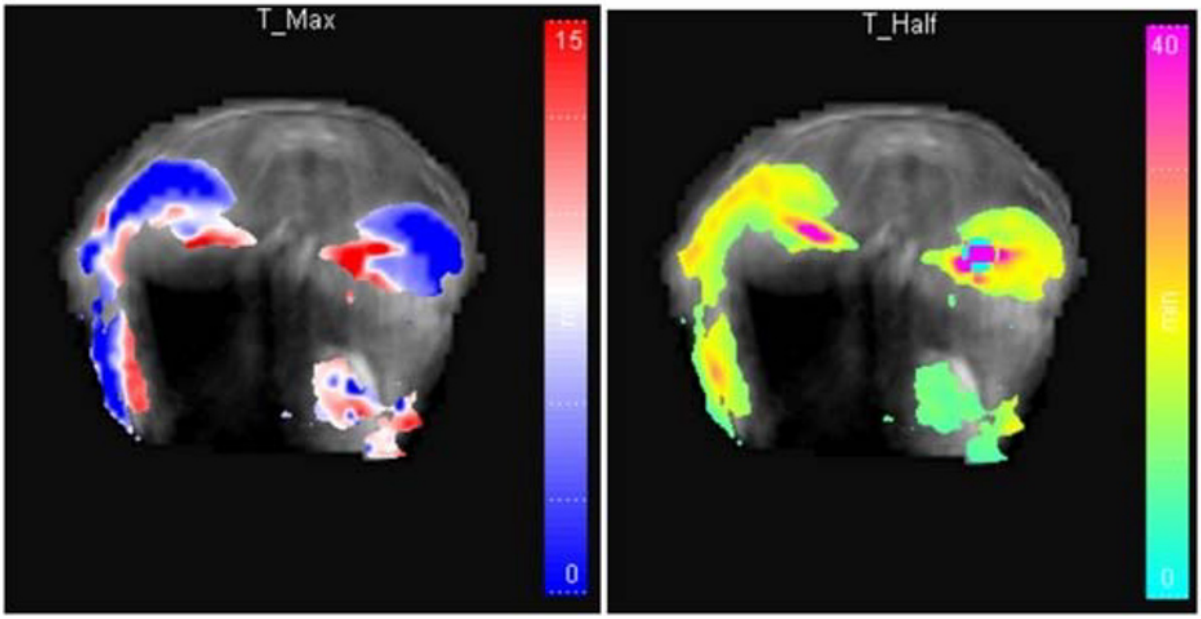

Parametric map of a cross-sectional image in the kidney area of a mouse. Parameters result from a PK modelling of an agent injection with a one-compartmental model, left image shows the time-to-peak while the right image shows the half-life in a respective pixel

Disclosure of author financial interest or relationships:
S. Morscher, iThera Medical, Employment; **W.H. Driessen**, iThera Medical, Employment; **N. Burton**, iThera Medical, Employment; **D. Razansky**, None; **V. Ntziachristos**, iThera Medical, Stockholder; SurgOptix BV, Consultant .

Presentation Number **P 549**
Poster Session 4
September 21, 2013 / 14:45-14:45 / Room: Exhibit Hall B

In vivo multi-photon molecular imaging visualizes inflammatory and immune cell cross-talks in metabolic disease

Satoshi Nishimura, *Mika Nagasaki, ther University of Tokyo, Tokyo, Japan. Contact e-mail: snishi-tky@umin.ac.jp*

To elucidate the underlying mechanisms of metabolic diseases based on chronic inflammation, it is vital to examine the multi-cellular kinetics in living animals. Therefore, we developed in vivo imaging technique based on single- and multi-photon microscopy, and we assessed dynamic immune and inflammatory cellular interplay in diseased conditions. Using this technique, we visualized cell kinetics in metabolic organs including adipose tissue (Fig a, b). Close interrelationships among metabolic elements including adipocytes, muscle, vessels, and nerves were visualized in vivo (Fig c). First, our imaging revealed close spatial and temporal interrelationships between angiogenesis and adipogenesis in obese adipose (2007 Diabetes, Fig d). These inflammatory cell clusters were closely associated with macrophage infiltrations. In addition, increased inflammatory cell interactions in the microcirculation of obese adipose were observed, indicating the inflammatory status in obese adipose (2008 JCI). We also found that CD8+ effector T cells infiltrated into obese adipose, and were essential for inflammatory processes (2009 Nat Med). We also developed FACS analysis methods of metabolic organs, and we identified a novel B cell subset that is abundant in adipose tissue. Adipose B cells also exhibited unique surface phenotypes, distinct from those of known regulatory B cell subsets. Our findings indicate that adipose B cells are a naturally occurring regulatory B cell subset that is essential for negative regulation of diet-induced adipose inflammation and maintenance of homeostasis within adipose tissue, and that B cell dysfunction pivotally contributes to the progression of inflammatory and fibrotic processes. Our results also clearly demonstrated the power of our imaging technique to analyze complex cellular interplays in inflammatory diseases, especially parenchymal and stromal cell cross talks, and to evaluate new therapeutic interventions against them.

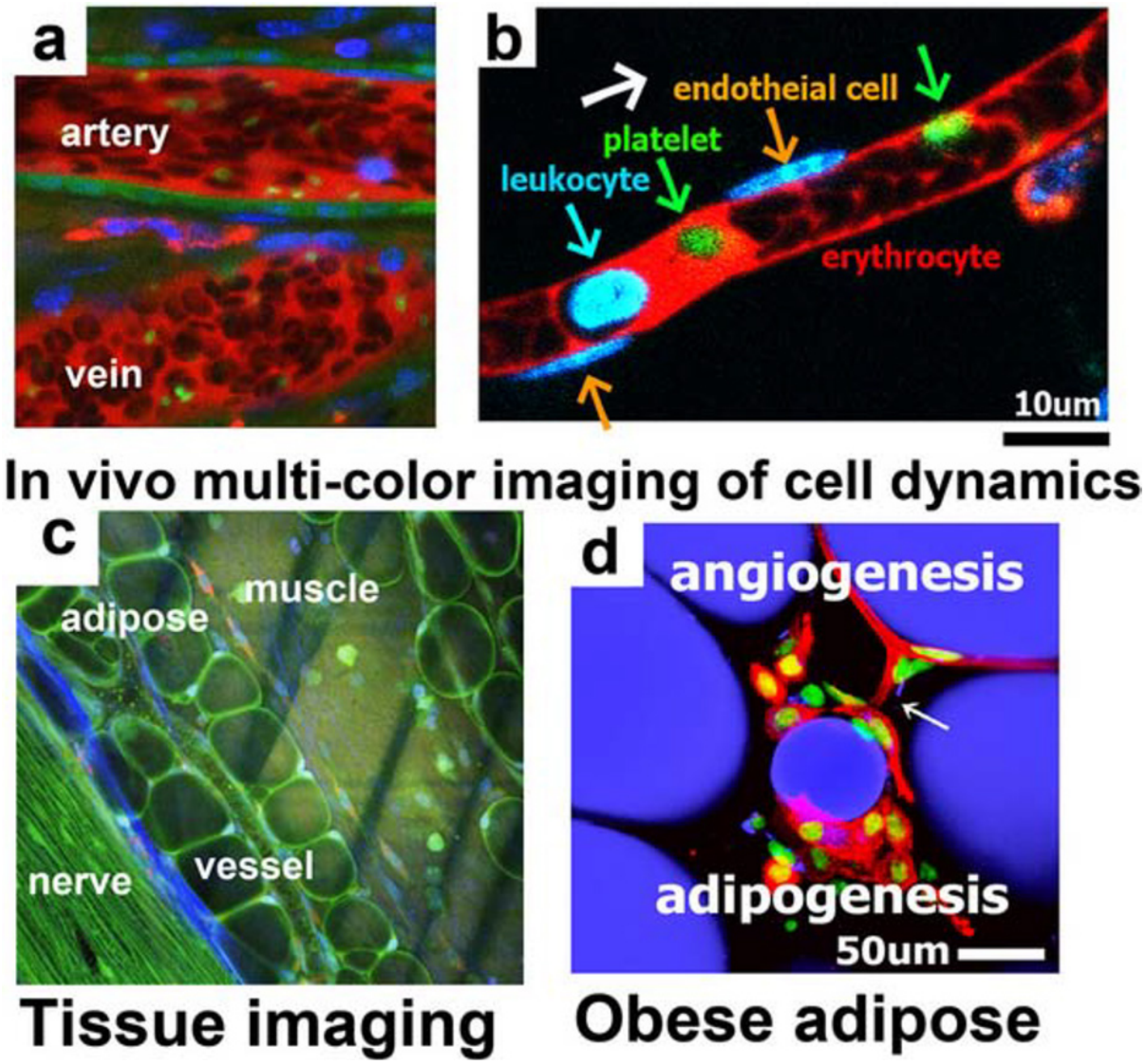

Disclosure of author financial interest or relationships:
S. Nishimura, None; **M. Nagasaki**, None.

Presentation Number **P 550**
Poster Session 4
September 21, 2013 / 14:45-14:45 / Room: Exhibit Hall B

Noninvasive Imaging of Cold Stress Responsive Reactive Oxygen Species

Rao V. Papineni, *University of Miami (adjunct), Branford, CT, USA. Contact e-mail: papineni@graduate.hku.hk*

Brown adipose tissue (BAT) thermogenesis is used by small mammals like mice to maintain core body temperature in response to cold temperature exposure. While in clinics, non-malignant 18FDG uptake by BAT clearly poses a challenge in PET interpretations. Pharmacological or physiological interventions to regulate thermogenesis may allow in development of strategies in obesity management and also in cogent PET diagnostics. Richly innervated by sympathetic nerves, the BAT contains high number of mitochondria. Thermogenesis is primarily mediated by uncoupling proteins (UCP) that directly convert the protons into heat. Vascular perfusion is however the ultimate event in this cold stress response. It allows the cold blood to enter and the warm blood to exit from BAT. This whole circuit during thermogenesis has the potential and the necessity in the rapid mobilization and activation of neutrophils and macrophages aiding in generation of reactive oxygen species (ROS) and the successive signaling cycles that include gene activation processes. Here, we evaluated the early changes in the ROS activity as a response to cold stress. The ROS activity was monitored real-time in vivo using L-012 (8-amino-5-chloro-7-phenylpyridol [3,4-d]pyridazine-1,4(2H,3H) dione), a chemiluminescence reporter, using planar multimodal imaging system. Athymic nude mice were subjected to cold stress for 10 min (40C), with the lower limbs directly exposed to cold. 0.1 ml of 1 mg/ml L-012 probe was injected (i.p.) to determine the initial changes in ROS activity. Noninvasive luminescence and X-ray images obtained show robust increase in ROS activity at BAT sites which is generally accumulated at the regions between the scapulae. Apart from the brown fat depot sites, increase in ROS activity was also observed at additional sites that include eyes. These real-time monitoring methodologies of ROS activity detection by in vivo imaging will greatly enhance the understanding of the early phase response to cold stress and aid in development of intervention strategies in several physiological and pathological processes.

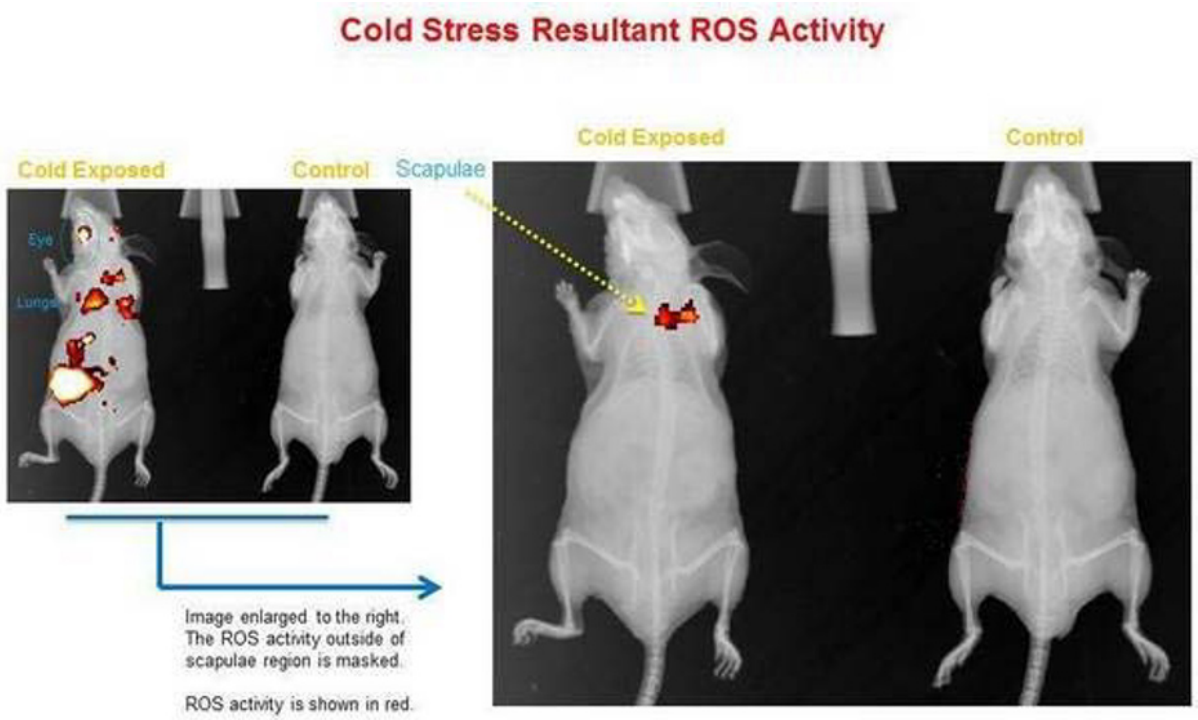

Disclosure of author financial interest or relationships:
R.V. Papineni, None.

Presentation Number **P 551**
Poster Session 4
September 21, 2013 / 14:45-14:45 / Room: Exhibit Hall B

Magnetic Nanoparticles Targeting GLP-1 Receptor For Pancreatic Islet Imaging

Ping Wang, *Byunghee Yoo, Xueli Zhang, Alana W. Ross, Pamela Pantazopoulos, Guangping Dai, Anna Moore, Radiology Department, MGH, Athinoula A. Martinos Center for Biomedical Imaging, Charlestown, MA, USA. Contact e-mail: peterw@nmr.mgh.harvard.edu*

OBJECTIVE—Non-invasive assessment of pancreatic beta-cell mass would tremendously aid in managing type 1 diabetes. Towards this goal we synthesized an iron oxide based probe targeting glucagon-like peptide-1 receptor (GLP-1R), which is highly expressed on beta-cell surface. As a targeting moiety we utilized Exendin-4, a GLP-1R agonist and a more stable analog of a naturally occurring GLP-1 peptide. METHODS—Iron oxide nanoparticles were synthesized and labeled with Cy5.5 followed by modification with N-succinimidyl S-acetylthioacetate hydrochloride (SATA) to introduce thiol group. N-[γ-maleimidobutyryloxy]succinimide ester (GMBS) was introduced to the side chain of lysine in Fmoc-protected Exendin-4. GMBS-conjugated Exendin-4 was loaded on iron nanoparticle through thioether formation. Next, experimental (MN-Ex-Cy5.5) and control (MN-Cy5.5) probes were tested for the binding with beta-cell line (βTC-6) and control cells lines. We also performed competitive inhibition assay to confirm probe specificity. Additional confirmation of probe accumulation in βTC-6 cells was obtained by fluorescence microscopy by co-localizing Cy5.5 signal with the staining of GLP-1R. In vivo experiments included tail vein injections of MN-Ex-Cy5.5 or MN-Cy5.5 in healthy six-week-old Balb/c mice (n=4/group; 10mgFe/kg). MRI was performed 1.5 and 3 hrs later using a 9.4T Bruker scanner. Imaging protocols consisted of T2-weighted spin echo, T2*-weighted gradient echo, and multislice multiecho T2 map. T2-weighted images were analyzed on a voxel-by-voxel basis by fitting the T2 measurements to a standard exponential decay curve, defined by the equation: [y = Aexp (-t/T2)]. We calculated T2 time in a region of interest surrounding the pancreases using Marevisi 3.5 software. Histology was performed on pancreatic frozen sections by staining for insulin and co-localizing it with Cy5.5 signal. RESULTS—In vitro studies demonstrated a concentration-dependent uptake of MN-Ex-Cy5.5 probes by βTC-6 cells. A competition assay using Exendin-4 as a blocking agent showed specific binding of MN-Ex-Cy5.5 to βTC-6 cells and no competition with control cells. Intracellular localization of the probe was confirmed by fluorescence microscopy with anti-GLP-1R antibody in βTC-6 cells. In vivo MRI demonstrated a significant post injection T2 shortening in the pancreas of mice injected with MN-Ex-Cy5.5 compared to control animals at 1.5 hr (20.42±2.76ms vs 26.78±3.41ms) and 3hr (16.63±4.22ms vs 24.83±4.04ms), reflecting significant accumulation of the targeted contrast agent in pancreatic beta-cells (Fig. 1A). Ex vivo histology confirmed considerable accumulation of MN-Ex-Cy5.5 in pancreatic beta-cells (Fig. 1B). CONCLUSIONS—Our data showed that in vitro uptake of MN-Ex-Cy5.5 by βTC-6 cells was dose-dependently inhibited by Exendin-4, suggesting a specific uptake of the probe. In vivo MRI showed significant accumulation of systemically delivered MN-Ex-Cy5.5 probe in the mouse pancreases compared to control group, which was further confirmed by histology. In our future studies we plan to utilize this probe as a therapeutic carrier to diabetic islets for efficient treatment of type 1 diabetes.

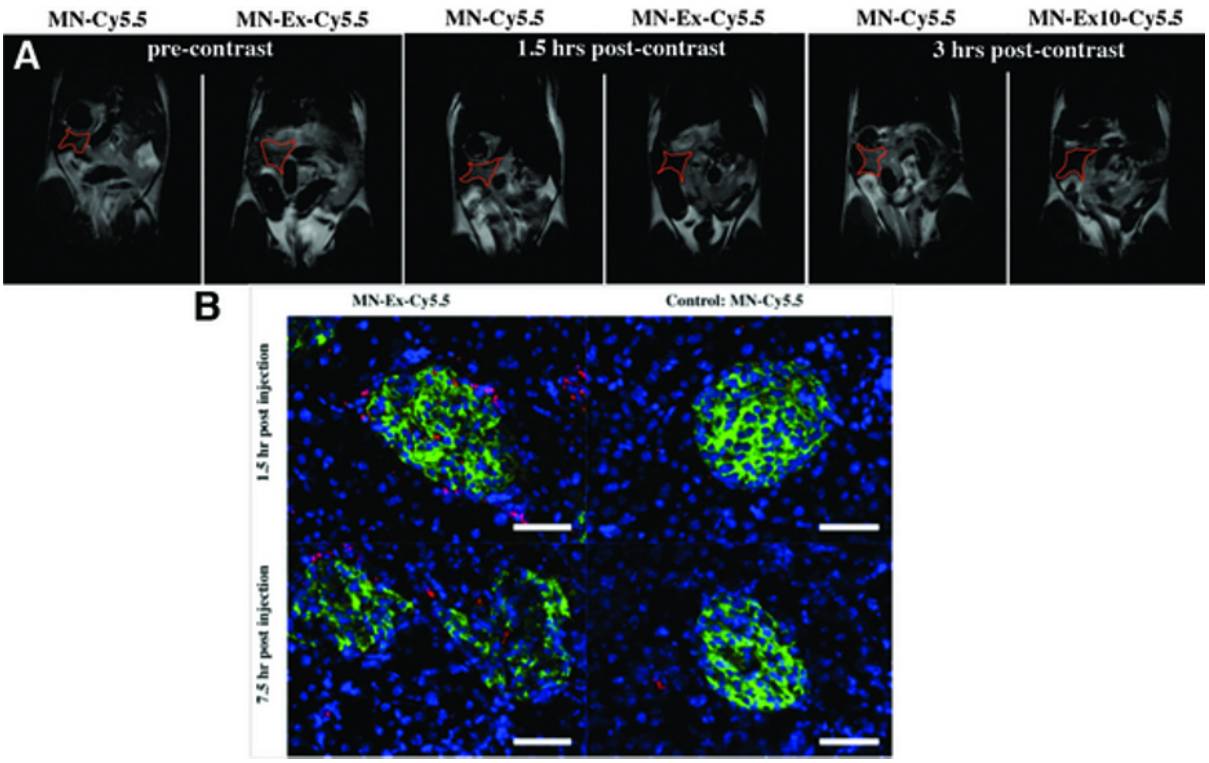

Disclosure of author financial interest or relationships:
P. Wang, None; **B. Yoo**, None; **X. Zhang**, None; **A.W. Ross**, None; **P. Pantazopoulos**, None; **G. Dai**, None; **A. Moore**, Fluoropharma, Grant/research support .

Presentation Number **P 552**
Poster Session 4
September 21, 2013 / 14:45-14:45 / Room: Exhibit Hall B

Effects of feeding conditions on the hepatic pharmacokinetics of radioiodine-labeled BMIPP in mice: Comparison with palmitic acid

Kazuaki Yamasaki, *Songji Zhao, Mie Nishimura, Yan Zhao, Wenwen Yu, Yoichi Shimizu, Ken-ichi Nishijima, Nagara Tamaki, Hiroshi Takeda, Yuji Kuge, Hokkaido University, Sapporo, Japan. Contact e-mail: k-yamasaki@med.hokudai.ac.jp*

Objects: Hepatic fatty acid (FA) metabolism plays important roles on energy homeostasis, and alteration in this metabolism leads to various diseases including hepatic steatosis. Therefore, understanding of hepatic FA metabolism is useful for diagnostic evaluation and therapy monitoring of the diseases. ^{123}I-15-(p-iodophenyl)-3(R,S)-methylpentadecanoic acid ([^{123}I]BMIPP), a FA analog, is widely used for the diagnosis of cardiac FA metabolism. We focused on this attractive compound [^{123}I]BMIPP which may also be applied to the imaging of hepatic FA metabolism. However, the intrahepatic kinetics has not been investigated in detail. Thus, in order to clarify potentials of [^{123}I]BMIPP for imaging hepatic FA metabolism, we determined hepatic distribution and metabolism of [^{125}I]BMIPP in mice at various metabolic conditions induced by fasting, and compared the results with those of [1-^{14}C]palmitic acid ([1-^{14}C]PA). **Methods:** Fed or fasted (6, 12, and 24 h fasting) male C57BL/6J mice at the age of 16 weeks were injected with [^{125}I]BMIPP or [1-^{14}C]PA. Radioactivity in the liver was measured at 1, 5, 10, 30, 60 and 120 min after the injection (n=5 in each designated time point in each group), and then AUC ([%ID/g/kg]•min) was calculated. Lipid components in the liver were extracted by using the Folch method, and radioactivity in each lipid component (e.g. unchanged [^{125}I]BMIPP/[1-^{14}C]PA, triglyceride(TG) and polar lipids) was analyzed by thin-layer chromatography (TLC). **Results:** Table shows AUC of radioactivity in the liver, TG-fraction, and polar lipid-fraction in each group. In mice given [^{125}I]BMIPP, the radioactivity in the liver and TG-fraction was higher in the fasted groups than the fed group, and this tendency was depending on the fasting time. Similarly in mice given [1-^{14}C]PA, radioactivity in the liver and TG-fraction was also increased depending on the fasting time. The radioactivity in the liver, TG-fraction, and polar lipid-fraction was higher in mice given [1-^{14}C]PA compared with mice given [^{125}I]BMIPP, and the difference was prominent on the polar lipid-fraction. As shown above, metabolic conversion of [^{125}I]BMIPP and [1-^{14}C]PA to TG-fraction was increased by fasting. It is known that FA released from adipose tissues can be re-esterified to produce TG in the liver under excessive fasting when influx of FA exceeds hepatic oxidation capacity, which may explain the present results. On the other hand, difference in the metabolic conversion to polar lipids may partly explain the difference in intrahepatic kinetics between [^{125}I]BMIPP and [1-^{14}C]PA. **Conclusion:** Hepatic radioactivity was increased by fasting in mice given [^{125}I]BMIPP, as well as in mice given [1-^{14}C]PA, which may be explained by the increased metabolic conversion of [^{125}I]BMIPP/[1-^{14}C]PA to TG. Thus, [^{125}I]BMIPP demonstrated the changes in hepatic FA metabolism induced by fasting, indicating potentials [^{123}I]BMIPP for imaging hepatic FA metabolism.

AUC of radioactivity in the liver, TG-fraction, and polar lipid-fraction in each group.

	[^{125}I]BMIPP administered groups			[1-^{14}C]PA administered groups		
	Liver	TG-fraction	Polar lipid -fraction	Liver	TG-fraction	Polar lipid -fraction
Fed group	34.7	5.6	3.1	100.2	20.5	45.2
6h-fasting group	45.1	12.7	3.6	100.7	39.2	36.7
12h-fasting group	50.4	31.6	1.3	116.0	61.8	25.8
24h-fasting group	58.5	37.6	2.3	121.1	67.7	27.4

AUC([%ID/g/kg]•min)

Disclosure of author financial interest or relationships:
K. Yamasaki, None; **S. Zhao**, None; **M. Nishimura**, None; **Y. Zhao**, None; **W. Yu**, None; **Y. Shimizu**, None; **K. Nishijima**, None; **N. Tamaki**, None; **H. Takeda**, None; **Y. Kuge**, None.

Presentation Number **P 553**
Poster Session 4
September 21, 2013 / 14:45-14:45 / Room: Exhibit Hall B

Can MR based body composition analysis help in identifying individuals at risk for developing metabolic diseases?

Rama Jayasundar[1], *Somenath Ghatak*[1], *Ankur Poddar*[2], *Ariachery Ammini*[3], *Ashok Mukhopadhyay*[4], [1]*Department of NMR, All India Institute of Medical Sciences, New Delhi, India;* [2]*Department of Biotechnology, All India Institute of Medical Sciences, New Delhi, India;* [3]*Department of Endocrinology, All India Institute of Medical Sciences, New Delhi, India;* [4]*Department of Lab Medicine, All India Institute of Medical Sciences, New Delhi, India. Contact e-mail: ramajayasundar@hotmail.com*

The social and economic consequences of ill health is becoming apparent with diseases like metabolic disorders emerging as both a public health and a clinical problem, affecting not only the health of individuals but also that of a nation's economy with their increasing healthcare cost. A typical example is diabetes, which has become a matter of great public health concern worldwide (1). There is now emerging evidence on the importance of preventability of diabetes and other metabolic disorders by identifying risk factors. In this regard, body composition analysis using MRI and MRS can play an important role by providing information on risk factors like regional and generalized adiposity. Given the known high predisposition of Indian male population to type 2 diabetes (2), the present study has evaluated, in this group, the predictive role of MR assessed adiposity in abdomen and thigh (full and mid-thigh) as an index of metabolic health by correlating it with biochemical metabolic risk factors such as insulin sensitivity, lipid profile, C-peptide and hormone levels. Twenty five normal Indian male volunteers without any history of diabetes and hypertension were studied. MR images were obtained at 1.5 T using the following parameters: TR of 650 ms, TE of 11 ms, 256 x 256 matrix and 8 mm contiguous slices. Transverse T1-weighted images were obtained from abdomen using breath hold sequence and also from thigh (full and mid-thigh). Area of subcutaneous fat (SF) was assessed by drawing regions of interest for each slice and fat volume was calculated. Single voxel proton MR spectroscopy (MRS) was carried out in five volunteers to assess the fat content in liver, pancreas and soleus muscle. Correlation between parameters was determined using Pearson's correlation coefficient. There was significant correlation between SF and the biochemical parameters. For example, insulin resistance showed significant positive correlation with SF in abdomen ($p < 0.05$) and mid-thigh ($p = 0.02$) but not with that from entire thigh region ($p = 0.21$). In the lipid profile, cholesterol showed significant association ($p < 0.05$) with SF in abdomen and thigh. There is growing evidence that South Asian men have a higher prevalence of insulin resistance, predisposing them to type 2 diabetes. Recent studies have shown that in this group, lower appendicular body fat as opposed to abdominal fat is associated with severity of insulin resistance (2). In this context, the results of the current study carried out on Indian males is relevant and interesting - in particular, the positive association of MRI assessed SF in mid-thigh with insulin resistance and other metabolic indices. SF (mid-thigh) measured using MRI could be an additional and independent risk factor and correlate of insulin resistance in Indian male population. Further in-depth studies on assessment of liver and pancreatic fat content using MRS are under way. 1. JE Shaw, RA Sicree, PZ Zimmet, Diab Res Clin Prac, 87, 4-14, 2010. 2. SM Balakrishnan, SM Grundy, A Islam et al., J Invest Med 60, 999-1004, 2012.

Disclosure of author financial interest or relationships:
R. Jayasundar, None; **S. Ghatak**, None; **A. Poddar**, None; **A. Ammini**, None; **A. Mukhopadhyay**, None.

Presentation Number **P 554**
Poster Session 4
September 21, 2013 / 14:45-14:45 / Room: Exhibit Hall B

MRI and Ayurveda: The odd match for phenotyping

Rama Jayasundar[1], *Somenath Ghatak*[1], *Ankur Poddar*[2], *Ariachery Ammini*[3], *Ashok Mukhopadhyay*[4], [1]*Department of NMR, All India Institute of Medical Sciences, New Delhi, India;* [2]*Department of Biotechnology, All India Institute of Medical Sciences, New Delhi, India;* [3]*Department of Endocrinology, All India Institute of Medical Sciences, New Delhi, India;* [4]*Department of Lab Medicine, All India Institute of Medical Sciences, New Delhi, India. Contact e-mail: ramajayasundar@hotmail.com*

With increasing interest in predictive and personalized medicine, the ayurvedic (traditional Indian medicine) concept of phenotyping an individual for personalizing treatment is evoking scientific curiosity. However, scientific validation of this ayurvedic concept and objective measurements for the same are required to make this a clinical feasibility. Ayurveda mentions 7 constitution phenotypes (labeled V, P, K, VP, PK, KV and VPK) based on a set of physical, physiological and psychological parameters. This study explores how MR can be used innovatively to measure some of these phenotyping indices. Healthy volunteers (19 males, 6 females) in the age group of 17-35 yrs, were recruited for the study. A questionnaire for phenotyping based on ayurvedic indices was used to assess the constitution types of the volunteers using a scoring method. MRI evaluation of regional (abdomen and thigh) subcutaneous fat (SF) was carried out at 1.5 T (Avanto, Siemens) using the following parameters: TR of 650 ms, TE of 11 ms, 256 x 256 matrix and 8mm contiguous slices. Area of SF was evaluated for each slice by drawing regions of interest and % fat was calculated with respect to the entire region. T1 and proton density weighted whole body MRI (10 mm contiguous slices in the coronal plane) were also carried out to evaluate the whole body fat and water distribution, respectively. In addition, BMI and body water content using Bio-Impedance Analyser were assessed. Human Leucocyte Antigen (HLA) DRB1 typing has also been carried out in peripheral blood samples of the volunteers by extracting genomic DNA and using PCR sequence specific primers and oligonucleotide probes. Of the 25 volunteers studied, 7 were phenotyped as KV, 6 as VP, 7 as PK , 2 as K, 2 as V and 1 as P. MRI assessed SF in K dominated type was maximum followed by P and V dominated phenotypes. These observations are in agreement with ayurvedic understanding of K and V dominated phenotypes as having contrasting physical attributes with P dominated as an intermediate. According to ayurveda, K dominated phenotypes are associated with presence of more fat (and pre-disposed to obesity and diabetes) as opposed to V types, who have very little fat and pre-disposed to diseases like osteoarthritis. Significant differences between constitution types and SF ($p < 0.02$) were observed in both abdomen and thigh (Fig. 1). Interestingly, significant associations were also observed between phenotypes considered in ayurveda to be predisposed to diabetes, and the MRI assessed regional & whole body subcutaneous fat distribution. The world is entering an era of personalized medicine and phenotyping individuals to customize treatments is being actively looked into. In this context, the comprehensive phenotyping in ayurveda has drawn much attention. This study reports a novel and interesting application of MRI in providing the much needed scientific validation and objective parameters for some of the ayurvedic phenotyping indices. Further studies using fMRI to evaluate the psychological parameters are under way.

Disclosure of author financial interest or relationships:
R. Jayasundar, None; **S. Ghatak**, None; **A. Poddar**, None; **A. Ammini**, None; **A. Mukhopadhyay**, None.

Presentation Number **P 555**
Poster Session 4
September 21, 2013 / 14:45-14:45 / Room: Exhibit Hall B

Detection of tumor hypoxia in a preclinical model of breast ductal carcinoma in situ with a fluorescent antibody targeting Carbonic Anhydrase IX

*Aram van Brussel[2,4], **Arthur Adams**[1], Jeroen F. Vermeulen[2], Sabrina Oliveira[4], Elsken van der Wall[3], Willem Mali[1], Paul J. van Diest[2], Paul M. van Bergen en Henegouwen[4], [1]Department of Radiology, University Medical Center Utrecht, Utrecht, Netherlands; [2]Department of Pathology, University Medical Center Utrecht, Utrecht, Netherlands; [3]Division of Internal Medicine and Dermatology, University Medical Center Utrecht, Utrecht, Netherlands; [4]Division of Cell Biology, Department of Biology, Utrecht University, Utrecht, Netherlands. Contact e-mail: a.adams@umcutrecht.nl*

Background Radical resection of breast ductal carcinoma *in situ* (DCIS) is difficult as it is non-palpable during surgery, and can thus necessitate re-excision. Real time visualization of DCIS during surgery by using near-infrared fluorescent probes could aid the surgeon in distinguishing tumor from non-affected tissue. As hypoxia inducing necrosis is a common phenomenon in DCIS, we investigated a fluorescent antibody specifically targeting an important marker of hypoxia, Carbonic Anhydrase IX (CAIX), in a mouse model of human DCIS. **Methods** We produced a monoclonal antibody against human CAIX, labelled it with the near-infrared fluorophore IRDye800CW, and characterized this tracer (MAbCAIX-IRDye800CW) in vitro. Mice bearing orthotopically transplanted human DCIS (MCF10DCIS.com) with (CAIX+) and without (DCIS) transduction of CAIX were injected with MAbCAIX-IRDye800CW in the tail vein. A clinically used multispectral fluorescence reflectance imaging (MFRI) system was used to monitor tracer uptake non-invasively and to determine tumor-to-normal tissue ratios (TNR) during surgery. Tumor uptake was visualized on tumor sections by the Odyssey imaging system, and quantified using an ex vivo biodistribution assay. **Results** The TNR of tumors that had hypoxic areas (DCIS+) reached a plateau level at 48 hours after injection of 2.1±0.1 (mean ± standard error of the mean), while tumors that did not have hypoxic areas (DCIS-) showed a TNR of 1.7±0.1. In vivo TNR of the CAIX+ tumors was 7.5±0.5. During surgery, TNR of CAIX+ tumors was 11.2±1.0 (96 hours after injection) and of DCIS+ tumors 2.9±0.1, compared to 1.5±0.1 for DCIS- tumors. Immunofluorescence on tumor sections showed specific uptake in hypoxic tumor regions, with higher contrast than conventional chromagen based immunohistochemistry. Biodistribution analysis confirmed tracer uptake with 56±8.0% ID/g in CAIX+, 11±1.1% ID/g in DCIS+, and 4±0.9% in DCIS- tumors, respectively. **Discussion** Molecular fluorescence imaging with MabCAIX-IRDye800CW can be successfully used to detect hypoxic DCIS before and during surgery in order to facilitate radical resection. Furthermore, it allows for optimized fluorescence guided sampling during pathology examinations and sensitive targeted immunofluorescence microscopy. **Acknowledgements** This research was supported by the Center for Translational Molecular Medicine (MAMMOTH).

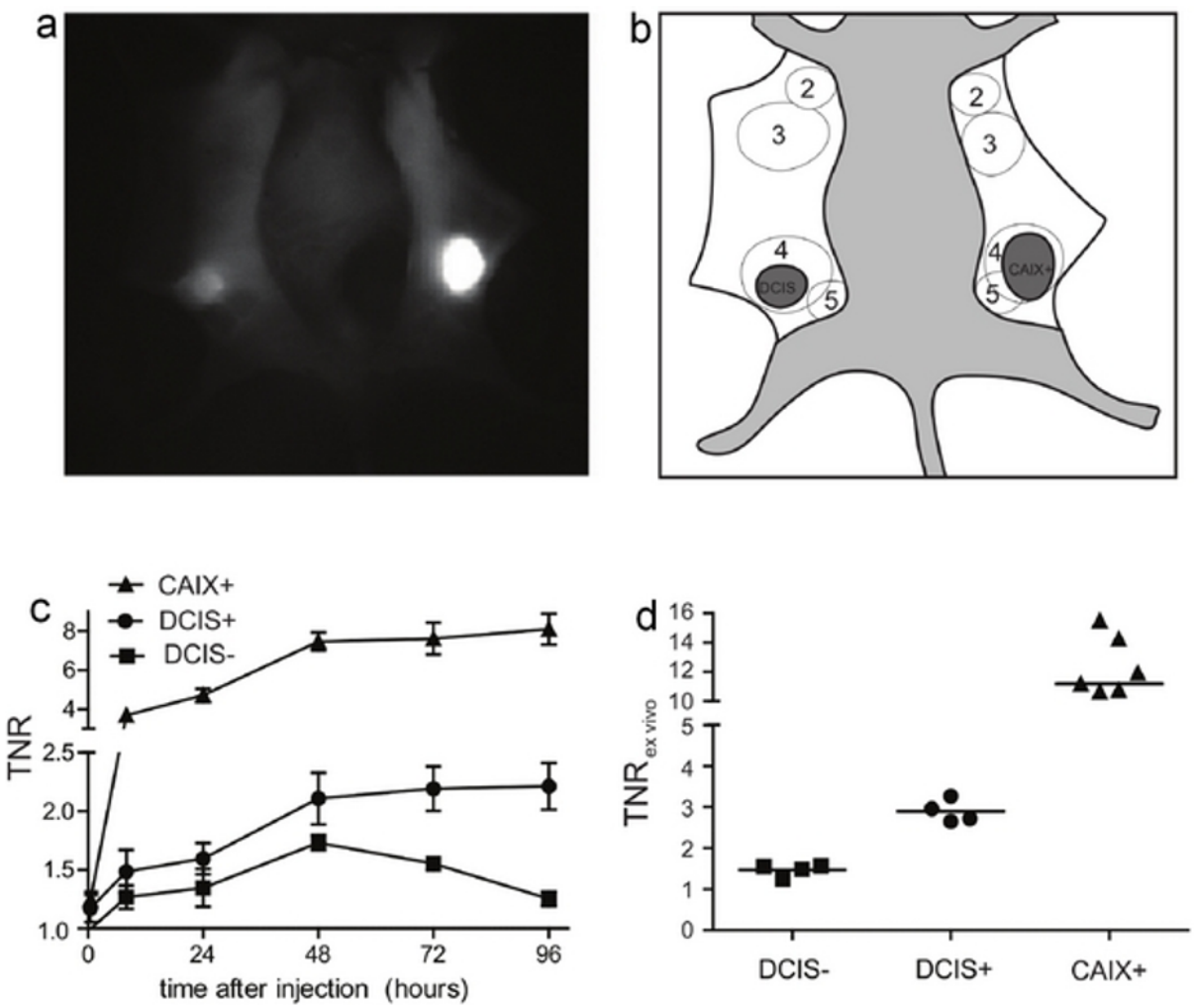

a. intra-operative imaging of MCF10DCIS.com xenografts. b. schematic drawing of position of mouse (light gray) and xenograft positions (dark grey) during intra-operative imaging. Skin and mammary glands in white. c. TNR measured in vivo after intravenous injection of 100 microgram MabCAIX between 0 and 96 hours after injection for DCIS tumors with CAIX transduction (CAIX+; triangle); for DCIS tumors with necrosis (DCIS+; circle); for DCIS tumors without necrosis (DCIS-; square). Error bars represent SEM. d. Individual values of intra-operative TNR in CAIX+, DCIS+ and DCIS- tumors. Horizontal bars represent the mean value.

Disclosure of author financial interest or relationships:

A. van Brussel, None; **A. Adams**, None; **J.F. Vermeulen**, None; **S. Oliveira**, None; **E. van der Wall**, None; **W. Mali**, None; **P.J. van Diest**, None; **P.M. van Bergen en Henegouwen**, None.

Presentation Number **P 556**
Poster Session 4
September 21, 2013 / 14:45-14:45 / Room: Exhibit Hall B

Radiation Necrosis as a Confounding Factor in ALA-mediated Fluorescence-Guided Surgery

Walter J. Akers[1], *Liya Yuan*[2], *Kyle Gullicksrud*[1], *Gail Sudlow*[1], *Jeffrey Bonin*[1], *Joel R. Garbow*[1], *Keith M. Rich*[2], [1]*Radiological Sciences, Washington University School of Medicine, St. Louis, MO, USA;* [2]*Neurologic Surgery, Washington University School of Medicine, St. Louis, MO, USA. Contact e-mail: akersw@mir.wustl.edu*

Glioblastoma multiforme (GBM) remains an incurable malignant brain cancer with limited treatment options. Therapy for GBM involves a multimodality approach with chemotherapy, external beam radiation and surgery. Despite these aggressive approaches, long-term survival rates remain dismal with less than 30% of patients surviving 2 years after diagnosis. Biomedical imaging (MRI, PET) plays a very important role for diagnosis and follow-up after therapy. The effects of therapy can be difficult to distinguish from tumor recurrence, leading to unnecessary additional surgery and/or radiation in some patients. In particular, radiation necrosis (RN), the inflammatory response in the brain after external beam radiation, gives similar enhancement on MRI as tumor tissue. This difficulty in defining the location of tumor tissue is also important in pre- and intra-operative imaging for guiding surgery. The success of surgical intervention in maximizing the extent of resection (EOR) is the primary prognostic factor and has been correlated with improved patient survival and quality of life. Due to the infiltrative nature of this cancer, identification of tumor margins for surgical resection can be difficult. Fluorescence-guided surgery (FGS) using photodiagnostic agents such as 5-aminolevulinic acid (ALA) is helpful for improving tumor resection and progression free survival time relative in GBM patients when compared with non-assisted surgery. In the case of ALA FGS, blue light excitation produces red fluorescence that is visualized by the surgeon, aiding the detection of tumor tissue in concurrence with preoperative imaging information. We endeavored to determine the potential impact of RN tissue on defining tumor margins using ALA-mediated fluorescence for surgical guidance in a mouse model. The right hemispheres of Balb/c mice were irradiated with 60 Gy in a single session using a micro-radiotherapy system. A second group of mice were implanted with DBT mouse glioblastoma tumors in the right hemisphere. At 6 weeks after radiation or 2 weeks post-implant, mice were imaged with MRI pre- and post-contrast. On the day following MRI, mice were injected with 100 mg/kg ALA, IP. Control groups for radiation and DBT tumors received no ALA. Mice were euthanized at 4 hr after ALA injection and whole brains gently dissected. Brain tissues were cooled briefly and sliced in 2 mm sections and imaged with fluorescence stereomicroscope and multispectral planar fluorescence imaging system for PPIX fluorescence. Fluorescence intensity values were calculated for regions of interest selected for each hemisphere and values compared for RN lesion, tumor and normal tissues for each group. Our results indicate that RN lesions accumulate significantly higher (~2-3X) PPIX after ALA administration relative to normal tissues while tumor tissues produced ~10X contrast. We concluded that RN may have a mild confounding effect on ALA-mediated fluorescence guided surgery of glioblastoma and this should be considered by the surgeon.

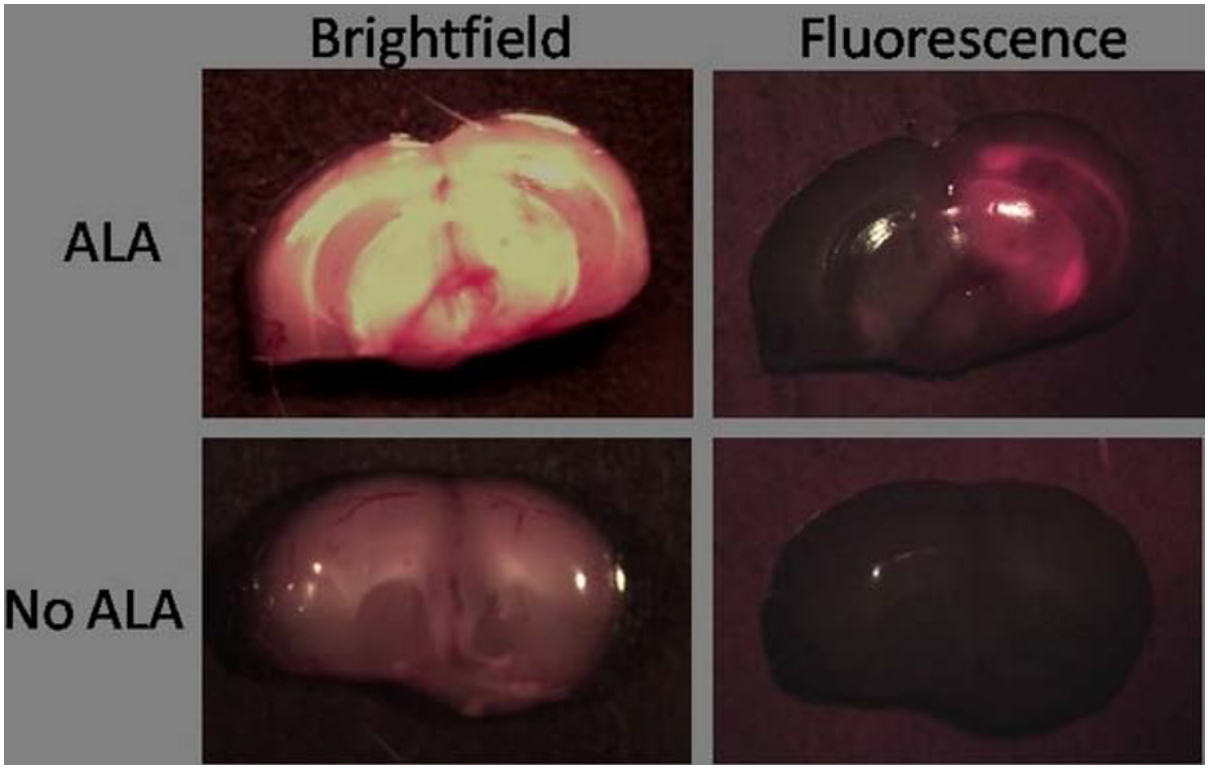

Disclosure of author financial interest or relationships:
W.J. Akers, None; **L. Yuan**, None; **K. Gullicksrud**, None; **G. Sudlow**, None; **J. Bonin**, None; **J.R. Garbow**, None; **K.M. Rich**, None.

Presentation Number **P 557**
Poster Session 4
September 21, 2013 / 14:45-14:45 / Room: Exhibit Hall B

Real-time fluorescein-guided sentinel node biopsy

Tessa Buckle[1], *Nynke S. van den Berg*[1], *Patrick T. Chin*[1], *Henk G. van der Poel*[2], *Fijs van Leeuwen*[1], [1]*Radiology, LUMC, Leiden, Netherlands;* [2]*Urology, Netherlands Cancer Institute (NKI-AvL), Leiden, Netherlands. Contact e-mail: t.buckle@lumc.nl*

Introduction Sentinel node (SN) biopsy was shown to be a valid alternative for the conventional regional lymph node dissection in a variety of malignancies. Conventionally, this procedure is performed using a combination of preoperative injection of radiocolloid and an intraoperative injection of vital blue dye. The latter allows intraoperative optical detection of the SN. However, for SN procedures of e.g. the prostate blue dyes have shown to be of limited value. An alternative to the conventional approach might be the use of fluorescence dyes. One such example is the near-infrared dye indocyanine green (ICG). Alternatively, the dye fluorescein might allow for optical SN detection. Compared to ICG, fluorescein has a much higher quantum yield. Moreover, fluorescein can be seen with the naked eye, this in contrast to ICG that requires the use of a near-infrared fluorescence camera. This study evaluated the value of fluorescein for intraoperative optical SN detection. Methods Non-tumor bearing male mice were anesthetized with a hypnorm/dormicum/water solution (1:1:2; 5ul/g). 10-20uL of fluorescein solution (1mg/mL) was injected into the left lobe of the prostate (n=6 or directly in the cortex of the kidney (n=3). After dye administration, the injection site was massaged for up to 1 minute. Intraoperatively dynamic fluorescence imaging was performed using a self-made fluorescence camera exciting fluorescein (ex = 488 nm; em = 520 nm). Results In all mice, directly after injection, drainage from the injection site into a lymphatic vessel could be visualized. In the prostate model, fluorescence imaging after injection of Fluorescein allowed real-time intraoperative visualization of the lymphatic vessels and the inguinal SNs. Dependent on the location of dye injection in the prostate or seminal vessels bi-lateral inguinal drainage and SN visualization was seen. When unilateral drainage was seen, re-injection in the contralateral lobe resulted in drainage to the contralateral SN. Compared to injection in the prostate, visualization of the SN after injection into the kidney proved to be more complicated, but feasible. Only in one of the animals a lymphatic vessel and SN located below the hilus were found. In the other animals drainage into a vessel was found, but the location of the possible SN was not explored. Conclusion Dynamic fluorescence imaging enabled real-time visualization of the draining lymphatic vessels into the SNs. From a clinical point of view this technique might allow for the detection of SNs during SN biopsy procedures in challenging malignancies such as the kidney and prostate.

Disclosure of author financial interest or relationships:
T. Buckle, None; **N.S. van den Berg**, None; **P.T. Chin**, None; **H.G. van der Poel**, None; **F. van Leeuwen**, None.

Presentation Number **P 558**
Poster Session 4
September 21, 2013 / 14:45-14:45 / Room: Exhibit Hall B

Combination Effects of Sorafenib with Ionizing Radiation on Human Oral Cancer

Betty Chang, *I-Tsang Chiang, Fei-Ting Hsu, Jeng-Jong Hwang, Biomedical Imaging and Radiological Sciences, National Yang-Ming University, Taipei, Taiwan. Contact e-mail: b3ttychang@gmail.com*

Purpose: Oral cancer is ranked the 5th cancer incidence in Taiwan. Current treatments for oral cancer are radiation, chemotherapy, and surgery, however, with poor prognosis. Radiation may induce radioresistance through upregulation of NF-κB signaling pathway. Sorafenib (Nexavar, BAY 43-9006), a multikinase inhibitor, has been approved by the US Food and Drug Administration (FDA) for the treatment of hepatocellular carcinoma (HCC) and renal cell carcinoma (RCC). Sorafenib can inhibit radiation induced NF-κB activation and its downstream proteins. Here, therapeutic efficacy of sorafenib combined with ionizing radiation in human oral carcinoma both in vitro and in vivo was evaluated. Materials and Methods: Human oral carcinoma SAS/tk-luc2 cell line was used in this study. Cytotoxcity of sorafenib alone and combined with radiation (pre-treat, concurrent and post-treat) were determined by MTT assay. On the other hand, apoptosis determined by DNA fragmentation and mitochondrial membrane potential (MMP), NF-κB/DNA binding activity assayed by electrophoretic mobility shift assay (EMSA), and Western blotting performed for NF-κB regulated downstream proteins were performed after treatment of SAS/tk-luc2 cells with15 μM sorafenib and 10 Gy. Therapeutic efficacy of the combination treatment was also evaluated by multimodalities of molecular imaging. Results: Cytotoxicity of SAS/tk-luc2 cells induced by sorafenib was increased with concentration in a dose dependent manner with IC50 (inhibition concentration at 50% survival) at 15 μM. Furthermore, sorafenib inhibited NF-κB/DNA binding activity and the expression of its downstream proteins including VEGF, MMP-9, XIAP, BCL-2, cyclin D1, COX-2, TNF-α, Caspase 8, Caspase 3,and Cytochrome C. Both DNA fragmentation and MMP showed that apoptosis was significantly increased by sorafenib. In addition, higher cell apoptotic percentage was found in combination group as compared with those treated with sorafenib and radiation, respectively. In addition, the similar results were found with an improved survival rate for the combination therapy as compared with sorafenib and radiation treatment alone. Conclusion: Radiation may activate NF-κB/DNA binding activity and the downstream effector proteins, which can be suppressed by sorafenib. Synergistic effect was found when sorafenib was combined with radiation for the treatment of human SAS oral carcinoma. (We thank the Taiwan Mouse Clinic which is funded by the National Research Program for Biopharmaceuticals (NRPB) at the National Science Council (NSC) of Taiwan for technical support in [18F]FDG/microPET imaging experiment.)

Disclosure of author financial interest or relationships:
B. Chang, None; **I. Chiang**, None; **F. Hsu**, None; **J. Hwang**, None.

Presentation Number **P 559**
Poster Session 4
September 21, 2013 / 14:45-14:45 / Room: Exhibit Hall B

Imaging evaluation of 188Re-HSA microsphere in hepatoma model by nano-SPECT/CT and 3D ultrasound

Liang-Cheng Chen, *Chia-Yu Yu, Wan-Chi Lee, Cheng-Hui Chuang, Chung Li Ho, Chih-Hsien Chang, Te-Wei Lee, Institute of Nuclear Energy Research, Taoyuan County, Taiwan. Contact e-mail: lcchen@iner.gov.tw*

Objectives: Nano-single photon emission computed tomography (Nano-SPECT)/computed tomography (CT) and ultrasound imaging are noninvasive imaging modalities for monitoring radioisotope-labeling drug distribution and tumor volume. The aims of this study were to investigate the ability of nano-SPECT/CT for quantitating intraarterial (i.a.) administration of 188Re-human serum albumin (188Re-HSA) microsphere and the utility of three-dimensional (3D) high-frequency ultrasound in the evaluation of radiotherapeutics in N1-S1 hepatoma model. Methods: Male SD rats were subcapsular inoculation with 2 x 106 N1-S1 cells. At 19 days after tumor inoculation, nano-SPECT/CT imaging was performed at 2, 24, 48 and 72 h after injection of 188Re-HSA microsphere. Each rat was i.a. injection of ~300-600 μCi/200 μL 188Re-HSA microsphere and scanned for 1-2 h. Percentage injection dose (%ID) of 188Re-HSA microsphere with the liver area was calculated from regions of interest analysis of the nano-SPECT/CT images. Longitudinal and sagittal-sectional ultrasound images of N1-S1 hepatoma acquired once a week. Results: In nano-SPECT/CT images, the obvious uptakes in liver area were observed from 2 to 72 h after injection of 188Re-HSA microsphere. The results of images quantification analysis were indicated that the %ID was maintained at 95%ID-88%ID from 2 to 72 h after injection of 188Re-HSA microsphere. To monitor the tumor growth, longitudinal tumor volumes were obtained from 3D segmentation of ultrasound imaging in the SD rat with N1-S1 hepatoma. The tumor volumes were decrease with time after i.a. injection of 188Re-HSA microsphere. Conclusions: Nano-SPECT/CT imaging can be used a noninvasive tool to localize and follow the radioisotope-labeling drug via i.a. injection in N1-S1 hepatoma model. The 3D high-frequency ultrasound with a high spatial resolution and contrast in soft tissue can become imaging modality for rat preclinical studies.

Disclosure of author financial interest or relationships:
L. Chen, None; **C. Yu**, None; **W. Lee**, None; **C. Chuang**, None; **C. Ho**, None; **C. Chang**, None; **T. Lee**, None.

Presentation Number **P 560**
Poster Session 4
September 21, 2013 / 14:45-14:45 / Room: Exhibit Hall B

Plasmonic Resonance Energy Transfer in Mesoporous Silica-Encased Gold Nanorod for Two-Photon-Activated Photodynamic Therapy

Nai-Tzu Chen[1,2], *Kuo-Chun Tang*[2], *Ming-Fang Chung*[1], *Shih-Hsun Cheng*[1,3], *Ching-Mao Huang*[1], *Chia-Hui Chu*[1], *Pi-Tai Chou*[2], *Jeffrey S. Souris*[3], *Chin-Tu Chen*[3], *Chung-Yuan Mou*[2], *Leu-Wei Lo*[1], [1]*Medical Engineering, National Health Research Institute, Miaoli, Taiwan;* [2]*Chemistry, National Taiwan University, Taipei, Taiwan;* [3]*Radiology, The University of Chicago, Chicago, IL, USA. Contact e-mail: ohnonancy@gmail.com*

The unique optical properties of gold nanorods (GNRs) have recently drawn considerable interest from those working in in vivo biomolecular sensing and bioimaging. Especially appealing in these applications is the plasmon-enhanced photoluminescence of GNRs induced by two-photon excitation at infrared wavelengths, owing to the significant penetration depth of infrared light in tissue. Unfortunately, many studies have also shown that often the intensity of pulsed coherent irradiation of GNRs needed results in irreversible deformation of GNRs, greatly reducing their two-photon luminescence (TPL) emission intensity. In this work we report the design, synthesis, and evaluation of mesoporous silica-encased gold nanorods (MS-GNRs) that incorporate photosensitizers for two-photon-activated photodynamic therapy (TPA-PDT). The photosensitizer, doped into the nano-channels of the mesoporous silica shell, can be efficiently excited via intra-particle plasmonic resonance energy transfer from the encased two-photon excited gold nanorod and further generates cytotoxic singlet oxygen for cancer eradication. In addition, due to the mechanical support provided by encapsulating mesoporous silica matrix against thermal deformation, the two-photon luminescence stability of GNRs was significantly improved; after 100 seconds of 800 nm repetitive laser pulse with the 30 times higher than average power for imaging acquisition, MS-GNR luminescence intensity exhibited ~260% better resistance to deformation than that of the uncoated gold nanorods. These results strongly suggest that MS-GNRs with embedded photosensitizers might provide a promising photodynamic therapy for the treatment of deeply situated cancers via plasmonic resonance energy transfer.

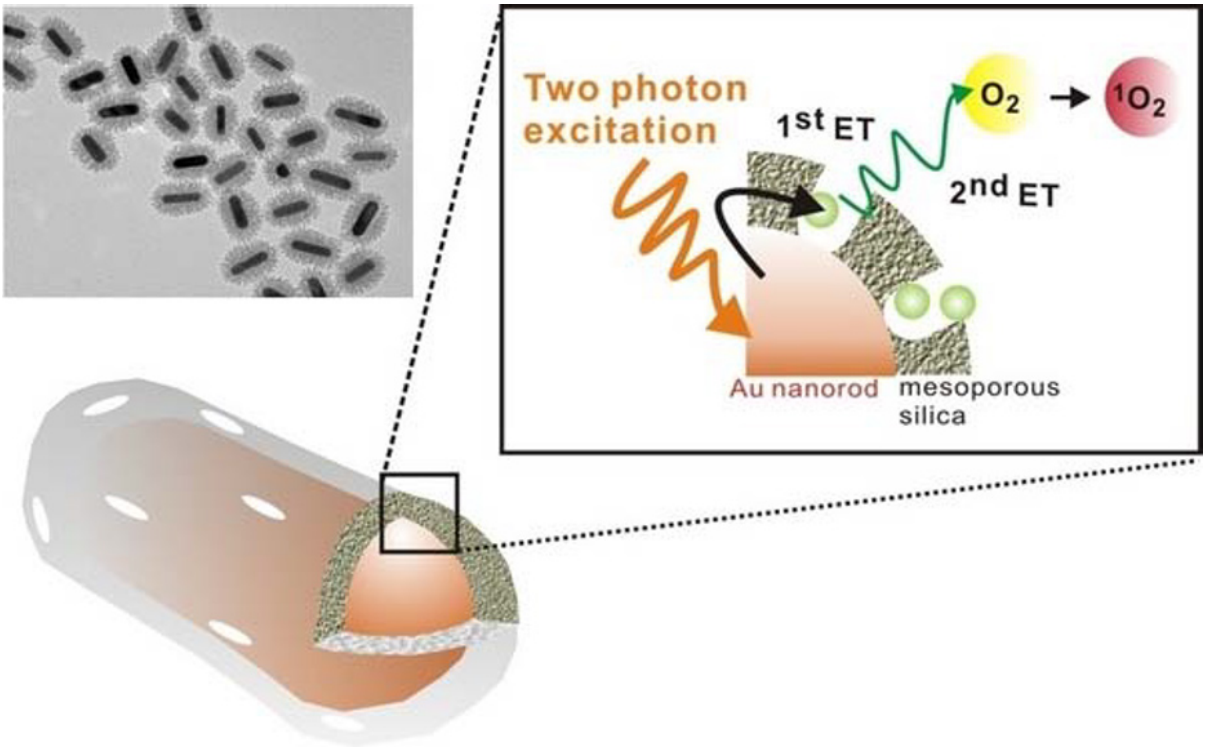

Schematic illustration of two-photon-activated photodynamic therapy (TPA-PDT) using mesoporous silica-encased gold nanorods.

Disclosure of author financial interest or relationships:
N. Chen, None; **K. Tang**, None; **M. Chung**, None; **S. Cheng**, None; **C. Huang**, None; **C. Chu**, None; **P. Chou**, None; **J.S. Souris**, None; **C. Chen**, Cell>Point, Grant/research support; RefleXion Medical, Consultant; DxRay/Photon Imaging, Consultant; **C. Mou**, None; **L. Lo**, None.

Presentation Number **P 561**
Poster Session 4
September 21, 2013 / 14:45-14:45 / Room: Exhibit Hall B

Imaging Various Levels of Heterogeneity within the Tumor Microenvironment by Multispectral Optoacoustic Tomography (MSOT)

Wouter H. Driessen[1,2], *Neal Burton*[1,2], *Stefan Morscher*[1,2], *Jing Claussen*[1,2], *Daniel Razansky*[1,3], *Vasilis Ntziachristos*[1,3], [1]*The Institute of Biological and Medical Imaging, Helmholtz Zentrum München, Neuherberg, Germany;* [2]*iThera Medical, Neuherberg, Germany;* [3]*Technische Universität München, München, Germany. Contact e-mail: wouter.driessen@ithera-medical.com*

Tumor tissue is variable in many aspects and in order to better understand this heterogeneity by (molecular) imaging, modalities with a temporal and spatial resolution appropriate for studying dynamic changes at sub-organ resolution are needed. Multispectral Optoacoustic Tomography (MSOT) is a novel biomedical imaging modality based on the photoacoustic effect: the conversion of absorbed electromagnetic energy (e.g. NIR light) to acoustic signals. During MSOT imaging, mice are illuminated with multiple wavelengths in the NIR window in biological tissue (680 - 980nm) and by detecting the acoustic waves with a 5MHz tomographic ultrasound array; multispectral whole animal cross-sectional images can be obtained at an in-plane resolution of 150µm in less than a second. Multispectral analysis allows for the specific identification of endogenous absorbers such as hemoglobin and melanin or injected contrast agents. In this work we studied various levels of heterogeneity within the tumor microenvironment by using a preclinical MSOT whole animal scanner. Firstly, we show inter- and intra-tumoral heterogeneity in the distribution of hypoxic pockets between various orthotopic tumors. In later stages of tumor development - as increased vascularization can no longer keep up with the growing tumor - a relative increase in deoxygenated hemoglobin can be observed. By determining oxy- and deoxy-hemoglobin ratios, hypoxic areas can be readily identified within tumors without the need of exogenous contrast agents. Secondly, we assessed heterogeneity in tumor perfusion by systemically administering Indocyanine Green (ICG), after which MSOT images were acquired at a frame rate of 10 Hz over 10 minutes. Region of Interest (ROI) analysis was performed at different regions throughout the tumor, thereby revealing a high degree of heterogeneity in dynamic contrast enhancement. Lastly, apoptotic regions within orthotopic tumors were visualized using a caspase-targeted probe and compared to the hypoxia status of each tumor region, before and after treatment with doxorubicin. We showed that in un-treated tumors, maximal apoptosis-signal was co-localized with more hypoxic regions in the tumor. However, overall signal intensity from apoptosis molecular probe was significantly increased after systemic treatment with doxorubicin. In summary, MSOT offers an imaging modality that can provide anatomical, functional, molecular and kinetic information at high temporal and spatial resolution. We used this modality to analyze three levels of heterogeneity within the tumor microenvironment by visualizing hypoxic pockets within orthotopic tumors without the use of contrast agents; determining heterogeneity in dynamic contrast enhancement by using the non-targeted perfusion marker ICG and by quantifying the extent of apoptosis in tumors in vivo.

Disclosure of author financial interest or relationships:
W.H. Driessen, iThera Medical, Employment; **N. Burton**, iThera Medical, Employment; **S. Morscher**, iThera Medical, Employment; **J. Claussen**, iThera Medical, Employment; **D. Razansky**, None; **V. Ntziachristos**, iThera Medical, Stockholder; SurgOptix BV, Consultant .

Presentation Number **P 562**
Poster Session 4
September 21, 2013 / 14:45-14:45 / Room: Exhibit Hall B

Murine Liver-Tumor Characterization by Ultrasound-Induced Biomarker Release

Aloma L. D'Souza[1], *Xinrui Yan*[1], *Huaijun Wang*[1], *Sanjiv S. Gambhir*[1,2], [1]*Radiology - Molecular Imaging Program, Stanford University, Stanford, CA, USA;* [2]*Bioengineering, Stanford University, Stanford, CA, USA. Contact e-mail: adsouza@stanford.edu*

Ultrasound at low frequencies is known to permeabilize cell membranes. We have shown that this bioeffect of ultrasound causes the extracellular release of protein and nucleic acid biomarkers when it is directly applied to tumor cells. We use this simple non-invasive method to amplify biomarker-release from and characterize mouse liver tumors. The ability to focus ultrasonic waves allows for the localization of the potential biomarker source *in vivo*. This novel strategy could lead to the earlier identification, characterization and localization of incidental lesions leading to earlier detection of cancer and other diseases. **Materials/Methods:** The colon cancer cell line LS174T transfected with firefly luciferase 2 and enhanced green fluorescent protein (luc2-eGFP) reporter gene was used to produce tumors within the liver of living mice. Three million cells suspended in matrigel were either injected directly or a piece of subcutaneous tumor was transplanted into the liver of nude mice. The tumor growth was followed using bioluminescence imaging and tumor size was determined using ultrasound imaging. The tumors (volume > 0.3 cm^3) were exposed to a low frequency (1 MHz) of ultrasound for 6 minutes and the release of the biomarkers was determined by analysis and comparison of serum from the mouse pre and post ultrasound treatment. Control serum samples were from tumor-bearing mice not treated with ultrasound. The released protein biomarkers, carcinoembryonic antigen (CEA) and cancer antigen 19-9 (CA19-9) were determined using an enzyme-linked immunosorbant assay. **Results:** Both the methods used to form the liver tumors showed an 80% rate of tumor establishment within 1 week when observed using bioluminescence. The other 20% of the mice also had tumors but they were slower growing and not easily visualized by either bioluminescence or ultrasound imaging. The transplantation of a previously established subcutaneous tumor fragment showed a better control of the tumor size when compared to a fixed number of cells injected. The tumors were followed over 3 weeks and showed exponential growth (week-3 mean tumor volume = 0.815 cm^3). The tumors showed significant increase in release of protein biomarkers when treated with ultrasound (CEA: $p<0.007$, $n=10$ and CA19-9: $p<0.002$, $n=6$), when comparing control and treated post-pre serum biomarker measurements. **Conclusions:** Increase in serum biomarker release from the liver tumor was observed when low frequency ultrasound was applied over the tumor. This would allow for the characterization of tumors depending on the amplification of specific blood biomarkers. These biomarkers can be protein or nucleic acids, like micro-RNA, and the use of an array for detection of markers can be used for tumor characterization. This model can be used to study orthotopic tumor characterization and has implications in diagnosis and monitoring of therapy of lesions. This novel method of tumor characterization has a clear pathway for the clinical applications for MRI-guided focused ultrasound, bringing together the fields of imaging and *in vitro* diagnostics.

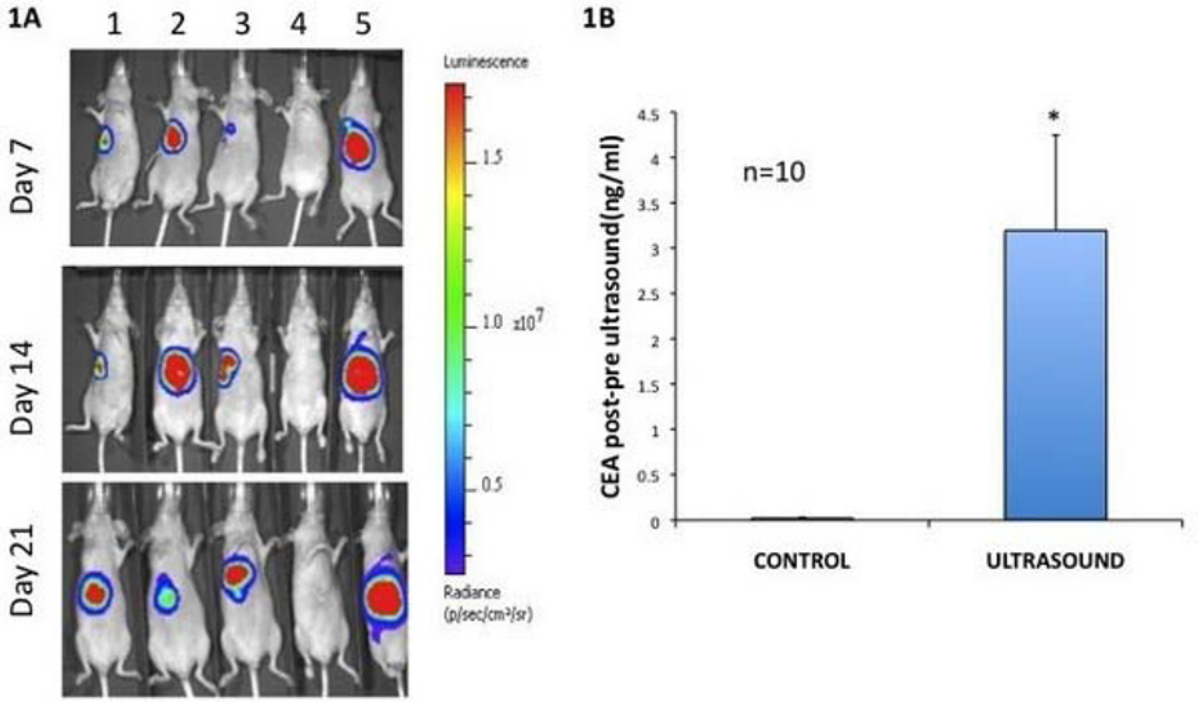

Fig 1A: Bioluminescence of mice with LS174T tumor-tissue implanted into the liver followed over 21 days. Fig 1B: Change in CEA concentration of control and ultrasound-treated groups. *p<0.007.

Disclosure of author financial interest or relationships:

A.L. D'Souza, None; **X. Yan**, None; **H. Wang**, None; **S.S. Gambhir**, Bracco Diagnostics, Consultant; Endra, Inc, Stockholder; Cellsight, Stockholder; Enlight, Inc., Stockholder; General Electric, Grant/research support; ImaginAb, Stockholder; MagArray, Inc., Stockholder; Sanofi-Aventis, US, Grant/research support; SiteOne Therapeutics, Stockholder; VisualSonics/Sonosite, Stockholder .

Presentation Number **P 563**
Poster Session 4
September 21, 2013 / 14:45-14:45 / Room: Exhibit Hall B

Ultrasound Contrast Agent Based Vascularity Measurements Versus Photoacoustic Derived Hemoglobin and Oxygenation Measurements in a Breast Cancer Model

John R. Eisenbrey[1], *Daniel A. Merton*[1], *Ji-Bin Liu*[1], *Traci B. Fox*[2], *Anush Sridharan*[1,3], *Flemming Forsberg*[1], [1]*Department of Radiology, Thomas Jefferson University, Philadelphia, PA, USA;* [2]*Department of Radiological Sciences, Jefferson College of Health Professions, Thomas Jefferson University, Philadelphia, PA, USA;* [3]*Department of Electrical and Computer Engineering, Drexel University, Philadelphia, PA, USA. Contact e-mail: john.eisenbrey@jefferson.edu*

Purpose: To compare tumor vascularity measurements derived via contrast-enhanced ultrasound (CEUS) with hemoglobin signal and oxygenation levels measured via photoacoustics in a breast cancer xenograft model. Materials and Methods: Eleven athymic, nude, female rats with subcutaneous MDA-MB-231 breast tumors implanted in the mammary pad were imaged using the nonlinear contrast mode on a Vevo 2100 ultrasound scanner (Visualsonics, Toronto, Canada). Rats received a 36 µl bolus injection of the contrast agent Definity (Lantheus Medical Imaging, North Billerica MA) during continuous CEUS imaging. Acoustic output power was set to 4%, frequency to 24 MHz, and contrast gain at 35 dB. Maximum intensity projections (MIP) were then generated over the tumor area using the VevoCQ contrast software and average enhancement in arbitrary units (a.u.) used as a measure of overall tumor vascularity. Following CEUS, photoacoustic imaging was performed using a photoacoustic probe (MS-250-PA, Visualsonics) on the Vevo2100. Ultrasound parameters were set to 21 MHz, with 100% power and a gain of 18 dB. Laser properties were set to 100% output power at wavelengths of 750 and 850 nm and a photoacoustic gain of 40 dB. Hemoglobin signal, oxygenation levels in detected blood (SO2 Avg), and oxygenation levels over the entire tumor area (SO2 Tot) were then calculated over 20 frames using the Oxygenation-Hemoglobin measurement package on the unit. For both CEUS and Oxy-Hemo measurements, contrast signal was overlaid on the concurrent B-mode images to validate tumor location and all imaging parameters were kept constant to maintain consistency. All measurements were repeated in triplicate and averaged. Results were compared using Pearson's correlation coefficient. Results and Discussion: Intratumoral contrast enhancement and photoacoustic signals were detected in all 11 tumors. Contrast-enhanced MIPs ranged from 0.1 to 8.7 a.u., with an average of 2.3 a.u. Hemoglobin signal ranged from 6980 to 13133 a.u. with an average of 8519 a.u. SO2 Avg values ranged from 13 to 58% with an average of 39% oxygenation, and SO2 Tot ranged from 2 to 19% with an average of 6% oxygenation. Significant correlation was observed between all three photoacoustic parameters and the CEUS MIP values (R= 0.61 for hemoglobin levels, R=0.56 for SO2 Avg, R= 0.64 for SO2 Tot). While signal location varied between imaging modes in some cases (presumably due to imaging of different planes after changing transducers), the positive correlations indicate that more vascular tumors (as gauged by CEUS) contain higher levels of hemoglobin and oxygenated blood. CEUS provided better overall resolution of the vasculature architecture, while photoacoustics inherently provided useful physiological information. Conclusions: CEUS vascularity measurements correlate well with functional oxygenation measurements obtained via photoacoustics and the two modes may be complementary. Acknowledgements: This work was supported in part by the U.S. Army Medical Research Material Command grants W81XWH-08-1-0503, W81XWH-11-1-0630 (supporting JRE), and NIH S10OD010408.

Disclosure of author financial interest or relationships:
J.R. Eisenbrey, None; **D.A. Merton**, None; **J. Liu**, None; **T.B. Fox**, None; **A. Sridharan**, None; **F. Forsberg**, Toshiba America Medical systems, Grant/research support; GE Healthcare, Grant/research support; Lantheus Medical Imaging, Grant/research support; AIUM, Other financial or material support .

Presentation Number **P 564**
Poster Session 4
September 21, 2013 / 14:45-14:45 / Room: Exhibit Hall B

Preclinical PET/CT evaluation of [18F]-D4-Choline as a diagnostic marker in non-small cell lung cancer

Rosy Favicchio[1], *Robin Fortt*[1], *Frazer Twyman*[1], *Juan Carlos Lacal*[2], *Eric O. Aboagye*[1], [1]*Surgery and Cancer, Imperial College London, London, United Kingdom;* [2]*Instituto de Investigaciones Biomédicas, Consejo Superior de Investigaciones Científicas (CSIC), Madrid, Spain. Contact e-mail: r.favicchio@imperial.ac.uk*

Choline kinase alpha (ChoKα) expression is strongly correlated to malignant progression in non-small cell lung cancer (NSCLC). This enzyme is the rate-limiting step in the Kennedy pathway and regulates the conversion of choline (Cho) to phosphocholine (PCho). PCho is metabolised to the membrane phospholipid phosphatidylcholine and is essential to proliferating cells, making ChoKα a promising biomarker in lung cancer. Here, the radiolabelled choline analogue [18F]-D4-choline was evaluated for its diagnostic potential and ability to predict therapeutic response in three models of NSCLC (H460, A549 and PC9), selected according to ChoKα expression levels (low, intermediate and high, respectively). Choline uptake (transport and phosphorylation) in cells treated with vehicle, cisplatin or the choline kinase inhibitor MN58b, was assessed by 60-min pulse-chase with radiolabelled choline *in vitro* following 3 or 13 hours of drug treatment. To enable clinical translation, we assessed drug treatment *in vivo* by [18F]-D4-choline Positron Emission Tomography/X-ray Computed Tomography (PET/CT) in mice bearing subcutaneous tumour xenografts. Dynamic imaging over 60 min was conducted in the mice following three daily doses of vehicle, cisplatin or MN58b. The initial choline uptake in cells following drug treatment correlated with growth inhibition at 72 hours in all three models. All three xenografts were detectable by [18F]-D4-choline-PET/CT with detection sensitivity dependent on ChoKα expression. Normalised tumour SUVmean, SUVmax, quartiles analysis (25th, 50th and 75th percentile), AUC and uptake rate values (%ID/cc) were used to assess response to therapy in the low (H460) and high (PC9) ChoKα expressing tumours. SUVmean(30-60min) values in treated PC9 tumours (2.7±0.01; 3.2±0.03; mean±SEM) were found to be significantly ($p<0.0001$) lower than vehicle treated tumours (4.2±0.01; mean±SEM). Identical treatment in H460 tumours showed a small increase in SUVmean(30-60min) [18F]-D4-choline following therapy (cisplatin: $p=0.02$; MN58b: $p=0.008$), however this indicator was insensitive to differences between uptake and retention. AUC and slope values were used to extrapolate an intriguing ($p<0.0001$) reversal in dynamics where cisplatin-treated tumours showed tracer washout whereas MN58b-treated tumours showed continuous uptake. Changes in radiotracer uptake occurred in parallel with long term tumour growth inhibition confirmed by calliper measurements and histology. Treatment with cisplatin and MN58b was found to reduce choline uptake in kidneys (10%-20%). Results were validated *ex vivo* by biodistribution and western blot. In conclusion, [18F]-D4-choline was established as a suitable tracer for diagnostic imaging of NSCLC linked to ChoKα expression. Uptake dynamics were predictive of therapeutic response to both the targeted ChoK inhibitor MN58b and to the alkylating agent cisplatin, with equal sensitivity, confirming the central role played by choline kinase in tumour progression and that exploitation of the Kennedy pathway provides the means to predict therapeutic efficacy.

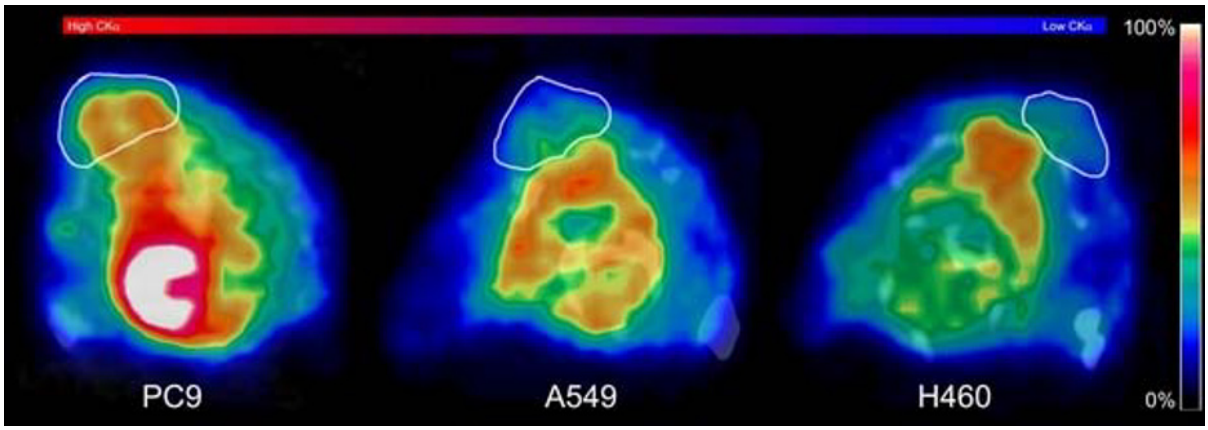

***In vivo* PET/CT axial image data for vehicle treated PC9, A549 and H460 tumours, white contour indicates tumour localisation**

Disclosure of author financial interest or relationships:
R. Favicchio, None; **R. Fortt**, None; **F. Twyman**, None; **J. Lacal**, TCD Pharma SL, Stockholder; **E.O. Aboagye**, None.

Presentation Number **P 565**
Poster Session 4
September 21, 2013 / 14:45-14:45 / Room: Exhibit Hall B

HIF signaling in the context of specific cancer-driving mutations

Catherine Germanier[1], *Ruth Keist*[1], *Manoj N. Desai*[1], *Georgios Batsios*[1], *Markus Rudin*[1,2], [1]*Institute for Biomedical Engineering, ETH Zurich, Zurich, Switzerland;* [2]*Institute for Pharmacology and Toxicology, University Zurich, Zurich, Switzerland. Contact e-mail: germanier@biomed.ee.ethz.ch*

Introduction The hypoxia inducible factor (HIF) is a transcription factor, which is usually stabilized in hypoxic conditions and enhances the transcription of genes involved in processes such as angiogenesis and glucose metabolism. HIF is a key player in the survival and in the adaptation of tumor cells to hypoxic conditions. However, it has been shown that tumor cells expressing mutated metabolic enzymes leading to alterations in the metabolite levels were able to stabilize HIF even under normoxic conditions, a step called pseudo-hypoxia[1]. As reprogramming of metabolism is considered a hallmark of cancer, the question arises how a specific alteration in metabolism may influence the signaling and vice versa. The aim of this project is to investigate the HIF signaling together with metabolic readouts in colon carcinomas with distinct cancer-causing mutations. Material and methods In this study, colon carcinoma cells with an activating mutation in the MAPK pathway, DLD-1 (Ras mutated) and RKO (Raf mutated) were used. In vitro regulation of HIF under hypoxic (DMOG stimulation and hypoxia chamber) and normoxic conditions was studied using Western Blot. To assess the HIF activity, tumor cell lines were stably transfected with a reporter gene containing three HRE (Hypoxia Responsive Element) sites in the promoter sequence driving the expression of a red fluorescent protein (mCherry). As a reference, the different cell lines were transfected with a CMV-mCherry reporter. Metabolic readouts were obtained by MRS experiments after the injection of hyperpolarized 1-13C-pyruvate in tumor-bearing nude mice. Results Proof-of-concept of the mCherry based HIF activity assay as readout of hypoxia signaling was established both in vitro and in vivo (in subcutaneous and orthotopic tumors) in mouse breast carcinoma using stably transfected 4T1 cells. Imaging data were validated by immunohistochemistry of tumor sections stained for hypoxia, HIF1α and HIF downstream gene products. Having demonstrated feasibility, the HIF assay has been translated to colon carcinoma cells. Preliminary results of in vivo MRS studies of subcutaneously implanted DLD-1 tumors hint towards a difference in the efficiency of pyruvate to lactate conversion between tumors grown from wild-type and mutated cells. Outlook The activity of HIF in colon carcinoma will be studied both in vitro and in vivo (subcutaneous tumors) and in analogy to the 4T1 study in vivo results will be validated using histological analysis with immunostaining for HIF-1α/HIF-2α, GLUT1 (glucose transporter), LDH, CA9 (downstream gene products of HIF), and pimonidazole (hypoxia marker). Comparing the HIF signaling and metabolic readouts in wild-type cells and in cells with a cancer-driving mutation will allow us to understand to what extent the specific genetic make-up of the tumor might modulate HIF activity.

Disclosure of author financial interest or relationships:
C. Germanier, None; **R. Keist**, None; **M.N. Desai**, None; **G. Batsios**, None; **M. Rudin**, Hoffmann-LaRoche AG, Basel, Switzerland, Grant/research support; Roche-Glycart AG, Schlieren, Switzerland, Grant/research support .

Presentation Number **P 566**
Poster Session 4
September 21, 2013 / 14:45-14:45 / Room: Exhibit Hall B

Evaluation of a method for assessing the heterogeneity impact on quantifying radiolabelled Annexin A5 uptake in xenografts in pre-clinical PET studies of induced cell death

Jonas Grafström[1], *Hanna-Stina Ahlzén*[2], *Sharon Stone-Elander*[1,3], [1]*Department of Clinical Neuroscience, Karolinska Institutet, Stockholm, Sweden;* [2]*Medical Biochemistry, Karolinska Institutet, Stockholm, Sweden;* [3]*Neuroradiologi, Karolinska University Hospital, Stockholm, Sweden. Contact e-mail: jonas.grafstrom@ki.se*

Radiolabelled Annexin A5 is used as an in vivo biomarker for induced cell death. Tumours are per se non-homogeneous tissues and drug-induced cell death can vary from tumour to tumour, between areas in the tumour and also throughout a therapeutic protocol. The heterogeneity of the region of interest (ROI) can thus have a large impact on the uptake quantification. The aim of this study was to assess the impact of varying tumour non-homogeneity on the calculated distribution volume ratio (DVR). A method to appraise the heterogeneity was developed. This method isolates the intensity deviation within the chosen ROI (in this case the tumour), and also normalizes for the size of the ROI. Methods: The study was performed with SCID mice and a microPET Focus 120 scanner. These mice were inoculated s.c. with FaDu (human head/neck carcinoma) tumour cells and after xenografts were established the mice were treated with doxorubicin. In order to isolate the ROI intensities, an if - statement was created using the Matrix Laboratory (MATLAB) software version 7.12. The intensity threshold was chosen as half the mean intensity. Each intensity gathered was associated with a location, and thus a distance from this intensity peak to the origin was calculated. The tumour size was also limited, i.e. a distance threshold was found, in order to avoid impact of varying tumour dimensions. The resulting distances were summed for each tumour, and subsequently normalized to the distance of the global mean. The DVR was calculated using the Siemens Inveon Research Workplace (IRW) software version 3.0. Results: Based on the range of the differences in DVRmax and DVRmean, the inhomogeneity had an impact of almost 8.5% on the DVR estimations. When the individually-calculated heterogeneity factor was applied to each corresponding DVR and compared to the mean, a quadratic fit was found most suitable describing the shape of the resulting scatter plot. This procedure gives a stepwise correction that follows the quantification results, but does not result in a simple, linear relationship for all the associated DVRs. Thus this method does not conclusively result in a generally working correction for non-uniform tissue. The fit does result in an approach to assess the DVR from the heterogeneity calculated as described above. Conclusions: This study has assessed one method for accounting for heterogeneity in these preclinical models. For more comprehensive corrections, other contributing factors such as specific activity and biologic individuality will also need to be considered.
Financed by SSF and Vinova

Disclosure of author financial interest or relationships:
J. Grafström, None; **H. Ahlzén**, None; **S. Stone-Elander**, None.

Presentation Number **P 567**
Poster Session 4
September 21, 2013 / 14:45-14:45 / Room: Exhibit Hall B

Multi-Modality Imaging (PET, CLI) of a PSMA-Targeted Cys-Diabody in Tumor-Bearing Mice

Harvey Hensley[1], *Mohan Doss*[2], *Jian Q. Yu*[1,2], *Derek W. Bartlett*[3], *Matthew K. Robinson*[1], [1]*Developmental Therapeutics Program, Fox Chase Cancer Center, Philadelphia, PA, USA;* [2]*Nuclear Medicine/PET Services, Department of Diagnostic Imaging, Fox Chase Cancer Center, Philadelphia, PA, USA;* [3]*Process Development & Translational Science, ImaginAb, Inglewood, CA, USA. Contact e-mail: harvey.hensley@fccc.edu*

Background: The purpose of this study was to: 1. Determine the ease of radiolabeling a NODAGA-conjugated anti-PSMA cys-diabody (NODAGA-Cys-Db) and 2. Determine the feasibility of using that radiotracer to image PSMA-positive human tumor xenografts in a mouse model of prostate cancer using both Positron Emission Tomography (PET) and Cerenkov Luminescence Imaging (CLI) Methods: NODAGA-Cys-Db was radiolabeled with 64CuCl2 to a specific activity of ~0.5 MBq/µg and its binding activity was verified in live-cell binding assays. Nu/Nu mice harboring PSMA-positive (22Rv1) and -negative (PC3) xenografts were then injected with 20 µg of radiolabelled NODAGA-Cys-Db. Serial images were acquired on both PET (2, 4, 16, and 26 hrs) and CLI (1, 4, 16 and 24 hrs) at various time points after i.v. injection of the radiotracer. The PET imaging was performed using a clinical PET/CT scanner (Biograph 16 Truepoint) with 10 minute PET acquisition. The CLI imaging was performed on an IVIS Spectrum. Images were made with a 300 second exposure, medium binning and a 19.6 cm field of view. Imaging results obtained at 24 hrs were compared to tissue uptake as quantified by biodistribution. Results: Labeling followed by an EDTA quench resulted in >98% radiochemical purity of the NODAGA-Cys-Db as quantified by ITLC. In preliminary studies, serial imaging of NODAGA-Cys-Db-injected mice over a 24 hr time period demonstrated selective targeting and effective multi-modality imaging (Figure 1). The decay-corrected tumor uptake determined from PET imaging increased to its peak value at about 4 hrs after injection and remained nearly steady until the end of the 24 hr study period. The activity in blood declined during this period, while kidney and liver uptakes were steady. In CLI images signal in PSMA-positive tumor and kidney peaked at 4 hrs with the maximum difference in average radiance between the PSMA-positive and -negative tumors occurring at 16 hrs post injection. Biodistribution results obtained immediately after the 24 hr imaging timepoint demonstrated NODAGA-Cys-Db reached levels of 5-fold selective uptake in 22Rv1 (8.1 %ID/g) vs PC3 (1.7 %ID/g). Kidneys, as seen both by imaging and biodistribution, represent the organs with highest level of uptake, consistent with the predicted first-pass renal clearance of this radiotracer. Conclusions: When radiolabeled with 64Cu the anti-PSMA targeted NODAGA-Cys-Db can selectively image PSMA-positive tumors in a nu/nu mouse model of prostate cancer via both PET and CLI, with the tumor uptake increasing and blood pool activity decreasing with time during the 24 hr period of the study. CLI permits a rapid and simple estimate of distribution of the imaging agent using widely available optical imaging systems, allowing one to determine optimal imaging times with precision. Additional studies are warranted to more fully evaluate the imaging capabilities of this radiotracer.

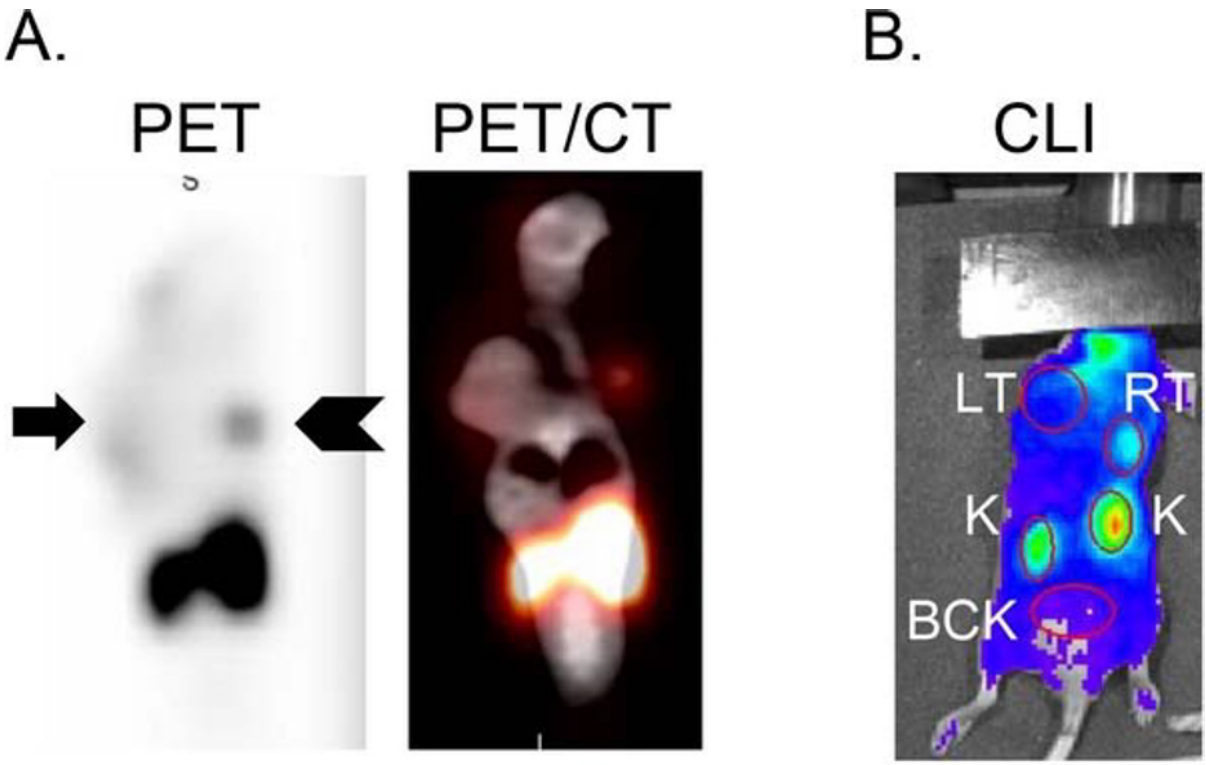

Figure 1: Multi-modality imaging of 64Cu-NODAGA-Cys-Db. A) PET/CT and B) CLI images depict same mouse ~16 hrs post i.v. injection. Regions of interest are labeled. The PSMA positive tumor (RT in CLI, chevron in PET) exhibits higher signal than the PSMA negative tumor (LT, arrow in PET). K=kidney, BCK=region for background

Disclosure of author financial interest or relationships:
H. Hensley, Imaginab, Grant/research support; **M. Doss**, Imaginab, Grant/research support; **J.Q. Yu**, None; **D.W. Bartlett**, ImaginAb, Inc., Employment; **M.K. Robinson**, ImaginAb, Grant/research support .

Presentation Number **P 568**
Poster Session 4
September 21, 2013 / 14:45-14:45 / Room: Exhibit Hall B

PET of VEGFR Expression with ^{61}Cu-Labeled Lysine-Tagged VEGF$_{121}$

Yin Zhang[1], *Hao Hong*[2], *Gang Niu*[3], *Xiaoyuan (Shawn) Chen*[3], *Todd E. Barnhart*[1], *Weibo Cai*[1,2], [1]*Medical Physics, University of Wisconsin - Madison, Madison, WI, USA;* [2]*Radiology, University of Wisconsin - Madison, Madison, WI, USA;* [3]*NIBIB, Bethesda, MD, USA. Contact e-mail: yzhang65@wisc.edu*

Objectives: Overexpression of vascular endothelial growth factor (VEGF) and VEGF receptors (VEGFRs) indicates poor prognosis in many tumor types. Noninvasive imaging and quantification of VEGFR expression is of paramount importance in cancer patient management and antiangiogenic drug development. Our goal is to develop a VEGFR-targeted positron emission tomography (PET) tracer based on VEGF$_{121}$, with three lysine residues fused to the N-terminus (denoted as K$_3$-VEGF$_{121}$), which can facilitate radiolabeling without affecting its VEGFR binding affinity. ^{61}Cu ($t_{1/2}$: 3.3 h; 62% β^+) was used as the radiolabel to match its uptake kinetics and minimize radiation dosimetry. Methods: Purified K$_3$-VEGF$_{121}$ was conjugated to 1,4,7-triazacyclononane-1,4,7-triacetic acid (NOTA) and labeled with ^{61}Cu. Cell binding assay was performed to compare the VEGFR-2 binding affinity of K$_3$-VEGF$_{121}$ and NOTA-K$_3$-VEGF$_{121}$. In vivo PET imaging, biodistribution, blocking, and histology studies were carried out in 4T1 murine breast tumor-bearing mice to evaluate the tumor targeting efficacy and in vivo specificity of ^{61}Cu-NOTA-K$_3$-VEGF$_{121}$. Radiation dosimetry was extrapolated to humans as well. Results: Based on cell binding assay using ^{125}I-VEGF$_{165}$ as the radioligand, the IC_{50} values of NOTA-K$_3$-VEGF$_{121}$ and K$_3$-VEGF$_{121}$ were comparable to VEGF$_{121}$ (1.50 nM and 0.65 nM, respectively). ^{61}Cu labeling was achieved with good yield (> 50 %) and specific activity. Serial PET imaging showed that the 4T1 tumor uptake of ^{61}Cu-NOTA-K$_3$-VEGF$_{121}$ was 3.4±0.5, 4.9±1.0, 5.2±1.0, and 4.8±0.8 %ID/g (n = 4) at 0.5, 2, 4, and 8 h post-injection respectively, consistent with biodistribution data measured by γ counting. Blocking and histology experiments confirmed VEGFR specificity of ^{61}Cu-NOTA-K$_3$-VEGF$_{121}$. Dosimetry calculation showed that the radiation dose was much lower than other VEGF-based tracers and that liver was the organ with the highest radiation dose. Conclusions: Successful PET imaging of VEGFR expression was achieved with ^{61}Cu-NOTA-K$_3$-VEGF$_{121}$, which retained high affinity to VEGFR and exhibited desirable radiation dosimetry. The use of ^{61}Cu as the radiolabel is optimal for small proteins like K$_3$-VEGF$_{121}$, which has much higher β^+ branching ratio than the commonly used ^{64}Cu (62% vs. 17%). Thus, it can offer stronger signal intensity and require lower tracer dose for PET imaging than ^{64}Cu, which is ideal for clinical translation.

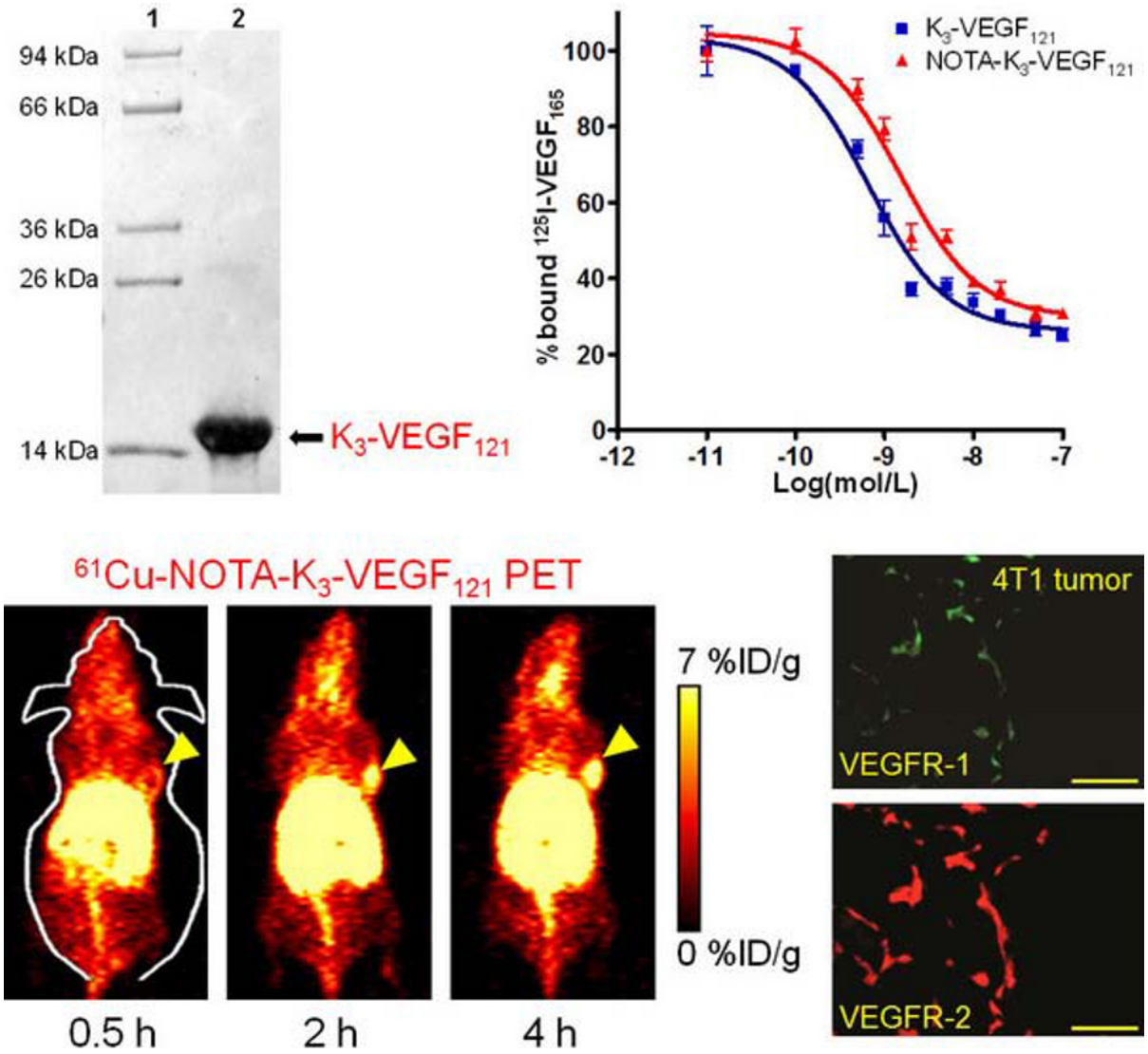

Disclosure of author financial interest or relationships:
Y. Zhang, None; **H. Hong**, None; **G. Niu**, None; **X. Chen**, None; **T.E. Barnhart**, None; **W. Cai**, None.

Presentation Number **P 569**
Poster Session 4
September 21, 2013 / 14:45-14:45 / Room: Exhibit Hall B

Detection of prostate tumor angiogenesis by volumetric molecular ultrasound imaging in an animal model

Kenneth Hoyt[1,2], *Anna G. Sorace*[2], *Marshall J. Mahoney*[2], *Kurt R. Zinn*[1], [1]*Radiology, University of Alabama at Birmingham, Birmingham, AL, USA;* [2]*Biomedical Engineering, University of Alabama at Birmingham, Birmingham, AL, USA. Contact e-mail: hoyt@uab.edu*

OBJECTIVE: Angiogenesis is critical for prostate tumor growth and represents an important target in drug development. The goal of this project was to evaluate volumetric molecular ultrasound ultrasound imaging of tumor vascularity in vivo using a preclinical model of prostate cancer. MATERIALS AND METHODS: Real-time volumetric molecular ultrasound imaging was performed using the BioSONIC VIEW system (Bioscan Inc) equipped with a broadband 4DL14-5/38 probe. A microbubble contrast agent sensitive harmonic imaging mode (transducer transmits at 5 MHz and receives at 10 MHz) was used to acquire real-time molecular ultrasound images of the entire 3-dimensional tumor burden. Nude athymic mice (N = 18) were implanted with 2 million prostate cancer cells (PC3) and tumors were allowed to grow for approximately 6 weeks. Microbubbles (Targestar-SA, Targeson) were conjugated with multiple antibodies targeting prostate tumor vascularity (αvβ3, p-selectin and VEGFR2) or with an IgG isotype control antibody. Following tail vein injection of microbubble contrast agent, a 2 min delay allowed systemic circulation and target receptor binding. Molecular ultrasound images were captured to determine the quantity of bound and flowing microbubbles. Then a high-intensity pulse via an external ultrasound transducer was administered to destroy all microbubbles, followed by an additional ultrasound scan to determine residual circulating contrast agent. Custom Matlab software was developed to determine overall intratumoral image intensity. Subtraction of ultrasound image data from before and after microbubble bursting yielded a measure of contrast agent bound to the targeted tumor receptors. All animals received both microbubble types following a 2 hour delay between injections. RESULTS: One animal was omitted from data analysis due to a bad tail vein contrast agent injection. Molecular ultrasound imaging of targeted contrast agent yielded a significant increase in intratumoral image enhancement over that obtained using control microbubbles as evident from segmented tumor data (mean image intensity of 97.1 ± 3.5 and 55.5 ± 2.2, respectively, $P < 0.001$). More specifically, molecular ultrasound image enhancement using targeted microbubbles was 1178.2 ± 393.9% when compared to control data from the same animal. Immunohistologic analysis confirmed biomarker presence. CONCLUSIONS: Whole tumor molecular ultrasound imaging is a promising strategy for assessing biomarkers of prostate cancer vascularity.

Disclosure of author financial interest or relationships:
K. Hoyt, None; **A.G. Sorace**, None; **M.J. Mahoney**, None; **K.R. Zinn**, None.

Presentation Number **P 570**
Poster Session 4
September 21, 2013 / 14:45-14:45 / Room: Exhibit Hall B

Multimodality functional imaging of tumor vasculature during antiangiogenic therapy

Yoshinori Kato[1,2], *Wenlian Zhu*[1], *Ronnie Mease*[3], *Marina Backer*[4], *Susanta K. Sarkar*[5], *Joseph M. Backer*[4], *Dmitri Artemov*[1,2], [1]*Division of Cancer Imaging Research, The Russell H. Morgan Department of Radiology and Radiological Science, The Johns Hopkins University School of Medicine, Baltimore, MD, USA;* [2]*Department of Oncology, The Sidney Kimmel Comprehensive Cancer Center at Johns Hopkins, Baltimore, MD, USA;* [3]*Division of Neuroradiology, The Russell H. Morgan Department of Radiology and Radiological Science, The Johns Hopkins University School of Medicine, Baltimore, MD, USA;* [4]*SibTech, Inc., Brookfield, CT, USA;* [5]*Translational and Experimental Medicine, Sanofi Oncology Division, Cambridge, MA, USA. Contact e-mail: ykato@mri.jhu.edu*

Noninvasive monitoring of functional changes in the tumor vasculature during the course of antiangiogenic therapy (AT) is critically important as they can provide an early marker of response. In addition, if AT is used in combination with traditional cytotoxic or nanocarrier-based chemotherapy, it is critical to set up appropriate treatment schedule because vasculature is essential for efficient drug delivery and possible vascular targeting. Multimodality imaging such as combination of MRI and nuclear imaging provides a sensitive and entirely noninvasive way to monitor these changes longitudinally in the subject (1-3). In this study, we monitored the expression of VEGFR2 vascular receptors and tumor perfusion in human breast cancer MDA-MB-231/luc xenografts grown in athymic female nude mice. The mice were treated with sunitinib tyrosine-kinase inhibitor that demonstrated significant antiangiogenic effect in animal models (2). Animals were imaged with micro PET using a ^{68}Ga-labeled single chain VEGF derivative (scVEGF), a ligand for VEGFR2 receptors, on day 0, 6, and 11. DCE-MRI with GdDTPA contrast agent was performed at 9.4T to assess tumor perfusion parameters, on day 1, 7, and 16. The treatment protocol included two cycles of therapy delivered daily for 5 days (80 mg/kg, orally) with a 6-day vacation between the cycles. At the endpoint, tumors were excised and stained for the expression of CD31 endothelial cell marker. Experimental results suggest a highly heterogeneous vascular regression response to the first round of treatment, with significant vascular regression as measured by decreased tracer uptake, tumor perfusion measured by GdDTPA kinetics, and by CD31 prevalence (**Fig. 1**). A significant vascular rebound was detected immediately after the vacation period in the treatment protocol as judged by the increase in tracer uptake and CD31 prevalence. The second round of treatment was significantly less effective than the first round as demonstrated by the sustained increase in tumor perfusion at day 16 (**Fig. 1A**). The ultimate goal of this project is to determine the optimal time for administration of the second cytotoxic component scVEGF-labeled targeted liposomes loaded with MRI contrast agents and paclitaxel. The studies to understand the effect of vascular regression and rebound caused by the AT vacation on the intratumoral delivery of scVEGF-targeted liposomes and on the therapeutic response are currently under way. Taken together, these results suggest that noninvasive molecular imaging of VEGF receptors reflects vascular regression and rebound in individual tumors and can provide clinically relevant information to monitor the response and to optimize scheduling of antiangiogenic therapy. This work was supported by NIH R01CA154738.
References 1. Blankenberg et al., *Transl. Oncol.* 3(1):56-64, 2010. 2. Levashova et al., *J. Nucl. Med.* 51(6):959-66, 2010. 3. Backer et al. *Nature Med.* 13(4):504-9, 2007.

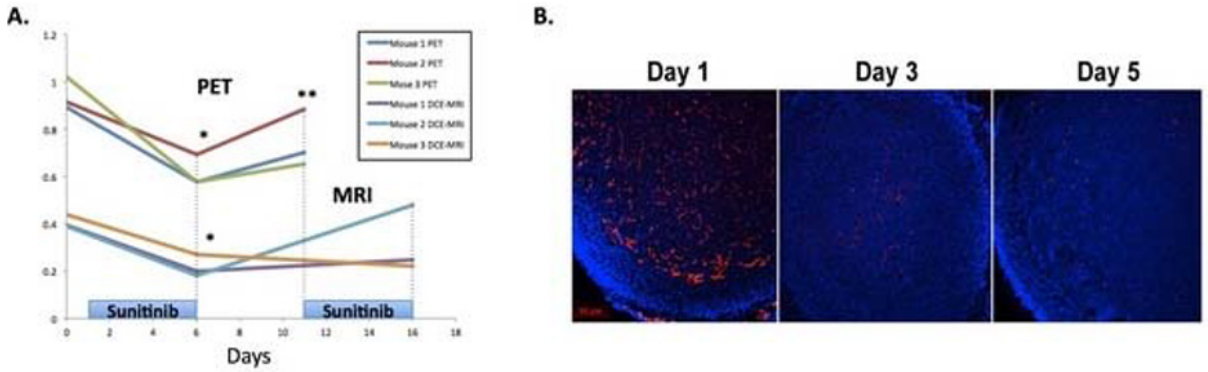

Figure 1. A. Modulation of the expression of VEGFR2 receptors by sunitinib AT reported by PET (injected dose of the probe was ~100 µCi, activity was integrated from 20 to 60 min after administration of the probe, * and ** denote significant changes $P < 0.05$). 3D DCE-MRI was performed after injection of 0.4 mmole/kg of GdDTPA with temporal resolution of ~30 sec. Area under the curve of the enhancement ratio was analyzed from 0 to 10 min after contrast administration. **B.** IHC of the pan-endothelial marker CD31 (red) during the course of sunitinib AT. Nuclei are counterstained with DAPI (blue).

Disclosure of author financial interest or relationships:
Y. Kato, None; **W. Zhu**, None; **R. Mease**, None; **M. Backer**, None; **S.K. Sarkar**, Sanofi, Employment; **J.M. Backer**, None; **D. Artemov**, None.

Presentation Number **P 571**
Poster Session 4
September 21, 2013 / 14:45-14:45 / Room: Exhibit Hall B

Cu 64 -ATSM PET/CT of Naturally Occurring Canine Soft Tissue Sarcomas: A translational model for hypoxic tumor imaging and therapy

Susan Kraft[1], *Takamitsu A. Kato*[1], *Elissa Randall*[1], *Nicole Ehrhart*[2], *Susan M. LaRue*[1], *Amanda Guth*[2], *Eugene Ehrhart*[3], *Luke Hetrick*[1], *Dayton D. McMillan*[1], *Dongqing Zhang*[1], *Takako Furukawa*[4], *Yasuhisa Fujibayashi*[4], [1]*Environmental and Radiological Health Sciences, Colorado State University, Fort Collins, CO, USA;* [2]*Clinical Sciences, Colorado State University, Fort Collins, CO, USA;* [3]*Microbiology, Immunology and Pathology, Colorado State University, Fort Collins, CO, USA;* [4]*Molecular Imaging Center, National Institute of Radiological Sciences, Chiba, Japan. Contact e-mail: susan.kraft@colostate.edu*

Introduction: Copper-64-diacetyl-bis (N4-methylthiosemicarbazone), or Cu 64 -ATSM, is a positron-emitting radiotracer that serves as a marker of hypoxic metabolism and is retained in cytochromal/microsomal hypoxic cell fractions. Based on studies in experimental tumor models, hypoxic tumor regions having high Cu 64 -ATSM uptake also harbor potential tumor stem cells. Cu 64 -ATSM tumor uptake may be a direct predictor of response and outcome, and also has the potential for internal radiotherapy. We have initiated Cu 64 -ATSM PET/CT studies in pet dogs with naturally-occurring soft tissue sarcomas as a large animal translational model to evaluate relative tumor uptake. These data will be used to determine the biodistribution for internal dosimetry modeling, and co-localization of Cu 64 -ATSM with regions of tumor hypoxia and potential stem cells in this natural hypoxic tumor model. Methods: Three canine patients with biopsy-proven sarcomas have been studied thus far. Tumor-bearing dogs underwent Cu 64 -ATSM -PETCT using a Philips Gemini TF Big Bore scanner. Whole body CT scan was acquired for attenuation correction, then a dynamic PET/CT study was obtained for one hour post-iv injection 0.17 mCi/kg Cu 64 -ATSM. The dynamic scan was centered over the cardiac apex, liver, and tumor to assess early tissue uptake and distribution. This was followed by the whole body PET scan using 5 minute bed times. Images were reconstructed and evaluated by region-of-interest analysis (Extended Brilliance Workstation, Philips) to determine degree and pattern of Cu 64 -ATSM uptake in the tumor relative to normal tissues. CT-guided needle aspirates and wedge biopsies were performed of two targeted tumor areas, for flow cytometry and immunohistochemistry. When possible, samples were obtained of tumor areas having high versus low Cu 64 -ATSM uptake for comparison. Those samples are being assessed by immunohistochemistry and flow cytometry for a number of tumor stem cell surface and hypoxia markers, but those results are pending and not available for this abstract. Results: The soft tissue sarcomas were large (up to 20 cm diameter), and included a Grade I myxosarcoma, osteosarcoma and Grade III soft tissue sarcoma. The Cu-64 blood pool dropped rapidly and distributed to the tumor, musculature and liver within the first 10 minutes, after which levels in these tissues stabilized. The majority of the activity went to the liver predominated by first pass effect. The ratio of Cu 64 -ATSM uptake in tumor to musculature was 5.07 +/- 2.08 SD (range 3.2 for the Grade I tumor - 7.31 for the Grade III tumor). The ratio of Cu 64 -ATSM uptake in tumor to liver was 0.16 +/- 0.11 SD (range 0.06 - 0.28). Conclusion and Ongoing Studies: Favorable tumor uptake relative to musculature can be achieved in this tumor model. Further strategies need to be developed to reduce liver activity to optimize the potential use for internal radiotherapy. Funding was provided by the National Institute of Radiological Sciences and Colorado State University Department of Environmental and Radiological Health Sciences.

Disclosure of author financial interest or relationships:
S. Kraft, None; **T.A. Kato**, None; **E. Randall**, None; **N. Ehrhart**, None; **S.M. LaRue**, None; **A. Guth**, None; **E. Ehrhart**, None; **L. Hetrick**, None; **D.D. McMillan**, None; **D. Zhang**, None; **T. Furukawa**, None; **Y. Fujibayashi**, None.

Presentation Number **P 572**
Poster Session 4
September 21, 2013 / 14:45-14:45 / Room: Exhibit Hall B

Image-Guided Small Animal Irradiation: Methods and Models

Sarah A. Krueger[1], *Jonathan Kane*[1,3], *Joshua Dilworth*[1], *Michael Chancellor*[2], *Jayabalan Nirmal*[2], *Gerard Madlambayan*[3], *Brian Marples*[1], *George D. Wilson*[1], [1]*Radiation Onocology, William Beaumont Hospital, Royal Oak, MI, USA;* [2]*Urology, William Beaumont Hospital, Royal Oak, MI, USA;* [3]*Biological Sciences, Oakland University, Rochester, MI, USA. Contact e-mail: sarah.krueger@beaumont.edu*

Objective/Purpose(s): The use of image-guided radiotherapy (IGRT) is widespread in clinical oncology. IGRT is utilized to create more accurate treatment plans, leading to minimization of radiation therapy (RT) related toxicities. In the pre-clinical setting however, the use of IGRT for radiation treatment is much less common. Traditional irradiation studies in animals have utilized crude lead jigs or other physical barriers to protect subjects from tissue toxicity during treatment. With the introduction of image-guided small animal irradiators, such as the Small Animal Radiation Research Platform (SARRP) or X-RAD 225 Cx, treatment of animal models of human cancers can now be more accurately planned and implemented. In addition, the use of targeted irradiation to mimic radiation-induced morbidities provides a powerful new tool in understanding changes in normal tissue following radiotherapy. Materials/Methods: Multiple animal models have been established in our institute to utilize image-guided irradiation on the SARRP. Investigations of different RT fractionation schemes have been examined in an orthotopic glioma tumor model in nude mice and in a model of orthotopic neuroblastoma implanted in the adrenal gland of SCID mice. The recruitment and localization of bone marrow (BM) derived progenitor cells within the tumor microenvironment in a mouse model of Lewis Lung Carcinoma (LLC) has been measured following targeted hypo-fractionated RT. Normal tissue studies have also been undertaken in the mouse brain to examine vascular changes following radiation and in normal rats to establish a model of radiation-induced hemorrhagic cystitis of the bladder. All models have been concurrently imaged with other modalities, including [18]F-FDG and [18]F-FMISO PET, CT, near-infrared imaging and MRI. All animal experiments were conducted with the approval and oversight of the institutional animal care and use committee. Results: In the orthotopic glioma model, animals treated on the SARRP exhibited increased survival and less neuronal damage following whole brain targeted RT as compared to animals treated with standard lead shielded RT. In the LLC ectopic model, bi-lateral tumors showed increased recruitment of BM derived stem-like cells to intratumoral sites of SARRP targeted irradiation. Validation of SARRP treatments is still on going in the orthotopic neuroblastoma model and rat radiation cystitis model. We anticipate demonstration of decreased tissue damage around the areas of targeted irradiation in the radiosensitive abdomen. Conclusions: Small animal IGRT allows for the use of better models of human disease states. Ongoing improvements in planning and treatment modules will increasingly allow the overlay of other imaging modalities, such as PET or MRI, into small animal treatment RT planning. Animal models of normal tissue damage following RT can be better achieved using target irradiation.

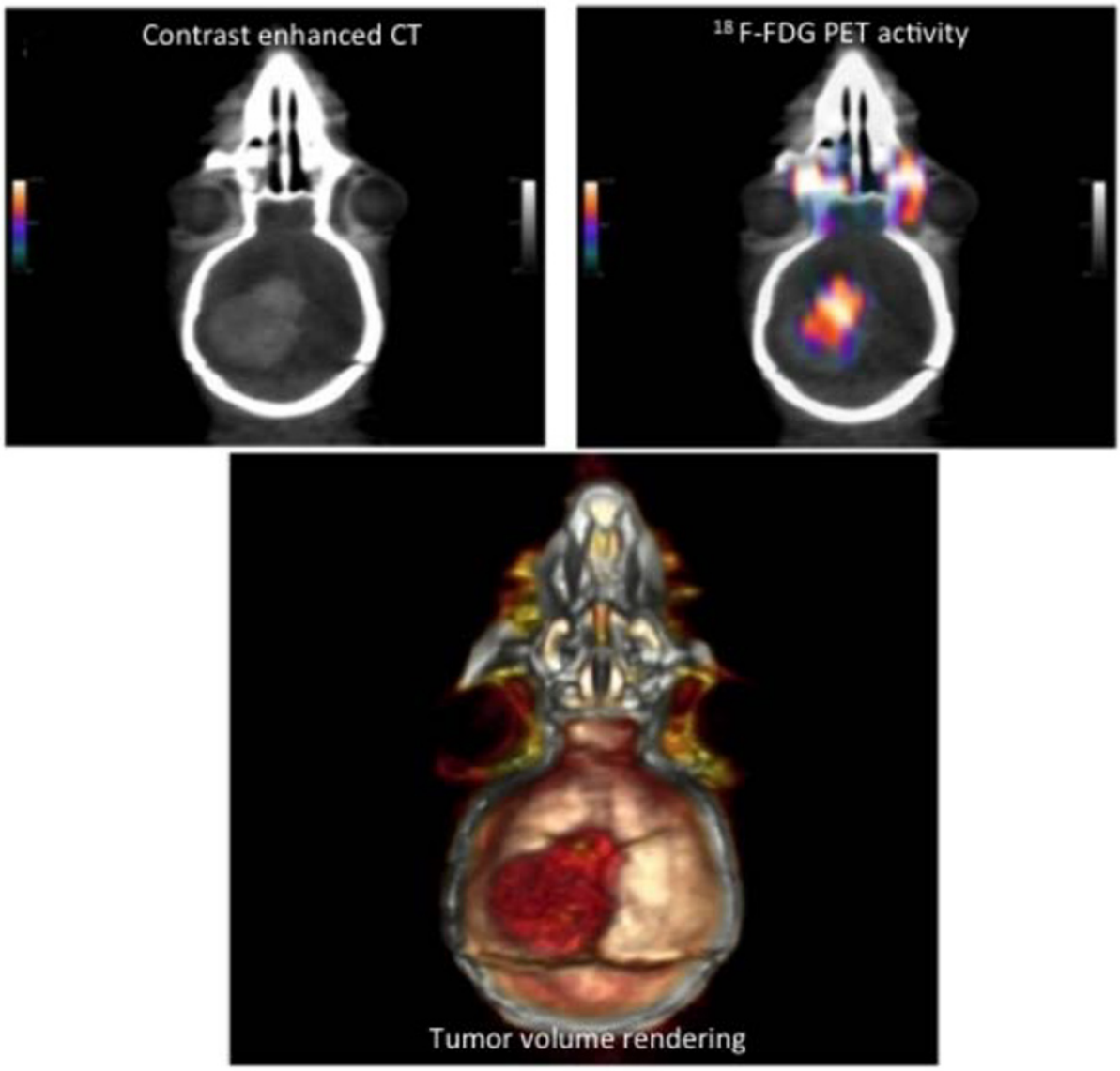

[18]F-FDG PET and CT images in orthotopic glioma mouse model Total tumor volume was measured by contrast enhanced CT and [18]F-FDG uptake was measured within the volume of interest to monitor changes in metabolic activity during and after radiotherapy.

Disclosure of author financial interest or relationships:
S.A. Krueger, None; **J. Kane**, None; **J. Dilworth**, None; **M. Chancellor**, None; **J. Nirmal**, None; **G. Madlambayan**, None; **B. Marples**, None; **G.D. Wilson**, None.

Presentation Number **P 573**
Poster Session 4
September 21, 2013 / 14:45-14:45 / Room: Exhibit Hall B

Photoacoustic Imaging for non-invasive characterization of the tumor microenvironment

Minalini Lakshman[1], *Andrew Heinmiller*[1], *Ines Lohse*[2,3], *David Hedley*[2,3], *Andrew Needles*[1], *Catherine Theodoropoulos*[1], [1]*FujiFilm VisualSonics, Inc., Toronto, ON, Canada;* [2]*Ontario Cancer Institute, Toronto, ON, Canada;* [3]*Campbell Family Research Institute, Toronto, ON, Canada. Contact e-mail: mlakshman@visualsonics.com*

Introduction: Abnormal metabolic changes are an underlying molecular pathology in resistance to standard radiation therapy. Personalised cancer management warrants imaging tools for non-invasive localization and characterization of this change. Tumor specific molecular information of this dynamic change can be delivered by photoacoustics (PA) imaging. PA harnesses spectral properties of endogenous or exogenous molecules and generates acoustic signatures to display molecular information at high spatial and temporal resolution of micro-ultrasound. In this work, we present two case studies of dynamic changes in the tumor microenvironment with histological validation. Non-invasive localization and characterization of hypoxic fractions will be discussed in human grafts of pancreatic cancer. Methods: Photoacoustic imaging was performed on the Vevo® LAZR system (Fujifilm VisualSonics Inc.) at 5-20 frames per second. Deep abdominal imaging was accomplished with a LZ250 probe at a center frequency of 21MHz and an axial resolution of 75 μm. The tumor model was generated in an immune compromised mouse by surgical implantation of primary patient derived tumors, in the pancreas. A subcutaneous model of Lewis Lung carcinomas (LLC) in the hind limb was exposed to breathing air of 100% and switched to 5% oxygen to induce hypoxia. Tumor perfusion was characterized in both models by contrast-enhanced ultrasound imaging using microbubbles. Multi wavelength PA images were analysed using the Vevo LAZR software to compute volumetrics and spectral changes. Results: Volumetrics analyses on B-mode images of the pancreatic tumors characterized them to be either small/non-palpable (18 cubic mm) or large tumors (> 200 cubic mm). The large tumors were more than 3 mm deep, and thereby occupy the entire abdominal cavity. Spectral imaging displayed a high to low gradient in oxygen saturation from the periphery towards the core. Multispectral imaging identified a sub region in the core with a four-fold signal only at 750 nm. A co-registered B-mode image of this region was shown to be echogenic and tissue remodeling was suspected. This echogenic region was identified with poor to negligible wash-in of microbubbles (Vevo MicroMarker® contrast agents, VisualSonics). Histology confirmed this region to be necrotic with signs of calcium deposit and neovascularization in the tumor core. Similar investigations in LLC model confirms in vivo PA changes associated with hypoxia. These changes were validated to induce hypoxia using immunebiomarkers. Conclusions: Spectral imaging for oxygen saturation in blood can characterize the tumor microenvironment into poorly and well oxygenated regions. These regions were validated by histology for hypoxia. Multispectral imaging identifies for the first time, molecular changes concurrent with tumor remodelling in these tumors. Taken together, non-invasive characterization of the tumor microenvironment using photoacoustics rendered spectral imaging of endogenous absorbers, a sensitive tool to monitor molecular changes representative of cancer progression.

Disclosure of author financial interest or relationships:
M. Lakshman, FujiFilm Visualsonics Inc.,, Employment; **A. Heinmiller**, FUJIFILM VisualSonics Inc., Employment; **I. Lohse**, None; **D. Hedley**, None; **A. Needles**, FUJIFILM VisualSonics, Inc., Employment; **C. Theodoropoulos**, Fujifilm VisualSonics Inc, Employment .

Presentation Number **P 574**
Poster Session 4
September 21, 2013 / 14:45-14:45 / Room: Exhibit Hall B

Characterization of Angiogenesis of Breast Cancer with Dynamic Contrast Enhanced MRI and a New Biodegradable Macromolecular Contrast Agent

Anthony Malamas, Erlei Jin, **Zheng-Rong Lu**, *Biomedical Engineering, Case Western Reserve University, Cleveland, OH, USA. Contact e-mail: zxl125@case.edu*

PURPOSE: In order to accurately characterize tumor angiogenesis with DCE-MRI, a new polydisulfide containing macrocyclic Gd(III) chelates was synthesized and evaluated as a safe and effective biodegradable macromolecular MRI contrast agent. Macrocyclic Gd(III) chelates have high kinetic stability against transmetallation, and the polydisulfide backbone of the agent allows breakdown of the polymers in the plasma and rapid excretion via renal filtration. The effectiveness of the agent for characterizing tumor angiogenesis with DCE-MRI was investigated in a mouse tumor model in comparison with a clinical small molecular contrast agent. METHODS: DOTA chelate was conjugated with the secondary amino group of diethylenetriamine (DETA) followed by condensation polymerization with 3,3-dithiolbispropionyl chloride (DTBPC). The biodegradable macromolecular contrast agent PolyDOTA-Gd was finally obtained after the complexation with gadolinium(III) acetate. The DCE-MRI study was performed in nude female mice bearing MDA-MB-231 human breast tumor model. Tumor angiogenesis biomarkers, endothelium transfer coefficient (Ktrans) and fractional tumor plasma volume (fPV) were calculated from the DCE-MRI data using a two-compartment model. RESULTS: Axial 2D MRI tumor images before and after injecting PolyDOTA-Gd and ProHance were shown in Fig. 1. The biodegradable macromolecular contrast agent showed greater and more prolonged enhancement in the tumor tissue than ProHance. Figure 1 B and C shows the Ktrans and fPV of the tumor tissue calculated from DCE-MRI data obtained with PolyDOTA-Gd and ProHance, respectively. The average Ktrans value from PolyDOTA-Gd was about 6 times lower than that from ProHance ($p < 0.05$), because the latter could extravasate through normal blood vessels. There was no significant difference in the fPV value between two contrast agents. CONCLUSION: The preliminary study indicates that the PolyDOTA-Gd is a promising contrast agent for characterizing tumor angiogenesis with dynamic contrast enhanced MRI.

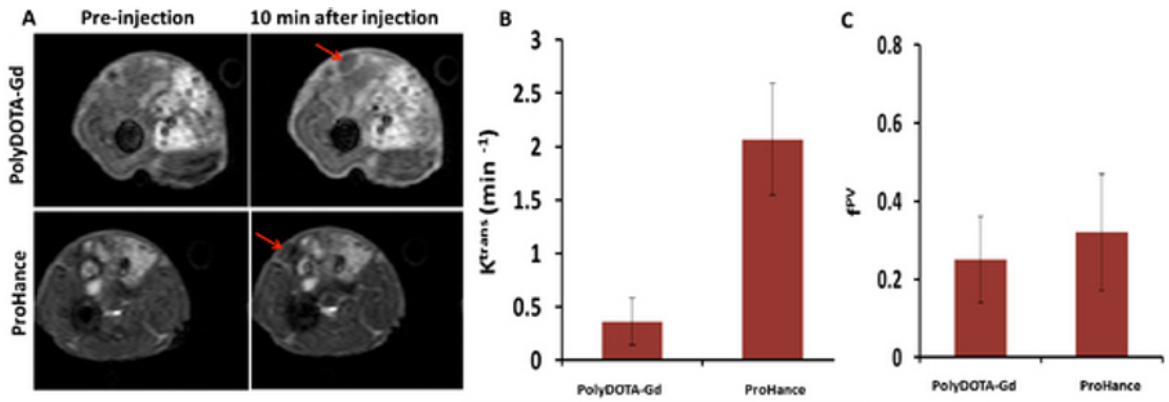

Figure 1. DCE-MRI images of tumor injected with PolyDOTA-Gd and ProHance (A, red arrows indicate tumors); K^{trans} values obtained from PolyDOTA-Gd and ProHance (B); f^{PV} values obtained from PolyDOTA-Gd and ProHance (C).

Disclosure of author financial interest or relationships:
A. Malamas, None; **E. Jin**, None; **Z. Lu**, None.

Presentation Number **P 575**
Poster Session 4
September 21, 2013 / 14:45-14:45 / Room: Exhibit Hall B

Increased Clinical Relevance of Orthotopic Glioma Models Through Bioluminescence and MR Imaging

Deanne Lister, *Jeni Baranski, Mary Anne Meade, Tracey Woolliscroft, Deepa Balagurunathan, Jeremy Castorena, Darren Shaw, Erin Trachet, Wilbur R. Leopold, Patrick McConville, Molecular Imaging, Inc., Ann Arbor, MI, USA. Contact e-mail: dlister@molecularimaging.com*

Glioblastoma multiforme (GBM) is the most common and most aggressive form of malignant primary brain tumors, affecting nearly 35,000 people in the United States. Most preclinical studies in glioma utilize survival as the primary endpoint to study, which provides limited information about disease progression, tumor burden response to treatment (a primary clinical end point). We have characterized two human glioma cell lines, Gli36 and LN827 that were modified to express luciferase in order to enable in vivo monitoring of disease progression and response to treatment using bioluminescence imaging (BLI). Anatomical magnetic resonance imaging (MRI) was also performed to directly correlate bioluminescence signal with tumor volume. Both models exhibited >90% tumor take-rate and responded to treatment with temozolomide, a clinical standard of care. Analysis of lifespan, tumor volume doubling times, and tumor growth delay all indicated that BLI is a reliable indicator of disease progression and response to treatment. BLI-based endpoints also showed good correlation with MR-based endpoints. These results support the use of in vivo imaging in these modified cell lines for longitudinal monitoring of tumor progression and response to therapy. Imaging was not only a reliable method for quantifying tumor burden, but enabled clinically relevant end points that could not be accessed through non-imaging means or lifespan determination alone. Further utility can be driven in these models through the use of other functional imaging end points.

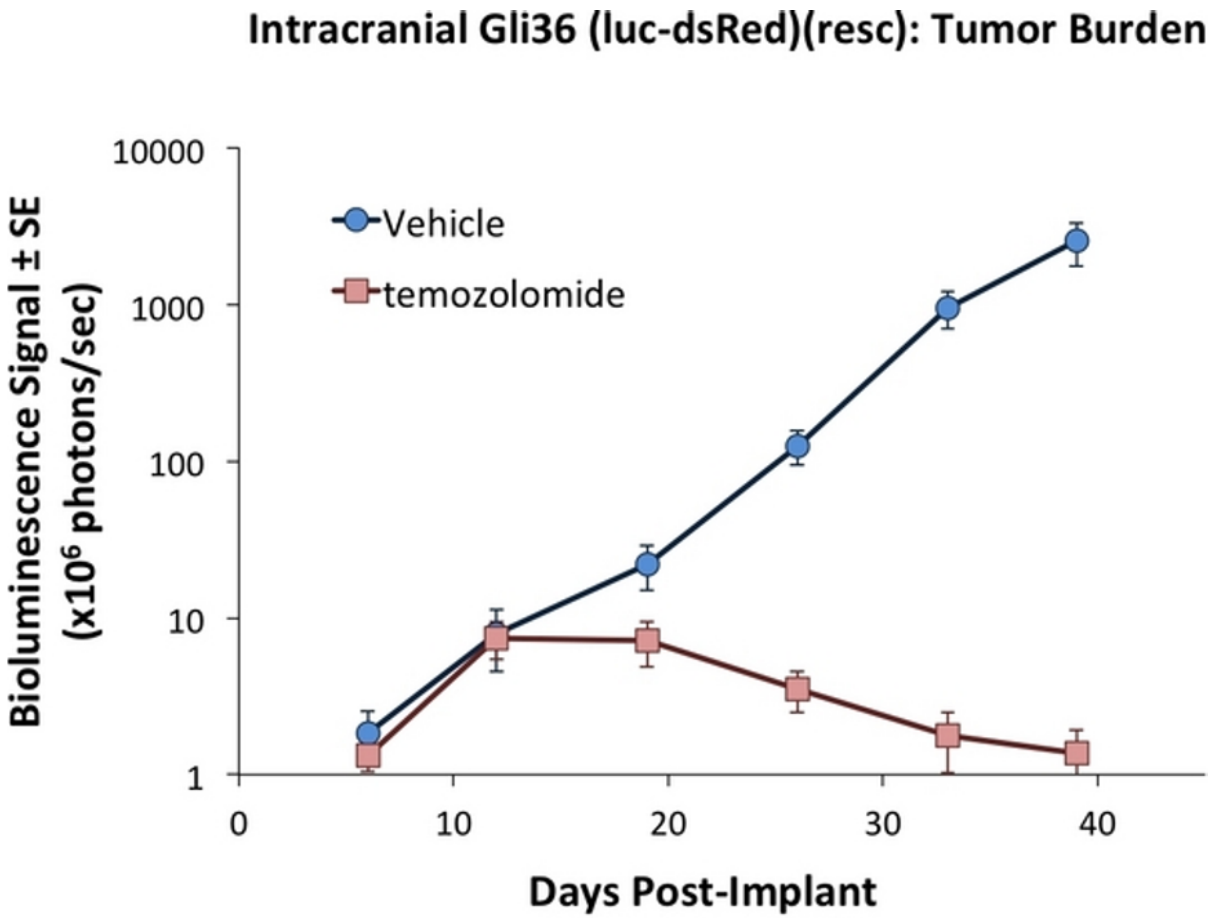

Intracranial Gli36 human glioma model: tumor burden by bioluminescence imaging and response to standard of care.

Intracranial Luciferase Expressing Glioma Models Characterization

Glioma Model	Take Rate	BLI Doubling Time (days)	Treatment	Median Lifespan (days)	BLI Tumor Growth Delay (days)
Gli36 (luc-dsRed)(resc)	94%	3.3	vehicle	41	-
			temozolomide, 100mg/kg, PO, QDx5	>83*	>53*
L1827 (luc-dsRed)(resc)	94%	2.9	vehicle	39	-
			temozolomide, 100mg/kg, PO, QDx5	>81*	>43*

*P<0.05 vs vehicle control

Disclosure of author financial interest or relationships:

D. Lister, None; **J. Baranski**, None; **M. Meade**, None; **T. Woolliscroft**, Molecular Imaging, Inc., Employment; **D. Balagurunathan**, None; **J. Castorena**, None; **D. Shaw**, None; **E. Trachet**, None; **W.R. Leopold**, None; **P. McConville**, Molecular Imaging, Inc., Employment .

Presentation Number **P 576**
Poster Session 4
September 21, 2013 / 14:45-14:45 / Room: Exhibit Hall B

In Vivo Imaging of Tissue Remodeling Activity Involving Infiltration of Macrophages by a Systemically Administered Protease-activatable Probe in Colon Cancer Tissues

Nobuhiko Onda[1], *Sayaka Kemmochi*[2,3], *Reiko Morita*[2,3], *Yasushige Ishihara*[1], *Makoto Shibutani*[3], [1]*Corporate R&D Center, Olympus Corporation, Tokyo, Japan;* [2]*Laboratory of Veterinary Pathology, Tokyo University of Agriculture and Technology, Tokyo, Japan;* [3]*Pathogenetic Veterinary Science, United Graduate School of Veterinary Sciences, Gifu University, Tokyo, Japan. Contact e-mail: nobuhiko_onda@ot.olympus.co.jp*

Recent progress on the development of fluorescent probes for molecular imaging enables visualization of cellular and molecular changes and provides valuable information regarding tumor development and its progression in living subjects. However, the cellular identity of a signal and the corresponding mechanism that renders biological images of target molecules of probes have remained enigmatic. Understanding the tumor detection mechanisms of probes is particularly important for the application to clinical cases as well as for improving probe performance. This study was performed to clarify the tumor detection mechanisms of *in vivo* imaging of systemically administered protease-activatable fluorescent probes using experimentally produced colon tumor tissues. For this purpose, the commercially available probe, ProSense, which was one the most used systemically applicable cathepsin protease-activatable probes for mice or rats and had been shown to visualize a variety of experimentally-induced tumors, was used. Time-course analysis of delivery and uptake of ProSense as well as the target protease and its cellular identity that gives rise to ProSense-cleaving activity were analyzed in a mouse xenograft tumor model using human colon tumor cell lines, HT29 and HCT116. *In vivo* imaging revealed the accumulation of ProSense signals within tumors, showing distribution preferentially in the vascular leakage area in parallel with the development of vasculature at the tumor periphery as revealed by vascular imaging probes. Immunohistochemically, cathepsin proteases targeted by ProSense, especially cathepsin B, were specifically distributed within macrophages in conjunction with the distribution of ProSense signals. Co-distribution of immunofluorescence for tenascin C and *in situ* zymography for fluorescein-quenched gelatin provided evidence of tissue remodeling in the infiltration areas of cathepsin B+ macrophages. Furthermore, *in situ* zymography revealed increased extracellular ProSense-cleaving activity in such areas. These results suggest that increase of tissue remodeling activity is a mechanism responsible for the capture of ProSense signals within tumors in a mouse xenograft tumor model. Because of the limitations of xenograft models that eliminate the principal mechanisms that govern the effects of inflammation and immunity on a tumor microenvironment, we further analyzed ProSense signals in an immunocompetent rat colon carcinogenesis model induced by azoxymethane. We could detect ProSense signals in the colon tumors in conjunction with the vascular leakage area at the tumor stroma, especially at the tumor margin showing cathepsin B+ macrophage infiltration. These results suggest that systemically administered protease-activatable fluorescent probes can effectively detect cancer invasive fronts, where tissue remodeling activity is high to facilitate neoplastic cell invasion. The clinical introduction of intraoperative protease imaging may have the potential to improve the accuracy of tumor resections.

Disclosure of author financial interest or relationships:
N. Onda, Olympus Corporation, Employment; **S. Kemmochi**, None; **R. Morita**, None; **Y. Ishihara**, Olympus Corporation, Employment; **M. Shibutani**, None.

Presentation Number **P 577**
Poster Session 4
September 21, 2013 / 14:45-14:45 / Room: Exhibit Hall B

A Targeted, Metalloprotein-Based MRI Contrast For Prostate Cancer Detection And Therapy

Keun C. Park[1], *David R. Mills*[2], *Edward Walsh*[3], [1]*Diagnostic Imaging, Rhode Island Hospital, Providence, RI, USA;* [2]*Medicine, Rhode Island Hospital, Providence, RI, USA;* [3]*Neuroscience, Brown University, Providence, RI, USA. Contact e-mail: kpark@lifespan.org*

Currently, prostate cancer poses a difficult challenge in providing effective diagnosis and treatment to most patients. Despite the fact that many technological and medical breakthroughs have recently been made, providing tools for accurate diagnosis and better treatment options remain elusive. PSA (prostate specific antigen) has been widely used as a prostate tumor marker for decades. But, it was found that BPH (benign prostatic hyperplasia) could also produce PSA, which resulted in over-diagnosing patients with the cancer and subsequently resorting to unnecessary treatment in many cases. The unmet medical need is large and urgent; therefore it is highly desirable to provide improvements in diagnosis and treatment in this field. Necl-5 is a cell surface glycoprotein that has been shown to promote cellular proliferation, migration and invasion of transformed cell lines. While Necl-5 is barely detectable in normal epithelial cells, it is dramatically upregulated in many human carcinomas including the common epithelial cancers including prostate. We obtained a genetically modified ferritin, originated from a hyper-thermophilic microbe called Archaoglobus Fulgidus, which encapsulates approximately 7,000 iron ions. The goals of this project are to demonstrate proof-of concept with respect to: i) specific targeting of Necl-5 (vide infra) positive tumor cells using the nanoconjugate MRI contrast agent in vivo, and ii) destroying the tumor cells selectively by applying a rapidly oscillating magnetic field, a method known as magnetic hyperthermia. The two components (Ferritin/Necl-5 antibody conjugate) have been chemically tethered, and the conjugate was tested for its specific binding to prostate tumor cells. The in vitro data suggests that the nanoconjugate can be used as a contrast agent for two MR contrast weightings (T2 and susceptibility). For in vivo study, immunodeficient mice were injected in the rear flank with PEC SAI cells (prostate epithelial cell soft-agar invasive, 10x106). Anti-Necl-5/ferritin nanoconjugate was injected via tail vein and animals scanned by MRI at 4 and 24 hours post injection. Nanoconjugate targeted tumor showed significant reduction of T2 signal at 4 hours (43.6±9.9 seconds) as compared to initial baseline value (72.8±11 seconds). No significant difference was observed in the control animal between baseline (62.8±8.3 seconds) and 4 hours (73.6±9.1 seconds). In vivo MRI of rat PEC SAI-derived tumor suggests utility of anti-Necl-5/ferritin nanoconjugate as a novel contrast agent. Furthermore, when a rapidly oscillating magnetic field was applied to ferritin, heat was generated in the surrounding sub-micron environment. Under the applied conditions (field strength = 350 oE, frequency = 162 kHz, duration = 3 min), a 25% increase in T2 and T2* was observed, which suggest that iron is shed from the heat-disrupted ferritin structure. As free iron ions are known to be toxic to cell survival, we are acutely interested in further investigating these observations in an animal tumor model. We will expand the scope of the studies to include a human tumor model that expresses CD155, the human ortholog of rat Necl-5.

Disclosure of author financial interest or relationships:
K.C. Park, None; **D.R. Mills**, None; **E. Walsh**, None.

Presentation Number **P 578**
Poster Session 4
September 21, 2013 / 14:45-14:45 / Room: Exhibit Hall B

Tumor Paint™ technology detects naturally occurring solid tumors in dogs

William S. Dernell[2], Janean Fidel[2], Katie Kennedy[2], Stacey Hansen[1], Valorie Wiss[1], Mark Stroud[1], **Julia Parrish-Novak**[1], [1]*Blaze Bioscience, Inc., Seattle, WA, USA;* [2]*College of Veterinary Medicine, Washington State University, Pullman, WA, USA. Contact e-mail: julie.novak@blazebioscience.com*

Background: Tumor Paint™ technology is designed to allow for real-time visualization of tumors during surgery at improved resolution over existing methods. BLZ-100 is a Tumor Paint product consisting of a chlorotoxin (CTX) peptide conjugated to a near-infrared (NIR) fluorophore that is being advanced toward clinical studies. CTX-based Tumor Paint products have been shown to illuminate a broad range of cancers—brain, colorectal, prostate, skin, head and neck, breast and lung—in mouse models. To facilitate clinical translation, a preclinical feasibility study is under way in dogs with naturally occurring solid tumors. Many types of canine tumors resemble human disease, including sarcomas, breast and lung cancers, mucosal squamous cell cancers, and gliomas. The diversity of tumor size and type, surrounding tissue, and patient body mass provides a model that is superior to the mouse in predicting the clinical characteristics of BLZ-100, including tumor penetration, background staining, and effective imaging dose. Methods: Dogs undergoing planned resection for any solid tumor were candidates for the study. All options were discussed and client consent was obtained under an approved IACUC protocol. Dogs received standard of care including tumor resection with intent to control or cure local disease. In the dose-ranging portion of the study, dogs received BLZ-100 intravenously 24-48 hours before surgery, and tissues were imaged *ex vivo* after surgery. *Ex vivo* imaging was performed on gross tissue specimens using the IVIS Spectrum (Caliper) and the Odyssey NIR scanner (Li-Cor) to determine overall signal in tumor and gross signal to background. Tissues were embedded in OCT, sectioned on a cryostat, and scanned on the Odyssey. Serial sections were stained with H&E, and comparison with the fluorescence scans was used to validate the specificity of BLZ-100 for tumor tissue. Results: To date, 13 dogs have been treated at doses from 0.01 to 0.1 mg/kg. Tumor types included sarcoma (6), mast cell tumors (2), adenocarcinoma (1), lung cancer (1), oral squamous cell carcinoma (1), and mammary cancer (2). Significant tumor fluorescence was detected in samples from dogs treated with 0.03 to 0.1 mg/kg. In this group, fluorescence was visible throughout viable tumor tissue. Tumor to normal tissue ratios in gross tissue imaging varied from 43:1 to 2:1 using the Spectrum and up to 257:1 using the Odyssey scanner. Conclusions: BLZ-100 is effective for differentiation of tumor tissue from surrounding normal tissue in canine cancer patients. The tumor specificity and high signal to background ratios attained thus far are encouraging, and intraoperative imaging will be incorporated into the next phase of the study. The information obtained in this study validates the breadth of tumor recognition seen in mouse studies, and provides data that will be valuable in clinical translation of the product. This project has been funded in whole with Federal funds from National Cancer Institute, National Institutes of Health, Department of Health and Human Services, under Contract No. HHSN2612012000054C

Disclosure of author financial interest or relationships:
W.S. Dernell, None; **J. Fidel**, None; **K. Kennedy**, None; **S. Hansen**, Blaze Bioscience, Inc, Employment; Blaze Bioscience, Inc., Stockholder; **V. Wiss**, None; **M. Stroud**, Blaze Biocsience, Inc., Stockholder; **J. Parrish-Novak**, Blaze Bioscience, Inc., Employment; Blaze Bioscience, Inc., Stockholder .

Presentation Number **P 579**
Poster Session 4
September 21, 2013 / 14:45-14:45 / Room: Exhibit Hall B

Metabolomic insights into pancreatic cancer-induced cachexia

Marie-France Penet[1], *Flonné B. Wildes*[1], *Yelena Mironchik*[1], *Tariq Shah*[1], *Dmitri Artemov*[1], *A. Maitra*[2], *Zaver M. Bhujwalla*[1], [1]*JHU ICMIC Program, Division of Cancer Imaging Research, The Russell H. Morgan Department of Radiology and Radiological Science, The Johns Hopkins University School of Medicine, Baltimore, MD, USA;* [2]*Departments of Pathology and Oncology, The Sol Goldman Pancreatic Cancer Research Center, The Johns Hopkins University School of Medicine, Baltimore, MD, USA. Contact e-mail: mpenet@mri.jhu.edu*

Pancreatic cancer is the fourth leading cause of cancer death in the USA. Early-stage pancreatic cancer is usually clinically silent, and most patients presenting symptoms attributable to pancreatic cancer have advanced disease and cachexia. Pancreatic cancer only becomes apparent after the tumor invades surrounding tissues or metastasizes to distant organs. Typical symptoms include abdominal or mid-back pain, obstructive jaundice, and weight loss that can arise from anorexia, maldigestion from pancreatic ductal obstruction, or from cachexia. Better understanding of the disease, effective early detection methods, and new therapeutic targets are urgently needed to improve its outcome. Here, our aims are to characterize the metabolism of multiple pancreatic ductal adenocarcinoma tumors with in vivo 1H magnetic resonance spectroscopic imaging (MRSI), ex vivo high-resolution magnetic resonance spectroscopy (MRS) and to assess the effect of tumors on body weight. We have also characterized the expression of choline kinase (Chk) and cyclooxygenase 2 (COX-2). Chk, the enzyme that converts free choline (Cho) into phosphocholine (PC), is known to be overexpressed in aggressive cancer, and COX-2 a critically important inflammation mediator, significantly influences cancer angiogenesis, invasion and metastasis. Pa02C, Pa04C, Panc1, and BxPC3 human pancreatic adenocarcinoma cell lines, obtained from Dr. Maitra at the Johns Hopkins University, were used in the study. Panc1 and BxPC3 were obtained originally from the ATCC. Pa02C and Pa04C originated from pancreatic ductal adenocarcinoma. Cells were inoculated subcutaneously in SCID male mice. Mouse weight was followed for approximately 6 weeks. Once tumors reached 500 mm3, the mice were scanned on a 4.7T spectrometer for 1H MRSI, and were then sacrificed and the tumors excised for immunoblot analyses, and high-resolution 1H MRS (1). Amongst the four cell lines tested, we observed a significant loss of weight in animals with Pa04C tumors (Figure 1). In vivo 1H MRSI revealed a high level of total choline in Panc1 and Pa04C tumors (Figure 2). The in vivo results were confirmed by ex vivo MRS analysis of the tumor extracts (Figure 3) that also revealed a similar trend with alanine. Immunoblots showed that Panc1 tumors exhibited high expression levels of COX-2 and the highest levels of Chk. Pa04C tumors showed low levels of those two proteins. The highest level of total choline observed in Panc1 tumors was mainly due to a high level of PC, and correlated with the high level of Chk observed in the immunoblots. Panc1 tumors were also characterized by a high level of lactate compared to the three other cell lines. Pa04C tumors that induced weight loss presented the second highest levels of total choline and lactate. No major differences in the lipid patterns were observed amongst the four tumor types. Our data identify increased total choline and lactate as potential imaging biomarkers to detect pancreatic cancer, and Chk and COX-2 as potential therapeutic targets of this devastating disease. (1) Penet et al., Cancer Res (2011) 71: 6948-56. This work was supported by NIH P50CA103175.

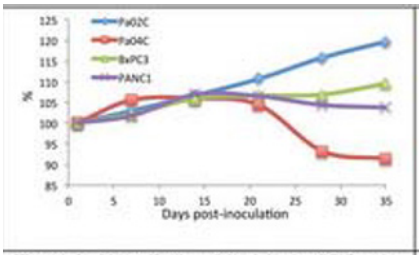

Figure 1: Normalized weight loss in SCID mice inoculated with Pa02C, Pa04C, BxPC3, and Panc1 cells (n = 6).

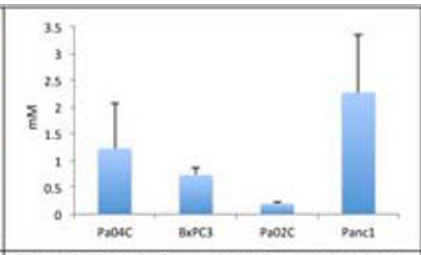

Figure 2: Total choline concentration measured *in vivo* with ^{1}H MRSI (mean ± sd) (n = 3)

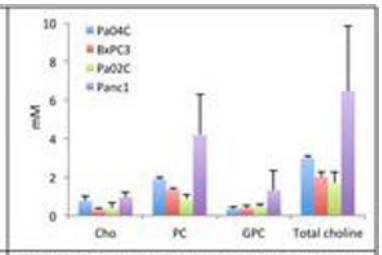

Figure 3: Metabolite quantification in tumor extracts with high-resolution ^{1}H MRS (Cho: free choline, PC: phosphocholine, GPC: glycerophosphocholine) (mean ± sem) (n = 3)

Disclosure of author financial interest or relationships:
M. Penet, None; **F.B. Wildes**, None; **Y. Mironchik**, None; **T. Shah**, None; **D. Artemov**, None; **A. Maitra**, None; **Z.M. Bhujwalla**, None.

Presentation Number **P 580**
Poster Session 4
September 21, 2013 / 14:45-14:45 / Room: Exhibit Hall B

Melanin Targeted PET Imaging for Liver Cancer Early Detection

Chunxia Qin[1,2], *Hongguang Liu*[1], *Xiang Hu*[1], *Xiaoli Lan*[2], *Yongxue Zhang*[2], *Zhen Cheng*[1], [1]*Molecular Imaging Program at Stanford (MIPS), Department of Radiology and Bio-X Program, Stanford University, Stanford, CA, USA;* [2]*Department of Nuclear Medicine, Union Hospital, Tongji Medical College, Huazhong University of Science and Technology, Wuhan, China. Contact e-mail: t0317008@163.com*

Introduction: Hepatocellular carcinoma (HCC) is highly aggressive and one of the most lethal cancers worldwide. Early diagnosis and accurate staging of HCC is crucial for improvement the management outcome of patients. Positron emission tomography (PET) is a very promising technology for non-invasively imaging tumor micrometastases. Currently, there is a strong need to develop PET probes for early detection of small HCC lesions. In this study, for the first time, we hypothesized that melanin is a new promising biomarker of HCCs and evaluated the feasibility of using a melanin targeted PET probe, N-(2-(diethylamino)ethyl)-18F-5-fluoropicolinamide (18F-P3BZA), for imaging of HCCs in mice models. Methods: Different cell lines including HCC (HepG2, Hep3B), positive control melanotic melanoma (B16F10) and negative control amelanotic melanoma A375M and prostate cancer PC3 cells were cultured and subcutaneous injected into mice to prepare different tumor models. The tumors were removed and their melanin expression was first evaluated by visual observation. Then paraffin sections of tumors were made to perform Fontana-Masson staining, and relative melanin expression levels in tissues were also measured using spectrophotometric method. 18F-P3BZA was radiosynthesized according to our previous published method. HepG2 and PC3 cell uptake of 18F-P3BZA studies were performed at different incubation time points. Small animal PET studies including static scan and dynamic scan were conducted on tumor (HepG2, Hep3B, B16F10, A375M or PC3) bearing mice (n=4 for each group). Biodistribution studies of 18F-P3BZA in HepG2 models at 0.5, 1 and 2 h after tail vein injection were also performed to verify the PET results. Tumors and normal tissues of interest were removed and weighed, and radioactivity was measured. Percentage of the injected radioactive dose per gram of tissue (%ID/g) was calculated. Results: Visual examination, Fontana-Masson staining and spectrophotometric measurement revealed that high melanin content are expressed in HepG2, Hep3B, B16F10, but not in A375M and PC3. Cell uptake studies further showed that melanotic HepG2 cell line had much higher uptake of 18F-P3BZA than that of PC3 (~20 fold, $p<0.05$). More importantly, PET and biodistribution studies demonstrated that 18F-P3BZA exhibited high tumor uptake in HCC models (~4%ID/g at 0.5 h in HepG2) and excellent tumor to background contrasts, whereas amelanotic tumors (A375M and PC3) could not be visualized by the probe. Conclusion: Melanin expression was confirmed in some HCC tumor models. Melanin avid PET probe 18F-P3BZA displayed excellent properties for imaging melanotic HCCs and melanomas. Melanin targeted PET may represent a new strategy for early detection and staging of HCCs.

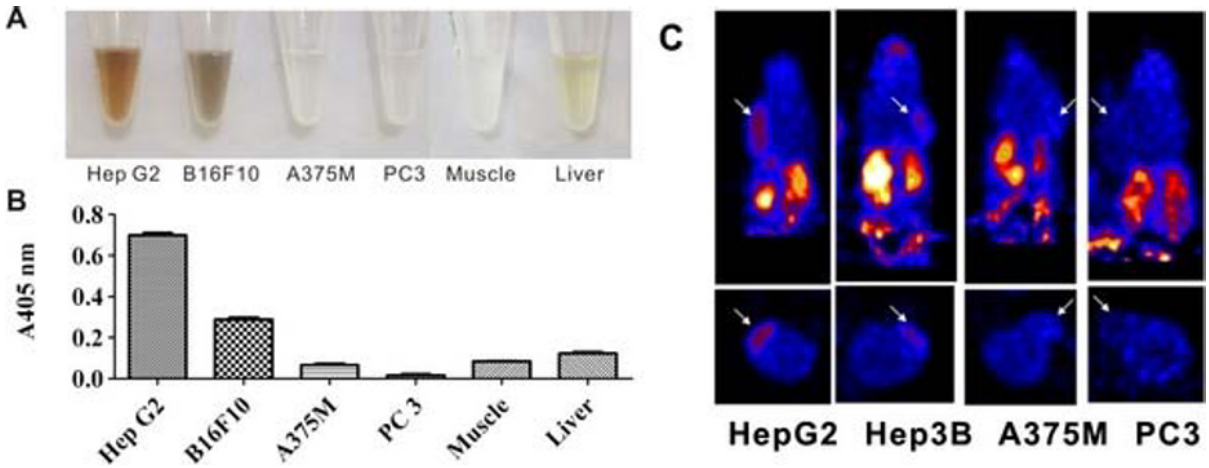

Figure 1. (A) Visual examination of different tumor and normal tissues; (B) Relative melanin expression level in different tissues measured by spectrophotometric method; (C) Decay corrected coronal and transverse PET imaging of HepG2, Hep3B, A375M and PC 3 tumor-bearing mice at 1 h after tail vein injection of about 3.7 MBq (100 mCi) of 18F-P3BZA (arrows indicate tumor).

Disclosure of author financial interest or relationships:
C. Qin, None; **H. Liu**, None; **X. Hu**, None; **X. Lan**, None; **Y. Zhang**, None; **Z. Cheng**, None.

Presentation Number **P 581**
Poster Session 4
September 21, 2013 / 14:45-14:45 / Room: Exhibit Hall B

TK-NTR Therapeutic Reporter Gene Fusion for Imaging GCV/CB1954 Dual-Prodrug Therapy in Triple Negative Breast Cancer

Thillai V. Sekar, *Kira Foygel, Ramasamy Paulmurugan, Departments of Radiology and Bioengineering, the Bio-X Program, Molecular Imaging Program at Stanford (MIPS), Stanford University School of Medicine, Palo alto, CA, USA. Contact e-mail: thillaiv@stanford.edu*

Gene directed enzyme prodrug therapy (GDEPT) is a novel approach for selective ablation of cancer by chemotherapy. More than 50 prodrugs and 12 different enzymes have been investigated so far. However, prodrug/enzyme combinations such as HSV-TK/GCV, NTR/CB1954, and CD/5-FC are the very few GDEPT systems reached clinical trial. The major limitations in achieving effective therapy by GDEPT system is either due to poor expression level of delivered therapeutic gene in the target tissues, or dose limited toxicity restricting the amount of prodrugs that can be used for treatment. To overcome these issues, a few dual-prodrug gene therapy approaches were developed, where two enzymes with their respective prodrugs have been attempted. We have recently reported that HSV-TK and NTR genes expressed as a fusion have high therapeutic value than either system alone, with the use of very low concentrations of GCV and CB1954. In this study, we explored the therapeutic potential of HSV-TK-NTR fusion to treat triple negative metastatic breast cancer, a highly resistant breast cancer sub-type. To characterize the therapeutic value of HSV1-TK-NTR fusion, we developed MDA MB231 triple negative breast cancer cell line stably expressing HSV-TK, NTR, and HSV-TK-NTR fusion, independently, and co-expressed FLUC-EGFP fusion to facilitate in vivo imaging. All three stable cell lines were functionally evaluated for the introduced therapeutic gene expression by ^{3}H-PCV uptake (HSV1-TK and HSV1-TK-NTR) and CytoCy5S substrate reduction (NTR and HSV1-TK-NTR) (Figure 1). ^{3}H-PCV uptake of MDA MB231 cells stably expressing TK-NTR fusion protein (17511cpm) showed 79.6 ± 3.62 fold higher than control cells, which is 1.28 ± 0.06 fold higher than MDA MB231 cells stably expressing TK alone (13670 cpm). MDA MB231 cells stably expressing NTR and TK-NTR fusion showed significant amount of Cy5 fluorescent signal through the reduction of CytoCy5S substrate. CB1954 in different doses (1, 5, and 10μM) either alone or in combinations with 1μM of GCV were assessed for cell death different time after treatment by propidium iodide (PI) based FACS analysis, and found maximum cell death from cells received 1μM GCV+10μM CB1954. To optimize the duration of treatment, three different combinations of GCV/CB1954 were used to treat the stable cells, and cell death was monitored for five consecutive days. The results showed significant cell death 72h after treatment with drug combinations. Percentage of cell death was higher in MDA MB231 cells stably expressing TK-NTR fusion protein, while MDA MB 231 cells stably expressing NTR and TK cells showed significantly low level of cell death as assessed by the FACS analysis of PI stained cells. TK-NTR expressing MDA MB231 cells showed 71.4% cell death 72h post-treatment, while cells expressing TK and NTR showed only 7.79 and 13.5% cell death respectively. These results clearly show the in vitro therapeutic efficacy of TK-NTR fusion against triple negative metastatic breast cancer. MDA MB231 cells stably expressing HSV1-TK-NTR fusion is currently under evaluation for therapeutic efficiency in a metastatic tumor model.

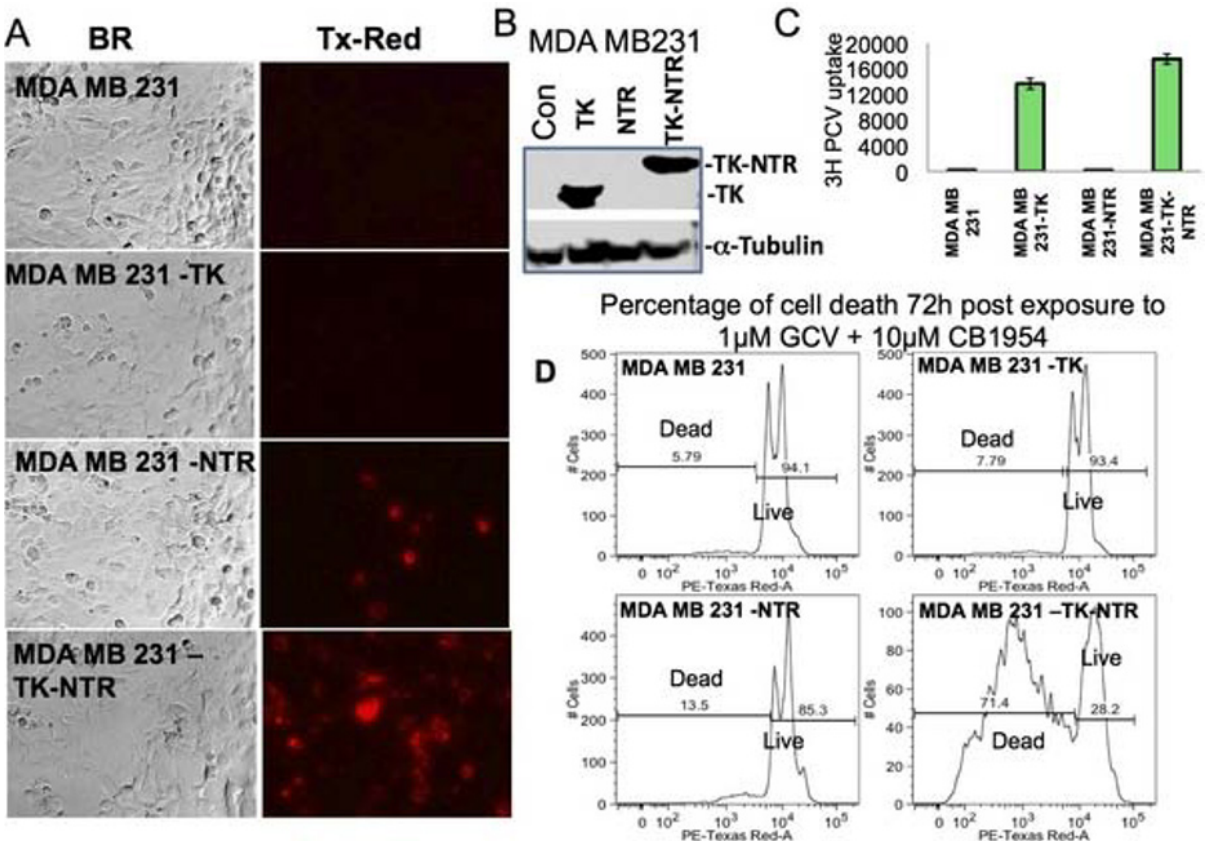

Disclosure of author financial interest or relationships:
T.V. Sekar, None; **K. Foygel**, None; **R. Paulmurugan**, None.

Presentation Number **P 582**
Poster Session 4
September 21, 2013 / 14:45-14:45 / Room: Exhibit Hall B

Noninvasive in vivo assessment of [131I]m-iodobenzylguanidine (mIBG) therapy using tumor volume and bioluminescence signal measurements in murine xenograft models

Youngho Seo[1], *Stephanie T. Murphy*[1], *Shorouk F. Dannoon*[1], *Shih-ying Huang*[1], *Henry F. VanBrocklin*[1], *W. Clay Gustafson*[2], *Erin A. Nekritz*[2], *Willam Weiss*[3], *Katherine K. Matthay*[2], [1]*Department of Radiology and Biomedical Imaging, University of California, San Francisco, San Francisco, CA, USA;* [2]*Department of Pediatrics, University of California, San Francisco, San Francisco, CA, USA;* [3]*Department of Neurology, University of California, San Francisco, San Francisco, CA, USA. Contact e-mail: youngho.seo@ucsf.edu*

Neuroblastoma is the most common extracranial cancer of childhood, derived from the sympathetic nervous system with a poor prognosis. A majority of children with high risk disease relapse after therapy. Targeted radiotherapy with ^{131}I-mIBG represents the most effective therapy for relapsed patients. We hypothesize that ^{131}I-mIBG will cooperate with targeted therapies to further enhance anti-tumor efficacy. A murine xenograft platform can help evaluate such synergistic therapeutic approaches for ^{131}I-mIBG therapy of drug resistant relapsed neuroblastoma. NB1691 luciferase transfected and human norepinephrine transporter transduced tumor cells (NB1691-luc-hNET) were implanted in mice subcutaneously and in the renal capsule. Tumor volume and bioluminescence signal measurements were made to assess ^{131}I-mIBG therapeutic effect. **Methods:** Intravenous administrations via tail vein were performed to infuse 2 mCi and 1 mCi of ^{131}I-mIBG as well as saline (sham) for the treatment. NaI solution (0.1 ml at 2.5 mg/ml) was injected intravenously to all animals to block the thyroid uptake of ^{131}I-mIBG, 50 minutes prior to the therapy. Caliper measurements of long and short axes for tumor volume calculation and D-luciferin (0.1 ml at 30 mg/ml) bioluminescence imaging (BLI) started on the day of therapy as baseline, and continued for 24 days posttherapy at 3 days per week interval. Volumes for subcutanoue tumors were normalized to the baseline measurement, and compared against the days posttherapy, followed by a regression analysis to find volume growth rate (mm^3/d). In addition, total flux (photons/s, or p/s) of BLI for both subcutaneous and renal capsule tumors were normalized to the baseline measurement, and compared against the days posttherapy, followed by a regression analysis to find the flux change rate (p/s/d). **Results:** The tumor volume growth rates were 0.11, 0.41, and 0.56 mm^3/d, respectively for 2 mCi (n=3), 1 mCi (n=4), and sham (n=2) cohorts of subcutaneous tumors, exclusive of tumors out of range (smaller than 50 mm^3 or larger than 300 mm^3 at baseline). The total flux change rates were 0.024, 0.064, and 0.65 p/s/d, respectively for 2 mCi (n=5), 1 mCi (n=4), and sham (n=4) cohorts of subcutaneous tumors, exclusive of tumors out of range (less than $8x10^8$ p/s total flux at baseline). The total flux change rates were 0.0067, 0.42, and 0.99 p/s/d, respectively for 2 mCi (n=5), 1 mCi (n=5), and sham (n=5) cohorts of renal capsule tumors. **Conclusion:** Both caliper measurement of tumor volumes and BLI total flux corresponded proportionally to the different dose levels of ^{131}I-mIBG treatments. We are extending our studies in larger cohorts, and plan to combine radiosensitizers or other novel anticancer drugs with ^{131}I-mIBG treatment in this established preclinical murine xenograft platform.

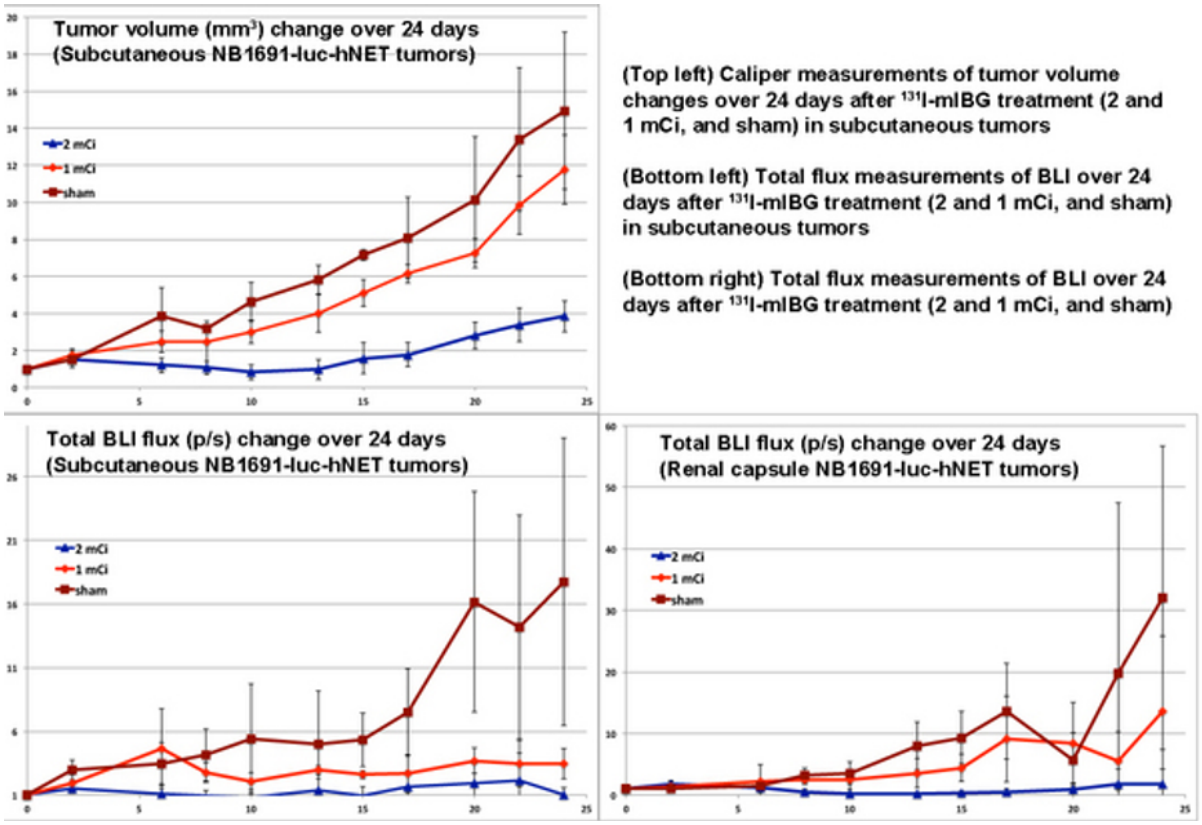

(Top left) Caliper measurements of tumor volume changes over 24 days after ^{131}I-mIBG treatment (2 and 1 mCi, and sham) in subcutaneous tumors

(Bottom left) Total flux measurements of BLI over 24 days after ^{131}I-mIBG treatment (2 and 1 mCi, and sham) in subcutaneous tumors

(Bottom right) Total flux measurements of BLI over 24 days after ^{131}I-mIBG treatment (2 and 1 mCi, and sham)

Disclosure of author financial interest or relationships:
Y. Seo, None; **S.T. Murphy**, None; **S.F. Dannoon**, None; **S. Huang**, None; **H.F. VanBrocklin**, None; **W. Gustafson**, None; **E.A. Nekritz**, None; **W. Weiss**, None; **K.K. Matthay**, None.

Presentation Number **P 583**
Poster Session 4
September 21, 2013 / 14:45-14:45 / Room: Exhibit Hall B

Hyperpolarized [1-13C]pyruvate as a probe of metabolic changes during pancreatic cancer progression

Eva Serrao[1,2], *Mikko I. Kettunen*[1,2], *Tiago B. Rodrigues*[1,2], *Ferdia A. Gallagher*[1,4], *Rebecca Harmston*[1], *David Tuveson*[3], *Kevin M. Brindle*[1,2], [1]*CRUK Cambridge Institution, University of Cambridge, Cambridge, United Kingdom;* [2]*Biochemistry Department, University of Cambridge, Cambridge, United Kingdom;* [3]*Cold Spring Harbor Laboratory, NY, NY, USA;* [4]*Radiology Department, University of Cambridge, Cambridge, United Kingdom. Contact e-mail: Eva.Serrao@cruk.cam.ac.uk*

Background: Pancreatic ductal adenocarcinoma (PDA) is the fourth leading cause of cancer-related deaths in the USA, with a 5-year survival of less than 5%. Early diagnosis has been hampered by the difficulties in establishing sensitive and specific biomarkers1,2. Like other tumors, PDA is believed to progress through precursor lesions termed pancreatic intraepithelial neoplasia (PanIN); non-invasive detection of PanIN before it progresses to PDA could improve mortality for this group of patients. An emerging technique for tumor imaging is dynamic nuclear polarization, which allows metabolism to be detected and imaged in real time using 13C-labelled magnetic resonance spectroscopy (13C-MRS). Hyperpolarized [1-13C]pyruvate is the most promising of the available DNP probes and has been used in the assessment of metabolic changes in animal models of cancer and has recently been translated into patient imaging3,4. The aim of this study was to identify metabolic signatures of the different stages of progression of PDA, using [1-13C]pyruvate as a 13C-labelled magnetic resonance spectroscopy probe, in well established genetically-engineered mouse models of pancreatic cancer. Methods:C57BL/6 mice with no pancreatic lesions, LSL-KrasG12D/+- p48Cre/+ (KC) mice (2-13 months old) with PanIN lesions2, LSL-KrasG12D/+ and p48Cre/+ control mice (age matched to KC mice), LSL-KrasG12/D+;LSL-Tpr53R172H/+;Pdx-1-Cre (KPC) mice (3-6 months old) with spontaneous pancreatic cancer5 and Pdx-1-Cre (PC) control mice (age matched to KPC) were used. KPC and C57BL/6 mice were used as models of established tumor and normal pancreatic tissue, respectively. KPC mice were enrolled when ultrasound examination showed the appearance of either a diseased pancreas or a sarcomatoid tumor. MRI was performed at 7T.A chemical shift image (TR 30ms;TE 1.5ms;FOV 40x40mm;data matrix 32x32;flip angle 5) was acquired from a single 4-8mm axial slice covering the pancreas 20 sec after injection of 0.3 mL of hyperpolarized [1-13C]pyruvate. [1-13C]Pyruvate, [1-13C]lactate and [1-13C]alanine signal intensities in the pancreas were analyzed. High-resolution 1H NMR spectra of pancreatic tissue extracts6, collected at different ages, were obtained at 14.1T (TR 12.5s). Lactate and alanine concentrations were calculated from the 1H NMR spectra. All pancreatic tissues were evaluated histologically. Results: A progressive reduction of the [1-13C]Ala/[1-13C]Lac ratio was observed with increasing disease burden, whereas no changes were observed in control mice. 1H NMR results revealed the same Ala/Lac signature. The Ala/Lac ratio was in agreement with histology, with higher values occurring in normal tissues. Conclusions: [1-13C]Pyruvate metabolism and the ratio of the subsequently formed [1-13C]Ala/[1-13C]Lac may form useful probes to detect and follow progression of pancreatic preneoplastic lesions, before any mass-forming lesion (tumor) can be detected by conventional imaging. This might offer an improved diagnostic tool in high-risk populations, such as patients with chronic pancreatitis or familial pancreatic cancer7, thereby helping to improve patient survival and prognosis.

Disclosure of author financial interest or relationships:
E. Serrao, GE Healthcare, Grant/research support; **M.I. Kettunen**, GE, Grant/research support; **T.B. Rodrigues**, None; **F.A. Gallagher**, GE Healthcare, Grant/research support; **R. Harmston**, None; **D. Tuveson**, None; **K.M. Brindle**, GE Healthcare, Grant/research support; GSK, Consultant .

Presentation Number **P 584**
Poster Session 4
September 21, 2013 / 14:45-14:45 / Room: Exhibit Hall B

PEGylated Mesoporous Silica Nanoparticle Targeting of Colorectal Cancer and Polyps

Jeffrey S. Souris[1], *Nai-Tzu Chen*[1,2], *Shih-Hsun Cheng*[1,2], *Vani Konda*[3], *Marc Bissonnette*[3], *Leu-Wei Lo*[2], *Chin-Tu Chen*[1], [1]*Department of Radiology, The University of Chicago, Chicago, IL, USA;* [2]*Division of Medical Engineering Research, National Health Research Institutes, Zhunan, Taiwan;* [3]*Department of Medicine, The University of Chicago, Chicago, IL, USA. Contact e-mail: sourisj@uchicago.edu*

To determine the utility of targeting aberrant glycosylation for the *in vivo* imaging of nascent colorectal cancers and polyps, we have recently begun to design, synthesize, and evaluate targeted fluorescent mesoporous silica nanoparticles (MSNs), for use as endoscopic contrast agents. Type MCM-41 MSNs were synthesized via conventional sol-gel chemistry, with the incorporation of fluorescein isothiocyanate (FITC) within the MSN's silica framework during co-condensation - to protect the fluorophore from photobleaching and O_2 quenching, and to maximize the nanoparticle's available surface area for targeting ligand conjugation. Following nanoparticle synthesis, the exteriors of MSNs were labeled with 5 kDa PEG and then conjugated, via maleimide/amine linkage, to the lectin *Ulex Europaeus Agglutinin 1* (UEA-1) to target α-L-fucose ($C_6H_{12}O_6$), a monosaccharide component of glycosylation that is known to be expressed on the luminal surface glycoproteins of colorectal dysplastic adenomas and cancers but largely absent from healthy colon tissue. Morphologies of MSNs were characterized by transmission electron microscopy (TEM), dynamic light scattering (DLS), N_2 adsorption-desorption isotherm analysis, and zeta potential measurement. TEM studies revealed discrete, uniformly sized mesoporous silica nanoparticles with an average pre-PEGylated diameter of 55 nm (average post-PEGylated diameter of 172 nm). N_2 adsorption-desorption isotherm studies yielded average MSN pore diameters of 4.7 nm, calculated using the Barrett-Joiner-Halenda (BJH) method, and average surface areas and pore volumes of 980 $m^2\ g^{-1}$ and 0.38 $cm^3\ g^{-1}$ respectively, calculated using the Brunauer-Emmett-Teller (BET) method. Zeta potential measurements varied little with PEGylation status, averaging -5.15 mV before and -6.57 mV following PEG + targeting ligand conjugation. *In vitro* studies of PEGylated MSN / cell binding specificity were conducted using α-L-fucose positive Caco-2 and α-L-fucose negative HCT116 human colorectal cancer cells, as well as fibroblasts. *In vivo* endoscopic exams were performed using a commercially available clinical colonoscope and probe-based confocal fluorescence microscope, with fasted/prepped A/J male mice that had been subjected to azoxymethane (AOM) / dextran sodium sulfate (DSS) treatments - a standard model for colitis-associated colorectal tumor development. As the cell studies and endoscopic images in the figure below illustrate, topical delivery of UEA-1 to both Caco-2 cells and AOM/DSS-induced colorectal polyps/tumors demonstrated significant binding and specificity to α-L-fucose. (Concentration / time-dependent blocking studies not shown.) Qualitative endoscopic comparison of PEGylated to unPEGylated FITC-MSN-UEA-1 nanoparticles revealed significantly greater binding of the former, suggesting that PEGylation can greatly enhance the transport of nanoparticles through colonic mucosa. Ongoing studies are aimed at quantifying and further enhancing our nanoplatform's transport through colon mucus, and extending its dwell-time once pathology bound.

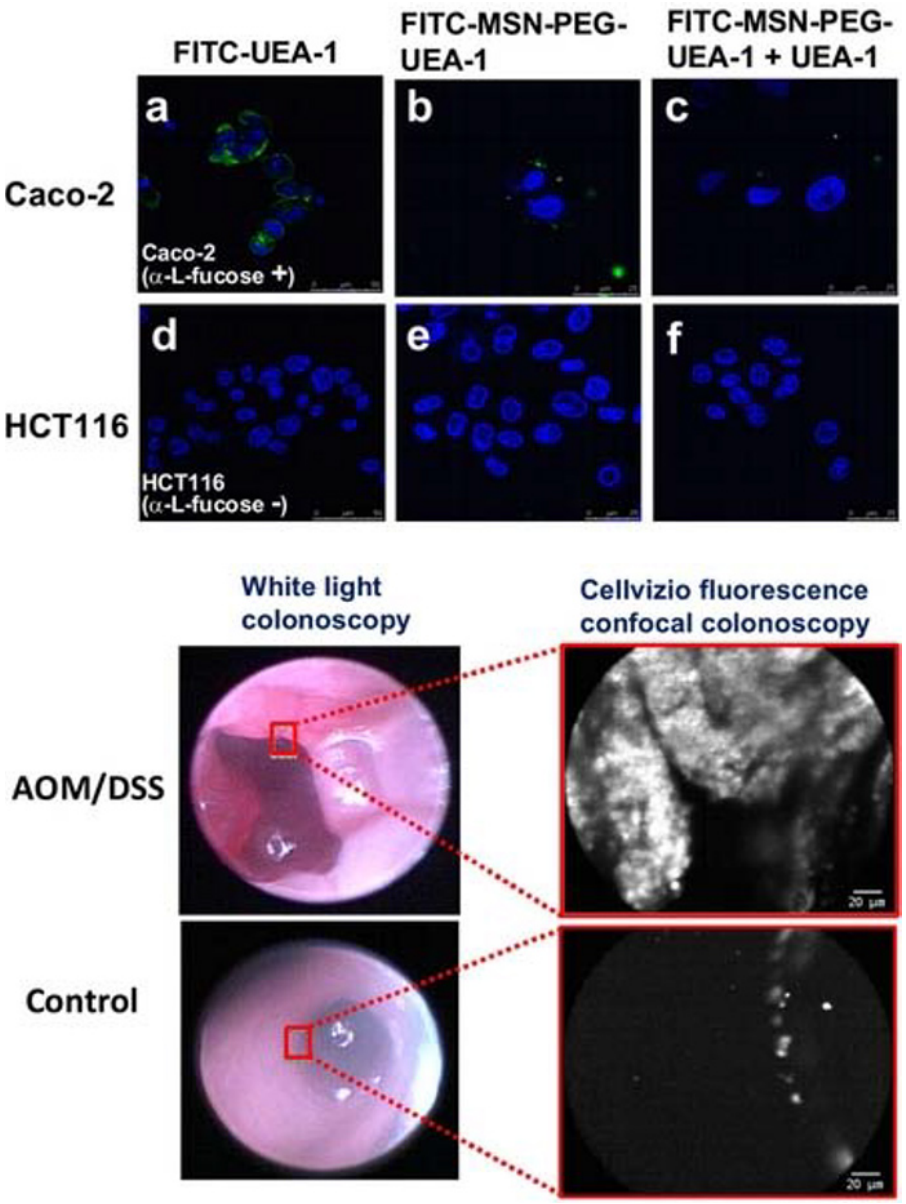

Figure 1. (Top) UEA-1 binding to α-L-fucose (+) Caco-2 (a,b,c) and α-L-fucose (-) HCT116 (d,e,f) human adenocarcinoma cells *in vitro*, with 1-hour blocking studies (e,f) using non-fluorescent UEA-1 pretreatment of cells. (Bottom) Fluorescence endoscopy *in vivo* confirmation of enhanced UEA-1 binding to AOM/DSS-induced colorectal polyps versus normal colonic mucosa in A/J mice.

Disclosure of author financial interest or relationships:

J.S. Souris, None; **N. Chen**, None; **S. Cheng**, None; **V. Konda**, Mauna Kea Teachnoloigies, Honoraria; Olympus, Grant/research support; **M. Bissonnette**, None; **L. Lo**, None; **C. Chen**, Cell>Point, Grant/research support; RefleXion Medical, Consultant; DxRay/Photon Imaging, Consultant .

Presentation Number **P 585**
Poster Session 4
September 21, 2013 / 14:45-14:45 / Room: Exhibit Hall B

Secondary Cerenkov-Induced Fluorescent Imaging for Multiple Biomarker and Quantitative Enzymatic Readout

Daniel L. Thorek[1], *Anuja Ogirala*[1], *Bradley J. Beattie*[2], *Jan Grimm*[1], [1]*Radiology, Memorial Sloan-Kettering Cancer Center, New York City, NY, USA;* [2]*Medical Physics, Memorial Sloan-Kettering Cancer Center, New York, NY, USA. Contact e-mail: thorekd@mskcc.org*

Nuclear imaging offers unparalleled sensitivity for whole body identification of disease in pre- and clinical applications. However, the physical basis of radioactive decay is a constant and cannot be manipulated for activatable imaging strategies. Thus, radiotracer imaging only indirectly reports metabolic or molecular activity through accumulation. Here, we have developed quantitative activatable imaging approaches that utilize nanoparticles (NP) for biologically specific fluorescent conversion of Cerenkov luminescence (an optical decay signal from PET tracers). We show that this method, Secondary Cerenkov-Induced Fluorescent Imaging, (SCIFI) enables us to combine a wide range of medically relevant isotopes (eg. 18-F, 68-Ga and 89-Zr) to excite and image small molecule (fluorescein and cyanine dyes) and NP (quantum dots). Significantly, this approach outperforms conventional fluorescent imaging in vitro and in vivo on the basis of signal-to-background. As SCIFI does not require external illumination we achieve approximately six-fold greater signal-to-background. We pursued application of SCIFI for tandem biomarker readout. 89-Zr trastuzumab with BT474 breast cancer xenografts could be used to excite co-localized RGD-QD605 but not non-specific RAD-QD605. This demonstrates hybrid concomitant visualization of multiple cancer relevant biomarkers (eg. Her2/neu and αvβ3). This significantly deviates from PET, which cannot distinguish between multiple targets at the same time. Finally, we investigated enzymatically activatable SCIFI. Fluorescein was conjugated to a peptide sequence cleavable by MMP-2, an enzyme whose overexpression contributes to cancer aggressiveness. When bound to a gold NP (Au-NP) the fluorescein is quenched, and after enzymatic cleavage, the fluorescein can be excited by Cerenkov luminescence and detected. When the quenched AuNP is co-administered with 18F-FDG, PET is unable to distinguish between MMP-2 low (BT-20) and MMP-2 overexpressing (SCC-7) lesions. However, cleavage of the fluorescein generates SCIFI signal specifically in SCC-7 tumors. We utilized the radiotracer quantitation inherent in PET with the integrated Frank-Tamm equation to quantify the light produced within a defined spectral window (matching SCIFI emission). Thus, we can quantitatively determine enzymatic activity in vivo. The quantitative SCIFI results (an average of 6.23 pmol of activated probe in SCC-7 tumors in comparison to 1.56 pmol in BT-20, $p<0.001$) correlate with the expression and gelatinolytic activity of excised tumors. Here, we demonstrate a novel approach for specific and activatable investigation of multiple biological signatures in vivo using radioactive decay signals. Imaging the fluorescence emission of Cerenkov excitation by PET radiotracers has significant clinically translatable potential as these agents are already clinically used (eg. FDA approved 18F-FDG and fluorescein with biologically inert AuNP). Clinical radiotracers in concert with optical sensors targeted to disease biomarkers have capacity to impact pre- and clinical science.

Disclosure of author financial interest or relationships:
D.L. Thorek, None; **A. Ogirala**, None; **B.J. Beattie**, None; **J. Grimm**, None.

Presentation Number **P 586**
Poster Session 4
September 21, 2013 / 14:45-14:45 / Room: Exhibit Hall B

Development of 5-Fu loaded PLA conjugated with humanized SM5-1 F(ab') fragments for HCC-LM3 liver tumor treatment

Xibo Ma, *Di Dong, Jie Tian, Medical Image Processing Group, Institute of Automation,CAS, "Beijing,100190", China. Contact e-mail: xibo.ma@ia.ac.cn*

Background and aims: SM5-1 is a humanized antibody which can specifically react with human hepatocellular carcinoma(HCC) cells. In this study, we prepared two drugs including 5-Fu loaded PLA conjugated with humanized SM5-1 F(ab') antibody fragments (PLA-5Fu-SM5-1) and 5-Fu loaded PLA(PLA-5Fu). The purpose of this study is to evaluate the therapeutic efficacy of PLA-5Fu-SM5-1and PLA-5Fu. Preparation of 5-Fu loaded PLA conjugated with humanized SM5-1 F(ab') fragments: SM5-1 antibody was kindly provided by Professor Yajun Guo of Shanghai Second Military Medical University [1, 2]. For targeted nanoparticles, antibody F(ab') fragments were covalently conjugated to nanoparticles using carbodiimide chemistry. Briefly, 1 mL PLA nanoparticle suspension (~5 mg/mL in 10 mmol/L NaH2PO4, pH 6.3) was incubated with 10 μL of 50 mg/mL 1-ethyl-3-3-dimethylaminopropyl carbodiimide and 10 μL of 50 mg/mL N-hydroxysuccinimide for 20 min at room temperature. The resulting N-hydroxysuccinimide-activated nanoparticles were covalently linked to 600 μL F(ab')fragments of humanized SM5-1 mAb (1 mg/mL in 50 mmol/L HEPES, pH 7.4). The resulting F(ab') fragment-nanoparticle bioconjugates were washed thrice to remove unbound F(ab'). After the final wash, no free F(ab')was detected in the supernatant by the Micro BCA assay kit (Pierce). The nanoparticles were lyophilized after washing. Three groups of HCC-LM3 tumor-bearing mice(n=5 per group) were treated with saline, PLA-5Fu-SM5-1, or PLA-5Fu (10mg/kg on four consecutive days). The tumor volume was estimated, assuming the tumors were ellipsoid, using the formula volume=4π/3(1/2 length×1/2width×1/2height). Tumor size was measured on day 3, 8, 13, 18, 23, 28 after treatment. Results: Contrast with PLA-5Fu, PLA-5Fu-SM5-1 clearly inhibited the tumor growth in vivo, although it was not able to completely ablate the tumor progression. Contrast with saline, PLA-5Fu-SM5-1 and PLA-5Fu induced a 14.17%±10.34% and 5.35% ±12.52% tumor growth inhibition rate on day 23 posttreatment (data was shown in Fig. 1). Conclusions: PLA-5Fu-SM5-1 obviously inhibited the tumor growth because antibody SM5-1 can target the HCC-LM3 tumor cell. This research reveal the application prospects of PLA-5Fu-SM5-1 on the treatment of HCC-LM3 liver tumor. We will deeply study the treatment mechanism of PLA-5Fu-SM5-1 on HCC-LM3 liver tumor and other tumors (such gastric tumor, colorectal cancer and so on) for further research. References [1] Geng Kou, Shuhui Wang, Changming Cheng, Jie Gao, Bohua Li, Hao Wang, Weizhu Qian, Sheng Hou, Dapeng Zhang, Jianxin Dai, Hongchen Gu, Yajun Guo, Develepment of SM5-1-conjugated ultrasmall superparamagnetic iron oxide nanoparticles for hepatoma detection, Biochemical and Biophysical Research Communications, 374:192-197, 2008. [2] Jie Gao, Geng Kou, Huaiwen Chen, Hao Wang, Bohua Li, Ying Lu, Dapeng Zhang, Shuhui Wang, Sheng Hou, Weizhu Qian, Jianxin Dai, Jian Zhao, Yanqiang Zhong, and Yajun Guo, Treatment of hepatocellular carcinoma in mice with PE38KDEL type I mutant-loaded poly(lacti-co-glycolic acid) nanoparticles conjugated with humanized SM5-1 F(ab') fragments, Molecular Cancer Therapeutics, 7(10): 3399-3407,2008.

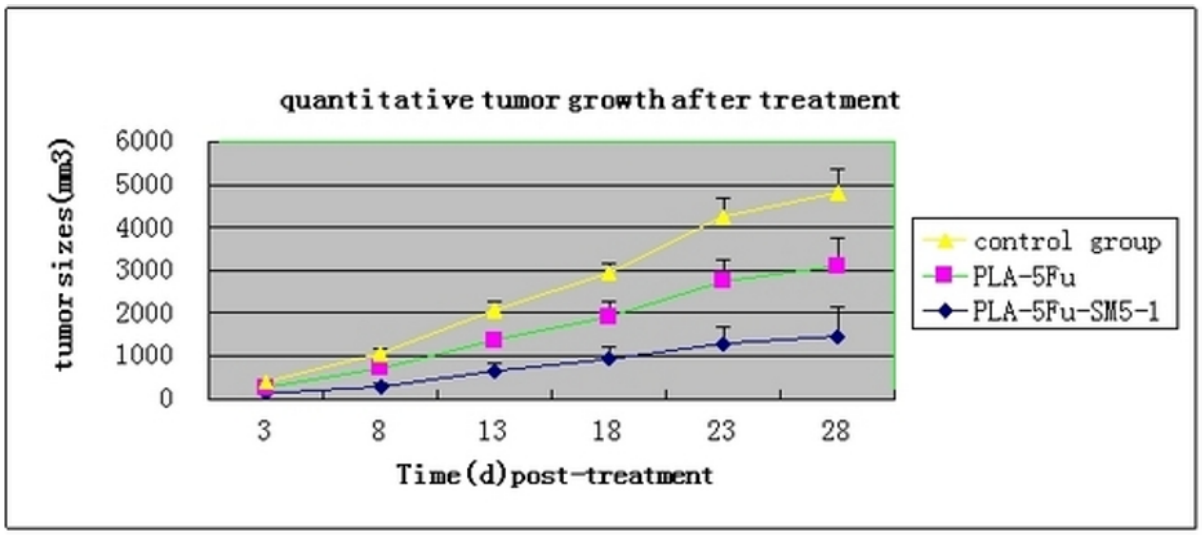

Fig. 1 HCC-LM3 tumor sizes of the nude mice that underwent saline, PLA-5Fu, or PLA-5Fu-SM5-1

Disclosure of author financial interest or relationships:
X. Ma, None; **D. Dong**, None; **J. Tian**, None.

Presentation Number **P 587**
Poster Session 4
September 21, 2013 / 14:45-14:45 / Room: Exhibit Hall B

Pharmacokinetics Evaluation of IL-4 receptor Targeting Liposome in a Human Brain Tumor-Bearing Mouse Model after Blood-Brain Barrier Disruption by Focused Ultrasound

Yu-Ling Hsieh[1], *Jia-Je Li*[1], *Wen Wei Lu*[1], *Ren-Shyan Liu*[2], *Maggie Jui-Mei Lu*[3], *Feng-Yi Yang*[1], *C. Allen Chang*[1], *Tai-Tong Wong*[5,4], *Hsin-Ell Wang*[1], [1]*Department of Biomedical Imaging and Radiological Sciences, National Yang-Ming University, Taipei, Taiwan;* [2]*Department of Nuclear Medicine and National PET/Cyclotron Center, Taipei Veterans General Hospital, Taipei, Taiwan;* [3]*Biomedical Technology and Device Research Laboratories, Industrial Technology Research Institute, Hsinchu, Taiwan;* [4]*Division of Pediatric Neurosurgery, Taipei Veterans General Hospital, Taipei, Taiwan;* [5]*Department of Surgery, Cheng Hsin General Hospital, Taipei, Taiwan. Contact e-mail: shieh910@yahoo.com.tw*

Objectives: The major limitation of conventional anticancer drug therapy of brain tumor is the blood-brain barrier (BBB). It has been shown that high-intensity focused ultrasound (HIFU) may facilitate the delivery of BBB impermeable drugs into the focal zone of brain tissue without appreciable disturbing the morphology of the path region. IL-4 receptor is highly expressed in glioblastoma (GBM). We have developed an AP1 (human atherosclerotic plaque-specific peptide-1)-conjugated liposomal doxorubincin (AP1-DO101) which can target IL-4 receptor on GBM. This study combined AP1-DO101 with HIFU to increase local drug accumulation in brain tumor lesion of GBM-bearing mice. Methods: Cnfocal fluorescence microscopic imaging was conducted after treating $1x10^7$ of BM8401-Luc cells with liposomal doxorubincin (DO101) and AP1-DO101 for 2 hours. The cellular uptake of their radioactive surrogates ^{111}In-DO101 and ^{111}In-AP1-DO101 (radiochemical purities ≥ 98%) in GBM8401 cell lines was studied. Biodistribution of ^{111}In-AP1-DO101 post intravenous injection in mice bearing orthotopic GBM8401-Luc brain tumor with or w/o HIFU were conducted. Immunohistofluorescence using cryostat sections of brain tumor post i.v. injection of AP1-DO101 was also studied. Results: Significantly higher uptake of AP1-DO101 compared with DO101 was observed based on the fluorescence of doxorubicin in GBM8401-Luc cells. The uptake of ^{111}In-AP1-DO101 in GBM8401-Luc cells (6.4±0.1 %AD/10^7 cells) was 5.3-fold higher than that of ^{111}In-DO101 (1.2±0.1 %AD/10^7 cells) after 8 h of incubation. These results indicate that conjugation with AP1 may improve the internalization of liposomal doxorubicin to tumor cells. The accumulation of ^{111}In-AP1-DO101 in mice bearing orthotopic GBM8401-Luc tumor with HIFU-induced BBB disruption was 1.7-fold higher than those without HIFU. The findings were consistent with those observed in immunohistofluorescence study of cryostat sections of brain tumor. Sonication does not alter the distribution of ^{111}In-AP1-DO101 in normal tissues. Conclusions: This study demonstrates that modifying PEGylated liposomes with AP-1 would increase the internalization of liposomal drugs to GBM cells. Irradiation with HIFU and modification with AP-1 provide physical and biological means to enhance the delivery and internalization of liposomal drugs into orthotopic GBM tumors in a mouse model, and may open a new window for clinical brain tumor therapy in the future.

Disclosure of author financial interest or relationships:
Y. Hsieh, None; **J. Li**, None; **W. Lu**, None; **R. Liu**, None; **M. Lu**, None; **F. Yang**, None; **C. Chang**, None; **T. Wong**, None; **H. Wang**, None.

Presentation Number **P 588**
Poster Session 4
September 21, 2013 / 14:45-14:45 / Room: Exhibit Hall B

A combination therapy of Fluorouracil (5-FU) and 188Re-liposome in C26 colonic peritoneal carcinomatosis mice

Mao-Feng Weng, *Chih-Hsien Chang, Te-Wei Lee, Institute of Nuclear Energy Research, Taoyuan County, Taiwan. Contact e-mail: mfweng@iner.gov.tw*

Nanoliposomes are designed as carriers capable of packaging drugs through passive targeting tumor sites by enhanced permeability and retention effects. The studies of therapeutic efficacy, biodistribution, pharmacokinetics, micro-SPECT/CT image, and dosimetry of 188Re-labeled nanoliposomes (188Re-liposomes) in the C26 colon carcinoma peritoneal metastasis mice model have been evaluated. In this study, we combined the clinical first-line drug Fluorouracil (5-FU) and 188Re-liposomes in the same animal model. 5-FU has been considered having not only the antineoplastic property but also as a radiosensitizer. Thus, we proposed that the combination therapy will reveal the additive therapeutic effect. Colon carcinoma peritoneal metastatic BALB/c mice were intraperitoneal (i.p) administrated with 188Re-liposomes and 5-FU. For the combination therapy, 5-FU was pre-treated at day(-2) and day(0) before of the administration of 188Re-liposomes. For therapeutic efficacy, the survival time of mice after respectively treating with 188Re-liposomes, fluorouracil (5-FU), and 188Re-liposomes combined with 5-FU were evaluated and compared. The results showed that 188Re-liposomes combined with 5-FU attained a longer life span in tumor-bearing mice than only chemotherapeutics of 5-FU and radiotherapeutics of 188Re-liposomes did. These results demonstrated that the pre-treatment and combination of 5-FU will enhance the therapeutic effect of 188Re-liposomes. This information will provide the ideal therapeutic strategy of the 188Re-liposomes in clinical application.

Disclosure of author financial interest or relationships:
M. Weng, None; **C. Chang**, None; **T. Lee**, None.

Presentation Number **P 589**
Poster Session 4
September 21, 2013 / 14:45-14:45 / Room: Exhibit Hall B

Predicting Response to MEK and PI3K Inhibitor Combination Treatment in Pre-Clinical Human Colorectal Tumours with [18F]-FLT PET

Ian Wilson[1], *Emma J. Haagensen*[1], *Huw D. Thomas*[1], *Suzannah J. Harnor*[2], *Kate S. Smith*[2], *Tommy Rennison*[2], *Sara L. Payne*[2], *Ross J. Maxwell*[1], *David R. Newell*[1], [1]*Northern Institute for Cancer Research, Newcastle University, Newcastle upon Tyne, United Kingdom;* [2]*School of Chemistry, Newcastle University, Newcastle Upon Tyne, United Kingdom. Contact e-mail: j.i.wilson@newcastle.ac.uk*

MR and PET imaging agents are important biomarkers for the evaluation of novel targeted cancer treatments. Ideally the imaging agent should give a pre-treatment signal which is specifically changed when the target is inhibited and predict response early so as to enable treatment modification in the absence of a biomarker change. Here we show how 18F-fluorothymidine positron emission tomography ([18F]-FLT PET) can achieve this goal for combined MEK and PI3K inhibitor treatment in a preclinical model system. Numerous small molecule inhibitors of specific signal transduction pathways have been developed; in particular, the PI3K pathway, a major survival pathway, and the MAPK pathway, a major mitogenic pathway, have been targeted in cancer. However, single agent clinical activity with these inhibitors has in general been modest, and hence combinations are being evaluated. The aim of this study was to measure [18F]-FLT uptake in HCT116 human tumour xenografts prior to and after treatment with the MEK inhibitor PD-0325901, the PI3K inhibitor GDC-0941 or a combination of both drugs. The PET data were compared with results from tumour growth delay studies to evaluate the ability of [18F]-FLT at predicting tumour response prior to tumour volume changes. Mice were implanted subcutaneously with HCT116 human tumour xenografts. When the tumours reached approximately 5mm in diameter they were given a 1 hour dynamic [18F]-FLT PET scan. Following this initial baseline scan mice were treated by oral gavage with 1 mg/kg PD-0325901, 100 mg/kg GDC-0941, the combination of both drugs or the vehicle once daily for 14 days. On day 2 of treatment mice were given a further [18F]-FLT dynamic PET scan. Tumour volume measurements were carried out and data evaluated as median relative tumour volumes (RTV), where the tumour volume in each mouse on initial day of treatment is assigned an RTV value of 1. The [18F]-FLT PET results (Figure 1) showed that there was no effect on the uptake of [18F]-FLT between the pre and 2 day post treatment scans in the single agents alone or vehicle control treated animals, whereas there was a statistically significant decrease in FLT uptake on day 2 when the animals were treated with the combination of the PI3K and MEK inhibitors. Statistical analysis was carried out on both the AUC data and the SUV mean at 1 hour. A similar decrease in FLT uptake was seen in both with the area under the curve 0-60 min (AUC) 18% and SUV mean at 1hr 24% ($p < 0.01$). The tumour growth delay studies demonstrated that single agent treatment caused tumour growth delay compared with vehicle treated control tumours, but that growth delay was greater with the combination. The PET results taken together with the tumour growth inhibition data indicate that the decrease in [18F]-FLT uptake on day 2 of treatment preceded tumour growth inhibition and thus [18F]-FLT PET can be used as an early surrogate response biomarker for combined PI3K and MEK inhibitor treatment. These studies confirm that dual targeting of PI3K and MEK can induce marked tumour growth inhibition in vivo, and that this anti-tumour effect can be predicted by measuring [18F]-FLT uptake.

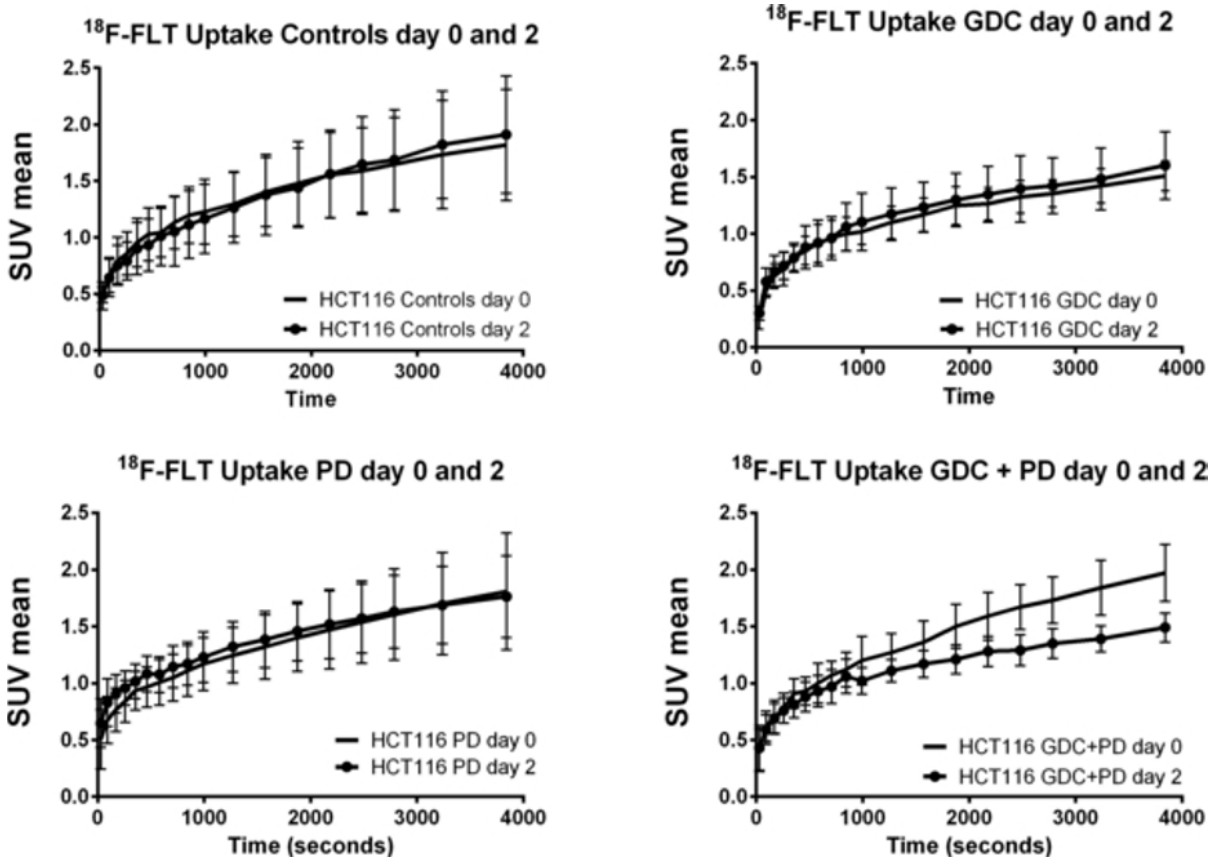

Figure 1. [18F]-FLT uptake in HCT116 human tumour xenografts at baseline and after 2 days of treatment with the PI3K inhibitor GDC-0941 and the MEK inhibitor PD 0325901, alone and in combination.

Disclosure of author financial interest or relationships:

I. Wilson, None; **E.J. Haagensen**, None; **H.D. Thomas**, None; **S.J. Harnor**, None; **K.S. Smith**, None; **T. Rennison**, None; **S.L. Payne**, None; **R.J. Maxwell**, Astex Pharmaceuticals, Grant/research support; **D.R. Newell**, Astex Pharmaceuticals, Grant/research support; Astex Pharmaceuticals, Consultant; Wilex, Consultant; Springer Verlag, Honoraria.

Presentation Number **P 590**
Poster Session 4
September 21, 2013 / 14:45-14:45 / Room: Exhibit Hall B

Functional Imaging of therapeutic effects of sunitinib in a renal cell carcinoma mouse model utilizing [^{18}F]FAZA and [^{18}F]FLT

Melinda Wuest[1], *David W. Chapman*[1,2], *John Mercer*[1], *Leonard I. Wiebe*[1], *Ronald B. Moore*[1,2], [1]*Dept. of Oncology, University of Alberta, Edmonton, AB, Canada;* [2]*Dept. of Surgery, University of Alberta, Edmonton, AB, Canada. Contact e-mail: mwuest@ualberta.ca*

Aim: Tyrosine kinase inhibitors (TKIs) are currently used as first line drug therapy for metastasizing renal cell carcinoma (RCC). TKIs target VEGF receptors in tumor as well as endothelial cells which lead to secondary effects observed as changes in tumor angiogenesis, proliferation, the tumor's microenvironment and metabolism. The goal of this study was to analyze changes in the tumor's hypoxia status and proliferation rate in a mouse RCC model during a therapy with the TKI sunitinib, utilizing positron emission tomography (PET) as a functional imaging tool. Materials and Methods: Dynamic and/or static PET imaging experiments were performed with [^{18}F]FAZA (up to 3 h p.i.) and [^{18}F]FLT (up to 1 h p.i.) in Caki-1 tumor-bearing BALB/c nu/nu mice. Half of which received sunitinib therapy (40 mg/kg/d i.p.) for 4 to 9 days and the other half served as a control group. Radiotracer uptake was analyzed during and after withdrawal of sunitinib therapy (10 to 12 days later). [^{18}F]FAZA uptake into Caki-1 tumors was compared with uptake of pimonidazole (3 h p.i.) analyzed with immuno-histochemical tissue staining. Results: After 5 days of therapy, [^{18}F]FAZA uptake reached a maximum after 60 min p.i. with a SUV_{mean} of 0.44±0.05 (n=4) in control Caki-1 tumors and remained relatively constant up to 3 h p.i. (0.42±0.05 (n=4) which was indicative for intracellular trapping. In sunitinib-treated animals [^{18}F]FAZA uptake reached its maximum after 30 min p.i. (SUV_{mean} of 0.38±0.02 (n=4), then decreased over the next 2.5 h to a final SUV_{mean} of 0.23±0.02 (n=4; $p<0.05$) at 3 h p.i., indicating reduced trapping of the radiotracer. These effects were consistent over the entire course of the sunitinib therapy regimen (79±4% of control after 9 days (n=8; $p<0.05$). When drug therapy was stopped, [^{18}F]FAZA uptake increased in the treated tumors again, and to even higher levels than in the control tumors, reaching 128±6% of the control (n=6; $p<0.05$). Pimonidazole staining analysis supported those results. In control Caki-1 tumors [^{18}F]FLT uptake continuously increased over time, reaching a $SUV_{mean,1h}$ of 1.08±0.04 (n=8). In sunitinib-treated tumors the $SUV_{mean,1h}$ was also reduced: 0.83±0.06 (n=8; $p<0.01$), indicating less proliferation during TKI therapy. After finishing sunitinib therapy, similar $SUV_{mean,1h}$ values were determined in both control and treated tumors: 0.97±0.06 and 0.98±0.06 (n=8), indicating an increase in cellular proliferation. Conclusion: Reduced trapping of [^{18}F]FAZA and [^{18}F]FLT indicates that therapy with the multitargeting TKI sunitinib leads to reduced hypoxia and proliferation in this RCC mouse model as detected with small animal PET. After stopping sunitinib therapy, these effects are reversed and as seen with [^{18}F]FAZA, hypoxia in these tumors increases even more. This corresponds well to the clinically observed TKI-withdrawal flare. Both PET radiotracers can be used clinically to observe the impact of TKI therapy in RCC patients. It also shows that small animal PET can be used as a functional tool to analyze the overall effects of TKIs in preclinical RCC models and to translate this into a clinical application.

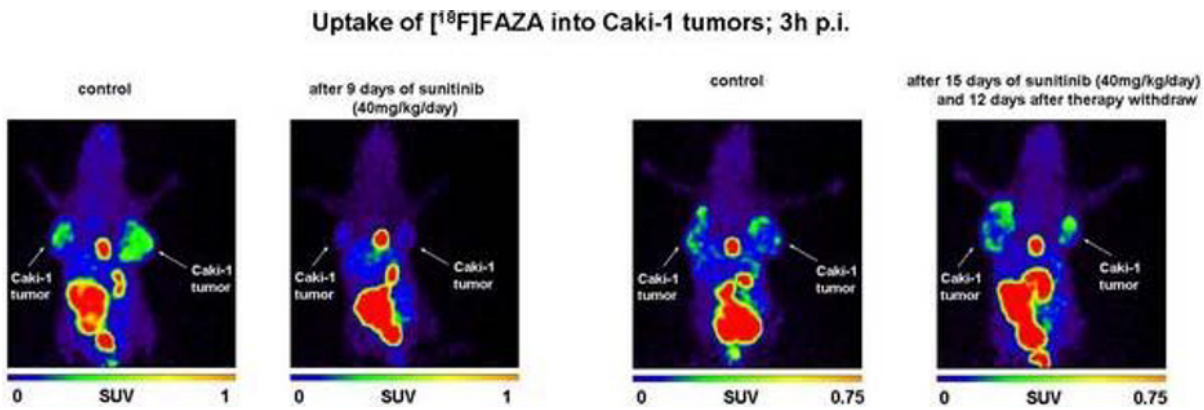

Disclosure of author financial interest or relationships:
M. Wuest, None; **D.W. Chapman**, None; **J. Mercer**, None; **L.I. Wiebe**, None; **R.B. Moore**, None.

Presentation Number **P 591**
Poster Session 4
September 21, 2013 / 14:45-14:45 / Room: Exhibit Hall B

Phosphatidylserine targeted multimodal imaging of brain metastases in mouse models

Dawen Zhao[1], *Heling Zhou*[1], *Nikolai V. Slavine*[1], *Jason H. Stafford*[2], *Philip E. Thorpe*[2], [1]*Radiology, UT Southwestern Medical Center, Dallas, TX, USA;* [2]*Pharmacology, UT Southwestern Medical Center, Dallas, TX, USA. Contact e-mail: Dawen.Zhao@UTSouthwestern.edu*

Brain metastasis is the most common intracranial malignancy in adults. The prognosis is poor, partly because most patients diagnosed with a solitary cerebral metastasis have undetected lesions, and current systemic therapies have limited access to occult metastases with an impermeable brain-tumor-barrier (BTB). Thus, there is an urgent need to develop new diagnostic and therapeutic agents that specifically target brain metastases. Phosphatidylserine (PS), normally restricted to the inner leaflet of the plasma membrane, becomes exposed on the outer surface of viable (non-apoptotic) endothelial cells in tumor vasculature. Vascular endothelium in normal tissues does not have exposed PS. In this study, we used a fully human monoclonal antibody, PGN635, that targets PS to identify brain metastases in mouse models. Brain-tropic human breast cancer MDA-MB-231/BR-GFP (231-Br) or mouse breast tumor 4T1 cells were injected directly into the left ventricle of a mouse heart under the imaging guidance of a small animal ultrasound machine. Multifocal lesions developed in the 231-Br mouse brain, while a solitary brain tumor was seen in 4T1 model by MRI scans. Fluorescence microscopy of sections of brain showed that there is extensive PS exposure (93 ± 5%) on vascular endothelial cells in the brain metastases but not in normal brain. Ex vivo imaging at 24 h post i.v. injection of PGN635F(ab')2 labeled with near infrared dye, IRDye800CW, allowed clear visualization not only of a single deep-seated 4T1 tumor (TNR = 5.8), but also individual brain metastases of 231-Br (TNR = 3.1). We have further exploited I-124 labeled PGN635F(ab')2 for in vivo PET imaging of brain metastases in the 231-Br model. PET/CT images were acquired 24 h and 48 h later. PET/CT merged images at 48 h showed a complete absence of uptake by the normal mouse brain. In contrast, multiple sites of localized uptake were observed in brains bearing metastases, indicating the uptake of I-124-PGN635F(ab')2 by the metastatic lesions. Specificity of PGN635 to brain metastases was further confirmed by ex vivo autoradiography. There was also spatial correlation between tumor lesions on MRI and the hot spots on the autoradiograph. Our study suggests that PS appears to be an excellent marker for the development of imaging and targeted therapeutics for brain metastases.
Acknowledgments: We thank Peregrine Pharmaceuticals Inc., Tustin, CA, for the provision of PGN635 antibody. This work was supported in part by DOD W81XWH-08-1-0583, DOD W81XWH-12-1-0317 and by the Meredith D. Chesler Foundation, Dallas, TX. Imaging was conducted by DOE grant #DE-FG02-05CH11280 and NIH BTRP # P41-RR02584.

Disclosure of author financial interest or relationships:
D. Zhao, None; **H. Zhou**, None; **N.V. Slavine**, None; **J.H. Stafford**, None; **P.E. Thorpe**, Peregrine Pharmaceuticals, Grant/research support; Peregrine Pharmaceuticals, Consultant; Peregrine Pharmaceuticals, Stockholder .

Presentation Number **P 592**
Poster Session 4
September 21, 2013 / 14:45-14:45 / Room: Exhibit Hall B

Non-invasive Quantitative Detection of Transferrin Receptor-mediated Internalization in Breast Cancer Cells using In Vivo NIR FRET Imaging

Lingling Zhao[1], *Ken Abe*[2], *Margarida Barroso*[2], *Xavier Intes*[1], [1]*Department of Biomedical Engineering, Rensselaer Polytechnic Institute, Troy, NY, USA;* [2]*Center for Cardiovascular Sciences, Albany Medical College, Albany, NY, USA. Contact e-mail: linglingzhao0121@gmail.com*

Introduction: Current tumor targeting strategies use existing proteins that show efficient cellular uptake at a targeted pathological site via receptor-mediated endocytosis. However, it is challenging to validate the efficiency of tumor targeting strategies in vivo due to the enhanced permeability and retention effect. The standard method to monitor whether internalization has actually occurred is via invasive and destructive biochemical in vitro analysis. To overcome this critical issue, we developed a novel near infrared Förster resonance energy transfer fluorescence lifetime imaging (NIR FRET FLIM) technique with wide-field illumination strategies. Herein, we employed NIR FRET FLIM to validate and characterize cellular uptake of transferrin (Tfn) in both cancer cells and normal cells in vitro and in vivo. Methods: Tfn has been used as a target in targeted delivery systems to carry anti-cancer drugs into cancer cells. The NIR FRET FLIM takes advantage of the dimeric nature of Tfn receptors to quantify the internalization by determining FRET between receptor-bound Tfn NIR donor and acceptor, based on the reduction of donor lifetime. We have selected a NIR FRET pair (Donor: Alexa Fluor 700 conjugated to Tfn, Acceptor: Alexa Fluor 750 conjugated to Tfn) based on its brightness, stability and lifetime contrast. T47D cells and HMEC were plated onto a 96-well plate and various acceptor: donor (A: D) ratios were internalized at 37oC for 1h. These cells were subjected to in vitro NIR FRET FLIM to determine the presence of FRET and to quantify the quenched donor fraction, which is an indicator of cellular internalization. Cancer cells exposed to Donor and Acceptor were fixed and resuspended in a Matrigel substrate for implantation in mice to establish the potential of in vivo NIR FRET FLIM. Results: The quenched donor fractions estimated in vitro increased linearly as the A: D ratios increased, demonstrating that we can detect and quantify Tfn binding and uptake into cancer cells using NIR FRET FLIM. Moreover, the NIR FRET FLIM data were successfully benchmarked with established microscopy spectral FRET analysis. Furthermore, similar results were obtained for the in vivo studies. Accurate quantification of the quenched donor fraction was achieved in vivo in agreement with the in vitro studies. These results validated our method as a non-invasive and quantitative method to quantify internalization of Tfn within live small animals. Conclusion: This work addresses one of the major problems in tumor targeting therapy development and optimization. The technique and methodology reported herein allows quantitatively determining the amount of molecules undergoing internalization and estimating the amount of the drug accumulating in the extracellular space and the amount internalized by tumor cells. This work, for the first time, establishes in vivo NIR FRET imaging in a relevant physiological system overcoming the limitation of penetration caused by visible FRET pairs. This work also provides the foundation for seamless translation from in vitro FRET assays to in vivo FRET studies in pre-clinical settings and potentially for clinical applications.

Disclosure of author financial interest or relationships:
L. Zhao, None; **K. Abe**, None; **M. Barroso**, None; **X. Intes**, None.

Presentation Number **P 593**
Poster Session 4
September 21, 2013 / 14:45-14:45 / Room: Exhibit Hall B

A Maximum A Posteriori (MAP) Algorithm for Estimating Blood Input Function and Myocardial Time Activity Curves in Dynamic SPECT

Mahmoud Abdalah[1], *Rostyslav Boutchko*[2], *Debasis Mitra*[1], *Chen Shi*[1], *Grant T. Gullberg*[2], [1]*Computer Science, Florida Institute of Technology, Melbourne, FL, USA;* [2]*Radiotracer Development and Imaging Technologies, Lawrence Berkeley National Laboratory, Berkeley, CA, USA. Contact e-mail: mabdalah2009@my.fit.edu*

INTRODUCTION The estimation of blood input function and tissues' time activity curves is essential for kinetic analysis in dynamic SPECT. In this work, we propose a Maximum A Posteriori algorithm (MAP) for estimating blood function and myocardial time activity curves from a very limited number of projections of acquired dynamic SPECT data. The algorithm was tested and validated against a numerically simulated dataset. The same method of TAC recovery is now applied to pinhole SPECT study of perfusion and innervation in a rat model. METHODS First, the problem was modeled using Factor Analysis of Dynamic Structures (FADS) technique. Then, a Maximum A Posteriori (MAP) algorithm was derived to solve the problem of estimating the temporal factors and their spatial coefficients. Dynamic SPECT problem is severally under-determined problem. Therefore, the algorithm imposes a number of constraints and regularization functions. Furthermore, the focus of this work is only to extract blood input function and myocardial time activity curves. The algorithm is designed to apply the proper regularization and constraints to the relevant regions of interest by incorporating a segmented reconstructed volume of the summed projections of the consistent later acquisitions of the dynamic data. In addition to the regularization application, the algorithm dynamically predicts and updates the value of each regularization parameter by keeping track of the noise level at each iteration. The MAP technique has some advantages for this problem over other techniques such as gradient search. For example, non-negativity constraint is implicitly embedded in the MAP algorithm. Imposing such a simple constraint can be very problematic in gradient search techniques, especially when the algorithm is searching or minimizing for two unknowns at the same time. Moreover, the MAP algorithm is much faster because it requires fewer matrix multiplications at each iteration. RESULTS To validate the algorithm, the method was tested on numerically generated datasets. Dynamic projections/sinogram was generated using the NCAT phantom and a set of chosen curves (blood and myocardium). The curves were generated using a two-compartment model to simulate the physiological activity of the tracer in blood and myocardium. After generating the dynamic sinogram, Poisson noise was added using the ImageJ tool. After running the method with the corrupted data with Poisson noise, the algorithm was able to recover those curves close to the original ones even with noisy and severely limited amount of input data.

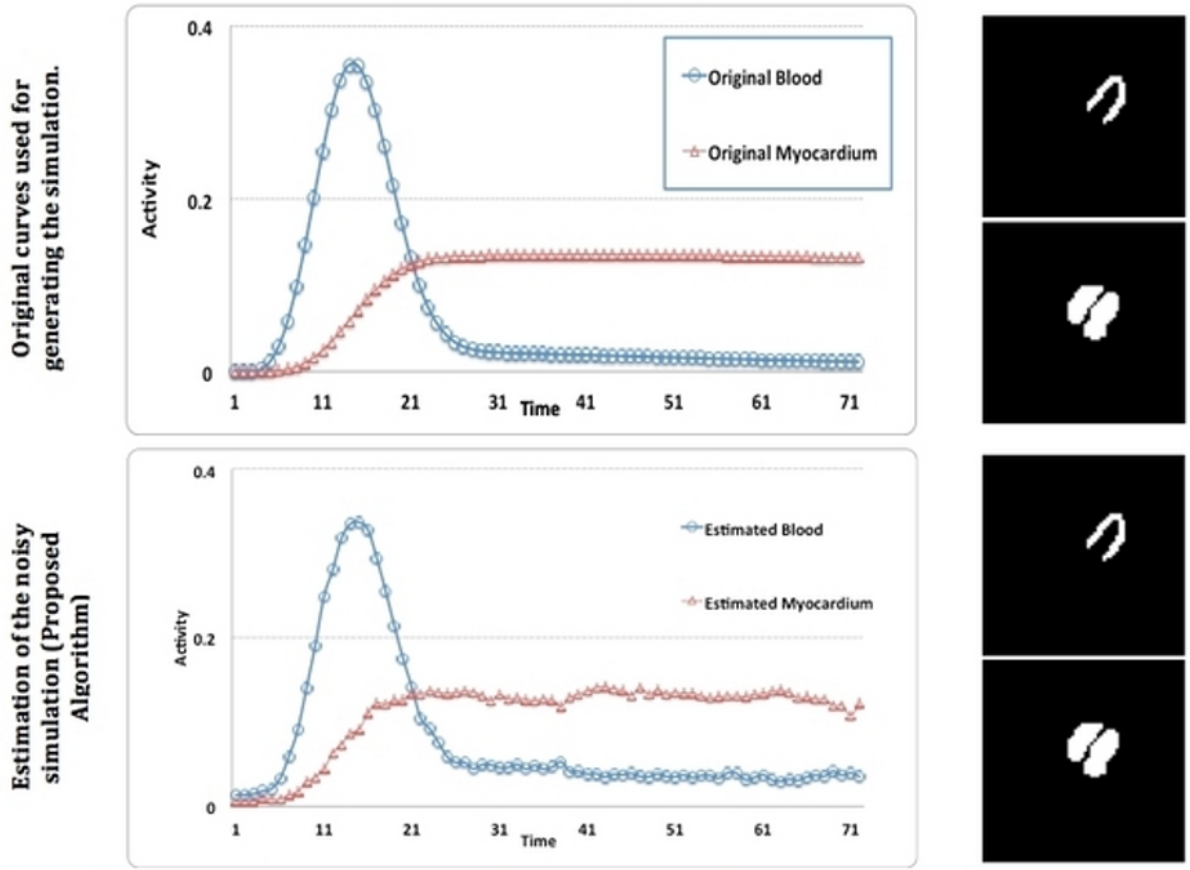

Curves: blood input function (blue) and myocardium time activity curve (red). Segmented image helped significantly to remove the spurious noise.

Coefficients of the curves.

Disclosure of author financial interest or relationships:
M. Abdalah, None; **R. Boutchko**, None; **D. Mitra**, None; **C. Shi**, None; **G.T. Gullberg**, None.

Presentation Number **P 594**
Poster Session 4
September 21, 2013 / 14:45-14:45 / Room: Exhibit Hall B

Characterization of Liver and Gallbladder Diseases Using Tracer Kinetics

Katuputhur Narayanan Srinivasan[1], Uma S. Ranjan[2], Sumana Srivatsa[3], **Smruthy Sivakumar**[3]*, Pooja Bhat[3], [1]G V N Institute of Oncology, Trichy, India; [2]Philips Electronics, Bangalore, India; [3]PESIT, Bangalore, India. Contact e-mail: smruthy90@gmail.com*

Biliary atresia, a common condition in infants and young children, can often lead to permanent liver damage if not treated correctly. The options for treatment of biliary atresia include stenting and /or a liver transplant. Even after a stenting, it is necessary to follow up the affected child to ensure that the liver is functioning well. A dynamic nuclear medicine scan with Tc99m-IDA is usually performed to determine the presence or absence of biliary atresia. In cases of mild atresia or where other complications like liver damage co-exist, qualitative view of the flow can be misleading, thereby leading to further damage. A quantitative measure of the effect of various factors affecting the liver and gall bladder is therefore necessary to determine an appropriate course of treatment. In the present work, we introduce a 3-compartment model to characterize the parameters related to liver functioning. While such models have been attempted earlier, the small volume of bile duct and gall bladder, especially in small children, has limited the numerical stability of the procedure. A crucial component of the model is the flow of bile between the common bile duct and gall bladder. In this work, we have overcome this limitation by splitting the model into two connected models - one involving the liver and the gall bladder and the second involving the liver and the common bile duct. In this work, we present the results of the first sub-system viz. the liver-gall bladder sub-system and its effectiveness in diagnosing and quantifying biliary atresia. The time activity curves from the Heart, Liver, common bile duct (CBD) and Gallbladder (GB) were fitted to a single input-three compartment model to compute the extraction and excretion efficiencies governing the overall functioning of the system under consideration. The method of least squares was used to estimate the kinetic parameters - k1 (between the Heart and the Liver), k2 and k3 (between the Liver and the CBD and k4 (between the Liver and Gallbladder). Dynamic HIDA scans were collected from 13 patients with varied clinical conditions including Liver Cirrhosis, Biliary Atresia, Cholestasis and Cholelithiasis. The transportation rates between Heart and Liver (k1) and between Liver and Gallbladder (k4) were significantly altered in Liver and Gallbladder associated diseases proving to be a good indicator of the severity of the conditions. The kinetic parameter k1 correlated well with cases showing a blockage such as Biliary Atresia and Cholecystisis. The negative value obtained in these patients may be attributed to the immediate saturation of the tracer in the Liver, which prevents further uptake of the tracer by Liver. On the other hand, in case of cirrhosis, due to lack of uptake of the tracer by the Liver, a low positive k1 was obtained in comparison to a negative value obtained for patients with blockages. In a patient with stenting a negative k1 value was observed which could be attributed to inadequate stenting. Therefore, k1 was used to characterize quantitative the extent of atresia and/or cirrhosis from normal patients.

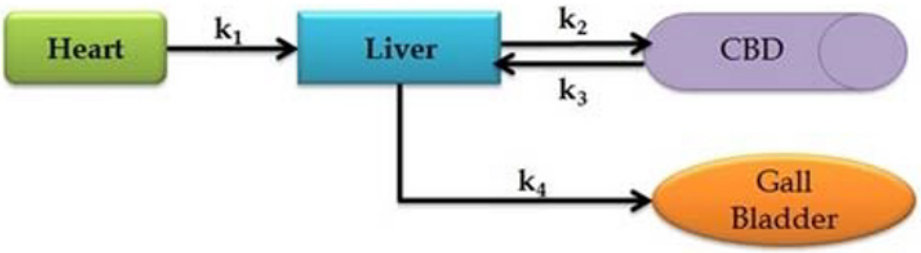

Single input - three compartment model

Disclosure of author financial interest or relationships:
K. Srinivasan, None; **U.S. Ranjan**, None; **S. Srivatsa**, None; **S. Sivakumar**, None; **P. Bhat**, None.

Presentation Number **P 595**
Poster Session 4
September 21, 2013 / 14:45-14:45 / Room: Exhibit Hall B

Reconstruction of freehand PET examinations

Aron Cserkaszky[1], *Benjamin Frisch*[2], *Milan Zvolsky*[3], *Giacomo Cucciati*[4], [1]*Technische Universität München, München, Germany;* [2]*CERN, Geneva, Switzerland;* [3]*DESY, Hamburg, Germany;* [4]*Milano-Bicocca, Milano, Italy. Contact e-mail: cserkaszky@yahoo.co.uk*

Purpose: Positron Emission Tomography (PET) is a leading diagnostic tool for numerous diseases. Extending its applications beyond the nowadays common gantry based PET scanners will allow for novel diagnostic methods to be discovered. In this work we present the freehand PET scanning approach and the challenges and a possible solution to reconstruct such unstructured PET data. In the freehand PET scenario the scanner consists of at least 2 coincidence coupled detector panels of arbitrary size. These detectors are moved freely during the acquisition in such way, that the line of responses (LOR) cross the volume of interest (VOI). An example to this approach is the EndoTOFPET-US project, where one detector matrix is attached to an endoscope and placed near the prostate or the pancreas inside the patient, while the other detector matrix is outside and placed adjacent to the patient's skin surface. During the acquisition the position of the detectors and the detected coincidences are collected in a time synchronized manner. Method: The reconstruction of such unstructured data is non trivial: assuming continuous motion of the detectors in the EndoTOFPET-US scenario leads to 2-7*10^7 possible unique LORs per second, which creates an unfeasibly large dataset. To solve this problem, we developed a method that structures the measurements by introducing virtual detector pixels around the VOI and remapping the actual LORs into the virtual LORs. A general way to construct the virtual pixels is to take a sphere around the VOI and map its surface by the Euler angles into surface segments, with sufficient resolution in the angles. Contrary to the 2D case, where the sinogram can represent a LOR with 2 variables (α, t), in 3D we need 4 [2d-2] variables, the 2 Euler angles for the entry and exit of the LOR to the sphere in this case. The virtual LORs, constructed by the virtual pixels, accumulate the number of detected counts and the total time when an actual LOR was corresponding to the virtual LOR. Taking into account this time is very important since the freehand scanning guarantees a very inhomogeneous sensitivity. In the reconstruction we can correct for this effect by adding time weights to the rows of the system matrix. Results: We tested and compared the freehand PET reconstruction to the usual reconstruction algorithms, with GATE simulated datasets, that contained only 8 detector poses around the VOI to allow for the efficient run of both methods. The cross-correlation error of the resulting images were 0.05% with a 0.1° Euler angle resolution after 10 iterations. The total runtime of the freehand reconstruction was 9% higher. Conclusions: The proposed method allows novel scanning geometries and possibly intraoperative applications by making fewer assumptions than the state of the art methods, while providing the same image quality.

Disclosure of author financial interest or relationships:
A. Cserkaszky, SurgicEye Gmbh., Employment; **B. Frisch**, None; **M. Zvolsky**, None; **G. Cucciati**, None.

Presentation Number **P 596**
Poster Session 4
September 21, 2013 / 14:45-14:45 / Room: Exhibit Hall B

Biopsy Guided by Molecular Breast Imaging (MBI)

James W. Hugg[1], *Rochelle Keen*[1], *David Beylin*[2], *Edward Anashkin*[2], *Eileen Millsap*[1], *Ronald Moore*[1], [1]*Research, Gamma Medica, Inc., Northridge, CA, USA;* [2]*Research, BLN Scientific, Inc., Bethesda, MD, USA. Contact e-mail: james.hugg@gammamedica.com*

Objectives: Molecular Breast Imaging (MBI) uses planar imaging with single gamma photon emission from an intravenous radiopharmaceutical, such as Tc99m-sestamibi or tetrofosmin, to visualize breast cancers that are often occult on mammography in the 40-50% of women (up to 70% of Asian women) with radiographically dense breasts. Mayo Clinic has reported successful dense-breast MBI screening trials using only 4-8 mCi of Tc99m-sestamibi (off-label), with a low whole-body dose approaching that of screening mammography. Our purpose was to provide and clinically validate MBI-guided biopsy capability for the ~15% of cases when an MBI-detected lesion is occult on ultrasound and mammography. Such lesions would previously go to MRI-guided biopsy, a more expensive and time-consuming procedure. Methods: MBI consists of a pair of opposed semiconductor (CZT, Cadmium Zinc Telluride) gamma photon cameras that mildly compress each breast between them in standard planar mammographic views. For 3D Cartesian (xyz) lesion targeting we also use a third small orthogonal CZT camera positioned between the two MBI cameras. A stereotactic needle guide provides lateral access between the two MBI cameras for hub-to-hub insertion of the biopsy sampling device parallel to the chest wall. The needle track is verified by imaging a rod source (typically Co57) prior to tissue sampling. MBI imaging of the biopsy sampled cavity and excised tissue samples provides verification of adequate sampling and guidance for histopathology analysis. Results: Laboratory testing with a point source and with breast simulating sponge phantoms containing Tc99m-labeled frozen gelatin lesions demonstrate that MBI is capable of guiding the biopsy sampling needle to within less than 4 mm of the target lesion. Measurements with a breast lesion phantom containing spherical chambers ranging from 3 to 10 mm in diameter enable determination of lesion contrast-recovery curves to characterize the performance of the MBI system. The biopsy guidance accessory is capable of targeting and sampling lesions throughout the breast. The setup and MBI-guidance procedure are simple and quick. In ongoing multi-site clinical tests, the trade-off of dose and procedure time is being optimized. We will present initial clinical cases to characterize the performance of the accessory and procedure. Conclusions: A simple and effective MBI-guided biopsy accessory has been built and tested in both the laboratory and clinic and is pending FDA 510(k) clearance. Along with the prior demonstration of low-dose dense-breast MBI screening in pilot studies, the next step toward FDA clearance for adjunctive MBI screening will be multi-center trials. Research Support: NIH National Cancer Institute grants R42-CA128407 and R44-CA143716; patent pending.

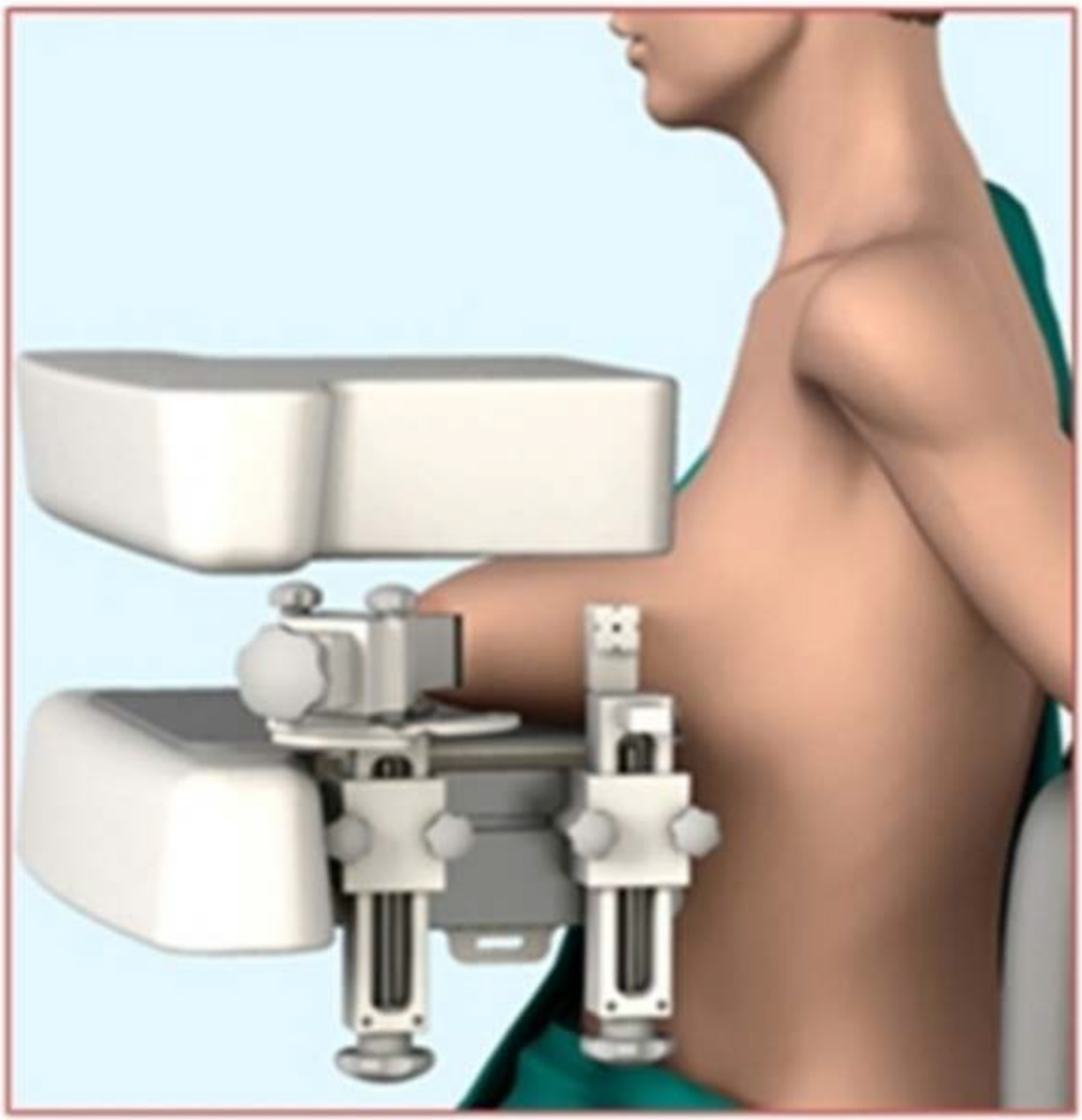

MBI-guided biopsy accessory: two CZT gamma cameras mildly compress the breast and determine xy position of MBI-detected lesion; CZT-targeting camera on left points toward MBI-detected lesion and determines z position of lesion; computer determines appropriate 3D xyz position of needle guide on right to guide biopsy needle to lesion.

Disclosure of author financial interest or relationships:
J.W. Hugg, Gamma Medica, Employment; Gamma Medica, Stockholder; **R. Keen**, Gamma Medica, Employment; **D. Beylin**, Gamma Medica, Inc., Consultant; **E. Anashkin**, Gamma Medica, Inc, Consultant; Weinberg Medical Physics, LLC, Consultant; **E. Millsap**, Gamma Medica, Employment; **R. Moore**, None.

Presentation Number **P 597**
Poster Session 4
September 21, 2013 / 14:45-14:45 / Room: Exhibit Hall B

Integration of a PSPMT/APD depth-encoding PET detector with a high-performance PET data acquisition system

Buddika Sumanasena[1], *Qiyu Peng*[2], *Felipe Godinez*[1], *Abhijit J. Chaudhari*[1], *Bill Moses*[2], *Ramsey D. Badawi*[1], [1]*Department of Radiology, University of California, Davis, Sacramento, CA, USA;* [2]*Lawrence Berkeley Lab, , Berkeley, CA, USA. Contact e-mail: bsumanasena@ucdavis.edu*

Poor spatial resolution, signal loss due to attenuation within the body, and poor sensitivity introduce limitations to using whole body PET scanners for imaging breasts and extremities - addressed by designing dedicated scanners optimized for those parts. Sensitivity and spatial resolution can be improved by scanners with smaller ring diameters. However, in these systems parallax errors reduce the resolution of the scanner towards the periphery of the field of view. If the depth at which the photon interacted with the crystal (depth of interaction or DOI) is known these parallax errors can be corrected. We developed a detector with hybrid readout for estimating DOI (1), but that implementation involved benchtop NIM electronics. The detector consists of an avalanche photodiode (APD) and a position sensitive photo-multiplier tube (PSPMT) coupled to either end of a 14×14 element array of unpolished 1.5 mm pitch, 20 mm thick lutetium orthosilicate (LSO) scintillation crystals, separated by 50 micron thick diffuse reflector material. NIM electronics is not scalable for a scanner with a large number of detectors. In this work we integrated the hybrid detector with the commercial Cardinal electronics suite which is suitable for data acquisition from a large number of detectors. The 4 position encoding signals from the PSPMT were read by Cardinal, but the electronics was not suitable for directly processing APD signals. Circuitry was designed to shape APD pulses to pulse-durations suitable for acquisition by Cardinal electronics. Let the energy of the four position encoding signals read-out from PSPMT be denoted by Ea, Eb, Ec and Ed, and the energy of the signal read-out from the APD be denoted by Eapd. Total energy read-out due to scintillation is E = Ea+Eb +Ec+Ed +KcEapd. The constant Kc accounts for the different gains of the two detectors and light propagation characteristics of individual crystals. It was evaluated for each crystal. The ratio D = KcEapd/E was used to estimate the DOI. DOI resolution of the hybrid detector was evaluated using the experimental setup shown in the figure (b). Acquisition of data was triggered by the single channel photo multiplier tube (SCPMT) coupled to a 0.6×20×30mm^3 LSO slab. Signals were acquired using the raw data acquisition mode of the Cardinal electronics. Starting at 2mm from the PSPMT-array data were acquired at 9 positions equally spaced by 2mm. The plot of the distribution of DOI ratios at a given depth versus depth was fitted to a straight line for each crystal. Interception Kic and slope Kgc of the linear plot thus obtained for each crystal was used to compute DOI. The mean FWHM DOI resolution computed over all depths and all crystals was 1.86mm. Mean FWHM energy resolution taken over all depths and all crystals was 17.0%. Using Cardinal electronics the detector provided satisfactory DOI and energy resolution for extremity or breast imaging. To the best of our knowledge, this is the first demonstration of read-out of a depth-encoding hybrid detector using the scalable Cardinal electronics suite. Refs:(1) Godinez F et al 2012 Phys. Med. Biol.57 (3435 3449), Research Support: NCI R01CA129561

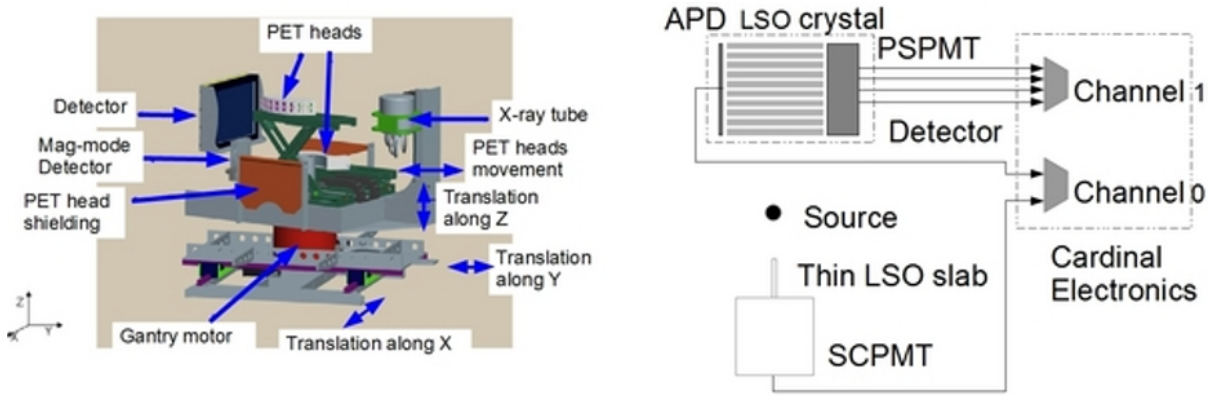

(a) PET/CT Scanner Gantry (b) Detector and the setup for DOI resolution evaluation

Disclosure of author financial interest or relationships:
B. Sumanasena, None; **Q. Peng**, None; **F. Godinez**, None; **A.J. Chaudhari**, None; **B. Moses**, None; **R.D. Badawi**, Philips Medical, Grant/research support; Toshiba Medical, Consultant; JNJ, Stockholder .

Presentation Number **P 598**
Poster Session 4
September 21, 2013 / 14:45-14:45 / Room: Exhibit Hall B

Simultaneous scanning of two mice in the Inveon small animal PET scanner: a quantitative assessment using experimental and simulated data

Frederic Boisson[1], Catriona J. Wimberley[2,1], David Zahra[1], Hasar Hamze[1], Marie-Claude Gregoire[1], Anthonin Reilhac[1], **Arvind Parmar**[1], [1]*LifeSciences, ANSTO, Kirrawee DC, NSW, Australia;* [2]*Brain and Mind Research Institute, University of Sydney, Sydney, NSW, Australia. Contact e-mail: arvind.parmar@ansto.gov.au*

Recently, some research groups have been investigating the feasibility of imaging several animals simultaneously in PET with the ultimate goal of increasing the throughput and reducing the cost of preclinical studies. However, simultaneous scanning of several animals lead to degraded imaging performance such as reduced signal to noise ratio caused by increased attenuation, scatter, randoms and dead-time, reduced spatial resolution and sensitivity due to the off-centre positioning of the animals. In the present study we assessed the feasibility of imaging two mice simultaneously using the Inveon small-animal PET scanner and determine the loss in statistical power induced by the performance degradation when 2 animals are present in the FOV. An Ultra-micro Derenzo phantom and the NU-4 Image Quality phantom were first imaged in both single and dual-mode acquisitions in order to evaluate performance degradation such as spatial resolution and statistical noise but also in order to assess the performance of data correction methods when 2 animals are present. This study was then followed by simulated biological study in mice, consisting of 4 groups of 8 replicates each of [^{11}C]Raclopride images with different Binding Potentials (BPs) in the striata was simulated using the PET-SORTEO Monte Carlo-based simulator recently validated for the Inveon system. The 4 groups (1 control group and 3 groups) shared the same true spatio-temporal activity distribution except for the striata where the employed TACs corresponded to increases of +5%, 10% and +30% (grp5%, grp10% and grp30%) of the corresponding BP from the control group (ctrl). Each simulation was performed twice: in single mouse mode where the mouse was centered in the FOV and in dual mice mode. The reference TACs used as input for the simulations were generated for tracer dose using the classical two-tissue compartment, five parameter model. Kinetic parameter values for the control group were taken from a study of [^{11}C]Raclopride in the rodent brain and from in vitro constants (Ross et al). Each simulated scan was histogrammed into 20 frames (10×1min, 10×5min) and reconstructed using FBP2D with all corrections applied. [^{11}C]Raclopride BP parametric map was then generated from each reconstructed dynamic image using the simplified reference tissue model (cerebellum). F-value and p-value (pFDR corrected) maps between each of the 3 groups with increased BP and the control group simulated in single and in dual mode settings were generated using R and RMINC. Results using actual phantom acquisitions showed that the data correction performed well in dual-mode acquisition. As expected, the off-centre positioning of each animal in dual mode setting lead to a decrease of the spatial resolution. More importantly, the simulated biological study showed that the performance degradation caused by the presence of 2 animal in the FOV induced an important loss of statistical power: see the F- and p-value (mean value for striata region) as a function of the simulated variation and for the single and dual mice mode.

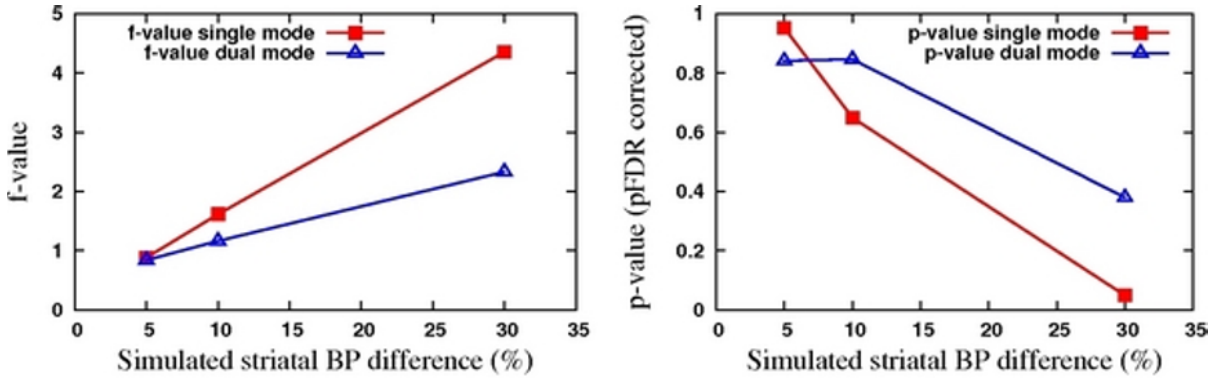

Figure1: F- and p-value (mean value for striata region) as a function of the simulated variation and for the single and dual mice mode.

Disclosure of author financial interest or relationships:

F. Boisson, None; **C.J. Wimberley**, None; **D. Zahra**, None; **H. Hamze**, None; **M. Gregoire**, None; **A. Reilhac**, None; **A. Parmar**, None.

Presentation Number **P 599**
Poster Session 4
September 21, 2013 / 14:45-14:45 / Room: Exhibit Hall B

An Automatic Synthesis Apparatus for Production of [68Ga] DOTA-peptide for PET

Hsin-Han Hsieh, *Ming-Hsin Li, Isotope Application, Institute of Nuclear Energy Research, Taoyuan, Taiwan. Contact e-mail: hsinhan@iner.gov.tw*

Objectives: An automatic synthesis apparatus is one of the most important technology to produce of [68Ga] DOTATATE for Positron emission tomography (PET), because it provides a fully automatic controlled system, employed for the synthesis of [68Ga] DOTATATE (1,4,7,10- tetraazacyclododecane-1,4,7,10- tetraacetic acid) which is mainly used for the diagnosis of tumor in brain and neuroendocrinology, granulomatous lymphomatosis and cancer of lung, breast and prostate. To meet the needs created by the rapid development of positron tomographic techniques, an automatic synthesis apparatus has been developed. Methods: Main procedures of the process include: (1) inject of [68Ga] ion; (2) oxidation reaction; (3) quench and neutralization with NaHCO3; (4) separation and collection. In easy terms, the actual operation procedures of this system can be divided into three steps. First, put the raw material into designed reaction bottle, afterward, turn on power button and run the executive program. Twenty minutes after this program is started, [68Ga] DOTATATE can be produced for clinical applications. Results: The automatic synthesis apparatus application of Ge-68/Ga-68 generator has been to produce medical radioisotopes as well as radiopharmaceuticals. 68Ga is an artificial radioisotope with half-life of 68 minutes and known to be incorporated into newly synthesized proteins, rendering it a potentially suitable tracer to image protein metabolism in vivo using PET. Conclusions: The automatic synthesis system at INER was used mainly for diagnostic purposes, such as DOTA-peptide labeling and so on. Moreover, other related radiopharmaceuticals will be explored and developed continuously

Disclosure of author financial interest or relationships:
H. Hsieh, None; **M. Li**, None.

Presentation Number **P 600**
Poster Session 4
September 21, 2013 / 14:45-14:45 / Room: Exhibit Hall B

Model-free analysis of PET and SPECT tracer kinetics in the isolated perfused rat heart using a hybrid maximum entropy method /non-linear least square algorithm

Erika Mariotti[1], *Joel T. Dunn*[1], *Rodolfo Medina*[1], *Zaitulhusna Md Safee*[1], *Maxwell G. Handley*[1], *Fiona Shaughnessy*[1], *Phil Blower*[1], *Thomas R. Eykyn*[1,2], *Richard Southworth*[1], [1]*Imaging Sciences and Biomedical Engineering, King's College London, London, United Kingdom;* [2]*Cancer Research UK and EPSRC Cancer Imaging Centre, Royal Marsden NHS Trust and The Institute of Cancer Research, Sutton, United Kingdom. Contact e-mail: erika.mariotti@kcl.ac.uk*

Introduction: Multi-compartmental modelling and spectral analysis are the most common approaches used in PET and SPECT to characterise tracer uptake, transport and clearance[1]. These methods require a priori assumption of the number of compartments involved in tracer kinetics or are limited to time-radioactivity curves with a positive second derivative[2]. We present a new method based on a hybrid Maximum Entropy/Non Linear Least Squares method[3] (MEM/NLS) for pharmacokinetic analysis of PET and SPECT tracers in the perfused rat heart that does not have any limitation on the type of time-radioactivity curve analysed and does not require any a priori assumption of the number of the kinetic rates. Methods: Monte Carlo Simulations: Ex vivo time-radioactivity curves were simulated using Eq. 1 (n=1000) with a time resolution $\Delta t=3$ ms., $f(t) = \Sigma i=1,k\ AiCm(t)*exp(-rit)$ (Eq.1) where k is the number of kinetic rates (k=1,2,3), Cm(t) is the blood input function and Ai is the characteristic amplitude of the rate ri and * is the convolution operator. Four different values were chosen for each rate ri (min-1) and seven different signal to noise ratios ($3<SNR<21$) were studied. Experimental datasets: A bolus (1 MBq in 100 µl KHB) of 64Cu-ATSM, 18FDG or 99mTc-Sestamibi was injected into the arterial line perfusing isolated rat hearts (n=4 for each tracer). The tracer accumulation in each heart was monitored during normoxia, and after 5 and 20 minutes anoxia ($\Delta t=3$ms). Data were fitted using the MEM/NLS algorithm [3]. Using this approach, the number of components characterising the data was determined iteratively, using the MEM fitting results as input parameters for NLS. Statistical analysis was performed using a two sample t-test. Datasets were simulated using a custom-made Matlab (MathWorks®) code. Results: Monte Carlo simulations showed that the hybrid MEM/NLS algorithm was able to derive the correct number of rates and to accurately estimate their value regardless of SNR studied (Fig.1). Three rates were identified for 18FDG and 99mTc-Sestamibi ex vivo time-radioactivity curves, whereas only two were derived from the 64Cu-ATSM curves. A number of significant differences were found for the rates and their amplitudes between normoxia and hypoxia in all three tracers studied. Conclusions: We demonstrate that the hybrid MEM/NLS method accurately quantified the kinetics of PET and SPECT tracers, enabling the distinction of the rate constants responsible for their retention or washout without a priori assumptions of what the rates might be. We also describe how these rates change during tissue hypoxia. This approach exhibits the potential to provide new insight into the trapping mechanisms of a variety of tracers which are currently poorly understood, like 64Cu-ATSM, or gain more detailed biological information from pharmacokinetics of established tracers, such as distinguishing trans-capillary transport from cellular transport for 18FDG, which we demonstrate here. References: 1.Cunningham et al., Journal of cerebral blood flow and metabolism 13, 15-23 (1993). 3. Steinbach et al., Biophysical journal 82, 2244-2255 (2002)

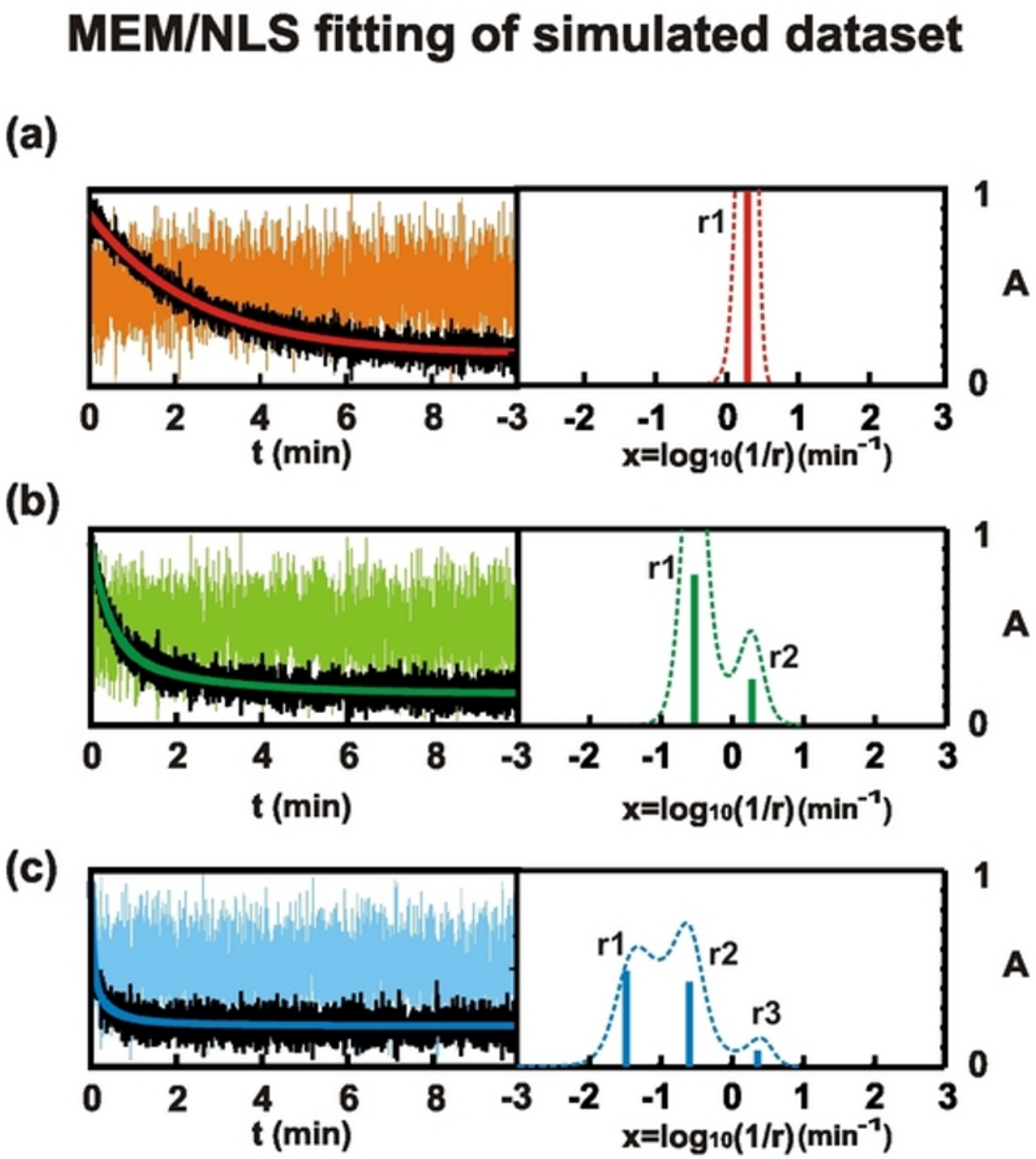

Figure 1: Representative results (SNR = 12) from the hybrid MEM/NLS fit of simulated datasets. Simulated data (black) are shown on the left with overlaid fits (red, blue and green). Residuals from the fitting are shown in the same window. MEM (dotted lines) and MEM/NLS (continuous lines) results for (a) mono- (b) bi- and (c) tri-exponential time-radioactivity curves.

Disclosure of author financial interest or relationships:
E. Mariotti, None; **J.T. Dunn**, None; **R. Medina**, None; **Z. Md Safee**, None; **M.G. Handley**, None; **F. Shaughnessy**, None; **P. Blower**, None; **T.R. Eykyn**, None; **R. Southworth**, None.

Presentation Number **P 601**
Poster Session 4
September 21, 2013 / 14:45-14:45 / Room: Exhibit Hall B

A Data Management System with Web Interface for Pre-clinical Multi-modality Imaging: ReMI

Debasis Mitra[1,2], *Hui Pan*[1], *Mahmoud Abdalah*[1], *Rostyslav Butchko*[2], *Grant T. Gullberg*[2], *Martin S. Boswell*[2], [1]*Computer Science, Florida Institute of Technology, Melbourne, FL, USA;* [2]*Radiotracer Development & Imaging. Life Sc. Div., Lawrence Berkeley National Laboratory, Berkeley, CA, USA. Contact e-mail: dmitra@cs.fit.edu*

Objectives: Molecular imaging research is an inter-disciplinary activity, where expertise may be distributed over multiple geo-locations. A well-designed database with web-access is very useful for this purpose. We are designing a database for pre-clinical imaging research in order to prevent data loss or corruption, and to enable re-use of the same data in different research projects while data may grow dynamically. Our e-science project is comparable to the ADNI database but we also archive raw scan data (anonymous for human). Methods: A generic and flexible architecture is being developed for the above purpose. The principal information about each imaging experiment was organized over multi-field meta-data (information about data). Well managed meta-data is a key to the reusability of any experimental data. A relational database (RDB) stores the metadata. It points to, as well as manages a file archive on a large server storing the experimental data. Typically experimental data are binary images and very large in size, but could be of any other types, e.g. source code. Results: A scalable model-view-controller architecture is used for integrating the system with a web-based GUI. The main meta-data fields in the RDB are: imaging modality, specific experiment's details (e.g. date), imaging subject data, instrumentation detail, and scan-specific protocol parameters. Currently available database entries include human, canine, and rodent SPECT-CT studies, microPET/CT studies, and diffusion tensor MRI data acquired both by our group and by our collaborators. Validation: The database ReMI (Research in Medical Imaging) is accessible at http://remi.lbl.gov, is being populated with data that can be shared within the community, and is ready to add new users and contributors. Current contributions of data are from Lawrence Berkeley National Lab, and Univ. of California, San Francisco. Two additional groups outside these labs, one from Shanghai, China and another from Florida, USA are using the data for cardiac dynamic imaging research. The architecture developed for ReMI [Figure 1] may be easily adapted and re-used in any similar projects for different types of scientific experiments. A clone of the database may be accessed at http://163.118.75.177:3000 with (guest-guest account-password), where all meta-data is similar to the actual database ReMI, but without the pointers to the actual data files as in the later. Conclusion: ReMI is fully functional now. (1) However, entering meta-data is a tedious and error prone process. Even though some amount of user-personalization is available currently, we would like to automatically extract as much meta-data as possible from relevant files by borrowing techniques from artificial intelligence. (2) A user should be able to quickly sample image data before deciding to go through the computationally expensive downloading process. Efficient online multi-modality image registration capability based on organ-specific atlas may be needed for this purpose. Research Support: NIH: R01 EB007219 and R01 HL60663 Director, & Office of Science, BER/DOE contract DE-AC02-05CH11231.

A Data Management System with Web Interface for Pre-clinical Multi-modality Imaging: ReMI

Image Attached to The Abstract, & referred in supporting document

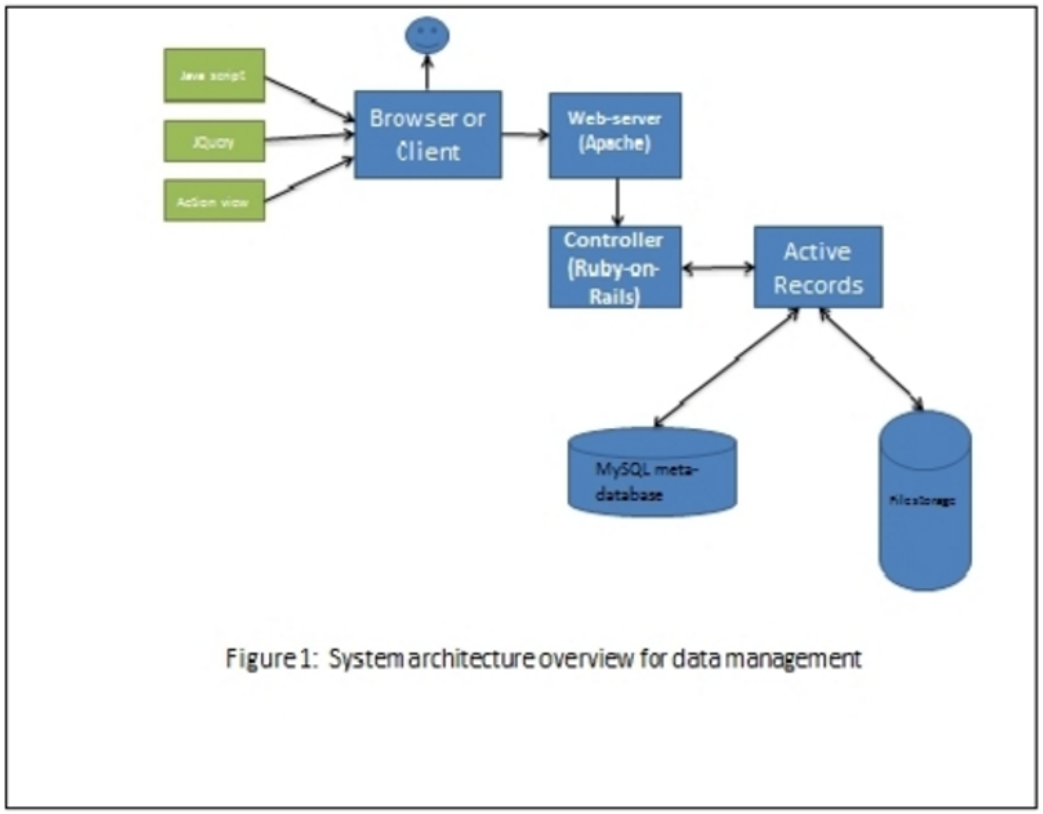

Figure 1: System architecture overview for data management

Authors: Debasis Mitra[1], Hui Pan[1], Mahmoud Abdalah[1], Rostyslav Boutchko[2], Martin Boswell[2], and Grant T. Gullberg[2]

[1]Florida Institute of Technology, [2]Lawrence Berkeley National Laboratory, CA

Disclosure of author financial interest or relationships:
D. Mitra, None; **H. Pan**, None; **M. Abdalah**, None; **R. Butchko**, None; **G.T. Gullberg**, None; **M.S. Boswell**, None.

Presentation Number **P 602**
Poster Session 4
September 21, 2013 / 14:45-14:45 / Room: Exhibit Hall B

Design of a High-Sensitivity, Multiple-Pinhole Scout Tube for MicroSPECT Imaging of Mice with a Conventional Triple-Head Camera

Stephen C. Moore[1,2], *Mi-Ae Park*[1,2], *Dan Xia*[3], *Scott D. Metzler*[3], [1]*Radiology, Brigham & Women's Hospital, Boston, MA, USA;* [2]*Radiology, Harvard Medical School, Boston, MA, USA;* [3]*Radiology, University of Pennsylvania, Philadelphia, PA, USA. Contact e-mail: scmoore@bwh.harvard.edu*

Introduction: We are developing a microSPECT system for targeted organ imaging of mice with <0.3mm reconstructed resolution and excellent sensitivity; the system is being designed as an upgrade for conventional triple-head clinical SPECT scanners. It will consist of two tungsten tubes of different diameter placed end-to-end along the scanner's central axis; each tube will contain many rectangular pinhole apertures. A mouse will be imaged sequentially in the two tubes, with no camera rotation. The first tube provides a whole-body scout image for rapidly locating the primary organ of interest (target). The mouse can then be moved to position the target in the center of the gantry for imaging by the other tube, which contains many more high-resolution (hi-res) pinhole apertures viewing the target region. The scout tube is also used to obtain data from background regions that are also necessary for quantitative reconstruction of the activity distribution within the target region. **Methods:** To obtain high sensitivity, the scout tube will provide a system resolution of 2.4 mm FWHM by all pinholes, whose central axes all point to the center of the gantry. To ensure that the whole mouse can be imaged well over the ~6cm axial range from which the hi-res pinholes can acquire background counts, the mean-squared error (MSE) of voxel activity estimates was minimized over this region by varying the pinhole radial distances, as well as the number and placement of pinholes within the tube, for a fixed detector radial distance of 17.2 cm. We simulated a digital mouse phantom (MOBY^{TM}) containing an organ activity distribution typical for ^{99m}Tc-sestamibi. Central-pinhole radial distances ranging from 4 to 5 cm were evaluated in 2mm increments; for each of these, the distances of the other pinholes from the center of the gantry were adjusted to provide good magnification with minimal spatial multiplexing by adjacent pinholes. Each pinhole size was then adjusted to provide 2.4mm system resolution at the center of the gantry. The axial separation of the two rings of pinholes was chosen so as to image a ~6-cm length of MOBY, with minimal overlapping of projections of the bladder through one pinhole ring and the heart through the other. As a final step to improve angular sampling and further diminish multiplexing, the two aperture rings were shifted with respect to each other in the tangential direction. Bias, precision, and MSE with respect to the simulated activity distribution were computed by quadrature averaging over all voxels, and over 20 independent Poisson noise realizations. **Results:** The central-pinhole radius yielding minimum MSE of whole-body voxel activity estimates was 4.4 cm; the radial distance of individual pinhole apertures ranged from 4.4 to 4.8 cm, respectively, for the central to outermost projections. A total of 30 pinholes (10 per detector) could be accommodated with limited multiplexing. The square pinhole sizes ranged from 1.39 mm (central) to 1.78 mm (outer), providing matched 2.4mm system resolution. The heart position could be easily identified in reconstructions of noisy data, which were of good quality with minimal artifacts.

Disclosure of author financial interest or relationships:
S.C. Moore, None; **M. Park**, None; **D. Xia**, None; **S.D. Metzler**, None.

Presentation Number **P 603**
Poster Session 4
September 21, 2013 / 14:45-14:45 / Room: Exhibit Hall B

Minimum Detectable Activity of a Preclinical PET/MR System

Kalman L. Nagy[1,2], *Judit Lantos*[1], *Péter Major*[1], *Gergely Patay*[1], *Christer Halldin*[2], *Balázs Gulyás*[2], [1]*Mediso ltd, Budapest, Hungary;* [2]*Dept. Clinical Neuroscience, Karolinska Institutet, Stockholm, Sweden. Contact e-mail: kalmanagy@gmail.com*

PET has very high sensitivity enabling imaging at low activity levels, utilized for example in cell trafficking studies or gene expression imaging. However, the widely used Lutetium-based scintillator materials (LSO, LYSO) have intrinsic radioactivity, causing a background signal. System noise and background due to intrinsic activity renders sensitivity at low activity levels into a separate quantity. A useful measure of low activity performance is the minimum detectable activity (MDA). We measured MDA of nanoScan® PET/MRI by Mediso [1]. MDA can be defined as the activity producing a signal 4.65 times the standard deviation of the background [2]. This is not an absolute quantity as it depends on the source distribution. We reproduced the setup of a previous study evaluating three instruments [3] for the sake of comparison. We filled seven wells of a 96 well plate with water and an eighth one with 18F-FDG. ([3] used several activity concentrations in the wells, but evaluated only the one with the highest activity). A scan of over 22 hours was binned into 20 minute frames using the default 400-600 keV energy window and reconstructed using 3D iterative reconstruction without attenuation or scatter correction. ROIs were defined according to [3]. MDA was evaluated by a fit to the signal-to-noise ratio. We also investigated how various reconstruction parameters influence the MDA. Using the well plate phantom, we found a MDA of 70 Bq. The MDA correlates weakly with the voxel volume as it is limited by the structured background signal. The MDA result verifies that the system investigated is suitable for PET applications involving imaging of low activities.

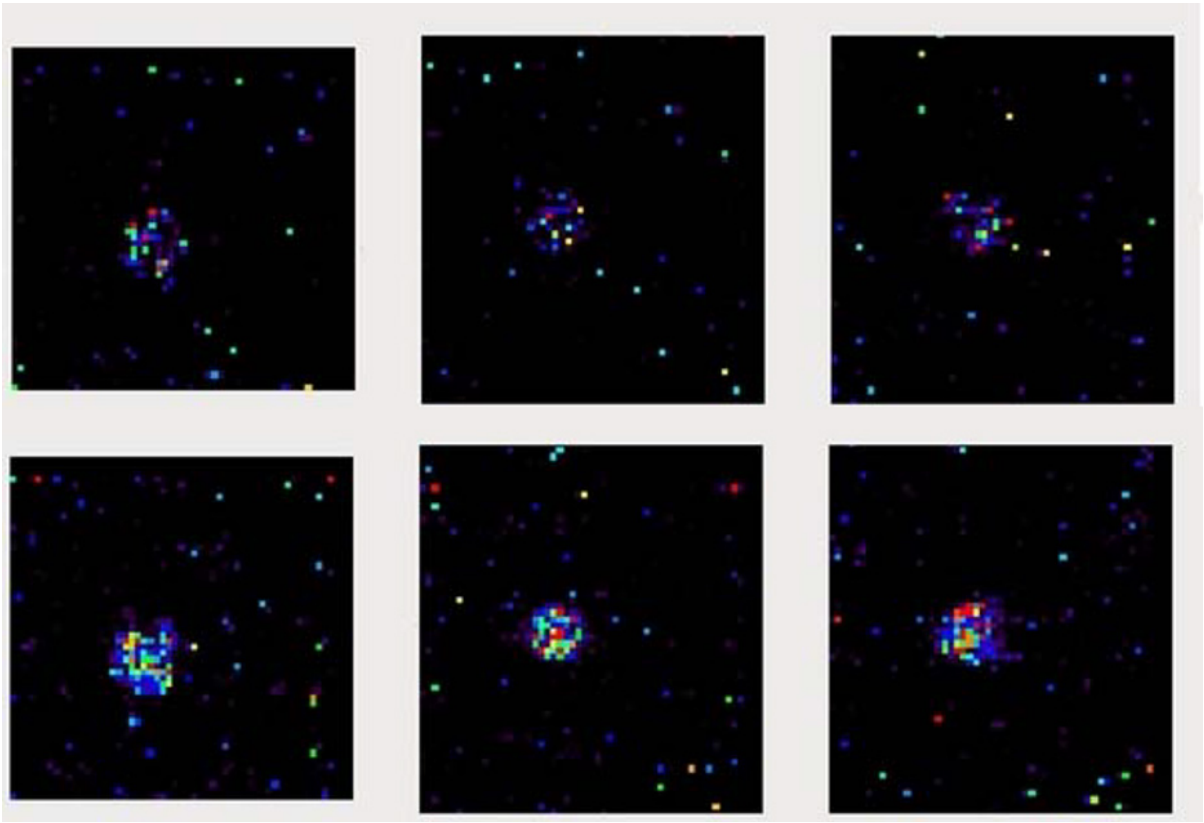

Three orthogonal planes through the sample at 10% below the minimum detectable activity level (top row) and at about 10% above it (bottom row).

Disclosure of author financial interest or relationships:
K.L. Nagy, Mediso ltd., Employment; **J. Lantos**, Mediso Ltd., Employment; **P. Major**, Mediso Ltd., Employment; **G. Patay**, Mediso Ltd., Employment; **C. Halldin**, None; **B. Gulyás**, None.

Presentation Number **P 604**
Poster Session 4
September 21, 2013 / 14:45-14:45 / Room: Exhibit Hall B

Determination of kinetic parameters in cardiac PET imaging of mice using Factor Analysis of Dynamic Sequences

Otman Sarrhini, *Suzanne Gascon, Jacques A. Rousseau, Jean-François Beaudoin, Roger Lecomte, Université de Sherbrooke, Sherbrooke, QC, Canada. Contact e-mail: otman.sarrhini@usherbrooke.ca*

Kinetic modeling in positron emission tomography (PET) imaging critically depends on accurate determination of the plasma input function (IF). While the gold standard to determine IF is an invasive arterial blood-sampling procedure, image-derived IF greatly simplifies imaging procedures. In small animal imaging, a major shortcoming of the image-derived IF method is that it is susceptible to spill-in and spill-out effects [Geworski et al. Eur J Nucl Med 27:161-169; 2000]. In this work, we show that the IF can be extracted from the blood pool of the left ventricle in the cardiac mice PET images by means of factor analysis of dynamic sequences (FADS) [Di Paola et al. IEEE Trans Nucl Sci 4:1310-1321; 1982; Benali et al. Phys Med Biol 38:1065-1080; 1993]. Blood-sampling and image-derived IFs were compared in terms of kinetic rate constants, such as myocardial glucose uptake (KFDG) derived from the Patlak graphical analysis, and the more challenging myocardial perfusion (K1) and myocardial oxygen consumption (k2) derived from a 3-compartment kinetic model analysis of 11C-acetoacetate. Ten Balb/c mice (23.5±2.3 g) were scanned in dynamic mode with 18F-FDG (n=5) during 60 min and with 11C-Acetoacetate (n=5) during 20 min using LabPETTM scanner [Bergeron et al. IEEE Trans Nucl Sci 56:10-16; 2009], having a spatial resolution of 1.3 mm. Blood samples were manually withdrawn during the scan to measure blood activity. Images were reconstructed into 43 and 27 frames for 18F-FDG and 11C-Acetoacetate, respectively. A region of interest (ROI) was manually drawn around the left ventricular (LV) tissue excluding all other structures. The time-dependent activity of the resulting voxels was decomposed using FADS procedure with two physiological components yielding to a "pure" blood pool image and a "pure" myocardial tissue image. Furthermore, a blood pool ROI was drawn on the blood component to determine the FADS IF and a tissue ROI was drawn on the measured myocardium to extract the tissue time activity curve. The FADS IF was corrected for the spill-out by means of a recovery factor estimated from images of spheres phantom. The estimated KFDG using FADS IF is 0.0929 ± 0.0103 (ml/g/min), which is comparable to the values reported by Zhong et al using a model-corrected blood input function [J Nucl Med 54:1-7; 2013] and by Wu et al. using an automated blood sampler [J Nucl Med 48:837-845; 2007]. On the other hand, our results show no significant difference of K1 and k2 for the FADS IF and blood-sampling IF (Fig. 1). In conclusion, kinetic parameters can be safely calculated using an image-derived IF with FADS analysis in cardiac PET imaging of mice without the need for invasive blood sampling.

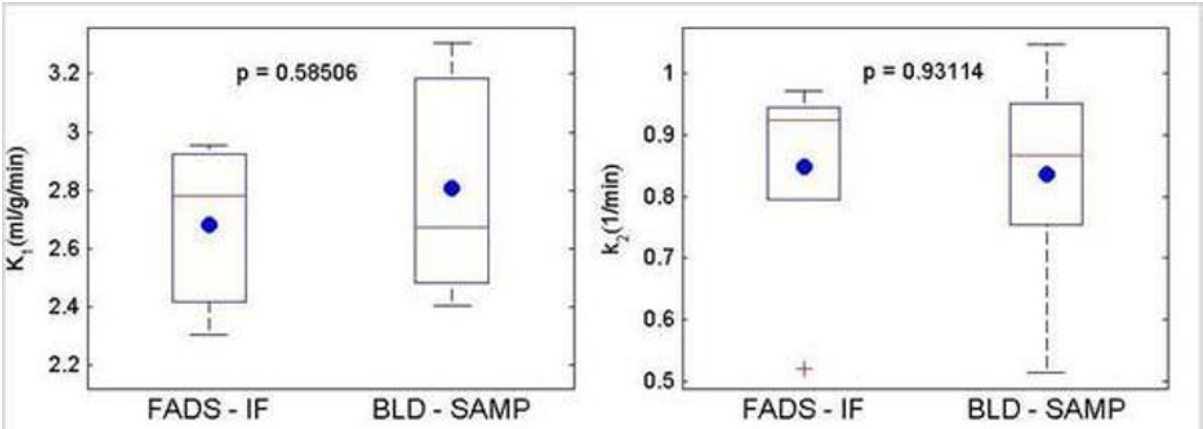

Fig. 1 Box plot of K_1 (left) and k_2 (right) as determined by a 3-compartment kinetic model for ^{11}C-Acetoacetate TACs using FADS IF (FADS – IF) and blood-sampling (BLD – SAMP). The solid blue circles in each group indicate the mean values over 5 mice. The two methods are equivalent as confirmed by p-value. The + is an outlier point of FADS-IF.

Disclosure of author financial interest or relationships:
O. Sarrhini, None; **S. Gascon**, None; **J.A. Rousseau**, None; **J. Beaudoin**, None; **R. Lecomte**, None.

Presentation Number **P 605**
Poster Session 4
September 21, 2013 / 14:45-14:45 / Room: Exhibit Hall B

A Method for Estimating Regional Tissue Blood Volumes with PET and 18F Albumin

Michael V. Green[1,2], *Jurgen Seidel*[1,2], *Elaine Jagoda*[1], *Falguni Basuli*[3], *Mark Williams*[1,2], *Gary L. Griffiths*[1], *Peter Choyke*[1], [1]*Molecular Imaging Program, NCI, NIH, Bethesda, MD, USA;* [2]*SAIC-Frederick, Inc., Frederick, MD, USA;* [3]*Imaging Probe Development Center, NHLBI, NIH, Bethesda, MD, USA. Contact e-mail: greenmich@mail.nih.gov*

Knowledge of total body and regional blood volumes are important clinically, e.g. in trauma and in the heart, and for research purposes where these variables can be altered by experimental conditions, e.g. changes in tumor blood volume with treatment. We have developed a tool for estimating these volumes based on count-rate measurements made on PET images of tissue regions containing blood uniformly labeled with 18F albumin. The principle upon which this method is based is well known: V = A/C, where V is the volume of distribution of the labeled compound (assumed to be the volume of blood in the tissue region), A is the total activity in this region and C is the (uniform) whole-blood tracer activity concentration in the region. Since both A and C can potentially be estimated from PET images alone, tissue blood volumes can be determined. We tested this method in three special cases that do not require attenuation correction: by (1), estimating the volumes of four small spheres filled with the same uniform concentration of 18F imaged in air and in a water-filled cylinder phantom, (2) by estimating the volume of fluid in an 80 cm length of 1.0 mm ID plastic tubing jumbled into a ball-like shape and imaged inside a water-filled cylinder and (3), by comparing the left ventricular (LV) and right ventricular (RV) stroke volumes (which must be equal) calculated from end diastolic (ED) and end systolic (ES) ECG gated cardiac images in each of four rats injected with 18F albumin. Total sphere count rates and tracer count rate concentration were determined by placing 3D regions of interest (ROIs) around each sphere and at the center of the largest sphere, respectively. Total count rate in the plastic tubing was determined by summing all images over the entire water-filled phantom. Tubing count rate concentration was determined by placing a 3D ROI at the center of the largest sphere located at the center of the same water-filled phantom used to image the tubing and with the same concentration of tracer as in the tubing. Total RV/LV count rates and tracer blood count rate concentration were determined by placing 3D ROIs around the RV and LV volumes at ED and ES and a 3D ROI at the center of the LV at ED, respectively. All images were reconstructed with the 2D OSEM algorithm (2 iterations, 16 subsets) and corrected for scatter. Sphere volumes in water were calculated from images with and without attenuation correction to verify that these special cases do not require attenuation correction as hypothesized (unlike the general case where both are required). True (T) sphere, stroke and tubing volumes and measured (M) sphere, stroke and tubing volumes were highly correlated (r = 0.99; M = 1.01 T - 0.7 microliters). With accurate scatter and attenuation correction, this count-rate based method may provide estimates of regional tissue blood volumes in animals and man when geometric methods fail, when whole organ (and in small animals, whole body) blood content is sought, and in other specialty circumstances, e.g. estimation of the actual volume of blood lost due to internal hemorrhage. Funded in part by NCI Contract HHSN261200800001E.

Disclosure of author financial interest or relationships:
M.V. Green, None; **J. Seidel**, None; **E. Jagoda**, None; **F. Basuli**, None; **M. Williams**, None; **G.L. Griffiths**, None; **P. Choyke**, None.

Presentation Number **P 606**
Poster Session 4
September 21, 2013 / 14:45-14:45 / Room: Exhibit Hall B

Flexible Geometry High Sensitivity SPECT System for Small Animal and Plant Imaging

Katherine L. Walker, *Jian Zhou, Jinyi Qi, Simon R. Cherry, Gregory S. Mitchell, Biomedical Engineering, University of California, Davis, Davis, CA, USA. Contact e-mail: katherine.leigh.walker@gmail.com*

Medical imaging systems using single gamma-ray emitting radioisotopes implement collimators in order to form images. However, a tradeoff in sensitivity is inherent in the use of collimators, and modern preclinical single photon emission computed tomography (SPECT) systems detect a very small fraction of emitted gamma-rays (~0.01%). We have built a prototype collimator-less system, which can reach sensitivity of 40% for Tc-99m imaging, while still producing images of sufficient spatial resolution for certain applications in "thin" objects such as mice, plant components, and well plates used for in vitro experiments. Our flexible geometry SPECT scanner consists of two large (5 cm x 10 cm), thin (3 mm and 5 mm), closely spaced, pixelated scintillation detectors of either NaI(Tl), CsI(Na), or BGO. The detectors are read out by two adjacent Hamamatsu H8500 multichannel photomultiplier tubes. The detector heads enable the interchange of scintillation detectors of different materials and thicknesses to optimize performance for a wide range of gamma-ray energies and imaging subjects. The detectors are horizontally oriented for animal imaging, and for plant imaging the system is rotated on its side to orient the detectors vertically. With a Co-57 source (122 keV), we measure energy resolution of 12.2% for our NaI(Tl) detectors and 25.5% for our CsI(Na) detectors. With a Cs-137 source (662 keV), we measure 16.1% energy resolution for the BGO detectors. We measured the intrinsic spatial resolution of the detectors using a phantom composed of capillary tubes (1 mm diameter) filled with either Tc-99m or In-111. With capillaries filled with In-111, we measure spatial resolution approaching 7 mm for the CsI(Na) detectors. While this collimator-less system is unable to approach the sub-mm spatial resolution obtained by the most advanced preclinical pinhole systems, the high sensitivity could enable significant and new use in molecular imaging applications which do not require good spatial resolution-for example, screening applications for drug development (small animals), for material transport and sequestration studies for phytoremediation (plants), or for counting radiolabeled cells in vitro (well plates). To demonstrate the potential for small animal imaging, we selected the Tc-99m labeled radiotracer MAG-3, a renal imaging probe. One healthy adult mouse received a 5 μCi tail vein injection, and was imaged for 15 minutes (rate ~33,000 cps per detector head). We observed 40% sensitivity on our collimator-less system, which is a 1000-fold increase in sensitivity compared to a commercial SPECT scanner with two 5-hole pinhole collimators. To demonstrate the capability of our system for plant imaging, Arabidopsis thaliana cuttings were incubated in dilute solutions (1 μCi/μL) of Tc-99m pertechnetate. The pertechnetate uptake was followed over several cm of transport in the shoots. Approaches for reconstructing tomographic images from the two opposing detector images currently are under development.

Disclosure of author financial interest or relationships:
K.L. Walker, None; **J. Zhou**, None; **J. Qi**, None; **S.R. Cherry**, GE Healthcare, Grant/research support; Perkin Elmer, Grant/research support; **G.S. Mitchell**, None.

Presentation Number **P 607**
Poster Session 4
September 21, 2013 / 14:45-14:45 / Room: Exhibit Hall B

Likelihood based Inter-crystal Compton Scatter and Pulse Pile-up Rejection for MR compatible Preclinical PET Insert

Christoph Lerche[1], Sarah Lodomez[2], **Jakob Wehner**[2]*, Benjamin Goldschmidt[2], Volkmar Schulz[1,2], [1]X-Ray Imaging Systems, Philips Research Europe, Eindhoven, Netherlands; [2]Experimental Molecular Imaging, RWTH, Aachen, Germany. Contact e-mail: jwehner@ukaachen.de*

Introduction For high-resolution preclinical PET scanner based on pixelated scintillation detectors, inter crystal Compton scatter events and event pile up causes energy to be deposited in more than one crystal [1]. This can be a source of substantial positioning errors and thus lead to spatial resolution and contrast to background ratio loss in the reconstructed image. At the moment, no available technology allows identifying the chronological order of two or more inter crystal Compton scattered events ore timely close pile up events. Therefore, these events have to be ignored for image reconstruction; otherwise they would lead to resolution degradation [2]. However, identification of these events is a challenging task. Method The presented method for reliable detection of such pile up events and inter crystal Compton scattered events is based on maximum likelihood gamma ray positioning for scintillation detectors of PET and SPECT cameras [3]. It allows to analyze the charge signals that are generated by the scintillation events and to assign them a likelihood value. This likelihood value is a measure for the similarity of the event's measured signal distribution to the expected signal distribution from a single impact. That is, this computed value is proportional to the probability that the charge pattern was generated by a pile up event or an inter crystal scattered event. From a calibration data set, reasonable threshold values are obtained and stored. During normal data acquisition, the likelihood value for each event is computed and compared to this threshold value. The event will be discarded, if it is below the threshold. The method was tested on a MR-silent and MR-hard preclinical PET insert for a human 3T MR scanner [4]. For this, a Na22 point source was scanned and the likelihood values for all coincident singles were computed. We established several likelihood threshold values in a way that 0 % to 50 % of all valid coincidences were filtered out, if the likelihood value of one of the singles falls below the established threshold. Results From the reconstructed images, the FWHM and FWTM values of the reconstructed point source was measured. We only considered a single scintillation detector module and measured the energy resolution for this module as a function of the filter fraction. We observed that energy resolution could be improved from 12.6 % for 0 % filtering to 11.9 % for 50 % filtering. Likewise, the FWHM value of the reconstructed point source improved from 1.68 mm to 1.54 mm and the FWTM value of the reconstructed point source improved from 5.4 mm to 4.0 mm. [1] Current Trends in Preclinical PET System Design, Levin et al, PET Clin 2, 2007, 125-160 [2] Effects of multiple-interaction photon events in a high-resolution PET system that uses 3-D positioning detectors, Gu et al, Med. Phys. 37, 5494 (2010); [3] Maximum likelihood based positioning and energy correction for pixelated solid state PET detectors, Lerche et al, IEEE Medical Imaging Conference Record, 2011, pp. 3610-3613. [4] A preclinical PET/MR insert for a human 3T MR scanner, Schulz et al, IEEE Medical Imaging Conference Record, 2009, pp. 2577 - 2579

Disclosure of author financial interest or relationships:
C. Lerche, Philips, Employment; **S. Lodomez**, None; **J. Wehner**, None; **B. Goldschmidt**, Philips, Other financial or material support; **V. Schulz**, Philips, Employment .

Presentation Number **P 608**
Poster Session 4
September 21, 2013 / 14:45-14:45 / Room: Exhibit Hall B

Quantification of low uptake cancer in gated PET imaging

Tae Won Nam, *Yong Jin Lee, Kyeong Min Kim, Ran Ji Yoo, Joo Hyun Kang, Sang Moo Lim, Sang-Keun Woo, Molecular Imaging Research Center, KIRAMS, Seoul, Republic of Korea. Contact e-mail: razr13@naver.com*

Gated PET imaging has been used widely for motion correction necessarily for quantitative analysis of tumor and it is affected by different activity and gated number. The purpose of this study was to compare the images acquired under the different conditions of intensity.Radioactive molecular sieves were inserted into lower liver region to track internal motion of rat. The sieves were classified two groups by high (0.67 MBq) and low (0.37 MBq) activity region. Operation was performed under 2% of isoflurane anesthesia. PET data was acquired from small animal PET scanner (InveonTM, Siemens) after injection of 37 MBq 18F-FDG for background activity. Respiratory and EKG signals were obtained and converted to trigger signals representing simultaneously motion by external trigger device (BioVet). Acquired sinogram data was reconstructed to gated PET images of 4 bin and 12 bin. The acquired list-mode data was reconstructed using fourier rebinning (FORE) and ordered subsets expectation maximization (OSEM) 2D algorithm with 4 iterations. Region of interest (ROI) was set to the sieve region as a target and background region of noise. Signal to noise ratio (SNR), standard uptake value (SUV) and full width at half maximum (FWHM) were measured to estimate the effect of intensity and the number of gating difference. Evaluated SNR value were decreased to 47.8%, 21.9% in high activity and decreased to 48.9%, 26.7% in low activity for 4bin and 12 bin to static image, respectively. SUV were 9.31, 8.12, 7.75 in high activity and 4.36, 4.17, 4.23 in low activity for static, 4 bin and 12 bin image, respectively. SUV of gated image was decreased to 83.2% in high activity and decreased to 97.0% in low activity. FWHM were 1.91, 1.72 in high activity and 2.18, 2.03 in low activity for static and 12 bin image, respectively. FWHM of gated image was improved of 10% in high activity and improved of 6.9% in low activity.Although SUV was decreased according to decrease of SNR and gating, FWHM was improved showing better result than static in both of high and low activity. Therefore PET gating acquisition is expected to be useful in early detection of low uptake cancer.

Disclosure of author financial interest or relationships:
T. Nam, None; **Y. Lee**, None; **K. Kim**, None; **R. Yoo**, None; **J. Kang**, None; **S. Lim**, None; **S. Woo**, None.

Presentation Number **P 609**
Poster Session 4
September 21, 2013 / 14:45-14:45 / Room: Exhibit Hall B

Development of a high resolution YSO single photon imaging system using 0.8mm pixels

Seiichi Yamamoto[1], *Hiroshi Watabe*[2], *Yasukazu Kanai*[2], *Katsuhiko Kato*[1], *Jun Hatazawa*[2], [1]*Nagoya University Graduate School of Medicine, Nagoya, Japan;* [2]*Osaka University Graduate School of Medicine, Suita, Japan. Contact e-mail: s-yama@met.nagoya-u.ac.jp*

YSO (Ce doped Y2SiO5) is a promising scintillator for single photon imaging system since it has relatively high light output and does not contain any natural radioactivity. YSO is not hygroscopic, so it may be possible to fabricate a block with small pixels for a high resolution system. For this purpose, we developed a high resolution single photon imaging system for small animals. The detector for the single photon imaging used 0.8 mm x 0.8 mm x 7 mm YSO pixels. All the surfaces of these YSO pixels were mechanically polished, combined with a 0.1mm thick BaSO4 reflector to form 48 x 48 matrix, and optically coupled to a high quantum efficiency 2-inch position sensitive photomultiplier tube (Hamamatsu Photonics H10966 A-100). The YSO block size was 43.2 mm x 43.2 mm. The YSO single photon imaging was encased in a 5mm thick tungsten container and parallel collimator was mounted on its front. The parallel hole collimator was made of 3-layer (each of the layer has 5mm thick) tungsten plate and each has 48 x 48, 0.6mm holes which is positioned one-to-one coupling with the YSO pixels. Even with the 0.8mm YSO pixels, we could resolve almost pixels clearly in 2-dimensional histogram with peak-to-valley ratio of 2.9 for 122-keV gamma photons. Energy resolution was 20.4% FWHM. Spatial resolution with parallel hole collimator 2mm from the collimator surface was 0.7mm FWHM and 1.3mm FWHM for 122-keV and 35-keV gamma photons, respectively. Phantoms and small animal images were successfully obtained with the single photon imaging system for 35-keV (I-125) and 122-keV (Co-57) gamma photons. We could successfully develop a high resolution YSO single photon imaging system employing 0.8mm pixels. The high resolution single photon imaging system will also be useful for developing a compact and high resolution SPECT system.

Disclosure of author financial interest or relationships:
S. Yamamoto, None; **H. Watabe**, None; **Y. Kanai**, None; **K. Kato**, None; **J. Hatazawa**, None.

Presentation Number **PLS 1**
Plenary Session 1
September 18, 2013 / 17:00-18:00 / Room: Ballroom B&C

Precision Medicine and Molecular Imaging: Quo Vadis?

Hedvig Hricak, *Memorial Sloan-Kettering Cancer Center, New York, NY, USA. Contact e-mail: hricakh@mskcc.org*

Summary: Revolutionary advances in molecular biology, biomedical imaging and information technology have opened up new avenues towards molecularly-based, "precision medicine," in which treatments are tailored to the specific biological features of disease in the individual patient. In oncology, the application of precision medicine offers tremendous potential for improving outcomes; however, it also poses great challenges. Cancers are genetically heterogeneous, undergoing constant evolution. Biological features differ within primary tumors, and in as many as 50% of cancers, metastases de-differentiate and demonstrate different features in different matrices (e.g., bone vs. liver vs. lung). Tissue and serum assays alone cannot sufficiently capture the spatial and temporal diversity of tumor biology. Spatially localized, molecularly-based evaluation of disease by imaging is essential. Conventional anatomic imaging will continue to be indispensible for localizing cancer and assessing its spread. At the same time, molecular imaging will become invaluable for improving our understanding of tumor biology through use of targeted probes and by allowing molecularly targeted biopsies. Molecular imaging will also improve our ability to monitor pharmacodynamics, expedite drug development, and, ultimately, enable evidence-based treatment decisions. Increasingly, descriptive and quantitative features from cross-sectional imaging will be supplemented by direct quantitative assessment of key cells and molecules. While the molecular imaging armamentarium still needs to be developed and validated, it is clear that there is no limit to what we can accomplish by bringing imaging and molecular biology together.

Presenter Bio: Dr. Hricak's work concerns the development of evidence-based imaging algorithms for improving the management of gynecological and genitourinary cancers. Her research focuses primarily on developing and validating prognostic, predictive, and early response biomarkers from both cross-sectional (ultrasound, MRI, CT) and molecular (DCE-MRI, MR spectroscopy, PET/CT and PET/MRI) imaging modalities. She seeks to use imaging to elucidate in vivo tumor biology and thus enable earlier and better tumor detection and characterization. Her recent work in radiogenomics has integrated pathology, genomics and molecular markers with multimodality imaging to gain insights into aspects of tumor heterogeneity (both spacial and temporal) that may predict treatment response or resistance and may therefore provide surrogate endpoints for next-generation clinical trials. With respect to prostate cancer imaging, her group's research focuses on the use of multiparametric quantitative MR imaging combining functional and metabolic methods (e.g., dynamic contrast-enhanced MRI, diffusion-weighted MRI and MR spectroscopy) to improve treatment selection for patients considering active surveillance of clinically low-risk prostate cancer. Her group is conducting studies involving high-resolution magic angle spinning spectroscopy of prostate cancer tissue, the findings of which can be translated to refine clinical spectroscopy.

Disclosure of author financial interest or relationships:
H. Hricak, None.

Presentation Number **PLS 2**
Plenary Session 2
September 19, 2013 / 09:00-09:45 / Room: Ballroom B&C

Targeting Cancer Cell Metabolism

Chi V. Dang, *Abramson Cancer Center of the University of Pennsylvania, University Park, PA, USA. Contact e-mail: dangvchi@exchange.upenn.edu*

Summary: Although the concept of targeting cancer metabolism has been explored for decades, therapeutic interventions that aim at metabolic enzymes has become more tangible as new concepts about metabolism are developed and new chemical entities have emergesd as drugs in clinical trials. In this regard, clinical imaging based on metabolic processes is essential for the direct assessment of clinical response and efficacy of this new class of drugs. The genetic and metabolic bases of cell growth will be discussed along with new therapeutic and imaging opportunities.
Presenter Bio: Chi Van Dang is Director of the Abramson Cancer Center of the University of Pennsylvania and the John H. Glick Professor. His career at Penn started in September 2011 after having been at Johns Hopkins when he was the Johns Hopkins Family Professor in Oncology Research and Vice Dean for Research of Johns Hopkins University School of Medicine. He directed the Hopkins Institute for Cell Engineering and was a Professor of Medicine, Pathology, Oncology, and Cell Biology with joint appointment in Molecular Biology and Genetics. Dr. Dang is Editor-in-Chief of Cancer & Metabolism, a scientific editor of Cancer Discovery and serves on editorial boards of Cancer Research, Clinical Translational Science, Current Cancer Therapy Reviews, eLIFE, Journal of Clinical Investigation, Journal of Molecular Medicine, Genes & Cancer, Molecular and Cellular Biology, Neoplasia, and Oncotargets. He has authored over 200 scientific and medical articles, book chapters and a book. He is a member of the Institute of Medicine of the National Academy of Sciences, American Academy of Arts & Sciences, National Cancer Institute Board of Scientific Advisors, American Society for Clinical Investigation (ASCI) and The Association of American Physicians. He was president of the ASCI (2003). He held an NIH/National Cancer Institute MERIT award, received a number of honors, and sponsored and mentored many NIH K08 physician-scientist awardees, Ph.D. doctorates and post-doctoral fellows. The Dang laboratory has contributed to the understanding of the function of the MYC cancer gene (www.myccancergene.org), which has emerged as a central transcription factor or gene switch in many different human cancers. His laboratory established the first mechanistic link between the MYC cancer gene and cellular energy metabolism, contributing to the concept that genetic alterations in cancers re-program fuel utilization by tumors and render cancers addicted to certain fuel sources. His laboratory is now exploiting these concepts for therapeutic targeting of cancer cell metabolism as a new way to treat cancer.

Disclosure of author financial interest or relationships:
C.V. Dang, None.

Presentation Number **PLS 3**
Plenary Session 3: Gold Medal Award Winners
September 19, 2013 / 16:45-17:22 / Room: Ballroom B&C

From Relaxation Enhancers to Frequency-Encoding Agents: How MRI Competes in the Molecular Imaging Arena

Silvio Aime, *University of Torino, Italy, Turin, Italy. Contact e-mail: silvio.aime@unito.it*

Summary: The possibility of exploiting the superb anatomical resolution of MRI continues to make this modality highly desirable for Molecular Imaging applications in spite of the low sensitivity of the currently available contrast agents. Whereas chemists have tackled this issue by designing novel structures endowed with enhanced sensitivity, important achievements have also been reached by using nanocarriers (e.g. apoferritin, LDL or liposomes, etc.) able to deliver a large number of paramagnetic agents at the targeting sites. This approach is bringing relevant insights to the emerging field of imaging-guided drug delivery ("theranostics"). Besides paramagnetic relaxation systems (e.g. Gd(III) or Mn(II) complexes), two new classes of frequency-encoding probes, namely the CEST agents (CEST= Chemical Exchange Saturation Transfer) and the class of hyperpolarized molecules, have been considered as powerful tools for Molecular Imaging applications. The use of frequency-encoding agents has opened the interesting perspective of detecting more than one agent in the same anatomical region. Moreover, hyperpolarized molecules have the potential for being a real breakthrough as diagnostic agents reporting on cellular metabolism and transport across cellular membranes. All together, the development in the design and testing of new probes has significantly improved the potential of MRI in respect to competing imaging modalities.

Presenter Bio: Silvio Aime received the Laurea degree from the University of Torino in 1971. Following a postdoctoral appointment at the University of East Anglia, he returned in 1974 to Torino where he has spent his entire career. He is currently Professor of General and Inorganic Chemistry at the Department of Molecular Biotechnologies and Health Sciences and Head of the Center of Excellence on Molecular Imaging of the University of Torino. Awards include Doctor honoris causa from the University of Debrecen (2010), Honorary Doctorate from Eindhoven Technical University (2011), Hans Fisher Senior Fellow, Institute of Advanced Study, Technical University Munich (2011), Distinguished Professor at the Eindhoven Technical University (2013). He is chairman of the EU-COST Action TD1004 "Theragnostics" and President of the European Society of Molecular Imaging (ESMI). Co-Editor in-chief of journal "Contrast Media and Molecular Imaging". He is author of over 550 peer-reviewed papers and 25 patents. His main research activities deal with the development of Lanthanide-based Imaging Probes (relaxation and CEST agents) for Molecular Imaging applications with the MRI modality. Other current research interests are in the field of hyperpolarized molecules (DNP and para-Hydrogen).

Disclosure of author financial interest or relationships:
S. Aime, None.

Presentation Number **PLS 4**
Plenary Session 3: Gold Medal Award Winners
September 19, 2013 / 17:22-18:00 / Room: Ballroom B&C

Design Concepts for MR Agents That Respond to Metabolism: How Far Have We Come - How Far Can We Go?

Dean Sherry, *University of Texas Southwestern Medical Center, Dalaas, TX, USA. Contact e-mail: Dean.Sherry@UTSouthwestern.edu*

Summary: It is often stated that magnetic resonance is too insensitive for molecular imaging because sensitivity comparisons with other imaging modalities, especially optical and nuclear, leave MR far short. Nevertheless, MR has many advantages over other imaging modalities including superb anatomical resolution, lack of ionizing radiation, and deep tissue penetration so the quest to develop methods to make MR more competitive in the world of molecular imaging continues. Given that water is the major component of most MR images, efficient transfer of tagged spins from specific pools of molecules to water is key to using the water proton signal as an efficient readout of metabolism and physiology. Although Gd3+-based contrast agents have been widely used as non-specific extracellular agents for over 25 years, the rate of water exchange in all clinically approved agents is too slow for many molecular imaging applications. This is an especially important parameter to consider in the design of new Gd3+ agents as responsive MR reporters. Paramagnetic lanthanide complexes that act as chemical exchange saturation transfer agents (PARACEST) have the opposite requirement. Here, the goal is to slow water exchange rates so that saturated spins can be efficiently transferred to water for MR readout. The chemistry of these novel reporters and their limitations for use in vivo to image tissue pH, redox, ROS and hypoxic tissues will be discussed. Other MR techniques, including imaging of diamagnetic CEST probes and hyperpolarized molecules also offer considerable potential for providing new insights into tissue metabolism and energetics. These newer technologies all contribute toward making MR more valuable as an effective tool for molecular imaging.

Presenter Bio: Short Bio: A. Dean Sherry, PhD, is Director of the Advanced Imaging Research Center at the University of Texas Southwestern Medical Center, Professor of Chemistry at the UT Dallas, and Professor of Radiology at UT Southwestern. He also holds the Cecil & Ida Green Distinguished Chair in Systems Biology at UT Dallas. He was one of four chemistry faculty to join the University of Texas at Dallas in 1972 to initiate a new department on that campus. Since that time, he helped build the undergraduate chemistry program and two graduate programs in Chemistry and served a department Chair for 12 years. Dr. Sherry has been recognized for his research in two major areas: the development of 13C NMR tracers of metabolism in animals and humans and in developing novel MRI agents that respond to physiology or metabolism including Gd3+-based agents, PARACEST agents and hyperpolarized MR agents. He currently serves on the Scientific Advisory Boards of the Molecular Imaging Program at NCI and the Ontario Institute for Cancer Research Institute. He also serves as Associate Editor of Contrast Media & Molecular Imaging and as a Deputy Editor for Magnetic Resonance in Medicine. He has won numerous awards, has published 380 scientific articles and 32 patents, mentored more than 100 graduate students & postdoctoral trainees. He participates annually in the NCI Cancer Imaging Bootcamp for introducing young biomedical scientists to molecular imaging. Dr. Sherry is the founding scientist of two companies related to molecular imaging, Macrocyclics, Inc. and Visual Metabolism, LLC. Both are located in Dallas, Texas.

Disclosure of author financial interest or relationships:
D. Sherry, None.

Presentation Number **PLS 5**
Plenary Session 4: Britton Chance Lecture for Advances in Basic Imaging Research
September 20, 2013 / 09:00-09:45 / Room: Ballroom B&C

Image-guided Nano Delivery

Katherine Ferrara, *University of California, Davis, Davis, CA, USA. Contact e-mail: kwferrara@ucdavis.edu*

Summary: In this session, we will explore the frontiers of image-guided nanodelivery with a particular focus on the use of ultrasound to enhance or assess therapeutic efficacy. In one scenario, ultrasound can be applied to locally release a drug from a delivery vehicle via thermal or mechanical means. We find that when ultrasound is combined with an engineered delivery vehicle, complete regression of established local cancers can be achieved. Also, the application of ultrasound can directly alter tissue properties through the application of mechanical forces or the generation of heat, and the current status and future opportunities for such techniques will be described. Further, the use of ultrasound to induce a systemic immune response and enhance immunotherapies will be described. Here again, multiple mechanisms are postulated for changes in immune cell phenotype and for the release of tumor antigen. In addition, molecular ultrasound imaging with targeted microbubbles is now undergoing clinical assessment and opportunities for disease detection and monitoring of therapeutic response will be described. Finally, combining ultrasound with MRI for treatment guidance or with PET to assess therapeutic delivery has been shown to have significant value. We will show that with such combinations, the ultrasound dose can be controlled within tight spatial, temporal and exposure limits and multi-fold delivery enhancements have been validated.
Presenter Bio: Katherine Ferrara received her Ph.D. in 1989 from the University of California, Davis. Prior to her PhD, Dr. Ferrara was a project engineer for General Electric Medical Systems, involved in the development of early magnetic resonance imaging and ultrasound systems. Following an appointment as an Associate Professor in the Department of Biomedical Engineering at the University of Virginia, Charlottesville, Dr. Ferrara served as the founding chair of the Department of Biomedical Engineering at UC Davis. She is a fellow of the Institute of Electrical and Electronics Engineers, American Association for the Advancement of Science, the Biomedical Engineering Society, the Acoustical Society of America and the American Institute of Medical and Biological Engineering. She is an author of more than 200 papers and her recent awards include the IEEE UFFC Achievement Award in 2012. Dr. Ferrara has served on numerous advisory boards including the National Advisory Council of the National Institute of Biomedical Imaging and Bioengineering and currently serves as the Chair of the Women in Molecular Imaging Society Interest Group. She is currently a Professor of Biomedical Engineering at UC Davis with research interests spanning imaging and drug delivery and serves as the principal investigator for a training program in molecular imaging.

Disclosure of author financial interest or relationships:
K. Ferrara, None.

Presentation Number **PLS 6**
Plenary Session 5: Jorge Barrio Lecture for Advances in Clinical Research
September 20, 2013 / 17:00-17:45 / Room: Ballroom B&C

Advances in MR/PET for Studies in Brain Function

Bruce Rosen, *Massachusetts General Hospital, Charlestown, MA, USA. Contact e-mail: bruce@nmr.mgh.harvard.edu*

Summary: The simultaneous acquisition of both positron emission tomography (PET) and magnetic resonance imaging (MRI) data offers an exciting opportunity to merge anatomical, physiological, metabolic, and molecular information in a single examination setting. This is especially relevant in studies of the brain, where many fundamental questions remain on the linkage between structure and function, and where even basic principals of the interactions between physiological changes such as cerebral blood flow, neuronal "activity", and neuroreceptor function are yet to be fully elucidated. This talk will first describe the technological principals underpinning such combined instruments, including changes in both the PET and MRI architectures which allow such instruments to be cross-compatible. The talk will then discuss how combining information from both modalities can be used to explore structure/function relationships, and how the simultaneous acquisition of data can provide information that is difficult to obtain using sequential acquisitions. Finally, some clinically relevant examples will be presented to highlight the future potential of this tool for advanced diagnostic evaluation of neurolopsychiatric diseases.

Presenter Bio: Dr. Rosen is Professor of Radiology at the Harvard Medical School and Professor of Health Science and Technology at the Harvard-MIT Division of Health Sciences and Technology. He is Director of the Athinoula A. Martinos Center for Biomedical Imaging at Massachusetts General Hospital. Dr. Rosen is a world-leading expert in functional neuroimaging. Over the past thirty years he has pioneered the development and application of many novel physiological and functional nuclear magnetic resonance techniques to measure hemodynamic and metabolic changes associated with brain activation and cerebrovascular insult as well as complementary tools to measure microvascular and microstructural morphology. These and other techniques he has developed are used by research centers and hospitals throughout the world to study and evaluate patients with stroke, brain tumors, dementia, and neurologic and psychological disorders. Most recently, Dr. Rosen's work has focused on the integration of fMRI data with information from other modalities, including positron emission tomography (PET), magnetoencephalography (MEG) and noninvasive optical imaging. By using fMRI tools to evaluate the linkage between neuronal and physiological (metabolic and hemodynamic) events during periods of increased neuronal activity, his studies will allow researchers to better interpret fMRI signal changes and develop new ways to probe brain function. Dr. Rosen leads the activities of several large interdisciplinary and inter-institutional research programs including the NIH Blueprint-funded Human Connectome Project, the NIBIB Regional Resource Center, the Center for Functional Neuroimaging Technologies (CFNT), and the Biomedical Informatics Research Network (BIRN) Collaborative Tools Support Network. He is Principal Investigator/Program Director for two neuroimaging training programs. He has authored more than 300 peer-reviewed articles as well as over 50 book chapters, editorials and reviews. Dr. Rosen is the recipient of numerous awards in recognition of his contributions to the field of functional MRI, including, most recently, the 2011 Outstanding Researcher award from the Radiological Society of North America (RSNA), and the Rigshospitalet's International KFJ Prize from the University of

Copenhagen/Rigshospitalet. Dr. Rosen is a Fellow and Gold Medal winner for his contributions to the field of Functional MRI from the International Society for Magnetic Resonance in Medicine, a Fellow of the American Institute for Medical and Biological Engineering, and a member of the Institute of Medicine of the National Academies.

Disclosure of author financial interest or relationships:
B. Rosen, Siemens, Consultant .

Presentation Number **PLS 7**
Plenary Session 6
September 21, 2013 / 09:00-09:45 / Room: Ballroom B&C

Liver Cancer Surgery Guided by in vivo ICG Fluorescence

Norihiro Kokudo, *The University of Tokyo, Bunkyo-ku, Japan. Contact e-mail: KOKUDO-2SU@h.u-tokyo.ac.jp*

Summary: This presentation describes one of the largest case series of clinical application of ICG fluorescent imaging in liver cancer surgery. ICG dye injected several days before liver resection is specifically accumulated in hepatocellular carcinoma (HCC) tissues or surrounding liver parenchyma around colorectal liver mets. These lesions are clearly visualized by a fluorescent camera. Video images of fluorescent lesions will be presented. This technique is also useful for visualizing cholestatic hepatic regions or evaluating liver congestion after division of major hepatic veins. Representative videos for such applications will also be presented.

Presenter Bio: Dr. Norihiro Kokudo earned his M.D. in 1981, and then Ph.D. in 1988 at University of Tokyo. From 1989 to 1991 he stayed at Department of Surgery, University of Michigan as a visiting research investigator. After 6 years at Cancer Institute Hospital, Tokyo, as a senior staff of GI surgery, he joined the current institution as an associate professor in 2001. He then rose to the current position in 2007. Dr. Kokudo has been conducting a number of research projects on surgical treatment of HCC, colorectal liver metastases, and living donor liver transplantation. His team started prospective studies on clinical application of ICG fluorescent imaging in April 2007 and has published a number of articles on this project including the world first report of HCC imaging. In April 2012, Dr. Kokudo was appointed as the President of Japan Surgical Society. He is a secretary elect for Asian-Pacific Hepato-Pancreato-Biliary Association (A-PHPBA) and a member-at-large of International Hepato-Pancreato-Biliary Association (IHPBA). He is also a member of International Society of Surgery and The Society of Surgical Oncology. He is an associate editor of Hepatology Research and Surgery Today, and on the editorial board of World Journal of Surgery, Journal of HPB Science, HPB, Japanese Journal of Clinical Oncology, and Hepatogastroenterology.

Disclosure of author financial interest or relationships:
N. Kokudo, None.

Presentation Number **PLS 8**

Closing Ceremony: Young Investigator Award Competition, Poster Awards, and Highlight Lecture

September 21, 2013 / 16:30-16:30 / Room: Ballroom B&C

Highlight Lecture

Sanjiv S. Gambhir, *Stanford University School of Medicine, Stanford, CA, USA. Contact e-mail: sgambhir@stanford.edu*

Summary: A summary will be presented of the top scoring abstracts presented at the meeting illustrating examples of developments in new imaging technology, novel assays, novel molecular imaging agents, and applications. The examples selected will be based on slides submitted by the abstract co-authors. The goal would be to provide the audience with an overview of some of the most exciting developments at the meeting. Due to time-constraints, not all of the exciting work will be able to be presented.

Presenter Bio: Dr. Gambhir received his MD/PhD from the UCLA Medical Scientist Training Program. He has over 400 publications in the field and over 40 patents pending or granted. His lab has focused on interrogating fundamental molecular events in living subjects. He has developed and clinically translated several multimodality molecular imaging strategies including imaging of gene and cell therapies. He serves on numerous academic advisory boards for Universities around the world and served on the Scientific Advisory Board of the National Cancer Institute for over 7 years. Among his many awards he is the recipient of the George Von Hevesy Prize and the Paul C. Aebersold Award for outstanding achievement in basic nuclear medicine science from the Society of Nuclear Medicine, Outstanding Researcher Award from the Radiological Society of Northern America in 2009, the Distinguished Clinical Scientist Award from the Doris Duke Charitable Foundation, the Holst Medal, the Tesla Medal, and the Hounsfield Medal from Imperial College, London. He was elected to the Institute of Medicine of the US National Academies in 2008.

Disclosure of author financial interest or relationships:

S.S. Gambhir, Bracco Diagnostics, Consultant; Endra, Inc, Stockholder; Cellsight, Stockholder; Enlight, Inc., Stockholder; General Electric, Grant/research support; ImaginAb, Stockholder; MagArray, Inc., Stockholder; Sanofi-Aventis, US, Grant/research support; SiteOne Therapeutics, Stockholder; VisualSonics/Sonosite, Stockholder .

Presentation Number **SS 1**
Scientific Session 01: First in Human & Clinical Studies - Oncology
September 19, 2013 / 10:30-10:45 / Room: 102

Imaging of Cytolytic T-Cells Therapy in Recurrent Glioma Patients using a PET Reporter Gene/Probe Strategy

Khun Visith Keu[1], *Shahriar Yaghoubi*[1], *Martin Allen-Auerbach*[4], *Xinrui Yan*[1], *Aileen Hoehne*[1], *Robert E. Reeves*[1], *Lindee Burton*[1], *Anita Kurien*[2], *Rachel Magnusson*[2], *John Williams*[4], *Frezghi Habte*[1], *Christine Brown*[3], *Jamie Wagner*[3], *Stephen Forman*[3], *Johannes Czernin*[4], *Michael Jensen*[2], *Behnam Badie*[2], *Sanjiv S. Gambhir*[1], [1]*Radiology, Stanford University, Palo Alto, CA, USA;* [2]*Neurosurgery, City of Hope, Duarte, CA, USA;* [3]*Hematology and Hematopoietic Cell Transplantation, City of Hope, Duarte, CA, USA;* [4]*Nuclear Medicine, UCLA, Los Angeles, CA, USA. Contact e-mail: kvkeu@hotmail.com*

Background: 9-[4-[18F]fluoro-3-(hydroxymethyl)butyl]guanine) or FHBG is the first human PET tracer approved by the FDA for imaging Herpes Simplex Virus 1 thymidine kinase (HSV1-tk) reporter gene expression. We employed CD8+ cytolytic T lymphocytes (CTLs) that are genetically engineered to express IL13-Zetakine chimeric immunoreceptors to recognize glioblastoma multiforme (GBM). CTLs were also electroporated with the HSV1-tk gene, encoding for an enzyme that selectively phosphorylates FHBG thereby trapping it within the cell. This study describes the role of FHBG PET for monitoring CTLs therapy in recurrent GBM patients resistant to conventional therapies. Methods: Six recurrent GBM patients (3M:3F, mean age:57 years) were enrolled into two separate trials to evaluate the safety and feasibility of intratumoral immunotherapy with CTLs. The first two patients received a total of $1x10^9$ autologous CTLs into the tumor resection cavity, while the subsequent 4 patients were infused with four injections of $1x10^8$ allogeneic CTLs into the site of tumor recurrence through a Rickham reservoir/catheter system over 2 weeks. Approximately 7.0 (±10%) mCi of FHGB was given iv for pre and post-therapy scans, FHBG PET images (2h post-iv) were acquired from vertex to mid-thighs. MRI and FDG PET scans were also performed in each patient. Results: CTLs transfected with HSV1-tk showed 4-fold higher FHBG uptake ($P<0.01$) in cell culture as compared to naïve CTLs. FHBG did not cause alterations in symptoms, vitals, ECGs, and blood labs in any patients. The biodistribution of FHBG was evaluated across all patients. Using a three-dimensional 50 mm diameter region-of-interest, the average (±SD) SUVmean was 0.04±0.01 for brain background, 0.22±0.04 for blood pool, 1.40±0.66 for hepatic dome and 0.28±0.10 for right thigh. For tumor quantification, no significant difference was observed for the average SUVmax or mean on pre and post-therapy scans (N=5); however, uptake volume (UV) after 50% maximum activity threshold, and total activity (i.e. SUVmean x UV) (TA) varied significantly. The percentage of SUVmax and TA changes were 5% (range:-57 to 47%) and 38% (range:29 to 60%) for pre and post CTLs imaging. The tumor and CTLs uptake were statistically higher ($P<0.05$) compared to the brain background (ratio:5.3±2.0), but similar to blood pool or muscles. The infusion techniques might also play a role in the homing to GBM and the survival of CTLs in vivo: convection-enhanced delivery (slow infusion) was used initially, but later changed for a fast infusion technique. In addition, CTLs might diffuse in the cerebrospinal fluid, thus reducing the concentration of CTLs locally. Therefore, TA values clearly better evaluate this issue than solely SUVmax. Conclusion: FHBG PET is a well-tolerated and non-invasive imaging technique to evaluate PET reporter gene expression of CTLs. These data suggests that percentage change of total uptake which takes into account the volume of uptake might be a promising tool for imaging CTLs delivery and survival. This is the first study we know of to use PET reporter gene/probe technology for the imaging of cell therapy in a pilot clinical trial.

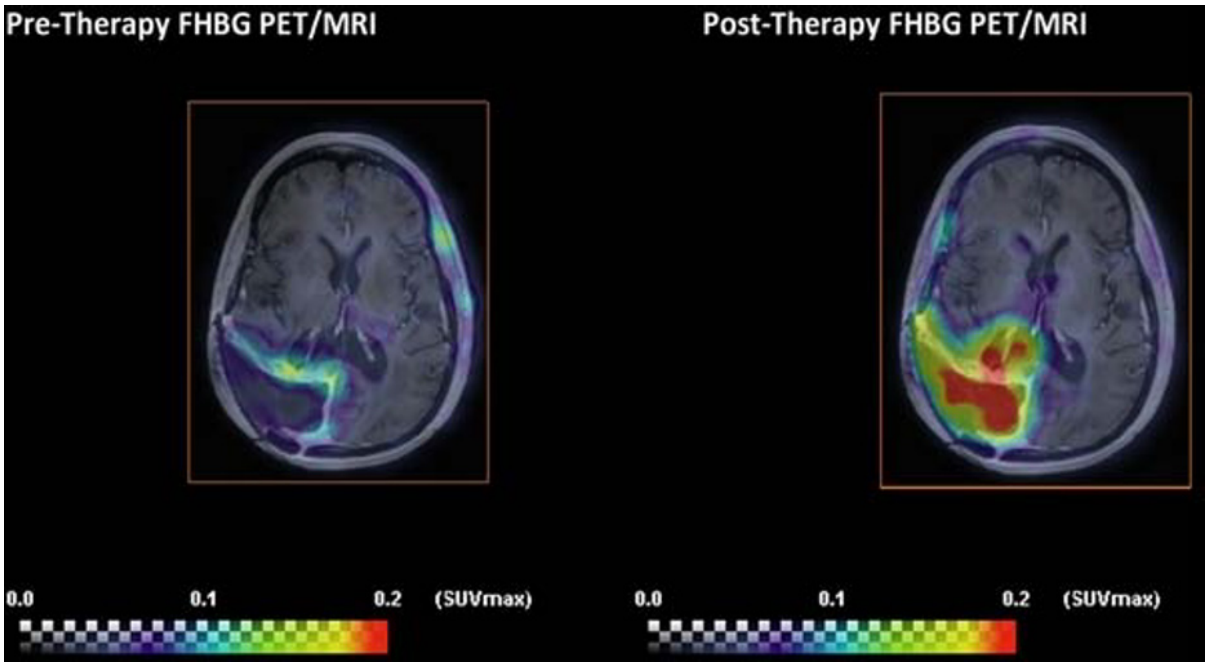

Figure 1: These figures are PET images 2.0 hours post-injection of FHBG fused to an MRI in patient-002 with a recurrent right occipital GBM. On the pre-therapy image where no cells express the HSV1-tk PET reporter gene, low activity is seen in the scalp muscle (physiological) and in the tumor cavity (likely increased blood pool activity secondary to inflammation). After CTLs therapy, a second PET scan demonstrates a significant increased FHBG activity in the right occipital region. Using a 50% maximum activity threshold, we evaluated the pre- and post-therapy SUVmax at 0.16 and 0.25, SUVmean at 0.10 and 0.16, the uptake volume at 116cc and 135cc, and the total activity (i.e. SUVmean x uptake volume) at 11.3 and 21.3.

Disclosure of author financial interest or relationships:

K. Keu, None; **S. Yaghoubi**, CellSight Technologies, Inc., Employment; CellSight Technologies, Inc., Stockholder; **M. Allen-Auerbach**, None; **X. Yan**, None; **A. Hoehne**, None; **R.E. Reeves**, None; **L. Burton**, None; **A. Kurien**, None; **R. Magnusson**, None; **J. Williams**, None; **F. Habte**, None; **C. Brown**, None; **J. Wagner**, None; **S. Forman**, None; **J. Czernin**, Sofie Biosciences, Stockholder; **M. Jensen**, ZetaRx Biosciences, Inc., Grant/research support; ZetaRx Biosciences, Inc., Stockholder; **B. Badie**, None; **S.S. Gambhir**, Bracco Diagnostics, Consultant; Endra, Inc, Stockholder; Cellsight, Stockholder; Enlight, Inc., Stockholder; General Electric, Grant/research support; ImaginAb, Stockholder; MagArray, Inc., Stockholder; Sanofi-Aventis, US, Grant/research support; SiteOne Therapeutics, Stockholder; VisualSonics/Sonosite, Stockholder .

Presentation Number **SS 2**
Scientific Session 01: First in Human & Clinical Studies - Oncology
September 19, 2013 / 10:45-11:00 / Room: 102

Optimization of near-infrared fluorescence cholangiography for open and laparoscopic surgery

Floris P. Verbeek[1], *Boudewijn Schaafsma*[1], *Quirijn Tummers*[1], *Joost van der Vorst*[1], *Wendeline J. van der Made*[1], *Coen I. Baeten*[1], *Bert A. Bonsing*[1], *John V. Frangioni*[2], *Cornelis J. van de Velde*[1], *Alexander Vahrmeijer*[1], *Rutger-Jan Swijnenburg*[1], [1]*Surgery, Leiden University Medical Center, Leiden, Netherlands;* [2]*Department of Radiology and Medicine, Beth Israel Deaconess Medical Center, Boston, MA, USA. Contact e-mail: f.p.r.verbeek@lumc.nl*

Introduction: During laparoscopic cholecystectomy, common bile duct (CBD) injury is a rare but severe complication. To reduce the risk of injury, near-infrared (NIR) fluorescent cholangiography using Indocyanine Green (ICG) has been presented as a novel method to visualize the biliary system during surgery. To date, several studies have shown feasibility of this technique with ICG being injected shortly prior to surgery. Hepatic clearance of circulating ICG into the bile allows imaging of the bile ducts, however, liver background fluorescence is a major problem. The aim of the current study was to optimize dosage and timing of ICG for NIR fluorescent cholangiography using a quantitative intraoperative camera system during open HPB surgery. Subsequently, these results were validated during laparoscopic cholecystectomy using a laparoscopic fluorescence imaging system. Methods: A total of 27 patients who underwent NIR fluorescence imaging during open HPB surgery were analyzed to assess optimal dosage and timing of ICG administration. ICG was intravenously injected at doses ranging from 5 to 20 mg at either 30 min (early) or 24 hours (delayed) preoperatively. Next, the optimal doses found for early (5mg/ 30 min) and delayed imaging (10mg/24hr) were applied to 2 groups of 6 patients (n=12) undergoing laparoscopic cholecystectomy. Results: Liver background fluorescence (normalized pixel value) was 8923 (sd 2143), 13941 (sd 8110), 726 (sd 758) and 928 (sd 433) for the 5mg/30min, 10mg/30min, 10mg/24hr and 20mg/24hr respectively. Mean fluorescence intensity of the liver was significantly lower 24 hours after administration ($p < 0.0001$). Importantly, no difference in CBD signal was observed between the groups, resulting in a significant increase in the CBD-to-liver contrast ratio during delayed imaging, which was optimal in the 10mg/24hr group ($p = 0.003$). Similarly, in the patients undergoing laparoscopic cholecystectomy liver signal was much reduced in the 10mg/24hr group, which enabled optimal discrimination of the bile ducts from surrounding tissue. Conclusions: To our knowledge this is the first study comparing the effect on dosage and timing of ICG administration for intraoperative NIR fluorescence cholangiography. During delayed imaging, minimal liver background signal is observed leading to improved CBD-to-liver contrast ratios. A dosage of 10 mg administered 24 hours before surgery seems optimal for NIR fluorescence cholangiography during both open and laparoscopic surgery.

Disclosure of author financial interest or relationships:
F.P. Verbeek, None; **B. Schaafsma**, None; **Q. Tummers**, None; **J. van der Vorst**, None; **W.J. van der Made**, None; **C.I. Baeten**, None; **B.A. Bonsing**, None; **J.V. Frangioni**, None; **C.J. van de Velde**, None; **A. Vahrmeijer**, None; **R. Swijnenburg**, None.

Presentation Number **SS 3**
Scientific Session 01: First in Human & Clinical Studies - Oncology
September 19, 2013 / 11:00-11:15 / Room: 102

Analysis of Circulating Tumor Cells and Tumor FDG PET Uptake in Stage I Non-small Cell Lung Cancer Patients

Mehran Jamali[5], *Khun Visith Keu*[6,5], *Viswam S. Nair*[1], *Madelyn S. Luttgen*[2], *Minal S. Vasanawala*[4,5], *Ware Kuschner*[3,1], *Andrei Iagaru*[5], *Joseph B. Shrager*[7,9], *Billy W. Loo*[8], *Peter Kuhn*[2], *Sanjiv S. Gambhir*[5], [1]*Medicine, Stanford University, Stanford, CA, USA;* [2]*Cell Biology, The Scripps Research Institute, La Jolla, CA, USA;* [3]*Medicine, VA Palo Alto Healthcare System, Palo Alto, CA, USA;* [4]*Nuclear Medicine, VAPAHCS, Palo Alto, CA, USA;* [5]*Radiology, Stanford University, Stanford, CA, USA;* [6]*Nuclear Medicine & Radiobiology, Centre Hospitalier de l'Université de Sherbrooke, Sherbrooke, QC, Canada;* [7]*Cardiothoracic Surgery, Stanford University, Stanford, CA, USA;* [8]*Radiation Oncology, Stanford University, Stanford, CA, USA;* [9]*Surgery, VA Palo Alto Healthcare System, Palo Alto, CA, USA. Contact e-mail: mjamali@stanford.edu*

Background: FDG PET uptake in non-small cell lung cancer (NSCLC) has previously been shown to associate with clinical outcome. Circulating tumor cells (CTCs) may play a role in tumor metastasis and clinical outcome. We therefore sought to associate enumerated CTCs with FDG PET uptake using a prospective study of treatment naive patients undergoing evaluation for NSCLC. Methods: We used a non-EpCAM based detection assay to detect putative CTCs (termed "High-Definition CTCs") from blood samples at two medical centers performing a prospective study of patients with a pulmonary nodule undergoing FDG PET-CT imaging for clinical evaluation. HD-CTCs were enumerated after standardization relative to white blood cells in circulation, both as individual cells and as clusters of cells (≥ 2 cells in direct contact with each other). PET-CT scanners were calibrated using an anthropomorphic thoracic phantom and images were extracted using PET VCAR™ software implemented on a GE AW workstation. HD-CTC quantities were then associated with FDG PET tumor uptake using uncorrected SUV_{max}, partial volume corrected SUV_{maxPVC}, and Total Lesion Glycolysis (TLG = SUV_{mean} x metabolic tumor volume) by Spearman rank correlation. Differences in groups were calculated using ANOVA or Chi-squared analysis, with the appropriate test applied based on the underlying distribution of the variable. Results: Sixty-three patients from two medical centers were eligible for this analysis. Forty-five patients had stage I NSCLC, 11 patients had more advanced stage NSCLC (II-IV) and 7 patients had non-NSCLC malignancies of the lung. No statistical differences were observed among groups for clinical, imaging, or CTC variables. Median tumor diameter was 2.2 cm (Interquartile range [IQR] 1.6-3.0) and 37 patients had adenocarcinoma compared to 12 with squamous histology and 7 with untyped NSCLC. CTCs were prevalent in stage I disease, with 64% (29/45) of tumors having > 2 CTCs/10M WBC and 53% (24/45) of tumors having > 5 CTCs per 10M WBC. Forty-nine percent of stage I tumors had CTC clusters. The median SUV_{max} was 4.6 (IQR 2.3-8.9), median SUV_{maxPVC} was 6.7 (IQR 4-11) and median TLG was 11 (2.8-26) for the primary tumor. CTCs correlated poorly with scalar imaging metrics SUV_{max}, SUV_{maxPVC} and CT diameter, as well as with volume metrics TLG and CT volume. Surprisingly, there was a wide distribution of HD-CTCs noted for a given FDG uptake or CT diameter in stage I disease (Figure 1). Conclusions: CTCs were prevalent in stage I disease when using a non-enriched CTC platform and there was a large range of CTCs for a given SUV_{maxPVC} or tumor diameter. Historically, these biomarkers associate with prognosis but they correlated poorly with each other in this study. These data suggest that non-invasive disease characterization using CTCs and metabolic activity of the tumor are two complementary diagnostic tools to describe NSCLC in its early stages.

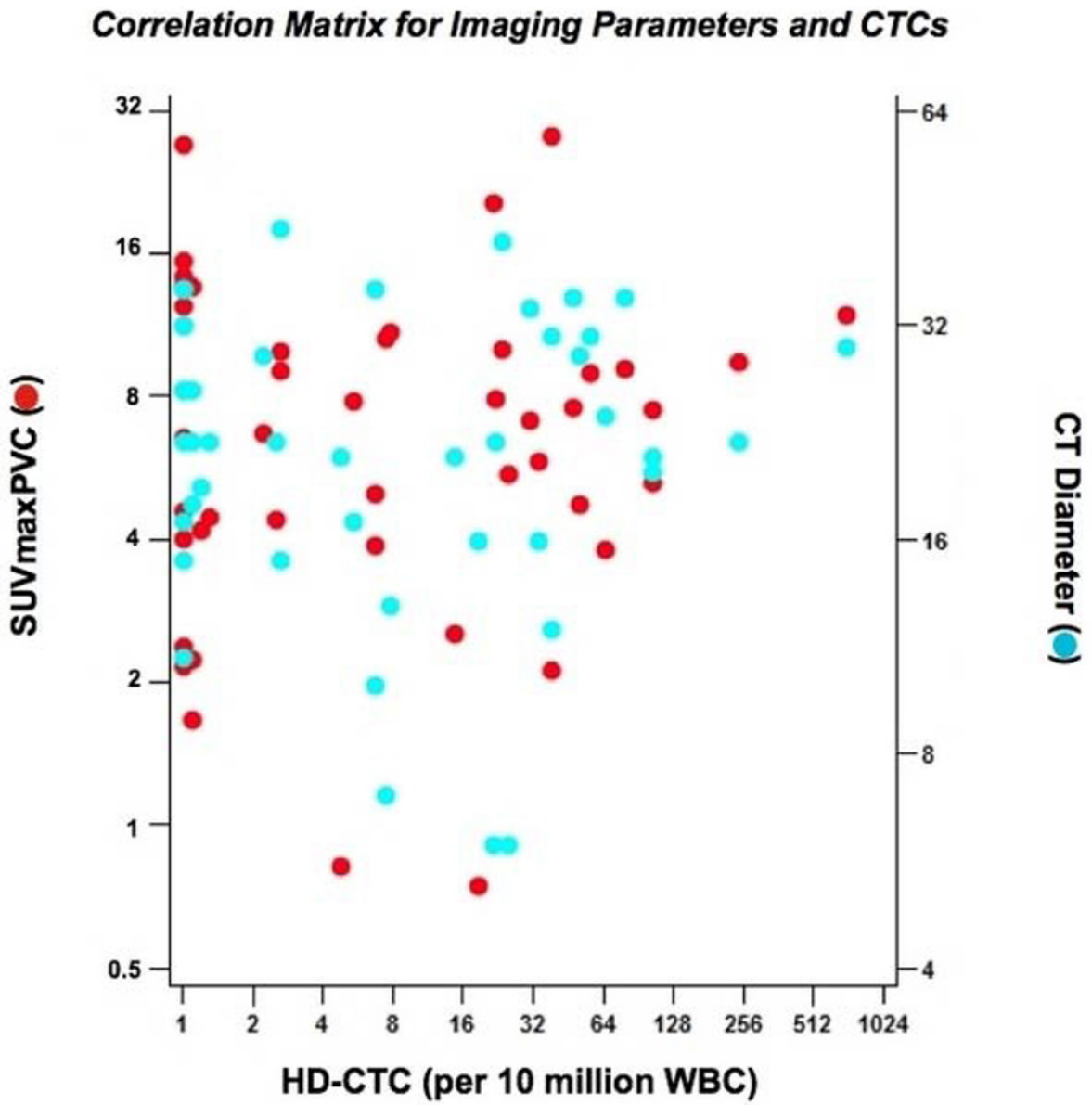

Circulating tumor cells (HD-CTCs) are shown with their respective tumor SUV_{maxPVC} (red) and CT diameter in millimeter (blue) for 45 stage I NSCLC patients. Axes are shown in their $log_2(x,y)$ form for ease of interpretation. Note the wide range of CTCs for a given tumor FDG uptake or diameter.

Disclosure of author financial interest or relationships:
M. Jamali, None; **K. Keu**, None; **V.S. Nair**, None; **M.S. Luttgen**, None; **M.S. Vasanawala**, None; **W. Kuschner**, None; **A. Iagaru**, None; **J.B. Shrager**, None; **B.W. Loo**, None; **P. Kuhn**, Epic Sciences, Inc., Stockholder; **S.S. Gambhir**, Bracco Diagnostics, Consultant; Endra, Inc, Stockholder; Cellsight, Stockholder; Enlight, Inc., Stockholder; General Electric, Grant/research support; ImaginAb, Stockholder; MagArray, Inc., Stockholder; Sanofi-Aventis, US, Grant/research support; SiteOne Therapeutics, Stockholder; VisualSonics/Sonosite, Stockholder .

Presentation Number **SS 4**
Scientific Session 01: First in Human & Clinical Studies - Oncology
September 19, 2013 / 11:15-11:30 / Room: 102

Pilot Prospective Evaluation of the Novel PET/CT Radiopharmaceutical 18F FPPRGD2 in Patients with Non-Small Cell Lung Cancer

Andrei Iagaru[1], *Guido Davidzon*[1], *Camila Mosci*[1], *Bin Shen*[2], *Frederick T. Chin*[2], *Sanjiv S. Gambhir*[1,2], [1]*Radiology, Nuclear Medicine, Stanford University Medical Center, Stanford, CA, USA;* [2]*Radiology, MIPS, Stanford University Medical Center, Stanford, CA, USA. Contact e-mail: aiagaru@stanford.edu*

Objectives: Angiogenesis is essential for tumor growth and the expression of activated αvβ3 integrins plays a key role in this process. 18F FPPRGD2 (US FDA IND #113269) is a novel PET radiopharmaceutical based on a dimeric RGD peptide sequence that targets the αvβ3 integrins. We now present data on its biodistribution, kinetics and lesion detection in patients with non-small cell lung cancer (NSCLC). Methods: We recruited 4 participants with NSCLC (2 women, 2 men), 55-76 year-old (average: 62.3 ± 9.4). One dynamic 18F FPPRGD2 PET and two static 18F FPPRGD2 PET/CT scans were obtained up to 3 hours post-injection. SUVmax values in the detected lesions, as well as in normal background areas were measured at 15 min, 30 min, 45 min, 60 min and 120 min after the radiopharmaceutical i.v. administration. Vital signs and EKGs were obtained at regular intervals. Blood samples were collected before injecting 18F FPPRGD2, at 24 hours and 1 week post-injection. Two participants were scanned before and at 1-week after starting bevacizumab treatment. Results: 18F FPPRGD2 was well tolerated, with no significant changes in vital signs, EKGs, or laboratory values. It had stable distribution in all patients, similar to the healthy volunteers data, with primary clearance through the kidneys, as well as the liver and bowel. 18F FPPRGD2 uptake was highest at 45 min in primary NSCLC lesions and metastases, with SUVmax values of 4.24 - 15.51 (average 10 ± 5.64) and 4.22 - 13.9 (average 8.33 ± 5), respectively. Background SUVmax values were 0 - 1.02 (average 0.53 ± 0.12) for cerebellum, 0.63 - 1.67 (average 1.29 ± 0.29) for aortic arch, and 2.29 - 4.11 (average 3.09 ± 0.7) for liver. The 18F FPPRGD2 uptake at 1 week after starting bevacizumab decreased by 29.5% in one patient and by 16.8% in the other. Conclusions: 18F FPPRGD2 is safe and has stable biodistribution and kinetics for imaging αvβ3 integrins expression as a surrogate biomarker of tumor angiogenesis. Evaluation of 18F FPPRGD2 in participants with NSCLC demonstrates high uptake in both the primary and metastatic lesions. Given the low uptake in normal background tissues, this may allow for patient selection prior to anti-angiogenesis treatments and for early assessment of response to such therapies.

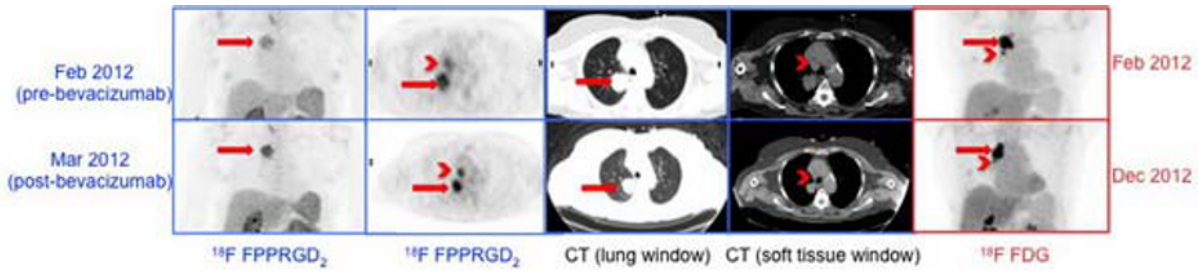

76 year-old woman with right lung NSCLC, treated with carboplatin, pemetrexed and bevacizumab, scanned before starting bevacizumab and 1-week after starting bevacizumab. Pre- and post-bevacizumab 18F FPPRGD2 images are highlighted in blue and show stable uptake post-treatment (change of 16.8%) in the lung mass (arrow) and nodal metastasis (arrowhead). Pre-bevacizumab and 10-month follow-up 18F FDG images are highlighted in red and also show stable uptake long-term post-treatment in the lung mass (arrow) and nodal metastasis (arrowhead).

Disclosure of author financial interest or relationships:

A. Iagaru, None; **G. Davidzon**, None; **C. Mosci**, None; **B. Shen**, None; **F.T. Chin**, Ground Fluor Pharmaceuticals, Consultant; **S.S. Gambhir**, Bracco Diagnostics, Consultant; Endra, Inc, Stockholder; Cellsight, Stockholder; Enlight, Inc., Stockholder; General Electric, Grant/research support; ImaginAb, Stockholder; MagArray, Inc., Stockholder; Sanofi-Aventis, US, Grant/research support; SiteOne Therapeutics, Stockholder; VisualSonics/Sonosite, Stockholder .

Presentation Number **SS 5**
Scientific Session 01: First in Human & Clinical Studies - Oncology
September 19, 2013 / 11:30-11:45 / Room: 102

Characterization of physiological 18F-FSPG uptake in healthy volunteers and comparison to 18F-FDG

Erik Mittra[1], *Meena Kumar*[1], *Camila Mosci*[1], *Kamilla Smolarz*[2], *Markus Schwaiger*[2], *Andrew Stephens*[3], *Ludger M. Dinkelborg*[3], *Sanjiv S. Gambhir*[1], [1]*Radiology, Stanford University, Stanford, CA, USA;* [2]*Nuclear Medicine, Technische Universitat Munchen, Munich, Germany;* [3]*Piramal Imaging GmbH, Berlin, Germany. Contact e-mail: erik.mittra@stanford.edu*

Objectives: (S)-4-(3-[18F] Fluoropropyl)-L-glutamic acid (FSPG) is a novel radiopharmaceutical for PET imaging. It is a glutamate analogue that is a marker of xC- transporter and CD44 expression that has a good dosimetric profile and shows promise for oncologic imaging. The purpose of this study is to understand the normal biodistribution and kinetics of FSPG and compare FSPG to 18F-FDG (FDG) in healthy volunteers. Methods: Eight (± 10%) mCi of FSPG was given IV to 5 subjects (3 women and 2 men; age range: 50-65 years-old) and 7 PET and 3 CT scans per volunteer were obtained 0-4 hours post-injection (p.i.). From the 45 minute (min) p.i. scan, we measured max and mean standardized uptake values (SUV) in 30 different regions of the body. A subset of these regions was analyzed over all 7 scans to evaluate tracer kinetics. FSPG SUV values at 45 min were compared with previously published FDG SUV values at 60 min. Results: On the 45 min p.i. scan, there was very low-grade background activity in most regions. There was prominent pancreatic uptake and renal clearance. Kinetic data showed rapid tracer clearance from blood pool and most organs except the pancreas (likely due to overexpression of xC-/CD44). Compared to FDG, FSPG showed less uptake in organs except the pancreas based on SUV mean, and higher uptake in organs except the brain based on SUV max. Notably, the brain takes up much less FSPG than FDG. Comparative SUVmax values are as follows (FSPG mean ± s.d., FDG mean ± s.d.): brain 0.31 ± 0.1, 3.87 ± 31.8; thyroid 1.84 ± 0.23, 0.93 ± 3.43; breast 1.15 ± 0.34, 0.27± 2.34; lung 0.79 ± 0.20, 0.33 ± 1.23; pancreas 17.68 ± 3.58, 0.97 ± 3.08; liver 3.36 ± 0.86, 1.59 ± 4.77; spleen 2.14 ± 0.79, 1.46 ± 3.80; and colon 1.53 ± 0.35, 0.69 ± 8.52. Similar findings have also been confirmed in 60 cancer patients. Conclusions: Understanding physiological uptake of this promising new tracer is critical for improved interpretative accuracy and understanding potential applications. Given low background activity, FSPG may be suitable for applications in a wide variety of malignancies with exception of the pancreas, kidneys and bladder.

Figure 1. Coronal Maximum Intensity Projection (MIP) Image (A) shows the biodistribution of 18F-FSPG 45 minutes after intravenous administration in a healthy volunteer. The principal organs/regions are labeled. The axial CT and PET images (B) further shows the distribution of 18F-FSPG at the brain (upper image), thorax (middle image) and upper abdomen (lower image). The labels are as follows: 1.brain, 2.oropharyngeal activity, 3.lung, 4.pancreas, 5.liver, 6.kidneys, 7.bladder, 8.heart.

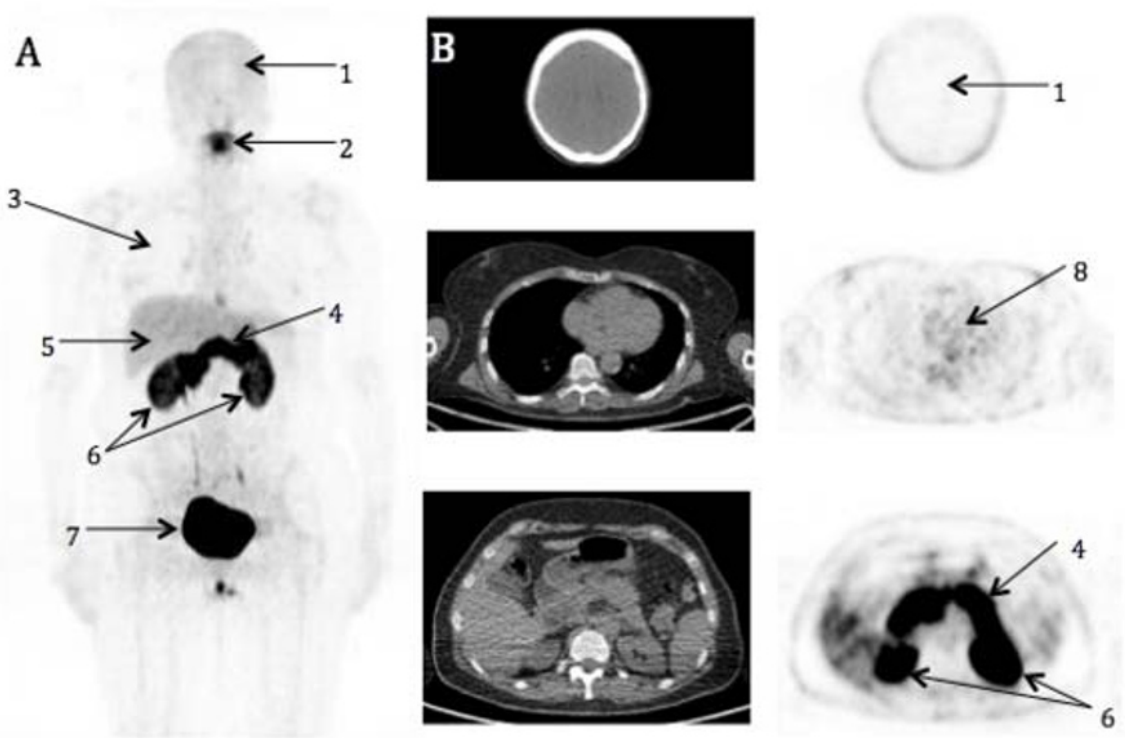

Disclosure of author financial interest or relationships:
E. Mittra, None; **M. Kumar**, None; **C. Mosci**, None; **K. Smolarz**, None; **M. Schwaiger**, Siemens Health care, Grant/research support; **A. Stephens**, Piramal Imaging, Employment; **L.M. Dinkelborg**, None; **S.S. Gambhir**, Bracco Diagnostics, Consultant; Endra, Inc, Stockholder; Cellsight, Stockholder; Enlight, Inc., Stockholder; General Electric, Grant/research support; ImaginAb, Stockholder; MagArray, Inc., Stockholder; Sanofi-Aventis, US, Grant/research support; SiteOne Therapeutics, Stockholder; VisualSonics/Sonosite, Stockholder .

Presentation Number **SS 6**
Scientific Session 01: First in Human & Clinical Studies - Oncology
September 19, 2013 / 11:45-12:00 / Room: 102

Proliferation rate assessed by [18F]fluorothymidine Positron Emission Tomography (PET) in paragangliomas is low and does not correlate with glucose metabolism as reflected by [18F]fluorodeoxyglucose PET

Elise M. Blanchet[1,4], *Corina M. Millo*[2], *Victoria Martucci*[1], *Maria J. Merino*[3], *Peter Herscovitch*[2], *Karel Pacak*[1], [1]*Program of Reproductive and Adult Endocrinology, NICHD, NIH, Bethesda, MD, USA;* [2]*PET Department, Clinical Center, NIH, Bethesda, MD, USA;* [3]*Laboratory of Pathology, NCI, NIH, Bethesda, MD, USA;* [4]*University Paris-Sud 11, Paris, France. Contact e-mail: eliseblanchet@gmail.com*

Objectives: The goal of this study was to image cellular proliferation in paragangliomas (PGL) using [18F]fluorothymidine (FLT) positron emission tomography (PET), in order to evaluate its potential in predicting tumor aggressiveness and to compare it with the information derived from [18F]fluorodeoxyglucose (FDG) PET. Material and Methods: Twelve patients with PGLs (7 metastatic and 5 non-metastatic) confirmed either by histology or by a combination of PET with PGL-specific tracers, anatomic imaging, biochemistry, medical history and follow-up, were scanned with both FLT and FDG. Uptake was assessed at a lesion level, visually and quantitatively by maximum standard uptake values (SUVmax) for both tracers. FLT uptake was compared to risk factors known to be linked to aggressiveness in PGLs (SDHB-mutated status, lesion size, dopaminergic phenotype) and with FDG uptake. Results: In 12 patients, 77 lesions were assessed. All lesions had low FLT uptake (median SUVmax of 2.25 and range of [0.7-4.5]). The only sites where a clear high FLT uptake was present were around bone lesions; this corresponded to non-specific bone marrow uptake at the periphery of lesions but not within. There was no elevation of FLT uptake in lesions believed to be aggressive. Most of the lesions showed a mismatch, with high FDG uptake (median SUVmax of 10.8 and range of 1.1-79.0) contrasting with low FLT uptake. Conclusions: FLT uptake was found to be very low in PGLs, whatever the status of the tumors. This appears to reflect the slow proliferation rate of all PGLs in the present study. These findings provide a new insight into PGL biological behavior and suggest that antiproliferative agents may not be useful for treatment of these tumors.

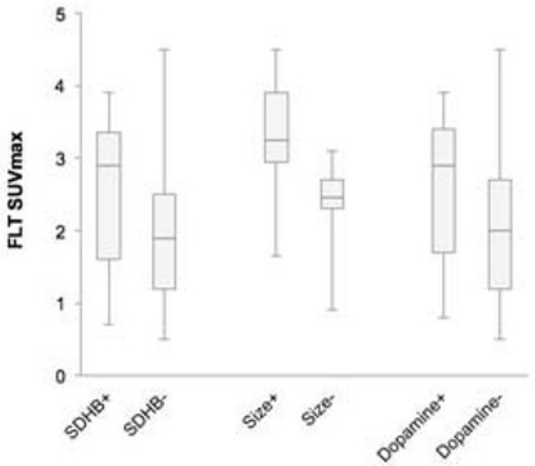

A: FLT SUVmax correlated to aggressiveness factors.

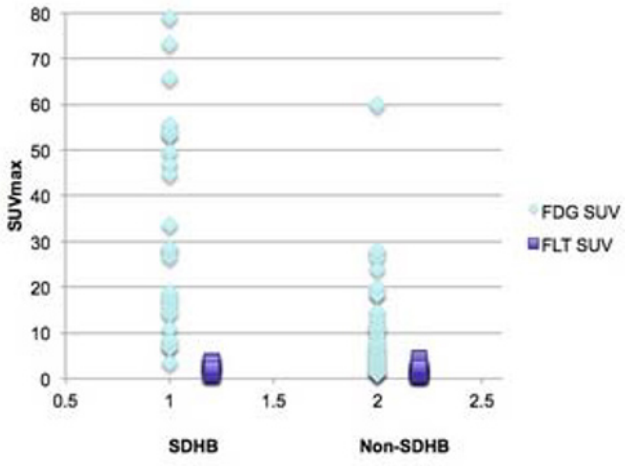

B: SUVmax values distributions for PGL lesion with both tracers (FDG and FLT) in SDHB and non-SDHB patients

Patients clinical characteristics

Patient	Age (years), sex	Germline mutation	Initial date of PGL onset	Initial presentation (size of the largest lesion in cm)	Status at the time of FLT and FDG PET	Dopamine secretion
#1	43, M	sporadic	2012	adrenal (4)	primary	normal
#2	43, M	SDHD	2012	head/neck (5)	primary	normal
#3	43, M	SDHD	2010	head/neck (5) + mediastinal + abdominal	primary	normal
#4	48, F	MEN2	1999	adrenal (12)	metastatic	normal
#5	47, M	sporadic	1995	adrenal (unknown)	metastatic	normal
#6	70, M	sporadic	2009	adrenal (34)	metastatic	normal
#7	50, F	sporadic	2005	abdominal (8)	metastatic	normal
#8	30, M	SDHB	2012	abdominal (2.5)	primary	normal
#9	27, M	SDHB	2012	mediastinal (3)	primary	normal
#10	35, M	SDHB	1996	abdomino-pelvic (8)	metastatic	increased
#11	35, M	SDHB	2002	abdominal (7)	metastatic	increased
#12	47, M	SDHB	2006	head/neck (3)	metastatic	normal

PGL: Paraganglioma.
SDHB: Succinate dehydrogenase subunit B.
SDHD: Succinate dehydrogenase subunit D.
MEN2: Multiple endocrine neoplasia 2.

Disclosure of author financial interest or relationships:
E.M. Blanchet, None; **C.M. Millo**, None; **V. Martucci**, None; **M.J. Merino**, None; **P. Herscovitch**, None; **K. Pacak**, None.

Presentation Number **SS 7**
Scientific Session 02: Preclinical in vivo Studies - Cardiology
September 19, 2013 / 10:30-10:45 / Room: 105

A Nanomedicine-based Treatment Paradigm for Rapid Remodeling of Atherosclerotic Plaques

Jun Tang[1,2], *Mark E. Lobatto*[1,3], *Susanne van der Staay*[1,3], *Sarian M. van Rijs*[1,3], *Sarayu Ramachandran*[1], *Wei Leong*[1,2], *Raphael Duivenvoorden*[3], *Ying Wang*[4], *Ira Tabas*[4], *Edward A. Fisher*[5], *David P. Cormode*[6], *Zahi A. Fayad*[1], *Willem J. Mulder*[1,3],
[1]*Translational and Molecular Imaging Institute, Icahn School of Medicine at Mount Sinai, New York, NY, USA;* [2]*Graduate School of Biomedical Sciences, Icahn School of Medicine at Mount Sinai, New York, NY, USA;* [3]*Department of Vascular Medicine, Academic Medical Center, Amsterdam, Netherlands;* [4]*Department of Medicine, Columbia University, New York, NY, USA;* [5]*Department of Medicine (Cardiology)(and Cell Biology, Marc and Ruti Bell Program in Vascular Biology, New York University School of Medicine, New York, NY, USA;* [6]*Department of Radiology, University of Pennsylvania, Perelman School of Medicine, PA, USA. Contact e-mail: jun.tang@mssm.edu*

Introduction: Atherosclerosis is an inflammatory disease. Its major clinical manifestation, coronary artery disease, is the leading cause of death in the western world. The disease is caused by the rupture of macrophage-laden and highly-inflamed atherosclerotic plaques, which are prone to rupture and cause myocardial infarctions. Oral statin therapy is widely used to reduce blood cholesterol levels in patients with atherosclerosis, and it is believed to have modest anti-inflammatory effects. We previously developed a strategy that aims at amplifying these anti-inflammatory effects through statin delivery to plaque macrophages using a reconstituted high density lipoprotein (rHDL) nanoparticle as a delivery vehicle. This statin rHDL ([S]-rHDL) nanotherapy reduced plaque macrophages by 80% (Supplementary). In the current study, we set out a novel nanomedical treatment paradigm, based on the aforementioned [S]-rHDL nanotherapy, which aims at realizing rapid remodeling of advanced atherosclerotic plaques towards a favorable phenotype in Apolipoprotein E-/- (ApoE KO) mice. Design and Results: ApoE KO mice received 26 weeks of high-cholesterol diet to develop advanced atherosclerotic plaques. After the diet, the mice first received high dose [S]-rHDL for a week (60 mg/kg simvastatin, 4 intravenous injections /week), followed by either low dose [S]-rHDL (15 mg/kg simvastatin, 2 intravenous injections /week), oral simvastatin (15 mg/kg/day), or no treatment for another 8 weeks (A). We evaluated the efficacies of the therapies during the course of the 9-week treatment with a MATLAB-assisted histological assessment of aortic roots, and CD68 immunostaining and hematoxylin phloxine saffron stain (HPS)) were performed (B). In vivo magnetic resonance imaging (MRI) of abdominal aortas and blood tests were done as well. After one week high dose [S]-rHDL treatment, macrophage levels in aortic roots were reduced by 70% ($P < 0.001$). The low levels were maintained by a subsequent 8-week low dose [S]-rHDL (48 % lower than control) or oral simvastatin treatment regimen (33% lower than control) (C). Importantly, both regimens resulted in an increase of connective tissue in the plaques at week 5 (D), indicative of plaque remodeling towards a favorable phenotype (E). Furthermore, the unchanged wall thickness in abdominal aortas suggested that the therapies affect plaque composition rather than plaque size. Finally, blood tests revealed no serious adverse effects. Conclusion and Clinical Perspective: We developed a [S]-rHDL nanotherapy treatment regimen that can rapidly reduce plaque inflammation in a week and subsequently promote plaque remodeling towards a favorable phenotype in 8 weeks. Clinically, this regimen could have implications for patients with acute coronary artery disease. The short-term intravenous infusion of [S]-rHDL could be applied to hospitalized patients and serve to rapidly reduce plaque inflammation, while subsequent high-dose oral statin treatment stabilizes the plaques. This new nanomedical treatment paradigm could be added to the current standard care of coronary artery disease and help reduce high recurrence rates.

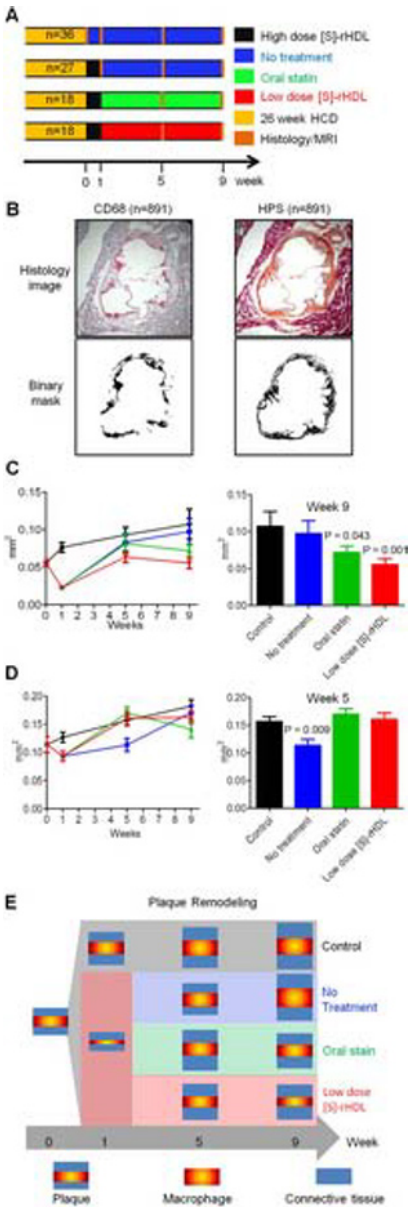

Disclosure of author financial interest or relationships:
J. Tang, None; **M.E. Lobatto**, None; **S. van der Staay**, None; **S.M. van Rijs**, None; **S. Ramachandran**, None; **W. Leong**, None; **R. Duivenvoorden**, None; **Y. Wang**, None; **I. Tabas**, None; **E.A. Fisher**, None; **D.P. Cormode**, Philips, Grant/research support; **Z.A. Fayad**, None; **W.J. Mulder**, None.

Presentation Number **SS 8**
Scientific Session 02: Preclinical in vivo Studies - Cardiology
September 19, 2013 / 10:45-11:00 / Room: 105

Nanoparticle targeting mechanism in experimental atherosclerosis

Mark E. Lobatto[1,2], *Claudia Calcagno*[1], *Antoine Millon*[1], *Max Senders*[1], *Francois Fay*[1], *Philip Robson*[1], *Sarayu Ramachandran*[1], *Erik S. Stroes*[2], *Zahi A. Fayad*[1], *Willem J. Mulder*[1,2], [1]*TMII, Mount Sinai School of Medicine, New York, NY, USA;* [2]*Vascular Medicine, AMC, Amsterdam, Netherlands. Contact e-mail: m.e.lobatto@gmail.com*

Introduction: The use of nanoparticles for drug delivery is well established in oncology, where accumulation of nanoparticles in tumors is attributed to the enhanced permeability and retention (EPR)-effect1. In a limited number of studies, long-circulating nanoparticles, such as PEGylated liposomes2, have been shown to accumulate in atherosclerotic plaques, though the mechanism of accumulation has not been elucidated. The aim of the current study was to systematically investigate how long-circulating nanoparticles accumulate in atherosclerotic lesions over time. Methods: Dynamic Contrast Enhanced-MRI (DCE-MRI) has been used to investigate permeability of atherosclerotic lesions in experimental atherosclerosis and patients. Due to the heterogeneity of atherosclerosis, we developed a 3D DCE-MRI protocol, to allow coverage over a large vascular region, e.g. the entire infra-renal aorta of an atherosclerotic rabbit, in a three-dimensional fashion. We first subjected atherosclerotic rabbits (n=8) to a 3D DCE-MRI scan on a 3T clinical scanner, from which area under the curves (AUC) were derived. After in vivo imaging we injected a fluorescent permeability dye, Evans Blue (EB), that stains dysfunctional endothelium. PEG-liposomes (LN) labeled with the fluorescent dye Cy7, were injected and allowed to circulate for different time points (½ hour, 6 hours and 24 hours) after which rabbits were sacrificed. IVIS optical imaging was used to quantify fluorescence of both EB and LN in excised abdominal aortas. Results: Excellent correlation of LN uptake after a ½-hour was seen when compared to both vascular permeability determined with EB ($r2 = 0.8$, $p<0.0001$) and by DCE-MRI ($r2=0.65$, $p=0.0009$). The correlation gradually decreased, though remained significant after 6 hours of LN circulation (EB: $r2=0.47$, $p=0.007$; AUC: $r2=0.53$, $p=0.003$), but became insignificant after 24 hours of LN circulation (EB: $r2=0.08$, $p=0.33$; AUC: $r2=0.08$, $p=0.33$). An example of in vivo 3D DCE-MRI (A), ex vivo EB (B) and LN (C) uptake after 6 hours shows permeability and LN uptake in the same regions. The correlation graphs of LN with EB and LN with DCE-MRI after 6 hours are shown in D and E, respectively. The decline in correlation over time led us to further investigate LN distribution at a microscopic level with fluorescence microscopy. We initially found LN confined to the vasculature. Gradual extravasation from the lumen and neovessels was observed at 6 hours (F), while LN was found throughout the plaque at 24 hours (G), corroborating in and ex vivo findings. Conclusion: In vivo 3D DCE-MRI correlates with ex vivo Evans Blue staining and can be used as an in vivo surrogate marker for vascular permeability. LN uptake correlates with endothelial permeability in atherosclerosis with in and ex vivo imaging, showing that LN uptake in atherosclerosis is very similar to EPR-facilitated targeting in cancer. Relevance: Long-circulating nanoparticles may be employed for local drug delivery to atherosclerotic plaques. Furthermore, 3D DCE-MRI might be a valuable in vivo tool to predict if a subject is amenable to nanoparticle therapy. 1Prabhakar U, Cancer Res 2013 2Lobatto ME, Mol Pharm 2010

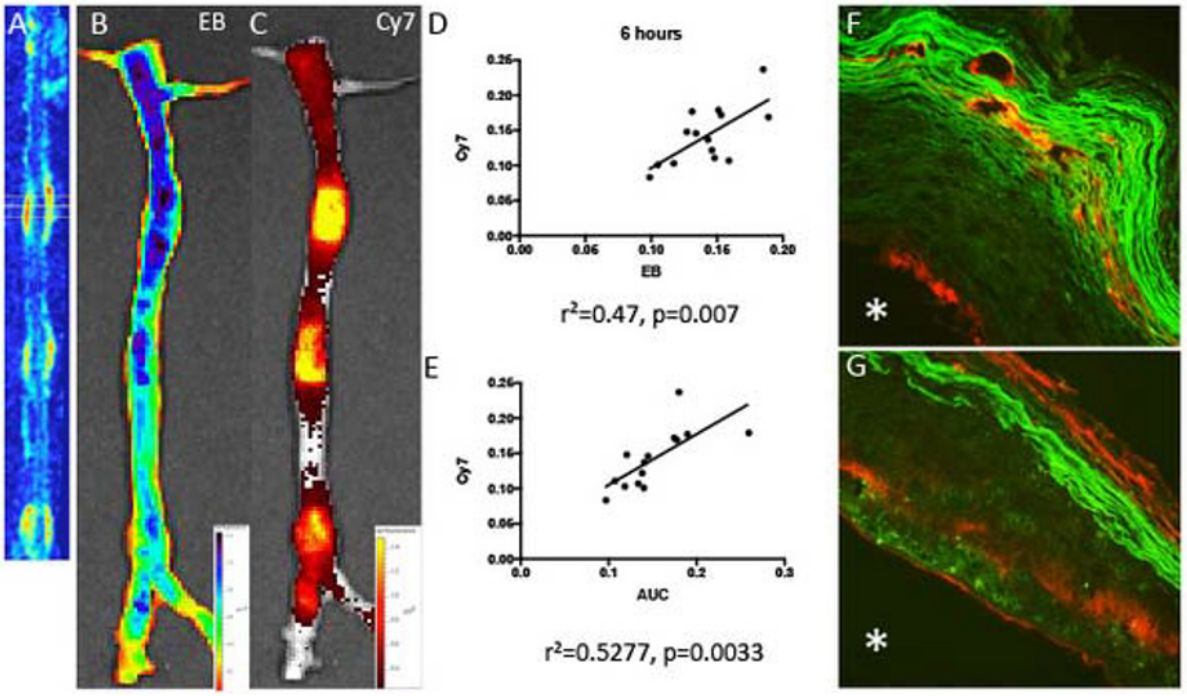

Disclosure of author financial interest or relationships:
M.E. Lobatto, None; **C. Calcagno**, None; **A. Millon**, None; **M. Senders**, None; **F. Fay**, None; **P. Robson**, None; **S. Ramachandran**, None; **E.S. Stroes**, None; **Z.A. Fayad**, None; **W.J. Mulder**, None.

Presentation Number **SS 9**
Scientific Session 02: Preclinical in vivo Studies - Cardiology
September 19, 2013 / 11:00-11:15 / Room: 105

Hybrid PET/MRI Cardiac Imaging in Canine Myocardial Infarction: Extent of Inflammation by 18FDG in no-reflow, hyper enhanced and remote myocardium as defined by late gadolinium enhanced MRI

Frank S. Prato[1,2], *James A. White*[1,4], *Martin Rajchl*[4], *Jane M. Sykes*[1], *John R. Butler*[1], *Kimberley Blackwood*[1], *R. Terry Thompson*[1,2], *Gerald Wisenberg*[1,3], [1]*Imaging, Lawson Health Research Institute, London, ON, Canada;* [2]*Medical Biophysics & Medical Imaging, Western University, London, ON, Canada;* [3]*Cardiology, LHSC, London, ON, Canada;* [4]*Imaging, Robarts Research Institute, London, ON, Canada. Contact e-mail: prato@lawsonimaging.ca*

The cell-mediated inflammatory response to myocardial infarction, particularly its time course and regional distribution, may be an important factor contributing to adverse myocardial remodeling and heart failure. Here we have used a canine model of myocardial infarction (permanent ligation of the left anterior descending coronary artery) to develop the methodology and image analysis tools to extract the time course of the inflammatory response within three myocardial zones (infarct without microvascular obstruction (IWMO), infarct with microvascular obstruction (MO) and remote myocardium (RM)). The infarct zones were defined based on their late gadolinium enhancement (LGE) pattern with precise co-registration of 18FDG PET and MR images using a whole body hybrid 3-Tesla MRI-PET scanner (Biograph mMR, Siemens Healthcare, Germany). Canines (n=5) underwent sustained occlusion of the LAD distal to the first diagonal branch and were imaged on the day of infarction and subsequently at days 7, 14 and 21. To suppress the normal myocardial uptake of FDG, animals were fasted for 12 hours and a fatty supplement was infused prior to administration of 18F-FDG, producing FDG images that primarily reflected activity within monocytes/macrophages. PET imaging was performed after injection of 10 MBq/kg of 18F labeled Fluro-2-deoxyglucose (FDG) administered at onset of the study. MR imaging was inclusive of: Dixon 2-point for attenuation correction, breath-held TrueFISP cines (short and long axis views), a 3D MRA and spatially matched 3D LGE imaging. The latter part of the protocol was performed using a high-resolution 3D (coronary) magnetic resonance angiography (MRA) sequence (ECG-gated 3D segmented FLASH with respiratory navigation, inversion pulse to suppress myocardial signal, and fat saturation) both during, and 20 minutes following infusion of 0.2 mmol/kg Gadolinium chelate (Magnevist, Bayer). ECG-gated PET was performed in list mode (binning of data according to cardiac cycle) simultaneous to 3D LGE imaging. Image analysis was performed using locally developed semi-automated software. Myocardial tissue and blood pool were segmented from 3D MRA and applied as constraints to the 3D LGE dataset following registration. Three myocardial zones were identified, as follows: i) IWMO defined as myocardial signal ≥5SD versus RM, ii) MO defined as regions of signal loss contained by the region of IWMO, and iii) RM was separated into five 3D shells, the first within 0 to 10 mm of the infarct edge and each subsequent shell 10 mm further removed. These tissue labels were registered to corresponding (inherently spatially registered) PET data for each of the 4-time points to derive an evaluation of FDG signal over time for each zone. Results are summarized in the figure and table, and demonstrate a) myocardial infarction induces an intense inflammatory reaction extending beyond the infarct, declining with increasing distance from the infarct edge b) this process evolves both in degree and extent over the first 3 weeks and c) perfusion is necessary for inflammation to occur. These techniques can be applied directly to the assessment of clinical infarction.

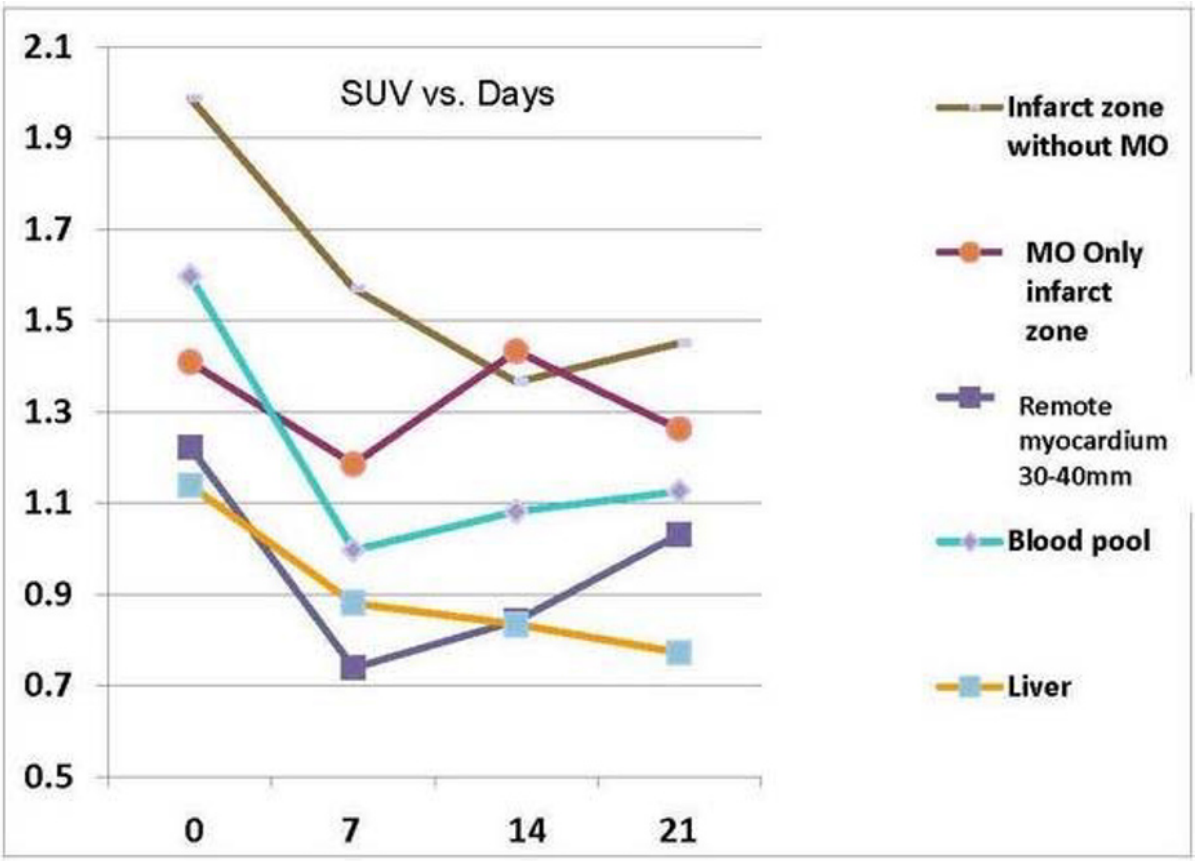

Graphic display of 18FDG SUV values for the five zones on days 0, 7, 14 and 21.

Average SUV In Remote Myocardium as a function of distance from infarct and days post infarction

Distance from Infarct	0 Days	7 Days	14 Days	21 Days
0 to 10mm	2.16	1.09	1.28	1.43
10 to 20mm	1.83	1.00	1.23	1.35
20 to 30mm	1.46	0.89	1.04	1.23
30 to 40mm	1.22	0.74	0.84	1.03
40 to 50mm	0.67	0.55	0.28	0.81

Rows correspond to days after the infarct (0,7,14 & 21 days) and columns correspond to distance of the remote myocardium from the infarction

Disclosure of author financial interest or relationships:

F.S. Prato, None; **J.A. White**, Bayer, Inc, Grant/research support; **M. Rajchl**, None; **J.M. Sykes**, None; **J.R. Butler**, None; **K. Blackwood**, None; **R. Thompson**, None; **G. Wisenberg**, None.

Presentation Number **SS 10**
Scientific Session 02: Preclinical in vivo Studies - Cardiology
September 19, 2013 / 11:15-11:30 / Room: 105

PET/CT imaging of activated platelets in murine carotid artery thrombosis using single-chain antibody labeled with the novel 64Cu-complexing chelator MeCOSar

Karen Alt[1,2], *Brett M. Paterson*[3], *Katie Ardipradja*[1,4], *Christine Schieber*[3], *Gojko Buncic*[3], *Graeme J. O'Keefe*[4,5], *Stan Poniger*[4], *Henri Tochon-Danguy*[4], *Andrew M. Scott*[4,6], *Uwe Ackermann*[4,5], *Karlheinz Peter*[2], *Paul S. Donnelly*[3], *Christoph E. Hagemeyer*[1], [1]*Vascular Biotechnology Laboratory, Baker IDI Heart and Diabetes Institute, Melbourne, VIC, Australia;* [2]*Atherothrombosis and Vascular Laboratory, Baker IDI Heart and Diabetes Institute, Melbourne, VIC, Australia;* [3]*School of Chemistry, Bio21, University of Melbourne, Melbourne, VIC, Australia;* [4]*Department of Nuclear Medicine and Centre for PET, Austin Health, Melbourne, VIC, Australia;* [5]*Department of Medicine, Dentistry and Health Scienes, University of Melbourne, Melbourne, VIC, Australia;* [6]*Ludwig Institute for Cancer Research, Austin Health, Melbourne, VIC, Australia. Contact e-mail: karen.alt@bakeridi.edu.au*

BACKGROUND: Platelets have an established role in haemostasis but it is becoming increasingly clear that they also have inflammatory functions. This makes molecular PET imaging of platelets very attractive as it opens up the possibility to detect not only acute thrombotic events in severe diseases such as stroke and myocardial infarction, but also to detect platelets in inflammatory disease such as arthritis and atherosclerosis. We previously generated a single-chain antibody (scFv) that specifically binds to the highly abundant platelets surface receptor GPIIb/IIIa in its active, ligand bound form (LIBS). The presented work reports on the generation of a novel 64Cu MeCOSar labeled scFvLIBS and the in vivo validation of the new radiotracer in acute thrombosis. METHODS: ScFvLIBS and non-binding control scFvmut were conjugated to the novel 64Cu chelator NHS-MeCOSar and loaded with 64Cu at room temperature at pH 8 for 30 min. The binding of the radiolabeled scFv to activated platelets was determined by flow cytrometry and the molar ratio of chelator to scFv determined by mass spectrometry. In vivo experiments were performed in a mouse model of acute thrombosis, where a platelet rich clot is formed in the carotid artery with FeCl3. Animals received an i.v. injection of 20ug radiolabeled scFv equivalent to 3-5 MBq 20 mins after injury. A 1h dynamic PET scan was acquired using a Bioscan NanoPET/CT system followed by obtaining a CT image for anatomical reference. After the scan a biodistribution was conducted. To demonstrate specificity of the radiotracer, blocking experiments with 200µg and 400µg non-radioactive scFv given 30 mins prior to injection of the radiolabeled scFv, were performed. RESULTS: The novel construct MeCOSar-scFvLIBS could be radiolabeled rapidly under mild conditions resulting in high specific activity. The biodistribution revealed a significant higher uptake of the scFvLIBS in the injured vessel (108.5 %ID/g ± 47.5) compared to the non-injured vessel (12.1 %ID/g ± 5.8) (p=0.001) and only minimal uptake of the scFvmut (8.5 %ID/g ± 8.4 (p=0.001). The binding of 64Cu-MeCOSar-scFvLIBS to its target receptor could be blocked with increasing concentrations of pre-injected non-radioactive scFv. Dynamic PET scans showed accumulation of scFvLIBS in the injured vessel over 60 mins but no uptake of scFvmut which only showed constant background signal. Presence of activated platelets was confirmed by histology. CONCLUSION: The observed high and specific uptake of the radiotracer in the mouse model of acute thrombosis establishes 64Cu-MeCOSar-scFvLIBS as an excellent imaging tool for the in vivo detection of activated platelets. PET visualisation of activated platelets in thrombosis and inflammation has the potential to identify patients with serious diseases much earlier than currently possible thereby enabling timely therapeutic interventions. To further increase the specific activity of the antibody tracer for even higher sensitivity imaging scFvLIBS-Dendrimer-MeCOsar constructs are currently under investigation.

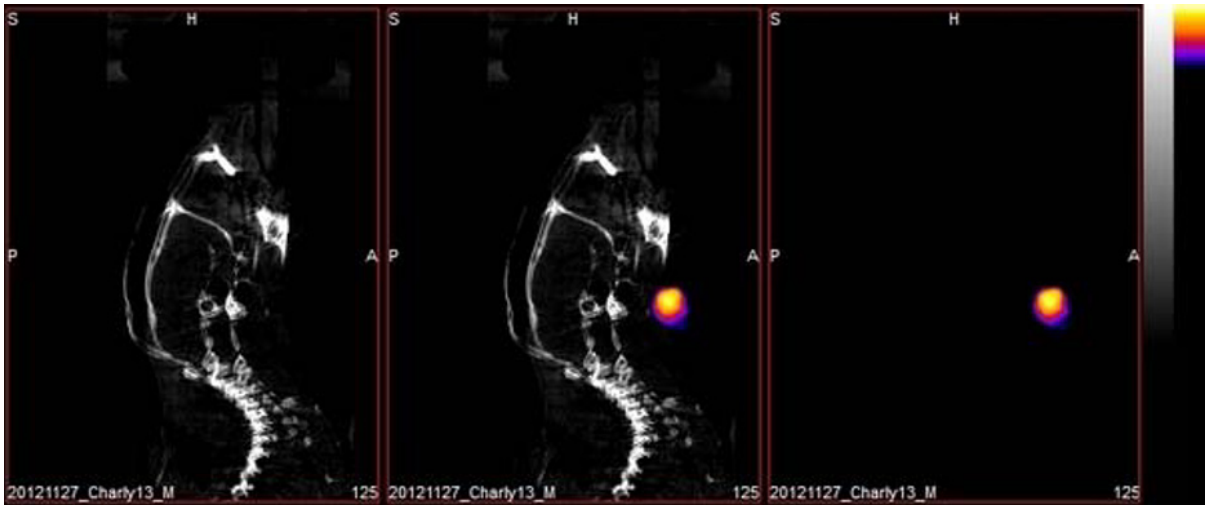

Disclosure of author financial interest or relationships:
K. Alt, None; **B.M. Paterson**, None; **K. Ardipradja**, None; **C. Schieber**, None; **G. Buncic**, None; **G.J. O'Keefe**, None; **S. Poniger**, None; **H. Tochon-Danguy**, None; **A.M. Scott**, None; **U. Ackermann**, None; **K. Peter**, None; **P.S. Donnelly**, Clarity Pharmaceuticals, Grant/research support; Clarity Pharmaceuticals, Consultant; **C.E. Hagemeyer**, None.

Presentation Number **SS 11**
Scientific Session 02: Preclinical in vivo Studies - Cardiology
September 19, 2013 / 11:30-11:45 / Room: 105

Molecular Imaging of Functional Microcirculation using a novel Chemical Exchange Saturation Transfer Encoded Steady State Cardiac MRI Pulse Sequence

Moriel Vandsburger[1], *Roni Oren*[1], *Katrien Vandoorne*[1], *Avigdor Leftin*[1], *Senzeni P. Mpofu*[1], *Fortune Kohen*[1], *Daniela Delli Castelli*[2], *Silvio Aime*[2], *Michal Neeman*[1], [1]*Biological Regulation, Weizmann Institute of Science, Rehovot, Israel;* [2]*Molecular Biotechnology Center, University of Torino, Torino, Italy. Contact e-mail: moriel.vandsburger@gmail.com*

Introduction: Chemical exchange saturation transfer (CEST) MRI is an emerging molecular imaging method by which to selectively visualize multiple targeted contrast agents or reporter genes in vivo (1). CEST-MRI typically employs a frequency-selective saturation preparation followed by rapid spin-echo readouts, and has been applied to stationary tissues, but is inapplicable to cardiac imaging due to contractile motion. We developed a CEST-encoded steady state MRI method that enables CEST imaging in the beating heart and free breathing mouse, and validated this method in vivo with a para-CEST agent. **Methods:** A pulse sequence was developed (Fig A) in which a saturation module is repeated prior to a constant TR gradient echo readout module in order to encode CEST contrast into the steady state longitudinal magnetization within the readout module (all parameters are detailed in supplemental data). Image reconstruction used the Bruker IntraGate system to retrospectively reconstruct cine cardiac images. Eu-HPDO3A (2), which generates CEST contrast at 15ppm offset from water at 37C, was dissolved in sterile water for intravenous (IV) administration. Male C57B6 mice (age 8-10 weeks) were imaged on a 9.4T Bruker Biospec (Ettlingen, Germany) scanner using a cylindrical volume coil for excitation and a single element surface coil for reception. Mice received an IV bolus injection of either Eu-HPDO3A (n = 6, 0.6 mg/g), Eu-HPDO3A 5 minutes after vasodilitation with dobutamine (40 mg/kg, n = 6), or saline (n = 5). Separately, myocardial infarction (MI) was surgically induced (n = 3) and cardiac CEST with Eu-HPDO3A was performed 28 days after MI. For all MRI experiments, pairs of cardiac CEST images (+15ppm, -15ppm offsets) were acquired prior to, and for 30 minutes following Eu-HPDO3A or saline injection. The asymmetric magnetization transfer ratio (MTRasym) was calculated on a pixel-wise basis as [S(-15ppm)-S(15ppm)]/S(-15ppm)*100, with S = signal intensity. Changes in MTRasym over time were calculated as the change over pre-contrast levels (Delta-MTRasym). **Results**: Pre-contrast MTRasym across all studies was 0.47 ± 0.48%. IV injection of Eu-HPDO3A induced a significant increase in MTRasym (Fig B, C), which was further enhanced in response to vasodilitation with dobutamine (Fig C, Fig S1). After MI, measurement of MTRasym elucidated the wash-in/out kinetics of Eu-HPDO3A from healthy myocardium, and accumulation of Eu-HPDO3A in infarcted myocardium (Fig S2,3). **Discussion:** In this study we demonstrated a novel method for CEST MRI in the mouse heart, and its application to probing microcirculatory function. Vasodilation with dobutamine generated an increase in MTRasym similar to measurements of myocardial perfusion reserve with dobutamine (3). Also, accumulation of Eu-HPDO3A within infarcted myocardium generated CEST contrast akin to that generated with delayed contrast-enhanced MRI. Cardiac CEST-MRI can serve as a powerful tool for pre-clinical cardiac research into heart failure and regeneration therapies. Refs: 1. Ward et al. JMR 2000; 2. Ferrauto et al. MRM 2012; 3. Vandsburger et al. EHJ 2007. Grant support is detailed in supplement.

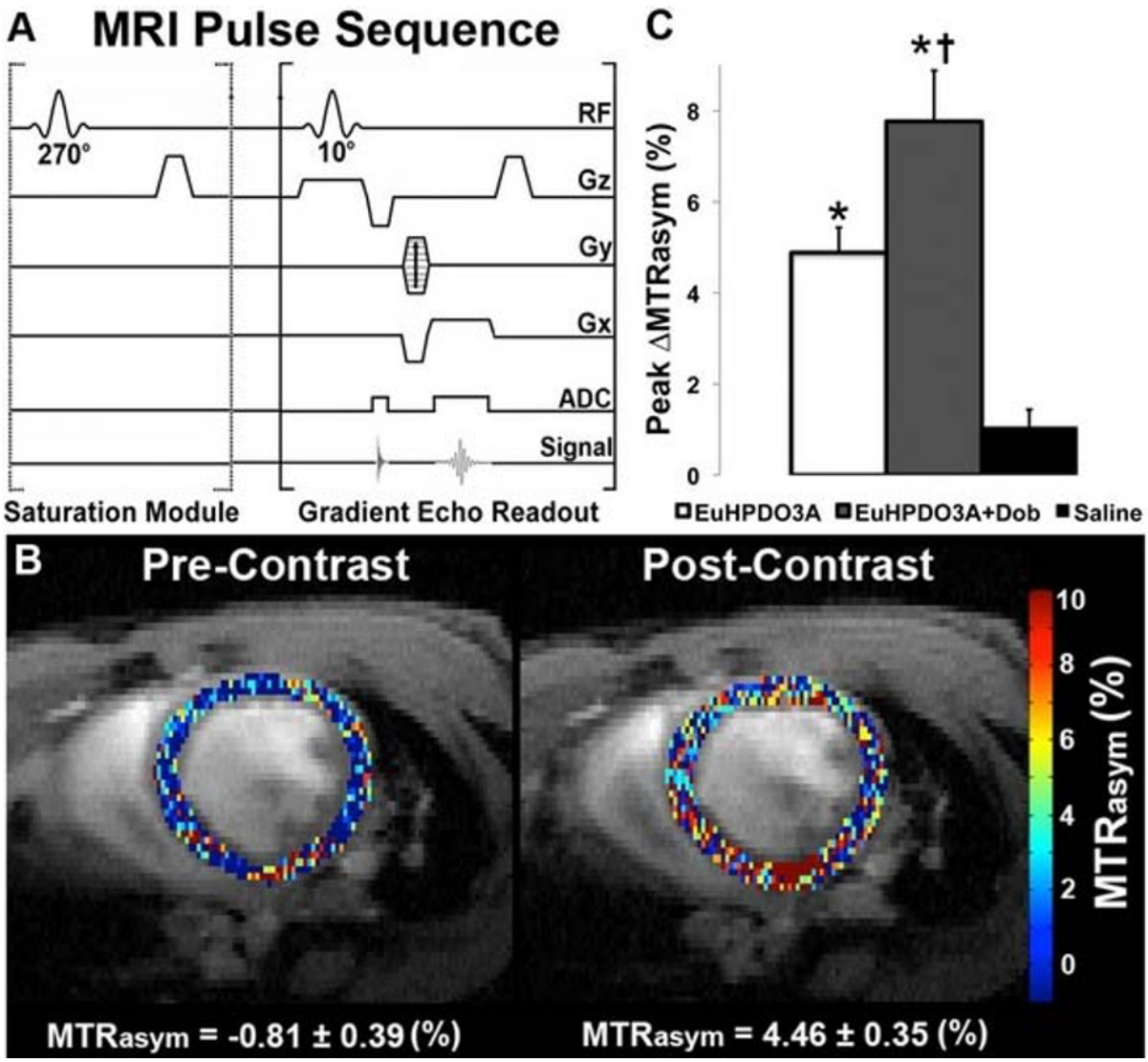

Figure. (A) Pulse sequence diagram for CEST-encoded steady state cardiac MRI. (B) MTRasym maps reveal significant CEST contrast following Eu-HPDO3A administration. (C) Peak Delta-MTRasym contrast after administration of either Eu-HPDO3A, saline, or Eu-HPDO3A following vasodilation with dobutamine (*P<0.05 vs. saline, †P<0.05 vs. Eu-HPDO3A).

Disclosure of author financial interest or relationships:

M. Vandsburger, None; **R. Oren**, None; **K. Vandoorne**, None; **A. Leftin**, None; **S.P. Mpofu**, None; **F. Kohen**, None; **D. Delli Castelli**, None; **S. Aime**, None; **M. Neeman**, None.

Presentation Number **SS 12**
Scientific Session 02: Preclinical in vivo Studies - Cardiology
September 19, 2013 / 11:45-12:00 / Room: 105

Multiplexed Molecular Imaging of the Cardioprotective Effect of Rapamycin in Ischemia Reperfusion Injury

Howard Chen[1,2], *Choukri Mekkaoui*[1,3], *Hoonsung Cho*[3,4], *Soeun Ngoy*[5], *Matthias Nahrendorf*[6], *Ronglih Liao*[5], *Lee Josephson*[1,4] *David E. Sosnovik*[1,2], [1]*Martinos Center for Biomedical Imaging, Massachusetts General Hospital, Harvard Medical School, Boston, MA, USA;* [2]*Center for Molecular Imaging Research, Massachusetts General Hospital, Harvard Medical School, Boston, MA, USA;* [3]*Department of Radiology, Massachusetts General Hospital, Harvard Medical School, Boston, MA, USA;* [4]*Center for Translational Nuclear Medicine and Molecular Imaging, Massachusetts General Hospital, Harvard Medical School, Boston, MA, USA;* [5]*Cardiovascular division, Department of Medicine, Brigham and Women's Hospital and Harvard Medical School, Boston, MA, USA;* [6]*Center for Systems Biology, Massachusetts General Hospital, Harvard Medical School, Boston, MA, USA. Contact e-mail: Chen.howard@mgh.harvard.edu*

Rapamycin is a modulator of mTOR (mammalian Target of Rapamycin) and exerts multiple effects on several molecular pathways including those that impact apoptosis and autophagy. Rapamycin is a FDA approved immunosuppressant but its therapeutic potential in cardiac protection is yet well characterized. In fact both protective and detrimental effects have been reported. Given prior reports of acute rapamycin treatment activating pro-survival factors such as AKT, we hypothesized that rapamycin could play a protective role in ischemia-reperfusion (IR) injury. We thus develop a multiplexed molecular imaging approach to investigate the complex cross-talk among cell death pathways in vivo. Cardiomyocytes (CMs) can die via apoptosis, autophagy and necrosis. We imaged apoptosis with an Annexin V construct conjugated to a near-infrared fluorochrome (ANX-750). Autophagy was imaged by a novel approach we developed targeting a cathepsin-activatable fluorochrome to the expanded lysosomal compartment (Figure 1A). Final infarct size was determined by TTC staining. The ischemic area-at-risk (AAR) was delineated with fluorescent microspheres. Cell death was imaged in three groups: 1) mice with IR injury, 2) IR mice injected with rapamycin 2 hours prior to coronary ligation (IR+preRAP), and 3) IR mice given rapamycin intravenously after coronary occlusion (IR+postRAP). ANX-750 was injected at the onset of reperfusion and fluorescence reflectance imaging of the heart was performed 4 hours later. A separate cohort of mice was sacrificed after 24 hours to measure infarct size by TTC staining. In the IR group, the area of positive annexin uptake encompassed almost the entire AAR (90.4+/-6.9%), but decreased significantly in both the IR+preRAP (74.8+/-8.0%) and IR+postRAP (69.3+/-5.9%) groups (Figure 1B-C). There was a reduction in the infarct size from 35.9+/-9.0% in the IR mice to 24.1+/-7.3% in the IR+preRAP mice and 19.6+/-5.6% in the IR+postRAP mice (Figure 1D-E). Rapamycin thus confers a robust cardioprotective effect reducing both annexin uptake (by 23%) and infarct size (by 45%). The observation that the protective effect persists when rapamycin is administered post ischemia is especially noteworthy. Interestingly, the area of annexin positivity (Figure 1B-C) was greater than the area of tissue necrosis (Figure 1D-E). This is consistent with previously published reports from other groups as well as our observation by molecular MRI. This suggests that not all CMs that become annexin positive undergo irreversible cell death/necrosis, and that a number of annexin-positive CMs remain viable. We show here that rapamycin treatment increases autophagy and reduces both apoptosis and infarct size in IR injured mouse hearts. Intravenous administration of rapamycin after ischemia is cardioprotective, suggesting a window of opportunity exists to slow cell death and ameliorate IR injury. Rapamycin is a clinically approved agent thus the translation of this approach is highly feasible. Furthermore, the multiplexed cell death imaging demonstrated here provides a general platform to investigate the complex interplay between cell death pathways in cardiovascular disease.

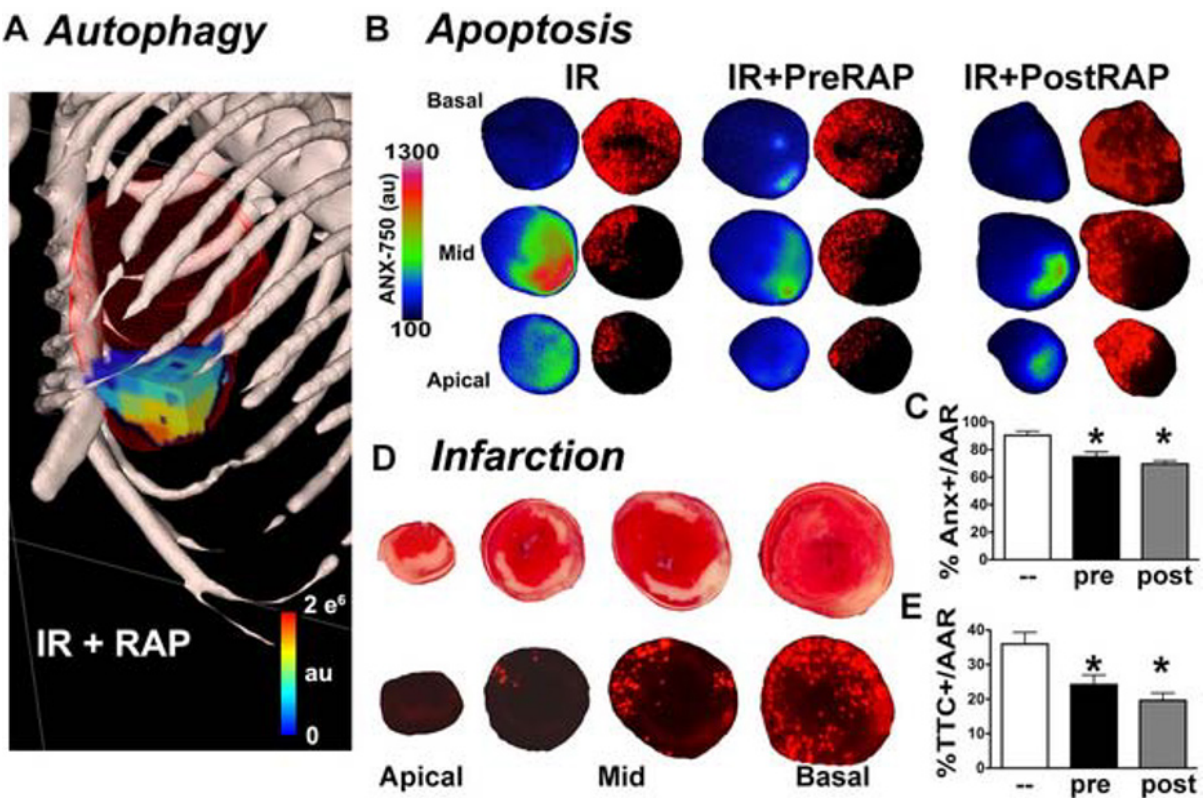

Disclosure of author financial interest or relationships:
H. Chen, None; **C. Mekkaoui**, None; **H. Cho**, None; **S. Ngoy**, None; **M. Nahrendorf**, None; **R. Liao**, None; **L. Josephson**, None; **D.E. Sosnovik**, Siemens Medical, Grant/research support .

Presentation Number **SS 13**
Scientific Session 03: Chemistry & Imaging Probes - Nuclear Imaging
September 19, 2013 / 10:30-10:45 / Room: 200

Evaluation of a [^{68}Ga]-labelled peptide antagonist to CXCR4 for preclinical PET imaging

Elizabeth Stevens, *Guillaume P. George, Quang-De Nguyen, Eric O. Aboagye, Comprehensive Cancer Imaging Centre, Department of Medicine, Imperial College London, London, United Kingdom. Contact e-mail: e.stevens09@imperial.ac.uk*

Introduction: The chemokine receptor CXCR4 is expressed in many cancer types, and is suggested to play a key role in the migration of tumour cells towards sites of metastasis along an SDF-1 chemokine gradient. Thus antagonists to CXCR4 have been investigated for their therapeutic potential. The selective molecular imaging of CXCR4 expression could be used to identify patients likely to respond to CXCR4-targeting therapies, or to detect metastases in known CXCR4-positive cancer patients. Recently published research has utilised antagonists to CXCR4 as PET and SPECT imaging probes to detect CXCR4 expressing tumours *in vivo*. It is the aim of this project to validate the suitability of CCIC16 (NOT2A-RR-2Nal-CY-Cit-KkPYR-Cit-CR-NH2), a novel T140-derived CXCR4 antagonist as a tracer for pre-clinical nuclear imaging of CXCR4 by the incorporation of radioisotopes into its chelating NOT2A group. **Methodology:** Antagonists were assayed for their ability to inhibit radioligand binding to CXCR4, and CXCR4-mediated migration in Jurkat cells. To analyse prospective radiotracers, we used human glioblastoma U87.CD4 and isogenic CXCR4 overexpressing U87.CD4.CXCR4 cells (NIH AIDS Reseach and Reference Reagent Program); the cells have markedly different CXCR4 mRNA and protein expression and therefore serve as cellular models of differential CXCR4 expression. *In vitro* uptake assays using these models were performed by incubation with 20μCi [^{68}Ga]Ga-CCIC16 for 60 minutes followed by measurement of bound radioactivity. For xenografts studies, 4.5×10^6 cells were injected subcutaneously on the back of female BALB/c nu/nu mice and once the tumours reached 80mm^3 in size, the mice were subjected to whole body PET imaging for 60 minutes after a 100μCi intravenous injection of [^{68}Ga]Ga-CCIC16. **Results:** High CXCR4 expression was confirmed in U87.CD4.CXCR4 cells compared to parental U87 and U87.CD4 cells; expression was also higher than untransfected Jurkat, MDA-MB-231 and MDA-MB-435S cells (supplementary data). Conjugation of the T140-derived CXCR4 antagonist to Ga^{3+}, $(AlF)^{2+}$, In^{3+}, and Cu^{2+} ions had little effect on CXCR4 receptor binding affinity; however ion chelation resulted in lower IC_{50} values for the inhibition of CXCR4-mediated migration. The *in vitro* uptake of [^{68}Ga]Ga-CCIC16 was, on average, 3.5-fold higher in U87.CD4.CXCR4 cells compared to U87.CD4 cells, indicating potential as a CXCR4-targeting PET tracer. The specificity of uptake in cells was confirmed via blocking with cold Ga-CCIC16. CXCR4-targeting was further confirmed by small animal imaging; [^{68}Ga]Ga-CCIC16 accumulated within U87.CD4.CXCR4 tumours at a significantly higher level than in U87.CD4 tumours (NUV60 of 3.73%ID/mL and 1.80%ID/mL respectively, $p<0.05$). Again specificity was demonstrated via blocking [^{68}Ga]Ga-CCIC16 in mice co-injected with cold Ga-CCIC16. Tracer elimination was both renal and hepatic. **Conclusion:** [^{68}Ga]Ga-CCIC16 is a T140-derived CXCR4 antagonist that can be used to differentiate tumours with high or low CXCR4 expression. Unlike an earlier T140-derived PET radiotracer, nonspecific red blood cell binding does not appear to affect discrimination of CXCR4 status.

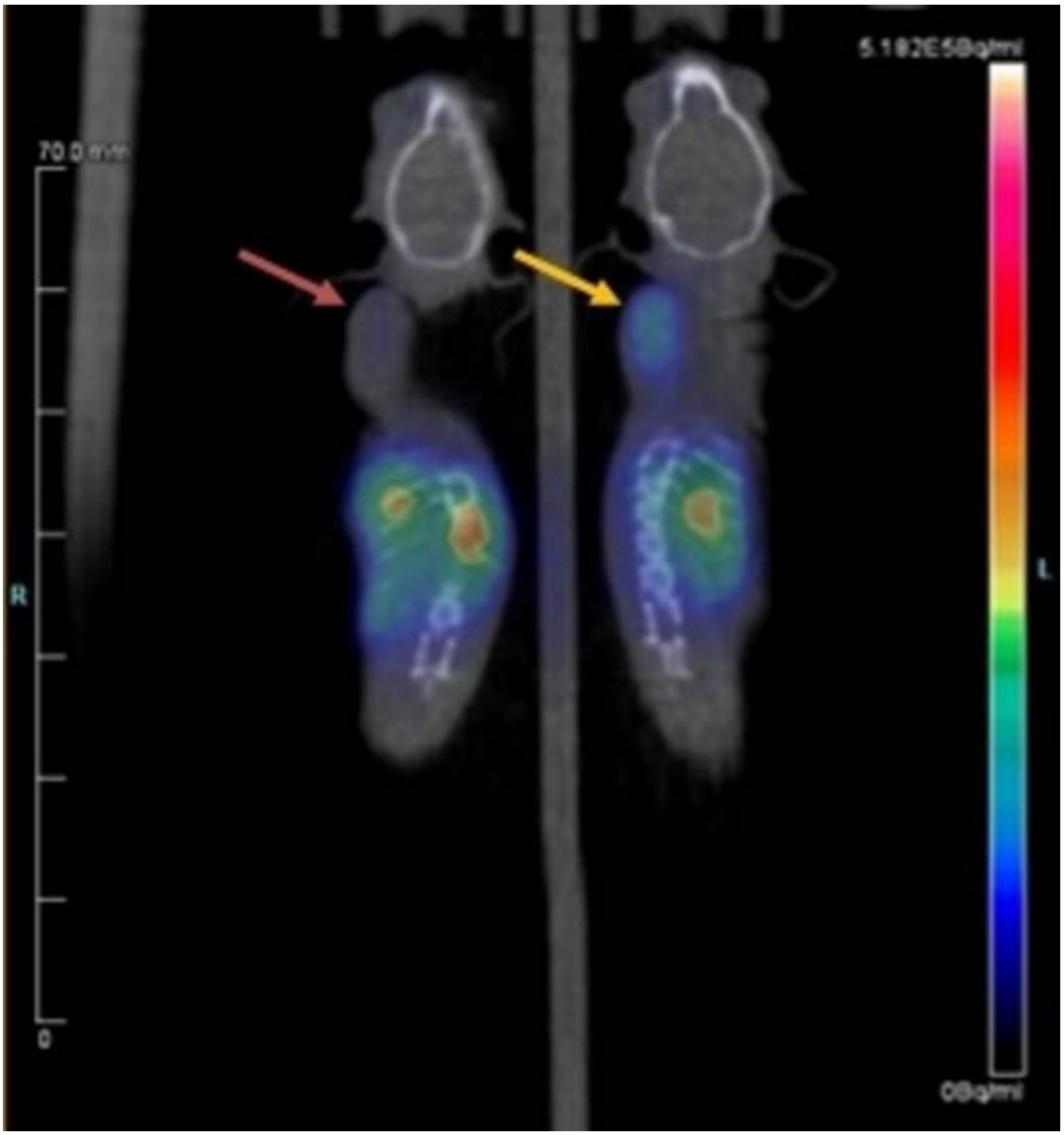

In vivo validation of [^{68}Ga]Ga-CCIC16 using U87.CD4 and U87.CD4.CXCR4 glioblastoma tumour models. BALB/c nu/nu mice were inoculated with 4.5×10^6 cells subcutaneously on the back, and imaged by CT/PET once the tumours had reached 80mm^3. Coronal view of merged PET-CT image showing [^{68}Ga]Ga-CCIC16 uptake in mice bearing U87.CD4 (red) or U87.CD4.CXCR4 (yellow) tumours, as visualised by 60 minute PET scan, following OSEM 3D reconstruction.

Disclosure of author financial interest or relationships:
E. Stevens, None; **G.P. George**, None; **Q. Nguyen**, None; **E.O. Aboagye**, None.

Presentation Number **SS 14**
Scientific Session 03: Chemistry & Imaging Probes - Nuclear Imaging
September 19, 2013 / 10:45-11:00 / Room: 200

PET imaging of VCAM-1 expression in atherosclerotic plaque with Cu-64 labeled VHPK-dendrimer

Jai Woong Seo[1], *Hyounggee Baek*[1], *Karen Gagnon*[1], *Lisa M. Mahakian*[1], *Sarah Tam*[1], *Brett Fite*[1], *Dong J. Son*[2], *Hanjoong Jo*[2], *Katherine Ferrara*[1], [1]*Biomedical Engineering, University of California Davis, Davis, CA, USA;* [2]*Coulter Department of Biomedical Engineering, Georgia Institute of Technology and Emory University, Atlanta, GA, USA. Contact e-mail: jwseo@ucdavis.edu*

VHPKQHR- was previously shown to bind to the vascular cell adhesion molecule (VCAM-1) on atherosclerotic plaque (1). Here we evaluate the targeting efficacy of this peptide by designing a multivalent dendrimer construct of VHPK peptides with an MMP cleavable site. A four-arm dendrimer was synthesized on solid phase and labeled with Cu-64 (t1/2 = 12.7 h). The accumulation of the radionuclide probes was assessed by in vivo and ex vivo imaging of plaque-containing aortae. Here, to validate the VCAM-1 expression in the aorta with PET, MR images were also acquired. Methods: (VHP)4-dendrimer ([VHPKQHR-miniPEG2]4-K2K-C(6-BAT)-miniPEG2-PLGLAG-C(SH)-NH2) and (NH3)4-dendrimer ([NH2miniPEG2]4K2K-C(6-BAT)-miniPEG2-PLGLAG-C(SH)-NH2) were synthesized on resins and isolated with HPLC (Figure 1a). Each dendrimer (4 nmol) was labeled with Cu-64 (5 Ci) and isolated with a C-18 cartridge. Cu-64 labeled dendrimers (0.3-0.2 μCi/mouse) were administered through the tail vein of the ApoE knockout mice, a left carotid artery ligated mouse model, fed with high fat diet for two weeks. PET images were acquired at 2 hours and the same mouse was immediately scanned with MRI to obtain anatomical information. The biodistribution of the two dendrimers was evaluated in the aortic arch, descending aorta and other organs at 3 hours after saline perfusion. PET images were reconstructed and co-registered with the MRI image with fiducials. Results: From the biodistribution study, the (VHP)4-dendrimer accumulated in the aortic arch (1.02 ± 0.20, n = 4) and in the descending aorta (0.45 ± 0.14 mCi, n = 4), where the accumulation was three and two times higher than the non-targeted dendrimer, respectively. Residual radioactivities of (VHP)4-dendrimer and (NH3)4-dendrimer in blood and muscle were similar, e.g. the blood activity for the (VHP)4-dendrimer and (NH3)4-dendrimer was 0.62 ± 0.14 %ID/cc and 0.49 ± 0.17, respectively. The accumulated (VHP)4-dendrimer in the heart was also three times higher than the (NH3)4-dendrimer. Interestingly, bone uptake of (VHP)4-dendrimer was 2.29 ± 0.53 mCi (n = 4), which was 10 times higher than that of (NH3)4-dendrimer. Discussion and conclusion: We synthesized Cu-64 labeled (VHP)4-dendrimer and evaluated VCAM-1 targeting efficacy with PET and biodistribution studies. Co-registration of PET and MR images enabled the visualization of VCAM-1 expression within the aortic arch (Figure 1b). The (VHP)4-dendrimer was designed to conjugate a potential cargo and to be cleaved by MMP. A (VHP)4-dendrimer conjugated with anti-miRNA will be applied to evaluate therapeutic response in atherosclerosis induced mice in future studies. Acknowledgement: This publication has been funded with funds from the National Heart, Lung, and Blood Institute, National Institutes of Health, Department of Health and Human Services, under Contract No. HHSN268201000043C. (1) Nahrendorf, M., Keliher, E., Panizzi, P., Zhang, H. W., Hembrador, S., Figueiredo, J. L., Aikawa, E., Kelly, K., Libby, P., and Weissleder, R. (2009) F-18-4V for PET-CT Imaging of VCAM-1 Expression in Atherosclerosis. Jacc-Cardiovasc Imag 2, 1213-1222.

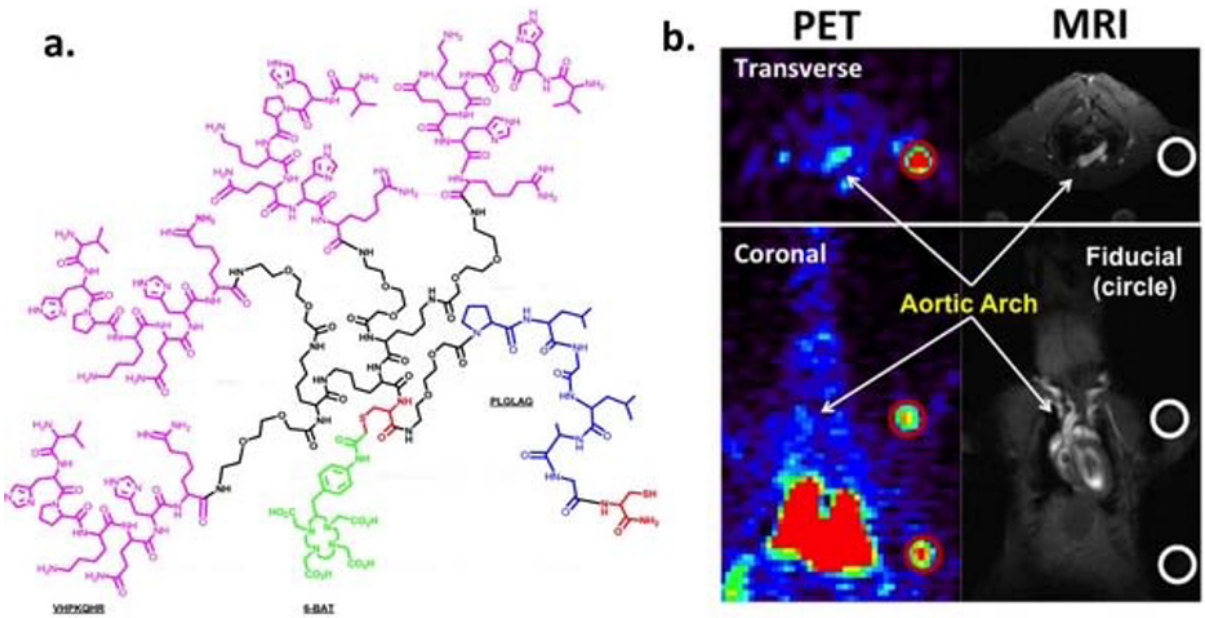

Figure 1. a. (VHPK)4-dendrimer b. PET and MR images of ApoE knockout mice after the administration of (VHPK)4-dendrimer

Disclosure of author financial interest or relationships:
J. Seo, None; **H. Baek**, None; **K. Gagnon**, None; **L.M. Mahakian**, None; **S. Tam**, None; **B. Fite**, None; **D.J. Son**, None; **H. Jo**, None; **K. Ferrara**, None.

Presentation Number **SS 15**
Scientific Session 03: Chemistry & Imaging Probes - Nuclear Imaging
September 19, 2013 / 11:00-11:15 / Room: 200

Measuring androgen receptor signaling in prostate cancer with zirconium-89 labeled radiotracers

Michael J. Evans, *Jason P. Holland, David Ulmert, Jason S. Lewis, Charles L. Sawyers, Memorial Sloan Kettering Cancer Center, New York, NY, USA. Contact e-mail: evansm1@mskcc.org*

As parallel advances in cancer biology and drug development continue to elevate the role of targeted therapies in oncology, the need for imaging biomarkers that systematically measure the biology associated with therapeutic intervention has become more urgent. Although the molecular imaging community has a commitment to develop technologies to this end, few investigational radiotracers directly measure the biology of common oncogenic signaling pathways often addressed by targeted therapies. For prostate cancer, we have addressed this challenge by developing a panel of radiotracers rationally designed to measure the patho-biology of the androgen receptor (AR), a nuclear hormone factor known to contribute to the progression of all stages of prostate cancer progression. The common design strategy among these radiotracer development programs is to exploit expression changes among "imageable" AR target genes to non-invasively measure the pathological activation (and pharmacological inhibition) of AR. For instance, 89Zr-J591 can be used to monitor the expression changes in prostate specific membrane antigen induced by androgen receptor inhibition with the antiandrogen enzalutamide. Moreover, 89Zr-5A10 can be used to monitor the expression changes in prostate specific antigen induced by androgen receptor inhibition with the antiandrogen enzalutamide. We have since shown that expression changes in other AR target genes can be measured with 89Zr-labeled biomolecules (e.g. STEAP1, hK2, MET), and a broader survey of prostate cancer models and treatments that impact AR signaling (e.g. radiation therapy) has shown that a panel of AR imaging tools may be required to effectively manage the disease. Adding excitement to these preclinical findings, two clinical trials have been initiated at MSKCC to image castration resistant prostate cancer with 89Zr-labeled antibodies (89Zr-J591, 89Zr-STEAP1), and the favorable initial results in man foreshadow a potentially landmark imaging study to monitor the impact of antiandrogens on AR biology directly with PET.

Disclosure of author financial interest or relationships:
M.J. Evans, None; **J.P. Holland**, None; **D. Ulmert**, None; **J.S. Lewis**, None; **C.L. Sawyers**, Aragon, Consultant; Aragon, Stockholder; Novartis Board of Directors, Other financial or material support .

Presentation Number **SS 16**
Scientific Session 03: Chemistry & Imaging Probes - Nuclear Imaging
September 19, 2013 / 11:15-11:30 / Room: 200

Novel LRRRLAHHHHHH Histidine-Tag Sequence for Improved Radiolabelling of the J591 ScFv anti PSMA Antibody Fragment with $[^{99m}Tc(CO)_3]^+$ for Imaging of Prostate Cancer

Jennifer D. Williams, *Florian Kampmeier, Margaret S. Cooper, Greg Mullen, Phil Blower, Imaging Sciences & Biomedical Engineering, King's College London, London, United Kingdom. Contact e-mail: jennifer.williams@kcl.ac.uk*

Introduction: Histidine tags incorporated into targeting proteins can be site-specifically radiolabelled with $[^{99m}Tc(CO)_3]^+$ for SPECT imaging but labelling efficiencies vary greatly between proteins. We have previously reported the discovery, based on a high throughput screening method, that polyhistidine peptide sequences modified to include a series of arginine residues offer significant improvements in radiolabelling efficiency and specific activity (up to an order of magnitude) compared to previously selected sequences. Here we report the first results documenting improvement in specific activity and labelling efficiency of a scFv antibody, based on J591 against the extracellular domain of the prostate specific membrane antigen (PSMA), incorporating the optimised arginine-rich high-pI His-Tag sequence has been compared to an analogue with a conventional His-Tag. **Method:** The J591 scFv antibody was engineered to contain the LRRRLAHHHHHH peptide sequence at the C-terminal. Other J591 and 6C7.1 scFv antibodies contain a generic His-Tag (RAAALEHHHHHHC and RAAALEHHHHHH respectively) at the C-terminal with a reduced number of adjacent arginine residues. Radiolabelling of the scFv antibodies with $[^{99m}Tc(CO)_3]^+$ was executed at 37°C in PBS at pH 7.4 with a final antibody concentration ranging from 17.5μM to 0.14μM in a 1:2 serial dilution. Analysis of the radiolabelled sample was performed after 60 minutes using iTLC-SA and citrate buffer as the mobile phase. The kinetic stability of the $[^{99m}Tc(CO)_3]^+$ labelled antibody was studied in serum over 4 hours using both iTLC-SA analysis and a gel purification method. **Results:** Radiolabelling the LRRRLAHHHHHH-J591 scFv antibody demonstrated a 25-30% increase in radiolabelling efficiency after 60 minutes in comparison to the generic His-Tagged J591 and 6C7.1 antibodies. Consequently, the arginine containing His-Tag yielded a 95% or more radiochemical yield at 17.5μM and 8.75μM concentrations and did not require the additional purification step needed for the other antibodies prior to use in vivo. In addition, a significant 5-fold higher specific activity was achieved with the $[^{99m}Tc(CO)_3]^+$ radiolabelling of the LRRRLAHHHHHH-J591 scFv antibody after 60 minutes ($p<0.0001$). The kinetic stability of the $[^{99m}Tc(CO)_3]^+$-LRRRLAHHHHHH-J591 in serum proteins remained at 100% for greater than 240 minutes. **Conclusion:** The combination of a His-Tag and an adjacent tri-arginine sequence offers a faster, more efficient and reliable labelling procedure yielding higher specific activity and reduced requirement for purification of proteins with $[^{99m}Tc(CO)_3]^+$, compared to conventional His-tagged proteins. It has the potential to become a potent tool to screen biological activities of recombinant proteins using ^{99m}Tc labelling and could also be translational to the use of therapeutic $^{186}/^{188}Re$ isotopes.

Disclosure of author financial interest or relationships:
J.D. Williams, None; **F. Kampmeier**, None; **M.S. Cooper**, None; **G. Mullen**, Mediso, Consultant; **P. Blower**, None.

Presentation Number **SS 17**
Scientific Session 03: Chemistry & Imaging Probes - Nuclear Imaging
September 19, 2013 / 11:30-11:45 / Room: 200

SPECT imaging of fibrin using ^{111}In-labeled fibrin-binding peptides: evaluation of EPep and FibPep in a carotid thrombosis rat model

Lucas Starmans[1], *Sander van Duijnhoven*[1], *Raffaella Rossin*[2], *Silvio Aime*[3], *Mat Daemen*[4], *Klaas Nicolay*[1], *Holger Gruell*[1,2], [1]*Biomedical Engineering, Eindhoven University of Technology, Eindhoven, Netherlands;* [2]*Minimally Invasive Healthcare, Philips Research, Eindhoven, Netherlands;* [3]*Department of Chemistry, IFM/ Center of Molecular Biotechnology, University of Torino, Torino, Italy;* [4]*Pathology, Academical Medical Centre, Amsterdam, Netherlands. Contact e-mail: l.w.e.starmans@tue.nl*

Introduction: Fibrin is a major constituent of thrombi and plays a key role in thrombosis. In addition, fibrin deposition in tumors and atherosclerotic plaques is associated with tumor angiogenesis and atherosclerotic plaque vulnerability, respectively. Noninvasive detection of fibrin in vivo using diagnostic imaging modalities may thus improve clinical decision making on possible therapeutic options in cancer, atherosclerosis and thrombus-related pathologies. The aim of this study was to compare the potential of FibPep, an ^{111}In-labeled fibrin-binding peptide previously reported for thrombus imaging in mice [1], to EPep for noninvasive visualization of fibrin using SPECT. EPep is a novel ^{111}In-labeled SPECT tracer for fibrin imaging based on the fibrin-binding amino acid sequence of the EP-2104R peptide [2], which has been used in numerous preclinical and clinical studies for molecular MRI of fibrin [3]. **Methods:** *Synthesis:* DOTA-conjugated EPep, FibPep and negative control NCFibPep were synthesized and radiolabeled with ^{111}In. *In vitro:* tracer stability was assayed in serum. In addition, the peptides were characterized with respect to *in vitro* fibrin and blood clot binding. *In vivo: In vivo* SPECT imaging of thrombi using the radiolabeled probes was performed using a $FeCl_3$-induced carotid thrombosis rat model. In addition, blood kinetic and biodistribution profiles were obtained. **Results:** *In vitro:* FibPep and Epep were stable (≥89% intact parent compound) after 90 minutes of incubation in human, rat and mouse serum, whereas NCFibPep was not (≤55%). FibPep and EPep showed similar binding to human blood clots (35 ± 4 and 30 ± 3% dose, respectively), whereas NCFibPep displayed significantly lower uptake (4 ± 2% dose, $p<0.01$; n=4). EPep bound to human, rat and mouse-derived fibrin with a dissociation constant (K_d) of 0.9, 1.2 and 1.4 μM, respectively. FibPep showed a comparable K_d for human and mouse fibrin (0.6 and 0.8 μM, respectively) whereas the K_d for rat fibrin was significantly higher (14 μM). NCFibPep bound at least 100 fold weaker to human, rat and mouse derived fibrin. *In vivo:* All probes displayed rapid blood clearance, low non-target organ uptake and were eliminated via the renal pathway. In vivo SPECT imaging using EPep allowed clear visualization of thrombi in rats, whereas FibPep and NCFibPep did not (Fig. 1). Ex vivo autoradiography of the excised carotids showed a significantly higher thrombus to contralateral carotid signal ratio for EPep (31.7 ± 16.0) in comparison to FibPep and NCFibPep (4.7 ± 1.1 and 1.7 ± 0.1, respectively; $p<0.01$ with respect to EPep; n=4). **Conclusions:** A novel fibrin-binding SPECT tracer, EPep, was synthesized and compared to FibPep. EPep displayed high affinity towards fibrin and allowed sensitive detection of thrombi using SPECT imaging in a carotid thrombosis rat model. FibPep did not allow detection of thrombi in rats, most likely due to its low affinity towards rat-derived fibrin. **References:** [1] Starmans LW, et al. Contrast Media & Molecular Imaging 2013, 8, 229-237. [2] Overoye-Chan K, et al. J. Am. Chem. Soc. 2008, 130, 6025-603. [3] Vymazal J, et al. Invest. Rad. 2009, 44, 697-704.

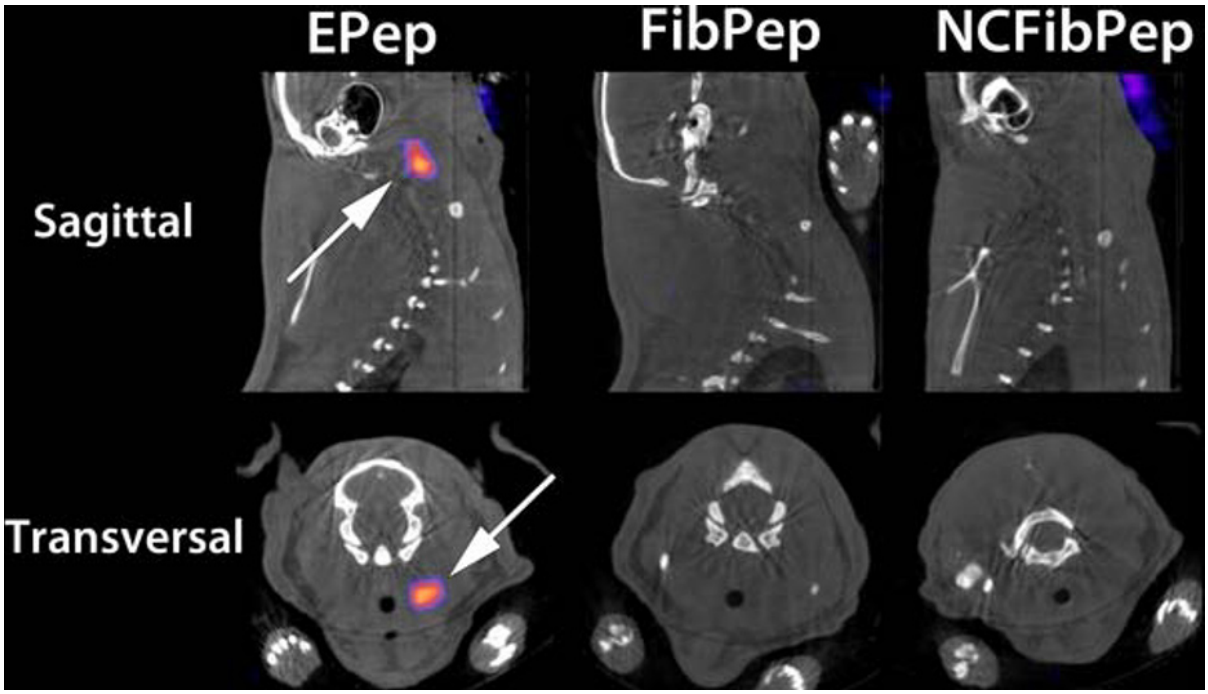

Figure 1. *In vivo* SPECT/CT imaging of the head/neck area using EPep, FibPep and NCFibPep in a carotid thrombosis rat model (3 hours post injection; transversal and sagittal slices). Arrows: increased uptake of tracer in the induced thrombus.

Disclosure of author financial interest or relationships:
L. Starmans, None; **S. van Duijnhoven**, None; **R. Rossin**, Philips, Employment; Tagworks Pharmaceuticals, Consultant; **S. Aime**, None; **M. Daemen**, None; **K. Nicolay**, None; **H. Gruell**, Eindhoven University of Technology, Employment; Philips, Employment .

Presentation Number **SS 18**
Scientific Session 03: Chemistry & Imaging Probes - Nuclear Imaging
September 19, 2013 / 11:45-12:00 / Room: 200

A binding-site barrier affects quantitative imaging capabilities of high-affinity amyloid reactive peptide radiotracer p5R

Jonathan S. Wall[1], *Angela Williams*[2], *Tina A. Richey*[2], *Alan Stuckey*[3], *Ying Huang*[3], *Craig Wooliver*[2], *Sallie D. Macy*[2], *Robert E. Heidel*[4], *Neil Gupta*[2], *Angela Lee*[2], *Brianna Rader*[2], *Emily B. Martin*[2], *Stephen J. Kennel*[1], [1]*Medicine and Radiology, University of Tennessee Graduate School of Medicine, Knoxville, TN, USA;* [2]*Medicine, University of Tennessee Graduate School of Medicine, Knoxville, TN, USA;* [3]*Radiology, University of Tennessee Graduate School of Medicine, Knoxville, TN, USA;* [4]*Surgery, University of Tennessee Graduate School of Medicine, Knoxville, TN, USA. Contact e-mail: jwall@utmck.edu*

Amyloid is a complex pathology associated with a growing number of diseases including Alzheimer's disease, type 2 diabetes, rheumatoid arthritis and myeloma. The distribution and extent of amyloid deposition in body organs establishes the prognosis and can define treatment options; therefore, determining the amyloid load by using non-invasive molecular imaging is clinically important. We have identified a heparin-binding peptide, designated p5, that, when radioiodinated, was capable of selectively imaging systemic visceral AA amyloidosis in a murine model of the disease [Wall *et al.* (2011) *PNAS* **108**(34): E586-594]. The p5 peptide was posited to bind effectively to amyloid deposits, relative to similarly charged polybasic heparin-reactive peptides, because it adopted a polar α helix secondary structure. To study this further, we synthesized a variant, p5R, in which the 8 lysine amino acids of p5 were replaced with arginine residues predisposing the peptide toward the α helical conformation in an effort to enhance the reactivity of the peptide with the amyloid substrate. The p5R peptide was shown by circular dichroism spectroscopy to have 2-fold greater helicity in physiological saline, relative to peptide p5, and exhibited higher binding affinities for both immobilized heparin (0.9 M vs 1.3 M) and AA amyloid-laden tissue extracts (0.4 M vs 0.9 M) as evidenced by the need for higher salt to prevent binding to these substrates. ^{125}I-p5R was shown to bind AA amyloid in mice by using SPECT/CT imaging accumulating 10-15% ID/g in amyloid-laden liver and pancreas. Microautoradiography was used to validate the microdistribution of radiotracer in the amyloid of visceral organs. In the spleen, where amyloid deposits are greatest the microdistribution was dramatically altered relative to ^{125}I-p5 (see figure). The ^{125}I-p5R peptide was seen as dense deposits in amyloid closely associated with the vasculature. This is likely due to its increased affinity and a resultant "binding site barrier" effect wherein the probe binds with high affinity to the first target encountered and thus does not penetrate the entire deposit. Analysis of the biodistribution of the tissue-associated radioactivity showed that as amyloid deposits became larger, the amount of ^{125}I-p5R peptide in the amyloid decreased relative to the p5 peptide. These data suggest that ^{125}I-p5R may be optimal for molecular imaging of discreet, perivascular amyloid, as found in the brain and pancreatic vasculature, by using molecular imaging techniques; however, peptide p5, due to its increased penetration, may yield more quantitative imaging of expansive tissue amyloid deposits.

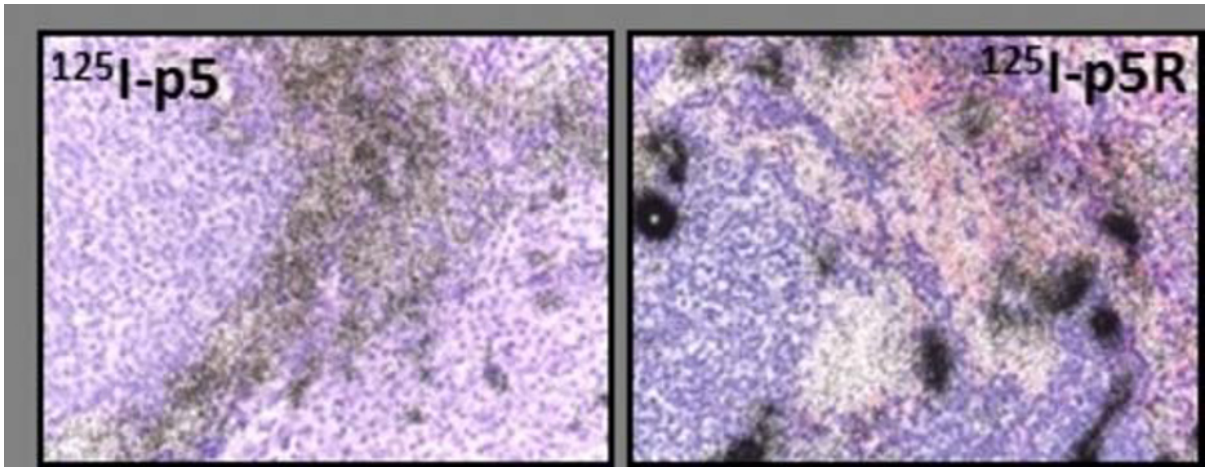

Disclosure of author financial interest or relationships:
J.S. Wall, Solex Inc, Stockholder; **A. Williams**, None; **T.A. Richey**, Solex Biomedical, Stockholder; **A. Stuckey**, Solex, LLC, Stockholder; **Y. Huang**, None; **C. Wooliver**, None; **S.D. Macy**, None; **R.E. Heidel**, None; **N. Gupta**, None; **A. Lee**, None; **B. Rader**, None; **E.B. Martin**, Solex LLC, Stockholder; **S.J. Kennel**, Solex,lld, Stockholder .

Presentation Number **SS 19**
Scientific Session 04: Preclinical in vivo Studies - Oncology (Targeted Imaging)
September 19, 2013 / 10:30-10:45 / Room: 203

Towards Early Detection of Pancreatic Cancers by CA 19-9 Conjugated Magnetic Nanoparticles and Active Feedback MR Molecular Imaging

Zhao Li, *Chao-Hsiung Hsu, Ryan Quiroz, Yung-Ya Lin, Chemistry and Biochemistry, UCLA, Los Angeles, CA, USA. Contact e-mail: zhaoli@chem.ucla.edu*

Purpose: Hope for mitigating pancreatic cancer (PC) arises from the early detection of small, resectable tumors through imaging modalities like MRI. Since late-stage PC exhibits chemo- and radiotherapy resistance, early detection of this malignancy using enhanced MRI imaging techniques increases not only the treatment options available, but also the patients' survival rate. This can be realized with antibody-conjugated superparamagnetic iron oxide (SPIO) nanoparticles capable of binding to early stage pancreatic cancer cells to improve imaging specificity and innovation methods that can sensitively detect SPIO to improve imaging sensitivity. The enhanced contrast from SPIO can then be used to visually assess the distribution and magnitude of SPIO-targeted tumor cells. Therefore, the purposes of this work are: (i) to enhance detection specificity through effective targeting of PC biomarkers, (ii) to enhance detection sensitivity through contrast-enhanced imaging of magnetic nanoparticles. Methods: (i) To enhance detection specificity, anti-CA 19-9 antibodies were conjugated to NH2-PEG-coated SPIO nanoparticles utilizing reductive amination chemistry, as detailed "Supplemental Data". (ii) To enhance detection sensitivity, we have developed a new approach, called "Active Feedback Magnetic Resonance". The general principle of the "Active-Feedback MR" is based on the feedback-induced nonlinear spin dynamics that we discovered, for examples [1-4]. Here, its specific applications to sensitively image SPIO/aggregates was developed. Our theoretical, numerical, and in vitro cellular imaging studies show that "Active Feedback MR" is sensitive to magnetic field fluctuations arising from diffusion motion within strong magnetic field gradients and thus can be applied to sensitively imaging magnetic nanoparticles. Results: In vivo images of human PC from both subcutaneous (top) and orthotopic (bottom) xenograft mouse models were carried out, where the PC were targeted by the SPIO-CA19-9 "molecular beacon" and imaged by the Active Feedback MR method. Discussion: Subcutaneous xenografts PC mouse models (top) show that, while T2-weighted image cannot clearly locate the magnetic nanoparticles, the active-feedback images successfully highlight the magnetic nanoparticles distribution with a close correlation with iron-stained histopathology. In addition, for the orthotopic xenografts PC mouse models (bottom), while CPMG-T2 weighted image cannot clearly locate the SPIOs, the "Active Feedback MR" images successfully highlight the SPIO distribution (red circles) with positive contrast and a close correlation with iron-stained histopathology. Conclusion: In vivo subcutaneous and orthotopic xenografts PC mouse models validated the superior contrast/sensitivity and robustness of this approach towards early PC detection. Statistical results (N>10) for PC mouse models at various cancer stages, and alternative active feedback pulse sequences with further improved performance will also be presented. Reference: [1] Science 290, 118 (2001) [2] Magn. Reson. Med. 56, 776 (2006) [3] Magn. Reson. Med. 61, 925 (2009) [4] J. Phys. Chem. B 110, 22071 (2006)

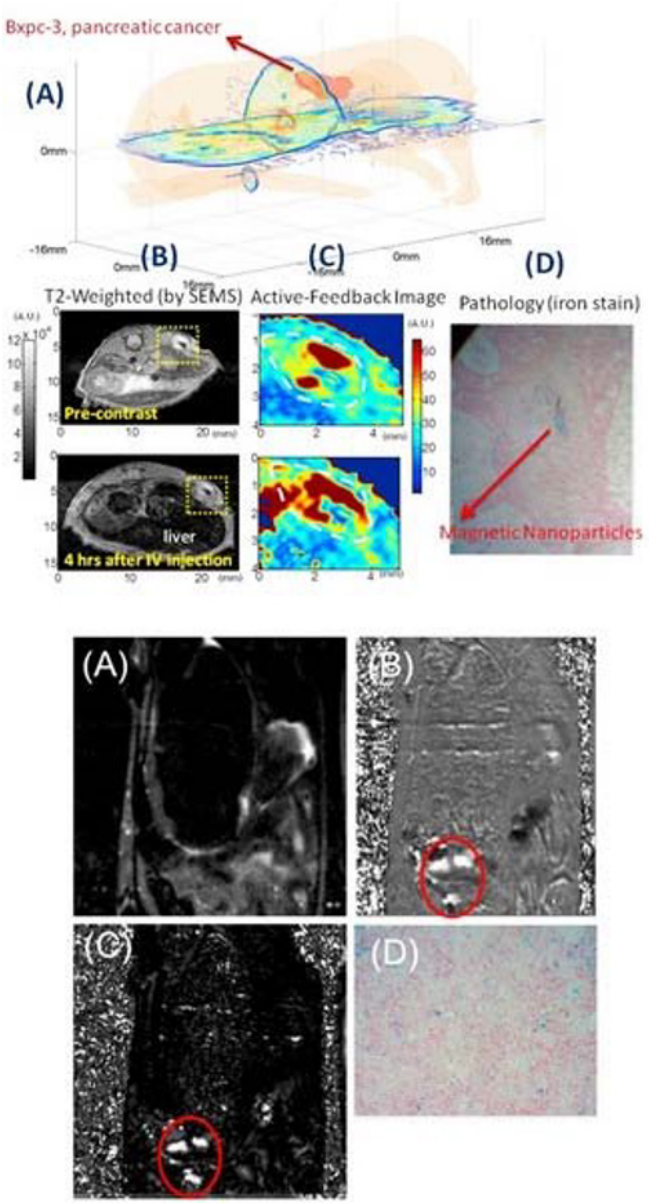

Top: Detection of pancreatic cancers in subcutaneous xenograft PC mouse models (A) by sensitive imaging of the dipolar fields induced by magnetic nanoparticles (D). The active feedback images show much improved post-injection contrast (C), compared with spin echo T2W images (B). Bottom: In vivo images of orthotopic mouse model bearing human PC (from CA 19-9 positive BxPC3 cell lines) labeled by SPIO were acquired. While CPMG-T2 weighted image cannot clearly locate the SPIOs (A), the "Active Feedback MR" images shown in (B) and (C) (acquired with two different active feedback pulse sequences) successfully highlight the SPIO distribution with positive contrast and a close correlation with iron-stained histopathology (D).

Disclosure of author financial interest or relationships:
Z. Li, None; **C. Hsu**, None; **R. Quiroz**, None; **Y. Lin**, None.

Presentation Number **SS 20**
Scientific Session 04: Preclinical in vivo Studies - Oncology (Targeted Imaging)
September 19, 2013 / 10:45-11:00 / Room: 203

Real-Time *In Vivo* Imaging of Hepatic Drug Metabolism

Adam J. Shuhendler, *Kanyi Pu, Lina Cui, Jianghong Rao, Radiology, Stanford University, Stanford, CA, USA. Contact e-mail: adam18@stanford.edu*

Introduction: It is estimated that only 10% of new drug candidates entering Phase I clinical trial are ever approved for human use. Additionally, drug-induced hepatotoxicity is the most common reason for withdrawal of FDA-approved drugs, accounting for more than 50% of acute liver failure cases in the US. Reactive drug metabolites underlie hepatotoxicity, among which reactive oxygen and nitrogen species (RONS) are common to both drug candidates and approved drugs alike. While *in vitro* assays have frequently been employed to screen for potentially hepatotoxic metabolites, extrapolation to *in vivo* metabolism is limited by impaired cell function, lack of tissue microenvironment integrity, and absence of non-parenchymal cells. Additionally, the low concentration and short half-lives of RONS prevents their detection by current *in vivo* metabolite sensing methods. The resultant high rates of hepatotoxicity and subsequent drug withdrawal suggest a critical gap in available technology for robust *in vivo* metabolism screening. **Aim:** To image hepatocyte-derived RONS *in vivo* and significantly impact our understanding of liver disease pathology and detection, reveal previously unattainable information regarding the propensity of xenobiotics for hepatotoxicity, and enhance the scrutiny of early drug candidate screening prior to clinical trial. **Methods:** To this end, a conjugated polymer-based nanoparticle probe has been engineered to sensitively and specifically report on hepatocyte RONS generation following *in vivo* drug challenge, and to discriminate oxidative stress from nitrosative stress, which differentially effect metabolism-induced hepatotoxicity. This discrimination is afforded by the dual optical modality-based reporting mechanism of our nanoprobe, simultaneously utilizing chemiluminescent and fluorescent resonant energy transfer (CRET and FRET) mechanisms differentially sensitive to specific RONS. **Results:** Active targeting of the nanoprobe to asialoglycoprotein receptors by galactose surface conjugation afforded a four-fold enhancement in hepatic uptake over untargeted nanoparticles. By challenging mice with the well-studied N-acetyl-p-aminophenol (APAP), the discrimination of toxic from non-toxic drug doses through real-time molecular imaging was achieved and was verified by histology. Inhibitors of APAP metabolism were also employed *in vivo*, including the reactive metabolite scavenger glutathione, the pan-CYP450 inhibitor 1-aminobenzotriazole, and the CYP2E1-specific inhibitor trans-1,2-dichloroethylene, resulting in the reduction of both oxidative and nitrosative stress as indicated by our nanoprobe. Finally, the toxicity of the anti-tuberculosis agent N-isonicotinyl hydrazine was assessed in mice, exhibiting a dose-dependent enhancement in hepatotoxicity observed through real-time *in vivo* molecular imaging, and confirmed by histology. **Conclusion:** These results demonstrate the specificity of our probe for drug metabolism-derived RONS, and for the first time prove that real time assays of drug metabolism previously confined to the *in vitro* space can now be performed in the more relevant *in vivo* environment.

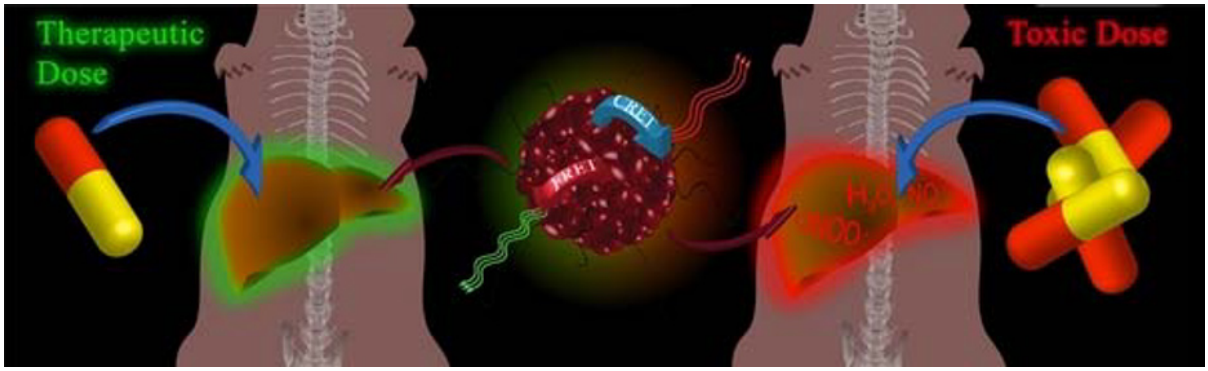

The *in vivo*, real-time monitoring of hepatic drug metabolism is now possible using a novel conjugated polymer-based nanoprobe. With a built-in dual optical modality sensing system, the differential detection of drug-induced oxidative stress and nitrosative stress can simultaneously be achieved through both chemiluminescent and fluorescent resonance energy transfer, respectively. With this new molecular imaging probe, more robust *in vivo* investigations of xenobiotic-induced hepatotoxicity are possible, ultimately enhancing the rational selection of early drug candidates for more successful clinical trial.

Disclosure of author financial interest or relationships:
A.J. Shuhendler, None; **K. Pu**, None; **L. Cui**, None; **J. Rao**, None.

Presentation Number **SS 21**
Scientific Session 04: Preclinical in vivo Studies - Oncology (Targeted Imaging)
September 19, 2013 / 11:00-11:15 / Room: 203

Tumor Targeting Kinetics of Ligand-Functionalized Nanoparticles Studied with Dynamic Contrast Enhanced Magnetic Resonance Imaging and Intravital Microscopy

Sjoerd Hak[1,2], *Jana Cebulla*[2], *Else Marie Huuse*[1,2], *Catharina D. Davies*[3], *Willem J. Mulder*[5], *Henrik B. Larsson*[4], *Olav Haraldseth*[1,2], [1]*MI Lab, Norwegian University of Science and Technology, Trondheim, Norway;* [2]*Department of Circulation and Medical Imaging, Norwegian University of Science and Technology, Trondheim, Norway;* [3]*Department of Physics, Norwegian University of Science and Technology, Trondheim, Norway;* [4]*Functional Imaging Unit, Glostrup University Hospital, Glostrop, Denmark;* [5]*Radiology, Mount Sinai School of Medicine, New York, NY, USA. Contact e-mail: sjoerd.hak@ntnu.no*

Targeted nanoparticles have been extensively studied as molecular imaging contrast agents for the detection of surface receptors on angiogenic endothelial cells. So far, little is known about the in vivo homing kinetics of such agents. These dynamics will not only depend on nanoparticle characteristics, but also on receptor binding and recycling kinetics. To address this we developed a multipronged approach based on combining intravital microscopy (IVM) in dorsal window chambers in mice[1], dynamic contrast enhanced magnetic resonance imaging (DCE-MRI), and compartment modeling. As a proof of concept we studied the in vivo targeting kinetics of αvβ3-integrin specific RGD-conjugated nanoemulsions (RGD-NE) in tumor bearing mice. Methods and Results A schematic of the nanoemulsion and its characteristics are depicted in Fig 1a. IVM (resolution: 2.5x2.5 μm, 325 frames of 3.94 s) was used to obtain vascular input functions (Fig 1b, used for compartment modeling) for RGD-NE (n=3) and non-conjugated nanoemulsion (CTRL-NE, n=5). Accumulation of RGD-NE and CTRL-NE (both n=4) in tumors was monitored with T1-weighted DCE-MRI (60 frames of 21.6 s, voxel: 0.45x0.45x1 mm3). Xenografts of the ovarian cancer TOV112D in female mice were used. Already 3 minutes post injection (20 s bolus, Gd dose: 20 μmol/kg) the RGD-NE exhibited a preference for the tumor rim, where angiogenesis is most predominant, whereas CTRL-NE distributed more evenly throughout the tumor. This indicted receptor binding to occur rapidly after injection, as has been demonstrated previously (Fig. 1c-d)[1]. DCE-MRI curves were extracted from ROIs containing 0.5-1 mm thick tumor rims (Fig 1d). Quantification of the accumulation rate (Ki) in the first 4.5 min post injection was achieved with the extended Tofts model[2] (Fig 1e), showing a much faster accumulation for the RGD-NE than for the CTRL-NE. This demonstrated that our approach can serve as a tool to optimize nanoparticle design for better targeting and potentially provide more quantitative information on in vivo receptor levels. Strikingly, in case of RGD-NE a periodicity in the accumulation rate was observed, which was not seen in case of CTRL-NE (Fig 1d). αvβ3-integrin is known to internalize and recycle back to the plasma membrane with a half-life of either 3 or 10 minutes[3]. Fourier analysis revealed the presence of frequencies with periods of 6.9 and 5.2 min in the RGD-NE accumulation, in the range of the integrin recycling half-lives. This indicated that after the observed initial binding and perhaps saturation of the integrin, recycling may have played a role in this periodicity. Conclusion We used a combination of IVM and DCE-MRI to study in vivo nanoparticle targeting kinetics. We observed a periodicity in the accumulation of αvβ3-integrin specific RGD-NE, which may be explained by αvβ3-integrin recycling kinetics. The initial targeting rate was quantified allowing for improvement of targeted nanoparticle design and potentially for better quantification of in vivo receptor levels. 1. Hak S, et al. (2012) ACS Nano 6 (6):5648-5658 2. Tofts PS (1997) JMRI 7 (1):91-101 3. Caswell PT, Norman JC (2006) Traffic 7 (1):14-21

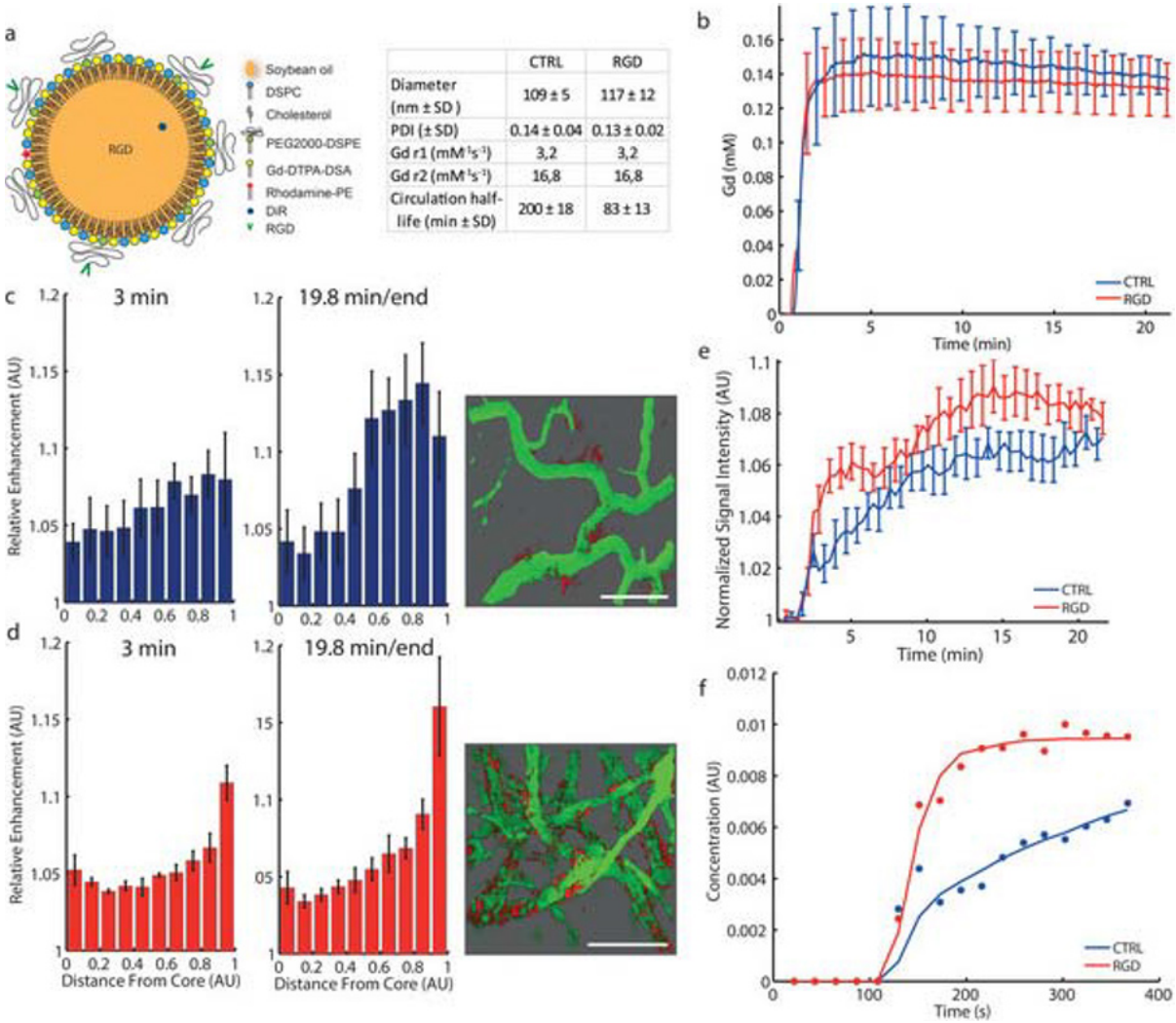

Figure 1 a: Nanoemulsion cartoon and characteristics. b: Average vascular input functions c: Relative enhancement in the tumor plotted as a function of the normalized distance from the tumor core at 2 time points post injection in the DCE-MRI for CTRL-NE (n=4). x=0 is at the tumor core and x=1 is at the tumor rim. The IVM image on the right shows CTRL nanoemulsion (red) extravasated from the tumor vasculature (green) d: As c but than for RGD-NE (n=4). The IVM image on the right in d shows RGD-NE (red) binding to the vasculature (green). d: Averaged normalized signal intensity in the tumor rim plotted versus time. e: Extended Tofts model fits (solid lines) to the first 4.5 min of DCE-MRI data (filled circles). Ki for RGD-NE was 8.43 whereas for CTRL-NE it was 1.98 ml/100g/min. Error bars represent standard error of the mean. The IVM images in c and d were reproduced from [1].

Disclosure of author financial interest or relationships:

S. Hak, None; **J. Cebulla**, None; **E. Huuse**, None; **C.D. Davies**, None; **W.J. Mulder**, None; **H.B. Larsson**, None; **O. Haraldseth**, None.

Presentation Number **SS 22**
Scientific Session 04: Preclinical in vivo Studies - Oncology (Targeted Imaging)
September 19, 2013 / 11:15-11:30 / Room: 203

Prolactin receptor-mediated internalization of imaging agents detects epithelial ovarian cancer with enhanced sensitivity and specificity

Karthik M. Sundaram[1,2], *Joseph A. Piccirilli*[2,5], *Ernst Lengyel*[3], *Brian B. Roman*[4], [1]*Pritzker School of Medicine - Medical Scientist Training Program, University of Chicago, Chicago, IL, USA;* [2]*Biochemistry and Molecular Biology, University of Chicago, Chicago, IL, USA;* [3]*Obstetrics and Gynecology, University of Chicago, Chicago, IL, USA;* [4]*Radiology, University of Chicago, Chicago, IL, USA;* [5]*Chemistry, University of Chicago, Chicago, IL, USA. Contact e-mail: ksundar@uchicago.edu*

Advanced OvCas with abdominal spread (stage III & IV) have 5-year survival rates of < 30%, while early cancers confined to the ovary and the pelvis (stage I and II) have 5-year survival rates of >70% (1). Because the ovaries and the fallopian tube are hidden in the peritoneal cavity, 75% of OvCas remain undiscovered until stage III or IV, after the tumor has metastasized (2). Thus, tumor detection poses one of the most important challenges to OvCa research and treatment. Two major goals for current detection methods include (i) detection of tumors when they are still small, confined to the pelvis, and curable and (ii) differentiation between benign and malignant ovarian tumors, which would drastically reduce the significant number of unnecessary surgeries (3). Bimanual pelvic examination, transvaginal ultrasound, and serum CA-125 levels have failed to consistently detect early ovarian malignancy, and advances in the serum biomarker field have been elusive (4). Therefore, new imaging modalities that address these concerns are urgently needed. Magnetic resonance imaging (MRI) provides several advantages in the imaging of the pelvis, providing high resolution images of anatomical structures with excellent soft tissue contrast without the use of ionizing radiation. Unfortunately, the diagnosis of malignant OvCa using gadolinium enhanced MRI still lacks sufficient specificity and sensitivity to distinguish healthy from cancerous tissue, leading to many unnecessary surgeries for a presumptive malignancy (3). One potential strategy is to create targeted molecular probes that imaging cell surface receptors expressed specifically on cancer cell surfaces. Here, we introduce the prolactin receptor (PRLR) as a high specificity biomarker for malignant OvCa that will serve as a vehicle for internalization of imaging agents into OvCa cells, engendering a new paradigm for targeted molecular imaging of OvCa. Our results indicate that > 98% of OvCas over-express PRLR regardless of stage, grade, and type. Using human placental lactogen (hPL), a specific and high affinity PRLR ligand, we show that hPL-gadolinium conjugates (and hPL-near-infrared probes conjugates) internalize efficiently into PRLR positive (PRLR+) cancer cells in OvCa mouse models and thereby enable detection of xenograft PRLR+ tumors in mice with substantially greater specificity and sensitivity than currently used clinical contrast agents. Molecular PRLR imaging holds the potential to achieve a more precise and earlier diagnosis of OvCa, which would reduce the number of unnecessary surgeries and increase patient survival. 1. Siegel, R., Naishadham, D. & Jemal, A. Cancer statistics, 2013. CA: A Cancer Journal for Clinicians 63, 11-30 (2013). 2. Lengyel, E. Ovarian cancer development and metastasis. The American Journal of Pathology 177, 1053-64 (2010). 3. Partridge, E. et al. Results from four rounds of ovarian cancer screening in a randomized trial. Obstetrics and Gynecology 113, 775-82 (2009). 4. Bast, R. C., Hennessy, B. & Mills, G. B. The biology of ovarian cancer: new opportunities for translation. Nature Reviews Cancer 9, 415-28 (2009).

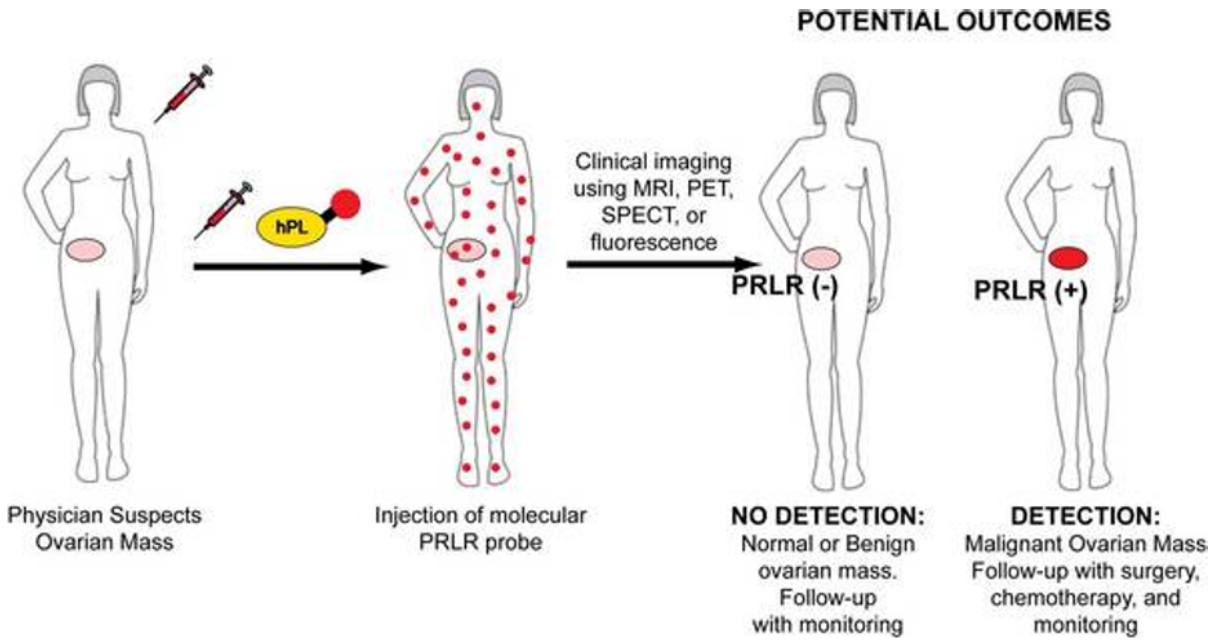

Molecular PRLR imaging with hPL-imaging conjugates holds the potential to achieve a more precise and earlier diagnosis of OvCa, which would reduce the number of unnecessary surgeries and increase patient survival.

Disclosure of author financial interest or relationships:
K.M. Sundaram, None; **J.A. Piccirilli**, None; **E. Lengyel**, None; **B.B. Roman**, None.

Presentation Number **SS 23**
Scientific Session 04: Preclinical in vivo Studies - Oncology (Targeted Imaging)
September 19, 2013 / 11:30-11:45 / Room: 203

111In-Bevacizumab Imaging as a Predictive Biomarker of Response to Anti-Angiogenesis Therapy: Preclinical Evaluation

Neel Patel[1,2], Sarah Able[1,2], Fergus Gleeson[2], Adrian L. Harris[2], **Katherine A. Vallis[1,2],** *[1]Gray Institute for Radiation Oncology and Biology, Oxford University, Oxford, United Kingdom; [2]Oncology, Oxford University, Oxford, United Kingdom. Contact e-mail: katherine.vallis@oncology.ox.ac.uk*

Background: Vascular endothelial growth factor (VEGF) and associated receptors play a critical role in tumor angiogenesis. The ability to image VEGF would enable prospective, non-invasive determination of response to antiangiogenesis therapy. Bevacizumab is a humanized monoclonal antibody that binds to VEGFA. The aim of this study was to investigate the use SPECT imaging with indium-labeled bevacizumab as a predictive biomarker. Methods: Bevacizumab was conjugated with benzyl-DTPA and radiolabeled with 111Indium (111In-BnDTPA-bevacizumab). Probe specificity was tested in vitro in competitive inhibition assays and in vivo by comparing uptake in Balb/c nude mice bearing tumours with variable VEGF expression with isotype-matched control antibody (111In-bnDTPA-IgG) and an excess of cold bevacizumab. Intratumoral VEGF was evaluated using ELISA and Western blot analysis. The effect of treatment on tracer uptake was tested by administering rapamycin (20 mg/kg) to mice bearing FaDu (squamous cell carcinoma) xenografts and compared to uptake of 111In-bnDTPA-IgG. Uptake was measured using gamma counting of ex-vivo tumours. Mice received anti-CD31 antibody intravenously for vessel analysis using confocal microscopy. Results: In inhibition assays the IC50 values for 111In-BnDTPA-bevacizumab and unmodified antibody were similar (0.85 nM and 1.0 nM, respectively). Specific uptake of 111In-BnDTPA-bevacizumab in VEGF-expressing tumors was observed (%ID/g in FaDu xenografts: 111In-BnDTPA-bevacizumab =20.25; 111In-bnDTPA-IgG=3.13; excess cold antibody=5.97). Rapamycin resulted in changes in tumor vascular morphology: relative vessel size increased (8.5 to 10.3, P=0.045) and mean relative vessel density decreased (0.27 to 0.22, P=0.0015), and was associated with increased tumor uptake of 111In-BnDTPA-bevacizumab (70% increase) but not 111In-bnDTPA-IgG. Intratumoral VEGF increased post-treatment (from 283+/-56 to 419+/-47 pg/g of protein). Western blot analyses showed the increase in VEGF was due mainly to VEGF165. Conclusion: 111In-BnDTPA-bevacizumab accumulates specifically in VEGF-expressing tumors and holds promise as an imaging tool for assessing response to therapy.

Disclosure of author financial interest or relationships:
N. Patel, None; **S. Able**, None; **F. Gleeson**, None; **A.L. Harris**, None; **K.A. Vallis**, None.

Presentation Number **SS 24**
Scientific Session 04: Preclinical in vivo Studies - Oncology (Targeted Imaging)
September 19, 2013 / 11:45-12:00 / Room: 203

HIF Silencing Reduces Total Choline, Metastatic Burden, and CD44 expressing cells in MDA-MB-231 Human Breast Cancers

Balaji Krishnamachary, *Santosh K. Bharti, Marie-France Penet, Flonne B. Wildes, Keve Zoltani, Yelena Mironchik, Zaver M. Bhujwalla, Radiology, Johns Hopkins University, Baltimore, MD, USA. Contact e-mail: bkrishn1@jhmi.edu*

Introduction: Hypoxia is frequently encountered in cancers and results in the stabilization of hypoxia inducible factors (HIF-1/2) that transcriptionally activate genes involved in invasion, metastasis, metabolism, and in the adaptation of cancer cells to the microenvironment. In breast cancer, stem-like breast cancer cells that survive, repopulate and metastasize to distant locations, have elevated expression of CD44. We observed elevated expression of CD44 in hypoxic tumor regions, and identified HIF-1α as a regulator of CD44 in breast cancer cells under hypoxic conditions [1]. Hypoxia has also been implicated in increasing the activity of choline kinase (Chk) - the enzyme responsible for elevated phosphocholine (PC) and total choline consistently observed in cancers [2]. Here, using non-invasive proton magnetic resonance spectroscopic imaging (1H MRSI), we have established the importance of HIF in reducing total choline and metastatic tumor burden, and have identified a role for CD44 in establishing lung metastasis. Methods: The establishment of MDA-MB-231 cells expressing shRNA against HIF-1α and HIF-2 α was done as previously described [1]. In vivo studies were performed using MDA-MB-23 1 human breast cancer cells and sub-lines silenced for HIF (-1, -2 or both), implanted in the mammary fat pad or injected intravenously in female severe combined immunodeficient (SCID) mice. MR experiments on size-matched tumors were performed on a Bruker 4.7T MR scanner using a home-built RF resonator. MR spectra were processed and analyzed with an in-house IDL program. Paraffin embedded adjacent sections of lung samples were stained for H&E and CD44. High-resolution digital scans of the stained sections were obtained using ScanScope (Aperio, Vista, CA). Images were processed and nuclei and membrane intensity quantified using ImageScope software and algorithm supplied by the manufacturer. Results: HIF silencing resulted in a significantly delayed tumor growth in mice. HIF-1α silencing decreased total choline and increased triglycerides compared to empty vector (EV) control tumors (Fig. 1A-D). Metabolic characterization of tumors with HIF-2 and both HIF-1 and 2 silenced are ongoing. Silencing HIF-1α, -2α or -1α and -2α resulted in a significant reduction of metastatic lung burden in mice (Fig. 1E). Additionally, HIF-2α silencing was more effective at reducing lung colonization than HIF-1α, while silencing both was the most effective. Although metastatic burden decreased in HIF-1α silenced cells, the percentage of cells with high CD44 expression in the metastatic foci was comparable to that in the wild type or EV foci. The percentage of high CD44 expression was significantly lower in HIF-2α and doubly silenced cells. These data support the importance of HIF and CD44 as targets to prevent lung colonization and disrupt the metastatic cascade. Acknowledgements: We thank Mr. Gary Cromwell for tumor inoculation and Dr. Dmitri Artemov for expert assistance. This work was supported by NIH R01CA136576 and P50 CA103175. References: 1. Krishnamachary, B., et al., PLoS One, 2012; 2. Glunde, K., et al., Cancer Res, 2008.

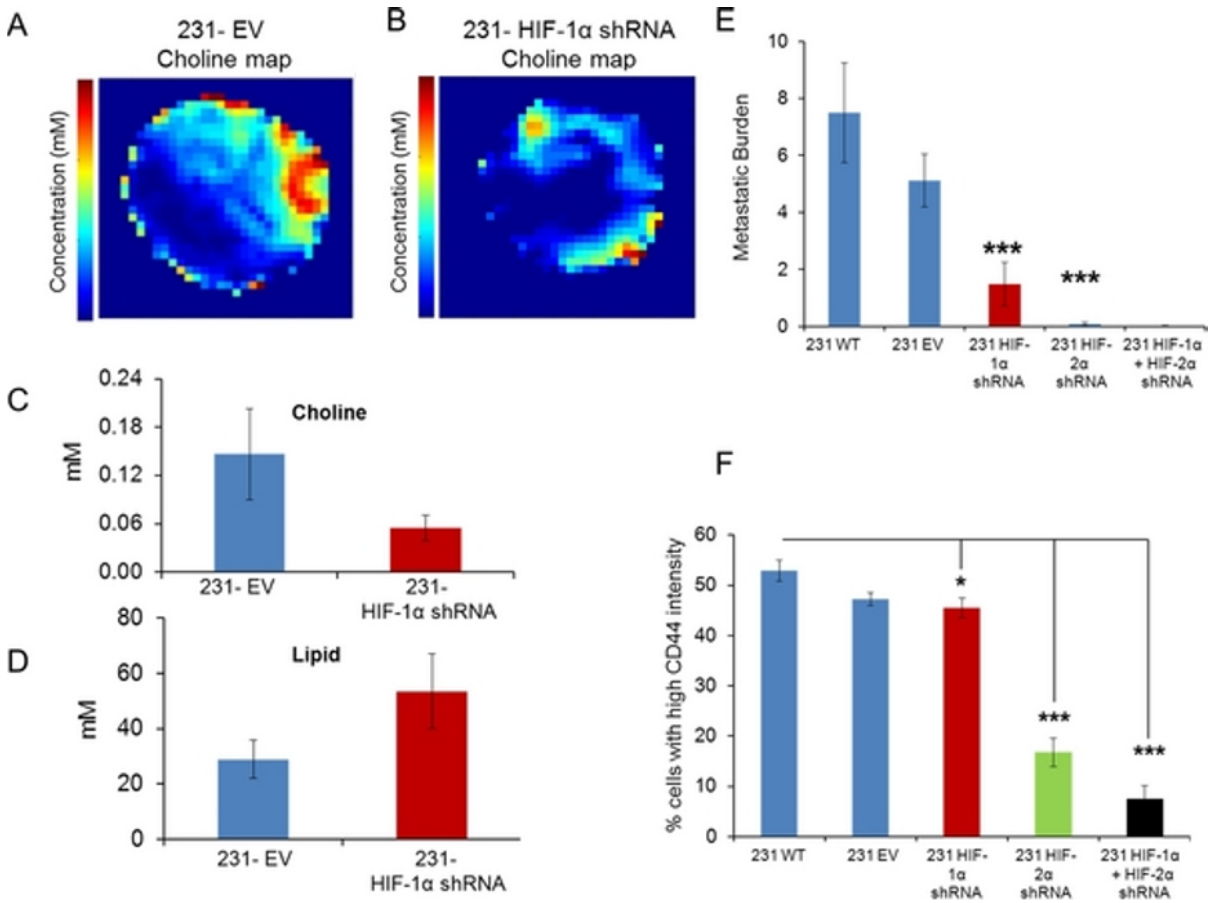

Disclosure of author financial interest or relationships:
B. Krishnamachary, None; **S.K. Bharti**, None; **M. Penet**, None; **F.B. Wildes**, None; **K. Zoltani**, None; **Y. Mironchik**, None; **Z.M. Bhujwalla**, None.

Presentation Number **SS 25**
Scientific Session 05: Chemistry & Imaging Probes - Optical Imaging
September 19, 2013 / 13:00-13:15 / Room: 102

NIRF Optical Peptide Probes Targeted against the Cholecystokinin-2/gastrin-Receptor with Variations of D-glutamine and D-glutamic Acid Sequences to Optimize Binding Affinity, Specificity and Pharmacokinetic Properties

Susanne Kossatz[1], *Rosalba Mansi*[2], *Martin Behe*[3], *Peter Czerney*[4], *Werner A. Kaiser*[5], *Ingrid Hilger*[1], [1]*Dept. of Experimental Radiology, Institute of Diagnostic and Interventional Radiology I, Jena University Hospital, Jena, Germany;* [2]*Institute for Nuclear Medicine, University Hospital Freiburg, Freiburg, Germany;* [3]*Paul Scherrer Institute, Center for Radiopharmaceutical Sciences ETH-PSI-USZ, Villigen-PSI, Switzerland;* [4]*Dyomics GmbH, Jena, Germany;* [5]*Institute of Diagnostic and Interventional Radiology I, Jena University Hospital, Jena, Germany. Contact e-mail: susanne.kossatz@med.uni-jena.de*

We adapted minigastrin peptides for optical imaging by equipping them with a near infrared fluorescent (NIRF) dye and making them available for fluorescence guided endoscopy and intraoperative real-time imaging of Cholecystokinin-2-receptor (CCK2R) expressing tumors. We designed optical minigastrin probes with different spacer sequences to identify probe variants with high target affinity and specificity. Additionally we were seeking for renal elimination and low nonspecific binding to exclude interfering fluorescence in the gastrointestinal tract during endoscopy in the prospective clinical application. We synthesized the following probe variants: "Q" with a six d-glutamine spacer (DY-754-(dQ)6-AYGWMNF-amide, "QE" with three alternating d-glutamines and d-glutamic acids (DY-754-(dQ-dE)3-AYGWMNF-amide and "bivQ" with a two minigastrins, each preceded by three d-glutamines (DY-754-2((dQ)3-AYGWNleNF-amid). They were tested for affinity and specificity in vitro on CCK2R expressing and non-expressing cells and for metabolic stability in liver homogenates. In vivo imaging was conducted with subcutaneous tumor bearing nude mice after i.v. probe injection (54-108 nmol/kg) and under competitive conditions with non-fluorescent minigastrin (n=5/group). Ex vivo we assessed probe biodistribution as well as NIRF distribution in tumor slides. The NIRF optical probes displayed high affinity binding with dissociation constants between 1.7 and 5.8 nM and high specificity for CCK2R binding. They were actively internalized at 37°C but not at 4°C and fluorescence accumulated intracellular. High binding specificity was confirmed, because a low competitor concentration of 16-17 nM led to a reduction of the initial binding by 50 %. Half times in liver homogenate were < 30 min ("bivQ), 187 min ("Q") and 347 min ("QE"). In vivo, highest tumor-to-background contrasts were observed for "QE" and "bivQ", but the strongest effect through competition was reported for the probe "Q". Ex vivo probe distribution showed selective accumulation in non-necrotic regions of CCK2R expressing tumors. Biodistribution analysis revealed strong kidney retention, which was further increased in the probe "QE". Importantly, the three probes showed an almost complete absence of fluorescence in the gastrointestinal tract. Although all NIRF optical probes showed high affinity binding, the highest affinity and highest in vivo specificity was found in the probe Q, with six uncharged d-glutamines as spacer. Introduction of d-glutamic acids into the spacer led to an increase in kidney fluorescence, but also to an increase in metabolic stability. Importantly, coupling of the dye moiety did

not lead to loss of affinity or specificity. The minigastrin probes displayed characteristics that are useful for future clinical applications of optical imaging, like rapidly achieved high contrast imaging of malignant tissue over healthy tissue and renal elimination. We showed that probe characteristics can be directed by introducing variants of d-glutamine or d-glutamic acid sequences into the construct, a concept that could also be applied to other small molecule probes.

Disclosure of author financial interest or relationships:
S. Kossatz, None; **R. Mansi**, None; **M. Behe**, None; **P. Czerney**, Dyomics GmbH, Stockholder; Dyomics GmbH, Employment; **W.A. Kaiser**, None; **I. Hilger**, None.

Presentation Number **SS 26**
Scientific Session 05: Chemistry & Imaging Probes - Optical Imaging
September 19, 2013 / 13:15-13:30 / Room: 102

A PSMA-Specific Theranostic Nanoplex For Molecular Targeting of Prostate Cancer

Zhihang Chen[1], *Marie-France Penet*[1], *Balaji Krishnamachary*[1], *Sangeeta Ray*[1], *Paul T. Winnard*[1], *Cong Li*[2], *Martin Pomper*[1], *Zaver M. Bhujwalla*[1], [1]*Department of Radiology and Radiological Science, Johns Hopkins University, Baltimore, MD, USA;* [2]*School of Pharmacy, Fudan University, Shanghai, China. Contact e-mail: zchen19@jhu.edu*

Prostate cancer (PCa) is the second leading cause of death from cancer in men in the U.S., and there is a compelling need for the development of effective treatments for metastatic PCa. Theranostic approaches that combine detection with treatment hold significant promise for cancer-cell-specific treatments especially with molecular reagents such as cDNA or siRNA that can increase or decrease the expression of genes of interest. We have reported on a prostrate-specific membrane antigen (PSMA)-based platform to deliver a prodrug enzyme and small interfering RNA (siRNA) to downregulate gene expression for theranostic imaging of metastatic PCa[1]. Here we expanded this platform for gene delivery and expression of tumor necrosis factor-related apoptosis-inducing ligand (TRAIL) cDNA. PSMA, which is highly expressed by castration-resistant PCa, was used for PCa-specific delivery and localization of the nanoplex that delivered TRAIL cDNA and a prodrug enzyme, bacterial cytosine deaminase (bCD). TRAIL has been reported to kill malignant cells specifically but to be relatively nontoxic to normal cells. The GFP-TRAIL cDNA used expresses a GFP-TRAIL fusion protein that can be detected with optical imaging to evaluate cDNA expression. The prodrug enzyme bCD converts the non-toxic prodrug 5-fluorocytosine (5-FC) to the active cytotoxic drug 5-fluorouracil (5-FU) that can be monitored by ^{19}F MRS. Our prototype nanoplexes were synthesized by conjugating: (i) a low molecular weight urea-based PSMA targeting moiety (2-(3-[1-carboxy-5-[7-(2,5-dioxo-pyrrolidin-1-yloxycarbonyl)-heptanoylamino]-pentyl]-ureido)-pentanedioic acid, (ii) the prodrug-activating enzyme bCD that converts nontoxic 5-FC to cytotoxic 5-FU, (iii) the near-infrared fluorescent probe Cy5.5 labeled linker poly-L-lysine (PLL), and (iv) the GFP-TRAIL cDNA delivery vector: PEI (polyethyleneimine)-PEG (polythethyeneglycol) co-grafted-polymer. A schematic representation of the structure of nanoplex is shown in **Figure 1A**. Imaging and therapy studies with nanoplexes were performed with PC3-PIP cells that overexpress PSMA, and non-PSMA expressing PC3-Flu cells. Cell imaging indicated that there was higher expression of GFP in PC3-PIP cells than PC3-Flu cells. In vivo images obtained from PIP and Flu tumors demonstrated increased accumulation of the nanoplex in PIP tumors (**Figure 1B**). Cell imaging studies indicated higher expression of GFP-TRAIL fusion protein in PC3-PIP cells. In vivo images obtained from PIP and Flu tumors demonstrated increased accumulation of the nanoplex in PIP tumors. In ex vivo imaging studies, increased uptake of the nanoplex as detected by Cy5.5 fluorescence, and higher expression of GFP in PIP compared to Flu tumors were observed. ^{19}F MRS indicated the prodrug enzyme bCD efficiently converted the prodrug 5-FC to 5-FU at 24 h. Tumor growth studies showed increased inhibition of PIP tumor growth. These data demonstrate the ability of our theranostic nanoplex to express a gene of interest in PSMA expressing prostate cancer cells. 1. Chen et al., ACS Nano, 2012. Support from NIH P50CA103175 is gratefully acknowledged

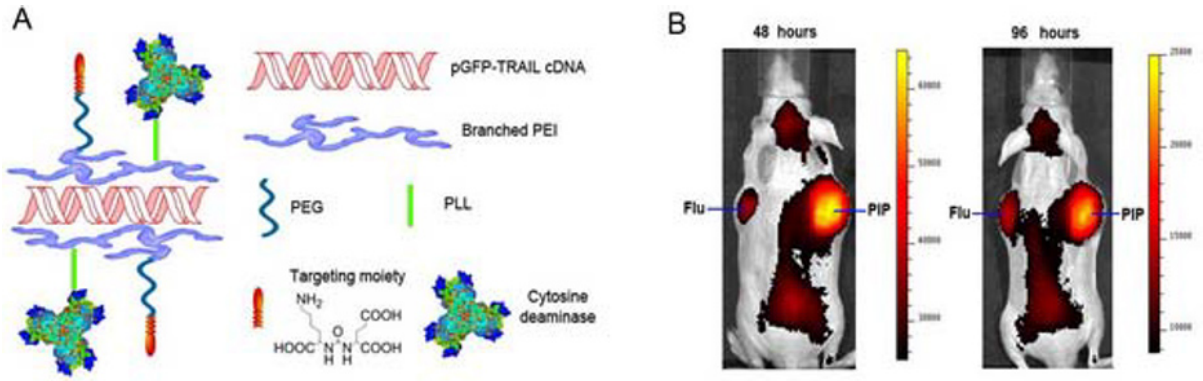

Figure 1: (A) Schematic representation of the nanoplex structure. **(B)** *In vivo* optical imaging (Cy 5.5 fluorescence) of SCID mouse bearing PIP and Flu tumor (injected iv with 150 mg/kg nanoplex).

Disclosure of author financial interest or relationships:
Z. Chen, None; **M. Penet**, None; **B. Krishnamachary**, None; **S. Ray**, None; **P.T. Winnard**, None; **C. Li**, None; **M. Pomper**, None; **Z.M. Bhujwalla**, None.

Presentation Number **SS 27**
Scientific Session 05: Chemistry & Imaging Probes - Optical Imaging
September 19, 2013 / 13:30-13:45 / Room: 102

Trapping and detection of circulating tumor cells using targeted magnetic and surface-enhanced-Raman-scattering nanopartic

Wei Shi, *Robert J. Paproski, Roger J. Zemp, Electrical & Computer Engineering, University of Alberta, Edmonton, AB, Canada. Contact e-mail: wshi2@ualberta.ca*

Detection of circulating tumor cells (CTC) is of great importance for tumor research since the CTCs are a marker of cancer metastasis and a source of biomarkers for research and diagnosis. However, in vivo detection of CTCs is difficult due to low concentration in blood. In 2009, Galanzha et.al (Nature Nanotech., vol. 4, 855-860, 2009) reported rapid photoacoustic detection of magnetically captured CTCs in vivo using magnetic and optically-absorbing nanoparticles (NPs). However, this and other approaches showed limited multiplexing ability to improve specificity of detection. Zavaleta et.al, (PNAS, vol. 106, no. 32, 13511-13516, 2009) demonstrated the ability to produce multiplexed in vivo images with 10 surface-enhanced Raman scattering (SERS) NP batches at picomolar sensitivities. Surface-enhanced Raman spectroscopy presents high multiplexing capabilities due to narrow spectral features of the Raman spectrum. To realize multiplexed detection of CTCs, we propose a combination of magnetic trapping and multiplex detection of CTCs by using targeted magnetic and SERS probes. Our Raman imaging setup is built using a custom Raman imaging spectrometer with EMCCD camera and a 785 nm excitation laser. A 1" cone magnet was used for magnetic trapping. Cell flow was controlled by using a syringe pump. In our experiments, SERS NPs composed of a 60 nm-diameter Au core with a Raman active molecular monolayer adsorbed onto it. Encapsulated with a 30 nm diameter silica shell, the entire SERS NP size was about 120 nm. Due to surface-enhanced Raman effects, the Au core metal substrate can enhance the Raman signal from the molecule layer by many orders of magnitude. De-mixing was based on classic least-squares methods. Estimated concentrations presented a highly linear relationship with actual concentrations of SERS NPs with R2=0.99 (Fig 1). The lowest concentration of SERS NPs detected by our imaging setup was 6 pM. The detection limit can be further improved by up to 160 times when using a fiber bundle to fully utilize the 160 channels on our EMCCD. Intralipid solution was used to mimic the turbidity of human tissue, where a maximum depth of 5 mm was observed by using 1.3 nM SERS NPs. To target CTCs with folate receptors, the thiolated SERS NPs were conjugated with maleimide-PEG-folate. HeLa (folate receptor positive) and ZR-75-1 (folate receptor negative) cell lines were incubated with serum free medium containing SERS NPs for 4 hours. The detected SERS signals from HeLa cells were 6 times higher than from ZR-75-1 cells (Fig.2). Magnetic NPs were targeted using maleimide-PEG-folate or anti-bodies. ZR-75-1 cells incubated with the magnetic NPs showed little magnetic trapping efficiency compared to HeLa cells. Mixtures of folate conjugated SERS NPs and folated conjugated magnetic NPs were investigated. Magnetic trapping during flow showed accumulation of cells exhibiting increasing SERS signals over time. By using multiple species of SERS NPs targeted to different targeting moieties, we plan to detect the trapped cells and identify CTC tumor type with high specificity.

Disclosure of author financial interest or relationships:
W. Shi, None; **R.J. Paproski**, None; **R.J. Zemp**, None.

Presentation Number **SS 28**
Scientific Session 05: Chemistry & Imaging Probes - Optical Imaging
September 19, 2013 / 13:45-14:00 / Room: 102

Encapsulation of a self-quenching Near-infrared Fluorescent dye in Liposomes enables reliable whole body Imaging of Inflammation upon in vivo fluorescence activation

Felista Tansi[1], *Ronny Rüger*[2], *Markus Rabenhold*[2], *Frank Steiniger*[3], *Werner A. Kaiser*[1], *Alfred Fahr*[2], *Ingrid Hilger* [1], *Experimental Radiology, Jena University Hospital, IDIR-I, Jena, Germany;* [2]*Department of Pharmaceutical Technology, Friedrich Schiller University, Jena, Jena, Germany;* [3]*Center for Electron Microscopy, Jena University Hospital, Jena, Germany. Contact e-mail: felista.tansi@med.uni-jena.de*

Introduction: Whole body fluorescence imaging allows the non-invasive detection and semi-quantitative analysis of inflammatory processes and tumors and is particularly suitable for intraoperative purposes [1, 2]. However, a hallmark of most available fluorescent probes is a rapid clearance in vivo, which hampers their application. The aim of this work was therefore the development of a fluorescence-activatable liposome, which enables discrimination between cellular internalized and non-internalized probes and a reliable whole body in vivo fluorescence imaging of inflammation over an adequate duration. Methods: Liposomes were prepared by the film hydration and extrusion method and encapsulated with high concentrations of the NIR fluorescent dye, DY-676-COOH [3]. The liposomes (termed Lip-Q) revealed a high level of fluorescence-quenching. Fluorescence activation upon release of the liposomal DY-676-COOH was demonstrated in vitro by spectro-fluorometry, cellular uptake and confocal microscopy and their accumulation in endo-lysosomes substantiated by use of chloroquine [4]. Lip-Q based in vivo imaging of zymosan-induced edema in mice was done by planar fluorescence reflectance imaging. The time-dependent fluorescence activation of Lip-Q in edema was analyzed semi-quantitatively. Furthermore, cells were isolated from zymosan-peritonitis mice models and characterized. Results: A 9-fold increase in fluorescence intensity of Lip-Q was detected after disruption with ethanol and Triton-X100. The liposomes were taken up predominantly by phagocytosis and could be detected in highly phagocytic macrophage and glioblastoma cell lines but not in the non-phagocytic fibrosarcoma cell line HT-1080. Cells treated with chloroquine prior to addition of Lip-Q revealed liposomal degradation in swollen phago-lysosomes. Furthermore, fluorescence activation of Lip-Q by the monocyte/ macrophage subset in vivo enabled distinct whole body fluorescence imaging of hind-leg edema, with the highest fluorescence intensities detected 8 h p.i. Monocytes/ macrophages isolated from zymosan-peritonitis mice models 6 h p.i. revealed liposomal-fluorescence of Lip-Q. Biodistribution studies exposed biliary clearance of Lip-Q. Conclusion: Lip-Q combines the advantage of prolonged stability and fluorescence activation upon internalization in cells and enables discrimination between internalized and non-internalized probe opposed to conventional non-activatable imaging probes. Furthermore, the clearance via the liver and kidney makes Lip-Q a potent non-invasive contrast agent for optimized NIRF imaging of inflammatory diseases located directly underneath the skin where NIR light can penetrate, for example rheumatoid arthritis. We strongly believe that Lip-Q constitutes a valuable tool relevant to research and clinical discovery. 1. Sevick-Muraca, E.M., et al., Curr Opin Chem Biol, 2002. 6(5): p. 642-50. 2. Luker, G.D. and K.E. Luker, J Nucl Med, 2008. 49(1): p. 1-4. 3. Fahr, A., et al., Eur J Pharm Sci, 2005. 26(3-4): p. 251-65. 4. Khalil, I.A., et al., Pharmacol Rev, 2006. 58(1): p. 32-45.

Disclosure of author financial interest or relationships:
F. Tansi, None; **R. Rüger**, None; **M. Rabenhold**, None; **F. Steiniger**, None; **W.A. Kaiser**, None; **A. Fahr**, None; **I. Hilger**, None.

Presentation Number **SS 29**
Scientific Session 05: Chemistry & Imaging Probes - Optical Imaging
September 19, 2013 / 14:00-14:15 / Room: 102

Luminescent imaging method to distinguish acute and chronic inflammation

Jen-Chieh Tseng[1], *Andrew L. Kung*[2], [1]*Radiology, Dana-Farber Cancer Institute, Boston, MA, USA;* [2]*Pediatric Hematology/Oncology/Stem Cell Transplantation, Columbia University Medical Center, New York, NY, USA. Contact e-mail: jen-chieh_tseng@dfci.harvard.edu*

Inflammation is a fundamental aspect of many pathological conditions in humans, including microbial infection, wound healing, diabetes, cancer, cardiovascular, neurodegenerative and autoimmune diseases. As it is a multi-stage process involving many cell types, inflammation is highly regulated to ensure proper tissue repair and disease resolution. Neutrophils and macrophages are two major phagocytic cell types that mediate inflammatory responses. During acute inflammation, neutrophils form the first line of defense. In response to tissue insult, neutrophils rapidly extravasate from the blood stream to the site of injury where the cells effectively engulf invading bacteria into phagosomes. The neutrophil phagosomes contain high levels of phagocyte NADPH oxidase (Phox) and myeloperoxidase (MPO) to produce toxic levels of superoxide (O2-) and hypochlorous acid (HOCl) for anti-microbial efficacy. As inflammation progresses, circulating monocytes gradually migrate to the site of infection and differentiate into macrophages. The phagocytic function of macrophages is important for cellular debris removal during tissue remodeling. In addition, macrophages play important roles in mediating late stage (chronic) inflammation. Macrophages regulate immune functions by producing extracellular reactive oxygen species (ROS) and anti-inflammatory cytokines. Thus, during the acute phase of inflammation, superoxide production in neutrophils directly participates in pathogen inactivation and elimination. In contrast, during late or chronic inflammation, macrophages assemble Phox in the plasma membrane to produce extracellular superoxide and various downstream ROS for regulating tissue repair. By taking advantage of the differential roles of superoxide during inflammation, we developed a luminescent imaging strategy to distinguish acute and chronic inflammatory status in living animals. The method involves the use of two superoxide-sensing chemiluminescent substrates: luminol (5-amino-2,3-dihydro-1,4-phthalazinedione) and lucigenin (bis-N-methylacridinium nitrate). Luminol is a small and uncharged molecule (MW = 177.16) that can easily penetrate both plasma and phagosome membranes. Since luminol bioluminescence requires phagosomal MPO activity, systemic delivery of luminol reveals regions of acute inflammation largely mediated by tissue-infiltrating neutrophils. In contrast, lucigenin is a larger compound with two positive charges and thus is less membrane-permeable. Injection of lucigenin enables detection of superoxide generated by macrophage Phox and its bioluminescence is closely associated with late phase or chronic inflammation. Together, we are able to visualize tissue inflammation resulting from wound healing, bacterial infection, foreign substance implantation, and antitumor immune responses. Given the central role of inflammation in a variety of human diseases, we believe this imaging method can help differentiate the roles of neutrophils and macrophages in various pathophysiological conditions.

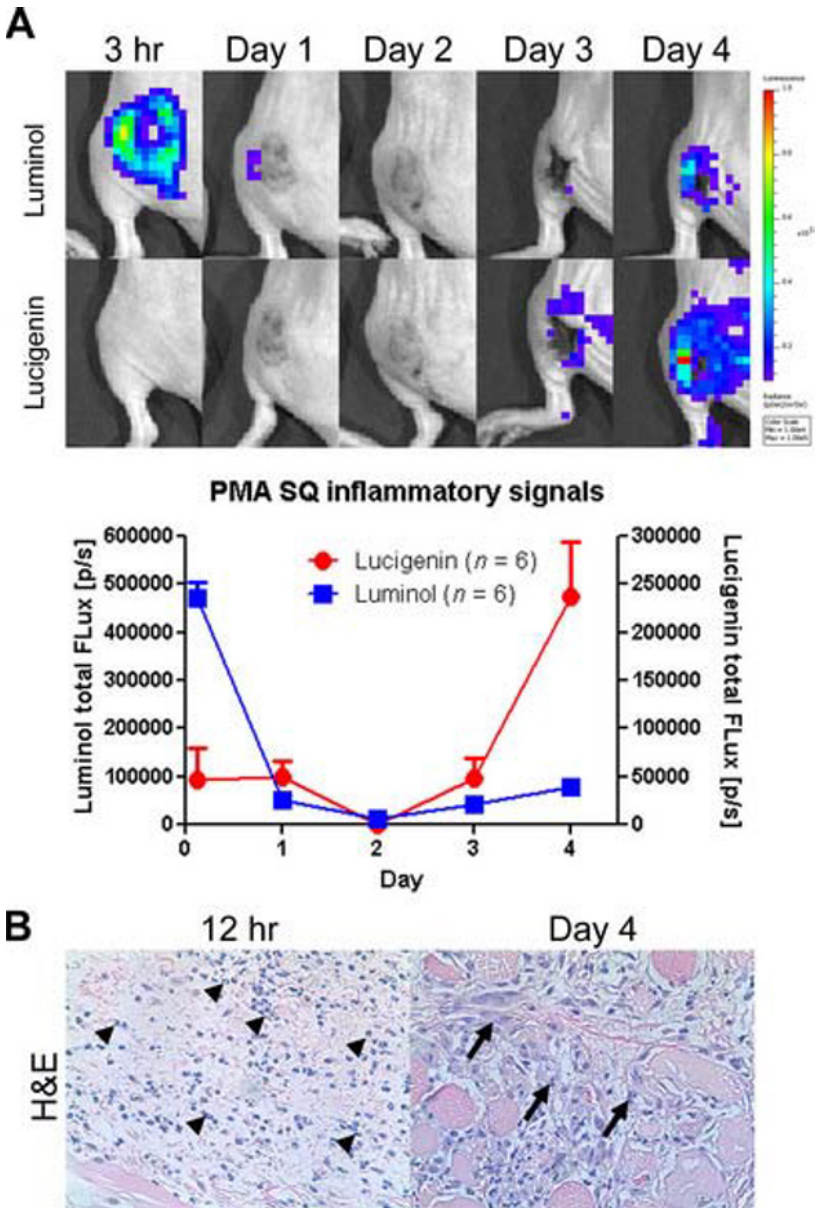

(A) Longitudinal bioluminescence imaging of acute and late phase inflammation. PMA (50 micrograms) was s.c. injected on the left flanks in NCr nude mice to induce local tissue inflammation. Starting 3 hr after PMA injection, we i.p. delivered luminol (100 mg/kg) or lucigenin (25 mg/kg) for bioluminescence imaging. Same imaging procedures were repeated daily for 4 consecutive days. Quantitative representation of the imaging data indicates that luminol bioluminescence correlates with acute inflammation, while lucigenin bioluminescence is associated with chronic or late stage of inflammation. (B) Skin samples were collected 12 hr or 4 days after s.c PMA injection. Tissue sections were prepared for standard H&E staining. We observed neutrophil infiltration (arrow heads) at the sites of PMA injection during acute phase of inflammation (12 hr), which was mostly replaced by macrophages (arrows) 4 days later.

Disclosure of author financial interest or relationships:
J. Tseng, None; **A.L. Kung**, None.

Presentation Number **SS 30**
Scientific Session 05: Chemistry & Imaging Probes - Optical Imaging
September 19, 2013 / 14:15-14:30 / Room: 102

Applying Advanced Spectroscopic Methods to Development of Degradable Polymeric Optical Probes

Tiffany P. Gustafson, *Young Lim, Fuwu Zhang, Jeniree A. Flores Delgado, Gyu Seong Heo, Shiyi Zhang, Sandani Samarajeewa, Jeffery E. Raymond, Karen L. Wooley, Departments of Chemistry and Chemical Engineering, Texas A&M University, College Station, TX, USA. Contact e-mail: tiffany.gustafson@chem.tamu.edu*

Successful development of degradable polymeric nanostructures as probes for optical imaging that can be realistically translated from the laboratory to in vivo imaging performance requires that one is able to distinguish between free optical contrast agents and the labeled polymeric materials as they undergo degradation. Within this body of work, we describe a series of nanoparticle systems in which dye labeling is assessed in a holistic manner. Specifically, we propose a combination of emission lifetime, anisotropy, anisotropy decay and steady-state techniques in which polymer nanoparticle-dye binding can be assessed independent of electrolyte gels. Such gels are conducted under non-physiological conditions that may promote accelerated degradation, affording misleading results, relative to in vivo translation of the nanomaterial optical probes. This ability to promote degradation makes the use of gentler spectroscopic methods particularly critical, especially as modern nanotheranostic polymer platforms transition to architectures intentionally reliant on built-in degradability. This degradability will be shown to be triggered by gel electrophoresis in several polymeric systems. Traditional non-degradable polymeric nanoparticles display different uptake characteristics in vitro, and longer clearance times in vivo, in comparison to free dye analogs. These differences have allowed for their use as optical probes largely without concern for the efficiency of dye conjugation and contamination by free optical dyes. When accurate evaluation of dye conjugation is necessary for these non-degradable systems, standard methods such as gel electrophoresis can be used. However, these same electrophoretic techniques trigger premature destabilization in degradable systems, making evaluation of dye conjugation more complex. More reliable, less destructive "gentle" methods of evaluation are, therefore, in high demand. Development and use of these gentler methods is particularly important in intelligently-designed, rapidly-degradable platforms. In these systems, polymeric optical probes may clear from biological systems quickly, making it impossible to distinguish between unconjugated and conjugated contrast agents in vivo. For example, materials prepared from cationic polyphosphoesters are shown to undergo degradation in vitro within 24 - 48 h. We have found that utilizing a combination of spectroscopic and microscopic techniques provides an accurate understanding of coupling efficiencies and dynamic interactions between contrast agents and polymeric nanoparticles. This array of complementary techniques is particularly critical in instances where gel electrophoresis is intrinsically unable to monitor the particle systems without triggering degradation during analysis. The improved understanding of the spectral signature-structure-function relationship this regime of assessment provides will enable an accurate evaluation of the in vitro and in vivo biodegradation characteristics of polymeric optical imaging platforms.

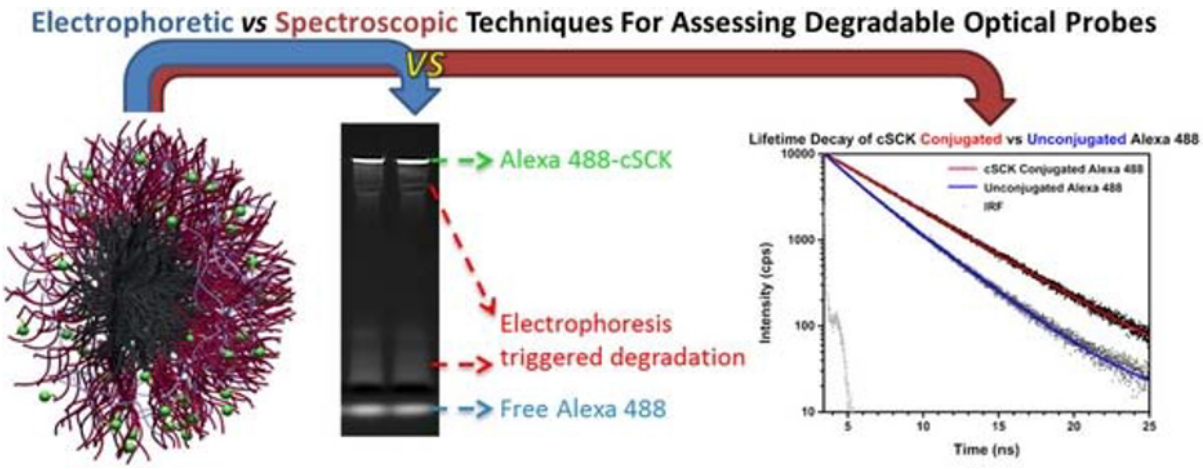

Disclosure of author financial interest or relationships:
T.P. Gustafson, None; **Y. Lim**, None; **F. Zhang**, None; **J.A. Flores Delgado**, None; **G. Heo**, None; **S. Zhang**, None; **S. Samarajeewa**, None; **J.E. Raymond**, None; **K.L. Wooley**, None.

Presentation Number **SS 31**
Scientific Session 06: Preclinical in vivo Studies - Neurology
September 19, 2013 / 13:00-13:15 / Room: 105

Molecular MRI and Immuno-Spin-Trapping used to Detect in vivo Membrane-Bound Radicals in a Mouse Model for ALS

Rheal Towner[1], *Nataliya Smith*[1], *Debra Saunders*[1], *Florea Lupu*[2], *Robert Silasi-Mansat*[2], *Melinda West*[3], *Dario C. Ramirez*[4], *Sandra E. Gomez-Mejiba*[4], *Marcelo G. Bonini*[5], *Ronald P. Mason*[6], *Marilyn Ehrenshaft*[6], *Kenneth Hensley*[7], [1]*Advanced Magnetic Resonance Center, Oklahoma Medical Research Foundation, Oklahoma City, OK, USA;* [2]*Cardiovascular Biology, Oklahoma Medical Research Foundation, Oklahoma City, OK, USA;* [3]*Free Radical Biology and Aging, Oklahoma Medical Research Foundation, Oklahoma City, OK, USA;* [4]*Laboratory of Experimental Medicine and Therapeutics, National University of San Luis, San Luis, Argentina;* [5]*DEpartments of Medicine and Pharmacology, University of Illinois, Chicago, IL, USA;* [6]*Laboratory of Pharmacology and Chemistry, National Institute of Environmental Health Sciences, Research Park, NC, USA;* [7]*Pathology, University of Toledo Health Sciences Center, Toledo, OH, USA. Contact e-mail: Rheal-Towner@omrf.org*

Introduction: Reactive oxygen (and nitrogen) species generated from oxidative stress play a crucial role either as modulators of signal transduction or as a cause of tissue injury in diseases. Monitoring in vivo radicals in a transgenic mouse model for amyo-trophic lateral sclerosis (ALS) by combining molecular magnetic resonance imaging (mMRI) and immuno-spin trapping (IST) technologies for the first time is possible. Methods: As a model for ALS, a human-G93A-SOD1 Tg mouse model was used, compared to wild-type (WT) controls. DMPO (5,5-dimethyl-pyrroline-N-oxide) was given for a week to maximize trapping of protein radicals prior to detection of DMPO-protein/lipid nitrone adducts at 120 days. For controls, G93A-SOD1 mice (n=5) were administered saline instead of DMPO, while WT mice (n=5) received DMPO. The contrast agent, biotin-anti-DMPO-BSA (bovine serum albumin)-Gd-DTPA (200µg anti-DMPO and 100µg biotin-BSA-Gd-DTPA), was used. Non-specific mouse-IgG conjugated to biotin-BSA-Gd-DTPA was synthesized by the same protocol. MRI experiments were performed on a Bruker Biospec 7.0 Tesla/30 cm horizontal small animal system. T1-weighted image was acquired with a repetition time (TR) of 2000 ms and an echo time (TE) of 17.5 ms, and the T2-weighted image with TR of 2000 ms and TE of 58.2 ms. mMRI was done with a variable-TR RARE sequence (rapid acquisition with refocused echoes), with TE of 15 ms and two transverse slices. Signal intensities were calculated in defined regions-of-interest (ROIs) in T1-weighed images. Relative probe (contrast agents) concentrations, C (units: M), were calculated for the selected ROI using the following formula: $C \propto [1/T1 \text{ (after)} - 1/T1(\text{before})]$, where 1/T1 (after or before) is the T1 taken at the different time points after or before injection of probe. Results: MRI was used to detect anti-DMPO adducts by either a significant sustained increase ($p<0.05$) in MR signal intensity (Fig. 1) or a significant decrease ($p<0.05$) in T1 relaxation. The biotin moiety of the anti-DMPO probe was targeted with streptavidin-fluorescently labeled to locate the anti-DMPO probe in excised tissues. As negative controls, either Tg ALS mice were initially administered saline rather than DMPO followed by the anti-DMPO probe, or wild-type mice were initially administered DMPO and then the anti-DMPO probe. DMPO adducts were also confirmed in disease/non-disease tissues from animals administered DMPO. Discussion: It is thought that only radical adducts that are membrane-bound (e.g. protein and/or lipid radical adducts) will be targeted by the Gd-based anti-DMPO probe and detected by MRI. Uptake of anti-DMPO probe into spinal cord tissue is thought to be due to a disrupted blood-spinal cord barrier (BSCB) and blood-brain barrier (BBB). We used a combination of mMRI and IST to show for the first time non-invasive in vivo detection of spin-trapped membrane-bound radicals in a mouse model for ALS. Using both mMRI and IST provides in vivo image resolution and spatial differentiation of regional events in heterogeneous tissues or organs and regional targeting of free radical mediated oxidation of cellular membrane components.

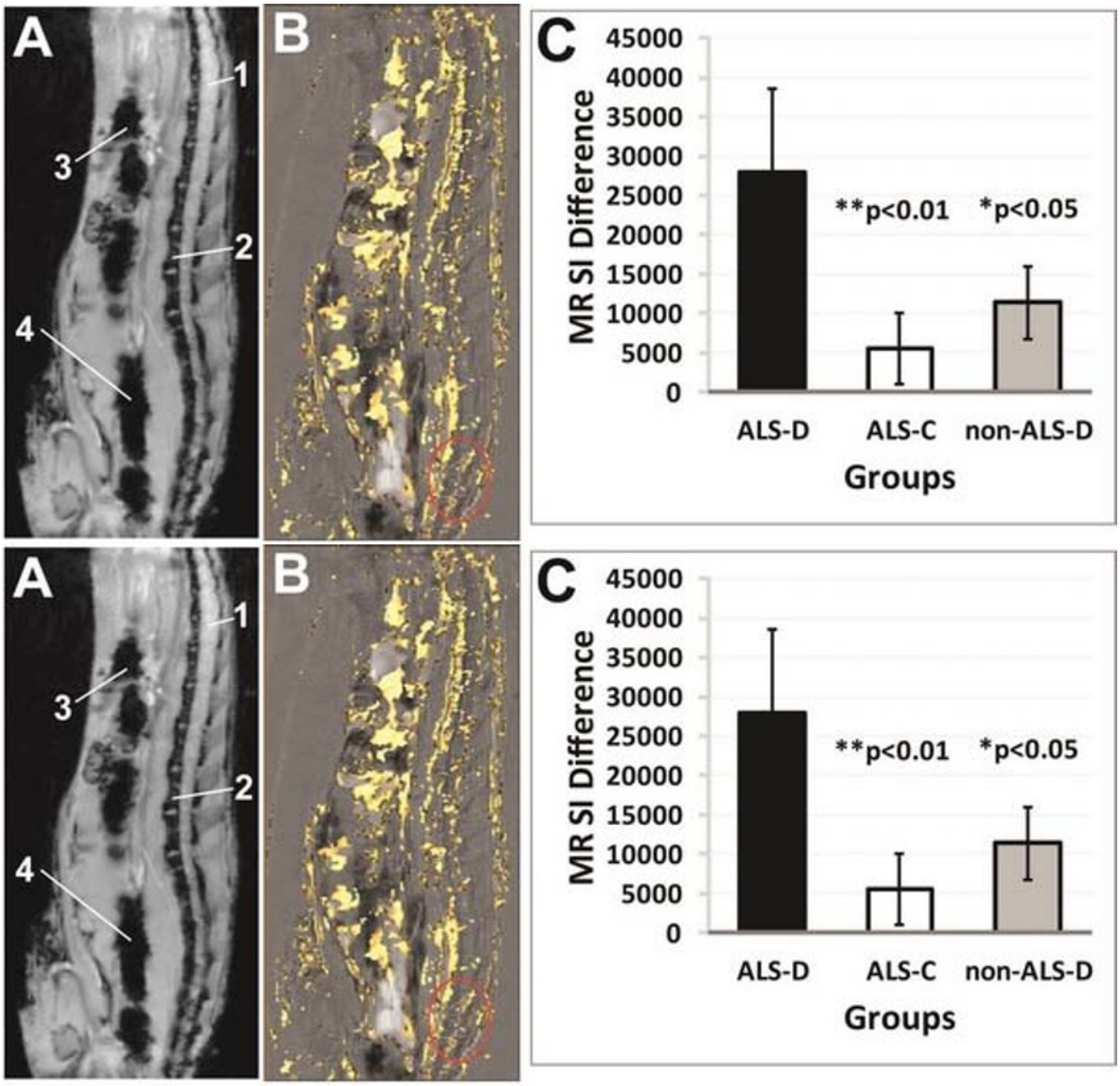

Disclosure of author financial interest or relationships:
R. Towner, None; **N. Smith**, None; **D. Saunders**, None; **F. Lupu**, None; **R. Silasi-Mansat**, None; **M. West**, None; **D.C. Ramirez**, None; **S.E. Gomez-Mejiba**, None; **M.G. Bonini**, None; **R.P. Mason**, None; **M. Ehrenshaft**, None; **K. Hensley**, None.

Presentation Number **SS 32**
Scientific Session 06: Preclinical in vivo Studies - Neurology
September 19, 2013 / 13:15-13:30 / Room: 105

In vivo imaging of dopaminergic and serotoninergic neurotransmission following long-term cerebral ischemia

Abraham Martin[1], *Vanessa Gómez-Vallejo*[2], *Boguslaw Szczupak*[1], *Eneko San Sebastián*[1], *Irati Markuerkiaga*[1], *Daniel Padró*[1], *Sandra Plaza*[1], *Jordi Llop*[2], [1]*Molecular Imaging, CICbiomaGUNE, San Sebastian, Spain;* [2]*Molecular Imaging, Radiochemistry, CICbiomaGUNE, San Sebastian, Spain. Contact e-mail: amartin@cicbiomagune.es*

Objectives: Neurotransmitter systems may play a key role in the functional recovery process and brain plasticity in response to cerebral ischemia. The aim of the present study is to study by positron emission tomography (PET) both the dopaminergic and serotoninergic neurotransmission to elucidate their relationship with brain perfusion, metabolism and functional recovery after long-term brain ischemia. Methods: Longitudinal PET imaging with [13N]ammonia, [18F]FDG, [11C]raclopride, [11C]DASB and [18F]altanserin was performed to explore the changes in cerebral perfusion, glucose metabolism, dopamine D2 receptor, serotonine transporter (SERT) and serotonine 5-HT2A receptor binding before and after 1, 3, 7, 14, 21 and 28 days following transient focal cerebral ischemia in rats. PET imaging studies were conducted in parallel with in vitro autoradiography by using [3H]Raclopride and inmunohistochemistry with tyrosine hidroxilase. Function recovery was carried out using a battery of neurologic and behavioral tests for rats. Results: In the ipsilateral hemisphere, PET [13N]ammonia showed a decrease of the signal at 1 day followed by the uppermost binding at day 7 after reperfusion. Surprisingly, a similar time course was observed in the contralateral hemisphere. The glucose metabolism of the ischemic territory evaluated by [18F]FDG showed a decrease at day 1 followed by a slight recovery around day 7-14 that did not reach control values. The [11C]Raclopride binding showed similar control values around day 1-7, after what signals dropped to 70% of control from days 14 to 28 in the ischemic striatum. Interestingly, a slight binding increase was observed at day 1-3 followed by the uppermost binding at day 7 in relation to control values in the contralateral to the lesion. In vitro binding of [3H]Raclopride and immunohistochemistry verified the in vivo PET results. The serotoninergic system also showed changes following brain ischemia. PET with [11C]DASB and [18F]altanserin showed a dramatic decline of both SERT and 5-HT2A binding potential in the ischemic hemisphere from day 1 to day 28 after cerebral ischemia. Interestingly, a slight increase of [11C]DASB binding was observed from days 7 to 21 followed by the uppermost binding at day 28 in the ipsilateral midbrain raphe nuclei. In contrast, no changes were observed in the contralateral hemisphere to the lesion by using both radiotracers. Both functional and behavior testing showed major impaired outcome at day 1 after ischemia onset followed by a recovery later on. Therefore, animals experienced a quasi-normal recovery of functional outcome that run in parallel with (i) an increase of whole brain perfusion, (ii) glucose metabolism recovery in the ischemic territory, (iii) over-expression of D2 dopaminergic receptor in the contralateral striatum and (iv) SERT binding increase in the ipsilateral midbrain following long-term cerebral ischemia. Conclusions: These results may provide new information about the key role of brain perfusion and both dopaminergic and serotoninergic neurotransmission in the recovery of brain function and may elucidate mechanisms involved in brain plasticity after stroke.

Disclosure of author financial interest or relationships:
A. Martin, None; **V. Gómez-Vallejo**, None; **B. Szczupak**, None; **E. San Sebastián**, None; **I. Markuerkiaga**, None; **D. Padró**, None; **S. Plaza**, None; **J. Llop**, None.

Presentation Number **SS 33**
Scientific Session 06: Preclinical in vivo Studies - Neurology
September 19, 2013 / 13:30-13:45 / Room: 105

MicroPET Assessment of Regional Brain Activation During Pavlovian Learning in Conscious Unrestrained Rats

Genevra Hart[1], *Georgios I. Angelis*[1,2], *Andre Kyme*[1,2], *Will Ryder*[1,2], *Steven Meikle*[1,2], *Arvind Parmar*[2,3], *Roger Fulton*[1,2], *Bernard Balleine*[1], [1]*Brain & Mind Research Institute, University of Sydney, Sydney, NSW, Australia;* [2]*Faculty of Health Sciences, University of Sydney, Sydney, NSW, Australia;* [3]*ANSTO LifeSciences, Australian Nuclear Science & Technology Organisation, Sydney, NSW, Australia. Contact e-mail: genevra.hart@sydney.edu.au*

Introduction: PET has proven vitally important for localising and quantifying dysfunctional neurotransmitter release and binding in disorders involving the dopaminergic and serotonergic systems. However, the inability to image moving subjects with PET has meant that much of this work has relied on a 'resting state' approach, despite the fact that many changes in brain function are only revealed during the dynamic engagement of some functional capacity. Recently, we have developed and validated a motion-compensation technique allowing PET imaging in awake, unrestrained rats. In this study, our aim was to use this capability to measure metabolic changes during expression of predictive (Pavlovian) learning. Methods: Two rats were trained inside a microPET scanner over several days to expect immediate, intra-oral delivery of sucrose during one sound (S+), and to expect nothing during a second sound (S-). Once rats could reliably predict sucrose delivery, they underwent imaging with 18F-FDG on two consecutive days with the sucrose-predictive tone (S+) and the non-predictive tone (S-), respectively. Imaging was performed in conjunction with head motion tracking (for motion compensation) and behavioural monitoring. The measured PET data were split into dynamic frames and the last 30 min (corresponding to tracer equilibrium) used for analysis. Image reconstruction was performed using an in-house list mode maximum likelihood expectation maximisation algorithm incorporating motion compensation. Reconstructed images from Day 1 and 2 for each rat were registered and then normalised to whole-brain uptake. Images were also registered to the Paxinos & Watson (6th Ed) rat atlas for visualisation and ROI generation. Thalamic and pre-frontal cortical ROIs were generated on the PET images and used to measure changes in FDG uptake during reward prediction (S+) relative to changes observed under identical conditions, but with no reward prediction (S-). Results: The image data were consistent across both rats for many key brain regions. Figure 1 shows normalised uptake in a sagittal brain slice (Bregma = 0.4) of the motion-corrected reconstruction for one rat. In the S- condition there was a strong band of activity in the anterior medial cortex, extending from the orbitofrontal cortex (OFC) back to the retrosplenial cortex (RSG). This activity was inhibited in the S+ condition. In contrast, the subcortical thalamic regions (CM, PF & SPF) showed higher activity in the S+ condition than in the S- condition. Overall, the results indicate a bidirectional change in metabolism in cortical and subcortical areas during reward prediction. Given that the thalamus is one of the few structures within the reward system that holds reciprocal connections with the prefrontal cortex, this pathway is of particular interest in future investigations. Conclusion: We have demonstrated, for the first time, the use of motion-compensated PET imaging in the context of animal learning experiments. Future research will focus on more targeted tracers to look specifically at changes in key dopaminergic and serotonergic transmission during reward prediction.

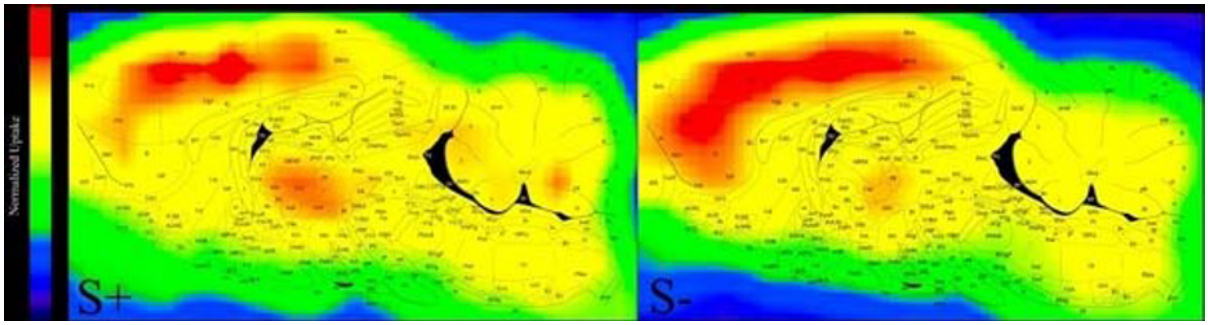

Figure 1. Sagittal slice showing normalised uptake in the motion-corrected reconstruction of the brain for one rat in the reward prediction (S+) and no reward prediction (S-) case.

Disclosure of author financial interest or relationships:
G. Hart, None; **G.I. Angelis**, None; **A. Kyme**, None; **W. Ryder**, None; **S. Meikle**, None; **A. Parmar**, None; **R. Fulton**, None; **B. Balleine**, None.

Presentation Number **SS 34**
Scientific Session 06: Preclinical in vivo Studies - Neurology
September 19, 2013 / 13:45-14:00 / Room: 105

PET/CT with [18F]ADAM using a biomarker for quantification of SERT change in the brain of PTSD rat model

Hsin-Hsien Yeh[1], *Tat-Wei D. Tan*[1], *Tso-Hao Tang*[2], *Hui-Ching Lin*[2], *Cheng-Ta Li*[3], *Ta-Kai Chou*[4], *Wen-Sheng Huang*[4], *Ren-Shyan Liu*[5], [1]*Biomedical Imaging and Radiological Sciences, National Yang-Ming University, Taipei, Taiwan;* [2]*Physiology, National Yang-Ming University, Taipei, Taiwan;* [3]*Psychiatry, Taipei Veterans General Hospital, Taipei, Taiwan;* [4]*Nuclear Medicine, National Yang-Ming University, Taipei, Taiwan;* [5]*Medicine, National Yang-Ming University, Taipei, Taiwan. Contact e-mail: skyeyeh@live.com*

Objectives: Post-traumatic stress disorder (PTSD) is a psychiatric disorder which can occur after a traumatic event such as assault or disaster. It has been proven that serotonin transporter (SERT) is implicated in PTSD pathophysiology. However, there is little known the change of SERT on PTSD. In this study, we aimed to investigate the dynamitic change of SERT in the brain of PTSD rat with increasing severity of disease by using [18F]ADAM PET which reflects the SERT density. Methods: The PTSD rat model was built up based on Pavlovian fear conditioning. SD rats (N=6/group) were conditioned with 3, 6 and 10 tone-shock pairings at 1 min intervals, and the freezing behavior was measured the percentage of time spent in freezing during 1 min interval. The animals were preformed static PET imaging for 10 min after administration of [18F]ADAM (150 μCi, 100μl, i.v.) at 30 min. One day later, the animals were sacrificed, brains grounded for the measurement of AMPA receptor trafficking. Results: The freezing behavior increased during 3, 6 and 10 tone-shock presentation. The conditioned 6 or10 tone-shock pairings evoked much stronger freezing behavior compared with 3 tone-shock pairings groups ($p < 0.01$). Compared to sham rats, [18F]ADAM accumulations decreased in the amygdala and hippocampus in the PTSD rats with a fear intensity-dependent manner (Fig.1). The phosphorylation of GluR1 at Ser831 which were subunits of AMPA was dramatically increased in the hippocampus of fear conditioning group compared with control group. Conclusions: The results support that 4-[18F]-ADAM PET could be used to monitor the change of SERT associated with the status of phosphorylation of AMPA receptor in the brain in PTSD animal.

Disclosure of author financial interest or relationships:
H. Yeh, None; **T.D. Tan**, None; **T. Tang**, None; **H. Lin**, None; **C. Li**, None; **T. Chou**, None; **W. Huang**, None; **R. Liu**, None.

Presentation Number **SS 35**
Scientific Session 06: Preclinical in vivo Studies - Neurology
September 19, 2013 / 14:00-14:15 / Room: 105

A novel hybrid MR and PET imaging with sequential inhalation of ^{15}O-labeled gaseous tracers on small animal model of cerebral vascular disease

Hidehiro Iida[1], *Jun-ichiro Enmi*[1], *Hajime Fukuda*[1], *Yoshiko Hashikawa*[1], *Masahiro Tsuji*[2], *Kazuhiro Koshino*[1], *Tetsuaki Moriguchi*[1], *Yuki Hori*[1], *Tsutomu Zeniya*[1], *Satoshi Iguchi*[1], *Akihide Yamamoto*[1], *Hidekazu Kawashima*[1], *Joji Nakagawara*[3], [1]*Department of Investigative Radiology, National Cerebral and Cardiovascular Center Research Institute, Suita City, Japan;* [2]*Department of Regenerative therapy, National Cerebral Cardiovascular Center, Suita City, Japan;* [3]*Integrative Stroke Imaging Center, Dept.of Neurosurgery, National Cerebral and Cardiovascular Center Research Institute, Suita City, Japan. Contact e-mail: iida@ri.ncvc.go.jp*

Backgrounds and objectives Hybrid MR and PET imaging provides valuable information in characterizing the disease status of cerebral diseases. Usage of ^{15}O-labeled gases such as $^{15}O_2$, $C^{15}O_2$, $C^{15}O$ enables quantitative assessment of regional cerebral metabolic rate of oxygen ($CMRO_2$), cerebral blood flow (CBF), and oxygen extraction fraction (OEF). These examinations are important, but requires further technical advances for small animals. This study was aimed at developing a dedicated device that enables the ^{15}O-PET scan at the same time as MR imaging on small animals. Validity and usefulness were examined on rat model of cerebral ischemic diseases. Materials and methods The device consists of a dedicated animal-holding container, ^{15}O-gas supply unit, miniature fabric-facemask, and air circulating unit. The container fits to the body coil of the 7T MRI (Biospin, Bruker) and also to Micro PET (CTI/Siemens, USA), thus allowing sequential MR/PET without moving animals. ^{15}O-containing nitrogen gas from the cyclotron target was mixed with 20% oxygen and 1-2% of isoflurane, and was supplied into the miniature fabric-facemask at 1 GBq/300mL/min. Air inside the holder was continuously circulated at 3L/min, so that contribution of gaseous radioactivity in PET FOV is minimal. MR/PET imaging was carried out on a normal rat (8 wo), and two rats (3 wo) after transient hypoxic stress (*Ohshima et al., Expr Neurol233: 481-489, 2012*). PET scans were carried out during continuous inhalation of $^{15}O_2$ and $C^{15}O_2$, from which semi-quantitative CBF, $CMRO_2$, OEF images were calculated, in which the input function was estimated from the radioactivity in the heart region at steady-state. T2-weighted (T2WI), fractional anisotropy (FA), apparent diffusion coefficient (ADC), and time-of-flight angiography (MRA) images were acquired using MRI. Results The present animal-holding device allowed easy and rapid repositioning of the small animals from PET to MRI and vice versa. The counting rate during the PET examination was 500 kcps for prompt, and the maximum dead time count loss less than 30%, supporting the accuracy of PET images. Semi-quantitative functional images of CBF, $CMRO_2$, and OEF calculated from buildup-phase appeared to be reasonably well, with averaged values of 1.0±0.25 ml/min/g for CBF, and 0.45±0.12 for OEF in control rat. Attention is needed for spillover from radioactivity in the paranasal sinuses into the frontal part of cerebral tissue regions. However, decreased CBF with preserved $CMRO_2$ at 1 hour after hypoxia stress, resulting in elevated OEF, and smaller decrease in CBF than $CMRO_2$, resulting in elevated OEF at 1 week were clearly observed in 1 week rat after hypoxia stress. Conclusion The animal-holding device developed in this study is useful in the hybrid imaging of MR and PET with ^{15}O-gases.This study suggested the validity and its feasibility for practical use.

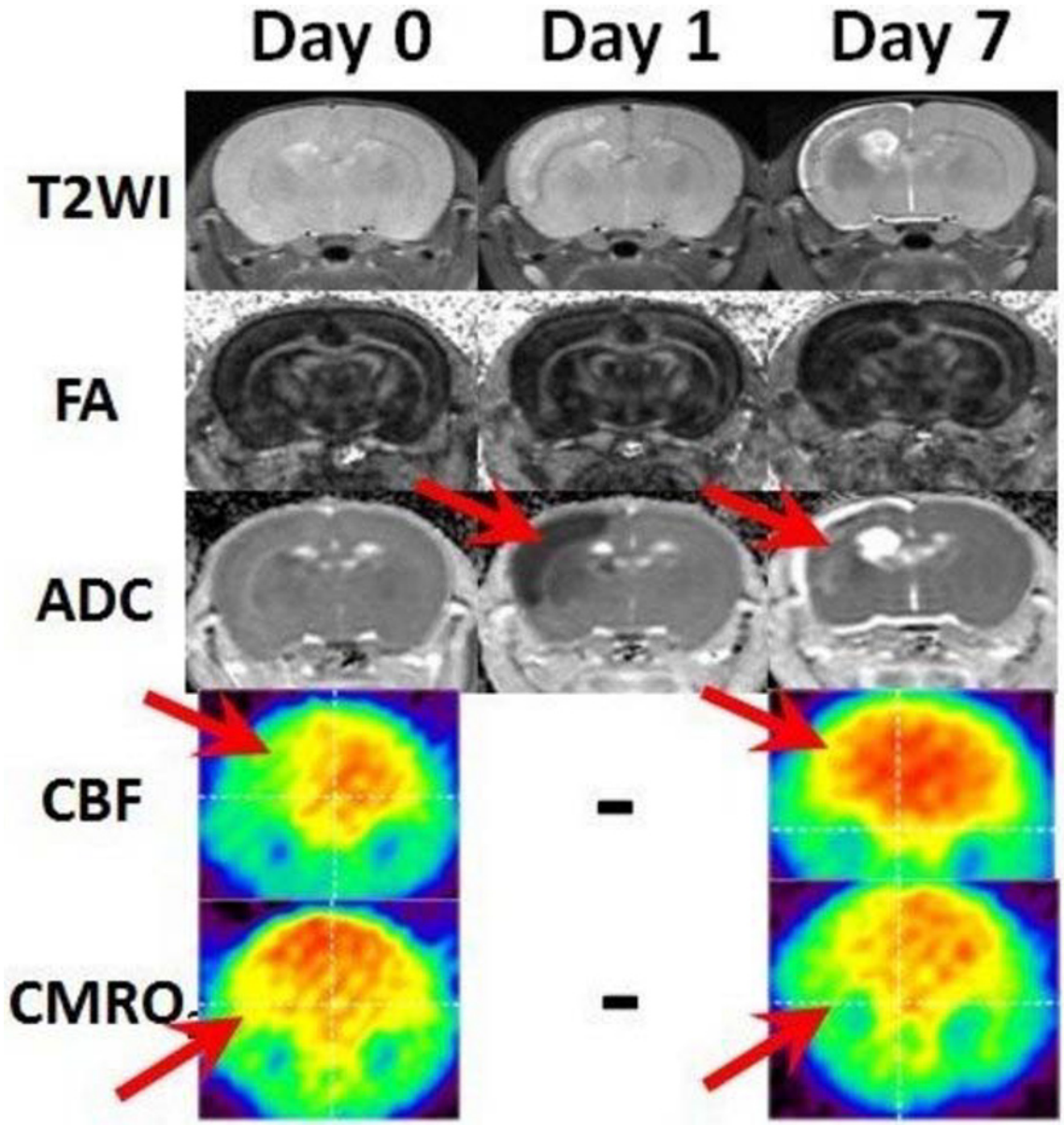

MRI (T1WI, FA, ADC) and PET (CBF. CMRO2) images of 3weel old rat after transient hypoxia stress. Reduced CBF with preserved CMRO2 is apparent immediately after the stress, where no abnormality is visible in MR. MR showed absormal signal after a day, and a week after, increased CBF in reduced CMRO2 area, where all MR images showed sign of cellular damage.

Disclosure of author financial interest or relationships:
H. Iida, None; **J. Enmi**, None; **H. Fukuda**, None; **Y. Hashikawa**, None; **M. Tsuji**, None; **K. Koshino**, None; **T. Moriguchi**, None; **Y. Hori**, None; **T. Zeniya**, None; **S. Iguchi**, None; **A. Yamamoto**, None; **H. Kawashima**, None; **J. Nakagawara**, None.

Presentation Number **SS 36**
Scientific Session 06: Preclinical in vivo Studies - Neurology
September 19, 2013 / 14:15-14:30 / Room: 105

Noninvasive Imaging of Angiogenesis with a αvβ3 Integrin-targeted Multi-modality Nanoprobe in Cerebral Ischemic Stroke Model

Bai Yingying, *southeast university, Naijing, China. Contact e-mail: yingying_bai@163.com*

Background: Angiogenesis is defined as blood vessel formation from a pre-existing vasculature, the formation of which can promote the recovery of cerebral blood flow after ischemic stroke. Proliferating endothelial cells highly express a number of integrins associated with angiogenesis, of which αvβ3 has been shown to be particularly important. Cyclic peptide containing an arginine-glycine-aspartic acid (cyclic RGD) sequence has a high affinity to αvβ3 integrin. The objective of this study was to design and develop a novel cyclic RGD probe based multi-modality imaging for evaluation of angiogenesis in cerebral ischemic stroke model. Methods and Meterials: The cyclic RGD, Gd-DOTA, IR783 and rhodamine were functionalized into the fifth generation PAMAM dendrimer to synthesize the aiming probe, and the control probe without cyclic RGD was synthesized in the same way. Cortical ischemic stroke was induced by photothrombosis in adult male C57BL/6 mice (8 weeks old, n=36). RGD probe (20mg/Kg) was intravenously injected into stroke mice on day 3, 7, 14 and 21. Magnetic resonance (MR) and near-infrared (NIR) fluorescence optical imaging were peformed 24 hours later at every time point. The gadolinium content in cerebral hemisphere with ischemic lesion was determined by ICP-MS. The expression of αvβ3 integrin and CD31 in cerebral hemisphere with ischemic lesion of stroke mice were detected by Western blot at different time points. Results: After injection of RGD probe, higher signal intensity appeared on peri-ischemic area on both MR and NIR fluorescence optical images, indicating more accumulation of RGD probe compared with control probe, which was confirmed in angiogenic region by immunofluorescence staining. The highest uptake in ischemic-angiogenic area was achieved on day 14, with gradually decrease by the 21th day. A linear correlation ($r2=0.7708$, $p<0.001$) was found between CNR on MR imaging and averaged fluorescent signal intensity on NIR optical imaging. The gadolinium content in cerebral hemisphere with ischemic lesion had linear correlations with both CNR on MR imaging ($r2=0.5728$, $p<0.005$) and average fluorescence signal intensity on NIR optical imaging ($r2=0.8696$, $p<0.001$). Pretreatment with intravenous injection of cyclic RGD at a dose of 200mg/Kg blocked most of the signal intensity enhancement both on MR and NIR imaging by αvβ3 integrin-targeted nanoprobe. Biodistribution analysis by fluorescence signal intensity showed that the probe predominantly located in kidney, liver and spleen of mice, and the kidney uptake was about four times higher than that in ischemic lesion, reflecting a renal excretion. Western blot analysis revealed that the expression of αvβ3 integrin and CD31 approached highest level on day 14. Conclusions: The αvβ3 integrin-targeted multi-modality imaging is a promising method for evaluation of angiogenesis in stroke model. It may provide a non-invasive method to directly monitor the effects of pro- or anti-angiogenesis therapy in patients in vivo.

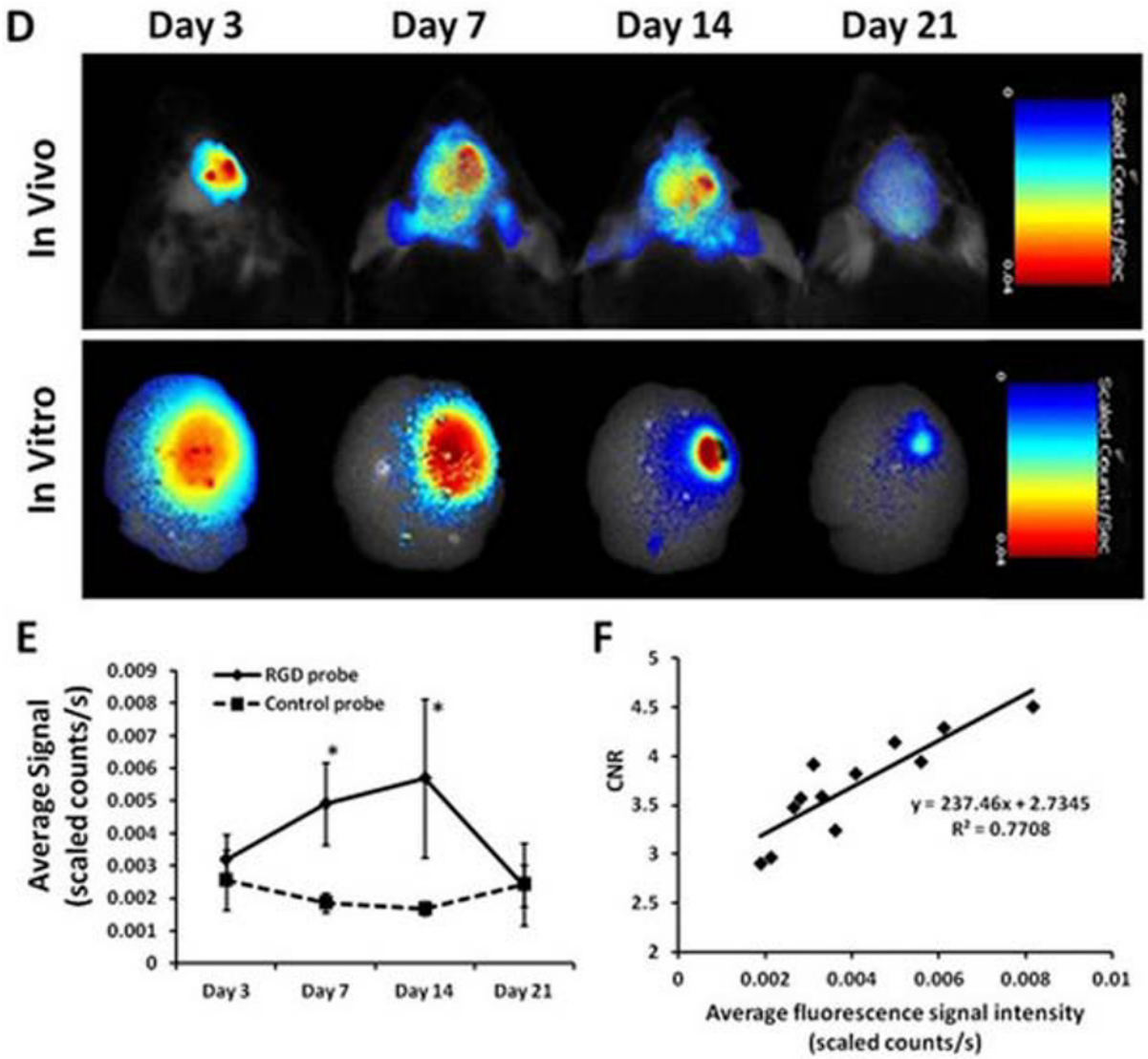

(D) NIR images of mice at different time points post RGD probe injection show peak signal intensity appeared at day 14. (E) The peak value of average fluorescent signal intensity was measured at day 14. Signal intensity changes from day 7 to day 14 in experiment group were statistically significant ($p<0.01$, $n=3$). (F) A liner correlation between CNR from MRI and average fluorescent signal intensity from NIR was detected ($r2=0.7708$, $p<0.001$).

Disclosure of author financial interest or relationships:
B. Yingying, None.

Presentation Number **SS 37**
Scientific Session 07: Chemistry & Imaging Probes - MRI
September 19, 2013 / 13:00-13:15 / Room: 200

Hyperpolarized [1 - ^{13}C] α-Ketoglutarate: a novel DNP probe for non-invasive assessment of IDH1 mutational status in glioma

Myriam M. Chaumeil[1], *Peder E. Larson*[1], *Hikari Yoshihara*[1], *Daniel B. Vigneron*[1], *Sarah J. Nelson*[1], *Russel O. Pieper*[2], *Joanna Phillips*[2,3], *Sabrina M. Ronen*[1,2], [1]*Radiology, UCSF, San Francisco, CA, USA;* [2]*Neurological Surgery, UCSF, San Francisco, CA, USA;* [3]*Pathology, UCSF, San Francisco, CA, USA. Contact e-mail: myriam.chaumeil@ucsf.edu*

INTRODUCTION In light of the prevalence and pathogenic role of isocitrate dehydrogenase 1 (IDH1) mutations in gliomas and upgraded glioblastomas (GBM)[1], mutant IDH1 inhibitors are developed as therapies, and non-invasive methods are needed to monitor IDH1 status *in vivo*. Whereas wild-type (wt) IDH1 converts isocitrate to α-ketoglutarate (αKG), mutant IDH1 reduces αKG into 2-hydroxyglutarate (2HG). To date, IDH1 status has been assessed by detecting 2HG using ^{1}H magnetic resonance spectroscopy (MRS) methods [2-4]. We showed that ^{13}C MRS of hyperpolarized (HP) αKG can inform on IDH1 status in lysed and live cells [5]. The goal of this study was to validate our method *in vivo* in orthotopic tumors at clinical field strength. **METHODS** U87 GBM cells were transduced with a lentiviral vector coding for wt IDH1 (U87IDHwt) or for mutant and wt IDH1 (U87IDHmut). Orthotopic tumors were implanted in the right putamen of rats. [1-^{13}C] αKG solution (53μL, 5.9M) was polarized using a Hypersense polarizer for 1h. After dissolution, HP αKG (100mM) was injected intravenously. Slab dynamic and 2D CSI ^{13}C data were acquired on a 3T GE MR system using sequences optimized for HP 2HG detection [6,7]. ^{13}C data were processed using the in-house SIVIC software. **RESULTS & DISCUSSION** HP [1-^{13}C] αKG, αKG hydrate and a resonance at 184ppm were detected in the slabs containing the tumor (Fig. A&B). Because the resonances of HP [5-^{13}C] αKG (δ=184ppm) and HP [1-^{13}C] 2HG (δ=183.9ppm) are only 0.1ppm apart, they cannot be resolved *in vivo* and appear as a single 184ppm resonance. The amount of HP αKG delivered to the brain was comparable between U87IDHwt and U87IDHmut rats (Fig. C). Importantly, in U87IDHwt rats, the 184ppm resonance presented a unimodal distribution corresponding to [5-^{13}C] αKG from the HP solution (Fig. D). In contrast, a bimodal distribution was seen in U87IDHmut rats, suggesting a delayed metabolic production of HP 2HG (max at 20s, Fig. D). When looking at the spatial distribution of metabolites (2D CSI), high levels of HP αKG were detected in the blood vessels under the brain but also in the tumor, confirming the delivery of αKG to the tumor site (Fig. E&F). Importantly, the 184ppm resonance was observed only in mutant tumors and not in normal tissues (Fig. G). Moreover, this resonance was detected in the tumor 20s post injection but not prior (Fig. H). Similar findings were made in all U87IDHmut rats (n=3, SNRmut=1.4±0.2 at 20s) and no 184ppm resonance was observed in U87IDHwt rats (n=3 SNRwt=1.0±0.1 at 20s, $P<0.05$), confirming that this resonance can be assigned to HP 2-HG. Collectively, our findings indicate that HP 2HG production from HP αKG can be detected *in vivo* using ^{13}C MRS and thus can serve to non-invasively inform on mutant IDH1 activity. **ACKNOWLEDGMENTS** SPORE CA097257, NIH R21 CA120010, NIH RO1 CA130819, ABTA fellowship, P41EB013598.
REFERENCES 1.Dang, L. Nature 462, 739-744 (2009) 2.Andronesi, O.C. Sci Transl Med 4, 116ra114 (2012). 3.Choi, C. Nat Med (2012) 4.Elkhaled, A. Sci Transl Med 4, 116ra115 (2012) 5.Chaumeil, M.M. ISMRM 4352 (Australia, 2011) 6.Larson, P.E.J Magn Reson 194, 121-127 (2008) 7.Xing, Y. J Magn Reson (2013).

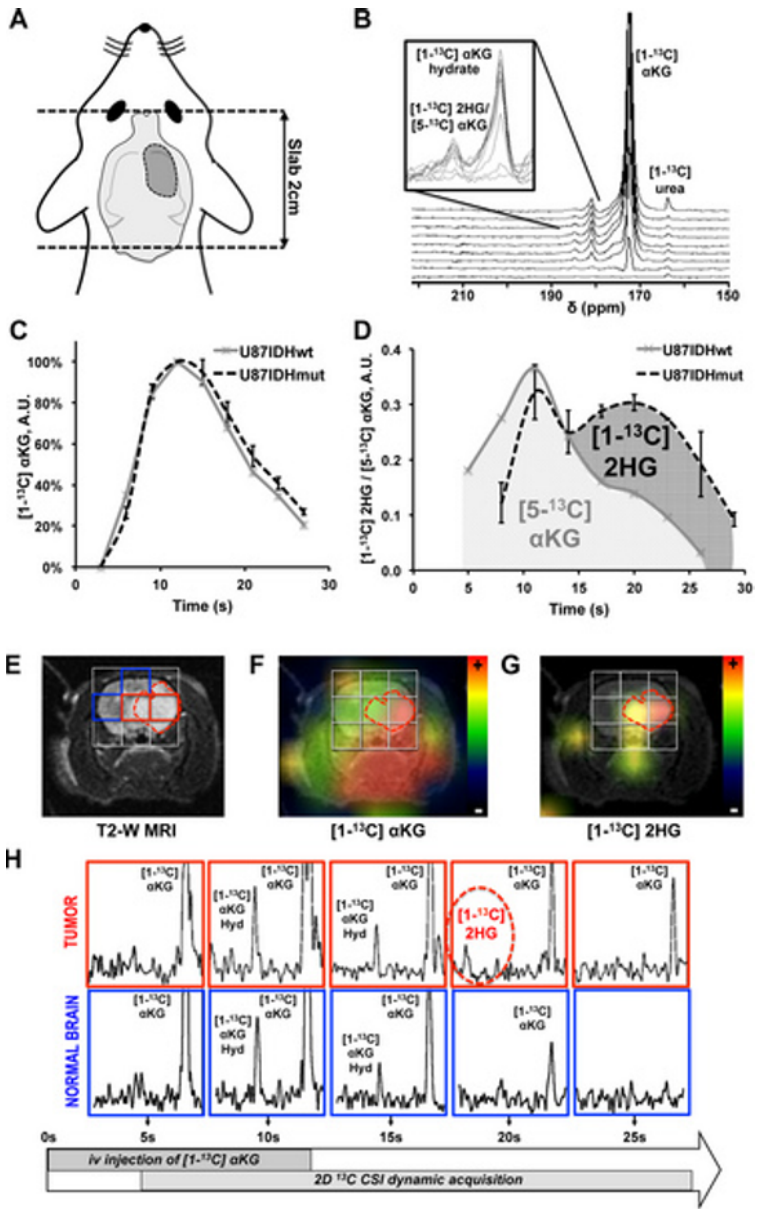

(A) Axial slab used for *in vivo* dynamic ^{13}C MR experiments. **(B)** Stack plot of *in vivo* ^{13}C MR spectra acquired from the slab following injection of HP αKG in a U87IDHmut rat. Integral of **(C)** HP αKG and of **(D)** the 184ppm resonance ([1-^{13}C] 2HG/ [5-^{13}C] αKG) as a function of time from dynamic ^{13}C spectra acquired in U87IDHmut (black) and U87IDHwt (grey) animals. **(E)** MR image of a U87IDHmut animal head overlaid with the grid used for 2D ^{13}C CSI acquisition (red tumor; blue normal brain). Corresponding heatmap of **(F)** HP αKG and **(G)** HP 2HG at 20s post injection. **(H)** HP ^{13}C MR spectra from a normal brain voxel (blue) and a tumor voxel tumor (red) showing the temporal evolution of metabolites and HP 2HG formation in the tumor at 20s post injection of HP αKG.

Disclosure of author financial interest or relationships:
M.M. Chaumeil, None; **P.E. Larson**, GE Healthcare, Grant/research support; **H. Yoshihara**, None; **D.B. Vigneron**, None; **S.J. Nelson**, GE Healthcare, Grant/research support; **R.O. Pieper**, None; **J. Phillips**, None; **S.M. Ronen**, None.

Presentation Number **SS 38**
Scientific Session 07: Chemistry & Imaging Probes - MRI
September 19, 2013 / 13:15-13:30 / Room: 200

Targeted and Responsive Magnetic Nanoparticles as High Sensitivity MRI Contrast Agents

Juan Gallo[1,2], *Nazila Kamaly*[2], *Quang-De Nguyen*[2], *Ioannis Lavdas*[2], *Marzena Wylezinska-Arridge*[3], *Eric O. Aboagye*[2], *Nicholas J. Long*[1,2], [1]*Chemistry, Imperial College London, London, United Kingdom;* [2]*Surgery and Cancer, Imperial College London, London, United Kingdom;* [3]*Imaging Sciences, Imperial College London, London, United Kingdom. Contact e-mail: j.gallo-paramo@imperial.ac.uk*

MRI is an imaging technique perfectly suited for its application in human disease diagnosis, but a major limitation of the technique is low sensitivity.(1) A number of strategies have been evaluated to overcome this problem, without a clear solution. We propose here that a new strategy combining magnetic nanoparticles, copper-free click chemistry and targeting peptides can significantly enhance the sensitivity of the MRI experiment. In this regard, 6 nm magnetic nanoparticles were synthesised following thermal decomposition protocols. Two families of targeted particles were prepared i.e. a) directed towards tumours via a peptide targeting the chemokine receptor CXCR4, and b) functionalised with matrix metalloproteinases (MMPs) cleavable sequences. CXCR4 and MMP are both overexpressed in many tumour cells and play important roles in invasion and metastasis.(2) One family of nanoparticles was further functionalised with an azide, and the other with a strained alkyne.(3) These two functional groups were able to react once MMPs have cleaved the ligands on the nanoparticle surface (Fig 1). In vitro analysis demonstrated that the hydrodynamic size of the particles had grown from 160 nm to around 1000 nm over 2h when incubated with MMP9 (sup. data, Fig. 1). This self-assembly process increased the contrast in T2 images because of higher local concentration of contrast agent, as well as higher relaxivity of the aggregates compared to those of individual particles.(4) The effect of the probes on MRI was further studied using model cell lines overexpressing CXCR4 (U87.CD4.CXCR4; NIH AIDS Research and Reference Reagent Program). U87.CD4.CXCR4 cells incubated with targeted nanoparticles showed a ΔR2/R2only cells decrease of ~160%. Only a small decrease of around 15% was observed with non-targeted nanoparticles or the targeted particles in CXCR4 negative cells (U87.CD4). The application of targeted nanoparticles without self-assembling capabilities decreased the contrast but in a less efficient way (ΔR2/R2only cells ~65%), showing the potential of the probes (sup. data, Fig. 2). Initial unoptimised in vivo data from BALB/c nude mice bearing U87.CD4.CXCR4 xenografts suggest that the targeted contrast agent is also able to decrease the T2 in tumours (ΔR2/R2baseline ~12%). Mice implanted with U87.CD4 cells showed no reduction in R2. References (1) Jokerst, J. V.; Gambhir, S. S. Acc. Chem. Res. 2011, 44, 1050. (2) Balkwill, F. R. J Pathol. 2012, 226, 148. (3) Agard, N. J.; Prescher, J. A.; Bertozzi, C. R. J. Am. Chem. Soc. 2005, 127, 11196. (4) Perez, J. M.; Josephson, L.; Weissleder, R. Chembiochem. 2004, 5, 261.

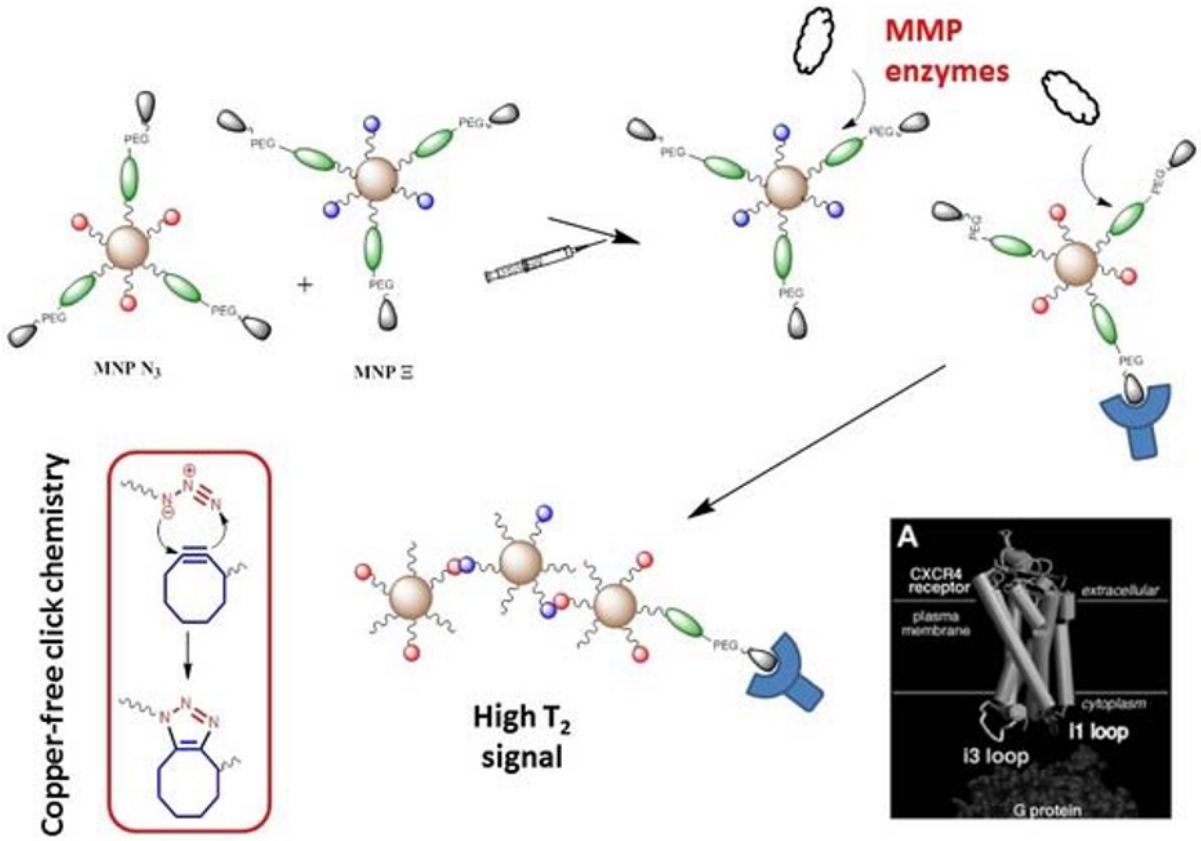

Fig. 1. Representation of the mechanism of action of targeted and responsive nanoparticles

Disclosure of author financial interest or relationships:
J. Gallo, None; **N. Kamaly**, None; **Q. Nguyen**, None; **I. Lavdas**, None; **M. Wylezinska-Arridge**, None; **E.O. Aboagye**, None; **N.J. Long**, None.

Presentation Number **SS 39**
Scientific Session 07: Chemistry & Imaging Probes - MRI
September 19, 2013 / 13:30-13:45 / Room: 200

A High Affinity and Selectivity MRI Contrast Agent for Targeting GRP Receptors on Prostate Cancer

Quanyu Cai[1,2], Fabio Gallazzi[3], James M. Guthrie[5], J David Robertson[3,5], Timothy Hoffman[2,4], **Lixin Ma**[1,2], *[1]Radiology, University of Missouri-Columbia, Columbia, MO, USA; [2]R&D, Harry S Truman VA Hospital, Columbia, MO, USA; [3]Chemistry, University of Missouri, Columbia, MO, USA; [4]Internal Medicine, University of Missouri, Columbia, MO, USA; [5]University of Missouri Research Reactor, University of Missouri, Columbia, MO, USA. Contact e-mail: mal@health.missouri.edu*

Introduction: Early detection of prostate cancer has not been successful due to the heterogeneities of prostate cancers and the lack of imaging contrast between cancerous and normal tissues in this disease. Therefore, there is a crucial need to develop prostate cancer specific imaging contrast agent (CA) for early and accurate detection and staging of prostate cancer in patients. Our objective is to develop a novel MRI CA based on Bombesin (BBN) that has very high binding affinity and specificity to gastrin releasing peptide receptor (GRPR) for early detection of both primary and metastatic prostate cancers. Methods: (Gd-DOTA)8-Bombesin[7-14]NH2 dendron was designed, synthesized and purified. The final product was characterized using MALDI-TOF mass spectroscopy. Number of Gd3+ ions per molecule was measured using inductively coupled plasma mass spectroscopy (ICP-MS). Relaxivity was determined at 1.5 T and 7 T at room temperature. In vitro binding affinity and selectivity was determined using competitive cell binding assay against 125I-Tyr4-BBN in PC-3 cells. In vivo MRI was performed using a T1-weighted (T1W) imaging sequence on a 7 T MRI small animal system. SCID mice bearing PC-3 flank-tumors were randomly assigned to three groups (n=4 per group): targeting group were injected with (Gd-DO3A)8-BBN, blocking group were pre-injected with 100μg unlabeled BBN[1-14] before (Gd-DO3A)8-BBN, and control group were injected with Gd-DTPA. After the baseline scan, mice were injected with 200 μl (600 nmol Gd/mouse) of CA via tail vein. T1W images were obtained for 60 minutes, and at 4 hour (h) after injection. Results: The molecule weight was 6534.4 (calculated MW: 6534). The number of Gd3+ ions per molecule was 8. The r1 relaxivity was 28.4±1.1 s-1 mM-1 for (Gd-DO3A)8-BBN compared with 3.8±0.1 s-1 mM-1 for Gd-DTPA at 1.5 T; and was 22.6±0.2 s-1 mM-1 for (Gd-DO3A)8-BBN at 7 T. The IC50 value was 2.0 nM against 125I-Tyr4-BBN in PC-3 cells. In vivo MRI showed that, in the uptake group, the tumor signal-enhancement-ratio (SER = (SIpost - SIpre)/SIpre × 100%) was increased to 50% at 1 h, and maintained 35% SER up to 4 h. In the blocking group, the tumor SER was 26% at 1 h and 18% at 4 h. In the control group (Gd-DTPA), the tumor SER was 21% at 1 h and decreased to the base level at 4 h. The tumor SER from the targeting group was significantly greater than those from the blocking and the Gd-DTPA control group ($P<0.01$ at 1h and 4 h). The Gd concentrations in tumor tissues were determined by ICP-MS and agreed with the MRI SER analysis. Conclusion: The r1 relaxivity of (Gd-DO3A)8-BBN was more than 7 times greater than that of a clinically used MRI contrast agents Gd-DTPA (Omniscan). Both in vitro and in vivo results showed high binding affinity and specificity to PC-3 prostate cancer. Grant support: DOD PCRP W81XWH-09-2-0176.

Disclosure of author financial interest or relationships:
Q. Cai, None; **F. Gallazzi**, None; **J.M. Guthrie**, None; **J. Robertson**, None; **T. Hoffman**, None; **L. Ma**, None.

Presentation Number **SS 40**
Scientific Session 07: Chemistry & Imaging Probes - MRI
September 19, 2013 / 13:45-14:00 / Room: 200

In Cellulo Assembly of Iron Oxide Nanoparticles Significantly Increases Their Accumulation and Enables Ultrasensitive Magnetic Resonance Imaging

Grigory A. Tikhomirov, *Radiology, Stanford University, Stanford, CA, USA. Contact e-mail: nanoassembly@gmail.com*

Magnetic resonance imaging (MRI) is a powerful tool for the diagnosis of disease and the study of biological processes such as cancer metastasis and inflammation. Superparamagnetic iron oxide nanoparticles (SPIONs) have been shown to be effective contrast agents for labeling cells to provide high sensitivity in MRI, but this sensitivity depends on the ability to label cells with sufficient quantities of SPIONs, which can be challenging for nonphagocytic cells such as cancer cells. Small SPIONs (20 nm) such as ferumoxytol undergo rapid endocytosis and endocytosis, while large SPIONs (200nm) undergo significantly slower endocytosis. An ideal nanoparticle for MRI labeling would combine rapid endocytosis and slow exocytosis. To address this issue, we developed "smart" nanoparticles (SNs) that form covalent clusters inside cells. Our SNs have record high iron uptake values and R2 contrast values in MRI. SNs were obtained by linking a molecule containing 2-cyano-6-aminobenzothiazole (CABT) and S-ethyl-cysteine to the surface of ferumoxytol, clinically approved SPIO. After cell uptake, and interaction with reducing medium within cancer cells, thiol and amino groups of cysteine become accessible and react with cyano group of CABT triggering clustering of SNs. SNs were characterized by transmission electron microscopy in vitro and in cellulo, infrared spectroscopy, and dynamic light scattering, and their uptake in HeLa cells was monitored with inductively coupled plasma mass spectrometry and T1 and T2 measurements over 48 hours. Record high uptake (3.2±0.3 pg/cell) and sixteen fold decreases in the transverse relaxation time (T2) were observed for cells labeled with SNs relative to cells labeled with ferumoxytol and other non-aggregatable control after just 24 hours. In addition SN oligomers have a very high reproducible value of T1/T2 ratio which gives labeled with SNs cells a unique magnetic signature that can be read by MRI. The trigger mechanism can customized via organic synthesis to target various biologically important processes, such as proteolytic activity of matrix metalloproteinases in cancer cells.

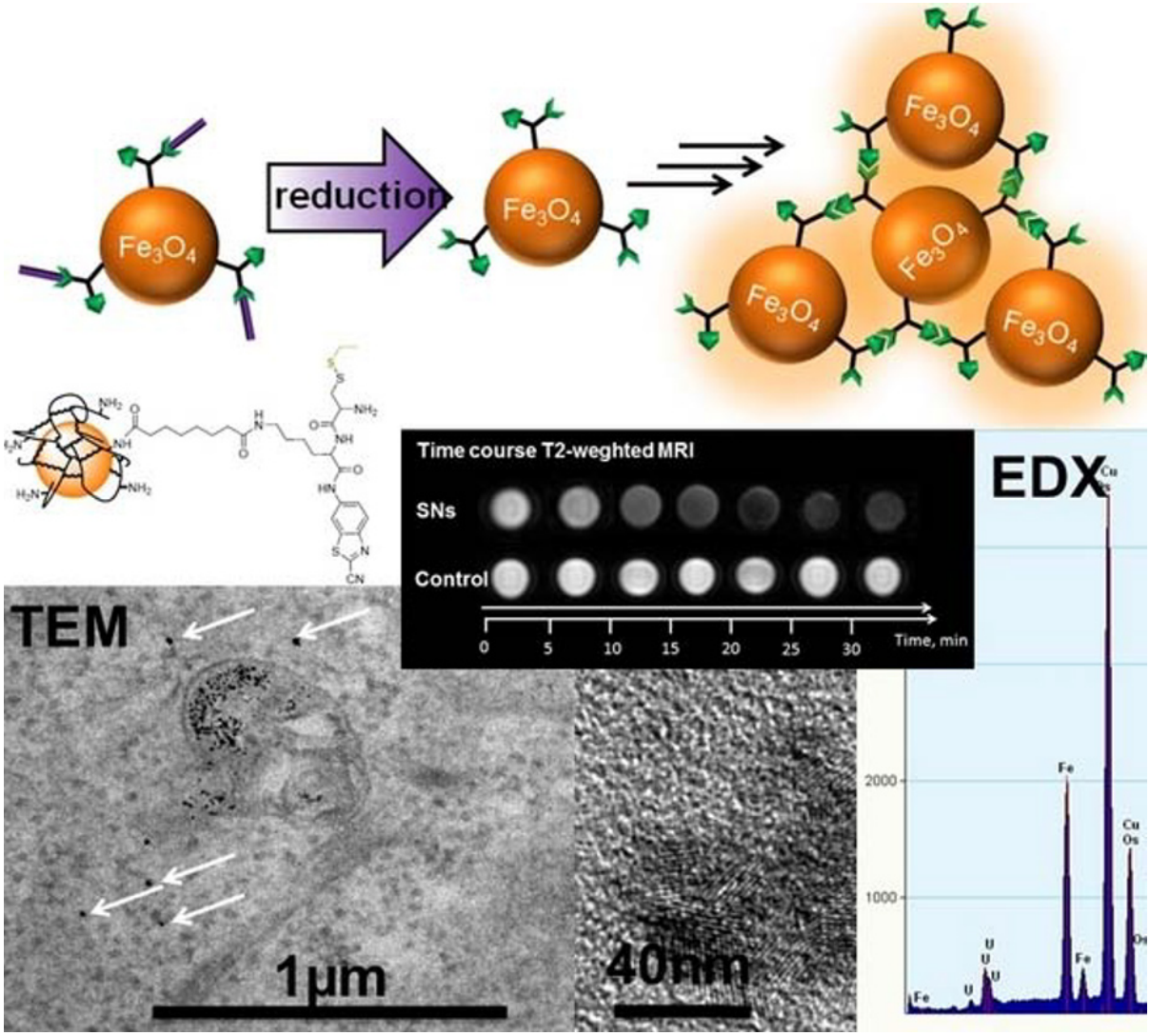

Disclosure of author financial interest or relationships:
G.A. Tikhomirov, None.

Presentation Number **SS 41**
Scientific Session 07: Chemistry & Imaging Probes - MRI
September 19, 2013 / 14:00-14:15 / Room: 200

Structure relaxivity relationships of new derivatives of the single amino acid Gd complex Gd(DOTAla) for high field, high relaxivity contrast agents

Eszter Boros, *Peter Caravan, Radiology, Massachusetts General Hospital/ Harvard Medical School, Charlestown, MA, USA. Contact e-mail: eboros@nmr.mgh.harvard.edu*

Magnetic resonance imaging (MRI) at high magnetic fields benefits from an increased signal to noise ratio, however T1 based MR contrast agents show decreasing relaxivity (r1) at higher fields. We have previously shown the design and characterization of a new Gd-based contrast agent, based on the single-amino acid Gd chelate Gd(DOTAla). Use of solid phase peptide synthesis allowed us to control the rotational dynamics (τR) of the molecule while maintaining a short water residency time (τM). We found that the trimeric structure Gd3L3 was superior to commercial contrast agents gadoteridol and serum albumin bound gadofosveset at high magnetic fields (1). In order to further explore this approach, we have synthesized two new derivatives of the ligand DOTAla and incorporated these into multimeric peptide structures. DOT3reo, a threonine derivative, provides even greater rigidity than the previously explored scaffold. DOTAlaP has one of the carboxylate groups replaced by a phosphonate, providing an altered water exchange rate and an overall negative charge of the corresponding Gd complex. The effect of these structural changes on water residency time (τM), rotational dynamics (τR), and field dependent relaxivity will be presented. Reference: (1) Boros E, Polasek M, Zhang Z, Caravan P. Gd(DOTAla) - A Single Amino Acid Gd-complex as a Modular Tool for High Relaxivity MR Contrast Agent Development. J Am Chem Soc. 2012;134(48):19858-68.

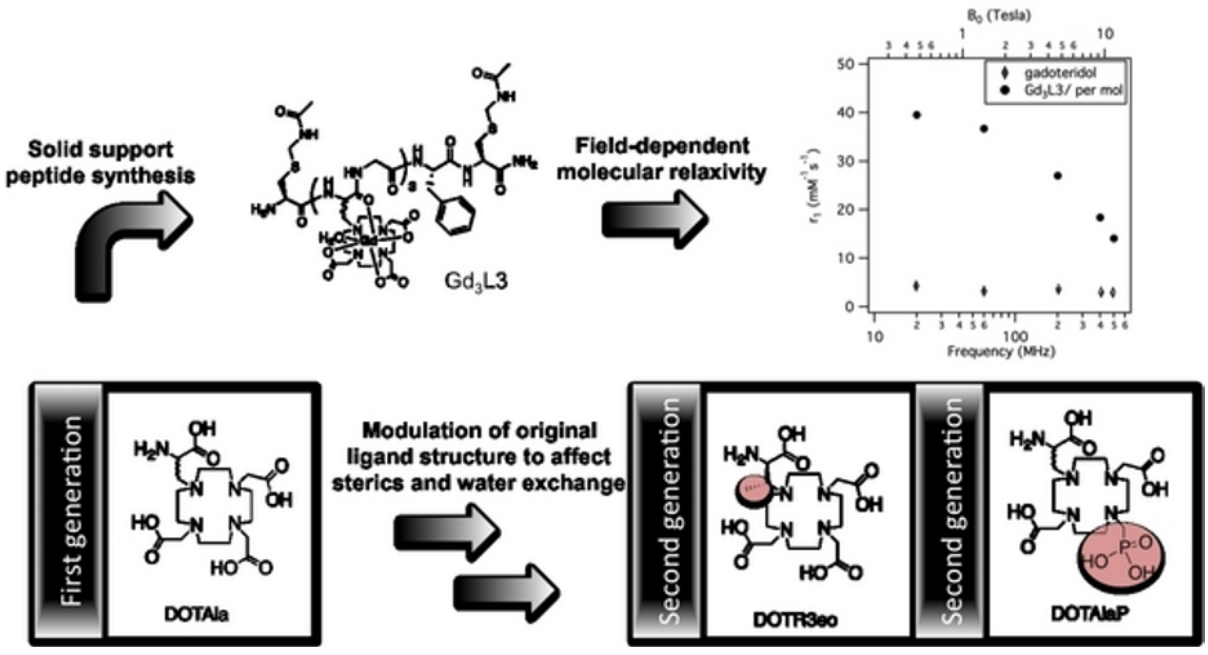

Disclosure of author financial interest or relationships:
E. Boros, None; **P. Caravan**, Sanofi, Grant/research support; Biogen Idec, Consultant; Factor 1A, Stockholder; Collagen Medical, Stockholder .

Presentation Number **SS 42**
Scientific Session 07: Chemistry & Imaging Probes - MRI
September 19, 2013 / 14:15-14:30 / Room: 200

New Nanoprobes for Magnetic Resonance Imaging of Dopamine Transporters

Gordana D. Vitaliano[1,2], *David Rios*[1], *Franco Vitaliano*[1], *Perry F. Renshaw*[3], *Martin H. Teicher*[1,2], [1]*Brain Imaging Center, McLean Hospital, Belmont, MA, USA;* [2]*Department of Psychiatry, Harvard Medical School, Boston, MA, USA;* [3]*The Brain Institute, University of Utah, Salt Lake City, UT, USA. Contact e-mail: gvitaliano@mclean.harvard.edu*

Background: Magnetic Resonance Imaging (MRI) is a noninvasive visualization technique with high spatial resolution, but low sensitivity for visualization of brain transporters and receptors. Gadolinium (Gd) contrast agents are used to improve MRI sensitivity, but they cannot cross an intact blood-brain-barrier (BBB). Our goal was to develop MRI Gd-nanoprobes with high T1 relaxivity that can cross an intact BBB and target dopamine transporters (DAT) in the rat brain. Method: Clathrin triskelia were conjugated to the gadolinium-2-(4-isothiocyanatobenzyl) diethylene-triamine-pentaacetic acid (Gd-DTPA-ITC) through reactive lysine residues. Arsenazo III assay was used to determine the chelate to protein molar ratio. Relaxivity of each sample was calculated by using T1 data and Gd concentrations as determined by NMR at 0.47 T. Clathrin nanoplatforms were radiolabeled with 153Gd-DTPA-ITC. DAT ligands (GBR-12935) were conjugated to clathrin cysteine residues via maleimide-PEGs. Biodistribution of DAT-nanoprobes was quantitatively assessed in rats at different time points after intravenous administration. Samples of blood, animal organs and brain regions (e.g., striatum and cerebellum) were removed and weighed, and their radioactivity measured with a gamma counter. Results: The PEGylated clathrin-nanoparticle was 36 nm in size. The mean chelate/protein molar ratio was 27±4.8/1. At 0.47 T, Gd-DTPA-ITC-Clathrin displayed relaxivity of 1,166 mM-1s-1 per particle, and 16 mM-1s-1 per Gd ion. Biodistribution studies showed a high accumulation of 153GdDTPA-DAT-nanoprobes in brain regions rich in DAT (e.g., striatum). The highest concentration of 153GdDTPA-GBR-nanoprobes was observed in the rat striatum 90 min after intravenous delivery (1.77 % ID/g). By contrast, brain regions with low concentrations of DAT (e.g., cerebellum) had a low accumulation of nanoprobes. Ninety minutes after intravenous delivery the concentration of 153GdDTPA-GBR-nanoprobes in the rat cerebellum was 0.70% ID/g. Conclusions: Clathrin triskelia can serve as robust MRI nanoplatforms onto which multiple functional motifs can be added through chemical modifications. Clathrin-nanoprobes displayed 300-fold greater molecular relaxivity than the MRI contrast agent gadopentetate dimeglumine and successfully crossed an intact BBB after intravenous administration. They were able to deliver adequate concentrations of Gd-contrast agent and DAT-ligand to the rat brain and to target dopamine transporters. These results should encourage further investigations into the use of clathrin as a new brain imaging and drug delivery nanoplatform. This technology may lead to development of non-radioactive, stable molecular nanoprobes to assist in early detection of neurobiological changes in dopamine related disorders (e.g., Parkinson's, Huntington's Disease, ADHD, drug addiction, psychotic disorders etc.); to monitor progression of the disease and recovery process; and to help evaluate the effectiveness of drugs aimed at treating these disorders.

Disclosure of author financial interest or relationships:
G.D. Vitaliano, EXQOR Technologies Inc., Stockholder; **D. Rios**, None; **F. Vitaliano**, ExQor Technologies, Inc., Stockholder; **P.F. Renshaw**, None; **M.H. Teicher**, None.

Presentation Number **SS 43**
Scientific Session 08: Preclinical in vivo Studies - Oncology (Targeted Imaging)
September 19, 2013 / 13:00-13:15 / Room: 203

A Novel Engineered anti-CD20 Tracer Enables Early Time PET Imaging in a Humanized Transgenic Mouse Model of Non-Hodgkins Lymphoma

Arutselvan Natarajan[1], *Benjamin Hackel*[1], *Sanjiv S. Gambhir*[1,2], [1]*Radiology, Stanford University, Stanford, CA, USA;* [2]*Bioengineering, Materials Science & Engineering, Stanford University, Stanford, CA, USA. Contact e-mail: anatarajan@stanford.edu*

Background: PET imaging at early time points is useful for effective patient management compared to antibody based immunoPET which requires very long times after tracer injection due to slow tracer clearance. The aim of this research was to develop and evaluate the use of a novel engineered anti-CD20 protein of the 10 kDa human fibronectin type 3 domain (FN3). PET was performed with ^{64}Cu-$FN3_{CD20}$and compared with ^{64}Cu-rituximab to measure CD20 in a humanized transgenic mouse model. **Methods:** The engineered $FN3_{CD20}$ and $FN3_{WT}$ were produced in E.coli cells of 2-5 mg/L, performed binder affinity assay by *in vitro* live cell binding and conjugated to DOTA. DOTA-FN3 was labeled with ^{64}Cu and used for PET imaging of huCD20 expression in B cells in a humanized transgenic mouse model. Each mouse (N=3) received ^{64}Cu-$FN3_{CD20}$or $FN3_{WT}$ (3.7 MBq/4 µg Do-FN3 in 200 µL PBS) via a lateral tail vein. The control mouse group (N=3) received a blocking dose (50-fold excess) of unconjugated FN_{CD20} two hours prior to radiotracer injection. PET imaging was carried out at 1, 2, 4, 16, and 24 h post-injections. **Results:** Cell culture assays demonstrated FN3 binds CD20 with 20 nM affinity on CD20-expressing cells. The ^{64}Cu-FN3 showed clear, high-contrast visualization of huCD20-expressing B-cells in the spleen of transgenic mice as early as 1 hour post-injection (38±3 %ID/g, Figure 1) and exhibited a spleen-to-blood ratio of 13 by 4 h. This is higher uptake (P = 0.04) and ten-fold greater signal-to-background (P = 0.04) than the ^{64}Cu-rituximab antibody radiotracer. **Conclusions:** The ^{64}Cu-Do-$FN3_{CD20}$ radiotracer represents a novel small, high affinity binder for imaging human CD20, which may be well suited for non-Hodgkin's lymphoma imaging in patients at early time points.

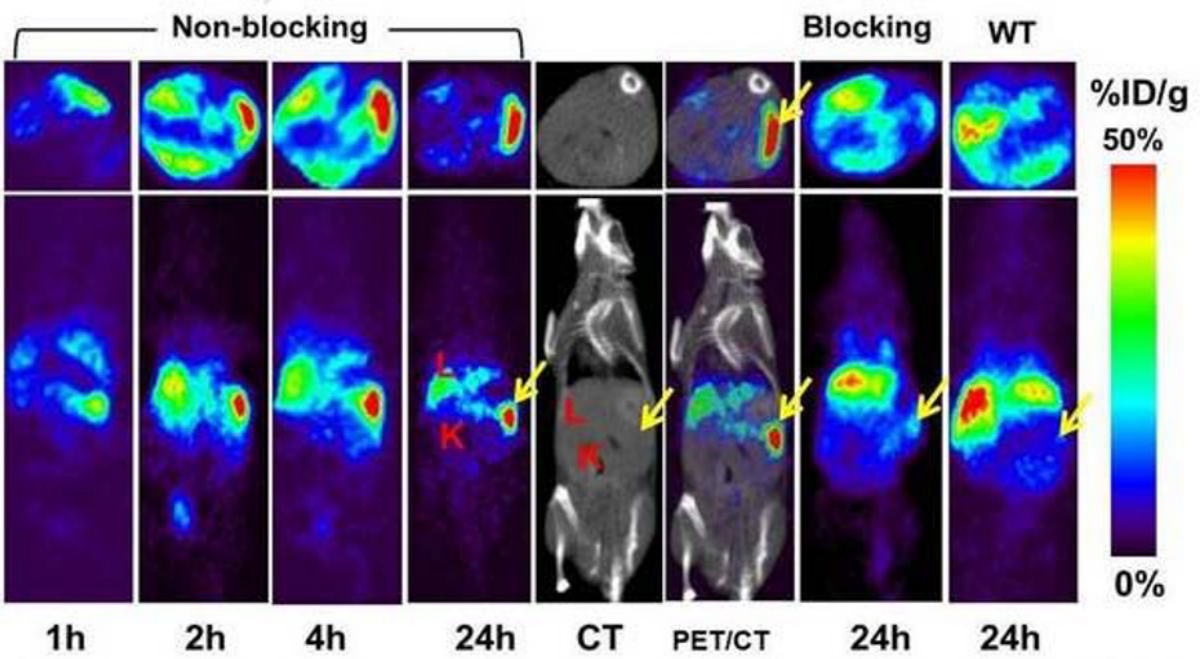

Figure 1. PET images show the ^{64}Cu-Do-FN3$_{CD20}$ tracer (3.7 MBq) in huCD20 transgenic mice (top = transverse, bottom = coronal). The CT and PET/CT co-registered images are shown at 24 h after tail-vein injection for organ identification. Non-blocking mice received tracer alone and blocking mice received 50-fold excess of unconjugated FN3$_{CD20}$ over tracer mass 2 h prior to tracer injection. Spleen (tracer targeting cells in this organ) is indicated by the yellow arrow. The other major clearance organs are marked in red fonts (*Liver* and *K*idney). WT: Wild type.

Disclosure of author financial interest or relationships:

A. Natarajan, None; **B. Hackel**, None; **S.S. Gambhir**, Bracco Diagnostics, Consultant; Endra, Inc, Stockholder; Cellsight, Stockholder; Enlight, Inc., Stockholder; General Electric, Grant/research support; ImaginAb, Stockholder; MagArray, Inc., Stockholder; Sanofi-Aventis, US, Grant/research support; SiteOne Therapeutics, Stockholder; VisualSonics/Sonosite, Stockholder .

Presentation Number **SS 44**
Scientific Session 08: Preclinical in vivo Studies - Oncology (Targeted Imaging)
September 19, 2013 / 13:15-13:30 / Room: 203

IR700-conjugated monoclonal antibody for CD44-targeted near-infrared photoimmunotherapy in breast cancer

Jiefu Jin[1], *Balaji Krishnamachary*[1], *Hisataka Kobayashi*[2], *Zaver M. Bhujwalla*[1], [1]*JHU ICMIC Program, Division of Cancer Imaging Research, The Russell Morgan Department of Radiology and Radiological Science, The Johns Hopkins University School of Medicine, Baltimore, MD, USA;* [2]*Molecular Imaging Program, Center for Cancer Research, National Cancer Institute, US National Institutes of Health, Bethesda, MD, USA. Contact e-mail: jjin@jhmi.edu*

Introduction: CD44 transmembrane glycolproteins are cell adhesion molecules that are closely related with cancer cell proliferation, migration and invasion.[1] CD44 expression is up-regulated in hypoxic microenvironments that promote tumor progression and metastasis.[1] Therefore, the CD44 family serves as an essential therapeutic target for breast cancer treatment. Molecular-targeted cancer therapies have been developed to minimize the side effects in normal tissues. Among the existing targeted therapies, monoclonal antibody (mAb)-based therapies have gained great successes in the clinic. However, high doses of mAb are required to achieve satisfactory therapeutic outcomes. Thus, there are increasing reports on the engineering of low doses of mAb as a vector for targeted delivery of various therapeutic agents, for example, photosensitizers.[2] However, conventional photosensitizers generally emit in the visible range, with limited tissue penetration. Moreover, they generate reactive oxygen species to cause cell death, which is only efficient when internalized into specific organelles.[2] Here we are developing a CD44 mAb-based targeted photosensitizer for photoimmunotherapy (PIT) in breast cancer. The mAb conjugate is activated by near-infrared (NIR) light, having phototoxic effects immediately after cell membrane binding and its NIR emission also leads to noninvasively monitoring of therapeutic outcome. **Method**: CD44 mAb was conjugated with a NIR phthalocyanine dye, IR700, to form CD44-IR700. Two wild-type human breast cancer cell lines, MB-MDA-231 (CD44 positive) and MCF-7 (CD44 negative) were selected for the cell studies. SDS-PAGE, UV spectroscopy and confocal fluorescence imaging were performed to determine the purity, composition and cellular localization of the conjugate. Microscopic observation and cell viability test by CCK-3 assay were performed to study CD44-specific cell death. **Results**: Figures 1a,b reveal the strong association of IR700 with CD44 antibody. Figure 1c shows the preferred binding of CD44-IR700 to MB-MDA-231 cell membrane. Figures 1d,e illustrate the CD44-specific cell death in response to CD44-IR700-mediated photoimmunotherapy (>90% of MB-MDA-231 cells killed immediately, while 88% of MCF-7 cells still alive). Control experiments show that irradiation itself (8 J/cm^2) is harmless to cells and there is no cytotoxicity associated with IR700 and CD44 antibody or with CD44-IR700 in the absence of irradiation. The percentage of cell death of MB-MDA-231 is dependent on the dose of irradiation or CD44-IR700 concentration. Additionally, phototoxicity of CD44-IR700 is inhibited by the excess of CD44 antibody in a dose-dependent manner. **Conclusion**: CD44-IR700 has an excellent CD44-specific phototoxicity for targeted PIT in cells. *In vivo* CD44-targeted PIT studies with tumor xenografts are currently underway. CD44-IR700 serves as a promising theranostic agent for targeting stem-like breast cancer cells. **References**: (1) Krishnamachary, B.*et al.*, *PloS one* **2012**, *7*, e44078. (2) Mitsunaga, M.*et al.*, *Nat Med* **2011**, *17*, 1685-1691. Supported by NIH R01 CA136576 and P50 CA103175.

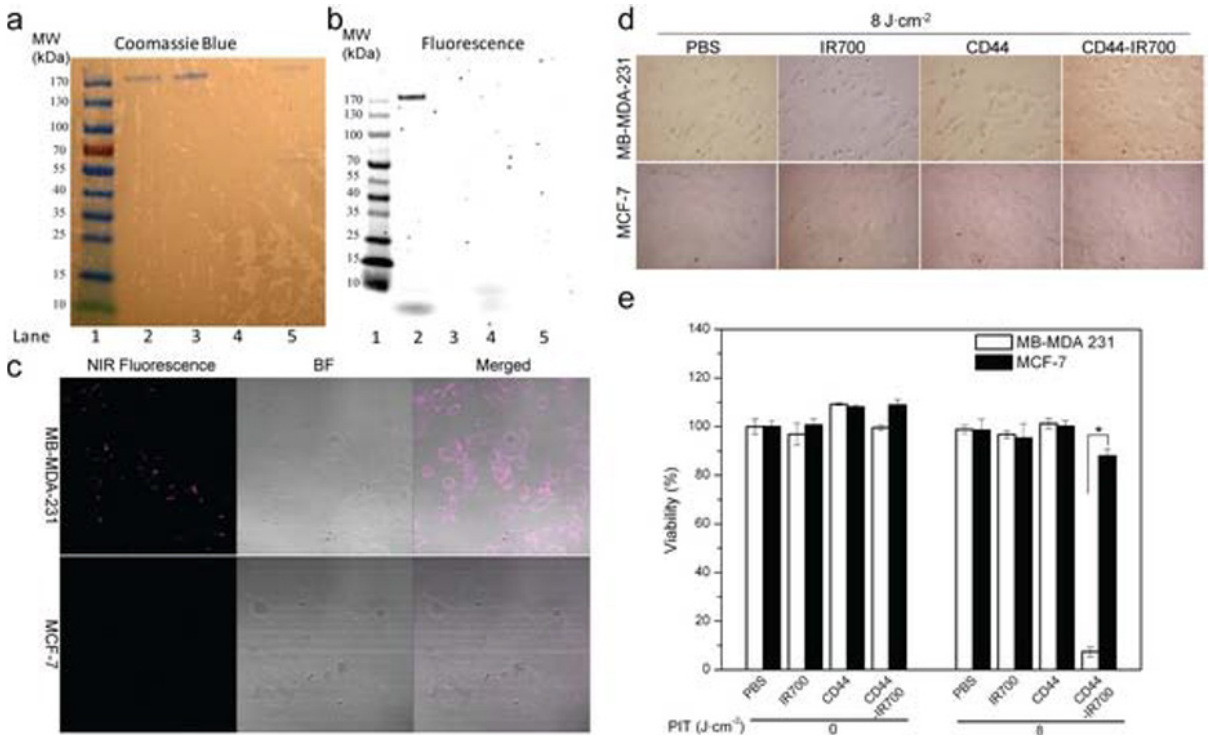

Figure 1. (a) SDS-PAGE gel stained with coomassie blue. (b) Gel checked with NIR fluorescence (λ_{ex} = 633 nm, λ_{em} = 650~700 nm). Lanes: 1, ladder; 2, CD44-IR700; 3, CD44 antibody; 4, IR700; 5, unpurified CD44 antibody. (c) Confocal NIR fluorescence microscopic images of MB-MDA-231 (upper) and MCF-7 (lower) cells after incubation of 10 μg/ml CD44-IR700 for 1 h at 37 °C. (d) Microscopic bright field images of MB-MDA-231 cells (upper) and MCF-7 cells (lower) after incubation with different reagents for 1 h at 37 °C and then irradiation at 8 J/cm^2. (Reagent code: PBS, left panel; IR700, left middle panel; CD44 antibody, 10 μg/ml, right middle panel; CD44-IR700, 10 μg/ml, right panel.) (e) Cell viability of MB-MDA-231 cells and MCF-7 cells upon incubation with different reagents before and after irradiation. *P<0.005.

Disclosure of author financial interest or relationships:

J. Jin, None; **B. Krishnamachary**, None; **H. Kobayashi**, None; **Z.M. Bhujwalla**, None.

Presentation Number **SS 45**
Scientific Session 08: Preclinical in vivo Studies - Oncology (Targeted Imaging)
September 19, 2013 / 13:30-13:45 / Room: 203

Molecular Imaging of Lung Cancer using a Fluorescent δ-Opioid Receptor Targeted Probe: Pharmacokinetics, Biodistribution, and Intraoperative Guidance

Allison S. Cohen[1], *Yolaine Jeune-Smith*[1], *Aimee Bode*[2], *Farah K. Khalil*[3], *Eric A. Welsh*[4], *Steven A. Enkemann*[5], *Noel Clark*[6], *Renata Patek*[8], *Eric B. Haura*[7], *Josef Vagner*[8], *David L. Morse*[1], [1]*Department of Cancer Imaging and Metabolism, H. Lee Moffitt Cancer Center & Research Institute, Tampa, FL, USA;* [2]*Department of Comparative Medicine, H. Lee Moffitt Cancer Center & Research Institute, Tampa, FL, USA;* [3]*Department of Anatomic Pathology, H. Lee Moffitt Cancer Center & Research Institute, Tampa, FL, USA;* [4]*Biomedical Informatics Shared Resource, H. Lee Moffitt Cancer Center & Research Institute, Tampa, FL, USA;* [5]*Molecular Genomics Shared Resource, H. Lee Moffitt Cancer Center & Research Institute, Tampa, FL, USA;* [6]*Tissue Core Shared Resource, H. Lee Moffitt Cancer Center & Research Institute, Tampa, FL, USA;* [7]*Department of Thoracic Oncology, H. Lee Moffitt Cancer Center & Research Institute, Tampa, FL, USA;* [8]*Bio5 Institute, University of Arizona, Tucson, AZ, USA. Contact e-mail: Allison.Cohen@moffitt.org*

Lung cancer is the leading cause of cancer deaths for men and women in the United States. Currently, the 5-year survival rate for this cancer is low. Imaging has the potential to improve the diagnosis and treatment of lung cancer. One of the major goals of molecular imaging of cancer is to develop imaging probes that target the tumor with high specificity and selectivity. The discovery of bona fide cell-surface markers for lung cancer is a key initial step in the development of lung cancer specific molecular imaging probes. Fluorescently labeled targeted probes can be developed for real-time surgical guidance through the use of endoscopic instruments with fluorescence capability. The delta opioid receptor (δOR) has been reported to be overexpressed in some lung cancers. Thus, we decided to develop a lung cancer specific imaging agent by targeting this receptor. δOR expression was verified in patient samples using immunohistochemistry of a lung cancer tissue microarray. We determined that 44% of lung tumors have elevated δOR expression. In this work, we describe the synthesis and evaluation of a novel agent for imaging of the δOR both *in vitro* and *in vivo*. This probe is based on a synthetic peptide δOR antagonist (Dmt-Tic) and our previously described Dmt-Tic-Cy5 imaging agent. To improve its potential for *in vivo* imaging and clinical translation, in this study we chose to conjugate Dmt-Tic to a near-infrared fluorescent dye (Licor IR800CW) with longer excitation and emission wavelengths than the previously reported Cy5 dye. We evaluated the binding affinity of the Dmt-Tic-IR800 probe *in vitro* using a competitive binding assay. Dmt-Tic-IR800 retains high binding affinity for the δOR (K_i = 1.43 ± 0.24 nM, n = 3). To determine selectivity of the probe *in vivo*, we used HCT-116 colorectal carcinoma cells and HCT-116/δOR engineered cells in a subcutaneous bilateral xenograft model. Dmt-Tic-IR800 targets the δOR+ tumor in this model. Using qRT-PCR we identified lung cancer cell lines with high and no endogenous expression of the δOR. Mice were injected subcutaneously with H1299 (δOR-) and DMS-53 (δOR+) cells in the left and right flanks, respectively. We determined that a 40 nmol/kg dose of Dmt-Tic-IR800 was optimal and used this dose to fully evaluate the pharmacokinetics (PK) and biodistribution (BD) of the probe. To study PK and BD, Dmt-Tic-IR800 was injected intravenously and fluorescence images were acquired at various time points from 0 to 48 hours (Fig. 1A and B). The largest fold of enhancement (4-fold) compared to δOR- tumor was observed at 24-48 h. Corresponding *ex vivo* fluorescence images were acquired for the δOR- and δOR+ tumors, lung, liver, kidneys, and GI tract (Fig. 1C). *Ex vivo* fluorescence signal in all organs except the δOR+ tumor and kidneys cleared to a baseline level by 24 h (Fig. 1D). We are currently studying Dmt-Tic-IR800 for imaging of orthotopic lung cancer models using fluorescence molecular tomography and for use in intraoperative guidance. In conclusion, fluorescent Dmt-Tic probes have high selectivity and affinity for the δOR. This should enable the use of these probes for guidance during lung cancer resection.

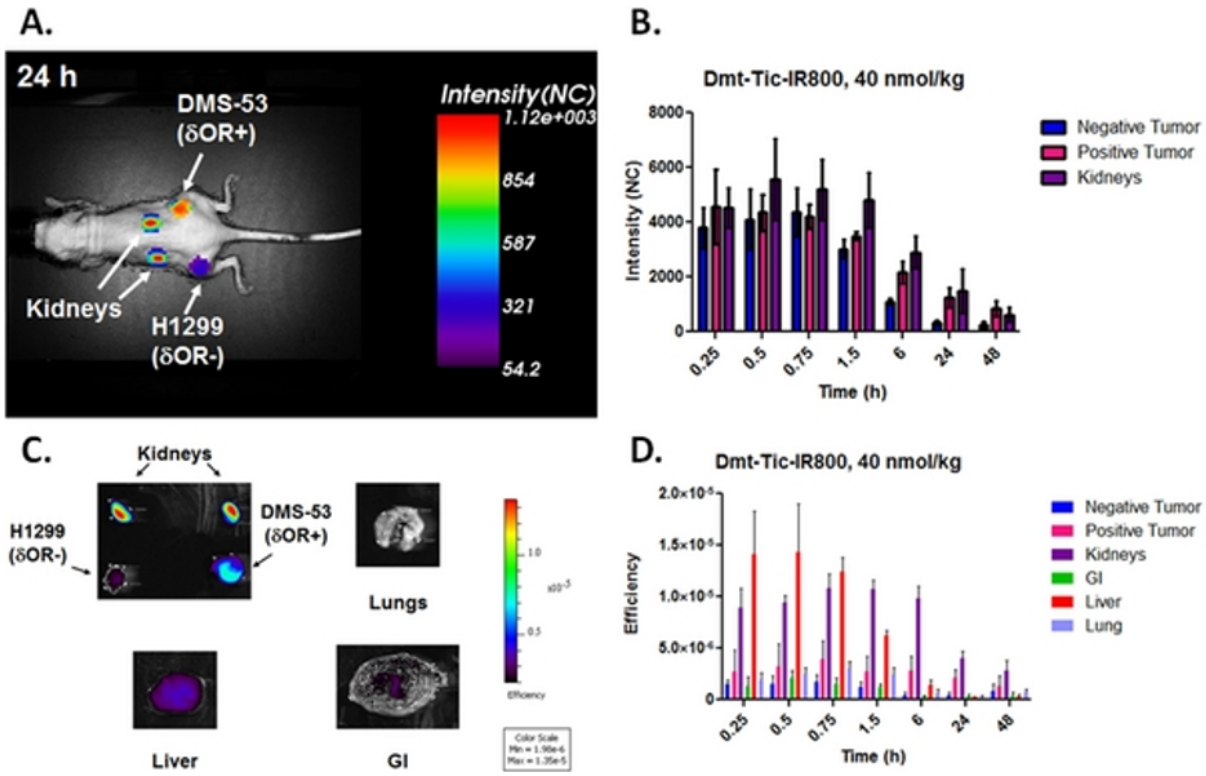

Figure 1: *In vivo* and *ex vivo* fluorescence imaging with Dmt-Tic-IR800 in subcutaneous tumor xenografts. The mice were injected with 40 nmol/kg Dmt-Tic-IR800 i.v. and images were acquired *in vivo* on the ART Optix MX3 and *ex vivo* on the IVIS 200 at various time points post-injection. Representative *in vivo* and *ex vivo* fluorescence images of a mouse and organs at 24 h post-administration of Dmt-Tic-IR800 (A and C, respectively). The graph (B) depicts the mean fluorescence intensity of the H1299 (δOR-) tumor (blue), DMS-53 (δOR+) tumor (pink), and kidneys (average of the signal from the left and right kidney) (purple) over a time course of 0-48 hours. The graph (D) depicts the mean fluorescence signal obtained from *ex vivo* imaging of the H1299 (δOR-) tumor (blue), DMS-53 (δOR+) tumor (pink), kidneys (purple), gastrointestinal tract (GI) (green), liver (red), and lungs (light blue) at various time points post-injection. Data are represented as mean ± sd.

Disclosure of author financial interest or relationships:
A.S. Cohen, None; **Y. Jeune-Smith**, None; **A. Bode**, None; **F.K. Khalil**, None; **E.A. Welsh**, None; **S.A. Enkemann**, None; **N. Clark**, None; **R. Patek**, None; **E.B. Haura**, None; **J. Vagner**, None; **D.L. Morse**, LiCor Biosciences, Grant/research support .

Presentation Number **SS 46**
Scientific Session 08: Preclinical in vivo Studies - Oncology (Targeted Imaging)
September 19, 2013 / 13:45-14:00 / Room: 203

Noninvasive quantification of receptor density using dynamic dual-tracer MRI-guided fluorescence tomography

Scott C. Davis[1], *Kimberley Samkoe*[2], *Kenneth M. Tichauer*[3], *Kristian Sexton*[1], *Tayyaba Hasan*[4], *Brian W. Pogue*[1], [1]*Thayer School of Engineering, Dartmouth College, Hanover, NH, USA;* [2]*Department of Surgery, Geisel School of Medicine at Dartmouth, Hanover, NH, USA;* [3]*Department of Biomedical Engineering, Illinois Institute of Technology, Chicago, IL, USA;* [4]*Wellman Center for Photomedicine, Harvard Medical School, Boston, MA, USA. Contact e-mail: Scott.C.Davis@Dartmouth.edu*

Abnormal receptor expression profiles which often arise as a result of cancer pathogenesis have become primary targets for new treatment strategies. As efforts to target these abnormalities accelerate, the need to quantify the availability of these drug targets in living tissue becomes increasingly acute. Current technologies which report receptor expression are non-quantitative or provide little information on the availability of receptor targets in vivo. While some ex vivo techniques can report total receptor density, this quantity is often different from the density of receptors available for binding in tissue. In vivo receptor-targeted imaging typically relies on single-tracer imaging of targeted contrast agents and are severely confounded by tracer transport behavior (e.g. extra- and intravasation rates). These phenomena often dominate the tracer distribution, making quantification of receptor density effectively intractable. To address these challenges, we have developed a noninvasive dual-tracer imaging technique capable of quantifying the density of receptors available for binding in vivo. This is accomplished by simultaneously imaging the kinetics of two co-administered fluorescent tracers, one targeted to a receptor of interest, and a non-targeted counterpart. By fitting the dynamic data to a dual-tracer compartment model, a parameter termed the binding potential can be estimated. This quantity is directly proportional to the density of receptors available for binding. To demonstrate the approach, mouse models with orthotopic gliomas which overexpress EGFR were imaged using an MRI-coupled spectrometer-based fluorescence molecular tomography (FMT) system capable of discriminating two fluorescent tracers. Study animals were positioned in the MRI-FMT system and administered a dual-tracer cocktail containing an EGFR-targeted tracer and a non-targeted counterpart. Dynamic FMT scanning started immediately after administration and continued for one hour at a rate of one frame every two minutes. Figure 1 shows a flowchart illustrating the process for combining MRI and optical data to recover receptor density. Optical data were processed by first spectrally decoupling the two tracer signals into independent channels. These data were then combined with the segmented MR images to recover three dimensional images of the fluorescence yield for each tracer at each frame. Finally, the time course data of both tracers in the tumor were extracted and fit to the dual-tracer compartment model, yielding estimates of available receptor density. Applying this approach resulted in a mean value for available receptor density of 2.3±0.5 nM in the population of mice (N=5). This value compared favorably with validation studies completed using dynamic dual-tracer data from exposed subcutaneous tumors, as well as ex-vivo analysis. These results have broad implications for both preclinical research and clinical developments in personalized cancer care. Specific applications include longitudinal tracking of receptor response to treatment in animals or humans undergoing treatment, and stratification of study patients for clinical trials.

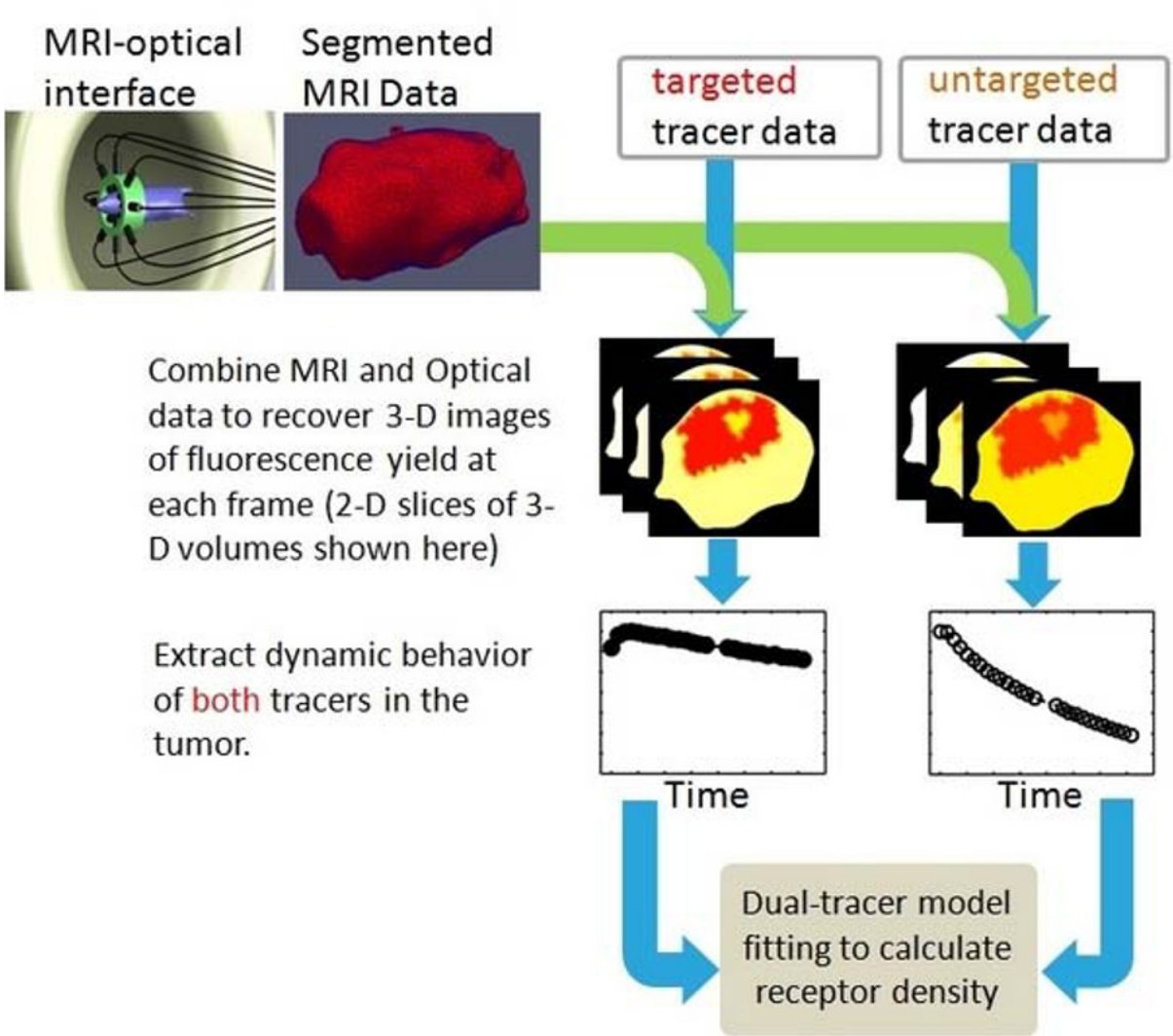

Figure 1. Flowchart illustrating the process for combining MRI and dynamic dual-tracer optical data to estimate the density of receptors available for binding in the tumor.

Disclosure of author financial interest or relationships:
S.C. Davis, None; **K. Samkoe**, None; **K.M. Tichauer**, None; **K. Sexton**, None; **T. Hasan**, None; **B.W. Pogue**, None.

Presentation Number **SS 47**
Scientific Session 08: Preclinical in vivo Studies - Oncology (Targeted Imaging)
September 19, 2013 / 14:00-14:15 / Room: 203

Imaging graded levels of CXCR4 expression in lung cancer models

Vishwa Kundoor, Mrudula Pullambhatla, Lauren Woodard, Ala Lisok, Martin Pomper, **Sridhar Nimmagadda***, Radiology, Johns Hopkins University, Baltimore, MD, USA. Contact e-mail: snimmag1@jhmi.edu*

The chemokine receptor 4 (CXCR4) is highly expressed in several cancers including small cell (SCLC) and non-small cell (NSCLC) lung cancers. CXCR4, with its ligand CXCL12, plays a critical role in tumor development, growth and metastasis. Lung tumors with high CXCR4 surface expression are more likely to metastasize and result in poor prognosis. CXCR4 based imaging probes can be used i) to evaluate primary tumors for elevated CXCR4 expression and therapeutic intervention and ii) to screen for secondary metastatic spread to local and distant sites. Here we demonstrate the potential of a CXCR4-based imaging agent to image graded levels of CXCR4 expression in subcutaneous and orthotopic SCLC and NSCLC xenograft models. Because CXCR4 is widely expressed on cells of hematopoietic origin, these studies were further validated in a syngeneic orthotopic lung tumor model (Lewis lung carcinoma, 3LL) in immunocompetent mice. AMD3465, a cyclam based CXCR4 inhibitor, was radiolabeled with $[^{64}Cu]Cu(OAc)_2$ at pH 5.5. SCLC cell lines H82($CXCR4^{low}$), H69($CXCR4^{high}$) and NSCLC cell line A549 ($CXCR4^{low\text{-}med}$) were used to generate subcutaneous and orthotopic xenografts, respectively in SCID mice. Similarly, 3LL cell line was used to generate orthotopic lung tumors in C57BL/6 mice. Whole body PET/CT imaging and biodistribution studies with selected tissue harvesting was carried out at 90 min post injection of $[^{64}Cu]$AMD3465. Regions of interest (ROI) were drawn over the whole tumors on PET images and radioactivity uptake values calculated as %ID/CC were used for analysis. CXCR4 expression in tumors and metastatic lesions was confirmed by immunohistochemistry and flow cytometry. Three to five animals were used per group. PET imaging and biodistribution studies demonstrated selective accumulation of activity in CXCR4 high expressing H69 compared to H82 tumors. The %ID/CC values were 9.3 ± 0.5 and 2.13 ± 0.2 %ID/CC, for H69 and H82 tumors, respectively. Accumulation of radioactivity was also observed in the orthotopic A549 lung tumors with an %ID/CC value of 10.5±0.9 compared to the contralateral lung at 3.1±0.08. In an A549 tumor mouse, elevated radioactivity accumulation was observed in lymph node metastases compared to the primary tumor. Similarly, 3LL lung tumors demonstrated %ID/CC values of 11.4±0.9 compared to contralateral lung at 2.3±0.4. Our findings demonstrate the feasibility of imaging graded levels of CXCR4 expression in lung tumors in immune -competent and -compromised mouse models.

Disclosure of author financial interest or relationships:
V. Kundoor, None; **M. Pullambhatla**, None; **L. Woodard**, None; **A. Lisok**, None; **M. Pomper**, None; **S. Nimmagadda**, BioMed Valley Discoveries, Consultant .

Presentation Number **SS 48**
Scientific Session 08: Preclinical in vivo Studies - Oncology (Targeted Imaging)
September 19, 2013 / 14:15-14:30 / Room: 203

Improved Diagnostic Accuracy of Ultrasound for Early Breast Cancer Detection using VEGFR2-targeted Contrast Microbubbles in a Transgenic Mouse Model

Sunitha Bachawal[1], *Kristin C. Jensen*[2], *Amelie M. Lutz*[1], *Sanjiv S. Gambhir*[1], *Francois Tranquart*[3], *Lu Tian*[4], *Juergen K. Willmann*[1], [1]*MIPS/Radiology, Stanford University, Stanford, CA, USA;* [2]*Pathology, Stanford University, Stanfrod, CA, USA;* [3]*Bracco research, Bracco research, Geneva, Switzerland;* [4]*Health Research and Policy, Stanford University, Stanford, CA, USA. Contact e-mail: bachawal@stanford.edu*

Background There is an increasing role of ultrasound for breast cancer screening in patients with dense breast; however current ultrasound techniques lack sensitivity and specificity for early breast cancer detection. The goal of our study was to assess the potential of molecular-ultrasound imaging using novel, clinically translatable microbubbles targeted to vascular endothelial growth factor receptor type 2 (MB-VEGFR2) to improve the diagnostic accuracy of ultrasound in earlier detection of breast cancer and ductal carcinoma in situ (DCIS) in transgenic mice. Methods A transgenic mouse model of breast cancer (FVB/N-Tg(MMTV-PyMT)634Mul) was used. In mice carrying the (MMTV/PyMT) transgene, breast cancer progression occurs through various histological stages, similar to disease progression in patients, including hyperplasia, DCIS, and invasive carcinoma. Our study was divided into three parts: In Part 1, binding specificity of MB-VEGFR2 to murine-VEGR2 was tested in 26 breast tumors with different sizes in transgenic mice (mean diameter, 7 mm; range, 3 - 12 mm). In Part 2, in vivo ultrasound molecular imaging signal was correlated with ex vivo histology, VEGFR2-expression and microvessel-density in 315 mammary glands. In Part 3, prospective screening was performed in 63 glands to access diagnostic accuracy of ultrasound molecular imaging. In vivo US imaging was performed on a dedicated small-animal US imaging system (Vevo 2100) Results Ultrasound imaging signal in glands with breast cancer was significantly higher ($P<0.001$) using MB-VEGFR2 compared to MB-Control and imaging signal significantly decreased ($P<0.001$) after administration of anti-VEGFR2 antibody. Ultrasound molecular imaging signal significantly increased ($P<0.001$) when breast tissue progressed from normal (1.65±0.17 a.u.) to hyperplasia (4.21±1.16), DCIS (15.95±1.31) and invasive breast cancer (78.1±6.31) and highly correlated with ex vivo VEGFR2-expression ($R2=0.84$; 95% CI, 0.72, 0.91; $P<0.001$). At an imaging signal threshold of 4.6 a.u.,ultrasound molecular imaging differentiated benign from malignant entities with a sensitivity of 84% (95% CI, 78, 88) and specificity of 89% (95% CI, 81, 94). In the prospective screening trail (n=63 glands) diagnostic performance of detecting DCIS and breast cancer was assessed and two independent readers correctly diagnosed malignant disease in >95% of cases and highly agreed between each other (ICC=0.98; 95% CI, 97, 99). Conclusion Our results suggest that VEGFR2-targeted ultrasound molecular imaging allows highly accurate and reliable detection of DCIS and breast cancer in a transgenic mouse model. Imaging tumor angiogenesis on a molecular level using ultrasound molecular imaging may be a promising approach for earlier detection and improved characterization of breast cancer in future clinical trials.

Disclosure of author financial interest or relationships:
S. Bachawal, None; **K.C. Jensen**, None; **A.M. Lutz**, None; **S.S. Gambhir**, Bracco Diagnostics, Consultant; Endra, Inc, Stockholder; Cellsight, Stockholder; Enlight, Inc., Stockholder; General Electric, Grant/research support; ImaginAb, Stockholder; MagArray, Inc., Stockholder; Sanofi-Aventis, US, Grant/research support; SiteOne Therapeutics, Stockholder; VisualSonics/Sonosite, Stockholder; **F. Tranquart**, Bracco Suisse SA, Employment; **L. Tian**, None; **J.K. Willmann**, Bracco, Consultant; Siemens, Grant/research support; Bracco, Grant/research support .

Presentation Number **SS 49**
Scientific Session 09: Technology & Software Developments - Optical Imaging
September 20, 2013 / 10:30-10:45 / Room: 102

Pulsed light imaging for fluorescence guided surgery

Scott C. Davis[1], *Kristian Sexton*[1], *David McClatchy*[1], *Pablo A. Valdes*[1,2], *Brian W. Pogue*[1,3], [1]*Thayer School of Engineering, Dartmouth College, Hanover, NH, USA;* [2]*Department of Surgery, Geisel School of Medicine at Dartmouth, Hanover, NH, USA;* [3]*Department of Neurosurgery, Dartmouth Hitchcock Medical Center, Lebanon, NH, USA. Contact e-mail: Scott.C.Davis@Dartmouth.edu*

Adding molecular-derived functional information to help differentiate diseased and normal tissue during surgical resection of cancer is one of the great of promises of fluorescence guided surgery. This potential has been the main driver of innovation in fluorescence imaging systems designed specifically for use in the operating room. The systems which are most effective and yet minimize the impact on current clinical practice are the most likely to be adopted by the surgical community. However, because fluorescence imaging requires detection of relatively small signals, most current-generation systems require the lights in the operating room to be dimmed, filtered, or shut off during fluorescence mode imaging, disrupting the normal clinical workflow. To address this challenge, we have developed a fluorescence imaging system which operates using high-intensity pulsed light and gated detection to allow fluorescence guide surgical imaging in the presence of ambient light. The experimental imaging system is shown in Figure 1 (a) and (b). Excitation is provided by an array of pulsed LED's and the remitted fluorescence light is collected by a low F# camera lens and passes through an 8-position motorized filter wheel before detection by an intensified CCD synchronized to the LED pulses. This gated imaging approach has several advantages over standard CW imaging, namely: (1) Pulsed-light imaging shortens the required exposure time for each frame while delivering the same irradiance, effectively reducing the relative intensity of background signal. (2) Further reduction in ambient signal is enabled by real-time background subtraction during which the camera collects light both when the LED's are on, and for an equal exposure time immediately after the LED's have been switched off. Subtracting these images dramatically reduces the contaminating signal from ambient light. (3) Imaging with real-time background subtraction can still be performed at video rate, which is generally not possible without gated detection. While these concepts are general known to the optical imaging community and have been discussed by others, to our knowledge, the system presented here represents the first realization of this approach for wide-field video-rate imaging for fluorescence guided surgery. We examined the ability of the gated system to image protoporphyrin IX (PPIX), an endogenous fluorophore currently under investigation for fluorescence guided resection of brain tumors, in realistic tissue-mimicking phantoms. Excitation was provided by pulsed 630 nm LED's and images collected for phantoms with varying concentrations of PPIX. A highly linear response to concentration was observed (Fig. 1 [c]), even under room light conditions. Furthermore, the minimum detectable concentration was found to be a factor of ten lower than a commercial system currently used in the clinic for this indication. These results suggest significant potential for rapidly translating this imaging approach to the clinic. Brain tumor resection studies in small animals are currently underway to establish the limits of detection under a variety of ambient light conditions.

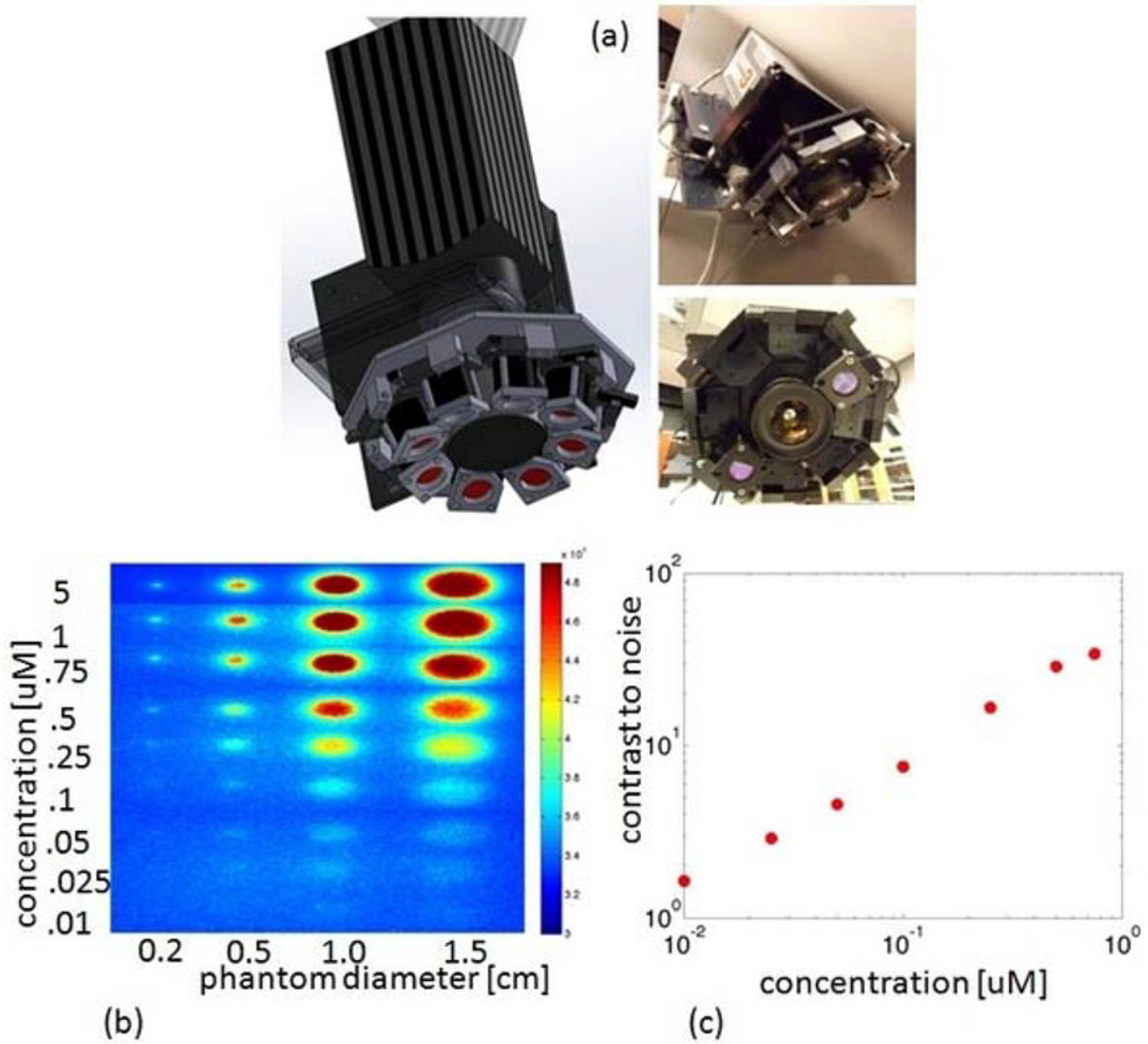

CAD rendering and photographs (a) of the surgical imaging system. Images of phantoms demonstrate system sensitivity to fluorescent objects of different sizes and contrasts (b). The system also demonstrates excellent linearity with fluorophore concentration (c).

Disclosure of author financial interest or relationships:
S.C. Davis, None; **K. Sexton**, None; **D. McClatchy**, None; **P.A. Valdes**, None; **B.W. Pogue**, None.

Presentation Number **SS 50**
Scientific Session 09: Technology & Software Developments - Optical Imaging
September 20, 2013 / 10:45-11:00 / Room: 102

Mechanical Molecular Imaging: Dynamically Imaging The Intracellular Mechanical Properties of Cancer in Living Subjects

Pei-Hsun Wu[2], Sanjiv S. Gambhir[1], Christopher Hale[2], Denis Wirtz[2], **Bryan R. Smith**[1], *[1]Radiology/Molecular Imaging, Stanford University, Stanford, CA, USA; [2]Chemical and Biomolecular Engineering, Johns Hopkins University, Baltimore, MD, USA. Contact e-mail: brsmith@stanford.edu*

Background: Molecular imaging traditionally enables scientists/clinicians to observe and quantify the presence of a particular molecule(s) within living subjects. Recently, the mechanical properties of biological tissues have been implicated in cancer initiation/growth. However, currently there exist no methods to examine mechanical properties in live subjects with high spatial resolution. Such techniques bring the promise to open entirely new avenues of inquiry for both disease diagnosis and treatment. Herein, we provide proof-of-principle of such a technique, and apply it to answer questions that were previously unresolvable about the dynamic stiffness of cancer as it converges and forms a solid tumor in vivo. Recent studies on cancer mechanics implicate mechanical parameters as major players in tumorigenesis. Yet these studies typically exploit cell culture and computer simulations. These systems are relatively simple and can not recapitulate the complexity of living subjects. To shed light on real tumor growth in live subjects, we developed and validated a new technique to examine the mechanical properties of implanted cancer cells in living subjects by combining multiple particle tracking microrheology (MPTM) with intravital microscopy (IVM). MPTM is a non-invasive optical technique that employs particles embedded within live cells to extract intracellular viscous and elastic information by tracking the particle movement. It has been applied in cell biology to study intracellular mechanics in cell culture. IVM has been used for decades to optically visualize microscale interactions in living subjects. We combined MPTM with IVM and developed algorithms to handle movements due to mouse heartbeat and breathing. We used EGFP-transfected MDA-MB-231 human breast cancer cells implanted into dorsal chambers of SCID mice for visualization using IVM. MDA-MB-231 cells were ballistically injected with 200 nm fluorescent nanoparticles (nps) into cell cytoplasm to perform MPTM on tumor cells containing nps in live subjects. We validated the technique using a variety of controls and computer simulations. Using this technique, we followed the initiation and growth of a tumor in N=4 mice from tumor cell implantation until 1 week post-implantation (Fig. 1 shows cell convergence). We found that tumor cells remain viscous and mechanically similar in the early stage of tumor formation (≤4 days), yet at 1 week post-implantation they stiffen, displaying viscoelastic character (significantly stiffer than previous days, $p<0.05$). We surprisingly demonstrated similarity between the compliance of cultured confluent cells and cells in living subjects, while cultured sub-confluent cells were significantly softer than both cells in live mice and confluent cultured cells ($p<0.001$). Conclusion: These results are the first to examine intracellular mechanical properties within live subjects, and they suggest that intravital particle tracking can be employed to investigate major hypotheses in cancer mechanics by studies in living animals. This will eventually have potential impact on understanding cancer cell biology and metastasis as well as optimizing cancer management.

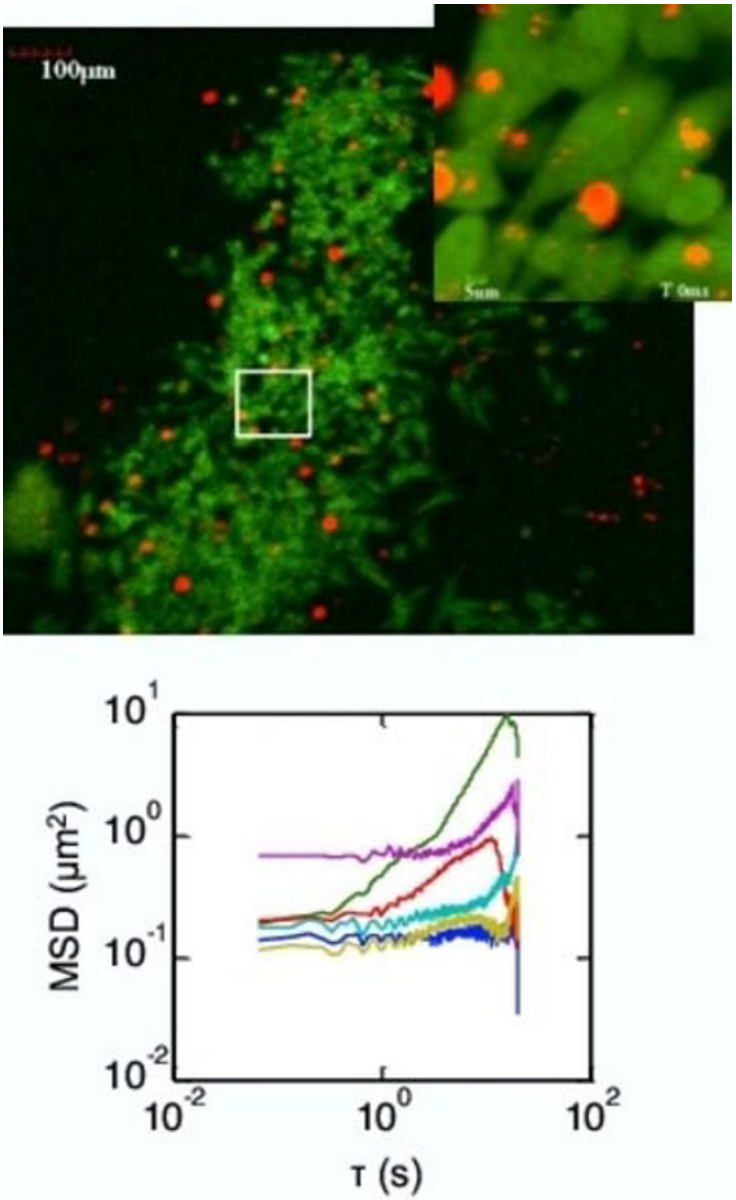

Figure 1. Tumor cells converging into a tumor on day 2 post-implantation and tracks of intracellular nanoparticles within living mice as imaged by intravital microscopy. (Top) 200 nm nanoparticles (red) are visible in tumor cells (green) - individual nanoparticles are the small red dots. These nanoparticles were tracked using high speed cameras, and their mean squared distances (MSDs) were plotted over time to yield the mechanical properties. (Bottom) Raw tracks of individual particles tracked using high-speed microscopy and custom software. These MSD tracks can be converted into local viscosity and elasticity of the cells within living subjects.

Disclosure of author financial interest or relationships:

P. Wu, None; **S.S. Gambhir**, Bracco Diagnostics, Consultant; Endra, Inc, Stockholder; Cellsight, Stockholder; Enlight, Inc., Stockholder; General Electric, Grant/research support; ImaginAb, Stockholder; MagArray, Inc., Stockholder; Sanofi-Aventis, US, Grant/research support; SiteOne Therapeutics, Stockholder; VisualSonics/Sonosite, Stockholder; **C. Hale**, None; **D. Wirtz**, None; **B.R. Smith**, None.

Presentation Number **SS 51**
Scientific Session 09: Technology & Software Developments - Optical Imaging
September 20, 2013 / 11:00-11:15 / Room: 102

Anatomically Guided Dynamic Fluorescence Molecular Tomography for Small Animal Imaging

Metasebya Solomon[1,2], *Walter J. Akers*[2], *Kooresh I. Shoghi*[2], *Samuel Achilefu*[1,2], *Joseph P. Culver*[1,2], [1]*Biomedical Engineering, Washington University in Saint Louis, Saint Louis, MO, USA;* [2]*Radiological Sciences, Washington University School of Medicine, Saint Louis, MO, USA. Contact e-mail: solomonm@mir.wustl.edu*

Dynamic fluorescence molecular tomography (DyFMT) including tracer kinetic modeling, can potentially provide powerful non-invasive quantification for molecular imaging analysis. Tracer kinetic modeling allows extraction of clinically or experimentally relevant information related to physiological and molecular processes. Kinetic models require two main measurements of tracer concentration over time as inputs: the arterial input function (AIF) and the tissue response kinetics. The AIF represents the tracer time course in arterial blood, which is used as a forcing function in fitting compartmental models to the tissue kinetics. The gold standard for obtaining an input function is through manual acquisition of arterial blood samples (ABS). Non-invasive imaging techniques, using factor analysis methods and region-of-interest (ROI) based input functions have been proposed to resolve the challenges associated with serial arterial blood sampling for routine implementation in small animal studies. Anatomically guided DyFMT provides a viable solution to obtain image derived input function (IDIF). Herein, anatomically guided DyFMT was made possible by combining our recently published fiber-based, video-rate FMT system (Solomon et. al. 2011) with preclinical NanoSPECT/CT to obtain complementary information. X-ray CT provides anatomical information for improved delineation of target tissues, while FMT provides dynamic functional information. In this work, we acquired dynamic tomography of fluorescent diagnostic imaging agents in healthy mice and in mice with FAS-targeted liver sepsis. We reconstructed the AIF from dynamic FMT images demonstrating, for the first time, the feasibility of implementing time traces extracted from highly vascularized ROI, the heart region, as an IDIF for DyFMT. For validation, temporal correlations were evaluated between the heart region time traces (IDIF) and the corresponding reference ABS. Time traces of the IDIF have high temporal correlation with their corresponding ABS, with $r=0.95 \pm 0.024$ and $r=0.86 \pm 0.083$ in healthy and diseased mice respectively. The high correlations validate the use of time courses from the heart region as an IDIF. We used the IDIF's with a two-compartment model to estimate ICG kinetic parameters of the target regions, the lung and liver. Each fitted ICG concentration curve showed high temporal correlation with the corresponding lung and liver ICG time courses data in both healthy and diseased mice. Moreover, the estimated ICG kinetic rate constants for the liver and lung demonstrated the feasibility of distinguishing different organs as well as healthy vs. diseased organs. The liver damage increased the overall rate constant of lungs and liver in diseased mice relative to healthy mice. In summary, DyFMT was shown feasibly with an image-derived input function, using a video-rate, fiber-based FMT. This provides a non-invasive in vivo imaging tool for quantitative pharmacokinetics and biodistribution studies using newly developed diagnostic optical agents. Further DyFMT has the potential for detecting the disease state affecting internal organs and monitoring their response to therapeutic agents.

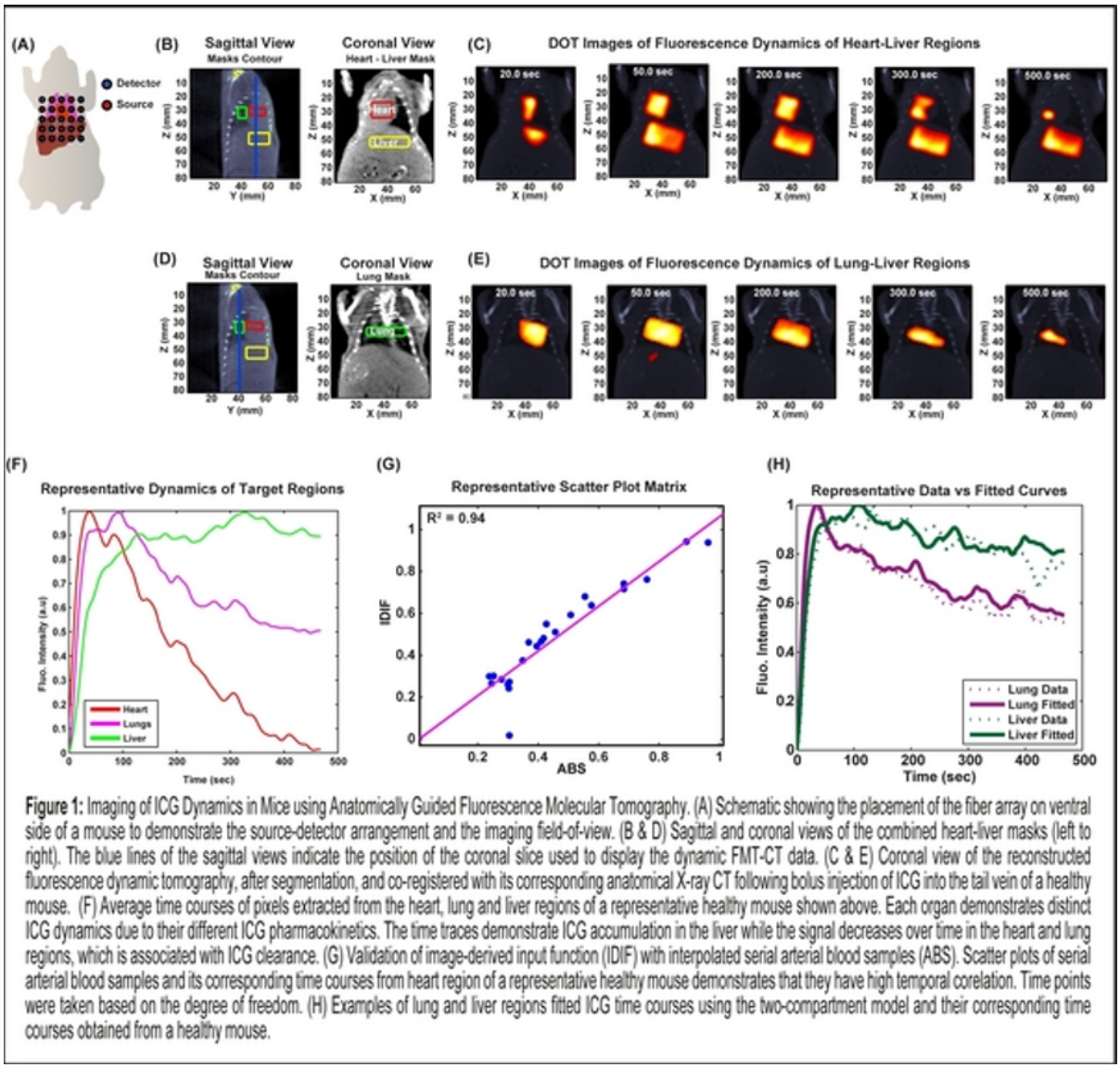

Figure 1: Imaging of ICG Dynamics in Mice using Anatomically Guided Fluorescence Molecular Tomography. (A) Schematic showing the placement of the fiber array on ventral side of a mouse to demonstrate the source-detector arrangement and the imaging field-of-view. (B & D) Sagittal and coronal views of the combined heart-liver masks (left to right). The blue lines of the sagittal views indicate the position of the coronal slice used to display the dynamic FMT-CT data. (C & E) Coronal view of the reconstructed fluorescence dynamic tomography, after segmentation, and co-registered with its corresponding anatomical X-ray CT following bolus injection of ICG into the tail vein of a healthy mouse. (F) Average time courses of pixels extracted from the heart, lung and liver regions of a representative healthy mouse shown above. Each organ demonstrates distinct ICG dynamics due to their different ICG pharmacokinetics. The time traces demonstrate ICG accumulation in the liver while the signal decreases over time in the heart and lung regions, which is associated with ICG clearance. (G) Validation of image-derived input function (IDIF) with interpolated serial arterial blood samples (ABS). Scatter plots of serial arterial blood samples and its corresponding time courses from heart region of a representative healthy mouse demonstrates that they have high temporal corelation. Time points were taken based on the degree of freedom. (H) Examples of lung and liver regions fitted ICG time courses using the two-compartment model and their corresponding time courses obtained from a healthy mouse.

Disclosure of author financial interest or relationships:
M. Solomon, None; **W.J. Akers**, None; **K.I. Shoghi**, None; **S. Achilefu**, None; **J.P. Culver**, Cephalogics, Stockholder .

Presentation Number **SS 52**
Scientific Session 09: Technology & Software Developments - Optical Imaging
September 20, 2013 / 11:15-11:30 / Room: 102

Quantitative *in-vivo* 3D image reconstruction of dual wavelength experiments from coregistered limited view projection FMT-XCT

Karin Radrich[2,1], *Pouyan Mohajerani*[1,2], *Vasilis Ntziachristos*[1,2], [1]*Institute of Biological and Medical Imaging, Helmholtz Zentrum München, Neuherberg, Germany;* [2]*Chair for Biological Imaging, Technische Universität München, Munich, Germany. Contact e-mail: karin.radrich@tum.de*

Introduction: Fluorescence Molecular Tomography (FMT) is an imaging modality that reconstructs fluorescence biodistribution in small animals using diffuse optical measurements. Recently, we have shown that coregistration of limited view projection FMT data to anatomical data from X-ray Computed Tomography (XCT) of disseminated devices significantly improves FMT reconstruction quality and accuracy. This was achieved by using the segmented XCT volume as functional and structural prior information to guide the fluorescence reconstruction. In this work we further investigated the ability of our method to quantitatively reconstruct fluorescence biodistribution in dual wavelength experiments. **Methods:** We simultaneously injected two near infrared dyes targeting different molecules into mice bearing deep seated KRas lung tumors or subcutaneously injected 4T1 tumors. For imaging, mice were anesthetized and placed in an imaging cassette consisting of transparent plates that immobilized the mice during both FMT and XCT acquisition. Raw FMT and XCT data were used for coregistration and hybrid reconstruction applying priors. To confirm *in-vivo* imaging results, mice were euthanized, frozen at -80°C and cryosliced employing a custom made fluorescence imaging cryotome. **Results:** Figure 1(a) depicts the reconstruction of a KRas lung tumor model injected with a probe targeting integrins and a nonspecific vascular probe, as well as the corresponding cryosections. The cryosections show that while the targeted probe accumulates in the tumors the vascular probe is distributed in the whole animal without significant accumulation in any tissue type. The reconstructed FMT images reflect these observations showing high fluorescence intensity in the lung (highlighted by arrows) for the integrin probe versus no regions of increased fluorescence activity for the nonspecific probe. The fluorescence intensity is shown to be lower for the vascular probe in both the cryosections and FMT images. Figure 1(b) depicts the reconstruction of a subcutaneous 4T1 tumor model injected with a probe targeting integrins and a probe targeting VEGF receptors. The high resolution cryosections of a 4T1 tumor indicate that the integrin probe is mainly accumulated within the tumor, while the VEGF probe shows increased intensity in the tumor periphery. Similarly to the lung tumor case, the FMT reconstructions do reflect this fluorescence intensity difference by depicting the integrin probe as being more distributed inside the tumor and the VEGF probe being concentrated at the tumor boundary. **Conclusion:** In this study we show that hybrid FMT-XCT imaging using priors is capable of accurately and quantitatively reconstructing fluorescence biodistribution of multiple fluorescence probes in the same animal. We also show that this method can be applied to very different types of tumor models and is therefore useful for a variety of *in-vivo* disease studies targeting more than one molecule.

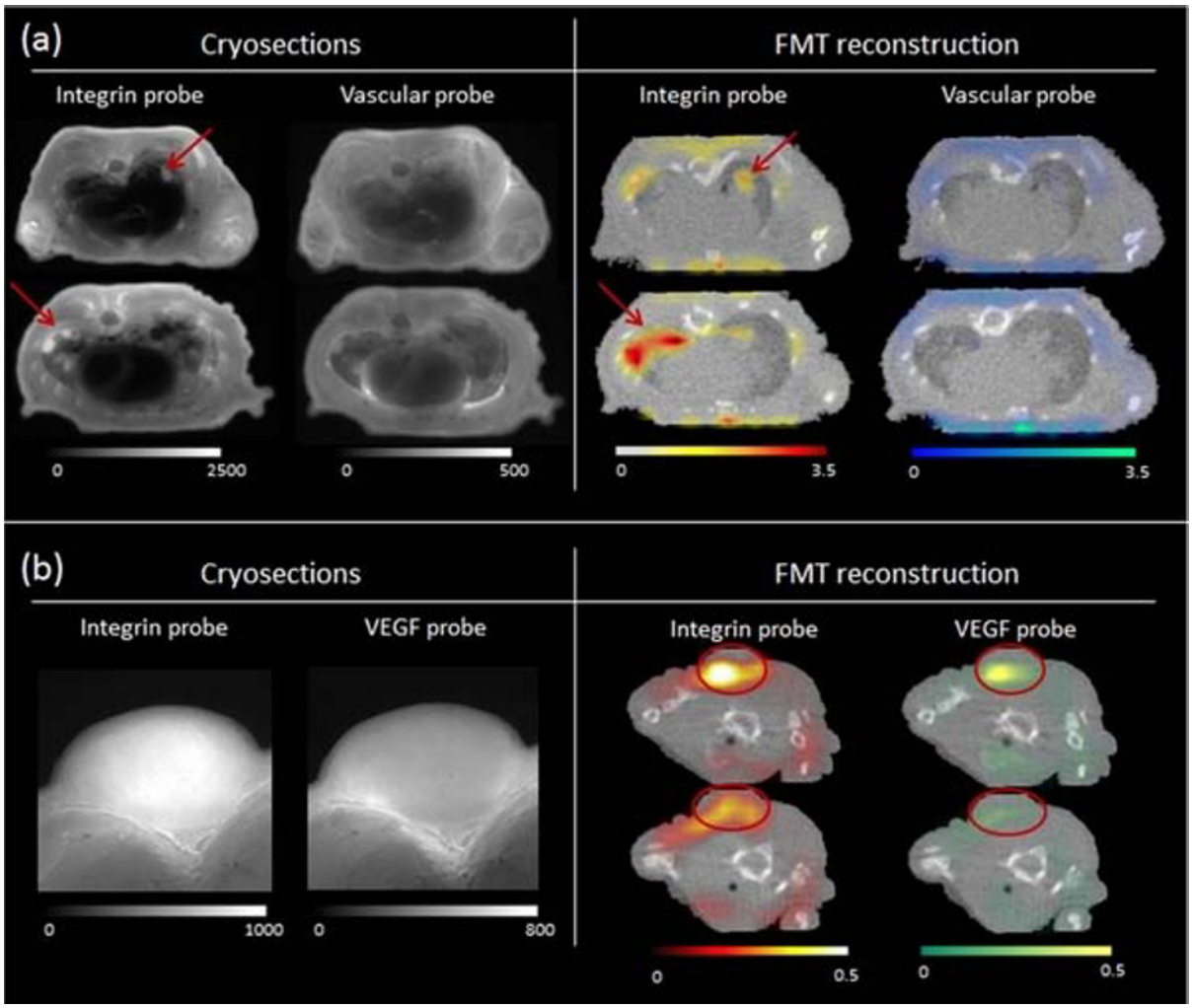

Figure 1: Exemplary slices of mice bearing Kras lung tumors (a) and a subcutaneous 4T1 tumor (b). Left in (a) and (b): Fluorescence images of cryosections. Units in camera counts normalized by exposure time. Right in (a) and (b): FMT reconstruction in arbitrary units.

Disclosure of author financial interest or relationships:
K. Radrich, None; **P. Mohajerani**, None; **V. Ntziachristos**, iThera Medical, Stockholder; SurgOptix BV, Consultant .

Presentation Number **SS 53**
Scientific Session 09: Technology & Software Developments - Optical Imaging
September 20, 2013 / 11:30-11:45 / Room: 102

Dual-Tracer Fluorescent Imaging Provides a Measure of Tumor Endothelial Marker Concentrations in Melanomas

Kenneth M. Tichauer[1,2], *Sophie J. Deharvengt*[3], *Kimberley Samkoe*[2], *Jason Gunn*[2], *Marcus W. Bosenberg*[5], *Mary Jo Turk*[2], *Tayyaba Hasan*[4], *Radu V. Stan*[3], *Brian W. Pogue*[2], [1]*Biomedical Engineering, Illinois Institute of Technology, Chicago, IL, USA;* [2]*Thayer School of Engineering, Dartmouth College, Hanover, NH, USA;* [3]*Pathology, Geisel School of Medicine, Hanover, NH, USA;* [4]*Wellman Institute of Photomedicine, Massachusetts General Hospital, Boston, MA, USA;* [5]*Dermatology, Yale University, New Haven, CT, USA. Contact e-mail: ktichaue@iit.edu*

Endothelial molecular markers on tumor-infiltrating blood vessel cells are being heavily explored in cancer research. They have been studied as accessible therapeutic targets, to understand biochemical effects of tumor growth on adjacent vasculature, and to facilitate extravasation of large molecule (e.g., nanoparticle) therapies that generally suffer from restricted leakage into the tumor parenchyma. While new tumor-specific endothelial markers are continually being identified, there exist no robust methods for quantifying levels of these markers non-invasively in vivo. This study presents a novel fluorescent imaging approach - based on our previous work in tumor cell receptor concentration imaging (RCI) - that is capable of providing the first-ever measures of tumor endothelial marker concentrations. Our approach to quantitative endothelial marker concentration imaging (EMCI) involves the simultaneous injection of two fluorescent tracers: 1) a tracer targeted to the endothelial marker of interest, and 2) a similar tracer that has no specific targeting but can be imaged simultaneously with the targeted tracer. The uptake of the untargeted tracer, when measured in conjunction with the uptake of the targeted tracer, can be used to account for non-specific uptake and retention of the targeted tracer, enabling the concentration of targeted endothelial marker to be measured through kinetic modelling. The EMCI approach was tested on triple mutant mice with melanomas induced on their right flank (n = 7). These inducible melanomas have been shown to overexpress PV1, which is an endothelial membrane protein that influences vascular leakiness in many cancers. In response, the targeted tracer employed in this studied was an antibody for PV1 labelled with the fluorophore, IRDye 800CW (LICOR), and the untargeted tracer was a negative control for anti-PV1 labelled with the fluorophore, IRDye 700DX (LICOR). One day prior to imaging, the right flanks of the mice were treated with a depilatory cream to expose the skin. Just prior to imaging, the mice were placed in a prone position in a two-channel fluorescence imaging system (Pearl Imager, LICOR Biosciences, Lincoln, NE), and then 5, 20, or 50 μg of targeted and untargeted tracers were injected intravenously into 2, 3, and 2 mice, respectively, and the uptake of each tracer was imaged at 1 min intervals up to 90 min in the tumor and surrounding healthy skin. The amount of tracer was varied to determine if PV1 saturation was occurring. Fluorescence of the targeted and untargeted tracers was much lower in the melanomas than in the surrounding skin (Fig. 1b, c, & f) caused by a large amount of fluorescence absorption by melanin in the tumors. Despite this dampening, the EMCI approach was able to image the increased levels of PV1 in the melanomas compared to the healthy skin (Fig. 1d, e, & g). The absence of a correlation between measured PV1 concentration and tracer dose suggested that the maximum dose of 50 μg was far from saturating. These preliminary results highlight the promise of using dual-tracer imaging to provide the first-ever means of quantifying intravascular marker concentrations in vivo.

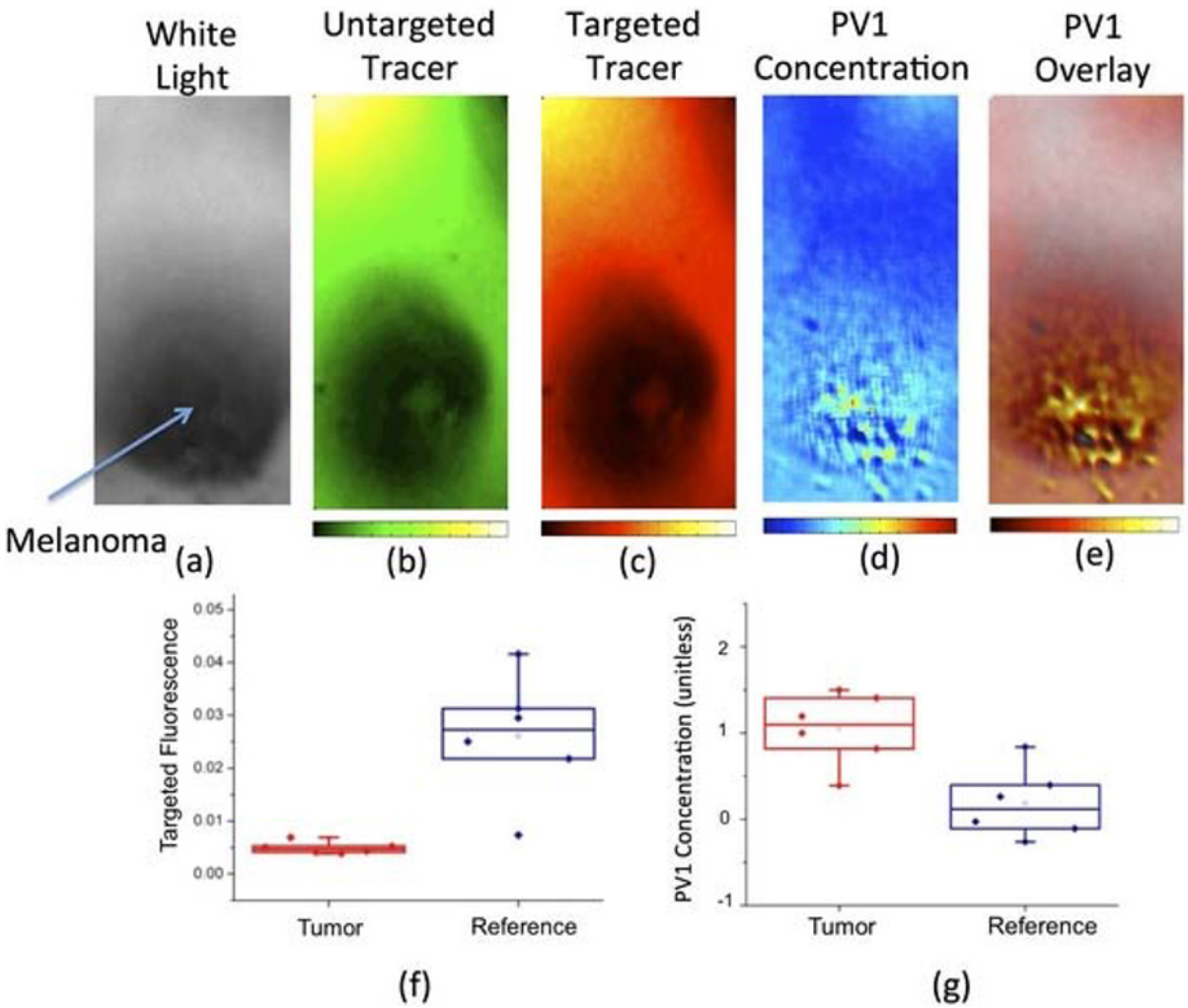

Disclosure of author financial interest or relationships:
K.M. Tichauer, None; **S.J. Deharvengt**, None; **K. Samkoe**, None; **J. Gunn**, None; **M.W. Bosenberg**, None; **M. Turk**, None; **T. Hasan**, None; **R.V. Stan**, None; **B.W. Pogue**, None.

Presentation Number **SS 54**
Scientific Session 09: Technology & Software Developments - Optical Imaging
September 20, 2013 / 11:45-12:00 / Room: 102

Fiber-Optic Catheter System for Dual Optical Imaging of Glucose Probes (18F-FDG and 6-NBDG) in Atherosclerotic Plaques

Raiyan Zaman[1,2], *Hisanori Kosuge*[1], *Guillem Pratx*[2], *Colin M. Carpenter*[2], *Lei Xing*[2], *Michael V. McConnell*[1], [1]*Cardiovascular Medicine, Stanford University School of Medicine, Stanford, CA, USA;* [2]*Radiation Physics, Stanford University School of Medicine, Stanford, CA, USA. Contact e-mail: rtzaman@stanford.edu*

Objectives: Atherosclerosis is a progressive inflammatory condition that underlies coronary artery disease—the leading cause of death in the USA and worldwide. The overall objective of this study is to improve the characterization of atherosclerotic plaques within the coronary arteries, using a novel fiber-optic molecular imaging system with high sensitivity to detect glucose uptake. Thus, the aims of this study are to (1) optimize a catheter-based optical/radionuclide imaging system with a novel scintillating balloon to detect both 18F-FDG and fluorescent glucose probes, (2) validate the system and demonstrate sensitivity on ex vivo plaques. Methods: The dual imaging system design (Fig. 1) uses a flexible fiber-optic catheter and enables both radio-luminescence imaging (e.g., 18F-FDG) and diffuse optical fluorescence imaging (e.g., 6-NBDG, a fluorescent glucose analog of 18F-FDG), the latter requiring fluorescence excitation light. The catheter system includes an emission filter inside a filter wheel placed between 35 mm and 8 mm fixed focal length lenses, connected to a CMOS camera and fiber holder. The proximal end of a leached image bundle was attached to the fiber holder and the distal ferrule was terminated with a wide-angle lens. Radio-luminescence detection requires a scintillator membrane in front of the wide-angle lens. For in vitro study, mouse macrophage cells (RAW264.7) were stimulated with/without lipopolysaccharide, LPS (100ng/ml) for 24 hours in 96-well plates (1x105/well) (Fig 2a). After washing and arresting in medium without glucose for 1 hour, cells were incubated with 6-NBDG at multiple concentrations (0-400 μM). One hour later, 6-NBDG uptake was assessed with IVIS-200. For ex vivo study, FVB mice (n=6) macrophage-rich carotid atherosclerotic lesions created by high-fat diet and diabetes induction (streptozotocin), followed 2 weeks later by left carotid ligation. Two weeks after ligation, mice were injected IV with either 6-NBDG (500 nmol) or 18F-FDG (1-1.4 mCi) after a 6-hour fast. One hour after injection, ligated left and non-ligated right (negative control) carotid arteries were harvested and cut longitudinally, then imaged (with the heart as positive control) using the fiber-optic catheter imaging system, as well as IVIS-200. Results: In vitro, LPS+ (LPS-activated) macrophages took up more than 2x 6-NBDG than LPS- macrophages (Fig. 2b). Ex vivo fluorescence imaging of 6-NBDG by IVIS-200 confirmed high signal from ligated left carotids compared to non-ligated right carotids, as well as high myocardial signal (Fig. 3). The fiber-optic catheter system showed high signal from ligated left carotids and myocardium, but no signal from the non-ligated right carotids (Fig. 4). Similarly, strong radio-luminescent signal from 18F-FDG was detected by the fiber-optic catheter imaging system for left carotid arteries and myocardium, with confirmation by IVIS-200 (Fig. 5). Conclusion: This novel fiber-optic catheter system for dual 6-NBDG and 18F-FDG detection in atherosclerotic plaques shows promising results for potential optical intra-coronary plaque characterization. Research Support: NIH Training Grant (T32EB009035).

Disclosure of author financial interest or relationships:
R. Zaman, None; **H. Kosuge**, None; **G. Pratx**, None; **C.M. Carpenter**, None; **L. Xing**, None; **M.V. McConnell**, GE Healthcare, Grant/research support .

Presentation Number **SS 55**
Scientific Session 10: Chemistry & Imaging Probes, Technology & Software Developments - Ultrasound
September 20, 2013 / 10:30-10:45 / Room: 105

Genetically Encoded Gas Nanostructures as Ultrasonic Molecular Reporters

Mikhail G. Shapiro[1,2], *Patrick Goodwill*[1,3], *Arkosnato Neogy*[3], *David V. Schaffer*[1,4], *Steven Conolly*[1,3], [1]*Bioengineering, UC Berkeley, Berkeley, CA, USA;* [2]*Miller Institute, UC Berkeley, Berkeley, CA, USA;* [3]*Electrical Engineering, UC Berkeley, Berkeley, CA, USA;* [4]*Chemical Engineering, UC Berkeley, Berkeley, CA, USA. Contact e-mail: mikhails@berkeley.edu*

Despite providing excellent resolution, sensitivity and convenience compared to other imaging modalities, ultrasound is currently limited in many molecular imaging applications by a lack of suitable nanoscale reporters. The basic physics of conventional "microbubble" contrast agents, which dictates sizes larger than one micron and half-lives shorter than a few hours, restricts their use as labels of specific cells and tissues outside the bloodstream. **Here, we introduce a new class of reporters for ultrasound based on genetically encoded gas nanostructures from buoyant bacteria and archaea.** These inherently stable nanoscale reporters overcome some of the main limitations of microbubbles, and raise the possibility of ultrasound contrast agents engineered and delivered to cells at the genetic level. - Gas vesicles (GVs) are gas-filled protein-shelled compartments 100-400 nm in size that exclude water and are permeable to gas. They are biosynthesized by photosynthetic cyanobacteria and halobacteria as a means to regulate buoyancy and thereby migrate to optimal aqueous depths for access to light and nutrients. GVs from different species have different shapes and sizes. Like microbubbles, GVs are gas-containing structures, but they exhibit different physics: they are smaller, the gas inside them is at equilibrium with the aqueous environment, they are inherently stable, and their shell is relatively inelastic. Here, we demonstrate the first use of GVs as ultrasound contrast agents. - Our results show that sub-nanomolar concentrations of GVs produce robust ultrasound contrast at frequencies of 5-17 MHz. Contrast mechanisms include linear scattering, attenuation and harmonics, enabling enhanced detection. GV contrast is readily observed *in vitro* and *in vivo*. Furthermore, differences in genetically-determined critical collapse pressures among GVs from different species enables multiplexed imaging through a serial *in situ* collapse paradigm. In addition, we show that clustering- dependent contrast enhancement permits the use of GVs as molecular biosensors and reporters of cellular integrity. These results highlight the potential of this new class of reporters to support unique modes of molecular imaging, and raise the intriguing prospect of genetically engineered and targeted reporters for ultrasound.

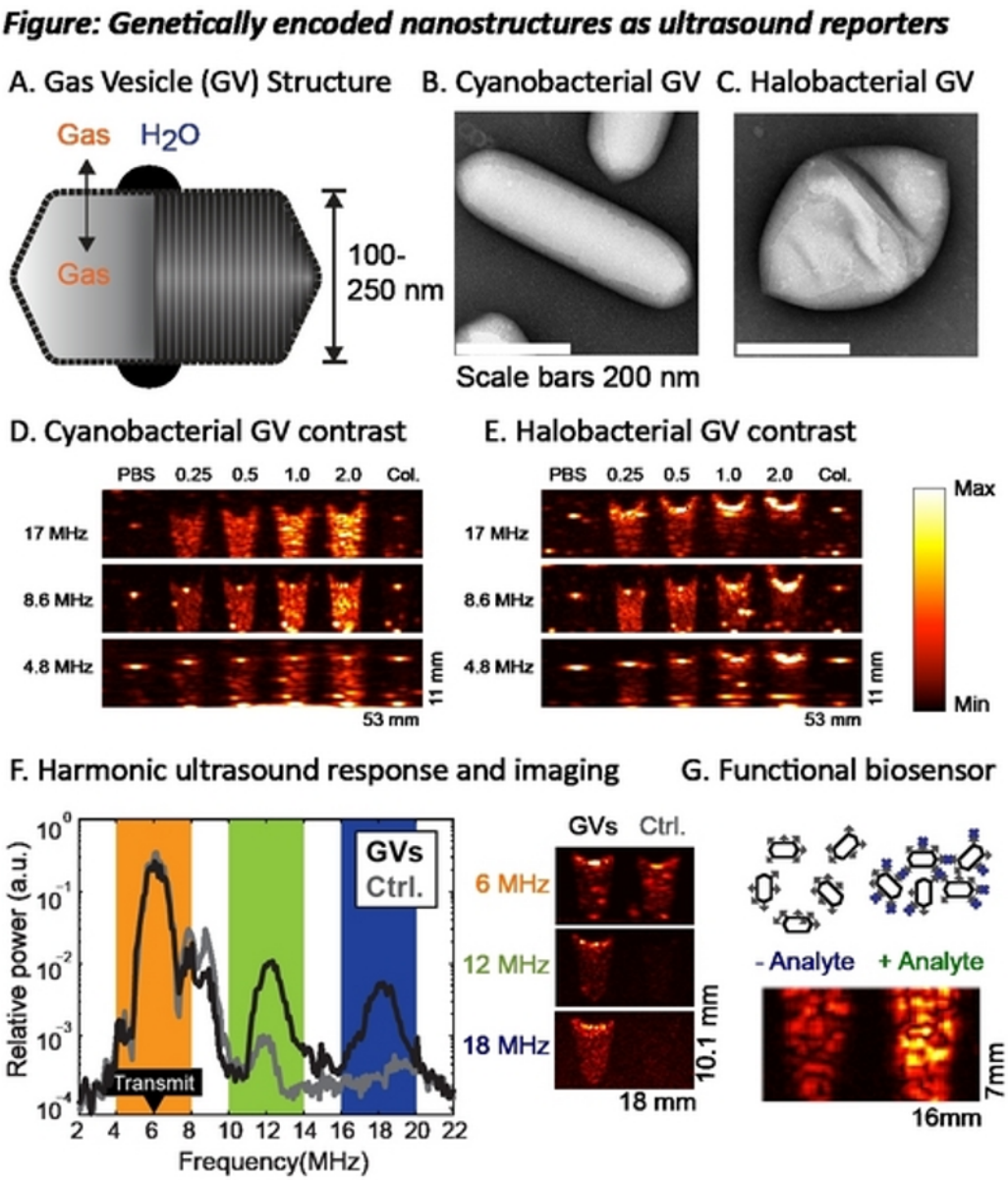

A. Diagram of a gas vesicle: a hollow gas nanocompartment surrounded by a gas-permeable protein shell. **B** & **C**. TEM images of GV purified from *A. flos-aquae* (B) and *H. salinarum* (C). **D**. Ultrasound images of a phantom containing *Ana* GVs at the indicated optical densities, collapsed *Ana* GVs (Col., OD 2.0) or buffer (PBS). Images were acquired at multiple frequencies, as indicated. **E**. Ultrasound images of *Halo* GVs arranged as described for (D). **F**. (left) Power spectrum of signal backscattered from *Halo* GVs (black) and 4.78 μm polystyrene (PS) microspheres (gray) in response to 6 MHz pulses. The orange, green and blue highlights correspond to frequency bands used to generate the images on the right. **G**. (top) Diagram of the designed aggregation interaction between surface-biotinylated GVs (hexagons with gray arrows) and streptavidin; (bottom) 17 MHz image of OD 1.0 biotinylated GVs in the absence or presence of streptavidin.

Disclosure of author financial interest or relationships:

M.G. Shapiro, Foundation Medicine, Stockholder; Afferent Pharmaceuticals, Stockholder; True & Company, Stockholder; **P. Goodwill**, None; **A. Neogy**, None; **D.V. Schaffer**, NIH, NSF, CIRM, Grant/research support; Bio-Rad, Avalanche, CellGS, Consultant; Valitor, Inc., Stockholder; **S. Conolly**, None.

Presentation Number **SS 56**
Scientific Session 10: Chemistry & Imaging Probes, Technology & Software Developments - Ultrasound
September 20, 2013 / 10:45-11:00 / Room: 105

Ultrasound Molecular Imaging Using a Dual-Selectin Targeted Contrast Agent versus FDG PET-CT Imaging for Assessment of Inflammation in a Murine Inflammatory Bowel Disease Model

Huaijun Wang[1], *Steven Machtaler*[1], *Thierry Bettinger*[2], *Amelie M. Lutz*[1], *Richard Luong*[3], *Philippe Bussat*[2], *Sanjiv S. Gambhir*[1], *Francois Tranquart*[2], *Lu Tian*[4], *Juergen K. Willmann*[1], [1]*Department of Radiology, Molecular Imaging Program at Stanford, Stanford University, Stanford, CA, USA;* [2]*Bracco Suisse SA, Geneva, Switzerland, Switzerland;* [3]*Department of Comparative Medicine, Stanford University, Stanford, CA, USA;* [4]*Department of Health, Research & Policy, Stanford University, Stanford, CA, USA. Contact e-mail: whjwang@stanford.edu*

Purpose: Inflammatory bowel disease (IBD) including Crohn's disease and ulcerative colitis is characterized by extensive inflammatory changes in the bowel wall and primarily affects young patients. Regular and accurate monitoring IBD is crucial for proper patient management. The adhesion molecules P- and E-selectin are overexpressed on inflamed vessels and help leukocytes roll and attach to inflamed vascular endothelial cells. Targeted contrast-enhanced (molecular) ultrasound (US) imaging is a non-invasive radiation-free technique and may be useful for quantitative monitoring of IBD especially in young patients. The purpose of this study was to evaluate the correlation between US molecular imaging using clinically translatable contrast microbubbles (MB) targeted at the inflammation markers P- and E-selectin ($MB_{Selectin}$) with a well-established molecular imaging modality, ^{18}F-FDG-PET, for inflammation quantification in a murine IBD model. Materials and Methods: Colitis was induced in 51 male BALB/c mice by rectal TNBS injection; rectal saline was injected in 19 control mice. The colitis mice were scanned either at day 1 (n=27) or day 5 (n= 24) after colitis induction. US molecular imaging was performed after i.v. injection of 5×10^7 $MB_{Selectin}$ using a small animal US system (Vevo2100; VisualSonics, Toronto, Canada) with a dedicated transducer (center frequency of 21MHz). Images were acquired at a high spatial resolution (lateral and axial resolution of 165µm and 75µm respectively; focal length, 8mm; transmit power, 10%; mechanical index, 0.2; dynamic range, 35dB). Within 3 hours on the same day of US, PET-CT was performed in all mice (200µCi FDG injected per mouse; 10-min static scan at 1 hour after the injection; Inveon; Siemens, Knoxville, TN). US signal was expressed in arbitrary units (a.u.) and FDG uptake in percentage of injected dose per gram (%ID/g). After the last imaging session, mice were sacrificed and colonic tissues were analyzed for presence of inflammation on H&E staining and for expression of P- and E-selectin using quantitative immunofluorescence. Results: US molecular imaging signal was significantly higher ($P<0.001$) in colitis mice at day 1 (173.8±134.8 a.u.) than in controls (5.0±4.5 a.u.) and significantly ($P<0.001$) decreased from day 1 to 5 (9.2±7.7 a.u) after TNBS induction with mice spontaneously recovering from colitis. Similarly, FDG uptake was significantly higher ($P<0.001$) in colitis (8.4±4.1%ID/g) compared to normal colon (2.6±1.3%ID/g) and significantly ($P<0.001$) decreased from day 1 to 5 (3.8±1.6 %ID/g). US imaging signal highly correlated with FDG uptake (rho=0.89; $P<0.001$). Ex vivo analysis confirmed inflammation in TNBS-treated mice on H&E staining and showed overexpression of selectins in inflamed bowel. Conclusion: US molecular imaging with $MB_{Selectin}$ allows non-invasive quantification of P- and E-selectin expression in a chemically-induced murine colitis model. US molecular imaging correlates well with FDG-PET uptake. Since US is widely available, relatively inexpensive, and radiation-free, US molecular imaging is a promising new, clinically-translatable approach for objective quantification in IBD.

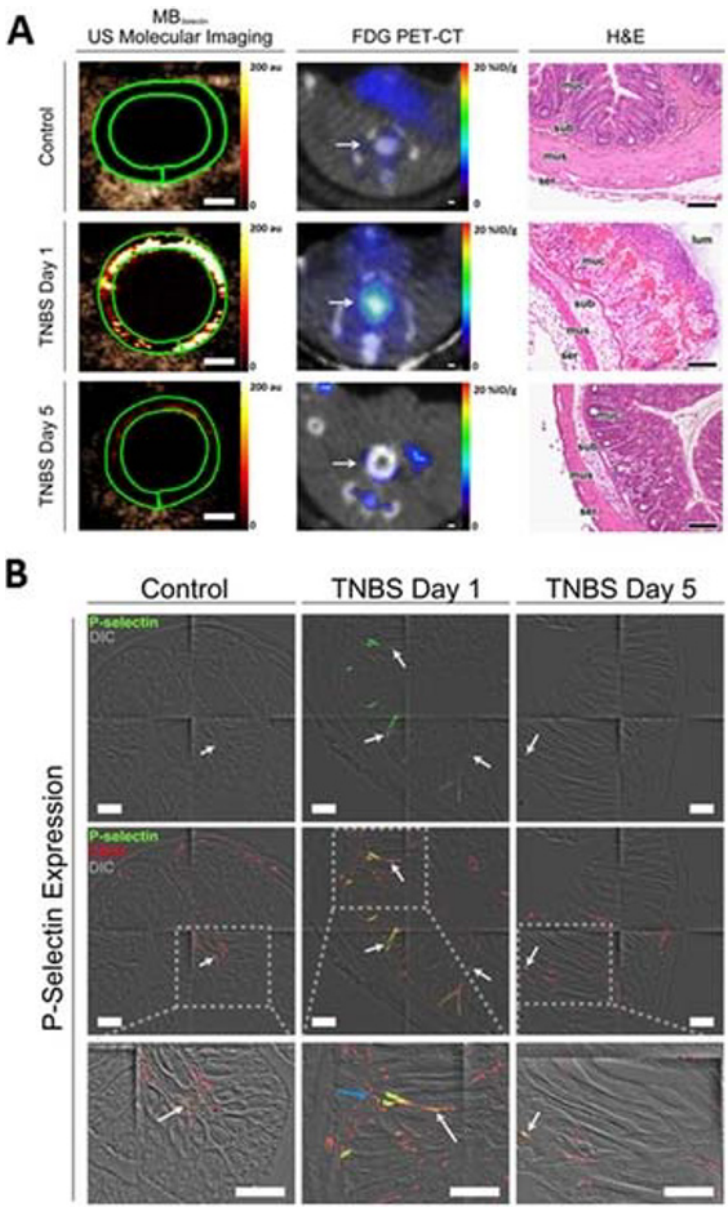

Disclosure of author financial interest or relationships:
H. Wang, None; **S. Machtaler**, None; **T. Bettinger**, Bracco Suisse SA, Employment; **A.M. Lutz**, None; **R. Luong**, None; **P. Bussat**, Bracco Suisse SA, Employment; **S.S. Gambhir**, Bracco Diagnostics, Consultant; Endra, Inc, Stockholder; Cellsight, Stockholder; Enlight, Inc., Stockholder; General Electric, Grant/research support; ImaginAb, Stockholder; MagArray, Inc., Stockholder; Sanofi-Aventis, US, Grant/research support; SiteOne Therapeutics, Stockholder; VisualSonics/Sonosite, Stockholder; **F. Tranquart**, Bracco Suisse SA, Employment; **L. Tian**, None; **J.K. Willmann**, Bracco, Consultant; Siemens, Grant/research support; Bracco, Grant/research support .

Presentation Number **SS 57**
Scientific Session 10: Chemistry & Imaging Probes, Technology & Software Developments - Ultrasound
September 20, 2013 / 11:00-11:15 / Room: 105

Multimodal detection of iron oxide nanoparticles in rat lymph nodes using Magnetomotive ultrasound imaging and Magnetic Resonance Imaging

Maria Evertsson[1], Magnus Cinthio[1], Pontus Kjellman[2,3], Rene in 't Zandt[2,4], Sarah Fredriksson[2], Fredrik Olsson[2], Hans W. Persson[1], **Tomas Jansson**[1], *[1]Electrical Measurements, Faculty of Engineering, Lund University, Lund, Sweden; [2]Genovis AB, Lund, Sweden; [3]Medical Radiation Physics IKVL, Lund University, Lund, Sweden; [4]Lund University BioImaging Center, Lund University, Lund, Sweden. Contact e-mail: tomas.jansson@med.lu.se*

Breast cancer and malignant melanoma spread mainly through the lymphatic system. If the cancer has spread it is most likely to find metastases in the sentinel lymph node (SLN), the first lymph node draining the tumor. In this study we aim to detect multimodal superparamagnetic iron oxide nanoparticles (SPIO-NP) in rat SLNs using both the new imaging technique magnetomotive ultrasound imaging (MMUS) and magnetic resonance imaging (MRI) (MMUS in situ, MRI in vivo). In MMUS a time-varying external magnetic field acts to move the NPs and, thus, the NP-laden tissue. This movement can be detected by proper processing of ultrasound data. Recently we developed a frequency and phase gated algorithm which efficiently reduce motion artifacts. The algorithm has shown promising results in phantom studies (IEEE Trans UFFC 2013, pp 481-491), but has not yet been verified in animals. If presence of adequate signal can be established in an animal model, there is a potential for MMUS to be used as a bed-side surgical guide, imaging the very same particles that were used in prior staging with other imaging techniques. Seven Wistar rats were subcutaneously injected with 100µL NP solution in their right hind paw, four with 31nm NPs and three with 67 nm NPs. Further, the injections were given as a low or a high concentration (0.3 and 3 mg iron /mL respectively). Only one animal received the low concentration 67nm NPs. 24 hours post injection the animals were anaesthesized and full body MR scans were acquired (2.4T Bruker Avance II system, 3D gradient echo, TE 6 ms, TR 27 ms). The rats were then sacrificed and imaged with a high frequency ultrasound scanner (Visualsonics VEVO 2100). Each rat was positioned between the transducer (center frequency 21 MHz) and a solenoid with a cone shaped iron core, imaging the popliteal lymph node, proximal to the injection site. The solenoid was excited with various voltages (10, 20, 30Vpp) and frequencies (5-15Hz, in steps of 2.5Hz). Acquired ultrasound data was analyzed offline. Fig.1A shows a T2* weighted MR image of a rat injected with 100µl 0.3mg/mL solution of 31nm NPs. SPIO-NP accumulation can be seen in the SLN in the right knee (arrow) due to lack of signal. Fig. 1B shows a B-mode ultrasound image of the SLN and Fig. 1C a MMUS image of the same area. Color represents magneto-motive displacement coded according to the color bar. The displacement is in the same order as in previous phantom studies. In the MMUS-images a tendency of decreasing displacement with increasing solenoid excitation frequency was found, as well as an increased displacement with increasing excitation voltage. The MR-images were affected to a higher degree, and the MMUS images showed a larger displacement, for both higher NP-concentration, and smaller NPs. We have established magnetic excitation parameters for successful MMUS imaging in a preclinical SLN model. Further, the results show that MMUS has potential as a stand-alone modality for other imaging applications, besides from SLN, such as stem cell tracking and cardiovascular research.

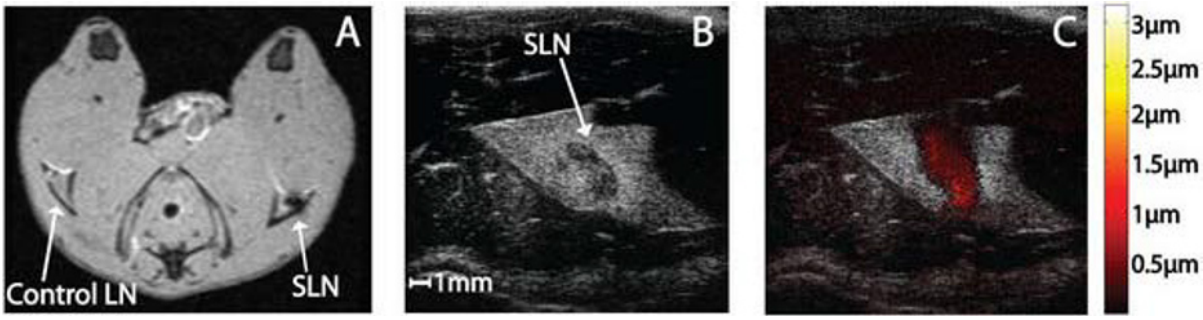

Disclosure of author financial interest or relationships:
M. Evertsson, Genovis AB, Other financial or material support; **M. Cinthio**, None; **P. Kjellman**, Genovis AB, Employment; **R. in 't Zandt**, Genovis AB, Employment; Genovis AB, Stockholder; **S. Fredriksson**, Genovis AB, Employment; **F. Olsson**, None; **H.W. Persson**, None; **T. Jansson**, None.

Presentation Number **SS 58**
Scientific Session 10: Chemistry & Imaging Probes, Technology & Software Developments - Ultrasound
September 20, 2013 / 11:15-11:30 / Room: 105

Ultrasound molecular imaging of the vascular activation marker Thy1 for the detection of pancreatic ductal adenocarcinoma in an orthotopic murine xenograft model

Steven Machtaler[1], *Kira Foygel*[1], *Huaijun Wang*[1], *Amelie M. Lutz*[1], *Ru Chen*[2], *Marybeth A. Pysz*[1], *Teresa Brentnall*[2], *Juergen K. Willmann*[1], [1]*Radiology, Stanford, Stanford, CA, USA;* [2]*Gastroenterology, Universityof Washington, Seattle, WA, USA. Contact e-mail: smachtal@stanford.edu*

Introduction Pancreatic ductal adenocarcinoma (PDAC) is the fourth leading cause of cancer related death in the USA with 43,920 new diagnoses and 37,390 deaths in 2012. Most often, PDAC is detected at advanced stages with a median survival of less than one year and only 5% of patients survive five years after the initial diagnosis. Therefore, earlier detection of PDAC offers our best hope to improve patient survival. Ultrasound (US) molecular imaging utilizes micron-sized, gas-filled contrast agents (microbubbles; MBs) that are modified to bind to vascular markers that are up-regulated due to disease or active biological processes. Here we describe the identification of a vascular tumor marker (Thy1/CD90) in human PDAC and assess the feasibility of using ultrasound molecular imaging directed against human Thy1 (hThy1) to detect pancreatic tumors in an orthotopic murine xenograft model. Methods Proteomic analysis was performed on whole tissues from patients with PDAC (n=5), chronic pancreatitis (n=5), and normal pancreas (n=10) using a LTQ-Orbitrap hybrid mass spectrometer coupled with a nano-flow HPLC. Out of a total of 118 proteins whose expression was increased by a factor of 2.0 or more in PDAC, hThy1 was chosen based on its vascular expression. Expression of Thy1 in human PDAC vasculature was verified by IHC of pancreatic tissue obtained from 4 normal patients; 15 primary chronic pancreatitis tissues; 21 PDAC patients; and in a commercial tissue microarray with 24 normal pancreatic tissues and 175 PDAC tissues. An orthotopic murine xenograft model was created to assess hThy1-specific in vivo MB binding. Orthotopic xenografts containing murine vascular endothelial (MS1) cells stably expressing human Thy1 and human AsPC1 PDAC cells were co-injected into the tail of the pancreas. In all PDAC xenografts, intra-animal comparisons of ultrasound imaging signals were performed following injection of bothMBThy1 and MBControl in a randomized order during the same imaging session using a VEVO2100 US system. Results IHC analysis verified the mass spectrometer data showing that the expression of hThy1 was significantly increased in the PDAC patients (score: 2.1±0.1, 81% of PDAC tumors were Thy1-positive) and was localized to the tumor vasculature (Figure 1A). Human Thy1 staining signal was minimal in normal tissue (score: 0.5±0.1; $P<0.0001$; 11% positive) and primary chronic pancreatitis (score: 0.6±0.15; $P=0.007$; 7% positive). In vivo binding of MBThy1 to hThy1 expressing orthotopic PDAC xenografts was assessed using US molecular imaging (Figure 1B). A targeted signal using MBThy1 of 7.7±2.3 au was observed in hThy1 expressing PDAC xenografts compared to 1.9±1.8 in control tumors and 1.4±2.2 using non-targeted MBs (Figure 1C). Conclusion These results illustrate the development of a translational US MB directed against a vascular tumor marker identified from screens of human PDAC and the development of a novel, orthotopic human PDAC model in mice that expresses hThy1 within the tumor vascular compartment, which may eventually aid in earlier detection of PDAC.

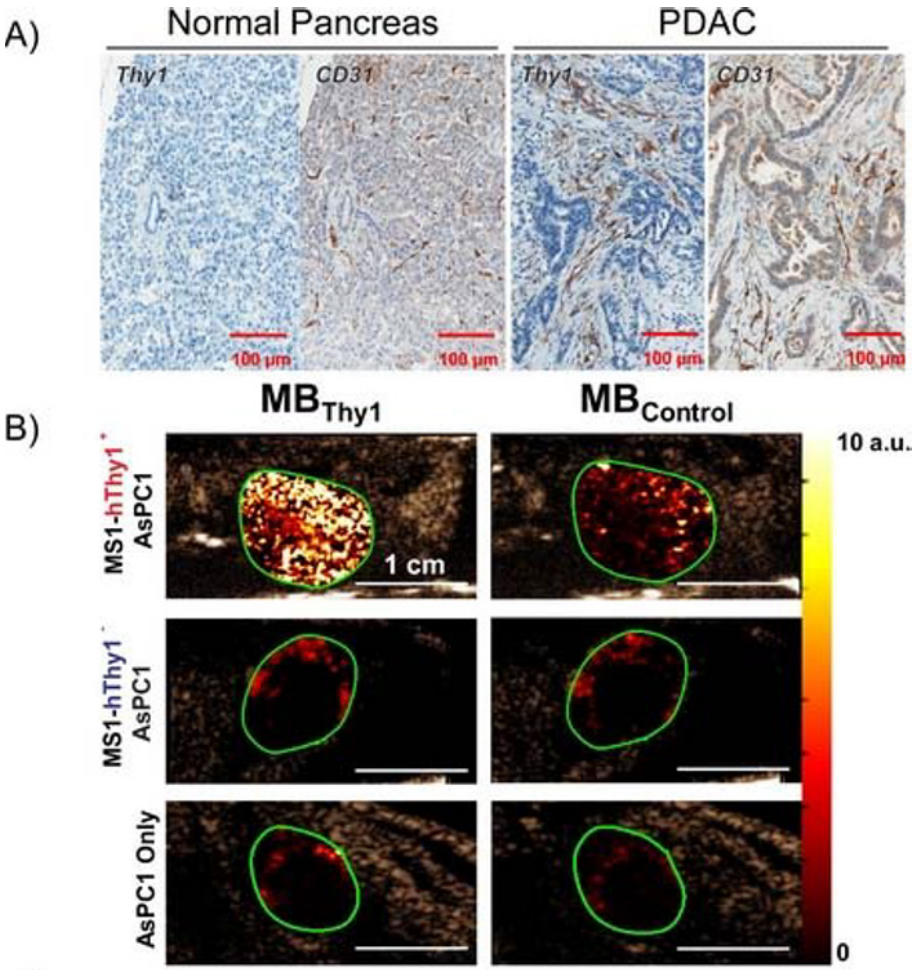

C)

	MB_{Thy1} signal (a.u.)	$MB_{Control}$ signal (a.u.)	P (MB_{Thy1} vs. $MB_{Control}$)
human Thy1 positive tumors (n=25)	7.7 ± 2.3	1.4 ± 2.2	<0.001
human Thy1 negative tumors (n=7)	1.9 ± 1.8	1.9 ± 1.7	1.0
AsPC1 control tumors (n=7)	1.7 ± 1.6	1.4 ± 0.6	0.68
Adjacent normal pancreas tissue (n=39)	1.7 ± 1.6	1.6 ± 2.2	0.37

Figure 1 Utilizing hThy1 as a vascular tumor marker for PDAC. A) IHC analysis of hThy1 expression within the vasculature (CD31) in normal pancreatic tissue and PDAC. B) US molecular images obtained using MB targeted to hThy1 (MBThy1, left pannels) or untargeted (MBControl, right pannels) in the murine PDAC orthotopic xenograft model. Top panel: Tumor consists of MS1 cells expressing human Thy1 with AsPC1 PDAC cells; Middle panel: Tumor consists of untransfected MS1 cells and AsPC1 cells; Bottom panel: Tumor consists of AsPC1 cells alone. C) Summary of US molecular imaging signals obtained in the murine PDAC orthotopic xenograft model.

Disclosure of author financial interest or relationships:

S. Machtaler, None; **K. Foygel**, None; **H. Wang**, None; **A.M. Lutz**, None; **R. Chen**, None; **M.A. Pysz**, None; **T. Brentnall**, None; **J.K. Willmann**, Bracco, Consultant; Siemens, Grant/research support; Bracco, Grant/research support .

Presentation Number **SS 59**
Scientific Session 10: Chemistry & Imaging Probes, Technology & Software Developments - Ultrasound
September 20, 2013 / 11:30-11:45 / Room: 105

Early Pancreatic Cancer Detection with VEGFR2-Targeted Ultrasonic Molecular Imaging

Steven Machtaler[1], *Marybeth A. Pysz*[1], *E. Scott Seeley*[3], *Francois Tranquart*[5], *Lu Tian*[4], *Teresa Brentnall*[2], *Juergen K. Willmann*[1], [1]*Radiology, Stanford, Stanford, CA, USA;* [2]*Gastroenterology, Universityof Washington, Seattle, WA, USA;* [3]*Pathology, UCSF, San Francisco, CA, USA;* [4]*Department of Health, Research & Policy, Stanford, Stanford, CA, USA;* [5]*Bracco Imaging, Bracco Suisse SA, Geneva, Switzerland. Contact e-mail: smachtal@stanford.edu*

Introduction Pancreatic ductal adenocarcinoma (PDAC) is the fourth leading cause of cancer-related death, with an average 5 year survival rate of 5%. Over 90% of diagnosed patients have non-resectable advanced disease (median survival, 4 to 6 months), and more than 65% of patients who had undergone surgery for removal of localized PDAC, will develop disease recurrence within 2 years post-surgery. Several studies have shown that long-term survival following PDAC resection increases with decreasing tumor size, with a 5-year survival time of more than 75% when the primary tumor is diagnosed with a diameter of less than 1 cm. Therefore, the development of a screening/surveillance approach for early pancreatic cancer detection holds promise for improving the patient outcome. Our approach for identifying these small tumors is to target vascular endothelial proteins from the developing blood vessels within the tumor. Once a developing tumor reaches a size of 1-2 mm, it becomes hypoxic and triggers the recruitment of new blood vessels though a process known as angiogenesis. The activation of this "angiogeneic switch" results in the expression of the growth factor receptor VEGFR2 on the luminal surface of the new blood vessels. The aim of this study was to develop and test an ultrasound (US) molecular imaging strategy which utilizes VEGFR2-targeted contrast microbubbles (VEGFR2-MB) for the identification of small pancreatic cancer in transgenic mice. Materials and Methods Transgenic mice (Pdx1-Cre; KRasV12G; Ink4a-/-) that spontaneously develop pancreatic cancer from age 4 weeks on were imaged using a dedicated small animal US system (21 MHz; Vevo2100; VisualSonics), following intravenous injection (dose: 5x107 MBs) of clinical grade VEGFR2-MB (BR55, Bracco Research) (Figure 1A). The pancreas in age-matched, wildtype littermates were scanned as controls. Pancreas tissues were analyzed ex vivo by histology (H&E staining) and immunostaining of CD31 (vascular endothelial cell marker) and VEGFR2. Results Ninety-five tumors (mean diameter: 2.7 ± 1.5 mm; range: 0.7 to 7.4 mm) were identified across the entire pancreas in 46 mice using B-mode US and later confirmed by histology. VEGFR2-targeted US signal intensity was significantly higher in small pancreatic tumors (4.1-fold higher; VEGFR2-US signal intensity: 6.0 ± 8.9 l.a.u.; range: 0 to 57.4 l.a.u; $P < 0.0001$) (Figure 1B) compared with VEGFR2-targeted signal intensity in normal pancreata of WT mice (VEGFR2-US signal intensity: 1.5 ± 1.4 l.a.u.; range: 0 to 4.5 l.a.u). Ex vivo immunostaining confirmed the expression of VEGFR2 on pancreatic tumor vessels (Figure 1C) and blood vessels in normal pancreas tissue as being VEGFR2-negative. Conclusions VEGFR2 expression in the developing vessels of early stage pancreatic cancer in transgenic mice results in a strong ultrasound molecular imaging signal compared to normal pancreatic tissue using VEGFR2-targeted MBs. These results suggest that ultrasound molecular imaging using VEGFR2-targeted MBs may be a useful imaging strategy for the identification of small pancreatic lesions.

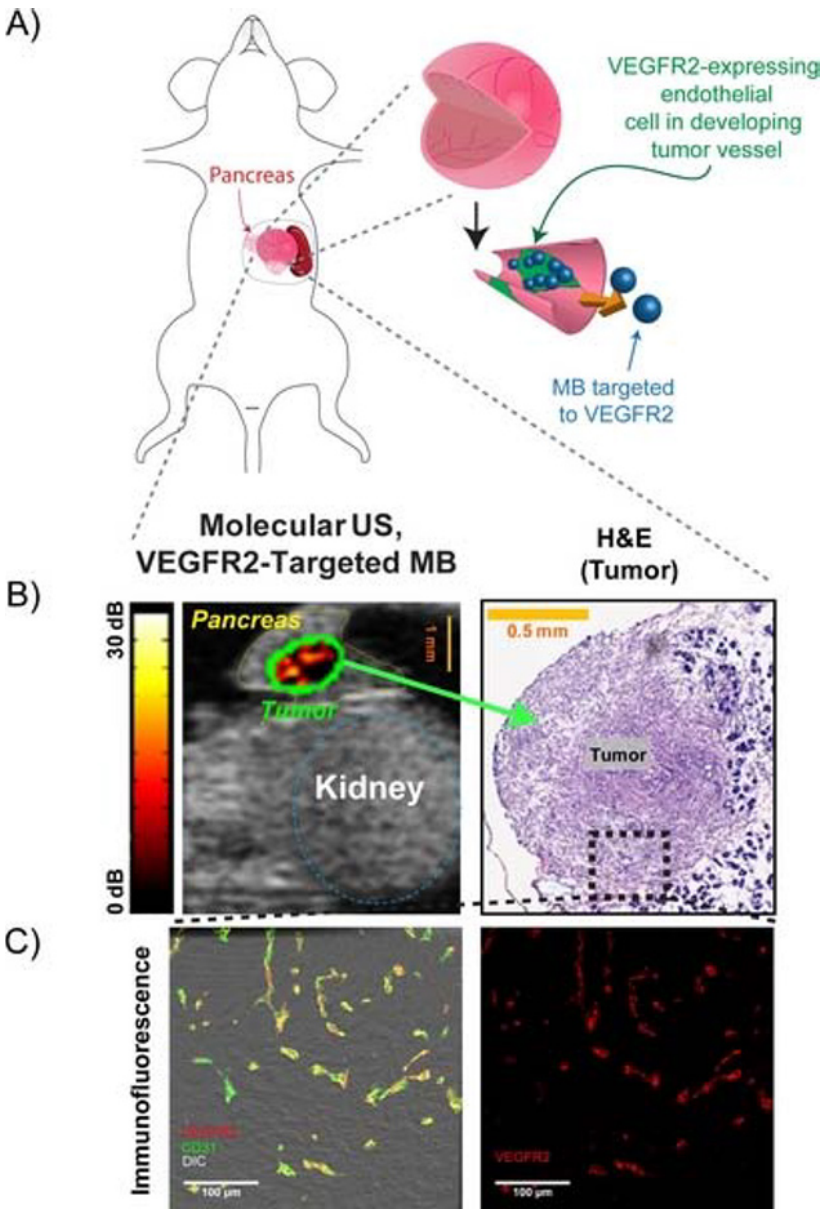

Figure 1 US molecular imaging of VEGFR2 in small pancreatic tumors. A) Overview of US molecular imaging strategy targeting VEGFR2 in developing vessels. B) US molecular imaging signal from a small pancreatic tumor (green ROI: left pannel) with accompanying histology (right panel). C) Validation of VEGFR2 expression (RED) within the tumor vessels (CD31:GREEN).

Disclosure of author financial interest or relationships:
S. Machtaler, None; **M.A. Pysz**, None; **E. Seeley**, None; **F. Tranquart**, Bracco Suisse SA, Employment; **L. Tian**, None; **T. Brentnall**, None; **J.K. Willmann**, Bracco, Consultant; Siemens, Grant/research support; Bracco, Grant/research support .

Presentation Number **SS 60**
Scientific Session 10: Chemistry & Imaging Probes, Technology & Software Developments - Ultrasound
September 20, 2013 / 11:45-12:00 / Room: 105

Peptide-Decorated Targeted Microbubbles for Ultrasound Molecular Imaging of VCAM-1 on Tumor Vascular Endothelium

Zhongmin Du, Galina B. Diakova, Sunil Unnikrishnan, **Alexander L. Klibanov***, Dept. of Medicine, Cardiovascular Div., University of Virginia, Charlottesville, VA, USA. Contact e-mail: sklib1@gmail.com*

VCAM-1 is a biomarker expressed on the surface of vascular endothelium in malignant tumors. Antibodies and nanobodies against VCAM-1 have been previously attached to microbubble shell, using avidin-biotin coupling scheme. Those targeted microbubble ultrasound molecular imaging preparations have been successfully tested in vitro and in murine models and described in the literature. To improve translatability of VCAM-1-targeted microbubbles and to simplify microbubble preparation, we formulated a targeted microbubble decorated with a previously described VCAM-1-binding peptide, VHPKQHRGGSKGC. Peptide was covalently conjugated to maleimide-PEG3400-DSPE lipid anchor via a C-terminal cysteine thiol and an extended PEG spacer arm, in a micellar aqueous phase under argon. Peptide-PEG-DSPE micelles were purified from excess free peptide by dialysis and lyophilized. To aid peptide quantification, lysine closest to C-terminus carried fluorescein. Microbubbles were prepared by a high-shear amalgamation mixing procedure in a sealed vial containing decafluorobutane gas headspace, and an aqueous phase containing normal saline and propylene glycol. Shell was stabilized with DSPC, PEG stearate and peptide-PEG-DSPE (1:1.1:0.2 mass ratio). Control bubbles were prepared with carboxy-PEG-DSPE instead of the peptide derivative. High yield of microbubble preparation was observed (>10^9/ml). Microbubbles were purified from unincorporated peptide conjugate and lipids by centrifugal flotation. Mean particle size was ~1.8 um (Coulter); over 99% of the bubbles were less than 4 um in diameter (volume distribution). Targeted microbubbles were carrying fluorescein-labeled peptide, as confirmed by fluorescence microscopy. Fluorescence spectroscopy of the infranatant following centrifugation determined that ~85% of the added peptide-anchor conjugate was associated with microbubbles; with this high coupling yield there is no need to remove unincorporated peptide from microbubbles. In vitro targeting tests with murine VCAM-1 fusion protein adsorbed onto polystyrene dish confirmed selective binding of targeted bubbles to the receptor, yet minimal adhesion to control albumin-only coated polystyrene dish surface. Following intravenous bolus of targeted or control microbubbles (2.10^7 particles per animal) to C57BL/6 mice (n=6) that carried subcutaneous MC38 tumor in the hind leg (generous gift of J. Schlom, NIH), enhanced accumulation of peptide-carrying but not control microbubbles in the tumor vasculature was observed by contrast ultrasound imaging (Siemens Sequoia, 15L8 probe, CPS mode) 10 min after injection, $p<0.0001$. At the 10 min time point, most of the circulating bubbles cleared from the bloodstream. Retention of targeted microbubbles in non-tumor tissue (contralateral hind leg muscle) was minimal, as compared with tumor ($p<0.0002$). In conclusion, we describe a simple peptide-based microbubble formulation for VCAM-1 targeting, suitable for clinical translation in the ultrasound molecular imaging setting. This approach paves the way for simplified preparation of translatable microbubble formulations with a wide variety of ligands suitable for clinical testing.

Disclosure of author financial interest or relationships:
Z. Du, None; **G.B. Diakova**, None; **S. Unnikrishnan**, None; **A.L. Klibanov**, Philips Research North America, Grant/research support; Targeson (NIH SBIR subcontract), Grant/research support; Targeson, Stockholder; AstraZeneca, Grant/research support .

Presentation Number **SS 61**
Scientific Session 11: Chemistry & Imaging Probes - Nuclear Imaging
September 20, 2013 / 10:30-10:45 / Room: 200

Novel fully human anti-MET cys-diabodies for in vivo PET imaging and therapy of non-small cell lung cancer

Keyu Li[1,2], *Richard Tavaré*[1,2], *Kirstin A. Zettlitz*[1,2], *Scott M. Knowles*[1,2], *Matthew Rochefort*[3], *Felix B. Salazar*[1,2], *Anna M. Wu*[1,2], *[1]Molecular and Medical Pharmacology, UCLA, Los Angeles, CA, USA; [2]Crump Institute for Molecular Imaging, UCLA, Los Angeles, CA, USA; [3]Department of Surgery, UCLA, Los Angeles, CA, USA. Contact e-mail: keyuli@mednet.ucla.edu*

MET, the receptor of hepatocyte growth factor, plays important role in embryogenesis, mesenchymal-epithelial interaction, and also tumorgenesis. Numerous cancers have been found to be associated with MET activation or over expression, and in non-small cell lung cancer, MET over expression is found to be an important mechanism for acquired resistance for anti-EGFR therapies, such as gefitinib and erlotinib. Recently, more and more MET inhibitors have shown therapeutic effects in multiple clinical trials. Therefore, a convenient method to quantify in vivo MET expression level is of great value for drug response evaluation and patient stratification. Here we report a study of in vivo PET imaging using fully human MET antibodies from a phage display library. Several anti-MET human scFvs were isolated from a human phage display library, and binding to cell surface target was confirmed by flow cytometry. Candidate scFvs were re-formatted into cys-diabodies (disulfide-linked covalent dimers of scFvs) and expressed by secretion from TG1 bacteria. Three clones, C2, H2 and H5, demonstrated high affinities to cell surface MET protein by flow cytometry, ranging from 0.6nM to 9nM. In vitro cell growth inhibition assays show inhibitory effects of H2 and H5 cys-diabodies on gefitinib resistant Hcc827 lines with MET amplification, while no effects were observed on other resistant lines lacking MET overexpression (H1975 and H1650). The H2 cys-diabody, with the highest affinity and cross-reactivity to mouse MET, was chosen for in vivo PET imaging studes. The resistant non-small cell lung cancer line, Hcc827-GR6 (~2.6 x 10^5 MET receptors per cell), and the sensitive parental line (~6.7 x 10^4 MET receptors per cell), were injected into immune-compromised mice to form subcutaneous tumors, and rat C6 glioma xenografts served as negative controls. H2 cys-diabody was site-specifically conjugated with deferoxamine-maleimide, and then radio labeled with Zr-89. PET scans were acquired at 4 hours and 20 hours post injection, and showed specific targeting to both the resistant and parental Hcc827 tumors. Biodistribution studies 20 hours post injection showed significant differences between uptake in the resistant vs parental tumors (n=4, P=0.0013; 1.8±0.2 %ID/gram uptake for Hcc827-GR6 tumors, and 1.1±0.1 %ID/gram uptake for Hcc827 tumor). In conclusion, these novel fully human anti-MET cys-diabodies not only show inhibitory effects on MET over-expressing cells, but also enable rapid in vivo PET imaging of subcutaneous xenografts. The significant difference between the uptakes of resistant and sensitive tumors indicates potential for drug response evaluation and patient stratification.

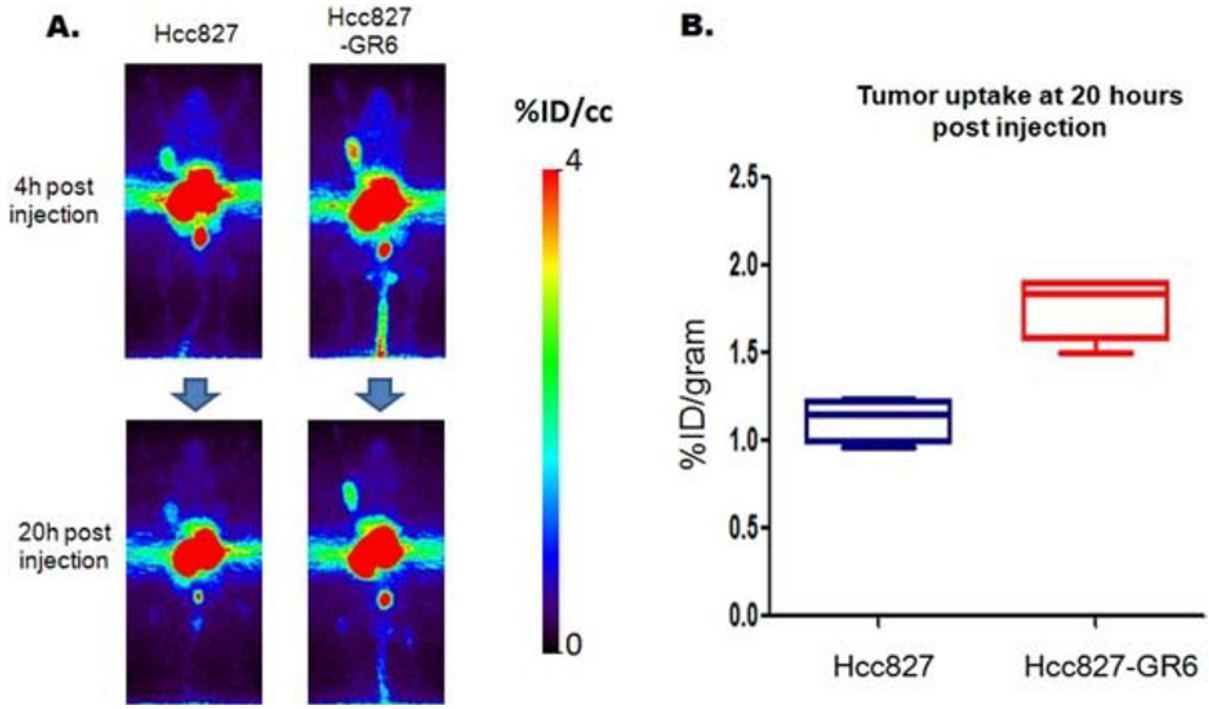

A. SCID mice were injected with either MET positive Hcc827 parental cells or Hcc827-GR6 resistant cells to the left shoulders, and C6 cells to the right shoulders as negative controls. Zr-89 labeled anti-MET H2 cys-diabody were injected through tail vein. Here shows two SCID mice with similar-sized MET positive tumors (Hcc827: 212mg; Hcc827-GR6: 262mg) scanned at 4 hours and 20 hours post injection. B. Ex vivo biodistribution study shows significant difference in tumor uptake for Hcc827 and Hcc827-GR6 (n=4, P=0.0013). The difference in tumor uptake level (Hcc827: 1.1±0.1 %ID/gram; Hcc827-GR6: 1.8±0.2 %ID/gram) agrees with the difference in MET expression level (Hcc827: 6.7 x 10^4; Hcc827-GR6: 2.6 x 10^5).

Disclosure of author financial interest or relationships:
K. Li, None; **R. Tavaré**, None; **K.A. Zettlitz**, None; **S.M. Knowles**, None; **M. Rochefort**, None; **F.B. Salazar**, None; **A.M. Wu**, ImaginAb, Inc., Stockholder; ImaginAb, Inc., Consultant; ImaginAb, Inc., Grant/research support; Daiichi Sankyo, Consultant; Sanofi, Consultant .

Presentation Number **SS 62**
Scientific Session 11: Chemistry & Imaging Probes - Nuclear Imaging
September 20, 2013 / 10:45-11:00 / Room: 200

PET imaging of integrin αvβ6 overexpression in a mouse model of cancer using novel ^{64}Cu-DOTA-cystine knot miniproteins: Modulating radiotracer pharmacokinetics by site-directed evolution

Richard Kimura[1,2], *Hongguang Liu*[1,2], *Zheng Miao*[1], *Bin Shen*[1], *Ananth Srinivasan*[1,2], *Frederick T. Chin*[1,2], *Zhen Cheng*[1,2], *Sanjiv S. Gambhir*[1,2], [1]*Radiology/Molecular Imaging Program at Stanford (MIPS), Stanford University, Palo Alto, CA, USA;*
[2]*Radiology/Canary Center for Early Cancer Detection, Stanford University, Palo Alto, CA, USA. Contact e-mail: rkimura1@stanford.edu*

Background: Integrin αvβ6 overexpression is a diagnostic hallmark of many cancers (lung, pancreas, epidermis, etc.). Using site-directed evolution, a small library of high-affinity cystine knot based positron emission tomography (PET) radiotracers were developed to image integrin αvβ6 *in vivo*. Cystine knot miniproteins (~4kDa) are characterized by a highly stabilized core structure of 3 interwoven disulfide bonds. Here, ^{64}Cu-DOTA-cystine knots were evaluated in mice bearing integrin αvβ6-positive A431 tumors. Methods: Yeast surface display and fluorescent activated cell sorting were used to engineer targeted cystine knot miniproteins with pharmacokinetics optimized for PET imaging. Binders were coupled to DOTA and labeled with Cu-64. Mice were imaged at 1, 2, 4 and 24 hours post injection (h, p.i.). At 24h p.i., excised tissues provided broader biodistribution profile, so that the effect of site-directed evolution on radiotracer uptake in tissues was quantified *in vivo*. Results: Three binders with single-digit nanomolar binding affinities (K_D~1nM) were evaluated *in vivo*. ^{64}Cu-DOTA-$R_0$1-MΔR demonstrated highest uptake in tumor tissue (~3.5%ID/g 1-24h, n=3) compared to ^{64}Cu-DOTA-$R_0$1-MΔG, and ^{64}Cu-DOTA-$R_0$1 (both ~2.5%ID/g, 1-24h, n=3 each) each differing by a single amino acid substitution at a specified position of the active loop-1. However, uptake of ^{64}Cu-DOTA-$R_0$1-MΔR was also higher in all normal tissues studied. For example, during 1-24h p.i., kidney uptake for ^{64}Cu-DOTA-$R_0$1-MΔR was ~180%ID/g to ~80%ID/g, but approximately 1/3 of those levels were observed for both ^{64}Cu-DOTA-$R_0$1 and ^{64}Cu-DOTA-$R_0$1-MΔG. Tumor-to-muscle contrast ratios were approximately 8:1 for all binders at all time points. Currently, different MΔR derivatives are undergoing further testing and lead development. Conclusion: ^{64}Cu-DOTA-R_0 1-MΔR produces excellent PET images for all time points. High-quality PET images at earlier time points open the possibility for shorter-lived radionuclides such as fluorine-18. Labeling and evaluation of $R_0$1-MΔR with F-18 groups, ^{18}F-fluoropropyl- and ^{18}F-AlF-NOTA-, are in progress.

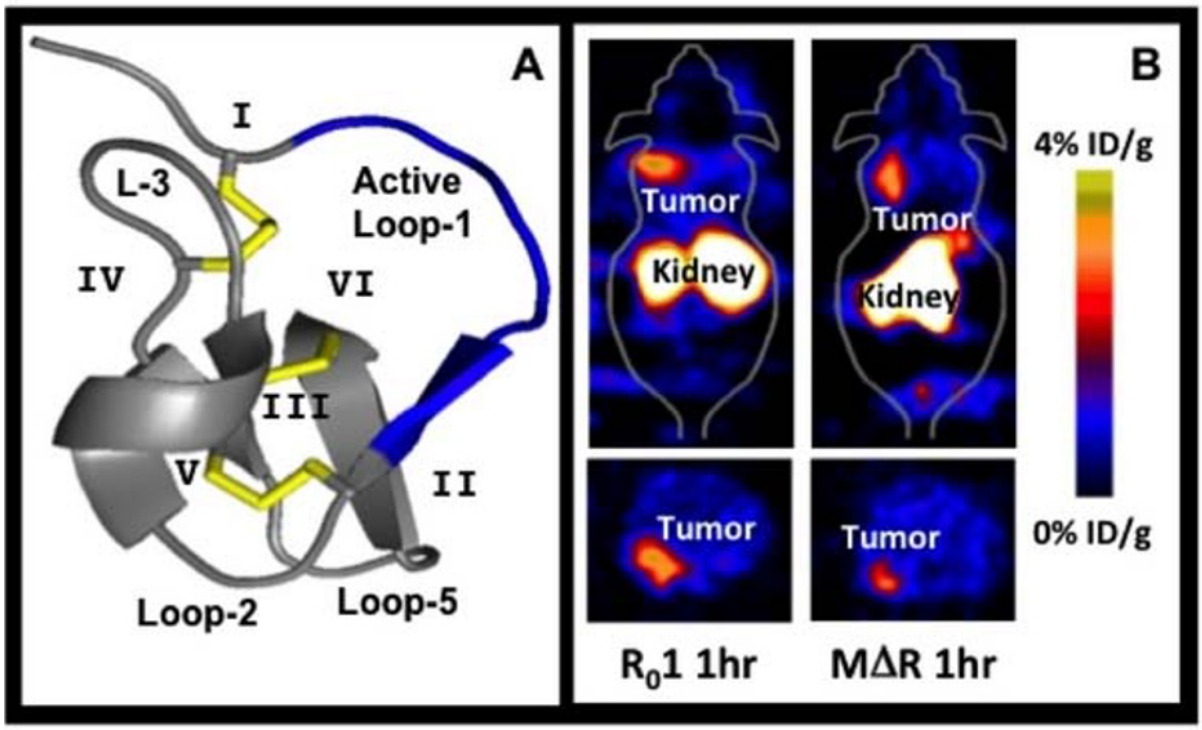

Figure 1. (A) Structure of cystine knot miniprotein. Cysteines are numbered I-VI, and the three interwoven or knotted disulfide bonds are show in yellow. Loop-1, shown in blue, was engineered to bind integrin αvβ6 with single digit nanomolar affinity. (B) PET images taken one hour after administration of ^{64}Cu-DOTA-$R_0$1 and ^{64}Cu-DOTA-$R_0$1-MΔR in mice bearing A431 xenografts clearly demonstrates excellent tumor-to-normal contrast.

Disclosure of author financial interest or relationships:
R. Kimura, None; **H. Liu**, None; **Z. Miao**, None; **B. Shen**, None; **A. Srinivasan**, None; **F.T. Chin**, Ground Fluor Pharmaceuticals, Consultant; **Z. Cheng**, None; **S.S. Gambhir**, Bracco Diagnostics, Consultant; Endra, Inc, Stockholder; Cellsight, Stockholder; Enlight, Inc., Stockholder; General Electric, Grant/research support; ImaginAb, Stockholder; MagArray, Inc., Stockholder; Sanofi-Aventis, US, Grant/research support; SiteOne Therapeutics, Stockholder; VisualSonics/Sonosite, Stockholder .

Presentation Number **SS 63**
Scientific Session 11: Chemistry & Imaging Probes - Nuclear Imaging
September 20, 2013 / 11:00-11:15 / Room: 200

Pycup - a new bifunctional cage-like chelate for coordination of Cu radioisotopes

Eszter Boros, *Peter Caravan, Radiology, Massachusetts General Hospital/ Harvard Medical School, Charlestown, MA, USA. Contact e-mail: eboros@nmr.mgh.harvard.edu*

Cu-64 has gathered great interest over the past decade for PET imaging of peptides and antibodies due to its favorable emission characteristics such as a suitable half-life of 12.7 hours and emission of a low energy positron similar to F-18. One of the great challenges for employing Cu-64 for targeted imaging is in overcoming the high lability of the Cu(II) ion. In the body, Cu(II) rapidly undergoes ligand exchange, even when complexed with ligands that form chelates with very high thermodynamic stability. Macrocyclic, cross-bridged (CB-TE2A) or cage-like (SarAr) complexes provide high thermodynamic stability, and importantly, high kinetic inertness with respect to dissociation (1). These ligands, however, are synthesized using low-yielding, multi-step procedures, which can limit donor atom versatility, and subsequently labeling conditions. Here we describe the macrobicyclic ligand system pycup and its corresponding derivatives as alternative bifunctional Cu-64 chelators. The Cu-64 complex of the non-derivatized di-acetato derivative showed rapid clearance from all organs including only 0.04 % ID/g activity in the blood after 2h in mice. A bifunctional version of this ligand (pycup1A1R) was also synthesized and successfully conjugated to a fibrin-targeted peptide for thrombus imaging. We will describe the labeling conditions, inertness, and biodistribution of these Cu-64 derivatives and their application in imaging of models of thromboembolic disease. Reference: (1) Wadas TJ, Wong EH, Weisman GR, Anderson CJ. Coordinating Radiometals of Copper, Gallium, Indium, Yttrium, and Zirconium for PET and SPECT Imaging of Disease. Chem Rev. 2010;110(5):2858-902.

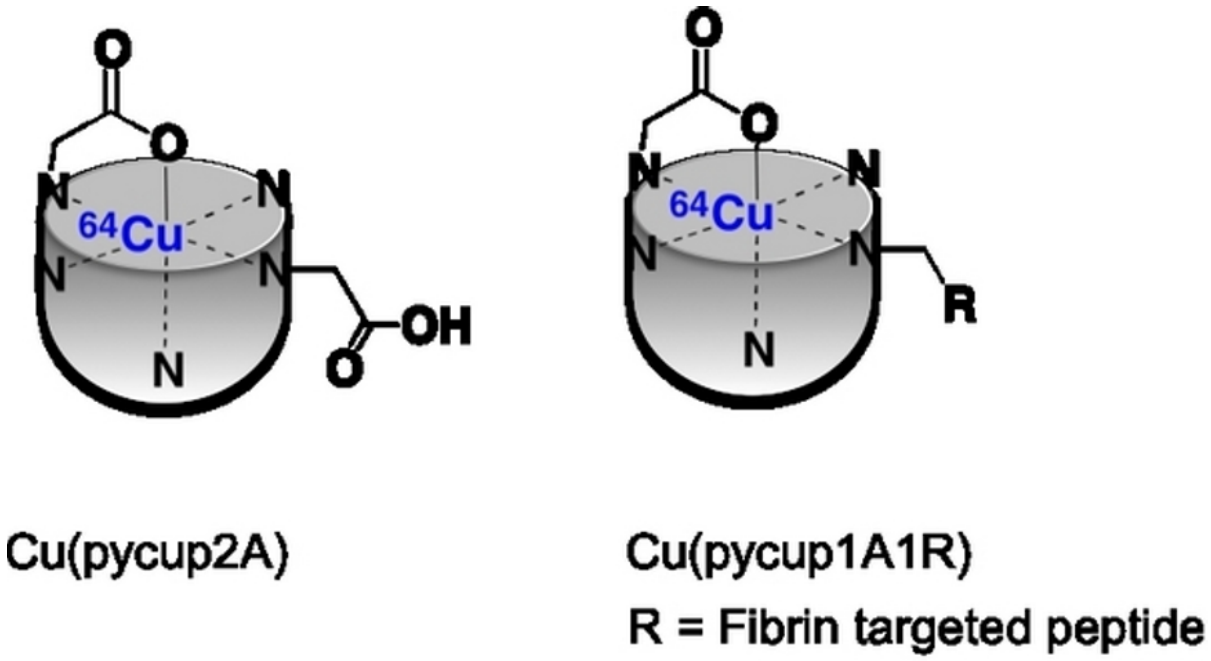

Disclosure of author financial interest or relationships:
E. Boros, None; **P. Caravan**, Sanofi, Grant/research support; Biogen Idec, Consultant; Factor 1A, Stockholder; Collagen Medical, Stockholder .

Presentation Number **SS 64**
Scientific Session 11: Chemistry & Imaging Probes - Nuclear Imaging
September 20, 2013 / 11:15-11:30 / Room: 200

Molecular imaging of breast cancer by targeting tumor angiogenesis

Tiemen R. van Mourik[1], *Tilman Läppchen*[2], *Raffaella Rossin*[2], *Klaas Nicolay*[1], *Holger Gruell*[1,2], [1]*Biomedical Engineering, Eindhoven University of Technology, Eindhoven, Netherlands;* [2]*Minimally Invasive Healthcare, Philips Research, Eindhoven, Netherlands. Contact e-mail: T.R.Mourik@tue.nl*

Introduction Angiogenesis, the formation of new blood vessels, is a hallmark of cancer and results in the overexpression of angiogenic markers. These markers are targets for therapy and diagnosis, e.g. with SPECT and PET. A suitable target is the angiogenic factor galectin-1, which is overexpressed on the membranes of tumor cells and activated endothelial cells. Anginex is a synthetic, beta-sheet forming peptide that acts as a cytokine to inhibit angiogenesis via binding to galectin-1. Aim of this project is to develop new imaging tracers to visualize tumor angiogenesis non-invasively using SPECT and PET. Methods DOTA-conjugated Anginex and the control βpep28 (Mayo, Angiogenesis 2001) were synthesized with solid phase techniques and radiolabeled with Indium-111 in NaAc buffer at 90°C for 5 min. 111In-Anginex binding to galectin-1 was tested in RF24 activated endothelial cells and in MDA-MB-231 (wild-type and LITG, galectin-1 +) and LS174T (galectin-1 -) tumor cells. Competition assays were carried out using an excess of non-radioactive Anginex and βpep28. The blood kinetics of 111In-Anginex were evaluated in MDA-MB-231-LITG and LS174T tumor-bearing BALB/c nu/nu mice (n = 3). Biodistribution experiments are ongoing and the results will be presented. Results The DOTA-conjugated peptides were successfully synthesized and labeled with In-111 (radiochemical purity >95%). 111In-Anginex showed significantly enhanced binding to the galectin-1 expressing cell lines (RF-24, MDA-MB-231-WT and MDA-MB-231-LITG) when compared to the galectin-1 negative tumor cell line LS174T (Fig. 1). Competition with a 1000-fold excess of non-radioactive Anginex led to a significantly reduced uptake of 111In-Anginex in all galectin-1 positive cell lines. An excess of βpep28 caused a reduction of 111In-Anginex binding, but to a lesser extent. In both tumor-models 111In-Anginex exhibited a rapid two-phase elimination from blood, with a slightly longer retention in mice bearing galectin-1 positive MDA-MB-231-LITG xenografts ($T1/2,\alpha$ = 3.9 min; $T1/2,\beta$ = 1h 21 min) with respect to the the mice bearing galectin-1 negative LS174T xenografts ($T1/2,\alpha$ = 2.8 min; $T1/2,\beta$ = 25 min). The preliminary biodistribution results showed low 111In-Anginex uptake in LS174T tumors (1.0 ± 0.6 %ID/g). Conclusion Indium-111 labeled Anginex showed specific binding towards galectin-1 in activated endothelial cells and in two tumor cell lines in vitro. Surprisingly, 111In-Anginex binding was partially blocked by an excess of βpep28, suggesting that this peptide is not a suitable negative control. The preliminary in vivo results show a slightly longer 111In-Anginex retention in the blood of mice bearing galectin-1 positive xenografts with respect to mice bearing galectin-1 negative xenografts (beta phase). This is possibly due to Anginex retention in the tumor followed by slow wash-out, which would make 111In-Anginex a suitable candidate for non-invasive tumor imaging with SPECT. These results provide an incentive for further evaluation of radiolabeled Anginex in vivo and conversion into a clinically more relevant PET tracer, when labeled with e.g. Fluorine-18.

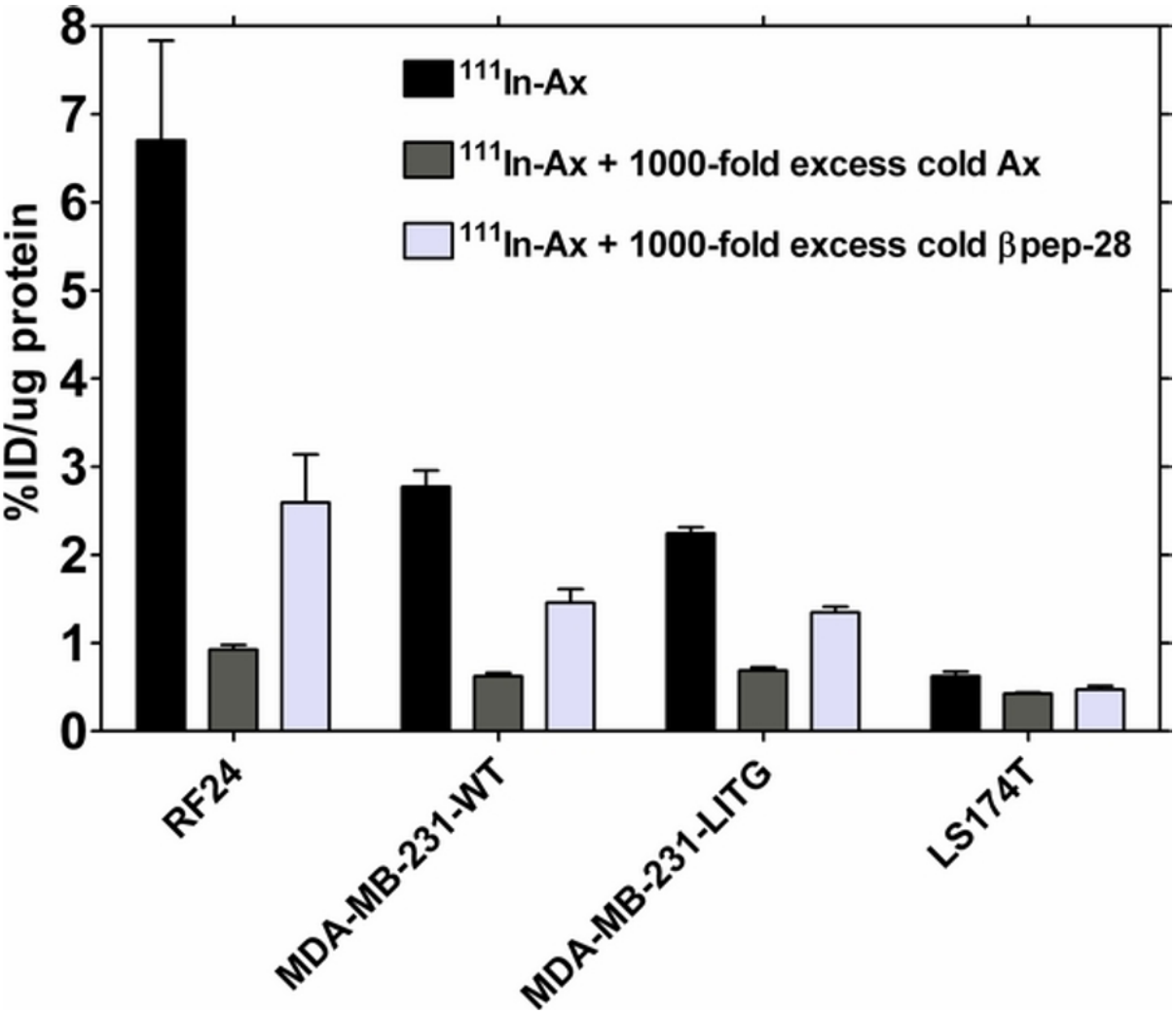

Figure 1: Incubation of 111Indium-labeled Anginex (10nM), 4 hours at 37°C, with and without competition with cold Anginex. Competition with cold Anginex and incubation in galectin-1- cells show a diminished binding, indicating specific and selective binding of the peptide to the target.

Disclosure of author financial interest or relationships:

T.R. van Mourik, None; **T. Läppchen**, Philips Electronics Nederland BV, Employment; **R. Rossin**, Philips, Employment; Tagworks Pharmaceuticals, Consultant; **K. Nicolay**, None; **H. Gruell**, Eindhoven University of Technology, Employment; Philips, Employment .

Presentation Number **SS 65**
Scientific Session 11: Chemistry & Imaging Probes - Nuclear Imaging
September 20, 2013 / 11:30-11:45 / Room: 200

A peptide-based positron emission tomography (PET) probe for caspase activity detection

Matthew R. Hight[1], *Yiu-Yin Cheung*[1], *Michael L. Nickels*[1], *Eric S. Dawson*[2], *Ping Zhao*[1], *Sam A. Saleh*[1], *Henry C. Manning*[1], [1]*Vanderbilt University Institute of Imaging Science, Vanderbilt University, Nashville, TN, USA;* [2]*Biochemistry, Vanderbilt University, Nashville, TN, USA. Contact e-mail: matthew.r.hight@Vanderbilt.Edu*

Deviations from normal apoptosis, or programmed cell death, programs tend to promote cell survival and are frequently associated with cancer. Accordingly, many anti-cancer therapies aim to induce apoptosis in tumor cells, making it possible to leverage the apoptosis pathway as a surrogate measure of response to therapeutic interventions in oncology. Cysteine aspartic acid-specific proteases, or caspases, are essential molecular determinants of apoptosis signaling cascades and represent promising targets for molecular imaging probe development. Here, we report development and *in vivo* validation of [^{18}F]4-fluorobenzylcarbonyl-Val-Ala-Asp(OMe)-fluoromethylketone ([^{18}F]FB-VAD-FMK), a novel molecular probe suitable for quantification of caspase activity *in vivo* using positron emission tomography (PET). [^{18}F]FB-VAD-FMK was prioritized for probe development based on computational modeling studies suggesting tolerance within the active caspase-3 binding domain to functionalization of the N-terminus of the VAD-FMK peptide with [^{18}F]fluorobenzoic acid, a prosthetic group commonly installed for PET imaging. Modeling studies were validated using live-cell caspase inhibition assays, which demonstrated that [^{19}F]FB-VAD-FMK inhibited caspase-3 with nanomolar affinity, and have been utilized to further explore the influence of peptide N-terminus modifications on specific binding through evaluation of other VAD-FMK analogues. For *in vivo* imaging studies, [^{18}F]FB-VAD-FMK was produced in high radiochemical yield and purity using a two-step, radiofluorination sequence which included the automated radiochemical synthesis of [^{18}F]N-succinimidyl-4-fluorobenzoate ([^{18}F]SFB) and subsequent conjugation of [^{18}F]SFB to VAD-FMK. In vivo biodistribution of [^{18}F]FB-VAD-FMK was evaluated in mouse models of human colorectal cancer (CRC) using microPET imaging. Interestingly, we found that accumulation of [^{18}F]FB-VAD-FMK closely reflected caspase activity in SW-620 and DLD-1 cell line xenografts treated with AZD-1152, an inhibitor of aurora kinase B. Interestingly, using Annexin V imaging, we were unable to discern a correlation between AZD-1152 treatment and cell death similar to that observed in this model by *in vivo* PET imaging and immunohistochemistry (IHC) analysis.

Expanding upon these findings, [^{18}F]FB-VAD-FMK has recently been utilized in other CRC small animal xenografts to evaluate early detection of cell death in correlation to single and combination agent drug therapies. These studies illustrate the feasibility of leveraging the VAD-FMK peptide as a scaffold for molecular imaging probe development and that non-invasive imaging of caspase activity may provide a sensitive and unique measure of apoptosis in tumor tissues. Thus, we envision that [^{18}F]FB-VAD-FMK is a promising PET imaging probe for non-invasive quantification of caspase activity and apoptosis in tumors and is a novel, potentially translatable biomarker of therapeutic efficacy in drug development.

Disclosure of author financial interest or relationships:
M.R. Hight, None; **Y. Cheung**, None; **M.L. Nickels**, None; **E.S. Dawson**, None; **P. Zhao**, None; **S.A. Saleh**, None; **H.C. Manning**, None.

Presentation Number **SS 66**
Scientific Session 11: Chemistry & Imaging Probes - Nuclear Imaging
September 20, 2013 / 11:45-12:00 / Room: 200

The importance of cardiac acidosis on the dissociation of hypoxia selective PET tracer ^{64}CuATSM

Fiona Shaughnessy, *Rodolfo Medina, Erika Mariotti, Thomas R. Eykyn, Phil Blower, Richard Siow, Richard Southworth, King's College London, London, United Kingdom. Contact e-mail: fiona.shaughnessy@kcl.ac.uk*

Background: ^{64}CuATSM is increasingly being used as a hypoxia-selective PET tracer. While lack of oxygen determines complex dissociation and radiocopper deposition, the biomechanism(s) which encourage radiocopper retention are poorly understood. It has been suggested that acidosis promotes protonation of the complex, accelerating the dissociation of radiocopper, thereby encouraging intracellular ^{64}Cu retention. We have monitored the progression of acidosis in a model of myocardial hypoxia using ^{31}P NMR spectroscopy to establish the importance of acidosis in ^{64}CuATSM dissociation. Further to this we used the ammonium prepulse technique to establish whether intracellular acidosis in the absence of hypoxia was sufficient to increase ^{64}Cu retention from ^{64}CuATSM. Methods: Isolated rat hearts (male Wistar 300g) were Langendorff-perfused with aerobic buffer (gassed with 95%O_2/5%CO_2) for 15 min, then anoxic buffer for 45 min (gassed with 95%N_2/5%CO_2). Cardiac contractile function was monitored via an intraventricular balloon. Cardiac ^{64}Cu retention from three 2MBq bolus injections of ^{64}CuATSM (during normoxia, and 5 and 20 mins of hypoxia) was monitored by NaI detectors. In parallel experiments, changes in intracellular pH, ATP and phosphocreatine (PCr) during this perfusion protocol were monitored using ^{31}P NMR spectroscopy (16 spectra acquired for 4 minutes each). To induce normoxic intracellular acidosis, further hearts were then perfused with aerobic buffer for 16 min, then NH_4Cl (20mM for 5mins) and sodium-hydrogen exchange inhibitor, zoniporide (1μM for 25 mins). Intracellular pH and cardiac energetics were measured as before. Results: Hearts retained significantly more ^{64}Cu during early and late hypoxia than normoxia (45±5.8%, 60±6.3% vs 14±4.9% control, $p<0.05$). PCr and ATP rapidly depleted after 4-8 min perfusion with hypoxic buffer, whereas Pi and sugar phosphate levels increased. While intracellular pH fell slightly and transiently within 8 minutes of hypoxia (7.0±0.08 vs 7.1±0.09 control), it did not reach statistical significance. In normoxic hearts infused with ammonium chloride and zoniporide, intracellular pH was lowered by almost 1 pH unit (from 7.2±0.04 to 6.3±0.09 after 16 mins acidosis, $p<0.05$). Conclusion: We have demonstrated a small transient decrease in intracellular pH in hypoxic isolated rat hearts. Although acidosis may promote protonation and dissociation of ^{64}CuATSM, we cannot conclude that the level of acidosis in this model is integral to the hypoxia selective ^{64}Cu retention seen. A more severe model of cardiac acidosis was therefore required. Here, the ammonium prepulse technique decreased intracellular pH in normoxic hearts to a much lower value. We intend to use this model to assess whether acidosis is a contributing factor to ^{64}CuATSM dissociation and ^{64}Cu retention during both normoxia and hypoxia.

Disclosure of author financial interest or relationships:
F. Shaughnessy, None; **R. Medina**, None; **E. Mariotti**, None; **T.R. Eykyn**, None; **P. Blower**, None; **R. Siow**, None; **R. Southworth**, None.

Presentation Number **SS 67**
Scientific Session 12: Preclinical in vivo Studies - Oncology (Staging and Image-Guided Surgery)
September 20, 2013 / 10:30-10:45 / Room: 203

Receptor concentration imaging provides a means of detecting cancer spread to sentinel lymph nodes in breast cancer

Kenneth M. Tichauer[1], *Kimberley Samkoe*[2,3], *Jason Gunn*[2], *Ramesh Govindan*[2], *Aravind Viswanathan*[2], *P. Jack Hoopes*[2,3], *Tayyaba Hasan*[4], *Peter A. Kaufman*[5], *Brian W. Pogue*[2,3], [1]*Biomedical Engineering, Illinois Institute of Technology, Chicago, IL, USA;* [2]*Thayer School of Engineering, Dartmouth College, Hanover, NH, USA;* [3]*Department of Surgery, Geisel School of Medicine, Lebanon, NH, USA;* [4]*Wellman Institute of Photomedicine, Massachusetts General Hospital, Boston, MA, USA;* [5]*Department of Medicine, Geisel School of Medicine, Lebanon, NH, USA. Contact e-mail: ktichaue@iit.edu*

Axillary lymph nodes drain roughly 75% of the breast tissue and are a prevalent site of breast cancer spread in metastatic disease. Accordingly, sentinel lymph node (SLN) dissection, i.e., the removal of the primary tumor-draining lymph node, is a commonly carried out during lumpectomy or mastectomy to stage the cancer and reduce the chance of secondary tumor formation. SLNs are typically located by tracking the drainage of blue dye or radioactive tracer injected into the primary tumor, and removed surgically. The problem with this approach is that only 40% of breast cancer patients have lymph node involvement, and removal of lymph nodes can lead to significant morbidity (e.g., lymphedema). In response, a receptor concentration imaging (RCI) approach was developed to non-invasively estimate the presence of cancer cells in tumor-draining lymph nodes to guide dissection decisions. The RCI approach consists of injected two imaging tracers simultaneously: 1) a tracer that is targeted to a molecular marker overexpressed by a patient's cancer; 2) a similar tracer that has no specific targeting but can be imaged simultaneously with the targeted tracer. By monitoring the uptake of the untargeted tracer along with the targeted tracer, it is possible to account for non-specific uptake and retention of the targeted tracer, enabling the concentration of targeted receptor to be measured through kinetic modelling. The receptor concentration can then be used to estimate tumor burden. To test the RCI approach, bioluminescent, metastatic human breast cancer cells (MDA-MB-luc-D3H2LN, Perkin Elmer) were implanted into the mammary fat pad of female athymic mice. The cell line is known to overexpress epidermal growth factor receptor (EGFR); therefore, the targeted tracer selected was IRDye-800CW (LICOR Biosciences) labelled erbitux - an EGFR specific antibody. The untargeted tracer was IRDye-700DX (LICOR) labelled mouse IgG (a negative control antibody of erbitux). Ten mice with cancer spread to the axillary lymph node, confirmed by bioluminescent imaging [bottom panel of Fig. 1(a)] were studied along with six tumor-free controls. The tracers were injected into the front footpad of the mice to encourage their drainage through the axillary lymph nodes, and their uptakes were imaged over 40 min at 1-min intervals using a two-wavelength fluorescence imaging system (Pearl Imager, LICOR). Fig. 1(b) and (c) demonstrate uptake of the targeted and untargeted tracers, respectively, at 40 min in one control (top panel) and one tumor-bearing (bottom panel) mouse. While the absence or presence of tumor is not obvious from either tracer image alone, the RCI approach yielding a map of EGFR concentration [Fig. 1(d)], demonstrated a clear difference between controls and tumor-bearing mice: 0.65 ± 0.59 nM vs. 0.05 ± 0.03 in tumor-bearing and control mice, respectively. Moreover, the measured EGFR concentration correlated well with the lymph node volume, an estimate of tumor burden [Fig. 1(e)]. These findings demonstrate the promise of the RCI approach, the first capable of quantifying cancer receptor concentrations in lymph nodes, to estimate SLN tumor-burden non-invasively.

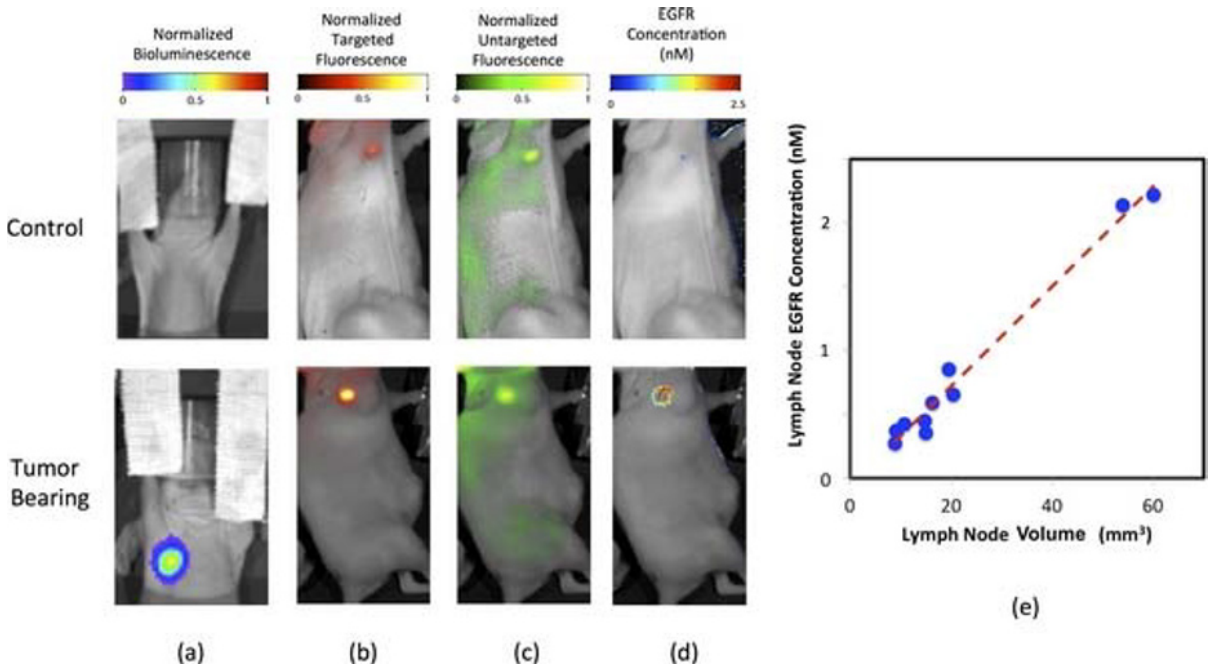

Disclosure of author financial interest or relationships:
K.M. Tichauer, None; **K. Samkoe**, None; **J. Gunn**, None; **R. Govindan**, None; **A. Viswanathan**, None; **P. Hoopes**, None; **T. Hasan**, None; **P.A. Kaufman**, None; **B.W. Pogue**, None.

Presentation Number **SS 68**
Scientific Session 12: Preclinical in vivo Studies - Oncology (Staging and Image-Guided Surgery)
September 20, 2013 / 10:45-11:00 / Room: 203

Relationship between tumor vasculature, interstitial fluid transport, malignant ascites and metastases

Marie-France Penet, *Zhihang Chen, Arvind P. Pathak, Dmitri Artemov, Zaver M. Bhujwalla, JHU ICMIC Program, Division of Cancer Imaging Research, The Russell H. Morgan Department of Radiology and Radiological Science, The Johns Hopkins University School of Medicine, Baltimore, MD, USA. Contact e-mail: mpenet@mri.jhu.edu*

Malignant ascites, a complication observed in terminal ovarian and prostate cancer, is a devastating condition that significantly contributes to poor quality of life and mortality. Once malignant ascites develops, treatment options for late-stage cancers are extremely limited and very invasive. New therapeutic strategies exploiting novel targets are urgently needed to minimize morbidity associated with this condition. Orthotopic implantation models, wherein tumor xenografts are implanted directly into the ovary or prostate of immunodeficient mice, result in metastases, and frequently induce the formation of malignant ascites. Here we combined in vivo MRI with optical imaging to characterize the relationship between tumor vasculature, interstitial fluid transport, malignant ascites formation and metastatic dissemination, using orthotopic human ovarian OVCAR3 and prostate PC3 tumor xenografts. By imaging the dynamics of the macromolecular contrast agent albumin-GdDTPA labeled with fluorescent rhodamine (1), it is possible to quantify the extravasation and transport of macromolecules from the tumor interstitium into malignant ascites. This enables us to gain insights into the role of tumor vascularization, tumor vessel permeability and interstitial fluid transport in the formation of malignant ascites and identify new therapeutic strategies. Orthotopic implantations were performed using a microsurgical method that avoids disseminating cancer cells as previously described (2). All MR imaging was performed on a Bruker 4.7T spectrometer when tumors were approximately 300-400 mm3. Vascular volume, permeability surface area product, number of draining and pooling voxels, draining and pooling rates and exudate volumes were measured from quantitative T1 maps obtained before and after intravenous administration of the albumin-GdDTPA-rhodamine (3). We related ascitic fluid accumulation to vascular volume, total permeability surface area product, efflux and influx rates and total draining and pooling volumes. The amount of rhodamine in ascites was quantified by spectrophotometry. Vascular permeability and efflux and influx rates tended to be higher in mice presenting with malignant ascites compared to those without ascites (Fig. 1). Albumin-GdDTPA-rhodamine was detectable 24 h post-injection in the tumor and lymph nodes (Fig. 2). Ascites volume ranged from 0 to 500 µl and was independent of tumor volume, indicating that an active process determines this build-up. . The ratio of ascites to injected solution rhodamine absorbance values were ~0.03 for the tumors with the largest fluid build-up, and 0.02 for the lowest build-up. We expect these ongoing studies to provide new insights into malignant ascites build-up. Eventually, these findings may result in new strategies to reduce morbidity and mortality from prostate and ovarian cancer.
References: (1) Dafni et al., Cancer Res (2002) 62:6731-9. (2) Penet et al., Cancer Res (2009) 69:8822-9. (3) Pathak et al., Cancer Res (2005) 65:1425-32. Acknowledgement: This work was supported by the HERA Foundation, the Honorable Tina Brozman Foundation, NIH P50CA103175, and NIH R01CA73850.

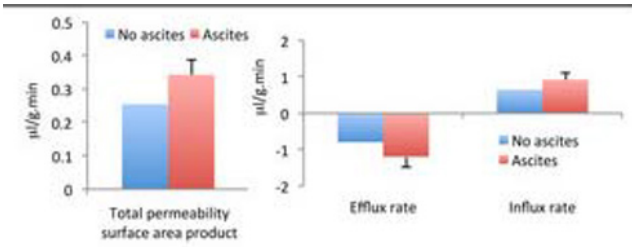

Figure 1: Total permeability surface area product and efflux and influx rates, *in vivo* in OVCAR3 xenografts implanted orthotopically without or with ascites (mean ± sem, n = 1 and n=5 respectively).

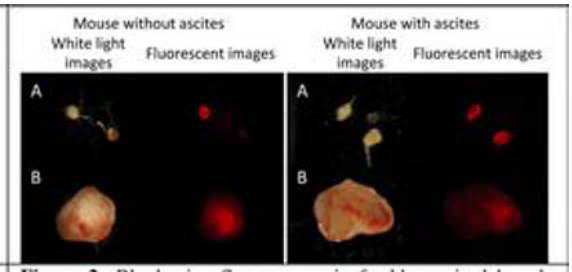

Figure 2: Rhodamine fluorescence in freshly excised lymph nodes (A) and orthotopic OVCAR3 tumor slices (B), 24 h after injection of the contrast agent.

Disclosure of author financial interest or relationships:

M. Penet, None; **Z. Chen**, None; **A.P. Pathak**, None; **D. Artemov**, None; **Z.M. Bhujwalla**, None.

Presentation Number **SS 69**
Scientific Session 12: Preclinical in vivo Studies - Oncology (Staging and Image-Guided Surgery)
September 20, 2013 / 11:00-11:15 / Room: 203

Receptor Targeted Nanoparticles and Spectroscopic Intraoperative Imaging Device for Image-guided Surgery of Breast Cancer

Weiping Qian[1], Zehong Cao[1], Aaron M. Mohs[5], Malgorzata Lipowska[3], Y. Andrew Wang[4], William C. Wood[1], Hui Mao[3], Shuming Nie[2], **Lily Yang**[1], *[1]Surgery, Emory University, Atlanta, GA, USA; [2]Biomedical Engineering, Emory University, Atlanta, GA, USA; [3]Radiology and Imaging Sciences, Emory University, Atlanta, GA, USA; [4]Ocean Nanotech, LLC, Springdale, AR, USA; [5]Biomedical Engineering, Wake Forest University, Winston-Salem, NC, USA. Contact e-mail: lyang02@emory.edu*

Significance:About 30% of breast cancer patients develop recurrent tumors after breast conserving surgery. The major challenges for breast cancer therapy include: 1) ineffectiveness of the conventional therapeutics in treating highly heterogeneous breast cancer cells; and 2) lack of sensitive and accurate methods to obtain intraoperative assessment of tumor margins and to identify small drug resistant residual tumors and tumor cell involved lymph nodes. Therefore, there is an urgent need to develop effective therapy and novel image-guided surgery. The objective of our study is to develop a novel image-guided surgical approach using receptor-targeted nanoparticle imaging probes or theranostic nanoparticles in combination with a clinically translatable hand-held spectroscopic imaging device for image-guided surgery. Methods: We have developed a class of dual optical and MR imaging nanoparticles using the receptor binding domain peptide of urokinase plasminogen activator (uPA) or single chain EGFR antibody. These targeting ligands are labeled with a NIR 830 dye with an emission wavelength of 825 nm on amphiphilic polymer-coated magnetic iron oxide nanoparticles (IONPs). Further encapsulation of chemotherapy drugs into the nanoparticles resulted in theranostic nanoparticles with the capability of both targeted tumor therapy and imaging. We examined target specificity in orthotopic mouse mammary tumor and human breast cancer xenograft models using handheld spectroscopic and Kodak FX in vivo optical imaging systems. The handheld spectroscopic device is a pen-sized fiber-optic probe device connected to a fiber optic cable for both laser excitation and light collection for real-time detection and imaing tumor lesions. Results: Systemic delivery of NIR-830 dye-labeled and uPAR or EGFR-targeted IONPs leads to the selective accumulation of the probes in orthotopic tumors in 4T1 mammary tumor model in Balb/c mice and in human breast cancer xenografts in nude mice. The spectroscopic device can sensitively detect the optical signal with a high tumor signal to skin background ratio (16 to 27 in Balb/c mice). It can detect as few as 5,000 NIR-830 dye-IONP-labeled tumor cells localized 2 mm depth under the skin. Spontaneous lung metastases and tumor-involved lymph nodes can also be detected either non-invasively or intraoperatively in the tumor bearing mice. Spectroscopic image-guided surgery significantly reduced the incidence and size of locally recurrent tumors in 4T1 mouse mammary tumor model. Furthermore, systemic delivery of targeted theranostic nanoparticles in orthotopic primary breast cancer xenograft models in nude mice significantly inhibited tumor growth. It is also feasible to detect drug resistant residual tumors in the surgical cavity for surgical removal by spectroscopic image-guided surgery. Therefore, novel NIR-830 dye labeled receptor-targeted imaging or theranostic nanoparticles in combination with the handheld spectroscopic imaging device should have great potential for targeted therapy, determining tumor margins, complete removal of residual tumor lesions, and therefore, increasing survival of breast cancer patients.

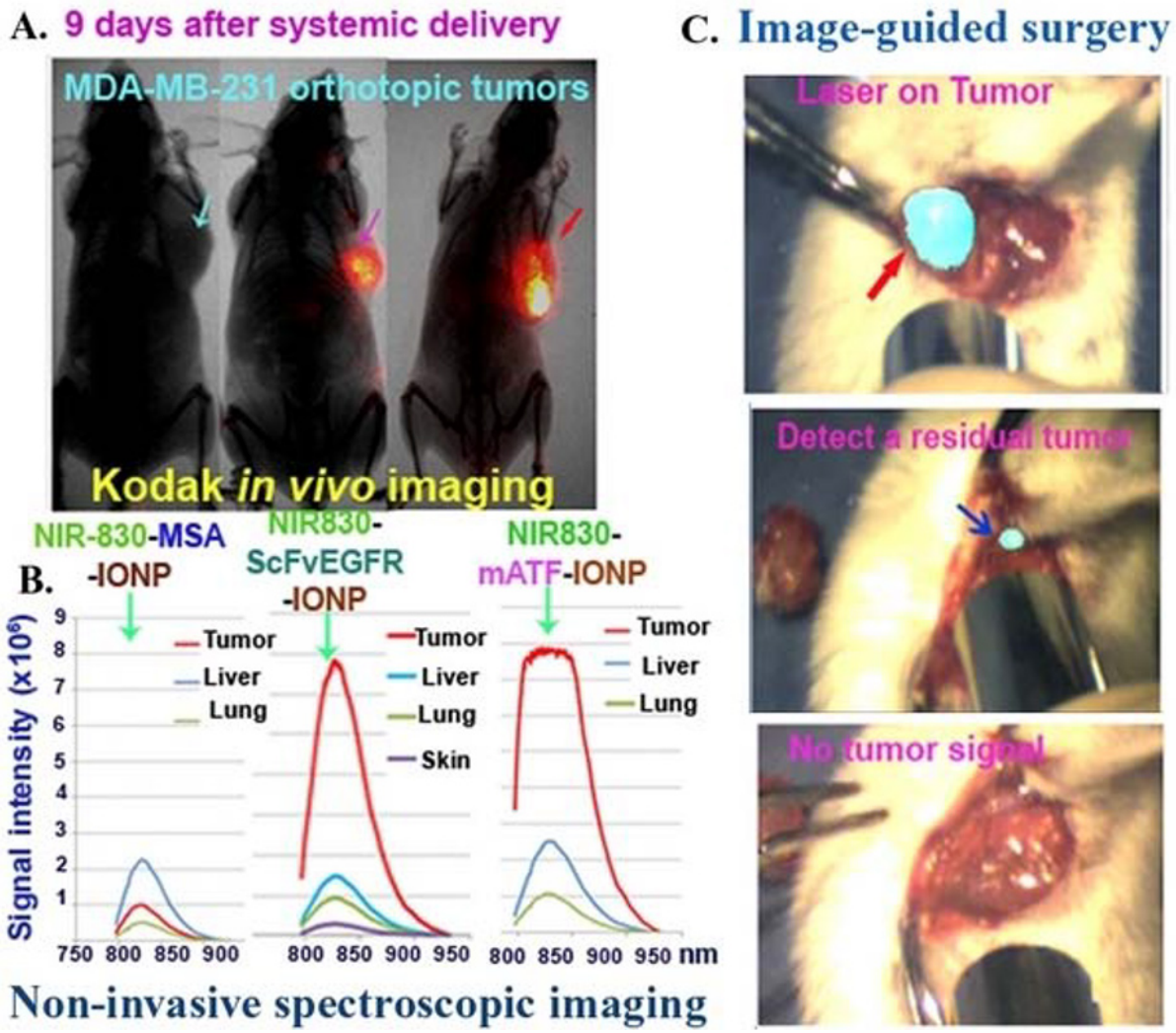

Disclosure of author financial interest or relationships:
W. Qian, None; **Z. Cao**, None; **A.M. Mohs**, Spectropath, Inc., Other financial or material support; **M. Lipowska**, None; **Y. Wang**, None; **W.C. Wood**, None; **H. Mao**, None; **S. Nie**, None; **L. Yang**, None.

Presentation Number **SS 70**
Scientific Session 12: Preclinical in vivo Studies - Oncology (Staging and Image-Guided Surgery)
September 20, 2013 / 11:15-11:30 / Room: 203

Ratiometric activatable cell-penetrating peptides (RACPPs) aid intraoperative detection and surgical removal of early stage salivary gland cancers

Timon Hussain[1], *Elamprakash N. Savariar*[2], *Julio A. Diaz-Perez*[1], *Roger Y. Tsien*[2,3], *Quyen T. Nguyen*[1], [1]*Department of Head and Neck Surgery, University of California, San Diego, San Diego, CA, USA;* [2]*Department of Pharmacology, University of California, San Diego, San Diego, CA, USA;* [3]*Howard Hughes Medical Institute, San Diego, CA, USA. Contact e-mail: tihussain@ucsd.edu*

Background and Objectives In cancers of the head and neck, complete resection is one of the most important prognostic factors for patient outcome. During parotidectomy, the proximity of the facial nerve and vasculature further increases the need for reliable identification of malignant tissues. Finally, decreasing time to tumor margin identification will decrease total operative time and associated cost. ACPPs are polycationic cell-penetrating peptides coupled to a neutralizing peptide by a linker cleavable by proteases characteristic of tumor tissue. We have shown that using fluorescently labeled ACPPs during surgery can increase tumor free survival after the resection of large invasive tumors in mice [1]. The aim of this study was to determine whether ratiometric ACPPs [2] could facilitate the intraoperative identification and resection of small (1-2mm) salivary gland tumors in mice. Methods 1x106 murine salivary cancer cells (SCA-9 clone 15) were injected into the right parotid gland of immunocompetent Swiss Webster mice (n=17). 14d after tumor implantation, 8 mice were intravenously injected with RACPPs and the remaining 9 mice served as controls. Tumor resection was then attempted using white light imaging for the control group and ratiometric fluorescence imaging for the RACPP group. In this latter group tissue foci with high ratio were resected. Histological analysis was performed by a pathologist blinded to RACPP status on all tissue samples. Results Operating time: Tumor identification after incision was faster with ratiometric fluorescence imaging compared to white light alone (6.1 minutes ± 2.6 (n=8) vs. 11.0 minutes ± 3.0 (n=9), p=0.0021). Tumor detection: Surgery with white light imaging resulted in the resection of 10 foci of high clinical suspicion (n=9 control mice). Of these, 50% (n=5/10) were histologically confirmed as malignant. In the 8 mice that received RACPPs, ratiometric fluorescence imaging revealed 8 high ratio foci. Of these, 75% (n=6/8) were histologically confirmed as malignant, suggesting that RACPPs can improve the detection specificity for small salivary gland tumors. Tumor detection specificity with RACPP was 75% (n=6/8). The two instances of high ratio foci with negative tumor histology were determined as auricular cartilage. Tumor detection sensitivity is currently assumed as 6/8 (75%) if all injected cells did form tumors, 2/8 (25%) of which were not detectable at the time of surgery. Long-term tumor free survival studies are ongoing to further evaluate this. Conclusion and Outlook We show that RACPPs aid the identification of small (1-2mm) salivary gland tumors. Ratiometric fluorescent imaging with RACPPs increased detection specificity of histologically confirmed malignant tissue compared to white light alone (75 % vs. 50%). Studies to monitor long-term tumor free survival are ongoing. References 1.Nguyen, Q.T., et al., Proceedings of the National Academy of Sciences of the United States of America, 2010. 107(9): p. 4317-22. 2. Savariar, E.N., et al., Cancer Res, 2013. 73(2): p. 855-64.

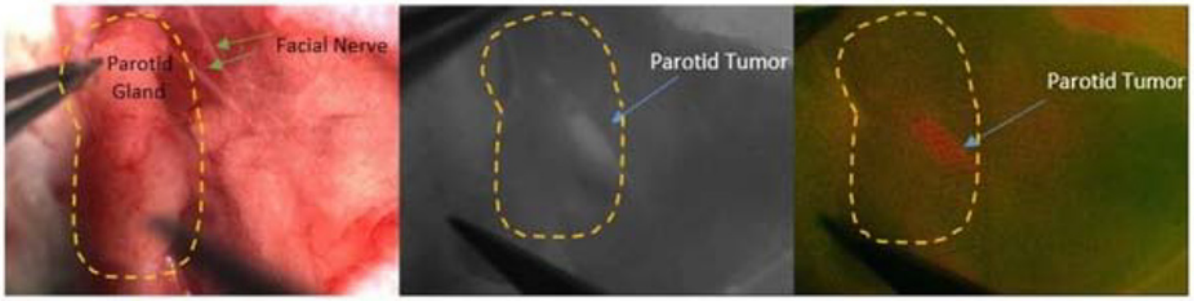

Parotid tumor imaging in a mouse model with molecularly targeted probes. White light reflectance image (left) showing the parotid gland contour (stippled yellow line) and branches of the facial nerve (solid green arrows). Ratiometric fluorescence image (center) of a parotid tumor (blue arrow) following systemic injection of Ratiometric Activatable Cell Penetrating Peptide (RACPP). Warm (yellow/orange) and cool (green/blue) colors in the color overlay image (right) designate high and low MMP2,9 activity, respectively. Skin (right upper corner) exhibits some autofluorescence.

Disclosure of author financial interest or relationships:
T. Hussain, None; **E.N. Savariar**, None; **J.A. Diaz-Perez**, None; **R.Y. Tsien**, Avelas Biosciences, Consultant; Avelas Biosciences, Stockholder; **Q.T. Nguyen**, Avelas Biosciences, Consultant; Avelas Biosciences, Stockholder .

Presentation Number **SS 71**
Scientific Session 12: Preclinical in vivo Studies - Oncology (Staging and Image-Guided Surgery)
September 20, 2013 / 11:30-11:45 / Room: 203

Image-guided Surgery with a Dual-modality CT and NIR Fluorescence Nano-agent

Jinzi Zheng[1], *Nidal Muhanna*[2,3], *Raquel De Souza*[1], *Mengqing Li*[1], *Margarete K. Akens*[3,4], *Michael Daly*[3], *Harley Chan*[3], *Michael Dunne*[1], *Hironobu Wada*[3,5], *Kazuhiro Yasufuku*[3,5], *Jonathan Irish*[2,3], *Christine Allen*[1,6], *David A. Jaffray*[1,7], [1]*STTARR Innovation Centre, Princess Margaret Hospital, Toronto, ON, Canada;* [2]*Surgical Oncology, Princess Margaret Cancer Centre, Toronto, ON, Canada;* [3]*Guided Therapeutics, Techna Institute / University Health Network, Toronto, ON, Canada;* [4]*Orthopaedic Surgery, Sunnybrook Research Institute, Toronto, ON, Canada;* [5]*Thoracic Surgery, Toronto General Hospital, Toronto, ON, Canada;* [6]*Pharmaceutical Sciences, University of Toronto, Toronto, ON, Canada;* [7]*Radiation Oncology, University of Toronto, Toronto, ON, Canada. Contact e-mail: jinzi.zheng@rmp.uhn.on.ca*

Introduction: The development of new imaging agents suitable for surgical guidance is a relatively unexplored and yet highly exciting area. Particularly in oncology, where effective screening programs and early diagnosis present surgeons with increasingly challenging cases of patients with small tumors that are non-visible and non-palpable. In addition, tissue-conserving surgeries require accurate identification of the tumor margins and knowledge of lymph node involvement in the operating room. We report here the development and preclinical characterization of a dual-modality computed tomography (CT) and near-infrared (NIR) fluorescence imaging agent (Nanovista-CF800) for pre-operative CT-based surgical planning and intra-operative optical guidance. **Methods:** Nanovista-CF800 is a liposome formulation that co-encapsulates iohexol and indocyanine green (ICG). The performance of Nanovista-CF800 for image-guidance in surgical applications was evaluated in three animal models of cancer: 1) a mouse xenograft model of SKOV-3/Luc ovarian adenocarcinoma, 2) a mouse xenograft model of LM2-4H2N metastatic breast cancer, and 3) a rabbit model of VX-2 buccal mucosa carcinoma. Bioluminescence (BLI), NIR fluorescence and CT images were acquired at 48h post i.v. administration of Nanovista-CF800 in the two mouse models. Pre-operative CT and intra-operative NIR fluorescence imaging were performed on the rabbit model at 4 days post Nanovista-CF800 administration. **Results:** In vitro photostability tests demonstrated that liposomal encapsulation protects ICG from photodegradation, even after repeated excitation. After 3 days of storage at room temperature, following 6 imaging sessions with high-power light exposure, and at a 100-fold dilution in water and a 1:10 ethanol/water mixture, Nanovista-CF800 (n=4) retained 78±8% and 92±11% of its original fluorescence signal, respectively. Free ICG diluted in water, a 1:10 ethanol/water mixture and a 0.5:10 iohexol/water mixture yielded only 8±2%, 3±1%, 7±2% of its original fluorescence, respectively. In vivo in the two mouse models of cancer, all 13 animals administered with Nanovista-CF800 displayed significantly higher NIR fluorescence signal in the tumor lesions compared to background (Fig. 1). Not all nodules were easily identifiable in CT. This is attributed to the heterogeneity and variability in liposome accumulation in these malignant lesions and the lower sensitivity of CT compared to fluorescence imaging. In the rabbit buccal mucosa tumor model, successful CT visualization of the contrast enhanced tumor and involved lymph nodes was achieved in the pre-operative setting (Fig. 2a). Intra-operatively, NIR fluorescence imaging also demonstrated successful detection of the surgical site containing the tumor and malignant lymph nodes enhanced with Nanovista-CF800 (Fig. 2b, 2c).

Conclusions: A novel CT/optical imaging agent was shown to possess high photostability after repeated light exposure compared to free ICG. It successfully localized in primary and metastatic tumor lesions in mouse and rabbit models of cancer and allowed for preoperative CT and intraoperative NIR fluorescence detection of the same lesions.

Disclosure of author financial interest or relationships:
J. Zheng, None; **N. Muhanna**, None; **R. De Souza**, None; **M. Li**, None; **M.K. Akens**, None; **M. Daly**, None; **H. Chan**, None; **M. Dunne**, None; **H. Wada**, None; **K. Yasufuku**, Olympus Medical Systems Corp, Grant/research support; **J. Irish**, None; **C. Allen**, None; **D.A. Jaffray**, Precision X-ray Inc., Other financial or material support .

Presentation Number **SS 72**
Scientific Session 12: Preclinical in vivo Studies - Oncology (Staging and Image-Guided Surgery)
September 20, 2013 / 11:45-12:00 / Room: 203

Thoracoscopic Color and Fluorescence Imaging System for Sentinel Node Mapping in Porcine Lung Using a Newly Developed Near-Infrared Fluorophore

Yujin Oh[2], *Hyun Koo Kim*[1], *Yun-Sang Lee*[3], *Yu Hua Quan*[1], *Yeonho Choi*[2], *Jae Min Jeong*[3], *Beop-Min Kim*[2], *Ji Ho Park*[4], [1]*Thoracic and Cardiovascular Surgery, Guro Hospital, Korea University Medical Center, Seoul, Republic of Korea;* [2]*Biomedical Engineering, Korea University College of Health Science, Seoul, Republic of Korea;* [3]*Nuclear Medicine, Seoul National University Hospital, Seoul, Republic of Korea;* [4]*Chemical Biomolecular Engineering, Korea Advanced Institute of Science and Technology, Daejeon, Republic of Korea. Contact e-mail: yjoh12@korea.ac.kr*

Introduction: We developed a thoracoscopic intraoperative combined color and fluorescence imaging system (ICFIS), providing convenient thoracoscopic sentinel lymph node (SLN) mapping conditions to the surgeons with merged images of surgical anatomy and pseudo-colored SLN fluorescence images in real-time. In this study, we evaluated clinical usefulness of newly developed fluorophore and conducted thoracoscopic SLN mapping in the big animal model, for demonstrating clinical feasibility using our thoracoscopic color and fluorescence imaging system. Method: A commercially available standard rigid thoracoscope is mounted to the established ICFIS. Mannose-binding human serum albumin (MSA) was synthesized by conjugating mannopyranosylphenylisothiocyanate to human serum albumin. ICG was noncovalently absorbed to mannose-binding human serum albumin (ICG:MSA). Total 10 porcine lungs were used for the SLN mapping with ICG:MSA and ICG. Results: A mean 20 minute after injection, the SLNs were identified using thoracoscopic ICFIS under in vivo conditions. 10 SLNs of 10 porcine lungs (100%) were identified well and dissected using video-assisted thoracoscopic technique Conclusion: We developed a newly developed mannose targeting fluorophore; ICG:MSA and built a thoracoscopic intraoperative color and fluorescence imaging system for lung cancer SLN mapping. We used commercially available thoracoscope connected to the system and mixed neomannosyl human serum albumin with FDA-approved ICG, indicating feasibility of prompt clinical translation for lung cancer SLN mapping.

Disclosure of author financial interest or relationships:
Y. Oh, None; **H. Kim**, None; **Y. Lee**, None; **Y. Quan**, None; **Y. Choi**, None; **J. Jeong**, None; **B. Kim**, None; **J. Park**, None.

Presentation Number **SS 73**
Scientific Session 13: Preclinical in vivo Studies - Inflammation/Immunology
September 20, 2013 / 10:30-10:45 / Room: Oglethorpe Auditorium

A Novel Strategy for PET Imaging of Graft Versus Host Disease in Living Subjects

John A. Ronald[1,2], *Byung-Su Kim*[3], *Mohammad Namavari*[1,2], *Xinrui Yan*[1,2], *Hui-Yen Chuang*[1,4], *Jonathan Benjamin*[3], *Robert Negrin*[3], *Sanjiv S. Gambhir*[1,2], [1]*Radiology, Stanford University, Stanford, CA, USA;* [2]*Molecular Imaging Program at Stanford, Stanford University, Stanford, CA, USA;* [3]*Division of Blood and Marrow Transplantation, Stanford University, Stanford, CA, USA;* [4]*Biomedical Imaging and Radiological Sciences, National Yang-Ming University, Taipei, Taiwan. Contact e-mail: jronald1@stanford.edu*

Graft versus host disease (GVHD) is a major complication of allogeneic tissue transplantation and is associated with significant morbidity and mortality rates. GVHD occurs when donor T cells react to "foreign" host cells, causing a wide spectrum of host tissue injuries. Currently, GVHD is diagnosed at late stages when symptoms such as gastrointestinal, liver or skin problems are apparent. Imaging strategies are needed to detect early GVHD so that existing interventions can be implemented in a timely fashion. We utilized a new tracer 2'-deoxy-2'-[18F]fluoro-9-β-D-arabinofuranosylguanine (18F-F-Ara-G), a fluorinated analog of arabinosyl guanine (Ara-G) proven to have selective toxicity towards T cells, and shown to have increased uptake in activated versus naïve T cells. Here we have evaluated the ability to image activated T cells using 18F-F-Ara-G in a mouse model of major mismatch acute GVHD (aGVHD). Methods and Results: Irradiated recipient Balb/c mice were implanted with bone marrow cells alone (Control; N=5) or both bone marrow cells and firefly luciferase-positive donor T cells from B6 L2G85 Thy1.1 CD45.1 mice (aGVHD Mice; N=5). Bioluminescence imaging of donor T cells revealed strong signal from spleen, mesenteric (MLN) and cervical lymph nodes (CLN) at day 3 (Figure 1A), which continued to increase over time and also spread to other organs. Importantly, as early as day 3 post cell-implantation, PET-CT images taken at 1 hour after 18F-F-Ara-G administration (200 μCi) revealed statistically increased uptake ($P<0.05$) in CLNs in aGVHD mice versus control mice (Figure 1B; n=3 for each group), and biodistribution at 90 minutes showed significantly increased uptake in both MLNs and CLNs ($p<0.05$), and a trend towards increased uptake in spleen ($p=0.12$). 18F-F-Ara-G PET-CT images on day 10 demonstrated even higher uptake in CLNs in aGVHD mice than control mice (Figure 1C; n=2 for each group), and biodistribution supported our imaging results with a trend towards higher uptake in MLNs and CLNs. Discussion: GVHD is a T cell mediated disease that can effect up to 30-40% of patients receiving related donor transplants and upwards of 80% in patients receiving unrelated donor transplants. Currently, there is no imaging method that can selectively image activated T cells in GVHD. Here we show that in aGVHD mice, 18F-F-Ara-G accumulated in lymphoid organs shown to harbor increasing numbers of activated T cells as the disease progressed. Furthermore, 18F-F-Ara-G PET images revealed significantly higher uptake in CLNs at both late (day 10) and early (day 3) time points following donor transplantion, the latter being a time point where overt symptoms in mice were absent. Future work will focus on monitoring the effects of novel immunosuppressive therapies in this model, and continued development of 18F-F-Ara-G as a selective T cell imaging agent in humans is ongoing. In conclusion, the ability to selectively image activated T cells using 18F-F-AraG at early stages of aGVHD may lead to more timely interventions, better monitoring of therapies, and ultimately improved patient outcomes.

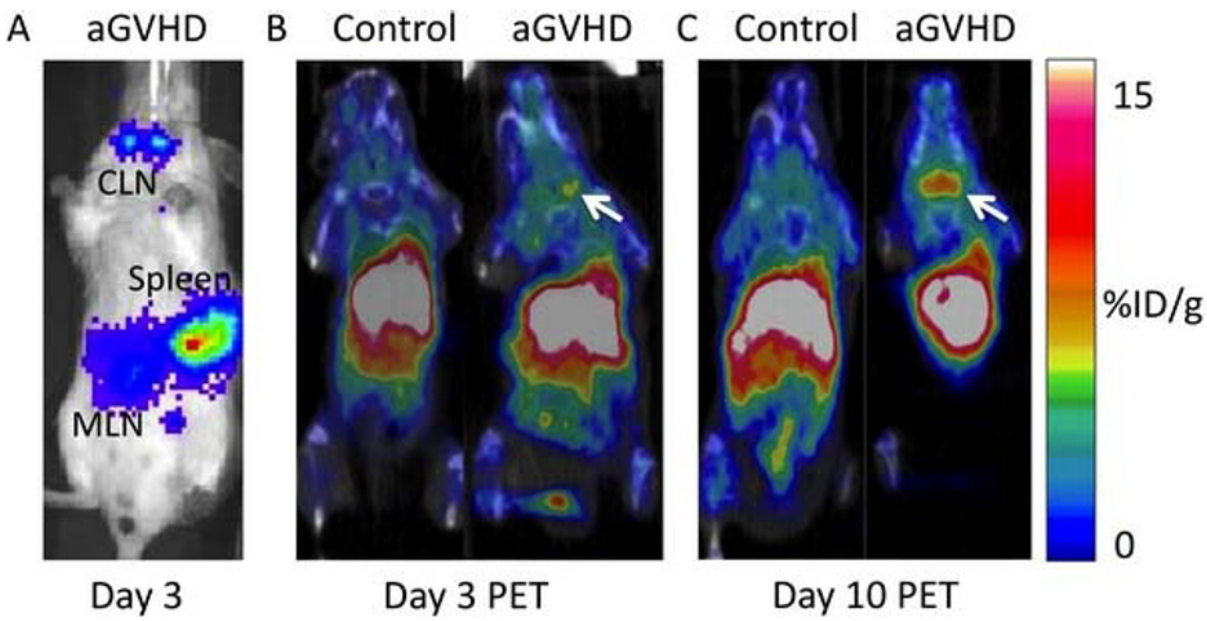

Figure 1 - A) Bioluminescence imaging of firefly luciferase-positive donor T cells in acute graft-versus-host disease (aGVHD) mice at day 3 after cell transplantation. CLN = cervical lymph node; MLN = mesenteric lymph node. 18F-F-Ara-G PET-CT images in control and aGVHD mice at days 3 (B) and 10 (C). Arrows indicate higher uptake in CLNs in aGVHD mice.

Disclosure of author financial interest or relationships:

J.A. Ronald, None; **B. Kim**, None; **M. Namavari**, None; **X. Yan**, None; **H. Chuang**, None; **J. Benjamin**, None; **R. Negrin**, None; **S.S. Gambhir**, Bracco Diagnostics, Consultant; Endra, Inc, Stockholder; Cellsight, Stockholder; Enlight, Inc., Stockholder; General Electric, Grant/research support; ImaginAb, Stockholder; MagArray, Inc., Stockholder; Sanofi-Aventis, US, Grant/research support; SiteOne Therapeutics, Stockholder; VisualSonics/Sonosite, Stockholder .

Presentation Number **SS 74**
Scientific Session 13: Preclinical in vivo Studies - Inflammation/Immunology
September 20, 2013 / 10:45-11:00 / Room: Oglethorpe Auditorium

Optoacoustic imaging and staging of arthritic inflammation

Nicolas Beziere[1], *Claudio von Schacky*[2], *Yvonne Kosanke*[2], *Melanie Kimm*[2], *Vasilis Ntziachristos*[1], *Reinhard Meier*[2], [1]*Institute for Biological and Medical Imaging, Neuherberg, Germany;* [2]*Radiology, Klinikum rechts der Isar, Munich, Germany. Contact e-mail: nicolas.beziere@helmholtz-muenchen.de*

With around 40 million people affected by the pathology, arthritis is one of the most frequent inflammatory diseases, causing pain and often disability in the affected joints. Early diagnosis is essential in order to increase the efficiency of symptomatic treatment. This relies on careful clinical examination and the use of MRI as an imaging gold standard, which is both expensive and time consuming. In an effort to provide the biomedical community with a more accessible way to assess arthritis advancement, we investigated the use of optoacoustic imaging in a murine model to visualize the extent of the inflammation in vivo through a L- and P-selectin targeting contrast agent. This preclinical imaging study was performed using multispectral optoacoustic tomography (MSOT), able to record the optoacoustic signal detected by a cylindrically focus 64-elements transducer after illumination by a tunable pulsed laser in the near infra-red range (680-900 nm), yielding transverse images of entire mice in real time1. The animal model used collagen injection in one leg to induce arthritis while keeping the other leg untouched as a reference2. The non-invasiveness of the imaging procedure allowed for imaging at difference stages of disease progression. A polyglycerol-sulfate grafted with near-infrared fluorophore was used (dPGS-ICG), allowing highlighting of the expression of L- and P-selectins3, directly correlating to the state of inflammation of the joint and surrounding tissue. Data was processed using a model-based image reconstruction algorythm followed by a spectral fitting method. Clinical and MRI assessment of arthritis as well as ex vivo planar fluorescent imaging was used to validate the results obtained by optoacoustic imaging. Careful observation of the images obtained from a number of animals at different stages of arthritic development showed that MSOT signal intensity directly and quantitatively correlated to the advancement of the disease in the joint. MSOT allowed clear identification of the probe over the anatomical signal without the need to rely in a pre- and post-contrast agent acquisition to highlight the inflamed area. The findings matched well with clinical evaluation of arthritis and MR imaging of synovial enhancement. Current effort is now turned toward systematic and user-independent staging of the development of the disease, which will be used for therapy evaluation and monitoring in similar animal models. In parallel, and given the current development of the imaging technology, it is expected that similar approaches will rapidly be translated in the clinic as a fast and relatively cheap staging procedure. 1 Ma, R., Taruttis, A., Ntziachristos, V. & Razansky, D. Multispectral optoacoustic tomography (MSOT) scanner for whole-body small animal imaging. Opt Express 17, 21414-21426 (2009). 2 Brand, D. D., Latham, K. A. & Rosloniec, E. F. Collagen-induced arthritis. Nature protocols 2, 1269-1275 (2007). 3 Dernedde, J. et al. Dendritic polyglycerol sulfates as multivalent inhibitors of inflammation. Proceedings of the National Academy of Sciences 107, 19679-19684 (2010).

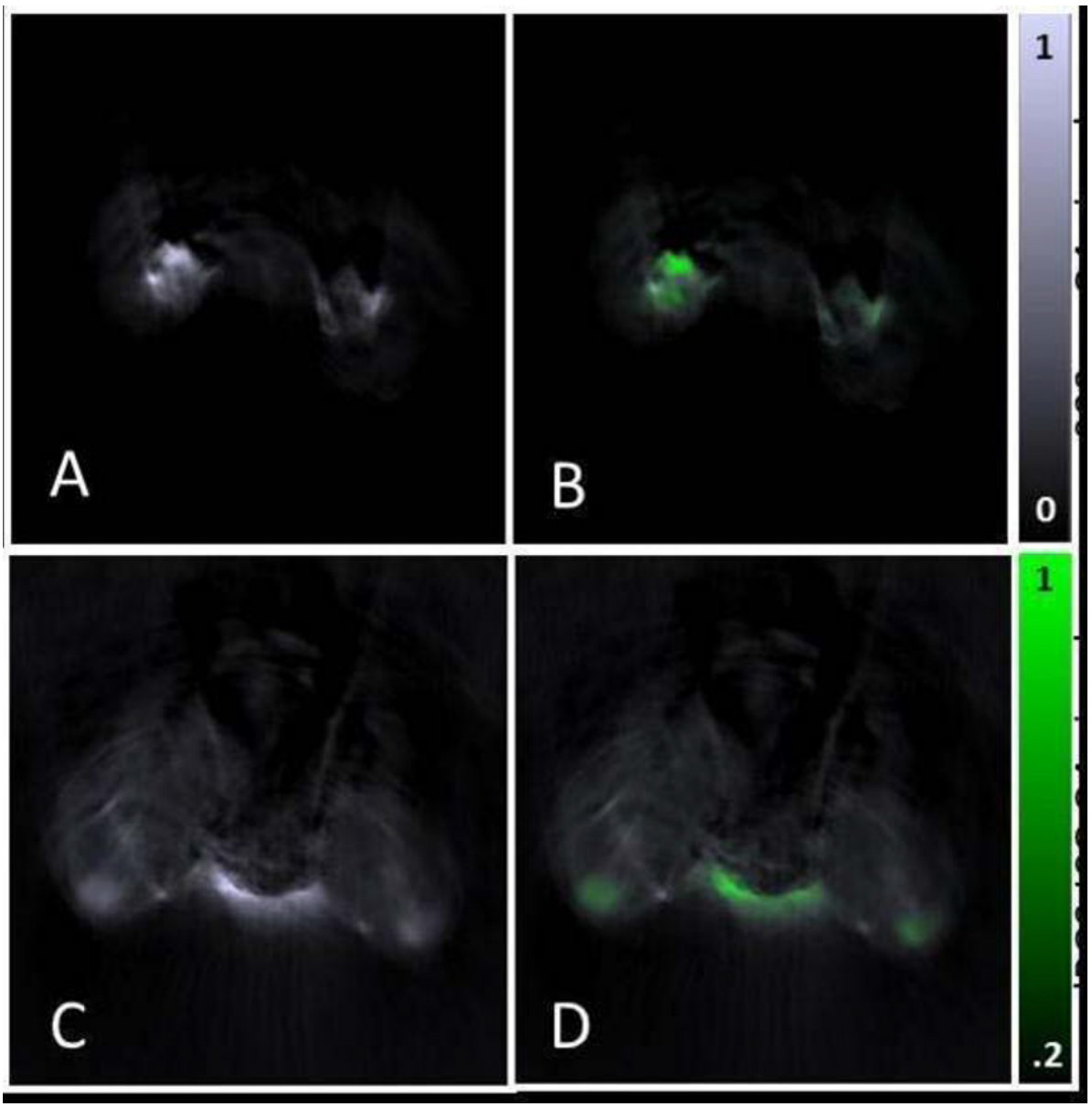

Multispectral Optoacoustic assessment of inflammation in an arthritic (left leg) and a healthy (right leg) mouse leg. Top row: transverse image of the ankle area acquired at 800 nm illumination (A) and overlayed with the dPGS-ICG signal (B). Bottow row: transverse image of the knee area acquired at 800 nm illumination (C) and overlayed with the dPGS-ICG signal (D).

Disclosure of author financial interest or relationships:
N. Beziere, None; **C. von Schacky**, None; **Y. Kosanke**, None; **M. Kimm**, None; **V. Ntziachristos**, iThera Medical, Stockholder; SurgOptix BV, Consultant; **R. Meier**, None.

Presentation Number **SS 75**
Scientific Session 13: Preclinical in vivo Studies - Inflammation/Immunology
September 20, 2013 / 11:00-11:15 / Room: Oglethorpe Auditorium

Cell imaging revealed differential homing of dendritic cells to lymphoid organs

Noriko Sato, *Peter Choyke, Molecular Imaging Program, NCI, Nat'l Inst of Health, Bethesda, MD, USA. Contact e-mail: saton@mail.nih.gov*

Antigen presenting cells play important roles in immune regulations. Dendritic cell (DC) based therapies that aim to modify immune responses against various malignancies and infectious diseases have been extensively investigated. In order for DCs to effectively control immune responses, such as to activate T cells against a specific target, it is important that the DCs delivered to patient migrate to secondary lymphoid organs. In clinic, DCs are administered via subcutaneous (s.c.), intravenous (i.v.) or intradermal (i.d.) routes. In case of preclinical studies using mice, intraperitoneal (i.p.) injections are commonly performed as well. Importantly, these studies often lack a system to monitor where the injected DCs migrate to and in what fraction. In order to better understand the migration of DCs following the transfer, we tracked the DCs labeled with In-111 oxine in mice after administration via various routes. Immature DCs generated from bone marrow and DCs matured by a Toll-like receptor (TLR) ligand were examined. Serial images were acquired using a small animal single photon computed tomography (SPECT) imager. In-111 oxine labeling did not affect the survival of DCs at the specific activity around 500 kBq per million cells. Five million labeled DCs were transferred per mouse. The imaging revealed significant difference in migration and homing of transferred DCs by administration route. Most of s.c. injected DCs failed to home to the adjacent lymph nodes and died at the injection site. DCs injected i.v. were initially trapped in the lungs, and then gradually migrated to the spleen and liver. Small fractions of the cells homed to lymph nodes. Interestingly, non-activated DCs egressed the lungs faster than activated DCs. By contrast, DCs administered i.d. and i.p. quickly entered the lymphatic system and homed to lymph nodes, including those far from the injection site. To examine the effect of distribution of transferred DCs on immune responses, wild type mice were transferred with CMFDA labeled OT-1 T cell receptor transgenic CD8 T cells specific for ovalbumin (OVA), followed by immunization with TLR ligand activated DCs loaded with OVA via different routs. Proliferation of OT-1 T cells analyzed by flow cytometry indicated that immunization through i.v. and i.p. routes triggered stronger and more systemic activation of T cells than that by s.c. and i.d. administrations. In summary, In-111 oxine cell imaging reveled differential homing of DCs by injection routs and maturation status of the cells. The choice of administration rout could determine the spatial distribution and degree of immune activation triggered by a DC-based immunization. Non-invasive monitoring of cell trafficking would provide important information for improvements of cell-based therapies.

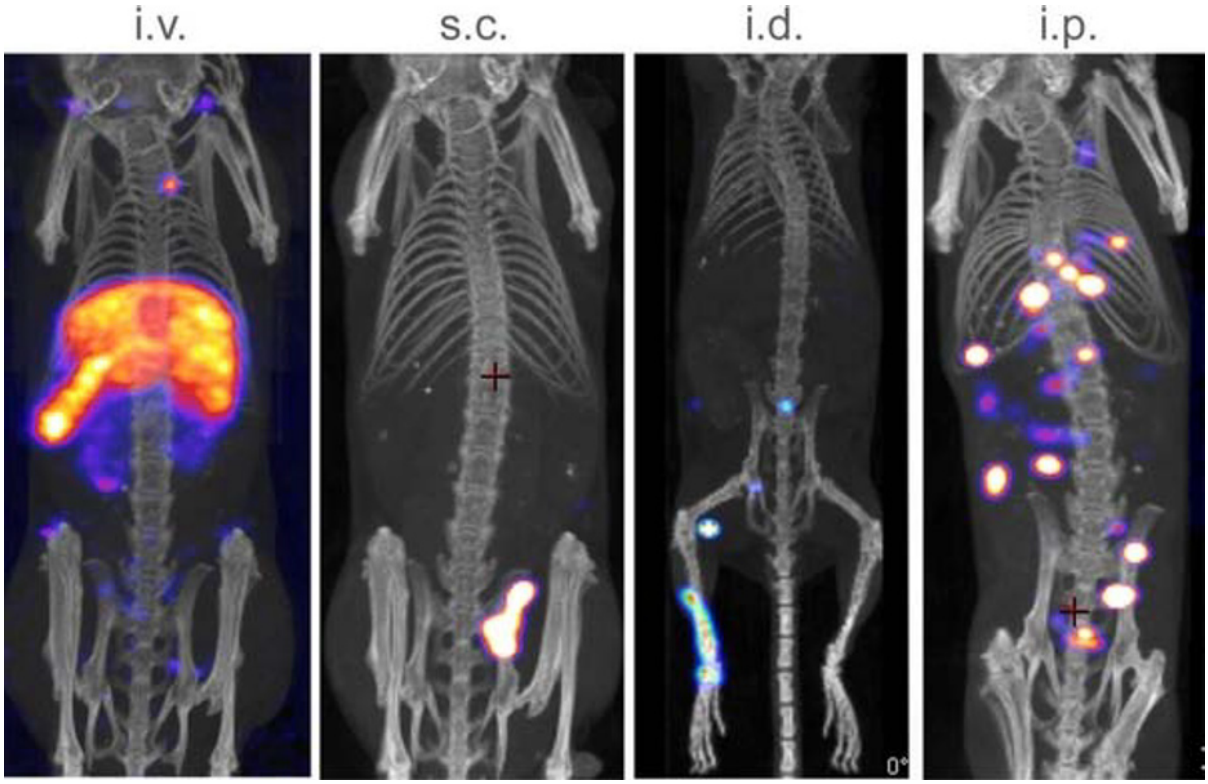

Migration of In-111 oxine labeled matured DCs 1 day after administration.

Disclosure of author financial interest or relationships:
N. Sato, None; **P. Choyke**, None.

Presentation Number **SS 76**
Scientific Session 13: Preclinical in vivo Studies - Inflammation/Immunology
September 20, 2013 / 11:15-11:30 / Room: Oglethorpe Auditorium

ImmunoPET imaging of CD8 expression using an anti-CD8 diabody

Richard Tavaré, *Kirstin A. Zettlitz, Felix B. Salazar, Anna M. Wu, Crump Institute for Molecular Imaging, UCLA, Los Angeles, CA, USA. Contact e-mail: rtavare@mednet.ucla.edu*

Antibodies and their engineered fragments, such as diabodies, are well suited for ImmunoPET imaging of cell surface proteins in vivo. Due to their rapid clearance, diabodies have been shown to enable high target-to-background PET images for antigen expression at much shorter times (4-44 hrs) than intact antibodies (5-7 days). Furthermore, the diabody antibody fragment does not contain an Fc domain and therefore lacks Fc dependent effector functions that are not desired in an imaging agent. Here, the variable domains of a depleting parental rat anti-mouse CD8 antibody (clone 2.43) have been reformatted into a Cys-diabody (cDb; ~51 kDa) for the targeting of murine CD8 in a range of animal models. The 2.43 cDb binds specifically CD8αLyt2.2 that is expressed on the mouse strains C57BL/6 and BALB/c but not CD8αLyt2.1 expressed on C3H and CBA/Ca mice. ImmunoPET imaging of CD8 expression in preclinical models can provide the ability to monitor therapies not only to $CD8^+$ T cell lymphoma models, but also to monitor the tumor infiltration of $CD8^+$ T cells in the context of immunotherapies, such as T cell and/or dendritic cell adoptive transfer and other antibody-based immunotherapeutics. In this study, the 2.43 cDb was site-specifically conjugated to either maleimide-DOTA or maleimide-DFO for the subsequent radiolabeling and ImmunoPET imaging with ^{64}Cu or ^{89}Zr, respectively. Both the ^{64}Cu-DOTA-2.43 cDb (3.2 μCi/μg, ~10μg injection) and the ^{89}Zr-DFO-2.43 cDb (3.4 μCi/μg, ~10μg injection) constructs targeted the spleen and lymph nodes of antigen-positive C57Bl/6 mice ($Lyt2.2^+$) but not antigen-negative C3H mice ($Lyt2.1^+$) at 4 hours post-injection. Axillary lymph node and spleen uptake for ^{64}Cu and ^{89}Zr radiolabeled 2.43 cDb ranged from 22.5(^{64}Cu)-39.3(^{89}Zr) %ID/g and 30.2(^{64}Cu)-44.2(^{89}Zr) %ID/g, respectively. Axillary lymph node- and spleen-to-blood ratios for ^{64}Cu and ^{89}Zr radiolabeled 2.43 cDb varied from 2.2(^{64}Cu)-3.4(^{89}Zr) and 2.9(^{64}Cu)-3.8(89Zr), respectively, in antigen-positive C57Bl/6 mice and 0.5(^{64}Cu)-0.7(^{89}Zr) to 0.4(^{64}Cu)-0.7(^{89}Zr) in antigen-negative C3H mice, demonstrating specific uptake in the lymphoid organs of $Lyt2.2^+$ mice. At only 4 hours post-injection, there is still ~10 %ID/g in the blood so images acquired at later time points will allow for more blood clearance and should yield higher target-to-background ImmunoPET images. These initial results are promising for the antibody fragment based detection of both $CD8^+$ lymphomas and tumor infiltrating $CD8^+$ T cells in preclinical models allowing for the non-invasive monitoring of immunotherapeutics in vivo.

Disclosure of author financial interest or relationships:
R. Tavaré, None; **K.A. Zettlitz**, None; **F.B. Salazar**, None; **A.M. Wu**, ImaginAb, Inc., Stockholder; ImaginAb, Inc., Consultant; ImaginAb, Inc., Grant/research support; Daiichi Sankyo, Consultant; Sanofi, Consultant .

Presentation Number **SS 77**
Scientific Session 13: Preclinical in vivo Studies - Inflammation/Immunology
September 20, 2013 / 11:30-11:45 / Room: Oglethorpe Auditorium

Paradoxical decrease in the capture and lymph node delivery of vaccine antigen induced by TLR4 agonists as visualized by dual-mode imaging

Deepak Kadayakkara[1], *Hyam I. Levitsky*[1], *Jeff W. Bulte*[2,3], [1]*Department of Oncology, Johns Hopkins School of Medicine, BALTIMORE, MD, USA;* [2]*Department of Radiology, Johns Hopkins School of Medicine, BALTIMORE, MD, USA;* [3]*Cellular Imaging Section, Institute of Cell Engineering, Johns Hopkins School of Medicine, BALTIMORE, MD, USA. Contact e-mail: dkadaya1@jhmi.edu*

Introduction: Non-invasive visualization of critical cellular events following vaccination can provide substantial insights into the development of novel vaccines and adjuvant systems. Toll-like receptor 4 (TLR4) is a specialized receptor expressed on antigen presenting cells (APC) that plays an important role in their activation and maturation. In this work, we evaluated the effect of the TLR4 agonist glucopyranosyl lipid A (GLA) as a tumor vaccine adjuvant using multi-modal imaging combining MRI and BLI. Methods: Mice were vaccinated in the right footpad with an irradiated engineered tumor cell vaccine against B16-mOVA melanoma expressing GM-CSF (GVAX) with or without GLA (20 μg/dose). For determining the optimal timing of adjuvant injection, GLA was administered 24 hrs pre-, together, or 24 hrs post-vaccination. For MRI, tumor cells were labeled with ferromagnetic iron oxide particle (FION, 100 μg/ml) by overnight incubation [1]. The magnetic vaccines release antigens along with iron oxide particles which are taken up by APCs and are then delivered to the popliteal lymph nodes (PLN) to prime T cells [2]. After magnetovaccination, mice were serially imaged using a T2*-weighted multi-gradient echo sequence (Bruker 11.7T), with the signal quantified as described previously [2]. MRI data were validated by FACS using iron oxide particles conjugated with evergreen fluorophore. CD8+ T cell response to vaccination was visualized by tracking ovalbumin specific CD8+ TCR transgenic T cells expressing firefly luciferase (OT1-Luci) which were transferred to non-transgenic mice 24 hours prior to vaccination,. Results: Paradoxically, combined administration of GLA with GVAX reduced antigen capture by APC and antigen delivery to the PLN (Fig. 1A,B,E). In both groups, signal within the PLN increased from day 3 to day 6 (Fig. 1E, n=3). These results were validated independently by FACS analysis (n=4) of CD11C+ APCs that captured iron-oxide particles with evergreen (Fig. S1). Based on these results, we hypothesize that premature maturation of APCs induced by GLA may be responsible for reduced antigen delivery to the PLN, because matured APCs are inefficient in phagocytosis as compared to immature APCs. Adjuvant timing study showed that injecting GLA 24 hrs following vaccination improved antigen delivery to the PLN (n=3) compared to GLA administered together or 24 hrs before vaccination (Fig1. C,D,E). BLI demonstrated that accumulation of OVA antigen-specific T cells in the PLN was proportional to the antigen delivery (Fig. 1F,G). Conclusions:, We have established a dual-mode imaging method to comprehensively visualize the afferent (APCs) and efferent arm (T cells) of vaccination. These tools will be invaluable to screen the efficacy of novel vaccine adjuvant systems non-invasively in vivo. Supported by U54 CA151838. References: 1. Nano Lett. 2012 13;12(6):3127-31, 2. Cancer Res 2009;69:3180-7

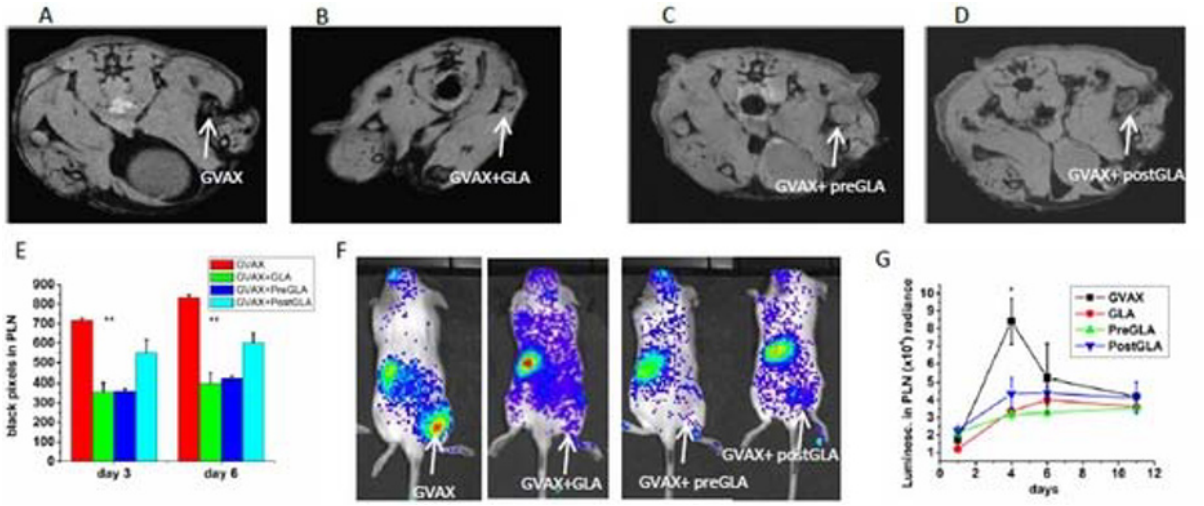

Figure 1: A and B) Representative MR images across the PLN showing that GLA adjuvant reduced the migration of antigen captured APCs compared to GVAX alone. D) GLA treatment 24 hrs post-vaccination shows improved antigen delivery to PLN compared to GLA pre-vaccination (C) or given together (B). E) Quantitative analysis of antigen captured APC migration to lymph nodes as determined by counting black pixels below the threshold from the adjacent muscle tissue in PLN (n=3, $P<0.01$, T test). F) BLI shows a correspondingly reduced accumulation of OT1 cells with GLA ($P<0.05$, T test), which is rescued by administering GLA 24 hours post vaccination. G) Quantitative longitudinal analysis of BLI signal in the PLN from the same cohort of mice that underwent MRI.

Disclosure of author financial interest or relationships:
D. Kadayakkara, None; **H.I. Levitsky**, Hoffmann La Roche, Employment; **J.W. Bulte**, None.

Presentation Number **SS 78**
Scientific Session 13: Preclinical in vivo Studies - Inflammation/Immunology
September 20, 2013 / 11:45-12:00 / Room: Oglethorpe Auditorium

In vivo PET-Imaging of Inflammation-induced Hypoxia during Experimental Arthritis: Comparison of [^{18}F]-Fluoromisonidazole ([^{18}F]FMISO) and [^{18}F]Fluoro-azomycin-β-deoxyriboside ([^{18}F]β-FAZDR)

Philipp Guenthoer[1], *Kerstin Fuchs*[1], *Manfred Kneilling*[1,2], *Denis Lamparter*[1], *Sandro Aidone*[1], *Daniel Bukala*[1], *Bernd J. Pichler*[1], *Gerald Reischl*[1], [1]*Preclinical Imaging and Radiopharmacy, University of Tuebingen, Tuebingen, Germany;* [2]*Dermatology, University of Tuebingen, Tuebingen, Germany. Contact e-mail: philipp.guenthoer@med.uni-tuebingen.de*

Rheumatoid arthritis (RA) is a systemic autoimmune disease characterized by progressive inflammation, erosive synovitis and consecutively joint destruction. Auto-antibodies against Glucose-6 phosphat-isomerase (GPI) induce arthritis in mice that closely resembles human RA. Hypoxia plays a major role in organ-specific autoimmune diseases such as GPI-arthritis and can induce angiogenesis via stabilization of the transcription factor HIF-1α. We compared the established hypoxia tracer [^{18}F]FMISO with the in our group newly developed hypoxia tracer [^{18}F]β-FAZDR in GPI-arthritis and analyzed the tracer kinetics and ability to quantify hypoxia *in vivo* at different time points after arthritis induction. Naïve BALB/c mice were injected with GPI- or control-serum to induce experimental arthritis. The course of ankle swelling was measured daily and static as well as dynamic *in vivo* PET-images were performed using [^{18}F]FMISO and [^{18}F]β-FAZDR on days 1, 3, 6 and 8 after arthritis induction. Both hypoxia tracers revealed, as early as 1 day after arthritis induction, a time point with hardly any ankle swelling, a 1.2-fold enhanced tracer uptake in arthritic ankles ([^{18}F]FMISO: 1.50±0.3%ID/cc, n=6; [^{18}F]β-FAZDR: 0.75±0.2%ID/cc, n=3) when compared to healthy control ankles ([^{18}F]FMISO: 1.28±0.3%ID/cc, n=4; [^{18}F]β-FAZDR: 0.63±0.1%ID/cc, n=3). Interestingly, the [^{18}F]FMISO uptake in ankles was 2-fold higher compared to [^{18}F]β-FAZDR, regardless whether ankles were inflamed or healthy. [^{18}F]FMISO and [^{18}F]β-FAZDR uptake further increased at day 3 after arthritis induction and displayed a 1.8-fold enhanced uptake in arthritic ankles for [^{18}F]FMISO (2.47±0.4%ID/cc, n=8) and 2.1-fold for [^{18}F]β-FAZDR (1.35±0.04%ID/cc, n=1), compared to control ankles. At day 6 the arthritic ankles to healthy control ratios were 2.2 for [^{18}F]FMISO and 1.9 for [^{18}F]β-FAZDR. The maximum [^{18}F]β-FAZDR uptake was observed at day 6 (1.46±0.1%ID/cc, n=6) and the maximum [^{18}F]FMISO uptake on day 8 after onset of RA (3.04±0.3%ID/cc, n=10). *In vivo* PET imaging confirmed a 2.1-fold higher [^{18}F]β-FAZDR and 2.2-fold higher [^{18}F]FMISO uptake in arthritic compared to control joints on day 8. [^{18}F]β-FAZDR demonstrated a faster tissue elimination and a reduced non-specific whole body uptake compared to [^{18}F]FMISO. In contrast, [^{18}F]FMISO indicated a more distributed uptake in the body of arthritic and healthy mice. Differences in tracer distribution could be explained by a higher hydrophilicity of [^{18}F]β-FAZDR compared to [^{18}F]FMISO. Most importantly, both tracers can be used to examine the early

effector phase and ongoing development of hypoxia *in vivo* in GPI-induced arthritis. Thus, non-invasive *in vivo* imaging of hypoxia-induced angiogenesis using [^{18}F]β-FAZDR and [^{18}F]FMISO appears to be a powerful tool to examine initial phases of hypoxia in autoimmune diseases during RA.

Disclosure of author financial interest or relationships:
P. Guenthoer, None; **K. Fuchs**, None; **M. Kneilling**, None; **D. Lamparter**, None; **S. Aidone**, None; **D. Bukala**, None; **B.J. Pichler**, Siemens, Grant/research support; Bayer, Grant/research support; AstraZeneca, Grant/research support; BoehringerIngelheim, Grant/research support; **G. Reischl**, None.

Presentation Number **SS 79**

Scientific Session 14: Technology & Software Developments - Clinical PET/SPECT, CT, Preclinical PET/SPECT

September 20, 2013 / 13:00-13:15 / Room: 102

Imaging the Breast: the ClearPEM Projects

Benjamin Frisch[1], *Pedro Almeida*[6], *Etiennette Auffray*[1], *Ricardo Bugalho*[3], *Claudia S. Ferreira*[3,6], *Nuno Ferreira*[7], *Valerie Juhan*[2], *Paul Lecoq*[1], *Olivier Mundler*[2], *Jorge A. Neves*[3], *Catarina Ortigão*[3], *Marco Pizzichemi*[5], *Jose C. Rasteiro da Silva*[1,3], *Pascale Siles*[2], *Rui Silva*[3], *Stefaan Tavernier*[4], *Laurent Tessonnier*[2], *Joao Varela*[3,1], *[1]CERN, Geneva, Switzerland; [2]Assistance Publique - Hopitaux de Marseille, Marseilles, France; [3]LIP, Lisbon, Portugal; [4]Vrije Universiteit Brussels, Brussels, Belgium; [5]University Milano-Biccoca, Milano, Italy; [6]University of Lisbon - FCUL - IBEB, Lisbon, Portugal; [7]ICNAS, Coimbra, Portugal. Contact e-mail: benjamin.frisch@cern.ch*

Breast cancer is the most frequent cancer amongst women. Since chances for full recovery are very good as long as it is detected at a sufficiently early stage, many countries have installed screening programs. However, classical techniques like X-ray mammography or ultrasound may have low sensitivity for patients with dense breasts, who have breast implants or had prior surgery. MRI is used as an additional tool, yet suffers from low specificity. Whole-body PET (WBPET), being the only technique that images metabolic processes, is handicapped by its low spatial resolution. Based on these considerations, we develop the ClearPEM, a PET dedicated to breast imaging. The patient is installed on a dedicated bed in the prone position. Two parallel detector plates rotate around the breast to acquire a full 3D image. ClearPEM also performs axillary exams by rotating its detector arm by 90 degrees, thereby shifting the plates to be on each side of the axilla. Currently, two prototypes have been installed in Coimbra, PT and Marseilles, FR. Since ClearPEM provides high-resolution metabolic information but lacks anatomical details, the ClearPEM-Sonic project extends the Marseilles prototype with an ultrasound elastography device. This aims at providing multimodal information allowing to exactly locate potential lesions in the surrounding anatomy and shall further improve the specificity with an exact measurement of tissue elasticity, reducing false positives from non-cancerous metabolically hyperactive tissue. Both prototypes have been successfully installed and commissioned. The PEM image resolution is determined to be better than 1.4 mm. The global detection efficiency of ClearPEM is around 1.5 % at the centre of the field of view. We use dedicated multimodal gelatine-Agar phantoms to objectively test the patient imaging performance of the machine. The PEM contrast recovery coefficient at an injected lesion-to-background ratio of 1:5 is above 80% for lesions bigger than 5 mm and above 20 % for lesions bigger than 3 mm. Multimodal phantom images confirm that ClearPEM-Sonic can co-register these images with a precision better than 2 mm. Both prototypes are in clinical trials that aim at determining the feasibility of ClearPEM exams on a total of 20 patients each. We present patient images and compare them to mammography, B-mode US, MRI and WBPET acquisitions. ClearPEM proves to be able to detect small lesions that are not visible with WBPET. We present cases where ClearPEM improves the specificity of the overall diagnostic process. ClearPEM is a project in the frame of the Crystal Clear Collaboration. ClearPEM-Sonic is a project in the frame of CERIMED.

ClearPEM-Sonic seen from the control room

N. ,

Disclosure of author financial interest or relationships:
B. Frisch, None; **P. Almeida**, PETSys, SA, Stockholder; **E. Auffray**, None; **R. Bugalho**, None; **C.S. Ferreira**, None; **Ferreira**, PETsys, Stockholder; **V. Juhan**, None; **P. Lecoq**, None; **O. Mundler**, None; **J.A. Neves**, None; **C. Ortigão** None; **M. Pizzichemi**, None; **J.C. Rasteiro da Silva**, None; **P. Siles**, None; **R. Silva**, None; **S. Tavernier**, PetSYS, Stockholder; **L. Tessonnier**, None; **J. Varela**, None.

Presentation Number **SS 80**
Scientific Session 14: Technology & Software Developments - Clinical PET/SPECT, CT, Preclinical PET/SPECT
September 20, 2013 / 13:15-13:30 / Room: 102

Potential of the wireless radiosensitive intracerebral probe PIXSIC to monitor PET radiotracers in anaesthetized and awake rat

Laure Balasse[1,2], Julia Maerk[3], Sylvain Fieux[2], Frederic Pain[1], Aurélie Genoux[1], Christian Morel[3], Pascale Gisquet-Verrier[4], Luc Zimmer[2], **Philippe Laniece**[1], [1]*IMNC - Imagerie et Modélisation en Neurobiolgie et Cancérologie, University Paris Sud /CNRS, Orsay, France;* [2]*CNRL- Neurosciences Center of Lyon- equipe BioRan, University Lyon 1 / CNRS, Lyon, France;* [3]*CPPM - Centre de Physique des particules de Marseille, Aix-Marseille Université, CNRS, IN2P3, Marseille, France;* [4]*CNPS - Neuroscience Center of Paris-Sud, University Paris Sud / CNRS, Orasay, France. Contact e-mail: laniece@imnc.in2p3.fr*

In neuroscience, functional imaging with positron emission tomography (PET) and behavioural assays in rodents are complementary approaches, despite the fact that they are rarely associated simultaneously because general anaesthesia inherent to PET precludes behavioural studies. To address this methodological limit, we have developped a radiosensitive pixelated intracerebral probe named PIXSIC that provides access to the combination of simultaneous observations of molecular and behavioural parameters on rodents. PIXSIC proposes a novel strategy for in vivo recording of the local time-activity curves of PET radiopharmaceuticals. It relies on a sub-millimetre pixelated probe of Si (200 µm thick, 690 µm wide and 17 mm long hosting 10 pixels with dimension 200 µm x 500 µm) implanted into the brain region of interest by stereotaxic surgery. Positrons resulting from decays of a PET radiotracer are detected by reverse-biased, high-resistivity silicon diodes. The system aims at time-resolved high sensitivity measurements in a volume of a few mm3 defined similarly as for the Beta-Microprobe by the positron range within tissues. The pixelated detection scheme adds "imaging" features as it allows recording of the time-activity curves in different brain regions along the probe position. PIXSIC has a compact and autonomous design based on a radiofrequency data exchange link that allows for full freedom in the animals motion and behavioural activity while limiting stress during acquisition. The first biological validations were performed on anaesthetized rats implanted with two probes, one in the region of interest (hippocampus or striatum, according to the radiotracer) and the other one in a control region (cerebellum). We used [11C]-raclopride for dopamine D2 receptors and [18F]-MPPF for serotonin 5HT1A receptors. According to our previous studies with the Beta-Microprobe (J Nucl Med 2002, 43(2):227-33; Eur J Nucl Med 2002 29(9) 1237-47), the radioactive signals measured with the PIXSIC pixels are reproducible and well-correlated with the distributions of the targeted receptors. The simultaneous measurement of implanted rats in a small animal PET camera confirmed the similarity between PIXSIC and microPET time-activity curves. Moreover, the binding curves highlighted the possibility for PIXSIC to distinguish different tracer kinetics within the structure of interest (cortex/striatum or cortex/hippocampus) in accordance to the stereotaxic location of the pixels. In addition, PIXSIC allowed us to perform the first kinetic measurements of [11C]-raclopride and [18F]-MPPF on awake and freely moving rats. In conclusion, PIXSIC constitutes an unprecedented instrumental methodology for connecting PET molecular imaging and behavioral measurements with freely-moving rodents.

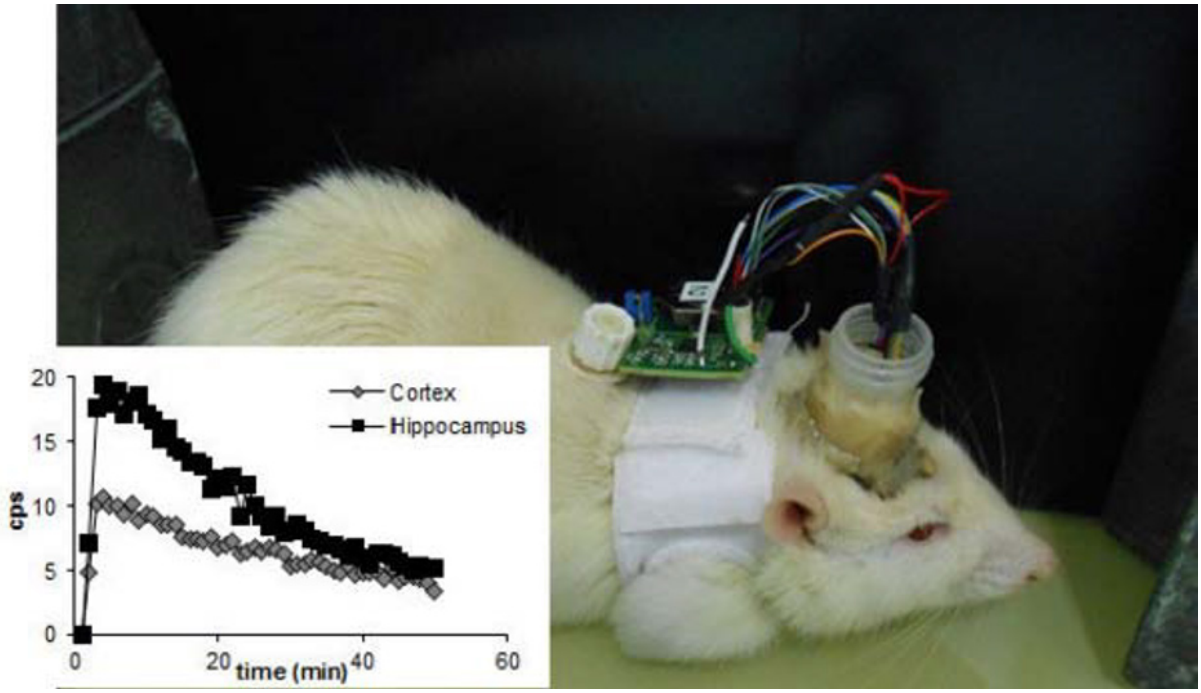

Figure: Photography showing a freely-moving rat equipped with PIXSIC's components and the first time-activity curves in the hippocampus and the cortex after bolus injection of 74 MBq (2mCi) [18F]-MPPF in awake freely-moving rats.

Gisquet-

Disclosure of author financial interest or relationships:

L. Balasse, None; **J. Maerk**, None; **S. Fieux**, None; **F. Pain**, None; **A. Genoux**, None; **C. Morel**, None; **P. Verrier**, None; **L. Zimmer**, None; **P. Laniece**, None.

Presentation Number **SS 81**
Scientific Session 14: Technology & Software Developments - Clinical PET/SPECT, CT, Preclinical PET/SPECT
September 20, 2013 / 13:30-13:45 / Room: 102

A Novel Collimation Technique for Molecular Breast Imaging

Olga Gopan[1], *David R. Gilland*[1], *Andrew Weisenberger*[2], *Brian J. Kross*[2], *Benjamin Welch*[3], [1]*Biomedical Engineering, University of Florida, Gainesville, FL, USA;* [2]*Thomas Jefferson National Accelerator Facility, Newport News, VA, USA;* [3]*Dilon Technologies, Inc., Newport News, VA, USA. Contact e-mail: ogopan@ufl.edu*

Purpose: Our purpose is to develop a gamma camera for molecular breast imaging (MBI) to perform high spatial resolution/sensitivity, limited angle SPECT. This system is designed to achieve 3D images of the breast while using a simplified detector motion and is furthermore conducive to both on-board biopsy and multi-modal imaging with mammography. Methods: The proposed gamma camera uses a novel collimation technique: a variable-angle, slant-hole (VASH) collimator, which is well suited for limited angle SPECT of a mildly compressed breast. Rather than rotate the camera around the breast, the VASH collimator allows tomographic acquisition (angular views of ±30°, ±45°) by changing the slant angle of its holes while the detector remains stationary and flush against the compression paddle. This simplified motion minimizes detector-to-object distance for high spatial resolution and/or sensitivity. Theoretical analysis and Monte Carlo simulations were performed assuming a point source and an isolated breast phantom. Spatial resolution and sensitivity were measured from the point source images and compared to theory. Contrast and signal-to-noise ratio (SNR) were measured from the reconstructed images of the breast phantom. Results were compared to both single-view, planar images and conventional SPECT images. For both conventional SPECT and VASH, data were reconstructed using an iterative algorithm. Finally, an experimental evaluation was performed using a proof-of-concept VASH collimator. The collimator was composed of brass and designed to image low energy emitters. Results: Results from Monte Carlo simulations studies showed good agreement with theory in terms of spatial resolution, including depth of interaction (DOI) effects, and sensitivity. The DOI effect resulted in roughly a 2 mm loss in spatial resolution only in the z-, or depth, dimension. Increasing the slant angle range from ±30° to ±45° improved spatial resolution in the z-dimension by roughly 1 mm. In reconstructed images of the breast phantom, VASH out-performed conventional SPECT in terms of SNR and contrast. VASH also achieved superior contrast and comparable SNR to planar scintimmammography. Finally, reconstructed images from the proof-of-concept VASH collimator system demonstrated reasonable depth resolution capabilities using a limited angle slant angle range. Conclusions: We conclude that this limited angle SPECT system using a VASH collimator can improve 3D image quality for MBI with a simple yet attractive design for clinical imaging.

	Planar	VASH, ±30°	VASH, ±45°	PH SPECT	Phantom
3 hours	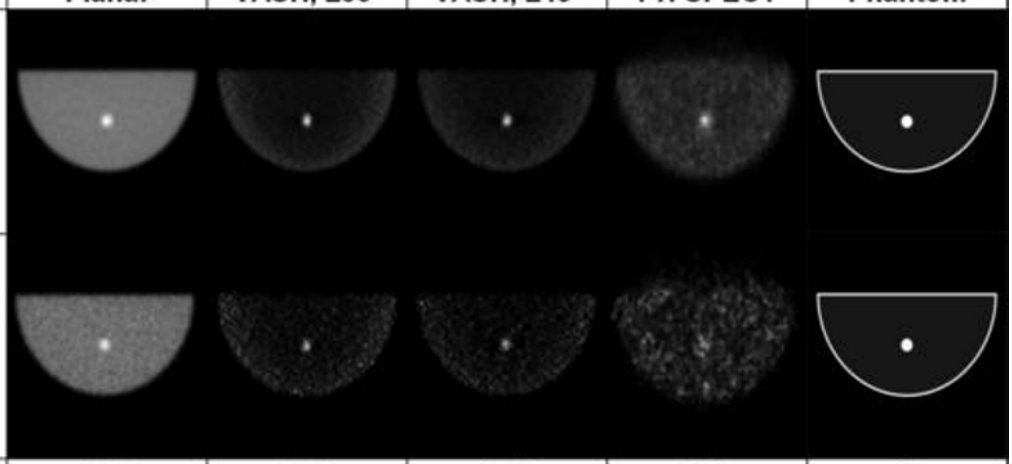				
20 minutes					
Contrast	0.94	9.60	9.45	3.11	10
Noise	0.03	0.25	0.32	0.29	0
SNR	34.25	41.04	31.84	10.94	Infinite

Contrast, noise and signal-to-noise ratio (SNR) results for the breast phantom in the x-y, or transaxial, plane.

Disclosure of author financial interest or relationships:
O. Gopan, None; **D.R. Gilland**, None; **A. Weisenberger**, None; **B.J. Kross**, None; **B. Welch**, Dilon Technologies, Employment .

Presentation Number **SS 82**
Scientific Session 14: Technology & Software Developments - Clinical PET/SPECT, CT, Preclinical PET/SPECT
September 20, 2013 / 13:45-14:00 / Room: 102

Sampling considerations for a sub-millimeter resolution zoom-in PET insert of a dedicated extremity PET/CT system

Shruti Agarwal, *Ramsey D. Badawi, Abhijit J. Chaudhari, Radiology, UC Davis School of Medicine, Sacramento, CA, USA. Contact e-mail: shagarwal@ucdavis.edu*

Objectives: We are fabricating a partial-ring, sub-millimeter resolution PET insert with zoom-in capability for integration into a dedicated extremity PET/CT system (Fig. 1A). The target application is for high resolution region-of-interest (ROI) molecular imaging in conditions such as breast cancer and arthritis. In this study we evaluated the sampling considerations for such an insert specifically in the context of maximizing the sensitivity for imaging and spatial resolution distribution of the imaged ROI. **Methods:** The zoom-in PET insert consists of 4 detector modules arranged in C-shape (Fig 1A). Each module has an array of 28x28 LYSO crystals (size 0.5x0.5x12 mm^3) coupled to a photomultiplier tube. The insert will substitute for a detector head of a dedicated extremity PET system (crystal pitch of 1.5 mm) built at our institution when high resolution scanning of an ROI is desired. The insert will be translated axially and rotated around the gantry center (O in Fig 1C). For this simulation study the cross-section of the PET insert (arc CD in Fig 1C) formed coincidence with the cross-section of the extremity PET detector head (arc AB in Fig 1C). The ring diameter and arc length of the extremity PET head (R_b=100 mm, S_b=176 mm respectively) and the arc length of the zoom-in PET insert (S_s= 64 mm) were fixed, while the ring diameter of the PET insert R_s was varied for optimization. Pixels that lie within the quadrilateral ACDB (Fig 1C) were considered in the analysis as they intersect all possible coincident lines of responses. This quadrilateral was further subdivided into four sub-planes (Fig 1C) with respect to the intersection point T. These four sub-planes were examined individually and the angular span of coincident lines through a given pixel was computed. **Results & Discussion**: Coincident lines crossing each pixel in various directions were obtained (Suppl. Fig 1A). System rotation was simulated over an angular range of $0 \leq \gamma \leq 180^o$ with steps of 4^o. The angular span of the coincident lines from each pixel was calculated (Suppl. Fig 1B & 1C). Based on the fan-beam sampling completeness condition, the minimum angular rotation of the system for full coverage of field of view was determined to be $\gamma_{min} = 215^o$. A sensitivity map (total number of coincident lines during 215^o rotation of the system) for each pixel is shown in Fig 1D. Intrinsic spatial resolution of the zoom-in PET insert along the center line in the image plane was calculated using an analytical formula. Fig 1B represents the variation in spatial resolution with respect to the pixel distance from the insert. The highest spatial resolution was 0.75 mm at the intersection point T in Fig 1C. **Conclusions:** In this study sampling constraints were evaluated and their impact on the sensitivity for zoom-in PET insert was determined. The change in the intrinsic spatial resolution across the field of view was evaluated. The results of this study are expected to provide a platform for evaluation of design trade-offs associated with such types of system. **Research Support:** California Breast Cancer Research Program grant #18IB-0018 and by NCI R01 CA129561.

Figure 1

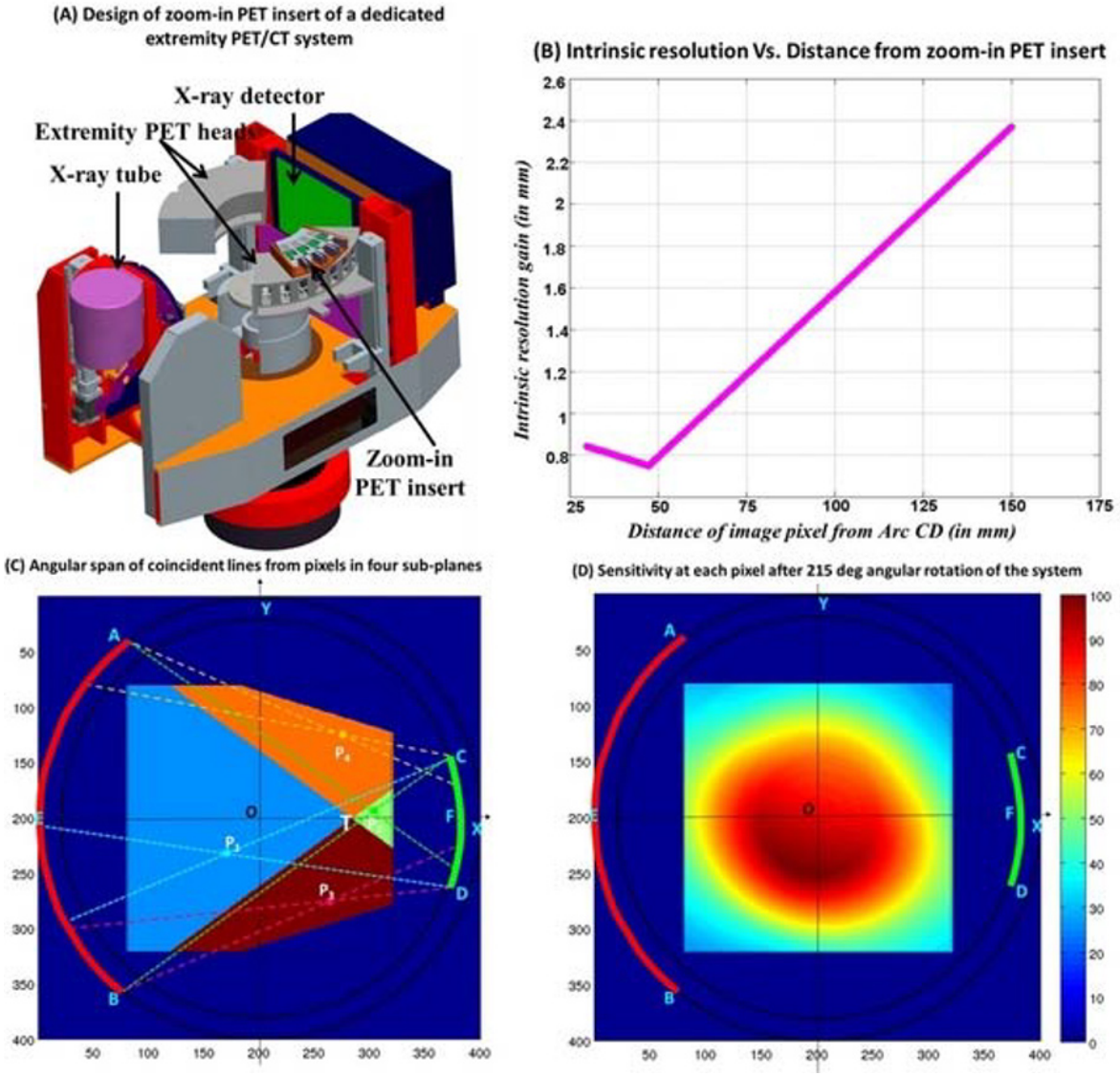

Figure 1: (A) Sub-millimeter resolution zoom-in PET insert of a dedicated extremity PET/CT system; **(B)** Intrinsic spatial resolution profile along the axial direction plotted w.r.t the distance of the pixel from a detector of the PET insert (note that parallax errors are not considered in this plot); **(C)** 2D tomographic image plane inside the planar span ACDB subdivided into four sub-planes (shown as number 1, 2, 3, 4) Illustrating the angular span of coincident lines from pixels in corresponding sub-planes; **(D)** Pseudo-color map shows the relative sensitivity values at each pixel (as a percentage of maximum value) when the system is continuously rotated by 215 degree.

Disclosure of author financial interest or relationships:
S. Agarwal, None; **R.D. Badawi**, Philips Medical, Grant/research support; Toshiba Medical, Consultant; JNJ, Stockholder; **A.J. Chaudhari**, None.

Presentation Number **SS 83**
Scientific Session 14: Technology & Software Developments - Clinical PET/SPECT, CT, Preclinical PET/SPECT
September 20, 2013 / 14:00-14:15 / Room: 102

A High Spatial Resolution PET Scanner Designed for Neuroimaging in Mice

Yongfeng Yang[1], *Julien Bec*[1], *Jian Zhou*[1], *Mengxi Zhang*[1], *Martin S. Judenhofer*[1], *Xiaowei Bai*[1], *Kun Di*[1], *Yibao Wu*[1], *Kanai Shah*[2], *Richard Farrell*[2], *Jinyi Qi*[1], *Simon R. Cherry*[1], [1]*Biomedical Engineering, UC Davis, Davis, CA, USA;* [2]*Radiation Monitoring Devices Inc., Watertown, MA, USA. Contact e-mail: yfyang@ucdavis.edu*

The spatial resolution of current commercial small-animal PET scanners is 1-2 mm. Small animal PET scanners with better spatial resolution and sensitivity would improve the quantification of signals by reducing the partial volume effects and increasing signal-to noise. This is particularly important if the power of PET methodology is to be successfully applied to the broad array of genetic models available for interrogating the mouse brain. The objectives of this work are to build and evaluate a prototype small-animal positron emission tomography (PET) scanner for imaging the mouse brain that approaches the resolution limits set by the physics of positron emission and annihilation. The scanner consists of 16 dual-ended readout tapered scintillation detectors arranged in a ring of diameter 61 mm. The scintillator arrays consist of 14×14 lutetium oxyorthosilicate (LSO) elements, with a crystal size of 0.43×0.43 mm^2 at the front end and 0.80×0.43 mm^2 at the back end. The crystal elements are 13 mm long. The axial field of view is 7 mm and transaxial field of view is 40 mm. The arrays are read out by an 8×8 mm^2 and a 13×8 mm^2 position-sensitive avalanche photodiodes placed at opposite ends of the scintillator array to provide depth-of-interaction information. The intrinsic spatial resolution, sensitivity and reconstructed spatial resolution of the scanner were measured. First phantom and in-vivo mouse images were acquired. The average detector intrinsic spatial resolution in the axial direction is 0.61 mm. The spatial resolution within a field of view that can accommodate the entire mouse brain is better than 0.6 mm using a ML-EM reconstruction algorithm of line/point sources. Sources were reconstructed in a warm background to ensure they were not artificially improved due to the non-negativity constraint in the ML-EM algorithm. Images of a micro hot-rod phantom showed that rods with diameter down to 0.5 mm can be resolved. First in vivo studies were obtained using 18F-fluoride and confirmed that 0.6 mm resolution can be achieved in the mouse head in vivo. The sensitivity of the scanner at center of the field of view is 1.1% for a lower energy threshold of 100 keV and 0.6% for a lower energy threshold of 250 keV. In conclusion, a prototype preclinical PET scanner dedicated to mouse brain imaging with a reconstructed spatial resolution less than 0.6 mm was developed and first animal studies performed. These are believed to be the highest resolution in vivo PET studies ever performed. We are currently improving the 3D ML-EM reconstruction by using the measured point spread function. Brain imaging studies with 18F-fluorodeoxyglucose as well as neuroreceptor ligands will be pursued. Future plans are to add more detector rings to extend the axial field of view of the scanner and increase sensitivity.

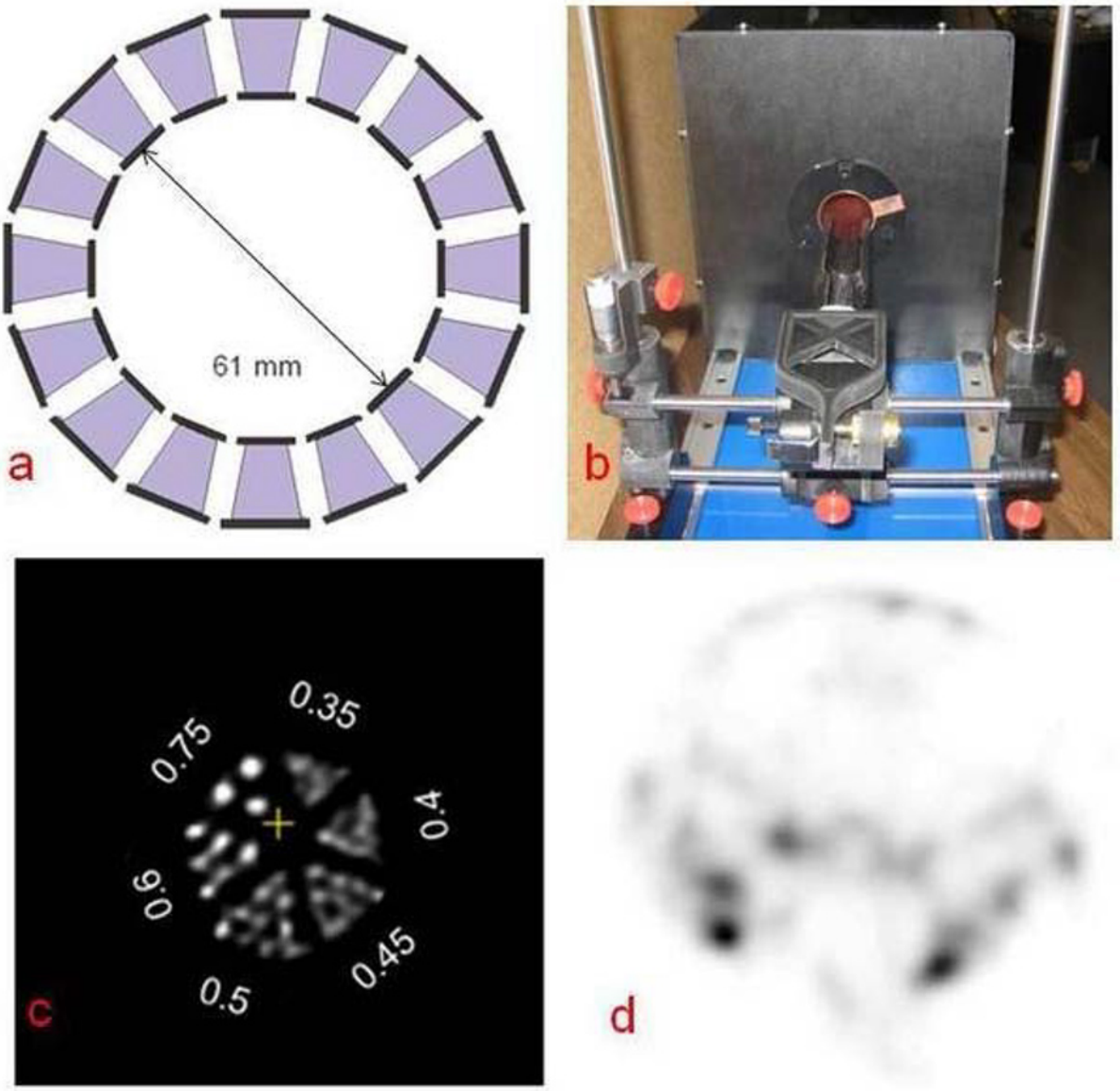

Figure: (a) Schematic of the prototype scanner showing the 16 dual-ended tapered detectors; (b) Photograph of completed scanner; (c) Image of a micro hot rod phantom showing that 0.5 mm are resolved; (d) Coronal section of juvenile mouse head showing the ability to image the 0.2-0.3 mm thick skull with 18F-fluoride.

Disclosure of author financial interest or relationships:

Y. Yang, None; **J. Bec**, None; **J. Zhou**, None; **M. Zhang**, None; **M.S. Judenhofer**, None; **X. Bai**, None; **K. Di**, None; **Y. Wu**, None; **K. Shah**, None; **R. Farrell**, None; **J. Qi**, None; **S.R. Cherry**, GE Healthcare, Grant/research support; Perkin Elmer, Grant/research support .

Presentation Number **SS 84**
Scientific Session 14: Technology & Software Developments - Clinical PET/SPECT, CT, Preclinical PET/SPECT
September 20, 2013 / 14:15-14:30 / Room: 102

Investigation of time-of-flight PET detectors with depth-encoding

Eric Berg, *Jeffrey P. Schmall, Junwei Du, Emilie Roncali, Varsha Viswanath, Simon R. Cherry, Biomedical Engineering, UC Davis, Davis, CA, USA. Contact e-mail: eberg@ucdavis.edu*

Introduction: Developing positron emission tomography (PET) detectors with time-of-flight (TOF) capability and depth-of-interaction (DOI) encoding is a key component in developing high resolution PET scanners for low dose imaging procedures while maintaining or exceeding existing spatial resolution standards. High sensitivity PET scanners with an extended axial field-of-view (FOV) require detectors capable of both TOF and DOI encoding in order for the reconstructed images to fully benefit from the increased sensitivity which places unique demands on the detector design. In this work, we evaluate two potential TOF-capable DOI encoding schemes and examine the impact of enabling DOI encoding on TOF capability. Methods: Single crystal timing resolution measurements were performed for crystals exhibiting no DOI encoding, discrete DOI encoding and continuous DOI encoding. For all measurements, 3 x 3 x 10 mm^3 LYSO crystals polished on all surfaces were used with a Hamamatsu R9800 photomultiplier tube (PMT) to read out the LYSO crystals. Coincidence timing resolution measurements for the non DOI crystals served as a baseline for comparison of DOI encoding crystals. The discrete DOI encoding detector consisted of two LYSO crystals coupled together to form a two segment, 20 mm long, crystal representative of a phoswich or dual layer offset scintillator array. For the continuous DOI timing measurements, a LYSO crystal was coated on the top surface and on the top half of the 4 side surfaces with a ~250 μm layer of cerium-doped yttrium-aluminum-garnet (YAG:Ce) phosphor compound. The phosphor absorbs and re-emits the scintillation light after a brief delay and at a longer wavelength. Sampling the decay curve of the output signal gave an estimate of the DOI in the crystal since the light emitted from the phosphor lengthens the signal decay time in a depth-dependent manner. Timing resolution data were acquired for the DOI encoding detectors using the non DOI detector as the reference detector. Results: A coincidence timing resolution of 373 ps was measured for the non DOI encoding detectors giving an intrinsic timing resolution of 260 ps for the non DOI detector. For the discrete DOI and continuous DOI detectors, intrinsic timing resolutions of 395 ps and 400 ps were calculated respectively. The DOI resolution for the phosphor coated LYSO crystal was based on sampling the PMT output signal decay curve to estimate the contribution of phosphor light to the overall signal and was estimated to be 3 mm. Discussion and Conclusion: We have shown that phosphor-coated scintillator crystals may be a viable solution for DOI-encoding TOF-capable PET detectors by exhibiting similar timing resolution to that of a dual-layer crystal while providing superior DOI resolution. Using these results, we plan to further examine and optimize the use of phosphor-coated crystals for TOF applications by examining various crystal surface treatments and phosphor coatings to give optimal TOF performance and DOI resolution. Based on these results, we will construct a prototype DOI-encoding TOF-capable block PET detector using an array of phosphor-coated LYSO crystals.

Disclosure of author financial interest or relationships:
E. Berg, None; **J.P. Schmall**, None; **J. Du**, None; **E. Roncali**, None; **V. Viswanath**, None; **S.R. Cherry**, GE Healthcare, Grant/research support; Perkin Elmer, Grant/research support .

Presentation Number **SS 85**
Scientific Session 15: Chemistry & Imaging Probes, Technology & Software Developments - Photoacoustic Imaging
September 20, 2013 / 13:00-13:15 / Room: 105

Genetically-Encoded Chromoproteins for Photoacoustic Imaging

Alexander Forbrich[1], *Yan Li*[2], *Jiahui Wu*[2], *Robert Campbell*[2], *Roger J. Zemp*[1], [1]*Electrical and Computer Engineering, University of Alberta, Edmonton, AB, Canada;* [2]*Department of Chemistry, University of Alberta, Edmonton, AB, Canada. Contact e-mail: aforbric@ualberta.ca*

Optical imaging of genetically-encoded reporter molecules such as green fluorescent protein (GFP) and its variants have allowed researchers to visualize and investigate a multitude of biological processes in vivo. Reporter molecules allow classification of specific cells within a larger population of cells and, if tagged to the protein of interest, reporter molecules can enable dynamic tracking of the sub-cellular localization of proteins. Although optical imaging of fluorescent proteins (FP) has substantially enhanced our understanding of biology, high optical scattering and absorption in tissues make high-resolution, non-invasive optical imaging below one transport mean free path (~1 mm) difficult. Photoacoustic (PA) microscopy offers a unique way to image reporter molecules at high depth-to-resolution ratios comparable to ultrasound imaging techniques with optical absorption contrast. PA imaging has already proven useful in providing structural and functional information of blood vessels and has been used to image gene expression of tyrosinase, lacZ, and some fluorescent molecules including mCherry, GFP, and infrared FP. Although these reporter molecules work well as PA markers, the products of tyrosinase and lacZ can be toxic to cells in high levels. FPs have limited photostability and exposure to laser energy causes substantial absorption-bleaching. Furthermore, the most commonly used FPs are all optimized for high fluorescence quantum yield (QY) and thereby exhibit inefficient energy conversion to heat and sub-optimal thermoelastic expansion necessary for PA imaging. Recently, several non-fluorescent chromoproteins with properties ideal for PA imaging have been identified. Ultramarine protein from coral and cjBlue protein from sea anemone have near-zero QY (< 0.001) and high extinction coefficients (~65,000 $M^{-1}cm^{-1}$) with peak absorption wavelength of 585 and 610 nm, respectively. These chromoproteins have been shown to have high photostability. Using a 25 MHz ultrasound transducer and a 10 Hz Nd:YAG laser with tunability provided by an optical parametric oscillator, we compare the PA signal of purified proteins and protein-producing E. coli. Specifically, we compare mCherry, yellow fluorescent protein (YFP), and a dark form of YFP to the chromoproteins ultramarine and cjBlue. The chromoproteins show an order of magnitude greater signal than the FP and are less prone to absorption-bleaching. Animal models were used to demonstrate the ability to image chromoproteins in vivo several millimeters below the tissue surface. We demonstrate that demixing algorithms can separate blood from ultramarine and cjBlue with minimal crosstalk. Finally, we are using directed evolution techniques and error-prone PCR to optimize cjBlue and ultramarine for PA imaging.

Our results show that imaging chromoproteins at the AINSI limit of ~20 mJ/cm^2 has a sensitivity of 140 nM and 98 nM for cjBlue and ultramarine, respectively, for unity signal-to-noise ratio (SNR). As reporter molecules for PA imaging, chromoproteins have demonstrated great potential having 14-60 fold greater SNR compared to other fluorescent molecules with minimal or no photobleaching effects.

Disclosure of author financial interest or relationships:
A. Forbrich, None; **Y. Li**, None; **J. Wu**, None; **R. Campbell**, None; **R.J. Zemp**, None.

Presentation Number **SS 86**
Scientific Session 15: Chemistry & Imaging Probes, Technology & Software Developments - Photoacoustic Imaging
September 20, 2013 / 13:15-13:30 / Room: 105

A high affinity, high stability photoacoustic agent for imaging gastrin-releasing peptide receptors in prostate cancer

Jelena Levi[1,2], *Ataya Sathirachinda*[1,2], *Sanjiv S. Gambhir*[1,2], [1]*Canary Center at Stanford, Palo Alto, CA, USA;* [2]*Molecular Imaging Program at Stanford, Stanford University, Palo Alto, CA, USA. Contact e-mail: jlevi@stanford.edu*

Background. Transrectal ultrasound (TRUS) is the most commonly used and ubiquitously spread out imaging technique for prostate cancer. When not accompanied by a biopsy, TRUS has a very limited diagnostic value as it provides only anatomical information. A closely related technique, photoacoustic imaging, can provide anatomical, functional and molecular information, the fusion of which can prove crucial for accurate non-invasive assessment of prostate cancer. Here we explore the ability of a novel photoacoustic agent that targets gastrin-releasing peptide receptor (GRPR) found in a great number of early prostate neoplasias, to enable molecular interrogation of prostate lesions. Methods. The imaging agent AA3G-740 was synthesized by conjugating a near infrared dye, ATTO-740, through a triglycine linker, to a GRPR antagonist peptide,dFQWAVGHStaL-NH2. The control agent, CAA3G-740 was synthesized in the same manner using a scrambled peptide sequence. The sensitivity of detection, stability in serum, as well as binding in cell culture were determined prior to testing the agents in mice bearing prostate cancer tumors. Results. The active agent showed a high stability in serum, strong binding to the GRPR expressing PC3 cells, and minimal attachment to low expressing LNCAP cells. The binding of the active agent to the PC3 cells was blocked by the addition of the high affinity ligand, bombesin, in a dose dependent manner, demonstrating the specificity of the agent for GRPR. The control agent did not show significant binding to PC3 cells. The photoacoustic signal had a linear response (R2=0.98) to the increasing concentration (50-250 pmol) of the imaging agent suggesting the possibility of inferring the levels of GRPR in a lesion based on the intensity of the photoacoustic signal. The lowest number of cells that could be photoacoustically detected in vitro was found to be 0.5 million. The ability of the imaging agent to bind to the receptors in vivo was tested by imaging PC3 tumors (~ 0.7cm in size) in mice (n=6) after a tail vein injection of 10 nmol of the agent (Figure1). Thirty minutes after the injection, an intense photoacoustic signal was observed in PC3 tumors of mice injected with the active agent while the injection of the control agent (n=4) did not lead to the appreciable signal. Concusion. The images obtained prior to injection of the agent clearly revealed vasculature in the PC3 tumors indicating the ability of photoacoustic imaging to provide anatomical and functional information about lesions. Supplemental molecular information was achieved through the use of GRPR-targeting agent that showed strong binding in vivo and allowed for high resolution imaging of the receptors. The combination of the high resolution, wealth of information and signal specificity promises a method for minimally invasive diagnosis of early prostate cancer.

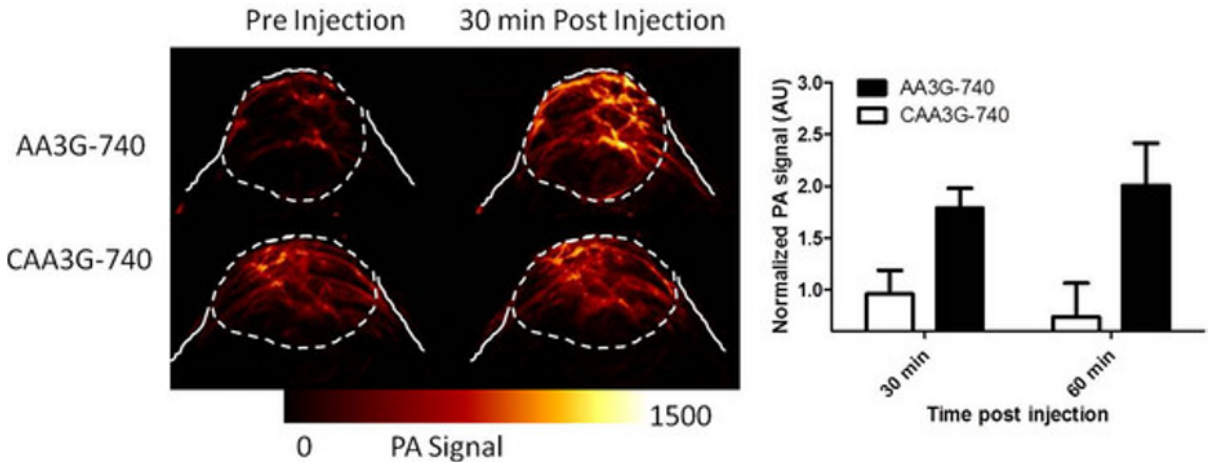

Figure 1. Photoacoustic imaging of the gastrin-releasing peptide receptors in PC3 prostate tumors in mice. Mice bearing subcutaneous PC3 tumors in the hind legs were photoacoustically imaged using 750 nm light before and after a tail-vein injection of 10 nmol GRPR-binding AA3G-740 and the control agent, CAA3G-740. The photoacoustic signal at 30 and 60 minutes post- injection was significantly higher for the active agent than for the control one. The error bars represent standard error (n=6 for the active, n=4 for the control agent, $p < 0.05$).

Disclosure of author financial interest or relationships:

J. Levi, None; **A. Sathirachinda**, None; **S.S. Gambhir**, Bracco Diagnostics, Consultant; Endra, Inc, Stockholder; Cellsight, Stockholder; Enlight, Inc., Stockholder; General Electric, Grant/research support; ImaginAb, Stockholder; MagArray, Inc., Stockholder; Sanofi-Aventis, US, Grant/research support; SiteOne Therapeutics, Stockholder; VisualSonics/Sonosite, Stockholder .

Presentation Number **SS 87**
Scientific Session 15: Chemistry & Imaging Probes, Technology & Software Developments - Photoacoustic Imaging
September 20, 2013 / 13:30-13:45 / Room: 105

Optoacoustic imaging of middle cerebral artery occlusion

Jake B. Turner[1,3], *Moritz Kneipp*[2,3], *Sebastian Hambauer*[4], *Jens Lehmberg*[4], *Ute Lindauer*[4], *Daniel Razansky*[2,3], [1]*Faculty of Electrical Engineering and Information Technology, Technische Universität München, München, Germany;* [2]*Faculty of Medicine, Technische Universität München, München, Germany;* [3]*Institute for Biological and Medical Imaging, Helmholtz Zentrum München, München, Germany;* [4]*Department of Neurosurgery, Klinikum rechts der Isar, Technische Universität München, München, Germany. Contact e-mail: jake.turner@helmholtz-muenchen.de*

Functional imaging of stroke aims at further understanding into the development of the ischemic lesion, which may lead to more effective treatment. However, imaging modalities commonly used for stroke visualization have generally high acquisition and running costs, with some also lacking the spatial and/or temporal resolution necessary for efficient investigations of disease progression in small animal models. Here a middle cerebral artery occlusion (MCAO) model was used to demonstrate the applicability of real-time multispectral optoacoustic tomography (MSOT) in identifying the ischemic lesion in vivo in the mouse model of MCAO. All animals studies were performed according to approved protocols (Regierung von Oberbayern, AZ 55.2-1-54-2531.2-6-10). This study saw eight nude unpigmented immunocompetent mice (Crl:SKH1-Hrhr strain) anesthetised with 1.5% isoflurane. The imaging system was a cross-sectional small animal MSOT scanner, which uses a 64-element ultrasonic array for real-time 2D imaging [1]. The scans were in vivo, whole-brain coronal tomographical slices acquired at 15 different excitation wavelengths between 710 and 850nm. The acquired data was reconstructed using a model-based algorithm [2] and spectrally unmixed for oxygenated- and deoxygenated-haemoglobin absorption spectra using linear regression with a non-negative constraint [3]. Following the preoperative control scan, the MCAO procedure was performed by introducing a filament into the common carotid artery and advancing it to the origin of the MCA [4]. After 60min of ischemia, the filament was retracted, the wound closed, and the animal allowed to survive for 24 hours. After 24h a final scan was performed under anesthesia. The animals were then sacrificed with their brains excised and frozen at -80° C. To validate the stroke area post mortem, H&E staining of coronal brain slices was performed and the infarct volumes were analyzed. When comparing the deoxygenated hemoglobin signal of the preoperative scans compared to the 24h time point, a clear asymmetry is visible (Fig. 1). The increase in the deoxygenated signal corresponded to part of the tissue suffering from hypoperfusion after the stroke. This signal did not correspond directly to the necrotic ischemic lesion found in the stained coronal slices, but to the immediate surroundings of the lesion. This area may represent part of the ischemic penumbra [5], consisting of hypoperfused and thus hypoxic tissue that is not completely destroyed, but may, depending on the course of the stroke, recover or become necrotic. In conclusion, it has been shown that, although the ischemic lesion was not directly detectable using MSOT, the adjacent penumbra was identifiable as a localised region of hypoxia. Furthermore, this shows potential for investigating the ability of acute stroke therapies to limit the lesion size. References: [1] Razansky et al. Nat Protoc 6, 1121-1129 (2011) [2] Rosenthal et al. IEEE Trans Med Imag 29(6): 1275-1285 (2010) [3] Razansky et al. Nat Phot 3, 412 - 417 (2009) [4] Hata et al. J Cereb Blood Flow Metab 18, 367-375 (1998) [5] Zhang et al. Brain Res 1343(2010) 143-152

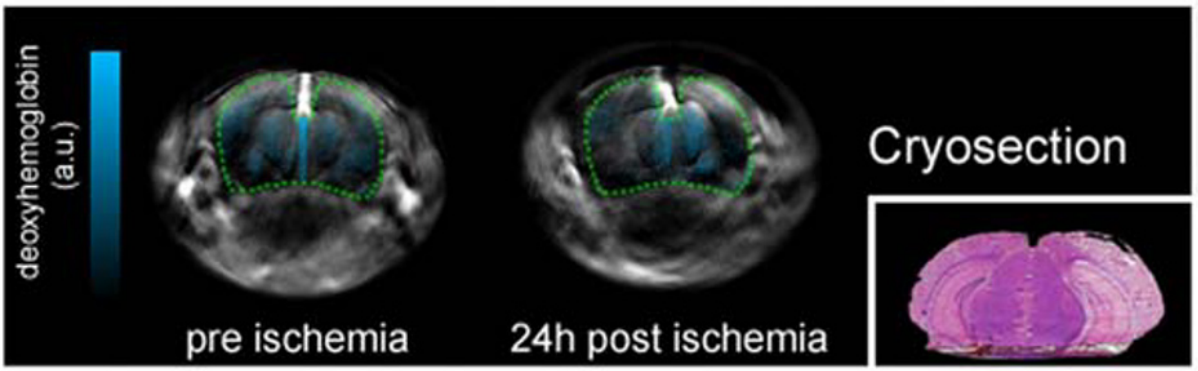

Disclosure of author financial interest or relationships:
J.B. Turner, None; **M. Kneipp**, None; **S. Hambauer**, None; **J. Lehmberg**, None; **U. Lindauer**, None; **D. Razansky**, None.

Presentation Number **SS 88**
Scientific Session 15: Chemistry & Imaging Probes, Technology & Software Developments - Photoacoustic Imaging
September 20, 2013 / 13:45-14:00 / Room: 105

ICG-Loaded Perfluorocarbon Nanodroplets for Molecularly Targeted Photoacoustic Imaging

Alexander Hannah, *Geoffrey Luke, Katheryne Wilson, Kimberly A. Homan, Stanislav Y. Emelianov, The University of Texas at Austin, Austin, TX, USA. Contact e-mail: hannahas@mail.utexas.edu*

Imaging contrast agents can localize diseased regions and enhance detection sensitivity, improving our ability to locate pathology at earlier stages. Photoacoustic imaging benefits from a dual optical and acoustic platform on which an imaging probe can be based. In this work we developed a dye-loaded nanodroplet, capable of enhancing contrast for both ultrasound (US) and photoacoustic (PA) imaging. The droplet consists of a perfluorocarbon core with dissolved indocyanine green (ICG) dye, surrounded by a shell of bovine serum albumin, Zonyl fluorosurfactant, or lipids. The perfluorocarbon core has a boiling point of 29C; however, due to the Laplace pressure imposed by the droplet's nanometer sized spherical shape, the droplets remain liquid beyond their boiling point, rendering them stable at physiological temperatures. To achieve molecular-specific imaging, an anti-EGFR antibody was attached to the surface of the lipid-coated droplet via a thiolester bond. Live cell microscopy was used to visualize the preferential attachment of the nanodroplets to human breast carcinoma cells. Furthermore, to determine the ability to visualize the droplets at greater depths, an emulsion of them was suspended in a polyethylene pipette, which was embedded in a polyacrylamide phantom. A control sample of blank perfluorocarbon droplets without ICG was also imaged, as well as a sample of blank droplets in aqueous ICG. These samples were imaged using both US and PA techniques. In their native liquid state, the droplets provided no US contrast; however, upon pulsed laser irradiation at their peak absorption wavelength of 780 nm, the nanodroplets were activated, inducing a liquid-to-gas phase change of the perfluorocarbon. The vaporization brought about a strong PA signal, and the resulting gas bubbles provided enhanced US contrast in the region of activation. To test the factors influencing vaporization efficiency, two experiments were conducted. First, the droplets were imaged at three temperatures: 23C, 37C, and 50C. While no change in US contrast was observed before activation, the droplets emitted a greater PA signal at higher temperatures, and the US contrast from bubbles was greater at higher temperatures. In addition, droplet samples were prepared using varying concentrations of ICG. With increasing amounts of ICG, the PA and US signals from vaporization increased, up to a point at which the droplets were saturated and further vaporization efficiency could not be achieved. These nanodroplets enhance both US and PA imaging contrast, and they have the capability to be molecularly targeted to specific cancer cell types. In addition, the encapsulated photoabsorber can be used for subsequent optical or photoacoustic imaging, which has applications for cancer detection in dense tissue. Lastly, the droplets may assist in therapy by encapsulating drugs or genetic material, rendering them remotely triggerable therapeutic delivery vehicles, and the gas bubbles can be combined with high intensity ultrasound to bring about cavitation. These dynamic nanoparticles have great potential in imaging and therapy of disease by providing targeted, controlled contrast.

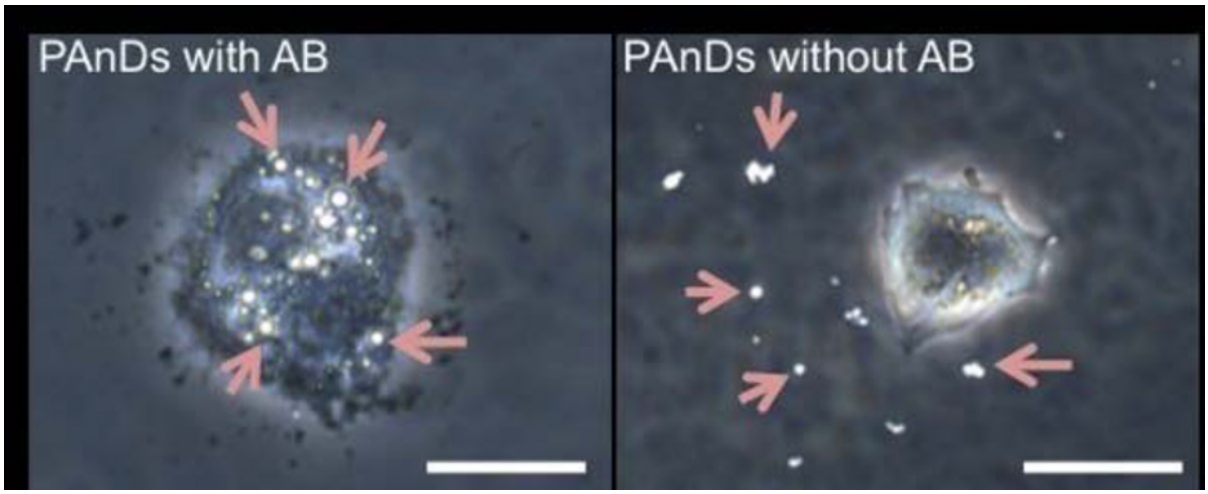

Disclosure of author financial interest or relationships:
A. Hannah, None; **G. Luke**, None; **K. Wilson**, None; **K.A. Homan**, NanoHybrids Inc, Grant/research support; **S.Y. Emelianov**, NanoHybrids, Inc, Stockholder .

Presentation Number **SS 89**
Scientific Session 15: Chemistry & Imaging Probes, Technology & Software Developments - Photoacoustic Imaging
September 20, 2013 / 14:00-14:15 / Room: 105

In vivo Cerebral Oxygen Consumption Estimation using Combined Photoacoustic and Doppler Ultrasound Imaging

Yan Jiang, *Roger J. Zemp, Electrical and Computer Engineering, University of Alberta, Edmonton, AB, Canada. Contact e-mail: yjiang5@ualberta.ca*

To maintain normal functions of the brain, continuous and efficient oxygen supply is necessary. Most common disorders of the brain, such as Alzheimer's, Parkinson's, and others have been found to be associated with alterations in the cerebral oxygen metabolism. Thus the ability to accurately and non-invasively measure the cerebral metabolic rate of oxygen (MRO2) is important for research and clinical practice related to brain functions. Since MRO2 can be quantified as the net oxygen flux of the blood vessels entering or exiting a well-defined tissue region, the cerebral MRO2 can be estimated from the cerebral blood flow rate and oxygen saturation of the carotid artery and jugular vein, which are the main arteriovenous blood vessels for the oxygen supply of the brain. We propose combined photoacoustic and Doppler ultrasound methods to non-invasively estimate the oxygen flux of the blood vessels. The imaging system uses a swept-scan 25MHz ultrasound transducer in combination with a light guide, and a pulse-sequencer which enables ultrasonic and laser pulses to be interlaced so that photoacoustic and Doppler ultrasound images are co-registered. The feasibility has been demonstrated by in vitro phantom experiments using sheep blood in our previous studies. In this work, a Sprague-Dawley (SD) rat (~50g in weight) was scanned across the neck by our combined system. The physiological conditions (hyperoxia, normoxia and hypoxia) of the rat are controlled by varying the oxygen concentration of the inhaled gases (pure oxygen and pure nitrogen are mixed at different flow rates). The blood flow speed is measured by a Doppler bandwidth broadening technique, and the direction of the flow is defined by a bi-directional motor scanning method. Thus the artery and vein can be distinguished and color mapped on the Doppler images. By interrogating the tissue at multiple wavelengths, the oxygen saturation (sO2) and total concentration of hemoglobin can be estimated. We produce co-registered photoacoustic, color Doppler, and power Doppler images of the vertebral artery and internal jugular vein. The artery is located at ~2mm depth. The size of the vessel is ~500μm, and the mean flow speed is calculated as 160mm/s. The vein is located at ~1mm with a size of ~1.5cm and mean flow speed of 130mm/s. The global arterial sO2 is measured using a pulse oximeter. The sO2 measured by a multi-wavelength photoacoustic method is quantified as oxygen fraction of breathing gases is varied. Estimated arterial sO2 shows good agreement with measurements from the oximeter. From measurements of all these parameters, the cerebral MRO2 is estimated with maximal variation of 0.5ml/100g/min. Cerebral MRO2 stays relatively constant during oxygen stress experiments, which is expected due brain auto-regulation mechanisms. Variations in measured MRO2 in future studies could lead to new ways to assess central nervous system disorders. Our photoacoustic methods could also be applied to other organs and tissues to extract information about local oxygen metabolism with a portable cost-effective system and in a way not presently available.

Disclosure of author financial interest or relationships:
Y. Jiang, None; **R.J. Zemp**, None.

Presentation Number **SS 90**
Scientific Session 15: Chemistry & Imaging Probes, Technology & Software Developments - Photoacoustic Imaging
September 20, 2013 / 14:15-14:30 / Room: 105

Human Prostate Imaging Using a Novel Integrated Transrectal Ultrasound and Photoacoustic Instrument

Sri Rajasekhar Kothapalli[1], *Jung Woo Choe*[2], *Anshuman Bhuyan*[2], *Byung Chul Lee*[2], *Te-Jen Ma*[2], *Amin Nikoozadeh*[2], *Jonathan Wu*[3], *Daniel Bui*[3], *Joseph C. Liao*[3], *James Brooks*[3], *Butrus T. Khuri-Yakub*[2], *Sanjiv S. Gambhir*[1], [1]*Radiology, Stanford University, Palo Alto, CA, USA;* [2]*Electrical Engineering, Stanford University, Palo Alto, CA, USA;* [3]*Urology, Stanford University, Palo Alto, CA, USA. Contact e-mail: ksraj@stanford.edu*

Background: The transrectal ultrasound (TRUS), current standard for tissue diagnosis of prostate cancer, enables visualization of the prostatic anatomy and guidance of needle placement. However, it does not assist with cancer detection or staging due to the lack of reliable contrast mechanisms that differentiate cancerous from non-cancerous tissue. Therefore novel imaging strategies are needed to visualize hallmarks of prostate cancer with high sensitivity and specificity. Methods: We developed a dual modality transrectal ultrasound and photoacoustic (TRUSPA) instrument (Fig. A) for human prostate imaging by integrating 1) two dimensional (2D) capacitive micromachined ultrasonic transducer (CMUT) arrays flip-chip bonded to front-end electronics, 2) optical fiber bundle coupled to a tunable (680 nm to 950 nm) nanosecond laser, and 3) multichannel data acquisition system. In addition, we also investigated the application of 1D CMUT arrays for prostate tissue imaging. Custom made software is used in all experiments for real-time dual modality image reconstruction and display. We first validated TRUSPA performance for deep tissue imaging using phantom models mimicking prostate tissue (Figs. B-D). With IRB approval, we further imaged human prostrates (N=2) derived from radical prostatectomy (supplementary figure). Spatial resolution, imaging depth, contrast and signal-to-noise ratio of this dual modality imaging system were quantified. Results: Experiments on phantoms with homogenous background containing indocyanine green (ICG) labeled fiducials placed at different depths, demonstrated that TRUSPA can detect about 100 uM concentration of ICG fiducial of 2 mm in size at ~5 cm depth with about 500 micron spatial resolution and 20 dB SNR. While 2D arrays demonstrated real time 3D imaging capabilities in both ultrasound (US) and photoacoustic (PA) modes, the experiments with 1D arrays in the human prostate containing optically absorbing fiducial tubes demonstrated clinical grade standard prostate anatomy in US mode and optical contrast of prostate in PA mode with imaging depth of ~2 cm. The observed contrast enhancement in left prostatic probe was consistent with the location of the cancer. Conclusion: We report the first demonstration of an integrated instrument capable of dual modality US and PA imaging using 2D CMUT arrays for use in applications such as transrectal prostate imaging. Our results demonstrate that CMUT arrays are an attractive choice for developing combined dual modality ultrasound and photoacoustic devices, especially for endoscopic applications, due to their low noise floor, wide bandwidth and small footprint allowing sufficient room for routing optical fibers. Currently we are optimizing the TRUSPA device using more sensitive CMUT arrays (2D as well as 1D) to further improve performance of deep tissue prostate imaging. A Fully optimized TRUSPA imaging system has the potential to provide new diagnostic and prognostic insights into prostate cancer screening and treatment by visualizing anatomical contrast in US mode and optical molecular contrast in PA mode leveraging the vascular, functional and molecular imaging strategies.

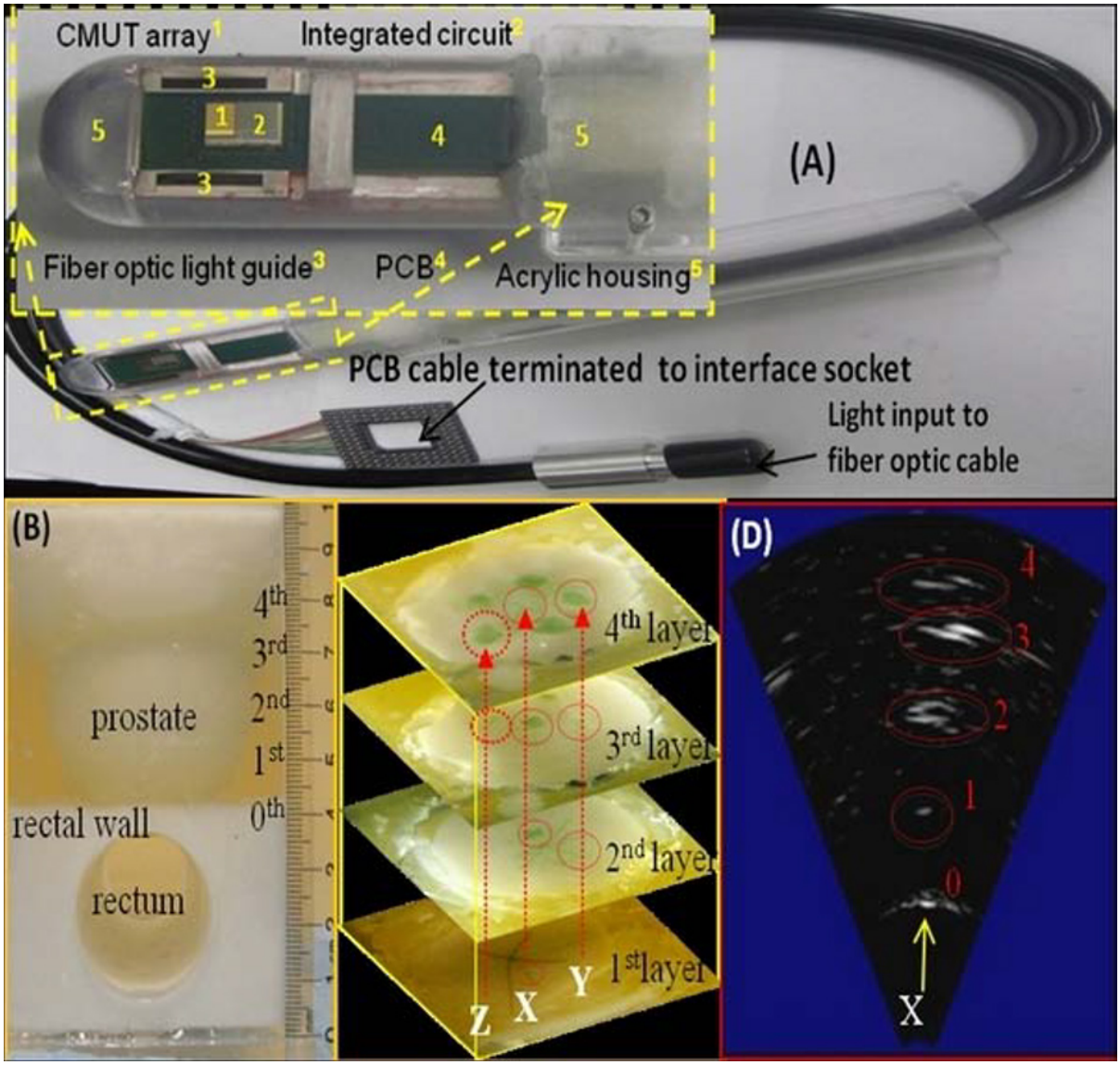

Figure: A) Transrectal Ultrasound and Photoacoustic (TRUSPA) device built using 2D-CMUT array flip-chip bonded to front-end electronic circuits and fiber optic light guide. The inset shows enlarged version of the device. B) Prostate phantom model that mimics ultrasound and optical properties of prostate tissue. C) Different layers (marked 1 to 4, 1 cm apart, starting from 5 cm on the ruler) inside the prostate, each layer containing different shapes and sizes of ICG-labeled optically absorbing objects. D) B-mode photoacoustic image, obtained when TRUSPA device touching the rectal wall is projected along the line X in C.

Disclosure of author financial interest or relationships:

S. Kothapalli, None; **J. Choe**, None; **A. Bhuyan**, None; **B. Lee**, None; **T. Ma**, None; **A. Nikoozadeh**, None; **J. Wu**, None; **D. Bui**, None; **J.C. Liao**, None; **J. Brooks**, None; **B.T. Khuri-Yakub**, None; **S.S. Gambhir**, Bracco Diagnostics, Consultant; Endra, Inc, Stockholder; Cellsight, Stockholder; Enlight, Inc., Stockholder; General Electric, Grant/research support; ImaginAb, Stockholder; MagArray, Inc., Stockholder; Sanofi-Aventis, US, Grant/research support; SiteOne Therapeutics, Stockholder; VisualSonics/Sonosite, Stockholder .

Presentation Number **SS 91**
Scientific Session 16: Chemistry & Imaging Probes - MRI
September 20, 2013 / 13:00-13:15 / Room: 200

Activatable MR probe for imaging acute thrombosis

Galen Loving, **Peter Caravan**, *Radiology, Massachusetts General Hospital, Charlestown, MA, USA. Contact e-mail: caravan@nmr.mgh.harvard.edu*

We report a novel activatable MR probe to be used for the visualization of acute thrombosis. Newly formed thrombi (blood clots) contain activated platelets which release an enzyme called Protein Disulfide Isomerase (PDI). This enzyme can serve as a useful biomarker of nascent clots since PDI activity is not present in mature clots. Our probe is a linear peptidomimetic species that contains a pair of disulfide bonds that mask two key cysteine residues required for fibrin binding (Figure). In the absence of PDI, the probe does not bind to fibrin and has no affinity for thrombus. However in the presence of activated platelets, PDI catalyzes an intramolecular cyclization reaction that results in new disulfide bridge formation between the cysteine residues. The cyclic product of this reaction exhibits a 1000-fold greater affinity for fibrin (Kd < 200 nM) than that of the linear precursor resulting in its selective retention at the site of the acute thrombus. Here we describe the synthesis and characterization of the probe, enzyme kinetics, and imaging proof-of-concept studies. Such a probe may play a useful role in revealing details of both the etiology and maturation of blood clots in a clinical setting.

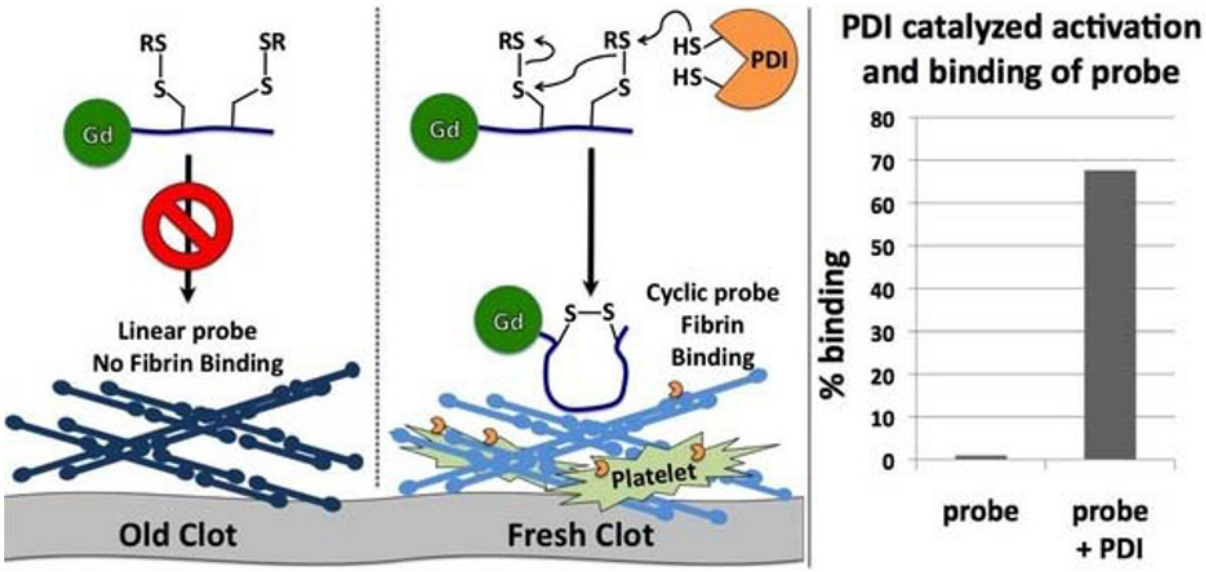

Disclosure of author financial interest or relationships:
G. Loving, None; **P. Caravan**, Sanofi, Grant/research support; Biogen Idec, Consultant; Factor 1A, Stockholder; Collagen Medical, Stockholder .

Presentation Number **SS 92**
Scientific Session 16: Chemistry & Imaging Probes - MRI
September 20, 2013 / 13:15-13:30 / Room: 200

Ca^{2+} Sensing Using ion Chemical Exchange Saturation Transfer (iCEST)- ^{19}F MRI

Amnon Bar-Shir[1,2], *Assaf A. Gilad*[1,2], *Kannie WY Chan*[1,3], *Guanshu Liu*[1,3], *Peter C. van Zijl*[1,3], *Michael T. McMahon*[1,3], *Jeff W. Bulte*[1,2], [1]*Division of MR Research, the Russell H. Morgan Department of Radiology and Radiological Sciences, the Johns Hopkins University School of Medicine, Baltimore, MD, USA;* [2]*Cellular Imaging Section, Institute for Cell Engineering, the Johns Hopkins University School of Medicine, Baltimore, MD, USA;* [3]*F.M. Kirby Research Center for Functional Brain Imaging, Kennedy Krieger Institute, Baltimore, MD, USA. Contact e-mail: abarshi2@jhmi.edu*

Introduction: Ca^{2+} play a crucial role in a myriad of biological processes, and the ability to monitor non-invasively real-time changes in Ca^{2+} levels is essential for understanding a variety of physiological events[1]. Currently, imaging dynamic changes in Ca^{2+} levels is restricted to fluorescence-based methodologies[2], which are limited by low tissue penetration and as a result do not allow in vivo Ca^{2+} imaging in deep tissues or organs. For this reason, there has been great interest to develop MRI-based sensors for Ca^{2+} monitoring[3-6]. We present here a novel chemical exchange saturation transfer (CEST) approach that combines ^{19}F- and CEST-MRI for specifically sensing the presence of Ca^{2+} ions through their substrate binding kinetics, which we have termed ion CEST (iCEST). Using RF labeling at the bound ion-^{19}F frequency, $\omega_{[Ca\text{-}5F\text{-}BAPTA]}$, and detection of label transfer to the free 5F-BAPTA ^{19}F frequency , $\omega_{5F\text{-}BAPTA}$ (0 ppm), we were able to amplify the signal of bound Ca^{2+} by a factor of 100 and demonstrate that the resulting Z-spectra display supreme specificity for bound Ca^{2+} as compared to other divalent cations. Results and discussion: Figure 1a illustrates the dynamic exchange process between the free 5-FBAPTA and M^{2+}-bound 5F-BAPTA, i.e., [M^{2+}-5F-BAPTA]. Interestingly, there is a chemical shift offset ($\Delta\omega$) between free 5F-BAPTA and bound M^{2+}-5F-BAPTA in the ^{19}F-NMR spectrum, with the $\Delta\omega$ values being unique for each M^{2+}[7]. In order to examine the possibility of detecting M^{2+} from [M^{2+}-5F-BAPTA] to free 5F-BATA we applied iCEST ^{19}F-MRI. As expected, no difference in contrast could be observed for the different tubes (Mg^{2+}, Zn^{2+}, and Ca^{2+}) on conventional ^{19}F-MRI (Figure 1c) as this detects only the free 5F-BAPTA. Figure 1d clearly demonstrates that when RF labeling is applied at the frequency offset of Ca^{2+}-5F-BAPTA (6.2 ppm), a saturation transfer effect is observed for the free 5F-BAPTA (0 ppm). Importantly, no CEST effect could be detected from Mg^{2+} or Zn^{2+}-containing solutions that experience fast and slow exchange with free 5F-BAPTA, respectively. The ^{19}F-iCEST properties of 5F-BAPTA in the presence of Ca^{2+} (slow-to-intermediate k_{ex}), Zn^{2+} (very slow k_{ex}), and Mg^{2+} (fast k_{ex}) are summarized in Figure 1e-g. A pronounced saturation transfer contrast was detected in the Ca^{2+} containing solutions (Figure 1e) but not for Mg^{2+} (Figure 1f) or Zn^{2+} (Figure 1g). Conclusion. We have developed a new approach for sensing low levels of Ca^{2+} using MRI, in which the conventional amplification strategy and exchange sensitivity of CEST are combined with the $\Delta\omega$ specificity of the ^{19}F frequency for free and bound substrate to obtain MR images of Ca^{2+} binding kinetics. Reference (1) Clapham, D. E. Cell 2007, 131, 1047. (2) Tsien, R. Y. Annu Rev Neurosci 1989, 12, 227. (3) Dhingra, K. et al. J Biol Inorg Chem 2008, 13, 35. (4) Li, W. H. et al. J Am Chem Soc 1999, 121, 1413. (5) Angelovski, G. et al. Bioorg Med Chem 2011, 19, 1097. (6) Atanasijevic, T. et al.

Proc Natl Acad Sci U S A 2006, 103, 14707. (7) Smith, G. A. et al. Proc Natl Acad Sci U S A 1983, 80, 7178. Supported by: MSCRFII-0161-00, R01EB012590, R01EB015031, R01EB015032 and MSCRFF-0103-00.

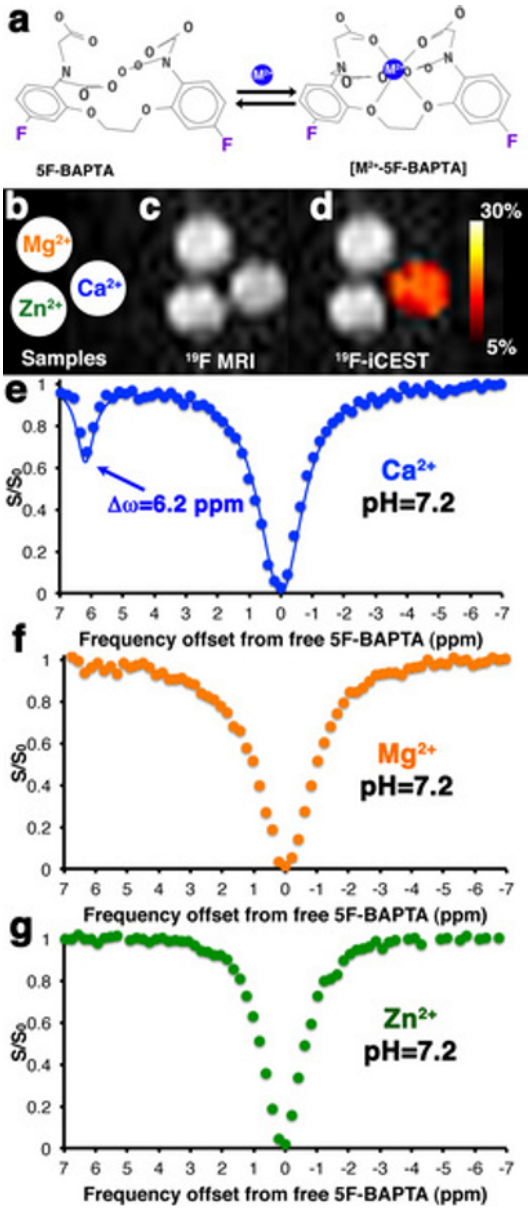

Figure 1: a) Schematic demonstration of the dynamic exchange process between M^{2+} and its complex [M^{2+}-5F-BAPTA]. b-d) Phantoms containing 10 mM of 5F-BAPTA and 50 μM of M^{2+} (pH=7.2). (b) Sample setup for MRI. (c) ^{19}F-MRI. (d) Merged image of the iCEST image (Δω=6.2 ppm) overlaid on ^{19}F-MRI shown in (c). e-g) 19F-iCEST Z-spectra of solutions in (b) at pH 7.2. Symbols represent the raw experimental data. For Ca2+, the blue solid line represents Bloch simulation and arrows point to the frequency of the [Ca^{2+}-5F-BAPTA] complex.

Disclosure of author financial interest or relationships:
A. Bar-Shir, None; **A.A. Gilad**, None; **K. Chan**, None; **G. Liu**, None; **P.C. van Zijl**, None; **M.T. McMahon**, None; **J.W. Bulte**, None.

Presentation Number **SS 93**
Scientific Session 16: Chemistry & Imaging Probes - MRI
September 20, 2013 / 13:30-13:45 / Room: 200

In vivo quantitative pH mapping with MRI using a new type of DIACEST agents

Xiaolei L. Song[1,2], *Xing Yang*[1], *Yuguo Li*[1,2], *Guanshu Liu*[1,2], *Sangeeta Ray*[1], *Martin Pomper*[1], *Michael T. McMahon*[1,2], [1]*The Russell H. Morgan Department of Radiology and Radiological Science, The Johns Hopkins University, Baltimore, MD, USA;* [2]*F.M. Kirby Research Center for Functional Brain Imaging, Kennedy Krieger Institute, Baltimore, MD, USA. Contact e-mail: lisasonger@gmail.com*

Introduction CEST-MRI has increasingly been drawing attention due to the unique characteristics including: 1) the ability to detect specific molecules with high sensitivity through exchange of their protons with water, amplifying MR contrast; and 2) the capability of designing highly pH-sensitive agents, offering a way to image the tumor microenvironment. Organic CEST agents have potential advantages over paraCEST agents, such as potential lower toxicity, ease of modification, and clearance during natural biochemical processes. We have developed a new type of organic agent, Imidazole-4,5-dicarboxamides (I45DCs) analogs, which possess the highest chemical shift (7.5ppm peak) reported so far (**Fig.a**). Use of these probes could significant reduce the problems caused by those with a smaller chemical shift, such as low spatial/temporal resolution, low CNR, and difficulties of being separated from other sources of water signal loss. **Owing to the multiple exchangeable protons on I45DCs and the high chemical shift, we aim to explore the ability of using these agents as a quantitative pH sensor in vivo**. **Material and Methods** *Phantom* One I45DC analog, I45DC-(Glu)2 was dissolved in PBS with concentrations from 5mM to 50mM and pH from 5.4 to 7.5. *Mice Preparation* BALB/c mice weighing 20-25 g (n=3) were anesthetized by isoflurane and placed in a 23 mm transmit/receive mouse coil, with breath rate monitored during MRI. A 100 uL I45DC solution of 0.25 M in water was slowly injected via a catheter into the tail vein. Imaging: Images were taken on Bruker 11.7T scanners, using a RARE sequence with CW saturation pulse of B1=5.9uT, Tsat=3s.For phantoms, saturation frequency incremented every 0.3 ppm from -15 to 15 ppm with TR/TE=6000 ms/17 ms, matrix size=64X48. For in vivo, CEST images with saturation frequencies of [±7.8ppm, ±7.5ppm, ±7.2ppm] and [±4.8ppm, ±4.5ppm, ±4.2ppm] were acquired repeatedly every 10 min pre- and post-injection. Image parameters are similar as for phantom except for TR/TE=5s/15ms and CEST contrast was quantified by MTRasym = (S-Δω-S+Δω)/S-Δω. **Results** MTRasym spectra of I45DC-(Glu)2 (Fig. a) show 2 broad peaks centered at 7.5 ppm and 2.4 ppm, with the 7.5 ppm peak increasing with pH while the 2.5 ppm-5 ppm portion of the spectrum remains relatively constant. As is shown in **Fig. b**, the ratio of MTRasym(7.5 ppm) to MTRasym(4.8 ppm) is linearly-correlated with pH in the physiological range of pH6-7.5 for B1=5. 9uT. The linear range is smaller for B1 = 3.6uT partially due to the relatively faster exchange rate of the heterocyclic NH (kex = ~ 4000). We performed in vivo studies for the purpose of determining renal pH, using a 6-offset collection scheme(**Fig.c**). A calibration function from PBS solutions using the same imaging conditions was applied for calculating pH, with pH = 5.37 + 0.88Xratio. The baseline of pre-injection contrast was subtracted using a simple average value for improving the CNR. The average kidney pH value was ~ 6.3, similar as ref.1. **Conclusions** I45DC can successfully generate pH maps in vivo. Future studies will involve testing these probes for imaging tumor pH. Ref. 1Longo DL, et.alMagn Reson Med 2011 65(1):202

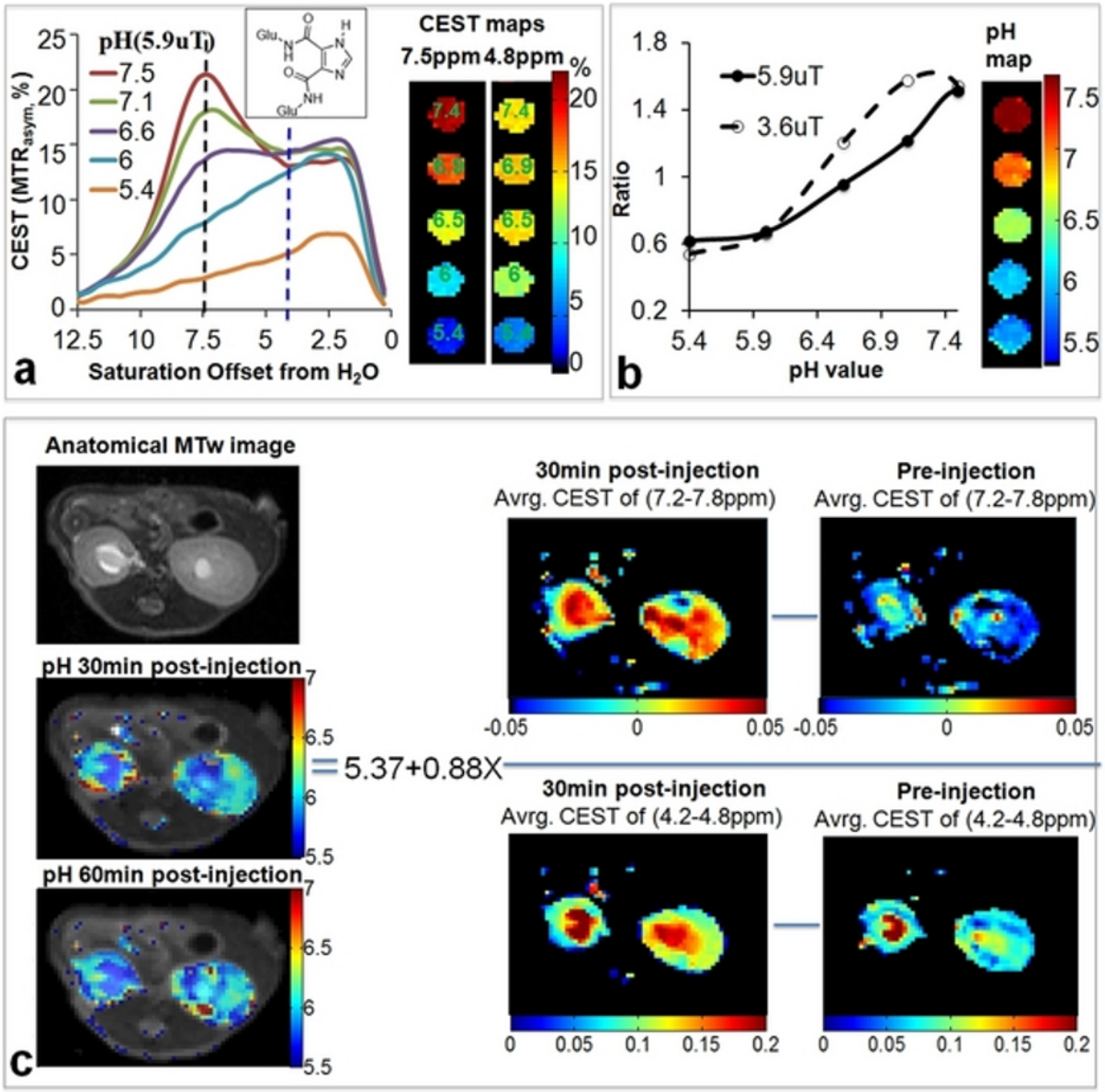

Figure a. CEST MTRasym for 25mM I45DC-(Glu)2 with different pH values.**b.** Calibrate pH use ratio of 2 CEST frequencies. **c.** In-vivo mice kidney pH mapping

Disclosure of author financial interest or relationships:

X.L. Song, None; **X. Yang**, None; **Y. Li**, None; **G. Liu**, None; **S. Ray**, None; **M. Pomper**, None; **M.T. McMahon**, None.

Presentation Number **SS 94**
Scientific Session 16: Chemistry & Imaging Probes - MRI
September 20, 2013 / 13:45-14:00 / Room: 200

The Development of Imidazole-based Small Molecule Probes for CEST-MRI Imaging

Xing Yang[2], *Xiaolei L. Song*[2], *Sangeeta Ray*[2], *Yuguo Li*[2], *Guanshu Liu*[1,2], *Martin Pomper*[2], *Michael T. McMahon*[1,2], [1]*F.M. Kirby Research Center, Kennedy Krieger Institute, Baltimore, MD, USA;* [2]*Radiology, Johns Hopkins School of Medicine, Baltimore, MD, USA. Contact e-mail: xyang45@jhmi.edu*

CEST-MRI has been developed as an important and sensitive new method to generate contrast in MRI. 1 Recently, organic CEST contrast agents have started to garner more attention, because of their lower toxicity, ease of modification and clearance compared with the paramagnetic metal containing paraCEST agents. However, currently reported organic CEST agents still suffer from sensitivity drawbacks, especially due to a small chemical shift difference between exchangeable proton and water. For the best agents reported so far, the CEST protons still resonate below 6 ppm.2 Azole N-H protons could potentially be a solution to that, because of the strong de-shielding effect from the azole ring. More interestingly, the acid and base property of azoles, especially the imidazoles, makes these compounds valuable pH sensors.3 However, most azole N-H's have a relative high proton exchange rate (30,000 s-1 or higher), which limits their practical application for existing CEST experimental protocols. In order to observe the CEST contrast, very high saturation power would need to be applied. Aiming to slow down the proton exchange rate to a useful level (100 Hz - 5000 Hz), we investigated modifying azoles. We have designed and screened a library of azole compounds, with the imidazole-4,5-dicarbonyl compounds (I45DCs) found to give a strong CEST contrast at 7.5 ppm from water while applying a relatively low saturation power, with their proton exchange rate ~3500 s-1. The contrast showed a significant dependence on pH, which could potentially be applied for tumor pH mapping (Figure a). Symmetrical or unsymmetrical I45DCs could easily be synthesized by reacting free amines with 5,10-dioxo-5H,10H-diimidazo[1,5-a:1'-5'-d]-pyrazine-1,6-dicarboxylic acid diphenyl ester (Figure c).4 The convenient method would allow the generation of different I45DCs for specific applications, such as receptor targeting, nanoparticle surface modification, multiple frequency CEST agent design, etc. Finally, I45DC-(Glu)2 was injected into mice, in order to evaluate the in vivo signal quality. CEST contrast of ~10 % was obtained in the kidney after 55 min (Figure c). Acknowledgements: Supported by NIH R01EB012590 and U54CA134675 References: 1. van Zijl, P. C.; Yadav, N. Magn. Reson. Med. 2011, 65, 927 - 948 2. a) Sherry, A. D.; Woods, M. Annu. Rev. Biomed. Eng. 2008, 10, 391-411. b) Bar-Shir, A; Liu, G.; Liang, Y; Yadav, N.; McMahon, M. T.; Walczak, P.; Nimmagadda, S.; Pomper, M. G.; Tallman, K. A.; Greenberg, M. M.; van Zijl, P. C.; Bulte, J. W.; Gilad, A. A. J. Am. Chem. Soc. 2013, 135, 1617-1624 3. van Sluis, R.; Bhujwalla, Z. M.; Raghunand, N.; Ballesteros, P.; Alvarez, J.; Cerdan, S.; Galons, J. P.; Gillies, R. J. Magn. Reson. Med. 1999, 41, 743-750. 4. Wiznycia, A. V.; Baures, P. W. J. Org. Chem. 2002, 67, 7151-7154

a) MTR asym of **I45DC-(Glu)2**

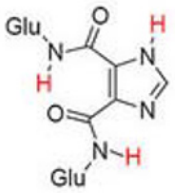

4,5-bis[(Glu)carbonyl]-1H-imidazole (**I45DC-(Glu)$_2$**)

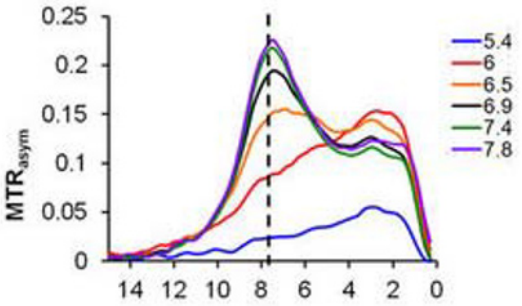

b) The convenient synthesis of **I45DCs**

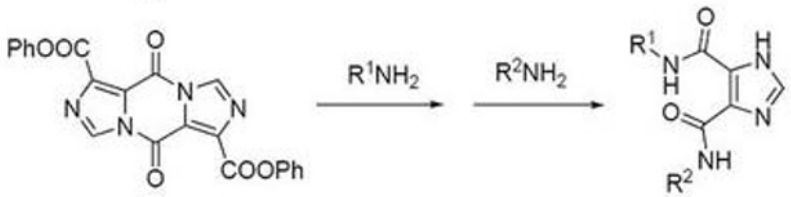

c) Tail vain injection of I45DC-(Glu)2 and watch accumulation in the kidney

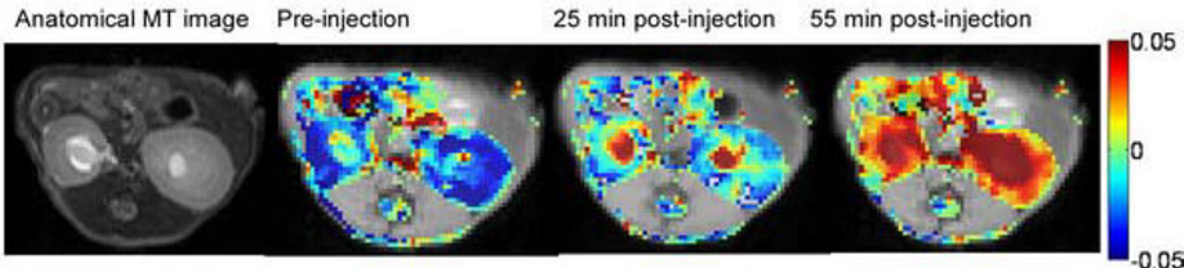

Disclosure of author financial interest or relationships:
X. Yang, None; **X.L. Song**, None; **S. Ray**, None; **Y. Li**, None; **G. Liu**, None; **M. Pomper**, None; **M.T. McMahon**, None.

Presentation Number **SS 95**
Scientific Session 16: Chemistry & Imaging Probes - MRI
September 20, 2013 / 14:00-14:15 / Room: 200

Lanthanide loaded Red Blood Cells for CEST MR imaging

Giuseppe Ferrauto[1], *Daniela Delli Castelli*[1], *Enza Di Gregorio*[1], *Sander Langereis*[2], *Dirk Burdinski*[2], *Holger Gruell*[2], *Enzo Terreno*[1], *Silvio Aime*[1], [1]*Molecular Biotechnology and Health Sciences, University of Torino, Torino, Italy;* [2]*Department of Minimally Invasive Healthcare, Philips Research Europe, Eindhoven, Netherlands. Contact e-mail: giuseppe.ferrauto@unito.it*

Introduction: Among the available MRI contrast agents (CAs), CEST ones have received much attention in virtue of their ability to generate a frequency encoded contrast that allows to switch "on" and "off" the contrast, upon changing the offset of the irradiation frequency. This characteristic is very important because it makes possible the simultaneous detection of multiple agents even co-localized in the same region. Unfortunately CEST agents suffer for a low sensitivity, lower than the one shown by T_1 and T_2 agents. In order to overcame this drawback, innovative systems bearing a very large numbers of equivalent exchanging protons have been proposed as high sensitivity CEST agents (e.g. LipoCEST).Herein we test the feasibility to exploit the large number of intracellular water protons as source of exchangeable proton pool to be irradiated. To shift this water signal in respect to the extracellular one, proper shift reagents (SRs) are internalized into the paramagnetic cells. **Methods:** Human erythrocytes have been isolated from healthy human donors' blood and labeled with SRs like Ln-HPDO3A complexes. The CEST visualization of cells has been carried out by acquiring the Z-spectra at 7T on a Bruker Avance 300MHz spectrometer (RARE spin-echo sequence RF 2-32, TE 3 ms, TR 5 s, isotropic 64 x 64 acquisition matrix with FOV of 10 mm and slice thickness of 1 mm). The whole sequence has been preceded by a saturation scheme (rectangular wave pulse 2 s long with an intensity of 3 μT). **Results:** By acquiring Z-spectra of Ln-HPDO3A-labeled RBC, it was possible to obtain good shifts of the intracellular water signal and good ST% values. In fig. 1, the Z-spectrum of Dy-HPDO3A-labelled RBCs is reported which shows a ST of ca. 50% at 3.6 ppm from water signal. By changing the lanthanide ions inside the cells it is possible to modulate the intracellular water proton chemical shift in according with the change of the effective magnetic moment of the paramagnetic metal ion. It is worth of note that the sign of the shift of the intracellular water resonance has been reversed by incorporating into the erithrocytes'membrane an anphiphilic Tm-DOTA-like complex which induces a magnetic anisotropy opposite to that of the cell membrane (fig.2). This information corroborates the idea that the observed shifts are mainly due to a bulk magnetic susceptibility (BMS) contribution that depends on the shape of the "container" in which the SRs are confined. Since cells are not spherical compartments, they should be able to orient themselves in the presence of a magnetic field and the ability to switch the sign of BMS upon incorporating Tm-complexes into the RBC membrane is the result of the change in the orientation of erythrocytes in the magnetic field. **Conclusions:** The herein reported work shows that, SR-loaded RBCs can be used as an innovative CEST contrast agent. At the best of our knowledge this is the first proof of concept demonstrating the possibility to use cells themselves as CEST agents. This new high sensitivity system may open new fields for the in vivo tracking of labeled cells.

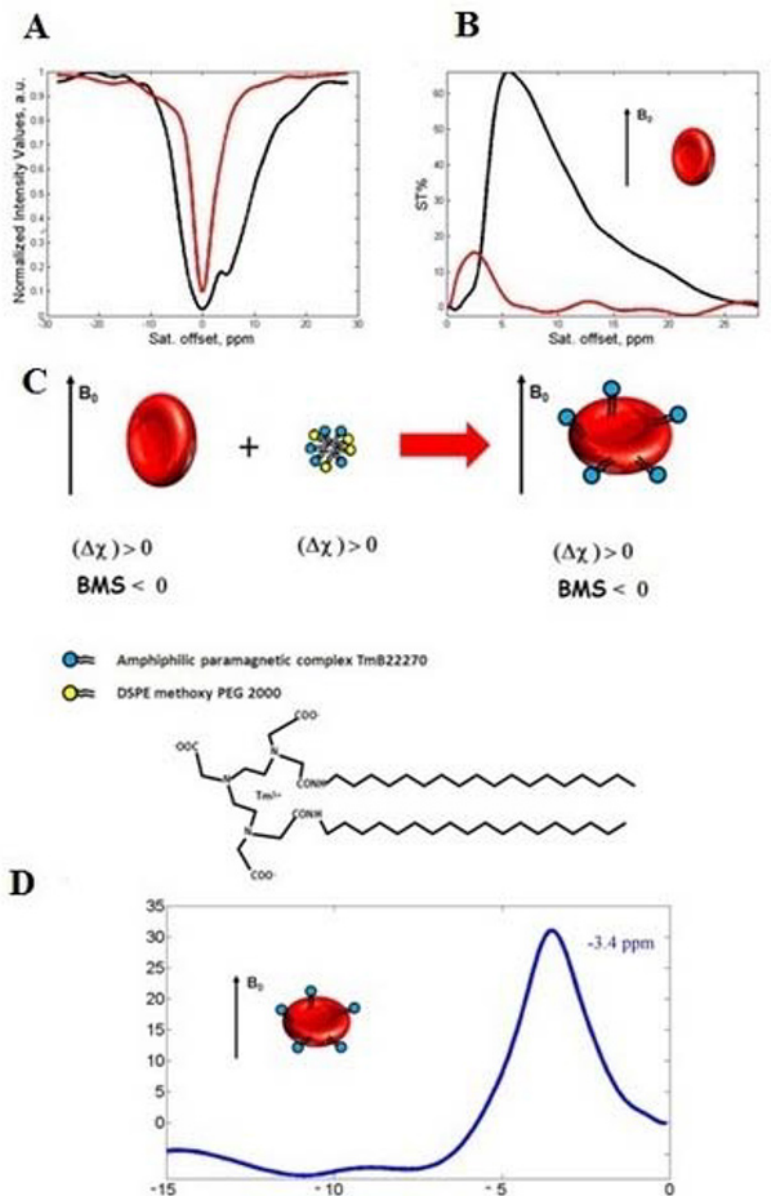

Z-spectrum (A) and ST profile (B) of control RBCs (red) and Dy-HPDO3A- labelled RBCs (black). (C)Scheme of the interaction between RBCs and Tm-containing micelles; (D) ST-spectrum of DyHPDO3A-labelled RBCs after interaction with paramagnetic micelles.

Disclosure of author financial interest or relationships:
G. Ferrauto, None; **D. Delli Castelli**, None; **E. Di Gregorio**, None; **S. Langereis**, Philips Research Europe, Employment; **D. Burdinski**, Philips Research (terminated), Employment; **H. Gruell**, Eindhoven University of Technology, Employment; Philips, Employment; **E. Terreno**, Bracco Imaging, Consultant; **S. Aime**, None.

Presentation Number **SS 96**
Scientific Session 16: Chemistry & Imaging Probes - MRI
September 20, 2013 / 14:15-14:30 / Room: 200

Encapsulated gadolinium and dysprosium ions within ultra-short carbon nanotubes for MR microscopy at 11.75 and 21.1 T

Jens Rosenberg[1,2], *Brandon T. Cisneros*[3,4], *Michael Matson*[3,5], *Fabian Calixto Bejarano*[1], *Michelle Sokoll*[1,2], *Afi Sachi-Kocher*[1], *Lon J. Wilson*[3], *Samuel C. Grant*[1,2], [1]*CIMAR, The National High Magnetic Field Laboratory, Tallahassee, FL, USA;* [2]*Chemical & Biomedical Engineering, The Florida State University, Tallahassee, FL, USA;* [3]*Department of Chemistry and The Smalley Institute for Nanoscale Science and Technology, Rice University, Houston, TX, USA;* [4]*Department of Surgical Oncology, University of Texas MD Anderson Cancer Center, Houston, TX, USA;* [5]*Department of Natural Sciences, University of Houston-Downtown, Houston, TX, USA. Contact e-mail: rosenberg@magnet.fsu.edu*

Introduction: Recently, biocompatible and multifunctional ultra-short single-walled carbon nanotubes (US-tubes) [1,2], have been applied to cellular MRI through the confinement of gadolinium ions (Gd^{3+}) within the tube structure [3]. Unlike Gd^{3+}, which displays decreased relaxation rates at high magnetic fields, ionic dysprosium (Dy^{3+}) demonstrates continued relaxation increases with field strength. This study builds upon previous work to evaluate Gd- and Dy-doped US-tubes (GNT and DNT) at 11.75 and 21.1 T both in solution and *in vitro*. In addition to field-related improvements in contrast due to the use of Dy^{3+}, the hollow interior and carbon surface of US-tubes may provide benefits at higher magnetic fields. **Methods:** GNTs and DNTs were synthesized by immersing homogenized US-tubes in aqueous $GdCl_3$ and $DyCl_3$ solutions, respectively. A biocompatible solution was made with a 1.0% (w/v) Pluronic solution using a sonicator. The suspension was centrifuged, and the supernatant was collected and dialyzed against running water to remove any excess surfactant [3,4]. MRI was performed on 11.75- and 21.1-T vertical magnets. For solution experiments, GNTs and DNTs were diluted serially to measure r_1 and r_2 relaxivity. For *in vitro* experiments, a rat Bv2 microglia cell line was used following methods outline previously [3, 5]. Bv2 cells were transfected for 12 h at a final lanthanide concentration of 17 μM. 150,000 labeled and unlabeled cells were washed, harvested and layered with 2% agarose solution. T_1, T_2 and T_2* relaxation measurements were performed along with a 3D gradient recalled echo (GRE) at 50-μm resolution (TE/TR = 7.5/150 ms). **Results and Discussion:** In solution, GNTs show an overall shorter T_1 that increases at 21.1 T. Consistent with theoretical expectations, DNTs, show a decrease in T_1 value [6,7]. For T_2, both samples show a reduction in the relaxation times at the higher field with DNT having a larger reduction. DNTs have a larger r_2 relaxivity at 21.1 T at 472 $mM^{-1}s^{-1}$ compared to DNT at 401 $mM^{-1}s^{-1}$. For r_1 relaxivity, GNTs still dominate with an r_1 = 8.31 $mM^{-1}s^{-1}$ compared to 0.89 $mM^{-1}s^{-1}$ for DNTs. In Bv2 cells, T_1 contrast is quenched while T_2 and T_2* contrasts are dominant (Fig 1b). DNTs are the more effective intracellular contrast agent with a 9% shorter T_2 and a much larger susceptibility effect with a 58% shorter T_2*. In conclusion, this study demonstrates that the DNTs provide a strong T_2/T_2*-agent at 21.1 T, potentially with higher contrast and detectability than the GNTs. Furthermore, both of these nanoparticle agents outperform many MRI contrast agents in a high magnetic field environment and should provide excellent cell detectability in vivo. **Acknowledgements & References:** Funding was provided by the NSF (DMR-0084173 and NHMFL User Collaborations Grant Program (to SCG), the American Heart Association (to SCG) and the Welch Foundation at Rice Univ (C-0627 to LJW). 1.Chen, J Am Chem Soc (2008) 2. Bianco, Curr Opin

Chem Biol (2005) 3. Tang, Contrast Media Mol. Imaging (2011) 4. Aschcroft, Nanothechnology (2006) 5. Rosenberg, Contrast Media Mol. Imaging (2011) 6. Rosenberg MRM (2010) 7. Woods, Dalton Trans (2005)

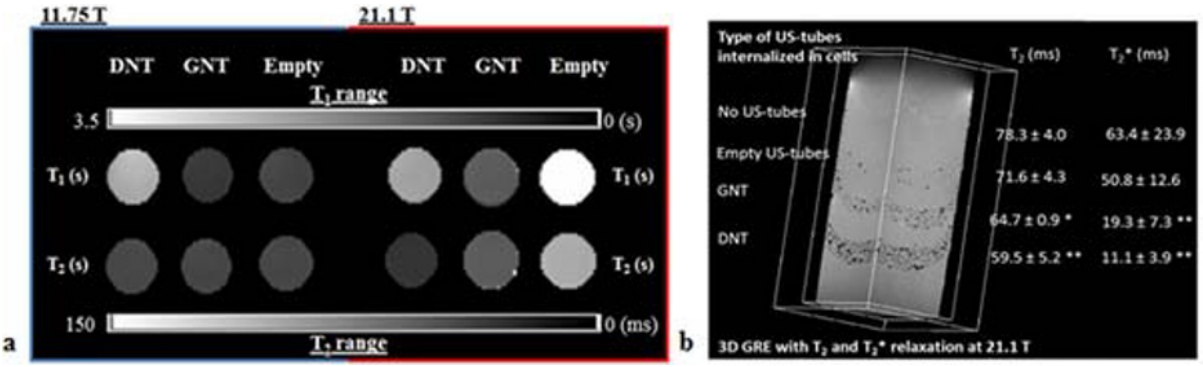

Figure 1a: T_1 and T_2 maps of DNT, GNT and Empty US-tubes at 11.75 (left) and 21.1 T (right) with stock solution corresponding to Dy^{3+} = 87.1 mM and Gd^{3+} = 83.7 mM. **b:** 3D GRE image of Bv2 cells labeled with GNT, DNT and Empty US-tubes at 21.1 T. The GNT and DNT are the only ones showing significant contrast as determined by ANOVA and LSD post hoc test ($P<0.05$) . TE=7.5 ms, TR=150 ms and 50-µm isotropic resolution.

Disclosure of author financial interest or relationships:
J. Rosenberg, None; **B.T. Cisneros**, None; **M. Matson**, None; **F. Calixto Bejarano**, None; **M. Sokoll**, None; **A. Sachi-Kocher**, None; **L.J. Wilson**, None; **S.C. Grant**, None.

Presentation Number **SS 97**
Scientific Session 17: Preclinical in vivo Studies - Neurology
September 20, 2013 / 13:00-13:15 / Room: 203

Longitudinal Monitoring of Intrastriatal Transplanted Retinal Pigment Epithelial Cells Survival In Vivo by 18F-P3BZA PET/CT

Lihong Bu[1,2], *Renfei Li*[2,1], *Hongguang Liu*[1], *Baozhong Shen*[2], *Zhen Cheng*[1], [1]*Department of Radiology and Bio-X Program, Molecular Imaging Program at Stanford (MIPS), Stanford, CA, USA;* [2]*Department of Radiology, the 4th hospital of Harbin Medical University, Harbin, China. Contact e-mail: bulihong@gmail.com*

Background: Human retinal pigment epithelial (hRPE) cells attached to gelatin microcarriers (GM) have been studied as a source of donor cells for neural transplantation for the treatment of Parkinson's disease (PD). In order to understand the anti-PD treatment efficacy of hRPE cells implantation, it is critical to develop a non-invasive imaging technique to detect the survival of hRPE cells following their implantation into the host brain accurately in vivo. Because hRPE cells contain high level of melanin, we hypothesized that the melanin targeted probe, N-(2-(diethylamino)ethyl)-18F-5-fluoropicolinamide (18F-P3BZA), could serve as a valid positron emission tomography (PET) probe for trafficking the implanted RPE cells in vivo. Methods: 18F-P3BZA was prepared by direct radiofluorination of the bromopicolinamide precursor. In vitro cell uptake of 18F-P3BZA was performed by incubation 18F-P3BZA with pRPE or control ARPE-19 cells (with or without 2 mM L-tyrosine pretreatment for 24 h). To assess the brain uptake and clearance of 18F-P3BZA in normal rat, dynamic PET/CT scans were initiated immediately after administration of 18F-P3BZA and terminated 60 min later. To validate the capability of 18F-P3BZA for visualizing the implanted RPE cells, normal rats were intrastriatally injected with pRPE-GM, ARPE-19-GM and GM, respectively.10 min-static PET/CT scans were performed at 48 h post implantation. Moreover, longitudinal PET/CT scans were acquired at day 2, 7 and 14. Postmortem analysis was performed subsequently. Results: Cell uptake studies demonstrated that 18F-P3BZA accumulated effectively in pRPE cells, which maximized at 1.97% and 7.19% applied dose (AD) within 30 min without or with tyrosine pre-treatment, respectively. Whereas ARPE-19 cells only exhibited 0.22% and 0.21% uptake, without or with tyrosine pre-treatment ($P < 0.01$). Further melanin assay confirmed that the amount of melanin in pRPE was 6-folder higher than that in ARPE-19 cells. L-Tyrosine pretreatment could dramatically increase the melanin production in pRPE but not in ARPE-19 cells. Time-brain activity curve from dynamic PET/CT demonstrated that 18F-P3BZA could pass through blood brain barrier and accumulate in the brain rapidly, peaked at 7.61±0.30 percentage of the injected radioactive dose per gram of tissue within the first 2 min, and then gradually decreased quickly over the remaining time of the scan. 18F-P3BZA-PET could clearly visualize the implanted pRPE cells, and the accumulation of the probe in the pRPE-GM was much higher than that of ARPE-19-GM or GM ($P < 0.05$) (Figure 1). Furthermore, longitudinal PET/CT scans revealed that little pRPE-GM cells survived long-term after transplantation, as evident by the significant reduced uptake of 18F-P3BZA uptake in the pRPE-GM transplantation sites. Lastly, autoradiography, H&E and Fontana-Masson staining further confirmed the in vivo imaging results. Conclusion: 18F-P3BZA PET/CT provides unprecedented opportunities to visualize, characterize and detected the long-term survival of implanted RPE cells via melanin targeting mechanism, and it may help to improve the therapeutic efficacy of hRPE cells for PD.

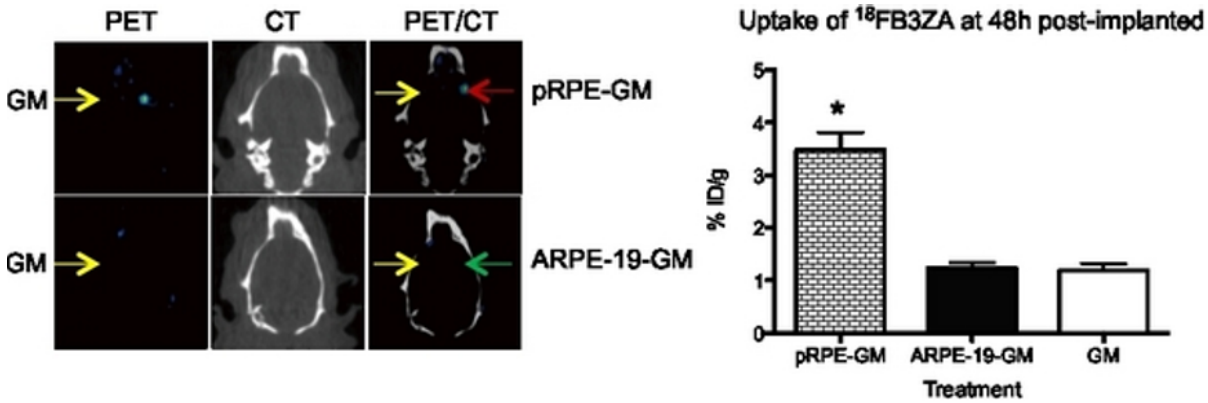

Figure 1. 18F-P3BZA PET/CT images at 48 h after cell implantation. (A). Representative decay-corrected coronal images of rats after transplantation of pRPE-GM (indicated by red arrows, top row) or ARPE-19-GM cells (indicated by green arrows, bottom row) in the right striatum and control GM in the left striatum (indicated by yellow arrows). (B) Quantification result of 18F-P3BZA PET/CT images. pRPE-GM cells show significant higher uptake than that of ARPE-19-GM and GM ($P < 0.05$)

Disclosure of author financial interest or relationships:
L. Bu, None; **R. Li**, None; **H. Liu**, None; **B. Shen**, None; **Z. Cheng**, None.

Presentation Number **SS 98**
Scientific Session 17: Preclinical in vivo Studies - Neurology
September 20, 2013 / 13:15-13:30 / Room: 203

Tracking of hMSCs in association with ischemic neuronal injury utilizing ^{1}H and ^{23}Na nuclei at 21.1T

Jens Rosenberg[1,2], *Katelyn L. Sellgren*[2], *Fabian Calixto Bejarano*[1], *Michelle Baird*[1], *Micheal Davidson*[1,3], *Teng Ma*[2], *Samuel C. Grant*[1,2], *[1]CIMAR, The National High Magnetic Field Laboratory, Tallahassee, FL, USA; [2]Chemical & Biomedical Engineering, The Florida State University, Tallahassee, FL, USA; [3]Department of Biological Science, The Florida State University, Tallahassee, FL, USA. Contact e-mail: rosenberg@magnet.fsu.edu*

Introduction: Human mesenchymal stem cells (hMSCs) are known to secrete factors for regulating inflammatory processes (1) in association with neural damage. In addition, hMSCs exposed to low oxygen tension (hypoxia), which is a native physiological condition, may enhance therapeutic effects. In this *in vivo* study, hMSCs exposed to normoxic and hypoxic conditions were transfected with superparamagnetic iron oxide (SPIO) nanoparticles and injected intra-arterially to treat ischemic stroke resulting from a middle cerebral artery occlusion (MCAO). Serial MRI at 21.1T was performed to acquire ^{1}H and ^{23}Na images of cell migration and lesion regression. **Methods:** hMSCs were (2) and transfected with 0.86-μm fluorescent iron oxides (Bangs Laboratory) for 12 h. Immediately following a 1-h transient MCAO (3), 1×10^{6} cells were injected intra-arterially through the exposed common carotid artery (CCA) of Sprague-Dawley rats. *In vivo* MRI was performed 24 h and 8 d after surgery utilizing high resolution, T_2-weighted (T_2W) spin echo, gradient recalled echo (GRE), 3D ^{23}Na GRE and diffusion weighted (DW) sequences at 21.1T for increased sensitivity. *Ex vivo* imaging was performed at 11.75T using a 100-μm 3D GRE sequence. Correlative histology was done on 20-μm brain sections treated with Hoechst nuclear stain and human antibody. Stroke lesion was determined based on volumetric changes on ^{1}H and ^{23}Na images. The apparent diffusion coefficient (ADC) was determined from DW images. **Results:** *In vivo* images of the ischemic stroke lesion (red circles in Fig 1) show increased signal as evidence of the influx of extracellular water and sodium. Increases in tissue sodium concentration (TSC) are seen by ^{23}Na MRI. SPIO-labeled cells are localized only within the stroked hemisphere, and after one week of initial MRI a decreases in SPIO contrast are evident on GRE images. Hypoxic and normoxic cells show significant ADC reduction compared to control (Fig 1b). Sodium images show significant reduction in lesion volume between hypoxic cells and normoxic treated cells (Fig 1c). Histological samples show SPIO-labeled hSMCs by the anti-human antibody and fluorescent SPIOs. **Conclusions:** This study shows that hypoxic cells provide improved lesion recovery compared to normoxic cells as measured with ^{1}H and ^{23}Na MRI. Cells are visible with GRE images and significant clearance within one week is seen and is confirmed with immunohistochemistry. A significant reduction in stroke ADC is seen for untreated and pretreated hMSCs. T_2W and ^{23}Na images show volumetric lesion reduction but the ^{23}Na is the only one showing significant recovery. The 21.1-T magnet provides increased ^{23}Na sensitivity for measurements of TSC, with potential for identifying penumbra regions (3) and recovery at earlier time points in stroke evolution. **Acknowledgement:** All work has been conducted in accordance with FSU Animal Care and User committee. Funding provided by the American Heart Association. **Reference:** 1. Pavlichenko, Brain Res (2008) 2. Grayson, Biotechnol Progres (2004) 3. Wetterling F et al MRM (2011)

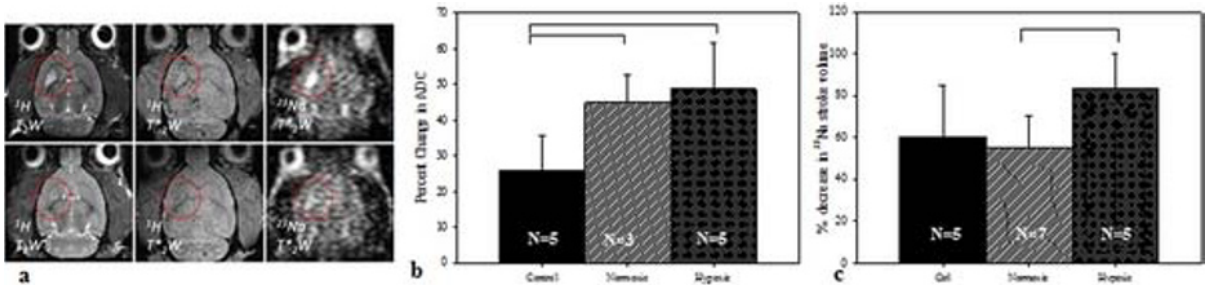

Fig 1a:T_2W, T_2*W sequences using ^{1}H and ^{23}Na nuclei showing the ischemic lesion and labeled cells (normoxic). Fig 1b & c:Graphs showing percent decrease in ADC (b) and ^{23}Na stroke lesion volume (c). Significance determined with one-way ANOVA and LSD posthoc test ($p<0.05$)

Disclosure of author financial interest or relationships:

J. Rosenberg, None; **K.L. Sellgren**, None; **F. Calixto Bejarano**, None; **M. Baird**, None; **M. Davidson**, None; **T. Ma**, None; **S.C. Grant**, None.

Presentation Number **SS 99**
Scientific Session 17: Preclinical in vivo Studies - Neurology
September 20, 2013 / 13:30-13:45 / Room: 203

Feraheme Nanoparticles for MRI-Guided Intra-arterial Injection to Target Specific Brain Regions: Implications for Stem Cell Delivery and Tumor Treatment

Piotr Walczak[1,5], *Miroslaw Janowski*[1,4], *Monica S. Pearl*[2,3], [1]*Division of MR Research, the Russell H. Morgan Department of Radiology and Radiological Sciences, Johns Hopkins University, Baltimore, MD, USA;* [2]*Interventional Neuroradiology, Johns Hopkins University, Baltimore, MD, USA;* [3]*Pediatric Neurointervention Department, Children's National Medical Center, Washington, DC, USA;* [4]*Neurorepair Department, Mossakowski Medical Research Centre, Warsaw, Poland;* [5]*Radiology, University of Warmia and Mazury, Olsztyn, Poland. Contact e-mail: pwalczak@mri.jhu.edu*

Introduction: Tremendous progress in interventional neuroradiology techniques allows for safe and precise positioning of catheters within the arterial system. Consequently, the intra-arterial route has become a promising pathway for the delivery of therapeutics to the brain including drugs or stem cells. However, current x-ray based monitoring of arterial flow has significant limitations in visualizing parenchymal perfusion. We hypothesized that the application of advanced ultra-fast MR imaging as well as Feraheme nanoparticles which are isotonic, biocompatible, and FDA-approved could be safely used to determine the parenchymal range after intra-arterial injection, thus precisely predicting the delivery of medicines to targeted brain areas. As a proof of principle experiment, we used Feraheme in a rabbit model to predict the area of mannitol-mediated blood brain barrier compromise; we also used this approach to target mesenchymal stem cells (MSCs) to the brain. Materials & Methods: Under fluoroscopic guidance, the left vertebral in rabbits was selectively catheterized with a 4 French catheter using femoral approach. Through the guide catheter, a 1.7F microcatheter was advanced into the left V4 segment or basilar artery under roadmap guidance. The rabbits were transported to a 3T (Magnetom Trio, Siemens) MRI for dynamic imaging and mannitol injection. Baseline horizontal T2 (TE/TR=105/1500) and T1 (TE/TR=9.1/300) images were obtained and were followed by intraarterial (IA) infusion of Feraheme (iron oxide nanoparticles, ~20 nm) at the rate 0.001-0.1ml/sec with dynamic GE-EPI images (TE/TR=30/3000; 60 measurements) for monitoring perfusion territory via the catheter. IA mannitol (25%, 0.005-0.05 ml/sec; 3ml total) was delivered. At the time of infusion, gadolinium (Magnevist) was injected iv (0.125 mmol/kg) Evans blue (EB) (2%, 2 ml/kg), was injected iv, and T1 post-gadolinium images were acquired. Iron oxide (Molday) labeled MSCs were infused IA and imaged with high resolution ex vivo MRI.The EB staining was evaluated post mortem on brain slices. Results: Catheter placement at desired levels of the artery was successful as visualized by x-ray angiography (A,D). Dynamic GE-EPI depicted the perfusion territory following Feraheme nanoparticle injection via the vertebral (B) or basilar (E) artery. Intra-arterial infusion of mannitol produced visible BBBD in the area previously pinpointed by the feraheme perfusion imaging. BBBD was visible as focal enhancement of the brainstem on gadolinium enhanced T1-weighted images (C,F). MSC infusion resulted in engraftment of cells in the brain with preferential accumulation in the area of BBBD (G) Conclusion: IA targeted delivery of Feraheme nanoparticles allows for the precise depiction of the brain territory supplied by a specific artery and with robust temporal resolution that enables the observation of local cerebral blood flow dynamics. This technique of guidance may be exploited for highly specific and efficient delivery of chemotherapeutic drugs for the treatment of brain tumors or other therapeutic agents including stem cells and neuroprotective factors.

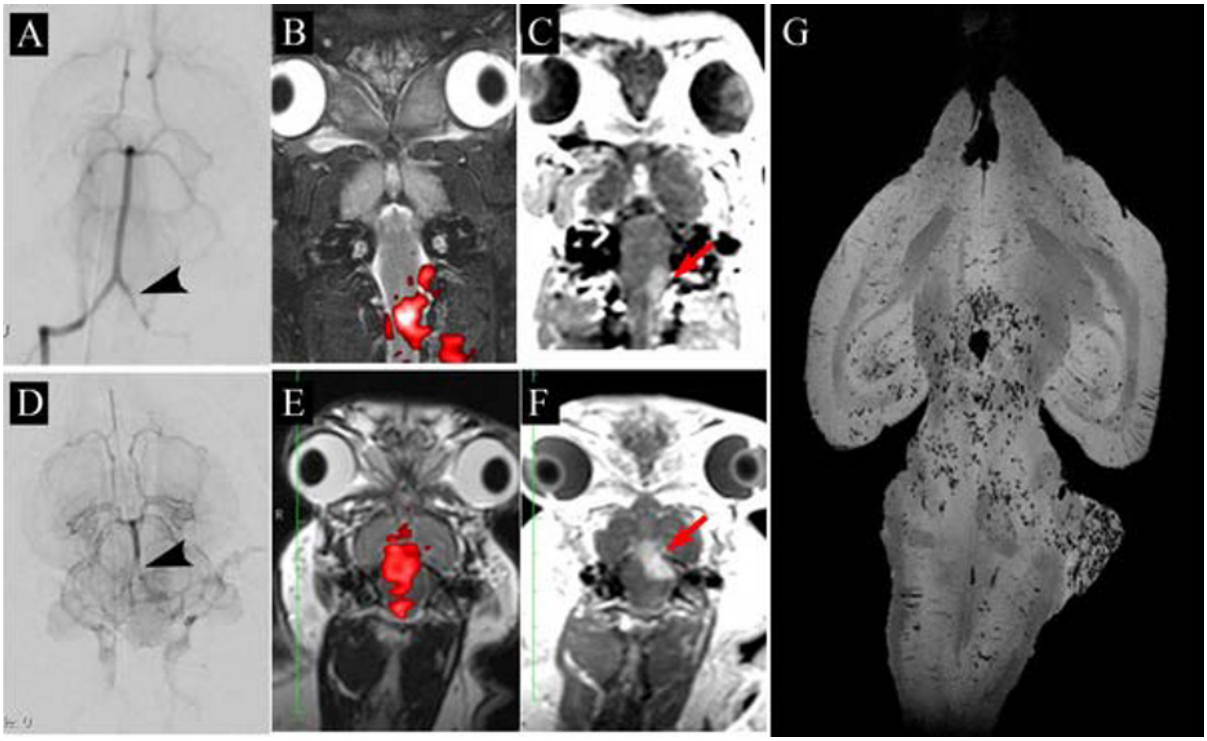

Injeciton via left vertebral artery (A-C) or basilar artery (D-F). Verterbral artery canulation visible on the x-ray angiography with a microcatheter tip marked by arrowhead (A). Perfusion imaging with feraheme showing enhancement in the medulla oblongata (B, substraction image color coded in red). T1-weighted MRI showing enhancement in the region previously pinpointed by feraheme perfusion (C, red arrow). Basilar artery canulation (D, arrowhead) resulted in completely different perfusion pattern (E, red). Also in this case, blood brain barrier disruption in T1-weighted MRI (F, red arrow) closely correlates to feraheme perfusion pattern. (G) iron oxide labeled mesenchymal stem cells are visualized as hypointensities on high resolution ex vivo T2*-weighted MRI. There is marked preference for the cells to localize in catheter perfused regions with BBBD.

Disclosure of author financial interest or relationships:
P. Walczak, None; **M. Janowski**, None; **M.S. Pearl**, None.

Presentation Number **SS 100**
Scientific Session 17: Preclinical in vivo Studies - Neurology
September 20, 2013 / 13:45-14:00 / Room: 203

Molecular imaging of genetically engineered mesenchymal stem cell for traumatic brain injury tropism and recovery

Zhe Wang, *Yu Wang, Gang Niu, Xiaoyuan (Shawn) Chen, National Institutes of Health, Bethesda, MD, USA. Contact e-mail: zhe.wang2@nih.gov*

Objective: Bone marrow derived mesenchymal stem cells (MSCs) appear to be the most appropriate stem cells for functional recovery of various cerebral injuries, such as traumatic brain injury (TBI). Unfortunately, limited number of cells can be eventually delivered to TBI area, and low cell viability after delivery further reduces MSCs' therapeutic capacity. In this study, we hypothesize that genetically engineering MSC to overexpress CXCR4 on cell surface membrane could significantly enhance the cell delivery efficiency to TBI area, and the extensive SDF1α/CXCR4 interaction could up-regulate downstream Akt activity to sustain MSC viability. Methods: CXCR4 gene was cloned into dual promoter vector by standard molecular cloning methods, followed by packaging into lentivirus. MSCs were isolated and pooled from bone marrow of transgenic FVB mice with β-actin promoter driving firefly luciferase, and underwent 5 passages before being infected by CXCR4 coding lentivirus twice. FACS and microscopy were employed to confirm the stem cell surface markers and differentiation ability. Transwell study was used to the chemotaxi of MSC. Immunoblots were conducted to stain specific proteins or chemokines. TBI in balb/c mice were induced by controlled cortical impact (CCI). In vivo bioluminescence imaging was conducted on IVIS System. Results: The expression of CXCR4 gene was promoted by MSCV promoter, which is stable and efficiency for most protein expressions in stem cells. FACS and immunoblots confirmed the almost 10-fold overexpression of CXCR4 on MSCs. Transwell study showed preferred migration of MSCCXCR4+ to SDF1α (50ng/ml). Immunoblotting revealed the activation of Akt and its associated downstream signaling pathway. The activated MSC, in turn, secreted proangiogenic chemokines to induce endothelial cells proliferation and tube formation through VEGFR2 signaling. Bioluminescence animal imaging study demonstrated improved accumulation of MSCCXCR4+ at TBI area over 21 days. Immunohistochemical staining revealed the preferable distribution of MSCCXCR4+ on peripheral site of TBI. In addition, MSCCXCR4+ also stimulated angiogenesis at the injury area as shown by blood vessel prevalence. Electrophysiological study showed that MSCCXCR4+ improved neural networking communication after TBI. Conclusion: Genetically engineered MSC to overexpress CXCR4 on surface membrane improved MSC migration and accumulation at TBI area, and enhanced therapeutical potency of MSC to TBI by activating Akt signaling pathway.

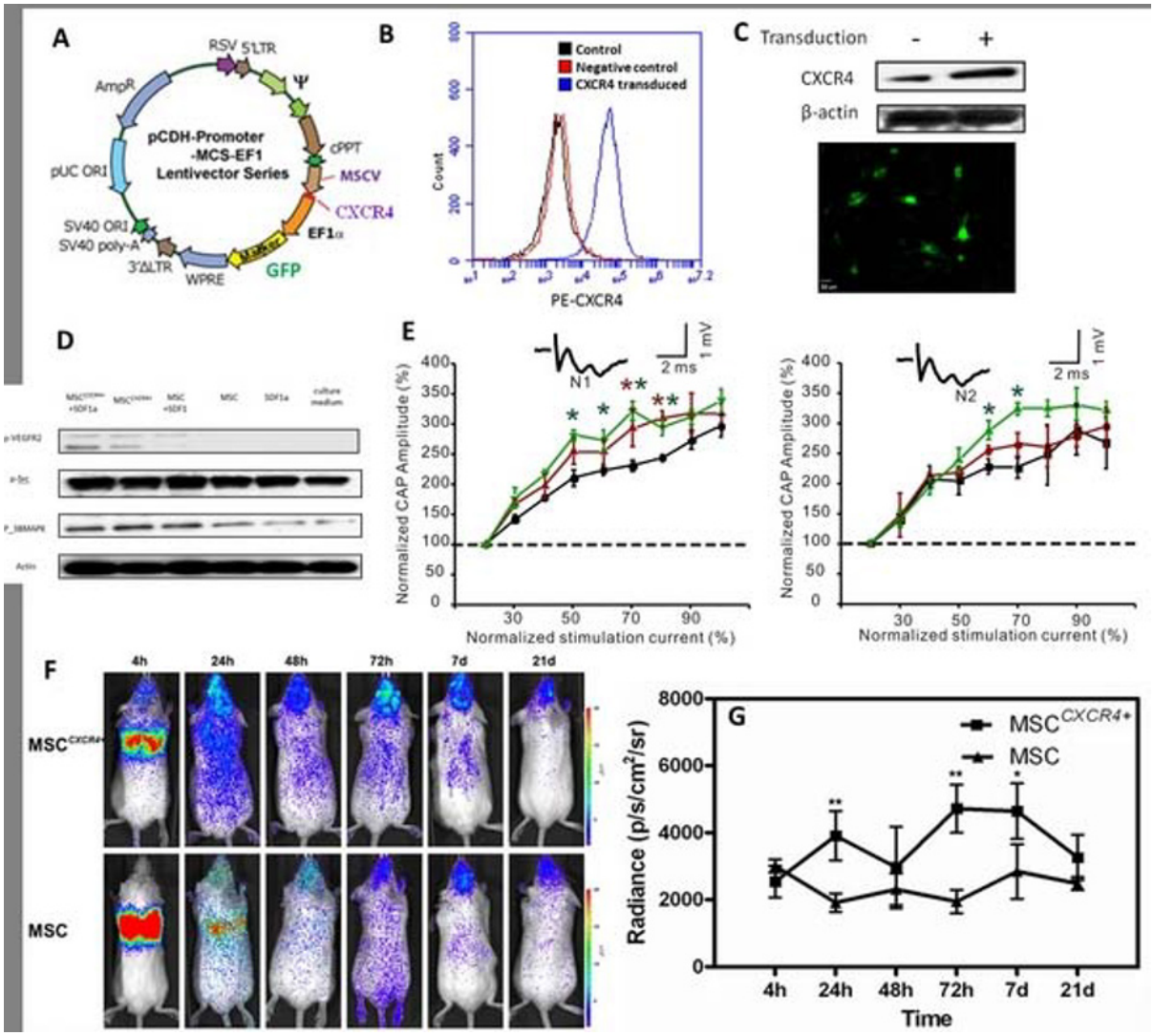

A) Gene map of dual promoter vector used in this study; B) FACS analysis of transduced MSC on surface overexpression of CXCR4; C) Western blot analysis of CXCR4 expression level; D) Fluorescence (GFP) image of transduced CXCR4 positive MSC; E) Electrophysiological analysis of TBI mice treated with CXCR4 infected (right) and non-infected (left) MSCs after 21 days; F) Bioluminescence imaging of the progression of intravenously administrated MSCCXCR4+ and MSC in TBI mice, respectively; G) Statistical analysis of BLI signals in the TBI areas.

Disclosure of author financial interest or relationships:
Z. Wang, None; **Y. Wang**, None; **G. Niu**, None; **X. Chen**, None.

Presentation Number **SS 101**
Scientific Session 17: Preclinical in vivo Studies - Neurology
September 20, 2013 / 14:00-14:15 / Room: 203

Monitoring myelination by transplanted glial progenitor cells in shiverer mouse brain using diffusion tensor MRI

Agatha Lyczek[1,2], *Jiangyang Zhang*[1,2], *Miroslaw Janowski*[1,2], *Jeff W. Bulte*[1,2], *Piotr Walczak*[1,2], [1]*Dept. of Radiology and Radiological Science, Johns Hopkins University, Baltimore, MD, USA;* [2]*Institute for Cell Engineering, Johns Hopkins University, Baltimore, MD, USA. Contact e-mail: alyczek1@jhu.edu*

Demyelinating disorders are characterized by neuroinflammation and oligodendrocyte loss and often result in the irreversible loss of neurological function with no effective treatment. A promising new approach is based on transplantation of progenitors restoring myelinating oligodendrocytes. There is evidence showing that transplantation of glial-restricted progenitor cells (GRPs) in rodent models results in the generation of new oligodendrocytes, myelination and therapeutic effect. In this study, we applied diffusion tensor MRI to monitor myelination by GRPs in dysmeylinated shiverer mice. GRPs were derived from transgenic mice expressing GFP under oligodendrocyte-specific PLP promoter (PLP-GFP) and transplanted into the lateral ventricles of neonatal rag2-/- shiverer mice (n=6). Age-matched non-transplanted rag2-/- shiverers (n=5) and C57BL/6 mice (n=5) were used as controls. MRI was performed at 11.7 T for grafted mice (n=6) and for age-matched control mice (n=10) 125 days post transplantation. In vivo 3D DTI was performed with TE/TR = 25/500 ms, 6 diffusion directions; b=3000 s/mm2; FOV = 16 mm x 16 mm x 17.5 mm, a matrix size of 128 x 128 x 70. Multi-slice T2-weighted images were acquired with TE/TR = 60/3800 ms, RARE-factor = 8, four signal averages, field of view (FOV) = 15 mm x 15 mm, in-plane resolution of 0.08 mm x 0.08 mm. Electron microscopy was performed on sagittal cross sections of corpus callosum. Histological analysis included immunostaining for Myelin Basic Protein (MBP). In vivo DTI showed different patterns of radial diffusivity, which reflects the extent of water molecule diffusion perpendicular to the direction of axons in white matter tracts and has been associated with myelin integrity in several other models, between transplanted and control shiverer mice. Several brain regions, primarily the corpus callosum and fimbria, showed decreased radial diffusivity (RD) and increased fractional anisotropy (FA) in transplanted mice indicating myelination. In histology, the distribution of engrafted, GFP+ cells was in good agreement with MRI findings. PLP-specific GFP expression correlated to immunohistochemistry against MBP confirming myelination by the graft. Average coronal profiles of FA and RD were generated across the cortex, corpus callosum and subcallosal gray matter (Fig. 1A). WT and transplanted shiverers had increased FA in the corpus callosum and fimbria (Fig. 1B, $p \leq 0.001$, $p \leq 0.001$, respectively) and decreased RD (Fig. 1C, $p \leq 0.001$, $p \leq 0.01$, respectively) as compared to non-transplanted shiverer controls. Normalized T2-w signal intensity profiles were generated across the corpus callosum and showed decreased signal intensity in the grafted group going towards WT values (Fig. 1D, $p \leq 0.01$). Electron microscopy was consistent with MRI findings, showing 10-13 myelin wraps per axon in WT mice, 2-4 wraps in shiverer controls, while grafted mice fell in the middle with 5-7 wraps. In conclusion, we demonstrated that transplanted GRPs are capable of myelinating shiverer mouse brain and that DTI is an excellent method for monitoring myelination. DTI MRI should be translatable for monitoring cell-based therapies in patients.

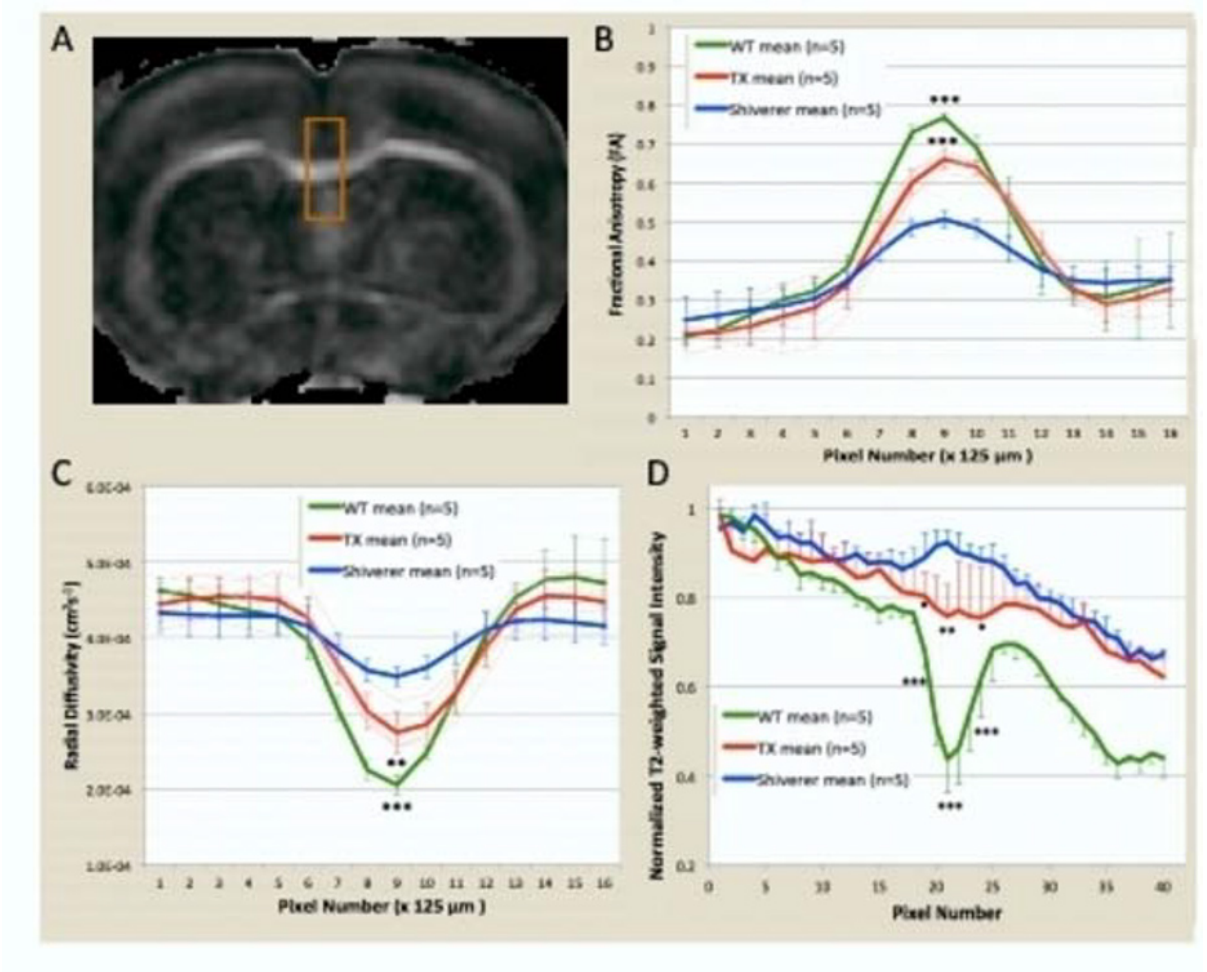

Figure 1: Average coronal profiles for C57BL/6 mice, Rag2 -/- shiverer controls and transplanted mice. Region of interest was selected across the corpus callosum at bregma 0.38mm (A). Fractional anisotropy (B) radial diffusivity (C) profiles differences in transplanted mice indicating myelination. Normalized T2-w signal intensity profile (D) showed decreased signal intensity in transplanted mice suggested increased myelin associated lipids in the area of the corpus callosum.

Disclosure of author financial interest or relationships:
A. Lyczek, None; **J. Zhang**, None; **M. Janowski**, None; **J.W. Bulte**, None; **P. Walczak**, None.

Presentation Number **SS 102**
Scientific Session 17: Preclinical in vivo Studies - Neurology
September 20, 2013 / 14:15-14:30 / Room: 203

Multiparametrical PET/MRI reveals that both β-amyloid load and loss of perfusion in the brain of transgenic AD mice reach a plateau phase

Florian C. Maier, *Hans F. Wehrl, Andreas Schmid, Stefan Wiehr, Carsten Calaminus, Bernd J. Pichler, Department of Preclinical Imaging and Radiopharmacy, Eberhard Karls University of Tübingen, Tuebingen, Germany. Contact e-mail: florian.maier@med.uni-tuebingen.de*

The availability of new treatment strategies targeting the cerebral β-amyloid burden in Alzheimers Disease (AD) emphasizes the need for the identification of a therapeutic window during disease progression. In AD patients it has been proposed that the most promising therapeutic window for secondary preventive therapies is represented by the linear growth phase of the β-amyloid burden - before further growth ceases and a plateau phase is reached. Thus, it is crucial to gain a deeper insight into the dynamics of β-amyloid deposition and physiological downstream events in the amyloid cascade. In this study, we present for the first time evidence for a plateau phase of the cerebral β-amyloid load in two different transgenic mouse models of AD, accompanied by a sigmoid decline of regional cerebral blood flow (rCBF) in the presence of cerebral amyloid angiopathy (CAA) - encompassing the entire course of the disease. Transgenic and littermate control APPPS1 and APP23 mice were i.v. injected with 7.2±2.5MBq [^{11}C]PIB for the determination of the β-amyloid burden growth rate and with 26.2±3.4MBq [^{15}O]H_2O for the measurement of rCBF. Quantitative [^{15}O]H_2O-PET data were cross-validated by an arterial spin labelling (ASL) MRI approach. PET and MRI data were acquired longitudinally for up to 20 months (n=5). During measurements, body temperature was maintained at 37±0.1°C. [^{11}C]PIB-PET data were quantified by the calculation of binding potentials (BP), [^{15}O]H_2O-PET analysis was conducted using an image derived arterial input function and ASL data were evaluated with a simplified version of the Bloch equation. Further, transgenic 2-,7-,12.5-,19-,21- and 24-months-old APPPS1 mice (n≤4) were examined histologically for the amyloid burden. The same applies for 2-,8-,18-,21-,27- and 30-months-old APP23 mice (n=3). We could clearly identify a linear growth phase of the amyloid burden in both APPPS1 (5.5-12.5 months, BP: 0.05±0.02 to 0.21±0.08, R^2=0.998) and APP23 (17-24 months, BP: 0.18±0.02 to 1.15±0.98, R^2=0.999) mice. Further, both mouse models show a subsequent plateau of the amyloid growth, confirmed by sigmoidal fitting of [^{11}C]PIB-PET (APPPS1: R^2=0.98, χ^2<0.01, BPmax=0.27±0.02; APP23: R^2=0.996, χ^2<0.01, BPmax=1.44±0.04; n=5) and histological data from amyloid immunohistochemistry (APPPS1: R^2=0.97, χ^2=1.40; APP23: R^2=0.999, χ^2=0.17; n≤4). In the presence of CAA (in APP23 mice), the sigmoidal growth of the amyloid burden is accompanied by a sigmoid decline of rCBF also reaching a plateau. Both measures are inversely correlated (R^2=0.96, χ^2=81, Pearsons corr. coef. p=-0.86). In the case of pure parenchymal amyloid deposition in APPPS1 mice, rCBF remained unchanged. This study provides first evidence for the proposed hypothetical model of sigmoidal AD biomarker dynamics in two distinctly

different AD mouse models. We demonstrate that the amyloid load reaches a plateau and reveal that there is a causal relationship between CAA presence and loss of perfusion, also reaching a plateau phase. Further, we demonstrate the presence of a linear growth phase of the amyloid burden which has been proposed as the ideal therapeutic window for amyloid targeting therapies.

Disclosure of author financial interest or relationships:
F.C. Maier, None; **H.F. Wehrl**, None; **A. Schmid**, None; **S. Wiehr**, None; **C. Calaminus**, None; **B.J. Pichler**, Siemens, Grant/research support; Bayer, Grant/research support; AstraZeneca, Grant/research support; BoehringerIngelheim, Grant/research support .

Presentation Number **SS 103**
Scientific Session 18: First in Human & Clinical Studies - Lymph Node Imaging and Tumor Staging
September 20, 2013 / 13:00-13:15 / Room: Oglethorpe Auditorium

Hybrid sentinel node biopsy; experience in 103 penile cancer patients

Nynke S. van den Berg[1,2], *Gijs H. KleinJan*[1,2], *Oscar R. Brouwer*[2], *Hanna M. Mathéron*[2], *Henk G. van der Poel*[3], *Renato A. Valdés Olmos*[2], *Fijs van Leeuwen*[1,2], *Simon Horenblas*[3], [1]*Radiology, Leiden University Medical Center, Leiden, Netherlands;* [2]*Nuclear Medicine, The Netherlands Cancer Institute-Antoni van Leeuwenhoek Hospital, Amsterdam, Netherlands;* [3]*Urology, The Netherlands Cancer Institute-Antoni van Leeuwenhoek Hospital, Amsterdam, Netherlands. Contact e-mail: N.S.van_den_Berg@lumc.nl*

Background: The sentinel node (SN) biopsy is routinely performed for staging patients with penile cancer with a clinically node-negative groin (cNO). Conventionally for SN mapping a combination of radiocolloid and blue dye is used. These are injected separately, which can lead to "staining" discrepancies. As alternative we use the fluorescent and radioactive tracer indocyanine green (ICG)-99mTc-nanocolloid. One injection of this hybrid tracer enables both preoperative SN mapping, and intraoperative radio- and fluorescence guidance towards the SNs. This study aimed to determine the additional value of the fluorescence in comparison with the blue dye during the SN biopsy procedure in patients with penile carcinoma. Methods: Between April 2011 and February 2013, 103 patients who underwent a SN biopsy of the cN0 groin and treatment of the primary tumour were prospectively included. 0.4mL of approximately 79,4 MBq ICG-99mTc-nanocoloid was injected peritumorally (3-4 deposits). After injection lymphoscintigraphy and SPECT/CT were routinely performed to identify the number and location of the SNs. Surgery was performed on the same or the next day. Patent blue dye was injected prior to the start of the operation. During the operation SNs were pursued via gamma tracing. The lymphatic tracts and the SNs could be visualized via fluorescence imaging and/or blue dye detection. A portable gamma camera was used to confirm excision of all SNs. Results: Preoperative imaging after injection of ICG-99mTc-nanocolloid enabled SN identification in all 103 patients (total 368 SNs distributed over 189 groins). Intraoperatively, all preoperatively defined SNs were localized using combined radio-, fluorescence and blue dye guidance. 93.2% of SNs could be visualized using fluorescence imaging whereas only 55% SNs had stained blue at the time of excision ($p<0.001$). Ex vivo, all excised SNs were both radioactive and fluorescent. As the fluorescent signal is limited to <0.5cm radioguidance cannot be omitted. Conclusion: The fluorescence feature of the hybrid tracer ICG-99mTc-nanocolloid has proven to be valuable for SN biopsy. Compared to fluorescence-based identification significantly fewer SNs had stained blue at the time of excision.

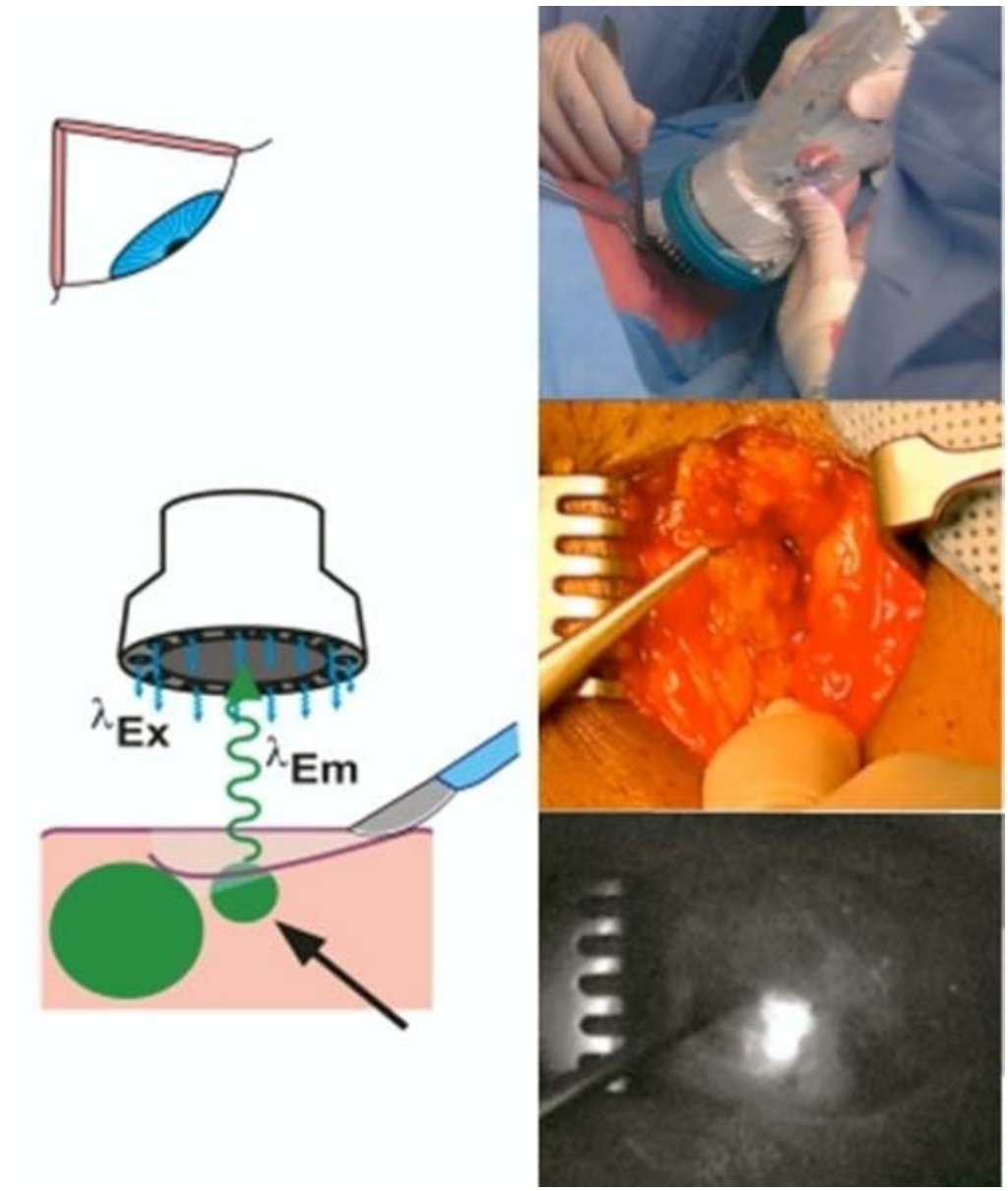

Disclosure of author financial interest or relationships:
N.S. van den Berg, None; **G.H. KleinJan**, None; **O.R. Brouwer**, None; **H.M. Mathéron**, None; **H.G. van der Poel**, None; **R.A. Valdés Olmos**, None; **F. van Leeuwen**, None; **S. Horenblas**, None.

Presentation Number **SS 104**
Scientific Session 18: First in Human & Clinical Studies - Lymph Node Imaging and Tumor Staging
September 20, 2013 / 13:15-13:30 / Room: Oglethorpe Auditorium

Integrated use of radioactivity and fluorescence during sentinel node biopsy in 109 melanoma patients

Nynke S. van den Berg[1,2], *Oscar R. Brouwer*[2], *Boudewijn Schaafsma*[4], *Hanna M. Mathéron*[2], *Gijs H. KleinJan*[1,2], *W Martin C. Klop*[3], *Michiel W. van den Brekel*[3], *Alfons J. Balm*[3], *Alexander Vahrmeijer*[4], *Omgo E. Nieweg*[5], *Renato A. Valdés Olmos*[1,2], *Fijs van Leeuwen*[1,2], [1]*Radiology, Leiden University Medical Center, Leiden, Netherlands;* [2]*Nuclear Medicine, The Netherlands Cancer Institute-Antoni van Leeuwenhoek Hospital, Amsterdam, Netherlands;* [3]*Head and Neck Surgery and Oncology, The Netherlands Cancer Institute-Antoni van Leeuwenhoek Hospital, Amsterdam, Netherlands;* [4]*Surgery, Leiden University Medical Center, Leiden, Netherlands;* [5]*Surgery, The Netherlands Cancer Institute-Antoni van Leeuwenhoek Hospital, Amsterdam, Netherlands. Contact e-mail: N.S.van_den_Berg@lumc.nl*

Background: Recently the hybrid tracer ICG-99mTc-nanocolloid was introduced for sentinel node (SN) biopsy in a variety of malignancies. Via one single injection, the radioactive component (99mTc-nanocolloid) allows for preoperative SN mapping, and intraoperatively, the near-infrared fluorescent component indocyanine green (ICG) allows for optical SN detection. This study evaluated the value of this hybrid tracer in a large cohort of melanoma patients. Methods: A total 109 patients with melanoma scheduled for a SN biopsy and re-excision of the melanoma scar were prospectively included in this study. Lesions were located in the head and neck (n=55), trunk (n=35) or on an extremity (n=19). On average 78MBq ICG-99mTc-nanocolloid was intradermally administered surrounding the melanoma scar (4 deposits of 0.1 mL). After injection lymphoscintigraphy and SPECT/CT were routinely performed to determine the number and location of the SN(s). The operation was carried out the same or the next day. Except in the 32 patients with melanoma on the face, prior to the start of the operation 1 mL patent blue dye was injected around the melanoma scar. The radioactive signal was detected by a portable gamma camera and the gamma probe, the latter transforming the radioactivity to a acoustic signal. Next to the use of blue dye fluorescence imaging was used to visualize the SNs. All harvested SNs were evaluated for radioactivity, fluorescence and blue dye staining. Results: In total 308 SNs were visualized in 109 patients. Of the excised SNs 95% was radioactive and 95% was fluorescent. In contrast, only 57% of the SNs was found to be blue. Conclusions: In melanoma patients the hybrid tracer outperforms blue dye. At the same time the optical component improves the detection sensitivity at sites of complex drainage were radioguidance is not sufficient.

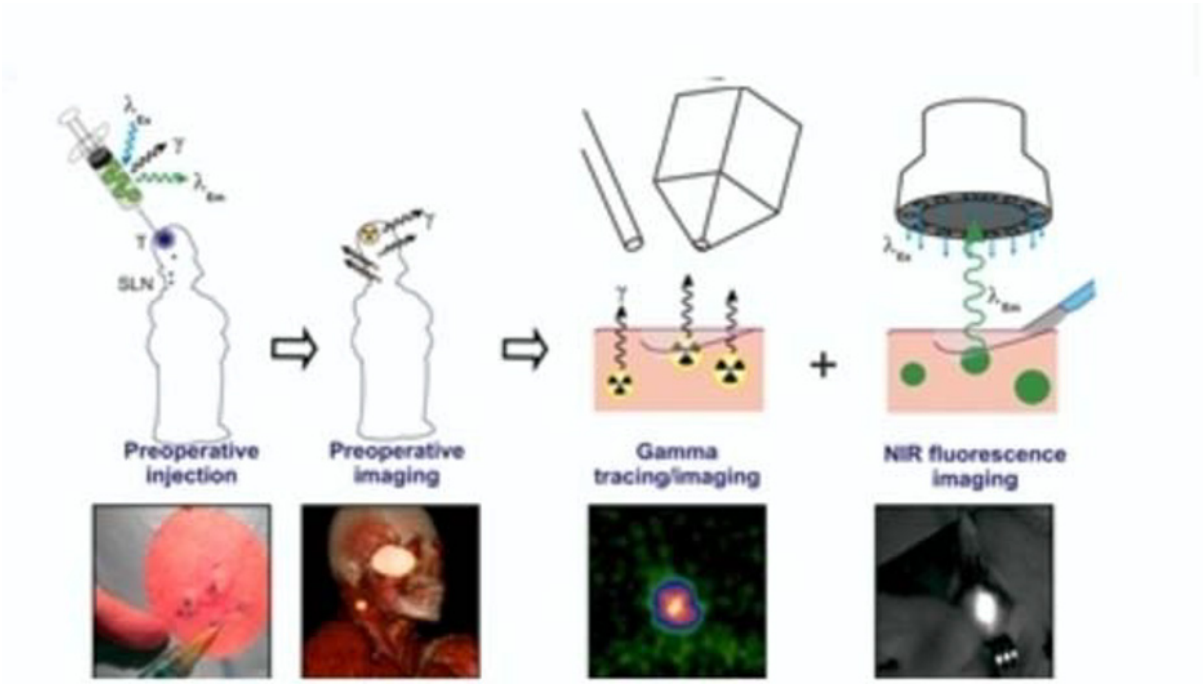

Schematic overview of the sentinel biopsy procedure for melanoma

Disclosure of author financial interest or relationships:
N.S. van den Berg, None; **O.R. Brouwer**, None; **B. Schaafsma**, None; **H.M. Mathéron**, None; **G.H. KleinJan**, None; **W.C. Klop**, None; **M.W. van den Brekel**, None; **A.J. Balm**, None; **A. Vahrmeijer**, None; **O.E. Nieweg**, None; **R.A. Valdés Olmos**, None; **F. van Leeuwen**, None.

Presentation Number **SS 105**
Scientific Session 18: First in Human & Clinical Studies - Lymph Node Imaging and Tumor Staging
September 20, 2013 / 13:30-13:45 / Room: Oglethorpe Auditorium

Phase I Study: BAY 1075553 PET/CT in Staging and Re - Staging of Prostate Cancer Patients - Comparison with 18F-Choline PET/CT

Mohsen Beheshti[1], *Thomas Kunit*[2], *Friedrich Fitz*[1], *Ray Valencia*[3], *Ludger M. Dinkelborg*[4], *Andrew Stephens*[4], *Andre Mueller*[4], *Werner Langsteger*[1], [1]*Nuclear Medicine & Endocrinology, PET - CT Center LINZ, St. Vincent's Hospital, Linz, Austria;* [2]*Urology, St. Vincent's Hospital, Linz, Austria;* [3]*Global Drug Discovery, Bayer Pharma AG, Berlin, Germany;* [4]*Radiopharmacology, Piramal Imaging GmbH, Berlin, Germany. Contact e-mail: mohsen.beheshti@bhs.at*

BAY1075553 ((2RS,4S)-2-[18F]Fluoro-4-phosphonomethyl-pentanedioic acid) showed increased uptake in prostate cancer cells corresponding to the PSMA expression in animal studies. In this prospective, first in man, study the diagnostic potential of PET/CT imaging with BAY1075553, as a novel PET tracer, was compared with 18F - Fluorcholine (FCH) . Material and Methods: 12 prostate cancer patients (9 primary staging, 3 Re-staging; mean age: 67 ± 8 yrs) were included. The mean PSA in the primary staging and restaging groups was 21.5 ± 12 ng/ml and 73.6 ± 33 ng/ml, respectively. The median Gleason score was 8 in both groups. From 24 hrs before to 5 - 8 days after BAY1075553 administration, all patients were clinically monitored (physical examination, ECG, laboratory parameters of different organs etc) and adverse events were documented. PET acquisition started 30 seconds after i.v. injection of 300 MBq of BAY1075553 or FCH with dynamic PET images in the pelvic region (8 x 30 sec. frames and 8 x 1 min. frames) followed by static semi - whole body acquisition. Radical prostatectomy and PLND was performed in the primary staging patients. Results: After i.v. administration of BAY 1075553 safety data showed no relevant changes in the sequential blood values, ECGs, urine testing or physical examination up to 5 - 8 days. In the prostate gland, there was a close correlation between detected lesions by means of both imaging modalities and histopathological results. Mean SUVmax in the prostate gland was higher on FCH PET (6.95 ± 1.6) than BAY1075553 PET (5.6 ± 2.4), p = n.s. Overall, 68 LNs were resected in 9 patients. The sensitivity and specificity of PET imaging for the detection of LN metastases was 42.9% and 100% by BAY1075553 vs. 81.2% and 50% by FCH. The findings of both modalities were closely correlated with each other in the detection of bone metastases; however, BAY1075553 could not detect a bone-marrow metastasis. Furthermore, degenerative bone lesions showed very often intensive uptake of BAY1075553. Conclusion: BAY1075553 showed no adverse effect and was well tolerated by all patients. BAY1075553 PET/CT was able to detect prostate cancer in patients with primary and advanced disease. However, FCH PET/CT showed superior results compared to BAY1075553 in particular with respect to the detection of LN and bone-marrow metastases. Furthermore, BAY1075553 seems to have limited specificity for detection of bone metastases mainly due to non-specific increased uptake in degenerative bone lesions.

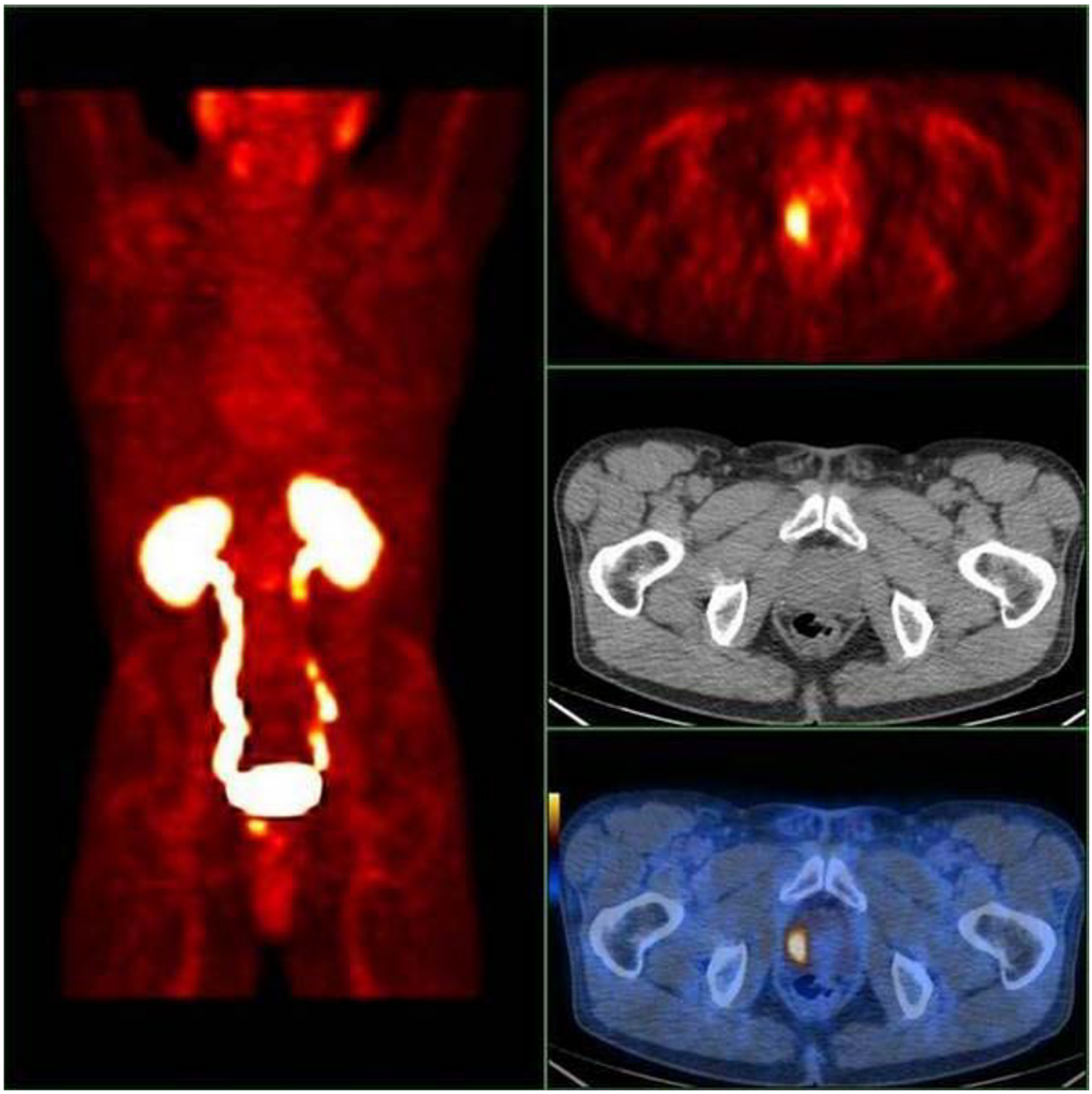

BAY 1075553 PET/CT in a prostate cancer patient, GSc 8 (4 + 4), PSA 22.6 ng/ml. Increased tracer uptake is evident on the right prostate lobe, highly correlated with histopathological findings.

Disclosure of author financial interest or relationships:
M. Beheshti, None; **T. Kunit**, None; **F. Fitz**, None; **R. Valencia**, Bayer Pharma AG, Employment; **L.M. Dinkelborg**, None; **A. Stephens**, Piramal Imaging, Employment; **A. Mueller**, Piramal Imaging, Employment; **W. Langsteger**, None.

Presentation Number **SS 106**
Scientific Session 18: First in Human & Clinical Studies - Lymph Node Imaging and Tumor Staging
September 20, 2013 / 13:45-14:00 / Room: Oglethorpe Auditorium

Novel Nanoparticle Enhanced Whole Body Tumor Scans for Staging of Children with Cancer

Christopher Klenk, *Rakhee Gawande, Deqiang Qiu, Andrew Quon, Jessica Donig, Daniel R. Owen, Ying Chen, Michael Moseley, Heike E. Daldrup-Link, Radiology, Stanford University, Stanford, CA, USA. Contact e-mail: cklenk@stanford.edu*

Purpose: Standard radiographic staging of children with cancer is associated with considerable radiation exposure and risk of secondary cancer development later in life. The purpose of this study was to develop an alternative radiation-free staging technique, based on whole body-magnetic resonance (WB-MR) imaging and the iron supplement ferumoxytol, used as a contrast agent. Methods: A novel WB-MR approach was established based on color-encoded, iron oxide nanoparticle-enhanced diffusion weighted (DW) scans for tumor detection, which were co-registered with iron oxide nanoparticle-enhanced T1-weighted MR scans for anatomical orientation. The Institutional Review Board, the Stanford Cancer Center and the US Food and Drug Administration (FDA) approved the study and following pulse sequence optimizations in nine healthy volunteers, eleven children and young adults with malignant lymphoproliferative disorders (11 malignant lymphomas, one burkitt leukemia) underwent WB-MR and PET/CT scans. Two experienced radiologists, blinded to clinical and other imaging data, determined in consensus the presence or absence of tumor deposits in eight different anatomical areas on WB-MR scans. These data were compared to corresponding evaluations of clinical routine 18F-FDG PET/CT scans. Histopathology and follow-up imaging served as the standard of reference. The disease stage of each patient was determined for WB-MR and 18F-FDG PET/CT, using the Anne Arbor classification system. Paired student's t-test was applied to asses agreement in staging evaluation and a p-value of <0.05 was chosen to indicate statistical significance. In addition the agreement between the tumor staging results of the two imaging tests was evaluated using Cohen's kappa statistics, with a score of 1.0 indicating perfect agreement. Results: Evaluations of volunteers revealed optimal pulse sequence parameters for axial WB-DW MR sequences with background suppression (DWIBS) as follows: repetition time (TR) of 3400 ms, an echo time (TE) of 60 ms, b-values of 50 and 600 s/mm2, a field of view (FOV) of 40cm, a slice thickness (SL) of 5mm and a bandwidth of 0.25kHz. Duration of the diagnostic procedure was 1-1.5 hours for WB-MR scans and 1.5-2.5 hours for 18F-FDG PET/CT scans (radionuclide injection + imaging). There was no statistically significant difference in staging outcome between WB-MRI and 18F-FDG PET/CT ($p < 0.0001$). The interobserver agreement between WB-MRI/DWIBS and 18F-FDG-PET/CT was good in evaluating staging according to the Ann Arbor classification with a weighted k value of 0.84. Conclusion: WB-MR may provide a radiation-free alternative to 18F-FDG PET/CT staging for children with malignant lymphomas. Funding: The authors acknowledge support from the Thrasher Fund and the Child Health Research Institute, Stanford University.

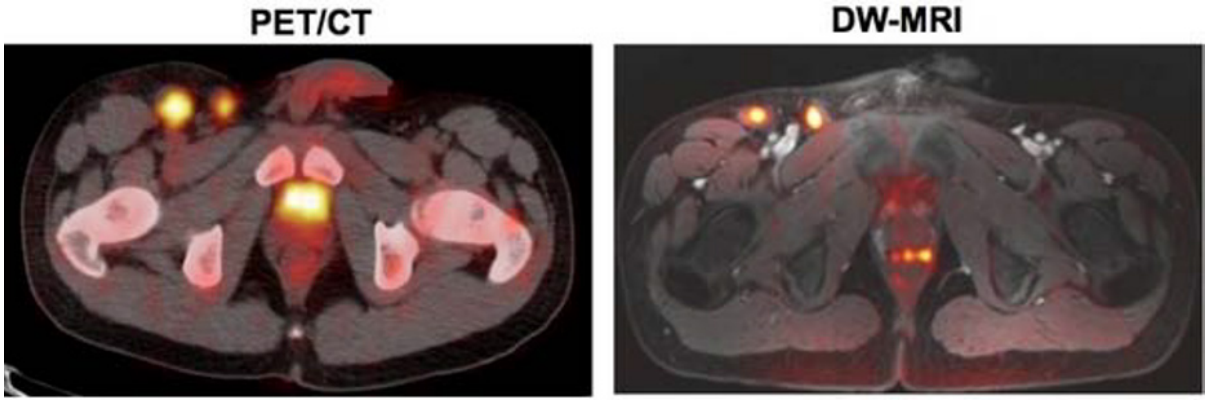

Example of a fused PET/CT image and a fused DW-MRI image to asses disease burden in a patient with Hodgkin's disease.

Disclosure of author financial interest or relationships:
C. Klenk, None; **R. Gawande**, None; **D. Qiu**, None; **A. Quon**, Lilly USA, Speakers bureau; Millenium, Grant/research support; Phillips, Consultant; GE Medical Systems, Consultant; **J. Donig**, None; **D.R. Owen**, None; **Y. Chen**, None; **M. Moseley**, None; **H.E. Daldrup-Link**, None.

Presentation Number **SS 107**
Scientific Session 18: First in Human & Clinical Studies - Lymph Node Imaging and Tumor Staging
September 20, 2013 / 14:00-14:15 / Room: Oglethorpe Auditorium

Near-infrared fluorescence sentinel lymph node mapping in breast cancer: a multicenter experience

Floris P. Verbeek[1], *Susan L. Troyan*[4], *Sven Mieog*[1], *Gerrit-Jan Liefers*[1], *Cornelis J. van de Velde*[1], *Alexander Vahrmeijer*[1], *John V. Frangioni*[2,3], [1]*Department of Surgery, Leiden University Medical Center, Leiden, Netherlands;* [2]*Department of Radiology, Beth Israel Deaconess Medical Center, Boston, MA, USA;* [3]*Department of Medicine, Beth Israel Deaconess Medical Center, Boston, MA, USA;* [4]*Department of Surgery, Dana-Farber/Harvard Cancer Center, Boston, MA, USA. Contact e-mail: f.p.r.verbeek@lumc.nl*

Background: The sentinel lymph node procedure plays an important role in the diagnosis and treatment of breast cancer. Currently, blue dyes or radiotracers or a combination are used as standard of care. However, these modalities have several disadvantages, including the use of ionizing radiation and tattooing of the breast up till several months after blue dye injection. Current identification rates are 93-96%. In case of non-identification of the SLN, an axillary lymph node dissection must be performed and is associated with a higher morbidity rate. Near-infrared fluorescence (NIRF) imaging has the potential to improve the sentinel lymph node (SLN) procedure by facilitating percutaneous and intraoperative identification of lymphatic channels and sentinel lymph nodes. Indocyanine green (ICG) is currently the only FDA and EMEA approved NIRF probe that can be used as a lymphatic tracer. Previous studies indicated that a dose of 500 μM ICG is optimal for SLN mapping in breast cancer. The current multicenter study validates these results in a large patient cohort. Methods: 95 breast cancer patients planned to undergo SLN procedure were included at the Dana-Farber/Harvard Cancer Center (Boston, MA USA) and the Leiden University Medical Center (Leiden, Netherlands) between July 2010 and January 2013. Patient characteristics were as follows: mean age = 56 years, mean tumor size = 13.7 mm, mean body mass index = 28. Patients underwent standard of care SLN procedure with lymphatic mapping using injection of 99Technetium-colloid, and in 33 (34%) patients, patent blue dye also injected. In addition, 1.6 mL of ICG (500 μM) was injected directly before surgical draping. For fluorescence guided sentinel node detection the Mini-FLARE™ camera system was used, which is capable of displaying real-time NIR signal and visible image simultaneously, and superimposing the NIR signal over the color video image. Results: Sentinel node mapping was successful in 94 of 95 patients using NIRF imaging or a combination of both NIRF imaging and radioactive guidance (identification rate = 99%). A total of 175 sentinel lymph nodes (mean = 1.9, range = 1-5) were detected: 96% hot, 98% fluorescent, and 76% blue. In one patient, the SLN was found only by fluorescence imaging. Time between skin incision and detection of SLN was 8 ± 4 minutes and was correlated to BMI ($P < 0.001$). In all patients that were treated with patent blue, the NIRF signal in the SLN was detected through the axillary fat considerably earlier than blue staining. The NIRF signal of the SLN was on average 11.7 ± 6.7 times higher than the surrounding axillary fat tissue. No adverse events related to indocyanine green injection were noted. Conclusion: This study demonstrates the safe and feasible introduction of NIRF imaging in order to detect the SLN in breast cancer patients with high identification rate using 500 μM ICG and the Mini-FLARE™ camera system.

Disclosure of author financial interest or relationships:
F.P. Verbeek, None; **S.L. Troyan**, None; **S. Mieog**, None; **G. Liefers**, None; **C.J. van de Velde**, None; **A. Vahrmeijer**, None; **J.V. Frangioni**, None.

Presentation Number **SS 108**
Scientific Session 18: First in Human & Clinical Studies - Lymph Node Imaging and Tumor Staging
September 20, 2013 / 14:15-14:30 / Room: Oglethorpe Auditorium

Application of Surgical Navigation System for Detecting the Sentinel Lymph Node in Breast Cancer Studies

Chongwei Chi[1], *Jinzuo Ye*[1], *Guojun Zhang*[2], *Jie Tian*[1], [1]*Medical Image Processing Group, Institute of Automation,CAS, "Beijing,100190", China;* [2]*The Cancer Hospital, Shantou University Medical College, Shantou, China. Contact e-mail: chichongwei@fingerpass.net.cn*

Introduction: In clinical applications, how to determine the boundaries of the tumor during surgery is an international hot and difficult problem. Radiology approaches such as X-rays, computed tomography (CT), magnetic resonance imaging (MRI) and ultrasound have been considered for use in assisting surgical procedures, but these were not applicable for intraoperative surgery. In order to assist the doctor to locate tumor during surgery, we developed a surgical navigation system which could provide real-time color and fluorescent video images. To prove its feasibility, the experiments on animals and patients for detecting the sentinel lymph node (SLN) in breast cancer with indocyanin green (ICG) were executed. Methods: A surgical navigation system was developed to perform intraoperative imaging. Firstly, the system was used to detect the lymphatic channels and lymph nodes in small animals including nude mice (n=5) and New Zealand rabbits (n=10). To explore an optimized dose/concentration for future use, a series titration of dose was administrated. Secondly, clinical studies were further conducted in breast cancer patients to evaluate the feasibility of the surgical navigation system in the detection of SLNs. Prior to surgery, 1 ml of ICG at 5mg/ml was intradermally injected into the areola and real-time color and fluorescent video images were acquired. Results: In the preclinical setting, 3-5 minutes later after injection of ICG at different dose, the lymphatic vessels and SLNs were visualized on the monitor in all 5 mice and 10 rabbits, the peak light intensities of the SLNs appeared about 10 minutes after injection with 1mg/ml as an optimized concentration. In breast cancer patients, 1 ml of ICG at 5mg/ml was given based on the recommendations from pre-clinical experiments. An average of 2.6 SLNs were found in 13 patients (detection rate = 100%). Conclusions: The lymphatic mapping and detection of the SLN in breast cancer by using the surgical navigation system were technically feasible. Clinicians could accurately locate the SLN in surgery with the system. The sensitivity and specificity of ICG imaging needs to be further determined in comparison to the use of methylene blue in early stage breast cancer patients. Index Terms—Near-infrared fluorescence, Image guided surgery, Sentinel lymph node mapping, Indocyanine green, Activatable probe

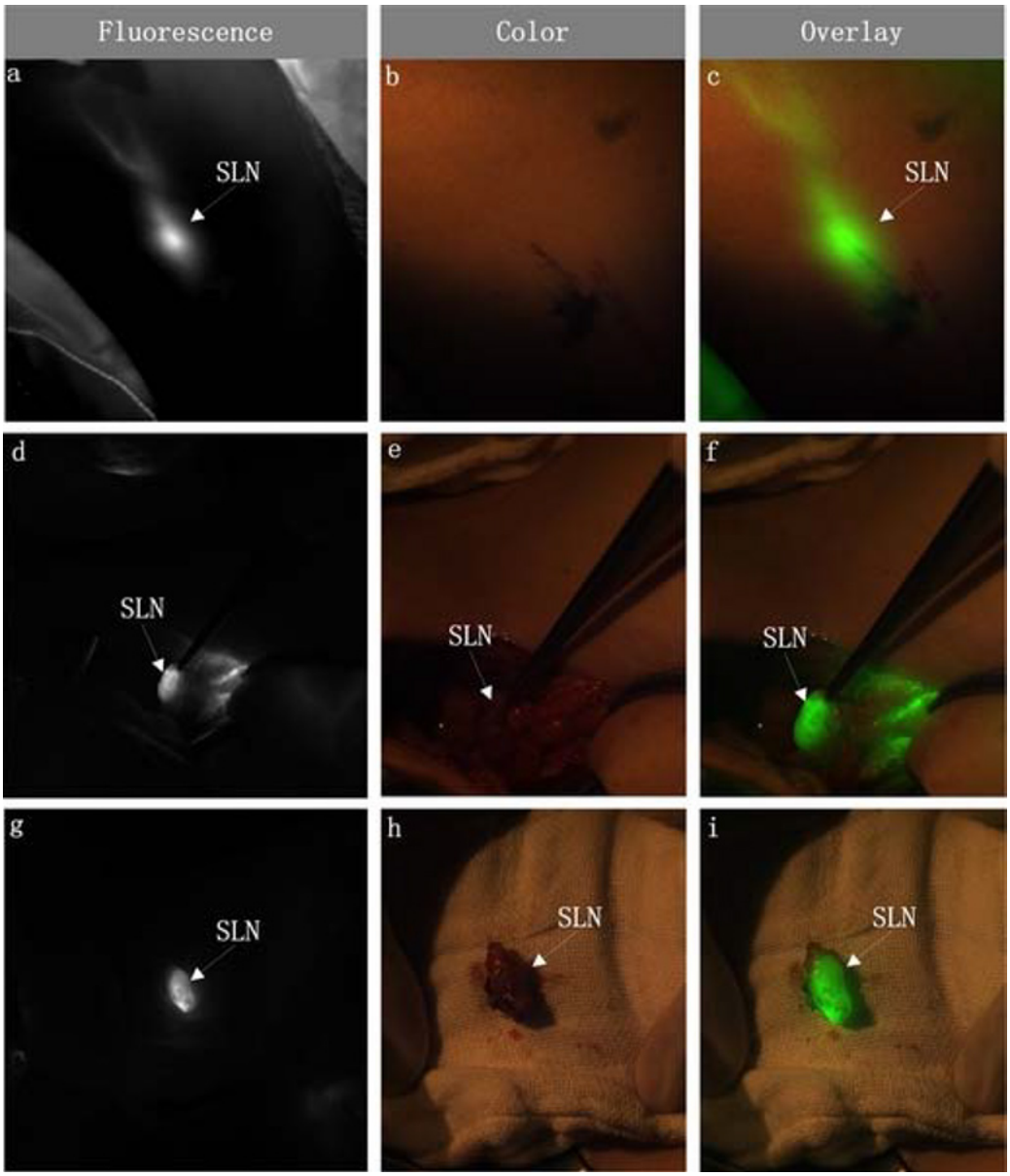

Disclosure of author financial interest or relationships:
C. Chi, None; **J. Ye**, None; **G. Zhang**, None; **J. Tian**, None.

Presentation Number **SS 109**
Scientific Session 19: First in Human & Clinical Studies - Multi-Organ Physiology and Metabolism
September 21, 2013 / 10:30-10:45 / Room: 102

Lung kinetics of autologous, radiolabelled, pure eosinophils and neutrophils in healthy and asthmatic volunteers. Feasibility and reproducibility study

Joanna J. Lukawska[2,1], *Lefteris Livieratos*[2,3], *Barbara M. Sawyer*[2], *Tak H. Lee*[4,2], *Michael O'Doherty*[3,2], *Phil Blower*[2], *Martin Kofi*[3], *James R. Ballinger*[2,3], *Christopher J. Corrigan*[1], *Greg Mullen*[2], [1]*Asthma, Allergy and Respiratory Science, Imaging Sciences, King's College London, London, United Kingdom;* [2]*Imaging Sciences and Biomedical Engineering, King's College London, London, United Kingdom;* [3]*Nuclear Medicine, Guy's & St Thomas' Hospital, London, United Kingdom;* [4]*Allergy Centre, HK Sanatorium and Hospital, Hong Kong, Hong Kong. Contact e-mail: joanna.lukawska@kcl.ac.uk*

Background: Cell therapies are attractive candidates for modulation and stimulation of the immune system and tissue repair in many disorders. However, demonstration of efficient cell migration to the target organ/regions, and avoidance of lung toxicity associated with cells' prolonged margination in pulmonary vasculature remains problematic. Here we demonstrate (1) feasibility and (2) baseline pulmonary kinetics of autologous radiolabelled eosinophils and neutrophils in healthy volunteers (non inflamed lungs) and volunteers with asthma (baseline inflammation). Methods: 105 mL of venous blood was obtained from healthy (4) and asthmatic (4) volunteers on two separate occasions. Granulocytes were separated using gradient Ficoll-Paque PLU 1.084 centrifugation. Superparamagnetic particles coupled to a monoclonal antibody against CD16, a surface marker present in neutrophils, were incubated with the granulocytes (mixed eosinophils and neutrophils). CliniMACS system (Miltenyi biotec, Bergisch-Gladbach, Germany) was used to obtain highly purified (>95.1% pure) human blood eosinophils (negative selection) or neutrophils (>97%, positive selection). Purified cells were labelled with Tc-99m HMPAO (Ceretec, GE Healthcare) under aseptic cGMP conditions and 75-100 MBq of labelled cells were administered intravenously. Dynamic lung images were acquired for the first 30 minutes. Further static scans of 5 minutes each were acquired at 1, 2 and 4 hours. Results: There was no evidence of prolonged lung margination of eosinophils or neutrophils in either group of volunteers. Lung migration of eosinophils differed significantly from that of neutrophils in both groups of patients. Migration of eosinophils in healthy volunteers followed clearance with T1/2 of 4.16 min whilst neutrophils T1/2 measured 13.72 min (p=0.0019). Similar results were obtained for eosinophils and neutrophils in stable asthmatics; T1/2 6.10 min measured for eosinophils and 14.01 min for neutrophils, p value = 0.0246. There were no statistically significant differences observed between healthy volunteers and stable asthmatics (eosinophils p=0.14 and neutrophils p=0.45). Conclusions: This technique provides an opportunity for rapid assessment of migration kinetics of pure cells used for immunotherapy or diagnostic purposes. It demonstrates the feasibility of using peripherally injected autologous, eosinophils and neutrophils in both healthy volunteers and volunteers with baseline lung inflammation. The technique establishes the basis for future spaciotemporal studies of pure cell kinetics.

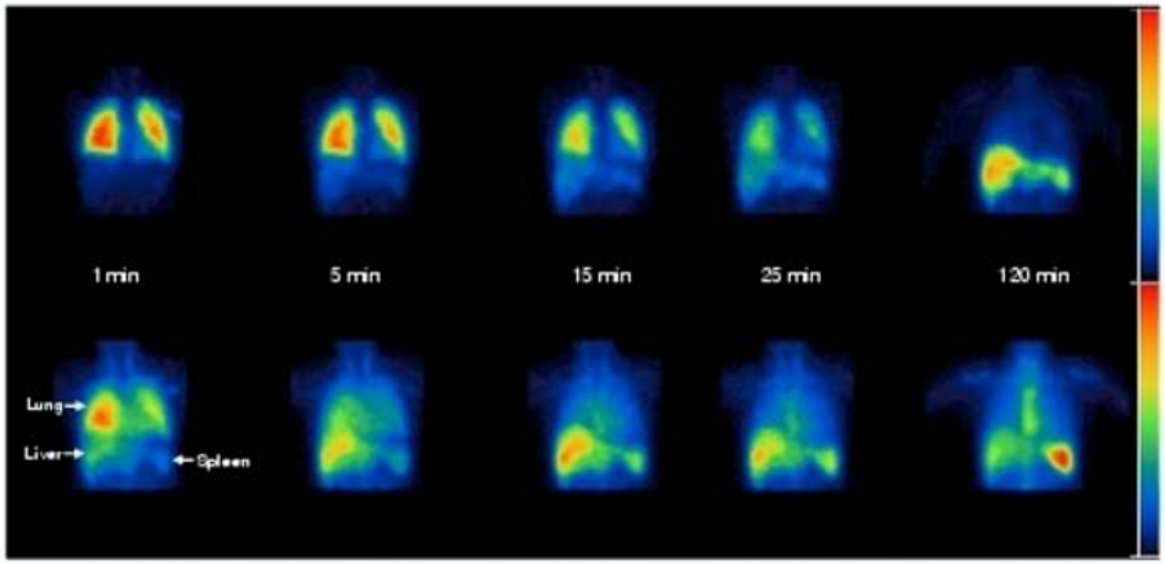

Representative images of biodistribution of 99mTc-HMPAO-labelled neutrophils and eosinophils in a normal volunteer at 1, 5, 15, 25 and 120 minutes

	T1/2 Healthy	T1/2 Asthma	p value
eosinophils	4.16 min	6.10 min	0.14
neutrophils	13.72 min	14.01 min	0.45
p value	0.0019	0.0246	

p values for T 1/2 of eosinophil and neutrophil lung kinetics in healthy and asthmatic volunteers

Disclosure of author financial interest or relationships:
J.J. Lukawska, None; **L. Livieratos**, None; **B.M. Sawyer**, None; **T.H. Lee**, None; **M. O'Doherty**, None; **P. Blower**, None; **M. Kofi**, None; **J.R. Ballinger**, GE Healthcare, Grant/research support; Imaging Equipment Ltd, Grant/research support; **C.J. Corrigan**, None; **G. Mullen**, Mediso, Consultant .

Presentation Number **SS 110**
Scientific Session 19: First in Human & Clinical Studies - Multi-Organ Physiology and Metabolism
September 21, 2013 / 10:45-11:00 / Room: 102

Quantitative perfusion $H_2{}^{15}O$-PET as an invaluable tool for the targeting of cerebral revascularization surgery and its correlation to clinical outcome in moyamoya disease

Geoff I. Warnock[1], *Thomas Schweingruber*[2], *Felix P. Kuhn*[3], *Alfred Buck*[1], *Nadia Khan*[2], [1]*Nuclear Medicine, University Hospital Zurich, Zurich, Switzerland;* [2]*Neurosurgery, Children's Hospital Zurich, Zurich, Switzerland;* [3]*Department of Medical Radiology, University Hospital Zurich, Zurich, Switzerland. Contact e-mail: geoffrey.warnock@usz.ch*

Background: Moyamoya disease (MMD) is an idiopathic intracranial angiopathy with a progressive spontaneous occlusion of the circle of Willis resulting in repeated ischemia if not diagnosed and treated early, especially in children. Prevention of stroke is achieved by revascularization of the affected cerebral regions. The pre-surgical management includes baseline neurological exam, MR scanning, angiography and hemodynamic evaluation, which is invaluable in assessing the regional cerebral baseline perfusion and reserves. Xenon CT and perfusion SPECT have been used to provide this functional information, but $H_2{}^{15}O$ PET allows regiospecific quantification of cerebral perfusion and in particular perfusion reserve (PR) after acetazolamide challenge, allowing surgery to be specifically targeted and personalized. Limited perfusion reserve can be used to identify regions at high risk of infarct. Furthermore, we hypothesize that PET can be used to define a particular pattern of perfusion deficits for diagnosis of MMD. Methods: Patients with diagnosed MMD underwent initial $H_2{}^{15}O$ PET scans at baseline and after stimulation with acetazolamide (AZA) and were subsequently selected for a tailor-made, multiple cerebral revascularization surgery. Postoperative assessment of clinical outcome was augmented with follow-up PET (median duration post-surgery: 10.4 months). Parametric images of cerebral blood flow were generated using a reported method [1] in which a standardized arterial input function and image scaling are used to derive $rCBF_{K1*s}$ and $rCBF_{k2*}$ images. Perfusion at baseline, after AZA and PR were compared for pre- and post-surgery scans. Six pre-defined brain regions (reflecting the areas supplied by the major cerebral arteries) were used and analysis limited to revascularized areas. Results: Parametric images reflecting PR clearly showed deficits in cortical but not subcortical regions or cerebellum, a pattern typical to confirmed MMD diagnosis. Perfusion deficits were most clear in middle (MCA) and anterior cerebral artery (ACA) regions, in agreement with the known pathology of MMD. Comparison of cerebral perfusion and PR between pre- and post-surgery scans in revascularized areas revealed a moderate improvement in baseline perfusion after surgery (ACA region, left: mean ± SD normalized perfusion pre- 0.81±0.26, post- 0.93±0.22, 2-sided paired t-test p=0.025; right: pre- 0.93±0.18, post- 0.97±0.20, p=0.319; MCA left: pre- 0.77±0.24, post- 0.90±0.20, p=0.006; right: pre- 0.91±0.17, post- 0.96±0.18, p=0.126) but only limited evidence for an increase in PR (ACA, left: pre- -21.5±11.5%, p=0.453; post- -24.0±16.4%, right: pre- -29.0±9.3%, post- -24.6±10.4%, p=0.152; MCA left: pre- -20.7±10.4 post- -21.0±14.9, p=0.933; right: pre- -26.6±8.5, post- -20.4±9.3, p=0.081). Conclusions: We demonstrate that quantitative $H_2{}^{15}O$ PET is a highly useful tool

to direct surgical intervention in MMD. Detailed quantitative analysis of changes in perfusion and PR after surgery supports a targeted surgical approach and correlates well with clinical outcome. [1] Treyer et al., Eur J Nucl Med Mol Imaging (2003) 30:572-580.

Disclosure of author financial interest or relationships:
G.I. Warnock, PMOD, Consultant; Swisstrace, Consultant; **T. Schweingruber**, None; **F.P. Kuhn**, None; **A. Buck**, None; **N. Khan**, None.

Presentation Number **SS 111**
Scientific Session 19: First in Human & Clinical Studies - Multi-Organ Physiology and Metabolism
September 21, 2013 / 11:00-11:15 / Room: 102

68Ga-PRGD2 PET/CT for integrin receptor imaging of myocardial infarction and follow-up

Yi Sun, *Zhaohui Zhu, Dept. Of Nuclear Medicine, Peking Union Medical College Hospital, Beijing, China. Contact e-mail: sunyi7290@126.com*

Purpose High expression of αvβ3-integrin receptor has been found at and surrounding the myocardial infarction (MI). This study was prospectively designed to investigate 68Ga-PRGD2, a novel PET tracer targeting αvβ3-integrin receptor, in assessment and follow-up of MI patients, and compared and correlated with the 99mTc-MIBI perfusion and 18F-FDG metabolism imaging. Methods Twenty-three MI patients underwent 68Ga-PRGD2 PET/CT for integrin receptor imaging 3 days to 2 years after the attack. Sixteen of the patients accepted dual-isotope myocardial SPECT imaging using 99mTc-MIBI/18F-FDG within one week, while the other 7 patients accepted post-meal 18F-FDG PET/CT. Seven patients accepted 68Ga-PRGD2 and 18F-FDG PET/CT follow-ups 3-10 months later. The 68Ga-PRGD2 images were co-registered and matched with the 99mTc-MIBI and 18F-FDG images for visual and semi-quantitative analysis. Results Most patients showed elevated 68Ga-PRGD2 uptake at the MI and peri-MI regions except for one patient at the 3rd day post a mild MI and two patients 1-2 years after MI attack. The maximum standardized uptake value (SUVmax) of 68Ga-PRGD2 ranged from 0.73-3.49 (2.21±0.68) and peaked at 1-3 weeks post MI. The uptake level of 68Ga-PRGD2 was in significant correlation with the longest diameter of MI measured on the 99mTc-MIBI images (P=0.004), but was not significantly correlated with the serum levels of myocardial enzymes and the ejection fraction measured by echocardiograph. In the 7 patients underwent follow-up studies, the 68Ga-PRGD2 uptake decreased in different degrees, and significantly less decrease was found in 3 patients still presenting angina pectoris (P=0.003). Conclusion This preliminary study indicated that 68Ga-PRGD2 PET/CT can provide valuable molecular information about MI status and recovery in vivo, which may be useful in diagnosis, prognosis, and personalized treatment of MI. Further investigations are needed.

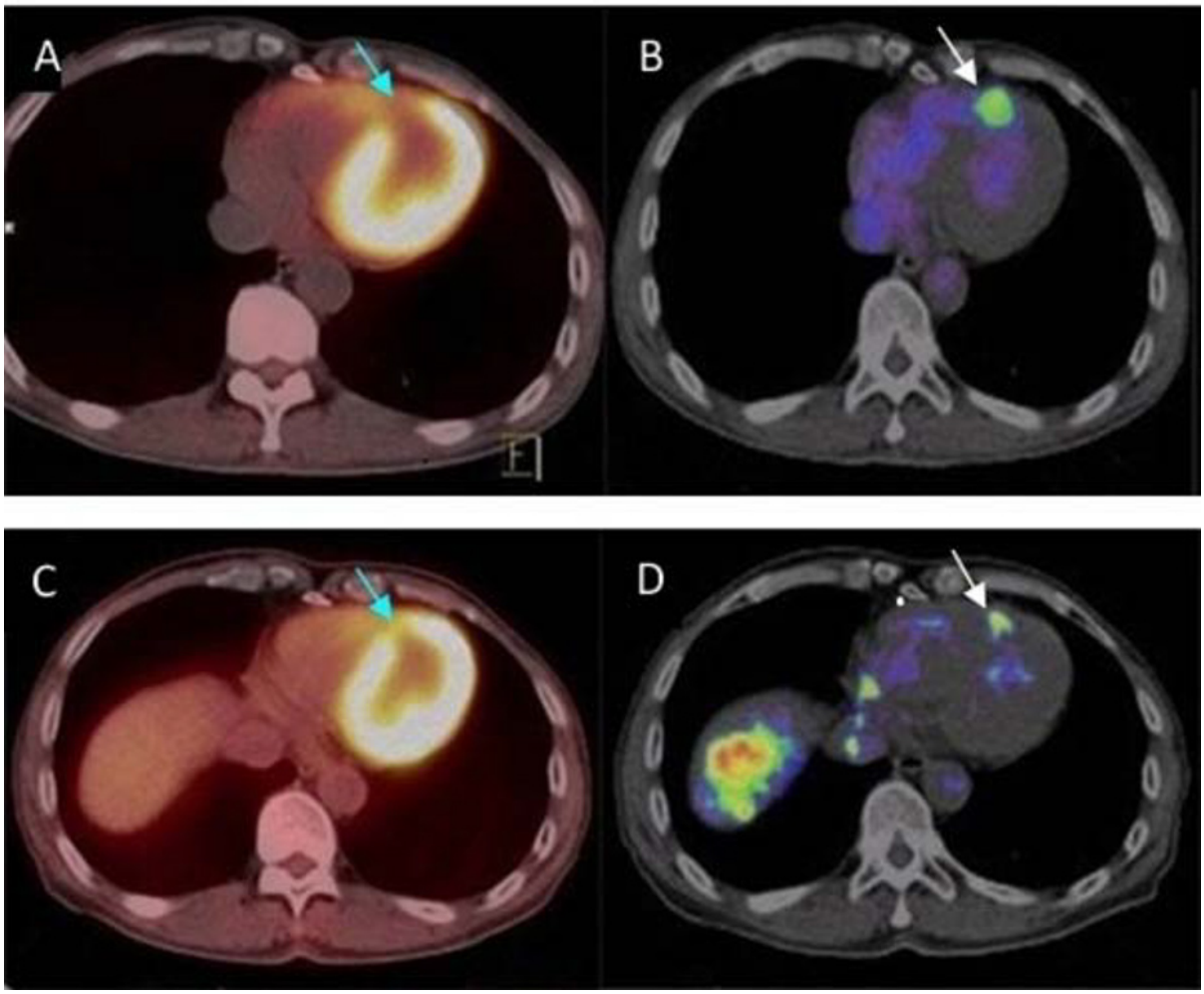

18F-FDG and 68Ga-PRGD2 PET/CT in a patient with myocardial infarction (MI). Upper row: Two weeks after MI attack, 18F-FDG PET/CT (A) showed an uptake defect area at the anterior septum of the left ventricle. 68Ga-PRGD2 PET/CT (B) showed a high RGD uptake at the edge of MI. Lower row: In the follow-up studies 10 months later when the patient still had strenuous chest pain, a smaller defect area was observed with increased 18F-FDG uptake (C) but high 68Ga-PRGD2 accumulation (D), indicating still existence of myocardial ischemia and repair.

Disclosure of author financial interest or relationships:
Y. Sun, None; **Z. Zhu**, None.

Presentation Number **SS 112**
Scientific Session 19: First in Human & Clinical Studies - Multi-Organ Physiology and Metabolism
September 21, 2013 / 11:15-11:30 / Room: 102

Imaging CXCR4-Chemokine Receptor Expression with [68Ga]CPCR4.2: Preclinical and First Clinical Results

Hans J. Wester[1,3], *Ulrich Keller*[2], *Ambros J. Beer*[3], *Margret Schottelius*[1], *Frauke Hoffmann*[1], *Horst Kessler*[4], *Markus Schwaiger*[3], [1]*Pharmaceutical Radiochemistry, Technische Universität München, Garching, Germany;* [2]*III. Medical Department, Technische Universität München, Munich, Germany;* [3]*Department of Nuclear Medicine, Technische Universität München, Munich, Germany;* [4]*Institute for Advanced Study, Department of Chemistry, Technische Universität München, Garching, Germany. Contact e-mail: h.j.wester@tum.de*

CXCR4 and its endogenous ligand CXCL12 are one of the major receptor/ligand systems consistently overexpressed in the majority of solid tumors and haematological malignancies such as B-cell lymphomas. CXCR4 is thought to contribute to tumorigenesis, cancer progression, vasculogenesis and tissue specific metastasis. Here we report on the preclinical evaluation of a new Ga-68-labeled PET probe, [68Ga]CPCR4.2, and first clinical PET results. The cyclic pentapeptide [68Ga]CPCR4.2 has emerged from the screening of a wide variety of cyclo(D-Tyr1-Arg2-Arg3-2-Nal4-Gly5) (FC131) derivatives. In competition binding studies using Jurkat cells and [125I]FC131 as radioligand, [68Ga]CPCR4.2 showed an IC50 of 5.0±07 nM (IC50 of FC131: 4.4±0.8 nM). In an inverse binding experiment (higher IC50 = stronger binding) with [125I]FC131 and [125I-Tyr1, natGa]CPCR4.2 as radioligands and FC131 as competitor, the CPCR4.2 analog showed 5 fold higher affinity (IC50 (inv.)=18.2±6.6nM vs 3.5±1.2nM (FC131)). These data indicate an improved affinity for Tyr1-iodinated [68Ga]CPCR4.2 which is accompanied by a decreased hyrophilicity (LogP [68Ga]CPCR4.2=-2.90 vs LogP [125I-Tyr1, natGa]CPCR4.2=-1.56). Binding studies on transiently transfected CHO-K1 cells revealed highly specific binding of [125I-Tyr1, natGa]CPCR4.2 to hCXCR4 and no binding to mCXCR4, rCXCR4 or hCXCR7. Based on excellent in vivo data in mice bearing OH1 hSCLC and HT19 colon cancer xenografts first CPCR4.2-PET scans were performed in patients with advanced malignancies at ~ 60 min. after injection of 101-145 MBq [68Ga]CPCR4.2. CPCR4.2-PET/MR revealed excellent image quality in a patient with chronic lymphocytic leukemia and suspected transformation into aggressive B-cell lymphoma, detecting all nodal lesions that were visible with even higher tracer uptake compared to [18F]FDG-PET/CT (SUVmean /SUVmax [18F]FDG: 3.66/5.94; [68Ga]CPCR4.2: 5.05/6.64). In a patient with histologically proven non-small cell adenocarcinoma of the lung and CD30-positive aggressive T-cell lymphoma CPCR4.2-PET/CT showed high tracer uptake in the lymphoma lesions (SUVmean /SUVmax [18F]FDG: 29.82/50.91; [68Ga]CPCR4.2: 9.91/16.95) but substantially lower uptake in the lung cancer lesions (SUVmean /SUVmax [18F]FDG: 26.36/38.57; [68Ga]CPCR4.2: 2.70/3.86). [68Ga]CPCR4.2 demonstrated only little to moderate uptake in normal organs and background tissue (SUVmean /SUVmax blood pool 1.87/3.38, muscle 0.77/1.38, lung 0.75/1.20, liver 1.46/2.99, spleen 5.69/7.53, bone marrow 4.00/5.05, kidney 5.06/11.89, bladder 36.4/71.0). Assessment of peripheral blood stem cell (PBSC) mobilisation using pre- and post-imaging standard CD34+ flow cytometry did not show any change in the frequency of PBSC. To the best of our knowledge we could demonstrate for the very first

time successful PET imaging of CXCR4 expression in humans. The cyclic pentapeptide probe [68Ga]CPCR4.2 exhibits high affinity and selectivity for CXCR4, excellent pharmacokinetics, low unspecific uptake and high target/non-target ratios. Based on the wide spectrum of diseases that has been linked with CXCR4 expression, [68Ga]CPCR4.2-PET opens a new and exciting field of clinical research.

Disclosure of author financial interest or relationships:

H.J. Wester, None; **U. Keller**, None; **A.J. Beer**, None; **M. Schottelius**, None; **F. Hoffmann**, None; **H. Kessler**, None; **M. Schwaiger**, Siemens Health care, Grant/research support .

Presentation Number **SS 113**
Scientific Session 19: First in Human & Clinical Studies - Multi-Organ Physiology and Metabolism
September 21, 2013 / 11:30-11:45 / Room: 102

In vivo hand-held optoacoustic tomography of the human thyroid

Alexander Dima[1,2], *Vasilis Ntziachristos*[1,2], [1]*Institute for Biological and Medical Imaging, Helmholtz Zentrum München, Neuherberg, Germany;* [2]*Electrical Engineering and Information Technology, Technical University of Munich, Munich, Germany. Contact e-mail: alexander.dima@helmholtz-muenchen.de*

Thyroid disorders are a wide spread cause of disease. According to the American Thyroid Association over 12% of U.S. citizens will be affect during their lifetime. Clinical diagnosis often involves blood tests for molecular parameters and imaging tests such as XCT, MRI or PET. Additionally, thyroid ultrasound, a more cost-effective and non-ionizing modality, is also often employed to evaluate anatomical features at high spatial resolution. Similarly, opotacoustic tomography is a non-ionizing imaging modality that combines ultrasound resolution and optical contrast. Thus, a high sensitivity to blood enables anatomical imaging of the thyroid, while the use of multi-spectral optoacoustic tomography (MSOT) offers sensitivity to disease specific molecular parameters. Here we present the first study on healthy human volunteers to showcase achievable optoacoustic imaging performance of the thyroid. To this end we have refined a previous design based on curved array detection and side-fire fiber bundle illumination. The new prototype can be held in one hand and achieves flexible water coupling by utilizing an optically and acoustically transparent foil to seal the curved-array cavity. By employing graphics card enhanced reconstruction the system is capable of displaying 10 image frames per second. Results clearly allow visual tracking of vascular features deep within the thyroid. Validation was performed by hand-held scanning of the probe in all directions and identifying continuous vascular features. Furthermore, we attempted validation by using directional Doppler Ultrasound and co-registering distinctive regions.

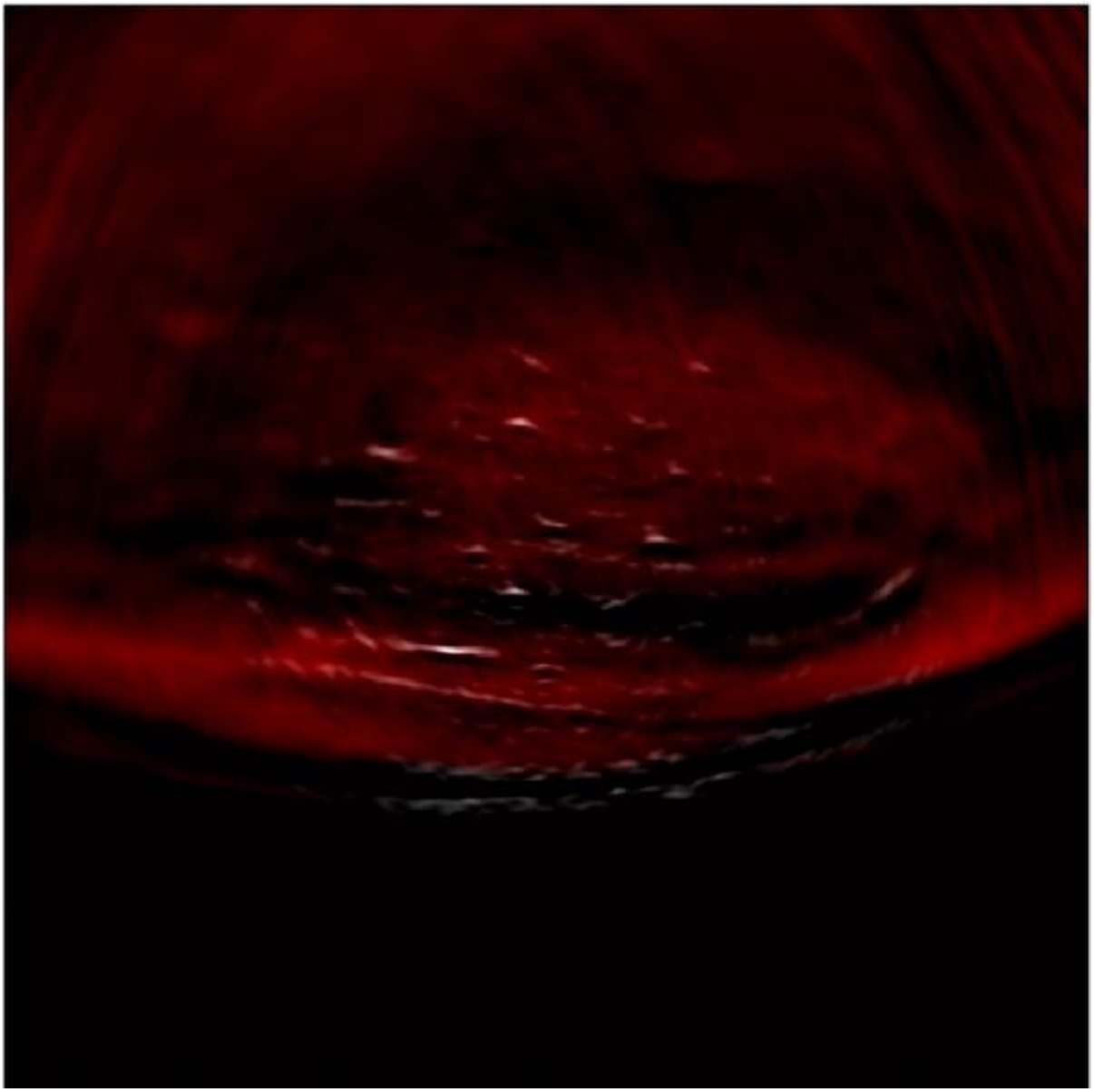

Thyroid gland of a female volunteer. The probe was located surrounding the image from the bottom. For better contrast smaller features are shown in bright white.

Disclosure of author financial interest or relationships:
A. Dima, None; **V. Ntziachristos**, iThera Medical, Stockholder; SurgOptix BV, Consultant .

Presentation Number **SS 114**
Scientific Session 19: First in Human & Clinical Studies - Multi-Organ Physiology and Metabolism
September 21, 2013 / 11:45-12:00 / Room: 102

Clinical handheld optoacoustic scanner for three-dimensional cardiovascular imaging in real time

X. Luís Deán-Ben, **Daniel Razansky**, *Technical University of Munich and Helmholtz Center Munich, Institute for Biological and Medical Imaging (IBMI), Neuherberg, Germany. Contact e-mail: dr@tum.de*

At present, the great potential of optoacoustic imaging that was showcased in preclinical research, have encouraged translation of this technology into clinical practice with multiple applications envisioned, from cardiovascular and cancer diagnostics to ophthalmology and endoscopic imaging. One of the key advantages of the optoacoustic imaging method is its intrinsic potential to deliver complete volumetric tomographic datasets from the imaged object with a single interrogating laser pulse, possibility that does not exist in other clinical imaging modalities. This capacity comes with important clinical advantages, such as ability to dynamically visualize biodistribution, reduce out-of-plane and motion artifacts, and accelerate clinical observations. However, multiple technical limitations hindered so far implementation of 3D optoacoustic imaging system suitable for dynamic visualization of human pathology in the clinical setting. Herein we report on the first hand-held optoacoustic imaging system for high resolution clinical 3D imaging at video rate. It utilizes an matrix of 256 ultrasonic detectors arranged upon a spherical surface with the excitation light from a pulsed laser delivered to the object through its center. A transparent membrane is used to enclose the active detection surface and provide an acoustic coupling medium. Raw optoacoustic data are simultaneously collected from all the detectors and processed in order to attain 3D image data at a rate of 10 frames per second. Spectral fitting of the images retrieved at several wavelengths can be further used to provide concentration maps of intrinsic tissue chromophores and extrinsic agents. Initial in-vivo demonstration experiments included tracking of deep vasculature in real time in a forearm of a healthy volunteer (Fig. 1). The laser wavelength was set at the isosbetic point of haemoglobin (797 nm), for which the exctinction coefficient of Hb and HbO2 is approximately the same. Real-time sequences of 3D images were acquired by moving the hand-held probe along the region of interest. Typical volumetric maximal intensity projection images from the forearm region, representing distinctive time points (snapshots), are shown in Fig. 1a. By combining images taken at different time points, one can capture a larger region, as shown in Fig. 1b with the corresponding photograph displayed in Fig. 1c. Here, the 3D image is further color-coded for depth to get a better impression of the volumetric vasculature distribution. In summary, we introduced a hand-held volumetric multispectral optoacoustic tomography system capable of real-time optoacoustic imaging of intrinsic anatomical and functional contrast as well as extrinsically-administered bio-markers in deep tissues. The proposed hand-held design combined with the real-time (video-rate) performance further make it highly effective for in vivo biological and clinical imaging in areas such as cardiovascular and breast diagnostics, imaging of neovasculature, inflammation, and lymphatic system.

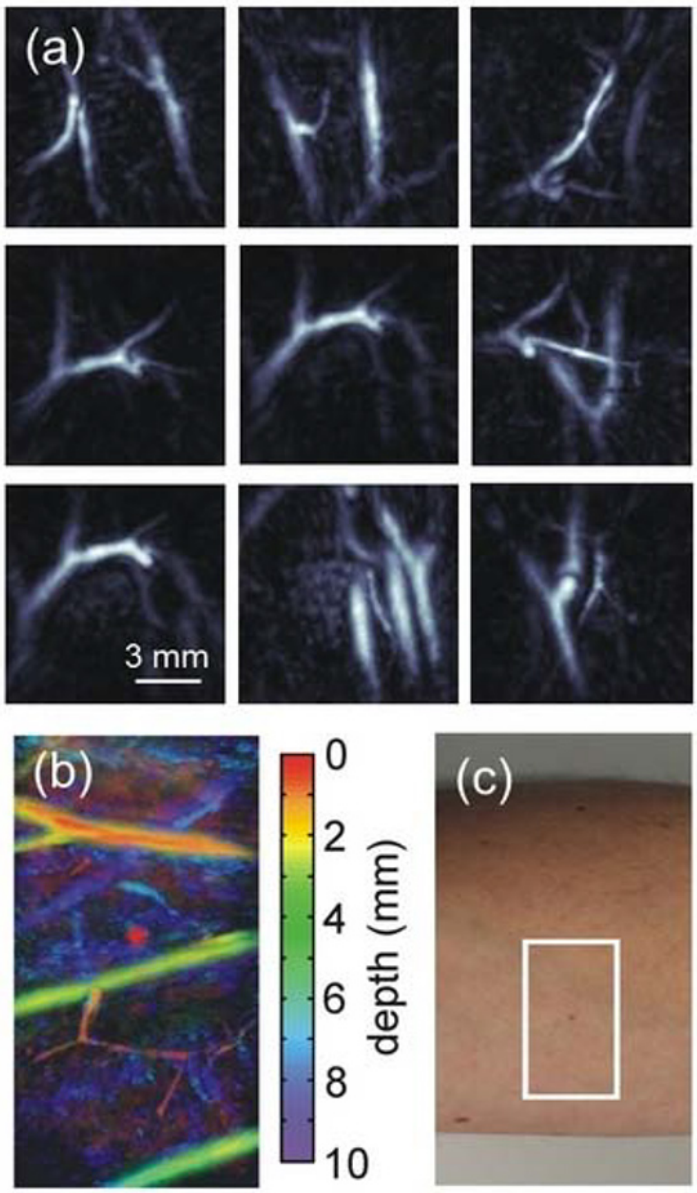

Disclosure of author financial interest or relationships:
X. Deán-Ben, None; **D. Razansky**, None.

Presentation Number **SS 115**
Scientific Session 20: Preclinical in vivo Studies - Oncology (Cells, Reporter Genes)
September 21, 2013 / 10:30-10:45 / Room: 105

Bacterium-Based Microrobot for Visualization of Tumor Targeting and Drug Delivery

Seung-Hwan Park[1], Sung Jun Park[2], Deok-Mi Kim[1], Jong-Oh Park[2], Sukho Park[2], **Jung-Joon Min**[1], [1]*Nuclear medicine, Chonnam National University, Gwangju, Republic of Korea;* [2]*Mechanical System Engineering, Chonnam National University, Gwangju, Republic of Korea. Contact e-mail: jjmin@jnu.ac.kr*

Objectives: Despite recent advances in drug delivery systems (DDS), drug delivery to cancer sites remains difficult because DDS lack active motility and because physical barriers, such as malformed blood vessels, elevated interstitial pressure, and large transport distances in the tumor interstitium, are encountered in solid tumors. The present study describes a bacterium-based microrobot (bacteriobot) in which the avirulent S. typhimurium is attached to a microstructure enabling the microrobot to swim toward tumors; the microstructure acts as a therapeutic molecule containing high amounts of drugs and/or imaging signals and the bacterium acts as a combination of microsensor and microactuator. Methods: We used a high-motility strain of attenuated S. typhimurium that expresses bacterial luciferase (lux) or green fluorescent protein (gfp). Strong attachment of the bacterium to the microstructure was achieved by exploiting the high-affinity interaction between biotin and streptavidin. In this case, bacteria were engineered to display biotin in the outer membrane proteins (omps), which are widely distributed on the bacterial surface; these bacteria were then attached to microstructures consisting of rhodamine-containing fluorescent polystyrene (PS) carboxylated microbeads that were covalently coupled to streptavidin-conjugated tandem fluorochrome composed of peridinin chlorophyll protein (PerCP), which was further labeled by Cy5.5 (PerCP-Cy5.5). The fluorophores were used to obtain a near-infrared fluorescence image for tracking purposes. Results: Tumor-targeting was evaluated on a flow-free chemotactic microfluidic chamber containing cell lysates or spheroids that allows diffusion of cell lysate molecules or cell spheroids in a manner that generates a chemical concentration gradient. Bacteriobots showed higher average velocity when migrating toward tumor cell lysates or spheroids than when migrating toward normal cell lysates or spheroids. Cy5.5-containing PS microbeads without bacterial attachment (microbeads only) showed no accumulation in tumor lysates or spheroids. To validate tumor targeting in vivo, bacteriobots were injected systemically into CT-26 tumor-bearing mice via tail veins. Bioluminescence was detected in the tumors from the bacteria- and bacteriobot-injected animals, but not in the tumors from the microbead-injected control animals. Subsequently, Cy5.5 fluorescence was observed in tumors from the bacteriobot-injected animals, but not in the tumors from the bacteria- or microbead-injected control animals, indicating successful tumor targeting by the bacteriobots. Immunofluorescence staining also supports this finding showing that the near-infrared fluorescence was measured only in tumors from the bacteriobot-injected animals. Conclusion: The present study suggests that the bacteriobot concept will be of great influence in the development of biomedical theranostic microrobots that can carry on versatile functions such as the detection and eradication of incurable malignancies.

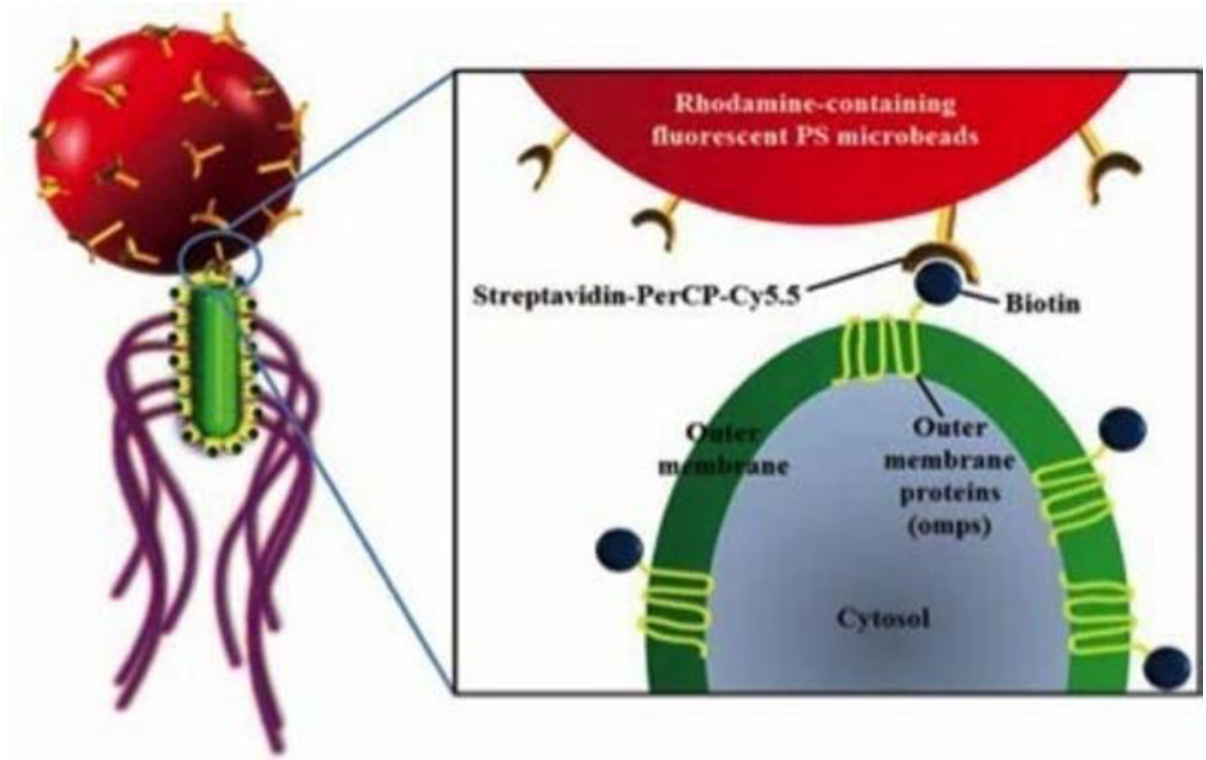

Development of bacteriobots using biotin-streptavidin conjugation

Disclosure of author financial interest or relationships:
S. Park, None; **S. Park**, None; **D. Kim**, None; **J. Park**, None; **S. Park**, None; **J. Min**, None.

Presentation Number **SS 116**
Scientific Session 20: Preclinical in vivo Studies - Oncology (Cells, Reporter Genes)
September 21, 2013 / 10:45-11:00 / Room: 105

Detection and quantitation of circulating tumor cells by bioluminescence imaging in an orthotopic mammary carcinoma model

Laura S. Sasportas[1,2], *Sharon S. Hori*[2], *Guillem Pratx*[3], *Sanjiv S. Gambhir*[2], [1]*Bioengineering, Stanford University, Stanford, CA, USA;* [2]*Radiology, Stanford University, Stanford, CA, USA;* [3]*Radiation Oncology, Stanford University, Stanford, CA, USA. Contact e-mail: lss@stanford.edu*

Background: Metastasis, the cause for 90% of cancer mortality, is a complex and poorly understood process involving the invasion of circulating tumor cells (CTCs) into blood vessels. These cells have potential prognostic value as biomarkers for early metastatic risk. Much of our current understanding of cancer metastasis and of the role of CTCs in this process comes from the study of mouse models. In order to probe CTCs in mouse models of metastasis, various techniques have been developed over the past 50 years. However, most of them (e.g., qPCR) do not allow recovery of live CTCs and can be extremely time consuming. Here we report on the development of a simple and fast CTC detection assay based on bioluminescence imaging (BLI). This assay takes advantage of the high sensitivity, specificity and quantitative capability of BLI to quickly detect and quantify rare CTCs in mouse blood samples. Methods: We developed a murine metastatic carcinoma cell line, 4T1-GL, strongly expressing a bifusion reporter of enhanced green fluorescent protein (eGFP) and firefly luciferase-2 (Luc2) driven by the ubiquitin promoter. Since all tumor cells are marked with the bi-fusion reporter, all CTCs will also express the bifusion reporter, allowing for their detection in the blood. Results: Using this cell line, we demonstrated that our CTC BLI assay could reliably quantify low number of CTCs (> 20 CTCs) spiked in mouse blood samples (R2=0.78) or in culture medium (R2=0.90) and could detect as low as 10 CTCs per 100 µL blood sample. We applied this assay to the detection of CTCs in an orthotopic 4T1-GL metastatic mouse mammary carcinoma model (n=7 mice). Using BLI, we monitored simultaneously the primary tumor growth, lung metastasis progression and the appearance of CTCs in blood samples (Fig. 1A). Early in tumor development (day 12), we observed low numbers of CTCs in 100 µL blood samples, coinciding with the appearance of lung metastasis. Bioluminescence microscopy of blood samples from day 23 confirmed our BLI CTC assay and identified single CTCs as well as clusters of CTCs or microemboli (Fig. 1B) producing BLI signal. Conclusion: These data represent the first reported use we know of for BLI to detect and quantify CTCs in any mouse model. Using this method we demonstrate that we can uncover the dynamics of CTCs during the progression of cancer from primary tumor to metastasis in a mouse model of breast cancer. Our novel BLI-based method will be particularly useful for rapidly assessing CTCs in mouse models of metastasis.

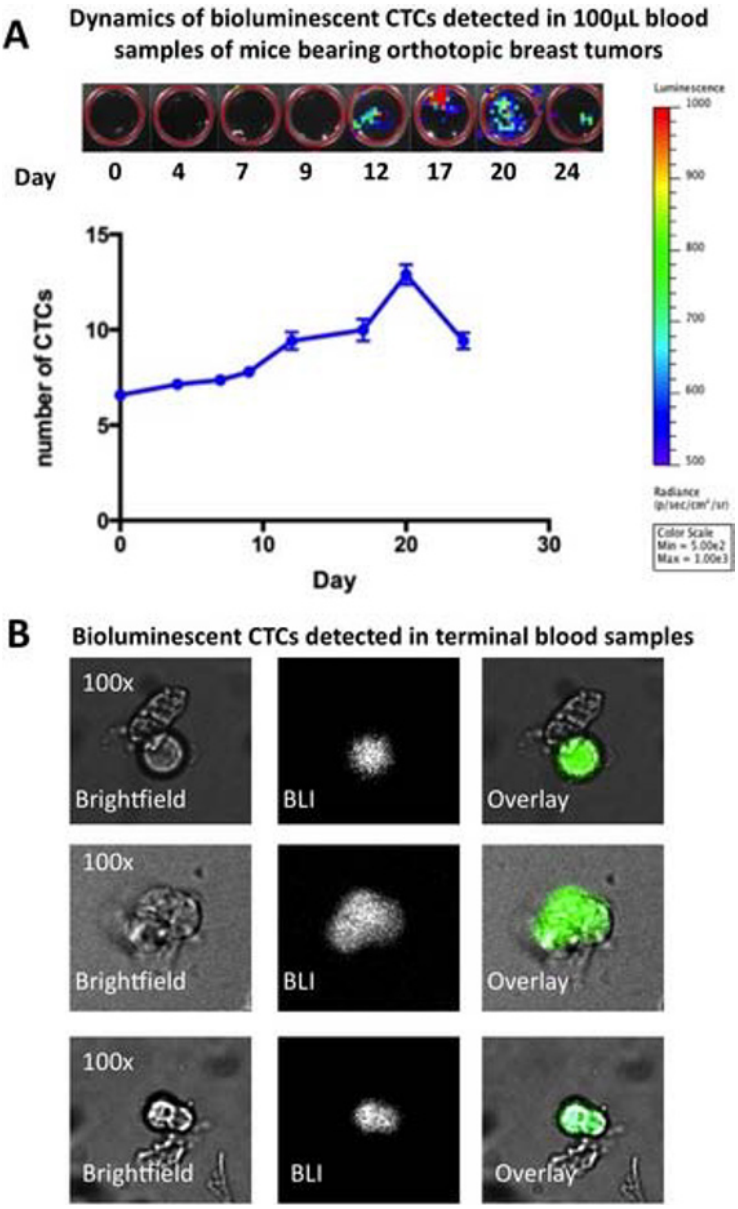

Figure. A. CTCs in 100 µL blood samples from the animals implanted orthotopically in the left mammary fat pad with 2 × 107 4T1-GL cells. CTC numbers were monitored and quantified using BLI B. CTCs and microemboli in terminal blood samples from animals bearing day 23 tumors, as imaged by bioluminescence microscopy.

Disclosure of author financial interest or relationships:

L.S. Sasportas, None; **S.S. Hori**, None; **G. Pratx**, None; **S.S. Gambhir**, Bracco Diagnostics, Consultant; Endra, Inc, Stockholder; Cellsight, Stockholder; Enlight, Inc., Stockholder; General Electric, Grant/research support; ImaginAb, Stockholder; MagArray, Inc., Stockholder; Sanofi-Aventis, US, Grant/research support; SiteOne Therapeutics, Stockholder; VisualSonics/Sonosite, Stockholder .

Presentation Number **SS 117**
Scientific Session 20: Preclinical in vivo Studies - Oncology (Cells, Reporter Genes)
September 21, 2013 / 11:00-11:15 / Room: 105

Non-invasive near-infrared imaging of dendritic cell trafficking in living mice

Fatma Youniss, *Ekaterine Goliadze, Gobalakrishnan Sundaresan, Li Wang, Georgi Gurili, Jamal Zweit, VCU, Richmond, VA, USA. Contact e-mail: younissfm@vcu.edu*

Immune cell therapies (ICT) aimed at increasing the frequency of tumor specific T-cells are promising methods to treat malignant tumors. Dendritic cells (DC), when loaded with an appropriate tumor Antigen (Ag) can prime T-cells that are capable of recognizing and killing tumor cells in an Ag-specific fashion. Moreover, DC-based immunization can lead to immunologic memory with protection against subsequent tumor challenges. However, for the effective use of DC based immunotherapy, it is important to better understand the dynamics and process of DC trafficking. The overall objective of this study is to non-invasively assess in vivo trafficking and targeting of DC labeled with a lipophilic near-infrared cell membrane dye. Methods: Bone marrow derived murine DC were grown in media containing GM-CSF and IL-4 for 7 days. TNF-α was added on day 5 for 48 hours. On day-7 DC were collected and direct cell membrane labeling was performed using a lipophilic near-infra red fluorescent dye, 1, 1-dioctadecyltetramethyl indotricarbocyanine iodide (DiR or DiLC18(7); absorption/ emission: 748/780nm). Various concentrations (15 to 350 ug/ml) of the DiR were used to determine the ideal concentration of the labeling solution. Labeling conditions were optimized on the basis of DC viability and NIR signal intensity, which were evaluated by luminescent cell viability assay and multi-spectral fluorescence imaging respectively. The trafficking pattern of labeled DC administered either by intravenous (IV) or by subcutaneous (SC) route was compared in naïve C57B/6 mice or C56B/6 mice with RM1 (murine prostate cancer cell line) tumor in the right flank. In vivo multi-spectral fluorescence imaging results were validated by ex vivo imaging of dissected organs and tissues from these animals. Results: The viability of DC was comparable to unlabeled cells when a 120 ug/ml NIR dye concentration was used at the time of labeling. DC labeled at this condition retained the NIR dye and showed persistence of the fluorescent signal up to 7 days both in vitro and in vivo. The labeled DC accumulated in the tumor area within 2 days following either route of DC administration. In the non-tumor bearing mice injected IV with labeled DC; the signal was greatest in the lungs followed by intestines and spleen. On the other hand following SC administration, lymph node signal was 2 times greater than signal by any other organ followed by the testes and then intestines. SC administration of labeled DC in the tumor bearing mice revealed lymph node signal 3 times than any other organ and tumor signal 2 times greater than all other organs. In the IV injected mice, highest signal was seen in the tumors, followed by lymph nodes, lungs and intestine Conclusions: Direct labeling of DC by a fluorescent dye yielded relatively stable labeling and provided in vivo data on trafficking of these cells up to 7 days at which point the study was ended. The SC and IV route in the non-tumor and tumor bearing mice showed higher signal of the labeled DC at the most effective sites such as the lymph nodes and tumor site.

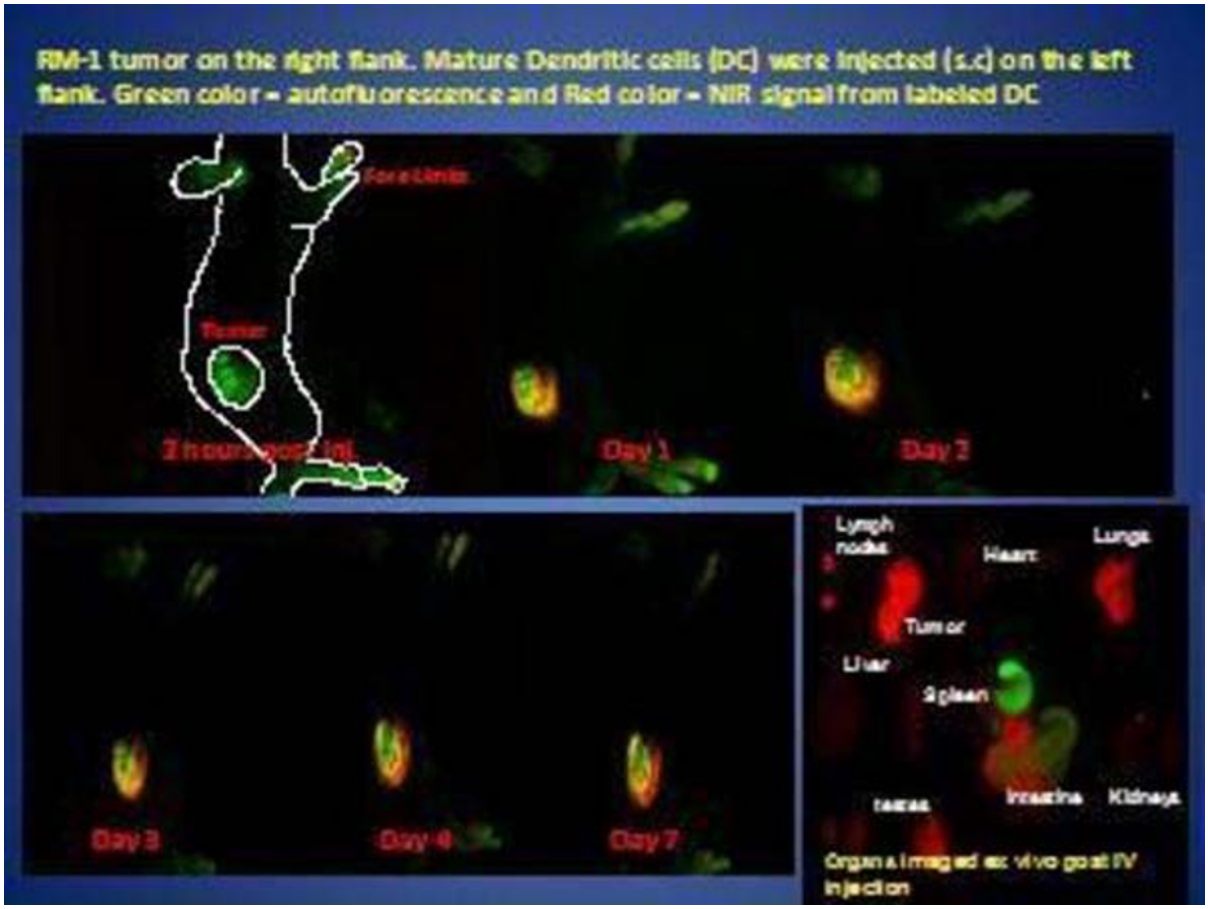

Disclosure of author financial interest or relationships:
F. Youniss, None; **E. Goliadze**, None; **G. Sundaresan**, None; **L. Wang**, None; **G. Gurili**, None; **J. Zweit**, None.

Presentation Number **SS 118**
Scientific Session 20: Preclinical in vivo Studies - Oncology (Cells, Reporter Genes)
September 21, 2013 / 11:15-11:30 / Room: 105

Proof of principle: Imaging of suicide gene therapy for glioblastoma

Cindy Leten[1], *Jesse Trekker*[1], *Tom Struys*[2], *Rik Gijsbers*[4], *Zeger Debyser*[4], *Ivo Lambrichts*[2], *Catherine M. Verfaillie*[3], *Uwe Himmelreich*[1], [1]*Biomedical MRI, KU Leuven, Leuven, Belgium;* [2]*Morphology, UHasselt, Diepenbeek, Belgium;* [3]*Embryo and stem cells, KU Leuven, Leuven, Belgium;* [4]*Laboratory for molecular virology and gene therapy, KU Leuven, Leuven, Belgium. Contact e-mail: cindy.leten@med.kuleuven.be*

Introduction A novel experimental therapeutic approach to treat glioblastoma (GBM) is suicide gene therapy, in which cells carrying a suicide gene, such as Herpes Simplex virus - thymidine kinase (HSV-TK) are administered to a glioma bearing individual. When the TK substrate, for instance ganciclovir (GCV) is provided, it causes chain termination, thus killing the transduced cells. Due to the bystander killing effect, by which GCV passively diffuses to glioma cells through gap junctions, also tumor cells can be killed [1]. So far, the delivery of GCV is empirical and not based on real time monitoring of the cells. To overcome this limitation, we have followed therapy by means of MRI and BLI using mouse Oct4+ bone marrow derived multipotent adult progenitor cells (m-Oct4(-)-BM-MAPCs) in a mouse glioblastoma model (GL261). M&M Stem cell preparation: m-Oct4(-)-BM-MAPCs were transduced with lentiviral vectors containing the EF1α-promotor and eGFP, Fluc and HSVtk or eGFP and Fluc genes. Subsequently cells were labeled with superparamagnetic iron oxide particles (SPIO's, in house synthetized [2]). Treatment: 2 weeks after stereotactical injection of 250.000 GL261 cells in the right striatum of female C57BL6/J mice, 500.000 transduced and labeled stem cells (1%) were injected into the tumor. Subsequently, mice received daily ip injections for 14 days of PBS or ganciclovir (GCV - 50mg/kg). (Figure 1A) Imaging: MRI was performed on a regular basis to assess, tumor growth, site of SC injection, temporal profile of SC location and treatment efficacy using a 9.4T Bruker Biospec MRI scanner. Furthermore, BLI was performed to assess stem cell viability using an IVIS 100. Results We have shown that injection of 1% of SPIO labeled eGFP-Fluc-HSVtk+ m-Oct4(-)-BM-MAPCs is sufficient for stem cell localization surrounding the tumour prior to starting GCV treatment, as the hypointense volume (0.30±0.04mm3) prior to stem cell injection was significantly different from post stem cell injection (1.82±0.12mm3) (Figure 1A+C Bottom). Furthermore, treatment of these cells with GCV in the GL261 model results in decreased tumour formation (responders (N=7): 2.44±1.10mm3 - non-responders (N=3): 33.10±11.7mm3) compared to PBS treated animals (33.17±15.37mm3) as determined by MRI (Figure 1B top+C top). In accordance with these results, the BLI signal from GCV treated animals (N=10) (Before: 1.37x108 ±7.02x107 - After: 2.7x105±2.1x105) decreased following GCV treatment but not in PBS treated animals did not (N=5) (Before: 4.24x107±2.67x107 After: 2.8x107±1.5x107). (Figure 1B bottom+1C middle) Conclusion In this study we have shown that labeling 1% of eGFP-Fluc-HSVtk+ m-Oct4 (-)-BM-MAPCs is sufficient for localizing therapeutic MAPCs in the brain. GCV was administered when cells surrounded the tumour. Furthermore, suicide gene therapy of glioblastoma with eGFP-Fluc-HSVtk+ m-Oct4(-)-BM-MAPCs was proven successful in the majority of the animals treated with GCV. Acknowledgment/References 1. Miletic, H et al., Mol Ther, 2007. 2. Trekker et al., IEEE Trans. Magn. 2013.

Figure 1:

A. Timeline of the experiment.
B. MRI and BLI of PBS and GCV treated animals.
C. Quantification of MRI and BLI.

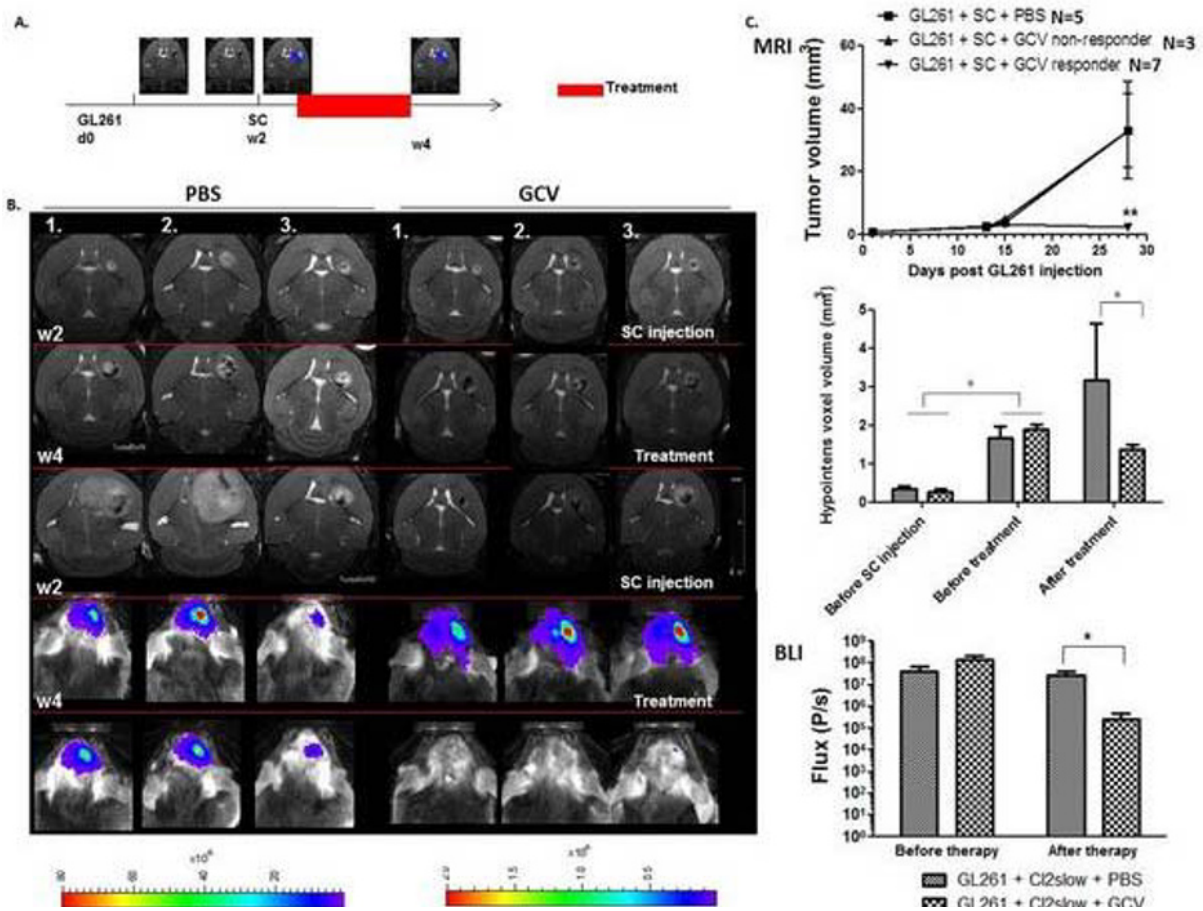

Disclosure of author financial interest or relationships:
C. Leten, None; **J. Trekker**, None; **T. Struys**, None; **R. Gijsbers**, None; **Z. Debyser**, None; **I. Lambrichts**, None; **C.M. Verfaillie**, ReGenesys, BVBA, Leuven BE, Grant/research support; ReGenesys BVBA, Leuven, BE, Consultant; **U. Himmelreich**, None.

Presentation Number **SS 119**
Scientific Session 20: Preclinical in vivo Studies - Oncology (Cells, Reporter Genes)
September 21, 2013 / 11:30-11:45 / Room: 105

Dual modality optical and radionuclide reporter gene imaging of heterogeneous chemotherapy response in different microenvironments

Gilbert O. Fruhwirth[1,3], *Seckou Diocou*[1], *Phil Blower*[1,3], *Tony Ng*[2,3], *Greg Mullen*[1], [1]*Deptartment for Imaging Chemistry and Biology, King's College London, London, United Kingdom;* [2]*Dimbleby Department of Cancer Research, King's College London, London, United Kingdom;* [3]*Comprehensive Cancer Imaging Centre KCL & UCL, King's College London, London, United Kingdom. Contact e-mail: gilbert.fruhwirth@kcl.ac.uk*

Longitudinal imaging of spontaneous cancer cell metastasis or heterogeneous responses of lesions to drug treatment in vivo is a difficult to achieve task. Therefore, we developed a new strategy for longitudinal in vivo imaging of cancer cells and used it to track spontaneous and distant metastasis in a murine xenograft model. It is based on breast cancer cells stably expressing the human sodium iodide symporter (NIS) fused to a red fluorescent protein thereby permitting radionuclide and fluorescence imaging. Using whole-body nanoSPECT/CT with [99mTc]-pertechnetate we followed not only primary tumour growth but also showed the reliable and highly sensitive detection of spontaneous metastasis. NIS imaging was used to classify organs as small as individual lymph nodes to be positive or negative for metastasis without any false positives as determined by confocal fluorescence microscopy. We found the NIS imaging approach to be superior to state-of-the-art FDG imaging in its ability to detect small tumours and metastasis due to improved signal-to-background. Furthermore, we applied this multimodal metastasis imaging approach to assess the treatment response to the neo adjuvant chemotherapy agent etoposide in this model. As etoposide was previously found to interfere with FDG imaging, we compared FDG-PET imaging with NIS-based SPECT imaging using [99mTc]-pertechnetate. In contrast to FDG-PET, NIS imaging allowed the reliable detection of spontaneous metastasis during etoposide treatment. Importantly, we also found that tumour cells in different microenvironments responded in a heterogeneous manner to etoposide treatment, which could only be determined by using this new NIS-based strategy but not by FDG imaging.

Disclosure of author financial interest or relationships:
G.O. Fruhwirth, None; **S. Diocou**, None; **P. Blower**, None; **T. Ng**, None; **G. Mullen**, Mediso, Consultant .

Presentation Number **SS 120**
Scientific Session 20: Preclinical in vivo Studies - Oncology (Cells, Reporter Genes)
September 21, 2013 / 11:45-12:00 / Room: 105

Monitoring the effect of mesenchymal stem cell therapy using cytosine deaminase-expressing MSC and 5-FC prodrug by PET/MR/BLI in orthotopic glioma model

Taemoon Chung[1,2], *Young Il Kim*[3,4], *Mi Jeong Kim*[1], *Dong Soo Lee*[1,5], *June-Key Chung*[1,7], *Sun Ha Paek*[6], *Hyewon Youn*[1,8], *[1]Nuclear Medicine and Cancer Research institute, Seoul National University College of Medicine, Seoul, Republic of Korea; [2]Biomedical science, Seoul National University College of Medicine, Seoul, Republic of Korea; [3]Radiology, Radiation Medicine, SNUMRC, Seoul, Republic of Korea; [4]Radiation Medicine, SNUMRC, Seoul, Republic of Korea; [5]Molecular Medicine and Biopharmaceutical Sciences, WCU Graduate School of Convergence Science and Technology, Seoul, Republic of Korea; [6]Neurosurgery, Seoul National University College of Medicine, Seoul, Republic of Korea; [7]Tumor Microenvironment Global Core Research Center, Seoul National University College of Medicine, Seoul, Republic of Korea; [8]Cancer Imaging Center, Seoul National University Cancer Hospital, Seoul, Republic of Korea. Contact e-mail: noenimy@snu.ac.kr*

Background: 5-Fluorouracil (5-FU) is one of the most frequently used anti-cancer drugs but its side effects cannot be avoided. To overcome this, nontoxic prodrug 5-Fluorocytosine (5-FC) can be used for an alternative choice. It is reported that cytosine deaminase (CD) has ability to convert non-toxic 5-FC to toxic 5-FU. Since mesenchymal stem cells (MSC) have ability to chase tumor cells, the combination therapy with CD-expressing MSC and 5-FC prodrug may reduce non-specific toxicity and increase therapeutic efficacy. Purpose: In this study, we evaluated the tumor suppression by the treatment of mesenchymal stem cell expressing CD (MSC/CD) with 5-FC prodrug in glioma using various imaging modalities. Methods: Human bone marrow derived MSCs were used for expressing CD and reporter genes. Human glioma cell lines (U373, U87MG) and primary glioma cells from a patient (GBM28, GBM37; before and after Temozolomide-radiation therapy) were used for this research. Luciferase expressing cells were established for bioluminescence imaging (BLI). The level of gene expression was measured by Real-Time PCR. For monitoring anti-cancer effect of MSC/CDs with 5-FC in vivo, MSC or MSC/CD cells were orthotopically transplanted into the cranial using stereotaxic frame. The tumor growth was monitored by 3T-MR or PET. Results: The bystander effects of MSC/CD against glioma were increased by 5-FC in a dose dependent manner and higher MSC/CD to tumor ratio. We found that the bystander effects are more effective in U87MG cells than U373 cells, and also in GBM37 than GBM28. The expression of dihydropyrimidine dehydrogenase (DPD), one of 5-FU metabolizing enzymes, was significantly reduced in U87MG cells than U373 cells, and also reduced in GBM37 than GBM28. These results indicate that DPD is a key enzyme to predict the effect of MSC/CD therapy with 5-FC prodrug. In glioma orthopotic model, trafficking ability of MSC/CD to the tumor was successfully monitored by BLI and effective inhibition of tumor growth was also observed by PET and MR. Conclusion: In this study, we could successfully visualize the therapeutic effect of MSC/CD therapy with 5-FC prodrug in vitro and in vivo tumor models. Furthermore, we showed that the bystander effects of MSC/CD have correlation with 5-FU metabolism related genes, especially DPD. Finally, we could conclude that MSC/CD therapy with 5-FC prodrug can be suggested as an option for glioma therapy, and higher tumor suppression can be expected in the DPD-less cells.

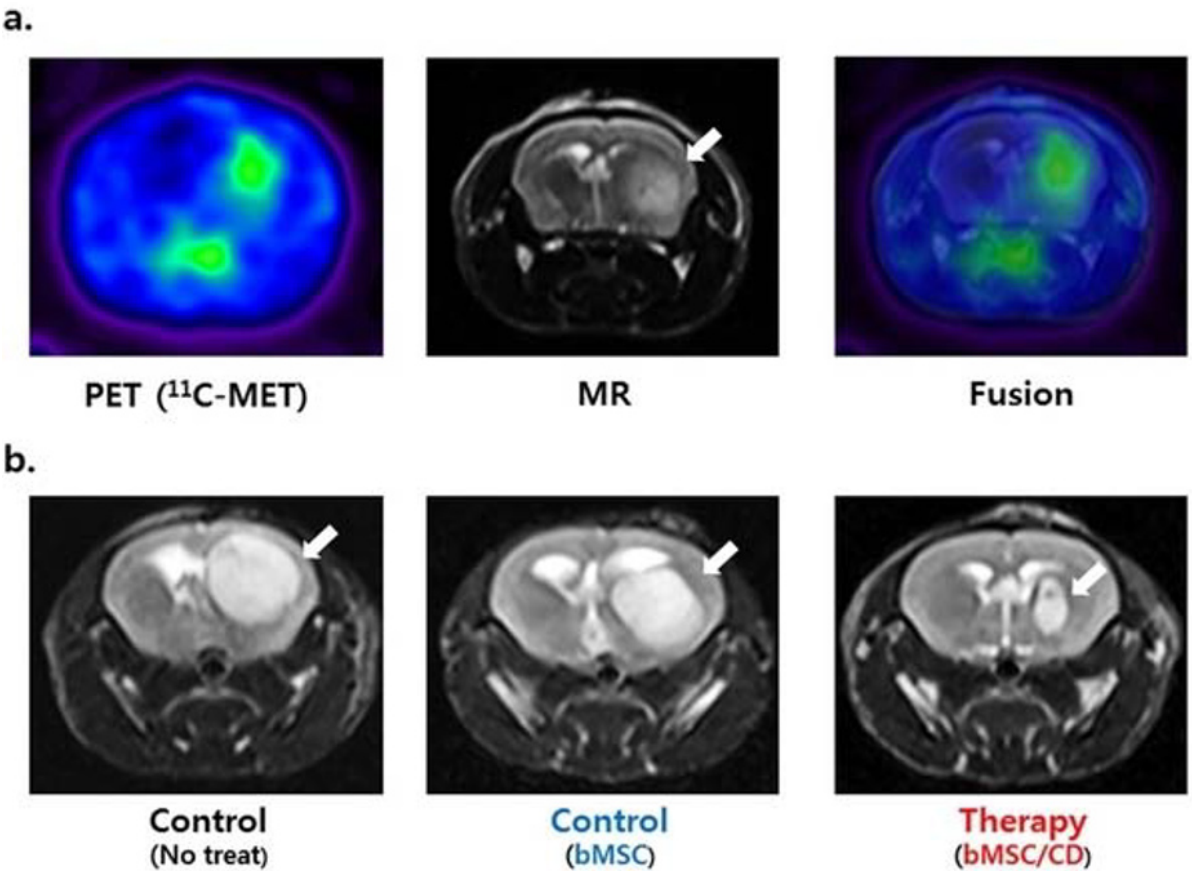

Disclosure of author financial interest or relationships:
T. Chung, None; **Y. Kim**, None; **M. Kim**, None; **D. Lee**, None; **J. Chung**, None; **S. Paek**, None; **H. Youn**, None.

Presentation Number **SS 121**
Scientific Session 21: Chemistry & Imaging Probes - CT & Multimodal
September 21, 2013 / 10:30-10:45 / Room: 200

In vivo monitoring of tumor response to chemotherapy by imaging cell death with a novel dual-function PET/NIRF probe

Kai Chen[1], *Brian D. Gray*[2], *Koon Y. Pak*[2], *Xinlu Wang*[1], *Guoquan Li*[1], *Peter S. Conti*[1], [1]*Department of Radiology, University of Southern California, Los Angeles, CA, USA;* [2]*Molecular Targeting Technologies, Inc., West Chester, PA, USA. Contact e-mail: chenkai@usc.edu*

Objectives: Phosphatidylserine (PS) exposure is one of the most prominent and ubiquitous fingerprints of dying cells, making it an attractive target for molecular imaging. Synthetic bis-zinc(II)-dipicolylamine (Zn-DPA) derivatives selectively bind to biological membranes enriched with PS. This study aims to apply PET/NIRF imaging with a novel DPA-containing probe (18F-PS-TumorVue®) to visualize and evaluate cell death induced by Paclitaxel in a U87MG tumor xenograft model. Methods: In vitro toxicity of Paclitaxel to U87MG cells was determined by a colorimetric assay. The response of U87MG cells to Paclitaxel treatment was determined by flow cytometry, fluorescence staining, and cell uptake study. Established U87MG tumors in nude mice were daily treated with a combination of All-Trans Retinoic Acid (ATRC) (1.5 μg/kg) and Paclitaxel (45 μg/kg). Longitudinal PET imaging was performed with 18F-PS-TumorVue® before treatment and at day 3, 6, and 9 after treatment. Following PET imaging, a direct tissue biodistribution study was performed to confirm the accuracy of PET quantification. NIRF imaging was carried out with 19F-PS-TumorVue® before treatment and at day 4, 7, and 11 after treatment. Results: U87MG human glioma cells are sensitive to Paclitaxel treatment. After being treated with Paclitaxel for 15 h, U87MG cells were stained with PSVue643, a DPA-containing dye. The strong red fluorescence signal was identified in the cytosol of the treated cells but not on the untreated cells, indicating Paclitaxel treatment induced PS externalization. Besides, the fluorescent signal was effectively blocked by co-incubation with excess amount of unlabeled Zn-DPA. For cell uptake study, about 1.5% of 18F-PS-TumorVue® uptake in Paclitaxel-treated U87MG cells was determined after 1 hr incubation, which is significantly higher than 0.69% and 0.39% observed for 18F-FP-DPA (single modality compound) and 18F-FP-Dye (negative control), suggesting that the Zn-DPA moiety is indeed the component binding to PS, and the cell uptake of 18F-PS-TumorVue® is significantly higher than that of 18F-FP-DPA. Daily treatment with ATRC and Paclitaxel effectively inhibited the growth of U87MG tumors by inducing cell death. The cell death was clearly visualized by 18F-PS-TumorVue® PET. The tumor uptake, which was observed at day 9 after treatment, was significantly higher than that in the untreated tumors (8.23±0.35 vs. 1.69±0.42%ID/g, $p<0.05$). The NIRF imaging results are consistent with the findings by PET. Conclusions: PET/NIRF imaging with PS-TumorVue® is sensitive enough to allow visualization of Paclitaxel induced cell death in U87MG tumor xenograft model. Fully quantitative imaging of tumor response to therapy with PS-TumorVue® offers the potential to provide early assessment of cancer treatment efficacy leading to individually tailored therapeutic plans with improved outcomes.

Disclosure of author financial interest or relationships:
K. Chen, None; **B.D. Gray**, Molecular Targeting Technologies, Inc, Employment; **K.Y. Pak**, Molecular Targeting Technologies, Inc., Stockholder; Molecular Targeting Technologies, Inc., Employment; **X. Wang**, None; **G. Li**, None; **P.S. Conti**, None.

Presentation Number **SS 122**
Scientific Session 21: Chemistry & Imaging Probes - CT & Multimodal
September 21, 2013 / 10:45-11:00 / Room: 200

Gene-evoked Melanin production: New reporter genes for Optical, Photoacoustic and Magnetic Resonance Imaging

Jochen Stritzker[1,2], Lorenz Kirscher[2], Miriam Scadeng[3], Nikolaos C. Deliolanis[4], Stefan Morscher[5,4], Panagiotis Symvoulidis[4], Karin Schaefer[4], Qian Zhang[1], Lisa Buckel[2], Michael Hess[2], Ulrike Donat[2], William G. Bradley[6], **Vasilis Ntziachristos**[4]*, Aladar A. Szalay[1,7], [1]Genelux Corporation, San Diego, CA, USA; [2]Department of Biochemistry, University of Würzburg, Würzburg, Germany; [3]Center for Functional MRI, University of California San Diego, San Diego, CA, USA; [4]Institute for Biological and Medical Imaging, Helmholtz Center and Technical University Munich, Munich, Germany; [5]iThera Medical, Munich, Germany; [6]Department of Radiology, University of California San Diego, San Diego, CA, USA; [7]Department of Radiation Oncology, University of California San Diego, San Diego, CA, USA. Contact e-mail: v.ntziachristos@tum.de*

Melanin pigments are produced virtually in all kingdoms of life. Their dark color renders them visible for optical imaging and the strong absorption of light (also in the near-infrared) enables them to be visualized by photoacoustic imaging. Moreover, the trapping of paramagnetic transition metal ions in melanin, generates high signals on T1-weighted magnetic resonance imaging. Here, we used recombinant oncolytic vaccinia virus as a backbone to express genes that lead to melanin production specifically in tumors and their metastases. We could show that insertion of murine tyrosinase (Tyr) into the viral genome resulted in high concentrations of melanin that was readily detectable by optical, photoacoustic and magnetic resonance imaging. Furthermore, additional expression of tyrosinase-related protein 1 (Tyrp1) enhanced the melanin specific signals. In conclusion, we suggest that gene-evoked melanin production could be a versatile alternative to the use of fluorescent proteins in imaging of cells in deeper tissues.

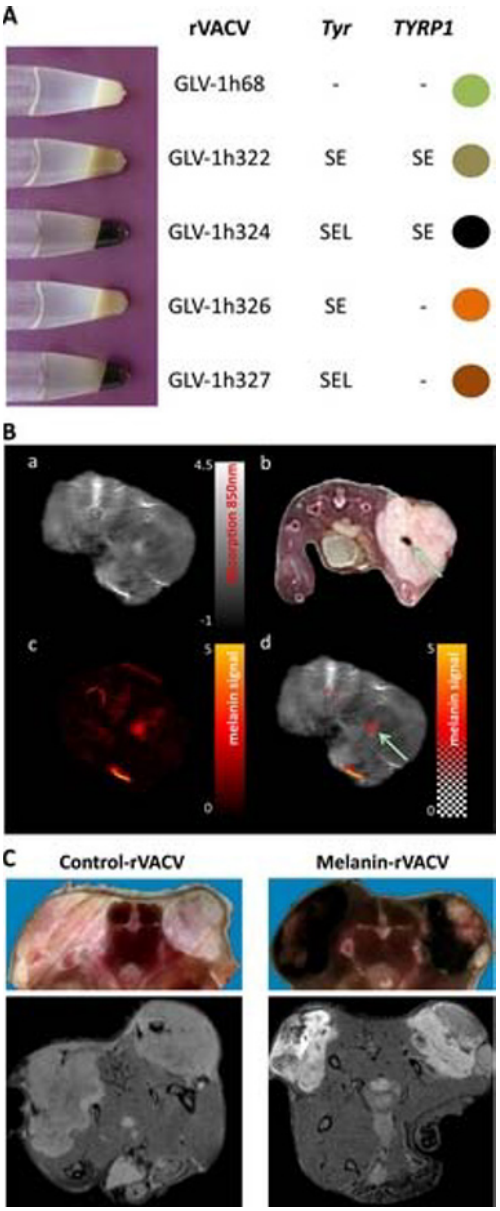

A) Production of melanin in cancer cells upon infection with Tyr/Tyrp1-encoding recombinant vaccinia virus strains (rVACV). B) Generation of melanin specific multispectral photoacoustic images: (a) Photoacoustic images at the exemplary wavelength of 850 nm; (b) cryosection of the same mouse that is shown in the other pictures at about the same plane; (c) melanin signal from multispectral imaging and (d) overlay of heat map from (c) over absorption scan image (a). C) Cryoslices (top) and T1-weighted magnetic resonance images (bottom) of tumor bearing mice injected with control- or melanin-rVACV.

Disclosure of author financial interest or relationships:
J. Stritzker, Genelux Corporation, Employment; Genelux Corporation, Stockholder; Genelux Corporation, Grant/research support; **L. Kirscher**, None; **M. Scadeng**, None; **N.C. Deliolanis**, None; **S. Morscher**, iThera Medical, Employment; **P. Symvoulidis**, None; **K. Schaefer**, None; **Q. Zhang**, Genelux Corporation, Employment; Genelux Corporation, Stockholder; **L. Buckel**, None; **M. Hess**, None; **U. Donat**, None; **W.G. Bradley**, None; **V. Ntziachristos**, iThera Medical, Stockholder; SurgOptix BV, Consultant; **A.A. Szalay**, Genelux Corporation, Stockholder; Genelux Corporation, Employment; Genelux Corporation, Other financial or material support .

Presentation Number **SS 123**
Scientific Session 21: Chemistry & Imaging Probes - CT & Multimodal
September 21, 2013 / 11:00-11:15 / Room: 200

Controlled in situ nano-aggregation of caspase-3/7 activatable fluorescent and MRI probes for dual-modality imaging of tumor cell death

Deju Ye, *Adam J. Shuhendler, Prachi Pandit, Kimberly D. Brewer, Brian K. Rutt, Jianghong Rao, Radiology, Stanford University, Palo alto, CA, USA. Contact e-mail: dejuye@stanford.edu*

Purpose: Tumor response to treatment often requires the iatrogenic induction of tumor cell death through apoptosis, noninvasive monitoring of which will provide important information for predicting therapy efficacy and for early screening of anti-cancer drugs. Herein, we report a novel caspase-3 controlled in-situ nano-aggregation strategy, with an integration of fluorescence and magnetic resonance (MR) modalities, for in vivo monitoring of tumor apoptosis under chemotherapy. Methods: The fluorescent (CaspAF) and MRI (CaspAM) probes are designed to comprise: (1) D-cysteine and 2-cyano-6-hydroxyquinoline (CHQ) moieties that can react intramolecularly to form a cyclic structure, (2) caging groups attached to the cysteine residue that can be removed by caspase-3 and intracellular glutathione, and (3) an imaging reporter of Cy5.5 for CaspAF or a Gd-chelate for CaspAM. Figure 1 depicts the general mechanism of the probes following intravenous administration to tumor accumulation via controlled self-assembly to form nano-aggregates in chemotherapy-induced apoptotic tumor cells. In apoptotic tumor cells, pro-caspase-3 is efficiently converted to active caspase-3, permitting cleavage of the L-DEVD capping group and promoting intramolecular condensation to form hydrophobic macrocycle 2. The cyclized products then self-assemble in situ into nanoparticles with a high density of bound reporter (fluorescent or MRI), resulting in prolonged retention in tumor tissue and enhanced imaging contrast. These probes were evaluated in female nude mice bearing subcutaneous HeLa tumors that received either i.v. chemotherapy consisting of three doses of 8 mg/kg doxorubicin (DOX) or saline. Probe 1 (CaspAF or CaspAM) was injected two days following the last DOX treatment, and whole animal fluorescence hyperspectral imaging was performed using a CRi Maestro system and MR imaging was scanned using a Bruker icon 1T desktop scanner with a multi slice spin echo sequence (TR/TE = 506/15 ms), respectively. Results: In vitro studies with CaspAF and CaspAM demonstrated that recombinant human caspase-3 can trigger macrocyclization and self-assembly into nanoparticles with diameters of less than 200 nm, providing a ~ 223% increase in r1 relaxivity at 1T for CaspAM after forming Gd-nanoparticles (from r1 = 12.57 mM-1s-1 to r1 = 28.02 mM-1s-1). When incubated with HeLa cells, both CaspAF and CaspAM were found to be preferentially retained to a significantly greater extent in DOX-induced apoptotic cells relative to viable cells, and this retention was blocked with the caspase-3 inhibitor. In vivo studies showed that both the extent of probe accumulation and retention were significantly greater in DOX-treated versus saline-treated tumors. Conclusion: Taking the advantage of fluorescence and MR imaging modalities, the combination of CaspAF and CaspAM under the same activation mechanism holds great promise as a new strategy for non-invasive in vivo monitoring of tumor cell death following chemotherapy.

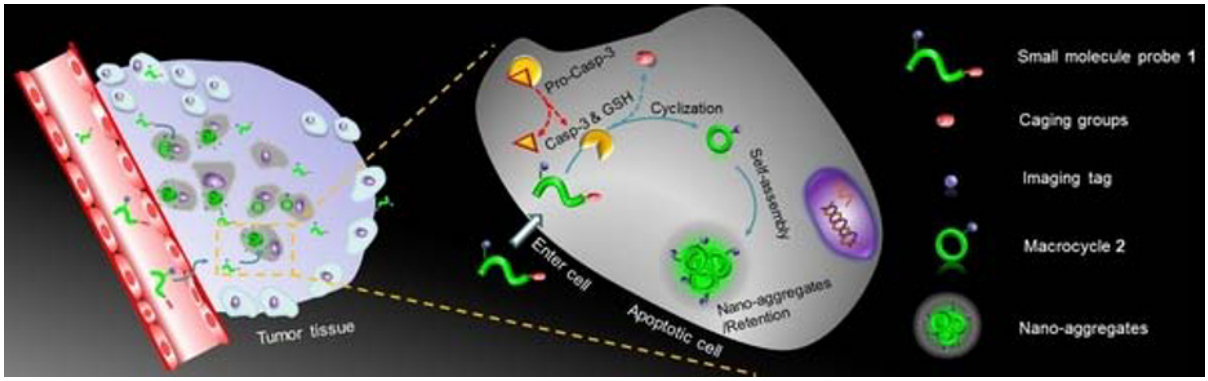

Figure 1. Principle of in vivo cancer chemotherapy response monitoring by probe 1.

Disclosure of author financial interest or relationships:
D. Ye, None; **A.J. Shuhendler**, None; **P. Pandit**, None; **K.D. Brewer**, Immunovaccine Inc., Employment; **B.K. Rutt**, GE Heathcare, Grant/research support; **J. Rao**, None.

Presentation Number **SS 124**
Scientific Session 21: Chemistry & Imaging Probes - CT & Multimodal
September 21, 2013 / 11:15-11:30 / Room: 200

A novel fluorine dendron based nanoprobe for tracking of mesenchymal stem cells with integrated 19F MRI and fluorescence imaging

Zhe Wang, *Xuyi Yue, Yu Wang, Pengfei Rong, Dale O. Kiesewetter, Gang Niu, Xiaoyuan (Shawn) Chen, NIBIB, National Institutes of Health, Bethesda, MD, USA. Contact e-mail: zhe.wang2@nih.gov*

Objective: Successful application of cell-based therapies requires the ability to monitor transplanted cell survival and integration non-invasively and dynamically with a high temporal and spatial resolution. In this study, we aimed to develop a dual functional fluorine dendron-based nanoprobe for in vivo tracking of mesenchymal stem cells (MSCs) with both 19F MRI and fluorescence imaging. Methods: We developed a series of symmetrically structured fluorine dendrons by a novel proportionate branching growth method. The synthesized 19F dendrons were screened by NMR to determine signal to noise ratio (S/N) and detection limitation. The ultimately selected 19F dendron was further functionalized by Cy5.5 fluorescence dye (F-Cy5.5). This molecule was encapsulated into self-assembled nanoparticles by modified solvent evaporation method (FNprobe). The size and morphology of the FNprobe were characterized by DLS and TEM. Loading content of F-Cy5.5 was analyzed by fluorine NMR. MSCs were isolated from 4-5 week old balb/c mice and underwent 5 passages prior to labeling. Confocal microscopy and FACS were used to confirm labeling efficiency. Traumatic brain injury (TBI) was induced by controlled cortical impact (CCI) on balb/c mice. 19F MRI imaging was conducted on PharmScan 7 T MRI. Cy5.5 fluorescence imaging was performed on Maestro II. Results: All the fluorine dendrons showed high 19F content in each molecule (>50%) with isotropic fluorine signal in spectrum. The conjugation with Cy5.5 retained the fluorine dendrons' properties. At the identical concentrations, the molecule containing 27 fluorine atoms showed the optimal S/N. FNprobe with 40% loading capacity was stable over a week at 4oC, and presented 130 nm in size with low size distribution (<0.2) in consistent to TEM image. Over 90% MSCs were extensively labeled after 24h incubation. Those labeled cells kept the distinctive cell surface markers, differentiation and migration abilities. Phantom MRI and optical imaging showed almost linear correlation between fluorine signal, fluorescence intensity and cell number. There is a significant correlation between fluorine signal and fluorescence intensity with an R2 value of 0.98. A high correlation of 19F MRI signal to fluorescence signal was confirmed by imaging of in vivo subcutaneous implants of the labeled MSCs. Transplantation of the labeled MSCs into TBI mouse brain showed the tracking progress of MSC over 7 days as shown by 19F MRI and fluorescence imaging. Conclusion: We synthesized symmetrically structured 19F dendrons bypassing the shortcomings of available 19F MRI contrast agents. One promising candidate was chosen to be loaded in an engineered nanoparticle for efficient MSC labeling and tracking both in vitro and in vivo. This nanoparticular dual modality imaging probe may open another avenue of integrated 19F MRI and optical imaging for quantitative and precise cell tracking in stem cell study.

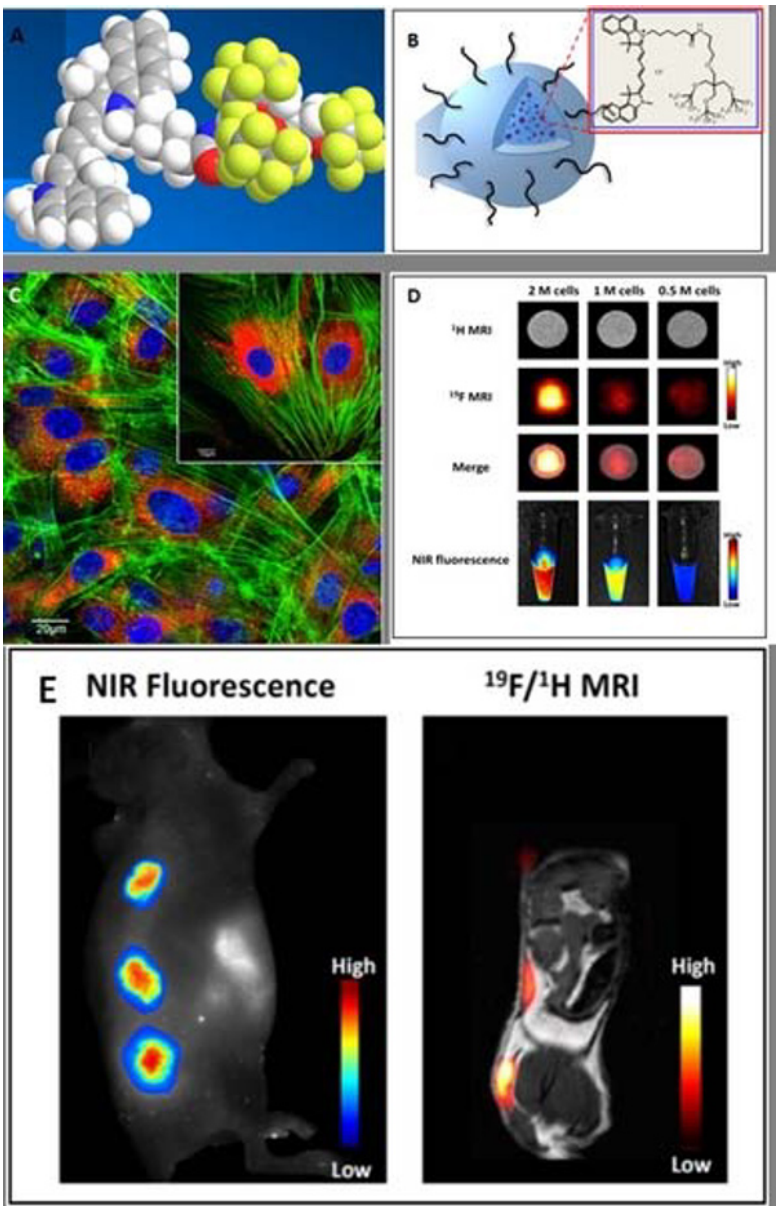

A) 3D modeling symmetrically structured small molecule for 19F-MRI and fluorescence imaging; B) self-assembled biodegradable nanoparticle sequestering the synthesized small molecule (F-probe); C) mesenchymal stem cell (MSC) uptake of F-probe over 24h incubation; D) Phantom 19F-MRI and fluorescence imaging of F-probe labeled MSC; E) in vivo subcutaneous implant of different number of F-probe labeled MSC for 19F-MRI and fluorescence imaging

Disclosure of author financial interest or relationships:
Z. Wang, None; **X. Yue**, None; **Y. Wang**, None; **P. Rong**, None; **D.O. Kiesewetter**, None; **G. Niu**, None; **X. Chen**, None.

Presentation Number **SS 125**
Scientific Session 21: Chemistry & Imaging Probes - CT & Multimodal
September 21, 2013 / 11:30-11:45 / Room: 200

Specific targeted contrast and high resolution - phase contrast CT with labeled macrophages in a preclinical asthma mouse model

Christian Dullin[1], *Simeone dal Monego*[3], *Emanuel Larsson*[4,6], *Sara Mohammadi*[4], *Martin Krenkel*[5], *Chiara Garrovo*[3], *Stefania Biffi*[3], *Andrea Lorenzon*[3], *Andrea Markus*[2], *Joanna Napp*[1,2], *Joachim Lotz*[1], *Tim Salditt*[5], *Frauke Alves*[2], *Giuliana Tromba*[4], [1]*Diagnostic Radiology, University Medical Center, Goettingen, Germany;* [2]*Hematology Oncology, University Hospital, Goettingen, Germany;* [3]*Optical Imaging, Cluster in Biomedicine, Trieste, Italy;* [4]*SYRMEP beamline, Synchrotron Elettra, Trieste, Italy;* [5]*X-ray physics, University Goettingen, Goettingen, Germany;* [6]*Architecture and Engineering, University of Trieste, Trieste, Italy. Contact e-mail: christian.dullin@med.uni-goettingen.de*

Here we present a novel approach to visualize both, morphological alterations as well as inflammatory processes in an asthma mouse model utilizing synchrotron radiation. We believe that this is of particular interest in the development of novel therapies, allowing the measurement of anatomical hallmarks of asthma and quantification of inflammation at the same time, which up to date was hampered by the small size of the mouse organs. Moreover, the contrast in X-ray imaging is, however, superior in spatial resolution, and is based on small x-ray attenuation differences within biological tissues. Therefore, the aim of this study was to validate a functional high resolution CT imaging approach by the use of barium labeled immortalized alveolar macrophages, applied intratracheally in ovalbumin induced asthmatic mice three days after the last antigen challenge. Immortalized alveolar macrophages (CRL-2019, ATCC) were maintained in culture and labeled in vitro for 24h with Micropaque (Guerbet), a barium sulfate containing, clinically approved contrast agent. Furthermore, membranes of cells were stained either with the fluorescent dye, DiD or DiO (Molecular Probes) for optical imaging. Six million labeled macrophages were injected intratracheally into mice 24h prior to sacrifice. Lungs were kept in situ and inflated with air at a physiological pressure of 30cm water column. Entire mouse samples were embedded in agarose gel and scanned at the SYRMEP beamline (Synchrotron Light Source "Elettra", Italy) with a sample-to-detector distance of 30cm, in order to use free propagation based phase contrast. The beamline was operated at 22keV, performing 1800 projections were acquired over 360 degrees with an exposure time 4s per projection. To cover the central lung area two slightly overlapping scans of approximately 4mm height each were performed and automatically stitched. The data was further processed using a phase retrieval algorithm, in order to remove the strong edge effects and decouple phase from absorbance information, thereby facilitating threshold based segmentation (Fig. A). The 3D phase distribution data sets were segmented and analyzed, and showed an increased barium and tissue content together with a reduced air volume in the asthmatic lung (Fig. B,D). Interestingly, injected macrophages were also detected inside the airway walls, thus suggesting a migration of macrophages to the lungs (Fig. B white arrows). This is consistent with published data demonstrating that macrophage migration is crucial for the development of asthma. Structural changes of the lungs could not only be detected in the larger bronchi, but also in smaller airways down to the alveolar level, which has not been reported before. The density of the tissue content in the asthmatic lung was found to be higher than in the controls, suggesting the presence of edema. All our observations are supported by NIR fluorescence and x-ray phase contrast microscopy performed on histological sections (Fig. C). We believe that our targeted contrast CT imaging technique would be beneficial in preclinical research to unravel mechanisms that are responsible for a variety of diseases.

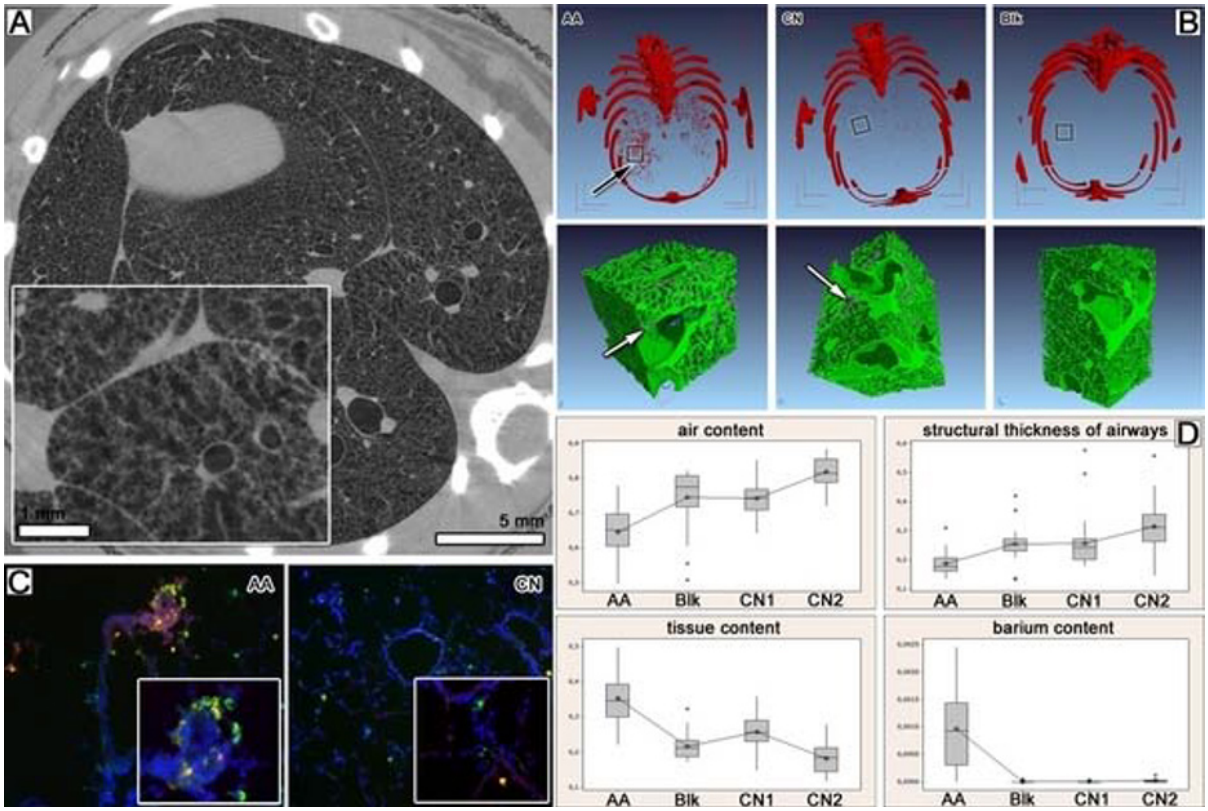

Disclosure of author financial interest or relationships:
C. Dullin, None; **S. dal Monego**, None; **E. Larsson**, None; **S. Mohammadi**, None; **M. Krenkel**, None; **C. Garrovo**, None; **S. Biffi**, None; **A. Lorenzon**, None; **A. Markus**, None; **J. Napp**, None; **J. Lotz**, None; **T. Salditt**, None; **F. Alves**, None; **G. Tromba**, None.

Presentation Number **SS 126**
Scientific Session 21: Chemistry & Imaging Probes - CT & Multimodal
September 21, 2013 / 11:45-12:00 / Room: 200

Monitoring macrophage migration in the liver in vivo with Contrast Enhanced micro CT

Anderson Peck[1], *Noel R. Monks*[2], *David Monsma*[3], *Anthony Chang*[1], [1]*Small Animal Imaging Facility, Van Andel Institute, Grand Rapids, MI, USA;* [2]*Laboratory of Translational Medicine, Van Andel Institute, Grand Rapids, MI, USA;* [3]*Preclinical Therapeutics Core, Van Andel Institute, Grand Rapids, MI, USA. Contact e-mail: anderson.peck@vai.org*

Introduction: The liver is a complex and important organ which is involved in many diseases including autoimmune disorders, drug toxicity, cancer and metastases. Within the liver, a large population of macrophage, Kupffer Cells, perform the important task of responding to foreign substances and neutralizing them through phagocytosis. As part of the complex response to pathogens and foreign cells, Kupffer cells play an important role in controlling various physiological mechanisms such as chemotaxis, angiogenesis, inflammation and others. Understanding the acute and chronic responses of Kupffer cells to disease will have a significant impact on the treatment of disease in the liver. To this end, we have developed a procedure for labeling Kupffer cells with a long lived CT contrast that allows a noninvasive, longitudinal in vivo observation. Method: A commercially available preclinical CT contrast agent (ViscoverTM ExiTronTM nano 6000; Miltenyi Biotec, Bergisch-Gladbach, Germany) labels Kupffer cells in the liver throughout the effective life of a mouse model. A pancreatic cancer liver metastasis model was used to evaluate the contrast. The mice were surgically implanted with either human pancreatic cancer cell line (L3.6pl) or saline (sham) within the spleen and monitored weekly by micro CT. Contrast injections and baseline scans were performed 1 day prior to surgery for both groups. A subset of each group of mice was sacrificed weekly after in vivo imaging for ex vivo high resolution micro CT imaging. Liver lobes were fixed whole in formalin and embedded in paraffin for routine processing. IHC staining was performed using the primary antibodies F4/80 to label Kupffer Cells and Human MHC Class 1 to label metastasis. Analysis was performed by viewing slices from micro CT imaging that correlated to the IHC slides. Results: Exitron nano 6000 provides a uniform contrast enhancement in healthy liver tissue at the time of injection. When mice are monitored longitudinally after a single contrast injection, the contrast remains homogeneously distributed in healthy mice but translocates in disease models with correlation to the movement of Kupffer Cells. CT contrast and Kupffer Cell co-location is confirmed with ex vivo analysis and IHC. IHC slides show small metastatic lesions, <100 cells, with rings of Kupffer cells surrounding them and amassing in large clusters nearby. Conclusion: Based on our study, in the period of weeks after injection, the population of Kupffer cells that were labeled at the time of injection can be seen migrating and conglomerating in areas that are sites of metastasis. This proves that Kupffer cell movement as an immune response to disease can be monitored over a period of weeks or months. This technique holds promise for the advanced understanding of Kupffer cell behavior, evaluation of the immune response, and the early detection of disease in the liver.

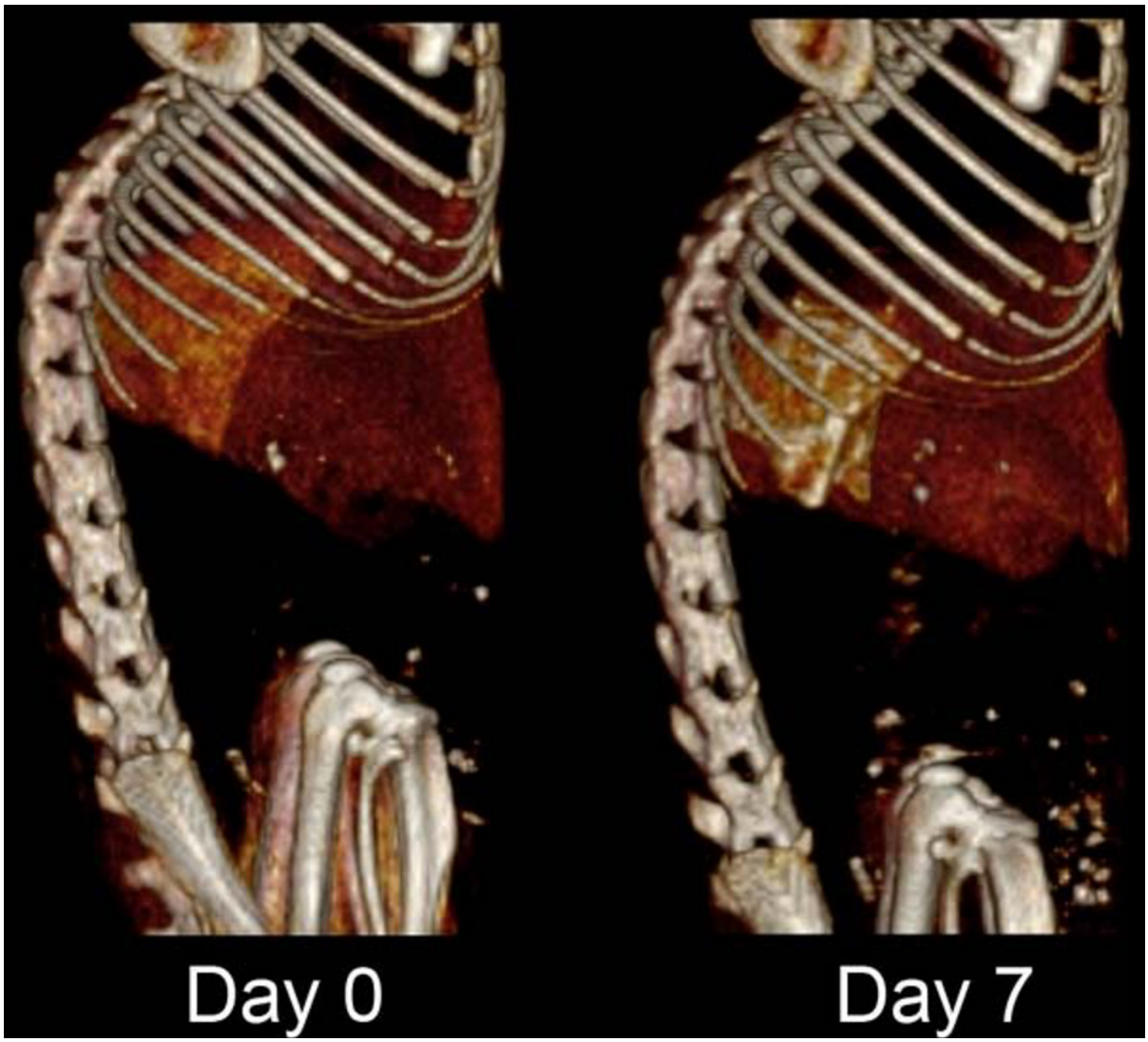

Contrast enhanced micro CT shows movement of Kupffer Cells in the right lobe of the liver from Day 0 to Day 7.

Disclosure of author financial interest or relationships:
A. Peck, None; **N.R. Monks**, None; **D. Monsma**, None; **A. Chang**, None.

Presentation Number **SS 127**
Scientific Session 22: Preclinical in vivo Studies - Oncology (Metabolic and Other)
September 21, 2013 / 10:30-10:45 / Room: 203

Correlation of MR Spectroscopy Measured 2-Hydroxyglutarate Concentration with Tumor Progression in Brain Tumors Carrying IDH1/2 Mutations

Liya Wang[1,2], *Juliya Kalinina*[3], *Run Lin*[1,2], *Shaoxiong Wu*[4], *Chad A. Holder*[1], *Jing Huang*[1,2], *Erwin G. Van Meir*[3], *Hui Mao*[1,2], *[1]Radiology and Imaging Sciences, Emory University, Atlanta, GA, USA; [2]Center for Systems Imaging, Emory University, Atlanta, GA, USA; [3]Neurosurgery, Emory University, Atlanta, GA, USA; [4]Chemistry, Emory University, Atlanta, GA, USA. Contact e-mail: lwang30@emory.edu*

Mutation in isocitrate dehydrogenase 1/2 (IDH1/2) is a prognostic marker of glioma patients. The mutant enzyme gains a novel activity of producing the oncometabolite, R(-)-2-hydroxyglutarate (2HG), which can be detected in vivo/ex vivo by magnetic resonance spectroscopy (MRS). However, the role of 2HG in tumor development and progression remains to be better understood. This study investigated the relationships of 2HG concentrations obtained from ex vivo MRS analysis with tumor progression features obtained from clinical pathology and radiology exams to explore the potential of using 2HG levels as a MRS measurable biomarker for predicting brain tumor prognosis and responses to the treatment. In tumor tissue samples selected for the study, we observed significantly elevated levels of 2HG in all gliomas carrying IDH1 mutations (n=38) comparing to the group without IDH1 mutations (n=34). Furthermore, we found the 2HG level is higher in tumors at higher grades (Grade II vs. Grade III). When comparing the 2HG level with tumor volume and tumor proliferation measurements of MIB index, it was found that 2HG level is associated with increased tumor volume (Fig. 1a) and is correlated to MIB index (Fig. 1b). Two cases of IDH mutation positive tumors were followed up. In first case, initial MRI exam at the diagnosis showed that there was a 4.2 x 5.1 x 4.2 cm3 mass with T1 hypointensity and T2 hyperintensity in right frontal lobe (Fig. 2a). There was no appreciable post contrast enhancement (Fig. 2b), suggesting a low grade tumor which is confirmed with pathology classification of Grade II oligodendroglioma. MR spectroscopic analysis of tumor tissue collected at the initial diagnosis reported a 2HG level of 3.5 mM. Two years later, MRI exam showed interval development of significant T1 hypointensity (Fig. 2c) and mass-effect centered in right frontal lobe with increased tumor size. The overall abnormal T1-hypointensity increased to approximately 9.0 x 6.3 x 6.0 cm. Furthermore, post-contrast MRI showed markedly nodular, irregular enhancements (Fig. 2d). NMR analysis of the tissue from the 2nd biopsy indicated that 2HG level was elevated to 8.5 mM. Changes of 2HG levels indicated by α-H of 2HG were shown in the NMR spectra (Fig. 3a). Pathology analysis confirmed that the tumor has developed to advance anaplastic oligodendroglioma (Grade III). Similarly in the 2nd case, the patient was diagnosed as oligoastrocytoma (Grade II) with no visible contrast enhancement (Fig. 2e-f). MR spectroscopic analysis showed a low 2HG level at 1.2 mM (Fig. 3b). However, when the tumor recurred two years later, increase of tumor volume (Fig. 2g-h) and elevated tumor grade (Grade IV) were reported. This was companied with a drastically elevated 2HG level. These two cases thus demonstrated patient specific examples to support the general finding that the 2HG level is increasing with the tumor grade. The results of this study provided the evidence that 2HG level has a strong correlation with several clinically important prognostic index, such as tumor size and MIB value. The excess 2HG accumulated in tumors may contribute to the formation and malignant progression of gliomas.

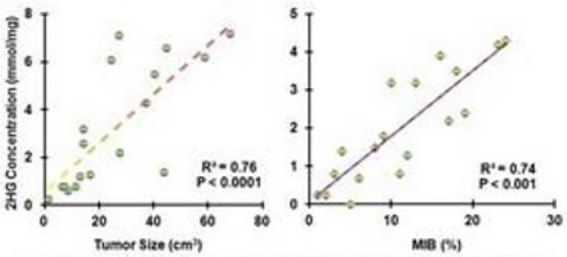

Fig. 1: There was a positive correration between 2HG level and tumor size from 18 available data sets (left panel) and MIB from 17 available data sets (right panel).

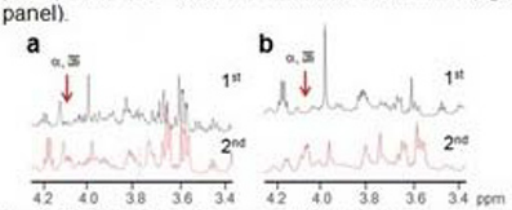

Fig. 3: The 2HG level increased after the tumors progressed to higher grade after two years. Case one (a) presented 2HG at 5.5 mM in the initial diagnosis but increased to 7.2 mM two years later showed 2HG increased to 20 mM after recurrence from 2.3 mM at the 1st exam (b).

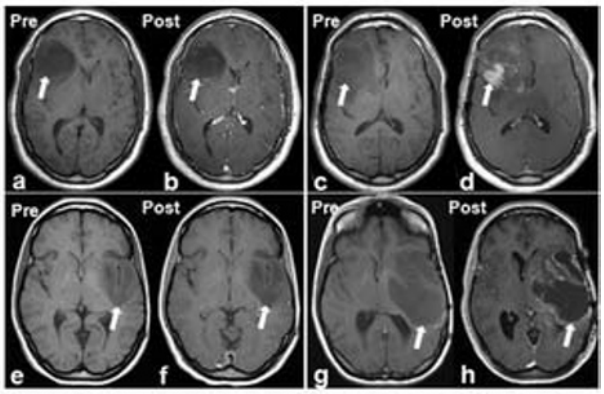

Fig. 2: Contrast enhanced MRI of two examples of low grade tumors harboring IDH mutation progressed to GBM (Grade IV) revealed the low signal lesion on pre T1WI (a, e) and no enhancement on post contrast T1WI (b, f). Two years later, same case showed the increased tumor size on T1WI (c, g), and strong contrast enhancement on post T1WI (d, h).

Disclosure of author financial interest or relationships:

L. Wang, None; **J. Kalinina**, None; **R. Lin**, None; **S. Wu**, None; **C.A. Holder**, None; **J. Huang**, None; **E.G. Van Meir**, None; **H. Mao**, None.

Presentation Number **SS 128**
Scientific Session 22: Preclinical in vivo Studies - Oncology (Metabolic and Other)
September 21, 2013 / 10:45-11:00 / Room: 203

EPR Oxygen Imaging Guided Treatment in Pancreatic Cancer

Shingo Matsumoto[1], *Keita Saito*[1], *Yoichi Takakusagi*[1], *Masayuki Matsuo*[1], *Jeeva P. Munasinghe*[2], *Nallathamby Devasahayam*[1], *Sankaran Subramanian*[1], *James B. Mitchell*[1], *Murali K. Cherukuri*[1], [1]*National Cancer Institute, NIH, Bethesda, MD, USA;* [2]*National Institute of Neurological Disorder and Stroke, NIH, Bethesda, MD, USA. Contact e-mail: matsumos@mail.nih.gov*

Aim: Pancreatic cancer is a malignant neoplasm with extremely poor prognosis. The 5-year overall survival rate is below 10%. A new drug TH-302 in combination with gemcitabine was approved for Phase 3 clinical trial in locally advanced or metastatic pancreatic adenocarcinoma in December 2012. TH-302 is a kind of drugs known as hypoxia-activated prodrug (HAP), which activated under hypoxia (low concentration of oxygen) and exhibits anti-tumor effect. A question derived is how clinicians select patients who receive most benefit from treatment with this hypoxia targeting new drug, instead of classical radiation therapy or gemcitabine monotherapy. Electron paramagnetic resonance imaging (EPRI) can non-invasively provide 3D absolute oxygen images. Here, we investigated if the EPR oxygen imaging can predict treatment benefit of oxygen dependent or independent therapies in three different pancreatic cancer xenografts. **Methods:** Three human pancreatic cancer cells Hs766t, MiaPaca2, and Su8686 were subcutaneously inoculated in hind leg of athymic nude mice. The tumor bearing mice were treated with TH-302 (80mg/kg, ip, 5 days), X-radiation (3Gy, 5 days), or gemcitabine (150mg/kg, ip, twice a week). Tumor oxygen imaging was conducted by a homemade 300 MHz pulsed EPRI scanner using an oxygen sensitive triarylmethyl probe OX063 (1), followed by anatomic MRI scan. **Results:** Three pancreatic cancer cell lines showed large difference in tumor oxygenation. Tumor median pO_2 values are 9.1±0.7 mmHg for Hs766t, 11.1±1.0 mmHg for MiaPaca2, and 17.6±1.1 mmHg for Su8686. TH-302 treatment provided survival benefic of 28.6 days in hypoxic Hs766t tumors but only 1.0 days in the most oxygenated Su8686 tumors. In contrast, tumor growth delay by radiotherapy was 10.3 days in Hs766t, 18.6 days in MiaPaca2, and 19.3 days in Su8686 tumors. Gemcitabine treatment was effective in both hypoxic and oxygenated tumors but there seemed to be most effective against the hypoxic Hs766t tumors. **Conclusion:** Quantitative oxygen images by EPRI can predict difference in the benefit from oxygen-dependent anti-tumor treatments in individual pancreatic tumor cell lines that may help properly choose the best treatment in patients with pancreatic cancer if EPRI is available in clinic.
References: 1. Matsumoto S et al. Low-field paramagnetic resonance imaging of tumor oxygenation and glycolytic activity in mice. J Clin Invest. 2008;118:1965-73.

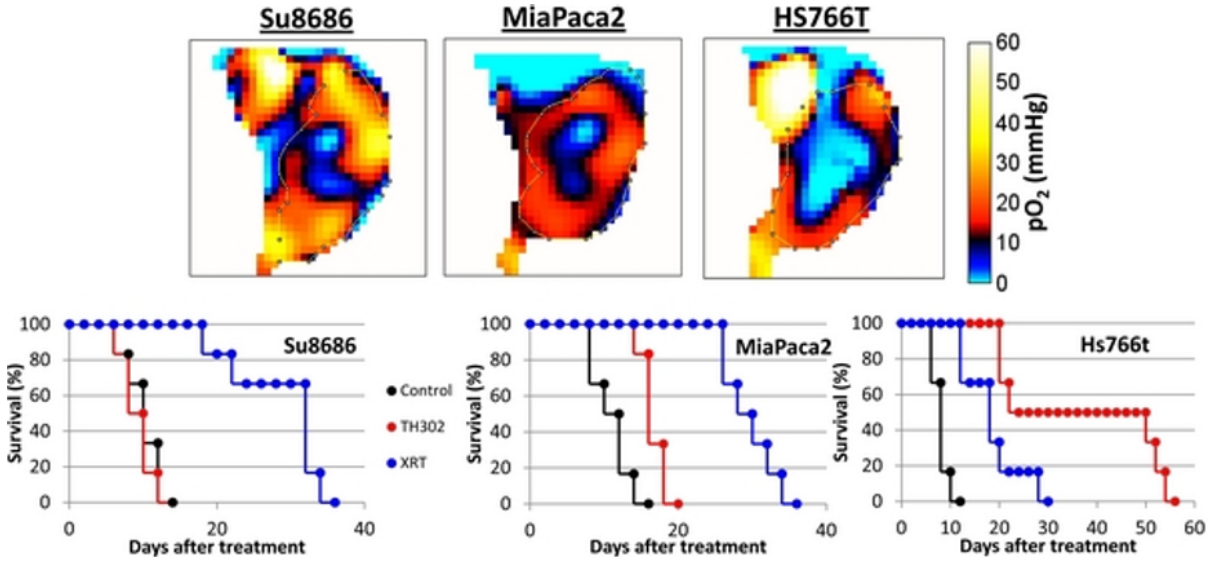

Fig.1 EPR oxygen images of three pancreatic tumor xenografts and treatment response to hypoxia activated prodrug TH-302 or fractionated radiation.

Disclosure of author financial interest or relationships:
S. Matsumoto, None; **K. Saito**, None; **Y. Takakusagi**, None; **M. Matsuo**, None; **J.P. Munasinghe**, None; **N. Devasahayam**, None; **S. Subramanian**, None; **J.B. Mitchell**, None; **M.K. Cherukuri**, None.

Presentation Number **SS 129**
Scientific Session 22: Preclinical in vivo Studies - Oncology (Metabolic and Other)
September 21, 2013 / 11:00-11:15 / Room: 203

Mapping pigment chemistry of melanoma in vivo with femtosecond pump-probe microscopy

Jesse W. Wilson[1], *Mary Jane Simpson*[1], *Simone Degan*[1], *Christina S. Gainey*[1], *Tanya Mitropoulos*[1], *Jennifer Y. Zhang*[2], *Warren S. Warren*[1,3], [1]*Chemistry, Duke University, Durham, NC, USA;* [2]*Dermatology, Duke University, Durham, NC, USA;* [3]*Radiology, Duke University, Durham, NC, USA. Contact e-mail: jesse.wilson@duke.edu*

Melanoma, a form of skin cancer that is particularly aggressive and resistant to chemotherapy, can usually be successfully treated if completely excised in its earliest stage (i.e. if tumor thickness < 1.0 mm). Though thin lesions comprise the majority of new cases, it is difficult to identify the 10% of thin lesions that will later present with metastatic disease [1]. In order to identify hallmark features of thin lethal melanomas, we have been developing a technique for in vivo observation of the progression of melanoma in mouse models of human melanoma, using noninvasive multiphoton microscopy to record changes both in morphology and pigment chemistry. We acquire molecular contrast between the pigments eumelanin, pheomelanin, and hemoglobin with a technique based on femtosecond pump-probe spectroscopy, which has been shown to differentiate melanoma from dysplastic nevi based on the microscopic distribution of melanin pigment chemistry in unstained biopsy slides [2]. In vivo microscopy is performed on anesthetized mice with a laser-scanning microscope equipped with three different imaging modalities, all driven by a femtosecond laser oscillator (SpectraPhysics Tsunami or Coherent Chameleon) supplying ~150 fs pulses at 810 nm. Structural contrast is acquired through two imaging channels, linear confocal reflectance, and combined multiphoton autofluorescence and second-harmonic generation, both employed in dermatology clinics worldwide [5]. Molecular contrast is provided by pump-probe microscopy, which uses second train of femtosecond laser pulses at 720 nm (generated by a Coherent Mira optical parametric oscillator), modulated at 2 MHz, to induce transient changes in optical absorption of the 810 nm pulses that are detected with a lock-in amplifier. Figure 1 shows the pump-probe imaging results for a xenograft, in which pigment chemistry is resolved by acquiring a stack of images, each with a different pump-probe time delay, and comparing each pixel's pump-probe signature to reference standards (sepia eumelanin and synthetic pheomelanin). We will also discuss validation of these results by comparing with histopathology, and characterizing changes in the pump-probe signatures of eumelanin and pheomelanin with respect to optical intensity, in order to account for higher-order nonlinearities. These results demonstrate pump-probe microscopy reveals useful information that is not provided by the traditional confocal reflectance and multiphoton techniques, and may even provide a means of monitoring treatment response. REFERENCES: 1. MF Kalady, et al. Ann Surg 238, 528-535 (2003). 2. TE Matthews, et al. Sci Transl Med 3, 71ra15 (2011). 3. Y Chudnovsky, et al. Nat Genet 37, 745-749 (2005). 4. D Dankort, et al. Nat. Genet 41, 544-552 (2009). 5. MJ Koehler, et al. Exp Dermatol 20, 589-594 (2011).

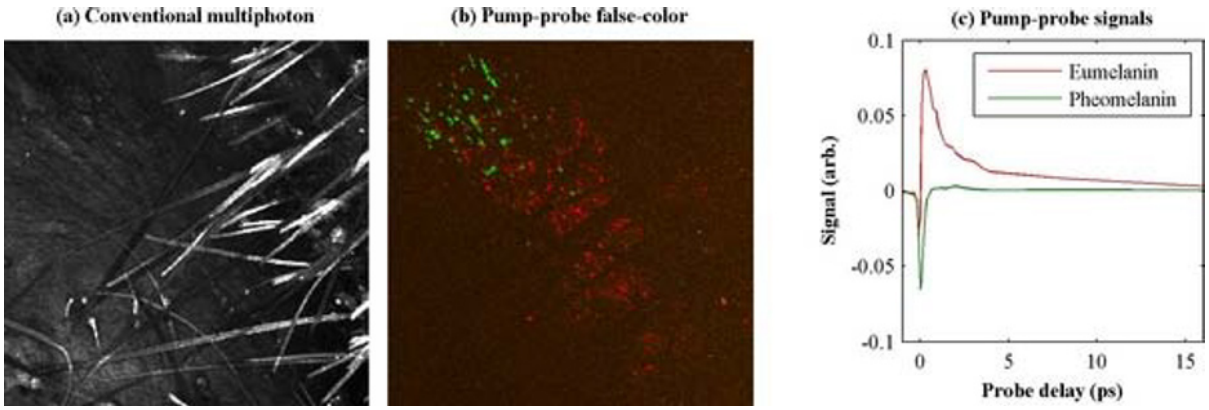

In vivo imaging of human skin xenograft melanoma model. (a) Multiphoton autofluorescence and second-harmonic generation. (b) False-color pump-probe image, pheomelanin shown in green, eumelanin shown in red. (c) Eumelanin and pheomelanin pump-probe signatures identified from the image stack used to generate (b).

Disclosure of author financial interest or relationships:
J.W. Wilson, None; **M. Simpson**, None; **S. Degan**, None; **C.S. Gainey**, None; **T. Mitropoulos**, None; **J.Y. Zhang**, None; **W.S. Warren**, None.

Presentation Number **SS 130**
Scientific Session 22: Preclinical in vivo Studies - Oncology (Metabolic and Other)
September 21, 2013 / 11:15-11:30 / Room: 203

Intratumoral *in vivo* phenotyping of breast cancer using a multiparametrical PET/MRI approach

Jennifer Schmitz[1], *Andreas Schmid*[1], *Julian Schwab*[1], *Jane Q. Chen*[2], *Neil E. Hubbard*[2], *Robert D. Cardiff*[2], *Alexander D. Borowsky*[2], *Bernd J. Pichler*[1], [1]*Department of Preclinical Imaging and Radiopharmacy, Eberhard Karls University of Tübingen, Tuebingen, Germany;* [2]*Center for Comparative Medicine, University of California, Davis, CA, USA. Contact e-mail: Jennifer.Schmitz@med.uni-tuebingen.de*

Introduction: One of the current challenges in cancer research is the diagnosis and therapy of heterogeneous tumors. Phenotypes are usually identified by invasive biopsies that produce major sampling errors. The Tg(PyV-mT) model develops spontaneous tumors along the mammary glands having a variety of phenotypic outcome in premalignant and malignant tumors, thus showing high levels of intratumoral heterogeneity. To develop a comprehensive tumor profile, we employed a variety of biomarkers for PET and MRI. Beside glucose metabolism, hypoxia, angiogenesis, proliferation, protein synthesis and diffusion was investigated, providing a basis for the *in vivo* identification of heterogeneous intratumoral phenotypes. **Methods**: 8 female C57BL/6:Tg(PyV-mT) mice at 19-22 weeks of age were scanned in a sequential PET/MRI setup. The animals were anesthetized with isoflurane and injected i.v. with 10±2MBq of [F-18]FDG, [F-18]FMISO, [Ga-68]NODAGA-RGD, [C-11]Choline and [C-11]Methionine. All molecular PET data were subsequently complemented with anatomical MRI. For data analysis the absolute uptake values (%ID/cc), the SUVs and the TMRs for the entire lesions and for each voxel were calculated. Image derived thresholds were computed to differentiate several phenotypes with various tracers and ADC maps. Following the last measurement, tumors were excised and prepared for histology and/or autoradiography. **Results**: MRI data revealed lesions from 3.4 to 772.0mm^3. PET tracer uptake varied strongly in individual lesions as well as within single regions. Highest uptake variations were achieved with [F-18]FDG ranging from 1 to 25 %ID/cc/voxel within single tumors. Analysis of the mean uptake values of the lesions was not feasible due to the strong intratumoral heterogeneity. Therefore, a voxel-based analysis was employed, providing an *in vivo* identification of different phenotypes using ADC, [F-18]FDG, [C-11]Choline and [C-11]Methionine. The ADC maps well differentiated between solid tissue (~0.1-0.5*$10^{-3}mm^2/s$) and cystic regions (>1*$10^{-3}mm^2/s$). In combination with PET, especially [F-18]FDG, these parameters enabled a differentiation of three different phenotypes (solid nodular, solid acinar, cystic hyperplasia), based on *in vivo* imaging and verified by histology and autoradiography. **Conclusion**: PET tracer uptake varies strongly within individual Tg(PyV-mT) tumors, making a comprehensive phenotypic analysis feasible only with combined PET/MRI. Single tracer analysis of these tumors is not sufficient to differentiate the heterogeneous tumor phenotypes *in vivo*. For a successful identification and characterization of intratumoral phenotypes, a set of multiple parameters combining tracer uptake, anatomical information and ADC values is necessary. Using the proposed setup a differentiation between hyperplasia and malignancy is

possible, and allows the detection of small malignancies within large hyperplastic lesions. In addition, the ability to distinguish between hyperplasia and malignancies at an early time point in neoplastic progression reveals great potential for further longitudinal studies to develop a full understanding of neoplastic progression.

Disclosure of author financial interest or relationships:
J. Schmitz, None; **A. Schmid**, None; **J. Schwab**, None; **J.Q. Chen**, None; **N.E. Hubbard**, None; **R.D. Cardiff**, None; **A.D. Borowsky**, None; **B.J. Pichler**, Siemens, Grant/research support; Bayer, Grant/research support; AstraZeneca, Grant/research support; BoehringerIngelheim, Grant/research support .

Presentation Number **SS 131**
Scientific Session 22: Preclinical in vivo Studies - Oncology (Metabolic and Other)
September 21, 2013 / 11:30-11:45 / Room: 203

High Frequency Oscillatory Ventilation: A Method to Reduce Respiratory Artifact in Micro CT Imaging

Brittany A. Holly, *Zachary Dieffenbach, Anderson Peck, Ryan A. Bozio, Anthony Chang, Small Animal Imaging Facility, Van Andel Research Institute, Grand Rapids, MI, USA. Contact e-mail: Brittany.Holly@vai.org*

Purpose: Micro computed tomography (microCT) can provide high resolution anatomical imaging of small animals. However, the resolution can be limited by the motion artifact caused by respiratory movement. This respiratory artifact is exhibited as a blurring or missing of anatomical features that would otherwise appear as well defined edges. Gating is a solution to this problem. However, significant extension to the total scan time, not being featured on most microCT scanners, and limited applicability on animals with extremely high breath rates, such as mice, are the main reasons that limit the usage of this technology. The method we proposed involves intubation of the mouse and the use of a ventilator capable of high frequency oscillatory ventilation. By ventilating oxygen at an ultra high frequency through the mouse lungs, the mouse will relinquish the control of breathing while maintaining a sufficient oxygen supply. This method uses equipment and procedures that can be reproduced for other imaging modalities to significantly reduce the respiratory artifact. Methods: All procedures were approved and overseen by the institute's IACUC committee and attending veterinarian. Intubation procedures were performed as previously described in literature and with ventilators manufacturer's recommendations. The ventilator (Micro Vent 1, Hallowell EMC, Pittsfield, MA) features 2 modes of ventilation; intermittent positive pressure ventilation (IPPV) and high frequency oscillatory ventilation (HFOV). IPPV imitates a natural breathing movement's volume and timing, while HFOV uses a much lower volume and a much faster timing to maintain oxygen supply with the least amount of movement. A pancreatic cancer liver metastasis mouse model was used to acquire quantitative results using a microCT scanner (Bioscan nanoSPECT/CT, Washington, DC). Adult female athymic nude mice received intrasplenic injections of 1 million cells, L3.6pl, 3 weeks prior to the imaging time point. CT liver contrast (Exitron nano 6000, Miltenyi Biotec, Auburn, CA) was injected via the tail vein 4 hours prior to imaging. MicroCT images were acquired in both IPPV and HFOV modes in successive scans for comparison. Images were selected for analysis of mice with tumors in the regions of the liver adjacent to the lungs. Edges of the tumors selected were analyzed to determine their width in pixels. Results: Mice were successfully intubated and ventilated using both IPPV and HFOV modes and recovered easily from the procedures. Analysis showed tumor borders in the liver had an average smaller width (2.62 ± 0.469 pixels or 0.526 ± 0.0938mm) when using HFOV over IPPV (6.833 ± 1.265 pixels or 1.366 ± 0.253mm). (see figure) Conclusion: HFOV is effective for significant improvement in micro CT image quality through the minimization of respiratory artifact. This provides a great advantage in evaluation of micro CT images and in small lesion detection within the thoracic and upper abdominal cavity. Mouse survivability is not threatened and long-term adverse effects of mechanical ventilation are not observed. This proves to be a beneficial tool in the field of small animal imaging.

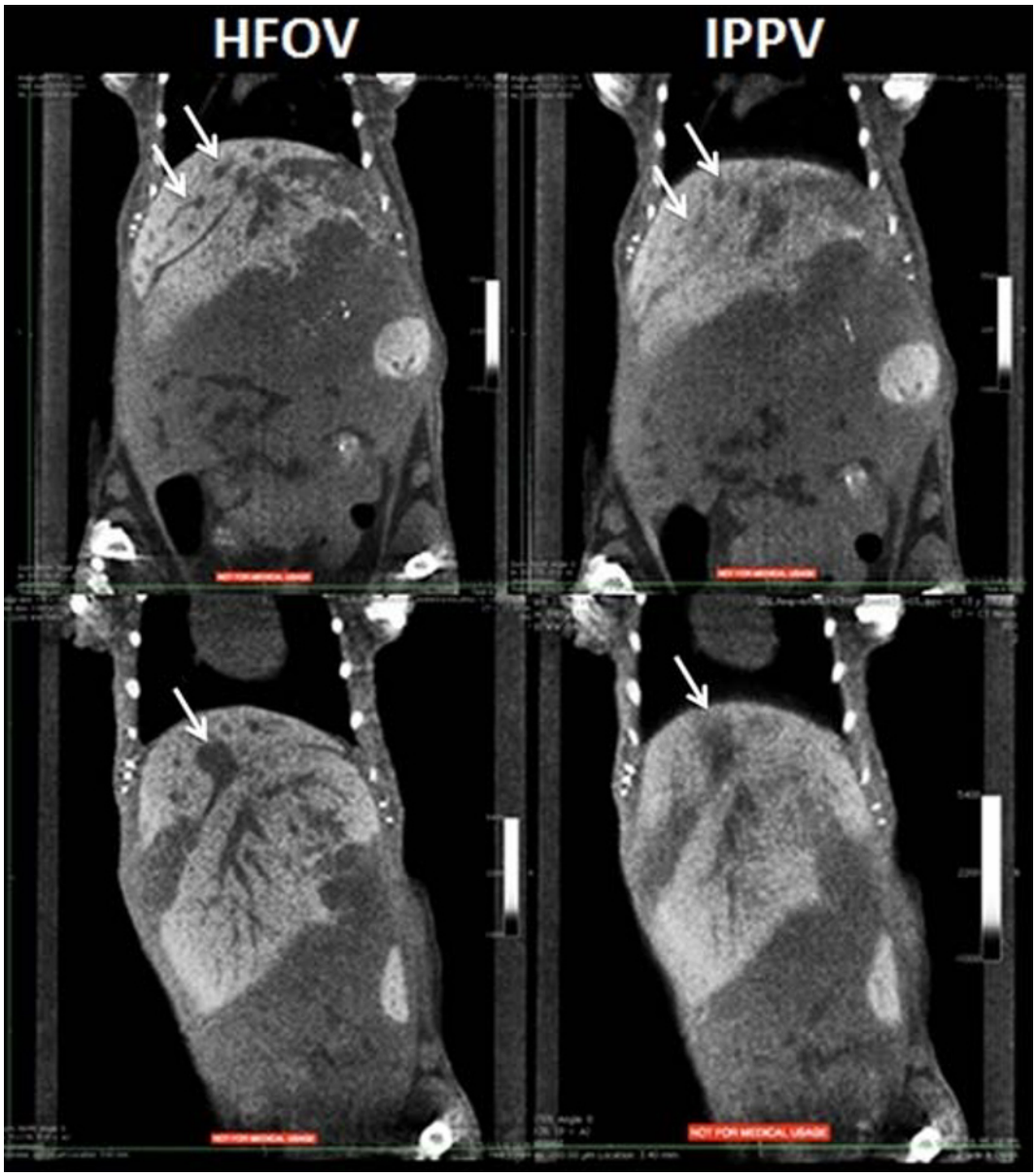

microCT images of 2 mice under mechanical ventilation. High frequency oscillatory ventilation (HFOV) shows significant increase in image quality and decrease in respiratory artifact, creating clear tumor borders within lung tissue. Intermittent positive pressure ventilation (IPPV) produces images with blurred tumor borders.

Disclosure of author financial interest or relationships:
B.A. Holly, None; **Z. Dieffenbach**, None; **A. Peck**, None; **R.A. Bozio**, None; **A. Chang**, None.

Presentation Number **SS 132**
Scientific Session 22: Preclinical in vivo Studies - Oncology (Metabolic and Other)
September 21, 2013 / 11:45-12:00 / Room: 203

MOLECULAR MRI DIFFERENTIATION OF VEGFR2 LEVELS IN FOUR DIFFERENT EXPERIMENTAL ANTI-GLIOMA THERAPIES WITHIN A GL261 MOUSE MODEL

Patricia Coutinho de Souza[1], *Krithika Balasubramanian*[1], *Nataliya Smith*[1], *Debra Saunders*[1], *Hong Chen*[2], *Yunzhou Dong*[2], *Rheal Towner*[1], [1]*Oklahoma Medical Research Foundation, Oklahoma City, OK, USA;* [2]*Cardiovascular Biology Research Program, Oklahoma Medical Research Foundation, Oklahoma City, OK, USA. Contact e-mail: csouzap@omrf.org*

Angiogenesis is essential to tumor progression and the precise imaging of the angiogenic marker vascular endothelial growth factor receptor 2 (VEGFR2) would provide an accurate evaluation for angiogenesis during a therapeutic response. In this study, we evaluated the molecular MRI differentiation of VEGFR2 levels in untreated gliomas and 4 different anti-glioma therapies in a GL261 mouse model (the nitrone OKN007, two different synthetic ubiquitin inhibitor peptides, and a combined therapy including OKN007 + ubiquitin inhibitor peptide). OKN-007 (2,4-disulfophenyl-PBN has demonstrated anti-glioma effects in several rodent models and is currently a clinical investigational drug for recurrent gliomas. The synthetic transduction peptides (Peptide 1 and Peptide 2) have anti-angiogenic properties via the Epsin-VEGF pathway and they target the ubiquitin interacting motif (UIM). METHODS GL261 cells were injected into the cortex of C57BL6 mice. For the OKN-007 treated group, the nitrone was given at a concentration of 0.018% (10 mg/Kg body weight/day) by drinking water and it was administered starting from 15 days after the glioma cell implantation. The synthetic UIM peptides 1 and 2 were administered i.v. via tail vein and repeated every 2 days for a total period of 15 days. The animals from this group were treated both with OKN-007 (via drinking water) and the synthetic peptide for a period of 15 days. Mice receiving normal drinking water were used as untreated tumor controls. MRI experiments were performed on a Bruker Biospec 7.0 T magnet system. The morphological imaging was taken by using double echo sequence. mMRI was performed with a variable-TR RARE sequence (rapid acquisition with refocused echoes, with TE of 15 ms and two transverse slices). Signal intensities were calculated in defined regions-of-interest in T1-weighed images. RESULTS The untreated tumor controls had a heterogeneous distribution of VEGFR2 in GL261 gliomas. All tumor VEGFR2 levels were significantly higher compared to the contralateral region, particularly in high signal tumor periphery and tumor interior regions. For the peptide 1 treatment group VEGFR2 levels were significantly increased in the tumor region ($p<0.001$), compared to untreated tumors. For peptide 2, VEGFR2 was significantly decreased ($p<0.0001$) in tumors, compared to untreated tumors. For OKN007, VEGFR2 was significantly decreased ($p<0.0001$) in tumors, compared to untreated tumors. When OKN007 and peptide 2 were combined, there was also a significant decrease ($p<0.01$) in VEGFR2 levels in tumor regions, compared to untreated gliomas. DISCUSSION Our study demonstrated differentiation in VEGFR2 levels within various tumor regions, which established the heterogeneous nature of angiogenesis within tumors. Measuring in vivo VEGFR2 levels using a targeted molecular imaging probe that can be detected by MRI provides an opportunity to assess anti-angiogenic therapies, as shown by the data. CONCLUSION Our study confirmed that in vivo VEGFR2 levels can be monitored as a function of therapeutic evaluation. Our study may also be of interest for using this method to target VEGFR2 to assess anti-angiogenic therapy.

Disclosure of author financial interest or relationships:
P. Coutinho de Souza, None; **K. Balasubramanian**, None; **N. Smith**, None; **D. Saunders**, None; **H. Chen**, None; **Y. Dong**, None; **R. Towner**, None.

Presentation Number **SS 133**
Scientific Session 23: Preclinical Cell & Tissue Level Studies - Oncology
September 21, 2013 / 10:30-10:45 / Room: Oglethorpe Auditorium

Hypoxic regions in breast cancer xenografts contain low collagen with disrupted water diffusion

Samata M. Kakkad[1,2], *Jiangyang Zhang*[1], *Alireza Akhbardeh*[1], *Meiyappan Solaiyappan*[1], *Venu Raman*[1], *Dieter Leibfritz*[2], *Kristine Glunde*[1], *Zaver M. Bhujwalla*[1], [1]*Russell H. Morgan Department of Radiology and Radiological Science, Johns Hopkins University SOM, Baltimore, MD, USA;* [2]*Department of Chemistry and Biology, University of Bremen, Bremen, Germany. Contact e-mail: skakkad1@jhmi.edu*

Introduction: Chaotic tumor vasculature leads to hypoxia which is associated with an aggressive phenotype and increased resistance to radiation and chemotherapy. Hypoxic tumor regions also contain very few collagen 1 (Col1) fibers, a major component of the tumor extracellular matrix (ECM). Here we examined the effects of hypoxia on water diffusion in a breast cancer xenograft model engineered to fluoresce under hypoxia. We observed, for the first time, that water diffusion and diffusion anisotropy were significantly lower in intensely fluorescing hypoxic regions compared to normoxic regions, which may be explained by the few Col1 fibers in hypoxic regions. Regions immediately adjacent to hypoxic foci showed a denser distribution of fibers around these hypoxic regions. Methods: Severe combined immunodeficient female mice were inoculated in the mammary fat pad with MDA-MB-231 cells stably expressing red fluorescent protein under the control of a hypoxia response element. Once tumor volume was approximately 300-400 mm3 the tumor was excised, fixed and imaged using high-resolution diffusion tensor imaging (DTI). The apparent diffusion coefficient (ADC) and fractional anisotropy (FA) maps were calculated. The tumor was then sectioned (1mm thick) for optical imaging in the bright field and fluorescence field to detect the RFP-containing hypoxic regions using a 1x lens. These sections were used to image Col1 fibers by second harmonic generation microscopy, acquiring a tile scan to cover the entire tumor section. Multimodality feature-based registration was performed to co-register optical and Col1 fiber images to DTI images. ADC and FA values were derived for hypoxic and normoxic regions. Results & Discussion: Heterogeneous ADC and FA value distributions were identified in the DTI data (Fig.1a,b,c). Red fluorescent hypoxic regions were identified from optical images (Fig.1d). Reregistration strength was confirmed by dice similarity index = 0.88, which is a good overlap for multimodality images (Fig.1e). The ADC map overlaid with the optical image demonstrates reduced ADC in hypoxic regions (Fig.1f). Overall, hypoxic regions had lower water diffusion (ADC) (Fig.1g) and diffusion anisotropy (FA) values (Fig.1h) than normoxic regions. A denser and altered fiber distribution was observed around hypoxic regions (Fig. 1i). Col1 fibers were significantly decreased in hypoxic regions, which could explain the lower ADC and FA values observed in these regions. Low ADC and FA values in low collagen hypoxic regions indicate a functional role of these fibers in molecular transport. Decreased diffusion of molecules due to fewer Col1 fibers in hypoxic regions may also contribute to poor drug delivery and tumor recurrence in hypoxic regions. Increased cellularity is thought to be one reason why lower ADC and FA values are observed in tumors. An even lower ADC within this backdrop may be due to hypoxic tumor regions. The denser fiber network in regions adjacent to hypoxic regions may facilitate the migration of aggressive cancer cells out of hypoxic tumor regions. Acknowledgement: This work was supported by NIH P50 CA103175; P30 CA006973.

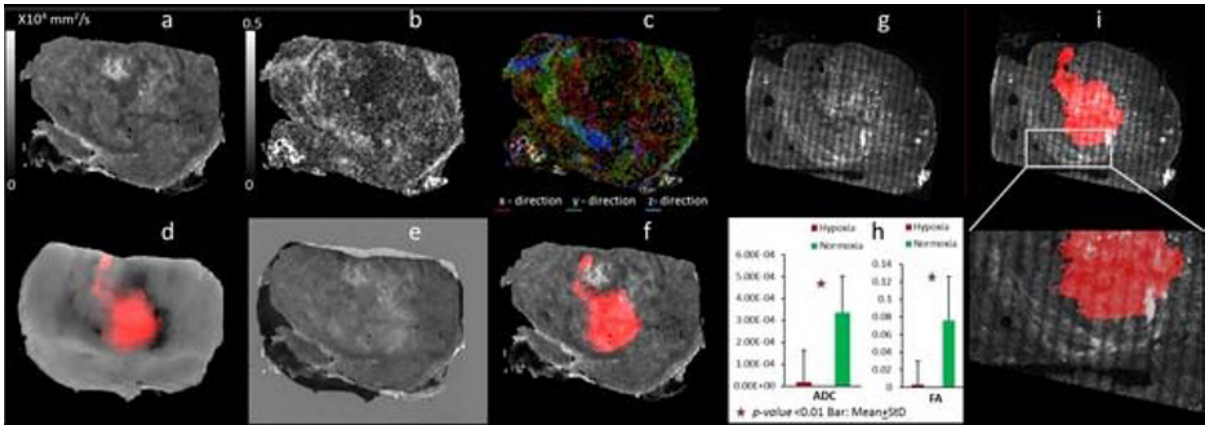

Figure 1: (a) Apparent diffusion co-efficient (ADC) map; (b) fractional anisotropy (FA) map; (c) DTI directions color-map; (d) corresponding registered optical bright field image overlaid with fluorescence field image; (e) ADC map overlaid with registered optical bright field section showing good co-registration; (f) registered hypoxic region overlaid with the ADC map; (g) corresponding registered SHG image showing Col1 fiber distribution; (h) ADC values in hypoxic and normoxic regions showing lower ADC with hypoxia; (h) FA values in hypoxic and normoxic regions showing relatively lower fractional anisotropy with hypoxia; (i) expanded region showing denser fibers around hypoxic tumor regions

Disclosure of author financial interest or relationships:
S.M. Kakkad, None; **J. Zhang**, None; **A. Akhbardeh**, None; **M. Solaiyappan**, None; **V. Raman**, None; **D. Leibfritz**, None; **K. Glunde**, None; **Z.M. Bhujwalla**, None.

Presentation Number **SS 134**
Scientific Session 23: Preclinical Cell & Tissue Level Studies - Oncology
September 21, 2013 / 10:45-11:00 / Room: Oglethorpe Auditorium

Topical Application of Activity-Based Probes for Rapid Detection of Non-Melanoma Skin Cancer in Human Skin Specimens

Yevgen (Eugene) Vykhovanets[1], *Margaret Mann*[2], *Galia Blum*[3], *Matthew Bogyo*[4,5], *James Basilion*[1,6], [1]*Radiology, CWRU, Cleveland, OH, USA;* [2]*Dermatology, CWRU, Cleveland, OH, USA;* [3]*Institute of Drug Research, The Hebrew University, Jerusalem, Israel;* [4]*Pathology, Stanford University, Stanford, CA, USA;* [5]*Microbiology and Immunology, Stanford University, Stanford, CA, USA;* [6]*Biomedical Engineering, CWRU, Cleveland, OH, USA. Contact e-mail: yvv@cwru.edu*

Objectives: Approximately 4 million people will be diagnosed with non-melanoma skin cancer this year in the US. Largely due to lesion size 75% of these patients are not candidates for more precise Mohs Micrographic Surgery (MMS) and will undergo traditional surgery, i.e. non-MMS, to remove the cancer. Non-MMS has lower cure rates and only assesses a limited portion (1%) of the margin days after surgery. Therefore there exists an unmet clinical need to more completely assess surgical margins during surgery to increase cure rates and minimize removal of normal tissue. Here we test the feasibility of topically applying a quenched near infrared (NIR) fluorescent contrast agent, GB119, to rapidly and globally detect cancer in skin specimens. Material & Method: We first characterized the feasibility of ex vivo applied GB119, to penetrate human skin tissue and "find" basal (BCC) or squamous carcinoma cells (SCC) in skin specimens. Detection of the cancer was measured by increased fluorescence resulting from specific activation and de-quenching of GB119 as it encounters active cathepsin associated with BCC and SCC. Samples were pre-imaged and then, using an applicator pad, GB119 was topically applied to excised skin specimens from patients previously diagnosed with either BCC or SCC. Activation and de-quenching of GB119 was measured over time by fluorescence imaging (Maestro, PerkinElmer, MA). Fluorescent "hot spots" on the surface of skin samples were marked with ink and the samples were frozen for routine histology and IHC. In the current study we analyzed excised skin specimens from 11 patents with BCC and 3 patients with SCC. Results: Twelve of 14 skin specimens produced robust fluorescence spots that were marked with pathology ink. Two samples did not produce any signal greater than pre-imaging auto-fluorescence (Fig.1A). H/E staining of marked skin specimens confirmed presence of ink nearby "nests" of cancerous tissue (Fig. 1B). The two skin samples that did not activate GB119 were determined by histology to be cancer free. Since it was not possible to detected GB119 fluorescence after H&E staining we developed an immunohistochemistry (IHC) assay to visualize the presence of activated de-quenched GB119 and used it pathologically correlate GB119 activation with cancer. Using an anti-Cy5 antibody (Sigma) our immunoassay detected primarily de-quenched GB119 (Fig. 2) and could be used to detect activated GB119 in tissue samples. Using this assay we detected low levels of GB119 activation in normal skin and cancer free samples form patients with BCC/SCC. However, high levels of GB119 activation were found within "nests" of cancerous tissue for both BCC and SCC specimens (Fig. 3). Conclusions: New tools to rapidly and completely assess cancer infiltrates in skin margins are essential to bring MMS advantages to non-melanoma skin cancer surgeries. These data confirm the feasibility of topically applying GB119 to excised skin cancer specimens to rapidly detect the presence of cancer within the margins of the samples. If successful this technology could potentially impact MMS-like precision to non-MMS surgical techniques.

Disclosure of author financial interest or relationships:
Y. Vykhovanets, None; **M. Mann**, None; **G. Blum**, None; **M. Bogyo**, None; **J. Basilion**, Akrotome Imaging, Consultant; Akrotome Imaging, Stockholder .

Presentation Number **SS 135**
Scientific Session 23: Preclinical Cell & Tissue Level Studies - Oncology
September 21, 2013 / 11:00-11:15 / Room: Oglethorpe Auditorium

Degron Based Protease Blockade Sensor to Image Histone Mehtylation

Thillai V. Sekar, *Kira Foygel, Ramasamy Paulmurugan, Departments of Radiology and Bioengineering, the Bio-X Program, Molecular Imaging Program at Stanford (MIPS), Stanford University School of Medicine, Palo alto, CA, USA. Contact e-mail: thillaiv@stanford.edu*

Histone methylation is an important post-translational modification (PTM) that governs the chromosome organization and gene regulation in cells. Histone lysine methylation identified as a watchdog for controlling growth and metabolic functions of normal and cancer cells. Due to regulatory role, histone lysine methylation turns out to be a promising therapeutic target, and to screen novel small molecule drugs capable of modulating this process. We developed a sensitive and robust optical imaging sensor to image histone lysine methylation in intact cells and in live animals. We adopted "degron protease blockade" as a concept to design our sensor. Degron is a specific amino acid sequence in proteins recognized by protease to initiate degradation. When a reporter protein is expressed as a fusion with the methylation domain and its substrate chromodomain along with the C-terminal degron sequence (Figure 1a), the conformational lock created by the interaction of methylated histone domain with its substrate chromodomain blocks the recognition and degradation of degron sequence by the protease. The sensor was constructed by expressing firefly luciferase (Fluc2) with chromodomain of methyltransferase (Suv39H1) and the first 13 amino acids of H3 protein (H3:K9) connected by a linker peptide [$(G_4S_3)_3$], and following C-terminal degron (FL2-Suv39H1-$(G_4S_3)_3$-H3K9-Degron). To show the specificity, we constructed mutant sensors where respective lysine at positions 4 and 9 were replaced with leucine (H3L4, H3L9 and H3KL4L9). Methylation sensors were studied in transient and stably transfected cells before and after treating with different epigenetic modulators (VPA, TSA and Chaetocin), and methyltransferase inhibitors. Wild-type methylation sensor yielded a specific signal ranging from $2.5x10^8 \pm 4.1x10^7$ p/sec/cm^2/sr, while K9 mutant and K4K9 mutant generated signals $4.4\ x10^7 \pm 1.6x10^6$ p/sec/cm^2/sr and $2.1\ x10^7 \pm 1.4\ x10^6$ p/sec/cm^2/sr respectively in HepG2 cells. Wild-type sensor showed luciferase signals which were 5.7 ± 0.22 fold higher than K9 mutant sensor and 11.8 ± 1.1 fold higher than K4K9 mutant sensor. The efficiency of these methylation sensors was studied in MDA MB231, HEK293 and MCF7 cells. Western blot analysis showed that wild-type sensor is resistant to proteolytic cleavage due to methylation mediated conformational blockade of protease recognition degron sequence, whereas mutant sensors with flexible open conformation are susceptible to proteolytic cleavage. The designed methylation sensors were highly competent and specific to sense changes in the methylation caused by methyltransferase enzymes specific to the H3:K9 which was further confirmed by treating cells expressing methyltransferase inhibitors, such as Bix01294 and UNC0638 and modulators like VPA, TSA. In vivo optical bioluminescence imaging in xenograft of stable cells expressing sensors found similar trend. The sensors developed from this study can be potentially used for the identification, and preclinical evaluation of drugs inhibiting methyltransferases, which can be used as therapeutic agents for treating various cellular diseases.

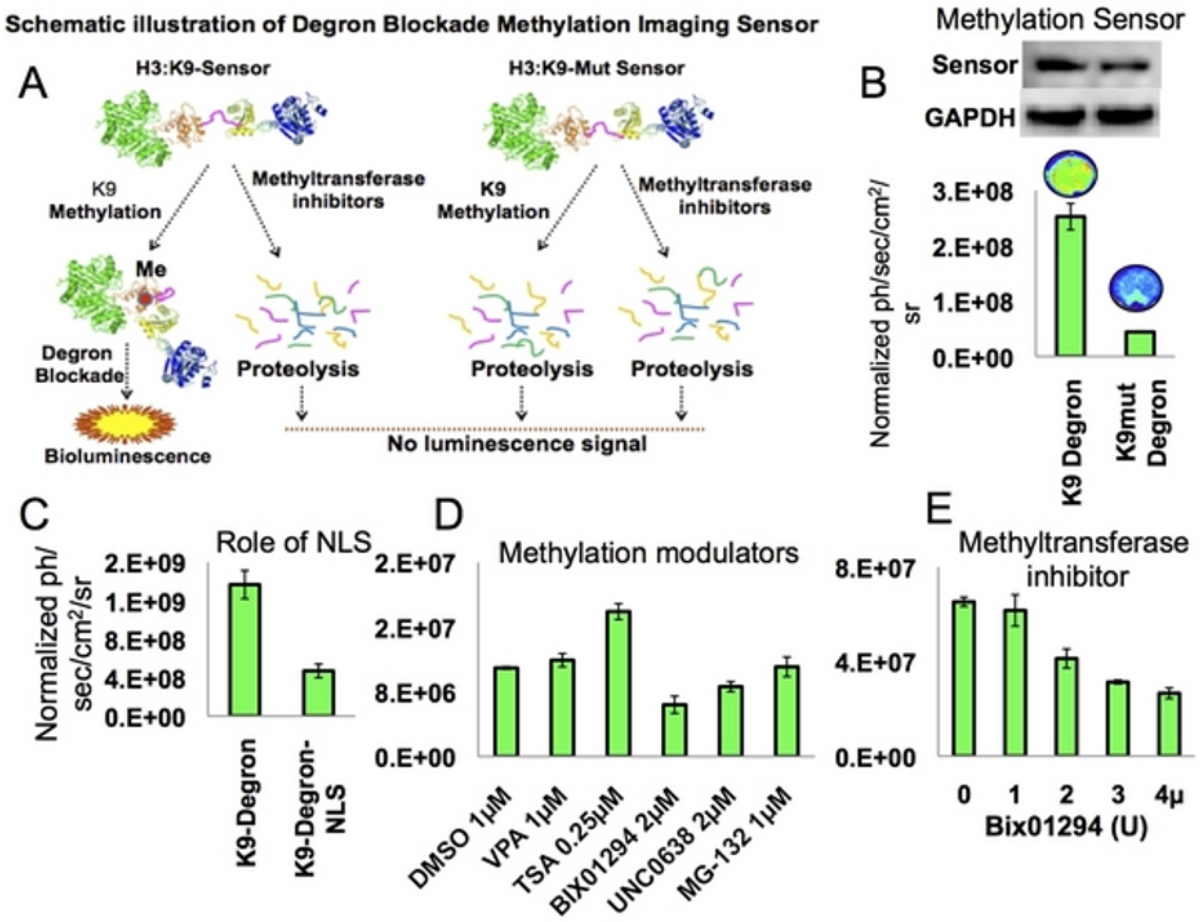

Disclosure of author financial interest or relationships:
T.V. Sekar, None; **K. Foygel**, None; **R. Paulmurugan**, None.

Presentation Number **SS 136**
Scientific Session 23: Preclinical Cell & Tissue Level Studies - Oncology
September 21, 2013 / 11:15-11:30 / Room: Oglethorpe Auditorium

Revealing Protein Biomarkers in Breast Tumor Models by combining MRSI and Mass Spectrometric Imaging

Lu Jiang[1], *Kamila Chughtai*[2], *Tiffany R. Greenwood*[1], *Gert B. Eijkel*[2], *Ron M. Heeren*[2], *Kristine Glunde*[1], [1]*Radiology Department - NMR Research - Oncology Section, JHU/APL, Baltimore, MD, USA;* [2]*Lab of Biomolecular Imaging Mass Spectrometry, FOM-Institute AMOLF, Amsterdam, Netherlands. Contact e-mail: ljiang12@jhmi.edu*

Introduction: The intensity of the total choline (tCho) signal in magnetic resonance spectroscopic imaging (MRSI) of tumors is elevated and spatially heterogeneous [1]. Our previous study [2] investigated the relationship between tCho and membrane phosphatidylcholine (PC) species detected by Matrix-assisted laser desorption ionization mass spectrometric imaging (MALDI-MSI). In this study, we further studied the correlations between tCho and proteins in a human breast cancer model by combining in vivo MRSI with ex vivo MSI. Methods: MDA-MB-231-HRE-tdTomato breast cancer cells were orthotopically grown in athymic nude mice. 3D MRSI to detect tCho was performed in vivo as previously described [3]. Each tumor was cryo-sectioned to perform MALDI-MSI on a Q-TOF instrument [2, 4] to detect trypsin-digested peptides. We fused MRI, MRSI, MSI images via fiducial markers and tumor shape characteristics [3]. 3D tCho volume was segmented into high-tCho (above 10% of the area under the histogram) and low-tCho areas. 2499 high- and 2500 low-tCho-containing voxels were selected randomly followed by principal component analysis (PCA) to reduce the data noise. 95% variance of the PCA projection data was analyzed by Fisher linear discriminant analysis (FDA) to classify high- and low-tCho-containing voxels. Loading spectra (m/z 1000-3000) of discriminant function 1 (DF1) were sorted to obtain the candidate m/z peaks that best differentiate between high- and low-tCho-containing voxels. These molecular m/z peak candidates were identified by searching a peptide AMT database with the resulting m/z values as keywords. Results: tCho (3.2 ppm) was observed by in vivo MRSI (Fig. A (1)). Peptides from hypoxia up-regulated protein 1 (HYOU1, m/z 1047.4) and from ribosomal proteins (m/z 1066.5, 1429.7, 2824.4) displayed the highest peaks in the DF1 loading spectrum. Fig. B shows the DF1 loading spectrum. Fig. C shows the scattering plot of FDA DF1 and DF2 scores. Fig. D lists the candidate molecular m/z peaks of tryptic peptides. Discussion and Conclusions: The HYOU1 peak (m/z 1047.4) was negatively correlated with tCho. HYOU1 is up-regulated by hypoxia [5] and is associated with poor prognosis in breast cancer [6]. However, in our previous study [3], tCho was increased in the hypoxic regions of breast tumors. The relative decrease of HYOU1 protein in high tCho regions is currently undergoing investigation in our lab. The ions m/z 1066.5, 1429.7, 2824.4 (ribosomal proteins) were positively correlated with high tCho regions. This suggests that increased biosynthesis of ribosomal proteins may happen in high tCho regions. All other identified tryptic peptides are currently undergoing further validation by ion fragmentation studies using MSI-based MS/MS methods. References: [1]. Glunde et al. (2011), NMR Biomed 24(6):673-90; [2]. Jiang et al. (2012), Abstract #: SS139, WMIC, Dublin, Ireland; [3]. Jiang et al. (2012), Neoplasia 14(8):732-41. [4]. Chughtai et al. (2012), Anal Chem, 84(4):1817-23. [5] Tamatani et al. (2001), Nature Medicine 7:317-323; [6] Stojadinovic et al. (2007), Med Sci Monit 13, BR231-239. Acknowledgements: This work was supported by NIH R01 CA134695.

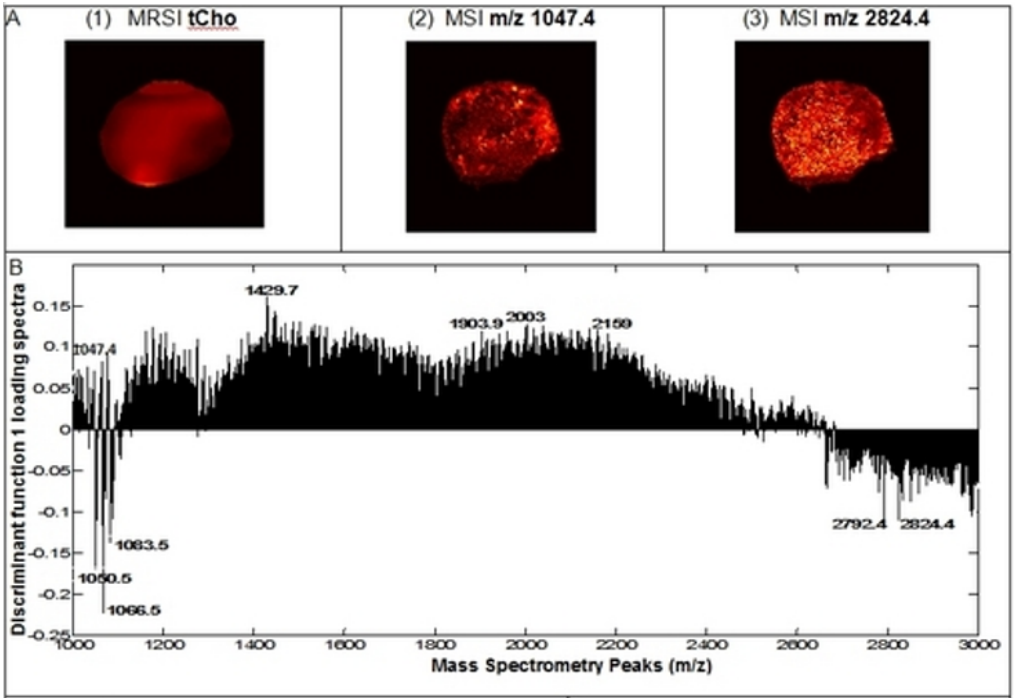

Candidate M/Z Peaks
1047.4
1050.5
1066.5
1083.5
1429.7
2159
2792.4
2824.4
2985.5

Figure A (1): MRSI tCho map (3.2 ppm) of breast tumor xenograft; and corresponding MALDI MSI map of m/z 1047.4 (Figure A (2)) and m/z 2792.4 (Figure A (3)). B: Discriminant function 1 loading spectra of 4999 randomly selected high-tCho-containing and low-tCho-containing voxels. C: Scattering plot of discriminant function 1 and function 2 scores obtained in the classification of high- and low-tCho-containing voxels. D: Candidate MALDI MSI peaks obtained by our data analysis.

Disclosure of author financial interest or relationships:

L. Jiang, None; **K. Chughtai**, None; **T.R. Greenwood**, None; **G.B. Eijkel**, None; **R.M. Heeren**, None; **K. Glunde**, None.

Presentation Number **SS 137**
Scientific Session 23: Preclinical Cell & Tissue Level Studies - Oncology
September 21, 2013 / 11:30-11:45 / Room: Oglethorpe Auditorium

Hyperpolarized MR/PET compatible bioreactor for mulit-modality investigation of metabolism in malignant cells and primary tissues

Kayvan Keshari, *Mark Van Criekinge, David M. Wilson, Zhen J. Wang, Bertram L. Koelsch, Renuka Sriram, Henry F. VanBrocklin, John Kurhanewicz, UCSF, San Francisco, CA, USA. Contact e-mail: rahimikk@mskcc.org*

Introduction: Aberrations in the metabolism of substrates, such as glucose and glutamine, have been linked to cancer and many other diseases[1]. As our knowledge of metabolism expands, platforms to facilitate non-invasive biochemical study and biomarker translation are needed. These systems, deemed bioreactors, provide an environment where cells and tissues can grow, and their response to perturbations studied[2]. Typically these systems are large and require a high cell-count (>10^8 cells) due to the low sensitivity of the techniques used. In this work, we report a novel 5mm MR/PET compatible bioreactor to explore the synergy of standard MR (Fig.A), hyperpolarized MR probes and PET in small cultures (~10^6 cells). We then extend this platform to living primary tissue slice cultures (TSCs) from prostate cancer patients. **Methods:** *Cell and TSCs:* PC-3 cancer cells were grown to 80% confluency in DMEM[2]. For TSCs, 8mm cores from radical prostatectomy specimens were sectioned and cultured[3]. *Bioreactor:*Cells were encapsulated in alginate[2]. TSCs were suspended in a custom designed cartridge. Both were perfused in an MR-compatible bioreactor[2]. *HP-MR:* Hyperpolarization was conducted by DNP using [1-^{13}C]pyruvate at 10mM[4]. PET: Studies used a small animal microPET/CT scanner. The bioreactor was perfused with medium containing 5μCi/mL of ^{18}FDG and washed out for 40min. *Correlative Studies:* Histology with H&E and KI-67. Lactate dehydrogenase (LDH) activity was assayed and qRT-PCR was used for the expression of GLUT1, HK2, monocarboxylate transporters (MCT1/4) and LDHA. **Results:** PC-3 cell encapsulates demonstrate reproducible ^{31}P NMR spectra similar to previously published, but here requiring a smaller culture (Fig.B). They demonstrated high conversion from HP pyruvate to lactate in real time, allowing for the capture of dynamic flux (Fig.C). HP Lactate generated was proportional to the cell density with a significant linear correlation. This same bioreactor was then placed inside a microPET detector and injected with FDG. After washout, uptake of FDG is observed in the bioreactor, scaling to cell density (Fig.D). Primary living human prostate TSCs were then studies in the bioreactor. TSC ^{31}P spectra, at only 4 slices and the equivalent of 20mg of tissue, demonstrated steady state bioenergetics analogous to significantly larger cultures[3]. Malignant TSCs demonstrated significantly increased HP lactate as compared to benign prostate (Fig.E). Interestingly, the level of HP lactate in the TSCs is nearly an order of magnitude lower than that of immortal cells when normalized to ATP. **Conclusions:** We have demonstrated the development and application of a novel combined MR/PET bioreactor capable of acquiring both MR and PET data on small cell cultures. It is amenable to translation to primary cultures and provides a multi-modality platform to explore the synergy of probes for the study of metabolism. Future work will apply novel probes to primary cultures and to assess response to therapy. **References:**[1]Ward Cancer Cell 2012 [2]Keshari Magn Reson Med 2010 [3]Keshari the Prostate 2013 [4]Keshari Cancer Res 2013 **Acknowledgements:** NIH K99EB014328, R21CA171766

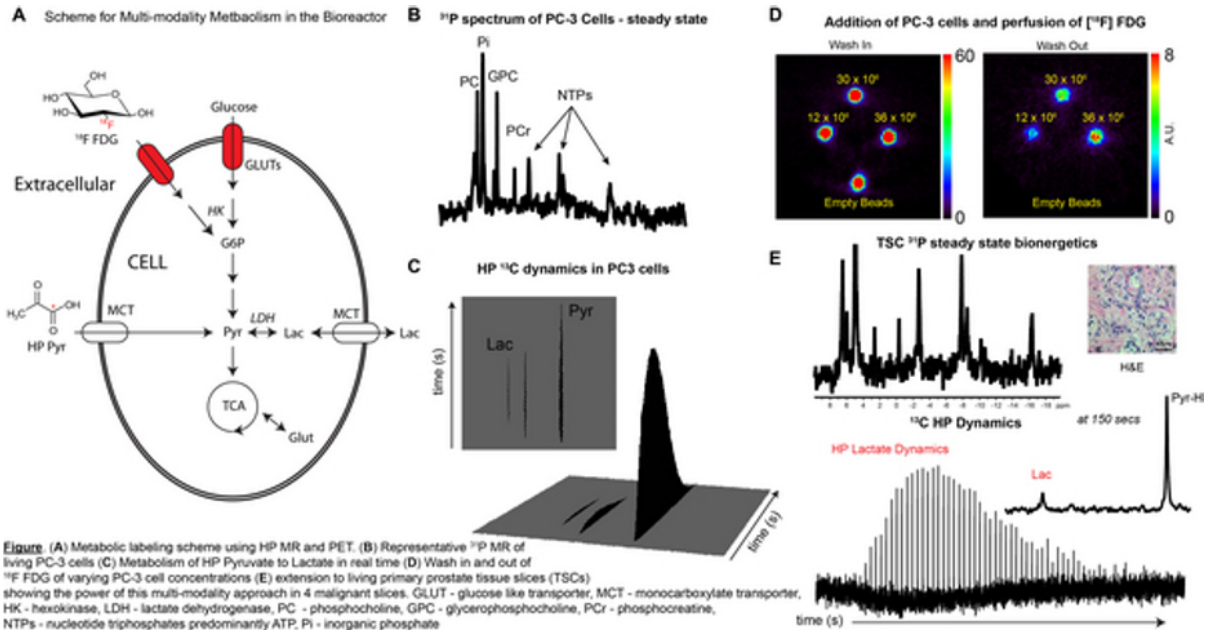

Figure. (**A**) Metabolic labeling scheme using HP MR and PET. (**B**) Representative ^{31}P MR of living PC-3 cells (**C**) Metabolism of HP Pyruvate to Lactate in real time (**D**) Wash in and out of ^{18}F FDG of varying PC-3 cell concentrations (**E**) extension to living primary prostate tissue slices (TSCs) showing the power of this multi-modality approach in 4 malignant slices. GLUT - glucose like transporter, MCT - monocarboxylate transporter, HK - hexokinase, LDH - lactate dehydrogenase, PC - phosphocholine, GPC - glycerophosphocholine, PCr - phosphocreatine, NTPs - nucleotide triphosphates predominantly ATP, Pi - inorganic phosphate

Disclosure of author financial interest or relationships:

K. Keshari, None; **M. Van Criekinge**, None; **D.M. Wilson**, None; **Z.J. Wang**, None; **B.L. Koelsch**, None; **R. Sriram**, None; **H.F. VanBrocklin**, None; **J. Kurhanewicz**, None.

Presentation Number **SS 138**
Scientific Session 23: Preclinical Cell & Tissue Level Studies - Oncology
September 21, 2013 / 11:45-12:00 / Room: Oglethorpe Auditorium

Rapid and Sensitive Imaging of Cancer Cells in Resected Human Breast and Lung Tissues by Novel Fluorescence Probes for GGT

Yasuteru Urano[1,5], *Mako Kamiya*[1], *Haruaki Hino*[1], *Koshi Mimori*[4], *Hiroki Ueo*[4], *Masayo Sakabe*[2], *Tetsuo Nagano*[2], *Hisataka Kobayashi*[3], [1]*Graduate School of Medicine, The University of Tokyo, Tokyo, Japan;* [2]*Graduate School of Pharmaceutical Sciences, The University of Tokyo, Tokyo, Japan;* [3]*National Cancer Institute, National Institute of Health, Bethesda, MD, USA;* [4]*Beppu Hospital, Kyushu University, Beppu, Japan;* [5]*Basic Research Program, Japan Science and Technology Agency, Tokyo, Japan. Contact e-mail: uranokun@m.u-tokyo.ac.jp*

We have synthesized and evaluated a series of hydroxymethyl rhodamine derivatives and found an intriguing difference of intramolecular spirocyclization behavior: the acetylated derivative of hydroxymethyl rhodamine green (Ac-HMRG) exists as a closed spirocyclic structure in aqueous solution at physiological pH, whereas HMRG itself takes an open non-spirocyclic structure. Ac-HMRG is colorless and non-fluorescent, whereas HMRG is strongly fluorescent. Based on these findings, we have developed a general design strategy to obtain highly sensitive fluorescence probes for proteases and glycosidases, by replacing the acetyl group of Ac-HMRG with a substrate moiety of the target enzyme. Specific cleavage of the substrate moiety in the non-fluorescent probe by the target enzyme generates a strong fluorescence signal. In order to confirm the validity and flexibility of our strategy, we designed and synthesized fluorescence probes for gamma-glutamyl transpeptidase (gGlu-HMRG), leucine aminopeptidase (Leu-HMRG), fibroblast activation protein (Ac-GlyPro-HMRG), and beta-galactosidase (bGal-HMRG). All these probes were almost non-fluorescent due to the formation of spirocyclic structure, but were converted efficiently to highly fluorescent HMRG by the target enzymes. We confirmed that the probes can be used in living cells. These probes offer great practical advantages, including high sensitivity and rapid response (owing to regulation of fluorescence at a single reactive site), as well as resistance to photobleaching. Among them, we have reported in the last WMIC meeting that gGlu-HMRG can visualize tiny tumor sites within a minute, even when they are less than 1 mm in size, by topically spraying onto tissue surfaces of cancer bearing mice that are suspected of harboring tumors. Furthermore, with many surgeons, we have been examining the efficacy of gGlu-HMRG with freshly resected real human tumor samples as an intraoperative tumor detecting agent. In this conference, we will discuss the results with resected human breast and lung cancer samples. We believe that the ease of spraying activatable fluorescence probes in open surgery or through catheters will provide alternative image guidance during treatment. References 1) T. Miura et al., J. Am. Chem. Soc., 125, 8666-8671 (2003). 2) Y. Urano et al., J. Am. Chem. Soc., 127, 4888-4894 (2005). 3) M. Kamiya et al., J. Am. Chem. Soc., 133, 12960-12963 (2011). 4) M. Sakabe et al., J. Am. Chem. Soc., 135, 409-414 (2013). 5) Y. Urano et al., Sci. Transl. Med., 3, 110ra119 (2011).

Disclosure of author financial interest or relationships:
Y. Urano, None; **M. Kamiya**, None; **H. Hino**, None; **K. Mimori**, None; **H. Ueo**, None; **M. Sakabe**, None; **T. Nagano**, None; **H. Kobayashi**, None.

Presentation Number **SS 139**
Scientific Session 24: Technology & Software Developments - Hybrid Multimodality, MRI
September 21, 2013 / 13:00-13:15 / Room: 102

Interventional Molecular MRI-Guided Local Delivery of Motexafin Gadolinium into Coronary Artery Walls

Yanfeng Meng[1], *Jinnan Wang*[2], *Jihong Sun*[1], *Feng Zhang*[1], *Patrick Willis*[1], *Jiakai Li*[1], *Han Wang*[1], *Tong Zhang*[1], *Stephanie Soriano*[1], *Bensheng Qiu*[1], *Xiaoming Yang*[1], [1]*Radiology, Univ Washington, Seattle, WA, USA;* [2]*Clinical Sites Research Program, Philips Research North America, Briarcliff Manor, NY, USA. Contact e-mail: mengyf@u.washington.edu*

Purpose: To develop a new technique, using interventional molecular MRI to monitor local agent delivery to coronary artery walls for potential molecular MRI-guided vascular gene therapy. Materials and Methods: The animal protocol was approved by the Institutional Animal Care and Use Committee. For in vitro confirmation, we used human arterial smooth muscle cells (SMCs) to determine (i) the capability of SMCs in uptake of Motexafin Gadolinium (MGd), a multifunctional intracellular T1 MR contrast/ anti-atherosclerotic agent; and (ii) the optimal MGd dose by exposing SMCs to MGd at different concentrations of 0, 50, 100, 150, 200, 300 μM and measuring T1 value of MGd at different concentration described above. For ex vivo evaluation, through a custom made infusion balloon, 2-mL MGd/trypan blue mixture was infused into the coronary arterial walls of six cadaveric pig heart under MRI monitoring by using either an MR imaging-guidewire (MRIG) and/or surface coils. For in vivo validation, the agent delivery balloon was placed into the coronary arteries of seven living pigs. MGd/blue mixture was infused into the arterial walls under MRI. Signal-to-noise ratio (SNR) and contrast-to-noise ratio (CNR) of the coronary arterial walls using different coils between pre- and post-agent infusion were compared, with subsequent histology confirmation. Results: SMCs could uptake MGd with the optimal concentration at 150μM. The average SNR with MRIG and surface coil combination was significantly higher than that with MRIG or surface coils only ($p<0.05$), and the average SNR and CNR of post-infusion images was significantly higher than that of pre-infusion images ($p<0.05$). Histology confirmed the successful intracoronary infiltration MGd/blue within the coronary arterial walls. Conclusion: This study demonstrates the possibility of interventional MRI to monitor the local delivery and distribution of multifunctional MGd in the coronary arterial walls, which establishes groundwork for development of interventional molecular MRI-guided local coronary gene therapy.

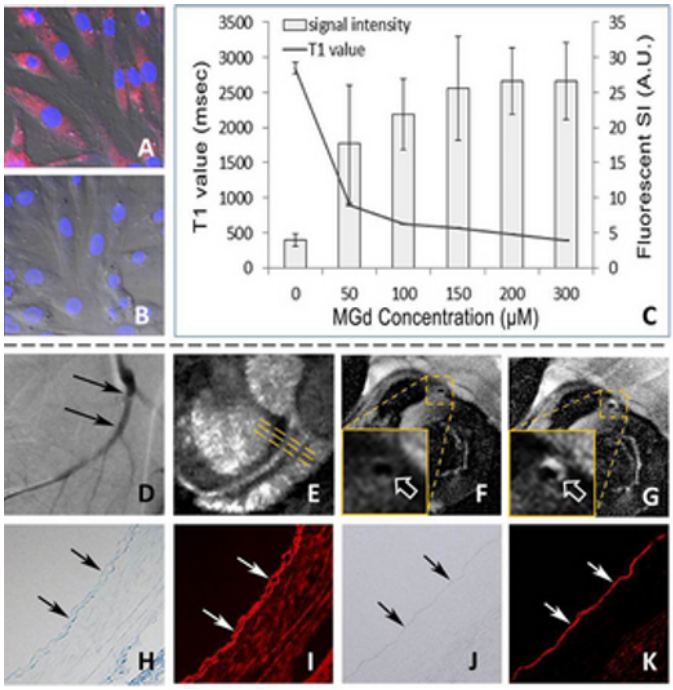

Figure: Upper row: (A&B) Confocal microscopy. MGd-exposed SMCs showed red fluorescent spots within the cytoplasm (A), compared to non-exposed control cells (B). Blue color indicates nuclei. (C) Average fluorescent signal intensity (SI) and T1 value plotted against MGd concentration for SMCs demonstrates that at 150-μM concentration SI begins to reach its maximum. Au=arbitrary unit. Lower row: In vivo MGd/blue infusion into the coronary artery walls. (D) Under X-ray imaging, the infusion balloon catheter is placed in the left anterior descending (LAD) coronary artery. Arrows indicate two markers of the balloon. (E) MR coronary angiogram shows the targeted LAD segment, cross which axial MRI is acquired. (F&G) Axial coronary arterial wall MRI pre-agent infusion (F) compared to post-agent infusion (G), showing enhancement of the artery wall (open arrows on insets of F and G). (H-K) Histology confirms blue dye deposit (H) and MGd-emitted red fluorescent spots (I) through the target coronary arterial walls, which are not seen in the control artery walls (J&K). Arrows indicate intima.

Disclosure of author financial interest or relationships:

Y. Meng, None; **J. Wang**, Philips Electronics, Employment; **J. Sun**, None; **F. Zhang**, None; **P. Willis**, None; **J. Li**, None; **H. Wang**, None; **T. Zhang**, None; **S. Soriano**, None; **B. Qiu**, None; **X. Yang**, None.

Presentation Number **SS 140**
Scientific Session 24: Technology & Software Developments - Hybrid Multimodality, MRI
September 21, 2013 / 13:15-13:30 / Room: 102

Reconstruction of Absorption and Scattering for Fluorescence Molecular Tomography

Felix Gremse[1], *Benjamin Theek*[1], *Sijumon Kunjachan*[1], *Wiltrud Lederle*[1], *Alessa Pardo*[2], *Stefan Barth*[2,3], *Uwe Naumann*[4], *Twan Lammers*[1,5], *Fabian Kiessling*[1], [1]*Experimental Molecular Imaging, RWTH Aachen University, Aachen, Germany;* [2]*Experimental Medicine and Immunotherapy, RWTH Aachen University, Aachen, Germany;* [3]*Pharmaceutical Product Development, Fraunhofer Institute for Molecular Biology and Applied Ecology, Aachen, Germany;* [4]*LuFG Informatik 12, RWTH Aachen University, Aachen, Germany;* [5]*Institute for Pharmaceutical Sciences, Utrecht University, Aachen, Germany. Contact e-mail: fgremse@ukaachen.de*

Introduction: Fluorescence molecular tomography (FMT) enables three-dimensional, non-invasive, highly sensitive and theoretically quantitative assessment of the fluorescence distribution in rodents. Its full potential for practical routine use is likely to be reached in combination with anatomical modalities such as Computed Tomography (CT), enabling unambiguous assignment of fluorescence to organs and lesions. Furthermore, the anatomical data can be used to derive an optical forward model useful for fluorescence reconstruction. Particularly absorption is strongly dependent on the hemoglobin concentration in tissue and therefore highly heterogeneous. In this study, we reconstruct the optical parameters and validate the absorption map against the relative blood volume determined with contrast enhanced µCT imaging. Furthermore, the effect on the fluorescence reconstruction is investigated. Methods: FMT-CT scans were performed using phantoms with a small inclusion filled with constant fluorescence and varying absorption. Similarly, 5 nude mice were imaged shortly after co-injection of CT and fluorescent blood pool contrast agents. Absorption and scattering maps were reconstructed by iterative minimization of a nonlinear cost function expressing the difference between predicted and measured boundary values. To compensate for ambiguities when separating absorption and scattering, regularization terms were included. To solve this complex and computationally demanding problem, algorithmic differentiation techniques were implemented on a massively parallel GPU-cluster. The relative blood volume (rBV) of several organs was determined by interactive segmentation and using the µCT data. Absorption, scattering and fluorescence were determined using the fluorescence reconstructions with and without using the absorption and scattering maps. Results: Phantom experiments show that absorption maps can be reconstructed qualitatively and quantitatively ($P<0.001$) with a voxel size of around 2.5 mm. Co-localized absorption significantly ($P<0.001$) reduces the fluorescence reconstructed using the normalized Born ratio. This is compensated using the reconstructed absorption and scattering maps. Usage of shape information improves the in vivo fluorescence reconstruction qualitatively. Reconstruction of absorption and scattering maps in vivo (mice, N=5) results in highly different and heterogeneous absorption across the analyzed organs ($P<0.05$) which correlates significantly with the CT-based relative blood volume ($P<0.001$). In vivo experiments show that the reconstructed fluorescence is significantly ($P<0.05$) suppressed in absorbing organs such as heart and liver when assuming homogeneous optical properties. Conclusion: Fluorescence reconstruction using the normalized Born ratio depends on a correct optical forward model to avoid systematic underestimation of fluorescence in strongly absorbing regions such as heart and liver. This may result in overly optimistic tumor-to-liver accumulation ratios when assessing the efficacy of fluorescence labeled agents. Reconstruction of absorption and scattering can provide such an optical model.

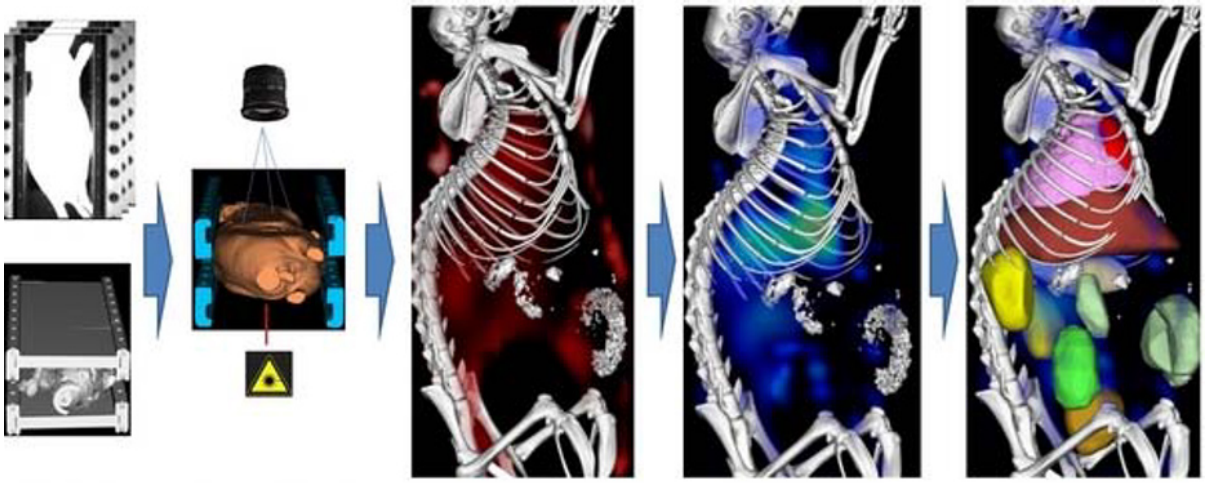

FMT-CT Imaging for biodistribution quantification. The image data is fused using markers in the multimodal mouse bed. Based on the µCT data, the mouse shape is segmented. Absorption and scattering are reconstructed based on the optical raw data and used as optical forward model for fluorescence reconstruction. Using interactive organ segmentation, the biodistribution is determined in vivo.

Disclosure of author financial interest or relationships:
F. Gremse, None; **B. Theek**, None; **S. Kunjachan**, None; **W. Lederle**, None; **A. Pardo**, None; **S. Barth**, None; **U. Naumann**, None; **T. Lammers**, None; **F. Kiessling**, None.

Presentation Number **SS 141**
Scientific Session 24: Technology & Software Developments - Hybrid Multimodality, MRI
September 21, 2013 / 13:30-13:45 / Room: 102

PET/MRI Insert Using Digital SiPMs: Investigation of MR-Compatibility

Jakob Wehner[1], *Bjoern Weissler*[1,2], *Peter Michael Dueppenbecker*[2,3], *Pierre Gebhardt*[3], *Walter Ruetten*[4], *David Schug*[1], *Fabian Kiessling*[1], *Volkmar Schulz*[1,2], [1]*Experimental Molecular Imaging, RWTH Aachen University Hospital, Aachen, Germany;* [2]*Philips Research Europe, Aachen, Germany;* [3]*King's College, London, United Kingdom;* [4]*Philips Research Europe, Eindhoven, Netherlands. Contact e-mail: jwehner@ukaachen.de*

Introduction To enable the full potential of hybrid PET/MR imaging, both imaging modalities have to work simultaneously. Especially fully digital Silicon photomultipliers (dSiPMs) offer a good timing, energy and spatial resolution and provide a good gain homogeneity which is essential for light-sharing techniques. They don't require complex protection against radio frequency (RF) disturbance and gradient switching, however they have the potential to generate digital electromagnetic noise patterns which might degrade the MR image quality. Thus proper PET system design and shielding is required to avoid interference between both imaging modalities. In this work, we present the current system design and investigations on interference between a fully digital PET scanner and a 3T clinical MRI. **Setup and Methods** The Hyperion-IID PET/MR insert (figure 1) consists of 10 PET Singles Detection Modules which are equipped with up to 2x3 detector stacks [1] whereas one of them consists of a crystal array, a light guide and an 8x8 dSiPM array [2,3,4]. The insert is designed to fit into a Philips Achieva 3T MRI system and is equipped with a dedicated PET transparent T/R mouse RF-coil (12 leg birdcage, high pass). The PET performance during simultaneous operation was studied with gradient dominated EPI sequences (EPI 9, TR=3s, slew rate: 198T/m/s) and RF intense TSE sequences (TSE 16, TEeff=402ms, TR=3s, FA=180°, B1= 25.7µT) while measuring a point source (2.8MBq) and Jaszczak phantom (6.9MBq). To investigate the RF interference on the MRI system, signal to noise ratio (SNR) measurements using SE sequences (TR/TE: 1000/50ms, VS: 0.25x0.25x1mm3, FA: 90°) as well as dedicated noise scans and experiments with sub-systems replacing the complete PET detector are performed. **Results and Discussion** A first evaluation of simultaneous acquired PET data shows no degradation of data quality and PET performance: flood map histograms, energy and spatial resolution remain unaffected during MRI acquisition. The singles data rates of the PET modules are stable even during harsh MRI sequences, but the SNR study of the acquired SE images (without and with PET) shows a degradation by a factor of two which is likely caused by common mode noise originating from the power supply unit (PSU) as experiments with resistive loads replacing the PET module have shown. First modifications of the PSU's shielding lead to a significant reduction of the RF interference. **Conclusion and Outlook** The PET detector initially performed stable even under harsh MRI sequences but causes a SNR decrease by a factor of two in the MR images. It could be shown that this SNR degradation is mainly caused by common mode noise originating from the power supply. First changes of the PSU's shielding show promising results. We will present a detailed interference and performance analysis at the conference.
References [1] Weissler et al., NSS/MIC 2012, M02-3; [2] Frach et al., NSS/MIC 2009, pp. 1959; [3] Degenhardt et al., NSS/MIC 2009, pp. 2383; [4] Dueppenbecker et al., NSS/MIC 2012, M18-2

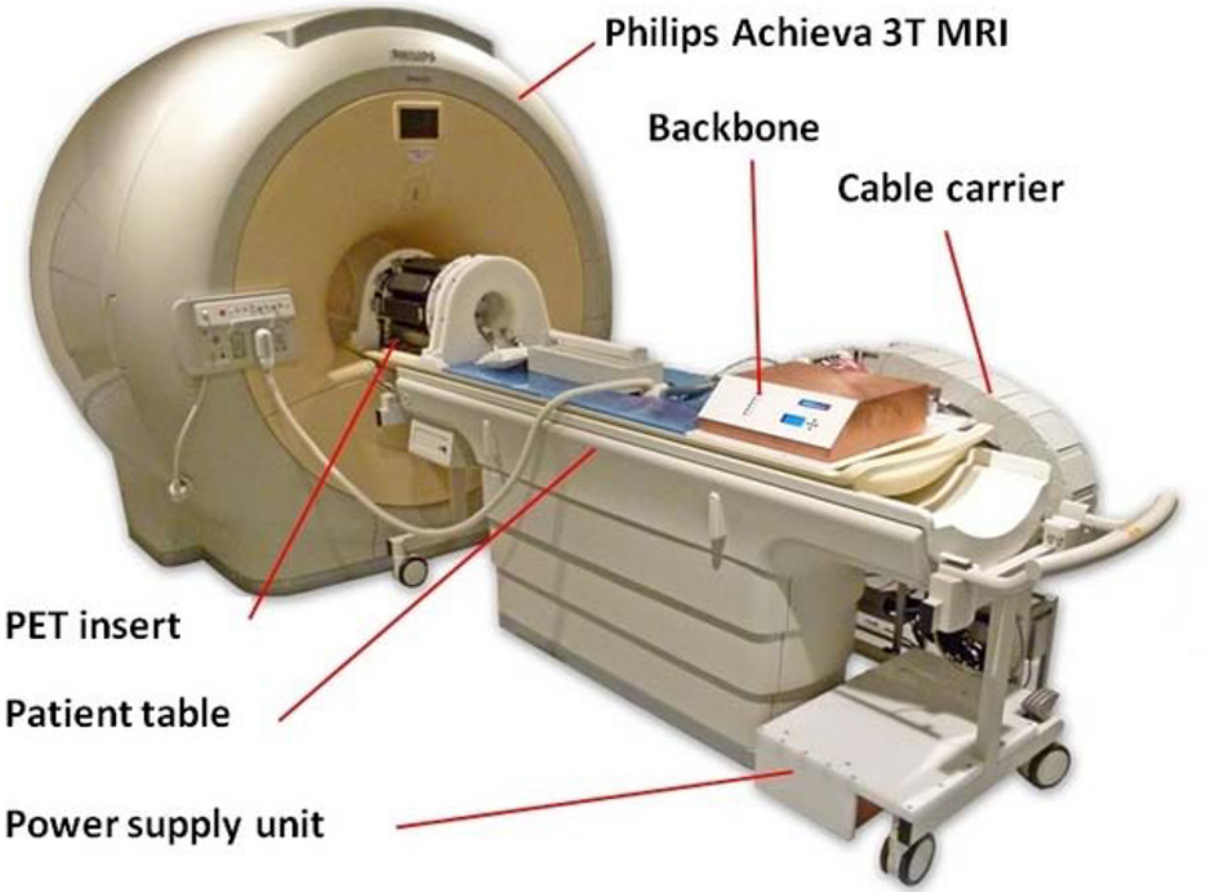

Figure 1: Hyperion-IID PET insert with 10 PET modules (2 stacks each) replacing the patient table top for a 3T clinical MRI

Disclosure of author financial interest or relationships:
J. Wehner, None; **B. Weissler**, Philips Research, Employment; **P. Dueppenbecker**, Philips Research Europe, Employment; **P. Gebhardt**, None; **W. Ruetten**, Philips Electronics Nederland B.V., (Philips Research), The Netherlands, Employment; Federal Ministry of Education and Research, Germany, Grant/research support; **D. Schug**, None; **F. Kiessling**, None; **V. Schulz**, Philips, Employment .

Presentation Number **SS 142**
Scientific Session 24: Technology & Software Developments - Hybrid Multimodality, MRI
September 21, 2013 / 13:45-14:00 / Room: 102

A Robust, Semi-Quantitative Imaging Strategy for Hyperpolarized MRI

Marc S. Ramirez[1], *Chris M. Walker*[1], *Jaehyuk Lee*[1], *Vlad C. Sandulache*[2,3], *Yunyun Chen*[2], *Stephen Y. Lai*[2], *James A. Bankson*[1], [1]*Department of Imaging Physics, The University of Texas M.D. Anderson Cancer Center, Houston, TX, USA;* [2]*Department of Head and Neck Surgery, The University of Texas M.D. Anderson Cancer Center, Houston, TX, USA;* [3]*Bobby R. Alford Department of Otolaryngology-Head and Neck Surgery, Baylor College of Medicine, Houston, TX, USA. Contact e-mail: marc.ramirez@mdanderson.org*

Introduction Hyperpolarized (HP) technology, such as dynamic nuclear polarization (DNP), can temporarily enhance the MR signal of exogenous 13C-labeled tracers, permitting noninvasive evaluation of metabolism in small-animal models of cancer. The rate of conversion from HP [1-13C]-pyruvate into HP lactate may be used as a biomarker of cancer since many malignant tumor cells maintain increased levels of anaerobic glycolysis. Unfortunately, there are limitations associated with HP 13C MRI, including a short activity time and irreversible signal loss due to radiofrequency (RF) excitation. Furthermore, optimal timing of the data sampling window depends on many biological and experimental factors, such as tracer handling, kinetics, and metabolism. We hypothesize that direct filtered backprojection (FBP) of radially-acquired HP data, acquired over the entire course of tracer activity, may provide a robust semi-quantitative estimate of tracer distribution that is insensitive to acquisition timing compared to traditional Cartesian encoding methods. Methods A numerical simulation was performed in which dynamic tracer curves were generated to correspond with regions of normal and tumor tissues in a two-compartment phantom. Evolution of tracer dynamics was based on a previously described kinetic model [1]. Variations in tracer arrival time, signal amplitude, and tracer activity were applied to increase phantom heterogeneity. Projections of the dynamic phantom were generated every 1 s, with 111° projection angle increments and constant 10° RF excitation angles. Metabolite images reconstructed by direct FBP were compared to the true mean polarization over time. In vivo imaging with this acquisition strategy was demonstrated in a mouse model of anaplastic thyroid cancer by using a radial echo planar spectroscopic imaging (EPSI) pulse sequence. Results Reconstructed pyruvate and lactate metabolite images from FBP data, that were sampled during the HP activity time-courses, are highly correlated ($R^2 = 0.92$) with the true mean over time. In vivo FBP metabolite images show elevated pyruvate signal in tissue proximal to cervical vessels and elevated lactate signal in tumor tissue. Conclusions Numerical simulations indicate a benefit for radial sampling of HP tracers compared to Cartesian sampling, where results depend heavily on the timing between tracer arrival and data acquisition through the center of k-space. Furthermore, radial spectroscopic imaging over the full duration of the polarized tracer is insensitive to the precise timing requirements of snapshot imaging, due to the continually changing ratio of HP pyruvate to HP lactate. References [1] Witney TH, et. al. Kinetic modeling of hyperpolarized 13C label exchange between pyruvate and lactate in tumor cells. J Biol Chem 2011;286(28):24572-24580. Funding sources include CPRIT grant RP101243-P5 and NCI grant P30-CA016672. Funding as an Odyssey Fellow was supported by the Odyssey Program and The Estate of C.G. Johnson, Jr.

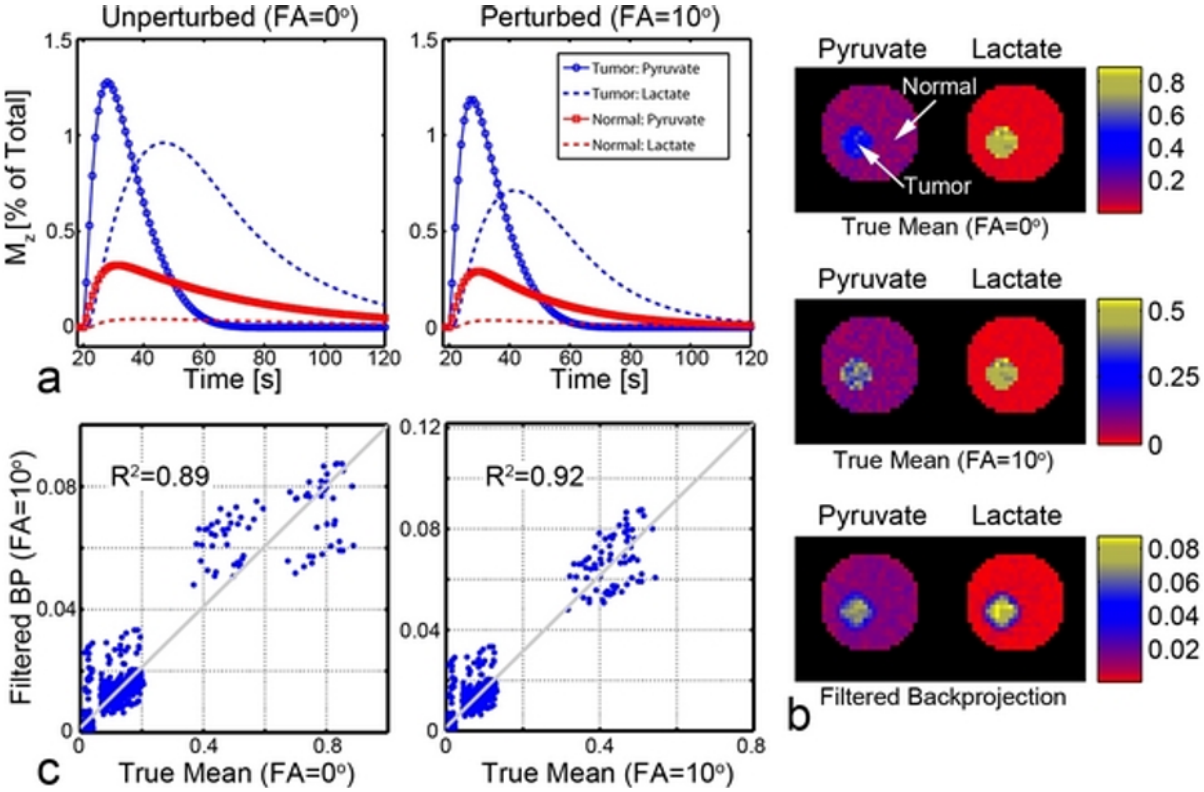

a) Representative time courses for normal and tumor compartments. Images of true temporal means are b) visually similar to FBP images and c) correlate well on a pixel-by-pixel basis.

Disclosure of author financial interest or relationships:
M.S. Ramirez, None; **C.M. Walker**, None; **J. Lee**, None; **V.C. Sandulache**, None; **Y. Chen**, None; **S.Y. Lai**, None; **J.A. Bankson**, None.

Presentation Number **SS 143**
Scientific Session 24: Technology & Software Developments - Hybrid Multimodality, MRI
September 21, 2013 / 14:00-14:15 / Room: 102

A MR-compatible PET Insert for Simultaneous High Resolution PET/MR Imaging

Martin S. Judenhofer[1], *Jian Zhou*[1], *Kun Di*[1], *Xiaowei Bai*[1], *Julien Bec*[1], *Yibao Wu*[1], *Yongfeng Yang*[1], *Richard Farrell*[2], *Kanai Shah*[2], *Jinyi Qi*[1], *Simon R. Cherry*[1], [1]*Department for Biomdecial Engineering, University of California, Davis, Davis, CA, USA;* [2]*Radiation Monitoring Devices, Inc, Watertown, MA, USA. Contact e-mail: msjudenhofer@ucdavis.edu*

We have built a next generation PET insert, which fits inside the 20 cm bore of a 7-T MRI scanner for simultaneous PET/MR imaging. This PET insert exhibits increased field of view and sensitivity as well as better spatial resolution compared to our previous system. The system employs a total of 96 block detectors arranged in 4 rings covering a FOV of 6.0 cm axially and 3.5 cm transaxially (limited by the RF coil). Each detector is composed of a 10x10 LSO array consisting of 1.2x1.2x14mm LSO crystal elements coupled to position sensitive avalanche photodiodes (PSAPD, 14x14 mm). The 4 anode contacts of each PSAPD are read out with charge-sensitive preamplifiers located inside the MRI but away from the MR iso-center leaving only LSO, PSAPDs, plastic support and RF shielding around the combined PET/MR imaging FOV. The PSAPDs are maintained at +5 C using chilled, dried air regulated by a temperature feedback loop. Using non-magnetic coaxial cable bundles all signals from the preamplifiers are carried outside the magnet to custom shaping electronics which process the signals to be accepted by dedicated PET processing electronics. MRI imaging is performed using a 35 mm ID RF transmit receive coil located within the PET insert. Comprehensive tests of the PET system comparing performance inside and outside the magnet were conducted. System performance and long term stability were investigated based on flood- and energy-histograms acquired with a cylindrical source (2 MBq) centered at the FOV while acquiring singles data. Imaging performance was evaluated based on measurements of a structured phantom and by imaging a mouse injected with [F-18]FDG inside the MRI scanner. For coincidence acquisitions a 350-650 keV energy window and 8 ns timing window was used. Phantom images were acquired at an initial activity of 8.5 MBq with and without MRI sequences running for 30 min each. A 21 g mouse was injected with 14 MBq of [F-18]FDG via the tail vein. After a 60 min conscious uptake period, PET and MR images were acquired simultaneously for 15 min. All data sets were reconstructed using a maximum likelihood expectation maximization (MLEM) algorithm with a direct data-based normalization. When inside the magnet, a PSAPD signal loss of 35% was experienced, which was compensated by a 10 V increase of the bias voltage. Average energy resolution (FWHM @ 511keV) of the system was 19% when measured outside and 22% when measured inside the magnet. Long term measurements showed good stability of the PET system with the average photopeak position variation remaining within 2%, both inside and outside the MRI. PET images (see figure) showed excellent quality (1.25 mm spatial resolution) with no visible artifacts introduced during MR imaging although a small count rate loss was observed during operation of MRI sequences. MR imaging was possible during PET data acquisition and PET/MRI data sets could be successfully fused. These initial results show excellent spatial resolution performance of this next generation PET insert covering a 6 cm axial FOV. Future work will focus on more detailed evaluation of the imaging performance and interference of the PET and MRI.

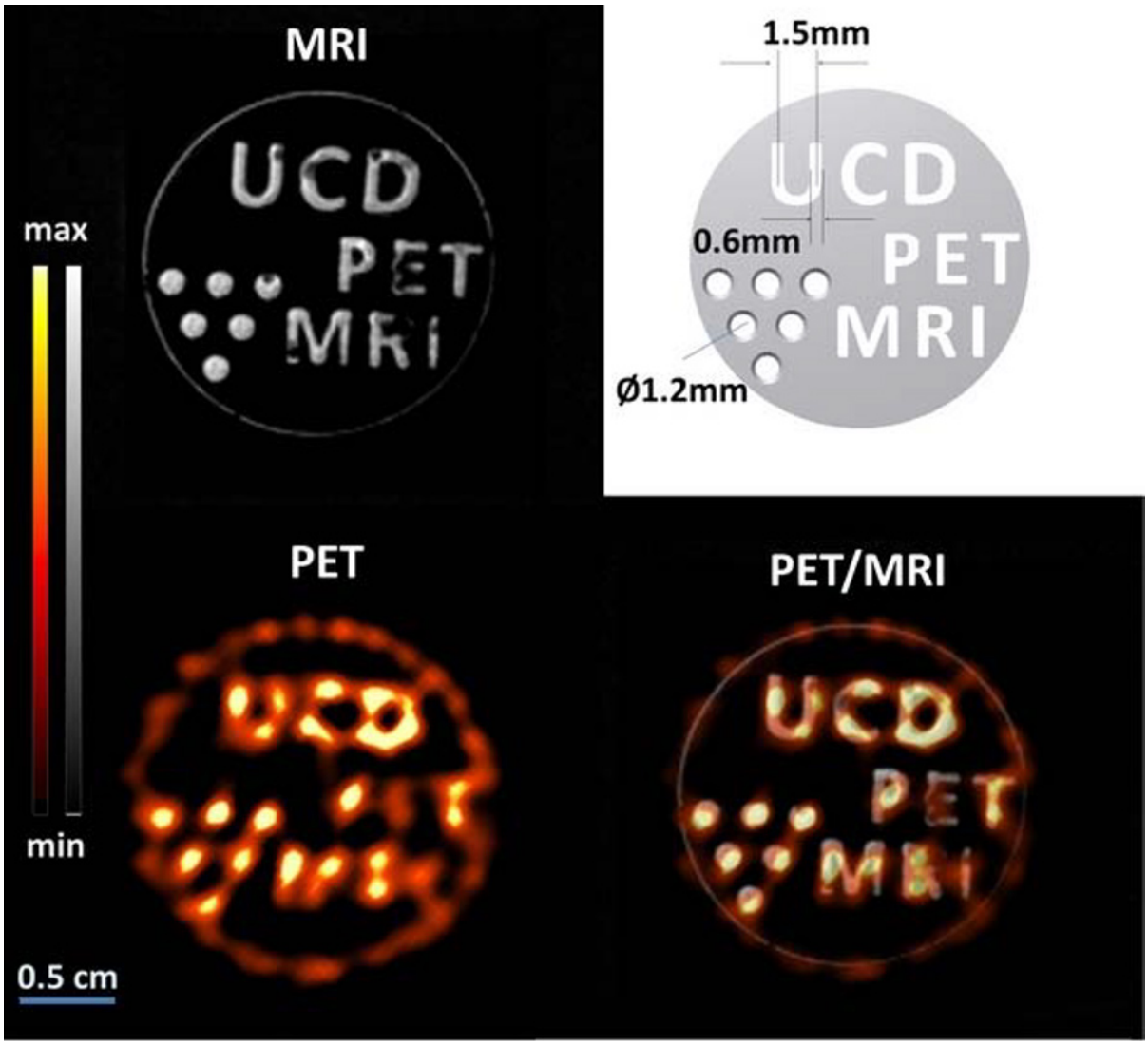

Simultaneous PET and MRI acquisition of a structured phantom filled with [F-18] solution. Structures down to 1.2mm can be separated in both, PET and MR

Disclosure of author financial interest or relationships:
M.S. Judenhofer, None; **J. Zhou**, None; **K. Di**, None; **X. Bai**, None; **J. Bec**, None; **Y. Wu**, None; **Y. Yang**, None; **R. Farrell**, None; **K. Shah**, None; **J. Qi**, None; **S.R. Cherry**, GE Healthcare, Grant/research support; Perkin Elmer, Grant/research support .

Presentation Number **SS 144**
Scientific Session 24: Technology & Software Developments - Hybrid Multimodality, MRI
September 21, 2013 / 14:15-14:30 / Room: 102

Evaluation of a Second Generation SPECT-MRI Insert for Simultaneous Dynamic SPECT-MR Imaging Studies of Small Animals

Benjamin M. Tsui, *Jingyan Xu, Andrew J. Rittenbach, AbdEL-Monem El-Sharkawy, William A. Edelstein, Department of Radiology, Johns Hopkins University, Baltimore, MD, USA. Contact e-mail: btsui1@jhmi.edu*

The aim is to evaluate a second generation SPECT-MRI Insert for simultaneous dynamic SPECT-MR imaging studies of small animals (SA). The second generation SPECT-MRI insert consists of 5 rings of 19 2.54x2.54 cm2, 16x16 pixels cadmium zinc telluride (CZT) detectors connected seamlessly. The CZT detectors directly convert incident photons into electric signals hence are minimally affected by the static magnetic field (Bo) of the MRI. A 36-pinhole (MPH) collimator was designed and constructed with a high-density tungsten powder and fitted with solid tungsten pinhole inserts. It had a 25 mm diameter common-volume-of-view (CVOV) with a target system resolution of 1.5 mm at its center. The geometric misalignment of the SPECT subsystem, uniformity and energy resolution of every detector pixel, and the Lorentz force effect were carefully measured, calibrated and corrected. Using a 3D quantitative sparse-view MPH ML-EM reconstruction method with modeling of the pinhole collimator detector response, artifact-free MPH SPECT images were obtained with no collimator or system rotation. A shielded transmit/receive RF coil for SA imaging fits inside the corresponding MPH collimator to improve SNR and to reduce interactions between the SPECT and MRI systems. The measured system resolution and sensitivity of the stand-alone SPECT subsystem with the 36-pinhole collimator agreed with the designed predictions and were measured to be ~1.25 mm and ~372 cps/MBq, respectively, at the center of the CVOV. Artifact-free high quality MPH SPECT images were obtained from experimental phantom studies using a Data Spectrum hot spot phantom and from small animal MPH SPECT studies using the SPECT subsystem. Placing the SPECT-MRI insert inside a 3T clinical MRI system, we demonstrated its feasibility for simultaneously SPECT-MR imaging study in experimental phantom studies. The simultaneously acquired SPECT, MR and the registered fused SPECT-MR images were in good agreement. In this work we performed a simultaneous dynamic SPECT-MRI kidney function study, a 30 min data acquisition in listmode format was initiated with a tail vein injection of ~2.5 mCi of 99mTc-MAG3. The listmode data were rebinned into 10-sec time frames before image reconstruction into 180 dynamic SPECT images showing the uptake and washout of 99mTc-MAG3 by the kidneys. Five 1-mm thick with 0.75 mm spacing coronal slices were acquired dynamically in 80 sec time frames for ~30 minutes using a multi-slice fast field echo (FFE) pulse sequence simultaneously with the SPECT data acquisition. The combined 30 min SPECT, MR and the fused SPECT-MR images again showed minimum artifacts and distortions. We continue to demonstrate the feasibility of simultaneous SPECT-MR imaging using the second generation SA SPECT-MRI insert. The 36-pinhole SPECT system allows dynamic data acquisition without collimator or system rotation. The high system resolution and detection efficiency with 25 mm diameter CVOV allows unprecedented high-resolution SA whole-body dynamic study as demonstrated by a 99mTc-MAG3 kidney function study in a mouse. Other SA applications using the SA SPECT-MR insert are being actively explored.

Disclosure of author financial interest or relationships:
B.M. Tsui, GE, Other financial or material support; Siemens, Grant/research support; Hybridyne Imaging Technologies, Consultant; Elmet, Consultant; **J. Xu**, None; **A.J. Rittenbach**, None; **A. El-Sharkawy**, None; **W.A. Edelstein**, None.

Presentation Number **SS 145**
Scientific Session 25: Preclinical Cell & Tissue Level Studies, Preclinical in vivo Studies - Infectious Disease, Reporter Genes & Signal Transduction
September 21, 2013 / 13:00-13:15 / Room: 105

Rapamycin Enhanced Adenovirus-mediated Cancer PET and Bioluminescent Imaging in Pre-Immunized Hosts

Ziyue Karen Jiang, *Diana Moughon, Lily Wu, Molecular Medical Pharmacology, University of California, Los Angeles, Los Angeles, CA, USA. Contact e-mail: jiangpkp@gmail.com*

Adenoviral vectors (Ads) that direct cancer-specific reporter gene expression are useful diagnostic tools. However, host immune responses against Ad have greatly limited the gene expression efficiency and clinical translation of viral vectors. Here, we explored the utilization of an immunosuppressant, rapamycin, to enhance the diagnostic applicability of Ads by augmenting both the robustness and the duration of Ad-delivered imaging reporter expression. Subcutaneous RM-9 tumors were established in their syngeneic immunocompetent hosts, C57BL/6 mice, and HSV-39tk-expressing PET-enabling Ad was administered intratumorally. Transient rapamycin treatment significantly enhanced reporter gene expression and thus permitted cancer PET imaging in all tested animals (n=4), which was not feasible in the control cohort (Fig. 1A). Next, immunocompetent C57BL/6 and FVB mice were inoculated intraperitoneally with Ad to develop pre-existing anti-Ad immunity 3 weeks before subcutaneous implantation of corresponding syngeneic prostate tumors. Firefly luciferase-expressing Ads were then intratumorally injected and bioluminescent imaging revealed that rapamycin pronouncedly augmented reporter gene expression and prolonged the imaging window from 7 to >21 days (Fig. 1B-C). Mechanistically, rapamycin dampened Ad-elicited innate immune reactions by inhibiting NF-κB activation and inflammatory cytokines secretion in BALB/c mice after intravenous viral administration. Furthermore, in the pre-immunization models, rapamycin not only markedly suppressed the secondary production of anti-Ad antibodies, but also retarded the infiltration and functional development of myeloid cells; the recruitment and activation of CD4+ T cells in the tumor as well as their responsiveness to Ad- and transgene-related stimuli were also repressed by rapamycin (Supplementary data). This study is the first to interrogate rapamycin's immunosuppressive effects in the context of Ad-based cancer molecular imaging with challenging host immunities. Rapamycin mitigated Ad-induced innate and adaptive immune responses, and thus increased the level and duration of Ad-conveyed reporter gene expression, rendering heightened imaging capability and diagnostic value of cancer-targeted Ad vectors in immunocompetent and pre-immunized murine hosts.

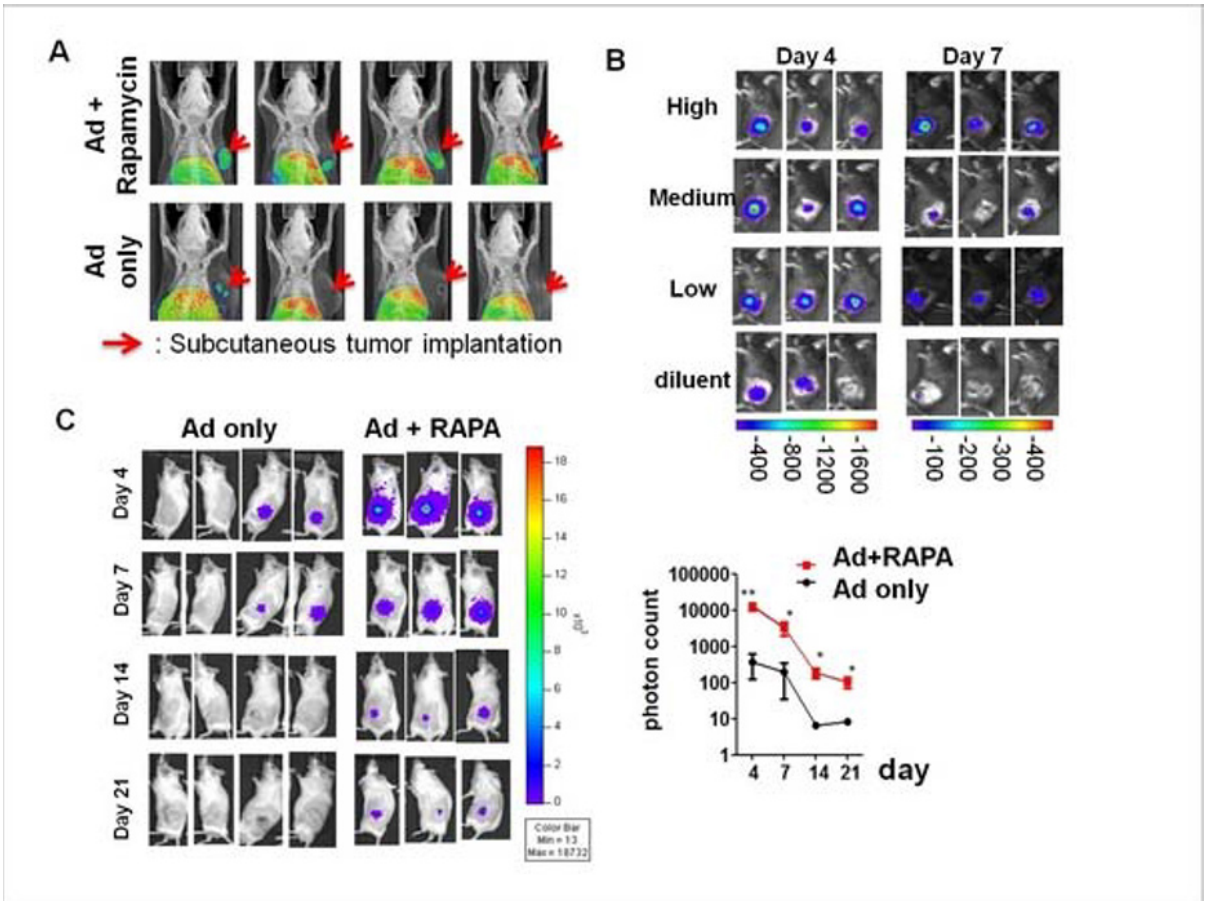

Rapamycin enhanced Ad-mediated cancer imaging. A. Male C57BL/6 mice carrying s.c. RM9 tumors received saline or rapamycin treatment for 4 days starting at 7 days post tumor implantation. Then, 5×108 PFU sr39tk-expressing Ad was injected intratumorally. PET imaging was performed 6 days later with 18F-FHBG. B-C. C57BL/6 (B) and FVB (C) mice were primed with an i.p. dose of 1×108 PFU Ad and, 3 weeks later, s.c. tumors were inoculated. RM9 tumors in C57BL/6 became palpable 4-5 days post implantation; MycCaP tumors in FVB became palpable in 5-7 days. Daily rapamycin or control treatment was then initiated and imaging Ads were administered 4 days later. Firefly luciferase bioluminescent imaging was conducted at indicated time points. High (5 mg/kg/day), medium (1.5) and low (0.5) doses of rapamycin were used for C57BL/6; 5 mg/kg/day rapamycin was used for FVB. Color bar: photon count. Error bars: mean ± SEM. * P<0.05, ** P<0.01 by two-tailed t test.

Disclosure of author financial interest or relationships:
Z. Jiang, None; **D. Moughon**, None; **L. Wu**, None.

Presentation Number **SS 146**
Scientific Session 25: Preclinical Cell & Tissue Level Studies, Preclinical in vivo Studies - Infectious Disease, Reporter Genes & Signal Transduction
September 21, 2013 / 13:15-13:30 / Room: 105

Increased brain phosphodiesterase type 4 (PDE4) in *Disc1* gene locus impairment mouse model imaged by [^{11}C](*R*)-rolipram PET

Talakad G. Lohith[1], *Tetsuya Tsujikawa*[1], *Sami S. Zoghbi*[1], *Hanna Jaaro-Peled*[2], *Yasuyuki Kimura*[1], *Cheryl L. Morse*[1], *Victor W. Pike*[1], *Akira Sawa*[2], *Robert B. Innis*[1], *Masahiro Fujita*[1], [1]*Molecular Imaging Branch, National Institute of Mental Health, Bethesda, MD, USA;* [2]*Department of Psychiatry, Johns Hopkins University School of Medicine, Baltimore, MD, USA. Contact e-mail: lohithtg@mail.nih.gov*

Purpose: The second messenger cyclic adenosine monophosphate (cAMP), a key signal transduction molecule is specifically hydrolyzed by phosphodiesterases (PDE). PDE type 4 (PDE4), which is selective to cAMP relative to cyclic guanosine monophosphate in brain, is regulated by protein kinase A (PKA) and by disrupted-in-schizophrenia 1 (DISC1). DISC1 suppresses the activity of PDE4, and mutations in DISC1 are involved in schizophrenia and mood disorders. Rolipram, a selective inhibitor of PDE4, has been labeled with carbon-11 ([^{11}C](*R*)-rolipram) for positron emission tomography (PET) imaging of in vivo activity of PDE4. By performing [^{11}C](*R*)-rolipram PET imaging of rat and by activating and deactivating PKA using dibutyryl-cAMP and Rp-adenosine-3',5'-cyclic monophosphorothioate, respectively, we showed for the first time that PDE4 is regulated by PKA in living animals (Itoh, et al. Synapse 2010). However, the role of DISC1 on PDE4 activity has not been shown in living animals. To investigate interactions between DISC1 and PDE4, this study compared [^{11}C](*R*)-rolipram binding in brain of *Disc1* gene locus impairment mice model lacking a large genomic region between exon 1 and 3 (DISC1 KO) and wild type (WT) mice. **Methods:** [^{11}C](*R*)-rolipram binding was measured by PET scanning under equilibrium achieved by bolus plus constant infusion for 90 min of the PET tracer in age-matched (3 months) DISC1 KO (n = 11) and WT (n = 9) C57BL/6 mice. Plasma levels of [^{11}C](*R*)-rolipram were measured in heart blood at the end of scan. [^{11}C](*R*)-rolipram binding in the whole brain was measured as total distribution volume V_T which is ratio of brain radioactivity in PET images to [^{11}C](*R*)-rolipram concentration in plasma at equilibrium. As only free ligand enters brain, V_T was corrected for plasma free fraction (f_P) of [^{11}C](*R*)-rolipram measured in a separate group of age-matched (3 months) DISC1 KO (n = 6) and WT (n = 7) mice. V_T/f_P equals B_{max}/K_D (binding site density / dissociation constant) plus nonspecific binding. **Results:** Average change in brain radioactivity per hour after 50 min scan time was -5 ± 6% for both mouse groups indicating equilibrium was achieved within the scan time. DISC1 KO mice showed a 41% significant increase in V_T (18 ± 6 vs. 13 ± 4 mL/cm^3, P = 0.04) compared to WT. The V_T/f_P, which more accurately reflects [^{11}C](*R*)-rolipram binding than V_T, showed a 73% significant increase (90 ± 31 vs. 52 ± 15 mL/cm^3, P = 0.004) in DISC1 KO compared to WT mice suggesting increased PDE4 activity in the presence of dysfunctional DISC1 protein. **Conclusion:** This study is the first to demonstrate that levels of PDE4, a key enzyme that regulates cAMP, is regulated by DISC1 in living animals. The increased rolipram binding to PDE4 in DISC1 KO mice is in line with several reports indicating that functional DISC1 represses PDE4 activity by binding to its active site. Combined with our previous work using PKA activator and inhibitor, we showed that PDE4 is regulated by both DISC1 and PKA in living animals. PET imaging of PDE4 activity

could facilitate development of drugs such as PDE4 inhibitors or monitor treatment in individuals affected with *DISC1* gene variants.

Disclosure of author financial interest or relationships:
T.G. Lohith, None; **T. Tsujikawa**, None; **S.S. Zoghbi**, None; **H. Jaaro-Peled**, None; **Y. Kimura**, None; **C.L. Morse**, None; **V.W. Pike**, None; **A. Sawa**, None; **R.B. Innis**, None; **M. Fujita**, None.

Presentation Number **SS 147**
Scientific Session 25: Preclinical Cell & Tissue Level Studies, Preclinical in vivo Studies - Infectious Disease, Reporter Genes & Signal Transduction
September 21, 2013 / 13:30-13:45 / Room: 105

Investigation of a novel PET tracer for imaging bacterial infections

Gayatri Gowrishankar[1], *Mohammad Namavari*[1], *Jonathan Hardy*[3], *Robert E. Reeves*[1], *Aileen Hoehne*[1], *Sanjiv S. Gambhir*[1,2], [1]*Radiology, Stanford University, Stanford, CA, USA;* [2]*Bioengineering, Stanford University, Stanford, CA, USA;* [3]*Pediatrics, Stanford University, Stanford, CA, USA. Contact e-mail: gayatrig@stanford.edu*

Background: The incidence of bacterial infections in hospitals worldwide is on the rise particularly with the emergence of several strains of resistant pathogenic bacteria (e.g., methicillin-resistant *Staphylococcus aureus*, multidrug-resistant *Streptococcus pneumoniae*, *Clostridium difficile*, etc.). Maltose is a natural substrate for most bacteria including many pathogenic strains of bacteria. These bacteria take up the maltose through a specific transport system which is absent in mammalian cells. We are developing a series of fluorinated PET tracers based on this bacteria-specific substrate. **Methods**: The uptake of 4-O-(α-D-glucopyranosyl)-6-deoxy-6-[18F]-fluoro-D-glucopyranoside (6-[18F]-fluoromaltose) was evaluated in bacterial and mammalian systems in culture. 5 x 10^6 colony-forming units (CFU) of a bioluminescent strain of *E.coli* was inoculated in the right thigh muscle of BALB/c mice (n=2). 24h later the mice were imaged on the IVIS 200 to check the viability of the bacteria. 100uCi of the 6-[18F]-fluoromaltose was then administered via tail vein and the mice were scanned on a small animal PET/CT scanner 45mins later. **Results**: The accumulation of 6-[18F]-fluoromaltose in the *E. coli* increased over time unlike in EL4 cells where its uptake was minimal at 60 mins post-incubation with tracer. The uptake in *E.coli* could also be blocked by a co-incubation with 1mM of cold maltose (98% blocking, $p < 0.0003$), the natural substrate of the transporter, confirming that the addition of the fluorine atom to maltose did not significantly perturb the transport of the tracer. The *in vivo* imaging showed that 6-[18F]-fluoromaltose clearly accumulated in the infected leg (Figure 1). ROI analysis showed that infected muscle had an average uptake of 7.7 ± 0.2 % ID/g (mean ± SD), 3.4 fold higher than the contra-lateral muscle. The route of clearance of the tracer is predominantly renal. **Conclusions**: 6-[18F]-fluoromaltose is a promising new tracer that is being evaluated for its ability to image and localize sites of bacterial infection. Our preliminary results *in vitro* and *in vivo* are encouraging and we are planning additional studies to evaluate the uptake of this class of tracers in a range of clinically relevant bacterial strains and murine models. These tracers will have potential impact in the clinical management of patients suspected of having bacterial infections. Determining the spread and extent of infection particularly in the case of patients admitted with wounds or with fever of unknown origin will help guide treatment protocols and reduce the morbidity and mortality associated with sepsis.

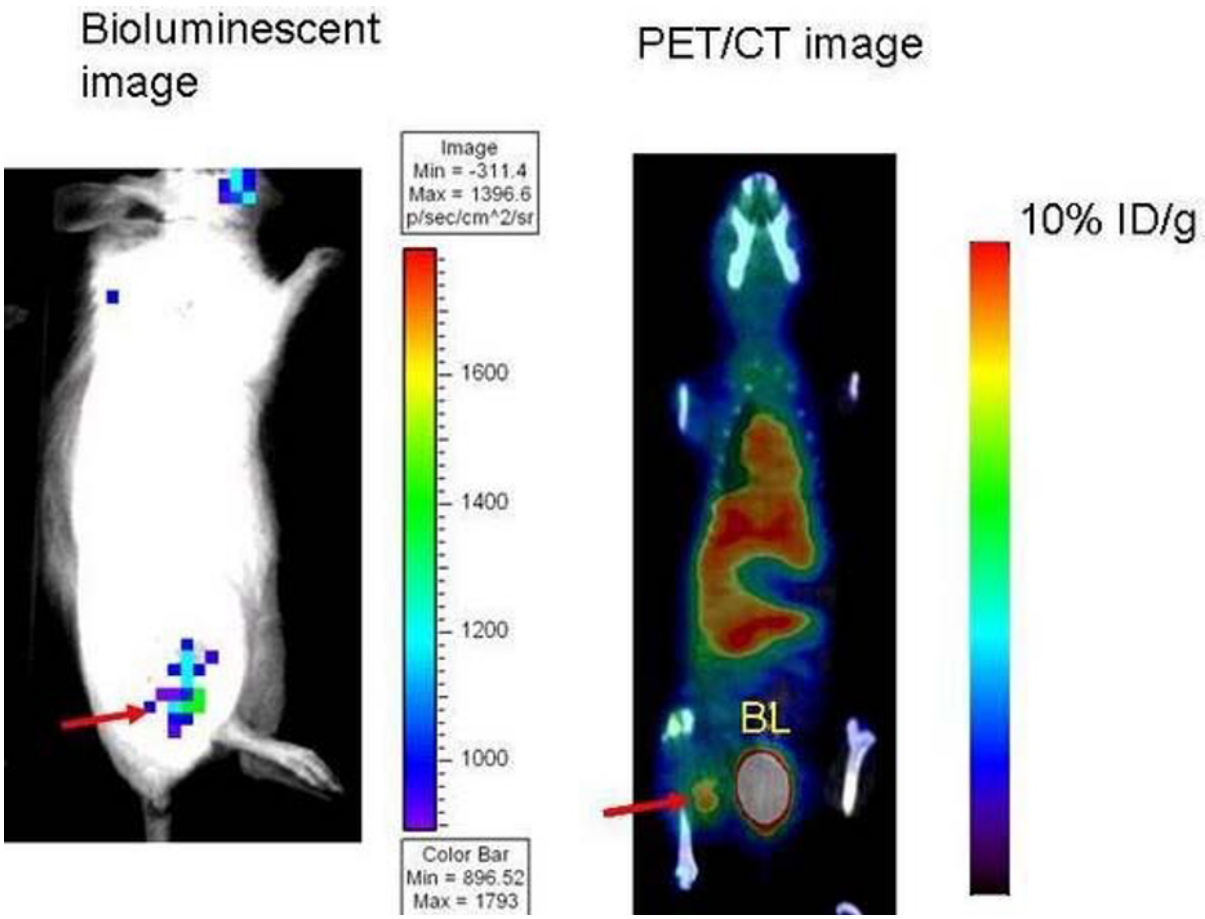

Figure 1: Bioluminescent image with mouse on its side and red arrow at infection site (left) and a coronal slice from a PET/CT image of a mouse with an E.coli infection on its right leg (arrow) 45mins after intravenous injection of 100uCi of 6-[18F]-fluoromaltose. Also seen is the bladder (BL).

Disclosure of author financial interest or relationships:

G. Gowrishankar, None; **M. Namavari**, None; **J. Hardy**, None; **R.E. Reeves**, None; **A. Hoehne**, None; **S.S. Gambhir**, Bracco Diagnostics, Consultant; Endra, Inc, Stockholder; Cellsight, Stockholder; Enlight, Inc., Stockholder; General Electric, Grant/research support; ImaginAb, Stockholder; MagArray, Inc., Stockholder; Sanofi-Aventis, US, Grant/research support; SiteOne Therapeutics, Stockholder; VisualSonics/Sonosite, Stockholder .

Presentation Number **SS 148**
Scientific Session 25: Preclinical Cell & Tissue Level Studies, Preclinical in vivo Studies - Infectious Disease, Reporter Genes & Signal Transduction
September 21, 2013 / 13:45-14:00 / Room: 105

SPECT Imaging of Bacterial Infection Using 111-Indium Labeled Molecular Probes

Douglas R. Rice[1], *Miles P. Smith*[2], *Yuzhen Wang*[2], *Adam J. Plaunt*[1], *Serhan Turkyilmaz*[1], *Mary Rusckowski*[2], *Bradley D. Smith*[1], [1]*Chemistry and Biochemistry, University of Notre Dame, Notre Dame, IN, USA;* [2]*Department of Radiology, University of Massachusetts Medical School, Worcester, MA, USA. Contact e-mail: drice1@nd.edu*

Purpose: Most molecular probes for infection imaging are unable to differentiate between inflammation and bacterial colonization. Zinc-dipicaloamine (Zn-DPA) ligands have high affinity for anionic cell membranes and fluorescent versions are known to selectively target bacterial cells over the nearly uncharged membrane surfaces of healthy mammalian cells. This study investigates SPECT imaging of gram-positive Streptococcus Pyrogenes (S. Pyrogenes) infection in mice using three novel Zn-DPA probes labeled with 111-In. Methods: Three Zn-DPA complexes were prepared and labeled with 111-In. Complex radiochemical purity was determined using reverse-phase HPLC. Direct tissue biodistribution studies were performed on CD-1 mice with an S. Pyrogenes leg infection 1 hour and 24 hours after dosing with probes (7 µg, 20 µCi). Whole body SPECT/CT imaging of CD-1 mice with a leg infection was obtained 0.8, 3.5 and 20 hours after intravenous probe injection (150 µg, 450 µCi). Results: All three Zn-DPA probes were complexed with radiopurities > 90%. Biodistribution studies revealed higher accumulation of probe in the infected leg than the blood and all organs other than the liver and intestines. High selectivity for the infected target leg (T) over the contralateral nontarget leg (NT) was reflected by T/NT ratios up to six. Whole-animal SPECT/CT imaging studies showed that intravenous dosing of Zn-DPA complex enabled detection of localized S. Pyrogenes infection with T/NT ratios up to four. Organ distribution varied greatly with probe structure suggesting that these probes have tunable properties for in vivo targeting optimization. Conclusions: Zn-DPA complexs are effective nuclear probes for detecting bacterial infection in living animals. With further development, these probes have potential utility as infection imaging agents within living patients.

Disclosure of author financial interest or relationships:
D.R. Rice, None; **M.P. Smith**, None; **Y. Wang**, None; **A.J. Plaunt**, None; **S. Turkyilmaz**, None; **M. Rusckowski**, None; **B.D. Smith**, None.

Presentation Number **SS 149**
Scientific Session 25: Preclinical Cell & Tissue Level Studies, Preclinical in vivo Studies - Infectious Disease, Reporter Genes & Signal Transduction
September 21, 2013 / 14:00-14:15 / Room: 105

2-[^{18}F]-Fluorodeoxysorbitol is a Novel PET Imaging Probe Specific for Enterobacteriaceae

Edward Weinstein[1,4], *Alvaro Ordonez*[2,4], *Elizabeth MacDonald*[2,4], *Mariah Klunk*[2,4], *Ronnie Mease*[3], *Sanjay K. Jain*[2,4], [1]*Medicine, Johns Hopkins University, Baltimore, MD, USA;* [2]*Pediatrics, Johns Hopkins University, Baltimore, MD, USA;* [3]*Radiology, Johns Hopkins University, Baltimore, MD, USA;* [4]*Center for TB Research, Johns Hopkins University, Baltimore, MD, USA. Contact e-mail: edward.a.weinstein@gmail.com*

Background: The Enterobacteriaceae is a family of gram negative bacteria that includes pathogens such as *Escherichia coli, Yersinia pestis, Klebsiella pneumoniae* and *Shigella*. Infection with these organisms is extremely serious with mortality approaching 50% in cases of sepsis. Early diagnosis of infection is essential for effective therapy, but traditional diagnostic methods are invasive, labor intensive, time consuming, and subject to incorrect sampling and contamination. As a result, imaging probes that can detect, quantify and monitor bacterial infections are urgently needed. Sorbitol is a sugar alcohol commonly used as a "sugar free" sweetener, yet is metabolized by prokaryotic-specific pathways. We describe our development of 2-[^{18}F]-fluorodeoxysorbitol ([^{18}F]FDS) as an imaging probe for infection by Enterobacteriaceae. Methods: We used a published method to generate [^{18}F]FDS from 2-[^{18}F]-fluorodeoxyglucose ([^{18}F]FDG) by chemical reduction in less than 30 minutes. Structure was confirmed by NMR and mass spectrometry. *In vitro* uptake assays exposed bacterial cultures to 0.037 Mbq per ml [^{18}F]FDS over 2 hours, then cells were washed and gamma counted. For *in vivo* studies, 5-6 week female CBA/J mice (n=3 per group) were immunosuppressed with cyclophosphamide then injected with 1x10^{7} *E. coli* in the right thigh and 50 µg LPS in the left thigh. 7.4 Mbq [^{18}F]FDS or [^{18}F]FDG was injected by tail vein 2 hours prior to collecting a static 15 minute frame. CT scans were performed for coregistration with PET images. Tissues were collected for direct gamma counting. Results: [^{18}F]FDS rapidly accumulated *in vitro* in *E. coli, K. pneumonia, C. freundii, S. enterica, E. cloacae*, but not in *S. aureus*, a gram positive control. *E. coli* yielded 68%±3% cell associated radioactivity at 120 minutes of exposure, and was therefore tested in an *in vivo* model. Immunosuppressed CBA/J mice were infected with live *E. coli* (right thigh) and LPS (left thigh). [^{18}F]FDS readily concentrated in the infected right thigh, gall bladder, intestine, and bladder, but not in the left thigh. [^{18}F]FDG produced an intense signal in the heart and bladder, but the infected right thigh was not easily distinguishable from other skeletal muscle. Following imaging, gamma counts of resected tissue indicated right thigh:left thigh SUV ratio of 16.37±3.38 for [^{18}F]FDS and 1.06±0.09 [^{18}F]FDG. Conclusion: [^{18}F]FDS is an easily synthesized, inexpensive probe that is selective for enterobacteria. The minimal background signal makes the probe an attractive candidate for visualizing infection in privileged compartments, such as the brain. The high signal to noise ratio is particularly promising at the high bacterial burden tested, but future studies will

aim to decrease the limit of bacilli detected. Clinically, the probe has numerous applications since the selection of antibiotics is roughly divided by activity against gram positive and negative organisms. Therefore, the distinction will dictate antibiotic choice and limit drug toxicity. Repeat imaging could monitor treatment efficacy, or suggest the presence of a drug resistant infection.

Disclosure of author financial interest or relationships:
E. Weinstein, None; **A. Ordonez**, None; **E. MacDonald**, None; **M. Klunk**, None; **R. Mease**, None; **S.K. Jain**
Grant/research support . , NIH,

Presentation Number **SS 150**
Scientific Session 25: Preclinical Cell & Tissue Level Studies, Preclinical in vivo Studies - Infectious Disease, Reporter Genes & Signal Transduction
September 21, 2013 / 14:15-14:30 / Room: 105

D-mannitol as a Bacteria-Specific Imaging Agent

Alvaro Ordonez[1], *Edward Weinstein*[2], *Sanjay K. Jain*[1], [1]*Department of Pediatrics, Johns Hopkins University, Baltimore, MD, USA;* [2]*Department of Medicine, Johns Hopkins University, Baltimore, MD, USA. Contact e-mail: aordone2@jhmi.edu*

Background While imaging has advantages of being rapid, non invasive and provides holistic whole organ/body analyses, standard anatomic imaging (CT, MRI) is neither sensitive nor specific for the diagnosis of bacterial infections. Moreover, though more sensitive, nuclear medicine imaging (99Tc-tagged WBC or [^{18}F]FDG-PET) have poor specificity in differentiating between sterile inflammation and infection. Therefore, bacteria-specific imaging tracers are required to discriminate infection from other disease processes, and to monitor treatment efficacy. Methods We performed an *in silico* analyses of over 400 radio-labeled random small molecules for participation in prokaryotic-specific metabolic pathways, absence of known eukaryotic metabolism, and evidence for bacterial accumulation. Potential candidates were then tested *in vitro* for intra-bacterial accumulation in exponentially growing bacterial cultures with 0.037 Mbq per ml [^{14}C] D-mannitol and in host-eukaryotic cells. Cells were washed and gamma counted. All assays were performed at least in triplicate. Results [^{14}C] D-mannitol was one of the most promising molecules identified by this screen. It accumulated rapidly and in significant amounts in all three models bacteria tested. Intracellular uptake was 66% ± 6%, 82% ± 7% and 83% ± 13% in *S. aureus*, *E. coli* and *M. smegmatis* respectively after only 2 hours of incubation. No uptake was observed in heat killed bacteria. Moreover, uptake in macrophage-like cells (J774) and human brain microvascular endothelial cells was <5% uptake at 2 hours. Presence of glucose in media did not decrease significantly the uptake of D-mannitol in *S. aureus* and *E. coli* indicating the existence of specific transport systems in these organisms. Conclusion D-mannitol is an inert sugar alcohol that has been extensively used in humans over the last 7 decades. It is neither synthesized nor metabolized by human cells but it is used as an energy source by bacteria. It is therefore a promising agent for development as a general bacteria-specific imaging tracer.

Disclosure of author financial interest or relationships:
A. Ordonez, None; **E. Weinstein**, None; **S.K. Jain**, NIH, Grant/research support .

Presentation Number **SS 151**
Scientific Session 26: Chemistry & Imaging Probes - Optical Imaging
September 21, 2013 / 13:00-13:15 / Room: 200

Dendritic upconverting nanoparticles - multiphoton probes for in vivo imaging and sensing

Tatiana V. Esipova[1], *Sava Sakadzic*[2], *Xingchen Ye*[3], *Joshua E. Collins*[4], *Christopher B. Murray*[3,5], *Sergei Vinogradov*[1],
[1]*Biochemistry and Biophysics, University of Pennsylvania, Philadelphia, PA, USA;* [2]*Optics Division, Athinoula A. Martinos Center for Biomedical Imaging, Massachusetts General Hospital/Harvard Medical School, Charlestown, MA, USA;* [3]*Chemistry, University of Pennsylvania, Philadelphia, PA, USA;* [4]*Intelligent Materials Solutions, Inc, Princeton, NJ, USA;* [5]*Material Science, University of Pennsylvania, Philadelphia, PA, USA. Contact e-mail: estachem@gmail.com*

We present a new class of optical imaging probes for in vivo depth resolved multiphoton microscopy. The probes comprise lanthanide-based upconverting nanoparticles (UCNPs), modified with biocompatible polyanionic dendrimers. UCNPs are capable of efficient upconversion of near-infrared excitation energy into visible light via multiphoton processes based on sequential absorption of two (or more) photons. Compared to conventional coherent multiphoton absorption, sequential absorption occurs via population of real (as opposed to "virtual") long-lived excited states of lanthanide ions. As a result, apparent two-photon absorption cross-sections of UCNPs are ~106-108 times higher than those of conventional dyes, making it possible to induce their emission using low-power continuous wave (cw) infrared sources. Such mode of excitation produces no auto-fluorescence and causes no photodamage, making UCNPs extremely attractive as probes for biological imaging. Unfortunately, lack of robust and efficient methods for UCNP solubilization and modification has significantly hampered their application in imaging. Here we show that shape-persistent dendrimers with rigid cores and multiple carboxylate groups at the periphery are able to tightly bind to surfaces of UCNPs pretreated with NOBF4, converting them in one step into stable water-soluble nanoprobes. Dendritic UCNPs possess excellent photostability, solubility and are directly suitable for in vivo applications. To demonstrate utility of the new agents, we used polyglutamic dendritic UCNPs and low power CW laser diode and performed mapping of mouse cortical vasculature with micron-scale resolution down to 400 μm under the brain surface, setting the first precedent of in vivo two-photon microscopy with CW sources. When cores of the dendrimers are chosen to be optically responsive to selected biological analytes (e.g. pH), UCNP-to-dendrimer energy transfer allows coupling UCNP emission to analyte-specific sensing via a unique ratiometric scheme. As an exmple, we demonstrate that UCNPs modified with polyglutamic porphyrin-dendrimers (UCNP/P-Glu4) are able to perform as multiphoton ratiometric pH-nanosensors. Such probes may find applications in multiphoton imaging of pH in tumors and other tissues where impaired metabolism results in acidification.

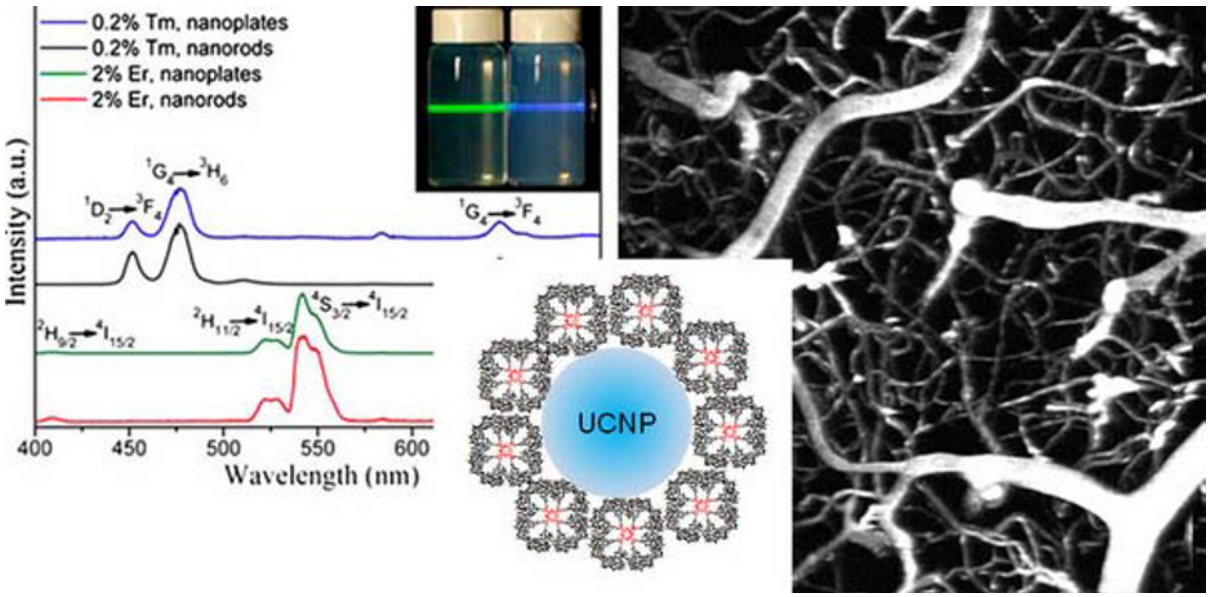

Disclosure of author financial interest or relationships:
T.V. Esipova, None; **S. Sakadzic**, None; **X. Ye**, None; **J.E. Collins**, None; **C.B. Murray**, None; **S. Vinogradov**, None.

Presentation Number **SS 152**
Scientific Session 26: Chemistry & Imaging Probes - Optical Imaging
September 21, 2013 / 13:15-13:30 / Room: 200

Distance Dependant Activatable Molecular Probes Powered by Cerenkov Radiation

Nalinikanth Kotagiri[1], *Dariusz M. Niedzwiedzki*[2], *Samuel Achilefu*[1], [1]*Radiology, Washington University School of Medicine, St. Louis, MO, USA;* [2]*Photosynthetic Antenna Research Center, Washington University in St. Louis, St. Louis, MO, USA. Contact e-mail: kotagirin@mir.wustl.edu*

Recently, Cerenkov radiation (CR) from highly energetic radioisotopes used in positron emission tomography (PET) has garnered attention because of its potential to serve as tissue depth-independent spontaneous light source. Thus, various forms of radiation or energy transfer processes can be used to excite molecular probes such as fluorescent dyes, nanoparticles, photosensitizers, and other light responsive materials at various tissue depths. We report herein for the first time an exciting discovery that spontaneous CR can be harnessed to report molecular events through distance-dependent activatable molecular constructs towards the development of optical-nuclear activatable probes powered by CR. Double stranded DNA (persistence length ~ 50 nm) was used as a ladder to control the distance of a PET isotope from quantum dots (QDs). Distance measurements of 64Cu-DOTA-ssDNA annealed at specified locations on the 99mer-QD adduct were determined through luminescence. At 1 nm distance, QD emission was 33±5% of the initial (control) value. Increasing the distance between radionuclide and QD surface from 1 nm to 31 nm resulted in a significant increase in the emission. In comparison to the control, the corresponding percentage values were 41±6, 47±3, 49±3, 52±3, 55±5, and 58±4 for 3.5 nm, 6 nm, 11 nm, 16 nm, 21 nm and 31 nm, respectively. Since Cu(II) is a known quencher, we investigated the effect of Cu(II) on the QD signal attenuation. Time resolved fluorescence studies determined the differences in the decay and fluorescence lifetime to be significant, from τ = 38.4 ns for the QD-DNA adduct to τ = 28.6 ns for the QD-DNA-Cu(II) construct. We suggest the quenching is due to ultrafast electron transfer from QD to Cu(II) via DNA facilitating charge separation followed by rapid non-radiative recombination with non-trapped hole leading to charge recombination from valence band in the QD. The PET-optical nanoruler was validated using both strand-displacement hybridization and hairpin probe approaches. In the strand displacement model, we observed a 45±7.5% increase in radiance after annealing the target 60mer to the 99mer that displaces the 10mer-DOTA-64Cu complex. In the hairpin probe design, upon annealing with its 60mer complement, luminescence increase of 22±6.5% relative to the initial value was observed. Therefore, integration of the design into simple DNA probes has yielded expected quenching and activation processes mediated by Cerenkov excitation. 64Cu can therefore serve as both a quencher and light source for highly sensitive detection of molecular processes. Careful alignment of the quencher groups at various distances from the QD provides distance-dependent quenching efficiency, allowing the use of CR in the design of activatable probes, with response up to 31 nm - a fit that is not attainable with traditional FRET systems. Importantly, the ensemble of the results holds promise for the potential use of the distance model to report molecular processes through tissue-depth independent excitation of activatable probes. We anticipate the application of this concept in optical-nuclear imaging of diseases and metabolic pathways in living systems.

Disclosure of author financial interest or relationships:
N. Kotagiri, None; **D.M. Niedzwiedzki**, None; **S. Achilefu**, None.

Presentation Number **SS 153**
Scientific Session 26: Chemistry & Imaging Probes - Optical Imaging
September 21, 2013 / 13:30-13:45 / Room: 200

Selective Bandwidth Quenching of Cerenkov Emission by Redox Activated Chromophores

Julie Czupryna, *Anatoliy V. Popov, Eric Blankemeyer, Alexander Kachur, Joel S. Karp, Edward J. Delikatny, Radiology, University of Pennsylvania, Philadelphia, PA, USA. Contact e-mail: czupryna@mail.med.upenn.edu*

Cerenkov emission occurs when charged β-particles emitted during radioactive decay exceed the speed of light in a dielectric medium, releasing the excess energy as photons. This phenomenon permits multimodal observation of β+-emitting probes, since in addition to PET imaging, the Cerenkov photons can also be imaged using bioluminescence optical imaging techniques routinely used in small animals. Cerenkov light emission is multispectral and continuous across the visible wavelengths. Thus absorption of a selected bandwidth of photons by a functional chromophore can attenuate the emission within a specific wavelength range and allow the measurement of a biological activity using a radiolabeled probe. This can be used to add real-time functional capabilities to PET imaging or as a stand-alone imaging modality. We have previously demonstrated the concept of selective bandwidth quenching by developing the first Cerenkov specific contrast agents. Electrophilically-fluorinated pH indicators were shown to report on pH both in vitro and in vivo through colorimetric quenching of Cerenkov emission. Here, we present the development of Cerenkov probes designed to report on another important biological phenomenon: the redox reaction. From cellular respiration to free radical interactions, the redox reaction is of great interest in vitro and in vivo. Using a similar model of colorimetric quenching, we show that Cerenkov emission can be selectively attenuated using two common cellular viability probes that report on mitochondrial function in whole cell in vitro assays: MTT and Alamar Blue. Reduction of these dyes leads to an irreversible color transition at wavelengths appropriate for Cerenkov imaging at redox potentials suitable for measuring biological function (Fig 1). In vitro, increasing the amount of reduced MTT quenched the Cerenkov emission from 18F-FDG in a dose-dependent manner. The reduction was greatest in the range 515-575 nm, near the maximum MTT absorption of 570 nm (Fig 1). No reduction in Cerenkov emission was seen at wavelengths greater than 650 nm, indicating that the selective bandwidth quenching has been achieved (Fig 1). With reduced Alamar Blue, the reverse effect was seen, a concentration-dependent increase in Cerenkov emission was observed in the 515-575 nm bandwidth corresponding with a change in maximum absorbance from 605 to 573 nm. Again, no reduction in Cerenkov emission was seen > 650 nm. When MTT was administered to intact MDA-MB-231 breast cancer cells in the presence of 18F-FDG, Cerenkov emission was selectively attenuated in proportion to the number of cells employed in the assay. These data indicate that redox status can be measured using Cerenkov imaging, and opens the possibility of measuring redox potential in vivo using radiolabeled redox probes. We believe that redox-sensitive Cerenkov probes could prove to be valuable in many areas of scientific research, ranging from antioxidant studies to oncology.

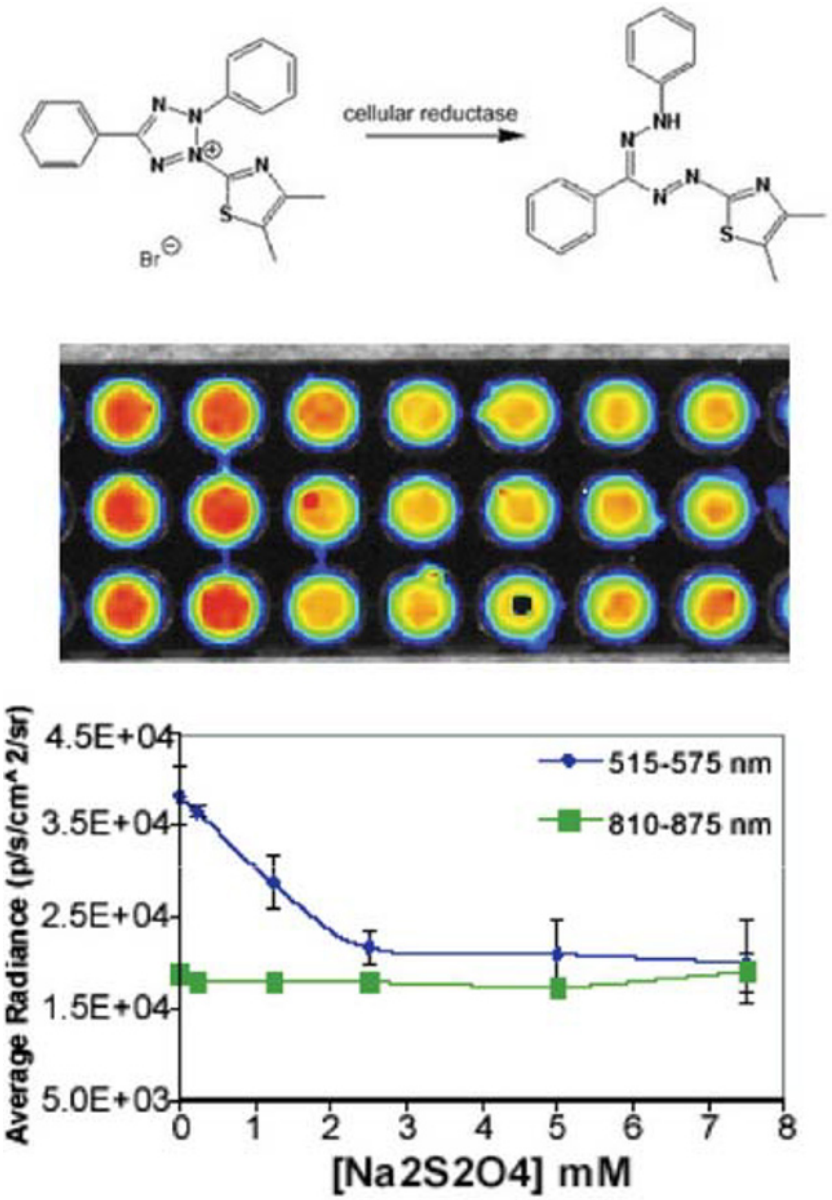

Figure 1 Top: Reduction of MTT by cellular reductases leads to the formation of a colored formazan dye with maximum absorbance at 570 nm (reaction scheme taken from Wikipedia). Middle: Reduction in Cerenkov emission (open filter) seen when 18F FDG is mixed with increasing amounts of reduced MTT. Bottom: Quantification of Cerenkov emission from 96 well plate data showing that emission is selectively quenched in the 515-575 nm bandwidth, near the MTT maximum absorption. No change is seen above 650 nm.

Disclosure of author financial interest or relationships:

J. Czupryna, None; **A.V. Popov**, None; **E. Blankemeyer**, None; **A. Kachur**, None; **J.S. Karp**, Philips Healthcare, Grant/research support; **E.J. Delikatny**, None.

Presentation Number **SS 154**
Scientific Session 26: Chemistry & Imaging Probes - Optical Imaging
September 21, 2013 / 13:45-14:00 / Room: 200

Polymer nanoparticle with persistent near-infrared luminescence shows potential for *in vivo* imaging

Mikael Palner, *Kanyi Pu, Jongho Jeon, Jianghong Rao, Radiology, Stanford School of Medicine, Stanford, CA, USA. Contact e-mail: mikael.palner@gmail.com*

Persistent luminescent materials have a prolonged emission of light after exposure to an excitation source, in contrast to fluorescence where immediate excitation/emission is required. Persistent luminescence is particularly useful for *in vivo* imaging, where enhanced signal to noise ratio is seen, because elimination of the immediate excitation lowers the background autofluorescence. Here we present the discovery and validation of a polymer nanoparticle (NP) with persistent near-infrared luminescence. The NP was produced using the reprecipitation method, with MEH-PPV as polymer, PS-PEG-COOH for the surface presentation of PEG, and a small molecule dye (NIR775) to enable near-infrared emission. The NP was excited with a 5 minute exposure to white-light from a surgical 3x60w spot light, and the luminescence and fluorescence emission spectra were recorded and compared. The NP clearly show persistent luminescence with an initial radiance of up to $1x10^7$ ($p/s/cm^2/sr$). The decay kinetics closely resembles a two-phase decay, which varies inversely with temperature changes; at RT, the first phase has a fast half-life of below 1 min and the second phase a slow half-life of 13-18 minutes. As control, no luminescence was detected from a similar NP using the polymer PFO-DPT. We injected four doses (5, 3.75, 2.5 and 1.75 µg) of excited NPs into the paws of two nude mice and imaged the luminescence with an IVIS-Spectrum bioluminescent imaging camera, using an acquisition time of 120 sec and open filter settings. The NPs were visible in the paw for at least one week (possibly because of continually excitation by room light). In another two nude mice we injected 15 ug excited NPs (1% EtoH:Saline) I.V. and followed the systemic distribution for over 25 minutes without the need for additional external excitation. MEH-PPV is known for its conducting and electro-luminescence abilities, also present in inorganic persistent luminescent materials. We propose — in a similar way as is described for persistent luminescent — that this conducting layer can absorb the energy from the excitation, and that the PS-PEG sidechains act as traps for the energy, releasing it slowly as luminescence. In conclusion, we present the first-generation of a novel polymer nanoparticle with persistent near-infrared luminescence and demonstrate a potential use as *in vivo* imaging probe. The big advantages of NPs over current inorganic persistent luminescent nanoparticles are; easier solvability, simpler conjugation chemistry for organic particles, modularity of the probe and tuning of emission wavelength through changing the encapsulated dye, and the resultant potential for multiplexed imaging. However, further experimentation into the luminescent mechanism is needed in order to optimize the polymer structure and produce brighter luminescence.

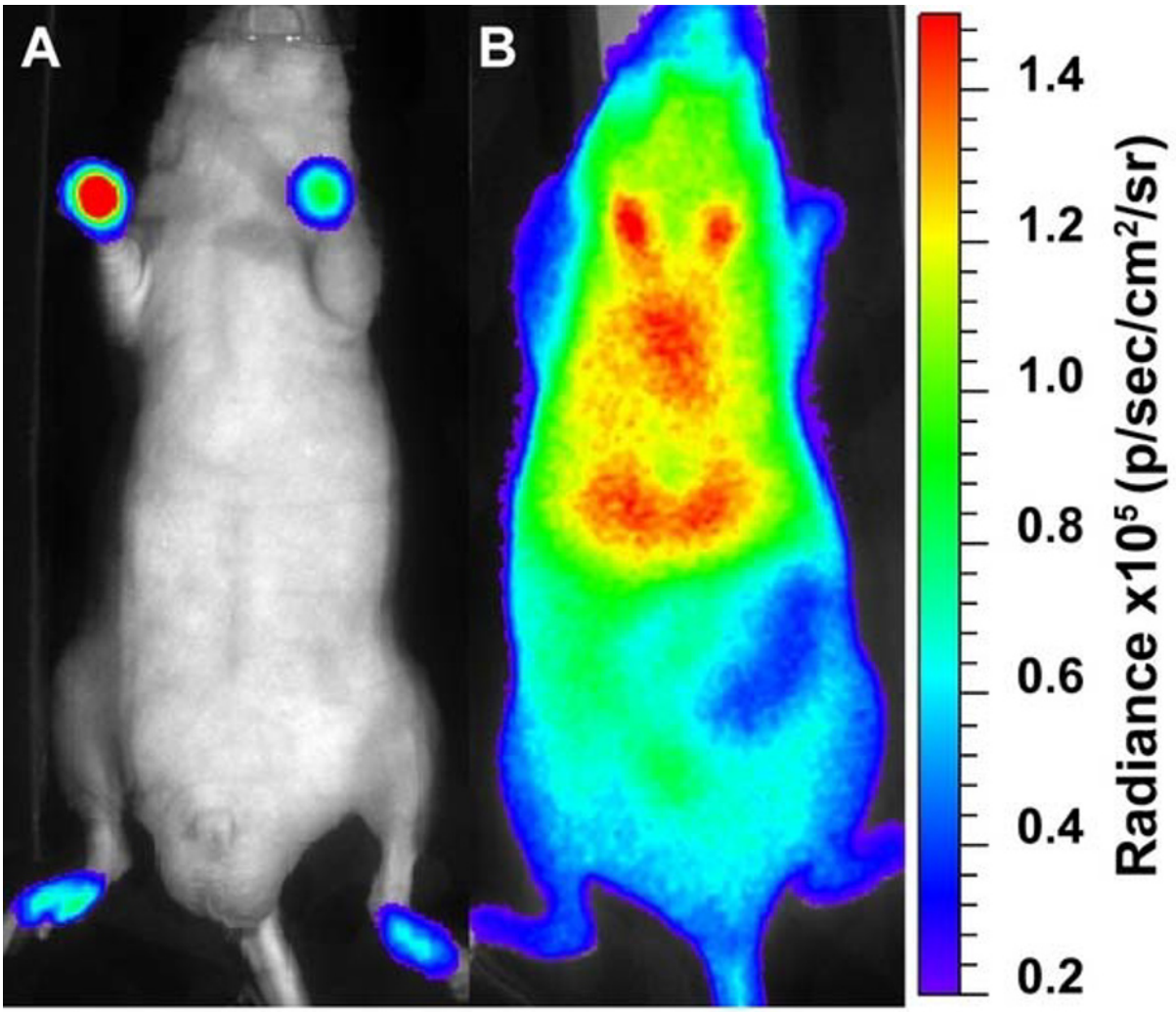

Two *in vivo* images, of a novel polymer nanoparticle with near-infrared persistent luminescent. Taken post injection of excited nanoparticles, with an acquisition time of 120 sec, using an IVIS Spectrum bioluminescent camera . A) At different concentrations (5, 3.75, 2.5 and 1.75µg) in the paws of a mouse. B) Systemic distribution in a mouse following I.V. injection of 15µg of nanoparticles.

Disclosure of author financial interest or relationships:
M. Palner, None; **K. Pu**, None; **J. Jeon**, None; **J. Rao**, None.

Presentation Number **SS 155**
Scientific Session 26: Chemistry & Imaging Probes - Optical Imaging
September 21, 2013 / 14:00-14:15 / Room: 200

Repeated Imaging of Cetuximab-IRDye800 in Non-Human Primates

Melissa L. Korb[1], *Sharon Samuel*[2], *Cheryl R. Killingsworth*[3], *David Dion*[4], *Trenton R. Schoeb*[5], *Eben L. Rosenthal*[6], *Kurt R. Zinn*[2], *[1]Surgery, University of Alabama-Birmingham, Birmingham, AL, USA; [2]Radiology, University of Alabama-Birmingham, Birmingham, AL, USA; [3]Animal Resources Program, University of Alabama-Birmingham, Birmingham, AL, USA; [4]Medicine-Division of Hematology and Oncology, University of Alabama-Birmingham, Birmingham, AL, USA; [5]Genetics Research Division, University of Alabama-Birmingham, Birmingham, AL, USA; [6]Surgery-Division of Otolaryngology, Head and Neck Surgery, University of Alabama-Birmingham, Birmingham, AL, USA. Contact e-mail: mlkorb@gmail.com*

Introduction: Near-infrared fluorescence imaging is a lucrative modality for real-time evaluation of blood flow and biomarkers associated with cancer detection and/or surgical resection. Little is known about this technology with respect to imaging whole animals or patients. There are also questions about the uptake of the imaging agents at wound sites, and the potential effect on wound healing. The goal of this experiment was to evaluate which organs may be visualized with the imaging bioconjugate cetuximab-IRDye800CW and how this agent affects wound healing in a preclinical model. Methods: Monoclonal antibody cetuximab was covalently linked to IRDye800CW (LICOR Biosciences) with confirmed antibody to dye ratio of 1.8, and retained immunoreactivity of cetuximab. Male cynomolgus macaques (n=4) were injected with cetuximab-IRDye800 at a dose of 20.83 mg/kg over 1 hour. SPY System (Lifecell, Branchburg, NJ) was used to collect images of the primates at several time points over a 15-day course. The images were analyzed for tissue fluorescence using Image J software with appropriate standards in the field of view. Results: Images of the thorax and abdomen had a homogenous and diffuse pattern of low-level fluorescence at each imaging point throughout the experiment; however, once the overlying tissues were removed at necropsy, the thymus, liver, and abdominal viscera had high fluorescence and appeared distinctly brighter than their surrounding tissues. Additionally, images of the oral cavity collected immediately pre- and post-mortem revealed that the post-mortem oral cavity had a substantial increase in fluorescence. Veterinary staff discovered that one submissive animal had minor abrasions on the right eye and left first digit from a dominant male. The injuries to the eye and digit were noted to have increased uptake of cetuximab-IRDye800CW, with wound to background ratios (WBR) of 3.0 and 4.6 respectively. Over the course of the experiment, complete healing was noted at both sites and the WBR decreased considerably. Conclusion: Tissue uptake of cetuximab-IRDye800 was high in areas that had undergone trauma; however the presence of the agent did not impair wound healing. The penetration of the imaging agent was severely limited by overlying tissues, despite high fluorescence in some of the underlying organs. These data represent novel findings in the area of near-infrared fluorescence imaging which will prove noteworthy as these agents move to the clinical realm.

Disclosure of author financial interest or relationships:
M.L. Korb, None; **S. Samuel**, None; **C.R. Killingsworth**, None; **D. Dion**, None; **T.R. Schoeb**, None; **E.L. Rosenthal**, None; **K.R. Zinn**, None.

Presentation Number **SS 156**
Scientific Session 26: Chemistry & Imaging Probes - Optical Imaging
September 21, 2013 / 14:15-14:30 / Room: 200

Investigation of Cyanine Dyes for *In Vivo* Optical Imaging of Altered Mitochondrial Membrane Potential in Tumors

Satoru Onoe, *Takashi Temma, Yoichi Shimizu, Masahiro Ono, Hideo Saji, Department of Patho-Functional Bioanalysis, Graduate School of Pharmaceutical Sciences, Kyoto University, Kyoto, Japan. Contact e-mail: onoe.satoru.67x@st.kyoto-u.ac.jp*

Objectives: Changes in mitochondrial membrane potential ($\Delta\psi_m$) due to mitochondrial dysfunction are associated with multiple characteristics of cancer, including reactive oxygen species production, oncogene expression, and increased cell proliferation. Therefore, *in vivo* imaging of $\Delta\psi_m$ could be applied to cancer diagnosis. For effective *in vivo* imaging, optical probes to detect $\Delta\psi_m$ should be lipophilic and cationic for efficient targeting to negatively charged mitochondria, and have fluorescence in the near-infrared (NIR) region. In this study, we designed cationic cyanine dyes with varying alkyl chain lengths (IC7-1 derivatives) that would have a wide range of lipophilicity and serum albumin binding rates with serum albumin functioning as an *in vivo* tumor targeting carrier, and evaluated their usefulness for *in vivo* $\Delta\psi_m$ imaging. Methods: IC7-1 derivatives having methyl to hexyl chains (IC7-1-Me to IC7-1-He) were synthesized and their optical properties in chloroform were measured. Cell microscopy was performed using HeLa cells incubated with IC7-1 derivatives. To evaluate the $\Delta\psi_m$ effect on cellular uptake of the IC7-1 derivatives, HeLa cells were treated with the probes and the uncoupler CCCP and the fluorescence intensities measured. The serum albumin binding rates of IC7-1 derivatives were evaluated using the albumin binding inhibitor warfarin and fluorescence measurement of probes in fetal bovine serum (FBS). For *in vivo* optical imaging, IC7-1 derivatives were intravenously administered to HeLa cell xenografted mice, and fluorescence images were acquired for 72 hr. For the *in vivo* blocking study, IC7-1-Bu and warfarin were co-administered to HeLa cell xenografted mice, and fluorescence images acquired for 72 hr. Results: IC7-1 derivatives showing maximum excitation and emission wavelengths of 823 nm and ~845 nm, respectively, were successfully synthesized. IC7-1-Me to Bu showed fluorescence in mitochondria that decreased with CCCP treatment in a concentration-dependent manner, showing that IC7-1-Me to Bu successfully indicated $\Delta\psi_m$. Warfarin significantly decreased the fluorescence of IC7-1-Bu in FBS compared to those of other derivatives, indicating a potent albumin binding rate of IC7-1-Bu. In an *in vivo* study, tumors were clearly visualized after IC7-1-Bu administration and tumor NIR fluorescence was sustained for up to 72 hr. In addition, co-administration of IC7-1-Bu and warfarin decreased IC7-1-Bu fluorescence at the tumor region. Conclusion: IC7-1-Bu showed fluorescence localized to the mitochondria of HeLa cells that was dependent on $\Delta\psi_m$. IC7-1-Bu also enabled clear tumor imaging *in vivo* using serum albumin as a drug carrier for effective tumor targeting. The results suggest that IC7-1-Bu is a promising NIR probe for *in vivo* tumor imaging.

Disclosure of author financial interest or relationships:
S. Onoe, None; **T. Temma**, None; **Y. Shimizu**, None; **M. Ono**, None; **H. Saji**, None.

Presentation Number **SS 157**
Scientific Session 27: Preclinical in vivo Studies - Oncology (Photoacoustic)
September 21, 2013 / 13:00-13:15 / Room: 203

Photoacoustic Imaging of Multiple Cell Biomarkers Within an in vivo Breast Cancer Model

Carolyn Bayer[1], *Geoffrey P. Luke*[2], *Stanislav Y. Emelianov*[1,2], [1]*Biomedical Engineering, The University of Texas at Austin, Austin, TX, USA;* [2]*Electrical and Computer Engineering, The University of Texas at Austin, Austin, TX, USA. Contact e-mail: carolynbayer@austin.utexas.edu*

Photoacoustic imaging with molecularly-targeted plasmonic nanoparticle contrast agents could provide a method to non-invasively diagnose and track the therapeutic response of breast cancer. To demonstrate multiplex photoacoustic molecular imaging, we have developed a mouse breast cancer model consisting of two tumor inoculations within the mammary fat pad region of a nude mouse - the first tumor was initiated with BT-474 cells, which over express the ErbB2/neu receptor, while the second tumor was initiated with MDA-MB-435 cells, which over express the αvβ3 integrin. After tumor growth, a mixed sample containing two specifically targeted silica-coated nanorods with optically distinguishable absorption spectra, was systemically introduced through a tail vein injection. By bioconjugating to monoclonal antibodies, one nanorod was targeted to the ErbB2/neu receptor, while the other was targeted to the αvβ3 integrin. Ultrasound and multiwavelength photoacoustic images were acquired using a Vevo 2100 small animal imaging system, with a 21 MHz linear array transducer custom-integrated with a Spectra Physics Nd:YAG with OPO tunable laser at different time points after the injection of the targeted contrast agents, and the wavelength-dependent photoacoustic signal was spectrally unmixed using a minimum mean squared error approach. The resulting correlations were used to identify endogenous contrast and the exogenous nanoparticles within the tumor regions. Immunohistochemistry and silver staining of tumor sections was used to confirm co-localization of nanoparticles and the over-expressed markers. The results (Figure 1) demonstrate that we are able to acquire strong photoacoustic signal within the tumor region. Additionally, we have acquired functional information from the same multiwavelength photoacoustic imaging data set; this functional information identifies the presence of regions of hypoxia within the tumor cores (Figure 1b), which is relevant to understanding the temporal changes in the tumor microenvironment. We are able to track the accumulation of specifically-targeted nanoparticles within the tumor regions (Figure 1c,d). Finally, we monitored the accumulation of the nanoparticles in tumors which have been treated with trastuzumab. As anticipated, the tumor overexpressing ErbB2/neu regresses with treatment, and shows decreased accumulation of the targeted nanorods over the course of one week. However, the αvβ3 integrin over-expressing tumor does not respond to trastuzumab. In summary, we present a model which can be used to demonstrate proof-of-principle, non-invasive multiplex photoacoustic imaging in vivo. We are using our model and imaging methods to elucidate functional and molecular information about tumors under treatment. Multiplex molecular imaging of breast cancer in vivo demonstrates progress towards a future where cancer therapies can be tailored to an individual's particular cancer phenotype. 1. Bayer CL, Luke GP, Emelianov S. Photoacoustic imaging for medical diagnostics. Acoustics Today. 2012;8(4):15-23.

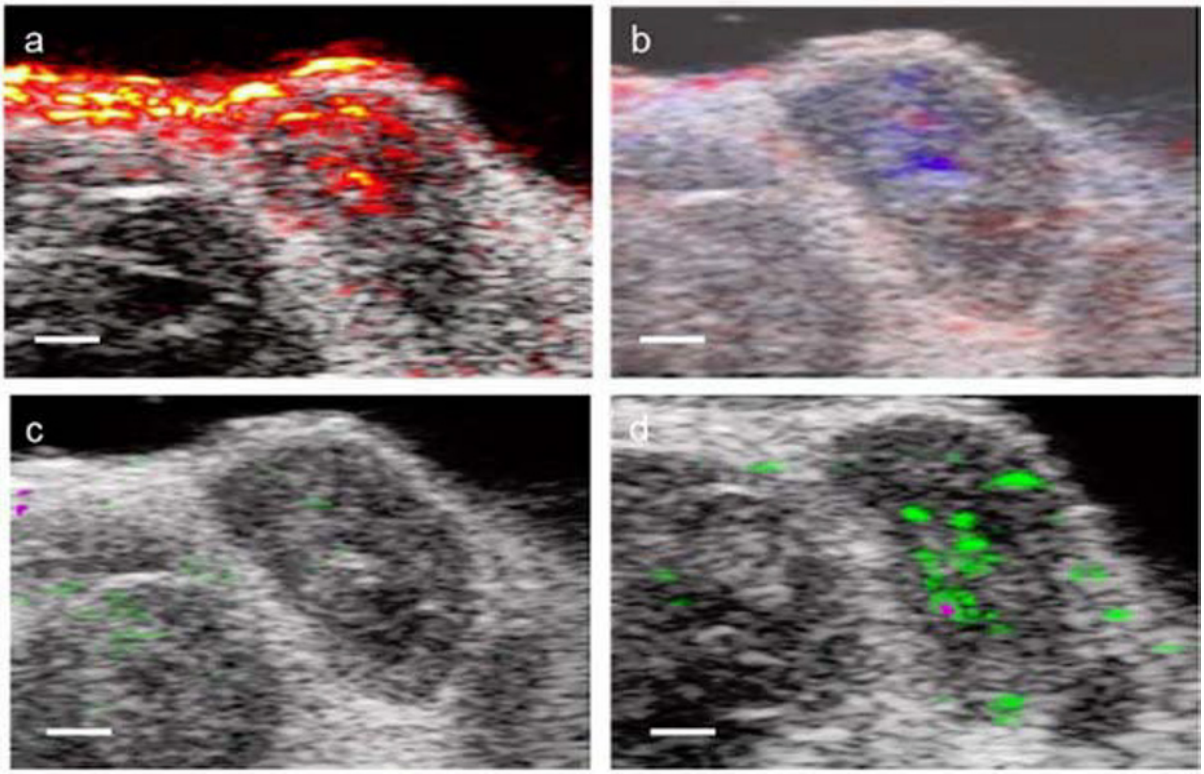

Figure 1: Combined ultrasound and photoacoustic imaging of a breast cancer tumor mouse model with multiplex photoacoustic contrast agents. a) Overlay of photoacoustic and ultrasound images of a ErbB2/neu tumor in vivo. b) Percent blood oxygen saturation maps from multiwavelength photoacoustic images show a hypoxic region within the tumors. c) Prior to nanoparticle injection, minimal photoacoustic signal can be seen matching the spectra of the injected contrast agents, while d) 24 hours after nanoparticle injection, a clear accumulation within the tumor region can be seen (1).

Disclosure of author financial interest or relationships:
C. Bayer, None; **G.P. Luke**, None; **S.Y. Emelianov**, NanoHybrids, Inc, Stockholder .

Presentation Number **SS 158**
Scientific Session 27: Preclinical in vivo Studies - Oncology (Photoacoustic)
September 21, 2013 / 13:15-13:30 / Room: 203

Photoacoustic molecular imaging and serum diagnostics rapidly detect response to anti-angiogenic therapy in ovarian cancer

Sarah Bohndiek[1,2], *Laura S. Sasportas*[1,2], *Steven Machtaler*[1,2], *Jesse V. Jokerst*[1,2], *Sharon S. Hori*[1,2], *Sanjiv S. Gambhir*[1,2], [1]*Radiology, Stanford University, Stanford, CA, USA;* [2]*Molecular Imaging Program at Stanford, Stanford University, Stanford, CA, USA. Contact e-mail: bohndiek@stanford.edu*

Introduction: There is an unmet clinical need to develop noninvasive biomarkers to detect early tumor responses to anti-angiogenic therapy. The combination of serum diagnostics, to monitor cancer-specific biomarkers in a low cost blood test, confirmed by photoacoustic imaging, to non-invasively visualize tumor vascular architecture and oxygenation, should yield a more effective approach than conventional measures of tumor volume. Trebananib is an angiopoietin 1 and 2 neutralizing peptibody in Phase III clinical trials, which displays potent antiangiogenic activity and has already shown efficacy in ovarian cancer patients (Phase II trial). The novel use of *in vitro* and *in vivo* biomarkers could help to select patients that will best respond to therapy, direct drug dosing and sensitively detect response to treatment. **Aim:** Our objective in this study is to assess the feasibility of photoacoustic imaging (*in vivo*) and serum diagnostics (*in vitro*) to monitor early response to Trebananib in ovarian cancer mouse models. These approaches could in the future be used in the clinic. **Methods:** Orthotopic ovarian tumors were established in nude mice by implanting $5x10^5$ 2008 human ovarian carcinoma cells stably expressing SEAP and FLuc-eGFP fusion protein directly into the ovary. Secreted alkaline phosphatase (SEAP) is a "gold standard" biomarker secreted from the ovarian cancer cells and was used to understand the impact of anti-angiogenic therapy on serum biomarker levels. Firefly luciferase (FLuc) was used to monitor tumor growth. The study design is shown in Fig. 1A; n=4 mice were used per treatment group. Photoacoustic imaging and a submandibular blood draw (<100 µL) were performed in mice with established tumors after each drug dosing of 5.6 mg/kg Trebananib or vehicle. Mice were sacrificed after 3 drug doses and tumors were excised for histopathology (H&E and CD31 staining). 3D regions of interest were drawn on reconstructed photoacoustic imaging volumes. SEAP concentration in plasma was evaluated using a chemiluminescence kit. **Results and Discussion:** No significant difference between treatment groups was observed based on tumor size (by BLI; $p=0.5$). The photoacoustic signal in the Trebananib treated group at 797 nm, representing total tumor hemoglobin concentration, declined by over 40 % by day 19 ($p<0.05$), while the ratio of the photoacoustic signals at 837 nm and 797 nm, representing oxygenation, increased significantly over the time course (2-way ANOVA; $p=0.01$). Uptake of intravenous indocyanine green (ICG, Fig.1B,C) was 40% lower in the treated group ($p<0.05$). Plasma SEAP concentration in the treated group was more than 30% lower at day 16, reaching a 40% reduction compared to vehicle at day 19 ($p<0.05$). These results were supported by a significant reduction in vessel density ($p<0.05$) by CD31 staining. Our data show that both photoacoustic imaging and serum biomarker measures can detect the changes in tumor vascular architecture after Trebananib treatment and may therefore provide sensitive biomarkers of response. Importantly, this work supports the use of both *in vitro* and *in vivo* diagnostics to monitor response to anti-angiogenic therapy.

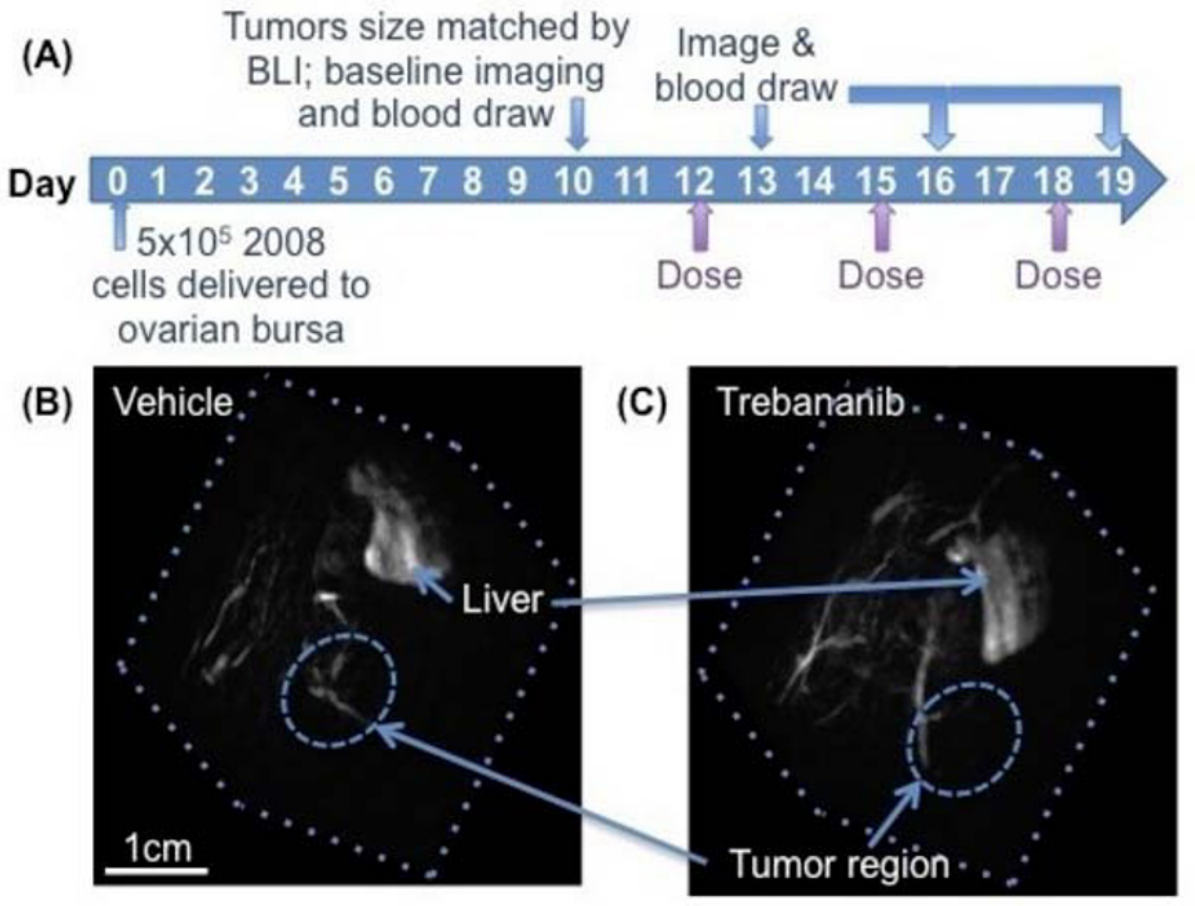

Figure 1: The study design is shown in (A). Tumors were size matched at day 10 by bioluminescence imaging (BLI) and divided into "Vehicle" or "Trebananib" treated groups (n=4 per group). Photoacoustic imaging was performed using both endogenous hemoglobin contrast (at 757, 797 and 837 nm) and injected indocyanine green (ICG; at 790 nm). Images shown in (B) and (C) were acquired on day 16 at 790 nm immediately post injection of ICG. The tumor region is outlined and the liver marked for anatomical reference. The uptake of ICG in the Trebananib treated tumor is clearly reduced compared to the vehicle treated control.

Disclosure of author financial interest or relationships:

S. Bohndiek, None; **L.S. Sasportas**, None; **S. Machtaler**, None; **J.V. Jokerst**, None; **S.S. Hori**, None; **S.S. Gambhir**, Bracco Diagnostics, Consultant; Endra, Inc, Stockholder; Cellsight, Stockholder; Enlight, Inc., Stockholder; General Electric, Grant/research support; ImaginAb, Stockholder; MagArray, Inc., Stockholder; Sanofi-Aventis, US, Grant/research support; SiteOne Therapeutics, Stockholder; VisualSonics/Sonosite, Stockholder .

Presentation Number **SS 159**
Scientific Session 27: Preclinical in vivo Studies - Oncology (Photoacoustic)
September 21, 2013 / 13:30-13:45 / Room: 203

Two in One: Gold Nanorods for Pre-Surgical Photoacoustics and Intra-Operative Raman

Timothy Larson, **Jesse V. Jokerst***, Adam J. Cole, Sanjiv S. Gambhir, Radiology, Stanford University, Stanford, CA, USA. Contact e-mail: jokerst@stanford.edu*

Introduction: Improved imaging approaches are needed for screening, diagnosis, staging and resection guidance in ovarian cancer patients. Ultrasound-based approaches are particularly useful due to the broad utility of that modality in gynecology. Here, we demonstrate gold nanorods that passively accumulate in ovarian cancer tissue and offer both photoacoustic properties for deep tissue imaging and surface enhanced Raman spectroscopy for image-guided resection. Materials and Methods: Gold nanorods (GNRs) were synthesized with through surfactant templating and were coated with IR792 as a Raman-active molecule. Subcutaneous tumor xenografts of the OV2008 cell line were created in nude mice and analyzed between 800 - 1200 mm3. Tomographic photoacoustic data was collected with a Nexus128 scanner from Endra LifeSciences. Results: Three batches of GNRs were examined with peak resonances between 680 - 760 nm. The batch at 756 nm had the strongest photoacoustic signal and was used for subsequent experiments. The intensity of the Raman signal was an order of magnitude larger than 60 nm gold core/silica shell nanoparticles and was stable for over 24 hours in 50% murine serum. The batch-to-batch reproducibility of four GNR batches had a relative standard deviation of 15.5% and 3.6% in the SERS and PA modalities. We injected 200 µL of 2.5, 5.4, and 16.8 nM GNRs into tumor-bearing mice via tail vein with n=3 mice at each concentration. Relative to baseline photoacoustic signal (A), these concentrations increased tumor signal 1.3-, 1.6-, and 2.5-fold, respectively (B). In all cases, maximum signal increase occurred within 2 hours of injection with elevated photoacoustic signal persisting for at least 24 hours. To validate that this signal increase was due to the presence of GNRs in the tumor and not due to changes in hemoglobin, tumors were analyzed for gold content at identical time points as the photoacoustic scans (see Supplement). There was strong correlation (R2>0.90) between gold content in tumor and photoacoustic signal. The same GNRs were suitable for optical imaging with Raman spectroscopy. Raman maps were created with least squares analysis. The spectrum at each point was compared to a reference spectrum and a high degree of similarity is indicated by a brighter pixel in D. By 24 hours, free GNRs had been sequestered to the liver and spleen as well as 2-3%ID/g immobilized in the tumor by the enhanced permeability and retention effect. This tumor gold signal remained elevated even after blood levels had returned to baseline suggesting extravasation. These GNRs produced Raman signal that could be used to identify tumor margins and also to monitor resection (Supplementary). Conclusion: The GNRs allow pre-surgical photoacoustic visualization for tumor staging as well as intra-operative Raman imaging to guide resection. GNRs with higher aspect ratios offered increased ex vivo and in vivo signal. Future work will study GNRs targeted to cell surface proteins to potentially increase tumor accumulation.

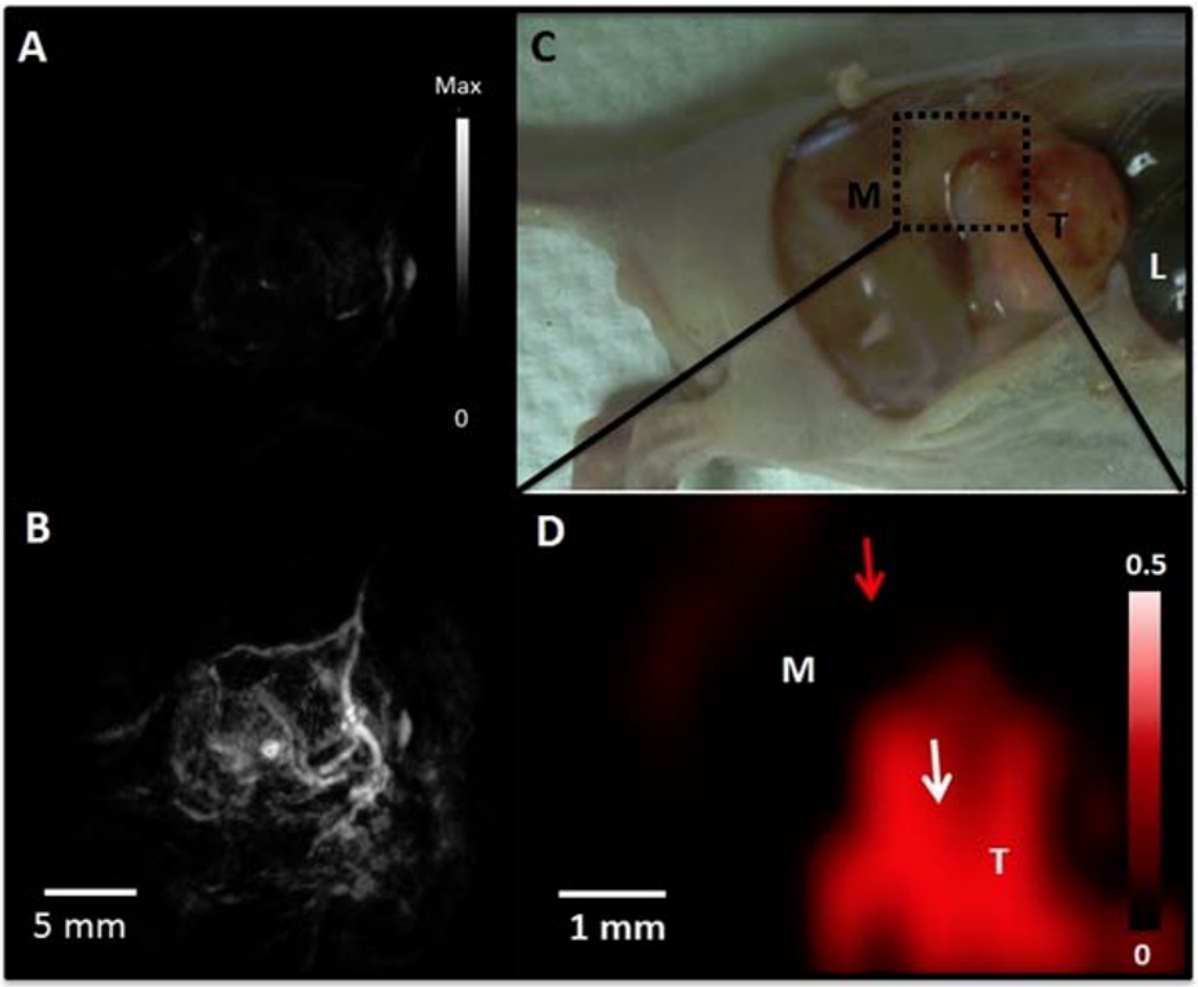

Figure 1. Photoacoustic imaging of xenograft ovarian tumor before (A) and three hours after (B) i.v. administration of 0.2 mL of 5.4 nM GNRs. Scale bar in B and intensity bar in A apply to both panels. The same contrast agent generates Raman signal for intra-operative imaging (C). The Raman modality (D) is useful for identifying tumor margins. M = muscle; T= tumor; L = liver.

Disclosure of author financial interest or relationships:

T. Larson, None; **J.V. Jokerst**, None; **A.J. Cole**, None; **S.S. Gambhir**, Bracco Diagnostics, Consultant; Endra, Inc, Stockholder; Cellsight, Stockholder; Enlight, Inc., Stockholder; General Electric, Grant/research support; ImaginAb, Stockholder; MagArray, Inc., Stockholder; Sanofi-Aventis, US, Grant/research support; SiteOne Therapeutics, Stockholder; VisualSonics/Sonosite, Stockholder .

Presentation Number **SS 160**
Scientific Session 27: Preclinical in vivo Studies - Oncology (Photoacoustic)
September 21, 2013 / 13:45-14:00 / Room: 203

Multimodality Imaging-based Characterization of a Xenograft Model of Metastatic Breast Cancer in Mice

Raquel De Souza[1], *Jinzi Zheng*[1], *Michael Dunne*[1], *Robert S. Kerbel*[2,3], *Christine Allen*[1,4], *David A. Jaffray*[1,5], [1]*STTARR Innovation Centre, Radiation Medicine Program, University Health Network, Toronto, ON, Canada;* [2]*Molecular and Cellular Biology Research, Sunnybrook and Women's College Health Sciences Centre, Toronto, ON, Canada;* [3]*Department of Medical Biophysics, University of Toronto, Toronto, ON, Canada;* [4]*Department of Pharmaceutical Sciences, University of Toronto, Toronto, ON, Canada;* [5]*Radiation Oncology, University of Toronto, Toronto, ON, Canada. Contact e-mail: Raquel.DeSouza@rmp.uhn.on.ca*

Introduction: Xenograft models of human cancers in mice have been widely used for assessment of novel anticancer therapies. However, growing demand exists for clinically relevant models of cancer, such as those displaying metastatic patterns that reflect the clinical scenario. A challenge in the use of these models is the monitoring of metastasis in vivo. In this study, non-invasive multimodality imaging is performed for visualization and characterization of primary and metastatic lesions in an orthotopic xenograft model of metastatic breast cancer in mice. Methods: The LM2-4H2N cell line is an erbB-2-positive, metastatic variant of the MDA-MB-231 human breast cancer cell line. The tumor inoculation protocol employed here was slightly modified from that originally reported by Dr. Robert Kerbel. Female SCID mice were injected with 50µL of 2 to 4x106 LM2-4H2N cells into their right inguinal mammary fat pad (MFP). Two weeks post-inoculation, primary tumors (250-400 mm3) were surgically resected. Prior to resection, tumor volumes were quantified using a µCT (GE Locus Ultra) data set. As the LM2-4H2N cell line stably expresses luciferase, bioluminescence imaging (BLI) was performed longitudinally to monitor primary and metastatic tumor growth. Mice were injected i.p. with 150mg/kg D-luciferin (Caliper) in phosphate buffer solution (PBS) 10 minutes prior to BLI acquisition. Bioluminescence signal was detected using an IVIS System (Xenogen, 5-10 second acquisition). At the study endpoint, a nanoparticle-based NIR fluorescence probe was administered i.v., and ex vivo 2-D visualization of metastatic lesions was performed using a Maestro system (Perkin Elmer). Results: All mice developed primary tumors in the inguinal MFP. Inoculation with 2x106 cells resulted in variable tumor growth curves, with primary tumors reaching the desirable size range of 200-400 mm3 within a broad timeframe (day 14 to 36). However, mice inoculated with 4x106 cells reached an average primary tumor volume of 398.3 ± 234.4 mm3 on day 14, at which point tumors were surgically resected. Metastatic lesions became apparent by BLI on week 5, 3 weeks after primary tumor resection, Fig 1b. Metastatic sites (Fig 1a, c) are consistent with previously published reports and accurately are a good representation of the clinical presentation of advanced-stage breast cancer. Primary tumors were detectable by BLI and µCT (Fig 2a), and metastatic lesions were readily identifiable in vivo with BLI and ex vivo with NIR fluorescence imaging (Fig 2b). In fact, BLI and NIR fluorescence imaging allowed for good visualization of lung metastasis, a type of lesion that is not easily identifiable. Conclusion: Our results demonstrate the feasibility of employing BLI, NIR fluorescence and µCT imaging to characterize metastatic tumor models and to monitor metastatic disease

progression over time. The combination of these imaging techniques allowed for non-invasive, accurate, real-time tracking of metastasis, overcoming limitations of endpoint-based studies. This demonstrates the feasibility of employing multimodality imaging for evaluation of treatment response in metastatic tumor models.

Disclosure of author financial interest or relationships:
R. De Souza, None; **J. Zheng**, None; **M. Dunne**, None; **R.S. Kerbel**, None; **C. Allen**, None; **D.A. Jaffray**, Precision X-ray Inc., Other financial or material support .

Presentation Number **SS 161**
Scientific Session 27: Preclinical in vivo Studies - Oncology (Photoacoustic)
September 21, 2013 / 14:00-14:15 / Room: 203

Multispectral optoacoustic tomography as novel imaging modality for pancreatic islets

Sven Gottschalk[1], *Neal Burton*[1], *Wouter H. Driessen*[1], *Daniel Razansky*[1,2], [1]*Institute for Biological and Medical Imaging, Helmholtz Zentrum München, Neuherberg, Germany;* [2]*School of Medicine, Technical University of Munich, Munich, Germany. Contact e-mail: sven.gottschalk@helmholtz-muenchen.de*

Multispectral optoacoustic tomography (MSOT) capitalizes on the unique combination of high resolution, representative of magnetic resonance imaging and X-Ray computed tomography, the molecular specificity of positron emission tomography and optical imaging techniques, and real-time imaging capacity of ultrasound imaging. Detection of exogenous contrast (fluorochromes, nanoparticles) as well as endogenous tissue chromophores (hemoglobin) with MSOT can be facilitated by applying multiple wavelength illumination and performing unmixing based on spectral signatures of the particular absorbers of interest [1]. In general, pancreatic tissue does not exhibit extensive endogenous contrast in MSOT, making the application of β-cell specific contrast agents essential for attaining detectable contrast. Here we used two targeted probes, the β-cell specific single chain antibody fragment SCA B1 [2] coupled to cobalt nanoparticles (NPs) and a fluorescent exendin-4 analog (coupled to AlexFluor®750) [3], kindly provided by U. Ahlgren, Umea, Sweden. Both probes were injected iv. into the tail vein of athymic nude-Foxn1nu mice. MSOT-measurements were done at 3 and 6 h post injection of 50 µg SCA B1-NP (corresponding to 1500 µg NP). For the exendin-4 probe (8 nmol), imaging was performed 90 minutes post injection. The real-time small animal MSOT scanner, used for the imaging, has been described elsewhere [4]. Multispectral acquisitions in an area of approx. 15 mm, encompassing both kidneys, with a step-size of 0.5 mm, were recorded. Figure 1A shows a maximum intensity projection of the spectrally unmixed data. Signal from the exendin-4 probe was primarily visualized in the kidneys, while signals originating from the pancreas area have very low intensity as compared to the surrounding tissues. A possible explanation for this could be low β-cell targeting. Yet, image acquisition at different time points or optimization of the dosing parameters might improve the visualization capacity. Figure 1B shows data acquired 6 h post injection of the SCA B1-NP probe similar to figure 1A. Very significant accumulation of the probe in the spleen is visible. Localization in the left kidney can also be observed. A clear signal in the supposable location of the pancreas can be seen. Region of interest analysis at the location of the splenic lobe of the pancreas in one slice (data not shown) revealed increases in signal intensities to 130±9% of control at 3h and to 193±8% of control at 6h post injection (n=2). Overall, MSOT was able to attain high resolution maps of the contrast agent distribution in pancreas and thus provide a qualitative assessment of the β-cell mass. Yet, certain challenges related to precise localization of the specific probe's contrast, need to be addressed in order to enable quantified visualization of β-cells in vivo using MSOT. We are therefore convinced that a more rigorous optimization of imaging and analysis parameters will unleash the full potential of MSOT for real-time in vivo β-cell imaging in mice. [1]Ntziachristos, Chem Rev 110(2010)2783; [2]Ueberberg, Diabetes 58(2009)2324; [3]Reiner, PNAS 108(2011)12815; [4]Razansky, Nat Prot 6(2011)1121;

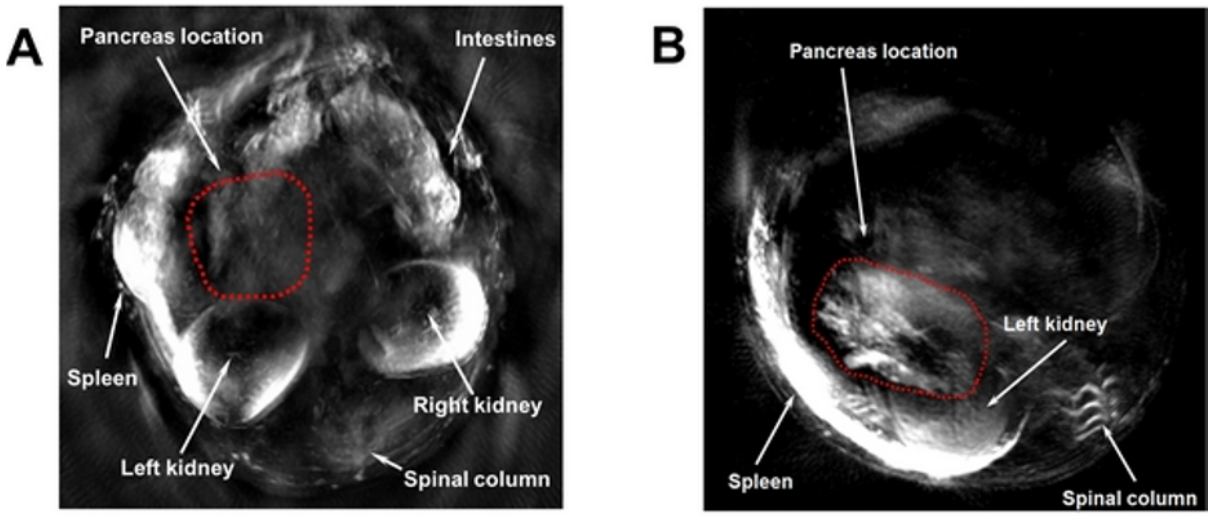

Figure 1: Maximum intensity projections of spectrally unmixed data (A) Exend-4 probe (B) SCA B1-NP probe

Disclosure of author financial interest or relationships:
S. Gottschalk, None; **N. Burton**, iThera Medical, Employment; **W.H. Driessen**, iThera Medical, Employment; **D. Razansky**, None.

Presentation Number **SS 162**
Scientific Session 27: Preclinical in vivo Studies - Oncology (Photoacoustic)
September 21, 2013 / 14:15-14:30 / Room: 203

In vivo Imaging of Tumor Vasculature and Nanoparticle Distribution Using Multispectral Optoacoustic Mesoscopy

Antonio Nunes[1], *Juan Salichs*[1], *Nicolas Beziere*[1], *Vladimir Ermolayev*[1], *Panagiotis Symvoulidis*[1], *Daniel Queiros*[1], *Neus Lozano*[2], *Kostas Kostarelos*[2], *Vasilis Ntziachristos*[1], [1]*Institute for Biological and Medical Imaging (IBMI), Technical University of Munich and Helmholtz, Neuherberg, Germany;* [2]*Nanomedicine Laboratory, Centre for Drug Delivery Research, UCL School of Pharmacy, London, United Kingdom. Contact e-mail: antonio.nunes@helmholtz-muenchen.de*

The introduction of imaging modalities for pre-, and post-operative diagnostic, as well as for real-time intra-operative visualization, is expected to enhance the effectiveness of the diagnostic techniques, in particular for tumor patients. Recently, a versatile technology- optoacoustic imaging- has emerged as an important tool for the study and monitoring of anatomical, functional and molecular changes in tumors. Optoacoustic imaging is a promising modality that bridges the gap between optical imaging, with an optical absorption generated contrast, and ultrasound imaging, with its ultrasound based detection system. Optoacoustic imaging could provide information regarding the localization of absorbing molecules in a living organism. Recent developments of the methodology also include a multispectral and tomographic approach, often called Multispectral Optoacoustic Imaging (MSOT). MSOT have been report as a novel and powerful imaging modality, which offers new tools for pre-clinical (and possibly clinical) cancer research. Herein, we have developed and explored the unique resources offered by MSOT (in particular mesoscopic MSOT) to simultaneous visualize, in terms of, in vivo high spatial and temporal resolution and in depth molecular imaging of absorbing compounds, the development of tumor vasculature. Particularly, we have investigated the dynamic enhancement of vasculature, characterization of the enhanced permeability and retention effect in tumors, as well as the oxygenated and deoxygenated hemoglobin mapping through whole tumor. Nanoparticle-based tracers were intravenous administered into the different SC tumor-bearing mice. Optical excitation was provided by an optical parametric oscillator laser with pulse duration of ns at repetition rate of 20Hz and a tunable range of 700 to 900nm. The ultrasonic detection was provided by high-frequency cylindrically focused transducer with a central frequency of 15MHz, allowing acquisition of coronal plane images of the tumor. The fiber bundle and transducer array were stationary, and the animal bed was rotational (360o) to acquire the whole tumor. Further to the investigation of the distribution of the probe, we also studied their permeability and retention effect in tumors. We correlated the in vivo signal detected acoustically with the one obtained after ex vivo cryo-slicing, regarding localization and extravasation of the probe into the tumor. Our results demonstrated the ability of the MSOT to offer high resolution and fidelity imaging of optical contrast with a direct impact on oncology research This study highlighted that MSOT is a powerful resource for biological applications, in particular for diagnosis or theranostics approaches on cancer research.

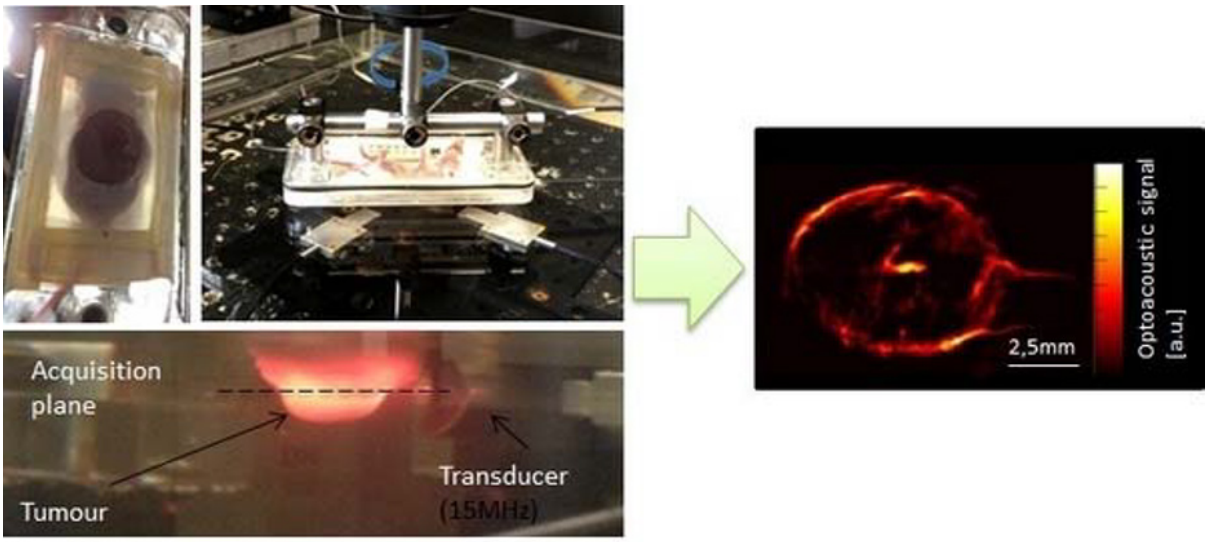

High resolution MSOT System. (left panel)Picture of a mouse during the scan in the MSOT showing the key components of the system. Mouse is placed in a rotational bed and 4 optical fibers homogenous illuminate the whole tumor. (right Panel) example of Optoacoustic image using mesoscopy MSOT.

Disclosure of author financial interest or relationships:
A. Nunes, None; **J. Salichs**, None; **N. Beziere**, None; **V. Ermolayev**, None; **P. Symvoulidis**, None; **D. Queiros**, None; **N. Lozano**, None; **K. Kostarelos**, None; **V. Ntziachristos**, iThera Medical, Stockholder; SurgOptix BV, Consultant .

Presentation Number **SS 163**
Scientific Session 28: Preclinical Cell & Tissue Level Studies, Preclinical in vivo Studies - Stem Cells
September 21, 2013 / 13:00-13:15 / Room: Oglethorpe Auditorium

Ultrasound guided photoacoustic monitoring of mesenchymal stem cells labeled with gold nanoparticles for tissue regeneration

Seung Yun Nam[1], *Laura M. Ricles*[2], *Laura J. Suggs*[2], *Stanislav Y. Emelianov*[2,1], [1]*Electrical and Computer Engineering, University of Texas at Austin, Austin, TX, USA;* [2]*Biomedical Engineering, University of Texas at Austin, Austin, TX, USA. Contact e-mail: snam@utexas.edu*

Stem cell therapy is a promising candidate for the novel alternative treatment of ischemic cardiovascular diseases. Medical imaging has an important role in stem cell therapy because stem cell behaviors and tissue regeneration indicators (e.g., neovascularization) need to be monitored for effective therapy following stem cell implantation. However, current imaging techniques for stem cell therapy using various contrast agents suffer from significant limitations such as short imaging duration (PET/SPECT), low cell detection sensitivity (MRI), and shallow penetration depth (optical microscopy). Ultrasound guided photoacoustic (US/PA) imaging has a great potential to overcome drawbacks of other stem cell imaging methods because it can achieve noninvasiveness with spatial resolution on the order of micrometers and great sensitivity/selectivity with various endogenous and exogenous contrast agents including hemoglobin and metallic nanoparticles. Therefore, we demonstrated that US/PA imaging is capable of longitudinal in vivo monitoring of migration of mesenchymal stem cells (MSCs) labeled with gold nanoparticles (AuNPs) and feasible of tracking the interaction of vascular growth with tissue regeneration (panel a). To verify longitudinal in vivo monitoring of stem cell distribution, the AuNP labeled MSCs (1×10^5 cells/mL, 3×10^4 cells) were injected intramuscularly in the hind limb of the Lewis rat and imaged at a range of wavelengths from 650 nm to 920 nm using a high frequency US/PA imaging system. The ultrasound image shows morphology of the lower limb, and the photoacoustic image represent various optical absorbers in the tissue which were distinguished as AuNP labeled MSCs (green), oxygenated (red) and deoxygenated hemoglobin (blue), and skin (yellow) by spectral analysis due to each unique optical absorbance (panel b). The 3D combined ultrasound and spectroscopic image shows not only distribution of MSCs but also microvasculature in the rat lower limb (panel c). After stem cell implantation, the AuNP labeled MSCs were able to be tracked for up to 10 days with a strong signal using US/PA imaging (Supporting Information). Based on quantitative analysis, the AuNP labeled MSCs can be imaged more than 10 days because of the excellent cell detection sensitivity of US/PA imaging. These results indicate that US/PA imaging has the capability of long-term noninvasive monitoring of stem cell migration and it also has a great potential to detect neovascularization if it is applied to ischemic muscle injury cases with high resolution and sensitivity.

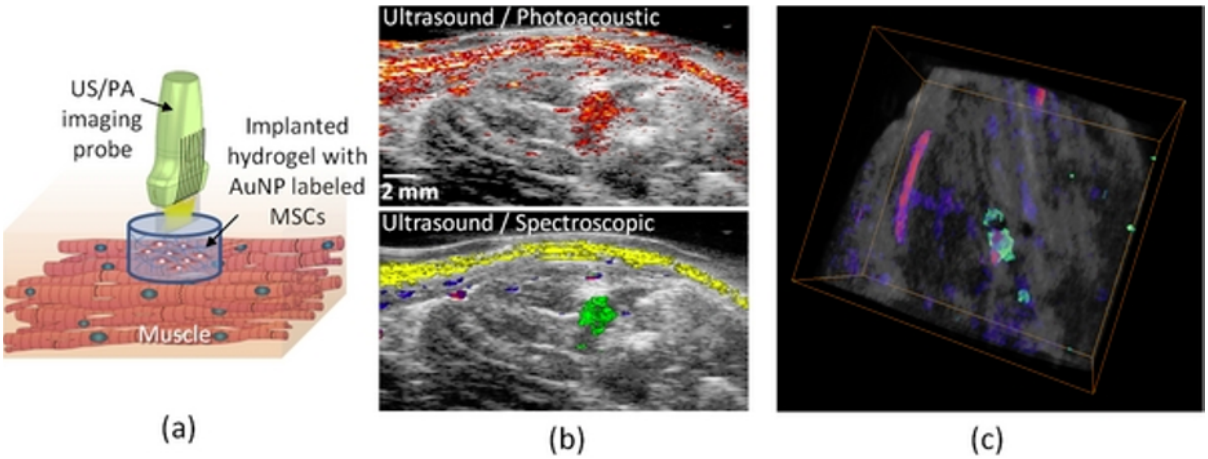

Disclosure of author financial interest or relationships:
S. Nam, None; **L.M. Ricles**, None; **L.J. Suggs**, None; **S.Y. Emelianov**, NanoHybrids, Inc, Stockholder .

Presentation Number **SS 164**
Scientific Session 28: Preclinical Cell & Tissue Level Studies, Preclinical in vivo Studies - Stem Cells
September 21, 2013 / 13:15-13:30 / Room: Oglethorpe Auditorium

In vivo iron loading of stem cells before their harvest enables MRI tracking after transplantation

Fanny Chapelin[1], *Aman Khurana*[1], *Olga D. Lenkov*[1], *Barbara Sennino*[2], *Paul J. Kempen*[3], *Heike E. Daldrup-Link*[1], [1]*radiology, stanford, Stanford, CA, USA;* [2]*Comprehensive cancer center, UCSF, San Francisco, CA, USA;* [3]*Materials Science and Engineering, Stanford, Stanford, CA, USA. Contact e-mail: chapelinfanny@hotmail.com*

PURPOSE: Novel stem cell therapies require in vivo tracking of the transplanted stem cells with non-invasive imaging technologies in order to monitor engraftment and exclude tumor formation. However, ex vivo contrast agent labeling involves stem cell manipulations between stem cell harvest and transplantation. This has led to safety concerns, such as possible contamination, alterations of stem cell biology or in vivo side effects of added transfection agents. The purpose of this study was to develop an immediately clinically applicable approach for labeling of bone marrow derived mesenchymal stem cells (MSC), which would not require ex vivo manipulations of harvested MSC. MATERIALS AND METHODS Sprague Dawley rats were injected IV with ferumoxytol (dose: 0. 5mmol/kg) 48 hours prior to bone marrow harvest from long bones (femur and tibia). Extracted cells were cultured for 7 days to allow MSC selection and expansion. Ferumoxytol labeling efficacy was assessed by fluorescence microscopy, confocal microscopy, MRI and Transmission Electron Microscopy (TEM). To assess if these in vivo ferumoxytol labeled cells could be tracked in vivo with MRI, osteochondral defects were created in the distal femur of six nude athymic rats and implanted with matrix associated stem cell implants (MASI) of either in vivo labeled MSC (right knee) or unlabeled MSC (left knee). Serial MR images were acquired up to 4 weeks after MASI, using a 7T GE MR scanner (T2 SE; TE-15, 30, 45, 60 ms TR-4000 ms NEX: 1). T2 relaxation time maps were generated and T2 relaxation times of labeled transplants and unlabeled controls were compared with a t-test. The knees were explanted for histopathologic evaluations of implant engraftment, iron labeling and chondrogenic differentiation. RESULTS Bone marrow MSC could be labeled through IV injection of ferumoxytol. Fluorescence microscopy and confocal microscopy confirmed the presence of ferumoxytol inside MSC and electron microscopy localized ferumoxytol nanoparticles in secondary lysosomes. The iron uptake per cell, as measured by ICP-OES, was significantly higher for in vivo labeled MSCs compared to unlabeled controls ($p<0.05$). Accordingly, MR imaging showed significant T2 shortening of labeled cell implants (15.459±0.729ms), but not unlabeled controls (24.423ms±1.213, $p=0.0002$), confirming possible MRI tracking in vivo. T2-signal effects of in vivo labeled MSCs remained significant over 4 weeks. Corresponding DAB-Prussian blue stains confirmed iron content of the labeled MSC at 4 weeks and H&E and Alcian Blue stains demonstrated integration and engraftment of the MASI with chondrogenic matrix production for both labeled in vivo and unlabeled MASI. CONCLUSION In vivo labeling of MSC is a novel, immediately clinically applicable approach for stem cell labeling with an FDA-approved iron supplement ferumoxytol, which allows in vivo MRI tracking after transplantation into arthritic joints. This approach could be widely used in patients for in vivo monitoring of MASI in various target tissues.

Disclosure of author financial interest or relationships:
F. Chapelin, None; **A. Khurana**, None; **O.D. Lenkov**, None; **B. Sennino**, None; **P.J. Kempen**, None; **H.E. Daldrup-Link**, None.

Presentation Number **SS 165**
Scientific Session 28: Preclinical Cell & Tissue Level Studies, Preclinical in vivo Studies - Stem Cells
September 21, 2013 / 13:30-13:45 / Room: Oglethorpe Auditorium

Preferential magnetic nanoparticles uptake by Bone Marrow Derived Macrophages Subpopulations: Effect of Surface Coating on Polarization, Toxicity and in vivo MRI Detection

Achraf Al Faraj, *King Saud University, Riyadh, Saudi Arabia. Contact e-mail: aalfaraj@ksu.edu.sa*

Introduction: Noninvasive imaging of macrophages activity has raised increasing interest for diagnosis of different diseases, which make them attractive vehicles to deliver contrast agents for diagnostic or drugs for therapeutic purposes. However, the effect of their labeling using superparamagnetic iron oxide (SPIO) nanoparticles needs further investigation. In this study, the effect of SPIO PEGylation and their further surface modification with carboxylic or amine groups on M1 and M2 bone marrow derived macrophages (BMDM) phenotype, labeling efficiency, toxicity and their in vivo MR detection were assessed. Methods: BMDM were first labeled with SPIO, SPIO-PEG, SPIO-PEG-COOH and SPIO-PEG-NH2 nanoparticles (100 nm) at 2 mM iron concentration. Macrophages uptake of magnetic nanoparticles (MNP) was determined using both Ferrozine-based spectrophotometry and magnetophoresis assays. Their biocompatibility was evaluated using MTT cell growth assay for cell viability, JC-1 fluorescence kit for mitochondrial membrane potential and 2',7' dichlorofluorescein diacetate (DCFDA) fluorogenic dye for Reactive oxygen species generation. Then, to characterize the phenotype of macrophages before and after their magnetic labeling, transmission electron microscopy, flow cytometry analysis of membrane receptor expression, and the measurement of iNOS and Arginase1 activity were performed. To further address the mechanistic nature of the nanoparticle uptake, macrophages were pretreated with different uptake inhibitors prior to particle incubation. Finally, to compare the biodistribution of intravenously injected macrophage subpopulations labeled with the different MNP, whole-body MRI investigation was performed on mice using a Bruker 4.7T scanner. Results: Spectrophotometer and magnetophoresis analysis revealed an enhanced and comparable uptake for both carboxylic and amine modified PEGylated SPIO by BMDM with a higher uptake for the M2 subsets. Biocompatibility evaluation showed no variation in cell viability and mitochondrial membrane potential as a hallmark for apoptosis and a low release of ROS. Surface membrane characterization assessed using flow cytometry and measurement of iNOS and arginase1 activity as marker of M1 and M2 macrophages polarization, confirmed that magnetic labeling of macrophages subsets did not affect their polarization. The uptake kinetics of SPIO in the presence of the inhibitors revealed that intercepting either scavenger receptor type A by polyinosinic acid or clathrin-dependent endocytosis by monodansyl cadaverine led to almost identical time-dependent inhibition of particle uptake by both M1 and M2 macrophages. Finally, no variation in the biodistribution of magnetic labeled macrophages, successfully monitored using noninvasive MRI, was observed. Conclusion: Carboxylic or amine modified PEGylated SPIO nanoparticles have been shown to be safe and having a higher labeling efficiency via clathrin-mediated, scavenger receptor A-dependent endocytosis pathway while not affecting neither the polarization nor the biodistribution of macrophages sub-populations.

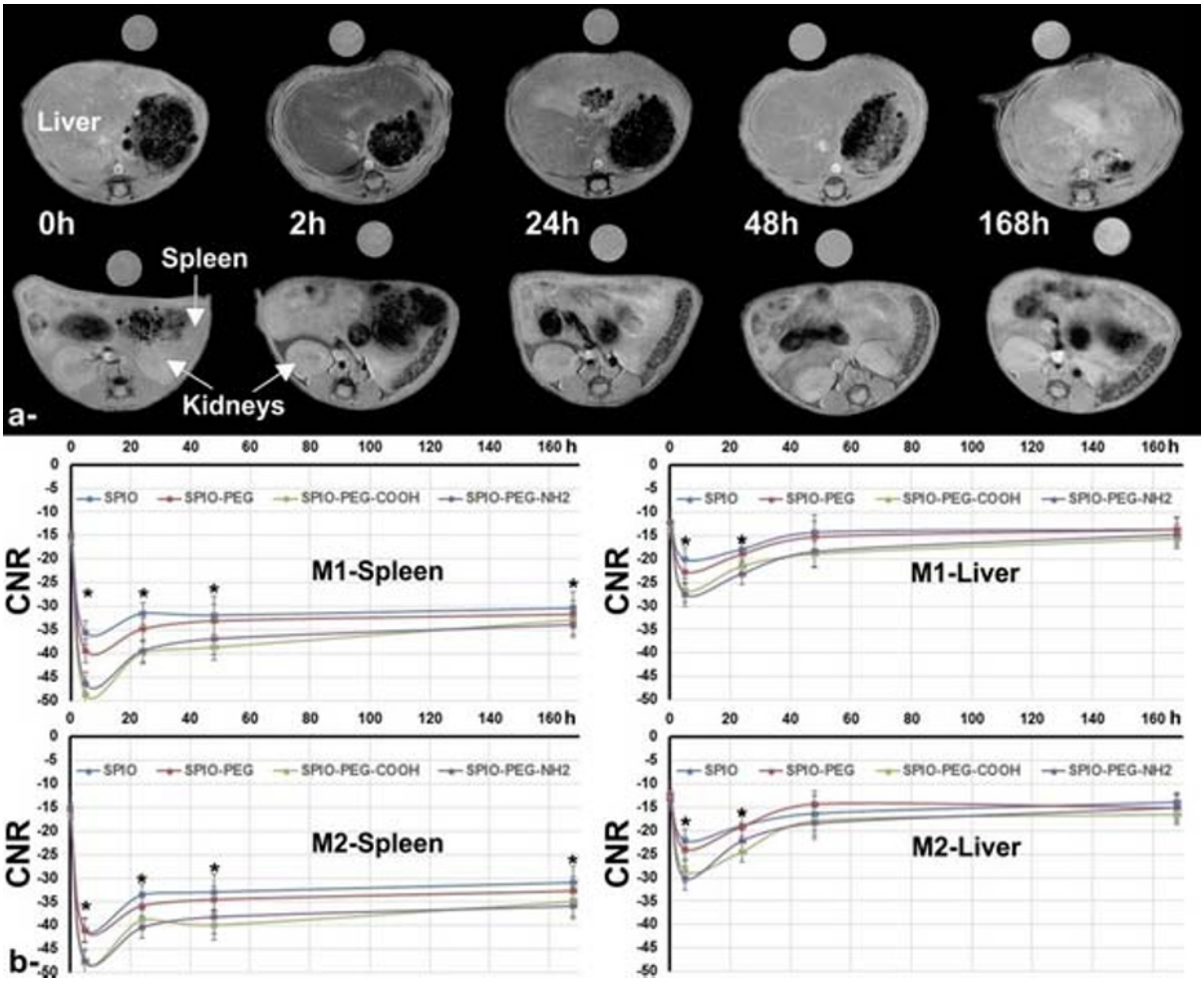

(a) MR images of liver, spleen and kidneys of SPIO-PEG-NH2 labeled M2 macrophages. (b) Contrast-to-noise (CNR) variation during the 7 days follow-up study for the spleen and the liver before and after injection of either M1 or M2 labeled macrophages.

Disclosure of author financial interest or relationships:
A. Al Faraj, None.

Presentation Number **SS 166**
Scientific Session 28: Preclinical Cell & Tissue Level Studies, Preclinical in vivo Studies - Stem Cells
September 21, 2013 / 13:45-14:00 / Room: Oglethorpe Auditorium

Multi-scale high-throughput cell culture monitoring by lensfree imaging

Srikanth Vinjimore Kesavan[1], *Cédric P. Allier*[1], *Fabrice P. Navarro*[2], *Mathilde Menneteau*[2], *Bernard Chalmond*[3,4], *Jean-Marc Dinten*[1], [1]*DRT Leti DTBS/STD/LISA, CEA, Grenoble, France;* [2]*DRT Leti DTBS/SBSC/LBAM, CEA, Grenoble, France;* [3]*Université de Cergy-Pontoise, Paris, France;* [4]*ENS-Cachan, Paris, France. Contact e-mail: srikanth.vinjimore@cea.fr*

Research is continuously developing new imaging methods to better understand the structure and function of biological systems at the microscopic scale. Despite our ability to peer through the cells using increasingly powerful optical instruments, fundamental biology questions remain unanswered at larger scales. Hence we are developing lensfree imaging as an alternative method bringing new perspectives, i.e. our system (Fig. 1a) aims at, 1. Multiscale observation capability across three orders of magnitude, e.g. from mm2 to µm2 2. Large field of view (larger than 20 mm2) 3. Live capture inside the incubator over several days (acquisition every 5 minutes) 4. Simplicity of use, small form factor (495cm3) and low cost (lesser than 200 Euros) In this presentation, we demonstrate the potentialities of lensfree imaging for cell culture monitoring and describe the innovative technologies that underpin its feasibility. The technique is based on inline holography as invented by Gabor. Albeit the existence of the method since 1970, the recent development of digital sensors, popularized by their use in cameras, helped realize the full potential of this method in the recent years. When illuminated with coherent light, cells diffract the incident wave and produce interferences that can be recorded by a sensor (Fig. 1b). LED, pinhole, and CMOS sensor are the three basic components of our lensfree imaging system. The absence of bulky optical components makes the system simple and hence it could be placed inside the incubator to monitor cells in real time. Several systems could also be placed simultaneously to observe several conditions in parallel (Fig 1c). The field of the view (FOV) of the system is 24 mm2, in other words, the system is capable of monitoring several thousands of cells at the same time. Hence it provides the ability to perform high throughput analyses (>5000 cells), e.g. cell tracking and cell density measurement. An automated reconstruction algorithm reconstructs the interference (holographic) patterns recorded over the entire field of view of the system (Fig 1d). When we digitally zoom into the reconstructed image (few mm2 FOV), cell-cell interaction, and cell division could be visualized in detail (Fig 1e). We could further zoom to obtain the morphology of the cells with a resolution close to 2 µm (Fig 1f). This allows the visualization of single cell motility with filopodial extensions and focal adhesion points. 3D reconstruction results from the calculation of phase with a precision of 1µm. Figure 1g shows, in 3D, a moving cell which later divides (marked by red arrow). Overall, the system offers a resolution close to 2µm over a field of view of 24mm2 which makes it capable of monitoring cell culture at different scales, from very large field of view (>20mm2) down to single cell. High through-put analysis of fundamental properties of cell populations could be performed without the necessity of markers, e.g. cell adhesion, cell division, cell migration and cell morphology.

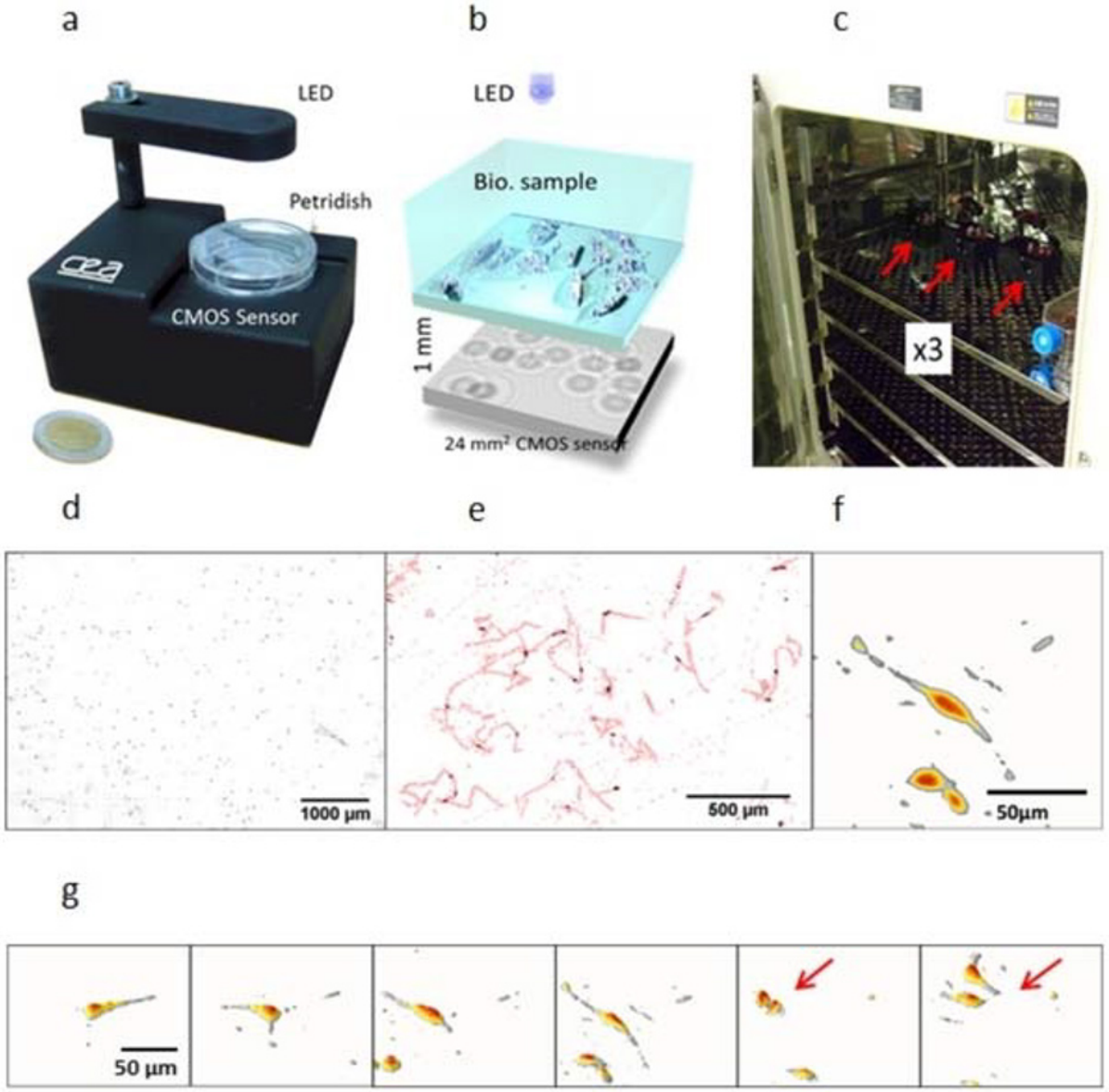

Photograph of the lensfree imaging system developed at CEA-Leti, (b) Schematic diagram explaining the principle of lensfree imaging system, (c)Photograph of three lensfree imaging systems inside the incubator, (d) Reconstructed image showing cells in a field of view of 24 mm2, (e) Trajectories followed by cells (reconstructed) during several hours of imaging inside the incubator, (f) Reconstructed image of a moving cell (filopodial extensions) and a dividing cell, (g)3D reconstruction montage of a moving cell which later divides (Red arrow)

Disclosure of author financial interest or relationships:
S. Vinjimore Kesavan, None; **C.P. Allier**, None; **F.P. Navarro**, None; **M. Menneteau**, None; **B. Chalmond**, None; **J. Dinten**, None.

Presentation Number **SS 167**
Scientific Session 28: Preclinical Cell & Tissue Level Studies, Preclinical in vivo Studies - Stem Cells
September 21, 2013 / 14:00-14:15 / Room: Oglethorpe Auditorium

Tracking Mesenchymal Stem Cell fate in Mouse Transplantation Models using Iron and Fluorine cellular MRI

Jeff M. Gaudet[1,2], *Emeline J. Ribot*[1], *Kyle M. Gilbert*[1], *Yuhua Chen*[1], *Paula Foster*[1,2], [1]*Imaging Research Laboratories, Robarts Research Institute, London, ON, Canada;* [2]*Medical Biophysics, University of Western Ontario, London, ON, Canada. Contact e-mail: jgaudet@robarts.ca*

Background: Stem cell therapy has the potential to revolutionize medicine and clinical trials are already underway. Still, there are questions about which parameters (numbers of cells, transplant route, timing) produce the best transplantation protocols. Most cellular MRI studies have used iron labels to image stem cells. This approach provides excellent cell detection sensitivity but suffers from low specificity. Fluorine-19 (^{19}F) MRI can address this limitation because of the potential for unambiguous detection and accurate quantification, since mammalian tissues have negligible ^{19}F. In this study we use MRI to detect mesenchymal stem cells (MSC) labeled with both iron and ^{19}F agents and track their fate over time to evaluate retention and distribution in vivo. **Methods:** We used two transplantation models (i) a xenograft - human MSC (hMSC) implanted into immune-compromised nude mice (n=4) and (ii) an allograft - mouse MSC (mMSC) implanted into immune-competent C57Bl/6 mice (n=5). MSC were labeled with either an iron oxide agent (Molday-rhodamineB) or a perfluorocarbon emulsion (Cell Sense). In the xenograft mice $1.5x10^6$ iron-labeled hMSC were implanted into the right quadriceps and $1.5x10^6$ ^{19}F-labeled hMSC were implanted into the left side. In the allograft model $2x10^6$ mMSC were implanted into the left quadriceps. Proton (^{1}H) and ^{19}F images were acquired at 9.4T with a dual-tuned ^{1}H/^{19}F mouse body coil using a 3D-balanced steady state free precession (bSSFP) sequence. Signal from iron-labeled cells was quantified by measuring the volume of the signal void in the ^{1}H images. Quantification of the ^{19}F signal was performed by measuring the signal in the region of interest and in a reference of known concentration. **Results:** The transplanted MSC were visible at the site of implantation on day 0 in all mice. Representative images are shown in Fig1. Signal was not observed in other parts of the mouse body. Over time the signal decreased. There was a notable difference in the retention of the ^{19}F signal when comparing the xeno-and allo-graft models. Signal from hMSC in nude mice persisted longer than the signal for mMSC in black mice (Fig2). No ^{19}F signal was detected in 2/3 mice in the allograft model at day 16. Another significant finding from this work was the difference in quantification between iron and ^{19}F labeled cells in the xenograft model (Fig3). On day 3 post implantation the iron void volume and ^{19}F signal are very similar; 80% of day 0. However, on day 12 the signal from iron-labeled cells has not changed whereas the 19F signal is at approx. 50% of day 0. Staining for human cells and fluorescence microscopy was used to validate ^{19}F images (Fig4). **Significance:** This is the first report of the use of the bSSFP sequence for ^{19}F cell detection. The very high SNR efficiency of this sequence improves ^{19}F imaging sensitivity. With ^{19}F MRI we were able to detect and quantify differences in the retention of MSC between xenograft and allograft transplant models. Our research addresses the pressing need for reliable methods to image cells in vivo, at multiple time points post-transplantation.

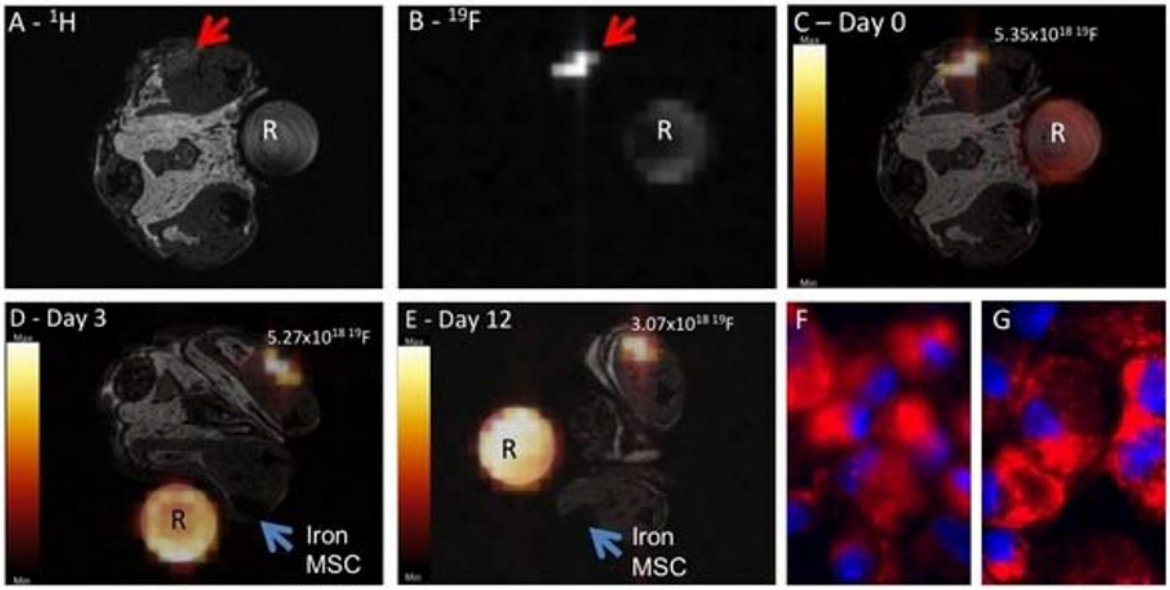

Figure 1: MRI of nude mouse injected with both Cell Sense- and Molday-labeled human MSC. For each mouse two MRI images were collected in the axial orientation, first a 1H image (A), then a 19F image (B). (A-C) show these images on day 0, the day of the cell implantation. The red arrow indicates the injection point of the 19F- Cell Sense labeled MSC. "R" denotes the reference tube for fluorine signal quantification purposes. (C) An overlay of the 19F signal due to MSC onto the 1H image provides anatomical context, with the 19F signal rendered in "hot-iron" color scale. The value 5.35 x 1018 indicates the number of 19F atoms measured in the region of interest (which extends into adjacent slices). (D&E) show images at days 3 and 12. The blue arrows indicate the signal voids due to iron labeled MSC. The number of fluorine atoms detected is reduced at day 12. (F&G) Fluorescence images of MSC labeled with the red fluorescent version of Cell Sense (F) and Molday-rhodamine B iron particles (G).

Disclosure of author financial interest or relationships:
J.M. Gaudet, None; **E.J. Ribot**, None; **K.M. Gilbert**, None; **Y. Chen**, None; **P. Foster**, None.

Presentation Number **SS 168**
Scientific Session 28: Preclinical Cell & Tissue Level Studies, Preclinical in vivo Studies - Stem Cells
September 21, 2013 / 14:15-14:30 / Room: Oglethorpe Auditorium

Novel Approach for Chondrogenic differentiation of induced pluripotent stem cells

Hossein Nejadnik, *Olga D. Lenkov, Ali Fathi, Ramasamy Paulmurugan, Heike E. Daldrup-Link, Radiology, Stanford University, Stanford, CA, USA. Contact e-mail: nejadnik@gmail.com*

Purpose: The goal of this study is to develop a novel approach for chondrogenic differentiation of hiPS cells which omits embryonic body formations and directly directs cell differentiation towards mesenchymal and chondrogenic lineages. Ongoing studies aim to detect the chondrogenic differentiation of hiPS cells in vitro and in vivo by using luminescent and fluorescent reporter gene imaging approaches. Materials and methods: hiPS-ASC3 cells were developed using established procedures in the Wu lab (Stanford University) and cultured as undifferentiated cells in matrigel coated petri dishes. At 40-50 percent confluency, mTeSR1 media was changed to hMSC culture media, cells were detached from the matrigel-coated petri dishes at day 5 and cultured in uncoated polysterene culture flasks. Pre-differentiated hiPS-cell derived MSC-like cells (P5) underwent chondrogenic differentiation using our established protocol. Pellets were harvested at day 0, 7, and 14 of chondrogenic differentiation for standard histopathology, immunohistochemistry, glycosaminoglycan quantification and gene expression analysis. After developing the chondrogenic differentiation methodology for hiPS cells, we aim to evaluate in vivo cartilage regeneration outcomes of different types of hiPS-derived cell derived MSC-like cells and chondrocyte precursors. In order to detect chondrogenic differentiation of these cells in vivo, our ongoing studies evaluate FLUC-eGFP reporter genes with Col2A1 promoters (experimental), CMV promoter (positive control) and reporter with no promoter (negative control). Results: Our results showed that the hiPS cells could be pre-differentiation to iPS-MSC like cells with subsequent differentiation to chondrocytes. Col2A1 gene expression of iPS-MSC like cells at day 14 significantly increased (20 fold) compared to hiPS cells at day 1 ($p<0.05$; Fig 1). Alcian blue staining and immunohistochemistry confirmed the production of proteoglycan and collagen type 2 as main components of hyalin cartilage matrix production (Fig 2). We produced our FLUC-eGFP reporter gene with Col2A1, CMV, and empty promoter and confirmed the functionality in ATDC5 cells (Fig 3). We are currently testing the transfected cells for the chondrogenic differentiation detection. Conclusion: We present a novel, immediately clinically applicable approach for cartilage repair by developing a simplified, high yield chondrogenic differentiation approach of iPS cells. We are in the process of developing and testing a reporter gene, which can detect the chondrogenic differentiation of these cells in vivo. This approach could be widely used to evaluate different approaches for iPS cell derived cartilage repair technique with non-invasive imaging techniques.

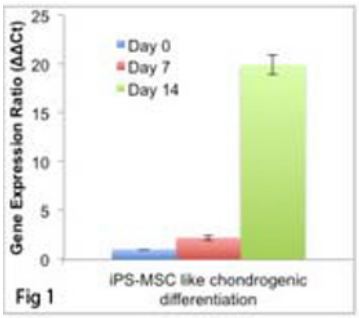

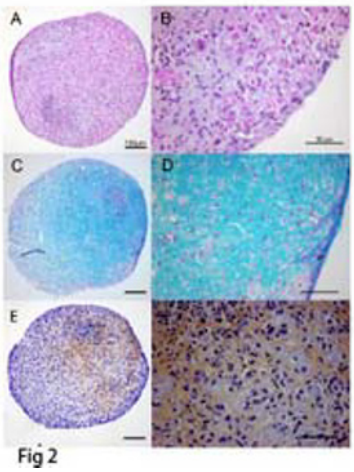

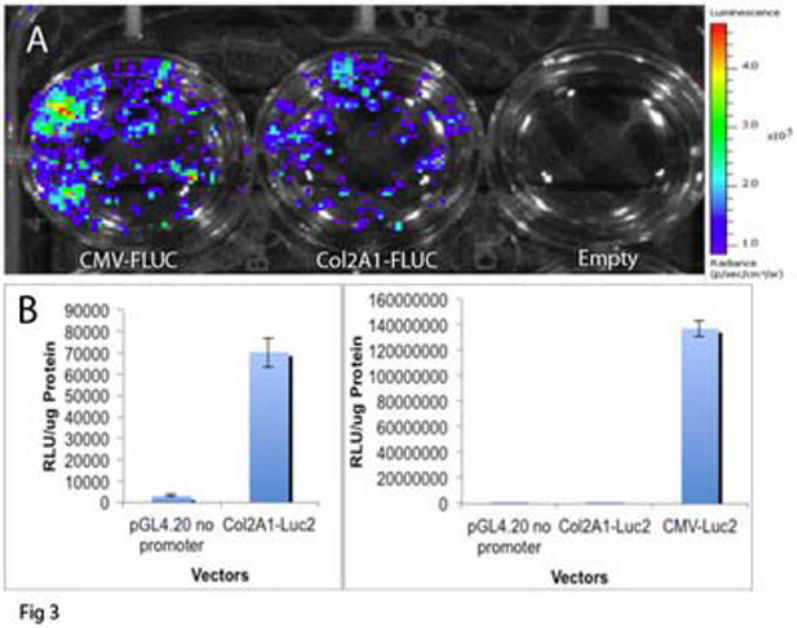

Figure 1. qPCR analysis of the gene expression of chondrogenic differentiated hiPS-MSC like cells. Relative gene expression of COL2A1. Figure 2. Histological evaluation of hiPS-MSC like cells after 21 days of chondrogenic differentiation induction. (A, B) H&E stain of chondrogenic differentiated hiPS-MSC like cells, (C, D) Alcian blue stain demonstrates the glycosaminoglycan production of chondrogenic differentiated cells, (E, F) immunohistochemistry of the pellets showed the production of the Collagen type II. Figure 3. Transient expression of the firefly luciferase (FLUC) in the cells transfected with reporter gene with CMV, Col2A1, and empty promoter. (A) bioluminescence imaging and (B) relative quantification of the FLUC expression which confirms the functionality of the vectors.

Disclosure of author financial interest or relationships:
H. Nejadnik, None; **O.D. Lenkov**, None; **A. Fathi**, None; **R. Paulmurugan**, None; **H.E. Daldrup-Link**, None.